Journal of Healthcare Engineering

Explainable Artificial Intelligence for Medical Applications

Lead Guest Editor: Enas Abdulhay
Guest Editors: Arunkumar N and Gustavo Ramirez

Explainable Artificial Intelligence for Medical Applications

Journal of Healthcare Engineering

Explainable Artificial Intelligence for Medical Applications

Lead Guest Editor: Enas Abdulhay
Guest Editors: Arunkumar N and Gustavo Ramirez

Contents

Contents

Contents

Contents

Contents

Contents

Contents

Contents

Contents

Contents

Contents

Contents

Hindawi
Journal of Healthcare Engineering
Volume 2023, Article ID 9826414, 1 page
https://doi.org/10.1155/2023/9826414

Retraction

Retracted: Clinical Care of Hyperthyroidism Using Wearable Medical Devices in a Medical IoT Scenario

Journal of Healthcare Engineering

Received 26 September 2023; Accepted 26 September 2023; Published 27 September 2023

This article has been retracted by Hindawi following an investigation undertaken by the publisher [1]. This investigation has uncovered evidence of one or more of the following indicators of systematic manipulation of the publication process:

(1) Discrepancies in scope
(2) Discrepancies in the description of the research reported
(3) Discrepancies between the availability of data and the research described
(4) Inappropriate citations
(5) Incoherent, meaningless and/or irrelevant content included in the article
(6) Peer-review manipulation

The presence of these indicators undermines our confidence in the integrity of the article's content and we cannot, therefore, vouch for its reliability. Please note that this notice is intended solely to alert readers that the content of this article is unreliable. We have not investigated whether authors were aware of or involved in the systematic manipulation of the publication process.

In addition, our investigation has also shown that one or more of the following human-subject reporting requirements has not been met in this article: ethical approval by an Institutional Review Board (IRB) committee or equivalent, patient/participant consent to participate, and/or agreement to publish patient/participant details (where relevant).

Wiley and Hindawi regrets that the usual quality checks did not identify these issues before publication and have since put additional measures in place to safeguard research integrity.

We wish to credit our own Research Integrity and Research Publishing teams and anonymous and named external researchers and research integrity experts for contributing to this investigation.

The corresponding author, as the representative of all authors, has been given the opportunity to register their agreement or disagreement to this retraction. We have kept a record of any response received.

References

[1] L. Wei, S. Hou, and Q. Liu, "Clinical Care of Hyperthyroidism Using Wearable Medical Devices in a Medical IoT Scenario," *Journal of Healthcare Engineering*, vol. 2022, Article ID 5951326, 10 pages, 2022.

Hindawi
Journal of Healthcare Engineering
Volume 2023, Article ID 9891861, 1 page
https://doi.org/10.1155/2023/9891861

Retraction

Retracted: Low Serum Albumin Is Associated with Poor Prognosis in Patients Receiving Peritoneal Dialysis Treatment

Journal of Healthcare Engineering

Received 15 August 2023; Accepted 15 August 2023; Published 16 August 2023

This article has been retracted by Hindawi following an investigation undertaken by the publisher [1]. This investigation has uncovered evidence of one or more of the following indicators of systematic manipulation of the publication process:

(1) Discrepancies in scope
(2) Discrepancies in the description of the research reported
(3) Discrepancies between the availability of data and the research described
(4) Inappropriate citations
(5) Incoherent, meaningless and/or irrelevant content included in the article
(6) Peer-review manipulation

The presence of these indicators undermines our confidence in the integrity of the article's content and we cannot, therefore, vouch for its reliability. Please note that this notice is intended solely to alert readers that the content of this article is unreliable. We have not investigated whether authors were aware of or involved in the systematic manipulation of the publication process.

Wiley and Hindawi regrets that the usual quality checks did not identify these issues before publication and have since put additional measures in place to safeguard research integrity.

We wish to credit our own Research Integrity and Research Publishing teams and anonymous and named external researchers and research integrity experts for contributing to this investigation.

The corresponding author, as the representative of all authors, has been given the opportunity to register their agreement or disagreement to this retraction. We have kept a record of any response received.

References

[1] Y. Shi, J. Cai, C. Shi, C. Liu, J. Zhou, and Z. Li, "Low Serum Albumin Is Associated with Poor Prognosis in Patients Receiving Peritoneal Dialysis Treatment," *Journal of Healthcare Engineering*, vol. 2022, Article ID 7660806, 6 pages, 2022.

Hindawi
Journal of Healthcare Engineering
Volume 2023, Article ID 9867826, 1 page
https://doi.org/10.1155/2023/9867826

Retraction

Retracted: Biomechanical Analysis and Training Method Research on Head Shot Strength of Football Players

Journal of Healthcare Engineering

Received 15 August 2023; Accepted 15 August 2023; Published 16 August 2023

This article has been retracted by Hindawi following an investigation undertaken by the publisher [1]. This investigation has uncovered evidence of one or more of the following indicators of systematic manipulation of the publication process:

(1) Discrepancies in scope
(2) Discrepancies in the description of the research reported
(3) Discrepancies between the availability of data and the research described
(4) Inappropriate citations
(5) Incoherent, meaningless and/or irrelevant content included in the article
(6) Peer-review manipulation

The presence of these indicators undermines our confidence in the integrity of the article's content and we cannot, therefore, vouch for its reliability. Please note that this notice is intended solely to alert readers that the content of this article is unreliable. We have not investigated whether authors were aware of or involved in the systematic manipulation of the publication process.

Wiley and Hindawi regrets that the usual quality checks did not identify these issues before publication and have since put additional measures in place to safeguard research integrity.

We wish to credit our own Research Integrity and Research Publishing teams and anonymous and named external researchers and research integrity experts for contributing to this investigation.

The corresponding author, as the representative of all authors, has been given the opportunity to register their agreement or disagreement to this retraction. We have kept a record of any response received.

References

[1] Y. Yao and S. Xiang, "Biomechanical Analysis and Training Method Research on Head Shot Strength of Football Players," *Journal of Healthcare Engineering*, vol. 2022, Article ID 7594124, 7 pages, 2022.

Hindawi
Journal of Healthcare Engineering
Volume 2023, Article ID 9836954, 1 page
https://doi.org/10.1155/2023/9836954

Retraction

Retracted: MiR-373 Inhibits the Epithelial-Mesenchymal Transition of Prostatic Cancer via Targeting Runt-Related Transcription Factor 2

Journal of Healthcare Engineering

Received 15 August 2023; Accepted 15 August 2023; Published 16 August 2023

This article has been retracted by Hindawi following an investigation undertaken by the publisher [1]. This investigation has uncovered evidence of one or more of the following indicators of systematic manipulation of the publication process:

(1) Discrepancies in scope
(2) Discrepancies in the description of the research reported
(3) Discrepancies between the availability of data and the research described
(4) Inappropriate citations
(5) Incoherent, meaningless and/or irrelevant content included in the article
(6) Peer-review manipulation

The presence of these indicators undermines our confidence in the integrity of the article's content and we cannot, therefore, vouch for its reliability. Please note that this notice is intended solely to alert readers that the content of this article is unreliable. We have not investigated whether authors were aware of or involved in the systematic manipulation of the publication process.

Wiley and Hindawi regrets that the usual quality checks did not identify these issues before publication and have since put additional measures in place to safeguard research integrity.

We wish to credit our own Research Integrity and Research Publishing teams and anonymous and named external researchers and research integrity experts for contributing to this investigation.

The corresponding author, as the representative of all authors, has been given the opportunity to register their agreement or disagreement to this retraction. We have kept a record of any response received.

References

[1] J. Pang, L. Dai, C. Zhang, and Q. Zhang, "MiR-373 Inhibits the Epithelial-Mesenchymal Transition of Prostatic Cancer via Targeting Runt-Related Transcription Factor 2," *Journal of Healthcare Engineering*, vol. 2021, Article ID 6974225, 9 pages, 2021.

Hindawi
Journal of Healthcare Engineering
Volume 2023, Article ID 9807423, 1 page
https://doi.org/10.1155/2023/9807423

Retraction

Retracted: Association of Pentachlorophenol with Fetal Risk of Prolonged Bradycardia: A Systematic Review and Meta-Analysis

Journal of Healthcare Engineering

Received 15 August 2023; Accepted 15 August 2023; Published 16 August 2023

This article has been retracted by Hindawi following an investigation undertaken by the publisher [1]. This investigation has uncovered evidence of one or more of the following indicators of systematic manipulation of the publication process:

(1) Discrepancies in scope
(2) Discrepancies in the description of the research reported
(3) Discrepancies between the availability of data and the research described
(4) Inappropriate citations
(5) Incoherent, meaningless and/or irrelevant content included in the article
(6) Peer-review manipulation

The presence of these indicators undermines our confidence in the integrity of the article's content and we cannot, therefore, vouch for its reliability. Please note that this notice is intended solely to alert readers that the content of this article is unreliable. We have not investigated whether authors were aware of or involved in the systematic manipulation of the publication process.

Wiley and Hindawi regrets that the usual quality checks did not identify these issues before publication and have since put additional measures in place to safeguard research integrity.

We wish to credit our own Research Integrity and Research Publishing teams and anonymous and named external researchers and research integrity experts for contributing to this investigation.

The corresponding author, as the representative of all authors, has been given the opportunity to register their agreement or disagreement to this retraction. We have kept a record of any response received.

References

[1] X. Song and X. Fu, "Association of Pentachlorophenol with Fetal Risk of Prolonged Bradycardia: A Systematic Review and Meta-Analysis," *Journal of Healthcare Engineering*, vol. 2022, Article ID 7552294, 9 pages, 2022.

Hindawi
Journal of Healthcare Engineering
Volume 2023, Article ID 9761938, 1 page
https://doi.org/10.1155/2023/9761938

Retraction

Retracted: Analysis of Systolic Blood Pressure Level and Short-Term Variability in Masked Hypertension

Journal of Healthcare Engineering

Received 15 August 2023; Accepted 15 August 2023; Published 16 August 2023

This article has been retracted by Hindawi following an investigation undertaken by the publisher [1]. This investigation has uncovered evidence of one or more of the following indicators of systematic manipulation of the publication process:

(1) Discrepancies in scope
(2) Discrepancies in the description of the research reported
(3) Discrepancies between the availability of data and the research described
(4) Inappropriate citations
(5) Incoherent, meaningless and/or irrelevant content included in the article
(6) Peer-review manipulation

The presence of these indicators undermines our confidence in the integrity of the article's content and we cannot, therefore, vouch for its reliability. Please note that this notice is intended solely to alert readers that the content of this article is unreliable. We have not investigated whether authors were aware of or involved in the systematic manipulation of the publication process.

Wiley and Hindawi regrets that the usual quality checks did not identify these issues before publication and have since put additional measures in place to safeguard research integrity.

We wish to credit our own Research Integrity and Research Publishing teams and anonymous and named external researchers and research integrity experts for contributing to this investigation.

The corresponding author, as the representative of all authors, has been given the opportunity to register their agreement or disagreement to this retraction. We have kept a record of any response received.

References

[1] Y. Hou and B. Liu, "Analysis of Systolic Blood Pressure Level and Short-Term Variability in Masked Hypertension," *Journal of Healthcare Engineering*, vol. 2022, Article ID 8016893, 9 pages, 2022.

Hindawi
Journal of Healthcare Engineering
Volume 2023, Article ID 9836380, 1 page
https://doi.org/10.1155/2023/9836380

Retraction

Retracted: ANOVA-Based Analysis of Early Blood Transfusions on Hemodynamics with Severely Injured Trauma Using Bedside Ultrasound Imaging

Journal of Healthcare Engineering

Received 8 August 2023; Accepted 8 August 2023; Published 9 August 2023

This article has been retracted by Hindawi following an investigation undertaken by the publisher [1]. This investigation has uncovered evidence of one or more of the following indicators of systematic manipulation of the publication process:

(1) Discrepancies in scope
(2) Discrepancies in the description of the research reported
(3) Discrepancies between the availability of data and the research described
(4) Inappropriate citations
(5) Incoherent, meaningless and/or irrelevant content included in the article
(6) Peer-review manipulation

The presence of these indicators undermines our confidence in the integrity of the article's content and we cannot, therefore, vouch for its reliability. Please note that this notice is intended solely to alert readers that the content of this article is unreliable. We have not investigated whether authors were aware of or involved in the systematic manipulation of the publication process.

In addition, our investigation has also shown that one or more of the following human-subject reporting requirements has not been met in this article: ethical approval by an Institutional Review Board (IRB) committee or equivalent, patient/participant consent to participate, and/or agreement to publish patient/participant details (where relevant).

Wiley and Hindawi regrets that the usual quality checks did not identify these issues before publication and have since put additional measures in place to safeguard research integrity.

We wish to credit our own Research Integrity and Research Publishing teams and anonymous and named external researchers and research integrity experts for contributing to this investigation.

The corresponding author, as the representative of all authors, has been given the opportunity to register their agreement or disagreement to this retraction. We have kept a record of any response received.

References

[1] L. Song, J. Zhang, and J. Liu, "ANOVA-Based Analysis of Early Blood Transfusions on Hemodynamics with Severely Injured Trauma Using Bedside Ultrasound Imaging," *Journal of Healthcare Engineering*, vol. 2021, Article ID 5263454, 6 pages, 2021.

Hindawi
Journal of Healthcare Engineering
Volume 2023, Article ID 9827564, 1 page
https://doi.org/10.1155/2023/9827564

Retraction

Retracted: Application of Clavien–Dindo Classification System for Complications of Minimally Invasive Percutaneous Nephrolithotomy

Journal of Healthcare Engineering

Received 8 August 2023; Accepted 8 August 2023; Published 9 August 2023

This article has been retracted by Hindawi following an investigation undertaken by the publisher [1]. This investigation has uncovered evidence of one or more of the following indicators of systematic manipulation of the publication process:

(1) Discrepancies in scope
(2) Discrepancies in the description of the research reported
(3) Discrepancies between the availability of data and the research described
(4) Inappropriate citations
(5) Incoherent, meaningless and/or irrelevant content included in the article
(6) Peer-review manipulation

The presence of these indicators undermines our confidence in the integrity of the article's content and we cannot, therefore, vouch for its reliability. Please note that this notice is intended solely to alert readers that the content of this article is unreliable. We have not investigated whether authors were aware of or involved in the systematic manipulation of the publication process.

In addition, our investigation has also shown that one or more of the following human-subject reporting requirements has not been met in this article: ethical approval by an Institutional Review Board (IRB) committee or equivalent, patient/participant consent to participate, and/or agreement to publish patient/participant details (where relevant).

Wiley and Hindawi regrets that the usual quality checks did not identify these issues before publication and have since put additional measures in place to safeguard research integrity.

We wish to credit our own Research Integrity and Research Publishing teams and anonymous and named external researchers and research integrity experts for contributing to this investigation.

The corresponding author, as the representative of all authors, has been given the opportunity to register their agreement or disagreement to this retraction. We have kept a record of any response received.

References

[1] X. Zhang, Z. Zhu, and J. Wu, "Application of Clavien–Dindo Classification System for Complications of Minimally Invasive Percutaneous Nephrolithotomy," *Journal of Healthcare Engineering*, vol. 2021, Article ID 5361415, 5 pages, 2021.

Hindawi
Journal of Healthcare Engineering
Volume 2023, Article ID 9823939, 1 page
https://doi.org/10.1155/2023/9823939

Retraction

Retracted: Targeting AraC-Resistant Acute Myeloid Leukemia by Dual Inhibition of CDK9 and Bcl-2: A Systematic Review and Meta-Analysis

Journal of Healthcare Engineering

Received 8 August 2023; Accepted 8 August 2023; Published 9 August 2023

This article has been retracted by Hindawi following an investigation undertaken by the publisher [1]. This investigation has uncovered evidence of one or more of the following indicators of systematic manipulation of the publication process:

(1) Discrepancies in scope
(2) Discrepancies in the description of the research reported
(3) Discrepancies between the availability of data and the research described
(4) Inappropriate citations
(5) Incoherent, meaningless and/or irrelevant content included in the article
(6) Peer-review manipulation

The presence of these indicators undermines our confidence in the integrity of the article's content and we cannot, therefore, vouch for its reliability. Please note that this notice is intended solely to alert readers that the content of this article is unreliable. We have not investigated whether authors were aware of or involved in the systematic manipulation of the publication process.

In addition, our investigation has also shown that one or more of the following human-subject reporting requirements has not been met in this article: ethical approval by an Institutional Review Board (IRB) committee or equivalent, patient/participant consent to participate, and/or agreement to publish patient/participant details (where relevant).

Wiley and Hindawi regrets that the usual quality checks did not identify these issues before publication and have since put additional measures in place to safeguard research integrity.

We wish to credit our own Research Integrity and Research Publishing teams and anonymous and named external researchers and research integrity experts for contributing to this investigation.

The corresponding author, as the representative of all authors, has been given the opportunity to register their agreement or disagreement to this retraction. We have kept a record of any response received.

References

[1] L. Li, C. Han, X. Yu, J. Shen, and Y. Cao, "Targeting AraC-Resistant Acute Myeloid Leukemia by Dual Inhibition of CDK9 and Bcl-2: A Systematic Review and Meta-Analysis," *Journal of Healthcare Engineering*, vol. 2022, Article ID 2842066, 7 pages, 2022.

Hindawi
Journal of Healthcare Engineering
Volume 2023, Article ID 9806292, 1 page
https://doi.org/10.1155/2023/9806292

Retraction

Retracted: Design and Implementation of Intelligent Monitoring System for Head and Neck Surgery Care Based on Internet of Things (IoT)

Journal of Healthcare Engineering

Received 8 August 2023; Accepted 8 August 2023; Published 9 August 2023

This article has been retracted by Hindawi following an investigation undertaken by the publisher [1]. This investigation has uncovered evidence of one or more of the following indicators of systematic manipulation of the publication process:

(1) Discrepancies in scope
(2) Discrepancies in the description of the research reported
(3) Discrepancies between the availability of data and the research described
(4) Inappropriate citations
(5) Incoherent, meaningless and/or irrelevant content included in the article
(6) Peer-review manipulation

The presence of these indicators undermines our confidence in the integrity of the article's content and we cannot, therefore, vouch for its reliability. Please note that this notice is intended solely to alert readers that the content of this article is unreliable. We have not investigated whether authors were aware of or involved in the systematic manipulation of the publication process.

In addition, our investigation has also shown that one or more of the following human-subject reporting requirements has not been met in this article: ethical approval by an Institutional Review Board (IRB) committee or equivalent, patient/participant consent to participate, and/or agreement to publish patient/participant details (where relevant).

Wiley and Hindawi regrets that the usual quality checks did not identify these issues before publication and have since put additional measures in place to safeguard research integrity.

We wish to credit our own Research Integrity and Research Publishing teams and anonymous and named external researchers and research integrity experts for contributing to this investigation.

The corresponding author, as the representative of all authors, has been given the opportunity to register their agreement or disagreement to this retraction. We have kept a record of any response received.

References

[1] Q. Liu, S. Hou, and L. Wei, "Design and Implementation of Intelligent Monitoring System for Head and Neck Surgery Care Based on Internet of Things (IoT)," *Journal of Healthcare Engineering*, vol. 2022, Article ID 4822747, 9 pages, 2022.

Hindawi
Journal of Healthcare Engineering
Volume 2023, Article ID 9761493, 1 page
https://doi.org/10.1155/2023/9761493

Retraction

Retracted: The Effect of lncRNA SNHG3 Overexpression on Lung Adenocarcinoma by Regulating the Expression of miR-890

Journal of Healthcare Engineering

Received 8 August 2023; Accepted 8 August 2023; Published 9 August 2023

This article has been retracted by Hindawi following an investigation undertaken by the publisher [1]. This investigation has uncovered evidence of one or more of the following indicators of systematic manipulation of the publication process:

(1) Discrepancies in scope
(2) Discrepancies in the description of the research reported
(3) Discrepancies between the availability of data and the research described
(4) Inappropriate citations
(5) Incoherent, meaningless and/or irrelevant content included in the article
(6) Peer-review manipulation

The presence of these indicators undermines our confidence in the integrity of the article's content and we cannot, therefore, vouch for its reliability. Please note that this notice is intended solely to alert readers that the content of this article is unreliable. We have not investigated whether authors were aware of or involved in the systematic manipulation of the publication process.

Wiley and Hindawi regrets that the usual quality checks did not identify these issues before publication and have since put additional measures in place to safeguard research integrity.

We wish to credit our own Research Integrity and Research Publishing teams and anonymous and named external researchers and research integrity experts for contributing to this investigation.

The corresponding author, as the representative of all authors, has been given the opportunity to register their agreement or disagreement to this retraction. We have kept a record of any response received.

References

[1] B. Kang, C. Qiu, and Y. Zhang, "The Effect of lncRNA SNHG3 Overexpression on Lung Adenocarcinoma by Regulating the Expression of miR-890," *Journal of Healthcare Engineering*, vol. 2021, Article ID 1643788, 9 pages, 2021.

Hindawi
Journal of Healthcare Engineering
Volume 2023, Article ID 9875409, 1 page
https://doi.org/10.1155/2023/9875409

Retraction

Retracted: Evaluation of Tresiba Combined with Six Ingredient Rehmannia Pill in the Treatment of Type 2 Diabetes

Journal of Healthcare Engineering

Received 8 August 2023; Accepted 8 August 2023; Published 9 August 2023

This article has been retracted by Hindawi following an investigation undertaken by the publisher [1]. This investigation has uncovered evidence of one or more of the following indicators of systematic manipulation of the publication process:

(1) Discrepancies in scope
(2) Discrepancies in the description of the research reported
(3) Discrepancies between the availability of data and the research described
(4) Inappropriate citations
(5) Incoherent, meaningless and/or irrelevant content included in the article
(6) Peer-review manipulation

The presence of these indicators undermines our confidence in the integrity of the article's content and we cannot, therefore, vouch for its reliability. Please note that this notice is intended solely to alert readers that the content of this article is unreliable. We have not investigated whether authors were aware of or involved in the systematic manipulation of the publication process.

In addition, our investigation has also shown that one or more of the following human-subject reporting requirements has not been met in this article: ethical approval by an Institutional Review Board (IRB) committee or equivalent, patient/participant consent to participate, and/or agreement to publish patient/participant details (where relevant).

Wiley and Hindawi regrets that the usual quality checks did not identify these issues before publication and have since put additional measures in place to safeguard research integrity.

We wish to credit our own Research Integrity and Research Publishing teams and anonymous and named external researchers and research integrity experts for contributing to this investigation.

The corresponding author, as the representative of all authors, has been given the opportunity to register their agreement or disagreement to this retraction. We have kept a record of any response received.

References

[1] J. Li and Q. He, "Evaluation of Tresiba Combined with Six Ingredient Rehmannia Pill in the Treatment of Type 2 Diabetes," *Journal of Healthcare Engineering*, vol. 2022, Article ID 2177176, 6 pages, 2022.

Hindawi
Journal of Healthcare Engineering
Volume 2023, Article ID 9873058, 1 page
https://doi.org/10.1155/2023/9873058

Retraction

Retracted: Effect Analysis of Epidural Anesthesia with 0.4% Ropivacaine in Transforaminal Endoscopic Surgery

Journal of Healthcare Engineering

Received 8 August 2023; Accepted 8 August 2023; Published 9 August 2023

This article has been retracted by Hindawi following an investigation undertaken by the publisher [1]. This investigation has uncovered evidence of one or more of the following indicators of systematic manipulation of the publication process:

(1) Discrepancies in scope
(2) Discrepancies in the description of the research reported
(3) Discrepancies between the availability of data and the research described
(4) Inappropriate citations
(5) Incoherent, meaningless and/or irrelevant content included in the article
(6) Peer-review manipulation

The presence of these indicators undermines our confidence in the integrity of the article's content and we cannot, therefore, vouch for its reliability. Please note that this notice is intended solely to alert readers that the content of this article is unreliable. We have not investigated whether authors were aware of or involved in the systematic manipulation of the publication process.

In addition, our investigation has also shown that one or more of the following human-subject reporting requirements has not been met in this article: ethical approval by an Institutional Review Board (IRB) committee or equivalent, patient/participant consent to participate, and/or agreement to publish patient/participant details (where relevant).

Wiley and Hindawi regrets that the usual quality checks did not identify these issues before publication and have since put additional measures in place to safeguard research integrity.

We wish to credit our own Research Integrity and Research Publishing teams and anonymous and named external researchers and research integrity experts for contributing to this investigation.

The corresponding author, as the representative of all authors, has been given the opportunity to register their agreement or disagreement to this retraction. We have kept a record of any response received.

References

[1] B. Hu, H. Wang, T. Ma, Z. Fu, and Z. Feng, "Effect Analysis of Epidural Anesthesia with 0.4% Ropivacaine in Transforaminal Endoscopic Surgery," *Journal of Healthcare Engineering*, vol. 2021, Article ID 2929843, 6 pages, 2021.

Hindawi
Journal of Healthcare Engineering
Volume 2023, Article ID 9858276, 1 page
https://doi.org/10.1155/2023/9858276

Retraction

Retracted: Antitumor Effects of 10058-F4 and Curcumin in Combination Therapy for Pancreatic Cancer In Vitro and In Vivo

Journal of Healthcare Engineering

Received 8 August 2023; Accepted 8 August 2023; Published 9 August 2023

This article has been retracted by Hindawi following an investigation undertaken by the publisher [1]. This investigation has uncovered evidence of one or more of the following indicators of systematic manipulation of the publication process:

(1) Discrepancies in scope
(2) Discrepancies in the description of the research reported
(3) Discrepancies between the availability of data and the research described
(4) Inappropriate citations
(5) Incoherent, meaningless and/or irrelevant content included in the article
(6) Peer-review manipulation

The presence of these indicators undermines our confidence in the integrity of the article's content and we cannot, therefore, vouch for its reliability. Please note that this notice is intended solely to alert readers that the content of this article is unreliable. We have not investigated whether authors were aware of or involved in the systematic manipulation of the publication process.

In addition, our investigation has also shown that one or more of the following human-subject reporting requirements has not been met in this article: ethical approval by an Institutional Review Board (IRB) committee or equivalent, patient/participant consent to participate, and/or agreement to publish patient/participant details (where relevant).

Wiley and Hindawi regrets that the usual quality checks did not identify these issues before publication and have since put additional measures in place to safeguard research integrity.

We wish to credit our own Research Integrity and Research Publishing teams and anonymous and named external researchers and research integrity experts for contributing to this investigation.

The corresponding author, as the representative of all authors, has been given the opportunity to register their agreement or disagreement to this retraction. We have kept a record of any response received.

References

[1] Z. Jie, Z. Jinna, Z. Jingjun et al., "Antitumor Effects of 10058-F4 and Curcumin in Combination Therapy for Pancreatic Cancer In Vitro and In Vivo," *Journal of Healthcare Engineering*, vol. 2022, Article ID 1620802, 8 pages, 2022.

Hindawi
Journal of Healthcare Engineering
Volume 2023, Article ID 9878935, 1 page
https://doi.org/10.1155/2023/9878935

Retraction

Retracted: Prescription of *Sageretia hamosa Brongn* Relieved Goiter through Promoted Apoptosis of Thyroid Cells via miR-511-3p and PTEN/PI3K/Akt Pathway

Journal of Healthcare Engineering

Received 1 August 2023; Accepted 1 August 2023; Published 2 August 2023

This article has been retracted by Hindawi following an investigation undertaken by the publisher [1]. This investigation has uncovered evidence of one or more of the following indicators of systematic manipulation of the publication process:

(1) Discrepancies in scope
(2) Discrepancies in the description of the research reported
(3) Discrepancies between the availability of data and the research described
(4) Inappropriate citations
(5) Incoherent, meaningless and/or irrelevant content included in the article
(6) Peer-review manipulation

The presence of these indicators undermines our confidence in the integrity of the article's content and we cannot, therefore, vouch for its reliability. Please note that this notice is intended solely to alert readers that the content of this article is unreliable. We have not investigated whether authors were aware of or involved in the systematic manipulation of the publication process.

Wiley and Hindawi regrets that the usual quality checks did not identify these issues before publication and have since put additional measures in place to safeguard research integrity.

We wish to credit our own Research Integrity and Research Publishing teams and anonymous and named external researchers and research integrity experts for contributing to this investigation.

The corresponding author, as the representative of all authors, has been given the opportunity to register their agreement or disagreement to this retraction. We have kept a record of any response received.

References

[1] Y. Deng, S. Chen, H. Wang, B. Wang, and K. Xiao, "Prescription of *Sageretia hamosa Brongn* Relieved Goiter through Promoted Apoptosis of Thyroid Cells via miR-511-3p and PTEN/PI3K/Akt Pathway," *Journal of Healthcare Engineering*, vol. 2021, Article ID 3506559, 13 pages, 2021.

Hindawi
Journal of Healthcare Engineering
Volume 2023, Article ID 9787369, 1 page
https://doi.org/10.1155/2023/9787369

Retraction

Retracted: The Role of Health Education in Vaccination Nursing

Journal of Healthcare Engineering

Received 25 July 2023; Accepted 25 July 2023; Published 26 July 2023

This article has been retracted by Hindawi following an investigation undertaken by the publisher [1]. This investigation has uncovered evidence of one or more of the following indicators of systematic manipulation of the publication process:

(1) Discrepancies in scope
(2) Discrepancies in the description of the research reported
(3) Discrepancies between the availability of data and the research described
(4) Inappropriate citations
(5) Incoherent, meaningless and/or irrelevant content included in the article
(6) Peer-review manipulation

The presence of these indicators undermines our confidence in the integrity of the article's content and we cannot, therefore, vouch for its reliability. Please note that this notice is intended solely to alert readers that the content of this article is unreliable. We have not investigated whether authors were aware of or involved in the systematic manipulation of the publication process.

In addition, our investigation has also shown that one or more of the following human-subject reporting requirements has not been met in this article: ethical approval by an Institutional Review Board (IRB) committee or equivalent, patient/participant consent to participate, and/or agreement to publish patient/participant details (where relevant).

Wiley and Hindawi regrets that the usual quality checks did not identify these issues before publication and have since put additional measures in place to safeguard research integrity.

We wish to credit our own Research Integrity and Research Publishing teams and anonymous and named external researchers and research integrity experts for contributing to this investigation.

The corresponding author, as the representative of all authors, has been given the opportunity to register their agreement or disagreement to this retraction. We have kept a record of any response received.

References

[1] M. Yao, X. Gu, Y. Mo, C. Xia, and L. Tang, "The Role of Health Education in Vaccination Nursing," *Journal of Healthcare Engineering*, vol. 2022, Article ID 6078846, 5 pages, 2022.

Hindawi
Journal of Healthcare Engineering
Volume 2023, Article ID 8231073, 13 pages
https://doi.org/10.1155/2023/8231073

Research Article

Portable Face-Shielding Device Based on sEMG Considering the COVID-19 Scenario

Tian Lyu,[1] **Dong Yang Liu**,[2] **Chen Shao**,[3] **and ZiJie Zhang**[4]

[1]*School of Mechatronics Engineering, Beijing Institute of Technology, 100081 Beijing, China*
[2]*Physics and Astronomy (PHYSX), Cardiff University, CF24 3AA, UK*
[3]*School of Mechanical Engineering, Xi'an Jiaotong University, Xi'an 710049, China*
[4]*City University of Hong Kong, Hong Kong 999077, Hong Kong*

Correspondence should be addressed to Tian Lyu; 1120181730@bit.edu.cn

Received 13 January 2022; Revised 1 March 2022; Accepted 2 April 2022; Published 8 July 2023

Academic Editor: Enas Abdulhay

Wearing a mask greatly reduced the possibility of infection during the COVID-19 pandemic. However, major inconveniences occur regarding patients with upper limb amputations, as they cannot independently wear masks. As a result, bacterial contamination is caused by medical staff touching the quilt when helping. Furthermore, this effect can occur with ordinary people due to accidental touch. This research aims to design an automatic and portable face shield assistive device based on surface electromyography (sEMG) signals. A concise face shield-wearing mechanism was built through 3D printing. A novel decision-making control method regarding a feature extraction model of 16 signal features and a Softmax classification neural network model were developed and tested on an STM32 microcontroller unit (MCU). The optimized electrode was fabricated using a carbon nanotube (CNT)/polydimethylsiloxane (PDMS). The design was further integrated and tested, showing a promising future for further implementation.

1. Introduction

In recent years, the COVID-19 epidemic has been rampant. As a result, face shielding has been effectively used to avoid the spread of the corresponding virus [1]. In the absence of a shelter-in-place strategy, infections, hospitalizations, and deaths were reduced by 37.7%, where the interquartile range (IQR) was 36.1–39.4%, 44.2% (IQR: 42.9–45.8%), and 47.2% (IQR: 45.5–48.7%), respectively, as nonmedical masks were worn by 75% of the population reduced [2]. The use of general facemasks has significant benefits, especially if they are adopted earlier, and at least some benefit is realized across a range of epidemic intensities. Furthermore, masks can be used in addition to other interventions, such as social distancing and hygienic measures, ultimately resulting in a nonlinear decrease in epidemic mortality and healthcare system burden [3]. During the COVID-19 outbreak, many new developments related to healthcare utilized electromyography (EMG) or electroencephalogram (EEG). Setiawan et al. proposed a stroke rehabilitation monitoring method using EEG [4], Bano and Hussain could identify patients that were infected by COVID-19 using the EMG technique [5], and L. Jiang et al. developed an advising device for at-home exercise using sEMG [6].

Some disabled and paralyzed patients, however, who have both arms amputated cannot wear face masks independently. According to the latest survey reported by China Disabled Persons' Federation, in 2010, China had 20.54 billion amputation patients [7], of which 2/3 were upper limb amputees [8]. In addition, there is a nonnegligible group that has a severe impairment of both upper-and triple-limb functions [9]. However, assistance in public places increases the risk of viral infection. Furthermore, cross-infection in hospitals when nurses take care of paralyzed patients and manually wear face shields can also occur. [10] Nevertheless, patients who cannot or have difficulties putting on masks by themselves arrive at hospitals without wearing masks or need to call a nurse for assistance at their home. As a result, the person can get infected if the nurse or people in the hospital are recessive carriers of COVID-19.

Many casual activities, such as dining and drinking, require that masks are constantly put on and off. However, some patients cannot be assisted by nurses all day. In some public places, directly touching the inside of a face shield by hand can contaminate this equipment, reducing its protection against infectious diseases and threatening health. We also believe that a new hand-controlled face-shielding device could be convenient for ordinary people. Hence, a noncontact wearable face-shielding-wearing system is proposed.

Heckendorn [11] and Backers Today [12] separately developed two automated face-shielding-wearing systems controlled through buttons. The automatic face shielding of Heckendorn is promising due to its mechanical structure and portability. Furthermore, the one designed by Backers Today is convenient for drinking water. These designs, therefore, reduce the possibility of contaminating face shields and are conducive for people with disabilities.

Huang developed an automask utilizing an ultrasonic sensor and an sEMG sensor that allowed the wearer to actuate when sneezing by contracting the abdominal muscle while manually covering the ultrasonic sensor [13]. This design could detect and avoid the sneeze spreading; however, the situations in which such devices can be applied are limited. Furthermore, the mask is not suitable for patients with upper limb amputations, as it can only be actuated by contracting the abdominal muscle while covering the ultrasonic sensor by hand. The utilization of an HC-SR04 ultrasonic distance sensor would significantly harm the cost efficiency of the design. The HC-SR04 module is an active measurement instrument [14] that continuously emits an echo pulse at a 40 kHz frequency [15]. Owing to the active detection limit, the power consumption of the HC-SR04 module is incessant during wearing. In contrast, the sEMG module is a passive measurement instrument whose power consumption is much lower; therefore, it is more suitable for casual wearing. Moreover, the ultrasonic distance sensor can be accidentally triggered from the outer environment, such as the clothing of the user or the impact caused by passing-by pacers. Furthermore, the signals of ultrasonic distance sensors commonly fluctuate (fluctuation phenomenon) [16], even though a threshold value is set to avoid accidental triggering. In addition, the control algorithm of the design involved no signal classification, increasing the risk of accidentally triggering the mechanism. The actuation and control of the servo motor without a signal classification are usually achieved by manually setting the threshold of the triggering voltage amplitude. [15] However, unwanted spike signals that trigger the actuators can be generated. For example, accidental pressing on the sEMG sensors or external force-induced position shift of the electrodes would create spikes and noise. Furthermore, the fluctuation phenomenon of the ultrasonic distance sensors contributes to more accidental actuation in Taliyah Huang's design. Finally, controlling the mask based on the abdominal muscle is not feasible, as the body fat at a selected abdomen position significantly varies depending on the person; therefore, the EMG signal cannot be commonly applied. Different factors, such as epidermal body fat, significantly influence the sEMG measurement, [17]. As lipids easily accumulate in the abdomen, the abdominal muscle EMG could be weak to be detected when facing thick abdominal fat tissue.

To solve these problems, we designed a portable, noncontact, and automatic face-shielding-wearing device that considers the EMG signals.

2. Background Knowledge

An electromyography instrument is used in EMG to record muscle bioelectric signals. These electrical signals can describe some characteristic behaviors of the human muscles. EMG signals can be used in many fields, such as clinical applications [18] and human-computer interaction [19]. More direct monitoring of the human body can be achieved through the analysis, processing, classification, and various signal analysis methods of these signals [20]. New implementations of EMG, such as muscular paralysis disease prediction using EMG, have been developed during the pandemic [21].

However, people who are inconvenienced by wearing masks often need to adapt themselves to EMG devices for a long time. Commercial electrodes are generally Ag/AgCl electrodes; however, these components should be avoided, as they cause damage to human skin [22]. As a result, we used carbon nanotubes, which are nontoxic, harmless, and pollution-free [23], as the primary material for the electrode, increasing its stronger skin affinity and allowing it to be more suitable for long-term use.

The proposed device collects and analyzes the human body EMG signal, realizing thereafter, through machine learning, the wearing and removal of the face shield according to the human body EMG signal. As a result, it does not need to be manually controlled. This study used the specific location of the muscle signal of a dual-channel sEMG detector. We also improved the electrode material in contact with the human body, resulting in a more suitable material for long-term use. Based on the corresponding signal feature processing and machine learning classification, noncontact automatic face shielding and wearing could be realized.

3. System Architecture and Methodology

The main objective of this study was to design a portable face-shielding device based on sEMG. The user of the proposed device could wear/undress the mask by contracting two specific muscles, fulfilling the noncontact demand for paralyzed patients with amputated upper limbs or ordinary people, therefore avoiding the accidental touch of the inner surface of the face shield. By selecting two independent muscles that do not usually form a synergic pattern, the device can be precisely actuated based on the corresponding gesture, thereby avoiding accidental triggers. To realize this purpose, at least three primary components were involved: data acquisition units, portable data processing units, and automatic face-shielding mechanisms.

A data flow chart of the designed system, composed of these primary components, is shown in Figure 1. We use a 2 MyoWare™ Muscle Sensor (AT-04-001) [24] to achieve

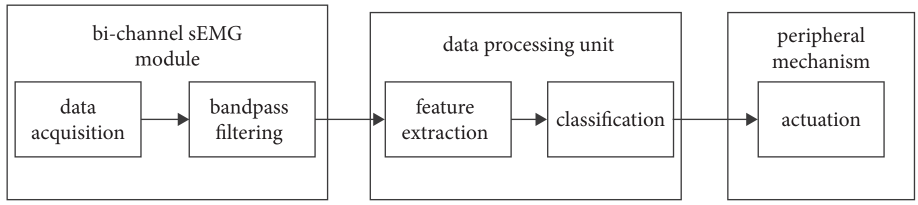

Figure 1: Data flow chart of the proposed device.

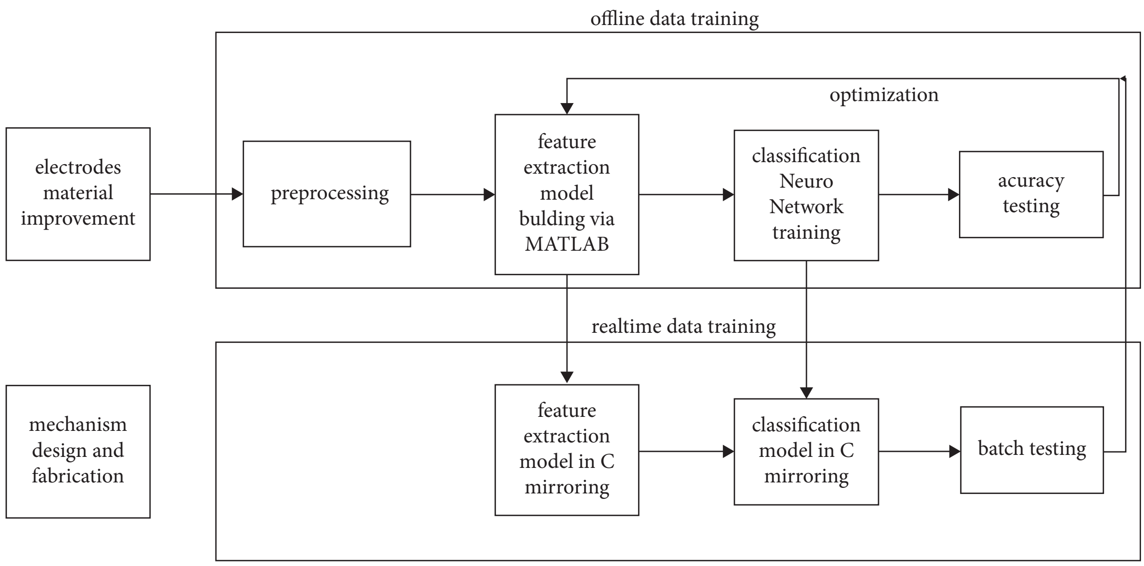

Figure 2: Research methodology diagram.

bichannel input of the sEMG signals, as the EMG signals of two independent muscles were detected. A hardware bandpass filtering circuit and rectifying and amplifying procedures were integrated into the MyoWare module. The analog sEMG signal was further converted to a digital signal through an analog to digital converter (ADC) on a STM32F103ZET6 microcontroller unit (MCU), which is a portable data processing unit. Based on the received data, our algorithm yields a decision that fulfills the user demand. Accordingly, the triggering signal is sent to the automatic face-shielding mechanism via IIC based on the corresponding gesture.

Many studies, among which the methodologies are profound examples of our research, have been conducted on implementations utilizing sEMG. References [25–28] investigated muscle selection for sEMG electrode placement or gesture selection. References [26–30] analyzed the sEMG signal preprocessing or segmentation. References [25–29] studied a feature extraction procedure of the signal and a classification method utilizing neural networks or a support vector machine (SVM), which was integrated into [25–29]. Based on the methodologies investigated, our research methodology can be summarized as indicated in Figure 2.

To increase the dermotropic property and electrical conductivity of the electrodes, we have investigated the improvement of the electrode material. The mechanical structural design targets a lightweight and conciseness compatible wearable mechanism. As shown in Figure 2, the model training of the EMG data flow can be divided into an offline data training process and a real-time model training.

In the offline model training procedure, the data were, first, preprocessed. Afterward, serial feature extraction based on the segmented data batches was conducted. The classification process was based on artificial neural networks (ANN) in this research.

Models are obtained through offline training, regardless of the real-time control of the mechanism and considering datasets stored on a personal computer (PC). Further development of these idealized models needs to be achieved and calibrated in the real-time training procedure. Their parameters were, therefore, carefully adjusted based on the actual performance of the device to achieve the optimized conditions.

Our experimental setups of the data flow model training are shown in Figure 3, which indicates the key components for the feature extraction model and the classification neural network training. The red arrows represent the power supply directions; the blue lines stand for data flows from the peripheral devices to the MCU. In contrast, the yellow arrows represent the opposite data flow. Both data flow represented by the yellow and blue arrows should be omitted during the real-time optimization to achieve the portability of the design. The green and grey arrows indicate the data flow between the MCU and peripherals.

To illustrate the hardware selection, two MyoWare™ muscle sensors (AT-04-001) were selected for the sEMG

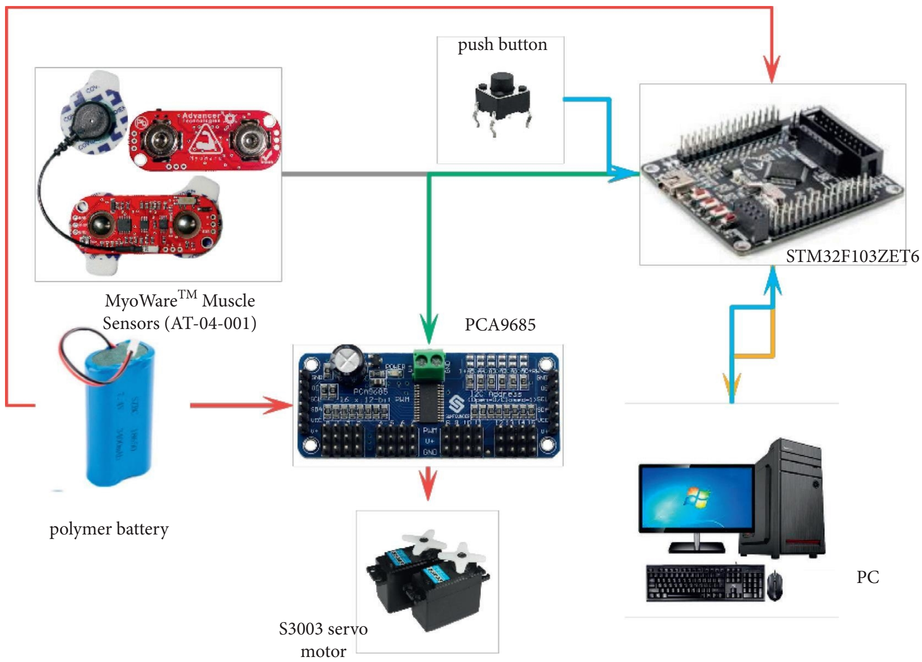

Figure 3: Experiment setups for feature extraction and classification model training.

signal detection. A 32-bit microcontroller composed of an ARM Cortex-M3 core STM32F103ZET6 [31] MCU module was selected to execute the computational tasks of this portable device, owing to its computational performance and stability. A push button, which was pressed to indicate the need for the shielding mask, was used for signal labeling. A 5 V polymer battery was needed for the power supply. The PCA9685 module is a 16-channel PWM output motor control module [32]. In this study, we realized control of a FUTABA Corp. S3003 servo motor through IIC communication and PCA9685.

4. Design of Mechanism

The mechanical design of the face-shielding device should promote function, reliability, and economic characteristics. To achieve a functional design, the basic motion form, as well as the main measurement of the device, should be analyzed based on practical applications. After completing the overall design of the device, which is usually idealistic and abstract, its reliability must be evaluated; therefore, specific parts, such as rockers and connectors, should be selected, and mechanical calculations and analyses are necessary to ensure the feasibility of movement. Certain elements might also be modified and optimized. Finally, the material and manufacturing process are were selected based on a limited budget.

Our face-shielding device must successfully take the face shield on and off. To simplify this situation, it can be assumed that the shield is moving around a fixed point. As this is the only movement required, the device can be designed as a planar mechanism, as shown in Figure 4(a). To further simplify the system, a rigid four-bar linkage was used as the basic structure.

As the only movement of the face shield is rotation, the mechanism has only one degree of freedom (DOF). To fulfill this requirement, a parallelogram form of the four-bar linkage was used, as shown in Figure 4(b)). Based on this adaptation, the rotary motion of the driver bar at the driven bar is duplicated, therefore creating a stable parallel relationship.

The planar DOF is governed by the following equation:

$$M = 3(L - 1) - 2J_1 - J_2, \quad (1)$$

where M is the DOF, L is the number of links, and J_1 and J_2 are the number of lower and higher pairs, respectively. In the parallelogram linkage, where one bar is already fixed, $L = 4$, $J_1 = 4$, and $J_2 = 0$; therefore, $M = 1$ based on equation (1). This value of DOF indicates that the four-bar linkage of the parallelogram fulfills the requirements of this study.

The concept of the planar mechanism was, thereafter, further refined into a 3D mechanism by adding two identical four-bar linkages connected by an axis, therefore completing the structure that could be fixed on the neck of the subject and achieving a rotary motion. The dimensions of the structure were based on the human face and actual movement. Figure 5(a) demonstrates the 3D version of the device constructed through SOLIDWORKS 2020. Two bases were placed on either side of the neck of the subject, and a servo motor was installed to drive rocker1, allowing it to complete the rotary motion. The face shield was placed between connecting rod3 and rod4.

However, according to our requirements, bar2 should be fixed to restrict the DOF to one. Moreover, the joints on which the connectors should be used have not been determined yet. As the stability of the structure must be ensured during operation, the movement of the bars moving along the axle cannot be executed. As a result, based on the

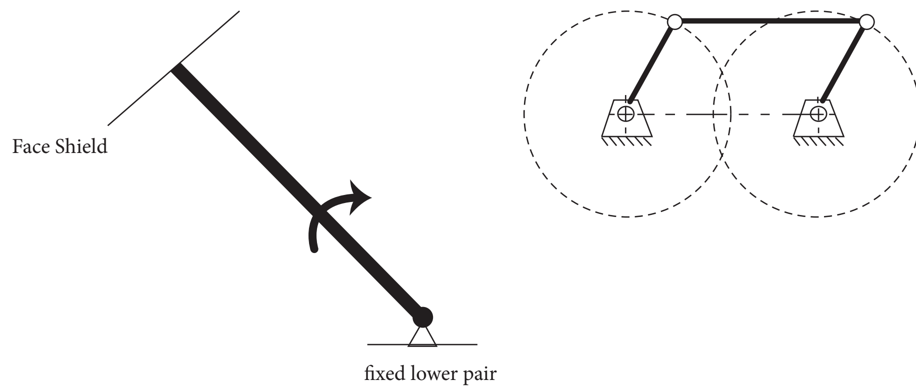

(a) (b)

Figure 4: Simplified model of the device. (a) Simplification of the motion form. (b) Parallelogram configuration of the four-bar linkage.

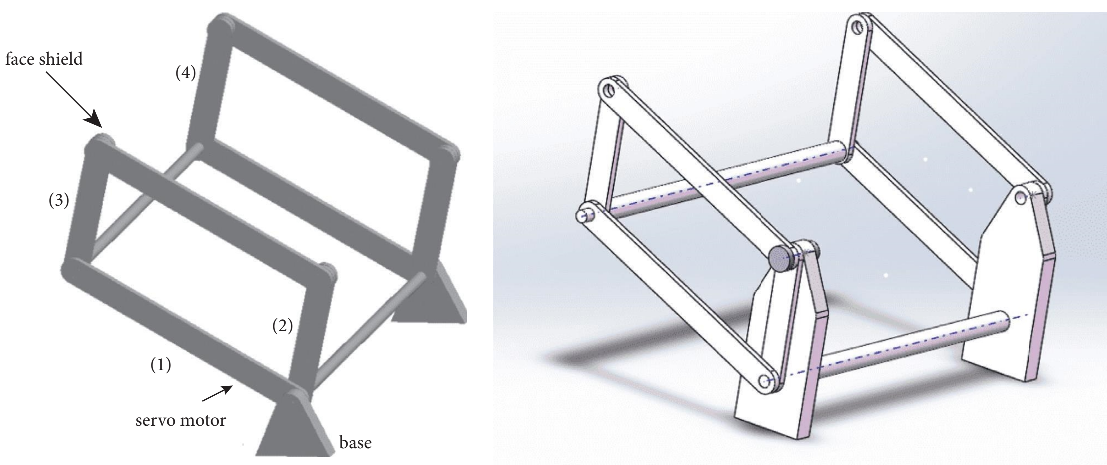

(a) (b)

Figure 5: Simulations of the device in SOLIDWORKS. (a) 3D mechanism of the face-shielding device, including two equal four-bar linkages, two bases, and two connecting axles. (b) Optimized mechanism containing connectors and new supporting bases.

reliability analysis, the joints were connected by bolts and nuts, a new base was designed to restrict the movement of bar2, and the diameters of the two axles were modified to ensure the axial constraint. The optimized mechanism is shown in Figure 5(b)).

In additive manufacturing (3D printing), simulations can be directly transformed into real objects, resulting in a swift process. The simulation in SOLIDWORKS was already implemented; therefore, due to the principle of economic design, additive manufacturing was selected as our manufacturing method. The material that has been frequently used in this process is resin, as it demonstrates suitable rigidity for the rotation of light objects, such as face shields. The accuracy of this method, however, is not satisfactory yet, which may result in higher dimensional and geometric tolerances in each part.

The proposed mechanism provides, therefore, a relatively effective procedure for taking the face shield on and off without requiring a complex structure. Furthermore, the material selected for the face-shielding device is light and the rigidity against the torque generated by the servo motor is sufficient, resulting in less stress for the subjects when using the device. However, the stability of the entire mechanism is not perfect owing to its simple structure, therefore requiring future improvements. Moreover, the mechanism might wear after a long-term operation due to the lack of protection.

5. Improvement of the Material of the Electrode

5.1. Background. The standard sEMG electrode commonly used in experiments is usually composed of gold (Au), silver (Ag), or silver-silver chloride (Ag/AgCl). Ag/AgCl is the most widely used material, as it has a lower baseline-noise interface than that of the other electrodes. Most Ag/AgCl on the market is present in the form of gel, for better maneuverability. This material can also be used in the surface coating of the electrode to reduce surface impedance and improve signal quality [33].

However, Ag/AgCl electrodes have several problems. The proposed equipment must be designed considering that people can wear it for a long time; however, the long use of an Ag/AgCl electrode can easily stimulate the skin and affect the signal quality after drying [34]. As a frequent replacement of new electrode sheets and stimulation of human skin are not considered in our design, an electrode that can be worn for a long time was developed [35].

Owing to the good dispersibility of carbon nanotubes (CNTs) and the flexibility of polydimethylsiloxane (PDMS), CNT/PDMS composites are considered good flexible conductors. The nanotubes dispersed in the electrode were in good contact with each other, forming a conductive path. Conductivity tests showed that the electrical performance depends on the concentration of carbon nanotubes. Furthermore, electrode materials are safe for biomedical applications, as they are not easily affected by sweat on the surface of the human body [36].

5.2. Materials and Methods

5.2.1. Material Parameters. The CNT used in the electrode was manufactured by Suzhou Tanfeng Tech. Inc., China. The purity and length of the carbon nanotube were over 95 wt% and 3–12 μm, respectively. The multiwall CNT was manufactured through vapor deposition. PDMS was manufactured by Shenzhen Xinwei New Material Co. Ltd. by using 909 potting glue.

5.2.2. Fabrication of Electrodes. The electrode was composed of an insulating layer, conductive film, and button electrode, as indicated in Figure 6.

The CNT was dispersed into the PDMS precursor (viscosity: 4000 ± 500,909-A, Xinwei New Material Co., Ltd.) and mixed through dispersion. A crosslinking agent (viscosity: 100 ± 10,909-B, Xinwei New Material Co., Ltd), whose ratio was 10 : 1, was solidified for 12 h at room temperature. When this agent could not solidify, the button electrode was embedded in the colloid and the solidification process occurred for 24 h. A 10 : 1 ratio of PDMS was used on the periphery, forming an insulating layer to facilitate contact between the electrode and the skin. Table 1.

As shown in Table 2, the specifications of the electrode sheet must be defined to enable the usage of the equipment for a long duration. The diameter of the conductive electrode part of the CNT/PDMS electrode sheet used in the experiment was 10 mm, which is a small part of the entire electrode. The conductive electrode (main body of the electrode), whose length and width were 36.5 mm and 30.2 mm, respectively, was composed of a PDMS solid gel. The overall thickness of the electrode sheet was 2 mm.

5.2.3. Electrical Test and Specification. The impedances of the electrodes were measured using an electric meter. Table 1 shows a test comparison diagram of commercial Ag/AgCl electrodes and CNT/PDMS electrodes considering the same specifications.

The transparent material in Figure 7 is the PDMS patch, and the black component corresponds to the CNT/PDMS electrode. The button electrode was connected on top of the CNT/PDMS to obtain an electrical signal from the device.

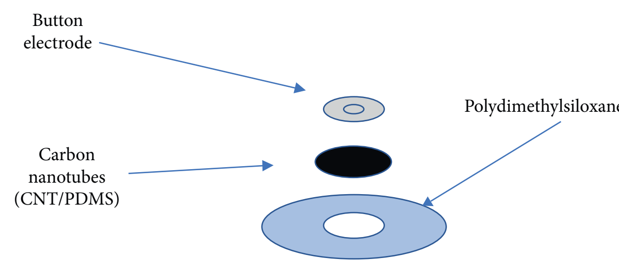

Figure 6: Design of CNT/PDMS composite electrodes.

Table 1: Resistance comparison.

Ag/AgCl electrodes	CNT/PDMS electrodes
600~800 Ω	200~300 Ω

Table 2: CNT/PDMS electrodes parameters.

Total size	Conductive diameter (mm)	Thickness (mm)	Doping quality
Length 36.5 mm, width 30.2 mm	10	2	Less than 1 g

Figure 7: Sample of CNT/PDMS electrode.

6. Electrode Positioning and Muscle Selection

The muscles were selected in this study by mainly two criteria: (1) if they are independent of each other; therefore, they ought not to collaborate to execute the same gesture, to reduce the possibility of accidentally actuating the mechanism; (2) if the selected gesture pattern is easy to achieve. Furthermore, face shielding should not affect the feasibility and regularity of the selected pattern.

The position and orientation of the muscle sensor electrodes significantly affect the strength of the signal. Owing to the differential detection mode of the sensors, two detection points and a reference position should be defined. The electrodes should be placed in the middle of the muscle body and aligned with the muscle fibers [25]. Meanwhile, the reference electrode should be placed on a separate section of the body, such as the bony portion of the elbow or a nonadjacent muscle. Due to the size of the MyoWare™ muscle sensors (AT-04-001), the sensors of the system are closely positioned (C-position). As a result, the differential voltage between the two points in the middle of the muscle body could be detected [37].

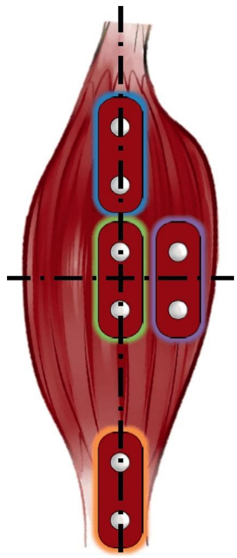

Figure 8: Electrode placement illustration.

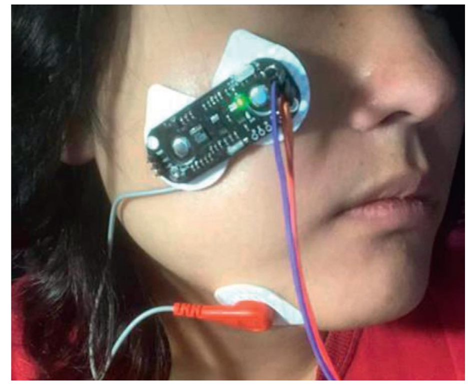

(a)

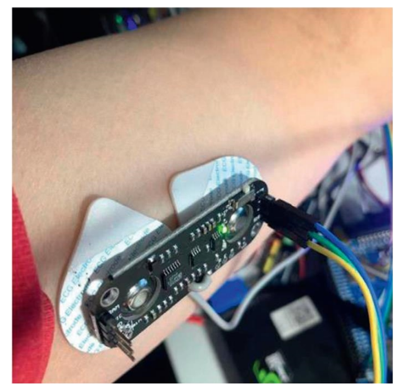

(b)

Figure 9: Muscle selection and electrodes placement. (a) Positioning of the electrode on zygomaticus. (b) Electrode positioning on the bicipital muscle of the arm.

Figure 8 shows the positions of the electrode placement based on the muscle. The green box indicates the correct positioning of the electrodes (midline of the muscle belly between the innervation zone and myotendinous junction) [24].

After comprehensive consideration of the two major factors affecting the positioning of the electrodes, the gesture pattern was defined based on the zygomaticus and bicipital muscle of the arm. In particular, these muscles were selected as they can be easily contracted and their gestures can be executed by different users, such as patients with upper limb amputation and ordinary people. The gesture pattern was defined as a signal trigger when both muscles simultaneously contracted. The detailed placement of the electrodes is shown in Figure 9. To preserve the accuracy and repeatability of the experiment, the contour of the electrode was marked by using a luminous pen after each test.

After attaching the electrodes to the surface of the muscles, a bichannel ADC function was completed on the MCU utilizing a timer interrupt and setting a sampling rate of 100 Hz. The sampled data were stored in an array for further processing.

7. Preprocessing and Feature Extraction

The preprocessing of the sEMG signal usually involves amplification [29], filtering [26, 27, 29], rectifying [26, 27], and segmentation (or windowing) [28, 38]. An instrumental amplifier, bandpass filter, and rectifying circuits were, therefore, integrated into the MyoWare™ Muscle Sensors (AT-04-001) [24]. As a result, only data segmentation could not be conducted directly by the sensor.

A fixed-length segmentation method [38] was applied in this study. The windowing length was restricted to the performance of the STM32 MCU. The coding process of the MCU was conducted using Keil MDK v5.26 Software. Only 64, 256, and 1024 points of fast Fourier transformation (FFT), which is a method to analyze the power-related characteristics of signals from the aspect of the frequency domain, were allowed on the F1 series of the STM32 [39]. Time-frequency analysis is an important key to EMG signal feature extraction [40, 41]. Due to the selected sampling rate and the requirement for a quick response, the FFT of 64 points was used in this study. To date, a windowing of 64 data points per batch has been set for feature extraction, indicating that the response time for pattern recognition is approximately 80 ms, based on a calculation machine cycle (MC).

The acquired voltage amplitude data of the two inputs and labeling data of the push button were sent from STM32F103ZET6 to the PC using a universal asynchronous receiver/transmitter (UART) and stored in text files (.txt). The files were later processed using MATLAB, as shown in Figure 10, where the vertical and horizontal axis indicates the amplitude and the timeline, respectively. The peaks in the figure are spiky as this dataset was composed of over 15000 points of data, resulting in a contraction in the horizontal display of the graph. The data sent to MATLAB were raw data that were not binned based on 64 batch sizes, as the segmentation of the data was performed via MATLAB2019a in this simulation stage.

During the feature extraction step of this study, the model was first simulated on a PC using MATLAB2019a to

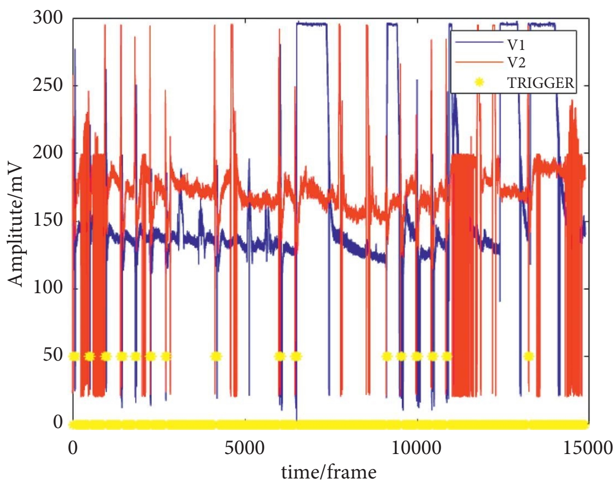

Figure 10: Raw data sent from the MCU to PC.

test the proposed concept. Afterward, the model was coded again using the C language and executed on MCU.

In this study, 16 features, of which 11 were based on the time domain and 5 on the frequency domain, were collected to analyze the binned datasets. The features based on the time domain were the integrated EMG (IEMG), mean absolute value (MAV), modified mean absolute value 1 (MMAV1) and 2 (MMAV2), mean absolute value slope (MAVS), root mean square (RMS), variance (VAR), waveform length (WL), threshold crossing (TC), Willison amplitude (WAMP), and simple square integral (SSI). Meanwhile, the features based on the frequency domain were the frequency median (FMD), frequency mean (FMN), modified frequency median (MFMD), modified frequency mean (MFMN), and frequency ratio (FR).

Equation (2) indicates the IEMG definition [42], where n is the batch size of the segmented data (64) and X_i represents i^{th} data in the dataset. The IEMG is the sum of the absolute value of the EMG signal, which can be treated as a signal power estimator [38].

$$\text{IEMG} = \sum_{i=1}^{n} |X_i|. \tag{2}$$

The MAV, MMAV1, and MMAV2 can be defined by equation (3) [43], equation (4), and equation (5) [44], respectively, where w_i is the i^{th} modified weight of the mean absolute value, which is an important characteristic of the sEMG signals that are based on the time domain.

$$\text{MAV} = \frac{1}{n}\sum_{i=1}^{n} |X_i|, \tag{3}$$

$$\begin{aligned} \text{MMAV1} &= \frac{1}{n}\sum_{i=1}^{n} w_i |X_i|, \\ w_i &= \begin{cases} 1, & 0.25n \le i \le 0.75n, \\ 0.5, & \text{otherwise}, \end{cases} \end{aligned} \tag{4}$$

$$\begin{aligned} \text{MMAV2} &= \frac{1}{n}\sum_{i=1}^{n} w_i |X_i| \\ w_i &= \begin{cases} 1, & 0.25n \le i \le 0.75n, \\ \dfrac{4i}{n}, & i < 0.25n, \\ \dfrac{4(i-n)}{n}, & i > 0.75n. \end{cases} \end{aligned} \tag{5}$$

The MAVS, which indicates the variation between two adjacent batches, can be correctly represented by equation (6) [38], where k represents the k^{th} batch in the dataset.

$$\text{MAVS}_k = \text{MAV}_{k+1} - \text{MAV}_k. \tag{6}$$

The RMS can be described by equation (7) [39]. This quantity is modeled as an amplitude-modulated Gaussian random process whose RMS is related to the constant force and nonfatigue contraction [38].

$$\text{RMS} = \sqrt{\frac{1}{n}\sum_{i=1}^{n} X_i^2}. \tag{7}$$

The VAR can be expressed by equation (8) [42]. This quantity indicates the difference between the signals in the dataset.

$$\text{VAR} = \frac{1}{n}\sum_{i=1}^{n} \left(X_i - \overline{X}\right)^2. \tag{8}$$

The WL is defined by equation (9). This value, which is the cumulative length of the waveform over a segment, is influenced by the waveform amplitude, frequency, and duration [43].

$$WL_k = \sum_{i=1}^{n-1} |X_{i+1} - X_i|. \tag{9}$$

The threshold crossings (TCs) are defined as the instances of the recorded data that crosses a threshold value during one batch.

Equation (10) represents the WAMP [39], which is the cumulative length of the waveform over a segment. This quantity indicates the number of times that the difference of consecutive amplitudes exceeded a predetermined threshold, ℓ.

$$\text{WAMP}_k = \sum_{i=1}^{n-1} f\left(|X_i - X_{i+1}|\right), f(x) = \begin{cases} 1, & x > \ell, \\ 0, & \text{otherwise}. \end{cases} \tag{10}$$

Equation (11) represents the SSI. This quantity is the cumulative length of the waveform over a segment. It also represents the accumulation of the bathed data power [38].

$$\text{SSI}_k = \sum_{i=1}^{n} \left(X_i^2\right). \tag{11}$$

Equations (12) and (13) indicate the FMN [38] and FMD [44], respectively. These quantities use FFT to calculate some properties regarding the power spectrum density (PSD). However, the Pwelch values must be obtained for the calculation of the PSD in MATLAB. This is a difficult task to be executed using an MCU, as similar results are difficult to be obtained. Hence, in this study, we obtained a resemblance [45] between the Pwelch method and the PSD calculated using FFT through equations (14) and (15), respectively. This procedure was added to the MCU using the built-in FFT library from the STM32 DSP.

$$\mathrm{FMN} = \frac{\sum_{i=1}^{n} f_i \mathrm{PSD}_i}{\sum_{i=1}^{n} \mathrm{PSD}_i},\quad f_i = \frac{i * \text{sampling\_rate}}{2 * n}, \tag{12}$$

$$\mathrm{FMD} = \frac{1}{2}\sum_{i=1}^{n} \mathrm{PSD}_i, \tag{13}$$

$$\mathrm{Pwelch} = 2\left(\left|fft\left(X_i\right)\right|\right)^2, \tag{14}$$

$$\mathrm{PSD} = \left(\left|fft\left(X_i\right)\right|\right)^2. \tag{15}$$

The MFMN and MFMD were proposed by Phinyomark et al. [44]. MFMN is calculated as the sum of the product of the amplitude spectrum and frequency divided by the sum of the spectral intensity. MFMD is defined as half of the sum of the amplitude spectrum [38]. As a result, the amplitude spectrum of the signal can result in a volatile FFT.

The frequency ratio (FR) [46] is calculated in equation (16), where $fft_{\max}$ and $fft_{\min}$, respectively, represent the maximum and minimum values of the dataset after the fast Fourier transformation.

$$\mathrm{FR} = \frac{fft_{\min}}{fft_{\max}}. \tag{16}$$

The flag label (FL) shown in equation (17) indicates the decision after evaluating the received data batch. When the dataset includes more than three sampled data points that are labeled, the entire batch is considered for the demand of the decision to trigger the actuator. This feature was omitted in practical scenarios, and it is only available for real-time calibration of the neural network classifier.

$$\mathrm{FL} = \begin{cases} 0, & f < 3, \\ 1, & f \geq 3. \end{cases} \tag{17}$$

The feature extraction was first built using MATLAB2019a considering a raw dataset stored in txt files. Each file contained more than 15000 samples of data. Sixteen feature extractions were applied for each channel of the sEMG signal, resulting in 32 features and one labeling data. These data were stored in csv files and were used, thereafter, in the classification stage.

After the offline data training procedure, the feature extracting model was coded again using the C language and downloaded into the MCU. The FFT was obtained by using the ARM_math and ARM_cFFT_Radix4 libraries [47]. 32 features were extracted from the two input channels. The output of the feature extraction was validated using a COM helper application and a JLINK debugger.

8. Classification

Many classification methods, such as k-nearest neighbours (k-NN) [26, 28], linear discriminant analysis (LDA) [26, 39], quadratic discriminant analysis (QDA) [28], support vector machine (SVM) [27, 28, 41], random tree (RT) [28], random forest (RF) [28, 41], artificial neural networks (ANN) [26, 38, 41], Bayes classifier [26, 38], self-organising map (SOP), and fuzzy classifiers [41], are available in the literature.

The Softmax classifier has outstanding performance when treating a multiclassification problem, as all types of features are normalized according to the number of classes. Furthermore, this classifier can clarify positive features [27]. In the binary classification problem in this study, the device is required to distinguish the triggering signal from the background noise, as the same triggering gesture pattern is used for the masking and unmasking actions. In this case, a Softmax classifier is adequate to solve this problem, as it yields fewer parameters than that of the other classifiers, owing to its simplicity. A large number of parameters would slow the computation speed and consume much flash memory of the MCU. In addition, the increase in complexity of the neural network results in the increase in difficulty to rewrite the model on a portable device.

We constructed the binary Softmax classifier using the 2.3.1 framework backend on TensorFlow 1.13.1. The IDE program on which the algorithm was developed was Pycharm 2020.3–Python version 3.7. No GPU was required, as the network structure and data type were not complicated.

For dataset recording, the person that tested the device was placed in a comfortable position and the electrode was firmly attached to the selected zygomaticus and bicipital muscles. A series of random movements of the limbs and changes in the countenance were performed while periodically executing the triggering pattern (simultaneous contraction of the zygomaticus and bicipital muscles). Whenever the targeting pattern was executed, the subject was requested to press the push button at the same time that he labels the corresponding data batch.

Throughout the offline model training stage, the features were extracted using MATLAB and stored in csv files, which were, thereafter, used in the training of the neural network. However, during the real-time optimization of the model, the features were directly extracted by the portable data processing unit and sent to the PC using UART. These data were again stored in txt files, which were, thereafter, converted into csv files for calibration. As a result, a more realistic dataset was acquired, and the Softmax classifier could be calibrated to achieve its best performance.

The accessed data were shuffled and, thereafter, divided into a training dataset and the test dataset using the K-fold method from the sklearn library. Meanwhile, the label value

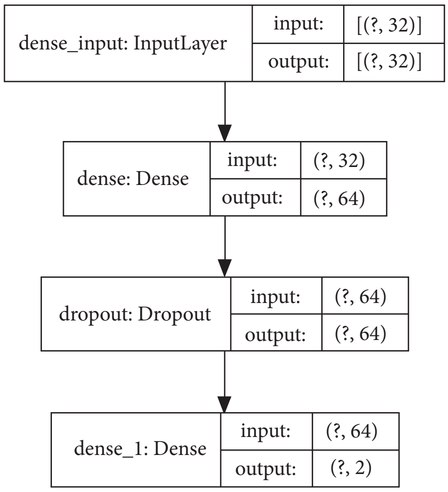

Figure 11: Neural network structure.

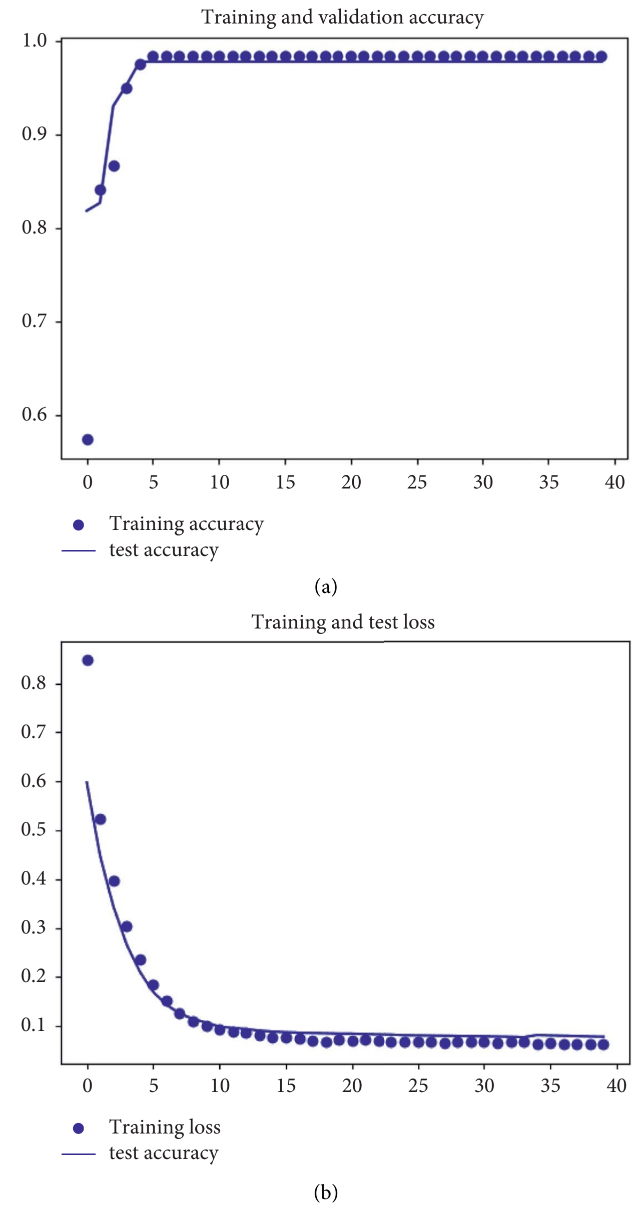

Figure 12: Assessment of the Softmax classifier. (a) Training and validation accuracy of the network. (b) Training and testing loss of the network.

was converted into a one-hot code using the built-in function of Keras.

The structure of the constructed binary Softmax classifier is shown in Figure 11. Overall, the classifier was composed of one input layer, one hidden dense layer, and one output layer. The input layer had a 1×32 input dimension and received a flattened array of 32 features related to the bichannel sEMG input, which could be fed to the network in single frames or catches. The hidden dense layer of the classifier outputted an array of data size 1×64. A drop-out method, whose ratio was 0.02, was introduced to the network to perform a regularization task, preventing the overfitting of the classifier. The output dimension of the network was the same as the class number (2).

For the neural network training process, 40 epochs of 50 batches for each step were implemented. A categorical loss function was used for the loss assessment. The Adam algorithm was implemented for optimization.

The performance analysis of the classifier is shown in Figure 12. Figure 12(a) shows the training and validation accuracy of the network. The average accuracy of 97.7% was achieved, and no significant difference was noticeable between the accuracies of the training and validation models, indicating that no overfitting or owe fitting occurred. Figure 12(b) displays the loss of the network during the training and test stages. Both losses converge to a single value.

The weights and biases of the trained model were, afterward, converted into array metrics. The copied network of the Softmax classifier was reconstructed using the C language, and the parameters were included. The resulting neural network was repeatedly calibrated considering real-time features sent from the MCU, which were updated to increase the accuracy.

Nevertheless, not all 16 features used in this study should be used during real clinical applications. The FMN shows no significant variation during the test, while the variation of the other features was noticeable. Accordingly, some of the 15 discussed features should be changed in clinical applications.

9. Experiment and Results

Based on the mechanical structure 3D printed and real-time models downloaded, a functioning prototype of the proposed device was built, as indicated in Figure 13.

The mechanism and circuitry of the device were welted on a 5 mm acrylic board using hot-melt adhesives. Actuation of the mechanism was accomplished using a pair of FUTABA S3003 servo motors. Two sets of 5 V batteries were affixed on the board due to the connection plugin shape variance. In the left corner of Figure 13(c), the JLink device, CH340 UART module, and push button were detached using the portable device. The white ropes shown in Figure 13 were used to fasten the device to the subject.

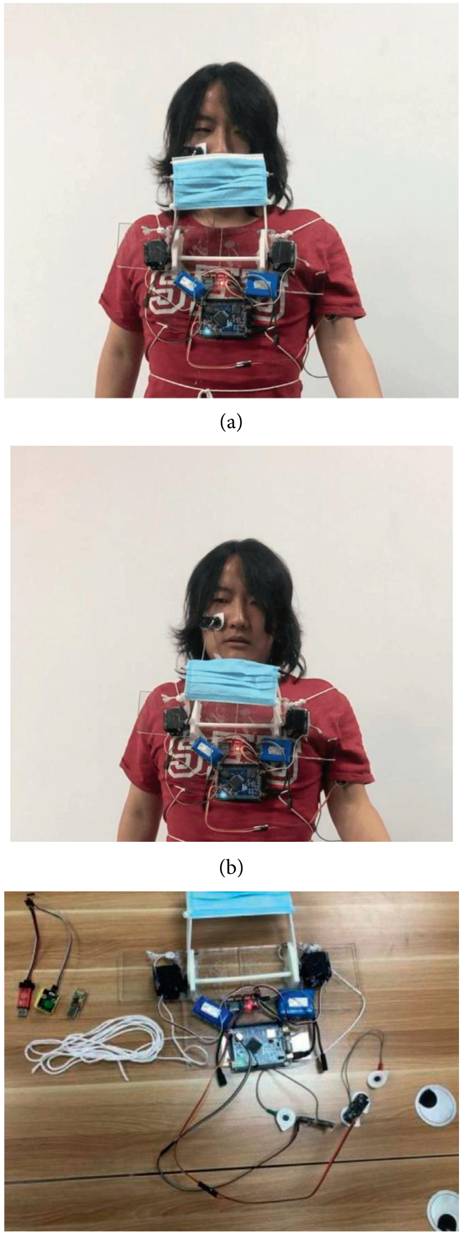

(a)

(b)

(c)

Figure 13: Test pictures of the prototype. (a) Unshielded status of the device. (b) Shielded status of the device. (c) Assembled device prototype.

To test the accuracy of the actual prototype, the accuracy was defined by [26]

$$\mathrm{ACC} = \frac{T_p}{T_p + F_N + F_P} \times 100\%, \quad (18)$$

where T_P, F_P, and F_N denote the number of correct recognitions, incorrect recognitions, and missed gestures. The subject wore the portable device for 1 min. The results are listed in Table 3.

Five tests were conducted considering a recording length of 1 min. Their overall average accuracy was 95.3%. During the test, the subject was asked to perform daily actions, such as drinking or walking, to simulate casual activities. The total number of gestures was not confined; therefore, the experiment could simulate casual activities within a fixed time interval. Based on the test results, therefore, the proposed portable face-shielding device was suitable for further implementation.

Table 3: Test result.

Number	T_P	F_N	F_P	ACC (%)
1	29	0	4	87.9
2	23	0	1	95.8
3	22	0	0	100
4	40	0	0	100
5	38	1	2	92.7

10. Conclusion

A portable face-shielding device utilizing sEMG was proposed, assembled, and proven to be feasible. The purpose of this research was to help disabled and paralyzed patients to independently wear face shields, reducing the risk of contamination due to the direct touch inside the face shield by the hands of ordinary people. Furthermore, new electrode materials using CNT/PDMS were proposed and tested to evaluate their dermotropic properties and electrical conductivity. The proposed device shows promising prospects for future implementation during the COVID-19 pandemic. Further product transitions are encouraged to target wear suitability and audience generalization.

Data Availability

The raw/processed data and program source code required to reproduce these findings are as follows: https://github.com/JasonLvernex/BMI_automatics-faceshielding-device.

Conflicts of Interest

The authors declare that they have no conflicts of interest.

Authors' Contributions

T. Lyu, D. Liu, and C. Shao helped with major contributions to this research, and Z. Zhang was partly involved in the research.

Acknowledgments

This study was supported by the CathayPath Institute of Science (CIS). The authors show their deepest gratitude to Prof. Jan Van Der Spiegel, who offered constructive guidance during this research.

References

[1] N. Zeng, Z. Li, S. Ng, D. Chen, and H. Zhou, "Epidemiology reveals mask wearing by the public is crucial for COVID-19 control," *Medicine in Microecology*, vol. 4, Article ID 100015, 2020.

[2] K. Zhang, T. N. Vilches, M. Tariq, A. P. Galvani, and S. M. Moghadas, "The impact of mask-wearing and shelter-in-place on COVID-19 outbreaks in the United States," *International Journal of Infectious Diseases*, vol. 101, pp. 334–341, 2020.

[3] S. E. Eikenberry, M. Mancuso, E. Boi et al., "To mask or not to mask: modeling the potential for face mask use by the general public to curtail the COVID-19 pandemic," *Infectious Disease Modelling*, vol. 5, pp. 293–308, 2020.

[4] A. F. Setiawan, A. D. Wibawa, M. H. Purnomo, and W. R. Islamiyah, "Monitoring stroke rehabilitation relearning program using EEG parameter: a preliminary study for developing self-monitoring system for stroke rehabilitation during new normal," in *Proceedings of the 2020 Int. Semin. Appl. Technol. Inf. Commun. IT Challenges Sustain. Scalability, Secur. Age Digit. Disruption, iSemantic*, pp. 620–624, Semarang, Indonesia, September 2020.

[5] S. Bano and S. F. Hussain, "Prediction of Covid-19 and post Covid-19 Patients with Reduced Feature Extraction Using Machine Learning Techniques," in *Proceedings of the 2021 International Conference on Frontiers of Information Technology (FIT)*, pp. 37–42, Islamabad, Pakistan, December 2022.

[6] L. Jiang, R. Li, Z. Wang, Z. Lin, and S. Li, "Healthy ways to cope with stress: home exercise advice for people during the COVID-19 by sEMG," in *Proceedings of the 2021 2nd International Conference on Big Data & Artificial Intelligence & Software Engineering (ICBASE)*, pp. 673–678, Zhuhai, China, September 2021.

[7] China Disabled Persons' Federation, "Total number of disabled persons in China at the end of 2010," 2010, https://www.cdpf.org.cn/zwgk/zccx/cjrgk/15e9ac67d7124f3fb4a23b7e2ac739aa.htm.

[8] F. Zhao, *fMRI Study of Functional Recombination of Primary Motor Cortex in Persons with Double Upper Limb Absence*, Zhejiang University, Hangzhou, China, 2010.

[9] China Disabled Persons' Federation, "Chinese standard for practical assessment of disabled persons," http://www.gov.cn/ztzl/gacjr/content_459939.htm?from=groupmessage&isappinstalled=0.

[10] ‘H. Whitlow, "A form of cross-infection in hospitals," 2021, https://www.cabdirect.org/cabdirect/abstract/19602700901.

[11] B. H. Hacks, "Auto-face shielding (Mark 1)," 2021, https://www.youtube.com/watch?v=DnJLAvsCGZU.

[12] B. Today, "Face mask that automatically makes you safe-AutoMask," https://www.youtube.com/watch?v=Tg7KHSHR5qw.

[13] T. Huang and C. Huang, "Auto mask," https://buildforcovid19.io/auto-mask/.

[14] S. M. Alan, *Measurement and Instrumentation Principles*, Elsevier, Amsterdam, Netherlands, 3rd edition, 2001.

[15] Q. Andrew, "STM32 and HC-SR04 ultrasonic ranging," https://blog.csdn.net/m0_37655357/article/details/72934643.

[16] Keydawg, "Emg_Motor_control," https://github.com/keydawg/EMG_Motor_control/tree/master/arduino/Motor_example.

[17] I. Tamanna, M. J. N. Mahi, S. Ahmed, M. Kader, A. Haque, and M. Biswas, "Controlling Body Sources of Noise Generated by Niddle Electrogram Machines: A New EMG Idea for Skipping Traditional Approaches," in *Proceedings of the2021 International Conference on Science & Contemporary Technologies (ICSCT)*, pp. 1–6, Dhaka, Bangladesh, August 2021.

[18] L. Hargrove, A. Simon, A. Young et al., "Robotic leg control with EMG decoding in an amputee with nerve transfers," *New England Journal of Medicine*, vol. 369, pp. 1237–1242, 2013.

[19] M. B. I. Reaz, M. S. Hussain, and F. Mohd-Yasin, "Techniques of EMG signal analysis: detection, processing, classification and applications," *Biological Procedures Online*, vol. 8, no. 1, pp. 11–35, Dec.

[20] "Wireless health monitoring system for Ecg, EMG and EEG Detecting|IEEE Conference Publication | IEEE Xplore," 2021, https://ieeexplore.ieee.org/abstract/document/8275879/.

[21] P. Subramani, K. Srinivas, R. B. Kavitha, R. Sujatha, and B. D. Parameshachari, "Prediction of muscular paralysis disease based on hybrid feature extraction with machine learning technique for COVID-19 and post-COVID-19 patients," *Personal and Ubiquitous Computing*, pp. 1–14.

[22] B. Grundlehner and V. Mihajlovic, *Ambulatory EEG monitoring," in Encyclopedia of Biomedical Engineering*, Elsevier, Oxford, UK, 2019.

[23] G. Ruffini, S. Dunne, F. Lluis et al., "First human trials of a dry electrophysiology sensor using a carbon nanotube array interface," *Sensors and Actuators A: Physical*, vol. 144, no. 2, pp. 275–279, 2008.

[24] Advancer Technologies, "MyoWareTM Muscle Sensor (AT-04-001) Datasheet," 2015.

[25] X. Liu, J. Sacks, M. Zhang, A. G. Richardson, T. H. Lucas, and J. V. D. Spiegel, "The virtual trackpad: an electromyography-based, wireless, real-time, low-power, embedded hand-gesture-recognition system using an event-driven artificial neural network," *IEEE Transactions on Circuits and Systems II: Express Briefs*, vol. 64, no. 11, pp. 1257–1261, 2017.

[26] J. Kim, S. Mastnik, and E. André, "EMG-based hand gesture recognition for realtime biosignal interfacing," in *Proceedings of the 2008 International Conference on Intelligent User Interfaces, January 13-16, 2008*, January 2008.

[27] S. Maier and P. S. V. Der, "Surface EMG suffices to classify the motion of each finger independently," in *Proceedings of the International Conference on Motion & Vibration Control DLR*, Germany, September 2008.

[28] S. Pancholi and A. M. Joshi, "Portable EMG data acquisition module for upper limb prosthesis application," *IEEE Sensors Journal*, vol. 18, no. 8, pp. 3436–3443, 2018.

[29] A. A. Abdhul, D. Subramani, J. Ganesan, S. Subramaniam, and K. G. Dharani, "Design and Development of EMG Based Prosthetic Arm," in *Proceedings of the 6th International Conference on Advanced Computing and Communication Systems*, pp. 502–504, ICACCS), Coimbatore, India, March 2020.

[30] F. Gao, B. Li, L. Chen, Z. Shang, X. Wei, and C. He, "A softmax classifier for high-precision classification of ultrasonic similar signals," *Ultrasonics*, vol. 112, Article ID 106344, 2021.

[31] "STMicroelectronics. STM32F1xx Datasheet ," 2008.

[32] N. X. P. Semiconductors, "PCA9685 Datasheet," 2015.

[33] J. G. Webster, "Medical instrumentation-application and design," *Journal of Clinical Engineering*, vol. 3, no. 3, p. 306, 1978.

[34] J.-Y. Baek, J.-H. An, J.-M. Choi, K.-S. Park, and S.-H. Lee, "Flexible polymeric dry electrodes for the long-term monitoring of ECG," *Sens. Actuators Phys.*vol. 143, no. 2, pp. 423–429, 2008.

[35] M. S. Fernandes, K. S. Lee, R. J. Ram, J. H. Correia, and P. M. Mendes, "Flexible PDMS -based dry electrodes for electro-optic acquisition of ECG signals in wearable devices," in *Proceedings of the Annual International Conference of the IEEE Engineering in Medicine and Biology*, pp. 3503–3506, Buenos Aires, Argentina, August 2010.

[36] H. C. Jung, J. H. Moon, D. H. Baek et al., "CNT/PDMS composite flexible dry electrodesfor long-term ECG

monitoring," *IEEE Transactions on Biomedical Engineering*, vol. 59, no. 5, pp. 1472–1479, 2012.

[37] W. J. Kang, J. R. Shiu, C. K. Cheng, J. S. Lai, H. W. Tsao, and T. S. Kuo, "The effect of electrode arrangement on spectral distance measures for discrimination of EMG signals," *IEEE Transactions on Biomedical Engineering*, vol. 44, no. 10, pp. 1020–1023, 1997.

[38] E. J. R. M. Ramirez and H. Hu, "Stages for Developing Control Systems Using EMG and EEG Signals," *A Survey*, vol. 1, 2011.

[39] C. S. D. N. YiLuXiangBeilm, "FFT-achieving with STM32F1+DSP library," https://blog.csdn.net/qq_27762895/article/details/103310598.

[40] S. Guria, P. M. Sai, and S. Lakshmi, "Brain-machine interface model to construct A prosthetic arm," in *Proceedings of the IEEE International Conference for Innovation in Technology (INOCON)*, pp. 1–5, Bangalore, India, November 2020.

[41] S. Inam, S. Inam, S A. Harmain et al., "A brief review of strategies used for EMG signal classification," in *Proceedings of the International Conference on Artificial Intelligence (ICAI)*, pp. 140–145, Islamabad, Pakistan, April 2021.

[42] H. P. Huang and C. Y. Chen, "Development of a myoelectric discrimination system for a multi-degree prosthetic hand," in *Proceedings of the 1999 IEEE International Conference on Robotics and Automation*, pp. 2392–2397, IEEE, Detroit, Michigan, USA, May 1999.

[43] K. Englehart and B. Hudgins, "A robust, real-time control scheme for multifunction myoelectric control," *Biomedical Engineering, IEEE Transactions on*, vol. 50, no. 7, pp. 848–854, 2003.

[44] A. Phinyomark, C. Limsakul, and P. Phukpattaranont, "A novel feature extraction for robust EMG pattern recognition," *Journal of Computing*, vol. 1, no. 1, pp. 71–80, 2009.

[45] weixin_34273046, "Units of PSD and its calculation method," https://blog.csdn.net/weixin_34273046/article/details/86003363.

[46] J. S. Han, W. K. Song, J. S. Kim, W. C. Bang, H. Lee, and Z. Bien, "New EMG pattern recognition based on soft computing techniques and its application to control of a rehabilitation robotic arm," in *Proceedings of the 6th International Conference on Soft Computing (IIZUKA2000)*, pp. 890–897, Fukuoka, Japan, October 2000.

[47] KALIENTEFft fft Stm32F103 willt6x Elite board, "ALIENTEK Source Code," https://download.csdn.net/download/weixin_42676678/25985028.

Hindawi
Journal of Healthcare Engineering
Volume 2023, Article ID 9860913, 1 page
https://doi.org/10.1155/2023/9860913

Retraction

Retracted: Study on Toll-Like Receptor 2-Mediated Inflammation-Induced Familial Hypertension Combined with Hyperlipemia and Its Mechanism

Journal of Healthcare Engineering

Received 11 February 2023; Accepted 11 February 2023; Published 18 February 2023

Journal of Healthcare Engineering has retracted the article titled "Study on Toll-Like Receptor 2-Mediated Inflammation-Induced Familial Hypertension Combined with Hyperlipemia and Its Mechanism" [1] due to concerns that the peer review process has been compromised.

Following an investigation conducted by the Hindawi Research Integrity team [2], significant concerns were identified with the peer reviewers assigned to this article; the investigation has concluded that the peer review process was compromised. We therefore can no longer trust the peer review process, and the article is being retracted with the agreement of the Chief Editor.

The authors disagree with the retraction.

References

[1] J. Liu, C. Li, Q. Wang, H. Hu, C. Li, and J. Qian, "Study on Toll-Like Receptor 2-Mediated Inflammation-Induced Familial Hypertension Combined with Hyperlipemia and Its Mechanism," *Journal of Healthcare Engineering*, vol. 2022, Article ID 1473597, 13 pages, 2022.

[2] L. Ferguson, "Advancing Research Integrity Collaboratively and with Vigour," 2022, https://www.hindawi.com/post/advancing-research-integrity-collaboratively-and-vigour/.

Hindawi
Journal of Healthcare Engineering
Volume 2023, Article ID 9879237, 1 page
https://doi.org/10.1155/2023/9879237

Retraction

Retracted: Clinical Efficacy and Safety of Percutaneous Spinal Endoscopy versus Traditional Open Surgery for Lumbar Disc Herniation: Systematic Review and Meta-Analysis

Journal of Healthcare Engineering

Received 27 January 2023; Accepted 27 January 2023; Published 2 February 2023

Journal of Healthcare Engineering has retracted the article titled "Clinical Efficacy and Safety of Percutaneous Spinal Endoscopy versus Traditional Open Surgery for Lumbar Disc Herniation: Systematic Review and Meta-Analysis" [1] due to concerns that the peer review process has been compromised.

Following an investigation conducted by the Hindawi Research Integrity team [2], significant concerns were identified with the peer reviewers assigned to this article; the investigation has concluded that the peer review process was compromised. We therefore can no longer trust the peer review process, and the article is being retracted with the agreement of the Chief Editor.

The authors do not agree to the retraction.

References

[1] X. Xu, C. Chen, Y. Tang, F. Wang, and Y. Wang, "Clinical Efficacy and Safety of Percutaneous Spinal Endoscopy versus Traditional Open Surgery for Lumbar Disc Herniation: Systematic Review and Meta-Analysis," *Journal of Healthcare Engineering*, vol. 2022, Article ID 6033989, 9 pages, 2022.
[2] L. Ferguson, "Advancing Research Integrity Collaboratively and with Vigour," 2022, https://www.hindawi.com/post/advancing-research-integrity-collaboratively-and-vigour/.

Hindawi
Journal of Healthcare Engineering
Volume 2023, Article ID 9864018, 1 page
https://doi.org/10.1155/2023/9864018

Retraction

Retracted: Analysis on Value of Applying Serum miR-144 and miR-221 Levels in Diagnosing Atherosclerosis

Journal of Healthcare Engineering

Received 12 November 2022; Accepted 12 November 2022; Published 30 January 2023

Journal of Healthcare Engineering has retracted the article titled "Analysis on Value of Applying Serum miR-144 and miR-221 Levels in Diagnosing Atherosclerosis" [1] due to concerns that the peer review process has been compromised.

Following an investigation conducted by the Hindawi Research Integrity team [2], significant concerns were identified with the peer reviewers assigned to this article; the investigation has concluded that the peer review process was compromised. We therefore can no longer trust the peer review process, and the article is being retracted with the agreement of the Chief Editor.

References

[1] J. Zhang, Q. Cao, Z. Zhang, C. Du, and L. Wang, "Analysis on Value of Applying Serum miR-144 and miR-221 Levels in Diagnosing Atherosclerosis," *Journal of Healthcare Engineering*, vol. 2022, Article ID 2261854, 7 pages, 2022.

[2] L. Ferguson, "Advancing Research Integrity Collaboratively and with Vigour," 2022, https://www.hindawi.com/post/advancing-research-integrity-collaboratively-and-vigour/.

Hindawi
Journal of Healthcare Engineering
Volume 2023, Article ID 9869635, 1 page
https://doi.org/10.1155/2023/9869635

Retraction

Retracted: LncRNA MAGI2-AS3 Suppresses the Proliferation and Invasion of Cervical Cancer by Sponging MiR-15b

Journal of Healthcare Engineering

Received 12 November 2022; Accepted 12 November 2022; Published 30 January 2023

Journal of Healthcare Engineering has retracted the article titled "LncRNA MAGI2-AS3 Suppresses the Proliferation and Invasion of Cervical Cancer by Sponging MiR-15b" [1] due to concerns that the peer review process has been compromised.

Following an investigation conducted by the Hindawi Research Integrity team [2], significant concerns were identified with the peer reviewers assigned to this article; the investigation has concluded that the peer review process was compromised. We therefore can no longer trust the peer review process, and the article is being retracted with the agreement of the Chief Editor.

References

[1] Y. Chai, L. Wang, Y. Qu, and Z. Hu, "LncRNA MAGI2-As3 Suppresses the Proliferation and Invasion of Cervical Cancer by Sponging MiR-15b," *Journal of Healthcare Engineering*, vol. 2022, Article ID 9707206, 9 pages, 2022.

[2] L. Ferguson, "Advancing Research Integrity Collaboratively and with vigour," 2022, https://www.hindawi.com/post/advancing-research-integrity-collaboratively-and-vigour/.

Hindawi
Journal of Healthcare Engineering
Volume 2023, Article ID 9873529, 1 page
https://doi.org/10.1155/2023/9873529

Retraction

Retracted: MicroRNA-517c Functions as a Tumor Suppressor in Hepatocellular Carcinoma via Downregulation of KPNA2 and Inhibition of PI3K/AKT Pathway

Journal of Healthcare Engineering

Received 12 November 2022; Accepted 12 November 2022; Published 29 January 2023

Journal of Healthcare Engineering has retracted the article titled "MicroRNA-517c Functions as a Tumor Suppressor in Hepatocellular Carcinoma via Downregulation of KPNA2 and Inhibition of PI3K/AKT Pathway" [1] due to concerns that the peer review process has been compromised.

Following an investigation conducted by the Hindawi Research Integrity team [2], significant concerns were identified with the peer reviewers assigned to this article; the investigation has concluded that the peer review process was compromised. We therefore can no longer trust the peer review process, and the article is being retracted with the agreement of the Chief Editor.

References

[1] L. Ma, C. Tao, and Y. Zhang, "MicroRNA-517c Functions as a Tumor Suppressor in Hepatocellular Carcinoma via Downregulation of KPNA2 and Inhibition of PI3K/AKT Pathway," *Journal of Healthcare Engineering*, vol. 2022, Article ID 7026174, 9 pages, 2022.

[2] L. Ferguson, "Advancing Research Integrity Collaboratively and with Vigour," 2022, https://www.hindawi.com/post/advancing-research-integrity-collaboratively-and-vigour/.

Hindawi
Journal of Healthcare Engineering
Volume 2023, Article ID 9803083, 1 page
https://doi.org/10.1155/2023/9803083

Retraction

Retracted: Investigation on the Effect of Graded Emergency Nursing Group under the Assistance of Multidisciplinary First Aid Knowledge Internet-Based Approach on the First Aid of Acute Myocardial Infarction

Journal of Healthcare Engineering

Received 12 November 2022; Accepted 12 November 2022; Published 26 January 2023

Journal of Healthcare Engineering has retracted the article titled "Investigation on the Effect of Graded Emergency Nursing Group under the Assistance of Multidisciplinary First Aid Knowledge Internet-Based Approach on the First Aid of Acute Myocardial Infarction" [1] due to concerns that the peer review process has been compromised.

Following an investigation conducted by the Hindawi Research Integrity team [2], significant concerns were identified with the peer reviewers assigned to this article; the investigation has concluded that the peer review process was compromised. We therefore can no longer trust the peer review process, and the article is being retracted with the agreement of the Chief Editor.

References

[1] L. Song, H. Lu, H. Ru, and X. Zhao, "Investigation on the Effect of Graded Emergency Nursing Group under the Assistance of Multidisciplinary First Aid Knowledge Internet-Based Approach on the First Aid of Acute Myocardial Infarction," *Journal of Healthcare Engineering*, vol. 2022, Article ID 8469930, 6 pages, 2022.

[2] L. Ferguson, "Advancing Research Integrity Collaboratively and with Vigour," 2022, https://www.hindawi.com/post/advancing-research-integrity-collaboratively-and-vigour/.

Hindawi
Journal of Healthcare Engineering
Volume 2023, Article ID 9829560, 1 page
https://doi.org/10.1155/2023/9829560

Retraction

Retracted: MiR-139-5p Inhibits the Development of Gastric Cancer through Targeting TPD52

Journal of Healthcare Engineering

Received 12 November 2022; Accepted 12 November 2022; Published 26 January 2023

Journal of Healthcare Engineering has retracted the article titled "MiR-139-5p Inhibits the Development of Gastric Cancer through Targeting TPD52" [1] due to concerns that the peer review process has been compromised.

Following an investigation conducted by the Hindawi Research Integrity team [2], significant concerns were identified with the peer reviewers assigned to this article; the investigation has concluded that the peer review process was compromised. We therefore can no longer trust the peer review process, and the article is being retracted with the agreement of the Chief Editor.

References

[1] Y. Li, Y. Sun, Z. Li, S. Li, and C. Wu, "MiR-139-5p Inhibits the Development of Gastric Cancer through Targeting TPD52," *Journal of Healthcare Engineering*, vol. 2022, Article ID 4033373, 10 pages, 2022.

[2] L. Ferguson, "Advancing Research Integrity Collaboratively and with Vigour," 2022, https://www.hindawi.com/post/advancing-research-integrity-collaboratively-and-vigour/.

Hindawi
Journal of Healthcare Engineering
Volume 2023, Article ID 9784985, 1 page
https://doi.org/10.1155/2023/9784985

Retraction

Retracted: Evidence-Based Care Can Improve Treatment Compliance and Quality of Life of Patients with Acute Pancreatitis

Journal of Healthcare Engineering

Received 12 November 2022; Accepted 12 November 2022; Published 25 January 2023

Journal of Healthcare Engineering has retracted the article titled "Evidence-Based Care Can Improve Treatment Compliance and Quality of Life of Patients with Acute Pancreatitis" [1] due to concerns that the peer review process has been compromised.

Following an investigation conducted by the Hindawi Research Integrity team [2], significant concerns were identified with the peer reviewers assigned to this article; the investigation has concluded that the peer review process was compromised. We therefore can no longer trust the peer review process, and the article is being retracted with the agreement of the Chief Editor.

References

[1] Q. Zheng, L. Cao, H. Ma et al., "Evidence-Based Care Can Improve Treatment Compliance and Quality of Life of Patients with Acute Pancreatitis," *Journal of Healthcare Engineering*, vol. 2022, Article ID 7621658, 8 pages, 2022.

[2] L. Ferguson, "Advancing Research Integrity Collaboratively and with Vigour," 2022, https://www.hindawi.com/post/advancing-research-integrity-collaboratively-and-vigour/.

Hindawi
Journal of Healthcare Engineering
Volume 2023, Article ID 9860692, 1 page
https://doi.org/10.1155/2023/9860692

Retraction

Retracted: The Exosomes Containing LINC00461 Originated from Multiple Myeloma Inhibit the Osteoblast Differentiation of Bone Mesenchymal Stem Cells via Sponging miR-324-3p

Journal of Healthcare Engineering

Received 12 November 2022; Accepted 12 November 2022; Published 25 January 2023

Journal of Healthcare Engineering has retracted the article titled "The Exosomes Containing LINC00461 Originated from Multiple Myeloma Inhibit the Osteoblast Differentiation of Bone Mesenchymal Stem Cells via Sponging miR-324-3p" [1] due to concerns that the peer review process has been compromised.

Following an investigation conducted by the Hindawi Research Integrity team [2], significant concerns were identified with the peer reviewers assigned to this article; the investigation has concluded that the peer review process was compromised. We therefore can no longer trust the peer review process, and the article is being retracted with the agreement of the Chief Editor.

References

[1] Y. Wu, Z. Zhang, J. Wu, J. Hou, and G. Ding, "The Exosomes Containing LINC00461 Originated from Multiple Myeloma Inhibit the Osteoblast Differentiation of Bone Mesenchymal Stem Cells via Sponging miR-324-3p," *Journal of Healthcare Engineering*, vol. 2022, Article ID 3282860, 7 pages, 2022.

[2] L. Ferguson, "Advancing Research Integrity Collaboratively and with Vigour," 2022, https://www.hindawi.com/post/advancing-research-integrity-collaboratively-and-vigour/.

Hindawi
Journal of Healthcare Engineering
Volume 2023, Article ID 9814987, 1 page
https://doi.org/10.1155/2023/9814987

Retraction

Retracted: The Effect of Acupuncture Combined with Aerobic Exercise for Coronary Heart Disease as Cardiac Rehabilitation

Journal of Healthcare Engineering

Received 12 January 2023; Accepted 12 January 2023; Published 21 January 2023

Journal of Healthcare Engineering has retracted the article titled "The Effect of Acupuncture Combined with Aerobic Exercise for Coronary Heart Disease as Cardiac Rehabilitation" [1] due to concerns that the peer review process has been compromised.

Following an investigation conducted by the Hindawi Research Integrity team [2], significant concerns were identified with the peer reviewers assigned to this article; the investigation has concluded that the peer review process was compromised. We therefore can no longer trust the peer review process, and the article is being retracted with the agreement of the Chief Editor.

References

[1] Y. Yang, Y. Li, Y. Zheng et al., "The Effect of Acupuncture Combined with Aerobic Exercise for Coronary Heart Disease as Cardiac Rehabilitation," *Journal of Healthcare Engineering*, vol. 2022, Article ID 4903265, 6 pages, 2022.

[2] L. Ferguson, "Advancing Research Integrity Collaboratively and with Vigour," 2022, https://www.hindawi.com/post/advancing-research-integrity-collaboratively-and-vigour/.

Hindawi
Journal of Healthcare Engineering
Volume 2022, Article ID 9864791, 1 page
https://doi.org/10.1155/2022/9864791

Retraction

Retracted: MiR-483 Promotes Colorectal Cancer Cell Biological Progression by Directly Targeting NDRG2 through Regulation of the PI3K/AKT Signaling Pathway and Epithelial-to-Mesenchymal Transition

Journal of Healthcare Engineering

Received 1 December 2022; Accepted 1 December 2022; Published 28 December 2022

Journal of Healthcare Engineering has retracted the article titled "MiR-483 Promotes Colorectal Cancer Cell Biological Progression by Directly Targeting NDRG2 through Regulation of the PI3K/AKT Signaling Pathway and Epithelial-to-Mesenchymal Transition" [1] due to concerns that the peer review process has been compromised.

Following an investigation conducted by the Hindawi Research Integrity team [2], significant concerns were identified with the peer reviewers assigned to this article; the investigation has concluded that the peer review process was compromised. We therefore can no longer trust the peer review process, and the article is being retracted with the agreement of the Chief Editor.

References

[1] X. Sun, K. Li, H. Wang, Y. Xia, P. Meng, and X. Leng, "MiR-483 Promotes Colorectal Cancer Cell Biological Progression by Directly Targeting NDRG2 through Regulation of the PI3K/AKT Signaling Pathway and Epithelial-to-Mesenchymal Transition," *Journal of Healthcare Engineering*, vol. 2022, Article ID 4574027, 9 pages, 2022.

[2] L. Ferguson, "Advancing Research Integrity Collaboratively and with Vigour," 2022, https://www.hindawi.com/post/advancing-research-integrity-collaboratively-and-vigour/.

Hindawi
Journal of Healthcare Engineering
Volume 2022, Article ID 9862727, 1 page
https://doi.org/10.1155/2022/9862727

Retraction

Retracted: Robotic-Assisted Laparoscopic Sacrocolpopexy for Pelvic Organ Prolapse: A Single Center Experience in China

Journal of Healthcare Engineering

Received 19 November 2022; Accepted 19 November 2022; Published 8 December 2022

Journal of Healthcare Engineering has retracted the article titled "Robotic-Assisted Laparoscopic Sacrocolpopexy for Pelvic Organ Prolapse: A Single Center Experience in China" [1] due to concerns that the peer review process has been compromised.

Following an investigation conducted by the Hindawi Research Integrity team [2], significant concerns were identified with the peer reviewers assigned to this article; the investigation has concluded that the peer review process was compromised. We therefore can no longer trust the peer review process, and the article is being retracted with the agreement of the Chief Editor.

The authors do not agree to the retraction.

References

[1] K. Niu, Q. Zhai, W. Fan et al., "Robotic-Assisted Laparoscopic Sacrocolpopexy for Pelvic Organ Prolapse: A Single Center Experience in China," *Journal of Healthcare Engineering*, vol. 2022, Article ID 6201098, 5 pages, 2022.

[2] L. Ferguson, "Advancing Research Integrity Collaboratively and with Vigour," 2022, https://www.hindawi.com/post/advancing-research-integrity-collaboratively-and-vigour/.

Hindawi
Journal of Healthcare Engineering
Volume 2022, Article ID 9780218, 1 page
https://doi.org/10.1155/2022/9780218

Retraction

Retracted: Research on the Current Situation of College Students' Physical Health under the Background of the Integration of Sports and Medicine

Journal of Healthcare Engineering

Received 19 November 2022; Accepted 19 November 2022; Published 8 December 2022

Journal of Healthcare Engineering has retracted the article titled "Research on the Current Situation of College Students' Physical Health under the Background of the Integration of Sports and Medicine" [1] due to concerns that the peer review process has been compromised.

Following an investigation conducted by the Hindawi Research Integrity team [2], significant concerns were identified with the peer reviewers assigned to this article; the investigation has concluded that the peer review process was compromised. We therefore can no longer trust the peer review process, and the article is being retracted with the agreement of the Chief Editor.

The authors do not agree to the retraction.

References

[1] Z. Lyu, Y. Hou, and Y. Wang, "Research on the Current Situation of College Students' Physical Health under the Background of the Integration of Sports and Medicine," *Journal of Healthcare Engineering*, vol. 2022, Article ID 1581282, 8 pages, 2022.

[2] L. Ferguson, "Advancing Research Integrity Collaboratively and with Vigour," 2022, https://www.hindawi.com/post/advancing-research-integrity-collaboratively-and-vigour/.

Hindawi
Journal of Healthcare Engineering
Volume 2022, Article ID 9765317, 1 page
https://doi.org/10.1155/2022/9765317

Retraction

Retracted: The Relationship between Thyroid-Stimulating Hormone and Insulin Resistance in Incipient Elderly Type 2 Diabetics with Normal Thyroid Function

Journal of Healthcare Engineering

Received 10 November 2022; Accepted 10 November 2022; Published 27 November 2022

Journal of Healthcare Engineering has retracted the article titled "The Relationship between Thyroid-Stimulating Hormone and Insulin Resistance in Incipient Elderly Type 2 Diabetics with Normal Thyroid Function" [1] due to concerns that the peer review process has been compromised.

Following an investigation conducted by the Hindawi Research Integrity team [2], significant concerns were identified with the peer reviewers assigned to this article; the investigation has concluded that the peer review process was compromised. We therefore can no longer trust the peer review process, and the article is being retracted with the agreement of the Chief Editor.

References

[1] Y. Zhang and L. Zhang, "The Relationship between Thyroid-Stimulating Hormone and Insulin Resistance in Incipient Elderly Type 2 Diabetics with Normal Thyroid Function," *Journal of Healthcare Engineering*, vol. 2022, Article ID 9447363, 6 pages, 2022.

[2] L. Ferguson, "Advancing Research Integrity Collaboratively and with Vigour," 2022, https://www.hindawi.com/post/advancing-research-integrity-collaboratively-and-vigour/.

Hindawi
Journal of Healthcare Engineering
Volume 2022, Article ID 9834370, 1 page
https://doi.org/10.1155/2022/9834370

Retraction

Retracted: Efficacy of Crizotinib Combined with Chemotherapy in Treating Advanced Non-Small-Cell Lung Cancer and Effect on Patients' Quality of Life and Adverse Reaction Rate

Journal of Healthcare Engineering

Received 10 November 2022; Accepted 10 November 2022; Published 23 November 2022

Journal of Healthcare Engineering has retracted the article titled "Efficacy of Crizotinib Combined with Chemotherapy in Treating Advanced Non-Small-Cell Lung Cancer and Effect on Patients' Quality of Life and Adverse Reaction Rate" [1] due to concerns that the peer review process has been compromised.

Following an investigation conducted by the Hindawi Research Integrity team [2], significant concerns were identified with the peer reviewers assigned to this article; the investigation has concluded that the peer review process was compromised. We therefore can no longer trust the peer review process, and the article is being retracted with the agreement of the Chief Editor.

References

[1] Z. Ma, Y. Wang, Y. Sun, G. Lin, and Z. Zhao, "Efficacy of Crizotinib Combined with Chemotherapy in Treating Advanced Non-Small-Cell Lung Cancer and Effect on Patients' Quality of Life and Adverse Reaction Rate," *Journal of Healthcare Engineering*, vol. 2022, Article ID 7898737, 5 pages, 2022.

[2] L. Ferguson, "Advancing Research Integrity Collaboratively and with Vigour," 2022, https://www.hindawi.com/post/advancingresearch-integrity-collaboratively-and-vigour/.

Hindawi
Journal of Healthcare Engineering
Volume 2022, Article ID 8280389, 8 pages
https://doi.org/10.1155/2022/8280389

Research Article

DPP-4 Inhibitor Improved the Cognitive Function in Diabetic Rats

Ying Hu,[1,2,3] Jiancheng Wang,[1,2,3] Jiao Wang,[1,2,3] Wen Chen,[1,2,3] and Qin Zhang[4]

[1]*Department of Endocrinology and Metabolism, First Affiliated Hospital of Nanchang University, Nanchang, Jiangxi 330006, China*
[2]*Jiangxi Clinical Research Center for Endocrine and Metabolic Disease, Nanchang, Jiangxi 330006, China*
[3]*Jiangxi Branch of National Clinical Research Center for Metabolic Disease, Nanchang, Jiangxi 330006, China*
[4]*Department of Anesthesiology, First Affiliated Hospital of Nanchang University, Nanchang 330006, Jiangxi Province, China*

Correspondence should be addressed to Qin Zhang; ndyfy03668@ncu.edu.cn

Received 13 January 2022; Accepted 2 March 2022; Published 18 November 2022

Academic Editor: Enas Abdulhay

Diabetes-associated cognitive dysfunction is a major problem of the international community. Dipeptidyl peptidase-4 (DPP-4) inhibitors are drugs with hypoglycemic effect widely used in diabetic treatment in clinic. In this article, we studied the effect of the DPP-4 inhibitor saxagliptin on cognitive function in diabetic rats. Firstly, to observe cognitive dysfunction caused by diabetes, we built the diabetic rat model. Subsequently, the effect of diabetes on cognitive function was evaluated by Morris Water Maze Task. Thirdly, the mechanism of the alleviation effect of DPP-4 inhibitor on cognitive dysfunction was investigated. Specifically, (1) the anti-inflammation mechanism was revealed by quantifying the accumulation of the inflammatory factor interleukin-1β (IL-1β) in the hippocampus area by western blotting and the glial fibrillary acidic protein (GFAP) by immunohistochemistry; (2) the anti-tau phosphorylation mechanism was revealed by quantifying phosphorylated tau by western blotting. This work represents the first study demonstrating the alleviation effect of DPP-4 inhibitor on cognitive dysfunction caused by diabetes. Results obtained here could be useful to seeking for a medical solution with high efficacy to the diabetes-associated cognitive dysfunction.

1. Introduction

Diabetes is one of the most ubiquitous chronic endocrine diseases in the world. According to the statistic, over 387 million people suffer from diabetes globally, and the incidence of diabetes in adults has reached up to 11.6% of the Chinese nation. It is estimated by 2035, the number of the diabetics in the world will exceed 600 million [1]. Diabetes is frequently accompanied by the incidence of cognitive dysfunction. It is due to the pathological changes in the microvessel caused by diabetes, which could lead to cerebrovascular damage and thus damage the central nervous system [2]. Cognitive dysfunction has many manifestations in clinic, including loss of memory, reduced recognition and understanding ability, and even the complete loss of daily activity [3]. Nevertheless, various complications of diabetes could deteriorate the progress of cognitive dysfunction [4]. The cognitive dysfunction makes the diabetics less able to realize they are sick, which could severely lower their compliance to therapy and diet control and result in the extreme fluctuation of the blood glucose level. The instability of the blood glucose level again deteriorates the cognitive dysfunction in return [5]. In such a vicious cycle, there is hardly a guarantee of full recovery from diabetes. Therefore, the prevention and treatment of the cognitive dysfunction caused by diabetes are of great significance. At present, the most widely used drugs in treating cognitive dysfunction include tacrine, rivastigmine, galanthamine, donepezil, memantine, etc. [6]. These drugs function as precursor of acetylcholine, inhibitor of acetylcholine esterase, and activator of cholinergic receptor, and thus only have the efficacy of temporarily alleviating clinical symptoms [7]. Seeking for an effective medical solution to the cognitive dysfunction, especially the diabetes-associated cognitive dysfunction, remains challenging.

Screening from the available antidiabetic drugs provides as the primary option to discover a specific compound with additional efficacy of improving the patient's cognitive function. Furthermore, investigating the mechanism of its pharmacological function will provide some leads in maintaining intact cognitive function of the diabetics in clinical treatment. Recently, researches have confirmed that the glucagon-like peptide 1 (GLP-1) plays an important role in treating degenerative diseases of the central nervous system such as Alzheimer, Parkinson, and vascular dementia, and thus could improve the patients' cognitive function [8].

In addition, hyper-phosphorylated tau has neurotoxicity, which can induce the neuronal necrosis [9]. Abnormal hyper-phosphorylation of tau affects its physiological function, thereby leads to the formation of neurofibrillary tangles, and consequently accelerates the deterioration of degenerative diseases [10]. Studies have shown inhibiting the hyper-phosphorylation of tau can effectively relieve patients' cognitive dysfunction and has therapeutic effects on Alzheimer's disease and other symptoms [11]. The level of dipeptidyl peptidase-4 (DPP-4) in some diabetic patients is elevated, and it is speculated that dipeptidyl peptidase-4 may be related to fat metabolism in diabetic patients [12]. The use of DPP-4 inhibitors can improve glycemic control in patients with type 2 diabetes [13]. The dipeptidyl peptidase-4 (DPP-4) inhibitors are new antidiabetic drugs which are effective in increasing endogenous GLP-1 availability [14, 15]. A variety of DPP-4 inhibitors have been widely used in the treatment of diabetes, among which the effect of saxagliptin on blood glucose control is higher than other oral hypoglycemic drugs [14, 16]. However, it remains unknown whether DPP-4 inhibitors are functional in treating diabetes-associated cognitive dysfunction.

Thus, in this work, we investigated the effect of the DPP-4 inhibitor saxagliptin on improving cognitive function in diabetic rats. Furthermore, we evaluated its efficacy in reducing inflammation and tau hyper-phosphorylation in the hippocampus of diabetic rats. The mechanism of the medical function of saxagliptin was finally discussed. The results obtained here provide information for the discovery and development of highly effective drugs to diabetes-associated cognitive dysfunction.

2. Materials and Methods

2.1. Animals. This study was performed in accordance with regulations for the Care and Use of Laboratory Animals and approved by the Animal Ethics Committee of Nanchang University. Forty-two adult healthy male Sprague-Dawley rats (160–200 g) used in this study were obtained from the Laboratory Animal Center of Nanchang University.

All the rats were bred under standard conditions (20–24°C, 55% ± 5% relative humidity, and 12-h/12-h dark/light cycle) with free access to food and water. All the rats were acclimated to laboratory conditions for 1 week prior to the experiment. At the beginning of the experiment, the rats were randomly divided into normal control group (NC, $n = 14$) and diabetic modeling group ($n = 28$). Rats in the NC group were fed with normal diet, while rats in the diabetic modeling group were fed with high sugar and high fat diet (composition: 67.5% normal feeds, 20% sucrose, 10% pig oil, and 2.5% powder of yolk). After 4 weeks of feeding, rats in the diabetic modeling group were fasted for 12 h but allowed free access to water, then injected with streptozotocin (STZ) intraperitoneally at a dose of 30 mg/kg (currently available, appropriate amount of STZ in the dark, 0.1 mol/L citric acid-sodium citrate in the buffer ice bath, pH = 4.4). 72 h after injection, rats with fasting blood glucose ≥16.7 mmol/L were randomly divided into diabetic model group (DM, $n = 12$) and DPP-4 inhibitor treatment group (DM-S, $n = 12$). Rats in the NC group were weighed and given corresponding dose of citric acid-sodium citrate buffer intraperitoneally instead of STZ. The DM-S group was given saxagliptin by intragastric administration at a dose of 10 mg/Kg/d for 12 weeks, while the NC group and the DM group were given an equal volume of normal saline in the same manner.

2.2. Morris Water Maze Task. 24 h after treatment with DPP-4 inhibitor, rats were subjected to the Morris Water Maze (MWM) test to evaluate the learning and memorizing abilities. A round, black painted pool (diameter, 180 cm; depth, 50 cm) was filled with water to a depth of 30 cm and the water was made opaque by the addition of black nontoxic ink. The water temperature was maintained at 24 ± 1°C. The pool was divided into four quadrants and a platform (diameter, 10 cm) was submerged approximately 2 cm below the water line in the center of one quadrant. Trials were started at 9 a.m. by releasing the rat into the water facing the outer edge of the pool at one of the quadrants (in a random sequence) and letting the rat escape to the submerged platform. Once the rat arrived at the platform, it was allowed to stay on it for 30 s. The rat was allowed to swim for a maximum time of 60 s in a trial. The time it spent in reaching the platform was defined as escape latency. Both the escape latency and the swimming distance were recorded. If the rat failed to get the platform within 60 s, it was manually guided to the platform and allowed to stay on it for 30 s and the escape latency was recorded as 60 s. All the tested rats received four training trials a day for 5 consecutive days, with 10- to 15-min interval between trials. On the sixth day, the platform was removed, and each rat was allowed to swim freely for 60 s. The number of times that the rat crossed over the previous platform site, the swimming distance, and swimming time in the target quadrant were all recorded and analyzed. Each rat's swimming path was tracked by a computerized video system (Electric factory of Anhui, China).

2.3. Measurement of Blood Glucose. Blood samples were collected from rats before and after treatment with DPP-4 inhibitor. The blood glucose level was measured using 3-uL drop of blood obtained by nicking the tail vein and a One Touch Ultra Link Blood Glucose Meter (Life Scan, Shanghai, China).

2.4. Tissue Preparation. After the MWM test, all rats were sacrificed by spinal dislocation. The brains from each group were harvested and the hippocampus was isolated from brain in the ice. The left half of the hippocampus placed in cryopreservation tube was frozen immediately in liquid nitrogen and then stored at −80°C for total protein extraction. Meanwhile, the right hippocampus was fixed in 10% formaldehyde, embedded in paraffin and coronally sectioned (4 μm) for hematoxylin-eosin (HE) staining.

2.5. HE Staining. Before immunostaining, 4-um-thick tissue sections were dewaxed in xylene and fixed on poly-L-lysine-coated slides. The tissue sections were dewaxed by xylene and gradient ethanol and stained with hematoxylin (Beyotime, Shanghai) for 3 min. It was differentiated with 1% ethyl alcohol hydrochloride for 30 s, then dyed with 0.5% eosin for 3 min, then dehydrated with gradient ethanol and xylene successively. After drying in a fume hood, the sheet was sealed with neutral gum. Neuronal damage in the hippocampus was analyzed at 400 × magnification (Nikon, Japan).

2.6. Immunohistochemistry. After MWM experiment and blood glucose measurement, six rats were randomly selected from each group and anesthetized by intraperitoneal injection of 0.5% sodium pentobarbital at a dose of 50 mg/kg. Their hearts were rapidly exposed, and an infusion needle was inserted into the ascending aorta via the left ventricular and infused with 200 ml of heparin saline (12.5 U/ml) rapidly until effluent liquid from the right atrial appendage was colorless and transparent. 4% paraformaldehyde fixative solution was reperfused slowly for about 30 min. Then their brains were rapidly removed and placed in fixation at 4°C for overnight. After dehydration in alcohol and xylene, the slices were embedded in paraffin and sectioned (4 μm thick).

Sections were deparaffinized, rehydrated with decreasing strengths of ethanol (100% to 50%), and then incubated with 3% H_2O_2 for 15 min at 37°C. Thereafter, brain tissue sections were placed in a 0.01 M citrate buffer, boiled at 95°C for 20 min, then cooled down to room temperature. After being sealed with normal goat serum at 37°C for 15 min, sections were probed with the primary antibody, rabbit anti-rat monoclonal antibody to GFAP (1 : 100, CST, Danvers, MA) overnight at 4°C. Then sections were incubated with the secondary antibody, horseradish peroxidase (HRP)-labeled goat anti-rabbit antibody (BL003A, Biosharp Biotech Co., Ltd., Hefei, China), for 30 min at 37°C. Sections were stained with diaminobenzidine (DAB; P0202; Beyotime Biotech Co., Ltd., Shanghai, China) for 5–10 min under microscope observation, counterstained with hematoxylin for 3 min, and then finally sealed. Five random fields from the CA1, CA3, and DG regions were selected respectively at 400 × magnification. The average optical density of GFAP-positive cells can reflect GFAP expression level and was calculated with Image-Pro Plus 6.0 software (Media Cybernetics, US).

2.7. Western Blotting. The hippocampus was harvested, homogenized in RIPA lysis buffer (RIPA: PMSF = 100 : 1) on ice for 15 min, and then centrifuged at 12,000 × g for 15 min at 4°C. The supernatant was collected and stored at -80°C. The total protein concentration was quantified by the BCA Protein Assay kit (Beyotime Institute of Biotechnology, China) following the manufacturer's instructions. 100 μg of protein per line was separated using 10% SDS-PAGE and then transferred to PVDF membranes (Millipore Co., Billerica, MA, USA). After blocking with 5% skim milk for 2 h, the membranes were incubated with primary antibodies overnight at 4°C.

The primary antibodies used in this study were as follows: anti-β-actin (1 : 1000; CST), anti-IL-1β (1 : 1000; CST), anti-tau (1 : 1000; CST), anti-p-tau (s202) (1 : 1000; CST), and anti-p-tau (s396) (1 : 1000; CST). The membranes were then washed with 1 × TBS/0.1% Tween 20 and then incubated with HRP-conjugated anti-rabbit IgG (secondary antibody, 1 : 3000; CST) or HRP-conjugated anti-mouse IgG (secondary antibody, 1 : 3000; CST) at room temperature for 2 h. Subsequently, membranes were washed with 1 × TBS/0.1% Tween 20 three times. Blots were visualized with an ECL detection kit (Beyotime Biotechnology, Shanghai, China) and analyzed using ImageJ software (National Institutes of Health, NIH).

2.8. Statistical Analysis. Results were analyzed using SPSS Statistics 23 software. Significant differences relative to the controls were determined using independent-samples *t*-tests. For multiple group comparisons, one-way ANOVA was used to determine the significant differences. All results were presented as mean ± standard. P values < 0.05 were considered to be statistically significant ($^*P < 0.05$, $\#P < 0.05$). Each experiment was repeated three times.

3. Results

3.1. Diabetes Caused Cognitive Dysfunction in Rats and DPP-4 Inhibitor Alleviated the Symptoms. To observe the effect of diabetes on cognitive function and further investigate the potential effect of DPP-4 inhibitor on diabetic cognitive dysfunction, we built diabetic rat model (see Materials and Methods section) and evaluated the rats' learning and recognition ability by MWM test. Comparative analysis was carried out on rats from three groups: the normal control group (NC), the diabetic model group (DM), and the saxagliptin-treated diabetic model group (DM-S). As shown in Figure 1, within the experimental time of 5 consecutive days, the NC group exhibited clearly patterned swimming path in all trials with an average escape latency of 6.1 s, suggesting conscious activity and unaffected recognition ability. However, rats from the DM group were unable to get to the platform and exhibited abnormal circulated swimming path which tended to be more abnormal with the progressing of the test. It seemed that the more high sugar and high fat diet they had eaten, the more confused they were. The average escape latency of the DM group was 56.5 s, which was 9.3 folds that of the NC group, whereas the daily shuttle times and total distance of the two groups were comparable. Thus, it appeared that DPP-4 treatment caused instant confusion

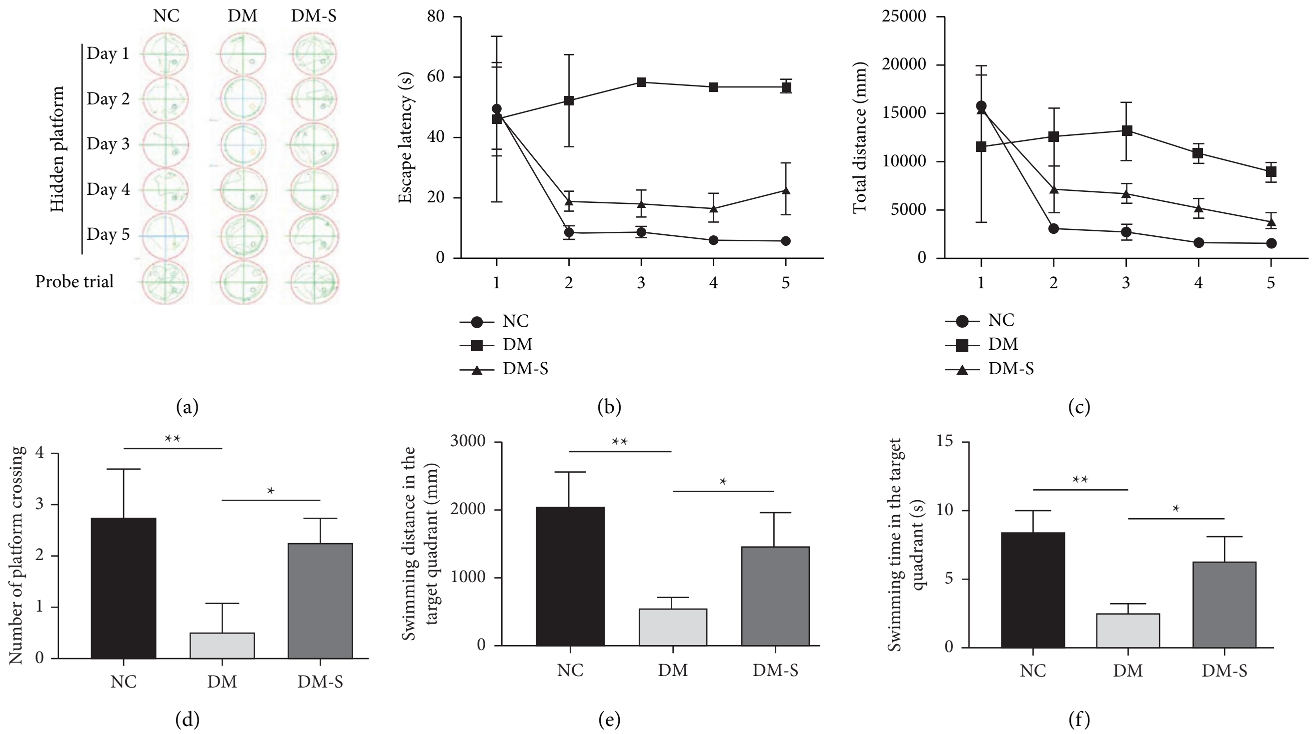

Figure 1: Results of Morris Water Maze Task. (a) The swimming path; (b) the escape latency; (c) the total distance; (d) number of platform crossings; (e) the swimming distance in the target quadrant; and (f) the swimming time in the target quadrant. The shown data represent the average of four parallel physiological replicates. In the experiment for 5 consecutive days, the NC group exhibited clearly patterned swimming path in all trials with an average escape latency of 6.1 s. However, rats from the DM group were unable to get to the platform and exhibited abnormal circulated swimming path. The average escape latency of the DM group was 56.5 s which was 9.3 folds that of the NC group, whereas the daily shuttle times and total distance of the two groups were comparable $^{*}P < 0.05$ $^{**}P < 0.01$.

and slight inactivity in the rats but did not cause the loss of cognitive function. As expected, but still astonishingly, the DM group exhibited disordered swimming path, and neither recovery of cognitive function nor effective physical activity was observed all over the experimental time period. It seemed that the diabetic rats were completely disabled, which was a definite demonstration of cognitive dysfunction. However, rats from the DM-S group exhibited obvious partial recovery of cognitive function along with the advance of time. These results demonstrated that diabetes could cause cognitive dysfunction in rats and DPP-4 inhibitor saxagliptin could alleviate such cognitive dysfunction symptoms caused by diabetes.

We evaluated the efficacy of daily intragastric administration of DPP-4 inhibitor saxagliptin in diabetic rats on blood glucose. The time points included the starting date of week 4 (before treatment) and 16 after intragastric administration of saxagliptin or saline. The fasting blood glucose of the NC group rats was lower than 10 mM before and after treatment. On the other hand, daily intragastric administration of saxagliptin significantly alleviated hyperglycemia of the diabetic rats, controlling the fasting blood glucose to ~7 mM from ~18 mM after 12 weeks of treatment. As a control, the fasting blood glucose increased from ~18 mM to ~24 mM after daily intragastric administration of saline (Figure 2). The preliminary results indicate that DPP-4 inhibitor saxagliptin can ameliorate high blood glucose status.

3.2. DPP-4 Inhibitor Prohibited Neuron Apoptosis in the Hippocampus Area of Diabetic Rats. To reveal the possible mechanism of how DPP-4 inhibitor saxagliptin alleviates cognitive dysfunction in the diabetics, we investigated the neuron apoptosis in the hippocampus area of these rats. We observed the morphology and structure of the hippocampus area of these tested rats under optical microscope after HE staining. As shown in Figure 3, significantly increased number of apoptotic cells was observed in the diabetic group (DM) as compared with the control group (NC), with the morphological change in scattering and decomposing, which demonstrated a severely deteriorated apoptotic process. However, the number of apoptotic cells of rats from the diabetic rats treated with DPP-4 inhibitor saxagliptin was comparable to that of the control group again, demonstrating a rescue from the diabetic status.

3.3. DPP-4 Inhibitor Reduced Inflammation in the Hippocampus in Diabetic Rats. Glial fibrillary acidic protein (GFAP) is the marker of astrocyte activation in the hippocampus, which could indicate the extent of the central inflammation in the hippocampus. Interleukin-1 (IL-1; sub-type IL-1β) is the major inflammatory factor closely related to cognitive function. Since glucagon-like peptide 1 (GLP-1) and its analogs were previously confirmed with an

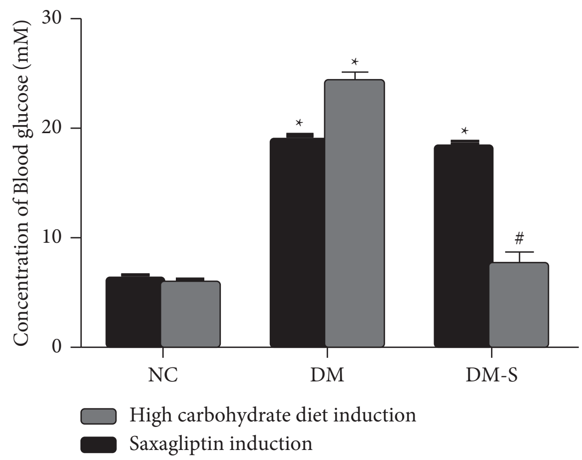

Figure 2: Changes in blood glucose before and after the treatment of rats. The fasting blood glucose of the NC group rats was lower than 10 mM before and after treatment. After daily administration of saxagliptin for 12 weeks in DM-S group, the fasting blood glucose was controlled to ~7 mM from ~18 mM. The fasting blood glucose of the DM group increased from ~18 mM to ~24 mM after daily intragastric administration of saline. $^*P < 0.05$, indicates a significant difference compared with the NC group; $\#P < 0.05$ indicates a significant difference compared with the DM group.

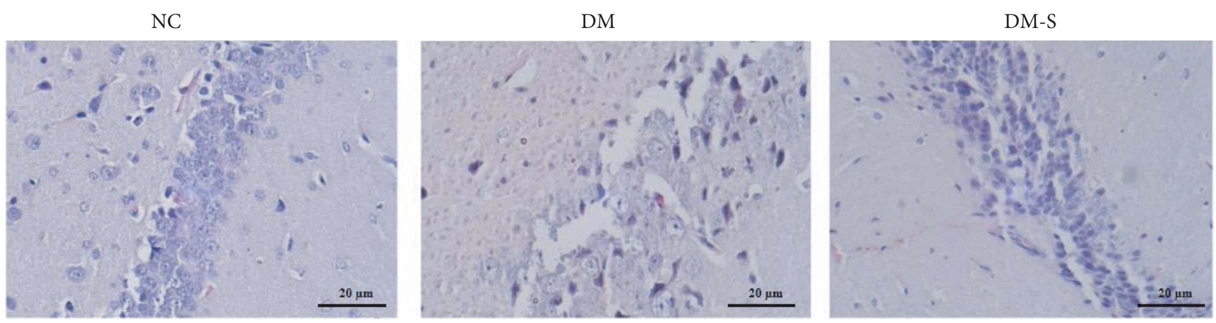

Figure 3: Morphology and structure of the hippocampus area by HE staining (400 × magnification). The significantly increased number of apoptotic cells was observed in the DM group as compared with the NC group, with the morphological change in scattering and decomposing. However, the number of apoptotic cells of rats from the diabetic rats treated with DPP-4 inhibitors was comparable to that of the NC group again.

inhibitory effect on the neural inflammation and DPP-4 inhibitor can increase the endogenous GLP-1 availability, we investigated the effect of DPP-4 inhibitor on neural inflammation in diabetic rats to further reveal the mechanism of its protective effect on cognitive function damaged by diabetes. The expression level of GFAP in the CA1, CA2, and DG regions of the brain was detected by immunohistochemistry. The level of inflammatory factor, IL-1β, in the hippocampus area of these rats was tested by the method of western blotting. As shown in Figure 4, a GFAP expression was increased by about 7 folds in rats from the diabetic group than in those from the NC group. However, the GFAP expression sharply decreased by half in the DM-S group compared with the DM group. As for IL-1β (Figure 5), increased IL-1β was detected in the DM group rats relative to the NC group. Whereas an obvious reduction in IL-1β accumulation was observed in rats from the DM-S group as in those from the DM group. These results suggested that diabetes could trigger inflammation and DPP-4 inhibitor could have an anti-inflammation effect on diabetic rats.

3.4. DPP-4 Inhibitor Reduced Tau Hyper-Phosphorylation in the Hippocampus. Hyper-phosphorylated tau has neurotoxicity which can induce the neuronal necrosis. Abnormal hyper-phosphorylation of tau affects its physiological function, thereby leads to the formation of neurofibrillary tangles and consequently accelerates the deterioration of degenerative diseases. We assume hyper-phosphorylation of tau might also be a factor in the incidence of cognitive dysfunction, thus we quantified hyper-phosphorylated tau by western blotting. As shown in Figure 5, the expression of the two forms of phosphorylated tau was abnormally high in rats from the diabetic group. DPP-4 inhibitor treatment has a reducing effect on phosphorylation of tau; however, the level of phosphorylated tau in rats from the DM-S group was still much higher than in those from the NC group.

4. Discussion

According to the WHO data, the number of diabetics worldwide is as high as 4.22 billion. Studies have shown that hyperglycemia, insulin resistance, inflammation, oxidative

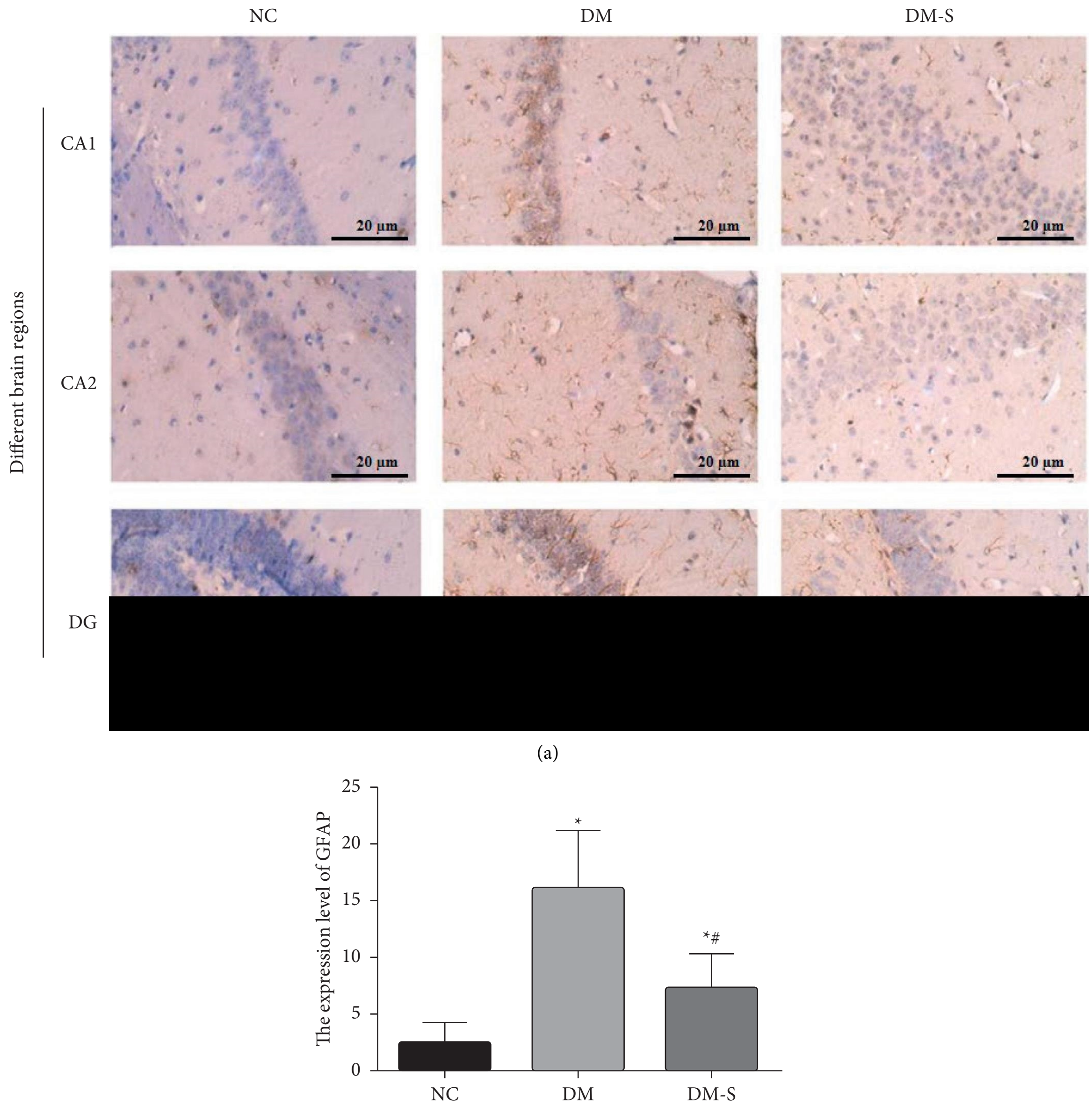

(a)

(b)

Figure 4: Effects of DPP-4 inhibitor inflammation in the hippocampus of diabetic rats. (a) Expression of GFAP in CA1, CA2, and DG regions of brain detected by immunohistochemistry (400 × magnification). (b) Quantification of GFAP expression. The GFAP expression was increased by about 7 folds in rats from the DM group than in those from the NC group. However, the GFAP expression sharply decreased by half in the DM-S group compared with the DM group. $^{*}P < 0.05$ indicates a significant difference compared with the NC group; $^{\#}P < 0.05$ indicates a significant difference compared with the DM group.

stress, and other factors all will affect cognitive function, so the probability of developing cognitive dysfunction, dementia, and other central nervous system diseases in patients with diabetes is significantly higher than that in normal people, and diabetes is also an independent risk factor for Alzheimer's disease [17, 18]. The cognitive dysfunction caused by diabetes seriously affects the quality of life of patients and their relatives, and greatly increases the burden of social medical care. Therefore, it is of great significance to study the cognitive dysfunction of diabetes.

It is acknowledged that both diabetes and Alzheimer cause cognitive dysfunction through over-activating the central inflammatory system or imbalancing the pro-inflammatory and anti-inflammatory systems, which could cause damage to the neuron [19]. Peripheral inflammatory mediators could directly enter the central nervous system or stimulate microglia and astrocyte in the hippocampus area to secrete inflammatory factors, causing local inflammation and thereby reducing cognition ability [20]. Since diabetes and Alzheimer's disease share many common physiological characteristics, and there are few breakthroughs in the treatment of Alzheimer's disease, many scholars try to use antidiabetics to treat the cognitive impairment of diabetes patients [21]. Clinical studies have found that among the

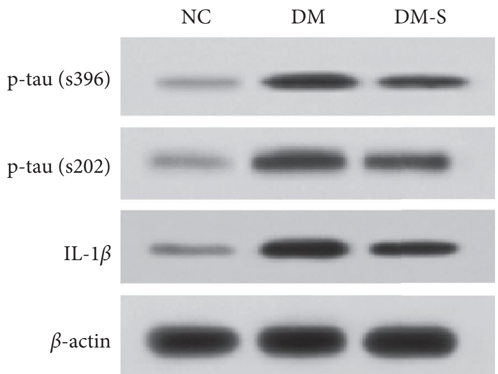

Figure 5: Western blotting of inflammatory factors and phosphorylated tau protein. The expression of the two forms of phosphorylated tau was abnormally high in rats from the DM group. After treatment with DPP-4 inhibitor, tau phosphorylation expression in DM-S group decreased, but it was still much higher than that in the NC group. As for IL-1β, increased IL-1β was detected in the DM group rats relative to the NC group. Compared with the NC group, IL-1β expression was increased in the DM group. The accumulation of IL-1β in DM-S group was significantly lower than that in the DM group.

antidiabetics, metformin, insulin, pioglitazone, sitagliptin, and other drugs can significantly improve the cognitive ability of diabetes patients [22].

Dipeptidyl peptidase-4 (DPP-4) inhibitors are a class of new oral antidiabetics for the treatment of type 2 diabetes mellitus (T2DM), which can not only regulate the metabolism of glucose and lipids in vivo, but also improve endothelial function and reduce the pro-oxidation and pro-inflammatory states of injured cells [23]. The clinical use of DPP-4 inhibitors includes vildagliptin, Alogliptin, etc., which has a significant therapeutic effect on diabetes without increasing the risk of infection [14, 24]. Saxagliptin as monotherapy or in combination with metformin reduces the risk of hypoglycemia in patients with type 2 diabetes. Saxagliptin is generally well tolerated in clinical trials, with relatively mild adverse reactions and high safety and efficacy. Therefore, this study chose saxagliptin as the research object to explore the therapeutic effect of saxagliptin, a DPP-4 inhibitor, on diabetes-related cognitive dysfunction.

In this study, a diabetic mouse model was established and treated with saxagliptin intragastric administration. The experimental results showed that the diabetic mice fed with high sugar and high fat had increased blood glucose, lost cognitive function, and swimming path disorder. The cognitive function of mice treated with saxagliptin was partially recovered and hyperglycemia was relieved. To further study the therapeutic mechanism of DPP-4 inhibitors, we examined the hippocampal area of diabetic rats. The results showed that saxagliptin treatment significantly inhibited neuronal apoptosis and the expression of inflammatory factors in the hippocampal area of diabetic mice, suggesting that DPP-4 inhibitor could effectively inhibit the inflammatory response and neuronal apoptosis induced by elevated blood glucose in diabetic mice. The detection of hyper-phosphorylated tau protein showed that the expression of phosphorylated tau protein in the hippocampal area of diabetic mice was abnormally high, while DPP-4 inhibitor treatment could effectively reduce the content of phosphorylated tau protein in mice. The above experimental results indicate that DPP-4 inhibitor can not only control blood glucose in diabetic mice, but also reduce neuronal apoptosis by inhibiting the expression of inflammatory factors and phosphorylated tau protein in the hippocampus of mice, thus improving the cognitive function of mice.

The limitation of this study is that GLP-1 levels in neuro inflammation have not been determined. However, our previous studies have shown that saxagliptin increases the level of active GLP-1 in the brain [25]. In conclusion, the treatment of diabetic mice with saxagliptin can improve hyperglycemia and partially restore cognitive function. DPP-4 inhibitors have therapeutic effects on diabetes-related cognitive dysfunction. This study provides a new idea for antidiabetics in the treatment of diabetes-related cognitive dysfunction and points out a new research direction for the treatment of Alzheimer's disease.

5. Conclusion

The results of this study suggest that DPP-4 inhibitors can improve the cognitive function of diabetic rats. After treatment with saxagliptin, the cognitive function of mice was partially recovered and the symptoms of hyperglycemia were relieved, so as to control the blood glucose of diabetic mice. Saxagliptin significantly inhibited the expression of phosphorylated tau protein and inflammatory factor IL-1β in hippocampal neurons of diabetic mice and reduced neuronal apoptosis, thus improving the cognitive function of mice.

Data Availability

The data used to support the findings of the research are included within this article.

Conflicts of Interest

The authors declare that they have no conflicts of interest.

References

[1] D. Lovic, A. Piperidou, I. Zografou, H. Grassos, A. Pittaras, and A. Manolis, "The growing epidemic of diabetes mellitus," *Current Vascular Pharmacology*, vol. 18, no. 2, pp. 104–109, 2020.

[2] F. Lyu, D. Wu, C. Wei, and A. Wu, "Vascular cognitive impairment and dementia in type 2 diabetes mellitus: an overview," *Life Sciences*, vol. 254, Article ID 117771, 2020.

[3] K. D. Mueller, B. Hermann, J. Mecollari, and L. S. Turkstra, "Connected speech and language in mild cognitive impairment and Alzheimer's disease: a review of picture description tasks," *Journal of Clinical and Experimental Neuropsychology*, vol. 40, no. 9, pp. 917–939, 2018.

[4] S.-C. Kuo, S.-W. Lai, H.-C. Hung et al., "Association between comorbidities and dementia in diabetes mellitus patients:

population-based retrospective cohort study," *Journal of Diabetes and Its Complications*, vol. 29, no. 8, pp. 1071–1076, 2015.

[5] G. J. Biessels and F. Despa, "Cognitive decline and dementia in diabetes mellitus: mechanisms and clinical implications," *Nature Reviews Endocrinology*, vol. 14, no. 10, pp. 591–604, 2018.

[6] M. U. Farooq, J. Min, C. Goshgarian, and P. B. Gorelick, "Pharmacotherapy for vascular cognitive impairment," *CNS Drugs*, vol. 31, no. 9, pp. 759–776, 2017.

[7] A. Dey, S. Hao, J. R. Erion, M. Wosiski-Kuhn, and A. M. Stranahan, "Glucocorticoid sensitization of microglia in a genetic mouse model of obesity and diabetes," *Journal of Neuroimmunology*, vol. 269, no. 1-2, pp. 20–27, 2014.

[8] J. Zhao, H. Christian, K. Liu, L. Li, G. L. Li, and Y. Liu, "Neuroprotective role of(Val8)GLP-1-Glu-PAL in an in vitro model of Parkinson's disease," *Neural Regeneration Research (English version)*, vol. 11, no. 2, pp. 326–331, 2016.

[9] D.-L. Ma, F.-Q. Chen, W.-J. Xu, W.-Z. Yue, G. Yuan, and Y. Yang, "Early intervention with glucagon-like peptide 1 analog liraglutide prevents tau hyperphosphorylation in diabetic db/db mice," *Journal of Neurochemistry*, vol. 135, no. 2, pp. 301–308, 2015.

[10] W. Xu, Y. Yang, G. Yuan, W. Zhu, D. Ma, and S. Hu, "Exendin-4, a glucagon-like peptide-1 receptor agonist, reduces Alzheimer disease-associated tau hyperphosphorylation in the Hippocampus of rats with type 2 diabetes," *Journal of Investigative Medicine*, vol. 63, no. 2, pp. 267–272, 2015.

[11] A. Boutajangout and T. Wisniewski, "Tau-based therapeutic approaches for Alzheimer's disease - a mini-review," *Gerontology*, vol. 60, no. 5, pp. 381–385, 2014.

[12] C. M. Valerio, J. S. de Almeida, R. O. Moreira et al., "Dipeptidyl peptidase-4 levels are increased and partially related to body fat distribution in patients with familial partial lipodystrophy type 2," *Diabetology & Metabolic Syndrome*, vol. 9, no. 1, p. 26, 2017.

[13] G. Crepaldi, M. Carruba, M. Comaschi, S. Del Prato, G. Frajese, and G. Paolisso, "Dipeptidyl peptidase 4 (DPP-4) inhibitors and their role in Type 2 diabetes management," *Journal of Endocrinological Investigation*, vol. 30, no. 7, pp. 610–614, 2007.

[14] C. I. Jarvis, A. Cabrera, and D. Charron, "Alogliptin," *The Annals of Pharmacotherapy*, vol. 47, no. 11, pp. 1532–1539, 2013.

[15] E. C. Rizos, E. E. Ntzani, N. Papanas et al., "Combination therapies of DPP4 inhibitors and GLP1 analogues with insulin in type 2 diabetic patients: a systematic review," *Current Vascular Pharmacology*, vol. 11, no. 6, pp. 992–1000, 2013.

[16] M.-M. Wang, S. Lin, Y.-M. Chen et al., "Saxagliptin is similar in glycaemic variability more effective in metabolic control than acarbose in aged type 2 diabetes inadequately controlled with metformin," *Diabetes Research and Clinical Practice*, vol. 108, no. 3, pp. e67–e70, 2015.

[17] L. A. Zilliox, K. Chadrasekaran, J. Y. Kwan, and J. W. Russell, "Diabetes and cognitive impairment," *Current Diabetes Reports*, vol. 16, no. 9, p. 87, 2016 Sep.

[18] M. Xue, W. Xu, Y.-N. Ou et al., "Diabetes mellitus and risks of cognitive impairment and dementia: a systematic review and meta-analysis of 144 prospective studies," *Ageing Research Reviews*, vol. 55, Article ID 100944, 2019.

[19] C. Infante-Garcia, J. J. Ramos-Rodriguez, L. Galindo-Gonzalez, and M. Garcia-Alloza, "Long-term central pathology and cognitive impairment are exacerbated in a mixed model of Alzheimer's disease and type 2 diabetes," *Psych Neuroendocrinology*, vol. 65, pp. 15–25, 2016.

[20] H. A. Rosczyk, N. L. Sparkman, and R. W. Johnson, "Neuroinflammation and cognitive function in aged mice following minor surgery," *Experimental Gerontology*, vol. 43, no. 9, pp. 840–846, 2008.

[21] M. Muñoz-Jiménez, A. Zaarkti, J. A. García-Arnés, and N. García-Casares, "Antidiabetic drugs in Alzheimer's disease and mild cognitive impairment: a systematic review," *Dementia and Geriatric Cognitive Disorders*, vol. 49, no. 5, pp. 423–434, 2020.

[22] B. Cao, J. D. Rosenblat, E. Brietzke et al., "Comparative efficacy and acceptability of antidiabetic agents for Alzheimer's disease and mild cognitive impairment: a systematic review and network meta-analysis," *Diabetes, Obesity and Metabolism*, vol. 20, no. 10, pp. 2467–2471, 2018 Oct.

[23] A. Avogaro, S. Kreutzenberg, and G. Fadini, "Dipeptidyl-peptidase 4 inhibition: linking metabolic control to cardiovascular protection," *Current Pharmaceutical Design*, vol. 20, no. 14, pp. 2387–2394, 2014.

[24] P. C. M. van Poppel, M. S. Gresnigt, P. Smits, M. G. Netea, and C. J. Tack, "The dipeptidyl peptidase-4 inhibitor vildagliptin does not affect ex vivo cytokine response and lymphocyte function in patients with type 2 diabetes mellitus," *Diabetes Research and Clinical Practice*, vol. 103, no. 3, pp. 395–401, 2014.

[25] N. M. Kamel, M. A. Abd El Fattah, H. S. El-Abhar, and D. M. Abdallah, "Novel repair mechanisms in a renal ischaemia/reperfusion model: s," *European Journal of Pharmacology*, vol. 861, Article ID 172620, 2019.

Hindawi
Journal of Healthcare Engineering
Volume 2022, Article ID 7598427, 14 pages
https://doi.org/10.1155/2022/7598427

Research Article

Microbial Characteristics of Common Tongue Coatings in Patients with Precancerous Lesions of the Upper Gastrointestinal Tract

Xiaoyu Kang,[1] Bin Lu,[2] Pan Xiao,[1] Zhaolai Hua,[2] Rui Shen,[1] Jianping Wu,[3] Juan Wu,[1] Zhenfeng Wu,[4] Chun Cheng ,[1] and Junfeng Zhang [1]

[1]*School of Medicine & Holistic Integrative Medicine, Nanjing University of Chinese Medicine, Nanjing 210000, China*
[2]*Department of Oncology, Yangzhong People's Hospital, Yangzhong, Jiangsu 212200, China*
[3]*Laboratory Animal Centre, Nanjing University of Chinese Medicine, Nanjing 210000, China*
[4]*Department of Surgical Oncology, Jiangsu Province Hospital of Chinese Medicine, Affiliated Hospital of Nanjing University of Chinese Me dicine, Nanjing 210029, China*

Correspondence should be addressed to Chun Cheng; ccheng@ntu.edu.cn and Junfeng Zhang; zhangjunfeng5_5@163.com

Received 8 January 2022; Revised 10 March 2022; Accepted 12 March 2022; Published 18 April 2022

Academic Editor: Enas Abdulhay

The tongue coating (TC) microbiota, a crucial component of the tongue coating, illustrates a huge microbial percentage of the body that mostly includes actinobacteria, bacteroides, firmicutes, and fusobacteria. The TC microbiota is closely related to the development of upper gastrointestinal malignancies, such as oral, gastric, and esophageal cancer. Nonetheless, the microbiological characteristics of common TCs in individuals with precancerous lesions of the upper gastrointestinal tract are still unclear. Herein, we designed a case-control study, recruiting 153 PLUGT patients with four different types of TCs, including 47 white-thin, 19 white-thick, 47 yellow-thin, and 40 yellow-thick, as well as 47 volunteers as controls. To analyze microbial characteristics, 16S rRNA microbiome approaches were used. An enzyme-linked immunosorbent assay (ELISA) was employed to assess serum IL-17A and total bile acid (TBA). According to the obtained results, *Leptotrichia* was found to be a promising biomarker for thin as well as thick yellow coatings. In comparison to the control TC microbiota, 39 different genera developed commensal networks in common TCs. *Lachnoanaerobaculum* and *pseudonocardia* were the most striking core bacteria. *Lachnoanaerobaculum* positively correlated with *Leptotrichia* in W-thin and Y-thick coatings, with *actinomyces* and *methylobacterium* in Y-thin coatings, with *Campylobacter* in Y-thick coatings, and with *Bradyrhizobium* in W-thick and Y-thick coatings. Serum IL-17A levels were greater in cases with W-thin coating than in controls, and serum IL-17A was positively linked with *Parvimonas* in patients with W-thick or Y-thin coating. In Y-thin coating, the oral dominating bacteria *Streptococcus* was negatively linked with serum TBA. Taken together, the promoted bacteria were found to be synergistically proliferative in the TCs of PLUGT patients. The diverse TCs had distinct bacterial commensal networks, whereas the common TCs were linked by specific bacteria to serum IL-17A and TBA.

1. Introduction

The upper gastrointestinal tract (GIT) includes the oral cavity, pharynx, esophagus, stomach, and duodenum. Gastric cancer (GC) and esophageal cancer (EC) are two of the most often seen cancers in clinical practice. Globally, GC is the third major reason for deaths related to cancer and the fifth most abundant sort of cancer, whereas EC ranks sixth in mortality and seventh in morbidity [1]. GC has the third greatest incidence and mortality rate of all malignant tumors in China, while EC has the seventh greatest incidence and the rate of mortality [2]. Numerous studies have demonstrated that early recognition and diagnosis of upper GIT cancer are critical strategies for lowering mortality and incidence rates and considerably increasing survival rates up to 5 years [3–5]. Precancerous lesions of the upper gastrointestinal tract (PLUGT) are a crucial stage in the transformation of the normal upper gastrointestinal mucosa into upper gastrointestinal cancer. Atrophy of the gastric glands associated with abnormal hyperplasia and/or intestinal metaplasia of the gastric mucosal epithelium is regarded as a precancerous lesion of gastric cancer (PLGC) [6, 7]. PLGC is the intermediate link in the transformation from gastritis to gastric cancer, and it is essential for reducing GC risk to timely and effective block or reverse the PLGC [8, 9]. Esophageal squamous cell carcinoma (ESCC) accounts for more than 85% of EC globally [10, 11]. ESCC precancerous and cancerous lesions are graded as follows: severe dysplasia/carcinoma, moderate dysplasia, mild dysplasia, and basal cell hyperplasia in situ [12]. Currently, the diagnosis of GC and EC initially depends on endoscopy and pathological biopsy, which has the characteristics of the invasive injury and high cost and leads to fear in patients; therefore, most patients with upper digestive tract cancer are clinically diagnosed at an advanced stage [13–15].

Tongue diagnosis is objective, simple, noninvasive, and rapid in traditional Chinese medicine (TCM) diagnostic methods and has a lengthy background. The holistic view of TCM believes that variable tongue coating (TC) is capable of reflecting the pathophysiological function of the spleen and stomach, which is mainly corresponding to digestive function [16–18]. Tongue diagnosis has great application value in many systemic diseases, systematically summarized in the classical book "*Bianshe Zhinan*" (referred to *Guide to Tongue Diagnosis*). In clinical TCM practices, TC is the key content of tongue diagnosis, and its characteristic (including thickness and color) is an important basis for syndrome differentiation and treatment for many digestive system diseases. The four most common syndromes are exterior cold syndrome, interior cold syndrome, exterior heat syndrome, and interior heat syndrome which are most commonly associated with white-thin (W-thin), white-thick (W-thick), yellow-thin (Y-thin), and yellow-thick (Y-thick) TCs, respectively.

Modern studies believe that TC consists of microorganisms (mainly bacteria and fungi), exfoliated epithelium, blood metabolites, and saliva derived from filamentous papilla [19]. A growing body of research in recent years has revealed a relationship between the TC microbiota and several systemic illnesses, such as malignant tumors and diabetes. The occurrence and progression of systemic disorders, as well as the treatment process, can be dynamically reflected by TC type and its microbiota. The tongue coating microbiota has been established as a possible gastritis biomarker [20] and has been shown to have prognostic significance for pancreatic head cancer [21] and gastric cancer [20]. The changes in the TC microbiota may be related to inflammation and the metabolome, and the bacteria can potentially act as a noninvasive biomarker for GC diagnosis, independent of lifestyle [22]. The tongue coating microbiota changes as halitosis progresses, and assessing tongue coating microbiome biomarkers could help predict the risk of halitosis in children [23]. Ye et al. [24] revealed a genus *Bacillus* that existed exclusively on the yellow tongue coating of cases suffering from chronic erosive gastritis. Both TC type and its microbiota can dynamically reflect the occurrence and development of systemic diseases and the treatment process. Cui et al. [20] found that the prevalence of TC *Campylobacter concisus* was significantly greater in intestinal metaplasia superficial gastritis, and atrophic gastritis compared to normal controls, and that the prevalence of *C. concisus* gradually increased with the progression of gastritis, including the precancerous cascade. Furthermore, TC microbiota has the potential to serve as biomarkers for several different types of systemic diseases, including malignant tumors [18, 25]. Wu et al. [26] found that the GC risk was related to increased *Firmicutes* and decreased *Bacteroidetes*. Xu et al. [22] found that the six TC bacterial genera combinations (*Fusobacterium, Megamonas*, *Rothia, Porphyromonas*, *Peptostreptococcus*, and *Peptococcus*) had a strong diagnostic value for GC risk. These results are further proof of the outstanding ability of tongue diagnosis in many systemic diseases besides malignant tumors. However, the microbial characteristics of the common TCs are still unclear.

Bacteria promote tumor formation by producing carcinogenic metabolites and inhibiting chronic and persistent inflammation, especially in organs exposed to microorganisms for a long time [27, 28]. Numerous studies showed that bile acid promoted intestinal metaplasia and GC [29, 30]. Karstens et al. [31] explored that the IL-17A level was reduced in cases with esophageal adenocarcinomas in comparison to healthy controls. And our previous study found that GC patients demonstrated a high level of serum IL-17A than the controls, and the patients with white coating had substantially lesser serum IL-17A levels compared to those with yellow coatings [32].

Therefore, this study comprehensively analyzed the microbial characteristics and potential biomarkers of common TC (Y-thin, Y-thick, W-thin, and W-thick) in PLUGT patients and explored the relationship between the different TC bacteria and the serum IL-17A and TBA. The results are expected to provide precise methods for the rapid and noninvasive diagnosis of PLUGT and embody the scientific connotation of tongue-diagnosis-assisting TCM syndrome differentiation and treatment.

2. Patients and Methods

2.1. Study Participants. The Clinical Ethics Committee at Yangzhong People's Hospital in Jiangsu Province (No. PHYC2018039) approved this study. From April 2019 to January 2020, the unified questionnaire was utilized for collecting clinical information from the upper gastrointestinal cancer screening of residents aged 40 to 70 in Yangzhong City. Endoscopy and pathologic biopsy were used to diagnose all PLUGT patients, who were histologically confirmed to have pancreatic lesions of gastric cancer (PLGC) and/or precancerous lesions of esophageal squamous cell carcinoma (ESCC). A total of 153 PLUGT patients were included in the case group, whereas 47 white-thin coating volunteers comprised the healthy control group. At the time of enrollment, all participants provided signed informed permission. All participants were excluded on the basis of the following criteria: (1) all participants who got probiotics, antibiotics, or both within the preceding 4 weeks and were diagnosed with periodontitis or another oral disease; (2) had any malignant tumor; (3) had a history of severe systemic diseases (Alzheimer's disease, liver cirrhosis, ulcerative colitis, etc.); and (4) unwillingness to cooperate. Furthermore, participants in the control group with severe digestive diseases, and significant gastrointestinal discomforts, including stomach pain, diarrhea, and abdominal pain, were excluded.

2.2. Sample Collection. All contributors were required to fast during the night hours (≥8 hours) and gargle with normal saline 2 to 3 times in the morning. Two traditional Chinese physicians with a combined clinical experience of >10 years independently diagnosed the TC type, and the TC images were photographed and analyzed using the DS01-B tongue diagnostic information acquisition system (DAOSH Co., Ltd, Shanghai, China). The patients were fit into this study when two physicians' diagnoses and DS01-B analysis were consistent. A sterile one-off toothbrush was used to collect each TC sample along the median groove of the tongue dorsum and suspended it into the sterile normal saline. After centrifugation of 5 min at 3000 r/min, the precipitates were collected as TC samples. All participants' peripheral blood (3–5 mL) was drawn and centrifuged for 10 min at 3000 r/min to achieve the serum. All the specimens were kept at −80°C within 2 h.

2.3. DNA Extraction, Polymerase Chain Reaction (PCR) Amplification, and Sequencing. The extraction of total TC DNA was performed in accordance with the manufacturer's procedure that used QIAamp DNA Mini Kit (Qiagen, Valencia, CA, USA). The V3–V4 region of the 16S (rRNA gene) was amplified employing the forward primer 341F (5′-CCTAYGGGRBGCASCAG-3′) and the reverse primer 806R (5′-GGACTACNNGGGTATCTAAT-3′). The PCR conditions were identical to those used in our previous study [19]. Electrophoresis on a 2% agarose gel was implemented to identify the products of PCR. AxyPrep DNA Gel Extraction Kit (Axygen Biosciences, CA, USA) was used to extract PCR products, and a QuantiFluor^{TM}-ST Assay Kit (Promega, WI, USA) was used to quantify them. The pooled DNA product was utilized for preparing the Illumina pair-end library in the same manner as the Illumina genomic DNA library preparation technique. Following that the library of the amplicon was sequenced paired-end on an Illumina MiSeq platform (Shanghai Biozeron Co., Ltd, Shanghai, China) employing standard guidelines. QIIME version 1.17 was employed to filter and remove low-quality sequencing reads (<200 bp), and UPARSE version 7.1 was implemented to cluster operational taxonomic units (OTUs) with 97% similarity cut-off after removal of chimeric sequences (http://drive5.com/uparse/). Taxonomic assessment was performed using the SILVA database, and each OUT was classified into the following five categories (phylum, class, order, family, and genus).

2.4. Laboratory Detection. Serum interleukin (IL)-17A (Human IL-17A ELISA KIT, ZC-32330) and total bile acid (TBA; Total Bile Acid ELISA Kit, MM-50350H1) levels were determined employing enzyme-linked immunosorbent assay (ELISA). All procedures were performed in metculous compliance with the manufacturer's instructions.

2.5. Bioinformatics and Statistical Analyses. The alpha diversity, community structure, and linear discriminant assessment of the effect size (LEfSe) were executed using the computer program Visual Genomics (Release1, Shanghai Infinity Biotechnology Co., Ltd, Shanghai, China). SPSS software version 26.0 was employed for statistical assessment. The student's t-test was implemented for normal distribution data, which were expressed as the mean ± standard deviation. The chi-square analysis was implemented for the grade data. Non-normal distribution data were assessed applying the Mann–Whitney U nonparametric assessment and represented as the median (interval value). The symbiotic networks were drawn using Spearman's correlation analysis and Cytoscape software (https://cytoscape.org/). GraphPad Prism 8 computer program was employed for drawing the point diagrams. The statistical result was two-sided, and $P < 0.05$ indicated statistically meaningful differences. Potential alterations in the microbiome at the functional level were appraised by implementing PICRUSt computer program and the Kyoto Encyclopedia of Genes and Genomes (KEGG) databank.

3. Results

The following section describes the core findings of the study.

3.1. Characteristics of the Study Population. A total of 153 PLUGT patients were categorized into four categories on the basis of the color and type of their TC (1) The W-thin group ($n = 47$) consisted of women and men (30 and 17), with an average age of 57.3 ± 7.2 years; (2) W-thick group ($n = 19$) included men and women (8 and 11), with an average age of 57.8 ± 8.4 years; (3) Y-thin ($n = 47$) included men and women (17 and 30), with an average age of 57.3 ± 7.7 years; and (4) Y-thick ($n = 40$) consisted of men and women (31 and 9), with an average age of 60.4 ± 5.8 years. The healthy controls ($n = 47$) included men and women (16 and 31), with an average age of 54.7 ± 8.8 years. In terms of age and sex, the W-thin, W-thick, and Y-thin groups have no meaningful differences with the control group ($P > 0.05$); however, the difference is significant in the case of the Y-thick group ($P < 0.05$).

3.2. Diversity of the Bacterial Community. Alpha diversity focuses on the richness and diversity of the microflora. Chao and ACE indices were employed to predict operational taxonomic units (OTUs) richness, whereas Shannon, Simpson, and Observed OTUs indices were implemented to appraise OTUs diversity. The Mann–Whitney U analysis was employed to scrutinize the discrepancy in alpha diversity between the control group and the four PLUGT patient groups (Table S1). Among the total five groups, there are meaningful discrepancies ($P < 0.05$) in Chao, Shannon, and Observed OTUs ($P < 0.05$). Compared with the control group, ACE, Chao, Shannon, and Observed OTUs of microorganisms in PLUGT patients were considerably enhanced ($P < 0.05$), whereas Simpson was considerably diminished ($P < 0.05$). In the W-thin and Y-thick groups, ACE, Chao, Shannon, and Observed OTUs enhanced substantially ($P < 0.05$), whereas Simpson reduced notably ($P < 0.05$). In the Y-thin group, Chao, Shannon, and Observed OTUs increased significantly ($P < 0.05$), whereas Simpson diminished remarkably ($P < 0.05$). The results suggested that the TC type was closely associated with the bacterial richness and diversity in PLUGT cases.

3.3. The Bacterial Community Structure of the Tongue Coating. Across all the TC samples, 13,774 OTUs belonged to 33 phyla, 75 classes, 189 orders, 268 families, and 657 genera. The predominant bacterial phyla and genera (relative abundance >1%) were similar among the five groups (Figure 1). At the phylum level, the cluster analysis found that all samples were categorized into two subgroups: the control group and the PLUGT group, and the bacteria of W-thin and W-thick got together, while the bacteria of Y-thin and Y-thick got together in the PLUGT group (Figure 1(a)). It was suggested that phyla-level bacterial composition was associated with the TC color transformation from white to yellow in PLUGT patients. Eighteen dominant bacterial genera (*Neisseria*, *Prevotella 7*, *Veillonella*, *Streptococcus*, *Haemophilus*, *Prevotella*, *Porphyromonas*, *Fusobacterium*, *Granulicatella*, *Leptotrichia*, *Rothia*, *Actinomyces*, *Alloprevotella*, *Peptostreptococcus*, *Gemella*, *Prevotella 6*, *Capnocytophaga*, and *Campylobacter*) were observed in the five kinds of TCs (Figure 1(b)).

3.4. Linear Discriminant Analysis (LDA) of the Microbiome of Tongue Coating. Based on the microorganisms of the controls, LDA was used to identify potential biomarkers for regular TCs in PLUGT cases. There were 5, 18, 3, and 25 marker bacterial taxa in the Y-thick groups, Y-thin, W-thick, and W-thin, accordingly. At the genus level, there were 10 potential biomarkers in the W-thin group: *Variovorax*, *Bradyrhizobium*, *Stomatobaculum*, *Taonella*, *Lachnoanaerobaculum*, *Prevotella 6*, *Actinomyces*, *Streptococcus*, *Parvimonas*, and *(Eubacterium) yurii group* (Figure 2(a)), *Ruminococcaceae UCG-014,* and *Kingella* were the potential biomarkers in the W-thick group (Figure 2(b)), there were five potential biomarkers in the Y-thin group: *Lachnoanaerobaculum*, *Campylobacter*, *Actinomyces*, *Leptotrichia*, and *Ralstonia* (Figure 2(c)), and *Leptotrichia* was a potential biomarker in the Y-thick group (Figure 2(d)). Therefore, *Leptotrichia* might be a potential biomarker of Y-thin and Y-thick groups in PLUGT cases.

To further study the relationship between coating color and TC microbiota, each group of TC was chosen for comparison with the other three converged groups. The microbial compositions among the four tongue coatings were further analyzed using the LefSe. LefSe analysis analyzed microbial dysbiosis, representing substantial discrepancies in the abundance of bacterial populations between the various groups. As a result of LefSe analysis, 32 bacterial taxa were identified. Among them, the relative abundances of 24 and 8 bacterial taxa were substantially increased and decreased, respectively (Figure 3). The comparative abundances of four bacterial genera (*Psychrobacter*, *Pelomonas*, *Aeromonas*, and *Pseudoramibacter*) were remarkably increased in the W-thin group (Figure 3(a)); the relative abundances of seven bacterial genera (*Clostridium sensu stricto 1*, *Burkholderia_Caballeronia_Paraburkholderia*, *Kingella*, *Parascardovia*, *Flaviflexus*, *Paraclostridium*, and *Thermus*) were significantly increased in the W-thick group (Figure 3(b)); the relative abundances of five bacterial genera (*Parvimonas*, *Prevotellaceae UCG-004*, *Salmonella*, *Dialister*, and *Filifactor*) were significantly increased in the Y-thick group (Figure 3(c)). However, no unique genus was found in the Y-thin group, which might have a similar bacterial community structure as the Y-thick group. The aforementioned results indicated that TC microbiota was closely related to the formation of TC color.

3.5. The Symbiotic Relationship of the TC Microbiome. In a normal circumstance, mixed bacteria have complex symbiotic relationships for maintaining the normal micro ecological balance, but in the disease condition, bacterial dysbiosis results in a distinct symbiotic relationship. Therefore, the symbiotic relationship may present a novel entry point for comprehending the microecological mechanism of disease occurrence. According to the controls' white-thin coating microbiota, Mann–Whitney *U*-test was conducted to screen the distinct bacterial genera in the four pathological TCs (Table S2). Spearman's association assessment was executed on the basis of distinct genera of each group, and the meaningful associations ($P < 0.05$) were presented as symbiotic networks (Figure 4). As shown in Figure 4, each node represents a genus and the genus's average relative abundance is represented by the size of each node. Nodes of the same color represent members of the same phyla. Edges illustrate relationships with values superior to 0.5 and P values lower than 0.05. Generally, most correlations were significantly positive, and only in W-thin coating did the negative correlations appear. As evident from the figure, the W-thick coating manifested the least number of correlations. In the PLUGT patients, the striking *Lachnoanaerobaculum* had the most complex symbiotic relationships. It was found to correlate positively with *Leptotrichia* in W-thin and Y-thick coatings, with *Actinomyces* and *Methylobacterium* in Y-thin coating, with *Campylobacter* in Y-thick coating, and with *Bradyrhizobium* in W-thick and Y-thick coatings. *Pseudonocardia* was the other significant promoted bacterial genus in the four common TCs, it positively correlated with *Methylobacterium* in W-thin coating, and positively correlated with *Variovorax* and *Bradyrhizobium* in Y-thin coating. As

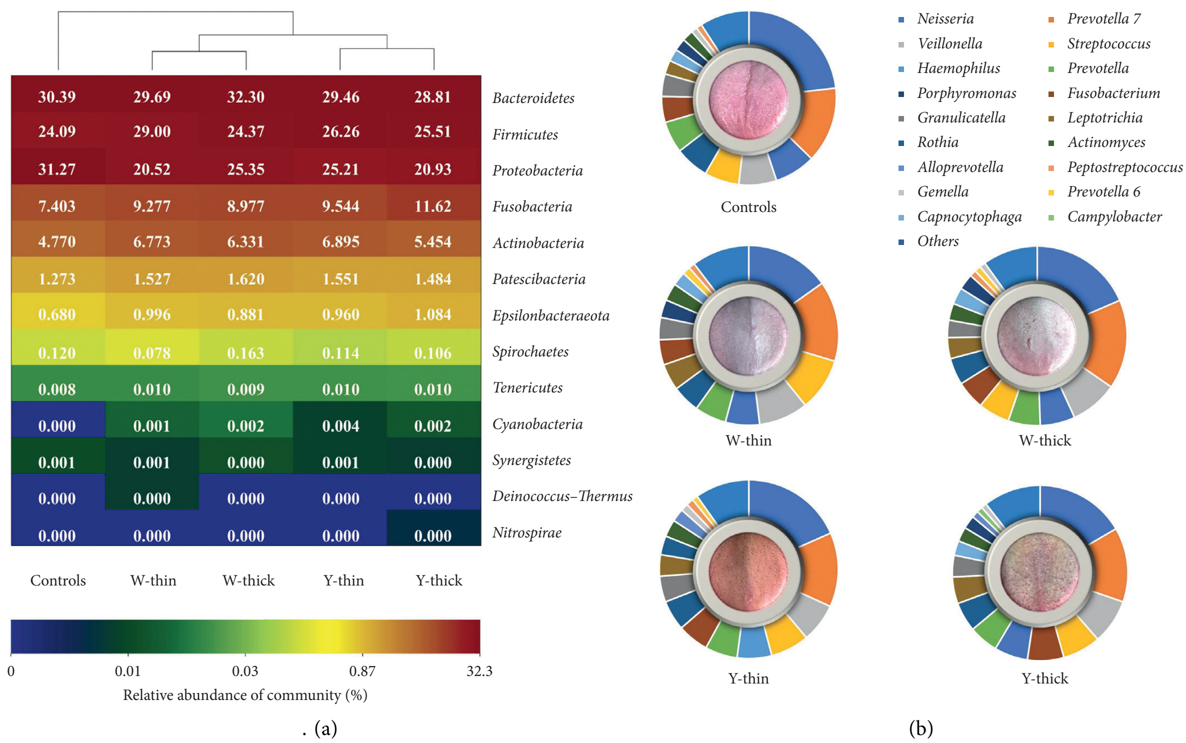

Figure 1: The composition and clustering analysis of TC microbiota in PLUGT patients and the controls. (a) The phylum-level heatmap. Cluster analysis is conducted based on the distance calculation using the Bray–Curtis method, and the results show that the same color TCs have similar microbial structures. (b) The genus-level doughnut chart. The size of bars represents the mean relative abundance of dominant bacterial genera. Each genus is represented by a different color. The image in the center of each doughnut chart is the typical TC.

shown in Figure 4, the *Prevotella* spp was found to have negative associations with *Methylobacterium and Variovorax. Leptotrichia* demonstrated negative correlations with *Streptococcus.* These results suggested that the promoted bacteria were synergistic proliferative.

Each node is related to a distinct genus. The size of each node illustrates the mean relative abundance of each genus. Nodes of the same color come from the same phylum. Relationships with values superior to 0.5 and P values lower than 0.05 are demonstrated as edges. The red edges mean a positive relationship and the blue edges mean a negative relationship.

3.6. Predictive Functional Analysis of the TC Microbiome. Potential biological functions of TC microbiota were evaluated using the KEGG database. Employing the Mann–Whitney U-test, four predictive functions were significantly different between the four PLUGT patients' groups in comparison to the control group ($P < 0.05$). They were betalain biosynthesis, fluorobenzoate degradation, indole alkaloid biosynthesis, and vasopressin-regulated water absorption (Figure S1). Using LDA, we found that changes in the five predictive functions of the Y-thick group also existed in the W-thin and Y-thin groups, including three reduced predictive functions (ABC transporters, phosphotransferase system, and transporters) and two enhanced predictive functions (chaperones and folding catalysts, and chromosome; Figure S2). However, no predictive function was found in the W-thick group, suggesting that a W-thick TC might be the basic pathological TC in PLUGT patients.

To further explore the unique functions of the four common TCs in PLUGT patients, each TC group was chosen for comparison with the other three converged groups. The Mann–Whitney U assessment revealed that the eight predictive functions were significantly different (Figure 5). Among them, the W-thick group manifested six significantly enhanced functions in comparison to the other three converged groups. These included the bacterial invasion of epithelial cells, benzoate degradation, germination, glycerolipid metabolism, *Staphylococcus aureus* infection, and steroid biosynthesis (Figure 5(a)–5(f)). The RIG-I-like receptor (RLR) signaling pathway was significantly enhanced in the W-thin group (Figure 5(g)). Cell motility and secretion were significantly enhanced in the Y-thick group (Figure 5(h)).

3.7. Serum IL-17Aand TBA Correlated with Distinct TC Bacteria. Serum levels of IL-17A and TBA were detected using ELISA. The Mann–Whitney U analysis was employed to ascertain if any two groups (PLUGT groups and controls) are considerably distinct from each other in terms of IL-17A and TBA levels. It was found that IL-17A levels in the W-thin group were substantially higher than

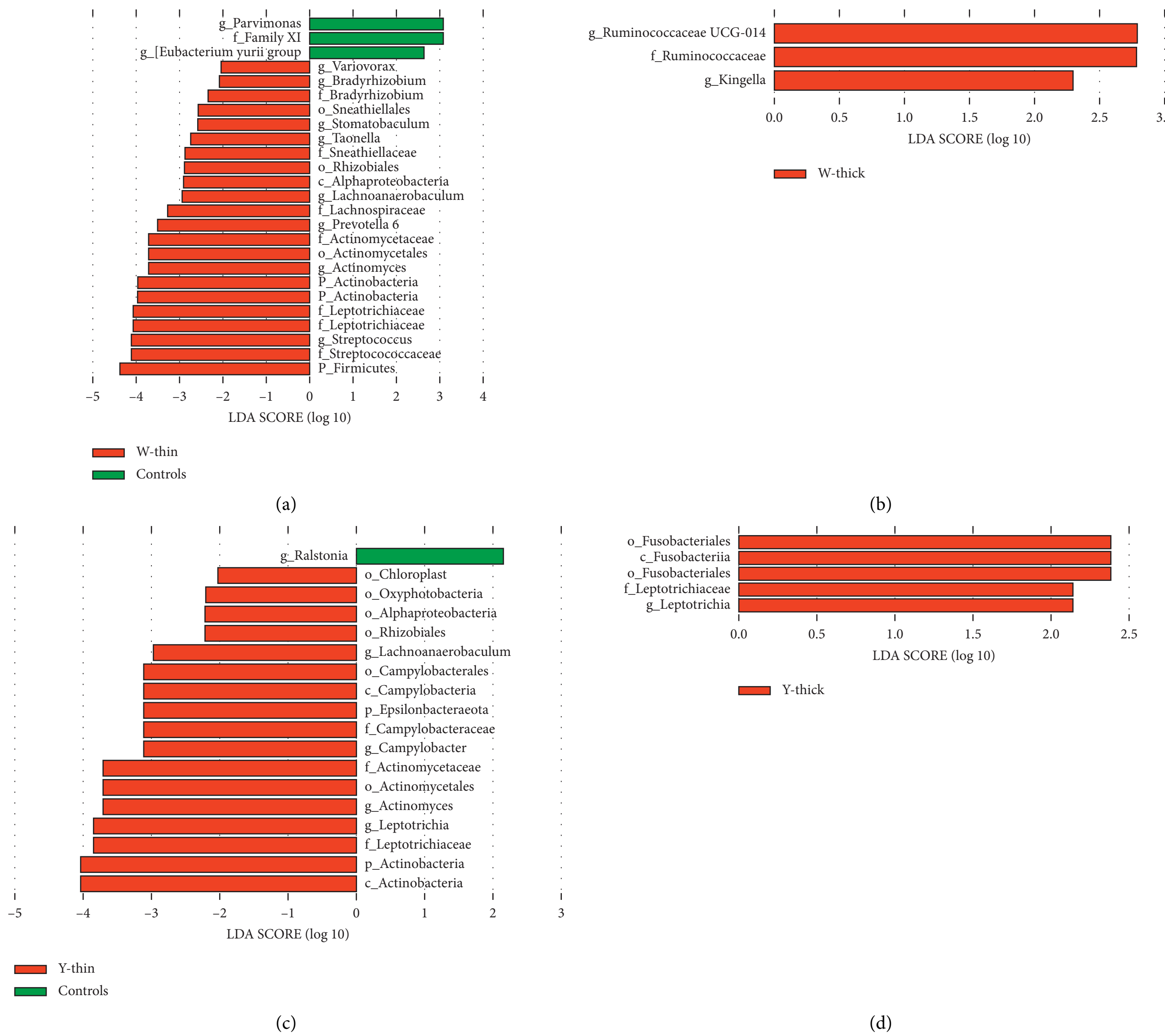

Figure 2: LDA assessment of TC microbiota between PLUGT patients and controls. Based on the controls, LDA analysis is conducted to screen potential biomarkers related to PLUGT with common TCs: (a) Y-thin group, (b) W-thick group, (c) Y-thin group, and (d) Y-thick group. Generally, LDA score means the significance of the microbial taxa. "*p*" refers to phylum, "*c*" refers to a class, "*o*" refers to order, "*f*" refers to family, and "*g*" refers to a genus.

those in the control group ($P < 0.05$), although there existed no remarkable discrepancy in serum TBA levels between the groups ($P > 0.05$; Figure 6(a)). Spearman's correlation analysis was employed for exploring the potential relationship between serum IL-17A, TBA, and the distinct genera (Table S2), and the meaningful relationships ($P < 0.05$) were created into symbiotic networks (Figure 6(b)). The results showed that *Parvimonas* positively associated with serum IL-17A in W-thick and Y-thin coatings. *Dialister* positively associated with serum TBA in W-thin and Y-thick coatings. Significantly, the oral dominant bacteria *Streptococcus* negatively correlated with both serum IL-17A and TBA in the control group, while negatively correlated with only serum TBA in Y-thin coating.

4. Discussion

Tongue diagnosis, or more accurately TC diagnosis, is one of traditional Chinese medicine's most essential diagnostic instruments. On the surface of the tongue, TC appears as a grayish-white deposit. The tongue coating is made up of blood cells, epithelial cells, vascular endothelial cells, bacteria, and a variety of metabolites.

Since the TC microbiota was firstly profiled by Jiang et al. [34], which indicated that different TCs link certain pathological status even in the same disease and occupy unique microbiota and commensal networks. Then, a great deal of literature presented the relationship between TC microbiota and systemic diseases, especially many digestive cancers and precancerous lesions [25]. As everyone knows, TC

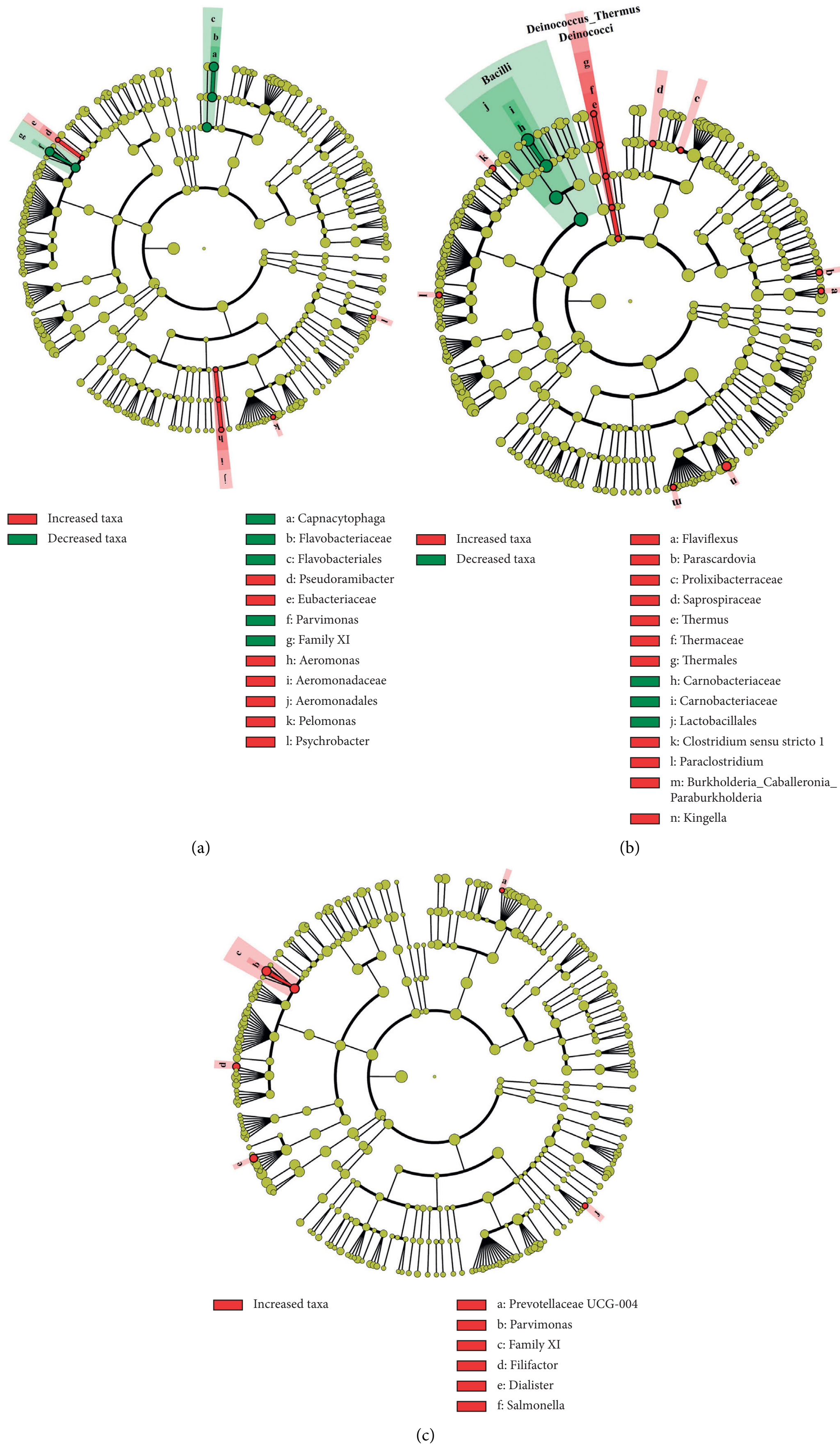

Figure 3: LEfSe analysis of TC microbiota in PLUGT patients. Each TC group is chosen for comparing with the other three converged groups in PLUGT patients. The LEfSe cladogram includes 5 layers of circles, which demonstrate 5 classifications (phylum, class, order, family, and genus) from the center to edge. (a) W-thin TC, (b) W-thick TC, and (c) Y-thick TC.

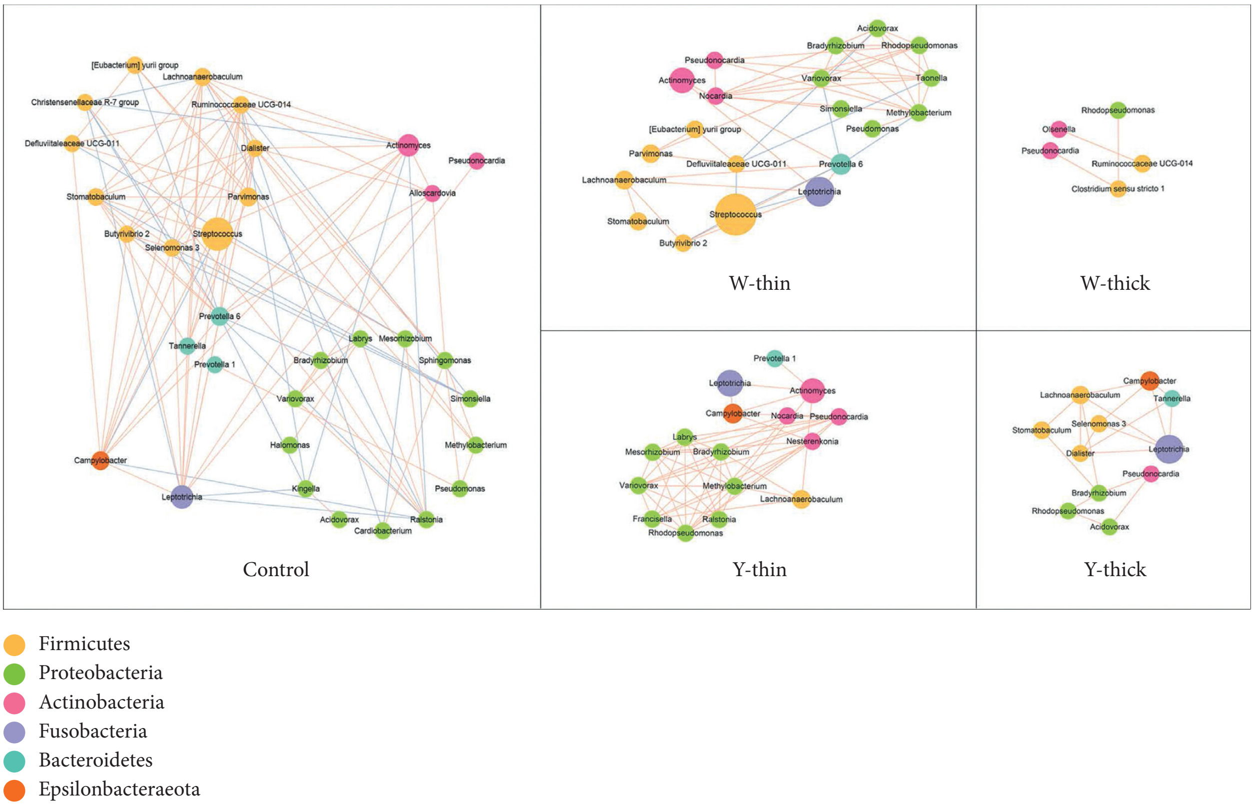

Figure 4: The symbiotic relationship of distinct genera from different TCs.

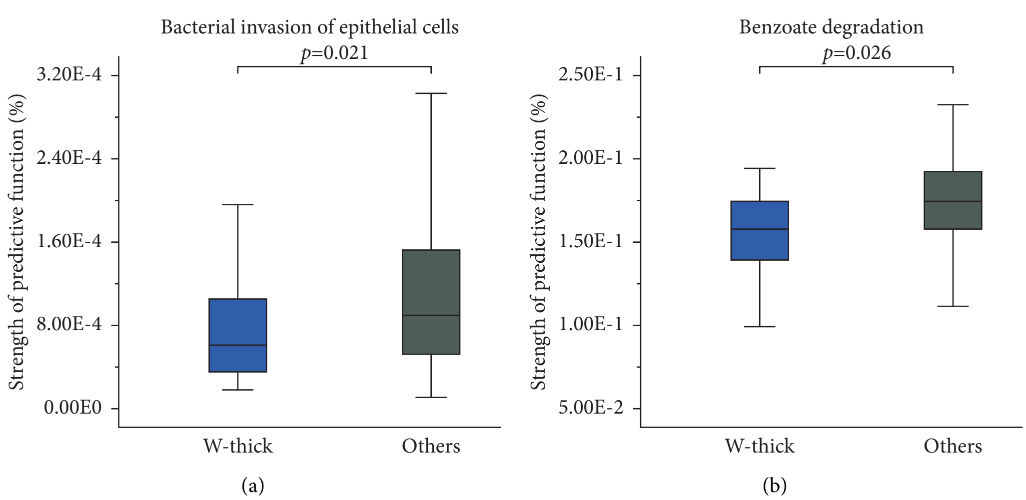

Figure 5: Continued.

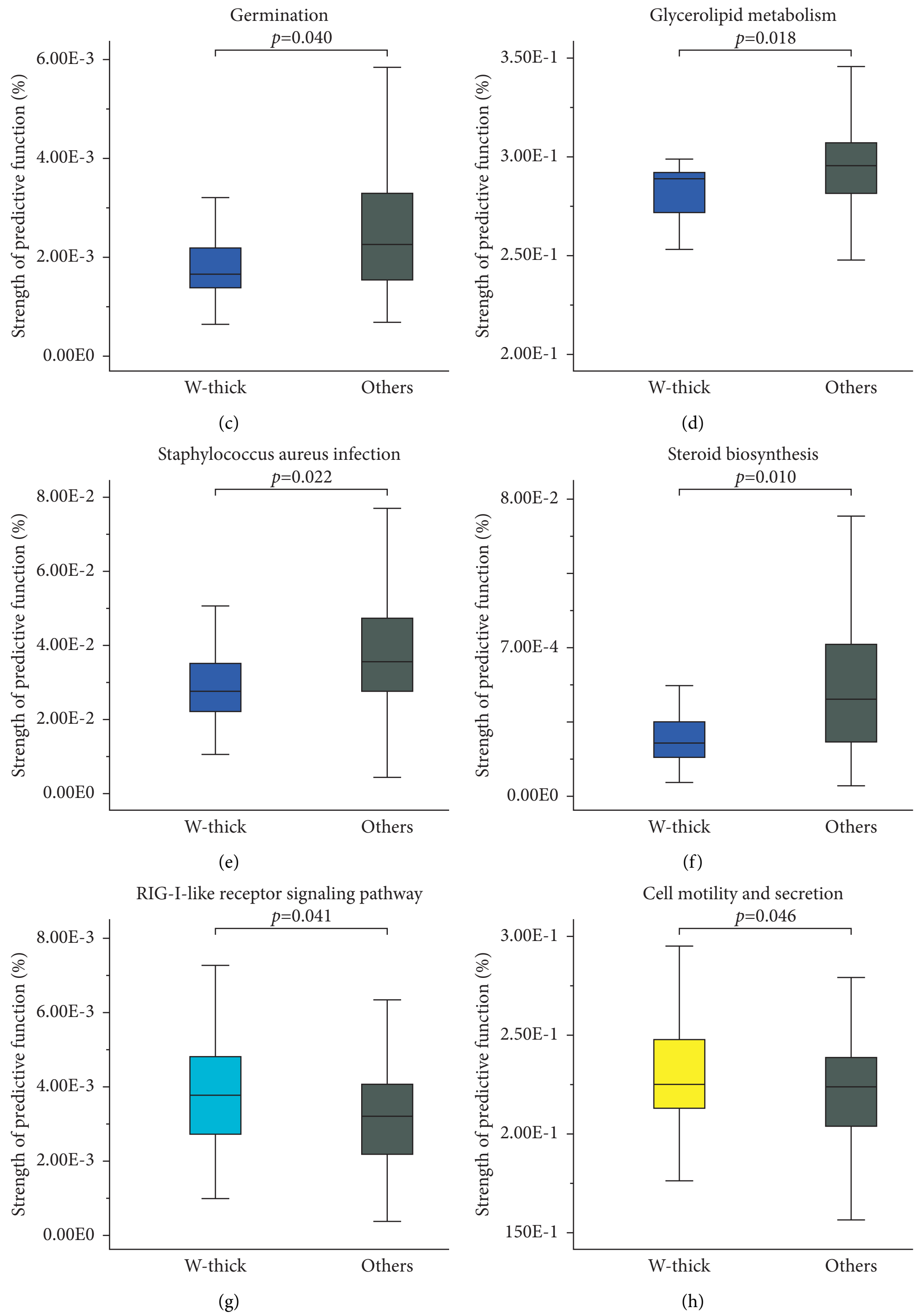

FIGURE 5: Eight predictive functions with significant differences based on TC microbiota in PLUGT patients. Each TC group is chosen for comparing with the other three converged groups in PLUGT patients. Differences between subgroups are evaluated through the Mann–Whitney U-test (only $P < 0.05$ are indicated).

microorganisms can enter the digestive tract with saliva and colonize the mucosal epithelium of the digestive tract. Therefore, here assumes that TC microbiota correlates to PLUGT progression, and analyzed the characteristics of the bacterial community of four common TCs in PLUGT patients to provide new potential biomarkers for accurate PLUGT diagnosis.

This exploration revealed that the bacterial richness and diversity of PLUGT cases were substantially superior to those of the control group. The bacterial richness and diversity in

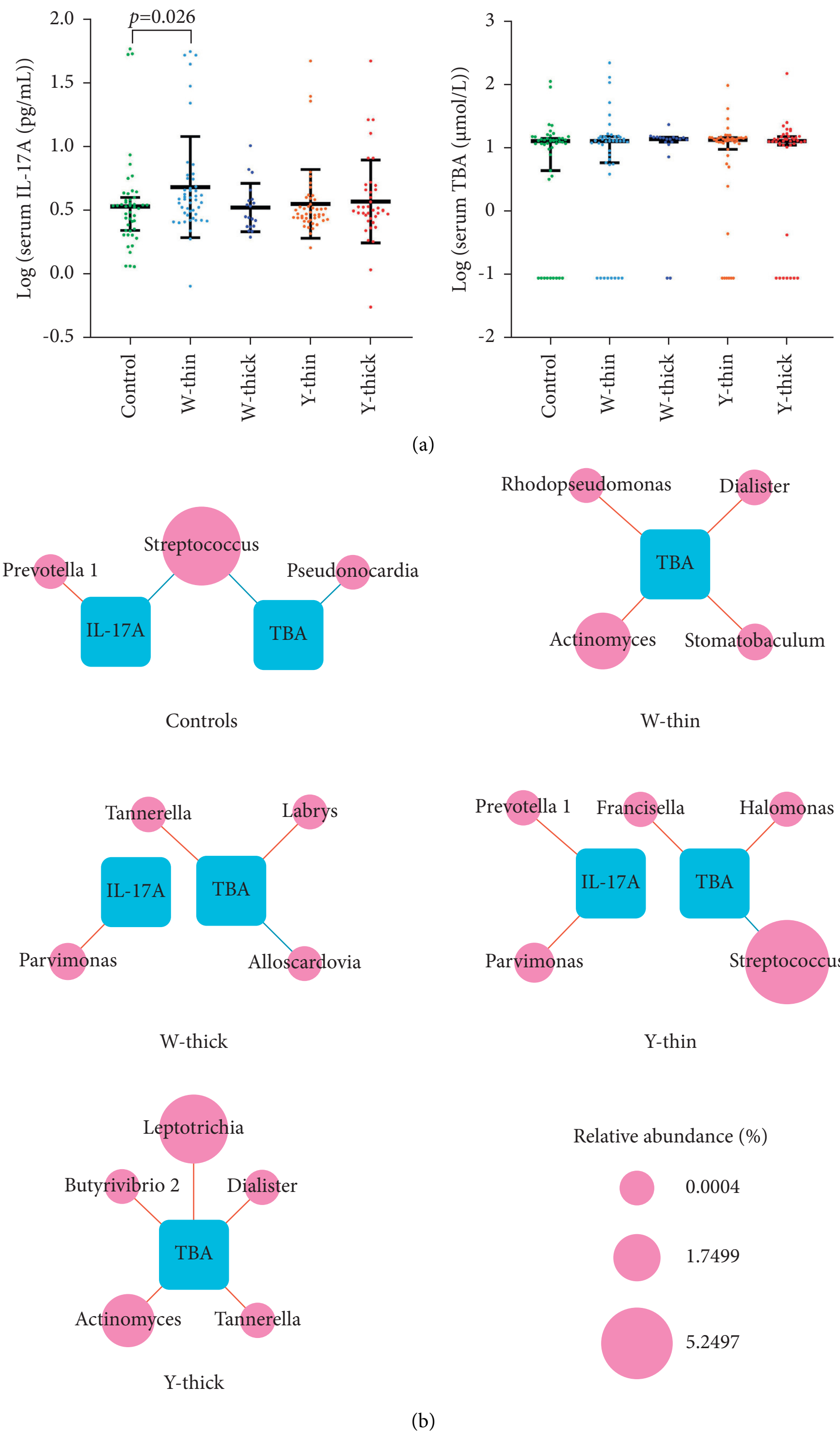

Figure 6: Correlation among serum IL-17A, TBA, and TCs distinct genera. (a) According to the Mann–Whitney U-test, the serum IL-17A was remarkably enhanced in the PLUGT cases with W-thin TC ($P < 0.05$); however, no discrepancies were detected in the serum TBA levels. (b) The commensal networks among serum IL-17A, TBA, and the distinct genera in the five groups. The size of node indicates the relative abundance, the red edges mean positive relationships, and the blue edges mean negative relationships ($P < 0.05$).

the W-thin, Y-thick, and Y-thin groups in PLUGT patients were remarkably superior to those in the control group. However, this result is inconsistent with the results of the already published investigations [19, 22, 35]. For example, Xu et al. [19] discovered that there existed no substantial discrepancy in the alpha diversity of microbiota in common TCs in GC patients, Xu et al. [22] found that GC patients had greater bacterial richness and lower bacterial diversity than those in the control group, Hu et al. [35] divulged that GC cases with thick TC demonstrated lesser bacterial diversity than the patients with thin TC and healthy controls. These inconsistent results may be related to complex factors including sex, age, region, and dietary habits.

In this study, it was found that the microbial community structure of PLUGT patients was similar to that of GC patients in previous studies [19, 35]. This finding suggests that tongue-coating microorganisms have potential diagnostic value for PLUGT. At the phylum level, cluster analysis revealed that the W-thin and W-thick groups were clustered together and the Y-thin and Y-thick groups were clustered together in PLUGT patients. Cheng et al. [36] found that the difference between white and yellow coatings in early gastric cancer patients was greater than that between thin and thick coatings. Jiang et al. [34] found that there were significant differences in the microorganisms of white-greasy and yellow-dense coatings in chronic gastritis (CG) patients. The aforementioned results indicate that the tongue coating color changes were related to the microbial community structure of the tongue coating. The changes in the microbial community in this study were similar to those observed in the esophageal mucosa of esophageal mucosal metaplasia patients [37]. The results suggested that the microbial community of the upper digestive tract, and the tongue coating might have similar changes in the progression of upper gastrointestinal cancer.

TCM believes that white and yellow coating represents cold and hot syndrome, respectively. In this study, *Leptotrichia* was a potential biomarker of Y-thin and Y-thick groups in PLUGT cases, and the relative abundance of *Leptotrichia* was considerably greater in them than in the control group. *Leptotrichia* has extensive genetic diversity. To date, six species belonging to this genus have been validly established [38]. *Leptotrichia* is an opportunistic bacterium that causes opportunistic infections when immune function is compromised by tumor chemotherapy and granulocytopenia disease [38–40]. *Leptotrichia* has strong immunogenicity and can stimulate a mucosal immune response, and anti-*Leptotrichia* antibody can be detected in serum [38]. It is speculated that the immune-inflammatory response resulting from *Leptotrichia* may promote carcinogenesis of the upper digestive mucosa. For instance, the relative abundance of *Leptotrichia* was significantly increased in colon cancer tissue, GC tissue, and mouthwash of pancreatic cancer patients [41–43]. A study showed that *Streptococcus* and *Leptotrichia* in saliva were positively correlated with the risk of pancreatic adenocarcinoma (PDAC), whereas *Veillonella* and *Neisseria* in saliva were negatively correlated with the risk of PDAC [44]. Furthermore, nonparametric test analysis found that the relative abundance of *Campylobacter* in Y-thin and Y-thick groups was significantly increased. Chen and Xie [45] found that rheumatoid arthritis (RA) activity was positively correlated with the degree of yellow tongue coating. Wang et al. [46] believed that RA patients with damp-heat obstruction regularly exhibited high disease activity. Damp and heat are often the causes of yellow-greasy coating formation [47]. Therefore, the tongue-coating type is closely related to RA activity. Previous studies found that the abundance of *Actinomyces* and *Campylobacter* in RA patients was significantly higher than that in healthy controls [48, 49]. The aforementioned results suggest that *Leptotrichia* and *Campylobacter* could be promising biomarkers of yellow coating and are related to the hot syndrome.

TCM regards the image of the tongue as a mirror image of the body's visceral functions. Changes in tongue coating reflect the pathophysiological status of the body. Tongue coating can be used to diagnose diseases and symptoms as a unique diagnostic indicator [25]. In this study, LEfSe analysis was used to analyze the unique biomarkers of regular tongue coatings in PLUGT patients. The unique biomarkers of the W-thin group include *Psychrobacter*, *Pseudoramibacter*, and *Aeromonas*. Kwon et al. [50] discovered that the abundance of *Psychrobacter* diminished in cervical swabs from cervical cancer patients. Gao et al. [51] explored that the abundance of *Psychrobacter* was diminished in cancerous tissues from colorectal cancer patients. Jia et al. [52] revealed that compared with intrahepatic cholangiocarcinoma (ICC) patients with vascular invasion (VI), the abundance of *Pseudoramibacter* in the intestines of ICC patients without VI was significantly higher; *Pseudoramibacter* was negatively correlated with plasma tauroursodeoxycholic acid, which was positively associated with tumor number and negatively associated with survival time. *Aeromonas* is one of the commonly occurring gastrointestinal pathogens associated with infections in animals and humans [53]. Moreover, numerous extracellular proteins, comprising hemolysin, endotoxins, and adhesion factors, are involved in the pathogenesis of *Aeromonas* [54–56]. Gao et al. [57] found that sleep deprivation significantly increased intestinal *Aeromonas* in mice. The unique biomarkers of the W-thick group include *C. sensu stricto 1, Kingella*, and *Thermus*. The relative abundance of intestinal *C. sensu stricto 1*increased in obese patients and was significantly positively correlated with body weight, blood lipid, and uric acid ($P < 0.0 5$) [58]. The increased oral abundance of Kingella is linked to a lower risk of head and neck squamous cell cancer (HNSCC), which could have implications for cancer prevention [59]. The genus *Thermus* is more abundant in tissues from developed lung cancer (IIIB, IV) patients, and it can perform a task in tumor development by means of different microbial functions, such as aldosterone-regulated sodium reabsorption, decreased signal transduction, amino acid metabolism, increased excretory system, and amoebiasis pathways [60].

Using KEGG predictive function analysis to explore the molecular mechanism of common TC formation in PLUGT patients, we found that the RLR signaling pathway in the W-thin group and cell motility and secretion in the Y-thick group were significantly enhanced. RLRs are important initiators of the innate immune response to RNA virus infection [61]. The RLR activates downstream transcription factors, leading to the generation of type-1 interferon and expression of an antiviral gene, eliciting an intracellular immune response capable of controlling viral infection [62]. Zhao et al. [63] found that cell motility (bacterial motility proteins) and membrane transport (secretion system) were enriched in chronic hepatitis B cases with yellow tongue coatings. The results provide clues for further exploration of the biological mechanism of the tongue coating that reflects the body's pathophysiological state and indicate that yellow coating could be substantially susceptible to bacterial colonization.

IL-17A performs a key task in host defense against fungal and bacterial infections, as well as in the development of autoimmunity, inflammation, and tumors. IL-17A greatly enhances protective immune responses in epithelial cells and keratinocytes by inducing the production of G-CSF, CXC chemokines, and antimicrobial peptides [64]. Our last research found that GC patients had an enhanced level of serum IL-17A [32], and here found that the PLUGT patients with W-thin TC had a greater serum IL-17A level than the controls ($P < 0.05$). The commensal networks presented that serum IL-17A positively correlated to *Parvimonas* in the W-thick group and Y-thin group and positively correlated to *Prevotella 1* in Y-thin group. Oral bacterium *Parvimonas* was found to be overexpressed in the gastric mucosa of GC patients and to have high centrality in the GC ecological network, indicating that it might act as a backbone for niche-specific connections and may exert considerable impact on the GC microbial ecology [65]. In addition, Zhao et al. [63] found an enhanced abundance of *Prevotella* in esophagitis or Barrett's oesophagus. Iwakura et al. [64] found salivary *Parvimonas micra* and *Prevotella* sp. were increased in periodontitis patients. A cohort study found that advanced periodontitis was associated with elevated risks of EC [65], and many kinds of research [66, 67] proved that a high level of oral IL-17 promoted the development of periodontitis via its pro-inflammatory and osteoclastogenic properties [68]. These results could assume that W-thick and Y-thin coatings may represent the oral pathogenic trait and inflammation, and simultaneously reflect the progress of upper digestive tract cancer.

Bile acids have a vital role in the development of gastric intestinal metaplasia (IM) and carcinogenesis of the gastric mucosa. Multiple studies have shown that cases with esophageal adenocarcinomas demonstrated lesser levels of IL-17A than healthy controls [29–31]. As our earlier study revealed that GC patients had substantially greater serum IL-17A levels than controls, while those with white coatings had remarkably lesser serum IL-17A levels than those with yellow coatings [32]. The current exploration discovered the association between unique TC bacteria and serum IL-17A and TBA levels, as well as the microbiological characteristics and potential biomarkers of common TC (W-thin, W-thick, Y-thin, and Y-thick) in PLUGT patients. According to the obtained results, the promoted bacteria were found to be synergistically proliferative in the TCs of PLUGT patients. In addition, the different TCs exhibited distinct commensal networks, whereas the common TCs were associated with serum IL-17A and TBA via specific bacteria. The findings are valuable because they can potentially furnish useful solutions to achieve a speedy and noninvasive diagnosis of PLUGT, as well as exemplify the scientific meaning of tongue diagnosis, thereby assisting in the differentiation and treatment of TCM syndromes.

5. Conclusion

This study examined the microbiological properties of four common TCs in PLUGT patients, as well as the relationship between the different TC bacteria and blood IL-17A and TBA, The potential biomarkers of common TC (W-thin, W-thick, Y-thin, and Y-thick) in PLUGT patients were also investigated. The findings add valuable information to our understanding of the biological mechanism of tongue coating development. Nevertheless, validation in a large population is needed due to the heterogeneity in individual habits, which impacts the universality of the study results. The results, however, are significant because they may provide effective ways for obtaining a quick and noninvasive diagnosis of PLUGT. Furthermore, the findings suggested that TC differentiation could provide a more accurate diagnostic for PLUGT clinical administration.

Data Availability

Data will be provided on request to the corresponding author.

Conflicts of Interest

The authors declare that they have no conflicts of interest.

Acknowledgments

This work was supported by the National Natural Science Foundation NSFC (grant no. 81473358); the Administrative Special Funding from the Nanjing University of Chinese Medicine; and the Chinese Medicine Science and Technology Program of Jiangsu Province (grant nos. MS20211003 and YB2020003).

Supplementary Materials

Figure S1. The significantly different predictive functions of TC microbiota between PLUGT patients and controls. *Figure S2*. LDA analysis of predictive functions of TC microbiota in PLUGT patients based on controls: (A) W-thin group, (B) Y-thin group, (C) Y-thick group, and (D) Venn analysis among the common TCs in PLUGT patients. *Table S1*. The alpha diversity of tongue-coating microbiota in the controls and common tongue coatings in PLUGT patients (relative abundance, median (P25, P75) %). *Table S2*. Mann–Whitney *U*-test of the distinct genera between PLUGT patients and the controls. (*Supplementary Materials*)

References

[1] F. Bray, J. Ferlay, I. Soerjomataram, R. L. Siegel, L. A. Torre, and A. Jemal, "Global cancer statistics 2018: GLOBOCAN estimates of incidence and mortality worldwide for 36 cancers in 185 countries," *CA: A Cancer Journal for Clinicians*, vol. 68, no. 6, pp. 394–424, 2018.

[2] R.-M. Feng, Y.-N. Zong, S.-M. Cao, and R.-H. Xu, "Current cancer situation in China: good or bad news from the 2018

Global Cancer Statistics?" *Cancer Communications*, vol. 39, no. 1, p. 22, 2019.

[3] X. Guo, X. Lv, Y. Ru et al., "Circulating exosomal gastric cancer-associated long noncoding RNA1 as a biomarker for early detection and monitoring progression of gastric cancer," *JAMA Surgery*, vol. 155, no. 7, pp. 572–579, 2020.

[4] M. di Pietro, M. I. Canto, and R. C. Fitzgerald, "Endoscopic management of early adenocarcinoma and squamous cell carcinoma of the esophagus: screening, diagnosis, and therapy," *Gastroenterology*, vol. 154, no. 2, pp. 421–436, 2018.

[5] W.-Q. Wei, Z.-F. Chen, Y.-T. He et al., "Long-Term follow-up of a community assignment, one-time endoscopic screening study of esophageal cancer in China," *Journal of Clinical Oncology*, vol. 33, no. 17, pp. 1951–1957, 2015.

[6] P. Correa, "Human gastric carcinogenesis: a multistep and multifactorial process--first American cancer society award lecture on cancer epidemiology and prevention," *Cancer Research*, vol. 52, no. 24, pp. 6735–6740, 1992.

[7] P. Correa, "A model for gastric cancer epidemiology," *The Lancet*, vol. 306, no. 7924, pp. 58–60, 1975.

[8] H. Song, I. G. Ekheden, Z. Zheng, J. Ericsson, O. Nyrén, and W. Ye, "Incidence of gastric cancer among patients with gastric precancerous lesions: observational cohort study in a low risk Western population," *BMJ*, vol. 351, p. h3867, 2015.

[9] J. L. Whiting, "The long term results of endoscopic surveillance of premalignant gastric lesions," *Gut*, vol. 50, no. 3, pp. 378–381, 2002.

[10] M. Arnold, I. Soerjomataram, J. Ferlay, and D. Forman, "Global incidence of oesophageal cancer by histological subtype in 2012," *Gut*, vol. 64, no. 3, pp. 381–387, 2015.

[11] M. Arnold, M. Laversanne, L. M. Brown, S. S. Devesa, and F. Bray, "Predicting the future burden of esophageal cancer by histological subtype: international trends in incidence up to 2030," *American Journal of Gastroenterology*, vol. 112, no. 8, pp. 1247–1255, 2017.

[12] M. Wang, J. S. Smith, and W. Q. Wei, "Tissue protein biomarker candidates to predict progression of esophageal squamous cell carcinoma and precancerous lesions," *Annals of the New York Academy of Sciences*, vol. 1434, no. 1, pp. 59–69, 2018.

[13] E. Van Cutsem, X. Sagaert, B. Topal, K. Haustermans, and H. Prenen, "Gastric cancer," *The Lancet*, vol. 388, no. 10060, pp. 2654–2664, 2016.

[14] X. Mu, C. Ji, Q. Wang et al., "Non-targeted metabolomics reveals diagnostic biomarker in the tongue coating of patients with chronic gastritis," *Journal of Pharmaceutical and Biomedical Analysis*, vol. 174, pp. 541–551, 2019.

[15] T. A. Ajayi, S. Cantrell, A. Spann, and K. S. Garman, "Barrett's esophagus and esophageal cancer: links to microbes and the microbiome," *PLoS Pathogens*, vol. 14, no. 12, p. e1007384, 2018.

[16] K. Liang, X. Huang, H. Chen et al., "Tongue diagnosis and treatment in traditional Chinese medicine for severe COVID-19: a case report," *Annals of Palliative Medicine*, vol. 9, no. 4, pp. 2400–2407, 2020.

[17] Z. Shu, Y. Zhou, K. Chang et al., "Clinical features and the traditional Chinese medicine therapeutic characteristics of 293 COVID-19 inpatient cases," *Frontiers of Medicine*, vol. 14, no. 6, pp. 760–775, 2020.

[18] S. Han, X. Yang, Q. Qi et al., "Potential screening and early diagnosis method for cancer: tongue diagnosis," *International Journal of Oncology*, vol. 48, no. 6, pp. 2257–2264, 2016.

[19] K. Seerangaiyan, F. Jüch, and E. G. Winkel, "Tongue coating: its characteristics and role in intra-oral halitosis and general health-a review," *Journal of Breath Research*, vol. 12, no. 3, p. 034001, 2018.

[20] J. Cui, H. Cui, M. Yang et al., "Tongue coating microbiome as a potential biomarker for gastritis including precancerous cascade," *Protein & Cell*, vol. 10, no. 7, pp. 496–509, 2019.

[21] G. D. Tribble, N. Angelov, R. Weltman et al., "Frequency of tongue cleaning impacts the human tongue microbiome composition and enterosalivary circulation of nitrate," *Frontiers in cellular and infection microbiology*, vol. 9, p. 39, 2019.

[22] S. Xu, C. Xiang, J. Wu et al., "Tongue coating bacteria as a potential stable biomarker for gastric cancer independent of lifestyle," *Digestive Diseases and Sciences*, vol. 66, no. 9, pp. 2964–2980, 2021.

[23] Y. Zhang et al., "Dynamic alterations of oral microbiota related to halitosis in preschool children," *Frontiers in cellular and infection microbiology*, vol. 11, p. 88, 2021.

[24] J. Ye, X. Cai, J. Yang et al., "Bacillus as a potential diagnostic marker for yellow tongue coating," *Scientific Reports*, vol. 6, no. 1, p. 32496, 2016.

[25] J. Wu, "Application value of tongue coating microflora in integration of traditional Chinese medicine and modern medicine," *TMR Theory Hypohesis*, vol. 2, pp. 229–240, 2019.

[26] J. Wu, S. Xu, C. Xiang et al., "Tongue coating microbiota community and risk effect on gastric cancer," *Journal of Cancer*, vol. 9, no. 21, pp. 4039–4048, 2018.

[27] A. Dzutsev, R. S. Goldszmid, S. Viaud, L. Zitvogel, and G. Trinchieri, "The role of the microbiota in inflammation, carcinogenesis, and cancer therapy," *European Journal of Immunology*, vol. 45, no. 1, pp. 17–31, 2015.

[28] C. H. Johnson, M. E. Spilker, L. Goetz, S. N. Peterson, and G. Siuzdak, "Metabolite and microbiome interplay in cancer immunotherapy," *Cancer Research*, vol. 76, no. 21, pp. 6146–6152, 2016.

[29] M. Tatsugami, M. Ito, S. Tanaka et al., "Bile acid promotes intestinal metaplasia and gastric carcinogenesis," *Cancer Epidemiology Biomarkers & Prevention*, vol. 21, no. 11, pp. 2101–2107, 2012.

[30] T. Matsuhisa, T. Arakawa, T. Watanabe et al., "Relation between bile acid reflux into the stomach and the risk of atrophic gastritis and intestinal metaplasia: a multicenter study of 2283 cases," *Digestive Endoscopy*, vol. 25, no. 5, pp. 519–525, 2013.

[31] K.-F. Karstens, J. Kempski, A. D. Giannou et al., "Systemic interleukin 10 levels indicate advanced stages while interleukin 17A levels correlate with reduced survival in esophageal adenocarcinomas," *PLoS One*, vol. 15, no. 4, p. e0231833, 2020.

[32] J. Zhang, "Expressing patterns of serum inflammatory factors in patients with gastric cancer with different types of tongue Fur," *Journal of Beijing University of Traditional Chinese Medicine*, vol. 41, no. 5, pp. 405–412, 2018.

[33] J. Xu, C. Xiang, C. Zhang et al., "Microbial biomarkers of common tongue coatings in patients with gastric cancer," *Microbial Pathogenesis*, vol. 127, pp. 97–105, 2019.

[34] B. Jiang, X. Liang, Y. Chen et al., "Integrating next-generation sequencing and traditional tongue diagnosis to determine tongue coating microbiome," *Scientific Reports*, vol. 2, no. 1, p. 936, 2012.

[35] J. Hu, S Han, Y Chen, and Z Ji, "Variations of tongue coating microbiota in patients with gastric cancer," *BioMed Research International*, vol. 2015, p. 173729, 2015.

[36] Y. Cheng, "Correlation between the Variety of Tongue Coating and Their Bacterial Community in the New Patients

with Gastric Cancer," *Journal of Nanjing University of Traditional Chinese Medicine*, vol. 4, 2018.

[37] L. R. Lopetuso, M. Severgnini, S. Pecere et al., "Esophageal microbiome signature in patients with Barrett's esophagus and esophageal adenocarcinoma," *PLoS One*, vol. 15, no. 5, p. e0231789, 2020.

[38] E. R. K. Eribe and I. Olsen, "Leptotrichia species in human infections," *Anaerobe*, vol. 14, no. 3, pp. 131–137, 2008.

[39] M. R. Couturier, E. S. Slechta, C. Goulston, M. A. Fisher, and K. E. Hanson, "Leptotrichia bacteremia in patients receiving high-dose chemotherapy," *Journal of Clinical Microbiology*, vol. 50, no. 4, pp. 1228–1232, 2012.

[40] S. Cooreman, C. Schuermans, J. Van Schaeren et al., "Bacteraemia caused by Leptotrichia trevisanii in a neutropenic patient," *Anaerobe*, vol. 17, no. 1, pp. 1–3, 2011.

[41] K. Kim, E. J. T. Castro, H. Shim, J. V. G. Advincula, and Y.-W. Kim, "Differences regarding the molecular features and gut microbiota between right and left colon cancer," *Annals of Coloproctology*, vol. 34, no. 6, pp. 280–285, 2018.

[42] N. Castaño-Rodríguez, "Dysbiosis of the microbiome in gastric carcinogenesis," *Scientific Reports*, vol. 7, no. 1, p. 15957, 2017.

[43] X. Fan, A. V. Alekseyenko, J. Wu et al., "Human oral microbiome and prospective risk for pancreatic cancer: a population-based nested case-control study," *Gut*, vol. 67, no. 1, pp. 120–127, 2018.

[44] A.-L. Wei, M. Li, G.-Q. Li et al., "Oral microbiome and pancreatic cancer," *World Journal of Gastroenterology*, vol. 26, no. 48, pp. 7679–7692, 2020.

[45] Y. Chen and L. Xie, "Research on connection between tongue presentations of dampness-heat blockage of rheumatoid arthritis and index of disease activity," *Liaoning Journal of Traditional Chinese Medicine*, vol. 26, p. 06, 2013.

[46] Z. Wang, Y.-f. Fang, and Y. Luo, "The objectivity research on 322 rheumatoid arthritis patients of dampness-heat impeding and cold-dampness impeding Chinese medical syndrome types," *Zhongguo Zhong xi yi jie he za zhi Zhongguo Zhongxiyi jiehe zazhi= Chinese journal of integrated traditional and Western medicine*, vol. 31, no. 4, pp. 466–470, 2011.

[47] X. Li and Z. J. Y. Yp, "Primary discussion of association of microecology and tongue coating," *LiaoNing J. Tradit. Chin. Med*, vol. 6, pp. 1102–1105, 2014.

[48] D. Manoil, N. Bostanci, G. Mumcu et al., "Novel and known periodontal pathogens residing in gingival crevicular fluid are associated with rheumatoid arthritis," *Journal of Periodontology*, vol. 92, no. 3, pp. 359–370, 2021.

[49] P. Frid, D. Baraniya, J. Halbig et al., "Salivary oral microbiome of children with juvenile idiopathic arthritis: a Norwegian cross-sectional study," *Frontiers in Cellular and Infection Microbiology*, vol. 10, p. 602239, 2020.

[50] M. Kwon, S. S Seo, M. K Kim, D. O Lee, and M. C Lim, "Compositional and functional differences between microbiota and cervical carcinogenesis as identified by shotgun metagenomic sequencing," *Cancers*, vol. 11, no. 3, 2019.

[51] Z. Gao, B. Guo, R. Gao, Q. Zhu, and H. Qin, "Microbiota disbiosis is associated with colorectal cancer," *Frontiers in Microbiology*, vol. 6, p. 20, 2015.

[52] X. Jia, S. Lu, Z. Zeng et al., "Characterization of gut microbiota, bile acid metabolism, and cytokines in intrahepatic cholangiocarcinoma," *Hepatology*, vol. 71, no. 3, pp. 893–906, 2020.

[53] C. Zhong, M Han, P Yang et al., "Comprehensive analysis reveals the evolution and pathogenicity of Aeromonas, viewed from both single isolated species and microbial communities," *mSystems*, vol. 4, no. 5, 2019.

[54] H. Körkoca, Y Alan, S Bozari, M Berktas, and Y Goz, "Detection of putative virulence genes in Aeromonas isolates from humans and animals," *Journal of infection in developing countries*, vol. 8, no. 11, pp. 1398–1406, 2014.

[55] J. M. Tomás, "The main Aeromonas pathogenic factors," *ISRN Microbiol*, vol. 2012, p. 256261, 2012.

[56] M. J. Albert, M. Ansaruzzaman, K. A. Talukder et al., "Prevalence of enterotoxin genes in Aeromonas spp. isolated from children with diarrhea, healthy controls, and the environment," *Journal of Clinical Microbiology*, vol. 38, no. 10, pp. 3785–3790, 2000.

[57] T. Gao, Z. Wang, Y. Dong et al., "Role of melatonin in sleep deprivation-induced intestinal barrier dysfunction in mice," *Journal of Pineal Research*, vol. 67, no. 1, p. e12574, 2019.

[58] Q. Zeng, D. Li, Y. He et al., "Discrepant gut microbiota markers for the classification of obesity-related metabolic abnormalities," *Scientific Reports*, vol. 9, no. 1, p. 13424, 2019.

[59] R. B. Hayes, J. Ahn, X. Fan et al., "Association of oral microbiome with risk for incident head and neck squamous cell cancer," *JAMA Oncology*, vol. 4, no. 3, pp. 358–365, 2018.

[60] G. Yu, M. H. Gail, D. Consonni et al., "Characterizing human lung tissue microbiota and its relationship to epidemiological and clinical features," *Genome Biology*, vol. 17, no. 1, p. 163, 2016.

[61] K. M. Quicke, M. S. Diamond, and M. S. Suthar, "Negative regulators of the RIG-I-like receptor signaling pathway," *European Journal of Immunology*, vol. 47, no. 4, pp. 615–628, 2017.

[62] Y.-M. Loo and M. Gale, "Immune signaling by RIG-I-like receptors," *Immunity*, vol. 34, no. 5, pp. 680–692, 2011.

[63] Y. Zhao, Y.-F. Mao, Y.-S. Tang et al., "Altered oral microbiota in chronic hepatitis B patients with different tongue coatings," *World Journal of Gastroenterology*, vol. 24, no. 30, pp. 3448–3461, 2018.

[64] Y. Iwakura, H. Ishigame, S. Saijo, and S. Nakae, "Functional specialization of interleukin-17 family members," *Immunity*, vol. 34, no. 2, pp. 149–162, 2011.

[65] O. O. Coker, Z. Dai, Y. Nie et al., "Mucosal microbiome dysbiosis in gastric carcinogenesis," *Gut*, vol. 67, no. 6, pp. 1024–1032, 2018.

[66] T. Kühn, M Stepien, M López-Nogueroles et al., "Prediagnostic plasma bile acid levels and colon cancer risk: a prospective study," *Journal of the National Cancer Institute*, vol. 112, no. 5, pp. 516–524, 2020.

[67] X. Meng, Z. Chang, N. Che, J. Wu, T. Dang, and J. Chai, "Acid/bile exposure triggers TRAIL-mediated apoptosis in esophageal cancer cells by suppressing the decoy receptors and c-FLIPR," *The International Journal of Biochemistry & Cell Biology*, vol. 122, p. 105736, 2020.

[68] J. H. Yu, J. B Zheng, J Qi et al., "Bile acids promote gastric intestinal metaplasia by upregulating CDX2 and MUC2 expression via the FXR/NF-κB signalling pathway," *International Journal of Oncology*, vol. 54, no. 3, pp. 879–892, 2019.

Hindawi
Journal of Healthcare Engineering
Volume 2023, Article ID 9787369, 1 page
https://doi.org/10.1155/2023/9787369

Retraction

Retracted: The Role of Health Education in Vaccination Nursing

Journal of Healthcare Engineering

Received 25 July 2023; Accepted 25 July 2023; Published 26 July 2023

This article has been retracted by Hindawi following an investigation undertaken by the publisher [1]. This investigation has uncovered evidence of one or more of the following indicators of systematic manipulation of the publication process:

(1) Discrepancies in scope
(2) Discrepancies in the description of the research reported
(3) Discrepancies between the availability of data and the research described
(4) Inappropriate citations
(5) Incoherent, meaningless and/or irrelevant content included in the article
(6) Peer-review manipulation

The presence of these indicators undermines our confidence in the integrity of the article's content and we cannot, therefore, vouch for its reliability. Please note that this notice is intended solely to alert readers that the content of this article is unreliable. We have not investigated whether authors were aware of or involved in the systematic manipulation of the publication process.

In addition, our investigation has also shown that one or more of the following human-subject reporting requirements has not been met in this article: ethical approval by an Institutional Review Board (IRB) committee or equivalent, patient/participant consent to participate, and/or agreement to publish patient/participant details (where relevant).

Wiley and Hindawi regrets that the usual quality checks did not identify these issues before publication and have since put additional measures in place to safeguard research integrity.

We wish to credit our own Research Integrity and Research Publishing teams and anonymous and named external researchers and research integrity experts for contributing to this investigation.

The corresponding author, as the representative of all authors, has been given the opportunity to register their agreement or disagreement to this retraction. We have kept a record of any response received.

References

[1] M. Yao, X. Gu, Y. Mo, C. Xia, and L. Tang, "The Role of Health Education in Vaccination Nursing," *Journal of Healthcare Engineering*, vol. 2022, Article ID 6078846, 5 pages, 2022.

Hindawi
Journal of Healthcare Engineering
Volume 2022, Article ID 6078846, 5 pages
https://doi.org/10.1155/2022/6078846

Research Article

The Role of Health Education in Vaccination Nursing

Mengjiao Yao, Xiaoping Gu, Yujie Mo, Chunjing Xia, and Liwei Tang

Jiangqiao Community Healthcare Center, Jiading, Shanghai, China

Correspondence should be addressed to Mengjiao Yao; yao_mengjiao@outlook.com

Received 3 December 2021; Accepted 15 January 2022; Published 18 April 2022

Academic Editor: Enas Abdulhay

The role of health education in vaccination is very important. Through various forms of activities, comprehensive and systematic education of health knowledge for people can promote students and others to be aware of vaccination and actively cooperate with vaccination work. Therefore, this article intends to conduct an in-depth study of the role of health education in prevention and treatment and to enhance people's awareness of vaccination. This article mainly uses questionnaire survey method, interview method, and controlled experiment to explain and analyze the effect of health education. The subjects of this questionnaire are students, parents, and staff. They have mixed reviews for its role in vaccination, but the overall situation is positive. 239 out of 500 people believe that health education can reduce allergic reactions and improve the effectiveness of vaccines. In the control experiment, after health education and publicity training, the parents of the observation group were significantly better than the control group in terms of mastering the relevant knowledge of vaccination, successfully vaccinating unplanned vaccines, etc. This shows that the importance of health education in vaccination care is incomparable.

1. Introduction

Our country's disease prevention work mainly focuses on public health. Factors such as large population, poor sanitation, and unbalanced economic development have affected people's understanding of disease knowledge. Health education is a kind of knowledge dissemination that focuses on prevention and combines prevention and treatment. It achieves the purpose of improving people's ideological awareness and enhancing the role of vaccines by cultivating and educating people in a certain degree of comprehensive physical and psychological qualities.

There are countless research results on the role of health education in vaccination care. For example, Wang et al. emphasized that in view of the problems existing in mass vaccination in schools, if targeted preventive care measures can be taken, the quality of medical care and the safety of vaccination can be greatly improved [1]. Tang pointed out that the scientific development of vaccination nursing work has a good effect on relieving the nervousness of children during vaccination, thereby promoting the success rate and safety of vaccination [2]. Yang and Wu explored the role of parental health education and nursing intervention in reducing the side effects of DPT vaccination among high school students. Parental health education and care intervention can significantly improve the understanding of the DPT vaccine among the parents of students who have received the DPT vaccine, thereby significantly reducing the awareness rate of the DPT vaccine [3]. Therefore, this article also follows the research line of other scholars and conducts in-depth exploration of the role of health education in vaccination care.

This article first studies the relevant theories and knowledge of health education. Then, a brief description of vaccination care is given. Afterwards, the function and performance of the design of the vaccination information management system were analyzed. Finally, through questionnaire surveys and experiments, an in-depth study of the role of health education in vaccination care was carried out, and data results were obtained [4]. The data show that through scientific health education, parents' cognition, the reduction of children's anxiety, and the success rate of vaccination can be significantly improved. The experiment proved the necessity of health education.

2. The Role of Health Education in Vaccination Care

2.1. Health Education. Health education is a scientific education that focuses on prevention and combines treatment. Its purpose is to let the audience have a correct and comprehensive understanding of the disease, improve people's self-protection ability, and enable them to receive effective care in social life. Health education is through the comprehensive and systematic shaping of people's physical and psychological factors so that they can establish a correct, positive, and self-improving ideology. The role of health education in vaccination care is very important [5, 6].

Health education is a systematic project, which requires systematic and planned planning as well as continuity. In terms of health knowledge, it mainly starts from the two perspectives of life care and social hygiene. As people's understanding of diseases continues to deepen, more and more knowledge about vaccination and nursing knowledge, methods, and approaches have begun to spread. The so-called health is a comprehensive good state of physique, psychological quality, and personality quality that combines a good mental state with a good physical shape [7, 8].

Health education can effectively improve people's misunderstanding of diseases, lifestyles, and behaviors, so as to achieve the purpose of vaccination and nursing. In health promotion and education, we must fully consider the individual differences of each patient, family environment, and other factors. Let more people in the whole society understand diabetes knowledge and prevention methods through publicity boards and playing video clips. Regularly organize "sports and fitness" activities to enable the general public to correctly understand the importance and role of sports in improving physical fitness. Actively cooperate with community neighborhood committees or residents' committees to conduct physical examinations for people with diabetes and guide them on how to vaccinate [9, 10].

In daily work, the importance of health education should be strengthened, and comprehensive and systematic publicity should be organized regularly to enable people to fully understand how to properly use and wear disease prevention equipment and related knowledge. At the same time, it can be spread through platforms such as WeChat official account.

Effective antibodies can be produced after vaccination, and such diseases will not occur after future contact, and vaccination is now free [11, 12].

Pay attention to the health education of parents. Parents should observe closely and do not give children antibiotics without authorization [13, 14].

Medical staff should pay attention to giving different nursing care to students' psychological reactions in different periods [15, 16].

2.2. Vaccination Care. Vaccination care refers to regular education of healthy patients so that they understand the disease and how to treat it and cultivate good habits in daily life. Through regular physical examinations, problems are found and solved in time.

Health education plays a very important role in vaccination care. It can help people understand their physical health and take corresponding measures to effectively control diseases. Nurses have a comprehensive knowledge and understanding of health education. In the actual nursing process, implement it to every construction worker, and all participants are required to strictly abide by the relevant regulations and take corresponding measures for different situations.

Regular lectures on vaccination and nursing knowledge: let parents and family members understand what problems need to be paid attention to in daily work and how to better and timely solve the various new situations in the medical history, discover potential risk factors, and control the development trend of the disease.

In health education, we can improve the staff's awareness of disease knowledge and awareness of disease prevention through professional training and qualification examinations. At the same time, it is necessary to strengthen communication with patients and their families.

Strengthen health education and publicity to train people through lectures, playing DVDs, etc., so that everyone can understand the importance of vaccination care and strengthen the relationship between people's disease and vaccination work. At the same time, some simple and easy-to-operate activities should be carried out in the hospital to increase the public's awareness of participation. Organize a regular theme activity with the theme of "Prevention and Treatment of Diseases" and distribute corresponding materials.

2.3. Design of Vaccination Information Management System

2.3.1. Data Mining Technology in the Management System. In the information management of vaccination, special technology is needed to sort and analyze the information and data. Based on the dimensionality of the data involved in the rule, association rules can be divided into single-dimensional and multidimensional. Its definition can be expressed as follows:

$$\begin{aligned}\text{Support}(P \Rightarrow Q) &= P(P \cup Q),\\ \text{Confidence}(P \Rightarrow Q) &= F(P \mid Q).\end{aligned} \tag{1}$$

Among them, the degree of support for association rules $P \Rightarrow Q$ is $F(P \cup Q)$. These data analysis techniques can be directly applied to the vaccination information data warehouse.

2.3.2. Vaccination Management. Vaccination is a welfare policy of the state to ensure the healthy growth of children and avoid contracting diseases. Vaccination information will be entered into the file as a required document for future enrollment. The production, packaging, and distribution of vaccines are also strictly controlled by the relevant departments, and the distribution is agreed.

In order to ensure the accuracy of each link in the vaccination process for children, each link will confirm the information and enter it into the computer, and the vaccine information will also be archived.

As for which vaccines to be vaccinated at different time periods, publicity brochures will also be formulated in advance and distributed to parents, which will also clearly indicate the adverse reactions of some vaccines.

The entire vaccination process plays a vital role in improving children's physical health and reducing the infection rate of group diseases and high-incidence diseases.

3. Experimental Investigation

3.1. Survey Object. This article first interviewed the vaccinated staff of the health center, mainly to explore the attitude and knowledge of the practitioners about the job. There is a total of 80 staff members under investigation. This article designs a relevant questionnaire to conduct a questionnaire survey on them.

Then, select 100 students who need vaccinations as the observation group. Among them, 52 were boys and 48 were girls. The vaccinated students are in good health and normal development. There is no special sensitivity reaction to vaccination. In addition, 90 students who need to receive vaccination were selected as the control group, of which 54 were boys and 46 were girls. There is no significant difference in gender between the two groups of experimental students, and they are comparable.

In addition, this article also invited the parents of the students to conduct surveys and interviews. Among the guardians of the survey subjects, there are up to 120 student mothers, 80 student fathers, and 30 grandparents.

3.2. Health Education Methods. Health education is a step that we all need to focus on throughout the vaccination process. Health education is not only a unilateral propaganda by medical staff but a mode of passive acceptance by parents. This mode can easily lead to parents' irritability and poor results.

Healthcare workers should consider innovative formats, such as educational video clips that encourage parents and children to watch together. In addition, you can also consider printing some storybooks and picture books to promote health education knowledge in the stories. Of course, giving children some small toys printed with health education can also have a good publicity effect.

Of course, the above method will inevitably incur costs, so the relevant part needs to issue funds to the community service station. Through the above methods, children can not only realize the harm of disease and can actively stay away from the source of disease in their daily life but also can enhance parents' awareness of vaccination.

3.3. Questionnaire Survey Method. The survey objects of this paper are parents and the staff of the community service station. The survey site is the community service station. The survey time is selected as weekends, because weekends are the peak time for parents to bring their children to vaccinate. In the form of face-to-face paper questionnaires, parents' real views on vaccination and health education, as well as their satisfaction with the vaccination process, were obtained.

In addition, we also distributed paper questionnaires to the staff of 10 community service workstations, mainly to investigate the difficulties they face during the usual vaccination process so as to propose solutions.

4. Analysis of Survey Results

4.1. Main Difficulties Faced by Vaccination. First of all, this article intends to analyze the main difficulties faced by vaccination. According to the survey data of the staff, we can see that 64 of the 90 staff are concerned about the 5 aspects of vaccination, namely, insufficient assistance, negative reports, noncooperation of the masses, weak team, and lack of salary and labor. There are great opinions on matches, etc. The specific data are shown in Table 1.

As shown in Figure 1, we can judge that the staff attach great importance to the problem of vaccination, and they believe that the two aspects of insufficient aid and the impact of negative reports have a negative impact on the work. This is enough to show that the health education work for vaccination is not yet in place, and the country's management is not perfect. Among them, only 14 people disagreed with these issues, and 12 others did not comment on it.

4.2. Parents' Satisfaction with the Work of Vaccination Clinic. Secondly, this article invites parents to conduct a questionnaire survey and found that the degree of satisfaction with the overall outpatient clinic, the number of consultations, waiting for observation, postevent precautions, sanitary conditions, and service procedures are also different. On average, about 160 people are satisfied with these 6 places, and about 42 people are dissatisfied with these places. The details are shown in Table 2:

As shown in Figure 2, we can clearly see that the parents are most satisfied with the sanitary condition of the vaccinated health center, and then they are satisfied with the service process. The most unsatisfactory thing is the number of visits in the outpatient department. As people are now more and more aware of the importance of vaccination, they attach great importance to vaccination. However, there is a time limit for vaccination, and there are not many consultations, so parents feel distressed about this.

4.3. Comparison of Effects between the Observation Group and the Control Group. Then, this article needs to understand the grouping situation. After conducting health education and publicity training for parents, 97 of the 100 parents of students in the observation group have knowledge of vaccination. 94 cases were successfully vaccinated with unscheduled vaccines, and 95 cases were qualified. Among the 100 parents of students in the control group, 61 parents successfully mastered vaccination-related knowledge. 68 students were successfully vaccinated with unscheduled vaccines, and 72 students passed the vaccine. According to

Table 1: Major difficulties faced in vaccination efforts.

	Agree	Disagree	General
Insufficient superior subsidies	18	4	1
Negative reports impact	19	2	1
The masses do not cooperate	13	3	2
Weak personnel team	6	2	3
Revenue is not linked to the workload	8	3	5

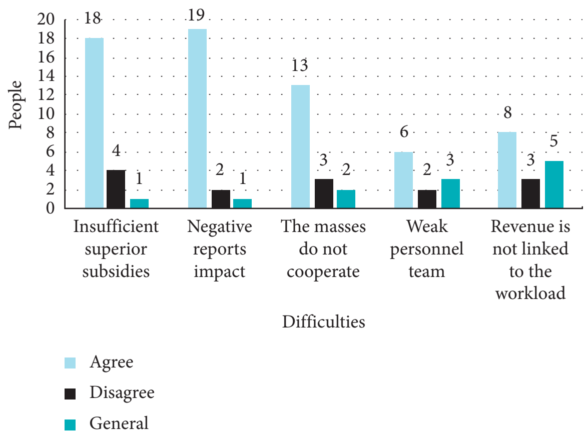

Figure 1: Major difficulties faced in vaccination efforts.

Table 2: Parents' satisfaction with the vaccination clinic work.

	Satisfied	Unsatisfied	General
General outpatient service	161	42	31
Number of opening visits	119	68	39
Waiting for planting to stay	142	61	32
Matters needing attention afterwards	163	36	26
Sanitary conditions	192	22	17
Service process	183	20	22

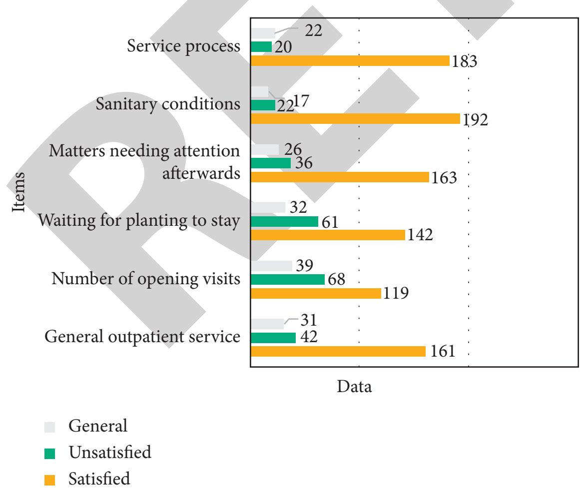

Figure 2: Parents' satisfaction with the vaccination clinic work.

the data comparison, it can be clearly seen that the inoculation effect of the observation group is better than that of the control group. The details are shown in Table 3.

Table 3: Effect comparison between the observed and control groups.

	Observation group	Control group
Number	100	100
Vaccine pass rate	95	68
Out planned qualified rate	94	72
Knowledge mastery rate	97	61

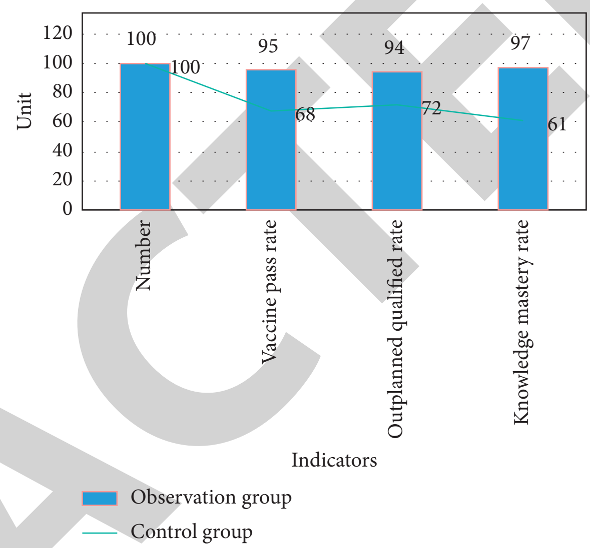

Figure 3: Effect comparison between the observed and control groups.

As shown in Figure 3, we can find that the vaccine qualification rate, unplanned qualification rate, and knowledge mastery rate of the observation group and the control group are better than those of the control group. In terms of vaccine qualification rate, the observation group is 27% larger, and in the unplanned qualification rate, the observation group is 22% larger. In terms of knowledge, the observation group can reach 97%. This shows that health education plays a great role in vaccination and can have an impact on the effectiveness of vaccines.

4.4. The Role of Health Education in Vaccination. Finally, this article conducts research on reducing adverse vaccine reactions, increasing satisfaction, improving vaccine effects, and reducing the occurrence of allergic reactions from the three perspectives of students, parents, and medical staff. From the data collection, it can be found that 142 people think that health education can reduce the occurrence of allergic reactions, 96 people think it can improve the effectiveness of the vaccine, and 153 people say it can increase satisfaction. Another 122 people said that health education would reduce the adverse effects of the vaccine. The details are shown in Table 4.

As shown in Figure 4, we can see that in the student population, most of them believe that health education can reduce the occurrence of allergic reactions. The proportion is 36.8%. In the parent group, most of them think that health education can improve their satisfaction and increase their

Hindawi
Journal of Healthcare Engineering
Volume 2023, Article ID 9891861, 1 page
https://doi.org/10.1155/2023/9891861

Retraction

Retracted: Low Serum Albumin Is Associated with Poor Prognosis in Patients Receiving Peritoneal Dialysis Treatment

Journal of Healthcare Engineering

Received 15 August 2023; Accepted 15 August 2023; Published 16 August 2023

This article has been retracted by Hindawi following an investigation undertaken by the publisher [1]. This investigation has uncovered evidence of one or more of the following indicators of systematic manipulation of the publication process:

(1) Discrepancies in scope
(2) Discrepancies in the description of the research reported
(3) Discrepancies between the availability of data and the research described
(4) Inappropriate citations
(5) Incoherent, meaningless and/or irrelevant content included in the article
(6) Peer-review manipulation

The presence of these indicators undermines our confidence in the integrity of the article's content and we cannot, therefore, vouch for its reliability. Please note that this notice is intended solely to alert readers that the content of this article is unreliable. We have not investigated whether authors were aware of or involved in the systematic manipulation of the publication process.

Wiley and Hindawi regrets that the usual quality checks did not identify these issues before publication and have since put additional measures in place to safeguard research integrity.

We wish to credit our own Research Integrity and Research Publishing teams and anonymous and named external researchers and research integrity experts for contributing to this investigation.

The corresponding author, as the representative of all authors, has been given the opportunity to register their agreement or disagreement to this retraction. We have kept a record of any response received.

References

[1] Y. Shi, J. Cai, C. Shi, C. Liu, J. Zhou, and Z. Li, "Low Serum Albumin Is Associated with Poor Prognosis in Patients Receiving Peritoneal Dialysis Treatment," *Journal of Healthcare Engineering*, vol. 2022, Article ID 7660806, 6 pages, 2022.

Hindawi
Journal of Healthcare Engineering
Volume 2022, Article ID 7660806, 6 pages
https://doi.org/10.1155/2022/7660806

Research Article

Low Serum Albumin Is Associated with Poor Prognosis in Patients Receiving Peritoneal Dialysis Treatment

Yanan Shi, Jiajie Cai, Chunxia Shi, Conghui Liu, Jingjing Zhou, and Zhongxin Li

Department of Nephrology, Beijing Lu-He Hospital, Capital Medical University, Beijing 101100, China

Correspondence should be addressed to Zhongxin Li; lhyy6806@ccmu.edu.cn

Received 21 December 2021; Accepted 18 March 2022; Published 18 April 2022

Academic Editor: Enas Abdulhay

Background. The number of patients receiving dialysis treatment is sustainably increasing, especially peritoneal dialysis. *Objectives*. It is necessary to find out potential factors that may indicate the prognosis of patients receiving peritoneal dialysis treatment. *Methods*. This study retrospectively involved 325 patients who received peritoneal dialysis treatment. *Results*.Low serum albumin (HR = 2.254; 95% CI: 1.534–3.311; $P < 0.001$) and high FBG (Fasting blood glucose) (HR = 1.474; 95% CI: 1.025–2.120; $P = 0.037$) were risk factors for death in patients receiving peritoneal dialysis treatment. Serum albumin (AUC = 0.683; $P < 0.001$) and creatinine (AUC = 0.625; $P < 0.001$) exhibited value of prognosis prediction. Both high FBG ($P = 0.005$) and low albumin ($P < 0.001$) were associated with poor prognosis, and low albumin predicted poorer survival. *Conclusions*. Low serum albumin and high fasting blood glucose were risk factors and associated with poor prognosis. Low albumin has a potential in predicting the prognosis of patients receiving peritoneal dialysis treatment.

1. Introduction

Dialysis is a renal replacement therapy (RRT), mainly including hemodialysis and peritoneal dialysis [1, 2]. The principle of peritoneal dialysis is the solutes and fluid exchange between the peritoneal capillary blood and the dialysis solution, in which the flow rate can be adjusted to achieve a maximum removal [2]. It is estimated that more than 272,000 patients are receiving peritoneal dialysis globally, accounting for approximately 11% dialysis patients worldwide (in 2017) [3]. The number of patients receiving dialysis treatment is sustainably increasing, especially peritoneal dialysis [4]. Among different countries, the selection of dialysis modality is dramatically different [3]. Different dialysis modalities bring important consequences for quality of life, patients' survival, financial implications, and logistics for the medical system [1, 5]. In Asia, the application of peritoneal dialysis ranges from 3% to 73%, and China has a fairly high peritoneal dialysis rate [3, 4, 6]. Notably, there is a steep rise in peritoneal dialysis utilization in China in the past decade [7].

Albumin is a single protein species and the most abundant plasma protein representing approximately 3/5 in quantity [8]. Albumin produced in the liver is an anionic, flexible, heart-shaped molecule with a molecular weight of ~65 kDa [9]. Normally, the serum albumin is about 45 g/L in human. Albumin plays an important role in maintaining an oncotic pressure difference between plasma and the interstitial space by regulating fluid exchange [10]. Besides, albumin carries a number of substances including bilirubin, fatty acids, ions, hormones, and drugs [8, 10]. Notably, low albumin in serum is in association with increased mortality [10].

It is necessary to find out potential factors that may indicate the prognosis of patients receiving peritoneal dialysis treatment. Herein, factors associated with the prognosis of patients receiving peritoneal dialysis treatment, such as serum albumin, creatinine, and fasting blood glucose, were evaluated. We also compared their abilities of prognosis prediction by ROC (receiver operating characteristic) analysis and survival analysis.

2. Materials and Methods

2.1. Patients. This study retrospectively involved 325 patients who received peritoneal dialysis treatment. Each patient had a complete record of dialysis during the period. All lab parameters were measured at admission as a baseline. The follow-up duration was 7 years.

Patients who were older than 18 years old and received peritoneal dialysis treatment for more than 3 months were included.

The exclusion criteria were as follows: incubation in other hospitals, hemodialysis to peritoneal dialysis, kidney transplant to peritoneal dialysis, annual follow-up <2, and missing baseline data.

2.2. Clinical Data Collection. After admission, the age of patients was recorded, and systolic pressure, diastolic pressure, and pulse were measured. Moreover, the patients received laboratory examination including total protein (g/L), albumin (g/L), Ca^{2+} (mmol/L), phosphate (mmol/L), K^+ (mmol/L), Na^+ (mmol/L), Cl^- (mmol/L), fasting blood glucose (FBG; mmol/L), blood urea nitrogen (BUN; mmol/L), creatinine (μmoI/L), hemoglobin (g/L), and parathyroid hormone (PTH; pg/mL) test. Normal, low, and high individual parameters were defined according to the clinical standard of the clinical lab of our hospital.

2.3. Statistical Analysis. Software SPSS 22.0 (IBM, USA) was used. Data were exhibited as mean ± SD. Quantitative data are expressed as mean ± standard deviation or median (interquartile range). Qualitative data are expressed as a rate or composition ratio. Differences between groups were analyzed by the *T*-test or analysis of variance. Survival risk analysis was performed using a cox risk regression model. The ROC (receiver operating characteristic) curve was used to predict the risk of death for patients receiving peritoneal dialysis treatment, and the AUC (area under curve) was calculated. $P < 0.05$ was considered statistically significant.

3. Results

3.1. Characteristics of Patients Receiving Peritoneal Dialysis Treatment. The summary of all the characteristics of patients receiving peritoneal dialysis treatment is shown in Table 1. The average age was 62.51 years old. Among the 325 patients, 147 were male and 178 were female. The average survival time was 892.36 days.

3.2. Differences between Survived Patients and Dead Patients. The subsequent comparisons between the survival and the death were further performed (Table 2). No significant differences were found in gender (P = 0.651), systolic pressure (P = 0.198), pulse (P = 0.745), total protein (P = 0.092), Ca^{2+} (P = 533), phosphate (P = 0.467), K^+ (P = 0.322), Na^+ (P = 0.260), Cl^- (P = 0.390), FBG (P = 0.333), BUN (P = 0.251), and PTH (P = 0.882). Survival time (P = 0.049) and diastolic pressure (P = 0.047) showed a little statistical difference. The hemoglobin (P = 0.038) was statistically different.

The age was significantly different (P < 0.001) as the dead patients (66.96 ± 13.89 years old) were much older than the survived patients (28.75 ± 13.13 years old).

The albumin was significantly different (P < 0.001) as the albumin in dead patients (32.98 ± 4.94 mmol/L) was much lower than that in survived patients (36.59 ± 4.85 mmol/L).

The creatinine was significantly different (P < 0.001) as the creatinine in dead patients (564.64 ± 268.80 μmoI/L) was much lower than that in survived patients (684.77 ± 271.00 μmoI/L).

3.3. Risk Factors for Death in Patients Receiving Peritoneal Dialysis Treatment. Based on the results of the comparison between survived patients and dead patients, we further analyzed the risk factors for death in patients receiving peritoneal dialysis treatment. As shown in Table 3, albumin, FBG, and creatinine were found to be significantly different.

However, the HR of creatinine was 0.999, with 95% CI of 0.998–1.000. Therefore, low albumin (HR = 2.254; 95% CI: 1.534–3.311; P < 0.001) and high FBG (HR = 1.474; 95% CI: 1.025–2.120; P = 0.037) were considered to be risk factors.

3.4. Prognosis Prediction in Patients Receiving Peritoneal Dialysis Treatment. To evaluate the prognosis prediction value of the observed risk factors, ROC curves were drawn (Figure 1). FBG did not show the prediction value (P = 0.593). Albumin (P < 0.001) and creatinine (P < 0.001) exhibited a value of prognosis prediction (Table 4). Of note, the albumin (with AUC of 0.683) showed a higher prognosis prediction value than creatinine (with AUC of 0.625).

3.5. Low Albumin and High FBG Were Associated with Poor Prognosis. Finally, the survival of patients receiving peritoneal dialysis treatment was analyzed (Figure 2). Both high FBG (P = 0.005) and low albumin (P < 0.001) were associated with poor prognosis, and low albumin predicted a poorer survival.

4. Discussion

In this study, we found age, albumin, and creatinine were significantly different between dead and survived patients receiving peritoneal dialysis treatment. Albumin and creatinine showed the value of prognosis prediction. Furthermore, low albumin and high fasting blood glucose were risk factors and associated with poor prognosis. Thus, it is suggested that low albumin has a potential in predicting the prognosis of patients receiving peritoneal dialysis treatment.

To some extent, the level of albumin represents nutrition status and infection [11, 12]. Renal handling of albumin can influence renal function by the effects of albumin. Albumin filtration in glomeruli and tubular reabsorption are two major processes in the renal handling of albumin. The dysfunction of them leads to an increased excretion of

Table 1: Characteristics of patients receiving peritoneal dialysis treatment.

Characters	Mean (median)	SD (quartile spacing)	n
Age	62.51	14.07	301
Male	—	—	147
Female	—	—	178
Survival time (d)	892.36	716.22	325
Systolic pressure (mmHg)	143.46	48.71	325
Diastolic pressure (mmHg)	80.81	14.73	325
Pulse (beat per minute)	77.83	11.60	313
Total protein (g/L)	65.54	25.18	323
Albumin (g/L)	34.89	5.20	323
Ca^{2+} (mmol/L)	2.21	0.28	323
Phosphate (mmol/L)	1.38	0.52	318
K^+ (mmol/L)	4.19	0.89	324
Na^+ (mmol/L)	139.79	2.93	323
Cl^- (mmol/L)	99.39	9.90	322
Fasting blood glucose (mmol/L)	7.63	3.92	323
Blood urea nitrogen (mmol/L)	19.68	32.59	323
Creatinine (μmoI/L)	628.24	276.15	323
Hemoglobin (g/L)	114.04	(101–129)	325
Parathyroid hormone (pg/mL)	146.90	(55.46–270.90)	325

Table 2: Comparisons between survival and death.

	Survival ($n = 173$)	Death ($n = 152$)	t (x^2)	P value
Age	28.75 ± 13.13	66.96 ± 13.89	5.267	<0.001
Male	78	67	0.859	0.651
Female	93	85		
Survival time (d)	965.59 ± 794.95	809.02 ± 606.39	1.975	0.049
Systolic pressure (mmHg)	146.72 ± 63.41	139.74 ± 22.05	1.289	0.198
Diastolic pressure (mmHg)	82.32 ± 16.01	79.08 ± 12.96	1.990	0.047
Pulse (beat per minute)	77.63 ± 11.21	78.05 ± 12.05	0.325	0.745
Total protein (g/L)	67.77 ± 33.77	63.04 ± 7.49	1.688	0.092
Albumin (g/L)	36.59 ± 4.85	32.98 ± 4.94	6.621	<0.001
Ca^{2+} (mmol/L)	2.22 ± 0.29	2.20 ± 0.26	0.624	0.533
Phosphate (mmol/L)	1.40 ± 0.51	1.36 ± 0.53	0.729	0.467
K^+ (mmol/L)	4.29 ± 0.84	4.09 ± 0.95	2.035	0.322
Na^+ (mmol/L)	139.97 ± 2.95	139.60 ± 2.91	1.128	0.260
Cl^- (mmol/L)	99.84 ± 9.24	98.89 ± 10.60	0.861	0.390
FBG (mmol/L)	7.43 ± 3.87	7.86 ± 3.97	0.970	0.333
BUN (mmol/L)	21.65 ± 44.15	17.47 ± 7.75	1.151	0.251
Creatinine (μmoI/L)	684.77 ± 271.00	564.64 ± 268.80	3.992	<0.001
Hemoglobin (g/L)	117.54 ± 23.72	112.19 ± 22.25	2.085	0.038
PTH (pg/mL)	212.30 ± 203.37	208.34 ± 275.71	0.148	0.882

Note. FBG: fasting blood glucose; BUN: blood urea nitrogen; PTH: parathyroid hormone.

Table 3: Risk factors for death in patients receiving peritoneal dialysis treatment.

		P value	HR	95% CI	
				Lower	Upper
PTH	75–150	0.410	1.000	—	—
	<75	0.110	1.481	0.915	2.398
	150–300	0.618	1.136	0.688	1.877
	>300	0.335	1.282	0.774	2.126
Albumin	Normal		1.000	—	—
	Low	<0.001	2.254	1.534	3.311
Cl^-	Normal	0.853	1.000	—	—
	Low	0.971	1.010	0.586	1.740
	High	0.574	1.201	0.634	2.275

Table 3: Continued.

		P value	HR	95% CI Lower	95% CI Upper
Na^+	Normal	0.357	1.000	—	—
	Low	0.947	0.974	0.442	2.143
	High	0.152	0.230	0.031	1.716
K^+	Normal	0.423	1.000	—	—
	Low	0.314	1.246	0.812	1.911
	High	0.433		0.335	1.598
Phosphate	Normal	0.313	1.000	—	—
	Low	0.747	1.075	0.692	1.671
	High	0.129	1.453	0.897	2.354
Ca^{2+}	Normal	0.347	1.000	—	—
	Low	0.788	0.946	0.629	1.422
	High	0.147	0.411	0.123	1.367
Hypertension	No		1.000	—	—
	Yes	0.789	1.048	0.741	1.483
Hemoglobin	Normal	0.386	1.000	—	—
	Low	0.531	0.841	0.489	1.445
	High	0.272	0.430	0.095	1.939
FBG	Normal	0.112	1.000	—	—
	Low	0.680	1.220	0.474	3.137
	High	0.037	1.474	1.025	2.120
Sex	Male		1	—	—
	Female	0.515	0.881	0.601	1.290
Age		0.102	0.966	0.978	1.002
Creatinine		0.022	0.999	0.998	1.000

Note. FBG: fasting blood glucose; PTH: parathyroid hormone.

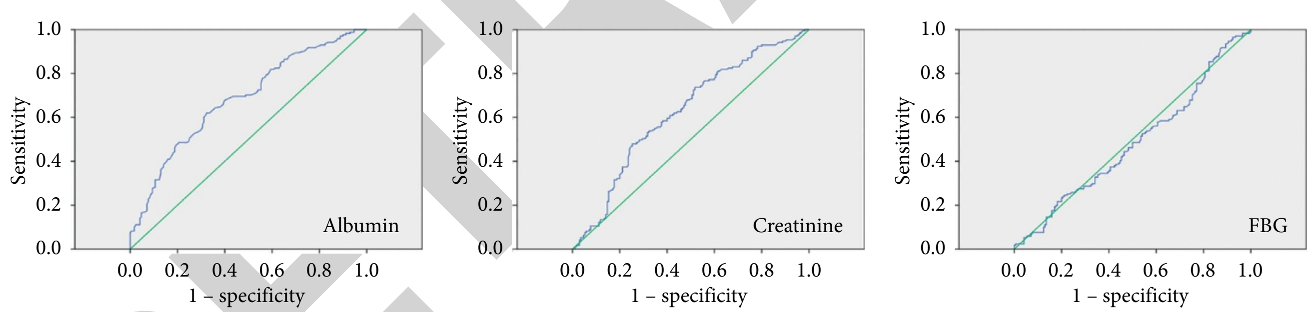

(a) (b) (c)

Figure 1: ROC curve of albumin (a), creatinine (b), and FBG (c) for death risks in patients receiving peritoneal dialysis treatment.

Table 4: ROC curve in patients receiving peritoneal dialysis treatment.

Predictors	ROC curves: Cut-off value	AUC	95% CI	p value
Albumin	35.75	0.683	0.626–0.739	<0.001
Creatinine	711.50	0.625	0.565–0.684	<0.001
Fasting blood glucose	4.44	0.483	0.422–0.545	0.593

albumin. Recently, Yamada et al. found lower serum albumin level is associated with an increased risk for loss of residual kidney function in patients receiving peritoneal dialysis treatment [13]. The loss of residual kidney function can make the general condition of patients worse and finally lead to the death. Our study goes further in exploring the prognosis prediction value of albumin by involving and considering the survival. Chiu et al. also reported lower serum albumin was associated with poorer survival [14]. Hao et al. used time-averaged albumin level and serum albumin reach rate as predictor variables and found higher serum albumin was associated with a lower all-cause mortality rate in patients undergoing long-term peritoneal dialysis treatment [15]. It is indicated that low serum albumin was a risk factor of both early and late death in incident peritoneal dialysis patients [16]. Interestingly, Singh et al. concluded that peritoneal dialysis is associated with

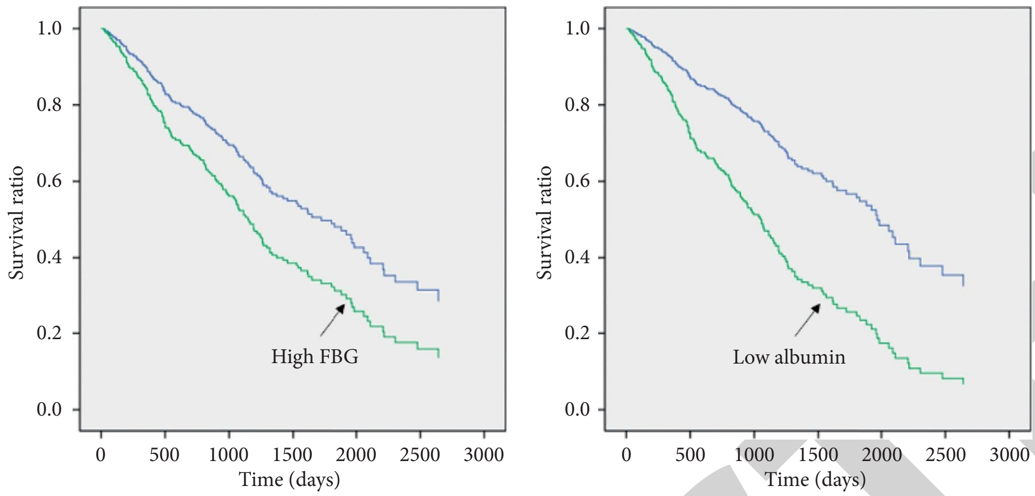

(a) (b)

Figure 2: (a) Survival of patients with high FBG (green line) and low and normal FBG (blue line). (b) Survival of patients with low albumin (green line) and high and normal FBG (blue line).

lower mortality than hemodialysis in patients with low serum albumin [17]. As for the study of serum creatinine, Inaquma et al. reported the ratio of blood urea nitrogen to serum creatinine is associated with mortality by conducting a multicenter prospective cohort study [18].

By comparison of the age between dead and survived patients receiving peritoneal dialysis treatment, we found the age may influence the clinical outcomes and mortality. Consistent with the study conducted by Sakaci et al., mortality was higher in elderly patients and low albumin levels affected mortality [19]. The treatment of peritoneal dialysis should be cautious and based on accurate assessment, because of a higher incidence of intestinal complications, previous history abdominal surgeries, multiple comorbidities, and other possible contraindications [20, 21]. Our result also revealed that high fasting blood glucose may be associated with poor prognosis. Chen et al. reported the association of impaired fasting glucose and mortality in nondiabetic patients on maintenance peritoneal dialysis [22]. The role of high blood glucose in cardiovascular complications and even mortality of peritoneal dialysis treatment needs to be studied.

A number of researchers focus on the study of risk factors for mortality in patients receiving peritoneal dialysis treatment. Female gender, lower Kt/V (weekly urea clearance), and WCCr (weekly creatinine clearance) were found to be risk factors [23]. Lower hemoglobin levels and the presence of diabetes were shown to be risk factors as well [16].

In this study, common laboratory test indicators were analyzed to predict the prognosis of patients with peritoneal dialysis, which is helpful to advance treatment intervention for patients with possible poor prognosis and improve the prognosis of these patients. For patients with hypoalbuminemia and/or high FBG, which may lead to poor prognosis, dietary modification, intravenous albumin supplementation, and more stringent measures of blood glucose control may be considered. However, further prospective studies are needed to confirm the clinical efficacy of these measures.

This is a retrospective study, which is the major limitation. In the future study, we plan to involve the complications and causes of death. It is known that peritonitis has a notable association with peritoneal dialysis treatment since technique failure of peritoneal dialysis treatment could lead to peritonitis [24, 25]. The cardiovascular complication is another severe risk for peritoneal dialysis treatment [26]. The association of albumin and complication of peritoneal dialysis treatment is not clear and remains to be further studied.

4.1. Implications. Low albumin and high fasting blood glucose were risk factors and associated with poor prognosis. Low albumin has a potential in predicting the prognosis of patients receiving peritoneal dialysis treatment.

Data Availability

The data used to support the findings of this study are included within the article.

Ethical Approval

The clinical study was approved by the Ethics Committee of Beijing Lu-He Hospital and was conducted in accordance with the provisions of the Declaration of Helsinki.

Consent

Written informed consent was obtained from all participants before enrolment.

Conflicts of Interest

The authors declare that there are no conflicts of interest.

Hindawi
Journal of Healthcare Engineering
Volume 2022, Article ID 1859747, 6 pages
https://doi.org/10.1155/2022/1859747

Research Article

The Efficacy of Rehabilitation Nursing Interventions on Patients with Open Lower Limb Fractures

Zengfen Pang,[1] Meimei Shan,[1] Yuanyuan Li,[1] Huan Zhang,[1] Amei Huang,[1] Yuping Liu,[2] and Xianghong Li[1]

[1]*The Affiliated Cancer Hospital of Shandong First Medical University, Jinan, Shandong, China*
[2]*Chinese Nursing Society, Beijing, China*

Correspondence should be addressed to Zengfen Pang; zfpang14@outlook.com

Received 14 January 2022; Revised 30 March 2022; Accepted 31 March 2022; Published 16 April 2022

Academic Editor: Enas Abdulhay

Objective. The study aims to analyze the efficacy of rehabilitation nursing interventions on patients with open lower limb fractures. *Methods*. From June 2020, patients who received RNI (observation group) were included and compared with patients who received routine nursing interventions (control group). The efficacy of different nursing modes was compared with several indicators. *Results*. One hundred patients were included in this study, 50 in each group. The baseline characteristics were not significantly different between the groups. Regarding the emotional scores, the Self-Rating Anxiety Scale (SAS) score (26.98 vs 43.47), and Distress Management Screening Measure (DMSM) score (8.01 vs 12.85) in the observation group were significantly lower than those in the control group, both $P < 0.05$. Regarding the postoperative related indexes, the postoperative pain score (10.13 vs 15.53), fracture healing time (6.32 vs 10.86 weeks), and postoperative complications rate (0 vs 12%) in the observation group were all significantly lower than those in the control group, all $P < 0.05$. Regarding the quality of life scores, the WHOQOL-100 score (94.12 vs 83.13) and PSQI score (6.43 vs 10.36) were both significantly better in the observation group, with both $P < 0.05$. *Conclusion*. Patients with open lower limbs who received RNI can help patients reduce postoperative anxiety and stress, promote postoperative rehabilitation and improve their quality of life.

1. Introduction

With the rapid development of China's construction industry and transportation industry, the incidence of open fractures of the lower limbs is also increasing year by year. The trauma caused by the fracture is large. Serious conditions such as tissue defects, bone fracture exposure, and wound infection may occur in these kinds of fractures, resulting in aggravating the pain of patients and delaying their postoperative recovery [1]. Even physical and psychological stress responses will occur in these patients [2].

In order to further reduce the complications and promote the recovery of lower limb function, it is necessary to find scientific measures for patients with open lower limb fractures. Researchers have identified the positive clinical value of rehabilitation nursing interventions (RNI) in patients who underwent general surgeries and orthopedic surgeries [3, 4]. The postoperative RNI may play an important role to ensure the quality of rehabilitation. However, studies about the efficacy of RNI on patients with open lower limb fractures are still rare. Therefore, we conducted a retrospective case-control study to explore the efficacy of RNI compared with routine nursing interventions, and the content is further discussed in this study.

2. Methods

The RNI was adopted in our department since 2020 June. The patients who received RNI after 2020 June were included in our study.

2.1. Case Selection Criteria

2.1.1. Inclusion Criteria. The inclusion criteria were as follows: (1) detailed imaging data can be obtained; (2) age ≥18 years old; (3) meet the standards of surgical operation and anesthesia; (4) has no treatment contraindications and midway withdrawal; (5) normal coagulation function, cardiopulmonary, liver, and kidney functions; and (6) patients or family members were aware of the study and signed the consent [5].

2.1.2. Exclusion Criteria. The exclusion criteria were as follows: (1) minors; (2) women in pregnancy and lactation; (3) with emotional and mental disorders; (4) with other fractures; (5) with blood disease; and (6) patients with malignant tumors [6].

2.2. Nursing Methods. Patients in the control group were given routine nursing and the corresponding nursing and guidance according to the patient's situation. Patients in the observation group provided RNI, the details are further discussed in this study [7].

2.2.1. Evaluation. The postoperative rehabilitation plan was conducted based on the data after a comprehensive examination of the patient's postoperative situation. Communication was strengthened to help patients improve their negative postoperative emotions. Nurses gave targeted nursing interventions for common postoperative complications. The patient's body position was adjusted in time. It is recommended to rest in a rigid bed within 3 weeks after surgery and turn over once every 2 hours. Family members were taught to massage their limbs to effectively prevent pressure sores. Good pain management was carried out for patients to relieve postoperative pain. If the patient took a flat rest, the elbow was extended with a back flexion of 30–40°. When taking the side position, the lower limb's joints were slightly flexed to avoid compression of the upper limbs. Some patients had obvious pain due to their own tolerance, and painkillers were taken under the guidance of the attending doctor to relieve the pain when necessary. When the patient was in pain, the pain pump was used to maximize the pain caregivers' acceptance of the patient. The patient was informed of the attention of the matters in the recovery process. The pain management methods and rehabilitation knowledge were explained, rehabilitation guidance and training were appropriately strengthened, and the patient's immunity was improved [8].

2.2.2. Psychological Nursing Care. Patients with an open fracture of the lower limbs often have severe pain after surgery, leading to a serious bad mood. This kind of bad mood is different from the concerns about surgery preoperatively. Therefore, the psychological counseling strategy adopted by nurses postoperatively is different from that of preoperatively. The proper pain relief guidance and detailed health education were based on timely counseling on patients' physical discomfort and pain condition. Nursing staff should communicate with patients actively to tell them the importance of postoperative medical and nursing cooperation. As a result, the patients' own medical compliance behavior was strengthened [9].

2.2.3. Pain Care. Nursing staff should determine the degree of postoperative pain and analyze the impact of pain symptoms on the quality of sleep.

In order to avoid the use of analgesics, nursing staff should explain how to divert pain attention to patients when the pain can be tolerated. The nursing staff were required to strengthen ward inspection [10] to inquire about the pain degree every day. If the VAS score exceeds 4 points, then report the pain to the doctor in time. After the feedback from the doctors, nursing staff should follow the doctor's advice to provide pain treatment if necessary.

2.2.4. Health Education. Nursing staff should explain the necessity of postoperative rehabilitation care, the high-risk factors that affect postoperative recovery, and the ways of postoperative rehabilitation care. Online consultation was also available for patients to clear up their doubts about the diseases and surgical treatment.

Nursing staff should guide the daily lives of patients to balance bed and activity. Exercise is necessary as soon as possible after the operation to promote blood circulation in the lower limbs. The amount of activity can be gradually increased according to the needs of rehabilitation and the condition of pain. Patients were advised to eat foods with high energy to promote the recovery of wounds. Smoking and drinking were forbidden during the rehabilitation period, and drinking more water was encouraged [11].

2.2.5. Prevention of Postoperative Complications. During the period of an indwelling catheter, nurses should carry out bladder training for the patient to prevent bladder muscle atrophy. After the patient's postoperative condition went well, intermittent catheterization was used to continuously strengthen its own urination function.

Nurses were required to advise patients and their family members of the guidance to avoid wound infection. The prevention methods include disinfecting and cleaning the pressed skin, informing patients not to scratch the wound with their hands, treating timely when the wound was contaminated by blood, and maintaining the skin dry.

There are four aspects to do a good job in the prevention of deep vein thrombosis (DVT). First of all, intravenous care. In order to prevent DVT, lower extremity puncture and infusion are avoided, especially repeated operations at the same location. When infusing drugs, the doctor's advice is followed to choose less irritating drugs for the patient to prevent the liquid from leaking out of the blood vessels. When using a touquet, it is necessary to reduce the binding time to avoid unnecessary damage to the distal and local blood vessels. The puncture site is closely observed, the inflammatory reaction is found and dealt with in time, and the venous channel is reselected. Secondly, lower extremity care. In order to effectively prevent deep venous thrombosis of the lower extremities, nurses instructed patients to raise the affected limb after surgery to facilitate the venous return of the lower extremities and prevent swelling. It should be careful not to compress the deep veins of the patient's legs. The color and temperature of the affected limb were observed, and the pulse of the dorsal foot artery was accurately recorded. On this basis, the cause of the abnormality in time was found and dealt with accordingly. When necessary, an intermittent inflation and compression device were used to perform periodic compression to improve the venous blood flow of the lower extremities and prevent deep vein thrombosis in the lower extremities. At the same time, medication guidance for patients with severe renal insufficiency or patients with thrombosis, unfractionated heparin can be used. The specific dosage depends on individual differences. The patient needs to be continuously monitored for coagulation indicators during the medication process to avoid medication risks. Low-dose heparin has a good effect of preventing thrombosis. It is recommended to use 5000 U subcutaneous injection 2 h before the operation and to monitor the patient's platelet function after the operation to avoid thrombocytopenia. Finally, mechanical prevention. Medical elastic stockings are used to apply external force to restrict venous pressure, promote venous return, and ensure the normal blood circulation function of the veins of the lower extremities, thereby exerting a preventive effect. At the same time, the use of intermittent inflation and compression devices to periodically pressurize patients can also improve the venous blood flow of the patients' lower limbs, increase blood flow, and prevent DVT [12].

2.2.6. Rehabilitation Guidance.

(1) Passive training program. After the operation, a rehabilitation training program was developed for the patient based on the preoperative examination results and the postoperative condition. On the first postoperative day, the patient's affected limb was properly raised and kept in a straightened state to avoid external rotation, and the patient's pain symptoms were evaluated. Patients were encouraged to take the initiative in bed activities. When the patient's pain is mild, their knee joints were passively moved, and ankle back extension exercises and quadriceps isometric exercise training were performed. Patients were instructed to perform ankle pump exercises and quadriceps contraction training to enable patients to master the essentials of movement to accelerate venous return. The patient was instructed to train for muscle tension and contraction. The affected limb was raised by 20~30°. Passive activities should be based on the comfort of the patient. Pillows were not put under the knees, letting the patients raise their entire lower limbs, and placing hard objects under the knees was avoided to avoid hitting the popliteal veins. Oppression was produced. Patients were instructed to press and rub the muscles of the lower limbs at the base of their palms to speed up blood flow, promote venous return, and prevent thrombosis. Patients were instructed to raise their straight legs, exercise their muscles, and prepare themselves for getting out of bed later. The condition of the dorsal artery of the device was closely observed to determine the degree of swelling of the limbs. If there was any abnormality, it was immediately notified to the doctor. On the 3rd day after the operation, the patient's knee joint passive training was carried out with the aid of the joint continuous passive activator. On the 4th to 7th day after the operation, the patient was given quadriceps isometric contraction exercise training, straight leg raising exercise training, and active knee flexion exercise training [13].

(2) Active training program: elastic bandages should be used when the patient goes down to the ground to reduce edema of the lower extremities, speed up the return of venous blood, and avoid thrombosis. According to the patient's postoperative recovery, the patient is guided to restore and contract the quadriceps, ankle joint, and gluteal muscles to avoid complications such as osteoporosis, venous thrombosis, and muscle atrophy. The changes in the recovery of the disease are observed, the patient's hip and knee joint flexion and extension strengths are trained in a timely manner, and the activities of the upper and lower joints of the fracture are carried out. According to the patient's recovery degree, the activity intensity can be appropriately increased to improve joint stiffness. Nursing staff should regularly perform related passive activities for the patient, and then gradually change to active activities, allowing the patient to lie on the bed to perform active leg elevation exercises, and assist them to restore their sitting ability until they can walk slowly and stand up. When the patient can stand autonomously and the affected leg can move forward, walking training is started. Limbs, standing, striding, and other exercises are guided, the patient's gait is observed, a walker is used to assist walking training at an appropriate time, or a small amount of support from family members is provided. Early walking training needs to pay attention to that the amount of activity should be moderate to avoid foot varus, and the patient is required to use the affected side of the lower limb to shift the center of gravity, and the healthy side of the lower limb cannot be used to help walk, to avoid gait instability, and to prevent the occurrence of spasm of the affected side of the lower limb. The range of movement of the uninvolved limb of the patient is controlled, requiring the patient not to move the uninhibited limb at will during training but to use the affected limb subconsciously [14].

2.3. Observation Indicators. The anxiety scores before and after nursing were compared using the Self-Rating Anxiety Scale (SAS). The critical value is 50 points: (1) mild anxiety: 50–59 points; (2) moderate anxiety: 60–69 points; and (3) severe anxiety: >69 score [8]. The psychological pain scores before and after the intervention were compared using the distress management screening measure (DMSM) scale; 0–10 points, 0 points for no psychological pain, and 10 points for extreme psychological pain [9]. The postoperative pain scores, fracture healing times, and times of the two groups of patients postoperative complications were compared. The quality of life scores of the two groups of patients before and after intervention were compared using the World Health Organization Quality of Life Scale (WHO-QOL-100 scale). There are a total of 25 subitems. Each subitem is evaluated according to the 0–4 point method. The total score is 100 points. The higher the score, the higher the quality of life. The comparison of the sleep quality scores of the two groups of patients before and after intervention, using the Pittsburgh Sleep Quality Index (PSQI) scale, 7 evaluation items, 0–3 points scoring method, a total score of 21 points; the lower the score, the better the sleep quality [15].

2.4. Statistics. In this study, SPPS20.0 was used for statistical analysis. The measurement data were described by the mean ± standard deviation ($\overline{x} \pm s$), and student's t test was used; the count data were described by example (%), and the χ^2 test was used. $P < 0.05$ means that the difference is statistically significant.

3. Results

3.1. Baseline Characteristics. In this study, 100 patients were included in this study. In the observation group, 50 patients with open lower limb fractures were included with men: women as 29 : 21. The mean age was 41.89 ± 1.38 years (a range of 25–70 years). The causes of fracture were as follows: 37 traffic accidents, 10 high falls, and 3 other causes. The fracture areas were as follows: 28 femur and 22 tibia. Fracture Gustilo–Anderson classification: 44 A and 6 B. In the control group, there were 32 men and 12 women aged 23–70 years on average (42.71 ± 1.29). Fracture causes were as follows: 34 traffic accidents, 12 falling injuries, and 4 other cases. The fracture areas were as follows: 30 femur and 20 tibia. Fracture Gustilo–Anderson classification: 42 A and 8 B. The two general data comparison results were $P > 0.05$, comparable.

3.2. Effects of RNI on Postoperative Emotional Scores. The comparison of SAS score (64.12 vs 64.30) and DMSM score (17.32 vs 17.46) had no significant difference between the two groups before nursing, with both $P > 0.05$. After the nursing intervention, the scores significantly improved compared with the same group before nursing, $P < 0.05$. Moreover, after the intervention, the abovementioned scores in the observation group decreased significantly more than in the control group (26.98 vs 43.47 and 8.01 vs 12.85), both $P < 0.05$ (Table 1).

3.3. Effects of RNI on Postoperative Related Indexes. The postoperative pain score (10.13 vs 15.53) and fracture healing time (6.32 vs 10.86 weeks) of the observation group were lower than those of the control group, $P < 0.05$; postoperative complications (0) in the observation group were lower than those of the control group (12.0%), $P < 0.05$ (Table 2).

3.4. Effects of RNI on Postoperative Life Quality Scores. The comparison of WHOQOL-100 scores and PSQI scores between the two groups before nursing had no significant difference with $P > 0.05$. After the nursing intervention, the PSQI score of the observation group was lower than that of the control group (94.12 vs 83.13), and the WHOQOL-100 score (6.43 vs 10.36) was higher than that of the control group with both $P < 0.05$ (Table 3) [13].

4. Discussion

Open fracture of the lower limbs is a common type of fracture in clinic practice, which can seriously damage the walking function and affect the daily life of patients. Although aggressive surgical strategies will be adopted, limb dysfunction will still occur in some patients. Moreover, the high risk of infection and strong traumatic stress response of patients was also associated with this kind of fracture [16]. Therefore, it is the common pursuit of orthopedic researchers to take effective measures to promote the prognosis of patients with lower limb fractures.

The concept of rehabilitation nursing focuses on applying multidisciplinary theories to formulate targeted treatment measures to reduce the psychological and physical stress and trauma caused by surgical operations on patients and to promote rehabilitation. [15] The efficacy of RNI has been identified in many fields. However, there is no systematic and authoritative research data about the efficacy of RNI in patients with open low limb fractures. Therefore, we conducted this study because we hypothesized that RNI may be helpful in improving the prognosis of patients with open low limb fractures. Finally, we identified that RNI can help patients reduce postoperative anxiety and stress, promote postoperative rehabilitation, and improve quality of life.

The psychological impact of open fracture surgery on patients is relatively large. Unhealthy emotions such as worry, anxiety, and depression may come from the burden of disease and economic conditions. The unhealthy emotions may decrease compliance and finally worsen the prognosis. Integrating postoperative psychological care into RNI is a supplementary nursing model for humanized nursing intervention. The model aims to help patients overcome their inner conflicts through communication and opinion exchanges. In previous studies, psychological nursing has been identified as playing an important role in the recovery of patients after surgery and in some chronic diseases. [17, 18] In our study, we also found emotional scores significantly improved after psychological nursing intervention in patients with open lower limb fractures.

Postoperative pain is a common phenomenon that often occurs within 3 days after an operation, and the incidence rate is as high as 95%. It is the result of the combined effects of fracture pain, surgical pain, postoperative swelling, and compartment syndrome. Severe pain after fracture is a

Table 1: Comparison of emotional scores between the two groups before and after nursing intervention ($\overline{x} \pm s$).

Group	SAS score (points)		DMSM score (points)	
	Before intervention	After the intervention	Before intervention	After the intervention
Observation group ($n = 50$)	64.12 ± 5.63	26.98 ± 2.12*	17.32 ± 1.25	8.01 ± 0.31*
Control group ($n = 50$)	64.30 ± 5.71	43.47 ± 3.41*	17.46 ± 1.33	12.85 ± 1.68*
t value	0.569	12.489	0.651	11.824
P value	0.239	0.000	0.304	0.000

Note: comparison results of before and after interventions within the group, $^*P < 0.05$; SAS = Self-rating Anxiety Scale; DMSM = distress management screening measure.

Table 2: Comparison of related indicators between the two groups before and after nursing intervention ($\overline{x} \pm s$).

Group	Pain score (points)	Fracture healing time (weeks)	Postoperative complications, n (%)
Observation group ($n = 50$)	10.13 ± 0.46	6.32 ± 0.33	0 (0)
Control group ($n = 50$)	15.53 ± 1.13	10.86 ± 0.78	6 (12.0)
t value	9.637	8.561	8.356
P value	0.000	0.000	0.008

Table 3: Comparison of sleep and quality of life scores between the two groups ($\overline{x} \pm s$).

Group	WHOQOL-100 score (points)		PSQI score (points)	
	Before intervention	After the intervention	Before intervention	After the intervention
Observation group ($n = 50$)	78.24 ± 3.63	94.12 ± 2.69*	14.32 ± 1.25	6.43 ± 0.12*
Control group ($n = 50$)	77.92 ± 3.77	83.13 ± 3.24*	14.46 ± 1.33	10.36 ± 0.68*
t value	0.639	13.826	0.639	15.278
P value	0.207	0.000	0.591	0.000

Note: comparison results of before and after interventions within the group, $^*P < 0.05$; WHOQOL-100 = World Health Organization Quality of Life Scale; PSQI = Pittsburgh Sleep Quality Index.

malignant stimulus, which can cause severe pain stress damage and traumatic pathological changes, such as increased systemic oxygen consumption, decreased body immunity, metabolic disorders, rapid loss of nutrients, high blood pressure, and shock response. It will damage the functions of various systems of the human body and affect the postoperative rehabilitation effects [19, 20]. Therefore, improving postoperative pain in patients with open lower limb fractures is of great significance for promoting postoperative recovery. The results of this study showed that RNI can significantly reduce the degree of postoperative pain in patients with open lower limb fractures.

Postoperative DVT is a common complication after surgery for open fractures of the lower limbs. It is generally recognized that early functional exercises and activities can reduce the incidence of postoperative complications [21]. Moreover, DVT can be prevented by many nursing interventions. In the conventional nursing mode, activities are restricted in the early stages after the operation. After the pain is relieved, the patient is encouraged to exercise moderately, but no specific requirements are made to avoid unnecessary trauma, which increases the risk of complications. RNI advocates early activities to avoid DVT caused by blood circulation disorders in the lower limbs. Therefore, DVT can be prevented by RNI [22]. The effects of RNI were identified in our study.

The quality of life and quality of sleep are very important evaluation indicators. Due to the reduced postoperative pain and complications, the WHOQOL-100 score and PSQI score improved significantly. The use of RNI is beneficial to the improvement of the quality of life and quality of sleep of patients with open lower limb fractures.

Our study had several limitations worth discussing. First, its retrospective nature prevented us from making stronger conclusions. The second limitation was the small sample size. Due to RNI being adopted in our hospital less than 2 years, the accumulated cases were not common in our center. Third, a lack of objective indicators may cause bias. More multicenter prospective studies with a large sample size are necessary to better understand the true value of RNI.

5. Conclusion

Based on a retrospective case-control study, we identified that patients with open lower limbs who received RNI can help reduce postoperative anxiety and stress, promote postoperative rehabilitation, and improve quality of life. More multicenter prospective studies with a large sample size are necessary to better understand RNI. More multicenter prospective studies with a large sample size are necessary to better understand the true value of RNI.

Data Availability

All the data generated or analysed during this study are included in this article.

Conflicts of Interest

The authors declare that they have no conflicts of interest.

References

[1] K. Al-Hourani, O. Pearce, and M. Kelly, "Standards of open lower limb fracture care in the United Kingdom," *Injury*, vol. 52, no. 3, pp. 378–383, 2021.

[2] A. Lee, L. Geoghegan, G. Nolan, K. Coopera, J. Supera, and M. Pearse, "Open tibia/fibula in the elderly: a retrospective cohort study," *JPRAS Open*, vol. 31, pp. 1–9, 2021.

[3] L.-L. Xia, T. Su, Y. Li, J.-F. Mao, Q.-H. Zhang, and Y.-Y. Liu, "Improving rehabilitation and quality of life after percutaneous transhepatic cholangiography drainage with a rapid rehabilitation model," *World Journal of Clinical Cases*, vol. 9, no. 34, pp. 10530–10539, 2021.

[4] Y.-L. Shen, Z.-Q. Zhang, L.-J. Zhu, and J.-H. Liu, "Timing theory continuous nursing, resistance training: rehabilitation and mental health of caregivers and stroke patients with traumatic fractures," *World Journal of Clinical Cases*, vol. 10, no. 5, pp. 1508–1516, 2022.

[5] M. Crotty, E. S. Gnanamanickam, I. Cameron, and M. Agar, "Are people in residential care entitled to receive rehabilitation services following hip fracture? Views of the public from a citizens' jury," *BMC Geriatrics*, vol. 20, no. 1, pp. 5–12, 2020.

[6] D. V. Dartel, M. Vermeer, E. C. Folbert, J. A. Arend, M. R. V. H. Miriam, and H. H. Johannes, "Early predictors for discharge to geriatric rehabilitation after hip fracture treatment of older patients," *Journal of the American Medical Directors Association*, vol. 22, no. 12, pp. 2454–2460, 2021.

[7] W. Y. Kuo, Y. Shyu, J. S. Wang, C. Min-Chi, W. Chi-Chuan, and C. Mei-Ling, "Adherence to home-based rehabilitation in older adults with diabetes after hip fracture," *Nursing Research*, vol. 68, no. 5, pp. 383–389, 2019.

[8] N. Mathilde, P. Louis, A. Laure, D. Eric, and V. Gilberto, "Lower extremity arterial disease in patients with diabetes: a contemporary narrative review," *Cardiovascular Diabetology*, vol. 17, no. 1, p. 138, 2019.

[9] W. D. Rinkel, T. M. Fakkel, M. C. Cabezas, E. Birnie, and J. H. Coert, "(Cost-)effectiveness of lower extremity nerve decompression surgery in subjects with diabetes: the DeCompression (DECO) trial study protocol for a randomised controlled trial," *BMJ Open*, vol. 10, no. 4, Article ID e035644, 2020.

[10] X. Meng, X. Chen, Z. Liu, and L. Zhou, "Nursing practice in stroke rehabilitation: perspectives from multi-disciplinary healthcare professionals," *Nursing and Health Sciences*, vol. 22, no. 1, pp. 28–37, 2020.

[11] C. E. Gonser, C. Bahrs, P. Hemmann, and D Körner, "Substantial decrease in paediatric lower extremity fracture rates in German hospitals in 2017 compared with 2002: an epidemiological study," *BMC Musculoskeletal Disorders*, vol. 21, no. 1, p. 357, 2020.

[12] H. Al-Thani, M. El-Matbouly, M. Al-Sulaiti, M. Asim, and A. El-Menyar, "Does perioperative hemoglobin A1c level affect the incidence, pattern and mortality of lower extremity amputation?" *Current Vascular Pharmacology*, vol. 17, no. 4, pp. 354–364, 2019.

[13] M. A. Griffioen, J. GluTtIng, R. V. OToole et al., "Transition from acute to chronic pain in lower extremity fracture patients: a pain phenotyping protocol," *Nursing Research*, vol. 69, pp. 149–156, 2020.

[14] J. Albareda, E. Ibarz, J. Mateo et al., "Are the unreamed nails indicated in diaphyseal fractures of the lower extremity? A biomechanical study," *Injury*, vol. 52, pp. S61–S70, 2021.

[15] J Lowe, S. M. Mitchell, S. Agarwal, and C. B. Jones, "The incidence of venous thromboembolism following pelvic and lower extremity trauma despite adherence to modern prophylactic protocols," *Journal of Orthopaedic Trauma*, vol. 34, no. 8, pp. 418–421, 2020.

[16] M. S. Hussain, F. R. Avilucea, and M. T. Archdeacon, "Effectiveness of the taut-line hitch knot in reducing and splinting lower extremity fractures," *Journal of Orthopaedic Trauma*, vol. 33, no. 1, pp. e31–e35, 2019.

[17] X. Yang, Y. Chen, S. Chen, and L. Pan, "Observation on clinical application effect of psychological nursing intervention in nursing care of elderly patients with chronic gastritis and analysis of nursing satisfaction," *Minerva Gastroenterologica*, 2021.

[18] R. Ma, R. Yu, Y. Yuan, B. Ren, and Y. Li, "Effects of traditional Chinese medicine for vaginal lavage combined with psychological intervention in postoperative patients with cervical cancer," *Evidence-based Complementary and Alternative Medicine: eCAM*, vol. 2021, Article ID 5751795, 17 pages, 2021.

[19] K. C. Vemulapalli, S. L. Davis, V. Mathews et al., "Treatment of periprosthetic nonunions of the lower extremity," *Orthopedics*, vol. 43, no. 4, pp. 209–214, 2020.

[20] L. Marcia and D. Y. Kim, "Predictors of peripheral vascular injury in patients with blunt lower extremity fractures," *Annals of Vascular Surgery*, vol. 57, pp. 35–40, 2019.

[21] H.-Y. Wang, G.-S. Yu, J.-H. Li, S.-X. Zhang, and Y.-B. Lin, "An updated meta-analysis evaluating limb management after total knee arthroplasty-what is the optimal method?" *Journal of Orthopaedic Surgery and Research*, vol. 14, no. 1, p. 97, 2019.

[22] S. Pesch, M. Hanschen, F. Greve et al., "Treatment of fracture-related infection of the lower extremity with antibiotic-eluting ceramic bone substitutes: case series of 35 patients and literature review," *Infection*, vol. 48, no. 3, pp. 333–344, 2020.

Hindawi
Journal of Healthcare Engineering
Volume 2022, Article ID 2113769, 12 pages
https://doi.org/10.1155/2022/2113769

Research Article

Psoriasis Vulgaris of Blood Heat Syndrome in Plasma Based on Widely Targeted Techniques

Xueyong Tang,[1] Juan Gong,[1] Yourang Jiang,[1] Xi Chen,[1] Dongwei Qi ,[1] and Xin Li [2]

[1]*Department of Dermatology, Chongqing Hospital of Traditional Chinese Medicine, Chongqing 400021, China*
[2]*Hunan University of Chinese Medicine, Changsha 410208, China*

Correspondence should be addressed to Dongwei Qi; qdw407@163.com and Xin Li; rheumatoidhn@163.com

Received 15 December 2021; Revised 22 February 2022; Accepted 7 March 2022; Published 15 April 2022

Academic Editor: Enas Abdulhay

Traditional Chinese medicine classifies psoriasis (Ps) according to clinical manifestations, and its different clinical manifestations imply the pathogenesis and material evolution basis of Ps, especially biomarkers that are meaningful to identification of Ps, treatment response, and elucidation of the pathogenesis of the disease. This study aims to screen differential metabolites in plasma of psoriasis vulgaris (PV) of blood heat syndrome based on a widely targeted metabolomic technique and to analyze syndrome metabolic markers and metabolic pathways. Forty-five PV patients were recruited, including 21 cases of the blood heat syndrome group (BH-PPG), 24 cases of the non-blood-heat syndrome group (NBH-PPG), and 30 healthy cases of the normal control group (NPG). The UPLC-MS/MS detection platform, a self-developed database, and multivariate statistical analysis were applied to investigate the plasma metabolic differences. The biomarkers related to blood heat syndrome were screened using the principal component analysis method. A total of 479 metabolites were detected in the three groups of plasma samples; 72 different metabolites were sorted out in the BH-PPG/NPG group, 82 in the NBH-PPG/NPG group, and 8 in the BH-PPG/NBH-PPG group. Differential metabolites mainly consist of metabolites of organic acids, amino acids, carbohydrates, and nucleotides. Multiple metabolites ginkgolic acid, pyrroloquinoline quinone, L-aspartic acid, and citramalic acid were expected to be the potential biomarkers of blood heat syndrome PV. The formation and evolution processes may be associated with disorders and regulation of metabolic pathways, ferroptosis, carbon metabolism, and purine metabolism.

1. Introduction

Psoriasis (Ps) is one of the most common chronic recurrent systemic dermatoses clinically [1], with a mounting incidence every year. The global prevalence rate is 0.51%–11.43% [2], and the recent incidence in China is 0.47% [3]. Because the disease has characteristics such as a long course, high recurrence rate, and low cure rate, it seriously impacts the physical and mental health of patients. Traditional Chinese medicine has unique advantages in the recognition and differentiation of this disease. Based on literature research and expert consensus, the clinical differentiation of psoriasis vulgaris (PV) presents three basic syndromes: blood heat syndrome, blood stasis syndrome, and blood dryness syndrome [4]. Zhao Bingnan was the first to put forward the basic pathogenesis of Ps that "there is long-term accumulated internal heat and stagnation of blood." Blood heat syndrome is the most important syndrome type in the progressive stage. It is not only the beginning of the onset but also essential to the transformation of the disease and syndrome [5]. However, the complexity of its pathogenesis, the internal reality and external deficiency of the syndrome, the multidimensional interface, the nonlinearity, and the formation and evolution of the syndrome need to be further clarified.

As the basic research of traditional Chinese medicine (TCM) syndromes and treatment on clinical metabolomics advances gradually, its advantages of multilevel, multitarget, and overall dynamics and temporal and spatial complexity have provided an effective solution for the investigation of the material basis and biomarker research of TCM syndromes [6]. In recent years, based on the metabolomics technique and bioinformatics methods, certain achievements have been made in research on the basis of Ps TCM syndromes and the efficacy evaluation of prescriptions [7]. However, the techniques of magnetic resonance imaging and nontargeted metabonomics methods, which have been mostly used, provide relatively low sensitivity and quantitative accuracy. Lately, the widely targeted metabolomics integrates the advantages of targeted and nontargeted ones, which is more applicable for the detection of low-to-medium abundant metabolites [8, 9]. Moreover, psoriasis vulgaris of blood-heat syndrome was diagnosed through different symptoms from the non-blood-heat syndrome [10]. It is assumed that differential metabolites are found between psoriasis vulgaris of blood-heat syndrome and non-blood-heat syndrome based on widely targeted metabolomics. The present study applies a widely targeted metabolomics approach and screens out differential metabolites and metabolic pathways in plasma samples of blood heat syndrome PV and intends to explore the material basis and evolution of PV syndrome based on the pathogenesis of blood heat syndrome.

2. Materials and Methods

2.1. Data Collection

2.1.1. Data Source. The 45 Ps volunteers were patients who visited the dermatology department of Chongqing Traditional Chinese Medicine Hospital (Daomenkou Division) from January to June 2019. There were 21 patients in the blood heat syndrome group (BH-PPG), and non-blood heat syndrome groups (NBH-PPG) included 13 for the blood stasis syndrome group (BS-PPG) and 11 for the blood dryness syndrome group (BD-PPG). There were also 30 volunteers in the normal control group (NPG) who were recruited from the physical examination center of this hospital and determined to be healthy during the same period. This project was approved by the Ethics Committee of Chongqing Traditional Chinese Medicine Hospital. All patients and healthy volunteers provided signed informed consent and volunteered to participate in this project.

2.1.2. Diagnostic Criteria. The western medicine diagnostic criteria for psoriasis vulgaris were referred to guidelines as previously published [11, 12]. Diagnosis of TCM syndromes referred to "Clinical Pathways of Traditional Chinese Medicine" diagnosis criteria of TCM clinical pathway syndromes of psoriasis (psoriasis vulgaris) [12]. Western medicine diagnosis and syndrome differentiation of cases were carried out by TCM researchers of attending physicians or above in the Department of Dermatology of this hospital who had been trained and who strictly implemented the previously described diagnostic criteria.

2.1.3. Inclusion Criteria. The inclusion criteria were as follows: ① patients should conform to the diagnostic criteria of western medicine diagnosis of PV and TCM blood heat syndrome, blood stasis syndrome, and blood dryness syndrome diagnosis of PV. ② Patients were of 18–65 years of age. ③ Patients should have no systemic diseases in the circulation, digestion, and endocrine systems, blood, and connective tissue and no other acute or chronic inflammatory or autoimmune dermal diseases except for Ps. ④ During the period from onset to treatment, no systemic or local medications including immunosuppressive agents, glucocorticoid steroid hormones, retinoids, antihistamines, biological agents, and traditional Chinese medicine should be administered, as well as no acceptance of physical therapy; ⑤ Patients should eat a light diet, take rest regularly, avoid bad habits such as smoking or drinking 6 weeks before onset. ⑥ Subjects are those who volunteered for the project and could enjoy the rights and fulfil the obligations as required. ⑦ Patients should have signed the informed consent.

2.1.4. Exclusion Criteria. Subjects with one or more of the previously described inclusion criteria that could not be met were excluded.

2.2. Sample Collection and Treatment. Both patients with PV syndromes and healthy volunteers fasted in the morning before collection of 3 to 5 mL of blood samples, which was carried out using tubes containing an anticoagulant. Immediately after blood collection, the tubes were gently inverted to mix the blood samples evenly 5 to 10 times to ensure the effect of the anticoagulant. The samples, after being collected within 30 min, were centrifuged at 3 000 rpm at 4°C for 10 to 15 min. Subsequently, 100 μL of the supernatant (plasma) was aspirated on ice, transferred to an EP tube, and stored in a refrigerator at −80°C for later use.

2.3. UPLC-MS/MS Analysis Conditions. The liquid phase conditions mainly include ① chromatographic column: Waters ACQUITY UPLC HSS T3 C18 1.8 μm, 2.1 mm $*$ 100 mm; ② mobile phase: phase A used ultrapure water (0.04% acetic acid), and phase B was acetonitrile purchased from Merck (0.04% acetic acid); ③ elution gradient: 0 min water/acetonitrile (95 : 5 V/V), 11.0 min 5 : 95 V/V, 12.0 min 5 : 95 V/V, 12.1 min 95 : 5 V/V, and 14.0 min 95 : 5 V/V; ④ flow rate was at 0.4 ml/min, with a column temperature of 40°C and injection volume of 2 μL. The standard reagent was chromatographically pure grade (China, BioBioPha). The experiment was performed on a shim-pack ultra-performance liquid chromatograph (Japan, SHIMADZU) and a QTRAP® 6500 + tandem mass spectrometer (USA, SCIEX). The mass spectrometry conditions mainly included the following: the temperature of the electrospray ionization source (ESI) is 500°C; the mass spectrum voltage is 5 500 V (positive) and −4 500 V (negative); and the pressure of ion source body I (GS I) is 55 psi, ion source body II (GSII) is 60 psi, and curtain gas (CUR) is 25 psi. The parameter of collision-induced ionization (CAD) was configured is high. Each ion pair of the QTRAP system was scanned based on the optimized declustering potential (DP) and collision energy (CE) [13].

2.4. Data Analysis. The metware database (MWDB), developed by MetWare Biotechnology Co. Ltd., was adopted for qualitative analysis using the retention time of the detected substance, the information of the precursor-product ion pair, and the secondary spectrum data. After obtaining the metabolite spectrum data of different samples, the characteristic ions of each substance were screened out using the QTRAP system. Analyst 1.6.3 and MultiQuant software were also applied to mass spectrometry quantitative analysis. Meanwhile, the construction of a reliable mathematical model adopted multivariate statistical analysis methods. Principal component analysis (PCA) was initially performed on the samples to observe the variability of the differentiated grouping samples. Based on the metabolite content, the range method was used for normalization, and the R software (https://www.r-project.org/) was applied to perform hierarchical cluster analysis (HCA) on the metabolites of different samples. Then, orthogonal partial least squares discriminant analysis (OPLS-DA) was used to distinguish the overall differences in metabolites between groups. Using the obtained multivariate analysis of the variable importance projection (VIP) of the OPLS-DA model, the metabolites of different species or tissues could be initially screened. Meanwhile, the p value or fold change in univariate analysis could be combined to further screen out the metabolites with VIP ≥1, fold change ≥2, or fold change ≤0.5 as significantly different metabolites.

3. Results

3.1. Clinical Baseline Comparison. The general data and disease conditions of the disease group and the normal control group are shown in Table 1. There are no significant differences in gender, age, and BMI between the control group and the disease group. In addition, there are also no significant differences in family history and BMI between BH-PPG and NBH-PPG, whereas significant differences are revealed in gender, age, course of disease, and psoriasis area severity index (PASI) scores.

3.2. Plasma UPLC-MS/MS Inspection Results

3.2.1. Sample Quality Control Analysis. The quality control sample (QC) was prepared by mixing the sample extracts, which was subsequently applied for monitoring the sample repeatability under the same processing method to obtain the trusted Internet connection (TIC) overlay detected by the mass spectrometry (Figure 1). The results indicate that the total ion current curves present a high overlap, detected using the metabolites, and the retention time and peak intensity are consistent, indicating that the signal stability is better when the mass spectrometer detects the same sample at different time points.

3.2.2. PCA and OPLS-DA Results between Groups. Pairwise comparison obtained the three-dimensional PCA structures of BH-PPG v NPG, NBH-PPG v NPG, and BH-PPG v NBH-PPG, and OPLS-DA scores and the S-plot (Figure 2), indicating an apparent trend of separation between groups. The results reveal that there is no crossover and overlap among the groups, with an apparent separation trend, and significant differences in plasma metabolites.

3.2.3. Differential Metabolite Screening Analysis. Based on OPLS-DA results, the metabolites with VIP ≥1, fold change ≥2, or fold change ≤0.5 were selected as significantly differentiated metabolites. Compared with the normal group, BH-PPG has 72 different metabolites, including ginkgolic acid and pyrroloquinoline quinone (Figure 3). They mainly consist of the metabolism of organic acids and their derivatives, followed by the metabolism of amino acids, carbohydrates, nucleotides, and their metabolites. There are 65 overlapped different metabolites with NBH-PPG (Table 2). BH-PPG presents 7 characteristic different metabolites compared with the normal group, including marked upregulation of L-petaminoacetic acid, L-amphetaminoacetic acid, and N-methyl-L-glutamic acid and marked downregulation of acadizine, 2-(methylthio)ethanol, neopterin, benzoic acid, and inositol; There are 17 different metabolites in the NBH-PPG group, including adenosine-3′-phosphate. Comparing the BH-PPG and NBH-PPG groups, four differential metabolites—1-naphthol, cortisol, inosine, and (±) 12-hydroxy-5Z, 8Z, 10E, 14Z-eicosatetraenoic acid—are markedly upregulated, whereas 4 differential metabolites—3,4,5-trimethoxycinnamic acid, 4-pyridoxic acid, mandelic acid, and p-hydroxyphenylacetic acid—are significantly downregulated, as shown in Table 3.

3.2.4. Metabolic Pathway Analysis. The KEGG database [14] was applied to annotate and enrich the selected differential metabolites, which were subsequently classified according to the types of pathways in KEGG (Figures 4 and 5). The results reveal that compared with the normal group, there are 23 entries of metabolic pathways in BH-PPG with differential metabolites ≥4 and 9 entries of metabolic pathways with p value ≤0.05 involve metabolic pathways, ABC transporters, antibiotic biosynthesis, carbon metabolism, ferroptosis, purine metabolism, galactose metabolism, glutathione metabolism, and phosphotransferase system (PTS). Among them, metabolic pathway q-values (corrected p-values), including ferroptosis (Figure 6) and carbon metabolism (Figure 7), are all less than 1, and the enrichment difference is significant.

4. Discussion

TCM diagnosis and treatment of psoriasis give priority to symptom differentiation and cause exploration of disease treatment with the corresponding prescriptions and syndromes. Syndrome is the starting point and the core of syndrome differentiation for disease treatment, and it is the bridge and key to the inheritance of principle, prescription, and medication [15]. The recent research on the standardization and material basis of psoriasis syndrome classification is mainly based on macroanalysis such as big data literature research and expert consensus. Despite that, there

Table 1: General data baseline comparison in each group.

Item	Normal control group (30 cases)	Disease group (45 cases)	Blood heat group (21 cases)	Non-blood heat group (24 cases)	Blood stasis group (13 cases)	Blood dryness group (11 cases)
Gender (male/female)	16/14	24/21	14/7**	10/14	4/9	6/5
Age (years)	36.90 [19, 56]	41.51 [18, 65]	35.95 [18, 54]**	46.38 [23, 65]	45.46 [25, 65]	47.45 [23, 65]
BMI index	21.68 [15.68, 25.68]	23.99 [15.57, 32.46]	24.20 [15.57, 32.46]	23.81 [17.96, 28.93]	23.71 [19.52, 28.13]	23.92 [17.96, 28.93]
Family history (yes/no)		18/27	10/11	8/16	3/10	5/6
Course (year)		10.02 [0.3, 30]	7.88 [0.5, 40]*	11.90 [0.5, 40]	11.65 [0.5, 36]	12.18 [4, 40]
PASI scores		13.62 [0.6, 28.8]	15.73 [0.6, 28.8]**	11.78 [1.8, 27.0]	11.41 [1.8, 22.5]	12.21 [2.6, 27.0]

Note. Except for gender and family history, the additional data of each item are represented by the median [minimum, maximum]; $^{*}p < 0.1$ and $^{**}p < 0.05$.

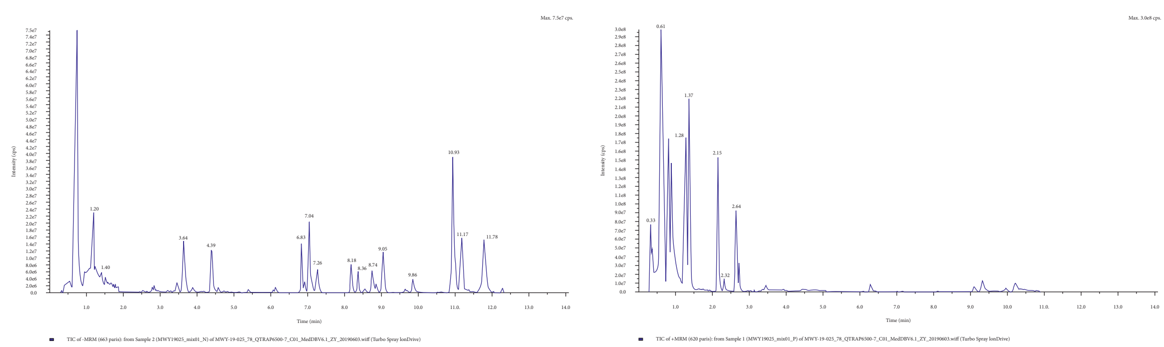

(a) (b)

Figure 1: QC sample TIC overlap detected by mass spectrometry. (a) QC_MS_TIC-N (normal control group) (b) QC_MS_TIC-P (disease group).

is some exploration on the microbiological basis of syndromes, and it is difficult to systematically clarify the formation and evolution mechanism of syndromes under the guidance of reduction theory [16]. Metabonomics starts from the terminal level of the human metabolic network, characterizes the response and regulation of the overall functional state of the body under the influence of pathogenic factors, and reveals essential metabolites closely related to disease and syndrome development. It also explores the formation and evolution of disease and syndrome [17, 18]. Based on a widely targeted metabonomics technique, this study analyzes plasma differential metabolites and screens specific key metabolic biomarkers for the pathogenesis and evolution of PV with blood heat syndrome.

Comparison of general data reveals that the condition is more serious in BH-PPG and the PASI scores are significantly higher than those of the NBH-PPG group. The total course of the disease is slightly short, with more men than women and younger age. These factors indicate that most of the blood-heat syndrome is in a progressive stage, which confirms that blood-heat syndrome is not only the beginning of the onset or recurrence of the disease but also key to the transformation of the disease. Analysis of widely targeted metabolomics shows that there are significant differences in plasma metabolism between BH-PPG, NBH-PPG, and the normal control groups. Comparing the syndrome group with the normal group, 65 overlapped differential metabolites including ginkgolic acid, pyrroloquinoline quinone (PQQ), L-aspartic acid, citramalic acid, and 3-hydroxybutyric acid are identified, and metabolic categories mainly involve organic acids, amino acids, carbohydrates, and nucleotides and its metabolites.

Organic acid is a carboxylic acid in the metabolism of amino acid, lipids, and sugar. It is widely distributed in plants. The human body develops disease due to certain enzyme depletion resulting from the accumulation of related carboxylic acids and their metabolites [19]. In this study, organic acids and their derivatives account for 23.29% of the different metabolite categories. The top 20 organic acids with significant differences include ginkgolic acid, PQQ, argininosuccinic acid, B-hydroxypyruvic acid, methyl isobutyrate, 2-hydroxybutyric acid, and methyl maleic acid. Among them, ginkgolic acid is present mostly in *Ginkgo biloba*. The research on the relationship of ginkgolic acid with diseases is mostly focused on its toxic and side effects such as sensitization, genotoxicity, and hepatorenal cytotoxicity [20, 21]. However, there are few studies on its metabolism in vivo and in vitro, and the apparent increase in plasma ginkgolic acid may be related to some drug oxidative metabolic enzymes. Abnormal expressions of CYP1A1 and CYP2E1, members of the cytochrome P450 (CYP450) family, are closely related to the occurrence and

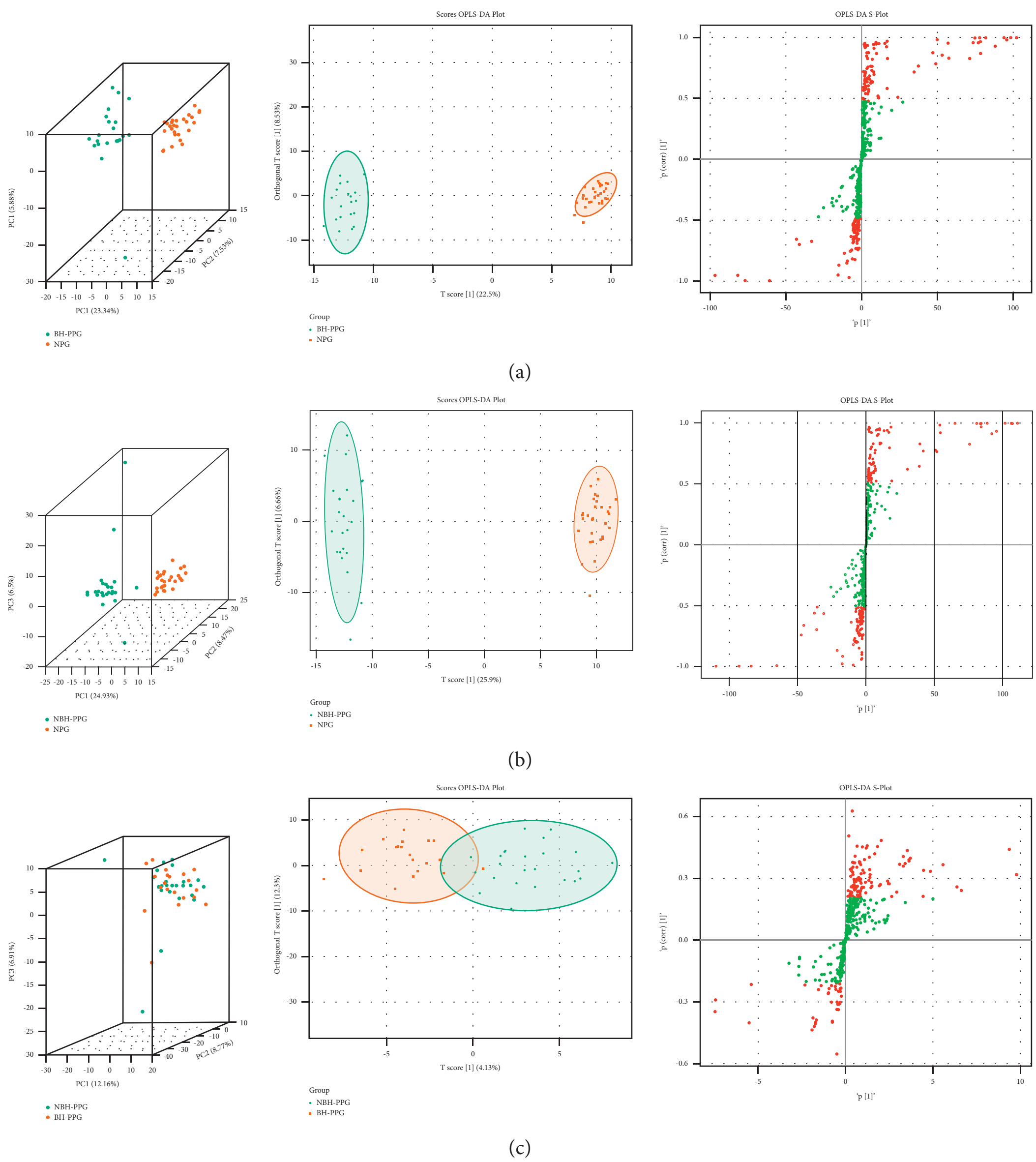

Figure 2: PCA and OPLS-DA plots of plasma samples in each group. *Note.* A1/B1, A2/B2, and A3/B3 represent the PCA three-dimensional structures, OPLS-DA scores, and S-plot of BH-PPG/NBH-PPG and the normal control group, respectively; C1, C2, and C3 represent the PCA three-dimensional structures, OPLS-DA scores, and S-plot of BH-PPG and NBH-PPG groups, respectively.

development of psoriasis [22], which may affect the normal metabolism of ginkgolic acid, thereby leading to a marked elevation in plasma expression levels. PQQ can scavenge intracellular oxygen-free radicals and avoid oxidative damage of tissues and cells, and it can repair mitochondrial dysfunction [23]. The marked increase in plasma PQQ expression may be involved in the inflammatory mechanism of Ps by affecting the function of mitochondria. Argininosuccinic acid ornithine is the intermediate product of circulation. As a precursor of arginine, it can be generated by the condensation of citrulline and aspartic acid under the action of argininosuccinate synthase in the liver and kidney. 3-hydroxybutyric acid is intimately correlated to energy metabolism disorders in organisms and diabetes. It can improve tissue damage, metabolic disorders, and protein metabolism as well as induce tumor cell apoptosis [24, 25]. Meanwhile, the downregulation of expression may be involved in the PV onset. The differential metabolism of some organic acids, namely, ginkgolic acid, selected in this study has not been reported in the previous literature, and its effect mechanism in the pathogenesis of PV or the formation of syndromes needs further exploration.

Second, 13 kinds of amino acids and their derivatives citramalic acid, L-aspartic acid, L-glutamic acid, and glutamate account for 19.18% of the differential metabolite categories. As the main place of amino acid metabolism in the human body, the liver plays an important role in the intake, synthesis, and secretion of amino acids. The level of amino acid metabolism directly reflects the state of liver cell metabolism. Studies have shown that patients with advanced

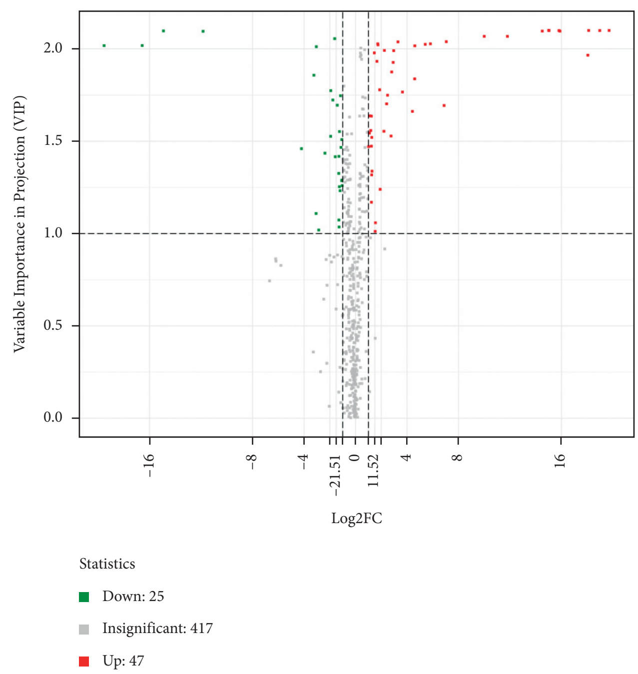

Figure 3: Differential metabolites' volcano map.

Table 2: Significantly different metabolites of BH-PPG and NBH-PPG from the normal control group.

Index	Differential metabolites	Metabolite categories	BH-PPG v NPG		NBH-PPG v NPG		Type
			VIP value	Log2FC	VIP value	Log2FC	
MEDN636	Ginkgolic acid	Organic acids and the derivatives	2.01	19.59	1.96	19.54	Up
MEDN196	Pyrroloquinoline quinone	Organic acids and the derivatives	2.01	16.57	1.96	16.65	Up
MEDN009	L-Aspartate amino	Amino acids and the metabolites	2.10	14.85	1.96	14.96	Up
MEDN195	Phosphopyridoxal	Pyridine and the derivatives	2.10	11.79	1.95	11.73	Up
MEDN499	Argininosuccinic acid	Organic acids and the derivatives	1.42	4.19	1.37	4.14	Up
MEDP443	Leucovorin	Pteridine and the derivatives	1.83	3.13	1.80	3.18	Up
MEDN506	N-Acetylglucosamine 1-phosphate	Carbohydrate and the metabolites	2.00	3.02	1.92	3.09	Up
MEDP831	DL-1-Amino-2-propanol	Alcohols	1.63	2.35	1.25	2.51	Up
MEDP016	L-Glutamic acid	Amino acids and the metabolites	1.79	1.90	1.61	1.72	Up
MEDP860	Glutamate	Amino acids and the derivatives	1.76	1.80	1.51	1.48	Up
MEDN206	Citromalic acid	Amino acids and the metabolites	2.10	−19.7	1.96	−19.7	Down
MEDN292	3-Hydroxybutyric acid	Organic acids and the derivatives	2.10	−18.98	1.96	−18.98	Down
MEDN244	Orotic acid	Coenzymes and vitamins	2.10	−18.11	1.96	−18.11	Down
MEDN484	B-Hydroxypyruvic acid	Organic acids and the derivatives	1.96	−18.05	1.83	−18.05	Down
MEDP718	Methyl isobutyrate	Organic acids and the derivatives	2.10	−15.88	1.96	−15.88	Down
MEDN283	2-Hydroxybutyric acid	Organic acids and the derivatives	2.10	−15.81	1.96	−15.81	Down
MEDN726	Capraldehyde	Aldehydes	2.10	−15.03	1.96	−15.03	Down
MEDN738	2, 6-Dimethylnaphthalene	Benzene and the derivatives	2.10	−15.01	1.96	−15.01	Down
MEDP151	2-Hydroxy-6-aminopurine	Nucleotide and the metabolites	2.10	−14.51	1.96	−14.51	Down
MEDN469	Citraconic acid	Organic acids and the derivatives	2.07	−11.55	1.96	−19.11	Down

Note. List of top 10 upregulated and downregulated differential metabolites.

psoriasis have abnormal amino acid metabolism and ratio imbalance [26] and liver and kidney amino acid metabolism disorders, so the abnormal expression of amino acid levels in plasma may be involved in the pathogenesis and progression of Ps [27]. This study reveals that the significant up-regulation of L-aspartic acid, L-glutamic acid, and glutamate is consistent with previous research results. The increased expression of aspartic acid and proline might be involved in the protein biosynthesis of Ps and excessive proliferation of keratinocytes [28, 29]. The expression level of glutamate is positively correlated with the severity of Ps lesions [30]. The expression of citramalic acid is markedly down-regulated. As an important node of the tricarboxylic acid (TCA) cycle, abnormal expression will disrupt the metabolism of the TCA

Table 3: Characteristic differential metabolites in BH-PPG and NBH-PPG.

Grouping	Index	Differential metabolites	Metabolite categories	VIP	Log2FC	Type
BH-PPG/NBH-PPG VS NPG	MEDP878	N-methyl-L-glutamate	Amino acids and the metabolites	1.38	1.10	Up
	MEDP037	L-Asparagine acetic acid - L-phenylalanine acetic acid	Amino acids and the metabolites	1.08	1.37	Up
	MEDP575	Acadesine	Nucleotide and the metabolites	1.09	−1.52	Down
	MEDN736	2-(Methyl thiyl) ethanol	Alcohols	1.61	−1.19	Down
	MEDP362	Neopterin	Pteridine and the derivatives	1.34	−1.16	Down
	MEDN084	Benzoic acid	Benzene and the derivatives	1.39	−1.02	Down
	MEDN808	Inositol	Carbohydrate and the metabolites	1.53	−1.02	Down
BH-PPG VS NBH-PPG	MEDN698	1-Naphthol	Phenols and the derivatives	1.07	3.2	Up
	MEDP889	Cortisol	Lipid	1.85	2.57	Up
	MEDP171	Inosine	Nucleotide and the metabolites	1.06	1.44	Up
	MEDN751	(±) 12-Hydroxy-5Z, 8Z, 10E, 14Z-eicosapentaenoic acid	Oxidized lipid	1.15	1.34	Up
	MEDN286	3,4,5-Trimethoxy cinnamic acid	Organic acids and the derivatives	1.81	−1.90	Down
	MEDP118	4-Pyrazole compound acid	Pyridine and the derivatives	1.69	−1.34	Down
	MEDN334	Mandelic acid	Organic acids and the derivatives	2.38	−1.04	Down
	MEDN097	p-Hydroxyphenylacetic acid	Benzene and the derivatives	2.24	−1.01	Down

Note. The upper part of the table presents the significantly differential metabolites of BH-PPG and NBH-PPG compared to the normal control group. The lower part of the table presents the differential metabolites of BH-PPG compared to NBH-PPG.

cycle, thereby affecting the glycolysis process. These metabolic changes enhance the production of mitochondrial reactive oxygen species and the unfolded protein response, which in turn causes an immunoinflammatory response in psoriasis marked by IL-23 and the onset of this disease [31].

In addition, nucleotides, carbohydrates, and their metabolites are in a higher proportion. Nucleotides are mainly involved in a variety of physiological functions, namely, energy metabolism and coenzyme regulation, the metabolism of which consists of three processes—synthesis, decomposition, and regulation. Some research evidence has indicated that abnormal purine nucleotide metabolism can affect the expression of genes and proteins by regulating signal transduction pathways, and a variety of enzymes involved in its metabolism are closely related to tumor cell proliferation, transformation, invasion, metastasis, and drug resistance [32]. Nucleotide metabolites in the BH-PPG group differ greatly from those of the normal group, including 2-hydroxy-6-aminopurine, guanine, guanosine, inosine, and arabinoinosine, suggesting that abnormal purine nucleotide synthesis and catabolism might be involved in Ps progression. Carbohydrates are the main components and major energy supplying substances of living cell structures, which have an important function of regulating cell activities. The metabolic processes contain sugar catabolism and anabolism. The oxidation and decomposition require multiple vitamins and metal ions as coenzymes. It is, therefore, the deficiency of coenzymes that can cause glucose metabolism disorders. Furthermore, the process is also affected by oxygen uptake, metabolic intermediates, hormones, and neurohumour of the body. The expressions of carbohydrate metabolites D-mannose, β-D-glucose, D-sorbitol, and N-acetylglucosamine 1-phosphate are significantly different, suggesting abnormal glucose metabolism in psoriasis with blood-heat syndrome.

Among the nine metabolic pathways with significantly enriched differential metabolites, ferroptosis [33], carbon metabolism [34], and purine metabolism [35] with q value < 1 are closely related to Ps pathogenesis. Among them, the ferroptosis metabolic pathway is mainly enriched with differential metabolites of the amino acid, including L-cystine, L-cysteine, reduced glutathione, glutamate, and L-glutamic acid. The carbon metabolism pathway is mainly enriched with β-D-glucose, L-cysteine, D-xylulose-5-phosphate, leucovorin, B-hydroxypyruvic acid, L-glutamic acid, glutamate, and L-aspartic acid. The purine metabolism pathway is mainly enriched with differential metabolites of the nucleotide, including guanine, hypoxanthine, inosine, guanosine, and adenosine. Metabolic pathway analysis indicated that the formation and evolution of psoriasis with blood-heat syndrome may involve a series of complex metabolic disorders and adjustment processes, namely, liver and kidney amino acid metabolism, energy metabolism, and coenzyme regulation related to nucleotides.

In conclusion, this study analyzes plasma metabonomics of PV with blood heat syndrome and screens multiple differential metabolites of ginkgolic acid, PQQ, L-aspartic acid, and citramalic acid. These metabolites are considered to be potential biomarkers of blood-heat syndrome PV. Specific disease and syndrome metabolic pathways contain carbon metabolism, ferroptosis, and purine metabolism. The exploration of these differential

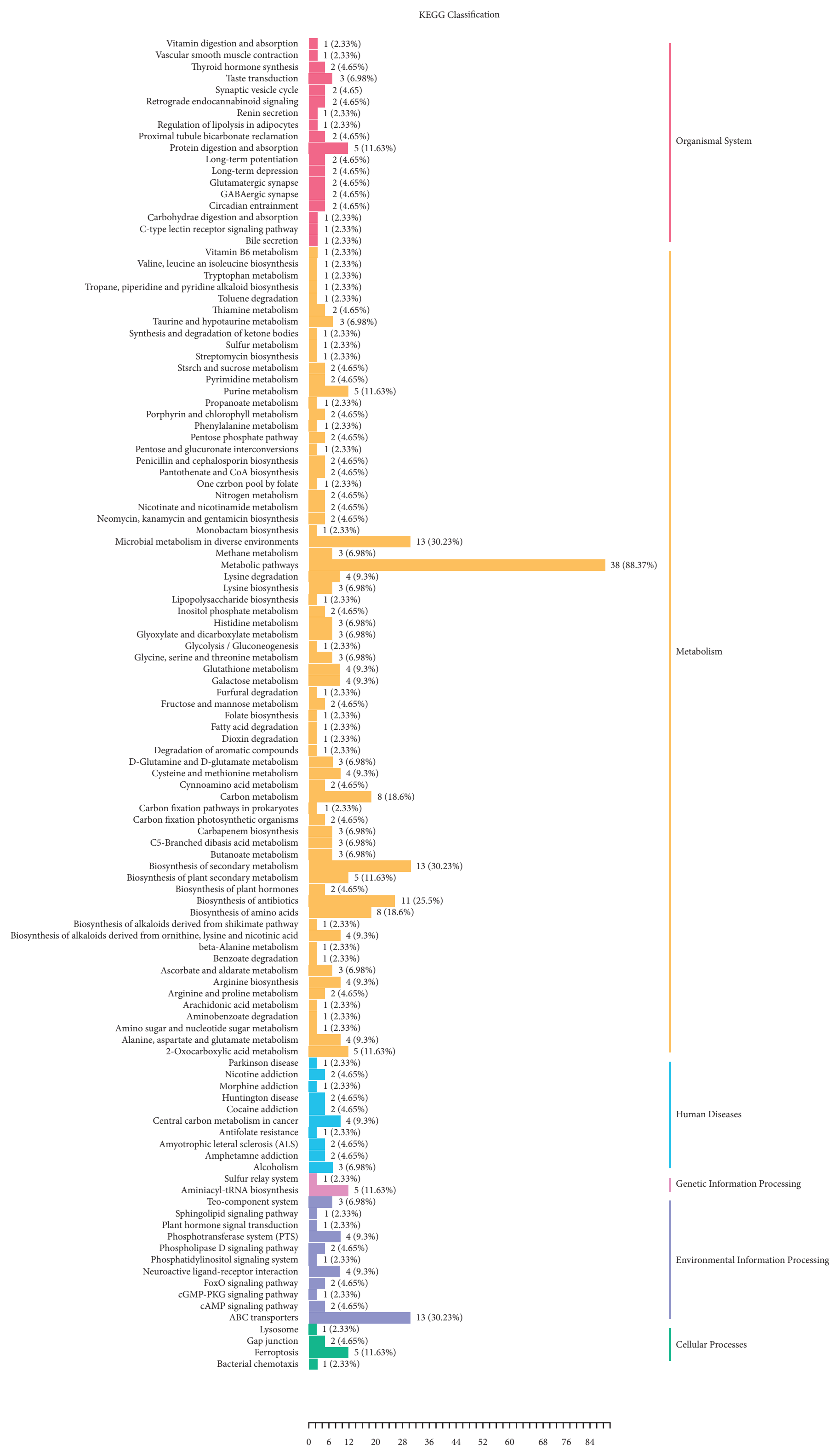

Figure 4: KEGG differential enrichment classification chart. Note: the vertical ordinate represents the KEGG metabolic pathways, and the horizontal axis represents the number of metabolites annotated to the pathway and the ratio to the total number of annotated metabolites.

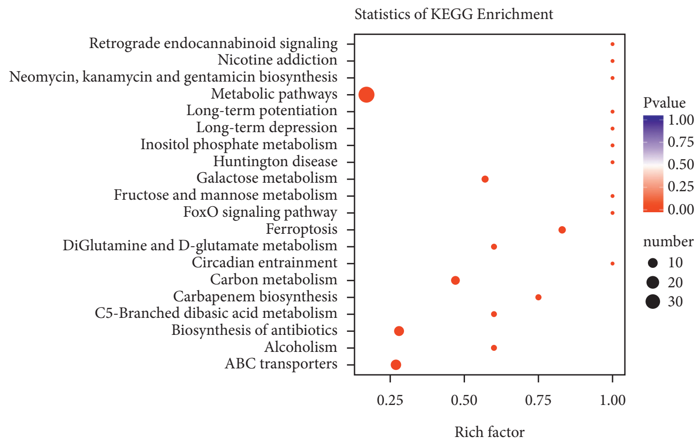

Figure 5: KEGG differential enrichment bubble chart. *Note.* The horizontal axis represents the corresponding rich factor of each pathway, and the vertical ordinate represents the pathways. The dot color represented p values; the darker the red, the more significant the enrichment. The dot size represents the number of enriched differential metabolites.

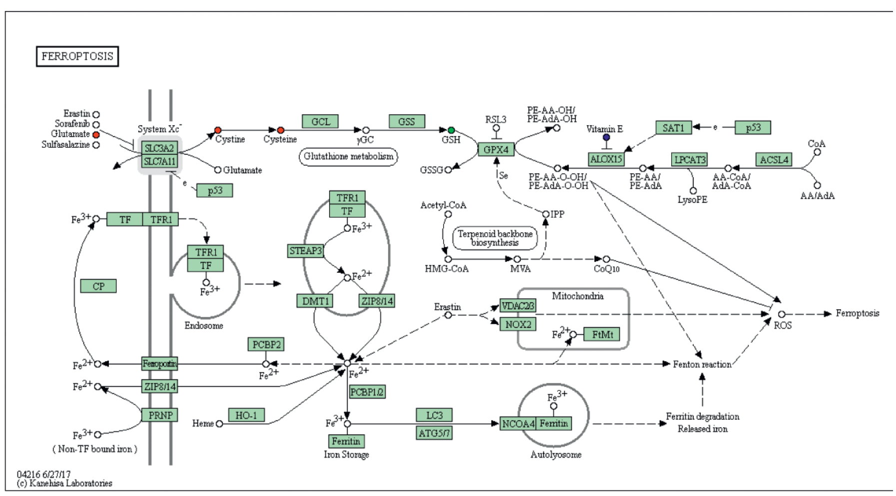

Figure 6: Ferroptosis metabolic pathway. *Note.* Red indicated markedly up-regulated content of metabolites in the experimental group. Blue indicated no marked change of the metabolite which had been detected. Green indicated markedly down-regulated content of metabolites in the experimental group. Cause for the phenotypic differences among the research subjects was identified through metabolic pathways.

metabolites and metabolic pathways can provide indicators for diagnosis and treatment of Ps-based blood-heat pathogenesis. Meanwhile, it also offers a new objective basis for revealing the material basis of the occurrence, development, and outcome of the pathogenesis of blood heat disease. Some potential markers for psoriasis have been identified at the genome, transcriptome, proteome, and metabolome level in previous research. This study not only explores the potential metabolic markers of PV based on the widely targeted metabolomic technique but also investigates the metabolic markers and metabolic pathways of two PV syndromes (blood heat syndrome and non-blood-heat syndrome) identified by TCM. Unfortunately, this study still has several limitations. The uncertainty of the dynamic changes during the metabolic process and the characteristics of multifactor interference of metabolites are the causes of difficulty in the reproducibility of metabolic data for subsequent research teams. Several differential metabolites have not been reported in the previous literature, and their effect mechanism in the pathogenesis or syndrome formation of psoriasis has not been further studied. In addition, despite that metabolic pathways and network analysis present some essential biological information, the clinical applicability of relevant evidence remains to be further explored. In subsequent projects, multisample, multilevel, and in-depth research can be performed using serum, urine, feces, saliva, and injured skin tissues to more comprehensively and accurately explore the mechanism of formation and evolution of the pathogenesis of blood heat PV.

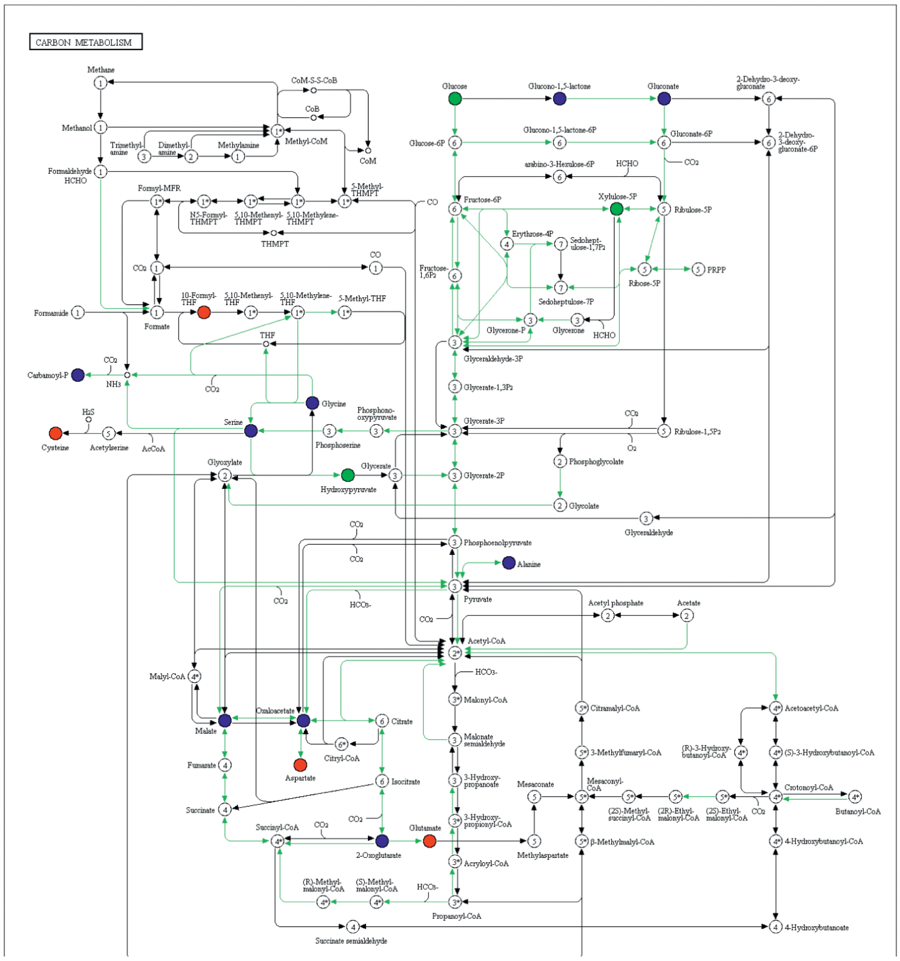

FIGURE 7: Carbon metabolic pathway. *Note.* Red indicated markedly up-regulated content of metabolites in the experimental group. Blue indicated no marked change of the metabolite which had been detected. Green indicated markedly down-regulated content of metabolites in the experimental group. Cause for the phenotypic differences among the research subjects was identified through metabolic pathways.

5. Conclusions

Here, we analyzed plasma metabonomics of PV with blood heat syndrome and found multiple differential metabolites of ginkgolic acid, PQQ, L-aspartic acid, and citramalic acid, which are considered to be potential biomarkers of blood-heat syndrome PV. It is helpful for western medicine to explore the identification of PV syndrome and the mechanism of disease progress, promote the development of western medicine in the identification of PV blood heat syndrome, and facilitate the progress of the PV diagnosis and treatment method.

Data Availability

All data are included in the article are also available upon request to the authors.

Disclosure

Xueyong Tang and Juan Gong are considered to be co-first authors.

Conflicts of Interest

The authors declare that there are no conflicts of interest.

Authors' Contributions

Xueyong Tang and Juan Gong contributed equally to this work. Tang Xueyong, Gong Juan, and Li Xin conceived this work and wrote this article; Jiang Yourang and Chen Xi collected and analyzed the data; and Qi Dongwei, Tang Xueyong, and Gong Juan revised this article.

Acknowledgments

This work was supported by https://doi.org/10.13039/501100005230 the Natural Science Foundation of Chongqing, China (cstc2019jcyj-msxmX0757), and https://doi.org/10.13039/501100001809 the National Natural Science Foundation of China (Grant No. 81704091).

References

[1] N. J. Korman, “Management of psoriasis as a systemic disease: what is the evidence?” *British Journal of Dermatology*, vol. 182, no. 4, pp. 840–848, 2020.

[2] I. M. Michalek, B. Loring, and S. M. John, “A systematic review of worldwide epidemiology of psoriasis,” *Journal of the European Academy of Dermatology and Venereology*, vol. 31, no. 2, pp. 205–212, 2017.

[3] X. Ding, T. Wang, Y. Shen et al., “Prevalence of psoriasis in China: a population-based study in six cities,” *European Journal of Dermatology*, vol. 22, no. 5, pp. 663–667, 2012.

[4] X. Yu, X. Wu, W. Xu, and T. Wang, “Literature research on common syndrome distribution characteristic of psoriasis vulgaris,” *China Journal of Traditional Chinese Medicine and Pharmacy*, vol. 27, no. 4, pp. 1008–1011, 2012.

[5] P. Li, J. Wang, J. Zhao et al., “Analysis of “toxin accumulation in blood” TCM pathogenesis in psoriasis,” *Journal of Capital Medical University*, vol. 30, no. 4, pp. 413–417, 2009.

[6] Y. Zhang, W. Zhang, and Y. Yang, *Application of systematic biology in Traditional Chinese Medicine*, Vol. 7, Science Publishing Company, , Beijing, China, 2017.

[7] X. Tang, X. Li, Z. Yang, and Q. Diao, “Research progress of traditional Chinese medicine syndrome therapy for psoriasis based on metabolomics,” *Chinese Journal of Information on Traditional Chinese Medicine*, vol. 27, no. 9, pp. 136–140, 2020.

[8] L. Cui, H. Lu, and Y. H. Lee, “Challenges and emergent solutions for LC-MS/MS based untargeted metabolomics in diseases,” *Mass Spectrometry Reviews*, vol. 37, no. 6, pp. 772–792, 2018.

[9] H. Takeda, Y. Izumi, M. Takahashi et al., “Widely-targeted quantitative lipidomics method by supercritical fluid chromatography triple quadrupole mass spectrometry,” *Journal of Lipid Research*, vol. 59, no. 7, pp. 1283–1293, 2018.

[10] N. Li, W. Zhao, J. Xing et al., “Chinese herbal Pulian ointment in treating psoriasis vulgaris of blood-heat syndrome: a multicenter, double-blind, randomized, placebo-controlled trial,” *BMC Complementary and Alternative Medicine*, vol. 17, no. 1, p. 264, 2017.

[11] C. Hongduo, *Clinical Practice Guidelines - Cutaneous And Venereal Diseases*, p. 109, People’s Medical Publishing House, Beijing, China, 2006.

[12] Medicine, *TCM Clinical Pathways for 95 Diseases in 22 Specialties*, p. 267, China Press of Traditional Chinese Medicine, Beijing, China, 2011.

[13] W. Chen, L. Gong, Z. Guo et al., “A novel integrated method for large-scale detection, identification, and quantification of widely targeted metabolites: application in the study of rice metabolomics,” *Molecular Plant*, vol. 6, no. 6, pp. 1769–1780, 2013.

[14] M. Kanehisa and S. Goto, “KEGG: kyoto encyclopedia of genes and genomes,” *Nucleic Acids Research*, vol. 28, no. 1, pp. 27–30, 2000.

[15] X. Geng and J. Zhang, “An attempt study on combination of disease and syndrome, corresponding prescription and treatment based on syndrome differentiation,” *Journal of Traditional Chinese Medicine*, vol. 49, no. 9, pp. 775–777, 2008.

[16] W. Xu, P. Li, and W. Liu, “Thoughts and methods exploration on syndrome standardization research,” *Beijing Journal of Traditional Chinese Medicine*, vol. 29, no. 5, pp. 343–346, 2010.

[17] A. Zhang, H. Sun, G. Yan, P. Wang, and X. Wang, “Metabolomics for biomarker discovery: moving to the clinic,” *BioMed Research International*, vol. 2015, Article ID 354671, 6 pages, 2015.

[18] X. Wang, A. Zhang, H. Sun, and G. Yan, “Precision diagnosis of Chinese medicine syndrome and evaluation of prescription efficacy based on chinmedomics,” *World Science and Technology-Modernization of Traditional Chinese Medicine*, vol. 19, no. 1, pp. 30–34, 2017.

[19] Y. Yang, “High risk screening on disorder of organic acid metabolism,” *Continuing Medical Education*, vol. 20, no. 17, pp. 35–39, 2006.

[20] Q. Q. Yao, Z. H. Liu, M. C. Xu et al., “Mechanism for ginkgolic acid (15:1)-induced MDCK cell necrosis: m,” *Chinese Journal of Natural Medicines*, vol. 15, no. 5, pp. 375–383, 2017.

[21] Q. Q. Yao, L. Li, M. C. Xu et al., “The metabolism and hepatotoxicity of ginkgolic acid (17:1) in vitro,” *Chinese Journal of Natural Medicines*, vol. 16, no. 11, pp. 829–837, 2018.

[22] A. S. Karadag, T. K. Uzunçakmak, S. Ozkanli et al., “An investigation of cytochrome p450 (CYP) and glutathioneS-transferase (GST) isoenzyme protein expression and related interactions with phototherapy in patients with psoriasis vulgaris,” *International Journal of Dermatology*, vol. 56, no. 2, pp. 225–231, 2017.

[23] A. Therianou, M. Vasiadi, D. A. Delivanis et al., “Mitochondrial dysfunction in affected skin and increased mitochondrial DNA in serum from patients with psoriasis,” *Experimental Dermatology*, vol. 28, no. 1, pp. 72–75, 2019.

[24] S. K. Shukla, T. Gebregiworgis, V. Purohit et al., “Metabolic reprogramming induced by ketone bodies diminishes pancreatic cancer cachexia,” *Cancer & Metabolism*, vol. 2, no. 1, p. 18, 2014.

[25] J. Su, J. Zeng, and L. Shao, “Effects of 3-hydroxybutyrate on growth and apoptosis of HeLa cells,” *Journal of Zhejiang Normal University*, vol. 42, no. 2, pp. 195–200, 2019.

[26] S. Cao and B. Li, “Study on amino acid metabolism in patients with psoriasis,” *Chinese Journal of Dermatology*, vol. 34, no. 2, p. 135, 2001.

[27] S. S. Li, Y. Liu, H. Li et al., “Identification of psoriasis vulgaris biomarkers in human plasma by non-targeted metabolomics based on UPLC-Q-TOF/MS,” *European Review for Medical and Pharmacological Sciences*, vol. 23, no. 9, pp. 3940–3950, 2019.

[28] A. W. Armstrong, J. Wu, M. A. Johnson et al., “Metabolomics in psoriatic disease: pilot study reveals metabolite differences in psoriasis and psoriatic arthritis,” *F1000Research*, vol. 3, p. 248, 2014.

[29] H. Kang, X. Li, Q. Zhou et al., “Exploration of candidate biomarkers for human psoriasis based on gas chromatography-mass spectrometry serum metabolomics,” *British Journal of Dermatology*, vol. 176, no. 3, pp. 713–722, 2017.

[30] E. P. Dutkiewicz, K.-T. Hsieh, Y.-S. Wang, H.-Y. Chiu, and P. L. Urban, “Hydrogel micropatch and mass spectrometry-assisted screening for psoriasis-related skin metabolites,” *Clinical Chemistry*, vol. 62, no. 8, pp. 1120–1128, 2016.

[31] D. A. Mogilenko, J. T. Haas, L. L'Homme et al., "Metabolic and innate immune cues merge into a specific inflammatory response via the UPR," *Cell*, vol. 177, no. 5, 2019.

[32] X. Yuan, "Research progress on the relationship between purine nucleotide metabolism and malignant tumors," *Oncology Progress*, vol. 17, no. 21, pp. 2498–2501, 2019.

[33] J. L. Arbiser, M. Y. Bonner, N. Ward, J. Elsey, and S. Rao, "Selenium unmasks protective iron armor: a possible defense against cutaneous inflammation and cancer," *Biochimica et Biophysica Acta (BBA) - General Subjects*, vol. 1862, no. 11, pp. 2518–2527, 2018.

[34] J. Bai, Y. Gao, L. Chen et al., "Identification of a natural inhibitor of methionine adenosyltransferase 2A regulating one-carbon metabolism in keratinocytes," *EBioMedicine*, vol. 39, pp. 575–590, 2019.

[35] Y. M. Moustafa, M. A. Elsaied, E. M. Abd Elaaty, and R. A. Elsayed, "Evaluation of serum adenosine deaminase and inflammatory markers in psoriatic patients," *Indian Journal of Dermatology*, vol. 64, no. 3, pp. 207–212, 2019.

Hindawi
Journal of Healthcare Engineering
Volume 2022, Article ID 7282453, 9 pages
https://doi.org/10.1155/2022/7282453

Research Article

The Therapeutic Effect of *Coriolus versicolor* Fruiting Body on STZ-Induced ICR Diabetic Mice

Fanxin Meng, Yumiao Lin, Lifu Hu, Wei Feng, Peiwen Su, and Liyan Wu

School of Pharmacy and Food Science, Zhuhai College of Science and Technology, Jinwan 519041, China

Correspondence should be addressed to Fanxin Meng; mfx@zcst.edu.cn

Received 16 December 2021; Revised 16 February 2022; Accepted 21 February 2022; Published 15 April 2022

Academic Editor: Enas Abdulhay

Coriolus versicolor is a natural drugs which has many pharmacological effects such as antitumor and enhanced immune activity. This paper studies the therapeutic effect of *Coriolus versicolor* fruiting body (CVFB) on streptozotocin (STZ)-induced Institute of Cancer Research (ICR) diabetic mice, the STZ solution was administered intraperitoneally at a dose of 150 mg/kg after fasting the mice, and ICR mice with fasting blood glucose >16.7 mmol/l were selected for research. Metformin was the positive control, and the dose of CVFB powder (1000 mg/kg, 2000 mg/kg, and 4000 mg/kg) for 28 consecutive days by gavage. The serum and liver of mice were collected for relevant index content testing. The results showed that CVFB can control or reduce the fasting blood glucose of mice and accelerate the rate of glucose metabolism, can reduce the levels of total cholesterol (T-CHO), triglyceride (TG), and high-density lipoprotein cholesterol (HDL-C) in mice, and regulate the abnormal symptoms of blood lipid metabolism commonly found in diabetes. It can increase the activity of superoxide dismutase (SOD) and glutathione peroxidase (GSH-Px) antioxidant enzymes and enhance the ability of antioxidative stress in diabetic mice. In the H&E staining and apoptosis experiments of pancreatic tissue, CVFB can greatly reduce the inflammatory factors present in islets, increase the islet cells, and reduce the apoptotic rate caused by diabetes. All data confirmed the therapeutic effect of CVFB on diabetic ICR mice. The present study provides a scientific basis for the development of drugs for the prevention and treatment of diabetes, it is of great significance to the in-depth study of *Coriolus versicolor*.

1. Introduction

According to the 9th edition of the Diabetes Map released by the International Diabetes Federation (IDF), diabetes is one of the most common chronic diseases in the world, and the number of adult patients with diabetes of the world is increasing year by year, while the number of adult patients with diabetes in China ranks first in the world, according to the noncommunicable disease.

Current research has not yet found a cure for diabetes drugs or treatment, controlling and treating diabetes are a long-term, ongoing, and slow-moving task, while most diabetes drugs have toxic side effects while treating the symptoms of hyperglycemia, long-term consumption of antidiabetic drugs will aggravate the burden on the liver and kidney, leading to a series of complications. Natural medicine is a kind of natural product with some pharmacological activities, including plants, animals, and minerals, and are easy to be absorbed and utilized by the human body and have stable effects and little toxic side effects on the body. The study found that many natural products have good hypoglycemic components, such as polysaccharides, polyphenols, flavonoids, alkaloids, and other compounds [1]. Therefore, in the prevention and treatment of diabetes, the full use of natural drug adjuvant therapy can improve the efficacy and reduce side effects.

Coriolus versicolor is a natural drug which has many pharmacological effects such as antitumor, ant-atherosclerosis, antiaging, antioxidation, and enhanced immune activity [2–9]. At present, the research on *Coriolus versicolor* is mainly focused on macromolecular compounds such as polysaccharide, glycopeptide, and glycoprotein, but *Coriolus versicolor*'s chemical composition is very complex.

Therefore, this article studies the therapeutic effect of the CVFB on ICR diabetic mice which is caused by streptozotocin (STZ); after the treatment, glucose metabolism, lipid metabolism, and antioxidant indexes of the experimental mice were detected, as well as further pathological analysis of the pancreas. This provides a scientific basis for the development of drugs for the prevention and treatment of diabetes and is of great significance for the in-depth study of CVFB.

2. Materials and Methods

2.1. CVFB Powder and Metformin Hydrochloride Preparation. *Coriolus versicolor* fruiting body powder: origin is Heilongjiang, purchased from Johncan International, Hangzhou, China.

Metformin hydrochloride tablets: Sino-American Shanghai Squibb Pharmaceuticals Ltd.

2.2. Development of Diabetic Mouse Models. A total of 120 four-week-old male ICR mouses ((SPF) grade, SCXK (YUE)-2013-0002) were adaptability to fed about 2 weeks. After 18 h fast (free access to water), mice of $22 + 2$ g were subjected to 150 mg/kg STZ solution intraperitoneally (except the NS group); the control group was injected with citric acid buffer; 2 h after administration, the mice were fed. After 7 days of feeding, fasting without water was done to measure fasting blood glucose. The fasting blood glucose value of mice ≥16.7 mmol/L was determined to be a successful model.

2.3. Drug Treatment Procedure. Diabetic mice were randomly divided into five groups with more than 12 mice in each group (to avoid death in the experiment). Normal mice served as the control group. The duration of drug administration was 28 days. Normal control group (normal saline, NS) and model group (diabetic control, DC) were given sterile normal saline gavage, and positive control group (positive control, PC) was given 200 mg/kg metformin hydrochloride by gavage; the drug group was intragastrically administrated with the CVFB at concentrations of 1000 mg/kg (low dose, LD), 2000 mg/kg (medium dose, MD), and 4000 mg/kg (high dose, HD). Routine diet was fed after administration. Water intake, food intake, weight, and fasting blood glucose were recorded regularly.

2.4. Oral Glucose Tolerance Test (OGTT). Oral glucose tolerance test (OGTT) is a glucose stress test used to determine whether an organism has diabetes to understand the function of pancreatic beta cells in vivo and the body's ability to regulate blood sugar. During the OGTT test, fasting without water for 6 h in the evening of the 26th day of the treatment period and fasting blood glucose values of diabetic mice in each group were measured in the morning of the 27th day. Each group was given 2 g/kg glucose by gavage at one time. Tail venous blood was taken, and blood glucose values of 30 min, 60 min, 90 min, and 120 min after glucose administration were measured by a blood glucose meter and recorded.

2.5. Sample Collection. At the end of the treatment period, the mice were weighed, and then mice were euthanized by ether, the blood was collected by eyeball extirpation, and the organs (liver, kidney, spleen, thymus, pancreas and heart) of the mice were collected and weighing. The pancreas was washed with cold saline and fixed with Carnoy's fluid for tissue sectioning. A small part of liver was washed with cold normal saline, and an appropriate amount of liver fragments were homogenized in cold 0.9% normal saline (liver (g):0.9% normal saline (mL) = 1 : 9). The homogenized mixture was centrifuged at 3000 RPM at 4°C for 10 min, and the supernatant was collected to obtain 10% liver homogenate. The samples were stored at −20°C.

2.6. Serum and Liver Homogenate Sample Index Detection. The contents of glycated serum protein (GSP), insulin (Ins), T-CHO, TG, HDL-C, low-density lipoprotein cholesterol (LDL-C), and blood urea nitrogen (BUN) in the serum and the contents of malondialdehyde (MDA), SOD, and GSH-Px in the serum and liver homogenate were detected by Nanjing Jiechen Kits (Nanjing Jiancheng Institute of Biological Engineering, Nanjing, China).

2.7. Pancreatic Histopathological Tests. Pancreatic tissue was fixed in Carnoy's fluid for 24 h, and the tissue was removed for dehydration, embedding, and sectioning. After the tissue sectioning was completed, some sections were stained with hematoxylin and eosin by H&E to observe the shape of pancreatic cells; the other sections were added with proteinase K and reacted with TUNEL kit (Roche) to observe the apoptosis of pancreatic cells.

2.8. Statistical Analysis. All data are expressed as mean ± standard error (S.EM.). SPSS 20.0 software was used for statistical analysis of the data. A one-way analysis of variance (ANOVA) and multiple comparisons were combined to calculate the significance of the data. In statistics, when $p > 0.05$, it is considered no significant difference, when $p < 0.05$, it is considered significant difference, when $p < 0.01$, it is considered very significant difference, and when $p < 0.001$, it is considered extremely significant difference.

3. Results

3.1. The Effects of the CVFB on Water Intake, Food Intake, Body Weight, and Organ Index of Diabetic Mice. During the treatment period, the water and food intake in the DC group increased significantly compared with the NS group. The body weight of mice in NS group was significantly different from that in 0 days of treatment ($p < 0.001$; Table 1, No. c) and increasing rate on day 28 of the treatment period was 58.0%, while there was no significant difference in the body weight of mice in DC group.

After 28 days of treatment, the water intake in 5 groups of diabetic mice increased significantly compared with 0 days of treatment ($p < 0.001$; Table 1, No. a). The body

TABLE 1: The effect of 28-day CVFB treatment on the water intake, food intake, body weights, and organ index of STZ-induced ICR diabetic mice ($n = 11$).

No.				NS	DC	LD	MD	HD	PC
a	Water intake (ml)	28 days	0	7.9 ± 0.2	45.6 ± 2.2	44.2 ± 2.6	50.8 ± 1.4	44.2 ± 2.4	46.5 ± 2.3
			7	$5.0 \pm 0.6^{**}$	46.9 ± 1.3	47.7 ± 0.8	50.0 ± 2.6	50.0 ± 4.2	50.0 ± 1.2
			14	$5.0 \pm 0.6^{**}$	$55.6 \pm 0.9^{***}$	$59.4 \pm 0.8^{***}$	$64.1 \pm 1.7^{***}$	$56.3.0 \pm 4.6^{***}$	$56.9 \pm 1.4^{***}$
			21	6.7 ± 1.2	$58.1 \pm 0.7^{***}$	$57.5 \pm 1.9^{***}$	$66.7 \pm 2.3^{***}$	$61.3 \pm 5.0^{***}$	$60.0 \pm 1.5^{***}$
			28	$4.2 \pm 0.3^{***}$	$62.5 \pm 0.6^{***}$	$63.1 \pm 1.1^{***}$	$66 \pm 1.4^{***}$	$61.9 \pm 3.7^{***}$	$61.8 \pm 1.6^{***}$
b	Food intake (g)	28 days	0	9.4 ± 0.1	11.9 ± 0.8	10.8 ± 0.5	11.3 ± 0.2	10.7 ± 0.4	10.2 ± 0.8
			7	5.2 ± 0.2	11.0 ± 0.8	9.8 ± 0.3	9.2 ± 0.4	10.1 ± 0.6	$8.1 \pm 0.3^{*}$
			14	5.8 ± 0.2	10.2 ± 0.1	11.6 ± 0.3	11.7 ± 0.3	11.3 ± 0.5	10.2 ± 0.7
			21	5.5 ± 0.2	10.5 ± 0.2	10.4 ± 0.3	10.1 ± 0.4	9.8 ± 0.4	9.2 ± 0.9
			28	$4.5 \pm 0.1^{***}$	11 ± 0.2	11.6 ± 0.2	11.0 ± 0.2	10.3 ± 0.3	9.1 ± 0.3
c	Body weights (g)	28 days	0	23.1 ± 0.8	25.2 ± 1.0	24.9 ± 0.9	24.0 ± 0.8	25.9 ± 1.4	25.4 ± 1.1
			7	$28.7 \pm 0.6^{***}$	23.1 ± 1.0	24.3 ± 0.7	24.2 ± 0.8	26.1 ± 1.0	24.1 ± 1.1
			14	$33.4 \pm 0.6^{***}$	26.6 ± 1.0	26.2 ± 0.9	$26.9 \pm 1.0^{*}$	$29.4.0 \pm 1.3^{*}$	$28.6 \pm 0.7^{*}$
			21	$31.6 \pm 0.7^{***}$	24.9 ± 1.0	$28.25 \pm 0.8^{**}$	$27.9 \pm 0.8^{**}$	25.9 ± 1.2	25.2 ± 0.4
			28 growth rate (%)	$36.5 \pm 0.8^{***}58.0$	$25.1 \pm 1.0–0.4$	$29.3 \pm 0.8^{**}17.7$	$29.7 \pm 0.9^{***}23.8$	$30.5 \pm 1.4^{**}17.8$	$29.8 \pm 0.9^{**}17.3$
d	Organ index (mg/g)		Liver	49.4 ± 1.8	53.0 ± 1.9	50.8 ± 1.9	47.3 ± 1.6	$48.9 \pm 1.8^{\#}$	49.8 ± 0.8
			Kidney	$14.1 \pm 0.3^{\#\#\#}$	18.4 ± 0.4	$19.9 \pm 0.4^{\#\#}$	18.6 ± 0.5	$17.2 \pm 0.4^{\#}$	17.6 ± 0.5
			Spleen	$2.8 \pm 0.3^{\#\#\#}$	1.7 ± 0.04	1.9 ± 0.1	1.6 ± 0.1	1.5 ± 0.1	2.0 ± 0.2
			Thymus	$1.0 \pm 0.1^{\#\#\#}$	0.4 ± 0.03	$0.7 \pm 0.1^{\#\#}$	0.5 ± 0.1	0.4 ± 0.1	0.4 ± 0.04
			Pancreas	6.3 ± 0.3	5.9 ± 0.3	5.9 ± 0.4	5.6 ± 0.2	6.1 ± 0.4	6.2 ± 0.3
			Heart	$4.6 \pm 0.1^{\#\#\#}$	3.6 ± 0.1	$3.9 \pm 0.1^{\#}$	3.5 ± 0.1	3.8 ± 0.1	3.7 ± 0.2

$^{*}p < 0.05$, $^{**}p < 0.01$, and$^{***}p < 0.001$ are the comparisons between within the group and day 0; $\#p < 0.05$, $\#\#p < 0.01$, and $\#\#\#p < 0.001$ versus DC group. Growth rate: body weights increment (day 28–day 0)/body weight (day 0)×100%.

weight of mice in the PC group and CVFB treatment group increased significantly compared with 0 days of treatment ($p < 0.01$; Table 1, No. c); compared with the DC group of mice, CVFB dosage group weight increased significantly after 28 days (29.3 ± 0.8; 29.7 ± 0.9, and 30.5 ± 1.4) having significant difference, in which the weight gain was similar to that of the positive control group (29.8 ± 0.9).

Compared with the NS group, the weight of the kidney index was significantly increased ($p < 0.001$; Table 1, No. d), the weight of the spleen, thymus, and heart index was significantly decreased ($p < 0.001$; Table 1, No. d), and the weight of the pancreas index was also decreased in the DC group.

After 28 days of administration of CVFB, it was found that CVFB could inhibit the trend of changing the direction of the organs in the DC group, and the indexes of related organs returned to normal level.

3.2. The Effects of the CVFB on Glucose Metabolism in Diabetic Mice. After 28 days of treatment, the fasting blood glucose concentration of diabetic mice treated with the CVFB decreased to the concentration of 0 days of treatment ($p > 0.05$; Table 2), and the fasting blood glucose concentration of the PC group was significantly different from that at 0 days of treatment ($p < 0.05$; Table 2).

Mice were given 2.0 g/kg glucose solution by gavage for OGTT test. After gavage, the blood glucose of each group increased significantly. After 30 minutes, the blood glucose value of each group showed a different trend to decrease; at 60 minutes, there was a significant difference in blood glucose between the PC group and the DC group ($p < 0.05$; Figure 1), and it was observed that the PC group had a greater tendency to decrease blood sugar than the DC group; at 90 min, the blood glucose levels of the HD group and the PC group were significantly different from those of the DC group ($p < 0.05$, $p < 0.01$; Figure 1).

After 28 days of administration, the CVFB groups and the PC group all decreased the levels of GSP to a certain extent ($p > 0.05$; Figure 2(a)) and had a certain degree of decline in INS content levels and MD and HD groups and PC groups had significant differences in the decline of INS content levels ($P < 0.05$; Figure 2(b)). HOMA-IR was decreased in the HD and PC groups ($P < 0.05$; Figure 2(c)).

3.3. The Effects of the CVFB on Lipid Metabolism in Diabetic Mice. After treatment, the concentrations of T-CHO ($p < 0.05$; Figure 3(a)), TG, and BUN ($p < 0.01$; Figures 3(b) and 3(e)) in diabetic mice were decreased, and the content of HDL-C was significantly increased ($p < 0.05$; Figure 3(c)), indicating that CVFB groups had a certain regulatory effect on lipid metabolism in diabetic mice.

3.4. The Effects of the CVFB on Antioxidant in Diabetic Mice. The serum and liver homogenate of mice were tested. In the serum test, it can be seen that the SOD activities of the MD and HD groups and PC group are all increased ($p < 0.001$; Figure 4(a)). The content of MDA in the LD, MD, and HD groups and the PC group decreased ($p < 0.05$, $p < 0.01$, $p < 0.001$, $p < 0.001$; Figure 4(b)); GSH-Px activity increased in the LD, MD, and HD groups and the PC group ($P < 0.05$, $p < 0.05$, $p < 0.01$, $p < 0.01$; Figure 4(c)).

In liver homogenate, SOD activity increased in the MD and HD groups and PC group ($p < 0.01$, $p < 0.001$, $p < 0.001$; Figure 4(a)). The content of MDA was decreased in the LD, MD, and HD of the CVFB group and the PC group ($p < 0.01$, $p < 0.001$, $p < 0.001$, $p < 0.001$; Figure 4(b)). The GSH-Px activity increased in the LD, MD, and HD groups and the PC group ($p < 0.01$, $p < 0.01$, $p < 0.001$, $p < 0.001$; Figure 4(c)).

The CVFB group and the PC group had certain antioxidant effects on diabetic ICR mice, and the positive drug metformin had better antioxidant properties than the CVFB groups, but there was no significant difference between them.

3.5. The Effects of the CVFB on Histopathology in Diabetic Mice

3.5.1. H&E Staining Results of Pancreatic Tissue Sections. It can be seen from Figure 5 that the number of pancreatic islet cells in the LD group is greatly reduced, and the interior and surrounding of the pancreatic islets are infiltrated by a large number of inflammatory cells, but the borders of the pancreatic islets can still be distinguished.

The pancreatic islets of the mice in the MD group were slightly atrophy, and there were inflammatory cells around the pancreatic islets. Compared with the negative control group, the inflammatory cells were greatly reduced. The structure of pancreatic islets in the HD group is relatively complete, with obvious borders, compared with the DC group, the islet cells are significantly increased, and the inflammatory cells are greatly reduced. However, there are still more inflammatory cells on the side of the islets.

With the concentration of CVFB increased, the number of inflammatory cells gradually decreased.

3.5.2. TUNEL Method to Determine the Results of Cell Apoptosis in Pancreatic Tissue. In the NS group (Figure 6), Normal cells are evenly distributed in mouse pancreatic islets; when there is inflammation, inflammatory cells are produced and pile up together; in the DC group (Figure 6), many inflammatory cell nuclei are distributed inside and outside the pancreatic islets. The *h* diagram shows that diabetes caused by STZ can cause cell apoptosis, and the apoptosis rate is significantly increased.

In the CVFB high-dose group (Figure 6), the inflammatory cells around the pancreatic islets of the mouse were significantly reduced, and the cells in the pancreatic islets were more evenly distributed. The apoptosis rate was significantly reduced (Figure 6).

Table 2: The effect of 28-day CVFB treatment on the fasting blood glucose of STZ-induced ICR diabetic mice ($n = 11$).

28 days	0	7	14	21	28
NS	6.3 ± 0.2	$8.5 \pm 0.3^{**}$	$7.9 \pm 0.5^{*}$	$8.4 \pm 0.5^{**}$	6.2 ± 0.4
DC	24.9 ± 1.3	$29.1 \pm 0.7^{*}$	$30.6 \pm 0.8^{**}$	$31.6 \pm 0.7^{**}$	27.4 ± 0.8
LD	23.4 ± 1.2	$27.8 \pm 0.9^{*}$	$29.7 \pm 0.8^{***}$	$28.5 \pm 0.8^{**}$	22.8 ± 1.1
MD	24.8 ± 0.8	$30.3 \pm 0.7^{**}$	$29.6 \pm 0.7^{**}$	$29.7 \pm 0.8^{*}$	24.2 ± 1.7
HD	24.4 ± 1.1	26.5 ± 1.1	27.48 ± 1.1	27.9 ± 1.2	22.8 ± 1.8
PC	25.3 ± 0.9	$28.9 \pm 0.7^{*}$	27.8 ± 1.0	26.7 ± 1.0	$22.2 \pm 1.5^{*}$

$^{*}p < 0.05$, $^{**}p < 0.01$, and $^{***}p < 0.001$ are the comparisons between within the group and day 0.

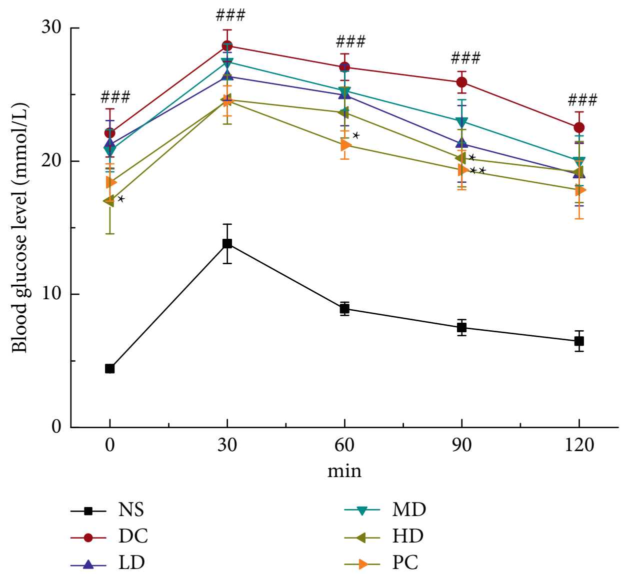

Figure 1: The effect of CVFB on OGTT of STZ-induced ICR diabetic mice. ###$p < 0.001$ versus NS group, $^{*}p < 0.05$, and $^{**}p < 0.01$versus DC group.

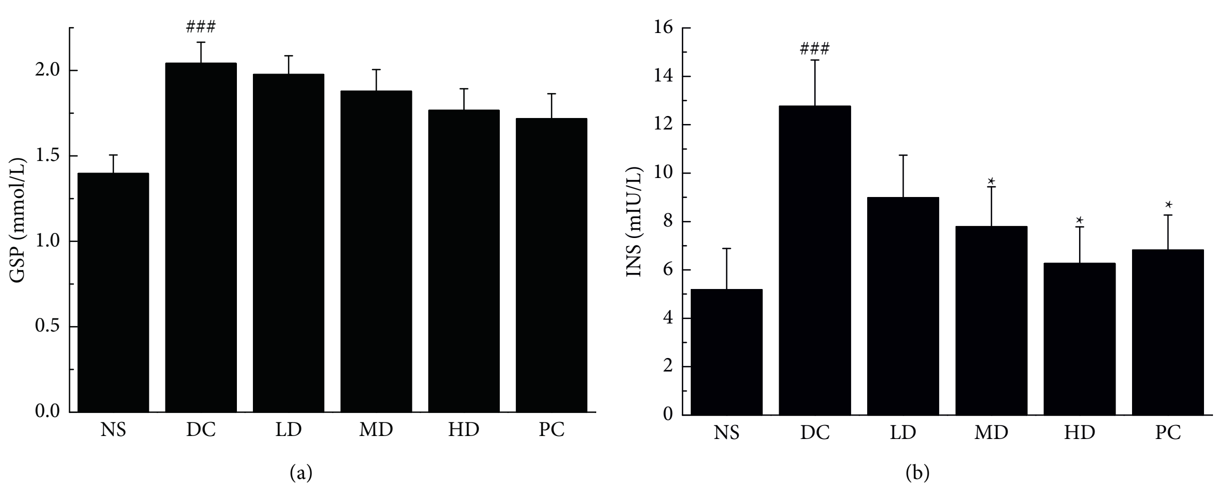

Figure 2: Continued.

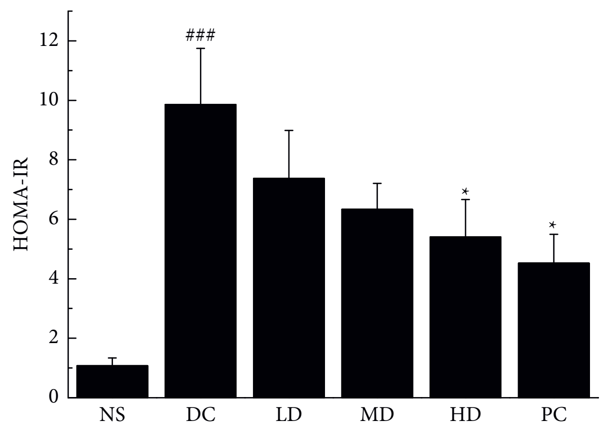

(c)

Figure 2: The effect of CVFB on the level of GSP (a), INS (b), and HOMA-IR (c) in the serum of STZ-induced ICR diabetic mice. ###$p < 0.001$ versus NS group. $^{*}p < 0.05$ versus DC group.

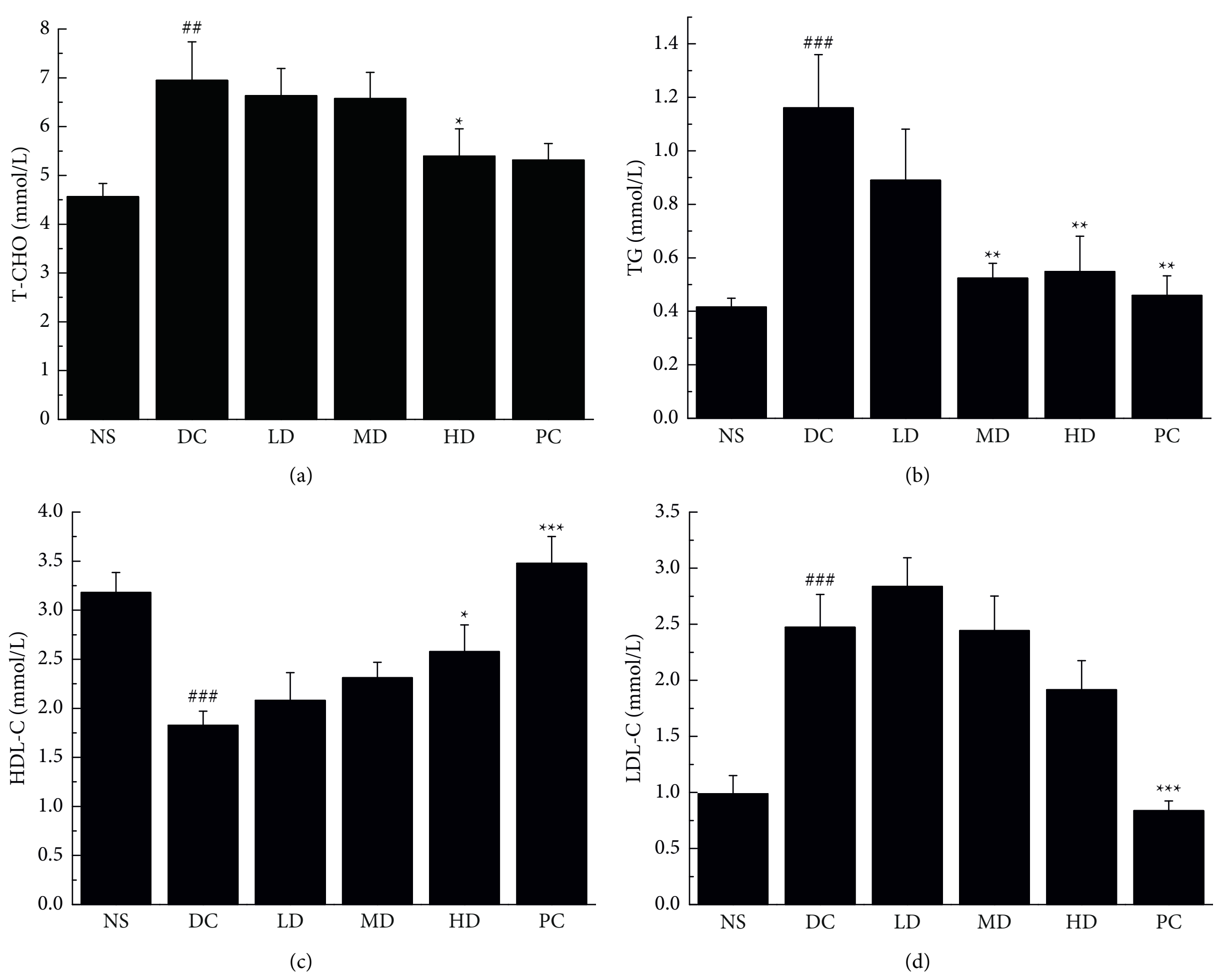

Figure 3: Continued.

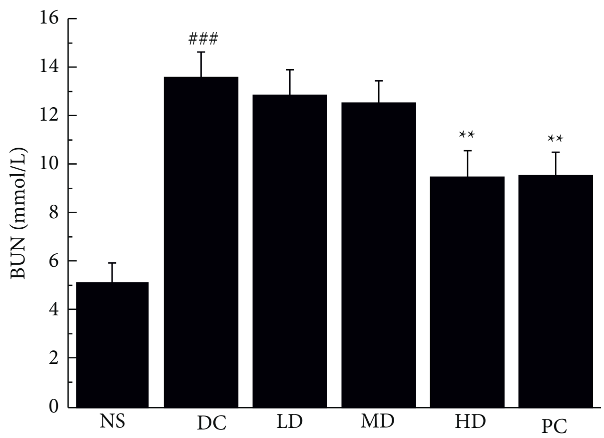

(e)

Figure 3: The effect of CVFB on the level of T-CHO (a), TG (b), HDL-C (c), LDL-C (d), and BUN (e) in the serum of STZ-induced ICR diabetic mice. ##$p < 0.01$ and ###$p < 0.001$ versus NS group; $^{*}p < 0.05$ and $^{***}p < 0.001$ versus DC group.

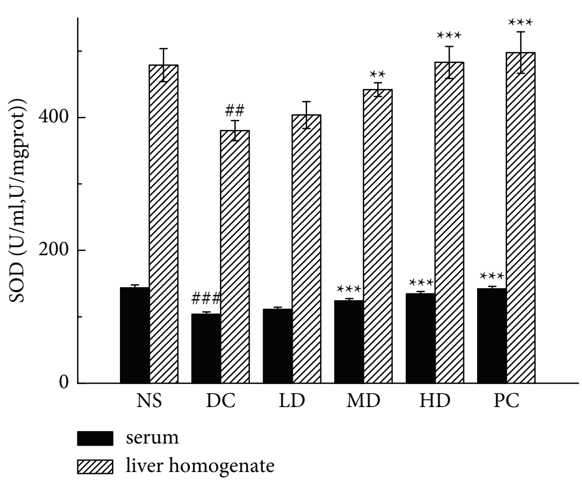

(a)

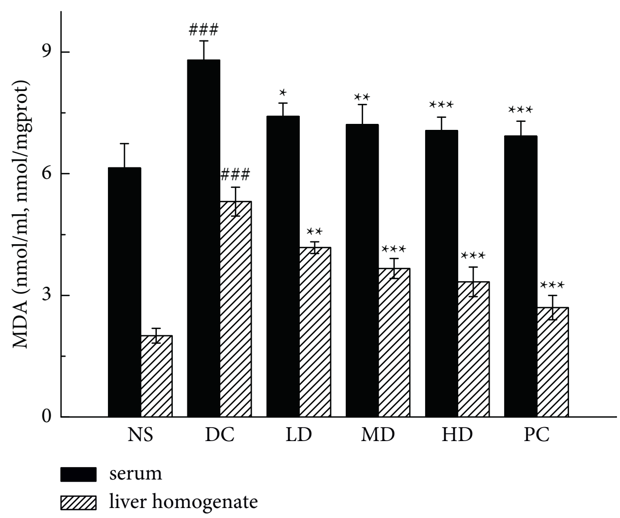

(b)

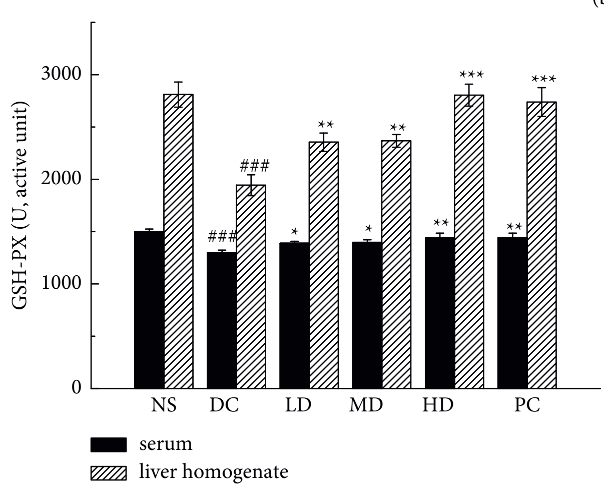

(c)

Figure 4: The effect of CVFB on the level of SOD (a), MDA (b), and GSH-Px (c) in the serum and liver homogenate of STZ-induced ICR diabetic mice. ##$p < 0.01$ and ###$p < 0.001$ versus NS group; $^{**}p < 0.01$ and$^{***}p < 0.001$ versus DC group.

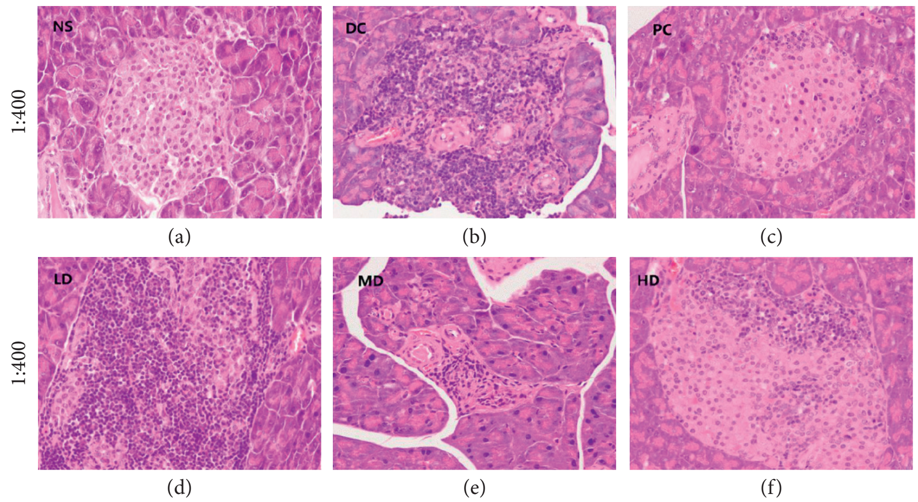

Figure 5: The picture of histopathological analysis in pancreas of STZ-induced ICR diabetic mice (×400).

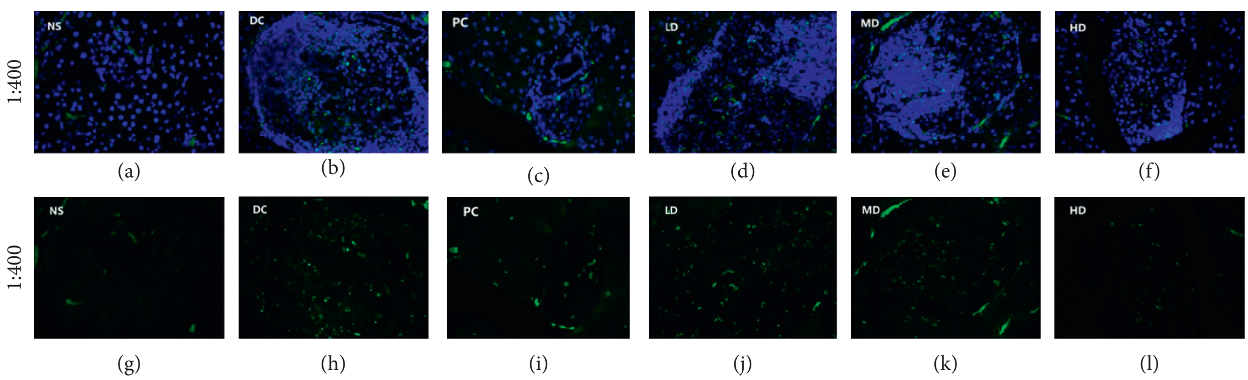

Figure 6: The picture of apoptosis analysis in pancreas of STZ-induced ICR diabetic mice (a–l).

4. Discussion

In this experiment, we used the STZ one-time high-dose injection method to build a diabetic ICR mouse model to explore the therapeutic effect of CVFB. Glucose metabolism, lipid metabolism, and antioxidant effects of diabetic ICR mice and the impact on mouse pancreas organs were analyzed by the daily living conditions.

Diabetes is a disease characterized by a relative or absolute lack of insulin, leading to hyperglycemia. Injecting large doses of STZ damages pancreatic β-cells, causing β-cell dysfunction and reducing insulin secretion, and inducing mice to become nonobese diabetic [10]. From the measurement results, we can see that CVFB can effectively control or reduce the fasting blood glucose of diabetic mice to a certain extent and reduce the levels of GSP and INS in the fasting serum. However, the sensitivity of related organs and tissues in diabetic mice to insulin is reduced, and insulin resistance promotes glucose uptake, which causes a variety of biochemical reactions in the body. Therefore, high levels of fasting plasma insulin can reflect insulin resistance [11]. The experimental results show that the HOMA-IR evaluation is reduced, indicating that CVFB can significantly improve insulin resistance and protect pancreatic β cells. At the same time, the OGTT test results show that CVFB can accelerate the decomposition and utilization of blood sugar and finally accelerate the glucose metabolism in diabetic mice.

Diabetes is one of the most common metabolic diseases, in which abnormal lipid metabolism is often an important factor in determining the direction and status of the disease [12]. The experimental results found that CVFB can reduce the content level of T-CHO, TG, BUN, and LDL-C, increase the content level of HDL-C, accelerate the metabolism of blood lipids in diabetic mice, and regulate the disorder of lipid metabolism in the body to reduce the incidence of hyperlipidemia and also reduce the risk of coronary heart disease, atherosclerosis, and diabetes complications.

Many researchers have proved that the oxidative damage associated with diabetes is caused by the production of reactive oxygen species. Therefore, increasing the activity of antioxidant enzymes can increase the body's antioxidant defense system's response to oxidative stress [13]. The experimental results found that CVFB can effectively increase the activity of antioxidant enzymes SOD and GSH-Px in the serum and liver homogenate of diabetic mice and reduce the level of MDA. MDA is the main product of lipid peroxides, which proves that diabetes is related to oxidative stress. The pancreas is an internal organ that produces insulin and glucagon, which regulates the body's blood sugar stability. Observing the H&E staining results and the apoptosis experiment of the pancreas tissue of diabetic mice, it can be seen that compared with the NS group, the CVFB group can reduce the inflammatory factors in the pancreatic islets in the pancreas of diabetic ICR mice and improve the damaged islet structure and increase the islet cells and the apoptosis rate was significantly reduced, indicating that CVFB has a protective effect on the pancreas of diabetic ICR mice.

In this experiment, we studied the therapeutic effect of CVFB on STZ-induced ICR diabetic mice and found that diabetic mice administered with CVFB can control or reduce the blood sugar level of diabetic mice, accelerate the rate of glucose metabolism, regulate the lipid metabolism disorder and abnormal blood lipid metabolism in the body, enhance the antioxidant capacity in mice, reduce oxidative stress damage, protect the pancreas organs, and repair and adjust the function of the pancreas to regulate blood sugar balance. In this experiment, we studied the therapeutic effect of CVFB on STZ-induced ICR diabetic mice and found that diabetic mice administered with CVFB can control or reduce the blood glucose level of diabetic mice and accelerate the rate of glucose metabolism, regulate the lipid metabolism disorder and abnormal blood lipid metabolism in the body, enhance the antioxidant capacity in mice, reduce oxidative stress damage, protect the pancreas organs, and repair and regulate the function of the pancreas to regulate blood sugar balance.

The above aspects show that CVFB has a therapeutic effect on diabetic mice, provides a scientific basis for the development of drugs for the prevention and treatment of diabetes, and is of great significance to the in-depth research of *Coriolus versicolor*.

Data Availability

The data used and analyzed during the current study are available from the corresponding author on reasonable request.

Conflicts of Interest

The authors declare that they have no conflicts of interest.

Acknowledgments

The research was supported by the Key Platforms and Major Projects of Guangdong Provincial Education Department (No. 2018KTSCX308); Zhuhai College of Jilin University Innovation Ability Cultivation Project (No. 2018XJCQ013); and Zhuhai College of Jilin University "Three Levels" Talent Construction Project.

References

[1] X. Z. Wang, "Research progress on hypoglycemic function factors of natural product," *Henan Journal of Preventive Medicine*, vol. 29, no. 4, pp. 241–243, 2018.

[2] W. J. Ge, Y. Zhao, B. Tolgor et al., "Antitumor effect of acid-soluble polysaccharides from *Trametes versicolor* (L.) Lloyd in H22 tumor-beaing mice," *Journal of Northwest A & F University(Natural Science Edition)*, vol. 46, no. 1, pp. 8–14, 2018.

[3] C.-H. Ko, G. G.-L. Yue, S. Gao et al., "Evaluation of the combined use of metronomic zoledronic acid and Coriolus versicolor in intratibial breast cancer mouse model," *Journal of Ethnopharmacology*, vol. 204, pp. 77–85, 2017.

[4] F. X. Nan and W. Shao, "Study on effects of polysaccharide krestin on mice antiaging," *Journal of Ningxia University (Natural Science Edition)*, vol. 26, no. 3, pp. 264–267, 2005.

[5] F. Y. Zhang, S. Zhang, J. F. Zeng, and W. J. Luo, "The effects of exopolysaccharides of c.versicolor, g.lucidum and a.cylindracea on fruit fly's life-span," *Life Science Research*, vol. 11, no. 2, pp. 130–133, 2007.

[6] F. F. Wang, L. M. Hao, Z. Z. Wang et al., "Comparison of antioxidation activities of the fermentation products of Coriolus versicolor and its polysaccharide," *Science and Technology of Food Industry*, vol. 34, no. 13, pp. 109–112, 2013.

[7] X. F. Xi, D. Y. Wang, and Z. Y. Xiong, "Effect of krestin polysaccharide on antioxidant capability and ATPase activity in brain tissues of rats with high intensity exercise," *Food Science*, vol. 33, no. 5, pp. 256–259, 2012.

[8] Y. Wang, Y. R. Bao, X. S. Meng et al., "Activation of spleen cells by Coriolus Versicolor polysaccharide," *Central South Pharmacy*, vol. 15, no. 3, pp. 284–287, 2017.

[9] L. X. Zhang, Y. L. Li, and W. X. Deng, "Effects of oral coriolus versicolor polysaccharide on the immune organ and CD^{4+} and CD^{8+} T cells in peripheral blood of mice," *Journal of Xinxiang Medical University*, vol. 27, no. 5, pp. 453–455, 2010.

[10] C. Gonzalez, S. Cuvellier, C. Hue-Beauvais, and M. L�vi-Strauss, "Genetic control of non obese diabetic mice susceptibility to high-dose streptozotocin-induced diabetes," *Diabetologia*, vol. 46, no. 9, pp. 1291–1295, 2003.

[11] G. Musen, A. M. Jacobson, N. R. Bolo et al., "Resting-state brain functional connectivity is altered in type 2 diabetes," *Diabetes*, vol. 61, no. 9, pp. 2375–2379, 2012.

[12] S. Gupta, S. B. Sharma, S. K. Bansal, and K. M. Prabhu, "Antihyperglycemic and hypolipidemic activity of aqueous extract of Cassia auriculata L. leaves in experimental diabetes," *Journal of Ethnopharmacology*, vol. 123, no. 3, pp. 499–503, 2009.

[13] Y. Liu, J. Sun, S. Rao, Y. Su, and Y. Yang, "Antihyperglycemic, antihyperlipidemic and antioxidant activities of polysaccharides from Catathelasma ventricosum in streptozotocin-induced diabetic mice," *Food and Chemical Toxicology*, vol. 57, pp. 39–45, 2013.

Hindawi
Journal of Healthcare Engineering
Volume 2022, Article ID 7640405, 13 pages
https://doi.org/10.1155/2022/7640405

Research Article

Quantitative Scintigraphy Evaluated the Relationship between 131I Therapy and Salivary Glands Function in DTC Patients: A Retrospective Analysis

Xiaolan Lv,[1,2] Liang Yin,[1,3] Weiming Wu,[1] Ning Li,[1] Ruyi Zhang,[1] Xue Li,[1] Qiang Jia,[1] Jian Tan,[1] Peng Wang,[1] Xiangqian Zheng,[4] Xianghui He,[5] Chao Huang,[6] Dihua Li,[7] Yan Wang ,[8] and Zhaowei Meng [1]

[1]*Department of Nuclear Medicine, Tianjin Medical University General Hospital, Tianjin 300052, China*
[2]*Department of Ultrasound, Affiliated Hospital of Hebei University, Baoding 071000, China*
[3]*Department of Nuclear Medicine, Pingjin Hospital, Characteristic Medical Center of Chinese People's Armed Police Forces, Tianjin 300162, China*
[4]*Department of Thyroid and Neck Tumor, Tianjin Medical University Cancer Institute and Hospital, National Clinical Research Center for Cancer, Key Laboratory of Cancer Prevention and Therapy of Tianjin City, Tianjin 300060, China*
[5]*Department of General Surgery, Tianjin Medical University General Hospital, Tianjin 300052, China*
[6]*Hull York Medical School, University of Hull, Hull, UK*
[7]*Tianjin Key Laboratory of Acute Abdomen Disease Associated Organ Injury and ITCWM Repair, Institute of Acute Abdominal Diseases, Tianjin Nankai Hospital, Tianjin, China*
[8]*Chinese Material Medical College, Tianjin State Key Laboratory of Modern Chinese Medicine, Tianjin University of Traditional Chinese Medicine, Tianjin 301617, China*

Correspondence should be addressed to Zhaowei Meng; zmeng@tmu.edu.cn

Received 28 December 2021; Accepted 18 February 2022; Published 14 April 2022

Academic Editor: Enas Abdulhay

Purpose. Quantitative scintigraphy to evaluate salivary gland function changes in patients with differentiated thyroid cancer (DTC) after iodine-131 (^{131}I) treatment. *Methods*. A total of 458 patients with DTC grouped by sex and age were included. Salivary gland scintigraphy was performed to evaluate salivary gland function before and after ^{131}I treatment. The uptake fraction (UF), uptake index (UI), and excretion fraction (EF) of two pairs of parotid glands and submandibular glands were measured and compared. The Chi-square test was conducted according to function impairment count. *Results*. Salivary gland function in different age groups and sexes were quite different, especially for women <55 years old, who had decreased UF, UI, and EF of all four glands without basal injury. The secretion or uptake function of some salivary glands with basic function impairment before ^{131}I treatment was increased after iodine treatment. Only a small percentage of males showed reduced functional parameters after several treatments. The most significant difference in the count of impairment for the four salivary glands were the first and third examinations, which was more evident in women. The submandibular gland had the most significant reduction in uptake. *Conclusion*. Changes in salivary gland function are more common in young females being treated for DTC. Impairment of salivary gland function is correlated with the number of treatments and the cumulative dose of ^{131}I. Some salivary gland functions impaired before ^{131}I treatment were enhanced in the early treatment.

1. Introduction

Differentiated thyroid cancer (DTC) is a common endocrine malignancy. According to statistics, 900,590 people were diagnosed with thyroid cancer in the United States. 52,070 people are expected to be diagnosed with thyroid cancer in 2019 [1]. Surgical treatment of thyroid cancer followed by removal of residual thyroid using iodine-131 (^{131}I) is a common treatment approach, but ^{131}I can induce salivary gland damage [2–4]. ^{131}I is absorbed on the membranes of thyroid follicular cells and cancer cells through the reactive sodium iodide transporter (NIS) [5]. Salivary glands expressing NIS can also absorb ^{131}I, and the accumulation of salivary gland ^{131}I is about 30 to 40 times that of plasma levels [6]. The radiation dose of high-concentration ^{131}I is sufficient to cause salivary gland damage and affect their function [7].

Salivary gland dysfunction is mainly reflected in decreased saliva secretion. Saliva is essential for the preservation of oral health. Saliva's functions include buffering, lubricating, mineralizing, and cleaning oral tissues [8]. Saliva also has antibacterial, antiviral, and antifungal properties [9]. Changes in the quantity or quality of saliva can affect the integrity of the oral tissues leading to the appearance of conditions like dental caries, periodontal diseases, and various other oral and pharyngeal disorders [10, 11]. In addition, salivary gland dysfunction is characterized by difficulty swallowing, dental disease, and loss of taste. DTC patients who had one or more ^{131}I treatments may experience the above discomfort [12–14]. Their quality of life was affected. Therefore, determining and protecting salivary gland function in DTC patients should not be ignored. There are many examinations to assess salivary gland function, including salivary gland scintigraphy with ^{99m}Tc-pertechnetate [3, 4, 15], neck ultrasonography [16], salivary flow rate measurement of the whole or individual gland [17]. ^{99m}Tc-pertechnetate is commonly used in hospitals. Because it can quantify the uptake or secretory from individual salivary glands and calculate their function [18–20].

Through salivary gland scintigraphy, we found that some patients had impaired salivary gland function before ^{131}I treatment. We defined it as an impairment of the basic function of the salivary glands. The Impairment of basic function could be associated with different factors, including Sjögren syndrome [21, 22], salivary gland obstructive disease [23], salivary gland infection [24], obesity and diabetes [25, 26], aging [27, 28] and so on. The changes in the salivary gland's function in these patients after ^{131}I treatment are worth discussing.

This study aimed to analyze the changes in salivary gland uptake and excretion function following ^{131}I treatment. And to study the relationships between the function change and different genders, age groups. The results provide clinical guidance for the protection of salivary function in DTC patients undergoing ^{131}I treatment.

2. Materials and Methods

2.1. Patients. A retrospective analysis of the hospital files from the Department of Nuclear Medicine of Tianjin Medical University General Hospital was in this study. The salivary gland scintigraphy parameters and inpatient treatment database of DTC patients from the hospital were used. We reviewed information for DTC patients who received ^{131}I therapy from November 2014 to December 2018. All enrolled patients had two or more pre-hospital scintigraphy of salivary glands. A total of 458 patients with DTC grouped by sex and age were included. Patients with the above information missing were excluded. Total thyroidectomy was performed for all patients by thyroid surgeons, and DTC was diagnosed by postoperative pathology. According to the ATA Guidelines, we selected N1b or M1 DTC patients [2]. All patients received ^{131}I treatment 6 weeks postoperatively. Before treatment with ^{131}I, patients were advised to have a low-iodine diet for 3 weeks. After the first radioiodine treatment, patients in the study received one or more radioiodine treatments. Salivary gland function parameters were recorded by 370 MBq (10 mCi) ^{99m}Tc-Pertechnetate salivary gland scintillation before ^{131}I treatment. The interval between each treatment was ~6 months. The protocol for evaluating salivary gland scintigraphy is shown in Figure 1. Patients with residual thyroid tissue were given 2.96 to 5.55 GBq (30–150 mCi) dosages for each treatment [2, 29].

2.2. Salivary Gland Imaging Protocol. According to our previous reports, pre-ablation salivary gland imaging was performed under thyroid-stimulating hormone (TSH) stimulation in the morning, 4 h before the first ^{131}I intake [3, 4]. Patients were asked to fast before salivary gland imaging. Single-photon emission computed tomography was performed on a Discovery NM/CT 670 (General Electric Medical Systems, Chicago, IL, USA) while subjects laid on their back. A low-energy, parallel hole, high-resolution collimator was used with a peak value of 140 keV and a window width of 20%. Each patient received 370 MBq ^{99m}Tc-pertechnetate intravenously through the cubital vein. After injection, the dynamic images were continuously shot on a 256×256 matrix at minute/frame with zoom 1.5 for 15 minutes. The patients were given 0.2 g oral vitamin C at the 8th minute after injection; they were instructed to chew quickly and then keep the tablet under the tongue for about 1 minute. To accurately calculate the delivered radioactivity dose, we measured the radioactivity count in the syringe before and after the injection. Patients underwent a radionuclide scan as described above before every ^{131}I treatment. Salivary gland imaging was also performed under TSH stimulation.

2.3. Image Analysis. First, circular regions of interest (ROIs) were manually drawn on the parotid and submandibular glands. Parotid glands showed a similar unified background area in the bilateral temporal-orbital region, while submandibular glands appeared as a similar unified background area in the bilateral supraclavicular region. The sizes and positions of these ROIs remained the same for each scanning session. An imaging system was used to generate time-activity curves for ^{99m}Tc-pertechnetate uptake and excretion in counts per minute. Based on these ROIs counts and the

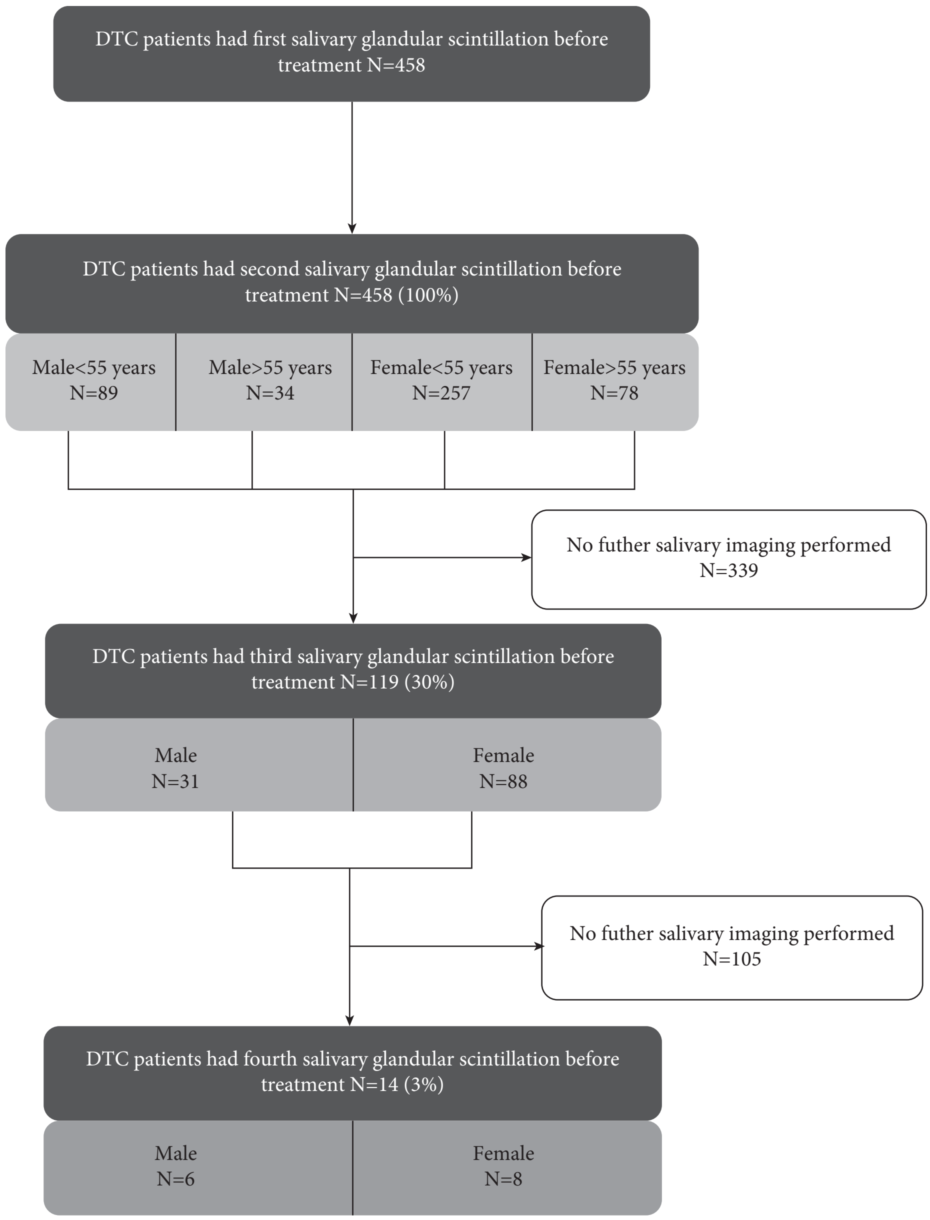

Figure 1: Case follow-up process. Salivary glandular scintillation imaging data were collected from DTC patients before the first, second, third, and fourth ^{131}I treatments. The group was compared according to the number of patients in each treatment course.

subsequent time-activity curves, the salivary gland functional indicators were derived using the following modified formulas [3, 4, 30, 31] (Figure 2):

2.3.1. Uptake Fraction (UF). UF = (salivary gland maximum count minute–salivary gland background count corresponding to maximum count minute)/(count in the syringe before injection–count in the syringe after injection)

2.3.2. Uptake Index (UI). UI = (salivary gland maximum uptake count minute–salivary gland background count corresponding to maximum uptake count minute)/salivary gland background count corresponding to maximum uptake count minute

2.3.3. Excretion Fraction (EF). EF = (salivary gland maximum uptake count minute–salivary gland minimum uptake count minute after vitamin C)/salivary gland background count corresponding to maximum uptake count minute

UI and UF reflect the uptake function of salivary glands, while EF reflects the secretion function.

2.4. Diagnostic Criteria for Salivary Gland Function. Salivary gland function impairment was established based on the diagnostic criteria of the Department of Nuclear Medicine, Tianjin Medical University General Hospital, with reference to previous studies and modified in our institute [18, 19, 32, 33]. Parameters obtained by salivary scintigraphy, the peak uptake (maximum salivary gland uptake count/second count at peak uptake) was set to <50 counts/s

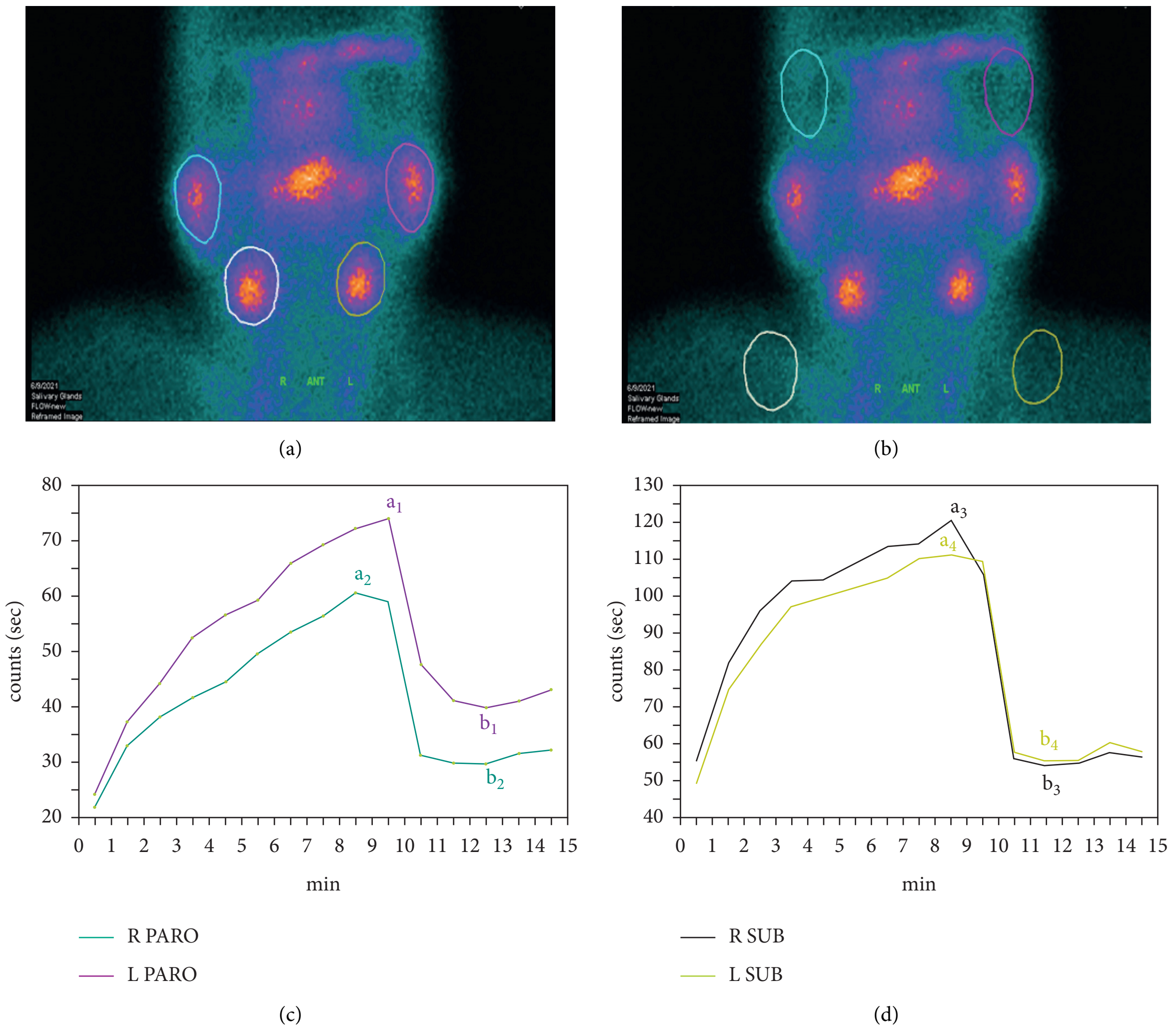

Figure 2: Physiological uptake and excretion of ^{99m}Tc-pertechnetate in parotid and submandibular salivary glands detected by dynamic salivary gland scintigraphy. (a) A clear depiction of the ROIs and ROIs of the salivary and mandibular glands was obtained from all frames. (b) The parotid gland was in the bilateral temporal-orbital region, and the mandibular gland was in the bilateral supraclavicular region to draw similar background areas, and the background ROIs count was recorded. (c-d) Time-activity curve of each salivary gland. The ordinate of a_1-a_4 corresponds to the maximum minute count of each salivary gland. The ordinate of b1- b4 corresponds to the count of each salivary gland at the minimum uptake minute after vitamin C.

with reduced intake function, and EF was set to <30% with reduced secretory function. A reduced diagnosis of either or both of these above salivary glands is dysfunction. The patients with salivary gland dysfunction before the first admission were those with impaired basic salivary gland function.

2.5. Statistical Analysis. All data for males and females were analyzed separately and are presented as either mean ± standard deviation or median (upper quartile, lower quartiles). Statistical analysis was performed by using Statistical Package for Social Sciences (SPSS version 25.0, IBM Corp., Armonk, NY, USA) software. Mann-Whitney U tests were used to compare values of the same patient before and after the first treatment. Kruskal-Wallis tests were performed to evaluate and compare salivary gland function in patients who underwent multiple ^{131}I treatments. After dividing men and women into separate groups, the distribution of salivary gland injuries before the first treatment and before the second to fourth treatments were analyzed by chi-square test.

3. Results

Among the 458 patients, most (72.9%) were female with a mean age of 46 ± 12 years (range 14–76 years). The lowest and highest doses of ^{131}I were 30 and 550 mCi, respectively. Patient demographic data are summarized in Table 1.

From the scintigraphy examinations, the analysis according to age and sex groups evidenced salivary gland function is more sensitive in females than in males. The sensitivity of salivary gland function was ranked from large to small, in order of <55 years female, ≥55 years female, <55 years male, ≥55 years male ($p = 0.05$). After treatment with

Table 1: Clinical characteristics of total patients.

Characteristic	Total	Male	Female	P
Age (years)	46 ± 12/14–76	46 ± 12/22–75	45 ± 12/14–76	0.442
Number/percentage		124/27%	334/73%	
^{131}I activity (mCi)	128 ± 78/30–550	131 ± 68/30–450	126 ± 80/30–550	0.145

Age and ^{131}I activity are stated as median ± standard deviation/range.

^{131}I, the UI, UF, or EF values of patients without impairment of basic salivary gland function tended to decrease. The secretion or uptake function of some salivary glands with basic function impairment before ^{131}I treatment was increased after iodine treatment. Table S1 summarizes the number of patients, age distribution, and cumulative dose before one or more ^{131}I treatments. The UI, UF, and EF of each group were compared before and after ^{131}I treatment (Tables 2–4).

We found that the difference between the first and third injury counts of salivary gland damage on salivary gland scintigraphy tests before hospitalization was the most significant. There were statistically significant differences between the four salivary glands in both the male and female groups. It was more pronounced in the female group (female, $P = 0.001$; male, $P < 0.05$). The percentage of damaged salivary glands increased with the number of treatments in both sexes, while the percentage of normal salivary glands gradually decreased (Table 5, Figure 1S). The cumulative dose of ^{131}I received by patients over several treatments is shown in Figure 2S. Chi-square test was performed to determine the relationship between the number of patients by sex and the impairment of salivary gland function before each ^{131}I treatment (Table S2). There was a statistical difference in the left submandibular gland injury count between sexes before the first treatment ($p < 0.05$).

4. Discussion

Salivary gland damage is a common manifestation of DTC patients after ^{131}I therapy [34]. ^{131}I is mainly concentrated in the duct system of the salivary glands. The radiation causes debris buildup that narrows the lumen, and this obstruction can lead to an injurious process that results in glandular degeneration. Salivary gland scintigraphy examination is necessary for the objective evaluation of the reproducibility of salivary gland function [20]. These measurement parameters mainly assess gland uptake and secretion capacity [15, 35, 36]. We performed salivary gland scintigraphy to identify relevant salivary gland parameters and then analyzed the factors that affect salivary gland function changes in DTC patients after each ^{131}I treatment.

4.1. Sex and Age. By comparing salivary glands without basic functional impairment, we found that functional changes were related to age and sex. The salivary glands of younger patients were more sensitive to ^{131}I treatment than older patients, and female patients were more likely to show decreased function. Other studies have examined age- and sex-dependent differences in salivary gland function changes. Liu et al. assessed iodine dynamics and salivary gland dosimetry after ^{131}I treatment and showed that women's parotid iodine intake was often higher than men's [37]. This suggests that female salivary glands are more susceptible to radiation, leading to decreased function following ^{131}I treatment. Almeida et al. found that patient sex was associated with the uptake phase on salivary glands scintigraphy. Intake of all major salivary gland was decreased in men compared with women. Patient age was the strongest predictor of parotid gland dysfunction as it affects the stage of parotid gland uptake and elimination on salivary gland scintigraphy [38]. Another study revealed the presence of epidermal and nerve growth factors (EGF and NGF) in salivary glands and described their roles in cell growth and differentiation. They are detected at higher levels in the submandibular glands of males than females [39], indicating that male salivary gland cells have stronger repair and regeneration abilities. Animal studies showed sex-attributed differences in wound healing patterns in submandibular glands between male and female mice. In males, the number of convoluted tubules rich in EGF and NGF (involved in cell proliferation and neurogenesis, respectively) was higher than that in females [40, 41]. These sex- differences observed in mice may help explain why the incidence of salivary gland disease tends to be much higher in women than in men (i.e., approximately 9:1) [42].

4.2. Different Basic Functions. Before the first ^{131}I treatment, we selected patients with basic impairment of salivary gland function. After the first ^{131}I treatment, some salivary gland parameters were different in the female group, with most changes in the group younger than 55 years old. After the second ^{131}I treatment, the bilateral submandibular gland EF values were different in females but not males. Interestingly, these altered functional parameters all showed an upward trend rather than the expected decline. We consider that this may be related to the compensatory increase in the function of glandular cells under certain stress states. Poradovskaia et al. showed that after ablating or removing one submandibular salivary gland in rats, the contralateral gland responded by increasing cell proliferation with concomitant increases in the size of the cells and nuclei by 10% and 17%, respectively. Burlage et al. observed that pilocarpine preconditioning induced proliferation of acinar and intercalated duct cells in rats, which could explain the observed enhanced compensatory response in salivary glands [43]. Compensatory proliferation is a mechanism to replace lost cells in rapidly cycling tissues [44]. After an initial singular dose ^{131}I dose of 100 mCi, the salivary glands might increase

TABLE 2: Comparison of salivary gland function in patients before secondary treatmen.

Scintigraphic parameters	Male under 55 years						Male older than or equal to 55 years					
	Damage before treatment	After firsttreatment	P	No damage before treatment	After firsttreatment	P	Damage before treatment	After firsttreatment	P	No damage before treatment	After firsttreatment	P
RP	Number:6			Number:83			Number:2			Number:32		
UF	0.039 (0.027–0.071)	0.057 (0.025–0.093)	0.173	0.043 (0.031–0.054)	0.039 (0.030–0.058)	0.806	0.016 (0.011–0.014)	0.018 (0.013–0.014)	0.180	0.047 (0.026–0.066)	0.043 (0.025–0.056)	0.100
UI	1.792 (1.337–2.293)	2.448 (1.117–4.080)	0.116	1.814 (1.425–2.377)	1.806 (1.424–2.423)	0.799	0.967 (0.589–0.862)	0.960 (0.707–0.732)	0.655	1.787 (1.176–2.175)	1.685 (0.974–1.949)	0.104
EF	0.109 (0.070–0.218)	0.501 (0.292–0.613)	0.046	0.473 (0.412–0.546)	0.461 (0.354–0.539)	0.064	0.306 (0.190–0.270)	0.268 (0.195–0.207)	0.655	0.444 (0.361–0.488)	0.396 (0.302–0.513)	0.161
LP	Number:3			Number:86			Number:2			Number:32		
UF	0.034 (0.019–0.048)	0.036 (0.016–0.040)	0.593	0.039 (0.030–0.050)	0.036 (0.027–0.050)	0.113	0.023 (0.011–0.023)	0.031 (0.012–0.034)	0.180	0.044 (0.034–0.072)	0.045 (0.025–0.067)	0.197
UI	0.805 (0.724–1.409)	1.197 (0.588–1.633)	0.285	1.874 (1.346–2.240)	1.689 (1.288–2.142)	0.079	1.072 (0.594–1.014)	1.312 (0.732–1.237)	0.180	1.858 (1.388–2.379)	1.567 (1.261–2.528)	0.443
EF	0.124 (0.104–0.154)	0.418 (0.132–0.443)	0.109	0.486 (0.427–0.544)	0.465 (0.377–0.549)	0.043	0.198 (0.053–0.244)	0.390 (0.227–0.358)	0.655	0.440 (0.359–0.511)	0.397 (0.304–0.498)	0.061
RS	Number:9			Number:80			Number:3			Number:31		
UF	0.033 (0.023–0.049)	0.024 (0.021–0.046)	0.767	0.058 (0.042–.0766)	0.048 (0.038–0.062)	0.000	0.023 (0.023–0.030)	0.036 (0.021–0.036)	0.285	0.057 (0.048–0.067)	0.045 (0.038–0.063)	0.011
UI	2.156 (1.363–2.733)	1.662 (1.297–2.530)	0.767	2.984 (2.540–3.957)	2.736 (2.209–3.705)	0.016	1.736 (0.886–1.989)	1.883 (1.282–2.093)	0.285	3.074 (2.399–3.531)	2.604 (2.127–3.239)	0.050
EF	0.171 (0.157–0.190)	0.194 (0.175–0.254)	0.066	0.388 (0.313–0.470)	0.347 (0.256–0.444)	0.020	0.152 (0.038–0.281)	0.196 (0.050–0.358)	0.593	0.374 (0.304–0.421)	0.339 (0.238–0.400)	0.264
LS	Number:10			Number:79			One case			Number:31		
UF	0.027 (0.020–0.034)	0.025 (0.021–0.041)	0.241	0.052 (0.044–0.071)	0.045 (0.035–0.059)	0.000				0.061 (0.045–0.069)	0.048 (0.040–0.066)	0.010
UI	1.882 (1.247–2.158)	1.794 (1.499–2.296)	0.139	3.056 (2.488–4.031)	2.914 (2.371–3.532)	0.055				3.1515 (2.683–3.707)	2.973 (2.481–3.797)	0.348
EF	0.168 (0.149–0.187)	0.192 (0.134–0.251)	0.110	0.377 (0.282–0.460)	0.343 (0.236–0.425)	0.005				0.362 (0.290–0.432)	0.345 (0.252–0.423)	0.367

Scintigraphic parameters	Female under 55 years						Female older than or equal to 55 years					
	Damage before treatment	After firsttreatment	P	No damage before treatment	After firsttreatment	P	Damage before treatment	After firsttreatment	P	No damage before treatment	After firsttreatment	P
RP	Number:13			Number:244			Number:4			Number:74		
UF	0.023 (0.016–0.049)	0.043 (0.022–0.051)	0.116	0.043 (0.032–0.057)	0.038 (0.030–0.049)	0.000	0.025 (0.010–0.044)	0.027 (0.015–0.036)	0.715	0.047 (0.034–0.058)	0.037 (0.029–0.057)	0.218
UI	1.714 (1.221–2.363)	1.946 (1.364–2.643)	0.133	2.105 (1.621–2.618)	1.920 (1.467–2.369)	0.000	1.314 (0.774–2.224)	1.169 (0.836–1.466)	0.465	1.868 (1.514–2.604)	1.712 (1.349–2.410)	0.243
EF	0.316 (0.118–0.437)	0.465 (0.241–0.521)	0.055	0.496 (0.428–0.560)	0.467 (0.404–0.533)	0.001	0.176 (0.091–0.255)	0.359 (0.143–0.473)	0.144	0.508 (0.444–0.556)	0.475 (0.409–0.541)	0.113
LP	Number:17			Number:240			Number:8			Number:70		
UF	0.023 (0.013–0.036)	0.032 (0.020–0.048)	0.407	0.038 (0.029–0.053)	0.036 (0.028–0.048)	0.000	0.020 (0.011–0.042)	0.031 (0.023–0.047)	0.069	0.044 (0.030–0.061)	0.035 (0.024–0.047)	0.000
UI	1.465 (1.308–2.291)	1.770 (1.368–2.305)	0.227	2.013 (1.569–2.548)	1.841 (1.464–2.347)	0.000	1.464 (0.940–2.044)	1.560 (1.012–2.049)	0.401	2.050 (1.427–2.531)	1.630 (1.243–2.134)	0.005
EF	0.225 (0.120–0.357)	0.383 (0.339–0.467)	0.001	0.494 (0.420–0.564)	0.468 (0.394–0.535)	0.000	0.188 (0.167–0.240)	0.390 (0.261–0.487)	0.208	0.504 (0.432–0.588)	0.472 (0.366–0.535)	0.008
RS	Number:39			Number:218			Number:5			Number:73		
UF	0.034 (0.028–0.042)	0.032 (0.026–0.049)	0.944	0.047 (0.035–0.061)	0.042 (0.033–0.052)	0.000	0.010 (0.009–0.026)	0.019 (0.015–0.029)	0.345	0.062 (0.050–0.078)	0.055 (0.047–0.070)	0.006
UI	1.780 (1.358–2.158)	2.018 (1.582–2.324)	0.024	2.490 (2.002–3.307)	2.401 (1.997–2.945)	0.001	1.205 (.699–1.960)	1.402 (0.846–1.937)	0.893	3.034 (2.607–3.986)	2.923 (2.405–3.742)	0.008
EF	0.157 (0.116–0.181)	0.255 (0.180–0.341)	0.000	0.377 (0.285–0.457)	0.344 (0.264–0.413)	0.000	0.132 (0.072–0.150)	0.174 (0.090–0.257)	0.043	0.432 (0.338–0.520)	0.383 (0.290–0.488)	0.005
LS	Number:50			Number:207			Number:7			Number:71		
UF	0.029 (0.024–0.035)	0.029 (0.023–0.037)	0.490	0.045 (0.035–0.060)	0.042 (0.032–0.053)	0.000	0.017 (0.012–0.033)	0.022 (0.018–0.034)	0.398	0.061 (0.044–0.082)	0.050 (0.036–0.062)	0.000
UI	1.917 (1.347–2.616)	2.015 (1.626–2.548)	0.420	2.877 (2.125–3.569)	2.630 (2.045–3.304)	0.004	1.974 (1.368–2.713)	2.239 (1.420–2.505)	0.735	3.120 (2.372–4.358)	2.809 (2.365–3.828)	0.003
EF	0.173 (0.139–0.198)	0.212 (0.171–0.291)	0.002	0.380 (0.306–0.475)	0.353 (0.277–0.428)	0.000	0.114 (0.063–0.174)	0.192 (0.142–0.336)	0.128	0.440 (0.324–0.499)	0.383 (0.275–0.462)	0.000

UF, UI, EF stated as median (upper quartile, lower quartiles), RP: Right parotid; LP: Left parotid; RS: Right submandibular; LS: Left submandibular; UF: Uptake fraction; UI: Uptake index; EF: Excretion fraction.

Table 3: Comparison of salivary gland function in patients before third treatment.

Scintigraphic parameters	Male group before third treatment								Female group before third treatment							
	Damage before treatment	After first treatment	After second treatment	P	No damage before treatment	After first treatment	After second treatment	P	Damage before treatment	After first treatment	After second treatment	P	No damage before treatment	After first treatment	After second treatment	P
RP		Number: 2				Number: 29				Number: 2				Number: 86		
UF	0.034 (0.018–0.033)	0.057 (0.019–0.067)	0.044 (0.012–0.055)	0.223	0.050 (0.031–0.068)	0.049 (0.032–0.060)	0.043 (0.026–0.061)	0.485	0.037 (0.010–0.045)	0.033 (0.010–0.039)	0.028 (0.008–0.034)	0.135	0.042 (0.031–0.055)	0.037 (0.028–0.048)	0.032 (0.021–0.041)	0.000
														III-II 0.005 III-I 0.000 ⋯ II-I 0.081		
UI	1.844 (1.054–1.712)	2.967 (0.865–3.586)	2.387 (0.864–2.717)	0.607	1.867 (1.527–2.391)	1.898 (1.440–2.819)	2.016 (1.277–3.038)	0.485	1.356 (0.673–1.360)	1.247 (0.533–1.336)	1.464 (0.588–1.607)	0.223	1.952 (1.549–2.479)	1.789 (1.460–2.188)	1.581 (1.137–2.102)	0.000
														III-II 0.014 III-I 0.000 II-I 0.098		
EF	0.254 (0.064–0.317)	0.506 (0.304–0.455)	0.299 (0.148–0.300)	0.607	0.486 (0.433–0.544)	0.478 (0.352–0.581)	0.493 (0.340–0.579)	0.422	0.194 (0.055–0.237)	0.418 (0.221–0.406)	0.412 (0.222–0.395)	1.000	0.485 (0.415–0.552)	0.4715 (0.419–0.539)	0.420 (0.246–0.521)	0.002
														III-II0.036 III-I 0.002 II-I 1.000		
LP		No case				Number: 31				Number: 5				Number: 83		
UF					0.041 (0.035–0.065)	0.045 (0.033–0.056)	0.036 (0.027–0.053)	0.206	0.019 (0.009–0.025)	0.025 (0.021–0.039)	0.021 (0.013–0.040)	0.165	0.040 (0.029–0.051)	0.034 (0.027–0.045)	0.032 (0.021–0.042)	0.000
														III-II 0.309 III-I 0.000 II-I 0.016		
UI					1.971 (1.523–2.460)	1.897 (1.348–2.457)	1.615 (1.359–2.576)	0.597	0.861 (0.687–1.776)	1.164 (1.010–1.879)	1.332 (.916–2.084)	0.247	2.006 (1.393–2.281)	1.717 (1.319–2.143)	1.686 (1.231–2.194)	0.008
														III-II 1.000 III-I 0.020 II-I 0.025		
EF					0.510 (0.442–0.558)	0.464 (0.402–0.550)	0.455 (0.347–0.545)	0.086	0.166 (0.102–0.382)	0.368 (0.292–0.439)	0.328 (0.173–0.458)	0.247	0.479 (0.420–0.544)	0.472 (0.394–0.523)	0.423 (0.326–0.514)	0.010
														III-II 0.392 III-I 0.008 II-I 0.392		
RS		Number: 2				Number: 29				Number: 6				Number: 82		
UF	0.034 (0.017–0.033)	0.033 (0.016–0.034)	0.032 (0.021–0.027)	1.000	0.058 (0.046–0.080)	0.054 (0.042–0.066)	0.051 (0.038–0.065)	0.018	0.050 (0.033–0.064)	0.044 (0.032–0.068)	0.044 (0.018–0.074)	0.607	0.052 (0.039–0.068)	0.048 (0.035–0.057)	0.043 (0.034–0.054)	0.000
						III-II 1.000 III-I 0.017 II-I 0.147								III-II 0.823 III-I 0.000 II-I 0.004		
UI	1.553 (0.664–1.665)	1.821 (0.961–1.770)	1.636 (1.189–1.265)	0.607	3.171 (2.438–3.936)	3.105 (2.284–3.663)	3.052 (2.415–3.624)	0.639	1.650 (1.266–2.771)	2.251 (2.099–3.090)	2.024 (1.318–3.273)	0.115	2.685 (2.161–3.528)	2.715 (2.021–3.318)	2.395 (2.010–3.092)	0.011
														III-II 0.930 III-I 0.009 II-I 0.153		
EF	0.096 (0.029–0.115)	0.122 (0.038–0.146)	0.073 (0.032–0.078)	0.223	0.381 (0.335–0.467)	0.375 (0.271–0.416)	0.396 (0.318–0.468)	0.343	0.159 (0.122–0.169)	0.339 (0.248–0.382)	0.343 (0.191–0.439)	0.042	0.404 (0.308–0.498)	0.367 (0.291–0.435)	0.332 (0.242–0.430)	0.000
										III-II 0.773 III-I 0.021 II-I 0.043 [b]				III-II 0.414 III-I0 .000 II-I0 .024		
LS		Number: 2				Number: 29				Number: 9				Number: 79		
UF	0.031 (0.011–0.036)	0.033 (0.009–0.040)	0.023 (0.009–0.025)	0.607	0.056 (0.044–0.079)	0.048 (0.040–0.065)	0.050 (0.040–0.059)	0.024	0.033 (0.023–0.051)	0.034 (0.020–0.040)	0.030 (0.021–0.043)	0.895	0.050 (0.039–0.068)	0.045 (0.034–0.055)	0.041 (0.033–0.054)	0.000
						III-II 1.000 III-I 0.018 II-I 0.018								III-II0.529 III-I 0.000 II-I 0.016		
UI	1.482 (0.656–1.568)	1.570 (0.645–1.711)	1.030 (0.421–1.125)	0.223	3.584 (2.667–4.089)	3.236 (2.655–3.797)	3.053 (2.546–3.685)	0.166	1.891 (1.437–2.864)	2.019 (1.591–2.928)	1.932 (1.408–2.687)	0.641	2.979 (2.219–3.580)	2.687 (2.140–3.362)	2.542 (1.977–3.191)	0.003
														III-II 1.000 III-I 0.003 II-I .051		
EF	0.169 (0.123–0.131)	0.072 (0.000–0.108)	0.034 (0.016–0.034)	0.223	0.418 (0.316–0.492)	0.372 (0.295–0.436)	0.404 (0.321–0.528)	0.166	0.169 (0.119–0.199)	0.336 (0.229–0.386)	0.235 (0.165–0.386)	0.050	0.395 (0.300–0.499)	0.365 (0.273–0.444)	0.323 (0.233–0.435)	0.000

UF, UI, EF stated as median (upper quartile, lower quartiles). Examination before first, second and third treatments expressed as I, II, and III. The values were p values after pairwise comparison of I, II, III. RP: Right parotid; LP: Left parotid; RS: Right submandibular; LS: Left submandibular; UF: Uptake fraction; UI: Uptake index; EF: Excretion fraction.

Table 4: Comparison of salivary gland function in patients before fourth treatment.

Scintigraphy parameters	Male group before fourth treatment number: 6					Female group before fourth treatment number: 8				
	Before treatment	After first treatment	After second treatment	After third treatment	P	Before treatment	After first treatment	After second treatment	After third treatment	P
RP										
UF	0.054 (0.024–0.072)	0.072 (0.035–0.089)	0.051 (0.025–0.077)	0.052 (0.015–0.076)	0.896	0.047 (0.043–0.056)	0.032 (0.031–0.046)	0.033 (0.018–0.037)	0.010 (0.009–0.042)	0.013
						VI-III 1.000 VI-II.231 VI-I .011 III-II 1.000 III-I .231 II-1 1.000				
UI	2.237 (1.492–2.725)	2.3137 (1.691–3.522)	2.252 (1.425–3.257)	2.127 (1.323–2.668)	0.706	2.371 (1.860–2.885)	1.690 (1.537–2.151)	1.388 (0.808–1.844)	0.707 (0.529–1.887)	0.003
						VI-III 1.000 VI-II0.317 VI-I .003 III-II 1.000 III-I 0.040 II-1 0.728				
EF	0.485 (0.330–0.559)	0.542 (0.460–0.705)	0.458 (0.364–0.547)	0.403 (0.004–0.548)	0.204	0.543 (0.500–0.567)	0.478 (0.439–0.487)	0.158 (0.023–0.446)	0.050 (0.022–0.407)	0.001
						VI-III 1.000 VI-II0.071 VI-I .006 III-II 0.199 III-I 0.022 II-1 1.000				
LP										
UF	0.040 (0.035–0.065)	0.052 (0.039–0.067)	0.041 (0.029–0.070)	0.031 (0.010–0.045)	0.849	0.041 (0.035–0.050)	0.035 (0.027–0.048)	0.033 (0.026–0.044)	0.025 (0.018–.035)	0.034
						VI-III 0.137 VI-II 0.231 VI-I 0.043 III-II 1.000 III-I 1.000 II-1 1.000				
UI	1.958 (1.661–2.357)	2.3628 (1.468–2.616)	1.623 (1.307–3.080)	1.675 (1.213–1.995)	0.978	2.051 (1.765–2.396)	1.684 (1.534–2.175)	1.635 (0.963–2.104)	1.576 (0.472–2.029)	0.010
						VI-III 1.000 VI-II 1.000 VI-I .040 III-II 1.000 III-I 0.012 II-I0.317				
EF	0.515 (0.480–0.589)	0.487 (0.385–0.575)	0.419 (0.216–0.548)	0.287 (0.047–0.48)	0.038	0.475 (0.454–0.526)	0.445 (0.297–0.485)	0.411 (0.031–0.501)	0.429 (0.016–0.518)	0.522
	I-III 1.000 VI-II 1.000 VI-I 0.044 III-II 1.000 III-1 0.152 II-1 1.000									
RS										
UF	0.053 (0.040–0.064)	0.057 (0.036–0.076)	0.050 (0.030–0.067)	0.040 (0.014–0.076)	0.284	0.052 (0.041–0.059)	0.039 (0.035–0.048)	0.043 (0.035–0.054)	0.037 (0.030–0.044)	0.021
						VI-III .043 VI-II .586 VI-I .043 III-II 1.000 III-I 1.000 II-1 1.000				
UI	2.147 (1.884–2.778)	3.041 (2.015–3.985)	2.703 (1.927–3.185)	2.726 (1.660–4.742)	0.572	2.988 (2.479–3.495)	2.465 (2.125–3.067)	2.649 (2.306–2.857)	2.447 (2.239–2.601)	0.119
EF	0.386 (0.338–0.444)	0.352 (0.246–0.471)	0.394 (0.315–0.466)	0.422 (0.181–0.475)	0.940	0.437 (0.373–0.455)	0.282 (0.254–0.352)	0.284 (0.218–0.405)	0.348 (0.143–0.437)	0.010
						VI-III 1.000 VI-II 1.000 VI-I 0.317 III-II 1.000 III-I0.040 II-1 0.012				
LS										
UF	0.052 (0.044–0.056)	0.045 (0.043–0.078)	0.054 (0.041–0.063)	0.045 (0.015–0.070)	0.849	0.049 (0.042–0.056)	0.042 (0.030–0.047)	0.042 (0.034–0.049)	0.037 (0.030–0.040)	0.392
UI	2.605 (1.676–3.068)	3.420 (2.807–3.783)	3.023 (2.450–3.487)	2.904 (2.145–3.613)	0.706	2.550 (2.338–3.107)	2.620 (1.897–3.204)	2.666 (2.135–3.045)	2.472 (2.344–2.949)	0.789
EF	0.397 (0.350–0.456)	0.371 (0.255–0.427)	0.420 (0.297–0.504)	0.376 (0.166–0.453)	0.392	0.332 (0.269–0.407)	0.289 (0.259–0.355)	0.274 (0.194–0.405)	0.327 (0.129–0.415)	0.327

UF, UI, EF stated as median (upper quartile, lower quartiles). Examination before first, second, and third treatments expressed as I, II, III, and IV. The values were P values after pairwise comparison of I, II, III, IV. RP: Right parotid; LP: Left parotid; RS: Right submandibular; LS: Left submandibular; UF: Uptake fraction; UI: Uptake index; EF: Excretion fraction.

Table 5: The number of salivary gland injuries before the last three treatments compared with the first treatment.

Scintigraphic parameters	Damage	Male									Female								
		First	Second	*P*	First	Third	*P*	First	Fourth	*P*	First	Second	*P*	First	Third	*P*	First	Fourth	*P*
RP	Hurt	8 (6.5%)	8 (6.5%)	1.000	8 (6.5%)	8 (25.8%)	0.005	8 (6.5%)	2 (33.3%)	0.069	17 (5.1%)	16 (5.1%)	0.859	17 (5.1%)	29 (33%)	0.001	17 (5.1%)	5 (62.5%)	0.001
	No hurt	115 (93.5%)	115 (93.5%)		115 (93.5%)	23 (74.2%)		115 (93.5%)	4 (66.7%)		318 (94.9%)	319 (94.9%)		318 (94.9%)	59 (67%)		318 (94.9%)	3 (37.5%)	
LP	Hurt	5 (4.1%)	9 (7.3%)	0.271	5 (4.1%)	7 (22.6%)	0.003	5 (4.1%)	3 (50%)	0.003	25 (7.5%)	23 (6.9%)	0.881	25 (7.5%)	24 (27.3%)	0.001	25 (7.5%)	2 (25%)	0.125
	No hurt	118 (95.9%)	114 (92.7%)		118 (95.9%)	24 (87.4%)		118 (95.9%)	3 (50%)		310 (92.5%)	312 (93.1%)		310 (92.5%)	64 (72.7%)		310 (92.5%)	6 (75%)	
RS	Hurt	12 (9.8%)	19 (15.4%)	0.179	12 (9.%)	8 (25.8%)	0.032	12 (9.8%)	2 (33.3%)	0.128	44 (13.1%)	48 (14.3%)	0.653	44 (13.1%)	36 (40.9%)	0.001	44 (13.1%)	2 (25%)	0.292
	No hurt	111 (90.2%)	104 (84.6%)		111 (90.2%)	23 (74.2%)		111 (90.2%)	4 (66.7%)		291 (86.9%)	287 (85.7%)		291 (86.9%)	52 (59.1%)		291 (86.9%)	6 (75%)	
LS	Hurt	11 (8.9%)	22 (17.9%)	0.040	11 (8.9%)	8 (25.8%)	0.027	11 (8.9%)	2 (33.3%)	0.112	57 (17%)	62 (18.5%)	0.613	57 (17%)	39 (44.3%)	0.001	57 (17%)	4 (50%)	0.036
	No hurt	112 (91.1%)	101 (82.1%)		112 (91.1%)	23 (74.2%)		112 (91.1%)	4 (66.7%)		278 (83%)	273 (81.5%)		278 (83%)	49 (55.7%)		278 (83%)	4 (50%)	

The sequence number of examinations before treatments. Expressed as number of cases (values of number of cases/total cases of this examination before treatments × 100%). RP: Right parotid; LP: Left parotid; RS: Right submandibular; LS: Left submandibular.

uptake to maintain secretory function [4]. Our results are consistent with those of the above-mentioned studies. It is believed that salivary glands with slight damage in the basal state have a certain compensatory function. After the initial radiation injury, the compensatory function of gland cells is activated by stress, manifesting as increased uptake or excretion. With the increase of radiation dose and the passage of time after ^{131}I treatment, this compensatory function gradually decreases or disappears. In this study, we also selected uninjured salivary glands and compared the functional parameters before and after ^{131}I therapy. Notably, these salivary glands were more likely to be affected than those that were already impaired before treatment. Most showed functional reduction without the phenomenon of functional compensatory increase. This provides new ideas for clinical treatment. For example, salivary gland protection should be strengthened during ^{131}I treatment, especially in patients with normal basal function.

4.3. Different Glands. The salivary gland imaging results after the first and second ^{131}I treatments showed that the submandibular glands are more sensitive than the parotid ones, and the most common change was a decreased UF value representing impaired uptake. We analyzed whether this difference was related to salivary gland cell characteristics and salivary gland structure. Damage to the microvascular endothelial cells in salivary glands caused by radiotherapy is one of the causes of impaired gland function [45, 46]. It leads to microvascular dysfunction and the production of ceramide and reactive oxygen species (ROS) that can induce gland dysfunction. ROS scavengers are used to protect salivary gland function in radiotherapy patients [47]. By inhibiting or eliminating aberrant oxidation reactions, it is possible to reduce damage to salivary gland function caused by radiation. One study found that levels of salivary non-enzymatic antioxidants and antioxidant enzymes in the saliva secreted by the parotid gland were higher than those secreted by the submandibular salivary glands [48]. Therefore, salivary gland function changes due to parotid microvascular injury are not as serious as those caused by submandibular microvascular injury. Another group showed that the saliva-to-serum ^{131}I concentration rates in the parotid gland of mice and humans were 0.59 and 4.6, espectively, while those in the submandibular gland were 5.1 and 6.9 [49]. The ^{131}I concentration was higher in the submandibular glands of both species. An investigation showed that murine duct cells in the different salivary glands varied greatly in their ability to concentrate iodide, so it could be shown that ^{131}I was mainly concentrated in the ducts of the submandibular glands in mice, with lower levels in the parotid gland and very little in sublingual gland ducts [50]. Because of their ability to concentrate ^{131}I, the submandibular glands are more susceptible to radiation damage.

After the first ^{131}I treatment, we performed a second scintigraphy scan. We found that the males younger than 55 and females older than 55 showed a tendency of decreased function of the left parotid gland compared to the right parotid gland. The differential changes in the left and right glands after radiation have been reported in several studies and may be due to the asymmetric concentration of radioactive iodine in the salivary glands [3, 15, 31].

4.4. Treatment Frequency and ^{131}I Dose. The Chi-square test showed that the difference between the number of damaged and undamaged salivary glands in males and females increased significantly with the increase of treatment times, and the percentage of damaged glands also increased gradually. The number of treatments was correlated with the ^{131}I cumulative dose. A correlation between radiation dose and salivary gland dysfunction was previously reported [51, 52]. A salivary glandular scintillation imaging study showed that ~30% of salivary parenchymal function was lost following a single ^{131}I dose of 6 GBq (162 mCi), with a cumulative dose of 35 GBq (945 mCi) resulting in complete loss of glandular function [53]. Parthasarathy and Crawford argued that significant side effects were rarely seen at doses <3.7 GBq (100 mCi) [54].

5. Limitations

Our results should be considered in the context of some limitations. First, this was a retrospective study with no survey to assess patient symptoms and signs, so it was not possible to add more conditions (e.g., dry mouth, difficulty swallowing, loss of taste) for case screening. Second, there was a small number of patients, especially among the group treated more than four times, which limited our analysis of salivary gland function in patients with DTC treated for more than 2–3 years. Third, clinical parameters and test data of some patients were missing. Finally, the lack of significant findings in males maybe because they only accounted for 27% of the study cohort.

6. Conclusions

This study quantitatively compared salivary scintigraphy parameters in DTC patients after multiple ^{131}I treatments. Salivary gland function sensitivities are quite variable in different ages and sexes, with the highest sensitivity in women younger than 55. After treatment, the uptake or secretion function of some salivary glands with impaired basic function increased. Decreased salivary gland function is significantly related to the number of ^{131}I treatments and the cumulative dose. The parotid glands have the most significant reduction in uptake.

Data Availability

The data generated in the study are included in this article. The database is available upon request.

Disclosure

XL and LY are co-first authors. ZM and YW are co-corresponding authors.

Conflicts of Interest

The authors declare that they have no conflicts of interest.

Authors' Contributions

XL and LY contributed equally to the study. ZM and YW contributed equally to the study.

Acknowledgments

This work was supported by the National Natural Science Foundation of China grants (#81571709 and #81971650 to Zhaowei Meng, #81872169 to Xiangqian Zheng) and the design of this research was funded by the Key Project of Tianjin Science and Technology Committee Foundation grant (#16JCZDJC34300 to Zhaowei Meng), Tianjin Science and Technology Committee Foundation grants (#19JCYBJC27400 to Xiangqian Zheng), Tianjin Medical University General Hospital New Century Excellent Talent Program (to Zhaowei Meng), Young and Middle-aged Innovative Talent Training Program from Tianjin Education Committee (to Zhaowei Meng), and Talent Fostering Program (the 131 Project) from Tianjin Education Committee and Tianjin Human Resources and Social Security Bureau (to Zhaowei Meng).

Supplementary Materials

Table S1 summarizes the number of patients, age distribution, and cumulative dose before one or more ^{131}I treatments. Table S2: Chi-square test was performed to determine the relationship between the number of patients by sex and the impairment of salivary gland function before each ^{131}I treatment. There was a statistical difference in the left submandibular gland injury count between sexes before the first treatment ($p < 0.05$). Figure S1: The percentage of damaged salivary glands increased with the number of treatments in both sexes. Figure S2: The cumulative dose of ^{131}I received by patients over several treatments. (*Supplementary Materials*)

References

[1] K. D. Miller, L. Nogueira, A. B. Mariotto et al., "Cancer treatment and survivorship statistics,," *CA: A Cancer Journal for Clinicians*, vol. 69, no. 5, pp. 363–385, 2019.

[2] B. R. Haugen, E. K. Alexander, K. C. Bible et al., "2015 American thyroid association management guidelines for adult patients with thyroid nodules and differentiated thyroid cancer: the American thyroid association guidelines task force on thyroid nodules and differentiated thyroid cancer," *Thyroid*, vol. 26, no. 1, pp. 1–133, 2016.

[3] A. Upadhyaya, P. Zhou, Z. Meng et al., "Radioprotective effect of vitamin E on salivary glands after radioiodine therapy for differentiated thyroid cancer," *Nuclear Medicine Communications*, vol. 38, no. 11, pp. 891–903, 2017.

[4] A. Upadhyaya, Z. Meng, P. Wang et al., "Effects of first radioiodine ablation on functions of salivary glands in patients with differentiated thyroid cancer," *Medicine*, vol. 96, no. 25, p. e7164, 2017.

[5] J.-K. Chung, H. W. Youn, J. H. Kang, H. Y. Lee, and K. W. Kang, "Sodium iodide symporter and the radioiodine treatment of thyroid carcinoma," *Nuclear Medicine and Molecular Imaging*, vol. 44, no. 1, pp. 4–14, 2010.

[6] R. K. Badam, J. Suram, D. B. Babu et al., "Assessment of salivary gland function using salivary scintigraphy in pre and post radioactive iodine therapy in diagnosed thyroid carcinoma patients," *Journal of Clinical and Diagnostic Research: Journal of Clinical and Diagnostic Research*, vol. 10, 2016.

[7] K. M. D. La Perle, D. C. Kim, N. C. Hall et al., "Modulation of sodium/iodide symporter expression in the salivary gland," *Thyroid*, vol. 23, no. 8, pp. 1029–1036, 2013.

[8] C. Llena-Puy, "The rôle of saliva in maintaining oral health and as an aid to diagnosis, Medicina Oral," *Patología Oral y Cirugía Bucal.*vol. 11, no. 5, 2006.

[9] E. Kaufman, I. B. Lamster, and I. B. Lamster, "The diagnostic applications of saliva- A review," *Critical Reviews in Oral Biology & Medicine*, vol. 13, no. 2, pp. 197–212, 2002.

[10] M. Lenander-Lumikari and V. Loimaranta, "Saliva and dental caries," *Advances in Dental Research*, vol. 14, no. 1, pp. 40–47, 2000.

[11] J. C. Atkinson, M. Grisius, W. Massey, and W. Massey, "Salivary hypofunction and xerostomia: diagnosis and treatment," *Dental Clinics of North America*, vol. 49, no. 2, pp. 309–326, 2005.

[12] E. N. Klein Hesselink, A. H. Brouwers, J. R. de Jong et al., "Effects of radioiodine treatment on salivary gland function in patients with differentiated thyroid carcinoma: a prospective study," *Journal of Nuclear Medicine*, vol. 57, no. 11, pp. 1685–1691, 2016.

[13] R. Solans, J. A. Bosch, P. Galofré et al., "Salivary and lacrimal gland dysfunction (sicca syndrome) after radioiodine therapy," *Journal of Nuclear Medicine: Official Publication, Society of Nuclear Medicine*, vol. 42, no. 5, pp. 738–743, 2001.

[14] S. Hyer, A. Kong, B. Pratt, C. Harmer, and C. Harmer, "Salivary gland toxicity after radioiodine therapy for thyroid cancer," *Clinical Oncology*, (Royal College of Radiologists), vol. 19, no. 1, pp. 83–86, 2007.

[15] J.-q. Wu, H.-j. Feng, W. Ouyang et al., "Systematic evaluation of salivary gland damage following I-131 therapy in differentiated thyroid cancer patients by quantitative scintigraphy and clinical follow-up," *Nuclear Medicine Communications*, vol. 36, no. 8, pp. 819–826, 2015.

[16] E. Horvath, V. Skoknic, S. Majlis et al., "Radioiodine-induced salivary gland damage detected by ultrasonography in patients treated for papillary thyroid cancer: radioactive iodine activity and risk," *Thyroid*, vol. 30, no. 11, pp. 1646–1655, 2020.

[17] D. Muralidharan, N. Fareed, P. V. Pradeep et al., "Qualitative and quantitative changes in saliva among patients with thyroid dysfunction prior to and following the treatment of the dysfunction," *Oral Surgery, Oral Medicine, Oral Pathology and Oral Radiology*, vol. 115, no. 5, pp. 617–623, 2013.

[18] T. Gupta, C. Hotwani, S. Kannan et al., "Prospective longitudinal assessment of parotid gland function using dynamic quantitative pertechnate scintigraphy and estimation of dose-response relationship of parotid-sparing radiotherapy in head-neck cancers," *Radiation Oncology*, vol. 10, no. 1, p. 67, 2015.

[19] T. Aksoy, P. O. Kiratli, B. Erbas, and B. Erbas, "Correlations between histopathologic and scintigraphic parameters of salivary glands in patients with Sjögren's syndrome," *Clinical Rheumatology*, vol. 31, no. 9, pp. 1365–1370, 2012.

[20] D. A. Anjos, E. C. S. C. Etchebehere, A. O. Santos et al., "Normal values of [99mTc]pertechnetate uptake and

excretion fraction by major salivary glands," *Nuclear Medicine Communications*, vol. 27, no. 4, pp. 395–403, 2006.

[21] G. B. Proctor, A. M. Shaalan, and A. M. Shaalan, "Disease-induced changes in salivary gland function and the composition of saliva," *Journal of Dental Research*, vol. 100, no. 11, pp. 1201–1209, 2021.

[22] J. Y. Barr, X. Wang, P. A. Kreiger, S. M. Lieberman, and S. M. Lieberman, "Salivary-gland-protective regulatory T-cell dysfunction underlies female-specific sialadenitis in the non-obese diabetic mouse model of Sjögren syndrome," *Immunology*, vol. 155, no. 2, pp. 225–237, 2018.

[23] Y. Q. Zhang, X. Ye, Y. Meng, Y. N. Zhao, D. G. Liu, and G. Y Yu, "Evaluation of parotid gland function before and after endoscopy-assisted stone removal," *Journal of Oral and Maxillofacial Surgery: Official Journal of the American Association of Oral and Maxillofacial Surgeons*, vol. 77, no. 2, 2019.

[24] A. Chern, A. O. Famuyide, G. Moonis, A. K. Lalwani, and A. K. Lalwani, "Sialadenitis: a possible early manifestation of covid -19," *The Laryngoscope*, vol. 130, no. 11, pp. 2595–2597, 2020.

[25] M. Knaś, M. Maciejczyk, K. Sawicka et al., "Impact of morbid obesity and bariatric surgery on antioxidant/oxidant balance of the unstimulated and stimulated human saliva," *Journal of Oral Pathology & Medicine: Official Publication of the International Association of Oral Pathologists and the American Academy of Oral Pathology*, vol. 45, no. 6, pp. 455–464, 2016.

[26] M. Maciejczyk, J. Matczuk, M. Żendzian-Piotrowska et al., "Eight-week consumption of high-sucrose diet has a pro-oxidant effect and alters the function of the salivary glands of rats," *Nutrients*, vol. 10, no. 10, 2018.

[27] J.-S. Choi, I. S. Park, S.-k. Kim, J.-Y. Lim, Y. M. Kim, and Y.-M. Kim, "Analysis of age-related changes in the functional morphologies of salivary glands in mice," *Archives of Oral Biology*, vol. 58, no. 11, pp. 1635–1642, 2013.

[28] W. Pedersen, M. Schubert, K. Izutsu, T. Mersai, E. Truelove, and E. Truelove, "Clinical science age-dependent decreases in human submandibular gland flow rates as measured under resting and post-stimulation conditions," *Journal of Dental Research*, vol. 64, no. 5, pp. 822–825, 1985.

[29] L. Lin and L. Sijin, "Clinical guidelines for 131I treatment of Graves' hyperthyoidism (2021 edition)," *Chinese Society of Nuclear Medicine*, vol. 41, no. 04, pp. 242–253, 2021, (in Chinese).

[30] B. Fallahi, D. Beiki, S. M. Abedi et al., "Does vitamin E protect salivary glands from I-131 radiation damage in patients with thyroid cancer?" *Nuclear Medicine Communications*, vol. 34, no. 8, pp. 777–786, 2013.

[31] Y.-S. An, J.-K. Yoon, S. J. Lee et al., "Symptomatic late-onset sialadenitis after radioiodine therapy in thyroid cancer," *Annals of Nuclear Medicine*, vol. 27, no. 4, pp. 386–391, 2013.

[32] K. Shizukuishi, S. Nagaoka, Y. Kinno et al., "Scoring analysis of salivary gland scintigraphy in patients with Sjögren's syndrome," *Annals of Nuclear Medicine*, vol. 17, no. 8, pp. 627–631, 2003.

[33] J. M. Roesink, M. A. Moerland, A. Hoekstra, P. P. V. Rijk, C. H. Terhaard, and C. H. J. Terhaard, "Scintigraphic assessment of early and late parotid gland function after radiotherapy for head-and-neck cancer: a prospective study of dose-volume response relationships," *International Journal of Radiation Oncology, Biology, Physics*, vol. 58, no. 5, pp. 1451–1460, 2004.

[34] G. Sunavala-Dossabhoy, "Radioactive iodine: an unappreciated threat to salivary gland function," *Oral Diseases*, vol. 24, no. 1-2, pp. 198–201, 2018.

[35] M. Caglar, M. Tuncel, R. Alpar, and R. Alpar, "Scintigraphic evaluation of salivary gland dysfunction in patients with thyroid cancer after radioiodine treatment," *Clinical Nuclear Medicine*, vol. 27, no. 11, pp. 767–771, 2002.

[36] K. S. Jo, Y.-S. An, S. J. Lee et al., "Significance of salivary gland radioiodine retention on post-ablation 131I scintigraphy as a predictor of salivary gland dysfunction in patients with differentiated thyroid carcinoma," *Nuclear Medicine and Molecular Imaging*, vol. 48, no. 3, pp. 203–211, 2014.

[37] B. Liu, R. Huang, A. Kuang et al., "Iodine kinetics and dosimetry in the salivary glands during repeated courses of radioiodine therapy for thyroid cancer," *Medical Physics*, vol. 38, no. 10, pp. 5412–5419, 2011.

[38] J. P. Almeida, Á. E. Sanabria, E. N. P. Lima, L. P. Kowalski, and L. P. Kowalski, "Late side effects of radioactive iodine on salivary gland function in patients with thyroid cancer," *Head & Neck*, vol. 33, no. 5, pp. 686–690, 2011.

[39] R. Levi-Montalcini and S. Cohen, "Effects of the extract of the mouse submaxillary salivary glands on the sympathetic system of mammals," *Annals of the New York Academy of Sciences*, vol. 85, pp. 324–341, 1960.

[40] R. L. Byyny, D. N. Orth, S. Cohen, and E. S. Doyne, "Epidermal growth factor: effects of androgens and adrenergic agents." *Endocrinology*, vol. 95, no. 3, pp. 776–82, 1974.

[41] D. N. Ishii and E. M. Shooter, "Regulation of nerve growth factor synthesis in mouse submaxillary glands by testosterone." *Journal of Neurochemistry*, vol. 25, no. 68, pp. 43–51, 1975.

[42] J. E. Brandt, R. Priori, G. Valesini, and D. Fairweather, "Sex differences in Sjögren's syndrome: a comprehensive review of immune mechanisms." *Biology of Sex Differences*, vol. 6, p. 19, 2015.

[43] F. R. Burlage, H. Faber, H. H. Kampinga, J. A. Langendijk, A. Vissink, and R. P. Coppes, "Enhanced proliferation of acinar and progenitor cells by prophylactic pilocarpine treatment underlies the observed amelioration of radiation injury to parotid glands," *Radiotherapy & Oncology*, vol. 90, no. 2, pp. 253–256, 2009.

[44] J. Denekamp, "Cell kinetics and radiation biology," *International Journal of Radiation Biology & Related Studies in Physics, Chemistry & Medicine*, vol. 49, no. 2, pp. 357–380, 1986.

[45] A. P. Cotrim, A. Sowers, J. B. Mitchell, B. J. Baum, and B. J. Baum, "Prevention of irradiation-induced salivary hypofunction by microvessel protection in mouse salivary glands," *Molecular Therapy*, vol. 15, no. 12, pp. 2101–2106, 2007.

[46] Z. Zhang, F. Cui, C. Cao, Q. Wang, and Q. Zou, "Single-cell RNA analysis reveals the potential risk of organ-specific cell types vulnerable to SARS-CoV-2 infections," *Computers in Biology and Medicine*, vol. 140, Article ID 105092, 2022.

[47] A. Mizrachi, A. P. Cotrim, N. Katabi et al., "Radiation-induced microvascular injury as a mechanism of salivary gland hypofunction and potential target for radioprotectors," *Radiation Research*, vol. 186, no. 2, pp. 189–195, 2016.

[48] K. Błochowiak and H. Witmanowski, "Ocena stężenia produktów peroksydacji lipidów w ślinie i w surowicy krwi u pacjentów ze złamaniami żuchwy," *Czasopismo Stomatologiczne*, vol. 63, no. 4, pp. 250–258, 2010.

[49] B. Cohen, N. B. Myant, and N. B. Myant, "Concentration of salivary iodide: a comparative study," *The Journal of Physiology*, vol. 145, no. 3, pp. 595–610, 1959.

[50] J. H. Logothetopoulos, N. B. Myant, and N. B. Myant, "Concentration of radio-iodide and 35-S-thiocyanate by the

salivary glands," *The Journal of Physiology*, vol. 134, no. 1, pp. 189–194, 1956.

[51] R. Solans, J. A. Bosch, P. Galofré et al., "Salivary and lacrimal gland dysfunction (Sicca syndrome) after radioiodine therapy," *Journal of Nuclear Medicine: Official Publication, Society of Nuclear Medicine*, vol. 42, pp. 738–743, 2001.

[52] C. Alexander, J. B. Bader, A. Schaefer, C. Finke, and C. M Kirsch, "Intermediate and long-term side effects of high-dose radioiodine therapy for thyroid carcinoma," *Journal of Nuclear Medicine: Official Publication, Society of Nuclear Medicine*, vol. 39, no. 9, pp. 1551–1554, 1998.

[53] W. Jentzen, E. Schneider, L. Freudenberg et al., "Relationship between cumulative radiation dose and salivary gland uptake associated with radioiodine therapy of thyroid cancer," *Nuclear Medicine Communications*, vol. 27, no. 8, pp. 669–676, 2006.

[54] K. L. Parthasarathy and E. S. Crawford, "Treatment of thyroid carcinoma: emphasis on high-dose 131I outpatient therapy," *Journal of Nuclear Medicine Technology*, vol. 30, no. 4, pp. 165–173, 2002, quiz 172-3.

Hindawi
Journal of Healthcare Engineering
Volume 2022, Article ID 1487212, 12 pages
https://doi.org/10.1155/2022/1487212

Research Article

Optimization-Based Ensemble Feature Selection Algorithm and Deep Learning Classifier for Parkinson's Disease

B. Sabeena,[1] **S. Sivakumari**,[1] **and Dawit Mamru Teressa**[2]

[1]*Department of Computer Science and Engineering, Avinashilingam Institute for Home Science and Education for Women, School of Engineering, Coimbatore, India*
[2]*Department of Chemical Engineering, College of Biological and Chemical Engineering, Addis Ababa Science and Technology University, Addis Ababa, Ethiopia*

Correspondence should be addressed to B. Sabeena; sabeena.bheeman@gmail.com and Dawit Mamru Teressa; dawit.mamiru@aastustudent.edu.et

Received 5 January 2022; Revised 4 February 2022; Accepted 22 February 2022; Published 13 April 2022

Academic Editor: Enas Abdulhay

PD (Parkinson's Disease) is a severe malady that is painful and incurable, affecting older human beings. Identifying PD early in a precise manner is critical for the lengthened survival of patients, where DMTs (data mining techniques) and MLTs (machine learning techniques) can be advantageous. Studies have examined DMTs for their accuracy using Parkinson's dataset and analyzing feature relevance. Recent studies have used FMBOAs for feature selections and relevance analyses, where the selection of features aims to find the optimal subset of features for classification tasks and combine the learning of FMBOAs. EFSs (ensemble feature selections) are viable solutions for combining the benefits of multiple algorithms while balancing their drawbacks. This work uses OBEFSs (optimization-based ensemble feature selections) to select appropriate features based on agreements. Ensembles have the ability to combine results from multiple feature selection approaches, including FMBOAs, LFCSAs (Lévy flight cuckoo search algorithms), and AFAs (adaptive firefly algorithms). These approaches select optimized feature subsets, resulting in three feature subsets, which are subsequently matched for correlations by ensembles. The optimum features are generated by OBEFSs the trained on FCBi-LSTMs (fuzzy convolution bi-directional long short-term memories) for classifications. This work's suggested model uses the UCI (University of California-Irvine) learning repository, and the methods are evaluated using LOPO-CVs (Leave-One-Person-Out-Cross Validations) in terms of accuracies, F-measure values, and MCCs (Matthews correlation coefficients).

1. Introduction

Parkinson's is a neurologic problem that involves tremors, rigidity, and problems moving, balancing, and coordinating. The signs of the disease normally appear slowly and continue to worsen. PD is a neurological malady classified as a motor system dysfunction. The patient's activities deteriorate with PD as it progresses. Patients are affected in their fundamental bodily systems, including breathing, balance, movements, and heart functioning [1], where, at initial stages, their speech flow gets hindered. The early diagnosis of PD leads to a longer life of patients, and the diagnostics require high precision and robust health informatics tools. Such solutions aim at assisting clinicians [2–4] who detect PD's severity using a range of sensors. This research work uses different speech signal processing methodologies to obtain PD's clinically relevant characteristics, which are then processed using learning algorithms to provide reliable detections of PDs.

The performances of computational algorithms are inextricably linked to the quality of input data. The manual identification of speeches or voices in a complex and intricate task can be executed efficiently by MLTs. Important features from voice signals can be identified by computer-based techniques, which may be one of the three categories, namely supervised, unsupervised, or semisupervised, based on the labeling of data. Filtering, wrapping, and embedding are the examples of supervised feature selection approaches.

Filtering strategies choose features that are unrelated to categorizations, while wrappers use the projected accuracies of previously determined values by algorithms for feature estimations. Embedded approaches like the filter models begin by selecting multiple potential feature subsets with specific cardinalities using statistical criteria, where subgroups with highest classification accuracies are finally selected. Unsupervised feature selections work on unlabeled data, however, evaluating the relevance of features is difficult for them. Using the labeled and unlabeled data and semi-supervised feature selections can evaluate feature relevance.

Computational methods based on biological evolutions provide a stronger basis for solving problems or taking decisions [5, 6]. EFSs boost the stability of feature selections as they take advantage of single approaches while overcoming their flaws. The analysis of features from datasets can be based on individual assessments or by the evaluation of subsets [7, 8]. Individual assessments create a rank of characteristics based on relevance, while alternative approaches employ search strategies to generate a series of feature subsets. These subsets are assessed iteratively using optimality criteria until they arrive at a final subset of selected characteristics [9]. This work's OBEFS framework guides the construction of EFSs that combine the benefits of several feature selection methods, avoid biases, and cover up their drawbacks.

The hierarchical layers of DNNs (deep neural networks), which are DLTs, manage to generate deep abstract representations of input features in applications. DLTs have been exploited in many applications, including speech recognition, image categorization, medication development, and genetic research [10]. Researchers have used DNNs for PD categorizations mainly because of their effectiveness [11, 12]. DNNs are very helpful classifiers in the case of PDs as they simulate complex and nonlinear data linkages. Previous research on PD classifications used single features like EEG data [11] and sensor activities [12] as inputs for CNNs (convolution neural networks), where the usage of unique parallel layers for classifications has not been tried. The study in [13] proliferated voices using more voice recordings of individuals in training and testing procedures with CVs (cross-validations), resulting in biased performance evaluations. Since the data had voice recordings of healthy persons and PD patients, LOPO-CVs were used to assess the performances of the proposed framework. LOPO-CVs removed examples from individuals in iterations in test sets while using other instances in training.

The suggested OBEFSs framework of this work selects features based on agreements. Instead of employing single feature selection approaches, the ensembles of feature selection methods aim to integrate numerous feature selection methods, such as FMBOAs, LFCSAs, and AFAs, whereas in OBEFSs, optimum features are utilized to train FCBi-LSTM classifiers. The proposed technique was trained using datasets from the UCI machine learning repositories, while its performance was validated using LOPO-CVs. This work's suggested model uses UCI learning repositories, and the methods are evaluated using LOPO-CVs in terms of accuracies, F-measure values, and MCCs.

2. Literature Review

In this part, we will outline some current works on PD classification that make use of machine learning techniques and discuss contemporary deep learning methods in PD classification. To evaluate speech recordings for PD classification, Alqahtani et al. [14] proposed classifications based on NNges (non-nested generalized exemplars), which, in spite of their capabilities, were not examined thoroughly. The study's experiments categorized healthy and PD using NNges and the algorithm's optimized parameters. Furthermore, the data was balanced using the synthetic minority oversampling technique (SMOTE) method. Finally, using the balanced data, NNge and ensemble algorithms, notably AdaBoostM1, were developed.

Using the sets of vocal data, Gunduz [15] used the dual frameworks of CNNs for identifying PDs, where different feature sets were generated but merged together. Their first architecture combined several feature sets before feeding them as inputs to 9-layered CNNs, while the second part fed feature set information directly to convolution layers in parallel. Hence, each parallel branch's deep features were obtained before their merger into layers. Their second showed highly promising results in tests as they learned deep features utilizing parallel convolutions. The extracted deep features were efficient in increasing the discriminative powers of classifiers in addition to differentiating patients with PDs from healthy people.

PDs were classified by Li et al. [16] by combining CART and ensemble learning. The study used CART to iteratively identify optimal training speech samples with high levels of differentiation. The study used ensembles, including RFs (random forests), SVMs (support vector machines), and ELMs (extreme learning machines) for learning optimal training data. The study classified test data using trained ensemble-learning systems. The study found that CART and RF combinations were stable when compared to other strategies and also improved PD predictions with speech data categorizations. Caliskan et al. [17] projected the diagnosis of PDs using speech impairments, the first indication of the disease. They used DNNs with stacked autoencoders and the softmax function for classifications. Their simulation results across two databases demonstrated the efficiency of DNN classifiers in comparison with other classification techniques.

For quickly detecting PDs, Cai et al. [18] proposed the usage of enhanced FKNNs (fuzzy K-nearest neighbors) combined with CBFOs (chaotic bacterial foraging optimizations) with Gauss mutations on voices data. Their CBFO-FKNN was an evolutionary instance-based learning methodology, where FKNN's parameters were tuned effectively by CBFOs. The study evaluated their suggested approach exhaustively on PD datasets in terms of classification accuracies, sensitivities, specificities, and AUCs (area under the receiver operating characteristic curves). The study aided physicians in making better clinical diagnostic judgments.

Castro et al. [19] classified PDs on UCI machine learning repository datasets with ANNs using MLPs (multilayer perceptrons). Their collections included voice recordings of patients with PDs along with control groups. The study used several networks and trained 10 to 6000 neurons, which were increased ten folds in the hidden layers. Their analyses of speech-related characteristics by ANNs could be used to assess patients' impacts of PDs. MLTs can identify other neurological disorders when biological data is made available. Disorders were classified by Abdurrahman and Sintawati, [20] where well-known speech characteristics were used in PD research, including jitters, shimmers, basic frequency parameters, and harmonicity parameters, and they assessed PDs using RPDEs (recurrence period density entropies), DFAs (detrended fluctuation analyses), and PPEs (pitch period entropies). PDs were classified using the XGBoost algorithm, which used identified baseline features, followed by feature selections executed from feature importance plots to enhance the model's performance. The resulting locShimmer features were eliminated from the model, and the efficacy of features was improved by XGBoost's assessments of feature importance to increase classification accuracies.

Karabayir et al. [21] examined PD data with multiple MLTs, including LGBs (light gradient boosts), EGBs (extreme gradient boosts), RFs, SVMs, KNNs, least absolute shrinkages, selection operator regressions, and LRs (logistic regressions). The study also conducted variable significance analyses to find important factors in people diagnosed with PDs. The study found that LGBs outperformed other MLTs in benchmarks and could be utilized to screen huge patient groups for PDs at low costs. Patra et al. [22] employed MLTs to assess the voices of patient datasets and identify PDs. The study's base classifiers were DTs (decision trees), LRs, and KNNs, which had their performances compared to ensembles like bagging, RFs, and boosts. Furthermore, the most important traits associated with classifications for PDs were discovered and prioritized, depending on feature importance with the aim of differentiating PD-affected patients by detecting dysphonia.

Parisi et al. [23] proposed the use of hybrid AIs (artificial intelligence) for examining the cases of PDs. The study used UCI's databases, where the dysphonic values of 68 patients' clinical ratings were considered for processing. The study's feature selections were based on MLP weights while ranking input features, where physiological and pathological patterns were given different weight values. This strategy reduced examinable features from 27 to 20, thus effectively reducing the dimensions for the learning of LSVMs (Lagrangian support vector machines). The proposed hybrid MLP-LSVMs performed well in benchmarks against the existing and previously proposed schemes and could be used in clinical environments for the detection of PDs.

Datasets with rich features were examined by Hasan and Hasan [24] using ANOVA (Analysis of Variance) F-score values to extract the top 50 features. Several MLTs were applied, and their results were compared to prior studies. Their experiments found that feeding select characteristics to RFs resulted in the greatest accuracy scores. Their use of ANOVA for feature extraction successfully retrieved important characteristics that distinguish PD patients from healthy persons while improving classification accuracy scores. Qasim et al. [25] suggested hybrid feature selection approaches for processing unbalanced PD datasets. SOMTE approach was used in the study to balance the dataset. Subsequently, RFEs (recursive feature eliminations) and PCAs (principal component analyses) were used to remove contradictions found in the dataset's features and reduce the processing times of PCAs. Their classifiers included bagging, KNNs, MLPs, and SVMs that worked on the acoustic recordings of PDs along with the patient's individual characteristics. Their idea of using SMOLTE with RFEs and PCAs in preprocessing datasets was also compared with other identifiers for PDs and general medical disorders found in people. The study was an asset to healthcare organizations.

Even though the first system integrates distinct selected features [15] prior to feeding them to a 9-layered CNN, the second model feeds feature sets to concurrent input layers that are directly connected to convolution layers. Before integrating deep features from each parallel connection in the merge layer, deep features from each parallel branch are extracted simultaneously. The suggested models are trained using information from UCI machine learning, and their results are verified using Leave-One-Person-Out Cross Validation (LOPO CV). The F-measure and Matthews correlation coefficient measure, as well as correctness, are employed to examine our data because of the imbalanced class distribution. This second model appears to be quite promising, as it is capable of learning feature representations from each set of features via concurrent convolution layers, according to experimental data.

3. Proposed Methodology

This research work proposes a new feature selection and classification framework for identifying PDs. This work uses five major steps, namely, the extraction of features based on voices, dimensionality reductions using KPCAs (kernel-based principal component analyses), the usage of proposed OBEFSs, LFCSAs, AFAs, and FCBi-LSTMs. Subsequently, the assessments are evaluated using LOPO-CVs. Figure 1 depicts the general flowchart of the proposed system.

3.1. PD Dataset. The PD dataset encompassed speech samples used by prior studies to diagnose PDs from UCI's machine learning repositories [13]. The data gathered at Istanbul University's Cerrahpasa Faculty of Medicine's Department of Neurology comprised 188 PD patients (107 men and 81 women) in the age range of [33, 87] and 64 healthy persons (23 men and 41 women) in [41, 82] age ranges. The voices were collected on 44.1 kHz (microphone's frequency), and three copies of the vowels of individuals were collected after doctor's examinations.

3.2. Feature Extractions. The dataset had baseline and temporal frequency features, MFCCs (Mel frequency cepstral coefficients), WTs (wavelet transforms), TQWTs (tunable Q-factor wavelet transforms), and vocal fold features:

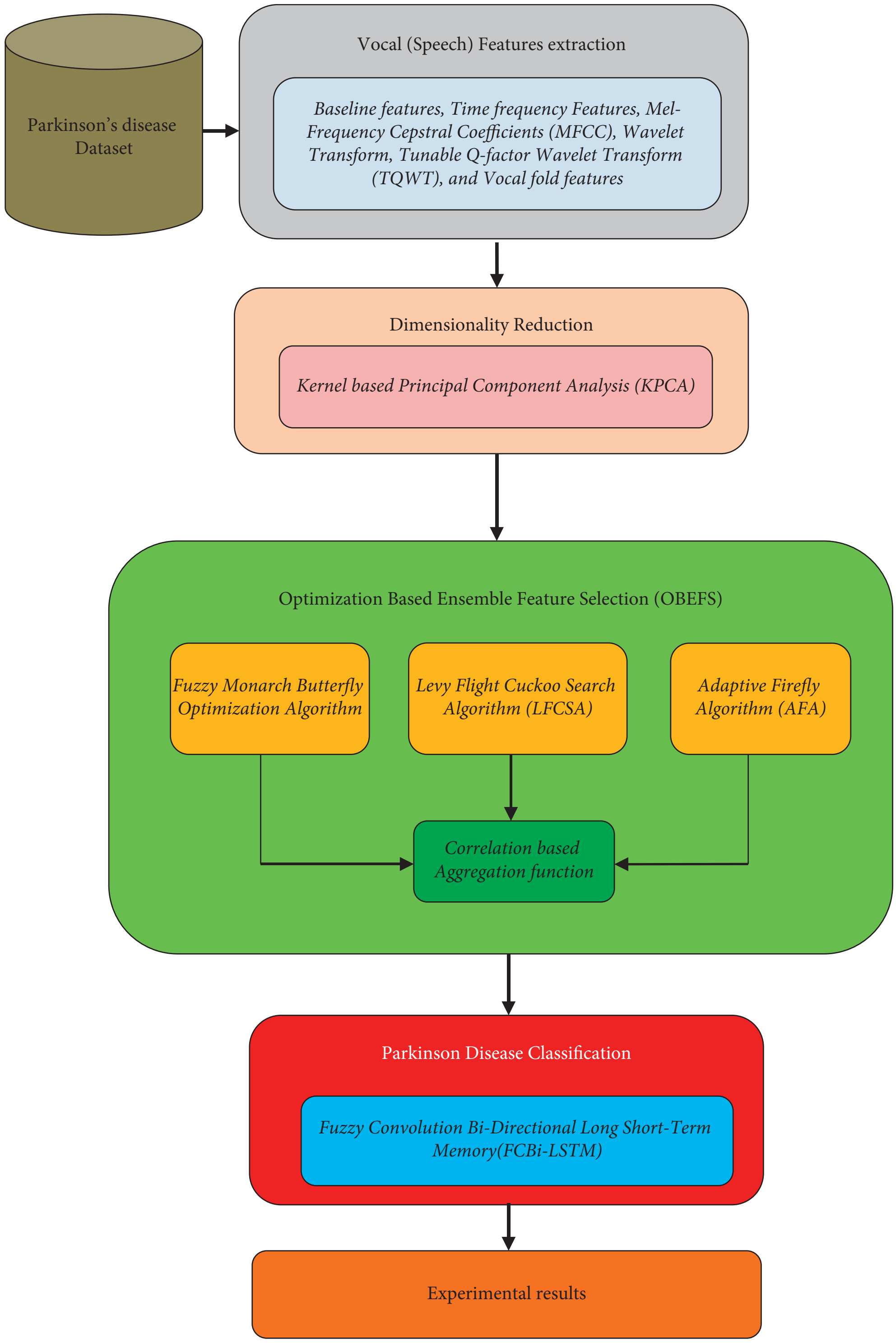

Figure 1: Overall flow of the proposed system.

(i) Baseline features: since PDs impede the speech of patients even in the early stages, speech characteristics were successfully used to evaluate PDs and track the disease's developments following medicinal therapies. The fundamental frequency parameters (#5), harmonicity parameters (#2), RTDEs (recurrence time density entropies) (#1), DFAs (detrended fluctuation analyses) (#1), and PPEs (#1) have been extensively utilized in characterizing speech-based PD researches [24, 26] and form the baseline features [13].

(ii) Time frequency features: intensity parameters (#3), formant frequencies (#4), and bandwidth (#4) are the examples of features.

(iii) MFCCs: MFCC-based extractions use triangular overlapped filter banks to combine cepstral analyses with spectral domain partitions. MFCCs can detect rapid deterioration in the movements of articulators in PDs like the tongues and lips, which are directly affected by the disease. The dataset had 84 characteristics related to MFCCs to identify the PD effects in the vocal tract (#84), and they were generated using the mean and standard deviation of initial 13 MFCCs along with the signal's log energies and $1^{st}/2^{nd}$ order derivatives [13], in addition to vocal folds.

(iv) WTs: generally, WTs are used to make decisions about signals and specifically on signals with minor fluctuations on regional scales. Several studies have utilized WT features obtained from a speech sample's raw fundamental frequencies (F0) to diagnose PD. This work produced 182 WTs characteristics from both approximations and detailed coefficients, including energies, Shannon's and log energy entropies, and Teager-Kaiser energies.

(v) TQWTs: the extraction of features using TQWTs improves signal qualities by adjusting three parameters, namely Q-factors (Q), redundancies (r), and a number of levels (J) based on the signal's behaviors. The oscillations in the time domain signals are proportional to Q-factors, while J stands for decomposed layer counts. On decompositions, J high-pass filters output $J+1$ sub-bands and one final low-pass filtered output. Ringing, controlled by r allows wavelet's localizations with respect to time [27]. This study's tests yielded 432 TQWT-related characteristics from the dataset [13].

(vi) Vocal fold features: the effects of noises on vocal folds were also investigated in this work using features based on vocal fold vibrations. The study extracted the following from the data [13]: glottis quotients (GQs) (#3), glottal-to-noise excitations (GNEs) (#6), vocal fold excitation ratios (VFERs) (#7), and empirical mode decompositions (EMDs).

(vii) Concat features: concat features are the combination of baseline, vocal fold, and time frequency features.

3.3. Dimensionality Reduction Using KPCAs. Approaches based on KPCAs are prominent for dimensionality reductions. KPCAs consider linear subspaces with reduced dimensionalities in the original sound's feature spaces, where new sound recordings of PDs show the greatest variance in features [28]. Assuming $\{a_i\}, i = 1, \ldots N$ is the PD dataset, where a_i represents D-dimensional sound recorded feature vectors, they have to be projected into M-dimensional sound reordered feature subspaces that are lesser than D, and reduced feature vectors of sound recordings are identified. These reduced dimensional feature sets are used by OBEFSs for selecting relevant features.

3.4. Feature Selections Using OBEFSs. The proposed OBEFSs integrate the normalized results of multiple feature selections to arrive at quantitative feature sets with ensemble significances. In the initial phase, the series of feature selectors are created for different outputs, followed by the aggregations of a single model's results. The aggregations of feature selections are accomplished using correlations or consensus on feature ranks or counting most selected features for determining consensus-based feature subsets. The proposed OBEFSs generate final consensus ranks by combining feature ranks supplied by single feature selectors: FMBOAs, LFCSAs, and AFAs.

3.4.1. FMBOAs. This work uses FMBOAs for the selection of feature subsets, where the characteristics for samples are considered based on the effects of feature existences in PDs. Classifiers then use these selected attributes from samples (m denotes the number of voice samples). Classifiers forecast their own class labels, and evaluations are made for ultimate selections. The original characteristics are given feature weights that indicate their significance to classifications, and features with the highest weights are chosen. MBOs are migration-based that are built on migration trends, where fitness and importance of selections are rated. When used without modifications, FMBOAs show good classification accuracy results, indicating that they balance their global and local searches. The global search components of MBOAs were tweaked in this study to provide more precise results and boost effectiveness in locating the right characteristics before resorting to local searches. Individual butterflies analyze attributes that interact with one another on local levels, disseminating information across swarms and resulting in the system's growing capabilities [29–31]. They are carried out with the help of two operations, namely migration operators and adjustments to butterfly operators.

3.4.2. LFCSAs. CSAs (cuckoo search algorithms) are motivated by the unusual habit of cuckoo species, known as obligatory interspecific brood parasitism [32]. These behavioral patterns are based on the fact that certain animals use suitable hosts to optimize the selections of characteristics from datasets to grow their progenies. CSAs avoid parental commitments in rearing their offspring while limiting the dangers of egg loss (irrelevant traits) to other species. The final characteristics are chosen by placing eggs (features) in a variety of nests. The method's purpose is to replace the present solutions with eggs (irrelevant features) previously placed in the nest with these new solutions connected with cuckoo eggs (features). This iterative replacement may undoubtedly increase the quality of the solution over iterations, finally leading to a very good solution of the feature. In particular, CSA is based on three idealized rules [33, 34], which are as follows:

(1) Cuckoos lay the eggs (features) in nests randomly (accuracies).

(2) Nests with the best eggs (quality of features) are considered for subsequent generations for producing better solutions (features).

(3 The host nest counts are set with probability $prb_a \in [0, 1]$. Hosts can find alien eggs (feature), a rule approximated by new nest replacements prb_a of the n available host nests. LFCSA algorithm initially begins with the N host. (1) gives the initial values of the k^{th} component of the j^{th} nest.

$$f_j^k(0) = \mu.\left(\mathrm{up}_j^k - \mathrm{low}_j^k\right) + \mathrm{low}_j^k, \quad (1)$$

where up_j^k is the k^{th} feature's upper bound, low_j^k is the k^{th} feature's lower bound, and μ is the uniform random variable in the range (0, 1). These parameters are adjusted for ensuring the feature values that exist with their feature spaces. The feature (egg), say i, randomly selected in the iteration, results in the solution f_i^{t+1}. The algorithm uses Lévy flights in place of random walks for efficient random searches. These flights, similar to random walks, are characterized by step sizes, following probability distributions with isotropic and random orientations. Lévy flights are depicted by

$$f_i^{t+1} = f_i^t + \alpha \oplus levy(\lambda). \quad (2)$$

The superscript t denotes the current generation, the symbol ⊕ denotes entry-wise multiplication, and $\alpha > 0$ denotes the step size. This step size specifies how far a particle (feature) may move in a certain number of iterations using a random walk. The Lévy distribution modulates the transition probability of the Lévy flights in

$$levy(\lambda) \sim g^{-\lambda}, \quad (1 < \lambda \leq 3), \quad (3)$$

The production of random numbers with Lévy flights has two basic phases from a computational standpoint, which are as follows:

To begin, a random direction based on a uniform distribution is selected.

Then, based on the chosen Lévy distribution, a series of steps is constructed.

For symmetric distributions, Mantegna's approach is employed [34]. This method uses an equation to calculate the factor,

$$\widehat{\phi} = \left(\frac{\Gamma(1+\widehat{\beta}).Sin(\pi.\widehat{\beta}/2)}{\Gamma\left((1+\widehat{\beta}/2).\widehat{\beta}.2^{\widehat{\beta}-1/2}\right)} \right)^{1/\beta}, \quad (4)$$

where the Gamma function is denoted by Γ, and since $\widehat{\beta} = 3/2$ was utilized in a recent study [34], this work used the same ranges here. By (5), this factor is utilized in Mantegna's procedure to compute the step lengths:

$$\varsigma = \frac{u}{|v|^{1/\beta}}, \quad (5)$$

where u and v are the zero mean and deviation normal distributions σ_u^2 and σ_v^2, respectively. $\sigma_v = 1$ and σ_u follow the Lévy distribution given by (4). The step size ζ is then computed using

$$\varsigma = 0.01\varsigma\left(f - f_{best}\right). \quad (6)$$

The obtained ς changes the value of dimension x to: $f \leftarrow f + \zeta.\Psi$, where Ψ stands for the solution's random vector, and the x value lies in the normal distribution in the range (0, 1). LFCSA approaches identify new solutions (feature selections) that are fit (accurate) with existing solutions, where new solutions replace older ones on improvements. Nests with the worst values are discarded for further iterations and replaced with randomized new solutions, where replacement rates are based on probabilities prb_a, which are tuned for optimality. Thus, in iterations, existing solutions (feature selections) are rated based on their fitness values (accuracies), and the best solutions (features) are attained and stored as feature vectors f_{best}. Iterations are continued until the defined stopping criteria are met. LFCSA's pseudocode is depicted as Algorithm 1.

3.4.3. AFAs. The firefly algorithm is based on the idealized behavior of firefly flashing [35]. For the core formulation of FA, the three rules idealized are as follows:

(i) Because all fireflies are unisex, they will attract each other regardless of their gender for the best feature selection from the dataset
(ii) The brightness (accuracy) of a firefly is related to its attractiveness, which decreases as the distance between two fireflies grows
(iii) The brightness of a firefly is controlled by the objective function (accuracy)

The light intensity (In) varies exponentially and monotonically with distance. Equation (7) is used to explain it.

$$\mathrm{In} = \mathrm{In}_0 e^{-\gamma r}, \quad (7)$$

where In_0 is the initial light intensity and γ is the light absorption coefficient. As a firefly's attractiveness is proportional to the light intensity seen by neighbor fireflies (features), define the attractiveness β of a firefly by

$$\beta = \beta_0 e^{-\gamma r^2}, \quad (8)$$

where $\beta_0 = 1$ is the attractiveness at $r = 0$. The movement of a firefly (feature) "i" is attracted to another more attractive firefly(feature) "j", which is determined by

$$x_i = x_i + \beta_0 e^{-\gamma r_{ij}^2}\left(x_i - x_j\right) + \alpha\varepsilon. \quad (9)$$

The third term is the randomization with the step α, being drawn from a Gaussian distribution.

FAs generically use (9) for iterative randomizations, resulting in uniform distributions in the interval [0, 1] range. Their step determinations are static/linear and are defined for unchangeable maximum generations. FAs begin with the same steps, and their values keep decreasing in iterations. As a result, it is possible that it will get stuck at the local optimum, causing premature convergence. Secondly, taking such a large stride may lead the firefly to miss the best option while it is still in the area of the firefly during the early phases of the search. As a result, search performance might be harmed.

Thus, (9) implies the benefits of explorations in FAs, where larger steps result in global optimum convergences.

(1) Begin
(2) Objective function $f(f)$, $f = (f_1, \ldots f_d)^T$ with $d = \dim(\Omega)$
(3) Generate initial population of N host nests $f_i (i = 1, \ldots N)$
(4) While ($t <$ MaxGeneration)
(5) Get a cuckoo (say i) randomly by Lévy flights
(6) Evaluate fitness F_i by the accuracy of the classifier
(7) Choose a nest among N (say j) randomly
(8 **) If** $(F_i > F_j)$
(9) Replace j with the new solution
(10) End
(11) A fraction (prb_a) of worse nest(features in the dataset) are abandoned and new features are built by
(12) Lévy Flights
(13) Keep the best solutions using the accuracy of the feature
(14) End while
(15) Postprocess the results and visualization
(16) End

Algorithm 1: Levy flights cuckoo search algorithm.

For steps with low values, considerable influence occurs on explorations and convergences of algorithms. The values keep declining slowly on more iterations, however, they are faster in reduced iterations. These issues have been overcome in this study by the usage of self-adaptive steps, where the firefly's unique experiences help in selecting the best features from the data.

Step settings should be used to remedy the difficulties listed above. The firefly step should be set to be far away from the ideal solution. Fireflies between the two are utilized to balance the global and local searches for the best feature selection from the dataset. As a result, the firefly's stride must be concerned with both its previous data and current circumstances. This work introduces the firefly's history data, which contains the optimal value of the previous two iterations. Based on the comments mentioned above and many experiments, the step α of each firefly is calculated by (10) and (11), respectively. It is discussed as follows:

$$h_i(t) = \frac{1}{\sqrt{\left(f_{\mathrm{pi}}(t-1) - f_{\mathrm{pi}}(t-2)\right)^2 + 1}}, \quad (10)$$

$$\alpha_i(t+1) = 1 - \frac{1}{\sqrt{\left(f_{\mathrm{best}}(t) - f_i(t)\right)^2 + h_i(t)^2 + 1}}, \quad (11)$$

where $h_i(t)$ is the past two iterations' history data of the i^{th} firefly. f_{pi} is the fitness value of the best solution of the i^{th} firefly. f_{best} is the fitness value of the best solution of population heretofore found, and f_i is the fitness value of the i^{th} firefly, which reflects the current data. The firefly's next iterations are self-adaptive and are decided by the gap between the current fitness values and the population's best fitness values. As a result, the firefly steps might change with repetitions, and each firefly's step is, likewise, changed at the same time.

(1) Begin
(2) Objective function $f(x)$, $x = (x_1, \ldots x_d)^T$
(3) Generate initial population of n fireflies $x_i (i = 1, \ldots n)$
(4) Formulate light intensity In by objective function $f(x)$
(5) While ($t <$ MaxGeneration)
(6) Define absorption coefficient γ
(7) Evaluate fitness F_i by accuracy of the classifier
(8) For $i = 1$ to n(n fireflies)
(9) For $j = 1$ to n(n fireflies)
(10) If $(I_j > I_i)$
(11) Move firefly i towards j
(12) End if
(13) Vary attractiveness with distance r via $\exp(-\gamma r^2)$
(14) Evaluate new selected features solutions and update light intensity
(15) Update the step of each firefly. The step is calculated by (10) and (11).
(16) End for j
(17) End for i
(18) Rank the best features and find the current best features
(19) End *while*
(20) Postprocessing the results and visualization
(21) End

3.4.4. Correlation Function. Correlations between the features are computed by ensemble feature selectors, where high similarities between the features award their eliminations. The features selected using three procedures form ensemble features, where only ideal feature sets are selected by majority votes and based on the outputs of individual feature sets. The correlation coefficient matrices for the features selected in the out-ensemble feature selection outputs are computed using

$$\text{correlation coefficient} = \frac{N\sum xy - (\sum x)(\sum y)}{\sqrt{\left[N\sum x^2 - (\sum x)^2\right]\left[N\sum y^2 - (\sum y)^2\right]}}, \tag{12}$$

where x and y are the attribute values under consideration, and N is the total number of instances. The feature set selected by the correlation-based ensemble feature selector is given as an input to the classification.

3.5. Classification of PDs Using FCBi-LSTMs. This work used FCBi-LSTMs for the classification of PDs. The suggested approach computes fuzzy weight with membership values that are adjusted for extracting the most relevant features with respect to PDs. FCBi-LSTMs and CNNs analyze the selected characteristics from PD datasets [36]. CNNs made of convolution and pooling layers convolute and pool where outputs are fed to subsequent convolution layers. CNNs offer significant advantages in terms of feature extractions as they use partial filters for convolutions based on their understanding of biological vision cells' local perception. The convolution layer is separated into many output matrices using filters to offer a better representation of the selected features from the PD dataset, with each output matrix having a size of $(Nm + 1)$. The pooling layer of CNN is a technique for reducing the dimension of a matrix while keeping the fundamental links between the features. Pooling layers are average pooling layers with inputs from convolution layers. In the Bi-LSTM data analysis technique, the output of the last convolution layer is used as an intermediate variable [37]. As a result, LSTM does more than just add a nonlinear element to the input and loop cell transformation. Fuzzy weights are computed using Gaussian membership functions, where Bi-LSTMs outperform unidirectional LSTMs as they capture more structural information. The final outputs of Bi-LSTMs are processed by CNN's convolution layers for diagnosing PDs. To combine features processed by CNN and features processed by Bi-LSTM, multimodal factorized bilinear pooling (MFB) is utilized.

4. Experimental Results

This section describes the experimental findings achieved by the proposed FCBi-LSTM classifier and compares them to approaches, such as FCLSTM-CNN (fuzzy convolution long short-term memory-based convolution neural networks), CNN, and SVM. Since the samples in the test sets were fewer, LOPO-CVs' performance was evaluated using the training set's remaining individual instances, as each individual had three recordings, and the class labels assigned to these recordings were used to establish the individual's class label. The MIT-BIH arrhythmia database was used to conduct the investigations on arrhythmia recognition and classification systems and MATrix LABoratory R2016a (MATLAB R2016a). The implementation has been done using the following system specifications: Intel (R) Core™i3-4160T CPU@3.10 GHz 3.09 GHz processor, 4.00 GB RAM, Windows 8.1 Pro, 64-bit operating system, and 1 TB hard disk.

4.1. Evaluation Metrics. To test the predictability of the classifiers, evaluation metrics are required. Although accuracy is a widely used statistic, it might produce deceptive findings when data has an imbalanced class distribution. Even when there is a class imbalance, evaluation measures like F-measure and MCCs may be used to assess how effectively a classifier can discriminate between distinct classes. Allow the confusion matrix in Table 1 to represent the numbers of properly and erroneously categorized occurrences per class for binary classification. The letters tp, fp, fn, and tn in the confusion matrix mean true positive (tp), false positive (fp), false negative (fn), and true negative (tn), respectively. Precision, recall, F-measure, accuracy, and error were calculated using the formulae based on these counts.

$$\text{Precision} = \frac{\text{tp}}{\text{tp} + \text{fp}}, \tag{13}$$

$$\text{recall} = \frac{\text{tp}}{\text{tp} + \text{fn}}, \tag{14}$$

$$F - \text{measure} = \frac{2^{*}\text{precision}^{*}\text{recall}}{\text{precision} + \text{recall}}, \tag{15}$$

$$\text{Accuracy} = \frac{\text{tp} + \text{tn}}{\text{tp} + \text{tn} + \text{fp} + \text{fn}}, \tag{16}$$

$$\text{error} = 100 - \text{Accuracy}. \tag{17}$$

MCCs, which take into consideration the tp, fp, fn, and tn counts and are frequently recognized as a balanced measure that may be employed even if the class distribution is uneven, are another statistic for evaluating the validity of binary classifications. MCCs are simply correlation coefficients ranging from −1 to +1 between the actual and predicted occurrences. A score of +1 indicates a perfect prediction, whereas a value of −1 indicates a discrepancy between the forecast and the actual labeling.

4.2. Results Comparison. Experimental evaluations of classifiers were executed with three types of features in terms of accuracy, error, F-measure, and MCC. The combination of MFCCs + Wavelets + Concated features with SVM resulted in the accuracy rate of 88.1294%, although the accuracy rate of MFCCs + Wavelets + Concated combination was 94.1752% for CNN. FCLSTM-CNN had the accuracy results of 93.0470%, 93.0854%, 93.1261%, and 95.1557%, respectively, for TQWT + MFCC + Wavelet, TQWT + Wavelet + Concat, TQWT + MFCC + Concat, and MFCC + Wavelet + Concat. The suggested FCBi-WLSTM classifier with MFCCs + Wavelets + Concated combinations achieved the highest accuracy rates of 98.7720% (F-measure rate of 98.5010% and 71.400% for MCC) (See Table 2).

Figures 2–5 show the F-measures, accuracies, MCCs, and errors of feature set combinations, where the TQWT + MFCC + Wavelet combination of feature sets yielded higher results of 98.3100 percent, 96.6381 percent, 74.300 percent, and 3.3619 percent for f-measures,

Table 1: Confusion matrix for two-class classification.

Actual/predicted as	Positive	Negative
Positive	tp	fn
Negative	fp	tn

Table 2: Results of classifiers with triple feature (KPCA + OBEFS).

Feature combination	F-measure	Accuracy	Error	MCC
SVM classifier (%)				
TQWT + MFCC + Wavelet	82.9150	85.1035	14.8965	56.2000
TQWT + MFCC + Concat	80.7960	83.6640	16.3360	54.6000
TQWT + Wavelet + Concat	86.3590	87.4662	12.5338	58.8000
MFCC + Wavelet + Concat	87.4510	88.1294	11.8706	59.7000
CNN classifier (%)				
TQWT + MFCC + Wavelet	85.8697	87.5696	12.4304	57.2007
TQWT + MFCC + Concat	90.2315	91.9315	8.0684	61.4600
TQWT + Wavelet + Concat	86.3695	88.0694	11.9306	63.3994
MFCC + Wavelet + Concat	92.4752	94.1752	5.8248	64.5384
FCLSTM-CNN classifier (%)				
TQWT + MFCC + Wavelet	94.2258	93.0470	6.9530	67.6669
TQWT + MFCC + Concat	91.5250	93.0854	6.9146	67.7060
TQWT + Wavelet + Concat	93.4200	93.1261	6.8739	65.4457
MFCC + Wavelet + Concat	91.6921	95.1557	4.8443	67.2960
FCBi-LSTM classifier (%)				
TQWT + MFCC + Wavelet	98.3100	96.6381	3.3619	74.300
TQWT + MFCC + Concat	96.5900	98.0244	1.9756	72.300
TQWT + Wavelet + Concat	97.5200	97.3457	2.6543	70.300
MFCC + Wavelet + Concat	98.5010	98.7720	1.2280	71.400

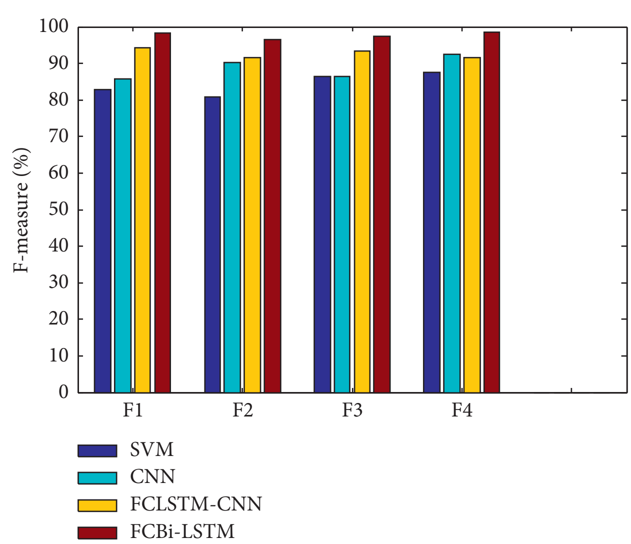

Figure 2: F-measure results of feature level combination vs. classifiers.

accuracies, MCCs, and errors, respectively, when compared to other combinations. Figure 2 compares the F-measure outcomes of four distinct feature level combinations using various classifiers. The proposed FCBi-LSTM with the first feature level combination achieved a higher F-measure value of 98.3100%, which was better than SVM, CNN, and FCLSTM-CNN, which achieved F-measures of 82.9150 percent, 85.8697 percent, and 94.2258 percent, respectively, at the first feature level combination.

Figure 3 depicts accuracies in the x-axis assessed using feature-level combinations on classifiers. FCBi-LSTM achieved 98.772 percent accuracy when compared to SVM, CNN, and FCLSTM-CNN, which achieved 88.1294 percent, 94.1752 percent, and 95.1557 percent accuracy, respectively, at the final feature level combination.

Figure 4 depicts error result comparisons of classifiers with four distinct feature level combinations. According to Figure 4, FCBi-LSTM results on final feature level

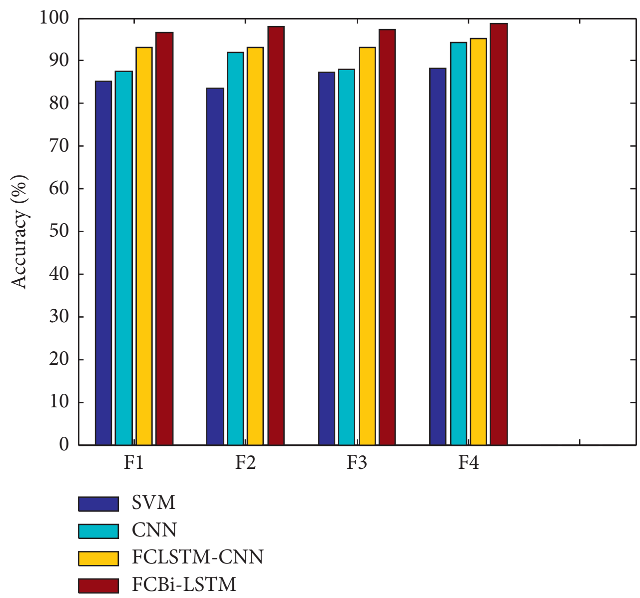

FIGURE 3: Accuracy results of feature level combination vs. classifiers.

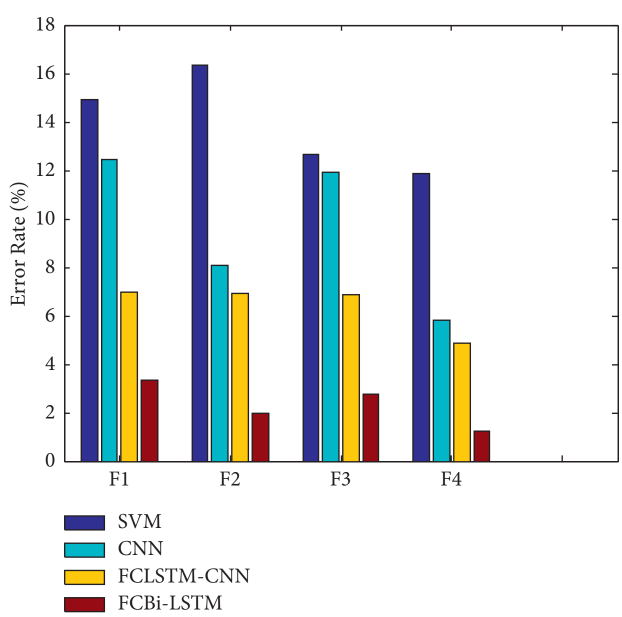

FIGURE 4: Error results of feature level combination vs. classifiers.

combinations produced reduced error values of 1.2280 percent, whereas SVM, CNN, and FCLSTM-CNN had higher error values of 11.8706 percent, 5.8248 percent, and 4.8443 percent, respectively, at the final feature level combination.

Figure 5 compares MCC results of TQWT + MFCC + Concat feature set, which yields a higher result of 74.30 percent for the proposed method, and 56.20 percent, 57.2007 percent, and 67.6669 percent for SVM, CNN, and FCLSTM-CNN classifiers, respectively (1^{st} feature level combination). Because feature selection is accomplished using the proposed approach achieves superior MCC outcomes for all classifiers (OBEFSs).

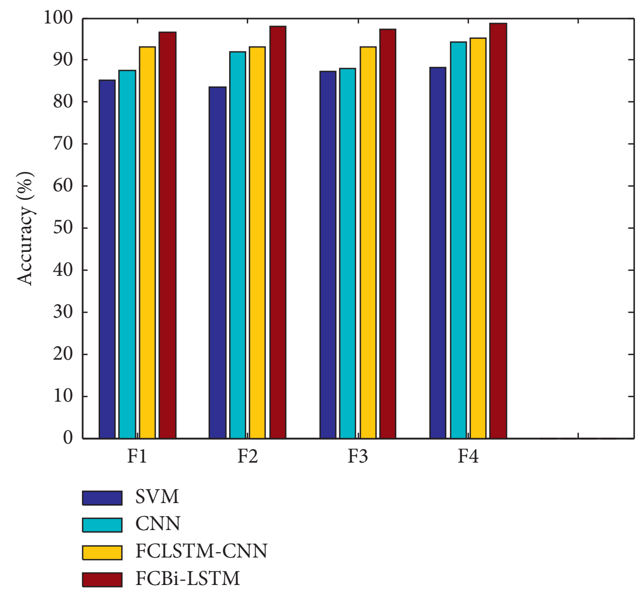

FIGURE 5: MCC results of feature level combination vs. classifiers.

5. Conclusion and Future Work

PD is the second most prevalent neurological ailment, causing considerable impairment, lowering the quality of life, and having no treatment. It is critical to diagnose PD early to use neuroprotective and early treatment techniques. In this research, a feature selection is used to present a multiclass classification challenge for PD analysis. For PD analysis, OBEFS and FCBi-LSTM are presented. The proposed OBEFS method is based on a number of algorithms, including FMBOA, LFCSA, and AFA. To execute OBEFS, the correlation function is utilized to choose optimum features from the three feature subsets. The FCBi-LSTM classifier is then used for PD diagnosis. It is an effective and accurate model for properly diagnosing the condition at an early stage, which might help doctors aid in the cure and recovery of PD patients. Classification algorithms were tested with UCI's machine learning libraries, and their performance is measured using precision, recall, F-measure, accuracy, and MCC. The results were compared to other existing techniques, and the findings show that the suggested model's accuracy is higher than the other current approaches. Deep learning has a bright future in engineering and medicine. In terms of future work, the goal is to extend existing research in novel ways. Different data types can be sent into the network as inputs at the same time using the proposed CNN's parallel convolution layers. It gives us the chance to utilize the multimodal data in PD classification. Also, the authors plan to use different deep learning models in the classification process.

Abbreviations

PD:	Parkinson's Disease
DMTs:	Data mining techniques
MLTs:	Machine learning techniques
EFSs:	Ensemble feature selections

OBEFSs: Optimization-based ensemble feature selections
LFCSAs: Lévy Flight Cuckoo Search Algorithms
AFAs: Adaptive firefly algorithms
FCBi-LSTMs: Fuzzy convolution bidirectional long short-term memories
UCI: University of California-Irvine
LOPO-CVs: Leave-One-Person-Out-Cross Validations
MCCs: Matthews correlation coefficients.

Data Availability

The datasets used and/or analyzed during the current study are available from the corresponding author on reasonable request.

Conflicts of Interest

The authors declare no conflicts of interest.

References

[1] T. V. S. Sriram, M. V. Rao, G. V. S. Narayana, and D. S. V. G. K. Kaladhar, "Diagnosis of Parkinson disease using machine learning and data mining systems from voice dataset," in *Proceedings of the 3rd International Conference on Frontiers of Intelligent Computing: Theory and Applications*, pp. 151–157, (FICTA), Berlin, Germany, January 2014.

[2] H. Gürüler, "A novel diagnosis system for Parkinson's disease using complex-valued artificial neural network with k-means clustering feature weighting method," *Neural Computing & Applications*, vol. 28, no. 7, pp. 1657–1666, 2017.

[3] M. Peker, "A decision support system to improve medical diagnosis using a combination of k-medoids clustering based attribute weighting and SVM," *Journal of Medical Systems*, vol. 40, no. 5, pp. 116–16, 2016.

[4] B. E. Sakar, G. Serbes, and C. O. Sakar, "Analyzing the effectiveness of vocal features in early telediagnosis of Parkinson's disease," *PloS one*, vol. 12, no. 8, pp. 1–18, 2017.

[5] B. Xue, M. Zhang, W. N. Browne, and X. Yao, "A survey on evolutionary computation approaches to feature selection," *IEEE Transactions on Evolutionary Computation*, vol. 20, no. 4, pp. 606–626, 2015.

[6] F. Moslehi and A. Haeri, "An evolutionary computation-based approach for feature selection," *Journal of Ambient Intelligence and Humanized Computing*, vol. 11, no. 9, pp. 3757–3769, 2020.

[7] B. Seijo-Pardo, V. Bolón-Canedo, I. Porto-Díaz, and A. Alonso-Betanzos, "Ensemble feature selection for rankings of features," *Advances in Computational Intelligence*, in *Proceedings of the International Work-Conference on Artificial Neural Networks*, pp. 29–42, Springer, Palma de Mallorca, Spain, June 2015.

[8] D. Guan, W. Yuan, Y.-K. Lee, K. Najeebullah, and M. K. Rasel, "A review of ensemble learning based feature selection," *IETE Technical Review*, vol. 31, no. 3, pp. 190–198, 2014.

[9] M. Mera-Gaona, D. M. López, R. Vargas-Canas, and U. Neumann, "Framework for the ensemble of feature selection methods," *Applied Sciences*, vol. 11, no. 17, pp. 1–16, 2021.

[10] S. L. Oh, Y. Hagiwara, U. Raghavendra et al., "A deep learning approach for Parkinson's disease diagnosis from EEG signals," *Neural Computing & Applications*, vol. 32, no. 4, pp. 1–7, 2020.

[11] C. R. Pereira, S. A. Weber, C. Hook, G. H. Rosa, and J. P. Papa, "Deep learning-aided Parkinson's disease diagnosis from handwritten dynamics," in *Proceedings of the 2016 29th SIBGRAPI Conference on Graphics, Patterns and Images*, pp. 340–346, (SIBGRAPI), Sao Paulo, Brazil, October 2016.

[12] B. M. Eskofier, S. I. Lee, J.-F. Daneault et al., "Recent machine learning advancements in sensor-based mobility analysis: deep learning for Parkinson's disease assessment," in *Proceedings of the 2016 38th Annual International Conference of the IEEE Engineering in Medicine and Biology Society*, pp. 655–658, (EMBC), Orlando, FL, USA, Augeust 2016.

[13] C. O. Sakar, G. Serbes, A. Gunduz et al., "A comparative analysis of speech signal processing algorithms for Parkinson's disease classification and the use of the tunable Q-factor wavelet transform," *Applied Soft Computing*, vol. 74, pp. 255–263, 2019.

[14] E. J. Alqahtani, F. H. Alshamrani, H. F. Syed, and S. O. Olatunji, "Classification of Parkinson's disease using NNge classification algorithm," in *Proceedings of the 2018 21st Saudi Computer Society National Computer Conference (NCC)*, Riyadh, Saudi Arabia, April 2018.

[15] H. Gunduz, "Deep learning-based Parkinson's disease classification using vocal feature sets," *IEEE Access*, vol. 7, pp. 115540–115551, 2019.

[16] Y. Li, L. Yang, P. Wang et al., "Classification of Parkinson's disease by decision tree based instance selection and ensemble learning algorithms," *Journal of Medical Imaging and Health Informatics*, vol. 7, no. 2, pp. 444–452, 2017.

[17] A. Caliskan, H. Badem, A. Basturk, and M. E. Yuksel, "Diagnosis of the Parkinson disease by using deep neural network classifier," *IU-Journal of Electrical & Electronics Engineering*, vol. 17, no. 2, pp. 3311–3318, 2017.

[18] Z. Cai, J. Gu, C. Wen et al., "An intelligent Parkinson's disease diagnostic system based on a chaotic bacterial foraging optimization enhanced fuzzy KNN approach," *Computational and mathematical methods in medicine*, vol. 2018, pp. 1–24, Article ID 2396952, 2018.

[19] C. Castro, E. Vargas-Viveros, A. Sánchez, E. Gutiérrez-López, and D.-L. Flores, "Parkinson's disease classification using artificial neural networks," *IFMBE Proceedings*, in *Proceedings of the Latin American Conference on Biomedical Engineering*, pp. 1060–1065, Springer, Cancun, Maxico, October 2019.

[20] G. Abdurrahman and M. Sintawati, "Implementation of xgboost for classification of Parkinson's disease," in *Journal of Physics: Conference Series*, vol. 1538, no. 1, p. 012024, IOP Publishing, 2020.

[21] I. Karabayir, S. M. Goldman, S. Pappu, and O. Akbilgic, "Gradient boosting for Parkinson's disease diagnosis from voice recordings," *BMC Medical Informatics and Decision Making*, vol. 20, no. 1, pp. 1–7, 2020.

[22] A. K. Patra, R. Ray, A. A. Abdullah, and S. R. Dash, "Prediction of Parkinson's disease using ensemble machine learning classification from acoustic analysis," in *Journal of Physics: Conference Series*, vol. 1372, no. 1, IOP Publishing, Article ID 012041, 2019.

[23] L. Parisi, N. RaviChandran, and M. L. Manaog, "Feature-driven machine learning to improve early diagnosis of Parkinson's disease," *Expert Systems with Applications*, vol. 110, pp. 182–190, 2018.

[24] K. A. Hasan and M. A. M. Hasan, "Classification of Parkinson's disease by analyzing multiple vocal features sets," in

Proceedings of the 2020 IEEE Region 10 Symposium (TENSYMP), pp. 758–761, Dhaka, Bangladesh, June 2020.

[25] H. M. Qasim, O. Ata, M. A. Ansari, M. N. Alomary, S. Alghamdi, and M. Almehmadi, "Hybrid feature selection framework for the Parkinson imbalanced dataset prediction problem," *Medicina*, vol. 57, no. 11, pp. 1–13, 2021.

[26] A. Tsanas, M. A. Little, P. E. McSharry, J. Spielman, and L. O. Ramig, "Novel speech signal processing algorithms for high-accuracy classification of Parkinson's disease," *IEEE Transactions on Biomedical Engineering*, vol. 59, no. 5, pp. 1264–1271, 2012.

[27] I. W. Selesnick, "Wavelet transform with tunable q-factor," *IEEE Transactions on Signal Processing*, vol. 59, no. 8, pp. 3560–3575, 2011.

[28] Q. Wang, "Kernel principal component analysis and its applications in face recognition and active shape models," 2012.

[29] M. Alweshah, "Solving feature selection problems by combining mutation and crossover operations with the monarch butterfly optimization algorithm," *Applied Intelligence*, vol. 51, no. 1, 2020.

[30] G GWang, X. Zhao, and S. Deb, "A novel monarch butterfly optimization with greedy strategy and self-adaptive," in *Proceedings of the Soft Computing and Machine Intelligence (ISCMI), 2015 Second International Conference on*, pp. 45–50, Hong Kong, China, November 2015.

[31] Y. Feng, G.-G. Wang, W. Li, and N. Li, "Multi-strategy monarch butterfly optimization algorithm for discounted {0-1} knapsack problem," *Neural Computing & Applications*, vol. 30, no. 10, pp. 3019–3036, 2018.

[32] A. Mesa, K. Castromayor, C. Garillos-Manliguez, and V. Calag, "Cuckoo search via Levy flights applied to uncapacitated facility location problem," *Journal of Industrial Engineering International*, vol. 14, no. 3, pp. 585–592, 2018.

[33] M. Guerrero, O. Castillo, and M. García, "Cuckoo search via Lévy flights and a comparison with genetic algorithms," in *Fuzzy Logic Augmentation of Nature-Inspired Optimization Metaheuristics*, pp. 91–103, Springer, Cham, 2015.

[34] M. Mareli and B. Twala, "An adaptive Cuckoo search algorithm for optimisation," *Applied computing and informatics*, vol. 14, no. 2, pp. 107–115, 2018.

[35] H. Wang, W. Wang, X. Zhou et al., "Firefly algorithm with neighborhood attraction," *Firefly algorithm with neighborhood attraction*, Information Sciences, vol. 382-383, , pp. 374–387, 2017.

[36] T. Chen, R. Xu, Y. He, and X. Wang, "Improving sentiment analysis via sentence type classification using BiLSTM-CRF and CNN," *Expert Systems with Applications*, vol. 72, pp. 221–230, Apr. 2017.

[37] S. Xingjian, Z. Chen, H. Wang, D. Yeung, W. Wong, and W. Woo, "Convolution LSTM network: a machine learning approach for precipitation nowcasting," in *Proceedings of the Advances in Neural Information Processing Systems*pp. 802–810, Montreal, QC, Canada, 2015.

Hindawi
Journal of Healthcare Engineering
Volume 2022, Article ID 9780218, 1 page
https://doi.org/10.1155/2022/9780218

Retraction

Retracted: Research on the Current Situation of College Students' Physical Health under the Background of the Integration of Sports and Medicine

Journal of Healthcare Engineering

Received 19 November 2022; Accepted 19 November 2022; Published 8 December 2022

Journal of Healthcare Engineering has retracted the article titled "Research on the Current Situation of College Students' Physical Health under the Background of the Integration of Sports and Medicine" [1] due to concerns that the peer review process has been compromised.

Following an investigation conducted by the Hindawi Research Integrity team [2], significant concerns were identified with the peer reviewers assigned to this article; the investigation has concluded that the peer review process was compromised. We therefore can no longer trust the peer review process, and the article is being retracted with the agreement of the Chief Editor.

The authors do not agree to the retraction.

References

[1] Z. Lyu, Y. Hou, and Y. Wang, "Research on the Current Situation of College Students' Physical Health under the Background of the Integration of Sports and Medicine," *Journal of Healthcare Engineering*, vol. 2022, Article ID 1581282, 8 pages, 2022.

[2] L. Ferguson, "Advancing Research Integrity Collaboratively and with Vigour," 2022, https://www.hindawi.com/post/advancing-research-integrity-collaboratively-and-vigour/.

Hindawi
Journal of Healthcare Engineering
Volume 2022, Article ID 1581282, 8 pages
https://doi.org/10.1155/2022/1581282

Research Article

Research on the Current Situation of College Students' Physical Health under the Background of the Integration of Sports and Medicine

Zenghui Lyu,[1] Yuanyuan Hou,[2] and Youwei Wang[1]

[1]*Anhui Medical University, Hefei 230000, Anhui, China*
[2]*Anhui Zhongao Institute Of Technology, Hefei 230000, Anhui, China*

Correspondence should be addressed to Youwei Wang; 58091698@qq.com

Received 8 January 2022; Accepted 10 February 2022; Published 13 April 2022

Academic Editor: Enas Abdulhay

As a health service model promoted by the "Healthy China 2030" plan, the integration of sports and medicine is of great significance to the reformation of college students' health management. Research shows that the general low health literacy, unhealthy lifestyle, significant decline in physical fitness, high incidence of subhealth, and prominent mental health problems are common among college students in China. This article comprehensively utilizes the literature data method, logical analysis method, and questionnaire survey method to analyze the health status of college students, the current status of the health management of college students, and outstanding issues and to focus on analyzing the current status of students' body shape, physical function, and physical fitness indicators. From the perspective of examining, reflecting, and exploring physical and medical integration, it is believed that the construction of students' physical health issues from the perspective of the development of the integration of sports and medicine is manageable and the interaction of medicine, health, and sports can be promoted. This article discusses the enlightenment of "sports–medicine integration" with school physical education, interprets the connotation of "sports–medicine integration", and analyzes the development direction of "sports–medicine integration" and physical education. In order to effectively strengthen school physical education work, we proposed to establish the concept of "sports and medical integration" sports health education, specifically the development strategy of school physical education, including promoting "sports integration," to improve the development of sports education, and establish a teaching service platform, providing ideas and suggestions for the development of national health strategies. In conclusion, colleges and universities should strengthen the construction of sports venues and facilities for physical education, increase students' enthusiasm for participating in physical exercise, and improve students' physical fitness.

1. Introduction

With the improvement in people's health awareness, all levels of the society are deeply aware of the importance of health. Sports and medical care are important pillars of social health, and "the integration of sports and medicine" has become a current research hotspot. Nowadays, people's dietary structure and lifestyle have undergone tremendous changes, and obesity has gradually become a serious problem in the field of public health. The obesity rate of college students continues to increase, and their physical fitness has been declining year by year. Some indicators are even inferior to that of middle school students. Obesity also makes college students low in self-confidence and prone to anxiety, which leads to interpersonal communication disorders. Moreover, the health of college students is also threatened by chronic diseases, and changes in lifestyle have made cardiovascular and cerebrovascular diseases, cancer, diabetes, and other diseases the "killers" that endanger college students; in addition, clinical medicine has little effect on such diseases. This gave birth to "physical medicine fusion" health promotion.

Since 1985, China has conducted four surveys on the health of college students. The results of the survey show that the physique of college students is gradually declining. The decline in college students' physique is not as simple as it seems. Countries are gradually paying attention to physical health. This is because of the poor psychological status of college students and their weak psychological endurance. It is also urgent to update school physical education. "Healthy China 2030" proposes "the integration of physical and medical care". The establishment of the Research Center for Promotion and Innovation of "Sports-Medical Integration" and other policy proposals indicate that the country has elevated health issues affecting the national strategy, which reflects the importance and timeliness of "sports–medical integration". The integration of sports and medicine has pointed out a new direction to our people for good health, and it has also brought new enlightenment to the physical education of our country's colleges and universities. The "Healthy China 2030" planning outline mentioned that health education should be incorporated into the national education system and a diversified health education model should be constructed, with health education as an important part of the education stage [1]. Zhang Jianwei started the concept and connotation of the integration of sports and medicine and put forward strategies based on the analysis of the development of the integration of sports and medicine and local practices: Sports and medical departments should work together, focus on the construction of talent teams, increase publicity and promotion, and explore and develop in accordance with local conditions [2]. Feng Zhenwei tried to use the symbiosis theory to construct a path for the integration of body and medicine. The research found that currently there are disadvantages in emphasizing medicine and neglecting the body, separation of industries, and insufficient laws and policies [3]. However, the current research results on the physical health of college students under the integration of sports and medicine and the research results on the reform of health management in colleges and universities are few. This article analyzes the current status of the physical fitness of college students across the country, analyzes the connotation of the integration of sports and medicine, and analyzes the integration of sports and medicine and physical education. At present, college students also lack the ability of self-decompression and psychological adaptation [4], and the proportion of dropouts due to psychological problems has also been increasing year by year [5]. On the basis of theoretically combing the correlation between the integration of sports and medicine and health management, the thought and feasibility of the reformation of the health management of college students under the integration of sports and medicine are promoted for the development of sports education and improving the physical health of college students. The comprehensive development of college students is promoted, references are provided, and ideas and suggestions are provided for the reformation of physical education.

2. Connotation and Development Status of the Integration of Sports and Medicine

The integration of sports and medicine has not only physical exercise methods but also the concept of medical services. It is a mode of operation that mainly provides nonprofit basic public services and is supplemented by profit-making methods such as the sports industry, that is, sports disciplines and medical disciplines. It is a model of mutual integration, mutual learning, and reference and mutual promotion of concepts, ideas, paths, and models. This model is very suitable for improving the physical health of students in college physical education. It is also one of the most effective ways to improve the physical health of college students. At the same time, it is an important tactical means of the "healthy China" strategy.

The main feature of the integration of sports and medicine is that "there is medicine in the body, and there is body in medicine;" the two are interdependent, permeable, and blended. It has high practical value in the promotion of sports and medical disciplines. "Physicians in sports" are mainly manifested in three aspects: competitive sports, mass sports, and school sports. In competitive sports, for athletes to achieve excellent results, they need not only the support of scientific research knowledge of sports but also the medical and health system to provide athletes with first aid and injury prescriptions; in mass sports, medical interventions are used to conduct physical fitness tests on the public and implement them. Medical supervision promotes scientific fitness for the masses. School physical education provides students with exercise programs with a certain exercise intensity to improve the effect of exercise on the basis of avoiding injuries. "Medicine in the body" is mainly manifested in three aspects: prevention, treatment, and rehabilitation. Prevention cannot rely solely on medical means but must be assisted with appropriate physical exercises and exercise prescriptions; the treatment of chronic diseases requires the use of exercise intervention methods. The effect is far better than that of drug treatment; sports rehabilitation should also be added to rehabilitation, which can accelerate the recovery from the disease and reduce the incidence of cancer.

At present, our school sports and social sports are not in touch with each other. There is a gap in the connection between school sports and social sports, and most students leave sports when they leave school. In the process of physical education, cultivating students' self-health and self-physical abilities is particularly important. The integration of physical and medical strategies and the idea of lifelong physical education influence each other and complement each other. We will take lifelong physical education as the main idea and the integration of physical and medical care as the main means to break the teaching situations that are too weak to deal with errands, deepen the reformation of physical education in an all-round way, and improve the health of students.

Most parents have low awareness of sports. During holidays, students and parents mostly sit quietly and move less. Sitting for a long time and moving less are prone to poor energy metabolism habits, which will also affect muscles and bones, because of which chronic diseases will follow. Studies have shown that the mortality rate of people who sit still and do not move is higher than that of people who exercise. The Institute of Physical Medicine Fusion proposes that reducing sitting and less movement is beneficial to the prevention of chronic diseases. In addition, to urge students to develop exercise habits is also the main task of physical education during holidays. Therefore, through the Internet's big data, the goal of physical education and the viewpoint of integration of sports and medicine are connected in order to achieve the goal of physical education and disseminate the viewpoint of integration of sports and medicine. The integration of sports and medicine has played an important role in improving the health of college students.

3. The Current Status of College Students' Physical Health

Every year, the Ministry of Education organizes health campaigns across the country to detect students' health problems, inputs the test results into a database with dynamic characteristics, and feeds them back to the national educational institutions and colleges and universities; the data indicators become important information to realize health assessment. The physical health of college students has always been an important content of physical education teaching in colleges and universities. In recent years, it has been found that the physical health of students has shown a downward trend through physical tests.

According to the survey, since 1985, the developmental indicators of students have not reached the standard and have been declining, including basic height, weight, vital capacity, and other tests. These declining data reflect that the status quo of students' physical fitness is extremely unoptimistic. A person's lack of self-confidence is largely related to one's appearance, and lack of self-confidence is the cause of many mental illnesses; hence, this also causes students' mental health to become less optimistic, and they lose the vitality that adolescents of the past had such as endurance, coordination, and hard-working spirit. Homework eats up a lot of sports time of young people. They don't have time to exercise, play, and reflect the vitality of young people. Instead, they are bound by scores. They are not released from this kind of major psychological pressure, which can only be accumulated in the bottom of their hearts. This leads to poor mental health. According to a survey, university students suffer from a variety of psychological problems and the rate of students with mental health problems is 12%. In severe cases, they commit suicide. The types of psychological problems of college students are more complicated, and the detection rate of psychological problems is ranked as obsessive-compulsive disorder, interpersonal sensitivity, hostility, depression, paranoia, and anxiety [6]. At the same time, college students are weak in psychological and social adaptability, and the incidence of psychological problems has been increasing year by year; there are also extreme situations in which "small things lead to catastrophes".

At present, about 50% of college students are living with cervical subhealth problems, and some have severe cervical degenerative characteristics [7]. More than 20% of college students suffer from various degrees of mental subhealth symptoms [8]. From a cognitive perspective, the percentage of college students who believe that they are in a subhealthy state is also as high as 52%. Studies have suggested that low sleep quality is the main threat to health, but the incidence of sleep disorders among college students is increasing. About 81.26% of them have sleep disorders, and the detection rate of low sleep quality is as high as 40.2% [9]. At the same time, the "report" pointed out that 30% of college students are dissatisfied with their sleep status, 68% go to bed between 23 : 00 and 24 : 00, and 18% go to bed after 24 : 00. Sleep disorders, low-quality sleep, and late sleep are the effects of these, which speeds up the subhealth state. Scholars have used a variety of theoretical models to conduct in-depth research on the development path of the integration of sports and medicine, enriching the connotation of the top-level design of the integration of sports and medicine and clarifying the development thinking.

The "Outline" proposes that China will carry out an action to popularize health knowledge and by 2030, the health literacy level of residents will not be less than 30%. However, the level of health literacy of college students is low, and there is a serious lack of healthy lifestyle and behavior literacy [10]. Studies have suggested that health literacy is highly positively correlated with autonomous exercise awareness [11], but college students' autonomous exercise awareness is weak, which hinders the improvement of health literacy levels [12]. At this stage, college students have only 9.1% of healthy lifestyle and behaviors, which is far from the national average of 17%. Studies have shown that unhealthy lifestyle is the main threat to health, and the "2020 China University Students Health Survey Report" published by China Youth Daily pointed out that unhealthy lifestyle is common among college students. For example, girls lose weight mainly by diet and meal replacement, but 30% of people do not lose weight but increase. The reason is that they consume too much junk food, eat fewer vegetables and fruits, and eat irregularly. At the same time, insufficient exercise is a risk factor for death. The total mortality rate is 5.5%. While more than 50% of college students in China never exercise or pay attention to their own health management, organ function problems such as abnormal liver function of college students caused by unhealthy lifestyle have also increased slightly in recent years [13]. 86% of college students said they had experienced health problems such as poor skin condition, lack of sleep, and emotional problems; 77% of college students said that a rich social life and various electronic products were the main factors leading to lack of sleep; 67% of college students said they would take action to improve their lifestyle; 64% of college students believe that taking care of the health should start at a young age and one should consciously maintain physical health [14]. These data show that the health problems caused by the irregular work and unhealthy lifestyle of college students have become a barrier to the construction of a healthy campus.

In order to tap sports talents, some colleges and universities blindly increase the intensity of sports training, causing students to feel exhausted and resist; other colleges and universities focus on the students' sports performance, and students perform mechanical exercises in order to obtain sports credits. Training: It is difficult to experience the fun of physical learning when the physical fitness level is not good. Even if the student's physical fitness level reaches the standard, it is difficult to carry out continuous exercise due to lack of exercise awareness and lack of self-discipline ability, resulting in the decline of the students' cardiopulmonary ability and physical fitness indicators in the later period. Analyzed from the perspective of the education system, more college students have suffered a serious decline in their physical health. The main reason is that the current model of exam-oriented education in our country has made physical activities inadequate.

A total of 400 questionnaires were randomly selected from freshmen and sophomore students in a university. A total of 400 questionnaires were distributed, 400 copies were returned, and 396 valid questions were obtained, with an effective rate of 99%.

A survey and analysis of the results of students' physical test results were conducted. From the survey results in Table 1, it can be seen that 19.9% of the students have excellent results in the physical test, 28.5% of the students are good, 31.8% of the students passed, and 19.7% of students failed. From this set of data, it can be seen that the current college students' physical fitness is not high and the students' physical test scores are between pass and good. The results of the physical test can reflect the physical health of the students. Improving the physical fitness of the students and improving the results of the physical test are challenges in the current college physical education teaching setup.

From the survey results in Table 2, it can be seen that 19.9% of students regularly participate in physical exercise, 16.4% of students regularly perform physical exercise, 45.2% of students occasionally perform physical exercise, and 18.4% of students hardly perform physical exercise. From this set of data, it can be seen that the current college students are less involved in exercise. In order to continuously improve the physical health of students, it is necessary to increase the time of students' physical exercise. Students need corresponding sports venues and sports equipment for physical exercise. Although colleges and universities continue to increase their investment in facilities and venue construction, there is still a shortage of supply. Although some colleges and universities have a relatively wide range of sports venues, it is difficult for the construction of facilities to meet the standards. Some colleges and universities have very strict management of facilities and venues due to the fear of loss and the lack of maintenance of sports facilities and rarely open them to students. In addition, some colleges and universities have physical teaching venues. All of the above-mentioned reasons make it difficult for students to meet their daily sport needs, resulting in low levels of physical fitness.

Table 1: Investigation and analysis of students' physical examination ($N = 396$).

Physical test results	Excellent	Good	Pass	Failed
Number of people	79	113	126	78
Percentage	19.9	28.5	31.8	19.7

Table 2: Investigation and analysis of students' extracurricular physical exercises.

Exercise frequency	Regular	Frequently	Occasionally	Almost not
Number of people	79	65	179	73
Percentage	19.9	16.4	45.2	18.4

4. Reformation Strategy of Health Education of "Integration of Sports and Medicine" in Physical Education in Colleges and Universities

The health problems of college students and the problems of health management of students in colleges and universities have seriously hindered the implementation of relevant policies of a healthy China and the progress of school sports and have become a necessary factor in the reformation and development of college students' health management.

The integration of sports and medicine is a new thinking in the development of health management. The "Outline" proposes to promote the formation of a disease management and health service model that integrates sports and medicine and to give full play to the active role of national scientific fitness in health promotion, chronic disease prevention, and rehabilitation. At present, the integration of sports and medicine has become a research hotspot. From the perspective of health elements, Guo and Zheng [15] proposed that the integration of sports and medicine is a model of using sports and medical methods to promote health and other aspects. In the context of the national health strategy and the construction of a healthy China, the integration of sports and medicine has been the health service model that the "Outline" has promoted. Its core is to actively mobilize the health promotion forces and resources of all parties under the integrated thinking and focus on the use of medicine. The scientific health promotion carried out by knowledge and sports science is a new model of health management development promoted by the state and is of great significance to the research on health management of college students.

Only when teachers reflect on teaching and discover and solve problems in time can the quality of college physical education be improved. Diversified teaching can ignite the sports enthusiasm of college students, allowing them to use their spare time for independent training. For example, teachers can use information-based teaching methods to broadcast corresponding sports games videos to cultivate students' sports spirit and promote tactical teaching. Colleges and universities must establish a sound physical and health education curriculum system.

We should promote traditional sports culture, enrich the content of school-based sports courses, and moderately increase burden on students. We also can set up "second classrooms" to meet students with different learning interests and sport needs, help them understand sports culture knowledge, cultivate their sports spirit and character, establish diversified sports clubs, and organize colorful athletic activities. Only by adhering to the educational philosophy of "health first and comprehensive education" can colleges and universities cultivate students' appropriate sports concepts, encourage them to integrate into physical education activities, make them feel the importance of sports to health, and improve their physical endurance, explosive power, and exercise speed.

First, colleges can increase the proportion of health education with the main teaching content of healthy physical fitness, health education, sports nutrition, physical and mental development characteristics of college students, chronic disease characteristics and prevention, etc., to improve the basic theoretical knowledge of sports and health of college students. Second, regular health lectures are to be held to inform college students of the relationship between their physical fitness level and work efficiency, competitiveness, quality of life, and the occurrence of chronic diseases in the form of cases so that college students will pay attention to learn health knowledge and skills from the ideological level and then achieve the goal of health education. Purpose: Third, carrying out various forms of fitness activities, after-school competitions, fun sports activities, etc., actively creates a platform to attract college students to participate in sports activities. The purpose and development target of physical education are all students. The main task of teaching is the acquisition of students' physical education. In teaching, teachers should provide timely and accurate feedback of students' learning changes to them so as to provide them with value for improving their learning status. Please refer to Figure 1 for relevant details.

The "five in one" public physical education curriculum system with equal emphasis on both inside and outside classes and a two-pronged approach between theory and practice [16] is shown in Figure 2. The class focuses on the combination of human science knowledge and special skills and incorporates the concept of integration of sports and medicine into the whole process of syllabus formulation, course goal setting, and teaching design. Based on the principles of fitness, culture, science, and teachability of the course content, the commonality of basic physical disciplines and basic medical disciplines is highlighted; taking the professional interest of medical students as the starting point, the teaching content is matched, and the scientific nature of the movement skills of medical students is improved so that they understand. Extracurricular: Relying on the advantages of the background of medical schools, the content related to sports prescriptions is incorporated into the development goals of the sports courses of medical schools using the student sports medicine club as the carrier; serving the school team, after-school exercise, and various sports events at all levels on the campus are used as the practice platform to strengthen the practical level of students' physical and medical integration skills. On the basis of exploring the relevance of the integration of sports and medicine and health management, combining the spirit of the "Outline" and the thinking of integrating sports and medicine, it is proposed to establish a "health management committee," reorganize the "health management center for integration of sports and medicine," build a "pyramid-style" health management model, build a "five-in-one" data platform, strengthen health education, cultivate healthy lifestyles and other reforms, and develop strategies for college students' health management.

According to the "Healthy China 2030" planning outline," the spirit of "Internet + health care" services is proposed, and the "integration of sports and medicine" construction model for college sports is established to establish an "integration of sports and medicine" smart health information platform for college students. Construction idea: When registering in the educational administration teaching system, each student enters the high-school and school physical examination information, physical fitness test data, personal health status, and physical experience after each exercise; the school hospital's health doctor estimates potential exercise risks. Sports health teachers put forward exercise prescriptions. Students choose appropriate venue facilities and exercise programs for scientific exercise through the suggestions of physical medicine teachers so as to realize the intelligent and convenient consultation and guidance of college teachers and accelerate the process of "Internet + physical medicine integration" in college sports. In order to promote the in-depth implementation of the new teaching reforms of physical education in colleges and universities, the physical fitness of college students should be improved, their physical test scores should be improved, and the failure rate should be reduced; college physical education teachers should promptly change their educational concepts and make up for their teaching shortcomings.

From Figure 3, we can see that the "sports–medical integration" platform service model is a systematic project, which consists of information–resource integration, exercise prescription formulation, fitness effect evaluation, process monitoring, and information feedback. (Health teachers and doctors and) college student groups participate in collaboration; increase publicity and promotion; compound talent training and administrative support; improve educational administration organization and management; and promote the integration and innovation of sports and hospitals so that lifelong sports and health education can be realized, as well as life education, physical fitness, disease prevention, and other educational demands.

5. The Guiding Significance of "Integration of Sports and Medicine" to the Reform of College Physical Education and Health Education

"Integration of sports and medicine" is one of the important means for the implementation of the sports curriculum construction strategy. It integrates scientific sports with the comprehensive sports curriculum construction service system for the trinity of prevention, treatment, and rehabilitation, which is important for the overall improvement of the health of the whole people. The integration of sports and medicine is not only a requirement for cultivating the builders of socialist modernization but also a key task in the implementation of the healthy China construction strategy. It is an all-round exploration of the basic path of the physical health promotion of

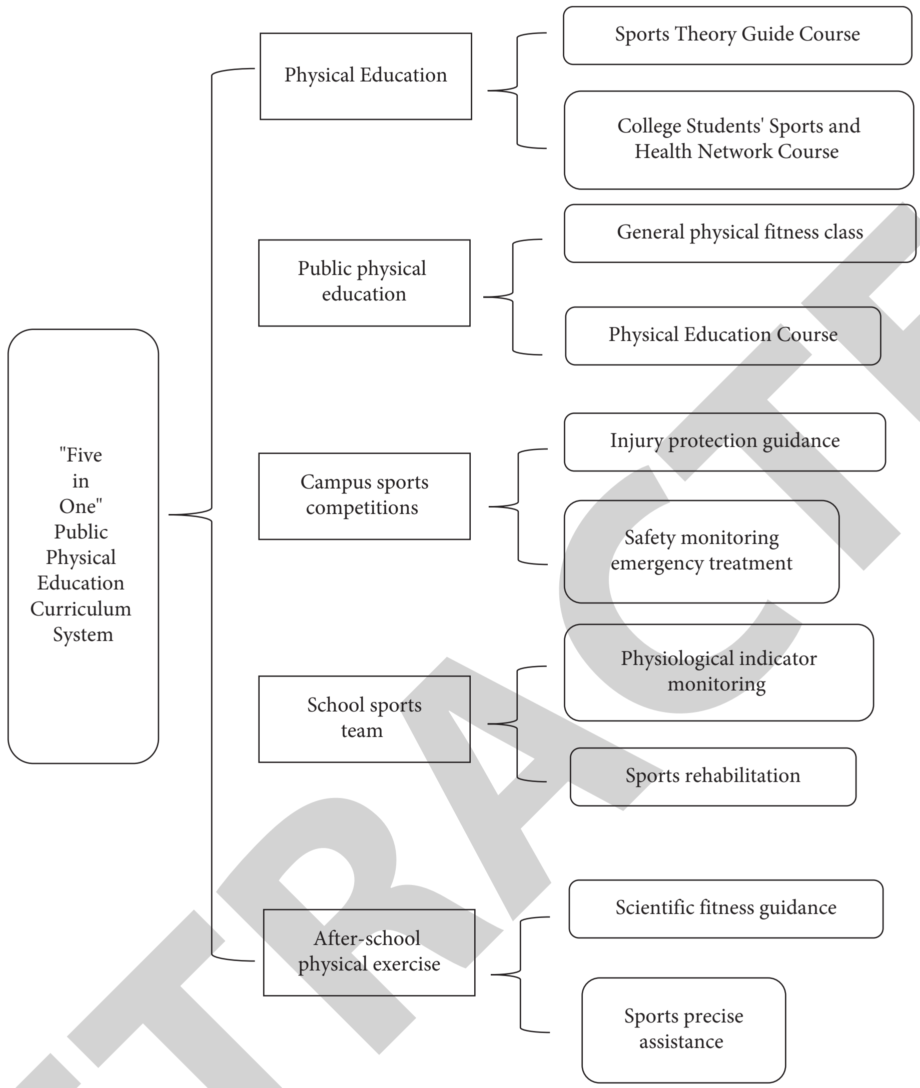

Figure 1: "Sports and medicine integration" sports health education system.

college students in order to promote the integration of sports and medicine.

Academic pressure is another major factor leading to the decline in physical health of college students. Before entering colleges and universities, students experienced three years of hardcore studies in high school and gave up a lot of exercise time in high school. Therefore, even after entering college, most students have lost the habit of exercising, and their physical fitness gradually deteriorated. In addition to the above-mentioned reasons, with the increasingly fierce social competition, more college students use their extracurricular time to study English and prepare for postgraduate entrance examinations and various qualification exams, which hinder students' physical exercise. Many college students approaching graduation, in order to be able to find the ideal job upon graduation, give up all the exercise time.

Nutrition has a basic material effect on the physical health of life and is the energy source for the main life activities of the human body. Balanced material nutrition is a material prerequisite for strengthening the system of college students and improving their health. Most college students live on campus, so it is often difficult to have a healthy life through diet. For this reason, major colleges and universities should strengthen the management of canteens. The scale of canteens should be expanded, attention should be paid to nutritional diet planning, and a healthy and balanced diet should be promoted.

For the effective development of sports activities, the strengths of all walks of life should be made to full use, taking into account the internal and external factors, to form a strong synergy and establish a three-dimensional pattern of physical health promotion of college students and a good environment and to make due contributions to cultivating college students' lifelong sports awareness. On the basis of the investigation of the status quo and analysis of the development trend of the "integration of physical education and medicine" teaching service model in college sports, full play will be given to the scientific and technological service

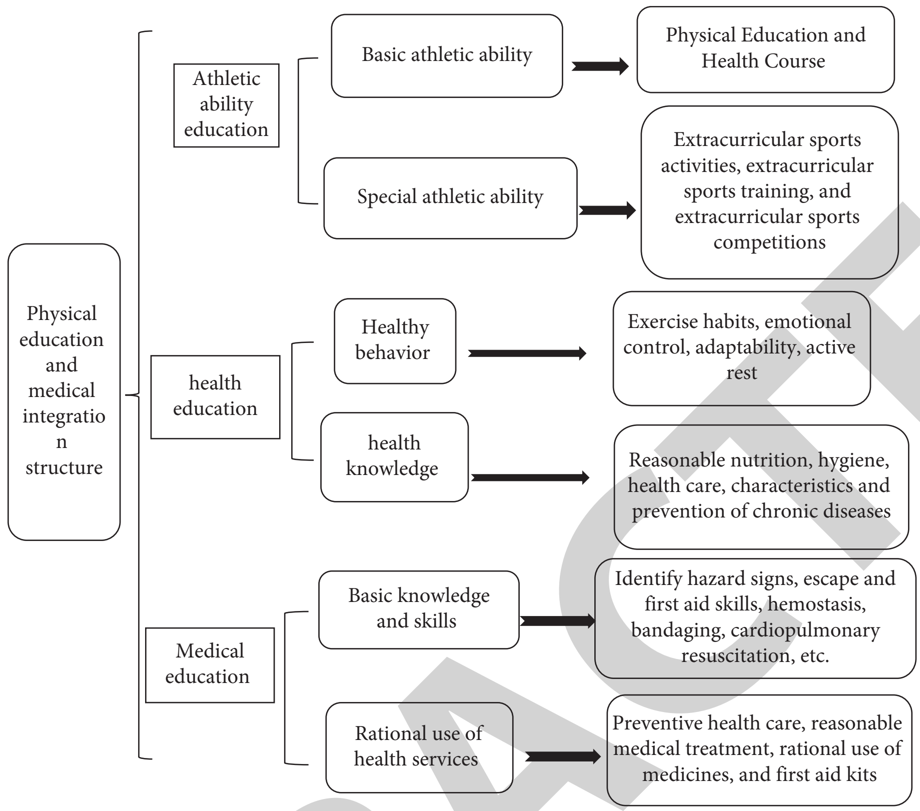

Figure 2: "Five-in-one" public physical education curriculum system.

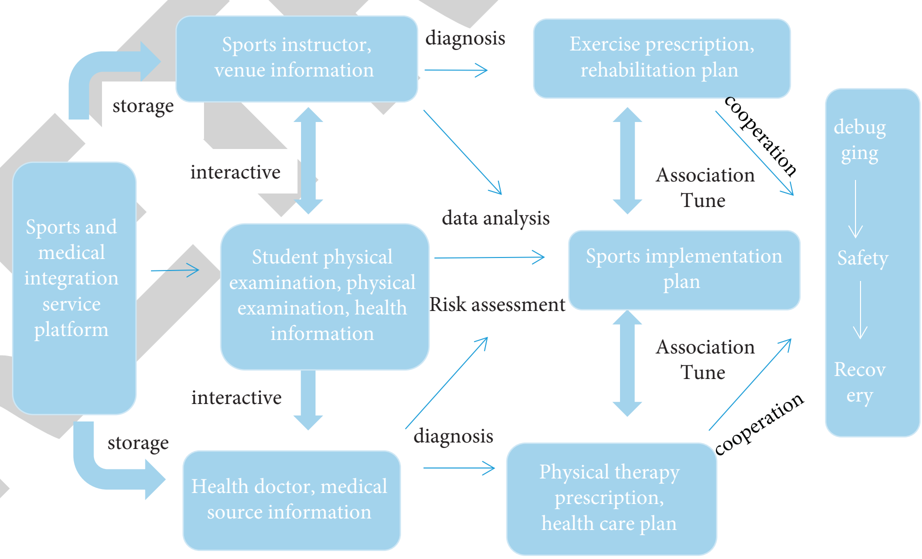

Figure 3: The framework of the teaching platform of "integration of sports and medicine" in colleges and universities.

advantages of the educational administration platform of colleges and universities and the importance of sports risk management and control will be advocated, with sports health programs as the starting point. A "sports–medical integration" teaching service platform that provides services such as exercise ability assessment and exercise prescriptions for students should be created.

6. Conclusion

The integration of physical and medical health promotion is a solution to college students under the new situation. The most obvious and effective method for improving physical fitness can be the fastest and most efficient way to meet the sports and health needs of college students. In order to

Hindawi
Journal of Healthcare Engineering
Volume 2022, Article ID 8256314, 16 pages
https://doi.org/10.1155/2022/8256314

Research Article

Single-Cell Sequencing Identifies the Heterogeneity of CD8+ T Cells and Novel Biomarker Genes in Hepatocellular Carcinoma

Hailei Wang,[1] Yang Fu,[2] Bin-Bin Da,[3] and Geng Xiong[4]

[1]*Kunming First People's Hospital, Kunming 650031, China*
[2]*CT Room, Kunming First People's Hospital, Kunming 650000, China*
[3]*Department of Minimally Invasive Interventional Medicine, Yunnan Cancer Hospital, Kunming 650118, China*
[4]*Third Department of General Surgery, Changde First People's Hospital, Changde 415003, China*

Correspondence should be addressed to Geng Xiong; xg491520@163.com

Received 21 December 2021; Revised 29 January 2022; Accepted 2 February 2022; Published 12 April 2022

Academic Editor: Enas Abdulhay

CD8+ T cells are required for the establishment of antitumor immunity, and their substantial infiltration is associated with a good prognosis. However, CD8+ T cell subsets in the tumor microenvironment may play distinct roles in tumor progression, prognosis, and immunotherapy. In this study, we used the scRNA-seq data of hepatocellular carcinoma (HCC) to reveal the heterogeneity of different CD8+ T cell subsets. The scRNA-seq data set GSE149614 was obtained from the GEO database, and the transcriptome and sample phenotypic data of TCGA-LIHC were obtained from the TCGA database. CD8+ T cell subtypes and metabolic gene sets were obtained from published reports. The data processing and analysis of CD8+ T cell groups was performed by *R* language. The PPI network was constructed to obtain the hub genes, and the KM survival curve of the hub genes was further plotted to determine the hub genes with differences in survival. CD8+ T cells in HCC were divided into 7 subsets, and the cytotoxic CD8 T cells 4 subset showed considerable differences between the TP53-mutant and nonmutant groups, as well as between different degrees of cirrhosis, HCC grades, stages, ages, and body weights. Cytotoxic CD8 T cells 4 differential genes were analyzed by TCGA-LIHC data and single-cell sequencing data set. 10 hub genes were found: FGA, ApoA1, ApoH, AHSG, FGB, HP, TTR, TF, HPX, and APOC3. Different subsets of CD8+ T cells were found to contribute to heterogeneous prognosis and pathway activity in HCC. Alterations in the cytotoxic and immune checkpoint gene expression during CD8+ T cell differentiation were also identified. We found that cytotoxic CD8 T cells 4 is closely associated with survival and prognosis of HCC and identified four differential genes that can be used as biological markers for survival, prognosis, and clinically relevant characteristics of HCC. Results of this study could help finding targets for immunotherapy of HCC and aid in the accelerated development of immunotherapy for HCC.

1. Introduction

Hepatocellular carcinoma (HCC) is a type of liver cancer that is extremely common [1]. Traditional treatment methods for HCC mainly include surgical treatment (liver resection, liver transplantation), radiofrequency, microwave ablation, embolization (transcatheter hepatic arterial chemoembolization, TACE), and sorafenib [2–6]. In the early stage of hepatocellular carcinoma, the symptoms are hidden without characteristics; hence, most of the patients have developed to the middle and late stage when diagnosed, most of them cannot accept radical treatment, and the prognosis is poor [7]. In recent years, immunotherapy has produced good therapeutic effects in the therapy of various malignant tumors, including melanoma and hematological malignancies, while the therapeutic effects in solid malignant tumors are not satisfactory, especially in HCC [8, 9]. On the one hand, this is related to the complex microenvironment in solid tumors, including low oxygen, high pH, nutritional deficiency, and immunosuppressive cells and factors [10–13]; and on the other hand, the disorder of the functional state of the relevant immune cells in the tumor is also an important factor leading to ineffective or inefficient immunotherapy [14].

Immune imbalance in the microenvironment of the tumor is one of the important characteristics of the tumor.

The adaptive immune response, which is mediated by immune cells, is important in the occurrence and development of tumors [15]. CD8+ T cells are the main antitumor effector cells [16]. The weakened antitumor immunity characterized by CD8+ T cell function disorder plays an essential role in the occurrence and development of hepatocellular carcinoma [17, 18]. CD8+ T cells from the circulation migrate and infiltrate into tumor tissues and are stimulated by contact with tumor antigens to become effective CD8+ T cells with the killing effect of tumor microcytes [19, 20].

In the process of antitumor immune response in normal organisms, antigen-presenting cells present tumor-specific antigen (TSA) as major histocompatibility complex (MHC) and bind to T cell surface TCR (T cell receptor) and then, under the action of various costimulatory signal molecules, activate T cells; activated T cells, mainly cytotoxic CD8+ T cells, bind to tumor cells via recognition of TSA on their surface and kill tumor cells after the costimulatory signal is activated [21, 22]. The activation of costimulatory signal plays an essential role in the killing of tumor by T cells [23]. In tumor microenvironment (TME) T cells, the expressions of costimulatory signal molecules including CD137, CD28, and OX40 are often significantly decreased [24–26], while the expressions of costimulatory signal molecules such as cytotoxic T-lymphocyte-associated protein 4 (CTLA4), programmed cell death protein 1 (PD-1), and T-cell immunoglobulin mucin-3 (TIM-3) are significantly increased [27–29]. These costimulating/inhibiting molecules are known as immune checkpoints, and the treatment of these signaling molecules is also known as immune checkpoint therapy.

Immunocheckpoint therapy has achieved a series of successes in the treatment of solid tumors, breaking through the original view that tumor immunotherapy may only be effective for immunogenic melanoma and kidney cancer [30]. Recent clinical studies have shown that monotherapy has achieved good efficacy in solid tumors such as non-small-cell lung cancer (NSCLC), colorectal cancer, and gastric cancer, and the safety of most immunotherapies has also been recognized [31–33]. The Food and Drug Administration (FDA) and the European Union have approved several immune checkpoint inhibitors and monoclonal antibodies for clinical tumor treatment, such as CTLA4 monoclonal antibody ipilimumab, PD1 monoclonal antibody nivolumab, etc. [34].

Like NSCLC and colorectal cancer, HCC cells also express a large number of co-inhibitory components such as PD-L1 on the surface, but unfortunately, the efficacy of immune checkpoint inhibitors has not been adequately evaluated in early clinical trials [35]. The current scRNA-seq technique is widely used in the study of cell heterogeneity. However, due to the need for preamplification of cDNA before library construction, poor amplification may lead to the loss of some information. To more comprehensively identify the differences among hepatocellular carcinoma cells, Xiao et al. [36] for the first time implemented the Holo-Seq technique to obtain the transcriptome information of mRNAs and small RNAs from a single cell at the same time and combined the information to determine intercellular heterogeneity. In this study, Holo-Seq technology was applied to analyze single cells of human liver cancer, and it was found that mitochondrial activity was downregulated in the early stage of liver cancer [36]. Moreover, tumor suppressor miRNA and tumor-promoting miRNA were upregulated earlier than the activation of classical tumor-promoting signaling pathway [36]. These findings provide important information and references for diagnosing liver cancer. Additionally, they drew a cluster map based on double transcriptional profiles of single-cell mRNAs and miRNAs in HCC [36]. Compared with single scRNA-seq clustering analysis, this approach enables a more complete understanding of the tumor cell heterogeneity in HCC and discover new cell subpopulations.

In this study, we used the scRNA-seq data of hepatocellular carcinoma to reveal the heterogeneity of different CD8+ T cell subsets. The cellular components of the CD8+ T cell subpopulation in liver cancer patients under different states of liver cirrhosis, grade, stage, age, and body weight were determined, and the activity analysis of metabolic pathway and hallmark pathway was carried out based on the pipeline analysis of pathway activity based on single-cell sequencing data. Cell differentiation trajectory and cell-cell interaction network analysis was performed, and the hub genes' expression in different cancers was determined for prognosis/treatment marker identification. Different subsets of CD8+ T cells were found to contribute to heterogeneous prognosis and pathway activity in HCC. Alterations in an immune checkpoint and cytotoxic gene expression during CD8+ T cell differentiation were also identified.

2. Materials and Methods

2.1. scRNA-seq and RNA-seq Data. HCC scRNA-seq was downloaded from the Gene Expression Omnibus (GEO) database (GSE149614), and a total of 34,414 cells from 10 HCC tissue samples were screened. From the TCGA Xena database (https://xenabrowser.net/datapages/), the transcriptome and sample phenotypic data of TCGA-LIHC were downloaded; a total of 424 samples were obtained, of which 374 were tumor tissues (6 of the samples had no survival information and were excluded from subsequent analysis) and 50 were normal tissues. The expressed value from log2 (count +1) were converted to count for subsequent analysis. CD8+ T cell subtypes were obtained from the study by Deng et al. [37]. A total of 85 metabolic gene sets were obtained from Xiao et al. [38], and a total of 50 hallmark gene sets were downloaded from h.all.v7.3.symbols.gmt from MSigDB.

2.2. Identification of CD8+ T Cell Subsets. The R package "Seurat" was used to map the expression profile of CD8A and CD8B (CD8+ T cell markers) and determine the CD8+ T cell population. CD8+ T cells were selected, and UMAP cluster analysis was performed again, and each cell subpopulation was annotated according to the expression distribution of CD8+ T cell subtypes. The proportion of each subtype of CD8+ T cells was counted, and a bar chart was drawn using the R package "ggplot2" for display. Hypervariable genes of each subtype were examined with the help of the Seurat package. To find all markers functions, the min.pct and logfc.threshold parameters set at 0.25 were used. The top 10 highly variable genes of each subtype were selected, and the R package "pheatmap" was used to draw the heatmap of gene expression. Marker genes of previously reported studies were employed to annotate subpopulations of CD8+ T cells including naive/memory CD8+ T cells (CCR7, IL7R, TCF7, SELL, SATB1, GPR183, LTB, LEF1, and S100A10), exhausted CD8+ T cells (CXCL13, HSPB1, IRF4, LAYN, GIMAP6, HSPH1, CXCR6, CTLA4, PDCD1, LAG3, HAVCR2, and TIGIT), and cytotoxic CD8+ T cells (PRF1, GZMA, GZMK, and NKG7).

2.3. The Cellular Components of the CD8+ T Cell Subpopulation. The Seurat package was used to obtain the hypervariable genes of each subtype of CD8+ T cells, and they were screened according to the Bonferroni correction P value <0.05. For screening of gene expression (count), CIBERSORTx (https://cibersortx.stanford.edu/) tools were used following the default parameters of CD8+ T cell subtype of liver cancer signature matrix file. The transcriptome data of TCGA-LIHC were collated, and the count was converted into CPM as the input file of CIBERSORTx to estimate the content of CD8+ T cell subtypes in liver cancer. The surv_cutpoint function was used to analyze the cell content of each subtype, and the cell content of TCGA-LIHC samples was divided into groups of high and low levels, and the survival curve of KM was plotted using Survival packet and survminer packet. The phenotypic data of TCGA-LIHC were sorted. Boxplots were drawn to show the difference in cell content between TP53 mutation and gender, and line plots were drawn to show the content of CD8+ T cell subtypes in liver cancer patients under different states of liver cirrhosis, grade, stage, age, and body weight.

2.4. Pathway Activity Analysis. For scRNA-seq data, the FindMarkers function of the Seurat package was used to obtain the hypervariable genes of each subtype of CD8+ T cells and screen them according to the Bonferroni correction P value <0.05. The ClusterProfiler package was used for Gene Ontology (GO) and Kyoto Encyclopedia of Genes and Genomes (KEGG) enrichment analysis, and then using ggplot2, a bubble chart was drawn to display the results. According to the research report of Xiao et al. [38], the activity analysis of metabolic pathway and hallmark pathway was carried out based on the pipeline analysis of pathway activity based on single-cell sequencing data.

2.5. Cell Differentiation Trajectory and Cell-Cell Interaction Network Analysis. Using the package's default parameters, the Slingshot package was utilized to assess the cell differentiation trajectory and the distribution of marker gene expression. The single-cell sequencing data of CD8+ T cells were collated, and the interaction network analysis of CD8+ T cell subtypes was conducted using CellPhoneDB software developed based on Python. The R package SCENIC was used to construct the gene regulation network of CD8+ T cell subtypes.

2.6. Prognosis/Treatment Marker Identification. CD8+ T cell subtypes with significant differences in survival analysis were selected and grouped according to the cell content of the cell subtypes. Differential analysis was performed on the TCGA-LIHC expression data (R package DESeq2), following |log2(-FoldChange)|>1 and corrected the P value <0.05 for differential genes screening. The protein-protein interaction (PPI) network was constructed using the String database (https://www.string-db.org/), and Cytoscape (v3.7.2) and cytoHubba plug-in were used to screen the hub genes. The hub genes were divided into two groups based on their expression levels: high and low according to the median number of hub genes. Kaplan–Meier (KM) survival curves were plotted using the survival package R and Survminer. Hub genes with survival differences were selected and single-gene gene set enrichment analysis (GSEA) was performed using the clusterProfiler package. According to different clinical features, ggstatsplot was used to plot boxplots to show hub gene expression levels with significant differences in survival. The TCGA pan-cancer data was downloaded from the TCGA Xena database, and hub gene expression in various tumors was shown in a bar graph.

2.7. Statistical Analysis. Genes differently expressed in different subsets, KEGG, GO, and GSEA analyses were analyzed statistically using the corresponding software packages or default methods in the software. Random arrangement tests exhibited statistical pathway activity. Student's test was used to assess the frequency of different cell types in normal and tumor samples; statistical analysis was also used to examine the levels of expression in tumors and normal tissue samples. The significance of the KM curves was tested using the log-rank test. The Kruskal–Wallis test was used to determine dynamic changes in cell proportion and levels of gene expression at various stages of pathology.

3. Results

3.1. Data Download and Preprocessing. For liver cancer, the scRNA-seq data set GSE149614 was downloaded from the GEO database (https://www.ncbi.nlm.nih.gov/geo/) and 10 liver cancer tissue samples were screened with a total of 34,414 cells. From the TCGA Xena database (https://xenabrowser.net/datapages/), the transcriptome and sample phenotypic data of the TCGA-LIHC were downloaded; a total of 424 samples were obtained, of which 374 were tumor tissues (6 samples had no survival information and were excluded from subsequent analysis) and 50 were normal tissues.

Single-cell sequencing results showed that the gene number of the samples was mainly distributed between 1000 and 8000, the gene count was mainly distributed between 100 and 50,000, and the mitochondrial proportion was mainly distributed between 0 and 5% (Figure 1). The correlation between the depth of the sequencing and the

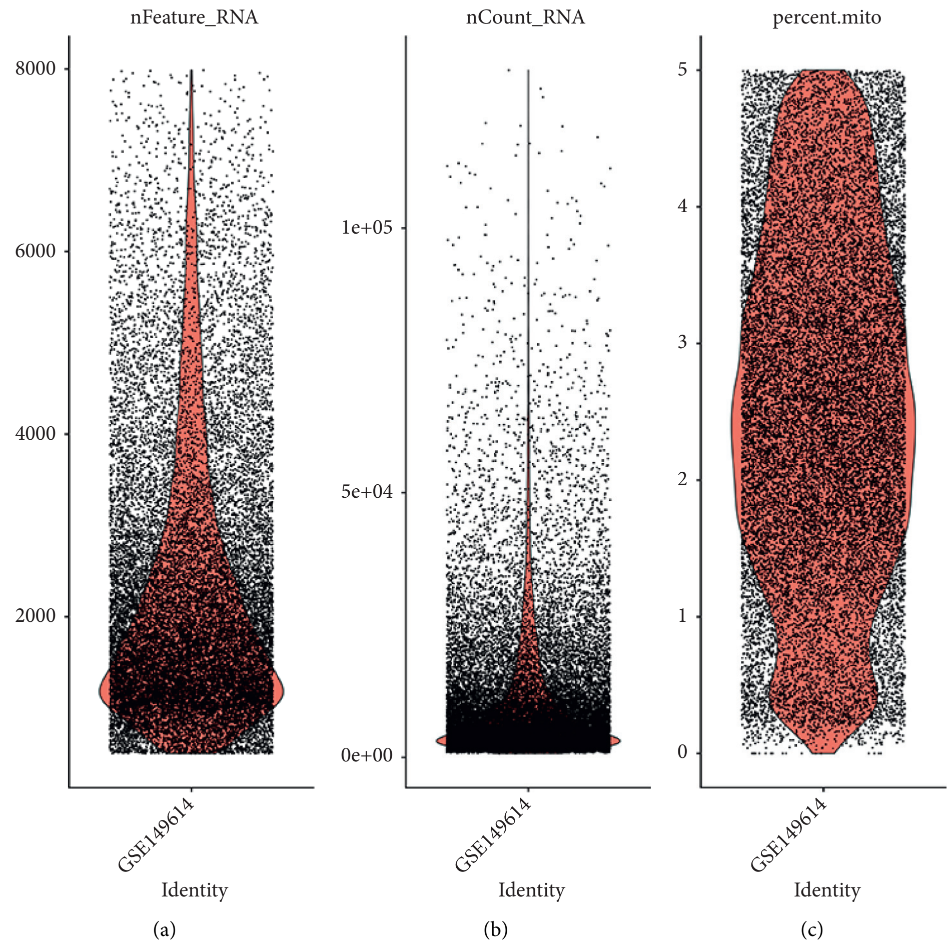

Figure 1: Quality control chart of GSE149614 single-cell data set. (a) The number of genes in a cell. (b) Count distribution of genes. (c) Figure: mitochondria percentage.

number of genes detected was 0.89, and between the sequencing depth and mitochondria was 0.16, indicating a positive correlation of sequencing depth with the number of measured genes (Figure 2). 2000 differentially expressed genes that are highly expressed were selected for principal component analysis (PCA), and the differences between the first 15 PCs were all highly significant, suggesting a considerable difference between theoretical and actual values, which was used for additional analysis (Figure 3).

3.2. CD8+ T Cell Extraction and Subpopulation Recognition. The UMAP method was used for clustering, and 26 clusters were obtained (Figure 4(b)). Because it was a tumor tissue sample, the heterogeneity was high (Figure 4(a)). CD8A and CD8B were mainly distributed in cluster 0, 6, 9, 16, and 24, with a total of 5062 cells (Figure 5). The cells of these groups were pulled out, and UMAP clustering was performed again to obtain 7 CD8+ T subgroups (Figure 6). CD8+ T cell subtype markers were obtained from the research report of Deng et al. [37], that is, markers of naive/memory CD8 T cells: CCR7, IL7R, TCF7, SELL, SATB1, GPR183, LTB, LEF1, and S100A10; the markers of cytotoxic CD8 T cells: PRF1, GZMA, GZMK, and NKG7; and the markers of exhausted CD8 T cells: CXCL13, HSPB1, IRF4, LAYN, GIMAP6, HSPH1, CXCR6, CTLA4, PDCD1, LAG3, HAVCR2, and TIGIT. Based on the expression of the above markers, 7 cell subgroups were annotated as follows: naive/memory CD8 T cells, exhausted CD8 T cells 1, exhausted CD8 T cells 2, cytotoxic CD8 T cells 1, cytotoxic CD8 T cells 2, cytotoxic CD8 T cells 3, and cytotoxic CD8 T cells 4.

3.3. Cell Proportion and Cell Marker Expression. The proportion of cells in each subpopulation was shown to be naive/memory CD8 T cells in the HCC TME. The proportion of the medium is the highest, followed by exhausted CD8 T cells 1, and the lowest is cytotoxic CD8 T cells 4 (Figure S1A of the supplementary information file). At the same time, the expression of top 10 differentially expressed genes in seven CD8+ T subsets was analyzed (Figure S1B). According to the transcriptome data of TCGA-LIHC, CIBERSORTx calculated that cytotoxic CD8 T cells 4 and exhausted CD8 T cells 2 accounted for the highest proportion (Figure S8, Table S1).

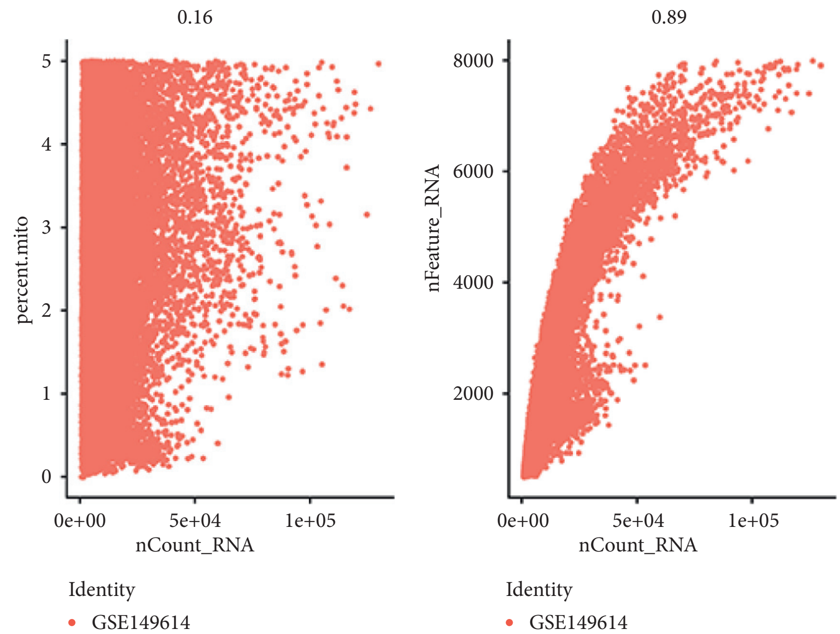

(a) (b)

Figure 2: GSE149614 single-cell data quality control chart. (a) Correlation between mitochondrial percentage and gene count. (b) Correlation between the number of genes and count.

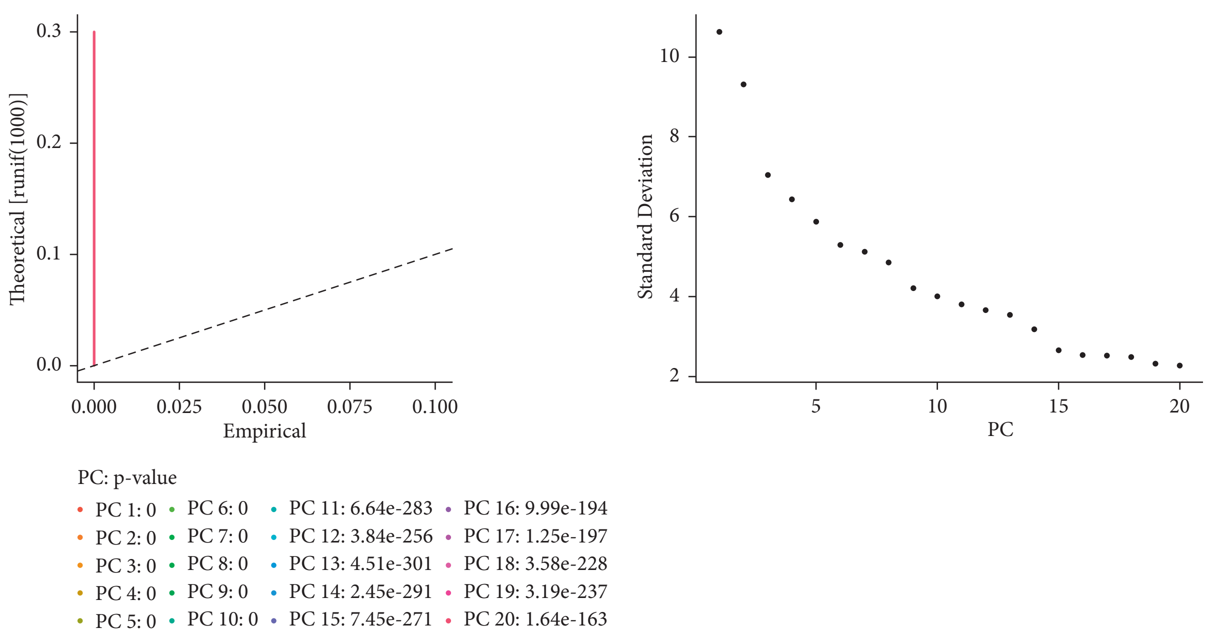

(a) (b)

Figure 3: PCA analysis. (a) The difference between the theoretical and actual values of the first 20 PCs. (b) Elbow plot.

3.4. Analysis of Prognosis and Clinical Correlation. The survival analysis was performed by log-rank test. The survival difference of the overall immune cell proportion group was statistically significant, and there was a significant survival difference between the groups with a high and low proportion of cytotoxic CD8 T cells 4. The survival difference between the exhausted CD8 T cells 2 and naive/memory CD8 T cells was not statistically significant (Figure S2, Table S2). Cytotoxic CD8 T cells 4 differed significantly between the TP53 mutant and nonmutant groups (nonparametric Wilcox rank-sum test) and between sex (Figures S9A and S9B). Among cirrhosis groups of different degrees, the proportion of cytotoxic CD8 T cells 4 increased first and was the lowest in nodular formation and

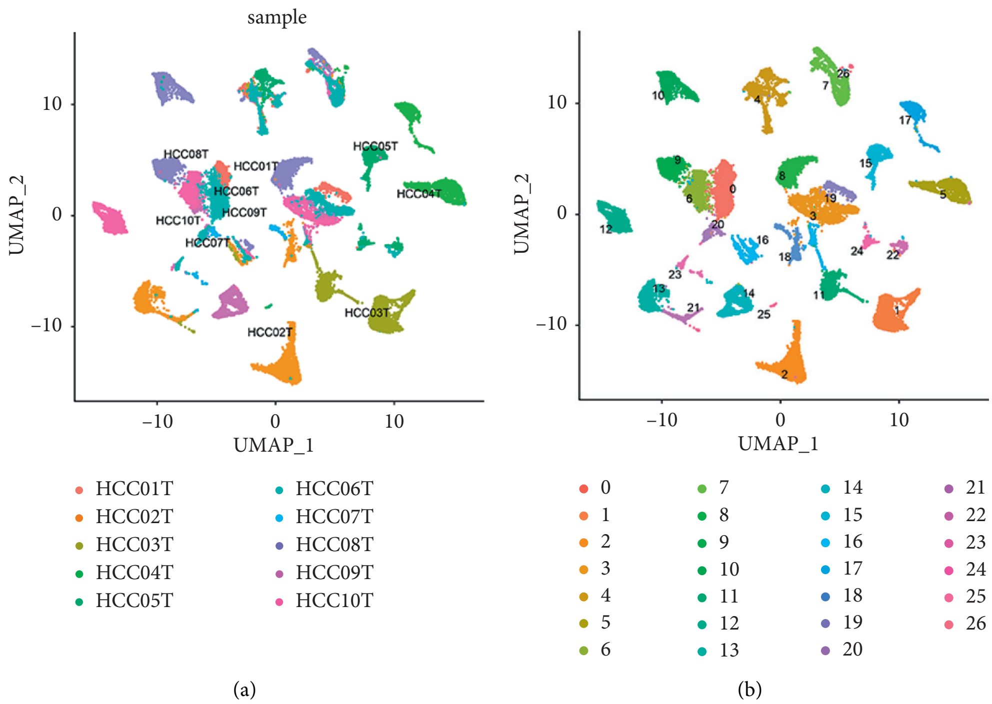

Figure 4: Clustering diagram of cells. (a) Labeled according to the sample name. (b) Labeled according to cluster ID.

incomplete cirrhosis (Figure S9C). In the grading of liver cancer, the ratio of cytotoxic CD8 T cells 4 was highest in G2 and then decreased progressively (Figure S9D). The proportion of cytotoxic CD8 T cells 4 decreased first and then increased in the stage of liver cancer (Figure S9E). The proportion of cytotoxic CD8 T cells 4 was lowest in the 40–60 years age group (Figure S9F). The proportion of cytotoxic CD8 T cells 4 increased with increasing body weight (Figure S9G).

3.5. The Landscape of Heterogeneous Pathway Activity. To investigate the presence of heterogeneous pathways in CD8+ T cell subsets, we used GO and KEGG analysis. GO analysis showed that cytotoxic CD8 T cells 4 had an obvious biological process, cellular component, and molecular function (Figures 7(a)–7(c), Table 1). KEGG results showed that cytotoxic CD8 T cells 4 were related to ribosomes (Figure 7(d), Table 1). To elucidate the heterogeneity of various subgroups further, we also performed the analysis of cell subgroup metabolic pathway activity and hallmark immune checkpoint pathway activity. The analysis of the metabolic pathway activity of cell subsets revealed that exhausted CD8 T cells 1, exhausted CD8 T cells 2, and cytotoxic CD8 T cells 3 had strong metabolic pathway activity, and cytotoxic CD8 T cells 2 had the lowest metabolic pathway activity (Figures S3A and S3B). Oxidative phosphorylation was significantly enriched in 7 CD8+ T cell subgroups (Figure S3C). Hallmark pathway activity analysis revealed that exhausted CD8 T cells 1, exhausted CD8 T cells 2, and cytotoxic CD8 T cells 3 had strong hallmark pathway activity, and cytotoxic CD8 T cells 2 had the lowest hallmark pathway activity (Figures 8(a) and 8(b)). HALLMARK_MYC_TARGETS_V1 was significantly enriched in 7 CD8+ T cell subgroups (Figure 8(c)).

3.6. Analysis of Cell Differentiation Trajectories and Cell Interaction Networks. The initial differentiation group is not specified and a lineage is obtained from exhausted CD8 T cells 1 to cytotoxic CD8 T cells 4, as shown in Figure S4A. The PRF1, GZMA, and NKG7 genes were first downregulated, then upregulated, and finally downregulated during the development of lineage (Figures S4B–S4E).The PDCD1, HAVCR2, LAG3, CD27, CTLA4, TIGIT, and TNFRSF9 genes remained unchanged during the predifferentiation process and significantly differentiated in the mid-term and then remained unchanged (Figures S4F–S4L).

Considering the heterogeneity of CD8+ T cell subsets, we analyzed their communication networks to identify the key ligand-receptor pairs and cell subsets that dominate the interactions. The results showed that cytotoxic CD8 T cells 2, cytotoxic CD8 T cells 1, and cytotoxic CD8 T cells 4 had the highest number of ligand receptors (Figure S5A). The ligand-receptor logarithm between exhausted CD8 T cells 2 and the other 6 subtypes was less (Figure S5B), and the regulatory factors JUND, EGR1, FOSB, IRF1, IRF8, and REL were highly expressed in cytotoxic CD8 T cells 1 (Figure S5C).

3.7. Prognosis/Treatment Marker Identification. Based on the results of significant differences in survival, the differentially expressed genes were calculated first by the TCGA database, and a total of 6813 differentially expressed genes were

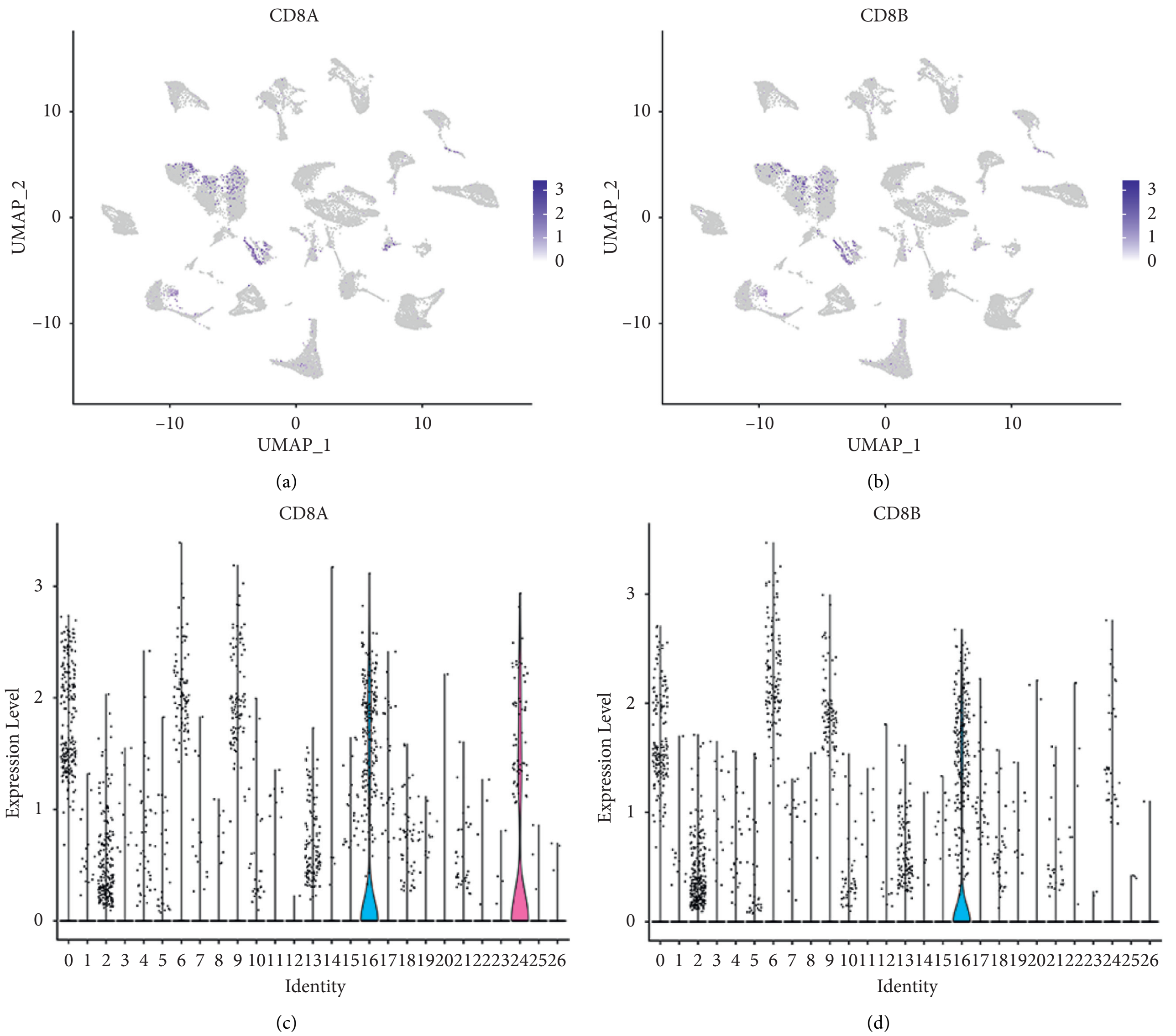

Figure 5: Expression and distribution of CD8+ T cell markers. (a, c) Expression distribution of CD8A. The darker the color, the higher the expression. (b, d) Expression distribution of CD8B.

obtained, of which 2378 were upregulated and 4435 were downregulated (Table S3). The expression of the first 50 differential genes is shown in Figures 9(a) and 9(b). Then, according to the results of significant differences in survival, the corresponding cell subsets and differentially expressed genes were selected, and the ligand receptors and transcription factors among them were given priority. If the subsequent analysis was not supported, only differentially expressed genes were selected, and a total of 168 differentially expressed genes were found. Since the survival analysis of 4 cases of cytotoxic CD8 T cells in the high and low groups showed significant survival differences, the expression of the first 50 differentially expressed genes of cytotoxic CD8 T cells 4 was selected for display (Figure S10). According to the obtained two groups of different genes, the PPI network was constructed and hub genes were identified. cytoHubba found 10 hub genes: FGA, APOA1, APOH, AHSG, FGB, HP, TTR, TF, HPX, and APOC3 (Figure 10). The log-rank test showed that APOC3 among the above 10 hub genes had statistically significant survival differences, while APOH, HPX, and FGB had significant survival differences (Figures 11(a)–11(d)). The Cox test showed that the P-values of APOC3, APOH, HPX, and FGB were 0.02, 0.14, 0.00067, and 0.034, respectively. Genetic GSEA of APOC3, APOH, HPX, and FGB was performed, and the first five enrichment items are shown in Figures 11(a)–11(d) and Table S4 in the supplementary file. Table S4 in the supplementary file shows the analysis results of single-gene GSEA of APOC3, APOH, HPX, and FGB. The expression levels of different genes in different clinical features were further analyzed, and the expression levels of genes APOC3, APOH, HPX, and FGB were significantly different in normal tissues and tumors , and were further analyzed whether TP53 mutation was present or not. There was a significant difference

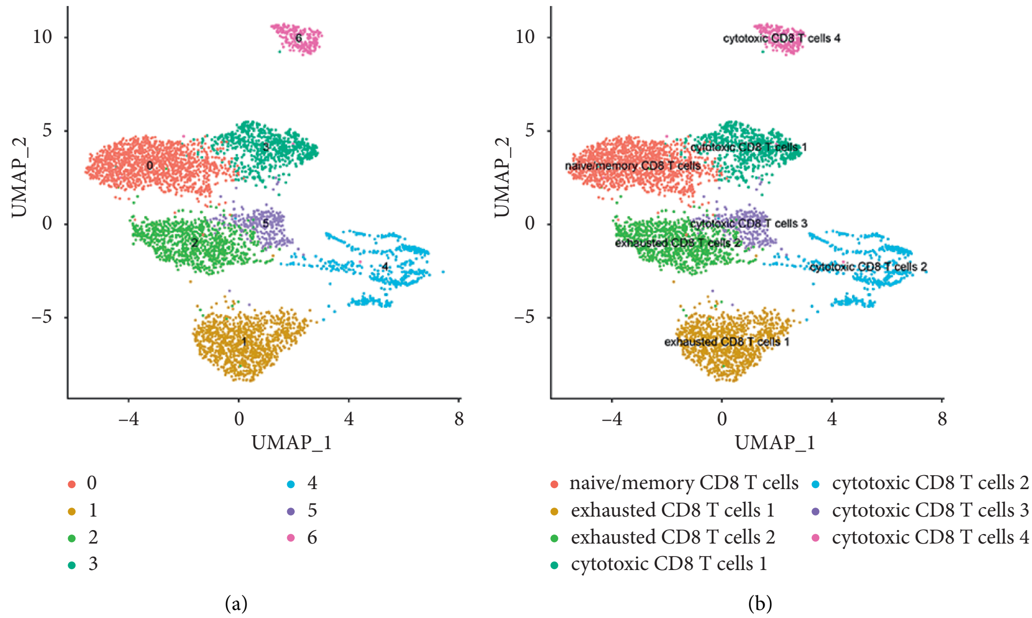

Figure 6: Cluster of CD8+ T cells. (a) An unannotated cluster diagram. (b) A cluster diagram annotated according to CD8+ T subtype markers.

($P = 0.0053$) in the expression of APOH among the sex groups. The expressions of APOC3, APOH, HPX, and FGB were not significantly different in different cirrhosis degrees and different ages ($P > 0.05$). There were significant differences in the grading and staging of liver cancer. The gene APOC3 had no significant difference among different body weights (Figures S6 and S11). Finally, the expression of different genes in different cancers was analyzed, and the results showed that the expression of genes APOC3, APOH, HPX, and FGB was the highest in liver hepatocellular carcinoma (LIHC), and the expression in normal tissues was higher than that in cancer tissues. Genes APOC3, ApoH, HPX, and FGB were also highly expressed in cholangiocarcinoma (CHOL), and their expression levels were higher in normal tissues than in cancer tissues (Figure S12).

4. Discussion

The role of tumor-infiltrating immune cells, particularly T cells, in tumor development has been revolutionized by a deeper understanding that has opened up new avenues for immunotherapeutic strategies. Previous studies have indicated that immune cells infiltrating tumors exhibit various levels of infiltration depending on the type of tumor and stages [39]. Immune-associated cells, including T cells and mast cells, have been shown to be novel prognostic markers in patients with HCC, further suggesting that the combination of immunoinfiltrating cells in tumor tissue can even predict the effects of chemotherapy and immunotherapy [40]. Due to the fact that CD8+ T cells are the most significant effector T cells in current tumor immunotherapy [41], CD8+ T cells detect tumor-associated antigens on the surface of cancer cells as major histocompatibility complex class I molecules [42].

It has been found that four coexpression genes (GZMA, C1QC, CD3D, and PSMB9) have been identified as CD8+ T cell coexpression genes that promote CD8+ T cell infiltration in HCC, and these coexpressed genes are favorably associated with the infiltration of CD8+ T lymphocytes during antigen presentation. This biological process may provide new directions for patients with stem cell cancers that are not sensitive to immunotherapy [43]. Thus, CD8+ T cells are essential for the formation of antitumor immunity, and their increased invasion is related with a favorable prognosis. CD8+ T cell subsets in the microenvironment of the tumor, on the other hand, may play distinct roles in tumor progression, prognosis, and immunotherapy. Cytotoxic CD8+ T cells have been reported to be associated with lymph node metastasis and other prognostic factors in breast cancer [44]. We found that cytotoxic CD8 T cells 4 differed significantly between the TP53-mutated and nonmutated groups, as well as with different degrees of cirrhosis, HCC grade, stage, age, and body weight. Cytotoxic CD8 T cells 4 differential genes were analyzed by the TCGA-LIHC data and single-cell sequencing data set. Finally, 10 hub genes were found: FGA, ApoA1, ApoH, AHSG, FGB, HP, TTR, TF, HPX, and APOC3. There were significant survival differences among APOC3, APOH, HPX, and FGB genes. Further analysis showed that APOC3, APOH, HPX, and FGB were significantly different in normal tissues and tumors irrespective of TP53 mutation, liver cancer grade, and stage. There was a significant difference in the expression of APOH among the sex groups. APOC3, APOH, HPX, and FGB expression levels were highest in HCC and were greater in normal tissues than that in cancer tissues. Additionally, it is significantly expressed in CHOL, and its level of expression is higher in normal tissues than that in cancer tissues. Apoprotein C3 (APOC3) is a key regulator of the

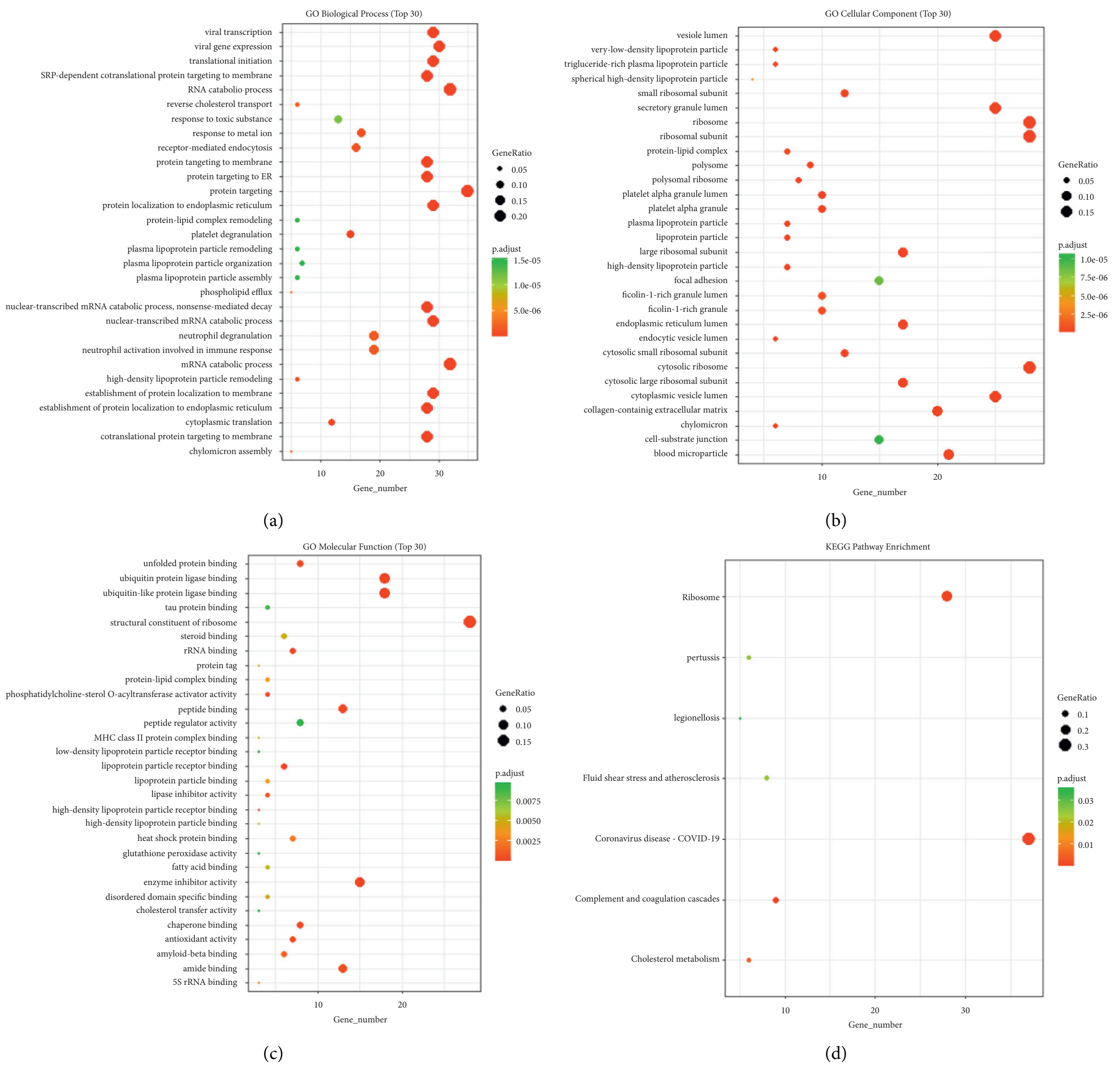

Figure 7: GO and KEGG enrichment analysis of the cytotoxic CD8 T cells 4 subgroup. (a) GO enrichment of biological process. (b) GO enrichment of cellular component. (c) GO enrichment of molecular function. (d) Enrichment of KEGG pathway. The vertical axis represents the enrichment items, the horizontal axis represents the number of different genes in the enrichment items, the size of the dot represents the ratio of the number of different genes in the enrichment items to the number of background genes, and the color represents the BH-corrected P value. The red color is directly proportional to enrichment.

metabolism of lipoprotein and has been demonstrated to be closely associated with hypertriglyceridemia [45]. β-2-glycoprotein 1 (APOH) has been shown to be associated with liver metastasis from colorectal cancer [46]. Hemopexin (HPX), which acts as a scavenger of toxic plasma heme and a transporter of it to the liver, has been demonstrated to be closely associated to the occurrence and development of breast cancer [47, 48]. Similarly, the fibrinogen β chain (FGB) gene has been revealed to be related with renal cell carcinoma invasion and metastasis [49]. All of these provide strong evidence that APOC3, APOH, HPX, and FGB can be used as biomarkers for hepatocellular carcinoma.

Tumor immunotherapy is a new method to treat cancer in recent years, which has greatly changed the prospect of cancer treatment [50, 51]. Although significant advances can be made in treatments such as immune checkpoint blockade, their efficacy varies greatly among different patients or cancer types [52]. A detailed understanding of the internal immune microenvironment of cancer tissue is of great reference value for the development of new immunotherapy. Single-cell sequencing technology can be used as an effective tool to study the immune microenvironment of liver cancer and plays an essential role in the process of immune cell therapy and antibody drug development of liver cancer.

Table 1: GO analysis and genomic encyclopedia (KEGG) analysis of cytotoxic CD8 T cells 4.

ID	Description	Gene ratio	Bg ratio	P value	p.adjust	Q value	Gene ID	Count
hsa05171	Coronavirus disease—COVID-19	37/113	232/8105	$5.79E-30$	$1.28E-27$	$1.11E-27$	2243/2244/718/2266/6189/712/4792/713/6173/6206/6158/6137/6171/6224/6143/6156/6181/6187/6139/5295/6202/7311/6161/3725/6192/6134/6135/6130/6159/6167/6228/6218/6133/6205/3921/6125/51065	37
hsa03010	Ribosome	28/113	158/8105	$7.35E-24$	$8.12E-22$	$7.08E-22$	6189/6173/6206/6158/6137/6171/6224/6143/6156/6181/6187/6139/6202/7311/6161/6192/6134/6135/6130/6159/6167/6228/6218/6133/6205/3921/6125/51065	28
hsa04610	Complement and coagulation cascades	9/113	85/8105	$2.45E-06$	0.000181	0.000158	2243/462/2244/7448/718/2266/712/713/1191	9
hsa04979	Cholesterol metabolism	6/113	50/8105	$6.20E-05$	0.003425	0.002985	350/345/335/341/348/336	6
hsa05133	Pertussis	6/113	76/8105	0.000636	0.025371	0.022114	718/712/713/805/3725/3659	6
hsa05418	Fluid shear stress and atherosclerosis	8/113	139/8105	0.000689	0.025371	0.022114	2938/4257/1843/805/5295/3725/3326/3320	8
hsa05134	Legionellosis	5/113	57/8105	0.001133	0.035775	0.031183	718/4792/1915/3329/3312	5

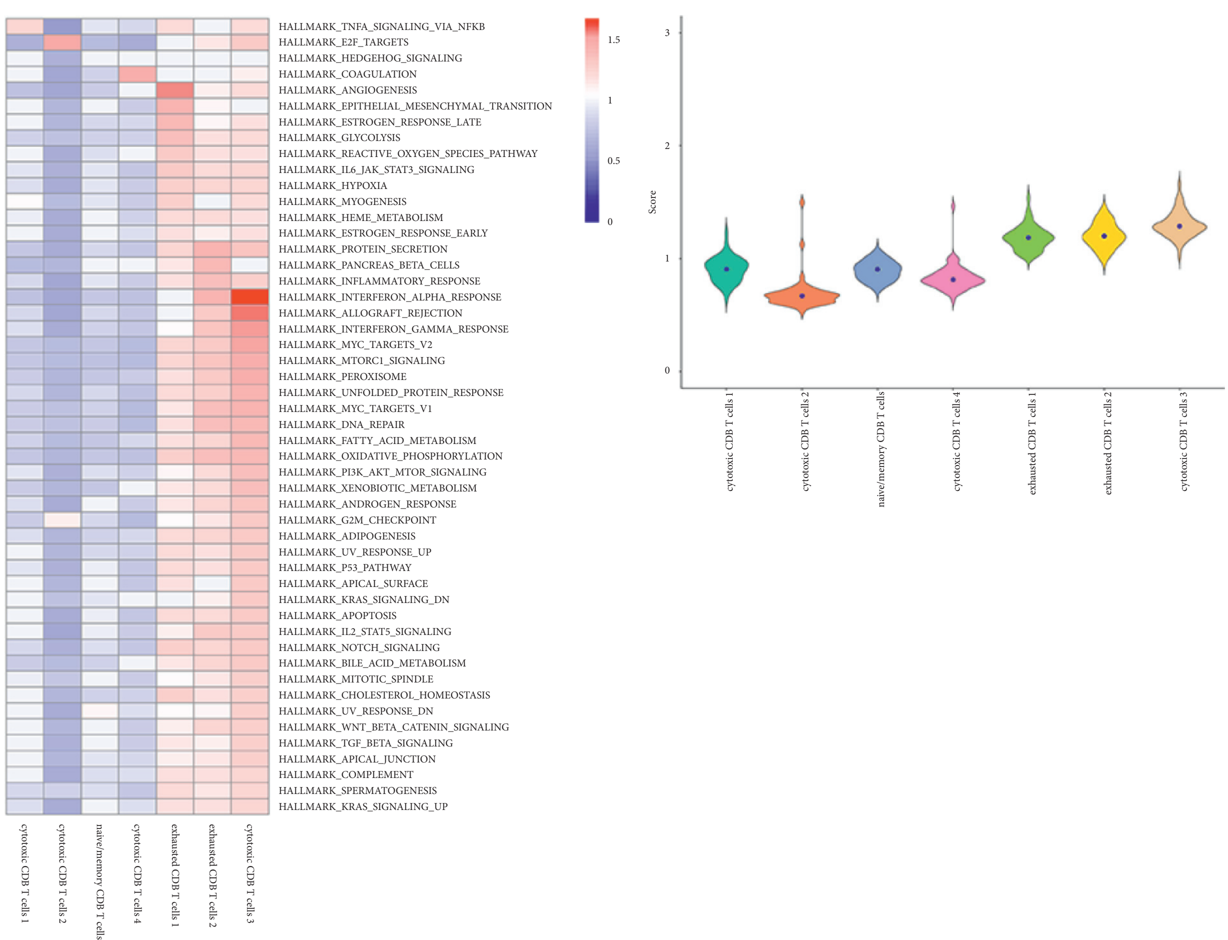

(a) (b)

Figure 8: Continued.

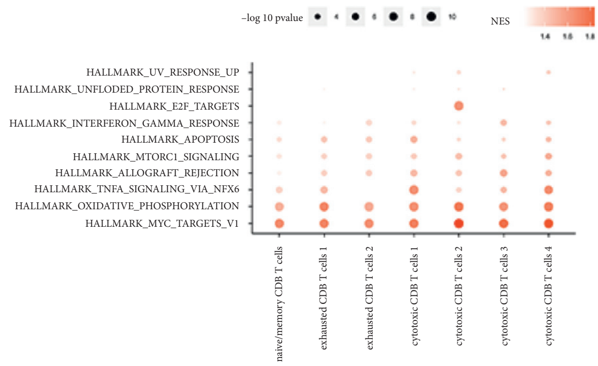

(c)

Figure 8: Hallmark pathway activity analysis of CD8+ T subsets. (a) Heatmap of hallmark pathway activity of CD8+ T subsets. (b) Active fiddle diagram of the hallmark pathway in CD8+ T subsets. (c) GSEA enrichment fractional point diagram of the CD8+ T subgroup.

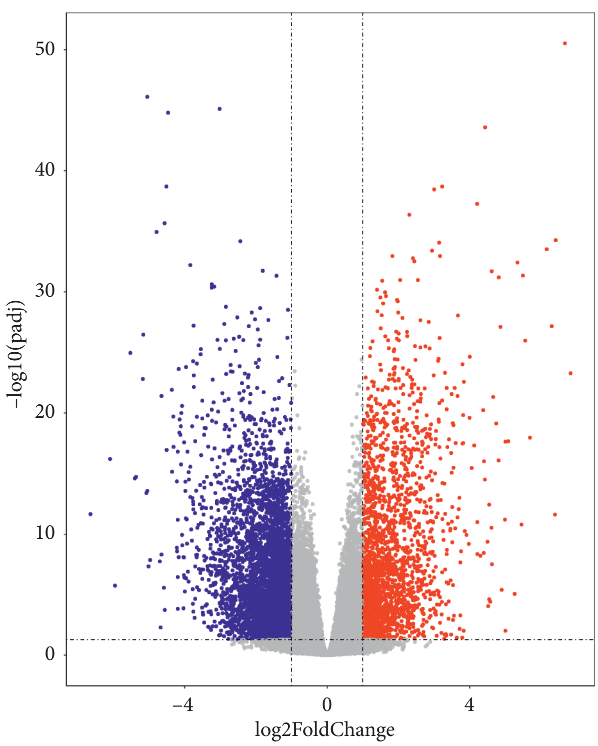

Figure 9: Differential analysis of TCGA-LIHC. (a) Volcanic map for TCGA-LIHC differential analysis. (b) Heatmap of differential gene expression. Differential gene screening criteria: |log2(FoldChange)|>1 and corrected P value <0.05.

The incidence and mortality of liver cancer are high [53, 54]. In order to understand the immune microenvironment of liver cancer and to find new targets and effective biomarkers for the immunotherapy of liver cancer, Zheng et al. [17] performed sRNA-seq on 5063 human T cells using the SMART Seq2 technique. Subpopulation classification of T cells based on single-cell transcriptional map showed that there were a large number of dysfunctional lethal CD8+ T cells and inhibitory T cells in tumor tissues. The gene Layilin was found to inhibit the killing function of CD8+ T cells by targeting the genes specifically expressed in these two

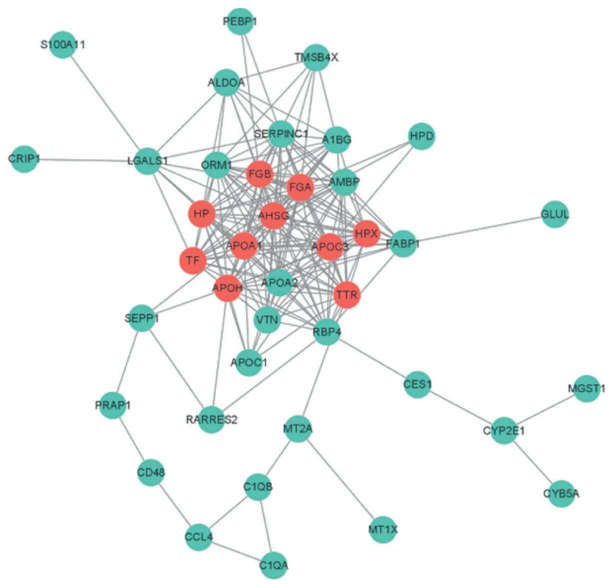

Figure 10: PPI network diagram.

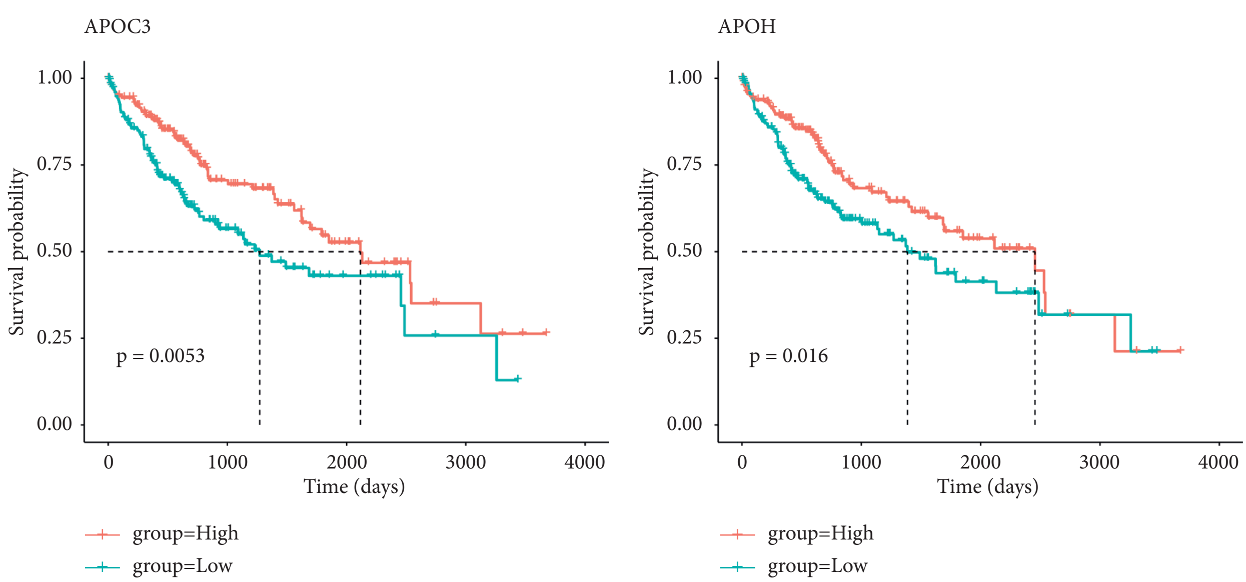

(a) (b)

Figure 11: Continued.

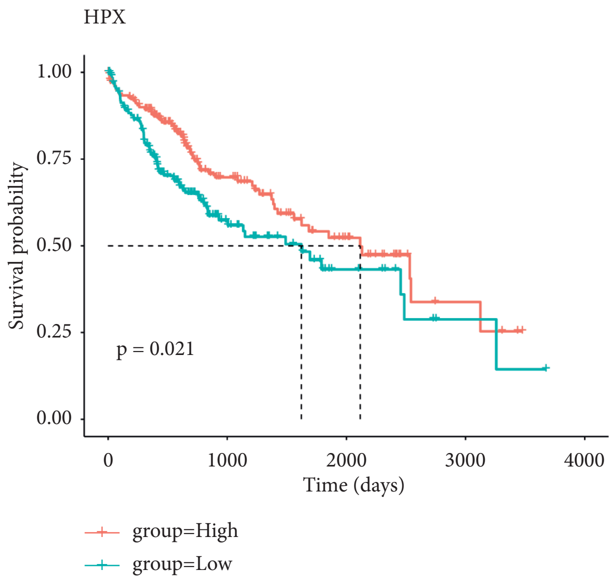

(c)

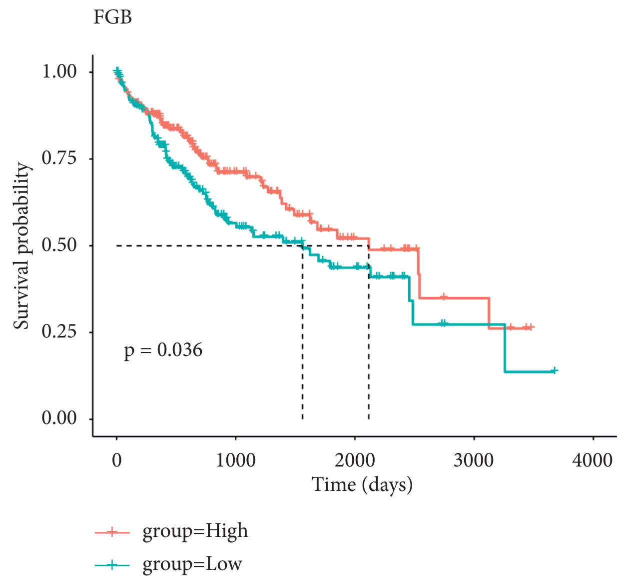

(d)

Figure 11: Hub gene survival analysis. (a) KM curve of APOC3 high- and low-expression groups. (b) KM curve of APOH high- and low-expression groups. (c) KM curve of HPX high- and low-expression groups. (d) KM curve of FGB high- and low-expression groups.

types of cells, which may be a new potential target for immunotherapy.

5. Conclusion

Immune-associated cells, including T cells, have been shown to be novel prognostic markers in patients with HCC, suggesting that the combination of immunoinfiltrating cells in tumor tissue can even predict the effects of chemotherapy and immunotherapy. Because CD8+ T cells are the most important effector T cells in the current tumor immunotherapy and they also recognize tumor-associated antigens as major histocompatibility complex class I molecules on the surface of cancer cells, we used scRNA-seq data of hepatocellular carcinoma (HCC) to reveal the heterogeneity of different CD8+ T cell subsets.CD8+ T cells in HCC were divided into 7 subsets, and the subset cytotoxic CD8 T cells 4 showed significant differences between the TP53 mutant group and the nonmutant group, as well as between different degrees of cirrhosis, HCC grades, stages, ages, and body weights. Hub genes were identified by TCGA-LIHC and single-cell sequencing data set analysis, and the genes APOC3, APOH, HPX, and FGB were identified as biological marker genes by the Cox test. The expression of APOC3, APOH, HPX, and FGB in normal tissues and tumors and TP53 mutation were significantly different. There was a significant difference in the expression of APOH among the sex groups. There were significant differences in the grading and staging of liver cancer. The gene APOC3 had no significant difference among different body weights. The expression levels of APOC3, APOH, HPX, and FGB were the highest in HCC and were higher in normal tissues than in cancer tissues. Moreover, it is also highly expressed in CHOL, and the expression level in normal tissues is higher than that in cancer tissues. We found that cytotoxic CD8 T cells 4 is closely associated with survival and prognosis of HCC and identified four differential genes that can be used as biological markers for survival, prognosis, and clinically relevant characteristics of HCC. This study could help to find effective targets for immunotherapy of HCC and accelerate the development of immunotherapy for HCC. At the same time, this work also outlines the map of the tumor-immune environment, which provides a basis for the future study of other tumor-immune microenvironments.

Abbreviations

CHOL: Cholangiocarcinoma
CTLA4: Cytotoxic T-lymphocyte-associated protein 4
FDA: Food and Drug Administration
GO: Gene Ontology
GSEA: Gene set enrichment analysis
HCC: Hepatocellular carcinoma
KEGG: Kyoto Encyclopedia of Genes and Genomes
LIHC: Liver hepatocellular carcinoma
NSCLC: Non-small-cell lung cancer
TACE: Transcatheter hepatic arterial chemoembolization
TSA: Tumor-specific antigen
MHC: Major histocompatibility complex
PD1: Programmed cell death protein 1
PCA: Principal component analysis
PPI: Protein-protein interaction
TIM-3: T-cell immunoglobulin mucin-3
TME: Tumor microenvironment
TCR: T cell receptor.

Data Availability

All data generated or analyzed during this study are included in this article and provided in the supplementary file.

Consent

Not applicable.

Conflicts of Interest

The authors declare that they have no competing interests.

Authors' Contributions

Hailei Wang and Yang Fu1 are responsible for data processing and analysis; Bin-Bin Da conducted writing, and Geng Xiong proofread the paper. All the authors read and approved the final manuscript.

Acknowledgments

This study is an opening project of Yunnan Organ Transplantation Clinical Medical Center in 2021, No. 2020SYZ-Z-011.

Supplementary Materials

Table S1: cell proportion and cell marker expression. Table S2: analysis of prognosis and clinical correlation. Table S3: prognosis/treatment marker identification. Table S4: genetic GSEA of APOC3, APOH, HPX, and FGB. Figure S1: the proportion and marker expression of CD8+ T subtypes. (A) Proportion bar chart of 7 CD8+ T subtypes. (B) Heat maps of 7 types of CD8+ T subtype markers. Figure S2: cell subpopulation survival analysis. (A) The KM curve of the whole immune cell proportion grouping. (B) The KM curves of cytotoxic CD8 T cells 4. (C) The KM curves of exhausted CD8 T cells 2. (D) The KM curves of naive/memory CD8 T cells. Figure S3: metabolic pathway activity analysis of CD8+ T subsets. (A) Heatmap of metabolic pathway activity of CD8+ T subsets. (B) Violin diagram of metabolic pathway activity of CD8+ T subsets. (C) GSEA enrichment fractional point diagram of CD8+ T subgroups. Figure S4: cell differentiation trajectory analysis and marker gene distribution. (A) Cell differentiation trajectories of seven CD8+ T subtypes. (B)–(L) Expression profile of marker genes in Lineage 1. Figure S5: cell-cell interaction network analysis. (A) Cell interaction network diagram. (B) Heatmap of ligand-receptor pairs between seven subgroups. (C) Regulators of seven subgroups. Figure S6: expression of genes HPX and FGB under different clinical characteristics. (A)–(H) Violin diagrams showing the expression differences of genes HPX (left) and FGB (right) in normal and tumor tissues, TP53-mutant and nonmutant patients, gender, degree of liver cirrhosis, cancer grade, cancer stage, different ages, and different body weights; the degree of liver cirrhosis was divided into no fibrosis, portal fibrosis, nodular formation and incomplete cirrhosis, and established cirrhosis; age: 0–20, 20–40, 40–60, 60–80 and 80–100; body weight: 40–60, 60–80, 80–100, 100–150, and 150–200. Figure S7: single-gene GSEA of hub genes. (A) APOC3 single-gene GSEA, showing the first 5 enrichment pathways. (B) ApoH single-gene GSEA, showing the first 5 enrichment pathways. (C) HPX single-gene GSEA, showing the first 5 enrichment pathways. (D) FGB single-gene GSEA, showing the first 5 enrichment pathways. Figure S8: proportion of TCGA-LIHC immune cells. (A) Boxplot of the proportion of cells of the seven CD8+ T subtypes. (B) Heatmap of the proportion of the seven CD8+ T subtypes. Figure S9: proportion of cytotoxic CD8 T cells 4 in different clinical features. (A), (B) Boxplots showing the ratio of CD8 T cells 4 with or without TP53 mutation and sex, respectively. (C)–(G) Line plots showing the proportion of cytotoxic CD8 T cells 4 in cirrhosis degree, grade, stage, age, and body weight. Figure S10: differential analysis of CD8+ T subsets. Figure S11: expression of genes APOC3 and APOH in different clinical characteristics. (A)–(H) Violin diagrams showing the expression differences of APOC3 (left) and APOH (right) in normal and tumor tissues, TP53-mutant and nonmutant patients, gender, degree of liver cirrhosis, cancer grade, cancer stage, different ages, and different body weights; the degree of liver cirrhosis was divided into no fibrosis, portal fibrosis, nodular formation and incomplete cirrhosis, and established cirrhosis; age: 0–20, 20–40, 40–60, 60–80 and 80–100; body weight: 40–60, 60–80, 80–100, 100–150, and 150–200. Figure S12: hub gene expression in different cancer types. (A) Expression of APOC3 in different cancer types. (B) Expression of ApoH in different types of cancer. (C) Expression of HPX in different types of cancer. (D) Expression of FGB in different cancer types. (*Supplementary Materials*)

References

[1] J. M. Llovet, A. Burroughs, and J. Bruix, "Hepatocellular carcinoma," *The Lancet*, vol. 362, no. 9399, pp. 1907–1917, 2003.

[2] J.-C. Nault, O. Sutter, P. Nahon, N. Ganne-Carrié, and O. Séror, "Percutaneous treatment of hepatocellular carcinoma: state of the art and innovations," *Journal of Hepatology*, vol. 68, no. 4, pp. 783–797, 2018.

[3] B. Guiu, "Stereotactic body radiation therapy vs. radiofrequency ablation in HCC: comparing noncomparable data," *Journal of Hepatology*, vol. 73, no. 3, pp. 727-728, 2020.

[4] F. Izzo, V. Granata, R. Grassi et al., "Radiofrequency ablation and microwave ablation in liver tumors: an update," *The Oncologist*, vol. 24, no. 10, pp. e990–e1005, 2019.

[5] A. Hiraoka, T. Kumada, K. Michitaka, and M. Kudo, "Newly proposed ALBI grade and ALBI-T score as tools for assessment of hepatic function and prognosis in hepatocellular carcinoma patients," *Liver Cancer*, vol. 8, no. 5, pp. 312–325, 2019.

[6] L. Wei, D. Lee, C.-T. Law et al., "Genome-wide CRISPR/Cas9 library screening identified PHGDH as a critical driver for Sorafenib resistance in HCC," *Nature Communications*, vol. 10, no. 1, p. 4681, 2019.

[7] F. Piñero, M. Dirchwolf, and M. G. Pessôa, "Biomarkers in hepatocellular carcinoma: diagnosis, prognosis and treatment response assessment," *Cells*, vol. 9, no. 6, p. 1370, 2020.

[8] A. Livingstone, A. Agarwal, M. R. Stockler, A. M. Menzies, K. Howard, and R. L. Morton, "Preferences for immunotherapy in melanoma: a systematic review," *Annals of Surgical Oncology*, vol. 27, no. 2, pp. 571–584, 2020.

[9] S. A. Holstein and M. A. Lunning, "CAR T-cell therapy in hematologic malignancies: a voyage in progress," *Clinical Pharmacology & Therapeutics*, vol. 107, no. 1, pp. 112–122, 2020.

[10] A. Sharma, J. F. Arambula, S. Koo et al., "Hypoxia-targeted drug delivery," *Chemical Society Reviews*, vol. 48, no. 3, pp. 771–813, 2019.

[11] S. K. Parks, J. Chiche, and J. Pouyssegur, "pH control mechanisms of tumor survival and growth," *Journal of Cellular Physiology*, vol. 226, no. 2, pp. 299–308, 2011.

[12] M. Pan, M. A. Reid, X. H. Lowman et al., "Regional glutamine deficiency in tumours promotes dedifferentiation through inhibition of histone demethylation," *Nature Cell Biology*, vol. 18, no. 10, pp. 1090–1101, 2016.

[13] X. Li, R. Liu, X. Su et al., "Harnessing tumor-associated macrophages as aids for cancer immunotherapy," *Molecular Cancer*, vol. 18, no. 1, p. 177, 2019.

[14] W. H. Fridman, L. Zitvogel, C. Sautès–Fridman, and G. Kroemer, "The immune contexture in cancer prognosis and treatment," *Nature Reviews Clinical Oncology*, vol. 14, no. 12, pp. 717–734, 2017.

[15] S. Hendry, J.-M. B. Pang, D. J. Byrne et al., "Relationship of the breast ductal carcinoma in situ immune microenvironment with clinicopathological and genetic features," *Clinical Cancer Research*, vol. 23, no. 17, pp. 5210–5217, 2017.

[16] A. M. van der Leun, D. S. Thommen, and T. N. Schumacher, "CD8+ T cell states in human cancer: insights from single-cell analysis," *Nature Reviews Cancer*, vol. 20, no. 4, pp. 218–232, 2020.

[17] C. Zheng, L. Zheng, J.-K. Yoo et al., "Landscape of infiltrating T cells in liver cancer revealed by single-cell sequencing," *Cell*, vol. 169, no. 7, pp. 1342–1356, 2017, e16.

[18] X. Wang, Q. He, H. Shen et al., "TOX promotes the exhaustion of antitumor CD8+ T cells by preventing PD1 degradation in hepatocellular carcinoma," *Journal of Hepatology*, vol. 71, no. 4, pp. 731–741, 2019.

[19] A. N. Henning, R. Roychoudhuri, and N. P. Restifo, "Epigenetic control of CD8+ T cell differentiation," *Nature Reviews Immunology*, vol. 18, no. 5, pp. 340–356, 2018.

[20] C. C. Zebley, S. Gottschalk, and B. Youngblood, "Rewriting history: epigenetic reprogramming of CD8+ T cell differentiation to enhance immunotherapy," *Trends in Immunology*, vol. 41, no. 8, pp. 665–675, 2020.

[21] Y. Li, G. Wang, X. Tan et al., "ProGeo-neo: a customized proteogenomic workflow for neoantigen prediction and selection," *BMC Medical Genomics*, vol. 13, no. Suppl 5, p. 52, 2020.

[22] N. Luckashenak, S. Schroeder, K. Endt et al., "Constitutive crosspresentation of tissue antigens by dendritic cells controls CD8+ T cell tolerance in vivo," *Immunity*, vol. 28, no. 4, pp. 521–532, 2008.

[23] C. Leibler, A. Thiolat, R. A. Elsner, K. El Karoui, C. Samson, and P. Grimbert, "Costimulatory blockade molecules and B-cell-mediated immune response: current knowledge and perspectives," *Kidney International*, vol. 95, no. 4, pp. 774–786, 2019.

[24] H. Wang, Z. Yan, J. Hao et al., "CD137 ligand feedback upregulates PD-L1 expression on lung cancer via T cell production of IFN-γ," *Thoracic Cancer*, vol. 10, no. 12, pp. 2225–2235, 2019.

[25] J. H. Esensten, Y. A. Helou, G. Chopra, A. Weiss, and J. A. Bluestone, "CD28 costimulation: from mechanism to therapy," *Immunity*, vol. 44, no. 5, pp. 973–988, 2016.

[26] K. Poropatich, D. Dominguez, W.-C. Chan et al., "OX40+ plasmacytoid dendritic cells in the tumor microenvironment promote antitumor immunity," *Journal of Clinical Investigation*, vol. 130, no. 7, pp. 3528–3542, 2020.

[27] C. S. Pai, D. M. Simons, X. Lu et al., "Tumor-conditional anti-CTLA4 uncouples antitumor efficacy from immunotherapy-related toxicity," *Journal of Clinical Investigation*, vol. 129, no. 1, pp. 349–363, 2019.

[28] Z. Y. Xu-Monette, J. Zhou, and K. H. Young, "PD-1 expression and clinical PD-1 blockade in B-cell lymphomas," *Blood*, vol. 131, no. 1, pp. 68–83, 2018.

[29] M. Das, C. Zhu, and V. K. Kuchroo, "Tim-3 and its role in regulating anti-tumor immunity," *Immunological Reviews*, vol. 276, no. 1, pp. 97–111, 2017.

[30] R. Grosser, L. Cherkassky, N. Chintala, and P. S. Adusumilli, "Combination immunotherapy with CAR T cells and checkpoint blockade for the treatment of solid tumors," *Cancer Cell*, vol. 36, no. 5, pp. 471–482, 2019.

[31] V. Velcheti, S. Chandwani, X. Chen, M. C. Pietanza, and T. Burke, "First-line pembrolizumab monotherapy for metastatic PD-L1-positive NSCLC: real-world analysis of time on treatment," *Immunotherapy*, vol. 11, no. 10, pp. 889–901, 2019.

[32] P. Pfeiffer, M. Yilmaz, S. Möller et al., "TAS-102 with or without bevacizumab in patients with chemorefractory metastatic colorectal cancer: an investigator-initiated, open-label, randomised, phase 2 trial," *The Lancet Oncology*, vol. 21, no. 3, pp. 412–420, 2020.

[33] C. S. Fuchs, T. Doi, R. W. Jang et al., "Safety and efficacy of pembrolizumab monotherapy in patients with previously treated advanced gastric and gastroesophageal junction cancer," *JAMA Oncology*, vol. 4, no. 5, Article ID e180013, 2018.

[34] H. A. Tawbi, P. A. Forsyth, A. Algazi et al., "Combined nivolumab and Ipilimumab in melanoma metastatic to the brain," *New England Journal of Medicine*, vol. 379, no. 8, pp. 722–730, 2018.

[35] Cancer Genome Atlas Research Network, "Electronic address, w.b.e. and N. cancer genome atlas research, comprehensive and integrative genomic characterization of hepatocellular carcinoma," *Cell*, vol. 169, no. 7, pp. 1327–1341 e23, 2017.

[36] Z. Xiao, G. Cheng, Y. Jiao et al., "Holo-Seq: single-cell sequencing of holo-transcriptome," *Genome Biology*, vol. 19, no. 1, p. 163, 2018.

[37] W. Deng, Y. Ma, Z. Su et al., "Single-cell RNA-sequencing analyses identify heterogeneity of CD8+ T cell subpopulations and novel therapy targets in melanoma," *Molecular Therapy - Oncolytics*, vol. 20, pp. 105–118, 2021.

[38] Z. Xiao, Z. Dai, and J. W. Locasale, "Metabolic landscape of the tumor microenvironment at single cell resolution," *Nature Communications*, vol. 10, no. 1, p. 3763, 2019.

[39] M. Simsek, S. B. Tekin, S. Basol Tekin, and M. Bilici, "Immunological agents used in cancer treatment," *The Eurasian Journal of Medicine*, vol. 51, no. 1, pp. 90–94, 2019.

[40] L. Chen, W. Zou, L. Zhang, H. Shi, Z. Li, and C. Ni, "ceRNA network development and tumor-infiltrating immune cell analysis in hepatocellular carcinoma," *Medical Oncology*, vol. 38, no. 7, p. 85, 2021.

[41] T. Bald, J. Landsberg, D. Lopez-Ramos et al., "Immune cell-poor melanomas benefit from PD-1 blockade after targeted type I IFN activation," *Cancer Discovery*, vol. 4, no. 6, pp. 674–687, 2014.

[42] S. Watanabe, H. Hayashi, K. Haratani et al., "Mutational activation of the epidermal growth factor receptor down-regulates major histocompatibility complex class I expression via the extracellular signal-regulated kinase in non-small cell lung cancer," *Cancer Science*, vol. 110, no. 1, pp. 52–60, 2019.

[43] Q. Pan, Y. Cheng, and D. Cheng, "Identification of CD8+ T cell-related genes: correlations with immune phenotypes

and outcomes of liver cancer," *J Immunol Res*, vol. 2021, Article ID 9960905, 2021.
[44] S. Ideyama, S. Moriwaki, and T. Horio, "[Experimental production of micropapular light eruption]," *Nihon Hifuka Gakkai Zasshi*, vol. 98, no. 3, pp. 341–344, 1988.
[45] G. Jo, S. Y. Kwak, J. Y. Kim, H. Lim, and M. J. Shin, "Association between genetic variant of apolipoprotein C3 and incident hypertension stratified by obesity and physical activity in korea," *Nutrients*, vol. 10, no. 11, p. 1595, 2018.
[46] T. Zhang, J. Guo, J. Gu et al., "Identifying the key genes and microRNAs in colorectal cancer liver metastasis by bioinformatics analysis and in vitro experiments," *Oncology Reports*, vol. 41, no. 1, pp. 279–291, 2019.
[47] P. Ascenzi and M. Fasano, "Heme-hemopexin: a 'Chronosteric' heme-protein," *IUBMB Life*, vol. 59, no. 11, pp. 700–708, 2007.
[48] N. Cine, A. T. Baykal, D. Sunnetci, Z. Canturk, M. Serhatli, and H. Savli, "Identification of ApoA1, HPX and POTEE genes by omic analysis in breast cancer," *Oncology Reports*, vol. 32, no. 3, pp. 1078–1086, 2014.
[49] Y. Chen, Y. Zhu, Y. Sheng et al., "SIRT1 downregulated FGB expression to inhibit RCC tumorigenesis by destabilizing STAT3," *Experimental Cell Research*, vol. 382, no. 2, Article ID 111466, 2019.
[50] S. Burugu, A. R. Dancsok, and T. O. Nielsen, "Emerging targets in cancer immunotherapy," *Seminars in Cancer Biology*, vol. 52, no. Pt 2, pp. 39–52, 2018.
[51] E. M. Ward, C. R. Flowers, T. Gansler, S. B. Omer, and R. A. Bednarczyk, "The importance of immunization in cancer prevention, treatment, and survivorship," *CA: A Cancer Journal for Clinicians*, vol. 67, no. 5, pp. 398–410, 2017.
[52] S. Schmid and M. Fruh, "Immune checkpoint inhibitors and small cell lung cancer: what's new?" *Journal of Thoracic Disease*, vol. 10, no. Suppl 13, pp. S1503–S1508, 2018.
[53] H. B. El-Serag, "Hepatocellular carcinoma," *New England Journal of Medicine*, vol. 365, no. 12, pp. 1118–1127, 2011.
[54] A. Villanueva and J. M. Llovet, "Mutational landscape of HCC-the end of the beginning," *Nature Reviews Clinical Oncology*, vol. 11, no. 2, pp. 73-74, 2014.

Hindawi
Journal of Healthcare Engineering
Volume 2022, Article ID 5087468, 9 pages
https://doi.org/10.1155/2022/5087468

Research Article

Application of Biomaterials in Tendon Injury Healing and Adhesion in Sports

Rui Zhang

Bengbu Medical College Sports and Art Department, Bengbu 233000, Anhui, China

Correspondence should be addressed to Rui Zhang; zr0206@bbmc.edu.cn

Received 11 January 2022; Revised 22 February 2022; Accepted 24 February 2022; Published 12 April 2022

Academic Editor: Enas Abdulhay

High-intensity sports make tendon injury of professional athletes occur frequently. However, tendon adhesion in the healing process of tendon injury seriously affects the normal functional training of athletes after rehabilitation. Therefore, based on the theory of tendon injury healing, the MRDM image data of tendon injury healing are obtained by using medical image analysis technology, and the useless image data are screened by using the RANSAC algorithm. Through the analysis of filtered MRDM image data, it is found that the application of biomaterials has a positive effect on promoting the stable healing of tendon. A multilevel model was used to evaluate the actual effect of several commonly used biomaterials in repairing tendon injury and adhesion. The results showed that sodium hyaluronate had the best repair effect on tendon injury.

1. Introduction

Sports are good for physical and mental health. After more than 100 years of development, there are many popular sports in the world, many of which have become one of the core events of the Olympic Games (Song) [1]. However, due to the high intensity of exercise itself, it is easy to cause damage to the body during exercise, among which tendon injury is the most prominent [2]. The following is tendon adhesion during tendon healing, which is a very common complication after tendon injury. Tendon adhesion directly affects the subsequent sports and technical competitions [3].

Therefore, how to prevent the healing of tendon injury has been a key research project of related researchers [4]. But so far, no simple and effective method for preventing tendon adhesion has been developed, and a stable healing of the tendon has been developed (Kang) [5]. With the development of modern medical technology, the use of biological materials to prevent the formation of tendon adhesion has made great progress (Zhang) [6].

After years of research, people have a clearer understanding of tendon adhesion (Gross and Hoffmann) [7]. First, the nutrient source required for tendon is that in addition to paratenon, retinaculum tendinum, and tendon bundle vessel, synovial is also a very important source of nutrients (Cheng and Jin) [8]. At the same time, tendon tissue itself can be self-healing. However, after the tendon injury, the tendon sheath is damaged and the synovial is reduced, resulting in insufficient nutrient supply, which slows the healing of the tendon tissue itself, and most of its repair process relies on peritendinous connective tissue for repair (Jia et al.) [9].

As a result, a large amount of scar tissue is produced, eventually forming adhesions (Yang et al.) [10]. Therefore, some scholars have proposed to intervene in the process of tendon healing through biological materials. The current mainstream practice is achieved through drug films (Nouiri et al.) [11]. The properties of this biomaterial are used to form a barrier to prevent the formation of adhesions, while at the same time directly affecting the healing of the tendons by drugs. In turn, a two-pronged approach is achieved to minimize the formation of adhesions (Han et al.) [12].

In this context, the application of biomaterials in the healing and adhesion of sports tendon injury was studied comprehensively. Through multiangle research and analysis, the advantages and disadvantages of current biomaterials for tendon adhesion repair are revealed, which provides the necessary theoretical basis for its future development (Zhang et al.) [13].

2. Related Work

For the repair principle of tendon, there are two different views in the academic world, one is the theory of endogenous healing and the other is the theory of exogenous healing (Lin et al.) [14]. Researchers supporting exogenous healing believe that tendons themselves are not self-healing and that fibroblasts that repair are produced from tendon sheaths and peritendon tissues (Moslehifard and Nokar) [15]. Adhesive bands from the tendon sheath and periorbital tissue are incorporated into the repair cells to achieve tendon repair (Koyanagi) [16]. Researchers believe that adhesions are necessary in the healing process, so it is impossible to completely prevent adhesions (Zhenyu et al.) [17]. Researchers who support the theory of endogenous healing have raised different opinions. During the study of the free tendon placed in the knee joint cavity, they found that the tendon survived on its own and also detected fibroblasts and newly formed collagen. These phenomena all indicate that tendons are self-healing (Guo et al.) [18]. In addition, researchers have found that human flexor tendons can be self-healing during the in vitro culture of human flexor tendons (Geng et al.) [19]. Researchers have also studied the collagen fibers secreted by tendon cells, which are found to be much larger than those produced by the outer membrane cells (Philip et al.) [20]. Moreover, when the newly formed collagen fibers are analyzed, it is found that the collagen fibers produced by the original tendon cells are arranged in the same manner. Therefore, some researchers believe that tendon cells themselves are also self-healing (as shown in Figure 1), can achieve self-proliferation, and self-repair by producing collagen by themselves.

According to research by relevant researchers, tendons can achieve endogenous healing. Therefore, improving the self-repairing efficiency of the tendon cells can effectively reduce the occurrence of adhesions. However, in the actual treatment process, endogenous healing and exogenous healing always exist simultaneously. This is because during the treatment of the tendon injury site, it is necessary to bring the drug into the tendon through the surrounding tissue. After the cut tendon sheath is sutured, there will still be some gaps. It may also be that after the synovial cells have fallen off, they are scattered in the synovial fluid and enter through them through the synovial. In another case, it is located in the tendon sheath. Due to the uneven cutting source and the internal friction of the sheath at the suture, it will cause a certain degree of wear on the inner surface of the sheath and then bring in foreign cells. Even if the tendon can be damaged and subcutaneous tissue, bone surface completely isolated, from the damaged place of the synovial sheath of the exogenous cells can still reach the damaged tendon, so there is no way to completely eliminate the entry of exogenous cells. As for the degree of exogenous healing is the majority or the degree of endogenous healing is the majority, it is judged based on the damage of the tendon, the nutritional status of the repair period, and the external environment. When the degree of exogenous healing is dominant, tendon adhesion will increase and vice versa. Taking into account the current level of medical technology, the best practice is to reduce exogenous healing as much as possible and increase the proportion of endogenous healing. Choosing the right biomaterial for treatment can achieve this goal well.

The properties of the biomaterial are utilized to form a barrier that prevents the formation of adhesions. At the same time, the drug directly affects the healing of the tendon, thereby achieving a two-pronged approach and minimizing the formation of adhesions. Since inflammation is highly likely to occur in areas where the tendon is damaged, inflammation causes the lymphatic vessels to be blocked by cellulose and proteins, resulting in hypoxia in the interior. Biomaterials allow the coverage area to maintain normal blood circulation and provide adequate oxygen supply for tendon repair. Not only that, but when inflammation occurs, it can destroy tissues such as giant cells, resulting in an increase in the concentration of the tissue fluid, an increase in the permeability of the capillaries, and an extravasation of a large amount of fluid, eventually resulting in edema. The use of biological materials here can accelerate blood circulation, resolve the problem of congestion, and eliminate edema. It is also possible to screen and isolate harmful active substances in blood vessels to ensure their recovery progress. In the process of using biological materials, due to its own physical characteristics, it can interfere with the transmission of painful impulses, thereby achieving the effect of relieving pain.

3. Theoretical Model Optimization

At present, the above tendon injury healing theory has been widely used in the medical field and has achieved good medical results. In order to verify the actual effect of biomaterials on the stable tendon healing of athletes, the MRDM image data of tendon injury healing were obtained by using medical image analysis technology to understand the tendon injury healing of patients (as shown in Figure 2). However, the collected data are mixed with a large number of worthless data. Therefore, it is necessary to use the RANSAC algorithm to filter worthless data.

The RANSAC algorithm is a data calculus method that uses an iterative random sampling method to extract and filter abnormal data to obtain a mathematical model. The implementation principle is mainly based on two different data types that exist in the sample data: (1) normal data model and (2) noise and abnormal data model. The algorithm believes that the data that cannot adapt to the mathematical model is mainly because the abnormal data may be caused by wrong assumptions in the process of mathematical model calculation or it is caused by the wrong way of calculation. However, these erroneous data often lack sufficient parameters to restore them. To this end, the algorithm restores its real data through multiple iterative

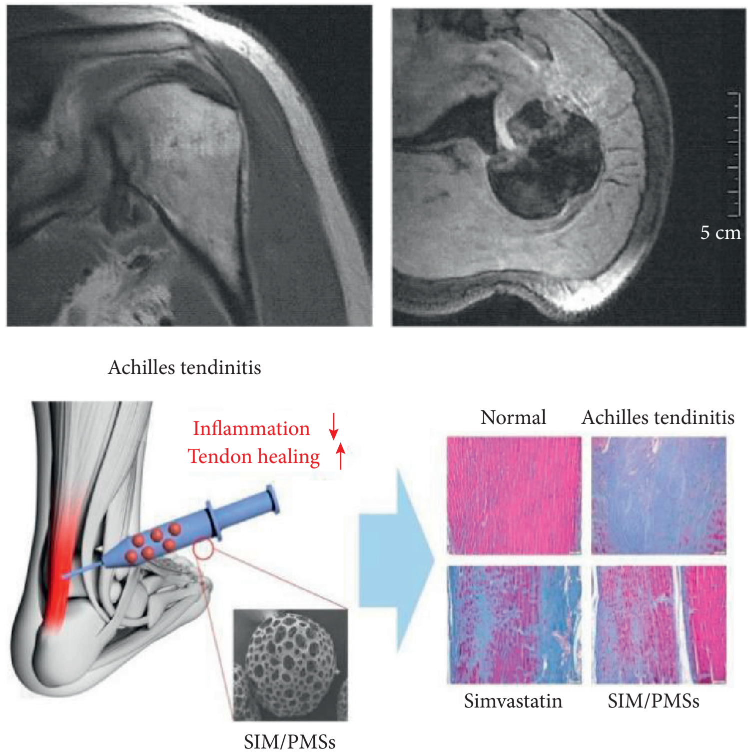

Figure 1: Self-repair of collagen fibers produced by tendon cells.

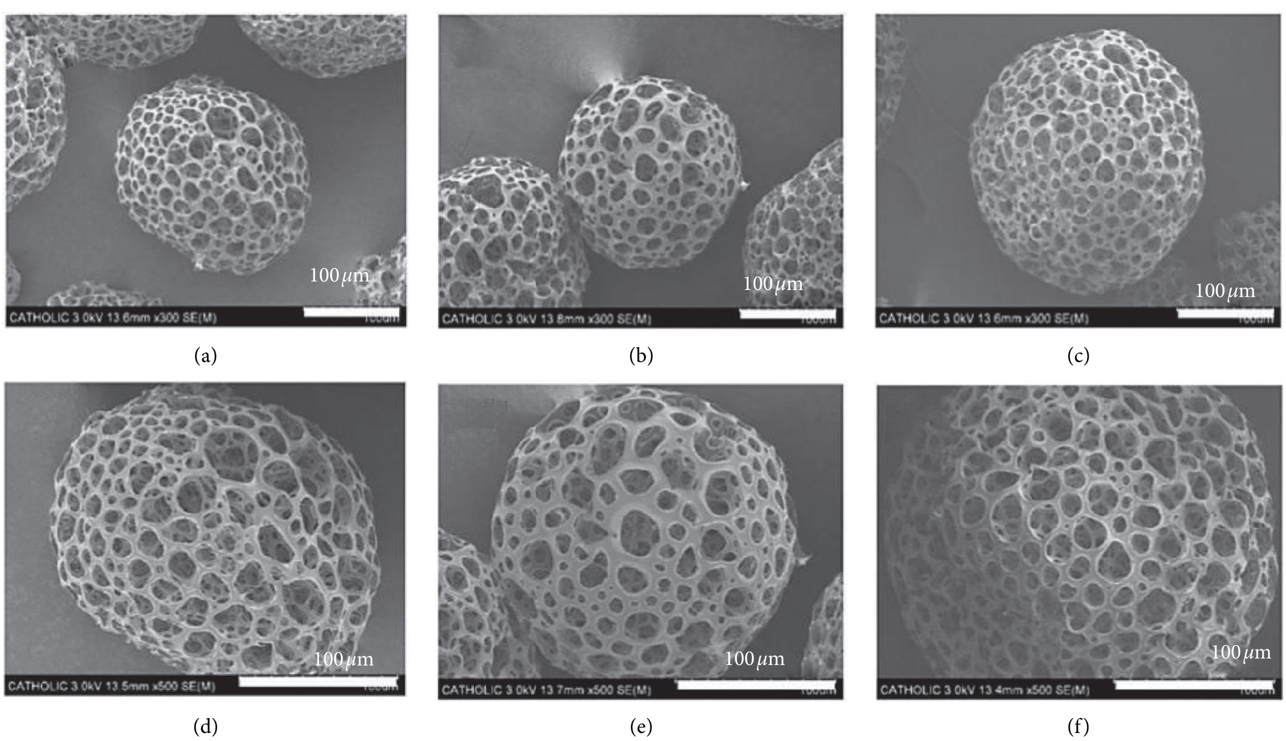

Figure 2: Continued.

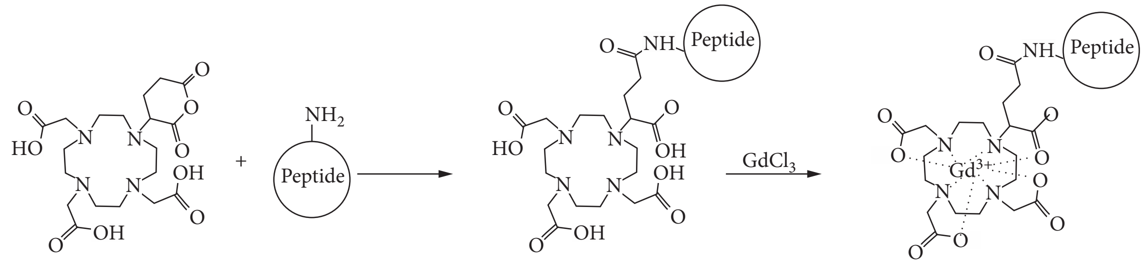

$C_{19}H_{30}N_4O_9$
Exact Mass: 458.2
Mol. Wt.: 458.46
m/e: 458.20 (100.0%), 459.20 (22.0%), 460.21 (4.0%)
C, 49.78; H, 6.60; N, 12.22; O, 31.41

$C_{147}H_{219}N_{43}O_{47}S$
Exact Mass: 3369.2
Mol. Wt.: 3372.71

Chemical Formula: $C_{148}H_{216}GdN_{42}O_{48}S^{3+}$
Exact Mass: 3539.47
Molecular Weight: 3540.86

(g)

Figure 2: The healing of tendon injury was obtained by medical image analysis.

screening methods. The RANSAC algorithm is mostly used in image processing in engineering. The basic implementation process is as follows:

It is needed to obtain necessary image data information, such as the edge of the object and the gray scale information. Whether the two information acquisitions are accurate or not will directly affect the accuracy of the detection. In general, when the system acquires graphics, it also needs to perform simple preliminary processing on the image, such as noise reduction. In this way, accurate information about the items to be inspected can be obtained accurately. The means of acquisition are mainly obtained by a CCD camera. Image enhancement is a very important step in image processing and one of the most used methods to improve image quality. There are two directions in this, one is to optimize the visual effect of the image and the other is to strengthen the characteristics of the image. Depending on the field of use, it can be divided into two types, one is airspace processing and the other is frequency domain processing. The former is processed directly on the image itself, while the latter is processed after the image is specially processed. The airspace processing formula is as follows:

$$g(x, y) = EH[f(x, y)], \tag{1}$$

where the image before enhancement is $f(\cdot)$, $g(\cdot)$ is the enhanced image, and EH is the enhanced operation.

The edge information of the image is able to directly reflect the shape of the object, and its importance is obvious. Moreover, it can display most of the information of the item only by the partial image information. But its acquisition has a lot of difficulties. The data obtained by the edge in the system behave as a discontinuous gray value. This requires a special algorithm to calculate its edges. It is usually calculated using the first derivative and the second derivative. The gradient corresponds to the first derivative, and the gradient operator is the first derivative operator. For a continuous function $f(x, y)$, its gradient at position (x, y) can be expressed as

$$\nabla f(x, y) = G(x, y) = \left[G_x G_y\right]^T = \left[\frac{\partial f}{\partial x}\frac{\partial f}{\partial y}\right]^T. \tag{2}$$

A gradient is a vector whose amplitude and direction angle are

$$\begin{aligned} |\nabla f| &= |G(x, y)| = \left[G_x^2 + G_y^2\right]^{\frac{1}{2}}, \\ \phi(x, y) &= \arctan\left(\frac{G_y}{G_x}\right). \end{aligned} \tag{3}$$

The approximate expression of the gradient is

$$\begin{aligned} G_x &= f[i, j+1] - f[i, j], \\ G_y &= f[i+1, j] - f[i, j]. \end{aligned} \tag{4}$$

Usually, in order to reduce the amount of calculation, the absolute value is usually used to approximate the gradient magnitude.

$$|G(x, y)| = \left|G_x\right| + \left|G_y\right|. \tag{5}$$

When analyzing an image, the approximate value is usually calculated using a small area template tape measure. One template is used for each of A and B, which requires two templates. According to the size of different templates, the calculation properties are different. Therefore, there are Robert operators, Prewitt operators, and Sobel operators.

Roberts operator: the Robe operator approximates the magnitude of the continuous gradient of the edge point, and its convolution template is as follows:

$$\begin{aligned} G_x &= \begin{bmatrix} 1 & 0 \\ 0 & -1 \end{bmatrix}, \\ G_y &= \begin{bmatrix} 0 & 1 \\ -1 & 0 \end{bmatrix}. \end{aligned} \tag{6}$$

The gradient templates in the horizontal and vertical directions of the Sobel operator are as follows:

$$G_x = \begin{bmatrix} -1 & 0 & 1 \\ -2 & 0 & 2 \\ -1 & 0 & 1 \end{bmatrix},$$
$$G_y = \begin{bmatrix} 1 & 2 & 1 \\ 0 & 0 & 0 \\ -1 & -2 & -1 \end{bmatrix}. \tag{7}$$

The gradient template in the two directions of the Prewitt operator is as follows:

$$G_x = \begin{bmatrix} -1 & 0 & 1 \\ -1 & 0 & 1 \\ -1 & 0 & 1 \end{bmatrix},$$
$$G_y = \begin{bmatrix} 1 & 1 & 1 \\ 0 & 0 & 0 \\ -1 & -1 & -1 \end{bmatrix}. \tag{8}$$

Then, the image content of the initial processing has been completed to extract corner points. It is assumed that variable I_x and variable I_y are used to represent the first-order partial derivative of image I in two different aspects of Cartesian coordinate x and y axes. Then, the function $w(x, y)$ can be used to represent a two-dimensional Gaussian smoothing function on Cartesian coordinates. The calculation process of this function is shown in the following two formulas:

$$M = \sum_{x,y} w(x, y) \begin{bmatrix} I_x^2 & I_x I_y \\ I_x I_y & I_y^2 \end{bmatrix},$$
$$R = \det M - k \cdot (\operatorname{trace} M)^2, k = 0.04 \sim 0.2. \tag{9}$$

Solving formula (15) can yield a specific number for each corner R on the image. Then, using the normalization idea to match the calculated corner points, the image corner point value can be obtained. The matching calculation equation is as follows:

$$NCC = \frac{\sum_i (I_1(x_i, y_i) - u_1)(I_2(x_i, y_i) - u_2)}{\sqrt{\sum_i (I_1(x_i, y_i) - u_1)^2 \sum_i (I_2(x_i, y_i) - u_2)^2}}. \tag{10}$$

It is worth noting that the results obtained by using the normalized thought tend to be mixed with some singularities. These singularities are the anomalous data belonging to the corner values of the image that are noisy and cannot be normally described by the mathematical model. Therefore, it is necessary to use the RANSAC algorithm to purify the image corner values (as shown in Figure 3). In the process of purification, the images should be considered separately according to the three color channels of red, green, and blue. Then, there is the following linear algebraic equation:

$$\begin{pmatrix} R_2 \\ G_2 \\ B_2 \end{pmatrix} = \begin{pmatrix} c_r & 0 & 0 \\ 0 & c_g & 0 \\ 0 & 0 & c_b \end{pmatrix} \cdot \begin{pmatrix} R_1 \\ G_1 \\ B_1 \end{pmatrix} + \begin{pmatrix} d_r \\ d_g \\ d_b \end{pmatrix}. \tag{11}$$

In the above formula, the variable R_2, the variable G_2, and the variable B_2, respectively, represent three color channels of red, green, and blue of the image. The variable $(R_2, R_1)_{\mathrm{n}}$ is mainly used to represent the transformation parameters of the linear equation (c, d). At this point, the purification is done by iterative summation as follows:

$$E = \sum T\left({d_n}^2\right), \tag{12}$$

In the above formula, when the condition satisfies ${d_n}^2 < \mathrm{Thre}^2$, then $T({d_n}^2) = {d_n}^2$, otherwise $T({d_n}^2) = \mathrm{Thre}^2$. Filter the corner points of the image that meet the conditions and continue the iterative calculation. The entire purification process is completed until the value of E does not change significantly. At this point, all data points belong to the data that can be normally described by the mathematical model. Finally, it is necessary to split the image. The effect of image segmentation is good or not will directly determine whether the analysis of the image is in place or not.

The similarity calculation is performed after the image is segmented, and the predetermined image in the database and the matching are performed according to the calculated result. The matching result of the image is extremely characteristic. The following function is used to measure the similarity between T and f:

$$SE(x, y) = \sum_{i=1}^{N} \sum_{j=1}^{N} [f(x - i, y - j) - T(i, j)]^2, \tag{13}$$

where the size of the image is $N \times N$, the above formula provides a measure of the degree of matching between the image T and the subgraph f at the (x, y) coordinate. Expand the above formula to calculate the matching result:

$$SE(x, y) = \sum_{i=1}^{N} \sum_{j=1}^{N} f^2(x - i, y - j) - 2 \sum_{i=1}^{N} \sum_{j=1}^{N} f(x - i, y - j) T(i, j) + \sum_{i=1}^{N} \sum_{j=1}^{N} T^2(i, j). \tag{14}$$

4. Experimental Results and Analysis

Sports posture is complex, and the amount of exercise is large. Because of the above reasons, professional athletes often have tendon injury in the process of sports. Tendon adhesion is a very common complication after tendon injury in the process of tendon healing and temporarily unable to recover, will affect the athlete's competition and training in varying degrees. Based on the above reasons and based on the theory of tendon injury healing, the MRDM image data of tendon injury healing were obtained by using medical image analysis technology, and the worthless image data were screened by using the RANSAC algorithm. Then, through the analysis of the filtered MRDM image data, it is found that the application of biomaterials can actively promote the stable healing of tendon. Finally, the clinical

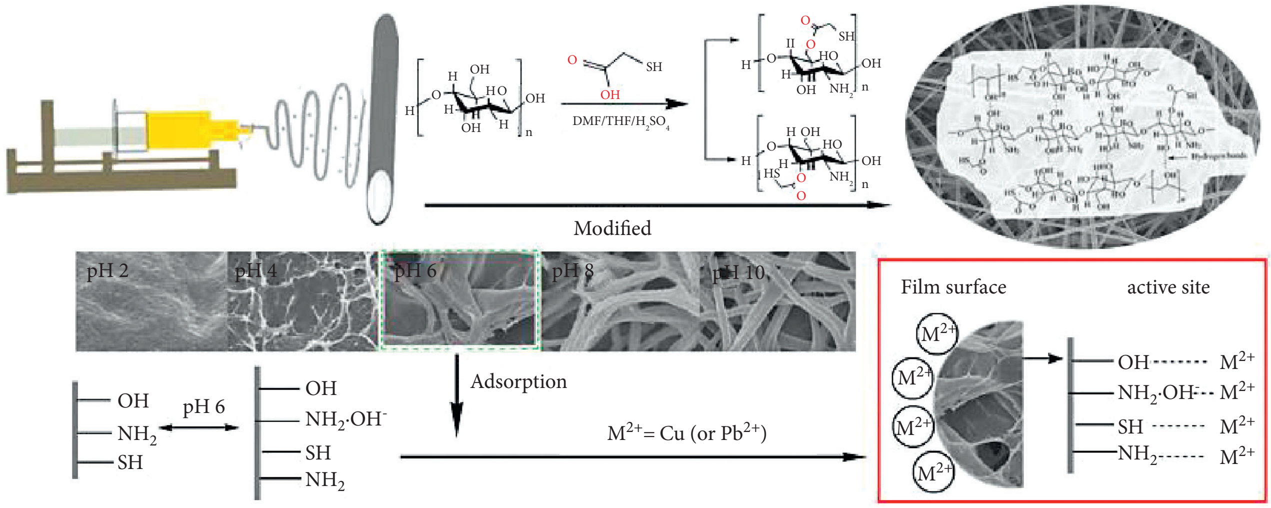

FIGURE 3: In the process of purification, the image should be considered separately according to the red, green, and blue channels.

application of biomaterials is listed, and the actual effect of several commonly used biomaterials to repair tendon injury and adhesion is evaluated by using the multilevel comprehensive evaluation model.

At present, the biological materials commonly used in medical clinics for repairing tendon injury healing adhesions (as shown in Figure 4) are mainly the following: (1) Chitosan: the biomaterial can effectively inactivate the fibroblasts at the site of the damage of the organism and inhibit the growth cycle of the fibroblasts. Furthermore, the proliferation time of endothelial cells is reserved for growth and self-repair of the human body. (2) Absorbable antiadhesion film: the biomaterial can also inactivate fibroblasts at the site of damage to the organism, and it can also act as a barrier to aid in the repair of the tendon. In addition, the absorbable antiadhesion film belongs to a biological material that can be absorbed and degraded by the living body. (3) Sodium hyaluronate: the biomaterial is a liquid material composed of a sodium salt and has high biocompatibility.

In order to more accurately screen out the biomaterials with the best effect on repairing tendon injury, the multilevel fuzzy comprehensive evaluation model is used to evaluate the actual effects of the above three biomaterials for repairing tendon injury healing. The multilevel fuzzy comprehensive evaluation model is an evaluation method based on cognitive science and fuzzy mathematics. The specific form is as follows:

$$\begin{pmatrix} a_{1,1} & a_{1,2} & \cdots & a_{1,n} \\ a_{2,1} & a_{2,2} & \cdots & a_{2,n} \\ \cdot & \cdot & \cdot & \cdot \\ a_{n,1} & a_{n,1} & \cdots & a_{n,n} \end{pmatrix}. \tag{15}$$

In the formula, ai, j represents the relative weight of indicator ai relative to indicator aj.

Calculate the product of each row element of the judgment matrix R,

$$M_i = \prod_{j=1}^{n} B_{ij}, i = 1, 2, \ldots, n. \tag{16}$$

Calculate the root in the times n of M_i,

$$\overline{w_i} = (M_i)^{\frac{1}{n}}, i = 1, 2, \ldots, n. \tag{17}$$

The normalization of $\overline{w_i}$ is as follows:

$$w_i - \frac{\overline{w_i}}{\sum_{i=1}^{n} \overline{w_i}}, i = 1, 2, \ldots, n. \tag{18}$$

Then, the weighting vector is $w = [w_1, w_2, \ldots, w_4]^T$.

The target criterion layer weight vector obtained according to the above method is as follows:

$$W = (w_1, w_2, w_3, \ldots, w_k). \tag{19}$$

w_i is the relative weight of the criterion layer indicator i in the criterion layer.

For the criterion level indicator of number k, the weight of the measure level under each criterion is as follows:

$$W_k = \left(w_{k1}, w_{k2}, w_{k3}, \ldots, w_{kp}\right). \tag{20}$$

In the hierarchical structure, the comprehensive weight calculation operator of the measure indicator j under criterion i is as follows:

$$w_{i,j} = w_i \cdot w_j. \tag{21}$$

After obtaining the weights of the respective indicators, the evaluation score can be finally calculated by multiplying the evaluation values. The calculation operator is as follows:

$$Ea = \left(w_{p,1}, w_{p,2}, \ldots, w_{p,n}\right)\left(v_{p,1}, v_{p,2}, \ldots v_{p,n}\right)^T. \tag{22}$$

$w_{p,i}$ is the comprehensive weight of the lowest level indicator i, and $w_{p,i}$ is its evaluation score.

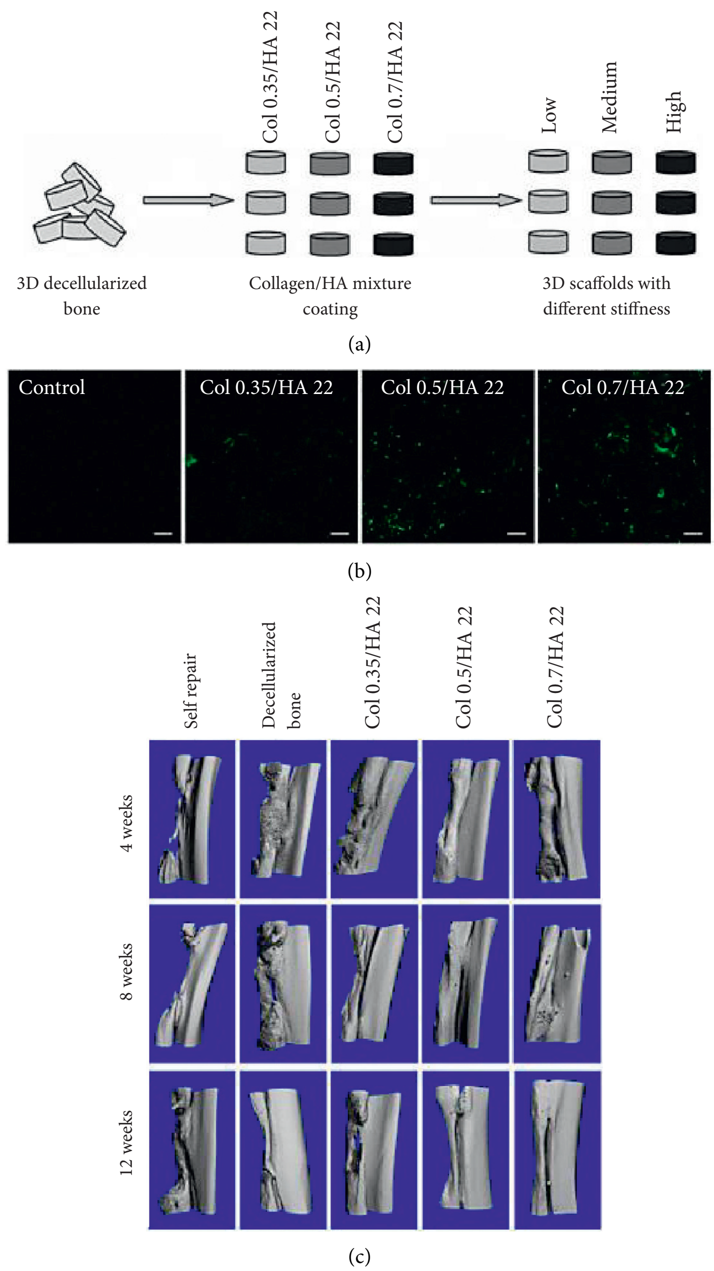

Figure 4: It is a common biological material used in repairing tendon injury and adhesion.

Substituting the data information recorded during the experiment into the above equation can obtain the evaluation result as shown in Figure 5. The data in the figure indicate that the three kinds of sodium hyaluronate in the biomaterials for repairing tendon injury healing have the best tendon damage repair effect.

In order to observe the effect of hyaluronic acid with different molecular weight, Hyalgan and Synvisc were used to evaluate the efficacy of knee osteoarthritis [21]. The rabbit knee osteoarthritis model was made by unilateral anterior cruciate ligament transection. Two weeks after operation, it was randomly divided into group A, group B, and control group (group C). Group A was given Hyalgan 0 2 ml, group B was given Synvisc 0 2 ml, and group C was given 0.2 ml of 0.9% sodium chloride injection. All patients received intra-articular injection once a week for 4 weeks. Three groups of animals were killed 10 weeks after operation, and articular cartilage was taken for gross observation and histological observation under the microscope. Mankin score—the results showed that group A and group B were significantly lighter than group C ($P < 0.05$), while group B was significantly lighter than group A ($P < 0.05$). Synvisc, a hyaluronic acid preparation with high molecular weight, has better short-term therapeutic effect on rabbit knee osteoarthritis than Hyalgan [22].

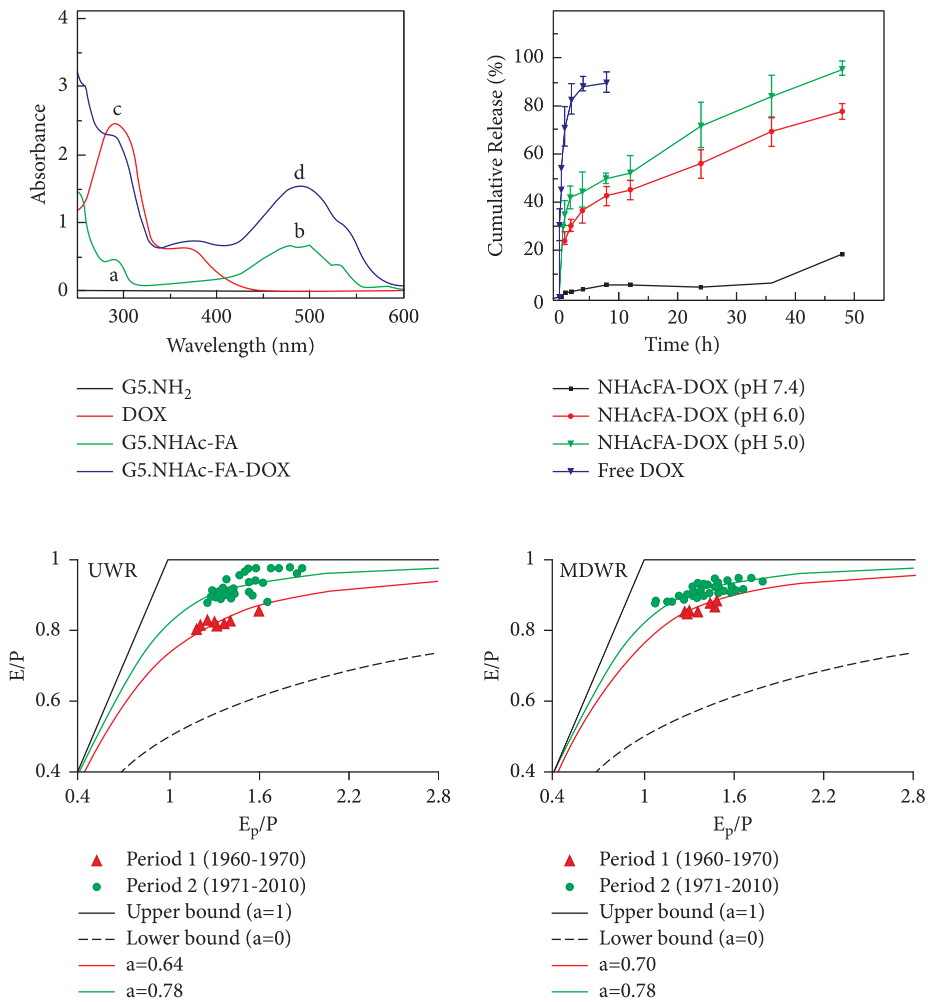

FIGURE 5: Evaluation of growth status of agrobacterium bisporus.

5. Conclusion

Professional athletes often encounter tendon injury in the process of exercise and then tendon adhesion occurs in the process of tendon healing. Tendon injury is a common complication after tendon injury. It is difficult to recover after a period of time, which has different effects on athletes' competition and training. Based on the above reasons, the theory of tendon injury healing has been deeply studied, and it is found that the biological barrier of biomaterials can effectively promote tendon repair and self-healing. In order to verify the actual effect of biomaterials on tendon healing, MRDM image data of tendon injury healing were obtained by medical image analysis technology for research and observation. The acquired MRDM image data contain a lot of useless information. For this reason, the RANSAC algorithm is used to filter the worthless image data and then in-depth analysis is carried out. The application of biomaterials can actively promote the stable healing of tendon. Then, the multilevel model was used to evaluate the actual effect of several biomaterials: (1) chitosan; (2) absorbable antiadhesion membrane; and (3) sodium hyaluronate, which is commonly used in the clinic to repair tendon injury and heal adhesion. The results showed that sodium hyaluronate was the best of the three biomaterials for tendon healing.

Data Availability

The data used in this paper to support the results of this study are included in this paper.

Conflicts of Interest

The authors declare that there are no conflicts of interest in this paper.

References

[1] Q. H. Song, "Application of artificial biomaterials to tendon injury," *Journal of Clinical Rehabilitative Tissue Engineering Research*, vol. 14, no. 12, pp. 2233–2236, 2018.
[2] G. P. Wang, K. F. Zhang, and G. F. Chen, "Application of artificial biomaterials for the treatment of tendon injury," *Journal of Clinical Rehabilitative Tissue Engineering Research*, vol. 13, no. 47, pp. 9345–9348, 2018.

[3] J. Dong, "Biomedical materials for adhesion repair after tendon injury," *Journal of Clinical Rehabilitative Tissue Engineering Research*, vol. 15, no. 47, pp. 8899–8902, 2018.
[4] N. Zhao, W. Chen, and T. Yan, "Application of different biomaterials in Achilles tendon repair for exercise injury," *Advanced Materials Research*, vol. 8, no. 6, pp. 329–332, 2018.
[5] D. Kang, "Anti-adhesion effect of absorbable biomaterials during tendon reconstruction," *Chinese Journal of Tissue Engineering Research*, vol. 12, no. 2, pp. 23-24, 2018.
[6] Z. F. Zhang, "Application of biomaterials in tendon adhesion following sports injury," *Journal of Clinical Rehabilitative Tissue Engineering Research*, vol. 13, no. 8, pp. 1549–1552, 2018.
[7] G. Gross and A. Hoffmann, "Therapeutic strategies for tendon healing based on novel biomaterials, factors and cells," *Pathobiology*, vol. 80, no. 4, pp. 203–210, 2018.
[8] R. Cheng and Y. Jin, "A social learning particle swarm optimization algorithm for scalable optimization," *Information Sciences*, vol. 291, no. 6, pp. 43–60, 2018.
[9] W. Jia, D. Zhao, T. Shen, S. Ding, Y. Zhao, and C. Hu, "An optimized classification algorithm by BP neural network based on PLS and HCA," *Applied Intelligence*, vol. 43, no. 1, pp. 176–191, 2018.
[10] S. Oranburg, "Distance education in the time of coronavirus: quick and easy strategies for professors," *Duquesne University School of Law Research Paper*, 2020.
[11] M. Nouiri, A. Bekrar, A. Jemai, S. Niar, and A. C. Ammari, "An effective and distributed particle swarm optimization algorithm for flexible job-shop scheduling problem," *Journal of Intelligent Manufacturing*, vol. 2, no. 3, pp. 603–615, 2018.
[12] D. Han, Y. Dai, T. Han, and X. Dai, "Explore Awareness of information security: insights from cognitive neuromechanism," *Computational Intelligence and Neuroscience*, vol. 15, no. 1, pp. 11–13, 2018.
[13] Q. He, K. Huo, X. Xu, Y. Yue, G. Yin, and M. Yu, "The square rod-shaped ionic polymer-metal composite and its application in interventional surgical guide device," *International Journal of Smart and Nano Materials*, vol. 11, no. 2, pp. 159–172, 2020.
[14] P. Venezia, F. Torsello, V. Santomauro, Dibello, and R. Cavalcanti, "Full digital workflow for the treatment of an edentulous patient with guided surgery, immediate loading and 3D-printed hybrid prosthesis: the BARI technique 2.0. a case report," *International Journal of Environmental Research and Public Health*, vol. 16, no. 24, p. 5160, 2019.
[15] E. Moslehifard and S. Nokar, "Designing a custom made gauge device for application in the access hole correction in the dental implant surgical guide," *Journal of Indian Prosthodontic Society*, vol. 12, no. 2, pp. 123–129, 2018.
[16] K. Koyanagi, "Development and clinical application of a surgical guide for optimal implant placement," *The Journal of Prosthetic Dentistry*, vol. 88, no. 5, pp. 548–552, 2018.
[17] H. F. Marei, A. Abdel-Hady, K. Al-Khalifa, and H. Al-Mahalawy, "Influence of surgeon experience on the accuracy of implant placement via a partially computer-guided surgical protocol," *International Journal of Oral & Maxillofacial Implants*, vol. 34, no. 5, 2019.
[18] L. Guo, J. Yang, and Y. Wang, "Accuracy evaluation of digital surgical template in angled implantation in the maxillary posterior region," *Journal of Prevention & Treatment for Stomatological Diseases*, vol. 35, no. 2, pp. 313–322, 2018.
[19] V. Alevizakos, G. Mitov, M. Stoetzer, and C. von See, "A retrospective study of the accuracy of template-guided versus freehand implant placement: a nonradiologic method," *Oral Surgery, Oral Medicine, Oral Pathology and Oral Radiology*, vol. 128, no. 3, pp. 220–226, 2019.
[20] A. A. Philip, A. A. Taofiki, and A. A. Bidem, "Artificial neural network model for forecasting foreign exchange rate," *World of Computer Science and Information Technology Journal*, vol. 26, no. 6, pp. 504–512, 2018.
[21] W. Wang, X. Zhang, and Z. Li, "Dendronized hyaluronic acid-docetaxel conjugate as a stimuli-responsive nano-agent for breast cancer therapy," *Carbohydrate Polymers*, vol. 267, Article ID 118160, 2021.
[22] C. Lei, X. R. Liu, Q. B. Chen et al., "Hyaluronic acid and albumin based nanoparticles for drug delivery," *Journal of Controlled Release*, vol. 331, pp. 416–433, 2021.

Hindawi
Journal of Healthcare Engineering
Volume 2022, Article ID 6955870, 10 pages
https://doi.org/10.1155/2022/6955870

Research Article

An Overview of the Implications for Perianesthesia Nurses in terms of Intraoperative Changes in Temperature and Factors Associated with Unintentional Postoperative Hypothermia

Fang Yang, Jing Wang, Jifang Cui, Jia Zhuan, Xiaoyan Hu, and Shuting Chen

Clean Operation Department, Qinghai People's Hospital, Qinghai 810000, China

Correspondence should be addressed to Fang Yang; fang_yang66@126.com

Received 14 January 2022; Revised 7 March 2022; Accepted 9 March 2022; Published 11 April 2022

Academic Editor: Enas Abdulhay

Patients undergo surgery and anaesthesia on a daily basis across the United States and throughout the world. A major source of worry for these patients continues to be inadvertent hypothermia, once core temperature <36°C (96.8°F). Despite well-documented adverse physiological consequences, anaesthesia nurses continue to have a difficult task in keeping patient warmth pre-/peri-/post-surgical procedure. Thermostasis within postoperative patient necessitates the collaboration of many individuals. In order to provide safe and high-quality treatment, it is essential to use the most up-to-date data to guide therapeutic procedures targeted at achieving balance body temperature in surgical patients. Providing a review of the physiology of perioperative temperature variations and the comorbidities linked with accidental intraoperative hypothermia, this article will also provide preventive and treatment methods.

1. Introduction

Patients undergoing surgery and anaesthesia often experience drops in core-body temperature to <36°C (96.8°F) [1–3]. Hypothermia is characterised by widespread metabolism reduction that affects all bodily systems at the same time. Between 50 and 90 percent of surgery patients suffer from hypothermia at some point throughout their recovery period [4, 5]. The consequence is significant physiological alterations, including changed heart function, fluctuations in state of awareness, shivering and extended plasma half-lives of medicines, which may also enhance oxygen consumption by up to 500 percent [6–8]. Hypothermia is linked with a number of additional negative outcomes, including an increase in the duration of hospital stay, an increase in infection rates, and an increase in cardiac events [9]. According to research, individuals who maintain a normal body temperature during the surgical process are less likely to get infections (64 percent), have 44 percent less cardiac problems, and are 34 percent fewer likely to need perioperative mechanical breathing. Furthermore, patients who got hypothermic were discharged from the hospital 40 percent sooner than those who did not become hypothermic [9, 10]. A solid understanding of the factors that contribute to perioperative hypothermia, as well as the mechanism of heat exchange in operating patients during their perianesthesia and post-surgical time frame, and also the physiologic changes related with this heat loss, are required for the implementation of guiding principles in the perianesthesia context [11]. It is also necessary to be familiar with the risk factors for hypothermia. Perianesthesia nurses continue to play a significant role in maintaining thermal balance in surgical patients. In the postoperative care of operating patients, via treatments targeted at reducing temperature loss, however preserving and/or recovering normothermia differentiates the difficulty faced by perianesthesia nurses from other types of challenges [11–13].

Herein, we first explained the temperature monitoring for patient undergoing anaesthesia and the basic science and temperature regulation physiology of heat lost from a patient to the environment. We explained the various risk factors to improve intraoperative heat control throughout the process.

Next, we highlight the perianesthetic heat loss and the phenomena, balance between thermolysis and thermogenesis and the physiological changes as a result of hypothermia, as well as the various variables for the improvement of perioperative hypothermia. Finally, we highlight the hypothermia and its consequences and provide the concluding remarks. This review will give readers an overview of the implications for perianesthesia nurses in terms of intraoperative changes in temperature and factors associated for unintentional post-operative hypothermia.

2. Temperature Monitoring

"Every patient undergoing anaesthesia should have his or her temperature monitored whenever clinically significant changes in body temperature are intended, expected, or suspected," as described by the American Society of Anesthesiologists' guidelines concerning fundamental anaesthetic observation [14]. Due to the fact that this recommendation does not specify the method of temperature monitoring to be used, when to monitor, or for how long to monitor, variability in patient safety and broad variance in clinical practise will result. The American Society of Perianesthesia Nurses (ASPAN) recommendations offer scientific proof guidelines for monitoring temperature in anaesthesia care settings[15].

Inner abdominal-area / thorax /neural tissue-temperature is defined as CT (CT). This temperature is carefully regulated, and it is typically 2 – 4°C (3.6 – 7.2 degrees Fahrenheit) elevated in comparison to dermal thermo-readings. During general anaesthesia, CTs remain frequently monitored across several sites such as the distal oesophagus, bladder (in instances of excessive urine flow), nasopharynx, and the pulmonary artery, among other places. The CT of people is the single greatest indication of their thermal state, despite the fact that it is not fully representative of their body heat content and distribution [16]. Axillary, rectal, bladder (having low urine flow), and mouth measures of near-CTs are more frequently utilised in regional anaesthetic patients during the perioperative period than other methods of temperature monitoring. This kind of measurement is usually less difficult to acquire, although it is influenced by external factors (such as the surrounding environment's temperature) and internal factors (such as the body's regional cutaneous blood flow). When it comes to axillary and oral temperatures, this concept makes sense, but the differences between bladder and rectal temperatures are less apparent. Temperatures in the rectal area are usually very closely related to CTs [17–19]. In the event of malignant hyperthermia (MH) and heat stroke, however, these precautions are not taken [20–22]. Furthermore, because rectal temperature lags after true CT during cardiac bypass, it is considered a near CT in patients who have been deliberately chilled. As a result, while taking rectal temperature readings, extreme care must be used. When urine flow is high, bladder temperature equals pulmonary artery thermal-reading / CT; however, upon reduced urine output, bladder temperature come close to rectal temperature [23, 24]. Beside this, temperature of bladder is also regarded to be a near-core metric because of its reliance on urine flow. As a result, the capacity of any of these measurements to represent CT is severely restricted. The most appropriate thermoregulatory monitoring location throughout periperative, intra-operative and after operation timeframes remains disputed, with the best source varying depending on the age of the patient. Preoperative temperature measures are most frequently taken by mouth for adults, oral or axillary temperature measurements are taken by mouth for paediatric patients, and axillary measurements are taken by hand for newborns. When feasible, an esophageal probes are employed for intra-surgical patient CT determinations. This technique is relatively safe / inexpensive, offering peak precise evaluation for thermo-readings available on the market. Furthermore, this measurement is the most precise when there are significant fluctuations in temperature. However, measuring the oesophagus is more difficult in patients receiving regional or controlled anaesthesia, as well as in those who are recovering from surgery. Except in the case of severe thermal disturbances, CTs may be calculated with acceptable precision from near-core observations taken near the core [25–27]. The application of a liquid-crystal temperature strip to the forehead is another popular method of thermal monitoring. These gadgets are low-cost, non-invasive, and simple to use, making them an excellent choice. Despite the fact that dermal thermo-reading remain significantly lesser in comparison to CT-readings, with increased vulnerability to environmental temperatures, these strips will offer a good approximation of CTs when regulated with a proper off-set (0.5uC in conscious individuals, 1uC in drowsy/anesthetized individuals) [28]. 19 When temperature fluctuations are more severe, for as during MH, liquid-crystal thermal-strips prove ineffective for noticing temperature rises within porcine models [29]. Such detectors were un-evaluated in people regarding this role, consequently not being recommended for human MH determination [30] . As a result of these considerations, CTs / near-CTs could become employed within the peri-surgical timeframes once risk-benefit analyses are concluded, knowing that clinical-setting situations could necessitate the use of a different technique.

The new AORN "Guideline for prevention of unintended patient hypothermia" gives guidelines in recognizing parameters related to intra-surgical hypothermia and its circumvention, teaching peri-surgical professionals regarding this issue, together with implementing applicable guidelines / protocols (Figure 1) [31].

3. Background Basic Science

There are four different ways through which heat may be lost from a patient to the environment. Radiation and convection are the most significant contributions to global warming [32]. Heat is emitted by any surfaces that are warmer than absolute zero, which is known as radiation (thermal) (infrared radiation). This emitted heat is absorbed by all surfaces in the immediate vicinity. As a result, the patient generates heat that is radiated into the surrounding environment. During surgery, radiation is most likely the most significant heat-loss source.

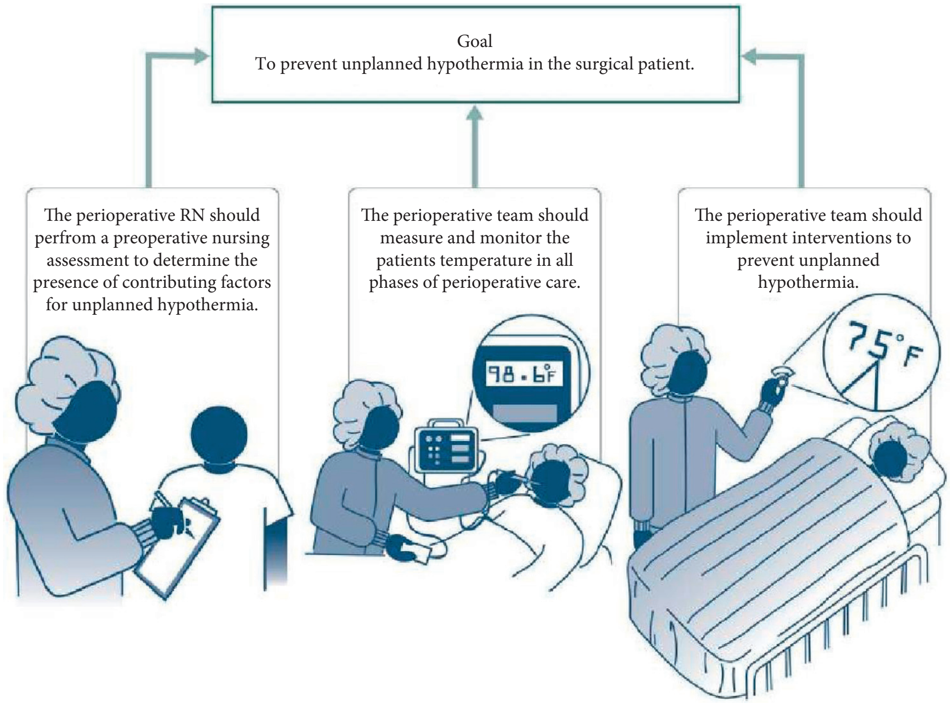

FIGURE 1: AORN Guideline for Prevention of Unplanned Patient Hypothermia. In briefly, peri-surgical registered nurse must conduct pre-surgical nursing assessment for ruling out risk factor manifestations driving unintentional hypothermia. Throughout peri-surgical period, the peri-surgical group must take and track patient thermal readings. The peri-surgical team should take preventative measures to avoid unintentional hypothermia.

3.1. Convection. Usually, minute layers of static-air in proximity to the dermal layer serve as insulation, preventing conduction-based heat from being transmitted through the skin to nearby air molecules. Once air currents pass across it, this layer is disturbed, the insulating qualities of the layer are significantly reduced, resulting in increased heat loss. Convection is the term used to describe this process, which is the foundation for the notion of wind cold factor. When it comes to non-OR hospital settings, room air is usually replaced four times per hour, whereas in distinctive operating room (OR), room air is circulated fifteen times per hour. Because of the little perceptible flow of air throughout the operating room, these rooms are perceived as being cooler. Surgical curtains serve as thermal insulators, reducing convective heat loss to a bare minimum. Contrary to popular belief, convection-based heat-loss forms 2nd paramount cause for thermal-losses within OR.

3.2. Conduction. Conduction can be described as thermal-transference through conductive media deprived of any discernible movement of the medium itself. Because of the temperature differential between two mediums and the material's heat conductivity, heat transfer occurs at a faster pace in certain cases. For the reason that the patient is in close touch with foam protecting sheet on the operating table, conduction contributes only a small portion of the heat loss during surgery.

3.3. Evaporation. This can be described as transformation of liquids into vapors once temperature is below the boiling point. As a result, molecules with the greatest kinetic energy can escape from a liquid's surface, decreasing the kinetic energy (KE) and therefore reduce the temperature. This kind of thermal loss is most often seen when sterile preparation solutions are used in the manufacturing process. It is possible that evaporative losses from surgical wounds will also be a factor [32].

3.4. Temperature regulation physiology. The human thermoregulatory system is capable of maintaining a constant body temperature inside under typical conditions; the usual body temperature is about 37°C. In the operating room, on the other hand, a collection of changed thermoregulatory mechanisms and lower ambient temperatures classically leads a reduction in CT. Hypothermia takes place once CT is less than 36°C, is a reasonably frequent occurrence within operating patients, with a frequency of up to 20% reported. Cases occur when healthy individuals experience CT drops of 0.5 - 1.5°C [33, 34] in the first hour after undergoing a surgical operation.

Physiologic thermoregulation is comprised of a system of afferent temperature sensing, efferent reactions and central regulation that works in concert. Thermosensing cellular populations found within spinal cord, brain, thorax, skin surface together with deep abdominal tissue are responsible for afferent thermal perception in hypothermia [35]. The hypothalamus, with reduced aid by the spinal cord, are responsible for central CT regulation. Endpoints to hypothermia in adults manifests itself mainly via behavioural change, although it may also express itself through vasoconstriction and shivering. Additionally, nonshivering thermogenesis is shown in neonates, and various physiological changes are associated with the with the hypothermia (Figure 2).

3.5. Thermoregulation and aesthetic effects. The body's temperature is well controlled under normal conditions by controlling blood flow using arteriovenous shunts, which have been located on the surface of skin and regulate blood flow. It is possible that this blood flow accounts for as much as 10% of the total cardiac output, and that vasoconstriction might cause an improvement in mean arterial blood pressure of about 15 mmHg [36–38]. Anesthesia has a significant impact on the body's thermoregulatory systems. The use of general anaesthetics may help prevent heat loss-driven vasoconstriction, leading to improvement in patient thermal regulation once they are exposed to a frigid environment. The heat produced by the body is not dispersed evenly. Relatively, heat is often focused within core-regions, namely the head / trunk regions, with peripheral regions remaining lower in temperature. It's important to observe that heat from the core is directed towards the periphery body-stress manifests by decreasing OR temperatures / vasodilation functions through generalized anaesthetic take effect due to a lack of sympathetic tone (Figure 3) [33]. Such change leads into fast CT drop, approximating 0.5-1.5°C (0.9–2.7°F), which may be detected within the first hour after surgery. As a consequence of the vasodilation characteristics of general anaesthetics, this redistribution hypothermia is not a true loss of heat, but instead of a transfer in heat energy from the central to the periphery, which causes the patient to become hypothermic. Following the administration of general anaesthesia, the warmer periphery created by the drug increases the likelihood that the patient may lose CT into external OR area.

Hypothermia under generalized anaesthesia follows distinct profiles, with early-phase fast drop in CT (Phase I), followed by more gradual decrease in CT (Phases II, III, and IV). A plateau-phase (Phase III) take place on process termination, during which CT stabilises (Figure 4). Thermal redistribution may be responsible for the fast heat loss seen during Phase I in the first hour. Phase II (heat transfer from the warmer perimeter to the rest of the environment) is characterised by a gradual linear decrease that occurs over a period of 2-4 hours, during which thermal loss surpasses metabolic heat generation [39–41]. Phase III (thermal homeostasis) starts following 3 - 4 h, once CTs of 33 to 35 degrees Celsius cause peripheral vasoconstriction [42, 43]. Neuraxial anaesthesia, like generalized anaesthesia, interferes with physiologic thermoregulation, but it does so via a different mechanism. The thresholds for tremors / vasoconstriction are lowered (approximately 0.6°C) with epidural 28,29 and spinal anaesthesia, respectively (1.08°F). Leg

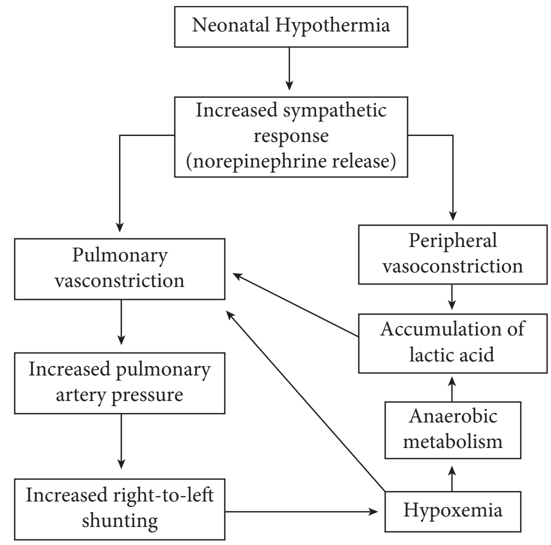

Figure 2: Neonatal physiological dysfunctions linked to hypothermia.

skin sensors provide afferent heat input is responsible for a large portion of the control of the CT. Within conventional ORs, constant cold-signals remain generating from peripheral regions, which are then processed [44]. Thermal input, on the other hand, is stopped across the blocked areas in regional anaesthesia. The lack of cold signals that results as a consequence of this is perceived centrally as relative leg warmth, which eventually lowers the shivering and vasoconstriction thresholds. Consequently, a patient who has been regionally anaesthetized may believe that he feels warm while are actually losing heat. Neuraxial anaesthesia is typically combined with sedatives / analgesics, which further compromise regulation by impairing the ability to regulate body temperature[45–48].

3.6. Risk Factors. Practitioners would, ideally, detect risk parameters leading to UPH before to performing any surgical operation for improving intra-surgical heat control throughout the process. When it came to identifying risk factors, ASPAN used an evidence-based practise approach [49, 50]. Following the evidence evaluation scale developed by colleagues and Stetler, this method evaluated the strength and quality of proof in descending order[51]. The American College of Cardiology/American Heart Association (ACC/AHA) categories were changed to address risk/benefit ratios, with considerable body of proof confirming such guidelines, and the amount of evidence supporting the recommendations. The following are the definitions for these classes[52]:

> Class I: The benefit exceeds the danger in this case, and the suggestion should be followed through on.

A suggestion falls into Class IIa if the profit exceeds the danger, and it is appropriate to carry out or administer the advise in question.

A suggestion falls into Class IIb if the profit outweighs the risk and it is not irrational to follow or implement the advice.

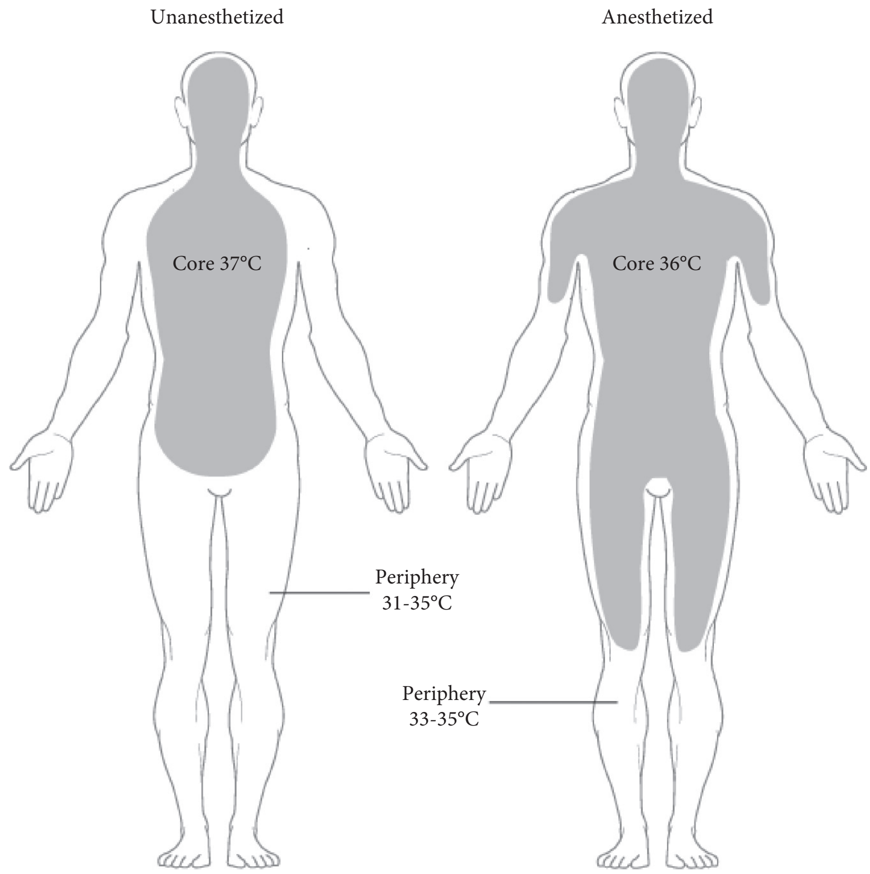

Figure 3: CT/heat re-distribution throughout generalized anaesthesia.

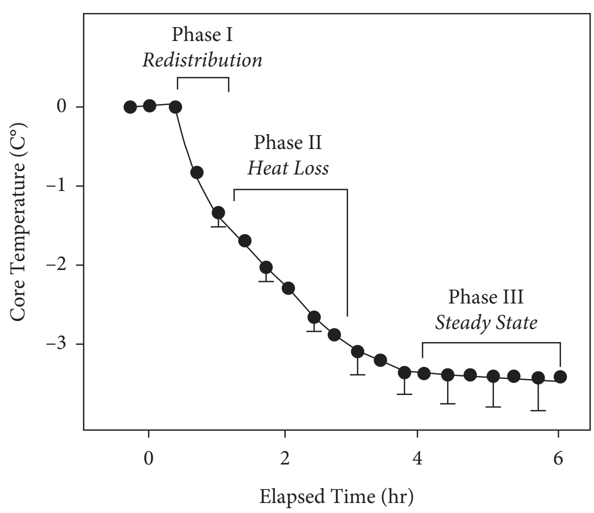

Figure 4: Typical thermal shift profiles observed during generalized anaesthesia. Reproduced with permission from [32].

Classes I, II, and III: The danger exceeds the advantage, therefore the advice would not be carried out or managed.

These suggestions are backed up by three different bodies of proof:

Level-A proof includes proof from several randomised trials / meta-analyses examining various (3–5) populi, having overall reliability in the direction and size of the impact.

A level B proof base would consist of proof from single randomised trials / non-randomized investigations assessing small (2 - 3) population samples.

The proof comes from case-based investigations, treatment quality levels, or skilled opinions containing relatively small (1 - 2) groups.

Unfortunately, neither one of the risk variables found is backed by solid proof, indicating that more study in this area is required. These variables suggest a connection but not necessarily a causal relationship; for example, one patient could carry risk parameters yet not develop hypothermia despite having them. Expectantly, by identifying individuals who are vulnerable to hypothermia during the preoperative evaluation, methods to assist maintain normothermic conditions throughout the peri-surgical phase may be devised.

3.7. Perianesthetic Heat Loss. The hypothalamus is in charge of regulating and maintaining body temperature, which is altered during the duration of perianesthesia [53–55]. The effects of generalized and regional anaesthesia on thermoregulation are similar. Generalized anaesthesia impairs the hypothalamus' capacity to control the small margin of temperature variation within which it operates [56, 57]. In turn, this leads in a suppression of both centrally mediated vasoconstriction and peripheral vasodilatation [58, 59]. Regional anaesthesia, on the other hand, causes a centrally mediated vasodilation that prevents peripheral vasoconstriction, resulting in re-distributing core-heat with consequent thermal losses throughout surgical procedure/s [53, 58]. According to research, the majority of patients have predictable patterns of heat loss due to anesthetic-driven thermoregulatory disruption coupled to body contact with colder OR ambient [60, 61]. During anaesthesia, there is a decrease of body heat that happens in 03 stages. During the first hour following operation, Phase I, or redistribution, occurs and anaesthesia due to fast systemic circulatory redistribution from patient core into peripheral areas throughout initial 60 minutes of surgery / anaesthesia. This is indicated through significant CT decrease (1 – 3°C) [58, 59]. In consequent 2 - 3 hours post-surgery, Phase II (linear phase) thermal losses remain, however, CT drops are less drastic/rapid and follows a linear trend. A decrease in the rate of decrease in the patient CT is caused by thermal losses surpassing the amount of heat produced by metabolic processes [58]. Eventually, within Phase III (the plateau-phase), thermostasis is achieved having the least amount of heat loss. When thermal loss matches metabolic heat generation, the body's CT remains constant [58].

The four main processes of thermal loss for operating patients will define the rate of heat loss throughout the linear phase: evaporation, conduction, convection, and radiation. Evaporation routes predominate thermal losses for operating patients.

Radiation, or the transmission of heat from one surface to another despite the presence of a constant ambient temperature, is the most significant source of thermal loss in patients undergoing surgery and anaesthesia. When it comes to heat loss in this population, convection is the second most frequent culprit. Conduction and convection both use heat transmission mechanisms that are quite similar. During surgery, the evaporation of physiological fluids during breathing offers an additional pathway for the loss of core body temperature (Figure 5).

3.8. Physiological Changes as a Result of Hypothermia. An association linked between hypothermia and the myriad of physiological effects that occur as a consequence of anaesthesia, and this connection is well established (Figure 6). The physiological consequences are characterised by a generalized slowing of metabolism that affects all bodily systems [58, 62, 63]. Apart from the physiological consequences of hypothermia, other possibly harmful consequences include myocardial infarction, impaired wound healing, coagulopathy, improved contagion rates and prolonged advent from anaesthesia due to reduced drug metabolism along with psychological consequences such as stress, pain and changed cognitive functioning [62]. However, while all patients are at increased risk of developing adverse physiological changes as a result of hypothermia, burns and trauma, senior and disabled, infants, mal-nourished patients are among those who are most likely to experience physiological changes as a result of the condition [56]. One study looking at prognostic variables in hypothermia identified patients >70 years had higher risks for adverse consequences linked to improvement of peri-surgical hypothermia [64].

3.9. Peri-surgical Hypothermia and Its Risk Factors. Many variables lead to the improvement of peri-surgical hypothermia, some of which are listed below. In accordance with current study and previous research, aetiology / connection of variables involved with accidental hypothermia are well understood and supported. Temperature and timing of the room natural light are critical. The ambient room temperature continues to be the most important interoperative variable in determining whether or not patients will develop hypothermic during surgery. In three landmark investigations, researchers discovered that all patients who entered operating rooms with external temperatures <70°F (21°C) were hypothermic [65–67]. As part of the research, there were no intra-surgical warming treatments given to the patients in this group. The findings revealed that the largest CT drops occurred within initial 60 minutes of presence inside OR [67]. This body of classic research, dating to 1960s - 1970s, provides substantial proof in support of regulating the ambient temperature aimed at preserving thermostasis across surgery cases. Despite this, present operating rooms remain chilly. Adjusting the operating room thermostat to 70°F (21°C) as soon as the patient enters OR could reduce risk of accidental hypothermia occurring. 18 Additional comfort will be provided by maintaining the patient swaddled as best-possible, as well as by decreasing thermal loss [68].

3.10. Anaesthetic Technique. Local and generalized anaesthesia both lead to the loss of body temperature in surgical patients by redistributing heat away from the body's centre and toward the periphery, respectively [69, 70]. Regional anaesthesia, on the other hand, causes heat loss mostly as a result of peripheral nerve block, rather than the change of the hypothalamus controlling centre for temperature regulation that happens with generalized anaesthesia [58]. Regional anaesthetic impairs the patient's capacity to constrict his or her blood vessels. When it comes to spinal and epidural anaesthesia, the legs are the primary organs responsible for the transfer of body heat. The use of generalized anaesthesia in conjunction with local anaesthetic allows for the maximum degree of heat loss in operating patients [53]. Understanding the kind of anaesthetic, a patient has had will assist the peri-surgical nurse and the perianesthesia team in developing a complete plan of care to maintain normothermia in the patient.

3.11. Hypothermia and Its Consequences. The goal of reducing peri-surgical hypothermia needs a collaborative effort all over the surgical process. When it comes to maintaining proper thermal balance in surgery patients, awareness and training of the whole operating team, containing preoperative, intra-surgical, and post-operative nurses as well as anaesthetic providers, surgeons, and surgery technicians, are essential. The frequency of this

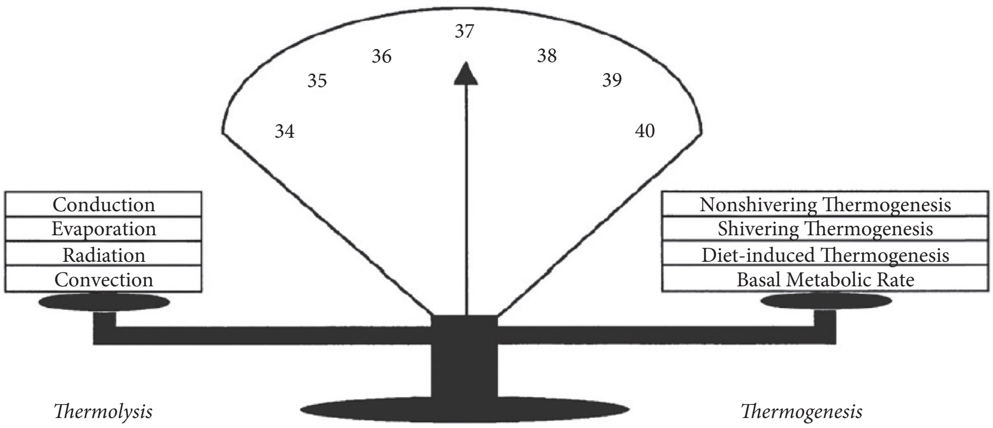

Figure 5: Balance between thermolysis and thermogenesis.

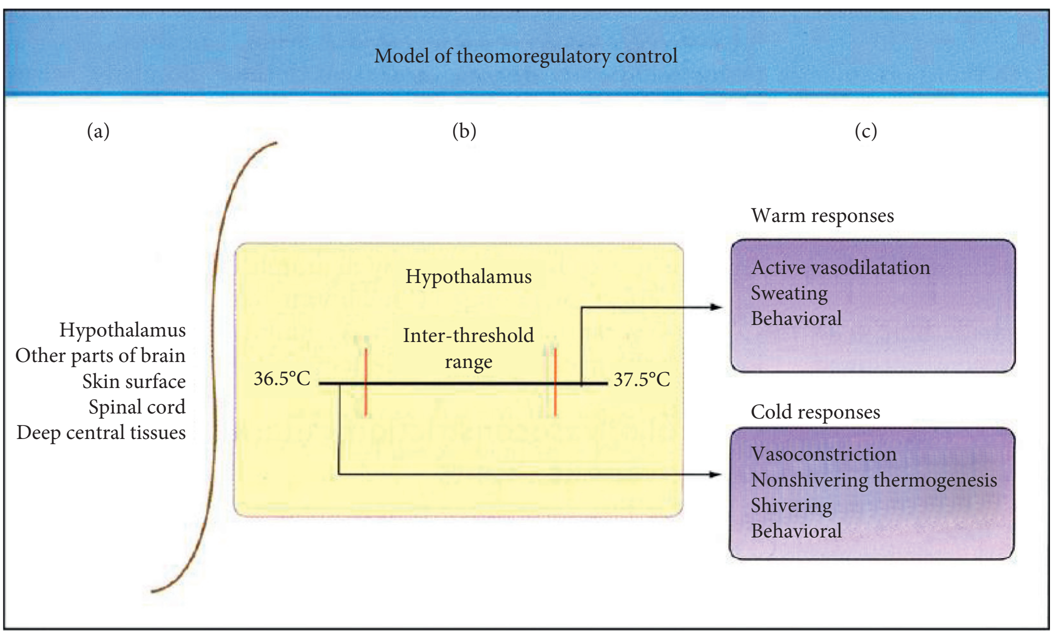

Figure 6: A model of thermoregulatory control.

avoidable illness will continue to rise unless efforts are made to educate all physicians who deal with operating patients before, during, and after surgical treatment about hypothermia and its potentially life-threatening consequences. The American Society of Plastic Surgeons (ASPAN) has well defined guidelines for avoiding hypothermia in surgery patients [71]. but, research aiming at demonstrating a link between these recommendations and a reduction in the prevalence of hypothermia has been difficult to conduct.

Preoperative some patients come in the operating room with hypothermia, but there is no information available on the prevalence of preoperative hypothermia. Showers in the morning, skin preparations, scant-clothing, together with vasodilator impact from pre-medication form variables that lead to a drop in body temperature. Preoperatively, one of the most essential goals should be to get the patient to surgery in a state of normal thermal balance. As a result, maintaining patients warm before entering the operating room highlights the requirement of early nurse involvement targeted at preserving normothermia in the patient [72, 73]. In order to maintain preoperative normothermia, blankets and forced-air warming equipment may be used, which could aid lower prevalence of peri-surgical hypothermia. Moreover, warming patients before they enter the operating room has been shown to have anxiolytic effects and to make the insertion of intravenous catheters easier [74]. In addition to caps and warming lights, which may be beneficial for babies, there is a paucity of research on their effectiveness.

3.12. Intra-surgical. Hypothermia during surgery may be substantially reduced if the operating room temperature is maintained at 70°F throughout the procedure [75, 76].

Although 70°F may appear excessively warm to the operating room personnel, maintain the environment warm until the incision could help to substantially minimise the first Phase I drop in body temperature after the incision. Warming blood products, IV fluids and irrigants may all help to keep the body's thermal balance in normal range. Anesthetic gases that have been heated and humidified also have a role an essential function in maintaining body temperature. Additionally, the use of warming blankets, layered draperies, and head coverings may help to offer extra thermal protection. Forcible warming has been shown to be one of the most efficient treatments for sustaining intra-surgical hypothermia, according to research [77]. The use of forcible heating equipment in the operating room helps to reduce radiant heat loss, which helps to keep the patient's body temperature stable [77].

4. Conclusion

Temperature regulation during the time of anaesthesia and peri-surgical care is affected by a variety of factors, and maintaining control over these factors is frequently challenging. When it comes to patient care, having a strong theoretical foundation is essential. Understanding the temperature physiology regulation and the risk factors linked with accidental hypothermia are important to have. Clearly, the body temperature of all operating patients, particularly those who are at risk of emerging hypothermia, must be closely monitored. The perianesthesia/peri-surgical team is in charge of putting in place preventative measures to keep the patient's body temperature as low as possible. According to the most recent research, rather than relying on a single preventative technique to reduce heat loss in the postoperative patient, it is essential to combine several methods for optimizing endpoints. In order to extend and support current data on treatments regarded most effective for reducing the prevalence of hypothermia all over the perianesthesia/peri-surgical cycle, further research is required. For example, research into preoperative treatments to guarantee that patients enter the operating room in near-normal thermal balance provides a chance to link the gap between research and practise in today's peri-surgical and anaesthetic settings. To use ideal proof to improve heat balance in the surgical patient necessitates the use of current and new investigation results throughout the whole perianesthesia/peri-surgical phase, which includes the full surgical procedure.

Data Availability

Data will be provided upon the corresponding author request.

Conflicts of Interest

Authors declare that they have no any conflict of interest.

References

[1] R. H. Morris, "Operating room temperature and the anesthetized, paralyzed patient," *Archives of Surgery*, vol. 102, no. 2, pp. 95–97, 1971.

[2] A. Kurz, "Physiology of thermoregulation," *Best Practice & Research Clinical Anaesthesiology*, vol. 22, no. 4, pp. 627–644, 2008.

[3] S. M. Frank, "Perioperative maintenance of normothermia reduces the incidence of morbid cardiac events," *JAMA*, vol. 277, no. 14, pp. 1127–1134, 1997.

[4] N. A. Blondin, "Diagnosis and management of periodic hypothermia," *Neurology: Clinical Practice*, vol. 4, no. 1, pp. 26–33, 2014.

[5] E. Zagkle, M. Grosiak, U. Bauchinger, and E. T. Sadowska, "Rest-phase hypothermia reveals a link between aging and oxidative stress: a novel hypothesis," *Frontiers in Physiology*, vol. 11, no. 1603, Article ID 575060, 2020.

[6] C. Tjoakarfa, V. David, A. Ko, and R. Hau, "Reflective blankets are as effective as forced air warmers in maintaining patient normothermia during hip and knee arthroplasty surgery," *The Journal of Arthroplasty*, vol. 32, no. 2, pp. 624–627, 2017.

[7] B. B. Koc, M. G. M. Schotanus, J.-P. A. P. A. C. Kollenburg, M. J. A. Janssen, F. Tijssen, and E. J. P. Jansen, "Effectiveness of early warming with self-warming blankets on postoperative hypothermia in total hip and knee arthroplasty," *Orthopaedic Nursing*, vol. 36, no. 5, pp. 356–360, 2017.

[8] E. Noll, S. Diemunsch, J. Pottecher et al., "Prevention of laparoscopic surgery induced hypothermia with warmed humidified insufflation: is the experimental combination of a warming blanket synergistic?" *PLoS One*, vol. 13, no. 7, Article ID e0199369, 2018.

[9] H. Shimaoka, T. Shiina, H. Suzuki, Y. Horii, K. Horii, and Y. Shimizu, "Successful induction of deep hypothermia by isoflurane anesthesia and cooling in a non-hibernator, the rat," *The Journal of Physiological Sciences*, vol. 71, no. 1, p. 10, 2021.

[10] H. Shimaoka, T. Kawaguchi, K. Morikawa et al., "Induction of hibernation-like hypothermia by central activation of the A1 adenosine receptor in a non-hibernator, the rat," *The Journal of Physiological Sciences*, vol. 68, no. 4, pp. 425–430, 2018.

[11] C. Li, B. Zhao, L. Li, G. Na, and C. Lin, "Analysis of the risk factors for the onset of postoperative hypothermia in the postanesthesia care unit," *Journal of Perianesthesia Nursing: Official Journal of the American Society of PeriAnesthesia Nurses*, vol. 36, no. 3, pp. 238–242, 2021.

[12] Y. A. Yitayew, E. B. Aitaye, H. W. Lechissa, and L. O. Gebeyehu, "Neonatal hypothermia and associated factors among newborns admitted in the neonatal intensive care unit of dessie referral hospital, amhara region, northeast Ethiopia," *International Journal of Pediatrics*, vol. 2020, Article ID 3013427, 2020.

[13] M. Liu and L. Qi, "The related factors and countermeasures of hypothermia in patients during the anesthesia recovery period," *American Journal of Tourism Research*, vol. 13, no. 4, pp. 3459–3465, 2021.

[14] B. Bindu, A. Bindra, and G. Rath, "Temperature management under generalized anesthesia: compulsion or option," *Journal of Anaesthesiology, Clinical Pharmacology*, vol. 33, no. 3, pp. 306–316, 2017.

[15] E. B. Card, N. Wells, P. Mesko, A. Eliades, R. MacDonald, and D. A. Krenzischek, "Perianesthesia nurses pain management practices: findings and recommendations from a national descriptive study of members of the American society of

perianesthesia nurses," *Journal of PeriAnesthesia Nursing*, vol. 36, no. 2, pp. 128–135, 2021.
[16] E. V. Osilla, J. L. Marsidi, and S. Sharma, *Physiology, Temperature Regulation*, Wiley, Hoboken, NJ, USA, 2021.
[17] F. Oguz, I. Yildiz, M. A. Varkal et al., "Axillary and tympanic temperature measurement in children and normal values for ages," *Pediatric Emergency Care*, vol. 34, no. 3, pp. 169–173, 2018.
[18] P. Kalasbail, N. Makarova, F. Garrett, and D. I. Sessler, "Heating and cooling rates with an esophageal heat exchange system," *Anesthesia & Analgesia*, vol. 126, no. 4, pp. 1190–1195, 2018.
[19] E. Madrid, "Active body surface warming systems for preventing complications caused by inadvertent peri-surgical hypothermia in adults," *Cochrane Database of Systematic Reviews*, vol. 4, Article ID Cd009016, 2016.
[20] C. M. House, M. J. Tipton, P. M. Hopkins, and D. Roiz de Sa, "Thermoregulation and markers of muscle breakdown in malignant hyperthermia susceptible volunteers during an acute heat tolerance test," *Journal of Science and Medicine in Sport*, vol. 22, no. 5, pp. 586–590, 2019.
[21] R. Gauer and B. K. Meyers, "Heat-related illnesses," *American Family Physician*, vol. 99, no. 8, pp. 482–489, 2019.
[22] N. Pumchandh, "Monitoring of the bed time body temperature and body weight to prevent the occurrence of heat stroke in the Royal Thai Army recruits, Lopburi Province, Thailand," *Medical Journal of the Medical Association of Thailand*, vol. 95, no. Suppl 5, pp. S1–S5, 2012.
[23] L. Xu, Z.-Y. Tao, J.-Y. Lu et al., "A single-center, prospective, randomized clinical trial to investigate the optimal removal time of the urinary catheter after laparoscopic anterior resection of the rectum: study protocol for a randomized controlled trial," *Trials*, vol. 20, no. 1, p. 133, 2019.
[24] M. Boisson, A. Alaux, T. Kerforne et al., "Intra-operative cutaneous temperature monitoring with zero-heat-flux technique (3M SpotOn) in comparison with oesophageal and arterial temperature," *European Journal of Anaesthesiology*, vol. 35, no. 11, pp. 825–830, 2018.
[25] S. Bayraktar, S. Balcı, and Z. Ince, "The effect of 2 humidifier temperature settings on inspired gas temperatures and the physiological parameters of preterm infants receiving mechanical ventilation therapy," *Advances in Neonatal Care*, vol. 21, no. 4, pp. 308–313, 2021.
[26] R. Magoon, "Precision cardiac anesthesia: welcome aboard!" *Journal of Cardiothoracic and Vascular Anesthesia*, vol. 34, no. 9, pp. 2551-2552, 2020.
[27] J. Daniels and E. Kulstad, "Further mechanistic evidence against luminal esophageal temperature monitoring?" *Journal of Cardiovascular Electrophysiology*, vol. 32, no. 6, pp. 1787-1788, 2021.
[28] M. Alhammoud, J. Oksa, B. Morel, C. Hansen, D. Chastan, and S. Racinais, "Thermoregulation and shivering responses in elite alpine skiers," *European Journal of Sport Science*, vol. 21, no. 3, pp. 400–411, 2021.
[29] H. Kim, S. Kim, M. Lee et al., "Smart patch for skin temperature: preliminary study to evaluate psychometrics and feasibility," *Sensors*, vol. 21, no. 5, 2021.
[30] P. E. A. Oliveira, G. H. M. Salvador, and D. P. Marchi-Salvador, "Malignant hyperthermia in bariatric surgery: a case study with clinical, pathophysiological, biochemical and biophysical correlations," *Journal of Medical Cases*, vol. 11, no. 12, pp. 379–387, 2020.
[31] M. A., Bashaw, "Guideline implementation: preventing hypothermia," *AORN Journal*, vol. 103, no. 3, p. 305, 2016.
[32] R. D. Miller, *Miller's Anesthesia*, p. 2827, Wiley, Hoboken, NJ, USA, 2010.
[33] T. Matsukawa, D. I. Sessler, A. M. Sessler et al., "Heat flow and distribution during induction of general anesthesia," *Anesthesiology*, vol. 82, no. 3, pp. 662–673, 1995.
[34] R. Chava, M. Zviman, F. R. Assis et al., "Effect of high flow transnasal dry air on core body temperature in intubated human subjects," *Resuscitation*, vol. 134, pp. 49–54, 2019.
[35] C. Jessen and G. Feistkorn, "Some characteristics of CT signals in the conscious goat," *American Journal of Physiology*, vol. 247, no. 3 Pt 2, pp. R456–R464, 1984.
[36] N. Columbano, L. R. Duffee, V. Melosu et al., "Determination of minimum alveolar concentration and cardiovascular effects of desflurane in positive-pressure ventilated sheep," *American Journal of Veterinary Research*, vol. 79, no. 7, pp. 727–732, 2018.
[37] N.-A. Hem, J. Phie, L. Chilton, and R. Kinobe, "A volume-pressure tail cuff method for hemodynamic parameters: comparison of restraint and light isoflurane anesthesia in normotensive male Lewis rats," *Journal of Pharmacological and Toxicological Methods*, vol. 100, Article ID 106601, 2019.
[38] M. Rufiange, V. S. Y. Leung, K. Simpson, and D. S. J. Pang, "Pre-warming before general anesthesia with isoflurane delays the onset of hypothermia in rats," *PLoS One*, vol. 15, no. 3, Article ID e0219722, 2020.
[39] K. Ohki, R. Kawano, M. Yoshida, I. Kanosue, and K. Yamamoto, "Normothermia is best achieved by warming above and below with pre-warming adjunct: a comparison of conductive fabric versus forced-air and water," *Surgical Technology International*, vol. 34, pp. 40–45, 2019.
[40] R. Santos, "Randomized clinical study comparing active heating methods for prevention of intra-surgical hypothermia in gastroenterology," *Rev Lat Am Enfermagem*, vol. 27, Article ID e3103, 2019.
[41] H. P. Thapa, A. J. Kerton, and P. J. Peyton, "Comparison of the EasyWarm self-heating blanket with the Cocoon forced-air warming blanket in preventing intraoperative hypothermia," *Anaesthesia & Intensive Care*, vol. 47, no. 2, pp. 169–174, 2019.
[42] K. J. Kaiyala and D. S. Ramsay, "Concentration-related metabolic rate and behavioral thermoregulatory adaptations to serial administrations of nitrous oxide in rats," *PLoS One*, vol. 13, no. 4, Article ID e0194794, 2018.
[43] B. Cobb, Y. Cho, G. Hilton, V. Ting, and B. Carvalho, "Active warming utilizing combined IV fluid and forced-air warming decreases hypothermia and improves maternal comfort during cesarean delivery," *Anesthesia & Analgesia*, vol. 122, no. 5, pp. 1490–1497, 2016.
[44] A. Rajek, R. Greif, and D. I. Sessler, "Effects of epidural anesthesia on thermal sensation," *Regional Anesthesia and Pain Medicine*, vol. 26, no. 6, pp. 527–531, 2001.
[45] T. Matsukawa, A. Kurz, D. I. Sessler, A. R. Bjorksten, B. Merrifield, and C. Cheng, "Propofol linearly reduces the vasoconstriction and shivering thresholds," *Anesthesiology*, vol. 82, no. 5, pp. 1169–1180, 1995.
[46] A. Kurz, J. C. Go, D. I. Sessler, K. Kaer, M. D. Larson, and A. R. Bjorksten, "Alfentanil slightly increases the sweating threshold and markedly reduces the vasoconstriction and shivering thresholds," *Anesthesiology*, vol. 83, no. 2, pp. 293–299, 1995.
[47] N. A. S. Taylor, Å Nykvist, N. Powers, and J. N. Caldwell, "Thermoeffector threshold plasticity: the impact of thermal pre-conditioning on sudomotor, cutaneous vasomotor and thermogenic thresholds," *Journal of Thermal Biology*, vol. 83, pp. 37–46, 2019.

[48] R. Lenhardt, "Body temperature regulation and anesthesia," *Thermoregulation: From Basic Neuroscience to Clinical Neurology, Part II*, vol. 157, pp. 635–644, 2018.
[49] V. D. Hooper, R. Chard, T. Clifford et al., "ASPAN's evidence-based clinical practice guideline for the promotion of perioperative normothermia," *Journal of PeriAnesthesia Nursing*, vol. 24, no. 5, pp. 271–287, 2009.
[50] A. M. Lepkowski and E. D. Maughan, "Introducing NASN's new evidence-based clinical guideline: students with seizures and epilepsy," *NASN School Nurse*, vol. 33, no. 6, pp. 345–350, 2018.
[51] C. B. Stetler, "Proof-based practice and the role of nursing leadership," *The Journal of Nursing Administration*, vol. 28, no. 7-8, pp. 45–53, 1998.
[52] K. A. Eagle, "Guidelines for peri-surgical cardiovascular evaluation for noncardiac surgery. Report of the American College of Cardiology/American heart association task force on practice guidelines (committee on peri-surgical cardiovascular evaluation for noncardiac surgery)," *Journal of the American College of Cardiology*, vol. 27, no. 4, pp. 910–948, 1996.
[53] P. Kiekkas and M. Karga, "Prewarming: preventing intraoperative hypothermia," *British Journal of Perioperative Nursing*, vol. 15, no. 10, pp. 444–451, 2005.
[54] K. K. Good, J. A. Verble, J. Secrest, and B. R. Norwood, "Postoperative hypothermia-The chilling consequences," *AORN Journal*, vol. 83, no. 5, pp. 1054–1066, 2006.
[55] T. L. Weirich, "Hypothermia/warming protocols: why are they not widely used in the OR?" *AORN Journal*, vol. 87, no. 2, pp. 333–344, 2008.
[56] B. Tander, S. Baris, D. Karakaya, E. Ariturk, R. Rizalar, and F. Bernay, "Risk factors influencing inadvertent hypothermia in infants and neonates during anesthesia," *Pediatric Anesthesia*, vol. 15, no. 7, pp. 574–579, 2005.
[57] A. Lewden, A. Nord, B. Bonnet, F. Chauvet, A. Ancel, and D. J. McCafferty, "Body surface rewarming in fully and partially hypothermic king penguins," *Journal of Comparative Physiology B*, vol. 190, no. 5, pp. 597–609, 2020.
[58] D. I. Sessler and M. M. Todd, "Perioperative heat balance," *Anesthesiology*, vol. 92, no. 2, p. 578, 2000.
[59] A. Taguchi and A. Kurz, "Thermal management of the patient: where does the patient lose and/or gain temperature?" *Current Opinion in Anaesthesiology*, vol. 18, no. 6, pp. 632–639, 2005.
[60] W. Koh, M. Chakravarthy, E. Simon et al., "Perioperative temperature management: a survey of 6 Asia-Pacific countries," *BMC Anesthesiology*, vol. 21, no. 1, p. 205, 2021.
[61] A. Ingram and M. Harper, "The health economic benefits of perioperative patient warming for prevention of blood loss and transfusion requirements as a consequence of inadvertent perioperative hypothermia," *Journal of Perioperative Practice*, vol. 28, no. 9, pp. 215–222, 2018.
[62] U. Ayres, "Older people and hypothermia: the role of the anaesthetic nurse," *British Journal of Nursing*, vol. 13, no. 7, pp. 396–403, 2004.
[63] W. Buhre and R. Rossaint, "Perioperative management and monitoring in anaesthesia," *The Lancet*, vol. 362, no. 9398, pp. 1839–1846, 2003.
[64] S. Kongsayreepong, C. Chaibundit, J. Chadpaibool et al., "Predictor of core hypothermia and the surgical intensive care unit," *Anesthesia & Analgesia*, vol. 96, no. 3, pp. 826–833, 2003.
[65] S. Kumar, P. F. Wong, A. C. Melling, and D. J. Leaper, "Effects of perioperative hypothermia and warming in surgical practice," *International Wound Journal*, vol. 2, no. 3, pp. 193–204, 2005.
[66] R. H. Morris and B. R. Wilkey, "The effects of ambient temperature on patient temperature during surgery not involving body cavities," *Anesthesiology*, vol. 32, no. 2, pp. 102–107, 1970.
[67] M. J. Goldberg and C. F. Roe, "Temperature changes during anesthesia and operations," *Archives of Surgery*, vol. 93, no. 2, pp. 365–369, 1966.
[68] J. Pich, "Intravenous nutrients for preventing inadvertent peri-surgical hypothermia in adults," *Journal of Perioperative Practice*, vol. 30, no. 1-2, pp. 11-12, 2020.
[69] P. Alfonsi, S. Bekka, and P. Aegerter, "Prevalence of hypothermia on admission to recovery room remains high despite a large use of forced-air warming devices: findings of a non-randomized observational multicenter and pragmatic study on perioperative hypothermia prevalence in France," *PLoS One*, vol. 14, no. 12, Article ID e0226038, 2019.
[70] Y. Li, H. Liang, and Y. Feng, "Prevalence and multivariable factors associated with inadvertent intraoperative hypothermia in video-assisted thoracoscopic surgery: a single-center retrospective study," *BMC Anesthesiology*, vol. 20, no. 1, p. 25, 2020.
[71] S. M. Burns, M. Wojnakowski, K. Piotrowski, and G. Caraffa, "Unintentional hypothermia: implications for perianesthesia nurses," *Journal of PeriAnesthesia Nursing*, vol. 24, no. 3, pp. 167–176, 2009.
[72] V. D. Wagner, "Unplanned perioperative hypothermia," *AORN Journal*, vol. 83, no. 2, pp. 473–476, 2006.
[73] L. Croke, "Guideline for prevention of hypothermia," *AORN Journal*, vol. 110, no. 1, pp. P8–p10, 2019.
[74] H. Xu, Z. Wang, X. Guan et al., "Safety of intraoperative hypothermia for patients: meta-analyses of randomized controlled trials and observational studies," *BMC Anesthesiology*, vol. 20, no. 1, p. 202, 2020.
[75] S. Collins, M. Budds, C. Raines, and V. Hooper, "Risk factors for perioperative hypothermia: a literature review," *Journal of PeriAnesthesia Nursing*, vol. 34, no. 2, pp. 338–346, 2019.
[76] L. Honkavuo and S. A. K. Loe, "Nurse anesthetists' and operating theater nurses' experiences with inadvertent hypothermia in clinical perioperative nursing care," *Journal of PeriAnesthesia Nursing*, vol. 35, no. 6, pp. 676–681, 2020.
[77] S. Cooper, "The effect of preoperative warming on patients' postoperative temperatures," *AORN Journal*, vol. 83, no. 5, pp. 1073–1084, 2006.

Hindawi
Journal of Healthcare Engineering
Volume 2023, Article ID 9761938, 1 page
https://doi.org/10.1155/2023/9761938

Retraction

Retracted: Analysis of Systolic Blood Pressure Level and Short-Term Variability in Masked Hypertension

Journal of Healthcare Engineering

Received 15 August 2023; Accepted 15 August 2023; Published 16 August 2023

This article has been retracted by Hindawi following an investigation undertaken by the publisher [1]. This investigation has uncovered evidence of one or more of the following indicators of systematic manipulation of the publication process:

(1) Discrepancies in scope
(2) Discrepancies in the description of the research reported
(3) Discrepancies between the availability of data and the research described
(4) Inappropriate citations
(5) Incoherent, meaningless and/or irrelevant content included in the article
(6) Peer-review manipulation

The presence of these indicators undermines our confidence in the integrity of the article's content and we cannot, therefore, vouch for its reliability. Please note that this notice is intended solely to alert readers that the content of this article is unreliable. We have not investigated whether authors were aware of or involved in the systematic manipulation of the publication process.

Wiley and Hindawi regrets that the usual quality checks did not identify these issues before publication and have since put additional measures in place to safeguard research integrity.

We wish to credit our own Research Integrity and Research Publishing teams and anonymous and named external researchers and research integrity experts for contributing to this investigation.

The corresponding author, as the representative of all authors, has been given the opportunity to register their agreement or disagreement to this retraction. We have kept a record of any response received.

References

[1] Y. Hou and B. Liu, "Analysis of Systolic Blood Pressure Level and Short-Term Variability in Masked Hypertension," *Journal of Healthcare Engineering*, vol. 2022, Article ID 8016893, 9 pages, 2022.

Hindawi
Journal of Healthcare Engineering
Volume 2022, Article ID 8016893, 9 pages
https://doi.org/10.1155/2022/8016893

Research Article

Analysis of Systolic Blood Pressure Level and Short-Term Variability in Masked Hypertension

Yinjing Hou and Bo Liu

Department of Geriatrics, Beijing Tongren Hospital, Capital Medical University, Beijing 100730, China

Correspondence should be addressed to Bo Liu; hyj2468@mail.ccmu.edu.cn

Received 14 January 2022; Accepted 2 March 2022; Published 9 April 2022

Academic Editor: Enas Abdulhay

Background. Patients with masked hypertension are at an elevated risk of cardiovascular events and all-cause death. This risk is close to that of sustained hypertension. The mean value and short-term variability of systolic blood pressure are considered to be risk factors for organ damage in hypertension. *Objective*. To investigate the mean value and short-term variability of systolic blood pressure in patients with masked hypertension. *Methods*. According to the results of in-clinic and ambulatory blood pressure measurement, participants were divided into four groups: normotension group, controlled hypertension group, masked hypertension group, and sustained hypertension group. The mean value and short-term variability of systolic blood pressure of masked hypertension group were evaluated by comparison with the other three groups. *Results*. A total of 250 subjects were enrolled, with an average age of 65.46 ± 8.76 years, and 166 (66.4%) were male, including 62 in the normotension group, 78 in the controlled hypertension group, 69 in the masked hypertension group, and 41 in the sustained hypertension group. Compared with the normotension group and controlled hypertension group, the mean value, blood pressure load, standard deviation, and coefficient of variation of systolic blood pressure over 24 hours and during the day and night, were all higher in the masked hypertension group ($P < 0.05$), while the rate of the nocturnal systolic blood pressure decline was lower ($P < 0.05$). There were no statistically significant differences in the above indexes between the masked hypertension group and sustained hypertension group ($P > 0.05$). *Conclusion*. There are higher mean value of systolic blood pressure and greater short-term variability in masked hypertension patients. Identification of masked hypertension is an important challenge in the clinic.

1. Introduction

Masked hypertension (MH) has recently been identified as a unique hypertension phenotype that occurs in both treated and untreated patients. MH is characterized by an elevated blood pressure when the patient is out of the clinic but a normal blood pressure when the patient is in the clinic. MH accounts for at least 15% of people with apparently normal blood pressure in the clinic [1, 2], but reports suggest that this figure may be an underestimate of its prevalence. Because MH patients can be in a state of elevated blood pressure for long periods of time, the clinical outcomes tend to be different from patients with true normotension. In particular, mounting evidence suggests that MH leads to increased risks of organ damages that are similar to those associated with sustained hypertension (SH) [2–4].

Although the harm of MH has been well recognized, limited research studies on the characteristics of systolic blood pressure (SBP) are available. Notably, multiple studies have shown that the elevated SBP impacts the risks of all-cause mortality, heart failure, stroke, and end-stage renal disease more than diastolic blood pressure does [5–7]. Accordingly, SBP tends to be the key target of blood pressure management in official guidelines [1, 2]. The level and variability of SBP are closely related to the progress of arteriosclerosis, which are the main predictive factors in predicting cardiovascular events and all-cause death [5]. Therefore, both the level of SBP and its variability may represent important factors affecting the prognosis of MH.

There are a few studies analyzing the differences of blood pressure variability among different phenotypes of hypertension [8, 9]. However, few studies have focused on the characteristics of SBP in patients with MH. The purpose of this study is to discuss the reasons for higher target organ damage of MH reported in the past by describing the differences in the average value and short-term variability of SBP over 24 hours and during the day and night among patients with normotension, controlled hypertension, MH, and SH.

2. Materials and Methods

2.1. Study Participants. A cross-sectional study was performed. Information was collected from patients hospitalized in Beijing Tongren Hospital whose vitals were stable from July 2020 to July 2021. This study was approved by Beijing Tongren Hospital Ethics Committee (no. TRECKY2021-192).

2.2. Inclusion and Exclusion Criteria. Details on the inclusion and exclusion of participants are shown in Figure 1. The inclusion criteria were as follows: age ≥45 years old, agreed to participate in the trial, and signed the informed consent form. The diagnostic criteria for hypertension were in line with the 2018 European Society of Cardiology/European Society of Hypertension (ESC/ESH) Guidelines for the Management of Arterial Hypertension [1] (hereinafter referred to as guidelines). The exclusion criteria were as follows: (1) diagnosis of SH; (2) glycosylated hemoglobin HbA1c >7.5%; (3) left ventricular ejection fraction ≤50%; (4) previous diagnosis of myocardial infarction and performing percutaneous intervention or coronary artery bypass grafting; (5) heart failure; (6) cerebrovascular disease, including stroke or transient ischemic attack; (7) carotid or cerebral artery revascularization; (8) hyperthyroidism (TSH <0.1 mU/L) or hypothyroidism (TSH >10 mU/L); (9) liver diseases (jaundice hepatitis, or cirrhosis, or liver failure); (10) chronic kidney disease 4 or above (eGFR <30 mL/min/1.73 m^2); (11) severe infectious diseases or autoimmune diseases; and (12) malignant tumors; mental disorders. Participants were constantly enrolled in the study. A total of 250 participants were eligible. All participants were collected a completed medical history survey and underwent laboratory examination and ambulatory blood pressure monitoring.

2.3. Data Collection

2.3.1. Epidemiological Questionnaire. A questionnaire was completed by participants and then verified by the study physician. The questionnaire items included demographic information, educational background, lifestyle (such as physical activities and use of alcohol or tobacco), types of antihypertension drugs and years medications were used, other complications, and family history. The use of alcohol was defined as having consumed alcohol more than 12 times in the past 12 months [10]. Physical activities were defined as at least 150–300 minutes of moderate-intensity aerobic activity per week; or at least 75–150 minutes of high-intensity aerobic activity [11].

2.3.2. Anthropometric and Biochemical Measurements. Standard instruments were used for all measurements. Anthropometry included height, weight, body mass index (BMI), and blood pressure. Biochemical tests included fasting blood glucose (FBG), HbA1c, triglycerides (TG), total cholesterol (TC), high-density lipoprotein cholesterol (HDL-C), and low-density lipoprotein cholesterol (LDL-C). The morning after an overnight fast, blood samples were collected from the forearm vein into vacuum tubes containing EDTA. FBG was measured by the hexokinase method. Determination of cholesterol and triglycerides were performed by enzymatic methods using commercially available kits (Beijing Tongren Hospital Clinical Laboratory).

2.3.3. In-Clinic Blood Pressure Measurements. Participants were instructed to rest in the sitting position for at least 5 minutes prior to measurements. Blood pressure was measured on the same arm throughout the study with a Hem-7051 blood pressure monitor (Omron, Kyoto, Japan). For each measurement, three consecutive blood pressure readings were obtained, and the average of these blood pressure readings was submitted to the clinic.

2.3.4. Twenty-Four-Hour Ambulatory Blood Pressure Monitoring. An ambulatory blood pressure monitor (Vasomedical BIOX Ambulatory Blood Pressure Monitor) was installed on the passive arm of each participant to automatically measure and record blood pressure. In the daytime, it was programmed to perform measurements every 20 minutes between 08:00 and 22:00. In the nighttime, it was programmed to perform measurements every 60 minutes after 22:00. Participants wore the ambulatory blood pressure monitor for 24 hours. If a record contained 70% of the programmed readings, the coverage time was greater than 20 hours and there were at least 20 readings during the day and at least 7 readings during the night, the record was considered effective [2]. Blood pressure values were weighted over the time interval between successive readings.

2.4. Grouping. The participants were divided into four groups according to in-clinic and ambulatory blood pressure values as guided by guidelines [1]. The four groups were assigned as follows. Group 1 was the normotension group: there was no history of hypertension, the blood pressure in the clinic was less than 140/90 mmHg, and the ambulatory blood pressure parameters were not within the range of hypertension. Group

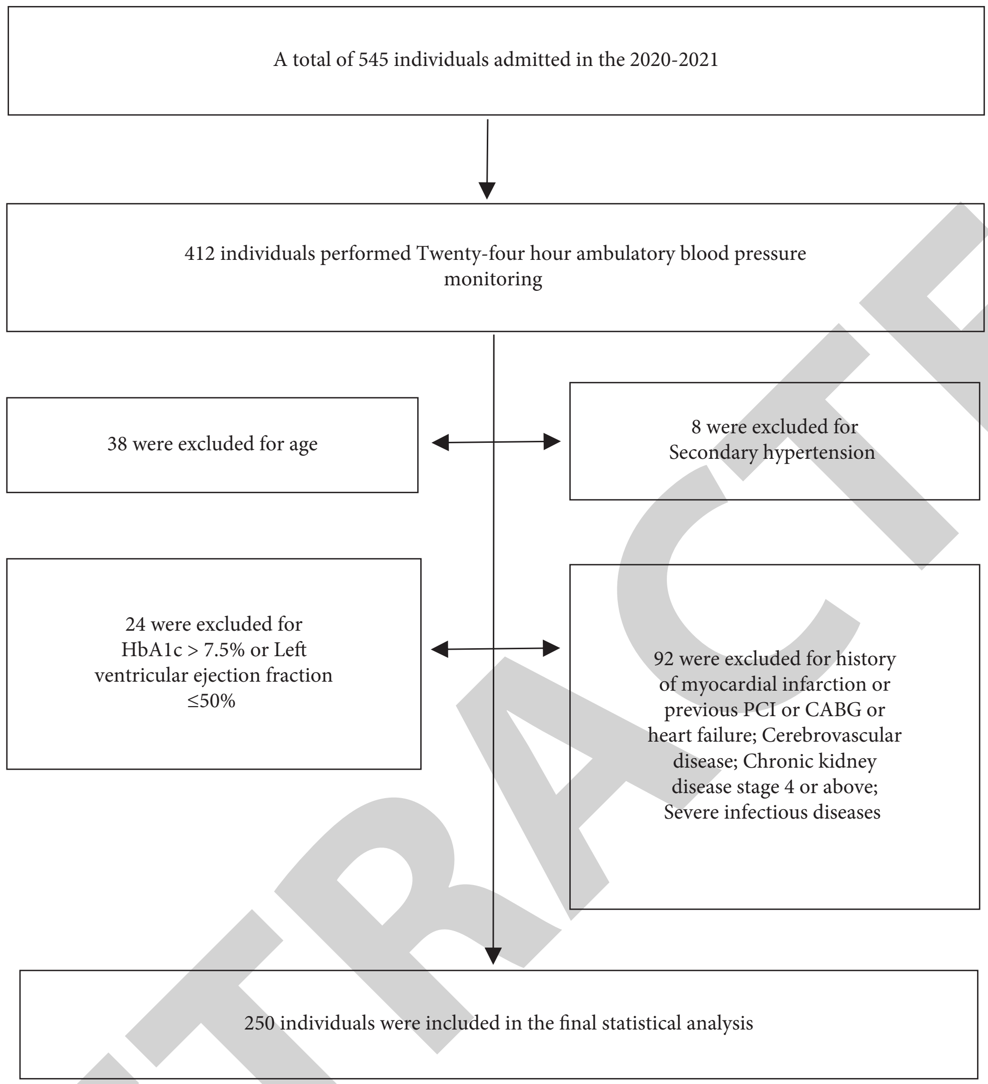

Figure 1: A flow chart of the current study.

2 was the controlled hypertension group: there was a history of hypertension, the blood pressure in the clinic was less than 140/90 mmHg, and the ambulatory blood pressure parameters were not within the range of hypertension. Group 3 was the MH group: the blood pressure in the clinic was less than 140/90 mmHg, and the ambulatory blood pressure parameters were within the range of hypertension. Group 4 was the SH group: the blood pressure in the clinic was greater than 140/90 mmHg, and the ambulatory blood pressure parameters were within the range of hypertension. Specifically, for ambulatory blood pressure parameters to be within the range of hypertension, the 24-hour average blood pressure was at least 130/80 mmHg, or the daytime average blood pressure was at least 135/85 mmHg, or the nighttime average blood pressure was at least 120/70 mmHg.

2.5. Statistical Analysis. The data were recorded by two people and consistency test was carried out. EpiData 3.1 was used to input data. The SPSS 22.0 statistical software was used to process descriptive statistics and difference analyses. Counting data were described by frequency distributions and were analyzed by chi-square tests. After a Kolmogorov–Smirnov normality test, the measurement data conforming to a normal distribution were expressed as $\bar{X} \pm \mathrm{SD}$, and the analysis of variance was used. The data that did not conform to a normal distribution were represented by the M ($Q1$, $Q2$) and were analyzed by the Mann–Whitney U test and the Kruskal–Wallis test. All factors were subjected to bilateral tests. Differences for which $P < 0.05$ were considered to be statistically significant.

3. Results

A total of 250 participants were included in this cross-sectional study. The average age of participants was 65.46 years, and 166 (66.4%) of the participants were male. The normotension group included 62 cases, the controlled hypertension group included 78 cases, the MH group included 69 cases, and the SH group included 41 cases. There were statistically significant differences in age, gender, BMI course of hypertension, number of antihypertension drugs, status of

Table 1: Comparison of baseline data of the four groups.

	Normotension group ($n=62$)	Controlled hypertension group ($n=78$)	Masked hypertension group ($n=69$)	Sustained hypertension group ($n=41$)	$t/Z/\chi^2$	P value
Age (years)	63 (54, 68)	65 (55.8, 74)	63 (57, 71)	75 (60, 77)	10.924	**0.012**
Male gender, n (%)	44 (71.0)	59 (75.6)	37 (53.6)	26 (63.4)	8.778	**0.032**
BMI (kg/m^2)	23.4 (21.6, 25.9)	25.1 (23.4, 26.7)	25.4 (23, 28.2)	25.5 (23.8, 28.3)	12.486	**0.006**
Never smoking, n (%)	31 (50.0)	49 (62.8)	39 (56.5)	29 (70.7)	5.412	0.144
Drinking, n (%)	15 (24.6)	13 (16.7)	19 (27.5)	8 (19.5)	5.677	0.460
Physical exercise, n (%)	55 (90.2)	61 (78.2)	53 (76.8)	33 (80.5)	4.538	0.209
Course of hypertension (years)	-	10 (3.8, 20)	5 (0, 18)	20 (10, 25.5)	123.735	**<0.001**
Number of antihypertension drugs, n (%)					94.635	**<0.001**
0	60 (96.8)	14 (17.9)	31 (44.9)	4 (9.8)		
1	2 (3.2)	23 (29.5)	15 (21.7)	16 (39.0)		
2	0	32 (41.0)	16 (23.2)	15 (36.6)		
3	0	9 (11.5)	6 (8.7)	4 (9.8)		
4	0	0	1 (1.4)	2 (4.9)		
Clinical history, n (%)						
Diabetes	13 (21.0)	32 (41.0)	42 (60.9)	18 (43.9)	21.435	**<0.001**
Hyperlipidemia	42 (67.7)	64 (82.1)	60 (87.0)	33 (80.5)	7.977	**0.046**
Chronic kidney disease	0	5 (6.4)	4 (5.8)	1 (2.4)	4.714	0.164
Hyperuricemia	18 (29.0)	13 (16.7)	8 (11.6)	7 (17.1)	7.001	0.072
Coronary heart disease	13 (21.0)	20 (25.6)	20 (29.0)	10 (24.4)	1.136	0.768
Sleep apnea syndrome	8 (13.1)	16 (20.5)	14 (20.3)	2 (4.9)	6.257	0.100
Laboratory parameters						
TG (mmol/L)	1.2 (0.8, 2)	1.5 (1.1, 2.1)	1.5 (1, 2.1)	1.2 (0.9, 1.6)	8.645	**0.034**
TC (mmol/L)	4.3 (3.7, 5)	4.1 (3.6, 4.5)	4.5 (3.7, 5)	4.1 (3.5, 5)	4.460	0.216
LDL-C (mmol/L)	2.5 (1.8, 3.1)	2.2 (1.8, 2.7)	2.7 (1.8, 3.1)	2.4 (1.8, 2.8)	4.945	0.176
HDL-C (mmol/L)	1.1 (0.9, 1.4)	1 (0.9, 1.2)	1 (0.9, 1.4)	1.1 (0.9, 1.3)	3.927	0.269
FBG (mmol/L)	5.1 (4.8, 5.7)	5.4 (4.9, 6.1)	5.7 (5.2, 7)	5.4 (4.9, 6.4)	13.950	**0.003**
HbA1c (%)	5.7 (5.5, 6.3)	6.1 (5.7, 6.6)	6.3 (5.9, 7)	6.1 (5.9, 6.8)	21.847	**<0.001**

Bold values represent the significant difference.

diabetes, and hyperlipidemia as well as levels of TG, FBG, and HbA1c among the four groups (Table 1).

The SBP parameters of ambulatory blood pressure monitoring among four groups are summarized in Figure 2. The average value, the standard deviation, and the coefficient of variation of SBP in all three time frames (24 hours, daytime, and nighttime) were significantly higher in the MH group compared with both the normotension group and the controlled hypertension group. The blood pressure load over all three time frames was also significantly higher in the MH group compared with both the normotension group and the controlled hypertension group ($P < 0.05$). The rate of the nocturnal SBP decline was lower in the MH group compared with both the normotension group and the controlled hypertension group. The above indexes regarding SBP in the MH group were not statistically different from those in the SH group ($P > 0.05$).

4. Discussion

In this study, we found that, as compared with participants with normal blood pressure or controlled hypertension, those with MH had a higher average value and blood pressure load and a higher standard deviation and coefficient of variation of SBP over all tested time frames. The rate of the nocturnal SBP decline was lower in participants with MH. These results suggest that the level of SBP and its short-term variability during all time periods (including night) are higher in patients with MH than in those with normal blood pressure. These differences support the idea that the blood pressure of people with MH, are in fact different from those of people with truly normal blood pressure. In addition, these differences in blood pressure suggest that their prognosis must be different. Therefore, it is important that we should pay much attention to identifying patients with MH.

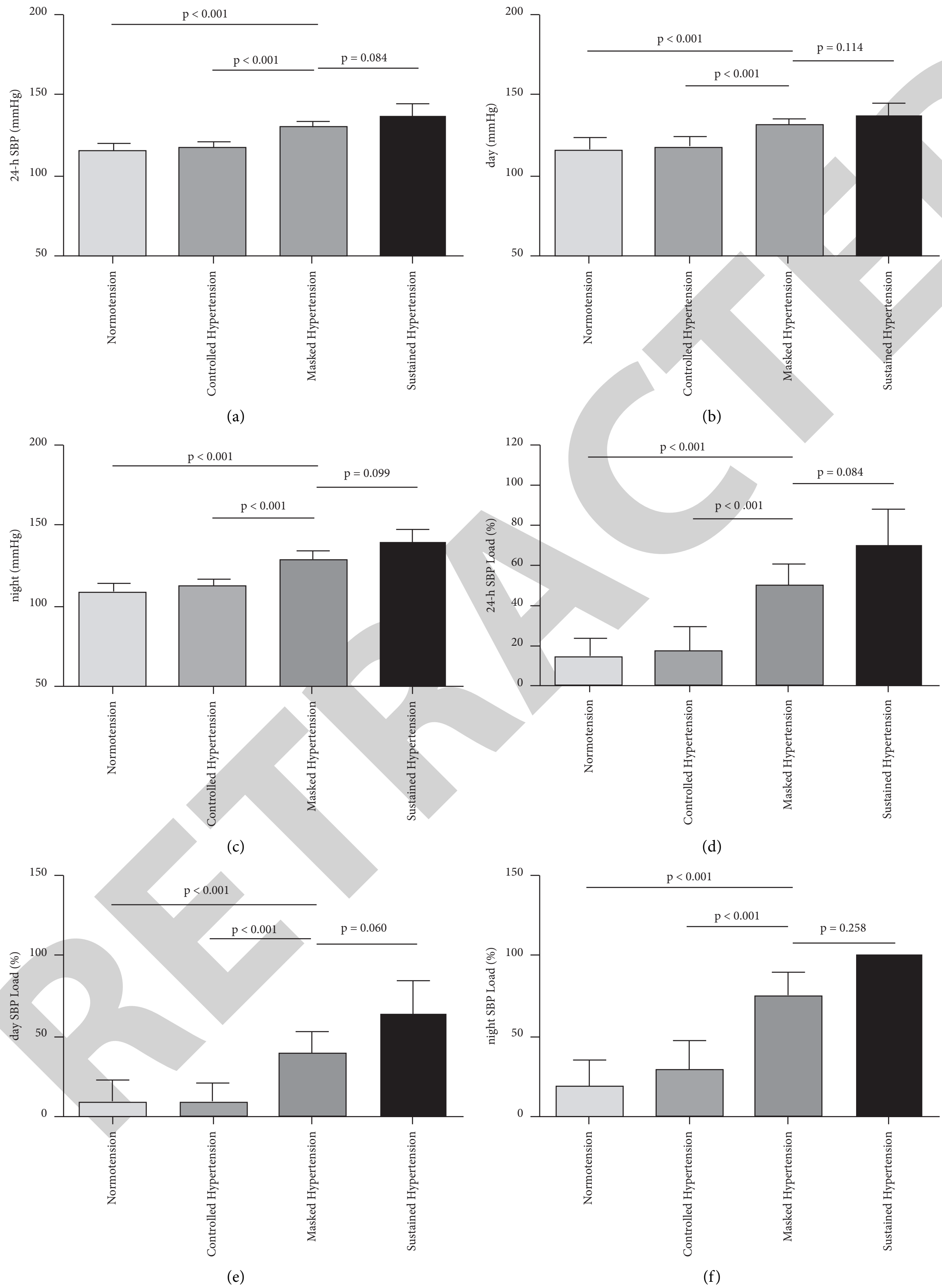

Figure 2: Continued.

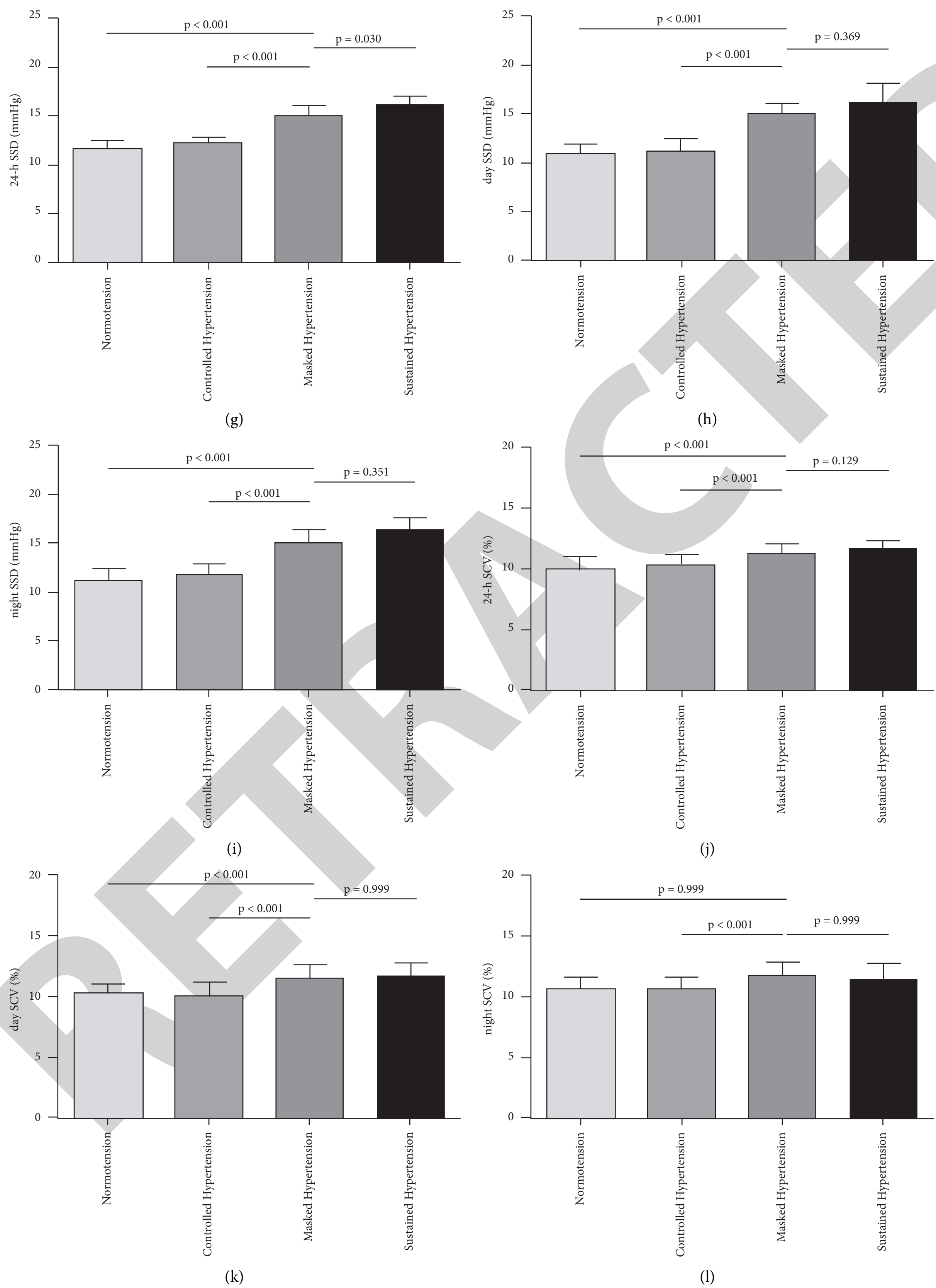

Figure 2: Continued.

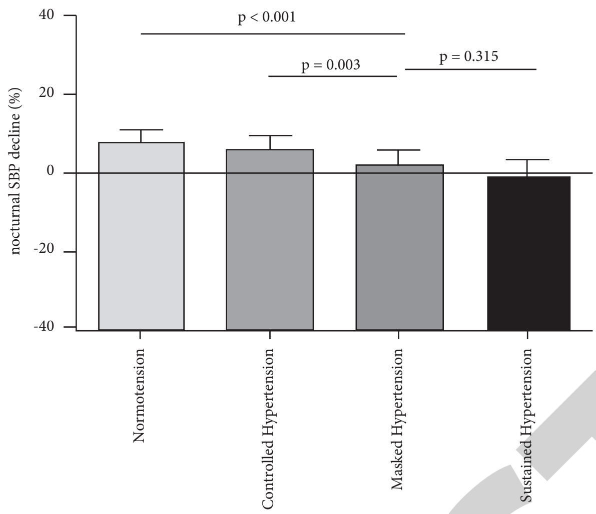

(m)

Figure 2: Comparison of systolic blood pressure parameters of ambulatory blood pressure monitoring in the four groups. (a) 24 h systolic blood pressure, (b) daytime systolic blood pressure, (c) nighttime systolic blood pressure, (d) 24 h systolic blood pressure load, (e) daytime systolic blood pressure load, (f) nighttime systolic blood pressure load, (g) 24 h systolic blood pressure standard deviation, (h) daytime systolic blood pressure standard deviation, (i) nighttime systolic blood pressure standard deviation, (j) 24 h systolic blood pressure coefficient of variation, (k) daytime systolic blood pressure coefficient of variation, (l) nighttime systolic blood pressure coefficient of variation, and (m) nocturnal systolic blood pressure decline rate.

In this study, we found that MH patients had generally a high SBP level, which would be expected to negatively impact blood vessels and to result in subsequent damage to multiple organs. High SBP has also been associated with the progression of arteriosclerosis. For example, in a meta-analysis, after adjusting for demographic indicators, a correlation was found between SBP and arteriosclerosis progression. Specifically, after adjusting for age, patients' pulse wave velocity was shown to increase by 1.14 m/s for every 20 mmHg increase in SBP. However, the correlation between mean arterial pressure or diastolic pressure and pulse wave velocity was weak [5]. Arteriosclerosis plays a key role in hypertension-related clinical outcomes and is a powerful predictor of cardiovascular events and all-cause death [12, 13]. Therefore, current hypertension guidelines identify arteriosclerosis as one of the markers of target organ damage. Similarly, these guidelines commonly advise to reduce arteriosclerosis by drastically lowering blood pressure, mainly SBP, to reduce the occurrence of serious organ damage [1, 2]. An important outcome of this study was that SBP tended to be high in patients with MH both during the daytime and nighttime, and the rate of the nocturnal SBP decline was low. These factors are bound to affect the prognosis of MH patients. Studies have shown that high nighttime blood pressure is more closely associated with risks of cardiovascular events and all-cause death than daytime blood pressure [14–16]. Both lifestyle factors, including work stress and lack of sleep, and biological factors, including metabolic syndrome and sleep apnea syndrome, are MH risk factors that all enhance the activities of nocturnal autonomic nerve, resulting in the increase of nighttime SBP. Therefore, controlling nighttime SBP, via the mitigation of risk factors and the appropriate timing of drug administration, will become one of the keys of MH management in the future.

We also found that MH patients have high SBP variability, which also helped to explain the previously reported high cardiovascular risks in MH patients. Multiple studies have demonstrated the links between SBP variability and risks of coronary heart disease, stroke, end-stage renal disease, and all-cause death that are stronger than SBP itself [17–19]. The blood pressure variability may be affected by both sympathetic regulation and arterial elasticity. The results of this study showed that the variabilities of SBP in the MH group and the SH group were similar, which were consistent with the results of previous studies [8]. It may be explained by a similar disturbance of the regulation of sympathetic function. Siddiqui et al. [17] compared the sympathetic nerve activities of patients with controlled hypertension and those with masked uncontrolled hypertension (MUCH) both in the clinic and out of the clinic. They found that blood pressure variability, urinary catecholamine, and urinary norepinephrine levels out of the clinic were significantly higher in patients with MUCH than those with controlled hypertension. It was therefore speculated that the enhancement of sympathetic nerve activities out of the clinic promoted the development of MUCH. Another study found that sympathetic nerve activities in patients with MH was significantly higher than those with normal blood pressure [20]. These studies showed abnormal sympathetic activities in MH patients that resulted in higher blood pressure variability as compared to patients with normal blood pressure.

On the other hand, although the effect of arteriosclerosis on blood pressure variability is not fully understood, the possibility of an alternate direction of causation cannot be ruled out. A major determinant of blood pressure variability depends on baroreceptor sensitivity [21]. When the vascular structure changes significantly, it may reduce the sensitivity of arterial baroreceptors by limiting the extension of baroreceptors, and the lower sensitivity would be expected to lead to increased blood pressure variability [22, 23]. Moreover, atherosclerosis itself may enhance blood pressure fluctuations associated with small changes in cardiac output. Notably, the inverse relationship between blood pressure variability and baroreceptor sensitivity has not been confirmed by prospective studies. However, no matter the reason, the increase of blood pressure variability in MH patients may cause vascular endothelial dysfunction or injury, promote inflammatory responses and immune activation, and lead to atherosclerosis, ischemic myocardial injury, or damage to target organs [24].

5. Limitations

This study had several limitations. First, the sample size of this study was small, and the participants were recruited from a city where inhabitants tended to receive optimal medical care, potentially leading to a certain survey bias. In the future, we plan to recruit participants from different regions of the country to further verify our conclusions. Second, the participants might have some activities during ambulatory blood pressure monitoring, which may affect the accuracy of the results and lead to a certain measurement bias. It is best to repeat ambulatory blood pressure monitoring in the future to ensure the accuracy of the results.

6. Conclusion

MH is a common state of hypertension. We found that the level and variability of SBP over the course of 24 hours and specifically during the daytime and nighttime in people with MH were higher than those in people with normotension or controlled hypertension. In addition, those indexes in people with MH were similar to people with SH. These findings may help to explain why people with MH have target organ damages that are similar to people with SH. However, it is often difficult to identify MH patients because of normal blood pressure in the clinic, which can lead to a relatively poor prognosis when finally diagnosed. Therefore, it is important to pay much attention to developing strategies to increase the clinical detection rate of MH. Screening, diagnostic, and treatment strategies need to be further explored. The results of this study suggest future studies to explore whether reducing the SBP level and variability in MH patients can improve clinical outcomes.

Data Availability

No data were used to support this study.

Disclosure

The funder had no role in the preparation, review, or approval of the manuscript and decision to submit the manuscript for publication.

Conflicts of Interest

The authors declare that there are no conflicts of interest.

Acknowledgments

The authors thank the funding supported by the Natural Science Research Foundation of Beijing Tongren Hospital, Capital Medical University (grant number 2021-YJJ-ZR-013), and Ministry of Science and Technology (grant no. 2020YFC2005200).

References

[1] B. Williams, G. Mancia, W. Spiering et al., "2018 ESC/ESH Guidelines for the management of arterial hypertension," *European Heart Journal*, vol. 39, no. 33, pp. 3021–3104, 2018.

[2] T. Unger, C. Borghi, F. Charchar et al., "2020 international society of hypertension global hypertension practice guidelines," *Hypertension*, vol. 75, no. 6, pp. 1334–1357, 2020.

[3] S. D. Pierdomenico, A. M. Pierdomenico, F. Coccina et al., "Prognostic value of masked uncontrolled hypertension," *Hypertension*, vol. 72, no. 4, pp. 862–869, 2018.

[4] D.-Y. Zhang, Q.-H. Guo, D.-W. An, Y. Li, and J.-G. Wang, "A comparative meta-analysis of prospective observational studies on masked hypertension and masked uncontrolled hypertension defined by ambulatory and home blood pressure," *Journal of Hypertension*, vol. 37, no. 9, pp. 1775–1785, 2019.

[5] J. Wilson and A. J. S. Webb, "Systolic blood pressure and longitudinal progression of arterial stiffness: a quantitative meta-analysis," *Journal of American Heart Association*, vol. 9, no. 17, Article ID e017804, 2020.

[6] D. E. Rifkin, R. Katz, M. Chonchol et al., "Blood pressure components and decline in kidney function in community-living older adults: the cardiovascular health study," *American Journal of Hypertension*, vol. 26, no. 8, pp. 1037–1044, 2013.

[7] R. Agarwal, "Blood pressure components and the risk for end-stage renal disease and death in chronic kidney disease," *Clinical Journal of the American Society of Nephrology*, vol. 4, no. 4, pp. 830–837, 2009.

[8] T. Gijón-Conde, A. Graciani, E. López-García et al., "Short-term variability and nocturnal decline in ambulatory blood pressure in normotension, white-coat hypertension, masked hypertension and sustained hypertension: a population-based study of older individuals in Spain," *Hypertension Research*, vol. 40, no. 6, pp. 613–619, 2017.

[9] C. Cacciolati, C. Tzourio, and O. Hanon, "Blood pressure variability in elderly persons with white-coat and masked hypertension compared to those with normotension and sustained hypertension," *American Journal of Hypertension*, vol. 26, no. 3, pp. 367–372, 2013.

[10] S. A. Cunningham, A. Mosher, S. E. Judd et al., "Alcohol consumption and incident stroke among older adults," *Journal of Gerontology: Serie Bibliographique*, vol. 73, no. 4, pp. 636–648, 2018.

[11] F. C. Bull, S. S. Al-Ansari, S. Biddle et al., "World Health Organization 2020 guidelines on physical activity and sedentary behaviour," *British Journal of Sports Medicine*, vol. 54, no. 24, pp. 1451–1462, 2020.

[12] G. F. Mitchell, N. Wang, J. N. Palmisano et al., "Hemodynamic correlates of blood pressure across the adult age spectrum," *Circulation*, vol. 122, no. 14, pp. 1379–1386, 2010.

[13] P. Meani, A. Maloberti, P. Sormani et al., "Determinants of carotid-femoral pulse wave velocity progression in

Hindawi
Journal of Healthcare Engineering
Volume 2022, Article ID 8424890, 7 pages
https://doi.org/10.1155/2022/8424890

Research Article

Application of *Anabaena azotica*- and *Chlorella pyrenoidosa*-Based Algal Biotechnology in Green Production of Algae-Rich *Crataegi fructus*

Kangjie Wang[1] **Beijuan Hu**[2] **Chuangang Zheng**[3] **Zhiyi Deng**[4] **Jian Duan**[5] **Kangxi Qin**[6] **Xinwei Cui**[6] **and Shifeng Li**[7]

[1]*Yuncheng Agriculture and Rural Bureau of Shanxi Province, Yuncheng 044099, China*
[2]*Key Laboratory of Poyang Lake Environment and Resource Utilization, Ministry of Education, Nanchang University, Nanchang 330031, China*
[3]*Agriculture Faculty, Xichang University, Xichang 615000, China*
[4]*Shanxi Province Jiangxian County Fruit Industry Development Center, Yuncheng 043699, China*
[5]*Yuncheng Difulai Biotechnology Development Co Ltd., Yuncheng 043699, China*
[6]*Shanxi School-Local Cooperative Microalgae Research Institute, Yuncheng 043699, China*
[7]*Vegetation Restoration Engineering Technology Research Center, China Agricultural University, Beijing 100091, China*

Correspondence should be addressed to Shifeng Li; lsf_68@126.com

Received 18 January 2022; Accepted 24 February 2022; Published 30 March 2022

Academic Editor: Enas Abdulhay

Nitrogen-fixing *Anabaena* and *Chlorella pyrenoidosa* algal biotechnology are known as new agricultural inputs due to their characteristics and are widely used in the field of agricultural planting. This paper discusses the application of algal biotechnology based on nitrogen-fixing *Anabaena* sp. The advantages of algal biotechnology based on nitrogen-fixing *Anabaena* and *Chlorella pyrenoidosa* in terms of yield, sugar content, polyunsaturated fatty acid content, and high-quality yield of hawthorn were compared.

1. Introduction

As for the fruit industry, one of the three major agricultural production industries worldwide [1], its development quality and development level are of great significance to rural revitalization. According to incomplete statistics, the planting area of *Crataegi fructus* has reached 7 million mu in China, accounting for about 10% of the total area of fruit trees planted; the industry scale reached about RMB 20 billion in 2020. *Crataegi fructus*, as a species of edible and medicinal plant, has been widely used in the pharmaceutical industry, food industry and light industry. However, with the continuous expansion of the planting scale, production problems such as the degradation of germplasm resources and increase of group diseases have taken place, especially the significant influence on the quality of *Crataegi fructus* due to the increasing use of fertilizers; therefore, it is urgent to study an ecological, green, efficient, and safe cultivation technology of *Crataegi fructus*, in which, it is quite important to use the new environmentally friendly biotechnology.

Qilipo in Wenxi County and Jiangxian County, Shanxi Province, located in the dominant production area of *Crataegi fructus* in China, have been respectively praised as "The First Village of *Crataegi fructus* Planting in Shanxi" and "The First County of *Crataegi fructus* Planting in China," both of which have planted about 150,000 mu of *Crataegi fructus* [2]. *Crataegi fructus*, as the local specialty product, is also the product protected by geographical indications of agricultural products and the backbone force for the revitalization of rural industries in the new era. In order to further improve the quality and reduce the use of fertilizers and pesticides, the local government has explored the planting technology of algae-rich *Crataegi fructus* based on *Anabaena azotica* and *Chlorella pyrenoidosa* while relying on the Central Geographical Indication Protection Project, following the "Five-Grade Mode" of the high-quality development of characteristic industries, and focusing on the quality [3]. As confirmed, this mode could significantly increase the yield, the content of unsaturated fatty acid, and sugar content, and also reduce the pesticide residue, thus making the quality of *Crataegi fructus* fundamentally different from that of the fruits in other regions. It is of great significance to create a county-specific brand of *Crataegi fructus* and improve the brand value of the product protected by geographical indications of agricultural products and the industrial competitiveness.

2. Selection of Carrier of Biotechnology

Microalgae, a general term for microorganisms, being rich in chlorophyll a and capable of photosynthesis, could absorb heavy metals and inorganic salts from sewage in paddy fields and also degrade organic substances such as pesticides, phenols, and alkanes [4]. The corresponding development and utilization was initiated in the United States, Japan, Germany, Israel, etc. in the 1940s. There are one million species of algae all over the world, over 40,000 of which are known microalgae. At present, the microalgae widely planted or produced with biotechnology mainly include *Chlorella vulgaris*, *Chlorella pyrenoidosa*, nitrogen-fixing blue-green algae, and *Anabaena*. The microalgae could be applied in green production of *Crataegi fructus* based on their own characteristics.

2.1. *Anabaena azotica*

2.1.1. Selection Basis. Strong biological nitrogen fixation of *Anabaena azotica* cells: with the nitrogen-fixing method of ($N_2 + 8e^- + 16MgATP + 8H^+ \longrightarrow 2NH_3 + H_2 + 16\ MgADP + 16Pi$), azotase contained could fix molecular nitrogen in the air and synthesize amino acids and proteins, thus reducing the plant's demand for nitrogen fertilizers by 10%–30% [5]; it could also dissolve the phosphorus fixed in the soil ($Ca_3(PO_4)_2 + CnOnH = H+ + 2PO_4^{3-} + CnOn\ - + 3Ca^{2+}$), and cell secretions can soak into the grid to activate potassium ions for direct absorption by plants so as to prevent the antagonism with other elements in the soil, activate the medium elements and trace elements in the soil, and transport them to the root system, thus promoting the absorption. The rich extracellular polysaccharide colloid EPS and growth stimulating substances could improve soil and improve the fertilizer and water retention capacity of soil.

2.1.2. Mechanism. The reverse carrier system of *Anabaena azotica* cells: The direction of the movement of substances across the membrane is opposite to the direction of ion transfer, namely, when the carrier binds to H+ and then other molecules or ions (such as Na+), they would be transported through the cell membrane in opposite directions. The reverse carrier system could promote the efflux of Na+ and reduce the accumulation of Na+ so as to increase the tolerance of blue-green algae to the salt environment; in addition, it could continuously transfer the extracellular H+ into the cells so as to adjust the balance of the pH value in the cells [6, 7].

2.2. *Chlorella pyrenoidosa*

2.2.1. Selection Basis. Chlorella pyrenoidosa, the microorganism with the largest surface area in the world, has been praised as the "canned sun" by scientists around the world [8]. It could realize photosynthesis under glimmer poor light, and the effect could be over 10 times the photosynthesis of plants. While being able to greatly improve the accumulation of organic matters in plants, provide rich and balanced natural nutrients, and improve the utilization of water by plants, it could also quickly adsorb various heavy metal ions and promote the excretion of harmful substances from plants. The unique active factor (C.G.F.) could repair the damaged cells, activate phagocytes and interferons, induce plant resistance, degrade the residues of pesticides and fertilizers, and convert them into the useable state beneficial to plants [5, 9].

2.2.2. Mechanism. Photosynthesis mechanism of chlorella (see Figure 1): $CO_2 + H_2O = (CH_2O) + O_2$ (conditional enzyme, chlorophyll). At the same time, *Chlorella pyrenoidosa* could make the cellular action of engulf bacteria or viruses active; as the direct user of harmful substances, it could reduce the contents of ammonia nitrogen and nitrite in *Crataegi fructus*. The ability of *Chlorella pyrenoidosa* cells to remove different forms of nitrogen in *Crataegi fructus* can be ordered as follows: ammonia nitrogen > nitrate nitrogen > nitrite nitrogen. The ability to remove different forms of phosphorus can be ordered as follows: orthophosphate > metaphosphate > pyrophosphate > organic phosphate [10].

2.2.3. Kinetic Study. "Severe heavy metal pollution of cultivated land" is one of the practical problems that should be resolved in China at present. The detailed results of the survey on soil pollution of cultivated land indicated that the main pollutants affecting the soil environment and quality of cultivated land were heavy metals, especially cadmium. The study on adsorption kinetics of *Chlorella* indicated that the chemical composition of the cytoderm of *Chlorella pyrenoidosa* had obvious advantages in the adsorption of heavy metals. Cells would continuously release various metabolites into the surrounding environment during growth, such as carbohydrates, amino acids, enzymes, vitamins, organic phosphoric acid, toxins, volatile substances, and inhibitory and promoting factors. As shown in the tracer experiment, at least 5%–10% of the carbon fixed by *Chlorella pyrenoidosa* cells would be released into the waters and soil in the form of DOC, and the value can be up to 10%–25% under better conditions. The adsorption of heavy metals by *Chlorella pyrenoidosa* cells can be ranked as follows: copper > tin > cadmium > nickel > lead > cobalt [11]. By

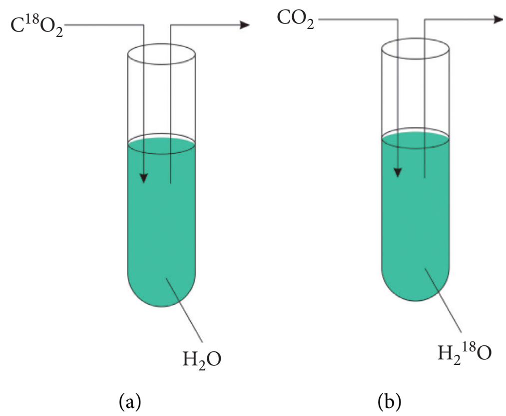

Figure 1: Photosynthesis of *Chlorella*.

means of active adsorption and passive adsorption, the cells can achieve adsorption and passivation of heavy metal ions, thus solving soil pollution of heavy metals.

3. Application Principle of Algae-Rich *Crataegi fructus* Technology Based on *Anabaena azotica* and *Chlorella pyrenoidosa*

3.1. Principle of Cell Fission and Oxygenation. The two kinds of cells would be subject to vegetative propagation and geometric fission after entering the soil. One cell would split into billions of cells in the soil, which would continuously release oxygen; the cell fission and reproduction could increase oxygen and ventilate the soil, thus enabling the original beneficial microorganisms multiply and inhibiting the activity of anaerobic bacteria; and bringing soil back to its original state by vital activity of the cells through increasing the organic matters, which can fundamentally solve the problems such as soil compaction, residual and safety, thus ensuring the natural, organic, nontoxic, and harmless nature of agricultural products.

3.2. Principle of Nutrient Equalization. The planting pattern of algae-rich *Crataegi fructus* based on *Anabaena azotica* and *Chlorella pyrenoidosa* could provide organic nitrogen, dissolve phosphorus, degrade potassium, and activate the medium and trace elements in the soil, thus promoting rapid growth of *Crataegi fructus* and helping to accumulate nutrients. While effectively promoting photosynthesis and providing comprehensive and balanced nutrients for the growth of *Crataegi fructus*, the organic matters generated could effectively adjust the soil acidity and make it neutral [12]. Active cells, with the phototaxis and chemotaxis, would reproduce by fission after entering the soil, thus promoting soil ventilation and water permeability, providing sufficient oxygen and organic nitrogen for soil, dissolving phosphorus and degrading potassium to activate the medium and trace elements in the soil, and help *Crataegi fructus* to accumulate nutrients. While effectively promoting photosynthesis, they could also provide comprehensive and balanced nutrients for the growth of *Crataegi fructus*, thus improving the quality, reduce the use of fertilizer, and realize high yield.

3.3. Principle of Metabolic Promotion. Terpenoids are widely distributed in nature, which could effectively improve the physiological activity of plants in growth metabolism. The planting pattern of algae-rich *Crataegi fructus* based on *Anabaena azotica* and *Chlorella pyrenoidosa* could assist in initiating plant secondary metabolism via the pathway of isoprene pyrophosphate, thus producing terpenoid polymers, which could increase the tolerance of plants to diseases, damage, drought, waterlogging, cold, and continuous cropping, and improve the quality of *Crataegi fructus*. Their application in the planting of *Crataegi fructus* could prolong the shelf life (due to the rich dry matters and increased soluble solids), make the appearance bright, and size uniform.

4. Selection of Manufacturers of Biological Fertilizers and Biotechnology

Yuncheng Biotechnology Development Co., Ltd. is a subsidiary of Microalgae Biological Times (Jilin) Ecological Technology Co., Ltd., a high-tech company integrating R&D, production and sales of algal active cell biological fertilizers. It takes the lead in R&D and application of nitrogen-fixing biological products and has three core technologies, namely metrocyte extraction, culture medium, and cell embedding. The development and application technology of algal active cell compound biofertilizers was evaluated as “domestic leading” by the Science and Technology Development Center of the Ministry of Agriculture, and listed as the main promotion technology by the Ministry of Agriculture in 2015. The production of *Anabaena azotica* and *Chlorella pyrenoidosa*-based biofertilizers adopts the single-cell rapid propagation technology. *Anabaena azotica* and *Chlorella pyrenoidosa* were respectively extracted under the microscope and cytoarchitecture analysis was performed, to select the optimal single-cell chain meeting the requirements as the metrocyte chain. After incubating in test tubes for 5–10 days, the cells were inoculated into a 100 ml flask for cultivating for 5–10 days and then inoculated into an 1-liter triangular flask for cultivating for 5–10 days, a 5-liter triangular flask for cultivating for 5–10 days, a 18-liter barrel for cultivating for 10–20 days, and a 1-ton barrel for cultivating for 20–100 days. The whole process was expanded step by step, with continuous illumination and constant temperature; the water and air should be filtered and purified to the required standard; finally, the amount of *Anabaena azotica* and *Chlorella pyrenoidosa* in biological fertilizers reached 8 million/ML, respectively.

5. Planting Experiment of Algae-Rich *Crataegi fructus* Based on *Anabaena azotica* and *Chlorella pyrenoidosa* in Wenxi County

5.1. Experiment Site and Farmer Information. Site: Duihou Village, Wenxi County, Shanxi Province (*experimental field of Wenxi County Half-mountain Crataegi fructus Planting Cooperative*) (see Figures 2–4).

Name and contact information of the farmer: Li Yuxian, 13834397137.

5.2. Experimental Design. In the treatment group, the soil was treated with *Anabaena azotica* and *Chlorella pyrenoidosa*, and in the control group, the *Crataegi fructus* plants were managed according to the management procedures of *Crataegi fructus* in Wenxi County. After the experiment, the results were compared by soil analysis and quality analysis. In order to ensure the accuracy of experimental results, during the whole growth process, soil tillage, weeding, irrigation, and pest control were carried out normally.

The *Crataegi fructus* experiment set a treatment group and a control group (covering an area of 1 mu), and the experiment was repeated for 3 times. The soil experiment set a treatment group and a control group (covering an area of 1 mu), and the experiment was also repeated for 3 times.

In each treatment and control group, all fruits of the trees in the east, west, south, north, and middle of the field were collected to determine the sugar content, polyunsaturated fatty acids and high-quality fruit rate; and the soil (1,000 cm^3) under these trees was collected for analysis.

5.3. Experimental Materials

5.3.1. Materials. "Dajinxing" *Crataegi fructus* in Duihou Village, Wenxi County, and the soil collected from the field of *Crataegi fructus* in Duihou Village, Wenxi County.

5.3.2. Experimental Materials. Anabaena azotica- and *Chlorella pyrenoidosa*-based biofertilizers were provided by Yuncheng Difulai Biotechnology Co., Ltd., with the single-cell rapid propagation technology, and *Anabaena azotica* and *Chlorella pyrenoidosa* cells reached 8 million/ML, respectively.

5.4. Type of Experimental Treatment.

5.5. Results and Analysis. As shown in Tables 1–3, for *Crataegi fructus* with 200 ml *Anabaena azotica* and *Chlorella pyrenoidosa*, the content of unsaturated fatty acid increased by 0.0041 g/100 g and the sugar content by 1.8% as compared with the control group.

Figure 2: Wenxi experimental field (overall field and performance of Dajinxing treated with biological fertilizers).

Figure 3: Wenxi experimental field (variety performance of Dajinxing treated with biological fertilizers).

Figure 4: Wenxi experimental field (variety performance of Dajinxing without being treated with biological fertilizers).

As shown in Table 4, the content of organic matters was increased by 0.18% in soil treated with 400 ml *Anabaena azotica* and *Chlorella pyrenoidosa*.

6. Experiment Effect of Algae-Rich *Crataegi fructus* Based on *Anabaena azotica* and *Chlorella pyrenoidosa* in Jiangxian County

6.1. Experiment Site and Farmer Information. Site: Zhengchai Village, Jiangxian County, Shanxi Province (see Figures 5–7).

Name and contact information of the farmer: Liu Shanfu 13934396508.

6.2. Experimental Materials

6.2.1. Materials. "Dajinxing" *Crataegi fructus* in Zhengchai Village, Jiangxian County, and the soil collected from the field of *Crataegi fructus* in Zhengchai Village, Jiangxian County.

6.2.2. Experimental materials. Anabaena azotica- and *Chlorella pyrenoidosa*-based biofertilizers were provided by Yuncheng Difulai Biotechnology Co., Ltd., with the single-cell rapid propagation technology, and *Anabaena azotica* and *Chlorella pyrenoidosa* cells reached 8 million/ML, respectively.

Table 1: Treatment of *Crataegi fructus*.

Treatment	Experiment treatment comparison
Treatment	*Anabaena azotica* and *Chlorella pyrenoidosa* + 70% conventional fertilization, once on August 1, 200 ml each of *Anabaena azotica* and *Chlorella pyrenoidosa*
Control	Conventional fertilization

Table 2: Soil treatment.

treatment	Experiment treatment comparison
Treatment	*Anabaena azotica* and *Chlorella pyrenoidosa* + 70% conventional fertilization, once on August 1, 400 ml each of *Anabaena azotica* and *Chlorella pyrenoidosa*
Control	Conventional fertilization

Table 3: *Crataegi fructus* results and analysis.

Item Treatment	Unsaturated fatty acid (g/100 g)	Sugar content (%)	High-quality fruit rate (%)
Treatment	0.0583	17.6	90
Control	0.0542	15.8	85

The detection method of unsaturated fatty acid adopted the first method in GB 5009.168–2016 and that of sugar content adopted the method in GB/T 10786–2006; the fruit greater than 0.15 kg was regarded as a high-quality fruit.

Table 4: Soil results and analysis.

Item Treatment	Sample state	Organic matter (%)
Treatment	Yellowish-brown	1.36
Control	Yellowish-brown	1.18

The detection of organic matters in the soil was performed according to the soil organic matter detection method in NY/T 85–1988 with 50 ml burettes.

Figure 5: Jiangxian experimental field (immature Dajinxing treated with biological fertilizers).

Figure 6: Appearance of "Dajinxing" treated with biological fertilizers.

Figure 7: Appearance of "Dajinxing" without being treated with biological fertilizers (control group).

6.3. Experimental Design. The *Crataegi fructus* experiment set two treatment groups and a control group (covering an area of 1 mu), and the experiment was repeated for 3 times. The soil experiment set two treatment groups and a control group (covering an area of 1 mu), and the experiment was also repeated for 3 times. In order to ensure the accuracy of experimental results, during the whole growth process, soil tillage, weeding, irrigation, and pest control were carried out normally.

In each treatment and control group, all fruits of the trees in the east, west, south, north, and middle of the field were collected to determine the sugar content, polyunsaturated fatty acids, and high-quality fruit rate; and the soil (1,000 cm^3) under these trees was collected for analysis.

Table 5: Treatment of *Crataegi fructus*.

Treatment	Experiment treatment comparison
Treatment 1	*Anabaena azotica* and *Chlorella pyrenoidosa* + 70% conventional fertilization, once on July 6, 200 ml each of *Anabaena azotica* and *Chlorella pyrenoidosa*.
Treatment 2	*Anabaena azotica* and *Chlorella pyrenoidosa* + 70% conventional fertilization, once on July 6, 400 ml each of *Anabaena azotica* and *Chlorella pyrenoidosa*.
Control	Conventional fertilization.

Table 6: Soil treatment.

Treatment	Experiment treatment comparison
Treatment 1	*Anabaena azotica* and *Chlorella pyrenoidosa* + 70% conventional fertilization, once on July 6, 200 ml each of *Anabaena azotica* and *Chlorella pyrenoidosa*.
Treatment 2	*Anabaena azotica* and *Chlorella pyrenoidosa* + 70% conventional fertilization, once on July 6, 600 ml each of *Anabaena azotica* and *Chlorella pyrenoidosa*.
Control	Conventional fertilization.

Table 7: *Crataegi fructus* results and analysis.

Item Treatment	Unsaturated fatty acid (g/100 g)	Diflubenzuron (mg/kg)	Chlordimeform (mg/kg)	Sugar content (%)	High-quality fruit rate (%)
Treatment 1	0.04430	Not detected	Not detected	15.25	91
Treatment 2	0.04735	Not detected	Not detected	15.60	90
Control	0.03890	0.0235	0.00981	14.80	84

Not detected indicated that the value was below the detection limit. The detection method of unsaturated fatty acid adopted the first method in GB 5009.168–2016, which of diflubenzuron and chlordimeform adopted the method in GB/T 20769–2008, and that of sugar content adopted the method in GB/T 10786–2006; the fruit greater than 0.15 kg was regarded as a high-quality fruit.

Table 8: Soil results and analysis.

Item Treatment	Sample state	Organic matter (%)
Treatment 1	Yellowish-brown	1.43
Treatment 2	Yellowish-brown	1.72
Control	Yellowish-brown	1.26

The detection of organic matters in the soil was performed according to the soil organic matter detection method in NY/T 85–1988 with 50 ml burettes.

6.4. Type of Experimental Treatment.

6.5. Results and Analysis. As shown in Tables 5–7, for *Crataegi fructus* with *Anabaena azotica* and *Chlorella pyrenoidosa*, the content of unsaturated fatty acid increased by 0.0054 g/100 g and 0.00845 g/100 g, the contents of diflubenzuron and chlordimeform decreased, and the sugar content increased by 0.45% and 0.80% as compared with the control group.

As shown in Table 8, the contents of organic matters were increased by 0.17% and 0.46% in soil treated with *Anabaena azotica* and *Chlorella pyrenoidosa* as compared with the control group.

7. Conclusion

7.1. Experimental Results. In conclusion, the one-year experiment on 'Dajinxing' treated with *Anabaena azotica* and *Chlorella pyrenoidosa* indicated that the use of *Anabaena azotica* and *Chlorella pyrenoidosa* could significantly reduce the pesticide residue on fruits; improve the appearance and quality of the fruits more significantly as compared with those with the use of chemical fertilizers; increase the content of unsaturated fatty acid, and improve the content of nutrients in the fruits; and obviously increase the content of organic matters in the soil.

7.2. Benefit Estimation. Within the growth cycle of *Crataegi fructus*, fertilization is generally performed twice (base fertilizer + flushing fertilize), with the average fertilizer cost of 500 yuan/mu/year; pesticides are generally sprayed for about 7 times, with the average cost of 350 yuan/mu/year (50 yuan each time); irrigation is generally performed for 4 times, with the average cost of 160 yuan/mu/year (40 yuan each time); therefore, the total cost is 1,100 yuan/mu/year. The cost of algal active cell biological fertilizer is 120 yuan/mu, and as calculated based on the reduction of fertilizers and pesticides by 30% (850×30% = 255), it can help the farmers to reduce the cost of 255–120 = 135 yuan per mu. The experimental results in 2020 and 2021 indicated that after using *Anabaena azotica* and *Chlorella pyrenoidosa*, the *Crataegi fructus* fruits were relatively uniform in size and good in color, and there were much more high-quality fruits. The average yield of 1,500 kg/mu in the experimental area, and the proportion of high-quality fruits without the use of biological fertilizer was about 85%; based on the unit price of high-quality fruits and non-high-quality fruits in the past two years, the benefit of *Crataegi fructus* per mu was 2,685 yuan. After using *Anabaena azotica* and *Chlorella pyrenoidosa*, the proportion of high-quality fruits increased to 90%, and the benefit was 2,790 yuan per mu. Therefore, the application of *Anabaena azotica* and *Chlorella pyrenoidosa* could reduce the cost of 135 yuan and increase the benefit of 105 yuan, with the total cost saving and efficiency increase of about 240 yuan. As calculated based on the area of 150,000 mu in the project area, the direct economic benefit of 36 million yuan could be increased each year. If calculated based on the area of 7 million mu in 2020, the economic benefit of cost saving and efficiency increase would be about 1.68 billion yuan as conservatively estimated; the specific benefits will be further verified and improved in subsequent promotion experiments.

7.3. Recommendations for Future Studies. In future, we will focus on the effects of nitrogen-fixing *Anabaena* and *Chlorella pyrenoidosa* on other fruits such as cherry, apple, and strawberry. If nitrogen-fixing *Anabaena* and *Chlorella pyrenoidosa* do have obvious improvement of content of polyunsaturated fatty acid on other fruits, it will have significant influence on the establishment of Chinese innovative fruit bands.

Data Availability

The datasets used and/or analyzed during the current study are available from the corresponding author on reasonable request.

Conflicts of Interest

The authors declare that they have no conflicts of interest.

References

[1] S. Y. Cao, A. D. Wang, and H. Yuan, "China forestry publishing house," *Atlas of Local Varieties of Crataegi Fructus in China*, 2018.

[2] K. J. Wang, "Shanxi people's publishing house," *Illustration of Agriculture Products Protected by National Geographical Indications in Yuncheng*, 2020.

[3] K. J. Wang, "Analysis on practical path of the innovation theory of "five-grade mode" in high-quality development of agricultural characteristic industries," *Sci-Tech Innovations and Brands*, vol. 11, no. 161, pp. 78–80, 2020.

[4] H. Y. Hu, X. Li, and J. Yang, "Coupling of wastewater deep purification and high quality biomass production based on microalgae cultivation," *Ecology and Environmental Sciences*, vol. 18, no. 3, pp. 1122–1127, 2009.

[5] Y. W. Shen, S. H. Li, S Song, X Xu, Q Ma, and Y Lu, "Sources, migration, accumulation and influence of microplastics in terrestrial plant communities," *Environmental and Experimental Botany*, vol. 192, 2021.

[6] H. Chen and Q. Wang, "Regulatory mechanisms of lipid biosynthesis in microalgae," *Biological Reviews*, vol. 96, no. 5, pp. 2373–2391, 2021.

[7] C. Zhang, X. Liu, C. Liu, and X. Luo, "Characterization of the complete mitochondrial genome of acanthacorydalis fruhstorferi van der Weele (megaloptera: corydalidae)," *Journal of the Kansas Entomological Society*, vol. 93, no. 4, 2021.

[8] X. Q. Chen and Y. C. Su, "Research progress on application of Chlorella," *Biology Teaching*, vol. 37, no. 1, 2012.

[9] M. Yang, Q. Kong, W. Feng, W. Yao, and Q. Wang, "Hierarchical porous nitrogen, oxygen, and phosphorus ternary doped hollow biomass carbon spheres for high-speed and long-life potassium storage," *Carbon energy*, vol. 4, 2021.

[10] Q. X. Kong, "Adsorption of heavy metals by chlorella," Master's thesis, , Master's thesis2016.

[11] S. M. Lee and C. M. Ryu, "Algae as new kids in the beneficial plant microbiome," *Frontiers of Plant Science*, vol. 12, 2021.

[12] L. X. Liu and M. Z. Liang, "An overview of plant secondary metabolism and its products," *Soil and Fertilizer Sciences in China*, vol. 46, no. 5, 2009.

Hindawi
Journal of Healthcare Engineering
Volume 2022, Article ID 9928546, 11 pages
https://doi.org/10.1155/2022/9928546

Research Article

Qi Sui Zhu Shui Plaster Inhibits AQP1 and MAPK Signaling Reduces Liver Damage Induced by Cirrhotic Ascites

Rong Zhen Zhang ,[1] Yin Liu ,[1] Min Li,[2] Yong Lin Huang,[3] and Zhen Heng Song[3]

[1]*Department of Hepatology, The First Affiliated Hospital of Guangxi University of Chinese Medicine, Nanning, China*
[2]*Department of Medical Laboratory, The First Affiliated Hospital of Guangxi University of Chinese Medicine, Nanning, China*
[3]*Department of Hepatology, Guangxi University of Chinese Medicine, Nanning, China*

Correspondence should be addressed to Yin Liu; linwys7@163.com

Received 29 December 2021; Revised 15 February 2022; Accepted 21 February 2022; Published 30 March 2022

Academic Editor: Enas Abdulhay

Objective. At present, there is no special treatment for cirrhotic ascites in modern medicine. Qi Sui Zhu Shui plaster (QSZSP) has been used in ascites. The purpose of this study was to investigate the mechanism of action of QSZSP in the treatment of cirrhotic ascites and its relationship with aquaporin 1 (AQP1). *Methods*. Twenty-four rats were divided into four groups, six rats in each group. Carbon tetrachloride-olive oil is injected into modeling. The control and model groups are treated with blank gel plaster (2 cm × 2 cm), QSZSP low-dose group is treated with Qi Sui Zhu Shui plaster (1 cm × 1 cm), and QSZSP high-dose group is treated with Qi Sui Zhu Shui plaster (2 cm × 2 cm). The changes in body weight and abdominal circumference were measured, the histopathological changes in liver, kidney, and peritoneum were observed in HE staining, the biochemical indexes related to liver function were detected, and the changes in AQP1 expression and the activation of MAPK pathway in the liver, kidney, and peritoneal tissues were evaluated in IHC staining and Western blot. *Results*. After one week of injection of carbon tetrachloride-olive oil, the rats in the model group increased their body weight slowly, the abdominal circumference of the model rats continued to increase with time. After 16 weeks of construction of the cirrhotic ascites model, the liver, kidney, and peritoneum were significantly damaged, and the serum levels of TBiL, AST, ALT, Cr, BUN, K, Na, and Ca in the rats were significantly higher ($P < 0.001$) and ALB levels were significantly lower ($P < 0.001$) than those in the control group. After 4 weeks of treatment, the liver, kidney, and peritoneal injury were improved. TBiL, AST, ALT, Cr, BUN, K, Na, and Ca levels were significantly lower ($P < 0.001$) and ALB levels were significantly higher ($P < 0.001$) than those in the model group. The protein expression of AQP1, p-ERK, p-JNK, and p-p38 was found to be inhibited in the liver, kidney, and peritoneum. *Conclusion*. QSZSP inhibits the protein expression of AQP1 and MAPK signaling pathway in the liver, peritoneum, and kidney to alleviate liver, kidney, and peritoneal injury caused by cirrhotic ascites, thus reducing the abnormal growth of abdominal circumference.

1. Introduction

Cirrhosis is a common clinical disease, which is caused by a series of pathological changes such as degeneration, necrosis, regeneration, and fibrous tissue proliferation of hepatocytes due to the persistent or repeated action of various pathogenic factors on the liver tissues, mainly manifesting as liver function decline [1]. The worldwide prevalence of cirrhosis is unknown. The prevalence of cirrhosis in the United States is about 0.15%–0.27% [2]. 69% of people do not know they have cirrhosis, and diabetes, alcohol abuse, hepatitis C and hepatitis B, being male, and being older are all associated with cirrhosis [3]. Regardless of the etiology, 50% of patients with cirrhosis will develop cirrhotic cardiomyopathy [4]. The 2017 National Vital Statistics Report for the United States reported that approximately 4.5 million adults, or 1.8% of the adult population, have chronic liver disease and cirrhosis. 41,473 people died from chronic liver disease and cirrhosis [5].

Ascites is the most prominent clinical manifestation of cirrhosis. It is the abnormal fluid accumulation in the abdominal cavity. About 60% of patients with compensatory cirrhosis develop abnormal peritoneal fluid accumulation within 10 years of diagnosis high incidence and poor prognosis of cirrhotic ascites, especially refractory ascites, can induce many fatal complications, which seriously affect the quality of life and survival rate of cirrhotic patients [7]. 90% of liver cancer cases are associated with the presence of cirrhosis [8].

Traditional Chinese medicine (TCM) has the effect of blocking or delaying malignancy and has low toxicity [9]. Long-term use of Chinese herbs can reduce the risk of cirrhosis in patients with chronic hepatitis B [10]. Qi Sui Zhu Shui plaster (QSZSP) consists of *Radix Astragali*, *Radix Kansui*, *Radix Aucklandiae*, *Poria*, *Herba Leonuri*, *Radix Salviae miltiorrhizae*, and *Pericarpium Arecae*. A previous clinical study found that QSZSP adjuvant treatment of patients with cirrhotic ascites resulted in improved urine output, 24 h urinary sodium excretion, reduced creatinine and total bilirubin levels, increased albumin content, and improved ascites recurrence rate after 3 months of continuous treatment with QSZSP [11]. There are few studies on QSZSP and cirrhotic ascites. In the history of research on the components in QSZSP and cirrhosis of the liver, Xiaozhang Tie as an adjuvant to primary therapy of cirrhotic ascites is safe [12]. Salviae miltiorrhizae significantly ameliorates cirrhosis and portal hypertension [13]. Further studies are needed on the agents of action of QSZSP in the treatment of cirrhotic ascites.

In 1991, CHIP28 was shown to function as a water channel, and subsequently, CHIP28 was renamed aquaporins [14, 15]. Thirteen aquaporins (AQP0-AQP12) have been identified [16–18]. Aquaporins have three isoforms. The first subtype transports only water molecules, the second subtype transports water molecules, urea, glycerol, etc., and the third subtype transports channels continuously open, without energy consumption or regulation [19–21]. Aquaporin 1 (AQP1) belongs to the first subtype, which exists as a tetramer and allows only water molecules to be transported across the membrane, and it is an independent water channel [22, 23]. The liver, peritoneum, and kidney are the organs in close contact, and AQP1 happens to be distributed in the liver, peritoneum, and kidney [24]. The water content of the human body is 70% of body weight, and abnormal water production-absorption-excretion in the peritoneal cavity is a key factor in the formation of ascites [19]. AQP1 is one of the aquaporins involved only in the transport of water molecules. Ascites in cirrhosis leads to increased accumulation of fluid in the liver, and the excess fluid is transferred to the peritoneum, which does not reabsorb enough water and eventually leads to increased reabsorption of water by the kidney, so AQP1 may be an important intermediate to study the metabolism of ascites.

Initially, cirrhosis leads to decreased liver function and increased fluid accumulation in the abdominal and thoracic cavities, forming ascites [25]. Ascites occurs commonly in cirrhosis [6]. Ascites is the abnormal fluid accumulation in the abdominal cavity [6]. Cirrhotic ascites can lead to kidney dysfunction [26]. In peripheral arterial vasodilation hypothesis, the kidney is involved in all 5 stages of ascites [27]. By linking AQP1 expression in the liver, peritoneum, and kidney, we propose a "liver-peritoneal-kidney" axis in cirrhotic ascites and suggest that it plays a critical role in the formation of cirrhotic ascites. It has been reported that AQP1 is regulated by MEK1/2 inhibitors in glial cells [28]. In prostate cancer cells, AQP1 protein expression levels are regulated by p38MAPK [29]. In human pleural mesothelial cells, peptidoglycan inhibits p38 MAPK regulation of AQP1 protein expression [30]. Therefore, the MAPK pathway would be a direction of AQP1 changes in the "liver-peritoneal-kidney" axis.

The role of QSZSP in the treatment of cirrhotic ascites and its relationship with AQP1 has not been reported yet. We speculate that the "liver-peritoneal-kidney" axis is a functional axis of water metabolism with aquaporins as the common material basis, which is involved in the "production-absorption-excision" of peritoneal fluid and plays a key role in the formation of cirrhotic ascites. The MAPK pathway may mediate QSZSP regulation of AQP1. Therefore, in this study, we treated rats with cirrhotic ascites *in vitro* with QSZSP, observed the histopathological changes in liver, kidney, and peritoneum, and evaluated the changes in AQP1 expression and activation of MAPK pathway in the liver, kidney, and peritoneal tissues to elucidate the effect of QSZSP in treating cirrhotic ascites and its mechanism.

2. Material and Methods

2.1. Regents. The reagents used are as follows: carbon tetrachloride (C805332) from Macklin, olive oil from Yihai Kerry Golden Dragon Fish Cereals, Oils and Foodstuffs Co., Ltd. (China), xylene and absolute ethanol from National Pharmaceutical Group Chemical Reagent Co., Ltd. (China), eosin (E8090) and neutral resin (G8590) from Solarbio (China), and hematoxylin (G1004) from Servicebio.

2.2. Qi Sui Zhu Shui Plaster Process. Qi Sui Zhu Shui plaster consists of Radix Astragali, Radix Kansui, Radix Aucklandiae, Poria, Herba Leonuri, Radix Salviae miltiorrhizae, and Pericarpium Arecae. The above seven Chinese medicines were purchased from the First Affiliated Hospital of Guangxi University of Traditional Chinese Medicine, in accordance with the provisions of the "Chinese Pharmacopoeia" 2010 edition.

12 ml of water is added to each 1 g of Radix Astragali, Poria, and Herba Leonuri and soaked for 30 min, water reflux extraction is repeated 3 times, 1.5 h each time, and the extracts are combined and filtered. 6 ml of 85% ethanol is added to each 1 g of Radix Kansui, Radix Aucklandiae, Radix Salviae miltiorrhizae, and Pericarpium Arecae and soaked for 30 min, water reflux extraction is repeated twice, 1.5 h each time, and the extracts are combined and filtered. The above two extracts were combined and dried under a vacuum to prepare dry powder. The base consists of 60% SodiuM acrylate, 30% carbomer, 10% Aluminium glycinate, and 6 times Glycerine. The penetration enhancer consists of 50% Azone and 50% propylene glycol. The base, penetration enhancer, and dry powder are mixed. Coater (RK-200, Tianjin Ruikang Babu Pharmaceutical Biotechnology Co.,

Ltd.) producing QSZSP is used. The hydrogel paste is prepared by RK-200 hydrogel coating machine (Tianjin Ruikang Babu Pharmaceutical Biotechnology Co.). Each tablet of this product contains Astragalus methyloside ($C_{41}H_{68}O_{14}$) in Radix Astragali, not less than 0.6932 mg, and Euphorbia grandis dienol ($C_{30}H_{50}O$) in Radix Kansui, not less than 1.4766 mg.

2.3. Animal. Animals from three Gorges University, twenty-four rats, male, weighing 200~250 g, were raised under the condition of no specific pathogen (specific pathogen free, SPF). The feeding environment is 22–26°C, 50%–60% of relative humidity. Modeling will begin in two weeks. Carbon tetrachloride-olive oil in 4 : 6 proportion, intraperitoneal injection dose of 3 mL/kg body weight, and injections were given twice a week (the four days and the seven days) for eleven weeks. For the control group, isotonic intraperitoneal injection of an equal amount of olive oil was given. The weight and abdominal circumference are measured before each injection. During the period, distilled water with 75% medical alcohol was used to prepare 10% concentration of drinking water for rats. Finally, four weeks of treatment, the body weight (Table 1), and abdominal circumference (Table 2) of the rats were measured twice a week for 15 weeks.

2.4. Treating and Sampling. Twenty-four rats were divided into four groups, six rats in each group, all rats were dehaired on the abdomen, and the dehairing area was 3 cm × 3 cm. Control group (Con) is treated with blank gel plaster (2 cm × 2 cm); model group (Mod), blank gel plaster (2 cm × 2 cm); QSZSP low-dose group, Qi Sui Zhu Shui plaster (1 cm × 1 cm); and QSZSP high-dose group, Qi Sui Zhu Shui plaster (2 cm × 2 cm). These were applied to the abdominal skin of depilated rats once a day for 6 h for 4 weeks. Carbon tetrachloride-olive oil was injected subcutaneously into the back once a week during treatment to prevent reversal of cirrhosis. After four weeks, the animals were killed by anesthesia and bloodletting. If the animals were not dead, the animals were anesthetized to death with pentobarbital sodium overdose (100 mg/kg). After anesthesia, the animals died without breathing or heartbeat. The filter paper method is used to obtain ascites. The blood from the abdominal aorta is collected and centrifuged, and serum is collected. An appropriate amount of liver tissue, kidney tissue, and peritoneal tissue is cut and fixed with 4% paraformaldehyde. In addition, the tissues of liver, peritoneum, and kidney were stored in an ultra-low-temperature refrigerator at −80°C. The fixed liver, kidney, and peritoneal tissues of rats were dehydrated and embedded in wax. The sections were frozen at −20°C and cut into a thickness of 3 μm, a water bath was used to stretch the sections, the sections were attached to slides, and the sections were stored at 4°C for backup.

2.5. Hematoxylin and Eosin (HE) Staining. The sections were stained in hematoxylin solution for 4 min, followed by rinsing with running tap water for 2 min and 15 s. The sections were then counterstained with eosin solution for 3 min. Cleaning was carried out at 80% and 95% ethanol, respectively, for 30 s each. The sections were then cleared in xylene for 3 s and mounted with neutral balsam. After staining, the sections were observed using a microscope, and Leica Application Suite was used to collect and analyze the relevant parts of the samples.

2.6. Biochemical Analysis. After the serum samples were thawed at 4°C, the serum samples were detected by Shenzhen Mindray BS420 Automatic Biochemical Analyzer, and TBiL, AST, ALT, ALB, Cr, BUN, K, Na, and Ca concentrations were determined with the Shenzhen Mairui (Shenzhen, China) Matching Biochemical Kit.

2.7. Immunohistochemical Staining. The protein expression of AQP1 in the liver, peritoneum, and kidney tissues was examined by immunohistochemistry. The slides were baked at 65°C for 1 h, soaked in xylene for 30 min, and hydrated in gradient alcohol. 1 mM Tris-EDTA buffer solution (G1203, Servicebio) was used for 18 min repair at 125°C and 103 kPa, incubated with 3% H_2O_2 (National Pharmaceutical Group Chemical Reagent Co., Ltd., China) for 10 min, incubated with 10% goat serum (SL038, Solarbio) for 30 min, and titrated with primary antibody AQP1 (PAB45863, Bioswamp), peritoneum dilution 1 : 250, and liver and kidney dilution 1 : 400 at 4°C overnight. The sections were transferred from 4°C to room temperature and left for 45 min. Treated with Max Vision TM HRP-Polymer anti-Rabbit secondary antibody (KIT-5020, MXB) for 60 min at 37°C. Treated with DAB (DA1010, Solarbio) until the sections change color. Soak the sections in turn, hematoxylin 3 min, 75% alcohol 5 min, 85% alcohol 5 min, 95% alcohol 5 min, 100% alcohol 10 min, xylene 10 min. Neutral resins seal sections. Leica Application Suite image system was used to capture the relevant parts of the sample. The nuclei were stained blue with hematoxylin, and the DAB showed positive brownish yellow.

2.8. Western Blot. The protein levels of p38, p-p38, ERK1/2, p-ERK1/2, JNK1/2/3, p-JNK1/2/3, and AQP1 in the liver, peritoneum, and kidney tissues were analyzed by Western blot. Tissue samples were homogenized in RIPA lysate (R0010, Solarbio) containing protease inhibitor at 4°C and centrifuged at 12000 g for 15 min. The concentration of the proteins was measured using the BCA Protein Assay Kit (PC0020, Solarbio). Proteins (20 μg) were separated by 12% sodium dodecyl sulfate-polyacrylamide gel electrophoresis and transferred onto polyvinylidene fluoride membranes (IPVH00010, Millipore). The membranes were blocked with 5% skim milk for 2 h at room temperature in Tris-buffered saline and incubated with primary antibodies against p-ERK1/2 (ab214036), JNK1/2/3 (ab208035), p-JNK1/2/3 (ab76572), and p-p38 (ab47363) from Abcam (UK), and ERK1/2 (MAB37123), p38 (PAB37381), AQP1 (PAB45863), and GAPDH (PAB36269) from Bioswamp (China), overnight at 4°C. GAPDH antibody (PAB36269, Bioswamp) was

Table 1: The changes in body weight (g) during 15 weeks.

Time (week)	Con	Mod	QSZSP low dose	QSZSP high dose
2	240.62 ± 8.76	231.97 ± 7.16	239.07 ± 8.88	241.32 ± 6.00
2.5	274.57 ± 13.79	244.28 ± 10.14	242.30 ± 14.88	246.90 ± 9.78
3	306.48 ± 11.66	240.08 ± 10.87	253.33 ± 20.08	250.90 ± 17.92
3.5	337.52 ± 13.11	244.98 ± 10.41	264.48 ± 14.18	252.92 ± 16.52
4	373.97 ± 13.15	246.87 ± 15.24	269.18 ± 22.74	262.25 ± 24.54
4.5	408.90 ± 14.12	259.20 ± 13.81	272.98 ± 14.06	262.88 ± 28.43
5	406.57 ± 14.39	263.95 ± 14.27	275.33 ± 15.39	265.90 ± 30.20
5.5	411.27 ± 18.97	266.62 ± 19.88	283.02 ± 14.66	269.65 ± 32.02
6	418.87 ± 19.39	267.30 ± 26.75	278.12 ± 19.41	265.18 ± 33.80
6.5	420.77 ± 23.51	270.97 ± 29.79	281.47 ± 18.66	267.65 ± 33.37
7	438.87 ± 24.75	266.90 ± 26.26	284.62 ± 22.64	269.08 ± 36.85
7.5	445.37 ± 30.10	275.10 ± 21.13	288.15 ± 20.96	271.12 ± 35.28
8	456.02 ± 34.16	279.10 ± 19.79	289.05 ± 14.94	267.52 ± 29.48
8.5	461.45 ± 39.24	277.60 ± 21.83	292.28 ± 17.86	272.82 ± 27.29
9	474.13 ± 43.54	282.35 ± 24.55	294.52 ± 20.95	270.83 ± 30.05
9.5	476.95 ± 45.68	285.43 ± 25.48	293.98 ± 17.88	273.87 ± 23.30
10	482.80 ± 38.05	283.07 ± 25.10	289.20 ± 19.57	273.80 ± 25.58
10.5	498.40 ± 37.98	279.98 ± 24.91	283.63 ± 27.88	268.77 ± 22.97
11	500.08 ± 34.11	276.07 ± 26.91	273.55 ± 27.04	273.88 ± 27.42
11.5	515.92 ± 40.80	275.50 ± 22.32	272.35 ± 33.01	276.53 ± 32.26
12	524.85 ± 38.18	274.00 ± 26.76	276.17 ± 27.98	272.23 ± 32.27
12.5	537.27 ± 36.80	271.18 ± 28.56	270.63 ± 25.96	272.13 ± 28.11
13	566.72 ± 37.67	284.08 ± 30.70	282.43 ± 29.67	301.62 ± 23.60
14	583.90 ± 34.03	296.22 ± 33.35	294.28 ± 33.14	329.77 ± 27.03
15	612.17 ± 41.29	332.53 ± 18.22	339.03 ± 10.94	394.83 ± 13.66
16	632.90 ± 42.57	341.47 ± 15.02	362.20 ± 9.71	427.40 ± 11.89

Data presented as mean ± standard deviation.

Table 2: The changes in abdominal circumference (mm) during 15 weeks.

Time(week)	Con	Mod	QSZSP low dose	QSZSP high dose
2	86.82 ± 10.10	83.42 ± 6.08	83.97 ± 2.57	88.95 ± 5.24
2.5	97.93 ± 8.89	91.67 ± 7.76	91.50 ± 3.84	88.97 ± 7.59
3	107.78 ± 7.12	84.52 ± 8.14	92.47 ± 8.92	91.57 ± 9.15
3.5	116.95 ± 8.95	92.30 ± 7.04	94.78 ± 7.58	93.72 ± 9.83
4	130.27 ± 8.90	97.50 ± 7.68	104.23 ± 6.31	98.73 ± 9.81
4.5	150.05 ± 12.11	100.03 ± 7.61	106.33 ± 4.13	103.20 ± 15.95
5	144.35 ± 14.13	108.78 ± 10.27	110.85 ± 7.32	108.58 ± 15.77
5.5	142.02 ± 11.11	110.63 ± 10.71	115.10 ± 8.89	111.40 ± 17.23
6	157.02 ± 9.70	109.18 ± 9.64	119.68 ± 10.69	115.10 ± 14.29
6.5	154.47 ± 13.95	116.42 ± 14.45	116.17 ± 8.02	112.65 ± 13.56
7	149.68 ± 8.13	114.72 ± 16.26	120.90 ± 11.55	114.57 ± 20.11
7.5	165.20 ± 12.73	124.82 ± 16.89	123.07 ± 12.84	118.77 ± 16.80
8	171.13 ± 7.42	125.50 ± 14.24	123.18 ± 9.90	120.28 ± 13.06
8.5	168.32 ± 22.96	136.28 ± 13.62	141.88 ± 11.82	124.18 ± 14.54
9	166.77 ± 25.63	137.53 ± 11.23	139.52 ± 6.78	128.63 ± 15.32
9.5	175.60 ± 19.28	137.00 ± 9.18	145.05 ± 6.80	127.73 ± 16.29
10	162.43 ± 13.10	140.27 ± 17.08	142.58 ± 9.35	134.80 ± 15.86
10.5	167.73 ± 12.37	143.18 ± 17.91	137.97 ± 15.70	132.43 ± 11.86
11	170.40 ± 17.75	133.67 ± 16.74	129.23 ± 13.34	135.38 ± 8.86
11.5	174.67 ± 16.79	131.15 ± 12.09	139.08 ± 15.77	130.03 ± 21.11
12	176.17 ± 18.18	131.75 ± 20.23	142.13 ± 18.74	137.10 ± 17.83
12.5	183.68 ± 16.49	132.83 ± 11.32	130.85 ± 19.06	135.52 ± 15.62
13	190.35 ± 20.90	155.17 ± 17.92	153.37 ± 12.49	149.97 ± 14.59
14	192.75 ± 16.63	170.27 ± 20.43	164.73 ± 11.44	161.17 ± 16.53
15	211.00 ± 14.26	198.93 ± 6.09	181.20 ± 8.63	177.73 ± 18.77
16	214.10 ± 17.34	213.80 ± 3.89	189.43 ± 7.17	185.03 ± 17.42

Data presented as mean ± standard deviation.

selected as an internal reference. All of the primary antibody dilution ratio is 1 : 1000. The membranes were then washed with Tris-buffered saline and incubated in goat anti-rabbit IgG secondary antibody (SAB43714, Bioswamp, 1 : 20000) for 2 h at room temperature. Immunoreactivity was visualized by the colorimetric reaction using Immobilon Western HRP (WBKLS0500, Millipore). The membranes were scanned with an Automatic Chemiluminescence Analyzer (Tanon 5200, Tanon).

2.9. Statistical Analyses. Statistical analyses were performed using SPSS 23.0 software. All data were presented as mean ± standard deviation (SD). Comparisons between the two groups were made using the independent-samples *t*-tests. The one-way ANOVA was used to compare differences among three or more groups, and the *post hoc* Fisher's least significant difference (LSD) test was used for the individual group comparisons. The values of $P < 0.05$ were considered statistically significant.

3. Results

3.1. Cirrhotic Ascites Lesions. As shown in Figure 1(a), the nucleus is stained with hematoxylin in a distinct blue color. The components in the cytoplasm and extracellular matrix were stained with eosin in different shades of red. The hepatocytes in the model group all showed steatosis, the pseudolobular structures were obvious in the fourth-week samples, and the sixth-week samples showed sclerotic necrotic features with disorganized hepatocyte arrangement, hepatocyte degeneration and necrosis, obvious proliferation of fibrous connective tissue, and extensive formation of pseudolobular structures. After ten weeks plus three days of carbon tetrachloride-olive oil injection, the rats in the model group increased their body weight slowly, and after the first week, a significant difference in body weight began to appear between the control group and the model group ($P < 0.001$), and the abdominal circumference coefficient (abdominal circumference/body weight) was calculated and found that the rats in the control group increased their abdominal circumference and body weight normally. On the contrary, the abdominal circumference of the model rats continued to increase with time. The increase in abdominal circumference was significantly greater in the model group than that in the control group at week 3 (Figure 1(b)). Thus, cirrhotic ascites can lead to an abnormal increase in abdominal girth and severe damage to the liver in rats.

3.2. QSZSP Alleviates Visceral Damage Caused by Cirrhotic Ascites. As shown in Figure 2, in the cirrhosis model group, the liver structure was disturbed and extensive vacuolar-like degeneration could be seen, and kidney tissue damage, glomerular hypertrophy, increase in the stroma of the thylakoid region, inflammatory cell infiltration, glomerular epithelial cell detachment, and the kidney tubules were dilated; peritoneal mesothelial cells were increased, the submesothelial stroma was thickened, and the peritoneal tissue was thickened. After four weeks of treatment with high-dose QSZSP, the liver tissue structure was basically intact, with centered nuclei and red-stained cytoplasm; most of the glomeruli had normal structure and normal tubules; peritoneal mesothelial cells were shed, and peritoneal tissue thickness was reduced compared with the model group.

3.3. QSZSP Regulates Liver Function-Related Factors in Rats with Cirrhotic Ascites. As shown in Figure 3, the concentrations of TBiL, AST, ALT, Cr, BUN, K, Na, and Ca in the model group were significantly higher ($P < 0.001$) than those in the control group and were significantly reduced after treatment with high doses of QSZSP. The concentrations of ALB in the model group were significantly lower ($P < 0.001$) than those in the control group, and their concentrations were significantly increased ($P < 0.001$) after treatment with a high dose of QSZSP. Combining the above two results, it can be found that QSZSP has the ability to modulate liver function-related factors to alleviate liver, kidney, and peritoneal damage caused by cirrhotic ascites.

3.4. QSZSP Regulates AQP1 Protein Expression in the Liver, Kidney, and Peritoneum. As shown in Figure 4, cirrhotic ascites leads to abnormally high expression of AQP1 protein in the liver, kidney, and peritoneum of rats ($P < 0.001$). Compared with the model group, AQP1 protein expression was reduced after treatment with a low dose of QSZSP and significantly reduced ($P < 0.001$) after treatment with a high dose of QSZSP, but AQP1 protein expression in the liver, kidney, and peritoneum was still higher than that in the control group at this time. QSZSP was able to inhibit AQP1 protein high expression caused by cirrhotic ascites.

3.5. QSZSP Inhibits the MAPK Signaling Pathway. As shown in Figure 5, the activation of p-ERK, p-JNK, and p-p38 in the model group was detected simultaneously in the liver, kidney, and peritoneum. The protein expression of p-ERK, p-JNK, and p-p38 was reduced after QSZSP treatment, and p-ERK, p-JNK, and p-p38 protein expression levels were significantly lower ($P < 0.001$) after a high-dose QSZSP treatment than those in the model group.

3.6. QSZSP Induces Abdomen Circumference in Rats with Cirrhotic Ascites. As shown in Figure 6, after four weeks of treatment, the model group's rat body weight is always lower than the other three groups, and after treatment with QSZSP at high dose, rats with cirrhotic ascites showed a significant increase in body weight, and the body weight of rats in the QSZSP low-dose treatment group was also higher than that of the model group (Figure 6(a)). Interestingly, the rats in the QSZSP high-dose group showed a decreasing trend in abdominal circumference along with an increase in body weight, and after four weeks of treatment, the rats in the QSZSP high-dose group were significantly lower than the model group. Combined with the results of HE staining, it could indicate that QSZSP alleviated the organ damage caused by cirrhotic ascites and reduced the abnormal growth of abdominal circumference.

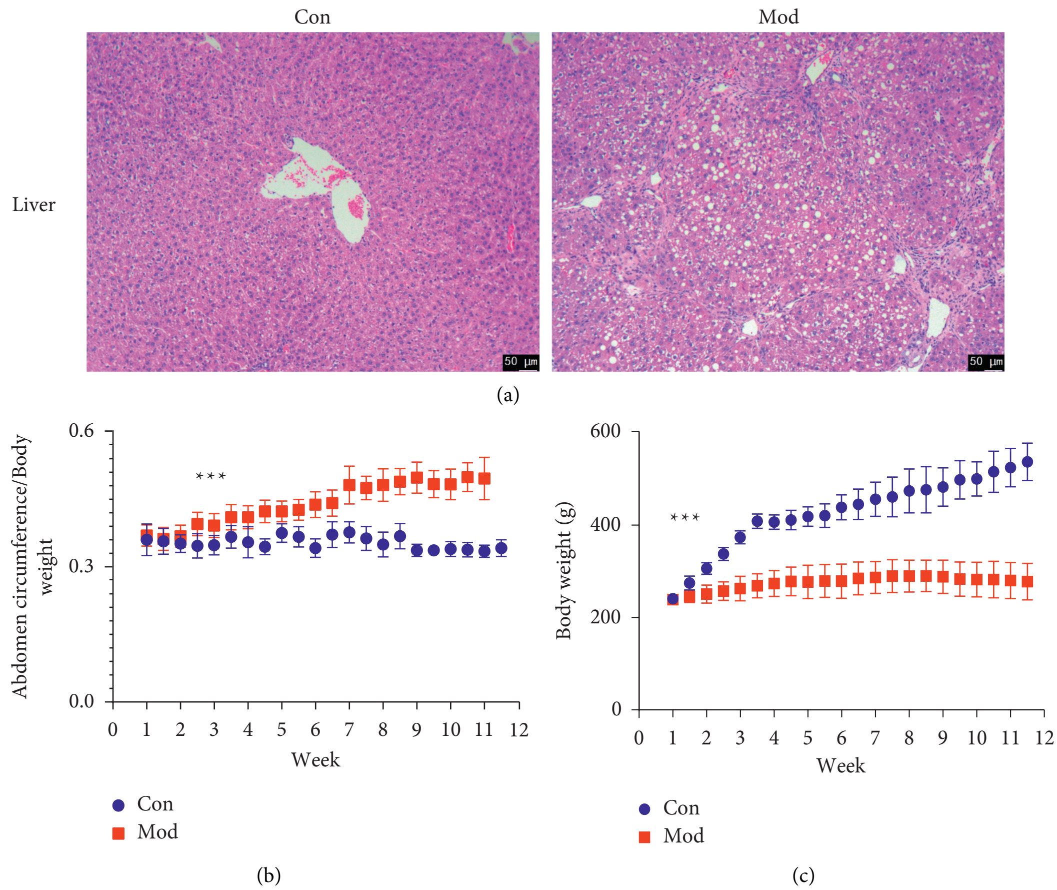

Figure 1: Cirrhotic ascites lesions. (a) HE staining of liver tissue at the fourteenth week (×100). (b) Abdominal circumference index (abdominal circumference/body weight) during modeling. (c) Body weight during modeling. Scale bar = 50 μm. $^{***}P < 0.001$ Con vs. Mod.

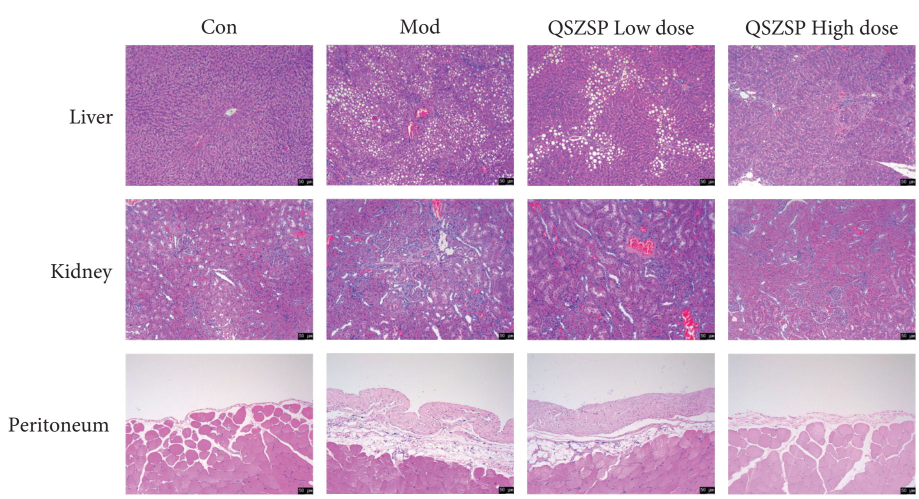

Figure 2: Tissues of liver, kidney, and peritoneum HE staining (×100). Scale bar = 50 μm.

4. Discussion

Cirrhosis ascites is a pathological phenomenon of fluid accumulation in the abdominal cavity caused by a combination of factors during the decompensated phase of cirrhosis and is the most common first event in the decompensated phase of cirrhosis. It not only brings unbearable pain to patients with liver disease and significantly reduces the quality of life, but also causes water-electrolyte disorders and deterioration of the body's internal environment, which can lead to serious complications such as liver encephalopathy, upper gastrointestinal bleeding, and hepatorenal syndrome, and is one of the main factors leading to death in patients with liver disease [31, 32]. Studies have

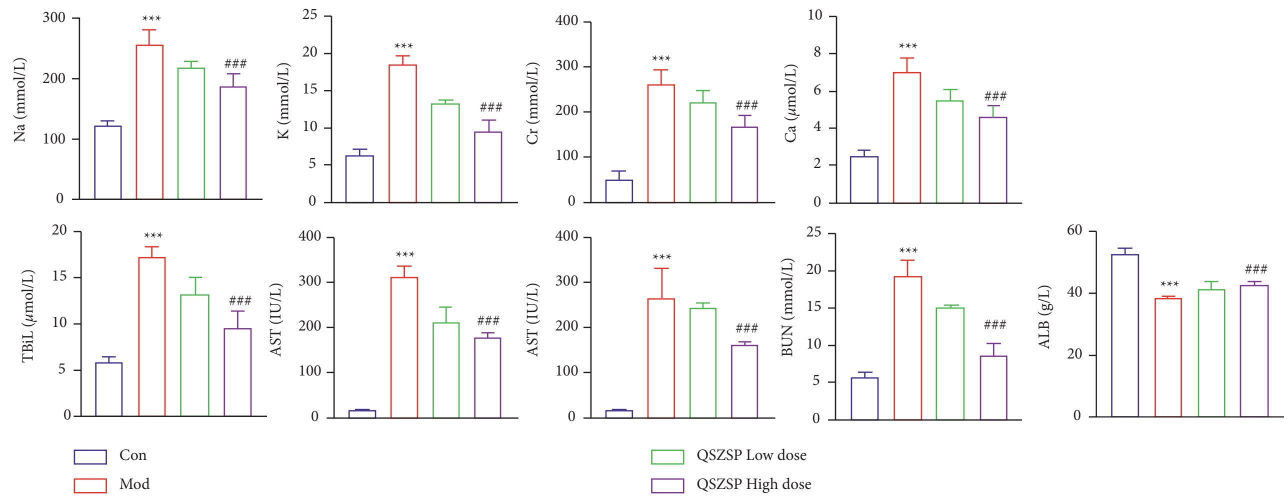

FIGURE 3: Concentrations of TBiL, AST, ALT, Cr, BUN, K, Na, Ca, and ALB in different treatment groups.

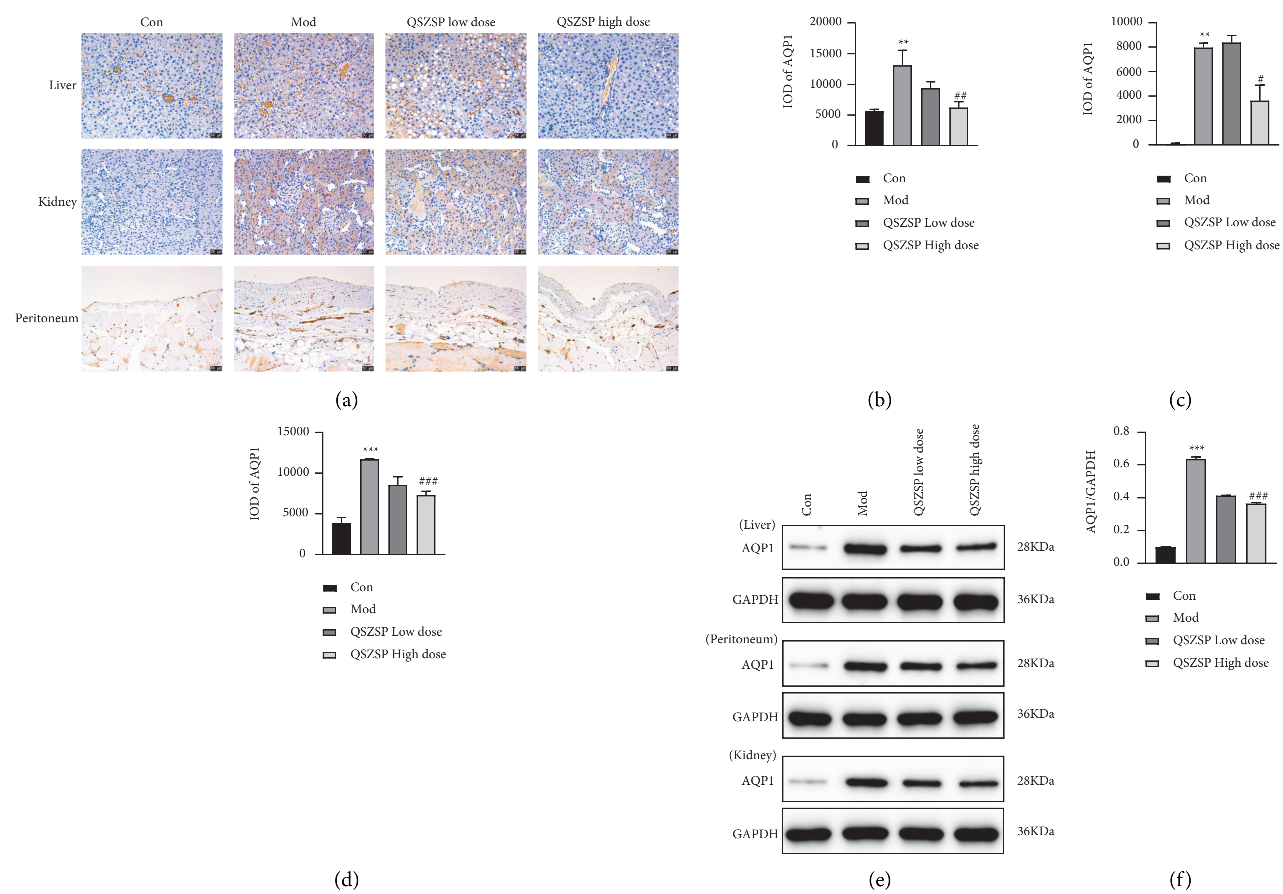

FIGURE 4: Continued.

Figure 4: QSZSP inhibits AQP1 protein expression in the liver, kidney, and peritoneum of cirrhotic ascites. (a) Expression of AQP1 protein in IHC staining (×100). Scale bar = 50 μm. (b) IOD of AQP1 in the liver. (c) IOD of AQP1 in the kidney. (d) IOD of AQP1 in the peritoneum. (e) Expression of AQP1 protein in Western blot. (f–h) Relative expression of AQP1 protein in the liver, peritoneum, and kidney, and GAPDH is loading control. $^{**}P < 0.01$ vs. Con, $^{***}P < 0.001$ vs. Con, $^{\#\#}P < 0.01$ vs. Mod, $^{\#\#\#}P < 0.001$ vs. Mod.

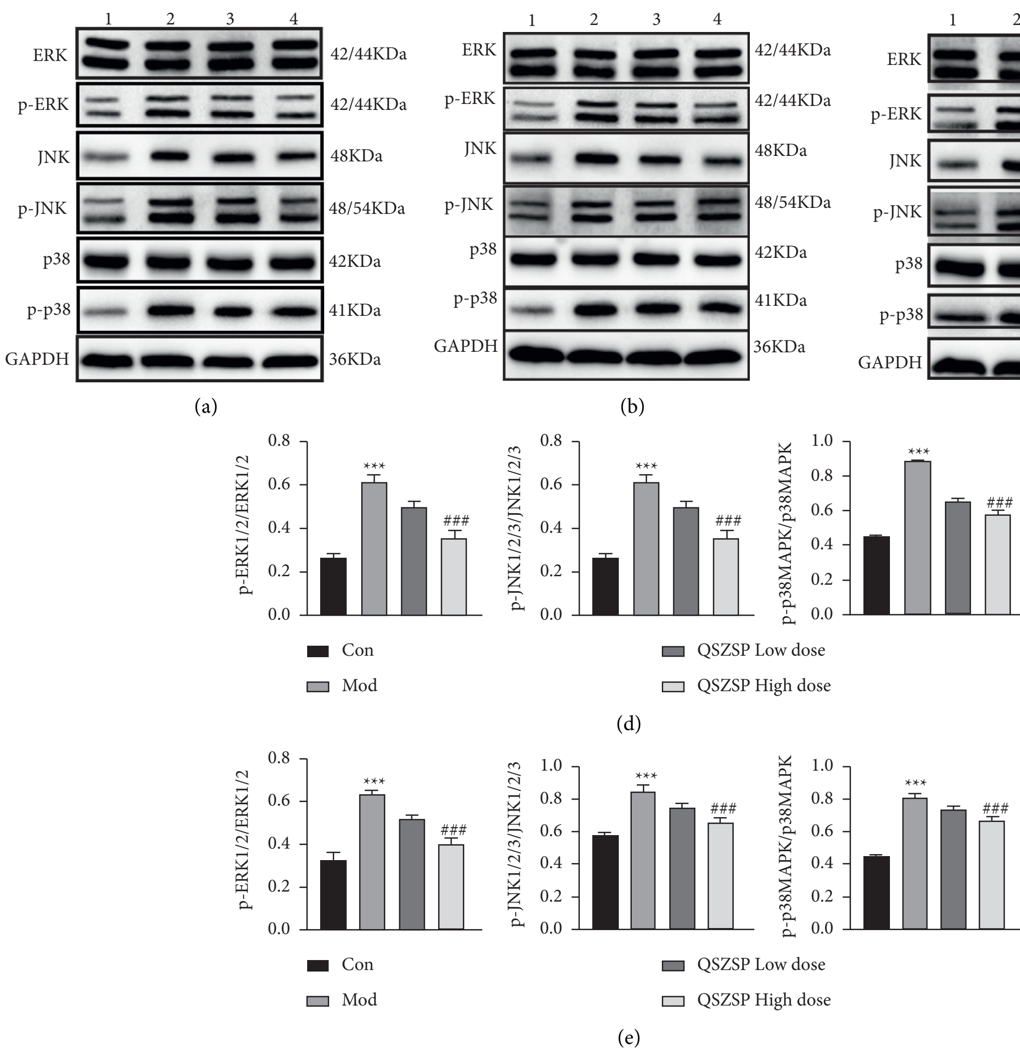

Figure 5: Continued.

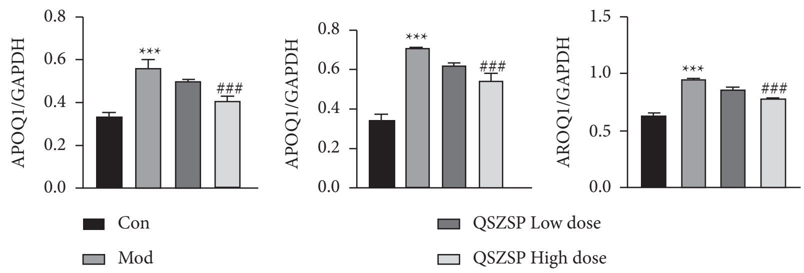

(f)

Figure 5: QSZSP inhibits the MAPK signaling pathway. (a, d) Expression of p-ERK1/2, p-JNK1/2/3, and p-p38 protein in the liver. (b, e) Expression of p-ERK1/2, p-JNK1/2/3, and p-p38 protein in the peritoneum. (c, f) Expression of p-ERK1/2, p-JNK1/2/3, and p-p38 protein in the kidney. $^{***}P < 0.001$ vs. Con, $^{###}P < 0.001$ vs. Mod. *Note.* 1: control group, 2: model group, 3: QSZSP low-dose group, and 4: QSZSP high-dose group.

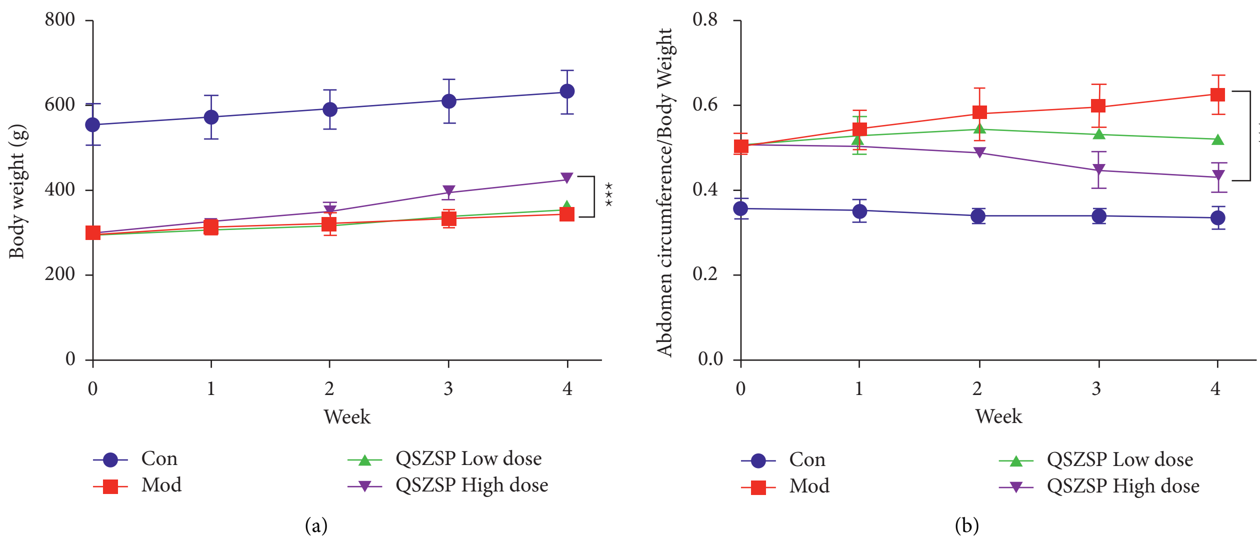

Figure 6: QSZSP induces abdomen circumference in rats with cirrhotic ascites. (a) The body weight of QSZSP after four weeks of treatment. (b) Abdominal circumference index (abdominal circumference/body weight) of QSZSP after four weeks of treatment. $^{***}P < 0.001$ Con vs. Mod.

shown that patients with cirrhotic ascites have a 3-year morbidity and mortality rate of 50% and a 5-year survival rate of only 5–10% [33]. This study not only found that cirrhotic ascites led to severe liver, peritoneum, and kidney damage, but also found that rats with cirrhotic ascites had slowed weight gain and excessive growth in abdominal circumference (Figure 1). After 4 weeks of treatment, the rats began to gain weight and their abdominal circumference was reduced (Figure 6).

Tie et al. [29] found that in prostate cancer cells, hypoxia induced AQP1 protein upregulation in a p38-dependent manner and that AQP1 was induced by hypoxia at the transcriptional level and that AQP1 regulation in PC-3M was dependent on calcium, PKC, and p38MAPK as well as oxygen tension. AQP1 is widely expressed in lymphatic vessels, capillaries, and endothelial cells of small veins and is distributed in the liver, peritoneum, kidney, pleura, respiratory tract, digestive tract from esophagus to colon, cardiac muscle, smooth muscle, and brain [24]. Huebert et al. [34] found that in the early stages of liver fibrosis, AQP1 expression on liver tissue cell membranes increased accordingly as the degree of liver fibrosis progressed. Liu et al. [30, 35] found that peptidoglycan is an inhibitor of the p38 MAPK transduction pathway and lipopolysaccharide is an inhibitor of the p38/JNK/ERK pathway ultimately acting on the AQP1 gene causing downregulation of AQP1 expression in human pleural mesothelial cells and that the reduction in AQP1 expression is dose-dependent and time-dependent. In this study, QSZSP was able to inhibit AQP1 protein high expression caused by cirrhotic ascites in the "liver-peritoneum-kidney" axis of cirrhotic ascites rats. QSZSP was able to inhibit AQP1 protein high expression caused by cirrhotic ascites, and the MAPK signaling pathway in the "liver-peritoneum-kidney" axis was also inhibited at this time. This demonstrated that the activation of MAPK signaling pathway was involved in organ damage in the "liver-peritoneum-kidney" axis of cirrhotic ascites rats and was associated with AQP1. Finally, it was found that the treated rats had lower Cr and TBiL and significantly higher ALB in serum, which, combined with the increase in body weight after treatment, indicated that QSZSP had some effect on improving the quality of life.

However, for the treatment of patients with cirrhotic ascites, medicine will obviously increase water intake, which contradicts the principle of water restriction in this disease; in particular, for patients with a large amount of ascites, medicine administration will further increase the patient's abdominal distension symptoms, and their compliance is poor. Chinese medicine is an important external treatment method in TCM, which can solve the contradiction between traditional Chinese medicine and the treatment of cirrhotic ascites with water restriction and can act directly on the diseased area. The development of the formulation process, quality standard, and safety of the gel form of QSZSP has been completed in the previous phase [36–39].

Previous studies on the mechanism of ascites formation in cirrhosis have mainly focused on the pathological role of the liver and kidney, such as the alteration of portal hemodynamics by cirrhosis, the water and sodium retention effect of the kidney, or the hormonal changes triggered by both, neglecting the role of the peritoneum and the role of the liver-peritoneum-kidney as an organic whole in the formation of ascites in cirrhosis.

Based on the previous study, this study took the pathological nature of water metabolism disorder in cirrhotic ascites as the starting point and was the first to propose the hypothesis that the "liver-peritoneum-kidney" axis is a functional axis of water metabolism that is involved in the "production-absorption-exhaustion" of peritoneal fluid with aquaporins protein as the common material basis and plays a key role in the formation of cirrhotic ascites. It was proved that QSZSP can inhibit the activation of MAPK signaling pathway and protect liver function in cirrhotic ascites rats, and it was found that AQP1 of "liver-peritoneal-kidney" axis plays a facilitating role in the process of ascites in cirrhosis ascites. The study also demonstrated that QSZSP regulates AQP1 expression in the "liver-peritoneal-kidney" axis, thus achieving the therapeutic effect of blocking ascites. It is clear that QSZSP inhibits AQP1 expression in the liver, peritoneum, and kidney, thus reducing abdominal girth. This process is related to the inhibition of MAPK pathway activation by QSZSP.

Many studies have found that the MAPK signaling pathway is involved in the regulation of ascites in cirrhosis. In this study, we found that the activation of MAPK signaling pathway was inhibited after QSZSP treatment, but whether QSZSP targets the MAPK signaling pathway for the treatment of cirrhotic ascites is unknown in this study. As a limitation of this study, perhaps the targeting relationship of MAPK signaling pathway in QSZSP for the treatment of cirrhotic ascites will be verified *in vitro* in future studies of liver.

5. Conclusion

QSZSP inhibits MAPK activation and AQP1 protein expression in the "liver-peritoneal-kidney" axis to alleviate ascites injury in cirrhosis.

Data Availability

The data used to support the findings of this study are available from the corresponding author upon request.

Additional Points

(i) Qi Sui Zhu Shui plaster inhibits MAPK activation in cirrhotic ascites rat. (ii) Qi Sui Zhu Shui plaster suppressed cirrhotic ascites-induced liver-peritoneum-kidney damage *in vivo*. (iii) Qi Sui Zhu Shui reduced abdominal circumference thickness by inhibiting the overexpression of AQP1.

Ethical Approval

All animal experiments are in line with the relevant provisions of the Ethical Certificate of Experimental Animals of the Animal Administration Commission of Hubei Province. The license number for laboratory animals is as follows: SYXK (E) 2018–0104.

Conflicts of Interest

The authors declare that there are no conflicts of interest.

References

[1] D. Schuppan and N. H. Afdhal, "Liver cirrhosis," *The Lancet*, vol. 371, no. 9615, pp. 838–851, 2008.
[2] B. Sharma and S. John, *Hepatic Cirrhosis. StatPearls*, StatPearls Publishing LLC., Treasure Island, FL, USA, 2022.
[3] S. Scaglione, S. Kliethermes, G. Cao et al., "The epidemiology of cirrhosis in the United States: a population-based study," *Journal of Clinical Gastroenterology*, vol. 49, no. 8, pp. 690–696, 2015.
[4] L. A. Lyssy and M. P. Soos, *Cirrhotic Cardiomyopathy. StatPearls*, StatPearls Publishing LLC., Treasure Island, FL, USA, 2022.
[5] A. Sharma and S. Nagalli, *Chronic Liver Disease. StatPearls*, StatPearls Publishing LLC., Treasure Island, FL, USA, 2022.
[6] F. A. Rochling and R. K. Zetterman, "Management of ascites," *Drugs*, vol. 69, no. 13, pp. 1739–1760, 2009.
[7] R. Planas, S. Montoliu, B. Ballesté et al., "Natural history of patients hospitalized for management of cirrhotic ascites," *Clinical Gastroenterology and Hepatology*, vol. 4, no. 11, pp. 1385–1394, 2006.
[8] A. Zanetto, E. Campello, F. Pelizzaro, and F. Farinati, "Hemostatic alterations in patients with cirrhosis and hepatocellular carcinoma: laboratory evidence and clinical implications," *Liver International: Official Journal of the International Association for the Study of the Liver*, 2022.
[9] Z. Yi, Q. Jia, Y. Lin et al., "Mechanism of Elian granules in the treatment of precancerous lesions of gastric cancer in rats through the MAPK signalling pathway based on network pharmacology," *Pharmaceutical Biology*, vol. 60, no. 1, pp. 87–95, 2022.
[10] Z. J. Hou, J. H. Zhang, X. Zhang et al., "Long-term traditional Chinese medicine combined with NA antiviral therapy on cirrhosis incidence in chronic hepatitis B patients in the real-world setting: a retrospective study," *Evidence-based Complementary and Alternative Medicine: eCAM*, vol. 2020, Article ID 3826857, 8 pages, 2020.
[11] H. Z. Qiu Hua and D. Mao, "Effects of TCM point application with QiSuiZuShui-paste on quality of life in patients with refractory ascites of cirrhosis," *Chinese Journal of Integrated Traditional Chinese and Western Medicine on Digestion*, vol. 17, no. 5, pp. 306–309, 2009.
[12] F. Xing, Y. Tan, G.-J. Yan et al., "Effects of Chinese herbal cataplasm Xiaozhang Tie on cirrhotic ascites," *Journal of Ethnopharmacology*, vol. 139, no. 2, pp. 343–349, 2012.

[13] H. Wang, X. P. Chen, and F. Z. Qiu, "Salviae miltiorrhizae ameliorates cirrhosis and portal hypertension by inhibiting nitric oxide in cirrhotic rats," *Hepatobiliary and Pancreatic Diseases International: HBPD INT*, vol. 2, no. 3, pp. 391–396, 2003.

[14] B. M. Denker, B. L. Smith, F. P. Kuhajda, and P. Agre, "Identification, purification, and partial characterization of a novel Mr 28,000 integral membrane protein from erythrocytes and renal tubules," *Journal of Biological Chemistry*, vol. 263, no. 30, pp. 15634–15642, 1988.

[15] P. Agre, S. Sasaki, and M. J. Chrispeels, "Aquaporins: a family of water channel proteins," *The American journal of physiology*, vol. 265, no. 3, Article ID F461, 1993.

[16] A. S. Verkman, M. O. Anderson, and M. C. Papadopoulos, "Aquaporins: important but elusive drug targets," *Nature Reviews Drug Discovery*, vol. 13, no. 4, pp. 259–277, 2014.

[17] Z. Draelos, "Aquaporins: an introduction to a key factor in the mechanism of skin hydration," *The Journal of clinical and aesthetic dermatology*, vol. 5, no. 7, pp. 53–56, 2012.

[18] A. S. Verkman, "More than just water channels: unexpected cellular roles of aquaporins," *Journal of Cell Science*, vol. 118, no. 15, pp. 3225–3232, 2005.

[19] M. Suzuki and S. Tanaka, "Structure and diverse functions of vertebrate aquaporins," *Seikagaku The Journal of Japanese Biochemical Society*, vol. 86, no. 1, pp. 41–53, 2014.

[20] A. D. Sales, C. H. Lobo, A. A. Carvalho, A. A. Moura, and A. P. R. Rodrigues, "Review Structure, function, and localization of aquaporins: their possible implications on gamete cryopreservation," *Genetics and Molecular Research*, vol. 12, no. 4, pp. 6718–6732, 2013.

[21] J. von Bülow, "Aquaporins--water channels in the cell membrane and therapeutic targets," *Medizinische Monatsschrift fur Pharmazeuten*, vol. 36, no. 3, pp. 86–94, 2013.

[22] A. Yool, "Functional domains of aquaporin-1: keys to physiology, and targets for drug discovery," *Current Pharmaceutical Design*, vol. 13, no. 31, pp. 3212–3221, 2007.

[23] G. Benga, "The first discovered water channel protein, later called aquaporin 1: molecular characteristics, functions and medical implications," *Molecular Aspects of Medicine*, vol. 33, no. 5-6, pp. 518–534, 2012.

[24] M. Y. S. Kalani, A. S. Filippidis, and H. L. Rekate, "Hydrocephalus and aquaporins: the role of aquaporin-1," *Acta Neurochirurgica Supplementum*, vol. 113, pp. 51–54, 2012.

[25] N. J. Shah, O. Y. Mousa, K. Syed, and S. John, *Acute on Chronic Liver Failure*, StatPearls Publishing LLC., Treasure Island, FL, USA, 2022.

[26] J. S. Pedersen, F. Bendtsen, and S. Møller, "Management of cirrhotic ascites," *Therapeutic advances in chronic disease*, vol. 6, no. 3, pp. 124–137, 2015.

[27] D. V. Garbuzenko and N. O. Arefyev, "Current approaches to the management of patients with cirrhotic ascites," *World Journal of Gastroenterology*, vol. 25, no. 28, pp. 3738–3752, 2019.

[28] E. McCoy and H. Sontheimer, "MAPK induces AQP1 expression in astrocytes following injury," *Glia*, vol. 58, no. 2, pp. 209–217, 2010.

[29] L. Tie, N. Lu, X. Y. Pan et al., "Hypoxia-induced up-regulation of aquaporin-1 protein in prostate cancer cells in a p38-dependent manner," *Cellular Physiology and Biochemistry: International Journal of Experimental Cellular Physiology, Biochemistry, and Pharmacology*, vol. 29, no. 1-2, pp. 269–280, 2012.

[30] L. Liu and C. Xie, "Effects of downregulation of aquaporin1 by peptidoglycan and lipopolysaccharide via MAPK pathways in MeT-5A cells," *Lung*, vol. 189, no. 4, pp. 331–340, 2011.

[31] J. Uriz, A. Cárdenas, and V. Arroyo, "Pathophysiology, diagnosis and treatment of ascites in cirrhosis," *Best Practice & Research Clinical Gastroenterology*, vol. 14, no. 6, pp. 927–943, 2000.

[32] W. Hou and A. J. Sanyal, "Ascites: diagnosis and management," *Medical Clinics of North America*, vol. 93, no. 4, pp. 801–817, 2009.

[33] B. S. Sandhu and A. J. Sanyal, "Management of ascites in cirrhosis," *Clinics in Liver Disease*, vol. 9, no. 4, pp. 715–732, 2005.

[34] R. C. Huebert, M. M. Vasdev, U. Shergill et al., "Aquaporin-1 facilitates angiogenic invasion in the pathological neovasculature that accompanies cirrhosis," *Hepatology*, vol. 52, no. 1, pp. 238–248, 2010.

[35] L. Liu, L. Du, Y. Chen et al., "Down-regulation of Aquaporin1 (AQP1) by peptidoglycan via p38 MAPK pathways in primary rat pleural mesothelial cells," *Experimental Lung Research*, vol. 40, no. 4, pp. 145–153, 2014.

[36] Q. H. Yuehong, "Study on ethanol extraction process for Qisui Zhushui gel cream," *Hunan Journal of Traditional Chinese Medicine*, vol. 30, no. 10, pp. 150–152, 2014.

[37] M. D. Qiu Hua, X. Liu, and Y. Guo, "Study on the water extraction technology of Qisui Zhushui gel ointment," *Guiding Journal of Traditional Chinese Medicine and Pharmacy*, vol. 21, no. 2, pp. 60–63, 2015.

[38] W. N. Qiu Hua, X. Liu, D. Mao, X. Xing, and Y. Guo, "Studies on the quality standard of the Qishui Zhushui gel ointments," *Journal of Liaoning University of Traditional Chinese Medicine*, vol. 18, no. 3, pp. 540–544, 2016.

[39] M. D. Qiu Hua, X. Liu, and Y. Guo, "The matrix formulation of Qishui Zhushui gel ointments optimized through orthogonal test," *Guangxi Journal of Traditional Chinese Medicine*, vol. 37, no. 5, p. 4, 2014.

Hindawi
Journal of Healthcare Engineering
Volume 2022, Article ID 9372807, 9 pages
https://doi.org/10.1155/2022/9372807

Research Article

Research on Data Analysis Network of TCM Tongue Diagnosis Based on Deep Learning Technology

Zongrun Li [1,2] Xiujuan Ren,[3] Lin Xiao,[4] Jing Qi,[5] Tianli Fu,[2] and Weihong Li [1]

[1] *Basic Medical College, Chengdu University of TCM, Chengdu, China*
[2] *School of Rehabilitation Medicine, Weifang Medical University, Weifang, China*
[3] *Administrative Office of Weifang People's Hospital, Weifang, China*
[4] *Basic Medical College, Weifang Medical University, Weifang, China*
[5] *School of Management, Weifang Medical University, Weifang, China*

Correspondence should be addressed to Weihong Li; lwh@cdutcm.edu.cn

Received 10 January 2022; Revised 18 February 2022; Accepted 23 February 2022; Published 29 March 2022

Academic Editor: Enas Abdulhay

The aim of the study is to build a tongue image intelligent analysis "end-to-end" deep learning network based on a tongue diagnosis image of traditional Chinese medicine. The tongue target region in the original image was segmented by the UNet tongue segmentation model at the front end of the network. After segmentation, the feature vector of the tongue target region was extracted by the ResNet network, and then the blood pressure on the day of shooting was fused with the feature vector extracted by the ResNet network through the convolution operation method to complete the extraction of two groups of data of tongue feature and fusion feature. Based on analyzing the data of blood pressure, tongue image, and their fusion at the end of the network, four regression analysis methods were used to predict the stage mean value. After training, the model is tested with the test set data, and the test results are evaluated with mean absolute error (MAE). The prediction error of the model based on the fusion data of tongue image and blood pressure on the day of shooting was lower than that of the other two data modes. The UNet tongue segmentation model combined with the ResNet network can realize the automatic extraction of tongue image features. The extracted features combined with machine learning modeling can be used to explore the complex hierarchical mathematical association between tongue image and clinical data. The experimental results show that the multimodal data fusion method is an important way to mine the clinical value of the TCM tongue image.

1. Introduction

Tongue diagnosis is an important part of Chinese medicine diagnosis, and the development of tongue diagnosis in Chinese medicine can be traced back to the Yin and Shang dynasties, after which generations of physicians have attached great importance to the application and research of tongue diagnosis, and it has been inherited as the core content of "diagnosis by looking," which is the first of the four diagnoses in Chinese medicine. A tongue image is the observation object of tongue diagnosis, and its theoretical body is mainly derived from the theory of holistic view of Chinese medicine, which means that the physiological state of the whole body can be detected by localization [1]. Based on the holistic view of Chinese medicine, the expression of the physiological functions of the human body by the tongue can be characterized as phased, comprehensive, and dynamic. Most of the clinical studies on the Chinese medicine tongue are based on the characteristics of the tongue, such as tongue texture, tongue coating, tongue shape, and other characteristics associated with clinical diseases, which to a certain extent limits the value of the tongue to the overall expression of human physiological information. In order to realize the efficient mining of valuable vital information contained in the tongue, this study combines the current information science hotspot "deep learning" technology to explore the intelligent analysis network of tongue image and verify the practicality of the network in tongue image data mining through clinical data.

1.1. "End-to-End" Model of Tongue Image Data Analysis. After decades of development, the modernization of Chinese medicine tongue diagnosis has made many achievements in data acquisition and data feature extraction, but the current research difficulties are mainly focused on the discovery of clinical information of tongue images [2]. Early studies on the objectification of tongue diagnosis mostly used quantitative methods to identify tongue features and thus achieve automated classification of tongue images. In recent years, with the development of machine learning technology, the objectification of tongue diagnosis has become more clinical, and it has become possible to use tongue images to understand the diagnosis and prognosis of diseases intuitively. In 2006, Hinton and Salakhutdinov [3] proposed the concept of layered neural networks, in which there are a large number of hidden layers in these layered networks to enhance the model learning ability. It further stereotyped the neural network by using deep hidden layers to enhance the learning ability of the network for stereoscopic data such as images, speech, and video [4], allowing the network to better handle medical image data such as tongue images. Thanks to the advancement of machine learning modeling, it is possible to mine clinical data of tongue images in an "end-to-end" mode from the input of the original image captured to the output of clinical data. This changes the traditional research paradigm of associating tongue images with clinical data.

1.2. Network Architecture for Intelligent Analysis of Tongue Clinical Information. Intelligent analysis of tongue clinical information refers to the separation of the tongue in the original image, then feature extraction of the target region of the tongue, and modeling analysis with clinical indicators, and finally yielding a prediction model of clinical indicators based on the tongue image. In this study, based on the data characteristics of clinical test indicators, which are mainly continuous variables, an intelligent tongue analysis network is constructed using a "dual-flow" network architecture. The network is composed of four different functional module groups (Figure 1).

One is the Unet tongue segmentation network model developed by our group [5], which is a deep learning network model consisting of 11 "convolution-pooling" layers (Figure 2). The semantic segmentation test results show that the model achieves a mean intersection ratio (MIoU) of 91% and a pixel accuracy (PA) of 93%.

The second is the feature extraction module for ResNet image data. In this module, data feature vector extraction is performed by multilayer residual network (ResNet) using pretrained weight values from ImageNet dataset. The ResNet structure is designed with 8 modules, connecting a convolutional layer from the input layer in turn, and then connecting Bottleneck1-4 modules, with a 1^*1 average pooling at the end of the Bottleneck4 output connection network to retain more coding information (Figure 3).

The third is the convolutional fusion module. To meet the need for further data mining, a convolutional fusion module is set up in the network architecture to integrate the tongue image with the associated data, and the fused data can be output as independent variables for regression modeling analysis. In this module, the collected clinical data are adjusted to 1^*2048 vectors by replication expansion, and then superimposed with the 1^*2048 vectors extracted by the above ResNet network, i.e., each vector channel is D before fusion and 2D after fusion. After completing the connection fusion, a 1^*1 convolutional kernel is used to do the dimensionality reduction in the channel dimension. The data obtained by convolutional fusion for the tongue image can be combined with a certain clinical data parameter to form a multimodal fusion data structure into the end-of-network regression analysis session.

The fourth is the regression modeling analysis part at the end of the network, which uses the tongue data features or the fused data of tongue data features and a certain clinical information as independent variables to carry out the prediction of the target physiological information. The regression analysis can select multiple machine learning models according to the data type, distribution pattern, and other characteristics combined with clinical information.

2. Web Application Experiment of Intelligent Analysis of Tongue Image Based on Deep Learning Technology

The tongue, as a muscular organ, in a healthy state, has a light red color due to the abundance of internal capillaries, i.e., the light red tongue image. In the pathological state, on the other hand, the tongue can take on a dark or light reddish-red, purple-dark, greenish-gray, or pale white color due to factors such as the amount of hemoglobin, impaired vascular circulation, or structural problems [6]. In Su Wen - Yin Yang Ying Xiang Da Lun, "The heart is the master of the tongue …… in the orifice for the tongue"; In Ling Shu - Pulse Degree, "The heart is connected to the tongue, the heart and the tongue can know the five tastes," on the basis of which later medical practitioners further condensed the relationship between the tongue and the heart as "the heart opens the orifice in the tongue, the tongue is the seedling of the heart." In recent years, it has been found that the initial pathological changes of primary hypertensive disease are mostly intermittent spasms of tiny arteries throughout the body [7], which can lead to organ damage after a period of time and the initial damage sites are mainly concentrated in the tiny arteries [8]. Microvascular lesions within the tongue can have an impact on tongue color, and the tongue, as a dense area of microcirculation in the body, has a complex intertwined network of vessels at all levels [9]. It is clear that changes in arterial blood pressure in the human body first affect the microcirculatory system, and the human tongue is the largest dense organ of microcirculation that we can visually and noninvasively observe, suggesting here that

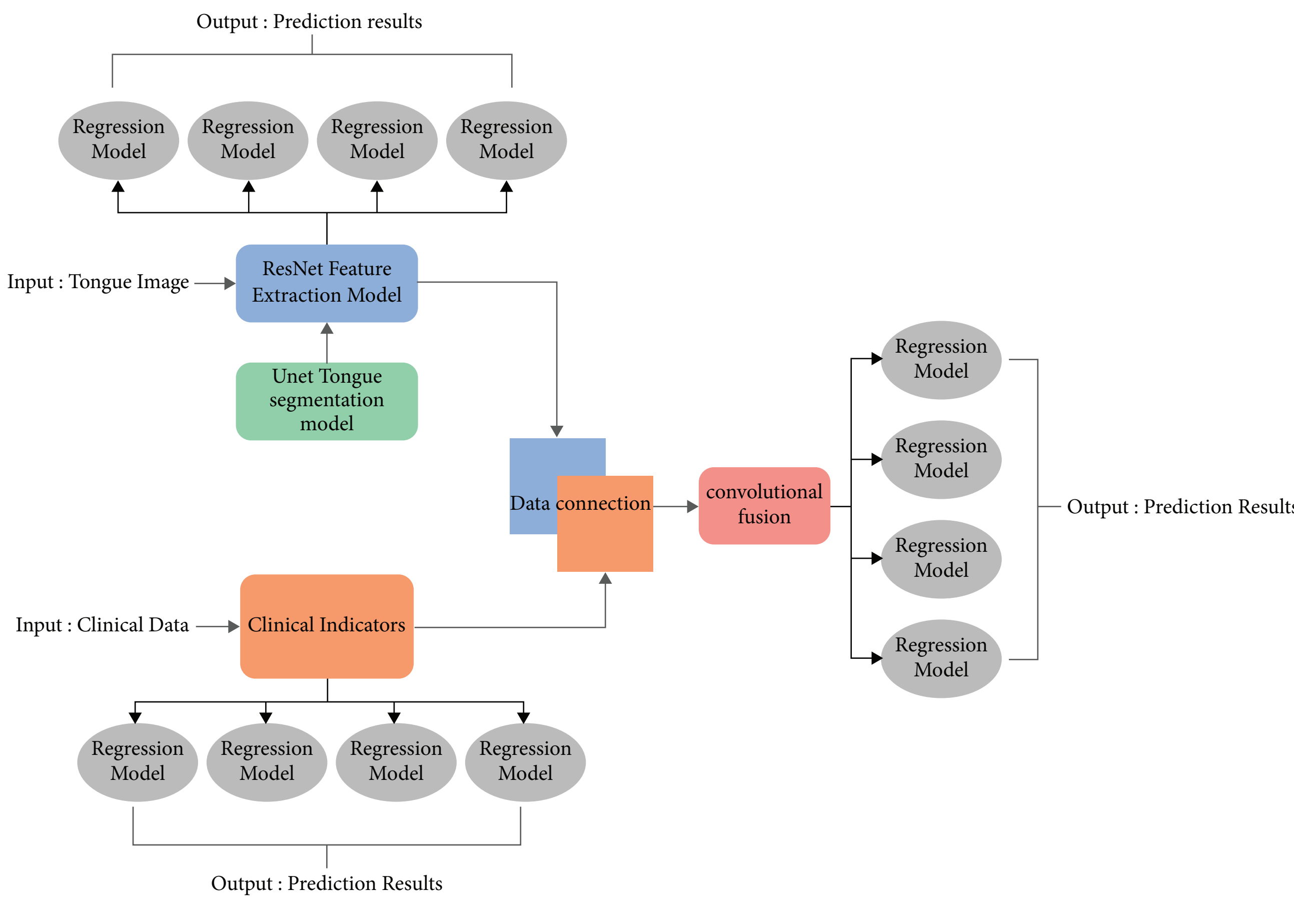

Figure 1: Dual path network architecture diagram.

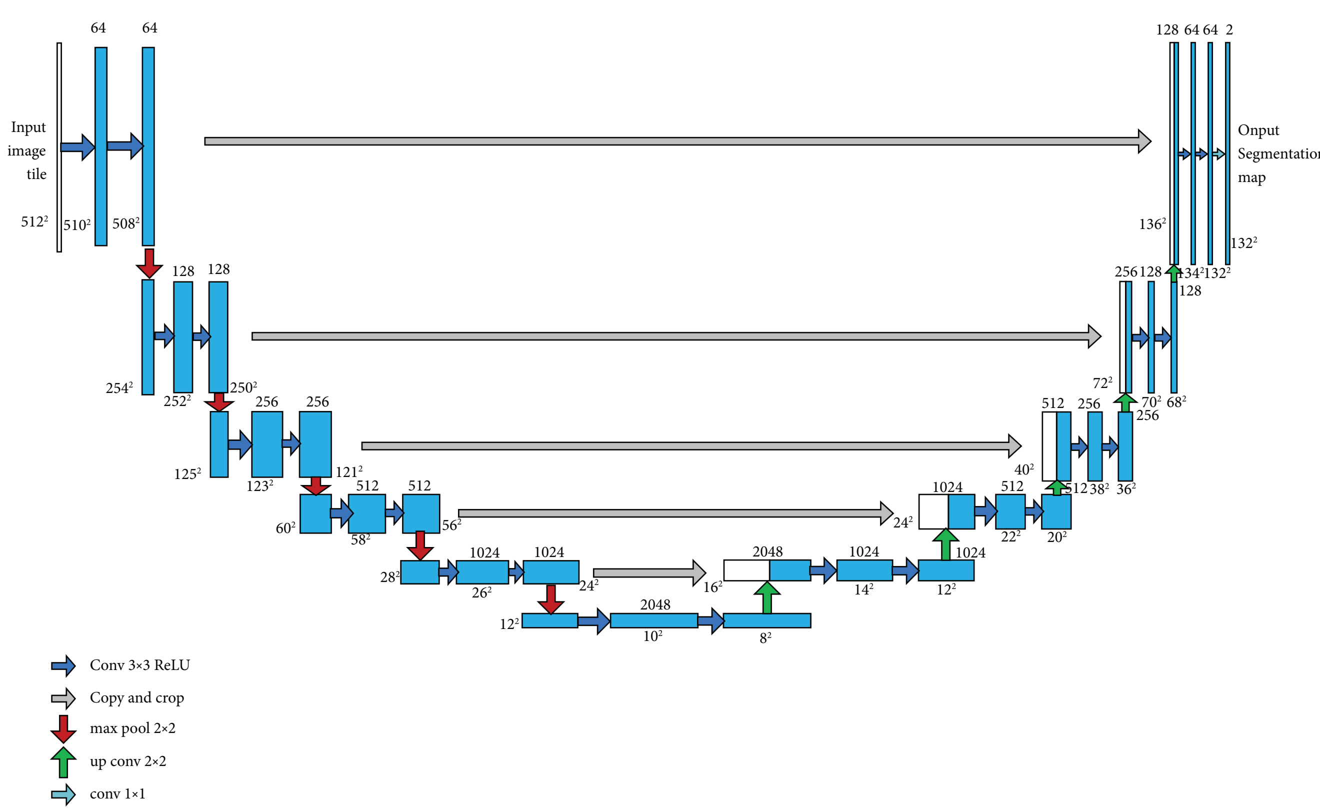

Figure 2: Unet tongue segmentation model.

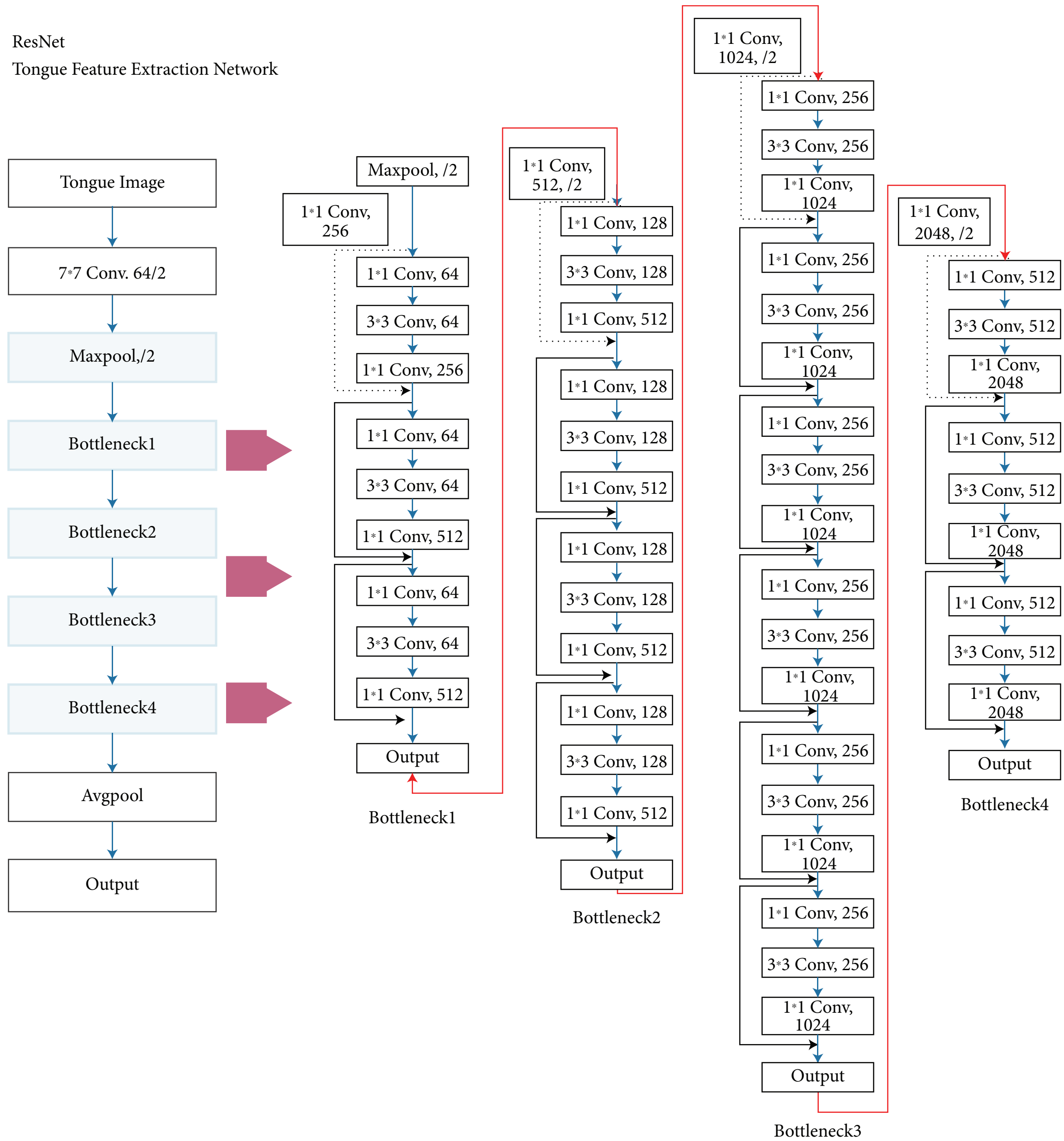

Figure 3: ResNet network structure.

there may be some correlation between tongue image and human blood pressure.

To further explore the application value of the intelligent analysis network of tongue images, a clinical experiment was set up in this study to combine the abovementioned Chinese medicine and modern medical theories for the constructed clinical data analysis network model of tongue images. The experiment was conducted with the mean value of the blood pressure values of the last 6 days of the week with staging diagnostic value as described in the Chinese Guidelines for the Prevention and Treatment of Hypertension 2018 Revision [2] as the target, and the blood pressure values of the day were collected using the tongue image and the tongue image overlay as the independent variables for the prediction experiment. To ensure the reliability and traceability of the experimental data and to reduce some interfering factors, the study population was selected from inpatients with type 2 diabetes mellitus in the Department of Endocrinology of the Affiliated Hospital of Chengdu University of Chinese Medicine. The input data of the dual-stream network were set up with two kinds of data: tongue image and blood pressure on the day of collection, and the network combined the two kinds of data into fused data by a convolutional fusion module. By comparing the prediction results of the three data, the value of tongue image in predicting the target data can be further illustrated, thus reflecting the correlation between the independent variable data and the dependent variable data to a greater extent.

The clinical trial was completed at the China Clinical Trials Registry in August 2018 (registration number: ChiCTR1800018090). The ethical review was approved by the Medical Ethics Committee of the Affiliated Hospital of Chengdu University of Traditional Chinese Medicine in July 2018 (Ethics Committee Approval Document No.: 2018KL-050). Tongue data and clinical data were collected from September 2018 to November 2019.

The tongue photo acquisition equipment used is the TFDA-1 desktop tongue diagnostic instrument developed by Shanghai University of Traditional Chinese Medicine, which consists of a CCD digital camera, LED light source, light shield, base, and curved reflector. The color temperature of the LED light is 5000K and the color rendering index is 97 as shown in Figure 4.

TFDA-1 usage and parameter settings: shooting parameters are M mode, shutter speed is 1/125; aperture value is F6.3; ISO sensitivity is 200; image size is L 5568*3712; central focus metering; automatic white balance. The collected raw tongue data are subject to regular quality control checks.

Clinical data were obtained from the inpatient medical record system of the Affiliated Hospital of Chengdu University of Traditional Chinese Medicine. The raw data were recorded in spreadsheet form using Microsoft Office Excel software and consisted of blood pressure records twice a day, morning and evening, during the patients' hospitalization. After collection, the data were randomly divided into training set (80%) and test set (20%) by inclusion number using Excel software.

2.1. Experimental Environment. The hardware configuration of the experimental computer is: Intel Core I7-9700 processor, Intel Q370 motherboard, NIVDA Geforce GT1080ti graphics card; the operating system is Ubuntu 9.04, the programming language is Python 3.7, and the model network is built through pytorch.

2.2. Regression Analysis. Since the data consisted of three categories, the regression modeling was performed in three groups, with each group modeling diastolic blood pressure and systolic blood pressure separately. The regression models used were identical for all three data categories, and only the input independent variables were changed in the experiment. The regression analysis process of the four models is described in detail in the following section, using "blood pressure on the day" as the independent variable, which is used as a reference for the other two data categories. The sample size of the training set used in this experiment was 260 cases. Since the blood pressure data were divided into diastolic and systolic blood pressure, we modeled the prediction of diastolic blood pressure and systolic blood pressure separately, so the methods used are exactly the same, and we will not describe the methods separately, but use "blood pressure" in the following.

FIGURE 4: TFDA-1 benchtop tongue diagnostic instrument.

2.3. Random Forest (RF). Random forests are reinforced classifiers consisting of multiple decision trees. The basic architecture is to form a model group of multiple decision tree classifiers and to "vote" on the output of these decision trees to determine the most optimal data processing result by the most votes [10]. A random forest of 10 trees was used for the regression experiments. The model training process is as follows:

(1) The value of blood pressure on the first day of the count is taken as the independent variable, x_i, and the mean of the patient's data from the second to the seventh day is taken as the dependent variable, y_i.

(2) For $i = 1,2, \ldots, 260$, the training set is randomly sampled for the ith time and a total of 260 acquisitions are made to obtain a sample set D_i containing 260 blood pressure data samples, and the ith tree model $T_i(x)$ is trained with the sample D_i. When training the tree model nodes, the features of some samples are randomly selected from all the blood pressure sample features on the nodes at the same time, and then an optimal feature is selected from them to be the left and right subtree division feature of the tree.

(3) The abovementioned tree model is averaged out, and the arithmetic average is considered directly here, so that the final output model $L(x) = 1/260\sum_{k=1}^{260} T_k(x)$ is the result.

2.4. Adaptive Enhancement Algorithm (AdaBoost). The adaptive boosting algorithm (AdaBoost) is trained with multiple weak classifiers in the training set and the sample weights are corrected according to the classifier error rate and then given to the next classifier, which forms a strong classification by combining multiple sets of weak classifiers [10] as follows:

(1) Initialize the weight matrix W of the blood pressure data. Each of the 260 data is assigned a weight $w_1 = 1/260$.

(2) Training the regression function f_i. The process is as follows: if a blood pressure sample point is correctly predicted by the regression function f_i, the corresponding weight is reduced for the next blood pressure training, and if it is incorrectly classified, the corresponding weight is increased. The updated blood pressure set is used to train the next classifier,

and so on iteratively. In this case, the error of the regression function f_i is

$$e_t = \sum_{i=1}^{260} w_{ii} I\left(H_t\left(x_i\right) \neq y_i\right), \tag{1}$$

where $I(\cdot)$ is the information function, $H(\cdot)$ is the entropy function, and W_{ii} is the weight of the ith iteration.

(3) The obtained regression function is combined, which is the final regression function:

$$D_{t+1} = \frac{D_t(i)\exp\left(-\alpha_t y_i H_t\left(x_i\right)\right)}{Z_t}, \tag{2}$$

where $Z_t = 2\sqrt{e_t\left(1 - e_t\right)}$ is the normalization constant.

2.5. Iterative Decision Tree (GBRT). GBRT is an integrated model consisting of numerous decision trees of shallow depth combined in a hierarchical connection [11], and the characteristics of GBRT are mainly focused on strong adaptability to various data categories and high accuracy of regression prediction, which is in line with the experimental design of this experiment in which prediction is carried out based on different categories of data. The decision tree model in the model group does not play the role of classification judgment, but carries out regression prediction, and this prediction process is carried out in each regression tree for the input data and more accurate prediction values are obtained through continuous correction. The calculation process in the experiment is as follows:

Input: Blood pressure data set. $D = \{(x_1, y_1), \ldots, (x_{260}, y_{260})\}$

Output: Return to lifting tree. $T_D(x)$

(1) Initialization $T_0(x) = 0$.

(2) For $n = 1, \ldots, 260$, the residual $r_{ni} = y_i - T_{n-1}(x_i)$ is calculated, and the residual is fitted to obtain the regression tree as $T(x; \Theta_m)$, and the update law as $T_m = T_{m-1} + T(x; \Theta_m)$.

(3) Obtaining regression tree $T_D(x) = \sum_{m=1}^{260} T(x; \Theta_m)$.

2.6. Support Vector Regression (SVR). SVR is a regression analysis, so there is only one type of sample points, and the total deviation of all sample points from the hyperplane is found to be the minimum distance in the regression process. For the consideration of linear distribution of blood pressure data, the kernel function is chosen as a linear type in this experiment. Moreover, $C = 1e3$, C represents the importance for outlier points. $\gamma = 0.01$ denotes the coefficient of the kernel function, which is too large to cause overfitting because it is a linear function, and is finally chosen to be 0.01. The blood pressure data are equivalent to solving the following constrained optimization problem in the SVR:

$$\begin{cases} \min\limits_{w,b} \dfrac{1}{2}\|\mathbf{w}\|^2, \\ \text{s.t.} \left|y_i - \left(\mathbf{w}\mathbf{x_i} + b\right)\right| \leq \varepsilon \quad i = 1, 2, \ldots, N, \end{cases} \tag{3}$$

where $\mathbf{w} = w \in R$ is the weight of the regression curve and ε is the maximum value of the distance from the curve to the blood pressure data point.

2.7. Evaluation Methods of Prediction Results. There are two commonly used regression prediction evaluation methods, namely, mean absolute error (MAE) and root mean square error (RMSE). In this experiment, mean absolute error [12] (MAE) was chosen to evaluate the test results, and the mean absolute error is the absolute average of the error between the prediction results and the real data, and the larger the mean absolute error is, the worse the prediction accuracy is proved to be. The use of MAE as a criterion for judging the error can better express the true error of data with 1-dimensional characteristics compared to RMSE [13] and facilitate the comparison between different data categories. The MAE formula is as follows:

$$\text{MAE} = \frac{1}{m}\sum_{i=1}^{m}\left\|y_{\text{test}}^{(i)} - \hat{y}_{\text{test}}^{(i)}\right\|_1. \tag{4}$$

3. Results

3.1. Data Acquisition Results. A total of 429 samples were collected according to the standardized data collection protocol described above, and 325 samples were screened after quality control to meet the study requirements, including 131 female samples and 194 male samples. The general statistics of the patients were as follows Tables 1–4.

3.2. Model Prediction Results. In this experiment, we used three kinds of data: "blood pressure of the day," "blood pressure of the day + tongue," and "tongue," and used four kinds of end-of-data regression models to predict the 6-day average of blood pressure. The prediction accuracy was assessed by the mean absolute error. The results are shown in Tables 5 and 6.

From the prediction trend, it was found that the prediction error performance was higher for the tongue data; the prediction error results were better for the blood pressure on the day of shooting than for the tongue data. The best prediction results were obtained with the fusion data of tongue image overlaid with blood pressure on the day of shooting.

In this study, the value of tongue image in the prediction of blood pressure stage mean was evaluated using the prediction results of the same-day blood pressure data modeling as a baseline. When the mean absolute error (MAE) of the same algorithmic model from the "same-day

Table 1: Age distribution of subjects.

N	Age	Max.	Min.
325	49.04 ± 13.50	75	34

Table 2: Distribution of subject's height (cm).

Gender (*N*)	Height	Max.	Min.
Male (194)	169.48 ± 5.76	185	153
Female (131)	157.12 ± 5.76	173	145

Table 3: Distribution of subjects' weight (kg).

Gender (*N*)	Weight	Max.	Min.
Male (984)	68.76 ± 16.72	120	49
Female (1064)	157.71 ± 5.97	95	41

Table 4: Subjects' education status.

Education level	*N*	Percentage
University	45	13.84%
High school (secondary school)	153	47.08%
Other	127	39.08%

Table 5: Mean absolute error of predicted systolic blood pressure (MAE) in mmHg.

Model data	SVR	RF	Adaboost	GBRT
Blood pressure for the day	7.13	6.54	5.91	6.25
Tongue image	15.41	10.39	10.22	9.61
Tongue image + blood pressure on the day	7.06	**5.49**	5.54	5.84

Table 6: Mean absolute error of predicted diastolic blood pressure (MAE) in mmHg.

Model Data	SVR	RF	Adaboost	GBRT
Blood pressure for the day	7.10	8.61	4.43	6.17
Tongue image	18.03	13.91	11.87	15.73
Tongue image + blood pressure on the day	6.32	8.54	**4.02**	5.91

blood pressure + tongue" and "tongue" data categories was lower than that of the "same-day blood pressure" model, it represented an improved value. On the contrary, if the MAE is higher than that of the "same-day blood pressure" model, it means that it has no value for blood pressure prediction. The prediction results showed that the MAE of each of the six predictions of systolic and diastolic blood pressure based on the "tongue image" data alone exceeded the prediction of blood pressure on the same day, and there was no significant advantage of using the tongue image alone to predict blood pressure for the next 6 days. The MAE of the model built with the fused tongue and blood pressure data was lower than that of the current day's blood pressure modelin (Figures 5 & 6).

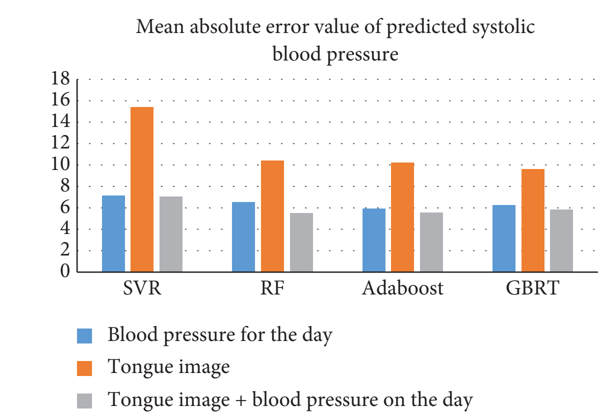

Figure 5: Comparison of mean absolute error in predicting systolic blood pressure prediction.

4. Discussion

In this experiment, we used a dual-input "two-stream network" analysis architecture for the two types of input data to perform blood pressure stage prediction using tongue image, current day blood pressure, and both fused data. The network is designed to use the "blood pressure of the day" prediction results as the baseline, and the cross-sectional comparison of the prediction results can further reflect the contribution of different data categories in prediction

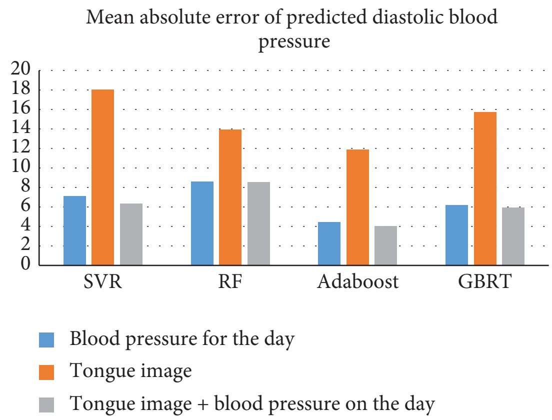

Figure 6: Comparison of mean absolute errors in predicted diastolic blood pressure.

accuracy. The models constructed from the fused data outperformed the models constructed from the same-day blood pressure data in all prediction results. The addition of tongue data contributes to the reduction of the error rate. Since the machine learning technique used is a "black-box" data processing model with uninterpretable complex hierarchical mathematical relationships, it is not possible to know which feature of the tongue data has a positive effect on the prediction of blood pressure. Here, this study argues that data convolution fusion makes the overall linear distribution of the fused data. The tongue image data, on the other hand, makes the amount of information increased by incorporating the information carried by features such as tongue morphology, color, and texture, which enhances the characteristics of the dimensionality of the data to some extent. Thus, the fused data incorporate a lot of lingual information compared to the same-day blood pressure data or the lingual image data only, and the overall data are still linearly distributed, which may be the reason why the fused data model is smaller than the two separate data models in terms of error. Through the above experiments, this study concluded that the multimodal data fusion method of "tongue +" mode can achieve more efficient data mining than the analysis of tongue data only. In the future, with the upgrade of data analysis capability, the tongue diagnosis data can be fused with various clinical data to form a big data matrix, and then the neural network can be used to carry out deep data mining, and its application will cover the auxiliary identification of Chinese medicine, physical determination, and the prognosis assessment of clinical indicators, radiotherapy, chemotherapy, and surgery in modern medicine.

5. Conclusion

Tongue diagnosis is an important part of Chinese medicine diagnosis, and the development of tongue diagnosis in Chinese medicine can be traced back to the Yin and Shang dynasties, after which generations of physicians have attached great importance to the application and research of tongue diagnosis, and it has been inherited as the core content of "diagnosis by looking," which is the first of the four diagnoses in Chinese medicine. The experimental results show that the tongue image overlaying the current day blood pressure can improve the prediction accuracy compared with the current day blood pressure data alone, suggesting the contribution of the tongue image to the improvement of the prediction accuracy and confirming that the data fusion model is an important way to explore the clinical value of the Chinese medicine tongue image.

Data Availability

The numerical dataset used to perform the study presented in the paper are available from the corresponding author upon request.

Conflicts of Interest

The authors declare that they have no conflicts of interest.

Acknowledgments

The study was supported by National Key Research and Development Program of China (No. 2017YFC1703304), and National Natural Science Foundation of China (No. 81873204).

References

[1] Xi Chen and P. Guijuan, "On the holistic view of Chinese medicine," *Liaoning Journal of Traditional Chinese Medicine*, vol. 35, no. 4, pp. 515–517, 2008.

[2] L. Breiman, "Random forests," *Machine Learning*, vol. 45, no. 1, pp. 5–32, 2001.

[3] G. E. Hinton and R. R. Salakhutdinov, "Reducing the dimensionality of data with neural networks," *Science*, vol. 313, no. 5786, pp. 504–507, 2006.

[4] L. Jiao, "70 years of Neural network: review and prospect," *Chinese Journal of Computers*, vol. 39, no. 8, pp. 1697–1716, 2016.

[5] Z. Li, W. Li, and J. Qi, "Research on tongue segmentation model based on multiple machine vision techniques," *Shi-Zhen Guomao*, vol. 32, no. 7, pp. 1768–1771, 2021.

[6] J. Li, "Exploring the mechanism of tongue color formation," *Chinese Journal of Basic Chinese Medicine*, vol. 6, pp. 72–75, 2013.

[7] L. Han, *Standardized Prevention and Treatment of Hypertension-From Guidelines to Practice*, L. Han, Ed., pp. 23-24, Peking University Press, Beijing, 2017.

[8] M. Kobayashi and S. Uesugi, "The role of hypertension as a risk factor of atherosclerosis. Rinsho byori," *The Japanese Journal of Clinical Pathology*, vol. 43, no. 2, pp. 104–110, 1995.

[9] Y. Zhang, "A method for building a three-dimensional vascular tree of the human lingual artery," *Journal of Engineering and Thermophysics*, vol. 11, pp. 120–122, 2008.

[10] Y. Cao, Q. Miao, and J. Liu, "Research progress and prospect of Adaboost algorithm," *J. Autom*, vol. 17, no. 23, pp. 342–351, 2013.

[11] J. H. Friedman, “Greedy function approximation: a gradient boosting machine,” *Annals of Statistics*, vol. 29, no. 5, pp. 1189–1232, 2001.

[12] J. Junping, H. Xiaoqun, and J. Yongjin, *Statistics*, Renmin University of China Press, Beijing, China, 4th edition, 2009.

[13] C. Willmott and K. Matsuura, “Advantages of the mean absolute error (MAE) over the root mean square error (RMSE) in assessing average model performance,” *Climate Research*, vol. 30, no. 1, pp. 79–82, 2005.

Hindawi
Journal of Healthcare Engineering
Volume 2023, Article ID 9807423, 1 page
https://doi.org/10.1155/2023/9807423

Retraction

Retracted: Association of Pentachlorophenol with Fetal Risk of Prolonged Bradycardia: A Systematic Review and Meta-Analysis

Journal of Healthcare Engineering

Received 15 August 2023; Accepted 15 August 2023; Published 16 August 2023

This article has been retracted by Hindawi following an investigation undertaken by the publisher [1]. This investigation has uncovered evidence of one or more of the following indicators of systematic manipulation of the publication process:

(1) Discrepancies in scope
(2) Discrepancies in the description of the research reported
(3) Discrepancies between the availability of data and the research described
(4) Inappropriate citations
(5) Incoherent, meaningless and/or irrelevant content included in the article
(6) Peer-review manipulation

The presence of these indicators undermines our confidence in the integrity of the article's content and we cannot, therefore, vouch for its reliability. Please note that this notice is intended solely to alert readers that the content of this article is unreliable. We have not investigated whether authors were aware of or involved in the systematic manipulation of the publication process.

Wiley and Hindawi regrets that the usual quality checks did not identify these issues before publication and have since put additional measures in place to safeguard research integrity.

We wish to credit our own Research Integrity and Research Publishing teams and anonymous and named external researchers and research integrity experts for contributing to this investigation.

The corresponding author, as the representative of all authors, has been given the opportunity to register their agreement or disagreement to this retraction. We have kept a record of any response received.

References

[1] X. Song and X. Fu, "Association of Pentachlorophenol with Fetal Risk of Prolonged Bradycardia: A Systematic Review and Meta-Analysis," *Journal of Healthcare Engineering*, vol. 2022, Article ID 7552294, 9 pages, 2022.

Hindawi
Journal of Healthcare Engineering
Volume 2022, Article ID 7552294, 9 pages
https://doi.org/10.1155/2022/7552294

Review Article

Association of Pentachlorophenol with Fetal Risk of Prolonged Bradycardia: A Systematic Review and Meta-Analysis

Xueyun Song and Xiaodong Fu

Department of Obstetrics, The Affiliated Hospital of Southwest Medical University, Luzhou, Sichuan Province, China

Correspondence should be addressed to Xiaodong Fu; dongerfu@163.com

Received 9 December 2021; Revised 13 February 2022; Accepted 21 February 2022; Published 27 March 2022

Academic Editor: Enas Abdulhay

Objective. This study explored the systematic evaluation and meta-analysis of different concentrations of PCP on the risk of long-term bradycardia in fetuses. *Methods*. Cochrane Library, Embase, PubMed, China Biomedical Literature Service, CNCNKI, and Wanfang database were computerized to collect all case-control studies on the association between variety classes and different concentrations of environmental pollutant gas to fetal of prolonged bradycardia. After evaluating the quality of the inclusion study and extracting valid data, meta-analysis was performed using Stata15 software. Relative hazards were calculated using the Mantel-Haenszel method and the random effect model, and P values and I^2 values were used for heterogeneity evaluation. When heterogeneity occurs, subgroup analysis and sensitivity analysis were used to explore the sources. *Results*. A total of 15 studies were included, including 1202 patients with fetal of prolonged bradycardia and 1380 in the control population. Meta-analysis showed that there was no statistical difference in PCP < 0.1 mg/L between the experimental group and control group (OR $= 1.03$, 95% CI (0.62, 1.72), $P = 0.90$, $I^2 = 0\%$, $Z = 0.13$), but there was a statistical difference in PCP > 5 mg/L (OR $= 1.73$, 95% CI (1.15, 2.58), $P = 0.008$, $I^2 = 0\%$, $Z = 2.65$), PCP > 10 mg/L (OR $= 1.75$, 95% CI (1.19, 2.57), $P = 0.004$, $I^2 = 14\%$, $Z = 2.85$), and PCP >15 mg/L (OR $= 2.02$, 95% CI (1.38, 2.95), $P = 0.0003$, $I^2 = 77\%$, $Z = 3.61$). *Conclusion*. In this study, we found that different concentrations of PCP increased the risk of long-term bradycardia in fetuses, and the risk coefficient increased with the increase of PCP concentration.

1. Introduction

Fetal bradycardia was defined as a fetal heart rate below 110 beats/min and with a duration longer than 10 min. The transient decline in fetal heart rate in middle and late pregnancies recovered in a short period of time and had a good prognosis [1]. Pathologic changes, such as sinus bradycardia, atrioventricular block, and long QT syndrome, should be considered when the fetal bradycardia continues. Persistent bradycardia is not common, accounting for about 5% of fetal arrhythmias, and can occur during various periods of the fetus [2]. The main disease accounts for about 14%, including atrioventricular septal defect, left atrial heterogeneous, and large artery abnormalities [3]. Abnormalities of these structures can cause interference with the electrophysiological continuity between the fetal atrium and ventricles, leading to arrhythmias. Fetuses combined with cardiac anatomical abnormalities have a relatively poor prognosis [4, 5].

Pentachlorophenol (PCP) is a white needle crystal, highly volatile, heated when irritant phenol odor, hardly soluble in water, and easy to be soluble in ether, acetone, benzene, and other organic solvents. Pentachlorophenol is widely used as pesticides, antibiotics, and preservatives, covering industrial and commerce, agriculture, water industry, and home life. Due to its high toxicity, long persistence, and difficult degradation, its extensive use and improper treatment lead to the pollution of soil and water resources and has become an environmental pollutant that cannot be ignored [6]. PCP and Na-PCP are slowly degraded in natural environments. It can be enriched in the bottom mud, and the long-term heavy use has caused environmental pollution and biological accumulation. Although many countries, including China, have banned the continued use of PCP, its residual effect will last for years or even decades [7]. A certain level of trichlorophenol can be detected in the water bodies, soil, and plants in the contaminated areas. Pentachlorophenol can have toxic and a series of adverse effects through direct contact (skin and respiratory tract) or food chain enrichment. Pentachlorophenol into the human body can accumulate in the liver, kidney, and adipose tissue for a long time, produce toxicity to the liver and kidney, improve the incidence of tumor, interfere with endocrine, affect immune function, and hinder reproductive development. Pentachlorophenol is not only a direct hazard to the human body, but may be potentially dangerous to electrophysiological function of fetal heart [8].

PCP has a strong uncoupling effect and can cause acute or chronic poisoning in humans and animals. In recent years, numerous studies have shown that PCP contains highly toxic dibenzene dioxin (PcDDs), tetrachloride diphenylfuran (TcBDFs), and other pollutants, especially the highly toxic tetrachlorodibenzene dioxin (TCDD). These substances have strong carcinogenic, teratogenic, mutagenic effects, with a greater impact on the reproductive system. Based on their strong biological stability, they will also be stronger and more durable. In addition, PCP has a strong adsorption to the soil and sediment; PCP water source irrigated crops will affect product quality; fishery will cause pollution to the environment of aquaculture waters, affect the healthy growth of fish, or cause death [9]. In the areas where PCP was used, the produced food PCP content, human daily intake, and urinary PCP concentration were significantly higher than that of the control region. After PCP enters the human body, it circulates to the tissues and organs of the whole body, most of which are discharged from the urine, and about 20% can accumulate in the body. Relevant investigation shows that the content of PCP in residents in polluted areas is significantly increased compared with the control area; therefore, attention should be paid to the potential health harm of food residual PCP to human body [10].

Although the use of PCP has been banned in China, its residual effect will persist for a long time; Na-PCP is still the best and cheapest sterilization effect in China, and this study was to explore the effects of different concentrations of environmental pollutants (PCP) on fetal bradycardia.

2. Materials and Methods

2.1. Search Strategy. Medline, Embase, Cochrane CENTRAL, Chinese Journal Full Text Database (CNKI), Chinese Biomedical Database (CBM), Chinese Science and Technology Journal Full Text Database (VIP), and Wanfang database were searched by computer. Manual retrieval of references is to important literature. Key search terms: “Environmental pollutant,” “Fetal bradycardia,” “Fetal arrhythmia,” and “Fetal prognosis”. All databases were searched from October 2000 to October 2021.

2.2. Literature Selection Criteria

(1) Inclusion criteria: all studies related to fetal bradycardia and environmental pollutants were selected in strict accordance with PRISMA statement, provide data on fetal arrhythmia and concentrations of targeted environmental pollutants, provide sufficient data to calculate OR and 95% CI, case-control study, get full text, duplicate publications from the same population were used, and the largest sample size was selected for inclusion in the study.

(2) Exclusion criteria: incomplete data, studies, case reports, reviews, reviews, summaries, and basic research based on pedigree data.

2.3. Data Extraction and Processing. Two researchers used a unified data extraction table to extract data independently and then cross-checked the data. If necessary, they contacted the authors of the original literature to determine the specific implementation process of the experiment. According to inclusion criteria, the following information was included: first author, year of publication, region, ethnicity, type of arrhythmia (fetal bradycardia and tachycardia), environmental contaminants and concentration detection methods, total number of cases, control group, study quality score, and cases. If two researchers have a dispute during data extraction, a third researcher will help resolve the discussion after referring to the original text.

2.4. Quality Evaluation of the Included Study. There are 3 researchers who independently evaluated the study based on a quality assessment form developed in the prior study quality. The score ranges from 0 to 13, with 0 being the lowest quality and 12 being the highest quality (Figure 1).

2.5. Bias Analysis. Heterogeneity between studies was assessed using I^2 statistics, and 25%, 50%, and 75% representing low, medium, and high heterogeneities, respectively; if I^2 50% and $P > 0.1$ between studies using fixed-effect models and if $I^2 > 50\%$ and $P < 0.1$ from chi-square analysis showed study heterogeneity, meta-analysis is by random effects models and searched for possible heterogeneity by subgroup analysis source. The sensitivity analysis removed the included literature one by one to see whether the pooled effect values were stable and reliable (Figure 2).

2.6. Statistical Analysis. RevMan 5.2 statistical software was used for meta-analysis. Heterogeneity was assessed by the t-test at a significant level $\alpha = 0.10$ ($P < 0.1$ or $I^2 > 50\%$). The results without heterogeneity were combined and analyzed by the fixed-effect model, while those with heterogeneity were analyzed by the random effect model. Mean difference (MD) and its 95% confidence interval (CI) combined effect were used for continuous variables with the same measurement units, and relative risk (RR) and its 95% CI combined effect were used for categorical variables.

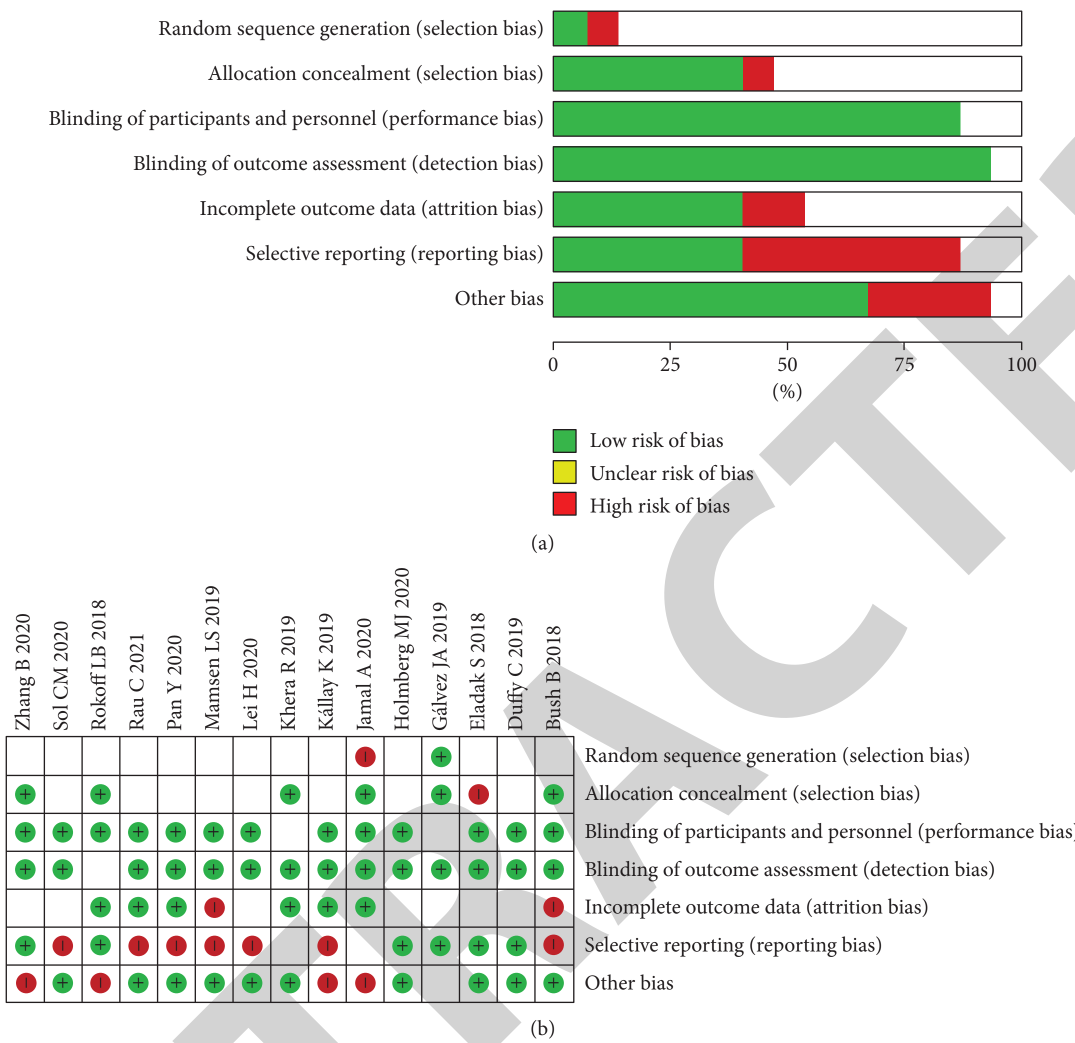

Figure 1: Literature quality evaluation chart. (a) Risk of bias graph. (b) Risk of bias summary.

3. Result

3.1. Retrieving the Results and Incorporating Basic Information in the Study. 359 literatures were obtained according to the retrieval strategy, and the remaining 108 literature entered the screening process after the exclusion of duplicate literature. 15 articles were selected for preliminary screening, among which two English articles were excluded due to lack of reported inclusion outcome indicators. 15 articles were finally included, with a total of 1397 patients [11–25]. There were 864 cases in the experimental group and 533 cases in the control group (Figure 3). Basic information of included studies is given in Table 1.

3.2. PCP < 0.1 mg/L. Among the 4 RCTs literature included in environmental pollutant concentrations with fetal risk of prolonged bradycardia, the heterogeneity test was carried out, and it was found that the heterogeneity of the selected studies was small, so meta-analysis with fixed models could be performed. Meta-analysis results showed that there was no statistical difference in PCP < 0.1 mg/L between the experimental group and control group (OR = 1.03, 95% CI (0.62, 1.72), $P = 0.90$, $I^2 = 0\%$, $Z = 0.13$) (Figure 4).

3.3. PCP > 5 mg/L. Among the 4 RCTs literature included in environmental pollutant concentrations with fetal risk of prolonged bradycardia, the heterogeneity test was carried out, and it was found that the heterogeneity of the selected studies was small, so meta-analysis with fixed models could be performed. Meta-analysis results showed that there was a statistical difference in PCP > 5 mg/L between the experimental group and control group (OR = 1.73, 95% CI (1.15, 2.58), $P = 0.008$, $I^2 = 0\%$, $Z = 2.65$) (Figure 5).

3.4. PCP > 10 mg/L. Among the 4 RCTs literature included in environmental pollutant concentrations with fetal risk of prolonged bradycardia, the heterogeneity test was carried out, and it was found that the heterogeneity of the selected studies was small, so meta-analysis with fixed models could be performed. Meta-analysis results showed that there was a statistical difference in PCP > 10 mg/L between experimental

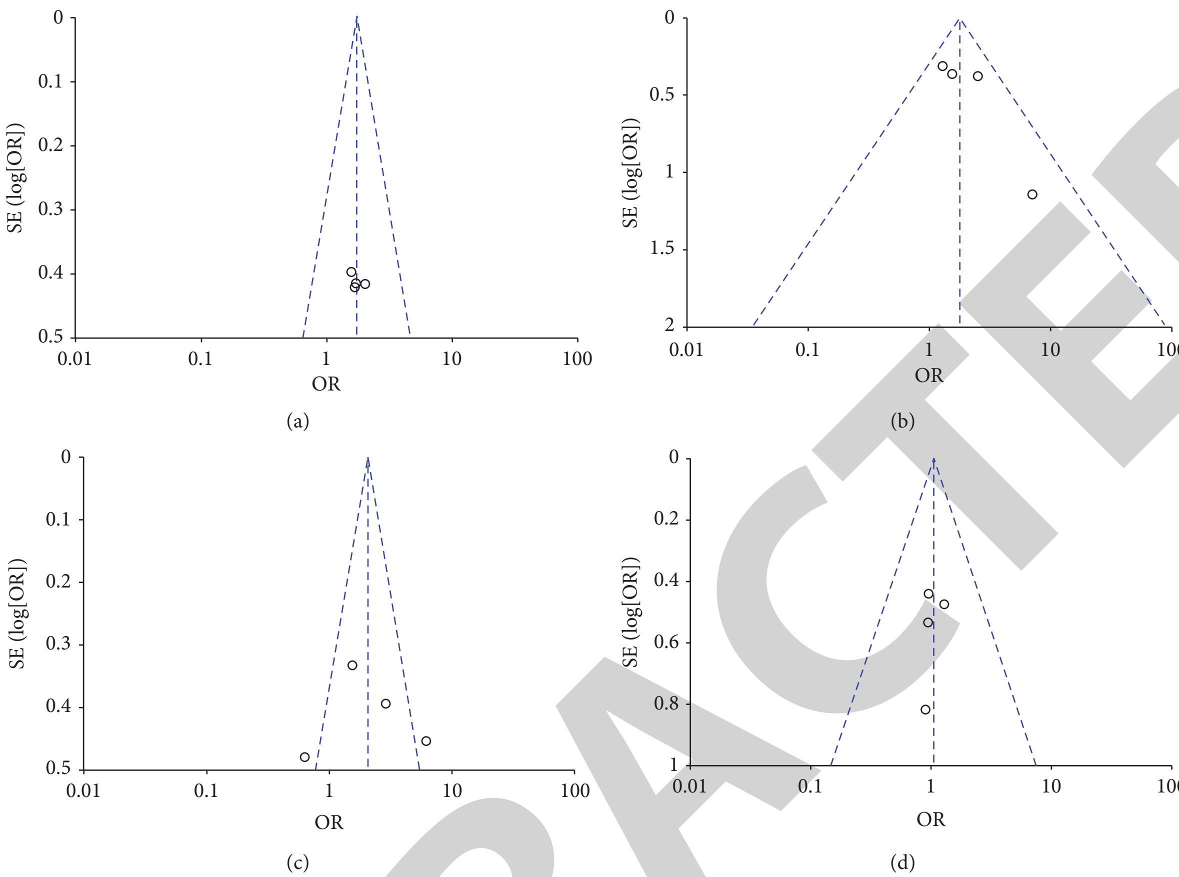

Figure 2: Funnel plot of literature publication bias for PCP < 0.1 mg/L (a), PCP > 5 mg/L (b), PCP > 10 mg/L (c), and PCP > 5 mg/L (d) between two groups.

the group and the control group (OR = 1.75, 95% CI (1.19, 2.57), P = 0.004, $I^2 = 14\%$, $Z = 2.85$) (Figure 6).

3.5. PCP > 15 mg/L. Among the 4 RCTs literature included in environmental pollutant concentrations with fetal risk of prolonged bradycardia, the heterogeneity test was carried out, and it was found that the heterogeneity of the selected studies was small, so meta-analysis with fixed models could be performed. Meta-analysis results showed that there was a statistical difference in PCP > 15 mg/L between the experimental group and control group (OR = 2.02, 95% CI (1.38, 2.95), P = 0.0003, $I^2 = 77\%$, $Z = 3.61$) (Figure 7).

4. Discussion

PCP in the environment mainly comes from the production and improper processing of the product. It is reported to produce 2,000 tPCP or Na-PCP, and the exhaust gas will contain 18tPCP, 9 t of other phenolic compounds. Na-PCP produces large amounts of PCP and other phenol wastewater; PCP can also be discharged directly into the environment by related industrial wastewater [26]. PCP-treated wood is also being released directly into the environment when used or burning.

Many animal experiments have confirmed that PCP has certain reproductive toxicity to organisms. For example, PCP can inhibit the growth and development of hamster oocytes; cows fed containing PCP found pathological changes such as luteal insufficiency and abnormal oocyte development [27]. After sexual maturation, ranging from 7 to 8 d, both the proportion of female mink receiving the second mating and the rate of lactation was decreased. R raised with feed containing PCP and necrolysis from the beginning of embryonic stage to week 28, the preferential margin of the scrotum increased, and the atrophy of the semen tube increased. The epididymal sperm density was decreased. In 2002, Bemard et al. fed 2 generations of SD rats with PCP, and reproductive toxicity tests showed that high-dose (60 mg/(kg.d)) feeding caused delayed sexual maturation, reduced sperm number, reduced prostate and testes, reduced embryo implantation capacity, and reduced litter production [28].

Similarly, in humans, with the deterioration of environmental quality, many environmental pollutants can pass through the way such as respiratory tract, the digestive tract, the skin into pregnant woman's body, and then through the limited tire barrier into fetal body because the fetus is sensitive to the chemical poison effect than adults; in the process of growth and development, if some poisonous substances contact within the womb, it may produce some effects, and adult contact with the substance is not the same as severe damage or even cancer [29, 30].

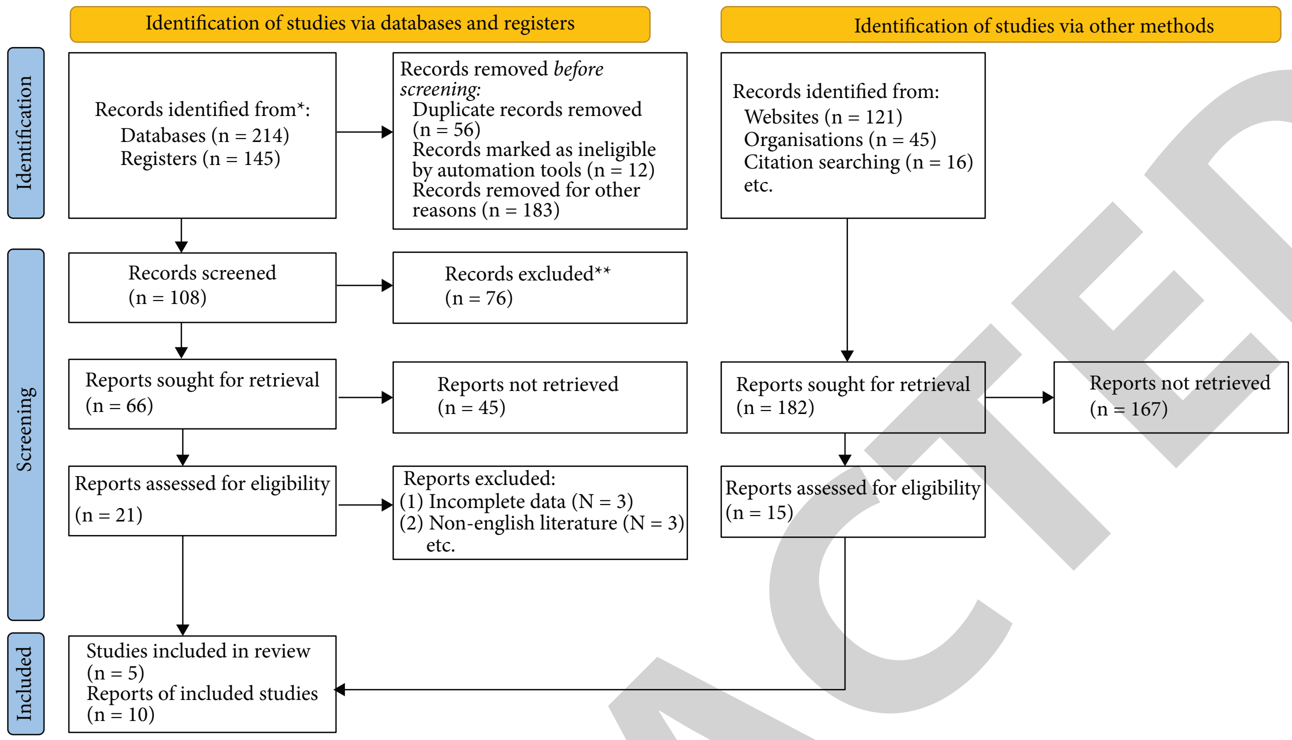

*Consider, if feasible to do so, reporting the number of records identified from each database or register searched (rather than the total number across all databases/registers).

**If automation tools were used, indicate how many records were excluded by a human and how many were excluded by automation tools.

Figure 3: Flowchart of the literature screening.

Table 1: Basic clinical features of 15 literature were included in our study.

Study	Pregnant time (W)	Environmental pollutant	Experimental group (*N*)	Control group (*N*)	NOS score	Research type	*P* values
Kállay K, 2019	23.71 ± 2.2	Pentachlorophenol (PCP)	96	75	8	RCT	0.35
Duffy C, 2019	25.65 ± 3.4	Pentachlorophenol (PCP)	86	63	8	RCT	0.02
Lei H, 2020	32.12 ± 4.5	Pentachlorophenol (PCP)	118	108	8	RCT	0.04
Holmberg, 2020	27.15 ± 4.5	Pentachlorophenol (PCP)	66	60	7	RCT	0.12
Khera R, 2019	32.45 ± 3.4	Pentachlorophenol (PCP)	58	73	8	RCT	0.06
Gálvez JA, 2019	24.26 ± 1.2	Pentachlorophenol (PCP)	54	65	7	RCT	0.02
Bush B, 2018	32.45 ± 2.2	Pentachlorophenol (PCP)	80	75	9	RCT	0.01
Rau C, 2021	32.51 ± 3.0	Pentachlorophenol (PCP)	80	63	8	RCT	0.02
Zhang B, 2020	27.25 ± 4.5	Pentachlorophenol (PCP)	41	56	7	RCT	0.14
Jamal A, 2020	26.22 ± 5.2	Pentachlorophenol (PCP)	64	70	8	RCT	0.23
Mamsen, 2019	31.35 ± 2.1	Pentachlorophenol (PCP)	108	100	7	RCT	0.01
Sol CM, 2020	27.65 ± 6.0	Pentachlorophenol (PCP)	96	77	7	RCT	0.25

Table 1: Continued.

Study	Pregnant time (W)	Environmental pollutant	Experimental group (N)	Control group (N)	NOS score	Research type	P values
Pan Y, 2020	25.65 ± 2.2	Pentachlorophenol (PCP)	22	25	8	RCT	0.14
Rokoff LB, 2018	24.62 ± 3.5	Pentachlorophenol (PCP)	44	32	8	RCT	0.07
Eladak S, 2018	31.46 ± 2.0	Pentachlorophenol (PCP)	25	30	8	RCT	0.35

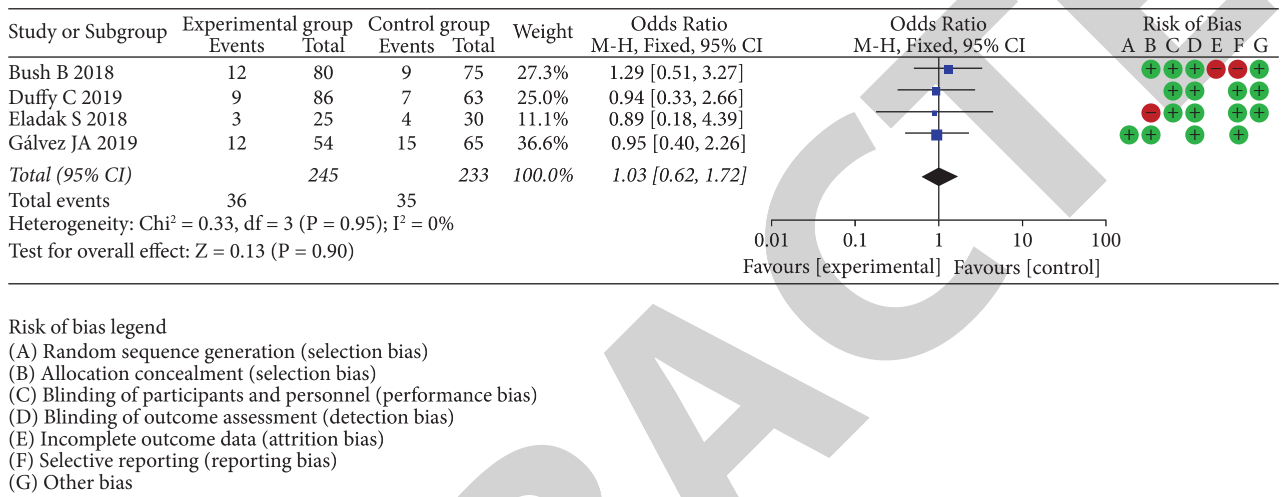

Figure 4: Meta-analysis of PCP < 0.1 mg/L between two groups.

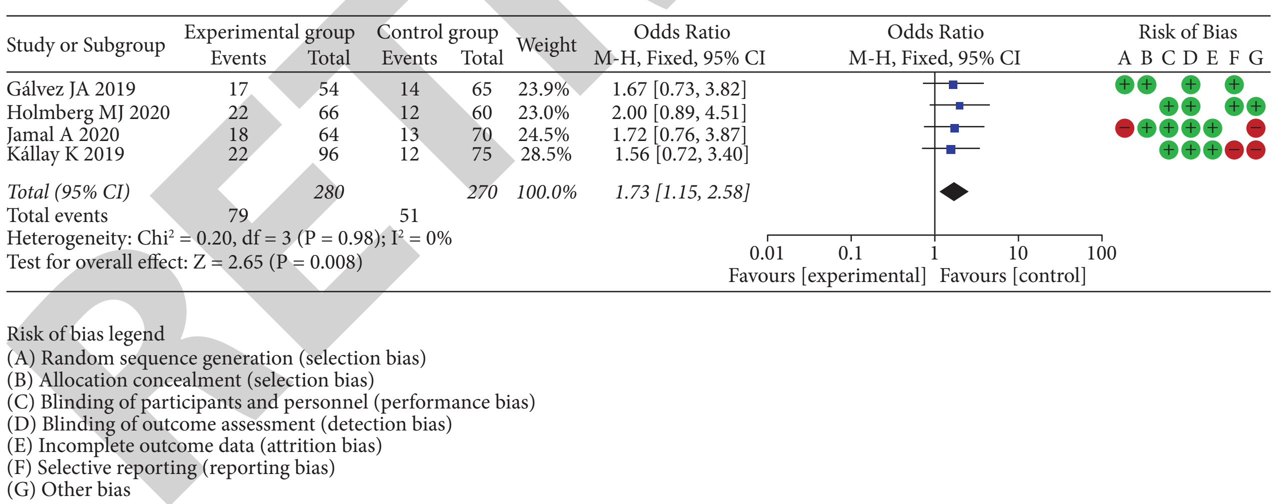

Figure 5: Meta-analysis of PCP > 5 mg/L between two groups.

PCP is an anticompetitive inhibitor of human placental alkaline phosphatase (PLAP). Toxicology tests show that PCP is a strong mitochondrial unconjugation agent that reduces plasma membrane mobility and also has a strong inhibitory effect in the acetylcholinesterase on the cell membrane [29]. Placental alkaline phosphatase is a metalloglycoprotein located on the membrane of late placental cells; in addition to catalytic function, some substances such as IgG, complement factor B, and cartilage matrix protein are related to fetal growth and development. Changes in the PLAP conformation can not only alter its function but also cause the structure and function of the placental cell membrane change, which must have adverse effects on the normal fetal development. In addition, PCP is a lipid-soluble substance that can enter the fetus through the placenta and have a direct

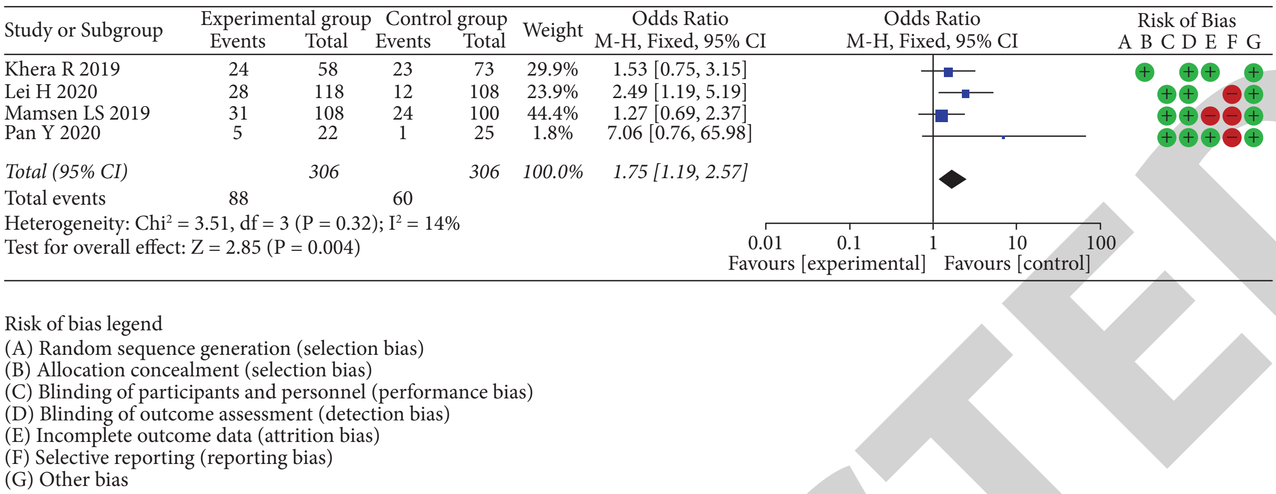

Figure 6: Meta-analysis of PCP > 10 mg/L between two groups.

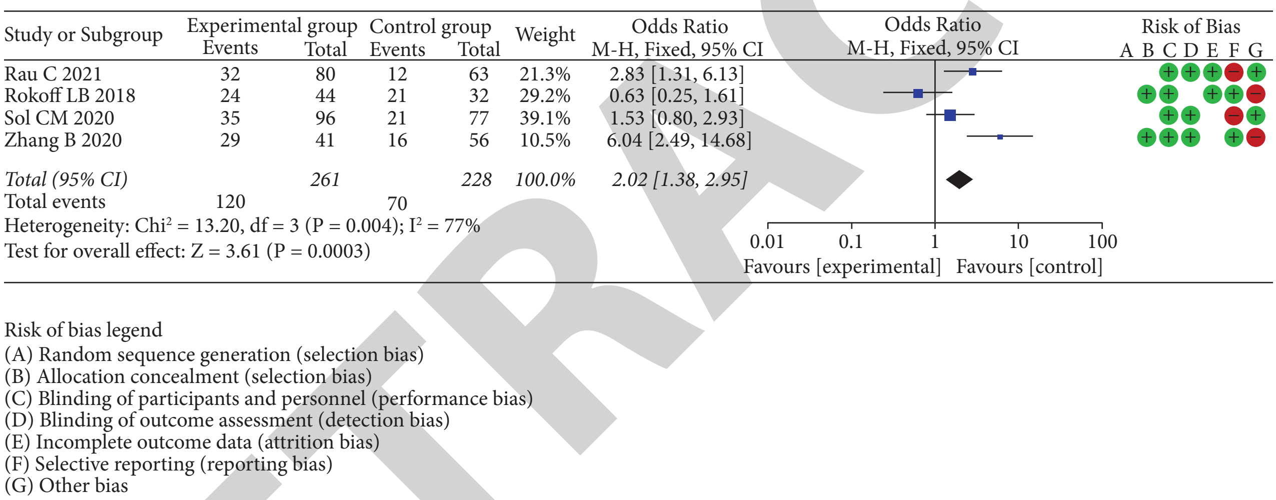

Figure 7: Meta-analysis of PCP > 15 mg/L between two groups.

toxic effect on the fetus [30]. In Heidelberg Hospital, Germany, during a physical examination of 65 women with a long history of PCP exposure, it was found that its serum PCP content was asked above 20 bucket g/L; thus, the exposure history of PCP in pregnant women will also have adverse effects on the fetus.

Fetal arrhythmias caused by the toxic effect of PCP are common in routine prenatal ultrasound screening and can occur throughout any stage of pregnancy, with the incidence reported in foreign literature during pregnancy of up to 1–3%. Fetal JbL, arrhythmias can be divided into three categories: irregular arrhythmias, tachycardia, and bradycardia, among which irregular arrhythmias are the most common, mainly caused by prephase contraction. The most common fetal tachycardia is intraventricular tachycardia and atrial fibrillation. The most common fetal bradycardia is complete atrioventricular block; the mother of children is with normal heart structure. There are high-efficiency anti-SSA antibodies or anti-SSB antibodies staring inside.

The limitations of this study are as follows: incorporating observational studies in the study is limited, the follow-up varies from 3 to 36 months, making the evaluation of long-term complications, the publication bias analysis is only qualitative and large personal factors, and the two techniques described in this study contain multiple surgical procedures, which may increase the bias of the article. Since the assessments were all based on a small number of studies [26–28], the results must be interpreted with caution. As the accumulated evidence grows, our conclusions may either be supported or overturned.

5. Conclusion

In conclusion, environmental pollutant PCP > 0.1 mg/L could increase the risk of fetal bradycardia, and it increased with the increase of PCP concentration. It is of great significance to evaluate the toxic effects of maternal exposure to environmental pollutants in order to reduce the health damage to the next generation.

Data Availability

The data used to support this study are available from the corresponding author upon request.

Conflicts of Interest

The authors declare that they have no conflicts of interest.

References

[1] J. L. Peel, M. Klein, W. D. Flanders, J. A. Mulholland, G. Freed, and P. E. Tolbert, "Ambient air pollution and apnea and bradycardia in high-risk infants on home monitors," *Environmental Health Perspectives*, vol. 119, no. 9, pp. 1321–1327, 2011.

[2] S. M. Cantanhêde, M. Hamoy, L. F. A. Montag, and L. L. Amado, "Electrophysiological responses in Amazonian fish species Bryconops caudomaculatus (Osteichthyes: characiformes) as biomarkers of xenobiotic toxicity," *Comparative Biochemistry and Physiology, Toxicology & Pharmacology: CB*, vol. 228, Article ID 108653, 2020.

[3] J. Widdicombe and L.-Y. Lee, "Airway reflexes, autonomic function, and cardiovascular responses," *Environmental Health Perspectives*, vol. 109, no. 4, pp. 579–584, 2001.

[4] V. A. Abrich, R. J. Le, S. K. Mulpuru et al., "Clinical outcomes of various management strategies for symptomatic bradycardia," *Clinical Medicine and Research*, vol. 18, no. 2-3, pp. 75–81, 2020.

[5] F. Suyama, K. Ogawa, Y. Tazaki et al., "The outcomes and risk factors of fetal bradycardia associated with external cephalic version," *Journal of Maternal-Fetal and Neonatal Medicine*, vol. 32, no. 6, pp. 922–926, 2019.

[6] L. Wong, W. T. Tse, C. Y. Lai et al., "Bradycardia-to-delivery interval and fetal outcomes in umbilical cord prolapse," *Acta Obstetricia et Gynecologica Scandinavica*, vol. 100, no. 1, pp. 170–177, 2021.

[7] J. Lepercq, M. A. Nghiem, and F. Goffinet, "Fetal heart rate nadir during bradycardia and umbilical artery acidemia at birth," *Acta Obstetricia et Gynecologica Scandinavica*, vol. 100, no. 5, pp. 964–970, 2021.

[8] L. Hruban, P. Janků, K. Jordanova et al., "The effect of transient fetal bradycardia and other heart rate changes during and after external cephalic version on perinatal outcomes," *European Journal of Obstetrics & Gynecology and Reproductive Biology*, vol. 245, pp. 39–44, 2020.

[9] A. Nakanomori, N. Nagano, A. Seimiya, A. Okahashi, and I. Morioka, "Fetal sinus bradycardia is associated with congenital hypothyroidism: an infant with ectopic thyroid tissue," *Tohoku Journal of Experimental Medicine*, vol. 248, no. 4, pp. 307–311, 2019.

[10] K. L. Thornburg, "Acute fetal hypoxic bradycardia: solving the chemoreception puzzle," *The Journal of Physiology*, vol. 598, no. 20, pp. 4433-4434, 2020.

[11] K. Kállay, D. Zakariás, K. Csordás et al., "Antithymocyte globuline therapy and bradycardia in children," *Pathology Oncology Research: POR*, vol. 25, pp. 487–492, 2019.

[12] C. Duffy, L. Hall, J. Godown, T. Koyama, and S. C. Borinstein, "Steroid-induced bradycardia during induction chemotherapy in children and young adults diagnosed with acute lymphoblastic leukemia and lymphoblastic lymphoma," *Journal of Pediatric Hematology*, vol. 41, no. 7, pp. 537–541, 2019.

[13] H. Lei, L. Chao, T. Miao et al., "Incidence and risk factors of bradycardia in pediatric patients undergoing intranasal dexmedetomidine sedation," *Acta Anaesthesiologica Scandinavica*, vol. 64, no. 4, pp. 464–471, 2020.

[14] M. J. Holmberg, C. E. Ross, T. Yankama, J. S. Roberts, and L. W. Andersen, "Epinephrine in children receiving cardiopulmonary resuscitation for bradycardia with poor perfusion," *Resuscitation*, vol. 149, pp. 180–190, 2020.

[15] R. Khera, Y. Tang, S. Girotra et al., "Pulselessness after initiation of cardiopulmonary resuscitation for bradycardia in hospitalized children," *Circulation*, vol. 140, no. 5, pp. 370–378, 2019.

[16] J. A. Gálvez, S. Acquah, L. Ahumada et al., "Hypoxemia, bradycardia, and multiple laryngoscopy attempts during anesthetic induction in infants: a single-center, retrospective study," *Anesthesiology*, vol. 131, pp. 830–839, 2019.

[17] B. Bush, J. D. Tobias, C. Lin et al., "Postoperative bradycardia following adenotonsillectomy in children: does intraoperative administration of dexmedetomidine play a role?" *International Journal of Pediatric Otorhinolaryngology*, vol. 104, pp. 210–215, 2018.

[18] C. Rau, S. Apostolidou, D. Singer, V. Avataneo, and R. Kobbe, "Remdesivir, sinus bradycardia and therapeutic drug monitoring in children with severe COVID-19," *The Pediatric Infectious Disease Journal*, vol. 40, no. 12, pp. e528–e529, 2021.

[19] B. Zhang, Y. He, H. Zhu et al., "Concentrations of bisphenol A and its alternatives in paired maternal-fetal urine, serum and amniotic fluid from an e-waste dismantling area in China," *Environment International*, vol. 136, Article ID 105407, 2020.

[20] A. Jamal, N. Rastkari, R. Dehghaniathar et al., "Prenatal urinary concentrations of environmental phenols and birth outcomes in the mother-infant pairs of Tehran Environment and Neurodevelopmental Disorders (TEND) cohort study," *Environmental Research*, vol. 184, Article ID 109331, 2020.

[21] L. S. Mamsen, R. D. Björvang, D. Mucs et al., "Concentrations of perfluoroalkyl substances (PFASs) in human embryonic and fetal organs from first, second, and third trimester pregnancies," *Environment International*, vol. 124, pp. 482–492, 2019.

[22] C. M. Sol, S. Santos, L. Duijts et al., "Fetal exposure to phthalates and bisphenols and childhood general and organ fat. A population-based prospective cohort study," *International Journal of Obesity*, vol. 44, no. 11, pp. 2225–2235, 2020.

[23] Y. Pan, M. Deng, J. Li et al., "Occurrence and maternal transfer of multiple bisphenols, including an emerging derivative with unexpectedly high concentrations, in the human maternal-fetal-placental unit," *Environmental Science & Technology*, vol. 54, no. 6, pp. 3476–3486, 2020.

[24] L. B. Rokoff, S. L. Rifas-Shiman, B. A. Coull et al., "Cumulative exposure to environmental pollutants during early pregnancy and reduced fetal growth: the Project Viva cohort," *Environmental Health*, vol. 17, no. 1, p. 19, 2018.

[25] S. Eladak, D. Moison, M.-J. Guerquin et al., "Effects of environmental Bisphenol A exposures on germ cell development and Leydig cell function in the human fetal testis," *PLoS One*, vol. 13, no. 1, Article ID e0191934, 2018.

[26] J. Guo, W. Miao, C. Wu et al., "Umbilical cord serum PBDE concentrations and child adiposity measures at 7 years," *Ecotoxicology and Environmental Safety*, vol. 203, p. 111009, 2020.

[27] M. C. O. Souza, M. C. P. Saraiva, M. Honda et al., "Exposure to per- and polyfluorinated alkyl substances in pregnant Brazilian women and its association with fetal growth," *Environmental Research*, vol. 187, Article ID 109585, 2020.

Hindawi
Journal of Healthcare Engineering
Volume 2023, Article ID 9858276, 1 page
https://doi.org/10.1155/2023/9858276

Retraction

Retracted: Antitumor Effects of 10058-F4 and Curcumin in Combination Therapy for Pancreatic Cancer In Vitro and In Vivo

Journal of Healthcare Engineering

Received 8 August 2023; Accepted 8 August 2023; Published 9 August 2023

This article has been retracted by Hindawi following an investigation undertaken by the publisher [1]. This investigation has uncovered evidence of one or more of the following indicators of systematic manipulation of the publication process:

(1) Discrepancies in scope
(2) Discrepancies in the description of the research reported
(3) Discrepancies between the availability of data and the research described
(4) Inappropriate citations
(5) Incoherent, meaningless and/or irrelevant content included in the article
(6) Peer-review manipulation

The presence of these indicators undermines our confidence in the integrity of the article's content and we cannot, therefore, vouch for its reliability. Please note that this notice is intended solely to alert readers that the content of this article is unreliable. We have not investigated whether authors were aware of or involved in the systematic manipulation of the publication process.

In addition, our investigation has also shown that one or more of the following human-subject reporting requirements has not been met in this article: ethical approval by an Institutional Review Board (IRB) committee or equivalent, patient/participant consent to participate, and/or agreement to publish patient/participant details (where relevant).

Wiley and Hindawi regrets that the usual quality checks did not identify these issues before publication and have since put additional measures in place to safeguard research integrity.

We wish to credit our own Research Integrity and Research Publishing teams and anonymous and named external researchers and research integrity experts for contributing to this investigation.

The corresponding author, as the representative of all authors, has been given the opportunity to register their agreement or disagreement to this retraction. We have kept a record of any response received.

References

[1] Z. Jie, Z. Jinna, Z. Jingjun et al., "Antitumor Effects of 10058-F4 and Curcumin in Combination Therapy for Pancreatic Cancer In Vitro and In Vivo," *Journal of Healthcare Engineering*, vol. 2022, Article ID 1620802, 8 pages, 2022.

Hindawi
Journal of Healthcare Engineering
Volume 2022, Article ID 1620802, 8 pages
https://doi.org/10.1155/2022/1620802

Research Article

Antitumor Effects of 10058-F4 and Curcumin in Combination Therapy for Pancreatic Cancer In Vitro and In Vivo

Zhang Jie,[1] Zhang Jinna,[2] Zhang Jingjun,[3] Li Pengcheng,[1] Yang Fang,[1] Chen Qinyang,[4] Chen Taiyu,[4] Jiang Hequn,[5] and Ren Tao[1]

[1]*Clinical Medical College and The First Affiliated Hospital of Chengdu Medical College, Si Chuan, China*
[2]*No.4 West China Teaching Hospital of Si Chuan University, Si Chuan, China*
[3]*The People's Hospital of JianYang City, Si Chuan, China*
[4]*Chengdu Medical College, Si Chuan, China*
[5]*South China Hospital of Shenzhen University, Guang Dong, China*

Correspondence should be addressed to Ren Tao; ren_tao66@163.com

Received 10 January 2022; Revised 28 February 2022; Accepted 2 March 2022; Published 24 March 2022

Academic Editor: Enas Abdulhay

Objectives of the Study. In vitro and in vivo evaluation of the antipancreatic cancer effects and benefits of the 10058-F4 and curcumin combination therapy. *Background*. Pancreatic cancer (PC) stands out as one of the most lethal cancers. Due to late diagnosis, only a fraction of patients can be resected. Although it still has significant adverse effects and poor results, the treatment is connected with better overall survival than the prior treatment. Thus, new alternative therapy for advanced PC is needed. *Materials/Methods*. The impact of 10058-F4 and curcumin combination therapy on apoptosis and cell growth in SW1990 pancreatic cancer cells were determined in vitro using the CCK-8 assay and flow cytometry of Annexin V-FITC/PI, and the in vivo antitumor effect was determined utilizing SW1990-bearing pancreatic tumor mouse models induced by subcutaneous implantation. *Results*. At concentrations of (10 mol/L+2 mol/L), 10058-F4+curcumin obtained the highest rate of SW1990 cell death, and they had a beneficial effect on SW1990 pancreatic tumor-bearing animals. Furthermore, c-Myc, Akt phosphorylation, and the expression of apoptosis-related molecular were reduced, and the combination therapy modified the expression of apoptosis-related molecular. *Conclusions*. In vitro and in vivo, the combination of 10058-F4 plus curcumin has antipancreatic cancer actions that are substantially effective.

1. Introduction

Pancreatic ductal adenocarcinoma (PDAC), having a 5-year survival rate of only 9%, is one of the fatal human cancers [1]. The only treatment that can potentially offer a cure for pancreatic cancer is surgical resection [2]. Immune checkpoint blockade therapies that are beneficial in other cancers have failed to benefit randomly selected PDAC populations in phase III trials [3]. As a proto-oncogene, c-Myc has been found to be activated in a variety of animal and human malignancies and is required for the metabolism, differentiation, apoptosis, and cell proliferation [4]. Previous research has established that overexpression of c-Myc has an involvement in the development and progression of PDAC [5, 6]. c-Myc downregulation impedes the development of PDAC [7, 8].

A small-molecule inhibitor of c-Myc-Max dimerization, referred to as 10058-F4, has been demonstrated to reduce cellular proliferation, increase apoptosis, and induce chemosensitivity [9–11]. Furthermore, no substantial tumor growth inhibition was observed after intravenous injection of either 20 or 30 mg/kg 10058-F4 into mice. The quick metabolism and low tumor concentration of 10058-F4 may have resulted in its lack of considerable antitumor effect in tumor-bearing mice [12]. The anticancer action of 10058-F4 has been reported in PDAC cell lines, and 10058-F4 therapy sensitizes PANC-1 and SW1990 cells to gemcitabine. In a subcutaneous xenograft model, 10058-F4 did not affect pancreatic carcinogenesis; however, when paired with 10058-F4, the anticancer impact of gemcitabine is more substantial [13].

Curcumin is a pure crystalline yellow pigment derived from the turmeric plant [14]. Curcumin possesses antitumor, antiangiogenesis, antiproliferative, and anti-inflammatory activities without causing cytotoxicity in normal cells [15, 16]. Curcumin has the potential to cause apoptosis in cancer cells [17]. Apoptotic proteins, inflammatory cytokines, transcription factors, and growth factors have all been shown to be modulated by curcumin. It can be an effective cancer therapy agent when used alone or in combination with other drugs [18]. Two reports indicate that curcumin regulates c-Myc [19, 20]. Curcumin inhibits gastric cancer cell proliferation by inhibiting the c-Myc/H19 pathway [19]. It can also have a strong inhibitory effect in three prostate cancer cell lines by upregulating miR-34a and downregulating β-catenin and c-Myc levels [20]. Curcumin has been found to have anticancer properties in PDAC cell lines. Interacting with the miR-340/XIAP signaling pathway has been demonstrated to promote apoptosis in pancreatic cancer cells in vitro [21].

Curcumin can also block EGF-induced pancreatic cancer cell invasion and migration by inhibiting the EGF/EGFR signaling pathway and downstream signaling molecules, for instance, ERK and Akt [22]. Curcumin inhibits the PI3K/Akt/NF-κB signaling pathway, preventing SOD-driven H_2O_2-induced pancreatic cancer metastasis [23]. Curcumin is shown to sensitize gemcitabine-resistant PDAC cell lines via an inhibitory effect on the PRC2-PVT1-c-Myc axis [24]. Such studies suggest that using curcumin in combination with chemotherapy to overcome chemoresistance in PDAC has therapeutic efficacy. Curcumin may inhibit c-Myc and improve the clinical therapeutic potential of the c-Myc inhibitor 10058-F4 in pancreatic cancer cells. This study used curcumin or 10058-F4 alone or in combination to treat SW1990 cells in vitro and in vivo. Curcumin therapy sensitized SW1990 cells to 10058-F4 for the first time.

2. Materials and Methods

2.1. Chemicals and Cell Culture. The Chinese Academy of Sciences (CAS) Cell Bank provided the pancreatic cancer cell lines PANC-1, SW1990, BxPC3, Capan-1, and Capan-2 (Shanghai, China). In a 5% CO_2 cell culture incubator at 37°C, cells were grown in high-glucose DMEMR or PMI-1640 media supplemented with 10% fetal bovine serum (FBS; Gibco) and 1% penicillin or streptomycin. In dimethylsulfoxide (DMSO) (Sigma), 100 mM stock solutions of curcumin and 100 mM stock solutions of 10058-F4 (Selleck) were produced.

2.2. Cell Proliferation Assay. 5,000 SW1990 cells were planted in individual wells of a 96-well plate, in 100 μl completed DMEM medium. Cells were monotreated with either 10058-F4 (10 μM) or curcumin (5 μM) for 48 hours before cotreatment with both 10058-F4 and curcumin. The Cell Counting Kit-8 (CCK-8, Dojindo) was employed to analyze cell proliferation, following the protocol elaborated by the manufacturer. Each well was filled with 10 μl CCK-8 solution and 90 μl DMEM. After oscillating for 15 seconds, the cell absorbance was measured at a wavelength of 450 nm (OD450) 2 hours later.

2.3. Colony Formation Assay. Different groups of people took part in the colony formation test. SW1990 cells were trypsinized and grown in 6-well plates at a density of 1,000 cells per well. Four groups of cells were created. The cells were monotreated with 10058-F4 (10 μM) or curcumin (5 μM) for 24 or 72 hours, later cotreated with 10058-F4 and curcumin twice. After 2 weeks, the colonies were fixed for 15 minutes with 4% (*w/v*) formaldehyde and stained for 15 minutes with 0.1% (*w/v*) crystal violet. Chemiluminescent image analysis photographs the colonies (Bio-Rad, ChemiDoc Touch, USA).

2.4. Flow Cytometry. SW1990 cells were trypsinized and grown in 6-well plates at a density of 2×10^5 cells per well. The cells were separated into four groups and treated with either 10058-F4 (10 μM) or curcumin (5 μM) alone or in combination for 48 hours. Trypsinization was used to harvest cells from four groups, and the cell density was maintained at 5×10^5 cells per ml. Centrifugation at 1200 rpm was used to wash the cell samples with phosphate-buffered saline (PBS). Following that, the Annexin V-FITC/PI Apoptosis Detection Kit (BD Pharmingen, CA, USA) was used to stain the cell samples as mentioned in the instructions provided by the manufacturer. After 30 minutes at 37°C in the dark, the stained cells were counted by making use of a FACS Calibur (BD Biosciences, San Jose, CA, USA) and analyzed through FlowJo software v.7.6.5 (Tree Star, OR, USA).

2.5. Xenograft Models of SW1990 Cells in Nude Mice. 12 male BALB/c nu/nu mice (5 weeks old and weighing around 18–22 g) were acquired from Shanghai Beijing Vital River Laboratory Animal Technology and kept within 12/12 h light/dark cycles with unrestricted supply of water and rat chow. The Medical Experimental Animal Care Commission approved the experimental methodology of Chengdu Medical College's First Affiliated Hospital. For producing the subcutaneous tumors, SW1990 cells (1×10^7 cells) in 0.2 ml PBS were injected into the right flank of test mice. Following one week, the mice were divided into four groups: the control group (with intraperitoneal and intravenous injections of equivalent solvent), the 10058-F4 group (with intravenous injections of 20 mg/kg 10058-F4 every other day), the curcumin group (with intraperitoneal injections of 25 mg/kg curcumin every other day), and the combination group (with intravenous injections of 20 mg/kg 10058-F4 and 25 mg/kg curcumin. Curcumin (25 mg/kg) was dissolved in 80% ddH_2O, 10% PEG300, 5% Tween 80, and 5% DMSO following the manufacturer's protocol. Dissolution of 10058-F4 (20 mg/kg) in a mixture of ethanol, Cremophor EL, and saline (1 : 1:8

v/v/v) to a final concentration of 2 mg/ml yielded the dosing solutions. Three mice from each group were slain three weeks later to obtain the implanted tumors.

2.5.1. Immunohistochemistry and Terminal Deoxynucleotidyl Transferase d-UTP Nick End Labeling (TUNEL) Staining. To eliminate endogenous peroxidase activity, the xenograft tumor tissues were cut into 4 μm thick slides after being embedded in paraffin and then treated with xylene to remove paraffin and rehydrate. The slides were incubated for 30 minutes at room temperature with 5% goat serum. A rabbit anti-PCNA antibody was used to treat the slides after being washed (1 : 100, Abcam, Cambridge, UK). As a final step, the Thermo Fisher Scientific HRP DAB (UltraVision Quanto Detection System) was employed for the detection of PCNA expression. Mayer's hematoxylin (Sigma-Aldrich, St. Louis, MO) was employed for counterstaining the slides, and neutral resins (Thermo Fisher Scientific, Pittsburgh, PA, USA) were used to attach coverslips. This study used the TdT-mediated d-UTP labeling approach to assess TUNEL staining, which was conducted in accordance with the manufacturer's instructions (Roche, Applied Biosystems). Apoptotic cell DNA fragments were tagged at free 3′-OH DNA ends and strand breaks, respectively. An antifluorescein antibody coupled with alkaline phosphatase was used to detect fluorescein. Light microscopy was used to examine the stained cells after the reaction with the substrate had taken place.

2.6. Western Blot. Using RIPA lysis buffer and protease/phosphatase inhibitor cocktail (MedChemExpress, NJ, USA) with 1 mM phenylmethyl sulphonyl fluoride PMSF (Beyotime Biotech, Shanghai, China), the whole protein in each cell sample was extracted and quantified with a BCA protein assay (Beyotime Biotech, Shanghai, China). After blocking the protein with the primary antibodies against c-Myc, SOX2, p-Akt (Ser473), Akt, MCL-1, Bcl-2, FAS, and cleaved-caspase 3 beta-actin (1 : 1000, Cell Signaling Technology, Danvers, MA USA), the incubation period was extended overnight at 4°C. Secondary antibody conjugated to HRP (Beyotime Biotech, Shanghai, China, 1 : 4000) was incubated for 2 hours at room temperature with protein. The eECL Western blot kit (Beyotime Biotech, Shanghai, China) was utilized to detect the protein.

3. Results

3.1. High Expression of c-Myc in Pancreatic Cancer. In prior research, the c-Myc gene is substantially expressed in pancreatic cancer cells [7, 8, 13]. It was shown that human pancreatic cancer cells overexpress c-Myc, as were normal pancreatic epithelial cell hTERT-HPNE in our investigation of 5 human pancreatic cancer cell lines (PANC-1, SW1990, BxPC3, Capan-1, and Capan-2 cells), as shown in Figure 1(a).

3.2. Curcumin Sensitized the Anticancer Influence of 10058-F4 in Pancreatic Cancer Cells. 10058-F4 is a c-Myc inhibitor [9, 10]. Curcumin also inhibits c-Myc [19, 20]. To further confirm the therapeutic value of targeting c-Myc, we attempted to sensitize the anticancer influence of 10058-F4 using curcumin and investigated the degree of inhibition of c-Myc using 10058-F4, curcumin, or a combination of both. First, we checked cell viability in 10058-F4 curcumin and combined treating SW1990 cells by detecting OD450 with CCK-8 reagent. Cell viability was gradually inhibited in the combination group (Figure 1(b)). The clonogenic assay results also confirmed the potent anticancer effect of the combination (Figure 2(a)). Since 10058-F4 and curcumin can induce apoptosis [9, 17], we postulated that the combination of 10058-F4 and curcumin might induce server apoptotic death in SW1990 cells. We used flow cytometry to directly examine the effects of 10058-F4 or curcumin treatment on early (Annexin V+/PI-) and late (Annexin V+/PI+) apoptosis on SW1990 cells. According to our findings, curcumin improved the sensitivity of 10058-F4 to SW1990 cells (Figure 2(b)).

3.3. In Vivo, Curcumin Increased the Therapeutic Efficacy of 10058-F4 in Pancreatic Cancer Cells. To further explore the effect of cotreatment with curcumin and 10058-F4 in vivo, SW1990 cells were implanted subcutaneously in Balb/c nu/nu mice ($n = 3$ for each group); one week later, the mice were treated with 10058-F4 by vein injection or curcumin alone by intraperitoneal injection or both 10058-F4 and curcumin every 3 days. After continuously treating the indicated drugs for 3 weeks, the combined group's average tumor weight was significantly lighter than in the monotherapy groups (Figure 3).

Additionally, PCNA and TUNEL labeling were used to detect cells in growth or death, respectively. Compared to the control group, the 10058-F4 and curcumin-treated groups have reduced the number of PCNA-positive cells and increased TUNEL-positive cells, but not the 10058-F4-treated group (Figure 4). As a result, our data established that the combination of 10058-F4 and curcumin had significant anticancer activity in vivo.

3.4. Curcumin Increased the Susceptibility of Pancreatic Cancer Cells to 10058-F4 by Inhibiting the Akt-Mediated Apoptotic Pathway. Accumulating evidence has shown that the Akt expression and phosphorylation are reduced by curcumin [22, 23] and upregulated by c-Myc [25]; we evaluated the expression levels of c-Myc, p-Akt, and Akt. As a result, we examined the expression levels of the apoptosis-related proteins Mcl-1, Bcl-2, Fas, and cleaved-caspase 3. Our findings showed that c-Myc and Akt phosphorylated protein levels were lower in SW1990 cells undergoing treatment with a combination of medicines than in cells treated with 10058-F4 alone (Figure 5(a)). Furthermore, the protein levels of Mcl-1 and Bcl-2 were dramatically reduced, whereas Fas and cleaved-caspase 3 were significantly enhanced in the combo treatment group (Figure 5(b)).

4. Discussion

The oncogene c-Myc is involved in cell proliferation, death, differentiation, and the sensitivity of cancer cells to

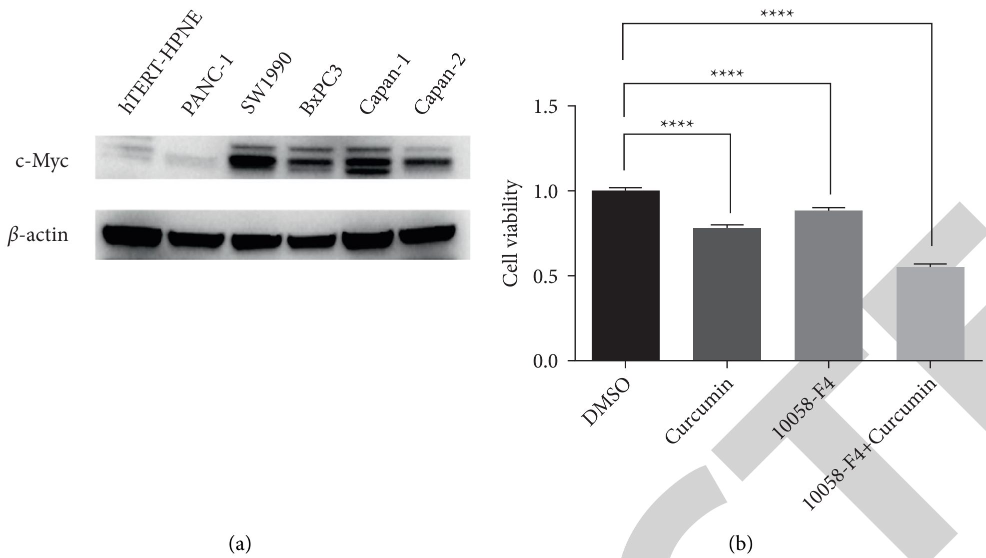

Figure 1: c-Myc highly expressed in pancreatic cancer (a) examined the expression of c-Myc in 5 human pancreatic cancer cell lines (PANC-1, SW1990, BxPC3, Capan-1, and Capan-2 cells) and normal pancreatic epithelial cell hTERT-HPNE. (b) Cell viability was inhibited in the combination group.

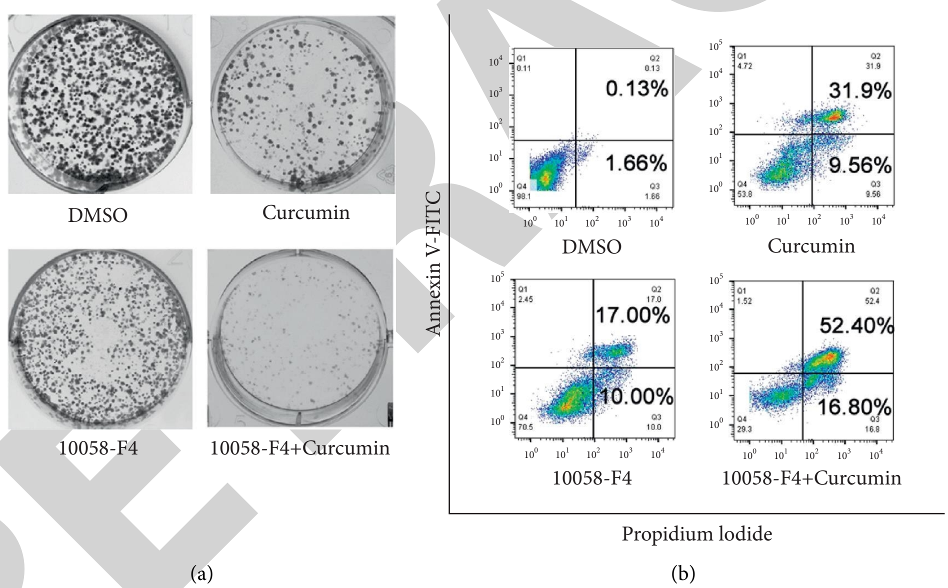

Figure 2: Curcumin sensitized the anticancer influence of 10058-F4 in pancreatic cancer cells. (a) Colonogenic assay for the potent anticancer effect of combination. (b) Curcumin enhanced the sensitization the sensitization effect of 10058-F4 on SW1990 cells.

chemotherapy [26]. 10058-F4 inhibits c-Myc, regressing human acute myeloid leukemia, hepatocellular carcinoma, and ovarian cancer cells [9, 10, 27]. In pre-B acute lymphoblastic leukemia cells, 10058-F4 can also intensify the antileukemic effect of vincristine [11].

However, on account of its quick metabolism and low concentration within tumors, no substantial anticancer effect is observed in vivo following exposure of mice to either 20 or 30 mg/kg 10058-F4 [12]. Curcumin has been used to treat numerous types of cancer, including colorectal cancer, either alone or in conjunction with other treatments [28, 29], breast cancer [30, 31], lung cancer [32], prostate cancer [33], and liver cancer [34]. The potent antineoplastic properties of curcumin against different cancers are due to proapoptotic, antiproliferative, proapoptotic, and anti-inflammatory mechanisms [15, 16, 35]. Emerging preclinical research suggests that curcumin-based combination treatments improve anticancer activity without increasing toxicity. Banerjee et al. [36] observed that treating prostate cancer (PC3) (DU145 and PC3) cells with a combination of curcumin (20 mM) and docetaxel (10 mM) for 48 hours substantially decreased proliferation and promoted apoptosis in comparison to docetaxel and curcumin alone. A study based on HepG2 and PLC/PRF/5 cells found that a

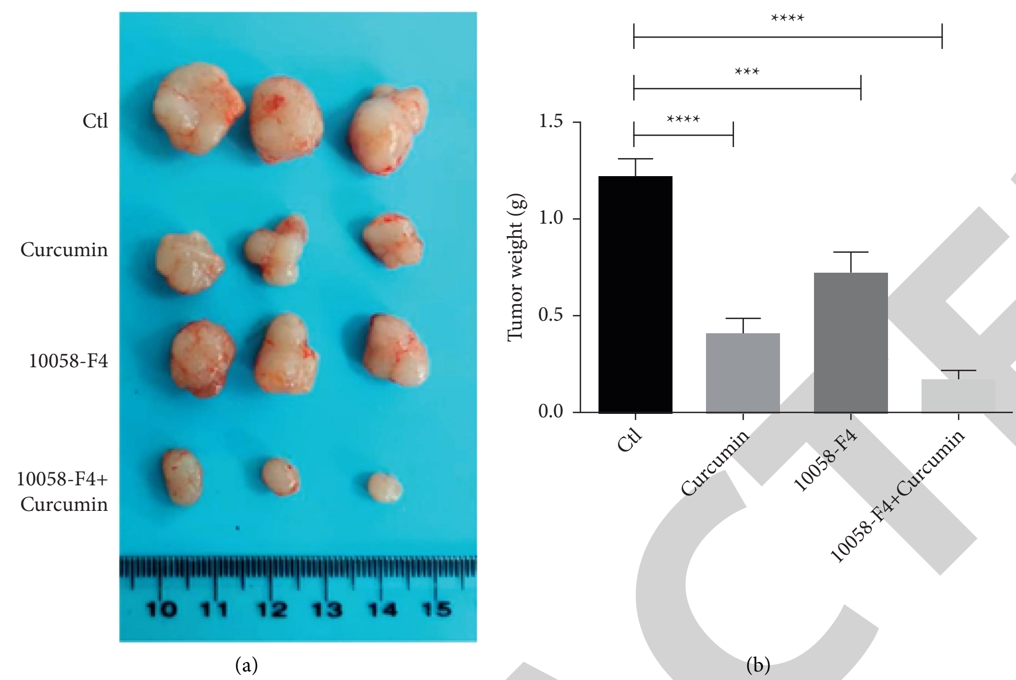

Figure 3: Tumor weight in the combination group and monotherapy groups.

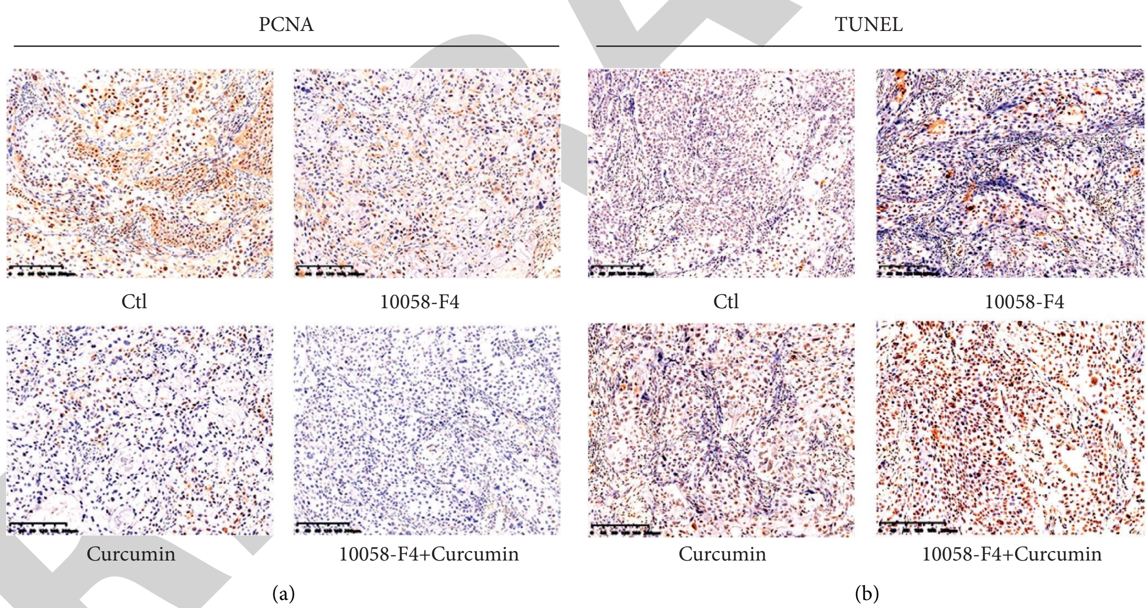

Figure 4: Detection of cells in proliferation or apoptosis by PCNA and TUNEL staining.

combination of curcumin (5 and 10 mM) and metformin (10 mM) can cause apoptosis and impede metastasis and invasion. Reduction of the epidermal growth factor receptor (EGFR)/STAT3 and NF–B/mTOR/Akt/PI3K inhibition of MMP2/9, vascular endothelial growth factor (VEGF), and vascular endothelial growth factor receptor 2 (VEGFR-2) and p53 and PTEN activation could all be contributors towards the anticancer effects.

Curcumin inhibits the expression of c-Myc in nonsmall cell lung cancer cells [36] and pancreatic cancer cells [24], in vitro and in vivo. In this work, we attempted to look into the impact of 10058-F4 combined with curcumin in PDAC, based on encouraging results obtained with c-Myc targeting techniques.

Consistent with previous reports [7, 8, 13], in most PDAC cell lines, c-Myc is amplified (Figure 1(a)). In vitro, 10058-F4 or curcumin alone reduced cell growth and induced apoptosis. Additionally, the combination-treated group's proliferation and apoptosis abilities were considerably altered (Figures 1(b) and 2). However, the 10058-F4

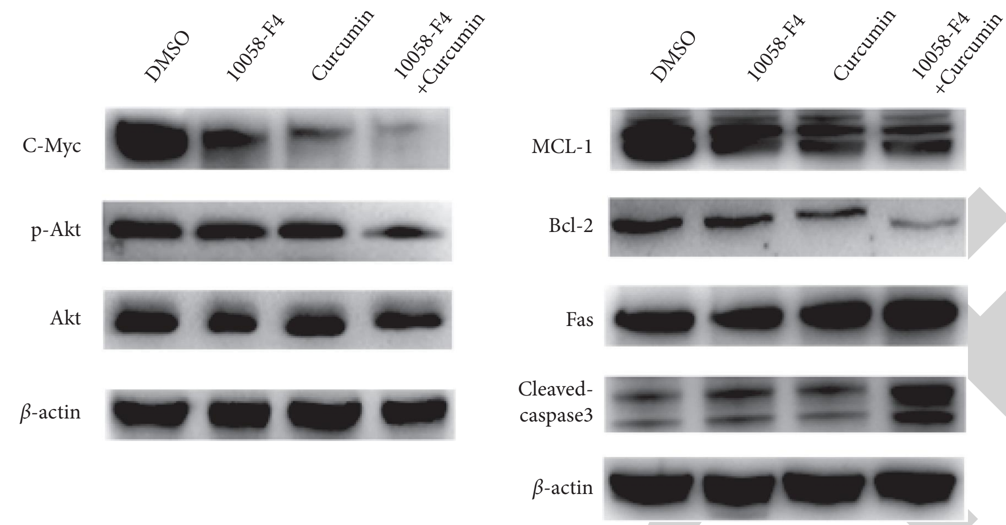

(a) (b)

Figure 5: Curcumin sensitized pancreatic cancer cells to 10058-F4 via inhibition of the Akt-modulated apoptosis pathway. (a) Protein levels of c-Myc and Akt phosphorylation in SW1990 cells treated with combination drugs and 10058-F4 alone. (b) Protein levels of Mcl-1 and Bcl-2 and the protein levels Fas and cleaved-caspase 3 in the combination treating group.

therapy had no discernible effect on the tumor burden. Compared to the control and 10058-F4 groups, combined curcumin plus 10058-F4 therapy substantially inhibited tumor growth (Figure 3). In the combination treatment group, the PCNA-positive cells were notably decreased, while the TUNEL-positive cells were considerably increased (Figure 4). This study also found that the combination of curcumin with 10058-F4 downregulated c-Myc and phosphorylation of Akt weakened Bcl-2 and Mcl-1 expression and increased Fas and cleaved-caspase 3 levels in SW1990 cells (Figure 5). Our findings show that curcumin induces tumor cell death and increases PDAC chemosensitivity to 10058-F4 through altering p-Akt and apoptosis-associated molecules. Importantly, our work furnishes sufficient in vivo evidence of the therapeutic potential of combined curcumin and 10058-F4 treatment in pancreatic cancer and shows cases a simple and convenient method for curcumin and 10058-F4 combinatorial therapy as a viable anticancer strategy in PDAC adjuvant therapy.

5. Conclusion

In conclusion, employing in vitro tests, we demonstrated the pharmacologic reduction of proliferation and induction of apoptotic effects of curcumin and 10058-F4, either alone or in combination. In vivo tests revealed that curcumin-induced tumor growth arrest boosted the anticancer efficacy of 10058-F4. However, additional tests, either in vivo or clinical trials, are a must to assess the effectiveness of the curcumin-10058-F4 combination and the safety of this technique in PDAC patients.

Data Availability

The data used to support the findings of this study are available from the corresponding author upon request.

Disclosure

Jiang Hequn and Ren Tao are the co-authors.

Conflicts of Interest

The authors declare that they have no conflicts of interest.

Authors' Contributions

Zhang Jie, Zhang Jinna, and Zhang Jingjun contributed equally to this study.

Acknowledgments

This study was supported by China's National Natural Science Foundation and the key project of the Sichuan Provincial Department of Science and Technology entitled 2019–2022 FOXM1/Dishevelled/Snail signal axis mediates the mechanism of EMT-induced metastasis and drug resistance in nonsmall cell lung cancer (2019YJ0370).

References

[1] R. L. Siegel, K. D. Miller, and A. Jemal, "Cancer statistics, 2020," *CA: A Cancer Journal for Clinicians*, vol. 70, no. 1, pp. 7–30, 2020.
[2] A. McGuigan, P. Kelly, R. C. Turkington, C. Jones, H. G. Coleman, and R. S. McCain, "Pancreatic cancer: A review of clinical diagnosis, epidemiology, treatment and outcomes," *World Journal of Gastroenterology*, vol. 24, no. 43, pp. 4846–4861, 2018.
[3] D. T. Le, J. N. Durham, K. N. Smith et al., "Mismatch repair deficiency predicts response of solid tumors to PD-1 blockade," *Science*, vol. 357, no. 6349, pp. 409–413, 2017.
[4] C. V. Dang, "c-Myc target genes involved in cell growth, apoptosis, and metabolism," *Molecular and Cellular Biology*, vol. 19, no. 1, pp. 1–11, 1999.

[5] C. Schleger, C. Verbeke, R. Hildenbrand, H. Zentgraf, and U. Bleyl, "c-MYC activation in primary and metastatic ductal adenocarcinoma of the pancreas: incidence, mechanisms, and clinical significance," *Modern Pathology*, vol. 15, no. 4, pp. 462–469, 2002.

[6] T.-L. He, Y.-J. Zhang, H. Jiang, X.-h. Li, H. Zhu, and K.-L. Zheng, "The c-Myc-LDHA axis positively regulates aerobic glycolysis and promotes tumor progression in pancreatic cancer," *Medical Oncology*, vol. 32, no. 7, p. 187, 2015.

[7] X. Liu, Y. Zhou, J. Peng, B. Xie, Q. Shou, and J. Wang, "Silencing c-myc enhances the antitumor activity of bufalin by suppressing the HIF-1α/SDF-1/CXCR4 pathway in pancreatic cancer cells," *Frontiers in Pharmacology*, vol. 11, p. 495, 2020.

[8] Y. Zang, L. Zhu, T. Li et al., "EI24 suppresses tumorigenesis in pancreatic cancer via regulating c-myc," *Gastroenterology research and practice*, vol. 2018, p. 2626545, 2018.

[9] M.-J. Huang, Y.-c. Cheng, C.-R. Liu, S. Lin, and H. E. Liu, "A small-molecule c-Myc inhibitor, 10058-F4, induces cell-cycle arrest, apoptosis, and myeloid differentiation of human acute myeloid leukemia," *Experimental Hematology*, vol. 34, no. 11, pp. 1480–1489, 2006.

[10] C.-P. Lin, J.-D. Liu, J.-M. Chow, C.-R. Liu, and H. Eugene Liu, "Small-molecule c-Myc inhibitor, 10058-F4, inhibits proliferation, downregulates human telomerase reverse transcriptase and enhances chemosensitivity in human hepatocellular carcinoma cells," *Anti-Cancer Drugs*, vol. 18, no. 2, pp. 161–170, 2007.

[11] N. Sheikh-Zeineddini, D. Bashash, A. Safaroghli-Azar et al., "Suppression of c-Myc using 10058-F4 exerts caspase-3-dependent apoptosis and intensifies the antileukemic effect of vincristine in pre-B acute lymphoblastic leukemia cells," *Journal of Cellular Biochemistry*, vol. 120, no. 8, pp. 14004–14016, 2019.

[12] J. Guo, R. A. Parise, E. Joseph et al., "Efficacy, pharmacokinetics, tisssue distribution, and metabolism of the Myc-Max disruptor, 10058-F4 [Z,E]-5-[4-ethylbenzylidine]-2-thioxothiazolidin-4-one, in mice," *Cancer Chemotherapy and Pharmacology*, vol. 63, no. 4, pp. 615–625, 2009.

[13] M. Zhang, H.-Y. Fan, and S.-C. Li, "Inhibition of c-Myc by 10058-F4 induces growth arrest and chemosensitivity in pancreatic ductal adenocarcinoma," *Biomedicine & Pharmacotherapy*, vol. 73, pp. 123–128, 2015.

[14] B. B. Aggarwal, C. Sundaram, N. Malani, H. Ichikawa, and H. Ichikawa, "CURCUMIN: the INDIAN solid gold," *Advances in Experimental Medicine and Biology*, vol. 595, no. 1, pp. 1–75, 2007.

[15] T. Kim, J. Davis, A. J. Zhang, X. He, and S. T. Mathews, "Curcumin activates AMPK and suppresses gluconeogenic gene expression in hepatoma cells," *Biochemical and Biophysical Research Communications*, vol. 388, no. 2, pp. 377–382, 2009.

[16] S. C. Gupta, S. Patchva, W. Koh, and B. B. Aggarwal, "Discovery of curcumin, a component of golden spice, and its miraculous biological activities," *Clinical and Experimental Pharmacology and Physiology*, vol. 39, no. 3, pp. 283–299, 2012.

[17] K. Mortezaee, E. Salehi, H. Mirtavoos-mahyari et al., "Mechanisms of apoptosis modulation by curcumin: implications for cancer therapy," *Journal of Cellular Physiology*, vol. 234, no. 8, pp. 12537–12550, 2019.

[18] P. Anand, C. Sundaram, S. Jhurani, A. B. Kunnumakkara, and B. B. Aggarwal, "Curcumin and cancer: an "old-age" disease with an "age-old" solution," *Cancer Letters*, vol. 267, no. 1, pp. 133–164, 2008.

[19] M. Zhu, Z. Zheng, J. Huang et al., "Modulation of miR - 34a in curcumin - induced antiproliferation of prostate cancer cells," *Journal of Cellular Biochemistry*, vol. 120, no. 9, pp. 15616–15624, 2019.

[20] G. Liu, T. Xiang, Q.-F. Wu, and W.-X. Wang, "Curcumin suppresses the proliferation of gastric cancer cells by downregulating H19," *Oncology Letters*, vol. 12, no. 6, pp. 5156–5162, 2016.

[21] D. Yang, Y. Li, and D. Zhao, "Curcumin induces apoptotic cell death in human pancreatic cancer cells via the miR-340/XIAP signaling pathway," *Oncology Letters*, vol. 14, no. 2, pp. 1811–1816, 2017.

[22] W. Li, Z. Wang, X. Xiao et al., "Curcumin attenuates hyperglycemia-driven EGF-induced invasive and migratory abilities of pancreatic cancer via suppression of the ERK and AKT pathways," *Oncology Reports*, vol. 41, no. 1, pp. 650–658, 2018.

[23] W. Li, Z. Jiang, X. Xiao et al., "Curcumin inhibits superoxide dismutase-induced epithelial-to-mesenchymal transition via the PI3K/Akt/NF-κB pathway in pancreatic cancer cells," *International Journal of Oncology*, vol. 52, no. 5, pp. 1593–1602, 2018.

[24] K. Yoshida, S. Toden, P. Ravindranathan, H. Han, and A. Goel, "Curcumin sensitizes pancreatic cancer cells to gemcitabine by attenuating PRC2 subunit EZH2, and the lncRNA PVT1 expression," *Carcinogenesis*, vol. 38, no. 10, pp. 1036–1046, 2017.

[25] J. Liu, W. Feng, M. Liu et al., "Stomach-specific c-Myc overexpression drives gastric adenoma in mice via AKT/mTOR signaling," *Bosnian Journal of Basic Medical Sciences*, vol. 21, no. 4, pp. 434–446, 2020.

[26] D. J. Liao, A. Thakur, J. Wu, H. Biliran, and F. H. Sarkar, "Perspectives on c-myc, cyclin D1, and their interaction in cancer formation, progression, and response to chemotherapy," *Critical Reviews in Oncogenesis*, vol. 13, no. 2, pp. 93–158, 2007.

[27] J. Wang, X. Ma, H. M. Jones et al., "Evaluation of the antitumor effects of c-Myc-Max heterodimerization inhibitor 100258-F4 in ovarian cancer cells," *Journal of Translational Medicine*, vol. 12, no. 1, p. 226, 2014.

[28] Z.-Y. He, C.-B. Shi, H. Wen, F.-L. Li, B.-L. Wang, and J. Wang, "Upregulation of p53 expression in patients with colorectal cancer by administration of curcumin," *Cancer Investigation*, vol. 29, no. 3, pp. 208–213, 2011.

[29] G. Mudduluru, J. N. George-William, S. Muppala et al., "Curcumin regulates miR-21 expression and inhibits invasion and metastasis in colorectal cancer," *Bioscience Reports*, vol. 31, no. 3, pp. 185–197, 2011.

[30] M. Kakarala, D. E. Brenner, H. Korkaya et al., "Targeting breast stem cells with the cancer preventive compounds curcumin and piperine," *Breast Cancer Research and Treatment*, vol. 122, no. 3, pp. 777–785, 2010.

[31] C. Wen, L. Fu, J. Huang et al., "Curcumin reverses doxorubicin resistance via inhibition the efflux function of ABCB4 in doxorubicin-resistant breast cancer cells," *Molecular Medicine Reports*, vol. 19, no. 6, pp. 5162–5168, 2019.

[32] J.-Y. Zhu, X. Yang, Y. Chen et al., "Curcumin suppresses lung cancer stem cells via inhibiting wnt/β-catenin and sonic hedgehog pathways," *Phytotherapy Research*, vol. 31, no. 4, pp. 680–688, 2017.

[33] H. Ide, S. Tokiwa, K. Sakamaki et al., "Combined inhibitory effects of soy isoflavones and curcumin on the production of Prostate-specific antigen (PSA)," *Journal of Men's Health*, vol. 6, no. 3, p. 248, 2009.

Hindawi
Journal of Healthcare Engineering
Volume 2022, Article ID 4034404, 9 pages
https://doi.org/10.1155/2022/4034404

Research Article

A Deep Learning Radiomics Analysis for Survival Prediction in Esophageal Cancer

Junxiu Wang[1,2] **Jianchao Zeng**[1] **Hongwei Li**[3] **and Xiaoqing Yu**[1]

[1]*Data Science and Technology, North University of China, Taiyuan, Shanxi 030051, China*
[2]*Department of Computer Engineering, Taiyuan Institute of Technology, Taiyuan, Shanxi 030008, China*
[3]*Shanxi Tumor Hospital, Taiyuan 030013, Shanxi Province, China*

Correspondence should be addressed to Jianchao Zeng; zjc@nuc.edu.cn

Received 11 January 2022; Accepted 3 March 2022; Published 24 March 2022

Academic Editor: Enas Abdulhay

The purpose of this study was to explore the deep learning radiomics (DLR) nomogram to predict the overall 3-year survival after chemoradiotherapy in patients with esophageal cancer. The 154 patients' data were used in this study, which was randomly split into training (116) and validation (38) data. Deep learning and handcrafted features were obtained via the preprocessing diagnostic computed tomography images. The selected features were used to construct radiomics signatures through the least absolute shrinkage and selection operator (LASSO) regression, maximizing relevance while minimizing redundancy. The DLR signature, handcrafted features' radiomics (HCR) signature, and clinical factors were incorporated to develop a DLR nomogram. The DLR nomogram was evaluated in terms of discrimination and calibration with comparison to the HCR signature-based radiomics model. The experimental results showed the outperforming discrimination ability of the proposed DLR over the HCR model in terms of Harrel's concordance index, 0.76 and 0.784, for training and validation sets, respectively. Also, the proposed DLR nomogram calibrates and classifies better than the HCR model in terms of AUC, 0.984 (vs. 0.797) and 0.942 (vs. 0.665) for training and validation sets, respectively. Furthermore, the nomogram-predicted Kaplan–Meier survival (KMS) curves differed significantly from the nonsurvival groups in the log-rank test (p value <0.05). The proposed DLR model based on conventional CT images showed the outperforming performance over the HCR signature model in noninvasively individualized prediction of the 3-year survival rate in esophageal cancer patients. The proposed model can potentially provide prognostic information that guides and helps the clinical decisions between observation and treatment.

1. Introduction

Esophageal cancer (EC) is the eighth most common malignancy and the sixth most common disease-related cause of death worldwide [1, 2]. The incidence of esophageal cancer is notably high in Asia and Iceland, as well as the United Kingdom and the United States [3–5]. In order to systemically control the disease, radiotherapy and neoadjuvant chemotherapy are commonly combined with surgery [6–8]. Regardless of its benefit for severe patients with a low survival rate, an aggressive treatment plan, including multiple cycles of treatment and adjuvant chemotherapy, is not suitable for the other patients with esophageal cancer [9]. Pre-identification for such patients having a low survival rate before surgery can help provide other suitable treatment regimens for these patients [10]. Therefore, identification of patients having a lower survival rate is vital to take benefit from additional treatment.

Radiomics features [11, 12] have been widely used as an extremely useful tool in quantitative analysis of medical imaging and in medical diagnosis [13, 14]. The traditional radiomics utilized handcrafted features, such as tumor shape and texture, obtained from medical images [11]. However, such handcrafted low-order features are not suitable to define intrinsic characteristics of intratumor imaging heterogeneity, limiting the applicability of the radiomics model [11–13]. Furthermore, the construction of handcrafted features is limited within the known knowledge of medical imaging.

Deep learning, especially CNN, has recently achieved promising results in medical image analysis [15–18]. Deep networks consist of multiple layers that can be learned from data [19, 20]. For example, prognostic tumor features can be extracted through hierarchical convolution operation on the medical images [21–24]. Compared with handcrafted features, DLR features contain more important tumor information that may help diagnose [25–27].

However, unlike handcrafted radiomics studied widely for radiological diagnosis and prediction [28], the application of deep learning in predicting overall survival in esophageal cancer has not been thoroughly explored yet. Hence, this study aims to develop and validate the deep survival prediction model based on a radiomics nomogram for individualized prediction of three years' overall survival in patients with esophageal cancer.

It is worthwhile to highlight three aspects of the contributions here. (1) This study investigated DLR features in the survival prediction of patients with esophageal cancer. Unlike the traditional handcrafted features, clinical target-oriented DLR features can be automatically learned from data. (2) Both HCR features and DLR features are considered in the prediction model to characterize the esophageal lesions thoroughly. The main reason is that the DLR and HCR can describe imaging heterogeneity of esophageal lesions in different levels. In particular, HCR comprise shape features, first-order statistics, and texture features; DLR contains the "real-world" textures, which are extracted from the pretrained DenseNet-169 network via transfer learning strategy. (3) This study develops a noninvasive predictive model that combines deep learning-based radiomics features, handcrafted features, and clinical factors to predict survival rates within three years at diagnosis of esophageal cancer. The DLR nomogram survival prediction of esophageal cancer patients can allow more proper treatment. The experimental results showed that the DLR nomogram outperforms the HCR model and the clinical model.

2. Materials and Methods

2.1. Patients. Esophageal cancer patients at Shanxi Cancer Hospital were the subject of our retrospective study. The patients were included according to the inclusion criteria: (a) patients who had pathologically confirmed esophageal cancer, (b) a standard CT scan performed before any treatment, and (c) clinical characteristics available. The patients were excluded with the following criteria: (a) too poor CT image quality, which may affect the diagnosis of the patient, (b) patients who had chemotherapy treatment at another institution, and (c) patients who are also suffering from other cancers.

The survival group includes patients who survived more than three years since the treatment, whereas the non-survival group includes patients who died within three years. A total of 154 esophageal cancer patients diagnosed from November 2012 to February 2015 participated in our retrospective study. Those data were grouped into two sets: training (116) and validation (38) data at a ratio of 3 : 1.

Baseline clinical data were collected via the electronic medical record system (EMRS) [29], including gender, BMI, age, M-stage, N-stage, T-stage, overall stage, and planning target volume (PTV). The picture archiving and communication system (PACS) was used to obtain CT images. The dataset was constructed and evaluated in April 2019, and all enrolled patients were followed for at least 3 years. The Institutional Review Board approved the study.

2.2. CT Image and Region of Interest (ROI) Acquisition. General Electric Light Speed RT16 was used for scanning, with a CT thickness of 5 mm. The primary tumor volumes for radiotherapy planning were set as the ROI to quantitatively analyze the images. Two skilled radiologists manually selected the three-dimensional tumor ROI using the software package 3D Slicer [30].

Training CT images were preprocessed to avoid accuracy degradation of DL models caused by noises introduced with the interval change, which include resampling, rescaling, and voxel normalization. Those CT images were reconstructed with a matrix of 512×512 and $0.5 \times 0.5\,\text{mm}^2$ pixel size, and the resampling with cubic interpolation to $1 \times 1 \times 1\,\text{mm}^3$ pixels was conducted, minimizing CT images variabilities [31].

The tumor area was located with a rectangle bounding box that covers the primary tumor area. The ROI for each patient was obtained with three cropped consecutive slices to avoid the bias of manual segmentation that affects the location of a bounding box. Lastly, the tumor image was resized to $224 \times 224 \times 3$ voxels.

2.3. Radiomics Feature Extraction. Phenotypic differences between tumors can be captured by a large number of quantitative radiomics features. In this study, deep learning features and handcrafted features were extracted to quantify tumor phenotype to enhance the learning efficiency of the radiomics model. Those two feature sets have complementary advantages that can be combined to improve the model. Also, expert knowledge on the esophageal cancer lesion can be reflected with shape and texture features. On the contrary, the high-level DLR features can significantly represent complex spatial features in both global and local perspectives.

The handcrafted feature extraction algorithm was standardized by referring to the Image Biomarker Standardization Initiative (IBSI) [32–34] and Radiomics Ontology [35]. For each CT ROI, 1,670 handcrafted features were extracted using Python implementation, including 18 first-order statistics, 16 geometric, and 1,564 texture features. The textural features include 14 gray-level dependence [36], 23 gray-level co-occurrence [37], 16 gray-level run-length [38], 16 gray-level size-zone [39], and 5 neighborhood gray-tone difference [40] matrices. Refer to the supplementary appendix of Lambing [41], for mathematical definitions of those features.

The DenseNet-169, designed for the image classification task, was adopted to extract DLR features. In the training cohort, data augmentation approaches including random rotation, random shear, and random zoom were employed before the training procedure. The deep learning model was pretrained on the ImageNet dataset, one of the largest image datasets, and then fine-tuned in a transfer learning strategy to avoid the overfitting problem [42]. The network was trained with cross-entropy loss function and Adam optimizer with a learning rate of 0.0001, a batch size of 16, and a regularization weight of 0.0001. The network was implemented on Keras (https://keras.io/) with the TensorFlow library as the backend (https://www.tensorflow.org/). As depicted in Figure 1, the tumor ROI was fed into the DenseNet-169, and the outputs of hidden layers were collected to obtain 1,664 features in total.

2.4. DLR Signature Building. In order to obtain the most effective feature, three stages of feature selection were carried out. First, features ($p < 0.05$) were obtained through the Mann–Whitney U (MWU) test. Then, the features were sorted based on the mutual information (MI) between features and the survival status using the minimum redundancy maximum correlation (mRMR) scheme [43]. It should be noted that, in this study, only the top 50 features in mRMR were retained. Lastly, the dimension of features is reduced by the LASSO to obtain optimal features [44]. The survival-related features were retained while the other features were removed by LASSO regression. The 10-fold cross validation was conducted with 100 iterations in LASSO regression. The obtained features are used to construct the DLR signature, and the HCR signature was constructed in a similar way for comparison.

2.5. DLR Nomogram Construction. A DLR nomogram was built by integrating DLR signature, HCR signature, and clinical features with a multivariable logistic regression model. Backward stepping selection was used with information criterion of Akaike as the stopping rule [45]. The variable multicollinearity in the multiple logistic regression model was checked by the variance inflation factor (VIF), where $VIF > 10$ indicates high multicollinearity [46]. A DLR nomogram was then built based on the multivariate logistic analysis, predicting the individual probability of survival in the training dataset.

2.6. Evaluation of the DLR Nomogram. Harrel's C -index was employed to evaluate the discrimination ability of the DLR nomogram in both training and testing datasets. The bootstrap method was used to resampling 1,000 times, and the C index in both cohorts was calculated with 95% confidence intervals. The AUC, accuracy, specificity, and sensitivity were calculated on the plotted ROC curves. The calibration ability of the DLR nomogram was evaluated using the calibration curve that depicts the consistency between predicted and actual survival probabilities. Hosmer–Lemeshow (HL) test [47] and decision curve analysis (DCA) [48] were utilized to evaluate the fitting accuracy and robustness of the DLR nomogram, respectively. Furthermore, KMS curves were constructed to predict survival status. Accordingly, the patients were predicted as survival or nonsurvival, and then, the difference in survival curves between the two groups was evaluated using the log-rank test.

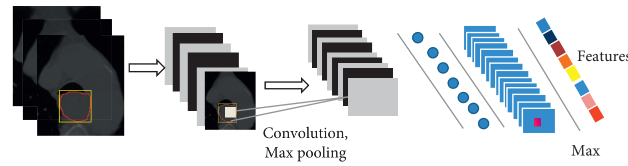

Figure 1: DLR feature extraction process.

2.7. Statistical Analysis. All the statistical analyses were conducted with R software (version 4.0.3; http://www.Rproject.org). MWU and Chi-square tests were adopted for univariate analysis, and Spearman's correlation rank was employed for correlation. The penalty parameter (λ) was tuned by LASSO logistic regression model. This study used the following packages for each analysis. "glomnet" package: LASSO logistic regression, "rms" package: nomograms and calibration plots, "ResourceSelection" package: HL test, "car" package: VIFs calculation, "survivalROC" package: AUC analysis, "survminer" package: KMS analysis, and "dca.R" function: DCA performance. This study utilized a bilateral statistical significance level p value <0.05.

3. Results

Figure 2 depicts the schematic diagram of the study.

3.1. Clinical Characteristics. Table 1 summarizes the clinical characteristics of the training and validation cohorts, where the Chi-square test (p value is 0.572) for two data shows no significant observable difference in the survival rate, 30.2% and 36.8%, for training and validation, respectively.

3.2. DLR Signature. Fifty features were obtained for each patient after survival-unrelated and redundant feature removal from 1,664 DLR features. Then, based on the training cohort, 33 potential predictors were selected by LASSO regression. Parameter (λ) selection and coefficients of LASSO are given in Supplementary Material (II). The DLR signature was constructed using the selected features.

The results show that scores of the survival group were higher than the nonsurvival group with a significant difference in terms of DLR signatures (1.10 ± 0.75 vs. -2.22 ± 0.75) in the training cohort and (0.15 ± 1.11 vs. -1.90 ± 1.12) in the validation cohort. MWU test was used with a p value <.001. Also, a significant correlation between DLR signature and survival status was found (C index: 0.729, $p = 0.035$ in the training data, and C index: 0.766, all $p < 0.001$ in the validation data).

The LASSO algorithm selected 18 handcrafted features to build HCR signatures. HCR signatures were also significantly different between survival and nonsurvival groups. In the training data, 0.68 ± 1.12 vs. -0.50 ± 1.03, p value <.001,

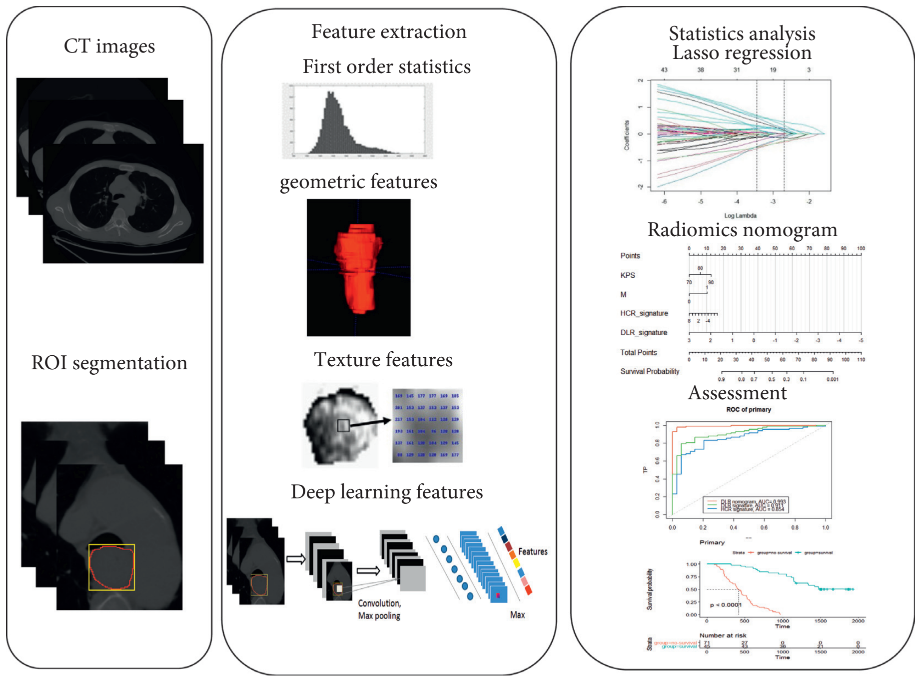

Figure 2: Schematic diagram of this study.

Table 1: Clinical characteristics of esophageal cancer patients.

	Training cohort ($n = 116$)			Validation cohort ($n = 38$)		
Characteristic	Nonsurvival (81)	Survival (35)	p	Nonsurvival (24)	Survival (14)	p
Gender						
Male: female	51 : 30	23 : 12	0.836	12 : 12	6 : 8	0.745
Age	67.96 ± 9.41	68.83 ± 8.80	0.644	66.54 ± 9.65	67.36 ± 7.09	0.785
BMI	21.70 ± 3.14	23.69 ± 4.25	0.006	23.04 ± 3.98	22.55 ± 3.24	0.702
T-stage						
T1	1 (1.2%)	2 (5.7%)		1 (4.2%)	0 (0.0%)	
T2	20 (24.7%)	16 (45.7%)	0.042	9 (37.5%)	7 (50.0%)	0.938
T3	43 (53.1%)	13 (37.1%)		10 (41.7%)	5 (35.7%)	
T4	17 (21.0%)	4 (11.4%)		4 (16.7%)	2 (14.3%)	
N						
N0	20 (25.0%)	14 (40.0%)	0.123	7 (29.2%)	6 (42.9%)	0.486
N1	60 (75.0%)	21 (60.0%)		17 (70.8%)	8 (57.1%)	
M						
M0	69 (85.2%)	35 (100.0%)	0.017	22 (91.7%)	14 (100.0%)	0.522
M1	12 (14.8%)	0 (0.0%)		2 (8.3%)	0 (0.0%)	
TNM						
I	0 (0.0%)	2 (5.7%)		0 (0.0%)	0 (0.0%)	
II	27 (33.3%)	19 (54.3%)	0.002	10 (41.7%)	8 (57.1%)	0.766
III	42 (51.9%)	14 (40.0%)		12 (50.0%)	5 (35.7%)	
IV	12 (14.8%)	0 (0.0%)		2 (8.3%)	1 (7.1%)	
PTV	379.62 ± 158.34	335.22 ± 179.33	0.186	382.56 ± 134.39	362.53 ± 166.27	0.687
HCR_signature	−0.50 ± 1.03	0.68 ± 1.12	<0.001	−0.23 ± 1.48	0.80 ± 1.26	0.035
DLR_signature	−2.22 ± 0.75	1.10 ± 0.75	<0.001	−1.90 ± 1.12	0.15 ± 1.11	<0.001

MWU test, and in the validation data, 0.80 ± 1.26 vs. -0.23 ± 1.48, p value = 0.035, MWU test. HCR feature selection by LASSO regression is described in detail in Supplementary Material (I).

3.3. DLR Nomogram. The DLR signature, HCR signature, and BMI were combined to construct a DLR nomogram, as shown in Figure 3. The VIFs of DLR signature, HCR signature, and BMI were 1.45, 1.41, and 1.07, respectively, indicating no severe collinearity in the regression model.

Figure 4 depicts ROC curves of the DLR nomogram for the DLR signature model and HCR signature model. The AUC was 0.984, 0.955, and 0.797 for the DLR nomogram, DLR signature model, and HCR signatures' model, respectively, in the training data. In the validation data, the

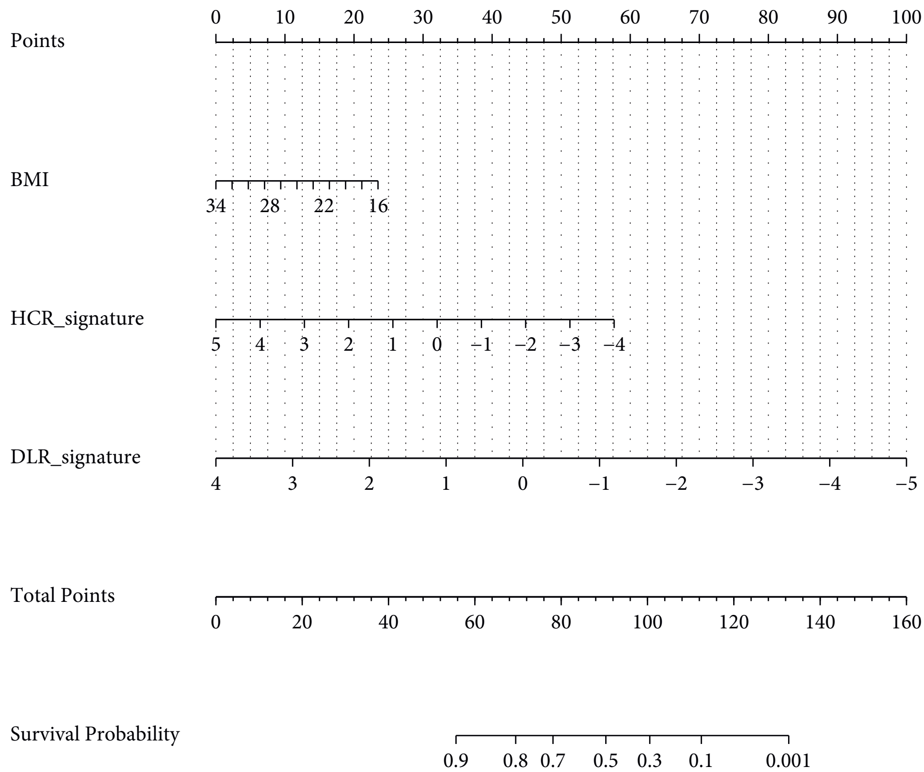

FIGURE 3: The construction of the DLR nomogram.

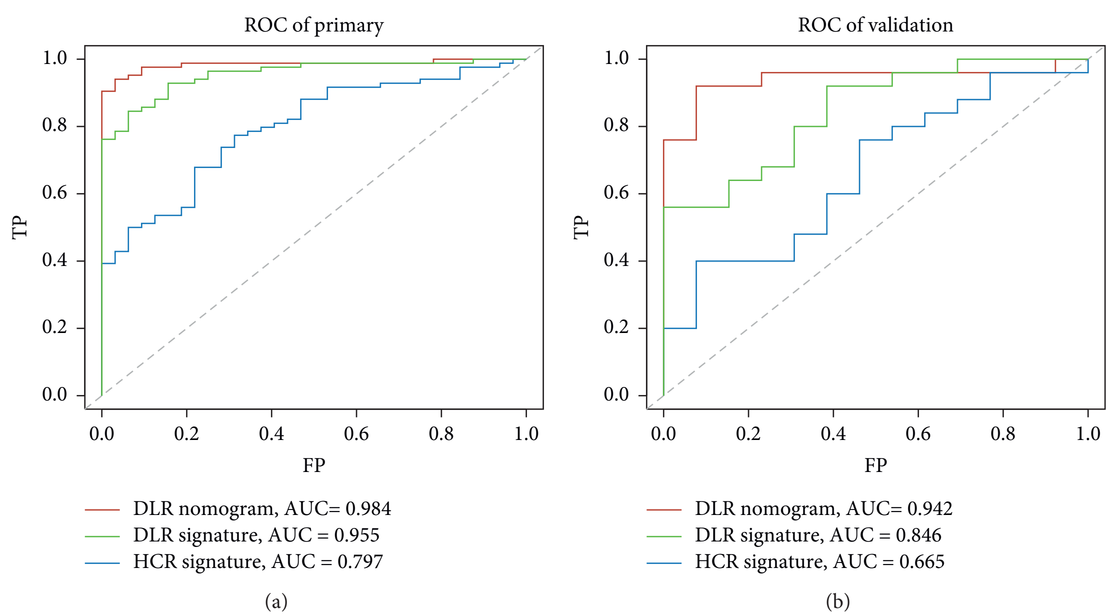

FIGURE 4: ROC curves for the DLR and HCR signatures for (a) training data and (b) validation data.

AUC was 0.942, 0.846, and 0.665 for the DLR nomogram, DLR signature model, and HCR signatures' model, respectively. The results indicate that the DLR nomogram model provides better discrimination ability (Harrel's concordance index, 0.76 and 0.784, for the training and validation data, respectively).

Figure 5 depicts the calibration curves, showing the consistency between predicted and actual survival rates. A nonsignificant statistic of the training cohort (p value = .563, HL test) showed no deviation from the ideal fit. In the validation cohort, the 3-year survival rate was also well-calibrated (p value = .648, HL test).

The DCA examined the clinical outcomes based on threshold probability at which a net benefit could be derived. Figure 6 depicts the DCA of the DLR nomogram, showing that the DLR nomogram obtained outstanding net benefits

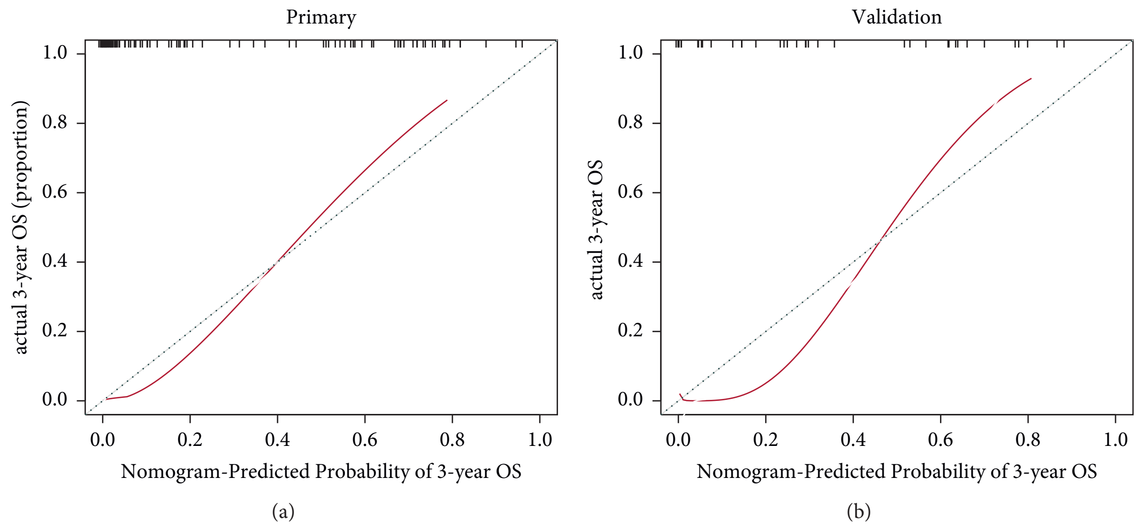

Figure 5: Calibration curves for the DLR nomogram for (a) training data and (b) validation data, where the x-axis and y-axis represent the predicted and actual rates. The solid red line is the performance of the DLR nomogram, and the dashed blue line is the ideal prediction. Closer the solid red line is to the dashed blue line, more accurate the prediction of the model.

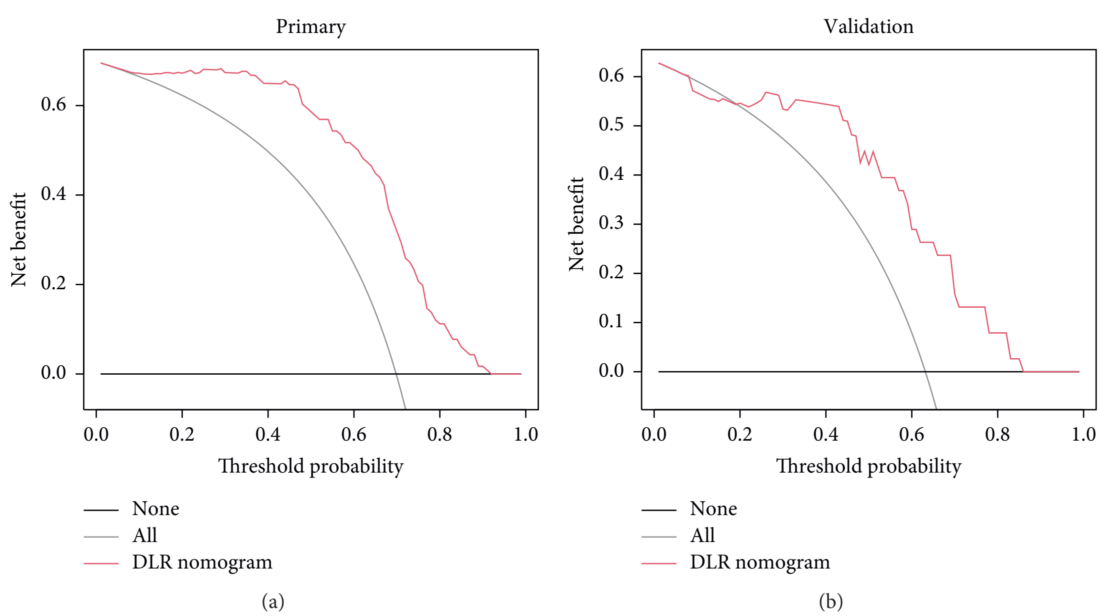

Figure 6: DCA for the DLR nomogram in (a) training and (b) validation data. The black and gray lines represent the hypothesis that all patients die and that no patient dies within three years, respectively. The red line represents the net benefit of the DLR nomogram.

over the other strategies: treat-all-patients and treat-none strategies. A significant difference (p value <.05, log-rank test) between prediction survival and nonsurvival groups was found in KMS curves (Figure 7).

4. Discussion

Treatment planning can be further individualized via preoperative prediction of three-year survival. In previous studies, handcrafted features were analyzed to predict survival rates. However, due to the limited feature extraction ability, the prediction accuracy was not high enough. In order to overcome such a limitation, this study investigated DLR features in the survival prediction of patients with esophageal cancer. Unlike the traditional handcrafted features, clinical target-oriented DLR features can be automatically learned from data [49].

Intratumor heterogeneity has been considered a potential prognosis factor. The DRL feature extraction can robustly characterize the intratumor heterogeneity noninvasively from the medical images [26]. The experimental results showed that the use of DLR features contributed to the performance of the model, which is also supported by recent studies that high-dimensional features can preserve more detailed cancer information, making them more sensitive when assessing survival status [24]. Therefore, by

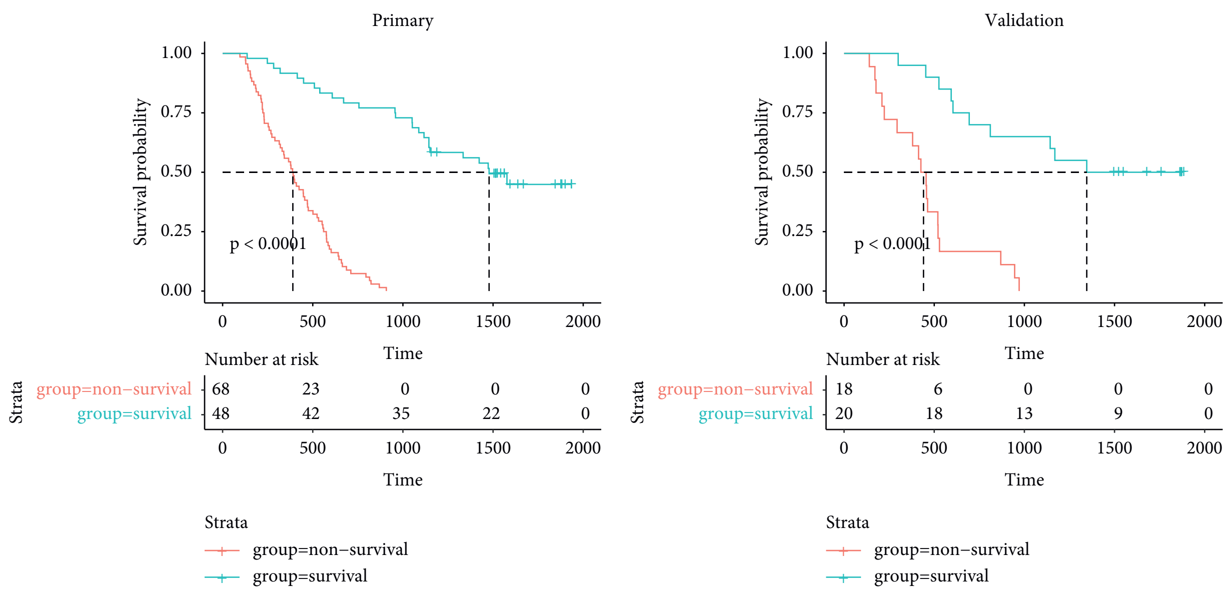

(a) (b)

Figure 7: KMS curves of the predicted survival and nonsurvival groups in (a) training and (b) validation data.

combining these DLR features, a DLR nomogram survival prediction of esophageal cancer patients can allow more proper treatment. The experimental results showed that the DLR nomogram outperforms the HCR model and the clinical model.

This study has several limitations, described as follows. First, only 154 patients were available for a three-year follow-up analysis. A larger amount of data is required to improve the performance of the model. Second, all the patients were collected to form a single-center, thereby limiting the generalizability of the DLR model. A more diverse dataset is required to validate the robustness and reproducibility of the DLR model. Third, our study did not consider genetic markers. Multiple factors should be considered for more personalized treatment, including biology, pathology, genomics [24, 26, 42–52], and imaging biomarkers [53]. In addition, this study was limited to CT images despite the essentiality of MIR images in surgical planning due to their excellent resolution for soft tissues. The focus should, therefore, be given towards developing an additional model combining CT and MRI image features. Finally, the primary tumor volumes were manually delineated for feature extraction. Even though the delineations are commonly used with confirmation by another radiation oncologist in radiotherapy planning, previous studies showed that semi-automatic tumor segmentation could reduce interobserver variability and therefore is more suitable for radiomics studies [54].

5. Conclusions

This study details the development of a noninvasive predictive model that combines deep learning-based radiomics features, handcrafted features, and clinical factors to predict survival rates within three years at diagnosis of esophageal cancer. The performance of the proposed DLR nomogram is superior to the traditional radiomics model in terms of Harrel's concordance index and AUC. The calibration curves show the good prediction performance of the nomogram. The nomogram-predicted Kaplan–Meier survival (KMS) curves differed significantly from the nonsurvival groups in the log-rank test (p value <0.05). The proposed model can present the basis for clinicians to make better treatment decisions and personalized diagnoses. Future works will include the model improvement based on larger data and complementary clinical factors.

Data Availability

The data used to support this research are included within the article.

Conflicts of Interest

The authors declare that there are no conflicts of interest regarding the publication of this paper.

Acknowledgments

This study was funded by National Natural Science Foundation of China (Grant no. 72071183) and Natural Science Foundation of Shanxi Province of China for Youths (Grant no. 201801D221209).

Supplementary Materials

(I) HCR feature selection using the least absolute shrinkage and selection operator (LASSO) logistic regression model. Figure S1. HCR feature selection using the LASSO logistic regression algorithm. (a) The penalization coefficient λ in the LASSO model was tuned by the binomial deviance minimization criteria. The binomial deviance metrics (the y-axis) were plotted against $\log(\lambda)$ (the bottom x-axis). The top x-axis indicates the number of predictors with the given $\log(\lambda)$. Red dots indicate average binomial deviance for each model at the given λ. Vertical bars through the red dots show the upper and lower values of the binomial deviance. The vertical black lines represent the optimal λ, where the model provides the best fit to the data. As a result, the optimal λ of 0.02373184 was selected. (b) LASSO coefficient profiles of the 50 radiomics features. For the optimal λ, eighteen features with nonzero coefficient were selected. (II) DLR feature selection using the least absolute shrinkage and selection operator (LASSO) logistic regression model. Figure S2. DLR feature selection using the LASSO logistic regression algorithm. (a) The penalization coefficient λ in the LASSO model was tuned by the binomial deviance minimization criteria. As a result, the optimal λ of 0.0445107 was selected. (b) LASSO coefficient profiles of the 50 radiomics features. For the optimal λ, thirty three features with nonzero coefficient were selected. (*Supplementary Materials*)

References

[1] P. C. Enzinger and R. J. Mayer, "Esophageal cancer," *New England Journal of Medicine*, vol. 349, no. 23, pp. 2241–2252, 2003.

[2] H. P. Van, M. C. Hulshof, J. V. Lanschot et al., "Preoperative chemoradiotherapy for esophageal or junctional cancer," *Journal of Medical Imaging & Radiation Oncology*, vol. 43, no. 2, pp. 215–219, 2012.

[3] B. W. Stewart and P. Kleihues, "World cancer report," Report, IARC Press, Lyon, France, 2003.

[4] B. Kumbasar, "Carcinoma of esophagus: radiologic diagnosis and staging," *European Journal of Radiology*, vol. 42, no. 3, pp. 170–180, 2002.

[5] R. Siegel, D. Naishadham, and A. Jemal, "Cancer statistics for hispanics/latinos, 2012," *CA: A Cancer Journal for Clinicians*, vol. 62, no. 5, pp. 283–298, 2012.

[6] K. Tanaka, H. Miyata, K. Sugimura et al., "Negative influence of programmed death-1-ligands on the survival of esophageal cancer patients treated with chemotherapy," *Cancer Science*, vol. 107, no. 6, pp. 726–733, 2016.

[7] T. N. Walsh, N. Noonan, D. Hollywood, A. Kelly, N. Keeling, and T. P. J. Hennessy, "A comparison of multimodal therapy and surgery for esophageal adenocarcinoma," *New England Journal of Medicine*, vol. 335, no. 7, pp. 462–467, 1996.

[8] B. H. Burmeister, B. M. Smithers, V. Gebski et al., "Surgery alone versus chemoradiotherapy followed by surgery for resectable cancer of the oesophagus: a randomised controlled phase III trial," *The Lancet Oncology*, vol. 6, no. 9, pp. 659–668, 2005.

[9] F.-L. Huang and S.-J. Yu, "Esophageal cancer: risk factors, genetic association, and treatment," *Asian Journal of Surgery*, vol. 41, no. 3, pp. 210–215, 2018.

[10] P. Lambin, J. Zindler, B. G. L. Vanneste et al., "Decision support systems for personalized and participative radiation oncology," *Advanced Drug Delivery Reviews*, vol. 109, pp. 131–153, 2017.

[11] H. J. W. L. Aerts, "The potential of radiomic-based phenotyping in precision medicine," *JAMA Oncology*, vol. 2, no. 12, pp. 1636–1642, 2016.

[12] J. Song, J. Shi, D. Dong et al., "A new approach to predict progression-free survival in stage IV EGFR-mutant NSCLC patients with EGFR-TKI therapy," *Clinical Cancer Research*, vol. 24, no. 15, pp. 3583–3592, 2018.

[13] D. Dong, L. Tang, Z.-Y. Li et al., "Development and validation of an individualized nomogram to identify occult peritoneal metastasis in patients with advanced gastric cancer," *Annals of Oncology*, vol. 30, no. 3, pp. 431–438, 2019.

[14] B. Zhang, J. Tian, D. Dong et al., "Radiomics features of multiparametric MRI as novel prognostic factors in advanced nasopharyngeal carcinoma," *Clinical Cancer Research*, vol. 23, no. 15, pp. 4259–4269, 2017.

[15] D. S. Kermany, M. Goldbaum, W. Cai et al., "Identifying medical diagnoses and treatable diseases by image-based deep learning," *Cell*, vol. 172, no. 5, pp. 1122–1131, 2018.

[16] S. Wang, J. Shi, Z. Ye et al., "Predicting EGFR mutation status in lung adenocarcinoma on computed tomography image using deep learning," *European Respiratory Journal*, vol. 53, no. 3, Article ID 1800986, 2019.

[17] S. Wang, M. Zhou, Z. Liu et al., "Central focused convolutional neural networks: developing a data-driven model for lung nodule segmentation," *Medical Image Analysis*, vol. 40, pp. 172–183, 2017.

[18] J. Gao, Q. Jiang, Q. Jiang, B. Zhou, and D. Chen, "Convolutional neural networks for computer-aided detection or diagnosis in medical image analysis: an overview," *Mathematical Biosciences and Engineering*, vol. 16, no. 6, pp. 6536–6561, Jul 15 2019.

[19] R. F. Thompson, V. Gilmer, C. D. Fuller, C. M. Carpenter, O. Morin, and S. Aneja, W. D. Lindsay, H. J. W. L. Aerts, B. Agrimson et al., "Artificial intelligence in radiation oncology: a specialty-wide disruptive transformation?" *Radiotherapy & Oncology*, vol. 129, 2018.

[20] X. Zheng, Z. Yao, Y. Huang et al., "Deep learning radiomics can predict axillary lymph node status in early-stage breast cancer," *Nature Communications*, vol. 11, no. 1, p. 1236, 2020.

[21] K. Chaudhary, O. B. Poirion, L. Lu, and L. X. Garmire, "Deep learning-based multi-omics integration robustly predicts survival in liver cancer," *Clinical Cancer Research*, vol. 24, no. 6, pp. 1248–1259, 2018.

[22] M. Jiang, C.-L. Li, X.-M. Luo et al., "Ultrasound-based deep learning radiomics in the assessment of pathological complete response to neoadjuvant chemotherapy in locally advanced breast cancer," *European Journal of Cancer*, vol. 147, pp. 95–105, 2021.

[23] Y. Hu, C. Xie, H. Yang et al., "Computed tomography-based deep-learning prediction of neoadjuvant chemoradiotherapy treatment response in esophageal squamous cell carcinoma," *Radiotherapy & Oncology: Journal of the European Society for Therapeutic Radiology and Oncology*, vol. 154, no. 1122–31, pp. 6–13, 2020.

[24] L. Zhang, D. Dong, W. Zhang et al., "A deep learning risk prediction model for overall survival in patients with gastric cancer: a multicenter study," *Radiotherapy & Oncology*, vol. 150, 2020.

[25] R. Poplin, A. V. Varadarajan, K. Blumer et al., "Prediction of cardiovascular risk factors from retinal fundus photographs via deep learning," *Nature Biomedical Engineering*, vol. 2, no. 3, pp. 158–164, 2018.

[26] Y. Zhu, C. Man, L. Gong et al., "A deep learning radiomics model for preoperative grading in meningioma," *European Journal of Radiology*, vol. 116, pp. 128–134, 2019.

[27] Z. Liu, Z. Jiang, L. Meng et al., "Handcrafted and deep learning-based radiomic models can distinguish GBM from

brain metastasis," *Journal of Oncology*, vol. 2021, no. 2, 10 pages, 2021.

[28] S. Bert-Ram, O. Kasia, S. Musib, C. J. R. Gary, and G. Vicky, "Radiomics in esophageal and gastric cancer," *Abdominal Radiology*, vol. 44, no. 6, pp. 2048–2058, 2019.

[29] J. Encinas de la Iglesia, M. A. Corral de la Calle, G. C. Fernández Pérez, R. Ruano Pérez, and A. Álvarez Delgado, "Esophageal cancer: anatomic particularities, staging, and imaging techniques," *Radiología*, vol. 58, no. 5, pp. 352–365, 2016.

[30] A. Fedorov, R. Beichel, J. Kalpathy-Cramer et al., "3D slicer as an image computing platform for the quantitative imaging network," *Magnetic Resonance Imaging*, vol. 30, no. 9, pp. 1323–1341, 2012.

[31] R. T. H. M. Larue, J. E. van Timmeren, E. E. C. de Jong et al., "Influence of gray level discretization on radiomic feature stability for different CT scanners, tube currents and slice thicknesses: a comprehensive phantom study," *Acta Oncologica*, vol. 56, no. 11, pp. 1544–1553, 2017.

[32] A. Zwanenburg, M. Vallières, M. A. Abdalah et al., "The image biomarker standardization initiative: standardized quantitative radiomics for high-throughput image-based phenotyping," *Radiology*, vol. 295, no. 2, pp. 328–338, 2020.

[33] A. Zwanenburg, S. Leger, L. Agolli et al., "Assessing robustness of radiomic features by image perturbation," *Scientific Reports*, vol. 9, no. 1, p. 614, 2019.

[34] S. Fiset, M. L. Welch, J. Weiss et al., "Repeatability and reproducibility of MRI-based radiomic features in cervical cancer," *Radiotherapy & Oncology*, vol. 135, pp. 107–114, 2019.

[35] J. J. M. van Griethuysen, A. Fedorov, C. Parmar et al., "Computational radiomics System to decode the radiographic phenotype," *Cancer Research*, vol. 77, no. 21, pp. e104–e107, 2017.

[36] C. Sun and W. G. Wee, "Neighboring gray level dependence matrix for texture classification," *Computer Vision, Graphics, and Image Processing*, vol. 23, no. 3, pp. 341–352, 1983.

[37] R. M. Haralick, K. Shanmugam, and I. H. Dinstein, "Textural features for image classification," *IEEE Transactions on Systems, Man, and Cybernetics*, vol. SMC-3, no. 6, pp. 610–621, 1973.

[38] M. M. Galloway, "Texture analysis using gray level run lengths," *Computer Graphics and Image Processing*, vol. 4, no. 2, pp. 172–179, 1975.

[39] G. Thibault, B. Fertil, and C. Navarro, "Texture indexes and gray level size zone matrix application to cell nuclei classification," in *Proceedings of the 10th International Conference on Pattern Recognition and Information Processing*, pp. 140–145, Minsk, Belarus, November 2009.

[40] M. Amadasun and R. King, "Textural features corresponding to textural properties," *IEEE Transactions on Systems, Man, and Cybernetics*, vol. 19, no. 5, pp. 1264–1274, 1989.

[41] P. Lambin, R. T. H. Leijenaar, T. M. Deist et al., "Radiomics: the bridge between medical imaging and personalized medicine," *Nature Reviews Clinical Oncology*, vol. 14, no. 12, pp. 749–762, 2017.

[42] F. Chollet, "Xception: deep learning with depthwise separable convolutions," 2017, https://arxiv.org/abs/1610.02357.

[43] H. Hanchuan Peng, F. Fuhui Long, and C. Ding, "Feature selection based on mutual information criteria of max-dependency, max-relevance, and min-redundancy," *IEEE Transactions on Pattern Analysis and Machine Intelligence*, vol. 27, no. 8, pp. 1226–1238, 2005.

[44] R. Tibshirani, "Regression shrinkage and selection via the lasso: a retrospective," *Journal of the Royal Statistical Society: Series B*, vol. 73, no. 3, pp. 267–288, 2011.

[45] H. Bozdogan, "Model selection and Akaike's information criterion (AIC): the general theory and its analytical extensions," *Psychometrika*, vol. 52, no. 3, pp. 345–370, 1987.

[46] M. H. Kutner, C. Nachtsheim, and J. Neter, *Applied Linear Regression Models*, McGraw-Hill/Irwin, New York, NY, USA, 2004.

[47] A. A. Kramer and J. E. Zimmerman, "Assessing the calibration of mortality benchmarks in critical care: the Hosmer-Lemeshow test revisited," *Critical Care Medicine*, vol. 35, no. 9, pp. 2052–2056, 2007.

[48] A. J. Vickers and E. B. Elkin, "Decision curve analysis: a novel method for evaluating prediction models," *Medical Decision Making*, vol. 26, no. 6, pp. 565–574, 2006.

[49] P. Afshar, A. Mohammadi, K. N. Plataniotis, A. Oikonomou, and H. Benali, "From handcrafted to deep-learning-based cancer radiomics: challenges and opportunities," *IEEE Signal Processing Magazine*, vol. 36, no. 4, pp. 132–160, 2019.

[50] The Cancer Genome Atlas Research Network, "Integrated genomic characterization of oesophageal carcinoma," *Nature*, vol. 541, pp. 169–175, 2017.

[51] H. Fei, W. Haojie, L. Yong et al., "SRPX2 knockdown inhibits cell proliferation and metastasis and promotes chemosensitivity in esophageal squamous cell carcinoma," *Biomedicine & Pharmacotherapy*, vol. 109, 2018.

[52] C. Ma, Z. Yao, Z. Yao, Q. Zhang, and X. Zou, "Quantitative integration of radiomic and genomic data improves survival prediction of low-grade glioma patients," *Mathematical Biosciences and Engineering*, vol. 18, no. 1, pp. 727–744, 2021.

[53] J. P. O'Connor, E. O. Aboagye, J. E. Adams et al., "Imaging biomarker roadmap for cancer studies," *Nature Reviews. Clinical Oncology*, vol. 14, pp. 169–186, 2017.

[54] C. Parmar, E. Rios Velazquez, R. Leijenaar et al., "Robust radiomics feature quantification using semiautomatic volumetric segmentation," *PLoS One*, vol. 9, no. 7, Article ID e102107, 2014.

Hindawi
Journal of Healthcare Engineering
Volume 2022, Article ID 7892408, 7 pages
https://doi.org/10.1155/2022/7892408

Research Article

Prior Distribution Estimation of Monitored Information in the Intensive Care Unit with the Hidden Markov Model and Decision Tree Methods

Xin Zhao[1] **Xiaokai Nie,**[2,3,4] **Guofei Pang,**[1] **Siyuan Qiu,**[1] **Kehan Shi,**[1] **Changqing Wang,**[1] **Bingqi Zhao,**[1] **and Yidan Huo**[1]

[1]*School of Mathematics, Southeast University, Nanjing 211189, China*
[2]*School of Automation, Southeast University, Nanjing 210096, China*
[3]*Key Laboratory of Measurement and Control of Complex Systems of Engineering, Ministry of Education, Southeast University, Nanjing 210096, China*
[4]*Shenzhen Research Institute, Southeast University, Shenzhen 518057, China*

Correspondence should be addressed to Xin Zhao; mmxinzhao@hotmail.com

Received 7 August 2021; Accepted 15 March 2022; Published 24 March 2022

Academic Editor: Ayush Dogra

In the intensive care unit, the monitored variables collected from sensors may have different behaviors among patients with different clinical basic information. Giving prior information of the monitored variables based on their specific basic information as soon as the patient is admitted will support the clinicians with better decisions during the surgery. Instead of black box models, the explainable hidden Markov model is proposed, which can estimate the possible distribution parameters of the monitored variables under different clinical basic information. A Student's *t*-test or correlation test is conducted further to test whether the parameters have a significant relationship with the basic variables. The specific relationship is explored by using a conditional inference tree, which is an explainable model giving deciding rules. Instead of point estimation, interval forecast is chosen as the performance metrics including coverage rate and relative interval width, which provide more reliable results. By applying the methods to an intensive care unit data set with more than 20 thousand patients, the model has good performance with an area under the ROC Curve value of 0.75, which means the hidden states can generally be correctly labelled. The significant test shows that only a few combinations of the basic and monitored variables are not significant under the 0.01 significant level. The tree model based on different quantile intervals provides different coverage and width combination choices. A coverage rate around 0.8 is suggested, which has a relative interval width of 0.77.

1. Introduction

In the intensive care unit (ICU), patients suffer from complications like sepsis and circulatory failure during surgery. Such complications will incur serious conditions out of medical control [1, 2]. Without fast and accurate disease diagnosis, patients face a high death rate due to lack of proper treatment. To improve the diagnosis efficiency, a prior information extraction method was developed in this research. As soon as the patients are admitted into the ICU, their basic clinical data can be checked from the medical information system. By giving the prior probability calculated from the basic clinical data, it can improve the posterior probability either diagnosed by the surgeons or by models like Bayesian.

The model developed during the training process in this research utilizes the basic clinical data before the surgery and the monitored data during the surgery. The data include two parts (1) the basic clinical data $B_{n,\cdot}$ for patient n including variables such as sex, age, weight, and height.

$$B_{n,\cdot} = \left[B_{n,1}, B_{n,2}, \ldots, B_{n,k}, \ldots\right], \quad (1)$$

where $n = 1, 2, \ldots, N$ and $k = 1, 2, \ldots, K$. (2) The monitored data during the surgery for patient n, including variables such as heart rate and cardiac output.

$$A_{n,\cdot,\cdot} = \begin{bmatrix} A_{n,1,1} & \cdots & A_{n,K,1} \\ A_{n,1,2} & \cdots & A_{n,K,2} \\ \vdots & \ddots & \vdots \\ A_{n,1,T_n} & \cdots & A_{n,K,T_n} \end{bmatrix}, \qquad (2)$$

where A_n refers to the matrix for the n^{th} individual containing all variables at all times. As the time length for patients differ, T_n is used to measure the time length for patient n. Without any extra information, the data for patient n are $\{B_{n,\cdot}, A_{n,\cdot,\cdot}\}$.

For diseases such as circulatory failure and sepsis during surgery, there are typical methods to diagnose their onset. For example, systemic inflammatory response syndrome (SIRS) and sequential organ failure asses (SOFA) are designed for sepsis detection. These are simple decision rules by including criteria like that the temperature is higher than 38 or lower than 36. These criteria are the general diagnosis standard when patients show obvious symptoms. In the early diagnosis of neonatal sepsis, the semiquantitative PCT test kit helps to exclude negative results [3]. Cheadle et al. [4] have surveyed a number of host defense parameters that pertain to an adequate immune response and developed an outcome predictive score, which can identify patients within hours of hospitalization who are at risk of subsequently developing overt clinical infection and sepsis. For observations $A_{n,\cdot,t}$ at time t, a response can be given according to the diagnosis standard as $y_{n,t}$. Until now, the data for patient n are $\{B_{n,\cdot}, A_{n,\cdot,\cdot}, y_{n,\cdot}\}$.

The current research for disease analysis by using the abovementioned data can be divided into three aspects, which are as follows:

(1) The relationship analysis of basic clinical data B and response variables such as survival rate. The models can be traditional biostatistics tests and machine learning methods [5]. For example, Chicco and Jurman [6] predict the survival rate of patients with sepsis from age, sex, and septic episode number alone.

(2) From the static aspect, the data A is regarded as a static multivariate time series, which assumes the data follow the same distribution without changing with time, thus a stationary process. Methods such as neural networks or ensemble learning technics such as the random forest or AdaBoost are used in the modeling process [7].

(3) From the dynamic aspect, the time series are regarded as dynamic multivariate variables, thus a nonstationary process [8]. Dynamic models are designed by giving model updating or retraining criteria. For example, Zhao et al. [9] use wavelet transform and decision tree-based methods to do interval forecasting for monitored data A. The input variables involved include A and sometimes B. For example, Esteban et al. [10] predict clinical events by combining static and dynamic information using recurrent neural networks. The data B is involved as an input layer in the neural network, resulting in an improvement in the performance. Bernhardt [11] proposes a two-part regression model composed of logistic regression and a truncated accelerated failure time model, which helps to use all of the available survival information. Instead of involving the data B in the existing model, Lin et al. [12] built a separate model to train B and combined it with the convolutional long short-term memory neural networks trained for A. In addition to the data A and B, pharmacy data are also used in the modeling process, as demonstrated by Hyland et al. [13].

Current research mainly concentrate on one specific disease with two states being safe or onset. But the reality is that multiple states may occur during the surgery process. Prediction of one specific state may reduce the data information utility and ignoring other states may bring more uncertainty to the health condition of the patients. In addition, the criteria of disease onset detection like SIRS may not cover all possible hidden conditions. The states can be regarded as hidden states that are not seen or cannot be measured directly while the monitored variables like A or basic information B are not hidden. One of the main hidden states model is the hidden Markov model. Christopher et al. give the initial probability distribution calculation method of the multi-Markov model for such data. Their following research can be seen from Christopher, Ieva et al. [14]. In this case, hidden state models are proposed in this research to label the state for each observation of each patient.

The distribution of data A is rarely studied among the researches, as most of the methods are nonparametric methods which have no parameter assumptions like some of the machine learning methods. But if the distributions can be estimated, the correlation of the basic clinical data B and the distributions of different state labels can be established. In that case, by giving the prior information of B, the clinicians can have the estimated posterior distribution of A of different disease states. For example, if females have an average higher heart rate than males, a heart rate value normal for females may be alerted for males. If the heart rate is not distinguished by sex, male patients may be delayed in medical treatment. So, in this research, the distributions of monitored data A are studied under different states' labels. The correlation between distribution parameters and basic clinical data is tested to distinguish their differences among different basic information.

The innovative aspects in this paper include the following: (1) the multivariable hidden Markov model is selected to discover the hidden states that may not be measured by the general standard rules. (2) The variables' distribution of A labelled with different states is estimated by the hidden Markov model under the Gaussian assumption. (3) The variables' distributions are compared under different prior basic clinic conditions to give a posterior information for clinical decision.

We introduce our basic model in Section 2, and apply it to the real data in Section 3. Some concluding comments appear in Section 4. All calculations were carried out using R

Core Team [15]; "depmmixS4" [16] was used for the hidden Markov model and "ctree" by Hothorn et al. [17] for the Ctree.

2. Methods

The hidden Markov model (HMM) origins from the research [18] for discrete observations and is further developed for time series; detailed study was carried out in [19]. The HMM has observations which are observable, such as the monitored variable heart rate which can be collected by sensors. The observations are generated by the corresponding states which are not observable, like the status of the patient as sick or healthy, as circulatory failure or normal. The HMM has three typical questions: likelihood, decoding, and learning. What is used in this research are decoding and learning, which are finding the most likely hidden status and learning the parameters of the model.

If the distribution of the observations are assumed to be Gaussian distribution, for patient n and monitored variable k at status s, by giving the parameters of initial distribution as π_s, Gaussian distribution as $\mu_{n,\cdot,s}$, $\Sigma_{n,\cdot,s}$, the conditional joint distribution is

$$f\left(A_{n,\cdot,\cdot}, y_{n,\cdot} | \pi_s, \mu_{n,k,s}, \sigma_{n,k,s}\right) = \prod_{t=1}^{T_n} \prod_{k=1}^{K} \pi_s^{I\left(y_{n,t}=s\right)} \mathcal{N}\left(A_{n,k,t} | \mu_{n,\cdot,s}, \Sigma_{n,\cdot,s}\right)^{I\left(y_{n,t}=s\right)}, \tag{3}$$

where $I(y_{n,t} = s)$ is the indicator variable showing whether the status of patient n at time t is s or not. If the variables are further assumed to be independent mutually, then the distribution is

$$f\left(A_{n,\cdot,\cdot}, y_{n,\cdot} | \pi_s, \mu_{n,k,s}, \sigma_{n,k,s}\right) = \prod_{t=1}^{T_n} \prod_{k=1}^{K} \pi_s^{I\left(y_{n,t}=s\right)} \left\{ \prod_{k=1}^{K} \mathcal{N}\left(A_{n,k,t} | \mu_{n,k,s}, \sigma_{n,k,s}\right) \right\}^{I\left(y_{n,t}=s\right)}. \tag{4}$$

By using the Baum–Welch algorithm (expectation maximization algorithm) and assuming the initial distribution is equally distributed, the Gaussian distribution parameters can be estimated for patient n, variable k, and state s as follows:

$$\left\{\widehat{\mu}_{n,k,s}, \widehat{\sigma}_{n,k,s}\right\}. \tag{5}$$

By applying the forward-backward algorithm, the best hidden states $\widehat{y}_{n,t}$ and its corresponding probability $p(y_{n,t} = s)$ can be estimated.

Since the hidden states are discrete, the metric AUC (area under the ROC curve) is chosen to measure the similarity between the real and estimated hidden states. A ROC curve (receiver operating characteristic curve) is a graph showing the performance of a classification model at all classification thresholds. AUC provides an aggregate measure of performance across all possible classification thresholds, which ranges in value from 0 to 1. A model whose predictions are 100 % wrong has an AUC of 0.0; one whose predictions are 100 % correct has an AUC of 1.0, while random guessing has an AUC of 0.5.

If the AUC results are acceptable, the estimated parameters $\left\{\widehat{\mu}_{n,k,s}, \widehat{\sigma}_{n,k,s}\right\}$ can be reliable. After that, the parameters are compared under different basic clinical data B. For example, the data $\widehat{\mu}_{\cdot,k,s}$ of variable k and state s are compared under different sex to test whether it has significant difference between female and male patients. The comparing methods include Student's t-test for discrete variables such as sex and the correlation test for continuous variables such as age, weight, and height. If the test shows significant results, the model decision tree is further conducted to find how the basic clinical variable influences the monitored variables' distribution, namely, the estimated parameters.

The model decision tree is a model of tree-like decision rules, which splits the sample space into subspaces by choosing the best split each time. Specifically, the model used in this research is a conditional inference tree (Ctree [17]). Ctree estimates a regression relationship by binary recursive partitioning in a conditional inference framework. The predictor variable, like the clinical basic variables, with the lowest p value is selected for splitting the response variable, for example, $\widehat{\mu}_{\cdot,k,s}$ of variable k and state s. The p value belongs to a split criterion which can be Spearman's correlation test, the Wilcoxon–Mann–Whitney test, the Kruskal–Wallis test, permutation tests, and so on. The stoping criteria are not constrained to the p value, but also include the max tree depth allowance. For example, a max tree depth of 5 means the tree can be no bigger than 5 in depth. Other stopping criteria may also be applied. A regression tree is formed by iteratively splitting nodes so as to maximize the decreased p value at each step.

For each observation, it will be split into one single terminal node. The observations in the same terminal node can be regarded as a set. By ranging the Y values in that set,

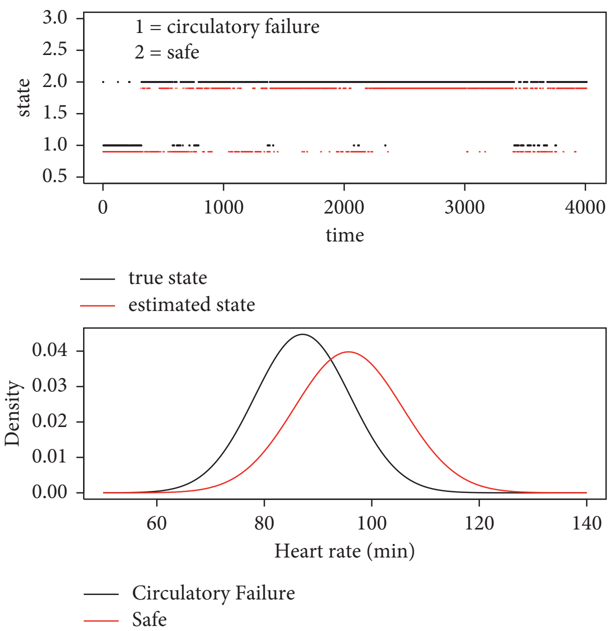

Figure 1: The hidden Markov model (HMM) result for one patient with multiple states. In the first figure, the HMM estimated red (below the black line) points are generally consistent with the black points (above the red line). Its corresponding AUC value is 0.8962. In the second figure, the right red Gaussian curve has the parameters $\mu = 95.675$ and $\sigma = 10.027$, and the left black curve has the parameters $\mu = 87.123$ and $\sigma = 8.918$. The observations of state circulatory failure have a relatively lower μ.

the quantile values can be selected as the forecast interval. For example, an 80 % interval has an upper value of 0.9 quantiles and a lower value of 0.1 quantiles. The width of the quantile interval is further standard adjusted to remove the influence of the different variable units by dividing their 0.9 quantile difference of the variable.

$$\text{Relative interval width} = \frac{\text{original interval width}}{0.95\ \text{quantile} - 0.05\ \text{quantile}}. \tag{6}$$

The coverage of the interval is as follows:

$$\text{coverage rate} = \frac{\text{number of observations in the interval}}{\text{total number of observations}}. \tag{7}$$

A wider interval has a high coverage when a new observation comes into the same terminal node, but at the cost of a higher width. An interval with good coverage and suitable width is suggested.

3. Real Data Analysis and Results

In the real data analysis, the circulatory failure data from Hyland et al. [13] are used. After deleting patients who have missing values, the data contains 22290 patients. The data include monitored variables A such as heart rate, systolic blood pressure (BP), diastolic BP, mean arterial pressure (MAP), and basic clinical data B such as sex, age, weight, height, and body mass index (BMI). Sepsis is a systemic inflammatory response syndrome caused by the invasion of

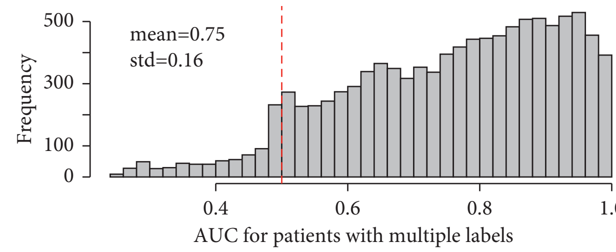

Figure 2: The area under the ROC curve (AUC) results for patients with multiple states. The AUC value of 0.5 means the model has a performance of random guessing. A value higher than that means the model has better performance.

pathogenic microorganisms such as bacteria into the body. Associated dysregulation of the inflammatory response has been thought to be directly associated with cardiomyocyte dysfunction. And heart rate reflects the frequency with which cardiomyocytes move. Systolic BP, diastolic BP, and MAP are related to blood volume, elasticity and tension of blood vessel walls, and cardiac output. They can all reflect well the ability of cardiomyocytes and can serve as an indicator of sepsis. For the state variable y, it is labelled generally according to the rule from [13]: $y_{n,t}$ is labelled as circulatory failure if MAP is ≤ 65 mmHg or (not exclusive) vasoactive/inotropic drugs are present and lactate is bigger than $2\ \mathrm{mmol\ l^{-1}}$. Under the other circumstances, $y_{n,t}$ is labelled as safe.

For the data $A_{n,\cdot,\cdot}$ of patient n, we train them with the model HMM under the Gaussian distribution assumption. The estimated states and the estimated parameters for the variable heart rate of one patient example are shown in Figure 1.

$$\hat{y}_{n,t} = f\left(A_{n,\cdot,\cdot}\right). \tag{8}$$

One thing that needs to be noticed is that the hidden state of not being safe is not constrained to circulatory failure but may also include others. The reason $y_{n,t}$ is labelled as circulatory failure is because circulatory failure is the main disease during the process. If it can be correctly labelled, the HMM results can be reliable. After the HMM processing, the AUC value is calculated for patients who have multiple states in $y_{n,\cdot}$. The patients with only circulatory failure or safe state, namely, $y_{n,}$ with only one label, are not involved in the AUC measurement. After that, the number of patients is 10406. The histogram of the results is shown in Figure 2.

The result shows that, the HMM model can efficiently recognize the patterns of the data, thus most of the states are labelled with the right tag. Since the AUC results are acceptable, the estimated parameters $\{\hat{\mu}_{n,k,s}, \hat{\sigma}_{n,k,s}\}$ can be reliable. After that, the t-test or correlation test is conducted to test whether the estimated $\hat{\mu}_{n,\cdot,s}$, $\hat{\Sigma}_{n,\cdot,s}$ have significant difference among different basic clinical settings. The results are shown in Table 1.

The results show that most of the parameters have a significant correlation with the clinical basic variables. By giving the clinical basic information, the parameters can have their values estimated, which can be regarded as the prior values for the monitored variables. Instead of

Table 1: The p value of the t-test or correlation test.

Variable	Heart rate				Systolic BP (invasive)				Diastolic BP (invasive)				MAP			
Parameter	μ		σ		μ		σ		μ		σ		μ		σ	
State	1	2	1	2	1	2	1	2	1	2	1	2	1	2	1	2
Sex	0.028	0.026	0.000	0.000	0.027	0.047	0.132	0.604	0.152	0.463	0.446	0.051	0.000	0.000	0.024	0.001
Age	0.000	0.000	0.000	0.000	0.309	0.365	0.000	0.000	0.000	0.000	0.001	0.000	0.000	0.000	0.000	0.000
Weight	0.113	0.163	0.000	0.000	0.029	0.025	0.000	0.001	0.000	0.001	0.000	0.008	0.023	0.014	0.022	0.325
Height	0.000	0.000	0.002	0.000	0.010	0.002	0.481	0.362	0.000	0.000	0.052	0.483	0.372	0.183	0.111	0.000
BMI	0.000	0.000	0.000	0.000	0.487	0.788	0.000	0.000	0.097	0.006	0.000	0.006	0.000	0.000	0.000	0.014
Variable	Cardiac output				SpO2				INR				Serum glucose			
Parameter	μ		σ		μ		σ		μ		σ		μ		σ	
State	1	2	1	2	1	2	1	2	1	2	1	2	1	2	1	2
Sex	0.000	0.000	0.000	0.000	0.001	0.000	0.610	0.895	0.667	0.434	0.531	0.130	0.014	0.000	0.000	0.000
Age	0.000	0.000	0.000	0.000	0.000	0.000	0.000	0.000	0.000	0.000	0.000	0.000	0.000	0.000	0.000	0.000
Weight	0.000	0.000	0.000	0.000	0.000	0.000	0.462	0.814	0.425	0.754	0.168	0.004	0.000	0.000	0.004	0.037
Height	0.000	0.000	0.000	0.000	0.019	0.001	0.863	0.999	0.218	0.097	0.195	0.007	0.000	0.014	0.000	0.000
BMI	0.000	0.000	0.000	0.000	0.000	0.000	0.312	0.783	0.585	0.552	0.280	0.066	0.000	0.000	0.000	0.000

BP: blood pressure MAP: mean arterial pressure BMI: body mass index INR: international normalized ratio.

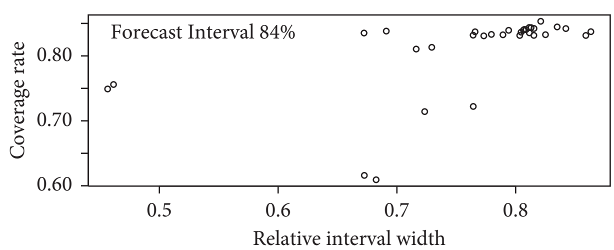

Figure 3: The coverage rate and relative interval width of the 32 monitored variables under the 84% forecast interval. The averaged relative interval width is 0.77, and the averaged coverage rate is 0.81.

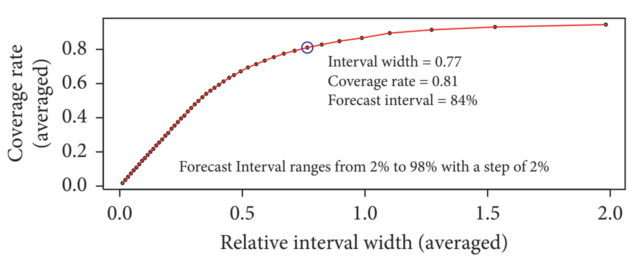

Figure 4: The averaged coverage rate and relative interval width of the 32 monitored variables under different forecast intervals.

point estimation, interval estimation is suggested to give more reliable support for clinicians. The model Ctree is applied, with the threshold chosen as 0.1 and the tree max depth as 5, which balances the performance and complexity of the model. For example, when the forecast interval is set as 84 %, the coverage rate and relative width across the 32 monitored variables are shown in Figure 3.

Since the correlation significant results differ across the monitored variables, the coverage rate and relative interval width have different performances. But the results are relatively acceptable as they are generally around 0.84, the preset forecast interval.

When the forecast interval changes, the averaged coverage rate and averaged relative interval width can be estimated. The results are shown in Figure 4. It can be shown that when the interval width increases, the coverage rate also increases, but at a decreasing speed. An increase of 0.1 may cost the width of 0.5 when coverage has reached 0.8. A result of around 0.8 is proposed, which has relatively high coverage but not that wider width. It should be noted that this study involves one disease, sepsis, but includes different stages of sepsis and has a large sample size to support the data, so the model is stable and can be generalized.

4. Conclusion

In order to calculate the prior distribution parameters of the monitored variables of different hidden states, this research gives a method by using the explainable HMM and Ctree models. The HMM finds the most possible hidden states, and the estimated states are compared with the true circulatory failure states, which results in an AUC of 0.75 in the real data analysis. Thus, the distribution parameters of the monitored variables learned by the HMM can be reliable. The t-test or correlation test is applied to test the significant relationship between the basic clinical variable and the distribution parameters of the monitored variables. Results show that most relationships are significant, which means the distribution of the monitored variables truly has some kind of dependence on the clinical basic information. To further explore the specific relationship, the model Ctree is conducted. Instead of point estimation, interval forecast is applied, along with the coverage rate and relative interval width as the performance metrics. Results show that, with a wider width, the coverage increases. But the increase decays when the coverage reaches a high level. A good coverage of 0.8 with a suitable width is suggested.

In further research, in terms of the method, the parameters of the monitored variables can be assumed to follow different distributions without being constrained to follow a Gaussian distribution. This can help extend the method for more general conditions. In terms of the variable relationship exploration part, the relationship test can be applied to a mixture of variables instead of one at a time. This helps explore more potential relationships among different variables. In the interval forecast method, point estimation can be conducted by including other input variables so as to get a good performance. In terms of sepsis, as it is a threat to the public health with high morbidity and mortality, further research can be extended from diagnosis assistance to also include prevention and treatment support. More machine learning methods can be developed to solve the potential problems incurred by the rapid development of medical technology.

The results of the research can not only be used for clinician support but also provide prior distribution for the models of state prediction during the monitoring process. This can improve the prediction accuracy at the beginning of the prediction process. If further pharmacy information is added, the research can also be used for exploring the influence of clinical basic information in the usage of drugs. Suitable and timely drug dosage provides the possibility of precision medicine. By combining machine learning technologies with medical demand, medical problems can be solved more automatically by modern algorithms, and less human resources are required. The method developed in this research can be also applied in other areas such as financial and economical areas, environmental regulation, and so on.

Data Availability

The source codes in the methods are available from the corresponding author upon request. The real data in the application can be requested from Hyland et al. [13] [20, 21].

Conflicts of Interest

The authors declare that they have no conflicts of interest.

Acknowledgments

Xin Zhao is grateful for the financial support of the Fundamental Research Funds for the Central Universities (no. 2242020R40073), the National Natural Science Foundation of China (12171085), the Natural Science Foundation of Jiangsu Province (BK20200347), and the Nanjing Scientific and Technological Innovation Foundation for Selected Returned Overseas Chinese Scholars (1107010306) during this research. Xiaokai Nie is grateful for the financial support of the National Natural Science Foundation of China (62103105), the Natural Science Foundation of Jiangsu Province (BK20210218), the Guangdong Basic and Applied Basic Research Foundation (2020A1515110129), Fundamental Research Funds for the Central Universities (MCCSE2021B02 and 2242020R10053), the Nanjing Scientific and Technological Innovation Foundation for Selected Returned Overseas Chinese Scholars (1108000241), the Jiangsu Province Foundation for Innovative and Entrepreneurial Doctor (1108000245), and Southeast University Zhishan Youth Scholar Foundation. Siyuan Qiu, Kehan Shi, Changqing Wang, Bingqi Zhao, and Yidan Huo are grateful for the financial support of the College Students Innovation and Entrepreneurship Training Program (202107024, S202110286069).

References

[1] K. Farrah, L. McIntyre, C. J. Doig et al., "Sepsis-associated mortality, resource use, and healthcare costs: a propensity-matched cohort study*," *Critical Care Medicine*, vol. 49, no. 2, pp. 215–227, 2021.

[2] T. Lafon, A. Appert, M. Hadj et al., "Comparative early hemodynamic profiles in patients presenting to the emergency department with septic and nonseptic acute circulatory failure using focused echocardiography," *Shock*, vol. 53, no. 6, pp. 695–700, 2020.

[3] N. Y. Boo, A. A. Nor Azlina, and J. Rohana, "Usefulness of a semi-quantitative procalcitonin test kit for early diagnosis of neonatal sepsis," *Singapore Medical Journal*, vol. 49, no. 3, pp. 204–8, 2008.

[4] W. G. Cheadle, M. Mercer-Jones, M. Heinzelmann, and H. C. Polk, "Sepsis and septic complications in the surgical patient," *Shock*, vol. 5, pp. S6–S9, 1996.

[5] S. Voicu, F. J. Baud, I. Malissin et al., "Can mortality due to circulatory failure in comatose out-of-hospital cardiac arrest patients be predicted on admission? a study in a retrospective derivation cohort validated in a prospective cohort," *Journal of Critical Care*, vol. 32, pp. 56–62, 2016.

[6] D. Chicco and G. Jurman, "Survival prediction of patients with sepsis from age, sex, and septic episode number alone," *Scientific Reports*, vol. 10, no. 1, Article ID 17156, 2020.

[7] S. L. Kausch, J. R. Moorman, D. E. Lake, and J. Keim-Malpass, "Physiological machine learning models for prediction of sepsis in hospitalized adults: an integrative review," *Intensive and Critical Care Nursing*, vol. 65, 2021.

[8] F. Van Wyk, A. Khojandi, and R. Kamaleswaran, "Improving prediction performance using hierarchical analysis of real-time data: a sepsis case study," *IEEE Journal of Biomedical and Health Informatics*, vol. 23, no. 3, pp. 978–986, 2019.

[9] X. Zhao, S. Barber, C. C. Taylor, and Z. Milan, "Interval forecasts based on regression trees for streaming data," *Advances in Data Analysis and Classification: Theory Methods and Applications in Data Science*, vol. 15, no. 1, p. 5, 2021.

[10] C. Esteban, O. Staeck, S. Baier, Y. Yang, and V. Tresp, "Predicting clinical events by combining static and dynamic information using recurrent neural networks," in *Proceedings of the 2016 IEEE International Conference on Healthcare Informatics (ICHI)*, pp. 93–101, Chicago, IL, USA, October 2016.

[11] P. W. Bernhardt, "Maximum likelihood estimation in a semicontinuous survival model with covariates subject to detection limits," *International Journal of Biostatistics*, vol. 14, no. 2, 2018.

[12] C. Lin, Y. Zhang, J. Ivy et al., "Early diagnosis and prediction of sepsis shock by combining static and dynamic information using convolutional-lstm," in *Proceedings of the 2018 IEEE International Conference on Healthcare Informatics (ICHI)*, pp. 219–228, New York, NY, USA, June 2018.

[13] S. L. Hyland, M. Faltys, M. Hüser et al., "Early prediction of circulatory failure in the intensive care unit using machine learning," *Nature Medicine*, vol. 26, no. 3, p. 364, 2020.

[14] F. Ieva, C. Jackson, and L. Sharples, "Multi-state modelling of repeated hospitalisation and death in patients with heart failure: the use of large administrative databases in clinical epidemiology," *Statistical Methods in Medical Research*, vol. 26, no. 3, pp. 1350–1372, 2017.

[15] R. Core Team, *R: A Language and Environment for Statistical Computing*, R Foundation for Statistical Computing, Vienna, Austria, 2018.

[16] V. Ingmar and S. Maarten, "depmixs4: an r package for hidden Markov models," *Journal of Statistical Software*, vol. 36, no. 7, 2010.

[17] T. Hothorn, K. Hornik, M. A. Van De Wiel, and A. Zeileis, "A lego system for conditional inference," *The American Statistician*, vol. 60, no. 3, pp. 257–263, 2006.

[18] L. Rabiner and B. Juang, "An introduction to hidden Markov models," *IEEE ASSP Magazine, ASSP Magazine, IEEE, IEEE ASSP Mag*, vol. 3, no. 1, pp. 4–16, 1986.

[19] W. Zucchini and I. Macdonald, *Hidden Markov Models for Time Series: An Introduction Using R*, Chapman and Hall/ CRC, Boca Raton, FL, USA, 2009.

[20] H. J. Christopher, "Multi-state models for panel data: the msm package for r," *Journal of Statistical Software*, vol. 38, no. 8, 2011.

[21] H. J. Christopher, D. S. Linda, G. T. Simon, W. D. Stephen, and C. Elisabeth, "Multistate Markov models for disease progression with classification error," *Journal of the Royal Statistical Society. Series D (The Statistician)*, vol. 52, no. 2, pp. 193–209, 2003.

Hindawi
Journal of Healthcare Engineering
Volume 2022, Article ID 1230812, 8 pages
https://doi.org/10.1155/2022/1230812

Research Article

Construction of a Prognostic Nomogram Model for Patients with Mucinous Breast Cancer

Xulong Zhu,[1,2] Ying Li,[3] Fende Liu,[1,3] Feifei Zhang,[1] Jianhui Li,[1] Chong Cheng,[1] Yanwei Shen,[1] Nan Jiang,[1] Jia Du,[1] Yajing Zhou,[1,3] and Binliang Huo[1]

[1]*Department of Surgical Oncology, Shaanxi Provincial People's Hospital, Xian 710068, China*
[2]*School of Life Science and Technology, Xi'an Jiaotong University, Xi'an 710049, China*
[3]*Graduate School, Xi'an Medical University, Xi'an 710068, China*

Correspondence should be addressed to Binliang Huo; huobinliang@163.com

Received 6 January 2022; Revised 28 February 2022; Accepted 2 March 2022; Published 23 March 2022

Academic Editor: Enas Abdulhay

Objective. The objective of the study is to develop a nomogram for estimating three- and five-year survival rates in mucinous breast cancer patients. *Methods*. Between 2010 and 2016, the National Cancer Institute's Surveillance, Epidemiology, and End Results (SEER) were searched as a data source for patients associated with mucinous breast cancer (MBC). A total of 3964 patients were recruited after screening. The multivariate Cox model and the univariate Kaplan-Meier (KM) approach were employed to evaluate the independent prognostic markers, followed by developing a nomogram for estimating three- and five-year survival rates in MBC patients. Consequently, the consistency index (C-index) was employed to assess the predictive accuracy of the generated nomogram. *Results*. Age, race, T stage, M stage, surgery, and radiotherapy were all independent predictive biomarkers for the MBC patients ($P < 0.05$). The nomogram was finally developed based on the underlined factors. Furthermore, the C-index of 0.803 and reliable calibration curves were obtained in the nomogram's assessment. *Conclusions*. In patients with mucinous breast cancer, the proposed nomogram provides a viable tool for accurate prognostic prediction. In clinical practice, it could serve as a personalized diagnosis tool, estimate prognosis, and help in suggesting treatment plans for patients with MBC.

1. Introduction

Mucinous breast cancer (MBC) is a rare and unusual type of breast cancer that manifests itself primarily by a huge percentage of extracellular mucins [1, 2]. It accounts for around 1%–6% of all primary breast cancers. MBC is more frequent in postmenopausal women and has a better survival [3]. MBC was shown to have elevated hormone receptor expression and decreased human epidermal growth factor receptor 2 expressions in prior research [4–6]. Because of the low incidence of MBC, it has different clinical, histopathological, and biological characteristics from common breast cancers in general [7], and there is a lack of reports of large sample studies on MBC, which predisposes to undertreatment or overtreatment. The prognosis of MBC is influenced by many factors at the same time. It is difficult to predict the actual situation of patients by one or several prognostic factors alone. The lack of a particular prognosis evaluation system for MBC has resulted in a uniform treatment for MBC, without any consideration of individual patient needs.

Nomograms have been developed as the new standard for predicting the occurrence and prognosis of certain cancers, and most cancer types have established prognostic nomograms [8, 9]. Such nomograms are considered a reliable tool that can help clinicians make accurate individualized predictions [10]. However, no satisfactory nomogram has yet been developed to predict survival in MBC. To solve the problem, this study attempts to establish a new nomogram-based prediction model for MBC that incorporates more than one clinical parameter in an attempt to individualize the estimation of prognosis for patients. It involves retrospective analysis of the data of MBC from 2010 to 2016 in the SEER database, screening independent prognostic factors, and, subsequently, constructing a nomogram prognostic model to provide a reference for clinicians to assess patient prognosis and develop individualized treatment plans.

2. Material and Methods

2.1. Source of Data. The data for the current study were attained from the SEER database of the US National Cancer Institute (NCI), and the data were obtained by SEER Stat 8.3.8 software.

2.2. Patient Inclusion and Information Extraction

2.2.1. Patient Inclusion and Exclusion Criteria. The data of MBC patients in the SEER database from 2010 to 2016 were collected. Inclusion criteria were as follows: (1) ICD-O-3 Hist/behave, malignant = "8480/3: mucinous adenocarcinoma"; (2) patients newly diagnosed with MBC; (3) patients with breast cancer as the only primary tumor; (4) patients with complete general clinicopathological information; (5) patients with complete follow-up (follow-up up to December 31, 2016). The exclusion criteria were given as follows: (1) male MBC patients; (2) confirmed patients of postmortem examination and death report; (3) patients with missing information and survival time less than 1 month (Figure 1).

2.2.2. Information Extraction. Extract the patient's age, race, marital status, tumor location (left breast, right breast), histological grade, TNM stage (7th edition AJCC-TNM staging system), ER status, PR status, HER-2 status, surgery, radiotherapy, chemotherapy, survival data, and other information.

2.3. Statistical Methods. Patients were randomly split into modeling and validation groups using *R* software. First, univariate analysis was conducted to evaluate the factors affecting the survival prognosis of patients in the modeling group, and variables that showed statistical significance on univariate analysis were also involved in the multivariate Cox proportional hazards regression (CPHR) model to determine the final independent prognostic factors, the effect of independent prognostic factors on the survival rate of MBC patients was shown by the KM method, and then, the nomogram was constructed using *R* software, and the consistency index was calculated, and the correction curve was drawn. The Bootstrap method was used to conduct internal and external validation for the modeling group and the validation group, respectively. In the calibration curve, the closer the curve is to the ideal 45° reference line, the closer the predicted value is to the actual observed value. *R* software (version 4.0.2) (http://www.r-project.org/) was employed to conduct the statistical evaluations.

3. Results

3.1. Clinicopathological Features of Included Patients. From 2010 to 2016, the SEER database yielded 3,964 eligible female MBC patients (2,776 in the modeling group and 1,188 in the validation group). It summarizes the sociodemographic and clinicopathological features of the two groups in Table 1. The 3,964 patients were followed up for a period of 1 to 83 months, with a mean follow-up of 39 months. Approximately three-quarters of patients were white ($n = 2{,}992$, 75.4%), more than one-half were Grade I ($n = 2{,}354$, 59.3%), and more than 90% were N0, M0, ER (+), PR (+), HER-2 (−). Other clinicopathological features are shown in Table 1.

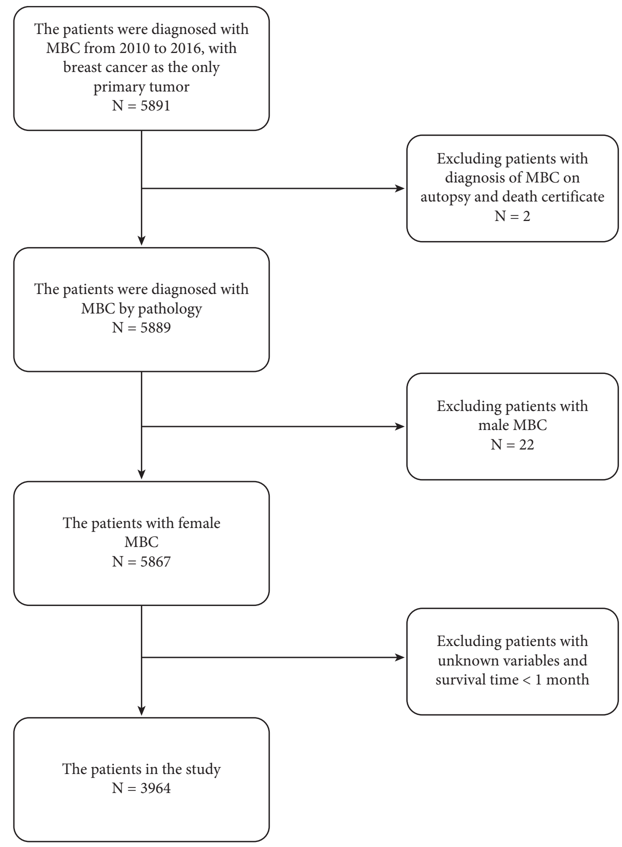

Figure 1: Flow chart of patient screening in SEER database.

3.2. Analysis of Influencing Factors of Survival Prognosis

3.2.1. Univariate Analysis Results. Univariate analysis of the survival of 2,776 MBC patients in the modeling group revealed that the 3- and 5-year survival rates of patients were linked to their age, ethnicity, marital status, T stage, N stage, M stage, surgery, radiotherapy, and chemotherapy ($P < 0.05$) but not to histological grade, lesion location, PR status, ER status, or HER-2 status ($P > 0.05$), as indicated in Table 2.

3.2.2. Results of Multivariate CPHR Analysis. Table 2 shows the results of multivariate CPHR analysis, which were based on the findings of univariate analysis. In this study, age, ethnicity, T stage, M stage, surgery, and radiotherapy were all found to be independent risk factors for MBC patients' prognosis ($P < 0.05$). The KM curve was used to demonstrate the impact of independent prognostic factors on MBC patient survival rates, as indicated in Figures 2(a)–2(f). In

Table 1: Clinicopathological features of patients in modeling and validation group (case (%)).

Clinicopathological characteristics	Modeling group ($n = 2776$)		Validation group ($n = 1188$)	
Age				
18–39	116	4.1	44	3.7
40–59	772	27.8	326	27.4
60–79	1448	52.1	605	50.9
≥80	440	15.8	213	17.9
Ethnicity				
White	2087	75.1	905	76.1
Black	343	12.3	144	12.1
Others	346	12.4	139	11.7
Marital status				
Married	1418	51.0	608	51.1
Unmarried	1358	48.9	580	48.8
Lesion location				
Left	1435	51.6	616	51.8
Right	1341	48.4	572	48.1
Histological grading				
I	1644	59.2	710	59.7
II	1030	37.1	428	36.0
III	100	3, 6	49	4.1
IV	2	0.1	1	0.1
T Stage				
T1	1776	63.9	795	66.9
T2	798	28.7	322	27.1
T3	153	5.5	56	4.7
T4	49	1.7	15	1.2
N Stage				
N0	2506	90.2	1068	89.8
N1	216	7.7	101	8.5
N2	32	1.1	16	1.3
N3	22	0.7	3	0.2
M Stage				
M0	2741	98.7	1174	98.8
M1	35	1.2	14	1.1
ER expression				
Negative	36	1.2	10	0.8
Positive	2740	98.7	1178	99.1
PR expression				
Negative	213	7.6	104	8.7
Positive	2563	92.3	1084	91.2
HER-2 expression				
Negative	2614	94.1	1131	95.2
Positive	162	5.8	57	4.7
Surgery				
Yes	2667	96.0	1150	96.8
None	109	3.9	38	3.1
Radiotherapy				
Yes	1419	51.1	624	52.5
None	1357	48.8	564	47.4
Chemotherapy				
Yes	381	13.7	157	13.2
None	2395	86.2	1031	86.7

each of the graphical representations, the horizontal axis (x-axis) represents time in months, and the vertical axis (y-axis) shows the probability of survival or the proportion of people surviving. A vertical drop in the curves indicates an event.

3.3. The Development of a Nomogram to Assess MBC Patients' 3- and 5-Year Overall Survival (OS) Rates. Age, ethnicity, T stage, M stage, radiation, and surgery were among the statistically significant prognostic factors in the multivariate CPHR model. A nomogram was constructed using *R* software. The predictive nomogram for the 3- and 5-year OS rates of MBC patients is shown in Figure 3. The nomogram is used by totaling the points identified on the top scale for each independent covariate. The score of each item of an individual can be obtained by projecting each clinicopathologic feature upwards to the score, and the total score is obtained by adding the scores of each item. There is a total points line at the bottom of the nomogram. The total points projected to the bottom scale indicate the % probability of 3-, 5-year ***overall survival (OS).***

The higher the total score, the worse the survival prognosis. The nomogram in Figure 3 shows that age at diagnosis is the greatest contributor to the prognosis, followed, respectively, by M stage, TNM stage, ethnicity, surgery status, and radiotherapy status. The nomogram shows that the use of radiotherapy is beneficial for patients with MBC.

3.4. Verification of Nomograms. We established a nomogram model integrating independent predictors of OS (e.g., age, tumor site, tumor size, tumor extension, and radiotherapy) to provide a visual statistical predictive tool for the survival of patients with MGCTB. We established a nomogram model integrating independent predictors of OS (e.g., age, tumor site, tumor size, tumor extension, and radiotherapy) to provide a visual statistical predictive tool for the survival of patients with MGCTB. We established a nomogram model integrating independent predictors of OS (e.g., age, tumor site, tumor size, tumor extension, and radiotherapy) to provide a visual statistical predictive tool for the survival of patients with MGCTB. We established a monogram model integrating independent predictors of OS (age, ethnicity, T stage, M stage, radiotherapy, and surgery) to provide a visual statistical predictive tool for the survival of patients with MBC. A calibration curve of the nomograph was drawn to evaluate the consistency between the observed and estimated survivals. The C-index calculated by *R* software was 0.803 (95% CI: 0.772–0.834) for the modeling group and 0.817 (95% CI: 0.768–0.866) for the validation group, suggesting that both had good predictive values and good discriminative ability. The bootstrap method was used for internal verification and external verification of nomogram. The self-sampling number $B = 1{,}000$. Figure 4 shows the calibration plots of the nomogram for predicting the probability of OS at 3 and 5 years. The calibration curves of 3- and 5-year survival rates in the modeling group and validation group were close to the ideal 45° reference line (Figure 4), suggesting that there was good consistency between the predicted value and the actual 3 and 5 years OS. Thus, the monogram has been internally and externally verified for both the modeling and validation group, respectively, showing good accuracy and clinical applicability. It can effectively predict OS in MBC patients, which may

Table 2: Results of univariate and multivariate analysis affecting the survival prognosis of 2776 patients in the modeling group.

Clinical pathology characteristics	Univariate analysis Hr value	95% confidence interval	P Value	Multivariate analysis HR value	95% confidence interval	P Value
Age						
18–39		1			1	
40–59	0.92	0.32–2.66	0.892	0.75	0.26 to 2.19	0.604
60–79	1.73	0.63–4.71	0.285	1.61	0.57–4.52	0.368
≥80	7.67	2.83–20.81	<0.001	5.34	1.89–15.08	0.002
Ethnicity						
White		1			1	
Black	1.07	0.73 to 1.57	0.725	1.17	0.79–1.74	0.434
Others	0.39	0.22–0.70	0.001	0.48	0.26 to 0.87	0.015
Marital status						
Married		1			1	
Unmarried	2.10	1.60–2.77	<0.001	1.22	0.91 to 1.64	0.184
Lesion location						
Left		1			1	
Right	1.14	0.88–1.48	0.311	1.88	0.91 to 1.55	0.205
Histological grading						
I		1			1	
II	1.09	0.83–1.44	0.522	1.00	0.76–1.33	0.978
III	1.62	0.90–2.93	0.110	1.98	0.63–2.28	0.584
IV	4.79	0.67–34.29	0.119	2.29	0.30–17.59	0.427
T Stage						
T1		1			1	
T2	1.93	1.45–2.57	<0.001	1.69	1.25–2.30	<0.001
T3	2.53	1.58–4.04	<0.001	1.77	1.05–2.97	0.031
T4	9.72	5.88–16.07	<0.001	3.54	1.86–6.73	<0.001
N Stage						
N0		1			1	
N1	1.60	1.06–2.41	0.025	1.37	0.88–2.15	0.168
N2	2.13	0.87–5.18	0.095	2.16	0.84–5.56	0.111
N3	3.71	1.52–9.02	0.039	0.35	0.12–1.07	0.066
M Stage						
M0		1			1	
M1	12.10	7.69–19.05	<0.001	7.22	3.98–13.12	<0.001
ER expression						
Negative		1			1	
Positive	0.72	0.27–1.93	0.514	0.70	0.23–2.11	0.529
PR expression						
Negative		1			1	
Positive	0.68	0.45–1.02	0.065	0.77	0.49 to 1.21	0.257
HER-2 expression						
Negative		1			1	
Positive	0.56	0.28–1.23	0.105	1.02	0.48–2.19	0.956
Surgery						
Yes		1			1	
None	6.69	4.59–9.76	<0.001	1.96	1.22–3.13	0.005
Radiotherapy						
Yes		1			1	
None	2.86	2.15–3.82	<0.001	1.86	1.37–2.51	<0.001
Chemotherapy						
Yes		1			1	
None	1.79	1.12–2.86	0.015	1.41	0.78–2.55	0.250

help clinicians personalize prognostic assessments and clinical decisions.

4. Discussions

MBC is a kind of breast cancer that is quite uncommon. It affects 1%–6% of all initial breast tumors. [1, 11] Relative to other kinds of breast cancer, MBC has a few distinct clinical characteristics. MBC is more common in postmenopausal and elderly women and has a satisfactory rate of survival. The positive rates of estrogen and progesterone receptors in MBC are substantial and demonstrate greater differentiation and a decreased rate of lymph node metastasis [6, 12, 13]. The underlined data showed consistency with the findings of

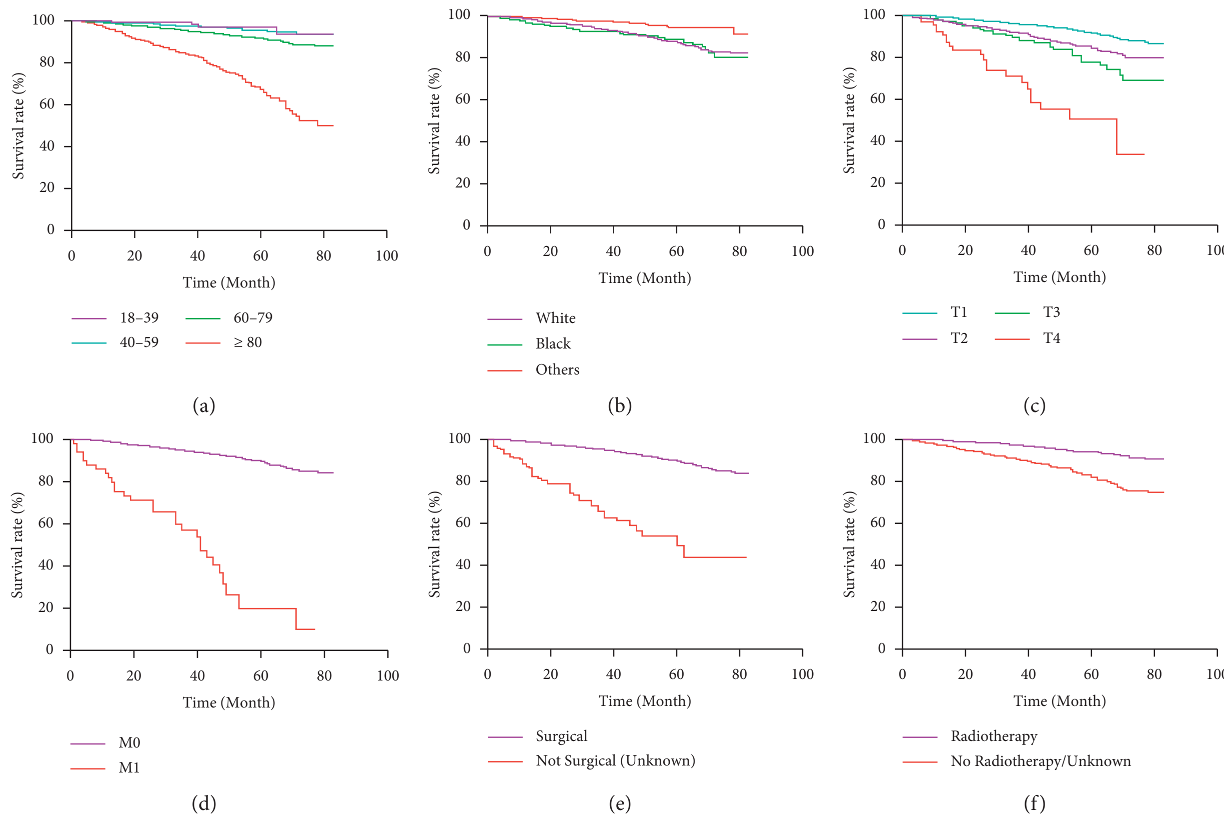

Figure 2: Kaplan-Meier curve of the effect of each independent risk factor on the prognosis of MBC. (a) Age; (b) ethnicity; (c) T stage; (d) M stage; (e) with or without surgery; (f) with or without radiotherapy.

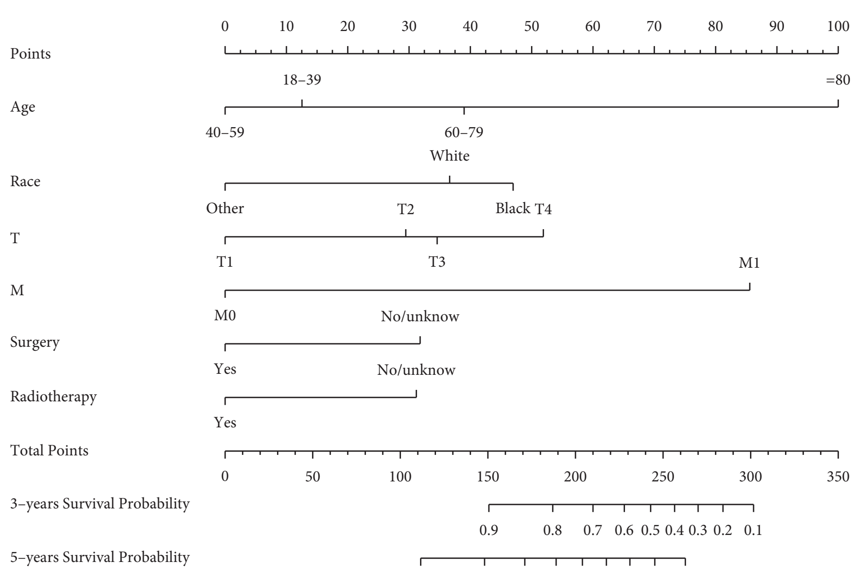

Figure 3: Prognostic nomogram models for 3- and 5-year OS rates of MBC patients. The nomogram is used by totaling the points identified on the top scale for each independent covariate. The total points projected to the bottom scale indicate the % probability of 3- and 5-year OS.

this study. Because of its rarity in the clinic, most studies on MBC have small sample sizes, relatively short follow-up times, and insufficient evidence on the clinical influencing factors and survival of MBC patients. Currently, data from invasive ductal carcinoma are used to generate guideline recommendations for both local and systemic adjuvant treatment of MBC, and the accuracy of survival prognostic information is influenced by physician experience, so a more accurate survival prediction model is lacking. In this study, an objective nomogram was constructed based on the SEER

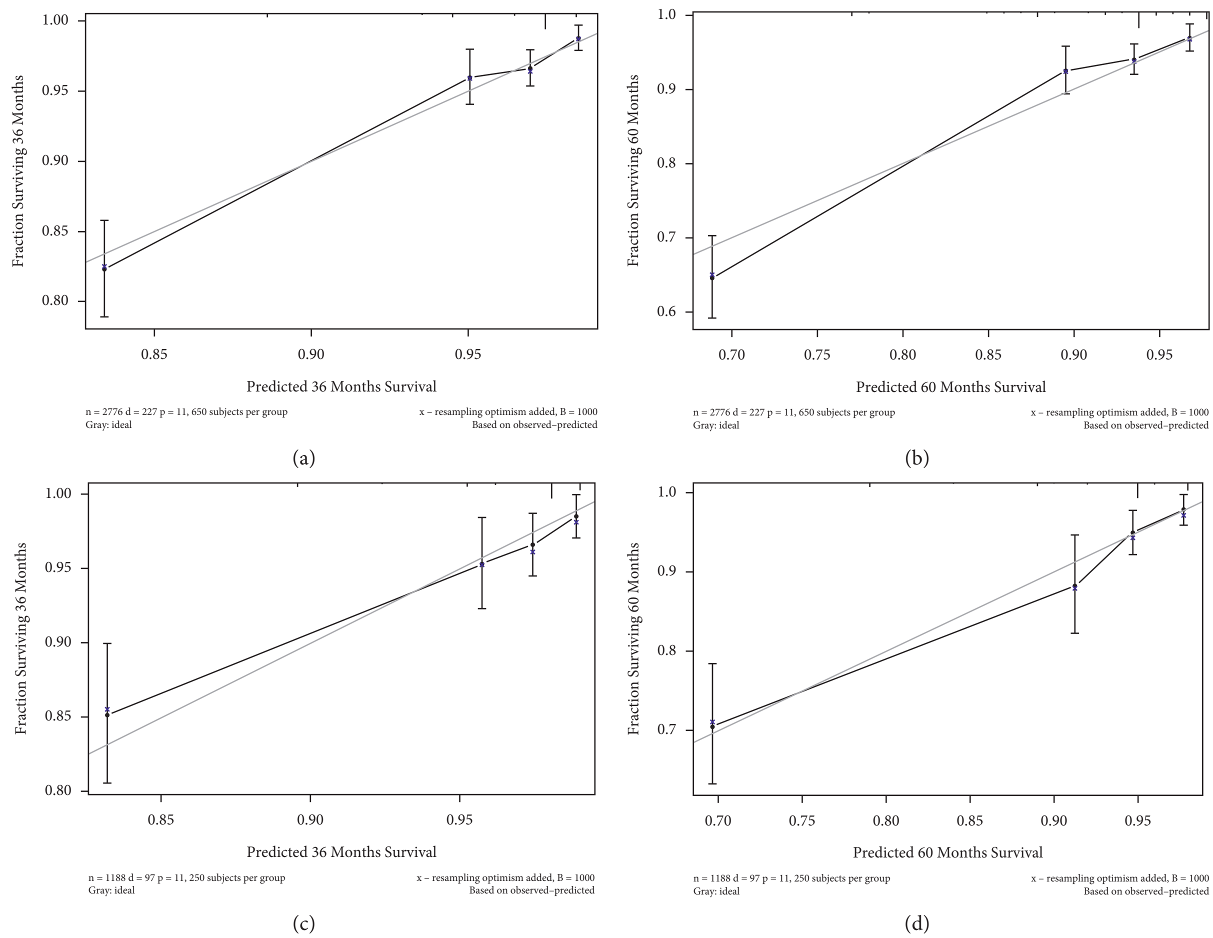

Figure 4: Calibration curve of the nomogram for predicting the probability of OS at 3 and 5 years. (a, b) modeling group; (c, d) validation group.

database to make a more accurate estimate of the 3- and 5-year survival rates of patients suffering from MBC, which improved the rationality of both doctors and patients for disease management and was important for clinical decision-making.

In this study, we analyzed multiple possible prognostic factors in MBC patients, and the results showed that age, ethnicity, T stage, M stage, surgery, and radiotherapy were all independent factors for patient survival prognosis. In our study, 68.1% of patients were over 60 years of age, and the prognosis was best for people aged 40–59 years, and previous studies have shown that MBC is common in older patients, and its incidence generally peaks after menopause [6, 14]. Patients with MBC had high ER or PR positivity (98.8% and 92.0% of ER and PR positivity, accordingly), low histological score (59.3% Grade I), and less lymph node metastasis (90.1% without lymph node metastasis). The findings of this study were consistent with the findings of previous research [2, 5, 15–17], which demonstrated that MBC patients had a substantial chance of surviving.

The predictive importance of tumor size in MBC patients is a point of contention. Patients with tumors greater than 2 cm were previously advised to take adjuvant chemotherapy, according to NCCN recommendations. However, the recommendations have been modified so that only lymph node involvement is considered chemotherapeutic, regardless of the T stage. While tumor size has been linked to the diagnosis of less aggressive tumors, its predictive value has been questioned due to the inclusion of extensive extracellular mucins in tumor size measurement [18]. As a result, tumor size measurements may not accurately reflect actual tumor size, making tumor size prediction problematic [19]. Furthermore, lymph node involvement was found to be unrelated to tumor size in one investigation [20]. T3 and T4 tumors had a worse prognosis than T1 and T2 tumors in our study, according to the nomogram. As a result, a tumor with a diameter of more than 5 cm may be associated with a bad prognosis.

At present, the treatment modalities for MBC patients are mainly surgery, chemotherapy, radiotherapy, and endocrine therapy. The choice of surgical approach also has a considerable influence on the subsequent treatment options of patients and the survival prognosis of patients. In this study, 3,817 patients (96.2%) received surgical treatment, and the nomogram showed that the prognosis of patients who received surgical treatment was better than that of patients who did not receive surgery. It has been shown that patients treated with breast-conserving surgery in stage T1-2

MBC have a better prognosis than those who undergo mastectomy, particularly in patients aged 50–79 years; [21] however, this study did not compare the specific modalities of surgery, and in the subsequent study, we will consider this aspect of the influencing factors. As a considerable adjuvant therapy, radiotherapy is commonly used in patients with high-risk factors post breast-conserving therapy or mastectomy for breast cancer [22]. However, there is a lack of clarity regarding the clinical value of radiotherapy in MBC. In the current study, a total of 2,043 (51.5%) patients received radiotherapy and 1,921 (48.4%) did not. The nomogram shows that the use of radiotherapy is beneficial for patients with MBC. It has been reported in the literature that [23, 24] the reason for the low efficacy of chemotherapy is that mucus accounts for most of the total volume in MBC cells, forming a large pool of mucin, resulting in inconsistency between clinical or imaging assessment of chemotherapy efficacy and mucinous carcinoma pathology. Despite the effective elimination of malignant cells by chemotherapy, the mucin pool remains [25].

However, this study has several limitations. First, important details such as treatment information (e.g., radiation dose, chemotherapy dose, targeted therapy, endocrine therapy, or immunotherapy) are missing in the SEER database because most patients with MBC are hormone receptor-positive. Patients who complete local therapy are likely to receive standard endocrine therapy, and the SEER database cannot provide data on endocrine therapy and is difficult to guide physicians in the treatment of patients of the same category. Second, the lack of information in the SEER database may affect the data of the CPHR model (such as Ki-67, tumor markers, and other related factors), and these important variables should be considered in future studies. Finally, the database does not perform specific pathological classification of MBC, such as pure mucinous breast carcinoma (PMBC) as well as mixed mucinous breast carcinoma (MMBC) [26], because MBC of different pathological types may have different prognoses. The nomograms in this study were internally and externally validated for the population of the SEER database. It is validated in the same population, and the validation of model performance can be biased. Hence, other multicenter data are needed for external validation to further test the predictive effect of nomograms.

5. Conclusion

Routine clinical data obtained from the SEER database were used to develop a useful clinical nomogram that could help clinicians treat MBC in their daily practice. The nomogram incorporates various clinicopathological indicators and can render great help in clinical decision-making thereby enabling individualized therapy and management of MCB patients.

The future directions of this work will potentially involve a larger sample size, including more related factors to further screen the independent influencing factors of the prognosis of MBC patients. In addition, we plan to carry out a multicenter prospective randomized controlled study to verify its predictive effect, improve the nomogram prognostic model, and provide a reference for the evaluation of the prognosis of MBC patients as well as the selection of personalized treatment plan.

Data Availability

Data will be provided on request.

Disclosure

Ying Li is co-first author.

Conflicts of Interest

The study has no financial conflicts of interest that would affect its scientificity and credibility.

Authors' Contributions

Xulong Zhu and Ying Li contributed equally.

Acknowledgments

This work was supported by the Xi'an City Innovation Ability Enhancement Basic Plan, Medical Research Project (No. 21YXYJ0092), Clinical Research Fund of Wu Jieping Medical Foundation (No. 320.6750.2021-10-39), and Beijing CSCO Clinical Oncology Research Foundation (No. Y-L2020-0013).

References

[1] N. Naqos, A. Naim, H. Jouhadi et al., "Mucinous carcinoma of the breast: clinical, biological and evolutive profile," *Cancer Radiotherapie*, vol. 20, p. 801, 2016.

[2] P. Skotnicki, B. Sas-Korczynska, L. Strzepek et al., "Pure and mixed mucinous carcinoma of the breast: a comparison of clinical outcomes and treatment results," *Breast Journal*, vol. 22, p. 529, 2016.

[3] S. G. Diab, G. M. Clark, C. K. Osborne, A. Libby, D. C. Allred, and R. M. Elledge, "Tumor characteristics and clinical outcome of tubular and mucinous breast carcinomas," *Journal of Clinical Oncology*, vol. 17, no. 5, p. 1442, 1999.

[4] SAUDADE, F. E. R. N. A. N. D. O. André et al., "Mucinous carcinoma of the breast: a pathologic study of 82 cases," *Journal of Surgical Oncology*, 1995.

[5] M. W. J. Louwman, M. Vriezen, M. W. P. M. V. Beek et al., "Uncommon breast tumors in perspective: incidence, treatment and survival in The Netherlands," *International Journal of Cancer Journal International Du Cancer*, vol. 121, no. 1, pp. 127–135, 2010.

[6] S. Di Saverio, J. Gutierrez, and E. Avisar, "A retrospective review with long term follow up of 11,400 cases of pure mucinous breast carcinoma," *Breast Cancer Research and Treatment*, vol. 111, no. 3, pp. 541–547, 2008.

[7] K. Y. Ha, P. Deleon, and W. Deleon, "Invasive mucinous carcinoma of the breast," *Baylor University Medical Center Proceedings*, vol. 26, no. 3, pp. 295–297, 2013.

[8] Y.-q. Huang, C.-h. Liang, L. He et al., "Development and validation of a radiomics nomogram for preoperative prediction of lymph node metastasis in colorectal cancer,"

Journal of Clinical Oncology, vol. 34, no. 18, pp. 2157–2164, 2016.

[9] W. Liang, L. Zhang, G. Jiang et al., "Development and validation of a nomogram for predicting survival in patients with resected non-small-cell lung cancer," *Journal of Clinical Oncology*, vol. 33, no. 8, pp. 861–869, 2015.

[10] G. Corso, P. Maisonneuve, G. Massari et al., "Validation of a novel nomogram for prediction of local relapse after surgery for invasive breast carcinoma," *Annals of Surgical Oncology*, vol. 27, no. 6, pp. 1864–1874, 2020.

[11] R. Ohashi, T. Sakatani, M. Matsubara et al., "Mucinous carcinoma of the breast: a comparative study on cytohistological findings associated with neuroendocrine differentiation," *Cytopathology*, vol. 27, no. 3, pp. 193–200, 2016.

[12] S. Y. Bae, M. Y. Choi, D. H. Cho et al., "Mucinous carcinoma of the breast in comparison with invasive ductal carcinoma: clinicopathologic characteristics and prognosis," *Journal of Breast Cancer*, 2011.

[13] H.-S. Tseng, C. Lin, S.-E. Chan et al., "Pure mucinous carcinoma of the breast: clinicopathologic characteristics and long-term outcome among Taiwanese women," *World Journal of Surgical Oncology*, vol. 11, no. 1, p. 139, 2013.

[14] C. I. Li, "Risk of mortality by histologic type of breast cancer in the United States," *Hormones and Cancer*, vol. 1, no. 3, pp. 156–165, 2010.

[15] T. Hanagiri, K. Ono, T. Baba et al., "Clinicopathologic characteristics of mucinous carcinoma of the breast," *International Surgery*, vol. 95, no. 2, p. 126, 2010.

[16] E. Avisar, M. A. Khan, D. Axelrod, and K. Oza, "Pure mucinous carcinoma of the breast: a clinicopathologic correlation study," *Annals of Surgical Oncology*, vol. 5, no. 5, pp. 447–451, 1998.

[17] I. Fentiman, R. Millis, P. Smith, J. Ellul, and O. Lampejo, "Mucoid breast carcinomas: histology and prognosis," *British Journal of Cancer*, vol. 75, no. 7, pp. 1061–1065, 1997.

[18] D. Kim, W.-H. Jung, and J. S. Koo, "Expression of MUC1, MUC2, MUC5AC and MUC5B in mucinous lesions of the breast," *Pathobiology*, vol. 79, no. 3, pp. 144–153, 2012.

[19] A. Ranade, R. Batra, G. Sandhu, R. A. Chitale, and J. Balderacchi, "Clinicopathological evaluation of 100 cases of mucinous carcinoma of breast with emphasis on axillary staging and special reference to a micropapillary pattern," *Journal of Clinical Pathology*, vol. 63, no. 12, pp. 1043–1047, 2010.

[20] J. C. Paramo, C. Wilson, D. Velarde, J. Giraldo, R. J. Poppiti, and T. W. Mesko, "Pure mucinous carcinoma of the breast: is axillary staging necessary?" *Annals of Surgical Oncology*, vol. 9, no. 2, pp. 161–164, 2002.

[21] P. Yu, P. Liu, Y. Zou et al., "Breast \ onserving therapy shows better prognosis in mucinous breast carcinoma compared with mastectomy: a SEER population-based study," *Cancer Medicine*, vol. 9, no. 15, 2020.

[22] F. Bernard, "Twenty-year follow-up of a randomized trial comparing total mastectomy, lumpectomy, and lumpectomy plus irradiation for the treatment of invasive breast cancer," *New England Journal of Medicine*, vol. 16, no. 347, 2002.

[23] G. Von Minckwitz, S. D. Costa, W. Eiermann et al., "Maximized reduction of primary breast tumor size using preoperative chemotherapy with doxorubicin and docetaxel," *Journal of Clinical Oncology*, vol. 17, no. 7, p. 1999, 1999.

[24] A. K. Lannigan, J. J. Going, E. Weiler-Mithoff, and T. G. Cooke, "Mucinous breast carcinoma," *The Breast*, vol. 11, no. 4, pp. 359–361, 2002.

[25] Didonato, S. H. A. P. I. R. O. Rosemarie et al., *Invasive Mucinous Carcinoma of the Breast and Response Patterns after Neoadjuvant Chemotherapy (NAC)*, Histopathology Official Journal of the British Division of the International Academy of Pathology, 2018.

[26] S. Kashiwagi, N. Onoda, Y. Asano et al., "Clinical significance of the sub-classification of 71 cases mucinous breast carcinoma," *SpringerPlus*, vol. 2, p. 481, 2013.

Hindawi
Journal of Healthcare Engineering
Volume 2022, Article ID 8331688, 4 pages
https://doi.org/10.1155/2022/8331688

Research Article

Study on the Efficacy of Electric Acupuncture in the Treatment of Premature Ejaculation Based on Testosterone Level

Xiangpeng Lu,[1] Hao Han,[1] Zhibiao Zhang,[1] Hao Chen,[2] Xingru Huang,[2] and Rui Zhang[1]

[1]*The Second Affiliated Hospital of Heilongjiang University of Chinese Medicine, Heilongjiang, China*
[2]*Heilongjiang Traditional Chinese Medicine Hospital, Heilongjiang, China*

Correspondence should be addressed to Rui Zhang; lxp15004687742@163.com

Received 5 January 2022; Revised 4 March 2022; Accepted 7 March 2022; Published 22 March 2022

Academic Editor: Enas Abdulhay

Objective. To investigate the clinical efficacy and possible mechanism of electroacupuncture in the treatment of premature ejaculation. *Methods*. 50 cases of premature ejaculation patients who met the diagnostic criteria were randomly divided into 2 groups with 25 cases in each group. The observation group was treated with electroacupuncture, and the control group was treated with Longdan Xiegan decoction. The treatment period was 4 weeks. Ejaculation latency (IELT), sexual satisfaction score of patients, sexual satisfaction score of partners, testosterone test, and drug safety assessment were performed in all 4 groups before and after treatment. *Results*. IELT was prolonged in all groups after treatment, the difference was statistically significant ($P < 0.05$). At the same time, the IELT of the observation group was significantly higher than that of the control group after treatment. Life satisfaction scores of patients and spouses in 2 groups were improved after treatment compared with before treatment, the difference was statistically significant ($P < 0.05$). After treatment, the satisfaction scores of patients and spouses in the observation group were higher than those in the control group, and the difference was statistically significant ($P < 0.05$). Before treatment, there was no significant difference in serum testosterone levels among all groups ($P > 0.05$). Serum testosterone levels in all groups were decreased after treatment compared with before treatment, with statistical significance ($P < 0.05$). After treatment, the serum testosterone level of the observation group was lower than that of the control group, and the difference was statistically significant ($P < 0.05$). During the treatment, the adverse reactions in each group disappeared after treatment, and no obvious abnormality was observed in the safety indicators. *Conclusion*. Electroacupuncture can improve the symptoms of premature ejaculation, which may be related to the regulation of serum testosterone by acupuncture.

1. Introduction

Premature ejaculation (PE) is a common disease in male sexual dysfunction, and its incidence rate is very high. PE refers to conditions in which the penis has not been inserted into the vagina, the parties have not contacted or have just been exposed to ejaculation, or ejaculation in less than 1 minute after insertion, resulting in an inability to perform normal sexual intercourse for more than 1 month. This disease is a common sexual dysfunction disease in adult men, and data show that about 75% of men will have premature ejaculation in their lifetime [1]. Among adult males, the incidence rate is 35%–50% [2]. Under the pressure of modern stressful life pace, the incidence rate of male premature ejaculation is on the rise every year, which greatly reduced the happiness in family.

At present, the treatment methods of Western medicine include psychotherapy and behavioral intervention, the application of antidepressants, the use of drug local anesthesia, and surgical treatment. Traditional Chinese medicine has a long history of treating the disease, accumulated rich clinical experience, and achieved good clinical efficacy. In traditional Chinese medicine, there are mainly traditional Chinese medicine, acupuncture, moxibustion, massage, umbilical therapy, acupoint application, acupoint embedding, and other relatively conservative treatment methods [3].

With the modern tense pace of life, physical overdraft, life pressure, air, food, and water pollution, and other factors, the incidence of male premature ejaculation has been increasing year by year, greatly affecting the quality of life of the couple and family happiness and stability. Now, there are many methods to treat premature ejaculation, and the application of antidepressants easily increases the misunderstanding of patients and increases the psychological burden. The curative effect of surgical therapy is not exact, and the harm is great. Psychological or behavioral treatment is difficult to operate clinically, long-term use of local anesthetics may cause erectile dysfunction, and to a certain extent, the internal environment of the woman has certain damage, affecting life. The operation of acupuncture and moxibustion is simple, and the deputy general use is small. Therefore, this study explores the efficacy of electroacupuncture in the treatment of premature ejaculation.

The etiology of premature ejaculation is complex, and the treatment is mainly based on serotonin reabsorption inhibitors. Studies have shown that low doses of testosterone combined with doxazosin in the treatment of premature ejaculation can achieve satisfactory results [4]. This study investigated 50 patients with premature ejaculation and observed the changes of IETE and spouse satisfaction and testosterone level in the two groups after treatment, which will provide more effective treatment methods for clinical application.

2. Methods

2.1. Ethical Statements. The included cases were from the outpatient department of acupuncture and moxibustion in our hospital from January 2019 to June 2021. The 50 patients who met the criteria for case selection were numbered from 1 to 50 according to the order of medical treatment. The odd and even numbers were divided into electroacupuncture group (hereinafter referred to as the observation group) and control group, with 25 patients in each group. All patients wrote the informed consent, and these studies were approved by the ethics boards of the hospital.

2.2. Diagnostic Criteria. “Chinese traditional medicine new medicine clinical research guiding principle” for premature ejaculation in Chinese medicine diagnosis standard was referred: during sexual intercourse, ejaculation when the penis has not been inserted into the vagina, or when both sides have not been contacted or just contacted, or ejaculation in less than 1 minute after inserting, as a result cannot have normal sexual intercourse, and lasting for more than 1 month are the diagnostic criteria for this disease. Inclusion criteria are as follows: (1) the patients meet the above diagnostic criteria for premature ejaculation; (2) age ≥24 years and ≤48 years and course of disease >3 months and <10 years; (3) married or with a regular sexual partner and sexual life for more than half a year; (4) no surgical treatment was performed; (5) patients who have not taken drugs or received other treatments recently (within 1 month before the treatment); and (6) voluntarily participate in the clinical study and signed informed consent.

Exclusion criteria are as follows: (1) ejaculation latency >1 min; (2) persons aged <24 or >48; course of disease ≤1 month or ≥10 years; (3) the penis and testicles have organic lesions, including phimosis, foreskin too long, foreskin frenulum too short, and cryptorchidism; (4) inflammation of the genitourinary system, such as prostatitis, seminal vesiculitis, vermontanetis, epididymitis, spermatic cord quietly varicose, and urethritis; (5) hyperthyroidism; (6) schizophrenics; (7) erectile dysfunction; (8) patients with abnormal blood lipid, blood glucose, and blood pressure; (9) patients with other diseases of brain, heart, liver, and kidney that affect the effectiveness evaluation of this treatment; (10) patients with neurological diseases (brain tumor, cerebrovascular disease, and spinal cord injury); (11) patients who have taken drugs or received other treatments recently (within 1 month before the treatment); (12) irregular sexual life; (13) the patient had undergone surgical treatment; and (14) needle sickness.

2.3. Treatment. The observation group was treated in the acupuncture points: Zhongji point (−) and Sanyinjiao point (+). The frequency was 2–100 Hz, the current intensity was 0.1 mA–1.0 mA, and the intensity was tolerated by patients with slight local beating. The needle was left for 30 min. Once a day, 6 times in a row, then rest for 1 day, 6 times in a course of treatment, a total of 4 courses. The control group was given one dose of Longdan Xiegan decoction every day, 300 ml of decoction, twice in the morning, and 1 hour after dinner.

2.4. Observation of Curative Effect Index. The changes of IELT before and after treatment were observed, and the average value of three sexual lives before and after treatment was taken as the value. The changes of sexual satisfaction scores of the patients and their spouses were observed before and after treatment. The sexual satisfaction scores of the patients were evaluated by 6, 7, and 8 points of the International Erectile Function Index (IIEF), with a total score of 0–15 points. The scores of 10, 13, and 14 in the IIEF table were used to evaluate the spouse’s sexual satisfaction with a total score of 0 to 15 points.

2.5. Sexual Satisfaction of Spouse. The observation form of spouse satisfaction was filled in. It was recorded once before the treatment, once at the end of the treatment, and follow-up was performed once 3 months after the treatment.

2.6. Determination of Serum Testosterone. The serum testosterone level of the selected subjects was measured by ELISA at 8–10 a.m., and the unit was nmol/*L*.

2.7. Safety Test. (1) The general physical examination items were checked (once before and after treatment). (2) Possible adverse reactions, such as diarrhea, abdominal pain, and abnormal discomfort of penile skin, were observed, and at the same time, whether women have abnormal discomfort of vagina, etc. was also observed.

2.8. Statistical Analysis. All data were analyzed with the SPSS18.0 statistical software. The counting data were analyzed by the chi square test. The measurement data were expressed in ($x \pm s$), and the difference was statistically significant ($P < 0.05$).

3. Results

3.1. General Information Comparison. There was no significant difference in the general information between the two groups, which was comparable ($P > 0.05$) (Table 1).

3.2. Comparison of IELT and Sexual Life Satisfaction Scores of Patients and Spouses between the Two Groups before and after Treatment. IELT was prolonged in both groups after treatment. At the same time, the IELT of the observation group was 3.28 ± 0.59, which was significantly higher than that of the control group (3.09 ± 0.62) after treatment. The sexual life satisfaction scores of patients and spouses in each group were 10.06 ± 1.28, which was significantly higher than those (6.85 ± 1.02) before treatment ($P < 0.05$). After treatment, the sexual life satisfaction score of patients and spouses in the observation group was 10.86 ± 1.49, which was higher than that (10.57 ± 1.75) in the control group ($P < 0.05$) (Table 2).

3.3. Comparison of Serum Testosterone Changes between the Two Groups before and after Treatment. Before treatment, there was no significant difference in serum testosterone levels among all groups ($P > 0.05$). The serum testosterone level after treatment in all groups (13.28 ± 3.15, 15.88 ± 4.71) was decreased compared with that before treatment (26.16 ± 5.26, 25.97 ± 5.58), with statistical significance ($P < 0.05$). After treatment, the level of serum testosterone in the observation group was 13.28 ± 3.15, which decreased significantly compared with the control group 915.88 ± 4.71) (Table 3).

3.4. Adverse Reactions. In the observation group, 5 cases had adverse reactions, including 2 cases of dizziness and 3 cases of subcutaneous hematoma. In the control group, there were 6 cases of malady, 4 cases of stomach discomfort, 1 case of mild diarrhea, and 1 case of dizziness.

3.5. Security Testing. Before and after treatment, no abnormality was found in blood, urine and stool routine tests, electrocardiogram, and liver and kidney functions in the two groups. After treatment, there were no serious adverse reactions in the two groups, and no patients were terminated due to adverse reactions.

4. Discussion

Traditional Chinese medicine believes that the etiology of premature ejaculation is caused by many aspects, which is most closely related to the center of the five Zang organs, liver, and kidney [5]. Its mechanism is in the heart, its movement is in the liver, and it is hidden in the kidney. If the functions of the heart, liver, and kidney are abnormal, such as pouring damp heat into the liver, uncomfortable liver Qi, and liver depression and fire; heart-kidney disharmony and hyperactivity of heart fire; and kidney deficiency, can lead to adverse catharsis, dereliction of duty in sealing and hiding, failure of God, resulting in no right to restrict Jingguan and premature ejaculation due to easy opening of Jingguan. Western medicine believes that the etiology and pathogenesis of this disease are complex, and the specific pathogenesis is inconclusive at present. There are various methods to treat the disease, but no curative effect has been widely recognized. Sertraline hydrochloride, as a highly selective serotonin reuptake inhibitor, can inhibit the reuptake of serotonin in ejaculatory central neurons so as to reduce the excitability of ejaculatory central neurons. On the other hand, sertraline has weak affinity for dopamine receptor, cholinergic receptor, histamine receptor, and adrenergic receptor and will not enhance the activity of catechol neurotransmitters so as to achieve the effect of treating premature ejaculation [6, 7]. However, the drug takes effect 1–2 weeks after taking, often including drowsiness, dry mouth, dizziness, nausea, diarrhea, decreased sexual desire, and nonejaculation [8, 9].

IELT and patient and spouse satisfaction score are commonly used to evaluate the efficacy of premature ejaculation. In this study, the IELT of each group was prolonged after treatment compared with that before treatment, and the difference was statistically significant, indicating that both traditional Chinese medicine and acupuncture had good therapeutic effects in the treatment of premature ejaculation, while electroacupuncture group had better efficacy compared between groups. The results showed that electroacupuncture treatment of premature ejaculation was better than traditional Chinese medicine in IELT and satisfaction score of patient and spouse. The adverse reactions of acupuncture were not significant. Erection is a prerequisite for sexual intercourse, and testosterone plays an important role in erection. Testosterone plays a central and peripheral regulatory role in penile erection response, and a certain level of testosterone is a necessary condition for maintaining sexual desire and penile erection [10]. Corona et al. [11] showed that high serum testosterone level is related to the occurrence of premature ejaculation, and delayed ejaculation is more likely to occur in patients with low serum testosterone. Sakamoto et al. [12] also found that the serum free testosterone level and serum FSH level of patients with premature ejaculation were significantly higher than those of patients without premature ejaculation, but there was no significant difference in the total serum testosterone level between them. In this study, serum testosterone in each group was lower after treatment than before, and the difference was statistically significant. After treatment, the decrease of serum testosterone in the electroacupuncture group was more obvious than that in the traditional Chinese medicine group. It is suggested that electroacupuncture may improve the symptoms of premature ejaculation by reducing the serum testosterone level to some extent. The mechanism of acupuncture in the treatment of premature ejaculation will be further studied in the future.

Table 1: General information comparison.

Group	No. of patients (n)	Age	Course of disease	No. of cases with different severity before treatment (n)		
				Light	Moderate	Severe
Observation group	25	32.68 ± 4.76	39.82 ± 7.95	18	6	1
Control group	25	33.57 ± 5.02	40.07 ± 8.75	17	7	1

Table 2: Comparison of IELT and sexual life satisfaction scores of patients and spouses between the two groups before and after treatment.

Item	Time	Observation group	Control group	P value
IELT	Before the treatment	1.08 ± 0.36	1.06 ± 0.44	$P < 0.05$
	After the treatment	3.28 ± 0.59	3.09 ± 0.62	
Patient satisfaction score of sexual life	Before the treatment	6.85 ± 1.02	6.91 ± 1.14	$P < 0.05$
	After the treatment	10.06 ± 1.28	9.86 ± 1.67	
Spouse's sexual satisfaction score	Before the treatment	4.85 ± 0.98	4.90 ± 1.04	$P < 0.05$
	After the treatment	10.86 ± 1.49	10.57 ± 1.75	

Table 3: Comparison of serum testosterone changes between the two groups before and after treatment.

Item	Time	Observation group	Control group	P value
Testosterone level	Before the treatment	26.16 ± 5.26	25.97 ± 5.58	$P < 0.05$
	After the treatment	13.28 ± 3.15	15.88 ± 4.71	

However, there are also limits in this study. The number of patients is small, which is not so scientific. Besides, the mechanism under this treatment was not clarified, which need further studies to explain it.

5. Conclusion

In conclusion, acupuncture therapy based on meridian points has definite curative effect in the treatment of premature ejaculation. Besides, acupuncture is relatively simple, convenient, and easy to implement, with minimal trauma and almost no side effects. Therefore, it is recommended to be popularized and applied in clinical practice. However, due to the small number of patients included in the current study, the overall level of the study is not high, and because there is no unified diagnostic standard and efficacy evaluation standard is inconsistent, the efficacy of each study is prone to bias, resulting in authenticity. Therefore, more researchers and patients need to join the clinical study for further verification.

Data Availability

The data used to support this study are available from the corresponding author upon request.

Conflicts of Interest

The authors declare that they have no conflicts of interest.

References

[1] S. E. Althof, C. H. N. Abdo, J. Dean et al., "International society for sexual medicine's guidelines for the diagnosis and treatment of premature ejaculation," *The Journal of Sexual Medicine*, vol. 7, no. 9, pp. 2947–2969, 2010.

[2] Z. C. Xin, W. S. Chung, Y. D. Choi, D. H. Seong, Y. J. Choi, and H. K. Choi, "Penile sensitivity in patients with primary premature ejaculation," *The Journal of Urology*, vol. 156, no. 3, pp. 979–981, 1996.

[3] Z. C. Xin, Y. D. Choi, D. H. Seong, and H. K. Choi, "Sensory evoked potential and effect of SS-cream in premature ejaculation," *Yonsei Medical Journal*, vol. 36, no. 5, p. 397, 1995.

[4] M. D. Waldinger, "The neurobiological approach to premature ejaculation," *The Journal of Urology*, vol. 168, no. 6, pp. 2359–2367, 2002.

[5] M. D. Waldinger, "Recent advances in the classification, neurobiology and treatment of premature ejaculation," *Sexual Dysfunction*, vol. 29, pp. 50–69, 2008.

[6] J. Buvat, F. Tesfaye, M. Rothman, D. A. Rivas, and F. Giuliano, "Dapoxetine for the treatment of premature ejaculation: results from a randomized, double-blind, placebo-controlled phase 3 trial in 22 countries," *European Urology*, vol. 55, no. 4, pp. 957–968, 2009.

[7] C. G. Mcmahon, S. E. Althof, M. D. Waldinger et al., "An evidence-based definition of lifelong premature ejaculation: report of the international society for sexual medicine (ISSM) ad hoc committee for the definition of premature ejaculation," *The Journal of Sexual Medicine*, vol. 5, no. 7, pp. 1590–1606, 2008.

[8] M. Peeters and F. Giuliano, "Central neurophysiology and dopaminergic control of ejaculation," *Neuroscience & Biobehavioral Reviews*, vol. 32, no. 3, pp. 438–453, 2008.

[9] C. F. Donatucci, "Etiology of ejaculation and pathophysiology of premature ejaculation," *The Journal of Sexual Medicine*, vol. 3, no. 4, pp. 303–308, 2006.

[10] F. Giuliano, "5-hydroxytryptamine in premature ejaculation: opportunities for therapeutic intervention," *Trends in Neurosciences*, vol. 30, no. 2, pp. 79–84, 2007.

[11] G. Corona, E. A. Jannini, E. Mannucci et al., "Different testosterone levels are associated with ejaculatory dysfunction," *The Journal of Sexual Medicine*, vol. 5, no. 8, pp. 1991–1998, 2008.

[12] H. Sakamoto, K. Takanami, D. G. Zuloaga et al., "Androgen regulates the sexually dimorphic gastrin-releasing peptide system in the lumbar spinal cord that mediates male sexual function," *Endocrinology*, vol. 150, no. 8, pp. 3672–3679, 2009.

Hindawi
Journal of Healthcare Engineering
Volume 2022, Article ID 9240569, 13 pages
https://doi.org/10.1155/2022/9240569

Review Article

Association of Insulin Resistance and Elevated Androgen Levels with Polycystic Ovarian Syndrome (PCOS): A Review of Literature

Yalan Xu[1,2,3,4,5] and Jie Qiao[1,2,3,4,5]

[1]Centre for Reproductive Medicine, Department of Obstetrics and Gynecology, Peking University Third Hospital, Beijing 100191, China
[2]National Clinical Research Centre for Obstetrics and Gynecology, Beijing 100191, China
[3]Key Laboratory of Assisted Reproduction (Peking University), Ministry of Education, Beijing 100191, China
[4]Beijing Key Laboratory of Reproductive Endocrinology and Assisted Reproductive Technology, Beijing 100191, China
[5]Research Units of Comprehensive Diagnosis and Treatment of Oocyte Maturation Arrest, Chinese Academy of Medical Sciences, Beijing, China

Correspondence should be addressed to Jie Qiao; jieqiao@21cn.com

Received 25 December 2021; Revised 8 February 2022; Accepted 12 February 2022; Published 21 March 2022

Academic Editor: Enas Abdulhay

The polycystic ovary syndrome (PCOS) is the disease featured by elevated levels of androgens, ovulatory dysfunction, and morphological abnormalities. At reproductive stage of women, the rate of PCOS occurrence is measured as 6–10% and the prevalence rate may be double. There are different pathophysiological factors involved in PCOS, and they play a major role in various abnormalities in individual patient. It is clear that there is noteworthy elevation of androgen in PCOS, causing substantial misery and infertility problems. The overexposure of androgen is directly linked with insulin resistance and hyperinsulinaemia. It has been reported previously that PCOS is related to cardiac metabolic miseries and potently increases the risk of heart diseases. Endometrial cancer is also a serious concern which is reported with exceedingly high incidence in women with PCOS. However, the overexposure of androgen has direct and specific influence on the development of insulin resistance. Although many factors are involved, resistance to the insulin and enhanced level of androgen are considered the major causes of PCOS. In the present review, we have focused on the pathophysiology and major revolutions of insulin resistance and excessive levels of androgen in females with PCOS.

1. Introduction

The polycystic ovary syndrome (PCOS) is the disease featured by elevated levels of androgens, ovulatory dysfunction, and morphological abnormalities. According to NIH (National Institutes of Health), it can be defined as "hyperandrogenism with ovulatory dysfunction." At reproductive stage of women, the rate of PCOS occurrence is measured as 6–10% and the prevalence rate may be double [1–4]. It is clear that there is noteworthy elevation of androgen in PCOS, causing substantial misery and infertility problems. Somehow, PCOS has also some environmental influences like obesity, as well as factors contributing to obesity. Most of the previous reports concluded that deformities associated steroidogenesis and follicular development are crucially involved in PCOS progression [4, 5]. PCOS generally exhibits constantly secreted levels of the gonadotropin-releasing hormone (GnRH), increased levels of the luteinizing hormone (LH), and insufficient follicle-stimulating hormone (FSH) secretion contributing to elevated secretions of the androgens and ovulatory dysfunction. Moreover, majority of the PCOS-suffering population develops insulin resistance, which in turn leads to the amplified secretion levels of the androgen, thereby decreasing the sex hormone-binding globulin secretions [6–11]. Genome research has been discovered numerous genes linked investigations such genes for the beta subunit of FSH, gonadotropin receptors, insulin receptor, neoplastic cells domain-containing protein

1A (DENND1A), differentially expressed in normal, and thyroid adenoma-associated protein (THADA). "Developmental programming" by environmental or hormonal influences may also add to the development of the PCOS. There are different pathophysiological factors involved in PCOS and they play a major role in various abnormalities in individual patient. It has been found that PCOS is related to cardiac metabolic miseries and potently increases the risk of heart diseases [11–16]. The mechanism of androgen biosynthesis in ovaries and adrenal gland is explained in Figure 1.

PCOS is found to be the major concern of women health and puts serious life-threatening conditions. Among the ratio of women suffering from PCOS, 50–80% are the obese women, 30–35% are those reported with impaired glucose tolerance, and 8–10% are found to be diabetic or having family diabetes history. The risk of PCOS is related to the history and severity of these influences [5, 16–20]. Generally, women with PCOS exhibit reduced levels of high-density lipoprotein (HDL) and amplified concentrations of triglycerides and low-density lipoproteins (LDL) cholesterols compared with normal women. LDL cholesterol differences appeared to play a significant role in PCOS, and it remains a major concern in most of women. However, sometimes LDL levels in normal range may lead to misconception as the activities of the LDL and HDL in PCOS women are sparse [21, 22]. The elevation of coronary artery calcium scores has been also described in PCOS women and high incidence is reported for the postmenopausal women with PCOS. Many reports provide evidence on the cardiovascular abnormalities in patients with history of PCOS. Endometrial cancer is also a serious concern which is reported with exceedingly high incidence in females with PCOS [21, 22]. The risk factors of the endometrial cancer in menopausal PCOS women include anovulation, heavy fats, and insulin resistance. The fear of chronic anovulation results in prolonged estrogen-mediated mitogenic activation of the endometrium with inadequate progesterone access to cause endometrial differentiation. Females with PCOS also face severe problems in pregnancy like risk of gestational diabetes mellitus, obstructive sleep apnea, and emotional distress [23–29]. Although many factors are involved, resistance to the insulin and high androgen are considered the major causes of PCOS. In the present review, we focus on the pathophysiology and major revolutions of insulin resistance and excessive levels of androgen in females with PCOS. The discussions are focused on insulin resistance, mechanism of insulin resistance, hyperandrogenism in PCOS, PCOS phenotypes, impacts of PCOS on physiological functions of the PCOS woman, and various treatments approaches for the treatment of PCOS, insulin resistance, and high secretions of androgens.

2. Insulin Resistance in PCOS

The actual understanding of insulin resistance can be explained by the requirement of excessive insulin for the metabolic activities, while, besides metabolic activities, insulin is also required for mitogenic and reproductive actions [24]. The rapid and fast glucose analysis make the researchers able to analyse insulin resistance. For this purpose, homeostatic model evaluation, quantitative insulin sensitivity check index, and fasting glucose and insulin levels have been established and utilized in clinical research and also metabolic investigations in PCOS [24–27].

In general, the obesity of abdomen in PCOS is the reason of insulin resistance possibly induced via subclinical swelling but whether the metabolically active intra-abdominal adipose tissues are augmented or not is unclear. However, it was previously investigated that the lower circulating adiponectin detection in PCOS justified subcutaneous adipose tissue as a dysfunctional adipose tissue compartment and having correlation with insulin resistance. Although different methods have been used for prevalence of insulin resistance, where it was found to be varied in PCOS women with respect to the detection method [28–31], more recent findings concluded that obesity is the main risk factor of insulin resistance in individuals suffering from PCOS. The investigations revealed that diagnostic criteria of insulin resistance have limited impact on the insulin resistance detection in PCOS women. Insulin resistance in PCOS patients is the main concern, and its prevalence and mechanism need to be investigated. In previous reports, it was found that large population of PCOS women is suffering from compromised glucose tolerance and type 2 diabetes mellitus (T2DM) [28, 29]. The statistically higher prevalence rate of the compromised glucose tolerance and T2DM serious threatening bell for healthy life. Few clinical studies have reported the glucose tolerance in PCOS women and T2DM risk in PCOS individuals. According to the findings of various studies, it was found that all those PCOS females who are obese and overweight are at greater risk of the disturbances in glucose metabolism and they required to check their glucose regularly with proper metabolic profiling [29–35].

3. Pathways of Insulin Resistivity in Patients with PCOS

Insulin is receptor binding hormone that binds to its membrane glycoprotein. This consists of two subunits α and β, associated with disulphide bonds. Subunit α is extracellular region responsible for the binding site, while subunit β is the intracellular region responsible for provoking intrinsic tyrosine kinase activity [36]. Ligand bindings lead to generating intrinsic tyrosine kinase activity in subunit β and initiate tyrosine phosphorylation. That further leads to the metabolic activities of insulin upon substrate binding, for example, glucose transport and glycogen synthesis [36, 37]. PCOS is a health issue for women and insulin resistance is one of the crucial issues that need to be emphasized. Insulin is an essential hormone for glucose metabolism and its sensitization is necessary for proper glucose uptake and metabolism [8, 38]. The cell surface receptor is homologous with the insulin-like growth factor 1 (IGF-1) receptor, so there is specific interaction for the binding of insulin to surface. The uptake of glucose is stimulated [19, 28, 39, 40]. The MAPK-ERK pathway initiation takes place, which

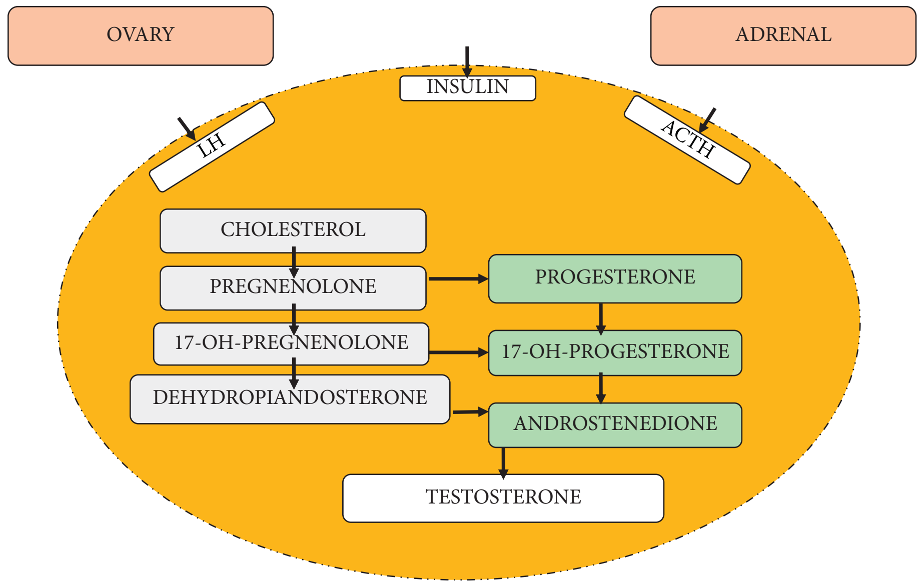

Figure 1: Production of androgen in ovaries and adrenal gland. Biosynthesis of the androgens associated with the ovary and the adrenal gland.

initiates stimulation of a series of enzymes cascades. In previous studies on PCOS women, cellular and molecular mechanism of insulin was highlighted and glucose uptake in insulin target tissues like adipose and skeletal muscles was evaluated in both lean and obese women [20, 25]. When observed in PCOS patients, it was concluded that although the receptors affinities of insulin are similar in both PCOS women and normal females, decreased insulin binding was recorded at pancreatic β-cell in adipose tissues resulting in low glucose uptake and insulin sensitivity in PCOSs females compared to normal females. The fact might be due the reduced abundance of GLUT4 in subcutaneous adipose tissues in PCOS patients, which leads to insulin insensitivity [19, 20, 25, 28, 41, 42]. Besides the reduction in sensitivity of insulin, β-cell dysfunction is also one of the reasons for low disposition. However, still it is unclear whether the subunit β defected function is the primary cause of insulin resistance or it is secondarily involved in insulin resistance [43, 44]. To analyse insulin resistance in PCOS patients, proinsulin and insulin ratio can be a marker. In PCOS women, the ratio of proinsulin and insulin can explain the insulin resistance and activity of β-cell. It was found that, in obese and overweight PCOS patients, there was increased secretion of insulin followed by the excessive levels of proinsulin, which results in insulin resistance and hyperinsulinaemia [19, 20, 25, 28, 39, 40]. These studies explained the dysfunction of β-cell in PCOS women and insulin resistance mechanism. PCOS is a genetically contributed disorder in its pathogenesis and considered a hereditary condition. It has been shown that first relatives of PCOS history will have reproductive and metabolic issues and more investigations revealed that hyperinsulineaemia will be developed in the early stages of life and remain persistent throughout the puberty of girls with hereditary history of PCOS. In such cases, the subjects are at high risk for hyperinsulinaemia and insulin resistance, even if they are not diagnosed with PCOS. The follow-up study of peripubertal adolescent girls whose mothers were suffering from PCOS presented reduced disposition index persistently which proposes the dysfunction of pancreatic β-cell and this might be one of the genetic causes in first-degree relatives of the PCOS population. Another probable hereditary reason for insulin resistance in PCOS is a significant rate of SH2 domain-containing adaptor protein (Lnk) activity in PCOS female's ovarian cell lines, which suppresses the MAPK-ERK and phosphatidylinositol 3-kinase-AKT signaling responses to insulin. Previously, skin fibroblasts were for the intrinsic problems in in insulin function in PCOS because both hyperandrogenism and hyperinsulinaemia affect insulin sensitivity. When PCOS fibroblasts were assessed for insulin stimulated receptors autophosphorylation, there was reduced receptors stimulation as well as minimal insulin sensitivity. More importantly, immunopurification studies revealed that there was no mutation in receptor gene of insulin in PCOS patients [19, 36, 38, 40, 41].

4. Hyperandrogenism and PCOS

The genetically determined excessive secretions of androgens from ovary are the major concern in clinical evaluation of PCOS [45, 46]. The secretions of androgen at early stages are generally considered premature in PCOS and though to develop insulin resistance in prior stages. In visceral adipocytes, the disturbances in lipid metabolism result in insulin resistance. Nevertheless, the overexposure of androgen has direct and specific influence on onset of insulin resistance [47–52]. The increased secretion of androgen is associated with malfunctioning of islets of Langerhans, thereby compromising the pancreatic metabolic functions and causing hyperinsulinaemia. In preclinical studies, in PCOS women, it was found to be a major cause of T2DM. These facts revealed the direct relationship of overexposure of androgens with hyperinsulinaemia, insulin resistance, and T2DM in PCOS population [45–59]. The impact of insulin on hypersecretion of LH and androgen and its correlation with ovary, pituitary gland, and adrenal gland are illustrated in Figure 2.

Androgens belong to the family of steroid hormones and oversecretion of androgens is considered the main clinical manifesto of the PCOS. So, how androgens are biologically manufactured and regulated should be understood. Since androgens are very important for women's reproductive hormonal system, their normal synthesis and secretion are of prime importance. Androgens are critical female reproductive endocrine system hormones. Androgens include androstenedione (A4), dihydrotestosterone (DHT), dehydroepiandrosterone (DHEA), testosterone (T), and dehydroepiandrosterone sulfate (DHEAS). A4, DHEA, and DHEAS are regarded as precursors of T and DHT. Among these, only DHT and T have a direction with androgenic receptors. Androgens are majorly prepared ovaries and adrenal glands, while steroidogenic enzymes regulate their synthesis [60–64].

Besides this, in PCOS gonadotropin releasing was seen to have much more secretions of luteinizing hormone (LH) with normal abundance of the follicle-stimulating hormone (FSH). The increase in LH secretions in PCOS women may be due to pulsatile increase in the secretions of gonadotropin-releasing hormone (GnRH). Previous analysis raises the point that the change in GRH secretion might be due to defects in hypothalamus in PCOS populations. However, these complications are not only concerned with PCOS, but such changes have been also observed with hyperandrogenism in other cases like ovarian cancer, where there are increased secretions of androgens. The discussion based on previous literature declares that GRH releasing behaviour in correlation with hyperandrogenism in PCOS may be the secondary issue not involved primarily [65, 66]. Women suffering from PCOS generally exhibit hyperandrogenism with increased ovarian androgen as illustrated in Figure 3. The theca cells are the cells of ovary which are responsible for the production of androgens; these cells secrete amplified levels of androgen (androstenedione) and 17-hydroxyprogesterone. 17-Hydroxyprogesterone is a steroidal intermediate for the biosynthesis steps of androgens and glucocorticoids to retort the LH. The questions arise that such abnormalities originate from the theca cells from the ovary of PCOS patients and chronic anovulation-PCOS or from theca cells of the normal ovaries [67–69]. Insulin can have mimicking influences on the LH in women with PCOS. When theca cells from women with PCOS were passaged in tissue culture, they demonstrated elevated activity of numerous steroidogenic enzymes: 3-hydroxysteroid dehydrogenase, 17-hydroxylase/17-20 lyase, and 17-hydroxysteroid hydrogenase. The previously published reports revealed the fact that the amplification of the steroidogenic activity is intrinsic and presumably genetic and leads to blemishes in PCOS. The PCOS might be a morphological associate of these steroidogenic abnormalities [56–62, 70].

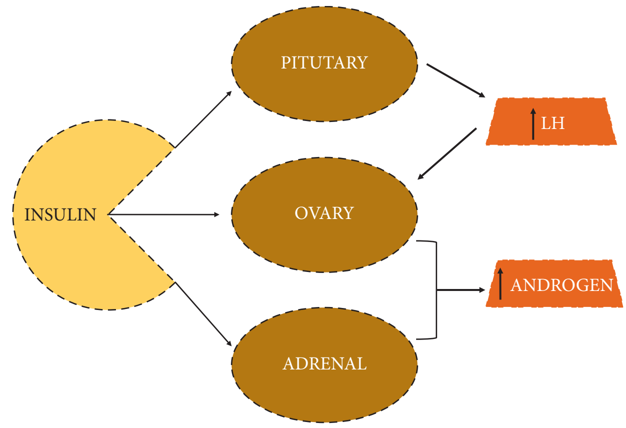

Figure 2: Impact of insulin on hypersecretion of LH and androgen.

5. PCOS Phenotypes

There are 4 various phenotypes of the PCOS identified up till now which are as follows: Type A: polycystic ovaries [PCO], chronic anovulation [CA], and Hyperandrogenism [H]; Type B: chronic anovulation [CA] and hyperandrogenism [H]; Type C: polycystic ovaries [PCO] and hyperandrogenism [H]; and Type D: polycystic ovaries [PCO] and chronic anovulation [CA] [70, 71]. The type of PCOS is related to metabolism and cardiovascular health, as it has been observed that most of the PCOS women are obese with severe or mild metabolic deformities [19, 70, 71] and often face problems of dyslipidaemia, hyperinsulinaemia, insulin resistance, and other metabolic disorders [20]. The major discussion is on fabricating how PCOS phenotypes can be related to aging. Patients with phenotype A are investigated to have high insulin resistance and overexposure of androgens as compared to phenotype B. Phenotype D is generally characterized by the insulin resistance in obese condition even if there is no overexposure of androgens. Meanwhile, in case of type C, the scenario is different where cardiovascular risk is high which may be due to lack of insulin resistance in PCOS. Dyslipidaemia is a serious metabolic issue in PCOS correlated with the HDL and LDL cholesterol levels. According to a research on the PCOS population, both lean and obese PCOS women exhibit aberrant phosphatidylcholine and polyunsaturated fatty acids (PUFAs) levels as well as free fatty acids [71–73].

6. Impact of PCOS on Physiologic Functions

PCOS is a heterogeneous disease of endocrine system which is followed by various clinical and physiological abnormalities. It exerts harmful and pervasive effects on physiological as well as metabolic system, and these characteristics categorise PCOS as a disorder associated with metabolism. Various dysfunctions like insulin resistance, hyperinsulinaemia, obesity, dyslipidaemia, hypertension, elevating risk of developing T2DM, endometrial hyperplasia, and coronary artery diseases. Here, we discussed the impact of the PCOS on various physiological functions of the body.

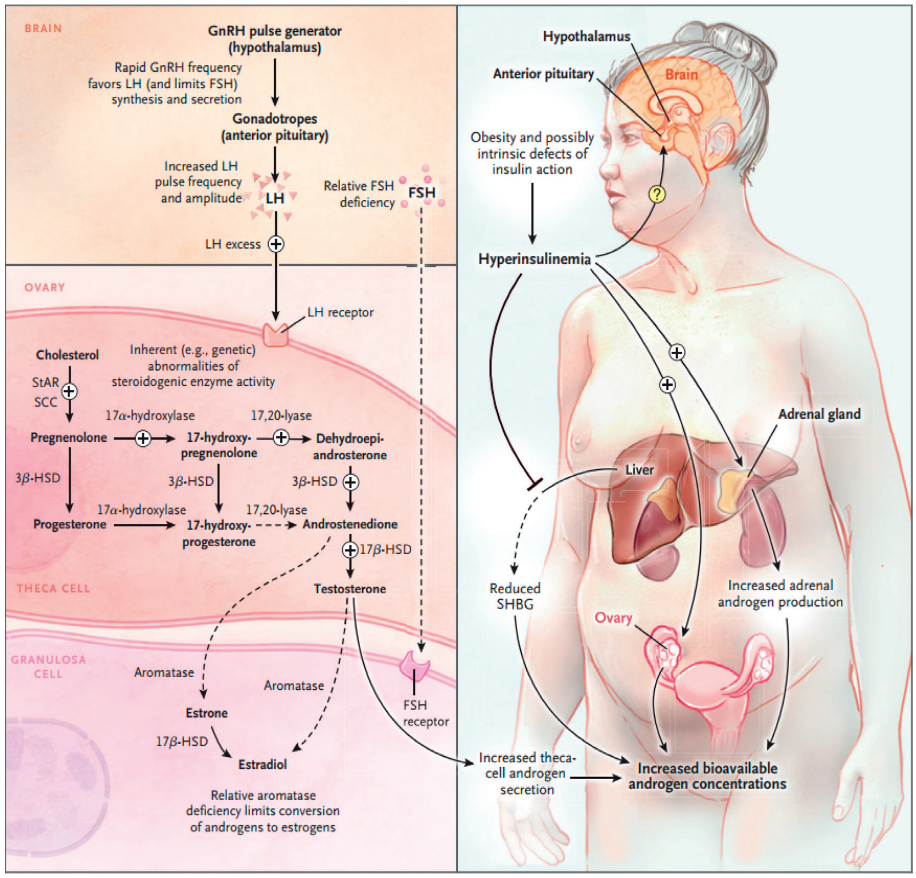

FIGURE 3: The basic mechanism of androgen overexposure in PCOS women [69]. The figure is cited with permission granted.

6.1. Liver Function. The excessive aggregation of fats in liver is called nonalcoholic fatty liver disease (NAFLD) and presents high risk of T2DM and CVS in PCOS. NAFLD is characterized by the presentation of insulin resistance and obesity. These issues are specifically related to abnormalities in liver metabolism. In PCOS population, there is always a high risk of NAFLD because PCOS women usually have insulin resistance with metabolic dysfunctions and unconditional obesity. So, PCOS consequences are found to be associated with NAFLD [74, 75].

6.2. Cardiac Functions. It was concluded that all the PCOS phenotypes have serious cardiovascular risks in PCOS patients. Phenotypes, insulin resistance, hyperinsulinaemia, overexposure of androgens, and ovaries function are reported to display increased cardiovascular health risk for PCOS women [76–78]. The insulin resistance is associated with the inactivation of NO after release from endothelial cells and decreased production of nitric oxide (NO) and synthesis of vasoconstricting agents in excessive amounts; all these defects lead to impaired vasodilatation and cardiac muscles stiffness [79, 80]. Insulin resistance and hyperinsulinaemia also display hypertrophic effect directly and proceed with the endothelial dysfunction. Clinical reports revealed increased risk of cardiac dysfunctions in PCOS population [77–81].

6.3. Reproductive Functions. PCOS is a primary disorder of the ovaries and will directly affect the reproductive system and functions. The excessive secretions of insulin have been observed to cause amplified levels of estrogens and progesterone secretions in women with PCOS. Insulin receptors are responsible for mediating these effects. It was reported that the insulin activity in in vitro granulosa cells can be treated with troglitazone, where IGF-1 mitogenic pathways are increased with the therapy. Besides this, there was an amplification in the IGF-1 receptor in the follicle cells of PCOS patient. This occurred in all stages of development in PCOS women [82]. In the recently reported data, it was concluded that the activity of cortisol is defective in follicular fluid and granulosa cells in PCOS population, where insulin resistance can further lead to tissue-specific insulin resistance. Endometrium cancer is a health-depriving deadly disorder and PCOS women are at high risk to develop endometrium cancer because of the high incidence of insulin resistance and hyperinsulinaemia together with overexposure of androgens. In PCOS, there is always increased upregulation of insulin receptors that have the direct implication of insulin signaling, thereby leading to cardiogenesis and development of endometrium cancer [83]. It might be due to metabolic defects, proteins expression in endometrium with insulin activity, and faulty glucose metabolism. Furthermore, the insulin receptor expression and IGF-1 signaling synergistically contribute to the development of endometrium cancer in PCOS population. So, PCOS is one of the major reasons for establishing endometrium cancer [82–84]. In Figure 4, the mechanism of PCOS associated infertility is illustrated, which displays the reproductive defects in PCOS women. The PCOS leads to increased production of androgens and decreased sensitivity of the follicle-stimulating hormone receptors (FSHR) as illustrated in Figure 4. The increased production of the androgens leads to failure in dominant follicles development and corpus luteum. It is responsible for decreased production of aromatase and progesterone. On the other hand, decreased sensitivity of the FSHR also leads to decreased aromatase production that further decreases the production of estrogens. So, overall, the syndrome leads to decreased production of the estrogens and progesterone followed by infertility.

6.4. PCOS and Hypertension. Hypertension is a persistently elevated blood pressure that affects a large human population and leads to serious health issues [84]. In PCOS population, the existence of systemic arterial hypertension (SAH) is more usual and has high incidence. A survey conducted on SAH in PCOS women demonstrated that there are 40% more chances of SAH occurrence in PCOS women than in the normal women. SAH has specific and central contribution in the development of PCOS and secondary cardiovascular disorders [84–88]. According to clinical investigational studies, there is a major and specific relationship between hypertension and endocrine system, so any abnormality in endocrine system will be definitely associated with the hypertension. In PCOS, the defective endocrine system is commonly observed leading to hypertension [85]. Besides this, insulin resistance and metabolic defects have also more commonly occurring issues in PCOS women, resulting in increased incidence of hypertension [84, 85]. The insulin resistance results in hyperinsulinaemia and increased production of LH, consequently increasing the androgen secretions causing persistently high blood pressure in PCOS women [89, 90]. The critical clinical studies show that there is a high occurrence of hypertension in females with PCOS. Moreover, it should be clearly understood that women suffering from PCOS should always monitor their blood pressure regularly in order to avoid delayed management [89–91].

6.5. Inflammation in PCOS. PCOS also promotes basis for chronic low-grade inflammation and inflammation pathways including interleukin-6 (IL-6), TNF-a, and type 2 TNF receptors. The circulating C-reactive protein (CRP) observation also leads to the point that PCOS is concerned with low-grade chronic inflammation [81, 91]. The basis can also be displayed from excessive adipose tissues which is direct producer of the CRP [92, 93]. Additionally, CRP has a physiological purpose by increasing lipid absorption into foamy macrophages inside atherosclerotic plaques. CRP is a direct and specific biomarker of abnormally low inflammation, according to a study [94, 95]. In general, PCOS patients have mild risk of chronic inflammation but it is not reflective at molecular levels.

7. Treatment Options for Hyperandrogenism, Insulin Resistance, and PCOS

7.1. Exercise and Weight Loss. Exercise is the best treatment modality for all the embolic manifestations and is recognized as necessary as food for human health. In PCOS, exercise and weight losing activities have supreme importance because they will help in lowering the adipose tissues having a major contribution to insulin resistance and androgenism [89, 96, 97]. The fats deposits are the key factors for insulin resistance, hyperinsulinaemia, hyperglycemia, T2DM, and oversecretion of androgen, so losing fats, specifically abdomen fats, has a direct and positive impact on all the major issues in PCOS women. It is also investigated that exercise not only diminishes fats but also promotes the normal endocrine and adrenal functions [97]. Physical exercises and weight losing activities can result in complete recovery from the clinical characteristics of PCOS.

7.2. Pharmacological Mediation. Drug therapy is always considered prime requirement for PCOS, where drugs like pioglitazone, inositol, and metformin isoforms have been recognized as therapeutic regimens for reproductive abnormalities and metabolic disorders in PCOS. Metformin is an insulin-sensitizing hormone that is used in PCOS even without diabetes and exerts actions on adipose tissue, skeletal muscles, ovary, and endothelium, impacted by insulin resistance. Prolonged use of metformin in PCOS treatment can augment ovulation rate, regulate menstrual cycle, and decrease the androgens secretions [87, 98–100]. The combinatorial regimen of clomiphene and metformin is considered more beneficial than single therapy of clomiphene or metformin for ovulation and pregnancy in PCOS women [101]. Metformin had no impact on fasting glucose, serum lipids, or anthropometric characteristics in women with PCOS, although it may postpone the advancement of glucose intolerance. Other insulin-sensitizing agents have also been shown to be effective in the treatment of PCOS [102]. Pioglitazone and rosiglitazone are also considered effective in eliminating insulin resistance, abnormal glucose tolerance, hyperandrogenaemia, ovulation rate, and menstrual regularity in PCOS patients. The combination of metformin and pioglitazone is also reported to have synergistic clinical profile in PCOS women's treatment; however, it should be avoided if pregnancy is desired due to teratogenic effects [103]. Inositol is another novel insulin-sensitizing agent that withholds superb insulin-sensitizing efficiency in PCOS women. Insulin resistance is troublesome along with hyperinsulinaemia for PCOS population and needs further research for the radical treatments. Hypersecretion of androgen in PCOS is considered fatal and hereditary. Therefore, there is an unmet need to evaluate the pathogenic and molecular network of this syndrome, insulin resistance, and excessive secretion of androgen [102, 103]. The metabolic irregularities and malfunctioning lead to complications like obesity, excessive lipids

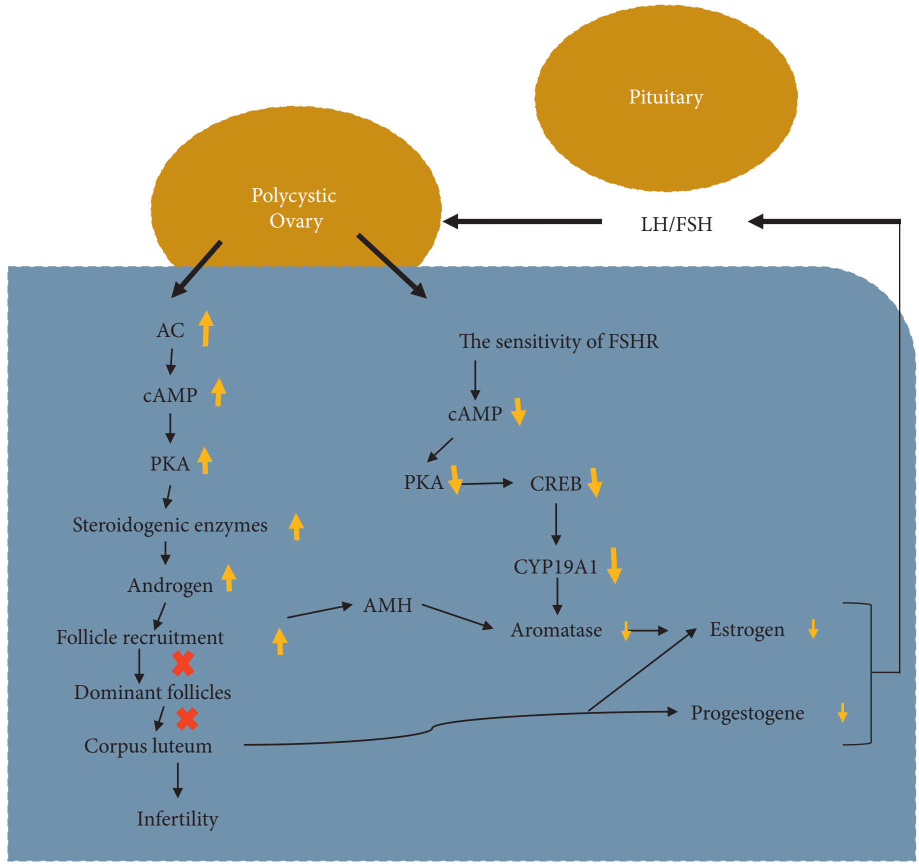

Figure 4: Schematic representation of PCOS associated infertility. The increased production of the androgens leads to failure in dominant follicles development and corpus luteum that is responsible for decreased production of aromatase and progesterone. Decreased sensitivity of the FSHR also leads to decreased aromatase production that further decreases the production of estrogens. So, overall the syndrome leads to decreased production of the estrogens and progesterone leading to infertility. H: anti-Mullerian hormone; PKA: protein kinase A; AC: adenylate cyclase; cAMP-response element binding protein:CREB.

aggregations, impaired glucose tolerance, hypertension, endometrium cancer, and hyperinsulinaemia [104, 105]. There is intended need for randomised clinical control trials for effective therapeutic approach in order to treat PCOS and its related complications.

7.3. Assisted Reproductive Technology (ART). Women infertility is also a major concern in PCOS, where assisted reproductive technology (ART) is employed for the fertility purposes. In ART, ovary is hyperstimulated in order to regulate the growth of multiple follicles, but it is ineffective in most cases due to augmented response to gonadotropins [106, 107]. In vitro maturation (IVM) methods have been employed for the fertilization of women with PCOS. IVF and IVM-IVF methods are also used for the embryo implantation to PCOS women [106–108]. However, further clinical research is aimed at yielding specified model for the success of ART in PCOS women to get fertilized.

7.4. Laparoscopic Ovarian Drilling (LOD). In 1984, laparoscopic ovarian drilling (LOD) was established to replace the invasive ovarian wedge resection surgery [109]. Currently, this technique is highly recommended and is developing pregnancy in 84% of the PCOS women who are facing infertility problems. LOD also augments insulin resistance and androgen production from ovaries. The improvements achieved with LOD have been observed to remain for a long time in 54% of the PCOS population. LOD is also a beneficial approach, as it results in low incidence of miscarriages in PCOS patients. LOD is also thought to be the first-line treatment when the CC treatment fails [26, 110–116]. These findings should be further evaluated for the confined use of LOD and its clinical benefits.

7.5. Oral Contraceptive Pills (OCPs). Oral contraceptives pills (OCPs) are regarded first-line therapy for people with PCOS who are not pursuing pregnancy. Not only are OCPs helpful in regulating the menstrual cycle, but also they reduce the secretion of androgens and regulate other physical activities [117]. OCPs have been reported which can significantly decrease the risk of endometrium cancer. OCPs are a combination of estrogen and progestogen, where estrogen is intended to decrease the levels of LH and FSH; the reduction in LH and FSH levels leads to suppression of T secretions and reduces the secretion of androgens.

Progestogen is generally recommended for low androgenic activity in women with PCOS [118, 119]. Three commonly used progestogens are desogestrel, cyproterone acetate, and drospirenone. As discussed earlier in this review, the PCOS population has high risk to develop disorders like insulin resistance, T2DM, hyperglycemia, abnormal glucose tolerance, enhanced levels of HDL and LDL cholesterols, hyperinsulinaemia, and so forth. Investigations in clinics revealed that OCPs can cause serious cardiac disorders like thrombosis, hypertension, insulin resistance, and myocardial infarction. These anomalies are thought to be having high risk in PCOS women compared to normal women and those who are on OCPs therapy. However, up till now, no clinical examination has been reported, to the best of our knowledge, regarding the metabolic effects of OCPs in PCOS population [118–122]. So, there is a great demand of clinical research in this area of interest because OCPs are the first-line treatment modality in females with PCOS. The recent interventions declared a new regimen with OCPs by adding metformin along with OCP, and the results found were satisfactory in reducing insulin resistance as well as decreasing the androgen production in PCOS population.

7.6. Dietary Therapy. Dietary therapy to reduce the weight of women with PCOS has a significant impact on metabolic conditions and is recognized to improve many PCOS issues like regulating androgen secretions, reducing insulin resistance, regularity of endocrine secretions, and menstrual cycle regulation [123, 124]. Weight loss can surely meet the goals of obtaining improved symptoms of PCOS and metabolic issues can intently resolve without medications. Moreover, the reproductive consequences in PCOS women can be improved with weight loss for those PCOS women who are interested in getting pregnant [123]. The weight loss results in high rates of pregnancy as well as decrease of the chances of miscarriages, suggesting weight loss significance for PCOS population. Dietary plan for weight loss is important and should be considered as first clinical regimen in order to live a healthy life with PCOS [125–128]. There is a need for clinical research and trials on the significance and effectiveness of dietary therapy for PCOS women.

8. Conclusion

Polycystic ovarian syndrome (PCOS) is considered as a major health issue. Women with PCOS face insulin resistance and overexposure of androgen, leading to a number of metabolic and reproductive abnormalities. These are considered the major causes of PCOS and other PCOS related manifestations. Herein, we have discussed the mechanism and treatment modalities of PCOS based on hypersecretion of androgen and insulin resistance. The current study gives concise and comprehensive outlook for the understanding of insulin resistance and androgen overexposure. We for the first time reported detailed review on the mechanism, pathophysiology, and treatment interventions for the insulin resistance and hypersecretion of insulin. The current study provides better understanding of the PCOS and provides a base for further exploration.

Data Availability

All the data can be requested from the corresponding author.

Conflicts of Interest

The authors declare that there are no conflicts of interest.

Authors' Contributions

YX and JQ collected the data and wrote the manuscript. JQ supervised the whole study.

Acknowledgments

This study was supported financially by the National Natural Science Foundation of China (no. 81730038) and CAMS Innovation Fund for Medical Sciences (no. 2019-I2M-5-001).

References

[1] S. Livadas and E. Diamanti-Kandarakis, "Polycystic ovary syndrome: definitions, phenotypes and diagnostic approach," *Frontiers of Hormone Research*, vol. 40, pp. 1–21, 2013.

[2] G. Conway, D. Dewailly, E. Diamanti-Kandarakis et al., "European survey of diagnosis and management of the polycystic ovary syndrome: results of the ESE PCOS Special Interest Group's Questionnaire," *European Journal of Endocrinology*, vol. 171, no. 4, pp. 489–498, 2014.

[3] R. Pasquali and A. Gambineri, "Glucose intolerance states in women with the polycystic ovary syndrome," *Journal of Endocrinological Investigation*, vol. 36, no. 8, pp. 648–653, 2013.

[4] J. K. Zawadski, *Diagnostic criteria for polycystic ovary syndrome: towards a rational approach; Polycystic ovary syndrome*, pp. 377–384, Blackwell Scientific Publications, Boston, 1992.

[5] E. S. Rotterdam, "Revised 2003 consensus on diagnostic criteria and long-term health risks related to polycystic ovary syndrome (PCOS)," *Human Reproduction*, vol. 19, pp. 41–47, 2004.

[6] R. Azziz, E. Carmina, D. Dewailly et al., "The androgen excess and PCOS society criteria for the polycystic ovary syndrome: the complete task force report," *Fertility and Sterility*, vol. 91, no. 2, pp. 456–488, 2009.

[7] E. Diamanti-Kandarakis and A. Dunaif, "Insulin resistance and the polycystic ovary syndrome revisited: an update on mechanisms and implications," *Endocrine Reviews*, vol. 33, no. 6, pp. 981–1030, 2012.

[8] A. Dunaif, K. R. Segal, D. R. Shelley, G. Green, A. Dobrjansky, and T. Licholai, "Evidence for distinctive and intrinsic defects in insulin action in polycystic ovary syndrome," *Diabetes*, vol. 41, no. 10, pp. 1257–1266, 1992.

[9] E. Carmina, S. Bucchieri, A. Esposito et al., "Abdominal fat quantity and distribution in women with polycystic ovary syndrome and extent of its relation to insulin resistance," *Journal of Clinical Endocrinology & Metabolism*, vol. 92, no. 7, pp. 2500–2505, 2007.

[10] A. N. Vgontzas, G. Trakada, E. O. Bixler et al., "Plasma interleukin 6 levels are elevated in polycystic ovary syndrome independently of obesity or sleep apnea," *Metabolism*, vol. 55, no. 8, pp. 1076–1082, 2006.

[11] L. Mannerås-Holm, H. Leonhardt, J. Kullberg et al., "Adipose tissue has aberrant morphology and function in PCOS:

enlarged adipocytes and low serum adiponectin, but not circulating sex steroids, are strongly associated with insulin resistance," *Journal of Clinical Endocrinology & Metabolism*, vol. 96, no. 2, pp. E304–E311, 2011.

[12] G. I. Shulman, "Ectopic fat in insulin resistance, dyslipidemia, and cardiometabolic disease," *New England Journal of Medicine*, vol. 371, no. 12, pp. 1131–1141, 2014.

[13] S. A. Morrison, A. M. Goss, R. Azziz, D. A. Raju, and B. A. Gower, "Peri-muscular adipose tissue may play a unique role in determining insulin sensitivity/resistance in women with polycystic ovary syndrome," *Human Reproduction (Oxford)*, vol. 32, pp. 185–192, 2017.

[14] P.-H. Ducluzeau, P. Cousin, E. Malvoisin et al., "Glucose-to-insulin ratio rather than sex hormone-binding globulin and adiponectin levels is the best predictor of insulin resistance in nonobese women with polycystic ovary syndrome," *Journal of Clinical Endocrinology & Metabolism*, vol. 88, no. 8, pp. 3626–3631, 2003.

[15] P. Vigil, P. Contreras, J. L. Alvarado, A. Godoy, A. M. Salgado, and M. E. Cortes, "Evidence of subpopulations with different levels of insulin resistance in women with polycystic ovary syndrome," *Human Reproduction*, vol. 22, no. 11, pp. 2974–2980, 2007.

[16] A. Dunaif, K. R. Segal, W. Futterweit, and A. Dobrjansky, "Profound peripheral insulin resistance, independent of obesity, in polycystic ovary syndrome," *Diabetes*, vol. 38, no. 9, pp. 1165–1174, 1989.

[17] T. M. Barber, J. A. Wass, M. I. McCarthy, and S. Franks, "Metabolic characteristics of women with polycystic ovaries and oligo-amenorrhoea but normal androgen levels: implications for the management of polycystic ovary syndrome," *Clinical Endocrinology*, vol. 66, pp. 513–517, 2007.

[18] S. Cassar, M. L. Misso, W. G. Hopkins, C. S. Shaw, H. J. Teede, and N. K. Stepto, "Insulin resistance in polycystic ovary syndrome: a systematic review and meta-analysis of euglycaemic-hyperinsulinaemic clamp studies," *Human Reproduction*, vol. 31, no. 11, pp. 2619–2631, 2016.

[19] R. S. Legro, A. R. Kunselman, W. C. Dodson, and A. Dunaif, "Prevalence and predictors of risk for type 2 diabetes mellitus and impaired glucose tolerance in polycystic ovary syndrome: a prospective, controlled study in 254 affected Women1," *Journal of Clinical Endocrinology & Metabolism*, vol. 84, no. 1, pp. 165–169, 1999.

[20] D. A. Ehrmann, R. B. Barnes, R. L. Rosenfield, M. K. Cavaghan, and J. Imperial, "Prevalence of impaired glucose tolerance and diabetes in women with polycystic ovary syndrome," *Diabetes Care*, vol. 22, no. 1, pp. 141–146, 1999.

[21] D. A. Ehrmann, K. Kasza, R. Azziz, R. S. Legro, and M. N. Ghazzi, "Effects of race and family history of type 2 diabetes on metabolic status of women with polycystic ovary syndrome," *Journal of Clinical Endocrinology & Metabolism*, vol. 90, no. 1, pp. 66–71, 2005.

[22] A. Gambineri, L. Patton, P. Altieri et al., "Polycystic ovary syndrome is a risk factor for type 2 diabetes," *Diabetes*, vol. 61, no. 9, pp. 2369–2374, 2012.

[23] R. J. Norman, L. Masters, and C. R. Milner, "Relative risk of conversion from normoglycaemia to impaired glucose tolerance or non-insulin dependent diabetes mellitus in polycystic ovarian syndrome," *Human Reproduction*, vol. 16, pp. 1995–1998, 2001.

[24] A. R. Saltiel and C. R. Kahn, "Insulin signalling and the regulation of glucose and lipid metabolism," *Nature*, vol. 414, no. 6865, pp. 799–806, 2001.

[25] B. Cheatham and C. R. Kahn, "Insulin action and the insulin signaling network*," *Endocrine Reviews*, vol. 16, no. 2, pp. 117–142, 1995.

[26] K.-M. Seow, C.-C. Juan, Y.-P. Hsu, J.-L. Hwang, L.-W. Huang, and L.-T. Ho, "Amelioration of insulin resistance in women with PCOS via reduced insulin receptor substrate-1 Ser312 phosphorylation following laparoscopic ovarian electrocautery," *Human Reproduction*, vol. 22, no. 4, pp. 1003–1010, 2007.

[27] T. P. Ciaraldi, V. Aroda, S. Mudaliar, R. J. Chang, and R. R. Henry, "Polycystic ovary syndrome is associated with tissue-specific differences in insulin resistance," *Journal of Clinical Endocrinology & Metabolism*, vol. 94, no. 1, pp. 157–163, 2009.

[28] A. Dunaif and D. T. Finegood, "Beta-cell dysfunction independent of obesity and glucose intolerance in the polycystic ovary syndrome," *Journal of Clinical Endocrinology & Metabolism*, vol. 81, no. 3, pp. 942–947, 1996.

[29] N. J. Wareham, C. D. Byrne, R. Williams, N. E. Day, and C. N. Hales, "Fasting proinsulin concentrations predict the development of type 2 diabetes," *Diabetes Care*, vol. 22, no. 2, pp. 262–270, 1999.

[30] D. Panidis, D. Macut, D. Farmakiotis et al., "Indices of insulin sensitivity, beta cell function and serum proinsulin levels in the polycystic ovary syndrome," *European Journal of Obstetrics & Gynecology and Reproductive Biology*, vol. 127, no. 1, pp. 99–105, 2006.

[31] T. Sir-Petermann, M. Maliqueo, E. Codner et al., "Early metabolic derangements in daughters of women with polycystic ovary syndrome," *Journal of Clinical Endocrinology & Metabolism*, vol. 92, no. 12, pp. 4637–4642, 2007.

[32] N. Raissouni, A. Kolesnikov, and R. Purushothaman, "Altered glucose disposition and insulin sensitivity in peripubertal first-degree relatives of women with polycystic ovary syndrome," *International Journal of Pediatric Endocrinology*, vol. 2012, p. 14, 2012.

[33] L. C. Torchen, N. R. Fogel, W. J. Brickman, R. Paparodis, and A. Dunaif, "Persistent apparent pancreatic β-cell defects in premenarchal PCOS relatives," *Journal of Clinical Endocrinology & Metabolism*, vol. 99, no. 10, pp. 3855–3862, 2014.

[34] A. Biyasheva, R. S. Legro, A. Dunaif, and M. Urbanek, "Evidence for association between polycystic ovary syndrome (PCOS) andTCF7L2and glucose intolerance in women with PCOS andTCF7L2," *Journal of Clinical Endocrinology & Metabolism*, vol. 94, no. 7, pp. 2617–2625, 2009.

[35] M. Hao, F. Yuan, C. Jin et al., "Overexpression of Lnk in the ovaries is involved in insulin resistance in women with polycystic ovary syndrome," *Endocrinology*, vol. 157, no. 10, pp. 3709–3718, 2016.

[36] G. A. Burghen, J. R. Givens, and A. E. Kitabchi, "Correlation of hyperandrogenism with hyperinsulinism in polycystic ovarian disease*," *Journal of Clinical Endocrinology & Metabolism*, vol. 50, no. 1, pp. 113–116, 1980.

[37] N. M. O'Meara, J. D. Blackman, and D. A. Ehrmann, "Defects in beta-cellfunction in functional ovarian hyperandrogenism," *Journal of Clinical Endocrinology & Metabolism*, vol. 76, pp. 1241–1247, 1993.

[38] K. S. Annika, T. Sascha, and O. Olaf, "Insulin resistance in patients with polycystic ovary syndrome," *Annals of Medicine*, vol. 36, pp. 426–439, 2004.

[39] R. N. Bergman, R. Watanabe, K. Rebrin, M. Ader, and G. Steil, "Toward an integrated phenotype in pre-NIDDM," *Diabetic Medicine*, vol. 13, pp. 67–77, 1996.

[40] D. A. Ehrmann, J. Sturis, M. M. Byrne, T. Karrison, R. L. Rosenfield, and K. S. Polonsky, "Insulin secretory defects in polycystic ovary syndrome. Relationship to insulin sensitivity and family history of non-insulin-dependent diabetes mellitus," *Journal of Clinical Investigation*, vol. 96, no. 1, pp. 520–527, 1995.

[41] A. Virkamäki, K. Ueki, and C. R. Kahn, "Protein-protein interaction in insulin signaling and the molecular mechanisms of insulin resistance," *Journal of Clinical Investigation*, vol. 103, no. 7, pp. 931–943, 1999.

[42] P. R. Shepherd and B. B. Kahn, "Glucose transporters and insulin action - implications for insulin resistance and diabetes mellitus," *New England Journal of Medicine*, vol. 341, no. 4, pp. 248–257, 1999.

[43] T. P. Ciaraldi, A. el-Roeiy, Z. Madar, D. Reichart, J. M. Olefsky, and S. S. Yen, "Cellular mechanisms of insulin resistance in polycystic ovarian syndrome," *Journal of Clinical Endocrinology & Metabolism*, vol. 75, no. 2, pp. 577–583, 1992.

[44] P. J. Marsden, A. Murdoch, and R. Taylor, "Severe impairment of insulin action in adipocytes from amenorrheic subjects with polycystic ovary syndrome," *Metabolism*, vol. 43, no. 12, pp. 1536–1542, 1994.

[45] J. K. Rodrigues, P. A. Navarro, M. B. Zelinski, R. L. Stouffer, and J. Xu, "Direct actions of androgens on the survival, growth and secretion of steroids and anti-Mullerian hormone by individual macaque follicles during three-dimensional culture," *Human Reproduction*, vol. 30, no. 3, pp. 664–674, 2015.

[46] A. Pierre, J. Taieb, F. Giton et al., "Dysregulation of the anti-müllerian hormone system by steroids in women with polycystic ovary syndrome," *Journal of Clinical Endocrinology & Metabolism*, vol. 102, no. 11, pp. 3970–3978, 2017.

[47] J. J. Lim, C. Y. Han, D. R. Lee, and B. K. Tsang, "Ring finger protein 6 mediates androgen-induced granulosa cell proliferation and follicle growth via modulation of androgen receptor signaling," *Endocrinology*, vol. 158, no. 4, pp. 993–1004, 2017.

[48] A. T. Nanba, J. Rege, J. Ren, R. J. Auchus, W. E. Rainey, and A. F. Turcu, "11-Oxygenated C19 steroids do not decline with age in women," *Journal of Clinical Endocrinology & Metabolism*, vol. 104, no. 7, pp. 2615–2622, 2019.

[49] H. Li, Y. Chen, L.-y. Yan, and J. Qiao, "Increased expression of P450scc and CYP17 in development of endogenous hyperandrogenism in a rat model of PCOS," *Endocrine*, vol. 43, no. 1, pp. 184–190, 2012.

[50] S. Bakhshalizadeh, F. Amidi, R. Shirazi, and M. Shabani Nashtaei, "Vitamin D3 regulates steroidogenesis in granulosa cells through AMP-activated protein kinase (AMPK) activation in a mouse model of polycystic ovary syndrome," *Cell Biochemistry and Function*, vol. 36, no. 4, pp. 183–193, 2018.

[51] A. Lerner, L. A. Owens, M. Coates et al., "Expression of genes controlling steroid metabolism and action in granulosa-lutein cells of women with polycystic ovaries," *Molecular and Cellular Endocrinology*, vol. 486, pp. 47–54, 2019.

[52] D. Salilew-Wondim, Q. Wang, and D. Tesfaye, "Polycystic ovarian syndrome is accompanied by repression of gene signatures associated with biosynthesis and metabolism of steroids, cholesterol and lipids," *Journal of Ovarian Research*, vol. 8, pp. 15–24, 2015.

[53] E. Gonzalez and F. P. Guengerich, "Kinetic processivity of the two-step oxidations of progesterone and pregnenolone to androgens by human cytochrome P450 17A1," *Journal of Biological Chemistry*, vol. 292, no. 32, pp. 13168–13185, 2017.

[54] H. Kakuta, T. Iguchi, and T. Sato, "The involvement of granulosa cells in the regulation by gonadotropins of Cyp17a1 in theca cells," *In Vivo*, vol. 32, no. 6, pp. 1387–1401, 2018.

[55] H.-M. Peng, S.-C. Im, N. M. Pearl et al., "Cytochrome b5 activates the 17,20-lyase activity of human cytochrome P450 17A1 by increasing the coupling of NADPH consumption to androgen production," *Biochemistry*, vol. 55, no. 31, pp. 4356–4365, 2016.

[56] Y. Nakamura, F. Fujishima, X.-G. Hui et al., "3βHSD and CYB5A double positive adrenocortical cells during adrenal development/aging," *Endocrine Research*, vol. 40, no. 1, pp. 8–13, 2014.

[57] K. Qin, D. A. Ehrmann, N. Cox, S. Refetoff, and R. L. Rosenfield, "Identification of a functional polymorphism of the human type 5 17β-hydroxysteroid dehydrogenase gene associated with polycystic ovary syndrome," *Journal of Clinical Endocrinology & Metabolism*, vol. 91, no. 1, pp. 270–276, 2006.

[58] K. Hattori, M. Orisaka, S. Fukuda et al., "Luteinizing hormone facilitates antral follicular maturation and survival via thecal paracrine signaling in cattle," *Endocrinology*, vol. 159, no. 6, pp. 2337–2347, 2018.

[59] J.-N. Xu, C. Zeng, Y. Zhou, C. Peng, Y.-F. Zhou, and Q. Xue, "Metformin InhibitsStARExpression in human endometriotic stromal cells via AMPK-mediated disruption of CREB-CRTC2 complex formation," *Journal of Clinical Endocrinology & Metabolism*, vol. 99, no. 8, pp. 2795–2803, 2014.

[60] N. Martinat, P. Crépieux, E. Reiter, and F. Guillou, "Extracellular signal-regulated kinases (ERK) 1, 2 are required for luteinizing hormone (LH)-induced steroidogenesis in primary Leydig cells and control steroidogenic acute regulatory (StAR) expression," *Reproduction Nutrition Development*, vol. 45, no. 1, pp. 101–108, 2005.

[61] L. S. Chow, D. G. Mashek, Q. Wang, S. O. Shepherd, B. H. Goodpaster, and J. J. Dubé, "Effect of acute physiological free fatty acid elevation in the context of hyperinsulinemia on fiber type-specific IMCL accumulation," *Journal of Applied Physiology*, vol. 123, no. 1, pp. 71–78, 2017.

[62] M. Li, K. Xue, J. Ling, F.-Y. Diao, Y.-G. Cui, and J.-Y. Liu, "The orphan nuclear receptor NR4A1 regulates transcription of key steroidogenic enzymes in ovarian theca cells," *Molecular and Cellular Endocrinology*, vol. 319, no. 1-2, pp. 39–46, 2010.

[63] X. Ma, E. Hayes, H. Prizant, R. K. Srivastava, S. R. Hammes, and A. Sen, "Leptin-induced CART (cocaine- and amphetamine-regulated transcript) is a novel intraovarian mediator of obesity-related infertility in females," *Endocrinology*, vol. 157, no. 3, pp. 1248–1257, 2016.

[64] F. Yang, Y.-C. Ruan, Y.-j. Yang et al., "Follicular hyperandrogenism downregulates aromatase in luteinized granulosa cells in polycystic ovary syndrome women," *Reproduction*, vol. 150, no. 4, pp. 289–296, 2015.

[65] W. K. McGee, C. V. Bishop, A. Bahar et al., "Elevated androgens during puberty in female rhesus monkeys lead to increased neuronal drive to the reproductive axis: a possible component of polycystic ovary syndrome," *Human Reproduction*, vol. 27, no. 2, pp. 531–540, 2011.

[66] K. H. Maas, S. Chuan, E. Harrison, H. Cook-Andersen, A. J. Duleba, and R. J. Chang, "Androgen responses to adrenocorticotropic hormone infusion among individual women with polycystic ovary syndrome," *Fertility and Sterility*, vol. 106, no. 5, pp. 1252–1257, 2016.

[67] M. W. O'Reilly, P. Kempegowda, and C. Jenkinson, "11-oxygenated C19 steroids are the predominant androgens in

polycystic ovary syndrome," *Journal of Clinical Endocrinology & Metabolism*, vol. 104, pp. 56–65, 2016.

[68] S.-H. Kim, J.-Y. Moon, H. Sasano, M. H. Choi, and M.-J. Park, "Body fat mass is associated with ratio of steroid metabolites reflecting 17,20-lyase activity in prepubertal girls," *Journal of Clinical Endocrinology & Metabolism*, vol. 101, no. 12, pp. 4653–4660, 2016.

[69] M. Cartney, C. Ru, and J. C. Marshall, "Polycystic ovary syndrome," *New England Journal of Medicine*, vol. 375, pp. 11–18, 2016.

[70] J. Idkowiak, Y. S. Elhassan, P. Mannion et al., "Causes, patterns and severity of androgen excess in 487 consecutively recruited pre- and post-pubertal children," *European Journal of Endocrinology*, vol. 180, no. 3, pp. 213–221, 2019.

[71] R. Azziz, K. S. Woods, R. Reyna, T. J. Key, E. S. Knochenhauer, and B. O. Yildiz, "The prevalence and features of the polycystic ovary syndrome in an unselected population," *Journal of Clinical Endocrinology & Metabolism*, vol. 89, no. 6, pp. 2745–2749, 2004.

[72] W. futterweit, "Polycystic ovary syndrome: a common reproductive and metabolic disorder necessitating early recognition and treatment," *Primary Care: Clinics in Office Practice*, vol. 34, no. 4, pp. 761–789, 2007.

[73] D. Cibula, R. Cifková, and M. fanta, "Increased risk of non-insulin dependent diabetes mellitus, arterial hypertension and coronary artery disease in perimenopausal women with a history of the polycystic ovary syndrome," *Human Reproduction*, vol. 15, no. 4, pp. 785–789, 2000.

[74] R. Azziz, E. Carmina, D. Dewailly et al., "Criteria for defining polycystic ovary syndrome as a predominantly hyperandrogenic syndrome: an androgen excess society guideline," *Journal of Clinical Endocrinology & Metabolism*, vol. 91, no. 11, pp. 4237–4245, 2006.

[75] A. Fraser, R. Harris, N. Sattar, S. Ebrahim, G. Davey Smith, and D. A. Lawlor, "Alanine aminotransferase, γ-glutamyltransferase, and incident diabetes," *Diabetes Care*, vol. 32, no. 4, pp. 741–750, 2009.

[76] K. Tziomalos, V. G. Athyros, and A. Karagiannis, "Non-alcoholic fatty liver disease in type 2 diabetes: pathogenesis and treatment options," *Current Vascular Pharmacology*, vol. 10, no. 2, pp. 162–172, 2012.

[77] D. Macut, K. Tziomalos, I. Božić-Antić et al., "Non-alcoholic fatty liver disease is associated with insulin resistance and lipid accumulation product in women with polycystic ovary syndrome," *Human Reproduction*, vol. 31, no. 6, pp. 1347–1353, 2016.

[78] M. W. O'Reilly, A. E. Taylor, and N. J. Crabtree, "Hyperandrogenemia predicts metabolic phenotype in polycystic ovary syndrome: the utility of serum androstenedione," *Journal of Clinical Endocrinology & Metabolism*, vol. 99, pp. 1027–1036, 2014.

[79] C. J. G. Kelly, A. Speirs, G. W. Gould, J. R. Petrie, H. Lyall, and J. M. C. Connell, "Altered vascular function in young women with polycystic ovary syndrome," *Journal of Clinical Endocrinology & Metabolism*, vol. 87, no. 2, pp. 742–746, 2002.

[80] E. Diamanti-Kandarakis, K. Alexandraki, C. Piperi et al., "Inflammatory and endothelial markers in women with polycystic ovary syndrome," *European Journal of Clinical Investigation*, vol. 36, no. 10, pp. 691–697, 2006.

[81] K. S. Bajuk, M. S. Jensterle, and M. Pfeifer, "Cardiovascular risk and subclinical cardiovascular disease in polycystic ovary syndrome," *Frontiers of Hormone Research*, vol. 40, pp. 64–82, 2013.

[82] A. Hurliman, J. Keller Brown, N. Maille, M. Mandala, P. Casson, and G. Osol, "Hyperandrogenism and Insulin resistance, not changes in body weight, mediate the development of endothelial dysfunction in a female rat model of polycystic ovary syndrome (PCOS)," *Endocrinology*, vol. 156, no. 11, pp. 4071–4080, 2015.

[83] S. Franks, J. Stark, and K. Hardy, "Follicle dynamics and anovulation in polycystic ovary syndrome," *Human Reproduction Update*, vol. 14, no. 4, pp. 367–378, 2008.

[84] X. K. Wu, S. Y. Zhou, J. X. Liu et al., "Selective ovary resistance to insulin signaling in women with polycystic ovary syndrome," *Fertility and Sterility*, vol. 80, no. 4, pp. 954–965, 2003.

[85] Q. Zhu, R. Zuo, Y. He et al., "Local regeneration of cortisol by 11β-HSD1 contributes to insulin resistance of the granulosa cells in PCOS," *Journal of Clinical Endocrinology & Metabolism*, vol. 101, no. 5, pp. 2168–2177, 2016.

[86] R. A. Wild, E. Carmina, E. Diamanti-Kandarakis et al., "Assessment of cardiovascular risk and prevention of cardiovascular disease in women with the polycystic ovary syndrome: a consensus statement by the androgen excess and polycystic ovary syndrome (AE-PCOS) society," *Journal of Clinical Endocrinology & Metabolism*, vol. 95, no. 5, pp. 2038–2049, 2010.

[87] E. Diamanti-Kandarakis, C. D. Christakou, E. Kandaraki, and F. N. Economou, "Metformin: an old medication of new fashion: evolving new molecular mechanisms and clinical implications in polycystic ovary syndrome," *European Journal of Endocrinology*, vol. 162, no. 2, pp. 193–212, 2010.

[88] Y.-W. Wang, S.-J. He, X. Feng et al., "Metformin: a review of its potential indications," *Drug Design, Development and Therapy*, vol. 11, pp. 2421–2429, 2017.

[89] C. L. Harrison, C. B. Lombard, L. J. Moran, and H. J. Teede, "Exercise therapy in polycystic ovary syndrome: a systematic review," *Human Reproduction Update*, vol. 17, no. 2, pp. 171–183, 2011.

[90] S. E. Inzucchi, R. M. Bergenstal, and J. B. Buse, "American DiabetesAssociation (ADA); European association for the study of diabetes (EASD). Management of hyperglycemia in type 2 diabetes: a patient-centered approach: position statement of the American diabetes association (ADA) and the European association for the study of diabetes (EASD)," *Diabetes Care*, vol. 35, pp. 1364–1379, 2012.

[91] R. S. Legro, S. A. Arslanian, D. A. Ehrmann et al., "Diagnosis and treatment of polycystic ovary syndrome: an endocrine society clinical practice guideline," *Journal of Clinical Endocrinology & Metabolism*, vol. 98, no. 12, pp. 4565–4592, 2013.

[92] K. Bajuk Studen, M. Šebeštjen, M. Pfeifer, and J. Preželj, "Influence of spironolactone treatment on endothelial function in non-obese women with polycystic ovary syndrome," *European Journal of Endocrinology*, vol. 164, no. 3, pp. 389–395, 2011.

[93] H. F. Escobar-Morreale, R. M. Calvo, G. Villuendas, J. Sancho, and J. L. San Millán, "Association of polymorphisms in the interleukin 6 receptor complex with obesity and hyperandrogenism," *Obesity Research*, vol. 11, no. 8, pp. 987–996, 2003.

[94] B. Peral, J. L. San Millán, R. Castello, P. Moghetti, and H. F. Escobar-Morreale, "The methionine 196 arginine polymorphism in exon 6 of the TNF receptor 2 gene (TNFRSF1B) is associated with the polycystic ovary syndrome and hyperandrogenism," *Journal of Clinical Endocrinology & Metabolism*, vol. 87, no. 8, pp. 3977–3983, 2002.

[95] G. Villuendas, J. L. San Millán, J. Sancho, and H. F. Escobar-Morreale, "The −597 G⟶A and −174 G⟶C polymorphisms in the promoter of the IL-6 gene are associated with hyperandrogenism," *Journal of Clinical Endocrinology & Metabolism*, vol. 87, no. 3, pp. 1134–1141, 2002.

[96] H. J. Moshage, H. M. J. Roelofs, J. F. van Pelt et al., "The effect of interleukin-1, interleukin-6 and its interrelationship on the synthesis of serum amyloid A and C-reactive protein in primary cultures of adult human hepatocytes," *Biochemical and Biophysical Research Communications*, vol. 155, no. 1, pp. 112–117, 1988.

[97] N. Ouchi, S. Kihara, T. Funahashi et al., "Reciprocal association of C-reactive protein with adiponectin in blood stream and adipose tissue," *Circulation*, vol. 107, no. 5, pp. 671–674, 2003.

[98] B. A. Gower, P. C. Chandler-Laney, F. Ovalle et al., "Favourable metabolic effects of a eucaloric lower-carbohydrate diet in women with PCOS," *Clinical Endocrinology*, vol. 79, no. 4, pp. 550–557, 2013.

[99] R. Pasquali, A. Gambineri, C. Cavazza et al., "Heterogeneity in the responsiveness to long-term lifestyle intervention and predictability in obese women with polycystic ovary syndrome," *European Journal of Endocrinology*, vol. 164, no. 1, pp. 53–60, 2011.

[100] T. I. Siebert, M. I. Viola, D. W. Steyn, and T. F. Kruger, "Is metformin indicated as primary ovulation induction agent in women with PCOS? A systematic review and meta-analysis," *Gynecologic and Obstetric Investigation*, vol. 73, no. 4, pp. 304–313, 2012.

[101] X. Tan, S. Li, Y. Chang et al., "Effect of metformin treatment during pregnancy on women with PCOS: a systematic review and meta-analysis," *Clinical and Investigative Medicine*, vol. 39, no. 4, pp. 120–131, 2016.

[102] S. T. Sharma, E. P. Wickham, and J. E. Nestler, "Changes in glucose tolerance with metformin treatment in polycystic ovary syndrome: a retrospective analysis," *Endocrine Practice*, vol. 13, no. 4, pp. 373–379, 2007.

[103] G. Valsamakis, K. Lois, S. Kumar, and G. Mastorakos, "Metabolic and other effects of pioglitazone as an add-on therapy to metformin in the treatment of polycystic ovary syndrome (PCOS)," *Hormones*, vol. 12, no. 3, pp. 363–378, 2013.

[104] G. Conway, D. Dewailly, E. Diamanti-Kandarakis et al., "The polycystic ovary syndrome: a position statement from the European Society of Endocrinology," *European Journal of Endocrinology*, vol. 171, pp. P1–P29, 2014.

[105] V. Unfer, J. E. Nestler, and Z. A. Kamenov, "Effects of inositol(s) in women with PCOS: a systematic review of randomized controlled trials," *The Internet Journal of Endocrinology*, vol. 2016, pp. 1849–1862, 2016.

[106] K. Elkind-Hirsch, O. Marrioneaux, M. Bhushan, D. Vernor, and R. Bhushan, "Comparison of single and combined treatment with exenatide and metformin on menstrual cyclicity in overweight women with polycystic ovary syndrome," *Journal of Clinical Endocrinology & Metabolism*, vol. 93, no. 7, pp. 2670–2678, 2008.

[107] M. Jensterle Sever, T. Kocjan, M. Pfeifer, N. A. Kravos, and A. Janez, "Short-term combined treatment with liraglutide and metformin leads to significant weight loss in obese women with polycystic ovary syndrome and previous poor response to metformin," *European Journal of Endocrinology*, vol. 170, no. 3, pp. 451–459, 2014.

[108] I. Tummon, L. Gavrilova-Jordan, M. C. Allemand, and D. Session, "Polycystic ovaries and ovarian hyperstimulation syndrome: a systematic review*," *Acta Obstetricia et Gynecologica Scandinavica*, vol. 84, no. 7, pp. 611–616, 2005.

[109] M. H. Choi, S. H. Lee, H. O. Kim et al., "Comparison of assisted reproductive technology outcomes in infertile women with polycystic ovary syndrome:In vitromaturation, GnRH agonist, and GnRH antagonist cycles," *Clinical and Experimental Reproductive Medicine*, vol. 39, no. 4, pp. 166–171, 2012.

[110] W.-Y. Son, J.-T. Chung, B. Herrero et al., "Selection of the optimal day for oocyte retrieval based on the diameter of the dominant follicle in hCG-primed in vitro maturation cycles," *Human Reproduction*, vol. 23, no. 12, pp. 2680–2685, 2008.

[111] H. Gjönnaess, "Polycystic ovarian syndrome treated by ovarian electrocautery through the laparoscope," *Fertility and Sterility*, vol. 41, no. 1, pp. 20–25, 1984.

[112] H. Gjønnaess, "Ovarian electrocautery in the treatment of women with polycystic ovary syndrome (PCOS). Factors affecting the results," *Acta obstetricia et gynecologica Scandinavica*, vol. 73, no. 5, pp. 407–412, 1994.

[113] R. Flyckt and J. Goldberg, "Laparoscopic ovarian drilling for clomiphene-resistant polycystic ovary syndrome," *Seminars in Reproductive Medicine*, vol. 29, no. 02, pp. 138–146, 2011.

[114] S. A. K. S. Amer, Z. Banu, T. C. Li, and I. D. Cooke, "Long-term follow-up of patients with polycystic ovary syndrome after laparoscopic ovarian drilling: endocrine and ultrasonographic outcomes," *Human Reproduction*, vol. 17, no. 11, pp. 2851–2857, 2002.

[115] M. J. Nahuis, N. Kose, N. Bayram et al., "Long-term outcomes in women with polycystic ovary syndrome initially randomized to receive laparoscopic electrocautery of the ovaries or ovulation induction with gonadotrophins," *Human Reproduction*, vol. 26, no. 7, pp. 1899–1904, 2011.

[116] K. A. Cocksedge, T.-C. Li, S. H. Saravelos, and M. Metwally, "A reappraisal of the role of polycystic ovary syndrome in recurrent miscarriage," *Reproductive BioMedicine Online*, vol. 17, no. 1, pp. 151–160, 2008.

[117] C. M. Farquhar, K. Williamson, and P. M. Brown, "An economic evaluation of laparoscopic ovarian diathermy versus gonadotrophin therapy for women with clomiphene citrate resistant polycystic ovary syndrome," *Human Reproduction*, vol. 19, no. 5, pp. 1110–1115, 2004.

[118] M. J. Nahuis, E. Oude Lohuis, N. Kose et al., "Long-term follow-up of laparoscopic electrocautery of the ovaries versus ovulation induction with recombinant FSH in clomiphene citrate-resistant women with polycystic ovary syndrome: an economic evaluation," *Human Reproduction*, vol. 27, no. 12, pp. 3577–3582, 2012.

[119] J. J. Schlesselman, "Risk of endometrial cancer in relation to use of combined oral contraceptives. A practitioner's guide to meta-analysis," *Human Reproduction*, vol. 12, no. 9, pp. 1851–1863, 1997.

[120] M. Vessey and R. Painter, "Oral contraceptive use and cancer. Findings in a large cohort study, 1968-2004," *British Journal of Cancer*, vol. 95, no. 3, pp. 385–389, 2006.

[121] P. C. Hannaford, S. Selvaraj, A. M. Elliott, V. Angus, L. Iversen, and A. J. Lee, "Cancer risk among users of oral contraceptives: cohort data from the Royal College of General Practitioner's oral contraception study," *BMJ*, vol. 335, no. 7621, pp. 651–658, 2007.

[122] A. A. Murphy, C. S. Cropp, B. S. Smith, R. T. Burkman, and H. A. Zacur, "Effect of low-dose oral contraceptive on gonadotropins, androgens, and sex hormone binding globulin in nonhirsute women∗∗Supported in part by the general research center grant PHS RR-00827 and grant NO1-HD-

32816 from the national institutes of health, bethesda, Maryland. ††Presented at the thirty-fifth annual meeting of the society of gynecologic investigations, march 18 to 20, 1988, baltimore, Maryland," *Fertility and Sterility*, vol. 53, no. 1, pp. 35–39, 1990.

[123] R. Azziz and F. Gay, "The treatment of hyperandrogenism with oral contraceptives," *Seminars in Reproductive Medicine*, vol. 7, no. 03, pp. 246–254, 1989.

[124] R. Azziz, "The evaluation and management of hirsutism∗1," *Obstetrics & Gynecology*, vol. 101, no. 5, pp. 995–1007, 2003.

[125] J. C. Crave, S. Fimbel, H. Lejeune, N. Cugnardey, H. Déchaud, and M. Pugeat, "Effects of diet and metformin administration on sex hormone-binding globulin, androgens, and insulin in hirsute and obese women," *Journal of Clinical Endocrinology & Metabolism*, vol. 80, no. 7, pp. 2057–2062, 1995.

[126] P. G. Crosignani, M. Colombo, and W. Vegetti, "Overweight and obese anovulatory patients with polycystic ovaries: parallel improvements in anthropometric indices, ovarian physiology and fertility rate induced by diet," *Human Reproduction*, vol. 18, no. 9, pp. 1928–1932, 2003.

[127] A. M. Clark, W. Ledger, C. Galletly et al., "Weight loss results in significant improvement in pregnancy and ovulation rates in anovulatory obese women," *Human Reproduction*, vol. 10, no. 10, pp. 2705–2712, 1995.

[128] S. Z. Yanovski and J. A. Yanovski, "Obesity," *New England Journal of Medicine*, vol. 346, no. 8, pp. 591–602, 2002.

Hindawi
Journal of Healthcare Engineering
Volume 2022, Article ID 3795060, 11 pages
https://doi.org/10.1155/2022/3795060

Research Article

lncRNA H19 Promotes Ox-LDL-Induced Dysfunction of Human Aortic Endothelial Cells through the miR-152/VEGFA Axis

Feng Tang,[1] Siqi Zhang,[2] Honghao Wang,[1] Shijia Xu,[1] Sen Yang,[1] Xiaohan Zhu,[1] Huan Zeng,[1] and Yongyao Yang[3]

[1]*Department of Cardiology, The Second People's Hospital of Guiyang, Guiyang 550023, China*
[2]*College of Life Science, Zhejiang University, Hangzhou 310058, China*
[3]*Department of Cardiology, Guizhou Provincial People's Hospital, Guiyang 550023, China*

Correspondence should be addressed to Yongyao Yang; yangyy18@outlook.com

Received 20 December 2021; Revised 23 February 2022; Accepted 25 February 2022; Published 19 March 2022

Academic Editor: Enas Abdulhay

Objective. lncRNA H19 (H19) elevation is related to the risk of coronary artery disease. DIANA-lncBase database analysis suggested that microRNA-152 (miR-152) and H19 have binding sites. Here, the effect and mechanism of H19 and miR-152 in the oxidized low-density lipoprotein (ox-LDL)-induced human aortic endothelial cells (HAECs) were explored. *Methods*. The expression of H19, miR-152, and vascular endothelial growth factor (VEGF)-A in the HAECs treated with 5 μg/mL ox-LDL was detected by qRT-PCR. MTT, wound-healing assay, and tube formation assay were analyzed to evaluate the angiogenic activity of H19 and miR-152 in the HAECs cells knocked down H19. Dual-luciferase assay was performed to verify the targeting relationship of miR-152 to either H19 or VEGFA, respectively. Western blot was used to detect the expression of epithelial-mesenchymal transition (EMT)-related proteins (E-cadherin and vimentin) and VEGFA protein in the cells. *Results*. After ox-LDL treatment, the expression of H19 and VEGFA was significantly increased, miR-152 expression was remarkably decreased. H19 was mainly expressed in the cytoplasm of HAECs. Knocking down H19 or overexpression of miR-152 significantly inhibited the cellular proliferation, migration, tube formation, and EMT trend of the HAECs. On the contrary, miR-152 interference reversed H19 silencing-mediated effects in the ox-LDL-induced HAECs. The dual-luciferase assay showed that miR-152 had a targeting relationship with H19 and VEGFA. MiR-152 was negatively corrected with the VEGFA expression. *Conclusion*. Ox-LDL negatively regulates miR-152 via H19, promotes the expression of VEGFA, and induces the dysfunction of HAECs.

1. Introduction

Cardiovascular diseases (CVDs) are characterized by high morbidity and mortality, which seriously threaten global adults and constitute a major socioeconomic burden on global economic growth [1]. Atherosclerosis is the major underlying cause of CVDs. Atherosclerosis is a widespread chronic inflammatory disease of the arterial wall, which usually leads to disability or even death [2]. Previous studies have shown that the main mechanism of atherosclerosis is lipid accumulation and chronic inflammation in the arterial wall, while atherosclerosis is usually associated with altered lipid metabolism and hypercholesterolemia [3]. Oxidized low-density lipoprotein (ox-LDL) is a known risk factor for CVDs, which expresses the heterogeneous oxidative changes of the lipid portion of LDL and apolipoprotein B (ApoB) [4]. Studies have pointed out that plasma levels of ox-LDL in patients with atherosclerotic CVDs are elevated. Moreover, clinically, the level of the ox-LDL or anti-ox-LDL antibody is selected as a biomarker for predicting cardiovascular events [5]. Overproduction of ox-LDL leads to abnormal proliferation, apoptosis, migration, angiogenesis, and inflammatory responses, all of which are responsible for endothelial cell dysregulation [6]. It is suggested that ox-LDL can be used as a new therapeutic target for the treatment of atherosclerosis and cardiovascular diseases.

Epithelial-mesenchymal transition (EMT) plays a crucial role in progress and destabilizing atherosclerotic plaques via infiltration of fibroblasts and upregulation of matrix metalloproteinase [7, 8]. Downregulation of E-cadherin is a hallmark of EMT [9]. Abnormality of E-cadherin in foam cells during the process of atherosclerosis suggests that lipid accumulation may relate to the reorganization of cellular interactions in atherogenesis [10]. In the EMT process, vimentin maintains intracellular homeostasis via regulation of cytoskeleton architecture and cellular force generation [11]. Gong et al. [12] recently showed that vimentin promotes atherogenesis in $ApoE^{-/-}$ mice. These data indicate that both E-cadherin and vimentin are important factors of EMT and have pathological activities in atherosclerosis.

lncRNA is a type of long-chain non-coding RNA larger than 200 nt. Early studies have confirmed that lncRNA can be used as a signal molecule to participate in cellular growth and development, as well as the occurrence and development of diseases [13]. Some studies have pointed out that lncRNA is an important information transmission mediator between cells and tissues, which can transmit information efficiently and accurately [14]. Studies have shown that lncRNA can promote tumor growth and metastasis. lncRNA MALAT1 can promote tumorigenesis through the Wnt/β-catenin pathway, EMT, phosphatidylinositol kinase (PI3K)/protein kinase B (AKT) pathway, extracellular regulatory protein kinase (ERK)/mitogen-activated protein kinase (MAPK) pathway, and angiogenesis [15]. lncRNA PCGEM1 is a specific lncRNA for prostate cancer, which can promote cell proliferation and reduce apoptosis induced by anticancer drugs [16]. A number of research have shown that the expression of lncRNA H19 (H19) in cancer cell lines and samples of patients with cancer is significantly upregulated [17]. After knocking down the H19, the viability, invasion, and migration ability of cancer cell lines were significantly reduced [18]. It shows that H19 has a great relationship with the biological activity of cells. Some studies reveal that increase of H19 is related to the risk of coronary artery disease [19]. Further, other scholars found that H19 is involved in the process of atherosclerosis. Sun et al. reported that knocking down the H19 can prevent atherosclerosis deterioration by increasing p53-mediated apoptosis in vascular smooth muscle cells [20]. Zhang et al. [21] revealed that knocking down H19 could regulate the proliferation and apoptosis of vascular smooth muscle cells induced by ox-LDL through the miR-148b/Wnt/β-catenin pathway. Thus, H19 is closely related to the formation of atherosclerosis and is an important mediator of the ox-LDL damaged vascular cells. At the same time, studies have found that H19 regulates the apoptosis of vascular endothelial cells in occlusive arteriosclerosis through the NF-κB pathway [22]. However, no research has revealed the role of H19 in the process of ox-LDL inducing vascular endothelial cells. Therefore, in order to explore the effect of H19 on atherosclerosis, this study aims to elucidate the pathological mechanism of ox-LDL-induced vascular endothelial cell lesions *in vitro*, which would provide new therapeutic targets for atherosclerosis.

2. Materials and Methods

2.1. Cell Culture and Grouping. Human aortic endothelial cells (HAECs) were purchased from the American Type Culture Collection (ATCC; Manassas, VA, USA). The cells were cultured in complete Dulbecco's modified Eagle's medium (DMEM) (Gibco, Waltham, MA, USA) containing 10% fetal bovine serum (FBS) (Gibco), 100 mg/mL penicillin, and 100 mg/mL streptomycin (Gibco) at 37°C and 5% CO_2 in an incubator (ThermoFisher Scientific, Waltham, MA, USA). Wild-type HAECs were used as negative controls (Control group). HAECs treated with 5 μg/mL of ox-LDL [23] (Feather biology, Shanghai, China) for 24 h were used as the ox-LDL group. H19 siRNA (si-H19) and siRNA scramble (si-NC), miR-152 inhibitor and NC inhibitor, miR-152 mimics and mimics NC, vascular endothelial growth factor (VEGF)-A overexpression plasmids (VEGFA) were all designed and synthesized by Guangzhou Ruibo Biotech (Guangdong, China) and transfected with Lipofectamine 3000 (ThermoFisher) by following the manufacture instructions in the ox-LDL-treated HAECs.

2.2. Quantitative Real-Time Polymerase Chain Reaction (qRT-PCR). The nucleus and cytoplasm of HAECs were isolated by a Subcellular Protein Fractionation Kit for Cultured Cells (ThermoFisher). Total RNA of the cells in each treatment group was extracted by TRIzol reagent (ThermoFisher) according to the instruction. The extracted RNA was detected by a NanoDrop microspectrophotometer (ThermoFisher), and cDNA was prepared according to the High-Capacity cDNA Reverse Transcription Kits (ThermoFisher). QRT-PCR analysis was performed according to the instructions of the SYBR GREEN kit (TaKaRa, Tokyo, Japan) to detect the expression levels of H19, miR-152, VEGFA mRNA, and other genes. Glyceraldehyde-3-phosphate dehydrogenase (GAPDH) was used as an internal reference control. Each experiment was set with 6 replicates. The experimental data obtained by qRT-PCR were calculated using the $2^{-\Delta\Delta Ct}$ method to calculate the relative expression of the target gene. The primer sequence is shown in Table 1.

2.3. Detection of Cellular Growth by Thiazolyl Blue (MTT) Staining. After treatment, each group of cells in the logarithmic growth phase was seeded in a 96-well plate at a density of 5000 cells/well, cultured in complete DMEM for 24, 48, and 72 h. 20 μL of 5 mg/mL MTT (Sigma-Aldrich, St. Louis, MO, USA) solution was added into each well of the cells and incubated in a 37°C incubator for 4 h. Following this, the supernatant was discarded, 150 μL of DMSO was added, and shaken for 15 minutes. The absorbance value of each well was measured with a wavelength of 570 nm in a microplate reader.

2.4. Wound-Healing Assay. Cells from each group were seeded into a 6-well plate, cultured to confluence. A 10 μL sterile pipette tip was used to scratch the diameter vertical to the horizontal plane of a single well. Cell debris and detached cells were removed by washing with PBS. Fresh serum-free medium was added, cultured for 24 h, and photographs were taken with an inverted microscope to record the experimental results. ImageJ software was used to calculate the

Table 1: qRT-PCR primers.

Target gene/RNA	Sequences (5′ to 3′)
lncRNA H19	F : ATCGGTGCCTCAGCGTTCGG R : CTGTCCTCGCCGTCACACCG
miR-152	F : CAGTGCATGACAGAACTTG R : GAACATGTCTGCGTATCTC
VEGFA	F : TTGCCTTGCTGCTCTACCTCCA R : GATGGCAGTAGCTGCGCTGATA
U6	F : ACCCGTTGAACCCCATTCGTGA R : GCCTCACTAAACCATCCAATCGG
GAPDH	F : CATCACTGCCACCCAGAAGACTG R : ATGCCAGTGAGCTTCCCGTTCAG

cellular migrated area on the scratched space. Each assay was repeated thrice.

2.5. Tube Formation Assay. 100 μL of Matrigel (HD Biosciences, San Diego, CA, USA) was added to each well of a 24-well plate and incubated at 37°C for 30 min. Cells treated with different conditions were resuspended in FBS-free DMEM and seeded at a concentration of 1×10^5 cells/well. After 6 h, the formation of capillary structures was counted under a light microscope, and scanning and quantification were performed. Each assay was repeated thrice.

2.6. Double-Luciferase Reporter Gene Assay. The sequence of H19, miR-152, and VEGFA binding site and their mutant sequences were inserted into the downstream of the firefly luciferase gene to construct an expression vector (Promega, Madison, Wisconsin, USA). MiR-152 mimics/mimics NC and mammalian cell miRNA reporter plasmid pmirGLO (Qincheng Biotechnology, Shanghai, China)-H19-WT/MUT recombinant plasmid, miR-152 mimics/mimics NC and pmirGLO-VEGFA-WT/MUT, and recombinant plasmid and Lipo2000 liposomes were mixed, respectively, and transfected into 293T cells (ATCC). After transfection 48 h, luciferase activity was detected according to the instructions of the Dual Luciferase Reporter Gene Assay kit (Promega).

2.7. Western Blot. Detecting cells were lysed by an RIPA reagent (Beyotime Biotechnology, Shanghai, China) to extract total protein. The protein concentration of the lysates was detected with a BCA kit (Abcam, Cambridge, British). Each 20 μg of the lysate protein was mixed with 4 x Protein Loading Buffer and boiled for denaturation, separated by SDS-PAGE, and was transferred on PVDF membranes. 5% skimmed milk was used to block the nonspecific proteins for 1 h. The primary antibody was reacted with the membrane overnight at 4°C. After washing, the membrane reacted with the secondary antibody for 1 h at room temperature. After washing, a chemiluminescence reagent (Haoxin-Biotech, Hanzhou, China) was applied to visualize the probed protein. The image was analyzed in an imaging system. Densitometry of the target protein bands was evaluated using ImageJ software, and the relative protein expression was calculated using β-actin as an internal reference.

2.8. Statistical Analysis. The tested results were analyzed by one-way ANOVA and independent samples *t-test* analysis with SPSS 26.0 (IBM-SPSS, Chicago, IL, USA). Results were expressed as mean ± standard deviation (SD). The correlation between miR-152 and H19/VEGFA was analyzed by the Pearson correlation analysis. $P < 0.05$ was used as the criterion for judging the significance of the difference.

3. Results

3.1. Ox-LDL Induced Upregulation of H19 Expression and Downregulation of miR-152 Expression in HAECs. DIANA-lncBase database (https://diana.e-ce.uth.gr/lncbasev3/interactions) predicted that miR-152 and H19 have binding sites (Figure 1(a)). QRT-PCR was performed to evaluate the H19 and miR-152 levels in the ox-LDL-treated HAECs. The results showed that compared with the control group, the expression of H19 in the ox-LDL group was significantly increased, but the expression of miR-152 was remarkably decreased (Figures 1(b) and 1(c), $P < 0.05$). This result indicates that H19 and miR-152 may involve the pathogenesis of the ox-LDL-induced atherosclerosis.

3.2. H19 Inhibited Cell Proliferation, Tube Formation, and Migration of the Ox-LDL-Induced HAECs. To further investigate the biological functions of H19 in the ox-LDL treated HAECs. We prepared H19 knockdown HAECs by H19 siRNA transfection. QRT-PCR analysis (Figure 2(a)) showed that compared with the siRNA scramble (si-NC) group, the expression of H19 in the H19 siRNA transfected (si-H19 group) HAECs were significantly downregulated. Further, compared with the siNC group, H19 knockdown significantly reduced cellular proliferation rate (Figure 2(b)), tube formation (Figure 2(c)), and cellular migration (Figure 2(d)) of the ox-LDL treated HAECs. E-cadherin and vimentin are reported to participate in the pathogenesis of atherosclerosis. Western blot detection indicated (Figure 2(e)) that compared with the siNC group, the E-cadherin protein expression in the si-H19 group cells was significantly increased, while vimentin expression was significantly reduced, indicating that knocking down H19 would reduce the epithelial-mesenchymal transformation (EMT) trend of the ox-LDL treated HAECs.

3.3. Expression of H19 Was Negatively Correlated to miR-152 in the Ox-LDL-HAECs. In order to study the molecular mechanism of H19, we determined whether H19 was expressed in the cytoplasm or the nucleus by qRT-PCR. The result showed that H19 was mainly expressed in the cytoplasm in the ox-LDL-HAECs (Figure 3(a)). Dual-luciferase experiment indicated that co-transfection of miR-152 mimics significantly inhibited the luciferase activity of the H19 vector (lncRNA H19-WT) but did not inhibit the luciferase activity of the lncRNA H19-MUT vector. Thus, the targeting relationship between H19 and miR-152 was confirmed (Figure 3(b)). In addition, compared with the siNC group, H19 knockdown significantly upregulated the expression of miR-152 (Figure 3(c)). The expression of H19

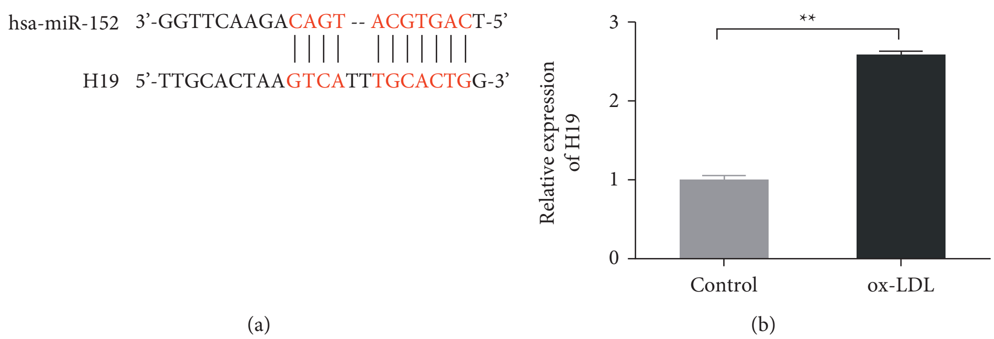

Figure 1: Ox-LDL induced upregulation of H19 expression and downregulation of miR-152 expression in ox-LDL-treated HAECs. A. Potential binding sites between miR-152 and lncRNA H19 (H19) were analyzed by DIANA-lncBase database. B. Expression of H19 was detected by qRT-PCR in the wild type HAECs (Control) and ox-LDL-treated HAECs. C. The expression of miR-152 was analyzed in the control and ox-LDL groups in HAECs. Each data were obtained from three different independent test results. $^{**}P < 0.01$.

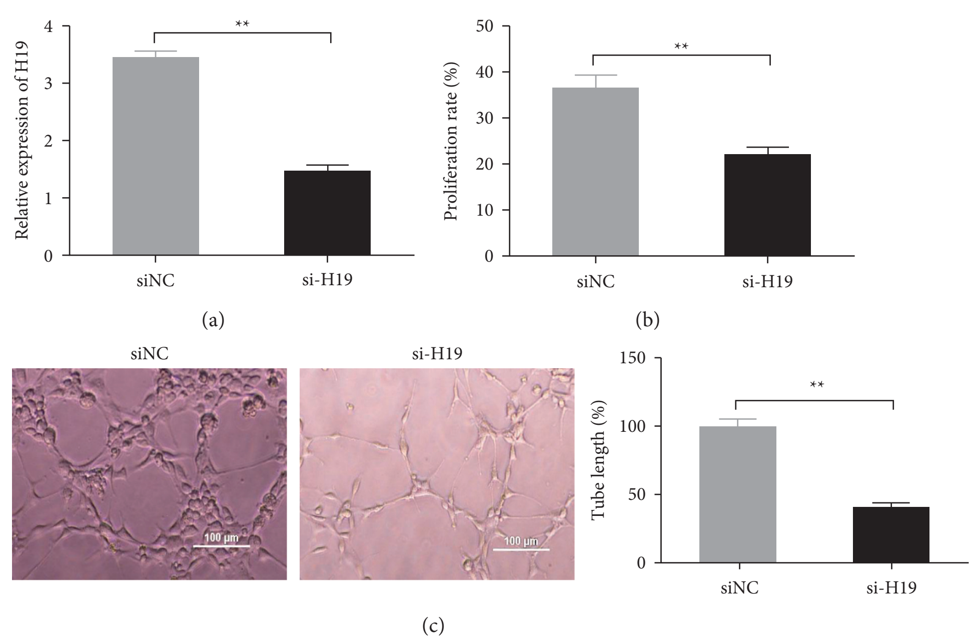

Figure 2: Continued.

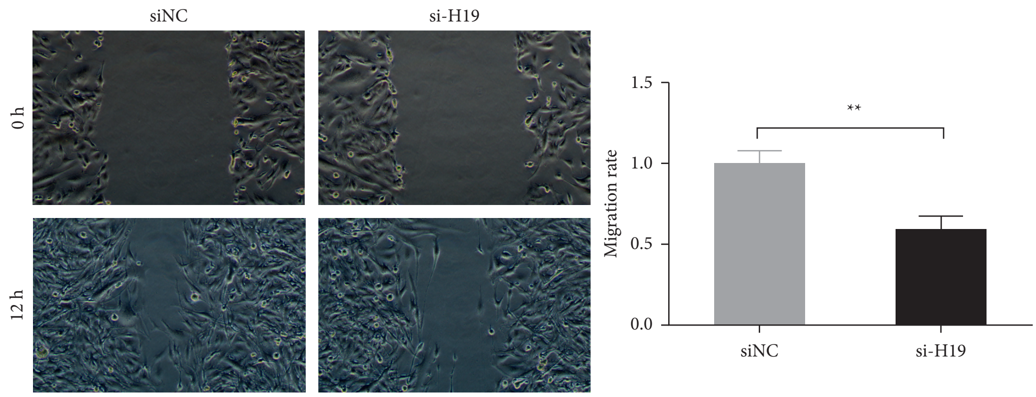

(d)

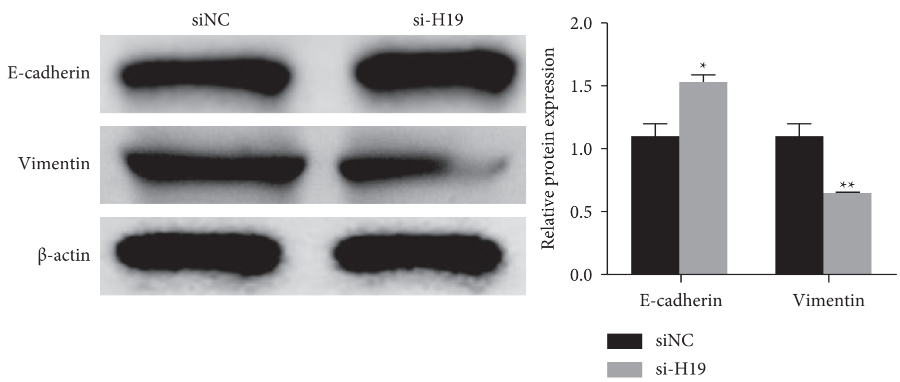

(e)

Figure 2: Knockdown of H19 inhibited the ox-LDL-induced proangiogenic activities of HAECs. (a). Efficiency of the si-lncRNA H19 (si-H19) was evaluated by qRT-PCR in the ox-LDL-HAECs. (b). Cellular proliferation was detected by MTT in the indicated cells. (c) Tube formation was performed to detect the angiogenesis ability in the indicated cells. (d) Cellular migration was evaluated by Wound-healing assay in the indicated cells. (e) Protein expression of E-cadherin and vimentin was analyzed by Western blot. $^{*}P < 0.05$ and $^{**}P < 0.01$ *vs.* siNC group.

was negatively correlated to the miR-152 in the ox-LDL-HAECs (Figure 3(d)).

3.4. Knockdown of miR-152 Attenuated the si-H19 Induced Antiangiogenic Activities in the Ox-LDL-HAECs. Compared with the siNC + NC inhibitor group, the proangiogenic activity (including cellular proliferation rate, migration ability, tube formation ability, and EMT trend) of the si-H19 + NC inhibitor group cells was significantly reduced. On the contrary, the cellular proliferation rate, migration ability, tube formation ability, and EMT trend of the ox-LDL-HAECs increased significantly after interference with miR-152. Interestingly, miR-152 inhibitor transfection attenuated the antiangiogenic activity induced by si-H19 in the ox-LDL-HAECs (Figures 4(a)–4(d)).

3.5. VEGFA Is the Target Gene of miR-152, Which Is Regulated by H19 via miR-152. TargetScan database (http://www.targetscan.org/vert_72/) was applied to predict the target genes of miR-152. The prediction results show that there is a binding site between VEGFA and miR-152 (Figure 5(a)). Dual-luciferase assay was then applied to verify this prediction, which showed that miR-152 mimics significantly inhibited the luciferase activity of the VEGFA-WT carrier but did not inhibit the luciferase activity of the VEGFA-mutation (VEGFA-MUT) carrier (Figure 5(a)). These results confirmed the targeting relationship between miR-152 and VEGFA. To further verify this relationship, qRT-PCR and Western blot were performed and showed that compared with the NC mimics group, miR-152 mimics transfection significantly inhibited the expression of VEGFA mRNA and protein in the ox-LDL-HAECs (Figures 5(b)–5(c)). Correlation analysis revealed that miR-152 was negatively correlated with VEGFA (Figure 5(d)). In addition, compared with the siNC group, the expression of VEGFA in the ox-LDL-HAECs was significantly reduced after interference with si-H19, and the expression of H19 and VEGFA was positively correlated (Figures 5(e)–5(f)). At the same time, after interfering with the miR-152, the expression of VEGFA in the cells increased significantly. However, compared with the si-H19NC inhibitor group, miR-152 inhibitor can reverse the expression of VEGFA (Figures 5(g) and 5(h)).

3.6. Antiangiogenic Activity of miR-152 Inhibits via Downregulating VEGFA in the Ox-LDL-HAECs. The angiogenic assay was further applied to determine whether miR-152

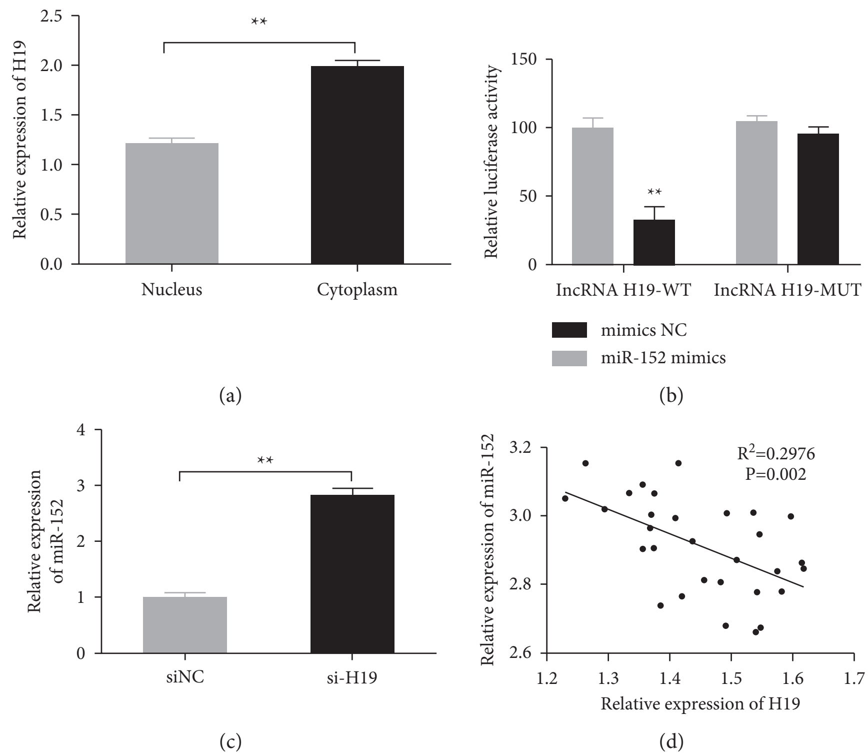

Figure 3: Expression of H19 was negatively correlated to the miR-152 in the ox-LDL-HAECs. (a) qRT-PCR detected the expression of H19 in the isolated cytoplasm and nucleus of the ox-LDL-HAECs. $^{**}P < 0.01$. (b) Binding relationship of the H19 and miR-152 were analyzed by Dual-luciferase assays. $^{**}P < 0.01$ *vs* mimics NC group. (c) qRT-PCR was used to detect the expression of miR-152 in the siNC group and si-H19 group in the ox-LDL-HAECs, $^{**}P < 0.01$. (d) Correlation between the expression of H19 and miR-152 was analysis by Pearson analyzes.

could regulate HAECs by targeting VEGFA. Compared with the NC mimics + vector group, the proliferation rate (Figure 6(a)), migration ability (Figure 6(b)), tube formation ability (Figure 6(c)), and EMT trend (Figure 6(d)) of the ox-LDL-HAECs were significantly reduced after miR-152 mimic transfection. While these activities and EMT trend were significantly higher in the VEGFA overexpressed ox-LDL-HAECs. At the same time, overexpression of VEGFA can reverse the effect of miR-152 upregulation on the angiogenic activity of the ox-LDL-HACEs.

4. Discussion

Atherosclerosis is a chronic multifactorial vascular disease and the root cause of cardiovascular disease. It is characterized by lipid accumulation and the formation of fatty plaques in blood vessels [24]. Despite advances in treatment, the morbidity and mortality of atherosclerosis are still at a high level. Therefore, there is an urgent need to reveal detailed mechanism of atherosclerosis and find effective treatment targets and methods for atherosclerosis.

Studies have shown that ox-LDL has a bidirectional effect on angiogenesis [25]. Low concentrations of ox-LDL (less than 5 μg/ml) stimulate VEGF expression, endothelial cell migration, and neocapillary formation [25, 26]. Therefore, in this study, 5 μg/ml was used to induce HAECs into an atherosclerosis cell model. Previous studies have shown that expression of H19 is upregulated in cardiovascular diseases, including vascular smooth muscle cells [27]. This study also found that H19 was significantly upregulated in HAECs induced by 5 μg/ml ox-LDL. Moreover, after knocking down the expression of H19, the proliferation, migration, and tube formation of ox-LDL-induced HAECs were significantly inhibited, which is similar to the role of the H19 in many cancer cells. For example, Zhao et al. found that knocking down H19 can significantly inhibit the proliferation and metastasis ability of lung cancer cell lines [28]. It is suggested that H19 has the potential to be a biomarker for diagnosing changes in the state of vascular endothelial cells, and H19 is related to the biological functions of cells.

According to previous research reports, lncRNA exhibits its activities in a variety of ways. It can participate in the regulation of protein before and after transcription to directly control the protein activity. It mainly includes direct binding to target protein to affect its function, or binding to miRNA or circRNA to participate in signal transduction and other ways [29]. Among them, miRNA is a type of short noncoding RNA with a length of about 22 nt [30]. Due to the high efficiency and specificity of miRNA, it is often used as a biomarker of disease [31]. Many studies have found that the expression of miR-152 is often downregulated in different solid tumors [32], suggesting that miR-152 can inhibit the biological activity of cancer, acting as a tumor suppressor.

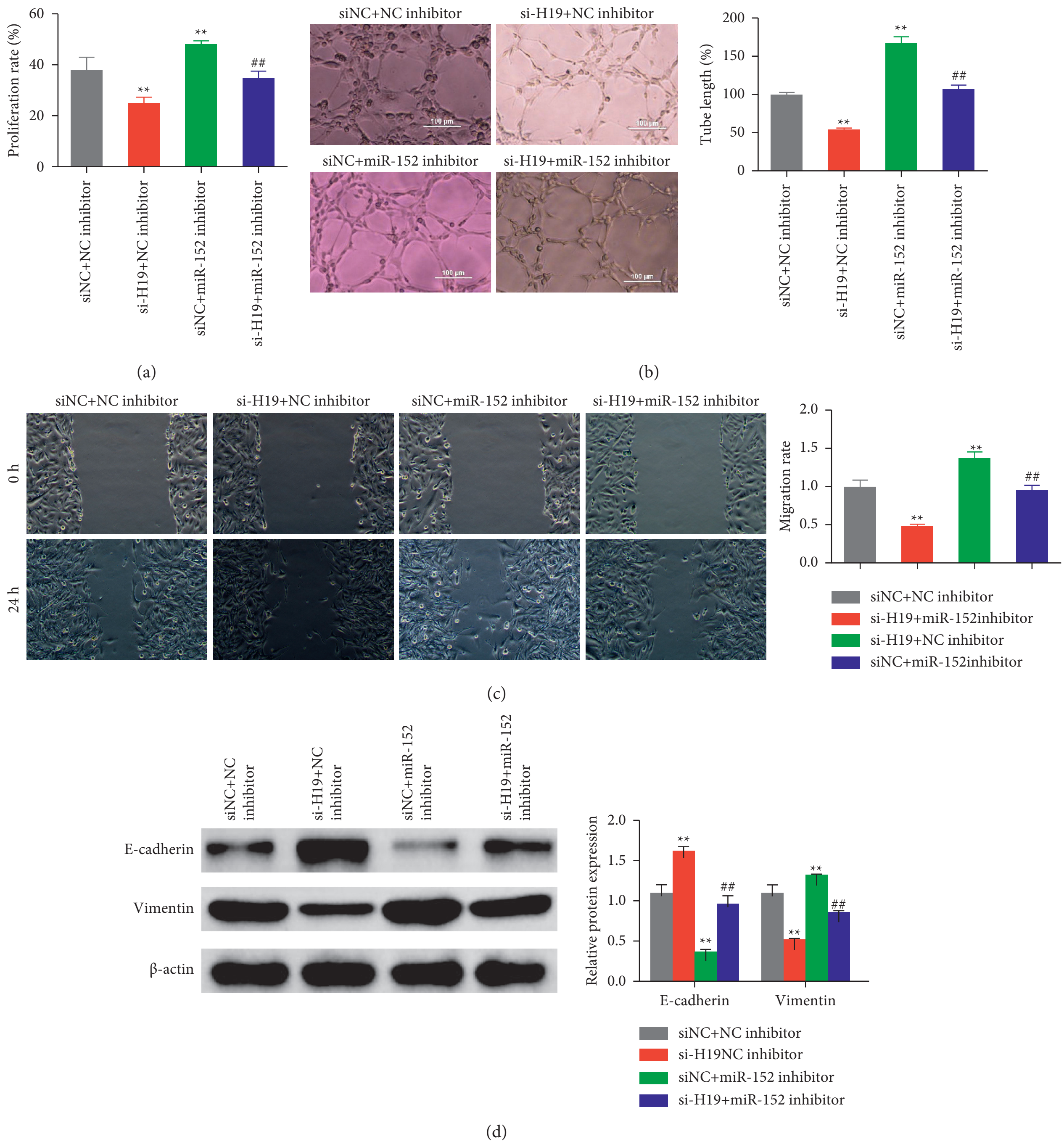

Figure 4: Low expression of miR-152 attenuated the si-H19-induced antiangiogenic activity in the ox-LDL-HAECs. Cellular proliferation, tube formation, migration, and protein expression of E-cadherin and vimentin were analyzed by MTT (a), Matrigel tuber formation (b), Wound-healing assay (c), and Western blot (d) in the ox-LDL-HAECs. $^{**}P < 0.01$ *vs* siNC + NC inhibitor group; ## $P < 0.01$ *vs* si-H19 + NC inhibitor group.

There have been some reports on the pathological regulation of the H19/miR-152 axis, which mostly involves cell proliferation, invasion, angiogenesis, and apoptosis. Li et al. [33] showed that in the study of diabetic foot ulcer repair, H19 inhibited the apoptosis and inflammation of fibroblasts by reducing the activity of miR-152-3p-mediated tensin protein homolog activity, thereby promoting wound healing of diabetic foot ulcers. In human glioma cells, the level of H19 increases, while the level of miR-152 decreases. Lowering H19 or increasing miR-152 can inhibit the proliferation and invasion of glioma cells to inhibit the growth of glioma cells [34]. The results of this study found that the expression of miR-152 was significantly downregulated in cardiovascular ox-LDL–treated HAECs. Dual-luciferase assay showed that H19 could bind miR-152. Knocking down H19 significantly upregulated miR-152 expression accompanied with

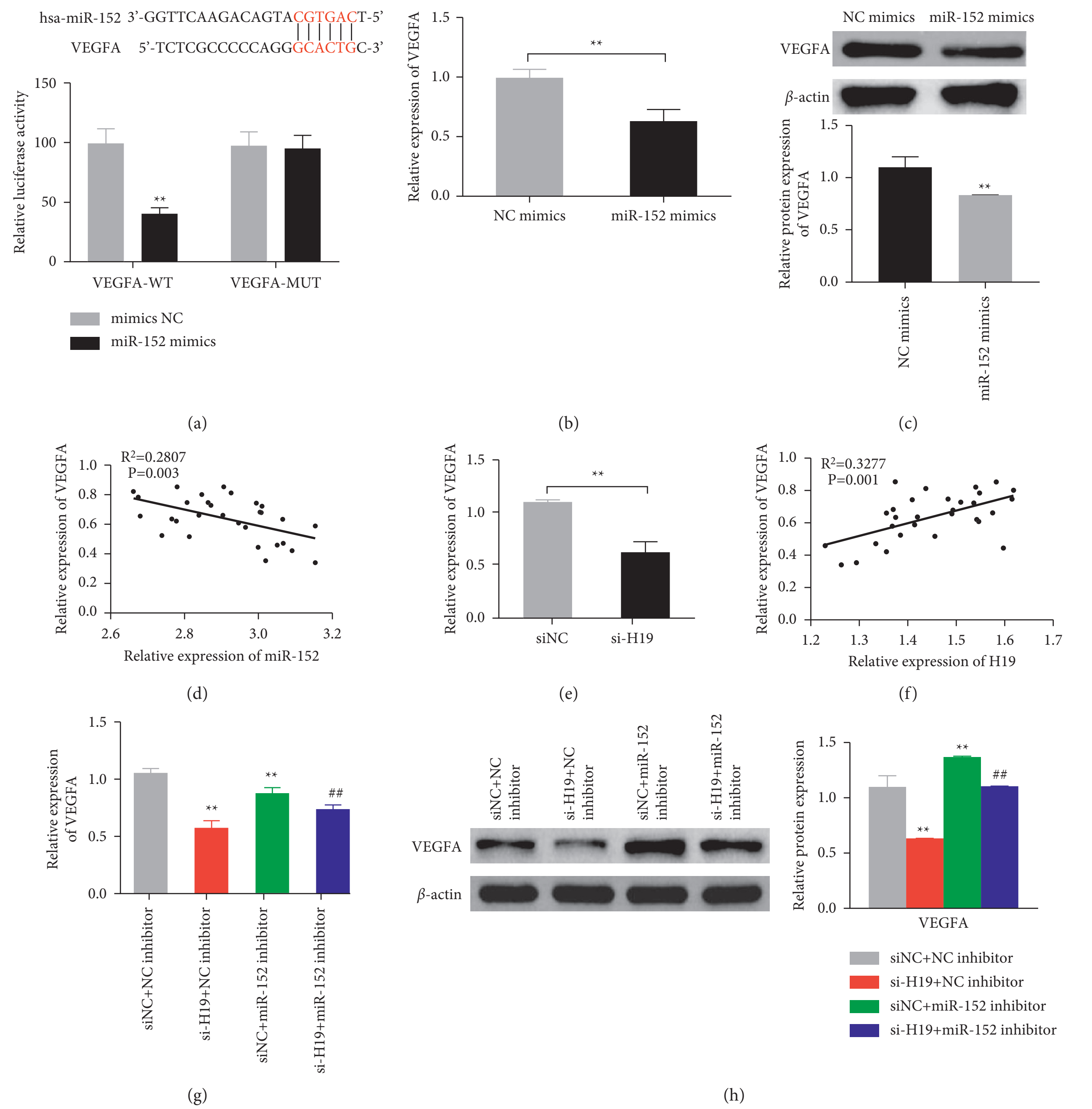

Figure 5: VEGFA is the target gene of miR-152, through which H19 can regulate the VEGFA expression. (a) Binding site between the miR-152 and VEGFA was predicated by TargetScan database analysis (up panel). Dual-luciferase analysis of miR-152 to VEGFA. $^{**}P < 0.01$ *vs* mimics NC. B–C. The expression of VEGFA mRNA and protein were analyzed by qRT-PCR (b) and Western blot (c) in the miR-152 mimics or mimics NC transfected ox-LDL-HAECs; $^{**}P < 0.01$. (d) Pearson analysis of the correlation between miR-152 and VEGFA expression. (e) VEGFA gene expression was detected by qRT-PCR in the si-H19 transfected ox-LDL-HAECs, $^{**}P < 0.01$. (f) Correlation of the expression of H19 and VEGFA was analyzed by Pearson analysis. **G-H**. VEGFA mRNA and protein expression were detected by qRT-PCR (g) and Western blot (h) in the indicated groups of the ox-LDL-HAECs. $^{**}P < 0.01$ *vs* siNC + NC inhibitor group, ## $P < 0.01$ *vs* si-H19 + NC inhibitor group.

antiangiogenic activity. Li et al. [35] showed that H19 can upregulate the expression of DNMT1 through sponge miR-152, thereby promoting the proliferation and invasion of breast cancer, suggesting that miR-152 is a key mediator for H19 to exert its biological functions. These data show that H19 has a negative regulatory effect on miR152. H19 is involved in the regulation of cell proliferation (vascular endothelial or tumor) through the negative regulation of miR152 to involve angiogenesis or tumor pathogenesis.

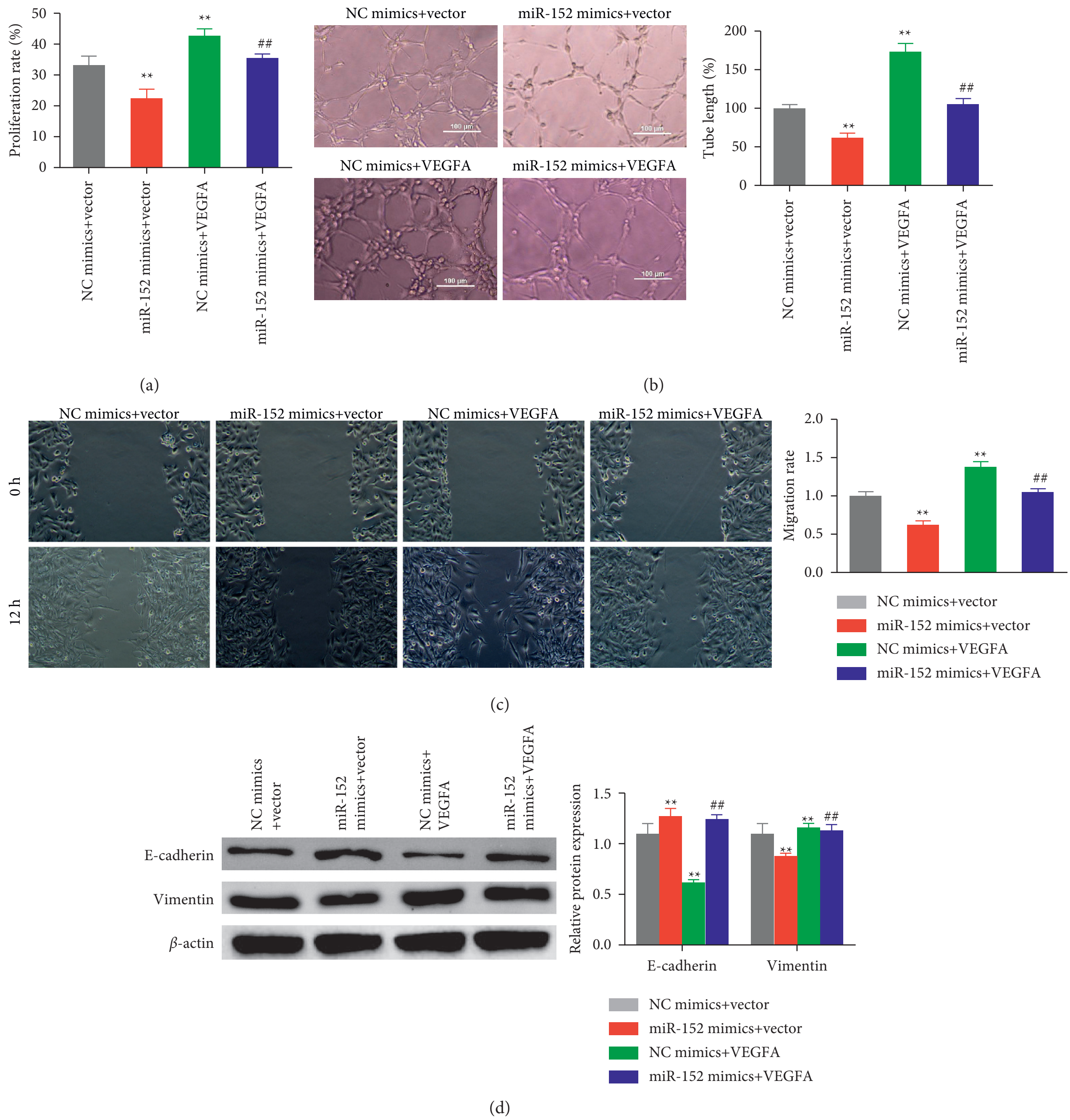

FIGURE 6: Antiangiogenic activity of miR-152 by downregulating VEGFA in the ox-LDL-HAECs. Cellular proliferation (a), tube formation (b), wound-healing assay (c) were detected in the indicated groups. (d) E-cadherin and Vimentin protein levels were analyzed by Western blot. $^{**}P < 0.01$ *vs.* NC mimics + vector group, ## $P < 0.01$ *vs.* miR-152 mimics + vector group.

According to previous research reports, miRNA can bind to the 3′-UTR of a specific mRNA through its seed sequence to inhibit the translation of the mRNA and participate in the regulation of cell life activities [36]. This study also showed that miR-152 has a target relationship with VEGFA that is an important signal molecule leading to atherosclerosis. Balance of VEGFA is crucial to maintaining the physiological vascular homeostasis of cells and tissues [37]. High expression of VEGFA is the direct cause activating vascular endothelial cells. Haque et al. found that overexpression of miR-152 can significantly inhibit the expression of VEGF and TGFβ1 in retinal endothelial cells [38]. Fu et al. [39] reported that overexpression of miR-152 can inhibit high glucose-induced angiogenesis in human retinal endothelium cells and retinal microvascular endothelial cell lines by targeting inhibition of VEGF signaling. All the data suggest that VEGF signal is the main target of miR-152 to inhibit angiogenesis.

5. Conclusion

In conclusion, H19 promotes cellular proliferation, migration, and angiogenesis through the miR-152/VEGFA axis in the ox-LDL-induced HAECs. These findings also suggested that H19 could be a target to regulate the biological activity of vascular endothelial cells. However, in order to reveal the relationship between ox-LDL and H19, further investigations are needed to more comprehensively elaborate the mechanism of ox-LDL causing changes in the activity of vascular endothelial cells.

Data Availability

The data used to support the findings of this study are available from the corresponding author upon request.

Conflicts of Interest

The authors declare that they have no competing interests.

Acknowledgments

This study was supported by Guizhou Science and Technology Plan Project Guizhou Ke-roots-ZK [2012] General 355.

References

[1] P. Joseph, D. Leong, M. McKee et al., "Reducing the global burden of cardiovascular disease, Part 1," *Circulation Research*, vol. 121, no. 6, pp. 677–694, 2017.

[2] J. Board, "Joint British Societies' consensus recommendations for the prevention of cardiovascular disease (JBS3)," *Heart*, vol. 100, pp. 1–67, 2014.

[3] K. A. Campbell, M. J. Lipinski, A. C. Doran, M. D. Skaflen, V. Fuster, and C. A. McNamara, "Lymphocytes and the adventitial immune response in atherosclerosis," *Circulation Research*, vol. 110, no. 6, pp. 889–900, 2012.

[4] V. I. Summerhill, A. V. Grechko, S. F. Yet, I. A. Sobenin, and A. N. Orekhov, "The atherogenic role of circulating modified lipids in atherosclerosis," *International Journal of Molecular Sciences*, vol. 20, no. 14, p. 3561, 2019.

[5] R. A. van Dijk, F. Kolodgie, A. Ravandi et al., "Differential expression of oxidation-specific epitopes and apolipoprotein(a) in progressing and ruptured human coronary and carotid atherosclerotic lesions," *Journal of Lipid Research*, vol. 53, no. 12, pp. 2773–2790, 2012.

[6] M. Zhang, Y. Xu, and L. Jiang, "Irisin attenuates oxidized low-density lipoprotein impaired angiogenesis through AKT/mTOR/S6K1/Nrf2 pathway," *Journal of Cellular Physiology*, vol. 234, no. 10, pp. 18951–18962, 2019.

[7] M. Wesseling, T. R. Sakkers, S. C. A. de Jager, G. Pasterkamp, and M. J. Goumans, "The morphological and molecular mechanisms of epithelial/endothelial-to-mesenchymal transition and its involvement in atherosclerosis," *Vascular Pharmacology*, vol. 106, pp. 1–8, 2018.

[8] C. Souilhol, M. C. Harmsen, P. C. Evans, and G. Krenning, "Endothelial-mesenchymal transition in atherosclerosis," *Cardiovascular Research*, vol. 114, no. 4, pp. 565–577, 2018.

[9] C. Y. Loh, J. Y. Chai, T. F. Tang et al., "The E-cadherin and N-cadherin switch in epithelial-to-mesenchymal transition: signaling, therapeutic implications, and challenges," *Cells*, vol. 8, no. 10, 2019.

[10] Y. Bobryshev, R. S. Lord, T. Watanabe, and T. Ikezawa, "The cell adhesion molecule E-cadherin is widely expressed in human atherosclerotic lesions," *Cardiovascular Research*, vol. 40, no. 1, pp. 191–205, 1998.

[11] C.-Y. Liu, H.-H. Lin, M.-J. Tang, and Y.-K. Wang, "Vimentin contributes to epithelial-mesenchymal transition cancer cell mechanics by mediating cytoskeletal organization and focal adhesion maturation," *Oncotarget*, vol. 6, no. 18, pp. 15966–15983, 2015.

[12] D. H. Gong, Y. Dai, S. Chen et al., "Secretory vimentin is associated with coronary artery disease in patients and induces atherogenesis in ApoE−/− mice," *International Journal of Cardiology*, vol. 283, pp. 9–16, 2019.

[13] F. Ferrè, A. Colantoni, and M. Helmer-Citterich, "Revealing protein-lncRNA interaction," *Briefings in Bioinformatics*, vol. 17, no. 1, pp. 106–116, 2016.

[14] S. Jathar, V. Kumar, J. Srivastava, and V. Tripathi, "Technological developments in lncRNA biology," *Advances in Experimental Medicine & Biology*, vol. 1008, pp. 283–323, 2017.

[15] J. Liu, W. X. Peng, Y. Y. Mo, and D. Luo, "MALAT1-mediated tumorigenesis," *Frontiers in Bioscience*, vol. 22, pp. 66–80, 2017.

[16] G. Petrovics, W. Zhang, M. Makarem et al., "Elevated expression of PCGEM1, a prostate-specific gene with cell growth-promoting function, is associated with high-risk prostate cancer patients," *Oncogene*, vol. 23, no. 2, pp. 605–611, 2004.

[17] X. Lan, W. Sun, W. Dong et al., "Downregulation of long noncoding RNA H19 contributes to the proliferation and migration of papillary thyroid carcinoma," *Gene*, vol. 646, pp. 98–105, 2018.

[18] Z. Liao, J. Zhao, and Y. Yang, "Downregulation of lncRNA H19 inhibits the migration and invasion of melanoma cells by inactivating the NF-κB and PI3K/Akt signaling pathways," *Molecular Medicine Reports*, vol. 17, no. 5, pp. 7313–7318, 2018.

[19] V. Simion, S. Haemmig, and M. W. Feinberg, "LncRNAs in vascular biology and disease," *Vascular Pharmacology*, vol. 114, pp. 145–156, 2019.

[20] H. Sun, Q. Jiang, L. Sheng, and K. Cui, "Downregulation of lncRNA H19 alleviates atherosclerosis through inducing the apoptosis of vascular smooth muscle cells," *Molecular Medicine Reports*, vol. 22, no. 4, pp. 3095–3102, 2020.

[21] L. Zhang, H. Cheng, Y. Yue, S. Li, D. Zhang, and R. He, "H19 knockdown suppresses proliferation and induces apoptosis by regulating miR-148b/WNT/β-catenin in ox-LDL -stimulated vascular smooth muscle cells," *Journal of Biomedical Science*, vol. 25, no. 1, p. 11, 2018.

[22] Z. F. Li, X. J. Shu, Y. W. Chang, S. Y. Liu, and W. H. Wang, "Effect of lncRNA H19 on the apoptosis of vascular endothelial cells in arteriosclerosis obliterans via the NF-κB pathway," *European Review for Medical and Pharmacological Sciences*, vol. 23, no. 10, pp. 4491–4497, 2019.

[23] A. Dandapat, C. Hu, L. Sun, and J. L. Mehta, "Small concentrations of oxLDL induce capillary tube formation from endothelial cells via LOX-1-dependent redox-sensitive pathway," *Arteriosclerosis, Thrombosis, and Vascular Biology*, vol. 27, no. 11, pp. 2435–2442, 2007.

[24] F. Schaftenaar, V. Frodermann, J. Kuiper, and E. Lutgens, "Atherosclerosis," *Current Opinion in Lipidology*, vol. 27, no. 3, pp. 209–215, 2016.

[25] A. Nègre-Salvayre, N. Augé, C. Camaré, T. Bacchetti, G. Ferretti, and R. Salvayre, "Dual signaling evoked by oxidized LDLs in vascular cells," *Free Radical Biology and Medicine*, vol. 106, pp. 118–133, 2017.
[26] C. Camaré, M. Trayssac, B. Garmy-Susini et al., "Oxidized LDL-induced angiogenesis involves sphingosine 1-phosphate: prevention by anti-S1P antibody," *British Journal of Pharmacology*, vol. 172, no. 1, pp. 106–118, 2015.
[27] A. A. Thomas, S. Biswas, B. Feng, S. Chen, J. Gonder, and S. Chakrabarti, "lncRNA H19 prevents endothelial-mesenchymal transition in diabetic retinopathy," *Diabetologia*, vol. 62, no. 3, pp. 517–530, 2019.
[28] Y. Zhao, C. Feng, Y. Li, Y. Ma, and R. Cai, "LncRNA H19 promotes lung cancer proliferation and metastasis by inhibiting miR-200a function," *Molecular and Cellular Biochemistry*, vol. 460, no. 1-2, pp. 1–8, 2019.
[29] E. K. Robinson, S. Covarrubias, and S. Carpenter, "The how and why of lncRNA function: an innate immune perspective," *Biochimica et Biophysica Acta (BBA) - Gene Regulatory Mechanisms*, vol. 1863, no. 4, p. 194419, 2020.
[30] M. Correia de Sousa, M. Gjorgjieva, D. Dolicka, C. Sobolewski, and M. Foti, "Deciphering miRNAs' action through miRNA editing," *International Journal of Molecular Sciences*, vol. 20, no. 24, p. 6249, 2019.
[31] J. Krol, I. Loedige, and W. Filipowicz, "The widespread regulation of microRNA biogenesis, function and decay," *Nature Reviews Genetics*, vol. 11, no. 9, pp. 597–610, 2010.
[32] Y. Liu, S. Gao, Q. Du, and M. Shao, "miR-146a and miR-152 in prostate cancer and clinicopathological parameters," *Journal of B.U.ON.: Official Journal of the Balkan Union of Oncology*, vol. 24, no. 4, pp. 1692–1699, 2019.
[33] B. Li, S. Luan, J. Chen et al., "The MSC-derived exosomal lncRNA H19 promotes wound healing in diabetic foot ulcers by upregulating PTEN via MicroRNA-152-3p," *Molecular Therapy - Nucleic Acids*, vol. 19, pp. 814–826, 2020.
[34] L. Chen, Y. Wang, J. He, C. Zhang, J. Chen, and D. Shi, "Long noncoding RNA H19 promotes proliferation and invasion in human glioma cells by downregulating miR-152," *Oncology Research Featuring Preclinical and Clinical Cancer Therapeutics*, vol. 26, no. 9, pp. 1419–1428, 2018.
[35] Z. Li, Y. Li, Y. Li et al., "Long non-coding RNA H19 promotes the proliferation and invasion of breast cancer through upregulating DNMT1 expression by sponging miR-152," *Journal of Biochemical and Molecular Toxicology*, vol. 31, no. 9, 2017.
[36] J. Lu, G. Getz, E. A. Miska et al., "MicroRNA expression profiles classify human cancers," *Nature*, vol. 435, no. 7043, pp. 834–838, 2005.
[37] A. P. Adamis and D. T. Shima, "The role of vascular endothelial growth factor in ocular health and disease," *Retina*, vol. 25, no. 2, pp. 111–118, 2005.
[38] R. Haque, E. H. Hur, A. N. Farrell, P. M. Iuvone, and J. C. Howell, "MicroRNA-152 represses VEGF and TGFβ1 expressions through post-transcriptional inhibition of (Pro) renin receptor in human retinal endothelial cells," *Molecular Vision*, vol. 21, pp. 224–235, 2015.
[39] X. Fu and B. Ou, "miR-152/LIN28B axis modulates high-glucose-induced angiogenesis in human retinal endothelial cells via VEGF signaling," *Journal of Cellular Biochemistry*, vol. 121, no. 2, pp. 954–962, 2020.

Hindawi
Journal of Healthcare Engineering
Volume 2022, Article ID 7369242, 9 pages
https://doi.org/10.1155/2022/7369242

Review Article

A Systematic Review and Meta-Analysis on Comparative Kinematics in the Lumbopelvic Region in the Patients Suffering from Spinal Pain

ZhiRui Zheng, YouQiang Wang, Tong Wang, Yue Wu, and YuHui Li

The Second Affiliated Hospital of Harbin Medical University Orthopedic Surgery Three Ward, Harbin, Heilonjiang, China

Correspondence should be addressed to ZhiRui Zheng; zhengzhirui824@163.com

Received 7 December 2021; Revised 6 January 2022; Accepted 7 January 2022; Published 19 March 2022

Academic Editor: Enas Abdulhay

Background. Lumbopelvic kinematics has been observed to include different parameters and directly relate to the movement of the hip spine. In the current scenario, more than 65 million people have been suffering from spinal pain, and 18% of adults experience chronic spinal pain. *Methods*. This systematic review and meta-analysis selected 9 studies for analysis via electronic databases like EMBASE, MEDLINE, Web of Science, Scopus, CINAHL, and Cochrane (CENTRAL). After collecting the data, the dataset has been systematically analyzed through statistical methodologies using RevMan and Stata. *Results*. Out of 116 studies initially scrutinized, nine were finally selected for the meta-analysis. When range of motion was studied via meta-analysis, it was noted that a considerable reduced movement was noted in the lumbar region of the spine when people were suffering from lower back pain in comparison to control group people. Hence, reduced lumbar range of motion, no difference in the angle of lordosis, and no significant difference in extension and rotation in people with lower back pain were found. However, variability was noted in people suffering from lower back pain for flexion and lateral flexion. A significant heterogeneity was found between the studies which lacked some details and standardization of the criteria which were used for defining patients with lower back pain or without them (control group). Results show that spinal pain is the main reason behind the limitation of lumbar range of motion. It is clear from the data set of mean and standard deviation, and this is clear to establish the relationship between the causes of pelvic and spinal pain. In flexion-based ROM, the mean difference was found to be −9.77 (95% CI: −21.86, 2.32). Similarly, for lateral flexion, the mean difference was found to be −5.58 (with 95% CI: −10.38, −0.79). *Conclusion*. It can be concluded that spinal disease is too influential for people; thereby, it affects day-to-day life activities by creating painful and restricted movements. It is concluded that people suffering from lower back pain have reduced proprioception and range of movement in the lumbar region when compared to control groups with no lower back pain, which mainly focus on flexion and lateral flexion.

1. Introduction

Lumbopelvic kinematics have been observed to include a wide range of parameters, such as lumbar and pelvic ROM, regional movement timing, and muscle activation. In addition to that, the duration of movement and postural position associated with the coordination of movement are also linked with lumbopelvic kinematics. The lumbopelvic rhythm for the coordination of the hip-spine can be described as the movement of the lumbar spine combined with the movement of the pelvis. The lower back muscle, called the erector spinae, contracts and relaxes to control the body's movement against gravity [1].

It has also been observed that the nerves in the pelvic region come from the lower back portion, and issues with the lumbar spine can contribute to the development of pelvic pain or spine pain. In addition to that, the other potential causes of lower back disorders associated with spine pain can be triggered by disc herniation, spinal stenosis, and pinched nerves [2]. This study will systematically review and provide a meta-analysis on the comparative kinematics in the pelvic region for patients who are suffering from spinal pain. In addition to that, this study will also shed light on the finding of possible solutions to mitigate the issues related to spinal pain [3].

This study aims to systematically review and produce a meta-analysis on the comparative research regarding kinematics in the lumbopelvic region for patients suffering from spinal pain. The key objectives of the study are as follows: (i) to analyze the current scenario of developing lumbopelvic disorders among patients suffering from spinal pain; (ii) to investigate the importance of kinematics in the lumbopelvic region; and (iii) to examine the possible ways of improving strategies to mitigate the issues associated with the lumbopelvic region.

Spinal pain has been observed to be a common disorder among adults from the age group of 40 to above 60. In the current scenario, more than 65 million people have been suffering from spinal pain. At the same time, 18% of adults have been found to experience chronic or persistent spinal pain because of certain daily activities [4].

Therefore, this has become a potential issue nowadays and needs to be controlled. In this regard, this study will systematically review and provide a meta-analysis on the comparative kinematics for the lumbopelvic region among patients suffering from spinal pain. This study will analyze different perspectives of other researchers through conducting a secondary systematic review that can contribute to finding something new in the process of creating this kind of spinal pain. Therefore, this study will also contribute to the development of strategies and procedures that can effectively reduce the number of individuals suffering from spinal pain through conducting a systematic review and meta-analysis.

2. Methodology

The methodology can be defined as conducting research, describing each step selected and completed in research. This study has been conducted with a systematic review of secondary sources that has presented a meta-analysis regarding the research topic [5].

2.1. Study Selection: Inclusion and Exclusion Criteria. The inclusion-exclusion criteria have been chosen to identify the selected population in this study as a reliable, consistent, uniform, and objective manager. At the same time, the selected source of data has also been passed through these inclusion and exclusion criteria. It has lowered the size of the population by removing the ineligible samples from the study. Databases such as EMBASE, MEDLINE, Web of Science, Scopus, CINAHL, and Cochrane (CENTRAL) were used for data extraction.

A PRISMA flow chart has been implemented to systematically include and exclude studies from this review work and meta-analysis. Records identified through electronic database searching have collected 113 studies from different sources. After that, three additional articles have also been included in this study from other sources.

Out of these 116 studies, 76 duplicate types of research were discarded. Following the inclusion criteria and eligibility standards, 40 studies were found applicable as per the aim of the current study. Articles were rejected as per their exclusion criteria, which were as follows: insufficient patient data, nonclinical studies, studies with no conclusions, review papers, abstracts, letters, or editorials were found to be 31 studies; therefore, nine studies were shortlisted for analysis (Table 1). The PRISMA statement flow chart shows this process (Figure 1).

In this systematic review and meta-analysis study, four major electronic databases have been searched systematically since November 2021. Electronic databases including PubMed, Google Scholar, ProQuest, and MEDLINE have been searched with specific combinations of keywords. The selection of articles from the data sources has been conducted with relieving the abstracts and titles of the journals.

Online data sources have contributed to this research and have helped the researchers conduct these meta-analyses and systematic reviews. During the data search, researchers selected only the journals related to this topic and used a bulletin table to search the most relevant journals [14]. In this secondary data collection, the researchers have also considered the relevance and eligibility of each online source that has been reviewed in this study. During the selection of online sources, the researchers chose different clinical studies, individual participant data, regulatory information, and other types of secondary data that are relevant to the review topic.

2.2. Data Extraction and Quality Assessment of the Study. Researchers have developed based on the checklist used in different articles and published the quality assessment tools to extract data from the collected sample. Data extraction and quality assessment have been necessary to reduce risk factors and bias in the systematic review while synthesizing the key findings. The characteristics included in the data extraction were the age of participants and the characteristics of the source. The other factors that have been included in the checklist for the text fraction include inclusion-exclusion criteria, along with the methods used in the studies [15]. The quality assessment has been conducted with the aim of reducing bias from the study based on the study population, LBP among the participants, measurement procedures, and assessor bindings to the presence of spine pain (yes/no) [16]. The analysis of studies has been conducted via RevMan and Stata where forest and funnel plots were drawn and interpreted [15]. However, the key focus of this meta-analysis and systematic review has been on the statistical data. Still, the thematic analysis has also allowed the researchers to establish a common link between different variables [17].

3. Results

3.1. Characteristics of Movement. A total of 1887 participants were divided into LBP groups ($n = 643$) and NoLBP groups ($n = 596$). The sample size ranged from 29 to 840.

A meta-analysis was performed for six studies where the angle of lumbar lordosis was compared in people with or

Table 1: The basic characteristics of the included studies.

Trial	Sample size (LBP/control)	Male/female	Age (y), mean ± SD, or range (LBP/control)	Main outcomes	Back pain duration	BMI (LBP/control)
Christie [6]	29 (19/10)	NR	18–46	①	8 years	24.7 ± 3.3/22.8 ± 2.3
Ng [7]	30 (15/15)	30/0	27.9 ± 6.7/27.8 ± 5.9	①④⑤	6.1 years	23.4 ± 1.9/22.7 ± 2.0
Norton [8]	188 (128/60)	85/103	42/39.3	①	7 weeks	NR
Nourbakhsh [9]	840 (420/420)	420/420	20–65	①	6 weeks	25.3/25.6
Youdas [10]	75 (30/45)	75/0	54.9 ± 9/54.8 ± 8.5	①②③	18.7 years	28.9 ± 5.7/26.1 ± 5
Youdas [10]	75 (30/45)	0/75	54.9 ± 8.5/53.4 ± 8.8	①②③	11 years	28.9 ± 5.7/26.1 ± 5
Crosbie [11]	38 (19/19)	13/25	34.0 ± 13.3/28.6 ± 5.4	②④⑤	6 months	24.5 ± 3.6/23.0 ± 2.4
Wong [12]	31 (21/10)	NR	34 ± 10/42 + −8	②③④⑤	1 year	23.6/24.7
Tsai [13]	32 (16/16)	32/0	48.6 ± 7.4/47.9 ± 8.3	③④⑤	2 years	27.9/26.7

NR: not reported; ①: lumbar lordosis; ②: flexion; ③: extension; ④: lateral flexion; ⑤: rotation.

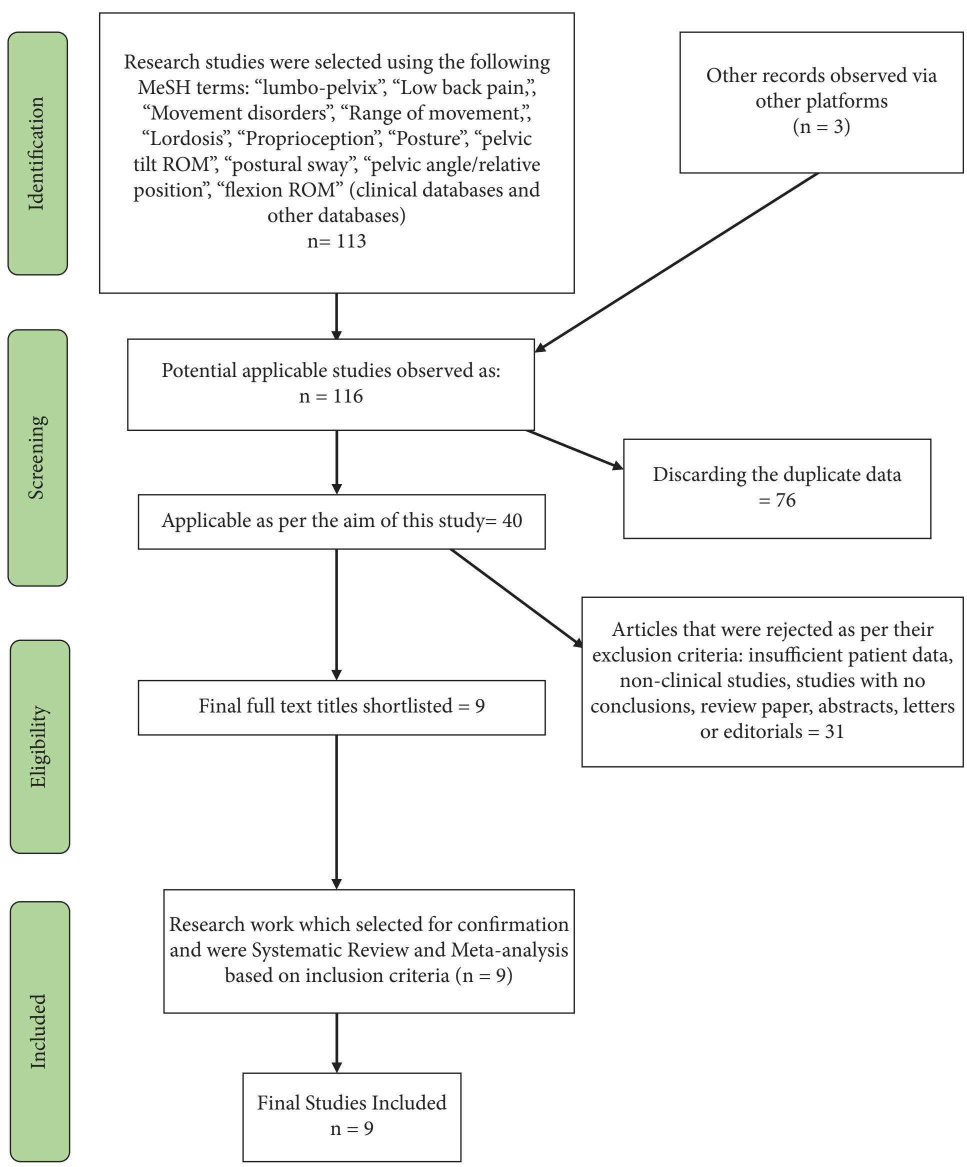

Figure 1: PRISMA study over the study methods.

Table 2: Comparing the angle of lumbar lordosis in the LBP group to the NoLBP-based group (control).

Study	LBP			Control		
	Mean	SD	Total	Mean	SD	Total
Christie [6]	26.4	9	19	19.3	9.2	10
Ng [7]	26	9	15	25	8	15
Norton [8]	42.5	15.2	128	40.2	14.8	60
Nourbakhsh [9]	37	13	420	38	14	420
Youdas [10]	39	8.1	30	37.5	11	45
Youdas [10]	55.5	10.4	30	52.7	15.3	45

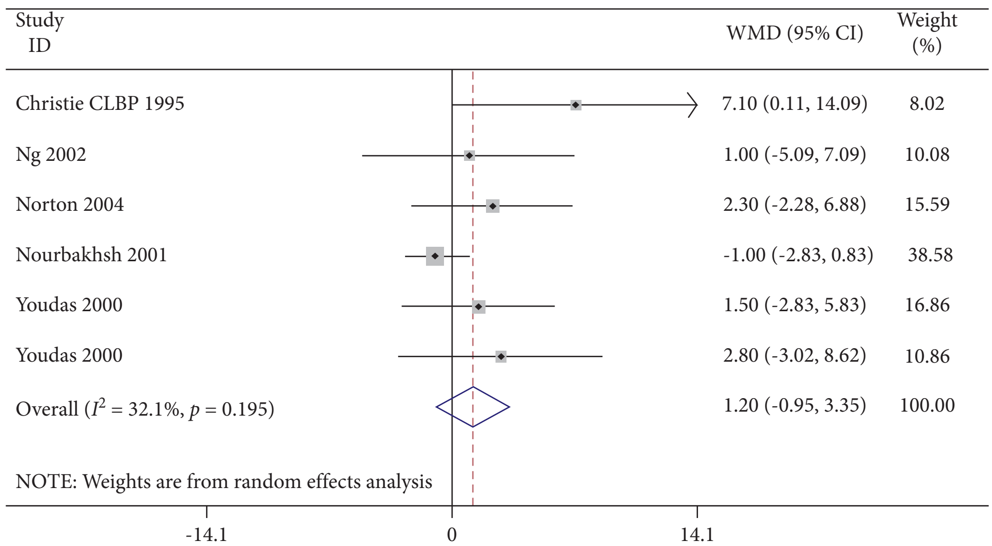

Figure 2: Forest plot analysis of lumbar lordosis in the LBP group to NoLBP on lumbar lordosis.

even without lower back pain, as shown in Table 2 and Figures 2 and 3. Most studies have reported small insignificant differences amongst groups.

3.2. Range of Motion. A meta-analysis of four studies was performed and it was found that there was a consistently reduced movement range in the lumbar spine region with people suffering from lower back pain. A meta-analysis has been performed in Table 3 with the findings listed in Figure 4 with forest and funnel plots. In some of the studies included the groups with chronic or acute lower back pain were compared with other groups showing no back pain signs. Variability was noted in people suffering from lower back pain during flexion. The meta-analysis showed that the flexion in the LBP group was significantly lower (WMD: −0.77; 95% CI: −21.86–2.32; $P \leq 0.001$, $I_2 = 95.2\%$) than that in the NoLBP group.

Studies which measured bilateral movement were meta-analyzed for extension (Table 4 and Figures 5 and 6), for lateral flexion (Table 5 and Figures 7 and 8), and for rotation (Table 6 and Figures 9 and 10). Meta-analysis showed that the lateral flexion in the LBP group was significantly lower (WMD: −5.58; 95% CI: −10.38 to −0.79; $P = 0.006$; $I_2 = 75.7\%$) than that in the NoLBP group. The studies selected were measured for their bilateral movement, that is, in both left and right rotations, and a mean difference was calculated. A significant relationship exists between lower back pain and movement restrictions along with dependent variables that not only efficiently but also effectively cause the same [18].

4. Discussion

4.1. Analysis of the Current Scenario for Growing of Lumbo-pelvic Disorder. In most cases, it has been seen that low back pain has contributed to pelvic disorders. The pelvic floor disorder has been noticed to be originating from the displacement of lumbar spines, which hardly has vivid symptoms in most human bodies. However, without or with the symptoms, this disorder reaches an extreme condition to some humans. It has been spotted from many discussions and scientific magazines and journals that the connection between the "low back pain" (LBP) or "spinal pain" and "pelvic floor dysfunction" (PFD) has been evident in the case of women's bodies [19]. The highest number of responses indicated the link between spinal pain and PFD, such as a considerable positive correlation.

4.2. Investigation on the Essence of Kinematics. Observing different studies, it has come to light that when the pelvic region muscles are unable to contract, it immediately causes a failure in the urinary tract contraction that results in

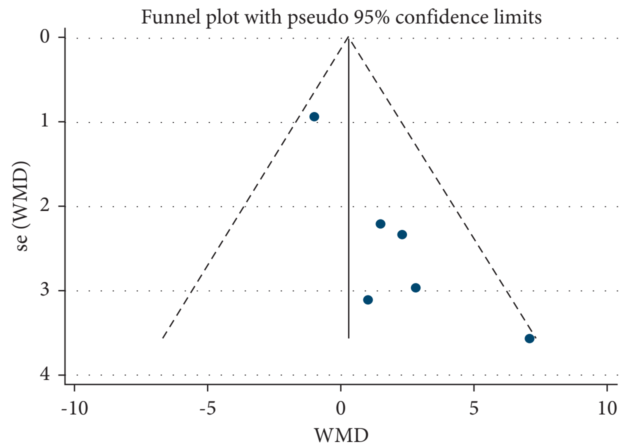

Figure 3: Funnel plot analysis of lumbar lordosis in the LBP group to NoLBP on lumbar lordosis.

Table 3: Flexion-based ROM meta-analysis.

Study	LBP			Control		
	Mean	SD	Total	Mean	SD	Total
Crosbie [11]	48	20	19	50	20	19
Wong [12]	29.8	11.9	20	61.9	9.9	17
Youdas [10] (female)	20.7	8.9	30	23	10.1	45
Youdas [10] (male)	28.6	6.6	30	31	5.7	45

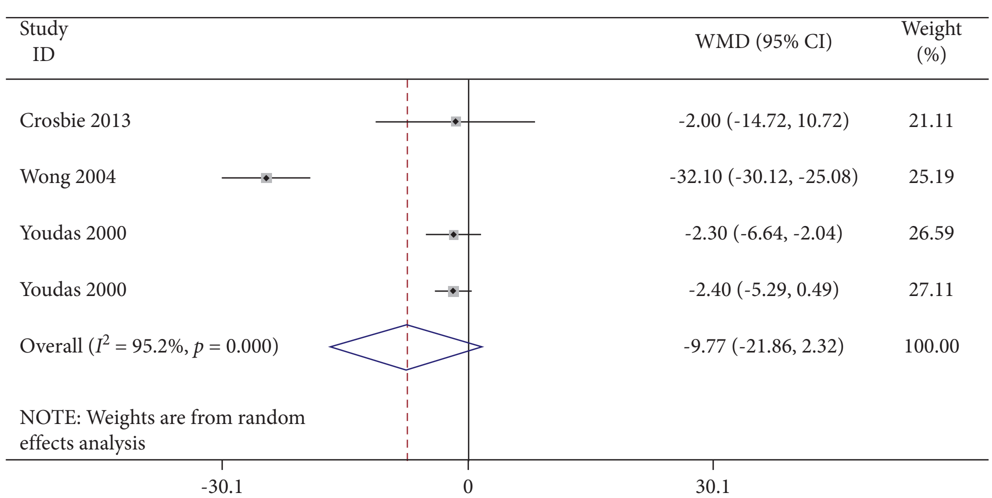

Figure 4: Forest plot analysis of lumbar lordosis in the LBP group to NoLBP on flexion.

Table 4: Extension-based ROM meta-analysis.

Study	LBP			Control		
	Mean	SD	Total	Mean	SD	Total
Tsai [13]	26	7	16	28	8	16
Wong [12]	12.7	5.9	20	15.5	7.4	17
Youdas [10] (female)	56	12	30	56.5	10.4	45
Youdas [10] (male)	42.7	8.8	30	50.1	9.2	45

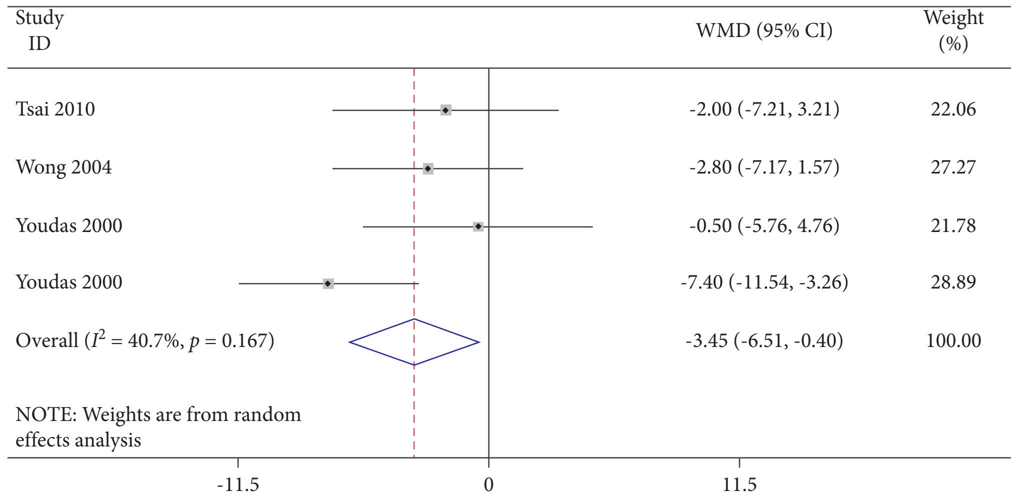

Figure 5: Forest plot analysis of lumbar lordosis in the LBP group to NoLBP on extension.

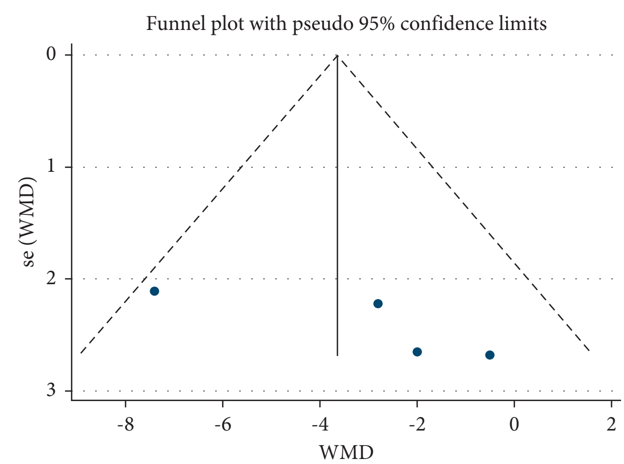

Figure 6: Funnel plot analysis of lumbar lordosis in the LBP group to NoLBP on extension.

Table 5: The lateral flexion-based ROM meta-analysis.

Study	LBP			Control		
	Mean	SD	Total	Mean	SD	Total
Crosbie [11]	23	11	19	28	13	19
Ng [7]	29.5	5.5	15	31	15	55
Tsai [13]	37	6.5	16	41	6	16
Wong [12]	12.8	4.7	20	23.7	5.4	17

urinary inconsistency. In the opinion of Aitken et al. [20], adding to it, it has been noticed that the pelvic organ starts prolapsing due to the same reason and gives rise to other abnormalities in the human body. It has been transparent that this phenomenon also disturbs the kinematics of the human body functions and causes PFD.

4.3. Analysis of Causes that Develop Further Issues in the Pelvic Region. Low back pain can be derived due to soft-tissue as well as mechanical issues, and these injuries can lead to more pain in their pelvic region. This has been the reason for coming up with more severity, which can lead to more suffering. Furthermore, they have been going through infections, and because of that, they have been facing more casualties.

Due to this reason, more complex problems have been coming up, which can lead to no proper movement of their lives [21]. Hence, it is clear from the discussion that issues developing due to derived spinal pain are related to the

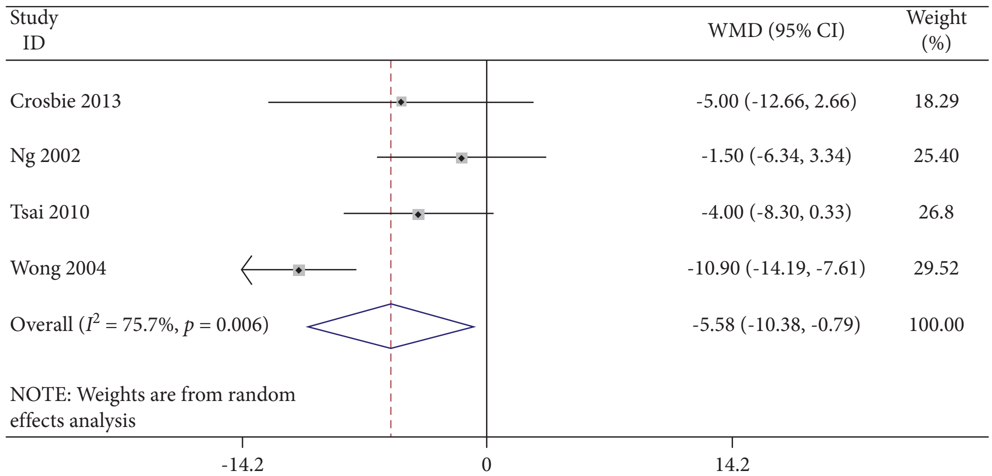

Figure 7: Forest plot analysis of lumbar lordosis in the LBP group to NoLBP on the lateral flexion.

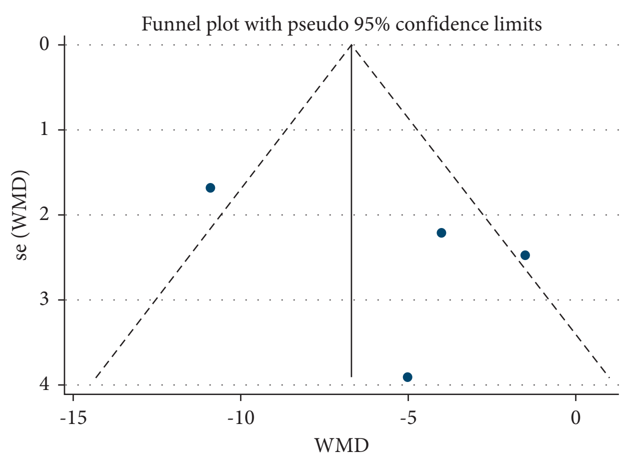

Figure 8: Funnel plot analysis of lumbar lordosis in the LBP group to NoLBP on the lateral flexion.

Table 6: The rotation-based ROM meta-analysis.

Study	LBP			Control		
	Mean	SD	Total	Mean	SD	Total
Crosbie [11]	12	6	19	12	6	19
Ng [7]	27.5	6.5	15	30.5	10	15
Tsai [13]	43	5	16	47	7	16
Wong [12] (LBP)	9	3.4	20	12.2	4.6	17

pelvic region. This may increase the severity of pain leading to suffering and infections, which might be the reason to other diseases.

4.4. Examination of Mitigation Strategies. Here, they should develop proper mitigation strategies at the beginning stage of the pelvic derivation of pelvic. Furthermore, they should

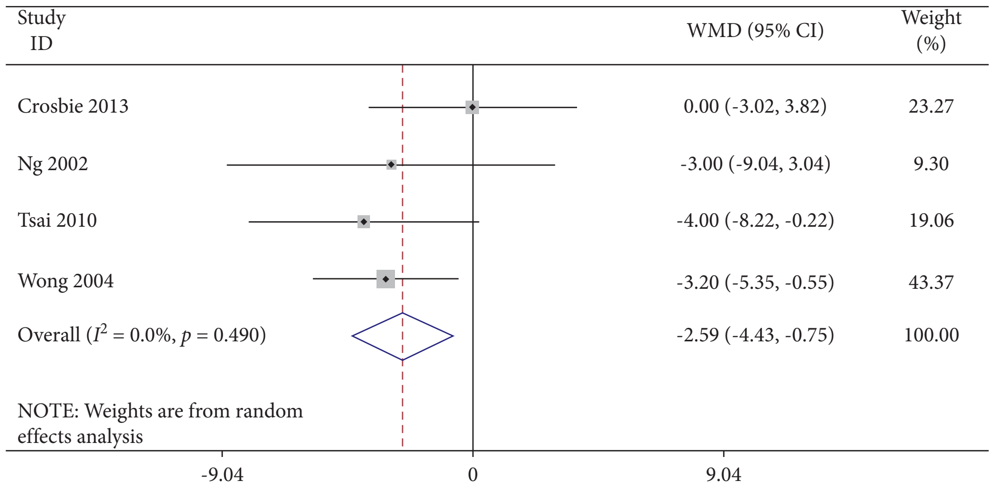

Figure 9: Forest plot analysis of lumbar lordosis in the LBP group to NoLBP on rotation.

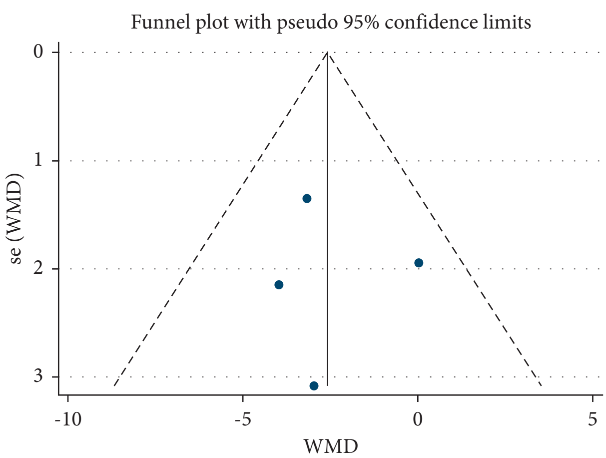

Figure 10: Funnel plot analysis of lumbar lordosis in the LBP group to NoLBP on rotation.

easily take physicians' appointments to solve their issues [22]. It is not possible to identify pelvic at their initial stage, but they should pay heed that they should not face any damage so that no issue or further complexity can be generated.

5. Conclusion

It can be concluded that lumbopelvic has been derived, so it is too problematic for people to lead their normal lives [23]. There are too many causes behind deriving pelvic disorders such as spinal stenosis, pinched nerves, and herniation. Here, proper analysis of the development of this disorder has been paid heed, and in this regard, it has been identified that spinal pain is the most significant cause [24]. Kinematics has become too vivid a reason for deriving this issue as well, and in this case, all of the explanation has been provided with giving analysis [25]. Possible strategies have been given heed to so that patients can get relieved from this kind of situation to a further extent. Here, for vivid results, primary data has been utilized and the data set given insight into mean and standard deviation values. The analysis of movement in the lumbopelvic region is based on the examination of kinematics such as posture, range of movement like flexion, and extension. This also includes a higher range of movements such as sequential and temporal patterns in case of proprioception, complex functions, physiological movements, or case of complex functions such as walking or lifting. Thus, analysis of all causes for developing various issues in the pelvic region among the patient is very effective, which is generated from spinal pain. It is concluded that people suffering from lower back pain have reduced proprioception and range of movement in the lumbar region when compared to control groups with no lower back pain, which mainly focus on flexion and lateral flexion [26].

Hence, it was concluded from the studies that people with lower back pain have a reduced range and speed of movement, but it is not significant for other characteristics of movement. But people suffering from lower back pain move slowly with low proprioception when compared to control group people. For patients with limited lumbar spine mobility, especially in forward flexion and lateral flexion, early intervention should be performed to reduce pain. For patients who already have low back pain, reducing forward flexion and lateral flexion activities may reduce the pain to a certain extent.

Data Availability

The data used to support this study are available from the corresponding author upon request.

Conflicts of Interest

The authors declare that they have no conflicts of interest.

References

[1] M. Sokouti and B. Sokouti, "A PRISMA-compliant systematic review and analysis on color image encryption using DNA properties," *Computer Science Review*, vol. 29, pp. 14–20, 2018.

[2] N. Panic, E. Leoncini, G. De Belvis, W. Ricciardi, and S. Boccia, "Evaluation of the endorsement of the preferred reporting items for systematic reviews and meta-analysis (PRISMA) statement on the quality of published systematic review and meta-analyses," *PLoS One*, vol. 8, no. 12, pp. 43–56, 2019.

[3] H. S. Krishna, P. V. Pramod, C. J. D'souza, S. Thomas, and A. Babu, "Hip rotation range of motion: a comparison between healthy individuals and patients with chronic low back pain," *Hip*, vol. 7, pp. 376–384, 2021.

[4] S. M. Tsang, G. P. Szeto, A. K. Yeung et al., "Recovery of the lumbopelvic movement and muscle recruitment patterns using motor control exercise program in people with chronic nonspecific low back pain: a prospective study," *PLoS One*, vol. 16, no. 11, pp. 322–328, 2021.

[5] C. Bauer, "Reliability and validity of lumbopelvic kinematics related to nonspecific low back pain," *Journal of Medical Advancement*, vol. 8, no. 1, pp. 121–133, 2018.

[6] H. J. Christie, S. Kumar, and S. A. Warren, "Postural aberrations in low back pain," *Archives of Physical Medicine and Rehabilitation*, vol. 76, no. 3, pp. 218–224, 1995.

[7] J. K.-F. Ng, C. A. Richardson, V. Kippers, and M. Parnianpour, "Comparison of lumbar range of movement and lumbar lordosis in back pain patients and matched controls," *Journal of Rehabilitation Medicine*, vol. 34, no. 3, pp. 109–113, 2002.

[8] B. J. Norton, S. A. Sahrmann, and L. R. Van Dillen, "Differences in measurements of lumbar curvature related to gender and low back pain," *Journal of Orthopaedic & Sports Physical Therapy*, vol. 34, no. 9, pp. 524–534, 2004.

[9] M. R. Nourbakhsh, S. J. Moussavi, and M. Salavati, "Effects of lifestyle and work-related physical activity on the degree of Lumbar Lordosis and chronic low back pain in a Middle East population," *Journal of Spinal Disorders*, vol. 14, no. 4, pp. 283–292, 2001.

[10] J. W. Youdas, T. R. Garrett, K. S. Egan, and T. M. Therneau, "Lumbar lordosis and pelvic inclination in adults with chronic low back pain," *Physical Therapy*, vol. 80, no. 3, pp. 261–275, 2000.

[11] J. Crosbie, R. de Faria Negrão Filho, D. P. Nascimento, and P. Ferreira, "Coordination of spinal motion in the transverse and frontal planes during walking in people with and without recurrent low back pain," *Spine*, vol. 38, no. 5, p. E286, 2013.

[12] T. K. T. Wong and R. Y. W. Lee, "Effects of low back pain on the relationship between the movements of the lumbar spine and hip," *Human Movement Science*, vol. 23, no. 1, pp. 21–34, 2004.

[13] Y.-S. Tsai, T. C. Sell, J. M. Smoliga, J. B. Myers, K. E. Learman, and S. M. Lephart, "A comparison of physical characteristics and swing mechanics between golfers with and without a history of low back pain," *Journal of Orthopaedic & Sports Physical Therapy*, vol. 40, no. 7, pp. 430–438, 2010.

[14] T. Meline, "Selecting studies for systemic review: Inclusion and exclusion criteria," *Contemporary Issues in Communication Science and Disorders*, vol. 33, no. 4, pp. 21–27, 2021.

[15] C. A. Bennett and N. L. Franklin, "Statistical analysis," *Chemistry and the Chemical Industry*, vol. 8, no. 12, pp. 342–354, 2021.

[16] E. R. Rodolfa, R. Vieille, P. Russell et al., "Internship selection: inclusion and exclusion criteria," *Professional Psychology: Research and Practice*, vol. 30, no. 4, pp. 236–241, 2019.

[17] D. Fryer, "Qualitative research methods in mental health and psychotherapy: a guide for students and practitioners," *Journal of Community and Applied Social Psychology*, vol. 24, no. 2, pp. 169–171, 2014.

[18] L. M. Villa, I. M. Goodyer, R. Tait et al., "Cognitive behavioral therapy may have a rehabilitative, not normalizing, effect on functional connectivity in adolescent depression," *Journal of Affective Disorders*, vol. 268, pp. 1–11, 2020.

[19] A. Karki, G. J. A. H. Wetzelaer, G. N. M. Reddy et al., "Unifying energetic disorder from charge transport and band bending in organic semiconductors," *Advanced Functional Materials*, vol. 29, no. 20, Article ID 1901109, 2019.

[20] M. Aitken, J. D. Haltigan, P. Szatmari et al., "Toward precision therapeutics: general and specific factors differentiate symptom change in depressed adolescents," *Journal of Child Psychology and Psychiatry*, vol. 61, no. 9, pp. 998–1008, 2020.

[21] S. Reynolds, F. Orchard, N. Midgley, R. Kelvin, and I. Goodyer, "Do sleep disturbances in depressed adolescents improve following psychological treatment for depression?" *Journal of affective disorders*, vol. 262, pp. 205–210, 2020.

[22] Y. Hu, L. Jiang, Q. Chen, J. Guo, and Z. Chen, "Direct observation of the dipole-induced energetic disorder in rubrene single-crystal transistors by scanning kelvin probe microscopy," *The Journal of Physical Chemistry Letters*, vol. 9, no. 11, pp. 2869–2873, 2018.

[23] S. P. Silfies, A. Bhattacharya, S. Biely, S. S. Smith, and S. Giszter, "Trunk control during standing reach: a dynamical system analysis of movement strategies in patients with mechanical low back pain," *Gait & Posture*, vol. 29, no. 3, pp. 370–376, 2019.

[24] C. W. Hunter, B. Stovall, G. Chen, J. Carlson, and R. Levy, "Anatomy, pathophysiology and interventional therapies for chronic pelvic pain: a review," *Pain Physician*, vol. 21, no. 2, pp. 147–167, 2018.

[25] M. Pavličev, R. Romero, and P. Mitteroecker, "Evolution of the human pelvis and obstructed labor: new explanations of an old obstetrical dilemma," *American Journal of Obstetrics and Gynecology*, vol. 222, no. 1, pp. 3–16, 2020.

[26] P. Roussouly, S. Gollogly, E. Berthonnaud, and J. Dimnet, "Classification of the normal variation in the sagittal alignment of the human lumbar spine and pelvis in the standing position," *Spine*, vol. 30, no. 3, pp. 346–353, 2005.

Hindawi
Journal of Healthcare Engineering
Volume 2022, Article ID 1033332, 7 pages
https://doi.org/10.1155/2022/1033332

Research Article

Association of Platelet-to-Lymphocyte Ratio with Stroke-Associated Pneumonia in Acute Ischemic Stroke

Wei Li and Cailian He

Department of Neurology, Beijing Shijitan Hospital, Capital Medical University, Beijing 100038, China

Correspondence should be addressed to Wei Li; liwei@bjsjth.cn

Received 9 January 2022; Revised 19 February 2022; Accepted 21 February 2022; Published 18 March 2022

Academic Editor: Enas Abdulhay

A common consequence of acute ischemic stroke (AIS), stroke-associated pneumonia (SAP), might result in a poor prognosis after stroke. Based on the critical position of inflammation in SAP, this study aimed to explore the correlation between platelet-to-lymphocyte ratio (PLR) and the occurrence of SAP. We included 295 patients with acute ischemic stroke, 40 with SAP, and 255 without SAP. The area under the receiver operating characteristic curve was used to determine the diagnostic value of SAP risk factors using binary logistic regression analysis. The comparison between the two groups showed that age, the baseline National Institutes of Health Stroke Scale (NIHSS) score, and the proportion of dysphagia, atrial fibrillation, and total anterior circulation infarct were higher, and the proportion of lacunar circulation infarct was lower in the SAP group ($P < 0.001$). In terms of laboratory data, the SAP group had considerably greater neutrophil counts and PLR, while the non-SAP group ($P < 0.001$) had significantly lower lymphocyte counts and triglycerides. Binary logistic regression analysis revealed that older age (aOR = 1.062, 95% CI: 1.023–1.102, $P = 0.002$), atrial fibrillation (aOR = 3.585, 95% CI: 1.605–8.007, $P = 0.019$), and PLR (aOR = 1.003, 95% CI: 1.001–1.006, $P = 0.020$) were independent risk factors associated with SAP after adjusting for potential confounders. The sensitivity and specificity of PLR with a cutoff value of 152.22 (AUC: 0.663, 95% CI: 0.606–0.717, $P = 0.0006$) were 57.5% and 70.6%, respectively. This study showed that high PLR is an associated factor for SAP in AIS patients. Increased systemic inflammation is linked to SAP in ischemic stroke. Inflammatory biomarkers that are easily accessible may aid in the diagnosis of high-risk SAP patients.

1. Introduction

Stroke is a common and leading cause of death and disability worldwide, imposing a heavy burden on society and the economy [1, 2]. Stroke-associated pneumonia (SAP) often occurs after a stroke; approximately 7%–38% [3–8] of stroke patients are diagnosed with SAP during hospitalization. Once a patient develops SAP, it leads to a poor prognosis and a prolonged hospital duration [9–12].Early diagnosis and preventive treatment are necessary for patients at high risk of SAP. Therefore, an effective biomarker is needed for risk assessment and early detection of SAP. Neurogenic immunosuppression is one of the critical mechanisms of increased susceptibility to postinfection [13, 14].

Platelet-to-lymphocyte ratio (PLR) is a novel and inexpensive biomarker that reflects systemic inflammation response [15, 16], which is affected by changes in lymphocytes and platelets after acute stroke. PLR is a sensitive marker to predict the occurrence and prognosis of cardiovascular events [16, 17], cerebrovascular diseases [18], poststroke depression [19],and pneumonia [20]. However, the association of PLR with SAP is uncertain. In light of this, we investigated the relationship of PLR with SAP in AIS patients.

In the proposed investigation, we discovered that high PLR is linked to SAP in AIS patients. PLR could be a useful tool for identifying high-risk SAP patients. It is more beneficial to improve results if SAP is detected early and well prevented. PLR was found to be considerably greater in the SAP group than in the non-SAP group in this study.

In the following section, we discuss the section-wise study. Section 2 discusses the materials and methods and also discusses the study subjects, clinical variables collection, laboratory parameters and clinical features, statistical analysis, and results. Section 3 defines the conclusion of the study. Finally, the research work is concluded in Section 4.

2. Materials and Methods

The overall quality of any research dissemination output is evaluated in this section and it reveals to readers what techniques, methodologies, designs, and treatments are used in the research, allowing us to repeat the results.

2.1. Study Subjects. Acute ischemic stroke patients in the Department of Neurology, Beijing Shijitan Hospital, were included in this study between March 1, 2018, and July 31, 2019. The study protocol was approved by the Scientific Research Ethics Committee of Beijing Shijitan Hospital Affiliated with Capital Medical University.

The inclusion criteria for enrolled patients are as follows:

(1) Hospitalization within 72 h after the onset of symptoms
(2) Patients diagnosed as new acute ischemic stroke by imaging examination (cranial magnetic resonance imaging or computed tomography) at the time of admission
(3) Modified Rankin scale (mRS) score<2 before admission
(4) Patients who were not discharged within 3 days before hospitalization

The exclusion criteria are as follows:

(1) The acute infections (vacuities, urinary, and infection of the upper or lower respiratory tract) within 2 weeks before the onset of the stroke
(2) Medical history of cancer, hematologic disease, severe liver and kidney dysfunction, and autoimmune disease

2.2. Clinical Variables Collection. Demographic data obtained at admission include age, sex, and the length of hospitalization. Premorbid history relevant risk factors contain current smoking, coronary heart disease, hypertension, diabetes, previous stroke, and atrial fibrillation.

2.3. Laboratory Parameters and Clinical Features. Within 24 h after admission, peripheral venous blood was collected from the participants and used for immediate biomarker detection. Laboratory data consisted of neutrophils, lymphocytes, platelets, total cholesterol (TC), triglycerides (TG), and low-density lipoprotein cholesterol (LDL-C). The PLR (defined as platelet/lymphocyte) was calculated. The clinical features of patients included dysphagia, the Oxfordshire Community Stroke Project (OCSP), and baseline National Institutes of Health Stroke Scale (NIHSS) score on admission.

According to clinical and laboratory examinations and chest X-ray or CT scan results retrospectively gathered from medical records, SAP was defined as a lower respiratory tract infection within the first 7 days of hospitalization after a stroke [21, 22].

2.4. Statistical Analysis. Normally distributed continuous variables were expressed as the mean ± standard deviation, while nonnormally distributed variables were expressed as the median (interquartile range). The Mann–Whitney *U* test was used to compare the clinical characteristics of continuous variables between groups. The chi-square test was used for categorical variables. Variables with $P < 0.05$ from the results of the univariate analyses were considered confounders in the multivariable logistic regression analysis. The association between different PLR and SAP risks was estimated using univariate analysis and binary logistic regression analysis. All patients were classified into two groups according to their median PLR (126.67), and the potential confounders of PLR were identified. We adjusted all potential confounding factors (parameters with $P < 0.05$ in univariate analysis). The results are presented in the form of an adjusted odds ratio (aOR) and 95% confidence interval (CI).

We conducted the receiver operative curve (ROC) and the area under the curve (AUC) to measure the specificity and sensitivity of PLR and obtained the optimal cutoff value of PLR. Results were considered significant at $P < 0.05$. The analysis of ROC was performed with MedCalc 15.6 (MedCalc Software, Belgium). Other statistical analyses were carried out using SPSS v23 (SPSS Inc., Chicago, IL).

3. Results

A total of 295 consecutive AIS patients were retrospectively included from March 1, 2018, and July 31, 2019, according to the inclusion and exclusion criteria, 40 (13.6%) of whom were diagnosed with SAP in the final analysis (Figure 1). The average age of patients was 69.5 ± 12.0 years, and 196 (66.4%) were male. The median length of hospitalization was 14.0 (11.0, 17.0) days. The comparison of demographic, clinical, and laboratory characteristics is given in Table 1. There were significant differences in age ($P < 0.001$) and baseline NIHSS score ($P < 0.001$) between the SAP group and the non-SAP group. The presence of dysphagia ($P < 0.001$), atrial fibrillation ($P < 0.001$), total anterior circulation infarction (TACI) ($P < 0.001$), and lacunar circulation infarction (LACI) ($P < 0.001$) were significantly different between the two groups. Neutrophil counts and PLR were significantly increased ($P \leq 0.001$; Figure 2), whereas lymphocyte counts and TG were significantly decreased in the SAP group ($P < 0.001$). The number of platelets in the patients with SAP was decreased, although not statistically significant.

The demographic and clinical characteristics (parameters with $P < 0.05$ in univariate analysis) in the high and low PLR groups are given in Table 2. We found that patients with the high PLR had high baseline NIHSS scores ($P = 0.047$) and low TG ($P = 0.004$). The prevalence of dysphagia ($P = 0.020$) was significantly higher in the high PLR group than in the low PLR group.

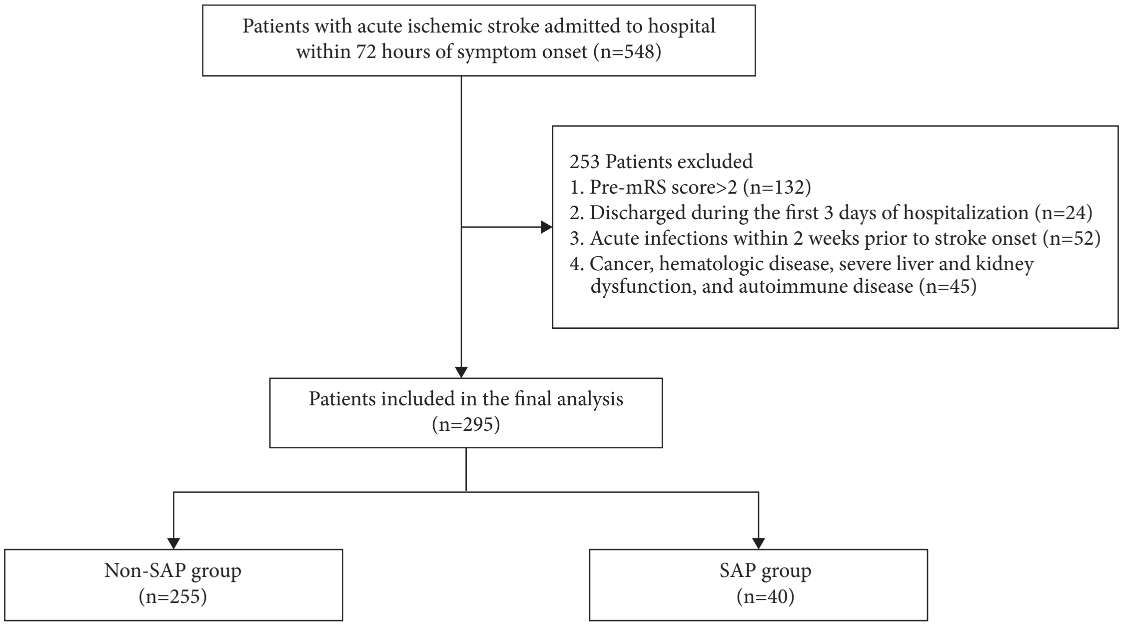

Figure 1: Flow diagram of the patient selection process.

Table 1: Comparison of the characteristics of AIS patients according to the onset of SAP.

Characteristics	Total ($N = 295$)	Non-SAP ($N = 255$)	SAP ($N = 40$)	P value
Age, years, mean ± SD	69.5 ± 12.0	68.1 ± 11.7	77.5 ± 10.6	<0.001 *
Male, n (%)	196 (66.4)	171 (67.1)	25 (62.5)	0.570
Length of hospitalization, days, median (IQR)	14.0 (11.0, 17.0)	14.0 (11.0, 16.0)	14.5 (9.0, 33.0)	0.241
Baseline NIHSS, median (IQR)	3 (1, 7)	3 (1, 5)	14 (7, 18)	<0.001 *
Dysphagia, n (%)	49 (16.6)	15 (5.8)	34 (85.0)	<0.001 *
Current smoking, n (%)	96 (32.5)	85 (33.3)	11 (27.5)	0.464
Coronary artery disease, n (%)	88 (29.8)	72 (28.2)	16 (40.0)	0.131
Hypertension, n (%)	229 (77.6)	196 (76.9)	33 (82.5)	0.426
Diabetes, n (%)	106 (35.9)	96 (37.6)	10 (25.0)	0.121
Previous stroke, n (%)	81 (27.5)	66 (25.9)	15 (37.5)	0.126
Atrial fibrillation, n (%)	46 (15.6)	29 (11.4)	17 (42.5)	<0.001 *
OCSP				
TACI, n (%)	15 (5.1)	5 (2.0)	10 (25.0)	<0.001 *
PACI, n (%)	90 (30.5)	78 (30.6)	12 (30.0)	0.940
POCI, n (%)	39 (13.2)	30 (11.8)	9 (22.5)	0.062
LACI, n (%)	151 (51.2)	142 (55.7)	9 (22.5)	<0.001 *
TC, mmol/L, median (IQR)	4.2 (3.5, 5.0)	4.3 (3.6, 5.0)	4.0 (3.1, 4.9)	0.086
TG, mmol/L, median (IQR)	1.2 (0.9, 1.7)	1.3 (1.0, 1.8)	0.9 (0.7, 1.3)	<0.001 *
LDL-C, mmol/L, median (IQR)	2.4 (1.8, 3.0)	2.4 (1.8, 3.0)	2.2 (1.8, 2.8)	0.306
Neutrophils, $\times 10^9$/L, median (IQR)	4.3 (3.3, 6.0)	4.0 (3.1, 5.3)	7.3 (6.0, 9.6)	<0.001 *
Lymphocytes, $\times 10^9$/L, median (IQR)	1.6 (1.3, 2.1)	1.8 (1.4, 2.1)	1.1 (0.9, 1.6)	<0.001 *
PLT, $\times 10^9$/L, median (IQR)	216.0 (179.0, 253.0)	216.0 (180.0, 253.0)	210.5 (152.3, 247.8)	0.137
PLR, median (IQR)	126.7 (99.6, 175.3)	123.2 (98.0, 163.8)	161.2 (114.1, 209.2)	0.001 *

NIHSS, National Institute of Health Stroke Scale; OCSP, Oxfordshire Community Stroke Project; TACI, total anterior circulation infarct; PACI, partial anterior circulation infarct; POCI, posterior circulation infarct; LACI, lacunar circulation infarct; TC, total cholesterol; TG, triglycerides; LDL-C, low-density lipoprotein cholesterol; PLT, platelet; PLR, platelet-to-lymphocyte ratio; SD, standard deviation; IQR, interquartile range; SAP, stroke-associated pneumonia. * P values less than 0.05 were considered statistically significant.

In the univariate analysis, the variables with $P < 0.05$ were used as covariates, and SAP was used as a dependent variable. As given in Table 3, after adjusting for the confounders of PLR, multivariate logistic regression analysis showed that PLR (aOR = 1.003, 95% CI: 1.001–1.006, $P = 0.020$), age (aOR = 1.062, 95% CI: 1.023–1.102, $P = 0.002$), and atrial fibrillation (aOR = 3.585, 95% CI: 1.605–8.007, $P = 0.019$) remained associated with SAP. In the ROC analysis, the best cutoff level of PLR was 152.22 ($P = 0.0006$), with 0.575 sensitivity and 0.706 specificity. The area under the ROC curve was 0.663 (95% CI: 0.606–0.717) (Figure 3).

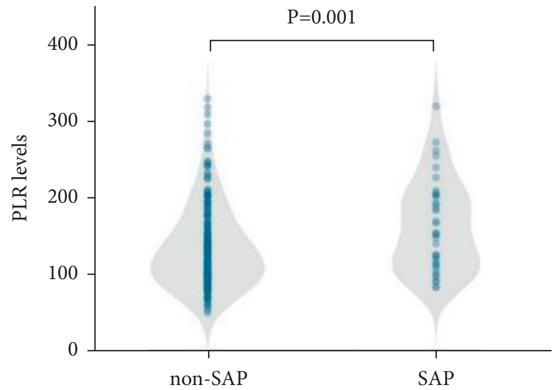

Figure 2: PLR levels and SAP. Violin plot of PLR distribution in patients with SAP and without SAP.

Table 2: Comparison of the characteristics between subgroups based on the median PLR.

Characteristics	Low PLR $N = 147$ (PLR<126.67)	High PLR $N = 148$ (PLR≥126.67)	P value
Age, years, mean ± SD	68.8 ± 12.2	70.0 ± 11.7	0.346
Baseline NIHSS, median (IQR)	3 (1, 5)	4 (2, 8)	0.047*
Dysphagia	17 (11.6)	32 (21.6)	0.020*
Atrial fibrillation, n (%)	17 (11.6)	29 (19.6)	0.057
TG, mmol/L, median (IQR)	1.2 (1.0, 1.8)	1.1 (0.8, 1.6)	0.004*

NIHSS, National Institute of Health Stroke Scale; TG, triglycerides; PLR, platelet-to-lymphocyte ratio; SD, standard deviation; IQR, interquartile range. *P values less than 0.05 were considered statistically significant.

Table 3: Multivariate logistic regression analysis of the associations between PLR and SAP.

Risk factors	B	SE	Wald	P value	aOR	aOR (95% CI)
Age	0.060	0.019	9.819	0.002*	1.062	1.023–1.102
Atrial fibrillation	1.277	0.410	9.699	0.019*	3.585	1.605–8.007
PLR	0.003	0.002	5.393	0.020*	1.003	1.001–1.006

PLR, platelet-to-lymphocyte ratio; SAP, stroke-associated pneumonia; SE, standard error; aOR, adjusted odds ratio. *P values less than 0.05 were considered statistically significant.

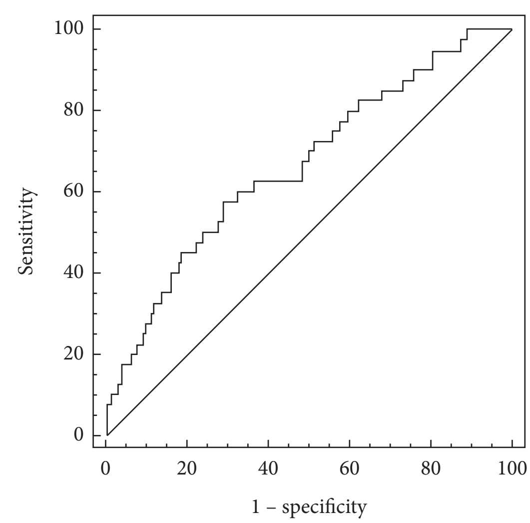

Figure 3: The receiver operating characteristic (ROC) curve analysis of platelet-to-lymphocyte ratio for predicting SAP.

4. Discussion

Based on increasing evidence, researchers reported the predictive effectiveness of PLR in the prognosis of artery diseases [16–18] and inflammation diseases. With reference to the studies by Turkmen et al. and Uslu et al. [23, 24] in the present study, we found that high PLR is associated with SAP in AIS patients. The results of multivariate analysis showed that PLR, a marker of systemic inflammation, is an independent risk factor for SAP, which further confirmed high PLR may be used as an effective indicator of inflammatory diseases.

Platelets have the function of regulating inflammation and immune responses, which play an important role in the formation of thrombosis in the arterial circulation. When AIS occurs, abnormal platelets are overactivated and accumulated [25], which may lead to thrombosis and vascular blockage and then vascular events [26]. Changes in circulating platelet counts are uncertain in diverse diseases. Platelets can increase in many inflammations with an acute phase. In the case of sepsis, the platelet count will increase due to the accelerated expression of platelets after the increase in their breakdown [27]. However, we found the platelet counts were decreased in AIS patients with SAP. There could be three reasons for this observation. The first reason is the particularities of AIS patients. When arterial platelet-fibrin thrombi are formed in AIS patients, a reduction of the circulation platelet counts occurs due to their increased consumption in the infarction area [28]. The second reason is that platelet count in AIS patients may correlate with disease severity. Ming Yang et al. showed that AIS patients in the lowest platelet count quintile had a higher risk of poor functional outcome [29]. In this study, SAP patients were severe, with high admission NIHSS scores, which lead to the reduction of platelet count. The third reason may be the effect of antithrombotic therapy of acute AIS on platelets. IVT using rt-PA influences peripheral blood platelet counts and lymphocyte concentrations, resulting in enhancing infection risk [30].

The lymphocytes belong to the adaptive immune cells, which influence the regulation of the inflammatory response. Lymphocytes were suggested to be a pivotal subtype that determined the severity of neuroinflammation in acute brain injuries. Urra et al. [31] suggested that lymphopenia in the early stages of stroke is a sign of persistent brain damage, stress response, and a greater possibility of infection. In addition, it has been reported that lymphopenia after reperfusion in vascular events can effectively predict the existence of microvascular occlusion in the early stage [32]. Konstantin et al. [33] reported apoptosis of lymphocytes after stroke, and catecholamine-mediated lymphocyte defect played an important role in stroke-associated infection. Recent studies in rodent models have shown that T cells accumulate early in the damaged area within the first 24 hours after the onset of a stroke, which causes lymphopenia in peripheral blood [34]. The stroke-induced lymphocyte apoptosis results in immune system suppression and inflammation [35, 36], shifting from a proinflammatory Th1 type response to an anti-inflammatory Th2 type response. Therefore, stroke causes local inflammation and leads to stroke-induced immunosuppressive syndrome (SIDS) [14]. SIDS then leads to the systemic inflammatory response through endocrine pathways involving the hypothalamic-pituitary-adrenal axis or activation of the sympathetic nervous system [33, 37, 38]. Meanwhile, SIDS results in decreased peripheral blood lymphocyte counts and functional T cell inactivation [39]. The results of this study further supported that lymphopenia caused by immunosuppression after stroke has a potential effect on SAP susceptibility.

PLR is a systemic inflammation index, which is calculated by dividing the platelet count by lymphocyte count. PLR represents the burden of systemic inflammation and combines platelet counts and lymphocytes counts to predict the prognosis of cardiovascular diseases [40] and ischemic stroke [41]. Altintas et al. found that high PLR values could reflect the infarcted size and poor recanalization rate in patients with thrombectomy therapy, supporting the view that PLR represents a prothrombotic inflammatory state [40]. In addition, PLR may provide important information for pulmonary diseases. Kumar et al. [42] showed that PLR could predict the 90-day mortality in patients with acute exacerbations of COPD. The PLR value can guide in diagnosing hypersensitivity pneumonia [43]. Kartal et al. showed that utilization of PLR may differentiate patients with community-acquired pneumonia [44]. Moreover, Jong-Han Lee et al. detected PLR might have diagnostic utilities such as CRP in the evaluation of the severity of pneumonia patients [45]. CRP has been reported to have a significant prognostic value and a useful adjunctive test as well as being a marker of treatment response in inflammation disease. The ability of PLR to predict infectious diseases is further proved by this indirect evidence. PLR was found to be considerably greater in the SAP group than in the non-SAP group in this study. However, Ahmet Adiguzel et al. found no correlation between the PLR level and SAP [46]. The possible reason for the different results is the difference in the severity of the stroke patients included. They included stroke patients with NIHSS >10 who were sicker than the patients in our study. Based on the discussion above, we speculated that there may be a correlation between high PLR and the occurrence of SAP, helping clinicians assess high-risk SAP in clinical works. The followings could be viewed as potential limitations to the study. First, selection bias is a concern because we undertook a single-center retrospective study. This study would have been more convincing if our sample size was enlarged. Second, as a retrospective study, some acute inflammation biomarkers were not incorporated for analysis. This could have a certain impact on the result. We will conduct prospective studies in the future to further prove this conclusion. Third, PLR was only measured at admission. Given the limitations related to the retrospective design, no data evaluating the dynamic change of PLR were available. In future studies, the hematologic markers during hospitalization should be dynamically measured to evaluate the predictive value of PLR for SAP. Fourth, we cannot rule out residual confounding or the effect of unmeasured confounders. Further studies need to record more potential risk factors for SAP.

5. Conclusion

In conclusion, our study showed that high PLR is associated with SAP in AIS patients. PLR may be a promising indicator to identify high-risk SAP patients. High PLR was found to be a risk factor for SAP in AIS patients in this investigation. In ischemic stroke, increased systemic inflammation is connected to SAP. Easy-to-find inflammatory biomarkers could aid in the diagnosis of high-risk SAP patients. It is more beneficial to improve results if SAP is detected early and well prevented.

Data Availability

The datasets used to support the findings of this study are available from the corresponding author upon request.

Conflicts of Interest

The authors declare that they have no conflicts of interest.

References

[1] GBD 2017 Disease and Injury Incidence and Prevalence, "Global, regional, and national age-sex-specific mortality for 282 causes of death in 195 countries and territories, 1980-2017: a systematic analysis for the Global Burden of Disease Study 2017," *Lancet*, vol. 392, no. 10159, pp. 1736–1788, 2018.

[2] V. L. Feigin, B. Norrving, and G. A. Mensah, "Global burden of stroke," *Circulation Research*, vol. 120, no. 3, pp. 439–448, 2017.

[3] O. Finlayson, M. Kapral, R. Hall, E. Asllani, D. Selchen, and G. Saposnik, "Risk factors, inpatient care, and outcomes of pneumonia after ischemic stroke," *Neurology*, vol. 77, no. 14, pp. 1338–1345, 2011.

[4] H. Harms, U. Grittner, H. Dröge, and A. Meisel, "Predicting post-stroke pneumonia: the PANTHERIS score," *Acta Neurologica Scandinavica*, vol. 128, no. 3, pp. 178–184, 2013.

[5] R. Ji, H. Shen, Y. Pan et al., "Novel risk score to predict pneumonia after acute ischemic stroke," *Stroke*, vol. 44, no. 5, pp. 1303–1309, 2013.

[6] A. Meisel and C. J. Smith, "Preventive antibiotics for stroke-associated pneumonia," *Nature Reviews Neurology*, vol. 11, no. 12, pp. 672-673, 2015.

[7] C. J. Smith, B. D. Bray, A. Hoffman, A. Meisel, P. U. Heuschmann, and C. D. Wolfe, "Can a novel clinical risk score improve pneumonia prediction in acute stroke care? A UK multicenter cohort study," *Journal of American Heart Association*, vol. 4, no. 1, Article ID e001307, 2015.

[8] R. Sui and L. Zhang, "Risk factors of stroke-associated pneumonia in Chinese patients," *Neurological Research*, vol. 33, no. 5, pp. 508–513, 2011.

[9] A. K. Kishore, A. Vail, B. D. Bray et al., "Clinical risk scores for predicting stroke-associated pneumonia: a systematic review," *European Stroke Journal*, vol. 1, no. 2, pp. 76–84, 2016.

[10] Y. Li, Y. Zhang, L. Ma, X. Niu, and J. Chang, "Risk of stroke-associated pneumonia during hospitalization: predictive ability of combined A2DS2 score and hyperglycemia," *BMC Neurology*, vol. 19, no. 1, p. 298, 2019.

[11] W. H. Teh, C. J. Smith, R. S. Barlas et al., "Impact of stroke-associated pneumonia on mortality, length of hospitalization, and functional outcome," *Acta Neurologica Scandinavica*, vol. 138, no. 4, pp. 293–300, 2018.

[12] J. Yang, Y. Dai, Z. Zhang, and Y. Chen, "Value of combination of the A2DS2 score and IL-6 in predicting stroke-associated pneumonia," *Neuropsychiatric Disease and Treatment*, vol. 16, pp. 2353–2359, 2020.

[13] A. Chamorro, X. Urra, and A. M. Planas, "Infection after acute ischemic stroke," *Stroke*, vol. 38, no. 3, pp. 1097–1103, 2007.

[14] S. Hoffmann, H. Harms, L. Ulm et al., "Stroke-induced immunodepression and dysphagia independently predict stroke-associated pneumonia - the PREDICT study," *Journal of Cerebral Blood Flow and Metabolism*, vol. 37, no. 12, pp. 3671–3682, 2017.

[15] B. Qin, N. Ma, Q. Tang et al., "Neutrophil to lymphocyte ratio (NLR) and platelet to lymphocyte ratio (PLR) were useful markers in assessment of inflammatory response and disease activity in SLE patients," *Modern Rheumatology*, vol. 26, no. 3, pp. 372–376, 2016.

[16] A. Temiz, E. Gazi, Ö Güngör et al., "Platelet/lymphocyte ratio and risk of in-hospital mortality in patients with ST-elevated myocardial infarction," *Medical Science Monitor: International Medical Journal of Experimental and Clinical Research*, vol. 20, pp. 660–665, 2014.

[17] E. H. Ozcan Cetin, M. S. Cetin, D. Aras et al., "Platelet to lymphocyte ratio as a prognostic marker of in-hospital and long-term major adverse cardiovascular events in ST-segment elevation myocardial infarction," *Angiology*, vol. 67, no. 4, pp. 336–345, 2016.

[18] O. Altintas, A. Tasal, E. Niftaliyev, O. T. Kucukdagli, and T. Asil, "Association of platelet-to-lymphocyte ratio with silent brain infarcts in patients with paroxysmal atrial fibrillation," *Neurological Research*, vol. 38, no. 9, pp. 753–758, 2016.

[19] J. Hu, W. Zhou, Z. Zhou, J. Han, and W. Dong, "Elevated neutrophil-to-lymphocyte and platelet-to-lymphocyte ratios predict post-stroke depression with acute ischemic stroke," *Experimental and Therapeutic Medicine*, vol. 19, no. 4, pp. 2497–2504, 2020.

[20] N. B. Akilli, M. Yortanlı, H. Mutlu et al., "Prognostic importance of neutrophil-lymphocyte ratio in critically ill patients: short- and long-term outcomes," *The American Journal of Emergency Medicine*, vol. 32, no. 12, pp. 1476–1480, 2014.

[21] C. J. Smith, A. K. Kishore, A. Vail et al., "Diagnosis of stroke-associated pneumonia," *Stroke*, vol. 46, no. 8, pp. 2335–2340, 2015.

[22] H.-R. Cheng, J.-Y. Song, Y.-N. Zhang et al., "High monocyte-to-lymphocyte ratio is associated with stroke-associated pneumonia," *Frontiers in Neurology*, vol. 11, Article ID 575809, 2020.

[23] K. Turkmen, F. M. Erdur, F. Ozcicek et al., "-----stage renal disease patients," *Hemodialysis International*, vol. 17, no. 3, pp. 391–396, 2013.

[24] A. U. Uslu, A. Küçük, A. Şahin et al., "Two new inflammatory markers associated with Disease Activity Score-28 in patients with rheumatoid arthritis: neutrophil-lymphocyte ratio and platelet-lymphocyte ratio," *International Journal of Rheumatic Diseases*, vol. 18, no. 7, pp. 731–735, 2015.

[25] X. Wang, T.-L. Yue, P. R. Young, F. C. Barone, and G. Z. Feuerstein, "Expression of interleukin-6, c-fos, and zif268 mRNAs in rat ischemic cortex," *Journal of Cerebral Blood Flow and Metabolism*, vol. 15, no. 1, pp. 166–171, 1995.

[26] Z. G. Franks, R. A. Campbell, A. S. Weyrich, and M. T. Rondina, "Platelet-leukocyte interactions link inflammatory and thromboembolic events in ischemic stroke," *Annals of the New York Academy of Sciences*, vol. 1207, no. 1, pp. 11–17, 2010.

[27] P. von Hundelshausen and C. Weber, "Platelets as immune cells," *Circulation Research*, vol. 100, no. 1, pp. 27–40, 2007.

[28] E. D'Erasmo, G. Aliberti, F. S. Celi, E. Romagnoli, E. Vecci, and G. F. Mazzuoli, "Platelet count, mean platelet volume and their relation to prognosis in cerebral infarction," *Journal of Internal Medicine*, vol. 227, no. 1, pp. 11–14, 1990.

[29] M. Yang, Y. Pan, Z. Li et al., "Platelet count predicts adverse clinical outcomes after ischemic stroke or TIA: subgroup Analysis of CNSR II," *Frontiers in Neurology*, vol. 10, p. 370, 2019.

[30] D. F. Draxler, F. Lee, H. Ho, C. B. Keragala, R. L. Medcalf, and B. e. Niego, "t-PA suppresses the immune response and aggravates neurological deficit in a murine model of ischemic stroke," *Frontiers in Immunology*, vol. 10, p. 591, 2019.

[31] X. Urra, Á. Cervera, N. Villamor, A. M. Planas, and Á. Chamorro, "Harms and benefits of lymphocyte subpopulations in patients with acute stroke," *Neuroscience*, vol. 158, no. 3, pp. 1174–1183, 2009.

[32] V. Bodí, J. Sanchis, J. Núñez et al., "Post-reperfusion lymphopenia and microvascular obstruction in ST-segment elevation acute myocardial infarction," *Revista Española de Cardiología*, vol. 62, no. 10, pp. 1109–1117, 2009.

[33] K. Prass, C. Meisel, C Höflich et al., "Stroke-induced immunodeficiency promotes spontaneous bacterial infections and is mediated by sympathetic activation reversal by post-stroke T helper cell type 1-like immunostimulation," *Journal of Experimental Medicine*, vol. 198, no. 5, pp. 725–736, 2003.

[34] R. Jin, G. Yang, and G. Li, "Inflammatory mechanisms in ischemic stroke: role of inflammatory cells," *Journal of Leukocyte Biology*, vol. 87, no. 5, pp. 779–789, 2010.

[35] D. S. Heffernan, S. F. Monaghan, R. K. Thakkar, J. T. Machan, W. G. Cioffi, and A. Ayala, "Failure to normalize lymphopenia following trauma is associated with increased mortality, independent of the leukocytosis pattern," *Critical Care*, vol. 16, no. 1, p. R12, 2012.

[36] T. Menges, J. Engel, I. Welters et al., "Changes in blood lymphocyte populations after multiple trauma," *Critical Care Medicine*, vol. 27, no. 4, pp. 733–740, 1999.

[37] Y. Hannawi, B. Hannawi, C. P. V. Rao, J. I. Suarez, and E. M. Bershad, "Stroke-associated pneumonia: major advances and obstacles," *Cerebrovascular Diseases*, vol. 35, no. 5, pp. 430–443, 2013.

[38] L. Li, L.-h. Zhang, W.-p. Xu, and J.-m. Hu, "Risk assessment of ischemic stroke associated pneumonia," *World Journal of Emergency Medicine*, vol. 5, no. 3, pp. 209–213, 2014.

[39] J. Klehmet, H. Harms, M. Richter et al., "Stroke-induced immunodepression and post-stroke infections: lessons from the preventive antibacterial therapy in stroke trial," *Neuroscience*, vol. 158, no. 3, pp. 1184–1193, 2009.

[40] O. Altintas, M. O. Altintas, A. Tasal, O. T. Kucukdagli, and T. Asil, "The relationship of platelet-to-lymphocyte ratio with clinical outcome and final infarct core in acute ischemic stroke patients who have undergone endovascular therapy," *Neurological Research*, vol. 38, no. 9, pp. 759–765, 2016.

[41] C. Chen, L. Gu, L. Chen et al., "Neutrophil-to-Lymphocyte ratio and platelet-to-lymphocyte ratio as potential predictors of prognosis in acute ischemic stroke," *Frontiers in Neurology*, vol. 11, Article ID 525621, 2020.

[42] P. Kumar, S. Law, and K. B. Sriram, "Evaluation of platelet lymphocyte ratio and 90-day mortality in patients with acute exacerbation of chronic obstructive pulmonary disease," *Journal of Thoracic Disease*, vol. 9, no. 6, pp. 1509–1516, 2017.

[43] F. Üçsular, G. Polat, G. Karadeniz et al., "Predictive value of platelet-to-lymphocyte ratio and neutrophil-to-lymphocyte ratio in patients with hypersensitivity pneumonia," *Sarcoidosis Vasculitis and Diffuse Lung Diseases: Official Journal of WASOG*, vol. 37, no. 4, Article ID e2020012, 2020.

[44] O. Kartal and A. T. Kartal, "Value of neutrophil to lymphocyte and platelet to lymphocyte ratios in pneumonia," *Bratislavske Lekarske Listy*, vol. 118, no. 9, pp. 513–516, 2017.

[45] J.-H. Lee, S. Song, S.-Y. Yoon, C. S. Lim, J.-W. Song, and H.-S. Kim, "Neutrophil to lymphocyte ratio and platelet to lymphocyte ratio as diagnostic markers for pneumonia severity," *British Journal of Biomedical Science*, vol. 73, no. 3, pp. 140–142, 2016.

[46] A. Adiguzel, E. M. Arsava, and M. A. Topcuoglu, "Temporal course of peripheral inflammation markers and indexes following acute ischemic stroke: prediction of mortality, functional outcome, and stroke-associated pneumonia," *Neurological Research*, vol. 44, no. 3, pp. 224–231, 2022.

Hindawi
Journal of Healthcare Engineering
Volume 2022, Article ID 8554188, 8 pages
https://doi.org/10.1155/2022/8554188

Review Article

Meta-Analysis of the Prognostic Value of Narcotrend Monitoring of Different Depths of Anesthesia and Different Bispectral Index (BIS) Values for Cognitive Dysfunction after Tumor Surgery in Elderly Patients

Na Chen[1] and Jing Lu[2]

[1]*School of Anesthesiology, Weifang Medical University, Weifang, China*
[2]*Department of Anesthesiology, Linyi People's Hospital, Linyi, China*

Correspondence should be addressed to Jing Lu; jinglu202112@163.com

Received 5 January 2022; Accepted 19 February 2022; Published 17 March 2022

Academic Editor: Enas Abdulhay

Objective. To study the effect of Narcotrend monitoring on the incidence of early postoperative cognitive dysfunction (POCD) under different bispectral index (BIS) conditions and the effect of different depths of anesthesia on the incidence of POCD. *Methods*. We performed a literature search of PubMed, Embase, OVID (database system made by Ovid Technologies, USA), CBM (Chinese Biomedical Literature database), CNKI (China National Knowledge Infrastructure), Wanfang, and VIP databases (full-text database of Chinese sci-tech journals), etc., from the date of the establishment of the database until December 31, 2020. Our meta-analysis was focused on the collection and study of Narcotrend monitoring of different depths of anesthesia. We carefully read the abstracts and full texts of randomized controlled trials on the incidence of POCD in the early postoperative period, and their references were tracked. Data extraction and quality evaluation of the included literature were also performed, and RevMan 5.3 software was used for analysis. *Results*. In the end, eight articles were included, with a total of 714 patients. The meta-analysis results showed that four articles (255 patients) compared the state of deep anesthesia (BIS 30–40) with conventional anesthesia (BIS 40–60 earlier) after POCD. Also, the incidence of POCD on the first day after deep anesthesia (Narcotrend stage (NTS): negative correlation is currently the most appropriate EEG description; Nd can subdivide the original EEG into six stages and 15 levels (Nd Sg, NTS), namely, A (state of wakefulness) state, B0 B2 (sedated state), C0 C2 (light anesthetic state), D0 D2 (general anesthesia), and E0–E1) was significantly lower than that of conventional anesthesia (NTS DO–D1) (odds ratio (OR) = 0.21, 95% confidence interval (CI): 0.13–0.35, $P < 0.00001$). Moreover, the incidence of POCD in deep anesthesia (NTS E1) at 7 days after surgery was significantly lower than that of conventional anesthesia (NTS D0) (OR (odds ratio) = 0.45, 95% CI: 0.23–0.91, $P = 0.03$), while the incidence of POCD 7 days after NTS D2 in conventional anesthesia was significantly lower than that of NTS D0 (OR = 0.42, 95% CI: 0.24–0.71, $P = 0.001$). *Discussion*. Deep anesthesia can reduce the incidence of POCD (OR = 0.40, 95% CI: 0.22–0.73, $P = 0.002$). This meta-analysis included three studies (216 patients) that compared the early postoperative POCD incidence of BIS 40–50 under conventional anesthesia and BIS 50–60; the BIS 40–50 did not significantly reduce the incidence of POCD (OR = 1.11, 95% CI: 0.24–5.24, $P = 0.9$). The incidence of POCD under deep anesthesia with Narcotrend monitoring was lower than that under conventional anesthesia.

1. Introduction

Postoperative cognitive dysfunction (POCD) is a postoperative complication of the central nervous system [1]. It is mainly manifested as differing degrees of obstacles such as memory, judgment, thinking, intelligence, orientation, etc., accompanied by a decline in social activity ability, and patients often experience anxiety, confusion, personality changes, and memory loss within 1 to 3 days after surgery. According to reports, the incidence of POCD within 1 week after major noncardiac surgery in elderly patients is as high as 25.8% [2]. Thus, POCD prevention has become a research hotspot, and there is currently no unified view on the impact of the depth of anesthesia on POCD.

This complication not only affects the patient's ability to take care of themselves, but also imposes a great burden on the family and society. As our society enters the aging stage of the population, the number of operations for elderly patients is gradually increasing. Thus, POCD prevention has become a research hotspot. Narcotrend monitoring is a novel anesthesia depth monitoring method that can subdivide the general anesthesia state into six stages and 15 sublevels of EEG (electroencephalogram) (Narcotrend stage, NTS). Among them, NTS D0–D2 (normal anesthesia state) and NTS E0–E2 (deep anesthesia state) are suitable for general anesthesia. The appropriate anesthesia depth can have the least impact on the postoperative cognitive function of the patient.

This study aims to systematically evaluate the effects of Narcotrend monitoring of different depths of anesthesia on POCD in order to provide a reference for clinical applications and further research. Studies have shown that maintaining an intraoperative bispectral index (BIS) value of 30–40 is more conducive to the recovery of early postoperative cognitive function. In this study, a meta-analysis was conducted to systematically evaluate the impact of different BIS values on POCD in order to provide a clinical reference [3].

2. Methods

2.1. Included Data. We performed a literature search for studies comparing Narcotrend monitoring under different BIS conditions in order to compare the incidence of early POCD in different patients. The treatment group received deep anesthesia surgery, while the control group received light anesthesia surgery.

The inclusion criteria were as follows: (I) patients aged >18 years old, without serious heart, liver, lung, nephropathy, or endocrine disease and no history of neuropsychiatry or anesthetic allergy; (II) patients with normal cognitive function before surgery who were planning to undergo elective surgery; and (III) postoperative patients with an incidence of early POCD ranging from 1 to 7 days. The exclusion criteria were as follows: (I) studies that did not provide a specific number of cases of cognitive dysfunction; and (II) studies that involved significant differences in the baseline data between the groups [4].

2.2. Detection Methods. We performed literature searches of the PubMed, Embase, OVID, CBM, CNKI, Wanfang, and VIP databases from the date of establishment of the database to December 2020. The English search terms included depth of anesthesia, postoperative cognitive dysfunction, cognitive function, cognitive dysfunction, cognitive impairments, mental disorders, and cognitive performance. The Chinese search terms included depth of anesthesia and postoperative cognition. There was no language restriction. The references of the retrieved documents were tracked, and the documents that met the inclusion criteria were included [5, 6].

2.3. Data Extraction. Two reviewers independently extracted data and evaluated the quality of the obtained literature. Differences of opinion were resolved by a third party ruling. The following data were extracted: (I) general information of the study, such as first author and year of publication; (II) research methods (such as retrospective research); (III) general information of the research subjects, such as age, gender, and ASA (American Society of Anesthesiologists) classification of the patient; (IV) treatment of the research object, such as the specific anesthesia methods; and (V) research results (such as the evaluation method of the research outcome and the research results (four-grid table data)).

The Jadad scale was used to evaluate the quality of the included literature. The scoring standards are as follows: randomization (0–2 points: 0 points for nondescription, 1 point for random descriptions only, and 2 points for random descriptions of normal methods); blinding method (0–2 points: 0 points for not stated, 1 point for blinding only, and 2 points for double-blind description); and loss to follow-up (including reasons, 0 or 1 point: 0 points for not stated and 1 point for narration). Literature with a score of 7 and a total score of 24 was considered high-quality research [7].

2.4. Statistical Analysis. Statistical analysis was performed using RevMan 5.3 statistical software provided by the Cochrane Collaboration. Measurement data were expressed in terms of the weighted mean difference (WMD) and its 95% confidence interval (CI), and count data were expressed in terms of odds ratio (OR) and its 95% CI. Subgroup and statistical homogeneity analyses were also performed, with $P > 1$ as the homogeneity test level. When the Q statistic of the heterogeneity test was $P > 0.1$, it was considered that there was no obvious heterogeneity between the studies, and the fixed-effects model was used for analysis. However, if the heterogeneity test statistic $P > 0.1$, it was considered that there was heterogeneity between the studies. In these cases, the sources of heterogeneity were divided into subgroups, and a random effects model was used.

3. Results

3.1. Retrieval Results and Quality Evaluation. A total of 551 documents were obtained from the initial search, including 114 from PubMed, 35 from OVID, 117 from CNKI, 97 from CBM, 137 from Wanfang, and 51 from VIP (Figure 1). After carefully reading the abstracts and full texts, a total of eight studies with a total of 714 patients met the inclusion criteria. The basic data of the included studies are shown in Table 1.

3.2. Meta-Analysis Results. A total of three studies compared the incidence of POCD on the first day after deep anesthesia (NTS E0–E1) and conventional anesthesia (NTS D0–D1). There was no significant heterogeneity between the studies

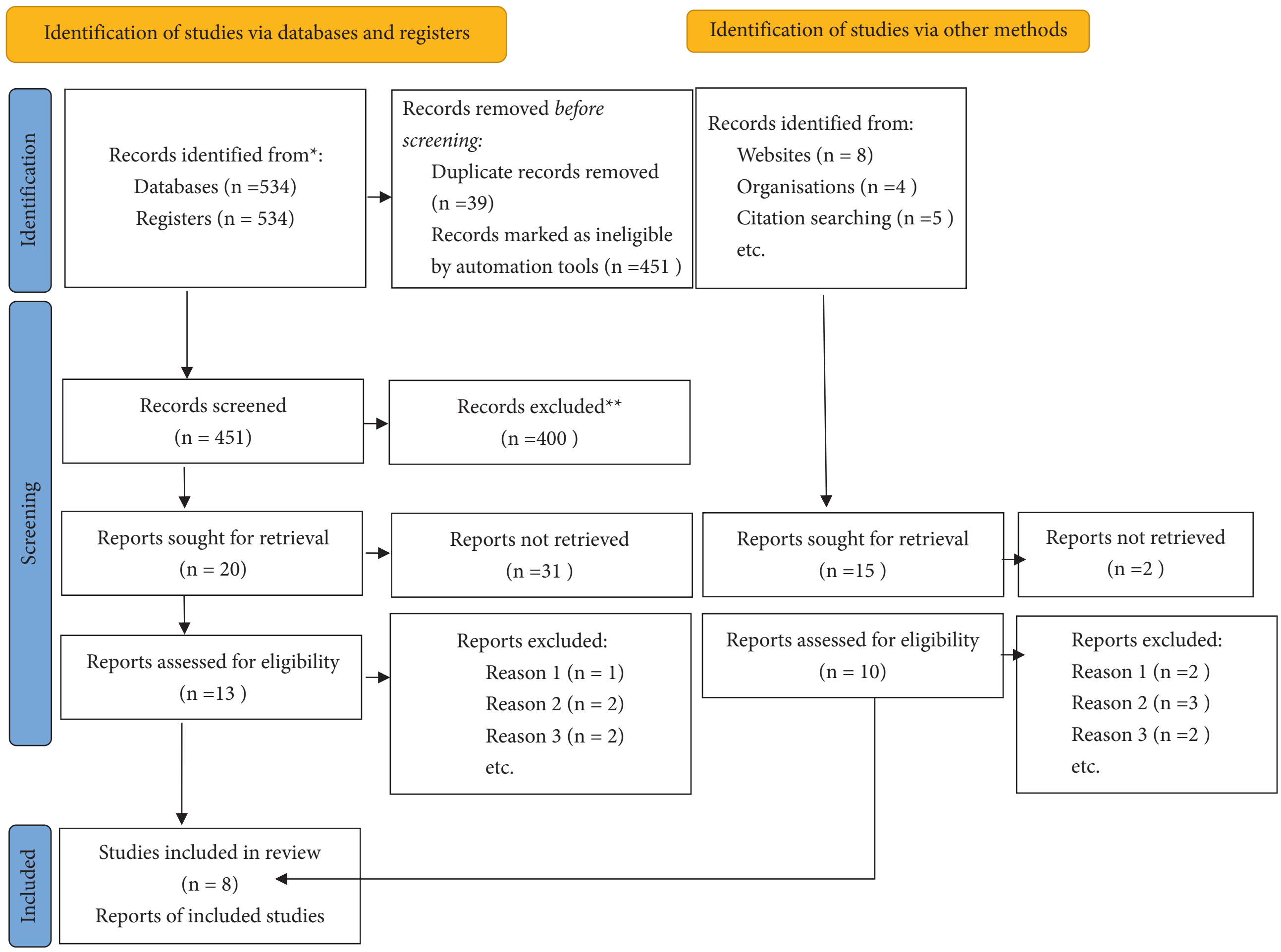

Figure 1: PRISMA flowchart. *Consider, if feasible to do so, reporting the number of records identified from each database or register searched (rather than the total number across all databases/registers). **If automation tools were used, indicate how many records were excluded by a human and how many were excluded by automation tools.

Table 1: Basic characteristics of the included studies.

Study	Age (years)	ASA rating (level)	Type of surgery	Research design	Detection indicator (ASA classification standard for anesthesia)	Detection time
Chengjin Le, 2019	>60	N–M	General anesthesia abdominal surgery	Random number table	(I)	Preoperative 1 day, after 1 day
Tao Feng, 2020	>70	I–M	Laparoscopic radical resection of bowel cancer	Random (unknown method) double-blind	(I), (II), (III), (IV), (V)	7 days before and after operation
Nian Liu, 2019	>60	I–M	Laparoscopic radical resection of bowel cancer	Random number table	(I), (II), (III), (IV), (V)	1 day before operation, 7 days after operation
Dongqing Wu, 2020	≥60	N–M	General anesthesia abdominal surgery	Random number table	(I)	Before operation and 1 day after operation
Yin Kang, 2018	60–92	I–M	Laparoscopic radical resection of bowel cancer	Computer random number method	(I), (II), (III), (IV), (V)	1 day before operation, 7 days after operation
Lingling Li, 2020	60–74	N–M	General anesthesia abdominal surgery	Random number table	(I)	Preoperative 1 day, after 1 day
Jia Deng, 2020	>65	I–N	Abdominal surgery	Random (method unknown)	(I), (VI)	1 day before operation, 7 days after operation
Shan Gao, 2019	3–65	I–N	Upper abdominal general surgery	Random (method unknown)	(I), (VI)	1 day before operation, 7 days after operation

Note: a total of three studies compared the state of deep anesthesia (NTSE1).

(P = 0.94, $I^2 = 0\%$), so a fixed-effects model was used for meta-analysis [8, 9]. The results showed that the incidence of POCD on the first day after deep anesthesia was significantly lower than that of conventional anesthesia (OR = 0.21, 95% CI: 0.13–0.35, $P < 0.00001$) (Figure 2).

Compared with conventional anesthesia (NTS D0), the incidence of POCD at 7 days postoperatively, there was no heterogeneity among the studies (P = 0.94, $I^2 = 0\%$), and the fixed-effects model was used for meta-analysis. The results showed that the incidence of POCD 7 days after deep anesthesia was significantly lower than that of conventional anesthesia (OR = 0.45, 95% CI: 0.23–0.91, P = 0.03) (Figure 3).

A total of five studies compared the incidence of POCD 7 days after surgery of NTS D2 and NTS D0 in conventional anesthesia. There was no heterogeneity among the studies (P = 0.87, $I^2 = 0\%$), and thus the fixed effects model was used for the meta-analysis. The results showed that the NTS POCD incidence of the postoperative NTS D2 group was significantly lower than the NTS D0 group (OR = 0.42, 95% CI: 0.24–0.71, P = 0.001) (Figure 4).

3.3. Sensitivity Analysis. A sensitivity analysis was carried out by changing the model, removing the maximum weight, and removing the minimum weight literature. The results showed that after three changes, the result has little change from the original OR value. Therefore, it can be considered that the sensitivity was low and the results of this study were relatively stable and reliable [10].

In the end, six studies met the inclusion criteria, including five Chinese studies and one English article, with a total of 521 patients. Four studies did not describe the method of random sequence generation, five studies did not describe the hiding of randomized sequences, and none of the studies described whether blinding was used; however, the subjects were blinded (i.e., single-blind) (Table 2). Furthermore, all of the included studies described the reasons for loss to follow-up as well as the treatment of these cases, and it could be considered that there is no incomplete data bias. The methodological quality evaluation of the included studies was detailed in four studies comparing the incidence of POCD on the first day after deep anesthesia (BIS 30–40) and conventional anesthesia (BIS 40–60). There was no heterogeneity among the studies, and the fixed effects model was used for the analysis. The results showed that under deep anesthesia, the incidence of POCD was significantly lower than that under conventional anesthesia (OR = 0.40, 95% CI: 0.22–0.73, P = 0.002) (Figure 5) [11–13].

The incidence of early postoperative POCD was compared between BIS 40–50 and BIS 50–60 in conventional anesthesia. There was heterogeneity among the research results, and thus, the random-effects model was used for analysis (Kant et al.) [14]. The results showed that there were no statistically significant differences in the incidence of early postoperative POCD between BIS 40–50 and BIS 50–60 (OR = 1.11, 95% CI: 0.24–5.24, P = 0.90) (Figure 6).

The deep anesthesia state (BIS 30–40) and the conventional anesthesia state (BIS 40–60) were compared on the third day after surgery, the incidence of POCD. There was no obvious heterogeneity between the studies, and the fixed-effects model was used for analysis. The results showed that after the first three deep anesthesias in anaesthetic-day conventional POCD, the difference in the incidence was not statistical significance (OR = 0.47, 95% CI: 0.13–1.71, P = 0.25) (Figure 7).

4. Discussion

At present, the pathogenesis of POCD is not clear. It may be based on the ageing of the nervous system, which is induced or aggravated by adverse stresses such as anesthesia and surgical trauma. Although the depth of anesthesia may have a certain relationship with the occurrence of POCD, there is currently no unified view. The intervention measures of this article are to perform anesthesia and surgical operations on patients, so it is difficult to double-blind the study subjects [14].

In this study, six articles with different BIS values were systematically evaluated, and the effects of different BIS values on the incidence of early postoperative POCD were compared. Four studies compared deep anesthesia (BIS 30–40) and general anesthesia (BIS 40–60) after the first day. At 1 day postoperatively, the incidence of POCD was significantly lower under general anesthesia than under deep anesthesia.

Systematic analysis of conventional anesthesia states such as BIS 40–50 and 50–60 showed that there was heterogeneity between the included studies. After analyzing and processing the existing heterogeneity, the results showed that there was no significant difference in the incidence of POCD under conventional anesthesia. This may be due to different studies using different surgical methods and anesthesia protocols. In addition, the sample size of this study is too small, which leads to deviations in the results.

This study further compared the incidence of POCD on the 3rd day after surgery under deep anesthesia (BIS 30–40) and conventional anesthesia (BIS 40–60), and the results showed that there was no significant difference between the two methods. This result may be compared with the literature method included in the study; poor learning quality is related to factors such as small sample size. Therefore, it is necessary to design more large-sample and high-quality randomized controlled trials for further systematic analysis.

In addition, this study found that under deep anesthesia, such as when BIS was 30–40, the incidence of POCD in the early postoperative period was lower than that of conventional anesthesia, which is consistent with the research conclusions. Previous studies have shown that deep anesthesia can significantly reduce the cerebral oxygen metabolism rate, thereby reducing the incidence of POCD in patients. Other studies have shown that deep anesthesia can inhibit the levels of cortisol, epinephrine, norepinephrine, etc., and reduce the body's stress response [15–17].

In summary, deep anesthesia has a certain effect on reducing POCD in the early postoperative period. However,

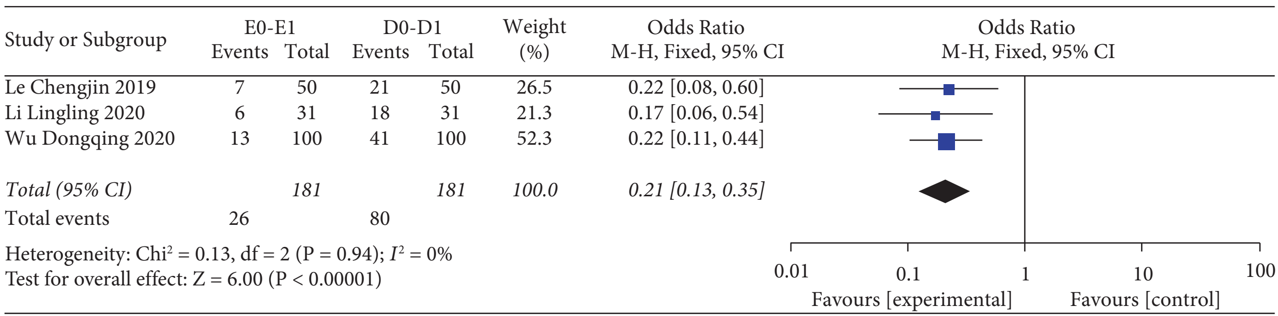

Figure 2: Forest plot of POCD incidence on day 1 after deep anesthesia and conventional anesthesia. POCD, postoperative cognitive dysfunction.

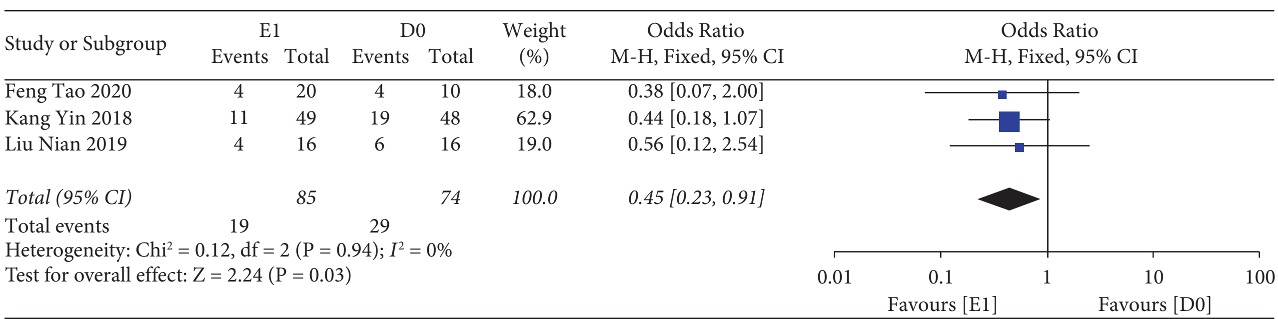

Figure 3: Forest plot of the incidence of POCD at 7 days after deep anesthesia and conventional anesthesia. POCD, postoperative cognitive dysfunction.

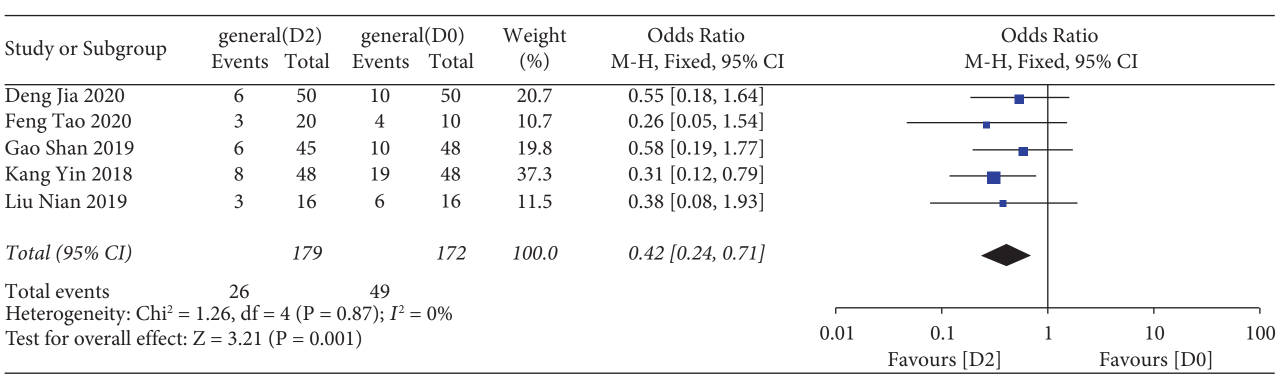

Figure 4: Forest plot of POCD incidence at 7 days after NTS D2 and NTS D0. POCD, postoperative cognitive dysfunction; NTS, XXXXX. NTS: negative correlation is currently the most appropriate EEG description; Nd can subdivide the original EEG into six stages and 15 levels (Nd Sg, NTS), or A (state of wakefulness) state, B0 B2 (sedated state), C0 C2 (light anesthetic state), and D0 D2 (general anesthesia).

Table 2: Methodological quality evaluation of the included studies.

Study	Random method	Blinding	Allocation hiding	Lost to follow-up/exit	Improved Jadad score
Xicai Li, 2020	Not sure	Not sure	Not sure	Without	3
Dong Hao, 2020	Not sure	Not sure	Not sure	Without	3
Bulong Bian, 2019	Computer random number method	Not sure	Not sure	Without	4
Feixiang Wang, 2019	Not sure	Not sure	Not sure	With	4
Bo Hong, 2020	Not sure	Not sure	Not sure	Without	3

due to the lack of multicenter studies in the literature included in this study, as well as the insufficient number and quality of randomized controlled trials, it was impossible to compare the incidence on the third or even the seventh day after surgery. Therefore, it is necessary to further develop rigorously designed and high-quality randomized controlled trials [18, 19].

POCD is the result of a combination of multiple factors, including the preoperative application of anticholinergic drugs, the patient's age, the preoperative underlying disease,

Study or Subgroup	Depth anesthesia Events	Depth anesthesia Total	General anesthesia Events	General anesthesia Total	Weight (%)	Odds Ratio M-H, Fixed, 95% CI
Bian Bulong 2019	6	25	19	50	26.5	0.52 [0.17, 1.52]
Hong Bo 2020	11	30	19	30	33.1	0.34 [0.12, 0.96]
Jiangxiong An 2020	4	40	11	40	27.2	0.29 [0.08, 1.02]
Li Xicai 2020	14	20	16	20	13.2	0.58 [0.14, 2.50]
Total (95% CI)		*115*		*140*	*100.0*	*0.40 [0.22, 0.73]*
Total events	35		65			

Heterogeneity: $Chi^2 = 0.82$, df = 3 (P = 0.85); $I^2 = 0\%$
Test for overall effect: Z = 3.02 (P = 0.002)

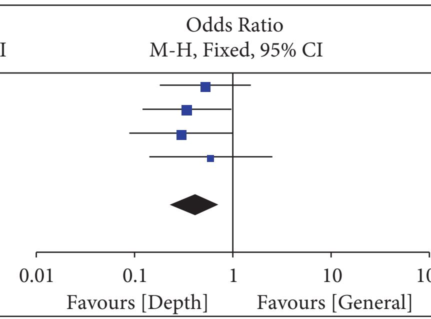

Figure 5: Comparison of the incidence of POCD on the first postoperative day between deep anesthesia and conventional anesthesia. POCD, postoperative cognitive dysfunction.

Study or Subgroup	Light anesthesia Events	Light anesthesia Total	Lighter anesthesia Events	Lighter anesthesia Total	Weight (%)	Odds Ratio M-H, Random, 95% CI
Bian Bulong 2019	5	25	14	25	31.5	0.20 [0.06, 0.69]
Hong Bo 2020	14	42	8	38	34.1	1.88 [0.68, 5.15]
Wang Feixiang 2019	19	44	8	42	34.4	3.23 [1.22, 8.56]
Total (95% CI)		*111*		*105*	*100.0*	*1.11 [0.24, 5.24]*
Total events	38		30			

Heterogeneity: $Tau^2 = 1.58$; $Chi^2 = 12.53$, df = 2 (P = 0.002); $I^2 = 84\%$
Test for overall effect: Z = 0.13 (P = 0.90)

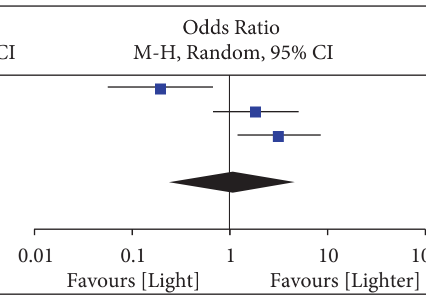

Figure 6: Comparison of the incidence of POCD in the early postoperative period between BIS 40–50 and BIS 50–60. POCD, postoperative cognitive dysfunction; BIS, bispectral index.

Study or Subgroup	Depth anesthesia Events	Depth anesthesia Total	General anesthesia Events	General anesthesia Total	Weight (%)	Odds Ratio M-H, Random, 95% CI
Hao Dong 2020	5	30	13	30	56.9	0.26 [0.08, 0.87]
Li Xicai 2020	4	20	4	20	43.1	1.00 [0.21, 4.71]
Total (95% CI)		*50*		*50*	*100.0*	*0.47 [0.13, 1.71]*
Total events	9		17			

Heterogeneity: $Tau^2 = 0.40$; $Chi^2 = 1.80$, df = 1 (P = 0.18); $I^2 = 44\%$
Test for overall effect: Z = 1.15 (P = 0.25)

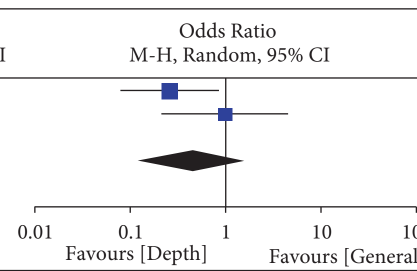

Figure 7: Comparison of the incidence of POCD between BIS 30–40 and BIS 40–60 on postoperative day 3. POCD, postoperative cognitive dysfunction; BIS, bispectral index.

the type of operation, the method and duration of anesthesia, the depth of anesthesia, as well as intraoperative hypotension and hypoxia. Older age is a definite influencing factor for the occurrence of POCD; the older the age, the higher the incidence of POCD and the longer the duration. The application of Narcotrend to select an appropriate depth of anesthesia is more conducive to reducing the incidence of various adverse reactions. Therefore, more attention should be paid to the influence of different depths of anesthesia on POCD [20, 21].

Narcotrend anesthesia trend is a new type of EEG/consciousness depth monitoring system with a professional EEG signal collection amplifier, which can accurately collect, monitor, and analyze real-time EEG signals at any position of the brain through ordinary ECG electrodes. Studies in China and abroad have found that Narcotrend can accurately reflect the changes in the depth of anesthesia during intravenous and inhalation anesthesia, and the depth of anesthesia is negatively correlated with NTS, which is currently the most suitable description for EEG [22, 23].

Narcotrend can subdivide the original EEG into six stages and 15 levels (NTS), namely, A (awake state), B0–B2 (sedation state), C0–C2 (light anesthesia state), D0–D2 (conventional anesthesia state), E0–E2 (deep anesthesia state), and F0–F2 (burst suppression state), and use the 0–100 dimensionless anesthesia depth index (Narcotrend index (NI)) to reflect the whole process from awake to deep anesthesia. Compared with BIS, Narcotrend not only distinguishes the state of consciousness over a large span but also provides the advantage of monitoring sudden changes in the depth of anesthesia [24, 25].

This study included eight articles and compared the effects of Narcotrend monitoring of different depths of anesthesia on POCD. The results showed that the incidence of early postoperative POCD under Narcotrend monitoring of deep anesthesia (E0–E1) was significantly lower than that of conventional anesthesia (D0–D1). The depth of anesthesia was maintained at the level of NTS D2 under conventional anesthesia. Compared with NTS D0, the incidence of postoperative POCD was significantly reduced.

Whether anesthesia has adverse effects on cognitive function is an area of particular interest for clinical anesthesiologists. The mechanism of deep anesthesia to protect cognitive function remains unclear. It may be that deep anesthesia reduces brain metabolism and produces neuroprotective effects, which further reduces the incidence of POCD in patients. In addition, surgery to stimulate the body's release of inflammatory factors and activation of glial cells can cause POCD cold. Studies such as FIDALGO have shown that an appropriate depth of anesthesia can also inhibit the inflammatory stress response and help protect the brain. However, in recent years, there have been limitations and controversies in the monitoring of the depth of anesthesia, and there are still reports of the awakening of patients under deep anesthesia. Therefore, this requires further study.

This systematic review has certain limitations that should be noted. At present, there are few studies on Narcotrend monitoring the influence of different depths of anesthesia on POCD in China and abroad. Due to the high literature requirements for meta-analysis, only eight articles met the final inclusion criteria. The sample sizes and the numbers of studies are insufficient, and thus, more large-sample and high-quality multicenter studies and randomized controlled trials need to be designed for further systematic analysis. In addition, due to the particularity of the anesthesia and surgeries to be performed on patients, it was difficult to implement rigorous blinding of the study subjects. The inclusion criteria did not report the allocation concealment, so the results of this study should be cautiously interpreted and applied [26].

In conclusion, deep anesthesia under Narcotrend monitoring can reduce the occurrence of early postoperative POCD, which can provide certain evidence-based medical assistance for the clinical work of anesthesiologists. Thus, deep anesthesia has a certain mitigating effect on POCD in the early postoperative period. However, the literature included in this study lacks multicenter research as well as a comparison of the incidences on postoperative days 3 or even 7, and therefore, more well-designed, high-quality controlled trials are needed to validate our findings.

Data Availability

The data used to support this study are available from the corresponding author upon request.

Conflicts of Interest

The authors declare that they have no conflicts of interest.

References

[1] J.-H. Shen, M. Ye, Q. Chen et al., "Effects of circadian rhythm on Narcotrend index and target-controlled infusion concentration of propofol anesthesia," *BMC Anesthesiology*, vol. 21, no. 1, 2021.

[2] D. Hight, C. Schanderhazi, M. Huber, F. Stuber, and H. A. Kaiser, "Age, minimum alveolar concentration and choice of depth of sedation monitor: examining the paradox of age when using the Narcotrend monitor: a secondary analysis of an observational study," *European Journal of Anaesthesiology*, vol. 39, no. 4, pp. 305–314, 2021.

[3] S. Heiderich, T. Ghasemi, N. Dennhardt et al., "Correlation of exhaled propofol with Narcotrend index and calculated propofol plasma levels in children undergoing surgery under total intravenous anesthesia - an observational study," *BMC Anesthesiology*, vol. 21, no. 1, 2021.

[4] J. F. Raue, J. Tünsmeyer, and S. B. R. Kästner, "Effects of isoflurane, remifentanil and dexmedetomidine on selected EEG parameters derived from a Narcotrend Monitor before and after nociceptive stimulation at different MAC multiples in cats," *BMC Veterinary Research*, vol. 16, no. 1, 2020.

[5] W. F. Puchner, M. W. Dünser, P. Paulus et al., "A comparative study on adequate anesthesia depth: clinical judgement and the Narcotrend measurement," *Canadian Journal of Anesthesia/Journal canadien d'anesthésie*, vol. 67, no. 6, pp. 664–673, 2020.

[6] E. K. Villa, D. Villa, and R. C. Bundoc, "Narcotrend-guided intraoperative care of a Trisomy 21 paediatric patient who underwent occipitocervical fusion," *BMJ Case Reports*, vol. 13, Article ID 231276, 2020.

[7] I. J. de Heer, A. T. Warmenhoven, and F. Weber, "Electroencephalographic density spectral array monitoring during propofol sedation in teenagers, using the narcotrend electroencephalographic monitor," *Minerva Anestesiologica*, vol. 86, pp. 601–607, 2020.

[8] K. Plaschke, A. Weiskircher, L. Benner et al., "Depth of anesthesia by Narcotrend and postoperative characteristics in children undergoing cardiac surgery under extracorporeal circulation: a retrospective comparison of two anesthetic regimens," *Perfusion*, vol. 35, no. 5, pp. 427–435, 2020.

[9] J. Berger-Estilita, K. Steck, C. Vetter et al., "A case report of several intraoperative convulsions while using the Narcotrend monitor," *Medicine*, vol. 98, no. 47, Article ID e18004, 2019.

[10] M. Zhang, J. Yuan, Q. Chen, Y. Qi, X. Jiang, and B. Liu, "Application of Narcotrend index and Richmond agitation-sedation score in sedation assessment of patients with short-term mechanical ventilation after pancreatoduodenectomy: a randomized controlled trial," *Zhonghua Wei Zhong Bing Ji Jiu Yi Xue*, vol. 31, pp. 737–741, 2019.

[11] K. Niu, C. Guo, C. Han, and S. Teng, "Equipment failure of intravenous syringe pump detected by increase in Narcotrend stage," *Medicine*, vol. 97, no. 47, Article ID e13174, 2018.

[12] N. Dennhardt, S. Arndt, C. Beck et al., "Effect of age on Narcotrend Index monitoring during sevoflurane anesthesia in children below 2 years of age," *Pediatric Anesthesia*, vol. 28, no. 2, pp. 112–119, 2018.

[13] N. Dennhardt, C. Beck, D. Boethig et al., "Impact of temperature on the Narcotrend Index during hypothermic cardiopulmonary bypass in children with sevoflurane anesthesia," *Perfusion*, vol. 33, no. 4, pp. 303–309, 2018.

[14] R. Kant, P. K. Dubey, and A. Ranjan, "Palonosetron pretreatment is not as effective as lignocaine for attenuation of pain on injection of propofol," *Turkish journal of anaesthesiology and reanimation*, vol. 48, pp. 196–201, 2019.

[15] N. Dennhardt, D. Boethig, C. Beck et al., "Optimization of initial propofol bolus dose for EEG Narcotrend Index-guided transition from sevoflurane induction to intravenous anesthesia in children," *Pediatric Anesthesia*, vol. 27, no. 4, pp. 425–432, 2017.

[16] J. Tünsmeyer, K. Hopster, and S. B. Kästner, "Clinical use of a multivariate electroencephalogram (narcotrend) for assessment of anesthetic depth in horses during isoflurane-xylazine anesthesia," *Frontiers in veterinary science*, vol. 3, 2016.

[17] K. A. Otto, "Differential effects of propofol and isoflurane on the relationship between EEG Narcotrend index and clinical stages of anaesthetic depth in sheep undergoing experimental cardiac surgery," *The Veterinary Journal*, vol. 208, pp. 87–89, 2016.

[18] J. Ji, G. Wang, K. Sun, G. Zhou, Z. Wang, and Y. Wang, "Application of dexmedetomidine combined with propofol in patients undergoing painless colonoscopy for colonic polyps resection under Narcotrend monitoring," *Nan Fang Yi Ke Da Xue Xue Bao*, vol. 35, pp. 264–267, 2015.

[19] C. X. Li and H. Li, "Determination of the 50% effective concentration of dexmedetomidine as an adjuvant in combined spinal-epidural anesthesia with Narcotrend," *Nan Fang Yi Ke Da Xue Xue Bao*, vol. 31, pp. 734–736, 2011.

[20] G. Duan, S. Guo, H. Zhan, D. Qi, Y. Zhang, and X. Zhang, "A new real-time method for detecting the effect of fentanyl using the preoperative pressure pain threshold and narcotrend index," *Medicine*, vol. 94, no. 1, Article ID e316, 2015.

[21] Y.-S. Qiu and Q. Xu, "Accuracy of narcotrend index in monitoring depth of anesthesia in diabetics: a case report," *Chinese Medical Sciences Journal*, vol. 29, no. 4, pp. 251-252, 2014.

[22] Z. Guo, L. Pang, X. Jia et al., "Intraoperative target-controlled infusion anesthesia application using remifentanil hydrochloride with etomidate in patients with severe burn as monitored using Narcotrend," *Burns*, vol. 41, no. 1, pp. 100–105, 2015.

[23] J. Shepherd, J. Jones, G. Frampton, J. Bryant, L. Baxter, and K. Cooper, "Clinical effectiveness and cost-effectiveness of depth of anaesthesia monitoring (E-Entropy, Bispectral Index and Narcotrend): a systematic review and economic evaluation," *Health Technology Assessment (Winchester, England)*, vol. 17, pp. 1–264, 2013.

[24] Y. Jiang, B. Qiao, L. Wu, and X. Lin, "Application of narcotrend monitor for evaluation of depth of anesthesia in infants undergoing cardiac surgery: a prospective control study," *Brazilian Journal of Anesthesiology*, vol. 63, no. 3, pp. 273–278, 2013.

[25] H. Rinösl, T. Fleck, and M. Dworschak, "Brain ischemia instantaneously tracked by the narcotrend EEG device," *Journal of Cardiothoracic and Vascular Anesthesia*, vol. 27, 2013.

[26] Z. G. Guo, X. Y. Wang, X. L. Lü, X. J. Su, and J. H. Hao, "Application of Narcotrend-assisted anesthesia in-depth monitor during escharectomy and skin transplantation in burn patients with target-controlled infusion of remifentanil hydrochloride and propofol," *Zhonghua Shaoshang Zazhi*, vol. 28, pp. 178–182, 2012.

Hindawi
Journal of Healthcare Engineering
Volume 2022, Article ID 9467568, 7 pages
https://doi.org/10.1155/2022/9467568

Research Article

Analysis of Clinical Outcomes of Different Fertilization Methods in Patients with ≤3 Eggs Retrieved

Shuang Wang, Xiaoyan Zhang, Hongchu Bao, and Yuanqing Cui

Department of Reproductive Medicine, Qingdao University Affiliated Yantai Yuhuangding Hospital, Yantai, Shangdong 264000, China

Correspondence should be addressed to Yuanqing Cui; yuanqing_cui@126.com

Shuang Wang and Xiaoyan Zhang contributed equally to this work.

Received 7 January 2022; Revised 16 February 2022; Accepted 21 February 2022; Published 16 March 2022

Academic Editor: Enas Abdulhay

Objective. To explore the intracytoplasmic sperm injection (ICSI) and *in vitro* fertilization (IVF) method on the clinical outcomes of infertile women with ≤3 eggs retrieved. *Study Design*. We retrospectively analyzed a cohort of female patients who received IVF/ICSI to assist pregnancy with retrieved eggs ≤3. The general conditions, i.e., two pronuclei (2PN) fertilization rate, abnormal fertilization rate, high-quality embryo rate, cycle cancellation rate, pregnancy rate of fresh embryo transfer, cumulative pregnancy rate, and miscarriage were compared between the two groups. *Results*. When the number of retrieved eggs was one, the fertilization rate of 2PN was higher and the cycle cancellation rate was lower in the ICSI group than in the IVF group ($P < 0.05$). The pregnancy rates of fresh embryo transfer, frozen-thawed embryo transfer, and the cumulative pregnancy rate were all higher in the ICSI group than in the IVF group ($P < 0.05$). When the number of retrieved eggs was two, the pregnancy rate of frozen-thawed embryo transfer and cumulative pregnancy rate in the ICSI group were higher than those in the IVF group ($P < 0.05$). When the number of retrieved eggs was three, the fertilization rate of 2PN and the pregnancy rate of frozen-thawed embryo transfer were higher in the ICSI group than those in the IVF group (all ($P < 0.05$)). *Conclusions*. For patients with one egg retrieved, ICSI fertilization can reduce abnormal fertilization rate and cycle cancellation rate and improve cumulative pregnancy rate significantly enhancing patients' benefits. However, increasing the number of eggs retrieved decreases the advantages of ICSI fertilization.

1. Introduction

With the development of assisted reproductive technology (ART), the clinical pregnancy rate has gradually increased. Studies have shown that the clinical pregnancy rate increases with the number of retrieved eggs [1, 2]. However, patients with decreased ovarian reserve function and low ovarian response have fewer eggs retrieved in a single operation, which is often less than or equal to 3. In these patients, fewer embryos can be transferred and the pregnancy rate is low [3]. Multiple egg retrieval operations are needed to achieve a successful pregnancy ultimately increasing the trauma of patients [4]. At present, the problem that needs to be solved is to improve the effective utilization of eggs when the number of eggs retrieved is low. An effective approach is to reduce the occurrence of abnormal fertilization, such as the occurrence of fertilization failure (zero pronucleus, 0PN) and multiple pronuclei (multi-PN, MPN) [5].

Intracytoplasmic sperm injection (ICSI) technology has been applied to non-male-derived infertility in the world, such as preimplantation genetic testing, failure of more than two ART assisted pregnancies, less than 5 eggs retrieved, patients ≥38 years old, and unexplained infertility [6]. The National Assisted Reproductive Technology Surveillance System (NASS) reported that the utilization rate of ICSI for male infertility had increased from 76.3% to 93.93% between 1996 and 2012. The utilization rate of ICSI in nonmale factor caused infertility had increased from 15.4% to 66.9% [7]. However, since ICSI is an invasive procedure, experts have different opinions on whether ICSI should be applied to patients with fewer eggs retrieved [8, 9]. In China, ICSI indications are relatively strictly controlled, and the increase of ICSI application rate is not as significant as that in Western countries. Scientists have discussed for many years whether ICSI indications should be extended to low retrieved egg number, poor fertilization history, and unexplained infertility. However, the conclusions remain controversial [10]. For the pregnancy outcome of patients with retrieved eggs ≤3, some studies suggest that ICSI can reduce the abnormal fertilization rate and cycle cancellation rate and improve the number of transferrable embryos and pregnancy rate [11, 12]. Other studies suggest that ICSI and IVF have no difference in pregnancy outcomes [13, 14]. Therefore, we retrospectively analyzed patients with retrieved egg number ≤3 and divided them into an ICSI group and an IVF group according to different fertilization methods they received. We matched the patients in the two groups based on age and ovulation induction scheme to reduce selection bias. By comparing the mature egg (MII) rate, 2PN fertilization rate, abnormal fertilization rate, high-quality embryo rate, cycle cancellation rate, pregnancy rate of fresh embryo transfer, miscarriage rate, cumulative pregnancy rate, and cumulative miscarriage rate, we investigated the effects of ICSI and IVF on the pregnancy outcomes of patients with retrieved eggs ≤3.

2. Materials and Methods

2.1. Research Subjects. This study was approved by the Ethics Committee of Qingdao University-affiliated Yantai Yuhuangding Hospital. All patients signed IVF or ICSI informed consent forms. Infertility patients who received IVF/ICSI in the Department of Reproductive Medicine, Qingdao University-affiliated Yantai Yuhuangding Hospital between January 2017 and June 2020 were selected for this study. Patients' inclusion was based on the following: (1) ≤3 retrieved eggs; (2) no abnormality in uterus and hysteroscopy showed that the endometrium was normal; (3) pituitary prolactin (PRL) was within normal range (6.0 ng/ml 29.9 ng/ml); and (4) normal thyroid function. Patients with (1) 42 years of age or above; (2) suffering from diabetes, hypertension, or other uncontrolled medical complications; and (3) received preimplantation genetic testing (PGT) were excluded from this study.

3. Research Methods

3.1. Grouping. The patients were divided into an ICSI group and an IVF group according to the different fertilization methods they received. After screening by inclusion and exclusion criteria, 326 cycles were included in the ICSI group, and 2,086 cycles that had ≤3 retrieved eggs were included in the IVF group.

3.2. Ovulation Induction Process. Ovulation induction treatment included microstimulation treatment, antagonist treatment, and natural cycle IVF.

(i) Microstimulation treatment: on the second day of the menstrual cycle, letrozole (0.5 mg/tablet, Furui, Hengrui Medicine, China) was given orally at 5 mg/d for 5 days After five days of letrozole treatment, urinary follicle stimulating hormone (75 IU/package, Lishenbao, Lizhu Medicine, China) for injection was initiated. The initial dose was 150–300 IU/d and continued until the day of HCG.

(ii) Antagonist treatment: on the second day of menstrual cycle, recombinant human follicle stimulating hormone (rFSH, 600 IU/package, Puregon, Organon, the Netherlands) was injected daily. The initial dose was 150–300 IU/d, and the dosage was adjusted according to the patient's condition until the maximum follicle diameter was 12 mm or E_2 level was higher than 1,468 pmol/L. Subsequently, GnRH antagonist (Ganirelix, 0.25 mg/package, MSD, USA) 0.25 mg/d was added to the treatment schedule until the day of HCG.

Follicular development was monitored by transvaginal ultrasound. When the diameter of at least one or two follicles was ≥1.8 cm, human chorionic gonadotrophin (hCG, 2,000 IU/package, Lizhu, Zhuhai, China) at 6,000 IU was injected subcutaneously to the patient. After 36 h, ultrasound-guided transvaginal egg retrieval was performed.

3.3. Fertilization and Embryo Transfer. IVF or ICSI was used according to the quality of semen. In IVF, 50 ul microdrop insemination technique was used. Sperm at the insemination concentration of 10,000 sperm/50 ul was added into the microdrop in insemination dish using a Pasteur pipette, and one oocyte was added to each microdrop. Before ICSI insemination, oocytes were degranulated. MII-stage oocytes were selected for ICSI insemination. After immobilization, the sperm was aspirated into an injection needle so that the sperm head was located at the tip of the injection needle. The tip of the needle was moved into the droplet containing an oocyte. The oocyte was fixed with the fix needle so that the first polar body was located at 11–12 o'clock position or 6 o'clock position. Next, the injection needle passed through the zona pellucida and entered the cytoplasm of the oocyte. After the oocyte membrane was broken, the sperm was slowly injected into the central area of the oocyte, and then, the injection needle was slowly withdrawn.

On the third day after oocyte retrieval, one or two embryos were transferred to the uterine cavity of the patient and the remaining embryos were cryopreserved. After embryo transfer, progesterone soft capsule (Utrogestan, 100 mg/capsule, Laboratoires Besins International, France) at 200 mg was given intravaginally, once every 8 h for luteal support. On the 14th day following embryo transfer, hCG levels of the patients were determined. The level of hCG >5.0 IU/L was considered biochemical pregnancy. On the 35th day after the embryo transfer, patients received ultrasonography, the appearance of the gestational sac confirmed clinical pregnancy. For frozen-thawed embryo transfer (FET), patients with regular menstrual cycle were treated with natural cycle plan for endometrial preparation, while patients with irregular menstrual cycles were treated with hormone replacement plan for endometrial preparation. The embryo transfer criterium was based on that the endometrium should be ≥8 mm with homogeneous echo.

3.4. Observation Index. The general conditions of the patients, including age, duration of infertility, type of infertility (primary/secondary), basic FSH, basic E_2, BMI, AMH, ovulation induction scheme, and abnormal semen of the male were observed. Laboratory and clinical outcomes were recorded, including MII rate (number of mature eggs/number of retrieved eggs), 2PN fertilization rate (2PN fertilized eggs/number of mature eggs), fertilization failure rate (number of mature eggs−number of 2PN fertilized eggs/number of mature eggs), high-quality embryo rate (number of high-quality embryos/number of 2PN cleaved embryos), cycle cancellation rate, pregnancy rate and miscarriage rate of fresh embryo transfer, pregnancy rate and miscarriage rate of frozen-thawed embryo transfer, miscarriage rate, and cumulative pregnancy rate. In this study, normal fertilization was defined as zygotes with 2PN following ICSI or IVF. Fertilization failure was defined as zero oocytes reaching the zygote stage with 2PN. The cycle cancellation rate only referred to the cycle cancelled due to the absence of transferrable embryos because of the failure of fertilization. The cumulative pregnancy rate referred to the total number of pregnancies achieved in all egg retrieval cycles analyzed in this study with normally fertilized embryos following fresh embryo transfer and frozen-thawed embryo transfer.

3.5. Statistical Analysis. The statistical software package (SPSS 20.0) was employed for statistical processing and analysis. Mean ± standard deviation ($\overline{x} \pm s$) was used for expressing measurement data, while percentage (%) was used for expressing count data. The analysis of the measurement data was carried out using independent sample *t*-test, while Fisher exact test and chi-square test were employed for the analysis of count data. ($P < 0.05$) was considered statistically significant.

4. Results

4.1. Comparison of General Data between the ICSI Group and IVF Group. After screening using inclusion and exclusion criteria, there were 326 cycles in the ICSI group and 2,086 cycles in the IVF group. There were no significant differences in age, infertility duration, body mass index (BMI), basic E_2, AMH, and ovulation induction scheme between the two groups with ($P > 0.05$) suggesting that the two groups were similar in terms of basic characteristics. However, the proportion of primary infertility was higher in the ICSI group than that in the IVF group ($P < 0.05$). The basic FSH value was higher in the ICSI group than that in the IVF group ($P < 0.05$). The proportion of abnormal semen of males in the ICSI group was also higher than that in the IVF group ($P < 0.05$). The details of patients' demographics and other characteristics are shown in Table 1.

4.2. Comparison of the Clinical Outcomes between the ICSI Group and IVF Group When ≤3 Eggs Were Retrieved. The fertilization rate of 2PN was higher in the ICSI group than that in the IVF group ($P < 0.05$). The cycle cancellation rate was markedly higher in the IVF group than that in the ICSI group ($P < 0.05$). The pregnancy rate and cumulative pregnancy rate were both higher in the ICSI group than that in the IVF group (($P < 0.05$), Table 2).

4.3. Comparison between the ICSI Group and IVF Group When the Number of Retrieved Eggs Were One, Two, and Three, Respectively. When the number of retrieved eggs was one, the fertilization rate of 2PN was higher in the ICSI group than that in the IVF group ($P < 0.05$). The cycle cancellation rate was higher in the IVF group than that in the ICSI group ($P < 0.05$). The pregnancy rates of fresh embryo transfer and frozen-thawed embryo transfer as well as cumulative pregnancy rate were all significantly higher in the ICSI group than that in the IVF group ($P < 0.05$).

When the number of retrieved eggs was two, the pregnancy rate of frozen-thawed embryo transfer and cumulative pregnancy rate were higher in the ICSI group than that in the IVF group ($P < 0.05$).

When the number of retrieved eggs was three, the fertilization rate of 2PN was significantly higher in the ICSI group than that in the IVF group ($P < 0.05$). The pregnancy rate of frozen-thawed embryo transfer was higher in the ICSI group than in the IVF group ($P < 0.05$). Detailed comparison between the groups is shown in Table 3.

5. Discussion

In the IVF cycle, if all or most of the eggs are not fertilized or fertilized abnormally and there is no transferrable embryo, it will bring a double blow to the patient economically and mentally [15]. The key to successful pregnancy for patients with ≤3 eggs retrieved is to obtain as many transferrable embryos as possible. The premise of obtaining transferrable embryo is to obtain normally fertilized embryo. Most of the patients whose number of retrieved eggs is ≤3 have poor ovarian function and low ovarian response. Studies have shown that the live birth rate in patients with poor ovarian function decreases. However, with the increase of the number of retrieved eggs, the cumulative live birth rate increases. At the same time, the proportion of cycles cancellation due to the lack of transferrable embryos decreases significantly [1]. Patients with ovarian dysfunction and low ovarian response often need multiple egg retrieval to achieve pregnancy. Multiple egg retrieval operations can cause enormous physical and psychological trauma and economic burden to the patients. How to improve the effective utilization of retrieved eggs and increase the pregnancy rate of patients with ≤3 retrieved eggs was the focus of this study.

According to the statistics of 2,414 cycles, the proportion of primary infertility was higher in the ICSI group than that

Table 1: Comparison of the general data between the ICSI group and IVF group.

Index	ICSI group $n = 326$	IVF group $n = 2086$	F/x^2	P value
Age (years, $\overline{x} \pm s$)	34.88 ± 3.82	35.11 ± 4.03	1.248	0.348
Duration of infertility (years, $\overline{x} \pm s$)	4.97 ± 3.35	4.80 ± 3.56	0.866	0.395
Infertility			8.050	0.005
Primary infertility (case (%))	175 (53.68)	944 (45.25)		
Secondary infertility (case (%))	151 (46.32)	1142 (54.75)		
bFSH (U/L, $\overline{x} \pm s$)	11.49 ± 5.89	10.55 ± 5.76	1.450	0.006
bE_2 (pg/ml, $\overline{x} \pm s$)	35.04 ± 17.10	34.66 ± 19.22	1.572	0.741
BMI (kg/m^2, $\overline{x} \pm s$)	23.79 ± 3.41	23.74 ± 3.56	2.853	0.814
AMH (ng/ml, M (P25, P75))	0.66 (0.32, 1.25)	0.73 (0.28, 1.43)	−0.283	0.812
	Ovulation induction scheme			
Microstimulation (case (%))	227 (69.63)	1,429 (68.50)	0.167	0.683
Antagonists (case (%))	71 (21.78)	494 (23.68)	0.569	0.451
Natural cycle (case (%))	28 (8.59)	163 (7.81)	0.232	0.630
Abnormal semen in male* (case (%))	201 (61.66)	433 (20.76)	243.396	<0.01

*Normal semen criteria: according to the WHO manual for the examination and processing of human semen (5th edition), semen was normal and there was no anti-sperm antibody. The details were as follows: concentration $>15 \times 10^6$/ml, total vitality >40%, premotor movement >32%, normal morphology >4%, and volume >1.5 ml. $P < 0.05$ was considered that the difference was statistically significant.

Table 2: Comparison of the clinical data and pregnancy outcomes between the ICSI group and IVF group when ≤3 eggs were retrieved.

Index	ICSI group (case) $n = 326$	IVF group (case) $n = 2,086$	P value
Gn time (d, $\overline{x} \pm s$)	8.21 ± 3.13	8.43 ± 3.34	0.298
Total Gn (IU, $\overline{x} \pm s$)	$1,878.37 \pm 1,001.69$	$1,854.62 \pm 1,007.40$	0.708
Number of eggs retrieved ($x \pm s$)	1.94 ± 0.82	1.94 ± 0.82	0.997
MII rate (case (%))	543 (85.78)	3,467 (85.58)	0.895
2PN fertilization rate (case (%))	477 (87.85)	2,775 (80.04)	<0.01
Abnormal fertilization rate* (case (%))	66 (12.15)	692 (19.96)	<0.01
High-quality embryo rate (case (%))	258 (56.70)	1544 (56.74))	0.993
Cycle cancellation rate** (case (%))	27 (8.28)	256 (12.27)	0.037
	Fresh embryo transfer		
Pregnancy rate (case (%))	30 (40.00)	178 (37.71)	0.705
Miscarriage rate (case (%))	4 (13.33)	27 (15.17)	0.794
	Frozen-thawed embryo transfer		
Pregnancy rate (case (%))	89 (48.63)	128 (29.63)	<0.01
Miscarriage rate (case (%))	13 (14.61)	13 (10.16)	0.321
Cumulative pregnancy rate (case (%))	119 (46.12)	306 (33.85)	<0.01
Cumulative miscarriage rate (case (%))	17 (14.29)	40 (13.07)	0.742

*(0PN + 1PN + multi-PN) fertilization. **Cancellation of cycles due to abnormal fertilization (multi-PN fertilization in the IVF group and 0PN + 1PN + multi-PN fertilization in the ICSI group).

in the IVF group. This is because the proportion of poor semen quality in the ICSI group was higher than that in the IVF group, and the proportion of infertility caused by male factors was also higher in the ICSI group. The basic FSH value in ICSI group was higher than that in the IVF group (11.49 ± 5.89 vs 10.55 ± 76) ($P < 0.05$). However, the number of eggs retrieved in enrolled patients was fixed, and there was no statistical difference in ovulation induction treatment and AMH value. Therefore, the basic FSH value had no impact on this study. The basic FSH values of the two groups were both higher than 10 IU/L, and the AMH values were both less than 1 ng/ml, suggesting that the ovarian reserve function was decreased in both groups.

In this study, in patients with ≤3 eggs retrieved, the 2PN fertilization rate was higher in the ICSI group than that in the IVF group ($P < 0.05$), while the cycle cancellation rate was higher in the IVF group than in the ICSI group ($P < 0.05$). The pregnancy rate of frozen-thawed embryo transfer and cumulative pregnancy rate were both higher in the ICSI group than in the IVF group ($P < 0.05$). However, after further grouping patients according to the number of retrieved eggs (one, two, and three), we found when the number of retrieved eggs was one that the pregnancy rates of fresh embryo transfer and frozen-thawed embryo transfer, and the cumulative pregnancy rate were all higher in the ICSI group than that in the IVF group ($P < 0.05$). When the number of retrieved eggs was two, the pregnancy rate of frozen-thawed embryo transfer and cumulative pregnancy rate of the ICSI group were higher than those of the IVF group ($P < 0.05$). When the number of retrieved eggs was three, the pregnancy rate of frozen-thawed embryo transfer in the ICSI group was higher than that of the IVF group ($P < 0.05$). Cycle cancellation can be caused by many reasons, including luteal phase ovulation induction, thin endometrium, and abnormal fertilization. Therefore, abnormal fertilization-caused cycle cancellation should be analyzed separately to reflect the difference of clinical outcomes caused by different fertilization methods. In this study, in

Table 3: Comparison of the clinical data and pregnancy outcomes between ICSI and IVF groups when the number of retrieved eggs was one, two, and three, respectively.

Index	One egg retrieved		P value	Two eggs retrieved		P value	Three eggs retrieved		P value
	ICSI group	IVF group		ICSI group	IVF group		ICSI group	IVF group	
Number of case	119	774		107	660		100	652	
Gn time (d, $\overline{x} \pm s$)	7.28 ± 3.67	7.77 ± 3.93	0.281	8.50 ± 2.75	8.59 ± 3.35	0.782	8.70 ± 2.84	8.87 ± 2.53	0.550
Total Gn (IU, $\overline{x} \pm s$)	1,500.88 ± 1,109.45	1,590.79 ± 1,120.78	0.489	2,002.14 ± 924.42	1890.06 ± 978.93	0.273	2,069.28 ± 900.86	2,056.24 ± 867.90	0.889
MII rate (case (%))	116 (97.48)	663 (85.65)	<0.01	176 (82.24)	1,127 (85.37)	0.234	251 (83.67)	1,677 (85.74)	0.344
2PN fertilization rate (case (%))	100 (86.21)	498 (75.11)	0.009	147 (83.52)	904 (80.21)	0.301	230 (91.63)	1373 (81.87)	<0.01
Abnormal fertilization rate* (case (%))	16 (13.79)	165 (24.89)	0.009	29 (16.48)	223 (19.79)	0.301	21 (8.37)	304 (18.13)	<0.01
High-quality embryo rate (case (%))	47 (50.54)	279 (56.47)	0.290	75 (54.35)	501 (56.67)	0.608	136 (60.71)	764 (56.88)	0.284
Cycle cancellation rate** (case (%))	17 (14.29)	177 (22.87)	0.035	9 (8.41)	60 (9.09)	0.820	1 (1.00)	19 (2.91)	0.268
Fresh embryo transfer									
Pregnancy rate (case (%))	8 (44.44)	18 (21.43)	0.042	10 (40)	52 (37.41)	0.516	12 (37.50)	108 (43.37)	0.191
Miscarriage rate (case (%))	1/8 (12.5)	4/18 (22.22)		1/10 (10.0)	7/52 (13.46)		2/12 (16.67)	16/108 (14.81)	
Frozen-thawed embryo transfer									
Pregnancy rate (case (%))	27 (42.19)	52 (28.26)	0.039	30 (46.88)	38 (28.57)	0.011	32 (58.18)	38 (33.04)	0.002
Miscarriage rate (case (%))	2/27 (7.41)	4/52 (7.69)		6/30 (20)	5/38 (13.16)		5/32 (15.63)	4/38 (10.53)	
Cumulative pregnancy rate (case (%))	35 (42.68)	70 (26.12)	0.004	40 (44.94)	90 (33.09)	0.043	44 (50.57)	146 (40.11)	0.076
Cumulative miscarriage rate (case (%))	3/35 (8.57)	8/70 (11.43)	0.652	7/40 (17.5)	12/90 (13.33)	0.535	7/44 (15.91)	20/146 (13.70)	0.713

$P < 0.05$ was considered that the difference was statistically significant. *(0PN+ 1PN + multi-PN) fertilization. **Cancellation of cycles due to abnormal fertilization (multi-PN fertilization in the IVF group and 0PN + 1PN + multi-PN fertilization in the ICSI group).

patients with one egg retrieved, 22.87% (177 cycles) of IVF group patients and 14.29% (17 cycles) of the ICSI group patients were cancelled due to abnormal fertilization. The patients who had no transferrable embryos due to abnormal fertilization needed to receive another ovulation induction and egg retrieval operation. The patients who have less transferrable embryos due to abnormal fertilization will lose the chance of frozen-thawed embryo transfer, which will reduce the cumulative pregnancy rate. It suggested that ICSI is a better fertilization method for patients with one egg retrieved.

In general, ICSI is more beneficial than IVF in patients with one egg retrieved when compared with patients with two or three eggs retrieved. It not only can improve the cumulative pregnancy rate and reduce the cycle cancellation rate but also can reduce the potential risk and trauma of multiple egg retrieval operations. In previous studies, whether ICSI can improve the pregnancy outcome of patients with ≤3 eggs retrieved remains controversial. Some researchers believe that ICSI can improve the number of transferrable embryos and the pregnancy rate [11, 12]. Some others consider that compared with IVF, ICSI has no significant impact on pregnancy outcome [13, 14]. In previous studies, it may be because the number of cycles with one, two, and three eggs retrieved was not consistent, e.g., there were more patients in the group with one egg retrieved. ICSI can provide more transferrable embryos and improve the cumulative pregnancy rate. ICSI can improve pregnancy outcome. In contrast, when most patients had 2 or ≥3 eggs retrieved, ICSI-provided improvement of pregnancy outcome was limited, which may be the reason for inconsistent statistical outcomes.

According to literature reports, in women with advanced age and nonmale factor infertility, ICSI does not significantly improve the embryo quality and clinical outcomes [16, 17]. Our study indicated that in patients with nonmale infertility, advanced age is not a criterion for whether choose ICSI as *in vitro* fertilization method. Patients with advanced ages can also obtain more than three embryos. Low number of retrieved eggs is the criterion for ICSI fertilization.

The damage of ICSI to oocytes remains controversial, and there is no clear evidence to show that ICSI can affect the health of offspring [18, 19]. In our study, when patients with ≤3 eggs retrieved, high-quality embryo rate was 56.70% in the ICSI group and 56.74% in the IVF group. There was no significant difference between the two groups. This result suggests that ICSI does not damage the quality of embryo. The miscarriage rate of fresh embryo transfer was 13.33% in the ICSI group and 15.17% in the IVF group, with no significant difference between the two groups. Regarding frozen-thawed embryo transfer, the miscarriage rate in the ICSI group and IVF group was 14.61% and 10.16%, respectively, with no significant difference between the two groups. The cumulative miscarriage rates were also similar between the two groups (14.29% in the ICSI group vs. 13.07% in the IVF group). These data suggest that ICSI does not increase the miscarriage rate. We will continue to track the impact of ICSI on the health of offspring.

The limitations of this study are as follows: (1) The difference between groups was not completely eliminated, especially the semen quality of the male, which is also a factor affecting the quality of pregnancy. Our next study is to use the randomized controlled trial (RCT) method to group patients to eliminate selection bias. (2) The dataset analyzed in this study was from a single center. Thus, the data are of limitation. The analytic results cannot represent the overall situation. However, our findings still provide a reference for clinical practice.

6. Conclusion

Patients with ovarian dysfunction and low ovarian response often need multiple egg retrieval to achieve pregnancy causing enormous physical and psychological trauma and economic burden to the patients. This study focused on the comparison of ICSI and IVF as effective utilization of retrieved eggs and increasing the pregnancy rate of patients with ≤3 retrieved eggs. Results of this study results show that for infertility patients with ≤3 eggs retrieved, ICSI can improve the normal fertilization rate and reduce the cycle cancellation rate caused by fertilization failure. In particular, for patients with one egg retrieved, the benefits of one egg retrieval cycle can be maximized so as to reduce the trauma and complications caused by multiple egg retrieval operations. However, with increased number of eggs retrieved, the advantages of ICSI fertilization decrease.

Data Availability

All the data generated or analyzed during this study are available from the corresponding author upon reasonable request.

Ethical Approval

The Ethics Committee of Qingdao University-affiliated Yantai Yuhuangding Hospital approved the current study.

Consent

All patients signed the IVF or ICSI informed consent form.

Conflicts of Interest

The authors declare that they have no conflicts of interest.

Authors' Contributions

All authors designed the study, evaluated the results, reviewed the manuscript, and approved the draft of the final manuscript. Shuang Wang played a major role in the manuscript's writing and carrying out the statistical analysis. Shuang Wang and Xiaoyan Zhang contributed equally to this work.

References

[1] P. Drakopoulos, C. Blockeel, D. Stoop et al., "Conventional ovarian stimulation and single embryo transfer for IVF/ICSI. How many oocytes do we need to maximize cumulative live

birth rates after utilization of all fresh and frozen embryos?" *Human Reproduction*, vol. 31, pp. dev316–376, 2016.
[2] Y.-h. Chen, X.-h. Xu, Q. Wang et al., "Optimum oocyte retrieved and transfer strategy in young women with normal ovarian reserve undergoing a long treatment protocol: a retrospective cohort study," *Journal of Assisted Reproduction and Genetics*, vol. 32, no. 10, pp. 1459–1467, 2015.
[3] S. Rasool and D. Shah, "Fertility with early reduction of ovarian reserve: the last straw that breaks the Camel's back," *Fertility research and practice*, vol. 3, pp. 1–12, 2017.
[4] A. Papathanasiou and N. Mawal, "The risk of poor ovarian response during repeat IVF," *Reproductive BioMedicine Online*, vol. 42, no. 4, pp. 742–747, 2021.
[5] S. Stigliani, C. Massarotti, F. Bovis et al., "Pronuclear score improves prediction of embryo implantation success in ICSI cycles," *BMC Pregnancy and Childbirth*, vol. 21, pp. 1–9, 2021.
[6] A. M. Quaas, "ICSI for non-male factor: do we practice what we preach?" *Journal of Assisted Reproduction and Genetics*, vol. 38, no. 1, pp. 125–127, 2021.
[7] S. L. Boulet, A. Mehta, D. M. Kissin, L. Warner, J. F. Kawwass, and D. J. Jamieson, "Trends in use of and reproductive outcomes associated with intracytoplasmic sperm injection," *JAMA*, vol. 313, no. 3, pp. 255–263, 2015.
[8] P. Drakopoulos, J. Garcia-Velasco, E. Bosch et al., "ICSI does not offer any benefit over conventional IVF across different ovarian response categories in non-male factor infertility: a European multicenter analysis," *Journal of Assisted Reproduction and Genetics*, vol. 36, no. 10, pp. 2067–2076, 2019.
[9] J. Y. Kim, J. H. Kim, B. C. Jee, J. R. Lee, C. S. Suh, and S. H. Kim, "Can intracytoplasmic sperm injection prevent total fertilization failure and enhance embryo quality in patients with non-male factor infertility?" *European Journal of Obstetrics & Gynecology and Reproductive Biology*, vol. 178, pp. 188–191, 2014.
[10] M. Haddad, J. Stewart, P. Xie et al., "Thoughts on the popularity of ICSI," *Journal of Assisted Reproduction and Genetics*, vol. 38, no. 1, pp. 101–123, 2021.
[11] J. Farhi, K. Cohen, Y. Mizrachi, A. Weissman, A. Raziel, and R. Orvieto, "Should ICSI be implemented during IVF to all advanced-age patients with non-male factor subfertility?" *Reproductive Biology and Endocrinology*, vol. 17, pp. 1–5, 2019.
[12] Y.-C. Ou, K.-C. Lan, F.-J. Huang, F.-T. Kung, T.-H. Lan, and S. Y. Chang, "Comparison of in vitro fertilization versus intracytoplasmic sperm injection in extremely low oocyte retrieval cycles," *Fertility and Sterility*, vol. 93, no. 1, pp. 96–100, 2010.
[13] S. Sunderam, S. L. Boulet, J. F. Kawwass, and D. M. Kissin, "Comparing fertilization rates from intracytoplasmic sperm injection to conventional in vitro fertilization among women of advanced age with non−male factor infertility: a meta-analysis," *Fertility and Sterility*, vol. 113, no. 2, pp. 354–363, 2020.
[14] T. Geng, L. Cheng, C. Ge, and Y. Zhang, "The effect of ICSI in infertility couples with non-male factor: a systematic review and meta-analysis," *Journal of Assisted Reproduction and Genetics*, vol. 37, no. 12, pp. 2929–2945, 2020.
[15] I. Kahyaoglu, B. Demir, A. Turkkanı et al., "Total fertilization failure: is it the end of the story?" *Journal of Assisted Reproduction and Genetics*, vol. 31, no. 9, pp. 1155–1160, 2014.
[16] S Tannus, WY Son, A Gilman, G Younes, T Shavit, and MH Dahan, "The role of intracytoplasmic sperm injection in non-male factor infertility in advanced maternal age," *Human reproduction (Oxford, England)*, vol. 32, pp. 119–124, 2017.
[17] B. Steinfeld, J. Scott, G. Vilander et al., "The role of lean process improvement in implementation of evidence-based practices in behavioral health care," *The Journal of Behavioral Health Services & Research*, vol. 42, no. 4, pp. 504–518, 2015.
[18] N. Pereira, C. O'Neill, V. Lu, Z. Rosenwaks, and G. D. Palermo, "The safety of intracytoplasmic sperm injection and long-term outcomes," *Reproduction*, vol. 154, no. 6, pp. F61–F70, 2017.
[19] S. R. Catford, R. I. McLachlan, M. K. O'Bryan, and J. L. Halliday, "Long-term follow-up of intra-cytoplasmic sperm injection-conceived offspring compared with in vitro fertilization-conceived offspring: a systematic review of health outcomes beyond the neonatal period," *Andrology*, vol. 5, no. 4, pp. 610–621, 2017.

Hindawi
Journal of Healthcare Engineering
Volume 2023, Article ID 9879237, 1 page
https://doi.org/10.1155/2023/9879237

Retraction

Retracted: Clinical Efficacy and Safety of Percutaneous Spinal Endoscopy versus Traditional Open Surgery for Lumbar Disc Herniation: Systematic Review and Meta-Analysis

Journal of Healthcare Engineering

Received 27 January 2023; Accepted 27 January 2023; Published 2 February 2023

Journal of Healthcare Engineering has retracted the article titled "Clinical Efficacy and Safety of Percutaneous Spinal Endoscopy versus Traditional Open Surgery for Lumbar Disc Herniation: Systematic Review and Meta-Analysis" [1] due to concerns that the peer review process has been compromised.

Following an investigation conducted by the Hindawi Research Integrity team [2], significant concerns were identified with the peer reviewers assigned to this article; the investigation has concluded that the peer review process was compromised. We therefore can no longer trust the peer review process, and the article is being retracted with the agreement of the Chief Editor.

The authors do not agree to the retraction.

References

[1] X. Xu, C. Chen, Y. Tang, F. Wang, and Y. Wang, "Clinical Efficacy and Safety of Percutaneous Spinal Endoscopy versus Traditional Open Surgery for Lumbar Disc Herniation: Systematic Review and Meta-Analysis," *Journal of Healthcare Engineering*, vol. 2022, Article ID 6033989, 9 pages, 2022.

[2] L. Ferguson, "Advancing Research Integrity Collaboratively and with Vigour," 2022, https://www.hindawi.com/post/advancing-research-integrity-collaboratively-and-vigour/.

Hindawi
Journal of Healthcare Engineering
Volume 2022, Article ID 6033989, 9 pages
https://doi.org/10.1155/2022/6033989

Review Article

Clinical Efficacy and Safety of Percutaneous Spinal Endoscopy versus Traditional Open Surgery for Lumbar Disc Herniation: Systematic Review and Meta-Analysis

Xingping Xu [1,2], Changwei Chen [1,2], Yong Tang [1,2], Fusheng Wang [1,2] and Yangsheng Wang [1,2]

[1] *Department of Orthopedics, 14F Yinzhou People's Hospital, No. 251 Baizhang East Road, Yinzhou District, Ningbo, Zhejiang Province, China*
[2] *The Affiliated People's Hospital of Ningbo University, Ningbo, Zhejiang Province, China*

Correspondence should be addressed to Xingping Xu; xxp13003776851@163.com

Received 29 November 2021; Revised 10 January 2022; Accepted 12 January 2022; Published 16 March 2022

Academic Editor: Enas Abdulhay

Objective. Systematic analysis of the incidence of percutaneous spinal endoscopic technique and traditional open surgery for lumbar disc herniation. *Methods*. A randomized controlled trial (RCT) and cohort study on complications related to traditional open surgery was searched on the MEDLINE, Cochrane Library, PubMed, Web of Science, Chinese journal full-text database (CNKI), Wanfang, and Embase database. Language is not limited. The quality of each study was evaluated, various complications were compiled into electronic baseline tables, and the data from these studies were available. Meta-analysis and synthesis were performed with the RevMan 5.3 software to evaluate the statistical significance of both surgical techniques in terms of various complications. *Results*. 12 studies were eventually included, and a total of 2,797 patients were included in the analysis. Meta-analysis results showed that there was no statistical difference in postoperative paresthesia between percutaneous spinal endoscopy and traditional open surgery (OR = 1.17, 95% CI (0.82, 1.66), $P = 0.38$, $I^2 = 0\%$, $Z = 0.88$), direct nerve root damage (OR = 0.79, 95% CI (0.58, 1.07), $P = 0.13$, $I^2 = 73\%$, $Z = 1.52$), and intraoperative hemorrhage and hematoma formation (OR = 1.00, 95% CI (0.67, 1.48), $P = 0.99$, $I^2 = 0\%$, $Z = 0.02$), but there was a statistical difference in disc recurrence (OR = 2.24, 95% CI (1.56, 3.21), $P < 0.0001$, $I^2 = 81\%$, $Z = 4.39$). *Conclusion*. Compared with the traditional open surgical treatment of lumbar disc herniation, percutaneous spinal endoscopic technology has obvious advantages in reducing nerve root injury, dural injury, and surgical area wound complications, but it is limited to preventing the technical characteristics of the surgical site, which is worse than that of open surgery.

1. Introduction

With the development of the time, the continuous promotion of the concept of minimally invasive surgery and the rapid development of surgical instruments, the increasingly mature minimally invasive spine technology has begun to attract attention [1]. Xin et al. [2] has treated the lumbar disc herniation (percutaneous endoscopic lumbar decompression, PELD, with the use of a combined percutaneous spinal endoscopic system with wide-angle visual decompression in the disc with the help of arthroscopy). It has become one of the important means to treat lumbar disc herniation and lumbar degenerative diseases [3]. However, most previous surgeons remain more focused on technological reform and innovations, surgical techniques, and clinical efficacy. There are few studies on complications of surgery, and previous reports have only studied the treatment of the procedure for lumbar disc herniation alone [4]. With the continuous development of percutaneous spinal endoscopic technology and the continuous expansion of the treatment scope, the indirect decompression from endoscopic disc resection to the direct expansion of the spinal canal, lateral crypt, and nerve root canal is also changing accordingly. For each clinical surgeon, the complications of surgery are a great challenge, so it is only fully and systematically important to know and grasp the surgical complications. The common complications of PELD are summarized to provide a reference for clinical surgeons [5].

Postoperative sensory abnormalities are a specific and common complication of PELD, which is generally considered to be associated with the stimulation of the dorsal root ganglion (DRG) during surgery. Some scholars have also referred to it as the "solar burning syndrome," with the incidence of about 2% to 17%. Kim et al. reported that with 93 laminina methods and 385 lamininal methods for lumbar disc disease, the incidences of postoperative sensory abnormalities were 16.13% and 7.53%, respectively. The reason may be caused by prolonged pulling stimulation of nerve roots during surgical operation [6]. Repeated positioning puncture, the use of microscopic abrasive, the use of ring saw and bone drilling for lamina and vertebral plate expansion, radiofrequency electrocoagulation, and rotation adjustment working casing to block the surrounding soft tissue may indirectly or directly stimulate the compression of nerve roots to make their ischemia and hypoxia and the corresponding symptoms. Anatomical changes in the lumbosacral nerve, lumbar trauma, and surgical history as well as foraminal size can also cause postoperative sensory abnormalities [7].

Most are because of direct damage to nerve roots during surgery and are one of the serious complications of PELD surgery. Cheng et al. [8] reported that the incidence of nerve root injury in 923 patients undergoing PELD for lumbar disc herniation was approximately 0.5%. Guo et al. [9] reported that the incidence of nerve root injury in 276 patients undergoing PELD for lumbar spinal stenosis was 1.1% [10]. The main reasons for its occurrence are summarized in the following points: anatomical structure factors, mainly including the anatomical variation in some patients and external physicians have an unclear understanding of the local anatomy, especially in the early stages of the technology, which eventually leads to nerve damage.

2. Materials and Methods

2.1. Search Strategy. This study was conducted according to the PRISMA systematic evaluation guidelines. Relevant meta-analysis and original literature were retrieved from the Medline, Cochrane Library, PubMed, Web of Science, Chinese journal full-text database (China National Knowledge Infrastructure, CNKI), Wanfang database, and Embase database. The time range is the library construction until November 2018. English retrieval keywords are Lumbar Discectomy Complication (s), Lumbar Discectomy Complication (s) and Outcome (s), and Lumbar and Discectomy or Percutaneous endoscopic lumbar discectomy and Complications (Figure 1).

2.2. Inclusion and Exclusion Criteria

(1) Inclusion criteria: randomized controlled trial (RCT) and cohort studies on percutaneous endoscopic discectomy and traditional open discectomy for the treatment of lumbar disc herniation (LDH) which are not limited in language. Subjects: unlimited gender, age older than 18 years, diagnosed with single segment lumbar disc herniation by physical examination and imaging examination (CT and MRI) and ineffective after 3 months of conservative treatment. Intervention group (the percutaneous spinal endoscopic technical group): discectomy with the following characteristics was defined as the meridian: the cutaneous spinal endoscopic discectomy places the working sleeve directly into the disc or canal, combined with the percutaneous puncture technique and then uses the suction, grasping, electrocoagulation, and other techniques to remove the diseased part of the disc. The control group (the traditional open surgery group): traditional open laminectomy, lamenestration, hemilaminectomy, and translaminectomy discectomy.

(2) Exclusion criteria: (1) randomized controlled trials (RCT) and cohort studies not related to the topic; (2) multisegment lumbar disc herniation, cauda equina syndrome, malignancy, spinal deformity, intervertebral hole injury, vertebral fusion, minimally invasive transabdominal and lumbar discectomy, and laminectomy; (3) preoperative studies with uncontrollable factors such as neurological injury, infection, or rheumatism; and (4) animal, in vitro, biomechanical studies were also excluded.

2.3. Evaluation of Literature Quality. The included literature was read in full and evaluated, and the disagreement is decided by discussion or by a third-party expert arbitration. Quality evaluation included in the RCT study was conducted according to the quality evaluation criteria recommended by the Cochrane system: (1) whether the randomization method is correct (selection bias); (2) adequate randomization concealment (selection bias); (3) whether the blinding method between participants and subjects is in place (implementation bias); (4) whether the blinding method of efficacy assessors is feasible (measurement bias); and (5) loss of visit. For the included observational studies and cohort studies, NOS can be used to evaluate the included studies. NOS adopts the semiquantitative principle of star system to make quantitative evaluation on the selection of research quality, comparability, and results (Figure 2).

2.4. Data Extraction and Analysis. Data were extracted and finally summarized and checked. Main observation indicators are total complications, postoperative sensory abnormalities (nerve root pain and burning nerve root pain), direct nerve root injury (any nerve root puncture or direct nerve root injury and nerve root displacement), dural injury (for perioperative dural damage and cerebrospinal fluid leakage), surgical area wound complications (including cellulitis, discitis, spondylitis, skin infection, superficial wound infection, suture granuloma, crack and hematoma),

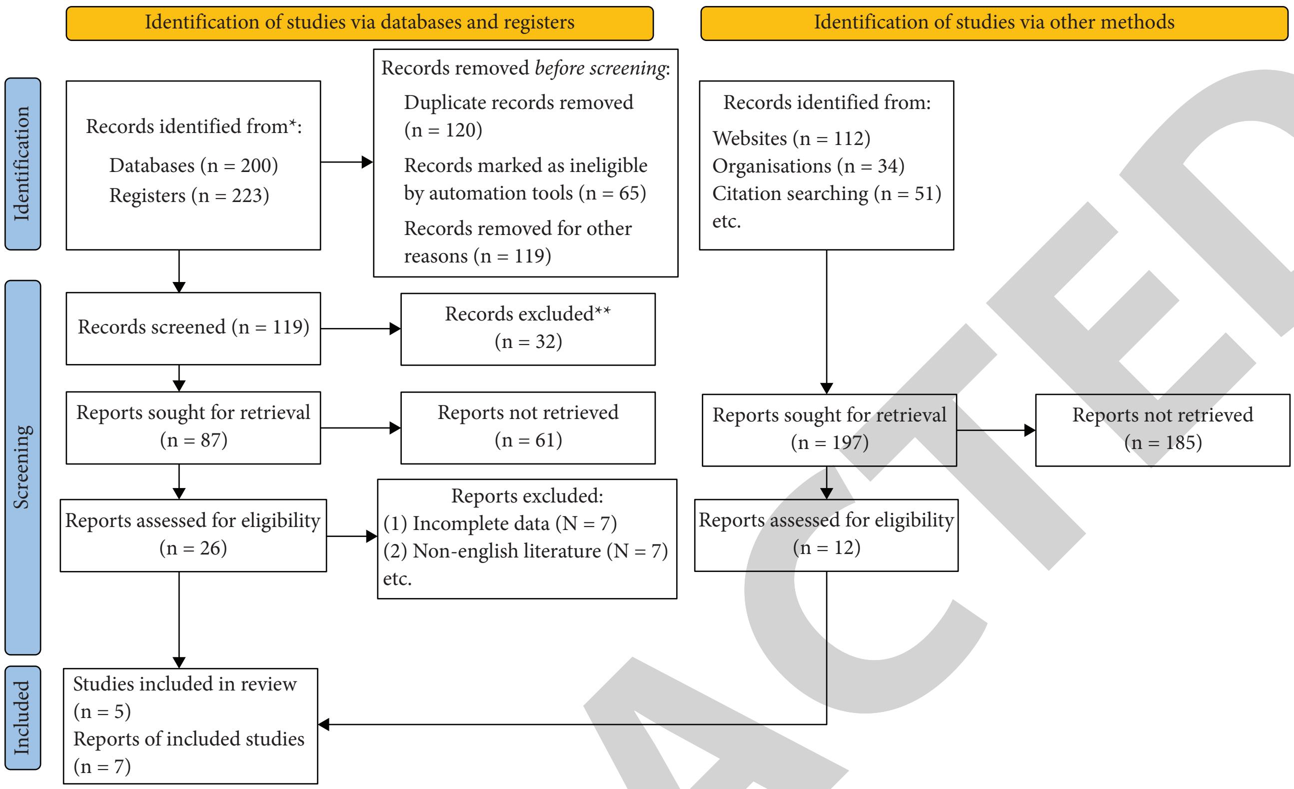

Figure 1: Flow chart of the literature screening.

intervertebral disc recurrence (complete remission of nucleus removal after the same space ipsilateral or contralateral lumbar disc herniation, with radiographic confirmation), residual nucleus pulposus (no remission or incomplete postoperative symptoms, confirmed by review MRI as residual compression of the nerve root), additional surgery of related complications (secondary surgery due to disc recurrence, nucleus pulposus residual, or other related complications). Among them, it is difficult to analyze and obtain the small sample size and low incidence of events, which is difficult to obtain reference data, so it will be integrated into other complications for analysis and discussion. Using the Cochran database, the extracted data were analyzed by using the RevMan 5.3.0 software. A chi-square test was first used to determine the heterogeneity of each study result. There was significant interstudy heterogeneity when included at $P < 0.1$ or $I^2 > 50\%$. For those with heterogeneity, the causes of heterogeneity were first analyzed, and subgroup analysis and sensitivity treatment were conducted. If it has clinical consistency, the analysis was combined with a random effect model. Fixed-effect models were used for the study data without heterogeneity.

2.5. Bias Analysis. The data in this study were all dichotomous variables, and odds ratio (OR) and 95% confidence interval (CI) were calculated. If the analysis showed statistically significant differences in complications among studies, a funnel plot was used to analyze whether publication bias existed. Sensitivity analysis was performed on the effects of studies of low quality, particularly high weight or results that differed from other studies (Figure 3).

3. Result

3.1. Characteristics and Quality Evaluation of the Included Literature. The initial examination obtained 423 documents by reading text questions, abstract, and full text and finally included 24 relevant research articles, 12 randomized controlled trials and 12 cohort studies [11–22]. A total of 2,797 patients were included in this study. Basic characteristics of the included study are as follows: there were no significant baseline differences in gender or age of the patients included in the literature (Table 1). For the 12 cohort studies included, the NOS score was 5–9. For the 12 included randomized controlled studies, the Cochrane Risk of Bias tool was used for risk assessment.

3.2. Postoperative Paresthesia. Among the 4 RCT literatures included in percutaneous spinal endoscopy versus traditional open surgery for lumbar disc herniation, the heterogeneity test was carried out and it was found that the heterogeneity of the selected studies was small, so meta-analysis with fixed models could be performed. Meta-analysis results showed that there was no statistical difference in postoperative paresthesia between percutaneous spinal endoscopy and traditional open surgery (OR = 1.17, 95% CI (0.82, 1.66), $P = 0.38$, $I^2 = 0\%$, $Z = 0.88$) (Figure 4).

Figure 2: Literature quality evaluation chart. (a) Risk of bias graph. (b) Risk of bias summary.

3.3. Direct Nerve Root Damage. Among the 4 RCT literatures included in percutaneous spinal endoscopy versus traditional open surgery for lumbar disc herniation, the heterogeneity test was carried out and it was found that the heterogeneity of the selected studies was small, so meta-analysis with fixed models could be performed. Meta-analysis results showed that there was no statistical difference in direct nerve root damage between percutaneous spinal endoscopy and traditional open surgery ($OR = 0.79$, 95% CI (0.58, 1.07), $P = 0.13$, $I^2 = 73\%$, $Z = 1.52$) (Figure 5).

3.4. Disc Recurrence. Among the 4 RCT literatures included in percutaneous spinal endoscopy versus traditional open surgery for lumbar disc herniation, the heterogeneity test was carried out and it was found that the heterogeneity of the selected studies was small, so meta-analysis with fixed models could be performed. Meta-analysis results showed that there was statistical difference in disc recurrence between percutaneous spinal endoscopy and traditional open surgery ($OR = 2.24$, 95% CI (1.56, 3.21), $P < 0.0001$, $I^2 = 81\%$, $Z = 4.39$) (Figure 6).

3.5. Intraoperative Hemorrhage and Hematoma Formation. Among the 4 RCT literatures included in percutaneous spinal endoscopy versus traditional open surgery for lumbar disc herniation, the heterogeneity test was carried out and it was found that the heterogeneity of the selected studies was small, so meta-analysis with fixed models could be performed. Meta-analysis results showed that there was no statistical difference in intraoperative hemorrhage and hematoma formation between percutaneous spinal endoscopy

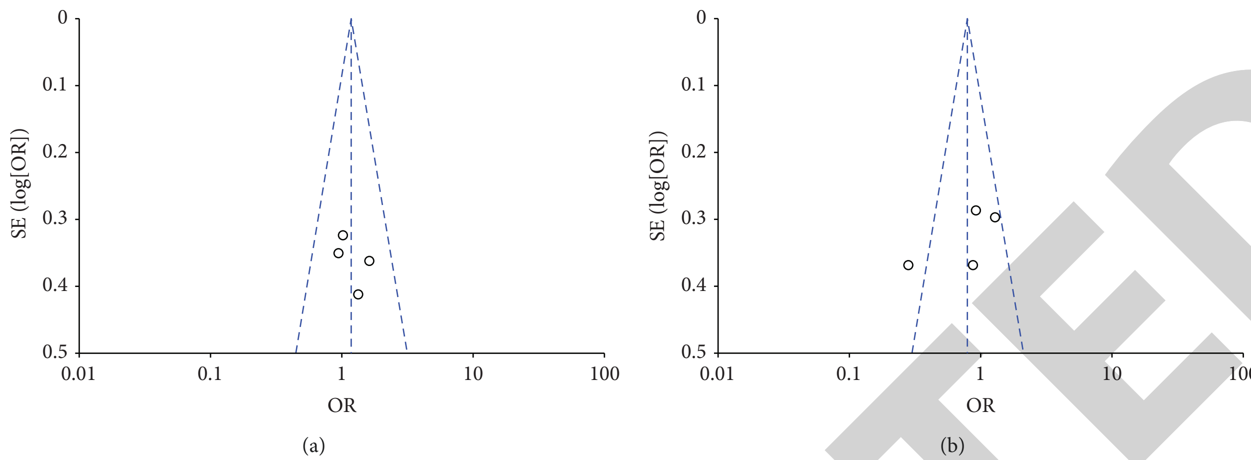

Figure 3: (a, b) Funnel plot of literature publication bias.

Table 1: Basic clinical features of 12 literatures included in our study.

Study	Age	Gender (man)	Experimental group (N)	Control group (N)	NOS score	Research type	P values of HWE
Heo et al. (2019) [11]	43.71 ± 12.2	45.25	96	75	8	RCT	0.35
Cheng and Chen (2020) [8]	45.65 ± 13.4	59.12	86	63	8	RCT	0.02
Lohre et al. (2020) [12]	62.12 ± 14.5	55.72	118	108	8	RCT	0.04
Carbó et al. (2019) [13]	57.15 ± 14.5	54.12	66	60	7	RCT	0.12
Wu et al. (2020) [4]	52.45 ± 8.4	54.89	58	73	8	RCT	0.06
Yang et al. (2020) [14]	64.26 ± 10.2	53.45	54	65	7	RCT	0.02
Ao et al. (2020) [15]	62.45 ± 12.2	48.10	80	75	9	RCT	0.01
Li et al. (2020) [16]	62.51 ± 13.0	58.75	80	63	8	RCT	0.02
Feng et al. (2020) [17]	47.25 ± 14.5	55.23	41	56	7	RCT	0.14
Li et al. (2020) [18]	56.22 ± 15.2	46.22	64	70	8	RCT	0.23
Wang et al. (2021) [19]	51.35 ± 8.1	54.16	108	100	7	RCT	0.01
Yu et al. (2020) [20]	57.65 ± 16.0	56.34	96	77	7	RCT	0.25

Study or Subgroup	percutaneous spinal endoscopy Events	percutaneous spinal endoscopy Total	traditional open surgery Events	traditional open surgery Total	Weight (%)	Odds Ratio M-H, Fixed, 95% CI
Ao S 2020	45	80	42	75	32.6	1.01 [0.54, 1.91]
Carbó Perseguer 2019	33	66	23	60	20.7	1.61 [0.79, 3.27]
Cheng XK 2020	56	86	42	63	29.1	0.93 [0.47, 1.85]
Feng WL 2020	22	41	26	56	17.5	1.34 [0.60, 3.00]
Total (95% CI)		*273*		*254*	*100.0*	*1.17 [0.82, 1.66]*
Total events	156		133			

Heterogeneity: $Chi^2 = 1.50$, df = 3 (P = 0.68); $I^2 = 0\%$

Test for overall effect: Z = 0.88 (P = 0.38)

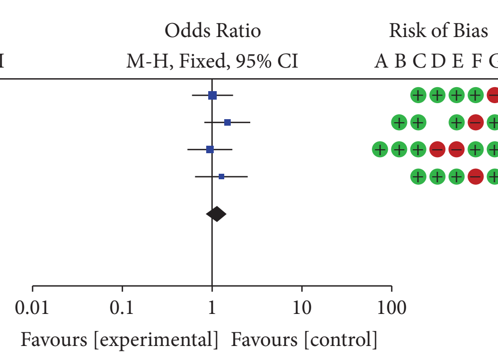

Risk of bias legend

(A) Random sequence generation (selection bias)

(B) Allocation concealment (selection bias)

(C) Blinding of participants and personnel (performance bias)

(D) Blinding of outcome assessment (detection bias)

(E) Incomplete outcome data (attrition bias)

(F) Selective reporting (reporting bias)

(G) Other bias

Figure 4: Meta-analysis of postoperative paresthesia between two groups.

Study or Subgroup	percutaneous spinal endoscopy Events	percutaneous spinal endoscopy Total	traditional open surgery Events	traditional open surgery Total	Weight (%)	Odds Ratio M-H, Fixed, 95% CI
Heo DH 2019	55	96	62	75	32.7	0.28 [0.14, 0.58]
Li XF 2020	42	64	48	70	17.3	0.88 [0.43, 1.80]
Lohre R 2020	88	118	75	108	21.9	1.29 [0.72, 2.31]
Wang Z 2021	65	108	62	100	28.2	0.93 [0.53, 1.62]
Total (95% CI)		*386*		*353*	*100.0*	*0.79 [0.58, 1.07]*
Total events	250		247			

Heterogeneity: $Chi^2 = 10.99$, df = 3 (P = 0.01); $I^2 = 73\%$

Test for overall effect: Z = 1.52 (P = 0.13)

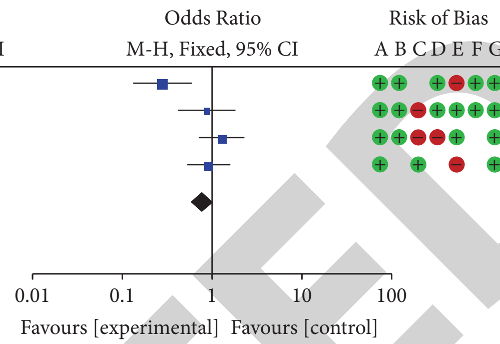

Risk of bias legend
(A) Random sequence generation (selection bias)
(B) Allocation concealment (selection bias)
(C) Blinding of participants and personnel (performance bias)
(D) Blinding of outcome assessment (detection bias)
(E) Incomplete outcome data (attrition bias)
(F) Selective reporting (reporting bias)
(G) Other bias

Figure 5: Meta-analysis of direct nerve root damage between two groups.

Study or Subgroup	percutaneous spinal endoscopy Events	percutaneous spinal endoscopy Total	traditional open surgery Events	traditional open surgery Total	Weight (%)	Odds Ratio M-H, Fixed, 95% CI
Lohre R 2020	89	118	85	108	54.4	0.83 [0.45, 1.55]
Wu D 2020	45	58	33	73	16.3	4.20 [1.94, 9.06]
Yang J 2020	51	54	47	65	5.9	6.51 [1.80, 23.53]
Yu KX 2020	78	96	45	77	23.4	3.08 [1.55, 6.11]
Total (95% CI)		*326*		*323*	*100.0*	*2.24 [1.56, 3.21]*
Total events	263		210			

Heterogeneity: $Chi^2 = 15.79$, df = 3 (P = 0.001); $I^2 = 81\%$

Test for overall effect: Z = 4.39 (P < 0.0001)

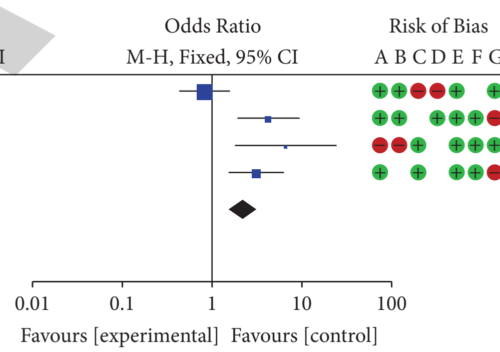

Risk of bias legend
(A) Random sequence generation (selection bias)
(B) Allocation concealment (selection bias)
(C) Blinding of participants and personnel (performance bias)
(D) Blinding of outcome assessment (detection bias)
(E) Incomplete outcome data (attrition bias)
(F) Selective reporting (reporting bias)
(G) Other bias

Figure 6: Meta-analysis of disc recurrence between two groups.

and traditional open surgery (OR = 1.00, 95% CI (0.67, 1.48), $P = 0.99$, $I^2 = 0\%$, $Z = 0.02$) (Figure 7).

4. Discussion

Surgical treatment of lumbar intervertebral disc herniation with the social development and scientific and technological progress has experienced from traditional to minimally invasive changes, and laminofenestration lumbar intervertebral disc resection is one of the classic traditional surgical treatments of LDH. Its clinical effect is satisfactory, but it causes lumbar rear muscle and bone structure damage, prone to lumbar instability and residual back pain [23]. At the same period, the technology was introduced into China, which favorably laid the foundation for the development of minimally invasive spine surgery technology in China. Wang et al. [24] invented the spinal endoscopic system (Thomas Hoogland Endoscopy Spine Systems, THESYS), which further developed as TESSYS. To enable the surgeon to reach the imaging and operating apparatus directly into the vertebral canal through the foramen to remove the protruding compressor, the technique is aided by a special multilayer drill hole which expands the foramen and the postoperative satisfaction rate can reach more than 80%

Study or Subgroup	percutaneous spinal endoscopy Events	percutaneous spinal endoscopy Total	traditional open surgery Events	traditional open surgery Total	Weight (%)	Odds Ratio M-H, Fixed, 95% CI
Ao S 2020	66	80	65	75	23.7	0.73 [0.30, 1.75]
Li XR 2020	47	80	39	63	36.3	0.88 [0.45, 1.72]
Yang J 2020	44	54	51	65	17.3	1.21 [0.49, 2.99]
Yu KX 2020	80	96	61	77	22.8	1.31 [0.61, 2.83]
Total (95% CI)		*310*		*280*	*100.0*	*1.00 [0.67, 1.48]*
Total events	237		216			

Heterogeneity: $Chi^2 = 1.30$, df = 3 (P = 0.73); $I^2 = 0\%$

Test for overall effect: Z = 0.02 (P = 0.99)

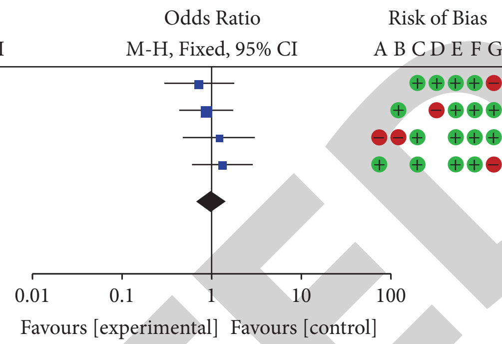

Risk of bias legend
(A) Random sequence generation (selection bias)
(B) Allocation concealment (selection bias)
(C) Blinding of participants and personnel (performance bias)
(D) Blinding of outcome assessment (detection bias)
(E) Incomplete outcome data (attrition bias)
(F) Selective reporting (reporting bias)
(G) Other bias

Figure 7: Meta-analysis of intraoperative hemorrhage and hematoma formation between two groups.

[25]. However, in the process of TESSYS application in clinical practice, various complications such as inaccurate puncture positioning, medical personnel damage due to too long perspective time, damage to nerve roots and dura, long channel establishment time, and other problems often occur. However, with the continuous development of percutaneous spinal endoscopic technology and the improvement of instruments, the efficacy and safety in the treatment of lumbar disc herniation are continuously improved [26].

Transcutaneous spinal endoscopic technology for lumbar disc herniation compared with traditional open surgical technology: its advantages are recognized by scholars, but its surgical complications are controversial. This study analyzed the percutaneous spinal endoscopic technology and traditional open surgery treatment of the LDH trial and cohort study [27], and the results show that the former in the total complications, direct nerve root injury, dural sac injury, and surgical wound complications were significantly better than the latter and in the myeloid residue inferior to the latter [28]. The results also showed no significant differences among the two technical methods in postoperative sensory abnormalities, disc recurrence, or other complications. Some scholars [29] believe that percutaneous spinal endoscopic technology after percutaneous puncture positioning casing and endoscopy directly by the foraminal area into the spinal canal and in the circulating water environment avoid large incision exposure, and timely debris, intraoperative bleeding point in the intraoperative area clearly visible, plasma bipolar radiofrequency hemostasis, and various conditions reduce the surgical area wound complications [30].

The total incidence of complications varied between the two surgical techniques in this study; however, due to the high heterogeneity, a subgroup analysis was performed and the results showed that percutaneous spinal endoscopic techniques outperform traditional open surgery in total complications. Also, it has statistical significance. However, percutaneous cohort endoscopy and traditional open surgery did not show significant advantages and disadvantages in the cohort study. The reason may be the large reporting bias in observational studies, leading to greater heterogeneity in the study. Due to the great controversy between the two techniques in postoperative disc recurrence, this study is hereby conducted according to the follow-up time subgroup analysis, and the results indicated no statistically significant complication incidence of postoperative disc recurrence between the two techniques.

The limitations of this study are as follows: (1) incorporating observational studies in the study is limited; (2) the follow-up varies from 3 to 36 months, making the evaluation of long-term complications; (3) the publication bias analysis is only qualitative and large personal factors; and (4) the two techniques described in this paper contain multiple surgical procedures, which may increase the bias of the study. Since the assessments were all based on a small number of studies, the results must be interpreted with caution. As the accumulated evidence grows, our conclusions may either be supported or overturned.

Compared with the traditional open surgical treatment of lumbar disc herniation, percutaneous spinal endoscopic technology has obvious advantages in reducing nerve root injury, dural injury, and surgical area wound complications, but it is limited to preventing the technical characteristics of the surgical site, which is worse than that of open surgery.

Data Availability

The data used to support the findings of this study are available from the corresponding author upon request.

Conflicts of Interest

The authors declare that they have no conflicts of interest.

Authors' Contributions

Xingping Xu and Chao Guo contributed equally to this work.

References

[1] M. Pan, Q. Li, S. Li et al., "Percutaneous endoscopic lumbar discectomy: indications and complications," *Pain Physician*, vol. 23, pp. 49–56, 2020.

[2] Z. Xin, P. Huang, G. Zheng, W. Liao, X. Zhang, and Y. Wang, "Using a percutaneous spinal endoscopy unilateral posterior interlaminar approach to perform bilateral decompression for patients with lumbar lateral recess stenosis," *Asian Journal of Surgery*, vol. 43, pp. 593–602, 2020.

[3] J. E. Kim, D. J. Choi, E. J. J. Park, H. J. Lee, J. H. Hwang, and M. C. Kim, "Biportal endoscopic spinal surgery for lumbar spinal stenosis," *Asian Spine J*, vol. 13, pp. 334–342, 2019.

[4] P. H. Wu, H. S. Kim, and I. T. Jang, "Intervertebral disc diseases part 2: a review of the current diagnostic and treatment strategies for intervertebral disc disease," *International Journal of Molecular Sciences*, vol. 21, 2020.

[5] J. Xue, H. Chen, B. Zhu et al., "Percutaneous spinal endoscopy with unilateral interlaminar approach to perform bilateral decompression for central lumbar spinal stenosis: radiographic and clinical assessment," *BMC Musculoskeletal Disorders*, vol. 22, 2021.

[6] H. S. Kim, N. Adsul, A. Kapoor, S. Siddiqui, I. T. Jang, and S. H. Oh, "Redefining the evolution of spinal discal cyst under percutaneous endoscopy: report of two cases," *Asian J Neurosurg*, vol. 14, pp. 890–893, 2019.

[7] Y. Liu, Y. Qi, D. M. Diaty et al., "Retraction Note: treatment for lumbar spinal stenosis secondary to ligamentum flavum hypertrophy using percutaneous endoscopy through interlaminar approach: a retrospective study," *Journal of Orthopaedic Surgery and Research*, vol. 16, 2021.

[8] X. K. Cheng and B. Chen, "Percutaneous endoscopic thoracic decompression for thoracic spinal stenosis under local anesthesia," *World Neurosurg*, vol. 139, pp. 488–494, 2020.

[9] C. Guo, D. Zhu, Q. Kong et al., "Transforaminal percutaneous endoscopic decompression for lower thoracic spinal stenosis," *World Neurosurg*, vol. 128, pp. e504–e512, 2019.

[10] Q. Yu, L. Shi, Z. Xu et al., "Therapeutic effectiveness of percutaneous endoscopic spinal surgery for intraspinal cement leakage following percutaneous vertebroplasty: an early clinical study of 12 cases," *Pain Physician*, vol. 23, pp. E377–E388, 2020.

[11] D. H. Heo, D. C. Lee, and C. K. Park, "Comparative analysis of three types of minimally invasive decompressive surgery for lumbar central stenosis: biportal endoscopy, uniportal endoscopy, and microsurgery," *Neurosurgical Focus*, vol. 46, 2019.

[12] R. Lohre, J. C. Wang, K. U. Lewandrowski, and D. P. Goel, "Virtual reality in spinal endoscopy: a paradigm shift in education to support spine surgeons," *J Spine Surg*, vol. 6, pp. S208–S223, 2020.

[13] J. Carbó Perseguer, A. Madejón Seiz, M. Romero Portales, J. Martínez Hernández, J. S. Mora Pardina, and J. García-Samaniego, "Percutaneous endoscopic gastrostomy in patients with amyotrophic lateral sclerosis: mortality and complications," *Neurologia*, vol. 34, pp. 582–588, 2019.

[14] J. Yang, C. Guo, Q. Kong et al., "Learning curve and clinical outcomes of percutaneous endoscopic transforaminal decompression for lumbar spinal stenosis," *International Orthopaedics*, vol. 44, pp. 309–317, 2020.

[15] S. Ao, W. Zheng, J. Wu et al., "Comparison of Preliminary clinical outcomes between percutaneous endoscopic and minimally invasive transforaminal lumbar interbody fusion for lumbar degenerative diseases in a tertiary hospital: is percutaneous endoscopic procedure superior to MIS-TLIF? A prospective cohort study," *International Journal of Surgery*, vol. 76, pp. 136–143, 2020.

[16] X. R. Li, J. Yu, W. Zhang et al., "Biomechanical model study of the effect of partial facetectomy on lumbar stability under percutaneous endoscopy," *World Neurosurg*, vol. 139, pp. e255–e264, 2020.

[17] W. L. Feng, J. S. Yang, D. Wei et al., "Gradient local anesthesia for percutaneous endoscopic interlaminar discectomy at the L5/S1 level: a feasibility study," *Journal of Orthopaedic Surgery and Research*, vol. 15, 2020.

[18] X. F. Li, L. Y. Jin, Z. D. Lv et al., "Efficacy of percutaneous transforaminal endoscopic decompression treatment for degenerative lumbar spondylolisthesis with spinal stenosis in elderly patients," *Experimental and Therapeutic Medicine*, vol. 19, pp. 1417–1424, 2020.

[19] Z. Wang, F. Jian, Z. Chen et al., "Percutaneous spinal endoscopic treatment of symptomatic sacral tarlov cysts," *World Neurosurg*, vol. S1878-8750, pp. 1720–1724, 2021.

[20] K. X. Yu, W. Z. Lu, C. M. Xiao et al., "Posterior percutaneous transpedicular endoscopic approach for treating single-segment cervical myelopathy," *BioMed Research International*, vol. 2020, Article ID 1573589, 2020.

[21] X. K. Cheng, Y. P. Cheng, Z. Y. Liu et al., "Percutaneous transforaminal endoscopic decompression for lumbar spinal stenosis with degenerative spondylolisthesis in the elderly," *Clinical Neurology and Neurosurgery*, vol. 194, 2020.

[22] D. Wu, J. Sun, W. Fan, and F. Yuan, "Unilateral or bilateral percutaneous endoscopic debridement and lavage treatment for lumbar spinal tuberculosis," *World Neurosurg*, vol. 140, pp. e73–e80, 2020.

[23] F. C. M. Torricelli, F. C. Vicentini, L. Zanetti et al., "Percutaneous nephrolithotomy in patients with spinal cord injury: should all these patients be automatically assigned a Guy's stone score of 4?" *World Journal of Urology*, vol. 39, pp. 2129–2134, 2021.

[24] Y. Wang, M. Deng, H. Wu, C. Guo, D. Zhang, and Q. Kong, "Short-term effectiveness of precise safety decompression via double percutaneous lumbar foraminoplasty and percutaneous endoscopic lumbar decompression for lateral lumbar spinal canal stenosis: a prospective cohort study," *BMC Musculoskeletal Disorders*, vol. 22, 2021.

[25] H. Li, Y. Ou, F. Xie, W. Liang, G. Tian, and H. Li, "Linical efficacy of percutaneous endoscopic lumbar discectomy for the treatment of lumbar spinal stenosis in elderly patients: a retrospective study," *Journal of Orthopaedic Surgery and Research*, vol. 15, 2020.

[26] O. Barzilai, M. H. Bilsky, and I. Laufer, "The role of minimal access surgery in the treatment of spinal metastatic tumors," *Global Spine Journal*, vol. 10, pp. 79S–87S, 2020.

[27] S. Wang, X. Zhang, B. Xiao, W. Hu, S. Chen, and J. Li, "Ultrasound-guided percutaneous nephrolithotomy for upper urinary tract calculi in patients with spinal deformity: a

Hindawi
Journal of Healthcare Engineering
Volume 2022, Article ID 3208780, 11 pages
https://doi.org/10.1155/2022/3208780

Research Article

Systematic Evaluation Meta-Analysis of the Efficacy of Recombinant Human Endostatin Combined with Gemcitabine and Cisplatin in Non-Small-Cell Lung Cancer

Li Zhang, Yuan He, ChengFeng Yi, and Mei Huang

Yunyang County People's Hospital Oncology Department, Chongqing, China

Correspondence should be addressed to Mei Huang; 2662508659@qq.com

Received 6 December 2021; Revised 16 January 2022; Accepted 7 February 2022; Published 15 March 2022

Academic Editor: Enas Abdulhay

Objective. To evaluate the efficacy of recombinant human endostatin combined with gemcitabine and cisplatin in the treatment of non-small-cell lung cancer (NSCLC). *Methods*. The databases of Cochrane Library, Embase, ClinicalTrials, PubMed, HowNet, Wanfang, and VIP were searched to collect randomized controlled trials (RCTs) of recombinant human endostatin combined with gemcitabine and cisplatin (experimental group) and gemcitabine combined with cisplatin (control group) for comparative study. The quality of literature was evaluated by bias risk assessment tools and related scales, and then meta-analysis was performed. *Results*. A total of 27 RCTs (1646 patients) were included. The results of meta-analysis showed that the effective rate ($P < 0.000\,01$) and benefit rate ($P < 0.000\,01$) of the experimental group were significantly higher than those of the control group, the incidence of leucopenia ($P = 0.79$), thrombocytopenia ($P = 0.39$), and gastrointestinal reaction ($P = 0.85$) were not statistically significant. *Conclusion*. The combination of recombinant human endostatin, gemcitabine, and cisplatin can increase the efficacy and safety of NSCLC patients.

1. Introduction

Nowadays, the prevalence trend and death status of lung cancer are not optimistic. Non-small-cell lung cancer (NSCLC) accounts for about 4/5 of all lung cancer patients, which is a cancer with high mortality in the world. The first-line chemotherapy of NSCLC is vinorelbine, gemcitabine, and cisplatin, which is widely used [1]. However, chemotherapy drugs are generally cytotoxic. Although they have a destructive effect on lung cancer cells, they also limit human immunity. In the process of lung cancer chemotherapy, it is a difficult problem for NSCLC to ensure the curative effect and reduce the adverse reactions as much as possible. Chemotherapy is the main treatment for advanced NSCLC patients. The standard treatment is 4–6 cycles of platinum combined with the third generation of cytotoxic drugs. The effective rate is 20.00%–30.00% [2]. The median survival time is 8–10 months, and the time of disease progression is 3–5 months. To some extent, the survival time of NSCLC patients can be prolonged, but the curative effect has reached the plateau [3, 4]. Therefore, in order to improve the survival and efficiency of patients with advanced NSCLC, we need to try new drugs and new chemotherapy regimens that are different from the existing treatment mechanisms. It is against this background that antitumor angiogenesis therapy is produced. Since the role of angiogenesis in tumor growth and progression was identified in the 1970s, the exploration of antiangiogenic drugs has not been interrupted [5]. With the progress of science and technology, many antiangiogenic drugs have been developed and applied in clinic. A large number of clinical studies have confirmed that the combination of molecular targeted drugs and chemotherapy can achieve the above therapeutic purposes, and some reports have shown that these drugs have a certain effect on tumor vascular normalization and can increase the sensitivity to chemotherapy and radiotherapy; when combined with chemotherapy, it has a positive synergistic effect. Recombinant human endostatin, also known as endostatin, is an angiogenesis inhibitor, which can inhibit angiogenesis and limit tumor angiogenesis. Nowadays, recombinant human endostatin can be used to intervene in NSCLC, gastric cancer, and so on [6]. Studies have shown that recombinant human endostatin and chemotherapy drugs can play a synergistic effect, making the efficacy increase. Although targeted therapy combined with chemotherapy has achieved a positive therapeutic effect in clinic, antiangiogenesis therapy has not achieved the obvious antitumor effect as in the animal experiment stage. There are many factors related to its possibility, but the difference in drug use is one of the most important factors [7]. Conventional drugs are treated by intravenous route. After the combination of drugs with plasma protein, the concentration of drugs distributed to the local tumor is significantly reduced, and the therapeutic effect of the tumor is not good. Interventional targeted therapy of tumor blood supply artery is a mature method of local perfusion chemotherapy [8]. This method is through superselective intubation to the target artery of tumor blood supply, a high concentration of therapeutic drugs is infused into the tumor area. Through the first-pass effect of drugs, the concentration of drugs in the tumor is increased; the action time is prolonged; the clinical side effects are reduced; and the tolerance of patients is increased. It is believed that endostatin combined with chemotherapeutic drugs can significantly increase the clinical therapeutic effect of NSCLC. In this study, we systematically reviewed the efficacy of recombinant human endostatin, gemcitabine, and cisplatin combined therapy and gemcitabine and cisplatin combined therapy in the treatment of NSCLC.

2. Information and Methods

2.1. Inclusion Criteria and Exclusion Criteria

2.1.1. Inclusion Criteria. The inclusion criteria are as follows: (1) randomized controlled trials (RCTs) were published in Chinese and English; (2) cytological or histopathological diagnosis of NSCLC was made, regardless of gender, age, course of disease, and so on; (3) the blood routine, heart, liver, kidney, and brain function were basically normal, and there were no structural or functional abnormalities of important organs; and (4) the period of treatment is no less than 2 cycles (1 cycle is 2 weeks).

2.1.2. Exclusion Criteria. The exclusion criteria are as follows: (1) the score of the Jadad scale was 0 or non-RCT literature, (2) repetitive literature, (3) descriptive research, (4) impossible to extract literature, and (5) animal experiments.

2.1.3. Method. The control group was treated with gemcitabine and cisplatin; patients in the experimental group were treated with gemcitabine, cisplatin, and recombinant human endostatin.

2.1.4. Outcome Measures. (1) Total effective rate, (2) benefit rate, (3) the incidence of leukopenia, (4) the incidence of thrombocytopenia, and (5) the incidence of gastrointestinal reactions are calculated. According to the new criteria for evaluation of solid tumor efficacy, the efficacy criteria were divided into complete remission (CR), partial remission (PR), steady (SD), and advanced (PD). Effective rate = (Cr + PR)/total cases × 100.00%; benefit rate = (Cr + PR + SD)/total cases × 100.00%; the incidence of leukopenia = 1–4 cases/total cases × 100.00%; and incidence of thrombocytopenia = cases of grade 1–4/total cases × 100.00%.

2.2. Literature Retrieval. A total of 501 databases of Cochrane Library, Embase, ClinicalTrials, PubMed, HowNet, Wanfang, and VIP are searched. Of these, 404 were included, and 97 were excluded. The Chinese keywords are "recombinant human angiostatin," "non-small cell lung cancer," "gemcitabine," "cisplatin," "meta-analysis," and so on. The English keywords are "recombinant human endostatin," "non-small cell lung cancer," "gemcitabine," "cisplatin," and "meta-analysis." The retrieval time period is from the establishment of each database to October 2020.

2.3. Screening of the Literature and Data. A total of three reviewers screened and checked the literature; two of them independently screened the literature according to the inclusion criteria and exclusion criteria; and two of them checked the literature. The third reviewer assisted in the case of different opinions. The extracted information included the year of publication, first author, sample size, age range, intervention method, disease stage, intervention course, outcome index, and so on.

2.4. Literature Quality Assessment. The Cochrane system version 5.1.0 was used to assess the risk of bias, whether the distribution was hidden, whether blinding was used (blinding of investigators and subjects and blinded assessment of the final results of the study), whether the results from the data were complete, whether the results of the study were selectively reported, and whether there were other sources of bias. Each item has a low risk of bias, ambiguity, and high risk of bias. Jadad scale was used to evaluate the quality of the study, including random sequence generation (appropriate 2 points, uncertain 1 points, and inappropriate 0 points), randomized concealment (appropriate 2 points, uncertain 1 points, and inappropriate 0 points), blind method (appropriate 2 points, uncertain 1 points, and inappropriate 0 points), withdrawal and withdrawal (description 1 points, no description, and 0 points). The score of low-quality research is less than 3, and that of high-quality research is 4–7.

2.5. Statistical Methods. Revman 5.3 software was used to analyze the data. The relative risk (RR) or odds ratio (or) and 95% confidence interval (CI) were used as the combined effect quantity if the included indexes were binary variables;

if the included research indicators were continuous variables, they were expressed by weight mean difference (MD) or standard mean difference (SMD) and 95% CI. For the heterogeneity analysis of the included studies, when the heterogeneity among the studies was low ($I^2 \leq 50\%$), the fixed-effect model was used for meta-analysis; when the heterogeneity among the studies was relatively high ($I^2 > 50\%$), the random-effects model was used for meta-analysis, and the incomplete data were used for descriptive analysis. The bias was analyzed qualitatively by funnel plot and quantitatively by state 12.0.

3. Results

3.1. Results of Literature Search. A total of 360 literature were collected, including 317 in Chinese and 43 in English. After reading the title and abstract, 81 related articles were obtained. After careful study of the full text, 27 articles were finally included, including 1,646 subjects, 830 patients in the experimental group, and 816 patients in the control group (Figure 1). The basic information of the study is shown in Table 1.

3.2. Assessment of the Quality of Included Studies. All studies were RCTs; among them, six studies involved randomized methods, and none of them involved allocation concealment, blind method, or other sources of bias. See Figures 2 and 3 for details.

3.3. Results of Meta-Analysis

3.3.1. Efficiency. Among them, 27 studies related to the effective rate, which had no statistical heterogeneity ($P = 0.99$, $I^2 = 0$). The fixed-effect model was used for the meta-analysis, as shown in Table 2. The results of meta-analysis showed that the effective rate of the experimental group was significantly higher than that of the control group, with statistical significance (RR = 1.67, 95% CI (1.48, 1.89), $P < 0.00001$).

3.3.2. Clinical Benefit Rate. Among them, 27 studies related to the benefit rate, which had no statistical heterogeneity ($P = 0.49$, $I^2 = 0$). The fixed-effect model was used for the meta-analysis, as shown in Table 3. The results of meta-analysis showed that the benefit rate of the experimental group was significantly higher than that of the control group (RR = 1.26, 95% CI (1.20, 1.33), $P < 0.00001$).

3.3.3. Incidence of Leukopenia. Among them, 19 studies related to the incidence of leukopenia, which was not statistically heterogeneous ($P = 1.00$, $I^2 = 0$). The fixed effect model was used for meta-analysis. Meta-analysis showed that the incidence of leukopenia among the groups was not statistically significant (RR = 0.98, 95% CI (0.88, 1.11), $P = 0.79$).

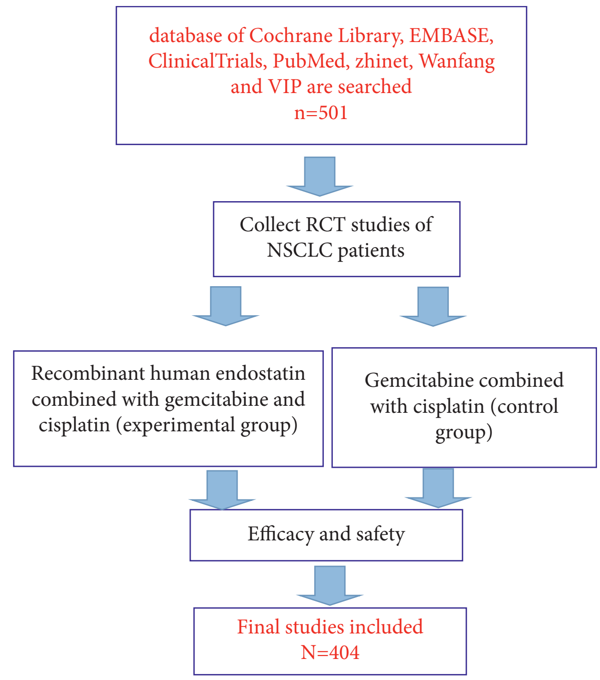

Figure 1: Flow chart.

3.4. Bias Analysis. Take the effective rate as an index and use the inverted funnel plot and Begg's test to analyze the bias, as shown in Figures 4 and 5. It can be seen from Figure 5 that all the scattered points in the study are within the scope of the inverted funnel diagram, and the distribution is basically symmetrical, indicating that there is a small possibility of bias in this study. Figure 5 shows that the P value of Begg's test is $0.084 > 0.05$, indicating that there is no obvious bias in this study.

4. Discussion

Lung cancer is the most malignant tumor in China and has the highest incidence rate in the world [9]. Most patients have an advanced tumor at the time of diagnosis, and NSCLC accounts for 80.00% of lung cancer in the late stage. Because the prognosis of NSCLC is not ideal, its treatment is very challenging [10]. Treatment of advanced NSCLC has also experienced a process. In 1980s, there were serious side effects of the first-generation chemotherapy drugs (cyclophosphamide, etc.); a clinical study showed that the prognosis after the first-generation chemotherapy drug treatment was not significantly improved compared with the patients with the best support treatment [11]. Therefore, it was generally considered that support therapy was the best treatment method for advanced NSCLC. The idea lasted until 1995; a meta-analysis published in the British Journal of medicine confirmed for the first time that platinum-containing chemotherapy significantly improved the survival time of patients with advanced NSCLC than the best support therapy [12]. This meta-analysis was selected into 52 randomized controlled studies, including 9,387 NSCLC patients. The results showed that the death risk and 1-year survival rate were improved by 10.00% ($P < 0.0001$) after

Table 1: Basic information of the study.

Year of publication and first author	Number of cases		Age (years)		Method		Intervention course (d)	Outcome measures	Jadad score (points)
	Control group	Experimental group	Control group	Experimental group	Control group	Experimental group			
Tan Yong in 2013	38	38	61.70 ± 9.80		Gemcitabine 1,000 mg, intravenous drip, once daily, d_{1-8} + cisplatin 25 mg/m^2, intravenous drip, once daily, D_{1-3}	The control group was treated with the chemotherapy regimen + recombinant human endostatin 7.50 mg/m^2, 0.9% sodium chloride injection 500 ml, intravenous drip, once a day, d_{1-14}	21	(1) (2) (3) (4) (5)	3
Xie Yanru in 2009	26	22	44.00–71.00	44.00–69.00	Gemcitabine 1,000 mg, D_1, D_8 + cisplatin 75 mg/m^2, divided into three days	The control group was treated with the chemotherapy regimen + recombinant human endostatin 15 mg, 0.9% sodium chloride injection 500 ml, intravenous drip, d_{1-14}	21	(1) (2) (3) (4) (5)	2
Chen Yongxing in 2010	25	30	49.00 ± 3.00	50.00 ± 2.00	Gemcitabine 1,000 mg, IV, D_1, D_8 + cisplatin 25 mg/m^2, IV, D_{1-3}	The control group was treated with the chemotherapy regimen + recombinant human endostatin 15 mg, added with 0.9% sodium chloride solution 500 ml, intravenous drip, d_{1-14}	21	(1) (2) (3) (4) (5)	1
Gu Ying in 2010	33	27	53.60		Gemcitabine 1,000 mg/m^2, D_1, D_8 + cisplatin 25 mg/m^2, intravenous drip, D_{1-3}	The control group was treated with the chemotherapy regimen + recombinant human endostatin 15 mg, added with 0.9% sodium chloride solution 500 ml, intravenous drip, d_{1-14}	21	(1) (2) (3) (4) (5)	1
Guo Hongbin in 2010	38	38	55.00 ± 12.00	53.00 ± 14.00	Gemcitabine 1,000 mg/m^2, intravenous drip, D_1, D_8 + cisplatin 30 mg/m^2, intravenous drip, D_{1-3}	The control group was treated with the chemotherapy regimen + recombinant human endostatin 15 mg, intravenous drip, d_{1-14}	21	(1) (2) (3) (4)	2
Wei Qihong in 2010	16	16	59.80		Gemcitabine 1 g/m^2, intravenous drip, D_1, D_8 + cisplatin 30 mg/m^2, intravenous drip, d_{2-4}	The control group was treated with the chemotherapy regimen + recombinant human endostatin 15 mg, intravenous drip, once a day, d_{1-14}	21	(1) (2) (3) (4) (5)	2
Xu Jian in 2010	20	20	64.00		Gemcitabine 1,000 mg/ M^2 + cisplatin 30 mg/m^2, tumor target artery perfusion, D_1, gemcitabine 1,000 mg/m^2, IV, D_8, 0.9% sodium chloride injection 500 ml, intravenous drip, D_{2-12}	The control group was treated with the chemotherapy regimen + recombinant human endostatin 15 mg/D, 0.9% sodium chloride injection 500 ml, intravenous drip, 2–12 days	36	(1) (2) (3) (4) (5)	2
Chen Qun in 2011	35	33	65	63	Gemcitabine 1,000 mg/m^2, intravenous drip, D_1, D_8 + cisplatin 80 mg/m^2, intravenous drip, D_1	The control group was treated with the chemotherapy regimen + recombinant human endostatin 15 mg, 0.9% sodium chloride solution 500 ml, intravenous drip, d_{1-14}, intermittent for 7 days	21	(1) (2) (3) (4) (5)	1

Table 1: Continued.

Year of publication and first author	Number of cases		Age (years)		Method		Intervention course (d)	Outcome measures	Jadad score (points)
	Control group	Experimental group	Control group	Experimental group	Control group	Experimental group			
Ruan Mei in 2011	19	17	58.50		Gemcitabine 1,000 mg/m^2, D_1, D_8 + cisplatin 75 mg/m^2, divided into three days	The control group was treated with the chemotherapy regimen + recombinant human endostatin 15 mg, 0.9% sodium chloride injection 500 ml, intravenous drip, d_{1-14}	21	(1) (2) (3) (4) (5)	1
Wang Fen in 2011	29	31	55.00	56.00	Gemcitabine 1,000 mg/m^2, IV, D_1, D_8 + cisplatin 75 mg/m^2, IV, D_1	The control group was treated with the chemotherapy regimen + recombinant human endostatin 15 mg, 0.9% sodium chloride solution 500 ml, intravenous drip, d_{1-14}, intermittent for 7 days	21	(1) (2)	1
Zheng Qingping in 2011	18	17	54.50	50.10	Gemcitabine 1,000 mg/m^2, intravenous drip, D_1, D_8 + cisplatin 20 mg/m^2, intravenous drip, D_{1-5}	The control group was treated with the chemotherapy regimen + recombinant human endostatin 15 mg/D, intravenous drip, d_{1-14}	21–28	(1) (2) (5)	1
Chen Bing in 2012	26	27	56.50 ± 7.30	55.70 ± 8.60	Gemcitabine 1,000 mg/m^2, 0.9% sodium chloride injection 100 ml, intravenous drip, D_1, D_8 + cisplatin 25 mg/m^2, 0.9% sodium chloride injection 500 ml, intravenous drip, d_{2-4}	The control group was treated with the chemotherapy regimen + recombinant human endostatin 15 mg, intravenous drip, once a day, d_{1-14}	14	(1) (2) (3) (4) (5)	1
He Rong in 2012	32	40	69.80 ± 5.50	70.50 ± 5.30	Gemcitabine 1,000 mg/m^2, D_1, D_8 + cisplatin 30 mg/m^2, d_{2-4}	The control group was treated with the chemotherapy + recombinant human endostatin 7.50 mg/m^2, $d_{1\sim14}$	21	(1) (2) (5)	1
Liu Jianwu in 2012	30	30	56.00	58.00	Gemcitabine 1,000 mg/m^2, IV, D_1, D_8 + cisplatin 75 mg/m^2, IV, D_1, D_2	The control group was treated with the chemotherapy + recombinant human endostatin 15 mg, D_{1-7}	21	(1) (2) (3) (4) (5)	2
Luan Wenqiang in 2012	27	25	40.00–67.00	42.00–68.00	Gemcitabine 1,250 mg/m^2, IV, D_1, D_8 + cisplatin 75 mg/m^2, IV, D_1	The control group was treated with the chemotherapy regimen + recombinant human endostatin 75 mg/m^2, added with 0.9% sodium chloride solution 500 ml, intravenous drip, d_{1-14}	21	(1) (2)	1
Yin Feng in 2012	90	94	49.30 ± 4.50	48.30 ± 5.20	Gemcitabine 1,000 mg/m^2, intravenous drip, D_1, d_8 + cisplatin 30 mg/m^2, intravenous drip, d_{2-4}	The control group was treated with the chemotherapy regimen + recombinant human endostatin 15 mg, 0.9% sodium chloride injection 500 ml, intravenous drip, once a day, d_{1-14}	21	(1) (2) (5)	1

Table 1: Continued.

Year of publication and first author	Number of cases		Age (years)		Method		Intervention course (d)	Outcome measures	Jadad score (points)
	Control group	Experimental group	Control group	Experimental group	Control group	Experimental group			
Almu Jiang in 2013	40	40	59.20 ± 9.50	58.30 ± 9.60	Gemcitabine 1.00 mg/m^2, 0.9% sodium chloride injection 250 ml, intravenous drip, D_1, D_{14} + cisplatin, 0.9% sodium chloride injection 500 ml, intravenous drip, D_{1-3}	The control group was treated with the chemotherapy regimen + recombinant human endostatin 15 mg, 0.9% sodium chloride injection 500 ml, intravenous drip, d_{1-14}	21	(1) (2) (3) (4) (5)	2
Zhang Yuanyuan in 2014	28	31	54.00	53.00	Gemcitabine 1,000 mg/m^2, D_1, D_8 + cisplatin 75 mg/m^2, divided into three days	The control group was treated with the chemotherapy regimen + recombinant human endostatin 15 mg, 0.9% sodium chloride injection 250 ml, intravenously pumped, d_{1-9}	21	(1) (2) (3) (4) (5)	2
Fu Hao in 2015	28	32	55.81	56.21	Gemcitabine 1,000 mg/m^2, intravenous drip, D_1, D_8 + cisplatin 25 mg/m^2, intravenous drip, D_{1-3}	The control group was treated with the chemotherapy regimen + recombinant human endostatin 15 mg, 0.9% sodium chloride injection 500 ml, intravenous drip, d_{1-14}, intermittent for 7 days	21	(1) (2) (3) (4) (5)	2
Liu Tao in 2015	32	32	No explanation		Gemcitabine 1,000 mg/m^2, intravenous drip, D_1, D_8 + cisplatin 80 mg/m^2, intravenous drip, D_1, D_2	The control group was treated with the chemotherapy regimen + recombinant human endostatin 15 mg, added with 0.9% sodium chloride injection 500 ml, d_{1-14}, repeated intermittently for 7 days	21	(1) (2)	2
Li Lihua in 2016	23	23	52.30 ± 10.60		Gemcitabine 1,000 mg/m^2, intravenous drip, D_1, D_8 + cisplatin 30 mg/m^2, intravenous drip, D_{1-3}	The control group was treated with the chemotherapy regimen + recombinant human endostatin 15 mg, 0.9% sodium chloride solution 500 ml, intravenous drip, d_{1-14}, intermittent for 7 days	21	(1) (2) (3) (4) (5)	3
Fangli in 2017	23	23	52.00	60.00	Gemcitabine 1,000 mg/m^2, intravenous drip, D_1, D_8 + cisplatin 75 mg/m^2, intravenous drip, D_{1-3}	The control group was treated with the chemotherapy regimen + recombinant human endostatin 7.5 0 mg/m^2, 0.9% sodium chloride injection 500 ml, once a day, d_{1-14}	21	(1) (2)	2
Jia Xiaoqiong in 2017	20	20	50.00 ± 2.00		Gemcitabine 1.00 mg/m^2, 0.9% sodium chloride injection 150 ml, intravenous drip, D_1, D_8 + cisplatin 25 mg/m^2, 0.9% sodium chloride injection 500 ml, intravenous drip, D_{1-3}	The control group was treated with the chemotherapy regimen + recombinant human endostatin 30 mg, 0.9% sodium chloride injection 110 ml, D_{1-7}	21	(1) (2) (3) (4) (5)	2

Table 1: Continued.

Year of publication and first author	Number of cases		Age (years)		Method		Intervention course (d)	Outcome measures	Jadad score (points)
	Control group	Experimental group	Control group	Experimental group	Control group	Experimental group			
Xu Li in 2017	30	30	54.10 ± 11.30		Gemcitabine 1.00 g/m^2, 0.9% sodium chloride injection 250 ml, intravenous drip, D_1, D_8 + cisplatin 30 mg/m^2, 0.9% sodium chloride injection 500 ml, intravenous drip, D_{1-3}	The control group was treated with the chemotherapy regimen + recombinant human endostatin 15 mg, 0.9% sodium chloride injection 500 ml, intravenous drip, d_{1-14}	21	(1) (2) (3) (4) (5)	3
Song Wencan in 2018	30	30	61.70	57.40	Gemcitabine 1,250 mg/m^2, intravenous drip, D_1, D_8 + cisplatin 25 mg/m^2, intravenous drip, D_{1-3}	The control group was treated with the chemotherapy regimen + recombinant human endostatin 15 mg/m^2, intravenous drip, D_{1-7}	21	(1) (2) (3) (4) (5)	1
Wang Zhifeng in 2018	30	34	55.45	55.97	Gemcitabine 1,000 mg/m^2, 0.9% sodium chloride injection 100 ml, intravenous drip, D_1, D_2 + cisplatin 75 mg/m^2, 0.9% sodium chloride injection 500 ml, intravenous drip, divided into 3 days	The control group was treated with the chemotherapy regimen + recombinant human endostatin 15 mg, 0.9% sodium chloride injection 250 ml, intravenously pumped, d_{1-9}	21	(1) (2) (3) (4) (5)	1
Zhong Li in 2018	25	25	70.34	70.21	Gemcitabine 1,000 mg/m^2, 150 ml of 0.9% sodium chloride injection, intravenous drip, D_1, d_8 + cisplatin 30 mg/m^2, 0.9% sodium chloride injection 500 ml, intravenous drip, D_{1-3}	The control group was treated with the chemotherapy regimen + recombinant human endostatin 7.50 mg/m^2, 0.9% sodium chloride injection 100 ml, intravenous drip, d_{1-14}	21	(1) (2) (3) (4) (5)	2

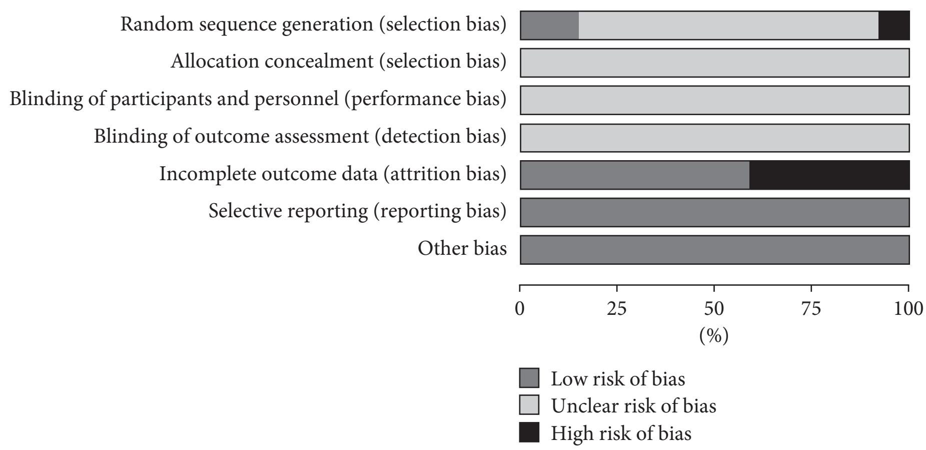

Figure 2: Bar chart of bias risk.

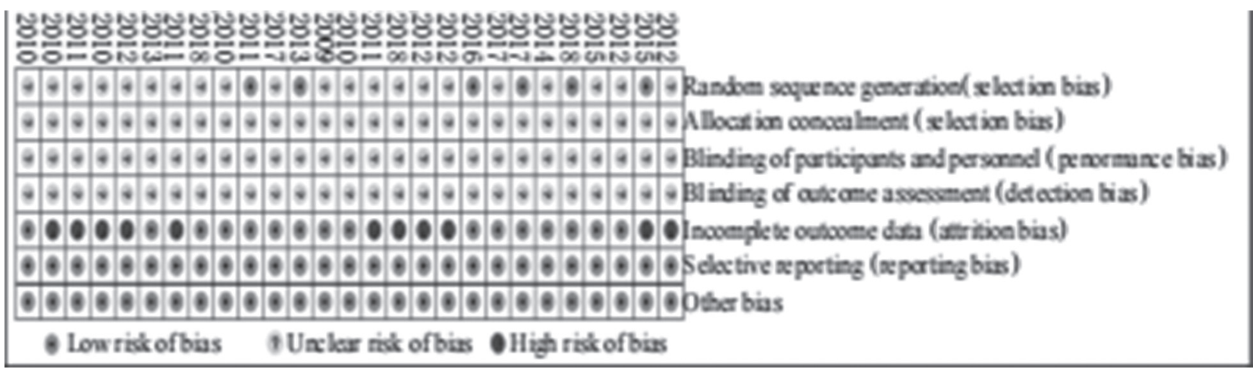

Figure 3: Bias risk diagram.

Table 2: Forest map of meta-analysis of patients' efficiency among groups.

Study details	Experimental		Control		Weight (%)	Risk ratio
	Events	Total	Events	Total		MH, fixed, 95% CI
Si Feng, 2012	17	40	9	32	4.1	1.51 [0.78, 2.93]
Fu Hao, 2015	19	32	9	28	3.9	1.85 [1.00, 3.40]
Jian-Wu Liu, 2012	12	30	11	30	4.5	1.09 [0.57, 2.07]
Liu Tao, 2015	21	32	13	32	5.3	1.62 [0.99, 2.63]
Song Wenxian, 2018	16	30	10	30	4.1	1.60 [0.87, 2.94]
Yuan-yuan Zhang, 2014	14	31	9	28	3.8	1.41 [0.72, 2.73]
Xu Li, 2017	11	35	8	35	3.2	1.38 [0.63, 3.00]
Fang Li, 2017	14	23	7	23	2.8	2.00 [0.99, 4.03]
Li Lihua, 2016	13	23	9	23	3.7	1.44 [0.77, 5.69]
LuanWenQiang, 2012	11	25	7	27	2.7	1.70 [0.78, 3.69]
Relapsed Chicken, 2012	67	94	31	90	12.9	1.76 [1.27, 2.44]
Hi-Feng Wang, 2018	19	34	9	30	3.9	1.88 [1.00, 3.47]
Wang Fang, 2011	13	31	11	29	4.6	1.11 [0.59, 2.06]
Mention, 2010	9	20	2	20	0.8	4.50 [1.11, 18.27]
Xie Yanru, 2008	9	22	7	26	2.6	1.52 [0.68, 3.41]
Tany, 2013	21	38	12	38	4.9	1.75 [1.01, 3.03]
Xiao-jing Jia, 2017	6	20	4	20	1.6	1.50 [0.50, 4.52]
Deng Qingping, 2011	5	22	2	18	0.8	2.65 [0.59, 11.88]

Heterogeneity: $chi^2 = 1.75$, $d_f = 2$ ($P = 0.42$), and $I^2 = 0\%$. Test for overall effect: $Z = 1.23$ ($P = 0.22$).

chemotherapy with platinum in patients with advanced NSCLC. The results of the analysis of the effects of chemotherapy on the survival of 2,714 patients with advanced NSCLC in 16 randomized controlled studies showed that chemotherapy combined with support therapy reduced the risk of death by 23.00% ($P < 0.0001$); the total survival time was prolonged by 1.50 months, and the 1-year survival rate was improved by 9.00% [13]. The results fully show that

Table 3: Forest map of meta-analysis of benefit rate between groups.

Study details	Experimental		Control		Weight (%)	Risk ratio
	Events	Total	Events	Total		MH, fixed, 95% CI
Si Feng, 2012	32	40	18	32	3.5	1.42 [1.01, 2.00]
Fu Hao, 2015	28	32	22	28	4.1	1.11 [0.88, 1.41]
Jian-Wu Liu, 2012	25	30	19	30	3.3	1.32 [0.96, 1.80]
Liu Tao, 2015	31	32	24	32	4.2	1.29 [1.05, 1.59]
Song Wenxian, 2018	25	30	22	30	3.9	1.14 [0.87, 1.49]
Yuan-yuan Zhang, 2014	22	31	19	28	3.5	1.05 [0.74, 1.47]
Xu Li, 2017	30	35	22	35	3.9	1.36 [1.02, 1.82]
Fang Li, 2017	20	23	12	23	2.3	1.54 [1.04, 2.28]
Li Lihua, 2016	23	23	22	23	4.0	1.04 [0.93, 1.18]
LuanWenQiang, 2012	20	25	14	27	2.4	1.54 [1.02, 2.33]
Relapsed Chicken, 2012	87	94	71	90	12.8	1.17 [1.04, 1.32]
Hi-Feng Wang, 2018	28	34	21	30	3.9	1.18 [0.89, 1.56]
Wang Fang, 2011	27	31	22	29	4.0	1.15 [0.90, 1.47]
Mention, 2010	20	20	18	20	3.3	1.11 [0.93, 1.31]
Xie Yanru, 2008	17	22	19	26	3.1	1.06 [0.76, 1.46]
Tany, 2013	34	38	24	38	4.2	1.42 [1.09, 1.85]
Xiao-jing Jia, 2017	16	20	12	20	2.1	1.33 [0.88, 2.03]
Deng Qingping, 2011	11	17	6	18	1.0	1.94 [0.92, 4.08]

Heterogeneity: $\text{chi}^2 = 1.75$, $d_f = 2$ ($P = 0.42$), and $I^2 = 0\%$. Test for overall effect: $Z = 1.23$ ($P = 0.22$).

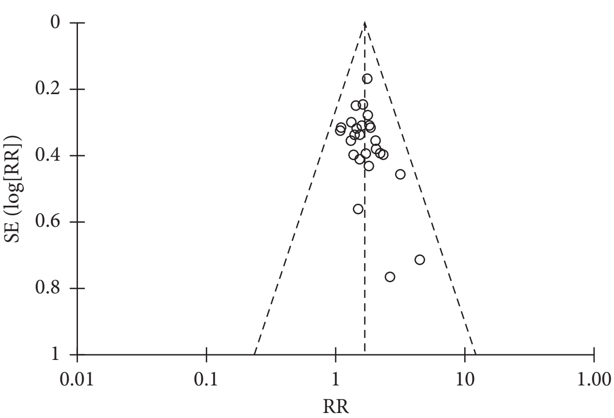

Figure 4: Inverted funnel plot of effective rate.

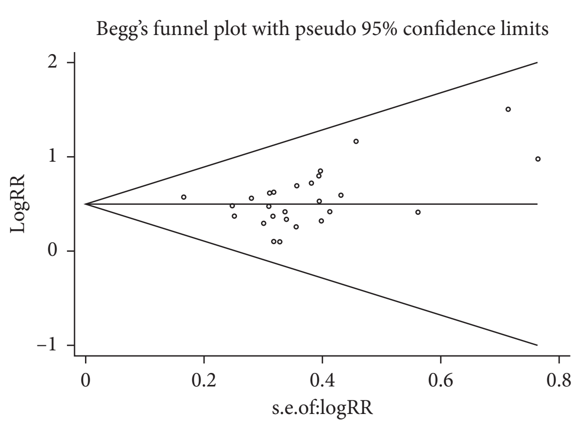

Figure 5: Efficient Begg's diagram.

chemotherapy based on platinum drugs can reduce the risk of death and bring obvious survival benefits to patients, thus promoting NSCLC treatment into platinum-containing chemotherapy era. Among the above chemotherapy schemes, gemcitabine + cisplatin (GP) has some advantages. In 2005, Le Chavalier et al. conducted a meta-analysis of a single study of gemcitabine plus platinum-based chemotherapy and other platinum-containing chemotherapy options to assess whether there is a treatment that is more advantageous in advanced NSCLC [14]. The meta-analysis was selected into 13 studies (4,500 cases), except for two phase II studies, all of which were phase III studies. Five studies were cisplatin single drug or first and second generation combined platinum-containing programs (1,900 cases), and 8 were third generation combined platinum (2,600 cases). The results showed that GP could significantly reduce the disease progression and death risk by 12.00% and 10.00%, respectively, compared with other chemotherapy schemes; compared with the first and second generation combined platinum-containing regimen, GP could significantly prolong the total survival period of patients ($P < 0.001$); and compared with other third-generation platinum-containing regimen without gemcitabine, gemcitabine significantly prolonged the progression-free survival period ($P < 0.001$). The results of this analysis fully confirm that gemcitabine plus platinum combined regimen can significantly prolong the total and progression-free survival of patients with advanced NSCLC compared with other platinum-containing schemes. In 2007, Grossi et al.'s meta-analysis compared the activity of gemcitabine with three other third-generation platinum-containing chemotherapy programs [15]. The meta-analysis included 48 studies, with 6,671 patients. The results showed that gemcitabine could significantly reduce the risk of disease progression by 14.00% compared with other third-generation platinum-containing chemotherapy. This meta-analysis study not only laid the foundation position of platinum-containing chemotherapy in advanced NSCLC treatment but also highlighted the treatment advantages of GP. Patients with advanced NSCLC received gemcitabine plus platinum first-line treatment, which can achieve a higher quality of life and longer life [16]. Therefore, GP with small side effects and good tolerance was used as chemotherapy. But there is no essential difference in efficacy between the third-generation chemotherapy drugs and platinum. The randomized controlled study ECoG 1594, published in the New England Journal of medicine in 2002, showed that there was no significant difference in the median OS between the four third-generation platinum-containing chemotherapy regimens (gemcitabine, paclitaxel, docetaxel, and vinorelbine combined with platinum) [17]. The treatment cycle of the first-line chemotherapy program and the combination of three chemotherapy drugs were also confirmed by the phase II clinical study of MPCRN cancer research network in the United States [18]. Therefore, if we want to further improve the chemotherapy effect of lung cancer, we must take new ideas.

The growth and diffusion of cancer cells depend on angiogenesis and tumor neogenesis, which is the most important antitumor method of vascular targeted therapy [19, 20]. In some studies, NSCLC patients were divided into 34 cases of platinum chemotherapy and 54 cases of platinum plus recombinant human endostatin [21–23]. It was found that the progression-free survival rate and overall survival rate of patients treated with combination therapy were significantly improved. Other related studies have pointed out that the efficacy of combined therapy is controversial and needs further study [24]. Gemcitabine is a substitute for inhibitory enzymes, which can inhibit the DNA replication of tumor cells in the process of DNA synthesis and repair. In order to study the curative effect of recombinant human endostatin in patients with NSCLC, this study summarized the randomized controlled trials of chemotherapy regimens in patients with NSCLC. The results showed that recombinant human endostatin combined with gemcitabine and cisplatin could significantly improve the total effective rate and benefit rate, and the bias analysis of funnel plot and Egger's test showed that the results were more reliable. The incidence of leucopenia, thrombocytopenia, and gastrointestinal reactions between the two groups were not statistically significant, indicating that the combination of recombinant human endostatin, gemcitabine, and cisplatin is safe [25].

Ouyang Lihui et al. conducted a meta-analysis in 2012 to compare the efficacy of gemcitabine + cisplatin + recombinant human endostatin (GPE) regimen and gemcitabine + cisplatin (GP) regimen in patients with NSCLC; GPE is superior to GP in total effective rate and disease control rate. Ma et al. included 9 studies and 839 patients with NSCLC [26]. The results showed that the GPE regimen did not increase the incidence of adverse reactions compared with the GP regimen. The combined results of 4 studies found that compared with the GP scheme, the GPE scheme led to increased arrhythmia, and the difference was statistically significant. This suggests that clinicians should pay close attention to the ECG of patients with NSCLC when using a GPE regimen to prevent serious adverse reactions of arrhythmia. At the same time, the log-rank test was used to compare the disease progression and overall survival of the two groups. It was found that recombinant human endostatin combined with GP regimen did not improve the overall survival of patients with advanced NSCLC, but it did not exclude the bias caused by the small sample size of this study, and it was also affected by the later treatment effect of patients. The main adverse reactions of recombinant human endostatin combined with GP regimen to patients with advanced NSCLC were myelosuppression and gastrointestinal reactions. A few patients had liver function damage and ECG changes, but there was no significant difference compared with patients treated with GP regimen alone.

The curative effect of recombinant human endostatin, gemcitabine, and cisplatin in the treatment of patients with NSCLC has been improved, without obvious adverse reactions. The disadvantages are as follows: firstly, the unpublished literature are not included; secondly, the comprehensive quality evaluation of the included literature is low; thirdly, the included literature are all Chinese literature, which are not suitable for foreign patients; and fourthly, the quality of life evaluation of patients is not involved.

5. Conclusion

The combination of recombinant human endostatin, gemcitabine, and cisplatin can increase the efficacy and safety of NSCLC patients.

Data Availability

The data used to support this study are available from the corresponding author upon request.

Conflicts of Interest

The authors declare that they have no conflicts of interest.

References

[1] L. Chen, X. Zhu, D. Li, and X. Cai, "Effect of thoracic hyperthermic perfusion with recombinant human endostatin plus nedaplatin in treating pleural effusion in patients with advanced non-small cell lung cancer," *Journal of BUON*, vol. 25, no. 6, pp. 2643–2649, 2020.

[2] S.-L. Zhang, C.-B. Han, L. Sun, L.-T. Huang, and J.-T. Ma, "Efficacy and safety of recombinant human endostatin combined with radiotherapy or chemoradiotherapy in patients with locally advanced non-small cell lung cancer: A pooled analysis," *Radiation Oncology*, vol. 15, no. 1, p. 205, 2020.

[3] L. Feng, Z. Wang, L. Jing et al., "Recombinant human endostatin combined with chemotherapy for advanced squamous cell lung cancer: A meta-analysis," *World Journal of Surgical Oncology*, vol. 19, no. 1, p. 64, 2021.

[4] K. Zhang, H. Wang, Z. Wang et al., "Intensity-modulated radiation therapy (IMRT)-based concurrent chemoradiotherapy (CCRT) with Endostar in patients with pelvic locoregional recurrence of cervical cancer: Results from a hospital in the Qinghai-Tibet Plateau," *Medicine*, vol. 99, no. 49, Article ID e21966, 2020.

[5] L. Guan, "Endostar rebuilding vascular homeostasis and enhancing chemotherapy efficacy in cervical cancer

treatment," *OncoTargets and Therapy*, vol. 13, no. 13, pp. 12811–12827, 2020.

[6] L. Lu, H. Chen, L. Wang et al., "A dual receptor targeting- and BBB penetrating- peptide functionalized polyethyleneimine nanocomplex for secretory endostatin gene delivery to malignant glioma," *International Journal of Nanomedicine*, vol. 15, no. 15, pp. 8875–8892, 2020.

[7] B. Wang, L. Xu, Q. Li et al., "Endostar continuous versus intermittent intravenous infusion combined with chemotherapy for advanced NSCLC: a systematic review and meta-analysis including non-randomized studies," *BMC Cancer*, vol. 20, no. 1, p. 1021, 2020.

[8] E. Idiiatullina, M. Al-Azab, W. Walana, V. Pavlov, and B. Liu, "EnDuo, a novel derivative of Endostar, inhibits the migration of colon cancer cells, suppresses matrix metalloproteinase-2/9 expression and impedes AKT/ERK activation," *Biomedicine & Pharmacotherapy*, vol. 134, no. 134, Article ID 111136, 2021.

[9] I. Z. Uras, H. P. Moll, and E. Casanova, "Targeting KRAS mutant non-small-cell lung cancer: past, present and future," *International Journal of Molecular Sciences*, vol. 21, no. 12, p. 4325, 2020.

[10] B. Li, L. Zhu, C. Lu et al., "circNDUFB2 inhibits non-small cell lung cancer progression via destabilizing IGF2BPs and activating anti-tumor immunity," *Nature Communications*, vol. 12, no. 1, p. 295, 2021.

[11] Y. Mu, X. Hao, P. Xing et al., "Acquired resistance to osimertinib in patients with non-small-cell lung cancer: mechanisms and clinical outcomes," *Journal of Cancer Research and Clinical Oncology*, vol. 146, no. 9, pp. 2427–2433, 2020.

[12] W. Hong, M. Xue, J. Jiang, Y. Zhang, and X. Gao, "Circular RNA circ-CPA4/let-7 miRNA/PD-L1 axis regulates cell growth, stemness, drug resistance and immune evasion in non-small cell lung cancer (NSCLC)," *Journal of Experimental & Clinical Cancer Research*, vol. 39, no. 1, p. 149, 2020.

[13] S. Kitagawa, T. Hakozaki, R. Kitadai, and Y. Hosomi, "Switching administration of anti-PD -1 and anti-PD-L1 antibodies as immune checkpoint inhibitor rechallenge in individuals with advanced non-small cell lung cancer: case series and literature review," *Thoracic Cancer*, vol. 11, no. 7, pp. 1927–1933, 2020.

[14] T. Le Chevalier, G. Scagliotti, R. Natale et al., "Efficacy of gemcitabine plus platinum chemotherapy compared with other platinum containing regimens in advanced non-small-cell lung cancer: a meta-analysis of survival outcomes," *Lung cancer*, vol. 47, no. 1, pp. 69–80, 2005.

[15] X. Wei, J. Yang, S. J. Adair et al., "Targeted CRISPR screening identifies PRMT5 as synthetic lethality combinatorial target with gemcitabine in pancreatic cancer cells," *Proceedings of the National Academy of Sciences*, vol. 117, no. 45, pp. 28068–28079, 2020.

[16] R. Nicolle, O. Gayet, P. Duconseil et al., "A transcriptomic signature to predict adjuvant gemcitabine sensitivity in pancreatic adenocarcinoma," *Annals of Oncology*, vol. 32, no. 2, pp. 250–260, 2021.

[17] T. S. Bekaii-Saab, J. W. Valle, E. Van Cutsem et al., "FIGHT-302: first-line pemigatinib vs gemcitabine plus cisplatin for advanced cholangiocarcinoma with FGFR2 rearrangements," *Future Oncology*, vol. 16, no. 30, pp. 2385–2399, 2020.

[18] R. Tang, J. Hua, J. Xu et al., "The role of ferroptosis regulators in the prognosis, immune activity and gemcitabine resistance of pancreatic cancer," *Annals of Translational Medicine*, vol. 8, no. 21, p. 1347, 2020.

[19] T. T. B. Ho, A. Nasti, A. Seki et al., "Combination of gemcitabine and anti-PD-1 antibody enhances the anticancer effect of M1 macrophages and the Th1 response in a murine model of pancreatic cancer liver metastasis," *Journal for immunotherapy of cancer*, vol. 8, no. 2, p. 1367, 2020.

[20] X. Chen, X. Wu, H. Wu et al., "Camrelizumab plus gemcitabine and oxaliplatin (GEMOX) in patients with advanced biliary tract cancer: a single-arm, open-label, phase II trial," *Journal for immunotherapy of cancer*, vol. 8, no. 2, p. 1240, 2020.

[21] Z. A. Wainberg, H. S. Hochster, E. J. Kim et al., "Open-label, phase I study of nivolumab combined with nab-paclitaxel plus gemcitabine in advanced pancreatic cancer," *Clinical Cancer Research*, vol. 26, no. 18, pp. 4814–4822, 2020.

[22] Z. Sadiq, E. Varghese, and D. Büsselberg, "Cisplatin's dual-effect on the circadian clock triggers proliferation and apoptosis," *Neurobiology of Sleep and Circadian Rhythms*, vol. 9, no. 9, Article ID 100054, 2020.

[23] H. Mei, L. Zhao, W. Li et al., "Inhibition of ferroptosis protects House Ear Institute-Organ of Corti 1 cells and cochlear hair cells from cisplatin-induced ototoxicity," *Journal of Cellular and Molecular Medicine*, vol. 24, no. 20, pp. 12065–12081, 2020.

[24] A. Taber, E. Christensen, P. Lamy et al., "Molecular correlates of cisplatin-based chemotherapy response in muscle invasive bladder cancer by integrated multi-omics analysis," *Nature Communications*, vol. 11, no. 1, p. 4858, 2020.

[25] X. Zhou, T. Teng, Y. Zhang et al., "Comparative efficacy and acceptability of antidepressants, psychotherapies, and their combination for acute treatment of children and adolescents with depressive disorder: a systematic review and network meta-analysis," *The Lancet Psychiatry*, vol. 7, no. 7, pp. 581–601, 2020.

[26] T. Chongqing, P. Liubao, Z. Xiaohui et al., "Cost–utility analysis of the newly recommended adjuvant chemotherapy for resectable gastric cancer patients in the 2011 Chinese national comprehensive cancer network (NCCN) clinical practice guidelines in oncology: gastric cancer," *Pharmacoeconomics*, vol. 32, no. 3, pp. 235–243, 2014.

Hindawi
Journal of Healthcare Engineering
Volume 2023, Article ID 9814987, 1 page
https://doi.org/10.1155/2023/9814987

Retraction

Retracted: The Effect of Acupuncture Combined with Aerobic Exercise for Coronary Heart Disease as Cardiac Rehabilitation

Journal of Healthcare Engineering

Received 12 January 2023; Accepted 12 January 2023; Published 21 January 2023

Journal of Healthcare Engineering has retracted the article titled "The Effect of Acupuncture Combined with Aerobic Exercise for Coronary Heart Disease as Cardiac Rehabilitation" [1] due to concerns that the peer review process has been compromised.

Following an investigation conducted by the Hindawi Research Integrity team [2], significant concerns were identified with the peer reviewers assigned to this article; the investigation has concluded that the peer review process was compromised. We therefore can no longer trust the peer review process, and the article is being retracted with the agreement of the Chief Editor.

References

[1] Y. Yang, Y. Li, Y. Zheng et al., "The Effect of Acupuncture Combined with Aerobic Exercise for Coronary Heart Disease as Cardiac Rehabilitation," *Journal of Healthcare Engineering*, vol. 2022, Article ID 4903265, 6 pages, 2022.

[2] L. Ferguson, "Advancing Research Integrity Collaboratively and with Vigour," 2022, https://www.hindawi.com/post/advancing-research-integrity-collaboratively-and-vigour/.

Hindawi
Journal of Healthcare Engineering
Volume 2022, Article ID 4903265, 6 pages
https://doi.org/10.1155/2022/4903265

Research Article

The Effect of Acupuncture Combined with Aerobic Exercise for Coronary Heart Disease as Cardiac Rehabilitation

Yan Yang, Yaoyao Li, Yuanyuan Zheng, Lei Zhang, Wei Ma, Lingling Shi, Jingjing Kong, Xiaoli Liu, and Hong Yu

Department of Cardiology, Shanghai Punan Hospital of Pudong New District, Shanghai 200125, China

Correspondence should be addressed to Yan Yang; 13816409220@163.com

Received 13 December 2021; Revised 8 January 2022; Accepted 12 January 2022; Published 15 March 2022

Academic Editor: Enas Abdulhay

Background. The mortality of coronary heart disease continues to rise. Cardiac rehabilitation intervenes the risk factors of cardiovascular disease, improves cardiopulmonary function, maintains healthy psychology, improves the quality of life of patients, and reduces cardiovascular mortality. *Objective*. To explore the effect of acupuncture combined with aerobic exercise on cardiopulmonary exercise ability, blood lipid, fatty acid oxidation, and psychology in patients with coronary heart disease. *Methods*. Sixty patients with coronary heart disease from February 2018 to October 2020 were randomly divided into two groups: the control group and experimental group. The control group was given an exercise prescription, and the experimental group was given acupuncture combined with an exercise prescription. Before and after the intervention, the cardiopulmonary exercise test, blood lipid, carnitine acyltransferase (CACT), the Self-Rating Somatic Symptom Scale (SSS), the Generalized Anxiety Disorder-7 (GAD-7), and the Patient Health Questionnaire-9 (PHQ-9) of the two groups were compared. *Results*. The PHQ-9 score was better in the experimental group than in the control group. In both groups, after the intervention, the peak oxygen uptake and anaerobic threshold were increased, and blood lipid and PHQ-9 scores were decreased. In the experimental group, the carbon dioxide metabolic equivalent was decreased, CACT was increased, and SSS and GAD-7 scores were decreased, with statistical difference ($P < 0.05$). *Conclusion*. Acupuncture combined with aerobic exercise can improve the cardiopulmonary exercise ability, increase fatty acid oxidation, decrease blood lipid, and ameliorate anxiety and depression symptoms of patients with coronary heart disease as cardiac rehabilitation.

1. Introduction

Cardiovascular disease is the leading cause of disability and death in Chinese residents [1]. There are more than 11 million people suffering from Coronary Artery Atherosclerotic Heart Disease (CHD) in China [2]. Despite the continuous development of drugs and interventional therapy, the mortality of coronary heart disease in China continues to rise [3]. The substantial decline in mortality of coronary heart disease in developed countries is due to coronary heart disease rehabilitation and secondary prevention [4]. China urgently needs to strengthen the prevention and rehabilitation of cardiovascular diseases. Cardiac rehabilitation applied drugs, exercise, nutrition, and psychological and behavioural intervention to comprehensively intervene the risk factors of cardiovascular disease, improve cardiopulmonary function, maintain healthy psychology, improve the quality of life of patients, and reduce cardiovascular mortality [5–7].

Acupuncture, having bidirectional regulatory ability and a much lower incidence of side effects, can treat a variety of diseases. It can intervene hypertension and psychological stress-induced cardiovascular reactivity to prevent cardiovascular disease and cardiovascular death [8]. It has been used as adjuvant therapy for chronic stable angina pectoris, which can reduce the frequency of angina attacks [9]. This study observed the effect of acupuncture treatment on cardiopulmonary exercise ability, blood lipid metabolism, and psychology of patients with coronary heart disease and explored rehabilitation strategy suitable for China's national conditions.

2. Subjects and Methods

2.1. Subjects. This study included sixty patients with stable coronary heart disease who were admitted to the Department of Cardiology, Punan Hospital, Pudong New District, Shanghai, from February 2018 to October 2020. Inclusion criteria: age >18 years and <85 years, stability of symptoms and dose for at least 2 weeks; coronary angiography showed at least one major coronary artery stenosis >50%; and obtained consent and sign informed consent. Exclusion criteria: those who are unwilling or unable to exercise or acupuncture treatment; there has been acupuncture treatment in the recent 6 months; bone and joint diseases affecting movement; aortic dissection; acute coronary syndrome; uncontrolled heart failure; and severe liver and renal dysfunction. Using random numbers, 60 cases were divided into the control group and experimental group.

2.2. Methods

2.2.1. Intervention Methods. All patients were treated with cardiac rehabilitation under the guidance of cardiac rehabilitation doctors. Exercise prescriptions were issued according to cardiopulmonary exercise test (CPXT). The control group received exercise rehabilitation, and the experimental group received acupuncture treatment and exercise rehabilitation. Exercise prescription: exercise intensity set anaerobic threshold heart rate as target heart rate; exercise frequency for 3–5 times a week, 20–30 minutes aerobic exercise, a total of 8 weeks; the form of exercise is mainly jogging and power cycling. Acupuncture acupoints were selected by acupuncture doctors according to the clinical symptoms of patients, and the selected acupoints were the following acupoint combinations. Chest discomfort acupoints: Nei guan, Ju Que, Shen men, Guan Yuan, Qi hai, and Da ling; insomnia acupoints: Bai hui, Zhao hai, and Tai Chong; shoulder pain acupoint: Jian yu, Jian Liao, Jian Zhen, Qu chi, and Wai guan; lower limb pain acupoint: Yin ling Quan, Chen shan, Tiao Kou, Zu san li, San yin jiao, Fu Tu, and Feng shi; and knee Joint pain acupoints: Nei Wai Xi Yan, Xue Hai, He Ding, Yang Ling Quan, etc. Acupuncture treatment was performed for 30 minutes each time, 1-2 times a week, for a total of 12 times.

2.2.2. Cardiopulmonary Exercise Test (CPXT). The Italian COSMED Cardiopulmonary exercise test system, exercise equipment for power cycling, with an increasing power (10–20 Watt Ramp) scheme for the symptom-limited maximum exercise load test, the V-slop method was used to calculate the anaerobic threshold (see Table 1).

2.2.3. Biochemical Indicators. All patients were taken fasting venous blood, Abbott C16000 automatic biochemical analyzer for blood lipid testing, triglycerides with the GPO-PAP method, total cholesterol with the enzyme method, low-density lipoprotein with the direct method-surfactant clearance method, high-density lipoprotein with the direct method-selective inhibition method, free fatty acids with the ACS-ACOD method, blood glucose with the glucose oxidase method, serum creatinine with the enzyme method, the uric acid kinase method, and homocysteine with the double-reagent circulation enzyme method. Glycosylated haemoglobin was measured by using the Arkray 8180 instrument and high-performance liquid chromatography. Serum CACT was determined by using the ELISA kit. The kit was provided by Shanghai Kamishu Biotechnology Co., Ltd.

2.3. Observation Indicators

2.3.1. CPXT Indicators. The CPXT indicators were peak oxygen uptake per kg body weight (VO2/kg), anaerobic threshold (AT) oxygen uptake, respiratory reserve, oxygen pulse, one-minute heart rate recovery, anaerobic threshold carbon dioxide ventilation equivalent (VE/VCO2 @ AT), and others.

2.3.2. Biochemical Indicators. The biochemical indicators were serum creatinine, uric acid, triglyceride, cholesterol, low-density lipoprotein, high-density lipoprotein, free fatty acids, serum carnitine acyltransferase, blood glucose, glycosylated haemoglobin, blood homocysteine, etc.

2.3.3. Psychological Assessment. Before and after the intervention, patients were asked to fill out the Self-Rating Somatic Symptom Scale (SSS), PHQ-9 health questionnaire (depression screening scale), and GAD-7 generalized anxiety disorder scale for psychological assessment.

2.4. Statistical Method. SPSS22.0 software was used. The measurement data were expressed as mean ± standard deviation, which was in line with normal distribution. A paired t-test was used for intragroup comparison, and an independent-sample t-test was used for intergroup comparison. Enumeration data were expressed as frequency and percentage. The Chi-square test was used for comparison between groups. $P < 0.05$ indicated statistical difference.

3. Results

3.1. Comparison of Baseline Basic Data between the Two Groups of Patients. There was no significant difference in gender, age, body mass index, history of hypertension, history of diabetes, homocysteine, creatinine, uric acid, triglyceride, cholesterol, low-density lipoprotein, high-density lipoprotein, free fatty acid, blood glucose, glycosylated haemoglobin (HbA1c), and other biochemical indicators between the two groups ($P > 0.05$), as shown in Table 2.

3.2. Comparison of the Cardiopulmonary Exercise Test. There was no significant difference between the two groups before and after intervention ($P > 0.05$). The peak oxygen

Table 1: Comparison of cardiopulmonary exercise parameters between the two groups of patients with coronary heart disease after and before treatment (mean ± standard deviation).

Groups	Cases	VO_2/kg peak (mL/min/kg)		VO_2/kg@AT (mL/min/kg)		VE/VCO_2@AT	
		Before treatment	After treatment	Before treatment	After treatment	Before treatment	After treatment
Trial groups	30	15.66 ± 4.63	16.75 ± 4.17*	12.64 ± 3.75	15.07 ± 4.09*	34.54 ± 5.98	32.89 ± 5.84*
Control groups	30	15.82 ± 2.46	18.45 ± 3.53*	12.91 ± 1.76	16.60 ± 3.88*	33.23 ± 3.01	33.49 ± 2.66
t value		−0.122	−1.231	−0.265	−1.033	0.781	−0.355
P value		−0.904	0.228	0.794	0.311	0.443	0.726

Compared with before treatment, $^*P < 0.05$.

Table 2: Basic information of the two groups.

	Acupuncture groups	Control groups
Number of people	30	30
Male	20	16
Age (years)	58.94 ± 13.53	62.60 ± 17.54
BMI (kg/m^2)	25.03 ± 3.39	24.83 ± 2.90
Hypertension	22	20
Diabetes	17	14
Homocysteine, umol/L	13.66 ± 11.39	11.39 ± 3.28
Creatinine, umol/L	70.71 ± 14.62	68.46 ± 17.51
Uric acid, umol/L	319.86 ± 62.71	313.46 ± 47.34
Triglyceride, mmol/L	1.53 ± 1.08	1.70 ± 0.54
Cholesterol, mmol/L	4.20 ± 1.32	4.70 ± 1.00
Low-density lipoprotein(LDL), mmol/L	2.69 ± 1.03	2.60 ± 0.79
High-density lipoprotein (HDL), mmol/L	1.08 ± 0.27	1.01 ± 0.24
Free fatty acid, umol/L	503.23 ± 195.96	598.31 ± 292.91
Blood glucose, mmol/L	6.5 ± 1.92	5.65 ± 0.90
HbA1c, %	6.99 ± 1.36	6.23 ± 1.17

uptake per kilogram (VO2/kg peak) and anaerobic threshold (VO2/kg @ AT) in the two groups were increased after intervention. The carbon dioxide ventilation equivalent (VE/VCO2 @ AT) in the experimental group decreased after intervention, with statistical significance ($P < 0.05$).

3.3. Comparison of Biochemical Indicators. There was no significant difference between the two groups in serum creatinine, uric acid, triglyceride, high-density lipoprotein, free fatty acid, blood glucose, glycosylated haemoglobin, and other biochemical indicators before and after intervention ($P > 0.05$). Compared within the group, the low-density lipoprotein and cholesterol in the two groups decreased after the intervention, and the serum carnitine acyltransferase in the experimental group increased after intervention, with a statistical difference ($P < 0.05$) (Table 3).

3.4. Comparison of Psychological Scales between the Two Groups. There was no significant difference between the two groups before intervention. After intervention, the acupuncture group improved PHQ-9 compared with the control group ($P < 0.05$). Compared within the group before and after intervention, the acupuncture group improved the Chinese somatization symptom checklist, PHQ-9 and CAD-7, and aerobic exercise improved PHQ-9 ($P < 0.05$), see Table 4.

4. Discussion

This study shows that aerobic exercise can improve peak oxygen uptake and anaerobic threshold in patients with coronary heart disease and reduce blood lipids. Aerobic exercise increases ventricular end-diastolic volume, myocardial contractility, and cardiac output through the sympathetic nerve and improves coronary artery circulation by increasing nitric oxide production and vasodilation; exercise can also reduce blood lipids and inflammation indicators [10]. Therefore, exercise is good medicine for heart rehabilitation. Based on a large number of clinical studies and systematic evaluation results in China, Europe, the United States, and other countries, guidelines for the prevention and rehabilitation of cardiovascular diseases based on exercise are introduced [11, 12].

This study found that acupuncture in the rehabilitation of patients with coronary heart disease can also bring three other benefits.

Fatty acid is an important source of muscle contraction energy, acetyl-CoA fatty acid is tranfered by the carnitine palmitoyl transferase system into mitochondrial oxidation. This study suggests that acupuncture can increase the concentration of serum carnitine acyltransferase, infer acupuncture promote fatty acid oxidation, and enhance myocardial and skeletal muscle energy supplement. Glucose is the main energy source during embryogenesis, and fatty acid oxidation is the main energy source after birth. The

Table 3: Comparison of blood cholesterol, low-density lipoprotein, and serum carnitine acyltransferase between the two groups (mean ± standard deviation).

Groups	Cases	Low-density lipoproteins		Cholesterol		Serum carnitine acyltransferase enzyme U/L	
		Before treatment	After treatment	Before treatment	After treatment	Before treatment	After treatment
Acupuncture group	30	2.69 ± 1.03	$1.88 \pm 0.67^*$	4.20 ± 1.32	$3.5 \pm 1.04^*$	189.09 ± 58.13	$216.64 \pm 57.36^*$
Control group	30	2.60 ± 0.79	$2.10 \pm 0.54^*$	4.70 ± 1.00	$3.89 \pm 0.58^*$	202.45 ± 60.83	208.60 ± 56.48
t value		0.274	−2.092	−1.128	−1.074	−7.13	0.45
P value		0.786	0.059	0.27	0.293	0.48	0.65

Table 4: Comparison of the two groups' psychological self-rating scale (mean ± standard deviation).

Groups	Cases	Somatic self-rating scale		PHQ-9		CAD-7	
		Before treatment	After treatment	Before treatment	After treatment	Before treatment	After treatment
Acupuncture groups	30	34.5 ± 5.98	$32.89 \pm 5.84^*$	4.91 ± 3.56	$2.1 \pm 1.85^*$	4.72 ± 5.04	$1.54 \pm 1.84^*$
Control groups	30	33.23 ± 3.01	33.49 ± 2.66	5.4 ± 3.06	$4.3 \pm 2.71^*$	3.30 ± 4.19	2.8 ± 3.22
t value		0.781	−0.355	−0.337	−2.119	0.701	−1.107
P value		0.443	0.726	0.74	0.048	0.492	0.283

Compared with before treatment, $^*P < 0.05$.

selection and change of myocardial energy substrates are the objects of myocardial metabolise in patients with ischemic heart disease and heart failure. Energy utilization efficiency and myocardial efficiency is a potential target for the treatment of heart failure and ischemia [13]. Animal experiments have found that the lack of carnitine palmitoyltransferase can lead to cardiac hypertrophy due to excessive pressure load caused by lipotoxicity [14]. Acupuncture treatment can regulate heart energy metabolism by affecting the key enzymes of fatty acid metabolism, with fewer adverse reactions and high safety.

Carbon dioxide ventilation equivalent (VE/VCO2) is the most widely studied ventilation efficiency parameter. The increase in VE/VCO2 is significantly associated with the mortality of patients, which is a reliable indicator for the prognosis of heart failure [15]. In this study, it was found that acupuncture treatment could reduce the anaerobic threshold carbon dioxide ventilation equivalent (VE/VCO2 @ AT), which was similar to the previous research results of acupuncture treatment for patients with heart failure in Germany [16]. The increase of VE/VCO2 was due to the increase of invalid ventilation residual cavity, mismatch of blood flow and ventilation, a decrease of skeletal muscle oxidation ability, and an increase of exercise lactic acid to stimulate breathing. Previous studies have found that acupuncture can reduce the production of lactic acid during exercise [17]. This study found that acupuncture can enhance fatty acid oxidation, so it is speculated that these two factors are the reasons why acupuncture can reduce VE/VCO2. Lowering VE/VCO2 may benefit, especially, cardiovascular patients who cannot exercise and have a poor response to treatment, suggesting that acupuncture can be used as a choice for rehabilitation.

Psychological anxiety, depression, and other emotional factors are not only risk factors for coronary heart disease but also closely related to the development of coronary heart disease. A systematic review [18] shows that exercise therapy may reduce depressive symptoms, while anxiety symptoms may be reduced in the short term (less than 12 weeks) and long-term outcomes are uncertain. By literature analysis [19] from 2011 to 2020, more and more studies have shown that acupuncture can be used as a potentially effective treatment for depression and improve depressive symptoms. Acupuncture treatment has positive results in the treatment of anxiety [20]. Metabonomics technology is used to analyze the body metabolism by acupuncture and moxibustion, which shows that acupuncture and moxibustion canchange plasma tryptophan and glutamate, regulate neurotransmitter, improve function, and promote health [21].

Acupuncture is based on the meridian theory, a guide for TCM dorctors to treat diseases, but the mechanism of acupunture is still unclarified; animal experiments have found that acupuncture activates the peripheral sensory nerve fibres of dorsal root ganglion and transmits the signals to the spinal cord and brain, thereby activating the peripheral autonomic nerve. Stimulating the acupoints of hind limbs (Zusanli) in mice can activate the vagal-adrenal anti-inflammatory pathway [22, 23]. Acupuncture and moxibustion activate the vagus nerve, reduce visceral immune cell production factors, reduce inflammatory factors, inhibit sympathetic nerve, and regulate neurohumoral factors, which can theoretically play more roles in cardiovascular diseases.

Therefore, acupuncture can improve the efficiency of exercise ventilation,promote fatty acid oxidation, improve anxiety and depression symptoms, and treat somatization symptoms in patients with coronary heart disease; combined with aerobic exercise can improve the cardiopulmonary exercise ability of patients and reduce blood lipids, which can be applied as cardiac rehabilitation technology.

The shortcomings of this study: (1) failure to set up a sham acupuncture control group because it was difficult to select acupoints in the sham acupuncture group during the preexperiment; (2) also, because there is no effect, patient compliance is not high in the sham acupuncture group after completing 1-2 times; and (3) the number of cases enrolled in this study is small; subsequent studies can expand the sample size and improve follow-up time to assess the long-term efficacy of acupuncture.

Data Availability

Data supporting the results of the study can be obtained by emailing the first author or corresponding author.

Conflicts of Interest

The authors declare no conflicts of interest.

Acknowledgments

This work was supported by the Fund Project: Training Plan of Excellent Young Medical Talents in Health System of Pudong New District, PWRq2016-31.

References

[1] D. Zhao, J. Liu, M. Wang, X. Zhang, and M. Zhou, "Epidemiology of cardiovascular disease in China: current features and implications," *Nature Reviews Cardiology*, vol. 16, no. 4, pp. 203–212, 2019.

[2] The China Cardiovascular Health and Disease Report Writing Group, "China cardiovascular health and disease report 2020 summary," *Chinese Journal of Circulation*, vol. 36, no. 6, pp. 521–545, 2021.

[3] J. Li, X. Li, Q. Wang et al., "ST-segment elevation myocardial infarction in China from 2001 to 2011(the China peace-retrospective acute myocardial infarction study): a retrospective analysis of hospital data," *Lancet*, vol. 385, pp. 441–451, 2015.

[4] N. J. Sethi, S. Safi, S. K. Korang et al., "Antibiotics for secondary prevention of coronary heart disease," *Cochrane Database of Systematic Reviews*, vol. 2, Article ID CD003610, 2021.

[5] D. J. Klionsky, A. K. Abdel-Aziz, S. Abdelfatah et al., "Guidelines for the use and interpretation of assays for monitoring autophagy," *Autophagy*, vol. 17pp. 1–382, 4th edition, 2021.

[6] C. Caffarelli, F. Santamaria, A. Vottero, and S. Bernasconi, "Progress in pediatrics in 2012: choices in allergy, endocrinology, gastroenterology, hematology, infectious diseases, neurology, nutrition and respiratory tract illnesses," *Italian Journal of Pediatrics*, vol. 39, p. 26, 2013.

[7] E. Rydwik, T. Gustafsson, K. Frändin, and G. Akner, "Effects of physical training on aerobic capacity in frail elderly people (75+ years). Influence of lung capacity, cardiovascular disease and medical drug treatment: a randomized controlled pilot trial," *Aging Clinical and Experimental Research*, vol. 22, pp. 85–94, 2010.

[8] H. R. Gao, Z. J. Wu, S. B. Wu et al., "Roles of central orexinergic system on cardiovascular function and acupuncture on intervention of cardiovascular risk: orexinergic system mediate the role of acupuncture?" *Neuropeptides*, vol. 87, Article ID 102132, 2021.

[9] L. Zhao, D. Li, H. Zheng et al., "Acupuncture as adjunctive therapy for chronic stable angina," *JAMA Internal Medicine*, vol. 179, no. 10, pp. 1388–1397, 2019.

[10] The Chinese Rehabilitation Society of cardiovascular disease professional committee Chinese Gerontology Society of cardiovascular and cerebrovascular disease professional committee, "Chinese expert consensus on the psychological prescription of patients in cardiovascular department," *Chinese Journal of Cardiovascular Disease*, vol. 42, no. 1, pp. 6–13, 2014.

[11] C. J. Lavie, R. Arena, D. L. Swift et al., "Exercise and the cardiovascular system," *Circulation Research*, vol. 117, no. 2, pp. 207–219, 2015.

[12] The Cardiovascular Society of Chinese Medical Association Cardiovascular Committee of Chinese Rehabilitation Medical Association Cardiovascular and Cerebrovascular Committee of Chinese Gerontology Society, "Chinese expert consensus on rehabilitation and secondary prevention of coronary heart disease," *Chinese Journal of Cardiovascular Disease*, vol. 41, no. 4, pp. 267–275, 2013.

[13] F. L. J. Visseren, F. Mach, Y. M. Smulders et al., "ESC Guidelines on cardiovascular disease prevention in clinical practice," *European Heart Journal*, vol. 42, no. 34, pp. 3227–3337, 2021.

[14] U. Corrà, P. G. Agostoni, S. D. Anker et al., "Role of cardiopulmonary exercise testing in clinical stratification in heart failure. A position paper from the committee on exercise physiology and training of the heart failure association of the European society of cardiology," *European Journal of Heart Failure*, vol. 20, no. 1, pp. 3–15, 2018.

[15] A. V. Kristen, B. schuhmacher, K. strych et al., "Acupuncture improves exercise tolerance of patients with heart failure: a placebo-controlled pilot study," *Heart*, vol. 96, no. 17, pp. 1396–1400, 2010.

[16] W. J. Hu, *Acupuncture Preconditioning on Exercise-Induced Fatigue Rat Heart protection and Serum Metabolomics Research*, Hubei University of Traditional Chinese Medicine, Wuhan, China, 2019.

[17] N. Fillmore, J. Mori, and G. D. Lopaschuk, "Mitochondrial fatty acid oxidation alterations in heart failure, ischaemic heart disease and diabetic cardiomyopathy," *British Journal of Pharmacology*, vol. 171, no. 8, pp. 2080–2090, 2014.

[18] L. He, T. Kim, Q. Long et al., "Carnitine palmitoyltransferase-1b deficiency aggravates pressure overload-induced cardiac hypertrophy caused by lipotoxicity," *Circulation*, vol. 126, no. 14, pp. 1705–1716, 2012.

[19] S. Verschueren, A. M. Eskes, J. M. Maaskant, A. M. Roest, C. H. M. Latour, and W. S. Op Reimer, "The effect of exercise therapy on depressive and anxious symptoms in patients with ischemic heart disease: a systematic review," *Journal of Psychosomatic Research*, vol. 105, pp. 80–91, 2018.

[20] H. Xiang, J. Li, B. Li, Q. Tan, and G. Cai, "Trends of acupuncture therapy on depression from 2011 to 2020: a bibliometric analysis," *Frontiers in Psychology*, vol. 12, Article ID 721872, 2021.

[21] D. Amorim, J. Amado, I. Brito et al., "Acupuncture and electroacupuncture for anxiety disorders: a systematic review of the clinical research," *Complementary Therapies in Clinical Practice*, vol. 31, pp. 31–37, 2018.

[22] X. L. Li, G. R. Huang, X. L. Wu et al., "An overview of the application of metabolomics technology in the study of acupuncture regulating metabolism in the past decade," *Global Chinese Medicine*, vol. 14, no. 7, pp. 1352–1357, 2021.

Hindawi
Journal of Healthcare Engineering
Volume 2022, Article ID 9248674, 14 pages
https://doi.org/10.1155/2022/9248674

Research Article

Using a System Pharmacology Method to Search for the Potential Targets and Pathways of Yinqiaosan against COVID-19

Li-hua Cao ,[1] Xing-yuan Jia,[2] Hong-juan He,[1] Zhen-zhen Wang ,[1] Yi-ying Zhao,[3] Xue Yang,[3] Xiu-min Li ,[4] and Ming-san Miao [1]

[1]*Academy of Chinese Medical Sciences, Henan University of Chinese Medicine, Zhengzhou 450046, Henan Province, China*
[2]*Department of Pharmacy, Henan Province Hospital of Traditional Chinese Medicine, Zhengzhou 450046, Henan Province, China*
[3]*School of Pharmacy, Henan University of Chinese Medicine, Zhengzhou 450046, Henan Province, China*
[4]*Microbiology and Immunology Department, New York Medical College, Valhalla, NY 10595, USA*

Correspondence should be addressed to Xiu-min Li; xiuminli@nymc.edu and Ming-san Miao; miaomingsan@hactcm.edu.cn

Received 19 November 2021; Revised 4 January 2022; Accepted 9 February 2022; Published 15 March 2022

Academic Editor: Enas Abdulhay

The first reported case of coronavirus disease 2019 (COVID-19) occurred in Wuhan, Hubei, China. Thereafter, it spread through China and worldwide in only a few months, reaching a pandemic level. It can cause severe respiratory illnesses such as pneumonia and lung failure. Since the onset of the disease, the rapid response and intervention of traditional Chinese medicine (TCM) have played a significant role in the effective control of the epidemic. Yinqiaosan (YQS) was used to treat COVID-19 pneumonia, with good curative effects. However, a systematic overview of its active compounds and the therapeutic mechanisms underlying its action has yet to be performed. The purpose of the current study is to explore the compounds and mechanism of YQS in treating COVID-19 pneumonia using system pharmacology. A system pharmacology method involving drug-likeness assessment, oral bioavailability forecasting, virtual docking, and network analysis was applied to estimate the active compounds, hub targets, and key pathways of YQS in the treatment of COVID-19 pneumonia. With this method, 117 active compounds were successfully identified in YQS, and 77 potential targets were obtained from the targets of 95 compounds and COVID-19 pneumonia. The results show that YQS may act in treating COVID-19 pneumonia and its complications (atherosclerosis and nephropathy) through Kaposi sarcoma-related herpesvirus infection and the AGE-RAGE signaling pathway in diabetic complications and pathways in cancer. We distinguished the hub molecular targets within pathways such as TNF, GAPDH, MAPK3, MAPK1, EGFR, CASP3, MAPK8, mTOR, IL-2, and MAPK14. Five of the more highly active compounds (acacetin, kaempferol, luteolin, naringenin, and quercetin) have anti-inflammatory and antioxidative properties. In summary, by introducing a systematic network pharmacology method, our research perfectly forecasts the active compounds, potential targets, and key pathways of YQS applied to COVID-19 and helps to comprehensively clarify its mechanism of action.

1. Introduction

Coronavirus infectious disease 2019 (COVID-19) is caused by 2019-nCoV virus and it seriously endangers human health. On January 12, 2020, the World Health Organization (WHO) confirmed and named its pathogen 2019-nCoV [1], which belongs to the novel coronavirus pneumonia of genus β. On January 31, 2020, it was designated a Public Health Emergency of International Concern (PHEIC). According to the latest statistics of the World Health Organization, as of October 28, 2021, there were approximately 244385444 confirmed cases and more than 4961489 deaths worldwide, including over 7053806 confirmed cases and over 108334 deaths in the United States.

The main clinical features of these cases are a high body temperature, cough without mucous, breathing difficulties (dyspnea), headache, and pneumonia. Disease attack may lead to progressive respiratory failure due to alveolar damage (which has been observed by transverse chest computerized tomography images) and cytokine storm syndrome and it could also develop a severe form with sometimes fatal outcomes [2, 3]. The cause of the disease was identified by clinicians as virus-induced pneumonia in line with the clinical signs and other standards, including increased body temperature, decreased lymphocytes and white blood cells (although the levels of the latter seemed normal sometimes), new pulmonary infiltrates on chest radiography, and no evident improvement after treatment with antibiotics for three days [4].

In traditional Chinese medicine (TCM), COVID-19 falls under the category of "pestilences," which occur because of direct or indirect contact with epidemic pathogens. Since the onset of the disease, the rapid response and intervention of TCM have played a vital role in effectively controlling the epidemic, and the classic prescription has become one of the highlights in preventing and controlling the epidemic [5, 6]. Yinqiaosan (YQS) is a traditional prescription for treating the influenza virus from the "Wen Bing Tiao Bian." YQS is a herbal formula comprised of 10 medicinal herbs (Jinyinhua (JYH, *Lonicera japonica* Thunb.), Lianqiao (LQ, *Forsythia suspensa* (Thunb.)), Jiegeng (JG, *Platycodon grandiflorum* (Jacq.) A. DC), Bohe (BH, *Mentha haplocalyx* Briq.), Dantouchi (DDC, *Glycine* max (L.) Merr.), Danzhuye (DZY, *Lophatherum gracile* Brongn.), Niubangzi (NBZ, *Arctium lappa* L.), Jingjie (JJ, *Schizonepeta tenuifolia* Eriq.), Lugen (LG, *Phragmites communis* Trin.), and Gancao (GC, *Glycyrrhiza uralensis* Fisch., *Glycyrrhiza inflata* Bat., or *Glycyrrhiza glabra* L.). The National Health Commission of the People's Republic of China and the National Administration of TCM issued the "Diagnosis and Treatment Program for COVID-19 (Trial Version 3)." They began to recommend TCM therapy, among which the recommended prescriptions are Maxing Shigan decoction and YQS.

Tang et al. [7], based on the TCMATCOV platform, analyzed the potential effects of commonly used traditional formulations for treating COVID-19 and discovered that YQS is a frequently used therapy for pneumonia. For the past few years, systems pharmacology [8, 9] means have been widely introduced in the prescription and mechanism of TCM. System pharmacology is an emerging systematic methodology and is guided by the "multicomponent multitarget network" theory, which conforms to the integrity and systematicity of TCM prescriptions. In addition, it combines oral bioavailability screening and multiple drug target prediction, providing an overall method for exploring the targets and potential mechanisms of TCM, and it can be used as an alternative strategy to analyze the therapeutic effects of the active ingredients [10, 11]. Wang et al. [12] discussed the targets and signaling pathways of Maxing Shigan decoction for treating pneumonia through systems pharmacology and found that the possible targets were IL-6, TNF, MAPK8, etc. Xia et al. found that Akt1 was a potential target of Lianhua Qingwen to treat and prevent COVID-19 using network pharmacology and molecular docking analyses [13].

Aiming to explore the possibility and mechanism of YQS in treating COVID-19, this paper uses systems pharmacology techniques and approaches to forecast the possible targets and signaling pathways of YQS and provides data for subsequent experimental research.

2. Materials and Methods

2.1. Finding Potential Targets of YQS. Taking the herbs (Jinyinhua, Lianqiao, Jiegeng, Bohe, Dantouchi, Danzhuye, Niubangzi, Jingjie, Lugen, and Gancao) in YQS as keywords, the TCMSP database (http://tcmspw.com/tcmsp.php) was used to retrieve their relevant chemical compositions, and oral bioavailability (OB) ≥ 30%, drug-likeness (DL) ≥ 0.18, and drug half-life (HL) ≥ 4 h were adopted as screening conditions to obtain active ingredients that meet the conditions [14–16]. Among them, the active ingredients of Danzhuye were obtained through a combination of a literature search [17] and the TCMSP database.

Through the TCMSP database and the PubChem database (https://pubchem.ncbi.nlm.nih.gov/) combined with the Swiss Target Prediction database, the targets of the active ingredients were obtained. UniProt KB (http://www.UniProt.org/), which prevents, for example, overannotation of semblable proteins such as paralogs and putative products of pseudogenes, was utilized to normalize gene names and organisms. Through the UniProt database (https://www.UniProt.org/), the species was set as "*Homo sapiens* (Human)" to standardize the obtained drug targets.

2.2. Screening of COVID-19-Associated Genes. Through the GeneCards database (http://www.genecards.org/) and OMIM (https://www.omim.org/) database, using "novel coronavirus pneumonia" as the keyword, COVID-19-related disease targets were retrieved and obtained. Only "*Homo sapiens*" proteins linked to COVID-19 were selected. The UniProt database was applied to standardize the obtained disease targets in *Homo sapiens*.

2.3. Screening of Candidate Targets. The acting targets of the active ingredients of YQS and the disease targets of COVID-19 were processed through Venny2.1 software (http://bioinfogp.cnb.csic.es/tools/venny/index.html) to acquire their common targets, which were taken as alternative targets of YQS for treating COVID-19, and its Venny map was also acquired.

2.4. Protein-Protein Interaction (PPI). The retrieved YQS active ingredient targets were linked to COVID-19 targets by the STRING (https://string-db.org/, ver.11.0) database [18]. The requirement was restrained to "*Homo sapiens*." In this paper, a high confidence score with a correlation degree ≥0.400 [19] as the cutoff value was set to obtain the network.

2.5. GO and KEGG Pathway Enrichment Analysis. Gene Ontology (GO) enrichment analysis was conducted using the OmicShare tools (http://www.omicshare.com/tools). The KOBAS 3.0 database was applied to analyze the KEGG pathway enrichment of the candidate targets, and the

RStudio 3.6.3 and ggplot2 packages were applied to illustrate the results.

2.6. Networks Construction and Analysis. Cytoscape 3.5.1, an open-source software platform to visualize complex networks, was employed to illustrate the networks. With this software, the network building was handled as follows: (1) compound-COVID19 PPI network, (2) compound-targets network, and (3) YQS (Yinqiaosan)-compound-targets-pathway network. In addition, four topological features of the hub network, such as "Degree" and "Betweenness Centrality," were determined to choose YQS alternative targets with topological significance [20, 21]. To determine the relationship between network clusters and to identify high-connectivity hub genes, "Cytohubba" (a plug-in of Cytoscape) was introduced to check the node element. The top 10 nodes were ranked by EPC [22].

2.7. Molecular Docking. For the sake of validation of the drug-targeted correlations, the molecular docking simulation further proceeded on every drug docking with their targets. Each drug molecule, such as luteolin, naringenin, acacetin, kaempferol, and quercetin, was downloaded from the TCMSP database and converted to a PDBQT file by Chimera (version 1.10.2).

The structures of the proteins in each alternative target were downloaded from the RCBS Protein Data Bank (http://www.rcsb.org/pdb), and every protein file was opened with ADT (version 1.5.6), a free GUI for AutoDock. In every file, the water molecules were canceled, the polar hydrogen atoms were increased, and then they were written to a PDBQT file.

The intersection of possible alternative targets and drug targets of PCOS was chosen for in-depth investigations. To validate the interaction and observe the docking sites between drugs and targets, molecular docking was performed by an open-source program called Autodock vina 1.1.2. The docking results were observed with ADT.

The foundation for developing medications for the clinical therapy of COVID-19 is shown in Figure 1.

3. Results

3.1. Active Components and Target Proteins of Yinqiaosan. By a systematic search of the public databases, 141 components were retrieved in JYH (17), LQ (11), JG (7), BH (10), DDC (2), DZY (4), NBZ (4), JG (9), LG (1), and GC (76), and the specific information of these components can be found in Table 1. After deleting the duplicate values, 117 active ingredients were acquired. Refer to the results in Figure S1. Through observation, it was discovered that some special compounds in this network interacted with multiple targets and took part in the regulation of multiple targets, such as luteolin, naringenin, acacetin, kaempferol, and quercetin.

A total of 810 targets were obtained from public databases, but not all information on all 810 targets is shown. The YQS compounds may jointly affect all of these targets, producing pharmacological impacts on COVID-19.

3.2. Screening Results of COVID-19-Related Disease Targets. The GeneCards database, as an online catalog of human genes and genetic illness, can enable effective navigation of gene-disease linkages [23]. The OMIM database deals with over 15,500 gene entries and concentrates on elaborating gene-phenotype correlations [24]. Through the two databases, we obtained 435 genes in total (not all shown).

3.3. Screening Results of Candidate Targets. Altogether, 77 overlapping genes were acquired by searching the overlaps of the aforementioned compound targets with the 435 COVID-19 gene targets. These genes included PIK3CD, PLA2G5, and ECE1 (Table S1, Figure 2(a)).

By importing compound-disease cotarget information into STRING, a compound-COVID-19 target PPI network was obtained. Taking a score ≥ 0.4 as the limiting condition [19], the interaction relationship of 77 targets obtained from the String network database was screened. Then, a network diagram of 77 targets protein interactions was obtained. Combined with Cytoscape 3.5.1 software, we obtained an interaction network graph of alternative targets of YQS for treating COVID-19, including 77 nodes and 719 edges. The node colors are illustrated from red to yellow in descending order of degree values (Figure 2(b)). Among the targets of YQS for treating COVID-19, the 5 targets with the highest degree were TNF, GAPDH, MAPK1, MAPK3, and EGFR.

3.4. Results of the Construction of the Compound-Target Network. The data of the active ingredients of YQS as well as its targets for treating COVID-19 were input into Cytoscape 3.5.1 software to obtain the network chart of active ingredient-acting targets. The active ingredients of YQS were represented by their Mol IDs. There were 173 nodes and 831 edges forming the compound-target network. The diamonds represent 95 active ingredients, and the ellipse indicates 77 targets of active ingredients (Figure 3).

3.5. Enrichment Analysis Results of Biological Processes and Pathways. To carry out an in-depth recognition of the biological functions of the above 77 potential targets in biological networks, a GO enrichment analysis was implemented with the OmicShare tools, a free online platform for data analysis (http://www.omicshare.com/tools) [25]. As shown in Figure 4, the results fell into three strata: biological processes (BP), cellular components (CC), and molecular functions (MF). The limiting condition was $P < 0.01$, where the smaller the P value is, the closer the relationship with YQS will be in treating pneumonia. The results show that the BP analysis mainly includes the response to organic substances, the cellular response to organic substances, and the cellular response to chemical stimulus (Figure 4(a)). The CC analysis mainly included membrane microdomains, membrane rafts, and membrane regions (Figure 4(b)). The MF analysis was mainly related to enzyme binding, phosphotransferase activities, alcohol groups as acceptors, and kinase activities (Figure 4(c)).

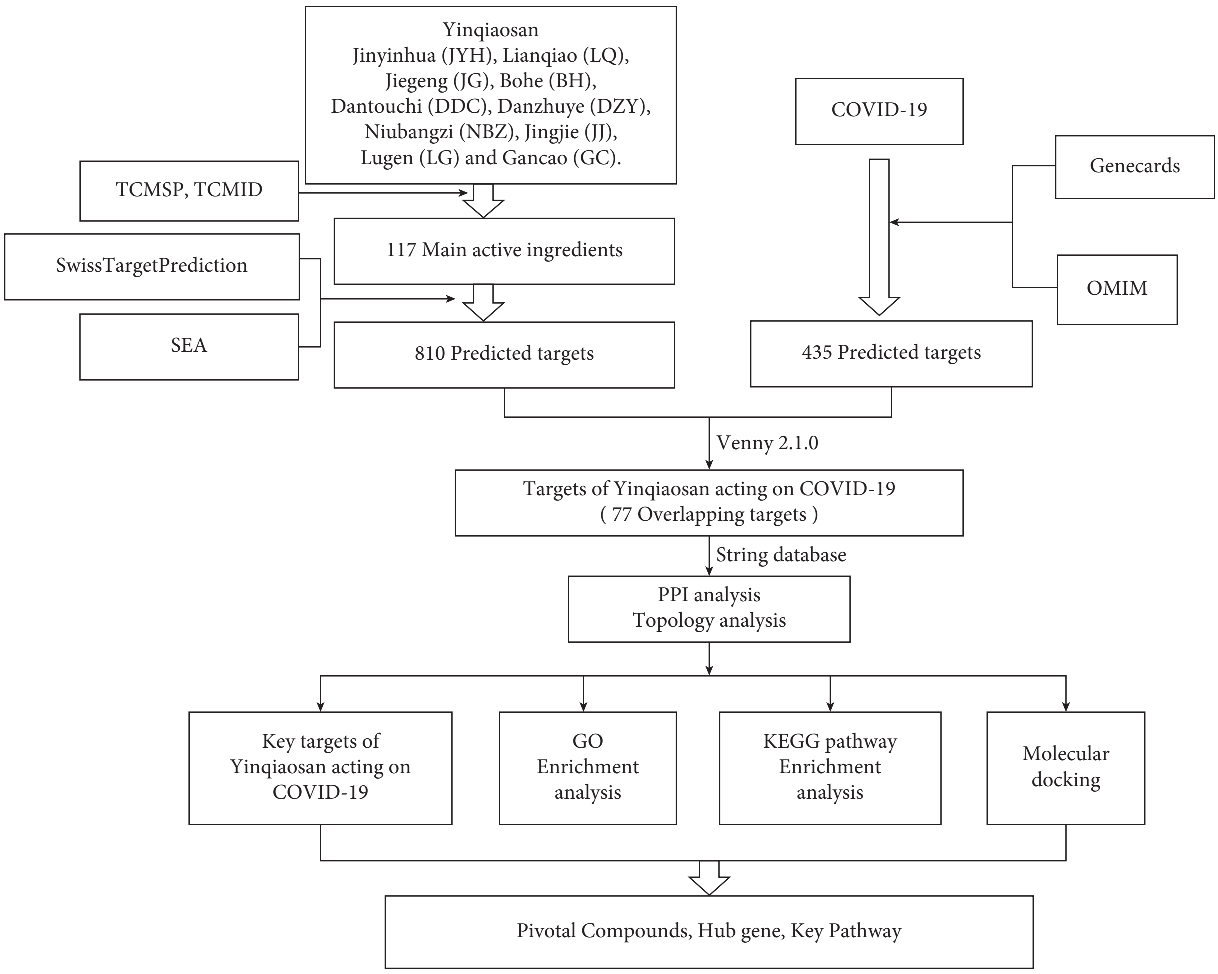

Figure 1: Process overview. To understand the active ingredients of each single drug in Yinqiaosan (YQS) through the TCMSP (Traditional Chinese Medicine Systems Pharmacology Database and Analysis Platform) and TCMID (Traditional Chinese Medicine Integrated Database), the targets of the active ingredients were identified by Swiss TargetPrediction and SEA (similarity ensemble approach). Similarly, COVID-19 targets were obtained through the GeneCards and OMIM (Online Mendelian Inheritance in Man) databases. Intersecting targets were then assessed by molecular docking and GO and KEGG enrichment analysis. GO (Gene Ontology) enrichment analysis was carried out with the OmicShare tools. The KOBAS 3.0 database was used for KEGG enrichment analysis, and RStudio was used to visualize the results. Molecular docking was conducted by an open-source program named Autodock vina 1.1.2. Networks were constructed to provide a visual view by Cytoscape 3.5.1 software.

Table 1: Active ingredients of Yinqiaosan (YQS).

Chinese herbs	Mol id	Molecule name	OB (%)	DL	HL(h)
JYH	MOL000006	Luteolin	36.16	0.25	15.94
JYH	MOL000098	Quercetin	46.43	0.28	14.4
JYH	MOL000358	Beta-sitosterol	36.91	0.75	5.36
JYH	MOL000422	Kaempferol	41.88	0.24	14.74
JYH	MOL000449	Stigmasterol	43.83	0.76	5.57
JYH	MOL001494	Mandenol	42	0.19	5.39
JYH	MOL001495	Ethyl linolenate	46.1	0.2	6.2
JYH	MOL002773	Beta-carotene	37.18	0.58	4.36
JYH	MOL002914	Eriodyctiol (flavanone)	41.35	0.24	15.88
JYH	MOL003006	(-)-(3R,8S,9R,9aS,10aS)-9-Ethenyl-8-(beta-D-glucopyranosyloxy)-2,3,9,9a,10,10a-hexahydro-5-oxo-5H,8H-pyrano[4,3-d]oxazolo[3,2-a]pyridine-3-carboxylic acid_qt	87.47	0.23	5.5
JYH	MOL003036	ZINC03978781	43.83	0.76	5.79
JYH	MOL003044	Chrysoeriol	35.85	0.27	16.31
JYH	MOL003059	kryptoxanthin	47.25	0.57	4.37

Table 1: Continued.

Chinese herbs	Mol id	Molecule name	OB (%)	DL	HL(h)
JYH	MOL003062	4,5′-Retro-.beta.,.beta.-Carotene-3,3′-dione, 4′,5′-didehydro-	31.22	0.55	5.39
JYH	MOL003095	5-hydroxy-7-methoxy-2-(3,4,5-trimethoxyphenyl)chromone	51.96	0.41	15.98
JYH	MOL003111	Centauroside_qt	55.79	0.5	5.18
JYH	MOL003124	XYLOSTOSIDINE	43.17	0.64	9.15
LQ	MOL000006	luteolin	36.16	0.25	15.94
LQ	MOL000098	quercetin	46.43	0.28	14.4
LQ	MOL000173	wogonin	30.68	0.23	17.75
LQ	MOL000211	Mairin	55.38	0.78	8.87
LQ	MOL000358	Beta-sitosterol	36.91	0.75	5.36
LQ	MOL000422	Kaempferol	41.88	0.24	14.74
LQ	MOL000791	Bicuculline	69.67	0.88	15.83
LQ	MOL003281	20(S)-Dammar-24-ene-3β,20-diol-3-acetate	40.23	0.82	9.14
LQ	MOL003315	3beta-Acetyl-20,25-epoxydammarane-24alpha-ol	33.07	0.79	7.82
LQ	MOL003365	Lactucasterol	40.99	0.85	5.53
LQ	MOL003370	Onjixanthone I	79.16	0.3	14.86
JG	MOL000006	Luteolin	36.16	0.25	15.94
JG	MOL001689	Acacetin	34.97	0.24	17.25
JG	MOL004355	Spinasterol	42.98	0.76	5.32
JG	MOL004580	cis-Dihydroquercetin	66.44	0.27	14.51
JG	MOL005996	2-O-Methyl-3—O-β-D-glucopyranosyl platycogenate A	45.15	0.25	6.03
JG	MOL006026	Dimethyl 2-O-methyl-3-O-a-D-glucopyranosyl platycogenate A	39.21	0.25	5.04
JG	MOL006070	Robinin	39.84	0.71	16.67
BH	MOL000006	Luteolin	36.16	0.25	15.94
BH	MOL000359	Sitosterol	36.91	0.75	5.37
BH	MOL000471	Aloe-emodin	83.38	0.24	31.49
BH	MOL001689	Acacetin	34.97	0.24	17.25
BH	MOL001790	Linarin	39.84	0.71	16.07
BH	MOL002881	Diosmetin	31.14	0.27	16.34
BH	MOL004328	Naringenin	59.29	0.21	16.98
BH	MOL005190	Eriodictyol	71.79	0.24	15.81
BH	MOL005573	Genkwanin	37.13	0.24	16.1
BH	MOL011616	Fortunellin	35.65	0.74	14.19
DDC	MOL008400	Glycitein	50.48	0.24	16.32
DDC	MOL011691	6′-O-Malonylglycitin	30.4	0.81	17.25
DZY	MOL000006	Luteolin	36.16	0.25	15.94
DZY	MOL000359	Sitosterol	36.91	0.75	5.37
DZY	MOL002322	Isovitexin	31.29	0.72	16.45
DZY	MOL003137	Swertiajaponin	32.12	0.78	16.28
NBZ	MOL000358	Beta-sitosterol	36.91	0.75	5.36
NBZ	MOL000422	Kaempferol	41.88	0.24	14.74
NBZ	MOL002773	Beta-carotene	37.18	0.58	4.36
NBZ	MOL010868	Neoarctin A	39.99	0.27	5.82
JJ	MOL000006	Luteolin	36.16	0.25	15.94
JJ	MOL000098	Quercetin	46.43	0.28	14.4
JJ	MOL000358	Beta-sitosterol	36.91	0.75	5.36
JJ	MOL000359	Sitosterol	36.91	0.75	5.37
JJ	MOL000449	Stigmasterol	43.83	0.76	5.57
JJ	MOL002881	Diosmetin	31.14	0.27	16.34
JJ	MOL005043	Campest-5-en-3beta-ol	37.58	0.71	4.43
JJ	MOL005100	5,7-Dihydroxy-2-(3-hydroxy-4-methoxyphenyl)chroman-4-one	47.74	0.27	16.51
JJ	MOL011856	Schkuhrin I	54.45	0.52	5.89
LG	MOL000449	Stigmasterol	43.83	0.76	5.57
GC	MOL000098	Quercetin	46.43	0.28	14.4
GC	MOL000211	Mairin	55.38	0.78	8.87
GC	MOL000239	Jaranol	50.83	0.29	15.5
GC	MOL000354	Isorhamnetin	49.6	0.31	14.34
GC	MOL000359	Sitosterol	36.91	0.75	5.37
GC	MOL000392	Formononetin	69.67	0.21	17.04
GC	MOL000417	Calycosin	47.75	0.24	17.1
GC	MOL000422	Kaempferol	41.88	0.24	14.74
GC	MOL000497	Licochalcone a	40.79	0.29	16.2
GC	MOL001484	Inermine	75.18	0.54	11.72

Table 1: Continued.

Chinese herbs	Mol id	Molecule name	OB (%)	DL	HL(h)
GC	MOL001792	DFV	32.76	0.18	17.89
GC	MOL002311	Glycyrol	90.78	0.67	9.85
GC	MOL002565	Medicarpin	49.22	0.34	8.46
GC	MOL003656	Lupiwighteone	51.64	0.37	15.63
GC	MOL003896	7-Methoxy-2-methyl isoflavone	42.56	0.2	16.89
GC	MOL004328	Naringenin	59.29	0.21	16.98
GC	MOL004805	(2S)-2-[4-Hydroxy-3-(3-methylbut-2-enyl)phenyl]-8,8-dimethyl-2,3-dihydropyrano [2,3-f]chromen-4-one	31.79	0.72	14.82
GC	MOL004806	Euchrenone	30.29	0.57	15.89
GC	MOL004808	Glyasperin B	65.22	0.44	16.1
GC	MOL004810	Glyasperin F	75.84	0.54	15.64
GC	MOL004814	Isotrifoliol	31.94	0.42	7.91
GC	MOL004815	(E)-1-(2,4-Dihydroxyphenyl)-3-(2,2-dimethylchromen-6-yl)prop-2-en-1-one	39.62	0.35	16.16
GC	MOL004824	(2S)-6-(2,4-dihydroxyphenyl)-2-(2-hydroxypropan-2-yl)-4-methoxy-2,3-dihydrofuro [3,2-g]chromen-7-one	60.25	0.63	4.31
GC	MOL004827	Semilicoisoflavone B	48.78	0.55	17.02
GC	MOL004828	Glepidotin A	44.72	0.35	16.09
GC	MOL004829	Glepidotin B	64.46	0.34	15.98
GC	MOL004835	Glypallichalcone	61.6	0.19	17.01
GC	MOL004838	8-(6-Hydroxy-2-benzofuranyl)-2,2-dimethyl-5-chromenol	58.44	0.38	8.71
GC	MOL004841	Licochalcone B	76.76	0.19	17.02
GC	MOL004848	Licochalcone G	49.25	0.32	15.75
GC	MOL004855	Licoricone	63.58	0.47	16.37
GC	MOL004856	Gancaonin A	51.08	0.4	16.82
GC	MOL004857	Gancaonin B	48.79	0.45	16.49
GC	MOL004860	Licorice glycoside E	32.89	0.27	25.39
GC	MOL004863	3-(3,4-Dihydroxyphenyl)-5,7-dihydroxy-8-(3-methylbut-2-enyl)chromone	66.37	0.41	15.81
GC	MOL004864	5,7-Dihydroxy-3-(4-methoxyphenyl)-8-(3-methylbut-2-enyl)chromone	30.49	0.41	14.99
GC	MOL004866	2-(3,4-Dihydroxyphenyl)-5,7-dihydroxy-6-(3-methylbut-2-enyl)chromone	44.15	0.41	16.77
GC	MOL004882	Licocoumarone	33.21	0.36	9.66
GC	MOL004883	Licoisoflavone	41.61	0.42	16.09
GC	MOL004884	Licoisoflavone B	38.93	0.55	15.73
GC	MOL004885	Licoisoflavanone	52.47	0.54	15.67
GC	MOL004891	Shinpterocarpin	80.3	0.73	6.5
GC	MOL004898	(E)-3-[3,4-Dihydroxy-5-(3-methylbut-2-enyl)phenyl]-1-(2,4-dihydroxyphenyl)prop-2-en-1-one	46.27	0.31	15.24
GC	MOL004903	Liquiritin	65.69	0.74	17.96
GC	MOL004907	Glyzaglabrin	61.07	0.35	21.2
GC	MOL004910	Glabranin	52.9	0.31	16.24
GC	MOL004912	Glabrone	52.51	0.5	16.09
GC	MOL004913	1,3-Dihydroxy-9-methoxy-6-benzofurano[3,2-c]chromenone	48.14	0.43	8.87
GC	MOL004914	1,3-Dihydroxy-8,9-dimethoxy-6-benzofurano[3,2-c]chromenone	62.9	0.53	9.32
GC	MOL004915	Eurycarpin A	43.28	0.37	17.1
GC	MOL004917	Glycyroside	37.25	0.79	14.62
GC	MOL004924	(-)-Medicocarpin	40.99	0.95	13.2
GC	MOL004935	Sigmoidin-B	34.88	0.41	14.49
GC	MOL004941	(2R)-7-Hydroxy-2-(4-hydroxyphenyl)chroman-4-one	71.12	0.18	18.09
GC	MOL004945	(2S)-7-Hydroxy-2-(4-hydroxyphenyl)-8-(3-methylbut-2-enyl)chroman-4-one	36.57	0.32	17.95
GC	MOL004948	Isoglycyrol	44.7	0.84	6.69
GC	MOL004949	Isolicoflavonol	45.17	0.42	15.55
GC	MOL004957	HMO	38.37	0.21	16.56
GC	MOL004959	1-Methoxyphaseollidin	69.98	0.64	9.53
GC	MOL004961	Quercetin der.	46.45	0.33	16.61
GC	MOL004985	Icos-5-enoic acid	30.7	0.2	5.28
GC	MOL004988	Kanzonol F	32.47	0.89	9.98
GC	MOL004989	6-Prenylated eriodictyol	39.22	0.41	16.52
GC	MOL004991	7-Acetoxy-2-methylisoflavone	38.92	0.26	17.49
GC	MOL004993	8-Prenylated eriodictyol	53.79	0.4	15.7
GC	MOL004996	Gadelaidic acid	30.7	0.2	5.25
GC	MOL005000	Gancaonin G	60.44	0.39	16.13
GC	MOL005001	Gancaonin H	50.1	0.78	16.64
GC	MOL005003	Licoagrocarpin	58.81	0.58	9.45

Table 1: Continued.

Chinese herbs	Mol id	Molecule name	OB (%)	DL	HL(h)
GC	MOL005007	Glyasperins M	72.67	0.59	15.57
GC	MOL005008	Glycyrrhiza flavonol A	41.28	0.6	13.71
GC	MOL005012	Licoagroisoflavone	57.28	0.49	19.64
GC	MOL005013	18α-Hydroxyglycyrrhetic acid	41.16	0.71	4.96
GC	MOL005016	Odoratin	49.95	0.3	16.35
GC	MOL005017	Phaseol	78.77	0.58	9.64
GC	MOL005018	Xambioona	54.85	0.87	14.5

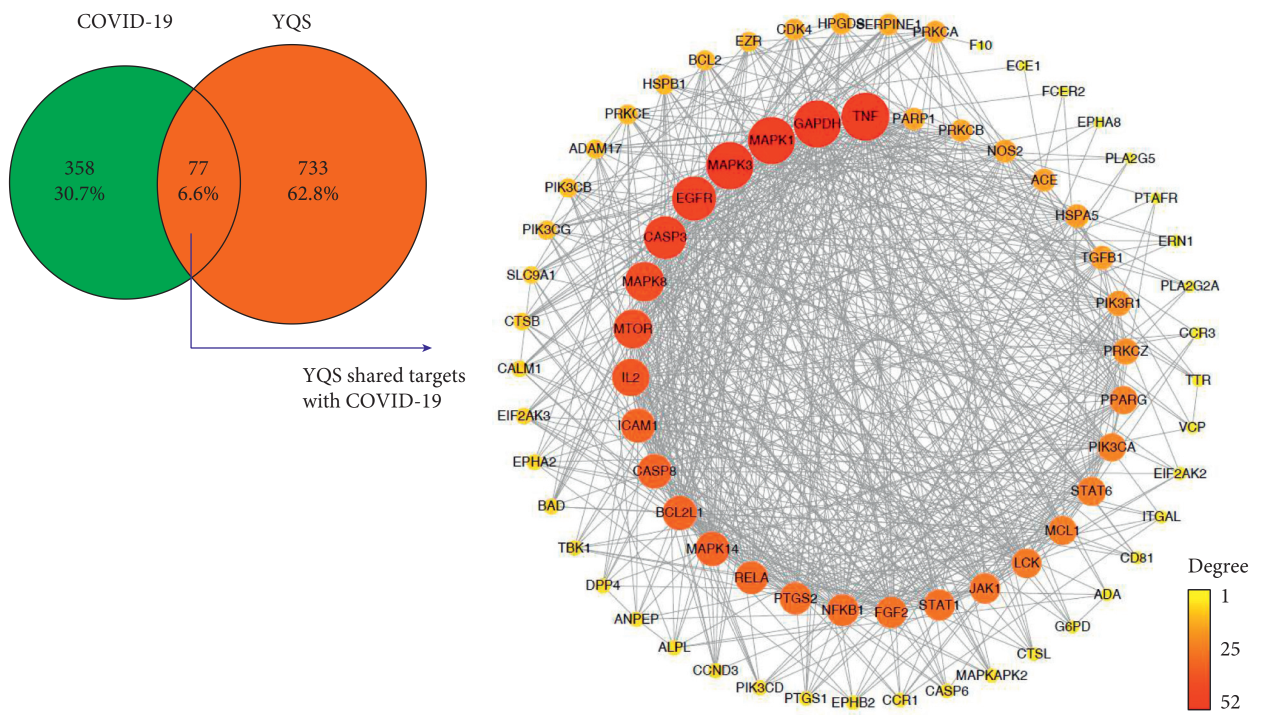

(a)

(b)

Figure 2: Overlapping targets (a) and the protein-protein network (b). Node colors change gradually from red to yellow, and node sizes are in proportion to their degree.

Utilizing the online platform KOBAS 3.0, 190 important KEGG pathways ($P < 0.01$) were found on the basis of differentially expressed coding transcripts. The most important pathways included Kaposi sarcoma-related herpesvirus infection, AGE-RAGE signaling pathways in diabetic complications, and pathways in cancer. The result was constructed by KOBAS 3.0, and the top 20 enrichment pathways were visualized by RStudio (Figure 5). This indicated that YQS might be a candidate for treating COVID-19 through these pathways.

3.6. Construction of "YQS-Compounds-Targets-Pathway" Network. The top ten channels in the enrichment analysis of the KEGG pathway and the compound and compound targets were imported into Cytoscape 3.5.1 software to build a "YQS-compounds-targets-pathway" network (Figure 6). The figure includes 194 nodes and 1185 edges. The red diamonds denote YQS, yellow hexagons represent the traditional Chinese herbs in YQS, green rectangles represent the potential active ingredients, blue ellipses represent YQS candidate treatment targets for COVID-19, and purple triangles represent the possible signaling pathways for the active ingredients to function. It can be seen from the figure that YQS includes 10 herbs and 95 active ingredients. It mainly acts on TNF, GAPDH, MAPK3, MAPK1, EGFR, CASP3, MAPK8, MTOR, IL-2, and MAPK14 and uses Kaposi sarcoma-related herpesvirus infection, AGE-RAGE signaling pathways in diabetic complications, pathways in cancer, apoptosis, hepatitis B, human cytomegalovirus signaling pathways such as infection, measles, and hepatitis C to treat pneumonia.

3.7. Molecular Docking. Molecular docking was further utilized in our research to estimate the interaction between components and targets to reduce the complexity and increase the precision of the constituent target network [26].

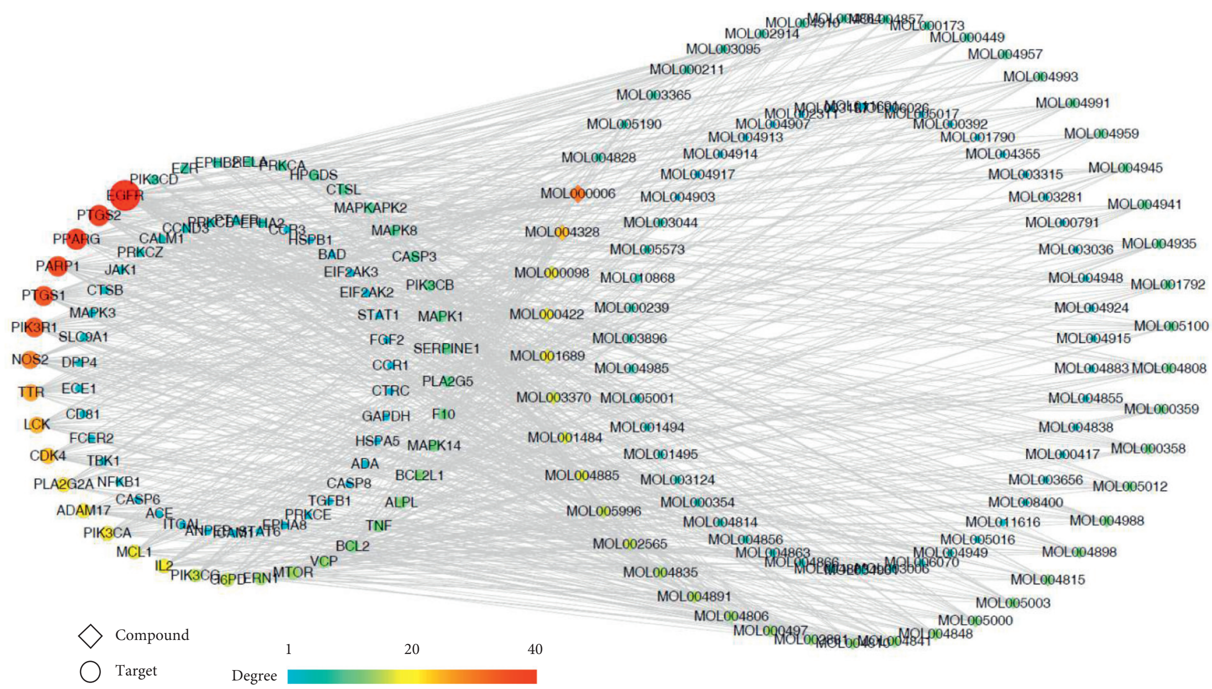

FIGURE 3: The compound-target networks of Yinqiaosan (YQS). The diamond nodes denote ingredients, and the circular nodes denote targets. The node colors from red to blue and node size are proportional to its degree.

The cytoHubba control panel is a useful tool to retrieve subnetworks from the whole large PPI set [27]. Hub gene recognition was processed by the cytoHubba plug-in in Cytoscape software. All active ingredients in the top 5 online pharmacology degrees of freedom were taken as the research object. To determine the valid connecting effects between YQS-main active ingredients and their predicted targets, molecular docking was assessed using the YQS-hub genes connecting the energy. Molecular docking analyzed 10 hub genes (CASP3, EGFR, GAPDH, IL-2, MAPK1, MAPK14, MAPK3, MAPK8, mTOR, and TNF) and 5 compounds (acacetin, kaempferol, luteolin, naringenin, and quercetin).

Zhou et al. [3] ascertained that 2019-nCoV makes use of the same cell entry receptor, angiotensin transforming enzyme II (ACE2), as SARS-CoV. 3CL hydrolase is the core protease of single-stranded RNA virus precursor polyproteolysis and it plays a vital role when replicating the single-stranded RNA virus [28]. Therefore, in this study, the 5 compounds were also molecularly docked with SARS-CoV-2 3CL hydrolase (Mpro) and ACE2 to provide references for treating COVID-19 by TCM.

The lower the binding energy, the more stable the conformation of the ligand-receptor binding [29]. When the binding energy is less than −5.0 kcal/mol, this suggests that the compound can bind to the target. When the binding energy is less than -7.0 kcal/mol, this suggests that the compound has a good ability to bind to the target. We selected the conformation with the lowest binding energy to analyze the docking binding mode and used Discovery Studio for mapping.

Molecular docking results showed that all five active ingredients could be combined with 10 hub genes (Table S2), Mpro or ACE2 (Table 2, Figure 7). Therefore, the 5 compounds could efficiently act on the 10 targets, especially TNF, MAPK14, MAPK3, and MAPK8. Kaempferol (Figures 7(a) and 7(b)) and Mpro have a better binding capacity, which is consistent with the docking results of the molecules discovered by Ling [30]. Acacetin (Figures 7(c) and 7(d)), luteolin (Figures 7(e) and 7(f)), and ACE2 have a better combining ability.

4. Discussion

At present, COVID-19 has expanded to over 200 countries and areas, and the lives and health of people around the world are under serious threat. Special drugs against COVID-19 are still under development. TCM adopts the principle of dialectical treatment with the characteristics of multiple targets and multiple pathways, and it plays a vital role in antiepidemic treatment [31–33]. The "COVID-19 Diagnosis and Treatment Program (Trial Ver. 3)" issued by the National Health Commission of the People's Republic of China pointed out that COVID-19 is categorized as a "pestile" in TCM, which happens under direct or indirect contact with epidemic pathogens. The main features are "damp, heat, poisonous, stasis." COVID-19 is divided into four types of TCM syndromes: cold-dampness stagnating in the lung, damp-heat accumulating in the lung, damp toxin stagnating in the lung, and internal blocking causing external collapse. The clinical symptoms of "damp-heat accumulating in the lung" are low body temperature or no fever, mild aversion to cold, fatigue, a heavy sensation in the head and body, dry coughs with scanty phlegm, sore throat, and a dry mouth with no wish to drink water. Alternatively, chest tightness, epigastric fullness, absence of sweating or

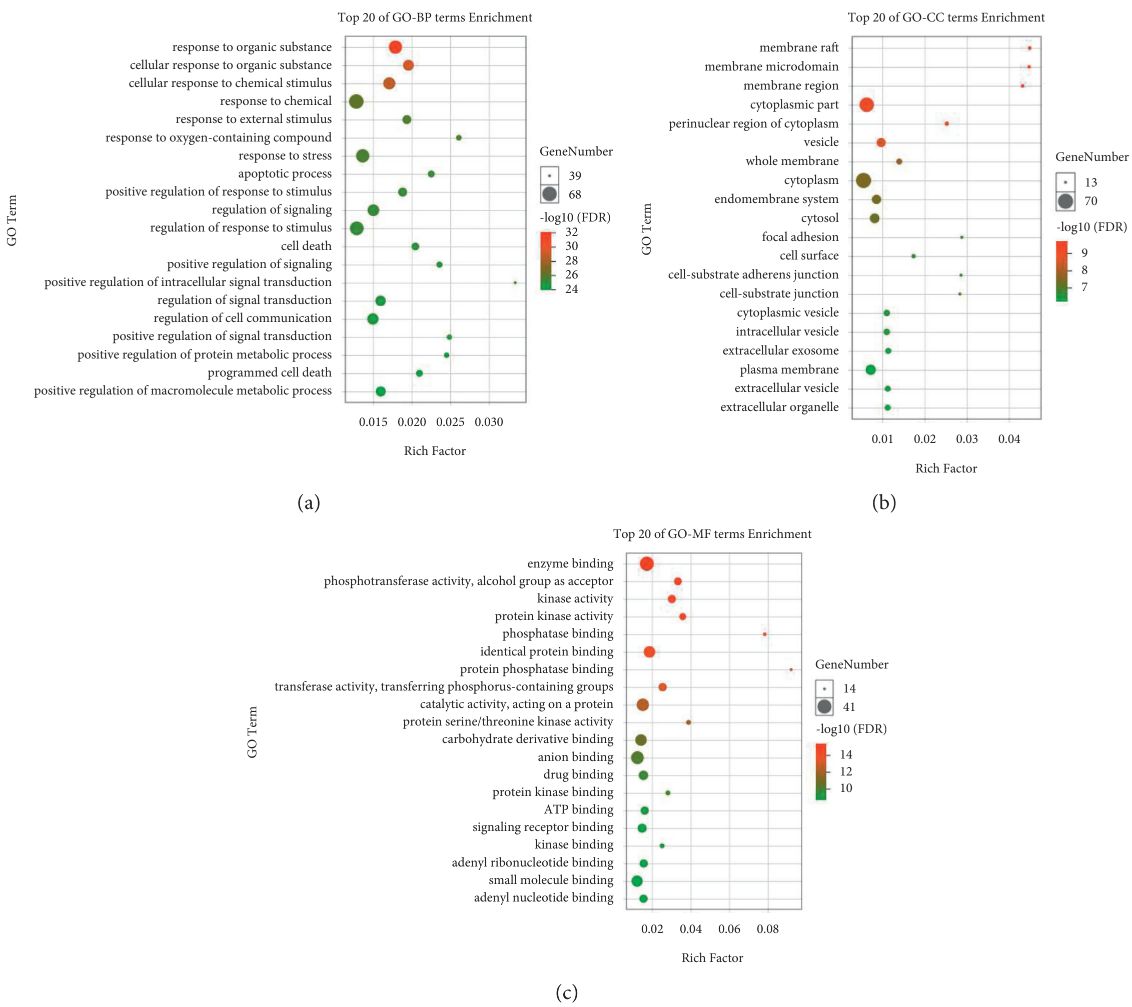

Figure 4: GO enrichment analysis of Yinqiaosan (YQS) targets. The three strata were biological processes (BP) (a), cellular components (CC) (b), and molecular functions (MF) (c). *Y*-axis: top 20 biological processes associated with the enriched targets. *X*-axis: enrichment factors (rich factors). Rich factors are proportional to the degree of enrichment. The node size shows the number of genes, and the larger the node is, the more the genes enriched in the term are. The color depth of the node demonstrates the significance level, and the redder the node is, the higher the significance will be to the term.

inhibited sweating, vomiting, a poor appetite, and loose stools or sticky stools with a feeling of incomplete bowel movement may also be present. The tongue is pale red with a white, thick, and greasy or thin, yellow coating. The pulse is soft or slippery and rapid. The recommended prescriptions are Maxing shigantang and YQS.

YQS was described by Wu in "Wen Bing Tiao Bian." He is a famous infectious febrile disease specialist. Part of the composition of the Lianhua Qingwen capsule comes from YQS, which is particularly effective in treating pneumonia. YQS is comprised of ten Chinese herbs, JYH, LQ, JG, BH, DDC, DZY, NBZ, JJ, LG, and GC, and mainly treats the manifestations caused by diseases such as damp-heat accumulation in the lung. Bohe and Niubangzi have flavor and cool properties and can help sore throats. Jingjie and Dandouchi can help the main medicine drive away damp heat. Dan Zhuye and Lugen can clear the heat, and Jiegeng and Gancao can relieve cough. YQS is commonly used in the clinic against influenza A virus infection [34–36].

This study uses network pharmacology to forecast the main active components and potential molecular mechanism of YQS against COVID-19. Through the TCMSP database, 141 active ingredients of each single medicine in Yinqiao powder were obtained, of which the five most powerful components were acacetin, kaempferol, luteolin, naringenin, and quercetin. Studies have shown that luteolin may suppress the infection of respiratory epithelial cells by *Escherichia coli* through immunomodulation [37]. Wu et al. established a mouse model of *Staphylococcus aureus* pneumonia and found that naringenin could significantly alleviate the disease [38]. Acacia has antibacterial, antioxidant, anti-inflammatory, antiviral, antipyretic, and analgesic effects [39]. It can protect against atherosclerosis by antagonizing the LysoPC-induced apoptosis of vascular smooth muscle cells and stimulating the antioxidant regulatory factor Nrf2 [40]. Kaempferol has an extensive scope of pharmacological activities, including antioxidant, anti-inflammatory, antimicrobial, etc. [41], and its derivatives are

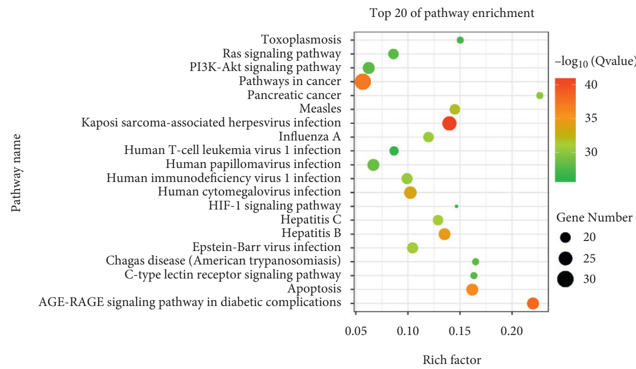

Figure 5: Analysis of the 20 most enriched KEGG pathways of candidate targets of Yinqiaosan (YQS) for COVID-19. The node size denotes the number of target genes that belong to the pathway. The X-axis denotes the enrichment factor (rich factor), that is, the number of genes in the pathway in the target gene/the number of genes contained in the pathway in the background gene set. The Y-axis denotes the pathway. The color depth of the node demonstrates the significance level, and the redder the node is, the higher the significance will be to the pathway.

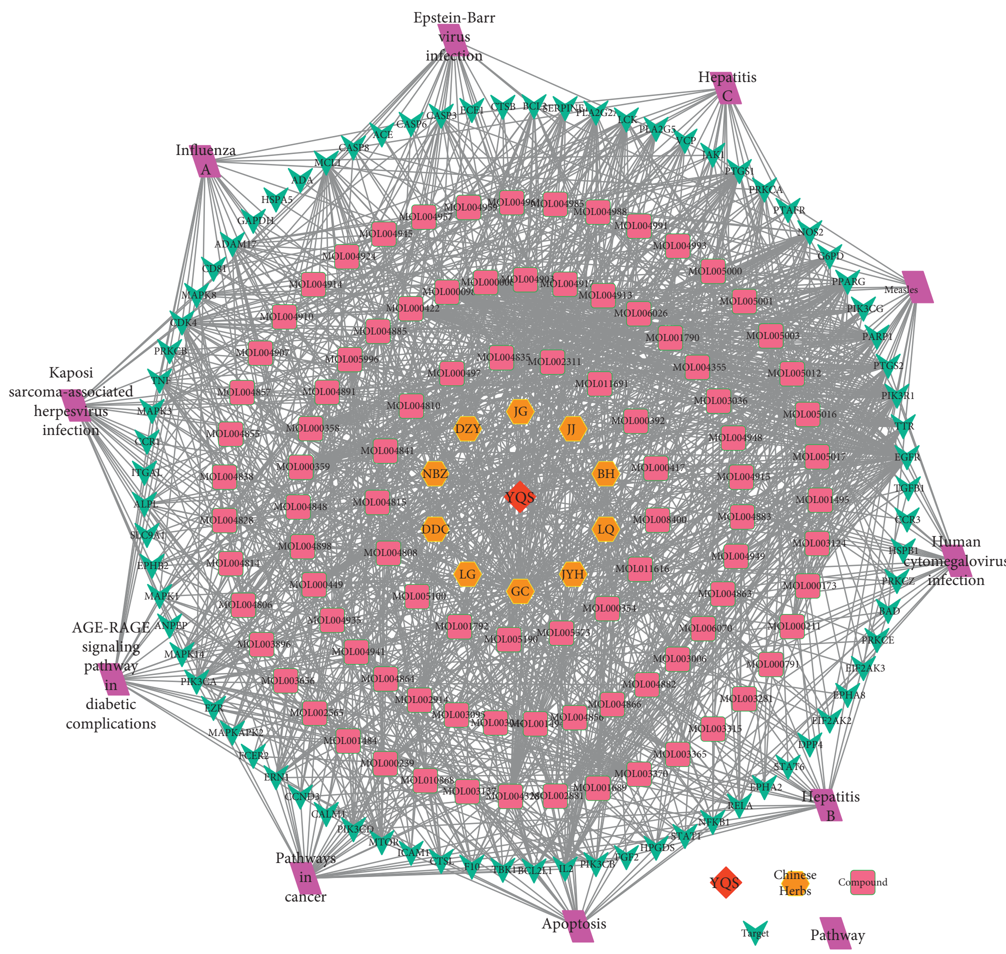

Figure 6: Yinqiaosan (YQS)-compound-target-pathway network. The red bubbles denote YQS (Yinqiaosan), the yellow bubbles denote Chinese herbs, the pink bubbles denote compounds, and the violet bubbles denote pathways.

used as antiviral drugs against coronavirus 3a channel protein [42]. Quercetin and its derivatives also have strong anti-inflammatory and analgesic pharmacological activities [43]. Wang et al. [12] found that active compounds such as quercetin, kaempferol, naringenin, and luteolin also played a pivotal role when treating COVID-19 using Maxing Shigan decoction. Kong et al. [44] discovered through molecular docking that kaempferol, quercetin, luteolin, and new coronavirus (SARS-CoV-2) 3CL hydrolase have good affinity.

There are 77 candidate targets for YQS in COVID-19 treatment. TNF, GAPDH, MAPK3, MAPK1, EGFR, CASP3,

Table 2: Docking results of main ingredients with target proteins.

No.	Ligand name	Mol id	Binding free energy/(kcal·mol^{-1}) Mpro	ACE2
1	Acacetin	MOL001689	−7.5	−8.8
2	Kaempferol	MOL000422	−7.9	−8.6
3	Luteolin	MOL000006	−7.4	−8.8
4	Naringenin	MOL004328	−6.8	−7.9
5	Quercetin	MOL000098	−7.5	−8.5

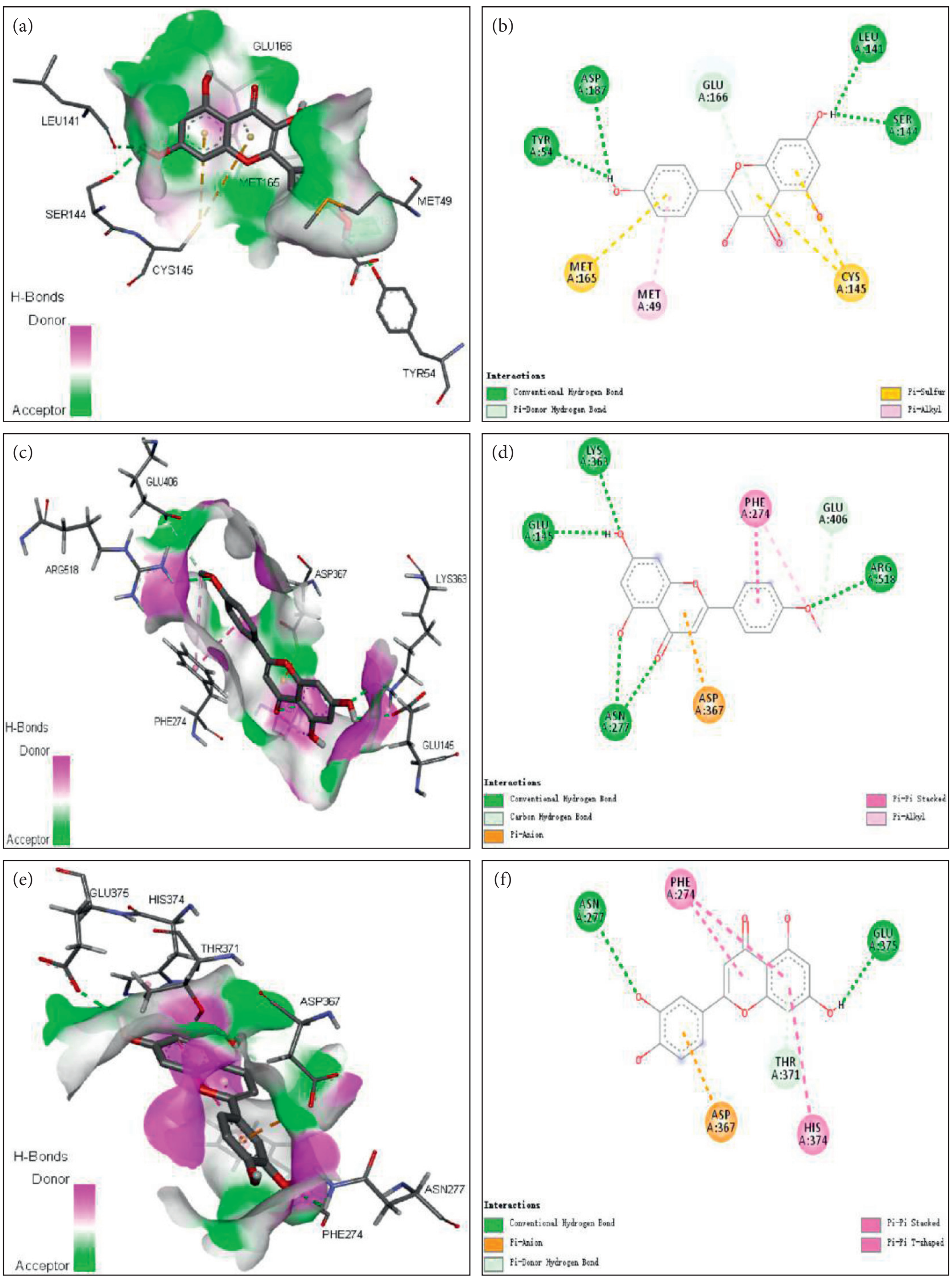

Figure 7: Molecular docking of compounds from YQS for COVID-19 targets. Predicted binding mode of Mpro (PDB id: 6lu7) with kaempferol in the active pocket (a). 2D binding view of kaempferol with Mpro (b). Predicted binding mode of ACE2 (PDB id: 1r4l) with acacetin in the active pocket (c). 2D binding view of acacetin with ACE2 (d). Predicted binding mode of ACE2 (PDB id: 1r4l) with luteolin in the active pocket (e). 2D binding view of luteolin with ACE2 (f).

MAPK8, mTOR, IL-2, and MAPK14 are important targets for YQS in COVID-19 treatment. COVID-19 is similar to other viral pneumonia conditions. Some scholars have found that cytokine storms (CSs) may affect the progression of COVID-19 illness [45]. The cytokines involved in CS mainly include six categories: tumor necrosis factor (TNF), interleukin (IL), interferon (IFN), colony stimulating factor (CSF), and growth factor (GF). The cytokine storm induced by SARS-CoV-2 includes the cytokine IL-2, and the TNF-α- and H7N9-induced cytokine storms include cytokines, including IL-2 [46]. Studies have shown that, in throat swabs and sputum specimens of 4 cases of COVID-19, the housekeeping gene GAPDH of human cells showed a typical amplification signal curve [47]. *Staphylococcus aureus* pneumonia and virulence factor A can stimulate the AMPK signaling pathway and inhibit the mTOR pathway to induce autophagy in alveolar epithelial cells, an important mechanism during early infection of *S. pneumoniae* [48]. Liu et al. [49] predicted MAPK1, MAPK3, and MAPK14 through network pharmacology as important targets for Dayuanyin to treat COVID-19. Huang et al. [4] predicted that MAPK1 and MAPK14 were important targets for Huanglian Jiedu decoction to treat COVID-19. Other studies have shown that EGFR may be a key factor in the inflammation caused by *Klebsiella pneumoniae* infection [50].

Furthermore, molecular docking results showed that the 5 compounds could efficiently act on the 10 targets, especially TNF, MAPK14, MAPK3, and MAPK8. Kaempferol and Mpro have a better binding capacity. Acacetin, luteolin, and ACE2 have a better combining ability. Whether they are docked with molecules of hub genes or docked with the proven targets of pneumonia, this shows the feasibility of using these five compounds to treat pneumonia. Reportedly, AGEs modulate COVID-19 pathogenesis and related comorbidities through their interactions with RAGE, among other molecules [51]. Interestingly, Yalcin Kehribar et al. [52] found that the RAGE pathway plays an important role in the aggravation of COVID-19. These reports provide strong evidence for our data.

To clarify the role of YQS in COVID-19 treatment based on gene functions and signaling pathways, this study performed GO functional enrichment and pathway enrichment analysis of the candidate targets. The GO enrichment analysis showed that the biological procedure of YQS against COVID-19 was mainly reflected in the positive regulation of the adhesion of white blood cells and vascular endothelial cells and the negative regulation of the apoptosis process of cholangiocarcinoma cells. The cellular components were mainly reflected in cytoplasmic vesicles, membrane rafts, and organelle membranes. The molecular functions were mainly reflected in phosphotransferase activity, alcohol receptor, and cytokine receptor binding. The results of KEGG pathway enrichment analysis show that YQS may comprehensively play a role in preventing and treating pneumonia by way of PTGS2, MAPK14, CCR1, CCR3, MAPKAPK2, MAPK3, MAPK1, ICAM1, JAK1, NFKB1, MAPK8, PIK3R1, MTOR, RELA, CASP3, FGF2, TBK1, EIF2AK2, CASP8, and CDK4 targets that are related to the Kaposi sarcoma-associated herpesvirus infection signaling pathway; TGFB1, MAPK14, SERPINE1, STAT1, PIK3CA, PIK3CB, PIK3CD, MAPK3, MAPK1, PIK3R1, NFKB1, RELA, ICAM1, PRKCA, PRKCB, PRKCE, PRKCZ, MAPK8, CASP3, TNF, CDK4, and BCL2 targets that are related to the AGE-RAGE signaling pathway; and TGFB1, MAPK14, SERPINE1, STAT1, PIK3CA, PIK3CB, PIK3CD, MAPK3, MAPK1, PIK3R1, NFKB1, RELA, ICAM1, PRKCA, PRKCB, PRKCE, PRKCZ, MAPK8, CASP3, TNF, CDK4, and BCL2 targets that are related to the pathways in cancer signaling pathways.

5. Summary

In summary, our study found that active ingredients such as luteolin, naringenin, farnesin, kaempferol, and quercetin can act on targets such as TNF, GAPDH, MAPK3, MAPK1, EGFR, CASP3, MAPK8, MTOR, IL-2, and MAPK14 to regulate signaling pathways such as Kaposi sarcoma-associated herpesvirus infection and AGE-RAGE, finally achieving the effect of curing COVID-19.

In the next step, further in vitro and in vivo experimental validation will be carried out to advance our research. The follow-up plan of our research group is to carry out more in-depth experimental research on YQS and to fully explore the mechanism of its efficacy.

Data Availability

All data included in this study are available upon request by contact with the corresponding author.

Conflicts of Interest

The authors declare that there are no conflicts of interest.

Authors' Contributions

Lihua Cao, Xingyuan Jia, and Yiying Zhao contributed to data curation. Lihua Cao and Xue Yang carried out formal analysis. Investigation was done by Zhenzhen Wang, methodology by Lihua Cao and Xing-yuan Jia, project administration by Miaosan Miao; software by Lihua Cao, Hongjuan He, Zhenzhen Wang, Yiying Zhao, and Xue Yang, and visualization by Lihua Cao and Hongjuan He. For writing, original draft was written by Lihua Cao and Yiying Zhao; review and editing were performed by Xiu-Min Li. All authors read the manuscript and agreed to publish it.

Acknowledgments

This work was supported by Henan Outstanding Foreign Scientist Studio (gzs2019006), Henan Province Emergency (201100312300); Zhengzhou Emergency Project (ZZKJ2020604), Jiansheng Fresh Medicine Innovation and Research Fund Project (jsyy-20200105-057); Key Scientific Research Projects of Colleges and Universities in Henan Province (20A360009, 22A360003); and Young Elite Scientists Sponsorship Program by Henan Association for Science and Technology (2022HYTP049). The authors would like to thank Henry Ehrlich for reading the manuscript. The authors also appreciate the support from International TCM Immunopharmacology Research Center, Henan University of Chinese Medicine, Drs. Lixiao Zhang, Jiang Yan Xu, and Erping Xu at Henan University of Chinese Medicine, and Raj Tiwary at Microbiology and Immunology Department, New York Medical College.

Supplementary Materials

Supplementary 1. Additional file 1: Fig. S1: YQS (Yinqiaosan) formula-active ingredient network diagram. Supplementary 2. Additional file 2: Table S1: the information of the related targets of YQS (Yinqiaosan). Supplementary 3. Additional file 3: Table S2: virtual docking of five bioactive ingredients from YQS for COVID-19 targets. (*Supplementary Materials*)

References

[1] N. Zhu, D. Y. Zhang, W. L. Wang et al., “A novel coronavirus from patients with pneumonia in China,,” *New England Journal of Medicine*, vol. 2020, no. 382, pp. 727–733, 2019.

[2] Y. Jamilloux, T. Henry, A. Belot et al., “Should we stimulate or suppress immune responses in COVID-19? Cytokine and anti-cytokine interventions,” *Autoimmunity Reviews*, vol. 19, no. 7, p. 102567, 2020.

[3] P. Zhou, X. L. Yang, X. G. Wang et al., “A pneumonia outbreak associated with a new coronavirus of probable Bat origin,” *Nature*, vol. 579, pp. 270–273, 2020.

[4] J. M. Ou, W. J. Ye, K. C. Zheng et al., “Epidemiological characteristics of an outbreak of 2019 novel coronavirus diseases (COVID-19) in FuJian, China,” *Chinese Journal of Zoonoses*, vol. 36, no. 5, pp. 366–371, 2020.

[5] L. S. Qiao, W. T. Huang, X. L. Zhang, H. Y. Guo et al., Evaluation of the immunomodulatory effects of anti-COVID-19 TCM formulae by multiple virus-related pathways,” *Signal transduct Tar*, vol. 6, no. 1, 2021.

[6] Y.-F. Huang, C. Bai, F. He, Y. Xie, and H. Zhou, “Review on the potential action mechanisms of Chinese medicines in treating Coronavirus Disease 2019 (COVID-19),” *Pharmacological Research*, vol. 158, p. 104939, 2020.

[7] X. Tang, L. Tong, F. F. Guo, S. H. Tang, and H. J. Yang, “Analysis of potential role of Chinese classic prescriptions in treatment of COVID-19 based on TCMATCOV platform,” *China Journal of Chinese Materia Medica*, vol. 45, no. 13, pp. 3028–3034, 2020.

[8] L. L. Huang, D. Xu, Y. W. Liu, and Z. Y. Liu, “Study on active compounds of yupingfeng san in preventing and treating COVID-19 based on network pharmacology and molecular docking Technology,” *Pharmacol Clin Mater Medica*, vol. 36, no. 2, pp. 116–121, 2020.

[9] H. Li and L. Zhang, “Study on the molecular mechanism of atractylodes lancea in treating novel coronavirus pneumonia based on network pharmacology,” *Chin herbal med*, vol. 43, no. 10, pp. 2610–2612, 2020.

[10] H. B. Xu, Z. S. Tang, Y. R. Liu et al., “Based on the network pharmacology method to predict the active components and potential targets of Weixuening Mixture in the prevention and treatment of new coronavirus pneumonia,” *Journal of Chinese Medicinal Materials*, vol. 43, no. 10, pp. 2602–2609, 2020.

[11] F. C. Meng and L. D. Tang, “Challenges and prospect in research of Chinese materia medica network Pharmacology,” *Chinese Traditional and Herbal Drugs*, vol. 51, no. 8, pp. 2232–2237, 2020.

[12] Z. Y. Wang, Y. Z. Sun, M. D. Qu et al., “Network pharmacological study on mechanism of Maxing Shigan Decoction in treatment of coronavirus disease 2019 (COVID-19),” *Chinese Traditional and Herbal Drugs*, vol. 51, no. 8, pp. 1996–2003, 2020.

[13] Q. D. Xia, Y. Xun, J. L. Lu et al., “Network pharmacology and molecular docking analyses on Lianhua Qingwen capsule indicate Akt1 is a potential target to treat and prevent COVID-19,” *Cell Proliferation*, vol. 53, no. 12, p. e12949, 2020 Dec.

[14] N. Wang, F. Zhu, M. Shen et al., “Network pharmacology-based analysis on bioactive anti-diabetic compounds in Potentilla discolor bunge,” *Journal of Ethnopharmacology*, vol. 241, p. 111905, 2019.

[15] J. Zhao, Y. Wang, W. Chen et al., “Systems pharmacology approach and experiment evaluation systems pharmacology approach and experiment evaluation reveal multidimensional treatment strategy of LiangXueJieDu formula for psoriasis,” *Frontiers in Pharmacology*, vol. 12, p. 626267, 2021.

[16] W. Zhang, Y. Chen, H. H. Jiang et al., “Integrated strategy for accurately screening biomarkers based on metabolomics coupled with network pharmacology,” *Talanta*, vol. 211, Article ID 120710, 2020.

[17] J. Zhang, Y. Wang, X. Q. Zhang, Q. W. Zhang, and W. C. Ye, “Chemical constituents from the leaves of Lophatherum gracile,” *Chinese Journal of Natural Medicines*, vol. 7, no. 6, pp. 428–431, 2009.

[18] D. He, J.-h. Huang, Z.-y. Zhang et al., “A network pharmacology-based strategy for predicting active ingredients and potential targets of LiuWei DiHuang pill in treating type 2 diabetes mellitus,” *Drug Design, Development and Therapy*, vol. 13, no. 1, pp. 3989–4005, 2019.

[19] O. Kuchaiev, M. Rašajski, D. J. Higham, and N. Pržulj, “Geometric de-noising of protein-protein interaction networks,” *PLoS Computational Biology*, vol. 5, no. 8, p. e1000454, 2009.

[20] R. Guo, X. Zhang, J. Su et al., “Identifying potential quality markers of Xin-Su-Ning capsules acting on arrhythmia by integrating UHPLC-LTQ-Orbitrap, ADME prediction and network target analysis,” *Phytomedicine*, vol. 44, pp. 117–128, 2018.

[21] D. Gary and C. W. H. Bader, “An automated method for finding molecular complexes in large protein interaction networks,” *BMC Bioinformatics*, vol. 4, no. 1, pp. 1–27, 2003.

[22] M. Clément-Ziza, C. Malabat, C. Weber et al., “Genoscape: a Cytoscape plug-in to automate the retrieval and integration of gene expression data and molecular networks,” *Bioinformatics*, vol. 25, no. 19, pp. 2617-2618, 2009.

[23] S. Fishilevich, S. Zimmerman, A. Kohn et al., *Genic Insights from Integrated Human Proteomics in GeneCards*, p. baw030, Database, Oxford, 2016.

[24] S. Boyadjiev and E. Jabs, “Online Mendelian Inheritance in Man (OMIM) as a knowledgebase for human developmental disorders,” *Clinical Genetics*, vol. 57, no. 4, pp. 253–266, 2000.

[25] Y. Zhang, T. Zhou, Z. Dai et al., “Comparative transcriptomics provides insight into floral color polymorphism in a pleione limprichtii orchid population,” *International Journal of Molecular Sciences*, vol. 21, no. 1, p. 247, 2019.

[26] L. Pinzi and G. Rastelli, “Molecular docking: shifting paradigms in drug Discovery,” *International Journal of Molecular Sciences*, vol. 20, no. 18, p. 4331, 2019.

[27] C.-H. Chin, S.-H. Chen, H.-H. Wu, C.-W. Ho, M.-T. Ko, and C.-Y. Lin, “cytoHubba: identifying hub objects and sub-

networks from complex interactome," *BMC Systems Biology*, vol. 8, no. S4, pp. 1–7, 2014.

[28] Y. Liu, C. Liang, L. Xin et al., "The development of Coronavirus 3C-Like protease (3CLpro) inhibitors from 2010 to 2020," *European Journal of Medicinal Chemistry*, vol. 206, p. 112711, 2020.

[29] M. Dos Santos Maia, G. C. Soares Rodrigues, A. B. Silva Cavalcanti, L. Scotti, and M. T. Scotti, "Consensus analyses in molecular docking studies applied to medicinal chemistry," *Mini Reviews in Medicinal Chemistry*, vol. 20, no. 14, pp. 1322–1340, 2020.

[30] X. Y. Ling, J. L. Tao, X. Sun, and B. Yuan, "Exploring material basis and mechanism of Lianhua Qingwen Prescription against coronavirus based on network pharmacology," *Chinese Traditional and Herbal Drugs*, vol. 51, no. 7, pp. 1723–1730, 2020.

[31] J.-l. Ren, A.-H. Zhang, and X.-J. Wang, "Traditional Chinese medicine for COVID-19 treatment," *Pharmacological Research*, vol. 155, p. 104743, 2020.

[32] Z. Zhao, Y. Li, L. Zhou et al., "Prevention and treatment of COVID-19 using Traditional Chinese Medicine: a review," *Phytomedicine*, vol. 85, p. 153308, 2021.

[33] Q. Tao, J. Du, X. Li et al., "Network pharmacology and molecular docking analysis on molecular targets and mechanisms of Huashi Baidu formula in the treatment of COVID-19," *Drug Development and Industrial Pharmacy*, vol. 46, no. 8, pp. 1345–1353, 2020 Aug.

[34] C. Bai, T. G. Liu, J. N. Xu et al., "Comparison of the mechanism of Yinqiao powder combined with modified sangju decoction, modified maxing shigan decoction and antiviral western medicine based on network pharmacology: taking the mild influenza in early winter of 2018 as an example," *Journal of Traditional Chinese Medicine*, vol. 60, no. 11, pp. 928–934, 2019.

[35] X. H. Guo, Y. L. Zhu, and Q. L. Cheng, "Study on the molecular docking of anti-influenza virus components in Yinqiao powder and neuraminidase," *Chinese Pharmacy*, vol. 29, no. 17, pp. 2351–2355, 2018.

[36] R. Guo, M. Zhao, H. Liu et al., "Uncovering the pharmacological mechanisms of Xijiao Dihuang decoction combined with Yinqiao powder in treating influenza viral pneumonia by an integrative pharmacology strategy," *Biomedicine & Pharmacotherapy*, vol. 141, p. 111676, 2021.

[37] Z. Y. Huang, F. J. Sun, X. Yuan, Y. Wang, L. R. Xiong, and W. Feng, "Effect of luteolin on reducing the infection of Escherichia coli in respiratory epithelial cells," *Chinese Journal of Hospital Pharmacy*, vol. 40, no. 7, pp. 781–785, 2020.

[38] W. W. Wu, S. X. Zheng, Q. Y. Weng, and D. M. Chen, "Naringenin alleviates the damage and mechanism of staphylococcus aureus pneumonia in mice," *Chin J Gerontol*, vol. 35, no. 14, pp. 3849-3850, 2015.

[39] N. Ma, Y. J. Li, and J. P. Fan, "Research progress on pharmacological action of acacetin," *Chin J Modern Applied Pharm*, vol. 35, no. 10, pp. 1591–1595, 2018.

[40] Y. D. Li, *Molecular Mechanism of Acacetin against Lysophosphatidylcholine-Induced Apoptosis in Cultured Rat Aortic Vascular Smooth Muscle Cells*, Xiamen University, 2018.

[41] K. P. Devi, D. S. Malar, S. F. Nabavi et al., "Kaempferol and inflammation: from chemistry to medicine," *Pharmacological Research*, vol. 99, no. suppl C, pp. 1–10, 2015.

[42] S. Schwarz, D. Sauter, K. Wang et al., "Kaempferol derivatives as antiviral drugs against the 3a channel protein of coronavirus," *Planta Medica*, vol. 80, no. 02/03, pp. 177–182, 2014.

[43] G. Carullo, A. R. Cappello, L. Frattaruolo, M. Badolato, B. Armentano, and F. Aiello, "Quercetin and derivatives: useful tools in inflammation and pain management," *Future Medicinal Chemistry*, vol. 9, no. 1, pp. 79–93, 2017.

[44] Y. Kong, H. W. Wu, Y. Chen, S. Lai, Z. M. Yang, and J. S. Chen, "Mechanism of Tanreqing Injection on treatment of coronavirus disease 2019 based on network pharmacology and molecular docking," *Chinese Traditional and Herbal Drugs*, vol. 51, no. 07, pp. 1785–1794, 2020.

[45] J. W. Zhang, X. Hu, and P. F. Jin, "Cytokine storm induced by SARS-CoV-2 and the drug therapy," *Chinese Pharmaceutical Journal*, vol. 55, no. 5, pp. 333–336, 2020.

[46] L. Gao, Q. Yang, Y. Huang, and C. Yi, "Application of traditional Chinese medicine to viral pneumonia based on cytokine storm theory," *Pharmacol Clin Mater Medica*, vol. 36, no. 2, pp. 17–23, 2020.

[47] W. Chen, C. Y. Zhang, Y. Zhu et al., "Comparison of throat swab and sputum specimens for viral nucleic acid detection in four cases of 2019-nCoV infection," *Chinese Journal of Zoonoses*, vol. 36, no. 5, pp. 354–358, 2020.

[48] X. G. Guo, *PAVA Induces Autophagy of Alveolar Epithelial Cells in the Infection of streptococcus Pneumoniae via AMPK/m TOR Pathway*, Southern Medical University, 2018.

[49] G. X. Liu and T. Zhang, "Feasibility of chai hu da yuan decoction treating COVID-19 based on network pharmacology and molecular docking Technology," *Pharmacol Clin Mater Medica*, vol. 36, no. 2, pp. 102–108, 2020.

[50] F. Xiao, E. L. Cao, N. B. Long, and S. L. Zheng, "Klebsiella pneumoniae capsular polysaccharide induces secretion of cytokines in bronchial epithelial cells via EGFR signaling pathway," *Chinese Journal of Pathophysiology*, vol. 36, pp. 514–518, 2020.

[51] D. Sellegounder, P. Zafari, M. Rajabinejad, M. Taghadosi, and P. Kapahi, "Advanced glycation end products (ages) and its receptor, rage, modulate age-dependent covid-19 morbidity and mortality. a review and hypothesis," *International Immunopharmacology*, vol. 98, p. 107806, 2021.

[52] D. Yalcin Kehribar, M. Cihangiroglu, E. Sehmen et al., "The receptor for advanced glycation end product (RAGE) pathway in COVID-19," *Biomarkers*, vol. 26, no. 2, pp. 114–118, 2021.

Hindawi
Journal of Healthcare Engineering
Volume 2023, Article ID 9867826, 1 page
https://doi.org/10.1155/2023/9867826

Retraction

Retracted: Biomechanical Analysis and Training Method Research on Head Shot Strength of Football Players

Journal of Healthcare Engineering

Received 15 August 2023; Accepted 15 August 2023; Published 16 August 2023

This article has been retracted by Hindawi following an investigation undertaken by the publisher [1]. This investigation has uncovered evidence of one or more of the following indicators of systematic manipulation of the publication process:

(1) Discrepancies in scope
(2) Discrepancies in the description of the research reported
(3) Discrepancies between the availability of data and the research described
(4) Inappropriate citations
(5) Incoherent, meaningless and/or irrelevant content included in the article
(6) Peer-review manipulation

The presence of these indicators undermines our confidence in the integrity of the article's content and we cannot, therefore, vouch for its reliability. Please note that this notice is intended solely to alert readers that the content of this article is unreliable. We have not investigated whether authors were aware of or involved in the systematic manipulation of the publication process.

Wiley and Hindawi regrets that the usual quality checks did not identify these issues before publication and have since put additional measures in place to safeguard research integrity.

We wish to credit our own Research Integrity and Research Publishing teams and anonymous and named external researchers and research integrity experts for contributing to this investigation.

The corresponding author, as the representative of all authors, has been given the opportunity to register their agreement or disagreement to this retraction. We have kept a record of any response received.

References

[1] Y. Yao and S. Xiang, "Biomechanical Analysis and Training Method Research on Head Shot Strength of Football Players," *Journal of Healthcare Engineering*, vol. 2022, Article ID 7594124, 7 pages, 2022.

Hindawi
Journal of Healthcare Engineering
Volume 2022, Article ID 7594124, 7 pages
https://doi.org/10.1155/2022/7594124

Research Article

Biomechanical Analysis and Training Method Research on Head Shot Strength of Football Players

Yipeng Yao [1] and Shanshan Xiang [2]

[1] *Guilin University of Aerospace Technology, Guilin, Guangxi, China*
[2] *Guangxi Normal University, Guilin, Guangxi, China*

Correspondence should be addressed to Shanshan Xiang; 2016402@guat.edu.cn

Received 12 January 2022; Revised 16 February 2022; Accepted 22 February 2022; Published 15 March 2022

Academic Editor: Enas Abdulhay

With the development of intelligent sports in China and the rapid improvement of the strength of colleges and universities, the reform of traditional football players' header shooting training methods is becoming more and more urgent in order to solve some problems in the development of sports and speed up the intelligent training of Chinese football players. Based on this, this paper studies the biomechanical analysis and training method based on the integration of header strength data of football players. A dynamic header tracking model of football players based on a local search algorithm is designed. The data collection is realized from the aspects of athletes' header shooting training, skill improvement, physical consumption, and trajectory. The biological data of header shooting power is comprehensively analyzed and evaluated by using a local search algorithm. The results show that the training system based on a local search algorithm has the advantages of high feasibility, high data accuracy, and fast response speed. It can effectively conduct accurate guidance and improve the shooting accuracy according to the biological characteristics of header shooting intensity. This paper studies the biological analysis and training method of header strength of football players based on a local search algorithm. This has certain reference significance for accelerating the construction of intelligent training of Chinese football players.

1. Introduction

Up to now, the teaching process of College Physical Education in China is mainly based on the traditional collective and group teaching, supplemented by the independent teaching of the main team members [1]. Since the reform and opening up, the rapid development of various information technologies in China has also led to the reform of China's football system and training methods. The emergence of modern football teaching methods such as team cooperation provides an opportunity for the large-scale development of new football courses in colleges and universities. Intelligence has become an important feature of China's current football training system [2]. At present, although the existing football training system provides a large number of football training methods, it is difficult for players to choose targeted football header shooting training methods according to their own strength structure and biological characteristics in the training process of header shooting and can not achieve the optimal football actual combat effect [3]. In this context, this paper studies the strength characteristics and biological characteristics of the headshot process of government and enterprise players and proposes a dynamic tracking training method of headshot based on the integration of football players' strength information.

The innovation of this paper is to propose a local search algorithm. On this basis, it can make full use of each player's strength training and biological energy characteristic information. Through real-time dynamic tracking, it can achieve the overall approach and quantitatively describe the degree of similarity between the comparison column and the reference column and the degree of agreement between the expected indicators with local correlation factors. By using quantitative indicators to complete the influence degree ranking of training system indicators, it can efficiently carry out customized analysis on the factors affecting players' skill level.

This paper studies the biological analysis of the headshot strength of football players and the construction of training methods, which is mainly divided into three parts. The first part introduces the research status of football training factors at home and abroad. In the second part, the dynamic tracking training model of football player's header shooting based on a local search algorithm is constructed, and the Laplace factor method is used to construct the evaluation index system of header shooting accuracy. The third part tests the evaluation index of the dynamic tracking training system of football players' heading and shooting strength and draws a conclusion.

2. Related Work

Since entering the twenty-first century, the training of sports players has encountered difficulties, especially in the construction of football teaching and training systems [4]. Columbia University scholars found that most football training still follows the traditional football training ideas, ignoring the cultivation of practical skills and comprehensive ability. Football training is mainly divided by basic football knowledge, basic football skills and professional knowledge, and broad football skills. Players are not interested in traditional football training. Scholars from Tokyo University of Japan teach according to the rules of football playing and put forward that we should pay attention to the development of classroom-based explanation or teaching video playback, strengthen the development and construction of professional football knowledge courses, and enhance the cognition and attention to football teaching, and the cultivation of football teachers' ability should be improved [5]. According to the multifactor relationship theory and local cooperation theory, a new multirelationship recommendation algorithm is proposed by scholars of Harvard University in the United States, The local weak relation recommendation algorithm has better heterogeneous information acquisition ability than the classical recommendation algorithm [6]. Scholars from Beijing Sport University of China adopted the local search algorithm based on multilocal high weight correlation factors, selected three characteristic parameters related to football players and training system influence indicators, and proposed a dynamic tracking training system for football players' heading and shooting based on local search algorithm for athletes' training characteristic parameters. Football training and other related theories improve the particle swarm optimization algorithm, construct the particle swarm optimization algorithm based on the traditional football training system, and explain the theoretical basis and practical significance of these changes in the algorithm performance with the theory of game theory. Experiments show that the improved algorithm has good local optimization performance [7]. Based on the kinematic theory, scholars from the University of London proposed a hierarchical football header shooting training method. Through the research and analysis of the dynamic differences of weight, height, body fat, and running speed of different football members, it is found that the algorithm can realize the personalized training improvement of hierarchical football players [8]. In order to improve the training efficiency and overall team coordination of football players, scholars from the University of Melbourne in Australia proposed a new team fusion intensive training system based on hyperchaotic mapping through the research of daily training, heading posture analysis and detection, and physical consumption, It is suitable for the analysis of football training and looking for the problems existing in training [9]. Scholars from the University of Toronto in Canada scramble the original football training method by using the transformed chaotic sequence. The results show that the innovative training system has a good overall coordination effect and can resist attack and defense. It can be used in the construction of a football training system [10]. Scholars from Waseda University in Japan proposed a new hyperchaotic cellular neural network football training algorithm to generate the keystream in the team defense stage of football training. The results show that, compared with other related algorithms, this algorithm has the advantages of key sensitivity and strong antiattack and is suitable for football training [11]. Based on the traditional football training fusion strategy technology, scholars from the University of California proposed a panoramic video football cross-border folding search algorithm, which clearly defined the hierarchical framework and index relationship of the whole football training system. This paper evaluates the system from multiple perspectives and provides a comprehensive index sample for the evaluation of the training system of intelligent Chinese football players. Then, it uses the local search algorithm to analyze the characteristics of the players' training results. The results show that the algorithm can effectively reduce the error of football search matching blocks and improve the training efficiency. It is conducive to improving the training skills of heading and shooting in football [12]. Scholars from the Northwestern University of the United States put forward the Fourier function algorithm, and the results show that the algorithm can effectively remove the inefficient cooperation events in the football training system [13]. In order to solve the problem of efficiency and tactical effectiveness of group training, scholars from Shanghai Jiaotong University of China proposed a football competition tactical method based on genetic algorithm and particle swarm optimization algorithm. Experiments show that the algorithm can effectively improve the practicability of football tactics [14]. Scholars from the Hong Kong Polytechnic University of China have realized the tactical evaluation basis in football training by simulating the "modeling structure diagram" in the process of football modeling and improved the flexible transformation from traditional football tactics to modern tactics [15].

To sum up, it can be seen that most of the current football training modes do not involve intelligent depth mining analysis and local search algorithms based on the dynamic training data of football players' heading and shooting. On the other hand, although China has done a lot of basic research, the specific quantitative dynamic evaluation of football intelligent training system and the improvement of football training effect research results are relatively less, and there is no research and related model construction on the intelligence of Chinese football players' heading and shooting training system.

3. Methodology

3.1. Application Principle of Local Search Algorithm in the Biomechanical Analysis Model of Heading Shot. In order to more intelligently and accurately analyze the specific effect of the signal processing link in the football header shooting, this paper uses the local search algorithm to detect and analyze the head dynamic signal of the football group in the daily football training process. The basic principle of the common local search algorithm is shown in Figure 1, in which DC is the search center.

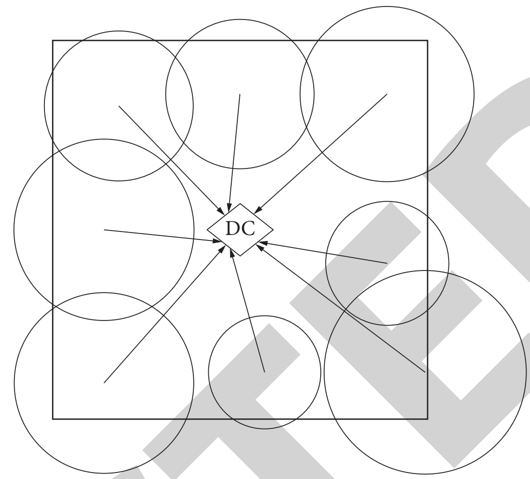

Figure 1: The basic principle of the local search algorithm.

In this study, the local search algorithm is to find the groups with high similarity of force signals in the process of header shooting from each football player and cluster them. Therefore, the probability of the standard motion data being selected for secondary or multiple detection and analysis is high. On the contrary, if the signal form with a low correlation of dynamic strength structure of football players is selected for secondary or multiple analysis, the probability will be very low. After many times of comparative analyses, the new generation of people with overlapping head ball posture features not only inherits the dynamic head data information of the previous round of intelligent screening but also has a better optimization degree than the information set of the previous generation of eliminated football signals. In this way, after several interactive cycles of two-way heading posture information, the specific information that meets the heading posture requirement conditions corresponding to the lowest normal football skills is finally generated; that is, the analysis value of the normal boundary of a certain football heading posture signal approximates the normal requirement value of the actual heading posture signal. In this way, we can analyze and record the unique heading posture information under the condition of "optimized local search algorithm," and the mode can also realize the function of self-storage and prediction. The more the process of accumulating the dynamic data of football players' heads, the stronger the self-learning ability and self-evaluation of the system. In addition, in the process of establishing this model, we found that, in the current Chinese long-term football and power sports groups, the analysis of most of the shooting posture of the head ball is based on the traditional detection equipment, and the detection process is mainly direct contact detection. However, noncontact real-time head ball attitude signal detection is rare. Therefore, in this model, a standard structure data evaluation model of football header shooting posture is set in advance (in order to determine the key detection nodes). Therefore, this paper studies the processing object based on the head ball poses randomly selected from the local multigroup head ball pose set of multiple targets to be detected. By comparing with the big data system of the real-time heading posture analysis model of football players, it is very easy to know through simulation that in the two groups with low similarity in the structure of heading posture, it is found that there is a great difference in the skill of shooting between them. And engaged in the football game, the difference in the way of attack will be relatively large.

The above is the basic principle of the local search algorithm used in the research of dynamic signal tracking and data processing of football players' headshots. Through the above optimized local search algorithm, the analysis process is shown in Figure 2, where BN is the connection center, and the rest (*a*, *b*, *c*, *d*, *e*, *f*, *g*, *h*, *i*, *k*) are the classification subcenters. Compared with the common head posture analysis method of football players, it can achieve more accurate analysis and strength correction, which plays a more effective role in the training process of football players' heading and shooting.

3.2. Implementation Steps of the Dynamic Tracking Training Model for Football Players' Heading and Shooting. In order to reduce the error analysis of the dynamic signal processing in the training process, we use the local search algorithm with adaptive characteristics. Aiming at the head ball posture signal analysis model of football players in the daily training process, firstly, we will use the big data information and intelligent analysis and processing of the heading posture corresponding to the existing skillful football movements to obtain the initial weight and the minimum threshold value of the heading posture requirement of normal football movement required in the optimized local search algorithm. Then, the local search algorithm is used to analyze and trace the demand degree of heading posture in accordance with the standard with secondary subdivision in the category group of a specific football player's heading posture information. Finally, the optimal solution is searched, and then the real-time dynamic range of heading posture data in the training process is screened out. The three simulation analysis results of the local search algorithm (TSBN, TSFA, and GCSA) are shown in Figure 3, where the horizontal axis

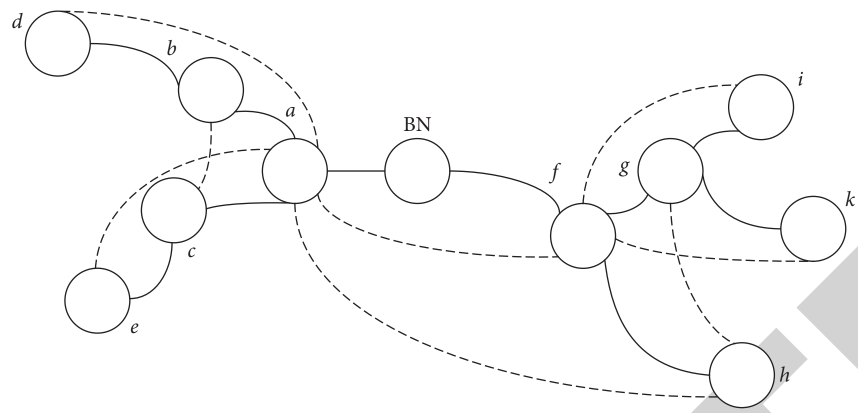

Figure 2: Analysis process of the local search algorithm.

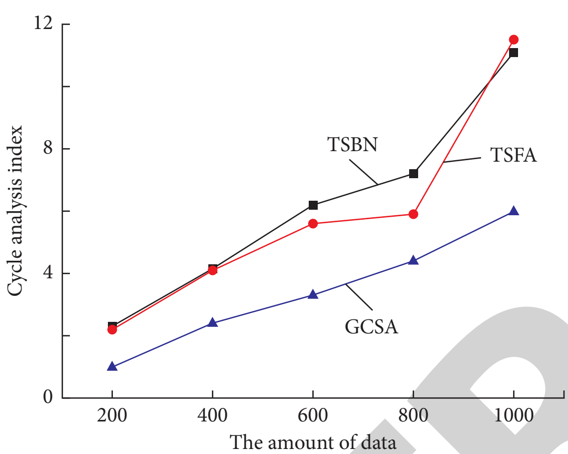

Figure 3: Three kinds of simulation analysis results of the local search algorithm.

is the amount of data and the vertical axis is the cycle index factor.

In the later simulation analysis process, we found that the effect of the traditional local search algorithm is not particularly good. Therefore, in order to improve the detection and intelligent analysis of the head dynamic signal in the football group through the local search algorithm, we need to optimize the local search algorithm, so we use the partial implementation process. In this process, the local search algorithm aims at the dynamic structure of the head ball and the realization process characteristics of the football movement analysis, which is based on the head ball posture information characteristics of the whole crowd target to carry out fuzzy random selection. The purpose of this fuzzy random selection process is to make the signal detection of the common heading posture of different football players more effective because the well-known local search algorithm is not based on a single target in a certain type of feature detection node of the overall target. But through the whole local group of football head ball posture of joint node structure type group to find and get the type of football head dynamic data detection and analysis, the value of the processing conforms to the standard value of the optimal data target. In the process of simulation, the headshot of a random group is taken as the control simulation object. At the beginning of the simulation, the competitive level of one group is lower than the average (the accuracy of the headshot is low), and the other group is lower than the average (the accuracy of the headshot is high). Through nearly 1000 times of simulation experiments and data training under the dynamic tracking model of football players' header shots based on a local search algorithm, it is found that the two groups of data have a great improvement in the comprehensive performance of the new football header shot strength analysis. Therefore, according to the simulation results, the head movement state and strength biological analysis model of the football player has a high accuracy when he is heading, which also shows that the model has good reliability.

Next, the implementation steps and results of the head dynamic signal processing model of football players in the process of training are shown in Figure 4 (under the three methods of TSBN, TSFA and GCSA, the horizontal axis is the amount of data, and the vertical axis is the cycle index factor).

3.3. Mathematical Algorithm of the Dynamic Tracking Training Model for Football Player's Headshot. The mathematical operation process is as follows when the dynamic tracking training model of a football player's headshot is realized. First, we need to initialize the parameters. First, let the initial parameter $x = 0$ set its judgment function as

$$F_{ij}(x) = \cos\frac{Nx}{x+1}, \tag{1}$$

where N is a constant, and $F_{00}(x) = 0$.

Next, the mathematical operation judgment process is verified, and the verification function is

$$H(x) = \sqrt{\left|\cos\frac{Nx}{x+1} - \sin\frac{Nx}{x+1}\right|}, \tag{2}$$

where N is a constant and x is the amount of information.

We also need to judge the constraints [16]. After the completion of the header shooting data information update, if the end condition is met, the constraint judgment and process update are carried out, and the judgment function is

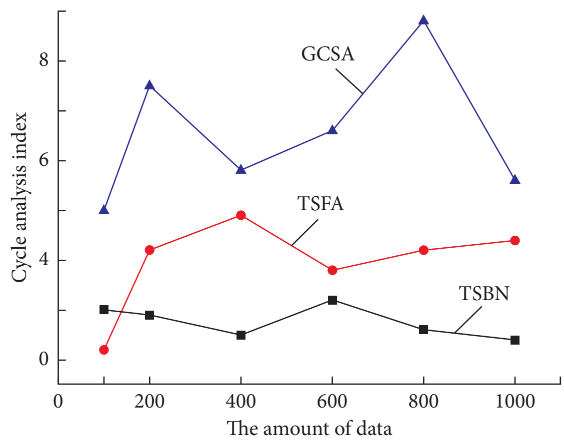

Figure 4: The process flow chart of the ant system algorithm.

$$Q(x) = \left| \frac{s - H(x)}{(s + 1)H(x)} \right|, \quad (3)$$

where s is determined by

$$s = (1 - \rho) * H(x) + \Delta\tau_{ij}. \quad (4)$$

Among them, $\Delta\tau_{ij} = \sum_{k=1}^{m} \Delta\tau_{ij}^{k}$, where τ_{ij} is the length of the current global optimal solution.

Finally, after the pheromone update is completed, the pheromone concentration on each side is limited between $[\tau_{ij\,\min}, \tau_{ij\,\max}]$, to avoid the pheromone on some sides being too large and reduce the pheromone gap on each side of the graph, so as to expand the search space of the solution, so as to complete the biological analysis of the header shot [17].

4. Results of Analysis and Discussion

4.1. Design Confirmatory Experiment. Based on the analysis of the above local search algorithms, the system compares the head ball attitude information data of the analyzed target in the process of processing the header shot signal of different players according to the optimized local search algorithm and the intelligent analysis mode of big data of real-time header shooting attitude information based on football players, so the multilevel comparative analysis can be realized. Under this model, there are different ways of heading posture of different football players and we need to know how to analyze whether the tested players' head posture conforms to the best degree of relevant football movements. Through the dynamic analysis model of football head posture after optimization based on multiple comparative analyses and screening, first, the signal similarity of the same football player in the dynamic training process is received, the data processing is carried out, and the relevant unique vector group is obtained. Then, the head ball attitude signal evaluation sample data of different football players are obtained. The data of the unique vector group of the specific single soccer head posture are processed uniformly and orthogonalized. Then, through the automatic comparison and analysis system of the head ball posture of normal football sport based on big data level and the intelligent combination mode of automatic two-way information interaction, and then through the detection and fuzzy processing of various header posture data of local football players, the minimum threshold of initialization weight and the prediction of head ball attitude signal data required by the optimized local search algorithm is realized. The parameter indexes are shown in Table 1.

In this verification experiment, in order to find the relationship between the headshot strength signal processing of football players and the spatial position of intelligent head ball posture, so that the analysis of football head ball posture can bring effective influence on the daily training of football players, this study calls on the local search algorithm, through the first screening and multilevel horizontal and vertical analysis and processing. The initialization weight and the actual threshold of the whole sample are optimized. The optimal vector obtained by the local search algorithm is transformed back as the optimal weight of the local search algorithm and the output average of the ball attitude structure data of football. Through the above process, the head ball posture analysis and the prediction of the future heading posture trend of football can be realized. According to the experimental results, we can find that the model can avoid some complicated links and achieve the same analysis effect or better processing effect in the process of real-time header attitude signal processing of football players. In the process of the research and establishment of the analysis model of the soccer players' real-time head gesture signal processing method, this paper establishes a unique fuzzy detection analysis and processing model from the aspect of the construction of the local search algorithm model.

4.2. Experimental Results and Analysis of the Analysis Model of Header Shooting Power. The experimental data of the key node signal under the local search algorithm is shown in Table 2.

The experimental results are shown in Figure 5. The horizontal axis is the number of experiments, and the vertical axis is the positive factor.

According to the results of Table 2 and Figure 5, when analyzing the movement process of different header shots in this football header shooting strength analysis model, we can accurately classify them according to the accuracy of shooting and update them according to the way of high shooting success rate, so as to analyze and summarize their internal verification relationship and continuity. Therefore, according to the experimental results, the dynamic signal detection analysis and processing model based on a local search algorithm can have good accuracy and reliability.

The accuracy results of the experimental results of the signals of key nodes under the local search algorithm are shown in Table 2.

The results of this experiment show that the model can compare and analyze the present state of the header shooting attitude of a specific target (football player) according to the information of key detection nodes, and then, we can know whether the skill of a target in football players is affected by the head ball posture. Therefore, the new method of dynamic

Table 1: Experimental data.

Group	Index 1	Index 2	Index 3	Index 4	Index 5
Test group	0.859	0.863	0.952	0.985	0.966
Control group	0.821	0.845	0.914	0.921	0.922

Table 2: Accuracy data of experimental results.

Accuracy	Test 1 (%)	Test 2 (%)	Test 3 (%)	Test 4 (%)	Test 5 (%)
Test group	86.9	88.9	95.8	84.0	93.8
Control group	85.8	85.5	89.9	83.9	91.6

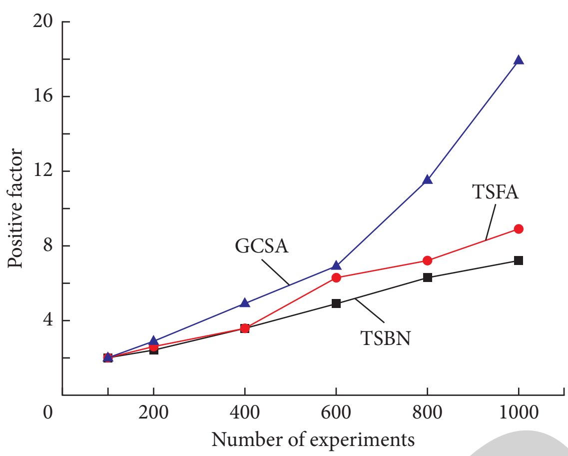

Figure 5: Experimental result.

signal processing of football players' headshots based on a local search algorithm can be applied to detect and process the real-time head ball attitude signal of professional football players and can complete the monitoring and data analysis of the athletes' posture and strength with high accuracy.

5. Conclusion

In this paper, the local search algorithm based on multiple related factors is used to analyze the header strength of football players. Three characteristic parameters related to header shooting and training system are selected, and a dynamic header shooting tracking training system for football players based on a local search algorithm is proposed. Through the research on the improvement of header shooting posture, header technology, and body consumption of football players, this paper expounds on the hierarchical structure and index relationship of the real-time header posture training system of football players. The local search algorithm and ant colony algorithm are used to analyze the characteristics of the screening results. Compared with the existing training search algorithm system, the training system can make full use of each player's football training and game characteristic information, realize the close combination of players, effectively analyze the factors affecting the player's technical level, and improve the player's football training level. However, this paper only focuses on the construction of a dynamic tracking training system for header shooting of football players, without considering the potential impact and overall cooperation of foreign header shooting. Therefore, the comprehensive analysis and evaluation of the index system need to be further studied.

Data Availability

The data used to support the findings of this study are included within the article.

Conflicts of Interest

The authors declare that they have no conflicts of interest.

References

[1] D. L. Yount, M. Jesunathadas, T. E. Plaisted et al., "Performance of a novel football helmet technology on head impact kinematics," *Sports Engineering*, vol. 24, no. 1, pp. 1–11, 2021.

[2] A. Hernandez-Martin, J. Garcia-Unanue, A. Martínez-Rodríguez et al., "The effects of football practice on nutritional status and body composition in children: a systematic review and meta-analysis," *Nutrients*, vol. 13, no. 8, p. 2562, 2021.

[3] M. Jamil, H. Liu, and A. Phatak, "An investigation identifying which key performance indicators influence the chances of promotion to the elite leagues in professional European football," *International Journal of Performance Analysis in Sport*, vol. 21, no. 4, pp. 641–650, 2021.

[4] L. Pirker, A. Gradišek, and B. Višić, "Nanoparticle exposure due to pyrotechnics during a football match," *Atmospheric Environment*, vol. 233, Article ID 117567, 2020.

[5] R. K. Le, M. N. Anderson, R. S. Johnson, L. B. Lempke, J. D. Schmidt, and R. C. Lynall, "On-field characteristics and head impact magnitude in youth tackle football," *Pediatric Neurology*, vol. 121, no. 5, pp. 33–39, 2021.

[6] J. A. Schneider, "Multiple pathologic pathways to dementia in football players with cte," *JAMA Neurology*, vol. 76, no. 11, p. 1283, 2019.

[7] J. L. Makovicka, A. Chhabra, K. A. Patel, S. V. Tummala, and D. E. Hartigan, "A decade of hip injuries in national collegiate athletic association football players: an epidemiologic study using national collegiate athletic association surveillance data," *Journal of Athletic Training*, vol. 54, no. 5, 2019.

[8] S. Lee, J. J. Shin, H. K. Kang et al., "Interfacial instability-driven morphological transition of prolate block copolymer particles: striped football, larva to sphere," *Macromolecules*, vol. 53, no. 16, 2020.

[9] H. Wang, L. Liang, P. Cai, J. Zhao, L. Guo, and H. Ma, "Associations of cardiovascular disease morbidity and mortality in the populations watching major football tournaments:

Hindawi
Journal of Healthcare Engineering
Volume 2022, Article ID 9174441, 9 pages
https://doi.org/10.1155/2022/9174441

Research Article

Effect of Ergonomics-Based Piano Teaching on Teachers' Physical and Mental Health and the Improvement of Sense of Happiness

Jian Pi

School of Preschool Education of Changsha Normal University, Changsha 410100, China

Correspondence should be addressed to Jian Pi; pijian188@outlook.com

Received 28 December 2021; Accepted 14 February 2022; Published 12 March 2022

Academic Editor: Enas Abdulhay

Background. As a special occupation of human beings, teachers have an important responsibility for society and students. As preachers, all their actions will affect the students. Teachers can be said to be the indicator of students' happy life. According to a survey by educational institutions, more than 90% of teachers believe that work pressure is increasing. 64.2% of teachers have experienced job burnout, and the status quo of teachers' professional well-being is worrying. So we must pay attention to teachers' happiness research. However, based on ergonomics, piano education is a kind of piano education to relieve fatigue and an important way to improve teachers' happiness. *Objective*. Using the self-designed questionnaire related to teachers' professional happiness, we investigated piano teachers in universities to understand the status quo of piano teachers' professional happiness, reduce the fatigue of piano teaching, explore the relationship between work fatigue and college piano teachers' professional happiness. *Methods*. This study combines qualitative and quantitative survey methods to make a qualitative analysis of the collected literature and survey and, at the same time, to make a quantitative survey of the collected data so as to get more scientific and accurate survey results. *Results*. According to the above analysis, this paper puts forward effective suggestions in order to reduce the fatigue of piano teaching and ultimately greatly improve the enthusiasm and efficiency of piano teaching, improve the professional happiness of piano teachers, and promote the effective progress of education. *Conclusions*. Through this study, the overall situation of piano teachers' professional happiness in H University is general and the evaluation of piano teachers' professional happiness in H University is mostly at the ordinary level. However, more than half of the teachers do not feel happy and excited at work, and some of them are tired and bored.

1. Introduction

Occupation refers to the exertion of individual personality and refers to the realization of human activities in life and sustainable life. The so-called professional happiness means that when human experimenters engage in specific professional activities, they have a sense of psychological satisfaction and joy, which is necessary for life and work. Their psychological activities not only show psychological satisfaction but also reflect their personal ability and give full play to their ability to get a higher sense of experience. At the same time, it is a kind of continuous happy life experience. From the perspective of subjective well-being, individuals are satisfied with the present working life and working state. From the perspective of satisfaction, it is a subjective experience of the working state.

1.1. Teachers' Professional Happiness. So far, there is no clear concept of teachers' professional happiness. For teachers, their professional happiness mainly comes from students' evaluation, satisfaction, and achievement in the teaching process, and recognition from colleagues and leaders in the school. Teachers also have their own career plans and goals. If they achieve them, it is also a source of their career happiness [1]. In fact, teachers' career happiness is closely related to students. Teachers, in the process of promoting the development of students, on the one hand, will make their own ability to develop, on the other hand, will also promote the development of students.

So far, there is no clear concept of teachers' professional happiness. For teachers, their professional happiness mainly comes from students' evaluation, satisfaction, and achievement in the process of education, as well as the understanding of school colleagues and leaders [2]. Every teacher has his own career plan and goal. If achieved, it is also a source of professional happiness. In fact, teachers' professional happiness is closely related to students. In the process of promoting the growth of students, on the one hand, teachers improve their ability. On the other hand, they also promote the development of students.

In general, it is a kind of spiritual happiness and satisfaction. It used to be thought that teachers' happiness is teachers' state. In other words, teachers have achieved certain results in life and work, so they often narrow the gap between their goals and understanding. But Durand et al. believe that when he feels happy as a teacher, his contribution is precious [3]. This is a model that benefits both sides. Mastering this sense of happiness is helpful for teachers and students to promote each other. As for the definition of teachers' professional happiness, Appannah and Biggs pointed out that this is their inner satisfaction in their work and life, and they have been realizing their ideals and goals [4], and, in this process, continue to play the greatest enthusiasm, to improve ability, and professional level of themselves [4]. They have been recognized and evaluated by all sides and received more joy and thanks. In this paper, this study adopts the definition of Mr. Wang.

1.2. Theoretical Basis of Teachers' Professional Well-Being. Subjective well-being is often defined in the field of western psychology. The focus of this definition is mainly related to the interaction between the internal environment and the external environment. The purpose is to investigate the influence of human personality factors on the social environment and the relationship between subjective well-being and some things in objective reality [5]. How people treat all kinds of personalities, reactions to things, and attitudes in all kinds of environments will affect their subjective well-being. This is the key research content in the field of western psychology. Through the study of subjective well-being, we can know the main source of happiness by studying people's various experiences of happiness. From the existing research results in the field of psychology at home and abroad, many different theories in the field of subjective well-being have been developed [6]. Based on these, many theoretical branches have been expanded. These theories discuss and analyze subjective well-being from different angles and draw some corresponding conclusions. It lays a specific foundation for the subjective well-being theory of University piano teachers, provides a lot of useful theoretical basis and information, and points out the direction for the follow-up research.

1.2.1. The Impact of Career Goals on Well-Being. As we all know, people's subjective well-being is closely related to a variety of people's personality, quality, environment, emotional state, and career goals. Therefore, the supporters of goal theory believe that personal career goals will have a great impact on career happiness, but also related to the personal environment, development direction, future, feelings, and other factors [7]. When each career goal is achieved, these factors are closely related. Then, in order to obtain personal subjective happiness, we must look forward. On the contrary, if an individual fails to achieve his or her goals, it will lead to a more negative emotional experience. Because different goals have different effects, the reasons for subjective well-being vary from person to person.

1.2.2. Theoretical Basis of Pedagogy. Life education theory is a good theoretical method. Its supporters believe that education is to cultivate people who can enjoy happiness, obtain happiness, understand happiness, and inherit happiness. Therefore, for teachers, students usually need to feel the happiness of learning. Happy student learning and happy teacher education are important channels and information sources for teachers to obtain professional happiness [8]. In a sense, teachers' happiness is the premise and foundation. Of course, different teachers have different levels of happiness because of their different morality and wisdom. Therefore, to make every teacher have a professional sense of happiness, we must constantly train and educate teachers to form a good moral character and realize the cultivation of wisdom [9]. Of course, all of these need to constantly pay attention to and improve the happiness level and professional level of teachers so that piano teachers can harvest the happiness of being a teacher.

Life education theory is used to criticize the neglect of life in modern education. Therefore, it is gradually formed and based on this continuous development. The theory of life education pays special attention to respecting life and pursuing life happiness. Life theory has the function of foresight. It may become a procedural theory, guiding teachers and students to pursue happiness has good traction [10]. The goal of this theory is to let teachers and students understand that the pursuit of happiness education is the common ideal and topic of teachers and students. At the same time, it also tells us that the pursuit of happiness, whether teachers or students, is the result of human nature. However, the premise of realizing teachers' professional happiness is the process of life education. Because people's life is the most important, so all this is based on cherishing life and promoting the good growth of personality. Otherwise, it is difficult for teachers and students to get happiness [11]. And it does not make sense. Therefore, for University piano teachers who want to achieve professional happiness, our teachers must adhere to the pursuit of happiness, and the pursuit process is based on the concern for life.

1.3. Overview of Ergonomics. Ergonomics includes human physiology, anthropometry, physiological anatomy, biomechanics, medicine, psychology, environmental science, management science, humanities, engineering science, etc., not only in the industrial sector but also in the research of work space, posture, seat, pedal work, operation method, workload, safety, working environment, work schedule, information operator, etc. In addition, it can also provide the design of management mode, the size parameters of "human" in industrial design, the reasonable scientific basis of "object," and the design guide of "environmental factors" [12]. The main research content can be summarized as the research of humans, including the physiological and psychological characteristics of humans, through the research of humans to solve the relationship between human and machine adaptation problem, to make workers healthy, comfortable, safe, and efficient in operation. Information communication design of the man-machine system, information exchange between man and machine, and reasonable consideration of environment are very important, which is very important in industrial design [13]. Therefore, in the design of the man-machine system, in order to meet the needs of man-machine, the functions of man and machine should be allocated reasonably. Workplace design includes the improvement of the workplace environment and the overall design of the workplace. Appropriate jobs can not only alleviate people's fatigue but also greatly improve work efficiency. In order to ensure the security and reliability of the system, the system security design not only greatly reduces the error rate but also meets the needs of society [14]. The overall efficiency of the system is designed by improving the operation method, optimizing the production or service process, and comprehensively improving the overall efficiency of the man-machine system. The main research methods are observation and investigation (including systematic observation and analysis, investigation, measurement, and recording), experimental method, graphic model method, and simulation method.

1.4. Research on Work Fatigue. Work fatigue is a physiological phenomenon that can be recovered through proper rest and adjustment. Due to the work itself, people's sports ability is temporarily reduced. A thorough exercise is a special form of burnout. That is to say, when you are tired, keep exercising until you cannot maintain the normal operation of your body [15]. The causes of work fatigue vary with the degree and place of occurrence. Generally speaking, the symptoms are weakness, hand tremor, waist pain, lower limb pain, yawning, carelessness, loss of memory, lack of thinking agility, etc. Bakker analyzed the executive control ability of piano staff before and after exercise fatigue and compared it with college students who did not receive professional training [16]. The results show that the executive control function of piano instructors and nonprofessional piano education and training students has been improved after work fatigue, and professionals show better executive control function. Yu Shuang's animal experiments show that job burnout may lead to poor learning ability and memory. In order to explore the mechanism of the brain regulating job burnout, Petrou et al. studied the brain function activities of seven healthy male college students before and after a thorough exercise of power bicycle and observed the active exercise in the brain field in the random running stage [17]. Through the use of whole-brain functional magnetic resonance imaging (fMRI) technology, it was found that there was no significant difference in the active parts of the brain before and after work fatigue in the execution stage of random movement, but the number of lines and thalamus in the active nucleus of the brain decreased, and gradually weakened. Tims's research is aimed at 800 m piano teachers [18]. Compared with quiet time, the connections between the primary motor area and cerebellum, somatosensory motor area and cerebellum, hippocampus/parahippocampal gyrus, and cerebellum became weaker after increasing exercise fatigue. At rest, the brain of the subjects formed a stable network system centered on the cerebellum, and the connection function decreased due to burnout and boredom. In short, there are differences in the effects of physical fatigue caused by piano teaching on psychological cognition, which may be related to exercise program, observation place, and detection method.

2. Methods

2.1. Participants. Based on the principle of research convenience, the piano teachers in H County colleges and universities are selected as the investigation object.

2.2. Process. In this study, 190 questionnaires were issued and 190 were recovered by random sampling. The recovery rate is 100%. Among them, 180 effective questionnaires were used, and the effective rate was 94.7%.

2.3. Research Design. Master the basic information of teachers such as gender, position, school type, school year, region, and income. There are 10 questions in this questionnaire, and there are several alternative answers after each question. Choose the answer that is consistent with the actual situation and the answer consistent with the situation of yourself. This paper uses the questionnaire of Andrews and wig from foreign countries to measure the overall occupational happiness of teachers [19]. The questionnaire has been evaluated highly internationally, and its reliability and appropriateness reach about 0.7. In this paper, the use of this intuitive graphic option avoids text deviation and improves the accuracy of the survey.

In order to promote the correctness of the investigation, this questionnaire specifically raises 30 specific questions and provides some answers to certain factors so as to better investigate the factors affecting the career happiness of university music teachers [20]. That is, it is divided into complete consistency, more consistent, unclear, no complete consistency, and complete inconsistency. The questioner uses the interview method to ask the teacher's occupational happiness question. In order to supplement the investigation of the influencing factors of the teacher's occupational happiness, let the teacher talk about his own ideas and suggestions so as to obtain a more accurate analysis.

2.4. Data Analysis. In this survey, the collected question list will be counted and processed scientifically through Excel and SPSS11.0 and analyzed and discussed by the analysis and processing of the collected data. Finally, based on ergonomics, the paper explores the relationship between alleviating the burnout of piano guidance and the happiness of teachers and makes a deep analysis.

3. Results

3.1. Analysis of Teachers' Subjective Occupational Happiness. Table 1 shows the statistical results of teachers' subjective occupational well-being towards their current work attitude. On the surface, 4.6% of teachers feel very happy. 34.6% of the teachers were happy, accounting for 39.2% of the total. 13.1% of the teachers were not very happy; 7.3% were unhappy; these two accounted for 20.4% of the total; the remaining 40.4% felt very ordinary.

The image description of teachers' subjective professional well-being survey is shown in Figure 1.

3.2. Subjective Factor Analysis. Table 2 shows the statistical results of teachers' response to whether they are satisfied in the workplace. 52.7% of the teachers are dissatisfied and basically dissatisfied in the workplace. In the process of work, 47.3% of teachers are always happy.

As shown in Table 3, the qualifications of music education managers based on ergonomics are not unified. Only three of them are high, and the moderate talents are the main ones, which has a certain impact on the popularization of music culture.

3.3. Objective Factor Analysis. In Table 4, "1" refers to teachers under 30 years old, "2" refers to teachers over 45 years old, and "3" refers to teachers over 46 years old. According to the table data, teachers under the age of 30 have the lowest professional well-being, with an average score of 2.286, while teachers over the age of 46 have an average score of 4.571. Second, the occupational well-being of 45-year-old teachers is also very high, with an average of 3.774 years old, but slightly lower than that of teachers over 46 years old.

The image description of the age difference of teachers' professional well-being is shown in Figure 2.

The average score and standard deviation of 180 effective question tables are investigated and analyzed, and a preliminary understanding of the status and characteristics of teachers' working fatigue is obtained. The specific results are shown in Table 5. When answering the questionnaire, use 5 grades of the scoring system. In this system, 1 is absolutely not, 2 is less than once a month, 3 is at least once a month, and 4 is at least once a week at least once a day. From Table 5, we can see that the overall situation of teachers' burnout is more than once a month, which shows that the teachers' burnout is in the middle and high level.

It can be seen from Table 6 that there is an obvious relationship between job burnout, job happiness, and turnover intention. In other words, there is a significant negative relationship between job burnout and job happiness and a significant positive correlation between job burnout and turnover intention. There is a significant negative relationship between job happiness and turnover intention.

Table 1: Questionnaire of teachers' subjective occupational happiness.

Your evaluation of your current job	Frequency	Percentage
Very happy	12	4.60
Relatively happy	90	34.60
General	105	40.40
Less happy	34	13.10
Very unhappy	19	7.30
Total	260	100.00

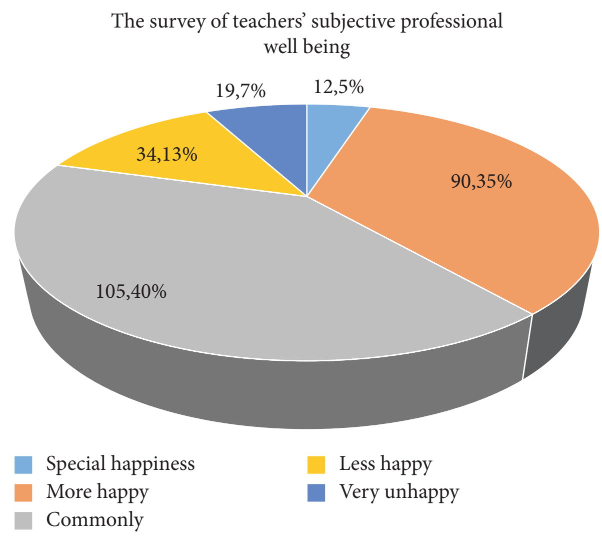

Figure 1: A survey of teachers' subjective professional well-being.

Table 2: Statistics of teachers' subjective feelings about work.

At work, you feel happy	Frequency	Percentage
Totally suitable	11	4.20
More in line with	112	43.10
Doesn't match	106	40.80
Totally inconsistent	31	11.90
Total	260	100.00

Table 3: Analysis on the qualification of piano teaching staff from the perspective of ergonomics.

Category	Statistics	Number of people
Age structure	50–59 years old	14
	40–49 years old	7
	30–39 years old	18
	Under 30	15
Title structure	Ortho height	3
	Subtropical high	18
	Lecturer	17
	Teaching assistant	14
	Teaching assistants	3
Academic structure	Postgraduate	23
	Undergraduate	24
	Specialist	9

Table 4: Age differences of teachers' professional well-being.

	N	Average	Standard deviation	95% confidence interval of average value		Minimum value	Maximum value
				Lower limit	Upper limit		
1	86	2.286	0.673	2.076	2.495	1.0	3.0
2	108	3.774	0.576	3.615	3.932	3.0	5.0
3	14	4.571	0.534	4.077	5.066	4.0	5.0
Total	208	3.216	1.611	3.017	3.414	1.0	5.0

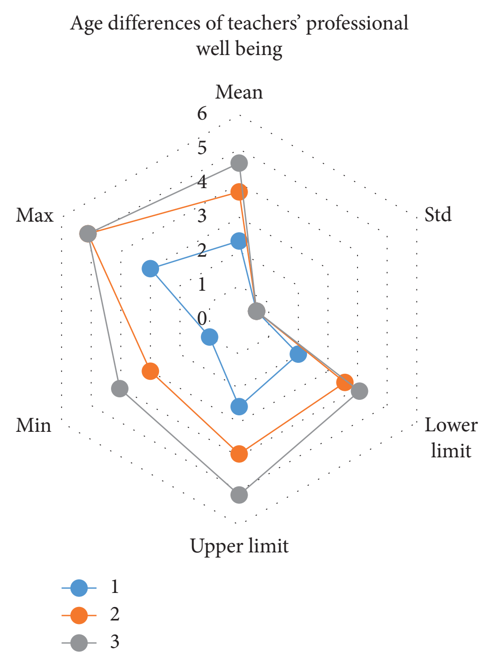

Figure 2: Age differences of teachers' professional well-being.

Table 5: Status quo of piano teaching fatigue based on ergonomics.

	Standard deviation (SD)	Average (M)	Number of items (n)	Average score of each question (m)
Physical work fatigue	3.463	20.22	6	3.370
Psychological work fatigue	3.585	19.34	6	3.224
Emotional work fatigue	2.932	18.57	6	3.092
General questionnaire	5.004	58.01	18	3.223

Table 6: Analysis of the relationship between piano teaching fatigue and teachers' happiness.

	Physical work fatigue	Psychological work fatigue	Emotional work fatigue	Total score	Turnover intention
Work value	−0.109	−0.213	−0.202	−0.167	−0.297
Welfare	−0.157	−0.243	−0.217	−0.190	−0.352
Prospects	−0.156	−0.17	−0.214	−0.186	−0.217
Environmental control	−0.309	−0.215	−0.296	−0.221	−0.186
Self-acceptance	−0.068	−0.024	−0.232	−0.177	−0.277
Interpersonal relationship	−0.245	−0.212	−0.317	−0.243	−0.408
Autonomy	−0.054	−0.258	−0.061	−0.167	−0.238
Total score for job well-being	−0.321	−0.225	−0.212	−0.245	−0.099
Turnover intention	0.277	0.138	0.355	0.237	

Table 6 shows the relationship between job burnout and job happiness. Seven aspects of job happiness (job value, welfare, development prospects, environmental control, self-acceptance, interpersonal relationship, and self-discipline), teachers' scores and the total scores of job happiness and job burnout (physical job burnout, mental job burnout, and emotional job burnout) [21], excluding self-discipline and physical job burnout, teachers' scores and the total scores of job happiness and job burnout (physical, mental, burnout). The relationship between self-discipline and emotional job burnout is not obvious. The rest has a negative correlation, and the correlation coefficient has reached a statistically significant level.

3.4. Frequency Table of Ways to Relieve Teachers' Work Fatigue. After classifying the collected questionnaires, the coping methods to reduce work fatigue are summarized and listed in Table 7 according to the frequency.

Table 7: Frequency of ways to relieve teachers' fatigue.

Solution	Frequency
Do sports	87
Objects (towels, etc.) relieved	35
Drink relief	134
Increase rest time	125
Distract attention from playing games	24
Ease	67
Improve lifestyle (more baths, etc.)	43
School organizes outdoor activities	105
School organization party	98
Schools send out more condolences	76
School lunch increases nutrition	69
Humanization of the school system	129
Others (basking in the sun, etc.)	109

4. Discussion

4.1. Job Fatigue Is Related to Teachers' Well-Being and Turnover Intention. Subjective well-being and teachers' turnover intention are the variables of job burnout. Through this study, we can find that the rationality and applicability of the concept of job burnout are influenced by turnover intention. Through the relevant investigation, we found that there is a correlation between teachers' work fatigue and work happiness. Seven aspects (work value, welfare, development prospects, environmental control, self-acceptance, interpersonal relationship, self-discipline) [22] were used to measure job happiness and job burnout (physical burnout, spiritual burnout, emotional burnout). There was no significant relationship between self-discipline and physical burnout except the total scores of self-discipline and emotional burnout. The other factors are negatively correlated with it, and the correlation coefficient is statistically significant.

There is a relationship between teachers' job fatigue and turnover intention. Teachers' turnover intention is related to all aspects of job burnout (physical job burnout, psychological job burnout, emotional job burnout) [23]. The correlation coefficient is statistically significant. There is a negative correlation between teachers' turnover intention and job happiness, between the seven dimensions of job happiness (work value, welfare, development prospects, environmental control, self-acceptance, interpersonal relationship, self-discipline) and teachers' job happiness, and between teachers' turnover intention (physical work fatigue, psychological work fatigue, emotional work fatigue). The correlation coefficient is statistically significant. These results show that job burnout plays an important role in teachers' job happiness and turnover intention [24].

The results show that job burnout has a negative predictive effect on teachers' work, and a positive predictive effect on teachers' turnover intention. Therefore, if enterprises want to improve teachers' job happiness and reduce teachers' turnover intention, they can consider it from the perspective of reducing teachers' job fatigue.

4.2. The Professional Well-Being of Piano Teachers Has Significant Differences. The happiness of female teachers is higher than that of male teachers. One of the reasons is that at this stage of society, the demand for men is much higher than that of women. For example, men's wages are higher than women's, and men's working conditions are generally worse than women's. Another reason is the decision and influence of the concept of ancient Chinese traditional culture [25]. In traditional China, it is generally believed that songs are not performed by boys but by girls. Music teachers must also be women. In this way, male teachers are not recognized by society, resulting in their own cognitive bias for their own identity.

Teachers under 30 have the best professional happiness. This is because young music teachers who have just graduated from universities and other roles have become teachers. They have a strong sense of freshness and pride, and they are very enthusiastic. The work of teachers is also very challenging, so it is easy to meet [26].

The higher the level of education, the lower the happiness of teachers. This is because, although the education background of teachers is low, their position is more correct, but they are most concerned about education, and they are also very competent in education business and satisfied with education. Teachers with higher education levels will have more expectations for work, which makes it difficult to get happiness.

Music teachers with the highest professional title have the strongest professional happiness, the second teacher with the lowest professional title, and the teacher with the middle professional title is between the lowest and the highest. For senior teachers, they are conscientious and responsible for their work, have a strong professional ability, have a higher status and understanding in society, and can win the respect and support of students and parents [27]. Wages and welfare are also guaranteed. The most important thing is to treat life, world outlook, and values correctly. That is to say, they have self-knowledge and have higher happiness. Teachers with primary professional titles, who have just taken office, have enthusiasm, are interested in identity changes, have a fresh sense, and their positioning is very correct, so happiness is very high [28]. Instead, if they are intermediate teachers, they have a rich educational experience, but they are older and have a lower sense of professional happiness due to their lazy education. Therefore, schools and governments should create a platform for teachers to improve their education level, constantly strive to inject positive energy into educational activities, and increase opportunities for teachers to continue research and further research.

The smooth development of educational activities is inseparable from teachers, and the educational activities of schools are closely related to teachers. Teachers' high vocational happiness can improve the quality of education to the greatest extent and enable students to grow up comprehensively [29]. In order to reflect the current situation of music teachers' professional happiness in a certain region, this paper will investigate and study the current situation of music teachers' professional happiness in some regions. A survey was conducted in a certain area by questionnaire. It provides the practical foundation for music teachers to obtain professional happiness.

4.3. Factors Affecting Teachers' Happiness. From the perspective of the whole social system, it is necessary to improve the economic treatment and social status of teachers. Economic treatment and social status are the important conditions and decisive factors to determine teachers' happiness. In essence, the direct reason for the decline of college music teachers' happiness is the widespread prejudice to overload work and society. Because of the particularity of the professional field, music teachers usually carry out school year music courses separately, and sometimes all music courses in the whole school will be implemented. This will bring great problems and pressure to music teachers in universities.

The current education reform originally put students aside but ignored the cultivation of teachers. The teacher's mood was not carefully considered. Music teacher is an awkward social role among teachers. Although university music teachers are engaged in heavy education and management work, their wages are still low. Needless to say, the benefits of welfare are out of proportion to their work intensity. The material basis determines the superstructure. Similarly, the basic prerequisite for teachers to achieve professional happiness is to have a specific material basis. Therefore, it is very necessary for teachers to create necessary material conditions and corresponding social status. Under the background of the market economy, the economic treatment of teachers must determine their professional happiness. Therefore, the most basic thing to really improve the happiness of teachers is to improve the economic and welfare treatment of teachers.

As a national central government, the education department should increase financial support, and the national government should formulate appropriate measures to ensure teachers' wages and gradually increase teachers' wages and social welfare. We should conscientiously implement the national financial expenditure and narrow the wage gap between teachers in different regions. Government departments continue to guarantee teachers' wages, but local autonomous bodies can also increase financial expenditure in order to increase teachers' wages. A powerful country must strengthen education. In order to strengthen education, it is necessary to increase investment in education. The top priority is to effectively improve teachers' wages and social low level. The state and government should narrow the wage gap of teachers in different regions through policy guarantees, and try their best to narrow the wage and subsidy gap of teachers in county-level cities, big cities, and local areas. To really improve the social status of teachers, so that teachers can feel their own value in the actual educational activities, so as to engage in educational activities at ease.

Society should give music teachers a relaxed environment, more understanding and support, less pressure and reprimand, and a reasonable and fair evaluation. Music teachers are not important to ordinary people. In fact, music teachers in universities are quasi-subject teachers. Music teachers are a troublesome social role among teachers, which generally leads to their low sense of self-existence and professional identity. So what do you say about professional happiness? Society should pay more attention to music teachers, treat their profession fairly, and create a good atmosphere of national trust. Let music teachers find their own professional identity in this atmosphere, urge teachers to regard education as their lifelong career pursuit, and let teachers get countless happiness in this professional education work.

Society needs to set correct and reasonable expectations for teaching staff. Students, families, and society should treat their responsibilities correctly, and teachers should not be excessively held responsible. Because education is not omnipotent, the cultivation of students is formed by the joint action of various facts, not only depending on teachers, but also the society should form the correct direction of teacher evaluation. Therefore, students, parents, schools, and society should have reasonable expectations for teachers, not too harsh. As social media, we cannot exaggerate individual phenomena unilaterally or convey negative energy to society. We must report it actively and objectively. Now some media exaggerate individual teachers' improper behavior to exaggerate the evaluation, which has a very bad impact on the society and even distorts the correct evaluation of teachers. Education reform is vigorously carried out throughout the country. Strengthening publicity, delivering positive energy to society, and forming a correct social atmosphere can gradually change people's wrong ideas.

4.4. Suggestions for Relieving Work Fatigue in Piano Teaching. In recent years, enterprises have paid more and more attention to the fatigue of teachers' work, but there is still much room for improvement. Therefore, business operators must take measures to solve these problems, including organizing more outdoor activities, such as going out, dinner, singing, and so on, and establishing effective reward and incentive mechanism. For example, when teachers are praised publicly, part of the bonus is used to comfort them, various bonus systems are set up, and more attention is paid to teachers' life and needs, so that teachers' life trends can be understood in detail. According to the operation of enterprises, within the limited scope of rights, teachers' personal requirements should be properly met, and teachers' interests should be maximized. In the daily work meal, give teachers continuous and reasonable nutrition distribution. Improve the company system, reduce inefficient, repetitive work, and effectively reduce the workload of teachers. The practice of "taking care of teachers" is rooted in the hearts of the people so that teachers can really feel the top-down care and respect, reduce the imbalance of teachers, and improve the happiness of teachers' work. Only when teachers feel the concern and respect of the company, can teachers have the best state in their work and will not bring too much pressure on themselves. This can not only improve teachers' working environment, reduce work fatigue, but also improve enterprise efficiency, increase teachers' sense of happiness, reduce teachers' desire to leave, improve teachers' sense of belonging, improve enterprise culture, and strengthen enterprise unity.

Most of the fatigue of teachers' work is related to their own cognition. Teachers can take various countermeasures to reduce and eliminate the fatigue of work. The general methods used are as follows: a combination of work and rest. Many people believe that when you work, you have to work crazily, and you will indulge in it when you rest and play. In fact, I do not recommend this approach. The best way to live a day is to learn how to combine work and rest. Work should be arranged in a reasonable time and priority, pay attention to rest, not to work in your life to rest. Usually, you can take part in sports activities such as running, swimming, playing ball, walking to ensure the rest time. Whether it is work or play, adults should ensure 7 hours of sleep, preferably not to take up sleep time. The best way to eliminate mental fatigue is to have plenty of sleep. Study work reasonable arrangement. Work and learning are the same, but both need to pay attention to the methods. As long as you have mastered the working methods, you can use less energy to do more, which can improve the efficiency of work and not overwork. Interpersonal communication also needs to be noted that people are social animals, and we can be supported and happy in society. When we have a good interpersonal relationship and work fatigue, chatting with friends and relatives helps to regulate and eliminate mental fatigue. Develop your own interests and hobbies. Whether it is concerned about work or ordinary concern for leisure and entertainment, it needs to be cultivated. It is not possible to be bored with the work of interest. Interest outside of work can also help relieve mental fatigue. When working very tired, you can rest properly, drink water, play games, read books, and distract your attention in order to alleviate the fatigue of work.

5. Conclusion

Through investigation and analysis, this study shows that there is no obvious correlation between teachers' professional happiness and their education background, professional title, school type, and educational experience. Teachers' professional happiness is obviously related to gender, age, teaching subjects and grades, school obligations, income, and other factors. In order to change the current situation, there are two main aspects to promote teachers' professional happiness. First, society should make a reasonable and fair evaluation of teachers; schools should take reasonable and objective measures, standardize the system and culture, and use ergonomics to improve teachers' happiness. The other is to improve teachers' own quality and psychological quality and improve their subjective sense of happiness. Although the posture of playing the piano should not be the focus of piano guidance, it is the basis of healthy piano playing. If the piano teachers can guide the learning of piano with the attitude of ergonomics in the basic piano education, reduce the phenomenon of giving up piano due to work fatigue so that more teachers can participate in music practice, improve the quality of music, and then get a sense of happiness. In future research, I will continue to pay attention to the cutting-edge theory of ergonomics and strive to obtain more experimental data to build a framework for the improvement of teachers' well-being.

Data Availability

The datasets used and/or analyzed during the current study are available from the author on reasonable request.

Conflicts of Interest

The author declares that there are no conflicts of interest.

References

[1] J. Wang, "The relationship between organizational support and professional well-being of special education teachers: An analysis of the chain mediation effect," *Chinese Journal of Clinical Psychology*, vol. 28, no. 6, p. 4, 2020.

[2] E. B. La, "Vulnérabilité en question? (Vulnerability in question?)," *Ethics Med Public Health*, vol. 3, pp. 365–373, 2017.

[3] L. Sun, "Research on the professional well-being of college teachers," *Journal of Baicheng Normal University*, vol. 35, no. 4, p. 5, 2021.

[4] A. Appannah and S. Biggs, "Age-friendly organisations: The role of organisational culture and the participation of older workers," *Journal of Social Work Practice*, vol. 29, no. 1, pp. 37–51, 2015.

[5] V. Lederer, P. Loisel, M. Rivard, and F. Champagne, "Exploring the diversity of conceptualizations of work (dis) ability: A scoping review of published definitions," *Journal of Occupational Rehabilitation*, vol. 24, no. 2, pp. 242–267, 2014.

[6] J. Marcus and B. A. Fritzsche, "One size doesn't fit all: toward a theory on the intersectional salience of ageism at work," *Organizational Psychology Review*, vol. 5, no. 2, pp. 168–188, 2015.

[7] P. Sevak, A. J. Houtenville, D. L. Brucker, J. O'Neill, and Y. Ben-Shalom, "Individual characteristics and the disability employment gap," *Journal of Disability Policy Studies*, vol. 26, no. 2, pp. 80–88, 2015.

[8] V. Sundar, J. O'Neill, A. J. Houtenville et al., "Striving to work and overcoming barriers: Employment strategies and successes of people with disabilities," *Journal of Vocational Rehabilitation*, vol. 48, no. 1, pp. 93–109, 2018.

[9] Y. Guo, "The influence of college teacher's professional identity on professional well-being and the path for improvement," *Xueyuan*, vol. 25, no. 17, p. 2, 2020.

[10] L. Schur, L. Nishii, M. Adya, D. Kruse, S. M. Bruyère, and P. Blanck, "Accommodating employees with and without disabilities," *Human Resource Management*, vol. 53, no. 4, pp. 593–621, 2014.
[11] S. Jiang, "Investigation and research on the professional well-being of female teachers in colleges and universities——Based on the research perspective of psychological capital," *Journal of Jilin Normal University: Humanities and Social Sciences Edition*, vol. 48, no. 6, p. 13, 2020.
[12] Bo. Tang, "Exploration on the way to obtain professional well-being of teachers of public courses in art higher vocational colleges," *Industry and Technology Forum*, vol. 19, no. 21, p. 2, 2020.
[13] S. Sun, J. Guo, and Y. Dong, "The construction of professional ideological and moral literacy of college teachers in the new era," *Caizhi*, vol. 37, no. 1, p. 1, 2020.
[14] C. Niessen, D. Weseler, and P. Kostova, "When and why do individuals craft their jobs? The role of individual motivation and work characteristics for job crafting," *Human Relations*, vol. 69, no. 6, pp. 1287–1313, 2016.
[15] M. Walk and F. Handy, "Job crafting as reaction to organizational change," *The Journal of Applied Behavioral Science*, vol. 54, no. 3, pp. 349–370, 2018.
[16] A. B. Bakker, A. Rodríguez-Muñoz, and A. I. Sanz Vergel, "Modelling job crafting behaviours: Implications for work engagement," *Human Relations*, vol. 69, no. 1, pp. 169–189, 2015.
[17] C. Yan and G. Xie, "Analysis on the construction of professional ethics for young college teachers in the new era," *Fortune Today*, vol. 46, no. 7, pp. 198-199+221, 2020.
[18] M. Tims, A. B. Bakker, and D. Derks, "The impact of job crafting on job demands, job resources, and well-being," *Journal of Occupational Health Psychology*, vol. 18, no. 2, pp. 230–240, 2013.
[19] Y. Li and Y. Zhang, "Why work: A research prospect of the career development management and work value orientation of young teachers in colleges and universities," *Journal of Inner Mongolia University of Finance and Economics (Comprehensive Edition)*, vol. 018, no. 1, pp. 35–38, 2020.
[20] X. Liu, "Looking at the job burnout of college teachers from the perspective of Maslow's hierarchy of needs," *Educational Research*, vol. 3, no. 10, pp. 46–48, 2020.
[21] A. Lazazzara, M. Tims, and D. de Gennaro, "The process of reinventing a job: a meta-synthesis of qualitative job crafting research," *Journal of Vocational Behavior*, vol. 59, no. 2, pp. 682–693, 2019.
[22] E. Demerouti and M. C. W. Peeters, "Transmission of reduction-oriented crafting among colleagues: A diary study on the moderating role of working conditions," *Journal of Occupational and Organizational Psychology*, vol. 91, no. 2, pp. 209–234, 2018.
[23] B. Wang, B. Xue, and J. Dang, "Investigation and analysis of the status quo of teacher's occupational happiness in private colleges and universities——Taking Q college as an example," *New Silk Road: Early Ten Days*, vol. 33, no. 11, p. 3, 2020.
[24] A. Z. Brzykcy, S. A. Boehm, and D. C. Baldridge, "Fostering sustainable careers across the lifespan: the role of disability, idiosyncratic deals and perceived work ability," *Journal of Vocational Behavior*, vol. 112, pp. 185–198, 2019.
[25] S. Dong, P. Geyer, T. Hinton, and A. Chin, "Accommodation request strategies among employees with disabilities: Impacts and associated factors," *Rehabilitation Counseling Bulletin*, vol. 63, no. 3, pp. 168–178, 2019.
[26] K. S. Markel and L. A. Barclay, "Professionals with disabilities: crafting a meaningful career," *Academy of Management Proceedings*, vol. 2015, no. 1, Article ID 11938, 2015.
[27] H. Gao, "The reasons for the lack of professional well-being of college teachers and the construction strategy of the mechanism of interest appeal," *Western Quality Education*, vol. 6, no. 8, p. 2, 2020.
[28] G. Hu, "The moderating and mediating effects of college teachers' psychological capital on work stress and occupational well-being," *Chinese Journal of Health Psychology*, vol. 42, no. 3, p. 5, 2020.
[29] F. Yao, "Strategies for improving the professional well-being of young teachers in colleges and universities: Based on the perspective of ERG needs theory," *Modern Communication*, vol. 37, no. 3, p. 3, 2020.

Hindawi
Journal of Healthcare Engineering
Volume 2022, Article ID 9087776, 9 pages
https://doi.org/10.1155/2022/9087776

Research Article

Empowerment of Primary Healthcare Providers on the Prevention and Management of Dental or Oral Health Issues among Postchemotherapy Patients in Pandemic

Premalatha Paulsamym,[1] Krishnaraju Venkatesan ,[2] Jamal Moideen Muthu Mohamed,[3] ShadiaHamoud Alshahrani,[1] Ramasubbamma Ramaiah,[1] Vigneshwaran Easwaran,[4] Mohamed El-Sherbiny,[5] Mohamed Dosoky,[6] Noohu Abdulla Khan,[2] Kousalya Prabahar,[7] Geetha Kandasamy,[2] and Kibebe Sahile [8]

[1]*College of Nursing, Mahalah Branch for Girls King Khalid University, Abha, Asir, Saudi Arabia*
[2]*Department of Pharmacology, College of Pharmacy, King Khalid University, Abha, Asir, Saudi Arabia*
[3]*College of Pharmacy, Shri Indra Ganesan Institute of Medical Science, Tiruchirappalli 620012, Tamil Nadu, India*
[4]*Department of Clinical Pharmacy, College of Pharmacy, King Khalid University, Abha, Saudi Arabia*
[5]*Department of Basic Medical Sciences, College of Medicine, AlMaarefa University, 71666 Riyadh, Saudi Arabia*
[6]*Department of Neuroscience Technology-College of Applied Sciences, Jubail Imam Abdulraman Bin Faisal University, Al Jubail, Saudi Arabia*
[7]*Department of Pharmacy Practice, Faculty of Pharmacy, University of Tabuk, Tabuk 71491, Saudi Arabia*
[8]*Department of Chemical Engineering, College of Biological and Chemical Engineering, Addis Ababa Science and Technology University, Addis Ababa, Ethiopia*

Correspondence should be addressed to Krishnaraju Venkatesan; kvenkatesan@kku.edu.sa and Kibebe Sahile; kibebe.sahele@aastu.edu.et

Received 4 January 2022; Accepted 8 February 2022; Published 10 March 2022

Academic Editor: Enas Abdulhay

Objectives. The study aim was to evaluate the empowerment of primary healthcare providers on the prevention and management of dental or oral health issues among postchemotherapy (PC) patients, in selected rural regions, India, during a pandemic. *Methods*. Initially, 240 PHPs were recruited by convenient and snow ball sampling with 90.3% response rate. A descriptive, cross-sectional study was adopted using a self-administered questionnaire with 5 sections: demographics, identification of dental/oral health issues, knowledge, attitude, and practice on prevention and management of dental/oral health problems in PC patients. Statistical Packages for Social Sciences (SPSS) version 23.0 was used for statistical analysis. *Results*. The overall knowledge was better among nurses (64.56%), followed by pharmacists (54.5%). 81.65% of PHPs were willing to learn more and expressed the need for collaboration with dentists. In the past 3 months, 18.81% of them had PC patients with dental/oral health issues, but only 3.5% of nurses and 0.8% of pharmacists treated them. The logistic regression model revealed higher scores in mucositis/mucosal pain (OR = 1.41), altered taste sensation (OR = 1.34), sensitive gums (OR = 1.71), and dental caries (OR = 1.32) domains ($p < 0.05$). Those who had readiness to learn (OR = 5.37), nurses and pharmacists, and having less years of experience (OR = 1.31) and higher degree (OR = 1.4) had a positive attitude ($p < 0.05$). *Conclusion*. PHPs had limited empowerment in terms of knowledge and practice but showed a positive attitude toward the prevention and management of dental/oral health issues of PC patients. For better practice, continuing education and collaboration with dental professionals is essential.

1. Introduction

Cancer is the second leading cause of mortality in developed countries, trailing only cardiovascular diseases. It is still a major public health concern. Oncology management encompasses a wide range of treatments addressing the preventive, curative, and rehabilitative aspects of cancer. Chemotherapy is one of the most effective treatment options [1]. Advances in cancer treatment have resulted in the longer survival of these patients. Nonetheless, the side effects of cancer therapies continue to be a major concern, as they may limit the effectiveness of the treatment and have a negative impact on the quality of life both during and after therapy.

The extent of chemotherapeutic agents' oral toxicity appears to be related to the dose and frequency of administration. They can cause direct damage to the soft and hard tissues of the oral structures, and their systemic toxicity can cause indirect damage. These oral complications, whether acute or chronic, can occur during or after cancer treatment. Many drugs target rapidly proliferating cells; however, they also have the same effect on rapidly proliferating normal tissues, such as the oral mucosa, and destroy the mucosal layer's basal cells. Their replacement or turnover is hampered, resulting in mucosal ulceration and decreased salivary function [2–4]. There is an indirect toxic effect that is caused outside the oral cavity such as myelosuppression or the destruction of immune cells. In general, more than 30–35% of cancer patients will experience mucositis, altered taste, xerostomia, sensitive gums, dental caries, speaking difficulties, and jaw pain [5, 6]. These side effects can have an implication on the patients' quality of life and as a whole clinical outcome.

The Global Burden of Disease Study (2017) reported that oral diseases affect 3.5 billion people worldwide. The prevalence of dental caries in patients who undergo chemotherapy was 37.3%. The oral cavity is extremely vulnerable to the direct and indirect toxic effects of chemotherapy due to the high cellular turnover rate, microflora, and oral tissue trauma associated with daily oral functions [7]. The estimated prevalence of oral complications ranges from 31 to 93% [8].

Effective oral health management prior to, during, and after treatment is therefore critical to improving patient well-being [9]. Each health professional engaged in the cancer care continuum ought to be aware of such specific oral health adverse reactions and be able to give the necessary precautions to avoid them. In 2020, an enigmatic virus known as SARS-CoV-2 confronted the medical community and wreaked havoc all over the world. According to the recently published data, COVID-19 patients have been prioritized over other patients, including cancer patients, due to the unforeseen conditions of the pandemic. The COVID-19 pandemic had a wide-ranging impact on healthcare services, beginning with disrupting regular patient flow to treatment centers, stressing and intimidating healthcare resources, and leading to the deployment of additional protective measures and social distancing with increased use of telehealth and virtual medicine. Access to healthcare and clinical services became difficult for cancer patients as well during the COVID-19 pandemic [10].

Due to the above-mentioned unprecedented circumstances, dental therapies have been halted in a lot of countries due to the role of saliva and aerosols in the spread of COVID-19. This has resulted in a disruption in the allocation of dental care to all patients, including postchemotherapeutic patients, for whom it is absolutely vital [11]. More importantly, postchemotherapeutic patients must have oral re-examinations every month for the first three months, then once in three months during the first year, and then every six months for the next three years. In this situation, the role of primary healthcare centers (PHCs) in providing adequate support for postchemotherapeutic oral ailments is critical.

In fact, in developing countries such as India, PHCs represent the first tier in healthcare system, providing a range of essential outpatient services to people living in the rural, suburban, and hard-to-reach areas. During the COVID-19 pandemic, the preparedness of PHCs in providing safe, patient-centered care and meeting the current health needs of the population is crucial. Hence, determining the empowerment of primary healthcare providers (PHPs) in terms of knowledge, attitude, and practice on the prevention and management of dental or oral health issues among postchemotherapy (PC) patients is the need of the hour.

2. Methods

2.1. Research Approach and Design. The research approach is quantitative. A descriptive, cross-sectional study was adopted for determining the empowerment of Primary Healthcare Providers (PHPs) in terms of knowledge, attitude, and practice on the prevention and management of dental or oral health issues among postchemotherapy (PC) patients.

2.2. Population and Setting. PHPs working in the rural regions of Tamil Nadu, India, were the population of the study. Three rural districts were selected and PHPs working in PHCs and subcenters were selected as samples for the study.

2.3. Sample Size and Sampling Process. The nonprobability convenient sampling technique was adopted to obtain samples from the three rural districts of Tamil Nadu, India.

The minimum suggested sample size was computed by Raosoft, an online sample size calculator having the overall population (approx. 681 PHPs) of three districts, a 95% confidence with margin of error as 5%, and the expected response rate of 60%. The calculated sample size was 240. Initially, 3 PHCs of each district were visited by one of the investigators personally to select the samples and the snow ball sampling technique was used to contact the rest of the participants. Registered nurses, pharmacists, and laboratory technicians who were willing to participate in the study were included in the study. PHPs who had basic professional training of less than 2 years were excluded from the study.

2.4. Data Collection Tools/Instruments. The self-administered tool consisted of 4 sections.

2.4.1. Section 1. Section 1 describes the demographic data of the participants.

2.4.2. Section 2. Section 2 describes a checklist for the identification of dental/oral health issues of post-chemotherapeutic patients.

2.4.3. Section 3. Section 3 describes knowledge on the prevention and management of dental/oral health problems of postchemotherapeutic patients. Among the dental and oral health problems, the most common and vital issues, such as mucositis/mucosal pain, dysgeusia/hypogeusia/altered taste sensation, xerostomia/dry mouth/hyposalivation, sensitive gums, and dental caries, were included in the knowledge questionnaire. It included 15 multiple-choice questions and each question had the score of "1" for the correct answer and "0" for the wrong answer.

2.4.4. Section 4. The attitude of the PHC providers toward the prevention and management of dental/oral health problems was assessed in this section. Participants assessed their attitude by themselves on a 5-point scale, with strongly agree – 5 to strongly disagree – 1. The participants' attitude was assessed by the mean scores of the 5 statements.

2.4.5. Section 5. The practice of PHC providers toward the prevention and management of dental/oral health problems of PC patients was evaluated with seven "yes" or "no" questions.

2.5. Reliability and Validity. The content validity of the tool was obtained from five experts in Nursing and one general physician and a Dental Specialist. The reliability of the tool was assessed by a pilot study by Cronbach's Alpha test (internal consistency) and the r value is 0.813, which was found to be highly reliable. The data were collected from the participants by electronic media such as WhatsApp, e-mail, and Instagram from February to April 2021. The PHPs were circulated with a Google Docs questionnaire and reminders were given thrice to complete and return the docs. Out of the 240 PHPs, 218 (90.8%) participants returned the completed tool.

2.6. Ethical Consideration. Official permission from the Medical Directors of the PHCs as well as ethical permission from the Institutional Ethical Committee with IEC/LCN/2021 was obtained. Consent from the participants was collected before starting the study by explaining the aim of the study, their role, confidentiality of the information, and their right to depart from the study at any point of data collection. The participants were given a soft copy of the study material after the data collection period in the form of a power point presentation on the prevention and management of dental/oral health among postchemotherapy patients for enhancing their knowledge on the same.

2.7. Statistical Analysis. The data were processed and analyzed by the SPSS software using descriptive and inferential statistics. Descriptive statistics, χ^2 tests (for categorical variables), and regression analysis were used to compare knowledge, attitude, and practice with demographics by SPSS 23.0 for Mac. $p < 0.05$ was considered to be significant in this study.

3. Results

3.1. Demographic Data of the Study Participants. The collected data from 218 PHPs were tabulated and the socio-demographic features of the study participants were tabulated in Table 1. Out of 240 PHPs, 218 responses were received with a response rate of 90.83%. Most of the participants (63.3%) were females and 23.4% of the participants were aged between 20 and 25 years. About 51.38% were nurses, 32.57% were pharmacists, and 16.05% were lab technicians. Among the PHPs, almost half (48.17%) of them had a diploma degree, and a small minority (6.42%) held postgraduate qualifications. Their work experience was variable, ranging from less than one year to greater than 10 years. More than half (53.67%) of them were getting 50 to 100 patients per day and more than two-thirds (77.99%) do not get any patients with postchemotherapy treatment. Among the PHPs, 18.81% of them had treated PC patients with dental or oral health issues.

3.2. PHPs' Knowledge on Dental- and Oral-Related Health Issues among PC Patients. Among the PHPs, most of them (88.53%) identified cachexia as one the major health issues among postchemotherapy patients followed by dental caries (85.78%). The least identified problem was mastication/jaw pain(26.15%) (Table 2).

The overall level of knowledge on dental or oral health was better among nurses (64.56%), followed by pharmacists (54.5%); lab technicians scored less (30.03%) comparatively. However, pharmacists had better knowledge (65.2% vs 63.0% and 27.7%) on mucositis/mucosal pain among the PHPs (Table 3).

3.3. PHPs' Attitude on Dental- and Oral-Related Health Issues among PC Patients. Figure 1 shows the PHPs' attitude toward the dental/oral healthcare among PC patients. Among these, 178 PHPs expressed positively of their willingness to learn more and also opined that having collaboration or telemedicine facility with dentists will enhance the PHPs' knowledge and skills to manage the dental/oral health of PC patients (151 PHPs). About the negative attitude, 125 PHPs had a negative opinion to handling the PC patients' dental/oral health issues effectively. This may occur due to inadequate knowledge and practice experience while handling PC patients with oral health problems.

Table 1: Demographic data of the PHPs.

Variables	No.	%
Age (years)		
20–25	51	23.4
26–30	40	18.3
31–35	69	31.7
>36	58	26.6
Sex		
Male	80	36.7
Female	138	63.3
Work experience		
Less than 1 year	84	38.5
1–3 years	77	35.3
4–6 years	37	17.0
7–9 years	11	5.1
≥ 10 years	9	4.1
Profession		
Nurses	112	51.4
Pharmacists	71	32.6
Lab technicians (LTs)	35	16.1
Level of education		
Diploma	105	48.2
Bachelor's degree	99	45.4
Master's degree	14	6.4
Approximate number of patients per day		
<10	51	23.4
10–50	117	53.7
51–100	42	19.3
>100	8	3.7
Do you get any patients with postchemotherapy treatment?		
Yes	48	22.0
No	170	78.0
If yes, did any of them attend the PHC with dental or oral health problems in the past 3 months?		
Yes	41	18.8
No	177	81.2

Table 2: Identification of dental- and oral-related health issues among PC patients.

S. no.	Dental/oral problems of PC patients	Yes	%
1	Mucositis/mucosal pain	137	62.84
2	Dysgeusia/hypogeusia/altered taste sensation	116	53.21
3	Xerostomia/dry mouth/hyposalivation	142	65.14
4	Sensitive gums	153	70.18
5	Dental caries	187	85.78
6	Oral candidosis	121	55.51
7	Bacterial sialadenitis	89	40.83
8	Cachexia	193	88.53
9	Trismus/fibrosis	94	43.12
10	Mastication/jaw pain	57	26.15

Table 3: Level of knowledge of PHPs on dental and oral health among postchemotherapy patients.

Knowledge	Nurses (%)	Pharmacists (%)	Lab technicians (%)
Mucositis/mucosal pain	63.0	65.2	27.7
Dysgeusia/hypogeusia/altered taste sensation	63.3	41.8	21.37
Xerostomia/dry mouth/hyposalivation	69.1	61.4	19.1
Sensitive gums	66.4	51.8	38.8
Dental caries	61.0	52.3	43.2
Overall knowledge	64.56	54.5	30.03

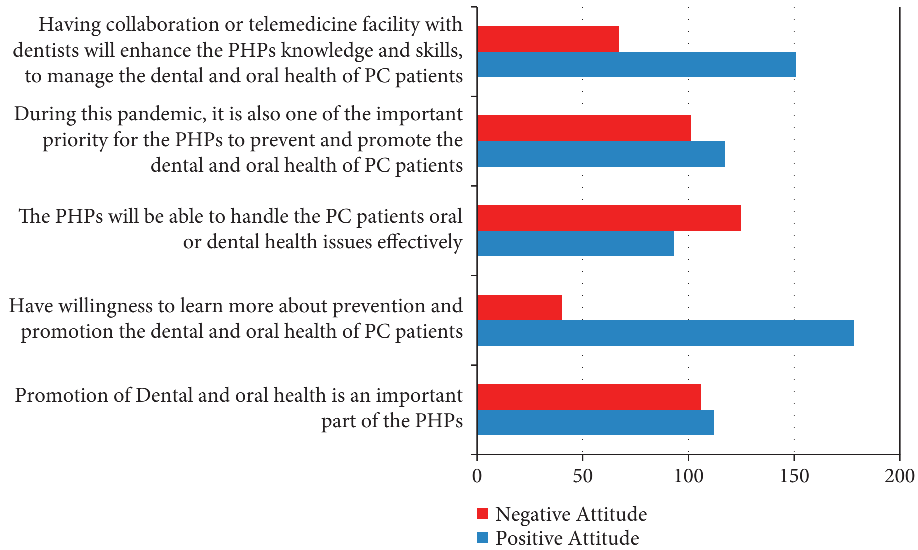

Figure 1: PHPs' attitude toward the dental/oral healthcare among PC patients.

3.4. PHPs' Practice on Prevention and Management of Dental and Oral Health Problems among PC Patients. Determining the practice of PHPs toward the prevention and management of dental/oral health problems of PC patients reveals that though 18.81% of them had PC patients with dental/oral health issues in the past 3 months, 65.1% of the nurses, 71.4% of the pharmacists, and 89.3% of the lab technicians never treated or counselled the PC patients (Table 4). Only 3.5% of the nurses and 0.8% of the pharmacists treated PC patients dental/oral issues often.

3.5. Multivariate Analysis. All variables were used in their continuous form except for profession, readiness to learn, and qualification. Goodness of fit with the Hosmer and Lemeshow test, (HL test) p- value = 0.13.

After controlling the demographic data of the PHPs, the logistic regression model revealed higher scores in the mucositis/mucosal pain (OR = 1.41, 95% CI: 1.13–1.61), altered taste sensation (OR = 1.34, 95% CI: 1.02–1.62), sensitive gums (OR = 1.71, 95% CI: 1.13–1.47), and dental caries (OR = 1.32, 95% CI: 1.27–1.52) domains with $p < 0.05$. Those who had greater readiness to learn more (OR = 5.37, 95% CI: 4.21–7.78) and nurses and pharmacists, i.e., the profession, were associated with a positive attitude toward the prevention and management of dental/oral health problems of PC patients (Table 5). Nurses and pharmacists with less years of experience (OR = 1.31, 95% CI: 1.43–3.11) and those who had higher degrees (OR = 1.4, 95% CI: 1.47–2.27) also had a more positive attitude toward the prevention and management of dental and oral health problems of PC patients than did those with a lower qualification ($p < 0.05$).

4. Discussion

The part of the oral cavity is teeth and gums which allows us to speak, smile, and chew. Cavities (tooth decay), gum (periodontal) disease, and oral cancer are some of the most common diseases affecting our oral health. Oral health is included as one of the 23 leading health indicators in Healthy People 2030. According to the World Health Organization (WHO), oral health is an important component of overall health and quality of life, and improving people's oral health around the world can improve their quality of life [12]. Good lifestyle choices, earlier diagnosis, and improved access to dentists during the pandemic are some of the key challenges in combating dental or oral issues of postchemotherapy, according to the State of Mouth Cancer UK Report 2020/21 [13].

In general, treating malignant diseases affects the mouth both directly and indirectly through effects on immune function or other systemic side effects. Pain, mucositis, salivary gland dysfunction, changes in taste, infections, difficulty in swallowing, fibrosis, soft tissue and/or bone necrosis, exacerbation of dental and periodontal diseases, and recurrent or secondary malignancy are all common oral complications [14]. Cancer survival has improved in recent decades as a result of evolving etiologies and treatment advancements, and the population of cancer survivors continues to grow [15]. This growing number of survivors presents new challenges, particularly in the care of patients with complex medical, oral/dental, and psychosocial needs. Oral complications in this population typically necessitate multidisciplinary collaboration among various professionals and healthcare providers. Primary healthcare professionals, such as nurses, pharmacists, and lab technicians, are "change agents" at the community level, and can thus collaborate to effectively implement oral health promotion strategies, with a key role in early prevention and referral oral health services.

4.1. Knowledge. The current study found that PHPs had a low level of oral health knowledge, as most of them could identify only dental caries as the major issue of PC patients. Other dental or oral issues such as mucositis/mucosal pain,

Table 4: Practice of PHPs toward prevention and management of dental and oral health problems of PC patients.

Statement of practice	Never (%)			Rarely (%)			Sometimes (%)			Often (%)			Always (%)		
	Nurses	Pharmacists	LTs	Nurses	Pharmacists	LTs	Nurses	Pharmacists	LTs	Nurses	Pharmacists	LTs	Nurses	Pharmacists	LTs
Have ever identified or diagnosed the dental or oral health problems of PC patients?	38.4	69.0	88.6	11.6	11.3	5.7	29.5	12.0	4.2	18.8	2.8	0	1.8	0	0
Have ever treated the dental or oral health problems of PC patients?	86.6	94.4	97.1	9.8	11.3	0	3.6	2.8	2.9	0	0	0	0	0	0
Have ever treated or given advise to prevent dry mouth to PC patients?	75.0	88.7	85.7	8.0	8.5	11.4	15.2	2.8	2.9	1.8	0	0	0	0	0
Have ever treated or given advise to prevent the loss of taste to PC patients?	83.0	97.2	94.3	6.3	0	0	8.0	2.8	5.7	2.7	0	0	0	0	0
Have ever treated or given advise to prevent mucositis to PC patients?	63.4	73.2	82.9	29.5	15.5	11.4	7.1	12.7	5.7	0	0	0	0	0	0
Have ever treated or given advise to prevent sensitive gums to PC patients?	36.6	36.7	94.3	47.3	15.5	5.7	10.7	43.7	0	0	2.7	0	0	0	0
Have ever treated or given advise to prevent dental caries to PC patients?	73.2	40.9	82.9	15.2	43.7	11.4	9.8	15.5	5.7	1.8	0	0	0	0	0

Table 5: Factors associated with PHPs' attitudes (positive/negative) toward the prevention and management of dental/oral health problems of PC patients controlling the demographic data by a logistic regression model.

	B.	S.E.	Sig	OR	95% CI for OR Lower	Upper
Mucositis/Mucosal pain	0.21	0.65	0.021	1.41	1.13	1.61
Altered taste sensation	0.31	0.07	0.000	1.34	1.02	1.26
Xerostomia/dry mouth/hyposalivation	0.09	0.04	0.173	1.03	0.91	1.31
Sensitive gums	0.13	0.06	0.023	1.17	1.13	1.47
Dental caries	0.16	0.21	0.05	1.32	1.27	1.51
Profession	0.7	0.31	0.000	1.59	1.09	2.43
Readiness to learn	1.970	0.22	0.000	5.37	4.21	7.78
Qualification	0.643	0.29	0.000	1.81	1.39	2.74

dysgeusia/hypogeusia/altered taste sensation, xerostomia/dry mouth/hyposalivation, jaw pain, etc. were least identified (Table 2). The overall level of knowledge on dental or oral health was better among nurses (64.56%), followed by pharmacists (54.5%); lab technicians scored less (30.03%) comparatively. However, pharmacists had better knowledge (65.2% vs 63.0% and 27.7%) on mucositis/mucosal pain among the PHPs (Table 3). Another study found similar results among primary care providers [16]. Wooten et al. reported that nurses have limited knowledge of oral health in a study of nurse practitioners' knowledge, opinions, and practice behaviors regarding oral disease and its outcomes [17].

Although the WHO recommends embedding oral health advancement with general preventive medicine and providing expert and policy support to nations to achieve this goal [18], our study found that primary healthcare providers receive limited training in this area [19, 20], notably in patients with postchemotherapy issues. This finding is also consistent with primary care healthcare professionals' lack of knowledge of pediatric OHC in a public healthcare setting in Tehran [16].

The WHO emphasized the importance of providing oral healthcare in developing countries as part of the primary healthcare programs [18]. During this COVID-19 pandemic, PHPs may be the only reliable source of oral health preventive care for PC patients, especially given the limited contact with oncology or dental professionals. PHPs can help diagnose oral health issues in their early stages and preclude their systemic effects in immunocompromised PC patients if they are given appropriate training in this field. According to studies, these PHPs have a significant impact on preventive activities and are a potential target for educational interventions [21–23].

4.2. Attitude. About the PHPs' attitude, most of them expressed positively toward their willingness to learn more and expressed the need for collaboration or telemedicine facility to manage the dental and oral health of PC patients. Nearly half of them had a negative opinion on handling PC patients' oral or dental health issues effectively (Figure 1). This may be due to the fact that they might have inadequate knowledge and practice experience of PC patients dental or oral health issues. The above attitude finding could be related to the PHPs' awareness of their lack of field knowledge. Our findings highlight the importance of adequate training and guidance for PHPs, a process that has proven effective to provide oral health promotion and disease prevention activities. Hence, primary healthcare professionals can make a team effort to effectively implement dental and oral health promotion approaches to PC patients.

4.3. Practice. Determining the practice as a part of empowerment of the PHPs toward the prevention and management of dental and oral health problems of PC patients reveals that though 18.81% of them had PC patients with dental or oral health issues in the past 3 months, Only 3.5% of the nurses and 0.8% of the pharmacists treated these patients' dental or oral issues often (Table 4). The results of a systemic review reported some empirical evidence that a dental health awareness campaign for care home nurses could enhance the nurses' oral healthcare knowledge and attitude [24]. If the PHPs' knowledge improves and gains positive attitude, this will enhance their practical skills as well. Because knowledge and attitude are directly interrelated to practice, there was a significant strong correlation between PHPs' knowledge and their attitude and practice [25–27].

4.4. Multivariate Analysis. The multivariate analysis shows that PHPs with higher knowledge scores, particularly in the mucositis/mucosal pain and dental domains, as well as those who were more willing to learn more about oral health had more positive attitudes toward the prevention and management of dental and oral health problems of PC patients (Table 5). Nurses and pharmacists with less years of experience and those who had higher degrees had a more positive attitude toward the prevention and management of dental and oral health problems of PC patients than did those with a lower qualification. Obtaining a higher degree may have improved their training, possibly due to their ability to search for the required information. In contrast to this study, the study by Rabiei S et al. [16] reported that nurses with a lower education (OR = 1.9) had a more positive attitude toward oral healthcare. Our findings call for training and continuing education for primary care providers about the oral health issues of PC patients, especially during this pandemic.

5. Clinical Relevance

5.1. Scientific Rationale for Study. PHPs not only play a role in the promotion of health, but also have a vital role in four levels of preventive care such as primordial, primary, secondary, and tertiary. In this scenario, information on the empowerment of PHPs in the dental/oral care of PC patients is still limited. In pandemic situations, especially in developing countries, the role of PHCs is important. Though their empowerment of knowledge in the dental/oral care of PC patients is a choice and cannot be ignored, this necessity provoked us to do the current study.

5.2. Principal Finding. The evidence for the role of PHPs in the oral care of PC patients is still limited in terms of knowledge, attitude, and practice on dental and oral health issues of PC patients.

5.3. Practical Implications. It is crucial that dental and oral health issues of PC patients be addressed during PHC visits to reduce the impact of these conditions on patients' morbidity, mortality, and quality of life, especially during this pandemic when there are limited points of referral or care. An educational intervention and continuous reinforcement on identification and management of these issues in collaboration with dental specialists, for the PHPs, can significantly reduce patients' agony, related morbidity as well as improve their quality of life.

6. Recommendations

(i) A similar study with larger samples in a wider population can be done

(ii) To improve the knowledge and skills of the PHPs; educational or training sessions with recent updates on research should be done to improve the quality of life of PC patients

7. Conclusion

Our study found that PHPs had limited empowerment with low level of knowledge in dental or oral health issues of PC patients while also displaying a generally positive attitude and a noteworthy readiness to obtain more training in this field. The findings of our study highlight the critical need for appropriate training and encouragement, particularly among PHPs working in PHCs, to promote oral health and provide appropriate conditions/care for PC patients.

Data Availability

The data presented in this study are available on request from the corresponding author.

Ethical Approval

Institution Ethical Committee gave an ethical clearance with IEC/LCN/2021.

Consent

Written informed consent was obtained from the participants of the study to publish this paper.

Conflicts of Interest

The authors declare that there are no conflicts of interest.

Authors' Contributions

All authors have read and agreed to the published version of the manuscript.

Acknowledgments

The authors extend their sincere appreciation to the Deanship of Scientific Research at King Khalid University (Grant number "RGP 2/186/42") for funding this study through the Large Research Group Project. The authors also deeply acknowledge the Researchers Supporting program (TUMA-Project-2021-3), Almaarefa University, Riyadh, Saudi Arabia, for supporting the steps of this work.

References

[1] A. Radha and O. Namrata, "Knowledge and practice on oral care among the patients receiving chemotherapy," *American Journal of Cancer Prevention*, vol. 2, no. 1, pp. 9–13, 2014.

[2] M. P. López-Galindo, J. V. Bagán, Y. Jiménez-Soriano, F. Alpiste, and C. Camps, "Clinical evaluation of dental and periodontal status in a group of oncological patients before chemotherapy," *Med Oral Patol Oral Cir Bucal*, vol. 11, no. 1, pp. E17–E21, 2006.

[3] S. A. Khan and J. R. Wingard, "Infection and mucosal injury in cancer treatment," *JNCI Monographs*, vol. 2001, no. 29, pp. 31–36, 2001.

[4] J. B. Epstein, A. H. F. Tsang, D. Warkentin, and J. A. Ship, "The role of salivary function in modulating chemotherapy-induced oropharyngeal mucositis: a review of the literature," *Oral Surgery, Oral Medicine, Oral Pathology, Oral Radiology & Endodontics*, vol. 94, no. 1, pp. 39–44, 2002.

[5] Scielo, "Revista Facultad de Odontología Universidad de Antioquia," 2019, http://www.scielo.org.co/scielo.php?script=sci_arttext&pid=S0121-246X2019000200178.

[6] U.S. Department of Health and Human Services, "Oral Health in America: A Report of the Surgeon General," *Executive Summary (2000) Rockville*, U.S. Department of Health and Human Services, National Institute of Dental and Craniofacial Research, National Institutes of Health, MD, USA, 2000.

[7] H. M. Wong, "Oral complications and management strategies for patients undergoing cancer therapy," *Science World Journal*, vol. 2014, Article ID 581795, 2014.

[8] B. Chaveli-Lopez, "Oral toxicity produced by chemotherapy: a systematic review," *Journal of Clinical and Experimental Dentistry*, vol. 6, no. 1, pp. e81–90, 2014 Feb 1.

[9] M. T. Brennan, F. K. L. Spijkervet, L. S. Elting, and L. S. Elting, "Systematic reviews and guidelines for oral complications of cancer therapies: current challenges and future opportunities," *Supportive Care in Cancer*, vol. 18, no. 8, pp. 977-978, 2010.

[10] M. Mitra and M. Basu, "A study on challenges to health care delivery faced by cancer patients in India during the COVID-

19 pandemic," *Journal of Primary Care and Community Health*, vol. 11, Article ID 215013272094270, 2020.
[11] A. S. Kochhar, R. Bhasin, G. K. Kochhar, and H. Dadlani, "Provision of continuous dental care for oral oncology patients during and after COVID-19 pandemic," *Oral Oncology*, vol. 106, Article ID 104785, 2020.
[12] World Health Organization (Who), "Oral Health," 2018, http://www.who.int/oral_healt h/en/.
[13] Centers for Disease Control and Prevention, "United States cancer statistics: data visualizations," 2018, https://gis.cdc.gov/Cancer/USCS/DataViz.html.
[14] J. B. Epstein, J. E. Raber-Drulacher, A. Wilkins, M.-G. Chavarria, and H. Myint, "Advances in hematologic stem cell transplant: an update for oral health care providers," *Oral Surgery, Oral Medicine, Oral Pathology, Oral Radiology & Endodontics*, vol. 107, no. 3, pp. 301–312, 2009.
[15] S. S. Baxi, L. C. Pinheiro, S. M. Patil, D. G. Pfister, K. C. Oeffinger, and E. B. Elkin, "Causes of death in long-term survivors of head and neck cancer," *Cancer*, vol. 120, no. 10, pp. 1507–1513, 2014.
[16] S. Rabiei, S. Z. Mohebbi, R. Yazdani, and J. I. Virtanen, "Primary care nurses' awareness of and willingness to perform children's oral health care," *BMC Oral Health*, vol. 14, no. 1, p. 26, 2014 Mar 26.
[17] K. T. Wooten, J. Lee, H. Jared, K. Boggess, and R. S. Wilder, "Nurse practitioner's and certified nurse midwives' knowledge, opinions and practice behaviors regarding periodontal disease and adverse pregnancy outcomes," *Journal of Dental hygiene: JDH*, Spring, vol. 85, no. 2, , pp. 122–131, 2011.
[18] P. E. Petersen, "Challenges to improvement of oral health in the 21st century - the approach of the WHO Global Oral Health Programme," *International Dental Journal*, vol. 54, no. 6 Suppl 1, pp. 329–343, 2004 Dec.
[19] J. W. Curtis Jr, R. S. Garrison Jr, and M. G. Camp, "Dentistry in medical education," *Academic Medicine*, vol. 60, no. 1, pp. 16–20, 1985 Jan.
[20] R. Kuronen, P. Jallinoja, and K. Patja, "Use of and attitudes toward current care guidelines among primary and secondary care nurses in Finland," *Clinical Nursing Research*, vol. 20, no. 3, pp. 310–325, 2011.
[21] E. Ponticelli, M. Clari, S. Frigerio et al., "Dysgeusia and health-related quality of life of cancer patients receiving chemotherapy: a cross-sectional study," *European Journal of Cancer Care*, vol. 26, no. 2, Article ID e12633, 2017.
[22] T. K. Houston, K. L. Delaughter, K. L. DeLaughter et al., "Cluster-randomized trial of a web-assisted tobacco quality improvement intervention of subsequent patient tobacco product use: a National Dental PBRN study," *BMC Oral Health*, vol. 13, no. 1, p. 13, 2013.
[23] C. R. Ford, K. T. Foley, C. S. Ritchie et al., "Creation of an interprofessional clinical experience for healthcare professions trainees in a nursing home setting," *Medical Teacher*, vol. 35, no. 7, pp. 544–548, 2013.
[24] K. H. M. E. de Lugt-Lustig, J. N. O. Vanobbergen, G.-J. van der Putten, L. M. J. De Visschere, J. M. G. A. Schols, and C. de Baat, "Effect of oral healthcare education on knowledge, attitude and skills of care home nurses: a systematic literature review," *Community Dentistry and Oral Epidemiology*, vol. 42, no. 1, pp. 88–96, 2014 Feb.
[25] R. Karbalaeifar, S. Kazempour-Ardebili, P. Amiri, S. Ghannadi, Z. Tahmasebinejad, and A. Amouzegar, "Evaluating the effect of knowledge, attitude and practice on self-management in patients with type 2 diabetes," *Acta Diabetologica*, vol. 53, no. 6, pp. 1015–1023, 2016.
[26] N. B. Kumar, "Assessment of malnutrition and nutritional therapy approaches in cancer patients," in *Nutritional Management of Cancer Treatment Effects*Springer, Berlin, Heidelberg, 2012.
[27] B. García-Chías, E. Figuero, B. Castelo-Fernández, J. L. Cebrián-Carretero, and R. Cerero-Lapiedra, "Prevalence of oral side effects of chemotherapy and its relationship with periodontal risk: a cross sectional study," *Supportive Care in Cancer*, vol. 27, no. 9, pp. 3479–3490, 2019.

Hindawi
Journal of Healthcare Engineering
Volume 2022, Article ID 9834370, 1 page
https://doi.org/10.1155/2022/9834370

Retraction

Retracted: Efficacy of Crizotinib Combined with Chemotherapy in Treating Advanced Non-Small-Cell Lung Cancer and Effect on Patients' Quality of Life and Adverse Reaction Rate

Journal of Healthcare Engineering

Received 10 November 2022; Accepted 10 November 2022; Published 23 November 2022

Journal of Healthcare Engineering has retracted the article titled "Efficacy of Crizotinib Combined with Chemotherapy in Treating Advanced Non-Small-Cell Lung Cancer and Effect on Patients' Quality of Life and Adverse Reaction Rate" [1] due to concerns that the peer review process has been compromised.

Following an investigation conducted by the Hindawi Research Integrity team [2], significant concerns were identified with the peer reviewers assigned to this article; the investigation has concluded that the peer review process was compromised. We therefore can no longer trust the peer review process, and the article is being retracted with the agreement of the Chief Editor.

References

[1] Z. Ma, Y. Wang, Y. Sun, G. Lin, and Z. Zhao, "Efficacy of Crizotinib Combined with Chemotherapy in Treating Advanced Non-Small-Cell Lung Cancer and Effect on Patients' Quality of Life and Adverse Reaction Rate," *Journal of Healthcare Engineering*, vol. 2022, Article ID 7898737, 5 pages, 2022.

[2] L. Ferguson, "Advancing Research Integrity Collaboratively and with Vigour," 2022, https://www.hindawi.com/post/advancingresearch-integrity-collaboratively-and-vigour/.

Hindawi
Journal of Healthcare Engineering
Volume 2022, Article ID 7898737, 5 pages
https://doi.org/10.1155/2022/7898737

Research Article

Efficacy of Crizotinib Combined with Chemotherapy in Treating Advanced Non-Small-Cell Lung Cancer and Effect on Patients' Quality of Life and Adverse Reaction Rate

Zaiqi Ma,[1] Yun Wang,[2] Yonghua Sun,[3] Gaoyang Lin,[1] and Zhenqing Zhao[1]

[1]*Cardiothoracic Surgery, Qingdao Hospital of Traditional Chinese Medicine (Qingdao Hiser Hospital), 4 Renmin Road, Qingdao City, Shandong Province, China*
[2]*Thoracic Surgery, No. 971 Hospital of PLA Navy, 22 Minjiang Road, Shinan District, Qingdao City, Shandong Province, China*
[3]*Pharmacy Department, Qingdao Hospital of Traditional Chinese Medicine (Qingdao Hiser Hospital), 4 Renmin Road, Qingdao City, Shandong Province, China*

Correspondence should be addressed to Zhenqing Zhao; zhao_zhenqing@126.com

Zaiqi Ma and Yun Wang are the equal contributors.

Received 2 December 2021; Revised 24 December 2021; Accepted 10 January 2022; Published 10 March 2022

Academic Editor: Enas Abdulhay

Purpose. To explore the efficacy of crizotinib combined with chemotherapy in treating advanced non-small-cell lung cancer (NSCLC) and its effect on patients' quality of life (QOL) and adverse reaction rate (ARR). *Methods*. 90 advanced NSCLC patients admitted to our hospital (from 01, 2019 to 01, 2020) were chosen as the research objects and randomly split into the control group (CG) and experimental group (EG) by flipping a coin, with 45 cases each. Chemotherapy was performed to CG, and the crizotinib treatment was introduced to EG on this basis, so as to compare their clinical efficacy, ARR and 3-year survival rate, and QOL before and after intervention by the Generic Quality of Life Inventory-74 (GQOLI-74). *Results*. Compared with CG, EG after treatment obtained obviously higher total clinical effective rate ($P < 0.001$), lower total ARR ($P < 0.05$), higher GQOLI-74 scores ($P < 0.001$), and higher 3-year survival rate ($P < 0.05$). *Conclusion*. Combining crizotinib with chemotherapy to advanced NSCLC patients can effectively improve the patients' level of quality of life, prolong the long-term survival rate, and present a better effect than single chemotherapy. Further study is conducive to establishing a better treatment scheme for advanced NSCLC patients.

1. Introduction

Lung cancer is currently the most common primary malignancy of the lung, originating from the bronchial epithelium [1, 2]. In recent years, lung cancer has seen a rapid increase in both prevalence and mortality in industrially developed countries [3]. According to statistics, lung cancer currently accounts for approximately 8.5% of all malignancies, and approximately 1.6 million people died of it around the world in 2012 [4, 5]. The lethality rate of lung cancer is also the highest among clinical malignancies at present, seriously threatening the life safety and reducing the quality of life (QOL) of patients [6, 7]. Currently, the pathogenesis of lung cancer has not been clarified, and most scholars believe that it is mostly related to smoking, stone sponges, ionizing radiation, and so on. Early lung cancer has no specific clinical conditions and is not easily sensed by patients, so usually the disease has progressed to the middle to late stage once diagnosed. According to the differentiation degree, it can be classified into small-cell lung cancer versus non-small-cell lung cancer (NSCLC). NSCLC refers to malignant tumors derived from the mucosal epithelium of organs, which mostly arise in the middle-aged and senior people and show the youth-oriented tendency [8, 9]. The clinical symptoms of advanced NSCLC include chest pain, cough, hemoptysis, and dyspnea, and in severe cases, even metastatic sites and other symptoms occur. At present, the main clinical treatments for NSCLC are radiation therapy, chemotherapy, targeted therapy, and surgical resection, but single chemotherapy has some limitations and can only kill a certain amount of cancer cells, resulting in poor treatment effect, which, combined with its greater general toxicity, is difficult in satisfying the clinical needs [10, 11]. It has been found that the introduction of crizotinib based on chemotherapy can largely alleviate the clinical symptoms of patients and enhance the body's immune function, which has a significant efficacy in the treatment of advanced NSCLC. Therefore, to further explore the efficacy of crizotinib combined with chemotherapy in treating advanced NSCLC and the effect on patients' QOL and ARR, 90 advanced NSCLC patients admitted to our hospital (from 01, 2019 to 01, 2020) were chosen as the research objects, with the results summarized as follows.

2. Materials and Methods

2.1. General Information. 90 advanced NSCLC patients admitted to our hospital (from 01, 2019 to 01, 2020) were chosen as the research objects and randomly split into the control group (CG) and the experimental group (EG) by flipping a coin, with 45 cases each.

2.2. Inclusion Criteria. ① Patients' survival was over 3 months after pathological diagnosis; ② the patients had no history of external injury or surgery within one month; ③ the study was approved by the Hospital Ethics Committee (approval no. 2020HC12LS001), and the patients and their family members understood the study purpose and process and signed the informed consent; ④ the patients had not received crizotinib treatment before; ⑤ the study met the World Medical Association Declaration of Helsinki [12]; ⑥ the patients were diagnosed with advanced NSCLC after pathological and laboratory examinations; and ⑦ the patients had measurable lesions after CT or MRI scan, and their clinical manifestations included hemoptysis, dyspnea, and loss of appetite.

2.3. Exclusion Criteria for the Patients. ① Severe brain, heart, kidney, and other organic diseases; ② allergy to the drugs; ③ other primary malignant tumors; ④ pregnant or lactating women; ⑤ confirmed interstitial fibrosis or interstitial lung disease; ⑥ mental disorders; and ⑦ nervous system metastasis and complicated severely impaired bone marrow haematopoietic function.

2.4. Methods. Patients in CG received chemotherapy. The patients were given 1,000 mg/m^2 of gemcitabine (manufactured: Jiangsu Hansoh Pharmaceutical Group Co., Ltd.; NMPA Approval No. H20030104; specification: 0.2 g) by intravenous infusion for 30 min per week for consecutive three weeks, and then the administration was stopped for a week. Such a course was repeated every four weeks. In addition, carboplatin (manufactured: Yunnan PHYTO Pharmaceutical Co., Ltd.; NMPA Approval No. H10950274; specification: 50 mg) was added on such basis, which was dissolved with 5% glucose (concentration: 10 mg/mL) and added to 250 mL–500 mL of 5% glucose injection for intravenous infusion, and the frequency was once per three to four weeks.

Additionally, patients in EG orally took crizotinib (manufactured: Pfizer Manufacturing Deutschland GmbH; Approval No. H20130076; specification: 200 mg × 60 s), with the dosage of 250 mg each time and twice a day.

The treatment duration of both groups was 60 days.

2.5. Observation Indicators. The clinical efficacy before and after treatment was compared between the two groups. Complete response (CR) referred to all measurable lesions disappeared and the diameter of all pathologic lymph nodes was reduced to less than 10 mm for over four weeks; partial response (PR) referred to ≥30% decrease SLD (the sum of the longest diameters) of all targeted lesions for more than 4 weeks; stable disease (SD) referred to no PR – no PD (progressive disease), and PD referred to ≥20% increase SLD compared with the smallest SLD in the study, or a 5 mm increase of SLD or one or more new lesions.

$$\mathrm{TER} = \mathrm{CR} + \mathrm{PR}, \tag{1}$$

where TER = total effective rate; CR = complete response; and PR = partial response.

Follow-up was conducted on all patients by means of telephone, WeChat, and interview for 7 times (once every three weeks) to record their adverse reaction rate (ARR) in detail. The adverse reactions included neurological abnormalities, gastrointestinal reactions, skin abnormalities, vision abnormalities, and liver function damage.

Patients QOL after the intervention was evaluated by referring to the Generic Quality of Life Inventory-74 (GQOLI-74) Scale [13], covering social function (social support, interpersonal skills, work and study, entertainment, marriage and family), physical function (sleep and vitality, physical discomfort, feeding function, sexual function, mobility and sensation function), psychological function (mental strain, negative emotions, positive emotions, cognitive function, and self-esteem), and material life (housing, social service, living environment, and financial situation). The total score was 100 points, with higher scores indicating better QOL.

The 3-year survival rates of the two groups were calculated by outpatient service and telephone followup.

2.6. Statistical Analysis. In this study, the data processing software was SPSS20.0, the picture drawing software was GraphPad Prism 7 (GraphPad Software, San Diego, USA), the items included were enumeration data and measurement data, the methods used were X^2 test, t-test, and normality test, and differences were considered statistically significant at $P < 0.05$.

3. Results

3.1. General Information. No significant between-group differences were presented in the age, gender, BMI, duration of disease, SAS scores, SDS scores, disease stage, or place of residence of patients ($P > 0.05$), which were comparable, see Table 1.

Table 1: Patients' general information.

	EG ($n = 45$)	CG ($n = 45$)	x^2 or t	P
Age (years old)	65.25 ± 3.32	65.33 ± 3.29	0.115	0.909
Gender			0.047	0.829
Male	28 (62.22)	27 (60.00)		
Female	17 (37.78)	18 (40.00)		
BMI (kg/m^2)	26.27 ± 1.59	25.89 ± 1.63	1.119	0.266
Duration of disease (months)	3.12 ± 1.21	3.13 ± 1.11	0.041	0.968
SAS score (points)	47.33 ± 0.51	47.17 ± 0.48	1.533	0.129
SDS score (points)	52.13 ± 1.61	52.21 ± 1.32	0.258	0.797
Disease staging			0.062	0.803
IIIb	35 (77.78)	34 (75.56)		
IV	10 (22.22)	11 (24.44)		
Place of residence			0.050	0.822
Urban area	31 (68.89)	30 (66.67)		
Rural area	14 (31.11)	15 (33.33)		

3.2. Clinical Efficacy. After treatment, the total clinical effective rate of EG was obviously higher than that of CG ($P < 0.05$), see Table 2.

3.3. ARR. After treatment, the total ARR of EG was obviously lower than that of CG ($P < 0.05$), see Table 3.

3.4. GQOLI-74 Scores. After treatment, the GQOLI-74 scores of EG were significantly higher than those of CG ($P < 0.05$), see Figure 1.

3.5. Long-Term Survival Rate. The study results showed that the median survival time of patients in EG was 21 months, with 41 survived cases and 91.11% of survival rate (41/45), and the median survival time of patients in CG was 18 months, with 27 survived cases and 60.00% of survival rate (27/45). The 3-year survival rate of EG was obviously higher than that of CG ($P < 0.05$), see Figure 2.

4. Discussion

NSCLC has a high mortality rate and an incidence rate accounting for 80% of lung cancer patients, which greatly endangers the life health and reduces the QOL of patients [14]. In addition, most patients tend to be at an advanced stage at the time of diagnosis because early NSCLC tumors do not involve the trachea, bronchial mucosa, surrounding blood vessels, and pleura and have no specific symptoms, thereby delaying the diagnosis to a large extent. At present, the clinical treatment modality for advanced NSCLC is mainly chemotherapy, which aims to inhibit tumor cell proliferation and control tumor growth. However, most advanced NSCLC patients are elderly, a group usually has multiple chronic diseases and poor body resistance, so they may obtain certain therapeutic effects but less than ideal remission rates and survival rates [15]. In chemotherapy, gemcitabine is metabolized to active diphosphate (dFdCDP) and triphosphate (dFdCTP) through the action of intracellular transnucleoside kinase, and dFdCDP and dFdCTP inhibit DNA synthesis through two mechanisms of action to achieve the cytotoxic effect of gemcitabine. Carboplatin, whose mechanism of action is similar to that of cisplatin, is a metal coordinating agent and targets the DNA of proliferating cells, which has a similar role of alkylating agent bifunctional groups and can bind the intracellular base, enable DNA molecular intra- and interchain cross bonds and changes of DNA chemical structure, thus affecting cell replication. Such chemotherapy has lower safety, for it can cause greater damage to both the tumor cells and normal cells, so it is aimed at prolonging the patients' survival time and improving QOL in the clinic [16]. As a clinically common antitumor drug, crizotinib has optimal efficacy, low toxicity, and high safety, which can not only inhibit ROS1, EML4-ALK, and other signaling pathways but also suppress tumor cell growth and prevent tumor formation [17]. In this experiment, EG was treated with crizotinib combined with chemotherapy and obtained a clinical overall response obviously higher than CG ($P < 0.05$), indicating that compared with the single treatment modality, the combined treatment presented a significant clinical treatment effect. Besides, chemotherapy treatment is less safe and causes adverse effects that lead to a serious impact on patients' QOL, while also reducing their treatment compliance, resulting in more negative emotions and adversely affecting the prognosis. Therefore, combining crizotinib with chemotherapy can accelerate the apoptosis of tumor cells, hinder the formation of tumors, inhibit the ALK and ROSI genes, and ensure a higher safety, which is easily accepted by clinical patients. The experiment demonstrated that the GQOLI-74 scores of EG were significantly higher than those of CG

Table 2: Between-group comparison of clinical efficacy (n (%)).

Group	n	CR	PR	SD	PD	Total effective rate
EG	45	22.22% (10/45)	37.78% (17/45)	17.78% (8/45)	22.22% (10/45)	60.00% (27/45)
CG	45	6.67% (3/45)	15.56% (7/45)	31.11% (14/45)	46.67% (21/45)	2.22% (10/45)
x^2						13.264
P						<0.001

Table 3: Between-group comparison of ARR (n(%)).

Group	n	Neurological abnormalities	Gastrointestinal reaction	Skin abnormalities	Vision abnormalities	Liver function damage	Total incidence rate
EG	45	2.22% (1/45)	2.22% (1/45)	0.00% (0/45)	0.00% (0/45)	0.00% (0/45)	4.44% (2/45)
CG	45	6.67% (3/45)	4.44% (2/45)	4.44% (2/45)	2.22% (1/45)	4.44% (2/45)	22.22% (10/45)
x^2							6.154
P							$P < 0.05$

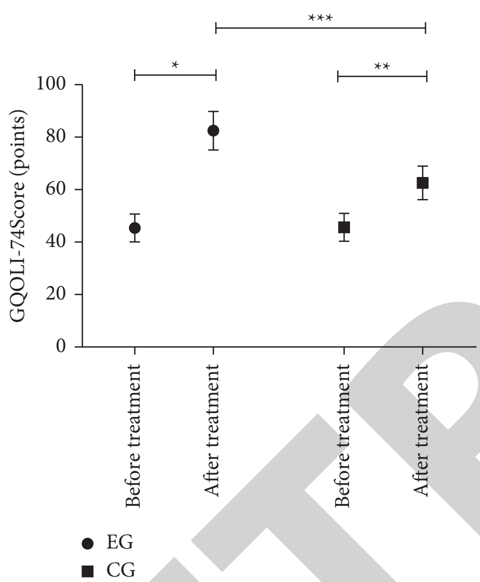

Figure 1: Between-group comparison of GQOLI-74 scores $(\overline{x} \pm s)$. Note: the horizontal axis indicated before and after treatment, and the vertical axis indicated the GQOLI-74 score (points). Before and after treatment, the GQOLI-74 scores of EG were 45.55 ± 5.31 and 82.75 ± 7.35, respectively. Before and after treatment, the GQOLI-74 scores of CG were 45.77 ± 5.32 and 62.77 ± 6.41, respectively. * indicated that the GQOLI-74 scores of patients in EG before and after treatment were significantly different ($t = 27.521$, $P < 0.001$); ** indicated that the GQOLI-74 scores of patients in CG before and after treatment were significantly different ($t = 13.690$, $P < 0.001$); and *** indicated that the GQOLI-74 scores of patients in both groups after treatment were significantly different ($t = 13.743$, $P < 0.001$).

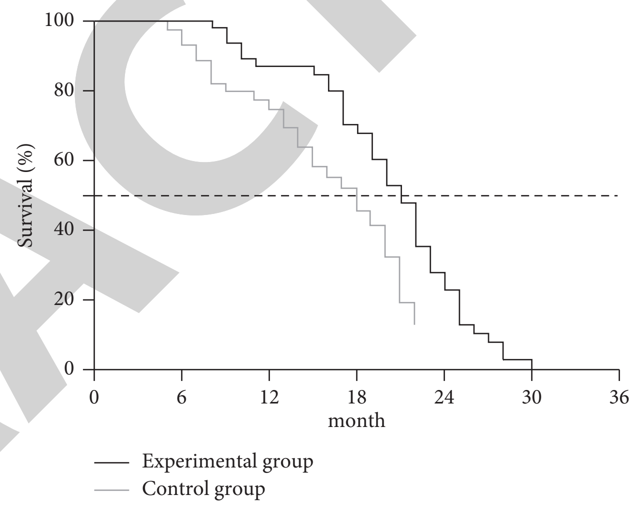

Figure 2: Between-group comparison of patients' long-term survival rates. Note: the horizontal axis indicated the survival time (months), and the vertical axis indicated the survival rate (%). The black line and the light gray line indicated the survival curves of EG and CG, respectively.

($P < 0.05$), indicating that crizotinib combined with chemotherapy could effectively improve QOL for advanced NSCLC patients. In addition, the combined treatment led to a significantly higher median survival time and a 3-year survival rate in EG ($P < 0.05$), implying that it could obviously prolong the survival time and improve the survival rate for patients. Also, the study results presented that the total ARR of EG was obviously lower than that of CG ($P < 0.05$), which was consistent with the founding of Van den Berg [18] et al. In their article, it was pointed out that "the difference in the ARR between the observation group and the control group was significant (8.33% vs 33.33%, $P < 0.05$)," which fully demonstrated that compared with the single treatment, the combined treatment of crizotinib and chemotherapy was safer.

5. Limitation of the Study

This study also has some shortcomings. As a retrospective study, it conducted both qualitative analysis and quantitative analysis, but the results related to treatment effect and ARR of EG were less accurate than in the clinical observational study. In addition, the small number of selected cases may lead to bias in the research results. Also, the cases selected were patients treated in our hospital, so the source of cases lacked diversity, and study design should be completed in the future. Therefore, multicenter, prospective, and large-N studies should be conducted in the future to promote the precision of results.

Hindawi
Journal of Healthcare Engineering
Volume 2022, Article ID 1363690, 10 pages
https://doi.org/10.1155/2022/1363690

Research Article

Research on Chorus Emotion Recognition and Intelligent Medical Application Based on Health Big Data

Yu Li and Yao Chen

School of Music, Sichuan Normal University, Chengdu 610000, China

Correspondence should be addressed to Yu Li; 20120111@sicnu.edu.cn

Received 19 November 2021; Accepted 8 February 2022; Published 9 March 2022

Academic Editor: Enas Abdulhay

In chorus activities, the conductor leads chorus members to recreate music works. If you want to interpret music works perfectly with sound, emotion and emotional expression are particularly important. In this paper, a cloud HBD (health big data) integration system based on ensemble learning is designed to realize the high-efficiency and high-precision integration of HBD. An emotional speech database containing three emotions such as pleasure, calmness, and boredom is established, and the corpus problems such as emotional feature analysis and extraction needed for chorus emotion recognition research are solved. It also studies the classification and decision-making in emotional changes, and a DBN (deep belief network) chorus emotion recognition algorithm based on multiple emotional features is proposed. Feature DBN (Deep Belief Network) Chorus Emotion Recognition Algorithm This paper extracts various robust low-level features according to different features' ability to describe emotions and then feeds them into the DBN network to extract high-level feature descriptors. Then, the classification results of ELM (extreme learning machine) are voted and fused with the idea of ensemble learning, and the effectiveness of the algorithm is proved on three public datasets.

1. Introduction

Chorus is a collective artistic activity, which emphasizes the commonality and unity of performers. When it comes to unity in chorus, it means not only breathing, articulation, articulation, speed, timbre, volume, and movement but also the unity of emotion and emotional expression [1]. Because in rehearsal and performance, in order to make the expressive force of chorus more perfect, we should not only train basic skills but also be good at mobilizing and unifying the emotions and feelings of chorus members, thus forming the resultant force of collective singing. However, while emphasizing the common features, we often ignore an important issue in music art: emotional expression [2]. This makes the supposed beautiful voice and ideological connotation lack verve and artistic appeal.

Information technology and Internet technology have been widely used in the field of intelligent medical care, and big data provides an opportunity to deeply explore the value of data in the field of intelligent medical care and health. Literature [3] looks at the scenarios and advantages of the application of IoT (Internet of Things), cloud computing, and big data in smart medical health. Literature [4] expounds on the technical route of big data in the field of intelligent medical health from the perspective of methodology. Literature [5] puts forward the life cycle model of smart medical big data and discusses the goals and measures of smart medical big data governance. Literature [6] puts forward a universal intelligent medical information management and service system, and points out the key problems and future research directions of universal intelligent medical computing. Literature [7, 8] put forward a classification method with pitch frequency related information as its main feature, analyze and study four emotional states: fear, anger, sadness, and pleasure, and point out in its research report that the maximum, minimum, and median pitch frequencies are prominent features in speech emotion recognition. Literature [9] in its experimental research, the cepstrum coefficient feature is used as the emotional feature to classify three kinds of emotions, namely sadness, anger, and calmness, and the recognition rate is about 64%, while the accuracy rate of voice samples used by the subjective judgment of people is only 70%. On the basis of statistical analysis of acoustic features related to duration, energy, fundamental frequency, and formant construction of continuous pronunciation, it is proposed that the difference in feature vector between emotional speech and calm speech is taken as an emotional feature vector. Literature [10–12] use principal component analysis to classify pleasure, surprise, anger, and sadness, and the recognition rate is close to 80%. By analyzing the big data of health intelligent medical care, we can find out the correlation and trend among the data, which is helpful to improve the health service and disease exploration process, to conduct disease diagnosis and treatment more scientifically, to improve the efficiency and quality of health intelligent medical care services, and to continuously meet diversified health needs [13]. However, the application of big data in the field of intelligent medical health is still in its infancy, and there is still a lack of general big data framework and standards, which leads to the inability of large-scale application across industries and regions, and the inability to really play the role of big data.

Emotion is an important instinct of human beings. Like rational thinking and logical reasoning ability, it plays an important role in people's daily life, work, communication, transaction processing, and decision making. Based on HBD (health big data), this paper is applied to the emotion recognition of choir for the first time and identifies six basic human emotions, such as joy, anger, surprise, sadness, fear, and calm. The chorus emotion recognition algorithm based on multifeature DBN has the advantages of fast convergence speed, high robustness, and strong global searching ability so as to optimize the connection weights of the neural network. It can not only give full play to the generalization ability of the neural network but also improve the convergence speed and learning ability of the neural network.

2. Research Method

2.1. HBD Integration System

2.1.1. System Architecture. In some chorus competitions and performances, we hear neat, unified, and beautiful voices without sincere feelings, and the facial expressions of the chorus members are not rich enough, which makes people feel the fly in the ointment. If you want to truly achieve harmony of voice and emotion, you must do a good job of second creation; then, the singer's ideological height, life experience, and artistic accomplishment play a leading role. An excellent chorus player should have rich cultural connotations and literary and artistic accomplishments besides music knowledge and high singing skills. To build a cloud-based HBD integration system, the framework diagram is shown in Figure 1.

The management layer, big data analysis layer, whole cloud HBD integration layer, and whole cloud HBD resource layer constitute a whole cloud HBD integration system. The four layers cooperate with each other to realize the collection, analysis, storage, and operation of the whole cloud HBD.

The interface for users to regulate and use the integrated system is the management operation layer, and the management, regulation, protection, and use of the whole cloud HBD integrated system are realized through the operation of the administrator on this layer [14].

The integrated HBD is stored in the temporary database and metadata of the cloud-wide HBD resource layer and then stored in the cloud-wide HBD integration layer, which is applied to practical application software to complete the integration of cloud-wide HBD based on integrated learning so as to ensure that the cloud-wide HBD resources have higher value embodiment and manageability when integrated [15, 16].

2.1.2. HBD Prediction Method. As chorus art is a form of collective singing, most chorus training emphasizes the common factors of chorus, such as the unity of strength, sound, and expression, to form the resultant force of collective singing. However, while emphasizing generality, emotional expression in music art is often neglected. This makes the sound that should be beautiful and full of ideological connotation lack charm and artistic appeal.

Health informatization has become the core power of innovation and development in the field of big health. Various information systems provide convenient services for the daily work of health and smart medical institutions and at the same time effectively improve their data collection and storage capabilities. Many dynamic nonlinear features are hidden in one-dimensional health sign data, which makes them nonstationary, complex, and unpredictable time series data.

Time series data refers to a series of data values indexed by time. It is common to sample at continuous and equally spaced moments to form a time series. The biggest feature of time series is uncertainty. However, there is a certain mapping relationship within the data. Using intelligent analysis and prediction methods to solve this specific relationship and dig out the potential laws can effectively grasp the future trend of the system.

From a qualitative point of view, if the system parameters and external conditions do not change, then the sampled sequence is stable. However, this kind of analysis is not reliable, and it needs certain statistical characteristics for auxiliary inspection.

For any m time series data $\{Y_t\}$, if its subset $\{Y_{t_1}, \ldots, Y_{t_n}\}$ and subset $\{Y_{t_{1+m}}, \ldots, Y_{t_{n+m}}\}$ are the same, then $\{Y_t\}$ is strictly stationary. The data with strict stationarity have no changing trend. In fact, this kind of data does not exist. Generally, the so-called stationary time series data are weak stationary time series data.

The expectation, variance, and covariance of weakly stationary time series data $\{Y_t\}$ do not change with time [17]. That is,

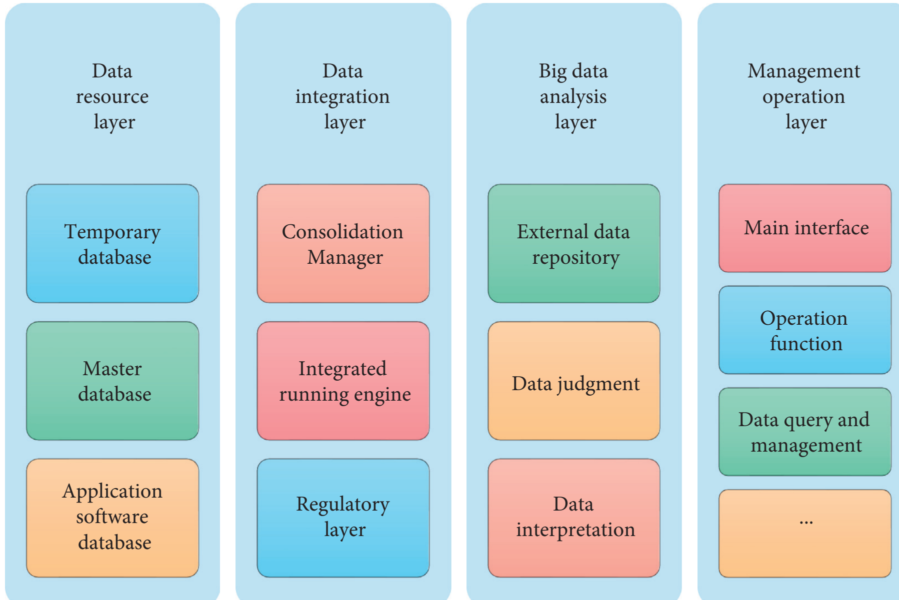

Figure 1: Framework diagram of HBD integration system.

$$E(y_t) = \mu,$$
$$Var(y_t) = \sigma^2, \quad (1)$$
$$Cov(y_t, y_s) = f(t-s).$$

After the time series has passed the stationarity check, the prediction model can be constructed through the relevant fitting model. For nonstationary time series data, it is necessary to process the stationarity and then rebuild the model.

The SARSA (state action reward state action) learning method is a complete state-action transition. When updating the current state action [18], this method does not use the state value function at the next moment but randomly selects actions to update the current state-action space according to a certain probability value and determines the execution action at the next moment when updating, which is the core of the SARSA method [19].The mathematical expression is described as follows:

$$Q(s,a) \leftarrow Q(s,a) + \alpha[r + \gamma Q(s',a') - Q(s+a)]. \quad (2)$$

In the above formula, (s,a) represents the state action at the current moment, (s',a') represents the state action at the next moment, r is the reward obtained after executing the action a, and α is the step size.

In this paper, a deep reinforcement learning method of SARSA based on "in-strategy" is proposed. The method proposed in this chapter is used to calculate the optimal decision. Let the current state be s, $\varepsilon - greedy$ as the selection strategy, the action be a, the current action report be r, and the next state be s'. Then, the current action value function $Q(s,a)$ is described as

$$Q^*(s,a) = E[r + \gamma Q(s',a')|s,a], \quad (3)$$

in which $Q^*(s,a)$ represents the optimal value of the current value function, and a' represents the optimal action selection at the next moment. Combined with CNN (convolutional neural network), if the network parameter is λ, the loss function in the j th iteration is defined as

$$L_j(\lambda_j) = \left(y_j - Q(s,a;\lambda_j)\right)^2, \quad (4)$$

in which $y_j = r + \gamma Q(s',a';\lambda_{j-1})$. By the differential solution of formula (4), the gradient of loss function can be obtained as follows:

$$\nabla L_j(\lambda_j) = \left(r + \gamma Q(s',a';\lambda_{j-1}) - Q(s,a;\lambda_j)\right)\nabla Q(s,a;\lambda_j). \quad (5)$$

The deep reinforcement learning process and its data flow based on the improved SARSA can be obtained from the formula above.

2.1.3. HBD Interpretation. In order to improve the accuracy and stability of the one-dimensional health sign data prediction model based on deep reinforcement learning, the data interpretation process shown in Figure 2 is designed.

Chorus health data analysis and processing system based on big data can provide health management services for chorus members. Through physical measurement, we can learn about chorus members' physical health status, build an interactive basic service and medical ecological platform [20, 21], and realize interactive sharing of key information between the system and the platform so as to provide efficient personalized physical health services for chorus members and promote optimal management of chorus members' self-health [22].

Because of the multifarious types of indicators, the interface display analysis is based on the body mass index. The

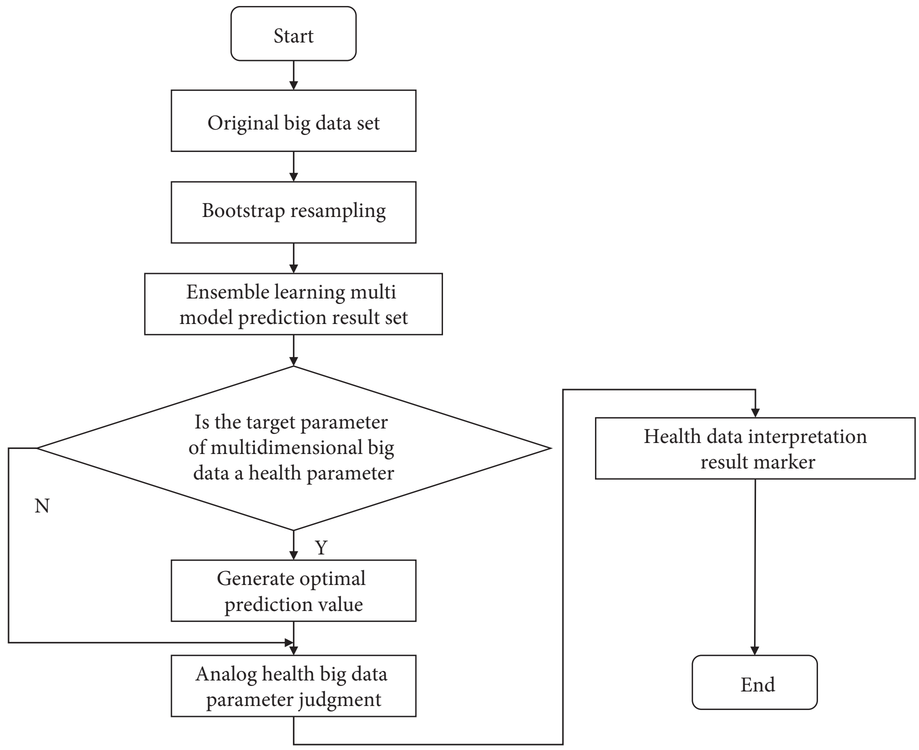

Figure 2: Data interpretation process.

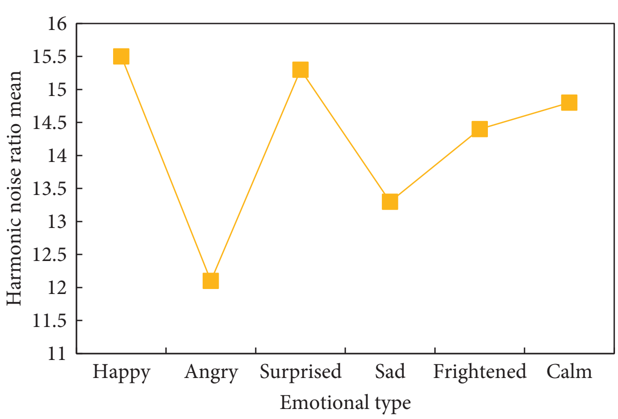

Figure 3: Harmonic noise ratio characteristics of emotion.

function module of weight increase is to increase the physical indicators of chorus members, set the corresponding threshold range reasonably, and dabble in data evaluation standards. In the system, the chorus's physical measurement data, that is, the score calculation, are mainly based on individual indicators and weights, or grades' scoring items and scoring weights, so as to obtain the chorus's total score.

2.2. Emotion Recognition of Chorus Staff. Emotion accompanies every moment of human life. About 38% of the information transmitted during human communication is carried by emotions. When people have a natural oral conversation, they not only convey the voice but also convey the speaker's emotional state, attitude, and intention.

The application of "emotion" in chorus can not only resonate with chorus members and audience but also realize the artistry of the chorus. In essence, emotional unity is a part of chorus unity. In the process of chorus rehearsal, we must follow the principle of chorus unity. The realization of chorus unity plays a very important role in the whole chorus rehearsal process.

In the process of chorus rehearsal, the chorus members should deeply understand the connotation of music and fully reflect the different attributes of each song so as to realize the resonance between the chorus members and the audience. Only in this way can we give full play to the artistry of chorus and achieve a perfect artistic realm.

This study mainly studies the algorithm of chorus emotion recognition. With the help of the excellent performance of neural network technology and the complementarity between different voice features, the idea of ensemble learning is introduced to complete the task of voice signal recognition under different emotions.

2.2.1. Emotional Feature Analysis. In chorus rehearsal, the commander should command the chorus's singing work on the one hand and interpret the music works on the other hand. Before chorus rehearsal, the commander should fully do desk work, get a deep understanding of the works of singing tracks and the background of the times, content forms, and cultures in which the singing tracks are produced, and put himself in another's shoes, understand the aesthetic requirements of songwriters for music, and realize the recreation of music on this basis.

Speech energy is one of the most important features in prosody, which is mainly determined by the vibration amplitude of the signal and reflects the strength of sound. In real life, people can feel that when a person expresses sad feelings, his voice is generally vague and low, while when he expresses happy and angry feelings, his voice is generally loud and bright. Therefore, different emotional voices have obvious differences in speech energy characteristics.

In view of which features in speech signals can effectively reflect emotion, researchers have carried out a lot of research from the perspectives of psychology and phonetic linguistics, but at present, they pay most attention to two types: prosodic features and sound quality features. This kind of feature and its derived parameters are most widely studied and applied in chorus emotion recognition. Sound quality features mainly refer to the timbre and spectrum of speech, so they are also called segmental features, which reflect the change of glottal wave shape during pronunciation (Figure 3).

If music only has notes and rhythms, it is just a shell. Only by giving rich emotions, the expression of music can be fuller and more perfect. Emotion and emotional expression run through the chorus. As chorus conductors, we should fully realize the importance of emotions and emotional expressions when interpreting chorus works and be good at unifying the emotions of members in the chorus process so as to make the chorus art more perfect.

Prosodic features and phonetic features are not isolated. Literature [23, 24] show that there is a certain correlation between prosodic features of speech signals and three emotional dimensions (valence dimension, activation dimension, and control dimension). Among them, the activation dimension is obviously related to prosodic features, and emotional states with similar activation dimensions have similar prosodic features, which are easy to be confused. By judging voiced and unvoiced speech signals, unnecessary calculation of the autocorrelation function of unvoiced frames can be effectively eliminated, and the calculation amount of pitch detection can be reduced.

The purpose of pitch detection preprocessing is to improve the accuracy of pitch detection by the autocorrelation method, which mainly includes band-pass filtering and nonlinear transformation. This paper only introduces the nonlinear transformation method. Commonly used nonlinear transformation methods include center clipping and three-level clipping. In this paper, the towel-center wave elimination method is adopted, and formula (6) is used as the central clipping function expression:

$$y(n) = \begin{cases} x(n) - L, & x(n) > L, \\ 0, & |x(n)| \le L, \\ x(n) + L, & x(n) < -L, \end{cases} \tag{6}$$

where $y(n)$ is the output of the central clipping function, and $x(n)$ is the input, which is the amplitude of n sample points in a frame of speech signal, and is the clipping level, which is a constant related to the maximum amplitude of the current frame. Usually, 60%–70% of the maximum amplitude is taken, and this paper takes 0.68.

The function definition of three-level clipping is

$$y(n) = \begin{cases} 1, & x(n) > L, \\ 0, & |x(n)| \le L, \\ -1, & x(n) < -L. \end{cases} \tag{7}$$

Comparing the expressions (6) and (7), it can be seen that the three-level clipping is a correction based on the central clipping, and the sample points exceeding the clipping level are assigned as 1 or -1, which can effectively reduce the multiplication in the calculation process of the autocorrelation function.

In order to analyze the relationship between formant-related features and emotional state, we extracted the first formant one by one from the emotional voice database. On this basis, the statistical characteristics of the first formant in different emotional states are statistically analyzed. Figure 4 shows the statistical analysis results of the mean value, dynamic range, and change rate of the first resonance peak.

It can be seen from the figure that the mean value of the first formant of pleasure and boredom is higher than that of the dynamic range, while the change rate is pleasure < calm < boredom, and the difference between the change rates of boredom and pleasure emotions is obvious.

2.2.2. Emotion Recognition of Chorus Based on Multifeature DBN. People can fully express their true feelings and thoughts through music. Emotion can be said to be the basic attribute of music. If a song lacks emotional integration, even if it has the best singing skills, it will be difficult for the audience to resonate with it. As music performers, musicians should fully tap the emotions in music, accurately understand the author's thoughts and feelings, and on this basis, organically integrate their feelings with music and recreate chorus music. Only in this way we can fully express the image that music wants to create and arouse the audience's resonance.

In this paper, we consider adopting the method of deep learning, extracting higher-level descriptors to represent more abstract concepts, and extracting more robust feature parameter factors through the multilevel representation of speech signals. The deep learning method has created the latest records in image processing, target location, detection, and other recognition and classification tasks, and DBN is one of the most representative networks.

The Boltzmann machine is an early component of the neural network, and its neurons are divided into two parts: explicit layer and implicit layer. The explicit layer is the input and output layer, which indicates the transmission of data, while the hidden layer is equivalent to the need to adjust the data in the transmission process, adding weight. The standard Boltzmann machine is a fully connected graph, and the complexity of the training network is very high. Therefore, in practice, the RBM (restricted Boltzmann machine) shown in Figure 5 is usually used for simplification.

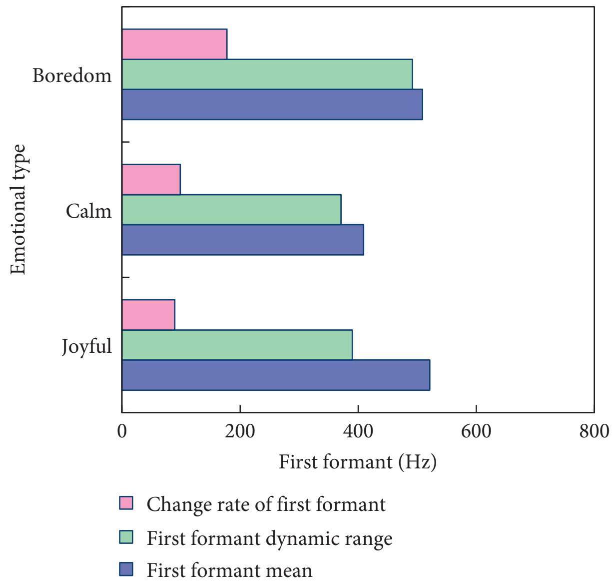

Figure 4: Comparison of the first formant characteristics of three emotions.

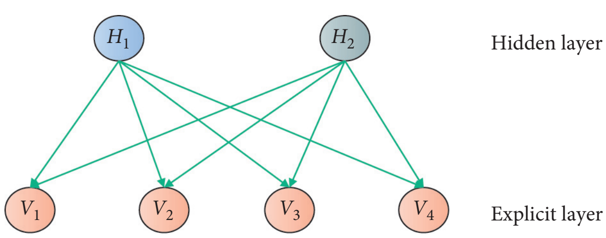

Figure 5: Restricted Boltzmann machine.

The construal divergence (CD) algorithm is often used to train constrained Boltzmann machines. Assuming that there are d neurons in the explicit layer and q neurons in the hidden layer in the network, let v and h represent the state vectors of the explicit layer and the hidden layer, respectively; then, because there is no connection in the same layer, there are

$$
\begin{aligned}
P(v|h) &= \prod_{i=1}^{d} P(v_i|h), \\
P(h|v) &= \prod_{j=1}^{q} P(h_j|v).
\end{aligned} \tag{8}
$$

The connection weight update formula is

$$\Delta w = \eta\left(vh^T - v'h'^T\right). \tag{9}$$

DBN (deep belief network) is connected by multiple RBM stacks, which can be trained effectively in a hierarchical way. Therefore, DBN has a strong learning ability and can learn high-level feature descriptors which are beneficial to the emotional recognition of chorus, as shown in Figure 6.

Firstly, it trains the first RBM with training samples and then uses the output of the first RBM as the input of the second RBM. Similarly, the output of the second RBM is used to train the third RBM. After each layer is pretrained, the whole network is trained by the BP algorithm.

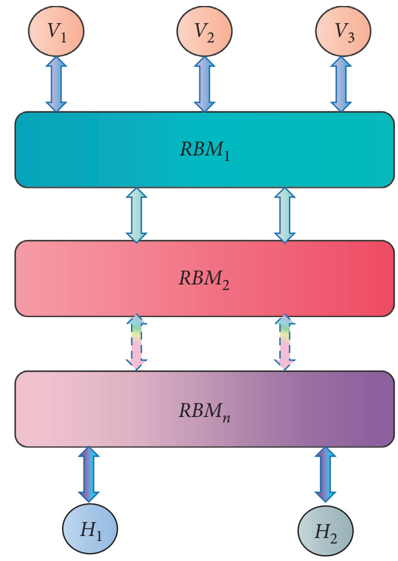

Figure 6: DBN structure diagram.

In this way, we can build a deep network model and then use the network model to obtain more robust high-level feature descriptors from low-level features.

In order to extract higher-level feature descriptors in speech emotion and ensure the diversity of base classifiers, inputting multiple features into the DBN network can solve the above problems. Therefore, this paper proposes a multifeature DBN method for chorus emotion recognition, which is composed of multifeature selection, DBN, and ELM (extreme learning machine) within the framework of set learning. The system framework is shown in Figure 7.

In this paper, we need to use spectrum sequence context (SSC) feature, power-normalized cepstral coefficient (PNCC), rhythm (Rhys) feature, Mel cepstrum coefficient (MFCC), and perceptual linear prediction (PLP), and then input these multiple features into the DBN network after feature selection so as to extract higher-level feature descriptors and create a better classifier.

Traditional hand-designed features do not perform well in emotion recognition tasks, mainly because they are low-level features, and it is difficult to fully describe the deep-seated information hidden in emotions [25]. Therefore, with the help of deep learning methods, a variety of traditional features are integrated with the DBN network to achieve better recognition results in emotion recognition tasks.

3. Discussion and Analysis

3.1. Comparison of Prediction Results. Based on the historical blood pressure data in the database of Literature [22], 221 experimental individuals, aged between 60 and 75 years, were preliminarily screened out. Predicting the blood pressure trend of these kind of people can help them control their blood pressure, guide their medication, and provide early risk warnings for some diseases.

Figure 8 shows the comparison between the actual value of blood pressure time series data and the prediction result of the model, and Figure 9 shows the error prediction model.

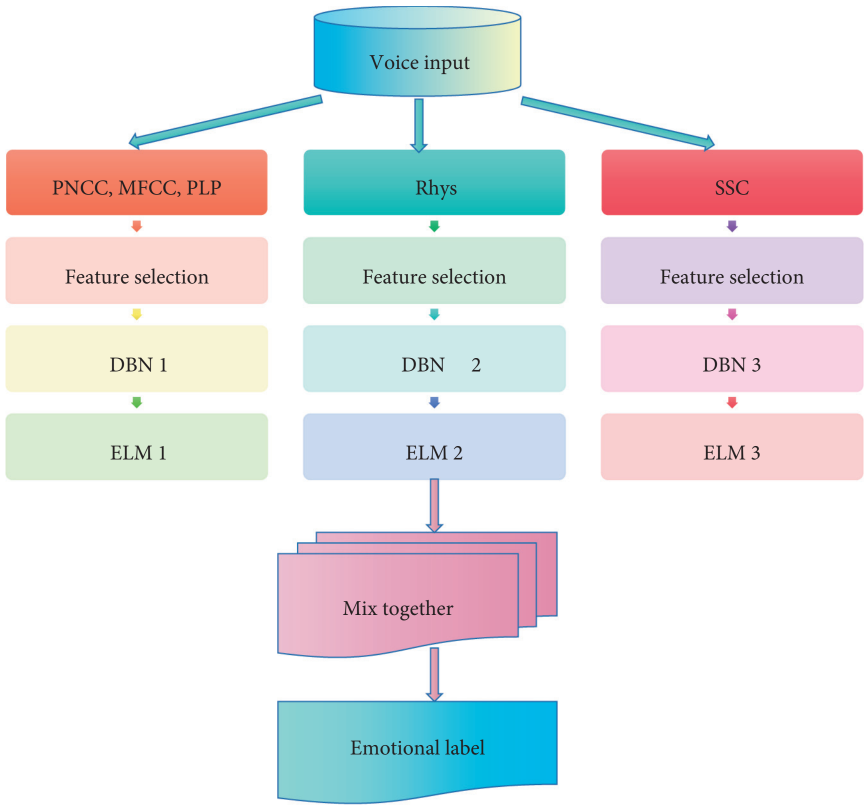

Figure 7: Flowchart of chorus emotion recognition based on multifeature learning.

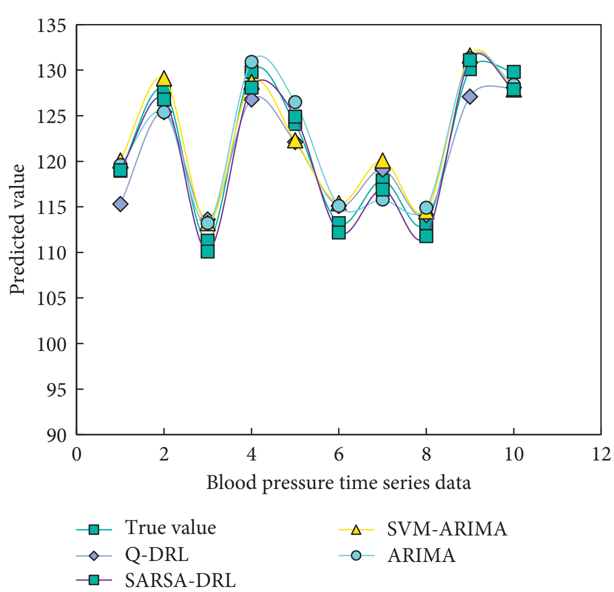

Figure 8: Comparison between actual values and model prediction results.

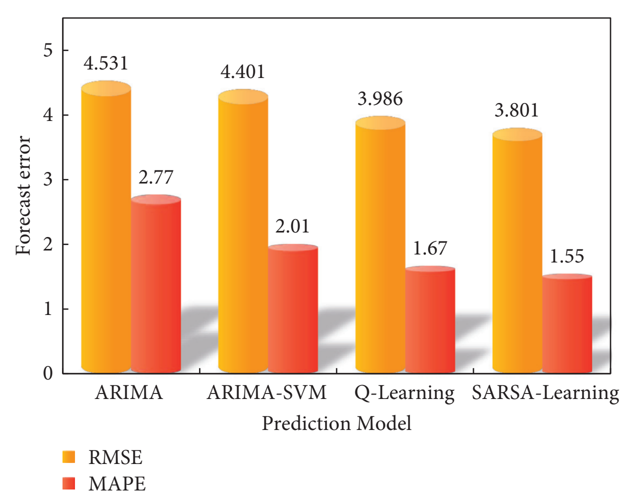

Figure 9: Comparison of final prediction errors of four models.

It can be seen from Figures 8 and 9 that the ARIMA-SVM model has higher prediction accuracy than the traditional ARIMA model and overcomes the limitations of the single model. Q-learning-based deep reinforcement learning and SARSA-based deep reinforcement learning are superior to the former two in high-dimensional spatial prediction, so the prediction accuracy is higher than the former two. Especially, the deep reinforcement learning method based on SARSA learning can fully express the hidden information in the original time series data of blood pressure.

3.2. Efficiency of HBD Integration. When the storage capacity of experimental big data is increasing, the two systems integrate the HBD efficiency of experimental logistics companies. The results are shown in Figure 10.

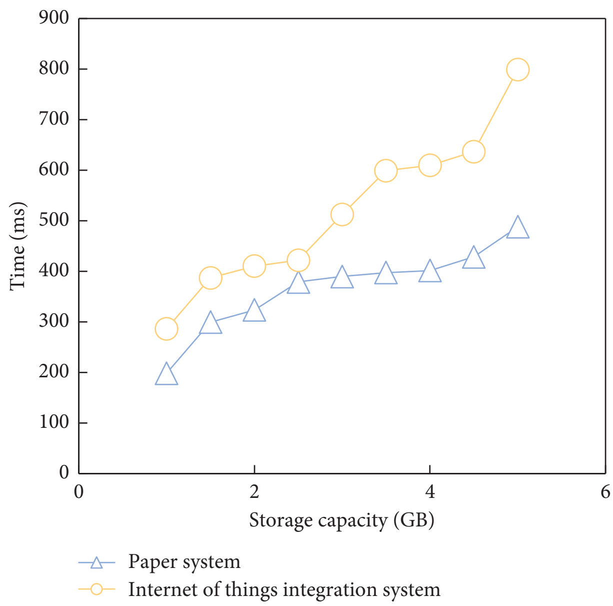

FIGURE 10: Efficiency of HBD integration.

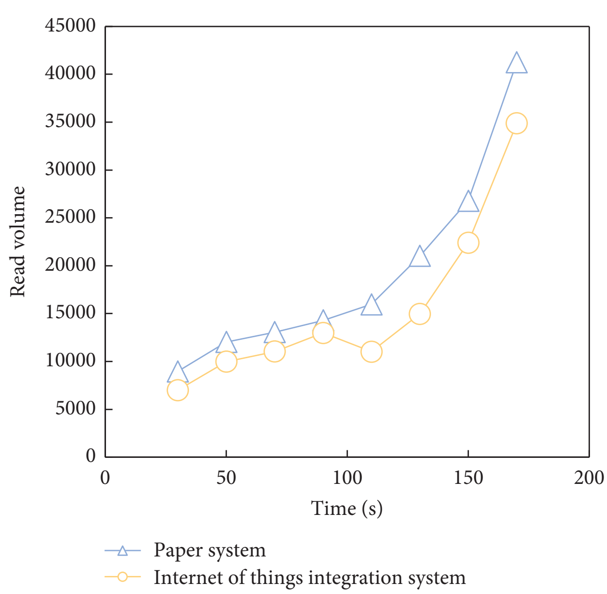

FIGURE 11: Test effect of integration system concurrency.

As can be seen from Figure 10, this system is highly efficient in integrating the whole cloud HBD.

The results of testing the concurrency of HBD integrated in this paper are shown in Figure 11.

According to the analysis of Figure 11, with the increase of time, the system in this paper is much larger than the HBD integration system based on IoT in processing the whole cloud HBD, which shows that the system in this paper has higher performance in processing the whole cloud HBD.

3.3. Analysis of Chorus Emotion Recognition. In order to verify the effectiveness of the spectral context features proposed in this paper in chorus emotion recognition, we compare the classical MFCC features and the combination

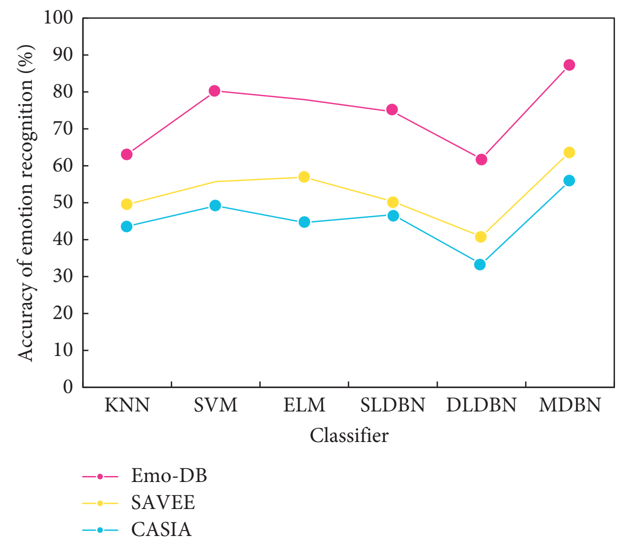

FIGURE 12: Comparison of emotional recognition accuracy of different classifiers.

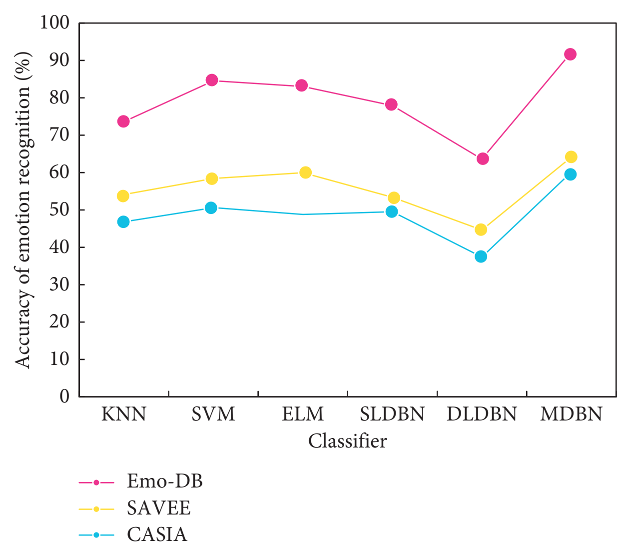

FIGURE 13: Comparison of emotional recognition accuracy of different classifiers.

of MFCC and delta features with the spectral context features on Berlin Emo-DB, SAVEE, and CASIA datasets, respectively. ELM classification is adopted in the classifier, with the number of hidden nodes being 6,000 and the activation function being hardlim. Figure 12 shows the comparison of the emotion recognition accuracy of different classifiers (speaker dependent).

In Figure 12, we compare the algorithm in this paper with KNN, SVM, ELM, single-layer DBN network (SLDBN), and double-layer DBN network (DLDBN). The experimental results show that the accuracy of the algorithm in this paper is greatly improved than the above methods, which shows that the algorithm in this paper can more effectively classify and recognize speech emotions.

In this experiment, 8 chorus samples were randomly selected from the Berlin Emo-DB dataset as the training set and the remaining 2 chorus samples as the test set. In order to avoid the error caused by the randomness of samples, we chose to repeat the experiment 5 times and calculate the average recognition accuracy. Figure 13 shows the comparison of emotion recognition accuracy of different classifiers (speaker independent).

Through Figure 13, we find that in the speaker independent experiment, the algorithm in this paper is compared with KNN, SVM, ELM, single-layer DBN network (SLDBN), and double-layer DBN network (DLDBN). The experimental results show that the algorithm in this paper is better than the above methods. Both have improved, indicating the effectiveness of the algorithm in this paper for the emotion recognition of chorus personnel.

4. Conclusion

If music only has notes and rhythm, it is just an empty shell. Only by giving rich emotions can the expression of music be fuller and more perfect. Emotion and emotional expression run through the chorus. The research work of emotional feature analysis and extraction is carried out in the established emotional voice database, and the changing rules of energy, fundamental frequency, formant, and other features in different emotional states are observed and analyzed. According to the statistical analysis results, the global statistical emotional features with emotional discrimination are selected and extracted. In this paper, according to the different abilities of different features to describe emotions, various robust low-level features are extracted, and then they are fed into the DBN network to extract high-level feature descriptors. Then, the ELM classification results are voted and fused with the idea of ensemble learning, and the effectiveness of the algorithm is proved on three public datasets.

Data Availability

The data used to support the findings of this study are included in this paper.

Conflicts of Interest

The authors declare that they have no conflicts of interest.

References

[1] K. Zhan, "Sports and HBD system based on 5G network and Internet of Things system," *Microprocessors and Microsystems*, vol. 80, no. 2, Article ID 103363, 2020.

[2] S.-Y. Choi and K. Chung, "Knowledge process of health big data using MapReduce-based associative mining," *Personal and Ubiquitous Computing*, vol. 24, no. 5, pp. 571–581, 2020.

[3] T. Yang, G. Yuan, and J. Yan, "Health analysis of footballer using big data and deep learning," *Scientific Programming*, vol. 2021, no. 2, pp. 1–8, Article ID 9608147, 2021.

[4] W. Xing and Y. Bei, "Medical HBD classification based on KNN classification algorithm," *IEEE Access*, vol. 22, no. 99, p. 1, 2019.

[5] R. K. Barik, H. Dubey, and K. Mankodiya, "GeoFog4Health: a fog-based SDI framework for geospatial HBD analysis," *Journal of Ambient Intelligence and Humanized Computing*, vol. 10, no. 2, pp. 551–567, 2019.

[6] S. Zhou, J. He, H. Yang, D. Chen, and R. Zhang, "Big data-driven abnormal behavior detection in healthcare based on association rules," *IEEE Access*, vol. 8, no. 99, p. 1, 2020.

[7] M. Christie and J. Lisa, "The intersection of mobile health and nursing knowledge: big data science," *Computers, informatics, nursing: CIN Plus*, vol. 37, no. 8, pp. 394-395, 2019.

[8] K. Han, L. Zhang, Z. Tian, and Y. Gu, "Human muscle measurement and big data health based on wireless sensors," *Microprocessors and Microsystems*, vol. 80, no. 1, Article ID 103580, 2021.

[9] R. Raja, I. Mukherjee, and B. K. Sarkar, "A systematic review of healthcare big data," *Scientific Programming*, vol. 2020, no. 6, 15 pages, Article ID 5471849, 2020.

[10] H. Q. Yu and F. Dong, "Semantic lifting and reasoning on the personalised activity big data repository for healthcare research," *International Journal of Web Engineering and Technology*, vol. 14, no. 2, 2019.

[11] B. Khan, R. Naseem, M. A. Shah et al., "Software defect prediction for healthcare big data: an empirical evaluation of machine learning techniques," *Journal of Healthcare Engineering*, vol. 2021, no. 2, pp. 1–16, Article ID 8899263, 2021.

[12] B. Xie, J. C. Kim, and C. H. Park, "Musical emotion recognition with spectral feature extraction based on a sinusoidal model with model-based and deep-learning approaches," *Applied Sciences*, vol. 10, no. 3, 2020.

[13] T. Schmidt, M. Schlindwein, K. Lichtner, and C. Wolff, "Investigating the relationship between emotion recognition software and usability metrics," *I-Com*, vol. 19, no. 2, pp. 139–151, 2020.

[14] W. Jiaqi, H. Liu, and B. Wang, "Extreme learning machine for emotion recognition of tactile gestures," *Caai Transactions on Intelligent Systems*, vol. 14, no. 1, pp. 127–133, 2019.

[15] K. Slimani, M. Kas, Y. E. Merabet, and Y. Ruichek, "Local feature extraction based facial emotion recognition: a survey [J]," *International Journal of Electrical and Computer Engineering*, vol. 10, no. 4, pp. 4080–4092, 2020.

[16] M. M. Nashipudimath, P. Pillai, A. Subramanian, and V. Nair, "Voice feature extraction for gender and emotion recognition," *ITM Web of Conferences*, vol. 40, no. 1, Article ID 03008, 2021.

[17] C. Deepika, "Speech emotion recognition feature extraction and classification," *International Journal of Advanced Trends in Computer Science and Engineering*, vol. 9, no. 2, pp. 1257–1261, 2020.

[18] S. Lawrence, T. Anjum, and A. Shabani, "Improved deep convolutional neural network with age augmentation for facial emotion recognition in social companion robotics," *Journal of Computational Vision and Imaging Systems*, vol. 6, no. 1, pp. 1–5, 2021.

[19] S. Hamsa, Y. Iraqi, I. Shahin, and N. Werghi, "An enhanced emotion recognition algorithm using pitch correlogram, deep sparse matrix representation and random forest classifier," *IEEE Access*, vol. 16, no. 99, p. 1, 2021.

[20] H. Luo and J. Han, "Nonnegative matrix factorization based transfer subspace learning for cross-corpus speech emotion recognition," *IEEE/ACM Transactions on Audio, Speech, and Language Processing*, vol. 19, no. 99, p. 1, 2020.

[21] W. C. Lin and C. Busso, "Chunk-level speech emotion recognition: a general framework of sequence-to-one dynamic temporal modeling," *IEEE Transactions on Affective Computing*, vol. 28, no. 99, p. 1, 2021.

[22] E. Mansouri-Benssassi and J. Ye, "Synch-graph: multisensory emotion recognition through neural synchrony via graph convolutional networks," *Proceedings of the AAAI Conference on Artificial Intelligence*, vol. 34, no. 2, pp. 1351–1358, 2020.

[23] H. Zang, S. Y. Foo, S. Bernadin, and A. M. Baese, "Facial emotion recognition using asymmetric pyramidal networks with gradient centralization," *IEEE Access*, vol. 9, Article ID 64487, 2021.

[24] V. Nair, P. Pillai, A. Subramanian, and V. Nair, "Voice feature extraction for gender and emotion recognition," *International Journal on Recent and Innovation Trends in Computing and Communication*, vol. 9, no. 5, pp. 17–22, 2021.

[25] G. Yan and R. Sha, "Autonomous learning of foreign language based on facial emotion recognition and cloud computing," *Journal of Intelligent and Fuzzy Systems*, vol. 25, no. 11, pp. 1–12, 2020.

Hindawi
Journal of Healthcare Engineering
Volume 2022, Article ID 5471575, 8 pages
https://doi.org/10.1155/2022/5471575

Research Article

Alternate Warm and Cold Therapy (AWCT) on Uricemia, Sleep, Pain, Functional Ability, and Quality of Life (USPFQoL) in Patients with Gout: A Path Forward

Premalatha Paulsamy,[1] Krishnaraju Venkatesan ,[2] ShadiaHamoud Alshahrani,[3] Fazil Ahmad,[4] Mohamed El-Sherbiny,[5] Vani Manoharan,[6] Kalaiselvi Periannan,[7] RashaElsayed Ahmed,[8] Kousalya Prabahar,[9] and Dawit mamiru teressa [10]

[1]*College of Nursing, Mahalah Branch for Girls King Khalid University, Abha, Asir, Saudi Arabia*
[2]*Department of Pharmacology, College of Pharmacy, King Khalid University, Abha, Asir, Saudi Arabia*
[3]*College of Nursing, Mahalah Branch for Girls, King Khalid University, Abha, Asir, Saudi Arabia*
[4]*Department of Anesthesia Technology, College of Applied Medical Sciences in Jubail, Imam Ab-dulrahman Bin Faisal University, P.O. Box 4030, Jubail, Saudi Arabia*
[5]*Department of Basic Medical Sciences, College of Medicine, Almaarefa University, P.O. Box 71666, Riyadh 11597, Saudi Arabia*
[6]*Georgia CTSA, Emory University Hospital, Atlanta, GA, USA*
[7]*Lecturer in Mental Health Nursing, Oxford School of Nursing & Midwifery, Faculty of Health and Life Sciences, Oxford OX3 0FL, UK*
[8]*Medical Surgical Nursing, College of Nursing Tanta University, Egypt and College of Nursing, Mahalah Branch for Girls King Khalid University, Asir, Saudi Arabia*
[9]*Department of Pharmacy Practice, Faculty of Pharmacy, University of Tabuk, Tabuk 71491, Saudi Arabia*
[10]*Department of Chemical Engineering, College of Biological and Chemical Engineering, Addis Ababa Science and Technology University, Addis Ababa, Ethiopia*

Correspondence should be addressed to Krishnaraju Venkatesan; kvenkatesan@kku.edu.sa and Dawit mamiru teressa; dawit.mamiru@aastustudent.edu.et

Received 11 January 2022; Accepted 8 February 2022; Published 9 March 2022

Academic Editor: Enas Abdulhay

Objective. To understand the impact of alternate warm and cold therapy (AWCT) on uricemia, sleep, pain, functional ability, and quality of life in gout patients. *Methods*. A quasiexperimental, nonequivalent control group, pre and posttest design was adopted among 120 gout patients. The data were collected on demographics, comorbidities, pain level, joint swelling/joint tenderness, patient global assessment of response to treatment (PGART), health-related quality of life (HRQoL) with SF-36, sleep quality by Pittsburgh Sleep Quality Index (PSQI), and serum uric acid and assessed. Descriptive and inferential statistics were used to analyze the data. *Results*. Patients had mean age of 58 and 61 years, mean number of comorbidities was 1.8 and 1.4, as well as presence of arthritic comorbidities except gout was 1.1 and 0.8 among study and control group participants, respectively. Pain ($p < 0.001$), PGART ($p = -0.01$), HRQoL, sleep quality, and level of SUA (mg/dl) improved significantly ($p < 0.01$) among the study group over study periods. It affirms that the AWCT is effective in reducing pain, functional disability, and SUA, as well as improving the sleep quality and HRQoL of the gout patients. There was a reduced incidence of gout flares ($p < 0.001$), and taking additional medicines for pain ($p < 0.01$) was statistically significant among study participants. Except social functioning, other domains of health were significantly ($p < 0.05$) affected by the comorbidities like hypertension, diabetes, heart disease, renal disease, and asthma/chronic obstructive pulmonary disease. *Conclusions*. Gout is independently associated with higher medical and arthritic comorbidity, and AWCT can be better and cost-effective alternative therapy for gout patients. In addition, it may lead to improved cardiac function, hypertension, and renal insufficiency.

1. Introduction

Gout is the most common form of inflammatory arthritis globally which is a metabolic disease marked by recurrent episodes of acute arthritis caused by inflammation caused by the formation, deposition, and release of monosodium urate crystals in one or more extremity joints [1–3]. It is the most common type of inflammatory joint disease in men over the age of 40, and it can affect women after menopause [4, 5]. Epidemiologic studies confirm a global distribution [5], with an estimated prevalence of 5.1 million people in the United States [6].

Gout is a common chronic crystal deposition disorder that affects 1–6.8% of the population, depending on the population studied. Serum uric acid (SUA) levels have been found to be high throughout the world, including the Philippines and Seychelles: 25%, USA: 21–22%, Japan: 20–26%, Indonesia: 18%, Russia and Nigeria: 17%, Brazil: 13%, Turkey: 12%, Taiwan: 10–52%, Thailand: 9–11%, Mexico: 11%, Sweden: 10–16%, Italy: 9–12%, Iran and Saudi Arabia: 8%, China: 6–25%, Spain: 5–11%, and South Korea: 5–25.8% [7].

Over the last 5–10 years, hospitalizations for gout have increased by 50–100% in the United Kingdom, the United States, and Sweden [8–11]. In these countries, gout now induces more hospitalizations than rheumatoid arthritis, and hospitalizations for gout increased more than for other rheumatological conditions between 2007 and 2012 [8].

The prevalence of self-reported, health professional diagnosed gout was 3.9% in the 2015–2016 National Health and Nutrition Examination Survey (NHANES), a stratified, multistage sample representative of the U.S. adult population [12]. Gout is also commonly associated with comorbidities such as cardiovascular disease (CVD), chronic kidney disease (CKD), obesity, and other conditions. As per a retrospective study in India, hyperuricemia (H.U.) was found in 33.6% of diabetics, 35.1% of hypertensives, and 34.4% of diabetic hypertensives, with the overall incidence of H.U. in patients attending screening programs being 25.8% [7].

Furthermore, cohort studies in the United States, Taiwan, and the United Kingdom have discovered that gout is linked to an increased risk of developing atrial fibrillation, obstructive sleep apnea (O.S.A.), venous thromboembolism (V.T.E.), and pulmonary embolism [13–19].The frequency of gout attacks usually increases with time in untreated patients. Hence, understanding trends in gout prevalence is critical for adequate global healthcare resource planning, not least even though gout can be "cured" with readily available and low-cost therapies.

There is a scarcity of information available on alternative therapies for the management of gout in the Indian population and its relationship with uricemia, pain, sleep, functional ability, and HRQoL. As a result, the current study was designed to evaluate the effect of alternating warm and cold therapy (AWCT) on uricemia, sleep, pain, functional ability, and quality of life (USPFQoL) gout patients: a path forward among Indian populace.

2. Methods

2.1. Research Approach and Design. For this study, quantitative research approach with a quasiexperimental, nonequivalent control group, pre and posttest design was used; only the experimental group received the intervention, while the control group received no intervention.

2.2. Participants and Setting. The study participants were both men and women diagnosed with gout and who were admitted as in patients for a minimum of 10 days and who agreed to participate in the study. Patients with illnesses such as open wounds and diabetic foot ulcers, peripheral vascular diseases, absence of tophi, and patients who are receiving physiotherapy were excluded from the study. The study was conducted in two orthopaedic hospitals, and one setting was used for the intervention group, and the other was for the comparison group to avoid contamination.

2.3. Sample Size and Sampling Process. The minimum recommended sample size was 60, as calculated by Raosoft's online sample size calculator, with a 95% confidence level and a 5% margin of error. In the first and second hospitals, 104 and 121 chronic gout patients were admitted during the study period. Among them, 120 samples were chosen by the nonprobability convenient sampling technique and distributed for experimental (60 participants) and control group (60 participants).

2.4. Data Collection Tools/Instruments. The data were collected on demographics and history of comorbidities, pain level using 10 points numerical scale, joint swelling/joint tenderness with a 4-point scale (0 = none to 3 = bulging beyond joint margins), and patient global assessment of response to treatment (PGART). The PGART was rated by patients using the visual analogue scale (VAS), a 15 cm horizontal line with marked anchors: 0 = very well and 100 = very poor. With these anchors, patients were asked to respond to the following: "Given all of the ways gout affects you, rate your performance on the following scale by placing a mark on the line." The health-related quality of life (HRQoL) was assessed, and the Medical Outcomes Study Short Form-36 (SF-36) consists of eight scaled scores, which are the weighted sums of the questions in their section. Assuming that each question carries equal weight, each scale is directly transformed into a 0–100 scale. The lower the score, the greater the disability, and the higher the score, the better the health. The SF-36 is a 36-item scale that assesses eight domains of health: physical functioning (10 components), physical role limitations (four elements), bodily pain (two elements), general health perceptions (five elements), energy/vitality (four elements), social functioning (two components), emotional role limitations (three elements), and mental health (five elements). Using the Pittsburgh Sleep Quality Index (PSQI), sleep quality was assessed.

Serum uric acid (uricase method) was measured. A high serum uric acid level is currently defined as a value of at least 6.8 mg per dl (405 μmol per L). These data were collected based on the core domains on that outcome measures in rheumatology (OMERACT) [20].

2.5. Assessment. Subjects completed and returned gout symptom diaries between follow-up visits, which the investigators reviewed at the next visit. The journals contained information such as the frequency, dates, duration, and severity of flares; the joint(s) affected; medications (both prescribed and over-the-counter); and whether the gout attack required a medical office contact or visit.

2.6. Intervention. Control group participants received standard care and consistent advice on diet, exercise, and weight management. The intervention group was given routine care and alternate warm and cold therapy twice a day, once in the morning and once before bedtime.Coconut oil was first applied to the lower legs and feet/the affected joints in the arm. The subjects subsequently plunged their toes and then both feet/arms, into 38° water, which was then adjusted to a comfortable temperature near 42°. The basin was covered with a plastic bag, as were the participants' legs/arms up to their knees/elbows. To allow the individual to maintain a comfortable position, a blanket and a pillow was placed beneath the knees/arms and the basin. For 4 minutes, the feet/arms were immersed. The feet/arm was then applied with cold therapy for 30 s until completing 5 cycles. Then, the feet/arms were cleansed with a foaming body shampoo and cotton gloves and dried dry with a towel.The complete procedure took 30 min and comprised a 5-minute oil rub, followed by 20 minutes of AWCT. To keep the techniques as equal as feasible, all AWCT were provided by the same person.This intervention was given for 7 days during their hospitalization, and the participants were advised to follow the same in the home after discharge in 5 days/week for one month. The baseline data and post hoc after one week and one month were assessed for both the control and study groups. Figure 1 shows the CONSORT diagram.

2.7. Ethical Consideration. Official permission to conduct the study and ethical approval was obtained from the Institutional Ethical Committee with ICE/LCN/2021–10 dated 20.09.2021. Consent from the participants was collected after explaining the aim of study, their role, confidentiality of the information, and their right to depart from the study. No harm certificate was obtained from an orthopaedician for the intervention. The control group also ensured that they were following the standard care protocol of the gout treatment. Confidentiality and beneficence were assured throughout the study period.

2.8. Statistical Analysis. The data were processed and analyzed by SPSS software using descriptive and inferential statistics. Analysis of data was by intention-to-treat. Analysis of variance was used to examine the main effects of AWCT among the two groups on the dependent variables. The t-test was used to compare differences between group means. Multiple regression analysis was used to examine the effect of AWCT and comorbidity on health-related quality of life in gout patients. All statistical tests used a significance of 0.05.

3. Results

The characteristics of study participants are given in Table 1. Most of the demographic and clinical characteristics were similar with study and control group, which is shown in the "Goodness of fit" test. Patients had a mean age of 58 and 61 years, 43 and 38 were men among study and control groups, respectively. Mean number of comorbidity was 1.8 and 1.4, as well as presence or absence of arthritic comorbidities except gout was 1.1 and 0.8 among study and control group participants, respectively.

As given in Table 2, the average pain score in baseline, after one week, and one month improved from 8.8 to 5.7 and 8.6 to 6.9 among the study and control groups, which is statistically significant at $p < 0.001$ among the study group.There were no differences between the mean values before AWCT in the score of joint swelling/joint tenderness among the control group. In the experimental group, the PGART score was decreased after the AWCT in the first week (74 (SD, 3)) and after one month (67 (SD, 6)), $p = -0.01$). Similarly, HRQoL, sleep quality, and level of serum uric acid (mg/dl) was improved significantly ($p < 0.05$) among study group participants, but there was no significant difference in the control group.

Table 3 provides the multivariable-adjusted effect of AWCT in gout patients. A multivariable model controlled the age, employment status, marital status, gender, education level, current medications, comorbidities, and arthritis comorbidity other than gout. Among the variables studied, there was a reduced incidence of gout flares ($p < 0.001$), and taking additional medicines, both prescribed and over-the-counter medications for pain ($p = 0.01$), was statistically significant among study participants. The number of joint(s) affected and hospital visits was not related significantly.

The effect of comorbidities on health-related quality of life in gout patients is given in Table 4 and Figure 2. The age, employment status, marital status, gender, education level, current medications, uric acid levels, and arthritis comorbidities other than gout were all controlled in a multivariable model. In this analysis, except social functioning, other seven domains of health status such as physical functioning, physical role limitations, bodily pain, general health perceptions, energy/vitality, emotional role limitations, and mental health were significantly ($p < 0.05$) affected by the comorbidities of the participants such as hypertension, diabetes, heart disease, renal disease, and asthma/chronic obstructive pulmonary disease.

4. Discussion

In the present study, 225 gout patients were screened. Among them, 120 samples were chosen by the non-probability convenient sampling technique and distributed

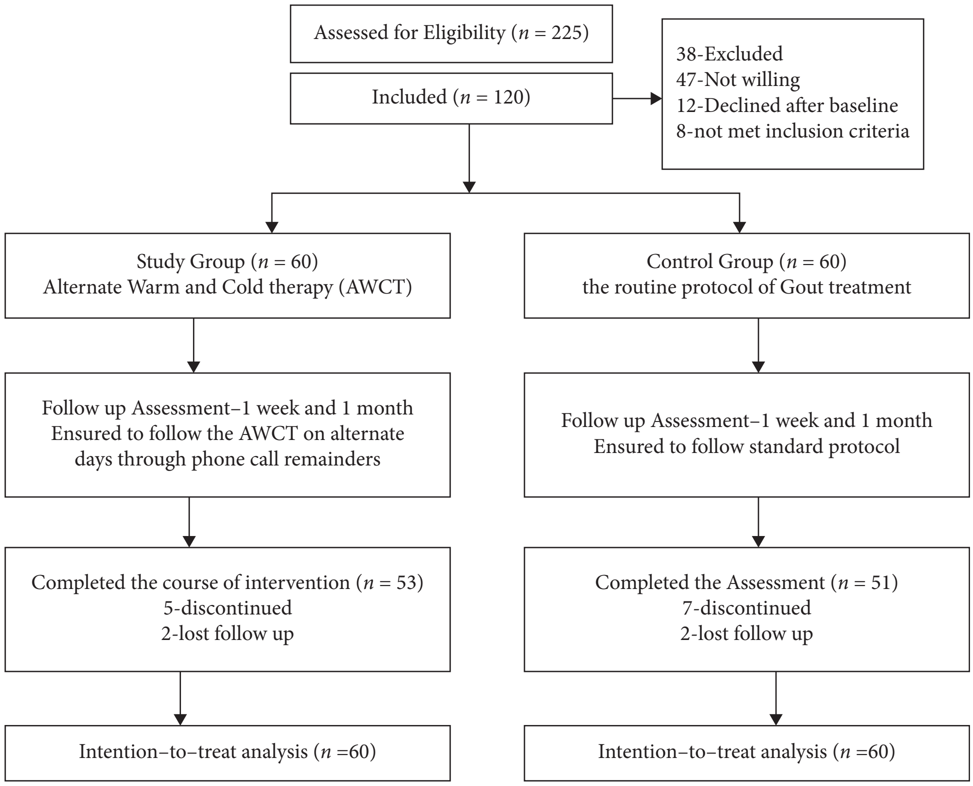

Figure 1: CONSORT diagram.

Table 1: Demographic and clinical data of study and control group participants.

Variables	Study group	Control group	P value
Age (in years), mean (SD)	58 (16)	61 (13)	<0.001
Employment status			
Employed	31	27	<0.001
Unemployed	18	19	<0.001
Retired	11	11	<0.001
Unknown	0	3	<0.001
Married	36	44	<0.001
Male	43	38	<0.001
Education level			
Less than 8th grade	25	21	<0.001
High school	8	14	<0.001
Higher secondary	13	7	<0.001
College	14	18	<0.001
Comorbidity	1.8 (1.3)	1.4 (1.7)	<0.001
Presence or absence of arthritic comorbidities except gout	1.1 (0.7)	0.8 (0.6)	<0.001

for experimental (60 participants) and control groups (60 participants) from two hospitals. The AWCT was given seven days during hospitalization and advised to follow the same at home for one month in the study group. The participants had 1.8 and 1.4 mean comorbidity and presence or absence of arthritic comorbidities, except gout was 1.1 and 0.8 among study and control group participants. A large study looked at the temporal relationships between the occurrence of comorbidities before and after gout diagnosis using data from the U.K. Clinical Practice Research Datalink (CPRD) [21–25]. This study confirmed the well-known association of gout with subsequent CVD and renal disease and hypertension, hyperlipidaemia, CVD, and renal disease as risk factors for gout. Cohort studies from the United Kingdom, the United States, and Canada have also validated the bidirectional relationship between gout and CKD, with CKD predisposing to gout, which increases the risk of CKD progression [26–28]. These findings show that gout can lead to these comorbidities or these comorbidities leads to gout. Hence, identifying and treating gout may be an excellent strategy to prevent the occurrence of these illnesses and can help to reduce the disease burden globally.

Table 2: Changes in the clinical data of study and control group participants over study periods.

Dependent variables: mean (SD)	Group	Baseline	1 week	1 month	P value
Pain score	AWCT	8.8 (0.8)	6.3 (1.1)	5.7 (0.9)	0.001
	Control	8.6 (1.2)	7.1 (1.3)	6.9 (1.02)	0.06
Joint swelling/joint tenderness	AWD	2.1 (0.4)	1.67 (0.13)	1.1 (0.3)	0.001
	Control	2.3 (0.2)	2.0 (0.7)	2.1 (0.5)	0.551
Patient global assessment of response to treatment (PGART)	AWD	81 (7)	74 (3)	67 (6)	−0.01
	Control	79 (11)	76 (9)	80 (4)	−0.971
HRQoL	AWD	57 (16)	61 (11)	69 (7)	0.01
	Control	54 (13)	57 (17)	56 (15)	0.819
Sleep quality	AWD	16 (3.1)	14 (1.8)	11 (0.5)	0.01
	Control	15.4 (4.3)	14.7 (1.8)	15.0 (0.9)	0.907
Serum uric acid (mg/dl)	AWCT	9.9 (1.4)	8.1 (0.9)	7.2 (1.1)	0.05
	Control	9.67 (2.1)	8.7 (1.8)	8.13 (2.2)	0.653

Table 3: Multivariable-adjusted effect of AWCT in gout patients.

	Multivariable adjusted			
	Study	Control	P value	Difference (%)
Incidence	2.69 (2.3–2.7)	3.52 (3.20–3.67)	0.001	34.11
No. of joint(s) affected	1.52 (1.45–1.58)	1.66 (1.27–2.05)	0.06	9.21
Taking additional prescribed and over-the-counter medicines	1.36 (1.48–1.83)	2.07 (1.82–2.33)	0.01	9.52
Hospital visits	2.08 (1.1–2.15)	2.3 (1.34–2.8)	0.21	16.21

Results are shown as mean (99% confidence intervals). Age, employment status, marital status, gender, education level, current medications, comorbidity, and arthritis comorbidity other than gout were all controlled in a multivariable model.

Table 4: Multivariable-adjusted effect of comorbidity on health-related quality of life in gout patients.

	Multivariable adjusted		
	Study	Control	P value
Physical functioning (P.F.)	51.6	47.3	0.01
Role physical (R.P.)	47.3	44.1	0.05
Bodily pain (B.P.)	49.3	43.6	0.001
General health (G.H.)	54.3	45.7	0.01
Vitality (VT)	43.9	40.8	0.05
Social functioning (S.F.)	68.3	67.9	NS
Role emotional (RE)	53.6	42.4	0.01
Mental health (MH)	73.1	66.9	0.05
Physical component summary (P.C.S.)	36.1	32.4	0.05
Mental component summary (M.C.S.)	51.8	42.1	0.01

Age, employment status, marital status, gender, education level, current medications, uric acid levels, and arthritis comorbidity other than gout were all controlled in a multivariable model.

As given in Table 2, pain ($p < 0.001$), PGART ($p = -0.01$), HRQoL, sleep quality, and level of SUA (mg/dl) improved significantly ($p < 0.01$) among study group participants, but there was no significant difference in the control group over study periods. It confirms that the AWAT effectively reduces pain, functional disability, and SUA and improves sleep quality and HRQoL in gout patients. According to Yamamoto and Nagata's study on physiological and psychological assessment of the wrapped warm footbath as a complementary nursing treatment to induce relaxation in patients with incurable cancer, the wrapped warm footbath reduced significantly sympathetic activity in hospitalized cancer patients, which can enhance relaxation and appears to provide pain relief as well as enhanced comfort [29].

Furthermore, a pilot study found a significant antihypertensive effect after 20 minutes of the steam spa. The hypotensive effect could be attributed to improved vascular endothelial function; nitric oxide produced by vascular endothelial cells causes vascular smooth muscle cells to relax [30, 31]. Though it is not the scope of the present study, this is a more significant finding as most of the study participants had the comorbidity of hypertension. This AWCT may help them reduce their blood pressure, and the effect on gout as its impact is bidirectional.

Functional disability [32], impairment of health-related quality of life (HRQoL), and increased mortality have all been reported in gout patients [33]. As a result, gout has emerged as a significant public health concern. The KING study data confirm the impact of gout on disability and

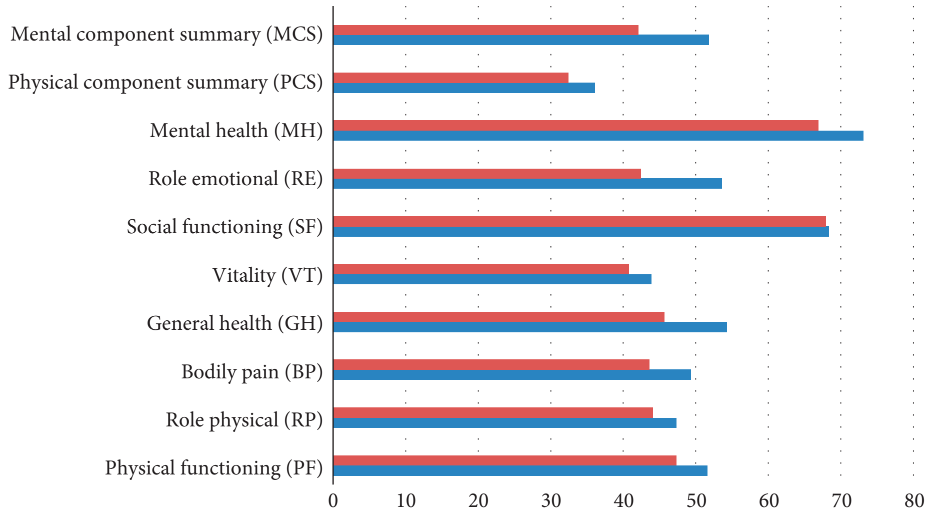

Figure 2: Effect of comorbidities on health-related quality of life in study and control groups.

provide evidence for an independent association of gout and gout-related features with functional outcome and HRQoL. This finding supports the need for better gout treatment [34]. As a nonpharmacological, safe, and simple application, footbaths can improve postmenopausal women's quality of life and prevent problems caused by insufficient sleep quality [35].

All study group patients reported significant pain relief in our preliminary investigation into whether patients receiving AWCT would report pain relief ($p < 0.001$). An increase in parasympathetic activity and a decrease in sympathetic activity would be expected to accompany pain relief-induced relaxation. The cause of the low parasympathetic activity is unknown. Still, the reduction in sympathetic nerve activity in patients may be due to the effects of soaking in warm water, alternate cold application, and tactile stimulation from massage [29]. This pain relief improved the sleep quality, functional ability, and HRQoL of the study group gout patients. However, efferent sympathetic nerve activity is increased by negative feelings in various pain disorders. Accordingly, it is supposed that the reduction in sympathetic nerve activity found in our subjects is the primary mechanism underlying both the relaxation and pain relief effects reported. Negative feelings or depression in patients, usually seen in chronic pain disorders, on the other hand, increase efferent sympathetic nerve activity. As a result, it is assumed that the decrease in sympathetic nerve activity observed in our subjects is the prime mechanism underlying both the reported improved sleep quality and pain relief effects.

Insomnia is a common sleep disorder in adults that can have various negative health effects. The total annual cost of direct and indirect insomnia healthcare costs has been estimated at USD 100 billion. Adding to the societal expenditure, insomnia harms patients' quality of life (QoL), including impaired social and occupational functioning or productivity and impaired cognition or mood. Insomnia can also worsen and increase morbidity and complications from psychological disorders like depression and have severe consequences like an increased risk of suicide [36, 37]. Hence, improving sleep quality is a significant investment in the perspective of the patients and the nation's economy.

In 85–90% of people, hyperuricemia is the major contributor to gout due to under excretion of urate. Sweat fluid comprises sodium chloride, potassium, and nitrogen metabolites like urea, ammonia, uric acid, and creatinine [38]. Besides, reduced sympathetic nerve activity results in increased renal excretory function by affecting the renal vasculature, the tubules, and the juxtaglomerular granular cells and impaired arterial baroreflex regulation. The significant reduction in SUA in the study group may be because of this effect, and AWCT increased sweat and thirst, consequently increasing fluid intake. The cold application increases the voiding sensation, thus enhancing the uric acid elimination in urine and sweat. However, further studies are required to investigate this supposition further.

5. Clinical Relevance

This study results can help healthcare professionals gain greater insight into alternative therapy for gout patients suffering from pain, sleep disturbance, reduced functional ability, and HRQoL. This technique can be used at home to alleviate problems, enhance their overall quality of life, and reduce healthcare costs, and this can provide an avenue for further research studies.

6. Conclusion

To summarize, the AWCT holds promise as a complementary intervention for inducing sleep, pain relief, and as a result, improved functional ability, HRQoL, and uric acid elimination in gout patients. As a result, the AWCT should be a proper adjuvant alternative method for gout patients. In addition, it may lead to improved cardiac function, hypertension, and renal insufficiency.

Data Availability

The datasets used and/or analyzed during the current study are available from the corresponding author upon request.

Ethical Approval

Institution Ethical Committee gave an ethical clearance with ICE/LCN/2021–10 dated on 20.09.2021.

Consent

Written informed consent was obtained from the study participants to publish this study.

Conflicts of Interest

The authors declare that they have no conflicts of interest.

Authors' Contributions

All authors have read and agreed to the published version of the manuscript. Premalatha Paulsamy conceptualised, investigated, validated, visualized, and supervised the study, performed formal analysis, developed methodology and software, administered project, collected resources, and wrote and reviewed the original draft. Krishnaraju Venkatesan conceptualised, validated, visualized, and supervised the study, performed formal analysis, developed methodology and software, administered project, collected resources, and wrote and reviewed the original draft. ShadiaHamoudAlshahrani conceptualized and visualized the study, developed methodology, administered project, and wrote and reviewed the article. VaniManoharan conceptualized and validated the study, curated data, developed methodology, administered project, and wrote and reviewed the article. Kalaiselvi Periannan curated data, performed formal analysis, developed methodology, administered project, validated and visualized the study, and wrote and reviewed the article. Kalpana Krishnaraju performed formal analysis, developed methodology and software, administered project, supervised and validated the study, and wrote and reviewed the study. RashaElsayed Ahmed curated data, performed formal analysis, developed methodology, administered project, collected resources, validation the study, and wrote and reviewed the article. Kousalya Prabahar conceptualised, investigated, supervised, validated, and visualized the study, developed methodology, administered project,, and wrote and reviewed the article.

Acknowledgments

The authors extend their sincere appreciation to the Deanship of Scientific Research at King Khalid University for funding this study through the Large Research Group Project (RGP 2/186/42).

References

[1] R. Roubenoff, "Gout and hyperuricemia," *Rheumatic Disease Clinics of North America*, vol. 16, no. 3, pp. 539–550, 1990.

[2] H. Ralph Schumacher, "Crystal-induced arthritis: an overview," *The American Journal of Medicine*, vol. 100, no. 2, pp. 46S–52S, 1996.

[3] R. A. Terkeltaub and M. H. Ginsberg, "The inflammatory reaction to crystals," *Rheumatic Disease Clinics of North America*, vol. 14, no. 2, pp. 353–364, 1988.

[4] M. D. Harris, L. B. Siegel, and J. A. Alloway, "Gout and hyperuricemia," *American Family Physician*, vol. 59, pp. 925–934, 1999.

[5] N. Schlesinger, "Management of acute and chronic gouty arthritis," *Drugs*, vol. 64, no. 21, pp. 2399–2416, 2004.

[6] H. M. Kramer and G. Curhan, "The association between gout and nephrolithiasis: the national health and nutrition examination Survey III, 1988-1994," *American Journal of Kidney Diseases*, vol. 40, no. 1, pp. 37–42, 2002.

[7] R. Porkodi, M. Parthipan, and S. Rukmangathararajan, "Clinical spectrum of gout in South India," *Journal of Indian Rheumatology Association*, vol. 10, pp. 61–63, 2002.

[8] G. M. Han, K. Michaud, F. Yu, S. Watanabe- Galloway, and T. R. Mikuls, "Increasing public health burden of arthritis and other rheumatic conditions and comorbidity: results from a Statewide Health Surveillance System," *Arthritis Care & Research*, vol. 68, pp. 1417–1427, 2016.

[9] A. A. Kiadaliri and M. Englund, "Temporal trends and regional disparity in rheumatoid arthritis and gout hospitalizations in Sweden, 1998-2015," *Clinical Rheumatology*, vol. 37, no. 3, pp. 825–830, 2018.

[10] S. Y. Lim, N. Lu, A. Oza et al., "Trends in gout and rheumatoid arthritis hospitalizations in the United States, 1993-2011," *JAMA*, vol. 315, no. 21, pp. 2345–2347, 2016.

[11] M. D. Russell, M. Yates, K. Bechman et al., "Rising incidence of acute hospital admissions due to Gout," *Journal of Rheumatology*, vol. 47, no. 4, pp. 619–623, 2020.

[12] M. Chen- Xu, C. Yokose, S. K. Rai, M. H. Pillinger, and H. K. Choi, "Contemporary prevalence of gout and hyperuricemia in the United States and decadal trends: the national health and nutrition examination Survey, 2007–2016," *Arthritis & Rheumatology*, vol. 71, pp. 991–999, 2019.

[13] J. D. Hasday and C. M. Grum, "Nocturnal increase of urinary uric acid:creatinine ratio. A biochemical correlate of sleep-associated hypoxemia," *American Review of Respiratory Disease*, vol. 135, pp. 534–538, 1987.

[14] G. Glantzounis, E. Tsimoyiannis, A. Kappas, and D. Galaris, "Uric acid and oxidative stress," *Current Pharmaceutical Design*, vol. 11, no. 32, pp. 4145–4151, 2005.

[15] H. E. Tzeng, C. C. Lin, I. K. Wang, P. H. Huang, and C. H. Tsai, "Gout increases risk of fracture," *Medicine*, vol. 95, no. 34, p. e4669, 2016.

[16] J. M. Paik, S. C. Kim, D. Feskanich, H. K. Choi, D. H. Solomon, and G. C. Curhan, "Gout and risk of fracture in women: a prospective cohort study," *Arthritis & Rheumatology*, vol. 69, no. 2, pp. 422–428, 2017.

[17] C. C. Huang, P.-H. Huang, J.-H. Chen et al., "An independent risk of gout on the development of deep vein thrombosis and pulmonary embolism," *Medicine*, vol. 94, no. 51, Article ID e2140, 2015.

[18] C.-C. Chiu, Y.-T. Chen, C.-Y. Hsu et al., "Association between previous history of gout attack and risk of deep vein thrombosis - a nationwide population-based cohort study," *Scientific Reports*, vol. 6, no. 1, Article ID 26541, 2016.

[19] L. Li, N. McCormick, E. C. Sayre et al., "Trends of venous thromboembolism risk before and after diagnosis of Gout: a general population-based study," *Rheumatology*, vol. 59, no. 5, pp. 1099–1107, 2020.

[20] N. Dalbeth, C. S. Zhong, R. Grainger et al., "Outcome measures in acute Gout: a systematic literature review," *Journal of Rheumatology*, vol. 41, no. 3, pp. 558–568, 2014.

[21] C.-F. Kuo, M. J. Grainge, C. Mallen, W. Zhang, and M. Doherty, "Comorbidities in patients with Gout prior to and following diagnosis: case-control study," *Annals of the Rheumatic Diseases*, vol. 75, no. 1, pp. 210–217, 2016.

[22] D. H. Jaffe, A. B. Klein, A. Benis et al., "Incident gout and chronic kidney disease: healthcare utilization and survival," *BMC Rheumatology*, vol. 3, no. 1, p. 11, 2019.

[23] T. Haque, S. Rahman, S. Islam, N. H. Molla, and N. Ali, "Assessment of the relationship between serum uric acid and glucose levels in healthy, prediabetic and diabetic individuals," *Diabetology & Metabolic Syndrome*, vol. 11, no. 1, p. 49, 2019.

[24] M. Roughley, A. A. Sultan, L. Clarson et al., "Risk of chronic kidney disease in patients with gout and the impact of urate lowering therapy: a population-based cohort study," *Arthritis Research and Therapy*, vol. 20, no. 1, p. 243, 2018.

[25] G. Billa, R. Dargad, and A. Mehta, "Prevalence of hyperuricemia in Indian subjects attending hyperuricemia screening programs-A retrospective study," *Journal of the Association of Physicians of India*, vol. 66, no. 4, pp. 43–46, 2018.

[26] V. S. Tan, A. X. Garg, E. McArthur, N. N. Lam, M. M. Sood, and K. L. Naylor, "The 3-year incidence of Gout in elderly patients with CKD," *Clinical Journal of the American Society of Nephrology*, vol. 12, no. 4, pp. 577–584, 2017.

[27] J. A. Singh and J. D. Cleveland, "Gout is associated with a higher risk of chronic renal disease in older adults: a retrospective cohort study of U.S. Medicare population," *BMC Nephrology*, vol. 20, no. 1, p. 93, 2019.

[28] T. Haque, S. Rahman, S. Islam, N. H. Molla, and N. Ali, "Assessment of the relationship between serum uric acid and glucose levels in healthy, prediabetic and diabetic individuals," *Diabetology & Metabolic Syndrome*, vol. 11, no. 1, p. 49, 2019.

[29] K. Yamamoto and S. Nagata, "Physiological and psychological evaluation of the wrapped warm footbath as a complementary nursing therapy to induce relaxation in hospitalized patients with incurable cancer," *Cancer Nursing*, vol. 34, no. 3, pp. 185–192, 2011.

[30] Y. Koike, H. Kondo, S. Kondo, M. Takagi, and Y. Kano, "Effect of a steam foot spa on geriatric inpatients with cognitive impairment: a pilot study," *Clinical Interventions in Aging*, vol. 8, pp. 543–548, 2013.

[31] Y. Kudo and M. Sasaki, "Effect of a hand massage with a warm hand bath on sleep and relaxation in elderly women with disturbance of sleep: a crossover trial," *Japan Journal of Nursing Science JJNS*, vol. 17, no. 3, Article ID e12327, 2020.

[32] P. M. ten Klooster, H. E. Vonkeman, and M. A. F. J. van de Laar, "Disability due to gouty arthritis," *Current Opinion in Rheumatology*, vol. 24, no. 2, pp. 139–144, 2012.

[33] X. Chen and P. K. Schadlich, "Association between Gout and all-cause as well as cardiovascular mortality: a systematic review," *Current Rheumatology Reports*, vol. 14, pp. 195–203, 2012.

[34] C. A. Scire, M. Manara, M. A. Cimmino et al., "Gout impacts on function and health-related quality of life beyond associated risk factors and medical conditions: results from the KING observational study of the Italian Society for Rheumatology (SIR)," *Arthritis Research & Therapy*, vol. 15, p. R101, 2013.

[35] V. Aghamohammadi, R. Salmani, R. Ivanbagha, F. Effati Daryani, and K. Nasiri, "Footbath as a safe, simple, and non-pharmacological method to improve sleep quality of menopausal women," *Research in Nursing & Health*, vol. 43, no. 6, pp. 621–628, 2020.

[36] L. K. Miyahara, R. Stefanini, V. M. Suguri, G. H. Wawginiak, R. A. Balsalobre, and F. L. M. Haddad, "Evaluation of sleep quality and risk of obstructive sleep apnea in patients referred for aesthetic rhinoplasty," *Sleep science (Sao Paulo, Brazil)*, vol. 12, no. 3, pp. 126–131, 2019.

[37] J. C. Ong and M. R. Crawford, "Insomnia and obstructive sleep apnea," *Sleep medicine clinics*, vol. 8, no. 3, pp. 389–398, 2013.

[38] K. Sato, "The physiology, pharmacology, and biochemistry of the eccrine sweat gland," *Reviews of Physiology, Biochemistry & Pharmacology*, vol. 79, pp. 51–131, 1977.

Hindawi
Journal of Healthcare Engineering
Volume 2022, Article ID 8362091, 6 pages
https://doi.org/10.1155/2022/8362091

Research Article

Genetic Programming-Based Feature Selection for Emotion Classification Using EEG Signal

Aditi Sakalle[1], **Pradeep Tomar**[1], **Harshit Bhardwaj**[1], **Asif Iqbal**[2], **Maneesha Sakalle**[3], **Arpit Bhardwaj**[4], and **Wubshet Ibrahim**[5]

[1]*CSE Department, University School of Information and Communication Technology, Gautam Buddha University, Greater Noida, India*
[2]*SDITS College of Engineering, Khandwa, India*
[3]*Department of Mathematics, SNGPG, College Khandwa, Khandwa, India*
[4]*CSE Department, BML Munjal University, Haryana, India*
[5]*Department of Mathematics, Ambo University, Ambo, Ethiopia*

Correspondence should be addressed to Aditi Sakalle; aditi.sakalle@gmail.com and Wubshet Ibrahim; wubshet.ibrahim@ambou.edu.et

Received 1 January 2022; Accepted 25 January 2022; Published 8 March 2022

Academic Editor: Enas Abdulhay

The COVID-19 has resulted in one of the world's most significant worldwide lock-downs, affecting human mental health. Therefore, emotion recognition is becoming one of the essential research areas among various world researchers. Treatment that is efficacious and diagnosed early for negative emotions is the only way to save people from mental health problems. Genetic programming, a very important research area of artificial intelligence, proves its potential in almost every field. Therefore, in this study, a genetic program-based feature selection (FSGP) technique is proposed. A fourteen-channel EEG device gives 70 features for the input brain signal; with the help of GP, all the irrelevant and redundant features are separated, and 32 relevant features are selected. The proposed model achieves a classification accuracy of 85% that outmatches other prior works.

1. Introduction

Due to the COVID-19 epidemic, all the governments in the world have to impose a lockdown. This strictness, however, affects the emotions of the people, and lots of people are feeling emotional imbalance [1]. The people are experiencing negative emotions, and their health and performance are degrading day by day. Emotion and mental awarenesses have become the primary concern for all the governments in the world because a lot of people are feeling stressed and alone [2].

To address the challenge as mentioned above, lots of researchers are applying classification algorithms to understand the emotion of the people [3]. Humans cannot classify these types of emotions; whereas, these classifiers can do this task very efficiently [4]. Recently, many expert systems and machine learning tools are gaining importance for the classification of medical data because they can learn from experience, past patterns, and examples [5–7]. Also, a more detailed medical data examination can be done in a shorter time with a reduced number of errors [8–10]. However, the problem with many features is that they are redundant. Because of that, they increase the error rather than reducing it [11, 12]. Feature selection can address this problem by selecting only relevant features for classification [13–15]. This improves the performance of the classifiers by removing similar features, shortening the training time. The techniques like evolutionary algorithms are gaining importance in feature selection because they can efficiently search the entire search space. There are few evolutionary algorithms, but genetic programming has shown good results on classification problems. Another advantage of using GP is that the classifier of GP has a tree structure [16], so we can recognize the features present in the best classifier. This will help, especially in the case of medical diagnosis, because we can determine which features are more important. In the last decade, there have been several reports on applying GP techniques to a range of medical data classification problems [17–19].

However, in this study, the genetic programming-based feature selection (FSGP) technique is proposed. It helps to improve the classification accuracy of the emotion recognition dataset by removing redundant and irrelevant characteristics in a single GP life cycle. An EEG dataset is created using brain signals [20]. The proposed algorithm yielded an accuracy of 85% for 80–20 training-testing partition. The results show that our approach works well with the EEG database and reduces the number of features with increased classification accuracy, confirming that it can be an excellent alternative to the well-known expert system and machine learning methods. The goal of our algorithm would be to correctly classify the samples as positive and negative emotions with an optimal number of features. The following few points highlight the difference between the current study and the existing ones in the literature. (i) How we can reduce the number of features and simultaneously increase the classification accuracy in a single genetic programming life cycle. (ii) The present study contains the result on the emotion recognition dataset created using the 14-channel EEG device. (iii) A reduced number of features are also presented along with the classification accuracy.

The rest of the study is described as follows: Section 2 gives the device and dataset description, Section 3 tells about the proposed algorithm, Section 4 presents the result of the proposed algorithm, and Section 5 compares the proposed algorithm with other machine learning algorithms.

2. Methods and Materials

This part provides information about the device, dataset used, and the classification algorithm.

2.1. Device Description. Emotiv EPOC is a 14-channel wireless headband for collecting brain signals shown in Figure 1. It is a portable device that has 14 electrodes following the American EEG Society Standard, as shown in Figure 2. This device can collect raw EEG data and generate the features from the signals. The total number of signals this device generates is 70. The five features are from every 14 channels, so 70 features.

The EEG signals are generated as a person experiences different emotions or feelings when exposed to situations or scenarios through visual content. We recognize an individual's emotions by analyzing brain waves while watching emotional or situational materials and classify the emotions into two classes, i.e., positive and negative. The elicitation materials included around 60 videos, which depict the dramatic person's predefined personality traits and are therefore recognized as the ground truth of this work's experimental procedure.

2.2. Dataset. Fifty (25 males and 25 females) nonclinical participants were considered for this research. The study was volunteered by participants, and an informed consent form was also concluded. All nonclinical participants from various cultures and education classes were Hindi speaking. However, 5 data samples were dropped as a result of failure in equipment or excessive EEG signal artifacts in the final analysis. The age group of participants is divided into three age groups as 15–20 years, 21–26 years, and 27–35 years.

Figure 1: 14-channel Emotiv EPOC.

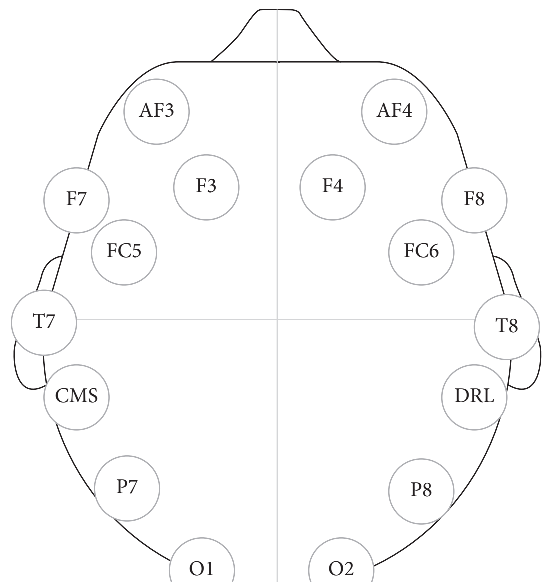

Figure 2: American Society Standard for putting 14-channel electrodes.

3. Proposed Method

For this research, fifty (25 males and 25 females) nonclinical participants involved. Participants volunteered for the study, and an informed consent form was also concluded—all nonclinical participants from various cultures and education classes were Hindi speaking. However, 5 data samples were dropped due to failure in equipment or excessive EEG signal artifacts in the final analysis; in total, 45 participants were considered for this research.

3.1. Initialization and Fitness. We generate the initial population using all features in the feature set and terminals in the terminal set. The ramped half and half method is used for initializing the population. We maintain the structural diversity of the people through all generations. To keep the variety, all the individuals are compared to ensure that no similar trees are generated. After generating the diverse initial population, we calculate the fitness of all the trees using the emotion recognition dataset. During training the individuals, we calculate the fitness using the training dataset.

3.2. Feature Selection. After evaluating the fitness of the classifiers, we perform our feature selection process. In this, we calculate the average fitness of the classifiers in the generation. After that, we select those classifiers whose accuracy (fitness) is more significant than average accuracy and named them Cgaa classifiers (classifier having accuracy greater than average accuracy). Then, we assign the weights to the features present in Cgaa classifiers. Initially, the weight of all the features is 0; then, we evaluate the number of times any feature is present in these Cgaa classifiers. The number of times the feature is present in the Cgaa classifier is the weight of that feature. This process is repeated for all the features, and their weights are evaluated. We repeat this process for 50% of the generation and evaluate the weight of all the features present in Cgaa classifiers. After getting the weight of all the features, we calculate their average. Those features whose weights are more significant than average weight is selected, and we named them suboptimal features (Fso). Then, we got two subsets of features: those whose weight is more significant than average weight (Fso) and those whose weight is not greater (Fno).

In the next generation, we replace all the (Fno) features with (Fso) features. To replace the (Fno) features with (Fso) features, we apply a modified mutation technique, in which we replace the single (Fno) feature with a single (Fso) feature randomly chosen from the (Fso) subset. Then, we compare the fitness of the newly generated tree with its parent. If the fitness of the tree is increased, then we stop; otherwise, we repeat this process till we get better offspring than a parent. In this way, all the unwanted (Fno) features are replaced by (Fso) features. Then, we allowed the GP life cycle to run till the last generation and obtain the best classifier in terms of fitness, and the features present in the best classifier are the optimal feature set. The advantage of this method is that we had done the feature selection and classification in one run of GP. The other benefit is that our process does not suffer from overfitting problems as happens in the case of wrapper approaches because of applying a similar algorithm two times, the first time for feature selection and the second time for classification. The flowchart of the proposed work is shown in Figure 3.

3.3. Genetic Operators. The three operators of genetic programming are applied to generate the following populations. Reproduction copies the best individual to the next generation. Crossover and mutation operators are improved to reduce the possibility of sending the lower fitness individuals to the next generations. The hill-climbing crossover and mutation operators [16] are used in this work. After doing the crossover and mutation, the offsprings are compared with their parents, and if their fitness is better than the parents, only the child is transferred to the next generation. Due to this property only, the exploitation of the solution is maintained.

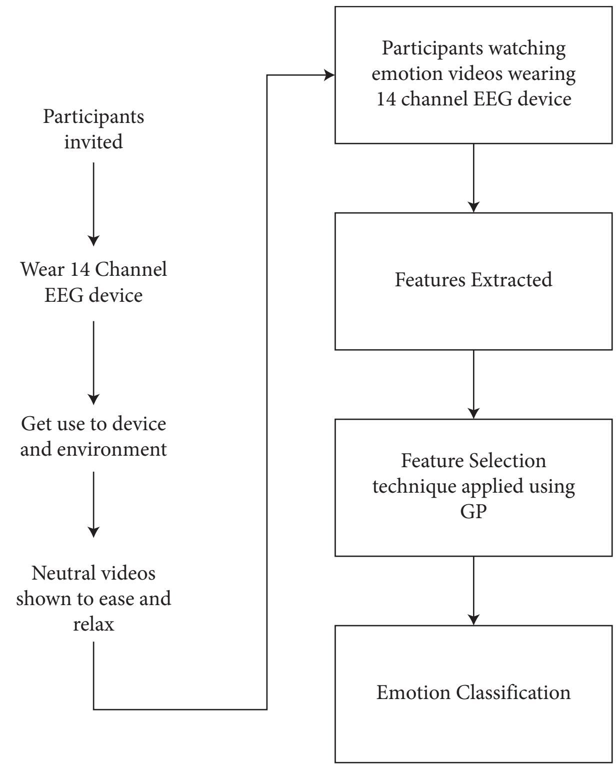

Figure 3: Flowchart of the proposed work.

3.4. Termination Criteria. The GP process is terminated as soon as the fitness reaches 100% accuracy.

4. Results

In this section, the FSGP model results are examined. The computer configuration consists of 64 GB RAM-based Python (3.8) for incorporating FSGP, GPmtfs, and another existing approaches, i.e., neural network, genetic programming, random forest, and SVM. These algorithms were applied to the EEG dataset for emotion recognition. Experimentation is carried out on the datasets with the parameters as given in Table 1.

In this study, the dataset is separated into two parts, i.e., in training and test sets. They are divided into different partitions to compare the training-testing outcomes to existing literature.

The performance assessment is conducted using a hold-out 80–20 validation scheme. In the 80–20 partition scheme, we have divided the dataset into two parts; the first part consists of 80%, which is used for training the model and the second part consisting of 20% is for model testing. The proposed FSGP and GPmtfs architecture were evaluated by calculating the performance metrics such as sensitivity,

Table 1: Parameter and values for the GP model.

Parameter	Value
Crossover probability	60%
Reproduction probability	20%
Mutation probability	20%
Population size	100
Initialization method	Ramped half and half
Initial maximum depth of a tree	10
Initial minimum depth of a tree	5

precision, and specificity values and are given in Table 2, and their mathematical expressions are given as follows.

$$\text{Recall} = \frac{TP}{TP + FN}$$
$$\text{Precision} = \frac{TP}{TP + FP} \quad (1)$$
$$\text{Specificity} = \frac{TN}{TN + FP}.$$

where TP is true positive, TN is true negative, FP is false positive, and FN is false negative.

In this section, we present the experimental results to test the behavior of the proposed genetic programming-based feature selection (FSGP) model, as well as to compare it with the classical multitree genetic programming-based FS (GPmtfs) model [14]. The results of classification accuracy of both the models are given in Table 3, with 80–20 training and testing data for the emotion recognition dataset. It is clear from the results that the FSGP model outperforms the classical GPmtfs in terms of classification accuracy for 80–20 training-testing data. It is also clear from the result that the average number of features selected by the FSGP model is less than the GPmtfs model, which shows that replacing the unwanted features in the middle stage with suboptimal features helps select the optimal set of features and improves the accuracy. Classification accuracy achieved by the FSGP model for 80–20 training-testing samples is 85% with 32 average number of features for the EEG dataset, which is very remarkable. It shows that the FSGP model has good adaptation generation capability and can select the optimal number of features if proper training data are provided. The result confirms the importance of appropriate training data for selecting the optimal features from the dataset.

This concludes that our FSGP can reduce the number of features with improved accuracy and show the important features in the dataset. Thus, our model can be a beneficial tool for physicians to diagnose the patient.

The GPmtfs model' maximum, average, and minimum classification accuracies for 80–20 training-testing partition achieved are 75%, 71%, and 68%, respectively.

The FSGP model' maximum, average, and minimum classification accuracies for 80–20 training-testing partition achieved are 85%, 82%, and 80%, respectively.

Table 4 provides the accuracy of the FSGP model on a different number of fitness evaluations. It is clear from the results that the model gives the best accuracy at 80000 fitness evaluations. The accuracy below those numbers is inferior, and after 80000 fitness evaluation, the accuracy is not improving. This suggests that our model converges at 80000 fitness evaluations.

Table 2: Comparison of performance measures.

Method	Sensitivity (%) Mean ± std	Precision (%) Mean ± std	Specificity (%) Mean ± std
GPmtfs	**70.29 ± 3.16**	**78.50 ± 3.42**	76.47 ± 2.36
FSGP	**84.29 ± 1.16**	**86.50 ± 1.42**	87.47 ± 2.36

Bold shows the maximum values.

Table 3: Classification accuracy comparison of GPmtfs and FSGP models for the emotion recognition dataset.

Method	No. of features	Accuracy		
		Max	Avg	Min
GPmtfs	42	75	71	68
FSGP	32	85	82	80

Table 4: FSGP model accuracy on different numbers of fitness evaluations.

Number of fitness evaluations	Accuracy (%)
50000	66
60000	68
70000	75
80000	85
90000	84
100000	84

Figure 4 shows the comparison of the accuracy of GPmtfs and FSGP on a different number of evaluations. Both algorithms do not seem to produce good results when the number of fitness evaluations is less. On increasing the fitness evaluations, the accuracy of both models increases; however, FSGP outperforms GPmtfs on every comparison. Both the models converged around 80000 fitness evaluations and marked their complete accuracy.

Figure 5 shows the accuracy and features of the FSGP model on a different number of fitness evaluations. The red line indicates the accuracy, and the blue line shows the features. It is clear from the figure that the FSGP model has the highest accuracy and the lowest features at 80000 fitness evaluations. The optimal number of fitness evaluations for the FSGP model is 80000 for emotion recognition data. This fitness evaluation gives the highest accuracy with an optimal number of features.

Table 5 provides the classification accuracy in the form of confusion matrix. It is clear from Table 5 that the sum of true positive and true negative is much better for FSGP as compared to GPmtfs. This again confirms the superiority of FSGP over GPmtfs. The Mann–Whitney confirms the statistical difference in result given in Table 6. The solution produced by our FSGP model is statistically different from the GPmtfs model for 80–20 training-testing partition for the emotion recognition dataset.

5. Discussion

This section compares the proposed model with the standard machine learning algorithms. The conventional algorithms

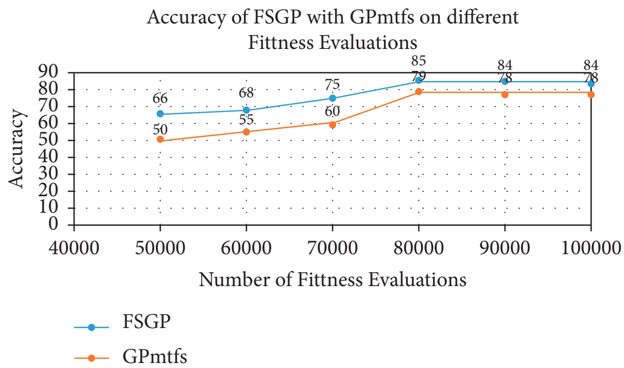

Figure 4: Accuracy of GPmtfs and FSGP on different fitness evaluations.

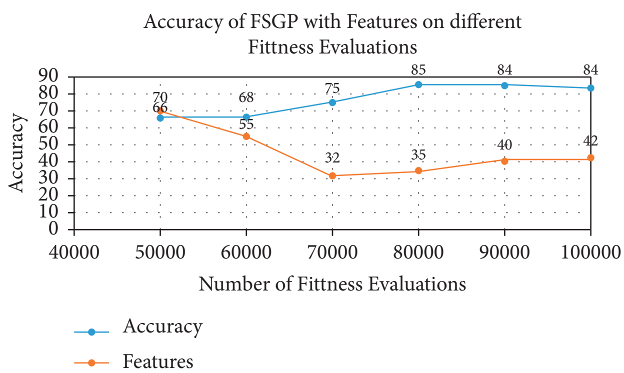

Figure 5: Accuracy of FSGP with features on different fitness evaluations.

Table 5: Confusion matrix of GPmtfs and FSGP models for the emotion recognition dataset.

	GPmtfs		FSGP	
	FP	FN	FP	FN
TP	42	75	71	68
TN	32	85	82	80

Table 6: *P* value for FSGP.

Method	Partition	*P* value
FSGP	70–30	2.871×10^{-11}

are also implemented using the same set of EEG features used to develop the proposed model. Table 7 provides the classification accuracy comparison of the proposed models on the 80–20 partition scheme.

5.1. Comparison. Various works from different authors on emotion recognition datasets are given in Table 7. Our proposed approach, FSGP, in which we have simultaneously done the feature selection and classification, is noteworthy in terms of classification accuracy than other approaches. Observations also show that our method removes the redundant and irrelevant features and finds the optimal number of features to classify the emotion recognition data.

Table 7: Classification accuracy comparison of existing approaches and MLSTM_3 classifier for two class of emotion classification to analyze the mental state during pandemic.

Method	Partition	Accuracy (%) Max
Neural network	80–20	74
Random forest	80–20	70
Genetic programming	80–20	79
SVM	80–20	76
FSGP	80–20	**85**

Bold shows the maximum value of accuracy.

The neural network, random forest, genetic programming, and SVM are the other state-of-the-art approaches used. To guarantee that the conclusions and comparisons given are explicit and accurate, the setting of parameters for all these classifiers has been implemented using the same method. It is evident from Table 7 that in the FSGP model, the classification accuracy was superior to all the other models for 80–20 training-testing partition. The second-best classification accuracy after FSGP is of genetic programming, and for the 80–20 training-test partition, the overall accuracy is 79%. Table 2 provides the values of FSGP and GPmtfs for 80–20 data partitioning scheme for sensitivity, precision, and specificity. It is clear from the result that FSGP outperforms the GPmtfs in all aspects.

Table 6provides the two-tailed Mann–Whitney test which shows the statistical result disparity [21]. The p value is computed using the Mann–Whitney test. If the p value is more significant than 0.05, the results do not alter considerably; nevertheless, if the p value is smaller than the value 0.001, the results are highly effective. The findings in Table 6 show that FSGP model results are statistically separate from GPmtfs for the 80–20 training-testing split. The results show a significant difference when these classifiers' p values are compared to FSGP. According to the evaluation findings, the suggested FSGP model for performance analysis of two classes of emotion, i.e., positive and negative classification, produces accurate output.

6. Conclusion

A novel approach for emotion recognition has been explored to extract important features and improve accuracy. This is done by removing the redundant and irrelevant features during 50% of the generation and forming a subset of suboptimal features rather than finding the optimal features that increase the classifier's accuracy after complete generation. Several experiments have been conducted with the proposed method, and a comparison has been presented with the classical GPmtfs model. The collected EEG dataset was used in this study.

Data Availability

The data used to support the findings of this are available from the corresponding author upon request.

Conflicts of Interest

The authors declare that they have no conflicts of interest.

References

[1] E. A. Holmes, R. C. O'Connor, V. H. Perry et al., "Multidisciplinary research priorities for the covid-19 pandemic: a call for action for mental health science," *The Lancet Psychiatry*, vol. 7, no. 6, pp. 547–560, 2020.

[2] Y. Ren, W. Qian, Z. Li et al., "Public mental health under the long-term influence of covid-19 in China: geographical and temporal distribution," *Journal of Affective Disorders*, vol. 277, pp. 893–900, 2020.

[3] Y. Gao, H. J. Lee, and R. M. Mehmood, "Deep learninig of eeg signals for emotion recognition," in *Proceedings of the 2015 IEEE International Conference on Multimedia & Expo Workshops (ICMEW)*, pp. 1–5, Turin, Italy, July, 2015.

[4] R. Li, C. Ren, X. Zhang, and B. Hu, "A novel ensemble learning method using multiple objective particle swarm optimization for subject-independent eeg-based emotion recognition," *Computers in Biology and Medicine*, vol. 140, Article ID 105080, 2022.

[5] T. Si, J. Bagchi, and P. B. C. Miranda, "Artificial neural network training using metaheuristics for medical data classification: an experimental study," *Expert Systems with Applications*, vol. 193, Article ID 116423, 2022.

[6] S. K. Mohapatra and M. N. Mohanty, "Big data classification with iot-based application for e-health care," in *Cognitive Big Data Intelligence with a Metaheuristic Approach*, pp. 147–172, Elsevier, Amsterdam, Netherlands, 2022.

[7] A. Sakalle, P. Tomar, H. Bhardwaj, D. Acharya, and A. Bhardwaj, "A lstm based deep learning network for recognizing emotions using wireless brainwave driven system," *Expert Systems with Applications*, vol. 173, Article ID 114516, 2021.

[8] C. Jaya Sudha and Y. S. Sneha, "Classification of medical images using deep learning to aid in adaptive big data crowdsourcing platforms," in *ICT with Intelligent Applications*, pp. 69–77, Springer, Berlin, Germany, 2022.

[9] G. Chandrashekar and F. Sahin, "A survey on feature selection methods," *Computers & Electrical Engineering*, vol. 40, no. 1, pp. 16–28, 2014.

[10] M. R. Ahmed, M. A. Ali, N. Ahmed, and T. Bhuiyan, "Computational intelligence approaches for prediction of chronic kidney disease," in *Advances in Distributed Computing and Machine Learning*, pp. 299–309, Springer, Berlin, Germany, 2022.

[11] H. Bhardwaj, A. Sakalle, A. Tiwari, M. Verma, and A. Bhardwaj, "Breast cancer diagnosis using simultaneous feature selection and classification: a genetic programming approach," in *Proceedings of the 2018 IEEE Symposium Series on Computational Intelligence (SSCI)*, pp. 2186–2192, IEEE, Bangalore, India, November, 2018.

[12] A. Jović, K. Brkić, and N. Bogunović, "A Review of Feature Selection Methods with Applications," in *Proceedings of the 2015 38th International Convention on Information and Communication Technology, Electronics and Microelectronics (MIPRO)*, pp. 1200–1205, Ieee, Opatija, Croatia, May, 2015.

[13] J. Yu, J. Yu, A. A. Almal et al., "Feature selection and molecular classification of cancer using genetic programming," *Neoplasia*, vol. 9, no. 4, pp. 292–IN3, 2007.

[14] D. P. Muni, N. R. Pal, and J. Das, "Genetic programming for simultaneous feature selection and classifier design," *IEEE Transactions on Systems, Man and Cybernetics, Part B (Cybernetics)*, vol. 36, no. 1, pp. 106–117, 2006.

[15] A. Hashemi, M. B. Dowlatshahi, and H. Nezamabadi-pour, "Ensemble of feature selection algorithms: a multi-criteria decision-making approach," *International Journal of Machine Learning and Cybernetics*, vol. 13, no. 1, pp. 49–69, 2022.

[16] A. Bhardwaj, A. Tiwari, M. V. Varma, and M. R. Krishna, "An analysis of integration of hill climbing in crossover and mutation operation for eeg signal classification," in *Proceedings of the 2015 Annual Conference on Genetic and Evolutionary Computation*, pp. 209–216, Madrid, Spain, July, 2015.

[17] A. Jain, M. Pandey, and S. Sahu, "A deep learning-based feature extraction model for classification brain tumor," in *Proceedings of Data Analytics and Management*, pp. 493–508, Springer, Berlin, Germany, 2022.

[18] D. Lavanya and D. K. U. Rani, "Analysis of feature selection with classification: breast cancer datasets," *Indian Journal of Computer Science and Engineering (IJCSE)*, vol. 2, pp. 756–763, 2011.

[19] A. Purohit, A. Bhardwaj, A. Tiwari, and N. S. Choudhari, "Removing code bloating in crossover operation in genetic programming," in *Proceedings of the 2011 International Conference on Recent Trends in Information Technology (ICRTIT)*, pp. 1126–1130, Chennai, India, June, 2011.

[20] A. Sakalle, P. Tomar, H. Bhardwaj, and A. Bhardwaj, "Emotion recognition using portable eeg device," in *Communications in Computer and Information Science*vol. 1434, , pp. 17–30, Springer, 2021.

[21] H. B. Mann and D. R. Whitney, "On a test of whether one of two random variables is stochastically larger than the other," *The Annals of Mathematical Statistics*, vol. 18, no. 1, pp. 50–60, 1947.

Hindawi
Journal of Healthcare Engineering
Volume 2022, Article ID 9765317, 1 page
https://doi.org/10.1155/2022/9765317

Retraction

Retracted: The Relationship between Thyroid-Stimulating Hormone and Insulin Resistance in Incipient Elderly Type 2 Diabetics with Normal Thyroid Function

Journal of Healthcare Engineering

Received 10 November 2022; Accepted 10 November 2022; Published 27 November 2022

Journal of Healthcare Engineering has retracted the article titled "The Relationship between Thyroid-Stimulating Hormone and Insulin Resistance in Incipient Elderly Type 2 Diabetics with Normal Thyroid Function" [1] due to concerns that the peer review process has been compromised.

Following an investigation conducted by the Hindawi Research Integrity team [2], significant concerns were identified with the peer reviewers assigned to this article; the investigation has concluded that the peer review process was compromised. We therefore can no longer trust the peer review process, and the article is being retracted with the agreement of the Chief Editor.

References

[1] Y. Zhang and L. Zhang, "The Relationship between Thyroid-Stimulating Hormone and Insulin Resistance in Incipient Elderly Type 2 Diabetics with Normal Thyroid Function," *Journal of Healthcare Engineering*, vol. 2022, Article ID 9447363, 6 pages, 2022.

[2] L. Ferguson, "Advancing Research Integrity Collaboratively and with Vigour," 2022, https://www.hindawi.com/post/advancing-research-integrity-collaboratively-and-vigour/.

Hindawi
Journal of Healthcare Engineering
Volume 2022, Article ID 9447363, 6 pages
https://doi.org/10.1155/2022/9447363

Research Article

The Relationship between Thyroid-Stimulating Hormone and Insulin Resistance in Incipient Elderly Type 2 Diabetics with Normal Thyroid Function

Yajing Zhang and Lin Zhang

NHC Key Laboratory of Hormones and Development Tianjin Key Laboratory of Metabolic Diseases Chu Hsien-I Memorial Hospital & Tianjin Institute of Endocrinology, Tianjin Medical University, Tianjin 300134, China

Correspondence should be addressed to Yajing Zhang; lianyajing@163.com

Received 25 November 2021; Revised 10 December 2021; Accepted 18 January 2022; Published 7 March 2022

Academic Editor: Enas Abdulhay

Objective. To explore correlations between serum thyroid-stimulating hormone (TSH) concentration within the normal range and insulin resistance and its possible mechanism in incipient type 2 diabetes in elderly patients. *Methods*. 453 elderly patients with type 2 diabetes were divided into four groups by the quartile of TSH. Body mass index (BMI), waist-to-hip ratio (WHR), fasting plasma glucose (FPG), fasting insulin (FINS), homeostasis model assessment of insulin resistance (HOMA-IR) and homeostasis model assessment of insulin secretion (HOMA-β), blood lipids, and other indicators were compared among all groups, and correlation and regression analysis were conducted. 3T3-L1 preadipocytes were induced into mature adipocytes in vitro, and different concentrations of bovine TSH were used to stimulate adipocytes. The levels of TNF-α in the culture medium were detected by ELISA. *Results*. (1) With the increase of TSH, TC showed an increasing trend. Compared with the G1 group (4.80 ± 1.08), G2 group (5.13 ± 1.16), G3 group (5.14 ± 1.39), and G4 group (5.38 ± 1.16), the difference was statistically significant ($P < 0.05$ or $P < 0.01$). The LDL also showed an increasing trend. Compared with the G4 group (3.47 ± 0.89), the G1 (3.12 ± 0.82) and G2 groups (3.14 ± 1.05) had a lower LDL, and the difference was statistically significant ($P < 0.01$). The BMI increased between the G4 group (26.7 ± 3.97) and the G1 group (25.6 ± 3.54), and the difference was statistically significant ($P < 0.05$). (2) The serum TSH level was positively correlated with FPG, FINS, HOMA-IR, TC, and LDL ($R = 0.292$, 0.271, 0.394, 0.195, and 0.178, all $P < 0.01$). (3) TSH is the dependent variable, other indicators are independent variables, and multiple stepwise regression analysis is performed; the results show that only HOMA-IR, TC, and LDL enter the regression equation. (4) The TSH stimulated TNF-α secretion of 3T3-L1 adipocytes in a dose-dependent manner. *Conclusion*. The TSH level was positively correlated with the insulin resistance and LDL in the elderly incipient type 2 diabetic patients. Higher levels of TSH may be involved in the development of insulin resistance in the elderly incipient type 2 diabetic patients.

1. Introduction

Type 2 diabetes mellitus (T2DM) is the most common type of diabetes in China, the majority of T2DM patients are middle-aged and elderly people, and the incidence is increasing year by year. Insulin resistance is the main pathophysiological basis of T2DM. In recent years, with the continuous in-depth research on the mechanism of insulin resistance, the role of thyroid-stimulating hormone (TSH) in the occurrence of insulin resistance has attracted much attention. The TSH binds to TSHR on the surface of adipocytes, then activates cyclic adenosine monophosphate-protein kinase A (cAMP-PKA) pathway, activates tumor necrosis factor-α (TNF-α) gene transcription and secretion of TNF-α, and further downregulates the expression of insulin receptor substrate-1 (IRS-1), which plays a role in insulin resistance. At present, under the premise of normal thyroid function, there are still few reports on the role of TSH in the onset of elderly type 2 diabetes patients. This study took newly-onset elderly type 2 diabetes patients as the research object and explored the correlation between serum TSH levels and insulin resistance and other metabolic indicators within the normal reference value range, in order to further understand the relationship between TSH and elderly type 2 diabetes and discuss its possible mechanism.

2. Method

2.1. Patients Test Indicators. From December 2018 to June 2020, 453 elderly patients with type 2 diabetes were enrolled in the study, who were first diagnosed during hospitalization in our hospital, aged 60 to 90 years old, with an average of 70.36 ± 7.19 years old. Among them, 236 were males and 217 were females. The diagnostic criteria for type 2 diabetes are in line with the 2013 American Diabetes Association (ADA). Diabetes is diagnosed by the following factors: fasting blood glucose ≥7.0 mmol/L and/or 2 h postprandial blood glucose ≥11.1 mmol/L [1]. None of the selected patients received any hypoglycemic drugs outside the hospital. Exclusion criteria for the patients include the following: patients with acute infection, diabetic hyperosmolar coma, diabetic ketoacidosis, acute and chronic heart failure, liver and kidney insufficiency, acute stroke patients, and patients with abnormal thyroid function during medication treatment.

Normal thyroid function is defined as TSH levels within 0.27–4.2 mIU/L, FT3 and FT4 are within the laboratory reference range (FT3 is 3.28–6.47 pmol/L and FT4 is 7.64–16.03 pmol/L). According to the patients' serum TSH levels, they were divided into four groups as follows: G1 group (TSH is 0.37–1.17 mIU/L), G2 group (TSH is 1.18–1.67 mIU/L), G3 group (TSH is 1.68–2.45 mIU/L), and G4 group (TSH 2.46–4.20 mIU/L). This study was approved by the Ethics committee of Zhu Xianyi Memorial Hospital, Tianjin Medical University. All patients signed the informed consent.

2.2. Detection of Indexes. Research subjects need to wake up in the morning, fasting, barefoot, and only wear underwear to measure height, weight, waist circumference, and hip circumference and calculate body mass index (BMI) and waist-hip ratio (WHR); at rest, the blood pressure (BP) was measured twice in the sitting position, and the average value was taken; fasting venous blood was taken, and biochemical indicators such as liver function, renal function, and blood lipid were measured by an automatic biochemical analyzer, and fasting plasma glucose (FPG) was determined by glucose oxidase method, and TSH, free triiodothyronine (FT3) and free thyroxine (FT4), fasting serum insulin (FINS), and glycosylated hemoglobin (HbA1c) were determined by chemiluminescence assay; using homeostasis model assessment for insulin resistance (HOMA-IR): HOMA-IR = FPG (mmol/L) × FINS (mIU/ml)/22.5 [2]. The homeostasis model was used to evaluate the insulin secretion index (HOMA-β): HOMA-β = 20 × FINS/(FPG-3.5) [3].

2.3. Culture and Induced Differentiation of 3T3-L1 Preadipocytes. The cells were inoculated in a cell culture flask at a cell density of $1.5 \times 104/\text{cm}^2$, and the cells were placed in a high-sugar DMEM medium containing 10% calf serum at 37°C and 5% CO_2 cell incubator for cultivation. The medium was changed every two days. When the cells grew to 60–70% confluence at the bottom of the culture flask in about 3-4 days, the cells were replaced with DMEM high glucose medium containing 0.5 mM IBMX, 1.0 M insulin, 0.25 M dexamethasone, and 10% FBS for 2 days (48 h). IBMX and dexamethasone were removed so that the complete medium contains only 1.0 M insulin. After 2 days, the medium was changed, and the insulin was removed. A complete medium is used without any inducer. The medium was changed every 2 days, and the differentiation was 8–10 days. Oil red O staining identification of induced differentiation 3T3-L1 cells was carried out.

2.4. Elisa Assay. After stimulation with different concentrations of bovine TSH (0.01 mIU/ml, 0.1 mIU/ml, and 1 mIU/ml) for 4 hours, the culture medium was collected strictly in accordance with the ELISA kit instructions. The enzyme-linked immunosorbent assay (ELISA) method was used to detect the concentration of TNF-α in the culture medium.

2.5. Statistical Methods. SPSS 20.0 software is used for statistical analysis. The data are represented by "". Non-normally distributed data are logarithmically transformed. Comparison between groups is performed by the analysis of variance. Pairwise comparison is performed by the LSD test. Correlation analysis is performed by the Pearson linear correlation analysis. Multivariate stepwise regression analysis was performed. The test level was $\alpha = 0.05$. $P < 0.05$ indicated that the difference was statistically significant.

3. Results

3.1. Comparison of General Information of Patients. There were no significant differences in gender, age, systolic blood pressure, diastolic blood pressure, BMI, WHR, liver function, renal function, FT3, FT4, triglyceride (TG), and high-density lipoprotein (HDL) among 4 groups ($P > 0.05$). With the increase of TSH, the TC showed an increasing trend. Compared with the G1 group, G2 group, G3 group, and G4 group, the difference was statistically significant ($P < 0.05$ or $P < 0.01$). The LDL also showed an increasing trend. Compared with the G4 group, the G1, G2, and G3 groups, the difference was statistically significant ($P < 0.01$). As the TSH level increased, BMI of G1, G2, G3, and G4 groups also showed an upward trend, and the difference between the G4 and G1 groups was statistically significant ($P < 0.05$) (see Table 1).

3.2. Comparison of TSH Levels and Related Indicators of Glucose Metabolism in the Normal Range of Elderly Patients with Incient Type 2 Diabetes. There was no statistically significant difference in LnHOMA-β and HbA1c between groups of patients ($P > 0.05$). With the increase in serum TSH levels, FPG, FINS, and HOMA-IR all showed an

Table 1: Comparison of clinical characteristics of different TSH patients.

Group	G1 (TSH 0.37–1.17 mIU/L)	G2 (TSH 1.18–1.67 mIU/L)	G3 (TSH 1.68–2.45 mIU/L)	G4 (TSH 2.46–4.20 mIU/L)
N ((F/M))	113 (51/62)	113 (52/61)	113 (59/54)	114 (56/58)
Age (year)	70.0 ± 7.09	70.6 ± 6.98	70.8 ± 8.08	70.1 ± 6.58
WHR (g/cm^2)	0.91 ± 0.08	0.92 ± 0.07	0.93 ± 0.07	0.91 ± 0.08
BMI (kg/m^2)	25.6 ± 3.54	25.8 ± 3.63	26.5 ± 3.57	26.7 ± 3.97^{a}
SBP (mmHg)	127 ± 15.7	127 ± 14.1	129 ± 14.0	126 ± 13.8
DBP (mmHg)	77.6 ± 9.69	75.6 ± 10.5	77.5 ± 9.91	77.0 ± 8.92
TG (mmol/L)	1.90 ± 1.33	2.14 ± 1.54	2.10 ± 1.24	2.08 ± 1.33
TC (mmol/L)	4.80 ± 1.08	5.13 ± 1.16^{a}	5.14 ± 1.39^{a}	5.38 ± 1.16^{b}
LDL (mmol/L)	3.12 ± 0.82	3.14 ± 1.05	3.27 ± 0.90	3.47 ± 0.89^{bd}
HDL (mmol/L)	1.33 ± 0.42	1.25 ± 0.29	1.26 ± 0.32	1.25 ± 0.28
FT_3 (pmol/L)	10.8 ± 6.25	10.1 ± 6.54	10.2 ± 6.50	9.53 ± 5.41
FT_4 (pmol/L)	12.1 ± 6.09	12.0 ± 6.67	11.6 ± 6.65	12.6 ± 5.67
ALP (U/L)	69.5 ± 15.7	71.4 ± 18.4	71.9 ± 19.6	73.3 ± 18.8
GGT (U/L)	35.2 ± 20.9	33.6 ± 20.9	32.8 ± 20.4	32.3 ± 18.8
ALT (U/L)	29.6 ± 18.6	26.3 ± 15.1	26.5 ± 16.6	27.3 ± 17.5
AST (U/L)	23.1 ± 13.3	20.8 ± 9.31	22.6 ± 13.8	20.9 ± 9.52
BUN (mmol/L)	5.60 ± 1.30	5.44 ± 1.32	5.45 ± 1.36	5.45 ± 1.64
Cre (umol/L)	67.2 ± 14.6	63.8 ± 15.4	64.3 ± 14.5	66.1 ± 20.6
UA (umol/L)	307 ± 96.5	305 ± 87.9	314 ± 92.5	312 ± 93.5

Note. Compared with G1, $^{a}P < 0.05$, $^{b}P < 0.01$; compared with G2, $^{c}P < 0.05$, $^{d}P < 0.01$; and compared with G3, $^{e}P < 0.01$.

upward trend. The pairwise comparison of G1, G2, and G3 groups showed no statistically significant difference ($P > 0.05$), while the comparison of the G4 group with G1, G2, and G3 groups showed statistically significant difference ($P < 0.01$), as shown in Table 2.

3.3. Correlation Analysis of Serum TSH Levels and Related Indicators. Correlation analysis of research subjects showed that serum TSH levels were positively correlated with FPG, FINS, HOMA-IR, TC, and LDL ($R = 0.292$, 0.271, 0.394, 0.195, and 0.178, all $P < 0.01$), and no correlation was found with HOMA-β, age, BMI, WHR, TG, HDL, SBP, DBP, and HbA1c, as shown in Table 3.

3.4. Multiple Stepwise Regression Analysis. Using TSH as the dependent variable, using FPG, FINS, HOMA-IR, TC, and LDL as independent variables, multiple stepwise regression analysis was performed. The results showed that HOMA-IR, TC, and LDL entered the regression equation; HOMA-IR, TC, and LDL were independently correlated with TSH. The regression equation was as follows: $Y = 0.393 + 0.187X1 + 0.103X2 + 0.092X3$ ($X1$: HOMA-IR; $X2$: TC; X3: LDL; $P < 0.05$).

3.5. Culture and Induced Differentiation of 3T3-L1 Preadipocytes. The morphology of mouse 3T3-L1 preadipocytes and fibroblasts is similar, as shown in Figures 1(a) and 1(b). After induction to the 10th day, lipid droplets of varying sizes were seen in most of the cells, and the cell volume increased to fill the intercellular space. After oil red O staining, there are bright red particles in the cytoplasm of induced differentiated mature adipocytes. After hematoxylin counterstaining, the nucleus was blue and deviated from the center of the cell. Observed under a 10x light microscope, randomly counted the proportion of adipocytes in the total number of cells in 10 nonrepetitive fields, and more than 95% showed adipocyte phenotype, which was further confirmed to be mature adipocytes.

3.6. Effect of TSH on the Secretion of TNF-α in 3T3-L1 Adipocytes. The 3T3-L1 adipocytes were stimulated with different concentrations of bovine TSH to induce differentiation and mature 3T3-L1 adipocytes for 4 hours, and the TNF-α level in the culture medium was detected. The results showed that, with the increase of TSH stimulation concentration, the TNF-α level showed an upward trend, and the difference was statistically significant as shown in Figure 1(c).

4. Discussion

Insulin resistance is an important pathophysiological basis for the occurrence of T2DM. The previous research centers on the pathogenesis of diabetes, most of the focus was on the secretion of inflammatory factors from adipocytes to cause insulin resistance, and then diabetes, ignoring that factors other than inflammatory factors would also participate in the occurrence of insulin resistance and metabolic disorders. In the past, thyroid disease was considered to be an endocrine metabolic disease independent of diabetes. In recent years, the relationship between TSH and diabetes and diabetic ischemic heart disease has gradually attracted attention. A large number of studies have shown that [4–6], diabetic patients, especially combined among diabetic patients with cardiovascular disease, the prevalence of abnormal thyroid function is significantly higher than that of nondiabetic patients.

In recent years, research on TSH levels and insulin resistance in people with normal thyroid function has gradually attracted attention. A study by Roos et al. on 2703 patients without thyroid disease and diabetes showed that

Table 2: Comparison of related indicators of glucose metabolism in different TSH patients.

Group	G1 TSH 0.37–1.17 mIU/L	G2 TSH 1.18–1.67 mIU/L	G3 TSH 1.68–2.45 mIU/L	G4 TSH 2.46–4.20 mIU/L
N ((F/M))	113 (51/62)	113 (52/61)	113 (59/54)	114 (56/58)
FPG (mmol/L)	8.42 ± 2.31	8.20 ± 2.24	8.37 ± 1.96	10.4 ± 3.09^{bde}
FINS (mIU/L)	9.03 ± 3.18	9.15 ± 5.02	9.24 ± 4.05	11.8 ± 4.27^{bde}
HOMA-IR	3.34 ± 1.39	3.30 ± 2.03	3.42 ± 1.71	5.37 ± 2.46^{bde}
LnHOMA-β	3.65 ± 0.66	3.63 ± 0.80	3.61 ± 0.71	3.57 ± 0.61
HbA_1c	8.76 ± 2.05	9.02 ± 2.11	8.90 ± 1.97	8.70 ± 1.95

Note. Compared with G1, $^aP < 0.05$ and $^bP < 0.01$; compared with G2, $^cP < 0.05$ and $^dP < 0.01$; and compared with G3, $^eP < 0.01$.

Table 3: Correlation analysis of serum TSH level.

Statistics	FPG	FINS	HOMA-IR	TC	LDL
r	0.292	0.271	0.394	0.195	0.178
P	<0.001	<0.001	<0.001	<0.001	<0.001

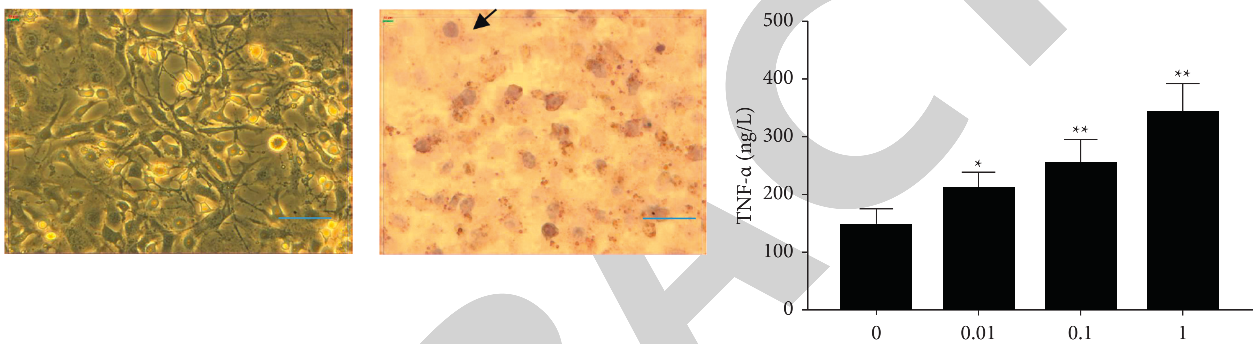

(a) (b) (c)

Figure 1: Culture and induced differentiation of 3T3-L1 preadipocytes. (a) 3T3-L1 preadipocytes (×100). (b) 3T3-L1 adipocytes (×100). (c) Different concentrations of TSH stimulated the level of TNF-α in the culture medium of 3T3-L1 adipocytes. $^*P < 0.05$ and $^{**}P < 0.01$.

serum TSH levels were significantly positively correlated with HOMA-IR [7]. Jayanthi R et al. found that serum TSH levels were positively correlated with plasma insulin level and significantly negatively correlated with the insulin sensitivity index with 530 normal, overweight, and obese adults [8]. Similarly, we also found in the previous study that the serum TSH level of T2DM patients was significantly higher than that of the normal control group [9]. In our previous study on diabetic rats, we found that the serum TSH level was negatively correlated with the insulin sensitivity index [10]. Preliminary research suggests that the TSH may be involved in the occurrence of insulin resistance and further development of type 2 diabetes. At present, the correlation between TSH and insulin resistance in elderly T2DM patients is still rarely reported. This study took newly onset elderly patients with type 2 diabetes as the research object, explored the correlation between serum TSH and insulin resistance and related metabolic indicators within the normal reference value range, and explored whether TSH is associated with the occurrence of newly onset elderly T2DM insulin resistance and abnormal lipid metabolism so as to provide a basis for further clinical treatment.

The results of this study suggest that, with the increase in serum TSH levels, BMI, TC, LDL, FINS, and HOMA-IR all showed an upward trend, while HOMA-β showed a downward trend, the TSH was within the normal range, and FNS and HOMA-IR are positively correlated in newly onset elderly patients with type 2 diabetes. Further cytological studies have shown that the TSH can stimulate 3T3-L1 adipocytes to secrete TNF-α in a dose-dependent manner ($P < 0.05$) and TSH can increase the activity of NF-κB. As can be seen from the gel electrophoresis pattern, the NF-κB/DNA probe binding bands gradually increased with the increase of TSH stimulation concentration. This effect was inhibited by a PKA inhibitor (H89). The possible mechanism is analyzed as follows: (1) our previous research results confirmed that there is the expression of thyroid-stimulating hormone receptor (TSHR) on the surface of adipocytes, TSH binds to TSHR on the surface of adipocytes, then activates the cyclic adenosine monophosphate-protein kinase A (cAMP-PKA) pathway [11–13], activates tumor necrosis factor-α (TNF-α) gene transcription and secretion of TNF-α, further downregulates the expression of insulin receptor substrate-1 (IRS-1), and interferes with the normal tyrosine phosphorylation of IRS-1, which plays a role in insulin resistance; (2) insulin resistance can lead to a compensatory increase in early insulin levels, and insulin increases TSH levels by affecting the level of leptin [14]; (3) overweight and obesity are one of the important causes of insulin resistance. This study found that, with the increase of TSH level, the BMI of patients showed an increasing trend, and the difference between the G4 group and the G1 group was statistically significant ($P < 0.05$). The reason may be that obesity leads to leptin resistance, resulting in serum leptin excess, which upregulates the expression of thyrotropin-releasing hormone and further increases serum TSH level [15, 16]. All of these mechanisms can lead to elevated TSH to further aggravate the occurrence of insulin resistance.

This study further found that the TSH is positively correlated with TC and LDL in the normal range. This may be because TSH directly acts on TSHR on liver cell membranes and stimulate cyclic adenosine mono-acyl-CoA reductase, and it also promotes cholesterol synthesis through the cyclic adenosine monophosphate/protein kinase A/cyclic adenosine phosphate response element-binding protein (cAMP/PKA/CREB) signaling system [17, 18]. Abnormal blood lipid metabolism may further damage the body's defense against oxidative stress, cause damage to the function of vascular endothelial cells and accelerate the formation of atherosclerosis, and increase the risk of cardiovascular disease.

To sum up, in the newly onset elderly type 2 diabetes patients with normal thyroid function, serum TSH levels are positively correlated with TC and LDL, and higher TSH levels within the normal reference value range may play a promoting role in the occurrence and development of insulin resistance through the abovementioned mechanisms. The elevated TC and LDL further participate in the pathological process of atherosclerosis occurs and increase the risk of cardiovascular disease in elderly patients with type 2 diabetes.

Therefore, it is necessary to strengthen thyroid function in elderly patients with type 2 diabetes. Monitoring and timely attention to the risk factors related to cardiovascular disease in patients with normal thyroid function and high serum TSH levels will play a positive role in preventing and delaying the occurrence of cardiovascular complications in elderly patients with type 2 diabetes.

Therefore, monitoring of thyroid function in elderly patients with type 2 diabetes should be strengthened, and timely attention should be paid to the risk factors related to cardiovascular disease in patients with normal thyroid function and high serum TSH levels, which will play a positive role in preventing and delaying the occurrence of cardiovascular disease in elderly patients with type 2 diabetes.

Data Availability

The data used to support the findings of this study are available on reasonable request from the corresponding author.

Conflicts of Interest

The authors declare that they have no conflicts of interest.

References

[1] American Diabetes Association, "Diagnosis and classification of diabetes mellitus," *Diabetes Care*, vol. 36, no. 1, pp. S67–S74, 2013.

[2] D. R. Matthews, J. P. Hosker, A. S. Rudenski, B. A. Naylor, D. F. Treacher, and R. C. Turner, "Homeostasis model assessment: insulin resistance and ?-cell function from fasting plasma glucose and insulin concentrations in man," *Diabetologia*, vol. 28, no. 7, pp. 412–419, 1985.

[3] S. M. Haffter, E. Kellledy, and C. Conzalez, "Aprospective analysis of the HOMA model. The Mexico city diabetes study," *Diabetes Care*, vol. 19, pp. 1138–1141, 1996.

[4] M. Li, X. Zhang, X. Zhou et al., "The association between serum thyrotropin within the reference range and metabolic syndrome in a community-based Chinese population," *Diabetes, Metabolic Syndrome and Obesity: Targets and Therapy*, vol. 13, pp. 2001–2011, 2020.

[5] A. Javed, P. B. Balagopal, A. Vella et al., "Association between thyrotropin levels and insulin sensitivity in euthyroid obese adolescents," *Thyroid*, vol. 25, no. 5, pp. 478–484, 2015.

[6] S. Ma, F. Jing, C. Xu et al., "Thyrotropin and obesity: increased adipose triglyceride content through glycerol-3-phosphate acyltransferase 3," *Scientific Reports*, vol. 5, no. 1, p. 7633, 2015.

[7] A. Roos, S. J. L. Bakker, T. P. Links, R. O. B. Gans, and B. H. R. Wolffenbuttel, "Thyroid function is associated with components of the metabolic syndrome in euthyroid subjects," *Journal of Clinical Endocrinology & Metabolism*, vol. 92, no. 2, pp. 491–496, 2007.

[8] R. Jayanthi, A. R. Srinivasan, and A. L. Maran, "Clinical sensitivity and specificity of serum total bilirubin – a study on thyroid status in clinically euthyroid non-obese, overweight, and obese type 2 diabetics," *International Journal of Health Sciences*, vol. 13, no. 4, pp. 22–28, 2019.

[9] H. Zhang, P. Fang, N. Zheng, and Z. Gao, "Analysis of thyroid function status in hospitalized patients with type 2 diabetes mellitus," *International Journal of Endocrinology and Metabolism*, vol. 27, pp. 139–141, 2007.

[10] Y. Zhang, W. Zhao, and H. Zhang, "Study on correlation between TSH and NF-κB, TNF-α protein levels in adipocytes," *Chinese Journal of Endocrinology and Metabolism*, vol. 29, pp. 74–76, 2013.

[11] Y. J. Zhang, W. Zhao, M. Y. Zhu, S. S. Tang, and H. Zhang, "Thyroid-stimulating hormone induces the secretion of tumor necrosis factor-α from 3T3-L1 adipocytes via a protein kinase A-dependent pathway," *Experimental and Clinical Endocrinology & Diabetes: Official Journal, German Society of Endocrinology [and] German Diabetes Association*, vol. 121, no. 8, pp. 488–493, 2013.

[12] Y. Zhang, L. Feng, W. Zhao, S. Tang, and H. Zhang, "Thyroid stimulating hormone down-regulates the expression of IRS-1 in 3T3-L1 adipocytes by promoting the secretion of TNF-α," *Chinese Journal of Endocrinology and Metabolism*, vol. 30, no. 1, pp. 65–68, 2014.

[13] Y. Zhang, W. Zhao, H. Zhang, X. Wu, and L. Jia, "Inhibitory effect of thyroid-stimulating hormone receptor on the expression of glucose transporter 4 in 3T3-L1 adipocytes," *Chinese Journal of Geriatrics*, vol. 32, no. 2, pp. 219–223, 2013.

[14] W. Tu, G. Zhang, and S. Yu, "Observations on factors that influence thyroid nodules in diabetic and non-diabetic patients in the Zhejiang province of China," *International Journal of Clinical and Experimental Medicine*, vol. 8, no. 10, pp. 19332–19338, 2015.

[15] C. Bétry, M. A. Challan-Belval, A. Bemard et al., "Increased TSH in obesity: evidence for a BMI-independent association with leptin," *Diabetes & Metabolism*, vol. 41, no. 3, p. 248, 2015.

[16] Y. S. Kushchayeva, S. V. Kushchayev, M. Startzell et al., "Thyroid abnormalities in patients with extreme insulin

Hindawi
Journal of Healthcare Engineering
Volume 2022, Article ID 1987917, 12 pages
https://doi.org/10.1155/2022/1987917

Review Article

Development of Advanced Artificial Intelligence and IoT Automation in the Crisis of COVID-19 Detection

Praveen Kumar Kollu,[1] Kailash Kumar,[2] Pravin R. Kshirsagar,[3] Saiful Islam,[4] Quadri Noorulhasan Naveed,[5] Mohammad Rashid Hussain,[5] and Venkatesa Prabhu Sundramurthy[6]

[1]*Department of Computer Science and Engineering, Velagapudi Ramakrishna Siddhartha Engineering College, Vijayawada, India*
[2]*College of Computing and Informatics, Saudi Electronic University, Riyadh 11673, Saudi Arabia*
[3]*Department of Artificial Intelligence, G. H. Raisoni College of Engineering, Nagpur, India*
[4]*Department of Civil Engineering, College of Engineering, King Khalid University, Abha 61411, Asir, Saudi Arabia*
[5]*College of Computer Science, King Khalid University, Abha 61413, Saudi Arabia*
[6]*Center of Excellence for Bioprocess and Biotechnology, Department of Chemical Engineering, College of Biological and Chemical Engineering, Addis Ababa Science and Technology University, Addis Ababa, Ethiopia*

Correspondence should be addressed to Pravin R. Kshirsagar; pravinrkshirsagarphd@gmail.com and Venkatesa Prabhu Sundramurthy; venkatesa.prabhu@aastu.edu.et

Received 12 November 2021; Revised 24 November 2021; Accepted 22 January 2022; Published 2 March 2022

Academic Editor: Enas Abdulhay

Internet of Things (IoT) is a successful area for many industries and academia domains, particularly healthcare is one of the application areas that uses IoT sensors and devices for monitoring. IoT transition replaces contemporary health services with scientific and socioeconomic viewpoints. Since the epidemic began, diverse scientific organizations have been making accelerated efforts to use a wide range of tools to tackle this global challenge and the founders of IoT analytics. Artificial intelligence (AI) plays a key role in measuring, assessing, and diagnosing the risk. It could be used to predict the number of alternate incidents, recovered instances, and casualties, also used for forecasting cases. Within the COVID-19 background, IoT technologies are used to minimize COVID-19 exposure to others by prenatal screening, patient monitoring, and postpatient incident response in specified procedures. In this study, the importance of IoT technology and artificial intelligence in COVID-19 is explored, and the 3 important steps discussed such as the evaluation of networks, implementations, and IoT industries to battle COVID-19, including early detection, quarantine times, and postrecovery activities, are reviewed. In this study, how IoT handles the COVID-19 pandemic at a new level of healthcare is investigated. In this research, the long short-term memory (LSTM) with recurrent neural network (RNN) is used for diagnosis purpose and in particular, its important architecture for the analysis of cough and breathing acoustic characteristics. In comparison with both coughing and respiratory samples, our findings indicate poor accuracy of the voice test.

1. Introduction

COVID-19 has been reported as a global epidemic by the World Health Organization (WHO), and it travels out across globe. 8.8 million cases were registered globally on June 30, 2020. With a record of 2.64 million cases and 128 lakhs of accidents, the United States is perhaps the most afflicted country in the region [1–3]. Health practitioners face many challenges such as identify signs, diagnose the condition, and take decisions. To overcome these problems, they use computer programs; they battle to ensure the virus identification, which is successful in this situation. In current trends, AI is a rising innovation; it is close to the intellect of man.

The human brain system illustrates the complex issues, but the lot of concerns increases the cost of solving that issue. AI is capable to concurrently quantify a range of issues and remedies. Many people just assume that AI is just about automation, but it is a computer that imitates human consciousness [4]. IoT connects the people worldwide for transmitting the data to the adjacent devices and systems [5]. The issue is a human who uses some sensors can be tracked regular with automatized devices. Original accusations are written to the framework [6]. IoT device operates with the technology and electronic hardware on the network accessible connected devices for the integrated devices. In recent times, IoT designed a new area of research, specifically in the field of medical services, as a modern subject of study in a broad array of academia and business. IoT development form, i.e., healthcare reform systems combine technical and socioeconomic resources [7]. It progresses from the traditional to much more adapted treatment programs wherein patients could be more easily spotted, managed, and tracked.

IoT is an emerging technology that consists of the set of links provided to interconnects with anything, anywhere, any connection, any device, and any period. IoT technology may affect the whole company range, since every device and entity in the digital Internet network might be identified as having huge benefits. Such benefits often include enhanced connection between services, devices, and systems that go beyond the machine status [8]. IoT delivers suitable solutions to a variety of software and systems. Pollution control, wearables, issues in traffic, defense, intelligent infrastructure, transit, disaster aid, healthcare, and commerce are the examples for IoT. Doctors and community care are one of the most intriguing areas of IoT applications. IoT can generate treatment services such as workout, geriatric therapy, remote monitoring systems, and chronic illness administration.

The emphasis can be made by an IoT framework, integrated with AI. Enhance social protection by using monitoring technologies, image-recognition technology, and the use of AI-enabled software and networks to provide, distribute, trace, and control people's access to the public places [6]. Usually, an IoT health service consists of several server-linked detectors. It provides real-time environmental or user tracking. In an epidemic, AI-assisted detectors can also be used to focus on indicators such as body temperature, respiratory rate, and cough habits of individuals.

A further helpful function might be monitoring people's geolocation. The difference between people could provide helpful info during epidemic of a deadly virus [4]. We will get a fair estimation about how much people share while moving in public spaces using technology like Ethernet.

It is also important to understand the protection and information security extensively during the implementation of certain applications in order to avoid the misuse of confidential data [5]. Authorities may continue to be using these resources and knowledge to continuously observe the actions of individuals after an epidemic. The healthcare sector has long been one of the major areas of application for the IoT. Based on the latest developments in AI and machine learning, eHealth has recently risen to greater heights. The COVID-19 pandemic strategy has provided shudders from several angles across the globe, such as its ability and deliverable, rapid reaction, connected information, and assessment.

The area of eHealth used by IoT and AI to healthcare has mainly become interdisciplinary and offered new horizons to problems during the COVID-19 pandemic [9]. In contrast, technology fields such as IoT and AI have been strongly encouraged to offer rapid and effective medical services, particularly with a view to COVID-19, frequently to automate and facilitate various activities for health professionals.

AI algorithms in particular forecasts play an important role in the study of epidemics. With enormous information on this pandemic, the machine learning methods assist to discover ways to prevent the transmission of the virus from taking prompt action [10]. This search uses the machine learning and deep learning methods to monitor everyday behavior in anticipation of COVID-19' future cross-country accessibility utilizing the official open information source in real-time. These models can predict the near future and help to reduce the harmful consequences of COVID-19. The advent of AI revolutionizes every social and personal sector. AI is designed to behave like a human brain and to mimic its processes of thinking that automate different jobs.

AI is data-driven and makes choices based on the data on which it has been trained. AI is needed to cope with the present epidemic since it has the advantage over the previously mentioned conventional methods. Although AI cannot supplant physicians, it helps them to make diagnostic choices efficient and accurate. Techniques may be used to change the healthcare sector. In pandemic conditions, the healthcare system is overburdened with the enormous number of patient demands, and AI can support them as quickly as practicable with minimal cost for diagnosis and treatment. AI algorithms, such as sensors and cameras, may be readily incorporated into the current infrastructure to automate the contact tracking process. AI helps to do simulations for the prospective medication during the vaccine development process to estimate its efficacy.

The WHO has reported the pivotal symptoms of COVID-19, including body pains, increased heart rate, strong coughing, and severe breathing difficulties [11]. Scientists believe that the respiratory system's audio noises may be identified and examined for the disease's existence. The absurd and stepped-up proliferation of the COVID-19 virus has led to enormous cooperation across many sectors to regulate and prevent the propagation of the virus on a daily basis. In addition, the solution will participate in the fight against COVID-19 in an innovative and the current manner by integrating AI and deep learning algorithms in the digital health district. There have been enormous executions of AI along with the techniques of deep learning (DL), which can be rational during the initial detection and monitoring processes of COVID-19 through the analysis of extracted features of coughing, breathing, and speech using the recurrent neural network (RNN) for coughing, breathing, and speech.

2. Review of Literature

Brem et al. [12] infection predictor to reduce the threat of predictive modeling with regard to sustainability variables has been introduced. They also developed to predict the hazards to the effects of chronic and to identify complications by using SVM classifications to identify the health conditions. Wu et al. [13] introduced a methodology for heart disease diagnosis to solve the medical challenges such as irregular heartbeat. To do this, they use the naive Bayesian method. This intelligent device evaluates and classifies data gathering. Rahman et al. [14] computerized improved teaching approach implemented including IoT computers. They used identities to classify the students' intelligibility and standard. This approach helps the students to evaluate without any public health consequences. Javaid et al. [15] suggested a framework to describe the geographic distribution of COVID-19 disease outbreaks.

Bayindir [16] suggested any IoT application to fight COVID-19. Javaid et al. [15] discussed how various 4.0 industries (e.g., IoT and artificial intelligence) might contribute to decrease the disease spread. Mokbel et al. believed that interaction tracking should be the duty of the utilities and offer a largely automated contact tracking design that is not dependent on user participation. Nasajpour et al. [17] discussed various IoT devices in three major phases: diagnosis, isolation, and healing. The application of ML, AI, and other intelligent methods for COVID-19 prognostics is discussed recently.

Dong and Yao [18] discussed about the promising IoT-based approaches to fight COVID-19 that have been developed. They provide a thorough investigation of current IoT systems at various levels, such as perception layers, network layers, and fog and cloud layers. They also explore uses of IoT in the diagnosis of COVID-19 signs. A four-layered architecture is built on the technology by IoT and blockchain to assist combat COVID-19. The chain-based approach for ensuring the confidentiality and security of physiological information exchanged between IoT nodes is suggested. It also includes the several apps designed to identify and trace the proposed approach with COVID-19. IoT's involvement is in the current digital healthcare system. It also discusses the consequences of IoT-generated data that permitted the healthcare system for policy-makers' choices. Additionally, current facilitators and obstacles to IoT-based healthcare are also included.

They identified the capability of the wireless connection and evaluated the network transfer to diagnose the area at greater hazard. They will also obtain greater attempts to monitor the spreading in some areas. Gupta and Johari [6] planned to identify the resource field utilizing IoT sensors including wireless communication technology 802.11 which was an IoT-based control mechanism. They built a modeling approach for tracking the small spaces. The sensors in light lamps have been fixed to track scheduling and the unnecessary use.

Siriwardhana et al. [4] addressed the production and implementation of IoT-based technology to combat the COVID-19 epidemic effectively. In particular, many scenarios and problems are raised, including how 5G and IoT may be candidates for creative technologies in diverse fields to tackle the pandemic. A systematic analysis has likewise been proposed to minimize the contribution made by big technological innovations including such 5G, artificial intelligence, UAV, Internet of Things, and blockchain.

Hussain et al. [5] emphasized using AI to tackle the epidemic COVID-19. This research offered an outline of different cognitive technologies for various types of epidemics dependent on clinical experience. The study classifies the current AI strategies in medical studies analyzes into neural systems, classical vector assistance, and pervasive processing. Last, a thorough explanation was given about the benefits of AI in the fight against related viruses.

Wu et al. [13] suggested a combined protection and health surveillance framework for IoT. The purpose was to increase safety in the open air. The framework contains two layers: one for gathering user information and the other for aggregating information gathered and over the Web. Wearable systems have been used to collect the public safety metrics and consumer health signs.

Afshar et al. [19] claimed that many research studies have been carried out in support of automatic diagnosis and screening of COVID-19. In the eHealth sector, AI can be gripped and pushed to help identify COVID-19 early by monitoring these three major sound systems, including cough, breath, and speech. In addition, pulmonary noises may include many indicators of the health status of human beings that can be identified and treated by the use of machine learning techniques. Consequently, doctors and experts have recently considered detecting COVID-19 from lung noises since before the large epidemic of COVID-19.

3. Conceptual Framework

3.1. Artificial Intelligence for COVID-19 Pandemic. AI has proven to be a scientific development. It is an incredibly powerful method to solve the COVID-19 epidemic if adequately used [5]. The following are the few present and ability for AI to support the officials in fighting successfully the COVID-19 epidemic:

(i) Monitoring of illness
(ii) Risk forecasting
(iii) Monitoring of surgical examination
(iv) Healing studies
(v) Study and simulation of the virus
(vi) Site recognition
(vii) False news for breaking
(viii) Implement the steps to shut down

Many of the above methods are discussed in depth in the following.

3.1.1. Monitoring of Illness. On December 31, 2019, a Toronto-based city health firm, Blue Dot, announced an imminent coronavirus outbreak. The Blue Dot AI system includes various machines learning and natural language processing (NLP) instruments to locate signs of infections that are developing. This ability allows Blue Dot to control the SARS-CoV-2 spread and predict that it would evolve long before pathologists. But this would not go so far as to suggest that there was no human experience to do so as well. Although your model of AI might forecast the epidemic, human knowledge of the model performance remained key. Figure 1 shows the interfacing of AI for COVID-19 pandemic.

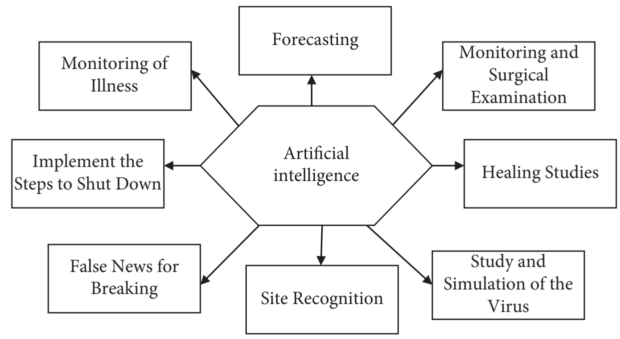

Figure 1: AI for COVID-19 pandemic.

3.1.2. Forecasting of the Risk. An important field of study was the use of prediction techniques to support hospital resource planning. The time-series analysis has been one of the most common methods used to generate short-term demand predictions since it offers thorough treatment for seasonality and serial correlations. For example [16], the prediction of short-term utilization of beds for various time-series techniques and historical average models was assessed [17]. Time-series techniques for predicting occupancy in an urgent ward are analyzed and demonstrated that they can offer meaningful data for up to one week. They exposed that the model generates excellent predictions, but in a crisis, it falls. On a separate line of research [20], patient-level data were used in a computationally expensive model to anticipate the demand at various hospital units.

3.1.3. Medical Diagnosis and Screening. Rapid COVID-19 diagnoses can permit authorities to take appropriate action to restrict the greater dissemination of the infection. Although, the scarcity of reagent kits internationally has complicated the success of huge diagnostic imaging by the officials. Most established AI techniques have been recast, whilst others will be developed to reduce this issue.

3.1.4. Healing Studies. As new, the lack of appropriate virus diagnostic and counseling procedures is one of the largest challenges with SARS-CoV-2. However, AI is known to have an achieve design to accelerate the manufacturing process by evaluating the latest COVID-19 instances as well as ongoing studies into viral infections. A variety of organizations and research laboratories have also used AI to classify new COVID-19 therapies. AI not only can speed things up in clinical trials but can also help to diagnose the established medicines.

3.1.5. Study and Simulation of Virus. Knowing the infection is just the secret to establishing the appropriate cure of COVID-19. Pathogens never replicate on their own, so that they can generate versions of their DNA using cell membranes. For this reason, an infection normally destroys the cell wall through a Keychain system by connecting itself with the host receptors. For most antibody substances, the operational function is to avoid this by removing the cell surface receptors. Therefore, researchers can design the consensus that exists in developing the successful inhibitors.

3.1.6. Site Recognition. The SARS-CoV-2 belongs to the beta-CoV tribe of attention and respect. Genotypes of such diseases usually consist of a combination of populations (bats and rodents). To present, an unexplained element is the biological host that made it easier to relay COVID-19 for humans. To correlate the bacterial vector efficiently and for recognition of differences among recognized viruses, machine learning algorithms have been used. The study proposes that the seasonal influenza species uses the decision tree algorithm. The SARS-CoV-2 can also be expanded to incorporate these versions.

3.1.7. False News for Breaking. Currently, it is unpredictable days since the COVID-19 epidemic have produced some theories and explanations of deception. There has been a lot of disinformation on social networking sites. Technology firms including Google, YouTube, and Facebook have used AI strategies to avoid the dissemination of such false information as well as provide checked facts. Both the networks have sought to filter the material with even the smallest disinformation. In fact, YouTube has put in place tough steps to gather some false video news.

3.1.8. Implement the Steps to Shut Down. A great several nations around the globe are using AI to encourage social dissociations and lock-up initiatives, including China, India, the United States, and the United Kingdom. In China, Baidu has established machine view (CV) operated infra-road monitors to search public areas, making it one of the biggest AI and network companies in the world. These devices not only recognize individuals with elevated physical heat but also distinguish residents who are not adopting the lock-down steps using their built-in face recognition system. A similar CV surveillance system was used to track the public dissociating steps taken by masses in Oxford, England.

3.2. Internet of Things Presence in Procedures for COVID-19. IoT offers strategically advanced forum for tackling the COVID-19 epidemic which overcomes the big lock-up difficulties [9]. This system aims to collect up-to-date information and displays the important functions that IoT is used during COVID-19 in the injured individual. IoT is being used to collect the healthcare information from different infectious patients' positions and to handle all the information through virtual management platforms in the first stage. This system enhances information management and coordination of the study. Figures 2 and 3 show interfacing of IoT to tackle the epidemic of COVID-19.

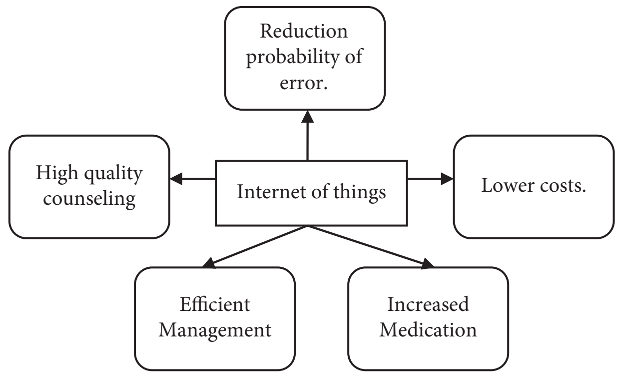

Figure 2: IoT tackles the epidemic of COVID-19.

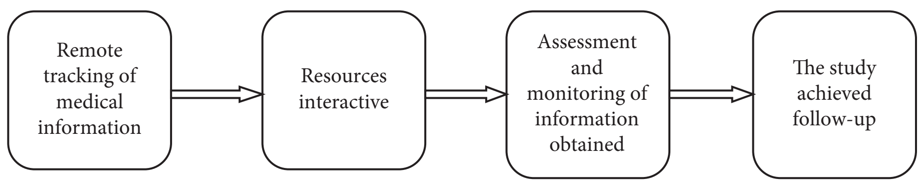

Figure 3: Increase IoT phase map to tackle the pandemic of COVID-19.

3.3. Impact of the COVID-19 Pandemic on the Global Economy. Due to the absence of every clear care plan, the greatest available method of protection against epidemic of COVID-19 was established at the time [5]. Nevertheless, the imperative of social distance forced policy-makers worldwide to implement the lockdowns that have signaled a significant split in the world economy. Both facilities that are nonessential were obliged to close down. It led the supply chain to destroy almost all businesses and thus to hazard losing their homes for people around the world.

3.3.1. Automotive Industry. Due to tight locking policies in many countries of the world, the car sector has undergone huge infrastructure delays to combat the epidemic. With social isolation imposed and people needed to stay at home, the use of vehicles, both commercial and personal, has diminished worldwide. The automobiles affiliated with essential services are the only cars still in use.

3.3.2. Aviation Industry. Atmospheric sector has been hit massively by the COVID-19 epidemic. The affected countries including virtually all states were compelled to both globally and domestically to implement a travel restriction. Critical lines of distribution serving cargo and freight planes are the only operational airways.

3.3.3. Tourism Industry. Since the epidemic of COVID-19, the tourist industry was one of the hardest hit sectors. Tourist industry sales make up to 10% of the worldwide GDP.

3.3.4. Construction Industry. Building businesses are expected to face serious disruptions and setbacks attributable to COVID-19 epidemic in existing ventures. As a result of the strict self-quarantine rules, most building companies will have to suspend their nonessential activities before the epidemic comes to an end. This is expected to lead a massive reprogramming of current programs that could lead to serious damages.

3.3.5. Healthcare and Medical Industry. The epidemic COVID-19 has a major impact globally upon these healthcare services, whereas the overeating induced by lockdown acts and travel restrictions has impacted other industries financially, and the safety sector is far from stagnating. Worldwide clinicians are now experiencing the need for COVID-19 patients to be managed by fans, intensive care units (ICUs), and personal protective equipment's (PPE).

3.4. Major Advantages of IoT for Pandemic COVID-19. Alsaeedy and Chong [21] All extremely dangerous patients are properly monitored via the Internet of Things. This technology is used to estimate biometric problems, such as hyperglycemia, pulse rate, and heart infections [22]. IoT is a creative and powerful phase in the fight against the COVID-19 epidemic and may make enormous problems during lockdown. This innovation is helpful in strengthening the infected patient's infinite data as well as other important data. Figure 4 shows the main advantages of IoT in the battle against COVID-19 pandemics.

3.5. Role of IoT Technologies and Tools in COVID-19 Pandemic. COVID-19 has a unique effect on society, and the economy of the effect of this epidemic nowadays has increased the use of numerous new technologies in combination with other technologies such as AI, data management, and cloud. IoT is of tremendous help in this disaster IoTs, utilized for epidemic monitoring. Important

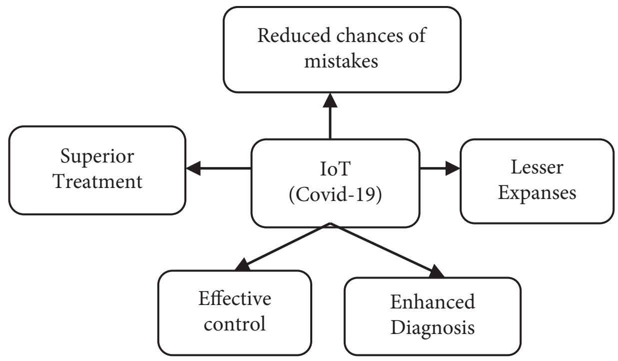

Figure 4: Major advantages of IoT for pandemic COVID-19.

IoT, AI, and big data innovations that assist with the COVID-19 problem and the several problems stated in that effort include telemedicine's for the prevention and management of disease, the prevention of outbreaks and the minimization or even stoppage of the transmission of the virus, the use of drones to monitor for isolation, and mask use. For COVID-19, primary IoT applications are the online clinics, remote consultations, fast screenings, and the smart monitoring of sick individuals and virus prediction [21], the real-time monitoring, patient monitoring, rapid diagnosis, patient education, testing and tracking, protection, and surveillance. There are additional concerns of confidentiality and protection related to the use of CR. The function of IoMT in monitoring patients from a distant location, the ordering of medical products, and the use of smaller devices to communicate patient data to the authorities concerned [4] focus on the peripheral system and improve quarantined sufferers for different metrics such as respiratory rate, air rate, and lung sound rate, tracking devices to identify infections and monitoring for remote access and diagnosing COVID-19 patients with mild symptoms and tele-health innovations. The function of IoT-based technologies in COVID-19 and the existing IoT solutions for the fight against COVID-19 were examined in three major stages; they separated IoT solutions into primary prevention, confinement period, and recovery. Each step was also shown using IoT-enabled devices including IoT controls, wearable, drones, robots, and smartphone apps.

Suraksha Kawach is an IoT device that is utilized by the Defense Research and Development Organization (DRDO), India, to monitor corona-affected individuals and to monitor them. This gadget may be used in the arm or knee and is a GSM and GPS device for reliable monitoring in real-time basis. The prototype of Suraksha Kawach gadget is shown in Figure 5(a).

In order to minimize healthcare personnel' danger, thermal sensors are used to monitor COVID-19 patients' body temperature. Figure 5(b) shows the temperature sensor of the sample. We have got wearable gadgets; next, these sensors measure various parameters such as temperature, heart rate, and pulse rate, and the measurement results may be utilized for action as soon as possible. These devices have an important role in containing COVID-19; the intelligent band is one of the wearable devices, as shown in Figure 5(c).

3.6. Techniques Used for Coronavirus Sample Collection. To prevent its fast spread, it is necessary to establish valid and realistic medications to treat SARS-CoV-2 disease in people. The nucleic acid test (NAAT) is recommended by the WHO which perhaps the most important model of SARS-CoV-2 detection for the effective SARS disease. These studies include the use of the nasopharyngeal swab procedure in which the cleaning solution is used in a specimen. This contains a combination of mucus and saliva.

In the event of significant breathing problems, the WHO advises that samples be taken from the nose and throat as well. Such specimens are taken to a specialist lab, where the polymerase chain reduction method is used to measure the existence of viral RNA. Table 1 provides the various techniques for coronavirus sample collection.

3.7. Using Artificial Intelligence to Detect, Respond, and Recover from COVID-19. AI systems observed that the epidemic of an unpredictable form of disease in the Chinese government before the world was ever conscious of the danger faced by the coronavirus (COVID-19). With the disease becoming a global epidemic, AI tools and techniques should be used to encourage actions by policy-makers. Furthermore, the health community and the society are essential to plan and control any step of the crisis: identifying, stopping, reacting to, and recovering and growing of COVID-19. Figure 6 shows the use of AI to detect, respond, and recover from COVID-19.

3.8. AI with IoT in Healthcare to Treatment of COVID-19. Since the main report of the 2019 coronavirus infection (COVID-19) in Wuhan, China, more than 200 countries and locations have been affected worldwide. Science and technology take on an important role in this perplexing battle. For example, as China began reacting to infection, it zeroed on brain research by monitoring polluted ancient times moving sick people, robots to convey food and medicines, automatons to clean open spots, and by watching and transmitting sound communication to the public to urge them to stay at home. Man-made knowledge was widely used to identify the new particles in transit to assist COVID-19. A number of experts uses AI to find new medicines and remedies alongside certain software engineering analysts that focus on the

(a) (b) (c)

Figure 5: (a) Suraksha Kawach device 5. (b) Sensor 5. (c) Smart band.

Table 1: Various techniques for coronavirus sample collection.

Technique	Analysis
NC	A collection of respiratory secretions from the back of the throat can be used for specific bacterial culture
NS	This approach includes having the breathing tube connected to a syringe, as opposed to nasopharyngeal swab procedure, for the processing of specimens from the nasopharynx
ETA	It is a bottom respiratory screening tool by means of a vertical pipe defined as bronchoscope that extracts the specimen from the lungs
BAL	A fiber-optical bronchoscope is transferred through nasal passage into the bronchoalveolary stress that after initiation of a sterile saline solution, a sample was obtained
Blood test	A pulse in the arm takes a blood sample

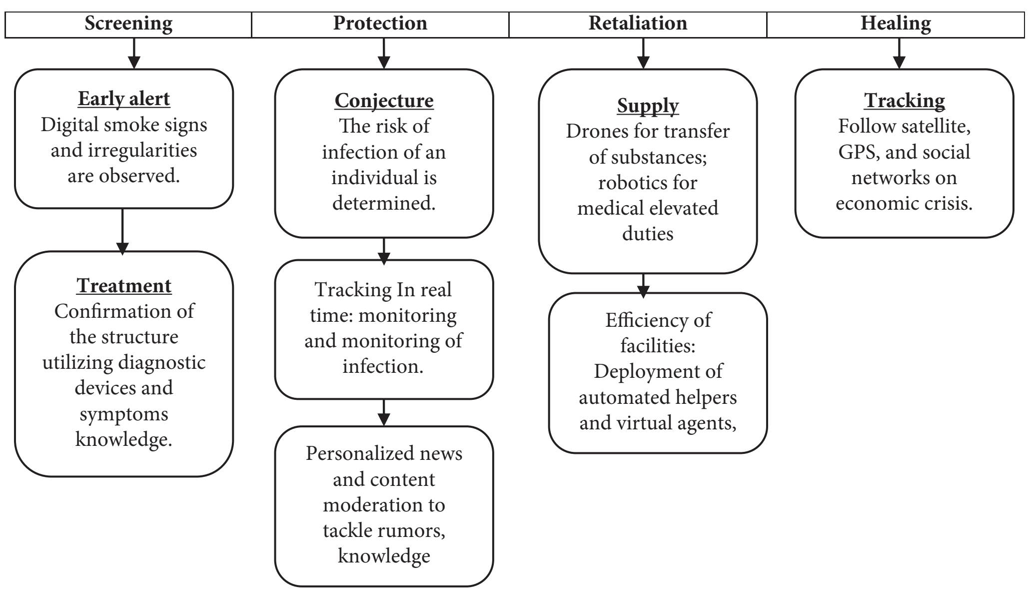

Figure 6: Use of AI to detect, respond, and recover from COVID-19.

identification of compelling patients via the preparation of a clinical image like X beams and CT filters [21].

In any case, computer-based intelligence follows the bands to assist group the isolated rule. Advanced mobile telephones and AI-enhanced heated cameras are being used to recognize fever and tinged people [19]. Nations such as Taiwan have combined the public knowledge based on clinical protection with input from the migration and customs data collection, thereby challenging the travel history and side effects of the COVID-19 patients. In all, AI is used to identify, monitor, and hypothesis flares and helps diagnose the illness.

It is used in the treatment of medical claims. Automobiles and robots are used to transport food and medicines, just as they are used to sanitize public areas. AI helps to create the medicines and COVID-19 antibodies using super PCs [17]. This present study focuses on the use of human-made pushes in the fight against the coronavirus epidemic. It provides an extensive review of the innovative drivers utilized to reduce and conceal the significant impact of the upheaval [5]. The motivation of current study is not only to assess the effect of presented methods but also to suggest their use.

4. Research Methodology

The program process entails the primary analyses and checks for modern sensors and intelligent systems. Research designs with AI techniques are designed to define a mechanism that underlies the number of environments in order to overcome the difficulty of the problem. The goal of the project is to explore the various sensing devices to gather the multiple information and utilizes the AI systems mostly on data sources. The key objective of the proposed work is to gather information upon this thermal and breathing level of the COVID-19 instances from various devices in real-time. In the data preprocessing, the recorded actual statistics shall be believed to reduce the error and extreme values from the principal component analysis (PCA). The third phase resulted in classifying the COVID-19 instances into three groups such as SIR, disease prone, affected and resuscitated (SIR). Then, in the fourth stage, the deep, simple RNN (recurrent neural network) predicts COVID-19 with past health data. Figure 7 shows the flow diagram for detection of COVID-19 using IoT and AI. The four steps of the model suggested are as follows:

(i) Data accession
(ii) Data accusation
(iii) Systemization
(iv) Forecasting

4.1. Recurrent Neural Network. The RNN is a class of the ANN that generates a graph structure for spatial and dynamic characteristics analysis. It assists to modeling the sequence information from transmission systems. The prediction findings are identical to the human brains. The processing of knowledge is clear. Assume an easy and simple given set of data feeding just one neuron. The method provides the performance in a typical neural net by increasing the input with the mass and creates strategies. An RNN returns this performance with the bunch of times. We call timestamp of the period, and the output is entered for the next multiplication of matrices. For illustration, the system consisted of one neuron in the image. The system measures the input/weight mathematical operations and applies nonlinearity with the enabling function. The performance at $t-1$ would be the same. This o/p is the i/p of the multiplication of the 2nd matrix. Figure 8 shows the recurrent neural network.

The proposed system consists of 6 neurons. Two important properties of the ANN are as follows.

(i) Data entered with the first weight set
(ii) Earlier production for a second weight collection

Notice that the quantities of the listed within the first flow forward which are null, and we have no quality present.

4.2. SIR Model. This framework is being implemented by Kermack and McKendrick, and it consists of the various classification COVID-19 situations, including such confirmed, contaminated, and rehabilitation instances. The disease deterministic method (Koike and Morimoto, 2018) is being implemented. The proposed method uses the SIR model as follows:

(i) Suspected (S): patients immediately suspected of disease by others
(ii) Infected (I): victims infected through whatever requires
(iii) Victims healed by infection, and patients accused of infection from others (R)

The design of the outbreak is mathematically written as follows:

$$\begin{aligned}\frac{\mathrm{d}s}{\mathrm{d}t} &= a - \mathrm{d}s - \lambda i + \beta,\\ \frac{\mathrm{d}i}{\mathrm{d}t} &= \lambda i - (d + m)i - T(i),\\ \frac{\mathrm{d}r}{\mathrm{d}t} &= mi - (d + \beta) + T(i),\end{aligned} \tag{1}$$

where a signifies the number of patients being tested; whereas i represent the relative state constant determined by $a1$, $a2$, the infection rate b parameter calculate is the rate of the victims not healed by loss of resistance, m is the normal patient's mortality rate, and T is a natural cure for the actual individuals diagnosed.

5. Result Analysis and Discussion

The table describes that the total population (sample size) of 227 among that population female population of 85 members and male population size of 135 members and other population size of 7 members and 30 members are below 18 years, between 19 and 30 years are 63 members, between 31 and 59 years are 92 members, and above 60 years are 42 members and 33 members having body temperature below 370°C, and 194 members having the temperature (380°C, 390°C, 400°C), and 123 members are infected with COVID-19, and 123 members are in danger zone; they are having different health abnormalities such as breathing problems.

Figure 9 shows COVID-19 effected cases. Figures 10 and 11 show the problematic cases and nonproblematic cases. Table 2 provides the forecasting of COVID-19 with the selective analytical aspects. Table 3 provides the COVID-19 effected cases. Table 4 provides problematic cases. Table 5 provides nonproblematic cases.

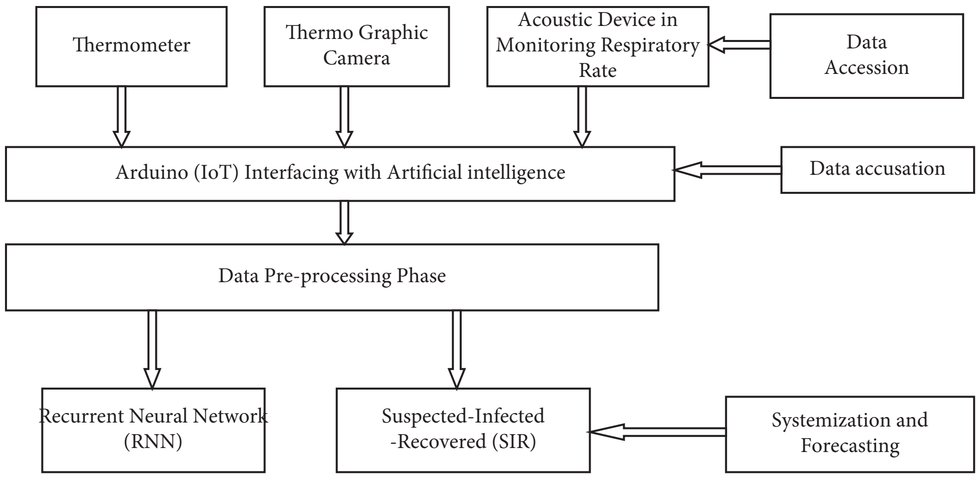

Figure 8: Flow diagram for detection of COVID-19 using IoT and AI.

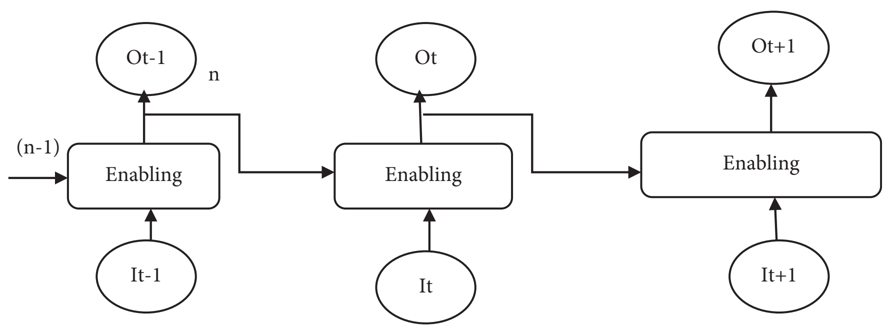

Figure 8: Recurrent neural network.

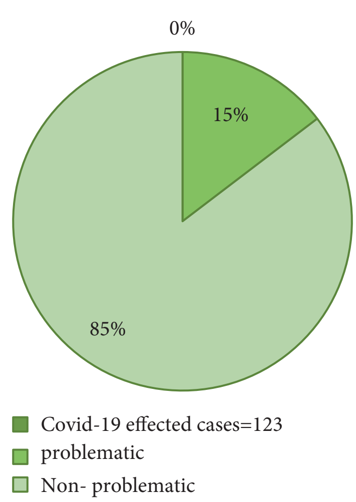

Figure 9: COVID-19 effected cases.

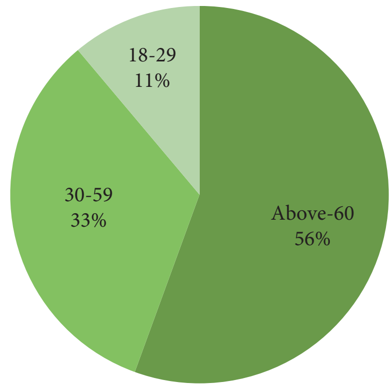

Figure 10: Problematic cases.

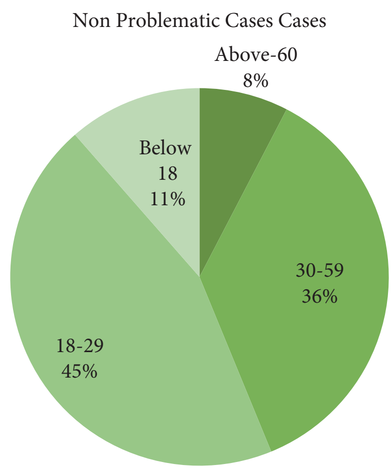

Figure 11: Nonproblematic cases.

Table 2: Forecasting of COVID-19 with the selective analytical aspects.

S. no.	Population characteristics	Classification	Frequency bands described
1	Gender	Female Male Others	Female = 85 Male = 135 Others = 7
2	Age	Below 18 Between 19 and 30 Between 31 and 59 Above 60	Below 18 = 30 Between 19 and 30 = 63 Between 31 and 59 = 92 Above 60 = 42
3	Temperature	Below 37 Above 38, 39, 40	Below 37 = 33 Above 38, 39, 40 = 194
4	Disease find	COVID-19 Others	COVID-19 = 123 Others = 104
5	Danger zone	Breathing problem/no breathing problem	Breathing problem = 18 No breathing problem = 105

Table 3: COVID-19 effected cases.

COVID-19 effected cases = 123	
Problematic	18
Nonproblematic	105

Table 4: Problematic cases.

Problematic cases = 18	
Age	Cases
Above 60	10
30–59	6
18–29	2

Table 5: Nonproblematic cases.

Nonproblematic cases = 105	
Age	Cases
Above 60	8
30–59	38
18–29	47
Below 18	12

6. Conclusion

The threat of the COVID-19 epidemic is still being faced by the universe that attempts complemented by numerous emerging innovations, including such IoT. These are being made by AI to mitigate their impact. Holding that, we have some recent observations of COVID-19 epidemic as the basis for this study. This study is initiated by an exhaustive analysis of COVID-19, wherein we discuss its medical characteristics, dissemination process, and the detection techniques.

For the population analysis, the SIR disease process is employed to identify the events under suspicion; the information is then fed into an LSTM RNN to estimate the COVID-19 instances with past data contained in the secret layer. The two stable problems in electronic enforcement, which requires adjustment, include confidentiality and faith. The migration of data also appears as an additional obstacle to solve interference and complexity by replacing evolutionary methods.

Data Availability

The datasets used and/or analyzed during the current study are available from the corresponding author upon request.

Conflicts of Interest

The authors declare that they have no conflicts of interest.

Acknowledgments

The authors extend their appreciation to the Deanship of Scientific Research at King Khalid University for funding and supporting this work under research grant award number RGP. 1/184/42.

References

[1] M. Pak and M. Shin, "Developing Disease Risk Prediction Model Based on Environmental Factors," in *Proceedings of the 18th IEEE International Symposium on Consumer Electronics (ISCE 2014)*, pp. 1-2, Jeju, Republic of Korea, June 2014.

[2] N. Repaka, S. D. Ravikanti, and R. G. Franklin, "Design and Implementing Heart Disease Prediction Using Naives Bayesian," in *Proceedings of the 2019 3rd International Conference on Trends in Electronics and Informatics (ICOEI)*, pp. 292–297, Tirunelveli, India, April 2019.

[3] A. Saxena, K. Shinghal, R. Misra, and A. Agarwal, "Automated Enhanced Learning System Using IOT," in *Proceedings of the 2019 4th International Conference on Internet of Things: Smart Innovation and Usages (IoT-SIU)*, pp. 1–5, Ghaziabad, India, April 2019.

[4] Y. Siriwardhana, C. De Alwis, G. Gur, M. Ylianttila, and M. Liyanage, "The _ght against the COVID-19 pandemic with 5G technologies," *IEEE Engineering Management Review*, vol. 48, no. 3, 2020.

[5] A. A. Hussain, O. Bouachir, F. Al-Turjman, and M. Aloqaily, "AI techniques for COVID-19," *IEEE Access*, vol. 8, pp. 128776–128795, 2020.

[6] A. K. Gupta and R. Johari, "IOT Based Electrical Device Surveillance and Control System," in *Proceedings of the 2019 4th International Conference on Internet of Things: Smart Innovation and Usages (IoT-SIU)*, Ghaziabad, India, April 2019.

[7] R. Vaishya, M. Javaid, I. H. Khan, and A. Haleem, "Artificial intelligence (AI) applications for COVID-19 pandemic," *Diabetes MetabolicSyndrome, Clinical Research Reviews*, vol. 14, no. 4, pp. 337–339, 2020.

[8] M. Abdulrazaq, N. Hazairin, S. Al-Zubaidi, S. Karim, S. Mustapha, and E. Yusuf, "Toward a novel design for coronavirus detection and diagnosis system using IoT based drone technology," *International Journal of Psychosocial Rehabilitation*, vol. 24, pp. 2287–2295, 2020.

[9] P. Chatterjee, L. J. Cymberknop, and R. L. Armentano, "IoT-based ehealth toward decision support system for CBRNE events," in *Enhancing CBRNE Safety & Security: Proceedings of the SICC 2017 Conference*, A. Malizia and M. D'Arienzoeds, Eds., Springer, Salmon Tower Building, NY, USA, pp. 183–188, 2018.

[10] S. Mifrah and E. H. Benlahmar, "Topic modeling coherence: a comparative study between lda and nmf models using COVID'19 corpus," *International Journal of Advanced Trends in Computer Science and Engineering*, vol. 9, no. 4, pp. 5756–5761, 2020.

[11] A. Shewalkar, D. Nyavanandi, and S. A. Ludwig, "Performance evaluation of deep neural networks applied to speech recognition: rnn, LSTM and GRU," *Journal of Artificial Intelligence and Soft Computing Research*, vol. 9, no. 4, pp. 235–245, 2019.

[12] A. Brem, E. Viardot, and P. A. Nylund, "Implications of the coronavirus (COVID-19) outbreak for innovation: which technologies will improve our lives?" *Technological Forecasting and Social Change*, vol. 163, Article ID 120451, 2021.

[13] F. Wu, T. Wu, and M. R. Yuce, "An internet-of-things (IoT) network system for connected safety and health monitoring applications," *Sensors*, vol. 19, no. 1, p. 21, 2019.

[14] M. S. Rahman, N. C. Peeri, N. Shrestha, R. Zaki, U. Haque, and S. H. A. Hamid, "Defending against the novel coronavirus (COVID-19) outbreak: how can the internet of things (IoT)

help to save the world?" *Health Policy and Technology*, vol. 9, no. 2, pp. 136–138, 2020.
[15] M. Javaid, A. Haleem, R. Vaishya, S. Bahl, R. Suman, and A. Vaish, "Industry 4.0 technologies and their applications in fighting COVID-19 pandemic," *Diabetes & Metabolic Syndrome: Clinical Research Reviews*, vol. 14, no. 4, pp. 419–422, 2020.
[16] L. Bayindir, "A survey of people-centric sensing studies utilizing mobile phone sensors," *Journal of Ambient Intell.SmartEnvrion*, vol. 9, no. 4, pp. 421–448, 2017.
[17] M. Nasajpour, S. Pouriyeh, R. M. Parizi, M. Dorodchi, M. Valero, and H. R. Arabnia, "Internet of things for current covid-19 and future pandemics: an exploratory study," 2020, https://arxiv.org/abs/2007.11147.
[18] Y. Dong and Y. D. Yao, "IoT platform for covid-19 prevention and control: a survey," 2020, https://arxiv.org/abs/2010.08056.
[19] P. Afshar, S. Heidarian, F. Naderkhani, A. Oikonomou, K. N. Plataniotis, and A. Mohammadi, "COVID-19-CAPS: a capsule network-based framework for identification of COVID-19 cases from X-ray images," *Pattern Recognition Letters*, vol. 138, pp. 1–5, 2020.
[20] WHO, "Coronavirus disease COVID-19 pandemic," 2020, https://www.who.int/emergencies/diseases/novel-coronavirus-2019.
[21] A. A. R. Alsaeedy and E. K. P. Chong, "Detecting regions at risk for spreading COVID-19 using existing cellular wireless network functionalities," *IEEE Open Journal of Engineering in Medicine and Biology, Healthcare*, vol. 8, no. 1, pp. 187–189, 2020.
[22] Z. Allam and D. S. Jones, "On the coronavirus (COVID-19) outbreak and the smart city network: universal Data Sharing Standards Coupled with Artificial Intelligence (AI) to Benefit Urban Health Monitoring and Management," 2020.

Hindawi
Journal of Healthcare Engineering
Volume 2022, Article ID 9091795, 7 pages
https://doi.org/10.1155/2022/9091795

Research Article

Career Development Anxiety and Mental Health Regulation of University Music Teachers

Hua Yan

School of Art, Zhejiang Yuexiu University, Shaoxing 312000, China

Correspondence should be addressed to Hua Yan; yanhua_edu@outlook.com

Received 30 December 2021; Revised 21 January 2022; Accepted 1 February 2022; Published 28 February 2022

Academic Editor: Enas Abdulhay

Mental health essentially refers to a state of mind. It means that an individual can keep a good or normal state in behavior. It is not only related to the overall development of the individual body and mind but also affects the construction of university teachers. This paper mainly studies the career development anxiety of music teachers in colleges and universities in China, analyzes its causes, and puts forward corresponding countermeasures and suggestions to alleviate the pressure and promote the physical and mental harmony of music teachers and the common growth of a good social atmosphere. The purpose is to help music teachers in colleges and universities better manage their mental health. This paper collects the data of occupational stress and mental health of 164 music teachers in many colleges and universities through the method of a questionnaire survey and processes the data with the analysis formula of sample variance and standard deviation. The analysis shows that a considerable number of the respondents have career development anxiety.

1. Introduction

The inequality between social progress and the reform of professional titles in higher education has always been a huge stone in the hearts of all teachers. In the past, we have always unilaterally emphasized that teachers should have the spirit of dedication but ignored the pressure they bear as a special social group and the reasonable demands for normal career development [1, 2].

After entering the new century, the research on the occupational stress of primary and secondary school teachers in China is gradually deepening, but the research on the occupational stress of college teachers has not attracted enough attention. Although university teachers do not face the pressure of students' entrance examinations, the students they face have more mature personalities, and the form of classroom teaching is more open. Students often put forward some problems that teachers cannot explain in class. All of these lead to the fact that college teachers are also suffering from unimaginable social and psychological pressure [3].

According to the survey data, more than 72.3% of young college teachers in China think that their work and academic research pressure is too high, which makes them often fall into more serious mental health problems [4]. In addition, many colleges and universities in our country adopt the incentive policy of "go or not", which makes young teachers in colleges and universities who are in deep trouble feel more confused about their career prospects.

A work stress survey of young university teachers found that the mental health of young university teachers has deteriorated year by year. Especially in recent years, the impact of pressure on young university teachers, such as low wages, difficulty in buying a house, and difficulty in promotion, has gradually increased. The state of mental health is getting more and more severe, as shown in Figure 1.

It can be seen from Figure 1 that the mental health index of young teachers in colleges and universities decreases year by year as the years increase. Taking 2015 as the best starting point for health, by 2021, the average health index has dropped by 30%. It can be seen that the mental health of young music teachers in colleges and universities is deteriorating rapidly.

The psychological state has an important influence on an individual's life and work. The influence of teachers' mental health on the sustainable development of education cannot be ignored [5, 6]. To pay attention to their mental health, and to achieve positive intervention on their mental health by building a good career development space and strengthening psychological counseling is a necessary way to improve the working state of college teachers in China [6, 7]. The mental health of university teachers will not only affect their own work and study but also bring great differences to students' learning moods and even their cognition of the world. There is an obvious positive relationship between the two. College teachers with good mental health will make students feel more sunshine in their studies and life, and vice versa [8, 9]. In many cases, these two opposite learning emotions will accompany students throughout their lives. Human resource management in colleges and universities, as an important entry point to improving the professional development space of college teachers, should not only focus on the teaching work and academic achievements and other hard indicators, but also expand to include the guidance and intervention of teachers' mental health so as to create a more three-dimensional and comprehensive work system of teachers' mental health and help college teachers to work more actively and effectively and improving their healthy psychological state to carry out education and teaching work. [10, 11].

As a nonmusic college, music teachers are a relatively special group. They are more in line with the perceptual cognition of university teachers: brilliant and easy to work with. As a result, their career development anxiety is more easily ignored by society [12, 13]. Paying attention to the mental health regulation of this group not only helps to solve the mental health problems they are facing, but also has a very important reference value for the mental health regulation of the whole team of university teachers.

2. Professional Development Anxiety and Psychological Adjustment of College Music Teachers

2.1. Characteristics of the Professional Development of College Music Teachers

2.1.1. Particularity of Music Teachers. Music teaching pays attention to aesthetics just like dance and art, and music learning is not a day's work. It requires years of learning. In addition, music learning is not only about professional knowledge, but more importantly, experience in life. The profession of a music teacher is different from other teachers, mainly in the following aspects.

First, after becoming a music teacher, you can combine your profession and expertise, find a suitable entry point, combine your expertise with teaching, and promote the continued development of music.

Second, there is a very close relationship between the professional development of music teachers and the school environment. These development environments mainly include the relationship between the internal environment and the external one [14, 15]. The internal environment mainly refers to people's innate sensitivity to music and various physiological conditions such as their voice, while the external environment mainly refers to people's in-depth research and pursuit of music.

Third, the professional development of music teachers has always been a straight line, and there are no other diversions. Despite this, music teachers also face all kinds of difficulties, but they still work hard to form their own unique teaching styles and models.

2.1.2. Features of Professional Development of Music Teachers in Colleges and Universities

Phased. Music teachers are of different ages, and their development will also show different developmental characteristics. At different ages, the problems they face will be different. This is the stage. According to research, 25–60 years old can be called an adult stage. Music teachers between the ages of 25–35. They are young and energetic and have innovative ideas in music. At this time, they are faced with problems in career planning, life planning, and family formation, such as employment, studying abroad, falling in love, and getting married. Music teachers at the age of 35–50 have completed family formation-related issues and accumulated a lot of social experience. They are calm and efficient in their work, and their bodies and spirits are at the peak of activeness. Music teachers at the age of 50–60 may not be as good as the previous two stages, but they have profound professional knowledge, the richest teaching experience, and the highest level of scientific research. According to the statistical results of university research institutions, it is found that the occupational anxiety of college music teachers will increase first and then decrease with age. The specific situation of anxiety is shown in Figure 2.

It can be seen from Figure 2 that the occupational anxiety value of young college music teachers between the ages of 30 and 35 reaches the highest level, and with the increase in age, the occupational anxiety value of college music teachers gradually decreases, reaching the lowest point at the age of 60.

Dynamic. Music teachers are also a group of society [16]. They are also in a social environment. Their career development cannot be separated from the influence of the environment, and this influence is also mutual. The activities of music teachers will also have an impact on the environment [17, 18]. The stages mentioned in the previous article also show that the professional development of music teachers is dynamic and constantly changing, which only shows that different ages lead to different environments, which will have an impact on the professional development of music teachers. In addition, when college music teachers leave the university campus, there are not many career choices. Maybe a certain institution becomes a training teacher. Therefore, it is best for college music teachers not to leave the university campus to develop independently.

Comprehensive. Comprehensiveness means that in the process of professional development, college music teachers

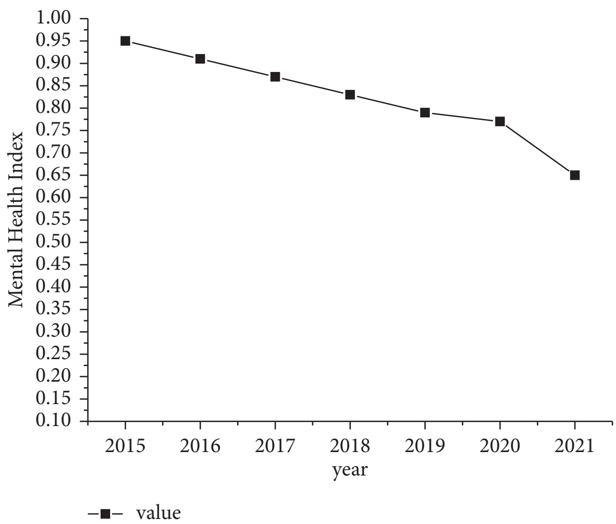

Figure 1: The mental health of young teachers in colleges and universities.

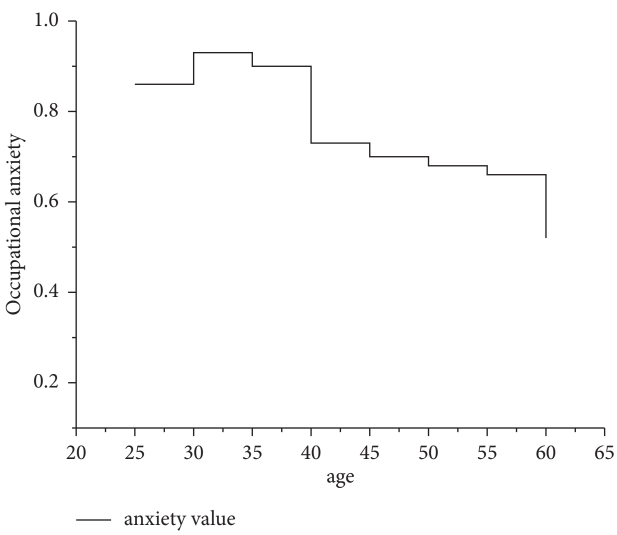

Figure 2: The changing trend of anxiety of college music teachers with increasing age.

must not only have their own unique professional style and authority but also have the knowledge and teaching management capabilities related to other disciplines [19]. As a teacher, they must have at least pedagogy-related knowledge, be good at getting along with students, discover the characteristics of students, and should know how to guide students with different physical conditions to guide their music professional learning. In addition, music teachers must have strong music creation abilities and practical abilities, and constantly improve their level of professional knowledge and innovative teaching methods.

2.2. Performance of College Music Teachers' Occupational Anxiety. Through the analysis of data from different institutions, it is shown that the performance of occupational anxiety of music teachers in colleges and universities is mainly divided into four types. Among them, the degree of influence of different types of anxiety on the teachers' mental health index is shown in Figure 3.

It can be seen from Figure 3 that the performance of college music teachers' occupational anxiety is mainly divided into four types. Among them, grumpy type anxiety has a high impact on teachers' mental health index, reaching 31.58%, while suspicious and uneasy types of anxiety have the lowest impact on teachers' mental health index, at only 19.3%.

It can be seen from Figure 3 that all kinds of anxiety will adversely affect the mental health of college music teachers. The specific types of anxiety involved are as follows.

Emotional Pessimism. When music teachers are dissatisfied with their current work, they will be pessimistic. They often feel exhausted, and it is difficult to show a happy expression about something. Most of the time, they see the negative side of things first. The time spent alone is prolonged, and interpersonal communication is extremely lacking. Too worried about the future and then become gloomy, even during the teaching period, they would not shy away from it. Over time, this emotion will infect students and other teachers.

Grumpy. Music is inherently unique in art, and music teachers also have very obvious personal characteristics. When society, parents, and schools intervene in their teaching too much, they feel that they cannot concentrate on studying music or even become secular. Sometimes they will become very irritable. In teaching, they will be more demanding on students. They will be less tolerant of students who make mistakes. They often become inexplicably angry. They will be self-centered, not cooperate, and not listen to other people's advice, which makes the job impossible. To proceed in an orderly manner, seriously interfering with teaching work.

Suspicious and Uneasy. When teachers are hit, they are prone to self-doubt or feel that others are deliberately targeting themselves, and when they start to think about themselves and their insecurity, the whole person's defensiveness becomes heavier and he is unwilling to communicate with others. In the long run, insomnia and overreaction are prone to occur, which seriously affects normal teaching and life, creates greater obstacles to professional development, and will aggravate teachers' professional anxiety.

Nervousness. Nervousness manifests itself as being overly entangled in something, speculating on the adverse consequences of the event, fear of making mistakes, excessive worry about the past and future, fear of losing face, always being cautious, and pursuing too much perfection.

2.3. Psychological Adjustment Countermeasures of College Music Teachers

2.3.1. Create an Environment Conducive to the Mental Health of Teachers. Teachers bear the heavy responsibility of preaching and receiving jobs, and their mental health has a

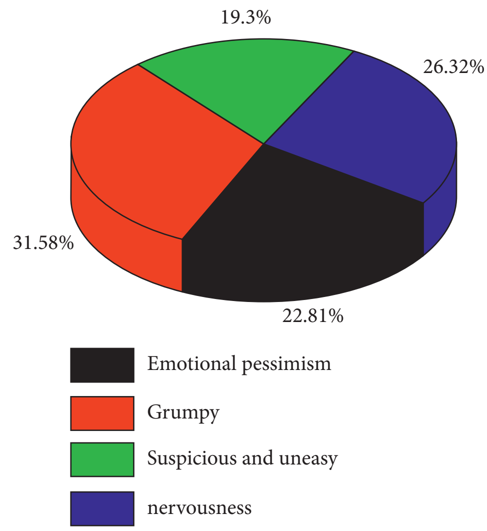

Figure 3: The degree of influence of different types of anxiety on teachers' mental health.

huge impact on society. Local governments should earnestly safeguard the rights and interests of teachers. To solve the psychological problems of music in colleges and universities, it is necessary to find the source of the problem, counter the medicine, create an easy-to-teach working environment for college music teachers, improve the salary and social status of college music teachers, and conduct regular mental health education for college music teachers. Practical actions should be taken to solve the difficulties that teachers encounter in life and work.

2.3.2. Adhering to the People-Oriented Education Management Method. In terms of adjusting the psychological state of music teachers in colleges and universities, it is necessary to optimize management methods and management models through local colleges and universities, always adhering to the people-oriented management philosophy, attaching great importance to the mental health of teachers, and carry out relevant training activities on a regular basis. In addition, formulate more scientific and reasonable teacher assessment standards and prohibit the establishment of standards that ignore reality. When recruiting teachers, we should also pay attention to the mental health of teachers and create a team of teachers with a good atmosphere. Formulate incentive policies that take into account teachers' contributions and achievements at work, and at the same time strictly require teachers' ethics and morality. They must also be rigorous in academic research to avoid mental health problems caused by bad academic habits. Reasonable control of the working hours, advocating the combination of work and rest, and holding faculty sports games or art evenings to provide teachers with more opportunities to show themselves.

2.3.3. Improving the Psychological Quality of Teachers Themselves. At the same time, teachers should also understand that their responsibilities are heavy, introspect in time, and improve their level of professional knowledge for teaching and ideological and moral cultivation. At the same time, they must also understand that they are the object of the students' respect, and they must be able to convey positive energy to the students rather than vent their negative emotions on the students. Survival of the fittest has always been the rule of the world. If they want to develop better, they must improve their overall quality, including psychological quality, in order to strengthen their professional knowledge. This requires teachers to learn to control their emotions and handle things calmly. To have a clear understanding of oneself, they should face up to one's own shortcomings and deficiencies, accept different opinions from the outside world, establish good interpersonal relationships with colleagues, treat students equally, and learn to tolerate others.

When the teachers realize that they are feeling irritable and stressed, they must learn to find solutions. Schools and students are the objects teachers can seek for help. Teachers should not feel ashamed to speak out when they have psychological problems. They should open their hearts to communicate with others. Closing themselves will only make the results worse and worse. They should learn to advance with the times, constantly improve themselves, and adapt to the surrounding environment. Actively participating in school activities, having the courage to show oneself, not caring too much about gains and losses, seeing the false name, teaching and educating people, and academic research are what teachers should care most about.

2.3.4. Developing Good Living Habits. Healthy living habits have always been an important prerequisite for physical and mental health. Music teachers or other teachers in colleges and universities will not change to tie themselves to research and professional titles. They must always be happy so that they can work in order to achieve the effect of getting twice the result with half the effort.

(1) Good sleeping habits can help music teachers in colleges and universities to be energetic and comfortable at work, reducing the intake of unhealthy stimuli such as coffee, tea, tobacco, and alcohol before going to bed, and forming and creating a suitable sleeping environment will also help;

(2) Scientific eating habits and scientific diets provide energy support for teachers to engage in heavy mental work. The specific requirements are timing, quantitative, reasonable collocation, no partial eclipse, and attention to food hygiene;

(3) Appropriate leisure activities can relax teachers' bodies and minds, satisfy hobbies, and experience the function of self-growth. Occasionally, a movie or drama, a walk in the park, a visit to a painting exhibition or a museum, etc., will make them feel physically and mentally happy and stress relieved;

(4) Reasonable physical exercise can strengthen the body, beautify the image, and at the same time help increase teachers' self-confidence, self-esteem, self-control, and self-satisfaction, and more importantly, relieve work and psychological pressure. Physical exercise is the best way to get rid of negative emotions and prevent depression, anxiety, and worries.

3. Investigation and Experiment on the Stress and Mental Health of Music Teachers in Colleges and Universities

3.1. Experimental Content. Music teachers are a group of teachers with distinctive personalities, but they are also prone to psychological problems. This experiment mainly selected 4 colleges and universities in the province as the experimental site, took the music teachers of these 4 colleges and universities as the research objects and investigated their occupational stress and mental health problems. This experiment adopts the experimental method of a questionnaire survey. A total of 175 questionnaires were distributed to music teachers in these 4 universities, and 164 valid questionnaires were returned. The survey tool used the SCL-90 symptom self-rating scale.

3.2. Experimental Process. The survey content was determined and the questionnaire questions were set up. The questionnaire is completed in accordance with the design criteria of the questionnaire. The survey subjects are communicated with before the survey, and after an agreement is made, the survey staff will hand out the questionnaire and the music teacher will fill it out on the spot. It took one week from the issuance of the questionnaire to the collection of the questionnaire. After that, the collected questionnaires were sorted out and the data was collected. The formula used in the data processing stage is as follows:

$$\text{Sample variance formula: } s^2 = \frac{\sum_{i=1}^{n}(x_i - x)^2}{n-1},$$

$$\text{Sample standard deviation formula: } s = \sqrt{s^2} = \sqrt{\frac{\sum_{i=1}^{n}(x_i - x)^2}{n-1}}. \tag{1}$$

4. Survey Results of the Professional Pressure and Mental Health of College Music Teachers

4.1. Survey on the Severity of Occupational Anxiety and Mental Health. The relevant standards of the SCL-90 symptom self-rating scale have stated that the factor score is greater than or equal to 2 as a mild symptom response. When the molecular factor is greater than or equal to 3, it means that the survey subject has a moderate or higher symptom response. Figure 4 shows the statistics based on the relevant standards of SCL-90:

Figure 4 shows that college music teachers may have various possible problems, including psychological problems such as somatization force, Interpersonal sensitivity, depression, anxiety, hostility, terror, paranoid, and psychotic.

Among the 164-people surveyed, 99 people had mild symptoms and 65 people had moderate or above symptoms. From this point of view, the professional pressure on music teachers in colleges and universities in the province is relatively high, and their mental health problems have gradually become prominent.

It can be seen from Figure 4 that among the mild symptom responses, the most prominent is the interpersonal relationship. The number is 90, which is more than half of the sample. Secondly, self-anxiety and physical factors are also compared among them.

Among the above-moderate reaction symptoms, self-anxiety is also the most prominent. The number of people with this factor is 25.

Through further analysis of the results of the questionnaire, the anxiety index is defined in the interval (0, 1), and then the value of a single survey result is quantified, compared with the quantified value of the entire survey sample, and the value of each survey sample is calculated. Anxiety values and the corresponding extreme values, average values, and anxiety states are analyzed and the specific display is shown in Table 1.

It can be seen from Table 1 that the lightest symptom of occupational anxiety for music teachers in colleges and universities is 0.18, and the worst symptom is 0.92. The average of the occupational anxiety symptoms of music teachers in colleges and universities is 0.72. Through the analysis of the mean value, it can be seen that the overall anxiety level of the 164 teachers in this survey is at an upper-middle level.

4.2. Attitudes of Music Teachers to Occupational Anxiety and Mental Health Problems. Figure 5 shows the survey results on the attitudes of music teachers to occupational anxiety and mental health problems. The figure shows that 68% of teachers adopt a positive and optimistic approach, and 16%

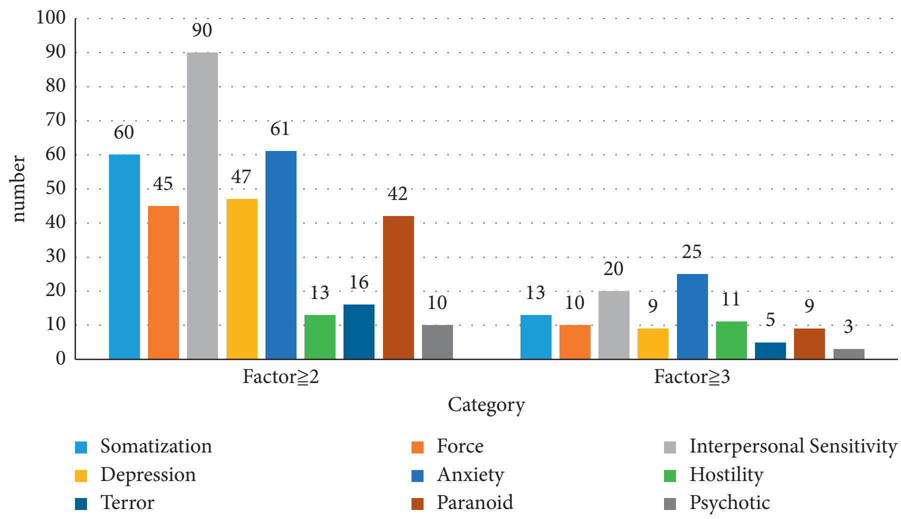

Figure 4: Distribution map of problem severity.

Table 1: Occupational anxiety index of college music teachers.

Number of respondents	Mean anxiety	Maximum anxiety	Anxiety minimal	General anxiety state
164	0.72	0.92	0.18	Middle

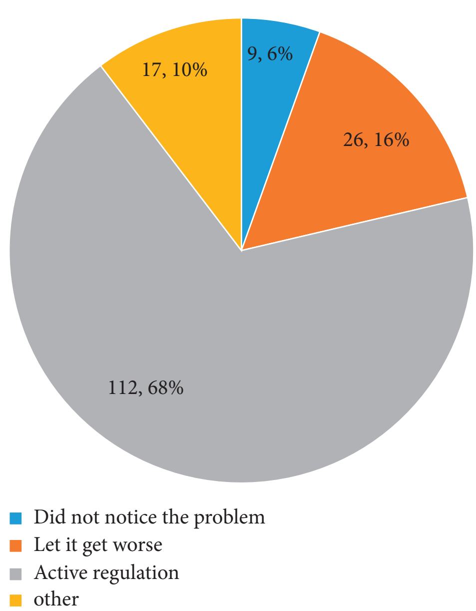

Figure 5: Music teachers' attitudes towards occupational anxiety and mental health problems.

of teachers feel that there is no need to pay attention and just let it develop. 6% of the teachers were unaware of the problem, and 10% of the teachers took other methods to solve it.

5. Conclusion

Music teachers are the most important team force to support music aesthetic education in colleges and universities. Their mental health will undoubtedly have a subtle impact on college students' studies and lives. Taking the opportunity of career development and reform, we must pay attention to the key topics of professional improvement and mental health adjustment of music teachers in colleges and universities. Teachers are humans too. Since they are humans, there are problems of survival and development. If these problems cannot be resolved in a timely and effective manner, psychological diseases may result. Patients suffering from severe psychological diseases may pose a certain threat to their family, society, and school. Music teachers in colleges and universities should pay attention to the improvement of their theoretical knowledge of mental health, and school management departments and society should also pay attention to the mental health of college music teachers, organizing various activities to improve teachers' mental health levels, promoting teachers' physical and mental health, and school education in a harmonious development.

Colleges and universities should create an environment conducive to the mental health of teachers and adhere to a people-oriented education management method. Music teachers in colleges and universities should also take the initiative to improve their own psychological quality and develop good living habits in peacetime. In short, the adjustment of the mental health of college music teachers requires the joint efforts of colleges and teachers. Only by maintaining a good mental state can college music teachers have better professional development.

Data Availability

The datasets used and/or analyzed during the current study are available from the corresponding author on reasonable request.

Conflicts of Interest

The authors declare that there are no conflicts of interest regarding the publication of this paper.

References

[1] M. Aitken, R. Martinussen, and R. Tannock, "Incremental validity of teacher and parent symptom and impairment ratings when screening for mental health difficulties," *Journal of Abnormal Child Psychology*, vol. 45, no. 4, pp. 1–11, 2016.

[2] F. Boman, M. Stafström, N. Lundin, M. Moghadassi, C. J Törnhage, and P. O Östergren, ""Comparing parent and teacher assessments of mental health in elementary school children," *Scandinavian Journal of Public Health*, vol. 1997, no. 2, pp. 168–176, 2016.

[3] J. H. Ohrt, J. D. Deaton, J. D. Guest, K. Linich, B. Wymer, and B. Sandonato, "Teacher training in K-12 student mental health: a systematic review," *Psychology in the Schools*, vol. 57, no. 4, pp. 1–20, 2020.

[4] Y. Jin, "Investigation and analysis of work stress and mental health status of music teachers in primary and secondary schools in Nan'an district of chongqing city," *Chongqing and the World*, vol. 33, no. 22, pp. 56–58, 2018.

[5] C. Gray, G. Wilcox, and D. Nordstokke, "Teacher mental health, school climate, inclusive education and student learning: a review," *Canadian Psychology*, vol. 58, no. 3, pp. 203–210, 2017.

[6] N. Nurbaiti, "Teacher's mental health in students perspective and its contribution to student's achievement of islamic religious studies," *Tazkiya Journal of Psychology*, vol. 23, no. 8, pp. 79–86, 2020.

[7] K. Coggins and K. Carnes-Holt, "The efficacy of child–teacher relationship training as an early childhood mental health intervention in head start programs," *International Journal of Play Therapy*, vol. 30, no. 2, pp. 112–124, 2021.

[8] S. Akbari-Zardkhaneh, S. M. Shahvarani, N. Mansurkiaie et al., "Psychometric properties of electronic mental health assessment device for high school students: teacher and parent form," *Iranian Journal of Psychiatry*, vol. 24, no. 3, pp. 324–339, 2018.

[9] S. Srinivasan, "A study of teacher's intelligence and emotional intelligence on students' mental health among higher secondary school of Thanjavur District," *American Journal of Educational Research*, vol. 6, no. 6, pp. 869–876, 2018.

[10] E. J. Nyavanga, "Factors that contribute to attitudes towards professional psychological help seeking for mental health issues among teacher trainees in Kenya," *American Journal of Applied Psychology*, vol. 6, no. 6, pp. 142–146, 2017.

[11] J. Zamarripa, I. Castillo, I. Tomás, and J. T. Rodriguez, "The teacher's role on the motivation and mental health in physical education students," *Salud Mental*, vol. 39, no. 4, pp. 221–227, 2016.

[12] H. Mayer-Benarous, X. Benarous, F. Vonthron, and D. Cohen, "Music therapy for children with autistic spectrum disorder and/or other neurodevelopmental disorders: a systematic review," *Frontiers in Psychiatry*, vol. 12, Article ID 43234, 2021.

[13] Y. Lin, "Research on the application of music therapy in mental health education in junior high schools," *Fujian Education*, vol. 45, no. 43, pp. 29-30, 2019.

[14] Q. F. Guo, "The cultivation of music appreciation for high school students' creative thinking," *Beauty and Times (Part 2)*, vol. 28, no. 5, pp. 89–91, 2020.

[15] Y. L. Jia, "Research on the application of music therapy in the rehabilitation of children with autism," *Teachers' Expo*, vol. 42, no. 3, pp. 82-83, 2021.

[16] N. Zhang, "Research on the role of music therapy in relieving the psychological pressure of college teachers," *Voice of the Yellow River*, vol. 51, no. 13, p. 146, 2020.

[17] J. J. Shen, "The application of background music in operating room work," *Industrial and Enterprise Medical Journal*, vol. 25, no. 1, pp. 87-88, 2012.

[18] S. L. Kong, "Tactics to relieve teachers' psychological pressure from the perspective of core literacy," *New Wisdom*, vol. 66, no. 4, pp. 63-64, 2021.

[19] Y. P. Yang, "Analysis of the status quo of primary and middle school teachers' mental health development and countermeasures," *Modern Teaching*, vol. 27, no. 24, pp. 36–39, 2020.

Hindawi
Journal of Healthcare Engineering
Volume 2022, Article ID 2354866, 8 pages
https://doi.org/10.1155/2022/2354866

Research Article

Optimal Medical Image Size Reduction Model Creation Using Recurrent Neural Network and GenPSOWVQ

Chethana Sridhar,[1] Piyush Kumar Pareek,[2] R. Kalidoss,[3] Sajjad Shaukat Jamal,[4] Prashant Kumar Shukla,[5] and Stephen Jeswinde Nuagah[6]

[1]*Department of Computer Applications, Sivananda Sarma Memorial R.V. College, Bangalore, Karnataka, India*
[2]*Department of Computer Science Engineering, Nitte Meenakshi Institute of Technology, Bangalore, Karnataka, India*
[3]*Sri Sivasubramaniya Nadar College of Engineering, Chennai, India*
[4]*Department of Mathematics, College of Science, King Khalid University, Abha, Saudi Arabia*
[5]*Department of Computer Science and Engineering, Koneru Lakshmaiah Education Foundation, Vaddeswaram, Guntur 522502, Andhra Pradesh, India*
[6]*Department of Electrical Engineering, Tamale Technical University, Tamale, Ghana*

Correspondence should be addressed to Stephen Jeswinde Nuagah; jeswinde@tatu.edu.gh

Received 1 November 2021; Accepted 3 January 2022; Published 26 February 2022

Academic Editor: Enas Abdulhay

Medical diagnosis is always a time and a sensitive approach to proper medical treatment. Automation systems have been developed to improve these issues. In the process of automation, images are processed and sent to the remote brain for processing and decision making. It is noted that the image is written for compaction to reduce processing and computational costs. Images require large storage and transmission resources to perform their operations. A good strategy for pictures compression can help minimize these requirements. The question of compressing data on accuracy is always a challenge. Therefore, to optimize imaging, it is necessary to reduce inconsistencies in medical imaging. So this document introduces a new image compression scheme called the GenPSOWVQ method that uses a recurrent neural network with wavelet VQ. The codebook is built using a combination of fragments and genetic algorithms. The newly developed image compression model attains precise compression while maintaining image accuracy with lower computational costs when encoding clinical images. The proposed method was tested using real-time medical imaging using PSNR, MSE, SSIM, NMSE, SNR, and CR indicators. Experimental results show that the proposed GenPSOWVQ method yields higher PSNR SSIMM values for a given compression ratio than the existing methods. In addition, the proposed GenPSOWVQ method yields lower values of MSE, RMSE, and SNR for a given compression ratio than the existing methods.

1. Introduction

Modern learning reports that the employment of imaging has increased significantly in the previous two decades [1]. In the United States, for example, there was a study by Smith-Brinman et al. [2]. It was reported in 2008 that CCTV images doubled and MRI images doubled. This growth is the effect of a quick overhaul of hardware as well as software to support imaging systems. In addition, the transition from analog to digital provides fast, stress-free, and accurate image development. All of these factors have supplied significantly to the group of images. Therefore, the byte of these images is received every year worldwide. Imaging technology is implemented by X-ray, ultrasound, MRI/fMRI (functional magnetic resonance image), nuclear medicine, PET (positron emission tomography), CT (computerized tomography) [3], and DXA (dual energy X-ray absorptiometry). The necessity of saving, distributing, and downloading these images in their own appearance has given to the picture archiving along with communication system

(PACS) a medical imaging skill that presents low-cost storage as well as access to useful images from many sources. Unluckily, the huge pixel size of these images severely limits the storage capacity [4–6]. For example, an emblematic NMR matrix dimension is 512×512 with 16 b [7].

A healthcare association that creates hundreds of images a week will need numerous megabytes of storage space. In a year, the total storage needed increases to a few gigabytes. This growth results in various terabit storage volumes per year. Moreover, a 56 kbps MRI band will take 12–15 minutes [8]. A lot of methods have been developed to reduce the size of these images, except that the major desirable novelty is the hybrid image production technique, in which the wavelet transform (DWT) along with vector quantization (VQ) as well as the loss [9] is preferred the most. In numerical analysis and function, DDD is a variation of spectacles in which the spectacles are precisely modeled and designed to process signals with a certain amount of time [10, 11].

In contrast to the discrete cosine transform (DCT) derived from the function of the base cosine, DWT is able to collect a few functions that meet the needs of multidimensional reaction analysis [12]. The origin of the image size reduction algorithm is to get an X input as well as produce an X demonstration that must need less bits for the representation. This went after recovery techniques that work on a compact X representation to produce a recovery , e.g., DWT offers a set of wavelet coefficients at various sizes showing various numerical types.

To propose the quantity for every set using the VQ technique, the bit value can significantly condense, devoid of affecting the excellence. Nevertheless, quantification leads to defeat of signal superiority. Consistent with Sannon, the dimensions of the selected vector have a significant influence on the quantitative efficiency. Larger vectors produce better quality than smaller vectors. For this reason, the purpose of this work is to develop a hybrid approach derived from discrete wavelet transforms and vector quantization to reduce the size of medical images with elevated compression rates and quality.

The main contributions of this paper are summarized as follows:

(i) Recurrent neural network is developed to compress the medical images.

(ii) A novel hybridized approach GENPSO is developed for optimizing the neural network parameters.

(iii) Using GENPSO, the hidden layer of recurrent neural network is compressed in more effective way to increase the compression ratio.

(iv) High compression ratio and better performance were achieved compared to the other existing approaches using wavelet vector quantization.

(v) The proposed method provides good results for real-time medical dataset.

The manuscript of this document is organized as follows: Section 2 discusses some of the relevant contemporary literature. Section 3 presents a detailed description of the proposed architecture. Section 4 presents the experimental results, which include the general operating results of comparing the performance of GENPSO and other compression methods previously published. Conclusion and future work are provided in Section 5.

2. Background

Juliet et al. [13] discussed a new approach, including Ripplet conversion, to ensure better image quality and higher compression levels. In this work, to achieve high compression, the image is presented in various weights and instructions. Cyriac et al. [14] developed a lossless compression technique to address the issue of expanding compression. In this article, the newly developed method is to reduce the image size sufficiently as well as speed up the hardware execution of the software in real time. Brahimi et al. [15] illustrated a new coding method in which both symbols along with images are compressed together with a codec. The major point of this method is to insert a rotten stray signal into the corrupted image, and the resulting image is employed for image size reduction.

Arif et al. [16] introduced an effective approach for minimizing fluoroscopic imaging. The retrieved ROI of this approach is minimized through a grouping of run length as well as hepatic coding. The final outputs show that the newly developed method offers a compression ratio of 400% compared to other traditional approaches. Das et al. [17] described a lossless medical imaging watermark (MIW) procedure that relies on the area of interest concept. The major purpose of this technique is to offer clarification to many issues related to the dissemination of medical data. This article uses seven various methods to display as well as compare outputs to demonstrate that the newly developed approach is easy and obvious in ensuring the security of the medical database.

Lucas et al. [18] introduced 3D lossless compression techniques 3-D MRP for high-volume medical imaging equipment. The presented technique relies on the minimum velocity forecasting mechanism (MRP). This article concludes that the demonstrated method can enhance the probability of error of the MRP as well as achieve higher image size reduction efficiency than ASS along with other standards for the depth of the medical signal. Špelič et al. [19] proposed new algorithms developed as voxel compression algorithms for 3D CT image compression for the broadcasting of graphics information acquired from CT scanners. This work illustrated the Hounsfield size being employed first for partial medicine, and then image size reduction is applied. In this work, a modeling method is employed to evaluate the effectiveness of the newly developed techniques.

Anusuya et al. [20] developed a new, lossless code employing a codec to reduce the size of 3D brain images. In this paper, MRI models are employed to analyze the effectiveness of the newly developed solution, and this paper focuses on sinking utilization time using parallel calculations. Xio et al. [21] introduced integrated tablets for compact image compression without data loss. The proposed technique integrates with integer maps for inefficient compaction. Amri et al. [22] introduced two lossless image size reduction techniques. In this work, demonstrated algorithms are employed to minimize image dimension and code algorithms for lossless image size reduction. It can be seen that the newly developed method can maintain image feature for elevated image size reduction levels and also provide different enhancements to the standard JPEG image size reduction.

Ramesh et al. [23] described a method for predicting wavelengths to minimize medical images. In this method, the forecast equations for each subline depend on the correlation analysis. Evaluation outputs show that the newly developed method offers a superior level of compression matched up to the standard SPHIT and JPEG2000. Ibrahim et al. [24] introduced two novel lossless image size reduction techniques based on logarithmic calculations. The proposed method can offer better image feature compared to conventional DWT. Avramovic et al. [25] developed a new loss-free image size reduction technique using context-based Internet converters. The proposed method relies on the concept of projection to eliminate the need for transparency in the image and to effectively compress the image without losing data. The conclusion is that the newly developed method can attain the similar results as high-class images like previous standard algorithms. Bairagi [26] accounted the idea of symmetry for medical imaging. The method shown here is lossless and can effectively remove unnecessary information from the image.

Zuo et al. [27] introduced an enhanced technique to IMIC-ROI medical imaging for efficient and effective medical imaging. The proposed technique is based on the concept of interest area (ROI) as well as non-ROI area. Srinivasan et al. [28] described encoders for compact electromagnetism (EEG) matrix. The method illustrated first two phases, the lost code layer (SPHIT) and the remaining coded layer. Taquet et al. [29] reported on hierarchical-oriented forecasting methods to allow scaling without loss and near-loss of medical imaging. It can be seen that the newly developed method is best employed for lossless image size reduction as it may offer superior or equivalent PSNR for higher bit rates compared to the JPEG 2000 standard.

Zanaty and Ibrahim [30] introduced a medical image compression technique based on combining region growing and wavelets algorithms. The authors have used a region growing algorithm where an image is portioned into two parts and the capability of the algorithm is justified.

3. Materials and Methods

3.1. Recurrent Neural Network. The recurrent neural network [31] is one of the neural networks which employs precedent data in a closed loop. It can be repeated through merely transmitting the network output or intermediate state as input. For instance, the input image of k-1 might be integrated into a network in kth step. This kind of network is suitable during short-term dependencies as it depends on other and does not perform better for long-term dependencies observed in compression. For this kind of network, there are issues in the training procedure, so throughout reproduction it can "disappear" or "explode." To avoid this limitation, this work uses a new approach called GenPSO and proposed vector quantization required to incorporate with neural network to manage the input and output image data. So in this work the codebook is generated using a novel hybrid GenPSO approach. Then this codebook is used in vector quantization for compressing the number of hidden neurons for increasing the compression ratio [32].

3.2. Updating Weights in Recurrent Neural Network Using GenPSO. In this step, the weight generated from the recurrent neural network is updated through the GenPSO method. The initial constitutive population of a chromosome has an evenly distributed random number. The chromosome represents the weight of the recurrent neural network. A crossover here can be defined as a crossover on a node. It is necessary to construct two springing from the parent node, with each node being retrieved from a hidden layer, and multiple outputs, randomly taken with equal probability. This node is considered a transit node [33]. The value of all input weights for that particular node is changed with the other master. This change can also be considered as a node change, in which all the incoming weights are for randomly selected active nodes. Finally, the PSO process is applied. The initial PSO population was determined by GA decision. Therefore, it can overcome the problem of slow convergence of the GPS network [34].

The algorithm for weights evolution by GenPSo in RNN is as follows.

The following steps are performed to determine the best weight value.

(i) For population of the XiMi, a solution, $i = 1, \ldots, \mu$, is started on area M with $R \in n$.

(ii) Two parents are randomly selected with a parent population distribution and two births will be generated by a crossover operator.

(iii) ereditary mutation of the offspring is performed.

(iv) Repeat step (ii) until the number of offspring μo is μ. Otherwise, go to step (v).

(v) Any parental decision, $i = 1, \ldots, \mu$ and progeny Xo, $o = 1, \ldots, \mu$, are estimated in light of objective function (X).

(vi) For mixed population Xm, m = 1,. . ., 2 μ, both the parent population and the population formed. They are randomly mixed so that parents and children mix up properly.

(vii) Each solution of Xm, $m = 1, \ldots, 2\mu$ is evaluated with 10% of the solutions of the other randomly selected solutions from a mixed population.

(viii) The highest earnings decision is reserved for the next generation of parents.

(ix) If the best chromosome difference for the N number of successive generations is less than the specified brightness, stop the process and the best chromosome of the last generation is the ideal weight. Otherwise, proceed to the next step.

(x) Beginning particle population and location and velocity are derived from the genetic algorithm.

(xi) Estimate the fitness value of all particles depending on the fitness function based on the objective of the optimization problem.

(xii) Compare the values of the fit of each particle and its holes. If the current value is better than pbest, then set the current fitness value to its pbest. Otherwise, the pbest will remain the same.

(xiii) Determine the current best fitness value among all fitness values of all particles in the population. Then, compare this value to Gebel and set the current value to Gebel if the current value is better than Gebet. Otherwise, leave it blank.

(xiv) Update the position and speed of each piece.

(xv) Stop if the best solution is found that matches the predefined minimum error or reaches the maximum number of repetitions. Otherwise, repeat the procedure from steps (x) to (xv).

3.3. Proposed Image Compression Using GenPSO Wavelet Vector Quantization Recurrent Neural Network Approach. The proposed technique for quantifying vectors using backward neural networks is summarized in the following steps:

Step 1. Apply wavelet transform to the image to produce transformed image.

Step 2. Get a pixel value (0 to 255) of the matrix.

Step 3. Now apply these values to the forward neural network. This network must have 64 input nodes since the detector is 8×8. Train the recurrent neural network using the training algorithm as explained in Section 3.2.

Step 4. Weight and tilt, updated by GPS, are fed to a hidden layer that can contain 2, 4, 8, 16, 32, and 64 hidden nodes. Encode these values with GenPSOWVQ

Step 5. Select the 8×8 printer in order after completing the training.

Step 6. Digital bits are now converted into real values.

Step 7. Finally, the call phase shows depressed images (output images) at the output of the nervous system's output layer. The conversion of a pixel to a true value and a true value to a pixel occurs during the compression and compression process.

4. Experimental Results

4.1. Dataset Used. Datasets of images which include chest radiographs, unenhanced brain CTs, mammograms, and abdominal CTs are used for experimenting this work. The performance of the proposed Int OPMICM method is evaluated using real-time medical images in terms of PSNR, MSE, SSIM, NMSE, SNR, and CR values [31]. These results are compared with those obtained by the existing algorithms, namely, FFNN, VQFFNN, optimized FFNN, and optimized VQFFNN. Figure 1 depicts the sample images from the real-time medical database [34].

4.2. Performance Metric. For the assessment of the compression approaches, this paper employs six metrics, namely, PSNR, MSE, SSIM, NMSE, SNR, and CR.

4.2.1. Peak Signal-to-Noise Ratio. The peak signal-to-noise ratio (PSNR) is used to evaluate the quality between the compressed image and the original image. The PSNR formula is defined as follows:

$$\log 10 \frac{255 \times 255}{1/H \times W \sum_{x=0}^{H-1} \sum_{y=0}^{W-1} \left[f(x, y) - g(x, y) \right]^2} \mathrm{d}B, \tag{1}$$

where H and W are the height and width of the image, respectively, and $f(x, y)$ and $g(x, y)$ are the grey levels located at coordinate (x, y) of the original image and compressed image, respectively.

4.2.2. Structural Similarity Index. The structural similarity index is a method for measuring the similarity between the compressed image and the original image.

$$SSIM(y, \hat{y}) = \frac{\left(2_{\mu_y \mu_{\hat{y}}} + c_1\right)\left(2\sigma_{y\hat{y}} + c_2\right)}{\left(\mu_y^2 + \mu_{\hat{y}}^2 + c_1\right)\left(\sigma_y^2 + \sigma_{\hat{y}}^2 + c_2\right)}, \tag{2}$$

where $\hat{Y}$ is the compressed image, Y is the original image, μ is the mean, and σ^2 is the variance.

4.2.3. Mean Square Error. The mean square error (MSE) is used to evaluate the difference between a compressed image and the original image. The MSE can be calculated by

$$\mathrm{MSE} = \frac{1}{n} \sum_{i=1}^{n} \left(\hat{Y}_i - Y_i\right)^2, \tag{3}$$

where $\hat{Y}\hat{Y}$ is the compressed image and Y is the original image.

4.2.4. Root Mean Square Error. The root mean square error (RMSE) is a frequently used measure of the difference between compressed image values and the original image values.

$$\mathrm{RMSE} = \sqrt{\frac{\sum_{i=1}^{n} \left(\hat{Y}_i - Y_i\right)^2}{n}}, \tag{4}$$

where $\hat{Y}\hat{Y}$ is the compressed image and Y is the original image.

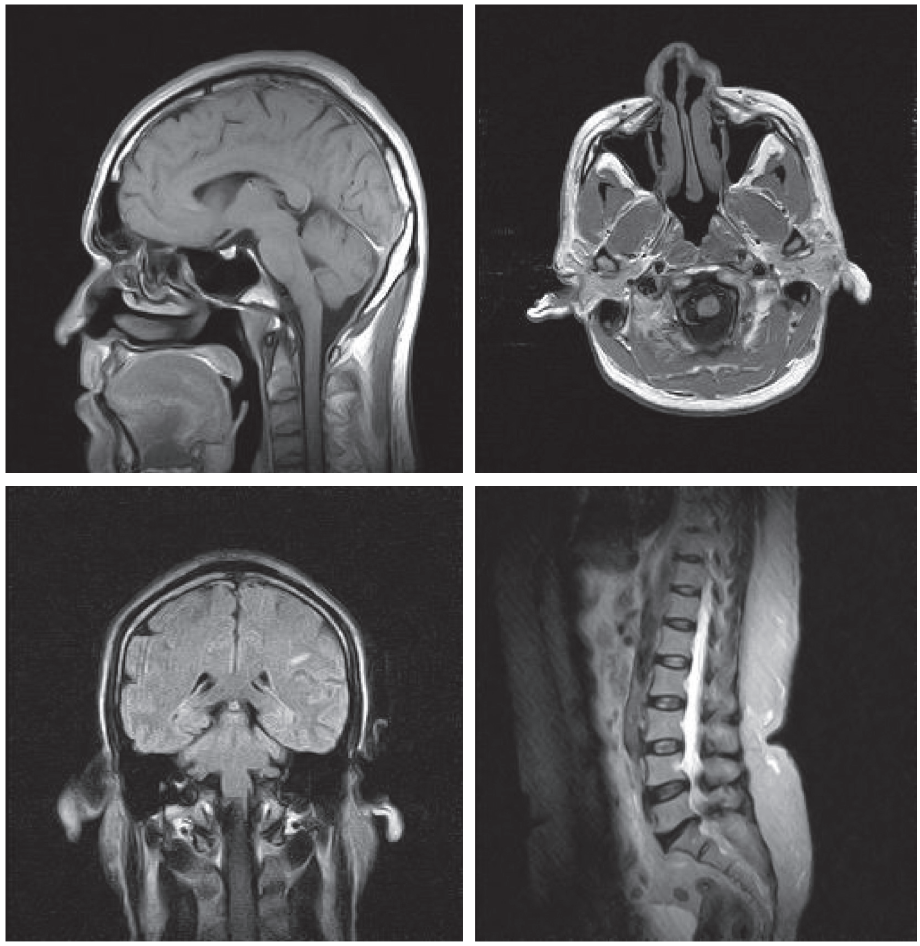

Figure 1: Experimental images.

4.3. Experimental Analysis

4.3.1. Experiment No. 1: Analysis of the Proposed GenPSOWVQ Compression Approach. In this experiment, we will evaluate the contribution of the proposed GenPSOWVQ compression approach. To evaluate the performance of this scheme, the PSNR, MSE, SSIM, NMSE, and SNR against 25% CR ratio are employed. This is shown in equations (1)–(4) correspondingly. This experiment will introduce the concept of GenPSOWVQ compression. It will be performed by estimating the performance of this scheme against a 25% CR ratio. Table 1 lists the PSNR, MSE, SSIM, NMSE, and SNR measures of GenPSOWVQ as well as the existing approaches.

The proposed GenPSOWVQ approach's performance is compared with traditional compression approaches through varying metrics, and the result is illustrated in Figure 2. The performance ratio of GenPSOWVQ has higher value than with traditional compression approaches. So it is proved that GenPSOWVQ is superior to traditional compression approaches.

4.3.2. Experiment No. 2: Performance of Best Chromosome Particles of GenPSO with Population Size of 50. The designed 2-2-1 feed forward architecture and the error value were developed according to the GenPSO method set out above. The population size was 50, and the termination rule is if the best error in the chromosome in the 50 successive generations is less than 0.00001. It is described in Figure 3.

The proposed GenPSO approach's performance is compared with varying population size, and the result is illustrated in Figure 3. The performance ratio of GenPSO has higher value than with traditional compression approaches. So it is proved that GenPSOWVQ is superior to traditional compression approaches.

4.3.3. Experiment No. 3: Performance of Best Chromosome Particles of GenPSO with Population Size of 100. The architecture of the best chromosome particle [35] distribution 2–2–1 was developed using the GenPSO method described above. The population size was 100, and the termination rule is if the 100 best chromosome errors continue to be less than 0.00001. It is described in Figure 4.

The proposed GenPSO approach's performance is compared with varying population size of 100, and the result is illustrated in Figure 4. The performance ratio of GenPSO has higher value than with traditional compression approaches. So it is proved that GenPSOWVQ is superior to traditional compression approaches.

Table 1: Analysis of PSNR, MSE, SSIM, NMSE, and SNR of GenPSOWVQ approach along with 25% CR ratio.

Dataset					
Compression approaches					
Metrics	OFFNN	VQFFNN	VQOFFNN	IntOPMICM	GenPSOWVQ
PSNR	36.80	48.12	49.65	52.4227	60.64
SSIM	0.20	0.43	0.53	0.6736	0.86
MSE	13.57	8.86	6.19	1.4164	0.83
RMSE	3.68	0.001	2.48	1.1901	0.0099
SNR	21.42	16.96	10.65	7.42	5.63

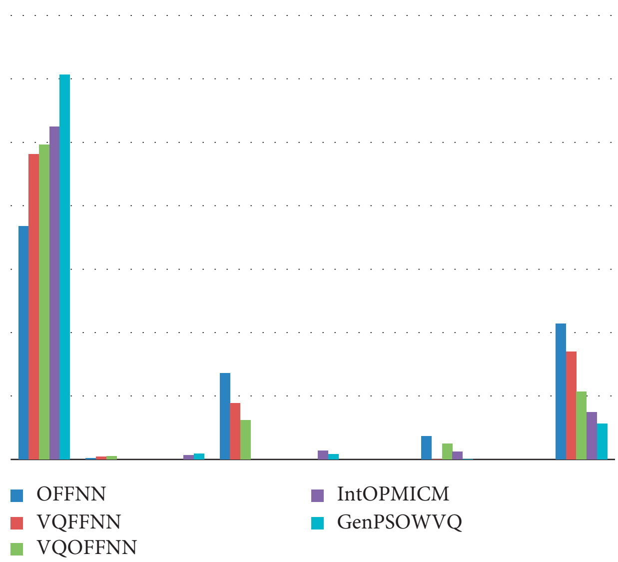

Figure 2: Analysis of PSNR, MSE, SSIM, NMSE, and SNR of GenPSOWVQ approach along with 25% CR ratio.

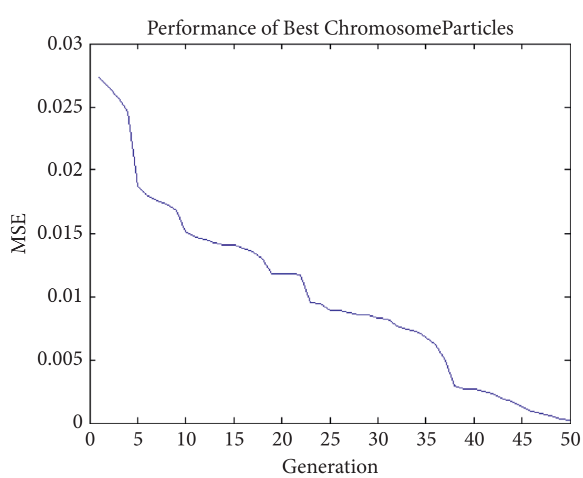

Figure 3: Analysis performance of best chromosome particles.

4.3.4. Experiment No. 4: Performance of Error of GenPSO with Population Size of 50. The designed 2-2-1 feed forward architecture and the error value were developed according to the GenPSO method set out above. The population size was 50, and the termination rule is if the best error in the chromosome in the 50 successive generations is less than 0.00001. It is described in Figure 5.

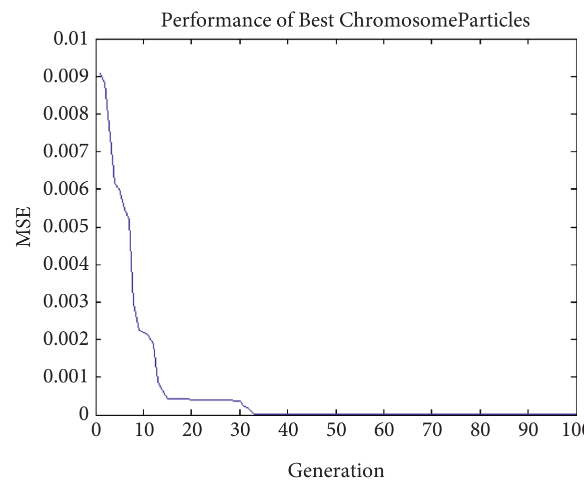

Figure 4: Analysis performance of best chromosome particles with 100 iterations.

The proposed GenPSO approach's performance is compared with varying population size of 50, and the result is illustrated in Figure 5. The performance ratio of GenPSO has higher value than with traditional compression approaches. So it is proved that GenPSOWVQ is superior to traditional compression approaches [36]. The proposed GenPSO achieves high performance against a large population size. This shows that it is superior to traditional compression approaches.

5. Conclusion

This article presents an image compression method for medical image compression using recurrent neural network. This recurrent neural network used a new image compression scheme called the GenPSOWVQ method which has been introduced using GenPSO with wavelet VQ. The codebook is built using a combination of fragments and genetic algorithms. The proposed method was tested using real-time medical imaging using PSNR, MSE, SSIM, RMSE, SNR, and CR indicators. Experimental results show that the proposed GenPSOWVQ method yields higher PSNR SSIMM values for a given compression ratio than the existing methods. In addition, the proposed GenPSOWVQ method yields lower values of MSE, RMSE, and SNR for a given compression ratio than the existing methods. This work can be further expanded to achieve the goal of creating optimal rules. The work can be extended for security in case

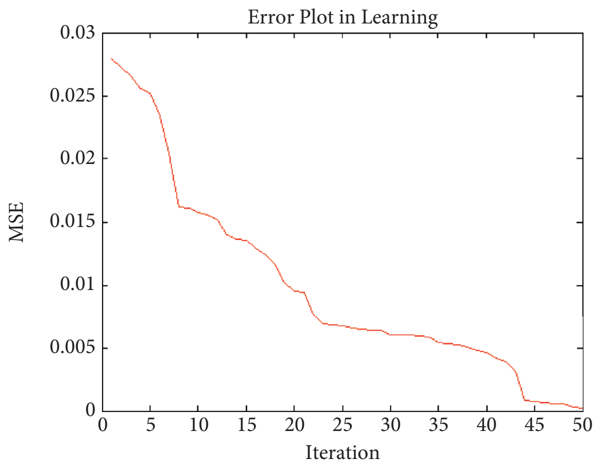

Figure 5: Analysis performance of best chromosome particles with population size of 50.

of image compression. Like the future work for this work, a new code of image compression is proposed using ambiguous logic. This research work has to be tested on large datasets and on a dynamic huge sample that is not tested and storage optimization that is not considered. The article presents a method for image compression using a recurrent neural network known as GenPSO. This method is built using a combination of genetic algorithms and fragments. The test results indicated that the proposed method achieves higher PSNR SSIMM values than the existing methods.

Data Availability

The data that support the findings of this study are available upon request from the corresponding author.

Conflicts of Interest

The authors of this manuscript declare that they do not have any conflicts of interest.

Acknowledgments

The authors extend their gratitude to the deanship of scientific research at King Khalid University for funding this work through research group program under Grant no. R.G.P. 2/48/42.

References

[1] R. Smith-Bindman, D. L. Miglioretti, E. Johnson et al., “Use of diagnostic imaging studies and associated radiation exposure for patients enrolled in large integrated health care systems,” *JAMA*, vol. 307, pp. 2400–2409, 2012.

[2] R. Smith-Bindman, D. L. Miglioretti, and E. B. Larson, “Rising use of diagnostic medical imaging in a large integrated health system,” *Health Affairs*, vol. 27, no. 6, pp. 1491–1502, 2008.

[3] T. Jones and D. Townsend, “History and future technical innovation in positron emission tomography,” *Journal of Medical Imaging*, vol. 4, no. 1, p. 011013, 2017.

[4] E. Reinhard, W. Heidrich, P. Debevec, S. Pattanaik, G. Ward, and K. Myszkowski, *High Dynamic Range Imaging: Acquisition, Display, and Image-Based Lighting*, Morgan Kaufmann, San Francisco, CA, USA, 2010.

[5] O. M. Al-Qershi and B. E. Khoo, “High capacity data hiding schemes for medical images based on difference expansion,” *J SystSoftw*, vol. 84, pp. 105–112, 2011.

[6] I. A. T. Hashem, I. Yaqoob, N. B. Anuar, S. Mokhtar, A. Gani, and S. Ullah Khan, “The rise of “big data” on cloud computing: review and open research issues,” *Information Systems*, vol. 47, pp. 98–115, 2015.

[7] M. J. House, S. J. Bangma, M. Thomas et al., “Texture-based classification of liver fibrosis using MRI,” *Journal of Magnetic Resonance Imaging*, vol. 41, no. 2, pp. 322–328, 2015.

[8] M. A. El Khaddar, H. Harroud, M. Boulmalf, M. Elkoutbi, and A. Habbani, “Emerging wireless technologies in e-health trends, challenges, and framework design issues,” in *Proceedings of the IEEE international conference on multimedia computing and systems (ICMCS)*, pp. 440–445, Tangiers, Morocco, May 2012.

[9] J. Spaulding, H. Noda, M. N. Shirazi, and E. Kawaguchi, “BPCS steganography using EZW lossy compressed images,” *Pattern Recognition Letters*, vol. 23, no. 13, pp. 1579–1587, 2002.

[10] S. G. Mallat, “A theory for multiresolution signal decomposition: the wavelet representation,” *IEEE Transactions on Pattern Analysis and Machine Intelligence*, vol. 11, pp. 674–693, 2009.

[11] M. Vetterli and C. Herley, “Wavelets and filter banks: theory and design,” *IEEE Transactions on Signal Processing*, vol. 40, pp. 2207–2232, 1992.

[12] I. Daubechies, *Ten Lectures on Wavelets*, Society for Industrial and Applied Mathematics, Philadelphia, PA, USA, 1992.

[13] S. Juliet, E. B. Rajsingh, and K. Ezra, “A novel medical image compression using Ripplet transform,” *Journal of Real-Time Image Processing*, vol. 11, no. 2, pp. 401–412, 2016.

[14] M. Cyriac and C. Chellamuthu, “A novel visually lossless spatial domain approach for medical image compression,” *European Journal of Scientific Research*, vol. 71, no. 3, pp. 347–351, 2012.

[15] T. Brahimi, L. Boubchir, R. Fournier, and A. Naït-Ali, “An improved multimodal signal-image compression scheme with application to natural images and biomedical data,” *Multimedia Tools and Applications*, vol. 76, no. 15, pp. 16783–16805, 2017.

[16] A. S. Arif, S. Mansor, R. Logeswaran, and H. A. Karim, “Auto-shape lossless compression of pharynx and esophagus fluoroscopic images,” *Journal of Medical Systems*, vol. 39, no. 2, p. 5, 2015.

[17] S. Das and M. K. Kundu, “Effective management of medical information through ROI-lossless fragile image watermarking technique,” *Computer Methods and Programs in Biomedicine*, vol. 111, no. 3, pp. 662–675, 2013.

[18] L. F. R. Lucas, N. M. M. Rodrigues, L. A. da Silva Cruz, and S. M. M. de Faria, “Lossless compression of medical images using 3-d predictors,” *IEEE Transactions on Medical Imaging*, vol. 36, no. 11, pp. 2250–2260, 2017.

[19] D. Špelič and Ž Borut, “Lossless compression of threshold-segmented medical images,” *Journal of Medical Systems*, vol. 36, no. 4, pp. 2349–2357, 2012.

[20] V. Anusuya, V. S. Raghavan, and G. Kavitha, “Lossless compression on MRI images using SWT,” *Journal of Digital Imaging*, vol. 27, no. 5, pp. 594–600, 2014.

[21] B. Xiao, G. Lu, Y. Zhang, W. Li, and G. Wang, “Lossless image compression based on integer Discrete Tchebichef Transform,” *Neurocomputing*, vol. 214, pp. 587–593, 2016.

[22] H. Amri, A. Khalfallah, M. Gargouri, N. Nebhani, J.-C. Lapayre, and M.-S. Bouhlel, “Medical image compression approach based on image resizing, digital watermarking and lossless compression,” *Journal of Signal Processing Systems*, vol. 87, no. 2, pp. 203–214, 2017.

[23] S. M. Ramesh and A. Shanmugam, “Medical image compression using wavelet decomposition for prediction method,” *International Journal of Computer Science and Information Security*, vol. 7, p. 1, 2010.

[24] M. S. Ibraheem, S. Z. Ahmed, K. Hachicha, S. Hochberg, and P. Garda, “Medical images compression with clinical diagnostic quality using logarithmic DWT,” in *Proceedings of the 2016 IEEE-EMBS International Conference on Biomedical and Health Informatics (BHI)*, pp. 402–405, IEEE, Las Vegas, NV, USA, February 2016.

[25] A. Avramović and G. Banjac, “On predictive-based lossless compression of images with higher bit depths,” *Telfor Journal*, vol. 4, no. 2, pp. 122–127, 2012.

[26] V. K. Bairagi, “Symmetry-based biomedical image compression,” *Journal of Digital Imaging*, vol. 28, no. 6, pp. 718–726, 2015.

[27] Z. Zuo, X. Lan, L. Deng, S. Yao, and X. Wang, “An improved medical image compression technique with lossless region of interest,” *Optik*, vol. 126, no. 21, pp. 2825–2831, 2015.

[28] K. Srinivasan, J. Dauwels, and M. RamasubbaReddy, “A two-dimensional approach for lossless EEG compression,” *Biomedical Signal Processing and Control*, vol. 6, no. 4, pp. 387–394, 2011.

[29] J. Taquet and C. Labit, “Hierarchical oriented predictions for resolution scalable lossless and near-lossless compression of CT and MRI biomedical images,” *IEEE Transactions on Image Processing*, vol. 21, no. 5, pp. 2641–2652, 2012.

[30] E. A. Zanaty and S. M. Ibrahim, “Medical image compression based on combining region growing and wavelet transform,” *International Journal of Medical Imaging*, vol. 7, no. 3, pp. 57–65, 2019.

[31] V. Roy, S. Shukla, P. K. Shukla, and P. Rawat, “Gaussian elimination-based novel canonical correlation analysis method for EEG motion artifact removal,” *Journal of Healthcare Engineering*, vol. 2017, Article ID 9674712, 11 pages, 2017.

[32] A. K. Saxena, S. Sinha, and P. Shukla, “Design and development of image security technique by using cryptography and steganography: a combine approach,” *International Journal of Image, Graphics and Signal Processing*, vol. 10, no. No.4, pp. 13–21, 2018.

[33] P. K. Shukla, J. Kaur Sandhu, A. Ahirwar, D. Ghai, P. Maheshwary, and P. K. Shukla, “Multiobjective genetic algorithm and convolutional neural network based COVID-19 identification in chest X-ray images,” *Mathematical Problems in Engineering*, vol. 2021, Article ID 7804540, 9 pages, 2021.

[34] P. K. Shukla, M. Agrawal, and A. U. Khan, “Stock price prediction using technical indicators: a predictive model using optimal deep learning,” *International Journal of Recent Technology and Engineering*, vol. 8, no. 2, pp. 2297–2305, 2019.

[35] P. Tiwari and P. Shukla, “Artificial neural network-based crop yield prediction using NDVI, SPI, VCI feature vectors,” in *Information and Communication Technology for Sustainable Development: Advances in Intelligent Systems and Computing*, M. Tuba, S. Akashe, and A. Joshi, Eds., vol. vol 933, Singapore, Springer, 2020.

[36] G. Khambra and P. Shukla, “Novel machine learning applications on fly ash based concrete: an overview,” *Materials Today Proceedings*, pp. 2214–7853, 2021.

Hindawi
Journal of Healthcare Engineering
Volume 2023, Article ID 9806292, 1 page
https://doi.org/10.1155/2023/9806292

Retraction

Retracted: Design and Implementation of Intelligent Monitoring System for Head and Neck Surgery Care Based on Internet of Things (IoT)

Journal of Healthcare Engineering

Received 8 August 2023; Accepted 8 August 2023; Published 9 August 2023

This article has been retracted by Hindawi following an investigation undertaken by the publisher [1]. This investigation has uncovered evidence of one or more of the following indicators of systematic manipulation of the publication process:

(1) Discrepancies in scope
(2) Discrepancies in the description of the research reported
(3) Discrepancies between the availability of data and the research described
(4) Inappropriate citations
(5) Incoherent, meaningless and/or irrelevant content included in the article
(6) Peer-review manipulation

The presence of these indicators undermines our confidence in the integrity of the article's content and we cannot, therefore, vouch for its reliability. Please note that this notice is intended solely to alert readers that the content of this article is unreliable. We have not investigated whether authors were aware of or involved in the systematic manipulation of the publication process.

In addition, our investigation has also shown that one or more of the following human-subject reporting requirements has not been met in this article: ethical approval by an Institutional Review Board (IRB) committee or equivalent, patient/participant consent to participate, and/or agreement to publish patient/participant details (where relevant).

Wiley and Hindawi regrets that the usual quality checks did not identify these issues before publication and have since put additional measures in place to safeguard research integrity.

We wish to credit our own Research Integrity and Research Publishing teams and anonymous and named external researchers and research integrity experts for contributing to this investigation.

The corresponding author, as the representative of all authors, has been given the opportunity to register their agreement or disagreement to this retraction. We have kept a record of any response received.

References

[1] Q. Liu, S. Hou, and L. Wei, "Design and Implementation of Intelligent Monitoring System for Head and Neck Surgery Care Based on Internet of Things (IoT)," *Journal of Healthcare Engineering*, vol. 2022, Article ID 4822747, 9 pages, 2022.

Hindawi
Journal of Healthcare Engineering
Volume 2022, Article ID 4822747, 9 pages
https://doi.org/10.1155/2022/4822747

Research Article

Design and Implementation of Intelligent Monitoring System for Head and Neck Surgery Care Based on Internet of Things (IoT)

Qiuxia Liu, Sujuan Hou, and Lili Wei

Department of Radiology, Tangshan Gongren Hospital, Angshan, Hebei 063000, China

Correspondence should be addressed to Sujuan Hou; 161842057@masu.edu.cn

Received 2 December 2021; Accepted 15 January 2022; Published 23 February 2022

Academic Editor: Enas Abdulhay

As a chronic disease, cervical spondylosis is prone to recurrent attacks as we age if we do not pay attention to protection, which can easily lead to symptoms such as osteophytes and herniated discs. In the early stage of cervical spondylosis, it is possible to alleviate the disease and prevent its aggravation by improving poor cervical posture and increasing cervical activities. This article analyzes the current situation and medical prospect of smart wearable devices with the prevention and treatment of cervical spondylosis in white-collar people as the starting point and smart wearable devices as the focus and provides a detailed analysis of the functions, categories, technologies, and applications of smart wearable devices to provide a technical theoretical basis for the construction of the subsequent research system. For the user's health state, some other physiological parameters are sent to data also through mobile Internet, and the user's physiological information is obtained on the computer database in also, which not only provides the monitoring function for the user's health but also provides the information of medical big data elements for medical and health institutions and so on. This article elaborates the requirement analysis of this system, based on which the system architecture design and module division are elaborated. It provides a practical and theoretical basis for further realizing the seamless integration of IoT technology and nursing information management system and improving its depth and breadth in the application of nursing information management system. From the perspective of the way of quantification of nursing practice activities, real-time monitoring, scientific management, and intelligent decision-making, it provides the basis for achieving the quality of nursing services, reducing errors, reducing labor intensity, and improving work efficiency and clinical research.

1. Introduction

With the rapid development of mobile technology and the widespread use of mobile Internet, the traditional Internet has slowly shifted to mobile Internet [1]. In this high-speed development trend, smart wearable devices are also growing rapidly and becoming a popular industry. In life, people want to use smart wearable devices to sense the outside world and their own information and to be able to process and communicate information more effectively with the help of computers, networks, and even other devices [2]. With the increasing awareness of health and health care requirements, all these are driving the medical model to shift from a symptom-centered treatment model to a prevention-centered, early diagnosis, and early treatment model, which has led to the focus on wearable products for health care. Smart wearable devices in the medical field have occupied an important position, and various medical devices such as smart blood pressure meter, smart blood glucose meter, and wrist-type ECG detector have emerged, making the seemingly professional medical devices start to come into ordinary people's homes [3]. Wearable health devices are devices that can be worn directly on the body or integrated into the user's clothes or accessories. Wearable medical devices can not only monitor blood sugar, blood pressure, heart rate, blood oxygen level, body temperature, breathing rate, and other human health indicators anytime and anywhere but also be used for the treatment of various diseases [4].

At present, wearable devices have made rapid development in the field of medical health, and smart wearable devices are moving from application research to practical application. In addition to monitoring users' personal health, they can also provide new diagnostic and treatment means for medical treatment, effectively solving the practical needs of clinical aspects, with good development prospects and broad market space. At the same time, the market scale of wearable mobile medical devices is expanding, and among the many mobile medical products, the most popular ones are wearable health products that provide medical services and monitoring for hospitals and patients [5]. In recent years, smart healthcare has been developing and growing, and smart ward systems in hospitals have attracted much attention. The construction of smart wards is developing rapidly. In smart wards, nursing staff can quickly access patient medical history information, doctors can use intelligent diagnostic data as auxiliary information for condition assessment and treatment, and patients can easily access health big data information in the process of medical treatment, so smart wards are an important part of realizing smart medical care [6]. Considering the special characteristics that the patient group has lower immunity and is more sensitive to environmental factors, the hospital ward environment is directly related to patients' health, and a good ward environment can create a good recuperation environment for patients. Therefore, a monitoring and control device is needed to monitor the environment in the ward in real time and strictly control the ward environment to meet the needs of patient recuperation. The continuous breakthrough of science and technology, the rise of artificial intelligence, the emergence of cloud computing and the Internet of Things, and the way of life in the ward have undergone further change and transformation, and the Internet of Things monitoring and control system with modern significance has gradually entered the ward [7]. IoT cloud platform is a kind of data processing and management platform that can provide services to consumers and enterprises. After cloud computing has been widely used, IoT technologies in logistics, education, agriculture, and many other fields have progressed. In these applications, the development cost of IoT can be high if it is arranged in local threads, while the cost is dramatically reduced by saving the transmitted data through the IoT cloud platform [8]. To network the physical endpoints, one needs IoT platforms to manage smart devices to achieve communication. The combination of IoT technology and cloud computing becomes inevitable [9]. Cloud computing adds fresh blood to the Internet and IoT development and also combines user applications with the currently popular web development technology, which makes the IT performance of products optimized, and consumers can get a good user experience and realize the cost optimization of enterprises [10].

The traditional intelligent system puts the server in the indoor environment and embeds it directly in the indoor gateway, which calculates, stores, and processes the indoor data, and the performance of the hardware gateway device cannot effectively meet the intelligent demand. On the other hand, due to the storage of data in indoor devices, it causes data disconnection, which is not conducive to the analysis and processing of user data. The rapid development of IoT cloud platform technology has strongly promoted the development of intelligent ward monitoring and control system. Based on the IoT cloud platform, intelligent management and control of equipment in wards can be realized, making the smart ward system solve the problem of data disconnection, and enterprises or users can simply and conveniently manage and control equipment, thus promoting the flow of the system into the market for mass production applications. Under the specific application scenario of the smart ward, the IoT monitoring and control system applied to the ward can integrate the current intelligent instruments, electrical resources, etc. To intelligently monitor and control the ward appliances. Users can view the working status of intelligent devices in wards in real time through cell phones and computers and can manipulate the operating parameters when the physical hardware is running, so as to get a good ward experience. The IoT cloud platform technology and system have scalable storage space and efficient data processing capability, providing a platform for the use of deep learning. The system can train artificial neural networks based on users' historical behaviors and users' interests, resulting in artificial network training models that enable users to understand their own habits of using equipment and also enable data prediction sharing through prediction of changes in environmental parameters, providing a foundation for future construction of intelligent wards. In the long-term direction, the system based on the IoT cloud platform has good security, data sharing, and fault tolerance features and has good development prospects and application value.

2. Related Work

Based on the requirement analysis of the IoT monitoring and control system applied to wards, the thesis designs the overall functional framework of the system. The thesis can be divided into two major parts: IoT hardware module and IoT software module [11]. Among them, the IoT software system includes the cloud platform server and the cloud platform client. Taking the ward application as the design background, different sensors of the ward environment monitoring module are used to collect the corresponding environmental parameters in the ward, including humidity, temperature, carbon dioxide concentration, and light intensity, connect to the network through WiFi wireless communication technology, upload the data to the TCP server inside the cloud server through TCP protocol, create a client in the TCP server, and transmit the data to the MQTT server, and the data information will be forwarded, processed, and stored in the TCP server [12]. The corresponding cloud platform client acts as a client of the MQTT server, and the MQTT client can subscribe to a topic to the MQTT server side, and once subscribed, it can publish messages to that topic, and any message that enters the subscribed topic will be printed to the JavaScript console, and the state changes of the sensor terminal and visual display data will be displayed in the cloud platform client web page in the form of animation. The same is true for reverse communication, which can be completed by the user clicking on the web interface to complete the control of the sensor terminal [13].

The behavior prediction module is based on an artificial neural network, using an attention model to complete the prediction of device usage, which is convenient for patients to understand their habits and provide direction for secondary development later. The system realizes the decoupling of heterogeneous hardware protocols by adding a cloud control software framework, which facilitates the management and control of information and makes the communication modules independent of each other and coordinates their work for easy development and use [14]. The core element and basic composition of IoT is still the Internet, which is an extension and expansion of the Internet and can realize information exchange, communication, intelligent positioning, and monitoring and control. In recent years, IoT has been widely used in production and life, introducing smart city, smart medical, smart energy management, smart transportation, and smart manufacturing into industrial and commercial fields. Currently, IoT platforms mainly consist of nonopen-source and open-source IoT platforms, and the following text briefly describes the two types of IoT platforms [15]. The computing mode of cloud computing is efficient, and IoT performs a lot of and fast computing, so consider combining IoT and cloud computing so that cloud computing provides a good application basis for IoT. Without the development of cloud computing, IoT cannot be successfully realized, and the development of IoT drives the progress of cloud computing technology; the two complement each other and are indispensable. Health care IoT is an important application area of IoT technology in the medical industry [16].

It is clearly proposed to “actively penetrate the medical consortium, use Internet technology to accelerate the interoperability and sharing of medical resources and information, achieve efficient business collaboration, and carry out more convenient telemedicine services” [17]. With the popularization of IoT technology and its full integration and application with 5G communication technology and computer technology such as cloud computing and big data, the influence of health care IoT is growing. Currently, China’s medical-related IoT can be roughly divided into three major application areas: smart hospital services, home health services, and public health services, covering multiple subapplications such as drug traceability, critical care, medical supplies management, and health management [18]. With the increase of people’s need for a better life, people’s demand for home health services is also gradually increasing, and the IoT platform for home health services has been given full attention. However, most of these applications still rely on the developed medical resources in the region to do some support, and the use is also very complicated, and the usage rate of IoT medical services is not high in areas with backward medical level [19]. At the same time, the user’s personal data involve personal privacy and interests; once leaked, they will have a serious impact on the user, and most of the current intelligent medical IoT products do not take into account the data security issues, many will even transfer the user’s data directly to the public cloud, and there are great hidden dangers [20]. Therefore, data security in smart medical is also the focus of attention of governments and researchers in various countries.

3. IoT Intelligent Assisted Head and Neck Care

3.1. Intelligent Monitoring of Head and Neck Wearable Devices. From the current point of view, the development of technology and the improvement of the quality of life also made wearable products available to people’s daily life, so that wearable devices are being known and applied by a large number of people; wearable products health care is the future direction of the development of intelligent wearable products. People use smart wearable devices to monitor various health and physiological indicators in real time, providing users with scientific guidance on health. Although there are many exploratory products in the field of posture monitoring, most of them focus on posture correction monitoring, mainly concerned with posture monitoring of the lumbar spine and other parts, by monitoring the user’s sitting posture, heart rate, breathing, and other data. The controller node can receive control commands sent from the cloud server to the hardware nodes, and the controller node performs the corresponding process according to commands such as switching on and off the fan and switching on and off the air humidifier. A two-directional control of the system is therefore achieved. However, for the user, the lack of data information from the information level to the transformation of action is precisely one of the reasons for the lack of user execution, mostly in giving advice and feedback, and not for the user to develop a corresponding improvement plan, the user needs to find their own way to make up for the shortcomings. At present, wearable monitoring products, monitoring posture, and other body indicators are very helpful to users, but considering that the daily scenarios of white-collar people are relatively irregular, interspersed with meetings, ambulatory work, leisure, study, and other scenarios, a single reminder mode sometimes becomes a disturbance and it may be necessary to consider setting the scenario mode to ensure that users have a good product experience. It is also necessary to integrate the corresponding ergonomics to ensure the comfort of the product.

The arrangement position of the neck ring monitoring node is directly related to the data collected by the sensor device to the model description; the closer to the monitoring target, the better the accuracy. Considering that the smart neck ring mainly monitors the cervical part of the human body, the product identification device can be placed near the cervical vertebrae, using the neck ring structure, which is conducive to the accuracy and fixity of identification. There is also an operation function area at the end of the neck ring, which can be used only through simple operation steps, and the whole process is easy and convenient. Information architecture is the process of normalizing the overall structure and specific functions of the application interface on the basis of the user task model. After the functional requirements of the smart neck ring application system are clear, the logic, hierarchy, and path of each information and element are presented by sorting out the relationship of the content information and elements of the system and constructing the relevant flowchart, making the target function and user’s needs reflected. The smart neck ring will be designed from the four modules of status, movement, discovery, and personal center, as shown in Figure 1.

With the continuous development of smart wearable devices in the medical field, the use of wearable devices to monitor and improve health has become a new way of health management, aiming to remind users to improve their poor lifestyle in real time by monitoring their behavioral data and providing targeted prevention and treatment suggestions. At present, it can detect blood sugar, blood pressure, heart rate, body temperature, human breathing, human posture, and other human physiological health indicators to provide users with scientific health guidance. In terms of cervical spine disease, wearable devices have already realized the monitoring of cervical spine dynamics, which can determine the posture and the activities of the wearer's cervical spine according to the position and angle of the wearer, providing a technical basis for wearable devices in the prevention and treatment of cervical spine disease. Combining with the characteristics and needs of white-collar people, the research and design of guardianship products can prevent and treat cervical spine disease for white-collar people, solve their cervical spine subhealth problems, let them maintain a good lifestyle while pursuing their ideals, and reduce the troubles of subhealth. It not only has social significance but also responds to the development of the times.

3.2. Wearable Device Sensor Node and Controller Node Design. The functionality of a hardware node is divided into two main parts: on the one hand, environmental parameters such as carbon dioxide concentration, light intensity, temperature, and humidity are to be recorded via sensor nodes and the collected data are uploaded to the cloud server via a WLAN module. The hardware notes in this white paper are complex and varied so that you can add new sensors and electrical devices depending on the environment and requirements or remove some sensors and corresponding electrical devices. After changing the devices, only some changes of the physical base interfaces are needed while agreeing on the message format for communication between the two sides, and then the design can be migrated to other physical bases, which is conducive to large-scale rollout. The sensor node includes a main control module, a WiFi networking module, a power and peripheral circuit module, a sensor module, and a controller module. The sensor module collects the environmental parameters in the ward, and the main control module converts the environmental parameters into the required physical quantities. The WiFi networking module can upload the processed data to the cloud server to complete data communication and also receive control commands from the cloud server to perform the corresponding control operations. The energy supply module is to provide various specifications of voltage requirements for each node device. The block diagram of sensor node and controller node structure is shown in Figure 2.

In the context of ward environment, the article requires large communication coverage, high transmission rate, good stability, and easy maintenance. WiFi is chosen as the

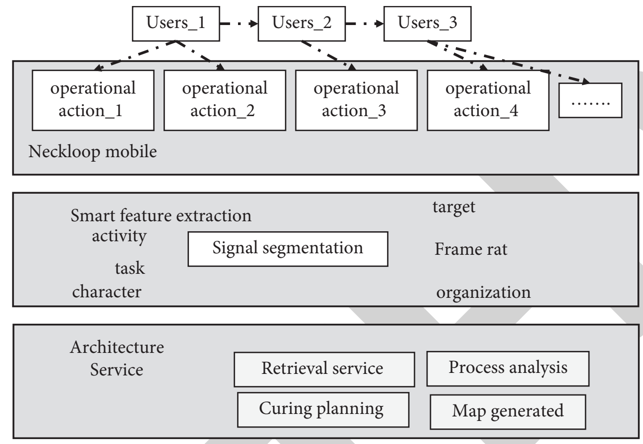

Figure 1: Neckloop mobile application state module information architecture.

wireless communication method for the IoT monitoring and control system in the ward. The USR-WIFI232-A2 is selected as the serial to WiFi communication module. The module is internally encapsulated and simple to set up to complete bidirectional data transmission between the serial device and the WiFi module. USR-WIFI232-A2, as a hotspot, can accommodate 32 WiFi clients at the same time and 32 TCP clients at the same time, providing convenience for the construction of the IoT system.

Several key elements in the recommendation system are defined:

$$T = \frac{\{T_1, T_2 \ldots T_n\}}{\sum_{i=1}^{N} Ti}. \tag{1}$$

User interest set for personalized fuzzy logic is as follows:

$$\mathrm{UT}(t_i) = \{w(u_i, t_i)\}. \tag{2}$$

The user is interested in personalized fuzzy logic set value.

When a user no longer has any user behavior on a resource to which a personalized fuzzy logic belongs after a certain time interval, we judge that the user's learning process for the resource has ended, and the interest value of the personalized fuzzy logic will follow.

$$w(u_i, t_i) = \frac{1}{1 + e^k} * \frac{t - t_0}{T}. \tag{3}$$

T is the time interval for the user's personalized fuzzy logic interest set to transfer; this interval is the time from the user's interest in a personalized fuzzy logic to the completion of the personalized fuzzy logic learning; t is the current time.

After the network parameters are set, restarting the WiFi module will complete the automatic network connection, at which time the WiFi module is accessed as a client and a connection is established with the cloud server. Take the fan as an example; its controller node receives the control command sent by the cloud server and sends the current state of the control node to the cloud server so that the server and the control node stay in sync and realize real-time update of the state information. Pulse width modulation

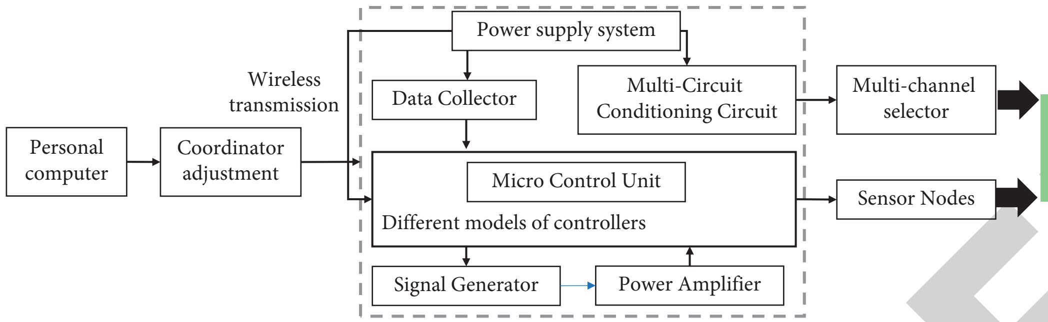

Figure 2: Sensor node/controller node architecture block diagram.

(PWM) technology is used to control the airflow for different gears. PWM technology is used to equate the required waveform by modulating the pulse width and then digitally encoding the analog signal level, i e., adjusting the information, energy, and other changes through the duty cycle to achieve different gears of airflow. At the fan hardware node side, the air conditioner switch is controlled by pressing the on/off button, real-time monitoring of the fan status is achieved by sending heartbeat packets, and the latest status of the node is sent to the cloud server in string format, which is stored, processed, and forwarded to the cloud platform client to achieve the animation display of the front-end page. The controller traffic change curve is shown in Figure 3. The controller nodes are monitored in real time to realize the transmission of status information of different sensor terminals and the execution of control commands from the server side, thus realizing the bidirectional control between the cloud server side and the sensor terminals.

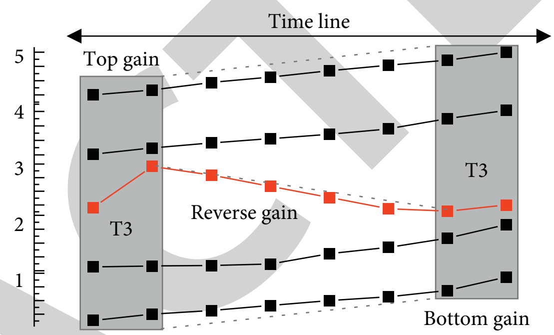

Figure 3: Flow gain selection timing diagram.

3.3. Design and Implementation of Cloud Server. Cloud servers provide interfaces to sensor devices and clients in stations where you can filter, store, and calculate data from sensor nodes and cloud platform clients. The article provides IoT systems on cloud platforms; cloud servers are data request and processing centers for the entire system while communicating with sensor nodes and, on the other hand, with cloud platform clients. Stores and processes requests and response signals from both sides. The two modules of the cloud server side are programmed using Python language to set shared variables and shared addresses in order to complete the communication between modules and realize two-way real-time communication and control transfer, which can be shown in Table 1.

Table 1: Real-time communication and control transfer.

Modules	Real-time communication	Control transfer
Node 1	NA	0.7739 ± 0.157
Node 2	NA	0.7652 ± 0.148
Node 3	0.6213 ± 0.269	0.6220 ± 0.169
Node 4	0.6349 ± 0.253	0.6539 ± 0.165
Node 5	0.7365 ± 0.183	0.8186 ± 0.129

The control transfer layer added between the cloud platform client and the sensor node can separate the client and the sensor node to achieve decoupling, thus allowing the two ends of the system to run separately during development and maintenance, reducing the coupling of the system. After the connection is completed, it is only necessary to negotiate and specify the communication protocol between the two sides and subscribe to it in the prescribed format, and the sensor nodes can quickly connect to the network to receive control commands and upload data to achieve bidirectional transmission of information between them. A block diagram of the cloud server architecture is shown in Figure 4.

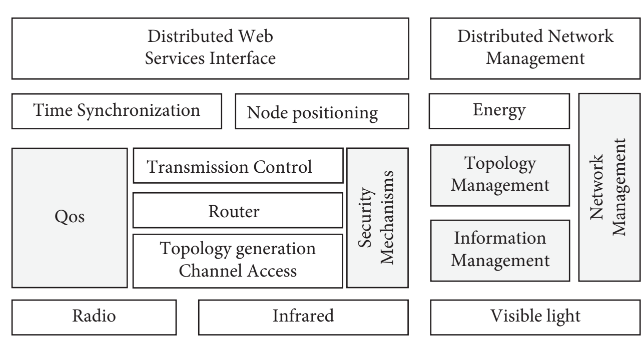

Figure 4: Block diagram of the cloud server architecture.

The cloud platform client acts as a client of the MQTT server and subscribes to the topic to the MQTT server side; once subscribed, it can post messages to the topic and any message that comes into the subscribed topic will be printed to the JavaScript console:

(1) Data messages based on the MQTT protocol are forwarded through the MQTT protocol proxy server to the MQTT client defined inside the TCP server, where they are forwarded, processed, and stored.

Then the data will be transmitted to the sensor nodes through the WiFi networking module via TCP protocol. The final realization of the cloud platform client real-time control sensor terminal execution.

(2) The same is true for the reverse data transfer, which is the transfer of sensor terminal data to the cloud platform client for presentation. The article selects the QoS1 level MQTT protocol, which completes the distribution at least once and ensures that the data from the sensor nodes must be sent out. Since the persistent communication between the client and the server requires constant message transmission, this makes the load on the server side increase.

(3) The article ensures that the signal changes can be listened to in real time by setting the heartbeat interval time, and that when there is no data transmission, the number of transmissions is reduced by lengthening the heartbeat interval time to maintain a continuous connection, achieving both minimizing the load on the server side and maintaining a two-sided connection. In the programming, the focus is on the four methods: connect, subscribe, publish, and disconnect.

4. Head and Neck Care Effectiveness Assessment and Testing

In the training parameters, the learning rate is set to 0.001 and the batch size is set to 128. According to the training curve, the model is better trained when the epoch is 5, and the switch threshold is set to 0.8. After the model training is completed, the trained model is called and tested using the test set. The accuracy of the test set for predicting the fan on/off state was 91.89% (accuracy is expressed as the ratio of the number of correctly predicted fan state samples to the total number of samples in the test set). For each predicted device, a binary model was trained, and a total of four models were trained in the article, each with the same training acquisition, to derive the accuracy of predicting the state of the device under the environmental state of the fan, air conditioner, smart lamp, and humidifier at a certain moment in the future, as shown in Figure 5.

The correlation between the air conditioner switch and the temperature value in the environmental parameters is relatively the greatest, and this chapter focuses on analyzing the correlation between the air conditioner switch and the temperature. The total number of times the air conditioner is turned on in different time periods in a week. The chart of the historical behavior of air conditioner switching in a week shows that the correlation between air conditioner switching and temperature values is low and not easy to predict, resulting in low accuracy of the test set. The results of user behavior prediction show that by fitting the historical serialized data with a neural network using the attention mechanism, the usage status of electrical devices at a future moment can be predicted with an accuracy of nearly 90%, as shown in Figure 6. The prediction accuracy can be improved in the future by improving the network structure and increasing the training set in an appropriate amount.

In several tests, it was found that when a sensor node is connected to the cloud server, when the node is disconnected due to an accident, the server is unable to determine whether the sensor is disconnected due to the lack of feedback. When the unexpectedly disconnected node is repowered, it reports an error because it already has a connection with the same name. The article solves this problem by sending "heartbeat packets," setting the TCP server to send a message to the sensor node every 20s, and if the sensor node receives it, it returns data to the TCP server, indicating that a connection exists. If the sensor node does not return a message to the TCP server after the TCP server sends a message to the sensor node, the connection is broken. At this time, close the connection channel and wait for the next reconnection to create a new channel; as shown in Figure 7, it can be seen that the connection can normally communicate again after the unexpected interruption. The above debugging shows that the two-way real-time communication between the server side and the sensor node is normal. This means that the integration of the two functional modules of the sensor node and the cloud server is successful.

Through research on the cervical spine subhealth of the white-collar population, the research was conducted around the psychological, physiological, behavioral and user needs of white-collar workers, and the real demands of users were discovered through questionnaires, in-depth interviews, and observation visits from which it was found that white-collar workers do not know and pay enough attention to their own cervical spine problems and have a long time of sedentary, lack of physical exercise, and lack of systematic and professional guidance on the prevention and treatment of cervical spine diseas and few of them really seek medical treatment. They usually relieve themselves by pressing the discomfort zone and sitting cervical spine exercises, as shown in Figure 8. Combined with the conclusions of the previous analysis, the overall product system design was carried out. The system includes the following: smart neck ring product hardware, R-neck software application, and the whole product system composition design. Taking into full consideration the actual requirements of white-collar workers in human-computer interaction, the product shape is chosen to be fashionable and lightweight, in line with the preferences and feelings of white-collar workers; in terms of software, according to the definition of product system functions and interaction methods, taking into account the busy nature of white-collar workers, a clear structure and hierarchical interface is designed to avoid interference from too many or overly complex factors, and relevant technical descriptions are made.

The system has several advantages over traditional IoT systems, (1) low coupling between client and sensor nodes, adding more control transfer layer than traditional architecture, which makes both sides function without affecting each other; (2) good platform migration, only needing to make some physical base interface changes and agree on the message format of the two sides of the communication to

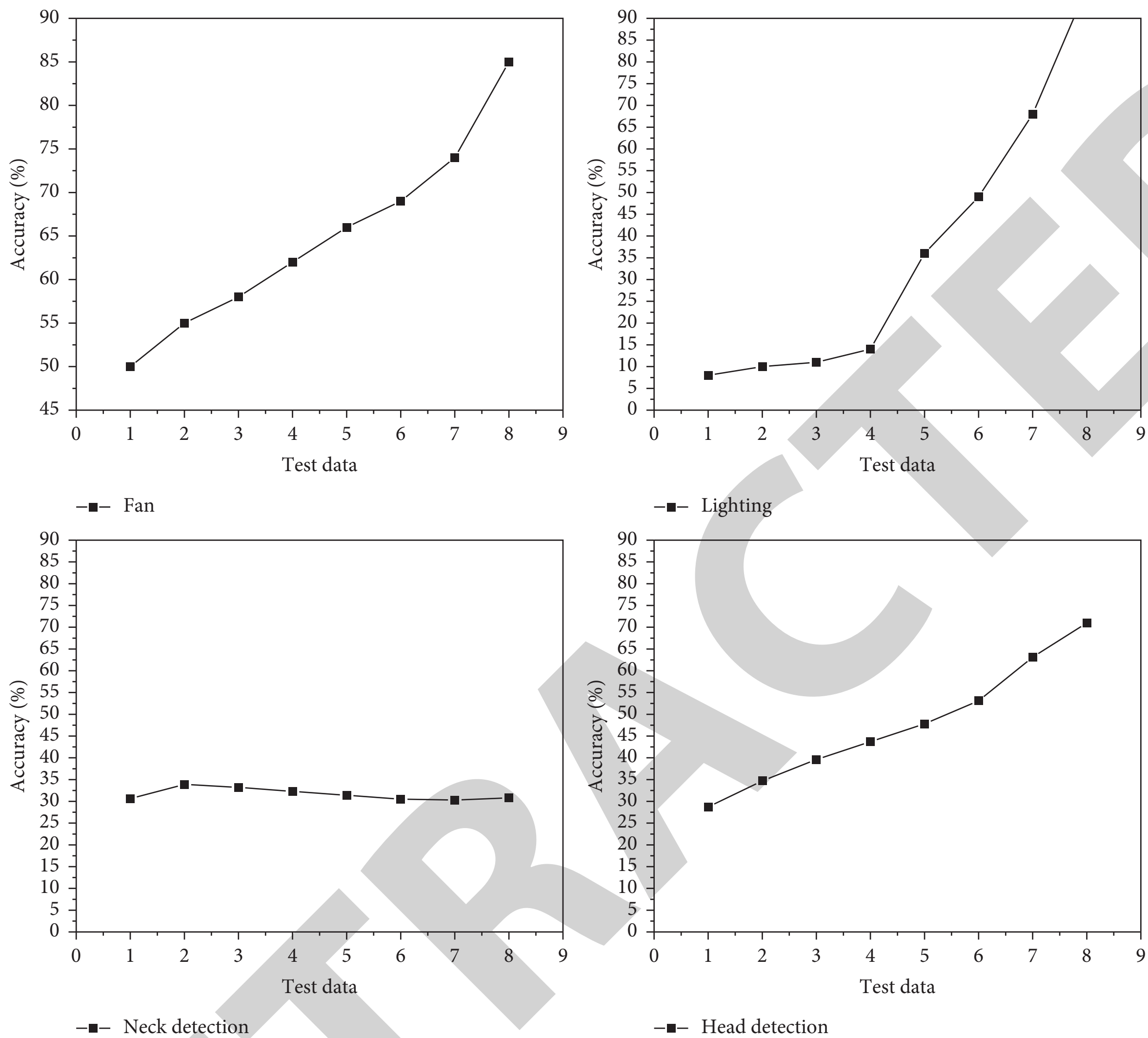

Figure 5: Device on/off test set accuracy.

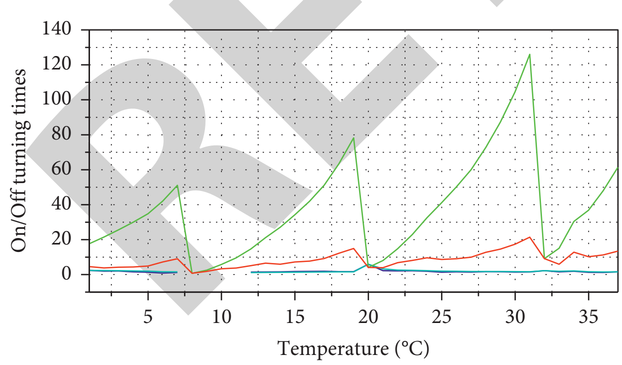

Figure 6: Chart of the total number of opens at different points in the week.

migrate the system design to other physical bases, unlike the traditional architecture which requires a lot of code changes; (3) friendly human-computer interaction, using the grid system to do a responsive layout to adapt to different screen sizes and real-time display of sensor node status through animation effects, you can click the animation to manipulate the sensor nodes. The client page display is further enriched and optimized by throttling and antishake and image preloading, which improves rendering efficiency and increases the dynamic web page effects intuitively and vividly, which improves the interaction friendliness and enhances user experience. (4) The system is predictive and uses an attention mechanism to achieve state prediction for different devices on the basis of artificial neural network. The accuracy rate of the test set is nearly 90%, which can meet the demand of patients and provide direction for the secondary development in the later stage. However, there are still problems in the system, which need to be improved continuously. There are some differences between the hardware and software of IoT devices; there are some delays that lead to miscalculations of information as the data are not updated in time. With regard to the optimization of the IoT control system for stations, there are few studies on scenarios where many users access simultaneously in a short time. Follow-up allows you to provide Nginx proxy web servers for load balancing to improve the responsiveness of your system to a large number of user data attacks in a short time. The behavior forecast

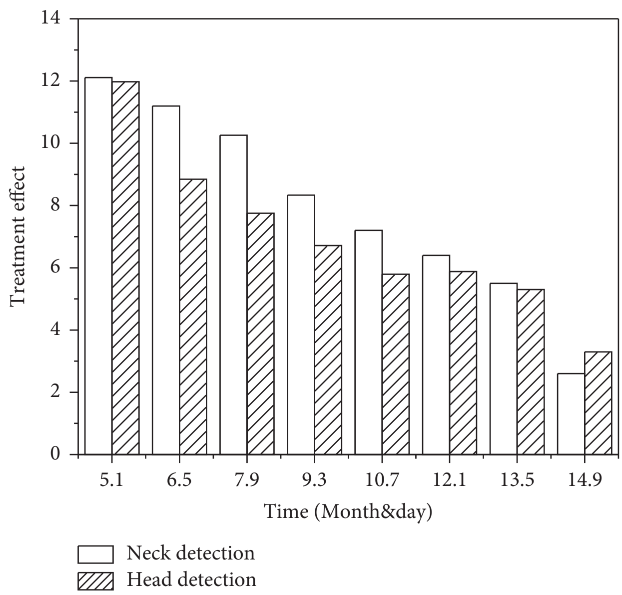

Figure 7: Change in head and neck treatment effect.

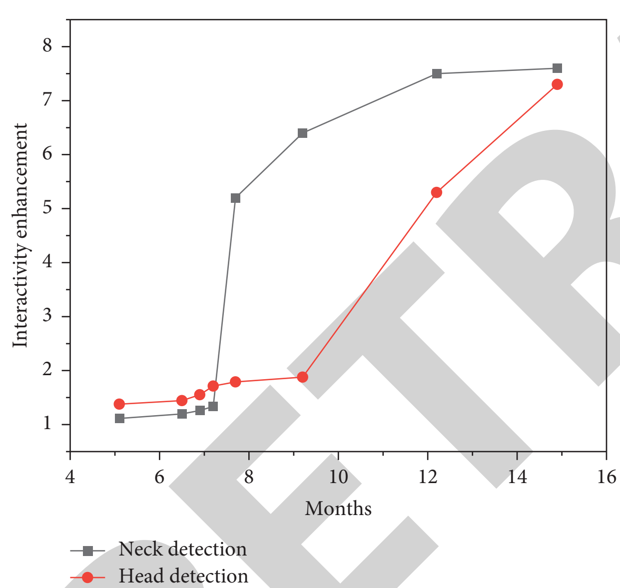

Figure 8: Changes in head and neck treatment interactivity enhancement.

module currently only implements device status forecasting. In later development, different input functions can be added based on the neuronal network model of the current attention mechanism.

5. Conclusion

In the IoT hardware system, the environmental monitoring node and the controller node are designed. The nodes include the main control module, WiFi networking module, power supply and peripheral circuit module, sensor module, and controller module. On the basis of hardware, software programs are written and the sensor node realizes the collection of environmental parameters in the ward, processes the environmental parameters using the main control module, and uploads the processed data information to the cloud service terminal through the WiFi module. In the IoT software system, the server-side publish-subscribe mode message transmission. The service handler is written in Python programming language to control and maintain the information of the management nodes, to complete the two-way communication between the server side of the cloud platform and the sensor terminals, and to realize the storage and management of the collected environmental data by building a database. Real-time animation display and control of sensor node status changes are realized using web development technology, and data are displayed in the form of visual images by ECharts js technology. In order to realize the user's personalized demand and make a differential response to the specified user, the attention mechanism is used to do data mining on the user's historical behavior, capture the key information that is helpful for the current behavior prediction, and complete the behavior prediction with an accuracy rate of 91.89%, which provides the basis and direction for future secondary development. The comprehensive test results of the system show that the system functions meet the expected objectives. The implementation of the IoT monitoring and control system applied to wards and the iterative improvement of its design methodology will be a reference for monitoring the ward environment, manipulating electrical equipment, and predicting future usage.

Data Availability

The data used to support the findings of this study are available from the corresponding author upon request.

Conflicts of Interest

The authors declare that they have no conflicts of interest.

Acknowledgments

This work was supported by Tangshan Gongren Hospital.

References

[1] M. Abdel-Basset and M. Mohamed, "RETRACTED: a novel and powerful framework based on neutrosophic sets to aid patients with cancer," *Future Generation Computer Systems*, vol. 98, no. 3, pp. 144–153, 2019.
[2] S. Bahl, R. P. Singh, M. Javaid, I. H. Khan, R. Vaishya, and R. Suman, "Telemedicine technologies for confronting COVID-19 pandemic: a review," *Journal of Industrial Integration and Management*, vol. 5, no. 4, pp. 547–561, 2020.
[3] A. M. Bur, M. Shew, and J. New, "Artificial intelligence for the otolaryngologist: a state of the art review," *Otolaryngology-Head and Neck Surgery*, vol. 160, no. 4, pp. 603–611, 2019.
[4] S. Garg, N. L. Williams, A. Ip, and A. P. Dicker, "Clinical integration of digital solutions in health care: an overview of the current landscape of digital technologies in cancer care," *JCO clinical cancer informatics*, vol. 2, pp. 11–19, 2018.

Hindawi
Journal of Healthcare Engineering
Volume 2023, Article ID 9826414, 1 page
https://doi.org/10.1155/2023/9826414

Retraction

Retracted: Clinical Care of Hyperthyroidism Using Wearable Medical Devices in a Medical IoT Scenario

Journal of Healthcare Engineering

Received 26 September 2023; Accepted 26 September 2023; Published 27 September 2023

This article has been retracted by Hindawi following an investigation undertaken by the publisher [1]. This investigation has uncovered evidence of one or more of the following indicators of systematic manipulation of the publication process:

(1) Discrepancies in scope
(2) Discrepancies in the description of the research reported
(3) Discrepancies between the availability of data and the research described
(4) Inappropriate citations
(5) Incoherent, meaningless and/or irrelevant content included in the article
(6) Peer-review manipulation

The presence of these indicators undermines our confidence in the integrity of the article's content and we cannot, therefore, vouch for its reliability. Please note that this notice is intended solely to alert readers that the content of this article is unreliable. We have not investigated whether authors were aware of or involved in the systematic manipulation of the publication process.

In addition, our investigation has also shown that one or more of the following human-subject reporting requirements has not been met in this article: ethical approval by an Institutional Review Board (IRB) committee or equivalent, patient/participant consent to participate, and/or agreement to publish patient/participant details (where relevant).

Wiley and Hindawi regrets that the usual quality checks did not identify these issues before publication and have since put additional measures in place to safeguard research integrity.

We wish to credit our own Research Integrity and Research Publishing teams and anonymous and named external researchers and research integrity experts for contributing to this investigation.

The corresponding author, as the representative of all authors, has been given the opportunity to register their agreement or disagreement to this retraction. We have kept a record of any response received.

References

[1] L. Wei, S. Hou, and Q. Liu, "Clinical Care of Hyperthyroidism Using Wearable Medical Devices in a Medical IoT Scenario," *Journal of Healthcare Engineering*, vol. 2022, Article ID 5951326, 10 pages, 2022.

Hindawi
Journal of Healthcare Engineering
Volume 2022, Article ID 5951326, 10 pages
https://doi.org/10.1155/2022/5951326

Research Article

Clinical Care of Hyperthyroidism Using Wearable Medical Devices in a Medical IoT Scenario

Lili Wei, Sujuan Hou, and Qiuxia Liu

Department of Radiology, Tangshan Gongren Hospital, Tangshan, Hebei 063000, China

Correspondence should be addressed to Sujuan Hou; 161842057@masu.edu.cn

Received 23 November 2021; Revised 14 January 2022; Accepted 20 January 2022; Published 23 February 2022

Academic Editor: Enas Abdulhay

This paper presents an in-depth study and analysis of clinical care of patients with hyperthyroidism using wearable medical devices in the context of medical IoT scenarios. According to the use scenario of the gateway and the connectivity of the equipment, the hardware architecture, hardware interfaces, functionality, and performance of the gateway were briefly designed, so as to monitor patients with hyperthyroidism more comprehensively and save labor costs. The gateway can provide access to different devices and adaptation functions to different hardware interfaces and provide hardware support for the subsequent deployment of the proposed new medical communication protocols and related information systems. A medical data convergence information system based on multidevice management and multiprotocol parsing was designed and implemented. The system enables the management and configuration of different medical devices and access to data through the targeted parsing of the underlying medical device communication protocols. The system also provides the automatic adaptation of multiple types of underlying medical device communication protocols and automatic parsing of multiple versions and can provide multiple devices to process fused data streams or device information and data from a single device. The use of event-driven asynchronous communication eliminates the tight dependency on service invocation in the synchronous communication approach. The use of a metadata-based data model structure enables model extensions to accommodate the impact of iterative business requirements on the database structure. Real-time patient physiological data transmission for intraoperative monitoring based on the MQTT protocol and video transmission for intraoperative patient monitoring based on the RTMP protocol were implemented. The development of the intelligent medical monitoring service system was completed, and the system was tested, optimized, and deployed. The functionality and performance of the system were tested, the performance issue of slow query speed was optimized, and the deployment of the project using Docker containers was automated.

1. Introduction

Relatively inexpensive domestic infusion monitoring devices have been marketed, but they can only be monitored individually and cannot be networked for systematic management [1]. Clinical infusion work still suffers from untimely fluid replacement, inaccurate infusion speed, and failure to detect infusion failure in time. With the frequent emergence of problems such as inefficient medical treatment caused by the insufficient and unreasonable allocation of total medical and health resources, inadequate medical risk control, weak primary health service system, imperfect medical security system, disorderly production and circulation of drugs and medical equipment, inflated prices, and serious disputes between doctors and patients, the problem of how to solve the "difficulty of seeing a doctor" and "expensiveness of seeing a doctor" caused by the imperfect medical system has become more acute [2]. The development and application of Internet of Things (IoT) technology in the medical field have emerged in the world, such as medical waste tracking management, special patient monitoring management, baby monitoring, and elderly vital signs' home monitoring. As IoT technology has precise sensing ability for mobile individuals, there are numerous mobile devices in the clinical medical field; thus, with the continuous development of IoT technology, it has successfully integrated into the clinical medical industry and has provided great help to the construction of smart therapy, which has now become one of the hot spots that the IoT field is concerned about [3].

A medical examination device with antidropping function for clinical use in hyperthyroidism and its control system includes a central processing and control module, a human body sensing module, an action recognition module, an overflow detection module, a height detection module, a sound alarm module, an opening and closing control module, a drive module, a status indication module, and a power supply module. The present invention can automatically identify human body movements, can realize automatic unpacking, and is convenient for putting the used syringes into the syringe storage box, making the recovery of the syringes convenient and preventing the inspectors from touching the intelligent storage box. For more safety and hygiene, the test tube holder and the intelligent storage box are fixed by the first electromagnet and the second electromagnet, which can make the placement of the test tube holder and the intelligent storage box more stable and prevent them from falling off during use; at the same time, the electromagnetic field is controlled by the control button. The working state of the body is convenient for taking the test tube holder and the intelligent storage box, and the practicability is higher. Cloud computing, big data, artificial intelligence, and so on have been the hot spots of general concern and technical research in various industries in recent years, and their related technologies have gradually become popular and mainstream application technologies in the process of informatization and intelligence in various industries. At the same time, in the medical field, large-scale regional medical and health information systems and large health care data centers are also under construction in full swing [4]. Nursing is an important part of health care delivery, and the application of information technology in nursing can reduce duplication of effort and nursing errors, allowing clinical nursing staff to spend more time caring for patients and substantially improving the quality of nursing services [5]. Therefore, nursing information competence has become a basic quality that every nurse must possess, and the improvement of information technology in medical services is a great driving force for the development of medical care. Through the study of nursing information competence theory and practice, a set of scientific and reasonable evaluation systems of nursing information competence of clinical nursing staff is developed [6]. The index system of nursing information competence of clinical nursing staff can provide an objective reference basis for clinical nursing staff and nursing managers on the one hand, and provide objective reference indicators for cultivating efficient clinical nursing staff and improve the overall information literacy of nursing staff on the other hand [7].

Wireless sensors used in the field of environmental monitoring such as temperature and humidity sensors are widely used in soil monitoring, infrared sensors are widely used in elevator escalator human detection, light sensors and sound sensors are widely used in intelligent electric lights, smoke sensors and flame sensors are widely used in security warning, and so on. These sensors use different networks to upload data and after processing and analysis to achieve real-time monitoring of human health and real-time monitoring of the environment. People from many remote areas flock to cities in search of a better medical environment and resources; especially in many cases, there is a need to ensure high-definition video call capability for ambulances to enable remote preemption. Establishing healthcare information systems that use Internet technology to connect hospitals to hospitals and hospitals to patients can greatly reduce the potential for unnecessary transportation, lodging, travel, and illness delays. However, there are still many shortcomings in the current healthcare information technology. Medical scenarios such as remote video suffer from certain delays due to limitations in network structure and medical informatics equipment. At the same time, there is a wide variety of medical informatics, which needs to be optimized for specific medical informatics scenarios.

2. Related Work

This section discusses the specific implementation of the Internet of Things in the health field and proposes a construction concept related to the smart hospital based on the Internet of Things [8]. It is considered that smart medicine is a medical system that combines electronic medical records, electronic health records, and medical Internet of Things with medical cloud data as the core and Internet of Things and data transmission and exchange as the technology to build medical and health services and optimal management [9]. Based on the new medical and health service model of "Internet + health care," the shortcomings of the traditional medical service model are analyzed, and the tasks of intelligent medical action are proposed, mainly including medical Informa ionization and medical body construction [3]. The construction of smart medical applications based on IoT technology, including mobile medical care, medical equipment management, and smart hospital service system, was elaborated to gradually realize the combination of IoT and medical services [10]. The purpose of cancer treatment is not only to prolong survival time but also to maintain and improve the quality of survival, which is not only in line with the natural law of cancer development but also consistent with the humanistic concept of "people-oriented" advocated by the state [11]. The evaluation of the quality of survival of cancer patients has become an important aspect of cancer care, but previously it mainly focused on common tumors such as gastric cancer, lung cancer, and breast cancer [12].

Since the incidence of thyroid cancer has shown a trend of increasing year by year in recent years and at the same time, with the advancement of medical screening, diagnosis, and treatment techniques, the postoperative survival of thyroid cancer is more considerable, many scholars have begun to focus on the study of the survival quality of thyroid cancer patients [13]. Medical process monitoring usually still uses manual rounds, transcription of infusion orders, and transcription of inpatient information small card, so the hospital ward nurses also need to blindly run back and forth between the nurse's station and the ward and cannot have a clear sense of the patient's various help but make the planning of the nurses work greatly reduced [14]. With the continuous development of smart mobile devices, mHealth has also begun to influence the way of medical management, doctor-patient communication mode, and health product innovation. Medical services and information are provided using computers, handheld mobile terminals, and software for smart devices combined with mobile communication technology connected to the network [15]. Later, as mobile communication technology continues to develop, increased hospitals are building mobile health care workstations using mobile devices such as PDAs.

The traditional infusion set is still the most used infusion tool in clinical care, and its monitoring method is based on manual inspection. During infusion, the bag or bottle is hung above the needle insertion site of the infuser, and the drip rate is set by the nurse according to experience by manually adjusting the pulley on the infusion tube. When the infusion is about to end or when discomfort occurs during the infusion, the patient or caregiver is required to manually notify the health care worker to come and deal with it in time. This not only increases the labor intensity of health care workers but also makes clinical safety not improved. The management system monitors the infusion status in real time in the field through wireless communication technology, calculates the end time of infusion, and gives an alarm to remind us when the infusion is finished. Any special situation during infusion can be contacted with the nurse main console through the patient call interconnection system. The system can not only reduce the labor intensity of nursing staff and improve work efficiency but also significantly reduce the hidden dangers that may occur during the infusion process, which is the future application trend of clinical medical nursing work.

3. Analysis of Clinical Care of Hyperthyroidism with IoT Wearable Medical Devices

3.1. Medical IoT for Wearable Medical Devices Design. The medical scenario considered in this paper is the scenario where multiple medical devices need to be connected and provide real-time monitoring to the patient, such as an operating room or emergency ward. In existing medical scenarios, it is often necessary to add multiple medical monitoring devices such as monitors, ventilators, and syringe pumps. In addition to this, there are also environmental monitoring devices such as cameras, monitor video encoding boxes, and environmental sensors. All these devices need to be set up independently on the device by the healthcare provider; for example, the monitor needs to be set up for network settings, IP settings, data display item settings, alarm settings, and so on, the syringe pump needs to be set up for push mode, drug settings, channel settings, alarm settings, and so on, the ventilator needs to be set up for ventilation mode, respiratory rate, airway pressure, tidal volume, alarm settings, and so on, and the camera and coding box need to be logged into the device access page for resolution, bit rate, push stream address settings, and so on.

At the same time, the medical process also requires medical personnel to always monitor the operating status of the equipment and alarm information to prevent medical accidents caused by unexpected equipment failures and parameter alarms. In addition, the maintenance of equipment also poses certain difficulties; after the failure of medical equipment, medical staff often need to consult the equipment manufacturer or hospital technicians to recover according to the equipment manual [16]. Environmental monitoring devices such as cameras also require login to the device page to enter a user name, password, and device IP before they can be accessed, as does the setup of the coding box.

At the same time, the unified management of devices such as device registration, device online, and device offline also needs the uniqueness of the device identification to be distinguished, how to ensure the uniqueness of the device is also a problem that needs to be studied, and a more reliable scheme is based on the device address (MAC address, USB address, and serial port address) and device protocol to register the device ID as shown in Figure 1.

There is more overlap in the way these three models apply IoT, and the main component of the project lies in the information system. Existing IoT products are mostly designed to solve specific challenges and hardly meet the needs of most healthcare organizations for system functionality. The deep integration and scale utilization of IoT and healthcare require a mature all-in-one applicable solution.

This paper examines the impact of IoT on the development of medical consortia on a macrolevel. There are various forms of IoT applications, which are currently divided into four categories, care management, medical device management, supply management, and wearable devices, and different applications have different impacts on medical consortia, while medical consortia are divided into four categories, medical groups, medical communities, specialty alliances, and remote collaboration networks, and different medical consortia have different needs for IoT [17]. So microscopic impact of IoT on the development of medical consortia is governed by the form of IoT and the type of medical consortia. In contrast, the study of the macroimpact is not influenced by these factors. In terms of aiding decision-making, the scores of macroimpact are categorized based on factors such as application technology and type of IoT project, and the conclusions of the analysis can be better used as a basis for decision-making. A neural network algorithm is used because our experimental data are limited, and only the algorithm using a neural network can get better results.

The ward call system is a comprehensive system project, which should be considered from various aspects such as its function, performance, cost, and application of modern related technology. Based on such requirements, it is suitable to develop an integrated intelligent medical call system that integrates the functions of bed call, bathroom call, and corridor screen display using CAN bus technology, as shown in Figure 2. As ZigBee technology itself is suitable for wireless data transmission in a small area, in an environment

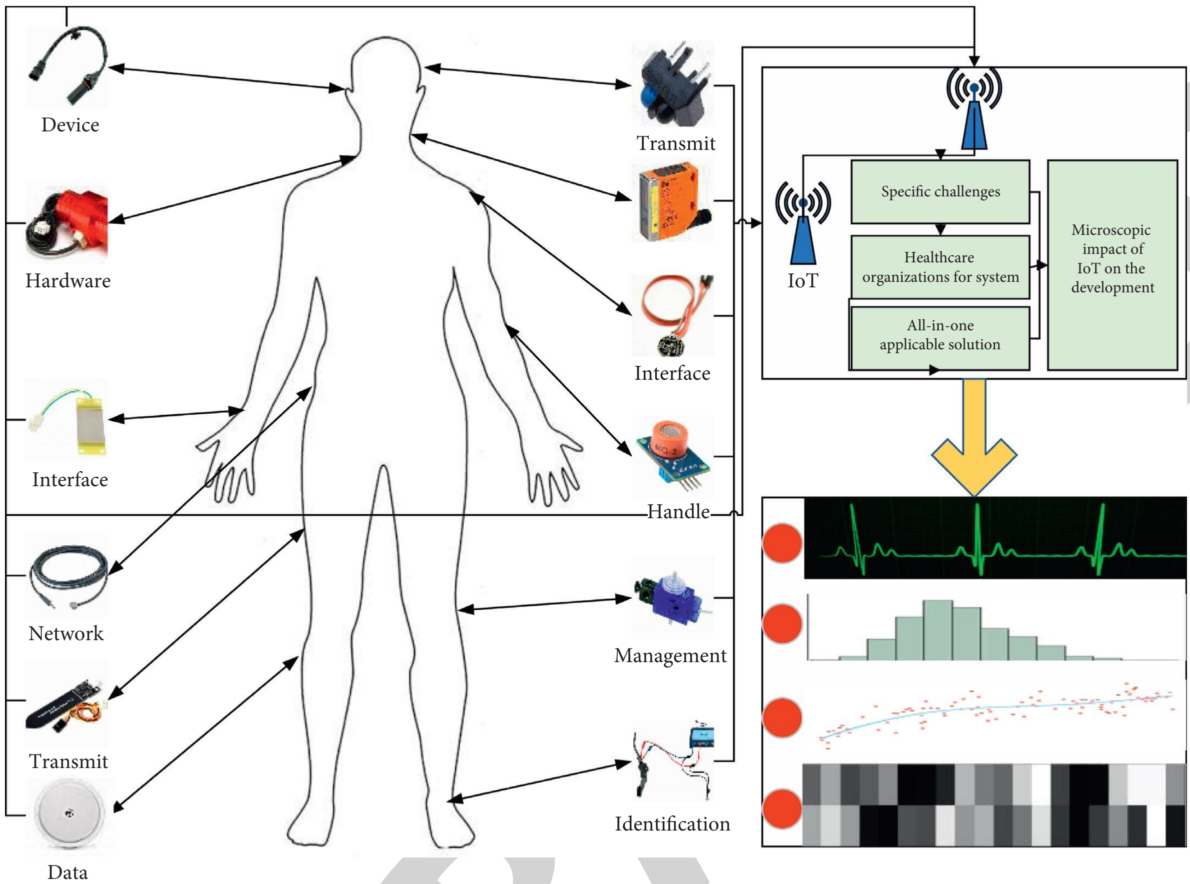

Figure 1: Medical IoT framework for wearable medical devices.

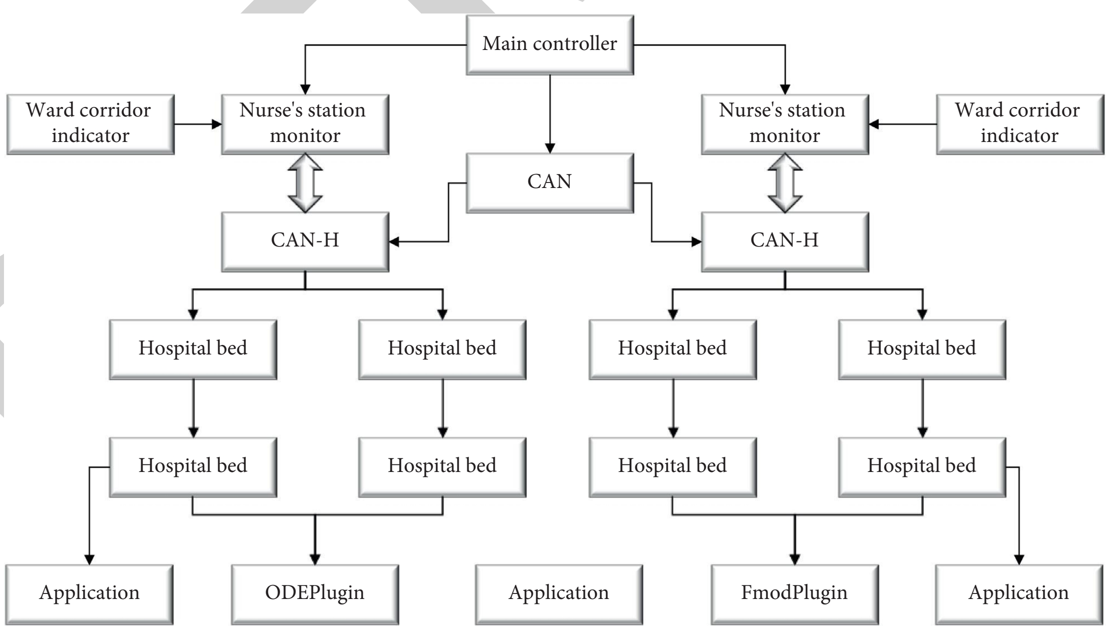

Figure 2: Signal transmission diagram of the call system.

with a large area and relatively complex building structure such as a hospital ward, the loss rate of wireless signals is inevitably high; if the data reception and forwarding capacity are increased by adding terminals, the problems of wireless signal collision and high probability of error codes cannot be solved; it is impossible to set up a large sensing network covering the whole hospital. It is impossible to set up a large sensor network covering the whole hospital.

The ZigBee terminals are wired and powered because they need to forward signals at any time and have high energy requirements. The ward call system uses the CAN bus for data transmission, which is mainly based on security considerations to ensure reliable transmission, but there are disadvantages such as poor system scalability and the need for wiring in the ward.

Any unit connected to the bus can start sending messages if the bus is idle, and if two or more units on the bus start sending messages at the same time, the priority can be determined by receiving or blocking the message according to its ID (identifier). In the ward call system, the call button located in the ward only needs to be pressed when the patient has an emergency to send a call message to contact the nurse and does not transmit the message at all times. The number of nodes that can be connected to the CAN bus is theoretically unlimited, but it is limited by the bus time delay and load capacity. If the number of connected nodes needs to be increased, then the communication speed can be reduced; conversely, if the transmission speed needs to be increased, then the number of connected nodes can be reduced.

For the award, the number of wards is relatively high. The main functions of the clinical medical information management system are to monitor the infusion status of patients in real time, to respond to patients' needs in time, to understand the situation and needs of each ward, and to realize scientific management of the whole ward and ward so that the efficiency of medical and nursing workers can be improved, the overall service quality of the hospital can be improved, and the medical safety and patient satisfaction can be enhanced.

3.2. Analysis of Clinical Care in Hyperthyroidism. With the continuous development of business, the amount of code of the whole system will become increasingly complex, and the system architecture will become increasingly complex. There are many problems faced by using monolithic architecture, such as low development efficiency, increasing maintenance cost, large deployment impact, poor scalability, and high technology selection cost. Therefore, at the beginning of the system design, the system should be split into multiple modules with the idea of microservices [18]. When the system is gradually upgraded with iterations, the vertical expansion of the system can be achieved by upgrading the in-service functionality of individual services. When the upgrade of existing microservices cannot meet the business needs of the system, new microservices can be added to provide new service capabilities to cope with complex business needs.

$$R_1 = \frac{V_{cc}^2 - V_F^2}{I_F^2}. \quad (1)$$

In the formula (1), R_1 represents the serial number 1 resistance, V_{cc}^2 represents the voltage difference, V_F^2 represents the negative voltage, and I_F^2 represents the current of the circuit. The way services communicate with each other also affects the degree of interdependence of the services.

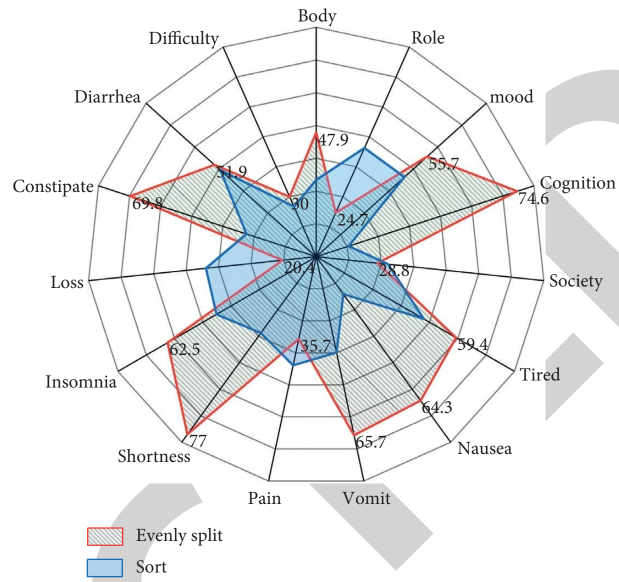

Figure 3: Status of quality of survival.

Synchronous and asynchronous communication are two ways to implement messaging between services. Rest HTTP is a request/response-based synchronous invocation method of communication that encapsulates parameters into JSON format for messaging. Although this communication method is simple to invoke, one party sends a request and waits for the request to be transmitted to the other party and waits until the other party returns after the request has been fully processed before proceeding to the next operation.

Another way of communication between services is asynchronous message invocation, and the message sender only needs to send the message and does not need to care which service is to receive this message; that is, the service does not know who they are called by and does not know which service they will call. Detaching the entire flow of business execution from the module reduces the coupling between the caller and the called, as shown in Figure 3.

It provides edge computing platform services, including support for edge application deployment, providing a unified portal for application deployment. It supports configuration distribution with streaming media equipment, and reports streaming configuration information to the dedicated network operation management platform. It also supportsthe provision of service capabilities, including location services, bandwidth management services, and wireless network information to industry applications through the wireless side or core network side interface. Based on specific business scenarios, it supports providing applications with capabilities such as video streaming and AI algorithm library to meet application requirements.

The scheduler can be seen as a parent node, and the queues/schedulers being scheduled are seen as children. The scheduler can schedule multiple queues and can schedule multiple schedulers. The parent node is the traffic convergence point for multiple child nodes. The classification rules of nodes at different levels can be oriented to different classification needs (e.g., users and business types), each

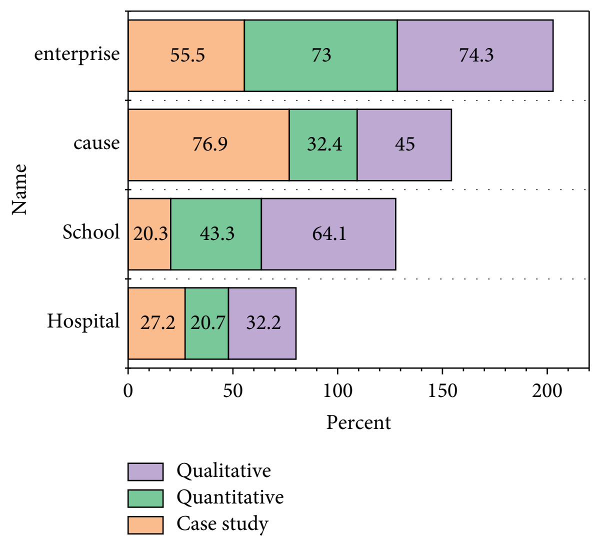

Figure 4: Proportion of data sources.

node can specify classification rules and control parameters to classify and control the traffic once, and different control actions can be done on the traffic at different nodes, thus realizing multiservice, multilevel, and multiuser management of the traffic.

$$\frac{R_{11}}{R_{10} - R_{11}} \cdot V_{cc} = 1000\, mV, \tag{2}$$

$$R_{10} \approx 8R_{11}. \tag{3}$$

In the formula (2), R_{11} represents the resistance between 1 and 2, R_{10} represents the resistance from the initial point to point 1, and the voltage value difference is 1000 mV. First, the subject of assessing the impact of IoT on the development of healthcare clusters is one or more healthcare clusters, with more than ten healthcare organizations in each cluster, and it is practical to use success rates as impact evaluation. Second, the market size in the field of medical IoT has maintained a 25% growth rate in 10 years and is forecast to remain the same in five years. Therefore, the proportion of IoT projects and the future changes in the development trend are not significant.

$$M(x) = w_2 \sigma(w_1 x), \tag{4}$$

where $M(x)$ represents the state at the X position, w_2 represents the weight of the second point, σ represents the state coefficient, w_1 represents the weight of the first point, and x represents the corresponding position. For IoT projects with high technology, the breakthrough products make a certain impact indicator score of 1, but the overall score tends to be close to 0 due to the difference in technology or application focus of other IoT projects. But because IoT technology is in the overall development stage, the overall change in the impact of IoT on healthcare in the next five years is small, and the impact of high technology projects, although growing faster, will not affect the overall statistical level as shown in Figure 4.

Firstly, based on the author's source, the data source, and the type of IoT projects, applied IoT technologies were counted, and percentage stacked bar graphs were plotted to understand the researcher's preference. After analysis, the researchers showed differences in the source of data and the two IoT technologies applied. Researchers from hospitals and schools were more likely to evaluate the impact of IoT on the development of healthcare clusters through qualitative methods, while researchers from the health sector and businesses were more likely to evaluate through case effects. Researchers from hospitals are mainly users of IoT products, researchers from schools are mostly product development designers, and the evaluation of the effects of IoT applications by these two types of researchers is more subjective. The technologies applied by researchers from hospitals and schools are mainly wearable devices, while health authorities and companies focus more on the integrated use of IoT technologies [6]. From Figure 4, it is known that researchers from schools and hospitals together account for 72.9% of the total researchers, so researchers from hospitals and schools will have more influence in the evaluation of the impact of wearable device cases on the development of health care clusters.

$$Q_N(w) = \frac{1}{2} \sum_{i,j} \left(1 + P_{ij}\right)^2 \left(m_i - m_j\right). \tag{5}$$

In formula (5), $Q_N(w)$ represents the state where the weight is w at the position of N, P_{ij} represents the weight component of the i-th row and j-th column, m_j represents the initial component, and m_i represents the end component [19]. The lack of interoperability of medical information systems has always been an important factor constraining the construction of health informatization, and there are two reasons for the difficulty in sharing information [20].

The study on the working status of the study subjects found that 53 cases (30.64%) were currently engaged in domestic work and 44 cases (25.43%) were still working, which was related to the fact that the survey subjects were mostly middle-aged women mainly from rural areas. The types of medical insurance of the survey respondents were mainly new rural cooperative medical insurance and urban employees, with 91 cases and 62 cases, accounting for 52.60% and 35.84%, respectively [8, 21, 22].

4. Analysis of Results

4.1. Performance of Medical IoT Systems for Wearable Medical Devices. As multiple surgeries are performed at the same time in a hospital, multiple monitoring devices are used to monitor the physiological status of the patient during each surgery. The real-time data transmitted from the gateway to the upper layer during the surgery includes both the physiological data of the patient collected by the monitoring device and the alarm information of the monitoring device. In addition to this, the client may also downlink the configuration information of the device at this time, so the concurrency of real-time data information received by the client at the same moment can be large. Using multiple

Figure 5: Real-time data display of the monitor.

threads to receive the patient's physiological data, alarm information, and configuration information separately, and using multiple threads to process the real-time data information, the CPU resource utilization can improve.

Considering that each time the real-time data arrives, a thread needs to be created to process the data, and after processing is complete, the thread must be destroyed to avoid resource usage; this process will keep consuming CPU resources, so a thread pool is used to implement a thread reuse mechanism and eventually interthread scheduling. The real-time curve board for ventilators and syringe pumps is designed according to the real screen of ventilator and syringe pump devices, and the expansion capability is reserved here to switch the display of different content on the page to accommodate the display of content for other types of device access. The real-time data display for the monitor is shown in Figure 5.

A complete test environment is set up in the laboratory as shown in Figure 5. The gateway communicates with the medical devices through the default intranet IP in the gateway, and the gateway, video encoding box, and network pushing camera are then connected to the laboratory LAN to achieve data and video transmission; the server and client are connected to the laboratory LAN to achieve system access and data communication with the gateway. The hardware environment is mainly a monitor connected to the gateway through the network port, a ventilator connected to the gateway through the serial port, and a syringe pump connected to the gateway through the USB port. Real-time data are collected by these three devices and collected by the

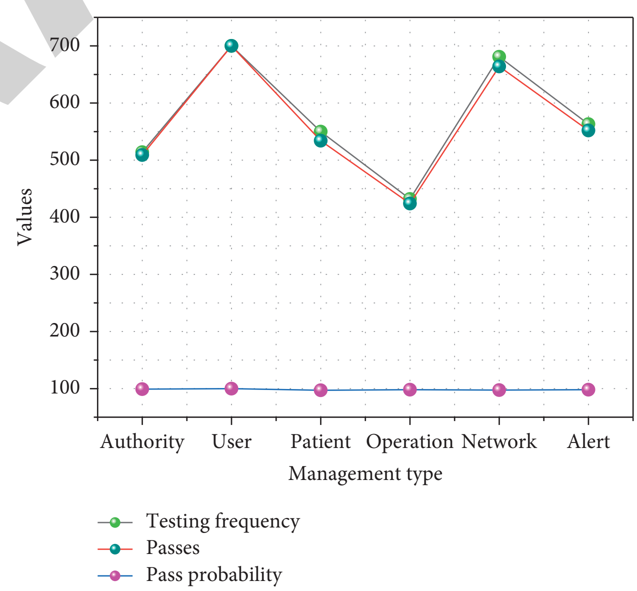

Figure 6: Graph of test results.

gateway, and then the gateway connects to the lab intranet through a wireless connection to realize data transmission with the server.

The video encoding box is connected to the monitor through a VGA port to collect the live video stream of the screen and then connected to the router through the network port to realize the live stream push. The webcam collects indoor scenes and connects to the router through the network port to realize the live streaming push of indoor scenes.

The operation functions of user management are routine operations, so there is no need to consider the concurrency problem, and only the feasibility of the function needs to be tested, as shown in Figure 6. The operation management module can complete the basic operation of the operation room and can realize the basic functions of intraoperative monitoring, which can enter the operation room to view the scene of the operation, perform the operation triggered by the key time points of the operation process, view the monitoring records and quality control records, view the live screen of the monitor screen and the live video broadcast of the scene captured by the camera, and view the real-time collected parameters of the anesthesia machine, the parameters of the syringe pump, the monitor parameters, and so on, and the basic functions of intraoperative monitoring can be achieved normally by changing different models of test devices during testing.

As the underlying gateway realizes the adaptation to different types of medical devices, the data collected by the devices are parsed and processed into a unified format and then sent to the server, and the gateway can realize the transmission of real-time data, so when the data are transmitted to the server, the differences between devices of different manufacturers are already shielded. The gateway and device management module realize the unified control of the gateway and various medical devices, and the system supports the management of various types of medical devices. Alarm management realizes the management of medical device alarms and abnormal alarms of physiological indicators of patients during surgery. In summary, the overall system function test pass rate is 100%, which means that all the modules of the system can be realized normally, and the system is currently applicable to all the gateways that have been successfully adapted to the devices.

4.2. Clinical Care Outcomes in Hyperthyroidism. Informatization of nursing services not only enhances efficiency and allows nursing staff to spend more time facing patients but also leads to higher patient satisfaction with the nursing staff. Therefore, the integration of healthcare services with Internet platforms is becoming the direction of information technology development in medium and large hospitals. Nursing staff plays an important role in hospitals, while some of our nursing staff have not yet been able to acquire some knowledge and skills in nursing informatics. As nursing staff should all need to master the professional knowledge and application related to nursing informatics as well as have the ethics related to nursing informatics.

It was concluded from reviewing a large amount of literature that the evaluation system of nursing information competency in China is necessary because it is less and one-sided compared to foreign studies. The nursing information competence evaluation index system established in this study can provide a theoretical basis for the development of a scientific and reasonable nursing informatics training program for nursing staff. The increasing number of hospitals applying 5G "Internet medicine" shows the importance of establishing a set of nursing informatics evaluation systems suitable for clinical nursing staff. The development of nursing informatics education and the improvement of nursing informatics personnel are effective means to reduce nursing errors and improve work, as shown in Table 1.

This study illustrates that the process of information technology construction must put the legality and security of information in the first place, information security is a prerequisite for the behavior of nursing information technology, and it is urgent to improve the awareness of information security of nursing staff; if there are information security problems, all information construction will be impossible to talk about, so it is necessary to first guarantee the security of nursing information and establish a security barrier to prevent nursing errors and management Vulnerability. The second level indicator is "nursing informatics awareness," and the weight coefficient of nursing staff's "subject awareness" is 0.1295, which indicates that nursing staff needs to constantly realize that they need to continuously learn to make up.

This indicates that nursing staff needs to be aware of the need for continuous learning to make up for their shortcomings, improve nursing information capabilities to enhance work efficiency, and realize the organic integration of information technology with nursing work and nursing management. "Knowledge of nursing informatics" has a low weighting factor compared with other indicators, but it is indispensable in nursing work. Without mastering the concepts, views, and theoretical systems of relevant theories and without a certain amount of relevant theoretical training, it is impossible to put forward any new views and concepts even if the practice time is longer and the practice is more, let alone put forward systemic new theories.

However, considering that all patients were aware of their thyroid ultrasound results before admission and with the increasing accuracy of medical technology, patients had a basic judgment of their condition before surgery; coupled with the health education of the medical staff, they had a scientific understanding of the good prognosis of thyroid cancer, as shown in Figure 7.

Knowledge of thyroid cancer disease is extremely low, and people fail to realize the closeness of these factors to the prognosis of the disease. Finally, the reason for the lack of statistically significant knowledge about the pathology of the disease may be related to the fact that some of the patients have postoperative pathological results of thyroid cancer, although their family members concealed the true nature of their pathology, considering that all patients knew the results of their thyroid ultrasound before admission, and with the continuous progress of medical technology ultrasound results becoming more and more accurate, patients have a basic judgment of their condition before surgery.

In life, the role of women is multiple; on the one hand, like men, they bear the important responsibility of promoting social development, and on the other hand, they also bear the sacred responsibility of taking care of their families and giving birth to and educating their offspring; at the same time, women have special body structure and physiological

Table 1: Multiple linear regression analysis.

Independent variable	B	Beta	FA	P
Constant	0.892	0.617	0.732	0.694
Hospital level	0.484	0.939	0.598	0.769
Does the hospital have	0.736	0.512	0.603	0.766
Information equipment	0.984	0.764	0.601	0.443

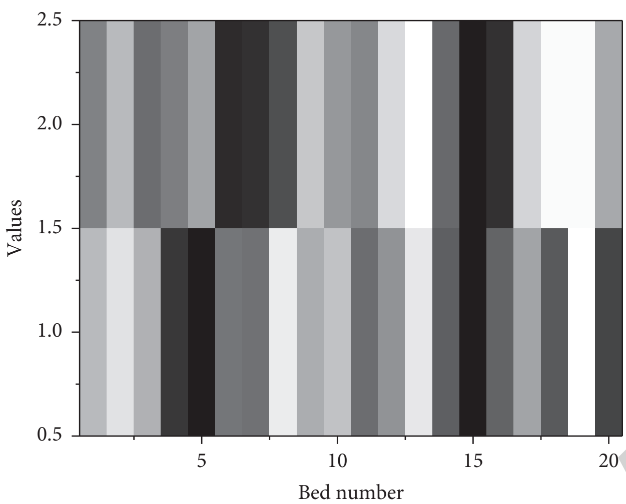

Figure 7: Outcome of care.

mechanism; therefore, the physical and mental health of women will be directly related to the harmony of a family or even the whole society. Strengthening the psychological care of female thyroid cancer patients will help to reduce the occurrence of anxiety, improve the quality of survival, and promote the prognosis of the disease.

5. Conclusion

In this paper, a new medical-oriented IoT gateway is proposed for the traditional medical scenario where the underlying medical devices are of various types and the data communication protocols used are closed to each other, the data cannot be processed and aggregated effectively, and the hardware, interface communication protocols, and information system of the gateway are designed and implemented. The gateway can provide a variety of hardware interfaces for device access and is equipped with a high-capacity lithium battery to cope with emergency emergencies. The internal information system can parse the protocols of the underlying medical devices that access the gateway to obtain medical monitoring data, and the interface communication protocol can provide data access interfaces and medical device management interfaces to external terminals. Therefore, the gateway can unify the management and configuration of all medical devices and IoT devices in the ward, automatically resolve the medical protocols of the underlying medical devices to obtain data, and realize the real-time pushing of data streams through the processing and fusion of data. By deploying the gateway in a hospital operating room for field testing, it is found that the gateway can effectively shield the differences of the underlying devices in the ward, the diversity of medical communication protocols, and the isolation of data and realize the unified management and configuration of devices, the automatic parsing of medical communication protocols, the secure encryption of data processing and fusion, and the real-time pushing of monitoring data of multiple devices in the ward. The relevant functions of the gateway have been effectively verified, and good remote real-time monitoring has been achieved. Our research results can be fully applied in practical situations.

Data Availability

The data used to support the findings of this study are available from the corresponding author upon request.

Conflicts of Interest

The authors declare that they have no known competing financial interests or personal relationships that could have appeared to influence the work reported in this paper.

Acknowledgments

This work was supported by the Tangshan Gongren Hospital.

References

[1] M. B. Shoemaker, R. L. Shah, D. M. Roden, and M. V. Perez, "How will genetics inform the clinical care of atrial fibrillation?" *Circulation Research*, vol. 127, no. 1, pp. 111–127, 2020.

[2] P. Borovska, I. Desislava, and I. Draganov, "Internet of medical imaging Things and analytics in support of precision medicine for early diagnostics of thyroid cancer," *Serdica Journal of Computing*, vol. 12, no. 1-2, pp. 047p–064p, 2018.

[3] E. Y. Wan, H. Ghanbari, and N. Akoum, "HRS white paper on clinical utilization of digital health technology," *Cardiovascular Digital Health Journal*, vol. 2, no. 4, pp. 196–211, 2021.

[4] P. Puri and S. Jha, "Artificial intelligence, automation, and medical education: lessons from economic history," *Journal of the American College of Radiology*, vol. 18, no. 9, pp. 1345–1347, 2021.

[5] L. Bakker, J. Aarts, C. Uyl-de Groot, and W. Redekop, "Economic evaluations of big data analytics for clinical decision-making: a scoping review," *Journal of the American Medical Informatics Association*, vol. 27, no. 9, pp. 1466–1475, 2020.

[6] C. O'Byrne, A. Abbas, E. Korot, and P. A. Keane, "Automated deep learning in ophthalmology: AI that can build AI," *Current Opinion in Ophthalmology*, vol. 32, no. 5, pp. 406–412, 2021.

[7] I. Masood, Y. Wang, A. Daud, N. R. Aijohani, and H. Dawood, "Privacy management of patient physiological parameters," *Telematics and Informatics*, vol. 35, no. 4, pp. 677–701, 2018.

[8] N. A. H. A. Pluymaekers, A. N. L. Hermans, R. M. J. van der Velden, and M. Gawalko, "Implementation of an on-demand app-based heart rate and rhythm monitoring infrastructure for the management of atrial fibrillation through teleconsultation: TeleCheck-AF," *EP Europace*, vol. 23, no. 3, pp. 345–352, 2021.

Hindawi
Journal of Healthcare Engineering
Volume 2022, Article ID 2129168, 9 pages
https://doi.org/10.1155/2022/2129168

Research Article

Pattern Recognition of Holographic Image Library Based on Deep Learning

Bo Wu [1,2] and Changlong Zheng [1]

[1] *Faculty of Education, Northeast Normal University, Changchun 130021, China*
[2] *High School Attached to Northeast Normal University, Changchun 130021, China*

Correspondence should be addressed to Changlong Zheng; zheng_changlong@outlook.com

Received 3 December 2021; Accepted 17 January 2022; Published 18 February 2022

Academic Editor: Enas Abdulhay

The final loss function in the deep learning neural network is composed of other functions in the network. Due to the existence of a large number of non-linear functions such as activation functions in the network, the entire deep learning model presents the nature of a nonconvex function. As optimizing the nonconvex model is more difficult, the solution of the nonconvex function can only represent the local but not the global. The BP algorithm is an algorithm for updating parameters and is mainly applied to deep neural networks. In this article, we will study the volume holographic image library technology, design the basic optical storage path, realize single-point multistorage in the medium, and multiplex technology with simple structure to increase the information storage capacity of volume holography. We have studied a method to read out the holographic image library with the same diffraction efficiency. The test part of the system is to test the entire facial image pattern recognition system. The reliability and stability of the system have been tested for performance and function. Successful testing is the key to the quality and availability of the system. Therefore, this article first analyzes the rules of deep learning, combines the characteristics of image segmentation algorithms and pattern recognition models, designs the overall flow chart of the pattern recognition system, and then conducts a comprehensive inspection of the test mode to ensure that all important connections in the system pass through high-quality testing is guaranteed. Then in the systematic research of this paper, based on the composite threshold segmentation method of histogram polynomial fitting and the deep learning method of the U-NET model, the actual terahertz image is cut, and the two methods are organically combined to form terahertz. The coaxial hologram reconstructs the image for segmentation and finally completes the test of the system. After evaluation, the performance of the system can meet the needs of practical applications.

1. Introduction

Image denoising is to reduce the noise in the image, and the low-resolution image is transformed to form a high-resolution image organically is the image superresolution technology [1]. Both can effectively improve image quality without changing the existing hardware equipment and imaging process [2]. In recent years, deep learning technology has achieved substantial breakthroughs and developments, bringing about tremendous changes in many fields [3]. Deep learning technology is derived from the second generation of neural network technology, which deepens the ability to process data through a deep network structure [4]. In the image field such as image noise and image superresolution, deep learning technology is developing rapidly and has achieved processing effects far exceeding traditional image processing technology. Add the existing deep learning segmentation algorithm to the 2.52 THz coaxial holographic image library for simultaneous processing [5]. Although the number of training samples is insufficient, U-NET can still accurately segment the electron microscope neuron image. According to the experiment in this article, for the real terahertz coaxial digital holographic image library, reconstruct the insufficient number of samples and analyze the U-NET segmentation results of the training set, loss function, and learning rate that affect the real terahertz image, so that it gets the best model. The experimental results show that the optimized U-NET model has the specific ability to distinguish between the image target and the background and at the same time has a specific noise reduction function, which can eliminate the more serious noise in the image [6]. It is proved that in the experiment, the noise in the gear image is basically eliminated, and the target is better retained. The segmentation result is better than the combined threshold segmentation method, but the seal image must be segmented by other algorithms [7]. The powerful Visual Studio development tool completes the development of the facial image pattern recognition system, with a high-quality interface and excellent friendliness. In the process of designing the system software, the confidentiality and special functions of police cases are integrated [8]. The customer adopts modular thinking in the design process to more easily identify the identity of others. It is composed of several important modules and is a kind of user-friendly approach. The database is mainly used to provide the client with interface configuration information, user credentials, and standard facial images. The database deployment in the system research is mainly used to save user credentials and login time and to compare with the recognized images. The design process of this article selects the SQL2008 database based on the skill level of the security assessment and the system survey.

2. Related Work

2.1. DnCNN Network. The literature introduces the application of deep convolutional neural network of DnCNN model to image denoising in terahertz image. First, the principle of noise suppression related to the network structure of the DnCNN network is studied [9]. Then optimize the network model from the relevant parameters of the neural network to obtain the most suitable denoising network for terahertz images [10]. Then the traditional denoising algorithms of NLM and BM3D are introduced, and their related parameters are optimized. Finally, the denoising effect of the DnCNN network is compared with the traditional denoising algorithm, and the denoising effect of the deep neural network model in this chapter is analyzed and compared [11]. The literature introduces the application of densely connected networks in the image superresolution of terahertz images [12]. First, we will introduce the network structure based on tightly connected networks and the principles of high-resolution networks. Then optimize the network model from the relevant parameters of the neural network to obtain the most suitable superresolution network for terahertz images [13]. Then introduced the traditional superresolution algorithm based on sparse representation and anchored neighborhood regression and optimized its related parameters. Finally, the denoising effect of the superresolution network of the dense residual network is compared with the traditional superresolution algorithm. The literature introduces the traditional terahertz image segmentation method and its improved algorithm. The composite threshold segmentation technique is used to characterize the actual holographic reconstructed terahertz image [14]. This means that when trimming and mirroring, the surrounding background will be removed first, and then filtering and denoising will be performed [15]. After the image is improved by grayscale stretching, a polynomial fitting histogram will be performed for threshold segmentation, and the two threshold methods and the Otsu method will be compared step by step [16].

2.2. U-NET Segmentation. The literature introduces the compound U-NET segmentation algorithm. Based on the research of segmentation of the holographic reconstructed terahertz image based on the combined threshold segmentation method and U-NET segmentation algorithm, the trimming and mirroring expansion steps, the NLM filter processing the terahertz image, and then the U-NET segmentation, repeat the experiment to the segmentation result is enlarged, the influence of the existing random features is reduced and the target is better maintained. The literature introduces the U-NET segmentation algorithm as a deep learning algorithm for segmentation of holographic reconstructed terahertz images [17, 18]. The deep learning segmentation algorithm learns and understands data by simulating the learning method of the human brain and can understand the training data before processing any other data. It has been partially applied [19]. U-NET relies on data expansion in order to use training images more effectively and accurately segment electron microscope neuron images from very few training images. This will reduce the sample size of the actual coaxial digital holographic terahertz reconstruction in this experiment [20]. In the experiment, we optimize by comparing and analyzing the results to obtain a model of the actual terahertz image that is particularly suitable for the experiment [21].

After reading the above literature, it can be determined that the main work of this paper includes Figure 1nodes.

3. Deep Learning and Pattern Recognition Technology of Holographic Image Library

3.1. Principles of Deep Learning. Artificial neural network originated from the mathematical bionic modeling of human nerves. Modern artificial neural network models are an important part of machine learning and an important foundation of deep learning.

The output of a single neuron can be expressed as (1)

$$y = f\left(\sum_{i}^{n} w_i x_i + b\right). \tag{1}$$

Artificial neural network fits the model through training, so as to achieve the purpose of learning. The training process of a single neuron can be expressed by (2). The network is trained by updating the weights each time the error between the network's predicted value and the true value. Among them, k represents the k training, i represents the ith data category, and λ represents the learning rate.

$$w^{(k+1)} = w^{(k)} + \lambda\left(y_i - \widehat{y}_i^{(k)}\right)x_i, \tag{2}$$

$\partial C/\partial w_i$ and $\partial C/\partial b_i$ are obtained by the chain derivation rule.

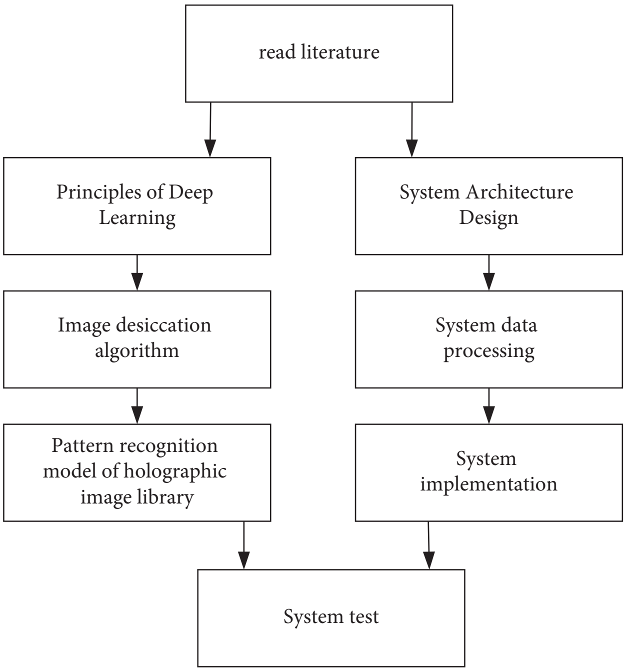

Figure 1: The main work of this paper.

$$w_i^+ = w_i + \Delta w_i = w_i - \lambda \frac{\partial C}{\partial w_i},$$
$$b_i^+ = b_i + \Delta b_i = b_i - \lambda \frac{\partial C}{\partial b_i}. \tag{3}$$

The loss of the network is propagated backward step by step through the chain derivation process, and the value of the parameters of each layer of the network from the back to the front is changed, so that the network can be trained.

$$\frac{\partial C}{\partial w_5} = \frac{\partial C}{\partial \mathrm{Out}_{o1}} \frac{\partial\, \mathrm{Out}_{o1}}{\partial \mathrm{Net}_{o1}} \frac{\partial \mathrm{Net}_{o1}}{\partial w_5}. \tag{4}$$

The formula of mean square error (MSE) corresponds to (4). The characteristic of using squaring to calculate the error is that when the difference between yi and (xi) is greater than 1, the squaring calculation will increase the error, giving it greater punishment, and speeding up the training. And when the difference between yi and (xi) is less than 1, the square calculation will reduce its error, thereby giving it a smaller punishment, and making the training more accurate. But at the same time, MSE will also give higher weight to abnormal points, which will reduce the overall performance of the model and lead to phenomena such as overfitting.

$$\mathrm{MSE} = \frac{1}{n} \sum_{i=1}^{n} \left(y_i - f(x_i)\right)^2. \tag{5}$$

Mean absolute error (MAE), its mathematical expression is as (5), minimizes the absolute value of the error to train the model. Unlike MSE, the gradient of MAE is equal everywhere, which also means that MAE will still give the same punishment to small losses as large losses, which is not conducive to the efficient convergence and learning of the model. But at the same time, because MAE gives all errors the same weight, it is not as sensitive to outliers as MSE. Using MAE to calculate loss is more conducive to learning from data with fewer outliers.

$$\mathrm{MAE} = \frac{1}{n} \sum_{i=1}^{n} \left|y_i - f(x_i)\right|. \tag{6}$$

L0optimizer was proposed by Louizos C et al. in 2017. Its mathematical expression is as in (7), where the term δ is a constant term of a hyperparameter, and δ is taken as 10^{-8} in the algorithm of this paper.

$$L0\mathrm{Loss} = \frac{1}{n}\sum_{i=1}^{n}\left(\left|y_i - f(x_i)\right| + \delta\right)^2,$$
$$L0\mathrm{Loss} = \frac{1}{n}\sum_{i=1}^{n}\left(\left(y_i - f(x_i)\right)^2 + \delta\left|y_i - f(x_i)\right| + \delta^2\right)^2, \tag{7}$$

tanh is a hyperbolic tangent function, proposed by Malfliet et al. in 2005, and its function expression is as (7)

$$f(x) = \frac{e^x - e^{-x}}{e^x + e^{-x}}. \tag{8}$$

But at the same time, the zeroing mechanism of the ReLU function also brings its shortcomings. If the back propagation process of the network (including the ReLU function) has large gradient fluctuations, the ReLU input distribution is concentrated in the almost negative area, then such A large number of negative inputs will cause a large number of outputs of the ReLU function to be 0. A large number of neurons are permanently closed because the gradient cannot be updated. This phenomenon is called Dead Relu. At the same time, unsuitable network parameter initialization methods, such as a large number of weights being initialized to 0, will also cause Dead Relu problems. Dead Relu can cause training problems such as vanishing gradients.

$$f(x) = \begin{cases} x, & \text{if } x > 0, \\ 0, & \text{if } x \le 0. \end{cases} \tag{9}$$

The ELU function was proposed by Clevert et al. in 2015. Its function expression is shown in (8)

$$f(x) = \begin{cases} x, & \text{if } x \ge 0, \\ \alpha\left(e^x - 1\right), & \text{if } x < 0. \end{cases} \tag{10}$$

PReLU was proposed by He K et al. in 2015. It is a variant function of the ReLU function. Its principle is the same as that of the Leaky ReLU function, which is to prevent the Dead ReLU problem in the ReLU function by giving a small slope to the negative input. But unlike the slope parameter in Leaky ReLU, which needs to be manually specified, the parameters in PReLU can be optimized through learning. Its function expression is as (9), where λ is a learnable parameter vector with the same shape as x.

$$f(x) = \begin{cases} x, & \text{if } x > 0, \\ \lambda x, & \text{if } x \le 0. \end{cases} \tag{11}$$

For a network that has not undergone batch normalization, take the sigmoid activation function as an example. If the data falls in the area with a small gradient, then the network may cause slow training due to the small gradient, or even cause the gradient to disappear. Training has stalled.

Use the mean and variance of each data batch to batch standardize the data to promote normal data distribution. The processed data are concentrated in the area with a large gradient at the center of the function.

However, the obtained normal distribution data may not achieve the best results. The gradient between the red dotted lines of the sigmoid function does not change much, so the effect of the non-linear transformation of the non-linear function cannot be reflected. Therefore, in the fourth step, the scale factor γ and the translation factor ß are introduced for batch standardization, which can be adjusted through training so that the network obtains the best distributed data. While preventing the gradient from disappearing, the non-linear function of the activation function is better utilized, which is more conducive to training.

3.2. Image Desiccation Algorithm. The DnCNN network is a deep convolutional neural network. It is based on the residual strategy used to remove noise from the image. It better solves the problem of neural network degradation caused by the gradient instability of the deep network and can be achieved at a deeper network depth—a stable convergence of the network under. It has achieved far more effects than traditional image denoising methods in image denoising [22].

The idea of the residual strategy mainly comes from the ResNet network. The ResNet network forms a residual block by adding a fast connection between every two convolutional layers to stabilize the gradient in the network. In the DnCNN network, the residual block design is not used, that is, the output of the network in the output layer is the noise part of the image [23]. And because the image and noise are additive, so to get the denoised picture, you only need to subtract the original picture from the noise picture output by the network. In the residual learning of ResNet, it can be proved that when the residual is very small, the layer-to-layer is close to the identity mapping, and the network at this time is very well trained. Therefore, in the DnCNN network, when the noise level is low, the error between the noise picture and the pure picture is also small, the network residual is also small, and the network training is simpler [24].

The simplified network structure of DnCNN is shown in Figure 2. In the DnCNN network, the main body of the network is the superposition of several identical convolutional layers. No pooling layer is added to the entire network. Each convolutional layer uses the "same" pattern to fill the edge of the feature map and ensures that the step size of each convolution kernel is 1 so that the size of the feature map is in the entire network keep constant. Except for the first and last convolutional layers, BN layers and activation function layers are added after each convolutional layer [25]. The number of convolution kernels in the termination stage of the convolutional layer is 1, and the purpose is to make the dimension of the final output tensor same dimension as the input image [26]. The final output of the network is the difference between the input image and the residual tensor of the last layer of convolution.

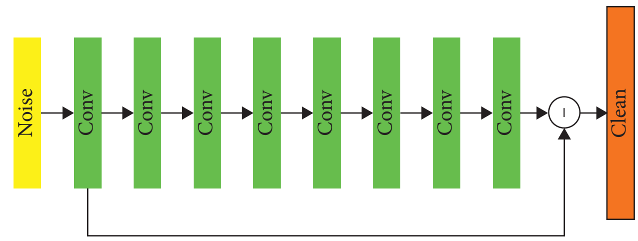

Figure 2: The structure of the DnCNN network.

Using MSE as the loss function training network, its denoising result index is shown in Table 1.

The network trained with MAE as the loss function, the index of the denoising result is shown in Table 2.

Using Looptimizer as the loss function training network, the index of the denoising result is shown in Table 3.

3.3. Pattern Recognition Model of Holographic Image Library. Feasibility study is the first task at the beginning of software development. If the problem cannot be solved, time, resources, and human resources are all wasted on software development. Nowadays, the optical image document recognition industry model has formed a certain theoretical tone through the development of recognition theory and image processing technology. Optical character recognition (OCR) continues to develop based on optical image processing and has taken a place in various fields of social life. Optical character recognition has the advantages of high speed, high efficiency, low error, and low cost of text input. As a new technology, various fields of social life are inseparable from document recognition based on optical character recognition. The characters on the ID card are unique documents, and the development of ID card recognition technology based on optical images has matured [27]. Therefore, the ID card information recognition system based on optical images is technically feasible. Currently, most ID card information is obtained by identifying high-frequency information embedded in the ID card or manually inputting it. The manual input method is inefficient and error-prone, so it will not be possible to obtain photo information [28]. On the other hand, the radio frequency identification method requires the increase of radio frequency chips for system identification and related application development, which promotes the increase of equipment costs. The effective use of computer technology in today's society, comprehensive, effective, fast and cheap access to personal data, verification, and management has become an urgent problem in the current population information flow management [29]. This theme is a very large application value theme and has high requirements in the fields of public safety, transportation, and services. By designing and implementing an ID card recognition system based on image processing and pattern recognition

Table 1: Denoising effect when the loss function is MSE.

Training times	PSNR	SSIM	Training times	PSNR	SSIM
200	17.3928	0.8907	250	17.1505	0.8887
100	17.1921	0.8782	275	16.9529	0.8858

Table 2: Denoising effect when the loss function is MAE.

Training times	PSNR	SSIM	Training times	PSNR	SSIM
125	16.4288	0.6829	275	16.4217	0.6822
300	16.4220	0.6822	200	16.4212	0.6823

Table 3: Denoising effect when the loss function is L0optimizer.

Training times	PSNR	SSIM	Training times	PSNR	SSIM
225	18.1851	0.8932	150	18.0801	0.8940
175	18.1754	0.8864	200	18.0481	0.8965

technology, we can provide the responsible department with an effective, fast, and cheap method of inputting personal ID card information. This method can facilitate the inquiry and verification of identity information and further promote the network and computerization of government agencies. Improving the cost and labor efficiency of services and government departments has important practical significance [30].

Table 4 shows the histograms of the R, G, and B channels. The histogram divides the illumination of the image into four areas. The first range is 0–25. This area mainly contains the black background and the text information on the ID card, which is the area with low gray value. The second area has a range of 25 to 50 and includes ID-specific information such as "name," "gender," and "ethnicity." The three channels in the third zone are slightly different, the blue channel is 50–120, and the red and green channels are about 50–150. The fourth is the remaining area with few pixels, which is the highlight area caused by uneven light in the image.

The image characteristic comparison table of the standard area and the highlight area is shown in Table 4. Comparing Table 4, it can be seen that in terms of gray mean, standard deviation, and average volatility, the standard area and the highlighted area are relatively close, but there is a big change in the average deviation. Therefore, by changing the average displacement rate, the highlight area of the ID card image can be corrected.

Define the average gray level of each channel as

Table 4: Image characteristics of ID card images.

Feature	Reference area			Highlight area		
	R	G	B	R	G	B
Mean	0.32	0.33	0.35	0.39	0.34	0.31
Standard deviation	0.01	0.03	0.01	0.02	0.01	0.01
Average volatility (%)	1.8	2.3	2.2	2.1	2.5	1.9
Average deviation rate (%)	—	—	—	121.1	95.5	101.0

$$\overline{I_x} = \frac{\sum_x N_x}{,} x = R, G, B. \tag{12}$$

Define the gray volatility rate of each channel:

$$K_x = \frac{l_x}{I_x}, x = R, G, B. \tag{13}$$

Define the color shift rate of each channel:

$$\mathrm{Rate}_x = \frac{I_x^s}{I_x^d}, x = R, G, B. \tag{14}$$

Use the highlight area shift rate to correct the highlight area. First, classify the light according to the intensity of the highlight area, calculate the average deviation rate of each layer, and correct the pixels with high gray values as follows:

$$I_{\mathrm{xnew}}^s = \frac{I_x^s}{\mathrm{Rate}_x}, x = R, G, B. \tag{15}$$

The global threshold method uses a variety of algorithms to determine a threshold T that is independent of pixel position. Methods for determining the value of T include Otsu's method and iterative algorithm. The Ostu method is also called the maximum difference between classes. It provides automatic selection of T by counting the histogram attributes of the entire image. If the threshold between the two categories is t, then the two categories are C_0 and C_1:

$$C_0 = \{0, 1, \ldots t\}, C_1 = \{t + 1, t + 2, \ldots, 255\}. \tag{16}$$

Then the Ostu method finds the maximum value of the following formula:

$$\eta = \frac{\sigma_B^2}{\sigma_T^2}. \tag{17}$$

The Bresen algorithm mainly uses the median between the maximum and minimum values of each pixel area as the segmentation threshold.

$$C(x, y) = G_{\max} - G_{\min} < l. \tag{18}$$

The new judgment criteria are as follows:

$$g(x, y) = \begin{cases} 0 & f(x, y) < (1-\beta)T, \text{ or }, \left(f(x, y) < T_{\mathrm{Bn}}(x, y), \text{ and }, (1-\beta)T \le f(x, y) \le (1+\beta)T\right), \\ 1 & f(x, y) > (1+\beta)T, \text{ or }, \left(f(x, y) \ge T_{\mathrm{Bn}}(x, y), \text{ and }, (1-\beta)T \le f(x, y) \le (1+\beta)T\right). \end{cases} \tag{19}$$

T_{bn} is determined by the following formula:

$$T_{Bn} = \operatorname*{avg}_{\substack{-w \leq \leq w \\ -w \leq j \leq w}} f(x+i, y+j). \tag{20}$$

β is determined by the following formula:

$$\beta = C1 \times \frac{(g2 - g1 + 1)}{128}. \tag{21}$$

The top-down layout analysis method is divided into two steps: row segmentation and column segmentation. The line segmentation can be obtained by analyzing the binarized image and projecting it vertically. Calculate the function as follows:

$$I(y) = \sum_{x=1}^{N} I(x, y), \tag{22}$$

$l_{(i,j)}(d)$ represents the fuzzy stroke length of the semicolon (i, j) of Chinese characters, defined as

$$l_{(i,j)}(d_0) = \max\left(l_{(i,j)}(d)\right). \tag{23}$$

4. Application of Holographic Image Library Pattern Recognition System Based on Deep Learning

4.1. System Architecture Design. Compared with the traditional print recognition, the ID card recognition system has undergone major changes. First, the font and size of the ID card information are already in a specific situation, and the position of the characters is also in a constant state, so the layout analysis of the ID card is relatively simple. However, contrary to ordinary printed Chinese character recognition, the Chinese characters on the ID card contain many rare characters. Due to the importance of identifying ID card information, the identification requirements for ID card characters must be very high, and the mismatch tolerance is also very low. In this article, we will use the following recognition process as shown in Figure 3to design an ID card recognition system based on optical images to realize the ID card recognition function.

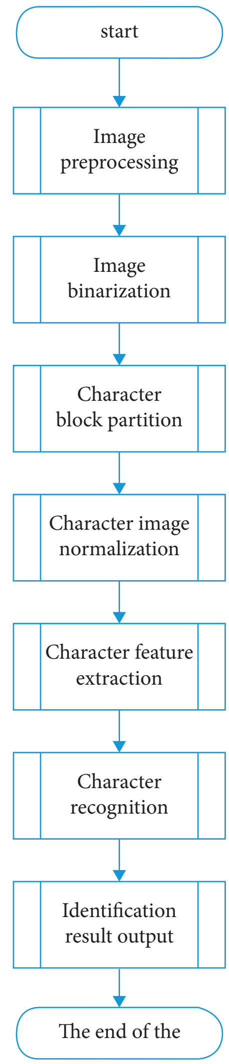

FIGURE 3: Flow chart of ID card recognition system based on optical image.

4.2. System Development Environment. By analyzing and summarizing the above, the ID card recognition software is developed and used. MATLAB is widely used in algorithm development, visualization, analysis, and calculation of data in engineering projects, with excellent interactive environment performance. The input of the software is the color ID card image, and the output is the ID card information that can be displayed. This article develops ID recognition software based on the MATLAB platform, and MATLAB 2013b is the design software.

4.3. System Data Processing. Image preprocessing includes two main parts: uneven light correction and image gray level. When correcting image unevenness, the color change rate is used as a reference for correcting the highlighted area of the image. The functional prototype is

Function Image out = getLightCorrect (Imagein).
%Input parameters:
%Imagein: The color image to be corrected.
%Output parameters:
%Image output: The color image has been changed.
The getLightCorrect function works as follows:

(1) Count the gray histograms of R, G, and B channels
(2) Calculate the forward difference and the backward difference of the gray histogram
(3) The point where the difference between the front and back is greater than 0 is regarded as the peak point
(4) As the starting point of color volatility statistical information, select the point closest to the gray value of 128 from the largest point and select the second largest point from the peak point as the gray value
(5) Starting from the statistical starting point, calculate the average color deviation by searching two

Table 5: The location of relevant information in the ID card (the vertical and horizontal coordinates of the image are all normalized to 1).

Name	X coordinate starting point	X coordinate end point	Y coordinate starting point	Y coordinate end point
"Name" image (name img)	0.1620	0.6173	0.0967	0.2028
"Sex" image (sex img)	0.1620	0.2293	0.2353	0.3317
"Nation" image (nation img)	0.3705	0.6173	0.2353	0.3317
"Birthday" image (birth img)	0.1620	0.6173	0.3514	0.4431
"Address" image (addr img)	0.1620	0.6173	0.4826	0.7616
"ID number" image (no img)	0.3134	0.8976	0.7976	0.9044

Table 6: Function test cases and qualification criteria.

Function name	Test case	Expected output	Eligibility criteria
getLightCorrect	Color ID card image in highlight area	Correct the image	Visually distinguish the corrected image of the highlight area
ImageDiv_ Otsu_ Bersen	ID card image after grayscale	Binarized image	The characters are clearly separated from most of the background
getLineDiv	Binarized image	Character row and column split data	Split characters correctly
getGridDiv	Unit number normalization graph	Character elastic grid segmentation results	The projections within the grid are roughly equal
getHanziLine	Unit number normalization graph	The four fuzzy stroke features of Chinese characters	The four stroke characteristics of Chinese characters are correctly extracted through visual discrimination
getHanziFeature	Unit number normalization graph	Chinese character characteristics	No criterion

directions in the histogram until the grayscale interval contains about half of the total number of pixels in the image as the reference point for color deviation statistics

(6) Use the average color change to correct the brightness of pixels with high gray values

Before binarizing the image on the ID card, first divide it into ID card information area. By using the prior knowledge of the ID card, the trouble of identifying ID card information can be reduced, the background that does not need to be identified can be reduced, and resources can be saved. Table 5 shows the approximate location of ID card-related information on the ID card image. In the identity recognition system, the image is converted according to the approximate position of the identity image where the prebinary ID card information is located.

4.4. System Implementation. The specific implementation of the key algorithm involved in identifying ID card information is described above. However, because the users of the ID card recognition system are not interested in specific recognition methods, the ID card software developed in this article executes the above algorithm in the background of the software, reads the image and outputs the recognition results, and saves the recognition results. The software interface includes three areas. The software title "ID Card Recognition System Based on Image Processing and Pattern Recognition" appears in the software title bar at the top. The center area is the event button, with three buttons: "Import Image", "Start Detection/Detection Complete" and "Save Results". The "Read Picture" button can select the picture on the badge that the user recognizes. The recognition start/recognition completion is used by the user to recognize the ID card information, and the recognition result is displayed on the user interface after the recognition is completed. After confirming that the ID card information has been correctly recognized, "Save Result" is used to save the recognition result in text format. The lower area is an information display area where the recognized image or result is displayed, and after the user determines the image to be recognized, the image to be recognized is displayed in the information display area. After the image is recognized and the user clicks the "Start Recognition" button, the software will start image preprocessing, character feature extraction, character recognition, and other algorithms. When the recognition of the ID card information is completed, the display of the "recognition start" button changes to "recognition end," and the recognition result is displayed in the information display area. This is because the ID card identification information may be incorrectly recognized. Therefore, the "ID Card Information View" window contains an interface for receiving string changes. Finally, the software has developed a function that can save the identification result of the ID card. When the user clicks the "Save Results" button, the software will automatically save the recognition results as a text file that other programs can access [31].

4.5. System Test. The test system has two aspects: basic function test and recognition index test. The basic function test includes some key functions of the test software and the output results of the test software. Test the recognition index by inputting a large number of ID card images to be recognized and statistically analyzing the possibility of correct recognition. The software identification index test does not have to separately test the system software output because the software output has actually been checked. The following is a brief introduction to the input and output test methods of each functional test [32].

As shown in Table 6, the optical image-based ID card recognition system mainly includes the following functional functions, and the functional test of these functions can be carried out using the black box test. In the functional black box test, specific inputs are passed to test whether the output meets the requirements.

5. Conclusion

This technology can provide a variety of conveniences for patients in the medical field. By integrating the data of each medical consortium, building a holographic view of patients based on the medical consortium, so that doctors can access all medical records of patients in the medical consortium, and diagnose the condition of a new patient as early as possible by comparing the diagnosis of other patients. At present, the mainstream application of this technology in the medical field is still in the direction of patient medical image recognition. Other directions such as on-axis holographic imaging detection on lensless sheets also have applications. Terahertz image segmentation based on coaxial reconstruction is an important research field of intelligent image recognition. In the experiment, the actual terahertz image is noisy, and the pixels are divided into target and background. However, when imaging, the laser energy of the seal image is insufficient, so there are grayscale pixels similar to the target pixels around the image. Using composite threshold segmentation method and U-NET segmentation method to segment the true coaxial terahertz holographic image can better maintain the target while eliminating heavy noise and surrounding background. Combine and apply the actual terahertz to segment the coaxial holographic reconstructed image and finally test the segmentation effect of the composite U-NET algorithm on the simulated image. A complete storage is established for the system, an automatic recognition function is added, and the corresponding control software is designed. According to experiments, the accuracy and recognition speed of target recognition based on the large-volume holographic image library are obtained. Based on the two exposure times, the impact of the test results on the detection is studied, and the angle multiplexing is extended to two-dimensional or angle fractal multiplexing, which greatly increases the single-point information storage capacity of the storage medium. Complete the establishment of the basic theoretical storage system, study the exposure method of the hologram with equal diffraction efficiency, analyze the noise source of the system in detail, and quantitatively calculate the influence of SLM and CCD parameters on the page, Using this technology not only costs less but also improves the accuracy of the diagnosis of patients' conditionsand also promotes the application of computer science in the medical field, providing reference for other scholars with experimental data.

Data Availability

The figure and table data used to support the findings of this study are included in the paper. In addition, the data and the models of analysis are available from the corresponding author upon request.

Conflicts of Interest

The authors declare that there are no conflicts of interest regarding the publication of this paper.

Acknowledgments

This research is funded by the National Nature Science and Technology Major Project of the Ministry of Science and Technology of China (no. 2016ZX05034-001).

References

[1] J. Wu, G. Wang, and G. Xu, "Color image encryption method combining computational holography and chaos," *Journal of Optics*, vol. 41, no. 19, pp. 113–132, 2021.

[2] M. G. Shan, X. L. Guan, L. Liu, and Z. Zhong, "Off-axis digital holographic imaging technology based on deep learning," *Laboratory Research and Exploration*, vol. 40, no. 10, pp. 1–5, 2021.

[3] Z. Meng, H. Ding, S. P. Nie, J. Ma, and C. J. Yuan, "Application of deep learning in digital holographic microscopy," *Advances in Lasers and Optoelectronics*, vol. 58, no. 18, pp. 166–184, 2021.

[4] Y. P. Liu, X. Wang, X. L. Liu, T. Jing, X. Y. Jiang, and X. P. Yan, "An image coding method for fusion display of virtual and real scenes with holographic stereoscopic view," *China Laser*, vol. 1-16, 2022.

[5] C. Zhao, S. M. Zhong, Q. S. Zhong, and K. B. Shi, "Synchronization of markovian complex networks with input mode delay and Markovian directed communication via distributed dynamic event-triggered control," *Nonlinear Analysis Hybrid Systems*, vol. 36, Article ID 100883, 2020.

[6] Y. Wang and L. X. Zhu, "Image adaptive information hiding technology based on holographic principle," *Computer Applications*, vol. 41, no. S1, pp. 131–136, 2021.

[7] Y. J. Cai and C. S. Wu, "Construction of 3D layout planning model of indoor scene based on laser technology holographic image," *Laser Journal*, vol. 42, no. 06, pp. 83–87, 2021.

[8] M. Z. Luo and C. Q. Yu, "Image reconstruction of millimeter wave holographic imaging with deep learning network," *Laser Journal*, vol. 42, no. 06, pp. 68–72, 2021.

[9] N. Polatidis and C. K. Georgiadis, "A multi-level collaborative filtering method that improves recommendations," *Expert Systems with Applications*, vol. 48, pp. 100–110, 2016.

[10] L. Qi, R. Wang, C. Hu, S. Li, Q. He, and X. Xu, "Time-aware distributed service recommendation with privacy-preservation," *Information Sciences*, vol. 480, pp. 354–364, 2019.

[11] L. Ren and W. Wang, "An SVM-based collaborative filtering approach for Top-N web services recommendation," *Future Generation Computer Systems*, vol. 78, pp. 531–543, 2018.

[12] F. Rezaeimehr, P. Moradi, S. Ahmadian, N. N. Qader, and M. Jalili, "TCARS: time- and community-aware

recommendation system," *Future Generation Computer Systems*, vol. 78, pp. 419–429, 2018.

[13] A. Stuart, "Rank correlation methods. By M. G. Kendall, 2nd edition," *British Journal of Statistical Psychology*, vol. 9, no. 1, p. 68, 1956.

[14] G. Tian, J. Wang, K. He, C. Sun, and Y. Tian, "Integrating implicit feedbacks for time-aware web service recommendations," *Information Systems Frontiers*, vol. 19, no. 1, pp. 75–89, 2017.

[15] Y. Wang and M. P. Singh, "Formal trust model for multiagent systems," in *Proceedings of the 20th international joint conference on Artifical intelligence (IJCAI'07)*, pp. 1551–1556, Morgan Kaufmann Publishers Inc., Hyderabad India, January 2007.

[16] X. Wang, J. Zhu, Z. Zheng, W. Song, Y. Shen, and M. R. Lyu, "A spatial-temporal QoS prediction approach for time-aware web service recommendation," *ACM Transactions on the Web*, vol. 10, no. 1, 2016.

[17] X. Wu, Y. Fan, J. Zhang, H. Lin, and J. Zhang, "QF-RNN: QI-matrix factorization based RNN for time-aware service recommendation," in *Proceedings of the 2019 IEEE international conference on services computing (SCC)*, pp. 202–209, Milan, Italy, July 2019.

[18] Z. Yang, B. Wu, K. Zheng, X. Wang, and L. Lei, "A survey of collaborative filtering-based recommender systems for mobile internet applications," *IEEE Access*, vol. 4, pp. 3273–3287, 2016.

[19] B. Yang, Y. Lei, J. Liu, and W. Li, "Social collaborative filtering by trust," *IEEE Transactions on Pattern Analysis and Machine Intelligence*, vol. 39, no. 8, pp. 1633–1647, 2017.

[20] A. Abbasi, H. Hsinchun Chen, S. Thoms, and T. Tianjun Fu, "Affect analysis of web forums and blogs using correlation ensembles," *IEEE Transactions on Knowledge and Data Engineering*, vol. 20, no. 9, pp. 1168–1180, 2008b.

[21] A. Aizawa, "An information-theoretic perspective of tf-idf measures," *Information Processing & Management*, vol. 39, no. 1, pp. 45–65, 2003.

[22] M. S. Akhtar, D. Gupta, A. Ekbal, and P. Bhattacharyya, "Feature selection and ensemble construction: a two-step method for aspect based sentiment analysis," *Knowledge-Based Systems*, vol. 125, pp. 116–135, 2017.

[23] S. Akhtar, T. Garg, and A. Ekbal, "Multi-task learning for aspect term extraction and aspect sentiment classification," *Neurocomputing*, vol. 398, 2020.

[24] O. Alqaryouti, N. Siyam, A. A. Monem, and K. Shaalan, "Aspect-based sentiment analysis using smart government review data," *Appl Comput Inform*, vol. 23, 2019.

[25] X. Bai, "Predicting consumer sentiments from online text," *Decision Support Systems*, vol. 50, no. 4, pp. 732–742, 2011.

[26] A. S. Cerqueira, D. D. Ferreira, M. V. Ribeiro, and C. A. Duque, "Power quality events recognition using a SVM-based method," *Electric Power Systems Research*, vol. 78, no. 9, pp. 1546–1552, 2008.

[27] C. C. Chang and C. J. Lin, "LIBSVM: a library for support vector machines," vol. 2, no. 3, 2011.

[28] J.-R. Chang, M.-Y. Chen, L.-S. Chen, and W.-T. Chien, "Recognizing important factors of influencing trust in O2O models: an example of OpenTable," *Soft Computing*, vol. 24, no. 11, pp. 7907–7923, 2020.

[29] P. Chaovalit and L. Zhou, "Movie review mining: a comparison between supervised and unsupervised classification approaches," in *Proceedings of the 38th Hawaii international conference on system sciences*, Big Island, HI, USA, January 2005.

[30] L.-S. Chen and C.-T. Su, "Using granular computing model to induce scheduling knowledge in dynamic manufacturing environments," *International Journal of Computer Integrated Manufacturing*, vol. 21, no. 5, pp. 569–583, 2008.

[31] L.-S. Chen, C.-C. Hsu, and M.-C. Chen, "Customer segmentation and classification from blogs by using data mining: an example of VOIP phone," *Cybernetics & Systems*, vol. 40, no. 7, pp. 608–632, 2009.

[32] L.-S. Chen, C.-H. Liu, and H.-J. Chiu, "A neural network based approach for sentiment classification in the blogosphere," *Journal of Informetrics*, vol. 5, no. 2, pp. 313–322, 2011.

Hindawi
Journal of Healthcare Engineering
Volume 2022, Article ID 7821525, 6 pages
https://doi.org/10.1155/2022/7821525

Research Article

A Cohort Study to Assess Cognitive Impairment and Its Effects on Older Patients in the Orthopedic Rehabilitation

Han Zhang, Bo Pang, Zheng Ma, Huimei Dong, Hongyi He, and Lan Jiang

Department of Rehabilitation Medicine, Shanghai Jiao Tong University Affiliated Sixth People's Hospital, Shanghai, China

Correspondence should be addressed to Lan Jiang; 7250003589@shsmu.edu.cn

Received 27 December 2021; Revised 7 January 2022; Accepted 18 January 2022; Published 18 February 2022

Academic Editor: Enas Abdulhay

Background. The cognitive role of older patients is regularly not investigated in orthopedic rehabilitation, after the elective as well as the nonelective operation. The objective of this research is to investigate the cognitive disorder and its influence over the duration of stay along with the functional consequences of the older patients who were admitted to orthopedic rehabilitation. *Material and Methods*. The inclusion criteria for this study were the patients with age above 50 years; who were admitted with the detection of orthopedic impairment and the surgery both elective and nonelective, investigated utilizing the MoCA (Montreal Cognitive Assessment) over admission, MBI (Modified Barthel Index), and FIM (Function Independent Measure) over admission and discharge status; and were discharged from the hospital. The demography, as well as the clinical data, comprising of the duration of stay, age and the detection was also reported. *Result*. Of the 109 admitted patients, 80 patients were included in the study where $n = 47$ (58.75%) patients were females and $n = 33$ (41.25%) were males. The age group range was 50 to 94 years with a mean age of 78.5 years (SD = 8.27). The diagnostic groups included for the study were fractured neck of femur ($n = 34$; 42.5%), orthopedic surgery ($n = 22$; 27.5%), and other orthopedic surgery ($n = 24$; 30%). The mean duration of rehabilitation stay was reported as 34 (4.39), where the MoCA was reported as 22.17 (2.44); functional independence measures were as follows: motor admission as 53.97 (7.55), motor discharge as 76.27 (5.35), cognitive admission as 30.71 (1.99), and cognitive discharge as 31.85 (1.94). Here, the diagnosis was done over the fractured neck of the femur (i.e., NOF being 34 (42.5%), elective surgeries 22 (27.5%), and other orthopedic as 24 (30%)). *Conclusion*. An excessive percentage of older-age patients in a rehabilitation unit with elective as well as nonelective diagnoses comprises the cognitive disorder. The cognitive screening was advised for all the older age patients in the rehabilitation units to report a specific rehabilitation plan to enhance the consequences along with the duration of stay. There is further study required to explore different cognitive strategies to enhance the rehabilitation consequences among older-age orthopedic patients.

1. Introduction

Cognitive impairment is a well-defined risk element for the damaging falls in older ages [1, 2]. As a consequence, it will be anticipated that chronic cognitive diseases like dementia or Alzheimer's are widely prevailing among older patients depending on multiple factors comprising of characteristic diagnostic parameters and the severity of the clinical manifestations. Postoperative cognitive disorders are frequently observed among elderly patients (age >65 years). These comprise mainly of degraded perception, information investigation, memory, concentrating strength, attention and focus, and the patient's response and reaction [3, 4].

The cases of cognitive disorders have been documented as independent risk measures for delirium, and the total case of the new delirium was remarkably observed higher among the older patients suffering from dementia, as compared to the older patients suffering from no dementia [5, 6]. Furthermore, the prefracture cognitive impairments along with the postfracture suffering of delirium were found to be strongly associated with the higher rate of mortality as well as the risk for the establishment, and the delirium may be an untimely indicator for the postdischarge cognitive degeneration [7, 8]. However, this can generate an outcome in the long-run cognitive degeneration, postoperative cognitive degeneration peripheral to the delirium which does not happen in all the patients.

The cognitive variations in the rehabilitation might be preexisting, which even may be an element causing orthopedic injury in a person [9, 10]. The rehabilitation from a therapy aspect might not individually focus on the cognitive impairment, instead, via the design of the rehabilitation program, assimilate the cognitive role to enhance the participation in the rehabilitation program, as a result of which improving the functional consequences [11]. The evidence proposes that the cognitively impaired suffering older patients can be benefitted from the specialized rehabilitation programs, which is more rigorous, with the patients with average-to-acute cognitive impairment determined to exhibit functional enhancements in the rehabilitation programs [12, 13].

The cognitive status can be a crucial predicting factor of the rehabilitation consequences, along with being aware of the information related to the cognitive abilities of the patient and the dimensions of deficiency facilitating the staff with the retrain in the useful task rendition, comprising of day-to-day activities like walking. To enhance the functional consequences of all the older patients with orthopedic conditions, a better comprehension of the cognitive abilities of the patient and how it can affect their process of rehabilitation is needed [14–16]. Various rehabilitation units implement the cognitive screens to help the decision-making procedure about both appropriateness of a patient who has to be admitted to a rehabilitation unit and the timing as well as assistance needed for discharge, although the screening tools implemented are not steady [17].

The objective of this study is to assess, through a cohort study, the association between the cognitions, calculated with the use of MoCA, and other functional outcomes, calculated using the FIM as well as the MBI, of the older patients with orthopedic condition, who were admitted into the rehabilitation, with the detection of the fractured neck of the femur, elective as well as other related orthopedic operations, and the duration of patient's stay [18]. The occupational therapists furnish the intervention associated to enhance the function in the orthopedic rehabilitation program. The occupational therapy involvement furnished the location of the study conducted and was constant beyond the detection, with the rehabilitation involvement specifically focusing on the requirements of the individuals.

It was hypothesized that the relation between the cognitive impairment and the consequences in the orthopedic rehabilitation may occur for the patients who were admitted with fracture injury, who inclined to be older and weaker, as compared to the ones who were admitted for the elective process.

2. Material and Methods

The audit was verified by the Research and the Ethics Committee, where the patients were recognized via the procedure of admission to the common rehabilitation unit. This unit was facilitated with the staff having a specialized multidisciplinary team, comprising physiotherapy, dietetics, social work, speech pathology, occupational therapy, and medical and nursing.

The inclusion criteria for this study were as follows: (1) the patients with age above 50 years; (2) the patients who were admitted with the detection of orthopedic impairment and the surgery both elective and nonelective, investigated utilizing the MoCA over admission, MBI as well as FIM over admission, and discharge status; and (3) the patients who were discharged from the hospital. The data for this cohort study was gathered through chart data entry and the status of admission and discharge data which is regularly gathered by the occupational therapy group.

The demography as well as the clinical data comprising of the duration of stay and age and the detection was also reported. The diagnosis was classified into subgroups: elective orthopedic surgery of hip as well as knee replacement, fractured neck of femur, and other associated orthopedic injuries comprising the orthopedic injury of the upper as well as the lower limbs along with the fractured pelvis.

The cognition was investigated over the admission utilizing the MoCA and the patients were classified into the groups of severity level as per the scale, to compare the variation between the diagnosis categorized in the range of 26 to 30 in the normal range followed by the range of 18 to 25 as the mild cognitive impairment, the score of 10 to 17 as the moderate cognitive impairment, and the score of 9 or below than that was the less severity of cognitive impairment.

Quantitative values were described using their number, mean, standard deviation, and median; MoCA scores on admission and discharge were compared using ANOVA with repeated measures, with age and education as covariables. Qualitative values were described using their number, frequencies, and centiles and were compared using the Chi^2 test or Fisher's exact test when necessary. To evaluate the change in MoCA score as a function of its baseline value, we split the study population into three subgroups with low (≤21), intermediate (≥22 and ≤25), and high (≥26) MoCA scores. All analyses were performed using SPSS software V22.0 (IBM SPSS Inc., Armonk, NY, USA).

3. Results

3.1. Patients' Characteristics. A total of 109 patients were admitted to the rehabilitation center from January to August 2019 where people with orthopedic injuries and surgeries were selected. Out of these, 29 patients were excluded who did not meet the criteria for inclusion (for not completing the MoCA). Of the 109 admitted patients, 80 patients were included in the study where $n = 47$ (58.75%) patients were females and $n = 33$ (41.25%) were males.

The age group range was 50 to 94 years with a mean age of 78.5 years (SD = 8.27). The diagnostic groups included for the study were fractured neck of femur ($n = 34$; 42.5%), orthopedic surgery ($n = 22$; 27.5%), and other orthopedic surgery ($n = 24$; 30%). The surgeries elected were planned prior to or scheduled. The patient's characteristics are presented in Table 1.

The clinical characteristics of the subgroups which are selected for diagnosis are shown in Tables 1 and 2. Collective MoCA score for the diagnosis was found to show mild impairment. A significant difference in FIM scores (both cognitive and motor), MBI scores at the time of admission or discharge, age, and diagnosis type was noted.

The post hoc analysis showed a significant difference in the scores of cognition where surgery patient scores were higher significantly in comparison to the patients with fractured neck of femur, though there was no other difference between fractured NOF or other orthopedic surgery patients. Statistical analysis has also shown that the FIM scores of cognition between fractured NOF and elective surgery patients were different (0.367). There was no significant change noted between patients with fractured NOF or other orthopedic cases or with elective surgery.

3.2. Significance between MoCA and FIM Scores and Their Functional Outcomes. The functional analysis was done on the basis of the FIM scores (motor) at the time of admission and discharge as well as the MBI scores at the time of admission and discharge were assessed. At the time of admission, a significant change in the FIM motor scores was noted on the basis of the diagnosis type. The post hoc analysis noted that patients with elective orthopedic surgery had a score significantly higher than the NOF cases of patients and with other orthopedic cases of patients.

No significant changes were noted in the FIM scores (motor) at the admission time for patients with fractured neck of femur and other patients with orthopedic cases. The post hoc analysis also revealed that the scores of elective orthopedic patients were higher significantly when compared with patients with fractured neck of the femur or other orthopedic surgery. In the discharge FIM scores (discharge), no difference was noted between orthopedic patients and fractured NOF.

The analysis revealed that the MBI scores were showing a significant difference between fractured NOF and elective orthopedic patients ($P = 0.001$). The analysis has no significant difference when MoCA scores showed no significant differences with the MBI change or FIM motor score (Table 2).

The median of MoCA for NOF and orthopedic surgery was 22 and that of other orthopedic surgeries was found to be 22. The median for FIM motor admission for NOF was 50.5, orthopedic surgery was 65, and another orthopedic surgery was found to be 50. The median for FIM cognition for admission in case of admission for NOF was 30, orthopedic surgery was 32.5, and another orthopedic surgery was 30, whereas the median for FIM cognition discharge for NOF was 31, orthopedic surgery was 33, and other orthopedic procedures was 30.

The median for FIM motor admission for NOF was found to be 71.5, orthopedic surgery was 81.5, and another orthopedic surgery was 76.5 (Table 2). MoCA scores and FIM cognition scores were compared against the functional variables where the association between cognition and discharge was linked significantly with the length of stay in the hospital. A marked association was seen in MoCA scores with FIM admission (motor), MBI discharge, and FIM admission/discharge (cognition, motor).

Table 1: Clinical characteristics of patients included in the study.

S. no.	Characteristic	Mean
(1)	Rehabilitation length of stay	34 (4.39)
(2)	Male	33
	Female	47
(3)	Montreal cognitive assessment	22.17 (2.44)
(4)	*Functional independence measure*	
	Motor admission	53.97 (7.55)
	Motor discharge	76.27 (5.35)
	Cognitive admission	30.71 (1.99)
	Cognitive discharge	31.85 (1.94)
		Number (%)
(5)	*Diagnosis*	
	Fractured neck of femur (NOF)	34 (42.5)
	Elective surgeries	22 (27.5)
	Other orthopedic	24 (30)

4. Discussion

In this study, it can be observed that a higher number of geriatric orthopedic older-age patients in the rehabilitation, in spite of the reason behind their admission, that is, either selective or nonselective operation, have experienced cognitive impairment ($n = 80$), as calculated by the MoCA. In this cohort analysis, we have indicated a median point with faint cognitive impairment, with fewer scores on the MoCA. The NOF group accounts for a larger proportion of fracture types and is associated with cognitive dysfunction in elective and other types of orthopaedic surgery.

There was zero significant variation found between the categories for their total MoCA scores, although there was a significant variation observed between the FIM cognitive score over the admission or the discharge status of patients, thus indicating the lower functional cognition of the patients with a fractured NOF as well as the other orthopedic status. With the scope of diagnosis for other orthopedic states and fractured NOF category, it can be presumed that these were because of the drops for which the precognitive state might have furnished to the risk of fall down.

The MBI was outstandingly varied between the three diagnoses, signifying that the calculation of function via observation, comprising of FIM as well as MBI, inspects the variations in the diagnostic categories. The FIM motor variations for all categories were considered clinically remarkable, thus assisting its implementation as a functional result calculated, on an orthopedic rehabilitation department.

The MBI variation from the status of admission of a patient to the discharge was remarkably varied with the highest development prevailing in the other orthopedic

Table 2: Detailed patient characteristics.

S. no.	Description	Fractured neck of femur (NOF) ($n = 34$)	Orthopedic surgery ($n = 22$)	Other orthopedic surgeries ($n = 24$)	P value
(1)	Age	50–98 72.79 (8.48)	71–89 81 (4.93)	73–92 84.33 (4.47)	0.001*
(2)	Length of stay	34 (4.48)	34 (3.38)	36 (4.90)	<0.001*
(3)	*Montreal cognitive assessment (MoCA)*		*Median, IQR (n %)*		
	Median (IQR)	22 (17–25)	22 (17–25)	22 (19–25)	
	Intact (n, %)	3 (8.82)	4 (18.18)	4 (16.66)	
	Mild (n, %)	14 (41.17)	13 (59.09)	11 (45.83)	0.105
	Moderate (n, %)	9 (26.47)	3 (13.63)	8 (33.33)	
	Severe (n, %)	1 (2.94)	1 (4.45)	1 (4.16)	
(4)	*FIM motor*	*Median*			
	Admission	50.5 (43–58)	65 (56–70)	50 (42–55)	<0.001*
	Discharge	71.5 (65–81)	81.5 (79–85)	76.5 (68–81)	<0.001*
	Change	25 (14–30)	12–24 (20.5)	25 (10–30)	0.016
(5)	*FIM cognition*	*Median*			
	Admission	30 (26–33)	32.5 (29–34)	30 (27–34)	0.014*
	Discharge	31 (28–35)	33 (30–35)	32 (29–34)	0.034*
	Change	0–2	0–1	0–2	0.367*
(6)	*MBI*				
	Admission				
	Minimal assistance	0	0	1 (4.16)	
	Mild dependence (n %)	12 (35.29)	7 (31.81)	12 (50)	
	Moderate dependence (n %)	15 (44.11)	11 (50)	7 (29.16)	<0.001*
	Severe dependence (n %)	4 (11.76)	4 (18.18)	3 (12.5)	
	Total dependence (n %)	2 (5.88)	0	0	
	Discharge				
	Independent (n %)	2 (5.88)	6 (27.27)	3 (12.5)	
	Minimal assistance (n %)	16 (47.05)	12 (54.54)	13 (5.42)	
	Mild dependence (n %)	9 (26.47)	2 (9.09)	4 (16.66)	0.001*
	Moderate dependence (n %)	5 (14.71)	1 (4.54)	3 (12.5)	
	Severe dependence (n %)	1 (2.94)	1 (4.54)	1 (4.16)	
	Total dependence (n %)	1 (2.94)	0	0	

category, densely followed by the fractured NOF category, assisting its utilization as a result measure of role among these patient populations. This also signifies that these patients experienced a better functional result, with alike cognitive capabilities to those allowed for the elective operation. As observed in other researches, the patients who were admitted with a fracture with a history of falls, usually had a failing function before their admission, which affects functional results, but it may even yield more chances for enhancement.

Furthermore, the patients who were admitted for elective operation might be prepared before admitting with social assistance, home set-up and on completion of the prior-admitting exercises, therefore possessing a greater initial point of function with slighter advancements quantifiable after the rehabilitation plan. Moreover, the results of MoCA, FIM movement variation, and MBI nonexpression did not help patients with severe cognitive impairment improvement during rehabilitation. However, a substantial specimen size with more practicality of cognition is needed.

The average duration of stay for those patients who were admitted with fracture NOF was a duration of 34 days and the other orthopedic patient for a duration of 36 days, while the elective orthopedic operation of the patients experienced a 34-day duration of stay. This was above and beyond the range of this project, although it might demonstrate the varied operations in rehabilitation or the patient parameters, like the high rate of cognitive impairment. This should be reported that the average age of these older patients who were admitted to these rehabilitation centers and assessed for this analysis was greater than the national average. Here, the national average age of orthopedic patients turns out to be 78.5 years (SD = 8.27).

The discoveries signify that all the cognitive computations, both MoCA and FIM cognitive scores, were linked with the duration of stay in the group total but not in individual diagnosis. This signifies that beyond both the elective and the nonelective orthopedic recognition, cognition can report the duration of stay. The correlation between cognition and hospitalization time shows that even the slightest reduction in cognition is also obvious, so it is necessary to reduce the cost of medical services.

This aids the advice of the cognitive partitions utilized with all the patients who are admitted to the geriatric orthopedic rehabilitation centers, despite the detection. This process of screening might help the programs to adapt how the rehabilitation is carried out, with respect to the functional context, specific prompts, as well as the assimilation of the cognitive training policies to make as large as possible for the functional results and then possibly diminish the duration of stay.

Cognition is majorly affected by age and it can impact the patient's potential to actively get involved in the process of rehabilitation goal setting, learning and deficient in the remembering skills, tough with the decision making the discharge site and the services needed. The outcomes signify that for the group of fractured NOF along with other groups of orthopedic, the MoCA scores were associated with the functional scores of the FIM (i.e., the admission and the discharge status) and the MBI (i.e., the discharge status), therefore signifying that the MoCA is functional in calculating the cognition before as well as after the rehabilitation as linked to the useful measures at both points.

Although, for the elective operation group, the FIM cognitive and not the MoCA, overadmitting was associated with the functional measures (i.e., FIM motor and the MBI over the admission of patients), but only the FIM motor overdischarge of patients. This proposes that for the elective operation group, the FIM cognitive is more functional in terms of measuring the cognitive potential, which will be associated with the functional behaviour.

There was no significant variation while drawing a comparison of the severity on the MoCA to the detection, and the breakdown of the scores on the basis of the assessing areas was further investigated, which would be advantageous to identify the aspects of cognition associated with the duration of stay. The MoCA scores and the location of discharge were found to be significantly different between those who were discharged directly to their homes and the ones discharged to any other location like a nursing center or an independent care unit or a hostel.

The details of specific cognitive deficiency were experienced by those patients who were admitted to the orthopedic units and would report the design of the rehabilitation program. Furthermore, with the fall as the primary reason for the orthopedic injury among the older patients, the fall prevention programs comprising of the education parameter were needed to count the cognitive elements to enhance their efficacy in lessening as well as preventing the falls. The experts promote the consideration of the role of technology in enhancing the results as well as the assistance of the older people to administer their process of rehabilitation.

Therefore, the implementation of the technology to report the rehabilitation for the people with cognitive modifications in orthopedic rehabilitation needs assessment. The additional study has to be conducted more efficiently to provide rehabilitation to those elder patients with orthopedic conditions, with cognitive impairment, who were likely excluded from the conducted rehabilitation trials.

5. Conclusion

To conclude, the geriatric patients with orthopedic conditions, who were admitted to the rehabilitation, were bestowed with the cognitive impairment beyond the detection and this was linked with the discharge location, useful outcomes, and the duration of stay. The cognitive screening is advised for all the older patients with orthopedic conditions who were admitted to the rehabilitation programs to report an individualized rehabilitation program in order to enhance the results and the duration of stay. Furthermore, the study is needed to investigate the cognitive plans to maximize the rehabilitation results among older patients with orthopedic conditions.

Data Availability

The data used to support this study are available from the corresponding author upon request.

Conflicts of Interest

The authors declare that they have no conflicts of interest regarding the publication of this paper.

References

[1] K. R. Suhrie, D. B. Hammers, S. M. Porter et al., "Predicting biomarkers in intact older adults and those with amnestic mild cognitive impairment, and mild Alzheimer's disease using the repeatable battery for the assessment of neuropsychological status," *Journal of Clinical and Experimental Neuropsychology*, vol. 43, pp. 1–18, 2022.

[2] L. Chen, N. J. Dar, R. Na et al., "Enhanced defense against ferroptosis ameliorates cognitive impairment and reduces neurodegeneration in 5xFAD mice," *Free Radical Biology and Medicine*, vol. 180, pp. 1–12, 2022.

[3] P. Hampel, T. Graef, B. Krohn-Grimberghe, and L. Tlach, "Effects of gender and cognitive-behavioral management of depressive symptoms on rehabilitation outcome among inpatient orthopedic patients with chronic low back pain: a 1 year longitudinal study," *European Spine Journal*, vol. 18, no. 12, pp. 1867–1880, 2009.

[4] R. Ingrid, "Postoperative cognitive dysfunction," *Dtsch Arztebl Int*, vol. 111, no. 8, pp. 119–125, 2014.

[5] R. A. Ruchinskas, H. K. Singer, and N. K. Repetz, "Cognitive status and ambulation in geriatric rehabilitation: walking without thinking?" *Archives of Physical Medicine and Rehabilitation*, vol. 81, no. 9, pp. 1224–1228, 2000.

[6] R. Nayoung, M. P. Jung, J. B. Min et al., "Coping with dementia in the middle of the COVID-19 pandemic," *Journal of Korean Medical Science*, vol. 35, no. 42, 2020.

[7] S. Lippke, J. P. Ziegelmann, and R. Schwarzer, "Behavioral intentions and action plans promote physical exercise: a longitudinal study with orthopedic rehabilitation patients," *Journal of Sport & Exercise Psychology*, vol. 26, no. 3, pp. 470–483, 2004.

[8] S. Scott, S. M. Friedman, D. A. Mendelson, K. W. Bingham, and S. L. Kates, "The 1-year mortality of patients treated in a hip fracture program for elders," *Geriatr Orthop Surg Rehabil*, vol. 1, no. 1, pp. 6–14, 2010.

[9] L. Patrick, F. Knoefel, P. Gaskowski, and D. Rexroth, "Medical comorbidity and rehabilitation efficiency in geriatric inpatients," *Journal of the American Geriatrics Society*, vol. 49, no. 11, pp. 1471–1477, 2001.

[10] H. D. Hari and C. Siddharth, "Management of traumatic brain injury patients," *Korean J Anesthesiol*, vol. 71, no. 1, pp. 12–21, 2018.

[11] N. J. Kirk-Sanchez and K. E. Roach, "Relationship between duration of therapy services in a comprehensive rehabilitation program and mobility at discharge in patients with orthopedic problems," *Physical Therapy*, vol. 81, no. 3, pp. 888–895, 2001.

[12] L. Tlach and P. Hampel, "Long-term effects of a cognitive-behavioral training program for the management of depressive symptoms among patients in orthopedic inpatient rehabilitation of chronic low back pain: a 2-year follow-up," *European Spine Journal*, vol. 20, no. 12, pp. 2143–2151, 2011.

[13] B. Apurba, C. Ahana, and B. Rohit, "Cognitive impairment and rehabilitation strategies after traumatic brain injury," *Indian Journal of Psychological Medicine*, vol. 38, no. 3, pp. 172–181, 2016.

[14] J. Paech and S. Lippke, "Social-cognitive factors of long-term physical exercise 7 years after orthopedic treatment," *Rehabilitation Psychology*, vol. 62, no. 2, pp. 89–99, 2017.

[15] C. Jimmy and W. Elizabeth, "Cognitive rehabilitation therapies for Alzheimer's disease: a review of methods to improve treatment engagement and self-efficacy," *Neuropsychology Review*, vol. 23, no. 1, pp. 48–62, 2013.

[16] P. Maresova, E. Javanmardi, S. Barakovic et al., "Consequences of chronic diseases and other limitations associated with old age - a scoping review," *BMC Public Health*, vol. 19, no. 1, p. 1431, 2019.

[17] P. Hampel and L. Tlach, "Cognitive-behavioral management training of depressive symptoms among inpatient orthopedic patients with chronic low back pain and depressive symptoms: a 2-year longitudinal study," *Journal of Back and Musculoskeletal Rehabilitation*, vol. 28, no. 1, pp. 49–60, 2015.

[18] N. Heyman, T. Tsirulnicov, and M. Ben Natan, "Prediction of geriatric rehabilitation outcomes: comparison between three cognitive screening tools," *Geriatrics and Gerontology International*, vol. 17, no. 12, pp. 2507–2513, 2017.

Hindawi
Journal of Healthcare Engineering
Volume 2022, Article ID 9055587, 6 pages
https://doi.org/10.1155/2022/9055587

Research Article

Risk Factors and Nursing Countermeasures of Ventilator-Associated Pneumonia in Children in the Intensive Care Unit

Rong Chen, Yu Liu, Xiaohong Zhang, Qin Yang , and Xiao Wang

Department of ICU, Xiangyang Central Hospital, Affiliated Hospital of Hubei University of Arts and Science, Xiangyang, Hubei 441021, China

Correspondence should be addressed to Qin Yang; yangqin6177@163.com and Xiao Wang; 1213081682@qq.com

Received 28 December 2021; Revised 12 January 2022; Accepted 17 January 2022; Published 17 February 2022

Academic Editor: Enas Abdulhay

Objective. This study discussed and analyzed the risk factors and nursing countermeasures of ventilator-associated pneumonia (VAP) in the children intensive care unit (ICU). *Methods*. In this study, 155 children with mechanical ventilation in the pediatric intensive care unit from Oct. 2018 to Oct. 2020 were chosen as research objects. We retrospectively analyzed the clinical data of children and divided them into VAP groups and non-VAP groups according to the occurrence of VAP. Subsequently, we adopted a univariate and multivariate logistic regression model to analyze and clarify the risk factors of VAP and formulated the corresponding nursing countermeasures. *Results*. 49 cases of total research objects had occurred VAP, with an infection rate of 31.62%. The primary pathogenic bacteria were Gram-negative bacteria (43/70, 61.43%). According to multivariate logistic regression analysis, the duration of mechanical ventilation, invasive procedures, and application of hormones and antacids are all independent risk factors for VAP in pediatric ICU. The VPA group had longer hospital stay than the non-VAP group, and the difference was statistically significant ((20.92 ± 4.16)d, (15.24 ± 3.77)d, $t = 8.4383$, $P \leq 0.001$). The hospitalization cost of the VPA group was substantially higher than that of the non-VAP Group ((45.8 ± 10.4) thousand Yuan, (33.2 ± 4.3) thousand Yuan, $t = 10.6822$, $P \leq 0.001$). *Conclusion*. Children admitted to the pediatric ICU have a high VAP incidence. The primary pathogenic bacteria are Gram-negative bacteria. As the occurrence of VAP is closely related to a variety of factors, we should take targeted nursing countermeasures to reduce the duration of mechanical ventilation and the frequency of invasive operations and use the hormone and antacids rationally to reduce the risk of VAP and improve the prognosis.

1. Introduction

Most children admitted to the pediatric intensive care unit (ICU) have severe pneumonia, myocarditis, encephalitis, hand-foot-and-mouth disease, etc. Children often need to use respiratory support to get through the dangerous period due to respiratory disorders or respiratory failure, but the application of ventilator is easy to cause complications such as pulmonary injury, displacement of tracheal intubation, septic shock, and respiratory-associated pneumonia (VAP) [1, 2]. VAP refers to pulmonary infection that occurs 48 h after endotracheal intubation or tracheostomy with mechanical ventilation or 48 h after removal of a mechanical ventilation tube, which has high morbidity and fatality rate [3, 4]. VAP prolongs the length of hospital stay and surcharges medical costs and increases the clinical mortality rate and affects the prognosis of children [5]. In recent years, the risk factors of VAP have been the hot spot in the analysis and research of the intensive care field. According to the work in [6–8], the occurrence of VAP is closely related to clinical nursing operations. Therefore, it is of great significance to take effective preventive and nursing measures to reduce VAP risks in the pediatric ICU. This study retrospectively analyzed the clinical data of the 155 mechanically ventilated children in the pediatric ICU of our hospital from Oct. 2018 to Oct. 2020, aiming to clarify the risk factors, pathogen distribution characteristics, and prognosis of children admitted in our pediatric ICU with VAP, meanwhile, to find targeted nursing countermeasures for the pediatric ICU of our hospital, and to provide a theoretical basis for clinical prevention of VAP.

2. Cases and Methods

2.1. General Data. 155 children with mechanical ventilation in the pediatric ICU from Oct. 2018 to Oct. 2020 were chosen as research objects. The objects included 81 males and 74 females, with an average age of (7.83 ± 2.46) years; the average duration of mechanical ventilation was (7.35 ± 3.12) d, and the average length of hospital stay was (18.52 ± 3.05)d. This study was carried out after acquiring approval from the ethics committee of our hospital.

2.2. Inclusion and Exclusion Criteria. Inclusion criteria: (1) the age of the patients ranged from 3 to 12 years; (2) all children were treated with invasive ventilation, and the duration of mechanical ventilation was ≥48 d; (3) children tended to be in stable conditions, or without progressive aggravation; and (4) the clinical data of children were complete.

Exclusion criteria: (1) children that were diagnosed with severe pneumonia before mechanical ventilation; (2) children with other serious diseases; (3) children with conscious or cognitive disorders, or with mental disorders; or (4) those discharged or died during treatment.

2.3. Diagnostic Criteria of VAP. We performed chest X-ray examination on children who have received mechanical ventilation for 48 h or within 48 h of withdrawing the ventilator and intubation. X-ray shows infiltrative shadows or new inflammatory lesions in the lungs, and moist rales could be heard during auscultation. According to the diagnostic criteria of VAP in *Guidelines for the Diagnosis and Treatment of Hospital-Acquired Pneumonia of the Chinese Society of Respiratory Medicine* [9], the child met any of the following two conditions simultaneously: (1) body temperature >38.5°C or <36.5°C, and there were no other obvious external causes; (2) the white blood cell (WBC) $>10 \times 10^9$/L or $<4.0 \times 10^9$/L; (3) increased or purulent respiratory secretions; and (4) new pathogenic bacteria were cultured in secretions.

2.4. Methods. We took 155 children with mechanical ventilation in the pediatric intensive care unit from Oct. 2018 to Oct. 2020 as research objects, retrospectively analyzed their clinical data, and divided them into VAP groups and non-VAP groups according to VAP occurrence. The children's general clinical data include gender, age, underlying diseases, blood transfusion experience, nutritional status, diagnosis, and treatment conditions such as nutritional support methods, intubation methods, application of antibiotics and hormones, and duration of mechanical ventilation retrospectively analyzed. We performed a single-factor analysis on the respective risk factors of the two groups and subsequently incorporated the obtained high-risk factors into the logistic regression model for analysis.

2.5. Statistical Analysis. We adopted the statistical software SPSS19.0 to analyze and process the data included. The measurement data were expressed as $(\overline{x} \pm s)$, and comparison between groups was by the t-test of independent samples; the enumeration data were described by percentage, and the results were taken by χ^2. $P < 0.05$ refers to the statistically significant difference. The multivariate logistic regression analysis included the selected statistically significant variables to determine independent risk factors by steps, and the significance level $\alpha = 0.05$.

3. Results

3.1. General Clinical Data in the Pediatric ICU. 49 cases of real research objects had occurred VAP, the infection rate was 31.62%, and a total of 70 pathogens were detected (Table 1). According to univariate analysis, the general clinical data of patients, including age, underlying diseases, experience of blood transfusion, and malnutrition, were all connected with the occurrence of VAP (Table 2).

3.2. Univariate Analysis of Medication and Diagnosis. Univariate analysis results indicated that the diagnosis and treatment, such as duration of mechanical ventilation, length of ICU stay, and application of invasive operations and hormones and antibiotics, were all concerned with the occurrence of VAP, as shown in Table 3. Variable assignment of VAP in the pediatric ICU: the variable assignment of VAP in the child intensive care unit is shown in Table 4. According to multivariate logistic regression analysis, the duration of mechanical ventilation, invasive procedures, and application of hormones and antacids are all independent risk factors for VAP in the pediatric ICU (Table 5).

3.3. Comparison of Treatment between the Two Groups of Children in the ICU. The VPA group had longer hospital stay than the non-VAP group, and the difference was statistically significant ((20.92 ± 4.16)d, (15.24 ± 3.77)d, $t = 8.4383$, $P \leq 0.001$); the hospitalization cost of the VPA group was substantially higher than that of the non-VAP group [(44.58 ± 1.04) ten thousand Yuan, (3.32 ± 0.43) ten thousand Yuan, $t = 10.6822$, $P \leq 0.001$) (Table 6 and Figure 1).

4. Discussion

Mechanical ventilation is a treatment that applies a ventilator to alter or replace patient's active breathing. It relies on auxiliary equipment to establish the pressure difference between the airway orifice and the alveoli of patient, thus alleviating the respiratory failure or dyspnea of the patient [10, 11]. According to the literature, over 20% children in the pediatric ICU will be treated with mechanical ventilation during treatment [12]. The complication of VAP in children often occurs with the widespread application of mechanical ventilation in the pediatric ICU. For every 24 h increase in

Table 1: Distribution of pathogenic bacteria of VAP in the pediatric ICU.

Species of pathogenic bacteria	Quantity	Composition ratio (%)
Gram-negative bacteria	43	61.43
Acinetobacter baumannii	19	27.14
Klebsiella pneumoniae	8	11.43
Pseudomonas aeruginosa	8	11.43
Stenotrophomonas maltophilia	4	5.71
Escherichia coli	3	4.29
Enterobacter cloacae	1	1.43
Gram-positive bacteria	23	32.86
Staphylococcus aureus	15	21.43
Staphylococcus epidermidis	5	7.14
Enterococcus	3	4.29
Fungi	4	5.71
Candida albicans	4	5.71
Total	70	100

Table 2: Univariate analysis of general clinical data on VAP in the pediatric ICU.

General clinical data	VAP group ($n = 49$)	Non-VAP group ($n = 106$)	X^2	P
Gender (cases)			0.0185	0.8918
Male	26	55		
Female	23	51		
Age (yd)			11.9029	0.0006
<7	28	30		
≥7	21	76		
Underlying disease (cases)			12.2373	0.0005
Yes	26	26		
No	23	80		
Experience of blood transfusion (case)			12.4831	0.0004
Yes	25	24		
No	24	82		
Malnutrition (cases)			5.7306	0.0167
Yes	13	12		
No	36	94		

time of mechanical ventilation, the probability of VAP will increase by 1% to 3%. According to related data [13], the incidence rate of VAP in children with mechanical ventilation was 9%–68%, the mortality was 24%–76%, and the incidence tends to increase year by year. Through the investigation of pathogenic bacteria changes in VAP children, it has been found in related studies that the primary pathogenic bacteria of VAP are Gram-negative bacteria, which have multiple drug resistance [14]. The primary pathogens of VAP in the pediatric ICU, of our hospital during the past 2 years, are *Acinetobacter baumannii*, *Staphylococcus aureus*, *Klebsiella pneumoniae*, and *Pseudomonas aeruginosa*. These results are consistent with those of most research [15–17].

The results of this study's univariate analysis and multivariate logistic regression analysis showed that the duration of mechanical ventilation, invasive operations, and the application of hormones and antacids are all independent risk factors for VAP in the pediatric ICU. The duration of mechanical ventilation is positively correlated with VAP incidence, and the incidence of VAP increases with the extension of mechanical ventilation. This is because the immunity of children under the growing and developing stage is weak due to incomplete body development. During mechanical ventilation, the normal physiological barriers of the nose, throat, and tracheal mucosa of the child are vulnerable to being damaged, which reduces the movement capacity of cilia and increases the viscosity of sputum, as well as chances pathogen invasion and reproduction, thus leading to the occurrence of nosocomial infection [18, 19]. The long-term mechanical ventilation also aggravates lung injury. The long-term upper respiratory tract stimulation of patients increases the accumulation of sputum and oesophagal reflux in children, which increases the probability of pathogens entering the lung tissues and terminal bronchi, thereby further increasing the risk of VAP [20]. Children with invasive operations are prone to VAP, which may be related to the aspiration and regurgitation of colonizing bacteria, the contamination of mechanical ventilation pipes, and the improper operations of medical staff [21, 22]. Glucocorticoids have effects of anti-inflammatory, antiviral, antishock, and immune suppression, but the inappropriate use will reduce the body defence function of children and interfere with electrolyte balance and energy metabolism in

Table 3: Univariate analysis of VAP diagnosis and treatment in the pediatric ICU.

Factors of diagnosis, treatment, and medication	VAP group ($n = 49$)	Non-VAP group ($n = 106$)	X^2	P
Methods of nutritional support (cases)			2.7389	0.0979
Parenteral nutrition	35	61		
Enteral nutrition	14	45		
Intubation method (cases)			1.2000	0.2733
Mouth	25	64		
Transnasal	24	42		
Duration of mechanical ventilation (cases)			10.9749	0.0009
<7 d	17	67		
≥7 d	32	39		
Duration of stay in the ICU (cases)			6.9206	0.0085
<48 h	18	63		
≥48 h	31	43		
Invasive operations (cases)				
Yes	38	53	10.4927	0.0012
No	11	53		
Application of antibiotics (cases)			0.8126	0.3674
Exclusive use	26	48		
Jointly use	23	58		
Application of hormone (cases)			22.0874	0.001
Yes	36	35		
No	13	71		
Application of antibiotics (cases)			20.8232	0.001
Yes	22	86		
No	27	20		
Atomizing inhalation (cases)			2.8590	0.0909
Yes	19	63		
No	30	43		

Table 4: Variable assignment of VAP.

Variables	Explanation of assignment
Age	<7yd = 1, ≥7 = 0
Underlying diseases	YES = 1, NO = 0
Experience of blood transfusion	YES = 1, NO = 0
Malnutrition	YES = 1, NO = 0
Duration of mechanical ventilation	≥7 d = 1, <7 d = 0
Time of admission to the ICU	≥48 h = 1, <48 h = 0
Invasive operations	YES = 1, NO = 0
Use of hormones	YES = 1, NO = 0
Application of antibiotics	YES = 1, NO = 0

the body. This will increase bacterial infection in children and lead to bacterial resistance, resulting in adverse outcomes such as severe pneumonia and immunodeficiency [23, 24] and rising VAP incidence in the pediatric ICU. The use of antacids increases VAP incidence, and its dominant reason may be that antacids can increase the PH value of gastric juice, thus weakening the gastric acid barrier in children. This can lead to gastrointestinal dysbacteriosis in children, leading to infections with multidrug-resistant bacteria such as *Acinetobacter baumannii* and *Klebsiella pneumonia*. On the other hand, the increased application of antacids may also lead to the displacement of the intestinal flora of children or the migration of colonizing bacteria to the lungs caused by oesophagal reflux, thus increasing VAP's probability [25, 26].

Given the independent risk factors for the occurrence of VAP in the pediatric ICU, our hospital has organized and formed the following targeted nursing countermeasures based on routine care. (1) Strengthening the humidification management of artificial airways and adjusting the total amount of humidification in line with the children's disease stouts and the viscosity of sputum. Appropriate airbag inflating pressure should be used, an adequate airtight artificial airway should be formed, the probability of external bacteria entering the respiratory tract should be reduced, and the respiratory infections caused by hand contamination should be prevented; subglottic sputum aspiration should be used, which can effectively clear the sputum and reduce the probability of pulmonary disease; intermittent shutdowns should be taken, the changes in the children's vital signs should be closely monitored, the intubation and ventilator should be removed as soon as possible to reduce the treatment time of mechanical ventilation, and the recovery of children's spontaneous breathing should be promoted [27, 28]. (2) The aseptic operations should be strictly followed when performing invasive operations. The pipeline should be checked immediately after operation to confirm whether it is polluted, the nursing should be strengthened, and the channel should be disinfected in time to prevent the reproduction of colonizing bacteria, thereby reducing the risk of VAP in children. (3) The sensitive drugs should be selected following the detection results of pathogenic bacteria in children, the changes and drug resistance of infected strains should be monitored by the dynamic method, and timely adjustments should be made to the types, duration, and dosage of hormones. (4) Gastric mucosal protectants instead of antacids should be used according to the child's condition to prevent

Table 5: Multivariate logistic regression analysis of VAP in the pediatric ICU.

Factor	β	S. E	Wald X^2	P	OR	95% CI
Mechanical ventilation	1.232	0.421	8.564	0.003	3.428	1.502–7.824
Invasive operations	1.496	0.425	12.390	≤0.001	4.464	1.941–10.286
Application of hormones	2.137	0.736	8.431	0.004	8.474	2.003–35.858
Application of antacids	1.535	0.524	8.581	0.003	4.641	1.662–12.962

Table 6: Comparison of the treatment of children in the ICU between the two groups.

Group	Length of hospital stay (d)	Hospital expenses (ten thousand Yuan)
VAP group ($n = 49$)	20.92 ± 4.16	4.58 ± 1.04
Non-VAP group ($n = 106$)	15.24 ± 3.77	3.32 ± 0.43
T	8.4383	10.6822
P	0.001	0.001

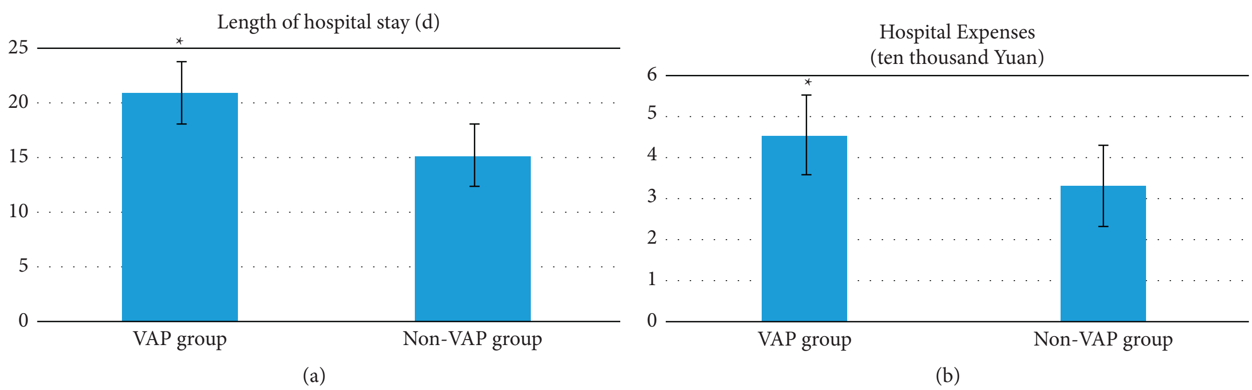

Figure 1: Comparison of the treatment of children in the ICU between the two groups. Compared with the non-VAP group, *$P < 0.05$.

gastrointestinal bleeding; dietary guidance and oral care should be strengthened. According to studies, the nursing countermeasures can remarkably reduce the incidence of VAP and prevent secondary infection, which is an effective measure to improve the patient's quality of life [29, 30].

5. Conclusions

To conclude, children admitted to the pediatric ICU have a high VAP incidence; the primary pathogenic bacteria are Gram-negative bacteria. As the occurrence of VAP is closely related to a variety of factors, we should take targeted nursing countermeasures to reduce the duration of mechanical ventilation and the frequency of invasive operations and use the hormone and antacids rationally to reduce the risk of VAP and improve the prognosis.

Data Availability

The data used to support this study are available from the corresponding author upon request.

Conflicts of Interest

The authors declare no conflicts of interest.

Authors' Contributions

Rong Chen and Yu Liu contributed equally to this study.

References

[1] R. X. Alecrim, M. Taminato, A. Belasco, M. C. B. Longo, D. M. Kusahara, and D. Fram, "Strategies for preventing ventilator-associated pneumonia: an integrative review," *Revista Brasileira de Enfermagem*, vol. 72, no. 2, pp. 521–530, 2019.

[2] C. F. de Lacerda Vidal, A. K. d. L. Vidal, J. G. d. M. Monteiro Jr et al., "Impact of oral hygiene involving toothbrushing versus chlorhexidine in the prevention of ventilator-associated pneumonia: a randomized study," *BMC Infectious Diseases*, vol. 17, no. 1, p. 112, 2017.

[3] M. Chomton, D. Brossier, M. Sauthier et al., "Ventilator-associated pneumonia and Events in pediatric intensive care," *Pediatric Critical Care Medicine*, vol. 19, no. 12, pp. 1106–1113, 2018.

[4] G. Vijay, A. Mandal, J. Sankar, A. Kapil, R. Lodha, and S. K. Kabra, "Ventilator associated pneumonia in pediatric intensive care Unit: incidence, risk factors and Etiological Agents," *Indian Journal of Pediatrics*, vol. 85, no. 10, pp. 861–866, 2018.

[5] G. L. Bassi, E. A. Xiol, F. Pagliara, Y. Hua, and A. Torres, "Body position and ventilator-associated pneumonia

prevention," *Seminars in Respiratory and Critical Care Medicine*, vol. 38, pp. 371–380, 2017.
[6] R. Soussan, C. Schimpf, B. Pilmis et al., "Ventilator-associated pneumonia: the central role of transcolonization," *Journal of Critical Care*, vol. 50, pp. 155–161, 2019.
[7] B. François, A. Cariou, R. Clere-Jehl et al., "Le Gouge A and CRICS-TRIGGERSEP Network and the ANTHARTIC study group prevention of Early ventilator-associated pneumonia after Cardiac Arrest," *New England Journal of Medicine*, vol. 381, pp. 1831–1842, 2019.
[8] Y. Fan, F. Gao, Y. Wu, J. Zhang, M. Zhu, and L. Xiong, "Does ventilator-associated event surveillance detect ventilator-associated pneumonia in intensive care units? A systematic review and meta-analysis," *Critical Care*, vol. 20, no. 1, p. 338, 2016.
[9] F. Álvarez-Lerma, M. Palomar-Martínez, M. Sánchez-García et al., "Prevention of ventilator-associated pneumonia: the Multimodal approach of the Spanish ICU "pneumonia Zero" Program," *Critical Care Medicine*, vol. 46, pp. 181–188, 2018.
[10] R. H. Kallet, "Ventilator Bundles in Transition: from prevention of ventilator-associated pneumonia to prevention of ventilator-associated Events," *Respiratory Care*, vol. 64, no. 8, pp. 994–1006, 2019.
[11] M.-Y. Wang, L. Pan, and X.-J. Hu, "Chest physiotherapy for the prevention of ventilator-associated pneumonia: a meta-analysis," *American Journal of Infection Control*, vol. 47, no. 7, pp. 755–760, 2019.
[12] C.-E. Luyt, G. Hékimian, D. Koulenti, and J. Chastre, "Microbial cause of ICU-acquired pneumonia," *Current Opinion in Critical Care*, vol. 24, no. 5, pp. 332–338, 2018.
[13] S. Burja, T. Belec, N. Bizjak, J. Mori, A. Markota, and A. Sinkovič, "Efficacy of a bundle approach in preventing the incidence of ventilator associated pneumonia (VAP)," *Bosnian Journal of Basic Medical Sciences*, vol. 18, pp. 105–109, 2018.
[14] E. Kocaçal Güler and G. Türk, "Oral chlorhexidine against ventilator-associated pneumonia and Microbial Colonization in intensive care patients," *Western Journal of Nursing Research*, vol. 41, pp. 901–919, 2019.
[15] A. Okgün Alcan, F. Demir Korkmaz, and M. Uyar, "Prevention of ventilator-associated pneumonia: use of the care bundle approach," *American Journal of Infection Control*, vol. 44, pp. e173–e176, 2016.
[16] A. Haghighi, V. Shafipour, M. Bagheri-Nesami, A. Gholipour Baradari, and J. Yazdani Charati, "The impact of oral care on oral health status and prevention of ventilator-associated pneumonia in critically ill patients," *Australian Critical Care*, vol. 30, no. 2, pp. 69–73, 2017.
[17] L. Ayzac, R. Girard, L. Baboi et al., "Ventilator-associated pneumonia in ARDS patients: the impact of prone positioning. A secondary analysis of the PROSEVA trial," *Intensive Care Medicine*, vol. 42, no. 5, pp. 871–878, 2016.
[18] N. Malhan, M. Usman, N. Trehan et al., "Oral care and ventilator-associated pneumonia," *American Journal of Therapeutics*, vol. 26, pp. 604–607, 2019.
[19] V. Kumar, "Ventilator associated pneumonia in children: Current status and Future Prospects," *Indian Journal of Pediatrics*, vol. 85, no. 10, pp. 830-831, 2018.
[20] A. Čiginskienė, A. Dambrauskienė, J. Rello, and D. Adukauskienė, "Ventilator-associated pneumonia due to drug-resistant Acinetobacter baumannii: risk factors and mortality relation with resistance Profiles, and independent predictors of in-hospital mortality," *Medicina (Kaunas, Lithuania)*, vol. 55, p. 49, 2019.
[21] R. Chacko, A. Rajan, P. Lionel, M. Thilagavathi, B. Yadav, and J. Premkumar, "Oral decontamination techniques and ventilator-associated pneumonia," *British Journal of Nursing*, vol. 26, no. 11, pp. 594–599, 2017.
[22] T. H. Craven, G. Wojcik, J. McCoubrey et al., "Ventilator-associated pneumonia surveillance using two methods," *Journal of Hospital Infection*, vol. 104, no. 4, pp. 522–528, 2020.
[23] D. P. Pozuelo-Carrascosa, Á. Herráiz-Adillo, C. Alvarez-Bueno, J. M. Añón, V. Martínez-Vizcaíno, and I. Cavero-Redondo, "Subglottic secretion drainage for preventing ventilator-associated pneumonia: an overview of systematic reviews and an updated meta-analysis," *European Respiratory Review*, vol. 29, no. 155, p. 190107, 2020.
[24] E. Iosifidis, G. Pitsava, and E. Roilides, "Ventilator-associated pneumonia in neonates and children: a systematic analysis of diagnostic methods and prevention," *Future Microbiology*, vol. 13, no. 12, pp. 1431–1446, 2018.
[25] Y. Xu, C. Lai, G. Xu et al., "Risk factors of ventilator-associated pneumonia in elderly patients receiving mechanical ventilation," *Clinical Interventions in Aging*, vol. Volume 14, pp. 1027–1038, 2019.
[26] M. Klompas, "Oropharyngeal decontamination with Antiseptics to prevent ventilator-associated pneumonia: Rethinking the Benefits of chlorhexidine," *Seminars in Respiratory and Critical Care Medicine*, vol. 38, no. 03, pp. 381–390, 2017.
[27] C. Cillóniz, C. Dominedò, and A. Torres, "An overview of guidelines for the management of hospital-acquired and ventilator-associated pneumonia caused by multidrug-resistant Gram-negative bacteria," *Current Opinion in Infectious Diseases*, vol. 32, pp. 656–662, 2019.
[28] A. Rouzé, I. Martin-Loeches, and S. Nseir, "Airway Devices in ventilator-associated pneumonia Pathogenesis and prevention," *Clinics in Chest Medicine*, vol. 39, pp. 775–783, 2018.
[29] S. Osman, Y. M. Al Talhi, M. AlDabbagh, M. Baksh, M. Osman, and M. Azzam, "The incidence of ventilator-associated pneumonia (VAP) in a tertiary-care center: comparison between pre- and post-VAP prevention bundle," *Journal of Infection and Public Health*, vol. 13, no. 4, pp. 552–557, 2020.
[30] A. Coppadoro, G. Bellani, and G. Foti, "Non-pharmacological Interventions to prevent ventilator-associated pneumonia: a literature review," *Respiratory Care*, vol. 64, no. 12, pp. 1586–1595, 2019.

Hindawi
Journal of Healthcare Engineering
Volume 2022, Article ID 1601354, 10 pages
https://doi.org/10.1155/2022/1601354

Research Article

Segmentation and Classification of Glaucoma Using U-Net with Deep Learning Model

M.B. Sudhan,[1] M. Sinthuja,[2] S. Pravinth Raja,[3] J. Amutharaj,[4] G. Charlyn Pushpa Latha,[5] S. Sheeba Rachel,[6] T. Anitha,[5] T. Rajendran ,[7] and Yosef Asrat Waji [8]

[1]*Department of Artificial Intelligence and Machine Learning, MVJ College of Engineering, Bangalore, Karnataka, India*
[2]*Department of Information Science and Engineering, M. S. Ramaiah Institute of Technology, Bangalore, Karnataka, India*
[3]*Department of Computer Science & Engineering, Presidency University, Bangalore, Karnataka, India*
[4]*Department of Information Science and Engineering, RajaRajeswari College of Engineering, Mysore Road, Bangalore, Karnataka, India*
[5]*Saveetha School of Engineering, Saveetha Institute of Medical and Technical Sciences (Deemed to be University), Chennai, Tamilnadu, India*
[6]*Department of Information Technology, Sri Sairam Engineering College (Autonomous), Chennai, Tamilnadu, India*
[7]*Makeit Technologies, Coimbatore, Tamilnadu, India*
[8]*Department of Chemical Engineering, College of Biological and Chemical Engineering Addis Ababa Science and Technology University, Addis Ababa, Ethiopia*

Correspondence should be addressed to T. Rajendran; rajendranthavasimuthuphd@gmail.com and Yosef Asrat Waji; yosef.asrat@aastu.edu.et

Received 2 December 2021; Revised 7 January 2022; Accepted 12 January 2022; Published 16 February 2022

Academic Editor: Enas Abdulhay

Glaucoma is the second most common cause for blindness around the world and the third most common in Europe and the USA. Around 78 million people are presently living with glaucoma (2020). It is expected that 111.8 million people will have glaucoma by the year 2040. 90% of glaucoma is undetected in developing nations. It is essential to develop a glaucoma detection system for early diagnosis. In this research, early prediction of glaucoma using deep learning technique is proposed. In this proposed deep learning model, the ORIGA dataset is used for the evaluation of glaucoma images. The U-Net architecture based on deep learning algorithm is implemented for optic cup segmentation and a pretrained transfer learning model; DenseNet-201 is used for feature extraction along with deep convolution neural network (DCNN). The DCNN approach is used for the classification, where the final results will be representing whether the glaucoma infected or not. The primary objective of this research is to detect the glaucoma using the retinal fundus images, which can be useful to determine if the patient was affected by glaucoma or not. The result of this model can be positive or negative based on the outcome detected as infected by glaucoma or not. The model is evaluated using parameters such as accuracy, precision, recall, specificity, and F-measure. Also, a comparative analysis is conducted for the validation of the model proposed. The output is compared to other current deep learning models used for CNN classification, such as VGG-19, Inception ResNet, ResNet 152v2, and DenseNet-169. The proposed model achieved 98.82% accuracy in training and 96.90% in testing. Overall, the performance of the proposed model is better in all the analysis.

1. Introduction

It is important to diagnose glaucoma early on, which can reduce damage and loss of vision and ensure prompt and appropriate care. The worldwide prevalence of glaucoma for people ages 40 to 80 years is 3.54%. Each one out of 200 individuals aged 40 have glaucoma, which ascends to one in eight by age 80 [1]. Various glaucoma-related risk factors have been established, where the elevated intraocular pressure (IOP) that damages the optic nerves and blood vessels is the significant one. It can lead to total damage to the optic nerves and cause vision loss, if glaucoma is left untreated. This gradual and complete damage to the optic nerves is often followed by only mild or no symptoms, so it is known as the "sneak thief of sight" [2].

Glaucoma is one of the most common causes of irreversible vision loss after cataracts worldwide, accounting for 12 percent of all blindness cases each year. The number of people affected by glaucoma between the ages of 40 and 80 is expected to rise to 111.8 million by 2040. Furthermore, 2.4 percent of all people and 4.7 percent of those aged 70 and up are at risk of developing the disorder. Glaucoma is defined as the degeneration of retinal ganglion cells (RGCs) caused by a variety of disorders. RGC degeneration may result in two major health concerns:

(i) Structural changes to the optic nerve head (ONH) and the nerve fiber layer

(ii) Concurrent functional failures of the field of vision

These two glaucoma side effects might induce peripheral vision loss and, if left unchecked, blindness. Besides early detection and treatment, there is no cure for glaucoma. It is essential in developing automated techniques for detecting glaucoma early on [3]. A retinal fundus image is an essential tool for documenting the optic nerve's health, vitreous, macula, retina, and blood vessels. Ophthalmologists used a fundus camera to take the retinal image. The retinal image was used to diagnose eye disease like glaucoma. Glaucoma is a significant cause of global blindness that cannot be cured. Glaucoma disease can change the cup region's shape, which is the center portion of the ONH. The changes can be used as a parameter for the early indicator of glaucoma. The ONH transmits visual information from retina to the brain [2]. Figure 1 shows the retinal fundus images.

There are no initial glaucoma symptoms but will gradually damage the optic nerves and then results in blindness. Thus, it is crucial to detect glaucoma as early as possible so that it can prevent visual damage. Physiologically, glaucoma is indicated by increased optic cup excavation. The increasing size of the optic cup will impact the size of the optic disc, and this relation is known as a cup-to-disc ratio (CDR). It means ophthalmologists can diagnose glaucoma progression using the value of CDR measurement. The optic cup and optic disc segmentation will support to calculate the CDR from the retinal image [3]. The most noticeable symptom of glaucoma is often a loss of side vision, which might go unnoticed as the condition progresses. This is why glaucoma is sometimes referred to as the sneaky thief of vision. In the case of extreme intraocular pressure levels, headache, sudden eye pain, impaired vision, or the formation of halos around lights might occur.

(i) Loss of vision

(ii) Eye redness

(iii) Hazy eyes (specifically in infants)

(iv) Vomiting or nausea

(v) Vision narrowing (tunnel vision) [4]

There are many forms of glaucoma, including angle-closure glaucoma (ACG), primary open-angle glaucoma (POAG), primary congenital glaucoma (PCG), normal-tension glaucoma (NTG), pseudoexfoliative glaucoma (XFG), traumatic glaucoma (TG), uveitic glaucoma (UG), pigmentary glaucoma (PG), and neovascular glaucoma. The forms vary between different ethnicities in intensity, complexity, and occurrence. Open-angle and angle-closure glaucoma are the two major forms of glaucoma [4]. Figure 2 is shown in optic nerve head structure.

The most common form of glaucoma is open-angle glaucoma also referred to as wide-angle glaucoma. It happens as a result of partial drainage canal blockage in which the pressure slowly rises as the fluid is not properly drained. Symptoms start from vision loss in the periphery and may not be detected until central vision is impaired. Angle-closure glaucoma caused by impulsive and aqueous drainage full blockage is often called acute glaucoma. The pressure increases exponentially, which quickly leads to vision loss. It is formed because of the angle of narrow drainage and the small and droopy iris. The iris is pulled inside the anterior angle of the eye against the trabecular mesh network (drainage canals) leading to blockage and bulging of the iris forward [5].

In most situations, this damage is caused by abnormal rise of the pressure inside the eye. The secretion rate is equalised to the drainage rate in healthy eyes. Glaucoma occurs when the drainage canal was partially or entirely blocked, leading to a surge in pressure known as intraocular pressure that affects the optic nerves used to relay signals to the brain where it is possible to perceive visual information. If this damage is left untreated, complete blindness will result. Hence, it is essential to diagnose glaucoma in early stage.

In this research, early prediction of glaucoma using deep learning technique is proposed. In this proposed deep learning model, the ORIGA dataset is used for the evaluation of glaucoma images. For segmentation, the U-Net segmentation model is implemented in this model and a pretrained transfer learning model, DenseNet-201, is used for feature extraction along with deep convolution neural network (DCNN). The DCNN approach is used for the classification, and the final results will be representing whether the glaucoma infected or not.

2. Related Works

Several study models have been developed by various authors for the segmentation and classification of glaucoma detection, each employing a different methodology and algorithm from the others. As will be detailed more, the majority of them are deep learning-based models with varying levels of performance analysis. The fact that retinal disease is such a terrible ailment makes it difficult to detect and distinguish between the two conditions.

The most common approach used in most of the studies to diagnose glaucoma was the acquisition of retinal scans using digital capture equipment for visual content, which was the most common procedure used in most of the studies. The scan images were then preprocessed to equalize the

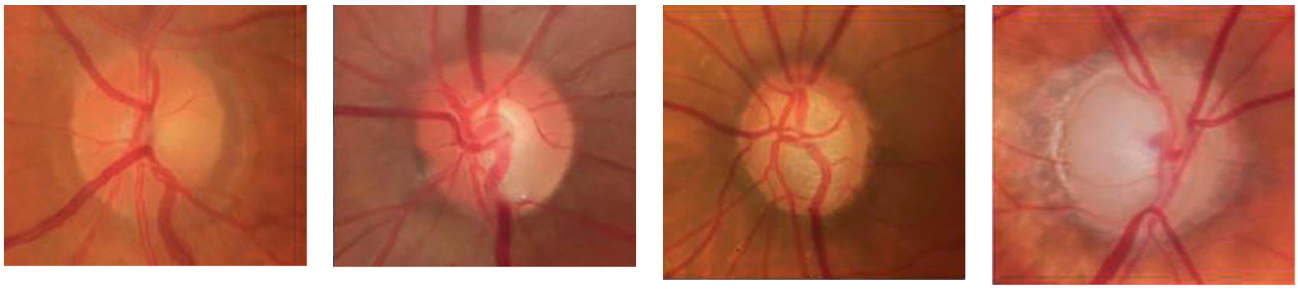

(a) (b) (c) (d)

Figure 1: Retinal fundus images: (a) healthy eye, (b) early glaucoma, (c) moderate glaucoma, and (d) deep glaucoma [2].

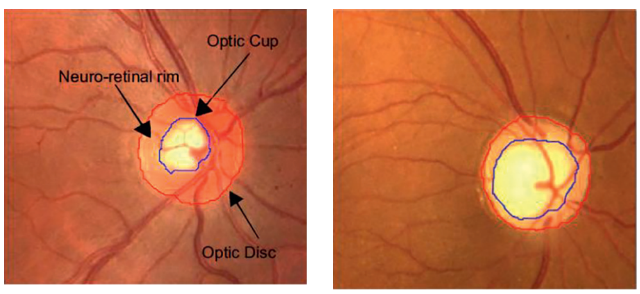

(a) (b)

Figure 2: Structure of optic nerve head: (a) normal and (b) glaucoma [3].

anomalies. During the preprocessing stage, blood vessels were segmented and depicted in order to create a vessel free image. Furthermore, feature extraction was utilized to efficiently reduce the dimensions of an image in order to represent the interesting areas of an image as a compact feature vector that could be used for precisely classifying the large amount of data collected. Techniques such as textures, pixel intensity values, FFT coefficients, and histogram models were employed in the process of feature extraction and classification. Data analysis and classification were accomplished through the use of image classification, which involved examining the numerical aspects of an image. The data set was divided into several classifications based on the results, such as normal or glaucoma, to facilitate analysis.

Prastyo et al. applied the U-Net segmentation technique to retinal fundus images in order to segment the optic cup. The segmentation of the optic cup and the optic disc aids in the achievement of improved performance in the detection of glaucoma disease. The ROI based on the optic disc image was cropped and segmented with the help of the U-Net algorithm. In order to obtain optimal training, an adaptive learning rate optimization technique was applied, and the model attained a dice coefficient rate of 98.42 percent and a loss rate of 0.15 percent during testing [6]. A model of attention-based CNN (AG-CNN) for identifying glaucoma was proposed by Li et al. and it was tested on a database known as the large-scale attention-based glaucoma database (LAG). The removal of large levels of redundancy from fundus images may result in a reduction in the accuracy and reliability of glaucoma identification. The AG-CNN model took this into consideration and made a decision on it. In this model, subnets of attention prediction, pathological region localization, and classification were combined to form an overall model. When it comes to detecting glaucoma, the model has a 96.2 percent accuracy rate and an AUC of 0.983. In several cases, the ROI was only partially highlighted, and the minor problematic regions were not correctly identified [7].

For the purpose of automatically segmenting the glaucoma images, MacCormick et al. developed a new glaucoma detection algorithm based on spatial detection. The method was developed on the basis of four assumptions: segmentation, deformation, shape, and size of the images were all taken into consideration. After a segmentation of the cup and disc of the retinal fundus images was completed, an estimation of the cup/disc ratio (CDR) in 24 cross sections was performed to generate the pCDR (CDR profile). The results were compared between healthy discs and glaucomatous discs on both external and internal validation, with the AUROC for internal validation being 99.6 percent and for external validation being 91 percent [8].

Juneja et al. proposed an artificial intelligence glaucoma expert system that was based on the segmentation of the optic cup and disc. In order to automate the identification of glaucoma, a deep learning architecture was designed, with CNN serving as the core element. In this model, two neural networks were integrated and used for segmenting images of the optic disc and cup of fundus, which were taken from different cameras. By examining 50 images, the model was able to segment the cup with 93 percent accuracy and the disc with 95.8 percent accuracy [9]. To diagnose glaucoma in retinal fundus images, Diaz-Pinto et al. used five ImageNet trained models, including the VGG-16, VGG-19, ResNet50, Inception-v3, and Xception, all of which were trained using ImageNet data. Performance study revealed that the Xception model outperformed the other models by obtaining better results, and the Xception model was then tested with five publicly accessible datasets for glaucoma diagnosis to confirm its superiority. The Xception model was more efficient than other commonly used models [10] due to its higher level of computing efficiency.

With the help of deep learning, SynaSreng et al. developed an automated two-stage model for glaucoma diagnosis and classification. Initially, the optic disc area was segmented using DeepLabv3+ architecture, but the encoder segment was replaced with several deep CNNs after the initial segmentation. For classification, a trained DCNN was employed with three approaches: transfer learning, feature descriptors learning using SVM, and constructing an ensemble of techniques in transfer learning and feature descriptors learning, respectively. It was possible to segment the optic discs using DeepLabv3+ and MobileNet architectures because of the integration of the two systems. Five separate glaucoma datasets were used in the classification process, which was done using an ensemble of algorithms. Finally, utilizing the ACRIMA dataset, DeepLabv3+ and MobileNet were able to achieve an accuracy of 99.7 percent for OD segmentation and 99.53 percent for classification using DeepLabv3+ and MobileNet [11].

To diagnose diabetic retinopathy, Mateen et al. developed a fundus image classification model that combined the VGG-19 with principal component analysis (PCA) and singular value decomposition (SVD) and used the VGG-19. The model's performance in region segmentation, feature extraction and selection, and classification has been improved by combining the Gaussian mixture model with the VGG, PCA, and SVD [12, 13]. Fu et al. employed two deep learning-based glaucoma detection techniques, multilabel segmentation network (M-Net) and disc-aware ensemble network, to detect the presence of glaucoma (DENet). Initially, M-Net was utilized to solve the segmentations of both the optic cup and the disc, and DENet was used to combine the deep hierarchical context of the global fundus image with the local optic disc region in the initial stages. The CDR was calculated based on the segmentation of the optic cup and disc in order to determine the glaucoma risk. It is possible to get accurate results from an image without segmenting it using the DENet [13].

Jiang et al. developed a new multipath recurrent U-Net model for segmenting retinal fundus image. The efficiency of the model was validated by the performance of two segmentation processes like optic cup and disc segmentation and retinal vessel segmentation. The model achieved 99.67% accuracy for optic disc segmentation, 99.50% for optic cup segmentation, and 96.42% for retinal vessel segmentation by using the Drishti-GS1 dataset [14].

Mahum et al. proposed an early-stage glaucoma diagnosis model based on deep learning-based feature extraction. Images were preprocessed in the first phase before the region of interest was retrieved using segmentation. Then, using the hybrid features descriptors, such as CNN, histogram of oriented gradients, local binary patterns, and speeded up robust features, characteristics of the optic disc were recovered from images including optic cup. Furthermore, HOG was used to extract low-level features, while the LBP and SURF descriptors were used to extract texture features. Furthermore, CNN was used to compute high-level characteristics. The feature selection and ranking technique of maximum relevance minimum redundancy was applied. Finally, multiclass classifiers such as SVM, KNN, and random forest were used to determine if fundus images were healthy or diseased [15].

Gheisari et al. proposed a new method for detecting glaucoma that combined temporal (dynamic vascular) and spatial (static structural) data. A CNN and recurrent neural network (RNN) classification model that extracts not just the spatial features in the fundus images but additionally the temporal features inherent in the consecutive images was developed. Because CNN was designed to diagnose glaucoma, it was built on spatial information encoded in images. CNN was used with RNN for increased performance in detecting glaucoma based on both temporal and spatial features [16].

3. Proposed Methodology

In this research, the deep learning-based models are proposed for segmentation and classification of glaucoma detection using retinal fundus images collected from ORIGA database. For segmentation, the U-Net architecture is used and a pretrained DenseNet-201 architecture was used to extract the features from the segmented image. For classification, the DCNN architecture is used to classify the images for detecting glaucoma.

3.1. Dataset Description. The ORIGA dataset is used in this research for evaluation [17]. The data set contains 650 images of the color retinal fundus with the extension (.jpg) and ground truth with the extension (.mat). The retinal images were collected by the Singapore Malay Eye Study (SiMES). ORIGA database shares clinical ground truth retinal images with the public and provides open access for researchers to benchmark their computer-aided segmentation algorithms. ORIGA dataset is open for online access upon request. After preprocessing, 650 image data were divided into 488 image data as training data, 162 image data as testing data [1, 6, 8, 11, and 13].

3.2. Segmentation Using U-Net. The deep learning algorithm-based U-Net architecture is implemented for optic cup segmentation. The U-Net architecture is the most widely used segmentation architecture for medical images. The architecture of the U-Net segmentation process is shown in Figure 3. The retinal fundus image is given as input; the ROI based on optical disc image is cropped and segmented using deep learning algorithm. The output of the segmentation will be based on the optic cup, where the optic cup outline is masked as shown in Figure 3.

Before segmenting the image, in preprocessing, the ground truth (mask) image was changed to (.png) so that an algorithm could process it. To get the Optic Disk (OD) mask, we used the equation (disc = double (mask > 0)), while for Optic Cup (OC), we employed the equation (cup = double (mask > 1)). After that, we took the region of interest (ROI) from the retinal fundus image by using the ground truth from OD to take OC's closest area.

A contracting path (left side) and an expansive path (right side) are included in this architecture, joined by multilevel skip connections (middle). Input to the contracting path is retinal fundus images, and predictions are generated from a final layer following the expansive path. Each convolution layer has filter banks, each applying 3×3 padded convolutions followed by a rectified linear activation unit whose functional form is $f(z) = \max(0, z)$ [18–20].

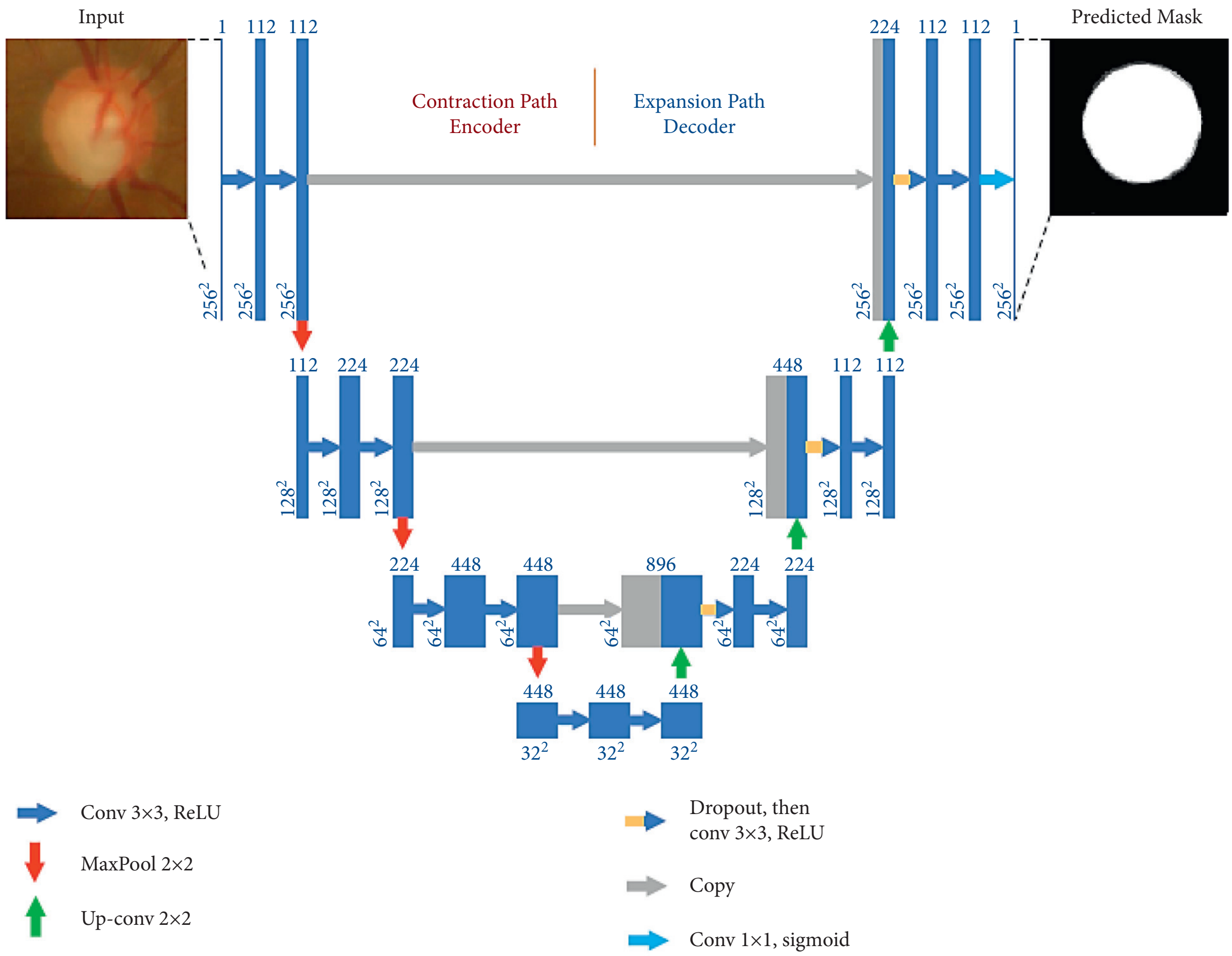

FIGURE 3: U-Net architecture of segmentation [6].

There are three convolutional blocks each in the contracting and expansive paths. Two convolutional layers consist of a block in the contracting path followed by a max-pooling layer with a pool size of 2×2. A block contains a 2×2 upsampling layer in the expansive path, a concatenation from the contracting path with the corresponding block (i.e., a merged layer), a dropout layer, and two convolutional layers. The connecting path includes two convolutional layers. Finally, a 1×1 convolutional layer with a sigmoid activation and a single filter to output pixel-wise class scores is the final output layer. Every convolution layer in blocks 1, 2, and 3 includes 112, 224, and 448 filters in the contracting path, while blocks 5, 6, and 7 include 224, 122, and 122 filters in the expansive path individually. There are 448 filters in every convolutional layer in the connecting path. The proposed DCNN differs from the original U-Net in the number of filters chosen for the model to fit into the GPU memory in each convolution layer and the use of dropouts in the expansive path.

3.3. DenseNet-201 with CNN. A DCNN model with pretrained DenseNet-201 is proposed in this research [21]. This DenseNet-201 model is based on deep transfer learning (DTL) as it is implemented to identify the glaucoma images from the input dataset by classifying the retinal fundus images. To extract features from the dataset, a pretrained DenseNet-201 model is used, and the DCNN model is used for classification. 256×256 is the input image size. The architecture of the DenseNet-201 with DCNN is shown in Figure 4.

DCNN usually performs well with a larger data set over a smaller one. TL could be useful in those CNN applications where the data set is not huge. For applications with comparatively smaller datasets, TL's concept utilizes the learned model from large datasets such as ImageNet. This removes the need for a large dataset and decreases the lengthy training time as needed when generated from scratch by the deep learning algorithm. TL is a deep learning method that uses a model trained for a single assignment as a starting point to train a model for a similar assignment. It is typically much quicker and simpler to fine-tune a TL network than training a network from scratch. By leveraging common models that have been already trained on large data sets, it allows the training of models using similar small labeled data. Training time and computing resources can be significantly decreased. With TL, the model does not need to be trained for as many epochs (a complete training period on the entire dataset) like a new model.

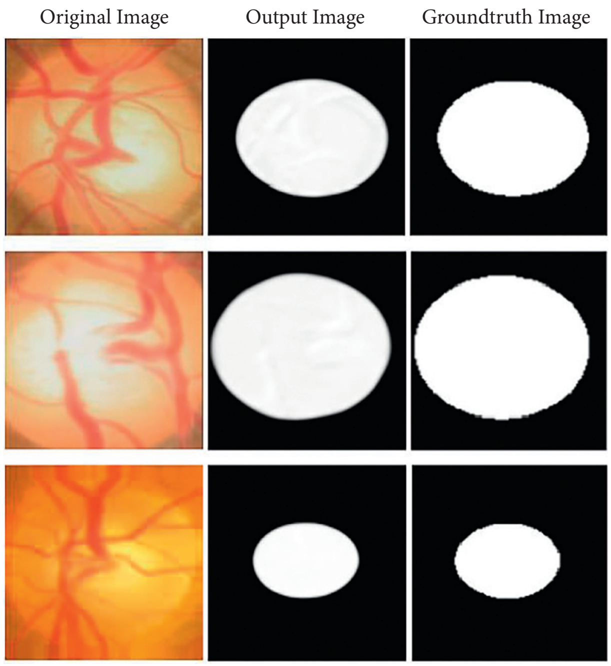

Figure 4: U-Net output image compared with ground truth image.

Because of the feature reuse possibility by various layers, the DenseNet-201 uses the condensed network that provides simple to train and highly parametrical effective models and expands variety in the following layer input and enhances the execution. On various data sets, such as CIFAR-100 and ImageNet, DenseNet-201 has shown remarkable results. Direct connections from each previous layer to every subsequent layer are added to boost connectivity in the DenseNet-201 model as shown in Figure 5.

The concatenation of feature can be mathematically expressed as

$$fc^i = \mathrm{NL}_i\left(fc^0, fc^1, \ldots, fc^{i-1}\right). \quad (1)$$

Here, $\mathrm{NL}_i(\bullet)$ was a nonlinear transformation that could be described as batch normalization (BN) composite function, accompanied by a rectified linear unit function (ReLU) and a (3×3) convolution layer.

For ease of implementation, $[fc^0, fc^1, \ldots, fc^{i-1}]$ indicates the feature map concatenation according to layers 0 to $i-1$ are combined into a single tensor. Dense blocks are generated in the network architecture for downsampling purposes, divided by layers known as transition layer consisting of BN followed by a 1×1 convolution layer and an average 2×2 pooling layer. DenseNet-201's growth rate defines how dense architecture produces better results, and the "H" hyperparameter denotes it. Because of its structure, where feature maps were regarded as a network's global state, DenseNet-201 performs adequately well even with a minimal growth rate. Therefore, all function maps of the preceding layers have access to each successive layer. Each layer includes "H" feature maps to the global state where each count of input feature maps at i^{th} layers $(fm)^i$ was expressed as

$$(fm)^i = H^0 + H(i-1). \quad (2)$$

Here, the input layer channels are given by H^0. A 1×1 convolution layer preceding each 3×3 convolution layer is added to increase computational performance, which reduces the input feature maps that were usually higher than the feature maps of output H. The 1×1 conv layer was known as the bottleneck layer and generates feature maps. FC layers act as a classifier in the classification stage. It uses extracted features and assesses the probability of a segment in the image. The architecture of DenseNet-201 is shown in Figure 6.

To create nonlinearity and to reduce overfitting, the activation function and dropout layer are typically used. Two dense layers of 128 and 64 neurons were implemented for classification. The DenseNet-201 feature extraction model was used for binary classification preceded by the sigmoid activation function to replace the softmax activation function utilized in the DenseNet-201 design. In the FC dense layer, every neuron was FC in the prior layer. The FC layer "i" whose input 2D feature map was extended to a 1D feature vector can be mathematically described.

$$\begin{aligned} v^{i-1} &= \mathrm{Bernoulli}(p), \\ z^{i-1} &= v^{i-1} * d^{i-1}, \\ z^i &= f\left(x^k z^{i-1} + u^i\right). \end{aligned} \quad (3)$$

Here, the Bernoulli function produces a vector $v^i = 1$ randomly with a certain probability that obeys the 0-1 distribution. The dimension of the vector is d^{i-1}. The dropout strategy is used by the initial two layers of the FC layer to randomly block some neurons based on a defined probability, which efficiently avoids overfitting situations in deep networks. The terms "x" and "u" describe the FC layer's respective weighting and offset parameters. The function of sigmoid activation was to convert nonnormalized outputs to 0 or 1 as binary outputs. Therefore, it helps to classify the images as nonglaucoma or glaucoma. The sigmoid function can be expressed as

$$S = \frac{1}{1 + e^{-\left(\sum x_i \cdot z_i\right)}}, \quad (4)$$

where the neuron output is S. The weights and inputs, respectively, represent x_i and z_i.

4. Performance Analysis

The performance analysis of the proposed DCNN with the U-Net and DenseNet-201 model is assessed using the dataset in this section. The model is evaluated using parameters such as accuracy, precision, recall, specificity, and F-measure. Also, a comparative analysis is conducted for the validation of the model proposed. The output is compared to other current deep learning models used for CNN classification, such as VGG-19, Inception ResNet, ResNet 152v2, and DenseNet-169. On the MATLAB 2019a Simulink toolbox, all the experiments are implemented and carried out. The dataset is split into 75% for training and 30% for validating the performance analysis.

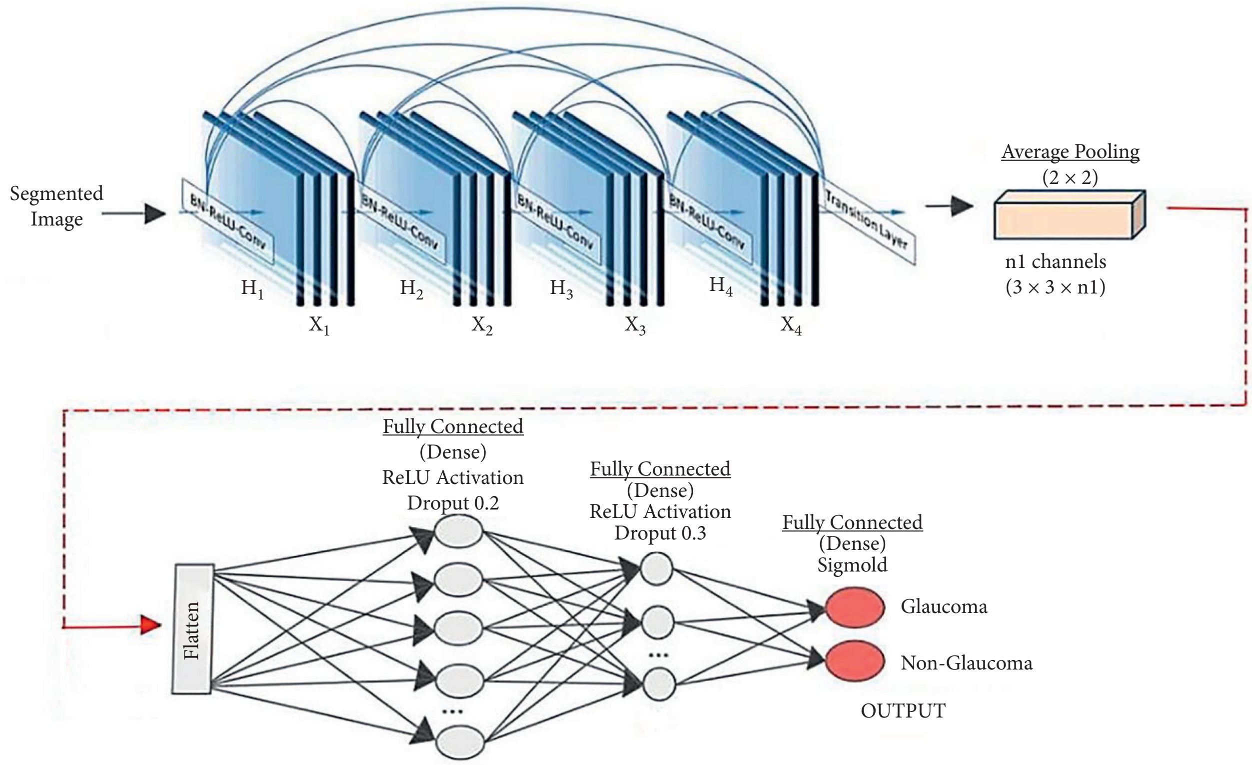

Figure 5: Feature extraction using pretrained DenseNet-201 model and classification using DCNN [21].

4.1. Performance Metrics. The primary objective of this research is to detect the glaucoma using the retinal fundus images, which can be useful to determine if the patient was affected by glaucoma or not. The result of this model can be positive or negative based on the outcome detected as infected by glaucoma or not. The true positive, true negative, false positive, and false negative are properly analyzed to estimate the outcome of this model.

TP: it indicates the total predictions correctly obtained in positive cases

FP: it indicates the total predictions incorrectly obtained in positive cases

TN: it indicates the total predictions correctly obtained in negative cases

FN: it indicates the total incorrect predictions in negative cases

Accuracy is the model's estimation of the performance subset. It is the primary output metric used to calculate the efficiency of the classification process. It is usually used to estimate when both the positive and negative classes are equally important. It is calculated using the following equation.

$$\text{Accuracy} = \frac{\text{TP} + \text{TN}}{\text{TP} + \text{TN} + \text{FP} + \text{FN}}. \quad (5)$$

As shown in Table 1, the proposed model achieved better classification accuracy in both training and testing for classifying the glaucoma fundus images. The model obtained 98.82% training accuracy, which is 1.09% to 3.96% improved compared with other techniques. The testing accuracy is 96.90%, which is 1.36% to 5.26% increased performance than the other existing compared models. The graphical chart of the comparison is plotted in Figure 7.

Precision is a positive predictive value. It is the measure of the cumulative predictive positive value of the correctly predicted positive observation. The lower precision value reflects that a large number of false positives have affected the classification model. The measure of precision can be computed using the following equation.

$$\text{Precision} = \frac{\text{TP}}{\text{TP} + \text{FP}}. \quad (6)$$

The estimation of precision is tabulated in Table 2, which shows that the proposed model has achieved better precision value than the compared models. The model obtained 98.63% precision rate in training, which was 1.1% to 4.8% improved compared with other techniques. The precision rate in testing was 96.45%, which was 1.08% to 4.9% increased performance than the other existing compared models. Figure 8 shows the comparison of precision analysis.

The sensitivity is also referred to as recall. It is the ratio of properly predicted positive evaluation of the overall positive predictive value. The lower recall value reflects that a large number of false negative values have affected the classification model. The recall estimation can be calculated using the following equation.

$$\text{Recall} = \frac{\text{TP}}{\text{TP} + \text{FN}}. \quad (7)$$

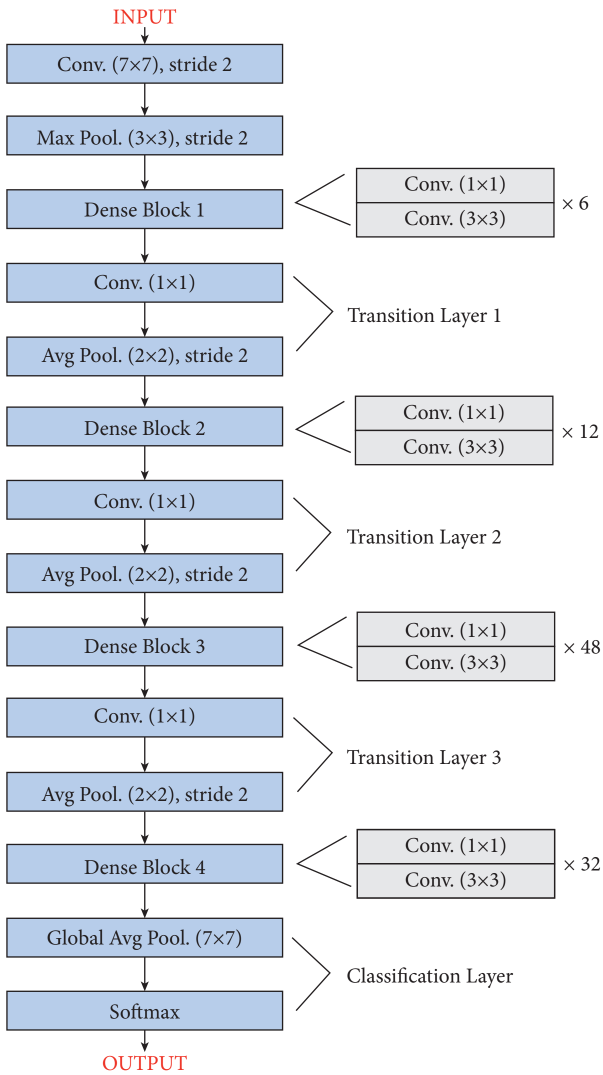

Figure 6: DenseNet-201 architecture [21].

Table 1: Performance analysis of accuracy.

Models	Training	Testing
VGG-19	97.73	95.54
Inception ResNet	94.86	91.64
ResNet 152v2	97.56	93.21
DenseNet169	97.14	95.45
Proposed	98.82	96.90

The proposed model has gained better recall or sensitivity rate as tabulated in Table 3. The model obtained 98.95% recall rate in training, which was 1.1% to 4.05% improved compared with other techniques. The recall rate in testing was 97.03%, which was 1.3% to 5.06% better performance than the other existing compared models. The comparison graph is plotted, as shown in Figure 9.

As per this model, specificity is the prediction that healthy subjects do not have the disease. It is the percentage of subjects with no illness that is tested as negative. The specificity estimation can be calculated using the following equation.

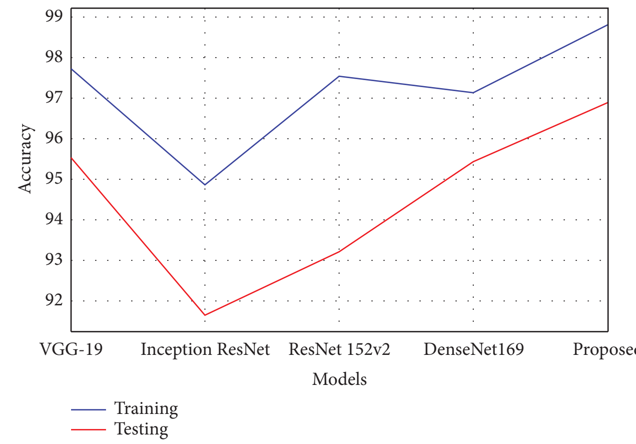

Figure 7: Graphical plot of accuracy.

Table 2: Performance analysis of precision.

Models	Training	Testing
VGG-19	97.30	94.70
Inception ResNet	93.81	91.52
ResNet 152v2	97.28	93.02
DenseNet169	97.49	95.37
Proposed	98.63	96.45

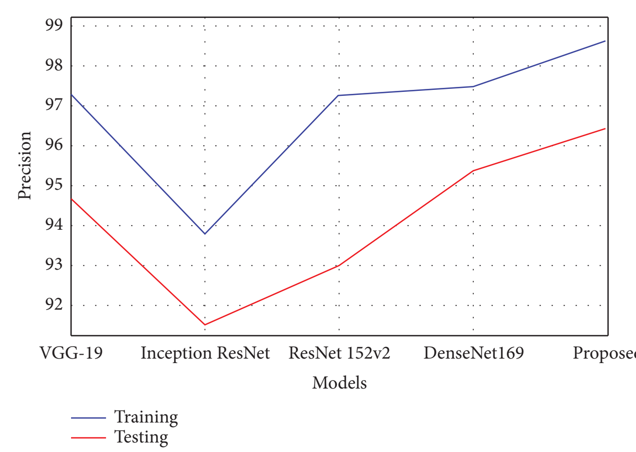

Figure 8: Graphical plot of precision.

Table 3: Performance analysis of recall.

Models	Training	Testing
VGG-19	97.84	95.62
Inception ResNet	94.90	91.97
ResNet 152v2	97.62	94.05
DenseNet169	97.35	95.69
Proposed	98.95	97.03

$$\text{Specificity} = \frac{TN}{TN + FP}. \tag{8}$$

As shown in Table 4, the proposed model has obtained a better specificity rate than the other comparative models of deep learning.

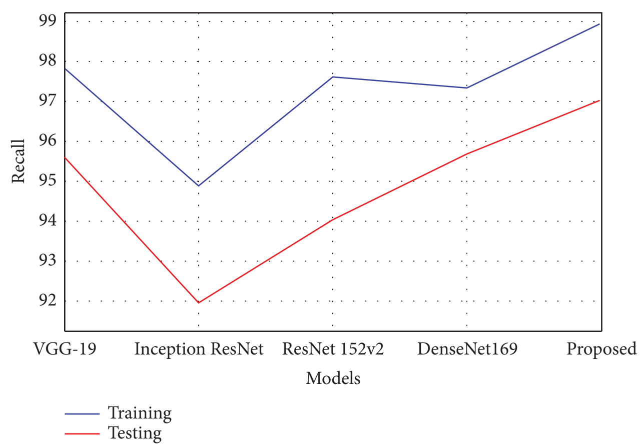

FIGURE 9: Graphical plot of recall.

TABLE 4: Performance analysis of specificity.

Models	Training	Testing
VGG-19	97.24	95.67
Inception ResNet	94.05	89.92
ResNet 152v2	97.28	92.73
DenseNet169	97.00	94.89
Proposed	98.15	96.33

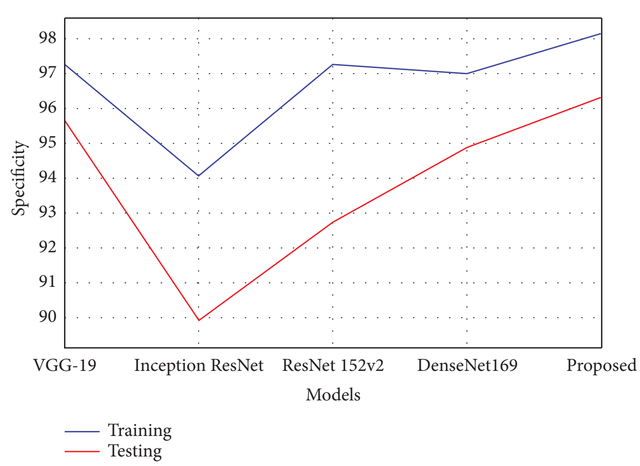

FIGURE 10: Graphical plot of specificity.

The model obtained 98.15% specificity rate in training, which was 0.8% to 4.1% improved compared with other techniques. The specificity rate in testing was 96.33%, which was 0.6% to 6.4% better performance than the other existing compared models. Figure 10 represents the comparison of specificity estimated.

The F-measure estimates the accuracy of the test and is defined as the weighted harmonic mean of the precision of the test and the recall. The accuracy does not take into account how the data was distributed. The F-measure is then utilized to manage the distribution problem with accuracy. When the data set has imbalance classes, it was useful. The F-measure estimation can be calculated using the following equation.

TABLE 5: Performance analysis of F-measure.

Models	Training	Testing
VGG-19	97.52	95.39
Inception ResNet	94.79	91.55
ResNet 152v2	97.35	93.14
DenseNet169	97.07	95.09
Proposed	98.50	96.28

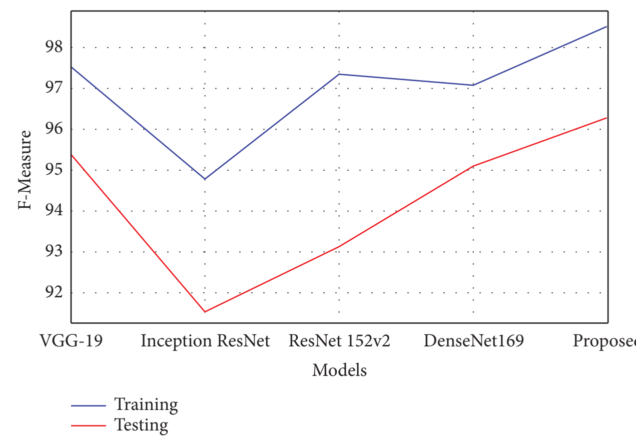

FIGURE 11: Graphical plot of F-measure.

$$\text{F} - \text{measure} = \frac{2 \times \text{Precision} \times \text{Recall}}{\text{Precision} + \text{Recall}}. \quad (9)$$

The F-measure estimation is tabulated in Table 5, which represents that the proposed model has achieved better F-measure value than the compared models. The model obtained 98.50% F-measure rate in training, which was 0.9% to 3.7% improved compared with other techniques. The F-measure rate in testing was 96.28%, which was 0.8% to 4.7% better performance than the other existing compared models. Figure 11 shows the comparison of F-measure analysis.

In this research, by comparing all the models like VGG-19, Inception ResNet, ResNet 152v2, and DenseNet-169, the proposed model has achieved better performance in both the training and testing stages. The least performance achieved model is Inception ResNet and DenseNet-169 has some close performance to the proposed model.

5. Conclusion

In this research, early prediction of glaucoma detection model using deep learning technique was proposed. In this proposed deep learning model, the ORIGA dataset was used for the evaluation of glaucoma images. 75% of the data was used for training and 25% of data was used for testing. For segmentation, the U-Net segmentation model was implemented in this model and a pretrained transfer learning model, DenseNet-201, was used for feature extraction along with DCNN. The DCNN approach was used to classify the images for glaucoma detection. The primary objective of this model was to detect the glaucoma using the retinal fundus images, which can be useful to determine whether the patient is affected by glaucoma or not. By segmenting the fundus images, the optic cup region was segmented and compared with ground truth images from the dataset. After segmentation, the features were extracted from the images using DenseNet model and classified using DCNN. The proposed model obtained 98.82% training accuracy, which was 1.09% to 3.96% higher compared with other models and the testing accuracy was 96.90%, which was 1.36% to 5.26% higher than the compared models. By analyzing the performance analysis, the results obtained by the proposed model are efficient and the reason for not achieving 100% results was due to the false positives and false negatives. In future, this imbalance issue will be sorted out by improving the classifier and reducing the threshold. This model can be useful for various medical image segmentation and classification processes like diabetic retinopathy, brain tumor detection, breast cancer detection, etc.

Data Availability

The datasets used and/or analyzed during the current study are available from the corresponding author on reasonable request.

Conflicts of Interest

The authors declare no conflicts of interest.

Authors' Contributions

Authors Sudhan M B and Sinthuja M are responsible for project design and concept. Authors Pravinth Raja S and J Amutharaj are responsible for surveys and content writing and proofreading. Authors Sheeba Rachel S and Charlyn pushpaLatha G are responsible for algorithm design, development, and proofreading.

References

[1] M. C. V. Stella Mary, E. B. Rajsingh, and G. R. Naik, "Retinal fundus image analysis for diagnosis of glaucoma: a comprehensive survey," *IEEE Access*, vol. 4, pp. 4327–4354, 2016.

[2] S. Anindita and H. Agus, "Automatic glaucoma detection based on the type of features used: a review," *Journal of Theoretical and Applied Information Technology*, vol. 72, no. 3, pp. 366–375, 2015.

[3] A. Sarhan, J. Rokne, and R. Alhajj, "Glaucoma detection using image processing techniques: a literature review," *Computerized Medical Imaging and Graphics: The Official Journal of the Computerized Medical Imaging Society*, vol. 78, Article ID 101657, 2019.

[4] B. N. Kumar, R. P. Chauhan, and N. Dahiya, "Detection of glaucoma using image processing techniques: a review," in *Proceedings of the 2016 International Conference on Microelectronics, Computing and Communications (MicroCom)*, pp. 1–9, Durgapur, India, January 2016.

[5] D. M. S. Barros, J. C. C. Moura, C. R. Freire, A. C. Taleb, R. A. M. Valentim, and P. S. G. Morais, "Machine learning applied to retinal image processing for glaucoma detection: review and perspective," *BioMedical Engineering Online*, vol. 19, no. 20, pp. 1–21, 2019.

[6] P. H. Prastyo, A. S. Sumi, and A. Nuraini, "Optic cup segmentation using U-net architecture on retinal fundus image," *Journal of Information Technology and Computer Engineering*, vol. 4, no. 2, pp. 105–109, 2020.

[7] L. Li, M. Xu, H. Liu et al., "A large-scale database and a CNN model for attention-based glaucoma detection," *IEEE Transactions on Medical Imaging*, vol. 39, no. 2, pp. 413–424, 2020.

[8] I. J. C. MacCormick, B. M. Williams, Y. Zheng et al., "Accurate, fast, data efficient and interpretable glaucoma diagnosis with automated spatial analysis of the whole cup to disc profile," *PLoS One*, vol. 14, no. 1, Article ID e0209409, 2019.

[9] M. Juneja, S. Singh, N. Agarwal et al., "Automated detection of Glaucoma using deep learning convolution network (G-net)," *Multimedia Tools and Applications*, vol. 79, no. 21-22, pp. 15531–15553, 2020.

[10] A. Diaz-Pinto, S. Morales, V. Naranjo, T. Köhler, M. Jose, and A. Navea, "CNNs for automatic glaucoma assessment using fundus images: an extensive validation," *BioMedical Engineering Online*, vol. 18, no. 29, pp. 1–19, 2019.

[11] N. M. SynaSreng, K. Hamamoto, and K. Y. Win, "Deep learning for optic disc segmentation and glaucoma diagnosis on retinal images," *Applied Sciences*, vol. 10, no. 4916, pp. 1–19, 2020.

[12] M. Mateen, J. Wen, S. Sun, and Z. Huang, "Fundus image classification using VGG-19 architecture with PCA and SVD," *Symmetry*, vol. 11, no. 1, pp. 1–12, 2019.

[13] H. Fu, J. Cheng, Y. Xu, and J. Liu, "Glaucoma detection based on deep learning network in fundus image," in *Deep Learning and Convolutional Neural Networks for Medical Imaging and Clinical Informatics, Advances in Computer Vision and Pattern Recognition*, L. Lu, X. Wang, G. Carneiro, and L. Yang, Eds., Springer, Cham, pp. 119–137, 2019.

[14] Y. Jiang, F. Wang, J. Gao, and S. Cao, "Multi-path recurrent U-net segmentation of retinal fundus image," *Applied Sciences*, vol. 10, no. 3777, pp. 1–17, 2020.

[15] R. Mahum, S. U. Rehman, O. D. Okon, A. Alabrah, T. Meraj, and H. T. Rauf, "A novel hybrid approach based on deep CNN to detect glaucoma using fundus imaging," *Electronics*, vol. 11, no. 1, Article ID 26, 2022.

[16] S. Gheisari, S. Shariflou, J. Phu et al., "A combined convolutional and recurrent neural network for enhanced glaucoma detection," *Scientific Reports*, vol. 11, no. 1945, pp. 1–11, 2021.

[17] Z. Zhang, F. S. Yin, J. Liu et al., "ORIGA(-light): an online retinal fundus image database for glaucoma analysis and research," *Annual International Conference of the IEEE Engineering in Medicine and Biology Society*, vol. 2010, no. 1, pp. 3065–3068, 2010.

[18] E. A. M. Yasir and H. I. Bashir, "Classification of diabetic retinopathy using stacked autoencoder-based deep neural network," *Journal of Computational Science and Intelligent Technologies*, vol. 1, no. 1, pp. 9–14, 2020.

[19] C. Narmatha, A. Hayam, and A. H. Qasem, "An analysis of deep learning techniques in neuroimaging," *Journal of Computational Science and Intelligent Technologies*, vol. 2, no. 1, pp. 7–13, 2021.

[20] P. Manimegalai and P. K. Jayalakshmi, "A study on diabetic retinopathy detection using image processing," *Journal of Computational Science and Intelligent Technologies*, vol. 2, no. 1, pp. 21–26, 2021.

[21] A. Jaiswal, N. Gianchandani, D. Singh, V. Kumar, and M. Kaur, "Classification of the COVID-19 infected patients using DenseNet201 based deep transfer learning," *Journal of Biomolecular Structure and Dynamics*, vol. 39, no. 1, pp. 1–8, 2020.

Hindawi
Journal of Healthcare Engineering
Volume 2023, Article ID 9829560, 1 page
https://doi.org/10.1155/2023/9829560

Retraction

Retracted: MiR-139-5p Inhibits the Development of Gastric Cancer through Targeting TPD52

Journal of Healthcare Engineering

Received 12 November 2022; Accepted 12 November 2022; Published 26 January 2023

Journal of Healthcare Engineering has retracted the article titled "MiR-139-5p Inhibits the Development of Gastric Cancer through Targeting TPD52" [1] due to concerns that the peer review process has been compromised.

Following an investigation conducted by the Hindawi Research Integrity team [2], significant concerns were identified with the peer reviewers assigned to this article; the investigation has concluded that the peer review process was compromised. We therefore can no longer trust the peer review process, and the article is being retracted with the agreement of the Chief Editor.

References

[1] Y. Li, Y. Sun, Z. Li, S. Li, and C. Wu, "MiR-139-5p Inhibits the Development of Gastric Cancer through Targeting TPD52," *Journal of Healthcare Engineering*, vol. 2022, Article ID 4033373, 10 pages, 2022.

[2] L. Ferguson, "Advancing Research Integrity Collaboratively and with Vigour," 2022, https://www.hindawi.com/post/advancing-research-integrity-collaboratively-and-vigour/.

Hindawi
Journal of Healthcare Engineering
Volume 2022, Article ID 4033373, 10 pages
https://doi.org/10.1155/2022/4033373

Research Article

MiR-139-5p Inhibits the Development of Gastric Cancer through Targeting TPD52

Yuanbo Li[1], Yan Sun[2], Zhenlu Li[1], Shikuan Li[1], and Changliang Wu[1]

[1]*The Department of Emergency Surgery, The Affiliated Hospital of Qingdao University, Qingdao, Shandong Province, China*
[2]*Neuroelectro Physiological Laboratory, People's Hospital of Linzi District, Zibo, Shandong Province, China*

Correspondence should be addressed to Changliang Wu; qdfywucl@qdu.edu.cn

Received 29 November 2021; Revised 30 December 2021; Accepted 17 January 2022; Published 16 February 2022

Academic Editor: Enas Abdulhay

Background. Many researchers have confirmed that miRNAs are involved in the pathogenesis of gastric cancer (GC). This study focused on investigating the specific functions of miR-139-5p in GC. *Methods*. MiR-139-5p and TPD52 expressions were observed by qRT-PCR or western blot in GC. The functional mechanism of miR-139-5p was explored by the luciferase reporter assay, transwell assay, and MTT assay. *Results*. MiR-139-5p downregulation and TPD52 upregulation were detected in GC. Adverse clinical features and prognosis in GC patients were related to low miR-139-5p expression. MiR-139-5p overexpression restrained GC cell proliferation and metastasis. Furthermore, miR-139-5p directly targeted TPD52. TPD52 silencing blocked GC progression. And TPD52 upregulation weakened the antitumor effect of miR-139-5p in GC. *Conclusion*. MiR-139-5p inhibits GC cell proliferation and metastasis through downregulating TPD52.

1. Introduction

Gastric cancer (GC) ranks third in human malignancies [1]. Moreover, it ranks first in gastrointestinal malignancies, accounting for 95% of gastric malignancies [2]. Now, surgery is still the most important treatment of early GC, and it is also the main method for the treatment of GC [3]. Due to the late detection of GC, the effect of surgery is not good. And 5-year survival rate is maintained at about 30% [4]. Additionally, patients with early GC have a better prognosis after treatment. The postoperative effect is better for patients over 60 years old, while patients under 30 years old tend to have poor prognosis [5]. Therefore, it is necessary to strengthen the attention to the symptoms of early GC and the monitoring of high-risk groups in order to increase the detection rate of patients with early GC.

MicroRNAs (miRNAs) regulate tumorigenesis by affecting their target genes [6–8]. Recently, more and more miRNAs are found to express abnormally in GC, such as miR-216a [9], miR-937 [10], and miR-1271 [11]. In particular, miR-139 participated in human GC development [12]. Moreover, abnormal miR-139-5p expression often occurs in various cancers and diseases, including neurodegeneration [13], breast cancer [14], glioblastoma [15], and thyroid carcinoma [16]. Recently, it has been reported that obesity was associated with miR-139-5p [17]. Collectively, miR-139-5p is an important biomarker for human diseases, including cancers.

It has been proposed that tumor protein D52 (TPD52), which belongs to the TPD52-like protein family, functions as an oncogene in prostate cancer [18]. Upregulation of TPD52 was first found in human breast cancer [19]. TPD52 overexpression was also detected in various human malignant tumors [20]. In addition, TPD52 expression was associated with the systemic progression of prostate cancer [21]. High TPD52 expression had an association with bad prognosis in breast cancer [22] and ovarian carcinoma [23] patients. More importantly, oncogenic TPD52 regulated cell metastasis in prostate cancer [24]. Nonetheless, the mechanism of TPD52 in GC is still unclear. Here, the functional mechanism of TPD52 and miR-139-5p was investigated in GC. The relationship between miR-139-5p and prognosis in GC patients was also analyzed.

2. Materials and Methods

2.1. Clinical Tissues. Sample tissues were obtained from sixty-seven GC patients in The Affiliated Hospital of Qingdao University. All participators provided informed consent. All GC patients only received surgery. Theses tissues were stored in a −80°C refrigerator. Our research was approved by the Institutional Ethics Committee of The Affiliated Hospital of Qingdao University.

2.2. Cell Culture and Transfection. HGC-27, SGC-7901, MKN-45, and AGS GC cell lines and GES-1 cells (ATCC, USA) were inoculated in the RPMI-1640 medium with FBS and incubated under suitable conditions (37°C, 5% CO_2).

MiR-139-5p mimics and inhibitor, TPD52 vector, and siRNA (GeneCopoeia, Guangzhou, China) were transfected in GC cells by using Lipofectamine 2000 (Invitrogen, Carlsbad, USA).

2.3. Transwell Assay. Transwell chamber (8 μm pore size; Millipore) is used to evaluate the migratory and invasive ability of GC cells. The upper chamber was put with 4×10^4 GC cells with the uncoated membrane. 10% FBS was added in the lower chamber. The coated membrane was used for the invasion assay. These cells were cultured for 24 h. Finally, moved cells were observed by using a microscope.

2.4. MTT Assay. Transfected cells (3×10^3 cells/well) were incubated in 96-well plates at 0, 24, 48, 72, and 96 h. Cell viability was evaluated by the MTT assay. The absorbance (OD = 490 nm) was examined with a spectrophotometer (Thermo Scientific).

2.5. Quantitative RT-PCR. TRIzol reagent (Invitrogen, Carlsbad, USA) was applied to extract total RNA containing miRNA. Quantitative RT-PCR was performed with SYBR Green PCR Master Mix and primers. GAPDH or U6 was used as an internal reference. MiR-139-5p and TPD52 expressions were assessed by the $2^{-\triangle\triangle ct}$ method. The primers are shown in Table 1.

2.6. Western Blot Analysis. RIPA lysis buffer was applied to extract protein samples. Protein was then separated by 10% SDS-PAGE and transferred into the PVDF membrane. Protein was incubated with anti-TPD52 (Abcam, Cambridge, USA) and anti-GAPDH antibodies (Epitomics, Burlingame, USA) at 4°C overnight. Next, the membrane was incubated with the corresponding secondary antibody (Abcam, Cambridge, USA). Finally, protein bands were observed by ECL (ECL, Pierce).

2.7. Dual-Luciferase Assay. pGL3 vectors (Promega, Madison, USA) with the 3′-UTR of wild-type or mutant TPD52 were built. GC cells with miR-139-5p mimics and the above vector were incubated for 48 h. Finally, luciferase activity was detected through the dual-luciferase assay system (Promega, USA).

2.8. Statistical Analysis. Data were calculated by SPSS 19.0 and GraphPad Prism 6. Differences were calculated by the chi-squared test. Survival analysis was performed by the Kaplan–Meier method with the log-rank test. All experiments were performed in 3 replicates. Significant difference indicated $P < 0.05$.

3. Results

3.1. MiR-139-5p Downregulation and TPD52 Upregulation Were Detected in GC. MiR-139-5p expression was evaluated in GC. MiR-139-5p in GC tissues was downregulated compared to the control (Figure 1(a), $P < 0.01$). Consistently, miR-139-5p was downregulated in HGC-27, SGC-7901, MKN-45, and AGS cells compared to GES-1 cells (Figure 1(b), $P < 0.05$ or 0.01). Meanwhile, the expression of TPD52 in GC was also detected. TPD52 upregulation was found in GC tissues (Figure 1(c), $P < 0.01$) and cells (Figure 1(d), $P < 0.05$ or 0.01). Additionally, lymph metastasis and TNM stage in GC patients were related to low miR-139-5p expression ($P < 0.05$, Table 2). And low miR-139-5p expression was related to worse prognosis (Figure 2) in GC patients.

3.2. MiR-139-5p Impeded GC Progression. The specific function of miR-139-5p in GC was investigated in HGC-27 cells containing miR-139-5p mimics or inhibitor. MiR-139-5p expression was enhanced by its mimics (Figure 3(a), $P < 0.01$) and lowered by its inhibitor (Figure 3(b), $P < 0.01$) in HGC-27 cells. Functionally, miR-139-5p overexpression restrained HGC-27 cell proliferation (Figure 3(c), $P < 0.01$). MiR-139-5p downregulation facilitated GC cell proliferation (Figure 3(d), $P < 0.01$). Meanwhile, miR-139-5p overexpression weakened the migratory and invasive abilities (Figures 4(a) and 4(b), $P < 0.01$) in HGC-27 cells, but miR-139-5p downregulation showed an opposite effect (Figures 4(a) and 4(b), $P < 0.01$). Collectively, miR-139-5p impeded GC progression.

3.3. TPD52 Was a Downstream Target of MiR-139-5p in GC. Furthermore, TargetScan (http://www.targetscan.org/vert_71/) shows that TPD52 can bind to miR-139-5p (Figure 5(a)). Luciferase reporter gene assay showed that miR-139-5p mimics blocked wild-type TPD52 luciferase activity (Figure 5(b), $P < 0.01$), which had little effect on that of mutant TPD52. Additionally, miR-139-5p had a negative association with TPD52 expression in GC tissues ($R^2 = 0.7531$, $P < 0.001$; Figure 5(c)). Consistently, miR-139-5p overexpression reduced TPD52 expression in HGC-27 cells when miR-139-5p downregulation accelerated TPD52 expression (Figures 5(d) and 5(e), $P < 0.01$). Therefore, miR-139-5p directly targets TPD52 and negatively regulates its expression in GC.

Table 1: Primer sequence.

	Primers	
MiR-139-5p	F: 5′-GCTCTACAGTGCACGTGTC-3′	R: 5′-GTGCAGGGTCCGAGGT-3′
TPD52	F: 5′-GGAAGAGGAGCAGGAAGAGC-3′	R: 5′-GATGACTGAGCCAACAGAG-3′
U6	F: 5′-CTCGCTTCGGCAGCACA-3′,	R: 5′-AACGCTTCACGAATTTGGT-3′
GAPDH	F: 5′-GCTGGCGCTGAGTATGGAGT-3′	R: 5′-CACAGTCTCTTGGTGATGG-3′

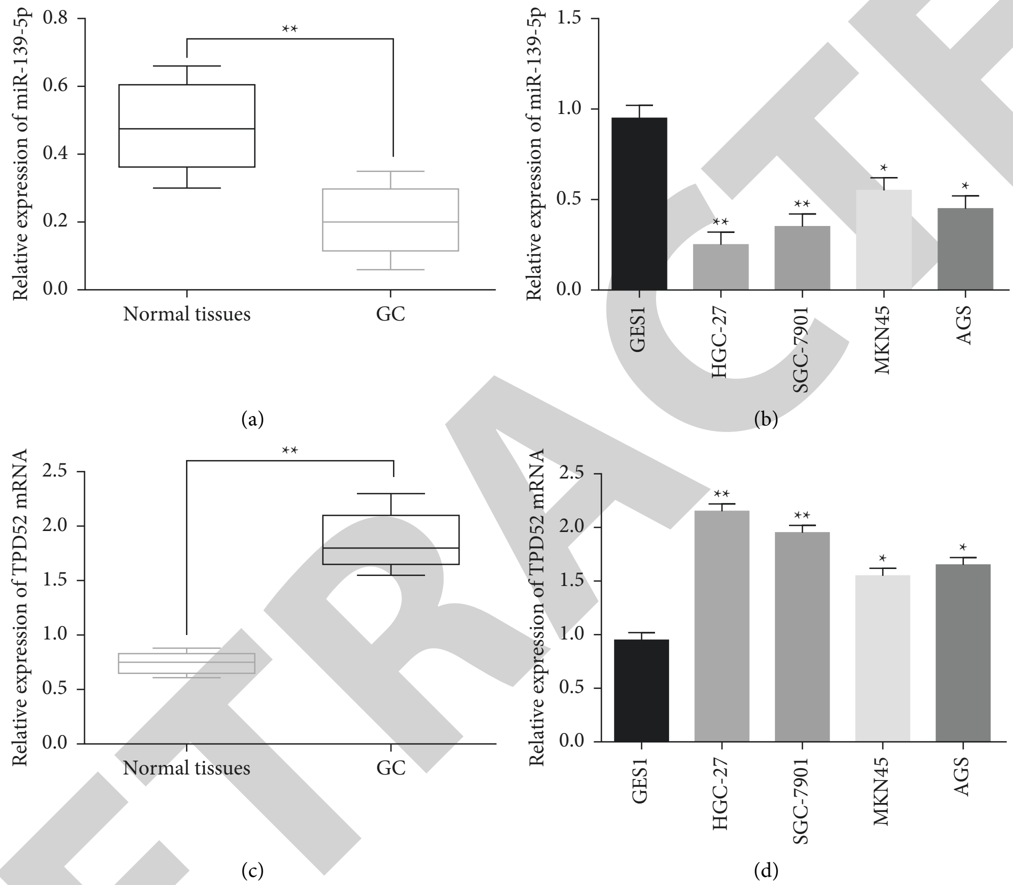

Figure 1: Downregulation of miR-139-5p and upregulation of TPD52 were detected in GC. (a) MiR-139-5p expression in GC tissues ($n = 67$). (b) MiR-139-5p expression in HGC-27, SGC-7901, MKN-45, AGS, and GES-1 cell lines. (c) TPD52 expression in GC tissues ($n = 67$). (d) TPD52 expression in HGC-27, SGC-7901, MKN-45, AGS, and GES-1 cell lines. $^{*}p < 0.05$ and $^{**}p < 0.01$.

3.4. TPD52 Silence Blocked GC Progression. Then, TPD52 function was investigated in HGC-27 cells with its siRNA. TPD52 expression was reduced by its siRNA (Figure 6(a), $P < 0.01$). Functionally, si-TPD52 restrained HGC-27 cell proliferation (Figure 6(b), $P < 0.01$). Meanwhile, HGC-27 cell migration was suppressed by si-TPD52 (Figure 6(c), $P < 0.01$). Similarly, downregulation of TPD52 also inhibited cell invasion in GC cells (Figure 6(d), $P < 0.01$). In brief, TPD52 silencing can inhibit cell proliferation and metastasis in GC.

3.5. Upregulation of TPD52 Partially Impaired the Antitumor Effect of MiR-139-5p in GC. Finally, HGC-27 cells with miR-139-5p mimics and TPD52 vector were employed to further explore their relationship. As we expected, TPD52 vector recovered the reduced TPD52 expression mediated by miR-139-5p mimics in HGC-27 cells (Figure 7(a), $P < 0.01$). Then, TPD52 vector lessened the suppressive effect of miR-139-5p on HGC-27 cell proliferation and metastasis (Figures 7(b)–7(d), $P < 0.01$). In brief, upregulation of TPD52 partially impaired the antitumor effect of miR-139-5p in GC.

4. Discussion

The high tumor recurrence rate and mortality of GC are mainly caused by systemic metastasis. Many researchers have proposed that abnormally expressed miRNAs can affect the occurrence and progression of GC [25, 26]. MiR-139-5p can affect the diagnosis, prognosis, and treatment of malignancy [27]. For instance, miR-139-5p affected cell metastasis in colorectal cancer [28]. Especially, miR-139 was

Table 2: Relationship between miR-139-5p expression and clinicopathological characteristics of GC patients.

Characteristics	Cases	MiR-139-5p		P value
		High	Low	
Age (years)				0.586
≥60	30	11	19	
< 60	37	17	20	
Gender				0.421
Male	40	18	22	
Female	27	10	17	
Tumor size (cm)				0.052
<5	42	18	24	
≥5	25	10	15	
TNM stage				0.038*
I + II	47	20	27	
III + IV	20	8	12	
Differentiation				0.199
Low	35	15	20	
Moderate or well	32	13	19	
Lymph metastasis				0.007*
Present	50	20	30	
Absent	17	8	9	

Statistical analyses were performed by the χ^2 test. $^*p < 0.05$ was considered significant.

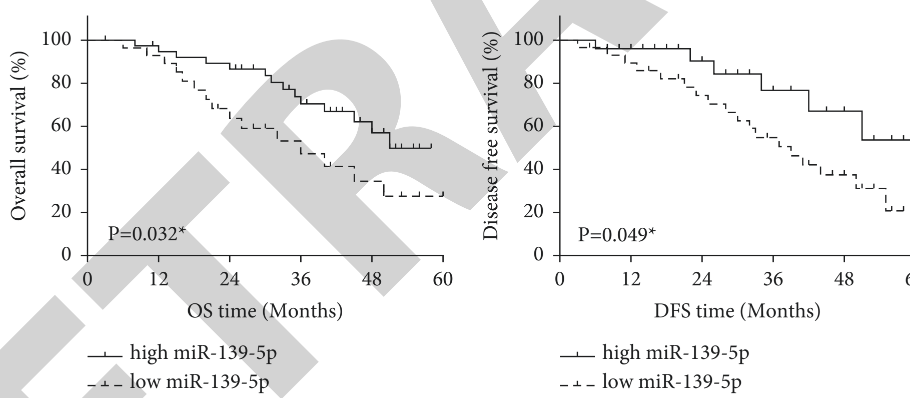

(a) (b)

Figure 2: MiR-139-5p could predict the prognosis of GC patients. (a) High-miR-139-5p-expression patients showed longer OS. (b) High-miR-139-5p-expression patients showed longer DFS.

associated with lymph node metastasis of human metastatic gastric tumors [29]. Moreover, miR-139-5p regulated aerobic glycolysis via inhibiting PRKAA1 in GC [30]. Thus, the role of miR-139-5p was explored in GC.

Here, miR-139-5p downregulation was detected in GC. Adverse clinical features and prognosis in GC patients were associated with its downregulation. The results are similar to previous studies [29]. Moreover, miR-139-5p overexpression restrained GC cell proliferation, migration, and invasion. Furthermore, miR-139-5p directly targets TPD52. More importantly, miR-139-5p hindered GC progression by downregulating TPD52. Similarly, miR-139-5p also repressed cell proliferation in uterine leiomyoma through mediating TPD52 [31]. In addition, we also found that TPD52 was upregulated in GC, and TPD52 silencing can block GC progression.

Previous studies have shown that TPD52 is a target of many miRNAs. Kumamoto et al. reported that TPD52 knockdown can restrain the metastasis of lung squamous cell carcinoma [32]. The same effect of TPD52 on GC was also identified in this study. Moreover, miR-34a and miR-449 repressed breast cancer cell metastasis via targeting the oncogenic TPD52 [33, 34]. MiR-218 also inhibited tumor growth through targeting TPD52 in prostate cancer [35]. These previous research studies are consistent with our conclusions in GC. In a word, the antitumor effect of miR-139-5p is affected by TPD52 in GC.

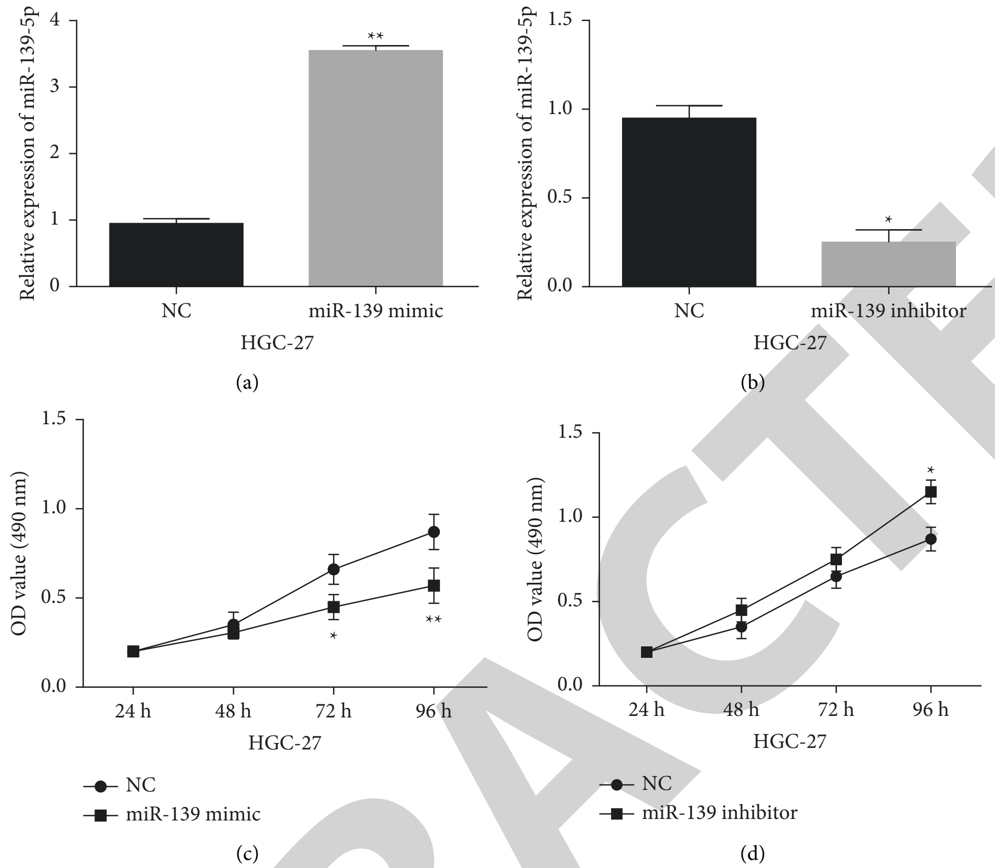

Figure 3: MiR-139-5p repressed cell proliferation in GC. ((a), (b)) MiR-139-5p expressions in HGC-27 cells with miR-139-5p mimics or inhibitor. ((c), (d)) Cell proliferation in HGC-27 cells with miR-139-5p mimics or inhibitor. $^{**}p < 0.01$.

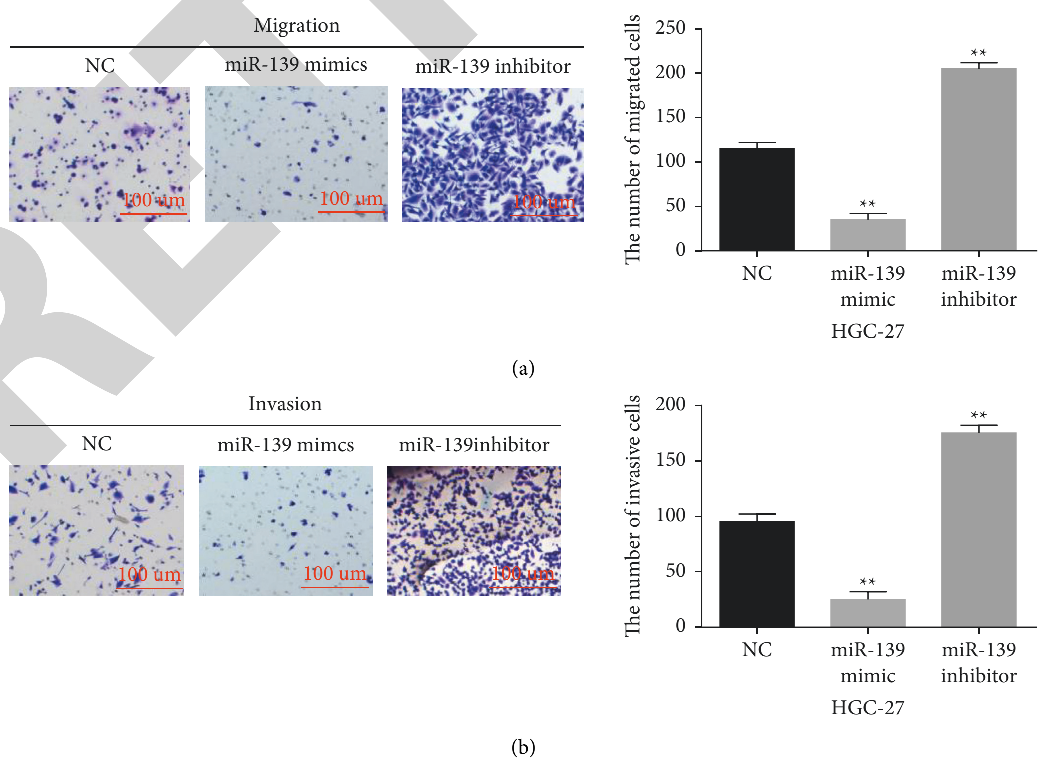

Figure 4: MiR-139-5p overexpression repressed cell migration and invasion in GC. ((a), (b) Cell migration and invasion in HGC-27 cells with miR-139-5p mimics or inhibitor. $^{**}p < 0.01$.

	Predicted consequential pairing of target region (top) and miRNA (bottom)
Position 1085-1092 of TPD52 3' UTR	5' ...AAACUGUAAAAUGAUACUGUAGA...
	|||||||
hsa-miR-139-5p	3' UGACCUCUGUGCACGUGACAUCU

(a)

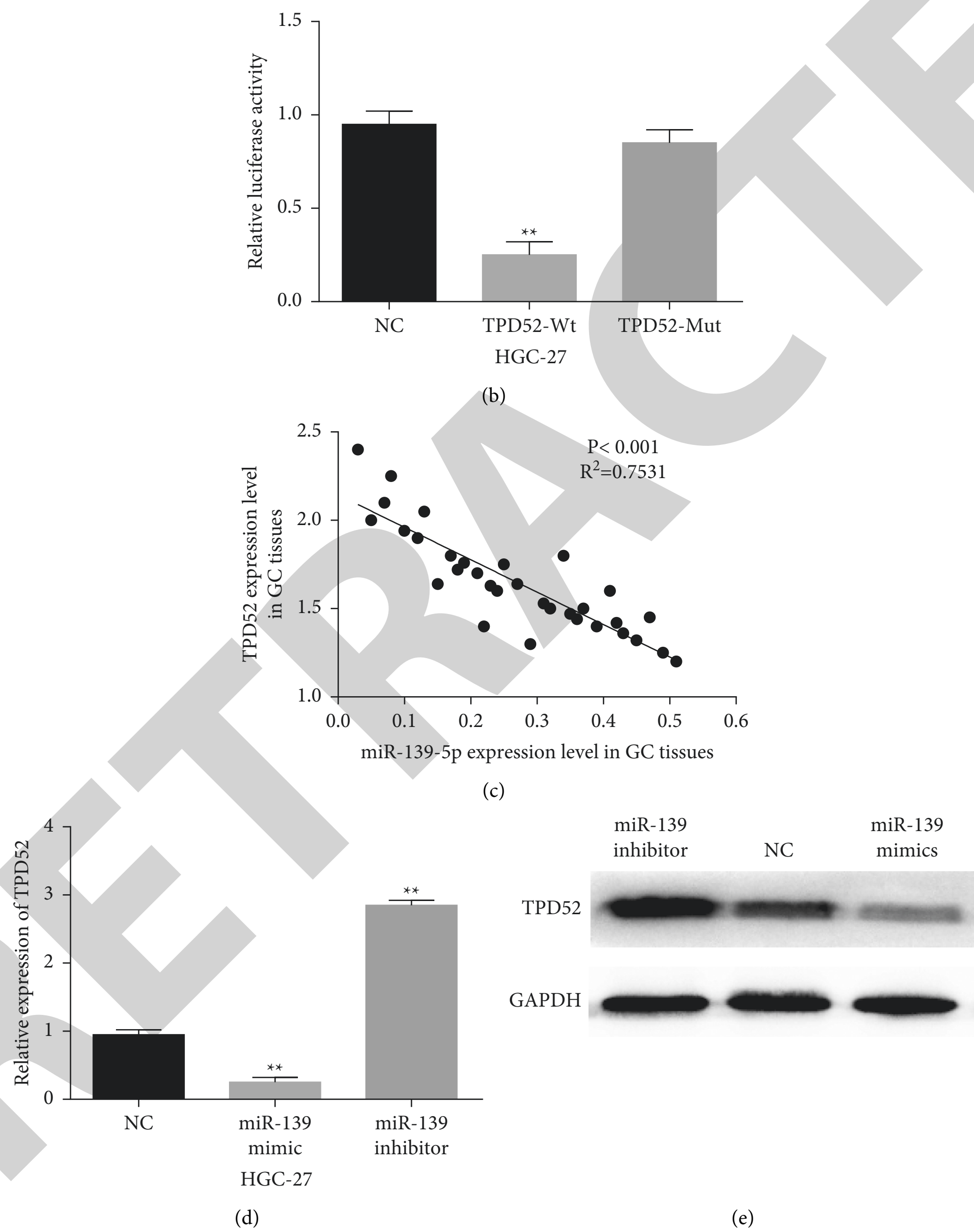

Figure 5: MiR-139-5p directly targets TPD52. (a) The binding site between miR-139-5p and TPD52. (b) Luciferase reporter assay. (c) The correlation between miR-139-5p and TPD52 expression. ((d), (e)) The mRNA and protein expression of TPD52 were analyzed in HGC-27 cells containing miR-139-5p mimics or inhibitor. $^{**}p < 0.01$.

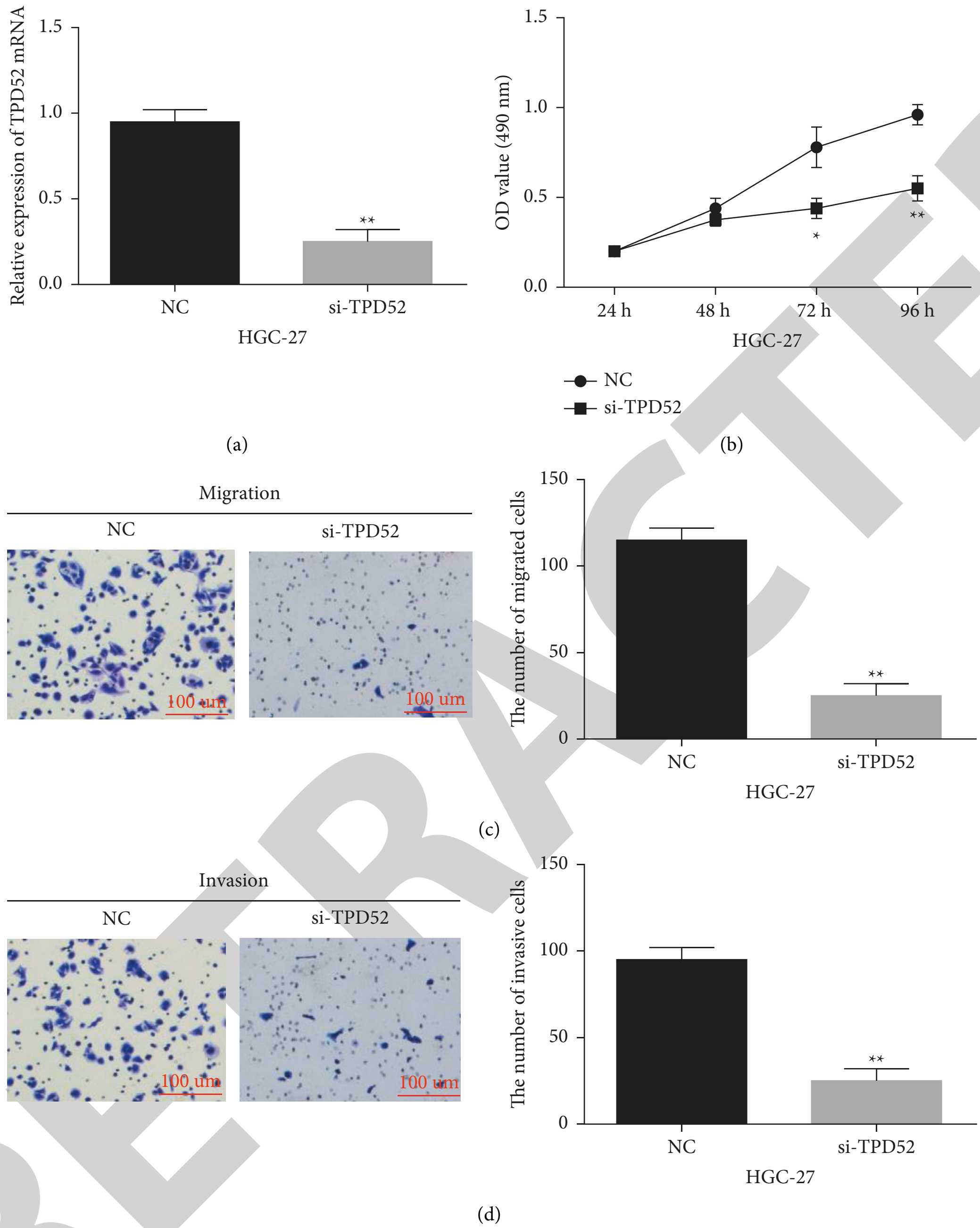

Figure 6: TPD52 silence blocked GC progression. (a) TPD52 expression in HGC-27 cells with TPD52 siRNA. ((b), (c), (d)) si-TPD52 regulated HGC-27 cell proliferation, migration, and invasion. $^{**}p < 0.01$.

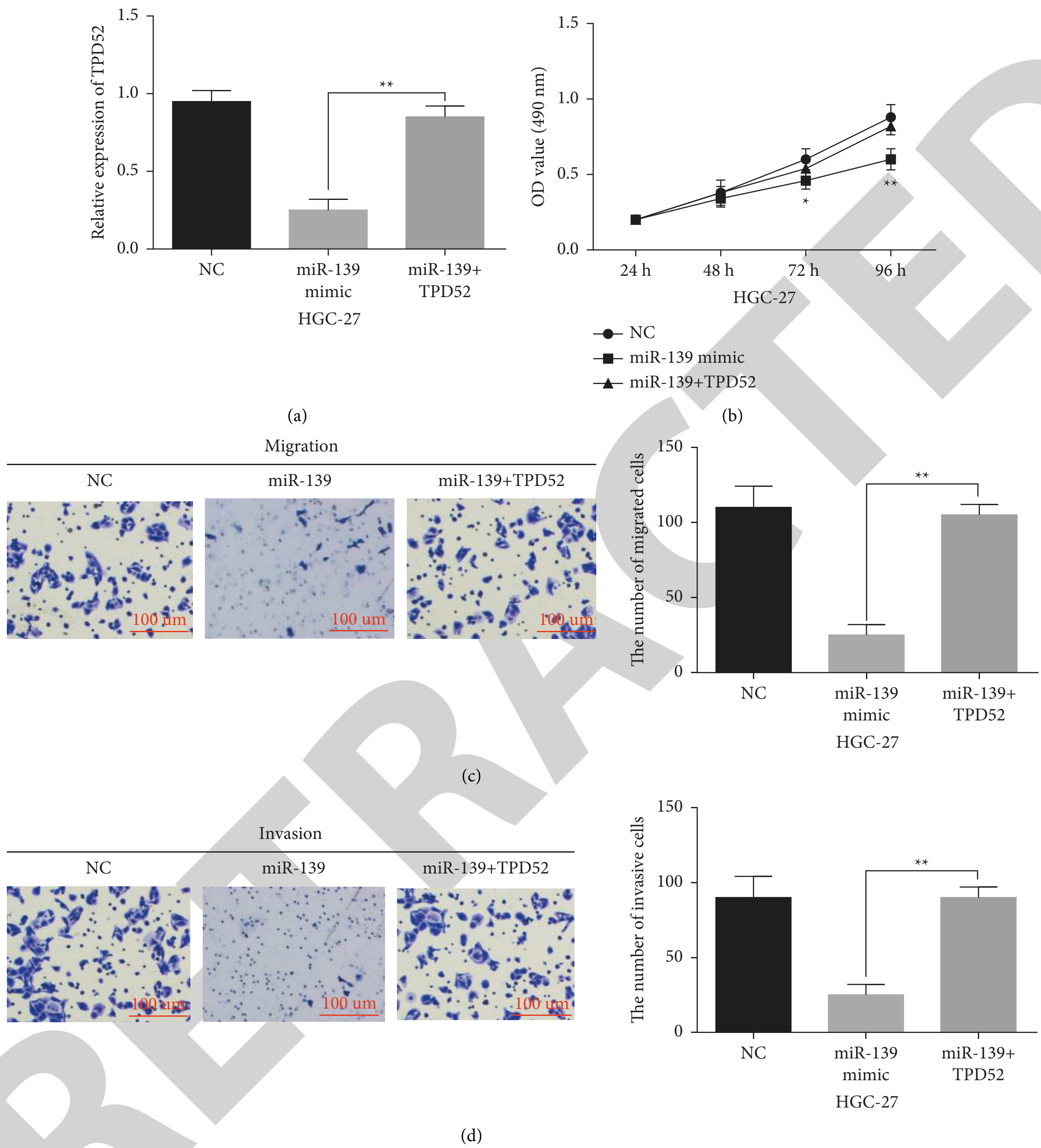

Figure 7: TPD52 upregulation impaired the inhibitory action of miR-139-5p in GC. (a) TPD52 expression in HGC-27 cells containing TPD52 vector and miR-139-5p mimics. ((b), (c), (d)) Cell proliferation, migration, and invasion in HGC-27 cells with the TPD52 vector and miR-139-5p mimics. $^{**}p < 0.01$.

5. Conclusion

In conclusion, miR-139-5p downregulation occurred in GC tissues and cells. Worse prognosis of GC patients was associated with miR-139-5p downregulation. Moreover, miR-139-5p restrained GC cell proliferation and metastasis through targeting TPD52. MiR-139-5p will develop into a therapeutic and prognostic marker for GC. However, the results of this study have not been verified in animals. Therefore, in vivo experiments still need to be done in the future.

Data Availability

The datasets used during the present study are available from the corresponding author upon reasonable request.

Ethical Approval

This study was approved by the Ethics Committee of The Affiliated Hospital of Qingdao University and conformed to the Helsinki Declaration and to local legislation.

Consent

Not applicable.

Conflicts of Interest

The authors declare that they have no conflicts of interest.

References

[1] R. L. Siegel, K. D. Miller, and A. Jemal, "Cancer statistics, 2015," *CA: A Cancer Journal for Clinicians*, vol. 65, no. 1, pp. 5–29, 2015.

[2] J. M. Marqués-Lespier, M. González-Pons, and M. Cruz-Correa, "Current perspectives on gastric cancer," *Gastroenterology Clinics of North America*, vol. 45, no. 3, pp. 413–428, 2016.

[3] R. Siegel, C. DeSantis, K. Virgo et al., "Cancer treatment and survivorship statistics, 2012," *CA: A Cancer Journal for Clinicians*, vol. 62, no. 4, pp. 220–241, 2012.

[4] F. De Vita, L. Vecchione, G. Galizia et al., "Perspectives in adjuvant therapy of gastric cancer," *Oncology*, vol. 77, no. 1, pp. 38–42, 2009.

[5] S. Kagawa, K. Shigeyasu, M. Ishida et al., "Molecular diagnosis and therapy for occult peritoneal metastasis in gastric cancer patients," *World Journal of Gastroenterology*, vol. 20, no. 47, pp. 17796–17803, 2014.

[6] G. A. Calin and C. M. Croce, "MicroRNA-cancer connection: the beginning of a new tale," *Cancer Research*, vol. 66, no. 15, pp. 7390–7394, 2006.

[7] H. Su, X. Wang, J. Song, Y. Wang, Y. Zhao, and J. Meng, "MicroRNA-539 inhibits the progression of wilms' tumor through down regulation of JAG1 and notch 1/3," *Cancer Biomarkers*, vol. 24, no. 1, pp. 125–133, 2019.

[8] X. Huang, L. Wang, W. Liu, and F. Li, "MicroRNA-497-5p inhibits proliferation and invasion of non-small cell lung cancer by regulating FGF2," *Oncology Letters*, vol. 17, no. 3, pp. 3425–3431, 2019.

[9] Y. Tao, S. Yang, Y. Wu et al., "MicroRNA-216a inhibits the metastasis of gastric cancer cells by targeting JAK2/STAT3-mediated EMT process," *Oncotarget*, vol. 8, no. 51, pp. 88870–88881, 2017.

[10] L. Yu, J. Chen, Y. Liu, Z. Zhang, and S. Duan, "MicroRNA-937 inhibits cell proliferation and metastasis in gastric cancer cells by downregulating FOXL2," *Cancer Biomarkers*, vol. 21, no. 1, pp. 105–116, 2017.

[11] X.-J. Xiang, J. Deng, Y.-W. Liu et al., "MiR-1271 inhibits cell proliferation, invasion and EMT in gastric cancer by targeting FOXQ1," *Cellular Physiology and Biochemistry*, vol. 36, no. 4, pp. 1382–1394, 2015.

[12] Y. Zhang, W.-L. Shen, M.-L. Shi et al., "Involvement of aberrant miR-139/Jun feedback loop in human gastric cancer," *Biochimica et Biophysica Acta (BBA) - Molecular Cell Research*, vol. 1853, no. 2, pp. 481–488, 2015.

[13] R. Saba, C. D. Goodman, R. L. C. H. Huzarewich, C. Robertson, and S. A. Booth, "A miRNA signature of prion induced neurodegeneration," *PLoS One*, vol. 3, no. 11, Article ID e3652, 2008.

[14] J. Guo, Y. Miao, B. Xiao et al., "Differential expression of microRNA species in human gastric cancer versus non-tumorous tissues," *Journal of Gastroenterology and Hepatology*, vol. 24, no. 4, pp. 652–657, 2009.

[15] R.-Y. Li, L.-C. Chen, H.-Y. Zhang et al., "MiR-139 inhibits Mcl-1 expression and potentiates TMZ-induced apoptosis in glioma," *CNS Neuroscience and Therapeutics*, vol. 19, no. 7, pp. 477–483, 2013.

[16] M. S. Dettmer, A. Perren, H. Moch, P. Komminoth, Y. E. Nikiforov, and M. N. Nikiforova, "MicroRNA profile of poorly differentiated thyroid carcinomas: new diagnostic and prognostic insights," *Journal of Molecular Endocrinology*, vol. 52, no. 2, pp. 181–189, 2014.

[17] L. Mi, Y. Chen, X. Zheng et al., "MicroRNA-139-5p suppresses 3T3-L1 preadipocyte differentiation through notch and IRS1/PI3K/akt insulin signaling pathways," *Journal of Cellular Biochemistry*, vol. 116, no. 7, pp. 1195–1204, 2015.

[18] M. A. Rubin, S. Varambally, R. Beroukhim et al., "Overexpression, amplification, and androgen regulation of TPD52 in prostate cancer," *Cancer Research*, vol. 64, no. 11, pp. 3814–3822, 2004.

[19] J. A. Byrne, S. Frost, Y. Chen, and R. K. Bright, "Tumor protein D52 (TPD52) and cancer-oncogene understudy or understudied oncogene?" *Tumor Biology*, vol. 35, no. 8, pp. 7369–7382, 2014.

[20] P. Tennstedt, C. Bölch, G. Strobel et al., "Patterns of TPD52 overexpression in multiple human solid tumor types analyzed by quantitative PCR," *International Journal of Oncology*, vol. 44, no. 2, pp. 609–615, 2014.

[21] T. Nakagawa, T. M. Kollmeyer, B. W. Morlan et al., "A tissue biomarker panel predicting systemic progression after PSA recurrence post-definitive prostate cancer therapy," *PloS one*, vol. 3, no. 5, Article ID e2318, 2008.

[22] M. Shehata, I. Bièche, R. Boutros et al., "Nonredundant functions for tumor protein D52-like proteins support specific targeting of TPD52," *Clinical Cancer Research*, vol. 14, no. 16, pp. 5050–5060, 2008.

[23] J. A. Byrne, S. Maleki, J. R. Hardy et al., "MAL2 and tumor protein D52 (TPD52) are frequently overexpressed in ovarian carcinoma, but differentially associated with histological subtype and patient outcome," *BMC Cancer*, vol. 10, no. 1, Article ID 497, 2010.

[24] Y. Goto, R. Nishikawa, S. Kojima et al., "Tumour-suppressivemicroRNA-224inhibits cancer cell migration and invasion via targeting oncogenicTPD52in prostate cancer," *FEBS Letters*, vol. 588, no. 10, pp. 1973–1982, 2014.

Hindawi
Journal of Healthcare Engineering
Volume 2022, Article ID 2761847, 9 pages
https://doi.org/10.1155/2022/2761847

Research Article

Investigations on Brain Tumor Classification Using Hybrid Machine Learning Algorithms

S. Rinesh,[1] K. Maheswari,[2] B. Arthi,[3] P. Sherubha,[4] A. Vijay,[5] S. Sridhar,[6] T. Rajendran ,[7] and Yosef Asrat Waji [8]

[1]*Department of Computer Science and Engineering, Jigjiga University, Jijiga, Ethiopia*
[2]*Department of Computer Science and Engineering, CMR Technical Campus, Hyderabad, Telangana, India*
[3]*Department of Computer Science and Engineering, College of Engineering and Technology, SRM Institute of Science and Technology, SRM Nagar,Kattankulathur,Kanchipuram, Chennai, Tamil Nadu, India*
[4]*Department of Information Technology, Karpagam College of Engineering, Coimbatore, Tamil Nadu, India*
[5]*Department of Business Administration and Information Systems, Arba Minch University, Sawla Campus, Ethiopia*
[6]*Department of Computer Science and Engineering, Saveetha School of Engineering, Saveetha Institute of Medical and Technical Sciences, Chennai, Tamil Nadu, India*
[7]*Makeit Technologies (Center for Industrial Research), Coimbatore, Tamil Nadu, India*
[8]*Department of Chemical Engineering, College of Biological and Chemical Engineering, Addis Ababa Science and Technology University,Addis Ababa, Ethiopia*

Correspondence should be addressed to T. Rajendran; rajendranthavasimuthuphd@gmail.com and Yosef Asrat Waji; yosef.asrat@aastu.edu.et

Received 2 December 2021; Revised 7 January 2022; Accepted 20 January 2022; Published 14 February 2022

Academic Editor: Enas Abdulhay

The imaging modalities are used to view other organs and analyze different tissues in the body. In such imaging modalities, a new and developing imaging technique is hyperspectral imaging. This multicolour representation of tissues helps us to better understand the issues compared to the previous image models. This research aims to analyze the tumor localization in the brain by performing different operations on hyperspectral images. The tumor is located using the combination of k-based clustering processes like k-nearest neighbour and k-means clustering. The value of k in both methods is determined using the optimization process called the firefly algorithm. The optimization processes reduce the manual calculation for finding K's optimal value to segment the brain regions. The labelling of the areas of the brain is done using the multilayer feedforward neural network. The proposed technique produced better results than the existing methods like hybrid k-means clustering and parallel k-means clustering by having a higher peak signal-to-noise ratio and a lesser mean absolute error value. The proposed model achieved 96.47% accuracy, 96.32% sensitivity, and 98.24% specificity, which are improved compared to other techniques.

1. Introduction

The increasing growth of medical image analysis uses various advanced image processing techniques [1]. Due to this development, incurable diseases can be cured nowadays. This development helps to cure most life-threatening diseases like tumors, blood clots, and cancer at the initial stages. These life-threatening diseases are confirmed with the help of images of the infected region and biopsy. Mostly, the infected region's images are the first step in diagnosing the conditions [2]. The diseases are confirmed with the help of a biopsy. In such a situation, the infected regions' modeling should be highly accurate and easily visualizable.

This paper discusses such modeling, which is called hyperspectral imaging, to locate the abnormal growth of cells in the brain. This hyperspectral image provides an accurate result compared with other images. In general, brain activities are recorded with the help of scanning and radiogram methods. The scanning so far used for the brain is the MRI scan and CT scan [3]. MRI is the abbreviation of magnetic resonance imaging, mainly used for the body's soft tissue analysis [4]. CT is the abbreviation of computed tomography imaging used to analyze the hard tissues of the body.

MRI scanning is mainly preferred for brain analysis. The advantages of this type of scanning are the ability to view the soft tissue clearly. It does not produce any side effects because of not using any ionizing radiation to visualize the brain regions. The MRI scan is highly used to locate the abnormal growth of cells in the brain. This imaging scheme produces the brain's imaging in a greyscale format [5], which medical experts can analyze. An in-depth diagnosis is required in this imaging model to locate the tumor.

Apart from MRI scanning, other types of scanning also produce the images in a greyscale format except for the color Doppler scan. However, alternative techniques like postprocessing for segmenting the tissue regions are not producing desired results. Hence, to overcome this drawback, a new imaging technique called hyperspectral imaging is used to analyze the body's soft tissues.

Hyperspectral imaging is used in remote sensing for vegetation classification by taking pictures of hundreds of bands' regions. This imaging process is also used for capturing the brain with 128 bands. Based on the image processing techniques, the hyperspectral image is classified. These hyperspectral images represent the brain regions in different colors, which effectively understand the brain tissues. This mainly helps the doctor during the surgery process to remove the abnormal tissues. This imaging technique also helps the patient understand the current stage of their diseases due to the representation of tissues in different colors. The high-resolution camera captures the brain tumor [6].

This paper discussed the mapping process of the brain to locate the abnormal tissues. The technique used for the mapping was noise removal to remove any artifacts in the images for postprocessing. The segmentation process was done using a hybrid k-based clustering process [4]. The algorithm for optimization was utilized to choose the value of clusters for the clustering process. The neural-based labelling process was to mention the tissues of the brain in different colors. Based on the image classification accuracy, the mean absolute error value, and the peak signal-to-noise ratio, the results are compared with existing image classification methods and neural network models.

This paper is organized as follows: Section 2 discusses the various research works of tumor localization. Section 3 presents a detailed explanation of the proposed methodologies. Section 4 discusses the comparison of various techniques by practical implementation and evaluation. Section 5 is about the conclusion statement based on the results and analysis.

2. Related Works

Hemanth et al. [1] proposed the abnormal brain image using the deep convolution method. This brain image was classified based on the dataset. The deep convolution neural network was applied to reduce design complexity. The convolution neural network model used a deep learning technique, that is, DCNN. The abnormal brain tumor dataset was used for classifying the image. Here, three layers in DCNN were carried out to perform the classification. The first layer was the convolution layer, which provides the higher-level features with trained parameters. The second layer was the ReLU Layer, which rectifies the linear unit layer. The final one was the Max-Pool layer. It was used after getting the four-cluster region. It classified the terms of metastasis, meningioma, glioma, and astrocytoma.

Deep-seated diseases like MS affect the nerve systems since they would be predicted earlier. Halimeh and Teshnehlab [2] proposed the tumors and MS simultaneous classification and diagnosis with the convolution neural network's help. Here, the image processing technique was used to classify that image, and it was diagnosed. Here, CNN was used. The MRI image was taken for the classification process of the internal image pixel's multiplications. This detects the infected area, lesion, and tumor after diagnosis.

Dong et al. [7] proposed a Farrow structure to apply the time delay filter contrary to a linear FIR structure to fulfill the requirement for real-time updates and be entirely suitable for the FPGA domain. Besides, another off-line approach was implemented to evaluate the Farrow filter coefficient if the coefficient was symmetric. Simulations have been generated to represent the structural model to the Farrow filter developed. The results likewise showed the Frost broadband adaptive antenna with a Farrow filter effectively diminishes the obstacle.

Choi and Jeong [8] proposed a model utilizing Speckle Reducing Anisotropic Diffusion (SRAD), guided filter, and soft thresholding to eliminate SAR image speckle noise while maintaining edge data efficiently. Initially, the generated procedure obtained a filtered image by executing an SRAD filter onto the noisy image. Thus, a logarithmic shift was used to change it to additional noise for future expulsion of the filtered image's multiplicative noise. The filtering image was transformed, using DWT, into multiresolution images. For each high and low-frequency, subimage soft thresholding and the directed filter were used. The denoised images were equipped with Inverse DWT (IDWT) and the exponential transform, showing that the procedure demonstrated superior function over the traditional filtering method and the output was both subjective and objective.

Mafi et al. [9] developed an image denoising technique within related speckle noise and Gaussian noises. The dual-tree complex wavelets transform was used on the images to accomplish a unique coefficient describing these noises. Hence, these isolated coefficients were evacuated by thresholding, and the inverse wavelet transform was executed to achieve the remake image. A connection between the dual-tree and standard wavelet-based denoising filter was applied depending on different basic parameters. Lastly, to expel some other existing noises, a spatial denoising filter was used on the image. The clinical ultrasound images are degenerated by the noise sequences. Such noise sequences helps the researchers' to understand the impacts of Gaussian and speckle noises with the help of most effective speckle and Gaussian denoising filters.

Choi and Jeong [10] proposed an algorithm utilizing SRAD and a guided filter for speckle noise decreasing and edge security. At first, speckle, which was a multiplicative noise, was detached by utilizing SRAD. The existing noise in the filtered image was transformed to added noise using algebraic transform. The additional noise that exists in the filtered image was further detached utilizing a guided filter. Lastly, the image without noise was derived utilizing aggressive transformation, indicating that the model have better noise reduction and edge-preserving capabilities than the standard filtering method.

Marie and Alalyani [11] proposed a novel firefly algorithm-based feature selection process. This also manages the Arabic text classification that was not successfully concentrated because of the Arabic language's inconvenience. This technique has been profitably tested in various complicated issues. Moreover, it has not been included in selecting feature methods to manage the classification of Arabic text. The SVM classifier was utilized as three-calculation parts for approving this method, including accuracy, recall, and F-measure. This work accomplished an accuracy of 0.994 using OSAC dataset.

Narayanan et al. [5] proposed a technique to access the standard EEG signal. At first, the peak EEG signal voltage estimation is computed. Finally, a developed time-frequency transformation method was used to send the signals into an image depending on the wavelet transform. Additionally, the S-transform access was planned to disengage the main features of signals to the classifier scheme. The firefly algorithm-based method was further treated to select the principal features of the signal utilized for training and testing the classifying method. In this method, the SVM, RF, and KNN methods were developed. Hence, the performance obtained an average accuracy of 80.39%. The performance affirmed that this method offered a better outcome on the chosen EEG signal.

Mashhour et al. [12] proposed a new classifier method depending on a firefly algorithm made as a managed learning algorithm. Hence, the analysis depended on the firefly algorithm created by simulating a firefly's character to bring different mates, dependent on intensity and distance. The procedure of this algorithm contained three stages. The feature selection stage was utilized to reduce the features and to select the most valuable features. The model development stage was significant in determining the firefly class moderators. The model forecast stage was utilized to apportion the testing or concealed sample in their related classes using class contributors. A few datasets ended up being related to the Ant-Miner technique. The experiment demonstrated that the firefly algorithm was the best.

Tawahid and Dsouza [13] presented an algorithm known as the Hybrid Binary Bat Enhanced Particle Swarm Optimization (HBBEPSO). In this method, a bat based genetic algorithm is used to analyze the feature space using echolocation and improved rendition of the PSO to achieve better solution in the search place. The algorithm's overall efficiency and technique were identified as the best compared to the other methods examined. Hence, the result has demonstrated the algorithm's capacity to discover the feature space for optimal feature sequence.

Sangaiah and Kumar [14] proposed an algorithm that used a relief attribute reduction with GA based on entropy for breasts cancer identification. This method's hybrid sequence was utilized to deal with the dataset with a higher dimension and concern. The information was accomplished from the WISCONSIN datasets, and the information has been classified depending on various properties. The technique was calculated and compared with the other notable feature selection processes. The experimental outcome indicates that the work has a remarkable capacity to create a decreased subspace of critical features while generating significant classifications accuracy for massive datasets.

Harithaa [15] presented the firefly and cuckoo search-based algorithms of feature selection with detached high accuracy and lower training upward for the PIMA Indian diabetic dataset from UCI. The empirical setup was made with the UCI dataset with the KNN classifier. The precision, accuracy, and recall were analyzed to calculate parameters, and the results were compared with those of the firefly and cuckoo search algorithms. This technique traditionally obtained high accuracy.

Long et al. [16] developed a heart disease diagnostic model with rough sets based on feature reductions and type 2 fuzzy logic (IT2FLS) intervals. Analysis among irregular groups based on feature reduction and IT2FLS targets address the issue and concern of high-dimensional datasets. IT2FLS used a hybrid teaching procedure to compose a fuzzy c-means clustering approach and the adjustment criterion by firefly chaos and hybrid genetic algorithms. This teaching procedure was costly in computational terms, especially when hired with a high-dimensional set of data. The rough set-based quality decline utilizing a chaos firefly approach was analyzed to detect an optimal reduction, reduce computational liability, and improve IT2FLS performance. Results explained remarkable device stability associated with numerous machine learning algorithms like Naive Bayes, ANN, and SVM. This model has been useful in diagnosing heart disease.

Cortes et al. [17] developed an approach for adaptively learning artificial neural networks (ADANET). It was based on analytical methods, including data-dependent generalized, which are proved in detail. The large-scale operations on the various binary division tasks are obtained using the CIFAR-10 dataset. Results explained that this technique could automatically learn network structures with very reasonable work accuracy when related to those obtained for neural networks.

Esfe et al. [18] analyzed nanofluids' thermal conductivity utilizing neural networks, test data, and correlativity for modeling thermal conductivity. Using a KD2-Pro thermal analyzer, the thermal conduction of $Mg(OH)_2$ nanoparticles with a 10 nm mean diameter isolated in ethylene glycol was solved. An experimental collaboration has been developed as far as volume fraction and temperature were concerned, based on observational information at other substantial volume portions and temperature. Therefore, the relative thermal conduction as temperature and volume fraction activities was proposed through a neural network depending on the analyzed information. A system with two layers hidden in each layer and five neurons has the slightest error and a high fitting coefficient. Besides correlating the model and the correlativity obtained from test knowledge, the neural network was highly accurate and predicted the thermal conduction of $Mg(OH)_2$-EG nanofluids.

Erkaymaz et al. [19] researched the work of two various feedforward neural networks (FFNN) for diabetes diagnosis. They used input as PIMA Indians Diabetic Dataset. The previous information indicated that the Watts–Strogatz small world FFNN delivered a good analysis work compared to traditional FFNN. Consequently, the result was associated with the Newman–Watts small world FFNN, and they demonstrated that the latter was even better. However, the Newman–Watts small world FFNN results from better output parameters were validated.

Torti et al. [20] executed an alternative analytical comprehension of the challenge from a smooth optimization perspective. Hence, the specific teaching of limited samples and acceptable conditions was analyzed using a critical point to set up any local minimal to be globally minimal. Additionally, an advanced algorithm, known as the Generalized Gauss-Newton (GGN), was returned as a surmised Newton's algorithm that moves the property of being locally united to a global minimum under the state of accurate teaching.

Hao et al. [21] proposed a glioblastoma brain tumor classification model using HSI images. The spatial and spectral features of HSI images were used by implementing various deep learning models for the detection of brain tumor. These features extracted could support obtaining accurate results in detecting brain tumor. The brain tumor detection process includes the processes like spectral phasor analysis and data oversampling, 1D-DNN-based spectral HSI feature extraction and classifications, 2D-CNN-based spectral-spatial HSI feature extraction and classifications, edge-preserving filtering-based classification results fusion and optimizations, and fully convolutional networks- (FCN-) based background segmentation.

3. Proposed Method

In this paper, a classification and detection model of brain tumor using hyperspectral imaging (HSI) is proposed. The brain tumor mapping technique was used in this work for improving the performance of the proposed model to achieve accurate results in terms of detecting brain tumor. The proposed model includes preprocessing, filtering, optimization, clustering, labelling, and classification processes in order to detect the brain tumor.

Mapping is the process, which represents the different regions of the same properties in different colors. This mapping process is used to understand the areas more effectively. This paper discusses such a mapping process for locating the abnormal tissues in the brain. The term abnormal tissue was the tumor cell whose growth was increasing without any ordered form [22, 23].

The mapping process is done on the hyperspectral image of the brain. The noise removal algorithm to remove any unwanted pixels or disturbance in the image processes the hyperspectral image. This noiseless image is suitable for a better mapping process. The mapping is carried out in two stages. The initial step is to group pixels of the same characteristics using an optimized hybrid k-based clustering process [24]. The second stage is to label the grouped pixels using the neural scheme. Figure 1 is the pictorial representation of the proposed system.

3.1. Image Modeling. The mapping of a brain region is done using hyperspectral images. The image used in this paper is obtained from the in vivo hyperspectral format. The input image consists of 128 bands, and its color wavelength ranges from 400 to 1300 nm, that is, the bandwidth of electromagnetic radiation.

NASA usually performs mapping in hyperspectral images remote sensing application form specifying the different crops. NASA is currently performing this mapping process in the mammogram images using the MEDSEG analyzer to represent the breast region's various tissues to detect the cancer part. The migration to hyperspectral medical imaging helps to capture the images in pixels and their wide range of frequencies.

Hyperspectral imaging's main advantage is to capture the spatial and spectral information of the images through spatial and spectral scanning of the body with different wavelengths.

The information is higher due to the capture of the body of more than eight bands. Each band of the hyperspectral image holds a different story on the brain's particular region, which is impossible in the other imaging models. This paper tests the proposed hybrid firefly and k-based mapping in the dataset used in the parallel k-means clustering process. The HSI brain image is obtained with a hyperspectral camera, and a technique like the one Vivo-based is used. It captures the brain region in 128 bands, and each band consists of different information about the brain. The process of each stage of the proposed method is elaborated in the following.

3.2. Conversion of the Hyperspectral Cube to RGB Format. Our research data preprocessing is one of the common process-forming concepts for the images mapping and noise removal sections. In the HSI RGB form, images have the maximum data in every pixel and color, typically 150 to 400 dimensional vectors were analyzed and configured. The reflection of the pixel consists of each wavelength.

In this preprocessing stage, two processes were performed under the following conditions:

(i) Greyscale process.

(ii) Noise removal process.

Previous research work was performed based on the greyscale process. Noise removal is acting under adaptive and Frost filters to get a better result. The adaptive filter uses an actual pixel integer concept that is replaced with an

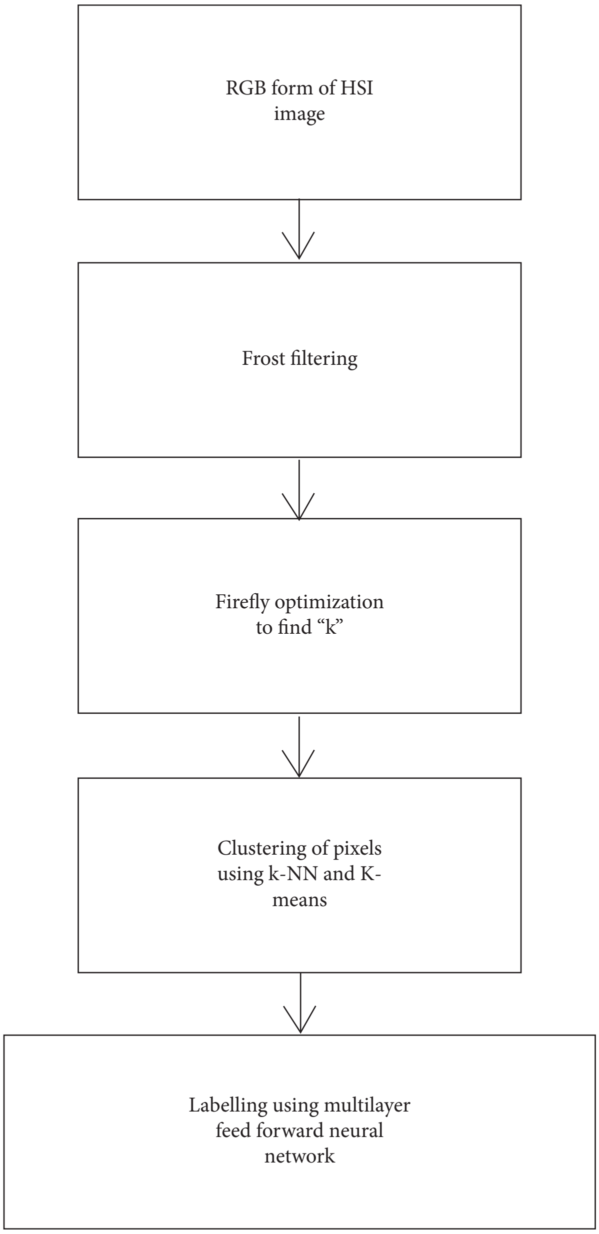

Figure 1: Flowchart for the mapping process.

advanced pixel integer concept, and it presents better results and high performance.

3.3. Frost Filtering. The Frost filter exchanges the pixel of interest with the moving (nXn) kernel's total weighted values. The weighting factor decreases as one moves away from the pixel of interest. As the variance of the kernel grows, the weighting factors for the central pixels will also grow. This filter was based on the statistics of multiplication and stationary noises.

Frost filter minimizes image edges speckle content. This type of filter is a damaged symmetric regular filter used for linear data. It was determining the accurate pixel here, replacing the filter and estimation based on filter distance.

Various order speckle pictures expressed the following equation:

$$J(m,n) = a(m,n).n(m,n), \tag{1}$$

where $J(m, n)$ is the speckle-noise image value corruption, $a(m, n)$ is the actual speckle free signal, and $n(m, n)$ is the speckle noise.

3.4. Feature Extraction. This process is to group the regions of the brain using an optimized k-means clustering technique. The term optimized refers to selecting the optimal clusters value for the k-means clustering process. This optimization approach helps to group the different regions of the brain, along with the tumor part.

Suppose local window size is $N \times N$ means; the result is expressed as

$$s(i, j) = \sum_{K=i-Nj}^{i+Nj} \sum_{i=j-Nj}^{j+N} h(k,l).I(k,l), \tag{2}$$

where

$$\begin{aligned} s(i, j) &= \sum_{K=i-Nj}^{i+Nj} \sum_{i=j-Nj}^{j+N} h(k,l).I(k,l), \\ d_{kj} &= \sqrt{(i-k)^2 + (j-l)^2}, \end{aligned} \tag{3}$$

where k is constant.

3.5. Firefly Algorithm (FA). Firefly algorithm is a meta-heuristic algorithm for the advancement of optimization. This concept is based on the speckle action of firefly insects. Xin-She Yang introduced this algorithm in 2008. Firefly algorithm (FA) uses speckle action to impress another firefly, naturally transmitting signals to differing gender. Firefly is of a similar gender; also, all fireflies can impress another firefly. This consists of brightness for all pairs of fireflies. A brighter firefly attracts another firefly; therefore, the minimum brighter ones are replaced with the brighter ones. The algorithmic flow of the firefly is given in Table 1. The fireflies' beginnings are based on the boundary's integer concept, which is the maximum and minimum limitation statement. The maximum and minimum limitation statements of the fireflies are 1 and 5.

The formula of a pair of two fireflies is expressed as follows:

$$x_i^{t+1} = x^t_{1+\beta\exp\left(-\gamma r_{ij}^2\right)} \left(x_{j}^t {}_{-x_i^t}\right) + \alpha_{t\,\varepsilon_t}, \tag{4}$$

which is optimized by

$$F(x) = (f1(x), f2(x), \ldots, fi(x), \quad i = 1, 2, 3, \ldots, m. \tag{5}$$

3.6. K-Means Clustering. It is the function of a similar pixel integer, and it is synthesis in one part. In our research work, an unsupervised method is referred to as clustering implemented in this section. The undefined address part of a

Table 1: Firefly algorithm pseudocode.

```
Begin
(1) Objective function: f (x), x = x1, x2, . . ., Xn;
(2) Generate an initial population of fireflies
Xi (i = 1, 2, 3).
(3) Formulate light intensity I so that it is associated with f (x)
(for example, for maximization problems, I α f (x) or simply I = f
(x);)
(4) Define absorption coefficient γ
  While (t < MaxGeneration)
    for i = 1: n (all n fireflies)
      for j = 1: i (n fireflies)
        if (i, j),
Vary attractiveness with distance r via Exp (−?, ?);
move firefly i towards j;
Evaluate new solutions and update light intensity;
        end if
      end for j
    end for i
Rank fireflies and find the current best;
  end while
Postprocessing the results and visualization;
end
```

picture is addressed by presenting the k-means clustering function about a centric portion.

This incorporates the pixel integer term of a picture-based k region, where k is several clusters in the picture and k calculates the firefly optimization function. The entire process is performing under the basis iteration still in the cluster form of every pixel picture. The clustering is one of the pixel properties, and by getting the k value of 3, the mapping region is performed based on the threshold method.

Addressing a function of the pixel term performs a k-cluster state. The centric portion calculated the choosing pixel property concept and the weight of both group concepts under the clustering condition.

The code profiling was performed using the dataset created by original HS images and assuming $k = 24$, min_error $= 10^{-3}$, and max_iter $= 50$.

3.7. Mapping the Regions. The affected region is mapped based on the neural network model, which uses a multilayer feedforward neural network. In the below discussion, the MFNN was described.

3.7.1. Multilayer Feedforward Neural Network (MFNN). Neural networks are computing systems made up of linked nodes that function similarly to neurons in the brain. Using the MFNN method, hidden patterns can be detected, correlations in raw data, cluster, and classifications can be performed, and the proposed MFNN continually learns and enhances over time. This is one of the popularised single-layer feedforward neural networks, naturally used in addressing the operation of the brain molecule. Testing the web is based on the brain's molecule and also the integer of the image. Dataset classification is based on testing and training based on the cross pleat estimation section. The neural network training is based on the training characteristics; the performance process and the results are produced based on those values.

In supervised learning, data labelling is an important component of data preparation. Every error or inaccuracy in this procedure might have a detrimental impact on the quality of a dataset. Furthermore, the overall performance of a predictive model might be lost, leading to errors. Taking this into account, for the ground truth in the tumor identification problem, the MFNN algorithm was applied, which labelled the data.

The multilayer feedforward neural network (MFNN) (refer to Figure 2) using the segmental feedback layer is given. The flow model is presented in the following figure. Here, it intimated the input process and the output process terms.

Multilayer feedforward neural network (MFNN) generates two classifications:

(i) Single multilayer feedforward neural network.

(ii) Multiple multilayer feedforward neural network.

The single-layer MFNN is helping the performance improvement to present the result alone. Another classification is multiple MFNN is used to find the difference between real integer resultant layers through the sigmoid activation process. The sigmoidal activation function in the MFNN presents an improved output with repespect to the individual input layers. In this investigation, MFNN is utilizing the testing and training sets of the image classification configuration. Meanwhile, 80% of the samples were utilized for training and 20% for testing. Input is one of the optimal features for the FNN from the objective of the research work. The trained single-layer feedforward neural network is tested on the feature extracted image. The performance metrics evaluate the results, and they are tabulated in the experimental part.

4. Experimental Analysis

In this, the Matrix laboratory software is utilized to execute the proposed technique in the simulation format. The proposed method is tested on the open-access brain tumor dataset (250 samples) collected from Kaggle data collection, which is used in the parallel k-means clustering for better analysis and comparison [25].

For training and testing, the dataset is split into 80% for training and 20% for testing. The following figures are the input and output of each stage of the proposed technique. The MFNN is reconfigured based on the features extracted by our proposed method. The reconfigured network was utilized for the training and testing of the data. The output of each process of the proposed method is shown in Figures 3–6.

The RGB format of the hyperspectral image is shown in Figure 3. The noisy image (refer to Figure 4) is preprocessed with a grayscale image shown in Figure 5. This noisy signal is processed with the GLCM method.

The filtered output image is shown in Figure 6. Based on these images, the mean absolute error value and peak signal-to-noise ratio are evaluated, and they are compared with the existing method, which is depicted in Table 2.

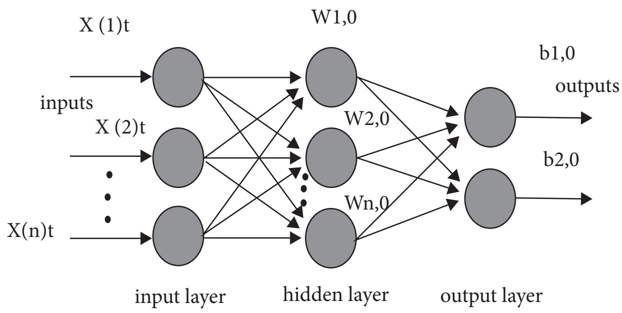

Figure 2: MFNN data flow model.

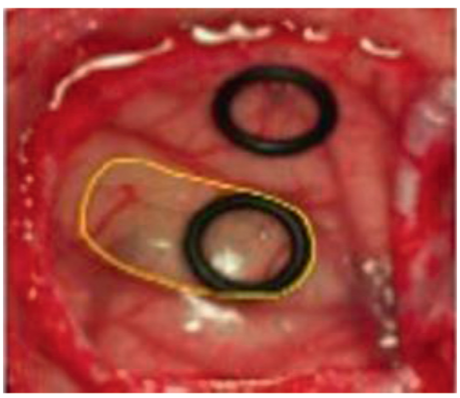
Figure 3: RGB format of HSI image.

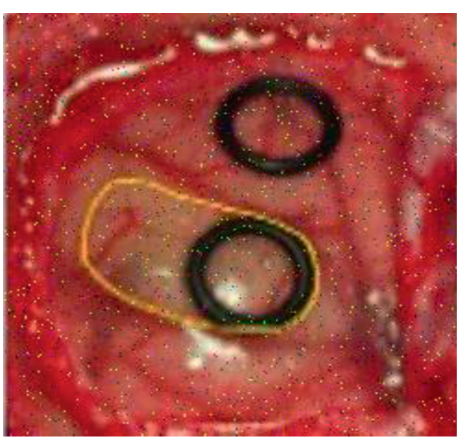
Figure 4: Noisy image.

The comparisons of the existing methods with the proposed method are made by calculating the following parameters:

MAE: MAE is the abbreviation of mean absolute error, which tells how much percentage of the detected labels has deviated from the original labels.

PSNR: PSNR is the abbreviation of the peak signal-to-noise ratio, which gives information about the image's quality after several processes to map the brain regions. The PSNR is increased in a hybrid firefly based on the k-means clustering technique by comparing the results. The results are compared with parallel k-means, optimized k-means, and SVM with k-means techniques. The mean absolute error is raised in the parallel k-means clustering technique and better in the proposed model (Table 2).

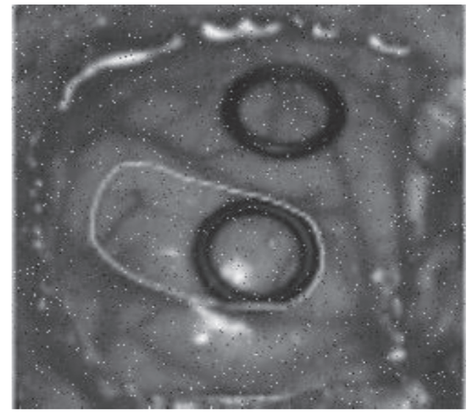
Figure 5: Preprocessed greyscale image.

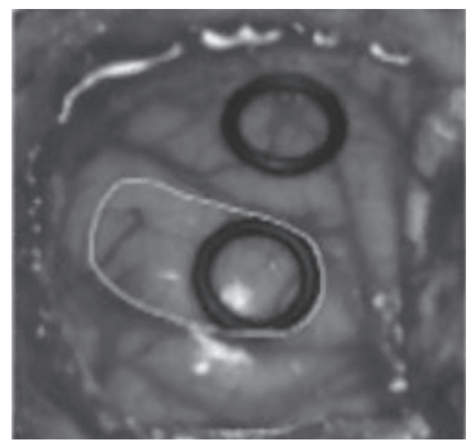
Figure 6: Postfiltered output.

The performance evaluation was carried out in order to assess the efficiency of the proposed model. Accuracy, sensitivity, and specificity are three performance measures used in the assessment. By merging specificity and sensitivity, a single metric, quality, may be obtained. Both metrics should have a value of one. These three comparable performance measuring evaluations are also used in this study, which are as follows:

$$\text{Sensitivity} = \frac{\text{TP}}{\text{TP} + \text{FN}}\%,$$
$$\text{Specificity} = \frac{\text{TN}}{\text{TN} + \text{FP}}\%, \tag{6}$$
$$\text{Accuracy} = \frac{\text{TP} + \text{TN}}{\text{TP} + \text{FP} + \text{TN} + \text{FN}}\%.$$

(i) TP: true positive was the total of truly identified brain tumor.

Table 2: Performance comparison results.

Parameters	Parallel k-means clustering	Optimized k-means clustering	SVM with k-means clustering	Hybrid firefly and k-based clustering
Mean absolute error value	75	70	68	65
Peak signal-to-noise ratio	72	75	80	85

Table 3: Comparison of performance analysis.

Classifiers	Accuracy	Sensitivity	Specificity
K-NN	94.93	94.26	94.55
DNN	95.30	94.85	97.70
PSO	95.11	94.71	97.01
Lagrangian SVM (LSVM)	93.34	91.22	96.69
DCNN [1]	94.50	95.10	95.86
Proposed method	96.47	96.32	98.24

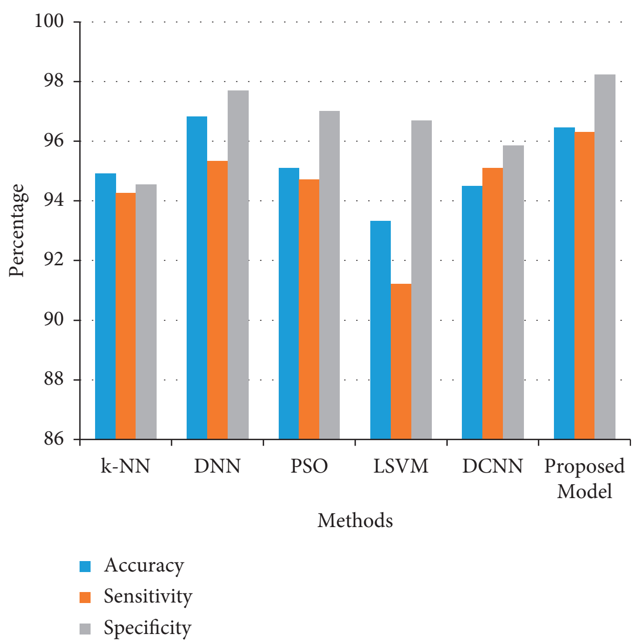

Figure 7: Graphical view of compared performance analysis.

(ii) FP: false positive was the total misclassified regions as a brain tumor.

(iii) FN: false negative was the total from inaccurately unidentified areas.

(iv) TN: true negative was the total of the truly identified nonbrain tumor.

In Table 3 and Figure 7, the comparisons of the performances analysis of the proposed model with other existing approaches were represented. Accuracy, sensitivity, and specificity are the parameters evaluated for this performance analysis. Based on the true positive and true negative values, the efficiency of the model was calculated. The proposed model is compared with k-NN, DNN, PSO, LSVM, and DCNN [1, 17–28]. The proposed model achieved 96.47% accuracy, which is 1.17% to 3.13% higher than other techniques, with a sensitivity of 96.32%, which is 2.06% to 5.1% better than other methods, and specificity of 98.24%, which is 0.5% to 3.6% improved compared to other techniques.

5. Conclusion

This research proposed an unsupervised approach for clinical treatment based on the patient's brain tumor estimation. The brain's mapping and localization are achieved using k-means clustering, firefly optimization, and MFNN. The proposed multilayer feedforward neural network (MFNN) addresses the brain-molecule optimization method's process and achieves minimum error and trial techniques. Hence, the proposed optimized mapping process produced improved outputs in every form, and it is suitable for mapping the molecules of the spectral medical image. The proposed model is compared with k-NN, DNN, PSO, LSVM, and DCNN. The proposed model achieved 96.47% accuracy, which is 1.17% to 3.13% higher than other techniques, with a sensitivity of 96.32%, which is 2.06% to 5.1% better than other methods, and specificity of 98.24%, which is 0.5% to 3.6% improved compared to other techniques. In future, to improve the performance, a hybrid deep learning method with a deep transfer learning model for the brain tumor classification process using related image datasets can be implemented. For the feature extraction process, a novel threshold-based method can be used [25–28].

Data Availability

The datasets used and/or analyzed during the current study are available from the corresponding author on reasonable request.

Conflicts of Interest

There are no conflicts of interest.

Authors' Contributions

S. Rinesh, K. Maheswari, and B. Arthi are responsible for data collection and validation. P. Sherubha and A. Vijay are responsible for surveys, content writing, and proofreading. S. Sridhar, Yosef Asrat Waji and T. Rajendran are responsible for algorithm design, development, and proofreading.

References

[1] D. J. Hemanth, J. Anitha, A. Naaji, and G. Oana, "A modified deep convolutionals neural networks for abnormal brain images classifications," *IEEE Access*, vol. 7, pp. 4275–4283, 2018.

[2] S. Halimeh and M. Teshnehab, "Diagnosing and classifications tumor and MS simultaneous of magnetics resonances image using convolutions neural networks," in *Proceedings of the 7th Iranian Joint Congress on Fuzzy and Intelligent System*, Bojnord, Iran, January 2019.

[3] H. Parikh, S. Patel, and V. Patel, "Analysis of denoising techniques for speckle noise removal in synthetic aperture radar images," in *Proceedings of the International Conference on Advances in Computing, Communications, and Informatics (ICACCI)*, Bangalore, India, September 2018.

[4] H. H. Sulthan, N. M. Saleem, and W. Al-Atabbany, "Multi classifications of brain tumors image using deep neural networks," *IEEE Access*, vol. 7, pp. 69215–69225, 2019.

[5] V. S. Narayanan, R. Elavarasan, C. N. Gnanaprakasam, N. S. M. Raja, and R. K. Kumar, "Heuristics algorithms based approach to classify EEG signal into normal and focals," in *Proceedings of the International Conferences on System, Computation, Automation, and Networking (ICSCA)*, Pondicherry, India, July 2018.

[6] T. Rajendran, K. P. Sridhar, S. Manimurugan, and S. Deepa, "Recent innovations in soft computing applications," *Current Signal Transduction Therapy*, vol. 14, no. 2, pp. 129–120, 2019.

[7] T. Dong, Q. Wang, Y. Zhao, L. Ji, and H. Zeng, "Broadbands frost adaptive arrays antennas with a Farrow delays filters," *International Journal of Antennas and Propagation*, vol. 2018, Article ID 3574929, 2018.

[8] H. Choi and J. Jeong, "Despeckling images using a preprocessing filter and discrete wavelet transform-based noise reduction techniques," *IEEE Sensors Journal*, vol. 18, no. 8, pp. 3131–3139, 2018.

[9] M. Mafi, S. Tabarestani, M. Cabrerizo, A. Barreto, and M. Adjouadi, "Denoising of ultrasound images affected by combined speckle and Gaussian noise," *IET Image Processing*, vol. 12, no. 12, pp. 2346–2351, 2018.

[10] H. Choi and J. Jeong, "Speckles noise reductions in ultrasounds image using SRAD and guided filtesr," in *Proceedings of the International Workshops on Advanced Images Technology (IWAIT)*, Chiang Mai, Thailand, January 2018.

[11] S. L. Marie-Sainte and N. Alalyni, "Firefly algorithms based features selections for Arabic texts classifications," *Journal of King Saud University-Computer and Information Sciences*, vol. 3, no. 3, pp. 320–328, 2018.

[12] E. M. Mashhour, E. M. El Houby, K. T. Wassif, and A. I. Salah, "A novel classifiers based on firefly algorithms," *Journal of King Saud University-Computer and Information Sciences*, vol. 2, no. 10, pp. 1173–1181, 2018.

[13] M. A. Tawahid and K. B. Dsouza, "Hybrid binary bats enhanced particles Swarm optimizations algorithms for solving features selections problem," *Applied Computing and Informatics*, vol. 16, no. 1-2, pp. 117–136, 2018.

[14] I. Sanghaiah and A. V. A. Kumar, "Improving medical diagnoses performances using hybrid features selections via relief and entropy-based genetics search (RF-EGA) approach: applications to breasts cancer predictions," *Cluster Computing*, vol. 22, no. 1, pp. S6899–S6906, 2019.

[15] R. Harithaa, D. S. Babu, and P. Samulal, "A hybrid approach for predictions of type-1 and type-2 diabetes using firefly and cuckoos search algorithm," *International Journal of Applied Engineering Research*, vol. 13, no. 2, pp. 896–907, 2018.

[16] N. C. Long, P. Meesad, and H. Unger, "A highly accurate firefly based algorithm for heart disease prediction," *Expert Systems with Applications*, vol. 42, no. 21, pp. 8221–8231, 2015.

[17] C. Cortes, X. Gonzalvo, V. Kuznetsov, M. Mohri, and S. Yang, "Adanet: adaptive structurals learning of artificial neural networks," 2016, https://arxiv.org/abs/1607.01097.

[18] M. H. Esfe, M. Afrand, S. Wongwises et al., "Applications of feedforward multilayer perceptron artificial neural networks and empirical correlation for prediction of thermal conductivity of Mg(OH) 2 -EG using experimental data," *International Communications in Heat and Mass Transfer*, vol. 67, pp. 46–50, 2015.

[19] O. Erkaymaz, M. Ozer, and M. Perc, "Performance of small-world feedforward neural networks for the diagnosis of diabetes," *Applied Mathematics and Computation*, vol. 311, pp. 22–28, 2017.

[20] E. Torti, G. Florimbi, F. Castelli et al., "Parallel K-means clustering for brain cancer detections using hyperspectral images," *Electron*, vol. 7, no. 283, pp. 2–19, 2018.

[21] Q. Hao, Y. Pei, R. Zhou et al., "Fusing multiple deep models for in vivo human brain hyperspectral image classification to identify glioblastoma tumor," *IEEE Transactions on Instrumentation and Measurement*, vol. 70, pp. 1–14, 2021.

[22] T. Anitha, G. C. P. Latha, and P. M. Surendra, "A proficient adaptive K-mean based brain tumors segmentations and detections using deep learning schemes with PSO," *J Comput Sci IntellTechnol*, vol. 1, no. 3, pp. 09–14, 2020.

[23] C. Narmatha and P. M. Surendra, "A review on prostate cancer detections using deep learning techniques," *J Comput Sci IntellTechnol*, vol. 1, no. 2, pp. 26–33, 2020.

[24] S. Shivaraj, R. Malamathanraj, and P. Palaniswamy, "Detecting anomalous growths of skin lesions using thresholds-based segmentations algorithms and fuzzy K-Nearests Neighbors classifiers," *Journal of Cancer Research and Therapeutics*, vol. 16, no. 1, pp. 40–52, 2020.

[25] Z. Cai, J. Guo, C. Wen et al., "An intelligent Parkinson diseases diagnostics systems based on a ChaoticsBacterials foraging optimizations enhanced fuzzy KNN approach," *Comput Math Method Med*, vol. 2018, Article ID 2396952, 2018.

[26] G. Jothi, "Hybrid Tolerances Roughs Sets–Firefly based supervised features selections for MRIs brain tumor images classifications," *Applied Soft Computing*, vol. 46, pp. 639–651, 2016.

[27] S. K. Paul and P. Bhaumik, "AIDCOR: artificial immunity inspired density based clustering with outlier removal," *International Journal of Machine Learning and Cybernetics*, vol. 9, no. 2, pp. 309–334, 2018.

[28] W. Zhang, S. Gong, and J. Zhang, "Effect of rubber particles and steel fibers on frost resistance of roller compacted concrete in potassium acetate solution," *Construction and Building Materials*, vol. 187, pp. 752–759, 2018.

Hindawi
Journal of Healthcare Engineering
Volume 2022, Article ID 7651549, 7 pages
https://doi.org/10.1155/2022/7651549

Research Article

Construction of a Comprehensive Mental Health Evaluation System for Clinicians

Wenjie Wang and Xumei Wang

Department of Psychiatry, Shengjing Hospital of China Medical University, Shenyang, China

Correspondence should be addressed to Xumei Wang; wangxm1124@163.com

Received 24 November 2021; Revised 13 January 2022; Accepted 17 January 2022; Published 14 February 2022

Academic Editor: Enas Abdulhay

Objective. To detect problems of mental health disorders early and actively by constructing a comprehensive evaluation system of mental health. *Methods*. The evaluation system was constructed by the Minnesota personality questionnaire (MMPI), the personality questionnaire (EPQ), and the depression experience questionnaire (DEQ). Total 341 interns and residents in a general hospital were investigated with the questionnaire about psychological status, and the results were analyzed by SPSS22.0. *Results*. The KMO was 0.879, and the factor load of the seven factors was 0.49 to 0.856. The cumulative variance contribution reached 72.18%, and the overall consistency coefficient was 0.871. The relationship, emotional disorder, paranoia, reflection, and positive response were 0.893, 0.614, 0.867, 0.771 and 0.621, respectively. In this study, the mental health composite scores of all study subjects met a normal distribution, so level 3 scores of clinical interns and residents were established according to the deviation method. *Conclusion*. The constructed index system contains comprehensive indicators, good reliability efficiency, and a level 3 score, which helps individuals and hospitals to detect problems early, and provide guidance and advice for active intervention.

1. Introduction

Mental health problems are prevalent in every working population of the world. The Organization for Economic Cooperation and Development (OECD) study showed that about 5% and 15% of the working population in high-income countries have serious and moderate mental health problems, respectively [1]. This problem is particularly prominent for physicians, with an increasing proportion of mental illness (such as anxiety, depression, and substance abuse) [2]. For example, in the UK, 10 to 20% of doctors become depressed at some stage of their career and are at higher risk of suicide than the general population; another online survey of UK physicians found that 68% of 116 respondents were diagnosed with depression and others with bipolar disorder, anxiety, eating disorders, and substance addiction [3]. A 2014 study by researchers from the American Medical Association (AMA) and Mayo Clinic showed that 54 percent of U. S. doctors are experiencing burnout, which is higher than in other industries [4]. The suicide rate was also high, with a 40-year review study of clinicians' suicides demonstrating that male clinicians had 70% more odds of suicide than the general population and 250%–400% higher for female clinicians [5].

Clinician mental health problems are mainly affected by the following factors: special occupational nature [6], growing working pressure, and inflexible working hours [7]. Because they know more and it is easier to access drugs, doctors are also more prone to substance addiction and abuse than the general population [8]. In addition, doctors rarely seek professional help because of the humiliation of mental illness [9].

The poor mental health state of clinicians simultaneously affects their work. Research has shown that poor mental health status will reduce the accuracy of clinical diagnosis and increase medical costs while reducing the quality of medical services that patients receive [10]. Although the mental health problems of clinicians have received wide attention, there is no relatively comprehensive evaluation method to comprehensively assess their mental health.

Therefore, how to evaluate and improve the mental health of hospital clinicians has become an urgent problem for individuals, families, hospitals, and even society. As it is difficult to comprehensively evaluate the individual mental health level if the individual psychological indicators are qualified or not, this study aims to explore the comprehensive mental health evaluation method and mental health status of clinicians so as to provide a reference for early problem detection and intervention.

2. Materials and Methods

2.1. Subject Investigated. A total of 353 clinical medical interns in a third-class hospital in Shenyang with standardized training, 12 invalid questionnaires were removed, and 341 valid questionnaires were obtained, with an efficiency of 96.6%. Among them, 128 were boys (37.5%) and 213 were girls (62.5%). Among them, 18 clinical medicine interns (52.8%) and 161 residents (47.2%) conducted standardized training. The age range was 21–35 years, and the mean age was 23.2 years.

2.2. Selection of the Study Indicators. Using the literature analysis method, the preliminary screening indicators were discussed by the expert group of the psychiatric department of the Grade A hospital and combined with the mental health quality of Chinese adults, five psychological indicators of personality characteristics, emotion, coping mode, interpersonal relationship, and reflection function were finally established to evaluate the mental health status of doctors.

2.3. Source of Indicators. Data on the subjects' age, gender, and specialty were collected. The Minnesota Muhiphasic Personality Inventory (MMPI) was prepared by S. R. Hathaway and J. C. Mckinley. Song Weizhen et al. revised 566 questions, including 4 validity scales and 10 clinical scales, showing good reliability and validity of each subscale. In this study, psychopathies, paranoia, and schizophrenia 3 subscales were used as evaluation tools for personality characteristics [11].

The Eysenck Personality Questionnaire (EPQ) was prepared by J. Eysenck and revised by Liu [12]. The questionnaire has 88 questions, including 4 subscales, of which scale E measures internal and external dimension; the P scale measures neuroticism dimension; the Q scale measures psychoplasm dimension; and the L scale mainly measures the concealment of subjects. It has good reliability and validity in the Chinese population. The Q scale was used as an assessment tool for personality characteristics in this study.

2.3.1. The Depression Experience Questionnaire (DEQ). Written by Blatt et al. and revised by Liu et al. [13], the DEQ had 66 questions and a graded Likert7 score with an internal consistency coefficient of 0.65–0.79 for the five factors included in the scale and 0.81 for the full scale. The five factors of the questionnaire were significantly associated with the total score of the depression self-rating scale, and the highest correlation coefficient between self-criticism factor and SDS was 0.508, followed by the helpless factor of 0.382, the dependent factor and SDS was 0.252, the autonomy factor was 0.298, and the satisfaction factor showed a significant negative correlation with SDS of −0.148.

2.3.2. State-Trait Anxiety Inventory (STAI). Prepared by Wang [14], it is made up of subscales evaluating two different anxiety types, with a total of 40 entries. Items 1–20 are the state anxiety subscales (STAI-Form Y-I, S-AI), and items 21–40 are the trait anxiety subscales (STAI-Form Y-II, T-AI).

2.3.3. Coping Style Questionnaire (CSQ). Prepared by Xiao Plan et al., the scale consists of 62 entries with only two answers each, including six subscales with good reliability and validity, and has been widely used [15].

2.3.4. Emotional-Social Loneliness Questionnaire (ESLI). The Emotion-Social Solitude Questionnaire (ESLI) is a multidimensional questionnaire distinguishing between the four types of loneliness: emotional isolation, social isolation, emotional loneliness, and social loneliness. The ESLI contains 15 pairs of descriptions, each with four-grade scores, from 3 (usually) to 0 (rarely) [14].

2.3.5. Reflective Functional Questionnaire-8 (RFQ-8). Written by Fonagy, and revised by Xu et al. [16], it is a self-assessment tool used to assess adult reflective function. The questionnaire consisted of eight entries, a Likert7 grade score, with options from "great disagreement" to "great consent." The score of entry 1,2,3,4,5,6 as "0,0,0,0,0,1,2,3" to form the excessive mentalization (certainty about mental states, RFQ-C) subscale; entry 2,4,5,6,8 as "3,2,1,0,0,0,0" and the entry 7 score as "0,0,0,0,1,1,2,3" to form the mentalization defect (uncertainty about mental states, RFQ-U) subscale. This study finally established five first-level psychological indicators, including personality characteristics, emotion, coping mode, interpersonal relationship, and reflective function, and 23 secondary psychological indicators, such as psychological metamorphosis, paranoia, schizophrenia, mental quality, anxiety state, and anxiety characteristics, as the mental health evaluation indicators of doctors. Index numbers are shown in Table 1.

2.4. Investigation Method. The method of random group sampling was applied with clinical medical interns and standardized training residents in Shenyang. Under the unified guidance of standardized trained researchers, the students were given appropriate time to let the research subjects complete the questionnaire independently and recycle the questionnaire on the spot after filling it in.

Table 1: Mental health evaluation indicators of physicians.

Level 1 indicators	Secondary indicators	Number
Personality characteristics	Metaphrenia	X1
	Bigoted	X2
	Split personality	X3
	Psychoticism	X4
	Anxiety state	X5
	Anxiety traits	X6
	Self-criticism	X7
Emotional state	Helplessness	X8
	Rely on	X9
	Autonomy	X10
	Satisfied	X11
	Solve the problem	X12
Coping style	Self-accusation	X13
	Turn to sb. for help	X14
	Illusion	X15
	Withdraw and keep off	X16
	Rationalization	X17
	Emotional isolation	X18
	Social isolation	X19
	Emotional loneliness	X20
	Social loneliness	X21
Reflect function	RFQC	X22
	RFQU	X23

2.5. Statistical Analysis. The data were entered using SPSS 22.0 software. The data were analyzed by descriptive statistical analysis, internal consistency test, and factor analysis, and the comprehensive scores of the study subjects were subjected to the normality test and the independent sample *t*-test.

3. Results

3.1. Distribution of Basic Sample Information. A total of 341 samples were collected in this study, including 180 clinical medicine interns and 161 residents with standardized training. The information distribution of the study subjects is shown in Table 2.

3.2. Data Standardization

3.2.1. Structural Validity. Because the data is not uniform in the indicators and there are positive and reverse indicators, the original data were assimilated and normalized first. Part of the raw data are shown in Table 3.

The KMO value of this study was 0.879 ($p < 0.01$), indicating the suitability for factor analysis.

3.2.2. Factor Extraction. The variance was decomposed by principal component analysis, and the resulting variable eigenvalues, variance contribution rate, and cumulative variance contribution rate are shown in Table 4. The cumulative contribution was required to be greater than 70% so that seven principal components were retained in this study. Combining the inflection point of the eigenvalue curve and the gravel diagram (scree plot, SP) of the eigenvalue (Figure 1), the figure shows from another side that the first 7 main components should be taken. To better explain the extracted factors, we maximized the orthogonal rotation of the extracted seven factors, and the eigenvalues of each factor after rotation are shown in Table 5. However, the factor load matrix obtained after rotation is shown in Table 6, indicating that the structural validity of the evaluation system in this study is good.

3.2.3. Factor Interpretation and Naming. According to the rotating factor load matrix, Factor Y1 was significantly associated with the indices X18, X19, X20, and X21; that is, Y1 is correlated with emotional loneliness and social loneliness. Factor Y1 is called a human relationship factor. Factor Y2 was significantly associated with metrices X5, X6, X7, X8, X9, and X10; that is, Factor Y2 is associated with anxiety and depression, and Factor Y2 is called an emotional dysregulation factor. Factor Y3 was significantly associated with the indices X13, X15, X16, and X17; that is Factor Y3 is associated with immature coping methods, and Factor Y3 is called a neurosis factor. Factor Y4 was significantly associated with metrices X1, X2, X3, and X4; that is, Factor Y4 is associated with severe psychotic symptoms, and Factor Y4 is called a paranoid factor. Factor Y5 was mainly significantly associated with metrices X22 and X23; that is, Factor Y5 is associated with reflective function, and Factor Y5 is called a reflective functional factor. Factor Y6 was significantly associated with metrices X12 and X14; therefore, Factor Y6 is related to problem solving and asking for help, and Factor Y6 is called an active response factor. Factor Y7 is associated with the indicator X11; that is, the factor Y7 is associated with self-satisfaction, and Factor Y7 is called a confidence factor.

3.3. Confidence Analysis. The internal consistency of the comprehensive evaluation system was tested, and the overall Cronbach α coefficient of the comprehensive mental health evaluation system was 0.871. The internal Cronbach α coefficient of interpersonal relationships, mood disorders, neurosis, paranoia, reflective function, and positive response to these six factors were 0.893, 0.614, 0.867, 0.771, 0.626, and 0.621, respectively, indicating the good reliability of the evaluation system.

3.4. The Clinician Mental Health Level 3 Score Was Established. The comprehensive scores were calculated for all study subjects and tested for normality with a Z-value of 0.044 ($p > 0.05$). Therefore, 3 all subjects scored normally distributed, and the histogram of the frequency distribution for 341 subjects is shown in Figure 2. The differences in mental health composite scores between genders and seniority were compared using independent sample *t*-tests, and the results showed that the differences in gender and seniority were not statistically significant; that is, the abovementioned factors had little impact on the mental health composite scores in this study.

Table 2: Distribution of basic information.

		Clinical intern		Chief physician	
		Example number	Percentage	Example number	Percentage
Sample		180	52.8	161	47.2
Sex	Male	70	38.9	58	36.1
	Female	110	61.1	103	63.9

Table 3: Standardized values for 23 index scores.

Subject investigated	1	2	3	4	5	6	7	. . .	341
X1	0.607	0.607	−1.498	0.607	−1.030	0.373	−0.563	. . .	0.841
X2	−0.624	1.500	0.286	−0.624	−1.230	−0.624	−1.534	. . .	1.803
X3	−0.906	−0.161	−0.906	−1.439	−1.013	−0.906	−1.119	. . .	2.609
X4	1.507	0.404	−0.698	−1.066	−0.698	−0.331	−0.331	. . .	1.874
X5	−2.037	−1.062	−1.842	−1.452	−1.355	−1.842	0.301	. . .	1.373
X6	−2.374	−0.699	−1.851	−2.060	−0.699	−1.327	−0.071	. . .	1.290
X7	−2.396	−1.782	−2.220	−1.782	−1.782	−1.255	−0.290	. . .	0.850
X8	−2.637	−1.960	−2.412	−0.943	−1.734	−1.621	−0.153	. . .	1.428
X9	−1.343	−1.118	−1.569	−0.442	−1.118	−1.794	−0.442	. . .	0.684
X10	1.791	1.259	1.791	1.259	1.614	1.791	1.259	. . .	−1.576
X11	0.405	1.208	−2.004	0.673	0.673	−1.201	0.673	. . .	−2.540
X12	−1.150	0.737	−0.678	−0.678	−0.206	0.266	0.737	. . .	0.266
X13	−1.087	−1.488	−0.687	−1.087	−1.087	−0.687	−1.087	. . .	2.120
X14	0.838	1.261	−0.853	−1.276	0.838	0.838	1.684	. . .	−0.430
X15	−1.147	−1.538	−0.756	−0.365	0.026	−1.147	−1.147	. . .	1.591
X16	−0.837	−2.178	−1.284	−1.284	−1.284	−1.731	−0.837	. . .	0.505
X17	−0.651	0.820	−0.284	−0.651	0.084	−1.387	−1.387	. . .	1.923
X18	−1.506	−1.506	−0.625	−0.625	0.036	−0.625	−1.506	. . .	1.578
X19	−1.207	−0.721	−0.721	−0.964	0.250	0.007	−1.207	. . .	1.221
X20	−1.101	−1.101	−0.371	−0.736	−0.188	−0.371	−1.101	. . .	1.639
X21	−1.118	−0.860	−0.603	−1.118	−0.345	−0.088	−1.118	. . .	2.488
X22	−1.193	−0.246	−2.376	−2.376	0.701	0.228	1.174	. . .	0.938
X23	−1.122	−0.380	−1.122	−1.122	−0.010	0.732	−1.122	. . .	−0.010

Table 4: Main component analysis table.

	Initial eigenvalue			Extract the sum of the square to load		
Element	Amount to	% of the variance	Accumulate (%)	Amount to	% of the variance	Accumulate (%)
1	7.667	33.336	33.336	7.667	33.336	33.336
2	2.397	10.420	43.756	2.397	10.420	43.756
3	1.765	7.672	51.429	1.765	7.672	51.429
4	1.413	6.146	57.575	1.413	6.146	57.575
5	1.236	5.372	62.947	1.236	5.372	62.947
6	1.209	5.255	68.201	1.209	5.255	68.201
7	0.915	3.978	72.180	0.915	3.978	72.180
8	0.797	3.467	75.647			
9	0.739	3.215	78.862			
10	0.629	2.736	81.597			
11	0.509	2.213	83.810			
12	0.468	2.035	85.845			
13	0.442	1.921	87.766			
14	0.403	1.754	89.520			
15	0.363	1.580	91.100			
16	0.344	1.494	92.594			
17	0.338	1.470	94.064			
18	0.321	1.397	95.461			
19	0.270	1.175	96.636			
20	0.252	1.096	97.731			
21	0.210	0.915	98.646			
22	0.202	0.876	99.522			
23	0.110	0.478	100.000			

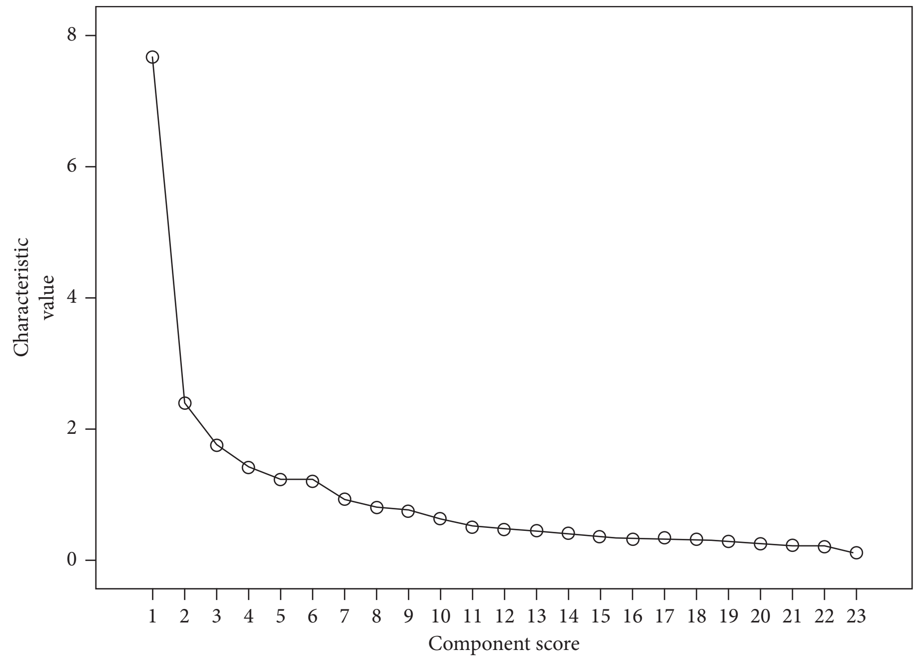

Figure 1: The inflection point of the eigenvalue curve and the gravel diagram (scree plot, SP) of the eigenvalue. Combining the inflection point of the eigenvalue curve and the gravel diagram (scree plot, SP) of the eigenvalue, the figure shows from another side that the first 7 main components should be taken.

Table 5: The rotational extraction factors are presented.

Factor	Eigenvalue	% of the variance	Accumulative total (%)
Y1	3.268	14.209	14.209
Y2	3.236	14.072	28.281
Y3	3.027	13.162	41.443
Y4	2.279	9.909	51.352
Y5	2.113	9.186	60.538
Y6	1.545	6.718	67.256
Y7	1.132	4.924	72.180

Table 6: Factor load matrix after rotation.

Variable	After rotation						
	Y1	Y2	Y3	Y4	Y5	Y6	Y7
X1	0.09	0.20	0.06	0.82	0.07	−0.03	0.12
X2	0.16	0.14	0.09	0.81	−0.01	−0.04	−0.18
X3	0.32	0.38	0.24	0.56	0.28	0.11	0.05
X4	0.18	0.13	0.14	0.51	0.18	0.23	0.36
X5	0.09	0.83	0.21	0.22	−0.09	0.20	−0.05
X6	0.12	0.82	0.20	0.23	−0.01	0.19	−0.05
X7	0.28	0.67	0.24	0.19	0.38	0.10	−0.04
X8	0.16	0.62	0.25	0.08	0.46	−0.10	−0.08
X9	0.21	0.49	0.21	0.06	0.25	−0.31	0.37
X10	−0.16	−0.51	−0.06	−0.14	−0.47	0.24	0.01
X11	0.04	−0.11	−0.02	0.01	−0.08	0.16	0.83
X12	0.14	0.19	−0.10	0.08	0.29	0.74	0.16
X13	0.16	0.28	0.75	0.19	0.15	0.05	−0.02
X14	0.28	0.02	−0.03	−0.01	−0.05	0.75	0.07
X15	0.10	0.22	0.80	0.09	0.23	−0.03	−0.05
X16	0.17	0.21	0.82	−0.01	0.09	−0.07	−0.09
X17	0.14	0.03	0.82	0.11	0.02	−0.07	0.18
X18	0.82	0.18	0.07	0.11	0.11	0.07	0.00
X19	0.86	0.07	0.12	0.06	0.00	0.15	0.09
X20	0.81	0.20	0.15	0.21	0.14	0.14	0.07
X21	0.80	0.09	0.22	0.14	0.07	0.09	−0.02
X22	0.01	0.12	0.18	−0.07	0.74	0.16	0.09
X23	0.15	0.03	0.13	0.28	0.77	0.05	−0.15

Table 7: Level 3 scoring criteria for physician mental health.

Grade	Range	Same as	Preferably
Standard	≥M + S	M − S~M + S	≤M − S
Standard mark standardized score	≥23.462	−23.461~23.462	≤−23.461

Note. M is the mean number, and S is the standard deviation.

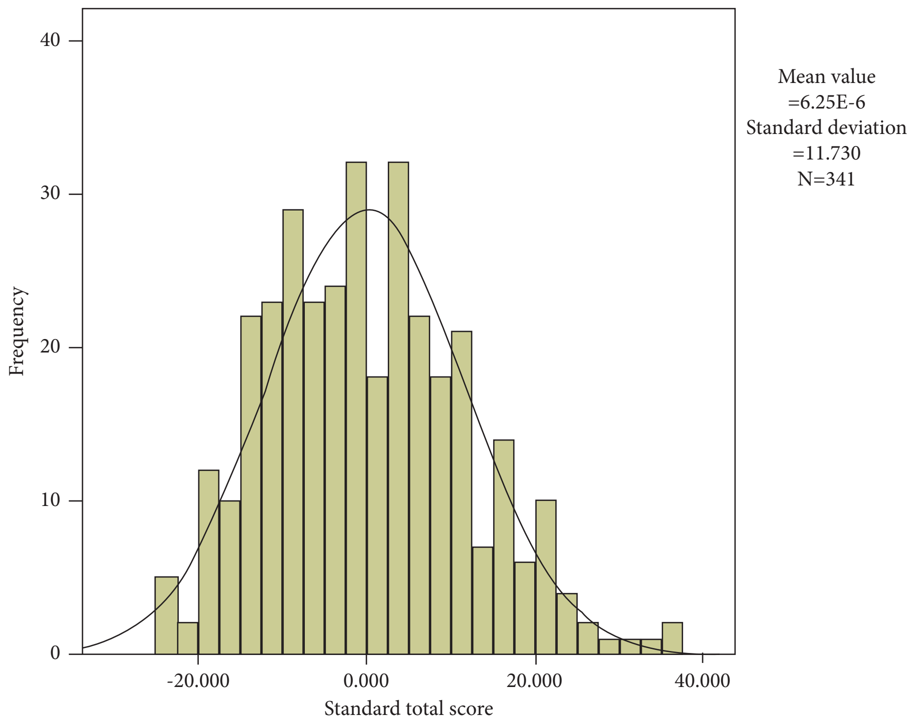

Figure 2: The histogram of frequency distribution of 341 study subjects in this study. Since the subjects fit a normal distribution, the level 3 score for establishing physician mental health with a standard deviation as a discrete distance according to the discrepancy method is shown in Table 7.

4. Discussion

Mental health problems are prevalent in every working population of the world [17]. It brings a great economic burden on individuals and families, but also brings huge economic losses to enterprises and society. This study completed the construction of a comprehensive evaluation system for physician mental health and was able to screen out doctors with mental health problems, contributing to early problem detection and active intervention.

In this study, we selected five psychological indicators, such as personality characteristics, emotion, coping mode, interpersonal relationship, and reflection function, and used widely used psychological measurement tools, such as the Minnesota Multiple Personality test (MMPI), the Eysenck Personality Questionnaire (EPQ), the Depression Experience Questionnaire (DEQ), and extracted psychological metamorphosis, paranoia, schizophrenia, schizophrenia, anxiety state, anxiety status, anxiety characteristics, and self-criticism as comprehensive evaluation theories [18]. A comprehensive evaluation system was built. Through the principal component analysis method, combined with the cumulative factor contribution rate, seven factors were extracted and rotated by the maximum orthogonal rotation method, which were named interpersonal factors, emotional dysregulation factors, neurosis factors, paranoid factors, reflective function factors, active response factors, and confidence factors, respectively. In study carried out by Liang [19], it is proposed that the mental health quality of Chinese adults is basically the same, indicating that the factors extracted from this study can comprehensively reflect the mental health status of individuals.

The KMO value in this study was 0.879. The factor load of the extracted factors ranged from 0.49 to 0.856. The cumulative variance contribution rate was 72.18%. It shows that the comprehensive evaluation system has a good structural validity; check the internal consistency of the comprehensive evaluation system. Among them, the overall Cronbach α coefficient of the comprehensive mental health evaluation system of clinicians was 0.871; the internal Cronbach of interpersonal relationships, emotional dysregulation, neurosis, paranoia, reflective function, and active response to these six factors, with coefficients of 0.893, 0.614, 0.867, 0.771, 0.626, and 0.621, respectively. It indicates that the evaluation system has a good reliability.

On the basis of the extracted 7 factors, the comprehensive scores of 341 subjects were calculated, and the data had a statistic Z-value of 0.044 ($p > 0.05$). The scores of 341 subjects were normally distributed, and they established a level 3 score of doctors with a standard deviation as a discretization to provide the basis for individual mental health evaluation. In addition, a comparison of mental health status between genders and posts showed that the differences in gender and posts were not statistically significant. Elwer et al. [20] studies showed that when individuals engage in nonsex-dominated occupations, their mental health is negatively affected and they are also more prone to absenteeism. But studies have also shown that men's mental health is largely unaffected when pursuing nongender-dominant occupations. However, in this study, significantly more women than men were present, so gender has no effect on mental health status, a conclusion that needs to be further confirmed in future studies.

This study has certain limitations: the survey was mainly of clinical interns and residents; limited by professional, age, education, and job category; failed to explore the influence of different education and postcategories for mental health status; and the measurement of mental health should be extended to more hospitals, professionals, and posts, to confirm the utility of clinicians' comprehensive mental health evaluation system.

5. Conclusion

This study constructed a comprehensive evaluation system of clinicians' mental health, different from the single evaluation index, using factor analysis to evaluate the mental health from interpersonal relationship, emotion, personality characteristics, reflection function, coping mode, and self-evaluation, which comprehensively reflected the mental health status of clinicians. The evaluation system has good credibility and accuracy and can classify clinicians' mental health status, providing reference for personal identification symptoms and hospital mental health screening [18, 21].

Data Availability

The data used to support this study are available from the corresponding author upon request.

Conflicts of Interest

The authors declare that they have no conflicts of interest.

References

[1] K. Memish, A. Martin, and L. Bartlett, "Workplace mental health: an international review of guidelines," *Preventive Medicine*, vol. 101, pp. 213–222, 2017.

[2] A. Haramati, S. Cotton, J. S. Padmore, H. S. Wald, and P. A. Weissinger, "Strategies to promote resilience, empathy and well-being in the health professions: insights from the 2015 CENTILE conference," *Medical Teacher*, vol. 39, pp. 118-119, 2017.

[3] L. Miller, "Doctors, their mental health and capacity for work," *Occupational Medicine*, vol. 59, no. 1, pp. 53–55, 2009.

[4] T. D. Shanafelt, G. Gorringe, R. Menaker et al., "Impact of organizational leadership on physician burnout and satisfaction," *Mayo Clinic Proceedings*, vol. 90, no. 4, pp. 432–440, 2015.

[5] T. Hampton, "Experts address risk of physician suicide," *Jama the Journal of the American Medical Association*, vol. 294, no. 10, pp. 1189–1191, 2005.

[6] R. Riley and M. C. Weiss, "A qualitative thematic review: emotional labour in healthcare settings," *Journal of Advanced Nursing*, vol. 72, pp. 6–17, 2016.

[7] L. Leape, D. Berwick, C. Clancy et al., "Transforming healthcare: a safety imperative," *Quality and Safety in Health Care*, vol. 18, pp. 424–428, 2009.

[8] Department of Health, *Mental Health and Ill Health in Doctors*, London, UK, 2008.

[9] A. I. Garelick, "Doctors' health: stigma and the professional discomfortin seeking help," *Psychiatrist*, vol. 36, pp. 81–84, 2012.

[10] M. J. Kreitzer and M. Klatt, "Educational innovations to foster resilience in the health professions," *Medical Teacher*, vol. 39, pp. 153–159, 2017.

[11] S. Ji and Z. Dai, *Minnesota Multiphasic Personality Survey-Recent Studies with Multiclass Scale Interpretation*, Science Press, Beijing, China, 2004.

[12] U. Liu, "Personality questionnaire and personality theory," *Chinese Journal of Psychiatrists*, vol. 17, no. 1, pp. 53–55, 1984.

[13] K. Smith and I. B.C De Torres, "A world of depression," vol. 515, no. 181, pp. 10–1038, 2014.

[14] X. Wang, *Mental Health Assessment Scale Manual (Supplement)*, Chinese Mental Health Journal, Beijing, China, 1999.

[15] X. Plan and X. Xiufeng,, "Validity and reliability of coping style questionnaire," *Chinese Journal of Mental Health*, no. 4, pp. 164–168, 1996.

[16] L. Xu, L. Guo, and J. Xia, "Reflective Functional Questionnaire-8 Chinese version of the revision and letter validity study," *Neurological Disease and Mental Health*, vol. 46, no. 10, pp. 878–881, 2017.

[17] W. Wang, L. Guo, J. Han, and X. Wang, "etc.Progress in studying factors affecting mental health in the working population," *Chinese Journal of Neuropsychiatric Disorders*, vol. 44, no. 10, 2018.

[18] X. Yu and T. Fu, "Review of multiindex comprehensive evaluation methods," *Statistics and Decision-making*, no. 11, pp. 119–121, 2004.

[19] B. Liang, "Basic concept, theory and formulation conception of mental health quality evaluation system," *Psychological and Behavioral Research*, vol. 10, no. 4, 2012.

[20] S. Elwér, L. Harryson, M. Bolin, and A. Hammarström, "Patterns of gender equality at workplaces and psychological distress," *PLoS One*, vol. 8, no. 1, Article ID e53246, 2013.

[21] J. Jia, X. He, and Y. Jin, *Statistics*, Renmin University of China Press, Beijing, China, 4th edition, 2009.

Hindawi
Journal of Healthcare Engineering
Volume 2023, Article ID 9784985, 1 page
https://doi.org/10.1155/2023/9784985

Retraction

Retracted: Evidence-Based Care Can Improve Treatment Compliance and Quality of Life of Patients with Acute Pancreatitis

Journal of Healthcare Engineering

Received 12 November 2022; Accepted 12 November 2022; Published 25 January 2023

Journal of Healthcare Engineering has retracted the article titled "Evidence-Based Care Can Improve Treatment Compliance and Quality of Life of Patients with Acute Pancreatitis" [1] due to concerns that the peer review process has been compromised.

Following an investigation conducted by the Hindawi Research Integrity team [2], significant concerns were identified with the peer reviewers assigned to this article; the investigation has concluded that the peer review process was compromised. We therefore can no longer trust the peer review process, and the article is being retracted with the agreement of the Chief Editor.

References

[1] Q. Zheng, L. Cao, H. Ma et al., "Evidence-Based Care Can Improve Treatment Compliance and Quality of Life of Patients with Acute Pancreatitis," *Journal of Healthcare Engineering*, vol. 2022, Article ID 7621658, 8 pages, 2022.

[2] L. Ferguson, "Advancing Research Integrity Collaboratively and with Vigour," 2022, https://www.hindawi.com/post/advancing-research-integrity-collaboratively-and-vigour/.

Hindawi
Journal of Healthcare Engineering
Volume 2022, Article ID 7621658, 8 pages
https://doi.org/10.1155/2022/7621658

Research Article

Evidence-Based Care Can Improve Treatment Compliance and Quality of Life of Patients with Acute Pancreatitis

Qiu Zheng,[1] **Li Cao**,[2] **Huanhuan Ma**,[1] **Yangyang Jin**,[3] **Yufei Gao**,[4] **Jiating Nie**,[5] **and Qingfeng Guo**[6]

[1]*Department of Gastroenterology, The Fourth Hospital of Harbin Medical University, Harbin 150001, Heilongjiang, China*
[2]*Department of Cerebral Surgery, The Fourth Hospital of Harbin Medical University, Harbin 150001, Heilongjiang, China*
[3]*Medical Oncology, The Fourth Hospital of Harbin Medical University, Harbin 150001, Heilongjiang, China*
[4]*Heilongjiang University of Traditional Chinese Medicine, Harbin 150040, Heilongjiang, China*
[5]*The Fourth Hospital of Harbin Medical University, Harbin 150001, Heilongjiang, China*
[6]*Department of Nursing Care, The Fourth Hospital of Harbin Medical University, Harbin 150001, Heilongjiang, China*

Correspondence should be addressed to Qingfeng Guo; guoqingfeng@ydsyy.org.cn

Received 27 November 2021; Revised 25 December 2021; Accepted 31 December 2021; Published 12 February 2022

Academic Editor: Enas Abdulhay

Acute pancreatitis represents a disease characterized by acute necro-inflammatory changes in the pancreas, which is histologically characterized by destruction of alveolar cells. We aim to explore whether evidence-based care can improve treatment compliance and quality of life of patients with acute pancreatitis. The changes of hemoglobin (HGB), serum pre-albumin (PAB), and serum albumin (ALB) before and after care were observed, as well as the incidence of complications after care, total effective rate after care, disease severity (bedside index for severity in acute pancreatitis, BISAP) before and after care, and psychological scores of the two groups before and after care were observed. Patients' compliance after care, self-management scores after care, and quality of life after care were compared between the two groups. After care, HGB, PAB, and ALB increased significantly in both groups ($p < 0.05$) and were higher in OG than CG. Compared with CG, OG had significantly lower incidence of complications ($p = 0.009$), significantly higher total effective rate ($p = 0.011$), significantly lower disease severity ($p < 0.05$), significantly better psychological condition scores ($p < 0.05$), significantly higher compliance scores ($p < 0.05$), higher self-management scores ($p < 0.05$), and significantly higher quality of life ($p < 0.001$). Evidence-based care can improve treatment compliance of patients with acute pancreatitis and can effectively improve their quality of life.

1. Introduction

Acute pancreatitis is a common digestive system disease, which is caused by abnormal digestive enzymes in the patient's own organs, resulting in inflammation of the pancreatic secretions [1]. The age range of the disease is wide, but most of the people who develop it are adults [2]. According to data, the incidence of acute pancreatitis is 34 cases per 100,000 in the general population and is increasing worldwide, and its incidence increases with age [3]. The main symptoms of acute pancreatitis are sudden onset of upper abdominal pain accompanied by nausea and vomiting [4], while patients with severe acute pancreatitis may be accompanied by hypotension or shock, leading to organ dysfunction and high mortality [5]. Patients need to be hospitalized immediately for diagnosis and treatment of the disease. Usually, symptomatic treatment and nonsurgical treatment are the main treatment methods [6]. Although most patients with acute pancreatitis have mild conditions and better treatment methods, there are still some patients with severe acute pancreatitis and the complications after treatment are very difficult [7]. Surgical treatment is required for complications, and the prognosis is poor [8]. Clinical data show that severe pancreatitis has a rapid onset and the patient is in dangerous condition, which causes a serious burden on pancreas, reduces patients' quality of life, and even endangers life [9].

Chronic alcohol ingestion, cholelithiasis, and overeating are usually the main causes of acute pancreatitis [10]. Therefore, choosing an appropriate nursing method is particularly important to improve the rehabilitation of acute pancreatitis and to avoid the continuous deterioration of the disease [11]. Over the past decade, cares in China have continued to shine in the treatment of clinical diseases, improving poor patient outcomes and enhancing the relationship between doctors and nurses [12], which greatly improves treatment compliance of patients and enhances treatment effects [13]. A review of previous studies suggested that evidence-based care based on evidence-based medicine is effective in constraining patient self-management and reducing disease complications [14]. Acute pancreatitis represents a disease characterized by acute necroinflammatory changes in the pancreas, which is histologically characterized by destruction of alveolar cells [15]. It is found that acute pancreatitis secondary to alcohol is more common in men and gallstone pancreatitis is more common in women [16]. At present, mild acute pancreatitis is usually treated with drugs, and the prognosis is generally good [17]. Moderate and severe acute pancreatitis should be treated according to the cause of disease, and if necessary, surgery should be performed, and the prognosis is generally poor due to frequent complications [18].

Besides, there are few clinical studies on the intervention effect of evidence-based care on patients with acute pancreatitis. Therefore, this experiment analyzes the effect of evidence-based care on patients with acute pancreatitis and observes the improvement of patients' compliance and quality of life, aiming at providing effective care for future clinical diagnosis and treatment of acute pancreatitis, so as to increase its recovery rate.

2. Materials and Methods

With deeper cognition of diseases and master of previous experience, the nursing staff can realize the adverse reactions of patients in time, adjust treatment strategies, closely cooperate with doctors, and improve the treatment effects from the patient's point of view [19], which is also suspected to be the main reason for the obvious improvement of disease status in OG after implementing care. Author Aviles et al. [20] pointed out that evidence-based care is of great help to promote the recovery of diseases by analyzing the effects of evidence-based care on enhancing the recovery of patients undergoing duodenectomy, which is similar to our experimental results.

A total of 117 patients with severe acute pancreatitis treated in our hospital from May 2017 to June 2019 were collected for prospectively analyzed, 65 of whom receiving evidence-based care during treatment were enrolled in the observation group (OG), and the other 52 patients receiving routine care during treatment were enrolled in the control group (CG). Note: this study has been approved by the Ethics Committee of our hospital.

2.1. Inclusion and Exclusion Criteria. Inclusion criteria were as follows: patients were diagnosed as severe acute pancreatitis after laboratory and imaging examination according to Chinese Journal of Pancreatology, patients were over 25 years old, patients underwent operation in our hospital, with stable vital signs, complete clinical data, and were in rehabilitation stage, and patients and their families knew and agreed to this experiment.

Exclusion criteria were as follows: patients had abnormal liver or renal function, other congenital diseases, or major diseases, patients did not have the ability to read and write, patients had immune dysfunction, and patients had drug allergy.

2.2. Nursing Methods. The team of Williams [21] also proposed that evidence-based care can effectively improve the recovery of patients after cardiac surgery, which has application value and supports this study. CG: routine care was adopted. The patients were assigned to the ward when they were admitted to the hospital. Then, the nursing staff followed the doctor's advice to monitor the vital signs of patients, performed routine examinations, made preparations before operation, and explained simple disease knowledge to the patients and their families. Besides, the nursing staff reminded patients of matters needing attention, performed routine care operations after operation, dispensed drugs, paid attention to the progress of the disease, and guided and restrained the behaviors and habits of the patients such as diet after operation.

OG: evidence-based care was given on the basis of routine care in CG. The nursing staff paid close attention to the patient's heart rate, blood pressure, and other vital signs before surgery, actively cooperated with the attending physician, registered, and completed the preoperative examination. The nursing staff should search for evidence based on previous nursing experience of acute pancreatitis and relevant literature, deepen their understanding of diseases, set reasonable care measures according to patients' own conditions, carry out disease education, psychological decompression, restrain misconduct, and perform other interventions, and closely grasp patients' first-hand information during and after operation. According to the patient's own situation and the requirements of the corresponding attending physician, the patient was given medication and diet control. The recovery of patients was also closely monitored by the nursing staff.

2.3. Outcome Measures. In the implementation of evidence-based care, nursing staff should closely observe patients' emotional changes, tell successful cases to patients before operation, enhance patients' self-confidence, reasonably regulate patients' diet and living habits after operation, and increase the doctor-patient relationship, so as to improve patients' cooperation and promote the treatment process [22]; the above are important factors in the value of evidence-based care. The changes of hemoglobin (HGB), serum pre-albumin (PAB), and serum albumin (ALB) before and after care were observed, as well as the incidence of complications after care, total effective rate after care, disease severity (bedside index for severity in acute pancreatitis, BISAPe) [23] before and after care, and psychological scores of the two groups before and after care were observed.

Patients' compliance after care, self-management scores [24] after care, and quality of life after care were compared between the two groups.

2.4. Statistical Methods. All statistical analysis of the experimental results was performed by using SPSS24.0 statistical software (Shanghai Yuchuang Network Technology Co., Ltd.). All graph results were plotted by Graphpad8 (SOFTHEAD Inc., Shenzhen). Enumeration data were expressed in the form of (%), and chi-square test was utilized for intergroup comparison. Measurement data were expressed in the form of (mean ± standard deviation), and t-test was used for intergroup comparison. Univariate analysis of variance (ANOVA) and LSD back testing were used for comparison among multiple groups. Repeated measures ANOVA and Bonferroni back testing were used for comparison between multiple time points. $p < 0.05$ was considered statistically significant.

3. Results

3.1. Patient Data. There was no statistic difference in age, gender, BMI, living environment, eating habits, smoking history, drinking history, family medical history, ethnicity, C-reactive protein, white blood cells, and so on ($p > 0.05$) as shown in Table 1.

3.2. Changes of HGB, PAB, and ALB in Two Groups before and after Care. The changes of HGB, PAB, and ALB before and after care were detected. The results showed that there was no statistic difference between the two groups before care ($p > 0.05$), but after care, HGB, PAB, and ALB in both groups increased ($p < 0.05$) and were higher in OG than CG ($p < 0.05$) as shown in Figure 1.

3.3. Incidence of Complications in Two Groups after Care. The incidence of complications after care in the two groups was observed. The total incidence of adverse reactions in OG was 2 (3.08%), while that in CG was 9 (17.31%), which was significantly lower in OG than CG ($p = 0.009$) as shown in Table 2.

3.4. Effective Rate of the Two Groups after Care. The effective rates of the two groups were observed after care. The markedly effective rate of OG was 75.38%, effective rate was 23.08%, and ineffective rate was 1.54%, with a total effective rate of 98.46%. The markedly effective rate of CG was 42.31%, effective rate was 44.23%, and ineffective rate was 13.46%, with a total effective rate of 86.54%. The total effective rate of OG was significantly higher than that of CG ($p = 0.011$) with statistic difference as shown in Table 3.

3.5. The Severity of Diseases in the Two Groups before and after Care. BISAP was used to analyze the disease severity before and after care. The results showed that there was no remarkable difference between the two groups before care ($p > 0.05$), but the scores of both groups decreased after care and were notably lower in OG than CG ($p < 0.05$) as shown in Figure 2.

3.6. Psychological Scores of the Two Groups before and after Care. The psychological status of the two groups of patients before and after care was observed. The results showed that there was no remarkable difference in psychological scores between the two groups before care ($p > 0.05$), but the psychological status scores of the two groups decreased after care, which were lower in OG than in CG ($p < 0.05$) as shown in Figure 3.

3.7. Comparison of Patients' Compliance after Care between the Two Groups. Comparison of the patients' compliance after care between the two groups showed that the compliance score of OG was notably higher than that of CG ($p < 0.05$) as shown in Figure 4.

3.8. Comparison of Self-Management Scores between the Two Groups after Care. After care, the self-management scores of patients in the two groups were observed. The results showed that the scores of disease management, diet management, medication management, and rehabilitation exercise management in OG were higher than those in CG, with statistical difference ($p < 0.05$) as shown in Figure 5.

3.9. Changes of Quality of Life after Care in Two Groups. By observing the quality of life of the two groups of patients after care, it could be seen that the scores of physical function, role physical, emotional function, cognitive function, social function, and other dimensions of the quality of life of the observation group after care were significantly higher than those of the control group ($p < 0.05$) as shown in Table 4.

4. Discussion

According to statistics, the mortality rate of patients with acute pancreatitis is estimated to be 5% [6], which seriously threatens the patient's life safety. It is known that poor diet and lifestyle are important factors in the onset of acute pancreatitis, so it is extremely important to improve bad habits after treatment for patients' rehabilitation, and a large number of documents have proved that effective care can effectively improve patients' quality of life during disease recovery period [25]. Therefore, this study focuses on evidence-based care in acute pancreatitis to improve patients' treatment compliance and quality of life, and the results are as follows: firstly, the changes of HGB, PAB, and ALB before and after care were detected. The results showed that there was no statistical difference between the two groups before care, but after care, HGB, PAB, and ALB in both groups increased and were higher in OG than CG, suggesting that evidence-based care can obviously improve the serum indexes of patients and promote the curative effect. We speculate that its value lies in the fact that evidence-based

Table 1: General data between observation group and control group (n [%]).

	Observation group ($n = 65$)	Control group ($n = 52$)	t or x^2	p
Age (years)			0.246	0.806
	46.8 ± 8.6	47.2 ± 8.9		
Gender			0.267	0.605
Male	43 (66.15)	32 (61.54)		
Female	22 (33.85)	20 (38.46)		
BMI (kg/cm^2)			0.748	0.456
	25.62 ± 3.05	26.16 ± 4.72		
Living environment			0.067	0.796
Town	41 (63.08)	34 (65.38)		
Countryside	24 (36.92)	18 (34.62)		
Dietary habit			0.007	0.933
Good	28 (43.08)	22 (42.31)		
Poor	37 (56.92)	30 (57.69)		
Smoking history			0.032	0.859
Present	44 (67.69)	36 (69.23)		
Absent	21 (32.31)	16 (30.77)		
Drinking history			0.178	0.673
Present	40 (61.54)	30 (57.69)		
Absent	25 (38.46)	22 (42.31)		
Family medical history			0.086	0.769
Present	10 (15.38)	7 (13.46)		
Absent	55 (84.62)	45 (86.54)		
Ethnicity			0.491	0.484
Han	56 (86.15)	47 (90.38)		
Minority	9 (13.85)	5 (9.62)		
C-reactive protein (mh/L)			0.142	0.888
	23.12 ± 5.34	23.26 ± 5.29		
White blood cell (×10^9/L)			1.121	0.265
	14.64 ± 2.31	15.11 ± 2.18		

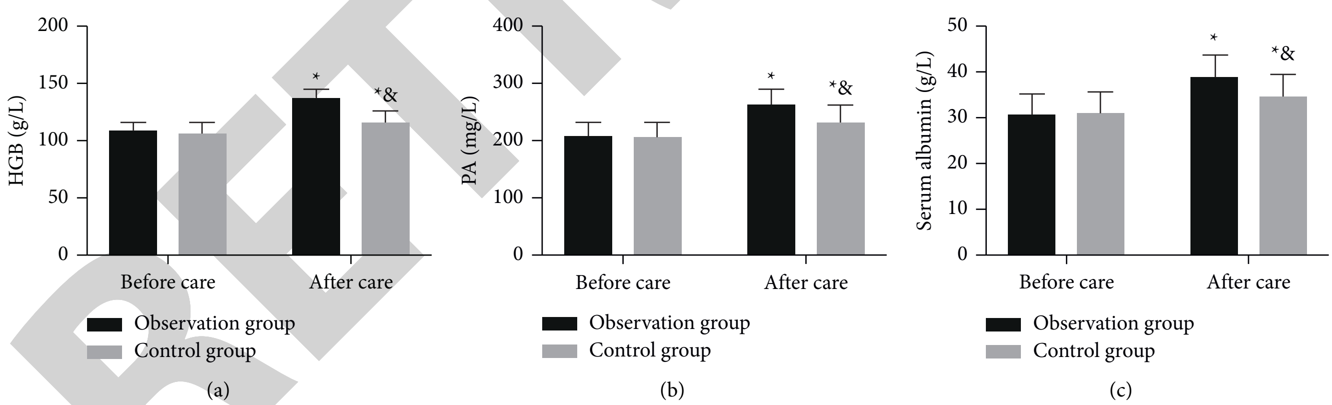

Figure 1: Changes of HGB, PAB, and ALB before and after care between observation group and control group. (a) HGB changes before and after care. (b) PAB changes before and after care. (c) ALB changes before and after care. *Note.* *denotes comparison with before care; & denotes comparison with observation group.

care follows the basis of evidence-based medicine, and patients can be treated according to different situations, including nutritional agent adjustment according to individual physical abnormalities and rational nutrition supply, so as to improve serum indexes and promote curative effects.

The incidence of complications after care in the two groups was observed. The total incidence of adverse reactions in OG was 2 (3.08%), while that in CG was 9 (17.31%), which was significantly lower in OG than CG ($p = 0.009$). The results indicated that evidence-based care can effectively improve prognosis of patients and reduce complications. Comparison of effective rate showed that the total effective rate of OG was 98.46%, which was notably higher than that of CG (86.54%), showing that evidence-based care has high clinical nursing value. We speculate that it is the efficient evidence finding of evidence-based care, summarizing previous care experiences, refining previous deficiencies, and formulating reasonable nursing interventions based on the individual's physical

Table 2: Adverse reaction rate after care between observation group and control group [n (%)].

	Observation group ($n=65$)	Control group ($n=52$)	x^2	p
Respiratory disorder	0 (0.00)	1 (1.92)		
Impaired cardiac function	0 (0.00)	2 (3.85)		
Gastrointestinal hemorrhage	1 (1.54)	3 (5.77)		
Renal dysfunction	1 (1.54)	3 (5.77)		
Total (%)	2 (3.08)	9 (17.31)	6.868	0.009

Table 3: Total effective rate of the two groups after care between observation group and control group [n (%)].

	Observation group ($n=65$)	Control group ($n=52$)	x^2	p
Markedly effective	49 (75.38)	22 (42.31)		
Effective	15 (23.08)	23 (44.23)		
Ineffective	1 (1.54)	7 (13.46)		
Total effective rate	64 (98.46)	45 (86.54)	6.447	0.011

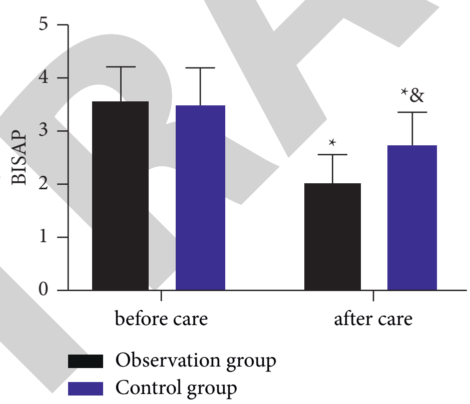

Figure 2: Recovery degree of the two groups before and after care. *Note.* *denotes comparison with before care; & denotes comparison with observation group.

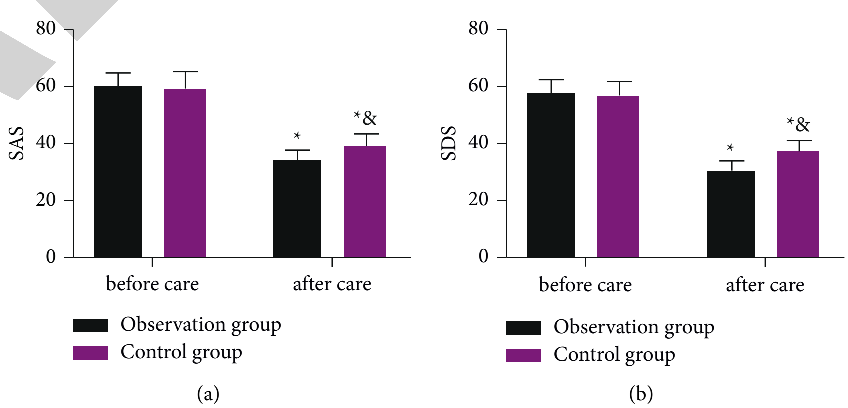

Figure 3: Psychological scores of two groups before and after care. (a) SAS score of the two groups before and after care. (b) SDS score of the two groups before and after care. *Note.* *denotes comparison with before care; & denotes comparison with observation group.

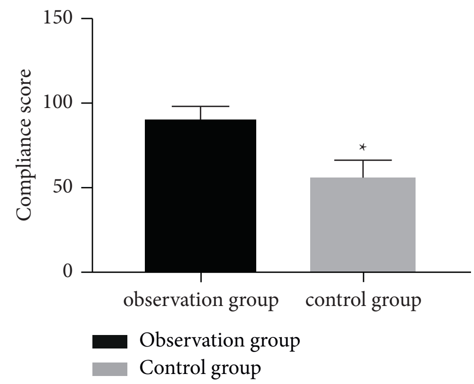

Figure 4: Comparison of patients' compliance after care between the two groups.

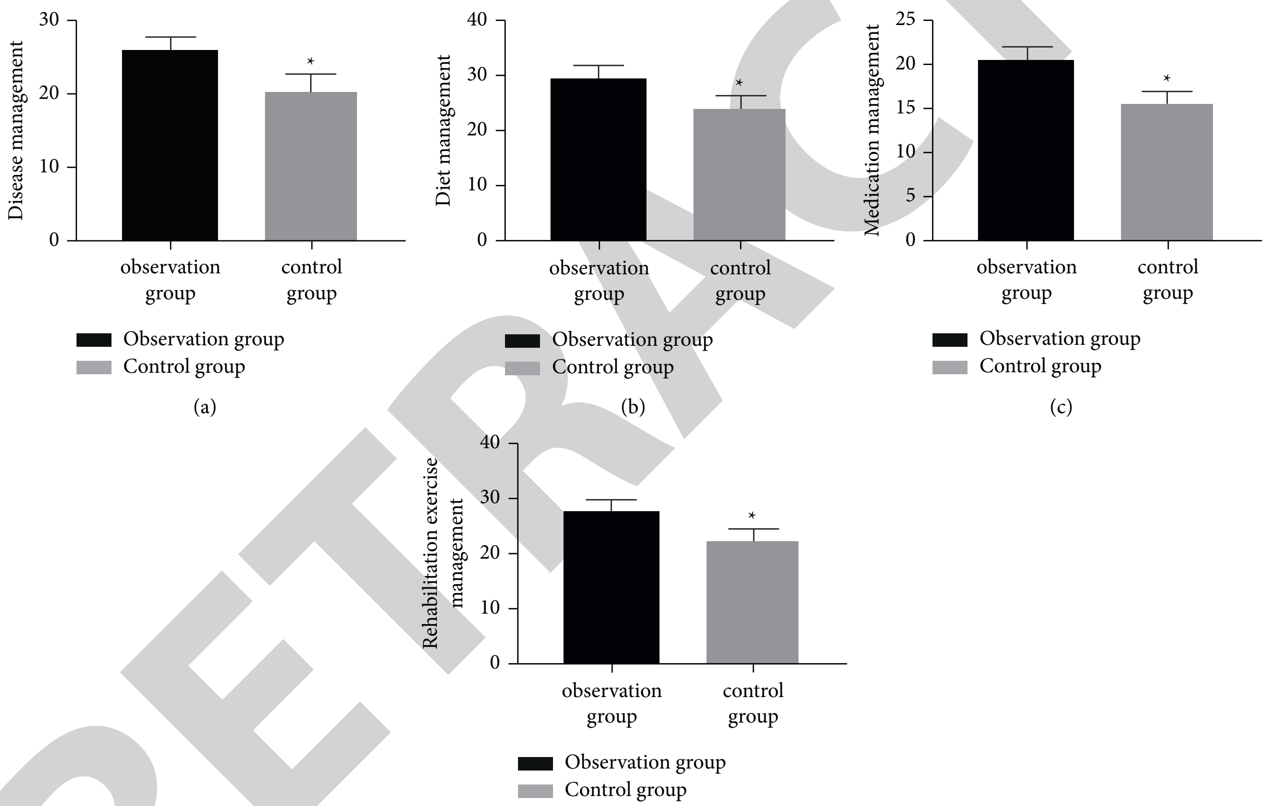

Figure 5: Comparison of self-management scores between two groups after care. (a) The score of disease management in the two groups after care. (b) The score of diet management in the two groups after care. (c) The score of medication management in the two groups after care. (d) The score of rehabilitation exercise management in the two groups after care.

Table 4: Comparison of quality of life between the two groups.

	Observation group ($n = 65$)	Control group ($n = 52$)	t value	p value
Physical function	91.23 ± 3.26	83.22 ± 3.37	13.010	<0.001
Role physical	85.52 ± 3.56	72.30 ± 3.14	21.020	<0.001
Emotional function	86.53 ± 3.25	70.74 ± 3.42	25.510	<0.001
Cognitive function	91.43 ± 3.59	83.34 ± 3.21	12.690	<0.001
Social function	65.55 ± 3.18	52.64 ± 3.24	21.640	<0.001

condition, thus further reduced the risk of complications and achieved consolidation of treatment outcomes. Then, we applied BISAP to analyze the degree of disease recovery before and after care. The results showed that there was no remarkable difference in BISAP between the two groups before care, but after care, the scores of both groups were reduced and were significantly lower in OG than CG, suggesting that evidence-based care can significantly reduce the severity of disease and relieve the pain of patients. Evidence-based care refers to the intervention of patients by consulting relevant disease data and combining with the actual situation of patients. Observation of psychological status of the two groups of patients before and after care showed that there was no remarkable difference in psychological scores between the two groups before care, but the psychological status scores of the two groups decreased after care, which were lower in OG than in CG. This result exemplifies the importance of evidence-based care in relieving patients' stress, anxiety, and other negative emotions. Comparison of the patients' compliance after care between the two groups also showed that the compliance score of OG was notably higher than that of CG, better reflecting the people-centered, comprehensive, and holistic interventions of evidence-based care. Finally, we observed the scores of self-management and the quality of life of patients in the two groups after care. The results showed that the scores of disease management, diet management, medication management, and rehabilitation exercise management in OG were higher than those in CG, and the quality of life was obviously better in OG than CG which further confirmed our above conjecture and showed that evidence-based care greatly improved the treatment outcome of patients.

5. Conclusion

In conclusion, evidence-based care can improve treatment compliance of patients with acute pancreatitis and can effectively improve their quality of life.

However, there are still some shortcomings in this experiment. For example, there are many nursing methods in clinic; the best nursing mode is still controversial. And the research objects in this paper are severe pancreatitis patients; it is not excluded that the application of evidence-based care in other diseases may be different from the experimental results. In addition, the time of this study was short, and long-term follow-up was not conducted. Hence, we will expand the sample size of the study as soon as possible, extend the experimental period, and conduct more detailed and comprehensive experimental analysis to obtain more perfect experimental results.

Data Availability

The datasets used and/or analyzed during the current study are available from the corresponding author on reasonable request.

Conflicts of Interest

The authors declare that they have no conflicts of interest.

Authors' Contributions

Qiu Zheng and Li Cao contributed to the paper equally as co-first authors.

References

[1] S. M. Van DIjk, N. D. L. Hallensleben, H. C. van Santvoort et al., "Acute pancreatitis: recent advances through randomised trials," *Gut*, vol. 66, no. 11, pp. 2024–2032, 2017.
[2] A. Shah, M. Mourad, and S. Bramhall, "Acute pancreatitis: current perspectives on diagnosis and management," *Journal of Inflammation Research*, vol. 11, pp. 77–85, 2018.
[3] P. J. Lee and G. I. Papachristou, "New insights into acute pancreatitis," *Nature Reviews Gastroenterology & Hepatology*, vol. 16, no. 8, pp. 479–496, 2019.
[4] M. Portelli and C. D. Jones, "Severe acute pancreatitis: pathogenesis, diagnosis and surgical management," *Hepatobiliary and Pancreatic Diseases International*, vol. 16, no. 2, pp. 155–159, 2017.
[5] A. Leppäniemi, M. Tolonen, A. Tarasconi et al., "2019 WSES guidelines for the management of severe acute pancreatitis," *World Journal of Emergency Surgery*, vol. 14, no. 1, p. 27, 2019.
[6] A. Garber, C. Frakes, Z. Arora, and P. Chahal, "Mechanisms and management of acute pancreatitis," *Gastroenterology Research and Practice*, vol. 2018, Article ID 6218798, 8 pages, 2018.
[7] R. Garg and T. Rustagi, "Management of hypertriglyceridemia induced acute pancreatitis," *BioMed Research International*, vol. 2018, Article ID 4721357, 12 pages, 2018.
[8] S. D. Crockett, S. Wani, T. B. Gardner et al., "American gastroenterological association institute guideline on initial management of acute pancreatitis," *Gastroenterology*, vol. 154, no. 4, pp. 1096–1101, 2018.
[9] P. Rawla, S. S. Bandaru, and A. R. Vellipuram, "Review of infectious etiology of acute pancreatitis," *Gastroenterology Research*, vol. 10, no. 3, pp. 153–158, 2017.
[10] E. Moggia, R. Koti, A. P. Belgaumkar et al., "Pharmacological interventions for acute pancreatitis," *Cochrane Database of Systematic Reviews*, vol. 4, no. 4, Article ID CD011384, 2017.
[11] S. Rijal, *Post-operative care in pancreatitis: nursing intervention*, Ph.D. thesis Arcada University of Applied Sciences, Helsinki, Finland, 2019, https://www.theseus.fi/handle/10024/163432.
[12] C. Johnstone, "Pathophysiology and nursing management of acute pancreatitis," *Nursing Standard*, vol. 33, no. 4, pp. 75–82, 2018.
[13] A. Z. Paredes, J. M. Hyer, E. W. Beal et al., "Impact of skilled nursing facility quality on postoperative outcomes after pancreatic surgery," *Surgery*, vol. 166, no. 1, pp. 1–7, 2019.
[14] B. E. Alving, J. B. Christensen, and L. Thrysøe, "Hospital nurses' information retrieval behaviours in relation to evidence based nursing: a literature review," *Health Information and Libraries Journal*, vol. 35, no. 1, pp. 3–23, 2018.
[15] A. T. Chatila, M. Bilal, and P. Guturu, "Evaluation and management of acute pancreatitis," *World Journal of Clinical Cases*, vol. 7, no. 9, pp. 1006–1020, 2019.
[16] M. Manrai, R. Kochhar, V. Gupta et al., "Outcome of acute pancreatic and peripancreatic collections occurring in patients with acute pancreatitis," *Annals of Surgery*, vol. 267, no. 2, pp. 357–363, 2018.
[17] S. G. Krishna, A. K. Kamboj, P. A. Hart, A. Hinton, and D. L. Conwell, "The changing epidemiology of acute

Hindawi
Journal of Healthcare Engineering
Volume 2023, Article ID 9875409, 1 page
https://doi.org/10.1155/2023/9875409

Retraction

Retracted: Evaluation of Tresiba Combined with Six Ingredient Rehmannia Pill in the Treatment of Type 2 Diabetes

Journal of Healthcare Engineering

Received 8 August 2023; Accepted 8 August 2023; Published 9 August 2023

This article has been retracted by Hindawi following an investigation undertaken by the publisher [1]. This investigation has uncovered evidence of one or more of the following indicators of systematic manipulation of the publication process:

(1) Discrepancies in scope
(2) Discrepancies in the description of the research reported
(3) Discrepancies between the availability of data and the research described
(4) Inappropriate citations
(5) Incoherent, meaningless and/or irrelevant content included in the article
(6) Peer-review manipulation

The presence of these indicators undermines our confidence in the integrity of the article's content and we cannot, therefore, vouch for its reliability. Please note that this notice is intended solely to alert readers that the content of this article is unreliable. We have not investigated whether authors were aware of or involved in the systematic manipulation of the publication process.

In addition, our investigation has also shown that one or more of the following human-subject reporting requirements has not been met in this article: ethical approval by an Institutional Review Board (IRB) committee or equivalent, patient/participant consent to participate, and/or agreement to publish patient/participant details (where relevant).

Wiley and Hindawi regrets that the usual quality checks did not identify these issues before publication and have since put additional measures in place to safeguard research integrity.

We wish to credit our own Research Integrity and Research Publishing teams and anonymous and named external researchers and research integrity experts for contributing to this investigation.

The corresponding author, as the representative of all authors, has been given the opportunity to register their agreement or disagreement to this retraction. We have kept a record of any response received.

References

[1] J. Li and Q. He, "Evaluation of Tresiba Combined with Six Ingredient Rehmannia Pill in the Treatment of Type 2 Diabetes," *Journal of Healthcare Engineering*, vol. 2022, Article ID 2177176, 6 pages, 2022.

Hindawi
Journal of Healthcare Engineering
Volume 2022, Article ID 2177176, 6 pages
https://doi.org/10.1155/2022/2177176

Research Article

Evaluation of Tresiba Combined with Six Ingredient Rehmannia Pill in the Treatment of Type 2 Diabetes

Jun Li[1] and Qingzhen He[2]

[1]*Department of Emergency, Xi'an No. 3 Hospital, Xi'an 710018, China*
[2]*Department of Endocrinology, Xi'an Gaoxin Hospital, Xi'an 710075, China*

Correspondence should be addressed to Qingzhen He; 161841186@masu.edu.cn

Received 29 November 2021; Revised 7 January 2022; Accepted 12 January 2022; Published 11 February 2022

Academic Editor: Enas Abdulhay

Objective. Insulin replacement therapy is the main treatment method for type 1 diabetes, and adjuvant comprehensive treatment to reduce the complications of diabetes is still the focus of research. The purpose of this study is to explore the clinical efficacy of Tresiba combined with Ingredient Rehmannia Pill in the treatment of type 1 diabetes. *Methods*. A total of 216 patients with type 2 diabetes admitted to our hospital from January 2019 to July 2019 were enrolled in this study. Patients in the control and observation groups were treated with Tresiba and Tresiba combined with Ingredient Rehmannia Pill, respectively. The change of TCM symptom score, blood glucose level and fasting insulin level before and after treatment were evaluated, and the insulin resistance index was calculated to observe the adverse reactions of patients. *Results*. After treatment, the TCM syndrome scores of the two groups decreased significantly, and the TCM syndrome scores of the observation group were significantly lower than those of the control group. The fasting blood glucose, 2 h postprandial blood glucose and insulin resistance index of the observation group were lower than those of the control group. The levels of FBG, 2 hBG and HbA1C in the observation group were significantly lower than those in the control group. The total effective rate of the observation group was 91.7%, which was significantly higher than that of the control group (77.1%). The adverse reactions of patients in the observation group were slightly more than those in the control group. *Conclusion*. Our study demonstrated that Ingredient Rehmannia Pill combined with Tresiba is effective in the treatment of type 2 diabetes, providing alternative therapies for the treatment of diabetes.

1. Introduction

Diabetes is the most common metabolic disease, which is characterized by partial or complete destruction of pancreatic cells leading to insulin deficiency [1]. Diabetic patients have impaired pancreatic islet function at a young age and may require lifelong insulin therapy [2]. According to the report of the International Diabetes Federation, approximately 542,000 children worldwide suffer from diabetes [3]. In addition, about 86,000 children under the age of 15 suffer from diabetes each year, with an estimated annual incidence of 3% worldwide. Complications of diabetes, such as ketoacidosis, should cause widespread concern during the treatment process [4]. Ketoacidosis is still the most common complication after discharge from hospital in diabetic patients [5]. Although insulin replacement therapy is the main treatment method for diabetes, adjuvant comprehensive treatment to reduce the complications of diabetes is still the focus of future research.

Tresiba is a long-acting human insulin analogue suitable for blood glucose control in diabetic patients [6]. There is a risk of hypoglycemia when using insulin to treat diabetes. The ideal insulin should reduce the risk of hypoglycemia while controlling blood sugar [7]. At present, the long-acting insulin commonly used in clinical diabetes treatment mainly include insulin glargine and insulin dete. Tresiba is a new type of long-acting insulin analogue, which can act for more than 24 h [8]. Many clinical studies [9, 10] and observational studies [11, 12] have shown that degu insulin can effectively treat type 1 diabetes and improve the quality of life of patients [13]. However, these drugs are not effective in treating diabetic complications.

Six Ingredient Rehmannia Pill is a famous prescription of “nourishing Yin and strengthening kidney” in traditional Chinese medicine books. Previous studies have demonstrated that Six Ingredient Rehmannia Pill has the effects of lowering blood sugar, preventing diabetes and complications [14]. Six Ingredient Rehmannia Pill combined with valsartan capsule can significantly improve the treatment effect of diabetic nephropathy [15]. It also can assist xiaoke pill in the treatment of type 2 diabetes to improve the efficacy and reduce adverse effects [16]. However, the efficacy of Six Ingredient Rehmannia Pill in the treatment of type 2 diabetes needs to be further verified. This study aimed to clarify the clinical effects of Six Ingredient Rehmannia Pill in the treatment of type 2 diabetes and its complications.

2. Materials and Methods

2.1. General Information. A total of 216 patients with type 2 diabetes admitted to our hospital from January 2019 to July 2019 were enrolled and divided into control group and observation group. The control group included 108 patients: 52 males and 56 females. The average age was 29.2 ± 15.9 years old. The average course of disease was 7.52 ± 0.71 years. The average body mass index was $21.92 \pm 2.63\,kg/m^2$. The observation group consisted of 53 males and 55 females. Mean age was 24.2 ± 13.8 years old, the average course of disease was 8.42 ± 1.35 years. The average body mass index was $21.39 \pm 2.71\,kg/m^2$. There was no significant difference in gender, age, disease course and body mass index between the two groups ($P > 0.05$).

2.2. Inclusion and Exclusion Criteria

Inclusion criteria: (1) the patient had symptoms of polydipsia, polyphagia, polyuria and other symptoms, such as easy to hunger, dry stool knot, red tongue, fear of heat, and upset, and fasting blood glucose was above 7.0 mmol/L. The patient was definitely diagnosed as diabetes; (2) good drug tolerance; (3) did not use glucocorticoids and other hormone drugs in the past month; (4) the patient is not insulin resistant; (5) the patients were informed and agreed to the study.

Exclusion criteria: (1) patients who do not follow the doctor’s advice to take drugs and test blood glucose and lipid; (2) patients with life-threatening serious complications during treatment; (3) patients with severe infectious diseases, renal failure, and immune system diseases; (4) combination of emotional tension and severe anxiety cannot cooperate; (5) women during lactation or pregnancy.

2.3. Treatment. Patients in the control group received routine Tresiba treatment with 0.4 U/kg once a day. Patients in the observation group were treated with Six Ingredient Rehmannia Pill (Henan Wanxi pharmaceutical co., LTD., specification: 240 pills, approval number: national drug approval Z41022128) orally three times per day and eight pills per time besides routine Tresiba treatment. Both groups were treated for 12 weeks.

2.4. Observation Indicators. According to the “Guiding Principles for Clinical Research of New Traditional Chinese Medicine” [17], the changes in TCM symptom scores before and after treatment were evaluated. Nine main syndromes: dry throat, dry mouth, heavy dizziness, sore waist and knees, chest tightness, chest pain, white and greasy tongue coating or less bitterness, heavy numbness of limbs, fatigue, fatigue, and obesity. These five symptoms include fever, insomnia and irritability, menstrual cramps or menstrual disorders, constipation, scaly skin and dryness. According to the severity of symptoms, the score was divided into four levels: none, mild, moderate, and severe. The main scores were 0, 2, 4, and 6 points, and the secondary scores were 0, 1, 2, and 3 points. The total score was 69 points. The blood glucose levels and fasting insulin levels before and after treatment were detected in the two groups, and the insulin resistance index was calculated. Insulin resistance index = (fasting insulin × fasting blood glucose)/22.5. The patient adverse reactions during treatment were observed. The fasting blood glucose, fasting blood glucose (FBG), 2 h postprandial blood glucose (2 HBG), and glycosylated hemoglobin (HbA1C) were detected before and after treatment.

All records are collected by our hospital and completed by trained and qualified investigators. Data management will be carried out under the guidance of medical statistics experts. To ensure the accuracy of the data, 2 data administrators will input and proofread the data.

2.5. Criteria for Therapeutic Effects. Significant effect was defined as the disappearance or improvement of clinical symptoms or signs, fasting blood glucose <7.2 mmol/L, and 2 h postprandial blood glucose <8.3 mmol/L. Effective was defined as significant improvement in clinical symptoms and signs, fasting blood glucose <10.0 mmol/L, and 2 h postprandial blood glucose <8.3 mmol/L. Ineffectiveness was defined as no improvement or aggravation of clinical symptoms and signs.

2.6. Data Analysis. SPSS 20.0 was used for statistical analysis. Quantitative data were used for independent t-test and qualitative data were used for χ^2 test. $P < 0.05$ was considered statistically significant.

3. Results

3.1. Comparison of TCM Syndrome Scores between the Two Groups before and after Treatment. No significant differences in TCM syndrome scores between the two groups before treatment were observed ($P > 0.05$, Figure 1 and Table 1). However, the treatment decreased TCM syndrome scores of the two groups significantly, TCM score of the observation group was significantly lower than that of the control group ($P < 0.05$).

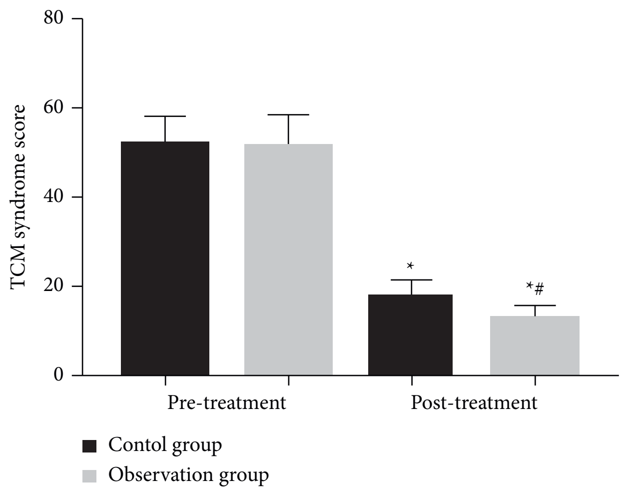

Figure 1: Comparison of TCM syndrome scores before and after treatment between the two groups. $^{*}P < 0.05$, compared with that before treatment; $^{\#}P < 0.05$, compared with the control group.

Table 1: Comparison of TCM syndromes before and after treatment between the two groups (mean ± standard deviation).

Group	Number	Before	After	T value	P value
Observation	108	51.63 ± 6.73	12.65 ± 2.77	36.489	0.000
Control	108	51.87 ± 6.29	18.97 ± 3.46	32.219	0.000
T value		0.178	7.936		
P value		0.428	0.000		

3.2. Comparison of Blood Glucose and Insulin Resistance Index before and after Treatment between the Two Groups (Mean ± Standard Deviation). Before treatment, there were no significant differences in fasting blood glucose, 2 h postprandial blood glucose, and insulin resistance index between the control group and the observation group ($P > 0.05$). After treatment, the fasting blood glucose, 2 h postprandial blood glucose and insulin resistance index of the observation group were significantly lower than those of the control group ($P > 0.05$, Table 2).

3.3. Comparison of FBG, 2 hBG and HbA1C between the Two Groups before and after Treatment (Mean ± Standard Deviation). As shown in Table 3, there was no significant difference in the levels of FBG, 2 hBG, and HbA1C before treatment between the two groups. After treatment, the levels of FBG, 2 hBG and HbA1C in the two groups decreased, and the levels of FBG, 2 hBG and HbA1C in the observation group were significantly lower than those in the control group ($P < 0.05$).

3.4. Comparison of Therapeutic Effect between the Two Groups. As shown in Table 4 and Figure 2, the total effective rate of patients in the observation group was 91.7%, which was significantly higher than that in the control group (77.1%) ($P < 0.05$).

3.5. Occurrence of Adverse Reactions During Treatment in the Two Groups. As shown in Figure 3, there were 3 cases of loose stools and 2 cases of anorexia the control group. The adverse reaction rate was 4.63% (5/108). In the observation group, there were 2 cases of nausea, 2 cases of headache, and 2 cases of bloating. The adverse reaction rate was 6.25% (6/108). The incidence of adverse reactions in the observation group was slightly higher than that in the control group (2 = 1.106, P = 0.293).

4. Discussion

As a systemic metabolic disease, diabetes mellitus is mainly manifested as elevated blood sugar [18], which is mostly caused by insufficient insulin secretion or dysfunction [19]. Diabetes is an autoimmune disease mediated by T lymphocytes. The destruction of β islet cells leads to inflammation, which leads to an absolute lack of insulin secretion, requiring lifelong treatment with exogenous insulin [20]. At present, insulin replacement therapy is the main treatment method for diabetes, but adjuvant comprehensive treatment to reduce the complications of diabetes is also the focus of research.

Previous studies have found that the intervention of Six Ingredient Rehmannia Pill can delay or prevent the occurrence of type 2 diabetes [21], and can improve the inflammatory response and increase the inflammation by regulating the expression of related genes, regulating cell apoptosis, and inhibiting the symptoms of liver and kidney yin deficiency caused by diabetes [22, 23]. In addition, compared with the use of metformin alone, Six Ingredient Rehmannia Pill combined with metformin have fewer adverse reactions, and the therapeutic effect is significantly improved [24, 25]. In this study, although the scores of TCM syndromes in the control group and the observation group were significantly reduced after treatment, the scores of the observation group were significantly lower than those of the control group, indicating that the therapeutic effect of Six Ingredient Rehmannia Pill combined with insulin degu was better than that of Degu insulin alone. Six Ingredient Rehmannia Pill combined with acarbose has accurate curative effect in the treatment of type 2 diabetes mellitus [26] and can be widely used in clinical practice, which further supports the conclusions of this study.

In addition, the comparison of fasting blood glucose, 2 h postprandial blood glucose and hba1c levels between the two groups and the clinical efficacy showed that Six Ingredient Rehmannia Pill had a significant treatment effect on type 2 diabetes. Although Six Ingredient Rehmannia Pill combined with Tresiba have more adverse reactions than Tresiba alone, the difference was not significant.

Our research has some limitations. The sample size of this research was limited. In the future, it is necessary to conduct a larger sample size research to further verify the conclusions of this research. At the same time, this study was not to verify the efficacy of Six Ingredient Rehmannia Pill on all complications of diabetes, which needs to be further verified by future studies.

Table 2: Comparison of blood glucose and insulin resistance index between the two groups before and after treatment.

Group	Fasting blood glucose (mmol/L)		2 h postprandial blood glucose (mmol/L)		Insulin resistance index	
	Before	After	Before	After	Before	After
Control	12.87 ± 1.24	6.35 ± 1.16	19.33 ± 3.27	7.87 ± 0.55	4.83 ± 0.84	2.83 ± 0.34
Observation	12.65 ± 1.37	5.12 ± 0.95	19.54 ± 3.35	6.35 ± 0.31	4.99 ± 0.78	2.27 ± 0.16
T value	1.165	5.667	0.163	17.002	0.911	10.691
P value	0.123	0.000	0.537	0.000	0.167	0.000

Table 3: Comparison of FBG, 2 hBG and HbA1C before and after treatment in the two groups.

Group	Number	Time	FBG (mmol/L)	2 hBG (mmol/L)	HbA_1C (%)
Control	108	Before	8.53 ± 1.59	14.15 ± 3.52	9.73 ± 2.13
		After	7.25 ± 0.58	10.26 ± 1.33	8.18 ± 1.60
Observation	108	Before	8.95 ± 1.63	14.83 ± 3.69	10.37 ± 2.06
		After	6.84 ± 0.50	9.26 ± 0.54	6.58 ± 1.20
t_1, P			5.31, <0.01	7.04, <0.01	4.08, <0.01
t_2, P			10.16, <0.01	10.48, <0.01	11.09, <0.01
t_3, P			1.35, >0.05	0.88, >0.05	1.56, >0.05
t_4, P			6.70, <0.01	4.75, <0.01	5.53, <0.01

(1) comparison before and after treatment in the control group; (2) comparison before and after treatment in the observation group; (3) comparison between groups before treatment; (4) comparison between groups after treatment.

Table 4: Comparison of therapeutic effect between the two groups.

Group	Number	Excellent	Effective	Ineffective	Total effective rate
Control	108	40	34	22	77.1
Observation	108	56	32	8	91.7*

* $P < 0.05$, compared with control group.

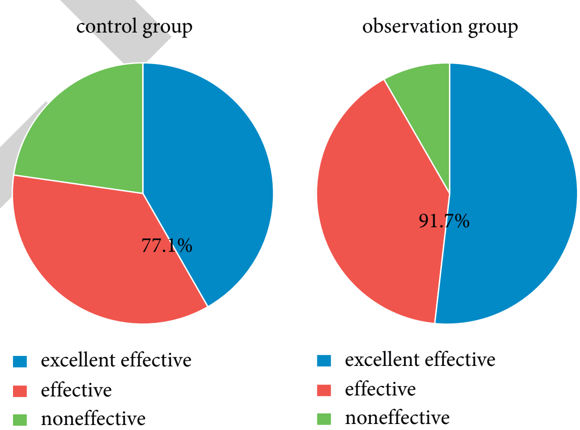

Figure 2: Comparison of therapeutic effect between the two groups.

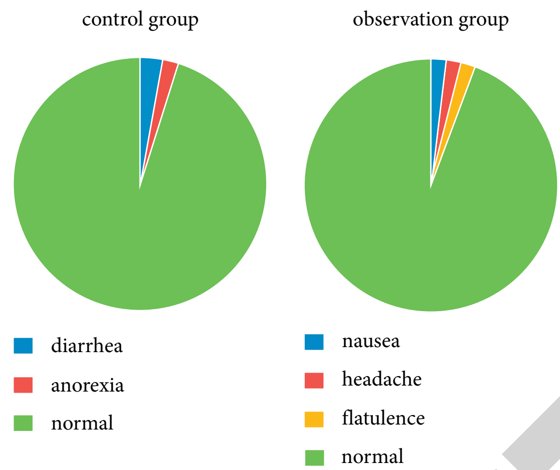

Figure 3: Occurrence of adverse reactions in the two groups.

5. Conclusion

In summary, Six Ingredient Rehmannia Pill combined with Tresiba has a significant therapeutic effect on type 2 diabetes and has the potential for clinical application. This research provided a research foundation for the future research on the treatment of diabetes and its complications.

Data Availability

The authors confirm that the data supporting the findings of this study are available within the article.

Conflicts of Interest

All authors declare no conflicts of interest.

Acknowledgments

This study was not supported by any grants.

References

[1] G. X. Ramalho and M. G. Dytz, "Diabetes of the exocrine pancreas related to hereditary pancreatitis, an update," *Current Diabetes Reports*, vol. 20, p. 16, 2020.

[2] A. Barker, A. Lauria, N. Schloot et al., "Age-dependent decline of β-cell function in type 1 diabetes after diagnosis: a multi-centre longitudinal study," *Diabetes, Obesity and Metabolism*, vol. 16, no. 3, pp. 262–267, 2014.

[3] I International Diabetes Federation, *International Diabetes Federation*, IDF Diabetes Atlas, Brussels, Belgium, 6th edition, 2013.

[4] M. J. Gan, A. Albanese-O'Neill, and M. J. Haller, "Type 1 diabetes: current concepts in epidemiology, pathophysiology, clinical care, and research," *Current Problems in Pediatric and Adolescent Health Care*, vol. 42, pp. 269–291, 2012.

[5] S. F. Farsani, K. Brodovicz, J. Marquard, E. Wissinger, and B. A. Maiese, "Incidence and prevalence of diabetic ketoacidosis (DKA) among adults with type 1 diabetes mellitus (T1D): a systematic literature review," *BMJ Open*, vol. 7, no. 7, Article ID e016587, 2017.

[6] G. M. Keating, "Insulin degludec and insulin degludec/insulin aspart: a review of their use in the management of diabetes mellitus," *Drugs*, vol. 73, no. 6, pp. 575–593, 2013.

[7] A. L. McCall, "Insulin therapy and hypoglycemia," *Endocrinology and Metabolism Clinics of North America*, vol. 41, pp. 57–87, 2012.

[8] V. Pandyarajan and M. A. Weiss, "Design of non-standard insulin analogs for the treatment of diabetes mellitus," *Current Diabetes Reports*, vol. 12, no. 6, pp. 697–704, 2012.

[9] S. Heller, J. Buse, S. Garg et al., "Insulin degludec, an ultra-longacting basal insulin, versus insulin glargine in basal-bolus treatment with mealtime insulin aspart in type 1 diabetes (BEGIN Basal-Bolus Type 1): a phase 3, randomised, open-label, treat-to-target non-inferiority trial," *The Lancet*, vol. 379, no. 9825, pp. 1489–1497, 2012.

[10] S. C. L. Gough, A. Bhargava, R. Jain, H. Mersebach, S. Rasmussen, and R. M. Bergenstal, "Low-volume insulin degludec 200 Units/mL once daily improves glycemic control similarly to insulin glargine with a low risk of hypoglycemia in insulin-naïve patients with type 2 diabetes," *Diabetes Care*, vol. 36, no. 9, pp. 2536–2542, 2013.

[11] K. Kaku and M. A. Eid, "Safety, efficacy, and early clinical experience of insulin degludec in Japanese people with diabetes mellitus: a first-year report from Japan," *Journal of diabetes investigation*, vol. 6, pp. 610–619, 2015.

[12] L.-H. Lena, "Changes in HbA1c, insulin dose and incidence of hypoglycemia in patients with type 1 diabetes after switching to insulin degludec in an outpatient setting: an observational study," *Current Medical Research and Opinion*, vol. 31, pp. 1487–1493, 2015.

[13] N. Freemantle, M. Evans, T. Christensen, M. L. Wolden, and J. B. Bjorner, "A comparison of health-related quality of life (health utility) between insulin degludec and insulin glargine: a meta-analysis of phase 3 trials," *Diabetes, Obesity and Metabolism*, vol. 15, no. 6, pp. 564–571, 2013.

[14] B. Wang, "Acupuncture combined with Six Ingredient Rehmannia Pill in the treatment of type 2 diabetes with lipid metabolism disorder and its effect on insulin resistance," *Chinese General Practice*, vol. 19, no. 31, pp. 3878–3882, 2016.

[15] Y. J. Dong, "Clinical observation on treatment of early diabetic nephropathy with six ingredient rehmannia pill and valsartan capsules," *Chinese Prescription Drugs*, vol. 9, pp. 63-64, 2015.

Hindawi
Journal of Healthcare Engineering
Volume 2022, Article ID 7872500, 9 pages
https://doi.org/10.1155/2022/7872500

Research Article

A Torn ACL Mapping in Knee MRI Images Using Deep Convolution Neural Network with Inception-v3

S. Sridhar ,[1] J. Amutharaj,[2] Prajoona Valsalan ,[3] B. Arthi ,[4] S. Ramkumar ,[5] S. Mathupriya,[6] T. Rajendran ,[7] and Yosef Asrat Waji [8]

[1]*Department of Computer Science and Engineering, Saveetha School of Engineering, Saveetha Institute of Medical and Technical Sciences, Chennai, India*
[2]*Department of ISE, RajaRajeswari College of Engineering,Mysore Road, Bangalore, Karnataka, India*
[3]*Dhofar University, Salalah, Oman*
[4]*Department of Computer Science and Engineering, College of Engineering and Technology, SRM Institute of Science and Technology (Deemed to Be University), Kattankulathur, Chennai, Tamilnadu, India*
[5]*Department of Computer Applications, Kalasalingam Academy of Research and Education (Deemed to Be University), Srivilliputhur, Tamilnadu, India*
[6]*Department of Computer Science and Engineering, Sri Sairam Institute of Technology (Autonomous), Chennai, Tamilnadu, India*
[7]*Makeit Technologies (Center for Industrial Research), Coimbatore, Tamilnadu, India*
[8]*Department of Chemical Engineering, College of Biological and Chemical Engineering, Addis Ababa Science and Technology University, Addis Ababa, Ethiopia*

Correspondence should be addressed to T. Rajendran; rajendranthavasimuthuphd@gmail.com and Yosef Asrat Waji; yosef.asrat@aastu.edu.et

Received 1 December 2021; Revised 7 January 2022; Accepted 17 January 2022; Published 8 February 2022

Academic Editor: Enas Abdulhay

The anterior cruciate ligaments (ACL) are the fundamental structures in preserving the common biomechanics of the knees and most frequently damaged knee ligaments. An ACL injury is a tear or sprain of the ACL, one of the fundamental ligaments in the knee. ACL damage most generally happens during sports, for example, soccer, ball, football, and downhill skiing, which include sudden stops or changes in direction, jumping, and landings. Magnetic resonance imaging (MRI) has a major role in the field of diagnosis these days. Specifically, it is effective for diagnosing the cruciate ligaments and any related meniscal tears. The primary objective of this research is to detect the ACL tear from MRI knee images, which can be useful to determine the knee abnormality. In this research, a Deep Convolution Neural Network (DCNN) based Inception-v3 deep transfer learning (DTL) model was proposed for classifying the ACL tear MRI images. Preprocessing, feature extraction, and classification are the main processes performed in this research. The dataset utilized in this work was collected from the MRNet database. A total of 1,370 knee MRI images are used for evaluation. 70% of data (959 images) are used for training and testing, and 30% of data (411 images) are used in this model for performance analysis. The proposed DCNN with the Inception-v3 DTL model is evaluated and compared with existing deep learning models like VGG16, VGG19, Xception, and Inception ResNet-v28. The performance metrics like accuracy, precision, recall, specificity, and F-measure are evaluated to estimate the performance analysis of the model. The model has obtained 99.04% training accuracy and 95.42% testing accuracy in performance analysis.

1. Introduction

ACL tear is a typical physical problem among young athletes with an annual occurrence of 0.8 per 1000 in the general population but as high as 100 for professional football players for every 1000. With the noncontact loading of a valgus knee, ACL injuries most commonly occur when turning the other direction, causing a constrained internal rotation of the tibia [1].

ACL tear might be partial and completely teared. Partial tear ranges from the small tears, including only few fibres, to a high-grade, near, and complete tear including practically the entire ACL fibres. A partial tear can include both or just a single bundle to a varying degree. In some cases, the plastic deformity of the ACL without fiber discontinuity can cause ACL insufficiency [2]. ACL tear detection depends on assessing the obliquely oriented structures on several images segments with various tissues contrast utilizing the integration of MRI discoveries such as discontinuity of fiber, contour changes, and abnormality of signal inside the injured ligaments [3].

Over the past decade, the role of imaging in osteoarthritis (OA) research has grown significantly. Magnetic resonance imaging (MRI) was one of the key components of large-scale longitudinal tests, providing a rich array of musculoskeletal tissue functional and structural characteristics that were previously unavailable. It is necessary to improve data management, quality assurance, automated postprocessing images pipelines, and multidimensionality feature space dissection methods in order to make better use of this data resource, which comes at a higher cost and contains more perplexing quantitative information volume [4]. When examining the tear in the ACL, the coronal, sagittal, and axial planes are taken into consideration. When the ligaments were first detected on the sagittal planes, they were followed from distal to proximal in order to evaluate where the rip had occurred. As a result, the sagittal and coronal planes were thoroughly analyzed in order to confirm the presence of the teared region. As soon as the spirally teared pattern was recognized, the middle part of the spiral was designated as the teared region [5].

MRI is a sort of medical imaging that is believed to be a successful method due to the fact that it is noninvasive and that it has superior soft-tissue contrast compared to other types of imaging. When compared to ionizing radiation-based methods, it does not alter the structure, construction, or properties of particles in the way that they do. As a result, magnetic resonance imaging (MRI) can provide a wealth of information on tissue structures, such as their size, shape, and location. Massive amounts of attention are drawn to magnetic resonance imaging (MRI) for medical procedures and CADe (computer-aided detection) [6].

Furthermore, the two factors that had the biggest impact on the results of medical image processing and analysis were the picture acquisitions and the image interpretations. It is commonly known that improved image quality leads to better results when photographs are processed, and this is true in this case. In many circumstances, the image quality was dependent on the quality of the image acquisition; in this way, better image acquisitions resulted in higher image quality overall. Not only does magnetic resonance imaging (MRI) have the advantages of being noninvasive and providing superior soft-tissue contrast, but it also does not expose patients to high levels of ionizing radiation. As a result, magnetic resonance imaging (MRI) could provide useful information about tissue structures; it is essential in medical image processing. As a result, MRI scans are the primary focus of this investigation. It is necessary to develop an image interpretation system that integrates a variety of functions such as image detection, segmentation, registration, and classification in order to obtain exact picture interpretation results. The deep learning model was used in this study in order to obtain the desired system. Figure 1 shows the difference betwwenNormal and torn ACL in MRI.

Deep learning (DL) is the subcategory of machine learning approaches in artificial intelligences (AI). If the number of layers increases in the network, it is known as deep learning. It is additionally called deep neural network (DNN). It can learn from unstructured data, likewise by utilizing fine-tuning that is done by the backpropagation approach. Deep learning might be utilized to discover features automatically from the provided dataset for each particular application [7, 8]. Inspired by the effective and reliable execution of deep learning systems, DCNN was implemented for MRI medical images classification to classify ACL ligament tears.

In this research, an Inception-v3 DTL model based on DCNN was proposed for the classification of ACL tear using MRI images. The most important aspect of this study was the detection of an ACL tear from MRI knee image, which could be beneficial in determining the nature of a knee anomaly. Data preparation is the first stage of the process. During preprocessing, noise and other artifacts were eliminated from the images, and the images were adjusted to be suitable for the intended classification work. Following the preprocessing stage, the next step is to extract the features of the image. To carry out this research, the Inception-v3 DTL model was employed, which extracted features from an input preprocessed image and then delivered those features to a DTL model for training. The model that was created as a result of this training was eventually put to the test by deploying the DCNN classification model to distinguish between images of normal and abnormal (torn) ACL. Finally, the proposed model's performance was compared to those of other existing models for validation.

ACL tears and their associated complications are covered in this section, which serves as an introduction to the topic. In the next sections, related works will be covered in Section 2, the proposed methodology will be discussed in Section 3, the experimental analysis of results will be discussed in Section 4, and the conclusion and future directions will be discussed in Section 5.

2. Related Works

Valentina Pedoia et al. used 3D CNN to detect and stage the severity of patellofemoral and meniscus joint cartilage morphological degenerative alterations in patients with osteoarthritis and anterior cruciate ligament rupture. The deep-learning pipeline in this model is comprised of segmenting cartilaginous and meniscus tissue and classifying lesions within the region of the tissue that has been segmented. The U-Net model was employed for automatic segmentation, and a "shallow" 3D CNN was used for the staging and identification of the severity of meniscus lesions. The conventions that were used for architectural visualization were very similar to those that were used for U-Net. The feature maps that were obtained were flattened into one-

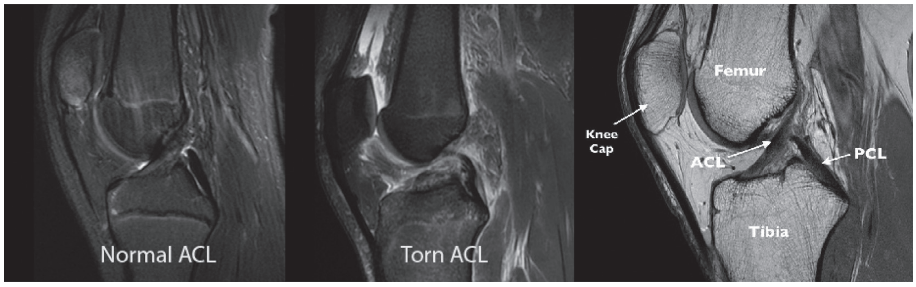

Figure 1: Difference between normal and torn ACL in MRI.

dimensional vectors and then used as inputs to a fully connected layer that created class probabilities based on the features that were obtained. A random forest was trained to make the final forecast after the probabilities were merged with demographic characteristics and coupled with the final prediction.

A DCNN classification approach based on three distinct CNN approaches for detecting ACL tears was proposed by Fang Liu et al., who used DenseNet, VGG16, and AlexNet to detect ACL tears. In this model, the classification models had to be trained separately, which resulted in a high training burden. In addition, the training y was inefficient, which can be improved with more practice. In general, the classification and detection of structural abnormalities present in the isolated ligament were performed correctly, and the results were satisfactory.

Rehan Ashraf et al. proposed a DCNN model for big data medical image classification using MRI images of various organs and tissues, which was tested in a real-world environment. The DCNN was used to carry out the feature extraction and classification steps in this particular model. An approach based on GoogleNet's pretrained GoogleNet layer classifier was used to extract the features, and a softmax layer classifier was used to extract deep features. A total of 144 layers, including convolution and fully connected layers, were used. When comparing the performance analyses from different classes, the model attained an overall accuracy of 98 percent in total.

Christoph Germann et al. employed the DCNN to diagnose ACL tears in MRI images as well. Using homogenous versus heterogeneous knee MRI cohorts with varied pulse sequenced methods and variable magnetic field strengths, a performance comparison was seen in this study [9], which compared the performances of the two groups.

Milica M.B. and Marko C.B. created a brain tumor classification algorithm based on CNN using MRI scans, which they believe will be successful. This model was proposed to classify three types of cancer in the brain tumor, and it was found to be effective. To obtain distinct viewpoints, the MRI scans were obtained in three separate planes: axial, coronal, and sagittal. Images with T1-W contrast enhancement were used to do the classification, which was done by comparing images from different databases. According to this model, CNN performed well with an accuracy of 97.28 percent when using 60 percent of training and 20 percent of validation and 20 percent of testing data. While taking additional approaches into consideration, it is possible to improve the generalization capability of the network [10].

CMAK Zeelan Basha employed machine learning methods to automate the classification of MRI images in this research. Using this model, a novel MRI image classification approach was developed for recognizing self-activation descriptions, which was then used to provide specialists and radiologists with a well-ordered selection devising result. In order to remove noisy data, a Gaussian filter was utilized, and the FCM technique was used for partitioning the data. The statistical features were retrieved with the use of mean, kurtosis, and median values, and the PNN, SVM, and K-NN algorithms were employed for classification. SVM with statistical characteristics outperformed the other two algorithms in terms of accuracy, with 93.1 percent accuracy [11].

In [12], a model for categorization and identification of anomalies in MRI brain images was suggested, which makes use of convolutional neural networks. A CNN containing feature maps that had been preprocessed in the curvelet domain was employed for MRI classification. Because of its multidirectional capability, the curvelet gave a good sparse representation, and the features recovered were more exact than those obtained using other standard methodologies. The accuracy of this curvelet domain combined with CNN was improved during the training and validation processes [12].

According to [13], a DCNN model has been developed for comparing the diagnostic interchangeability and image quality of nonaccelerated images to 15-layered DCNNs or 3-layered CNNs images with the optimal number of layers for a sixfold acceleration of the knee MRI dataset, with the optimal number of layers being three.

Mazhar Javed Awan et al. suggested an automatic detection algorithm for ACL tears based on deep learning techniques. In this study, two models of CNN technique were used, one of which was a regular CNN model and the other was a customized CNN model. ACL MRI pictures were classified using a conventional model with five layers and a customized model with eleven layers. Both models were tested for classification using ACL images. According to [14], the modified CNN model has produced superior results than the regular CNN model in terms of learning rate, accuracy, and other factors.

3. Proposed Methodology

A DCNN model with pretrained Inception-v3 is proposed in this research. This Inception-v3 model is based on DTL as it is proposed to identify the ACL ligament tears from the input dataset by classifying the MRI scan images. To extract features from the dataset, a pretrained Inception-v3 model is used, and the DCNN model is used for classification. $299 \times 299 \times 3$ is the input image resolution. DCNN usually performs well with a larger dataset over a smaller one. TL could be useful in the CNN applications where the dataset is not huge [13]. For applications with comparatively smaller datasets, the concept of TL utilizes the learned model from large datasets such as ImageNet. This removes the need for a large dataset and decreases the lengthy training time as needed when generated from scratch by the deep learning algorithm. TL is a deep learning method that uses the model trained for the single assignment as ainitial point to train the model for a similar assignment. It is typically much quicker and simpler to fine-tune a network with TL than training a network from scratch. By leveraging standard models that have already been trained on large datasets, it allows training models using similar small labeled data. Training time and computing resources can be significantly decreased. With TL, the model does not need to be trained for as many epochs (a complete training period on the entire dataset) like a new model.

There are many kinds of transfer learning; an effective way was to initialize from pre-rained models the parameters of deep architectures and thus fine-tune learning parameter for making it adaptable for the target domains. This technique was used if the dataset was smaller, and, related to feature spaces or tasks, the target domains shared similarities with the domain sources. In image, lower-level characteristics were generally among various classes of image like edges, curves, gradients, and so on; thus higher-level features were classes-specific. The pretrained deep architecture for the classifications of ACL MRI images was modified based on this assumption. TL is an efficient way of achieving meaningful results in classification issues with small data size. Also, the hypertuning of DTL models will further enhance the performance. A DTL model-based Inception-v3 is implemented in this work. The proposed model is used for feature extraction by utilizing its learned weights on the ImageNet dataset together with a convolution neural network. The proposed DCNN technique with Inception-v3 architecture for the classification of ACL images is shown in Figure 2.

Inception-v3 based DCNN model is considered for retraining; this model consists of AvgPool, convolution, maxpool, concat Layer, dropout, fully connected layer, and softmax function.

3.1. Average Pooling. It is a 2-dimensional (2D) function with a pool size of (8×8), which decreases the data variance and the computational complexity. This layer allows the outcome to flow to the next layer.

3.2. Convolution. A $299 \times 299 \times 3$ input size is used by convolution function, and this layer generates the feature maps through convolving the input data.

3.3. Maxpool. It is a two-dimensional maxpooling function and it reduces the variance at data and the computational complexity. The maxpooling is used to extract essential features such as edges, and average pooling is used to extract features smoothly.

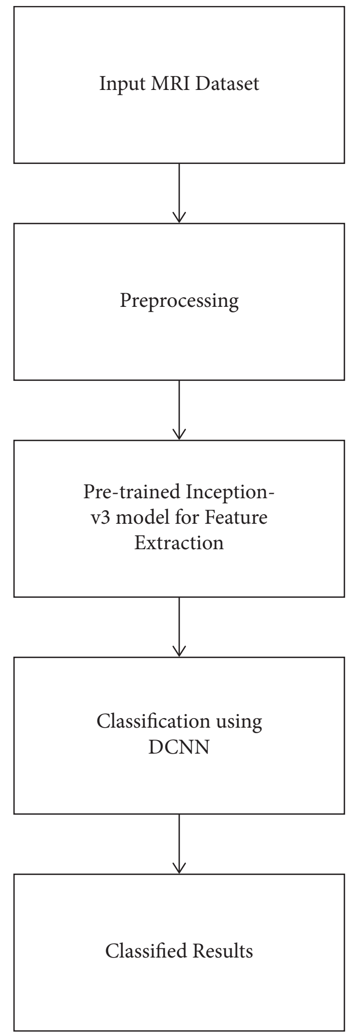

Figure 2: Proposed model.

3.4. Concatenation. This layer is used to concatenate its several input blobs into a single blob of output, and it takes a list of tensors as the input, where all have the same type of shape expect concatenation axis. It returns an output of a single tensor while concatenating all the inputs.

3.5. Dropout. It is considered as the regularization approach to minimize overfitting in the ANNs by overcoming complexed coadaptations from the training data. Here, the dropout scale is considered as 0.4, and it was the very effective method for executing averaging with the neural network model. Moreover, dropout refers to dropout of the units such as visible and hidden sides in a considered neural network.

3.6. Fully Connected. This is used to connect all neurons to one layer and another layer, which works based on a conventional multilayer-preceptor (MLP) neural network.

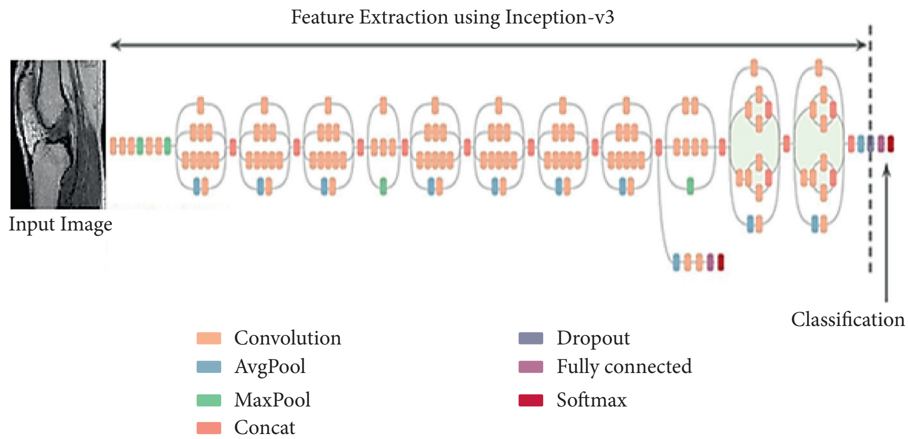

Figure 3: Architecture of the proposed model.

3.7. Softmax. The softmax function is used like the output function, which works similarly to maxlayer when it was variable for training via gradient descents. The exponential functions would cause an increment in the probability of preceding layers and compared to the other values; correspondingly, all output summations will always be equal to one [15].

In general, a two-dimensional plane can form many independent neurons, and the DCNN was made of several layers in which multiple 2D feature mapping planes structure. There are four core segments of the DCNN. The first segment was the local perceptions that the global image does not need to be interpreted by each neuron in neural networks, yet just local and global information waacquired by collecting local data. Next was the method of convolutions. The convolution functionality which was for extracting features of image is shown in Figure 3, and, by using convolution kernel, the total parameters could be reduced higher. Weight sharing is third. It means that parameters of the similar convolution kernels were utilized for the entire image and because of different positions in an image, the weights in the convolution kernels would not be modified. In addition, convolution operations' weight sharing will significantly reduce the parameters of the convolution kernel. Pooling is the final segment. The pooling layer was normally set in the CNN behind the convolution layer, which could be utilized for decreasing feature dimensions of the performance of previous layer's convolution layer, simultaneously to retain adequate key images information details.

To evaluate the dot products of the weights and the values in the input, a filter, which was an array of weights, was used in a convolutional layer, which slides over the input from a previous layer. These weights are discovered through the process of backpropagation of errors. After applying an activation function that incorporates element-wise nonlinearity, a feature map is produced, with each entry representing an individual neuron output from a tiny local region of the input. The feature map was then used to train a neural network.

As filters are considered, if the number of filters is higher, then it is possible to extract more feature mappings, and the better the model performances are. The comparative trails of 32-32-64, 32-32-32, 64-64-64, and 64-64-128 filters were therefore used for selecting the most appropriate filters on the conditions that both resources of computing and DCNNs network performances were considered on holding the different hierarchical structures and various influencing unchanged factors. 64-64-64 was therefore chosen as convolution layer filters, considering the performance considerations, and every receptive field size is 5×5 [16].

In the case of Inception-v3, the probability of every label $k \in \{1, \ldots, K\}$ for every training example is calculated by

$$Q(k \mid z) = \frac{\exp(y_k)}{\sum_i^K \exp(y_i)}, \tag{1}$$

where y represents the nonnormalized log probabilities. Distribution of ground truth over labels $p(k \mid z)$ was normalized; hence, that $\sum_k p(k \mid z) = 1$. For this system, the loss was provided by cross-entropy:

$$C = \sum_{k=1}^{K} \log(q(k))p(k). \tag{2}$$

For logits yk, the cross-entropy loss is differentiable and can therefore be used for deep model gradient training, where the gradients have the simple form of $\partial C/\partial y_k = q(k) - p(k)$, bound between -1 and 1. Normally, this means that the log-probability of the correct label is maximized when the cross-entropy is minimized. Thus, it can produce few overfitting issues. Inception-v3 considered the distributions over label with a smooth parameter ϵ independent of training examples *v(k)*, where, for training instance, the label distributions $p(k \mid z) = \partial_{k,z}$ were exchanged by

$$p'^{(k \mid z)} = (1 - \epsilon)\partial_{k,z} + \epsilon v(k), \tag{3}$$

which is a mixture of the original $p(k \mid z)$ distribution with 1- ϵ weights and the *v(k)* fixed distribution with ϵ weights.

For a uniform distribution *v(k) = 1/K*, the label-smoothing regularization was applied such that it becomes

$$p'^{(k|z)} = (1-\varepsilon)\delta_{k,z} + \frac{\varepsilon}{K}. \quad (4)$$

Alternately, this could be interpreted like cross-entropy as

$$H(p', q) = -\sum_{k=1}^{K} \log(q(k))p'^{(k)} = (1-\epsilon)H(p', q) + \epsilon H(v, q). \quad (5)$$

On the activation layer, there are several activation features, such as sigmoid, ReLU, and softmax. Its functionality was to combine nonlinear factors for improving the model's conditions; hence it needs to be nonlinear. The activation function of the sigmoid function can be expressed as

$$f(x) = \frac{1}{1+e^{-x}}. \quad (6)$$

The activation function of ReLU is expressed as follows:

$$f(x) = \begin{cases} 0, & x \le 0, \\ x, & x > 0. \end{cases} \quad (7)$$

The activation function of the softmax layer is expressed as follows:

$$f(x_j) = \frac{e^{x_j}}{\sum e^{x_i}}. \quad (8)$$

In these above equations, *f(x)* is the activation function, and x is the activation function input.

It is a nonlinear function like ReLU or sigmoid, which is applied to the elements of a convolution and was known as the activation function. When one or more pooling layers were deployed to the feature maps generated by the convolutional layers, the computational difficulty of a CNN was reduced. This was accomplished by decreasing the size of the maps created by the convolutional layers. The methods of maximum pooling and average pooling are the most widely utilized. The output layer has as many nodes as the number of classes in the dataset, which was one hundred. The output was classified using the softmax function, which was implemented in the proposed work. The number of epochs defines the number of times that the neural network will be trained and validated before it is performed. It may take thousands of epochs for an algorithm to converge on a set of weights that provides an acceptable level of accuracy. In neural network's training and validation, the batch size is defined as the number of samples in the dataset that will be loaded and propagated throughout the training and validation of the neural network.

The learning rate regulates the size of weight and bias changes in the training algorithm's learning as it progresses. It was the value that should be specified at the level low enough to allow the neural network to converge while also being high enough to avoid spending an excessive amount of time training it. Hidden layer count refers to the number of FC layers in the neuron which have a specified weight for every identified neuron, which was updated as the training durations are completed. Every neuron has an activation value, which was determined depending on the values of its inputs and the weights assigned to them. When this calculation was completed, it returns a value that was used as input for the final layer, which uses the softmax function to classify MRI images into two categories: normal and torn ACL.

4. Performance Analysis

The performance analysis of the proposed DCNN with the Inception-v3 model is assessed using the dataset in this section. The model was evaluated using parameters such as accuracy, precision, recall, specificity, and F-measure. Also, a comparative analysis was conducted for the validation of the model proposed. The output is compared to other current deep learning models used for classification, such as VGG16, VGG19, Xception, and Inception ResNet-v28. On the MATLAB 2019a Simulink toolbox, all the experiments are implemented and carried out. The dataset is split into 70 percent for training and 30 percent for testing the performance analysis.

4.1. Dataset Description. The dataset used in this work is collected from the MRNet database. It is an open-access database for the knee MRI dataset. It can be downloaded from https://stanfordmlgroup.github.io/competitions/mrnet/site.

The MRNet dataset includes 1,370 knee MRI images diagnosed at Stanford University Medical Center. There are 1,104 (80.6%) abnormal images, 319 (23.3%) ACL tears, and 508 (37.1%) meniscal tears in this dataset; labels were acquired from clinical reports through manual extraction.

Acute and chronic pain, follow-up or preoperative assessment, and injury/trauma are the most common indications for knee MRI examinations included in this dataset. GE scanners (GE Discovery, GE Healthcare, Waukesha, and WI) were used for examination with a regular knee MRI coil and a routine noncontrast knee MRI protocol that included the following sequences: coronal T1 weighted, sagittal proton density (PD) weighted, axial PD weighted with fat saturation, coronal T2 with fat saturation, and sagittal T2 with fat saturation. A total of 775 (56.6%) used a 3.0 T magnetic field; the remaining used a 1.5-T magnetic field for examination. This model uses 70% of data (959 images) for training and testing and 30% of data (411 images) for performance analysis [17, 18].

4.2. Performance Metrics. The proposed DCNN with the Inception-v3 DTL model is proposed in this research and compared with deep learning models like VGG16, VGG19, Xception, and Inception ResNet-v28. The performance metrics like accuracy, precision, recall, specificity, and F-measure are evaluated to estimate the performance analysis of the model. For every validation, both training and testing results are evaluated and compared. The primary

Table 1: Performance analysis of training evaluation.

Models	Accuracy	Precision	Recall	Specificity	F-measure
VGG16	95.13	95.05	94.64	96.25	94.72
VGG19	95.66	94.22	94.80	96.90	95.39
Inception ResNet-v28	90.74	89.90	89.26	91.72	90.56
Xception	92.48	91.94	91.67	93.36	92.07
Proposed	99.04	98.96	98.45	99.18	98.81

Table 2: Performance analysis of testing evaluation.

Models	Accuracy	Precision	Recall	Specificity	F-measure
VGG16	85.45	85.74	84.23	85.67	85.19
VGG19	87.90	87.50	86.06	88.72	86.09
Inception ResNet-v28	89.91	89.32	88.35	90.43	89.24
Xception	92.25	91.48	91.29	93.11	91.92
Proposed	95.42	95.02	95.13	96.34	94.83

objective of this research is to detect the ACL tear from MRI knee images, which can be useful to determine the abnormality of the patient. The result of this model can be based on the outcome detected as normal or abnormal. The true positive, true negative, false positive, and false negative are correctly analyzed to estimate this model's outcome [19–21].

True Positive (TP): It represents the total correct predictions in abnormal cases.

False Positive (FP): It represents the total incorrect predictions in abnormal cases.

True Negative (TN): It represents the total correct predictions in normal cases.

False Negative (FN): It represents the total incorrect predictions in normal cases.

Accuracy is the model's estimation of the performance subset. It is the primary output metric used to calculate the efficiency of the classification process. It is usually used to estimate when both the positive and negative classes are equally important. It is calculated using the following equation:

$$\text{Accuracy} = \frac{TP + TN}{TP + TN + FP + FN}. \tag{9}$$

Precision is a positive predictive value. The preciseness of the classification model is calculated using it. It is the measure of the cumulative predictive positive value of the correctly predicted positive observation. The lower precision value reflects that a large number of false positives affected the classification model. The measure of precision can be computed using the following equation:

$$\text{Precision} = \frac{TP}{TP + FP}. \tag{10}$$

The sensitivity is also referred to as recall. It is the proportion of correctly predicted positive observation of the overall positive predictive value. The lower recall value reflects that a large number of false-negative values affected the classification model. The recall estimation can be calculated using the following equation:

$$\text{Recall} = \frac{TP}{TP + FN}. \tag{11}$$

As per this model, specificity is the prediction that healthy subjects do not have an abnormality. It is the percentage of subjects with no injury/trauma that is tested as abnormal. The specificity estimation can be calculated using the following equation:

$$\text{Specificity} = \frac{TN}{TN + FP}. \tag{12}$$

The F-measure estimates the accuracy of the test and is defined as the weighted harmonic mean of the precision of the test and the recall. The accuracy does not take into account how the data is distributed. The F-measure is then used to manage the distribution problem with accuracy. The F-measure estimation can be calculated using the following equation:

$$F - \text{measure} = \frac{2 \times \text{Precision} \times \text{Recall}}{\text{Precision} + \text{Recall}}. \tag{13}$$

As shown in Tables 1 and 2, the proposed DCNN-Inception-v3 model achieved better performance in training and testing for classifying the ACL tear MRI images. The model obtained 99.04% training accuracy and 95.42% testing accuracy, which is 3.1% to 9.9% increased performance compared to the other existing compared models. VGG16, VGG19, Inception ResNet-v28, and Xception achieved 95.13%, 95.66%, 90.74%, and 92.48% in training and 85.45%, 87.90%, 89.91%, and 92.25% in testing performance, respectively. Inception-ResNet-v28 and Xception model achieved better performance in testing compared to the training performance. The performance was the same as accuracy for other parametric evaluations like recall, precision, specificity, and F-measure.

Compared with both testing and training results, the VGG16 approach achieved the least performance in every parameter, and the Xception model has achieved close results to the proposed model. The graphical chart of the comparison is plotted in Figures 4 and 5.

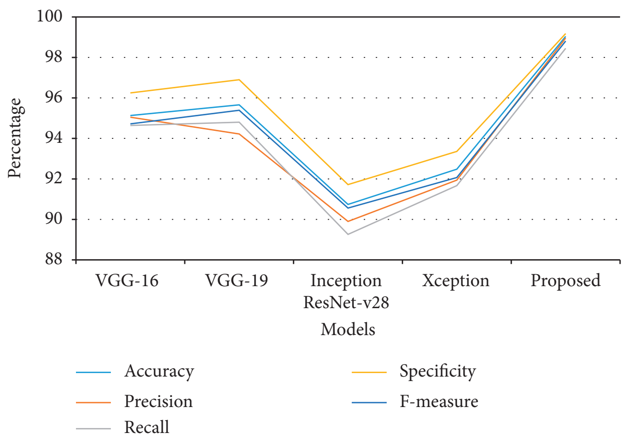

Figure 4: Graphical plot of performance analysis of training.

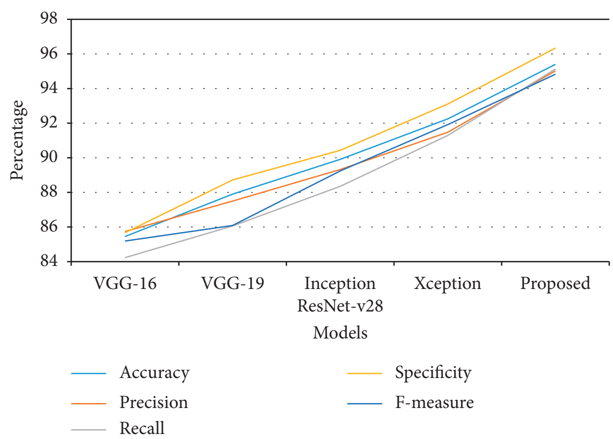

Figure 5: Graphical plot of performance analysis of testing.

5. Conclusion

In this research, a DCNN based Inception-v3 DTL model was proposed for classifying the ACL tear MRI images. The proposed model was executed in four stages. Data preprocessing is the initial stage. After preprocessing, the next stage is to extract the features of image and then to deliver the features extracted into the model to train. The trained model was finally tested. The dataset used in this work was collected from the MRNet database. It is an open-access database for the knee MRI dataset. A total of 1,370 knee MRI images were used for evaluation. 70% of data (959 images) were used for training and testing and 30% of data (411 images) were used in this model for performance evaluation. The proposed DCNN with the Inception-v3 DTL model was assessed and correlated with existing deep learning models like VGG16, VGG19, Xception, and Inception ResNet-v28. The performance metrics like accuracy, precision, recall, specificity, and F-measure were evaluated to estimate the performance analysis of the model. For every validation, both training and testing results were evaluated and compared. The model has obtained 99.04% training accuracy and 95.42% testing accuracy, which was 3.1% to 9.9% higher than the other existing compared models in performance. However, this model was proposed to classify the ACL tear injuries from knee MRI images and has obtained better results in validation. In the future, the proposed model can be used to find any abnormalities present in various body organs by using different datasets like a brain tumor, heart disease, lung cancer, and so forth. The performance can be further increased by implementing a new deep transfer learning model with better classification performance.

Data Availability

The datasets used and/or analyzed during the current study are available from the corresponding author upon reasonable request.

Conflicts of Interest

There are no conflicts of interest.

Authors' Contributions

S. Sridhar, J. Amutharaj, and Prajoona Valsalan are responsible for data collection and validation. B. Arthi, and S. Ramkumar are responsible for surveys and content writing and proof reading. S. Mathupriya, Yosef Asrat Waji, and Rajendran T are responsible for algorithm design, development, and proofreading.

References

[1] N. Rory, T. Pete, and G. Alan, "The effects of anterior cruciate ligaments reconstruction on the progressions of osteoarthritis," *The Open Orthopaedics Journal*, vol. 6, no. 3, pp. 506–510, 2012.

[2] H. A. N. Wing, F. G. James, H. Y. H. Esther, P. Bhawan, K. Y. L. Billy, and S. H. Y. Patrick, "Imaging of the anterior cruciate ligaments," *World Journal of Orthopedics*, vol. 2, no. 8, pp. 75–84, 2011.

[3] F. Liu, B. Guan, Z. Zhou et al., "Fully automated diagnoses of anterior cruciate ligaments tear on knee MR image by using deep learning," *Radiology: Artificial Intelligence*, vol. 1, no. 3, pp. 1–10, 2019.

[4] P. Valentina, N. Berk, N. M. Sarah, D. B. Matthew, M. L. Thomas, and M. Sharmila, "3D convolutional neural network for detections and severity stagings of meniscus and PFJ cartilages morphological degenerative change in osteoarthritis and anterior cruciate ligaments subject," *Journal of Magnetic Resonance Imaging*, vol. 49, no. 2, pp. 400–410, 2019.

[5] P. L. Jelle, N. M. Douglas, and S. D. Gregory, "The locations of anterior cruciate ligaments tear: a prevalence study using magnetic resonance imaging," *The Orthopaedics Journal of Sport Medicines*, vol. 5, no. 6, pp. 1–9, 2017.

[6] D. Priyanka and R. Rajesh, "An introduction to deep learning application in MRI image," in *Proceedings of the 2nd International Conferences on Power Energy, Environments and Intelligent Controls*, pp. 458–465, IEEE, Greater Noida, India, October 2019.

[7] L. Jin, P. Yi, L. Min et al., "Application of deep learning to MRI image: a survey," *Big Data Mining and Analytics*, vol. 1, no. 1, pp. 1–8, 2018.

[8] R. Ashraf, M. A. Habib, M. Akram et al., "Deep convolution neural networks for big data medical images classifications," *IEEE Access*, vol. 8, pp. 105659–105670, 2020.

[9] C. Germann, G. Marbach, F. Civardi et al., "Deep convolutional neural networks–based diagnosis of anterior cruciate ligaments tear: performances comparison of homogenous versus heterogeneous knee MRI cohorts with different pulses sequence protocol and 1.5-T and 3-T magnetic field strength," *Investigative Radiology*, vol. 55, no. No.8, pp. 499–506, 2020.

[10] M. B. Milica and C. B. Marko, "Classifications of brain tumor from MRI image using a convolutional neural networks," *Applied Sciences*, vol. 10, no. 1999, pp. 1–13, 2020.

[11] Z. B. Cmak, A. Likhitha, P. Alekhya, and V. Aparna, "Computerised classifications of MRI image using machine learning algorithm," in *Proceedings of the 2020 International International Conferences on Electronic and Sustainable Communication System*, pp. 80–85, IEEE, Coimbatore, India, July 2020.

[12] P. M. Krishnammal and S. S. Raja, "Convolutional neural networks-based images classifications, and detections of abnormalities in MRI brain image," in *Proceedings of the 2019 International Conferences on Communication and Signal Processing*, pp. 548–553, Chennai, India, April 2019.

[13] N. Subhas, H. Li, M. Yang et al., "Diagnostics interchangeability of deep convolutional neural network reconstructed knees MR image: preliminary experiences," *Quantitative Imaging in Medicine and Surgery*, vol. 10, pp. 1748–1762, 2020.

[14] M. J. Awan, M. S. M. Rahim, N. Salim, A. Rehman, H. Nobanee, and H. Shabir, "Improved deep convolutional neural network to classify osteoarthritis from anterior cruciate ligament tear using magnetic resonance imaging," *Journal of Personalized Medicine*, vol. 11, no. 11, p. 1163, 2021.

[15] C. B. Viswanath and C. P. Priyadarshini, "An efficient food images classification by inception-V3 based CNNs," *International Journal of Scientific & Technology Research*, vol. 9, no. No.3, pp. 6987–6992, 2020.

[16] H. Mahbub, J. B. Jordan, and R. F. Diego, "A study on CNNs transfer learning for image classifications," in *Advance in Computational Intelligences System. UKCI 2018*, A. Lotfi, H. Bouchachia, A. Gegov, C. Langensiepen, and M. McGinnity, Eds., Advance in Intelligent System and Computing, Biloba, Spain, 2019.

[17] N. Bien, P. Rajpurkar, R. L. Ball et al., "Deep-learning-assisted diagnoses for knee magnetic resonances imaging: development and retrospectives validation of MRNet," *PLOS Medicines*, vol. 15, no. 11, pp. 1–19, 2018.

[18] T. Chen-Han, K. Nahum, K. Eli, E. Iris, and M. Arnaldo, "Knees injury detections using MRIs with efficiently-layered networks (ELNet)," *Proceeding of the Third Conferences on Medical Imaging with Deep Learning*, vol. 121, pp. 784–794, 2020.

[19] S. Manimurugan, "Classification of Alzheimer's disease from MRI Images using CNN based Pre-trained VGG-19 Model," *Journal of Computational Science and Intelligent Technologies*, vol. 1, no. 2, pp. 15–21, 2020.

[20] S. Manimurugan and P. M. Surendra, "A new modified recurrent extreme learning with PSO machine based on feature fusion with CNN deep features for breast cancer detection," *Journal of Computational Science and Intelligent Technologies*, vol. 1, no. 3, pp. 29–34, 2020.

[21] E. Sreenivas and J. Praveena, "Performance analysis of deep belief neural network for brain tumor classification," *Journal of Computational Science and Intelligent Technologies*, vol. 1, no. 3, pp. 29–34, 2020.

Hindawi
Journal of Healthcare Engineering
Volume 2022, Article ID 7309387, 9 pages
https://doi.org/10.1155/2022/7309387

Research Article

Psychological Health Intervention of Rural Art and Cultural Communication of Dihuagu in Nanxian County under the Background of Network

Jie Liu

Academy of Music and Dance, Changsha Normal College, Changsha 410100, China

Correspondence should be addressed to Jie Liu; liu_jie188@outlook.com

Received 10 December 2021; Revised 12 January 2022; Accepted 15 January 2022; Published 8 February 2022

Academic Editor: Enas Abdulhay

Background. With the development of the Internet, people are facing greater pressure. People in modern society are facing the threat of mental illness. For people with poor mental health, it is necessary to take an appropriate psychological intervention. Nanxian dihuagu is not only a form of folk dance but also a collection of local people's artistic wisdom. Now, Nanxian dihuagu artists use network media to record it. *Objective*. Introduce the cultural connotation and value function of dihuagu dance in Mingnan county. *Methods*. In this paper, literature and field survey methods, according to the logical analysis method of dance point of view, a detailed analysis of multiculture, from the perspective of comprehensive academic research methods, explore the value and cultural significance of dance. *Results*. The Internet has promoted the exchange of local art and culture, and the effective communication has been formed under the promotion of network media. But the Internet age has also led to some problems, and psychological intervention can effectively improve the psychological problems caused by the network. *Conclusions*. In this paper, the research process is not limited to the dance itself, at the same time, starting from the local folk customs, focusing on the analysis of the significance and value function of dance culture, which provides a reference for the development and optimization of folk customs. And through the analysis of Nanxian dihuagu, we can know more about the national culture and promote the development of Chinese national culture.

1. Introduction

Nanxian dihuagu is a dance performance art with local ethnic characteristics, which is usually held in the traditional Lantern Festival, Spring Festival, wedding, and funeral. It is formed on the basis of the original folk dance and folk musical instruments while absorbing a variety of cultural arts. This kind of art is not only happy and beautiful in music melody but also natural in dance action and full of rich breath of life and unique artistic style, which is deeply loved by people.

1.1. The Origin and Development of Dihuagu in Nanxian County. Nanxian dihuagu is a folk art invented by people who work every day. It is close to people's living conditions. This form of folk song and dance art inherits the living state and shows people's real living state by relying on the body language recorded from generation to generation. The inheritance and development of dihuagu in Nanxian County have experienced more than 200 years, and its development process can be roughly divided into five stages: the enlightenment period of the Jiaqing era of the Qing Dynasty, the prosperity period from the Xianfeng era to the Tongzhi era of the Qing Dynasty, the peak period from the early Republic of China to the postliberation period, the decline period from the Cultural Revolution to the end of the 20th century, and the revival period in the new century.

1.2. Definition of Psychological Intervention. Psychological intervention is based on psychological consultation and cognitive psychology, using social psychology to design the intervention process of mental health problems in detail so as to influence their action level (i.e., using specific methods) and adjust their mental state in order to lead their mental state to the expected target state.

Due to the increasing pressure of people's lives and the influence of various environmental factors, people under the background of the modern network are often affected by some bad emotions, thus damaging their mental health [1]. Timely psychological intervention can help to prevent personal injury caused by excessive action, form correct self-awareness and self-evaluation, promote communication with the outside world, and improve the quality of life of intervention objects. Taking into account the characteristics of the Internet age, in previous studies, due to the lack of expansion of art therapy methods such as Internet new media and apps, people receiving treatment are vulnerable to psychological intervention, and flower drum practitioners can express their ideas more simply.

1.3. The Influence of Psychological Intervention on the Dissemination of Rural Art and Culture. Rural art is a form of artistic expression, and people can obtain the required network information in a short time and pass on the network information that psychological interveners want to convey to the intervened objects in a convenient way [2]. Now, there are some preliminary exploratory studies on the application of psychotherapy suggestions on dihuagu. However, the research is usually a one-way psychological intervention method, most of which is to discuss the two-way interaction between the psychological intervener and the object, without a detailed discussion of the application of dihuagu in the psychological intervention [3]. From the perspective of reception aesthetics, artistic creation is a process in which the audience and the author create a horizon according to their own psychological understanding, which requires the interaction between them. They can create the color, action, emotion, and other aspects of spiritual communication in the process of interaction and guide the next iteration of creation. In this process, their mental state is constantly improved.

The purpose of this study is to make a detailed theoretical analysis of the psychological cognitive characteristics of various groups and design the most suitable interactive psychological intervention method for various groups [4]. Moreover, through the experiment of color, material, form of expression, work content, and psychological intervention effect of qualitative and quantitative analysis, it has certain guiding significance for psychological intervention. On the other hand, the use of interactive gradient has a very practical significance for psychological intervention. It can be directly used in the process of psychological diagnosis, psychological consultation, and psychotherapy to effectively and appropriately support the intervention objects to improve their mental health indicators.

1.4. Cultural Communication of Dihuagu in Nanxian County under the Background of Network. As a representative of the traditional dance of the Han nationality in Hunan Province, the dihuagu of Nanxian County has been inherited with vivid performance forms and rich and varied songs, which is a vivid portrayal of the culture of Nanxian County. In Nanxian County, the protection of flower drum can activate the national art, promote the development of national culture, and build a harmonious socialist society [5]. First, the flower drum ecosystem must be protected. In Nanxian County, the living environment of Huagu was combined with the natural environment to establish a complete ecological protection area, which saved Huagu culture and became a park to protect Huagu culture.

Fundamentally speaking, as intangible cultural heritage, Nanhua drum dance reflects the collective life, thoughts, feelings, and cultural spirit of the people in Nanxian County. It is the crystallization of the wisdom and great spirit of the people. The content of its dance performance is a mirror of the human spiritual lifestyle. It inherits a prosperous and unique cultural spiritual home [6]. In different historical periods, it has the most typical regional characteristics and is the continuation of history. It reflects the world outlook and living conditions of the people in Nanxian County, reflects the collective spirit and action mode of the people in this fertile land, and improves people's understanding of vision and lifestyle, so it has high historical value.

Nanxian dihuagu dance is the great spiritual and cultural wealth of Nanxian people, the living fossil of local folk culture, the crystallization of working people's wisdom, and the primitive cultural gene of Southwest China [7]. The protection and development of traditional ecological culture can improve the cultural awareness of the whole society and contribute to the recovery and development of culture, as well as the planning and construction of cultural ecology. This dance reflects the way of thinking, aesthetic, and social development of the Nanxian people and also reflects the unique historical and cultural charm of this area, showing its unique cultural value.

Nanxian dihuagu dance is a kind of Han nationality dance with distinctive performance and rich songs. It has unique local characteristics, unique dance art style, rich life taste, and deep mass foundation [8]. At the Gutian Meeting in 1929, Comrade Mao Zedong advised the Red Army soldiers to sing "flower drum" and other recreational activities. Exploring, rescuing, and protecting Huagu have played a certain role in promoting national art, inheriting national culture, and building socialist spiritual civilization. The essence of Nanxian dihuagu culture is reflected in Nanxian's history, thoughts, habits, etiquette, education, production, and life. We should organize cultural education, cultivate folk artists of Nanxian dihuagu dance, and do our best to explore, rescue, and protect the ecological culture of dance.

2. Methods

2.1. Participants. In order to better study the use of new online media in Nanxian County, the author has carried out preparations many times, taking the method of going to the scene in person, going to Nanxian County, conducting surveys on local residents, interviewing key figures, and distributing questionnaires to a large number of residents. Surveys and other methods to obtain a large number of documents required information.

2.2. Process. According to statistics, a total of 280 paper questionnaires were distributed, and 270 were recovered. According to statistics, Nanxian villagers posted 506 WeChat messages, including 92 students, 280 migrant workers, 54 migrant workers, 42 fishery professionals, 18 pure farmers, and 20 businessmen. According to the characteristics of the questionnaire, the coverage of this questionnaire is wide enough.

2.3. Research Design. The survey is analyzed and implemented from four aspects. First of all, it is necessary to understand the understanding of new online media in Nanxian County and the daily use of new online media. Second, it is necessary to understand the characteristics and hotspots of new media users in the Nanxian network [9]. Third, it is necessary to understand the new media users' understanding of the dissemination of national traditional culture. Fourth, it is necessary to understand the impact of online new media users on national culture.

2.4. Data Analysis. SPSS16.0 and Amos 7.0 software were used for data analysis. First, record the statistical questionnaire data, extract the data, and conduct statistical analysis. Then, according to the results of questionnaire statistics and statistical analysis, exploratory factor analysis and confirmatory factor analysis were used to verify the suitability and reliability of each measurement scale.

3. Results

3.1. Analysis of the Respondents' Understanding of Dihuagu in Nanxian County. According to Table 1, 96.6% of respondents knew or did understand the traditional culture, while only 3.40% did not know the traditional culture at all. Generally speaking, the respondents have a high understanding of traditional culture, but some people do not fully understand the traditional culture. The results show that the investigation content is comprehensive and reliable, which may reflect the original intention of the investigation.

3.2. Descriptive Statistical Analysis on the Dissemination of Rural Art and Culture. When establishing the influencing factor model, the author assumes that the level of the communication process and audience level have a certain impact on the social level and verifies the correlation through the correlation analysis between the influencing factors [10]. Based on SPSS, the author analyzes the relationship among personal level, social level, and communication process level. From the data in Table 2, it can be seen that personal concern is obviously related to other factors except communication ability, and government policy at the social level is significantly related to media technology at the communication process level [11]. The cultural environment at the social level is significantly related to the media technology and communication ability at the communication process level, and the media technology and communication ability at the communication process level at the social level are also significantly related. The results show that there is an obvious correlation among personal level, communication process level, and social level.

3.3. Time Distribution of Internet Use among Survey Population. From the questionnaire, it can be seen that a total of 515 people were surveyed. 196 people surf the Internet every day, accounting for 38.74%. 138 people (27.2%) used the Internet frequently. 156 people did not surf the Internet, accounting for 30.83%. 16% of the elderly could not access the Internet. Most of them can use the network independently. Therefore, the new Internet media has played a positive role in the popularization of Nanxian culture. Among them, 180 people use the Internet for 1–3 hours a day, accounting for 35.57%, 120 people for 3–5 hours, accounting for 23.7%, and 112 people for less than 1 hour, accounting for 22.3%. From the data, young people use the Internet for a long time (Table 3).

3.4. Survey and Analysis on the Installation of Network Tools among the Survey Population. With the use of mobile phones at the same time, WeChat, QQ, Weibo, and many other types of software were downloaded. WeChat, in particular, can greatly promote people's lives and bring convenience to the communication between the two. In addition, it is also an indispensable communication software in production and life [12]. Among 446 people, 88.14% used instant software, and 238 and 226 people used social networks and video websites, accounting for 47.04% and 44.66% of the total, respectively. Like TikTok, it is fun and popular, and many young people love it. Because of the fast pace of work, many people in Nanxian love it and help Nanxian culture expand rapidly (As shown in Table 4).

3.5. Analysis of the Cognition of the Survey Population to the Spread of Dihuagu Culture in Nanxian County. Of the 506 surveyed, 298 people barely know their own culture, accounting for 58.89%. 162 people know their own culture, especially Jienan county culture, accounting for 32.02%, and only 9.09% of the people do not understand the culture of Nanxian County. More than 90 percent of people know their own culture. Of the 506 respondents, 354 responded to spreading the culture of Nanxian County to other countries through various forms of network, accounting for 69.96% [13]. 152 people said their culture was not broadcast abroad, accounting for 30.04 percent. Therefore, most people like to inherit their own culture, which plays a positive role in the popularization of Nanxian culture. Of the 534, 304 used WeChat and TikTok, accounting for 85.88%, while 50 used BBS to contribute only 14.25%. But WeChat is worth mentioning. Because WeChat can send photos and videos through moments, a large number of users from different cultures have poured in, and WeChat has gradually promoted cultural exchanges. The details are shown in Table 5.

3.6. Analysis of the Types of Cultural Transmission of the Investigation Population to the Drum Culture. About using the new media channel of the network to spread Nanxian

Table 1: Statistical results of respondents' understanding of dihuagu in Nanxian County.

The level of understanding of Nanxian dihuagu	Frequency	Percentage	Effective percentage	Cumulative percentage
Know very well	30	11.2	11.2	11.2
Have a certain understanding	228	85.4	85.4	96.6
Do not understand at all	9	3.4	3.4	100.0
Total	267	100.0	100.0	

Table 2: Descriptive statistics on the dissemination of rural art and culture.

	Mean value	Standard deviation	N
Interest	3.9	952	267
Government policy	4.03	975	267
Cultural environment	3.23	1.589	267
Network media content	3.61	1.246	267
Network media technology	3.58	1.258	267
Network communication talents	3.57	1.176	267

Table 3: Time distribution of the Internet use among survey population.

Category item	Number of people	Proportion (%)
1–3 hours	180	35.57
3–5 hours	120	23.72
Less than 1 hour	112	22.13

Table 4: Questionnaire on the installation of Internet tools.

Category item	Number of people	Proportion (%)
Instant software	446	88.14
Social network	238	47.04
Video site	226	44.66

Table 5: The cognition of the investigated people on the spread of dihuagu culture in Nanxian County.

Category item	Number of people	Proportion (%)
Barely know	298	58.89
Special understanding	162	32.02
Do not understand	46	9.09

culture, 354 people know these methods, 294 people know the method of using photos, accounting for 83.05%, and 270 people choose text communication, accounting for 76.27%. A total of 230 people chose video communication, accounting for 63.97%, and 122 people chose audio communication, accounting for 34.46%. Because of the intuitive nature of the photos, the spread is relatively simple and high speed, so the acceptance of netizens and fans is relatively high [14]. The best way to transmit is to use language and photos. The effect is better. There are short videos with images and sounds in the videos. You can also use music, especially wedding pictures. The effect is very beautiful. In the circle of friends, the relevant videos and pictures were made public, which provided great convenience for the popularization of Nanxian culture (as shown in Table 6).

Table 6: Communication types of dihuagu culture among the investigated people.

Category item	Number of people	Proportion (%)
Pictures and photos	294	83.05
Text spread	270	76.27
Video dissemination	230	63.97
Audio transmission	122	34.46

3.7. Analysis of Rural Network Use Problems and Psychological Intervention Needs. According to the survey data, people with network psychological problems mainly use the network to play games and chat to make friends, and the proportion of playing games is the highest, accounting for 80%, and making friends accounts for 14.3%. This shows that people with psychological problems due to the Internet like the entertainment function of the Internet [15]. On the contrary, nonnetwork causes psychological problems. In order to achieve the purpose of learning, people tend to use the network to understand and obtain information. On the other hand, the proportion of people who have psychological problems due to the network and those who do not have psychological problems is very high, which is worthy of attention [16]. As shown in Table 7, playing games ranks first among the people who have psychological problems, which indicates that online games are an important factor causing middle school students' psychological problems on the Internet.

4. Discussion

4.1. Strengthen the Innovation of Communication Means of Dihuagu Culture in Nanxian County

4.1.1. New Style of Dance Vocabulary of Dihuagu in Nanxian County. Nanxian dihuagu, as a folk dance, can be properly and skillfully disassembled and reconstructed, which can not only enrich the vocabulary of dance but also be theoretically constructed for "poetry and painting." In the process of adaptation and innovation, we can start from the following points.

First, perform the best combination of actions. On the basis of traditional sports, change the original range of movement, intensity, rhythm development, and innovation [17]. On the basis of not changing the basic rhythm, it produced a new dance vocabulary and expanded along the trend to make it more emotional. For example, you can see the combination of simple step and long step squat.

Secondly, break the fixed mode of thinking, and make the dance more professional and artistic. According to the characteristics of the performers, Nanxian dihuagu designs dance movements, which can give full play to their

Table 7: Questionnaire of psychological problems in the process of rural network use.

	There is no need for psychological intervention	Need psychological intervention	x	P
Play online games	85 (16.2%)	28 (80%)		
Audiovisual entertainment	162 (30.8%)	2 (5.7%)		
Chat and make friends	114 (21.7%)	5 (14.3%)	85.286	0
Network information search	98 (18.6%)	0		
Learning and knowledge	67 (12.7%)	0		

respective advantages. The props and movements used by various roles of men and women can learn from each other, strengthen the fluency of movements, and enrich the vocabulary of dance [18]. For example, in traditional dance performance, dance can fully demonstrate the lifestyle of modern people. The foot movement is more flexible, adding a specific jump action. When dancing, the movements are relaxed, broad, open, and smooth. In addition, acrobatic movements such as "exploring the sea" and "front bridge" were added to improve dance appreciation and professional awareness [19]. Clowns can change the original dance movements. We can give full play to the talents of the actors and choose some specific skills and movements, such as flying feet, rotating feet, sweeping feet, and turning upside down so as to make the warm atmosphere of the scene further rise and fully show the positive and optimistic spirit of Nanxian people.

Finally, it can add luster to other arts. The creative ideas, processing means, and action design of dance are very innovative, which is the feeling of the current era, the pulse of the times and the action after the processing of modern dance vocabulary [20]. Today's square dance has caused a national fitness heatwave. It can selectively absorb the popular modern dance, hip-hop dance, and square dance, as well as the dance elements of teenagers, middle-aged, and elderly people. With the feelings of modern people, we can make the rhythm of original dance, combine simple movements and famous popular songs, and combine them closely with the modern life of young people [21]. Mix modern elements to show the charm of new art. In order to let people all over the country and even the world know this art form, we must depend on the original taste of Nanxian Dihua drum dance and get people's attention through a number of innovations.

4.1.2. Clever Use of Dihuagu Props and Lighting in Nanxian County. The use of beautiful dance composition, creating beautiful movements, and strengthening the innovation of small tools are helpful to strengthen the stage art performance of Nanhua drum dance. Compared with the "Er Ren Zhuan" in the northeast, the dance skills of Dihua drum dance in Nanxian are insufficient; that is to say, there are few "unique skills" [22]. Nanxian flower encouragers hope to show excellent skills and stage performance and cannot be satisfied with playing flower fans and other original performance skills. In addition to handkerchiefs, flowers, wine cups, chopsticks, umbrellas, and other small props, we must also maximize the use of a variety of small props. For example, in the handkerchief, the traditional flower fan dance has only one simple "rotation" [23]. You can learn skills from the northeast "Errenzhuan," such as adding a handkerchief around the shoulder and other physical activities to perform. Because the Nanxian Wai drum can be used as exaggerated dance props, it can expand the space of stage performance, and the dance pictures will become more overlapping.

Stage design enriches the role of dance, produces artistic concepts, stimulates imagination, and improves the overall charm of dance. For example, the accompaniment of Lang's seeing his sister in Gaopo is composed in accordance with the local folk song Lang's seeing his sister in Gaopo. It is just that the sisters who wash clothes by the river become "sisters who put clothes by the river" [24]. When performing on the stage, using new multimedia technologies such as stage lighting and scenery, the background of the stage becomes the scene of lyrics, which fascinates the audience and directly feels the beautiful feelings.

4.1.3. Innovation of Performance Program of Dihuagu in Nanxian County. At the first Nanxian dihuagu Art Festival, Yiyang Ziyang District Cultural Center's "drag bench" and so on can break Nanxian's traditional dance performance projects. In this program, the movement of dance elements and the traditional Nanxian dihuagu movement are retained, focusing on the details of the interaction between the dancers and the clowns [25]. As a flower drum performance, although the changes of dance modeling are relatively scattered, the movements are consistent with the rhythm of fixed music, and the whole is beautiful, neat, and hierarchical. The clown rolls forward from the bench, mastering somersault and other skills, combining with the characteristics of sports, adding a specific story performance plot, setting special performance skills, making the scene warm and the audience in a high mood, meeting the expression of modern people's emotion, temperament, spirit, and sense of rhythm to the greatest extent, and meeting the aesthetic psychology and needs of modern people [26].

Nanxian dihuagu dance can be transformed into a family comedy stage, creating new scripts and beautiful songs. The traditional dihuagu dance can be integrated into family comedy, and the accompaniment music can be integrated into chorus or Male Solo and female lead singing. Various dance segments, such as group dance and double dance, are added to enhance the artistic charm and stage performance of Nanxian dihuagu dance by using multimedia technologies such as stage space layout, original configuration, stage lighting, and scenery [27].

All the traditional dance projects of the Nanhua drum in Nanxian County need to be sorted out and maintained. For those that are still preserved, they should be selectively absorbed by all means of criticism and modernization and optimized in combination with modern aesthetics. It can adjust and transform the original music songs and movements and create new dance works [28]. Only in this way can we maintain the original vitality of the dance and inherit the traditional art of the country.

We should comprehensively study the contents and forms of flower drum and folk art in different times, regions, and styles, learn the advantages of others, make up for our own weaknesses, absorb the essence, eliminate the bad content, and optimize and improve them in the largest scope [29]. Although the content has changed, the essence remains unchanged. The function of dihuagu dance in Xinnan county still maintains the excellent characteristics of traditional culture, reflects the cultural connotation of the nation, and can adapt to the modern aesthetic and promote the development of modern culture.

4.2. Strengthen the Construction of Network Media Tools and Talent Quality in Rural Art Communication. With the development and application of network, human society takes knowledge and network information as the main resources to participate in the construction of a network information society. In the network information society, the relevant talents of Nanhua drum can not only learn multimedia technology and computer network technology and other professional skills but also face a large number of pieces of network information, know how to effectively obtain and identify network information, process network information, express network information creatively, and send network information [30]. Facing the severe challenges brought by the network information age, it is a new historical mission for modern educators to teach students to acquire, evaluate, and apply network information.

4.2.1. Cultivate Network Information Retrieval Skills of Talents Related to Dihuagu in Nanxian County. Before the emergence of the network, the network information retrieval skills mainly refer to the library information retrieval skills for the relevant talents of Nanxian dihuagu University, but now the network environment contains more important network information retrieval skills. This paper mainly introduces the network information retrieval skills under the network environment.

Network information is very rich in content and form, including politics, economy, sports, entertainment, medical care, education, science, and technology, mainly including color photos, text, audio, and video. Faced with the vast amount of network information, if we do not have the ability to search for network information resources, we will not only be unable to obtain effective network information, but also consume a lot of precious time [31]. Many talents associated with dihuagu in Nanxian originally intended to use the network to obtain learning resources, but in the face of many network connections, they did not know how to choose and finally turned their attention to other pieces of external network information; the loss exceeded the gain. Therefore, for educators, it is particularly important to cultivate talents related to Nanhua drum network information retrieval skills. In the network environment, the forms of network information retrieval include search engine and electronic database. Educators should not only teach students how to use search engines and electronic databases to obtain network information methods and skills but also let students quickly and effectively obtain the necessary network information.

4.2.2. Cultivate Network Information Evaluation Skills of Talents Related to Dihuagu in Nanxian County. Although the network information on the network is rich but complex, there are also a large number of pieces of unfiltered fake network information and pornographic network information [32]. Educators teach students to evaluate the reliability, appropriateness, and correctness of network information from the collected network information so as to prevent students from indulging in the virtual world. Students need to use critical thinking to evaluate these pieces of network information so as to avoid losing the sense of active participation or forming the character of indifference, isolation and lack of responsibility.

4.2.3. Cultivate Network Information Application Skills of Talents Related to Dihuagu in Nanxian County. The cognitive impairment caused by the Internet has sounded the alarm for educators. Therefore, education should not only let students understand the ability to obtain and evaluate network information but also creatively apply network information. Facing the network information, students cannot use it for their own purposes. Educators must guide students to reorganize the network information and combine the new network information with the original knowledge background. Students can use the network information reasonably and effectively, instead of being subordinate to the network information, and can become masters, so as to creatively construct the network information system owned by students.

In the process of cultivating students' network information literacy ability, educators should not put it in the priority of classroom education but should combine it with daily education. Let students develop excellent network information literacy ability unconsciously. In addition, considering the poor level of network dependence, in order to use and rationalize the network as a tool, the relevant talents of Nanhuagu need to introduce network information literacy education in the freshman year.

4.3. Reduce the Problems in the Process of Network Culture Communication through Psychological Intervention. The implementation of psychological intervention is to analyze the causes of psychological problems and formulate the exercise plan related to the success or failure of intervention. The causes of psychological problems caused by the Internet are quite different, and the people who have psychological problems seek different satisfaction on the Internet. Some people want to seek new stimulation on the Internet, some want to make more friends through the Internet, some want to reflect their own values, and some want to ease the pressure of reality through the Internet. Sports are also very rich and can provide athletes satisfaction, which is not the same. In order to interfere with the psychological problems caused by the Internet, we use the conditional emotional response to intervene, specifically analyze the specific causes caused by psychological problems, suggest the intensity of exercise, and formulate a specific intervention plan. It is suggested that the conditional emotional response intervention method should be used in the temporary improvement of psychological problems caused by the network in Nanxian County, and the necessary and appropriate differential treatment should be carried out.

4.3.1. The Psychological Problems Caused by the Internet Can Be Divided into Mild, Moderate, and Severe Psychological Problems. According to the research results, the intervention effect of a conditional effective response is better than that of moderate network psychological problems for mild network psychological problems. It is suggested that intervention should be carried out at the beginning of the problem. Even if there are no psychological problems, colorful sports activities and games will also be used to enrich students' spare time life. On the other hand, it also reduces the students' time using the Internet and the bad behaviors caused by the psychological problems caused by the Internet.

4.3.2. Suggestions on Adjusting the Psychological Problems of Network Culture Communicators through Psychological Intervention. Considering that the change of action needs a long-term accumulation process, we need to use the conditional emotional response intervention method to improve the psychological problems of talents in the Nanhua drum for a short time. The content of training needs to be adjusted according to the degree, reason, and interest caused by the network.

Nanxian dihuagu related talents have psychological problems due to network reasons; most of them have serious negative self-knowledge, often think that they cannot do it and give up, considering that they have been used to self-verification, or blame the failure caused by some factors on their own failure, and verify that they cannot do it. In order to temporarily improve the psychological problems caused by the Internet, it is suggested to use the conditional emotional response intervention method, and they can doubt their ability. However, please do not let them have absolutely impossible reasons, and only give them a chance to self-verify.

In the experimental study, if we consider that the subjects may change their physical and mental states due to training or other factors, we need to use the conditional emotional response intervention method to temporarily correct the psychological problems caused by network talents. Grasp the feedback information of the test object at any time, understand the physical and mental state of the test object, and formulate, adjust, and implement a timely, scientific, reasonable, and flexible intervention plan according to the feedback network information of the test object.

Considering the important intervention effect of this experimental study, it is suggested that it is necessary to use the conditional emotional response intervention method to temporarily correct the psychological problems caused by the talent network of dihuagu in Nanxian County. According to the actual situation of different individuals, different periods, and different stages, we should appropriately choose the content and time arrangement of this experimental study.

4.4. The Influence of Network New Media on the Dissemination of Rural Art and Culture in Nanxian County

4.4.1. The Network New Media Has Expanded the Dissemination Scope of Nanxian Culture. Nanxian people want to promote fish skin painting and other products, basically through radio and television teaching, not only spending time and labor but also spending a lot of money. As we all know, the advertising price on TV is very high, the economic burden of the people in Nanxian County has increased greatly, the product price has risen, and the sales volume has decreased greatly. Through the new media on the Internet, all problems can be solved simply. In the traditional way of communication, there are also people communicating with each other, but this way of communication has fewer people to understand, less influence, high cost, heavy economic burden, and high product cost. After adding new online media, you only need to take photos and videos through your mobile phone, add appropriate instructions, set up a web page, publish Weibo and WeChat, or use a social network platform, which can be seen by a large number of people. Moreover, the people of Nanxian County can record the life of the people of Nanxian County for the first time, anytime and anywhere, and they can also sell their own products. We all know the importance of smartphones in real life, which can be applied to all aspects of life. Now, people's communication completely depends on mobile phones, which is very convenient. Through QQ and WeChat, it is more convenient for people to communicate with each other and spread network information faster. At the same time, the network can connect the whole world, and the space distance between the whole Earth is reduced. With the help of network technology, network new media is moving towards a higher, faster, and stronger direction. The two combinations combine perfectly. As the popularization speed and scope of network information have been greatly improved, Nanxian County has ushered in a good development opportunity. Therefore, the emergence of new network media provides great convenience for the dissemination of Nanxian culture.

4.4.2. The Network New Media Has Promoted the Dissemination Speed of Nanxian Culture. The new network media is very convenient, and now, everyone has a mobile phone, no matter when and where all parts of life can be recorded. The

Wurigong meeting of Nanxian County will be held in Zhangjiakou. It is a comprehensive meeting, including religious belief, sports performance, clothing display, food feast, national song, and dance. The people of Nanxian County are singing and dancing, very lively. People who are not in Zhangjiakou cannot see it on the spot, but in the new media on the Internet, Nanxian culture lovers can enjoy this grand banquet by forwarding the videos, sounds, and photos of mobile phone videos to the Internet. The audience looked at Nanxian County from different perspectives. The grand event was displayed in an all-round way, achieving a good viewing effect and meeting the strong curiosity of the masses and Nanxian cultural lovers. Spreading to the outside world through the new media on the Internet is not only an important channel but also a window for the outside world to understand Nanxian. Nowadays, many ethnic minorities use the new media on the Internet to introduce their national habits and works of art. It provides an excellent platform for the display of minority culture, the interweaving and collision of various cultures, and the integration and exchange of various cultures. It greatly promotes the exchange and cooperation of national culture and constantly innovates and develops national culture. All these are the benefits of new media on the Internet to cultural development.

4.4.3. The Network New Media Has Widened the Digital Channel of Cultural Communication in Nanxian County. The so-called digitization means that, with the development of science and technology, computers can convert multiple sound signals, image signals, and other signals into digital signals. Compared with the analog signal, the digital signal has made great progress. It can transform numerous complex network information into binary digital code or data format and process multiple sound and image signals on a computer. Due to the existence of a large number of computer storage devices, it is very important for the digitization of Nanxian culture. This means that the national culture can always record the life of the people in Nanxian County and keep many beautiful things, regardless of regional and time restrictions. At the same time, the Nanxian people's marriage habits and other digital forms can also be promoted. This kind of record not only records the grand wedding on the wedding day but also records the preparations before marriage, including how to worship ancestors and the details of married life. It can record all the things about marriage habits from a complete perspective, and it can be spread on the Internet through video. The masses and Nanxian culture lovers can turn on their computers at any time, and they can find pictures and videos of marriage in Nanxian County without time and place restrictions. Such a media digital platform has created many favorable conditions for the continuous inheritance and rapid popularization of Nanxian culture. On the other hand, this network is widely used to shorten the Earth space distance and can spread information to any place on the Earth.

5. Conclusion

The basic conclusion of this study is that the Internet era must inherit excellent local traditional culture. This paper adopts the method of literature analysis and visiting survey, starting from the characteristics of rural art, carries out a detailed analysis of multiculturalism, and discusses the value and cultural significance of dance from the perspective of comprehensive academic research methods. This is not only a requirement of the Internet age but also because the local tradition contains the cultural truth of human existence. The culture of the Internet age is not imagined but produced at historic moments according to local traditions. Culture is not a rootless tree. Local tradition is the root of culture in the Internet age, providing valuable cultural resources for cultural construction and development in the Internet age. In the Internet age, people's cultural behavior is bound to be restricted by traditional culture. In the Internet age, people realize the urgency and importance of inheriting the excellent traditional Chinese culture. It is imperative to build the cultural spirit of the Internet age, and traditional regional culture cannot be fully absorbed. Guided by the materialist dialectics of Marxism and the methodology of seeking truth from facts, we must earnestly study and analyze the excellent cultural essence of local traditions, inherit the reasonable and beneficial culture of local traditions, and improve people's overall cultural level.

Data Availability

The datasets used and/or analyzed during the current study are available from the author on reasonable request.

Conflicts of Interest

The author declares no conflicts of interest.

Acknowledgments

This work was supported by "Study on the "2 + 1 + X" Communication and Learning Strategy of Dihuagu in Nanxian County under the Internet + Situation" (no. 19B046), Scientific Research Excellent Youth Project of the Hunan Education Department.

References

[1] H. Chen, J. Song, X. Lu, L. Liu, Q. Jiang, and N. Li, "A systematic review of the effect of individual cognitive stimulation therapy on mental health intervention in patients with dementia," *Journal of Nursing*, vol. 36, no. 24, pp. 72–76, 2021.

[2] M. Lu, "Research on effective methods of mental health intervention for peizhi lower grade students in Gannan Tibetan area," *New Curriculum*, vol. 48, no. 48, p. 14, 2021.

[3] Z. Liang, T. Xue, and L. Ma, "Talking about the current situation and perfect countermeasures of mental health work in higher vocational colleges," *Caizhi*, vol. 22, no. 32, pp. 125–127, 2021.

[4] L. Wang, N. Zhang, Y. Liu, and Y. Qian, "Progress of mental health intervention for children and adolescents under the

new crown pneumonia epidemic," *Science and Technology Herald*, vol. 39, no. 18, pp. 25–33, 2021.
[5] J. Chen, "A systematic evaluation of baduanjin's intervention effect on college students' mental health," *Journal of Longyan University*, vol. 39, no. 5, pp. 102–111+117, 2021.
[6] B. Xia, "Analysis of the clinical effect of mental health intervention in patients with cerebral infarction complicated with tonsil enlargement," *Chinese Medical Abstracts (Otolaryngology)*, vol. 36, no. 5, pp. 212-213+216, 2021.
[7] P. Huang, "Research on online learning and student mental health education intervention," *New Curriculum*, vol. 13, no. 36, p. 239, 2021.
[8] Y. Huang and J. Ye, "College students' mental health intervention from the perspective of positive psychology," *Reference for Middle School Political Teaching*, vol. 27, no. 33, p. 82, 2021.
[9] X. Yang, "Discussion on the intervention of reading therapy on the mental health of left-behind children in rural areas," *Teacher*, vol. 15, no. 10, pp. 9-10, 2021.
[10] B. Yin, "Analysis of the mental health of college students in major emergencies," *Fortune*, vol. 23, no. 3, pp. 105-106, 2021.
[11] L. Wang and J. Li, "Intervention strategies for college students' mental health based on the influence of social media," *Comparative Research on Cultural Innovation*, vol. 5, no. 6, pp. 186–188, 2021.
[12] Y. Liu, X. Li, A. Li et al., "Evaluation of the effect of mental health intervention skills training on improving the mental health of clinical nurses," *Shanxi Medical Journal*, vol. 49, no. 9, pp. 1084–1086, 2020.
[13] S. Ji, "Research on the cross-cultural communication of documentaries from the perspective of semiotics: taking "approaching daliangshan" as an example," *Audio Visual*, vol. 8, no. 1, pp. 110–112, 2022.
[14] Q. Xu, "Research on the communication strategy of intangible cultural heritage in the new media environment—taking the Northeast drum as an example," *Communication and Copyright*, vol. 19, no. 1, pp. 109–111, 2022.
[15] X. Yan, "Chinese and western silk road spice trade and buddhist culture spread in sui and tang dynasties," *Wutaishan Research*, vol. 21, no. 4, pp. 11–18, 2021.
[16] S. Xie, "The enlightenment of Korean tea culture dissemination to Chinese tea culture under the 5W model," *Fujian Tea*, vol. 44, no. 1, pp. 4–6, 2022.
[17] H. Yining, "The value of English teaching in higher vocational colleges for the dissemination of tea culture under the background of "one belt, one road"," *Fujian Tea*, vol. 44, no. 1, pp. 170–172, 2022.
[18] H. Yang, "Research on translation practice innovation of children's picture books in the context of cross-cultural communication," *Journal of Zaozhuang University*, vol. 39, no. 1, pp. 57–62, 2022.
[19] L. Hong, "Red culture communication in jinggangshan red film text narrative," *Journal of Yuzhang Normal University*, vol. 36, no. 6, pp. 36–39, 2021.
[20] F. Li, "An analysis of the red culture communication ability of the docents of the red memorial hall," *PR World*, no. 24, pp. 128-129, 2021.
[21] Ji Li, "Research on the realization path and value of archives cultural dissemination from the perspective of Northeast Revitalization," *Urban Construction Archives*, vol. 31, no. 12, pp. 130-131, 2021.
[22] H. Chen, "Research on the inheritance and innovative development of jinxiu yao weaving and embroidery art under the rural revitalization strategy," *Comedy World (Second Half Month)*, vol. 35, no. 11, pp. 62–64, 2021.
[23] J. Gao and P. Wei, "Research on the intervention of music and art in southwestern Hubei on the strategy of rural revitalization," *Art Review*, vol. 37, no. 21, pp. 167–169, 2021.
[24] P. Li and Y. Qin, "Research on the innovation and inheritance of local opera art under the background of rural revitalization," *Journal of Shandong Agricultural Engineering Institute*, vol. 38, no. 11, pp. 68–72, 2021.
[25] Y. Zhang, "Education to revitalize the countryside and art to serve the people," *Journal of the Central Conservatory of Music*, vol. 6, no. 4, p. 2+161, 2021.
[26] R. Wang, "The practical application of cultural tourism art in rural revitalization in Henan," *Rural. Agriculture. Peasants (version B)*, vol. 33, no. 10, pp. 42-43, 2021.
[27] M. Qu, "From the perspective of creative tourism geography to explore the model of art revitalization in rural areas," *Public Art*, vol. 42, no. 5, pp. 24–39, 2021.
[28] Y. Wang, "Discussion on the value and countermeasures of strengthening the mental health education of contemporary college students," *Shanxi Youth*, vol. 45, no. 23, pp. 171-172, 2021.
[29] S. Yi, "Constructing a new model of college students' mental health education in the network environment," *Theoretical Research and Practice of Innovation and Entrepreneurship*, vol. 4, no. 22, pp. 124–126, 2021.
[30] D. Li, "Research on primary school mental health education under the Internet background," *Anhui Education and Research*, vol. 24, no. 23, pp. 100-101, 2021.
[31] L. Dong, "Innovative integration of ideological and political education in the Internet age," *Chinese Journal of Multimedia and Network Teaching (Mid-Term)*, vol. 47, no. 7, pp. 80–83, 2021.
[32] Q. Hou, "Innovation of ideological and political education model in the Internet age," *Journal of Honghe University*, vol. 19, no. 3, pp. 119–121, 2021.

Hindawi
Journal of Healthcare Engineering
Volume 2022, Article ID 5466853, 7 pages
https://doi.org/10.1155/2022/5466853

Research Article

Intratumoral Microbiota Impacts the First-Line Treatment Efficacy and Survival in Non-Small Cell Lung Cancer Patients Free of Lung Infection

Miao Zhang,[1] Yan Zhang ,[1,2] Yi Sun,[2] Shaochun Wang,[2] Huan Liang,[2] and Yaguang Han[2]

[1]*Department of Oncology, Graduate School, Hebei Medical University, Shijiazhuang 050017, China*
[2]*Department of Oncology, Shijiazhuang People's Hospital, Shijiazhuang 050030, China*

Correspondence should be addressed to Yan Zhang; zhangyan201810@163.com

Received 28 December 2021; Revised 7 January 2022; Accepted 17 January 2022; Published 7 February 2022

Academic Editor: Enas Abdulhay

Background. It has been known that there are microecology disorders during lung cancer development. Theoretically, intratumoral microbiota (ITM) can impact the lung cancer (LC) survival and treatment efficacy. This study conducted a follow-up investigation of non-small cell lung cancer (NSCLC) patients without lung infection to prove whether ITM indeed impacts the first-line treatment efficacy and survival. *Methods*. We enrolled all patients diagnosed with NSCLC in our department from 2017 to 2019, whose tumor samples were available (through surgery or biopsy) and sent for pathogen-targeted sequencing. All patients received the first-line treatment according to the individual situation. In the short term, the efficacy of the first-line treatment was recorded. During the follow-up, the survival status, progress events, and overall survival (OS) period were recorded if a patient was contacted. *Results*. Firstly, 53 patients were included, and our following analysis focused on the stage III and stage IV cases with ADC, SCC, or ASC tumors (47 cases). Several bacteria are associated with the LC status and progression, including N stages, metastasis sites, epidermal growth factor receptor (EGFR) mutation, first-line outcome, and later survival. The risk bacteria include *Serratia marcescens*, *Actinomyces neesii*, *Enterobacter cloacae*, and *Haemophilus parainfluenzae*; and the protective (against LC development and progression) ones include *Staphylococcus haemolyticus* and *Streptococcus crista*. In the logistic regression, the two-year survival can be predicted using the results of four bacteria (*Haemophilus parainfluenzae*, *Serratia marcescens*, *Acinetobacter jungii*, and *Streptococcus constellation*), with an accuracy rate of 90.7%. *Conclusion*. ITM have links to malignancy, EGFR mutation, first-line outcome, and survival of NSCLC. Our results implied the potential anti-NSCLC activity of antibiotics when used reasonably. It is still necessary to deepen the understanding of the characteristics of ITM and its interactions with NSCLC tumors and the immune cells, which is significant in individualized approaches to the LC treatment.

1. Introduction

Lung cancer (LC), especially non-small cell lung cancer (NSCLC), is one of the primary causes of global death. Traditionally, the carcinogenic factors of LC mainly include genetic factors and environmental factors. In recent years, it has been realized that microbial flora possibly impacts LC development [1]. The role of the microbiome has become increasingly clear, and variation of the microecology has been noticed in LC patients [2]; different clinicopathologies may be related to different conditions of the lung microbiota (LM) [3]. LM is also involved in LC onset and malignant progression. Understanding the diverse contributions of the bacterial microbiota to carcinogenesis is of great importance in LC diagnosis and treatment. Currently, studies do not distinguish LC cases with or without lung infection (LI). Bacterial and viral infections had influence on the patients' prognosis, affecting the immune system and impairing the outcome of anticancer treatments [4]. These cases have two major diseases, and the situation should be more complicated than LC alone. For patients free of LI, the features of tumor-associated microbiota are particularly informative in the investigation of tumorigenesis driven by LM. Additionally, published studies concerning the intratumoral microbiota (ITM) mainly focused on the basal clinical characteristics. Theoretically, IMT may impact the immune response and inhibit the treatment efficacy. So far, these factors and consequences are poorly understood in LC. It is reasonable to evaluate whether these interactions can impact the LC survival and treatment efficacy. However, very limited studies have analyzed the prognosis and investigated these potential influences induced by ITM.

Here, we conducted this 5-year follow-up study of NSCLC patients without respiratory infection and proved that ITM indeed impacts the first-line treatment efficacy and survival, which will show the potential anti-NSCLC activity of antibiotics. It is still necessary to deepen the understanding of the characteristics of ITM and its interactions with NSCLC tumors and the immune cells, which is significant in individualized approaches to the LC treatment.

2. Materials and Methods

2.1. Patients. We enrolled all patients diagnosed NSCLC in our department since 2017, whose tumor samples were available (through surgery or biopsy) and sent for pathogen-targeted sequencing. The inclusion criteria are as follows: (1) patients diagnosed with lung cancer, including adenocarcinoma (ADC), squamous cell carcinoma (SCC), and adenosquamous carcinoma (ASC) and (2) patients with the basic demographic information and tumor characteristics. The exclusion criteria are as follows: (1) patients diagnosed with a definite respiratory infection and other system disease. The smoking history and average number of cigarettes smoked every year were acquired. The EGFR and TP53 mutation features were extracted from the electronic medical record system. In addition, 5 μm paraffin-embedded tumor-tissue sections were prepared, and the PD-L1 expression in the immunohistochemistry analysis was acquired from the Department of Pathology. All patients received the first-line treatment according to an individual situation. In the short term, the efficacy of the first-line treatment was recorded. During the follow-up (at most 5 years), the survival status, progress events, progression-free survival (PFS), and overall survival (OS) period were recorded if a patient was contacted.

2.2. Targeted Sequencing of Intratumoral Microbiota (ITM). We used all the collected tumor samples to perform the pathogen-targeted sequencing. The sequencing process was performed in the Pathogeno One Pan-Infectious Pathogen high-throughput sequencing system by Shanghai Bingyuan Medical Technology Co. The report of each patient was acquired and documented in the dataset. For each known pathogenic microorganism, two fields were used for analysis: the reads of known bacteria and the presence of each microorganism.

2.3. Outcome Measures. 53 patients were included, and 47 cases were followed for analysis.

The risk bacteria include *Serratia marcescens*, *Actinomyces neesii*, *Enterobacter cloacae*, and *Haemophilus parainfluenzae*; the protective (against LC development and progression) ones include *Staphylococcus haemolyticus* and *Streptococcus crista*.

Table 1: Clinical characteristics of NSCLC patients.

Characteristics		Case number	%
Total cases		53	100
Gender	Male	38	71.7
	Female	15	28.3
Smoking history	Never smoking	21	39.6
	Smoking	31	58.5
	Smoking quitted	1	1.9
Major stage	I	1	1.9
	II	2	3.8
	III	25	47.2
	IV	25	47.2
Pathological type	ADC	26	49.1
	SCC	21	39.6
	ASC	3	5.7
	Others	3	5.7
PD-L1 positive		13	24.5
EGFR mutation		12	22.6
Metastasis	Mediastinal lymph nodes	11	20.8
	Lung	11	20.8
	Bone	10	18.9
	Liver	7	13.2
	Brain	6	11.3
	Pleura	3	5.7
	N	Mean	SD
Age (years)	53	66.08	8.786
Cigarettes per year	53	385.85	436.813

2.4. Statistical Analysis. The data are expressed as numbers with proportions (%), mean with SD, or median with 95% confidence interval (CI). The differences in values derived from categorical variables were compared using the chi-squared test. One-way ANOVA was used for three or four groups. Overall survival (OS) in relation to the bacterial result was evaluated by Kaplan–Meier survival curve and log-rank test. The Cox proportional hazard model was also used to discover the potential risk of the relationship between multiple factors and the overall postoperative survival. Statistically significant prognostic factors identified by univariate analysis were further included in the multivariate analysis. A P value <0.05 was considered statistically significant.

3. Results

3.1. Clinical Characteristics of Enrolled NSCLC Patients. Firstly, 53 patients were included, and the clinical features are presented in Table 1. There were 38 (71.7%) males and 15 (28.3%) females. About 40% of patients were smokers. There were 25 (47.2%) stage III and 25 (47.2%) stage IV cases. Only three patients were in stage I or II. The pathological types were as follows: the numbers for adenocarcinoma (ADC), squamous cell carcinoma (SCC), and adenosquamous carcinoma (ASC) were 26 (49.1%), 21 (39.6%), and 3 (5.7%), respectively. Besides, there were three cases of other types, including two poorly differentiated carcinomas and one large cell lung cancer. The main metastasis sites were mediastinal lymph nodes, lung, bone, liver, and brain.

3.2. Association between Intratumoral Microbiota (ITM) and Disease Characteristics. Given there were only three stage-I/II cases, and only three cases had the other pathological types (including poorly differentiated carcinoma and large cell lung cancer), our following analysis focused on the stage III and stage IV cases with ADC, SCC, or ASC tumors (47 cases). If some microbiota had no more than four positive cases, the results might be unreliable. Therefore, those microbiota results with rare cases were culled from the raw data. First, the association between the microbiota and the pathological type was probed. Among ADC, SCC, and ASC, the ASC tumors had a higher abundance of *Serratia marcescens* (2.67 ± 4.619 counts) versus ADC (0.27 ± 0.962 counts, $P < 0.05$) and SCC (0 counts, $P < 0.05$). However, the case number of ASC was three, and this conclusion is still to be verified. Next, there was no association between ITM and the major stage (T stage and M stage). But for N stages, among N0 to N3, we noticed different features in the presence of *Actinomyces neesii* and *Haemophilus* (Table 2). These two bacteria were negatively related to the metastasis in the lymph node ($P < 0.01$). Next, the main metastasis organs/tissues (including mediastinal lymph nodes, lung, bone, liver, brain, and pleura) showed noticeable association with the ITM. Tumors with *Serratia marcescens* were more likely to develop brain metastasis ($P < 0.01$, Table 3), and those with *Enterobacter cloacae* were more likely to develop metastases to the mediastinal lymph node ($P < 0.05$, Table 3). Moreover, for the first time, we noticed that ITM can link to the EGFR mutation (Table 4). For example, EGFR mutation was negatively related to *Haemophilus parainfluenzae* ($P < 0.05$) but positively with *Serratia marcescens* ($P < 0.01$). Furthermore, *Acinetobacter jungii* was positively correlated with PD-L1 expression (PD-L1 positive/negative = 4/8) in *Acinetobacter jungii*-positive cases, in comparison with 7/41 in *Acinetobacter jungii*-negative cases, (chi-square = 4.168, $P = 0.041$). Collectively, ITM is notably associated with disease characteristics of NSCLC.

3.3. Association between ITM and the First-Line Treatment Outcomes. Next, we evaluated whether ITM may impact the efficacy of first-line treatments (targeted therapy or chemotherapy). Also, only stage III and IV cases were analyzed. Overall, there is no association between ITM and the response to the first-line treatment. However, in the hierarchical analysis, we noticed that the presence of *Haemophilus parainfluenzae* was negatively correlated with response to the first-line treatment for stage IV patients (Table 5). The patients with intratumoral *Haemophilus parainfluenzae* had a poorer control rate (3/6 vs 18/19).

Table 2: Association between ITM and N stages.

Bacteria		N0	N1	N2	N3	Chi-square	*P* value
Actinomyces neesii	−	0	1	28	8	18.875	<0.001
	+	1	1	1	0		
Haemophilus	−	0	2	25	8	8.473	0.037
	+	1	0	4	0		

Table 3: Association between ITM and metastasis sites.

Bacteria		No	Yes	Chi-square	*P* value
		Brain			
Serratia marcescens	−	39	4	8.136	0.004
	+	1	2		
		Mediastinal lymph node			
Enterobacter cloacae	−	36	6	6.031	0.014
	+	2	3		

Table 4: Association between ITM and EGFR mutation.

Bacteria		WT	Mutant	Chi-square	*P* value
Haemophilus parainfluenzae	−	24	12	4.924	0.026
	+	11	0		
Serratia marcescens	−	34	9	9.093	0.003
	+	0	3		

Table 5: Association between *Haemophilus parainfluenzae* and the first-line outcome in stage IV.

Bacteria		PD	SD	PR	Chi-square	*P* value
Haemophilus parainfluenzae	−	1	10	8	6.877	0.032
	+	3	2	1		

Table 6: Association between *Haemophilus parainfluenzae* and the PFS in stage IV.

Outcome	Median	95% CI		Log-rank chi-square	*P* value
−	7 months	4.891	9.109	3.940	0.047
+	4 months	1.600	6.400		

3.4. Association between ITM and Survival. Initially, we used the Kaplan–Meier method to evaluate the association between ITM and survival in stages III and IV. If any case, the number of the ITM/target event (progressed or death) double-positive set was not more than two, this index was omitted. Similar to the response to the first-line treatment outcomes, the presence of *Haemophilus parainfluenzae* was related to the poorer PFS of stage IV patients (Table 6 and Figure 1(a)). When stage III and IV cases were pooled together, we found that *Staphylococcus haemolyticus* infection was linked to the longer PFS (Table 7 and Figure 1(b)). Meanwhile, for pooled cases (stage III and IV), *Serratia marcescens* was related to better OS (Table 8 and Figure 1(c))

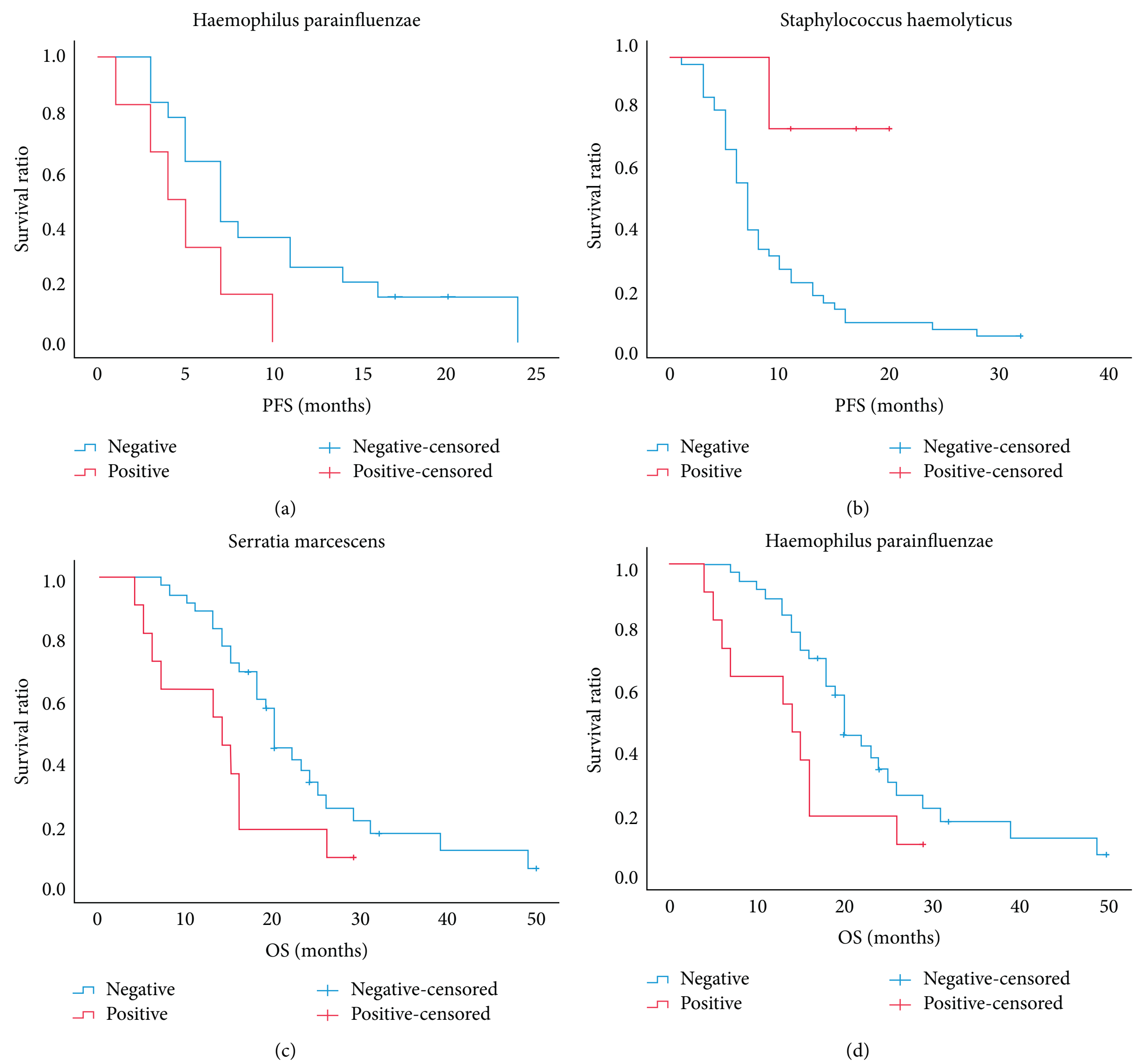

Figure 1: The association between intratumoral microbiota and survival in stage III and IV non-small cell lung cancer patients using the Kaplan–Meier method. (a) The presence of *Haemophilus parainfluenzae* was related to poorer PFS (only for stage IV patients). (b) *Staphylococcus haemolyticus* infection was linked to longer progression-free survival (PFS). (c) *Serratia marcescens* was related to better overall survival (OS). (d) *Haemophilus parainfluenzae* was related to poorer OS.

Table 7: Association between *Staphylococcus haemolyticus* and the PFS.

Outcome	Median	95% CI		Log-rank chi-square	*P* value
–	7 months	6.102	7.898	5.887	0.015
+	Not reached				

Table 8: Association between *Serratia marcescens* and the OS.

Outcome	Median	95% CI		Log-rank chi-square	*P* value
–	18 months	15.107	20.893	6.995	0.008
+	49	N.A.	N.A.		

and the presence of *Haemophilus parainfluenzae* was related to the poorer OS (Table 9 and Figure 1(d)). Also, the Cox regression analysis (using the Enter model) showed that, besides *Staphylococcus haemolyticus*, *Streptococcus crista* is also associated with better PFS (Table 10). On the contrary, *Haemophilus parainfluenzae* and *Corynebacterium jergeri* were two risk factors for OS (Table 11). Finally, in the logistic regression model, the two-year survival was predicted (for stage III or IV patients with ADC, SCC, or ASC), using the following seven variables: age, major stage, pathological type, and the results of four bacteria (*Haemophilus parainfluenzae*, *Serratia marcescens*, *Acinetobacter jungii*, and *Streptococcus constellation*). The variables and their contribution are listed in Table 12. Using this regression, the

Table 9: Association between *Haemophilus parainfluenzae* and the OS.

Outcome	Median	95% CI		Log-rank chi-square	P value
−	20 months	18.676	21.324	4.933	0.026
+	14 months	5.368	22.632		

Table 10: Cox regression analysis of PFS based on IMT results.

Bacteria	B	Wald	P value	Exp (B)
Enterococcus	−0.199	0.131	0.717	0.820
Streptococcus crista	−1.216	3.951	0.047*	0.297
Acinetobacter jungii	0.380	0.379	0.538	1.462
Aerococcus light green	0.115	0.041	0.840	1.121
Staphylococcus haemolyticus	−2.588	5.715	0.017*	0.075
Haemophilus haemolyticus	0.267	0.209	0.648	1.306
Actinomyces neesii	0.643	0.696	0.404	1.901
Corynebacterium pseudodiphtheriae	0.468	0.614	0.433	1.596
Streptococcus constellation	0.217	0.091	0.762	1.242
Streptococcus pneumoniae	0.102	0.048	0.827	1.107
Haemophilus parainfluenzae	0.966	2.681	0.102	2.627
Prevotella II	0.460	0.497	0.481	1.584
Haemophilus influenzae	0.463	0.502	0.479	1.589
Haemophilus	0.018	0.001	0.978	1.018
Corynebacterium jergeri	0.450	0.612	0.434	1.569
Enterobacter cloacae	−1.070	2.556	0.110	0.343
Serratia marcescens	−0.881	1.410	0.235	0.415

predicted results (at the cutoff value 0.5) are as follows: 31 true-negative cases, 1 false-positive case, 3 false-negative cases, and 8 true-positive cases (with an accuracy rate of 90.7%).

Table 11: Cox regression analysis of OS based on IMT results.

Bacteria	B	Wald	P value	Exp (B)
Enterococcus	0.161	0.079	0.778	1.175
Streptococcus crista	−1.592	4.151	0.042*	0.203
Acinetobacter jungii	0.042	0.005	0.946	1.043
Aerococcus light green	−0.670	0.962	0.327	0.512
Staphylococcus haemolyticus	−13.925	0.002	0.964	0.000
Haemophilus haemolyticus	0.974	2.297	0.130	2.649
Actinomyces neesii	−0.725	0.741	0.389	0.484
Corynebacterium pseudodiphtheriae	0.973	1.644	0.200	2.646
Streptococcus constellation	−0.776	0.816	0.366	0.460
Streptococcus pneumoniae	−0.777	1.980	0.159	0.460
Haemophilus parainfluenzae	1.396	4.771	0.029*	4.038
Prevotella II	0.092	0.015	0.904	1.096
Haemophilus influenzae	−0.527	0.377	0.539	0.590
Haemophilus	0.278	0.130	0.718	1.320
Corynebacterium jergeri	1.997	6.086	0.014*	7.366
Enterobacter cloacae	−0.799	1.629	0.202	0.450
Serratia marcescens	−13.556	0.003	0.960	0.000

Table 12: Logistic regression analysis of 2-year survival based on general information and IMT results.

Variables	B	Wald	P value	Exp (B)
Age	−0.189	2.512	0.113	0.827
Major stage	−1.118	0.513	0.474	0.327
Pathological type		0.000	1.000	
ADC	−21.501	0.000	0.998	0.000
SCC	−19.736	0.000	0.999	0.000
ASC	−20.288	0.000	0.999	0.000
Haemophilus parainfluenzae	−0.049	0.001	0.974	0.952
Serratia marcescens	41.742	0.000	0.999	1.3*10^18
Acinetobacter jungii	0.336	0.029	0.864	2.1*10^9
Streptococcus constellation	19.164	0.000	0.998	2.1*10^8

4. Discussion

It has been recognized that LC has non-negligible links to pathogenic microorganisms, such as *Haemophilus influenzae*, *Moraxella catarrhalis*, *Granulicatella*, *Abiotrophia*, *Streptococcus*, and *Mycobacterium tuberculosis* [5–8]. With the development of sequencing technology, their relationships have been increasingly clear. However, there are still problems to be solved. One of the most important questions is whether and how ITM affect the treatment and prognosis of lung cancer. We here innovatively observed the link between ITM and disease characteristics and combined the results of ITM to construct a prognostic model. Overall, several bacteria are associated with the LC status and progression, including N stages, metastasis sites, EGFR mutation, first-line outcome, and later survival. Seemingly, the risk bacteria include *Serratia marcescens*, *Actinomyces neesii*, *Enterobacter cloacae*, and *Haemophilus parainfluenzae*; and the protective (against LC development and progression) ones include *Staphylococcus haemolyticus* and *Streptococcus crista*. So far, all the abovementioned associations were highly novel findings, so supporting evidence are limited. *Haemophilus parainfluenzae* has been regarded as an indicator of LM changes triggered by preoperative prophylaxis in LC patients [9]. It was observed in 43.3% to 63.3% cases of LC patients [9], and it is reasonable to believe that this bacterium is a cancer-promoting strain. Interestingly, there are also some seemingly unsupportive evidence. For example, prodigiosin is a secondary metabolite, isolated from a culture of *Serratia marcescens*. It induces LC apoptosis in both caspase-dependent and caspase-independent pathways [10]. It is still early to tell whether *Serratia marcescens* has a driving or suppressive effect on LC. However, based on Table 3, if *Serratia marcescens* drives LC progression, a possible pathway is metastasis in the brain. Similarly, as shown in Table 2, the reason for the driving effect by *Actinomyces neesii* may be due to the promotion of lymph node metastasis. Also, *Haemophilus parainfluenzae*, as a risk factor to survival, may promote the EGFR-WT carcinomas but not EGFR mutant ones, and these cases cannot be treated by targeted TKIs, which is a possible reason for the poor survival.

The mechanisms underlying the impact of ITM on survival may include the following and various aspects. First, ITM (as well as bacteria outside the tumor) may drive carcinogenesis directly. It is estimated that 20% of cancers are caused by infectious agents [11]. The dysbiosis of some carcinogenic microbiomes causes direct DNA damage and inflammation [12]. Moreover, inflammation triggered by microbial dysregulation can largely impact invasion and angiogenesis, which significantly drives the malignant progression. Known targets of microbiome-induced inflammation include TLRs, NF-κB, and STAT3 [13–15]. These direct effects exerted by microbes are highly possibly carcinogenic. Also, there are some indirect mechanisms. For example, through modulation of immune response, the response to treatment and prognosis can be influenced. Besides, the inflammatory effect triggered by IMTs, their inhibitive effects on the immune system can also play an essential role [12]. At least partially, ITM can result in the exhaustion of immune cells, and they inhibit antitumor immunity together with the tumor cells. For example, they may exert suppress NK cells [16]. However, given the digestive tract has more abundant flora, most attention to the relationship between microbiome and cancer has been paid to colorectal cancer and gastric cancer. There are limited data about the impact of ITM on the prognosis of LC, but related research can be used as reference. Recently, a Chinese study found nine enriched bacteria in the lung of NSCLC patients [17]. Also, the analysis of T cells and B cells implied that these bacteria in the lung may change the immune cell infiltration in LC tissues. Recently, a retrospective study of 69 NSCLC reported that patients treated with anti-PD-1 antibodies receiving antibiotics had greatly decreased objective response rate, OS, and PFS compared to those who did not use antibiotics [18]. This result highlights that inappropriate usage of antibiotics may influence the flora of the tumor environment and impair the treatment effect. Indeed, the use of antibiotics has been reported to be associated with an elevated risk of LC onset [19, 20]. Moreover, when not limited to the local lung tissue, another interesting issue is whether the gut-lung axis may impact the outcome of chemotherapy and later survival through the impact of microbiota. This issue is being investigated by a multicenter, prospective, double-blind randomized trial [21], but the final result has not yet been announced.

Still, the present study has some limitations. The main shortcoming is the small sample size. The number of many classification results was around 5 in one cell, which is the major reason for the inconsistency between the univariate analysis and binary regression analysis. Also, due to the limited sample size, the performance of bacteria in the 2-year prediction model is not outstanding enough, and we cannot divide the dataset into the training set and test set; hence, the scalability of the model is still unclear.

5. Conclusion

This novel study proved that ITM was related to malignancy, EGFR mutation, first-line outcome, and survival of NSCLC. Also, our results implied the potential anti-NSCLC activity of antibiotics when used reasonably. It is still necessary to deepen the understanding of the characteristics of ITM and its interactions with NSCLC tumors and the immune cells, which is significant in individualized approaches to the LC treatment.

Data Availability

The data used to support this study are available from the corresponding author upon request.

Conflicts of Interest

The authors declare that they have no conflicts of interest.

References

[1] G. Liu, A. Gu, and M. E, “Mechanism and research progress of microbiome in the development of lung cancer,” *Zhongguo Fei Ai Za Zhi*, vol. 23, no. 11, pp. 948–953, 2020.

[2] Z. Ran, J. Liu, F. Wang et al., “[Analysis of pulmonary microbial Diversity in Patients with advanced lung cancer Based on high-throughput sequencing technology],” *Zhongguo Fei Ai Za Zhi*, vol. 23, no. 12, pp. 1031–1038, 2020.

[3] D. Huang, X. Su, M. Yuan et al., “The characterization of lung microbiome in lung cancer patients with different clinicopathology,” *American journal of cancer research*, vol. 9, no. 9, pp. 2047–2063, 2019.

[4] L. Belluomini, A. Caldart, A. Avancini et al., “Infections and immunotherapy in lung cancer: a bad relationship?” *International Journal of Molecular Sciences*, vol. 22, no. 1, p. 42, 2020.

[5] F. C. Lin, J.-Y. Huang, S.-C. Tsai et al., “The association between human papillomavirus infection and female lung cancer: a population-based cohort study,” *Medicine (Baltimore)*, vol. 95, no. 23, p. e3856, 2016.

[6] K. L. Greathouse, J. R. White, A. J. Vargas et al., “Interaction between the microbiome and TP53 in human lung cancer,” *Genome Biology*, vol. 19, no. 1, p. 123, 2018.

[7] L. X. Jiang, R. X. Ren, H. J. Zhou et al., “Simultaneous detection of 13 key bacterial respiratory pathogens by combination of multiplex PCR and capillary electrophoresis,” *Biomedical and Environmental Sciences*, vol. 30, no. 8, pp. 549–561, 2017.

[8] H. D. Hosgood, A. R. Sapkota, N. Rothman et al., “The potential role of lung microbiota in lung cancer attributed to household coal burning exposures,” *Environmental and Molecular Mutagenesis*, vol. 55, no. 8, pp. 643–651, 2015.

[9] U. Kosikowska, A. Biernasiuk, P. Rybojad, R. Łoś, and A. Malm, “Haemophilus parainfluenzae as a marker of the upper respiratory tract microbiota changes under the influence of preoperative prophylaxis with or without postoperative treatment in patients with lung cancer,” *BMC Microbiology*, vol. 16, p. 62, 2016.

[10] E. Llagostera, V. Soto-Cerrato, B. Montaner, and R. Pérez-Tomás, “Prodigiosin induces apoptosis by acting on mitochondria in human lung cancer cells,” *Annals of the New York Academy of Sciences*, vol. 1010, pp. 178–181, 2003.

[11] J. Vande Voorde, J. Balzarini, and S. Liekens, “Mycoplasmas and cancer: focus on nucleoside metabolism,” *Excli j*, vol. 13, pp. 300–322, 2014.

[12] N. Keren, F. M. Konikoff, Y. Paitan et al., “Interactions between the intestinal microbiota and bile acids in gallstones patients,” *Environ Microbiol Rep*, vol. 7, no. 6, pp. 874–880, 2015.

[13] V. García-Castillo, E. Sanhueza, E. McNerney, S. A. Onate, and A. García, "Microbiota dysbiosis: a new piece in the understanding of the carcinogenesis puzzle," *Journal of Medical Microbiology*, vol. 65, no. 12, pp. 1347–1362, 2016.
[14] V. Sethi, S. Kurtom, M. Tarique et al., "Gut microbiota promotes tumor growth in mice by modulating immune response," *Gastroenterology*, vol. 155, no. 1, pp. 33–37.e6, 2018.
[15] M. Y. Wei, S. Shi, C. Liang et al., "The microbiota and microbiome in pancreatic cancer: more influential than expected," *Molecular Cancer*, vol. 18, no. 1, p. 97, 2019.
[16] S. V. Rajagopala, S. Vashee, L. M. Oldfield et al., "The human microbiome and cancer," *Cancer Prevention Research*, vol. 10, no. 4, pp. 226–234, 2017.
[17] Y. S. Chang, M. H. Hsu, S. J. Tu et al., "Metatranscriptomic analysis of human lung metagenomes from patients with lung cancer," *Genes*, vol. 12, no. 9, p. 1458, 2021.
[18] K. Hamada, K. Yoshimura, Y. Hirasawa et al., "Antibiotic usage reduced overall survival by over 70% in non-small cell lung cancer patients on anti-PD-1 immunotherapy," *Anticancer Research*, vol. 41, no. 10, pp. 4985–4993, 2021.
[19] G. Ternák, K. Berényi, A. Sümegi et al., "Antibiotic consumption patterns in European countries may Be associated with the incidence of major carcinomas," *Antibiotics*, vol. 9, no. 10, p. 643, 2020.
[20] A. Halley, A. Leonetti, A. Gregori et al., "The role of the microbiome in cancer and therapy efficacy: focus on lung cancer," *Anticancer Research*, vol. 40, no. 9, pp. 4807–4818, 2020.
[21] Q. Xia, G. Chen, Y. Ren et al., "Investigating efficacy of "microbiota modulation of the gut-lung Axis" combined with chemotherapy in patients with advanced NSCLC: study protocol for a multicenter, prospective, double blind, placebo controlled, randomized trial," *BMC Cancer*, vol. 21, no. 1, p. 721, 2021.

Hindawi
Journal of Healthcare Engineering
Volume 2022, Article ID 2345600, 7 pages
https://doi.org/10.1155/2022/2345600

Review Article

Implementation of Whale Optimization for Budding Healthiness of Fishes with Preprocessing Approach

Pravin R. Kshirsagar[1] **Hariprasath Manaoharan,**[2] **Vineet Tirth,**[3] **Saiful Islam,**[4] **Sandeep Srivastava,**[5] **Varsha Sahni,**[6] **M. Thangamani,**[7] **M. M. Khanapurkar,**[8] **and Venkatesa Prabhu Sundramurthy**[9]

[1]*Department of Artificial Intelligence, G.H. Raisoni College of Engineering, Nagpur, India*
[2]*Department of Electronics and Communication Engineering, Audisankara College of Engineering and Technology, Gudur, Andhra Pradesh, India*
[3]*Mechanical Engineering Department, College of Engineering, King Khalid University, Abha 61411, Asir, Saudi Arabia*
[4]*Civil Engineering Department, College of Engineering, King Khalid University, Abha 61411, Asir, Saudi Arabia*
[5]*MCA Department, GL BAJAJ Institute of Technology & Management, Greater Noida, India*
[6]*Department of Computer Science and Engineering, CT Group of Institute (CTIEMT), Shahpur, I.K.Gujral Punjab Technical University, Jalandhar, Pin 144603, India*
[7]*Department of Information Technology, Kongu Engineering College, Perundurai, Tamilnadu, India*
[8]*G.H. Raisoni College of Engineering, Nagpur, India*
[9]*Center of Excellence for Bioprocess and Biotechnology, Department of Chemical Engineering, College of Biological and Chemical Engineering, Addis Ababa Science and Technology University, Addis Ababa, Ethiopia*

Correspondence should be addressed to Pravin R. Kshirsagar; pravinrkshirsagarphd@gmail.com and Venkatesa Prabhu Sundramurthy; venkatesa.prabhu@aastu.edu.et

Received 12 November 2021; Revised 14 December 2021; Accepted 18 December 2021; Published 2 February 2022

Academic Editor: Enas Abdulhay

This article examines distinctive techniques for monitoring the condition of fishes in underwater and also provides tranquil procedures after catching the fishes. Once the fishes are hooked, two different techniques that are explicitly designed for smoking and drying are implemented for saving the time of fish suppliers. Existing methods do not focus on the optimization algorithms for solving this issue. When considering the optimization problem, the solution is adequate for any number of inputs at time *t*. For this combined new flanged technique, a precise system model has been designed and incorporated with a set of rules using contention protocols. In addition, the designed system is also instigated with a whale optimization algorithm that is having sufficient capability to test the different parameters of assimilated sensing devices using different sensors. Further to test the effectiveness of the proposed method, an online monitoring system has been presented that can monitor and in turn provides the consequences using a simulation model for better understanding. Moreover, after examining the simulation results under three different scenarios, it has been observed that the proposed method provides an enhancement in real-time monitoring systems for an average of 78%.

1. Literature: A Brief Review

For applying the proposed indication on monitoring fisheries with smoking and cutting methods, many existing methodologies have been analyzed, and they are discussed in this section. Since many accurate predictions are needed under water, a smart quality sensor has been designed with a new adaptive system model [1]. The major exertion has concentrated on analyzing the varying nature of fishes, and an ice storage system has been used for storage where only a limited number of measurements have been provided. Consequently, association between index quality and standard quality is provided by selecting a sequencing method that validates calibration and corroboration of sensors. Also, wireless sensors have been integrated, and their performance on water quality has been checked in the western region of Andhra Pradesh where direct field visits have been made for designing an autonomous mode of operation [2]. The researchers examined and created an autonomous vehicle that is capable of traveling inside water and reports corresponding information to the base station. This type of system has been inspected in India for the first time, and it is significantly supportive for all aqua farmers to lead a better quality of life. A review has been prepared by comparing different methods for monitoring the health parameters of each fish [3] that are present inside the water. This type of review provides complete information on the usage of low-power devices that requires only minimum water for improving the productivity in farms. Moreover, the impact of freshwater has also been discussed, but only a small area has been considered, and it is not enough to make a prudent decision since the area of monitoring is much important for aquaculture research.

Moreover, an analytical method for monitoring water quality has been examined [4] under four different categories that even include the existence and nonexistence of different contaminants. For monitoring both physical and biological contaminants, a high-end network setup is needed with low-cost sensors. The major reason for using high-quality setup is to avoid microbes that affect the aqua farms, but the cost of implementation is higher when a high-end network setup is established. Once the fishes are gathered, they should be desiccated for a period of time; therefore, a smoking machine is established [5], which observes only a small quantity of water. However, the setup consists of a closed-loop circulation with Arduino Uno sustenance where high-cost pipes and chambers are established. This method serves as a basic perception of desiccating the fishes within three hours, and it can even be changed from one place to another. Even during the smog period, the fishes can be dehydrated for six hours, but the amount of energy that is consumed for this process is much higher due to the existence of a huge chamber. Therefore, to overcome the drawback of the big-sized chamber that cannot be used in the indoor environment, a machine learning algorithm for smoking fishes has been created [6]. This procedure uses the concept of k-nearest neighbor for receiving the data from the chamber with help of low-cost sensors. But, in most methods, only a binary value is not sufficient to determine the simplicity of prediction. The researchers have also rationalized the old technique of image classification to the video detection method [7] where an automated detection scale has been presented with different time scales. One additional advantage of the aforementioned method is that it paves way for transferring the video to all cable telescopes. But a high number of video nodes is needed for underwater, and it will be difficult to integrate all information from several nodes.

In a fish processing survey, it is observed that most of the fishes are smoked and expurgated before reaching the final stage [8] that is not good for health. Therefore, it is necessary to monitor the amount of proteins that are present in each fish, and they should be extracted for use in other sources. Furthermore, the researchers have explored that the amount of freshness in fish fillets should also be monitored [9] that is significantly useful for improving the accuracy of the entire system. This procedure can be implemented with multiple ethereal that can store fishes for a period of 12 days, and the high amount of power will be consumed during this process when images are extracted. For both assessment and data processing techniques the components of machine vision applications are extracted [10] that include the size and volume of fishes to be smoked. This type of machine vision application serves as an important component for the automatic processing of aqua food processing techniques. Moreover, for measuring both quality and quantity of fishes, an electronic sensor device has been implemented that detects tongue and nose for electronic authentication process [11]. This type of high advancement needs metal-oxide-semiconductor field-effect transistor electrochemical sensors to be implemented at a high cost.

Additionally, control guidance by the food processing industry for storing vulnerabilities has been provided [12] that serve as a contrivance for all countries to follow highly defined standards in aqua farms. By following these standards, an investigation has been made in the Mediterranean Sea [13] where attrition is prevented and fishes are protected in prematured stage itself. Since most of the process is implemented with sensors, a new system model is necessary; therefore, a semiconductor sensor model has been created [14], and it is integrated with machine vision algorithms. Besides, this system an agent-based simulator has also been introduced in the current system process that provides an inherent mechanism for monitoring fishes [15]. This type of model is having many hidden layers, and all these layers are fulfilled only using the cost of communication channels.

To improve the health of fishes in underwater, whale optimization algorithm is used. In this study, the behavior of fishes and their presented environment, that is, underwater, are analyzed for the number of sensors deployed. Both environment and fish-related information are analyzed using the sensors. Based on the current state, the performance of optimization is achieved using the sensors.

The rest of this paper is organized as follows. Section 2 summarizes the precise design methodology in which the proposed system overview is detailed. Section 4 discusses the proposed optimization algorithm for using the fishers improvement analysis. Section 5 discusses the results and discussion for the proposed methodology in which the overall results of the designed methodology are highlighted in detail, and finally, the system is concluded with the conclusions and further enhancements.

2. Precise Design Methodology

For designing a precise methodology, it is much important to calibrate the sensors, and all the decompositions that are used for smoking fishes must run in a parallel manner. Since parallel operations are performed, a likelihood model has to be formed that performs different sensor operations when data is distributed individually. Therefore, the likelihood function can be established using the following equation:

$$f(i) = \sum_{i=1}^{n} \frac{(\mu_i - p_i)^2}{\sigma_i^2}, \quad (1)$$

where p_i denotes the prediction of sensors for distributed data. μ_i and σ_i represents the mean and variance of given likelihood functions.

Equation (1) denotes that variation in size of fishes with different sizes in the smoking process has been considered using mean and variance functions. Also, during the cutting process, it is difficult to cut the fishes of the same size; therefore, for proper examination of length and breadth, data are predicted using a contact distance sensor that is indicated as LVDT has been integrated inside the corresponding cutting machines. After unknown likelihood values are known in the next step, all measurement counts gained during the cutting process have to be calculated using the following equation:

$$\frac{\mathrm{d}c_i}{\mathrm{d}t_i} = \mu_i\left(1 - 10^{m_i(t)}\right), \quad (2)$$

where $m_i(t)$ denotes various concentrations in the population of fishes at time $t = 0$ inside the smoking chamber. Equation (2) indicates that all concentrated population values will be segregated with respect to time, and it will be multiplied with mean values that are obtained from equation (1). One major reason for considering all segregated values in terms of time is that each fish will be kept inside the chamber at different times, and for each time, a separate size cannot be given as input likelihood values. Therefore, for cutting the fishes in equal size, it is necessary to separate fishes of different sizes, and all can be kept inside the chamber by following different time periods. In addition, for taking all measurements, it is obligatory to observe that output voltage of sensors during the temperature setting process. Thus, the output voltage in terms of time can be represented as follows:

$$\max \mathrm{volt}_i = \sum_{i=1}^{n} \frac{298K \times e^{\mathrm{temp}_i\left(1/t_1 - 1/t_0\right)}}{e^{\mathrm{temp}_i\left(1/t_1 - 1/t_0\right)} \times g_i}, \quad (3)$$

where $298K$ represents the initial temperature when fishes are kept inside the chamber for the smoking process. temp_i denotes distinguishing temperatures between 1,000K and 3,000K. t_1 and t_0 signify different timing characteristics when fishes are smoked inside the chamber. g_i represents greater resistance that is provided when corresponding voltages are divided.

Equations (1)–(3) indicates that the prediction of sensors should be a variable process and it should be eminent using a statistical test that follows a chi-square distribution as indicated in the following equation:

$$S_i^2 = \sum_{i=1}^{n} \frac{(E_i - P_i)}{P_i^2}, \quad (4)$$

where S_i^2 denotes the corresponding sampling times. E_i and P_i represent the observed and predicted values from LVDT sensors, respectively.

In order to establish the relationship between input and output variables, it is necessary to integrate a polynomial regression that is nonlinear in nature as given in the following equation:

$$\theta_i = \sum_{i=1}^{n} \gamma_i \tau_i, \quad (5)$$

where γ_i denotes the scaled cutting factor of fishes. τ_i represents the enduring measurement values of LVDT sensors.

If equation (5) is established correctly, then it indicates that the efficiency of the entire process is going to be decided using inclinations of the water quality process where high velocity needs to be applied for smoking fishes by integrating wide channels. Also, it is necessary to find the activity of each fish that is present inside the pond using two different parameters since cutting and smoking methods are used.

$$a_i = \sum_{i=1}^{n} e^{\omega_i * \vartheta_i}, \quad (6)$$

where ω_i represents the average swimming time of different fishes inside the pond. ϑ_i denotes the swimming speed of each fish.

Equation (6) is specified to calculate the speed and time of spinning for each fish since it is necessary to differentiate different types of fishes that are present inside the pond. Once the activities of different fishes are known, then the total area of the tarn will be monitored, and the rapidity of the airstream will be converted using control rule as follows:

$$R(i)_{100\,\mathrm{m}} = \aleph_{25} + \frac{E_{i25\,\mathrm{m}}}{E_{i14.4\,\mathrm{m}}}, \quad (7)$$

where $\aleph_{25}$ represents the rapidity of the air stream at an altitude of 25 meters. $E_{i25\,\mathrm{m}}$ and $E_{i14.4\,\mathrm{m}}$ represent the rapidity of the air stream at an altitude of 25 meters and 14.4 meters, respectively.

Equation (7) indicates the control rule where sensors are placed at an altitude of two different meters such as 25 meters and 14.4 meters. After establishing the altitude of each pond, measurement and regulation of the feed process for each fish have to be calculated; this is designed using the following equation:

$$\mathrm{feed}_i = 1 - \left(i_{\max} - i_{\min}\right), \quad (8)$$

where $i_{\max}$ and $i_{\min}$ denotes the maximum and minimum intestine values of each fish, respectively.

Equation (8) denotes that difference between the maximum and minimum intestine values will provide the amount and regulation of feed using calcium-sensing receptors. The perception behind this calculation is to determine the amount of water that is absorbed by each fish in its intestine. In addition, the sensitivity of absorbed water will be measured at various luminescence levels that are exposed by calcium receptors.

3. Optimization Algorithm

In this section, an optimization process is introduced for integrating the system model for defined objective functions such as monitoring of pond, measurement, and regulation of feed with proper natural contaminant proportions. Therefore, in the first step, a set of rules have been defined using contention protocols since the load of measurement is higher. For making this contention protocol work, the main node will be divided into many subnodes that is termed as adaptive tree method. The protocol is designed to distribute the work allocated to each sensor node and to provide a collision-free technique, while packets are distributed to intended recipients. With the use of collision-free protocols, collisions do not occur, and the CSMA/CD and CSMA/CA use the possibility of the collisions for the transmission channel that is acquired using any station. Therefore, for every successful packet transmission, an optimal path will be selected, and it can be given statistically as follows:

$$\mathrm{Prob}_i = \sum_{i=1}^{n} \left[\frac{z_i - 1}{z_i} \right], \tag{9}$$

where z_i represents a number of stations struggling to get channel access from the central node.

Suppose if a station is connected to the corresponding channel in the specified first slot, then the probability rate can be given as follows:

$$z_i \mathrm{prob}_i \left(1 - \mathrm{prob}_i\right)^{z_i - 1}. \tag{10}$$

Since many subnodes are present in the media access control sublayer for monitoring the condition of fishes that are present in underwater, the expected number of uniformly distributed stations must be discovered. This is expressed using the following:

$$U_i = \log_2 z_i. \tag{11}$$

For monitoring the entire pond, which is present in underwater using wireless sensors, four different steps are followed in every transmission cycle. In the first phase of transmission, a request for sending data will be sent, and in the next phase, once the request is accepted, entire data will be discarded in current node, and it will be sent back to the requested nodes. In the third and fourth phase data, acknowledgment will be sent from each subnet node that is connected in a pipe-like structure. Moreover, contention-free protocols will use the concept of time-division multiple access where each and every node will be allotted a separate slot for data transmission. At the final stage, all packets will be combined for providing suboptimal congestions, and it can be expressed using the following condition:

$$T_{i,j} = \sum_{i=1}^{n} \mathrm{Prop}_i + \mathrm{Prop}_j + T_{i0} + T_{j0}, \tag{12}$$

where Prop_i and Prop_j denote the propagation delay in seconds. T_{i0} and T_{j0} represents the delay from first i^{th} and j^{th} nodes, respectively.

Whenever protocols are defined using wireless sensors, a large computational complexity will be present that can be solved by the application of the corresponding algorithm. Therefore, in the proposed method, a whale optimization algorithm [16, 17] will be incorporated for optimizing the schedules in control and data transmission phases. The major advantage of selecting a whale optimization algorithm is that it provides an accurate system for allocating different resources in underwater that are consumed by fishes. In addition, the implemented algorithm is having the ability to provide solutions using very few parameters, and even global solutions can be obtained within less period of time. Since the problem is linear, it is necessary to calculate capacity constraints as follows:

$$\sum_{i,j=1}^{n} TW_{ij} \geq AW_{ij}, \tag{13}$$

where TW_{ij} denotes total water supply resource from i^{th} to j^{th} node. AW_{ij} represents available water supply resource from i^{th} to j^{th} node.

Equation (13) denotes that the total water supply should be greater than or at least equal to the available water supply in different resources. To calculate the current precise solution, distance between whale and generated prey should be observed. This can be calculated using the following equation:

$$\Delta_i = \left| d_w(t) - d_p(t) \right|, \tag{14}$$

where $d_w(t)$ and $d_p(t)$ represent the distance of whale and prey with respect to time.

Subsequently, it is necessary to explore the solution in whale optimization algorithm using exploration phase where two different coefficient will be used for performing a global search that can be expressed using the following equation:

$$d(t+1) = \overline{d_t} - i.j. \tag{15}$$

Here i, j represent two different coefficient that are used in the exploration phase.

Consequently, the aforementioned protocol and algorithm have to be implemented with a system model with different objectives. Therefore, step-by-step implementation is elucidated in Figure 1.

4. Results and Discussion

In this section, validation of the system model after integrating whale optimization algorithm by defining a set of rules has been deliberated. Since the proposed method is deciphering multiple objectives, the following three major scenarios are considered:

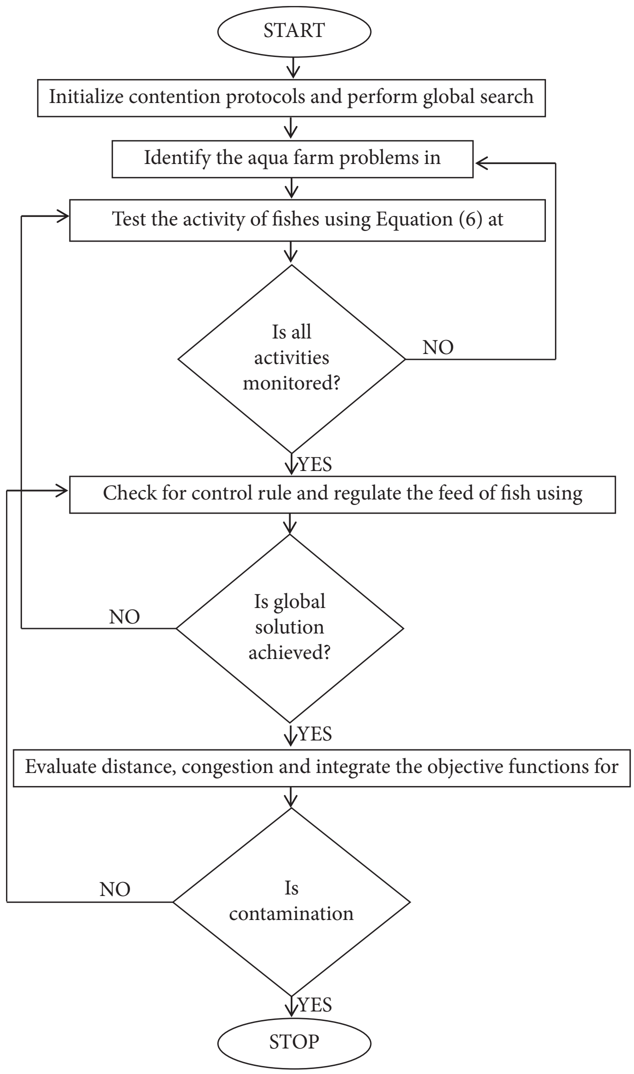

Figure 1: Implementation of WOA for monitoring activities of fishes.

(i) Scenario 1: surveillance of tarn
(ii) Scenario 2: regulation of feed
(iii) Scenario 3: proportion of natural contaminant

For these aforementioned scenarios, simulation analysis is performed by incorporating the corresponding hardware setup with Node-RED, and the reproduction is performed offline using MATLAB for better indulgence of day-to-day activities of fishes in underwater.

4.1. Scenario 1. In this scenario, the basic parameter that is necessary for monitoring the fish pond is investigated. Since more number of fishes is present in underwater, there is a necessity for monitoring the turbidity level of water inside the tarn. In the proposed exploration, fishes that are present inside the pond are monitored for a period of 20 days uninterruptedly, and all observed data have been stored in the online monitoring system. The data have been imported using MATLAB, and simulation results for scenario 1 have been reflected in Figure 2. If the turbidity level of water is reduced, then fishes can stay inside the water for a long period of time, and hence, level of health can also be increased.

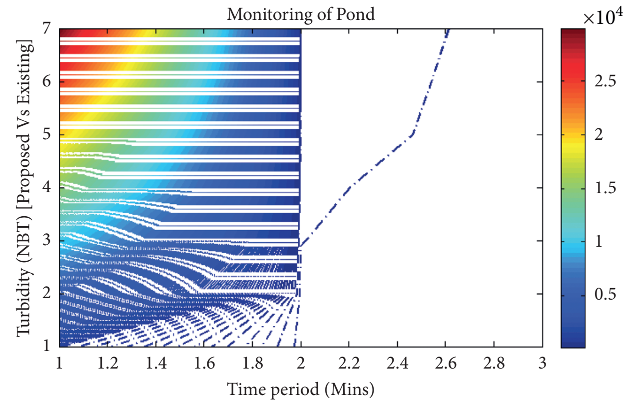

Figure 2: Turbidity level of the fish pond.

From Figure 2, it can be observed that for every time period, the maximum and accurate turbidity levels are monitored. Also, if an intelligent sensing device is present, it is possible to evaluate the precise value of turbidity level; therefore, in Figure 2, time period of sensors is reserved for one alignment, and turbidity values that are measured in NBT are reticent for another alignment. After examining the simulated results, it is ascertained that the proposed method using an intelligent sensing device performs well when compared to the existing method. For example, if the time period of sensors is 15,000 minutes, then the level of turbidity for an existing method is 168 NBT, but the proposed method provides the exact turbidity level that is observed as 108 NBT. This proves that within the selected time period and even if the time period is poignant, the proposed method can provide exact turbidity values without any error.

4.2. Scenario 2. After examining the turbidity level, the amount of feed that is supplied to fishes must be counteracted; this is examined in this scenario. If the amount of feed is much higher than the body length of fishes, then they cannot move to the exact position, and if it moves inside high depth, then it is difficult for fishermen to catch fishes.

Therefore, this method has been monitored using an intelligent sensing device, and simulation results for determining the amount of feed has been provided in Figure 3. Figure 3 is plotted by considering the body length of fishes that are measured in meters. By measuring the body length of fishes, the amount of feed that is supplied for each fish should be either increased or decreased. From Figure 3, it can be observed that only sensors can monitor the amount of feed in a precise way as compared to the existing method in absence of the intelligent sensing device. For example, if the body length of fish is 13.5 meters, then the amount of feed that needs to be supplied for a day is 10, but in existing methods, only 9 times the fishes are nourished. This will affect the health, and furthermore, it will decrease the lifetime of fishes. Since the proposed method can regulate

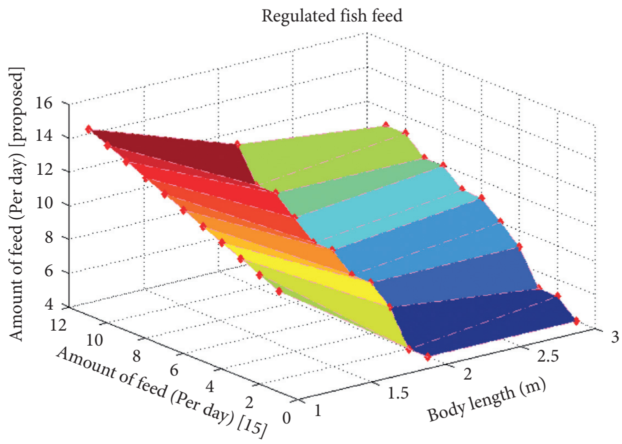

Figure 3: Level of regulating fish feed.

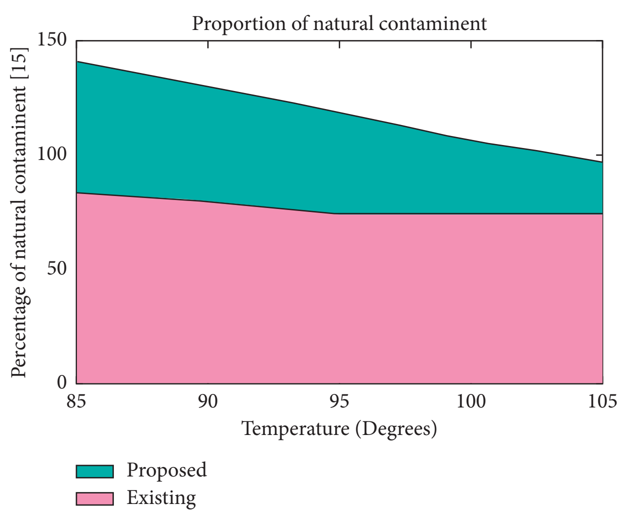

Figure 4: Percentage of contaminants in underwater.

the correct amount of feed, it can be preferred for real-time monitoring in underwater.

4.3. Scenario 3. This scenario examines the third major parameter that defines the maximum natural contaminant that is present in underwater. In real-time application of fisheries, natural contaminant should be much lesser for preventing the fishes before it enters the red zone region. Therefore, careful experimentation has been processed by establishing sensors, and the percentage of natural contaminant that is mixed with undesirable content has been observed. To realize the percentage of mixture simulation results using observed values are plotted in Figure 4.

Figure 4 is plotted by considering the temperature that is present in underwater where it is varied between 85° and 105°. The major reason for considering the temperature is that for each period of time, the level of contaminants will vary, and if the temperature is much higher, then the original contaminant level will be further reduced.

The growth of fishes will be much higher only when it is present in the bottom layer of water, and if natural contaminants are reduced, fishes will come up to the top level, and in early stages, they will be hooked. Therefore, to avoid this, the proposed method provides the exact amount of natural contaminants that are present in the pond. In this scenario, the proposed method performs much better than the existing method in terms of percentage identification of contaminants and prevents the fishes before it enters the upper layer.

5. Conclusions

A new flanged real-time monitoring and examination of fishes in underwater have been introduced with the simulation model in this article. Even though many methods are available for monitoring the state of fishes that are present in underwater, it is necessary that remote checks should be performed using intelligent monitoring devices. Therefore, the major advantage of the proposed method is that it reduces the time of fish vendors as they can able to smoke and dry the fishes within a short period of time. Since this new technique combines monitoring the health of fishes with cutting and smoking techniques a set of rules has been designed with contention protocols since large data is processed. This technique is also integrated with Node-RED for storing central data where users can able to access it using an authentication key. Subsequently, this online monitoring system can provide day-to-day results, and they are integrated with simulation fragments that are executed using MATLAB. It has been experiential that the integrated whale optimization algorithm that is integrated with system model can provide improved results around 78% that is much higher than existing methods. In future, the proposed method can be protracted by introducing robotic technology to further reduce the export time of vendors.

Data Availability

The data sets used and/or analyzed during the current study are available from the corresponding author upon reasonable request.

Conflicts of Interest

The authors declare that there are no conflicts of interest.

Acknowledgments

The authors gratefully acknowledge the Deanship of Scientific Research, King Khalid University (KKU), Abha-Asir, Kingdom of Saudi Arabia, for funding this research work (Grant no. RGP.2/58/42).

References

[1] M. R. García, M. L. Cabo, J. R. Herrera, G. Ramilo-Fernández, A. A. Alonso, and E. Balsa-Canto, “Smart sensor to predict retail fresh fish quality under ice storage,” *Journal of Food Engineering*, vol. 197, pp. 87–97, 2017.

[2] Z. Shareef and S. R. N. Reddy, “Wireless sensor network for aquaculture: review, survey, and case study of aquaculture

practices in western Godavari region," *Journal of Ambient Intelligence and Smart Environments*, vol. 10, no. 5, pp. 409–423, 2018.
[3] F. Akhter, H. R. Siddiquei, M. E. E. Alahi, and S. C. Mukhopadhyay, "Recent advancement of the sensors for monitoring the water quality parameters in smart fisheries farming," *Computers*, vol. 10, no. 3, pp. 26–20, 2021.
[4] X. Su, L. Sutarlie, and X. J. Loh, "Sensors, biosensors, and analytical technologies for aquaculture water quality," *Research: Ideas for Today's Investors*, vol. 2020, Article ID 8272705, 15 pages, 2020.
[5] T. A. D. Jayanti, A. Sudarmanto, and M. I. Faqih, "Cold smoking equipment design of smoked fish products with closed circulation using temperature and concentration monitoring system based on Arduino Uno," *IOP Conference Series: Materials Science and Engineering*, vol. 846, no. 1, Article ID 12025, 2020.
[6] J. H. Cho, "Detection of smoking in indoor environment using machine learning," *Applied Sciences*, vol. 10, no. 24, pp. 8912–8917, 2020.
[7] S. Marini, E. Fanelli, V. Sbragaglia, E. Azzurro, J. Del Rio Fernandez, and J. Aguzzi, "Tracking fish abundance by underwater image recognition," *Scientific Reports*, vol. 8, no. 1, pp. 1–12, 2018.
[8] A. E. Ghaly, V. V. Ramakrishnan, M. S. Brooks, S. M. Budge, and D. Dave, "Fish processing wastes as a potential source of proteins, amino acids and oils: a critical review," *Journal of Microbial & Biochemical Technology*, vol. 5, no. 4, pp. 107–129, 2013.
[9] S. Khoshnoudi-Nia and M. Moosavi-Nasab, "Prediction of various freshness indicators in fish fillets by one multispectral imaging system," *Scientific Reports*, vol. 9, no. 1, pp. 1–11, 2019.
[10] B. Gümüş, M. Ö Balaban, and M. Ünlüsayin, "Machine vision applications to aquatic foods: a review," *Turkish Journal of Fish AquatScience*, vol. 11, pp. 171–181, 2011.
[11] J. L. Z. Zaukuu, G. Bazar, Z. Gillay, and Z. Kovacs, "Emerging trends of advanced sensor based instruments for meat, poultry and fish quality- a review," *Critical Reviews in Food Science and Nutrition*, vol. 60, no. 20, pp. 3443–3460, 2019.
[12] FDA, *Fish and fishery products hazards and controls guidance*, US Dep Heal Hum Serv Food Drug Adm Cent Food SafApplNutr, Silver Spring, MD, USA, 4th Edition, 2020.
[13] S. Sendra, L. Parra, J. Lloret, and J. M. Jiménez, "Oceanographic multisensor buoy based on low cost sensors for posidonia meadows monitoring in mediterranean sea," *Journal of Sensors*, vol. 2015, Article ID 920168, 23 pages, 2015.
[14] S. Seto, H. Kawabe, L. Shi, Y. Shimomura, T. Oyabu, and T. Katsube, "Mathematical model of semiconductor gas sensor," *Sensors and Materials*, vol. 18, no. 1, pp. 1–16, 2006.
[15] I. García-Magariño, R. Lacuesta, and J. Lloret, "Abs-Fishcount: an Agent-Based simulator of underwater sensors for measuring the amount of fish," *Sensors*, vol. 17, no. 11, p. 2606, 2017.
[16] Z. Yan, S. Wang, B. Liu, and X. Li, "Application of whale optimization algorithm in optimal allocation of water resources," *E3S Web of Conferences*, vol. 53, pp. 4019–4025, 2018.
[17] S. Mirjalili and A. Lewis, "The whale optimization algorithm," *Advances in Engineering Software*, vol. 95, pp. 51–67, 2016.

Hindawi
Journal of Healthcare Engineering
Volume 2022, Article ID 3384102, 11 pages
https://doi.org/10.1155/2022/3384102

Research Article

Speckle Noise Algorithm-Based Ultrasound Imaging in Evaluating the Therapeutic Effect of Blood Purification on Children with Kidney Failure and Analysis of Its Correlation with Serum Inflammatory Factor Levels

Xueqin Li ,[1,2] Hui Guo ,[1,2] Soinam Songjin ,[3] Ning Mo ,[4] and Xiuying Chen [1,2]

[1]*Department of Pediatrics Nephrology Nursing, West China Second University Hospital, Sichuan University/West China School of Nursing, Sichuan University, Chengdu 610041, Sichuan, China*
[2]*Key Laboratory of Birth Defects and Related Diseases of Women and Children (Sichuan University), Ministry of Education, Chengdu 850002, Sichuan, China*
[3]*Department of Pediatric Nephrology, The Second People's Hospital of Tibet Autonomous Region, Lhasa, Tibet Autonomous Region 610041, China*
[4]*Department of Pediatric Nephrology, Chengdu Western Angel Child Maternity Hospital, Chengdu 610041, Sichuan, China*

Correspondence should be addressed to Xiuying Chen; 13115051729@sdupsl.edu.cn

Received 30 August 2021; Revised 6 December 2021; Accepted 7 January 2022; Published 29 January 2022

Academic Editor: Enas Abdulhay

The study focused on the therapeutic effect of clinical treatment on urinary calculi with kidney failure and its relationship with the serum inflammatory factor levels. 90 children with melamine urinary calculi were selected as research subjects. Of them, 52 cases were in group 1 (nonrenal failure), and 38 cases were in group 2 (combined with renal failure). In addition, 35 hospitalized children with no history of melamine-contaminated milk feeding during the same period were used as healthy controls. They all underwent ultrasound imaging examination based on the speckle noise algorithm, and the prognosis was analyzed. It was found that the peak signal-to-noise ratio (PSNR), structural similarity (SSIM), and local edge preservation index (EPI) of the algorithm in this study were significantly greater than other algorithms ($P < 0.05$). The admission age of the children in group 1 was significantly younger than that of group 2, the bilateral stone rate was significantly higher than that in group 2, and the difference was statistically significant ($P < 0.05$). Of the 52 children in group 1, the stone disappeared in 25 cases after treatment, the stone was reduced in 20 cases, and the stone remained unchanged in 7 cases. The total effective rate of treatment was 88.46%. Of the 38 cases in group 2, the stone disappeared in 22 cases after treatment, the stone was reduced in 12 cases, and the stone remained unchanged in 4 cases. The total effective rate of treatment was 89.47%. No difference was noted in blood urea nitrogen (BUN), blood creatinine (Cr), TNF-α, and C-reactive protein (CRP) levels in group 1, group 2, and the healthy control group ($P > 0.05$). Hence, the denoising algorithm in this study has better denoising effects on ultrasound images than traditional algorithms, with higher definition and less noise and artifacts. The clinical treatment of children with urinary calculi and renal failure is highly effective, the renal function and serum inflammatory factor levels return to the normal range, and the inflammatory response is weakened.

1. Introduction

Kidney failure is a decline in kidney function that occurs when the kidneys are unable to maintain metabolism and water and electrolyte balance. Renal failure is divided into acute renal failure and chronic renal failure [1, 2]. Acute renal failure arises from the rapid decline of glomerular filtration rate, accumulation of nitrogenous waste in the body, water and sodium retention, and electrolyte imbalance, and patients will have symptoms such as reduced urine output or even anuria, general edema, and heart failure [3]. Acute renal failure is also known as acute kidney injury, and its causes include prerenal, renal parenchymal, and postrenal factors [4, 5]. Acute kidney injury caused by prerenal and postrenal factors is reversible but timely diagnosis and active treatment contribute to a good prognosis and in most cases can restore the kidney function to normal [6–8]. In clinical practice, chronic renal failure is common in nephrology, mainly arising from kidney damage and serious destruction of the nephron, which then lead to endocrine disorders, nitrogen metabolite storage disorders, and water electrolyte and acid-base balance disorders. In the case of chronic renal failure, the body's immunity and resistance will decrease significantly, and the internal environment disorders caused by renal excretion and metabolic dysfunction will further make the body's response to infection abnormal. Worse still, the clinical application of antibiotics is subject to various limitations [9]. Clinical treatment of acute renal failure and chronic renal failure generally uses hemodialysis. Hemodialysis is a renal replacement treatment for patients with acute and chronic kidney failure. It can drain blood from the body to the outside of the body and pass it through a dialyzer composed of countless hollow fibers. The electrolyte solution (dialysis solution) with a similar concentration of the blood exchanges substances with the blood to remove metabolic waste, maintain electrolyte and acid-base balance, and at the same time remove the excessive water [10]. In the study, hemodialysis was performed on children with urinary stones and renal failure.

With the continuous advancement of science and technology, medical ultrasound imaging technology has made great progress in both imaging quality and imaging speed [11]. Ultrasound has become one of the commonly used examination methods for kidney diseases due to its advantages of noninvasiveness, convenience, low cost, and reproducibility, and whether there are congenital malformations, cystic lesions, and stones can be determined by observing the shape of the kidney. In the meanwhile, it can also be used for the auxiliary examination of acute renal failure [12, 13]. However, due to the limitations of ultrasound imaging mechanisms, ultrasound images have inherent disadvantages. A large amount of speckle noise often appears in the original ultrasound image, reducing the readability, and it is impossible to observe the tiny structural edges and lesion areas, which increases the risk of misdiagnosis [14–16]. The removal of speckle noise in ultrasound images has always been a topic of great concern in the medical field. Traditional ultrasound image denoising techniques are mainly image filtering techniques in the spatial domain, such as classic median filtering, mean filtering, and Wiener filtering. However, these methods face an obvious contradiction between noise filtering and edge preservation, so they have certain limitations. Speckle noise algorithm solves the initial value of the partial differential diffusion equation of the original image and takes different diffusion coefficients and the numbers of iterations to generate the corresponding scale image and further produce the final filter image by image transformation. This kind of algorithm is not influenced by the filtering window and the shape. When applied to process ultrasonic images, it can effectively suppress noise while preserving image details and even enhance contrast and improve image quality, which can overcome the difficulties existing in traditional algorithms.

The study aimed to analyze the effect of clinical treatment of urolithiasis complicated with renal failure and the changes of serum inflammatory factors, expected to provide a reference for the clinical treatment of children with renal failure. Ninety children with melamine urinary calculi who were admitted to the hospital were selected as the research subjects. According to the presence or absence of renal failure, 52 cases were in group 1 (nonrenal failure), and 38 cases were in group 2 (combined with renal failure). They all underwent ultrasound imaging examination based on the speckle noise algorithm. The effect of clinical treatment was evaluated, factoring into the effective rate, prognosis, renal function, and changes in inflammatory factor levels. Additionally, the relationship between urinary calculi combined with kidney failure and serum inflammatory factor levels was analyzed.

2. Materials and Methods

2.1. Research Subjects. Ninety children with melamine urinary calculi who were admitted to the hospital from May 3, 2019, to January 15, 2021, were selected as the research subjects, including 53 males and 37 females. According to the presence or absence of renal failure, 52 cases were in group 1 (nonrenal failure), and 38 cases were in group 2 (combined with renal failure). In addition, 35 hospitalized children who had no history of drinking melamine-contaminated milk and were free of urinary tract diseases during the same period were selected as the healthy control group, including 23 males and 12 females. This study has been approved by the Medical Ethics Committee of the hospital, and the subjects and their family members fully understood the situation of the study and had signed an informed consent form.

Inclusion criteria were as follows: (I) children with complete clinical data; (II) children who had signed an informed consent form; (III) children under 3 years of age; (IV) imaging examination that confirmed the presence of urinary calculi; and (IV) hematuria examination showing normal red blood cell morphology. Exclusion criteria were as follows: (I) hematuria of glomerular origin; (II) children with urinary tract malformations; (III) children who withdrew from the experiment midway; and (IV) children with metabolic diseases.

2.2. Ultrasound Examination. Color Doppler ultrasound system was used to perform urinary tract ultrasound examination on the child with a probe frequency of 3.5 MHz. Before the examination, the child was allowed to drink a proper amount of water to fill the bladder. During the examination, the child was in a lateral position. The probe was placed in the double kidney area to scan the kidneys. Then, it walked along the renal hilum, renal pelvis, and ureter to check the junction of the renal pelvis and ureter and the upper part of the ureter. Next, in the supine position, the outer edge of the rectus abdominis was compressed. After the walking direction of the abdominal aorta was identified, the intestine was opened, and the probe walked along the ureter to scan the abdominal segment, pelvic segment, second stricture, and terminal segment of the ureter. Next, the bladder above the symphysis pubis was scanned, and the angle was adjusted to display the opening of the bilateral ureters in the bladder wall. Subsequently, the presence or absence of urinary calculi and the presence or absence of dilation of the collecting system of the kidneys and the ureter were observed. If there were urinary tract stones, the size, number, location, shape, and internal echo of the urinary tract were recorded, and it was checked whether there were urinary tract malformations.

2.3. Ultrasound Denoising Algorithm Based on Shearlet Transform and KDA Model. Shearlet transform (ST) [17] is a new type of multiscale geometric analysis tool. Compared with contourlet transform, it has lower time complexity and unlimited number of directions. However, ST does not have translation invariance, and the pseudo-Gibbs phenomenon will occur during image reconstruction. Therefore, in this study, the nonsubsampled shearlet transform (NSST) is introduced to optimize it.

First, the two-dimensional compound expansion affine system can be expressed as follows:

$$\lambda_{PQ}(\omega) = \left\{\omega_{i,j,n}(x)|\det P|^{1/2}\omega\left(Q^k P^i x - n\right):\ i,k \in W, n \in W^2\right\}, \quad (1)$$

where P and Q represent a 2×2 invertible matrix, $|\det P| = 1$, and both n and k are constants. If $\lambda_{PQ}(\omega)$, there is

$$\sum_{i,k,n}\left|\left(h,\omega_{i,k,n}\right)\right|^2 = \|h\|^2. \quad (2)$$

Then, the elements of the system are called composite wavelets. P^i is related to scale changes and Q^k is associated with geometric transformations with constant area. Let $P = P_0$ *or* P_1, $Q = Q_0$ *or* Q_1, $P_0 = \left\langle\begin{smallmatrix}5 & 0\\ 0 & 3\end{smallmatrix}\right\rangle$, $P_1 = \left\langle\begin{smallmatrix}3 & 0\\ 0 & 5\end{smallmatrix}\right\rangle$, $Q_0 = \left\langle\begin{smallmatrix}2 & 2\\ 0 & 2\end{smallmatrix}\right\rangle$, and $Q_1 = \left\langle\begin{smallmatrix}2 & 0\\ 2 & 2\end{smallmatrix}\right\rangle$; then, the set in (1) is a shear wave, $P = P_0$ or P_1 is an anisotropic stretching matrix, and $Q = Q_0$ or Q_1 is a shear matrix. Then, the shear wave transform function is as follows:

$$\begin{aligned}\omega^{(0)}_{i,k,n}(x) &= 2^{3i/2}\omega^{(0)}\left(Q_0^k P_0^i x - n\right),\\ \omega^{(1)}_{i,k,n}(x) &= 2^{3i/2}\omega^{(1)}\left(Q_0^k P_0^i x - n\right),\end{aligned} \quad (3)$$

where $i \geq 0$, $-2^i \leq k \leq 2^i$, $\omega^{(0)}(\beta) = \omega^{(0)}(\beta_1.\beta_2) = \omega_1(\beta_1)\omega_2(\beta_2/\beta_1)$, and $\omega^{(1)}(\beta) = \omega^{(1)}(\beta_1.\beta_2) = \omega_1(\chi_2)\omega_2(\beta_2/\beta_1)$. For any $(\beta_1.\beta_2) \in C_0$, $C_0 = \{(\beta_1.\beta_2) \in \mathfrak{R}^2 ||\beta_1| \geq 1/Q, |\beta_2/\beta_1| \leq 1\}$, $C_1 = \{(\beta_1.\beta_2) \in \mathfrak{R}^2 ||\beta_1| \geq 1/Q, |\beta_2/\beta_1| \leq 1\}$ constitutes the supporting domain of $\omega^{(0)}_{i,k,n}(x)$ and $\omega^{(1)}_{i,k,n}(x)$. Figure 1 shows the support frequency domain of the shear wave in the $\mathfrak{R}^2$ plane. The yellow line represents C_1, and the green line represents C_0.

Thus, for any image h $i \geq 0$, $-2^i \leq k \leq 2^i$, the ST can be expressed as follows:

$$\text{Shearlet}_\omega h_{(i,k,n)} = \left(h, \omega^{(c)}_{i,k,n}\right). \quad (4)$$

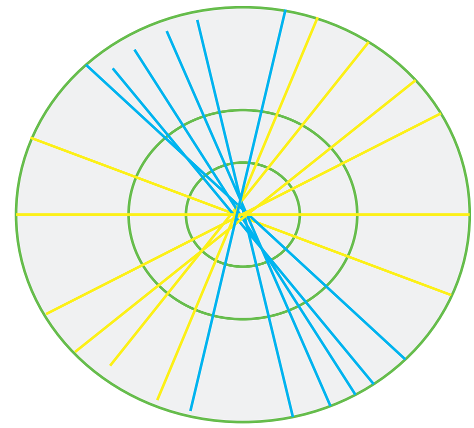

Figure 1: Shear wave support frequency domain in the $\mathfrak{R}^2$ plane.

The NSST transform discretization constructs the algorithm together with the Laplacian pyramid and the directional filter [18]. First, the image is decomposed by the Laplacian pyramid to obtain a high-frequency subband and a low-frequency subband. The subband represents the edge detail information in the image, and the low-frequency subband represents the overview of the original image. Then, the high-frequency subband is divided by directions with a directional filter to obtain the directional detail information in the image. Next, the low-frequency subband is further decomposed, and the above steps are repeated (Figure 2).

The threshold function is weighted by scale to prevent the decrease of noise pollution level with the reduction of resolution [19], and the scale function controls the size of the threshold under the resolution to effectively filter out the noise under each resolution. Therefore, the scaling function is defined as follows:

$$W(r) = \sqrt{\alpha\log\left(\frac{r+1}{r}\right)}, \quad (5)$$

where r represents the scale where the NSST transform coefficients are located, $r = 1$ represents high resolution, and α represents the attenuation degree parameter. Then, the hard threshold method is introduced for improvement, expressed as follows:

$$S_{i,j} = \theta W(r)\phi_i, \phi_j, \quad (6)$$

where θ is the constant that controls the global threshold, $W(r)$ represents the scale weighting function, ϕ represents the standard deviation of the noise image, and $\phi^2_{i,j}$ represents the noise variance in the NSST transform decomposition subband. The noise variance can be expressed as follows:

$$\phi^2_{i,j} = \frac{\sqrt{\sum_{x=1}^{Z_l}\sum_{y=1}^{Z_l} J^{\text{NSSST}}_{i,j}(x,y) J^{\text{NSSST\#}}_{i,j}(x,y)}}{Z_j}, \quad (7)$$

where $J^{\text{NSSST}}_{i,j}(x,y)$ represents the NSST transform coefficient of the j-th scale in the i-th direction, $J^{\text{NSSST\#}}_{i,j}(x,y)$ is the resurrection yoke of $J^{\text{NSSST}}_{i,j}(x,y)$, and Z_j represents the length of the subband.

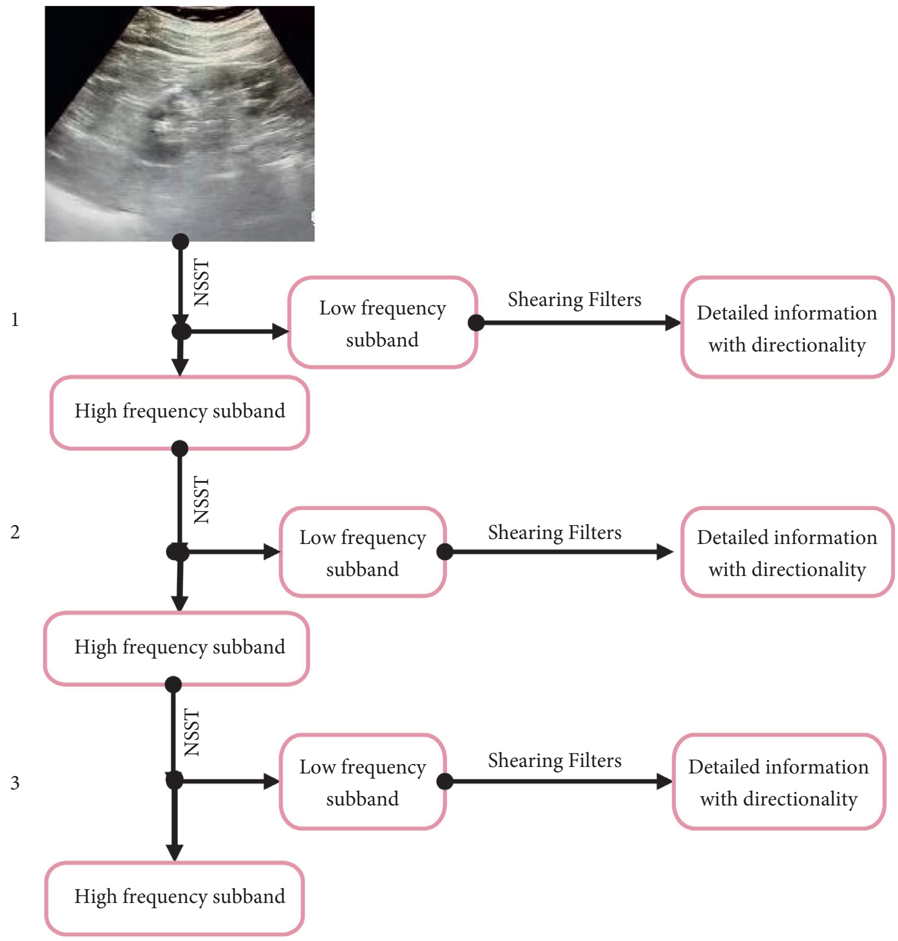

FIGURE 2: High- and low-frequency subband processing flow based on NSST transform.

Finally, the threshold of the high-resolution NSST coefficients is solved to obtain the denoising coefficients at various high resolutions. The NSST coefficients after threshold denoising can be expressed as follows:

$$\overrightarrow{J}^{\mathrm{NSSST}}_{i,j}(x,y) = \begin{cases} J^{\mathrm{NSSST}}_{i,j}(x,y), \left|J^{\mathrm{NSSST}}_{i,j}(x,y)\right| \geq S_{i,j} \\ 0 \end{cases}. \quad (8)$$

The above is the optimization process of the NSST. A larger threshold value is used at high resolution, and a smaller threshold value is used at lower resolution to effectively filter out the noise at each high resolution.

However, the low-resolution coefficients after the optimization still retain less low-frequency noise, so further processing is necessary. Therefore, the NSST coefficients are combined with the nuclear anisotropic diffusion model to perform anisotropic diffusion denoising on the NSST coefficients of the low-frequency subbands so that the low-frequency noise is filtered out and the low-frequency details are also well preserved. Next, the NSST coefficients substitute the two-dimensional image, and the new nuclear anisotropic diffusion model can be expressed as follows:

$$\begin{aligned} &J^{\mathrm{NSST}}(e=0) = J^{\mathrm{NSST}}{}_{0}, \\ &\frac{\partial J^{\mathrm{NSST}}(x,y)}{\partial e} = \mathrm{Div}\left[c\left(\left\|\nabla\Phi\left(J^{\mathrm{NSST}}\right)\right\|\right)\nabla J^{\mathrm{NSST}}\right], \\ &\left\|\nabla\Phi\left(J^{\mathrm{NSST}}\right)\right\|_{u} = \left[\frac{\sum_{v\in\lambda_u}\left\|J_u^{\mathrm{NSST}} - J_v^{\mathrm{NSST}}\right\|^2}{\left|\lambda_u\right|}\right]^{0.5}, \end{aligned} \quad (9)$$

where J^{NSST} represents the NSST coefficient matrix in the low-frequency subband after the ultrasound image is decomposed by NSST, Φ is the mapping function, $\|\nabla\Phi(J^{NSST})\|$ represents the nuclear gradient modulus in the eigenspace determined by the mapping function, λ_u represents the field of u, and $|\lambda_u|$ represents the size of the field. Then, kernel replacement is performed, and the square of the gray difference in a certain characteristic direction in the feature space can be expressed as follows:

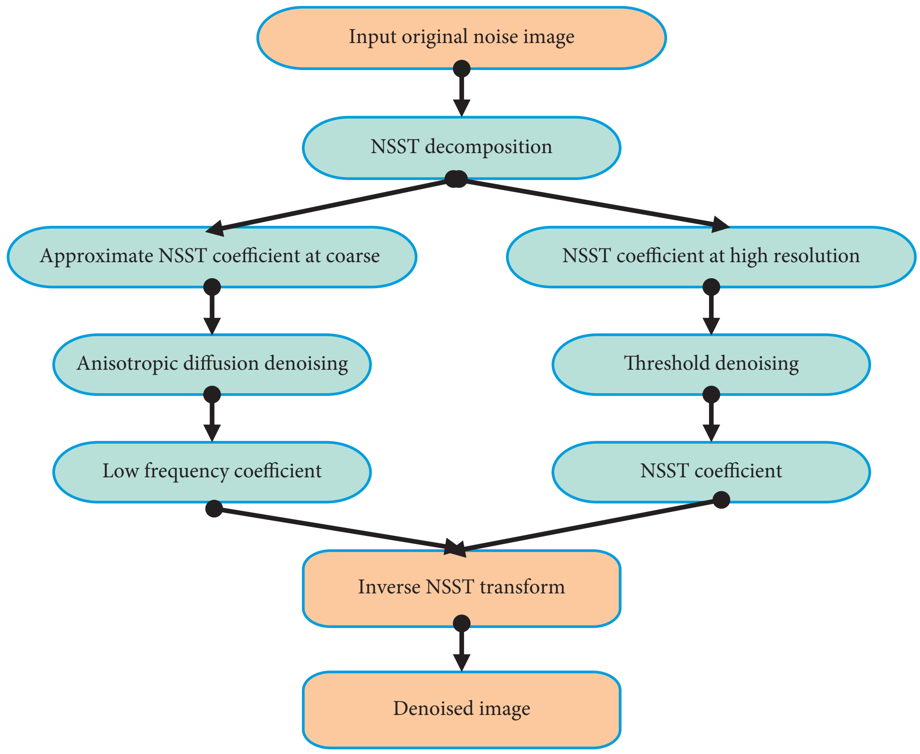

Figure 3: Image denoising process based on NSST coefficients and nuclear anisotropic diffusion model.

$$\begin{aligned}\left\|\Phi\left(J_u^{\mathrm{NSST}}\right)-\Phi\left(J_v\right)\right\|^2 &= F\left(J_u^{\mathrm{NSST}},J_u^{\mathrm{NSST}}\right)+F\left(J_v^{\mathrm{NSST}},J_v^{\mathrm{NSST}}\right)+F\left(J_u^{\mathrm{NSST}},J_v^{\mathrm{NSST}}\right),\\ \left\|\nabla\Phi\left(J^{\mathrm{NSST}}\right)\right\|_u &= \left[\frac{\sum_{v\in\lambda_u}F\left(J_u^{\mathrm{NSST}},J_u^{\mathrm{NSST}}\right)+F\left(J_v^{\mathrm{NSST}},J_v^{\mathrm{NSST}}\right)+F\left(J_u^{\mathrm{NSST}},J_u^{\mathrm{NSST}}\right)}{\left|\lambda_u\right|}\right]^{0.5}.\end{aligned} \tag{10}$$

To better control the degree of local diffusion, the grayscale and nuclear gradient models are jointly used to control the degree of diffusion of the image. Then, the optimized diffusion equation is as follows:

$$c\left(\left\|\nabla\Phi\left(J^{\mathrm{NSST}}\right)\right\|\right)=\exp\left(-\left(\frac{\phi_F\left\|\nabla\Phi\left(J^{\mathrm{NSST}}\right)\right\|}{4\tau}\right)^2\right), \tag{11}$$

where ϕ_F^2 represents the local grayscale variance of the image and τ represents the diffusion threshold, expressed as follows:

$$\tau=\mathrm{median}\left(\left\|\nabla\Phi\left(J^{\mathrm{NSST}}\right)\right\|\right)-\mathrm{median}\left(\left\|\nabla\Phi\left(J^{\mathrm{NSST}}\right)\right\|\right), \tag{12}$$

where median represents the median function.

Combining the NSST coefficients with the nuclear anisotropic diffusion model can realize high-quality denoising of ultrasound images. Figure 3 shows the specific process.

2.4. Observation Indicators. Basic information of groups 1 and 2 was recorded, such as the admission age, bilateral stone rate, feeding time, amount of milk taken, and feeding methods (mixed feeding and artificial feeding). Then, groups 1 and 2 were compared for the effective rate (disappearance of stones, reduction of stones, and no change in stones) and prognosis (discharge rate with stones, stone disappearance rate after 1 year, discharge rate with water accumulation, and water disappearance rate after 1 year). Next, the renal function indexes (blood urea nitrogen (BUN) and blood creatinine (Cr)) and serum inflammatory factors (TNF-α and C-reactive protein (CRP)) of group 1, group 2, and the healthy control group were recorded after treatment.

2.5. Statistical Methods. The data was processed by SPSS19.0 version statistical software, the measurement data were expressed by the mean ± standard deviation ($\bar{x} \pm s$), and the count data were expressed by the percentage (%). One-way analysis of variance was used for pairwise comparison. The difference was statistically significant at $P < 0.05$.

3. Results

3.1. Denoising Results. The Lena images and Barbara images with different degrees of Gaussian white noise pollution (noise standard deviations were 5, 15, and 25, resp.) were used as samples, and the original images were all grayscale images with a size of 521×521. The anisotropic

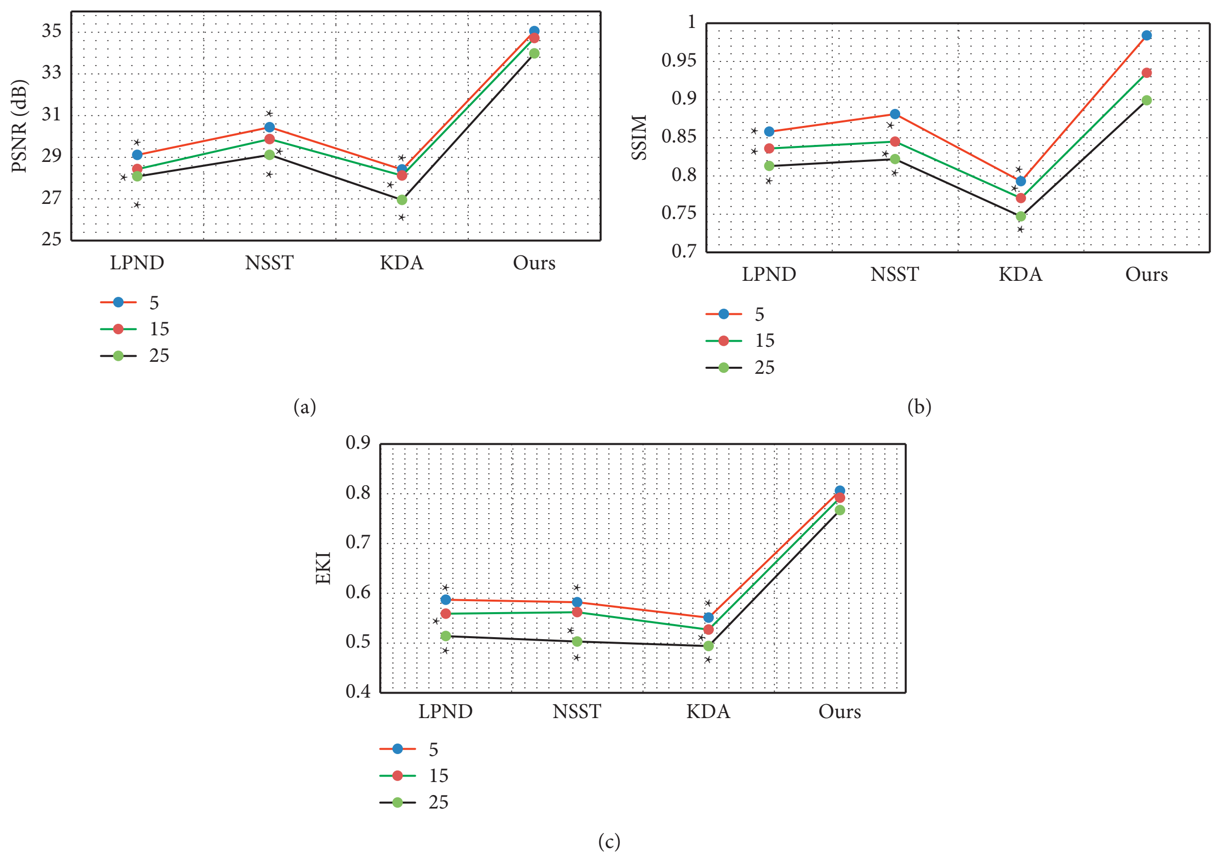

FIGURE 4: The denoising performance of the four algorithms for Lena images with different degrees of Gaussian white noise pollution: (a) PSNR; (b) SSIM; (c) EPI.*The difference compared with the algorithm in this study is statistically significant ($P < 0.05$).

diffusion denoising algorithm based on LPND, the denoising algorithm based on the traditional NSST transform, and the denoising algorithm based on KDA were introduced to compare with the algorithm of the study. The four algorithms were then compared for the PSNR, SSIM, and EPI [20].

As shown in Figure 4, for the Lena images with different degrees of Gaussian white noise pollution, the PNSR, SSIM, and EPI indicators of the four algorithms all decreased as the noise standard deviation increased. The indexes of PSNR, SSIM, and EPI of the algorithm in this study were always greater than those of LPND, NSST, and KDA, and the difference was statistically significant ($P < 0.05$).

As shown in Figure 5, for the Barbara images with different degrees of Gaussian white noise pollution, the PNSR, SSIM, and EPI of the four algorithms all decreased as the noise standard deviation increased. The PNSR, SSIM, and EPI of the algorithm in this study were always greater than those of the LPND, NSST, and KDA algorithms, and the difference was statistically significant ($P < 0.05$).

3.2. The Denoising Effect of the Algorithm for the Ultrasound Images of Children. Figure 6 shows the denoising performance of four algorithms for ultrasound images of renal failure. It was noted that the image noise and artifacts were significantly reduced versus the original image after being processed by the four algorithms, and the image quality was improved. Of the four algorithms, the algorithm in this study demonstrated the best denoising effects, with higher definition and less noise and artifacts.

Further quantitative comparison found (Figure 7) that the PNSR, SSIM, and EPI of the algorithm in this study were significantly greater than those of the LPND, NSST, and KDA algorithms, and the difference was statistically significant ($P < 0.05$).

3.3. Comparison of Clinical Data between Group 1 and Group 2. Figure 8 shows the clinical data of the children in groups 1 and 2. It was noted that the admission age of the children in group 1 was significantly younger than that of group 2, the bilateral stone rate was significantly higher than that in group 2, and the difference was statistically significant ($P < 0.05$). There were no statistically significant differences in the feeding time, the amount of milk taken, and the feeding methods of the children in groups 1 and 2 ($P > 0.05$).

Figure 9(a) is an ultrasound image of a child with melamine urinary calculi, and it shows dilated ureter and hyperechoic echo with acoustic shadow, central echo separation, and anechoic area around the kidney. Figure 9(b) is an image of a child with melamine urinary calculi and renal failure. It was noted that the kidney was slightly enlarged, the

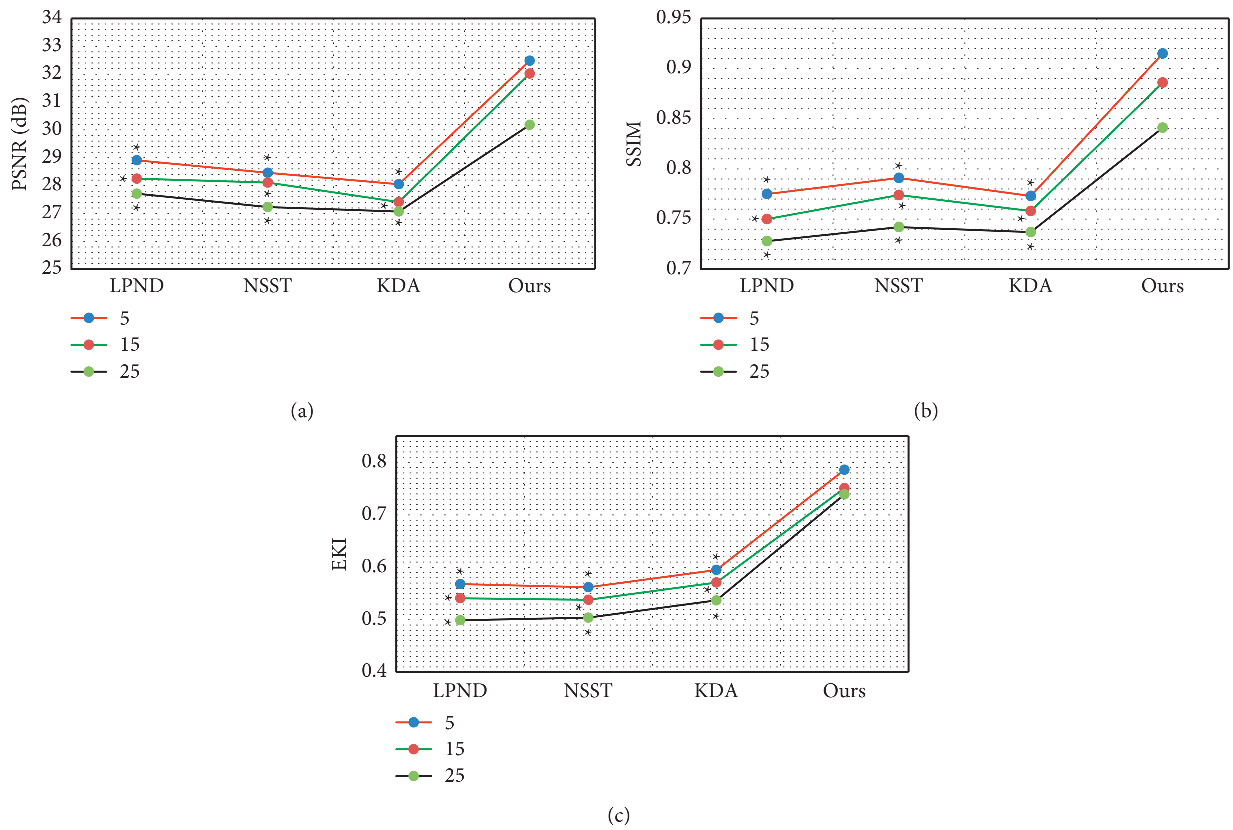

Figure 5: The denoising performance of the four algorithms Barbara images with different degrees of Gaussian white noise pollution: (a) PSNR; (b) SSIM; (c) EPI. *The difference compared with the algorithm in this study is statistically significant ($P < 0.05$).

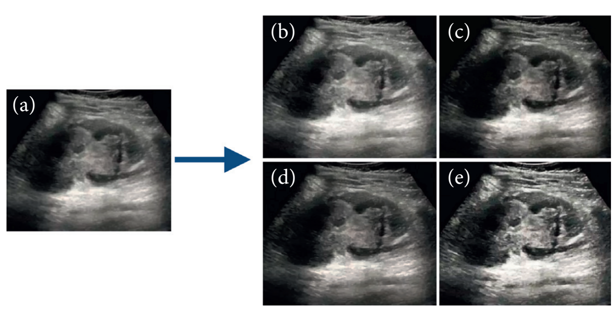

Figure 6: Denoising performance of four algorithms on ultrasound images of renal failure. (a)–(e) are the original image, image processed by the LPND algorithm, image processed by the NSST algorithm, image processed by the KDA algorithm, and image processed by the algorithm in this study.

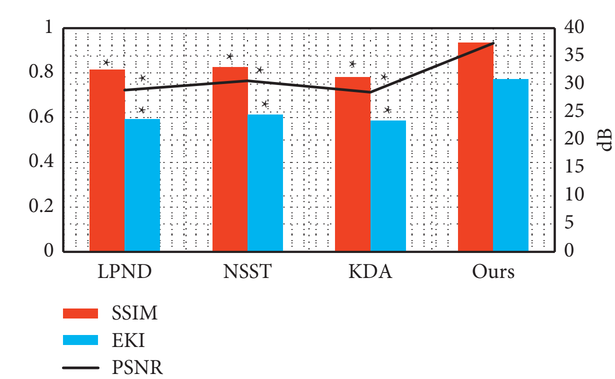

Figure 7: The denoising performance of four algorithms on ultrasound images of renal failure. *The difference compared with the algorithm in this study is statistically significant ($P < 0.05$).

cortex was thickened, the cortex and medulla were clearly demarcated, and the medulla contour was obviously enlarged.

3.4. Total Effective Rate of Treatment for Children in Groups 1 and 2. It was noted from Figure 10 that, of the 52 children in group 1, the stone disappeared in 25 cases after treatment, the stone was reduced in 20 cases, and the stone remained unchanged in 7 cases. The total effective rate of treatment was 88.46%. Of the 38 cases in group 2, the stone disappeared in 22 cases after treatment, the stone was reduced in 12 cases, and the stone remained unchanged in 4 cases. The total effective rate of treatment was 89.47%. There was no statistically significant difference in the total treatment effective rate between the two groups of children ($P > 0.05$).

3.5. Comparison of Prognosis of Children in Groups 1 and 2. Figure 11 shows the prognosis of children in groups 1 and 2. No difference was noted in the rate of discharge with stones, the rate of stone disappearance after 1 year, the rate of

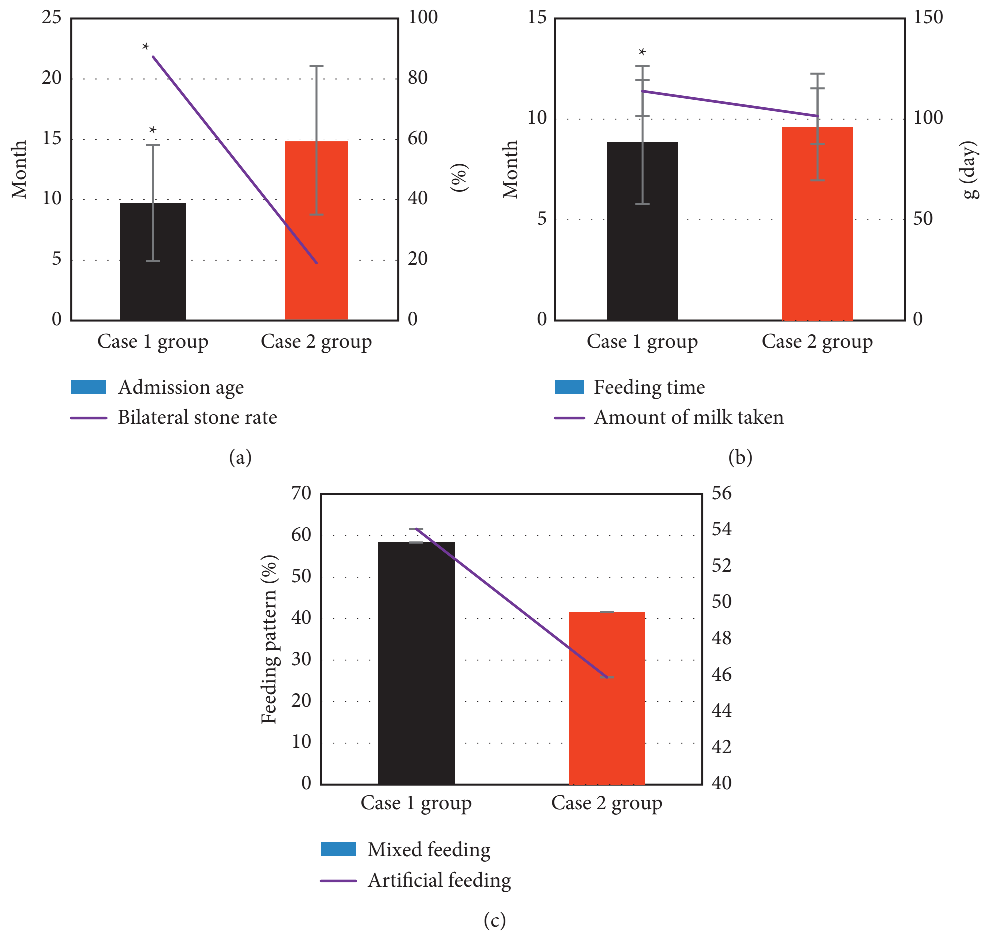

Figure 8: Comparison of clinical data between groups 1 and 2: (a) the age of admission and the rate of bilateral stones; (b) the feeding time and the amount of milk taken; (c) the feeding methods (mixed feeding and artificial feeding).

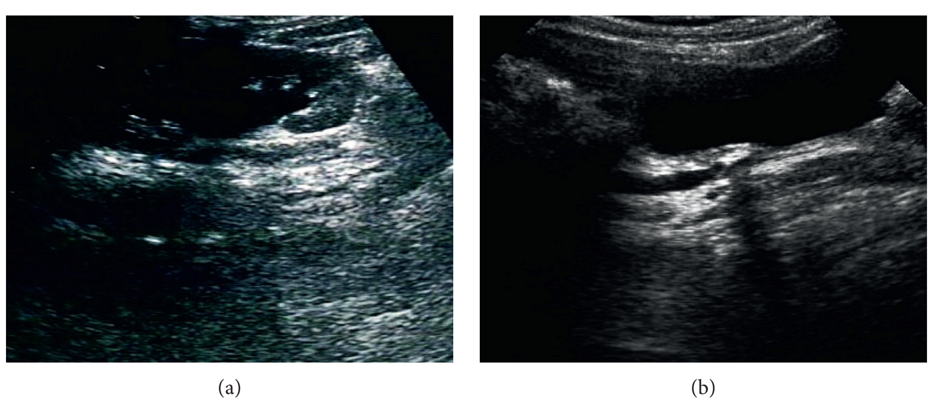

Figure 9: Ultrasound images of the patients: (a) an ultrasound of a child with melamine urinary calculi; (b) an ultrasound of a child with melamine urinary calculi and renal failure.

discharge with water accumulation, and the water loss rate after 1 year ($P > 0.05$).

3.6. Comparison of Renal Function of Children in Group 1, Group 2, and the Healthy Control Group. Figure 12 shows the renal function of children in group 1, group 2, and the healthy control group after treatment. No difference was noted in the blood BUN and blood Cr of the children in group 1, group 2, and the healthy control group after treatment ($P > 0.05$).

3.7. Comparison of Serum Inflammatory Factors in Children of Groups 1 and 2 after Treatment with the Healthy Control Group. Figure 13 shows the serum inflammatory factors in

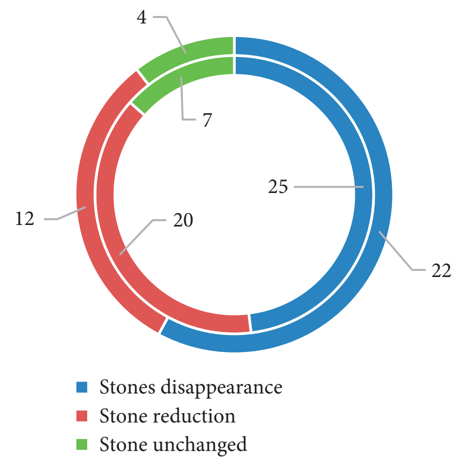

FIGURE 10: The total effective rate of treatment for children in groups 1 and 2. The inner circle represented group 1, and the outer circle represented group 2.

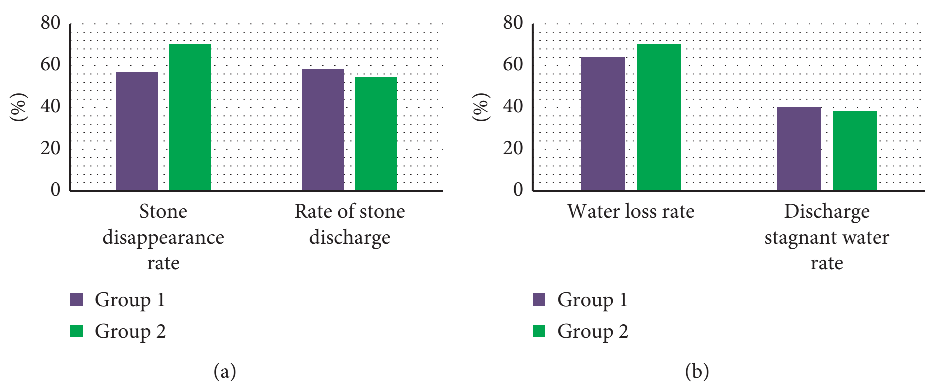

FIGURE 11: Comparison of prognosis of children in groups 1 and 2: (a) rate of discharge with stones and rate of stone disappearance after 1 year; (b) rate of discharge with water accumulation and rate of water loss after 1 year.

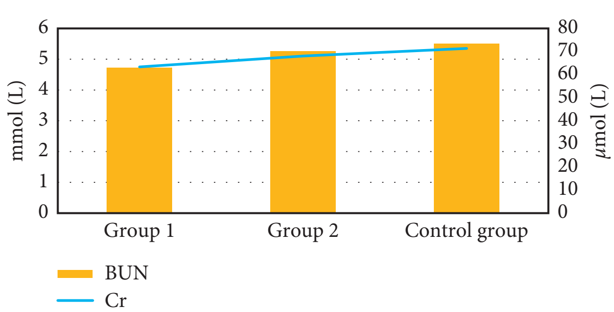

FIGURE 12: Comparison of kidney function of children in group 1, group 2, and the healthy control group.

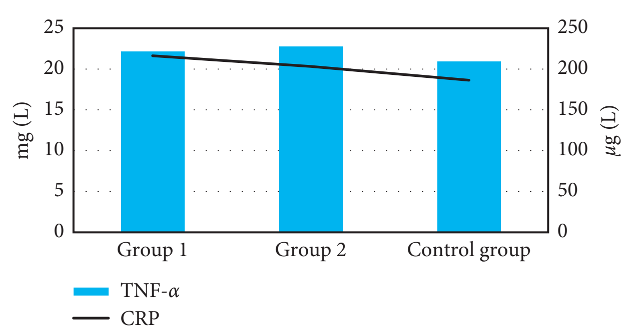

FIGURE 13: Comparison of serum inflammatory factors in children of group 1, group 2, and the healthy control group after treatment.

children of groups 1 and 2 and the healthy control group after treatment. No difference was noted in the TNF-α and CRP levels of children between group 1, group 2, and the healthy control group after treatment ($P > 0.05$).

4. Discussion

Acute renal failure is a common kidney disease, and it is associated with many factors, such as changes in human hemodynamics and injury from toxic substances [21]. The clinical manifestations of urinary calculi in children are often atypical and easily confused with other abdominal diseases. If diagnosis and treatment are delayed, it may be complicated by acute kidney failure [22]. In this study, 90 children with melamine urinary calculi were selected as research subjects. Of them, 52 cases were in group 1 (nonrenal failure), and 38 cases were in group 2 (combined with renal failure). In addition, 35 hospitalized children with no history of melamine-contaminated milk feeding during the same period were used as a healthy control. They all underwent ultrasound imaging examination based on the speckle noise algorithm, and the prognosis was analyzed. Firstly, the Lena images and Barbara images with different degrees of Gaussian white noise pollution (noise standard deviations were 5, 15, and 25, resp.) were used as samples. It was found that the PNSR, SSIM, and EPI indicators of the four algorithms all decreased as the noise standard deviation increased. The indexes of PNSR, SSIM, and EPI of the algorithm in this study were always greater than those of LPND, NSST, and KDA, and the difference was statistically significant ($P < 0.05$). This was in line with the research results of Li et al. (2016) [23] that compared with the traditional ultrasonic denoising technology, this algorithm can overcome the contradiction between noise filtering and entry edge reservation, indicating that the algorithm in this study had a good denoising effect on images with different degrees of noise pollution. After the algorithms were applied to ultrasound images of renal failure, it was noted that the image noise and artifacts were significantly reduced versus the original image after being processed by the four algorithms, and the image quality was improved. Of the four algorithms, the algorithm in this study demonstrated the best denoising effects, with higher definition and less noise and artifacts [24].

The clinical data of the children in groups 1 and 2 were compared, and it was found that the admission age of the children in group 1 group was significantly younger than that in group 2, the bilateral stone rate was significantly higher than group 2, and the difference was statistically significant ($P < 0.05$), which indicated that renal failure might be related to the age [25]. Of the 52 children in group 1, the stone disappeared in 25 cases after treatment, the stone was reduced in 20 cases, and the stone remained unchanged in 7 cases. The total effective rate of treatment was 88.46%. Of the 38 cases in group 2, the stone disappeared in 22 cases after treatment, the stone was reduced in 12 cases, and the stone remained unchanged in 4 cases. The total effective rate of treatment was 89.47%. There was no statistically significant difference in the total treatment effective rate between the two groups of children. In this study, hemodialysis was used for children with renal failure, and there was no bleeding or infection during the treatment, and the treatment effect was good. As for the prognosis, no difference was noted in the rate of discharge with stones, the rate of stone disappearance after 1 year, the rate of discharge with water accumulation, and the water loss rate after 1 year ($P > 0.05$). It suggested that children with renal failure had a good prognosis after treatment, and most of the symptoms disappeared or were alleviated [26]. No difference was noted in the blood BUN and blood Cr of the children in group 1, group 2, and the healthy control group after treatment ($P > 0.05$). It suggested that the renal function of children with renal failure recovered after treatment to normal. In terms of the comparison of serum inflammatory factors, no difference was noted in the TNF-α and CRP levels of children between group 1, group 2, and the healthy control group after treatment ($P > 0.05$). It also showed that the serum inflammatory factor levels returned to normal after treatment, and the inflammatory response was weakened [27].

5. Conclusion

In this study, 90 children with melamine urinary calculi were selected as research subjects. Of them, 52 cases were in group 1 (nonrenal failure), and 38 cases were in group 2 (combined with renal failure). In addition, 35 hospitalized children with no history of melamine-contaminated milk feeding during the same period were used as a healthy control. They all underwent ultrasound imaging examination based on the speckle noise algorithm, and the prognosis was analyzed. The results showed that the denoising algorithm based on ST and KDA model in this study had good denoising effect on ultrasound images than traditional algorithms, with higher definition and less noise and artifacts. It has been proved that the clinical treatment of children with urinary calculi and renal failure is highly effective, the renal function and serum inflammatory factor levels return to the normal range, and the inflammatory response is weakened. However, some limitations in the study should be noted. The sample size is small, which will reduce the power of the study. In the follow-up, an expanded sample size is necessary to strengthen the findings of the study. In conclusion, this study provides good theoretical support for the clinical diagnosis and treatment of urinary calculi complicated with renal failure.

Data Availability

The data used to support the findings of this study are available from the corresponding author upon request.

Conflicts of Interest

The authors declare that there are no conflicts of interest.

Acknowledgments

This work was supported by grants from the Science and Technology Bureau of Sichuan Province (21ZDYF1329).

References

[1] R. Ryšavá, "Renal failure in multiple myeloma and its treatment," *Vnitřní Lékarství*, vol. 66, no. 7, pp. 425–431, 2020.

[2] S. Watanabe, "Low-protein diet for the prevention of renal failure," *Proceedings of the Japan Academy, Series B*, vol. 93, no. 1, pp. 1–9, 2017.

[3] P. Forget, J. A. Borovac, E. M. Thackeray, and N. L. Pace, "Transient neurological symptoms (TNS) following spinal anaesthesia with lidocaine versus other local anaesthetics in adult surgical patients: a network meta-analysis," *Cochrane Database of Systematic Reviews*, vol. 12, no. 12, Article ID CD003006, 2019.

[4] M. Stanak, S. Wolf, H. Jagoš, and K. Zebenholzer, "The impact of external trigeminal nerve stimulator (e-TNS) on prevention and acute treatment of episodic and chronic migraine: a systematic review," *Journal of the Neurological Sciences*, vol. 412, Article ID 116725, 2020.

[5] D. K. Wells, M. M. van Buuren, K. K. Dang et al., "key parameters of tumor epitope immunogenicity revealed through

a consortium approach improve neoantigen prediction," *Cell*, vol. 183, no. 3, pp. 818–834, 2020.

[6] D. S. Thommen, V. H. Koelzer, P. Herzig et al., "A transcriptionally and functionally distinct PD-1+ CD8+ T cell pool with predictive potential in non-small-cell lung cancer treated with PD-1 blockade," *Nature Medicine*, vol. 24, no. 7, pp. 994–1004, 2018.

[7] M. D. Wellenstein, S. B. Coffelt, D. E. M. Duits et al., "Loss of p53 triggers WNT-dependent systemic inflammation to drive breast cancer metastasis," *Nature*, vol. 572, no. 7770, pp. 538–542, 2019.

[8] J. Fan, K. Hu, X. Li et al., "A qualitative study of the vocational and psychological perceptions and issues of transdisciplinary nurses during the COVID-19 outbreak," *Aging*, vol. 12, no. 13, pp. 12479–12492, 2020.

[9] J. J. McGough, A. Sturm, J. Cowen et al., "Double-blind, sham-controlled, pilot study of trigeminal nerve stimulation for attention-deficit/hyperactivity disorder," *Journal of the American Academy of Child & Adolescent Psychiatry*, vol. 58, no. 4, pp. 403–411, 2019.

[10] D. Toomey, E. Wiener, N. Greene, A. Weisman, K. Wittels, and S. R. Wilcox, "Mystery medications and renal failure," *Journal of Emergency Medicine*, vol. 58, no. 5, pp. 807–809, 2020.

[11] M. Brennan, S. T. O'Keeffe, and E. C. Mulkerrin, "Dehydration and renal failure in older persons during heatwaves-predictable, hard to identify but preventable?" *Age and Ageing*, vol. 48, no. 5, pp. 615–618, 2019.

[12] H.-P. Marti, V. Serebruany, and D. Atar, "Challenging anticoagulation in advanced renal failure," *The American Journal of Medicine*, vol. 132, no. 11, pp. 1258-1259, 2019.

[13] K. M. Van de Velde-Kossmann, "Skin examination: an important diagnostic tool in renal failure patients," *Blood Purification*, vol. 45, no. 1-3, pp. 187–193, 2018.

[14] S. Rocchi, P. Tacchetti, L. Pantani et al., "Safety and efficacy of daratumumab in dialysis-dependent renal failure secondary to multiple myeloma," *Haematologica*, vol. 103, no. 6, pp. e277–e278, 2018.

[15] P. Sookaromdee and V. Wiwanitkit, "Renal failure in advanced cholangiocarcinoma: magnitude," *Saudi Journal of Kidney Diseases and Transplantation*, vol. 29, no. 2, p. 485, 2018.

[16] A. Gonzalez, R. Krieg, H. D. Massey et al., "Sodium butyrate ameliorates insulin resistance and renal failure in CKD rats by modulating intestinal permeability and mucin expression," *Nephrology Dialysis Transplantation*, vol. 34, no. 5, pp. 783–794, 2019.

[17] R. Khatri, M. R. Afzal, M. A. Qureshi, A. Maud, D. Huanyu, and G. Jose Rodriguez, "Pre-existing renal failure increases in-hospital mortality in patients with intracerebral hemorrhage," *Journal of Stroke and Cerebrovascular Diseases*, vol. 28, no. 2, pp. 237–242, 2019.

[18] R. Li, Q. F. Wang, W. W. Li, and X. C. Niu, "Effect of treating renal failure with decorin gene therapy," *European Review for Medical and Pharmacological Sciences*, vol. 22, no. 8, pp. 2483–2489, 2018.

[19] Z. Lv, D. Chen, R. Lou, and A. Alazab, "Artificial intelligence for securing industrial-based cyber-physical systems," *Future Generation Computer Systems*, vol. 117, no. 1, pp. 291–298, 2021.

[20] C. J. Long and D. K. Bowen, "Predicting and modifying risk for development of renal failure in boys with posterior urethral valves," *Current Urology Reports*, vol. 19, no. 7, p. 55, 2018.

[21] D. Ferreira, "Renal failure in decompensated heart failure patients: double trouble," *Revista Portuguesa de Cardiologia*, vol. 37, no. 2, pp. 167-168, 2018.

[22] I. Auge, "Renal failure in focus," *Acta Physiologica*, vol. 232, no. 1, Article ID e13645, 2021.

[23] P. Neves, "Post cardiopulmonary bypass renal failure - do we need goal directed perfusion?" *Rev Port Cir Cardiotorac Vasc*, vol. 26, no. 2, pp. 91-92, 2019.

[24] J. A. Oud, D. Evers, R. A. Middelburg et al., "Association between renal failure and red blood cell alloimmunization among newly transfused patients," *Transfusion*, vol. 61, no. 1, pp. 35–41, 2021.

[25] J. Lujan Varas, G. Morales Varas, and A. Paredes Sánchez, "Obstructive renal failure as a complication of anticoagulant therapy," *Intensive Care Medicine*, vol. 45, no. 4, p. 520, 2019.

[26] S. Chand, S. Thapa, S. Kon et al., "Hantavirus infection with renal failure and proteinuria, Colorado, USA," *Emerging Infectious Diseases*, vol. 26, no. 2, pp. 383–385, 2020.

[27] R. Bhattacharyya and L. E. Miller, "Pre-existing renal failure increases in-hospital mortality in patients with intracerebral hemorrhage," *Journal of Stroke and Cerebrovascular Diseases*, vol. 28, no. 8, p. 2360, 2019.

Hindawi
Journal of Healthcare Engineering
Volume 2022, Article ID 7011836, 6 pages
https://doi.org/10.1155/2022/7011836

Research Article

Mediating Role of Mental Resilience between Sleep Quality and Mindfulness Level of Pregnant Women Screened by Prenatal Diagnosis

Jinhan Liu,[1] Xiaoxin Yan,[1] Liangliang Chu,[2] Chang E. Li,[2] Jiamin Hu,[1] and Shengqiang Zou[1]

[1] *Department of Nursing, The Affiliated Third hospital of Zhenjiang, Jiangsu University, Jiangsu, Zhenjiang 212013, China*
[2] *Department of Nursing, The First Affiliated Hospital of Shandong First Medical University, Shandong, Jinan 250014, China*

Correspondence should be addressed to Shengqiang Zou; shengqiang1121@163.com

Received 22 November 2021; Revised 28 December 2021; Accepted 7 January 2022; Published 28 January 2022

Academic Editor: Enas Abdulhay

Objective. To explore the status quo of psychological resilience, mindfulness level, the sleep quality of pregnant women by Prenatal Diagnosis Screening, and the mediating effect of psychological resilience on sleep quality and mindfulness. *Methods*. A survey of 298 pregnant women was conducted using the psychological resilience scale, Pittsburgh sleep quality index, and the concise version of the five-factor mindfulness scale. *Results*. The total score of psychological resilience of pregnant women was (68.96 ± 17.27), mindfulness was (77.25 ± 12.65), the median of total sleep quality was 6, and the detection rate of sleep disorders was 31.9%. The sleep quality of pregnant women was negatively correlated with mindfulness level and psychological resilience ($p < 0.01$), and mindfulness level was positively associated with psychological resilience ($p < 0.01$). Bootstrap analysis showed that psychological resilience played an 14.1% mediating role between mindfulness and sleep quality. *Conclusion*. The psychological resilience of pregnant women is low, sleep quality is poor, and mindfulness is mild to moderate. Psychological resilience plays an important role in mediating between mindfulness level and sleep quality that suggests nursing staff should pay attention to and improve the psychological resilience of pregnant women screened by prenatal diagnosis to improve the mindfulness level and sleep quality of pregnant women screened by prenatal diagnosis.

1. Introduction

Studies at home and abroad show that about 78% to 87% of pregnant women have sleep problems during pregnancy [1, 2]. The sleep survey reported that nearly 80% of women complained about disturbed sleep during pregnancy [3]. This will increase the risk of comorbidities in pregnant women and increase the likelihood of preterm birth [4]. Clinically, pregnant women usually refuse to use psychotropic medications to treat sleep problems during pregnancy due to concerns about fetal growth and development. Mindfulness is to purposefully focus your attention entirely on the present, without attaching any judgment, perception, or awareness. Mindfulness interventions as effective drug alternative therapies have been shown to improve sleep quality [4]. Mindfulness meditation is becoming a method of mental health intervention, and theoretical concepts related to it have an effect on psychopathology [5]. Psychological resilience is a dynamic process that takes shape as a change allowing people to find balance and to evolve positively [6]. It is the product of the interaction between individuals and the environment. Improving psychological resilience help individuals reintegrate and grow in the face of difficulties [7, 8]. Psychological resilience can effectively enhance changes in the hormonal levels caused by sleep disorders. Therefore, this paper aims to understand the status of sleep quality, mindfulness level, and psychological resilience in prenatal diagnosis screening of pregnant women, and to explore the role of psychological resilience between mindfulness level and sleep quality, to provide a reference to improving the sleep quality of screening pregnant women with prenatal diagnosis.

2. Materials and Methods

2.1. Subjects. From July to September 2020, 298 pregnant women were selected from the outpatient department of obstetrics and gynecology in a tertiary hospital.

Inclusion criteria are as follows: (1) age >18 years old; (2) smooth language communication; (3) pregnant women who voluntarily participate in the study and actively cooperate; and (4) elected prenatal diagnostic screening.

Exclusion criteria are as follows: (1) pregnant women with previous mental illness; (2) low intelligence or combined with severe complications; (3) communication impairment and hearing impairment. There were no ethical conflicts in "Materials and methods."

2.2. Study Tool. General data shall be designed by the researcher, including basic data of age, education level, address, living status, working status and monthly family income, pregnancy week, adverse pregnancy history, mode of pregnancy, and other relevant data.

2.2.1. Five Facet Mindfulness Questionnaire-Short Form (FFMQ-SF). The scale consists of five dimensions: observation, description, perceived action, no judgment, and no behavior, with a total of 24 items. Using a grade Likert5 score method with a total score of 24 to 120, higher scores represent higher levels of individual mindfulness [9].

2.2.2. Connor Davidson Resilience Scale (CD-RISC). Connor and Davidson developed Connor Davidson Resilience Scale (CD-RISC) in 2003 [10]. Yu and Zhang [11], a Chinese scholar, introduced and Chineseizing it. The Cronbach's alpha of the Chinese version was 0.916, and the test-retest reliability was 0.821. The scale includes three dimensions: toughness, optimism, and self-improvement, with a total of 25 items. The Likert 5-level scoring method is used, with a total score of 100 scores. The higher the score, the higher the mental Resilience.

2.2.3. Pittsburgh Sleep Quality Index (PSQI). Applied Liu and Tang's Chinese version to evaluate the sleep quality in the past month. The scale includes 19 self-assessment items and 5 other-assessment items, and the scoring items are the top 18 items in the self-assessment items. Scoring items contain 7 factors, each factor 0~3 scores, total score range 0~21 scores, the higher the score, the worse the sleep quality [12]. PSQI total score greater than 7 scores for poor sleep quality [13].

2.3. Study Method. Researchers and trained nurses distributed the questionnaire. Unified guidance is adopted. On the premise of obtaining their consent, the corresponding help was given in the questionnaire filling process, and the empty items were filled again after the inquiry. All questionnaires are returned on the spot after completion and check the completeness and quality. A total of 300 questionnaires were distributed, and 298 were effectively recovered, with an effective rate of 99.3%.

2.4. Statistical Method. SPSS22.0 was used for statistical analysis. Counting data were tested by the number of people, in percentage description. Measurement data are described by mean and standard deviation. Pearson correlation analysis was used to analyze the correlation between mindfulness level, psychological resilience, and sleep quality of pregnant women in prenatal diagnosis screening. The hierarchical regression analysis was used to analyze the mediating effect of psychological resilience [14], and the structural equation model was established by AMOS23.0 software. The Bootstrap method is used to further verify the result.

3. Results

3.1. General Data of Prenatal Diagnosis Screening for Pregnant Women. A total of 298 pregnant women for prenatal diagnostic screening were included in this study. Age: less than 25 years old, 1 person, 0.3%; aged 25–30, 228 person, 75.7%; aged 30–35, 67 people, 22.3%; older than 35 years, 2 people, 0.7%. Education: students in junior high school and below, 2 people, 0.7%; high school, 28 people, 9.4%; specialized schools, 96 people, 31.9%; undergraduate, 161 people, 53.5%; masters or above, 11 people, 3.7%. Address: rural areas, 44 people, 14.6%; township, 120 people, 39.9%; urban areas, 134 people, 44.5%. Living status: with parents, spouses, 70 people, 23.3%, with spouses, 211 people, 70.1%; separated from spouses, basically live alone, 17 people, 5.6%. Family monthly income: less than 5000 yuan, 22 people, 7.3%; 5000–10000 yuan, 112 people, 37.2%; 10000 to 20000 yuan, 111 people, 36.9%; 20000 to 30000 yuan, 46 people, 15.3%; more than 30000 yuan, 7 people, 2.3%. Working situation: 216 employees, 71.8%; 82 nonemployees, 27.2%. Only child: 172, 57.1%; No, 126, 41.9%. Whether the pregnancy is planned: yes, 193,64.1%; No, 105,34.9%. The mode of delivery: 234 natural births, 77.7%; 64 births by cesarean section, 21.3%. Adverse pregnancy: yes, 2, 0.7%; no, 296, 98.3%. Pregnant week: less than 13 weeks, 78 people, 25.9%; 13–28 weeks, 188 people, 62.5%; more than 28 weeks, 32 people, 10.6%. Satisfaction degree of husband-wife relationship: 250 people were satisfied, accounting for 83.1%; 48 people, general, 15.9%.

3.2. Prenatal Diagnosis and Screening of Pregnant Women for Psychological Resilience (Table 1). The dimension score of the optimistic, self-improvement, as well as the tough and tensile group, was 10.59 ± 3.08, 22.46 ± 5.89, and 35.93 ± 8.94, respectively. The item average score of the optimistic, self-improvement, as well as the tough and tensile group, was 2.65 ± 0.77, 2.81 ± 0.74, and 2.76 ± 0.69, respectively.

3.3. Prenatal Diagnosis and Screening of Pregnant Women for Sleep Quality. The total Pittsburgh sleep quality score and the score of all dimensions of pregnant women with prenatal diagnosis is shown in Table 2, with 95 sleep disorders detected, 31.9%.

Table 1: Total score of psychological resilience and scores of all dimensions of pregnant women screened after prenatal diagnosis ($n = 298$).

Project	Number of entries	Score range (scores)	Dimension score ($\overline{x} \pm s$, component)	Item average score ($\overline{x} \pm s$, component)
Optimistic	4	1~15	10.59 ± 3.08	2.65 ± 0.77
Self-improvement	8	3~31	22.46 ± 5.89	2.81 ± 0.74
Tough and tensile	13	6~48	35.93 ± 8.94	2.76 ± 0.69
Total scores	25	12~92	68.96 ± 17.27	2.76 ± 0.69

Table 2: Total scores of sleep quality and all dimensions of pregnant women with prenatal diagnosis ($n = 298$).

Project	Median
Sleep quality	1.00
Sleep time	1.00
Hours of sleep	0.00
Sleep efficiency	0.00
Dyssomnia	1.00
Hypnosis drugs	0.00
Day dysfunction	1.00
Total scores	6.00

3.4. Prenatal Diagnosis and Screening for Maternal Mindfulness Levels (Table 3). The dimension score of the observational dimensions, describe dimensions, known dimension of action, do not judge dimensions as well as do not judge dimensions was 15.16 ± 2.94, 16.70 ± 3.45, 13.46 ± 5.00, 13.58 ± 3.59, and 18.36 ± 3.62, respectively. The item average score of the observational dimensions, describe dimensions, known dimension of action, do not judge dimensions as well as do not judge dimensions was 3.79 ± 0.73, 3.34 ± 0.69, 2.69 ± 0.10, 2.71 ± 0.72 as well as 3.67 ± 0.72, respectively.

3.5. Prenatal Diagnosis and Screening of Mindfulness Level, Sleep Quality, and Psychological Resilience. The results of person correlation analysis showed that PSQI was negatively correlated with the CD-RISC score range in prenatal diagnosis screening pregnant women ($r = -0.426$, $p < 0.01$). The PSQI was negatively associated with the FFMQ-SF score ($r = -0.429$, $p < 0.01$), and the FFMQ-SF was positively associated with the CD-RISC score ($r = 0.373$, $p < 0.01$).

3.6. Test of the Mediating Effect of Maternal Psychological Resilience between Sleep Quality and Mindfulness Levels. The results showed that the negative effect of mindfulness level on sleep quality decreased from −0.429 to −0.314, and the effect was still significant ($p < 0.01$), indicating that psychological resilience played a partial mediating role in the prediction of mindfulness level on sleep quality in pregnant women screened by prenatal diagnosis, as shown in Table 4. This conclusion needs to be further verified.

3.7. Validation of Mediating Effect Model of Psychological Resilience between Mindfulness Level and Sleep Quality in Prenatal Diagnosis Screening Pregnant Women. The structural equation model of psychological resilience, mindfulness level, and sleep quality of prenatal diagnosis screening pregnant women was established. The maximum likelihood method and AMOS23.0 software were used for mediating effect test. The path analysis is shown in Figure 1. The model absolutely fits the exponential $x^2/df = 3.067$, GFI (adaptation index) = 0.890, AGFI (adjusted fitness index) = 0.831, IFI (value is configuration) = 0.937, RMSEA (progressive square and square root) = 0.096, NFI (standard adaptation index) = 0.919, showing good data fit. As can be seen from Figure 1, the direct effect of mindfulness level on sleep quality is 0.28, and the indirect effect of psychological resilience on sleep quality is 0.141 (product of 0.47 and −0.30), accounting for 34.49% of the total effect, suggesting that psychological resilience plays a partial role between sleep quality and mindfulness level. Further interval estimation was performed using the variation correction bootstrap confidence region estimation method with a sample size selection of 5000 [15]. Under 95% CI results, the mediation of psychological resilience between sleep quality and mindfulness level was −0.146, the interval did not contain 0 (LLCI = −0.248, ULCI = −0.069), suggesting a mediation effect of psychological resilience between mindfulness level and sleep quality; the direct effect of mindfulness level on sleep quality was −0.251 and the interval did not contain 0 (LLCI = −0.435, ULCI = −0.047), indicating a significant direct effect.

4. Discussion

4.1. The Psychological Resilience Level of Pregnant Women with Prenatal Diagnosis Screening Is at a Relatively Low Level. This study showed that the psychological resilience of pregnant women in prenatal diagnosis screening was low, which was consistent with the results of Zhong et al. [16]. The score of optimism dimension was the lowest (10.59 ± 3.08), which was consistent with the study of Shang et al. [17]. The reason may be that prenatal diagnosis during pregnancy and screening of pregnant women need to face both physical and psychological pressure. As the growth of pregnancy week, pregnant women will have early pregnancy reaction, insomnia, anemia, urinary frequency, oedema, constipation, stature change, changes in hormone levels, and lack of awareness of pregnancy and childbirth. The fear of prenatal diagnosis results, resulting in negative emotions such as anxiety. Pregnant women's lack of confidence in a successful pregnancy weakened their psychological resilience. Clinical nursing staff should take positive and effective measures to establish mutual communication groups, on-demand education in pregnant schools, and one-to-one psychological counseling. While improving the nursing ability, help prenatal diagnosis screening pregnant women

Table 3: Total scores of mindfulness levels and all dimensions of pregnant women screened after prenatal diagnosis ($n = 187$).

Project	Number of entries	Score range (scores)	Dimension score ($\overline{x} \pm s$, component)	Item average score ($\overline{x} \pm s$, component)
Observational dimensions	4	6~20	15.16 ± 2.94	3.79 ± 0.73
Describe dimensions	5	7~24	16.70 ± 3.45	3.34 ± 0.69
Known dimension of action	5	5~23	13.46 ± 5.00	2.69 ± 0.10
Do not judge dimensions	5	7~23	13.58 ± 3.59	2.71 ± 0.72
Do not act dimension	5	7~25	18.36 ± 3.62	3.67 ± 0.72
Total	24	50~107	77.25 ± 12.65	3.09 ± 0.51

Table 4: Results of stratified regression analysis of mindfulness level, psychological resilience, and sleep quality for prenatal diagnosis ($n = 298$).

Project	Dependent variable	Argument	β price	t price	p price	R^2 price	F Price	p price
Step 1	Sleep quality (Y)	Mindfulness level (X)	−0.429	−8.181	0.000	0.182	66.933	0.000
Step 2	Psychological resilience (M)	Mindfulness level (X)	0.373	6.918	0.000	0.136	47.863	0.000
Step 3	Sleep quality (Y)	Mindfulness level (X)	−0.314	−5.874	0.000	0.262	53.596	0.000
		Psychological resilience (M)	−0.309	−5.746	0.000			

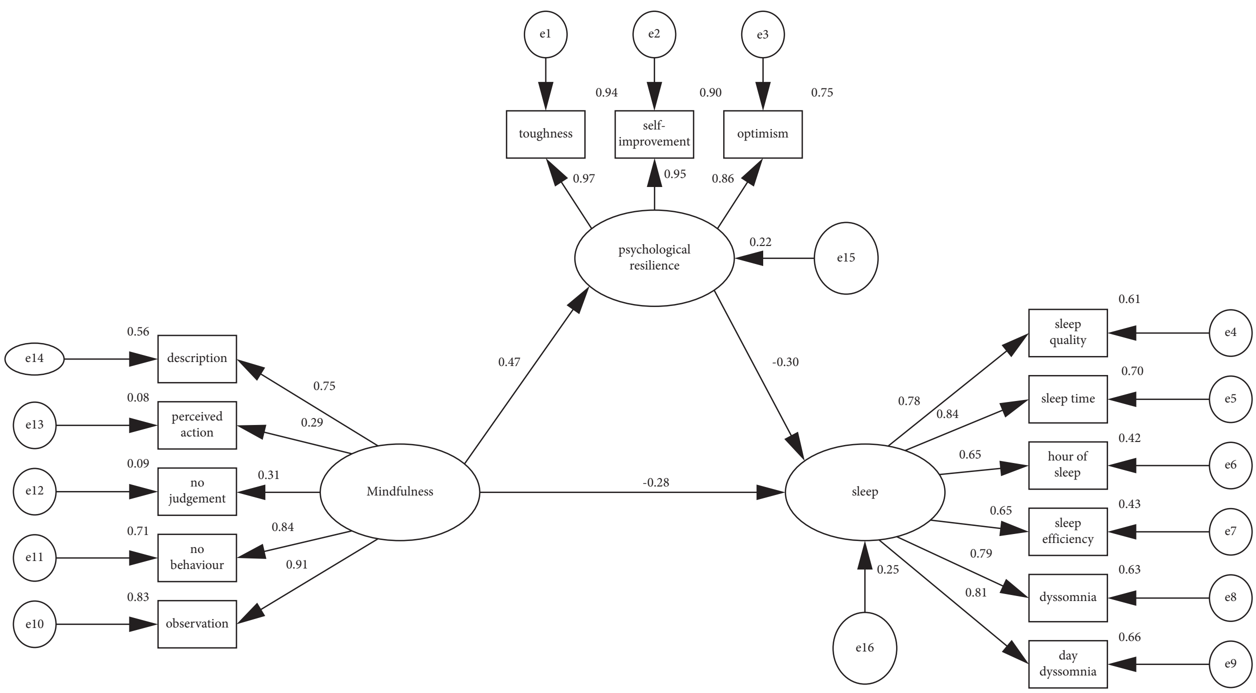

Figure 1: Antenatal diagnostic screening for maternal psychological resilience between mindfulness level and sleep quality.

understand pregnancy and prenatal diagnosis-related knowledge, establish confidence in a successful pregnancy, and then improve the negative emotions of pregnant women.

4.2. Mindfulness Levels in Pregnant Women Screened for Prenatal Diagnosis Are Low. This study showed a prenatal diagnostic screening of pregnant women with mindfulness levels at a lower level, lower than related studies [18]. The mindfulness level of pregnant women with prenatal diagnosis is at the middle level, indicating that their self-regulation and cognitive ability need to be improved. The level of mindfulness affects individuals' cognitive patterns and negative emotions caused by sleep problems. The higher the level of mindfulness, the stronger the self-regulation ability, and the more optimistic and positive they can face difficulties [19]. The level of mindfulness can be improved through learning, and long-term mindfulness practice can give practitioners peace and tranquility [20]. Mindfulness helps sleep by detecting sleep problems and not responding to any emotions or thoughts that arise. It is also necessary to explore patterns of prenatal diagnostic screening for pregnant women to improve sleep quality through mindfulness practice. Medical staff can screen pregnant women for mindfulness levels as early as possible in prenatal diagnosis and use the hospital-community and network resources to develop appropriate interventions to bring mindfulness into life and improve sleep quality through continuous learning and self-practice in prenatal diagnosis screening pregnant women.

4.3. Pregnant Women Have Poor Sleep Quality. This study showed that the median sleep quality of prenatal diagnostic screening was 6 score, and the detection rate of sleep disorders was 31.9%. The results showed that the three factors namely, sleep time, sleep disorder, and daytime dysfunction scored higher, consistent with Tan et al. [21]. The causes of sleep problems in pregnant women include fear of prenatal diagnosis screening results, increased nocturia, difficulty to find a comfortable sleeping position, physical pain, and discomfort, resulting in prolonged sleep time and sleep disorders. With the development of society, more and more professional women in the workplace need to work at high intensity while taking into account, their pregnancy [2, 22, 23]. Excessive energy into work may lead to daytime dysfunction. Therefore, we should attach great importance to sleep factors during pregnancy. Clinical medical staff should thoroughly evaluate the sleep status of pregnant women in prenatal diagnosis screening. Given the relevant influencing factors, early identification and intervention should be carried out to shorten sleep latency, control sleep disorders, and reduce the incidence of daytime sleep disorders to better improve pregnant womens sleep quality in prenatal diagnosis.

4.4. Relevant Analysis between Sleep Quality, Mindfulness Level and Psychological Resilience. Pearson correlation analysis showed that the sleep quality of pregnant women screened by prenatal diagnosis was negatively correlated with psychological resilience. Sleep quality is negatively correlated with mindfulness and positively associated with resilience. Sleep quality was negatively correlated with mindfulness levels and positively correlated with psychological resilience. This indicates that higher the mindfulness, the better the sleep quality, and higher the psychological resilience, the higher the mindfulness. The results of hierarchical regression analysis, structural equation model, and bootstrap method show that psychological resilience is the intermediary variable of the sleep quality and mindfulness level of prenatal diagnosis and screening of pregnant women and plays a partial intermediary role, accounting for 33.49% of the total effect. This indicated that psychological resilience, as a protective factor within individuals, can enhance the positive function of the mindfulness level. In the face of pregnancy-related problems, at the same mindfulness level, pregnant women with high psychological resilience levels can take a relatively more positive attitude and response way to adapt to the current state, less affecting sleep quality. On the contrary, pregnant women with poor psychological resilience are more likely to produce destructive emotions or even psychological problems and then appear sleep disorders. Consistent with the results [24], studies have shown that psychological resilience is the protective resource for the prenatal diagnosis and screening of the sleep quality of pregnant women. For pregnant women with low mindfulness levels, the mindfulness level can be improved by improving psychological resilience and sleep quality. The limit of the study is that this study is short of scientific experiments, which made the result not so solid. Further studies are needed to confirm the opinion of these reports.

4.5. Summary. In conclusion, prenatal diagnostic screening for maternal psychological resilience plays a significant mediating effect between mindfulness and sleep quality. Clinical nursing staff should pay attention to improving the psychological resilience of pregnant women in prenatal diagnosis and screening, and fully explore and utilize the integration of social resources so that pregnant women in prenatal diagnosis and screening can enhance their ability to cope with state changes, maintain good mental health, and improve the mindfulness level of pregnant women, and improve sleep quality. In this study, we only selected pregnant women with prenatal diagnosis and screening in a tertiary hospital as the research object. The sampling may be biased and cannot fully represent pregnant women with prenatal diagnosis and screening. In future studies, multi-center selection samples are needed for further exploration.

Data Availability

The data used to support this study are available from the corresponding author upon request.

Conflicts of Interest

The authors declare that they have no conflicts of interest.

Acknowledgments

This paper was funded by China Hepatitis Prevention and Control Fund Project (WBEXJS2018001) and Zhenjiang Key R & D and Development Plan Social Development Project (SH2018028).

References

[1] H. Skouteris, C. Germano, E. H. Wertheim, S. J. Paxton, and J. Milgrom, "Sleep quality and depression during pregnancy: a prospective study," *Journal of Sleep Research*, vol. 17, no. 2, pp. 217–220, 2008.

[2] J. A. Mindell, R. A. Cook, and J. Nikolovski, "Sleep patterns and sleep disturbances across pregnancy," *Sleep Medicine*, vol. 16, no. 4, pp. 483–488, 2015.

[3] V. Bacaro, F. Benz, A. Pappaccogli et al., "Interventions for sleep problems during pregnancy: a systematic review," *Sleep Medicine Reviews*, vol. 50, Article ID 101234, 2020.

[4] F. L. Facco, W. A. Grobman, K. J. Reid et al., "Objectively measured short sleep duration and later sleep midpoint in pregnancy are associated with a higher risk of gestational diabetes," *American Journal of Obstetrics and Gynecology*, vol. 217, no. 4, pp. 447.e1–447.e13, 2017.

[5] J. Wielgosz, S. B. Goldberg, T. R. A. Kral, J. D. Dunne, and R. J. Davidson, "Mindfulness meditation and

psychopathology," *Annual Review of Clinical Psychology*, vol. 15, no. 1, pp. 285–316, 2019.

[6] A. Sisto, F. Vicinanza, L. L. Campanozzi, G. Ricci, D. Tartaglini, and V. Tambone, "Towards a transversal definition of psychological resilience: a literature review," *Medicina*, vol. 55, no. 11, p. 745, 2019.

[7] M. C. Johnston, T. Porteous, M. A. Crilly et al., "Physical disease and resilient outcomes: a systematic review of resilience definitions and study method," *Psychosomatics*, vol. 56, no. 2, pp. 168–180, 2015.

[8] G. E. Richardson, "The metatheory of resilience and resiliency," *Journal of Clinical Psychology*, vol. 58, no. 3, pp. 307–321, 2002.

[9] Y. Wu, *Intervention Study on Mindfulness-Based Stress Reduction Therapy in Community Patients with Type 2 Diabetes*, Nanjing University of Traditional Chinese Medicine, Nanjing, China, 2019.

[10] K. M. Connor and J. R. T. Davidson, "Development of a new resilience scale: the connor-davidson resilience scale (CD-RISC)," *Depression and Anxiety*, vol. 18, no. 2, pp. 76–82, 2003.

[11] X. N. Yu and J. X. Zhang, "Resilience-The psychological mechanism of recovery and growth under stress," *Psychological Science Progress*, vol. 5, pp. 658–665, 2005.

[12] X. C. Liu and M. Q. Tang, "Reliability and validity of pittsburgh sleep quality index," *Chinese Journal of Psychiatry*, vol. 29, no. 2, p. 5, 1996.

[13] H. Y. Zhou, G. P. Li, P. Li, and H. L. Yang, "The relationship between pregnancy perceived stress and sleep quality of pregnant women-the mediating role of psychological distress," *Chinese Journal of Mental Health*, vol. 30, no. 12, p. 5, 2016.

[14] Z. Wen and B. Ye, "Analyses of mediating effects: the development of methods and models," *Advances in Psychological Science*, vol. 22, no. 5, pp. 731–745, 2014.

[15] X. M. Yan, Q. Peng, X. Li, and J. P. Su, "Psychological Resilience plays an intermediary role between sleep quality and care burden of main caregivers of patients with esophageal cancer," vol. 3, pp. 153–157, 2019.

[16] J. Zhong, Y. F. Zhou, L. L. Li et al., "Psychological Resilience of pregnant women with gestational diabetes mellitus and its influencing factors," *Journal of Nursing*, vol. 4, pp. 74–78, 2019.

[17] N. Shang, H. F. Zhang, and S. W. Dong, "Study on the correlation between Resilience and anxiety in late pregnancy," *Tianjin Nursing*, vol. 5, pp. 509–513, 2019.

[18] G. Jia and Y. Xiao, "Analysis of the correlation between mindfulness level and sleep quality in middle and late pregnancy," *General nursing*, vol. 20, pp. 2440–2443, 2019.

[19] S. L. Shapiro, L. E. Carlson, J. A. Astin et al., "Mechanisms of mindfulness," *Journal of Clinical Psychology*, vol. 62, no. 3, pp. 373–386, 2010.

[20] W. R. Qian, *Effects of Mindfulness Training on College Students' Positive Emotions*, Zhejiang University of Technology, Hangzhou, 2016.

[21] L. W. Tan, H. J. Shi, Y. Wang et al., "Sleep quality of pregnant women in early and middle pregnancy in Shanghai and related social structural factors," *Shanghai Preventive Medicine*, vol. 3, pp. 207–211, 2018.

[22] B. Gelaye, Y. V. Barrios, Q. Y. Zhong et al., "Association of poor subjective sleep quality with suicidal ideation among pregnant peruvian women," *General Hospital Psychiatry*, vol. 37, no. 5, 2015.

[23] J. A. Mindell and B. J. Jacobson, "Sleep disturbances during pregnancy," *Journal of Obstetric, Gynecologic, and Neonatal Nursing*, vol. 29, no. 6, 2000.

[24] Q. P. Gao, P. Chen, B. Zhou, J. Wang, Y. Z. Wei, and G. L. Jiao, "Effects of resilience, anxiety, and depression on sleep quality of first-line medical staff during the period of new coronavirus pneumonia," *Chinese convalescent medicine*, vol. 11, pp. 1153–1155, 2020.

Hindawi
Journal of Healthcare Engineering
Volume 2022, Article ID 9864791, 1 page
https://doi.org/10.1155/2022/9864791

Retraction

Retracted: MiR-483 Promotes Colorectal Cancer Cell Biological Progression by Directly Targeting NDRG2 through Regulation of the PI3K/AKT Signaling Pathway and Epithelial-to-Mesenchymal Transition

Journal of Healthcare Engineering

Received 1 December 2022; Accepted 1 December 2022; Published 28 December 2022

Journal of Healthcare Engineering has retracted the article titled "MiR-483 Promotes Colorectal Cancer Cell Biological Progression by Directly Targeting NDRG2 through Regulation of the PI3K/AKT Signaling Pathway and Epithelial-to-Mesenchymal Transition" [1] due to concerns that the peer review process has been compromised.

Following an investigation conducted by the Hindawi Research Integrity team [2], significant concerns were identified with the peer reviewers assigned to this article; the investigation has concluded that the peer review process was compromised. We therefore can no longer trust the peer review process, and the article is being retracted with the agreement of the Chief Editor.

References

[1] X. Sun, K. Li, H. Wang, Y. Xia, P. Meng, and X. Leng, "MiR-483 Promotes Colorectal Cancer Cell Biological Progression by Directly Targeting NDRG2 through Regulation of the PI3K/AKT Signaling Pathway and Epithelial-to-Mesenchymal Transition," *Journal of Healthcare Engineering*, vol. 2022, Article ID 4574027, 9 pages, 2022.

[2] L. Ferguson, "Advancing Research Integrity Collaboratively and with Vigour," 2022, https://www.hindawi.com/post/advancing-research-integrity-collaboratively-and-vigour/.

Hindawi
Journal of Healthcare Engineering
Volume 2022, Article ID 4574027, 9 pages
https://doi.org/10.1155/2022/4574027

Research Article

MiR-483 Promotes Colorectal Cancer Cell Biological Progression by Directly Targeting NDRG2 through Regulation of the PI3K/AKT Signaling Pathway and Epithelial-to-Mesenchymal Transition

Xifeng Sun,[1] **Kun Li**,[2] **Huiling Wang**,[3] **Yifang Xia**,[4] **Ping Meng**,[5] **and Xiaogang Leng**[6]

[1]*Department of Clinical Laboratory, Weifang People's Hospital, Weifang 261041, China*
[2]*Department of Anesthesia, Zhangqiu District People's Hospital, Jinan 250200, China*
[3]*Department of Infectious Diseases, Zhangqiu District People's Hospital, Jinan 250200, China*
[4]*Department of Imaging, Zhangqiu District People's Hospital, Jinan 250200, China*
[5]*Department of Burn and Plastic Surgery, Zhangqiu District People's Hospital, Jinan 250200, China*
[6]*Department of Anus and Intestine Surgery, Weifang People's Hospital, Weifang 261041, China*

Correspondence should be addressed to Xiaogang Leng; lengxiaogang@sdwfph.cn

Received 1 December 2021; Accepted 10 January 2022; Published 27 January 2022

Academic Editor: Enas Abdulhay

Background. Colorectal cancer is the third frequent tumor in the whole world. MiR-483, located at the 11p15.5 locus, acts as an oncogene in multiple tumors. The purpose of this study is to explore the important roles of miR-483 in colorectal cancer. *Materials and Methods*. RT-qPCR and western blot were applied to calculate the mRNA levels of miR-483 and genes. The Kaplan–Meier method was conducted to calculate the survival of patients with colorectal cancer. The proliferation and invasive abilities were measured by Methyl Thiazolyl Tetrazolium (MTT) and transwell assays. *Results*. MiR-483 was upregulated in colorectal cancer tissues, and the upregulation of miR-483 predicted poor prognosis of colorectal cancer patients. NDRG2 was a target gene of miR-483 in colorectal cancer. Furthermore, miR-483 has been reported to promote colorectal cancer cell proliferation and invasion through targeting NDRG2 by the PI3K/AKT pathway and epithelial-to-mesenchymal transition (EMT). In addition, the overexpression of miR-483 promoted xenograft growth of LOVO cells. *Conclusion*. MiR-483 promoted cell proliferation through the NDRG2/PI3K/AKT pathway and invasion-mediated EMT in colorectal cancer. In view of the multiple mechanisms of molecular immunotherapy, it is necessary to further study the relationship between miR-483 and colorectal cancer, so as to find a more direct and effective treatment method to prevent colorectal cancer.

1. Introduction

Colorectal cancer (CRC) is a type of gastrointestinal cancer that is the third frequent tumor in the whole world [1, 2]. Despite the increase of treatment modalities, the metastasis remains to be a challenge for the treatment of colorectal cancer [3]. Therefore, it is urgent to investigate the new biomarkers for the early diagnosis and metastasis of colorectal cancer.

MicroRNAs (miRNAs) are noncoding RNAs with a length of 18–25 nucleotides, which repressed gene expression through directly binding to the mRNA 3′-untranslated region (3′-UTR) at the posttranscriptional level [4, 5]. MiRNAs may act as tumor suppressors or oncogenes to regulate the tumor process including growth, differentiation, and metastasis [6, 7]. A previous study has reported several miRNAs played important roles in colorectal cancer, including miR-483 [8]. MiR-483, which has been reported to be located at the 11p15.5 locus, plays important roles in multiple tumors, including breast cancer, nasopharyngeal carcinoma, and anaplastic thyroid cancer [9–11]. Yang et al. have revealed that, in prostate cancer, miR-483 promoted cell proliferation and invasion [12]. Similarly, Tang et al. have illuminated that miR-483 promoted the proliferation, migration, and invasion and inhibited the apoptosis in hepatocellular carcinoma [13]. Even in colorectal cancer, miR-483 was overexpressed and mediated cellular proliferation by directly targeting DLC-1 [14]. Therefore, we conjectured that miR-483 may promote cell proliferation and metastasis through regulating the PI3K/AKT pathway and EMT in colorectal cancer.

N-Myc downstream-regulated gene 2 (NDRG2) belongs to the NDRG family and is a newly identified differentiation-related gene whose promoter has hypermethylation [15, 16]. NDRG2 played a vital role in multiple biological processes including cell growth, metastasis, and apoptosis [17]. Tamura et al. have indicated that loss of NDRG2 enhanced the metastasis potential in oral squamous cell carcinoma [18]. Moreover, Yamamura et al. have revealed that the suppression of NDRG2 was associated with poor prognosis in gastrointestinal cancer [19]. Even in colorectal cancer, Ali Golestan indicated that overexpression of NDRG2 promoted cell proliferation and invasion [20]. Moreover, Claire Agosta has illuminated that miR-483 promoted the migration and invasion through directly binding to NDRG2 in adrenocortical cancer [21]. Thus, we firmly believe that miR-483 may play an important role in carcinogenesis through NDRG2 in colorectal cancer. In this study, we revealed that miR-483 was upregulated in colorectal cancer and the overexpression of miR-483 predicted poor 5-year survival. MiR-483 promoted the proliferation and invasion in colorectal cancer. In addition, miR-483 promoted growth of CRC cell xenograft.

2. Materials and Methods

2.1. Sample Collection. Cancer tissue samples from 47 patients with colorectal cancer were collected from Weifang People's Hospital. Meanwhile, we also collected the 47 control tissues which were obtained from nonnecrotic colon patients. Patients were excluded if they received chemotherapy or radiation therapy before the blood was drawn. All the samples were immediately frozen in liquid nitrogen and stored at −80°C. Informed consent was obtained from all individual participants included in the study. All the specimens of this study were approved by the Ethical Committee of Weifang People's Hospital.

2.2. Cell Culture. Two human colorectal cancer cell lines (LOVO and SW480) and a normal colorectal epithelial cell line CCD-18Co were obtained from the American Type Culture Collection (ATCC, Manassas, VA, USA). All the cells were cultured in the RPMI-1640 medium (Hyclone, UT, USA) with 10% fetal bovine serum (FBS), 100 U/ml penicillin, or 100 mg/ml streptomycin at 37°C in humidified air with 5% CO_2.

2.3. Cell Transfection. The miR-483 mimic and the miR-483 inhibitor, as well as their negative control (NC), were synthesized and purchased from GenePharma (Shanghai, China), which were transfected into colorectal cancer cells VOLO to up- or downregulate the expression of miR-483. The transfection was performed using Lipofectamine 2000 Reagent (Invitrogen, Carlsbad, CA) pursuant to the command of the manufacturer.

2.4. RNA Extraction and Real-Time Quantitative Polymerase Chain Reaction (RT-qPCR). For the miRNAs, total miRNAs were extracted utilizing the miRNeasy Mini Kit (Qiagen, Hilden, Germany) from tissues or cell lines. The reverse transcription was carried out to synthesize the first cDNA chain using the TaqMan miRNA Reverse Transcription Kit (Applied Biosystems, Foster City, CA, USA). Then, the qPCR was performed using the miRNA-specific TaqMan miRNA Assay Kit (Applied Biosystems) on an ABI7500 real-time PCR system (Applied Biosystems). The relative levels of miRNA were derived using the $2^{-\Delta\Delta Ct}$ method with U6 small nuclear RNA as normalization.

For the mRNAs, the TRIzol reagent (Invitrogen) was applied to extract total RNA. The Omniscript Reverse Transcription Kit (Qiagen) was utilized to synthesize the first cDNA chain from total RNAs. The qPCR was carried out using the QuantiTect SYBR Green PCR Kit (Qiagen) on a Quantitect SYBR green PCR system (Qiagen). A method was used for the mRNA quantification, which was normalized by GAPDH. We analyzed the data using the $2^{-\Delta\Delta Ct}$ method for relative quantification. The sequences of primers were as follows: miR-483 forward 5′-AGTTGGCTCACGGTTCTTTCAA-3′, reverse 5′-ATCGCCATGGCCCGCATGTCGG-3′; U6 forward 5′-GC TTCGGCAGCACATATACTAAAAT-3′, reverse 5′-CGCT TCAGAATTTGCGTGTCAT-3′; NDRG2 forward 5′-CCT CACCTC TTCCATTCC-3′, reverse 5′-TATCACCTC CACG CTCAA-3′; and GAPDH, forward 5′-CGGAGTCAACG GATTTGGTCGTAT-3′, reverse 5′-AGCCTTCTCCATGGT GGTGAAGAC-3′.

2.5. Western Blotting. Total proteins were extracted using the RIPA buffer (Beyotime, Nantong, China), and then, we tested the protein concentration by bicinchoninic acid protein assay (BCA). Equal amounts of proteins were isolated by 10% sodium dodecyl sulfate polyacrylamide gel electrophoresis (SDS-PAGE) and transferred onto a polyvinylidene fluoride (PVDF) membrane (Millipore, Boston, MA, USA). After blocking with 5% nonfat dried milk for 1h, the membrane was incubated with the primary antibody against NDRG2 (1 : 1000; ab174850, Abcam, Cambridge, USA), E-cadherin (1 : 1000; ab197751, Abcam), N-cadherin (1 : 1000; ab256744, Abcam), vimentin (1 : 1000; ab92547, Abcam), p-PI3K (1 : 1000, 17366, Cell Signaling, San Jose, CA, USA), PI3K (1 : 1000, 3821, Cell Signaling), p-AKT (1 : 1000, 5197, Cell Signaling), AKT (1 : 1000, 4685, Cell Signaling), and GAPDH (1 : 3000, Cell Signaling) at 4°C overnight. Subsequently, the membranes were incubated with the secondary HRP-conjugated antibody (Beyotime) for 2 h at room temperature. Finally, the protein signal was determined with the enhanced chemiluminescence (ECL) kit (Pharmacia Biotech, Arlington, USA).

2.6. CCK-8 Assay. The ability of cell proliferation was measured by CCK-8 assay. In brief, 300 μl cell suspension with a concentration of 80% was seeded in each well of the 96-well plates. Meanwhile, CCK-8 reagent (Dojindo, Kumamoto, Japan) was added after 24 h, 48 h, 72 h, or 96 h of culture, and the absorbance at a wavelength of 450 nm was evaluated using a Model 680 Microplate Reader (Bio-Rad, Hercules, CA).

2.7. Transwell Assay. Transwell insert (8 μm pore filters, BD Bioscience, Bedford, MA) with a Matrigel (BD Biosciences)-coated membrane was used to calculate the invasion and migration assay. Cells suspended in serum-free media were seeded to the upper chamber, while a normal RPMI-1640 medium with 15% FBS was added in the lower chamber. After incubating for about 24 h at 37°C, the invasive cells were fixed and stained by 4% paraformaldehyde and 10% crystal violet, respectively. Finally, we photographed and counted the invasive cells in five random fields under a microscope (Tokyo, Japan).

2.8. Dual-Luciferase Reporter Assay. NDRG2 was predicted to be a potential downstream target of miR-483 using TargetScan (https://www.targetscan.org). The binding sequences were mutated from 5′-AGGGCAGA-3′ to 5′-AGGCGUCA-3′ to validate whether miR-483 directly binds to NDRG2 in colorectal cancer cells. Subsequently, the wild type and the mutant 3′-UTR of NDRG2 were inserted into the dual-luciferase reporter vectors, which were designated as WT or MUT. For the luciferase assay, Lipofectamine 3000 Reagent (Invitrogen, USA) was employed to be cotransfected with the miR-483 mimic and the WT or MUT plasmid into VOLO cells. Then, the luciferase activity was measured on a dual-luciferase reporter assay system (Promega, USA).

2.9. Xenograft Tumor Formation Assay. Four-week old nude mice were purchased from Charles River Laboratories (Beijing, China). VOLO cells (5×10^6 cells) were subcutaneously injected into one side of the axillae of the nude mice. The length and the width of the xenograft tumor were evaluated and recorded every 3 days after completing the transplant tumor model. The volume of the xenografts was calculated as the square of length multiplied by the width divided by two. The experiment was terminated after culturing for 26 days, and the xenografts were incised. All animal experiments were performed in the animal laboratory center of Weifang People's Hospital and approved by the Animal Care and Use Committee of Weifang People's Hospital.

2.10. Statistical Analysis. All data are expressed as the means ± standard deviation (SD) of at least three independent experiments. Statistical analysis was performed using SPSS 16.0 software (IBM, Armonk, NY, USA). The differences between two or more groups were compared using Student's *t*-test or one-way ANOVA. The association between the expression of miR-483 and the overall survival for colorectal cancer patients were assessed by the Kaplan–Meier curve and log-rank test. Results were considered statistically significant if $P < 0.05$. Each experiment was repeated three times.

3. Results

3.1. Upregulation of MiR-483 Predicted Poor Prognosis of Colorectal Cancer. The mRNA level of miR-483 was calculated in 47 pairs of colorectal cancer and nonnecrotic colon tissues. As expected, the expression of miR-483 was higher in colorectal cancer tissues in comparison with corresponding nonnecrotic colon tissues ($P < 0.05$) (Figure 1(a)). In addition, the overexpression of miR-483 predicted poor 5-year survival in colorectal cancer ($P < 0.05$) (Figure 1(b)).

3.2. MiR-483 Promoted the Proliferation and Invasion in Colorectal Cancer Cells. The expression of miR-483 was assessed in two colorectal cancer cell lines (LOVO and SW480) and a normal colorectal epithelial cell line CCD-18Co. Similar with the findings in tissues, miR-483 was overexpressed in CCD-18Co cells compared with colorectal cancer cell lines LOVO ($P < 0.05$) and SW480 ($P < 0.05$) (Figure 2(a)). To explore the functions of miR-483 in colorectal cancer, the miR-483 mimic or the miR-483 inhibitor was transfected in LOVO cells to up- ($P < 0.01$) or down-regulate ($P < 0.05$) miR-483 (Figure 2(b)).

MTT assay revealed that the miR-483 mimic promoted cell proliferation ($P < 0.05$), while the cell proliferative ability was suppressed by the miR-483 inhibitor in LOVO cells ($P < 0.05$) (Figure 2(c)). Furthermore, transwell assay illuminated that the miR-483 mimic enhanced the cell invasive ability ($P < 0.01$) while the miR-483 inhibitor suppressed ($P < 0.05$) (Figure 2(d)). All the findings elucidated that miR-483 promoted the capacities of proliferation and invasion in colorectal cancer cell line LOVO.

3.3. MiR-483 Regulated the Expression of NDRG2 through Directly Binding to the 3′-UTR of NDRG2 mRNA. TargetScan predicted NDRG2 was a target gene of miR-483 and the binding site was located at 3′-UTR of NDRG2 mRNA. To validate miR-483 direct binding to the potential binding site of NDRG2, the binding sequences were mutated from 5′-AGGGCAGA-3′ to 5′-AGGCGUCA-3′ and then inserted into the luciferase vectors (Figure 3(a)). The luciferase reporter assay indicated that the luciferase activity of LOVO cells transfected with the wild-type NDRG2 3′-UTR was decreased by miR-483 mimic ($P < 0.05$), while the miR-483 mimic has no effect on the luciferase activity of cells transfected with mutant NDRG2 3′-UTR ($P < 0.05$) (Figure 3(b)). Furthermore, the mRNA levels of NDRG2 were measured when transfected with the miR-483 mimic or the miR-483 inhibitor in LOVO cells. As expected, the overexpression of miR-483 enhanced the mRNA level of NDRG2 ($P < 0.05$), while the knockdown of miR-483 inhibited the expression of NDRG2 in LOVO cells ($P < 0.05$) (Figure 3(c)). All the results illuminated that miR-483 regulated the expression of NDRG2 in colorectal cancer cell line LOVO.

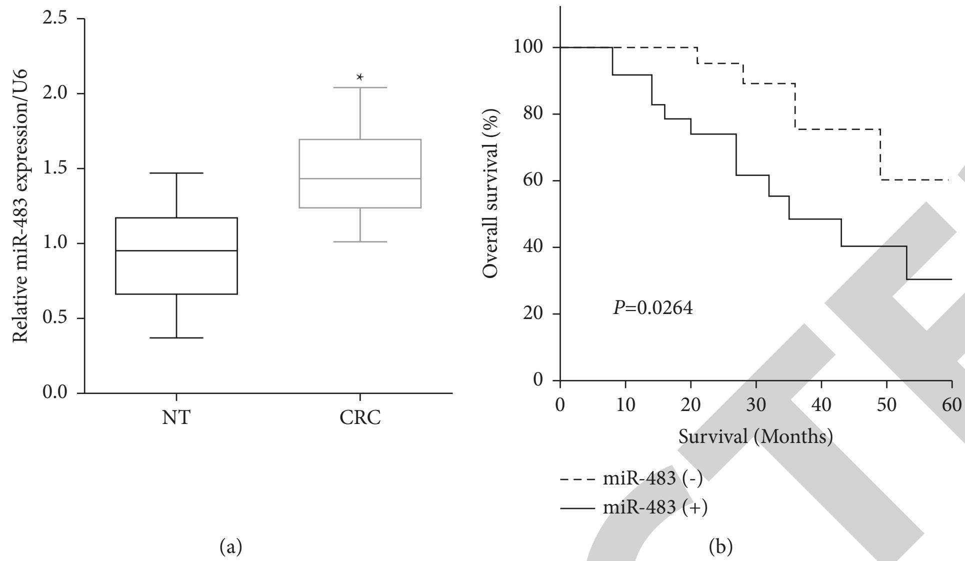

Figure 1: Upregulation of miR-483 predicted poor prognosis of colorectal cancer. (a) The expression of miR-483 was higher in colorectal cancer tissues than in the nonnecrotic colon tissues. (b) Overexpression of miR-483 predicted poor 5-year survival of colorectal cancer patients. $^*P < 0.05$. NT: normal tissues; CRC: colorectal cancer.

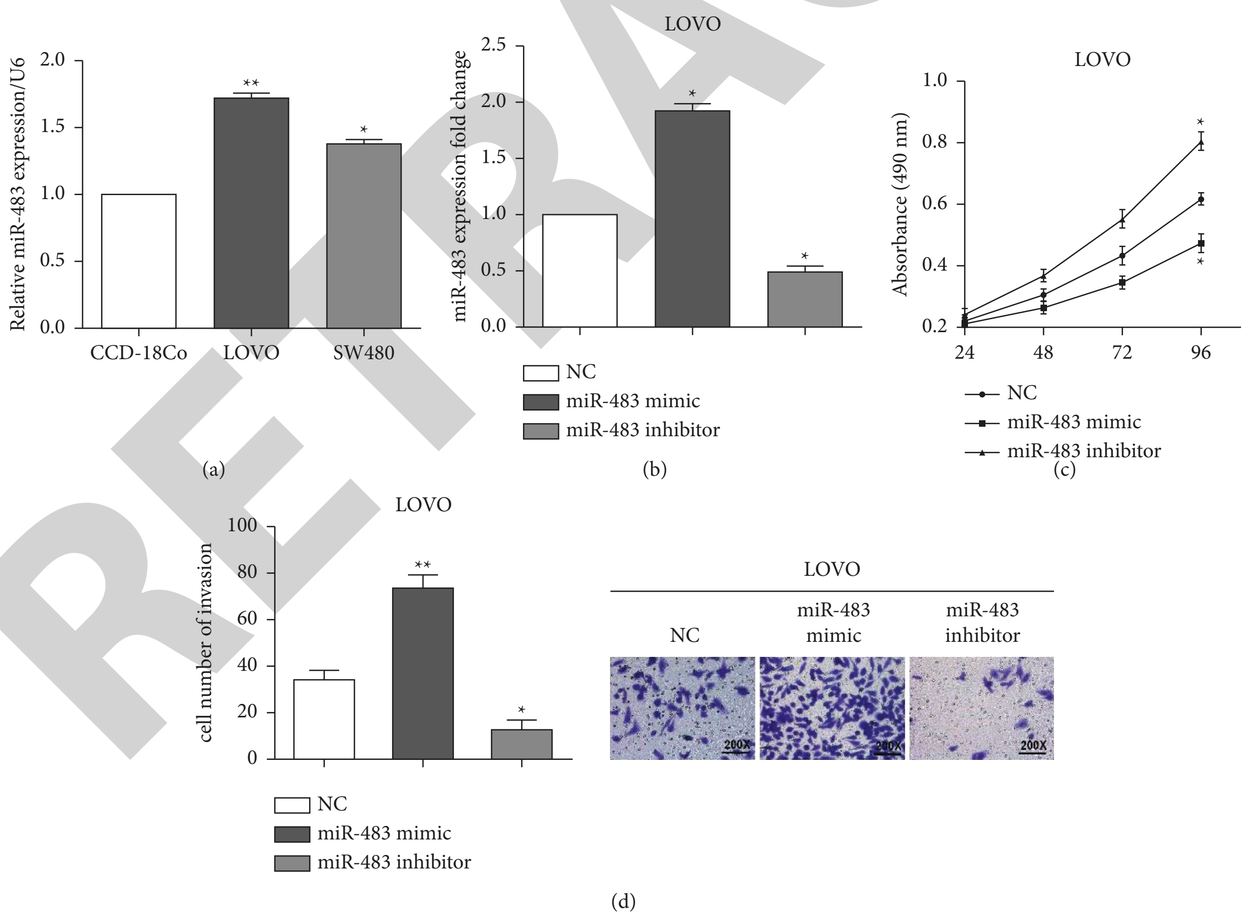

Figure 2: MiR-483 promoted the proliferation and invasion in colorectal cancer cells. (a) MiR-483 was overexpressed in CCD-18Co cells versus LOVO and SW480 cells. (b) The miR-483 mimic or the miR-483 inhibitor was transfected to up- or downregulate miR-483 in LOVO cells. (c) MTT assay revealed that the miR-483 mimic promoted the proliferation in LOVO cells. (d) The invasive ability was enhanced by the miR-483 mimic cell, while it was inhibited by the miR-483 inhibitor in LOVO cells. $^*P < 0.05$; $^{**}P < 0.01$.

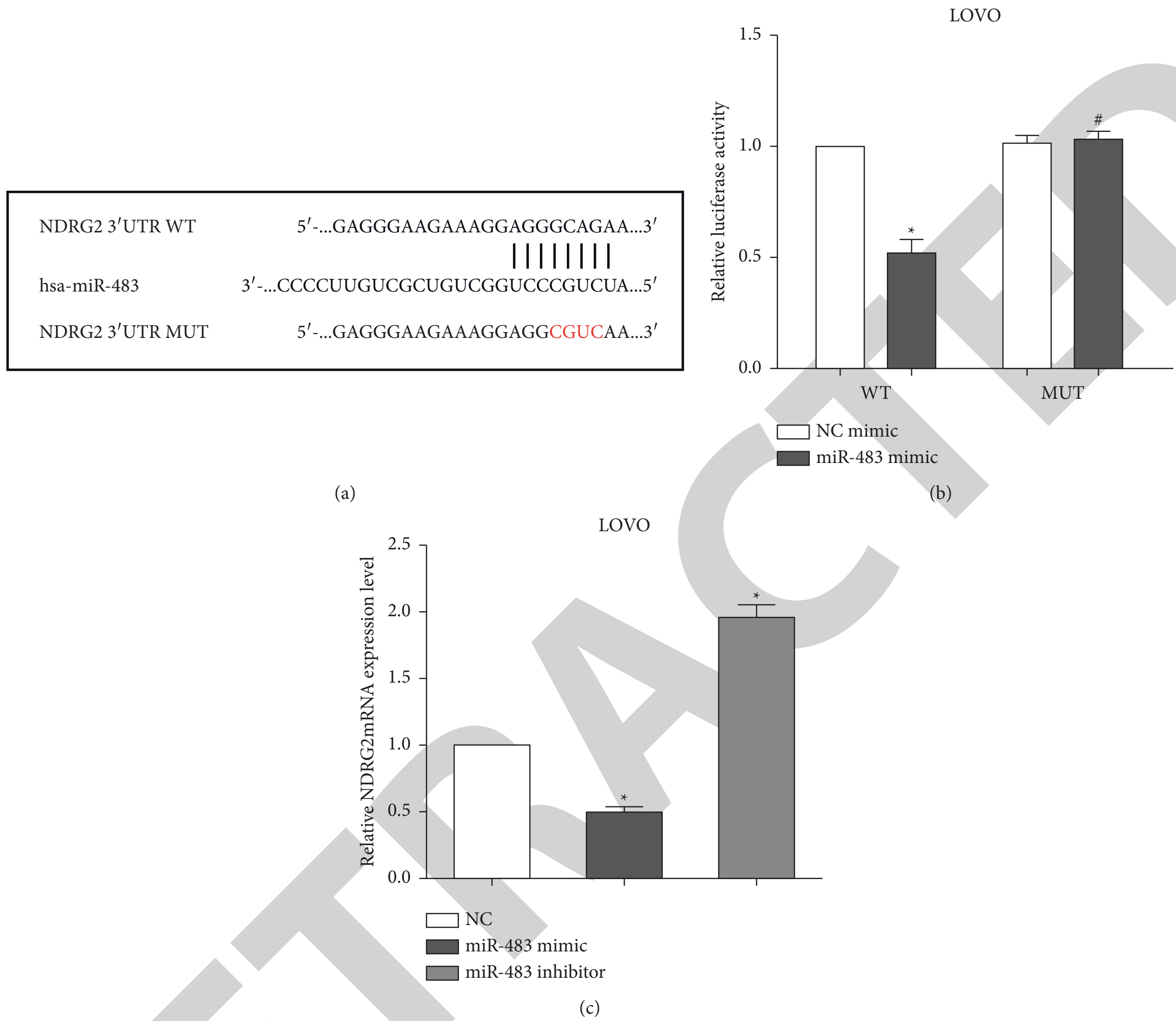

Figure 3: MiR-483 regulated the expression of NDRG2 through binding to NDRG2 mRNA 3′-UTR. (a) TargetScan predicted NDRG2 was a target gene of miR-483 and the binding site was located at the 3′-UTR of NDRG2 mRNA. (b) The luciferase reporter assay indicated that miR-483 directly targeted NDRG2 in LOVO cells. (c) Overexpression of miR-483 enhanced the mRNA level of NDRG2, while the knockdown of miR-483 inhibited the expression of NDRG2 in LOVO cells. $^*P < 0.05$; $^{\#}P < 0.05$.WT: wild type; MUT: mutant type.

3.4. MiR-483 Promoted the EMT and Activated the Phosphorylation of the PI3K/AKT Signaling Pathway. The relative mRNA level of NDRG2 was calculated, and it was found to be upregulated in nonnecrotic colon tissues in comparison with that of colorectal cancer tissues ($P < 0.05$) (Figure 4(a)). Also, the expression of NDRG2 was detected in normal colorectal epithelial cell line CCD-18Co and two human colorectal cancer cell lines LOVO and SW480. Not unfortunately, the expression of NDRG2 was lower in LOVO ($P < 0.05$) and SW480 ($P < 0.05$) cells than that in CCD-18Co cells (Figure 4(b)). Moreover, western blot was conducted to assess the expressions of EMT and PI3K pathway associated proteins in LOVO cells. We discovered that the miR-483 mimic promoted the EMT via NDRG2 by suppressing the expression of NDRG2 and N-cadherin while improving the expression of E-cadherin in LOVO cells (Figure 4(c)). Phosphorylation of PI3K and AKT promoted cell growth, proliferation, and survival [22]. As we expected, the overexpression of miR-483 enhanced the expression of p-PI3K and p-AKT in LOVO cells (Figure 4(d)), which elucidated that miR-483 activated the phosphorylation of the PI3K/AKT signaling pathway.

3.5. MiR-483 Enhanced the Xenograft Growth In Vivo. LOVO cells stably transfected with the miR-483 mimic, or control plasmid was applied to inject into the nude mice subcutaneously. The xenograft tumor volume was calculated every 3 days, and the group of transfecting the miR-483 mimic had a higher growth rate than the control group (Figure 5(a)). After dissecting the nude mice, the xenograft tumors were collected and the volumes were calculated.

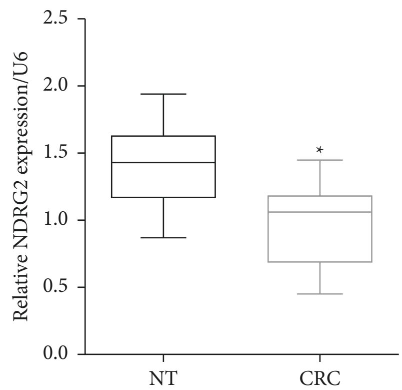

(a)

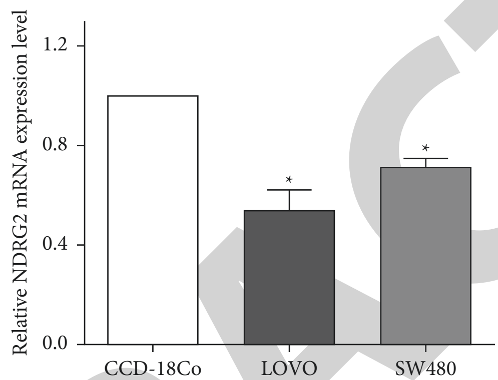

(b)

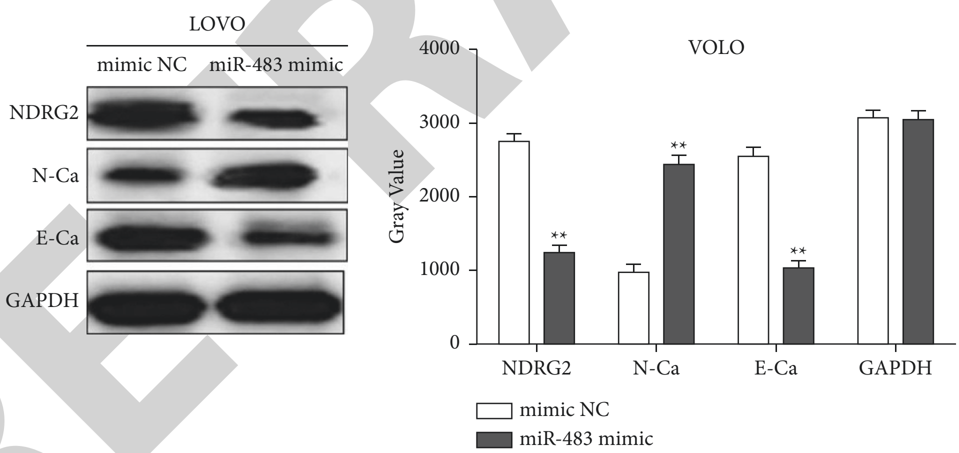

(c)

Figure 4: Continued.

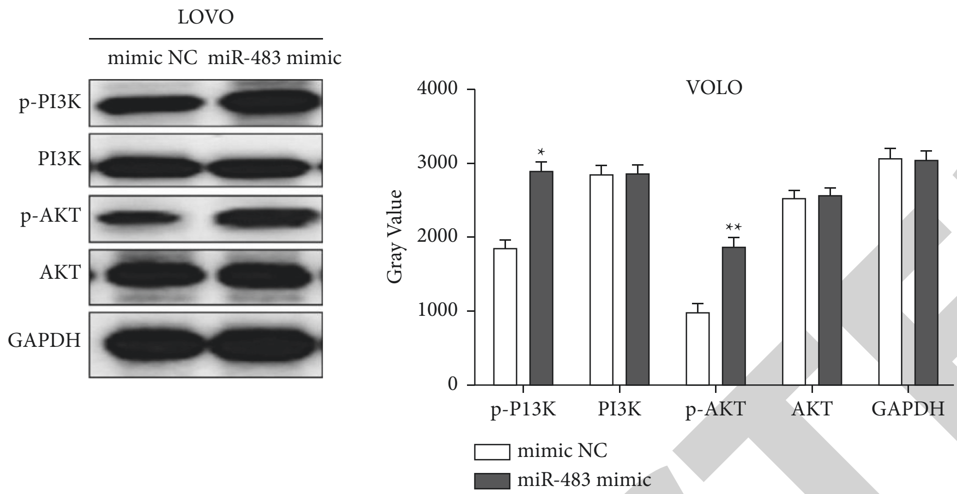

(d)

Figure 4: MiR-483 promoted the EMT and activated the phosphorylation of the PI3K/AKT signaling pathway. (a) The mRNA level of NDRG2 in nonnecrotic colon tissues was higher than that in colorectal cancer tissues. (b) NDRG2 was lowly expressed in colorectal cancer cells than normal cells. (c) Western blot illuminated that miR-483 promoted the EMT through NDRG2. (d) MiR-483 activated the PI3K/AKT pathway. $^{*}P < 0.05$. NT: normal tissues; CRC: colorectal cancer; N-Ca : N-cadherin; E-Ca : E-cadherin; and GAPDH: glyceraldehyde-phosphate dehydrogenase.

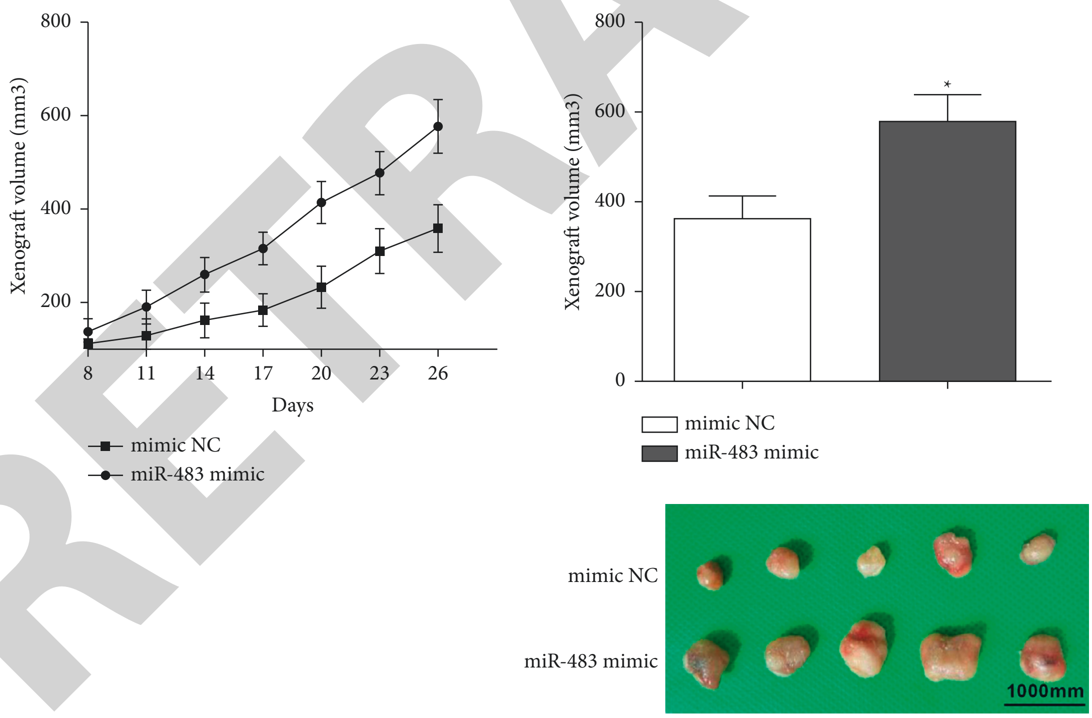

(a) (b)

Figure 5: MiR-483 enhanced the growth of xenograft in vivo. (a) MiR-483 promoted colorectal cancer growth in vivo. (b) The tumor volume of cells overexpressing miR-483 was bigger than the control group. $^{*}P < 0.05$.

Also, we discovered the tumor volumes of cells overexpressing miR-483 was bigger than that of the control group, which indicated that miR-483 mimic promoted the growth of colorectal cancer xenograft ($P < 0.05$) (Figure 5(b)).

4. Discussion

Colorectal cancer is the third frequent tumor and one of the leading causes of cancer-related death worldwide [1, 2]. The morbidity and mortality of colorectal cancer caused by metastasis are increasing rapidly [3, 23]. Therefore, it is urgent to explore the early diagnosis and metastasis of newly biomarkers for colorectal cancer.

MiRNAs repressed the protein degradation and translation through directly binding to the 3′-UTR of target mRNA at the posttranscriptional level [24]. MiR-483 which acted as a prognostic biomarker was upregulated in esophageal squamous cell carcinoma [25]. Consistent with the findings, we discovered that miR-483 was upregulated in colorectal cancer tissues in comparison with the nonnecrotic colon tissues. Moreover, miR-483 may act as a prognosis marker and the overexpression of miR-483 predicted a poor 5-year overall survival of colorectal cancer patients, which was the first time to propose the association between miR-483 and the survival of CRC. Furthermore, miR-483 played an oncogenic role and promoted cell proliferation and migration in esophageal squamous cell carcinoma [26]. In adenocarcinoma, Song et al. indicated that miR-483 promoted cell invasion and the EMT [27]. Our results were consistent with all the findings that the overexpression of miR-483 in colorectal cancer promoted cell proliferation and invasion, while the reverse was downregulation. However, miR-483 served a tumor suppressive role in glioma [28], and we speculated that miR-483 has a tissue-specific expression. In addition, we first proposed that miR-483 promoted the growth of colorectal cancer cell xenografts.

NDRG2 is a gene with promoter hypermethylation and is a newly identified differentiation-related gene [15, 16]. In esophageal cancer, NDRG2 inhibited cell proliferation, migration, invasion, and the EMT [17]. NDRG2 was a target gene of several miRNAs including miR-141b, miR-375, miR-301, and miR-650 [29–32]. Consistent with the findings of Claire Agosta in adrenocortical cancer [21], we discovered that NDRG2 was a target gene of miR-483 and miR-483 mediated the expression of NDRG2 in colorectal cancer. The expression of NDRG2 was lower in colorectal cancer tissues than in nonnecrotic colon tissues. Moreover, miR-483 promoted colorectal cancer cell proliferation, invasion, and EMT through targeting NDRG2 and activated the PI3K/AKT pathway.

5. Conclusions

MiR-483 promoted colorectal cancer cell proliferation, invasion, and EMT through directly targeting NDRG2 and activated the PI3K/AKT pathway. In addition, the overexpression of miR-483 promoted the growth of LOVO cells xenograft. Our data suggest that miR-483 is a prognostic predictor and can serve as a potential therapeutic target of colorectal cancer.

Data Availability

Data supporting the findings of this study are available on reasonable request from the corresponding author.

Conflicts of Interest

The authors have no conflicts of interest to declare.

References

[1] H. Brenner, M. Kloor, and C. P. Pox, "Colorectal cancer," *The Lancet*, vol. 383, no. 9927, pp. 1490–1502, 2014.

[2] J. Ferlay, I. Soerjomataram, R. Dikshit et al., "Cancer incidence and mortality worldwide: sources, methods and major patterns in GLOBOCAN 2012," *International Journal of Cancer*, vol. 136, no. 5, pp. E359–E386, 2015.

[3] M. Worni, K. N. Shah, and B. M. Clary, "Colorectal cancer with potentially resectable hepatic metastases: optimizing treatment," *Current Oncology Reports*, vol. 16, no. 10, p. 407, 2014.

[4] E. C. Lai, "Micro RNAs are complementary to 3′ UTR sequence motifs that mediate negative post-transcriptional regulation," *Nature Genetics*, vol. 30, no. 4, pp. 363-364, 2002.

[5] F. Xiao, Z. Zuo, G. Cai, S. Kang, X. Gao, and T. Li, "miRecords: an integrated resource for microRNA-target interactions," *Nucleic Acids Research*, vol. 37, no. Database, pp. D105–D110, 2009.

[6] B. D. Adams, A. L. Kasinski, and F. J. Slack, "Aberrant regulation and function of microRNAs in cancer," *Current Biology*, vol. 24, no. 16, pp. R762–R776, 2014.

[7] R. Rupaimoole, G. A. Calin, G. Lopez-Berestein, and A. K. Sood, "miRNA deregulation in cancer cells and the tumor microenvironment," *Cancer Discovery*, vol. 6, no. 3, pp. 235–246, 2016.

[8] Y. Zhu, Q. Peng, Y. Lin et al., "Identification of biomarker microRNAs for predicting the response of colorectal cancer to neoadjuvant chemoradiotherapy based on microRNA regulatory network," *Oncotarget*, vol. 8, no. 2, pp. 2233–2248, 2017.

[9] K. Cui, H. Zhang, and G. Z. Wang, "MiR-483 suppresses cell proliferation and promotes cell apoptosis by targeting SOX3 in breast cancer," *European Review for Medical and Pharmacological Sciences*, vol. 23, pp. 2069–2074, 2019.

[10] Y. Tian, M. Yan, J. Zheng et al., "MiR-483-5p decreases the radiosensitivity of nasopharyngeal carcinoma cells by targeting DAPK1," *Laboratory Investigation*, vol. 99, 2019.

[11] X. Zhang, L. Liu, X. Deng et al., "MicroRNA 483-3p targets Pard3 to potentiate TGF-β1-induced cell migration, invasion, and epithelial-mesenchymal transition in anaplastic thyroid cancer cells," *Oncogene*, vol. 38, no. 5, pp. 699–715, 2019.

[12] Z.-G. Yang, X.-D. Ma, Z.-H. He, and Y.-x. Guo, "miR-483-5p promotes prostate cancer cell proliferation and invasion by targeting RBM5," *International Braz J Urol*, vol. 43, no. 6, pp. 1060–1067, 2017.

[13] S. Tang, Y. Chen, S. Feng et al., "MiR-483-5p promotes IGF-II transcription and is associated with poor prognosis of hepatocellular carcinoma," *Oncotarget*, vol. 8, no. 59, pp. 99871–99888, 2017.

[14] H. Cui, Y. Liu, J. Jiang et al., "IGF2-derived miR-483 mediated oncofunction by suppressing DLC-1 and associated with colorectal cancer," *Oncotarget*, vol. 7, no. 30, pp. 48456–48466, 2016.

[15] V. Melotte, X. Qu, M. Ongenaert et al., "The N-myc downstream regulated gene (NDRG) family: diverse functions, multiple applications," *The FASEB Journal*, vol. 24, no. 11, pp. 4153–4166, 2010.

[16] Y. Deng, L. Yao, L. Chau et al., "N-Myc downstream-regulated gene 2(NDRG2) inhibits glioblastoma cell proliferation," *International Journal of Cancer*, vol. 106, no. 3, pp. 342–347, 2003.

[17] C.-L. Yang, X.-L. Zheng, K. Ye et al., "NDRG2 suppresses proliferation, migration, invasion and epithelial-

Hindawi
Journal of Healthcare Engineering
Volume 2022, Article ID 9188553, 11 pages
https://doi.org/10.1155/2022/9188553

Research Article

Data Mining and Meta-Analysis of Psoriasis Based on Association Rules

Jiarui Ou[1] and Jianglin Zhang[2]

[1]*Department of Detmatology Xiangya Hospital, Central South University, Changsha, Hunan 410008, China*
[2]*Department of Detmatology, Shenzhen People's Hospital (The Second Clinical Medical College,Jinan University; The First Affiliated Hospital,Southern University of Science and Technology), Shenzhen, Guangdong 518020, China*

Correspondence should be addressed to Jianglin Zhang; zhang.jianglin@szhospital.com

Received 4 November 2021; Accepted 22 December 2021; Published 27 January 2022

Academic Editor: Enas Abdulhay

Psoriasis is a common chronic and recurrent disease in dermatology, which has a great impact on the physical and mental health of patients. Meta-analysis can evaluate the effectiveness and safety of defubao in the treatment of psoriasis vulgaris. This article observes psoriasis skin lesions treated with topical defubao and the changes in blood vessels under dermoscopy. Considering that the Apriori algorithm and the existing improved algorithm have the problems of ignoring the weight and repeatedly scanning the database, this paper proposes a matrix association rule method based on random forest weighting. This method uses the random forest algorithm to assign weights to each item in the data set, and introduces matrix theory to convert the transaction data set into a matrix form and store it, thereby improving operating efficiency. This article included 11 studies, of which 7 studies used the indicator "Researcher's Overall Assessment" (IGA) to evaluate the efficacy, 5 studies used the "Patient Overall Assessment" (PGA) as the efficacy evaluation index, and Loss Area and Severity Index (PASI) was used as an observation index to evaluate the efficacy. Seven studies conducted safety comparisons. In this paper, IGA and PGA were used as evaluation indicators. The treatment effect of the defubao group was better than the calcipotriol group and the betamethasone group. The differences were statistically significant. The effect of the Fubao treatment for 8 weeks is significantly better than that of 4 weeks and 2 weeks, and the differences are statistically different. Using PASI as the evaluation index, a descriptive study was carried out, and it was found that after 4 weeks of treatment for psoriasis vulgaris, the average PASI reduction rate of patients was higher than that of the calcipotriol group and the betamethasone group. The safety evaluation found that after 8 weeks of treatment, the incidence of adverse events in the defubao group was significantly lower than that in the calcipotriol group.

1. Introduction

How to discover these hidden and valuable relationships has always been a research hotspot in the field of data mining [1, 2]. Among them, data mining technology refers to a large number of data sets, through association rule mining, classification, aggregation and outlier detection and other methods, to find the internal relationship between the data in the data set without obvious characteristics, so as to guide people in subsequent production activities. For example, in the typical case of retail data on beer and diapers, if the decision-makers did not use data mining technology to effectively analyze the retail data, how could they find that people who bought beer would also buy diapers? Among them, in the case of beer and diapers, association rules technology is used, which is a very practical data mining technology [3–5]. This mining technology has been widely used in many fields such as store layout, consumer behavior, accident data analysis, and fraud detection [6, 7].

Psoriasis, known as "white boil" in traditional Chinese medicine, is a common chronic, inflammatory, and recurrent skin disease [8]. It is characterized by red papules or plaques with multiple layers of silvery white scales covering the limbs. Extensive side, scalp and back, severe skin lesions can spread all over the body, accompanied by varying degrees of itching [9, 10]. The disease can be seen in all races, and the prevalence varies among different regions and races. Psoriasis is clinically divided into 4 types, including vulgaris, erythroderma, pustular, and articular types, among which vulgaris is the most common, accounting for more than 97% of all patients [11]. Common TCM syndrome differentiation mainly includes blood syndrome, blood heat syndrome, blood dryness syndrome, blood deficiency syndrome and blood stasis syndrome [12]. However, psoriasis persists for a long time and the pathogenesis is complicated. Only four types cannot meet the complex and changeable clinical syndrome differentiation needs of psoriasis vulgaris. At present, our country is in a period of social transformation and rapid economic growth, and the subsequent air pollution, water pollution and increasing living pressure have laid hidden dangers for the occurrence of this disease [13]. Therefore, the need for research and treatment of this disease is more urgent than in any previous period. Modern medicine has been continuously exploring and researching the disease, and there have been a lot of research results. However, the etiology and pathogenesis of psoriasis are still unclear. Its treatment has large side effects and lacks safe, effective and satisfactory long-term curative effects. This article aims to systematically collect patients' symptoms, related factors, and analyze the distribution characteristics of pathogenic factors, combination characteristics, distribution of related factors and typical symptoms caused by pathogenic factors as comprehensively as possible, and discuss the differentiation of psoriasis vulgaris [14]. Element characteristics, using the simple, flexible, accurate, and comprehensive characteristics of syndrome elements to describe the pathogenesis of psoriasis vulgaris, provide a basis for more accurate and effective differentiation and treatment of psoriasis vulgaris [15]. In this way, the complex pathogenesis is divided into several syndrome differentiation elements of the combination of syndromes, and the precise differentiation of syndromes can be used to guide the treatment more accurately, so as to be beneficial to more in-depth research on the disease and to further improve the clinical efficacy of the disease. At present, the common indicators for evaluating the severity of psoriasis include skin lesion area and severity index, the researcher's overall assessment, the patient's overall assessment, and the target skin lesion score. The first three indicators are to observe and evaluate the overall severity of the patient. Target lesion scores are widely used to assess the severity of specific lesions in psoriasis. It includes erythema, scale, and infiltration. TLS observes specific local skin lesions. Therefore, when it is necessary to combine auxiliary examination methods to dynamically observe and record changes in diseases or skin lesions, TLS is more intuitive and comparative.

Calcipotriol has been widely used in the treatment of psoriasis, and its efficacy and safety have been recognized by doctors and patients. Local topical glucocorticoids are also the first choice for the treatment of psoriasis. Before the advent of defubao, the effect of using glucocorticoid in the morning and calcipotriol at night was significantly better than using calcipotriol or glucocorticoid alone twice a day. Topical calcipotriol and glucocorticoids have been used as classic first-line drugs for the treatment of psoriasis for several years. Calcipotriol is a vitamin D derivative, which can regulate the proliferation and differentiation of epidermal cells, as well as the production and release of proinflammatory cytokines. Local topical glucocorticoid therapy will have a wide range of biological effects, such as inhibiting the production and migration of inflammatory cells, regulating the release of cytokines (such as IL-2) and chemokines, and regulating DNA synthesis. However, external hormones alone have side effects, including skin atrophy, telangiectasia, and uneven pigmentation. Defubao is a compound preparation of betamethasone and calcipotriol, containing calcipotriol 50 μg/g and betamethasone dipropionate 0.5 mg/g. Defubao was approved by the State Food and Drug Administration for the treatment of psoriasis vulgaris. In theory, it has both calcipotriol's prokeratinocyte differentiation effect and betamethasone anti-inflammatory effect, which combines the advantages of the two drugs and complements the side effects of the two drugs. However, the effectiveness and safety of defubao still need strong evidence-based medical evidence to objectively evaluate.

2. Related Work

Many scholars have proposed binding and nonbinding association rules [16–18]. For example, they add restrictions on the number of transactions and transaction time to each item in the database to reduce the number of association rules, generate only interesting rules, generate only nonredundant rules, or use sampling to display association rules, or generate only those that meet certain requirements [19].

Relevant scholars have adopted the maximum utility value strategy, and proposed the LQS-tree storage structure, item connection and sequence connection to expand the sequence, and also provided width pruning and deep pruning to prune undesirable sequences [20]. Related scholars have proposed a four-stage MapReduce framework, which is completely based on the famous Spark platform for mining HUSP [21]. The framework provides more efficient and faster mining performance for processing large data sets. It includes four stages: initialization, mining, update, and generation. It is based on the MapReduce framework running on the Spark platform to process large data sets.

At present, most of the algorithms are mainly focused on HUSP mining in static databases, without considering streaming data. In streaming data, unlimited data appears continuously and at a high speed, which will increase the difficulty of mining. Based on this, related scholars have proposed a HUSP-UT algorithm, which is based on a data stream tree structure [22, 23]. A large number of experiments on real data sets show that HUSP-UT can effectively identify high-efficiency sequences. In addition, the article also proposes a new upper bound-sequence expansion utility. A variety of pruning strategies are further adopted [24].

In the real world, the time interval between elements is also very important. However, the existing HUSP mining algorithms cannot extract sequential patterns of this nature. The researchers took into account the utility of the elements and the time interval, and proposed a sequential pattern mining algorithm with the nature of time interval [25, 26]. In addition, four time constraints are used to process the time intervals in the sequence to extract more meaningful patterns. In addition, two upper bounds of utility are proposed, namely the upper bound of residual utility (RUUB) and the upper bound of co-occurrence utility (CUUB) to prune hopeless candidates. Under the assumption that multiple events can occur simultaneously and persist for different periods of time, considering the utility of events, a pattern mining algorithm based on high-efficiency intervals, HUIPMiner, is proposed [27, 28].

Relevant scholars believe that psoriasis is related to the five internal organs, and is most closely related to the liver [29]. The main factors are that the liver controls drainage, the blood storage in the liver, and the pathological interaction between the liver and other internal organs. Scholars used a multi-center randomized controlled method for clinical observation [30]. The treatment group was mainly given the prescription of cooling blood and detoxification, the liver-clearing and purging gunpowder was used for the blood-heat syndrome, the liver-releasing and qi-regulating medicine was used for the blood stasis syndrome, and the liver-softening detoxification was used for the blood-dry syndrome [31–33]. All were treated with medicine that was soothing to the liver and relieved depression. The improvement of DLQI scores in the treatment group was better than those in the control group. Therefore, the treatment of psoriasis from the liver theory based on Liangxue Jiedu Decoction can effectively improve the degree of skin lesions, TCM syndromes and quality of life [34, 35].

The TCM syndrome differentiation type included in the literature lacks objective and unified standardized standards. The outcome index adopts the comprehensive curative effect evaluation index, and the improvement of symptoms is based on the subjective judgment of the investigator, which makes the judgment of curative effect lack objectivity. In addition, in the trial design, most of the literature lacks long-term follow-up, which affects the combined analysis of the long-term efficacy of external use of traditional Chinese medicine in the treatment of psoriasis vulgaris. This may be related to the long treatment period of traditional Chinese medicine and the relatively difficult follow-up. A small part of the literature even lacks the description of the adverse reaction, and most of the literature lacks objective basis when describing the adverse reaction, which reduces the completeness of the data.

3. Method

3.1. Mining Based on Apriori Text Association Rules. The following introduces the related concepts of Apriori and the main algorithm process in two parts.

(1) Support: For a given data set, how often certain features are found. Support is defined as follows:

$$\text{support}(A, B) = P(A \subseteq B) \cup P(A \cap B). \tag{1}$$

Among them, A and B are itemsets.

(2) Confidence degree: It reflects the certainty of the reflection rules on the basis of frequent itemsets. The confidence is defined as follows:

$$\text{Confidence}(A, B) = P(A \cup B) \cap P(A \cap B). \tag{2}$$

(3) Frequent itemsets: Frequent itemsets find the set of data that is not less than the minimum support degree.

(4) Strong association rules: On the basis of frequent itemsets, strong association rules also meet artificially set thresholds.

Apriori's algorithm uses the candidate function to generate frequent itemsets. The function first counts the number of occurrences of each element in the itemsets (also known as support count), and finds the frequent itemsets. Then the function rescans the data set, using the iterative layer-by-layer method until there is no maximum itemset generated. The calculation process of Apriori is shown in Figure 1.

3.2. Diagnostic Model Construction Method. RNN and DBN can also achieve better experimental results in practical applications. However, these two methods still have problems in processing text data. In view of the shortcomings of the above methods, CNN, as a typical neural network, can solve the above problems well. As a feedforward network, it has outstanding performance in reducing weights and computational complexity.

The input data has a certain format, and the image itself is composed of multiple pixels, so it has certain regularity. For text data, the converted word vector is generally used as input data.

To extract the features of the input data $x(i)$, the discrete convolution formula is

$$y(n) = \prod_{i=0}^{\infty} [h(n-i+1) \bullet x(i+1)]. \tag{3}$$

Among them, $h(n-i)$ is the convolution kernel.

A filter is also called a convolution kernel. Assuming that the length of the input data is n and the size of the convolution kernel is m, the feature length after the convolution operation is $n-m+1$. However, this situation will reduce the length of the feature. CNN adopts an expansion method, that is, filling the boundary of the input data to prevent problems caused by size changes.

The feature matrix obtained by convolution has a relatively large dimension and cannot accurately describe data features. After pooling, more accurate features can be obtained, which is convenient for subsequent work.

TextCNN optimizes the standard CNN convolutional layer structure, which uses simple models to achieve excellent results in multiple data sets, achieves end-to-end classification effects, and makes it better to process text content. Compared with CNN, the network structure is simple, and the input data is one-dimensional data. The biggest feature of TextCNN is to classify text. The data are mapped to a low-dimensional space for encoding through

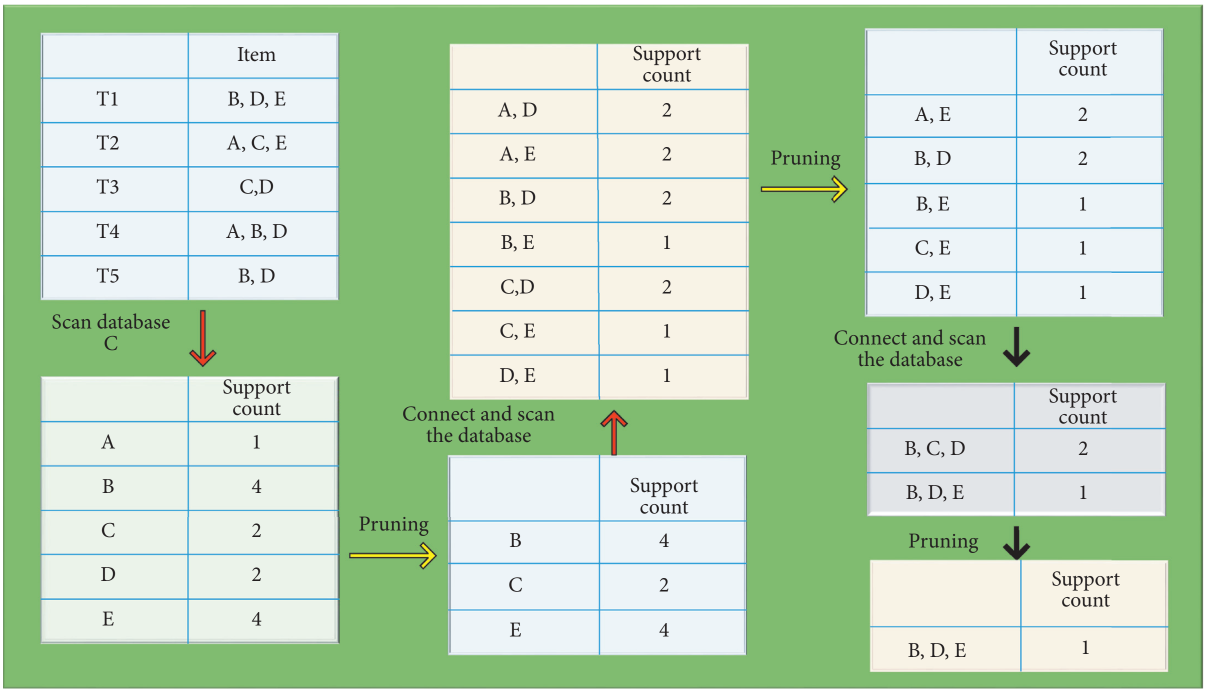

Figure 1: Apriori calculation process.

the feature extractor of the embedding layer. Figure 2 shows the architecture of the psoriasis data mining system based on association rules.

3.3. Random Forest Algorithm.

The algorithm principle is as follows:

(1) The sample is replaced with n samples randomly selected as the training set.

(2) Use the training set to construct a decision tree, and randomly extract features during the construction process.

(3) Repeat the above process to generate multiple decision trees.

(4) Integrate all decision trees to predict new data (the majority vote is generally used for classification).

The random forest algorithm can effectively weigh each feature in the data set. The main idea is to calculate the average contribution of each feature in the random forest for all trees in the random forest. The Gini index is commonly used as a measurement indicator. The process of random forest algorithm is shown in Figure 3.

Here, VIM is used for variable importance measures, and GI is used for Gini index. Taking a data set containing n features as an example, the calculation method of the j-th feature Gini index score $\mathrm{VIM}_j(\mathrm{Gini})$ is:

$$GI_m = \prod_{k=0}^{K}\prod_{k'=1}^{K}\left(p_{mk}p_{mk'}\right), \tag{4}$$

where K represents the number of categories included, and P_{mk} represents the probability of randomly sampling two samples of different categories from node m. The importance of feature X_j to node m is:

$$\mathrm{VIM}_{jm}^{Gini} + GI_l = 2GI_r + GI_m. \tag{5}$$

Here, GI_l and GI_r, respectively, represent the Gini index of the new node after branching. If the node of feature X_j in decision tree i belongs to set M, then the importance of X_j to the i-th tree is:

$$\begin{aligned}\mathrm{VIM}_{ij}^{Gini} &= \prod_{m \longrightarrow M}\left(\mathrm{VIM}_{jm}^{Gini} + GI_l + GI_r + GI_m\right),\\ \mathrm{VIM}_{j}^{Gini} &= \prod_{i=0}^{n-1}\left(\mathrm{VIM}_{ij}^{Gini} - GI_l - GI_r - GI_m\right).\end{aligned} \tag{6}$$

3.4. Design of Matrix Association Rule Algorithm Based on Random Forest Weight.

The traditional Apriori algorithm and the existing improved algorithm have problems such as low operating efficiency, and many redundant rules. In response to these problems, this section combines the random forest algorithm with matrix theory, proposes a matrix association rule algorithm based on random forest weights, and designs and implements related comparative experiments.

Due to the introduction of weights, the traditional support and confidence are no longer applicable. In addition, the transformed matrix needs to be compressed according to related properties to further obtain frequent itemsets. Therefore, this paper defines the weighted support and weighted confidence, and provides related definitions and proofs for matrix compression.

$W(X)$ is recorded as the weight of item set X, which represents the sum of the weights of all items in item set X:

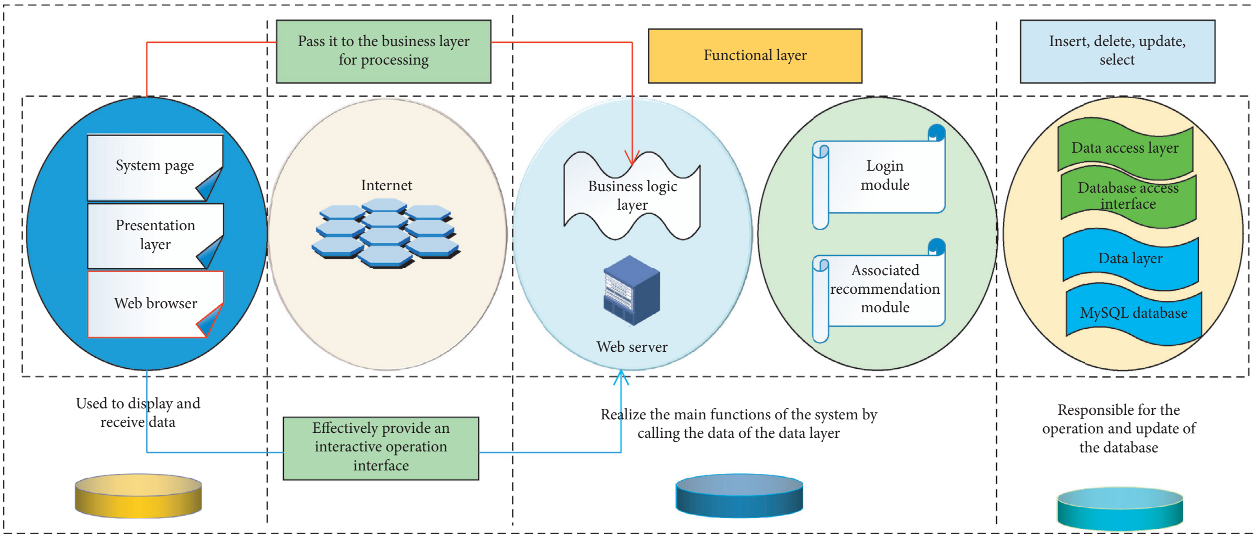

Figure 2: Architecture of psoriasis data mining system based on association rules.

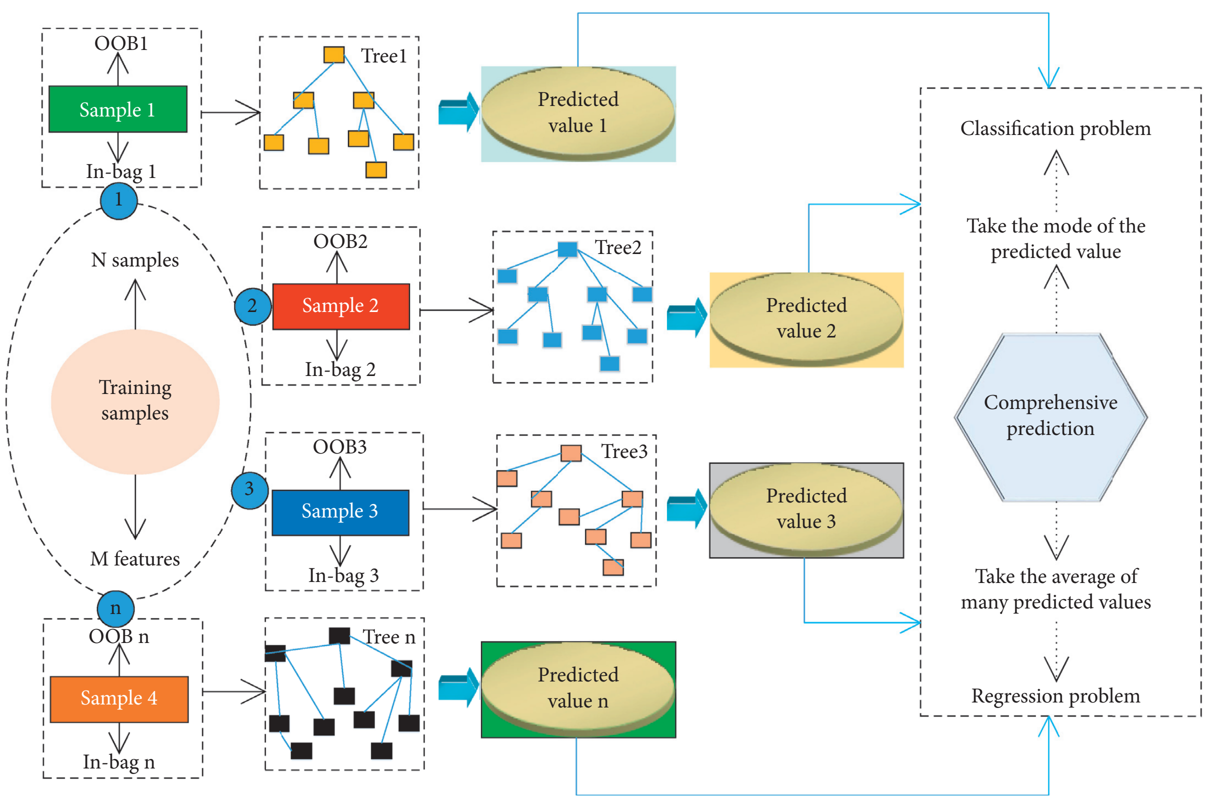

Figure 3: Random forest algorithm process.

$$W(X) = \sum_{i,I(X)} \left[W(i_j) + GI_l + GI_r + GI_m\right] \Big| \prod_{i,I(X)} W(i_j). \quad (7)$$

$WSup(X)$ is recorded as the weighted support of item set X:

$$WSup(X) = W(X) \bullet W(X) \bullet Sup(X). \quad (8)$$

If $WSup(X) > \text{minsup}$ (customized minimum weighted support), then the item set X is called a weighted frequent set. The weighted confidence of the association rule X-Y is:

$$WConf(X \mapsto Y) = WSup(X \cap Y) | WSup(X \cup Y). \quad (9)$$

Suppose there is a transaction data set $D = \{t1, t2, t3, t4, t5\}$, and its corresponding item set is I = {I1, I2, I3, I4, I5}. First, we scan the transaction data set D, and obtain the weight of each feature through the above random forest method. The conversion method is, if the j-th item exists in the i-th transaction, we set the value of the i-th row and the j-th column of the matrix to 1, otherwise set its value to 0. The transformed transaction matrix D1 is shown in Table 1.

Table 1: Transaction matrix D1.

	I1	I2	I3	I4	I5
T1	1	2	1	2	1
T2	2	1	1	1	2
T3	2	1	1	2	1
T4	1	2	2	1	2
T5	1	2	2	1	1

On the basis of the converted matrix, we add two new rows Sup and WSup, and add a new column sum_c, where sum_c is used to record the total number of items contained in each transaction, and Sup and WSup are used to record the support of different items, respectively.

We set the minimum weighted support min_wsup, compare the support number of each item recorded in the last row, if the support number of an item is not less than min_sup, it will be recorded as frequent 1 item set, otherwise the corresponding column will be deleted. If the value corresponding to an element is 0, we delete the corresponding row to obtain a new transaction matrix.

This process is repeated all the time, resulting in frequent k itemsets ($k \geq 2$). We delete the matrix column corresponding to the item Ij that appears less than k in the frequent $k-1$ item set and recalculate the sum_c column of the matrix. According to property 2, if the value of an element is less than k, we delete the corresponding row of the element in the matrix. If the value of an element is less than min_sup, we delete the column corresponding to the element.

3.5. Statistical Processing. RevMan 5.3 software was used for meta-analysis of the data. First, X2 is used to evaluate the heterogeneity between similar studies. If $P \geq 0.1$ and $I2 \leq 50\%$, it means that there is homogeneity between the studies, and the fixed effects model is used for meta-analysis; if $P < 0.05$, $I2 > 75\%$, it is considered that there is heterogeneity between the studies and the heterogeneity should be analyzed. After subgroup analysis is conducted according to the research design and different treatment options, and after eliminating the problems of the quality of the research design and different treatment options, the random effects model can be used to combine the effect size, and the research results can be explained carefully. Sensitivity analysis is performed on the heterogeneity caused by different research methods, and different model calculations are performed to evaluate the stability of the meta-analysis results. The outcome variables of this study are all two-category count data, and the odds ratio and 95% confidence interval are used as the analysis statistics. For those with insufficient data in clinical trials, only descriptive analysis will be performed.

4. Results and Discussion

4.1. Effectiveness Analysis. There are 4 randomized trials to evaluate and compare the effectiveness of defubao and betamethasone in the treatment of psoriasis vulgaris through IGA indicators. According to the course of treatment, they are divided into 3 subgroups: treatment for 2 weeks, treatment for 4 weeks, and treatment for 8 weeks. After 2, 4, and 8 weeks of treatment, the proportion of patients in the defubao group whose IGA assessment changed to "regression of skin lesions" or "very mild skin lesions" was significantly higher than that of the betamethasone group. The group had no heterogeneity in each outcome index, so fixed effects models were used for meta-analysis. The results showed that whether the treatment course was 2 weeks or 8 weeks, the treatment effect of defubao was significantly better than that of betamethasone, and the difference was statistically significant. The IGA used the IGA as an indicator to evaluate the asymmetry of the funnel chart between the defubao group and the betamethasone group at 8 weeks, and there is a publication offset in the study, as shown in Figure 4. However, in the subgroup comparing the efficacy of 4 weeks, the Cochrane Q analysis suggests that the combined data of the three groups are significantly heterogeneous, so the 4-week period is valid. The conclusions reached suggest that after 4 weeks of treatment, the treatment effect of the defubao group is better than that of the betamethasone group.

Three trials compared the effectiveness of defubao and calcipotriol (1 time/day) using IGA as an observation indicator. According to the different treatment time, they are divided into 3 subgroups and compared separately. The difference in curative effect of treatment for 2 weeks, treatment for 4 weeks, and treatment for 8 weeks is mainly compared. The 2-week curative effect subgroup and the 8-week curative effect subgroup, respectively. A fixed effects model was used for data analysis. As shown in Figure 5, the funnel graph is asymmetric, and the research has a publication offset. There is significant heterogeneity in the three groups of data compared between the four-week efficacy subgroups, and the random effects model is selected for data analysis. The results showed that the treatment with defubao was applied in 2 weeks [OR = 5.49, 95%CI (4.27, 7.05), $P < 0.001$], 4 weeks [OR = 4.67, 95%CI (3.31, 6.57), $P < 0.001$], and 8 weeks [OR = 3.44, 95% CI (2.78, 4.25), $P < 0.001$], and the effective rate of treatment was significantly better than that of calcipotriol, and the differences were statistically significant. In addition, the efficacy of defubao (1 time/day) and calcipotriol (2 times/day) was compared.

Five randomized controlled trials compared the effect of defubao and other drugs by comparing the baseline change rate of PASI before and after 8 weeks of treatment. Based on the provided clinical trial data, we conducted a descriptive analysis of the trial results, as shown in Figure 6.

4.2. Security Analysis. Six studies compared the safety issues of using defubao and calcipotriol. Three randomized experiments compared the safety difference of treatment for 4 weeks, and 3 randomized controlled experiments compared the safety difference of treatment for 8 weeks. Meta-analysis uses a fixed-effects model to compare the occurrence of adverse events. The results suggest that the defubao group was used for 4 weeks or 8 weeks. The incidence of adverse

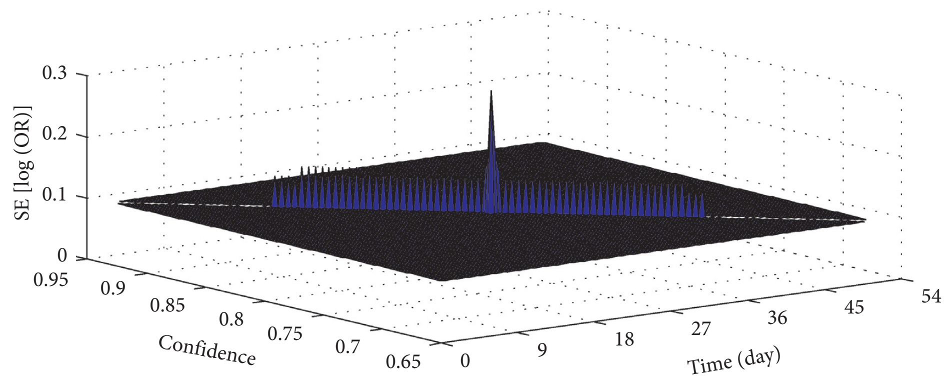

Figure 4: IGA as an indicator to evaluate the 8-week defubao group and the betamethasone group.

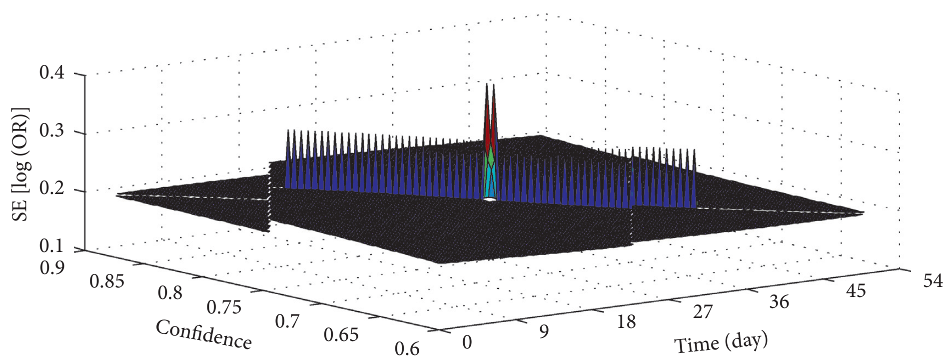

Figure 5: IGA was used to evaluate the 8-week defubao group and the calcipotriol group.

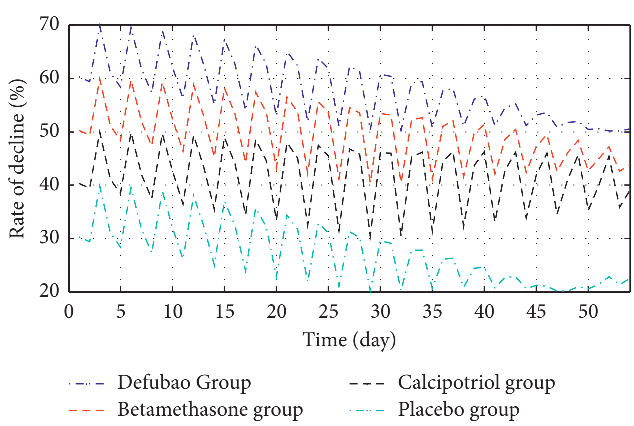

Figure 6: PASI reduction rate for 8 weeks of treatment.

events was significantly less than that of the calcipotriol group. The funnel chart shows asymmetry, and there is a publication offset in the research, as shown in Figure 7.

Four randomized controlled trials compared the safety of defubao and betamethasone for 8 weeks of treatment, that is, the proportion of at least one adverse event. The results showed that after 8 weeks of treatment with defubao and betamethasone, there was no statistical difference in the incidence of adverse reactions between the two. Two randomized controlled trials compared the incidence of adverse reactions after using Defabao and placebo for 4 weeks. Through data analysis, it was found that the proportion of adverse events in the placebo group was significantly higher than that in the defubao group. The results of different groups for 8 weeks are shown in Figure 8. In addition, the safety analysis and comparison results are shown in Table 2.

4.3. Discussion. Relevant scholars observed the changes in clinical PASI score and vascular dilatation under dermatoscope after treatment, and the relative index was used to calculate the evaluation index [36]. Many published evaluation indicators for observing curative effect are compared with the decline rate. In the initial stage of the trial design, this article consulted a large number of domestic and foreign literatures and found that even if the psoriatic skin lesions appear normal to the naked eyes, the capillaries still have different degrees of expansion under dermoscopy [37]. With drug treatment, the skin lesions of psoriasis improved, and the improvement of skin lesions reduced the release of vascular growth factors and inflammatory mediators, which in turn changed the state of intravascular microcirculation of the whole body skin, and the intravascular microcirculation of the skin surrounding the skin lesions. It will change accordingly, that is, the “normal skin data around the skin lesion” will change. The comprehensive evaluation compared the relative index algorithm and the decline rate algorithm [38]. In this experiment, the decline rate was selected as the evaluation index, the target skin lesion score (TLS) was observed to evaluate the severity of the skin lesion, and the diameter of the vascular bulb was used to evaluate the degree of vasodilation, respectively.

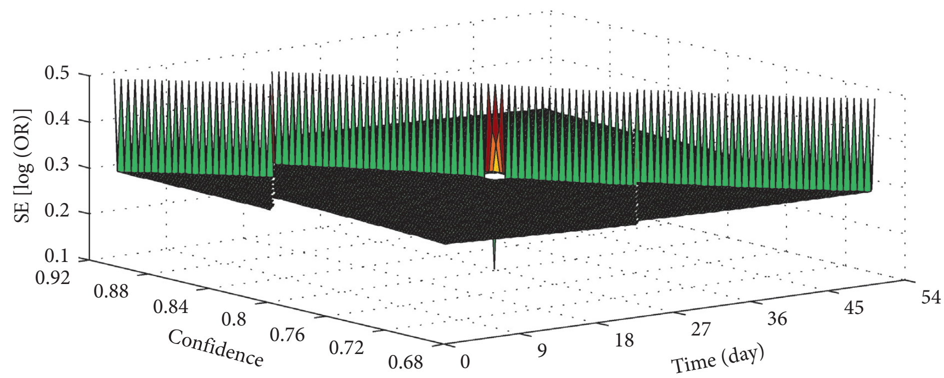

Figure 7: Safety analysis of the 8-week defubao group and the calcipotriol group.

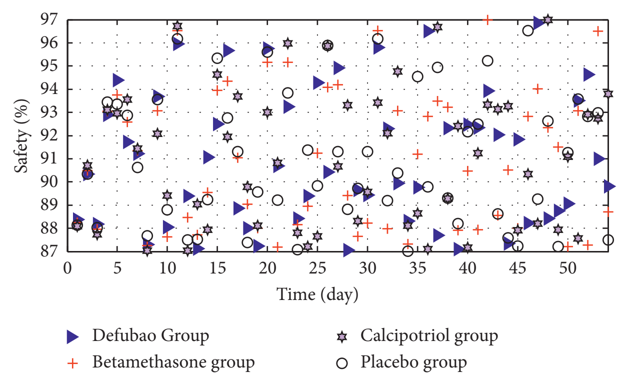

Figure 8: Safety analysis results of different groups in 8 weeks.

Table 2: Comparison results of safety analysis.

Outcome indicators	χ^2	Heterogeneity p	OR	0.95CI	Z	P
Defubao vs placebo 4 weeks	0.01	0.52	0.61	(0.41,0.89)	2.3	0.02
Defubao vs betamethasone 8 weeks	0	0.93	0.92	(0.84,1.1)	0.56	0.16
Defubao vs calcipotriol 8 weeks	0.65	0.03	0.57	(0.48,0.66)	6.4	0.011
Defubao vs calcipotriol 4 weeks	0.32	0.21	0.52	(0.42,0.61)	5.2	0

In addition, in order to be able to observe the overall condition of the skin lesions under a dermatoscopic field of view, and reduce the error caused by the difference in the observation field, the area of the psoriasis skin lesions selected in this experiment is 4–9 cm^2, which makes the data obtained more objective. However, this experiment only observed the changes in specific skin lesions of patients with psoriasis after treatment with defubao, and did not observe and evaluate the overall disease severity of the patients. In the study included in Study 1 (meta-analysis) of this article, it was found that the PASI score of patients with psoriasis vulgaris was significantly decreased after topical application of defubao. Because previous studies have found that in mouse experimental models, the inhibitory effect of steroid hormones on DNA synthesis can be observed even if they are far away from the site where steroid hormones are used [39]. In addition, the improvement of psoriasis plaques reduces the release of vascular growth factors and inflammatory mediators, and the intravascular microcirculation of the whole body skin will be improved.

The two main immunohistological changes in psoriasis are the changes in the skin microvascular system and the abnormal differentiation of the epidermis in the end-stage. The capillary loops in the dermal papilla can be seen elongated, bent and dilated. Relevant scholars have found that in the early stage of psoriasis, the skin lesions and surrounding capillaries dilate and abnormal blood flow precede the inflammatory manifestations and hyperplasia of the skin lesions [40]. With the treatment, the skin lesions improved, the plaque disappeared, and the degree of vasodilation and function also gradually recovered. The researchers compared the blood vessel diameters of scalp lesions in healthy people, patients with seborrheic dermatitis, and patients with psoriasis through dermoscopy, and found that the diameters of scalp capillaries in the seborrheic dermatitis group and the healthy group were similar [41]. There was a significant difference between the capillary diameter of the group and the former two, and the vascular bulb was significantly expanded. In recent years, the use of noninvasive examination methods to evaluate the efficacy of drugs has increasingly appeared in several skin diseases including psoriasis. After local or systemic drug treatment, the researchers evaluated the effect of the drug by evaluating the change in the diameter of the capillary globules in psoriasis or the number of capillary globules per unit field of view before and after the treatment [42].

This article compares the effectiveness and safety differences of defubao, calcipotriol, betamethasone, and placebo in the treatment of psoriasis vulgaris. Regardless of the treatment for 2 weeks, 4 weeks, or 8 weeks, compared with the calcipotriol group, the betamethasone group, or the placebo group, the efficacy of the defubao group was more significant. Topical calcipotriol and glucocorticoids are classic drugs for the treatment of psoriasis, but calcipotriol requires an alkaline environment to maintain stability, and betamethasone can be more effective in an acidic environment. The two are incompatible when mixed, and it is difficult to have both. For this reason, the researchers developed a unique and stable excipient to overcome the incompatibility barrier of the two, and finally form a formulation containing stable active ingredients. This not only gives play to the advantages of the two drugs, makes the treatment effect stronger, but also reduces the amount of topical glucocorticoids, thereby reducing the risk of hormone-related adverse reactions. This may be the reason why defubao is better than calcipotriol and betamethasone. In addition, meta-analysis found that after 4 weeks of treatment, the effective rate of the defubao group (1 times/day) was 1.72 times that of the calcipotriol group (2 times/day), which provides powerful clinical guidance for medication However, the low frequency of medication and the significant effect are more acceptable to patients. From the perspective of pharmacoeconomics, it can reduce costs and is more beneficial to patients. The study found that the incidence of adverse events in the calcipotriol group was significantly higher than that in the defubao group, while the difference in adverse events between the defubao group and the betamethasone group was not statistically significant. Moreover, it is mentioned in the literature that long-term use of defubao will not increase the risk of glucocorticoid-related adverse events compared with nonglucocorticoid topical drugs. This shows that the safety of defubao treatment is worthy of recognition.

This study found that within 8 weeks of medication, the curative effect increased with the time of medication, 8 weeks curative effect >4 weeks curative effect >2 weeks curative effect, and the difference between them was statistically significant. However, there is a lack of longer-term efficacy data. Therefore, clinical observations of a longer course of treatment are needed to determine the optimal medication time for treatment with defubao. This meta-analysis only compares the efficacy of defubao, calcipotriol and betamethasone, and does not compare with other topical drugs. This study included 11 studies, divided into multiple subgroups. When designing the study, the publication bias was tested by formulating detailed search strategies, searching literature from multiple libraries, formulating inclusion and exclusion criteria, sensitivity analysis, and making funnel charts. The number of studies included in some subgroups is small, which affects the results of heterogeneity testing. In addition, this study only retrieved Chinese and English articles, and did not retrieve research conclusions in other languages. All of the above may cause bias.

This study evaluated the efficacy of topical defubao on psoriasis vulgaris. Through clinical observation and dermoscopic observation, it was found that defubao had a significant effect on psoriasis skin lesions. The treated psoriasis plaques improved in all patients, and at the same time, the diameter of the capillary bulbs under dermoscopy gradually decreased.

However, there is a big difference between the speed and intensity of the improvement of the diameter of the capillary bulb under the dermoscopy and the clinical TLS score. After 4 weeks of treatment, the TLS score was 25/32 of "completely healed skin lesions" and "significantly improved", which reached almost 78%, while the spheroid diameter score was much lower than 10%. After 6 weeks of treatment, the target skin lesions of 26 patients had completely disappeared. Under dermoscopic imaging observations, only 5 patients returned to normal vascular diameters, while in other patients, even those whose clinical skin lesions disappeared completely, there were still significant telangiectasias.

There may be two mechanisms for the difference in results between the two. One possibility is that we have observed that the psoriasis skin lesions have subsided clinically, but there may still be slight keratinocyte proliferation or low-level growth factor secretion in the skin lesions. These small changes may continue to stimulate blood vessel formation. Another possibility is that the regulation speed of the keratinocyte proliferation cycle is faster than the speed of capillary remodeling or disappearance, the proliferation cycle of keratinocytes has returned to normal, but the expanded capillaries still exist. After treatment, some psoriasis skin lesions have dilated capillaries that can become smaller, but they cannot return to their normal size. As we all know, all clinical treatment observations are performed with standard doses within the safe range of each drug, so it cannot be excluded that increasing the dose of the drug can improve the microcirculation changes of the psoriasis skin lesions and make it possible for the dilated blood vessels to return to normal.

This article not only searched the English database, but also searched the Chinese database. The included studies are more comprehensive and involve more ethnic groups. The comparisons were made with PASI, IGA, and PGA as evaluation indicators, and the results obtained were more comprehensive and objective. The included articles are all high-quality randomized controlled trials, divided into multiple subgroups, and stratified analysis of the difference in efficacy of 2 weeks, 4 weeks, and 8 weeks of treatment.

5. Conclusion

This paper studies the classic algorithm Apriori in association rules, points out the insufficiency of this algorithm and the existing improved algorithms in dealing with unbalanced medical data sets, and then proposes a new scheme of mining association rules after balancing first to improve it. A new scheme for mining association rules that balances first and then mines is proposed. In the data balance part, aiming at the blind sampling problem of the traditional SMOTE algorithm, a balance improvement algorithm based on the combination of K-means and SMOTE is proposed. Defubao was safer than calcipotriol and placebo. The difference was statistically significant, but there was no statistical difference from betamethasone. Defubao is more advantageous than calcipotriol or betamethasone in the treatment of psoriasis vulgaris. High-quality systematic reviews provide an effective and objective choice for the choice of clinical external medications. Two randomized controlled trials were conducted to compare the efficacy of defubao in the treatment of psoriasis vulgaris in 2, 4, and 8 weeks. A fixed-effect model was used for data analysis, and the results showed that the efficacy after 4 weeks of use was better than that after 2 weeks of use [OR = 0.73, 95% CI (0.61, 0.86), $P < 0.01$]. The curative effect after 8 weeks of use was significantly better than that after 4 weeks of use [OR = 0.68, 95% CI (0.47, 0.98), $P < 0.01$]. The curative effect after 2 weeks of use was significantly weaker than that after 8 weeks of use [OR = 0.49, 95% CI (0.41, 0.58), $P < 0.01$]. After topical treatment of psoriasis skin lesions with defubao, the clinical observation showed that the skin lesions subsided and the diameter of the vascular bulb became smaller under dermatoscope, suggesting that defubao is effective in treating psoriasis vulgaris. There is a positive correlation between the target skin lesion score of a specific skin lesion in psoriasis and the diameter of the vascular bulb. As the treatment time increases, the correlation between the two increases. The reduction rate of the clinical target skin lesion score after treatment of psoriasis skin lesions is significantly greater than the reduction rate of vascular globule diameter. The microvascular healing of the skin lesions is later than the clinical cure. The observation of skin lesion vascular changes can be used to evaluate the condition of psoriasis and guide drug selection. However, this study only compared the efficacy of defubao, calcipotriol and betamethasone, and did not compare with other topical drugs. Further research is needed. In addition, there is also a lack of data to study the longer-term efficacy of defubao.

Data Availability

Relevant data require the consent of the corresponding author to obtain it.

Conflicts of Interest

The authors declare that there are no conflicts of interest.

Acknowledgments

This work was supported by the project of Xiangya Hospital, Central South University.

References

[1] Y. Fu, C.-H. Lee, and C.-C. Chi, "Association of psoriasis with inflammatory bowel disease," *JAMA dermatology*, vol. 154, no. 12, pp. 1417–1423, 2018.

[2] N. Rajesh and A. A. L. Selvakumar, "Association rules and deep learning for cryptographic algorithm in privacy preserving data mining[J]," *Cluster Computing*, vol. 22, no. 1, pp. 119–131, 2019.

[3] S. Hussain, N. Abdulaziz Dahan, F. M. Ba-Alwi, and N. Ribata, "Educational data mining and analysis of students' academic performance using WEKA," *Indonesian Journal of Electrical Engineering and Computer Science*, vol. 9, no. 2, pp. 447–459, 2018.

[4] A. W. Armstrong, L. Puig, A. Joshi et al., "Comparison of biologics and oral treatments for plaque psoriasis," *JAMA dermatology*, vol. 156, no. 3, pp. 258–269, 2020.

[5] V. Nourani and A. Molajou, "Application of a hybrid association rules/decision tree model for drought monitoring," *Global and Planetary Change*, vol. 159, pp. 37–45, 2017.

[6] K. S. Lakshmi and G. Vadivu, "Extracting association rules from medical health records using multi-criteria decision analysis," *Procedia Computer Science*, vol. 115, pp. 290–295, 2017.

[7] S. Vaengebjerg, L. Skov, A. Egeberg, and N. D. Loft, "Prevalence, incidence, and risk of cancer in patients with psoriasis and psoriatic arthritis," *JAMA dermatology*, vol. 156, no. 4, pp. 421–429, 2020.

[8] S. Das, A. Dutta, R. Avelar, K. Dixon, X. Sun, and M. Jalayer, "Supervised association rules mining on pedestrian crashes in urban areas: identifying patterns for appropriate countermeasures," *International Journal on the Unity of the Sciences*, vol. 23, no. 1, pp. 30–48, 2019.

[9] J. Silva, J. Cubillos, J. V. Villa, L. Romero, D. Solano, and C. Fernández, "Preservation of confidential information privacy and association rule hiding for data mining: a bibliometric review," *Procedia Computer Science*, vol. 151, pp. 1219–1224, 2019.

[10] H. Kaiser, J. Abdulla, K. M. A. Henningsen, L. Skov, and P. R. Hansen, "Coronary artery disease assessed by computed tomography in patients with psoriasis: a systematic review and meta-analysis," *Dermatology*, vol. 235, no. 6, pp. 478–487, 2019.

[11] A. M. Trafford, R. Parisi, E. Kontopantelis, C. E. M. Griffiths, and D. M. Ashcroft, "Association of psoriasis with the risk of developing or dying of cancer," *JAMA dermatology*, vol. 155, no. 12, pp. 1390–1403, 2019.

[12] P. Ungprasert and S. Raksasuk, "Psoriasis and risk of incident chronic kidney disease and end-stage renal disease: a systematic review and meta-analysis," *International Urology and Nephrology*, vol. 50, no. 7, pp. 1277–1283, 2018.

[13] Z. K. Jabbar-Lopez, Z. Z. N. Yiu, V. Ward et al., "Quantitative evaluation of biologic therapy options for psoriasis: a systematic review and network meta-analysis," *Journal of Investigative Dermatology*, vol. 137, no. 8, pp. 1646–1654, 2017.

[14] L. Sawyer, I. Fotheringham, E. Wright, N. Yasmeen, C. Gibbons, and A. Holmen Møller, "The comparative efficacy of brodalumab in patients with moderate-to-severe psoriasis: a systematic literature review and network meta-analysis," *Journal of Dermatological Treatment*, vol. 29, no. 6, pp. 557–568, 2018.

[15] M. T. Patrick, P. E. Stuart, H. Zhang et al., "Causal relationship and shared genetic loci between psoriasis and type 2 diabetes through trans-disease meta-analysis," *Journal of Investigative Dermatology*, vol. 141, no. 6, pp. 1493–1502, 2021.

[16] L. M. Sawyer, L. Cornic, L. A. Levin, C. Gibbons, A. H. Møller, and G. B. Jemec, "Long-term efficacy of novel therapies in moderate-to-severe plaque psoriasis: a systematic review and network meta-analysis of PASI response," *Journal of the*

European Academy of Dermatology and Venereology, vol. 33, no. 2, pp. 355–366, 2019.

[17] T. Li, "Mining association rules on enrollment information of higher vocational colleges using the Apriori algorithm," *Journal of Advanced Computational Intelligence and Intelligent Informatics*, vol. 23, no. 4, pp. 775–781, 2019.

[18] A. Mourad, S. Straube, S. Armijo-Olivo, and R. Gniadecki, "Factors predicting persistence of biologic drugs in psoriasis: a systematic review and meta-analysis," *British Journal of Dermatology*, vol. 181, no. 3, pp. 450–458, 2019.

[19] C.-C. Chi, T.-H. Chen, S.-H. Wang, and T.-H. Tung, "Risk of suicidality in people with psoriasis: a systematic review and meta-analysis of cohort studies," *American Journal of Clinical Dermatology*, vol. 18, no. 5, pp. 621–627, 2017.

[20] N. D. Loft, S. Vaengebjerg, A. S. Halling, L. Skov, and A. Egeberg, "Adverse events with IL-17 and IL-23 inhibitors for psoriasis and psoriatic arthritis: a systematic review and meta-analysis of phase III studies," *Journal of the European Academy of Dermatology and Venereology*, vol. 34, no. 6, pp. 1151–1160, 2020.

[21] M. Augustin, D. Jullien, A. Martin, and C. Peralta, "Real-world evidence of secukinumab in psoriasis treatment - a meta-analysis of 43 studies," *Journal of the European Academy of Dermatology and Venereology*, vol. 34, no. 6, pp. 1174–1185, 2020.

[22] M.-J. Huang, H.-S. Sung, T.-J. Hsieh, M.-C. Wu, and S.-H. Chung, "Applying data-mining techniques for discovering association rules," *Soft Computing*, vol. 24, no. 11, pp. 8069–8075, 2020.

[23] J. Rauch, "Expert deduction rules in data mining with association rules: a case study," *Knowledge and Information Systems*, vol. 59, no. 1, pp. 167–195, 2019.

[24] H. Shang, D. Lu, and Q. Zhou, "Early warning of enterprise finance risk of big data mining in internet of things based on fuzzy association rules," *Neural Computing & Applications*, vol. 33, no. 9, pp. 3901–3909, 2021.

[25] C. Théréné, E. Brenaut, T. Barnetche, and L. Misery, "Efficacy of systemic treatments of psoriasis on pruritus: a systemic literature review and meta-analysis[J]," *Journal of Investigative Dermatology*, vol. 138, no. 1, pp. 38–45, 2018.

[26] G. Xu, M. Xia, C. Jiang et al., "Comparative efficacy and safety of thirteen biologic therapies for patients with moderate or severe psoriasis: a network meta-analysis," *Journal of Pharmacological Sciences*, vol. 139, no. 4, pp. 289–303, 2019.

[27] M. Mamizadeh, Z. Tardeh, and M. Azami, "The association between psoriasis and diabetes mellitus: a systematic review and meta-analysis," *Diabetes & Metabolic Syndrome: Clinical Research Reviews*, vol. 13, no. 2, pp. 1405–1412, 2019.

[28] C. Cameron, B. Hutton, C. Druchok et al., "Importance of assessing and adjusting for cross-study heterogeneity in network meta-analysis: a case study of psoriasis," *Journal of comparative effectiveness research*, vol. 7, no. 11, pp. 1037–1051, 2018.

[29] D.-L. Miholca, G. Czibula, and I. G. Czibula, "A novel approach for software defect prediction through hybridizing gradual relational association rules with artificial neural networks," *Information Sciences*, vol. 441, pp. 152–170, 2018.

[30] A. Attia, A. I. Abushouk, H. Ahmed et al., "Safety and efficacy of brodalumab for moderate-to-severe plaque psoriasis: a systematic review and meta-analysis," *Clinical Drug Investigation*, vol. 37, no. 5, pp. 439–451, 2017.

[31] M. T. Patrick, R. Bardhi, K. Raja, K. He, and L. C. Tsoi, "Advancement in predicting interactions between drugs used to treat psoriasis and its comorbidities by integrating molecular and clinical resources," *Journal of the American Medical Informatics Association*, vol. 28, no. 6, pp. 1159–1167, 2021.

[32] J. C. E. Lane, J. Weaver, K. Kostka et al., "Risk of depression, suicide and psychosis with hydroxychloroquine treatment for rheumatoid arthritis: a multinational network cohort study [J]," *Rheumatology*, vol. 60, no. 7, pp. 3222–3234, 2021.

[33] M. Cesaroni, L. Seridi, and M. J. Loza, "Suppression of siγ levels as a potential measure of response to ustekinumab treatment in patients with systemic lupus erythematosus," *Arthritis & Rheumatology*, vol. 73, no. 3, pp. 472–477, 2021.

[34] H. Johns, J. Bernhardt, and L. Churilov, "Distance-based Classification and Regression Trees for the analysis of complex predictors in health and medical research," *Statistical Methods in Medical Research*, vol. 30, no. 9, pp. 2085–2104, 2021.

[35] C. Yu, T. Zhang, S. Shi, T. Wei, and Q. Wang, "Potential biomarkers: differentially expressed proteins of the extrinsic coagulation pathway in plasma samples from patients with depression," *Bioengineered*, vol. 12, no. 1, pp. 6318–6331, 2021.

[36] K. A. Yunanto, N. N. Waspodo, F. Tabri, and F. Ilyas, "Obesity as a comorbid factor in a boy with psoriasis vulgaris," *Enfermería Clínica*, vol. 30, pp. 259–262, 2020.

[37] B. Hsa, C. Sb, and C. Baa, "Lésions jauntres de psoriasis révélant une métaplasie lipomateuse dermique - ScienceDirect[J]," *Annales de Dermatologie et de Vénéréologie*, vol. 147, no. 1, pp. 46–49, 2020.

[38] P. C. M. van de Kerkhof, "Translational research and drug development in psoriasis by collaborative efforts of academia and industry," *Journal of Investigative Dermatology*, vol. 140, no. 3, pp. 524–526, 2020.

[39] P. C. Ma, B. Abg, C. Jc et al., "Measuring psoriatic arthritis symptoms: a core domain in psoriasis clinical trials[J]," *Journal of the American Academy of Dermatology*, vol. 82, no. 1, pp. 54–61, 2020.

[40] A. Arakawa, E. Reeves, S. Vollmer et al., "ERAP1 controls the autoimmune response against melanocytes in psoriasis by generating the melanocyte autoantigen and regulating its amount for HLA-C $*$ 06:02 presentation," *The Journal of Immunology*, vol. 207, no. 9, pp. 2235–2244, 2021.

[41] R. Aschoff, A. Martorell, T. Anger, D. Chayer, and A. Bewley, "Real-world experience using topical therapy-calcipotriol and betamethasone dipropionate foam in adults with beyond-mild psoriasis," *Dermatology and therapy*, vol. 11, no. 2, pp. 555–569, 2021.

[42] A. A. Hernández-Collazo, O. Pérez-Méndez, V. López-Olmos et al., "Association between rs662 (A> G) and rs854560 (A> T) polymorphisms in PON1 gene and the susceptibility for psoriasis in mestizo population of Western Mexico[J]," *Molecular Biology Reports*, vol. 48, no. 1, pp. 183–194, 2021.

Hindawi
Journal of Healthcare Engineering
Volume 2023, Article ID 9860692, 1 page
https://doi.org/10.1155/2023/9860692

Retraction

Retracted: The Exosomes Containing LINC00461 Originated from Multiple Myeloma Inhibit the Osteoblast Differentiation of Bone Mesenchymal Stem Cells via Sponging miR-324-3p

Journal of Healthcare Engineering

Received 12 November 2022; Accepted 12 November 2022; Published 25 January 2023

Journal of Healthcare Engineering has retracted the article titled "The Exosomes Containing LINC00461 Originated from Multiple Myeloma Inhibit the Osteoblast Differentiation of Bone Mesenchymal Stem Cells via Sponging miR-324-3p" [1] due to concerns that the peer review process has been compromised.

Following an investigation conducted by the Hindawi Research Integrity team [2], significant concerns were identified with the peer reviewers assigned to this article; the investigation has concluded that the peer review process was compromised. We therefore can no longer trust the peer review process, and the article is being retracted with the agreement of the Chief Editor.

References

[1] Y. Wu, Z. Zhang, J. Wu, J. Hou, and G. Ding, "The Exosomes Containing LINC00461 Originated from Multiple Myeloma Inhibit the Osteoblast Differentiation of Bone Mesenchymal Stem Cells via Sponging miR-324-3p," *Journal of Healthcare Engineering*, vol. 2022, Article ID 3282860, 7 pages, 2022.

[2] L. Ferguson, "Advancing Research Integrity Collaboratively and with Vigour," 2022, https://www.hindawi.com/post/advancing-research-integrity-collaboratively-and-vigour/.

Hindawi
Journal of Healthcare Engineering
Volume 2022, Article ID 3282860, 7 pages
https://doi.org/10.1155/2022/3282860

Research Article

The Exosomes Containing LINC00461 Originated from Multiple Myeloma Inhibit the Osteoblast Differentiation of Bone Mesenchymal Stem Cells via Sponging miR-324-3p

Yang Wu, Zhemei Zhang, Jing Wu, Jinxia Hou, and Guosheng Ding

Clinical Laboratory Center, Gansu Provincial Hospital, Lanzhou 730000, Gansu, China

Correspondence should be addressed to Guosheng Ding; dinggs2021@163.com

Received 1 December 2021; Revised 24 December 2021; Accepted 31 December 2021; Published 25 January 2022

Academic Editor: Enas Abdulhay

Multiple myeloma is one of the hematological malignancies and inhibited osteoblast differentiation of bone marrow mesenchymal stem cells (BM-MSCs) which has been proved as a major complication of the patients with multiple myeloma. However, the pathomechanism of symptom remains unclear. Besides, several studies have indicated that LINC00461 plays an important role in the progression of multiple tumors. Hence, this study attempted to reveal the role of LINC00461 in the osteoblast differentiation of MSCs. In this study, the expression level of LINC00461 in the exosomes of multiple myeloma cells was measured, and BM-MSCs were cultured with the exosomes to observe the change of cellular phenotype. Moreover, downstream target of LINC00461 was searched and verified with dual-luciferase reporter assay, and the activation of the Wnt/β-catenin pathway was also observed by Western blot. The results showed that the isolated BMSCs exhibited special biomarkers of MSCs. LINC00461 was significantly upregulated in the exosomes originated multiple myeloma cells, and increased LINC00461 significantly impeded the osteoblast differentiation of MSCs. Moreover, LINC00461 could significantly suppress the activation of the Wnt/β-catenin pathway in MSCs. In conclusion, this study suggested that LINC00461 in exosomes of multiple myeloma could reduce the activity of the Wnt/β-catenin pathway to inhibit the osteoblast differentiation of BM-MSCs via targeting miR-324-3p.

1. Introduction

Multiple myeloma is the most dangerous malignant hematological diseases with high morbidity. Statically, more than 100000 people have been diagnosed with multiple myeloma, and approximately 2% cancer-related death in the world is caused by this disease each year [1, 2]. At present, even with the current therapeutic strategies, including radiotherapy, chemotherapy, and drug intervention, the prognosis of the patients with multiple myeloma remains unsatisfactory [3]. According the recent study, the 5-year survival rate of the multiple myeloma is less than 40% [4]. Therefore, investigating more effective intervention techniques for multiple myeloma are urgent.

The failure of osteoblast differentiation is a major reason causing the bone-related complications of the patients with multiple myeloma, such as osteoporosis and osteodynia, which is also related with the malignant progression and of multiple myeloma [5]. The osteoblast differentiation of human mesenchymal stromal cells (hMSCs) serves as an important role in maintaining the stability of skeletal internal environment [6]. Recently, increasing studies have indicated that multiple myeloma cells can remarkably inhibit the differentiation of MSCs, and the intervention on osteoblast differentiation of MSCs has also been confirmed as a promising strategy for alleviating the poor prognosis of the patients with multiple myeloma [7, 8]. Several studies have indicated the aberrant expression of some noncoding RNAs, such as long noncoding RNA (lncRNA) and micro-RNA (miRNA). lncRNA consist of almost 200 ribonucleic acids, and miRNA contains approximately 22 ribonucleic acids [8, 9]. lncRNA and miRNA involve the progression of cellular development and differentiation, and lager studies in recent ten years have illustrated that those aberrant noncoding RNAs involve the formation and development of multiple diseases [8, 10].

LINC00461 has been confirmed as a tumor promoter involving the malignant progressions of many cancer cells [11]. However, few studies have revealed the functions of LINC00461 in multiple myeloma. Thus, this study attempted to investigate the role of LINC00461 in multiple myeloma cells and then reveal the molecular mechanism of LINC00461 on osteoblast differentiation of BM-MSCs.

2. Materials and Methods

2.1. BM-MSCs Isolation and Osteogenic Differentiation. This study was approved by the hospital ethic committee, and the human-related experiments were performed following the Declaration of Helsinki protocol. The primary CD 138$^+$ BM cells were isolated from mononuclear cells of the patients and normal donors. The BM-MSCs obtained from the patients and health donors were cultured with Dulbecco's modified Eagle medium (DMEM) with 20% fetal bovine serum (FBS).

After cell attachment, BM-MSCs were cultured with the osteogenic induction medium (full culture medium containing 10^{-2} M β-sodium glycerophosphate, 50 mg/mL L-ascorbic acid, and 10^{-7} M dexamethasone) to induce the progression of osteoblast differentiation. After culture for 21 days, BM-MSCs were strained with alizarin red S (Beyotime), and then, the osteoblast mineralization in three random microscopic regions was imaged and quantified with Image-Pro Plus 6.0 software. Finally, the relative mineralized regions were calculated.

2.2. Cell Culture and Translation. Human normal plasma cell line (nPCs) and human myeloma cell lines including H929 and U266 cell lines purchased from Tongpai Biotechnology Co., Ltd (Shanghai, China), and the cells were cultured with the 1640 medium containing 10% FBS. All cells were cultured in an incubator with 5% CO_2 and 37°C. The cells subculture was performed when the confluence of the cells was at 90%.

The cell transfection was performed when cellular confluence was at 70%. In brief, 4 μg of DNA or 100 pmol RNA was incubated with 250 μl serum-free mediums for 5 min and then was mixed and incubated with isometric serum-free containing 10 μl Lipofectamine 2000 at 25°C for 20 min. Finally, the mixtures were added into each well, and the cells were further incubated for 24 hours.

2.3. Exosomes Isolation. U266 cells were cultured with FBS-free 1640 medium, and the culture medium was collected and centrifuged at 800 g for 5 min, followed by 3000 g for 10 min and 10000 g for 60. After that, total exosome isolation reagent (Cat#: 4478359; Thermo Fisher Scientific) was used for isolation of exosomes from the supernatants. Afterward, exosomes were harvested from the pellets and resuspended in PBS. Then, 0.22 μm pore size polyvinylidene difluoride (PVDF) membrane filters (Cat#: GVWP04700; Millipore Sigma) were used to filter any remaining cells or debris. The concentration of exosome was quantified through the BCA kit.

2.4. Cells Differentiation and Observation. The MSCs were cultured and induced with osteogenic differentiation medium, including alpha-minimum essential medium containing 10% FBS, 2 mM L-glutamine, 100 mM dexamethasone, 0.2 mM L-ascorbic acid, and 10 mM β-glycerophosphate. The osteogenic differentiation of BM-MSC cells were observed after alizarin red staining. In brief, the MSCs were fixed with 1% formaldehyde for 15 min after inducing with osteogenic differentiation medium, and then, the cells were rinsed with double distilled water. After that, the cells were stained with 2% alizarin red S solution (pH = 4.2, Shanghai Zeye Biotechnology Co., Ltd, Shanghai, China) for 10 min. Finally, after rinsing with double distilled water for three times, the cells were imaged and then quantified with decalcification solution at 405 nm.

2.5. qRT-PCR. For RNA extraction, the total RNAs of the cells were isolated with TRIzol reagent. The total RNAs were transcribed as cDNA by a PrimeScript® RT reagent Kit (Thermo Fisher, Massachusetts, the USA). The reaction system including primers, cDNA, dNTPs, and Taq DNA polymerase were prepared according the instruction of the qRT-PCR kit (Sigma-Aldrich, Missouri, USA). After that, qRT-PCR was performed according to the following program: denaturation at 95°C for 3 min, followed by amplification for 40 cycles at 95°C for 12 s and at 53°C for 40s and 70°C for 30s. The relative levels of miRNA or mRNA were calculated with the $2^{-(\Delta\Delta Ct)}$ method. The sequences of the primers are given in Table 1.

2.6. Western Blot. The total proteins of the cells were extracted with RIPA buffer on the ice, and then, the concentration of the extracts was measured with the BCA kit. The protein was added with loading buffer and then boiled at 100°C for 5 min. After that, 30 μL of the symbol was separated by SDS-polyacrylamide gel electrophoresis (SDS-PAGE), and then, the proteins in the gels were transferred on the polyvinylidene difluoride membranes by the wet transfer method. The membranes were blocked with 5% fat-free milk at 4°C for 2 hours and then were incubated with the related primary antibodies at 4°C overnight. Subsequently, the membranes were washed with TBST for three times, and then, the membranes were incubated with the second antibodies. Finally, the expressions of the related proteins were observed with a chemiluminescence detection system.

2.7. Dual-Luciferase Reporter Gene Assay. The binding sites of LINC00461 and miR-324-3p were obtained from the NCBI database (https://www.ncbi.nlm.nih.gov/) and used for synthetizing the mutant sequences of LINC00461. The mutant type and wild type of LINC00461 were, respectively, cotransfected with miR-324-3p mimics or the miR-NC into

Table 1: Primer sequences of LINC00461, miR-324-3p, and U6.

Name of primer	Sequences
LINC00461-F	5′-GCGTGGACTACTCTGATG-3′
LINC00461-R	5′-CCAAGTGCTTACTGTCT-3′
miR-324-3p-F	5′-ATTAGCCCACTGCCCCAGGT-3′
miR-324-3p-R	5′-CCCACTGCCCCAGGTGCTGCTGG-3′
U6-F	5′-CTCGCTTCGGCAGCACA-3′
U6-R	5′-AACGCTTCACGAATTTGCGT-3′

HEK-293T for 48 hours. After that, a dual-luciferase reporter assay system was used to observe the luciferase activity of HEK-293T.

2.8. Data Analysis. The experiments in this study were performed 3 times, independently. The data analysis was performed with SPSS 20.0 with the chi-squared test or ANOVA with Tukey's post hoc-test and then were graphed with GraphPad Prism 8.0. Moreover, $P < 0.05$ meant that the statistically significance existed in two groups.

3. Results

3.1. LINC00461 Was Upregulated in the Exosomes of Multiple Myeloma Cells. To analyze the role of LINC00461 in multiple myeloma cells, the expression levels of LINC00461 in cells and pathological symbol were measured with qRT-PCR. The result showed that LINC00461 was significantly upregulated in multiple myeloma cells, compared with the normal cells (Figure 1(a), $P < 0.01$). Moreover, the increased LINC00461 was also found in the exosomes originated from multiple myeloma cells (Figure 1(b), $P < 0.01$). Those observations suggested that LINC00461 may involve the progression of multiple myeloma and was abundant in the exosomes of multiple myeloma cells.

3.2. The Exosomes of Multiple Myeloma Cells and LINC00461 Inhibited the Osteoblast Differentiation of MSCs. To investigate the mechanism of multiple myeloma cells on blocking the osteoblast differentiation of MSCs, the exosomes originated from MSCs were used to culture MSCs cells. The results showed that compared with normal MSCs, the expression levels of RUNX2 and ALP were downregulated, significantly (Figures 2(a)–2(c), $P < 0.01$). Moreover, compared with the cells transfected with negative control of LINC00461, MSCs transfected with LINC00461-expressed vectors exhibited poor progression of osteoblast differentiation (Figure 2(d), $P < 0.01$). Those observations suggested that LINC00461 was the main substance in the exosomes, which could restrain the osteoblast differentiation of MSCs.

3.3. MiR-324-3p Was a Downstream Target of LINC00461. To reveal the regulation mechanism of LINC00461 in development of multiple myeloma, the downstream targets of LINC00461 were searched and matched with TargetScan, an online database. The results showed that miR-324-3p was a potential downstream target of LINC00461 (Figure 3(a), $P < 0.01$). The binding effect of LINC00461 and miR-324-3p was verified by dual-luciferase reporter assay, and the results showed that LINC00461 could directly target 3′-UTR of miR-324-3p. Moreover, the expression level of mi-485-5p was also detected with qRT-PCR. The results showed that miR-324-3p was significantly downregulated in MSCs after transfecting with LINC00461-expressed vectors (Figure 3(b), $P < 0.05$). Those observations suggested that miR-324-3p was a downstream target of LINC00461, and miR-324-3p also involved in the progression of multiple myeloma.

3.4. MiR-324-3p Reversed the Effect of LINC00461 on the Osteoblast Differentiation of the MSCs. To further confirm whether miR-324-3p is involved in the regulation of LINC00461 on osteoblast differentiation of MSCs and proosteocytic cells, the miR-324-3p inhibitors and miR-324-3p mimics were cotransfected into cells. The results showed that compared with LINC00461-negative cells, the levels of RUNX2 and ALP in MSCs cotransfected with LINC00461-expressed vectors and miR-324-3p mimics were reversed, partly (Figures 4(a)–4(c), $P < 0.01$). Moreover, the inhibited osteoblast differentiation of MSCs treated with exosomes of multiple myeloma cells was remarkably reversed after transfecting with miR-324-3p mimics (Figure 4(d), $P < 0.01$). Those observations supported that LINC00461 could inhibit the osteoblast differentiation of MSCs and proosteocytic cells via targeting miR-324-3p.

3.5. LINC00461 Reduced the Activity of Wnt/β-Catenin Pathways via Targeting miR-324-3p. To delve the regulation mechanism of LINC00461 in the progression of multiple myeloma, the activities of the Wnt/β-catenin pathway were observed by Western blot. The study showed that Wnt and β-catenin were remarkably downregulated in MSCs after transfecting with LINC00461-expressed vectors (Figure 5, $P < 0.01$). Moreover, to further investigate whether miR-324-3p was involved in the regulation of miR-324-3p on multiple myeloma cells, the LINC00461-expressed vectors and miR-324-3p mimics were cotransfected into MSCs, and Western blot showed that the effect of LINC00461 on multiple myeloma could be reversed by increased miR-324-3p (Figure 5, $P < 0.01$). Those observations suggested that LINC00461 could inactivate the Wnt/β-catenin pathway via targeting miR-324-3p.

4. Discussion

Multiple myeloma is still a malignant plasma cell disorder, which seriously threatens the health of people, and several studies have indicated that the suppressed osteoblast differentiation of the MSCs induced by multiple myeloma can promote the progression of bone-related disease [12]. lncRNA and miRNA involve in the life activities of cells, and the aberrant expression of those noncoding RNA may serve as a key biomarker and drug target reference for clinical treatment [13]. This study proved the relationship of LINC00461 and multiple myeloma and the revealed the regulation mechanism of LINC00461 on osteoblast differentiation of the MSCs.

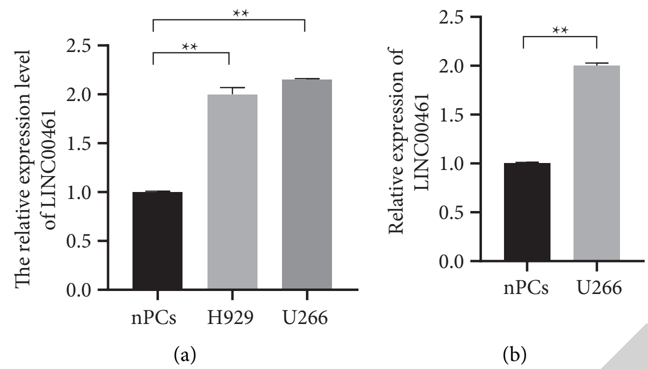

Figure 1: LINC00461 significantly upregulated in the multiple myeloma cells and their exosomes. (a) The relative expression level of LINC00461 in normal and multiple myeloma cell lines. (b) The relative expression level of LINC00461 in the exosomes originated from nPCs and U266.

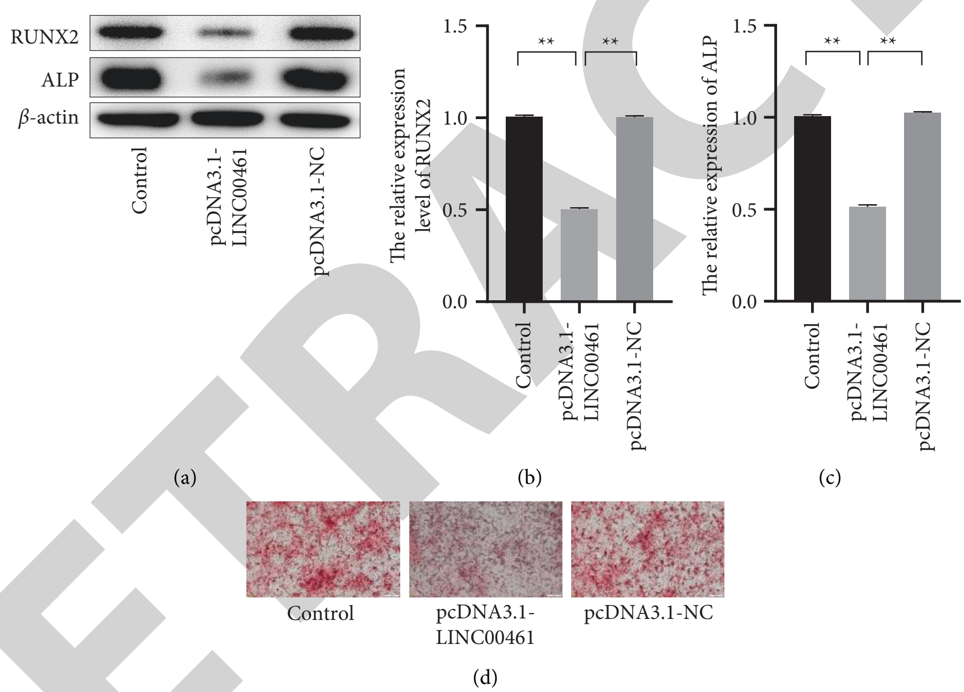

Figure 2: LINC00461 inhibits the osteoblast differentiation of MSCs. (a)–(c) The relative expression levels of RUNX2 and ALP measured with Western blot. (d) The osteoblast differentiation of MSCs observed by alizarin red staining.

lncRNA disorder is closely related with the progression of multiple myeloma [14]. In this study, it was found that LINC00461 was significantly upregulated in the multiple myeloma cells and their exosomes. Several studies have indicated that LINC0046 plays a tumor promoter role in some cancer cells and involves the multiple malignant behaviors of the tumor cell, including drug resistance, proliferation, and migration [15]. Qu et al. confirmed that LINC00461 is extremely upregulated in the rectal cancer cells and could decrease the sensitivity of tumor cells on cisplatin via mediating the miR-593-5p/CCND1 pathway [11]. The failure of osteoblast differentiation induced by multiple myeloma has been identified as a major reason leading the poor prognosis of the patients [16]. Increased RUNX2 and ALP have been confirmed as the biomarker events for the differentiation of BMSCs [17]. This study also found that the exosomes originated from multiple myeloma cells or upregulation of LINC00461 could obviously inhibit expression of RUNX2 and ALP. Exosomes, the nanometre-sized membranous vesicles with a diameter of about 30–100 nm, are secreted through the endocytic pathway [18]. The exosomes containing some cancerogenic factors can be released by tumor cells and then may promote angiogenesis and stromal remodelling. Liu et al. indicated that the exosomes derived from multiple myeloma could effectively block the differentiation of BMSCs [19]. Therefore, those study suggested that LINC00461 silence induced the differentiation of osteoblast.

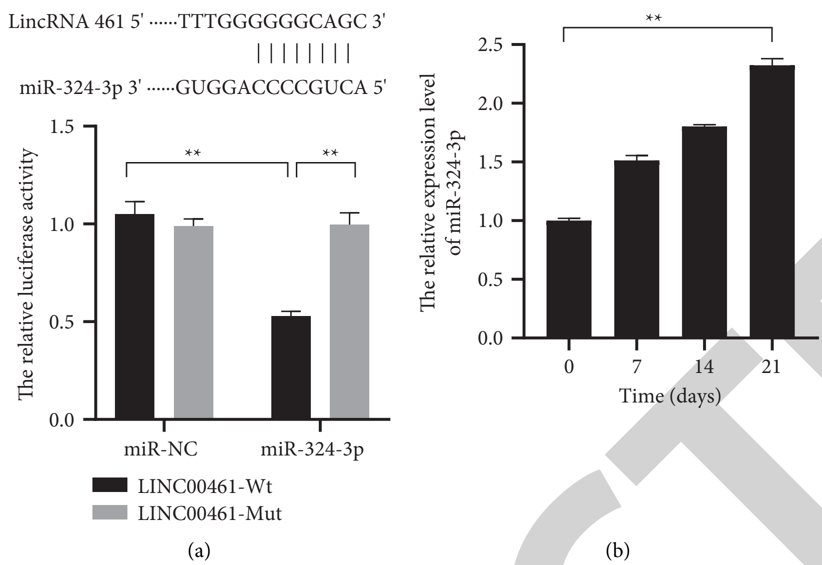

FIGURE 3: MiR-324-3p was a target of LINC00461, and miR-324-3p was related with osteoblast differentiation of MSCs. (a) The binding effect of LINC00461 and miR-324-3p observed by dual-luciferase assay. (b) Increased miR-324-3p observed in MSCs during the osteoblast differentiation.

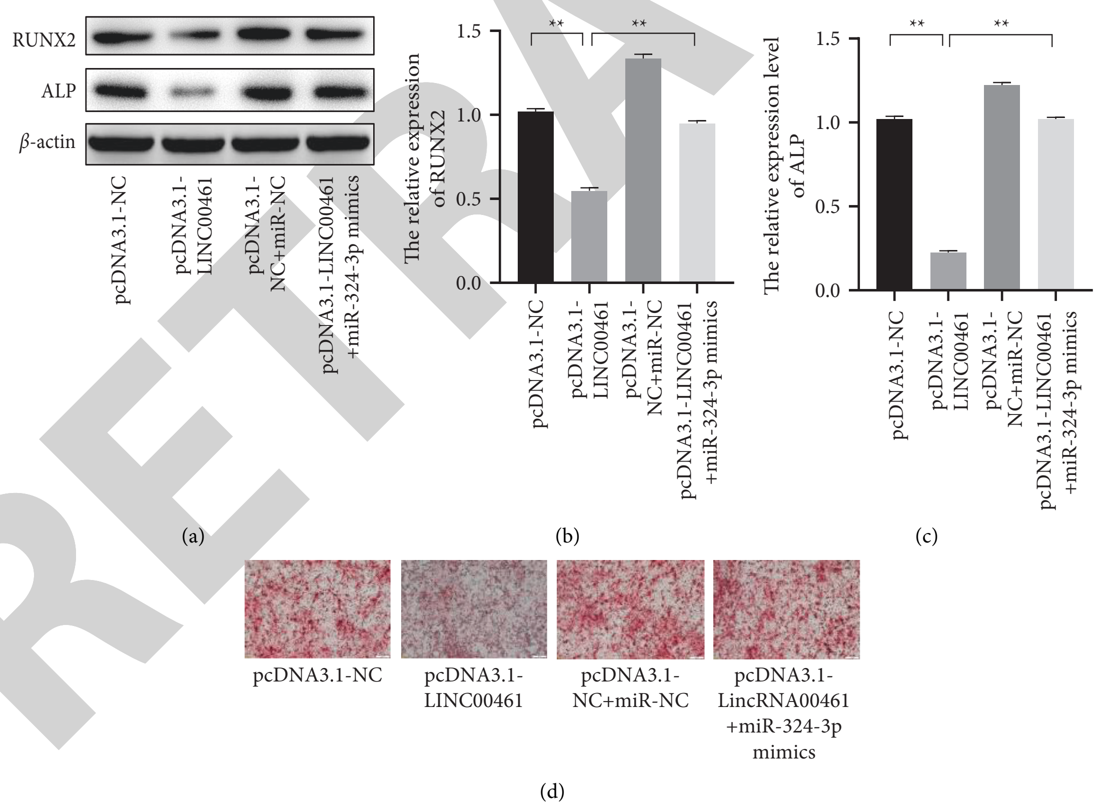

FIGURE 4: LINC00461 inhibits the osteoblast differentiation of MSCs via targeting miR-324-3p. (a)–(c) The relative expression levels of RUNX2 and ALP measured with Western blot. (d) The osteoblast differentiation of MSCs observed by alizarin red staining.

lncRNAs are characterized by regulating the cellular activities via serving as a molecular sponge to specially combine with the related mRNAs and miRNAs. Dong et al. indicated that LINC00461 promotes the proliferation and migration via regulating miR-30a-5p/integrin β3 axis [20]. The studies have indicated that miR-324-3p serves as a tumor inhibitor to impede the progression of some cancer cells. Zhao et al. observed that miR-324-3p was remarkably downregulated in thyroid cancer, and increased miR-324-3p could effectively block the

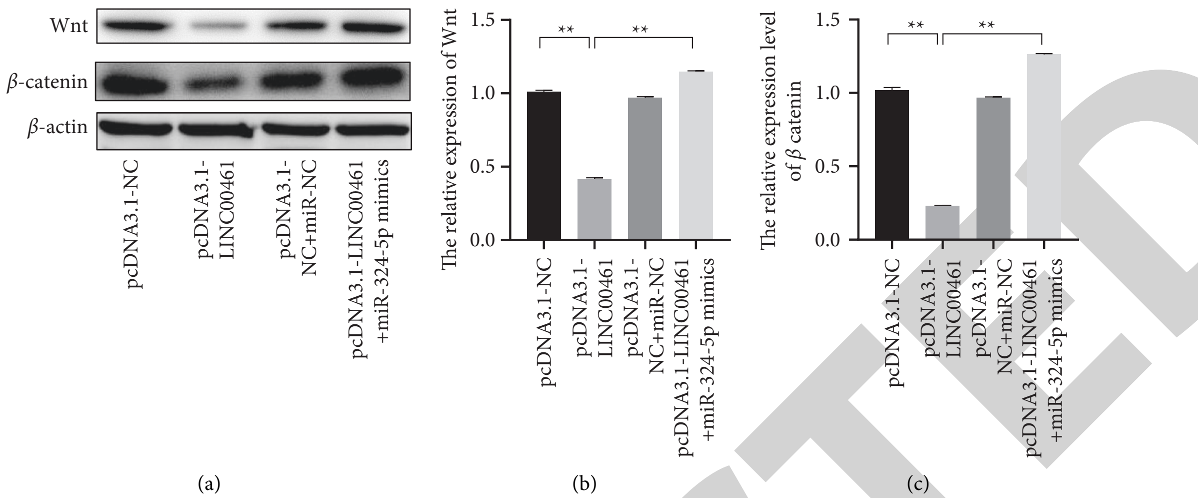

Figure 5: LINC00461 inhibits Wnt/β-catenin via targeting miR-324-3p. (a)–(c) The expression levels of Wnt and β-catenin measured by Western blot.

progression of hemangioma via targeting PDRG1 [21]. In this study, it was found that LINC00461 could directly target the 3′-UTR of miR-324-3p. It was also found that miR-324-5p was downregulated in the MSCs cells transfected with LINC00461-expressed vectors, and miR-324-3p could partly reverse the effect of LINC00461 on the osteoblast differentiation of MSCs. Kocijan et al. [22] confirmed that the expression of miR-324-3p was correlated with formation and development of the patients with postmenopausal osteoporosis. Moreover, the study also confirmed that miR-324-3p upregulation could partly reverse the effect of LINC00461 on osteoblast differentiation of MSCs. Those proofs suggested that LINC00461 in the exosomes originated from multiple myeloma cells could impede the osteoblast differentiation of MSCs via targeting miR-324-5p.

Cell differentiation involves the changes of multiple signaling pathways, and increasing studies have indicated that the activation of the Wnt/β-catenin pathway is responsible for osteoblast differentiation [23]. The study has indicated that the antagonists produced and secreted by multiple myeloma cells may block the progression of osteoblast differentiation via inactivating the Wnt/β-catenin pathway in MSCs [24]. In this study, it was found that the expression levels of Wnt and β-catenin in MSCs were obviously downregulated after treating with the exosomes of multiple myeloma cells and LINC00461-expressed vectors, suggesting that LINC00461 regulates the osteoblast differentiation of MSCs via inactivating the Wnt/β-catenin pathway. Moreover, it was also observed that increased miR-324-3pcould partly reverse the inactivated Wnt/β-catenin pathway [25]. Razny et al. indicated that miR-324-3p was significantly downregulated in the progression of osteoblast differentiation, which may be related with the activation of the Wnt/β-catenin pathway [26]. Thus, those proofs suggested that LINC00461 could inactivate the Wnt/β-catenin pathway to suppress the osteoblast differentiation of MSCs via targeting miR-324-3p.

Data Availability

The data used to support the findings of this study are available from the corresponding author upon request.

Conflicts of Interest

The authors declare that they have no conflicts of interest.

Acknowledgments

This study was supported by the Lanzhou Science and Technology Planning Project (2020-ZD-25).

References

[1] E. Terpos, G. Morgan, M. A. Dimopoulos et al., "International Myeloma Working Group recommendations for the treatment of multiple myeloma-related bone disease," *Journal of Clinical Oncology*, vol. 31, no. 18, pp. 2347–2357, 2013.

[2] L. Burgos, N. Puig, M.-T. Cedena et al., "Measurable residual disease in multiple myeloma: ready for clinical practice?" *Journal of Hematology & Oncology*, vol. 13, no. 1, p. 82, 2020.

[3] K. Shires and T. Van Wyk, "The role of Cancer/Testis Antigens in Multiple Myeloma pathogenesis and their application in disease monitoring and therapy," *Critical Reviews in Oncology*, vol. 132, pp. 17–26, 2018.

[4] H. Ludwig, S. Novis Durie, A. Meckl, A. Hinke, and B. Durie, "Multiple myeloma incidence and mortality around the globe; interrelations between health access and quality, economic resources, and patient empowerment," *The Oncologist*, vol. 25, no. 9, pp. e1406–e1413, 2020.

[5] J. Adamik, S. Jin, Q. Sun et al., "EZH2 or HDAC1 inhibition reverses multiple myeloma-induced epigenetic suppression of osteoblast differentiation," *Molecular Cancer Research*, vol. 15, no. 4, pp. 405–417, 2017.

[6] B. M. Abdallah, A. M. Alzahrani, and M. Kassem, "Secreted Clusterin protein inhibits osteoblast differentiation of bone marrow mesenchymal stem cells by suppressing ERK1/2 signaling pathway," *Bone*, vol. 110, pp. 221–229, 2018.

Hindawi
Journal of Healthcare Engineering
Volume 2023, Article ID 9823939, 1 page
https://doi.org/10.1155/2023/9823939

Retraction

Retracted: Targeting AraC-Resistant Acute Myeloid Leukemia by Dual Inhibition of CDK9 and Bcl-2: A Systematic Review and Meta-Analysis

Journal of Healthcare Engineering

Received 8 August 2023; Accepted 8 August 2023; Published 9 August 2023

This article has been retracted by Hindawi following an investigation undertaken by the publisher [1]. This investigation has uncovered evidence of one or more of the following indicators of systematic manipulation of the publication process:

(1) Discrepancies in scope
(2) Discrepancies in the description of the research reported
(3) Discrepancies between the availability of data and the research described
(4) Inappropriate citations
(5) Incoherent, meaningless and/or irrelevant content included in the article
(6) Peer-review manipulation

The presence of these indicators undermines our confidence in the integrity of the article's content and we cannot, therefore, vouch for its reliability. Please note that this notice is intended solely to alert readers that the content of this article is unreliable. We have not investigated whether authors were aware of or involved in the systematic manipulation of the publication process.

In addition, our investigation has also shown that one or more of the following human-subject reporting requirements has not been met in this article: ethical approval by an Institutional Review Board (IRB) committee or equivalent, patient/participant consent to participate, and/or agreement to publish patient/participant details (where relevant).

Wiley and Hindawi regrets that the usual quality checks did not identify these issues before publication and have since put additional measures in place to safeguard research integrity.

We wish to credit our own Research Integrity and Research Publishing teams and anonymous and named external researchers and research integrity experts for contributing to this investigation.

The corresponding author, as the representative of all authors, has been given the opportunity to register their agreement or disagreement to this retraction. We have kept a record of any response received.

References

[1] L. Li, C. Han, X. Yu, J. Shen, and Y. Cao, "Targeting AraC-Resistant Acute Myeloid Leukemia by Dual Inhibition of CDK9 and Bcl-2: A Systematic Review and Meta-Analysis," *Journal of Healthcare Engineering*, vol. 2022, Article ID 2842066, 7 pages, 2022.

Hindawi
Journal of Healthcare Engineering
Volume 2022, Article ID 2842066, 7 pages
https://doi.org/10.1155/2022/2842066

Research Article

Targeting AraC-Resistant Acute Myeloid Leukemia by Dual Inhibition of CDK9 and Bcl-2: A Systematic Review and Meta-Analysis

Linzhang Li, Chengwu Han, Xueying Yu, Jun Shen, and Yongtong Cao

Department of Laboratory Medicine, China-Japan Friendship Hospital, Beijing, China

Correspondence should be addressed to Yongtong Cao; caoyongtong100@sina.com

Received 14 November 2021; Revised 13 December 2021; Accepted 3 January 2022; Published 25 January 2022

Academic Editor: Enas Abdulhay

Purpose. This study aims to determine the influence of targeting araC-resistant acute myeloid leukemia by dual inhibition cyclin-dependent protein kinase (CDK9) and B-cell lymphoma-2 (Bcl-2). *Method.* The c-Myc inhibitor 10058-F4 and the CDK9 inhibitor AZD4573 were used to determine the cell cycle arrest and apoptosis. *Results.* 10058-F4 reduces c-Myc protein levels and suppresses HepG2 cell proliferation, possibly by upregulating cyclin-dependent kinase (CDK) inhibitors, p21WAF1, and reducing intracellular alpha-fetal protein (AFP) levels. *Conclusion.* The combination of AZD4573 and 10058-F4 has a synergistic anti-araC-resistant AML activity, providing a solid database for the aforementioned scientific hypothesis.

1. Introduction

Hematopoietic stem cells can self-renew and differentiate, and their control regulates their proliferation speed [1, 2]. When hematopoietic stem cells show malignant proliferation, leukemic cells are characterized by abnormal proliferation, impaired differentiation, and blocked apoptosis. The proliferation and accumulation of leukemic cells are substantially held in the bone marrow and other hematopoietic tissues and proceed to infiltration in other body tissues and organs, thus affecting the normal physiological function of the human body. Common clinical symptoms of leukemia are various anemic blood pictures, uncertain bleeding, common infections and body fever, and enlargement of vital body organs, including liver, spleen, lymph adenomegaly, and skeletal pain [3–6]. Acute myeloid leukemia (AML) is a cancer of blood cell myeloid cell lines defined by the rapid growth of abnormal leukocytes, accumulating in the patient's bone marrow and interfering with the normal blood cells production, and its incidence increases with age [7–10]. In our country, 3-4 people develop leukemia per 100,000 people. Leukemia ranks sixth among female malignancies, seventh among men, and first among children and adults under 35. Therefore, it is urgent to develop more effective treatment strategies to enhance the therapeutic effect of leukemia and reduce mortality. Currently, the primary treatment of AML is "7 + 3" therapy combined with HSCT [11]. Although most patients can achieve complete remission after chemotherapy, most of these patients will relapse with complications. In addition, approximately two-thirds of older patients (over 60 years old) with AML are refractory to standard chemotherapy and have a poor prognosis [12]. Currently, the five-year overall survival in adult AML is only about 25% and about 65% in pediatric patients. Therefore, it is of great scientific and clinical importance to find new AML therapies, develop new therapeutic strategies to prolong the survival rate of AML patients, and ultimately improve their cure rates.

2. Method

The Bcl-2 protein family comprises antiapoptotic proteins (Bcl-2, Bcl-xL, Mcl-1, Bcl-w etc.) and proapoptotic proteins (Bim, Bak, Bad, Bax, etc.), and the two classes of protein ratios determine cell survival or cell death [13, 14]. The aberrant expression of antiapoptotic Bcl-2 family proteins is firmly linked with chemoresistance and poor prognosis [15]. 10058-F4 is a c-Myc inhibitor that explicitly inhibits c-Myc-

Max interactions and prevents the transcriptional activation of c-Myc target gene expression [16–19]. 10058-F4 can promote caspase-3-dependent apoptosis and regulate autophagy. 10058-F4 inhibited leukemic cell growth and inhibited Myc and Max dimerization. Cell cycle arrest and apoptosis were induced by 10058-F4 in AML cells. AML cells stalled by 10058-F4 in the cell cycle phase of G0/G1 downregulated the expression of c-Myc and upregulation of CDK inhibitors, including p21 and p27 [20].

3. Results

Meanwhile, the apoptosis was induced by 10,058-F4 performing mitochondrial pathway activation, and downregulation of Bcl-2, upregulation of Bax, cytochrome C release within the cytosol, and cleavage of caspase 3, 7, and 9 were observed. In addition, bone marrow cell differentiation is also induced by10058-F4, perhaps by activating multiple transcription factors. Similarly, 10058-F4 acts on primary AML cells to cause apoptosis and differentiation. 10058-F4 reduces c-Myc protein levels and suppresses HepG2 cell proliferation, possibly by upregulating cyclin-dependent kinase (CDK) inhibitors, p21WAF1, and reducing intracellular-alpha-fetal protein (AFP) levels [21]. The human telomerase reverse transcriptase (hTERT) downregulated at the transcriptional level by the treatment of 10058-F4. Besides inhibiting He 2 cell proliferation, HepG8-F4 is used to enhancing its sensitivity and responsiveness against conventional chemotherapeutics, including doxorubicin, 5-fluorouracil (5-FU), and cisplatin. It has also been shown that Mcl-1 causes the tolerance of tumor stem cells to chemotherapeutic agents by enhancing mitochondrial oxidative phosphorylation [22].

Moreover, Bcl-2 was also overexpressed in human AML stem cells, and inhibition of Bcl-2 selectively eradicated quiescent AML stem cells by inhibiting mitochondrial oxidative phosphorylation [23–25]. The above studies suggest that targeting both Bcl-2 and Mcl-1 induces apoptosis through the mitochondrial pathway. On the other hand, it inhibits mitochondrial oxidative phosphorylation while killing AML primary cells and stem cells [26]. Our previous work demonstrated that the FLT3 inhibitors midostaurin and gilteritinib can downregulate Mcl-1 and synergy with anti-F LT 3 mutation-positive AML activity with ABT-199 [27]. Still, studies of their combined application on AML stem cell killing activity are lacking.

CDK is a cyclin-dependent kinase that functions to activate the phosphorylation of downstream cell cycle-associated proteins while regulating its activity itself, influenced by phosphorylation and nonphosphorylation [28]. Its activity control points are mainly summarized as follows: (1) the concentration of cyclin because CDK needs to bind to some cyclins to produce activity; (2) CDK phosphorylation sites; (3) the regulation of CDK repressors, such as CDK repressor CKI; and (4) the control of protein catalytic factors.

AZD4573 is a potent CDK9 inhibitor with high selectivity. Scheme 1

In cells, the short-term treatment of AZD4573 can decrease intracellular pSer2-RNAPII (concentration and time correlation), with the activation of caspase 3 and apoptosis in most hematologic blood cancer cell lines. In various human blood cancer cells, AZD4573 induced rapid caspase activation (6 h) and lost survival viability (24 h), with little effect on solid tumors. Cyclin-dependent kinases (CDK) are a wide range of key proteins that perform cellular activities and function, including cell division and transcription. Dysregulation is identified as an important tumorigenesis driver. Additionally, the role of CDK in cancer and its involvement in the transcriptional process has been demonstrated recently. In most cancers, CDKs openly used as vital transcriptional regulators (e.g., CDK9) for consistent production of short-lived gene products that support cell survival [29]. Therefore, CDK9 pathway dysregulation is seen in various malignancies, making it a key anticancer target [30]. This approach has been used to initiate the discovery of CDK9 inhibitors by conducting human clinical trials [31].

Protein kinases are an important name in the CDK9 inhibitors list. These are the large family of enzymes and are responsible for the regulation of most eukaryotic cellular functioning and regulate cell signaling pathways by protein phosphorylation. This process is responsible for enzymes activation or inhibition, increasing protein-protein interactions, alteration of cellular localization, or generation of protein recruitment sites. Regulation of protein kinases itself is generated by various transcriptional and posttranslational modifications. The overall outcome of the whole process is the regulation of cellular functioning, including proliferation, apoptosis, and differentiation. The encoding of the human genome includes more than 500 genes of protein kinase. Because of its key function, dysregulation of protein kinase due to gene mutations or lack of negative regulators is associated with many pathological diseases (e.g., cancer and inflammatory diseases). A protein-dependent kinase (CDK) is a serine (Ser)/threonine (Thr) protein kinase activated by the regulatory cyclin. The encoding of 20 CDK (numbers 1–20) of the human genome belongs to the CDK and CDK-like clades of the CMGC. CMGC is a subfamily of human cell kinases, such as cyclin-dependent, glycogen synthase, mitogen-activated, and CDC-like kinases.

CDK and its cyclin partners perform their particular roles in many cellular functioning, including cell division and cell transcription, responding to intracellular and extracellular cell signaling. The structure of CDK protein is a double-leaf, and the active site is sandwiched between the (amino) N-terminal lobe, particularly comprising sheet B and the (carboxyl) C-terminal lobe of the helix. The CDK regulation is initiated by cyclin subunits binding, which is itself regulated by formation and degradation, and the phosphorylation of the conserved residues in the T-and glycine (G) rich loop structures of CDK. Due to the evolutionary connection and key functional roles, CDKs can be categorized into two major groups: CDKs that are responsible for the cell cycle regulation, including CDKs 1–7 and 14–18, and CDKs for transcription regulation, including CDKs 7–13 and 18–20. Due to these central regulatory activities, dysregulation of CDK is closely linked to human

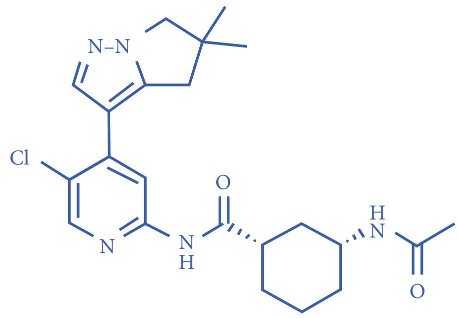

Scheme 1: Chemical structure of AZD4573. AZD4573 is a novel and selective inhibitor of CDK9, exhibiting rapid cell-death induction in most hematologic blood cancer cell lines.

cancers or malignancies. This is especially true of CDK9, where CDK9 is a key transcriptional regulator in which cancer cells openly utilize to continuously produce short-lived proteins that sustain survival. During transcription elongation, a component called P-TEFb is a major target of DRB. A protein obtained from the human immunodeficiency virus 1 (HIV1), called the transcriptional transactivator (TAT), performs a vital role in HIV1 viral transcription by creating a complex containing P-TEF.

Based on the above literature analysis and preliminary research basis, we propose the scientific hypothesis of this project (Figure 1). In araC-resistant AML, applying AZD4573 and 10058F4 to downregulate c-Myc and Mcl-1 to inhibit Bcl-2 simultaneously and, on the other hand, to induce apoptosis by the activation of the endogenous apoptotic pathway. We demonstrated in our previous work that the combination of AZD4573 and 10058-F4 has a synergistic anti-araC-resistant AML activity, providing a solid database for the aforementioned scientific hypothesis.

For a comprehensive validation of the above hypothesis, this study will focus on addressing three key scientific issues: ① in araC-resistant AML, AZD4573 downregulated c-Myc and Mcl-1. Thus the molecular mechanism of inducing apoptosis in AML cells in coordination with 10058-F4;② effects of AZD4573 and 10058-F4 on the energy metabolism of Arac-resistant AML cells further illustrate the molecular mechanism of the AZD4573 and 10058-F4 synergy against araC-resistant AML;③ the in vivo activity of the combination of AZD4573 and 10058-F4 and the effects on araC-resistant AML cells.

4. Discussion

Cells in the human blood are all derived from pluripotent HSCs in the bone marrow. Pluripotent hematopoietic SCs differentiate into myeloid progenitors, and after a series of differentiation maturation processes, myeloid progenitors eventually become erythrocytes, granulocytes, monocytes, and platelets, while lymphoid progenitors differentiate into lymphocytes and plasma cells [32–35]. Each blood cell has important and unique physiological functions, and blood cell abnormalities can lead to the occurrence of disease. Leukemia is triggered if blood cell precursor cells arrest and proliferate malignantly. Leukemic cells are able to inhibit the generation of normal blood cells and infiltrate other

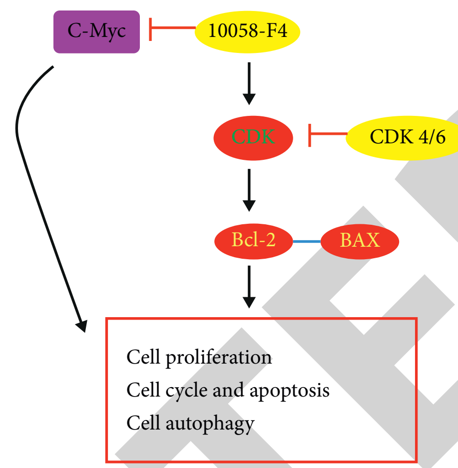

Figure 1: In araC-resistant AML, we apply AZD4573 and 10058F4 to downregulate c-Myc to inhibit Bcl-2 and affect the cell proliferation, cell cycle and apoptosis, and cell autophagy.

healthy tissues and organs, causing hematopoietic dysfunction. The clinical manifestations of patients with leukemia are usually anemia, easy fatigue, fever, bleeding points, pain in limbs, infection, hepatic manifestations, and splenomegaly. The exact etiology of leukemia is currently unclear, with smoking, ionizing radiation, exposure to certain chemical reagents, viruses, and genetic factors being possible triggers of leukemia. About 75,000 new leukemia patients occur in China every year, while 53,000 individuals die of leukemia every year. In the past two years, the incidence of leukemia in China has been on the rise.

Leukemia can be categorized into acute leukemia and chronic leukemia according to the fast and slow course of the disease. Abnormal proliferating cells of acute leukemia are not mature and make rapid clinical progress; blood cells with abnormal proliferation of chronic leukemia develop more mature but do not have the anti-infection ability of normal leukocytes, and the clinical progress is slow. Leukemia can be divided into myeloid leukemia and lymphoid leukemia according to the origin of the onset cell. By combining the incidence rate with the cellular source, leukemia can be divided into four types, as shown in Table 1:

Acute myeloid leukemia (AML) is a highly malignant hematological disease with abnormal proliferation, blocked differentiation, and high cell heterogeneity. Routine treatment of AML is divided into two stages. The first stage is the induced remission phase, and the primary aim is to reduce the number of AML main cells to achieve complete remission, where AML cells are not detectable in both the bone marrow and peripheral blood, and healthy blood cells return to normal levels. Commonly used drugs are cytarabine (cytarabine, araC) and anthracyclines such as daunorubicin (daunorubicin, DNR), idarubicin, and mitoxantrone. The conventional chemotherapy regimen was a 7-day continuous intravenous infusion of standard-dose cytarabine (100–200 mg/m2/d) plus daunorubicin continuous intravenous infusion (60–90 mg/m 2/d), also known as "7 + 3" therapy.

The second stage of AML treatment is the postremission treatment. A small number of undetectable AML cells will

Table 1: The classification of leukemia.

Number	Disease	Popular
1	Acute lymphoid leukemia	Children aged 3–7 years; is relatively rare in adults
2	Acute myeloid leukemia	67–70 years old, especially the elderly over 65; is rare before 45 years old
3	Chronic lymphoid leukemia	Frequently occurring in adults, occasionally in adolescents; it is extremely rare in children
4	Chronic myeloid leukemia	Extremely rare among children with a median age of onset over 70 years

still exist in vivo after complete remission. Without further treatment, AML will relapse within weeks to months. There are two strategies after remission: the first is consolidation therapy, which refers to the same or higher intensity of chemotherapy with chemotherapeutic drugs without cross-resistance as the chemotherapeutic drugs used for inducing remission therapy. Suitable for AML patients under 60 years of age, who are highly tolerated and can continue to receive 2–4 cycles of araC after remission. The other is to find a suitable bone marrow donor for bone marrow transplantation. Patients need a feasibility and risk assessment to decide on a bone marrow transplant. Bone marrow transplant patients need to remove AML cells before bone marrow transplantation, and not all patients can withstand this treatment, and there is a certain risk of surgical failure. Patients with AML may still relapse even with the most effective after remission therapy. Although most patients can achieve complete remission after chemotherapy, most of these patients will relapse with complications. In addition, approximately two-thirds of older patients (over 60 years old) with AML are refractory to standard chemotherapy and have a poor prognosis. Currently, the five-year overall survival in adult AML is only about 25% and about 65% in pediatric patients. Therefore, it is of great scientific and clinical importance to find new AML therapies, develop new therapeutic strategies to prolong survival in AML patients, and ultimately improve their cure rates.

Acute myeloid leukemia (AML) is initiated by the abnormal myeloblasts accumulation, primarily in the bone marrow, which leads to bone marrow failure and finally causes death [36–39]. Involvement of peripheral blood is frequent in AML, while infiltration of vital body organs (most ominous, brain and/or lungs) is quite rare; the most common sign in AML patients is high blood cell count (e. g., >50,000/L). Granulocytic sarcoma (GS), also referred to as AML, that confined to bone marrow or blood does not progress to organs. GC usually developed involvement of bone marrow within 1 year time and is generally treated as myeloid-involved acute myeloid leukemia. The 2016 World Health Organization (WHO) criteria for acute myeloid leukemia define at least 20 percent of bone marrow (or blood) cells (MFCs). The exception to the 220% standard was CBF acute myeloid leukemia including cytogenetic abnormalities (t [8; 21], or inv [16], or t [16; 16]), NPM1 mutant AML, or acute promyelocyte leukemia; in each case, the diagnosis of acute myeloid leukemia was not dependent of % of blast seen. Occasionally myeloid blasts may also have T-cell or B-cell markers for the identification or may have distinct myeloid and lymphoid populations [40–43]. These AML cases are identified as "mixed phenotypic acute leukemia." It is still unclear whether it requires simultaneous treatment as acute myeloid leukemia, lymphoblastic leukemia, or both. Treatment dependence is based on the extent to which the myeloid or lymphatic component is dominant. Cases with fibroblasts of over 20% but lack markers are called acute undifferentiated leukemia, often treated as acute myeloid leukemia.

The prognosis of AML patients ranges from the death of treatment to within days, i.e., treatment-related mortality to cure it, possibly. The main reason for patients is treatment resistance and often presents as relapse after remission rather than a TRM with decreasing incidence even in older patients. Knowledge of the various premutational states of gene therapy improves our ability to assign initial treatments. More importantly, whether ostensibly patients have measurable residual disease in time in remission should affect subsequent management. The US Food and Drug Administration has approved several new drugs, discussing their role in treatment.

Based on data that indicate predictive covariates, the following factors are more important than the difference in acute myeloid leukemia—MDS disease, and some centers treated patients with blast number >10% as acute myeloid leukemia, even if they were treated by the WHO as a blast number of more than 2. From a biological perspective, the pattern of acute myeloid leukemia mutations occurring after previous hematological disorders (e. g., myeloid marrow dysplasia) is generally more similar to that found in MDS than primary (new) acute myeloid leukemia.

As research advances, many new therapies have been constantly proposed and applied to clinical experiments, such as small-molecule inhibitor-targeted therapies, immunotherapy. Among them, small-molecule inhibitor-targeted treatment is even more popular and highly concerned. Small molecule inhibitor-targeted treatment mainly suppresses cell growth, proliferation, and survival by targeting relevant cell signaling pathways (for example, kinase pathway, apoptosis pathway, DNA damage repair-related pathway) to achieve the effect of treating AML [44–47]. At present, the research of such new therapies has also achieved gratifying results. In recent years, the FDA has successively approved multiple small-molecule targeting inhibitors to treat AML, such as the Bcl-2-selective inhibitor venetoclax, the FLT-3 inhibitor midostaurin and gilteritinib [48].

Traditionally, new drugs have been tested in newly diagnosed cases of acute myeloid leukemia with relapse or at risk of disadvantage [12, 49–51]. One possibility is on the MRD setting. This practice may tend to abandon these drugs, but in less advanced diseases, they may act better. However, the registration of many new drug trials is limited to morphological relapse (>5% fibroblasts) [52]. The response rate to new therapeutics may be higher if tested in MRD cases, and MRD is the only evidence of disease. It is the rationale for relapse that the predictive value of positive MRD trials is very high, particularly in individuals taking pretreatment of ELN 2017 year confrontation, the interval between MRD emergence and morphological relapse is usually short (<1 year), and the side effects of "targeted" therapy are generally limited, thus creating a favorable risk ratio when used for the MRD treatment. It is most likely that more targeted therapies for MRD will follow in the next few years. In recent years, it has also been seen to detect recurrence by bone marrow morphological evaluation of technical partial replacement criteria based on MRD; it seems that when MFC results are negative, the morphology of the cell will inevitably present with <5% of fibroblasts, which is below the morphological recurrence threshold. When the identical drug treatment is used to treat MRD relapse only and morphological degeneration, AML patients who only treat MRD will compare outcomes. It will also allow testing the very plausible yet unproven hypothesis that reduced MRD will generate better results. The next step will allow the piloting of new therapeutics with MRD negative cases but having a high risk of recurrence based on the pretreatment markers.

Finally, we may have overestimated our knowledge of targeted therapeutic targets. We note that the above beneficial effects of sorafenib, commonly considered as FLT 3 inhibitors, and, by adding to 7 + 3, appear to be the same in the population, regardless of whether they have FLT3 ITD or not. Therefore, there may have potential value once the outcome of targeted therapy. However, the limit is that there are not enough solid data that support the opinion, which suggest us to conduct further experiments to confirm this.

Data Availability

The data used to support this study are available from the corresponding author upon request.

Conflicts of Interest

The authors declare that they have no conflicts of interest.

Acknowledgments

This paper was funded by the China-Japan Friendship Hospital research fund (2018-1-QN-7) (Linzhang Li), the National Natural Science Foundation of China (82072337) (Yongtong Cao), and Key Clinical Specialty Project of Beijing 2020.

References

[1] J. Chen, Y. Dong, J. Peng et al., "Notch signaling mitigates chemotherapy toxicity by accelerating hematopoietic stem cells proliferation via c-Myc," *American Journal of Translation Research*, vol. 12, pp. 6723–6739, 2020.

[2] J. J. D. Roo and F. J. T. Staal, "Cell signaling pathway reporters in adult hematopoietic stem cells," *Cells*, vol. 9, 2020.

[3] O. Gorshkova, J. Cappai, L. Maillot, and A. Serge, "Analyzing normal and disrupted leukemic stem cell adhesion to bone marrow stromal cells by single-molecule tracking nanoscopy," *Journal of Cell Science*, vol. 134, 2021.

[4] B. Zhang, L. X. Truong Nguyen, D. Zhao et al., "Treatment-induced arteriolar revascularization and miR-126 enhancement in bone marrow niche protect leukemic stem cells in AML," *Journal of Hematology & Oncology*, vol. 14, p. 122, 2021.

[5] O. Ilhan, Z. Narli Ozdemir, K Dalva et al., "Leukemic stem cells shall be searched in the bone marrow before "tyrosine kinase inhibitor-discontinuation" in chronic myeloid leukemia," *Int J Lab Hematol*, vol. 43, pp. 1110–1116, 2021.

[6] P. W. Krenn, S. Koschmieder, and R. Fassler, "Kindlin-3 loss curbs chronic myeloid leukemia in mice by mobilizing leukemic stem cells from protective bone marrow niches," *Proceedings of the National Academy of Sciences of the U S A*, vol. 117, pp. 24326–24333, 2020.

[7] P. Makowka, V. Stolp, K. Stoschek, and H. Serve, "Molecular determinants of therapy response of venetoclax-based combinations in acute myeloid leukemia," *Biological Chemistry*, vol. 402, pp. 1547–1564, 2021.

[8] D. Padmakumar, R. C. Vineetha, G. Preethi, R T. V. D. Akhila, and R. J. A. Geetha, M. S. Mahitha, P. Amritha, and S. Hariharan, A concise review on the molecular genetics of acute myeloid leukemia," *Leukemia Research*, vol. 111, Article ID 106727, 2021.

[9] M. Maleki Behzad, M. Abbasi, I. Oliaei, S. Ghorbani Gholiabad, and H. Rafieemehr, "Effects of lifestyle and environmental factors on the risk of acute myeloid leukemia: result of a hospital-based case-control study," *Journal of Research in Health Sciences*, vol. 21, Article ID e00525, 2021.

[10] B. Aqil, J. Gao, M. Stalling et al., "Distinctive flow cytometric and mutational profile of acute myeloid leukemia with translocation(8;16)(p11;p13)," *American Journal of Clinical Pathology*, 2021.

[11] J. L. Carter, K. Hege, J. Yang et al., "Targeting multiple signaling pathways: the new approach to acute myeloid leukemia therapy," *Signal Transduct Target Ther*, vol. 5, p. 288, 2020.

[12] M. Stanchina, D. Soong, B. Zheng-Lin, J. M. Watts, and J. Taylor, "Advances in acute myeloid leukemia: recently approved therapies and drugs in development," *Cancers*, vol. 12, 2020.

[13] S. Cang, C. Iragavarapu, J. Savooji, Y. Song, and D. Liu, "ABT-199 (venetoclax) and BCL-2 inhibitors in clinical development," *Journal of Hematology & Oncology*, vol. 8, p. 129, 2015.

[14] Y. Wei, Y. Cao, R. Sun et al., "Targeting bcl-2 proteins in acute myeloid leukemia," *Frontiers Oncology*, vol. 10, Article ID 584974, 2020.

[15] S. Thomas, B. A. Quinn, S. K. Das et al., "Targeting the Bcl-2 family for cancer therapy," *Expert Opinion on Therapeutic Targets*, vol. 17, pp. 61–75, 2013.

[16] R. Ghaffarnia, A. Nasrollahzadeh, D. Bashash, N. Nasrollahzadeh, S. A. Mousavi, and S. H. Ghaffari, "Inhibition of c-Myc using 10058-F4 induces anti-tumor effects in ovarian cancer cells via regulation of FOXO target genes," *European Journal of Pharmacology*, vol. 908, Article ID 174345, 2021.

[17] M. Sayyadi, A. Safaroghli-Azar, M. Safa, H. Abolghasemi, M. Momeny, and D. Bashash, "NF-kappaB-dependent mechanism of action of c-myc inhibitor 10058-F4: highlighting a promising effect of c-myc inhibition in leukemia cells, irrespective of p53 status," *Iranian Journal of Pharmaceutical Research*, vol. 19, pp. 153–165, 2020.

[18] M. Sayyadi, A. Safaroghli-Azar, A. Pourbagheri-Sigaroodi, H. Abolghasemi, A. Arash Anoushirvani, and D. Bashash, "c-Myc inhibition using 10058-F4 increased the sensitivity of acute promyelocytic leukemia cells to arsenic trioxide via blunting PI3K/NF-kappaB Axis," *Archives of Medical Research*, vol. 51, pp. 636–644, 2020.

[19] N. Sheikh-Zeineddini, A. Safaroghli-Azar, S. Salari, and D. Bashash, "C-Myc inhibition sensitizes pre-B ALL cells to the anti-tumor effect of vincristine by altering apoptosis and autophagy: proposing a probable mechanism of action for 10058-F4," *European Journal of Pharmacology*, vol. 870, Article ID 172821, 2020.

[20] R. Pan, R. Vivian, and H. Mu, J. D. Leverson, G. Nichols, J. C. Reed, M. Konopleva, and M. Andreeff, Synthetic lethality of combined bcl-2 inhibition and p53 activation in AML: mechanisms and superior antileukemic efficacy," *Cancer Cell*, vol. 32, p. 748, 2017.

[21] R. Pan, L. J. Hogdal, J. M. Benito et al., "Selective BCL-2 inhibition by ABT-199 causes on-target cell death in acute myeloid leukemia," *Cancer Discovery*, vol. 4, pp. 362–375, 2014.

[22] L. Han, Q. Zhang, M. Dail et al., "Concomitant targeting of BCL2 with venetoclax and MAPK signaling with cobimetinib in acute myeloid leukemia models," *Haematologica*, vol. 105, pp. 697–707, 2020.

[23] D. Sharon, S. Cathelin, S. Mirali et al., "Inhibition of mitochondrial translation overcomes venetoclax resistance in AML through activation of the integrated stress response," *Science Translational Medicine*, vol. 11, 2019.

[24] K. Ishitsuka, S Mirali, T J.M Di, D.J Yanofsky, K.A Keon, and J.L Rubinstein, "Targeting Bcl-2 family proteins in adult T-cell leukemia/lymphoma: in vitro and in vivo effects of the novel Bcl-2 family inhibitor ABT-737," *Cancer Letters*, vol. 317, pp. 218–225, 2012.

[25] S. Peirs, V. Frismantas, F. Matthijssens et al., "Targeting BET proteins improves the therapeutic efficacy of BCL-2 inhibition in T-cell acute lymphoblastic leukemia," *Leukemia*, vol. 31, pp. 2037–2047, 2017.

[26] H. E. Ramsey, M.A Fischer, T Lee et al., "A novel MCL1 inhibitor combined with venetoclax rescues venetoclax-resistant acute myelogenous leukemia," *Cancer Discovery*, vol. 8, pp. 1566–1581, 2018.

[27] D. A. Luedtke, Y Su, J Ma et al., "Inhibition of CDK9 by voruciclib synergistically enhances cell death induced by the Bcl-2 selective inhibitor venetoclax in preclinical models of acute myeloid leukemia," *Signal Transduct Target Ther*, vol. 5, p. 17, 2020.

[28] F. Morales and A. Giordano, "Overview of CDK9 as a target in cancer research," *Cell Cycle*, vol. 15, pp. 519–527, 2016.

[29] E. M. Beauchamp, "Identification and targeting of novel CDK9 complexes in acute myeloid leukemia," *Blood*, vol. 133, pp. 1171–1185, 2019.

[30] W. L. Huang, T. Abudureheman, J. Xia et al., "CDK9 inhibitor induces the apoptosis of B-cell acute lymphocytic leukemia by inhibiting c-myc-mediated glycolytic metabolism," *Frontiers in Cell and Developmental Biology*, vol. 9, Article ID 641271, 2021.

[31] S. Boffo, A. Damato, L. Alfano, and A. Giordano, "CDK9 inhibitors in acute myeloid leukemia," *Journal of Experimental & Clinical Cancer Research*, vol. 37, p. 36, 2018.

[32] G. A. Mora-Roldan, D. Ramirez-Ramirez, R. Pelayo, and K. Gazarian, "Assessment of the hematopoietic differentiation potential of human pluripotent stem cells in 2D and 3D culture systems," *Cells*, vol. 10, no. 11, 2021.

[33] A. Yuzuriha and K. Eto, "Revised "hPSC-Sac method" for simple and efficient differentiation of human pluripotent stem cells to hematopoietic progenitor cells," *Methods in Molecular Biology*, 2021.

[34] X. Lei, C Ma, Y Cao, Y Xiong, J.V Zhang, and E Duan, "High-efficiency differentiation of human pluripotent stem cells to hematopoietic stem/progenitor cells in random positioning machine bioreactors," *Methods in Molecular Biology*, 2021.

[35] K. Fortschegger, A. M. Husa, D. Schinnerl, K. Nebral, and S. Strehl, "Expression of RUNX1-JAK2 in human induced pluripotent stem cell-derived hematopoietic cells activates the JAK-STAT and MYC pathways," *International Journal of Molecular Sciences*, vol. 22, 2021.

[36] C. Ustun, C Ustun, S Williams et al., "Allogeneic NK cells eradicate myeloblasts but not neoplastic mast cells in systemic mastocytosis associated with acute myeloid leukemia," *American Journal of Hematology*, vol. 92, pp. E66–E68, 2017.

[37] T. Kupsa, J. Vanek, Z. Pavel, L. Jebavy, and J. M. Horacek, "Serum levels of soluble adhesion molecules in newly diagnosed acute myeloid leukemia and in complete remission suggest endothelial cell activation by myeloblasts," *Biomed Pap Med Fac Univ Palacky Olomouc Czech Repub*, vol. 161, pp. 92–99, 2017.

[38] G. He, G He, C Wang et al., "Clinical and laboratory features of seven patients with acute myeloid leukemia (AML)-M2/M3 and elevated myeloblasts and abnormal promyelocytes," *Cancer Cell International*, vol. 14, p. 111, 2014.

[39] M. A. Jacoby, J P R.E De, J Shao et al., "The DNA double-strand break response is abnormal in myeloblasts from patients with therapy-related acute myeloid leukemia," *Leukemia*, vol. 28, pp. 1242–1251, 2014.

[40] K. K. Kannan, P Vellanki, S Isom et al., "Re-induction therapy in adult patients with acute myeloid leukemia with </=20 % blasts: a retrospective cohort study," *Leukemia Research*, vol. 111, Article ID 106731, 2021.

[41] C.-M. Aanei, R. Veyrat-Masson, L. Rigollet et al., "Advanced flow cytometry analysis algorithms for optimizing the detection of "different from normal" immunophenotypes in acute myeloid blasts," *Frontiers in Cell and Developmental Biology*, vol. 9, Article ID 735518, 2021.

[42] C. T. Kuo, R. J. Lee, and R. Garzon, "Correction to: methods used to make lipid nanoparticles to deliver LNA gapmers against lncRNAs into acute myeloid leukemia (AML) blasts," *Methods in Molecular Biology*, vol. 2348, p. C1, 2021.

[43] V. Dembitz, H. Lalic, B. Tomic, T. Smoljo et al., All-trans retinoic acid induces differentiation in primary acute myeloid leukemia blasts carrying an inversion of chromosome 16," *International Journal of Hematology*, 2021.

[44] U. F. Ndiokwelu, L. A. Ogunkanmi, J. B. Minari, and I. C. Uzoma, "Allium sativum aqueous extract does not have chemo-protective effect on etoposide induced therapy-related DNA damage leading to Acute Myeloid Leukemia in albino-wistar rats," *African Health Sciences*, vol. 21, pp. 673–682, 2021.

[45] Y. Han, X. Hu, X. Yun et al., "Nucleolar and spindle associated protein 1 enhances chemoresistance through DNA damage repair pathway in chronic lymphocytic leukemia by binding with RAD51," *Cell Death & Disease*, vol. 12, p. 1083, 2021.

[46] M. Henklewska, A. Pawlak, R.-F. Li, J. Yi, I. Zbyryt, and B. Obmińska-Mrukowicz, Benzyl isothiocyanate, a vegetable-derived compound, induces apoptosis via ROS accumulation and DNA damage in canine lymphoma and leukemia cells," *International Journal of Molecular Sciences*, vol. 22, 2021.

Hindawi
Journal of Healthcare Engineering
Volume 2023, Article ID 9864018, 1 page
https://doi.org/10.1155/2023/9864018

Retraction

Retracted: Analysis on Value of Applying Serum miR-144 and miR-221 Levels in Diagnosing Atherosclerosis

Journal of Healthcare Engineering

Received 12 November 2022; Accepted 12 November 2022; Published 30 January 2023

Journal of Healthcare Engineering has retracted the article titled "Analysis on Value of Applying Serum miR-144 and miR-221 Levels in Diagnosing Atherosclerosis" [1] due to concerns that the peer review process has been compromised.

Following an investigation conducted by the Hindawi Research Integrity team [2], significant concerns were identified with the peer reviewers assigned to this article; the investigation has concluded that the peer review process was compromised. We therefore can no longer trust the peer review process, and the article is being retracted with the agreement of the Chief Editor.

References

[1] J. Zhang, Q. Cao, Z. Zhang, C. Du, and L. Wang, "Analysis on Value of Applying Serum miR-144 and miR-221 Levels in Diagnosing Atherosclerosis," *Journal of Healthcare Engineering*, vol. 2022, Article ID 2261854, 7 pages, 2022.

[2] L. Ferguson, "Advancing Research Integrity Collaboratively and with Vigour," 2022, https://www.hindawi.com/post/advancing-research-integrity-collaboratively-and-vigour/.

Hindawi
Journal of Healthcare Engineering
Volume 2022, Article ID 2261854, 7 pages
https://doi.org/10.1155/2022/2261854

Research Article

Analysis on Value of Applying Serum miR-144 and miR-221 Levels in Diagnosing Atherosclerosis

Jianxiu Zhang,[1] Qian Cao,[1] Zhenying Zhang,[1] Chenguang Du,[2] and Lizhong Wang[1]

[1]*Cardiac Rehabilitation Centre, Beijing Rehabilitation Hospital of Capital Medical University, Beijing 100144, China*
[2]*Cardiac Rehabilitation Centre, College of Traditional Chinese Medicine, North China University of Technology, Tangshan, Hebei Province 063210, China*

Correspondence should be addressed to Lizhong Wang; wanglizhong@bjkfyy.org.cn

Received 2 December 2021; Revised 24 December 2021; Accepted 31 December 2021; Published 25 January 2022

Academic Editor: Enas Abdulhay

Objective. To explore the value of serum miR-144 and miR-221 in diagnosing atherosclerosis (AS). *Methods*. The clinical data of 52 AS patients treated in the department of cardiovascular medicine of our hospital from August 2019 to August 2020 were retrospectively analyzed, and 53 healthy persons were selected from the physical examination center at the same period as the control group. By measuring the indicators including the serum vascular endothelial growth factor (VEGF), superoxide dismutase (SOD), miR-144, and miR-221 in patients of both groups, their value of diagnosing AS was analyzed. *Results*. Compared with the control group, the AS group obtained significantly higher serum miR-221 and miR-144 expression levels ($P < 0.001$), significantly higher mean serum homocysteine (Hcy) level value ($P < 0.001$), lower mean serum SOD level ($P < 0.001$), and significantly higher level values of serum VEGF, nuclear factor-kappaB (NF-kB), and transforming growth factor-β (TGF-β) ($P < 0.001$), and the area under ROC curve, sensitivity, and specificity of combining miR-221 with miR-144 were significantly higher than those of single diagnosis. *Conclusion*. Serum miR-221 and miR-144 expression levels are increased in AS patients, and combining the two indicators in diagnosis is more accurate and can provide an accurate basis for diagnosis and condition assessment of AS.

1. Introduction

Atherosclerosis (AS) is a slowly progressive cerebrovascular disease. Research and investigations have revealed that [1, 2] approximately 20 million people worldwide die from the disease each year, which is an important cause of diseases including angina, coronary heart disease, and sudden cardiac death, as well as a leading cause of death in the elderly population. Although the fatality rate of AS shows a decreasing trend with modern medical treatment technology advancing day by day, its incidence rate is still increasing. Traditionally, AS is assessed mainly by imaging methods such as ultrasound vascular examination or X-ray, but quantitative indexes of assessment are lacking. According to the research finding [3], the incidence of AS is closely related to vascular inflammation, cell proliferation and apoptosis, and lipid metabolism, which is a complex and slow process. Recently, with the intensive research on exosomes, it has been found that exosomes can act as an important medium of intercellular communication and plays a major role in the occurrence and progression of AS. Micro-RNAs (miRNAs), stably present in various body fluids as the biomarker for various types of diseases, involve in the formation of AS as the key signaling and molecular regulator (Figure 1) [4–6]. miR-144 is structurally highly conserved and involves in the occurrence and progression of cancer, and cardiovascular diseases. Foreign scholars have confirmed [7] the down-regulation of miR-144 in plasma of patients with medullary carcinoma of thyroid, which in turn led to the development and progression of thyroid cancer; other studies have proved that [8] miR-144 played the role of cancer suppressor gene in cervical cancer, which provided a new direction in the later diagnosis and treatment for cardiovascular diseases. It has been proved that miR-211 is expressed abnormally in patients with epithelial ovarian cancer and closely related to the processes such as incidence, invasion, and metastasis of such disease [9, 10]. Currently, the diagnostic efficacy of miR-144 and miR-221 in AS is rarely studied, and therefore, it was

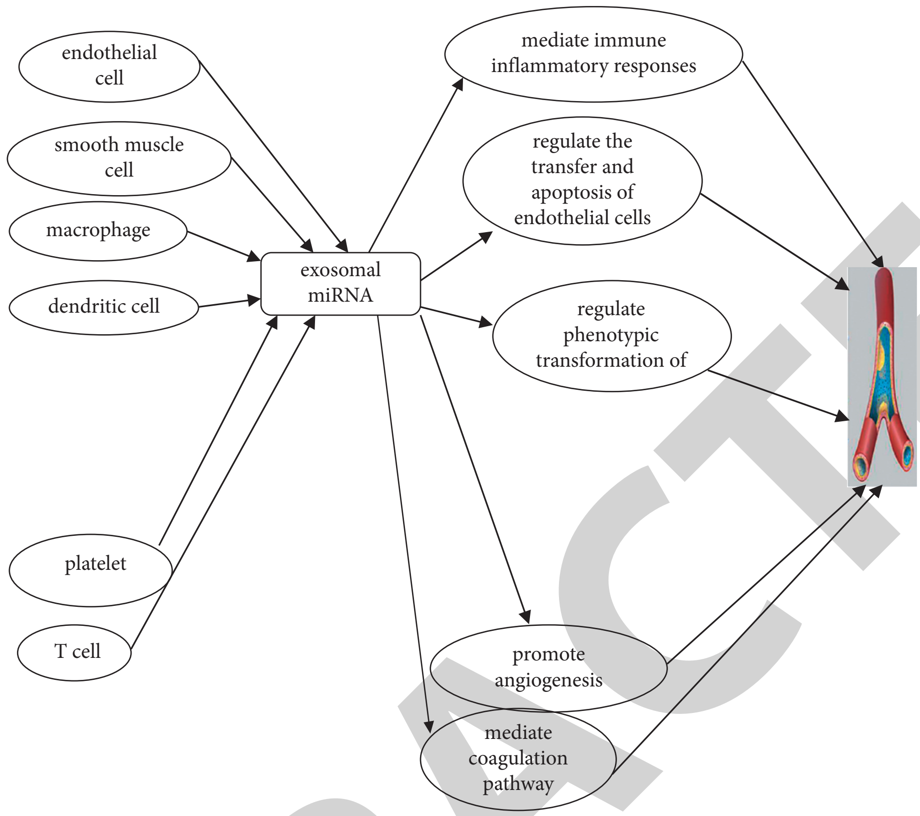

Figure 1: Effect of exosomal miRNA on AS progression.

analyzed herein to prevent and treat relevant cardiovascular diseases by target regulating miR-144 and miR-221 expression levels.

2. Data and Methods

2.1. General Information. The study was reviewed and approved by the hospital ethics committee. The clinical data of 52 AS patients treated in the department of cardiovascular medicine of our hospital (08.2019–08.2019) were selected for the retrospective study, and 52 healthy persons were screened from the physical examination center at the same period as the control group. Patients in the AS group met the diagnosis criteria of the disease, namely, abnormal blood lipid indexes and vascular stenosis lesions found in arteriography, and their clinical manifestations included angina, arrhythmia, headache, and fainting. Those with heart failure, angina, heart disease, hypertension, kidney function obstacle, and other cardiovascular diseases were excluded. Under the condition that all subjects signed the informed consent and agreed to join the study, the retrospective analysis and physical examination were conducted to all enrolled subjects, and their gender, age, BMI values, and other indicators were recorded.

2.2. Index Detection

2.2.1. Detection of miR-221 and miR-144 Level Values. The subjects fasted for more than 10 h. Before blood drawing, relevant instruments were prepared as required. The patients took the sitting position, with an arm extended straight on the table and the tourniquet tied at the upper arm; they were instructed to repeatedly make a fist to fill the vein, a cotton stick moistened with iodophor was used to make a ring disinfection treatment at the site for venipuncture with a syringe to collect 10 ml of venous blood, blood was placed in a procoagulant containing blood collection tube, and after centrifugation at 3,500 r/min for 10 min in an intelligent high-performance centrifuge (Beckman Coulter China branch; model: Avanti JXN-30/26), the serum from the upper layer was collected for relevant index detection [11, 12].

The extraction of RNA in serum was conducted according to the specification of blood RNA extraction kit (Shanghai GenePharma Co., Ltd.). The extracted RNA was collected and reversely transcribed into cDNA with the genome removal reverse transcription kit (Shanghai Ruifen Biotechnology Co., Ltd.). The expression levels of serum miR-221 and miR-144 were detected by the real-time fluorescent quantitative PCR method.

2.2.2. Detection of Serum Superoxide Dismutase (SOD) and Homocysteine (Hcy) Levels. The level values of serum SOD and Hcy were detected with the automatic biochemical analyzer (Shanghai Huanxi Medical Device Co., Ltd.; model: LW C200E).

2.2.3. Detection of Vascular Endothelial Growth Factor (VEGF), Nuclear Factor-Kappa B (NF-kB), and Transforming Growth Factor-β (TGF-β) Levels. The cytokine levels were detected by enzyme-linked immunosorbent assay (ELISA), the VEGF and NF-kB kits were purchased from Shanghai Zhen Ke Biological Technology Co., Ltd., the FGF-β kits were purchased from Shanghai Win-Win Biotechnology Co., Ltd., and all operations were carried out according to the kit instructions.

2.3. Statistical Processing. The statistical analysis and processing of experimental data were conducted with SPSS 21.0 software, the picture drawing software was GraphPad Prism 7 (GraphPad Software, San Diego, USA), the diagnosis value was analyzed by the Mann–Whitney U test, and the area under receiver operating characteristic curve (ROC curve), the measurement data examined by the t-test and expressed by ($\overline{x} \pm s$), and differences were considered statistically significant at $P < 0.05$.

3. Results

3.1. Between-Group Comparison of Basic Clinical Information. Other than various blood lipid indicators, no obvious between-group differences in the gender ratio, mean age, BMI value, smoking history, and drinking history were observed ($P < 0.05$), as given in Table 1.

3.2. Between-Group Comparison of Serum miR-221 and miR-144 Levels. Compared with the control group, the AS group had significantly higher miR-221 expression level and significantly lower miR-144 expression level ($P < 0.001$), as shown in Figure 2.

3.3. Between-Group Comparison of Serum SOD and Hcy Level Values. Compared with the control group, the AS group presented significantly higher mean serum Hcy level values ($P < 0.001$) and significantly lower mean serum SOD level values ($P < 0.001$), as shown in Figure 3.

3.4. Between-Group Comparison of Serum VEGF, NF-kB, and TGF-β Level Values. The serum VEGF, NF-kB, and TGF-β level values were significantly higher in the AS group than in the control group ($P < 0.001$), as given in Table 2.

3.5. Diagnosis Value of Serum miR-221 and miR-144 Levels for AS. The areas under the ROC curves of serum miR-221 and miR-144 levels for the diagnosis of AS was 0.670 and 0.613, respectively, and the area under the ROC curve of combined diagnosis was 0.858 (Table 3 and Figures 4–6).

4. Discussion

AS will cause arterial wall thickening, vessel stenosis, and vascular elasticity decrease, which is the main pathological basis of coronary heart disease, cerebral infarction, and peripheral ischemic vascular disease [13] and chronic inflammatory disease triggered by various factors. Since the early symptoms of the disease are not obvious, most patients have entered middle and late stages when diagnosed, seriously affecting the prognosis. Intravascular ultrasound (IVUS) examination is a common method for the diagnosis of AS [14–16], but it cannot accurately obtain the internal fine structure of local plaques, has less significance for identifying their vulnerability, and is an invasive tomographic technique [17]. On people's deeper exploration of serum biology, it is found that inflammation extends through the whole occurrence and progression process of AS, a long-term formed and progressed chronic inflammatory response, while serum marker levels are relatively stable and less affected by other factors, presenting higher sensitivity and specificity. Studies have shown that multiple cell-derived exosomal miRNAs are involved in this inflammatory process [18], exacerbating the disease progression of AS by causing inflammatory responses in its targeted cells and then leading to the formation of endothelial cell insufficiency, monocyte adhesion, foam cell, and vascular remodeling in the arterial wall. Among them, miR-221 accelerates the progression of AS by participating in the inflammatory response, activating its target genes, and causing dysfunction of the vascular endothelial membrane in patients. In the study conducted by foreign scholars [19] on a rat model of inflammation caused by chronic intake of sucrose, by detecting the exosomes in rats' blood, it was found that their miR-221 expression in plasma was significantly elevated, from which it could be speculated that miR-221 in plasma exosomes might be involved in the inflammatory response. Another study also found [20] that upregulated miR-221 expression could inhibit the cell cycle regulator p27kip1 in vascular smooth muscle cells, thereby mediating vascular calcification to cause atherosclerosis and stenosis. In this study, by detecting the expression levels of serum miR-221 in AS patients and in healthy persons, it was found that the miR-221 expression level was significantly higher in AS patients ($P < 0.001$), which was proved in the study by Elbaek et al. [21].

As an evolutionarily highly conserved miRNA, miR-144 is mapped on chromosome 17 in humans and exists as a miR-144/miR-451 gene cluster [22]. miR-144 levels in tissues are also of a great value in the diagnosis and prognosis evaluation of malignant tumors, and its clinical utility has been demonstrated in diseases such as breast cancer, oral squamous cell cancer, and colon cancer cancer [23]. Studies have found that [24] miR-144 is highly expressed in cardiomyocytes, and its high expression level can promote myocardial oxidative stress, thereby inducing myocardial injury related diseases, and its key role in the occurrence and progression of cardiovascular diseases have been confirmed by several foreign clinical trials. In this study, it was found that the serum miR-144 expression level in AS patients was significantly higher than that in the healthy group, and Lu et al. [25] in their study found that miR-144 expression in AS plaques and vascular smooth muscle cells (VSMCs) would gradually elevate as the disease progressed, presumably due to the imbalance of methylation and demethylation systems in vivo causing increased methylation of the miR-144 promoter.

An ideal serum marker shall have high specificity and sensitivity. In this study, miR-144 was found to be under

Table 1: Between-group comparison of basic clinical information (n (%), $\bar{x} \pm s$).

Item	AS group ($n = 52$)	Control group ($n = 53$)	X^2/t	P
Gender			0.094	0.759
Male	30 (57.69%)	29 (54.72%)		
Female	22 (42.31%)	24 (45.28%)		
Mean age ($\bar{x} \pm s$, years)	64.37 ± 3.26	64.42 ± 3.31	0.078	0.938
BMI ($\bar{x} \pm s$, kg/m^2)	21.19 ± 1.02	21.23 ± 1.04	0.199	0.843
Smoking history	29 (55.77%)	31 (58.83%)	0.079	0.778
Drinking history	32 (61.54%)	28 (52.83%)	0.813	0.367
Total cholesterol ($\bar{x} \pm s$, mmol/L)	5.22 ± 0.47	3.52 ± 0.46	18.731	<0.001
Triacylglycerol ($\bar{x} \pm s$, mmol/L)	1.62 ± 0.46	0.84 ± 0.21	11.212	<0.001
LDL-C ($\bar{x} \pm s$, mmol/L)	3.56 ± 0.35	2.26 ± 0.17	24.280	<0.001
HDL-C ($\bar{x} \pm s$, mmol/L)	1.12 ± 0.31	1.34 ± 0.23	4.135	<0.001

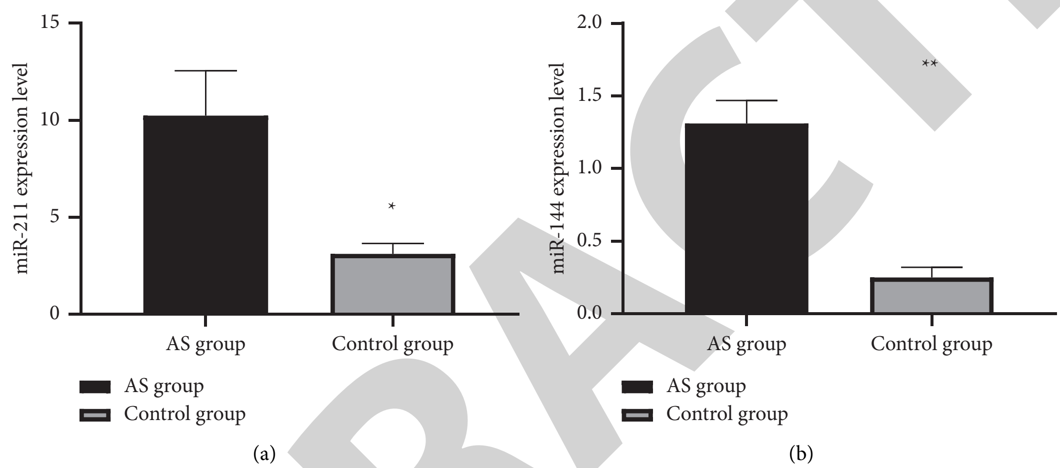

Figure 2: Between-group comparison of serum miR-221 and miR-144 levels ($\bar{x} \pm s$). (a) The between-group comparison of miR-221 expression levels. The horizontal axis denotes the AS group and control group, and the vertical axis denotes the level. The miR-221 expression level of the AS group and control group was 10.24 ± 2.31 and 3.12 ± 0.54, respectively, and * indicates the significant between-group difference in the miR-221 expression levels ($t = 21.841$, $P < 0.001$). (b) The between-group comparison of miR-144 expression levels. The horizontal axis denotes the AS group and control group, and the vertical axis denotes the level. The miR-144 expression level of the AS group and control group was 1.31 ± 0.16 and 0.25 ± 0.07, respectively, and ** indicates the significant between-group difference in the miR-144 expression levels ($t = 44.122$, $P < 0.001$).

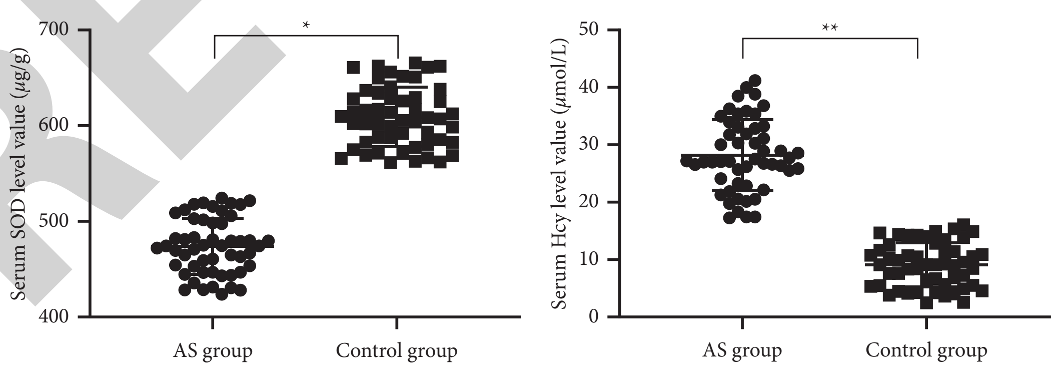

Figure 3: Between-group comparison of serum SOD and Hcy level values ($\bar{x} \pm s$). (a) The between-group comparison of serum SOD level values. The horizontal axis denotes the AS group and control group, and the vertical axis denotes the value (μg/g). The mean serum SOD level values of the AS group and control group were (477.30 ± 31.19) and (606.65 ± 32.00), respectively, and * indicates the significant between-group difference in mean serum SOD level values ($t = 20.970$, $P < 0.001$). (b) The between-group comparison of serum Hcy level values. The horizontal axis denotes the AS group and control group, and the vertical axis denotes the value (μmol/L). The mean serum Hcy level values of the AS group and control group were (28.17 ± 6.20) and (9.09 ± 3.85), respectively, and ** indicates the significant between-group difference in mean serum Hcy level values ($t = 18.983$, $P < 0.001$).

Table 2: Between-group comparison of serum VEGF, NF-kB, and TGF-β level values ($\bar{x} \pm s$).

Group	n	VEGF (pg/ml)	NF-kB (ng/L)	TGF-β (ng/L)
AS group	52	432.25 ± 35.64	1.69 ± 0.36	257.83 ± 5.27
Control group	53	142.56 ± 24.26	1.04 ± 0.29	67.48 ± 4.58
T		48.770	10.198	197.662
P		<0.001	<0.001	<0.001

Table 3: Diagnosis value of serum miR-221 and miR-144 levels for AS.

Indicator	Area under ROC curve	Positive rate (%)	95% CI	Sensitivity (%)	Specificity (%)
miR-221	0.670	24.76	0.566–0.774	86.75	81.26
miR-144	0.613	21.90	0.505–0.721	79.25	74.27
miR-221 + miR-144	0.858	43.81	0.781–0.935	93.25	85.37

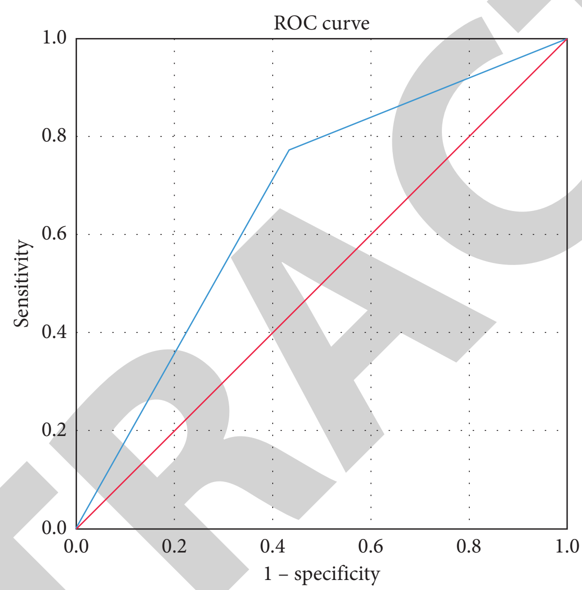

Figure 4: ROC curve of diagnosing AS with serum miR-221 expression level.

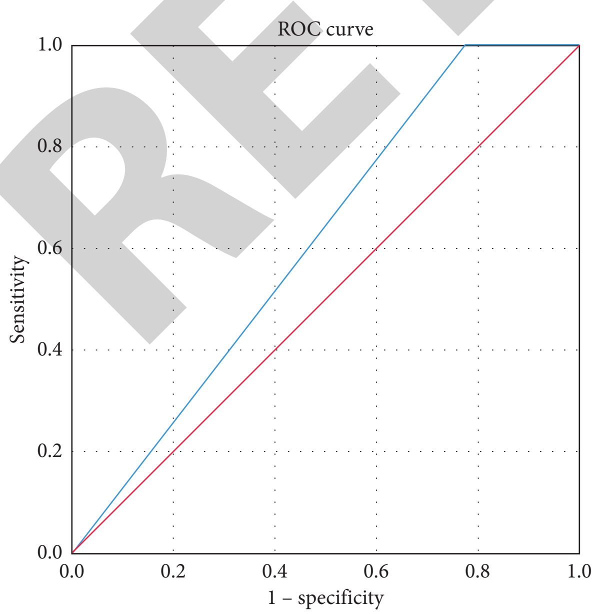

Figure 5: ROC curve of diagnosing AS with serum miR-144 expression level.

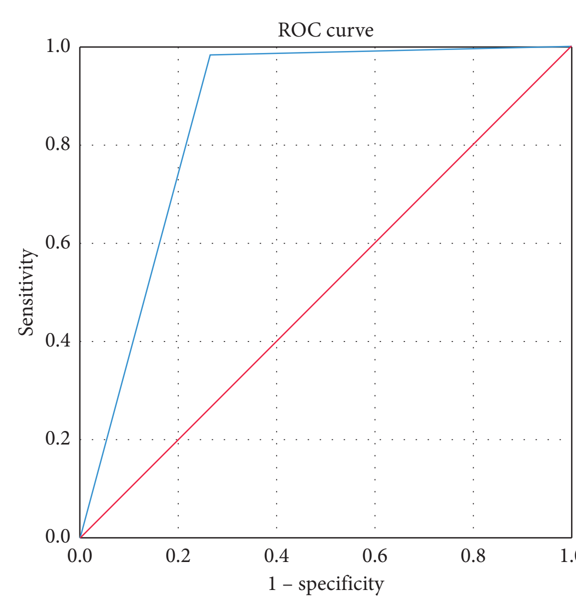

Figure 6: ROC curve of diagnosing AS with miR-221 + miR-144 expression level.

expressed in the serum of AS patients, and its area under the ROC curve for the diagnosis of AS was 0.613, whereas miR-221 had an area under the ROC curve of 0.670, which was higher than that of miR-144. But considering the low specificity of miR-144 in the diagnosis of AS, miR-221 was adopted for combined diagnosis, and as a result, the combination could improve the specificity and sensitivity of miR-144 for the diagnosis of AS, with an area under the ROC curve of 0.858. Deficiency of this study is that the small number of cases selected and the failure to consider the effect of disease type and stage on the results of the study are prone to bias of conclusions.

In conclusion, both miR-144 and miR-221 participate in the occurrence and progression of AS, and the combination of the two has a higher diagnosis value and can provide a new direction for the clinical diagnosis of AS.

Data Availability

The data used to support the findings of this study are available from the corresponding author upon request.

Conflicts of Interest

The authors declare that they have no conflicts of interest.

References

[1] W. Gong, J. Li, Y. Wang, and Z. Guangying, "miR-221 promotes lens epithelial cells apoptosis through interacting with SIRT1 and E2F3," *Chemico-Biological Interactions*, vol. 306, pp. 39–46, 2019.

[2] H.-Z. Ni, Z. Liu, L.-L. Sun et al., "Metformin inhibits angiogenesis of endothelial progenitor cells via miR-221-mediated p27 expression and autophagy," *Future Medicinal Chemistry*, vol. 11, no. 17, pp. 2263–2272, 2019.

[3] Y. Fu, F. Li, P. Zhang et al., "Myrothecine a modulates the proliferation of HCC cells and the maturation of dendritic cells through downregulating miR-221," *International Immunopharmacology*, vol. 75, Article ID 105783, 2019.

[4] A. S. Abo El Atta, Y. B. M. Ali, I. H. Bassyouni, and R. M. Talaat, "Upregulation of miR-221/222 expression in rheumatoid arthritis (RA) patients: correlation with disease activity," *Clinical and Experimental Medicine*, vol. 19, no. 1, pp. 47–53, 2019.

[5] X. Tang, G. Tu, G. Yang et al., "Autocrine TGF-beta 1/miR-200s/miR-221/DNMT3B regulatory loop maintains CAF status to fuel breast cancer cell proliferation," *Cancer Letters*, vol. 452, pp. 79–89, 2019.

[6] G. Ravegnini, C. Serrano, V. Simeon et al., "The rs17084733 variant in the KIT 3' UTR disrupts a miR-221/222 binding site in gastrointestinal stromal tumour: a sponge-like mechanism conferring disease susceptibility," *Epigenetics*, vol. 14, no. 6, pp. 545–557, 2019.

[7] J. Feng, M. Wang, M. Li et al., "Serum miR-221-3p as a new potential biomarker for depressed mood in perioperative patients," *Brain Research*, vol. 1720, Article ID 146296, 2019.

[8] Y. Higashi, S. Mummidi, S. Sukhanov et al., "Minocycline inhibits PDGF-BB-induced human aortic smooth muscle cell proliferation and migration by reversing miR-221-and-222-mediated RECK suppression," *Cellular Signalling*, vol. 57, pp. 10–20, 2019.

[9] Z. Cheng and D. Xing, "Ginsenoside Rg3 inhibits growth and epithelial-mesenchymal transition of human oral squamous carcinoma cells by down-regulating miR-221," *European Journal of Pharmacology: International Journal*, vol. 853, pp. 353–363, 2019.

[10] K. Srinoun, N. Sathirapongsasuti, K. Paiboonsukwong, S. Sretrirutchai, M. Wongchanchailert, and S. Fucharoen, "miR-144 regulates oxidative stress tolerance of thalassemic erythroid cell via targeting NRF2," *Annals of Hematology*, vol. 98, no. 9, pp. 2045–2052, 2019.

[11] M. R. Siddiqui, S. Akhtar, M. Shahid, M. Tauseef, K. McDonough, and T. P. Shanley, "miR-144-mediated inhibition of ROCK1 protects against LPS-induced lung endothelial hyperpermeability," *American Journal of Respiratory Cell and Molecular Biology*, vol. 61, no. 2, pp. 257–265, 2019.

[12] J. Liu, L. Feng, H. Zhang et al., "Effects of miR-144 on the sensitivity of human anaplastic thyroid carcinoma cells to cisplatin by autophagy regulation," *Cancer Biology & Therapy*, vol. 19, no. 4/6, pp. 484–496, 2018.

[13] M. Zhao, J. Huang, K. Gui et al., "The downregulation of miR-144 is associated with the growth and invasion of osteosarcoma cells through the regulation of TAGLN expression," *International Journal of Molecular Medicine*, vol. 34, no. 6, pp. 1565–1572, 2014.

[14] M. Kalimutho, G. Del Vecchio Blanco, S. Di Cecilia et al., "Differential expression of miR-144 as a novel fecal-based diagnostic marker for colorectal cancer," *Journal of Gastroenterology*, vol. 46, no. 12, pp. 1391–1402, 2011.

[15] F. Gao, T. Wang, Z. Zhang, R. Wang, Y. Guo, and J. Liu, "Regulation of activating protein-4-associated metastases of non-small cell lung cancer cells by miR-144," *Tumor Biology*, vol. 37, no. 12, pp. 15535–15541, 2016.

[16] F. Liu, J. Wang, Q. Fu et al., "VEGF-activated miR-144 regulates autophagic survival of prostate cancer cells against Cisplatin," *Tumor Biology*, vol. 37, no. 12, pp. 15627–15633, 2016.

[17] A. Hartley, D. Haskard, and R. Khamis, "Oxidized LDL and anti-oxidized LDL antibodies in atherosclerosis - novel insights and future directions in diagnosis and therapy,," *Trends in Cardiovascular Medicine*, vol. 29, no. 1, pp. 22–26, 2019.

[18] J. W. Eikelboom, S. J. Connolly, J. Bosch et al., "Bleeding and new cancer diagnosis in patients with atherosclerosis," *Circulation*, vol. 140, no. 18, pp. 1451–1459, 2019.

[19] Y. Zhang, C. Zhang, H. Li, and J. Hou, "The presence of high levels of circulating trimethylamine N-oxide exacerbates central and peripheral inflammation and inflammatory hyperalgesia in rats following carrageenan injection," *Inflammation*, vol. 42, no. 6, pp. 2257–2266, 2019.

[20] V. Van De Pol, M. Vos, M. C. Deruiter, M. J. Goumans, C. J. M. De Vries, and K. Kurakula, "LIM-only protein FHL2 attenuates inflammation in vascular smooth muscle cells through inhibition of the NFκB pathway," *Vascular Pharmacology*, vol. 125-126, Article ID 106634, 2020.

[21] E. Mette Vestergaard, S. Anders Lindholm, and H. C. Hasselbalch, "Cardiovascular disease in chronic myelomonocytic leukemia: do monocytosis and chronic inflammation predispose to accelerated atherosclerosis?" *Annals of Hematology*, vol. 98, no. 1, pp. 101–109, 2019.

[22] M. Yu, Y. Niu, D. Zhou et al., "Hyaluronic acid-functionalized gadolinium doped iron oxide nanoparticles for atherosclerosis-targeted Mr imaging," *Journal of Biomedical Nanotechnology*, vol. 15, no. 1, pp. 127–137, 2019.

[23] S. Sheng, L. Xie, Y. Wu, M Ding, T Zhang, and X Wang, "MiR-144 inhibits growth and metastasis in colon cancer by down-

Hindawi
Journal of Healthcare Engineering
Volume 2022, Article ID 1892123, 7 pages
https://doi.org/10.1155/2022/1892123

Research Article

Application of Internet of Things on the Healthcare Field Using Convolutional Neural Network Processing

J. Mohana,[1] Bhaskarrao Yakkala,[1] S. Vimalnath,[2] P. M. Benson Mansingh,[3] N. Yuvaraj,[4] K. Srihari ,[5] G. Sasikala,[6] V. Mahalakshmi,[6] R. Yasir Abdullah,[7] and Venkatesa Prabhu Sundramurthy [8]

[1]*Department of Electronics and Communication Engineering, Saveetha School of Engineering, SIMATS, Chennai, Tamil Nadu, India*
[2]*Department of Electronics and Communication Engineering, Erode Sengunthar Engineering College, Erode, Tamil Nadu, India*
[3]*Department of Electronics and Communication Engineering, Sri Ramakrishna Institute of Technology, Coimbatore, Tamil Nadu, India*
[4]*Research and Publications, ICT Academy, IIT Madras Research Park, Chennai, Tamil Nadu, India*
[5]*Department of Computer Science and Engineering, SNS College of Technology, Coimbatore, Tamil Nadu, India*
[6]*Department of Electronics and Communication Engineering, Vel Tech Rangarajan Dr. Sagunthala R&D Institute of Science and Technology, 400 Feet Outer Ring Road,Avadi, Chennai 600062, Tamil Nadu, India*
[7]*CSBS, Sri Krishna College of Engineering and Technology, Coimbatore, Tamil Nadu, India*
[8]*Center of Excellence for Bioprocess and Biotechnology, Department of Chemical Engineering, College of Biological and Chemical Engineering, Addis Ababa Science and Technology University, Addis Ababa, Ethiopia*

Correspondence should be addressed to Venkatesa Prabhu Sundramurthy; venkatesa.prabhu@aastu.edu.et

Received 20 November 2021; Revised 6 January 2022; Accepted 7 January 2022; Published 25 January 2022

Academic Editor: Enas Abdulhay

Population at risk can benefit greatly from remote health monitoring because it allows for early detection and treatment. Because of recent advances in Internet-of-Things (IoT) paradigms, such monitoring systems are now available everywhere. Due to the essential nature of the patients being monitored, these systems demand a high level of quality in aspects such as availability and accuracy. In health applications, where a lot of data are accessible, deep learning algorithms have the potential to perform well. In this paper, we develop a deep learning architecture called the convolutional neural network (CNN), which we examine in this study to see if it can be implemented. The study uses the IoT system with a centralised cloud server, where it is considered as an ideal input data acquisition module. The study uses cloud computing resources by distributing CNN operations to the servers with outsourced fitness functions to be performed at the edge. The results of the simulation show that the proposed method achieves a higher rate of classifying the input instances from the data acquisition tools than other methods. From the results, it is seen that the proposed CNN achieves an average accurate rate of 99.6% on training datasets and 86.3% on testing datasets.

1. Introduction

Data collection has become much easier, thanks to the rise of smart Internet-of-Things (IoT) devices and sensors. However, the analysis and utilization of data still face challenges associated with incorrect feature extraction. When faced with these difficulties, researchers and specialists began looking for optimal solutions that allow extraction of most possible data from a given dataset. Our ability to learn more about our surroundings has improved since the invention of AI in the late twentieth century.

Ongoing advancements in artificial intelligence (AI) have been implemented in numerous industries, including the education and medical field. According to numerous studies [1–3], AI has shown the ability to outperform humans and information systems at most cases [4–8]. It is a mechanical, electrical, and chemical organism that constitutes the human body [5]. Electrocardiogram (ECG) signals are a biophysical indicator of the electrical activity of the heart. It shows how the beating of the heart changes over time [9–13]. Automated systems have a difficult time spotting anomaly. External noise and the body response to different physical conditions are examples of this [6–8].

To our knowledge, convolutional neural network (CNN) works well with ECG recordings from the data acquisition IoT devices. Appropriate ECG signal processing with the CNN learns features using patient needs with abnormalities in arrhythmia and heart failure [14–16].

In this paper, we develop the convolutional neural network (CNN) architecture, which we examine in this study to see if it can be implemented. The study uses the IoT system with a centralised cloud server, where it is considered as an ideal input data acquisition module.

The main contribution of the work involves the following:

(i) The authors develop a sparse CNN with autoencoding properties in order to improve the accuracy of classification.

(ii) The speed and reliability of IoT systems are heavily dependent on the speed and reliability of the internet connection used. Smart gateway devices lack the processing power to execute CNN methodologies.

(iii) The study uses cloud computing resources by distributing CNN operations to the servers with outsourced fitness functions to be performed at the edge. It is therefore enabling improved system availability by making decisions at the local level.

(iv) An ECG classification using input IoT data acquisition modules is evaluated in terms of response time and accuracy in a real-world case study.

2. Background

Each of the six waves in the ECG waveform is separated into two waves, two segments, and one complicated wave. During the initial electrical activity of the human heart, which is known as the PR interval, the right atrium chamber depolarizes, causing deoxygenated blood to exit via the vena cava into the right ventricle. It is at this point that two distinct pumping mechanisms kick into high gear: one to move deoxygenated blood to the lungs for oxygenation and the other to move oxygenated blood throughout the remaining part of the body. To begin another heartbeat cycle, the heart ventricles must be repolarized during the QT interval including the QRS complex, the ST segment, and the *T*-wave.

Some of the most critical and subtle ECG signals may be missed by commonly used applications that only count the number of beats per second and ignore the ECG signal pattern morphology that changes without altering the cycle normal time. A great deal of effort has gone into figuring out how to get useful information out of such sensitive medical records. Several methods utilizing the feature extraction based on features, feature combinations, or a selection of features were presented [17]. Time-frequency analysis of ECG signals can be done using wavelet transforms developed by the authors in [18]. In this paper, ECG classification using a CNN is presented to address these shortcomings. CNNs are a type of hierarchical artificial neural networks (ANNs) [19, 20] that use downsampling and convolutional layers to alternately mimic the human visual cortex cells.

3. Proposed Method

Figure 1 shows an autoencoder with the hidden layer for learning features from the input x if there are data $x = \{x_1, x_2, x_3, x_4, x_5\}$ available. All three layers are referred to as input, hidden, or reconstitution layers. The input layers are connected directly with layer 2 or hidden layers, where it performs various operations of autoencoding, and then layer 3 performs the process of providing the outputs of the hidden layers.

The goal of the reconstitution layer is to minimize the error between the layers. The hidden layer can be thought of as a different way to represent data because the essential characteristics of the data can be extracted from it.

Autoencoder networks are actually designed to learn the activation function $h_{W,b}(x) \approx x$. The limited neurons in the hidden layer extract the hidden features. As an example, 1024 neurons can be used to process a 32×32 matrix image. In a similar way to PCA and other dimension reduction methods, this is what this does. However, the hidden layer contains only a few neurons. According to this constraint, any network can be made to become sparse if the activation value of each hidden layer j^{th} neuron is a_j.

$$\rho_j = \frac{1}{m}\sum_{i=1}^{m} a_j x_i, \tag{1}$$

where m is the input layer neurons and ρ_j is the sparse constraint constant (like 0.05).

The study uses the KL distance function to optimise ρ_j when solving the hidden layer.

$$\mathrm{KL}\left(\rho\rho_j\right) = \rho \log\frac{\rho}{\rho_j} + (1-\rho)\log\frac{1-\rho}{1-\rho_j}. \tag{2}$$

CNNs use a spatiotemporal convolution kernel to specify the feature map in their convolution layer. Each feature map output of the last subsampling layer l consists of the bias term b_j^{ℓ} and convolution kernel W_{ij}^{ℓ} only if there exist input feature maps N_{in}. The formula for estimating the feature map X_j^{ℓ} of output j is as follows:

$$X_j^{\ell} = f\left(\sum_{i=1}^{N_{in}} \alpha_{ij}\left(X_i^{\ell-1} * W_{ij}^{\ell}\right) + b_j^{\ell}\right). \tag{3}$$

Additionally, it must adhere to the following rules:

$$\begin{gathered}\sum_i \alpha_{ij} = 1,\\ 0 \le \alpha_{ij} \le 1.\end{gathered} \tag{4}$$

Backpropagation begins with determining how each subsampling layer (l) is connected to its next convolution layer, and this must be done before we can begin the process, so as to conduct backward the next layer residual $\delta^{\ell+1}$. To determine the feature map of the j^{th} residual (δ_j^{ℓ}) layer, we can apply the gradient descent method. Suppose the layer activation function f which is the derivative of $f'(z_j^{\ell})$ has the input z_j^{ℓ}. The formula for the calculation is as follows:

$$\delta_j^{\ell} = f'\left(z_j^{\ell}\right) \cdot \operatorname{conv2}\left(\delta_j^{\ell+1}, \operatorname{rot180}\left(W_j^{\ell+1}\right)\right). \tag{5}$$

In the above process, the convolution kernel conv2 $(\cdot)$ must be rotated in order to perform cross-correlation calculations.

The sparse constraint is imposed on the output of the sparse autoencoder neural network. However, in this case, the input is limited to a sparse set of values. These two modes of operation are distinct, but they accomplish the same thing. Features can be extracted from input data using sparse autoencoder neural networks. Spatiotemporal convolution is a major change in this framework because all of the previous layer input feature maps are used as inputs for each output feature map. Due to the sparse constraints, the feature maps can be fed to the output map, and this is limited extremely.

3.1. Event Recognition Using the CNN. In the above framework, we feed the CNN seven consecutive 64×64-pixel frames in order to capture ECG data encoded in the input image frame, with the current image frame serving as the centre of attention. Assume that each frame in the input set is a 64×64 greyscale image with the same dimensions. Scaling is required if the dimensions are different from one another.

Convolution kernels of the form $7 \times 5 \times 5$ can be used by the C1 layer to obtain 36 feature maps to extract 36 different features from the input frames. As complicated as action event classification is, the 36 feature maps are perfectly capable of classifying the simple action. On the contrary, the convolution kernel is 5×5 in the space dimension. In other words, each C1 layer feature map is linked to all seven 5×5 image blocks. The C1 layer produces 36 number of 60×60-pixel feature maps as a result.

It is a sampling layer, the S1 layer. Accordingly, the C1 layer feature maps are rescaled to improve the CNN resilience to scale changes and minor deformations. The subsampling layer scaling factor cannot be too large.

4. Results and Discussion

In this section, the entire simulation is conducted in the Python environment to study the effectiveness of the proposed model. Table 1 shows the proposed CNN which is compared with existing image classification models such as VGG-16, ResNet-50, Inception V3, EfficientNetB0, and EfficientNetB7, the parameters of which are given in Table 1.

The proposed CNN is compared with existing methods such as VGG-16, ResNet-50, Inception V3, EfficientNetB0, and EfficientNetB7 in terms of various performance metrics including accuracy, precision, recall, *F*-measure, and percentage error. Moreover, the running time of the proposed method is tested on training and testing times.

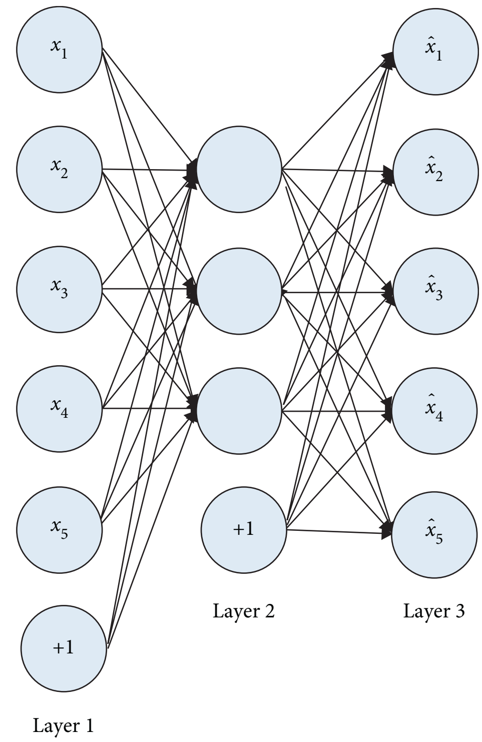

Figure 1: Sparse CNN of autoencoding type.

Table 1: Deep learning parameters.

Model	Parameters
VGG-16	138 million
ResNet-50	25 million
Inception V3	24 million
EfficientNetB0	5.3 million
EfficientNetB7	66 million
Proposed CNN	60,000

Table 2 shows the results of accuracy between the proposed CNN and existing methods such as VGG-16, ResNet-50, Inception V3, EfficientNetB0, and EfficientNetB7. The results of the simulation are conducted on both training and testing stages. The results of accuracy show that, at the time of training, the study has more accuracy than at the testing stage. Moreover, it is seen that the proposed CNN has higher classification accuracy than other methods.

Table 3 shows the results of run time between the proposed CNN and existing methods such as VGG-16, ResNet-50, Inception V3, EfficientNetB0, and EfficientNetB7. The results of the simulation are conducted on both training and testing stages. The results of run time show that, at the testing stage, it has higher run time than the training stage. Moreover, it is seen that the proposed CNN has reduced run times than other methods.

Figure 2 shows the results of precision between the proposed CNN and existing methods such as VGG-16, ResNet-50, Inception V3, EfficientNetB0, and

Table 2: Accuracy (%) of training and testing.

Model	Accuracy with training datasets	Accuracy with testing datasets
VGG-16	75.0	74.5
ResNet-50	87.0	76.3
Inception V3	90.7	77.15
EfficientNetB0	93.8	78.8
EfficientNetB7	94.9	84.4
Proposed CNN	99.6	86.3

Table 3: Running time (ms) of training and testing.

Model	Running time with training datasets	Running time with testing datasets
VGG-16	352,628	793,412
ResNet-50	38,797	117,167
Inception V3	15,652	97,854
EfficientNetB0	10,422	79,485
EfficientNetB7	5252	43,685
Proposed CNN	4556	42,965

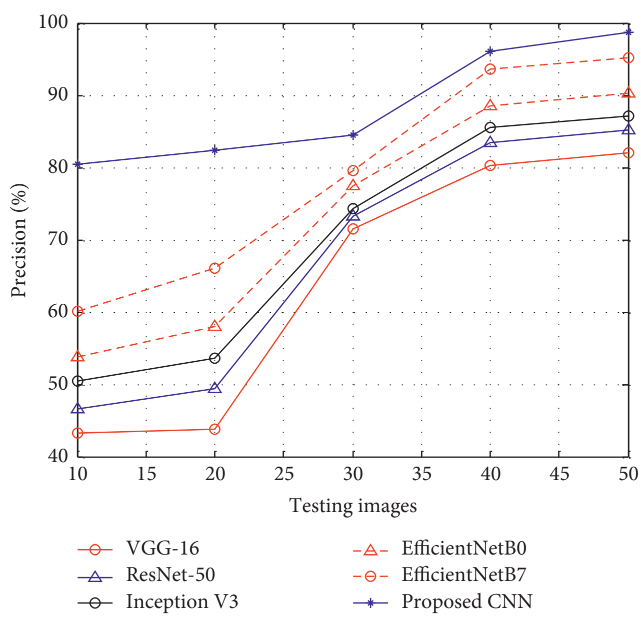

Figure 2: Precision.

EfficientNetB7. The results of precision show that, at the time of the testing stage, the proposed CNN has higher precision rate than other methods.

Figure 3 shows the results of recall between the proposed CNN and existing methods such as VGG-16, ResNet-50, Inception V3, EfficientNetB0, and EfficientNetB7. The results of recall show that, at the time of the testing stage, the proposed CNN has higher recall rate than other methods.

Figure 4 shows the results of *F*-measure between the proposed CNN and existing methods such as VGG-16, ResNet-50, Inception V3, EfficientNetB0, and EfficientNetB7. The results of *F*-measure show that, at the time of the testing stage, the proposed CNN has higher *F*-measure rate than other methods.

Figure 5 shows the results of MAE between the proposed CNN and existing methods such as VGG-16, ResNet-50, Inception V3, EfficientNetB0, and EfficientNetB7. The results of MAE show that, at the time of the testing stage, the proposed CNN has reduced MAE than other methods.

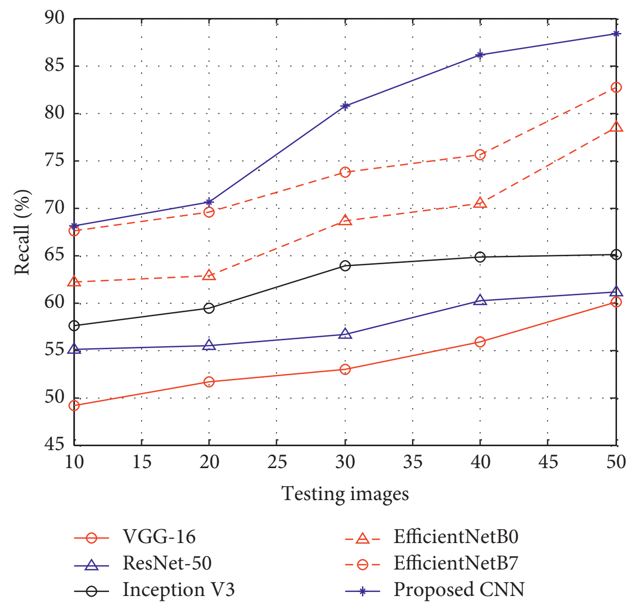

Figure 3: Recall.

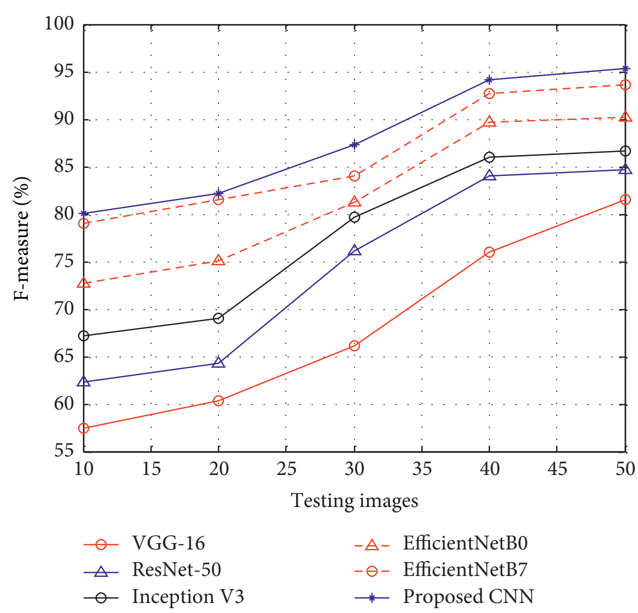

Figure 4: F-measure.

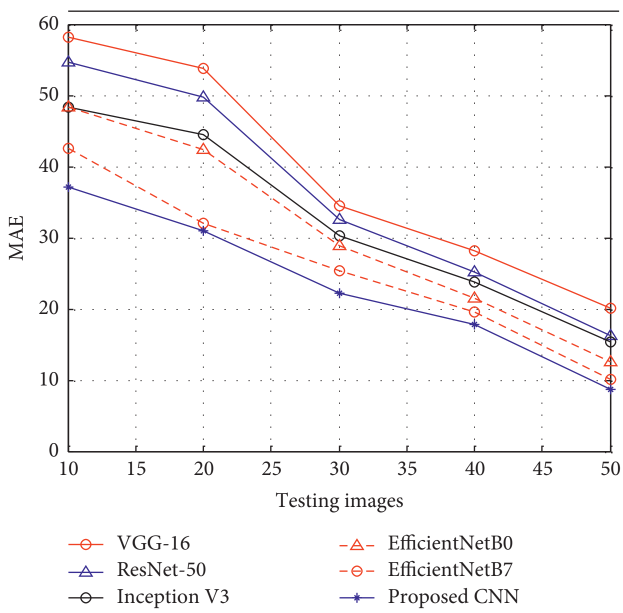

Figure 5: MAE.

5. Conclusions

In this paper, CNN examines the input signal from the IoT devices, where ECG data are classified to detect the presence of arrhythmia and heart failure from the image dataset. The classification of the dataset on two different heartbeat signals enables faster training and testing packages. The utilization of cloud resources to perform the CNN classification shows fastest classification process without lags. The simulation is conducted to test the efficacy of the CNN against ECG image datasets. The simulation shows that the proposed CNN classifies well the instances than other existing methods. The results of the simulation show an improved accuracy rate of 98% than image ECG classification models. In the future, federated learning can be used to examine the multimodal signals for the purpose of improved classification of instances in case of arrhythmia and heart failure.

Data Availability

The datasets used and/or analyzed during the current study are available from the corresponding author upon reasonable request.

Conflicts of Interest

The authors declare no conflicts of interest.

References

[1] N. Du, Q. Cao, L. Yu et al., "FM-ECG: a fine-grained multi-label framework for ECG image classification," *Information Sciences*, vol. 549, pp. 164–177, 2021.

[2] P. Kanani and M. C. Padole, "ECG image classification using deep learning approach," in *Handbook of Research on Disease Prediction through Data Analytics and Machine Learning*IGI Global, PA, USA, 2021.

[3] Q. Cao, N. Du, L. Yu et al., "Practical fine-grained learning based anomaly classification for ECG image," *Artificial Intelligence in Medicine*, vol. 119, Article ID 102130, 2021.

[4] A. Ullah, S. M. Anwar, M. Bilal, and R. M. Mehmood, "Classification of arrhythmia by using deep learning with 2-D ECG spectral image representation," *Remote Sensing*, vol. 12, no. 10, p. 1685, 2020.

[5] B. A. Teplitzky, M. McRoberts, and H. Ghanbari, "Deep learning for comprehensive ECG annotation," *Heart Rhythm*, vol. 17, no. 5, pp. 881–888, 2020.

[6] N. Nonaka and J. Seita, "In-depth benchmarking of deep neural network architectures for ECG diagnosis," in *Proceedings of the Machine Learning for Healthcare Conference*, pp. 414–439, PMLR, Beijing, China, August 2021.

[7] M. Jangra, S. K. Dhull, and K. K. Singh, "ECG arrhythmia classification using modified visual geometry group network (mVGGNet)," *Journal of Intelligent and Fuzzy Systems*, vol. 38, no. 3, pp. 3151–3165, 2020.

[8] D. A. Abdullah, M. H. Akpınar, and A. Şengür, "Local feature descriptors based ECG beat classification," *Health Information Science and Systems*, vol. 8, no. 1, pp. 20–10, 2020.

[9] P. Wang and J. Li, "Implementation of real-time medical and health data mining system based on machine learning," *Journal of Healthcare Engineering*, vol. 2021, Article ID 7011205, 5 pages, 2021.

[10] M. Y. Li, D. J. Zhu, W. Xu, Y. J. Lin, Y. Kai-Leung, and A. W. H. Ip, "Application of U-net with global convolution network module in computer-aided tongue diagnosis," *Journal of Healthcare Engineering*, vol. 2021, Article ID 5853128, 15 pages, 2021.

[11] Y. Zeng and F. Cheng, "Medical and health data classification method based on machine learning," *Journal of Healthcare Engineering*, vol. 2021, Article ID 2722854, 5 pages, 2021.

[12] Y. Ren, H. Yu, and L. Cong, "Application value of a deep convolutional neural network model for cytological assessment of thyroid nodules," *Journal of Healthcare Engineering*, vol. 2021, Article ID 6076135, 6 pages, 2021.

[13] S. Hamida, O. E. Gannour, B. Cherradi, A. Raihani, H. Moujahid, and O. Hassan, "A novel COVID-19 diagnosis support system using the stacking approach and transfer learning technique on chest X-ray images," *Journal of Healthcare Engineering*, vol. 2021, Article ID 9437538, 17 pages, 2021.

[14] T. Wang, C. Lu, Y. Sun, M. Yang, C. Liu, and C. Ou, "Automatic ECG classification using continuous wavelet transform and convolutional neural network," *Entropy*, vol. 23, no. 1, p. 119, 2021.

[15] Q. Wu, Y. Sun, H. Yan, and X. Wu, "ECG signal classification with binarized convolutional neural network," *Computers in Biology and Medicine*, vol. 121, Article ID 103800, 2020.

[16] V. Gliner, N. Keidar, V. Makarov, A. I. Avetisyan, A. Schuster, and Y. Yaniv, "Automatic classification of healthy and disease conditions from images or digital standard 12-lead electrocardiograms," *Scientific Reports*, vol. 10, no. 1, p. 16331, 2020.

[17] Z. Ahmad, A. Tabassum, L. Guan, and N. M. Khan, "ECG heartbeat classification using multimodal fusion," *IEEE Access*, vol. 9, pp. 100615–100626, 2021.

[18] A. Josko and R. J. Rak, "Effective simulation of signals for testing ECG analyzer," *IEEE Transactions on Instrumentation and Measurement*, vol. 54, no. 3, pp. 1019–1024, 2005.

[19] A. B. Asgharzadeh, M. C. Amirani, and A. Mehri, "Spectral entropy and deep convolutional neural network for ECG beat classification," *Biocybernetics and Biomedical Engineering*, vol. 40, no. 2, pp. 691–700, 2020.

[20] Y. Zhao, J. Cheng, P. Zhan, and X. Peng, "ECG classification using deep CNN improved by wavelet transform," *Computers, Materials and Continua*, vol. 64, no. 3, pp. 1615–1628, 2020.

Hindawi
Journal of Healthcare Engineering
Volume 2022, Article ID 9904870, 12 pages
https://doi.org/10.1155/2022/9904870

Research Article

Artificial Intelligence-Based Smart Comrade Robot for Elders Healthcare with Strait Rescue System

Golda Dilip,[1] Ramakrishna Guttula,[2] Sivaram Rajeyyagari,[3] Hemalatha S,[4] Radha Raman Pandey,[5] Ashim Bora,[6] Pravin R Kshirsagar ,[7] Khanapurkar M M,[8] and Venkatesa Prabhu Sundramurthy [9]

[1]*Department of Computer Science and Engineering, SRM Institute of Science and Technology, Vadapalani Campus, Chennai, India*
[2]*Aditya College of Engineering, Surampalem-533437, Chittoor, Andhra Pradesh, India*
[3]*Department of Computer Science, College of Computing and Information Technology, Shaqra University, Saudi Arabia*
[4]*Department of Computer Science & Engineering, Panimalar Institute of Technology, Chennai, Tamil Nadu, India*
[5]*Advanced Institute of Technology and Management, Hodal, Delhi, India*
[6]*Department of Mathematics, Diphu Government College, Diphu, Assam, India*
[7]*Department of Artificial Intelligence, G. H. Raisoni College of Engineering, Nagpur, India*
[8]*G. H. Raisoni College of Engineering, Nagpur, India*
[9]*Center of Excellence for Bioprocess and Biotechnology, Department of Chemical Engineering,College of Biological and Chemical Engineering, Addis Ababa Science and Technology University, Addis Ababa, Ethiopia*

Correspondence should be addressed to Pravin R Kshirsagar; pravinrkshirsagarphd@gmail.com and Venkatesa Prabhu Sundramurthy; venkatesa.prabhu@aastu.edu.et

Received 11 November 2021; Revised 24 November 2021; Accepted 28 December 2021; Published 25 January 2022

Academic Editor: Enas Abdulhay

A rising proportion of older people has more demand on services including hospitals, retirement homes, and assisted living facilities. Regaining control of this population's expectations will pose new difficulties for lawmakers, medical professionals, and the society at large. Smart technology can help older people to have independent and fulfilling lives while still living safely and securely in the community. In the last several decades, the number of sectors using robots has risen. Comrade robots have made their appearance in old human life, with the most recent notable appearance being in their care. The number of elderly individuals is increasing dramatically throughout the globe. The source of the story is the use of robots to help elderly people with day-to-day activities. Speech data and facial recognition model are done with AI model. Here, with the Comrade robotic model, elder people's healthcare system is designed with better analysis state. The aim is to put in place a simple robotic buddy to determine the health of the old person via a headband that has been given to them. Comrade robot may do things like senior citizens home automation, home equipment control, safety, and wellbeing sensing, and, in emergency situation, routine duties like navigating in the outside world. The fear that robotics and artificial intelligence would eventually eliminate most of the jobs is increasing. It is anticipated that, in order to survive and stay relevant in the constantly shifting environment of work, workers of the future will need to be creative and versatile and prepared to identify new business possibilities and change industry to meet challenges of the world. According to the research, reflective practice, time management, communicating, and collaboration are important in fostering creativity.

1. Introduction

Technology is a trend that affects human existence in every part of the world. Robots are an exciting example of what the future of technology holds. Robotics has enhanced human life and industry significantly, thanks to the technology [1]. Adults with autism are already a regular thing in many industries, including healthcare, military service, and domestic assistance. The global population is growing, therefore making the requirements of this demographic an increasingly significant issue for health providers, government officials, caretakers, and families. Due to these reasons, buddy robots (which serve as aids to elderly people) are often seen as having an authoritarian function in helping individuals do their caring duties without assistance. An increased old population is often brought up as a method of dealing with the rising number of senior persons. Actually, robots are becoming more prevalent in the senior care sector. We should have been aware of certain ethical issues that have recently been brought to light as a result of these advances. Artificial intelligence approaches are applicable for various fields of utility. Digital smart systems, medical data analysis, healthcare system, and other applications are possible with AI model. Specifically, disease diagnosis with deep learning, radiology model with ML, automatic systems, and so forth are the most utilized healthcare systems of AI.

A rising need for new technology has emerged for older adults because of the greying of our current generation. The primary reasons in favour of this are that there are too few hospital workers and many individuals want to live as independently as possible rather than be placed in an institution [2]. Additionally, we will need an adequate supply of healthcare professionals together with the use of cutting-edge technology. Robotics is playing a significant role in helping older people these days. A household use robot that is particularly intended for use at home may be regarded as a level of service robot. The business of making robots specifically for the house is expanding from scientific and commercial standpoints. In order for Comrade robot to be the most effective in the house, it should be able to carry out several activities such as home monitoring, gadget management, personal assistance, and entertaining. When more and more robots are developed to engage with a human being to give the sort of care that is often provided by a licensed therapist, the lack of healthcare and the standard of living for the elderly will both improve [3]. Designing a providing assurance "robotic arm" to supervise the old person is the method being used. The overall aim is to create a low rental Comradeship robot to assist an elderly person with daily home automation.

In the end, the house robot could traverse the usual home settings without any human assistance, carrying out duties such as senior citizens monitoring devices, home gadget management, and security and stability sensing, as well as in the case of an attack. This document has two distinct sections. One is a Comrade robot, while the other is a health monitoring band. A Comrade robot does so in the form of "making itself helpful"; that is, it is capable of assisting people in a household setting. The old person is constantly being kept under constant supervision by the Comrade robot [4]. With the sensors incorporated in the design, the leaving comments industrial vehicle ensures both safe and secure environment in the family environment. Trespassers, gas leaks, and fire are all on the list. In the creative and emotional realm, Comrade robots and emotional synthetic avatars have now been created for graduate training. It may be difficult to extract a ministry of planning from both materials; therefore, teams that want to build Comrade robots must create their own website from scratch. Of course, there are many representations of structure for Comrade robot, but it is also tough to locate how the actual ones operate. Most articles concern themselves with how well an overall behavior performs, with little emphasis on the detailed architecture needed for replication.

This article, covering the themes of the first twenty months of exercises of RoboCare, explains the kind of programs the group has done so far and the subjects in which they have focused. The RoboCare program is dedicated to creating distributed applications where programming and autonomous agents all work together to accomplish an overall objective, which is to provide a supply of services that are ready for use in settings where people may need help and direction. While we are also interested in supporting endangered elderly individuals to enjoy an inclusive environment in their own homes, our primary focus is on bringing the concept to market [5]. According to recent data, Europe and Japan are gradually growing older. In order to increase public attention to this matter of "independence" and "ageing at home," new ways of supporting the seniors and persons with disabilities have been created.

This is why when it comes to RoboCare, most of the study deals with two potential situations, which are referred to as the RoboCare Household Atmosphere and the Quality of Life Institution setting [6]. Robotic frameworks, wearable devices, activity monitoring in complicated settings, and human relationships are the main components of strong reliance for the future of robotic care. Here we will give the reader a short summary of the key findings that we have discovered so far and many lessons we have learnt from those efforts to custom-tailor AI for assisted living. Remote sensing data-based applications, image processing, video and audio recognition system, security system, and so forth are the applications of this research field. The major objective is to improve the performance state of medical data analysis and the robot model construction with efficient analysis is designed. This research contributes to improving the robot technology and availability of AI in medical healthcare system. Comrade robot model with AI utility helps to obtain a better performance result.

The remainder of the paper is organized as follows. Section 2 analyzes various review papers related to the topic. The overview of robot model is studied in Section 3. The module performance and architecture of Comrade robot are described in Section 4. Section 5 analyzes the AI technology in the healthcare system. Specifically, the elder healthcare system is designed. Section 6 presents the methodology, and Section 7 evaluates the analyzed performances result. Section 8 concludes the proposed work.

2. Review of Literature

Lifespans across the globe are rising, and therefore the percentage of the people in retirement ages is growing (Moyle et al. [6]). As visual acuity in older adults diminishes, this necessitates the provision of more services and has a larger impact on budgets for healthcare provision. The older population needs more research to help them retain emotional human fellow. Robotic technology may be used to assist both rehabilitative and sociable robots in relieving strain on social care facilities. Large data processing, overlapping issue, and feature set analysis difficulties are the major problem of conventional work.

You may also look into Comradeship robotics, which are little robots that are made to look and behave like animals (Pu et al [4]). They aid creatures during rodent therapy by decreasing the dangers for the mammals individually. In general, Schrödinger, the mechanical seal, is a famous example. The advantages of getting to know Paro, a simulated nursing care Comrade for elderly people, include decreased irritation as well as depressive disorder in cognitive impairment, better immune responses, less burden on care providers, and enhanced affect and information exchange among both elderly people and their day care providers. Furthermore, paracetamol may help to minimize the need for hallucinogenic and analgesia medications and may help to lower cholesterol levels.

The authors in [7] and others examine the main methodologies, including designation as well as learning algorithms, which are essential in the development of developing quantum computing, as well as designation and learning algorithms, and computational efficiency that are applicable in the field of growing artificial intelligence and intricate their use [8–10]. Research methods employed in data security, personal computing, and cloud services provide better findings, as diverse assessment criteria are taken into consideration.

The impact of robot animals upon autonomous older adults was examined in a clinical trial (Abubshait et al. [11]), and also the researchers reported that robotic dogs may offer social enjoyment and relationships. While practical assistance was very attractive, the fact that the robot looked and felt more like a human created a conflict. People preferred soft fur and recommended play elements, such as plush toys, as potential improvements for the Comrade robots that are presently available. When new, brightly colored, child-oriented dogs were used, this restricted the kind of impressions respondents might create. Note that although older persons and individuals with memory are incorporated throughout Comrade robot creation, they are seldom, if ever, offered the opportunity to be engaged. Interaction typically happens in the project design whenever healthcare services are engaged.

It was recommended that the construction of something like an everyone around collapse detection technique be undertaken (Celis et al. [12]). Utilizing just one aeration rate, an innovative wearable gadget for the detection of falls was created. Ubiquitous computing Remote Monitoring for the Old capable of detecting an individual's fall as maintaining the health of the patients. An Intelligent Home Security System based on GSM and ARM Architectural design: Industrial robots have lately been created utilizing a range of technologies, including the Web, wireless communications, wirelessly, and speech recognition.

3. General Overview of Robots

The word robot was originally derived from the Czech word robot, which means forced labor. Karel Capek, the Czech writer, introduced the term robot in his play "R.U.R." Capek used the term robotic in a series called "Rossum's Universal Robots" that premiered in Prague in 1921. The robots in R.U.R were built by man, and they were supposed to work for humanity. Thus, from generations to generations, human people have made use of robots to do various jobs. However, there is just no generally accepted definition for robots [11]. Despite this disagreement, the University of the Robot Society still sees a robot as a multipurpose fully programmable tool that is used to transfer credible commitments, tools, or optical disks in various ways using preprogrammed movements. This concept differentiates robots from other automated machines, because they are programmable. A robot may be described as an upgradeable, complex nervous, sentient, and transportable machine that uses energy to do work. Regardless of its form and size, a robot has seven major elements. This collaboration serves a particular goal. Figure 1 depicts the parts of a robot.

3.1. Controller. The commander is in charge of coordinating the robot's movements. The operational environment refers to the area within which a robot may operate [13]. The microcontroller is also in charge of collecting input first from surrounding environment via the use of its sensing.

3.2. Power Conversion Unit. The fusion reactor supplies the robot's controls. Electricity, combustible materials, and battery storage are all commonplace power stations in robots [14]. Most of the electricity that is provided to a building comes from the grid, and, in order to power the building, the system uses an AC/DC electrical power converter to change the AC electricity into DC electricity.

3.3. Manipulator. The robotics have had the capacity to pick up, alter, and blow things up. The robot's manipulation imitates outstretched arm of something like a human individual. Manipulators typically refer to the joints connecting the arms with the upper arms, elbows, and wrists. Joints tend to be either rotational or sliding [4]. Reaction kinetics refer to the way wherein the joints are arranged to define the potential stepper motor.

3.4. End Effector. The final part of the system, which connects to the input device, is known as the manipulation link. The instrument handle's link is known as an actuation. It imitates the mechanical arm, mimicking the results obtained.

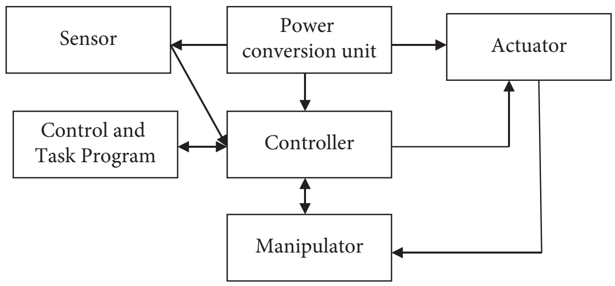

Figure 1: Components of a robot.

3.5. Sensors. Robots may now have the sensor take a specific measurements of the surroundings, with the sensing' data helping to shape the robot's behaviors. To guarantee the robot's security, this is often done. Devices utilize a robot to respond to environmental variations.

3.6. Actuator. In most of the robots, the actuators are often known as the muscles of the robot. The conversion takes place by using the energy that drives your robot's mobility.

3.7. Control and Task Program. A collection of commands from the manufacturers of the robot's controller are known as the management plan, while a sequence of questions typically supplied by the user are called the task programme [15]. To accomplish a particular job, the manipulator must carry out the movements task programmed by the task programme.

4. Architecture of Comrade Robot

To develop up with a proper Comrade robot structure, we also must research the many needs that Comrade robots may have. Just one "perfect" Comrade robot might fulfill all these criteria. Meanwhile, theoretically speaking, the need of a Comrade robot does not quite apply; in reality, one is still required [16]. The specifications for a given robot rely on a variety of different variables, including the kind of intended application and also the particular hardware components that are required. Here we provide a comprehensive list of all potential criteria an engineer should consider while designing a generic structure. The main task of the Comrade robot is to sense the environment around it, including hearing, seeing, and touching. Intercultural competence calls for synchronizing data; thus, various kinds of data need attention. In addition, inputs processing may be programmed to target specific sensor data, in response to predictions from a mixing process. Significance must be verified on every piece of data received, and all information collected must also be classified before it can be kept.

The Comrade robot was able to have a classroom discussion with the user. What this implies is not just to create effective sentences and also to take fundamental principles of communicating into consideration [17]. A Comrade robot should constantly be likely to preserve the dialogue flowing in order to sustain a strong connection. The usage of live interaction also incorporates elements like this; for instance, in order to prevent boring or misunderstanding the user, lengthy pauses should not be present in a discussion. It should be able to communicate across all modalities and should do so in a logical and reasonable manner. Speech would overlap with proper lip motions, which have been prioritized about the present face animations and the robot dealing with the lips both of it. We illustrate the construction of a Comrade robot in Figure 2 and address the specifications outlined above. However, observe that perhaps the design is abstracted from the specifics of various kinds of friend robotics, allowing its application to diverse kinds of robot Comrades. We are emphasizing again here that it was for a Comrade robot that also has an "overall" personality; nevertheless, you may build various parts without putting any content into them. Initial set of data processing uses dialogue engine and reasoning engine. Depending on the goals, rules, memory unit, and emotion recognitions are taken with heuristics approach. After that, the input and output processing states are determined with facial recognition with animation approach. Dataset uses source from camera, sound, and so forth and the speech recognition and facial recognition data are synchronized. With the low-level behavior, the animation controls are processed. Here this conflict scheduler, the performance of output state is determined.

5. AI and Robotic Technology in Elder Healthcare

By building a framework that incorporates current state-of-the-art AI technologies from an off way, RoboCare aims to help service providers fully appreciate the kind of assistance resources available [18]. The difficult part is to find out whether the methods listed above might help create educational software parts that can be purchased off market. Robotic systems now provide us the ability to create robotic system with very accurate survival skills. We have effectively implemented these systems in both the home and hospital facility settings thanks to a variety of methods.

The professional diagnosis and management Comrade robot is able to provide guidance on prevention and prognosis by collecting data like clinical findings, a client's medical records, and previous medical instances. The robot was created by the robotics and artificial intelligence, that is, related to clinical texts, two million clinical data, and many individual instances [19–22]. The hospital is conducting a pilot programme in which people participate to evaluate the robot. When interacting with a client all through physical diagnosis, the robot "pays attention" to the dialogue and takes the sensor readings along with source information to help the clinician diagnose and prescribe medication [19]. The clinician then collects information to interact with the clinician. It is anticipated that the robot would assist doctors to come to a conclusion about the cause of the patient's symptoms quicker and cut down on mistakes.

The Health System Mechanism, shown in Figure 3, is made up of several AI industrial robots. To arrive at a prognosis, the speech based EHR system and image natural antibiotic are both utilized. Comrade proposes a diagnosis and therapy in which all relevant information is collected.

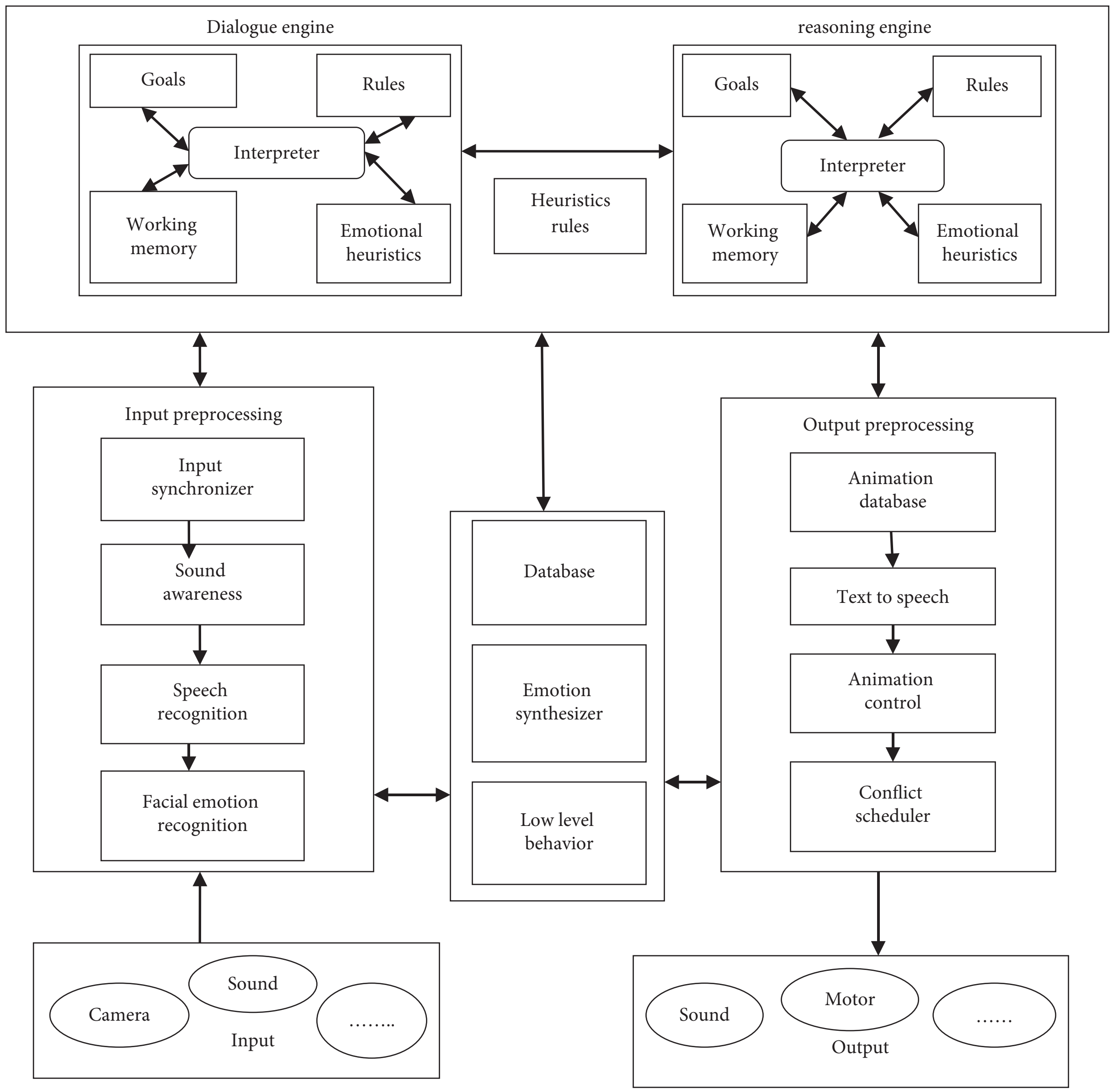

Figure 2: Architecture of Comrade robot.

Thanks to advancements in technology, it is now possible to provide ambient independent living solutions to help seniors in their dwellings [23]. The multidisciplinary approach that is required for robotics technology problems includes knowledge from fields like building, fashion, psychological, law, and ethics, as well as technology, computer programming, science, and medicine. In order to benefit everyone, robots and information and communication technology (ICT) must be made accessible across the populace at school, in hospitals, in home languages, and in smart neighborhoods. A high degree of acceptance and usefulness for the users may be achieved by integrating these approaches in the development of the surroundings.

Some basic suggestions for social order, together with technological and legal troubles, may be discovered through the applying load with actual customers in some kind of a contemporary context.

5.1. Society Centered Design. Robotic technologies should be planned, manufactured, and deployed to assist people in the day-to-day tasks in a societal architecture. The intelligent machines must be able to go from a user-centered design process to a social system design process, at which development process is properly considered and is further integrated with the society's requirements [24]. Many of the ideas shown in the previous sections included users throughout the whole development process, starting with the study of end-users' requirements and leading all the way through the assessment of the prototype system for valuable suggestions.

5.2. Stakeholder Readiness. It is also essential to consider the speed to market in evaluating integrated services. That level of readiness indicates how soon the individuals and

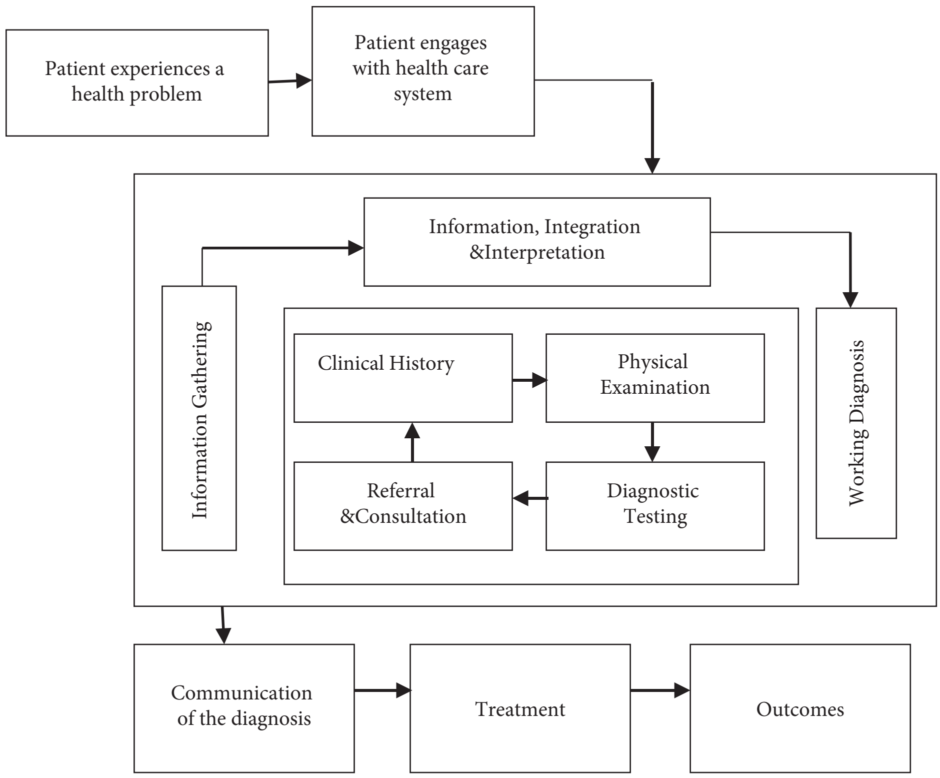

Figure 3: AI robotic systems in elder healthcare process.

organizations are prepared to take and spread the technologies. The gap among study and implementation is the only problem with this topic.

5.3. Low Cost. Considering that personalized robotics are meant to be used by the individual, the price must be in line with their financial capability, in place to encourage for broad service usage. Robotic alternatives incur a reduced cost for the sake of a costing system [25]: they are costly owing to the increased components they employ, but then on the other hand they are less costly for the public health system. Cloud automation solution models may enable a new breed of personalized robots for businesses.

5.4. Customizability, Flexibility, and Modularity. The requirements of the users will fluctuate. Having provided component services, it is essential to offer one that can respond to customer requirements and competences that vary.

5.5. Robustness, Dependability, Safety, and Security. Because the test equipment is expected to engage with those who are vulnerable and aged, it must have been secure and dependable.

5.6. Autonomy. Robotics institutions are expected to move independently and make choices based on the needs of consumers. They ought to be capable of identifying errors that users have made or they have made and make corrections on their own when required.

5.7. Social Informatics of Knowledge Embodiment. Our study has significance that are present in the system; it is applied to other comparable systems. Nonetheless, in order to validate our results, further research with healthcare practitioners in the field is required [26]. In our research of AI-infused autonomous vehicles, we disregarded electronic archives, too. The usage of other things, like computers, may be affected by AI industrial robotics; however, in our research paper, we have not seen this. The possibility of further study includes research that compares cognitive manifestation in various entities in order to learn about how they support or replace one another. Lastly, we have not investigated the nature of senior executives' interest in, or usage of, AI machines. Understanding the four forms of information embodiment as a generative framework for finding motivators may be the most useful. Mechanistic explanation of cognitive immersion should rely on knowing the motive.

From a social bioinformatics viewpoint, AI technology is relevant in the context. It is vital to understand the socio-spatial relationships AI has with people in order to fully comprehend its true worth. STIN analytic approach is particularly helpful, since it offers a paradigm for incorporating various social actors' perspectives while considering technologies [20]. An excellent illustration of our findings is that, in contrast to the robots that were intended to make people's job and emphasizing, the AI humanoid systems that operate as rivals and magisters encounter greater opposition from economic systems than those that work as collaboration and guild mates. This STIN study also showed that the automation technologies supplier has a minimal but nonetheless significant impact on the market.

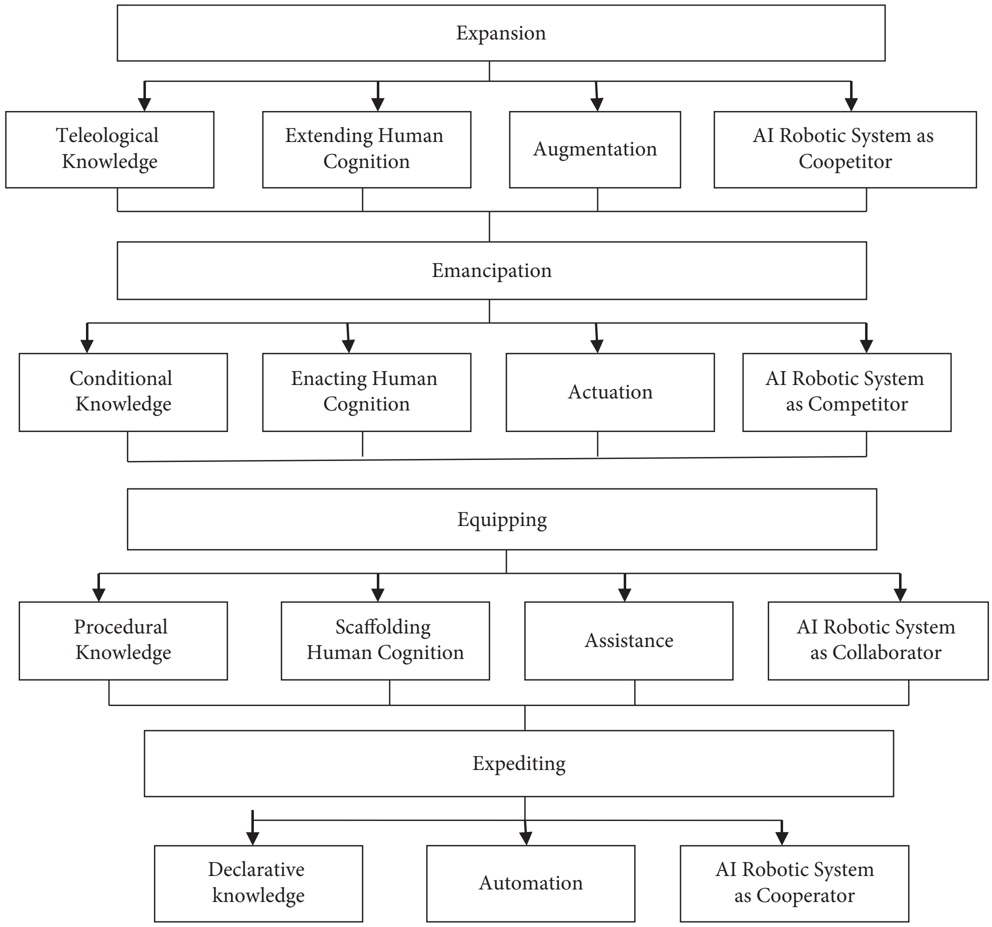

Figure 4: Overview of social informatics of knowledge embodiment.

Requiring timely deployment of AI mobile robots for skilled employees, the supplier highlighted the technologies' complimentary and nonconfrontational character to help people gain confidence. This research confirms that our awareness of the use of AI industrial robotics in intellectual work requires a social information systems viewpoint.

By using powerful computers like AI robotic systems, researchers are showing that they can behave as an independent social actor in addition to just being a tool for humans. When humans and robots interact more naturally and intuitively, the difference between the humanity and the machine may become obsolete. Further refinement of the notion of interconnections in social bioinformatics as interpersonal relations and living organism connection converge may be required in order to help more people have social networks [8]. A manifestation of information changes understanding labor, and the introduction of new privacy practices is probable. Since making scientific have yet to comprehend the consequences of artificial intelligence, it is possible that the necessary training activities may need new methods of collecting, analyzing, and displaying data at employment. Social and community customers frequently need to work with machines, as well. Because of the resulting shift in the organization, in other words, the dissemination of materials is most likely to be caused.

Figure 4 shows major module utilizing expansion, emancipation, equipping, and expediting. Speech data with knowledge analysis, human cognition, augmentation, and AI robot are analyzed in expansion set. Actuation and competitor design of emancipation is determined. Assistance and automation model uses the procedural knowledge and final declaration.

6. Methodology

Robotic systems that utilize the making plans, observation, concurrence, and successive cognitive orientations review process acquire questionnaire questions from guardians and carry out the intellectual orienting examination control and experimental group. The robot then engages in a discussion with the user and gathers feedback. When the robot has finished evaluating the responses, it reports back to those same caregivers with the results [25]. This section describes the cognitive assessment method and the communication mechanisms platform. Our Friend Robotic, a 3D-printed desk device, is fitted with a cognition assessment process. The capacitive touch screen is linked to an ARM-based microcomputer executing Android platform, and the interaction is shown on it. In addition to having a 3D camera, this robot is equipped with a vision circuit composed of an RGB-D camera for image recognition and four loudspeakers that help with sound localization. We have also included voice and physical movement detection in our robot arm, as can be seen in Figure 5. The cognitive orientation assessment method has seven critical features: a development tool, inquiry and response creation, agreement between two parties, excessive screen, Internet computer vision, answer appraisal, and intelligence score [15]. An online dataset and native databases are required for the relational database. In the public cloud, Q&A worksheets containing users' accounts and summaries of memory score are stored, along with cognitive orientations evaluations. These may be revised and checked by a caretaker. The personal dataset provides the user's focus strategy, test timetables, and Q&A answers.

6.1. Modeling and Formulations of Comrade Robots. The study of bending moment enables one to approach performs of large masses. According to the current motion, one may see the position, orientations, and higher incidence as having evolved through time. Dynamics in robotics are used to build up basic equations of controls, with the dynamic transfer function for deceivers acting as the explanation governing motion. Torque is the mechanism that is responsible for producing the dynamic movement of both manipulating arms in a robot's arm [24]. Dynamic modeling is involved in the development of the differential equations of the manipulation as a function of something like the displacements acting on it. In dynamic modeling, the robotics manipulator's components are constrained to a set of forces and; as a result, the locations, velocities, and deceleration are determined:

(i) People who have torque needed to achieve certain end-effector movements are all determined by this calculation (the direct dynamic problem)
(ii) The elastic scattering issue is modeled mathematically, and there are a variety of control methods which use the model
(iii) It enables the calculation of the real manipulation to be done using a control scheme

Lagrange's integrated model may be used to construct Euler equations and manipulate Lagrange's movement. Joint characteristics and characteristics of the manipulation define the motion.

A communication model with overall energy K and gravitational potential V is shown as follows. Lagrange refers to

$$L(q, \dot{q}) = K(q, \dot{q}) - \mathrm{V}(q). \tag{1}$$

It is a simple procedure using the Lagrangian differential equation derived.

$$\frac{\mathrm{d}}{\mathrm{d}t}\frac{\partial L}{\partial \dot{q}} - \frac{\partial L}{\partial q} = \mathrm{Q}_i. \tag{2}$$

The general force that corresponds to the generalized coordinate q_i is referred to as Q_i. Connection I has kinetic and potential energy provided.

$$\begin{aligned} K_i &= \frac{1}{2}\,\mathrm{trace}\left[\sum_{j=1}^{i}\sum_{k=1}^{i}\frac{\partial T}{\partial \mathrm{Q}_i}J_i\frac{\partial T}{\partial q_k}\dot{q}_j\dot{q}_k\right], \\ V_i &= -m_i g^T T_I r^{-(i)}. \end{aligned} \tag{3}$$

A second-order linear evolution equation may be used to describe the Lagrangian equations of motion for the n-th links manipulators.

$$\sum_{j=1}^{n} B_{ij}\ddot{q}_j + \sum_{j=1}^{n}\sum_{K=1}^{n} C_{ijk}\dot{q}_j\dot{q}_j + g_i = \mathrm{Q}_i, \tag{4}$$

where

$$\begin{aligned} B_{ij} &= \sum_{k=\max(i,j)}^{n}\mathrm{trace}\left[\frac{\partial T_k}{\partial q_i}J_k\frac{\partial T_k}{\partial q_i}^{T}\right], \\ C_{ijk} &= \sum_{k=\max(i,j,k)}^{n}\mathrm{trace}\left[\frac{\partial T_h}{\partial q_i}J_n\frac{\partial^2 T_h}{\partial q_i \partial q_k}^{T}\right], \\ g_i &= \sum_{k=1}^{i} m_i g^T \frac{\partial T_k}{\partial q_{ki}} r^{-(i)}. \end{aligned} \tag{5}$$

6.2. Evaluation Process. Google has published a new open software speech recognition processing framework, known as SyntaxNet, to the public. Syntax Net's main purpose is to find out the words and phrases, and each word is clearly shown in phrase. A parser is capable of determining the morphological purpose of any single phrase, including conjunctions, in the phrase. In addition to providing an also before the model named Parse McParseface, Goggling also offers a grammar models, known as Parsey McParseface, that is developed. No matter how complicated the root of a phrase may be, SyntaxNet is able to recognize it [15]. It is able to trace out the connection between the word meaning and each individual word in the phrase. This study aimed to use SyntaxNet, so that the customer's voice communication may be processed genuinely. To illustrate, a phrase will be spoken, at which point the voice activation component will transform textual content, which is then processed by SyntaxNet for deeper comprehension. To put a POS on a word, SyntaxNet examines the whole phrase as well as the word's semantics. Similarly, since SyntaxNet can correctly predict the calculated value used when a machine evaluates the provided response with the right answer, assessing answers that utilize math is quite simple. The capabilities of SyntaxNet may also be utilized to detect whether there is negativity in the word but when the phrase has a pejorative perception.

The programming language we use to describe paragraph characteristics is called SyntaxNet. Step one is answering the question, and step two is evaluating the response. Next, the input is examined and processed using SyntaxNet to identify both user responses and right answers. Long computational network and right answer structure are created from the interpreted results. Those trees stand for the concept of a "pos" and how words relate to one other [26].

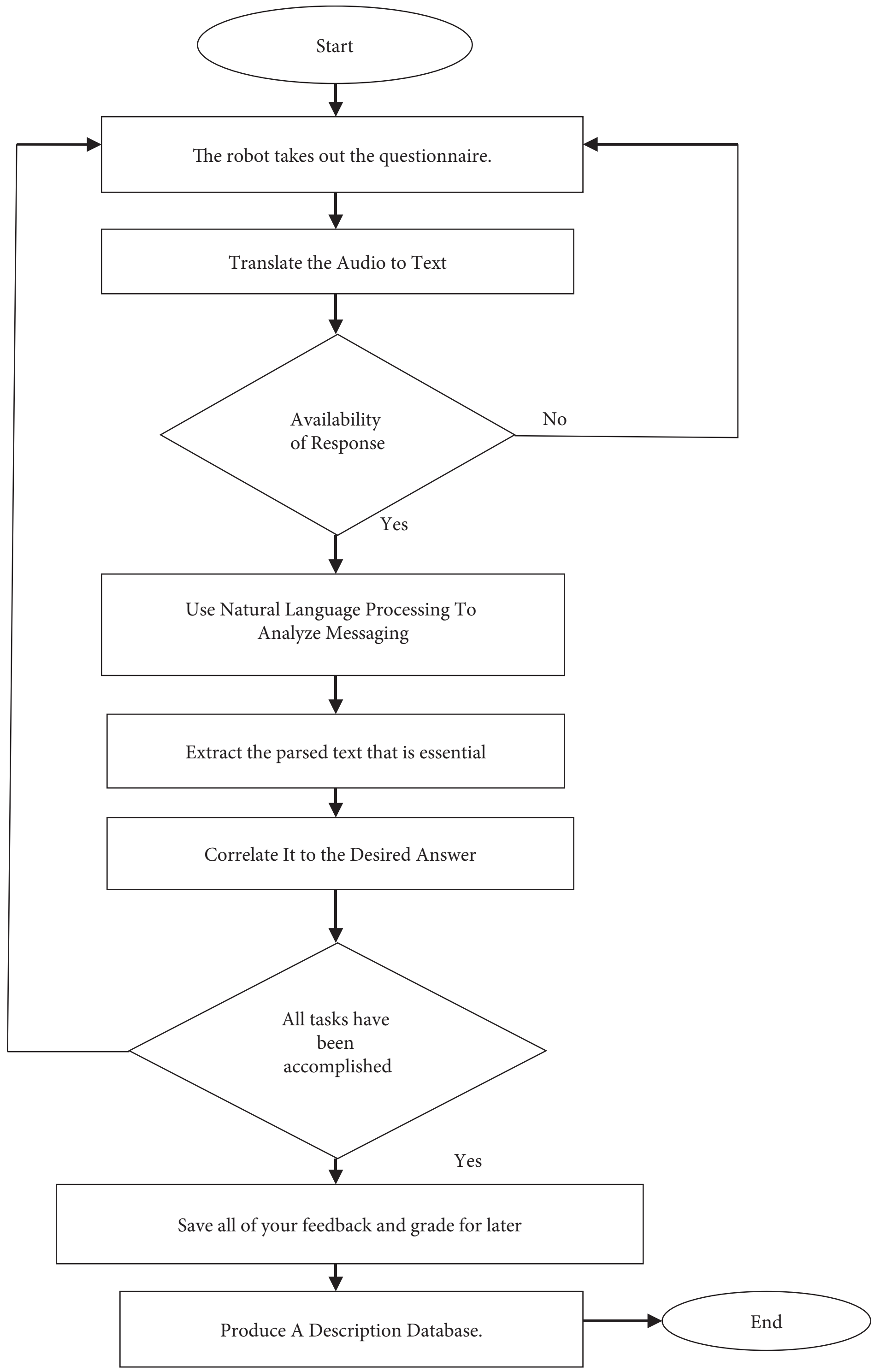

Figure 5: Cognitive assessment of Comrade robot for elder healthcare.

The second step in the algorithm is to connect two trees, and the saplings are compared using a mating Canadian land. A compatibility score is given for these tree trunks, depending on their resemblance. The robot gives a score of 1 to a right answer tree and a score of 0 to an erroneous solution tree. A partial number may be given if the answer matches both trees; however, the progress and achievement are used to evaluate the two trees. To determine the user's cognitive score, the participant's characteristics and a caregiver-determined criterion are utilized.

Recognition state of robot has various questionnaires, which translates the audio data to text data. Depending on the availability of given response, the NLP is performed and messages are taken with NLP analysis model. The parsed text is extracted with the feature set of given database. These correlated results are analyzed and desired answers are taken for the task accomplishment. Feedbacks are saved; then the respective description database assessment result is produced.

7. Result and Discussion

The robots were selected based on the category of robotic systems for old, meaning they may help elderly individuals feel more at ease with one another. The many robots attempted to encompass several diverse settings linked to ageing, such as healthcare, recreation, and commercial work [24]. There were three types of robots: Comrades, service, and factory. The researchers checked all of the materials that the groups debated about which robot should best suit each particular task and put it to the blackboard. We should also point out that respondents were not encouraged to do so, and they did not identify a robot for every activity. A second advantage of having several robots on hand is that they may choose to do multiple activities with each one. In order to prevent pressuring individuals while being indecisive, the course designed was used in this phase.

The data gathered from the activities performed by the respondents were studied by the psychologist from this research. The behaviors generated from the chalkboard and or the edited version of the meetings originated from two separate sources. The whole group meeting was recorded and mapped onto the blackboard with the included assignments [17]. Participants developed 85 activities that included a majority over and over again. The main objective of this study would be to provide light on a variety of activities, and thus the researchers focused on just the activities that were being performed on a regular basis. Thus, only 75 quasi tasks were actually and categorized to collect data. A structure for ageing in place was created so that groups of actions may be classified thus according to both purpose and environment.

Basic Activities of Daily Living. This would be the minimum set of fundamental tasks a person should have been able to do while living on their own (e.g., bathing).

Instrumental Activities of Daily Living. The capacity to carry out effective instrument tasks is an important part of enjoyable life (e.g., managing a medication regimen).

Enhanced Activities of Daily Living. Independence includes time for interests, social interaction, and personal development. It also incorporates interests, social interaction, and personal growth that extend beyond functional needs. These are obligations that go hand in hand with large and important tasks (e.g., buying groceries).

Social Activities. Those practices are intended to promote social connectedness, such as maintaining connections through talking with people. This component was incorporated to the structure for elderly people with robot as per the suggestions gathering of data.

Table 1: Number of activities yield by older adults.

S. no.	Name of the activity	Number of activities
1	IADL	29
2	BADL	20
3	EADL	13
4	SA	13

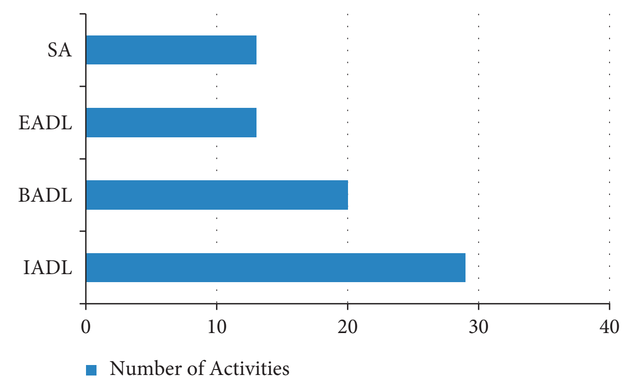

Figure 6: Number of activities yielded by older adults.

7.1. Activities for Ageing in Place with Robots. Table 1 and Figure 6 show that older adults do the same activities every day; they refer to around 29 different daily tasks and use the term Instrumental Activities of Daily Living (20), followed by Basic Activities of Daily Living (or BADL) and then the terms Enhanced Activities of Daily Living (or EADL) and Social Activities (or SA).

7.2. Chosen Robots according to the Different Types of Activities. Table 2 and Figure 7 show that Paro (50%), Pleo (47%), and Emys (55%) are the robots selected by the majority of participants in IADL; Paro (49%), Pleo (42%), and Emys (48%) are the robots chosen by the majority of participants in BADL; and Paro (37%), Pleo (36%), and Emys (32%) are the robots chosen by participants in EADL.

7.3. Accuracy Response of Robots (Comrade and Service) with Different Activities. The activity of ageing in robot model is analyzed with the name and respective value of activity. Different types of activities are evaluated with robot model. The performance states and graph model of Paro, Pleo, and Emys Comrade robots are obtained. Depending on the service type, the accuracy response is obtained and activities of IADL, BADL, EADL, and SA are obtained with two different states. Table 3 and Figure 8 describe that, in IADL, Comrade robot gives highest accuracy response with percentage of 99% compared to service robot;, in BADL, Comrade robot gives highest accuracy response with percentage of 99% compared to service robot; and, in IADL, Comrade robot gives highest accuracy response with percentage of 92% compared to service robot; in EADL, Comrade gives highest accuracy response with percentage of 77% compared to service robot; and, in SA, Comrade robot gives accuracy response with percentage of 64%.

Table 2: Chosen robots according to the different types of activities.

Robot	Activity			
	IADL (%)	BADL (%)	EADL (%)	SA (%)
Paro (Comrade)	50	49	37	12
Pleo (Comrade)	47	42	36	13
Emys (Comrade)	55	48	32	11

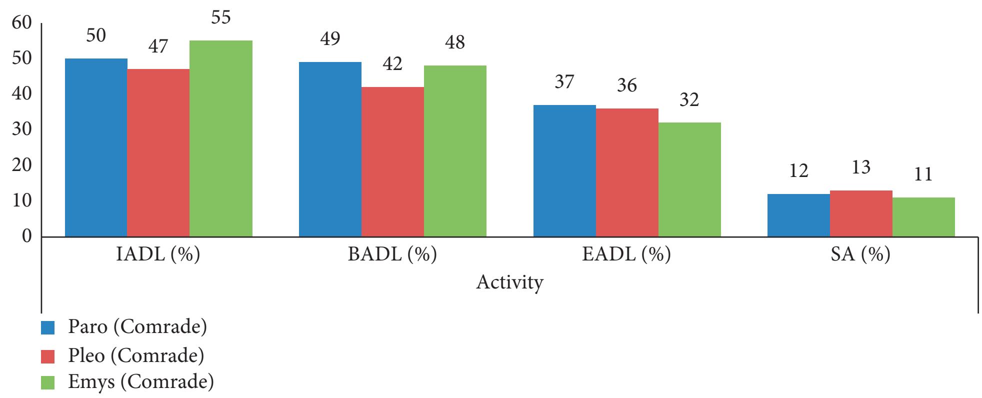

Figure 7: Chosen robots according to the different types of activities.

Table 3: Accuracy response of robots with different activities.

Activity	Accuracy response	
	Comrade robot	Service robot
IADL	99	91
BADL	92	88
EADL	77	23
SA	64	65

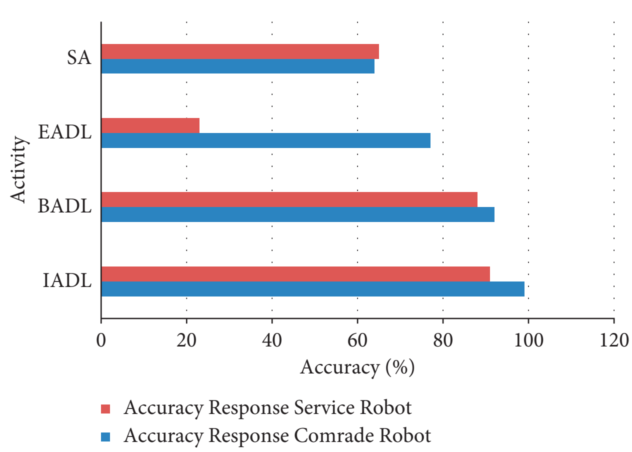

Figure 8: Accuracy response of robots with different activities.

8. Conclusion

Artificial intelligence is a rapidly expanding area of research, which has implications in many sectors, such as medical services, and to provide pharmaceutical aid. It is well established that the area of healthcare is a dynamic market for AI. In this article, a robotics framework is created which uses human messages between a human and a robot to carry out cognitive orientation evaluation. SyntaxNet, which enables the robots to comprehend programming knowledge naturally, helped carry out natural language processing. The Comrade robot was created from the ground up to handle this entire ecosystem. We do not need outside assistance in order to conduct a cognitive orientation evaluation, since the system is capable of doing it. This research sought to elicit tasks where a certain robot aids with increasing the quality of life (QoL) and assisting with an autonomous, healthy ageing. This research presents occupations that are an important component of the lives of older people in all the secondary classrooms. This study demonstrates that it is possible to use technologies with an eye on improving the quality of life for older people. At a profound level, elderly people need robots to do more complex tasks. In the future, the research work may be adopted with big data analysis, image processing, and statistical analysis reviewed with comparative analysis of machine learning approach.

Data Availability

The datasets used and/or analyzed in this study are available from the corresponding author upon reasonable request.

Conflicts of Interest

The authors declare that there are no conflicts of interest.

References

[1] B. Kartal, E. Nunes, J. Godoy, and M. Gini, "Monte Carlo tree search with branch and bound for multi-robot task allocation symposium conducted at the meeting of the the IJCAI-16 workshop on autonomous mobile service robots," vol. 30, no. 1, 2016, http://www-users.cs.umn.edu/%7Ebilal/papers/AAAI16_MCTS.pdf.

[2] M. Sg, T. Ak, A. St, S. Sv, and O. Mj, “Role of artificial intelligence in health care,” *Biochemistry Ind Journal*, vol. 11, no. 5, pp. 1–14, 2017.

[3] D. SverreSyrdal, J. Saunders, and K. Dautenhahn, K. L. Koay and N. Burke, “Teach me–show me””“—”end-user personalization of a smart home and comrade robot”,” *IEEE transactions on Human Machine Systems*, vol. 46, no. 1, 2016.

[4] L. Pu, W. Moyle, C. Jones, and M. Todorovic, “The effectiveness of social robots for older adults: a systematic review and meta-analysis of randomized controlled studies,” *Gerontologist Jan*, vol. 59, no. 1, pp. e37–51, 2019.

[5] P. R. Kshirsagar, H. Manoharan, F. Al-Turjman, and K. Kumar, “Design and testing of automated smoke monitoring sensors in vehicles,” *IEEE Sensors Journal*, vol. 1, p. 1, 2020.

[6] W. Moyle, C. Jones, L. Pu, and S. C. Chen, “Applying user-centred research design and evidence to develop and guide the use of technologies, including robots, in aged care,” *Contemporary Nurse*, vol. 54, pp. 1–3, 2018.

[7] G. Yang, Z. Pang, M. J. Deen et al., “Homecare robotic systems for healthcare 4.0: visions and enabling technologies,” *IEEE Journal of Biomedical and Health Informatics*, vol. 24, pp. 2535–2549, 2020.

[8] F. Al-Turjman and J. P. Lemayian, “Intelligence, security, and vehicular sensor networks in internet of things (IoT)-enabled smart-cities: an overview,” *Computers & Electrical Engineering*, vol. 87, Article ID 106776, 2020.

[9] S. M. Mortazavi, F. Aminiazad, H. Parsaei, and M. A. Mosleh-Shirazi, “An artificial neural network-based model for predicting annual dose in healthcare workers occupationally exposed to different levels of ionizing radiation,” *Radiation Protection Dosimetry*, vol. 189, 2020.

[10] B. Zohuri and M. Moghaddam, “Neural network driven supper artificial intelligence based on internet of things and big data,” *Business Resilience System (BRS)*, vol. 1, 2018.

[11] A. Abubshait, E. Wiese, and Y. L. Human, “You look human, but act like a machine: agent appearance and behavior modulate different aspects of Human-Robot interaction,” *Frontiers in Psychology*, vol. 8, 2017.

[12] J. Celis, S. Castro, and D. Guevara, “Voice processing with Internet of Things for a home automation system,” in *Proceedings of the International conference on Electronics, Electrical engineering and computing*, pp. 8–10, IEEE, Lima, Peru, August 2018.

[13] S. Montani, R. Bellazzi, A. Riva, C. Larizza, L. Portinale, and M. Stefanelli, “Artificial intelligence techniques for diabetes management: the T-IDDM project. ECAI,” in *Proceedings of the 14th European conerence on Artificial Intelligence*, pp. 1–5, Berlin, Germany, August 2000.

[14] H. Manoharan, Y. Teekaraman, P. R. Kshirsagar, S. Sundaramurthy, and A. Manoharan, “Examining the effect of aquaculture using sensor-based technology with machine learning algorithm,” *Aquaculture Research*, vol. 51, no. 11, pp. 4748–4758, 2020.

[15] J. Sensmeier, “Harnessing the power of artificial intelligence,” *Nursing Management*, vol. 48, no. 11, pp. 14–19, 2017.

[16] B. Mesko, “The role of artificial intelligence in precision medicine,” *Expert Rev Precis Med Drug Dev*, vol. 2, pp. 239–241, 2017.

[17] A. Davison, *Introduction to Robotics, Department of Computing*, Imperial College, London, UK, 2016.

[18] H. Boz, U. Kose, Emotion extraction from facial expressions by using artificial intelligence techniques,” *Broad Research in Artificial Intelligence and Neuroscience*, vol. 8, pp. 5–16, 2017.

[19] W. Yu, A. Kapusta, J. Tan, C. C. Kemp, G. Turk, and C. K. Liu, “Haptic simulation for robot-assisted dressing,” in *Proceedings of the IEEE International Conference on Robotics and Automation*, pp. 6044–6051, Singapore, May 2017.

[20] R. Bhatnagar and D. Batra, “Robotic process automation in healthcare-a review,” *International Robotics & Automation Journal*, vol. 5, 2019.

[21] H. Ashrafian, A. Darzi, and T. Athanasiou, “A novel modification of the Turing test for artificial intelligence and robotics in healthcare,” *International Journal of Medical Robotics and Computer Assisted Surgery*, vol. 11, pp. 38–43, 2015.

[22] K. Hameed, I. S. Bajwa, S. Ramzan, W. Anwar, and A. Khan, “An intelligent IoT based healthcare system using fuzzy neural networks,” *Scientific Programming*, vol. 2020, Article ID 8836927, 15 pages, 2020.

[23] P.-P. C. F. Rudzicz and S. Raimondo, “Ludwig: a conversational robot for people with alzheimer’s,” *The Journal of the Alzheimer’s Association*, vol. 13, 2017.

[24] C. G. Viejo, D. D. Torrico, F. R. Dunshea, and S. Fuentes, “Development of artificial neural network models to assess beer acceptability based on sensory properties using a robotic pourer: a comparative model approach to achieve an artificial intelligence system,” *Beverages*, vol. 5, 2019.

[25] M. M. A. D. Graaf, S. B. Allouch, and J. A. G. M. V. Dijk, “Why would I use this in my home? a model of domestic social robot acceptance,” *Human-Computer Interaction*, vol. 34, pp. 115–173, 2019.

[26] J. Cowie, “Evaluation of a digital consultation and self-care advice tool in primary care: a multi-methods study,” *Inter. Jour.of Environ Res Public Health*, vol. 15, 2018.

Hindawi
Journal of Healthcare Engineering
Volume 2023, Article ID 9869635, 1 page
https://doi.org/10.1155/2023/9869635

Retraction

Retracted: LncRNA MAGI2-AS3 Suppresses the Proliferation and Invasion of Cervical Cancer by Sponging MiR-15b

Journal of Healthcare Engineering

Received 12 November 2022; Accepted 12 November 2022; Published 30 January 2023

Journal of Healthcare Engineering has retracted the article titled "LncRNA MAGI2-AS3 Suppresses the Proliferation and Invasion of Cervical Cancer by Sponging MiR-15b" [1] due to concerns that the peer review process has been compromised.

Following an investigation conducted by the Hindawi Research Integrity team [2], significant concerns were identified with the peer reviewers assigned to this article; the investigation has concluded that the peer review process was compromised. We therefore can no longer trust the peer review process, and the article is being retracted with the agreement of the Chief Editor.

References

[1] Y. Chai, L. Wang, Y. Qu, and Z. Hu, "LncRNA MAGI2-As3 Suppresses the Proliferation and Invasion of Cervical Cancer by Sponging MiR-15b," *Journal of Healthcare Engineering*, vol. 2022, Article ID 9707206, 9 pages, 2022.

[2] L. Ferguson, "Advancing Research Integrity Collaboratively and with vigour," 2022, https://www.hindawi.com/post/advancing-research-integrity-collaboratively-and-vigour/.

Hindawi
Journal of Healthcare Engineering
Volume 2022, Article ID 9707206, 9 pages
https://doi.org/10.1155/2022/9707206

Research Article

LncRNA MAGI2-As3 Suppresses the Proliferation and Invasion of Cervical Cancer by Sponging MiR-15b

Yiqing Chai,[1] Lili Wang,[2] Yanwen Qu,[3] and Zhixia Hu[4]

[1]*Department of Ultrasound, Tianjin Central Hospital of Gynecology Obstetrics, Tianjin 300000, China*
[2]*Department of Gynaecology and Obstetrics, Rizhao Hospital of TCM, Rizhao 276800, Shandong, China*
[3]*Department of Gynecological Oncology, Affiliated Qingdao Central Hospital, Qingdao University, Qingdao 266000, China*
[4]*Department of Prices and Charges Management Division, Shandong Provincial Hospital Affiliated to Shandong First Medical University, Jinan 250021, Shandong, China*

Correspondence should be addressed to Zhixia Hu; huzhixia@sdphospital.cn

Received 2 December 2021; Accepted 6 January 2022; Published 25 January 2022

Academic Editor: Enas Abdulhay

Background. Cervical cancer is the leading cause of cancer deaths among women, and more than 85% of cervical cancer deaths occur in low and middle-income countries. The purpose of this study is to investigate the functions of MAGI2-AS3 and miR-15b in cervical cancer. *Materials and Methods*. The mRNA levels of MAGI2-AS3, miR-15b, and CCNE1 were evaluated using RT-qPCR assay. Dual-luciferase reporter gene assay was used to confirm whether miR-15b binds to CCNE1. *Results*. LncRNA MAGI2-AS3 was downregulated, while miR-15b was upregulated in cervical cancer. Cervical cancer patients with low expression of MAGI2-AS3 have a poor prognosis. Upregulation of MAGI2-AS3 inhibited proliferative and invasive abilities of HeLa cells via regulating the expression of miRNA-15b. MiR-15b inhibitor suppressed cell proliferation and invasion. CCNE1 was a direct target gene of miR-15b, which binds to the 3'-UTR of its mRNA. MiR-15b partially reversed the inhibitory effect of overexpression of MAGI2-AS3 on the proliferation and invasion of HeLa cells. MAGI2-AS3 mediated the expression of CCNE1 in HeLa cells. *Conclusion*. LncRNA MAGI2-AS3 inhibits the proliferation and invasion of cervical cancer cells via the miRNA-15/CCNE1 axis. Our results illustrates that MAGI2-AS3 can be used as a useful clinical predictor for early diagnosis and prognosis assessment of cervical cancer.

1. Introduction

Cervical cancer (CC) is the fourth most commonly diagnosed cancer in women and one of the most common cancers in the world. There were approximately 570,000 new cases worldwide in 2018, and 311,000 died of cervical cancer [1, 2]. There are two main types of cervical cancer: cervical squamous cell carcinoma (CSCC), which accounts for approximately 80% to 85% of cervical cancer cases, and the remainder are cervical adenocarcinoma (CAC) [3]. Although treatments such as chemotherapy, radiation, and surgical resection have improved the prognosis of early-stage cervical cancer, the metastasis and recurrence of cervical cancer are the cause of most deaths [4]. Thus, it is urgent to investigate the biomarkers related to cervical cancer metastasis.

Long non-coding RNAs (lncRNAs) belong to noncoding RNAs that are greater than 200 nucleotides in length [5]. Increasing evidence has proven that lncRNAs were involved in range of biological processes, including differentiation, tumorigenesis, and metastasis [6]. For instance, lncRNA-H19 activated the CDC42/PAK1 pathway to promote cell proliferation, migration, and invasion by targeting miR-15b in hepatocellular carcinoma [7]. Long noncoding RNA DSCAM-AS1 contributed to tumorigenesis to enhance cell proliferation, migration, and invasion ability in cervical cancer [8]. LncRNA MAGI2-AS3 suppressed cell viability and migration via miR-374b/SMG1 signaling pathway in hepatocellular carcinoma [9]. In addition, MAGI2-AS3 inhibited cell proliferation and invasion through miRNA-23a-3p/PTEN axis in non-small cell lung carcinoma [10]. Therefore, exploring the mechanism of action of lncRNA

MAGI2-AS3 may provide new ideas for the clinical treatment of cervical cancer.

LncRNAs always regulate cell progression via spongy micro-RNAs [11]. Micro-RNAs (miRNAs) are short noncoding RNAs with a length of approximately 22–25 nucleotides [12]. MiRNAs functioned as regulators in tumorigenesis by cleaving mRNA and suppressing translation [13]. MiR-15b enhanced cell cycle from G1 phase to S phase and reduced cell apoptosis in the treatment of renal cell carcinoma with sunitinib [14]. However, miR-15b represses cell proliferation, migration, invasion, senescence, and apoptosis of ovarian cancer [15].

The cyclin E1 (CCNE1) belongs to the highly conserved cyclin family, whose members are characterized by a dramatic periodicity in protein abundance through the cell cycle [16]. CCNE1, acted as a regulator of CDK kinases, whose activity is required for cell cycle G1/S transition [17]. Overexpression of CCNE1 has been observed in many tumors, which can lead to chromosome instability, and thus may contribute to tumorigenesis. In this study, we found that upregulation of MAGI2-AS3 inhibited the proliferative and invasive abilities of HeLa cells via regulating the expression of miRNA-15b. LncRNA MAGI2-AS3 inhibited cell proliferation and invasion of cervical cancer via the miRNA-23a-3p/PTEN axis.

2. Materials and Methods

2.1. Clinical Samples. During 2015 to 2018, we collected 47 cervical cancer patients from Shandong Provincial Hospital Affiliated to Shandong First Medical University and obtained pairs of cervical cancer tissues and corresponding normal tissues. The excised tissue samples are frozen in liquid nitrogen, followed by cryopreservation. All patients did not receive any therapy before surgery. Our study was approved by the Ethics Committee of Shandong Provincial Hospital Affiliated to Shandong First Medical University, and all patients signed written informed consent.

2.2. Cell Culture and Transfection. A normal cervix epithelial Ect1/E6E7 cell and three cervical cancer cell lines HeLa, SiHa, and CaSki were obtained from American Tissue Culture Collection (ATCC, USA). All cells were cultured in RPMI-1640 (Hyclone, USA) containing 10% fetal bovine serum (FBS) in a humidified atmosphere with 5% CO_2 at 37 °C.

MAGI2-AS3 overexpression vector (pEX-MAGI2-AS3) and the control vector were purchased from Ribobio (Guangzhou, China). The miR-15b mimic, miR-15b inhibitor, and the corresponding controls (NC) were synthesized by GenePharma (Shanghai, China). Lipofectamine 2000 (Invitrogen Life Technology) was used to transfect pEX-MAGI2-AS3, miR-15b mimic, and miR-15b inhibitor into HeLa cells. All cells were harvested at 48 h after transfection.

2.3. RNA Extraction and Real-Time Quantitative Polymerase Chain Reaction (RT-qPCR). The TRIzol reagent (Invitrogen Life Technology) was used to isolate total RNA from HCC tissues or cells. The RT-PCR kit (Takara, Dalian, China) or Hairpin-it miRNA qPCR quantitation kit (GenePharma) was used to perform the reverse-transcription and synthesize the first cDNA chain. The SYBR Green-based PCR kit (TAKARA Biotechnology, Dalian, China) was conducted to carry out the qPCR in an iQ5 Multicolor real-time PCR detection system (Bio-Rad Laboratories, Hercules, CA). The primers were MAGI2-AS3: forward, 5′-CACCTTGCTTGACAACTTGA-3’ and reverse, 5′-CATTACAGCTCGGCTACTGC-3’; glyceraldehyde 3-phosphate dehydrogenase (GAPDH): forward, 5′-ACCACAGTCCATGCCATCAC-3′ and reverse, 5′-TCCACCACCCTGTTGCTGTA-3’; miR-15b: forward, 5′-CTCAACTGGTGTCGTGGAGTCGGCAATTCAGTT-GAGTGTAA-3′ and reverse, 5′-ACACTCCAGCTGGGT-TAGCAGCACATC-3’; U6: forward, 5′-ATTGGAACGATACAGAGAAGATT-3′ and reverse, 5′-GGAACGCTTCACGAATTTG-3’.

2.4. Transwell Assay. Cell invasion assay was carried out using Transwell inserts (Corning, Blacksburg, VA, USA) with a filter of 8 μm pores (BD Biosciences, San Diego, CA) according to the manufacturers' instructions. The upper chamber was added 200 μl medium containing 5×10^5 cells without serum, and the lower chamber was filled with 600 μl medium with 20% FBS. After 24 h of incubation, the invaded cells were fixed and stained with methanol and crystal violet. A light microscope (Olympus Corporation, Tokyo, Japan) was used to count the number of the invading cells.

2.5. Cell Counting Kit-8 (CCK-8). Cell counting kit-8 (CCK-8; Dojindo Laboratories, Kumamoto, Japan) was conducted to evaluate cell proliferation following manufacturer's instructions. Each well was added with 10 μl CCK-8 solution, and then the absorbance was measured using a spectrophotometer (Thermo Fisher Scientific, MA, USA).

2.6. Luciferase Reporter Assay. StarBase v2.0 (http://starbase.sysu.edu.cn/) software predicted the putative miRNA binding sites in the MAGI2-AS3 sequences. HeLa cells were seeded in 6-well plates. The wild-type (WT) or mutant (MUT) MAGI2-AS3 binding sites and the miR-15b mimic or NC (GenePharma Biotechnology, Shanghai, China) were cotransfected in HeLa cells using Lipofectamine 2000 according to the manufacturer's instructions. Cells were harvested 48 h after transfection, and assayed using a luciferase reporter assay system (Promega, Madison, WI, USA) according to the manufacturer's instructions.

2.7. Statistical Analysis. GraphPad Prism software, version 5.0 (GraphPad Software, La Jolla, CA) was used to perform the statistical analyses. The data are expressed as the mean ± standard deviation (SD). The difference between two or more groups was compared by Student's *t*-test and a one-way analysis of variance. Spearman's correlation analysis was used to assess the relationships between MAGI2-AS3 and miR-15b. $P < 0.05$ is considered to be of statistical significances. Results were from at least three independent experiments.

3. Results

3.1. MAGI2-As3 Expresses Low Expression in Cervical Cancer. RT-qPCR was conducted to measure the expression of MAGI2-AS3 in tissues and cell lines. As expected, the expression of MAGI2-AS3 in cervical cancer tissues was lower than that of matched adjacent normal tissues (Figure 1(a)). Moreover, MAGI2-AS3 has been found to be downregulated in cervical cancer patients at III-IV stage compared with the I-II stage (Figure 1(b)). Similarly, the expression of MAGI2-AS3 was lower in cervical cancer cell lines HeLa, SiHa, and CaSki than the normal cervix epithelial Ect1/E6E7 cells (Figure 1(c)). Kaplan–Meier curve was employed to evaluate the overall survival of cervical cancer patients, indicating that downregulation of MAGI2-AS3 predicted a worse prognosis (Figure 1(d)).

3.2. Overexpression of MAGI2-As3 Suppresses the Proliferative and Invasive Abilities in HeLa Cells. The transfection efficacy of pEX-MAGI2-AS3 transfected in HeLa cells was determined by RT-qPCR assay (Figure 2(a)). CCK-8 and transwell assays were applied to assess the cell proliferative and invasive capacities. Cell proliferation was inhibited by transfecting with pEX-MAGI2-AS3 in comparison with negative control (Figure 2(b)). Similarly, the invasive ability of HeLa cells was attenuated by overexpressing MAGI2-AS3 (Figure 2(c)).

3.3. MAGI2-As3 Sponges MiRNA-15b as a ceRNA. The expression of miR-15b was calculated after altering MAGI2-AS3, and we are surprised to discover that the expression of miR-15b was reduced when overexpression of MAGI2-AS3 in HeLa cells (Figure 3(a)). The expression of miR-15b was increased in HeLa, SiHa, and CaSki cells versus normal cervix epithelial cell Ect1/E6E7 (Figure 3(b)). Likewise, the expression of miR-15b was also measured, and we found that miRNA-15b was upregulated in cervical cancer tissues compared with the paracancerous tissue samples (Figure 3(c)). Due to the expression of MAGI2-AS3 and miR-15b in cervical cancer tissues, the correlation analysis was measured. Not unfortunately, it has a negative correlation between the mRNA level of MAGI2-AS3 and miR-15b in cervical cancer tissues (Figure 3(d)). Thus, all the results demonstrated that MAGI2-AS3 sponged miRNA-15b and negatively regulated its expression in cervical cancer.

3.4. Knockdown of MiR-15b Suppresses the Proliferation and Invasion in HeLa Cells. To investigate the functions of miR-15b, the expression of miR-15b was reduced by miR-15b inhibitor ($P < 0.05$) (Figure 4(a)). Cell proliferation was inhibited after miR-15b was knocked down compared with the negative control ($P < 0.05$) (Figure 4(b)). Similarly, miR-15b inhibitor reduced the invasive ability of HeLa cells ($P < 0.05$) (Figure 4(c)). All the findings suggested that silencing miR-15b suppressed HeLa cell proliferation and invasion.

3.5. MiR-15b Restores the Inhibitory Effect of MAGI2-As3 on HeLa Cells. In order to find out whether miR-15b has an effect on the function of MAGI2-AS3, miR-15b mimics were transfected into MAGI2-AS3 overexpressing HeLa cells, and the transfection efficiency was calculated by RT-qPCR ($P < 0.05$) (Figure 5(a)). CCK-8 results demonstrated that retransfection of miR-15b mimic enhanced cell viability versus only transfected pEX-MAGI2-AS3 group ($P < 0.05$) (Figure 5(b)). Moreover, HeLa cells cotransfected with miR-15b mimic and pEX-MAGI2-AS3 cause a great increase of cell invasion compared with pEX-MAGI2-AS3 group ($P < 0.05$) (Figure 5(c)). The results revealed that miR-15b restored the inhibitory effect of MAGI2-AS3 on the proliferation and invasion in HeLa cells.

3.6. CCNE1 Is a Direct Target of MiR-15b. Next, we designed to explore how MAGI2-AS3 and miR-15b were involved in the cervical cancer progression. TargetScan analysis showed that there was an evolutionarily conserved miR-15b binding site in the 3'-UTR of CCNE1 mRNA (Figure 6(a)). Subsequently, the luciferase reporter assay indicated that the luciferase activity of wild-type CCNE1 was decreased. Meanwhile, miR-15b mimic does not alter the luciferase activity of the mutant CCNE1, which demonstrated specific binding of CCNE1 3'-UTR to miR-15b (Figure 6(b)). Furthermore, the expression of CCNE1 was reduced after transfection with miR-15b inhibitor (Figure 6(c)). In addition, the expression of CCNE1 was increased by knockdown of MAGI2-AS3, while it was decreased by overexpressing MAGI2-AS3 (Figure 6(d)). All results exhibit that CCNE1 is a target gene of miR-15b, and its expression is mediated by MAGI2-AS3.

4. Discussion

Increasing evidence indicated that lncRNAs played vital functions in the progression of cervical cancer [18,19]. For instance, lncRNA-CTS promoted metastasis and epithelial-to-mesenchymal transition through regulating miR-505/ZEB2 axis in cervical cancer [20]. Long noncoding RNA ZNF667-AS1 inhibited tumor invasion by counteracting downregulation of micro-RNA-93-3p-dependent PEG3 in cervical cancer [21]. In our study, we discovered that MAGI2-AS3 was low expressed in cervical tissues. Also, through comparing the expression of MAGI2-AS3 in different stage, we found that the expression of MAGI2-AS3 was lower in III-IV stages than I-II stages. The overall survival of cervical cancer patients were calculated and compared its relationship with the expression of MAGI2-AS3. The results indicated that low expression of MAGI2-AS3 was associated with poor prognosis. Previous studies demonstrated that MAGI2-AS3 played tumor suppressive roles in high-grade serous ovarian carcinoma and breast cancer [22,23]. Consistent with the previous studies, we discovered that upregulation of MAGI2-AS3 suppressed cell proliferation and invasion in HeLa cells. However, MAGI2-AS3 promoted progression of gastric cancer and colorectal cancer [24,25]; thus, we conjectured that MAGI2-AS3 might have tissue specificity.

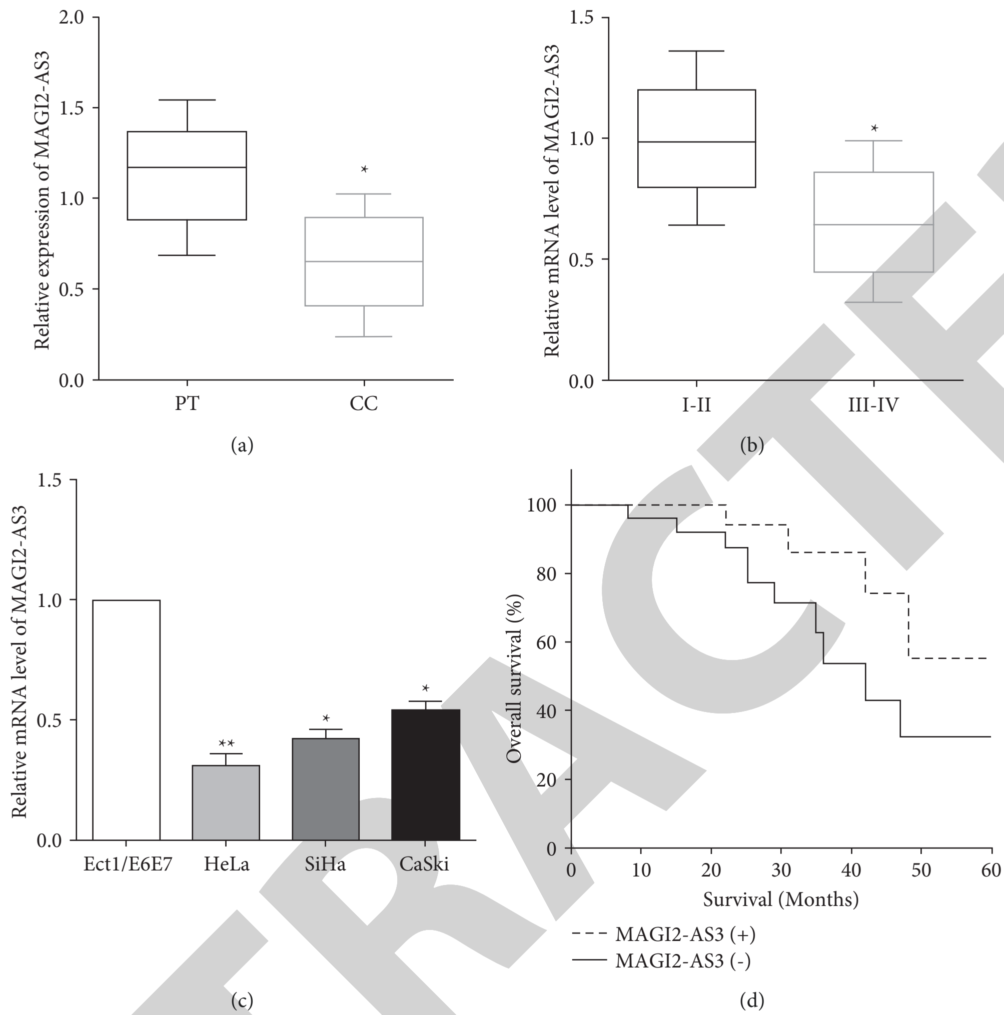

Figure 1: MAGI2-AS3 exhibits low expression in cervical cancer (a) MAGI2-AS3 has a lower expression in cervical cancer tissues than matched adjacent normal tissues. (b) MAGI2-AS3 was downregulated in cervical cancer patients at III-IV stage compared with the I-II stage. (c) MAGI2-AS3 expression was lower in cervical cancer cell lines than the normal cervix epithelial cells. (d) Kaplan–Meier curve indicated that downregulation of MAGI2-AS3 predicted a worse prognosis.

LncRNAs often acted as the endogenous competitive RNA (ceRNAs) of miRNA. LncRNA MAGI2-AS3 inhibited cell invasion and migration via sponging microRNA-374a [26]. Similarly, the spongy of MAGI2-AS3 miR-15b inhibited the progression of bladder cancer [27]. In this study, we discovered that overexpression of MAGI2-AS3 reduced the expression of miR-15b. Evidence showed that miR-15b promoted cell proliferation and invasion by targeting AXIN2 in liver cancer [28]. However, the expression of miR-15b inhibited tumor progression via directly targeting MYCN in neuroblastoma [29]. But the expression of miR-15b in cervical cancer is unknown; thus, we conducted RT-qPCR to assess miR-15b. We found that the expression of miR-15b was higher in cervical cancer cells and tissues. Moreover, the expression of MAGI2-AS3 has a negative connection with miR-15b in cervical cancer tissues. However, we have no evidence to prove whether MAGI2-AS3 and miR-15b directly bind, which was a limitation in this study. Next, the functional tests were performed after knockdown miR-15b in HeLa cells. We discovered that miR-15b inhibitor can impair cell proliferation and invasion of HeLa cells. Furthermore, miR-15b partially reversed the promotive functions of MAGI2-AS3 on HeLa cell viability and invasion. MiR-15b regulates cell differentiation and survival by targeting CCNE1 in APL cells [30]. Consistent with the above findings, miR-15b was confirmed to be directly binding to the 3’UTR of CCNE1 by luciferase report assay. The expression of CCNE1 was suppressed by upregulating miR-15b in HeLa cells. Meanwhile, overexpression of MAGI2-AS3 enhanced the expression of CCNE1, and low expression of MAGI2-AS3 reduced the expression of CCNE1. Thus, we proposed that MAGI2-AS3 enhanced cervical cancer cell proliferation and invasion via regulating the miR-15b/CCNE1 axis.

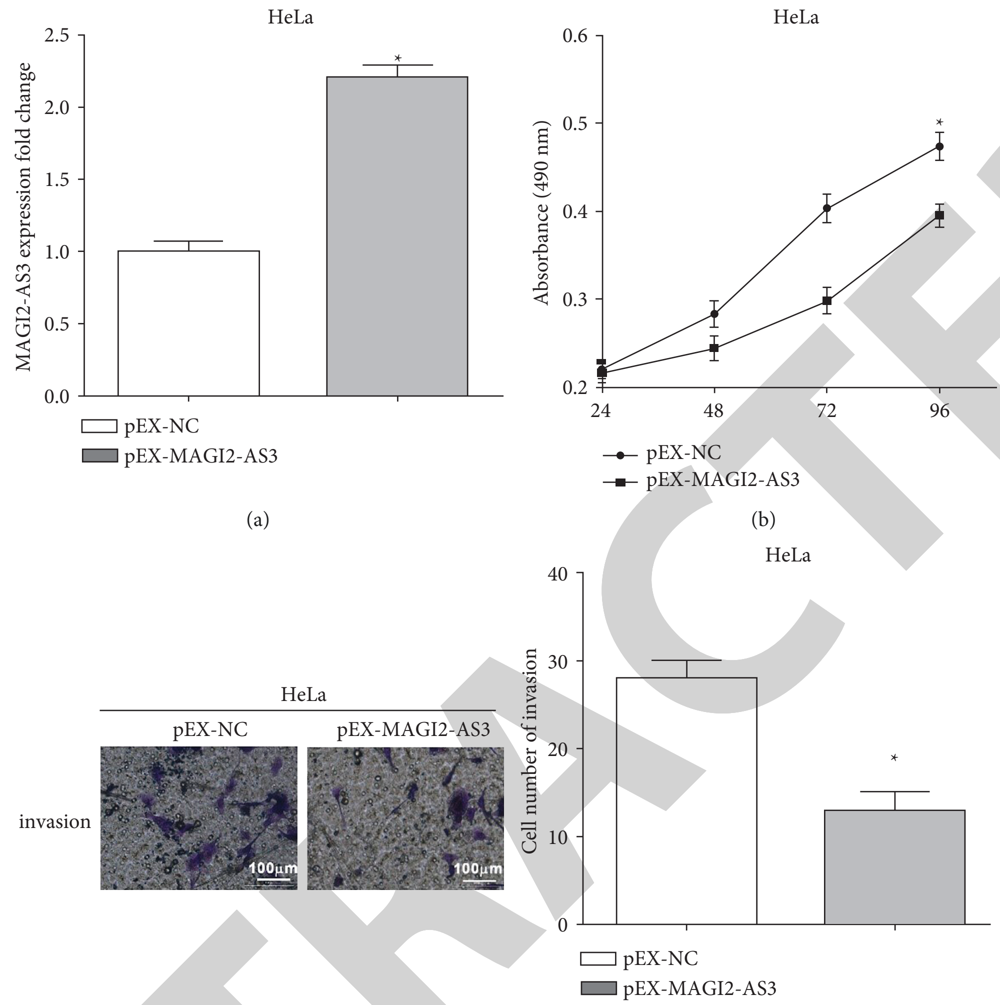

Figure 2: Overexpression of MAGI2-AS3 suppresses the proliferative and invasive abilities in HeLa cells (a) The transfection efficacy of transfection of pEX-MAGI2-AS3 in HeLa cells using RT-qPCR assay. (b) Cell proliferation was inhibited by transfecting with pEX-MAGI2-AS3 in comparison with negative control. (c) The invasive ability of HeLa cells was attenuated by the overexpression of MAGI2-AS3.

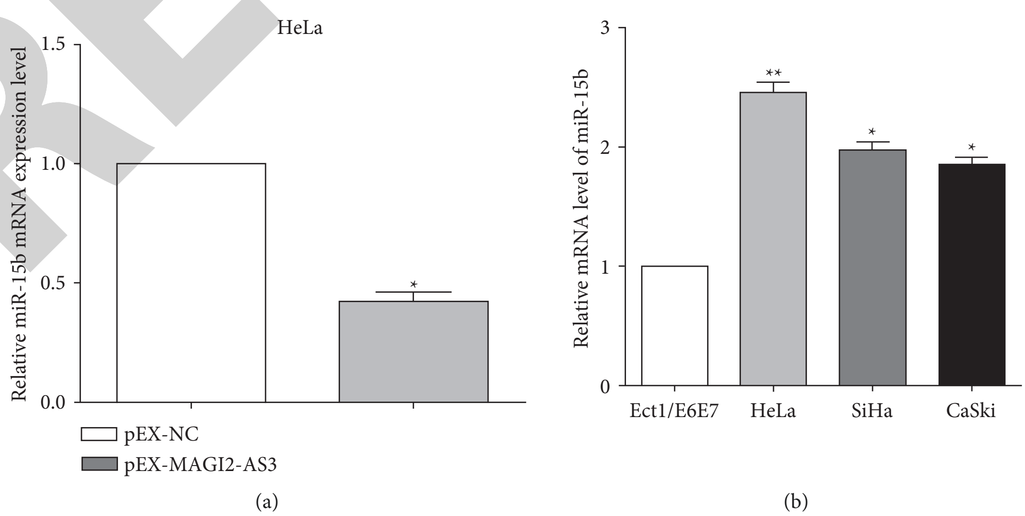

Figure 3: Continued.

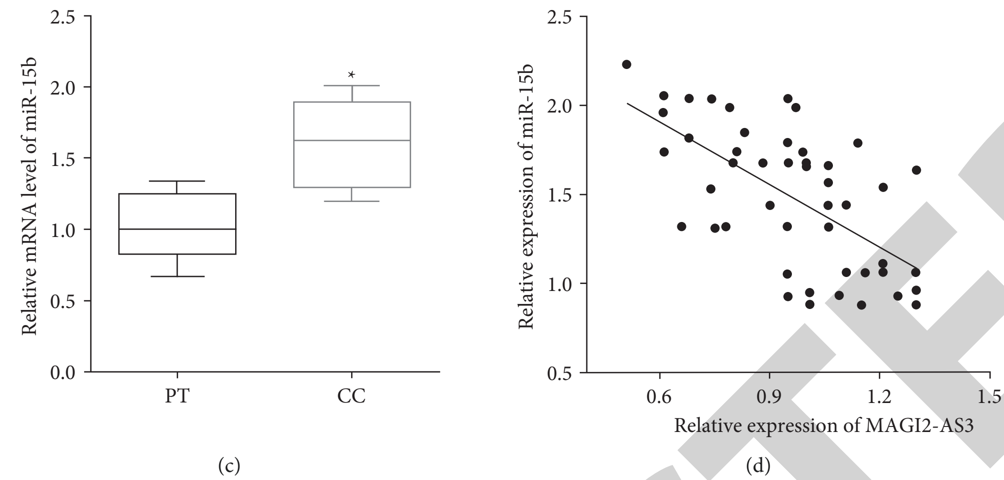

Figure 3: MAGI2-AS3 sponges miRNA-15b as a ceRNA. (a) The expression of miR-15b was reduced when overexpression of MAGI2-AS3 in HeLa cells. (b) The expression of miR-15b was increased in cervical cancer cells versus normal cervix epithelial cell. (c) MiRNA-15b was upregulated in cervical cancer tissues compared with the paracancerous tissue samples. (d) It has a negative correlation between the mRNA level of MAGI2-AS3 and miR-15b in cervical cancer tissues.

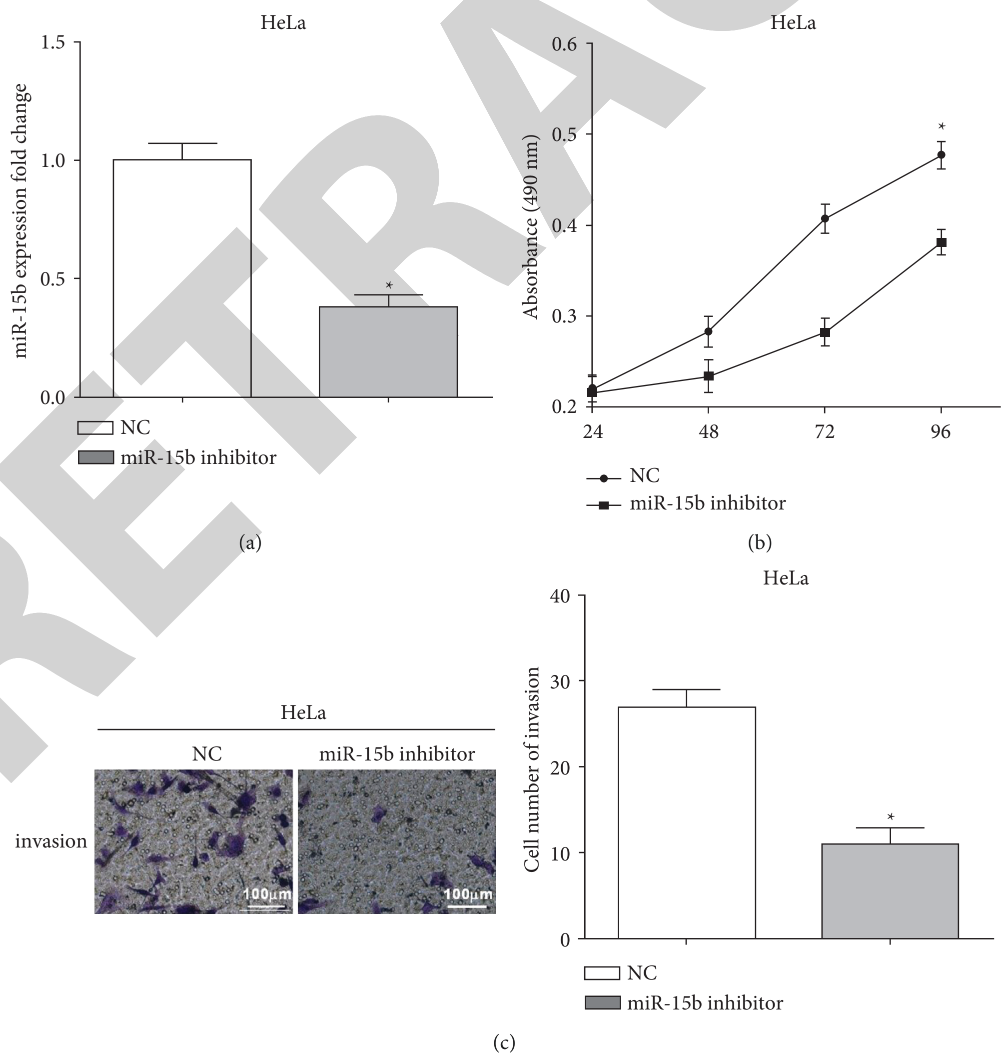

Figure 4: Knockdown of miR-15b suppresses the proliferation and invasion in HeLa cells. (a) The expression of miR-15b was reduced by miR-15b inhibitor. (b) Cell proliferation was inhibited after knockdown miR-15b. (c) MiR-15b inhibitor reduced the invasive ability in HeLa cells.

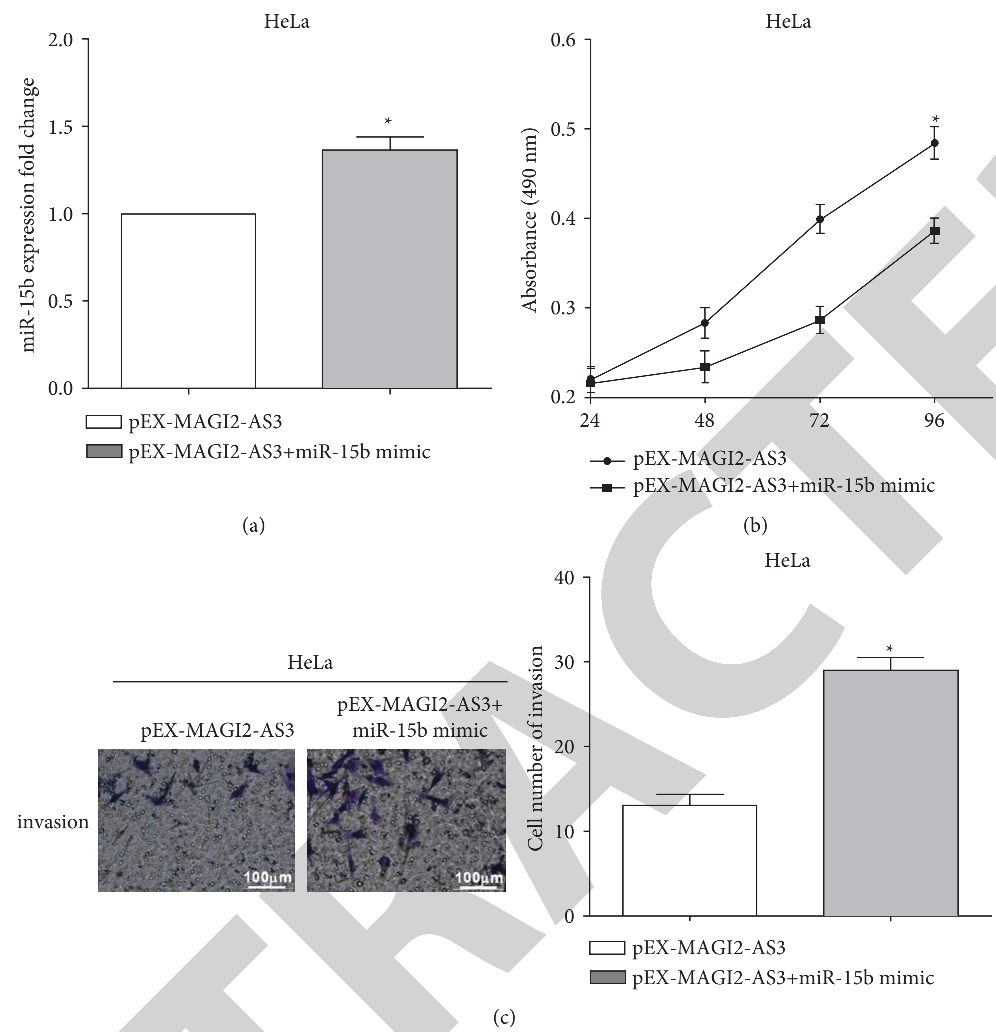

Figure 5: MiR-15b restores the inhibitory effect of MAGI2-AS3 on HeLa cells. (a) MiR-15b mimics were transfected into MAGI2-AS3 overexpressing HeLa cells. (b) Retransfection of miR-15b mimic enhanced cell viability. (c) Cotransfected with miR-15b mimic and pEX-MAGI2-AS3 cause a great increase of cell invasion compared with pEX-MAGI2-AS3 group.

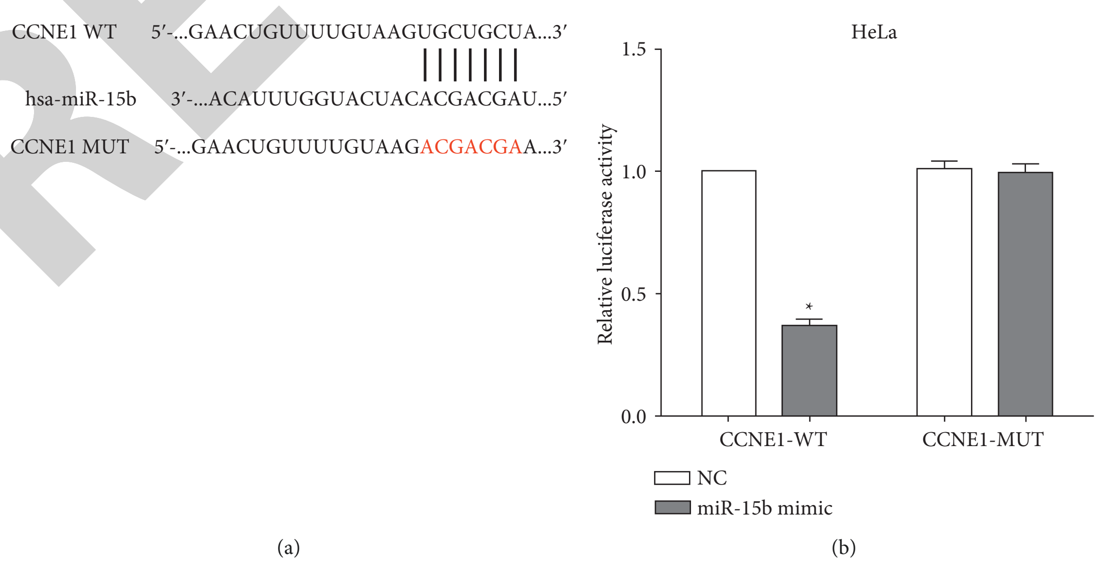

Figure 6: Continued.

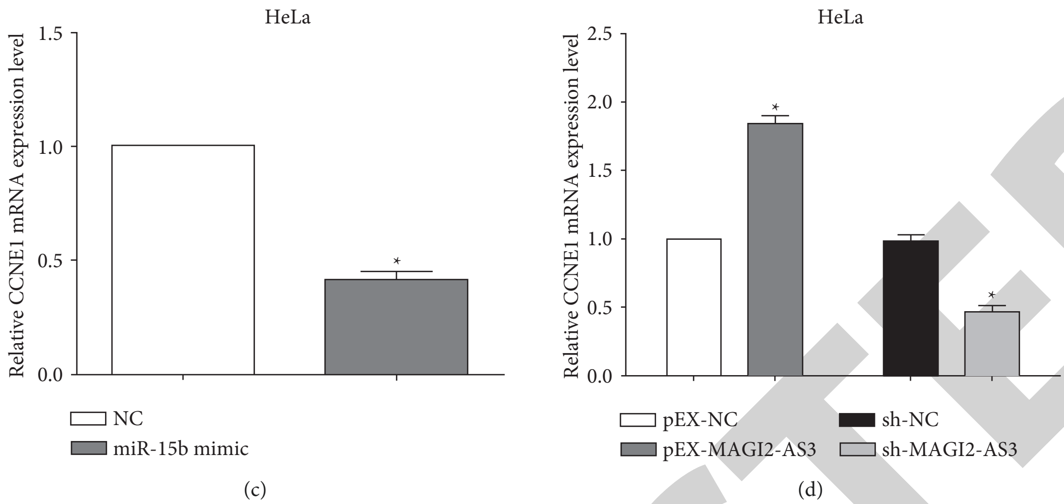

Figure 6: CCNE1 is a direct target of miR-15b. (a) TargetScan analysis showed that there was an evolutionarily conserved miR-15b binding site in the 3'-UTR of CCNE1 mRNA. (b) Luciferase reporter assay indicated that CCNE1 3'-UTR bound specifically to miR-15b. (c) The expression of CCNE1 was reduced after transfecting miR-15b inhibitor. (d) The expression of CCNE1 was increased by knockdown of MAGI2-AS3, while it was decreased by overexpressing MAGI2-AS3.

5. Conclusion

We found that MAGI2-AS3 inhibited the growth and invasion of cervical cancer by regulating the miR-15b/CCNE1 pathway. The findings of this study provide new insights into how MAGI2-AS3 could be an effective target for the diagnosis of cervical cancer. However, it is not enough to support the clinical application of MAGI2-AS3, and more research is urgently needed.

Data Availability

Data to support the findings of this study are available on reasonable request from the corresponding author.

Conflicts of Interest

The authors have no conflicts of interest to declare.

References

[1] F. Bray, J. Ferlay, I. Soerjomataram, R. L. Siegel, L. A. Torre, and A. Jemal, "Global cancer statistics 2018: GLOBOCAN estimates of incidence and mortality worldwide for 36 cancers in 185 countries," *CA: A Cancer Journal for Clinicians*, vol. 68, no. 6, pp. 394–424, 2018.

[2] H. Li, X. Wu, and X. Cheng, "Advances in diagnosis and treatment of metastatic cervical cancer," *Journal of gynecologic oncology*, vol. 27, no. 4, p. e43, 2016.

[3] S. S. Wang, M. E. Sherman, A. Hildesheim, J. V. Lacey, and S. Devesa, "Cervical adenocarcinoma and squamous cell carcinoma incidence trends among white women and black women in the United States for 1976-2000," *Cancer*, vol. 100, no. 5, pp. 1035–1044, 2004.

[4] K. Matsuo, M. Shimada, T. Saito et al., "Risk stratification models for para-aortic lymph node metastasis and recurrence in stage IB-IIB cervical cancer," *Journal of gynecologic oncology*, vol. 29, no. 1, p. e11, 2018.

[5] K. Schaukowitch and T.-K. Kim, "Emerging epigenetic mechanisms of long non-coding RNAs," *Neuroscience*, vol. 264, pp. 25–38, 2014.

[6] G. A. Calin, C.-g. Liu, M. Ferracin et al., "Ultraconserved regions encoding ncRNAs are altered in human leukemias and carcinomas," *Cancer Cell*, vol. 12, no. 3, pp. 215–229, 2007.

[7] Y. Zhou, R.-G. Fan, C.-L. Qin, J. Jia, X.-D. Wu, and W.-Z. Zha, "LncRNA-H19 activates CDC42/PAK1 pathway to promote cell proliferation, migration and invasion by targeting miR-15b in hepatocellular carcinoma," *Genomics*, vol. 111, no. 6, pp. 1862–1872, 2019.

[8] J. Liang, S. Zhang, W. Wang et al., "Long non-coding RNA DSCAM-AS1 contributes to the tumorigenesis of cervical cancer by targeting miR-877-5p/ATXN7L3 axis," *Bioscience Reports*, vol. 40, 2019.

[9] Z. Yin, T. Ma, J. Yan et al., "LncRNA MAGI2-AS3 inhibits hepatocellular carcinoma cell proliferation and migration by targeting the miR-374b-5p/SMG1 signaling pathway," *Journal of Cellular Physiology*, vol. 234, no. 10, pp. 18825–18836, 2019.

[10] X. Z. Hao and K. Yang, "LncRNA MAGI2-AS3 suppresses the proliferation and invasion of non-small cell lung carcinoma through miRNA-23a-3p/PTEN axis," *European Review for Medical and Pharmacological Sciences*, vol. 23, no. 17, pp. 7399–7407, 2019.

[11] M. S. Ebert and P. A. Sharp, "Roles for microRNAs in conferring robustness to biological processes," *Cell*, vol. 149, no. 3, pp. 515–524, 2012.

[12] H. Guo, N. T. Ingolia, J. S. Weissman, and D. P. Bartel, "Mammalian microRNAs predominantly act to decrease target mRNA levels," *Nature*, vol. 466, no. 7308, pp. 835–840, 2010.

[13] W. C. S. Cho, "MicroRNAs: potential biomarkers for cancer diagnosis, prognosis and targets for therapy," *The International Journal of Biochemistry & Cell Biology*, vol. 42, no. 8, pp. 1273–1281, 2010.

[14] L. Lu, Y. Li, H. Wen, and C. Feng, "Overexpression of miR-15b promotes resistance to sunitinib in renal cell carcinoma," *Journal of Cancer*, vol. 10, no. 15, pp. 3389–3396, 2019.

Hindawi
Journal of Healthcare Engineering
Volume 2023, Article ID 9803083, 1 page
https://doi.org/10.1155/2023/9803083

Retraction

Retracted: Investigation on the Effect of Graded Emergency Nursing Group under the Assistance of Multidisciplinary First Aid Knowledge Internet-Based Approach on the First Aid of Acute Myocardial Infarction

Journal of Healthcare Engineering

Received 12 November 2022; Accepted 12 November 2022; Published 26 January 2023

Journal of Healthcare Engineering has retracted the article titled "Investigation on the Effect of Graded Emergency Nursing Group under the Assistance of Multidisciplinary First Aid Knowledge Internet-Based Approach on the First Aid of Acute Myocardial Infarction" [1] due to concerns that the peer review process has been compromised.

Following an investigation conducted by the Hindawi Research Integrity team [2], significant concerns were identified with the peer reviewers assigned to this article; the investigation has concluded that the peer review process was compromised. We therefore can no longer trust the peer review process, and the article is being retracted with the agreement of the Chief Editor.

References

[1] L. Song, H. Lu, H. Ru, and X. Zhao, "Investigation on the Effect of Graded Emergency Nursing Group under the Assistance of Multidisciplinary First Aid Knowledge Internet-Based Approach on the First Aid of Acute Myocardial Infarction," *Journal of Healthcare Engineering*, vol. 2022, Article ID 8469930, 6 pages, 2022.

[2] L. Ferguson, "Advancing Research Integrity Collaboratively and with Vigour," 2022, https://www.hindawi.com/post/advancing-research-integrity-collaboratively-and-vigour/.

Hindawi
Journal of Healthcare Engineering
Volume 2022, Article ID 8469930, 6 pages
https://doi.org/10.1155/2022/8469930

Research Article

Investigation on the Effect of Graded Emergency Nursing Group under the Assistance of Multidisciplinary First Aid Knowledge Internet-Based Approach on the First Aid of Acute Myocardial Infarction

Lili Song, Han Lu, Hong Ru, and Xue Zhao

Department of Emergency, Beijing Hospital, National Center of Gerontology, Institute of Geriatric Medicine, Chinese Academy of Medical Sciences, No.1 Da HuaRoad, DongDan, Beijing 100730, China

Correspondence should be addressed to Lili Song; songlili@bjhmoh.org

Received 29 November 2021; Revised 16 December 2021; Accepted 27 December 2021; Published 18 January 2022

Academic Editor: Enas Abdulhay

Objective. To analyze the effect of a graded emergency nursing group under the assistance of multidisciplinary first aid knowledge Internet-based approach on the first aid of acute myocardial infarction (AMI). *Methods*. The clinical data of 90 AMI patients treated in our hospital from March 2019 to March 2020 were selected for the retrospective analysis, and the patients were divided into the observation group and the routine group according to the first aid order, with 45 cases each. The patients in the routine group received the conventional first aid measures, and the graded emergency nursing group mode with the help of multidisciplinary first aid knowledge Internet-based approach was adopted for those in the observation group so as to compare the prognosis, nursing satisfaction scores, etc., between the two groups. *Results*. Compared with the routine group, patients in the observation group obtained significantly lower various fast reaction indicators and quality of life score ($P < 0.001$), higher nursing satisfaction score ($P < 0.001$), lower total complication rate ($P < 0.05$), higher successful rescue rate ($P < 0.05$), and lower AMI recurrence rate and PCI reuse rate ($P < 0.05$). *Conclusion*. Rescue measures by the graded emergency nursing group with the help of multidisciplinary first aid knowledge Internet-based approach are a reliable method for improving AMI patients, and such strategy greatly promotes patients' quality of life and reduces the PCI reuse rate. Further research will be conducive to establishing a better solution for AMI patients.

1. Introduction

Acute myocardial infarction (AMI), the myocardial ischemic necrosis resulting from the blockage of coronary arteries, is a common critical illness with the characteristics such as rapid disease progression, poor clinical prognosis, and high mortality [1, 2]. Early reperfusion is the key to rescuing patients, and studies have found that [3] the case fatality rate reaches 6% in those who received reperfusion with onset >6 h and decreases to 2% in those who received reperfusion with onset <1 h, indicating that prompt rescue is significant in reducing the mortality of AMI patients [4, 5]. Routine first aid processes are cumbersome and significantly delay the rescue time, so optimization is necessary [6, 7]. For patients with critical, urgent, and complex condition, instead of single department working alone, multiple departments must jointly carry out first aid by the way of consultation to exploit their advantages to the full, thereby taking effective first aid measures with the shortest time and improving the success rate of first aid to the greatest extent through close cooperation. With the help of the modern Internet assistance model, an emergency network consisting of the emergency center, clinic, community medical service, primary hospital, and ambulance is connected, thus helping rescue staff to drive out to the emergency scene precisely and quickly and greatly reducing the time from patients' onset to admission. The treatment effect has been proved in the first aid of severe craniocerebral trauma and chest pain [8]. In addition, investigations found that triage and first aid for patients with different degrees of critical diseases can maximize the first aid efficiency of nurses at different grades and that the implementation of graded first aid nursing in the rescue process can effectively shorten the rescue time, which has been confirmed in the rescue of patients with abdominal trauma accompanied by hemorrhagic shock [9]. At present, there are fewer reports about the graded emergency nursing group with the help of multidisciplinary first aid knowledge Internet-based approach in the first aid of AMI, and the following study was carried out on the basis of the background.

2. Materials and Methods

2.1. General Data. The clinical data of 90 AMI patients treated in our hospital from March 2019 to March 2020 were selected for the retrospective analysis, and the patients were divided into the observation group and the routine group according to the first aid order, with 45 cases each. The study met the World Medical Association Declaration of Helsinki (2013) [10].

2.2. Inclusion and Exclusion Criteria. Inclusion criteria were defined as follows: (1) the patients who were diagnosed with AMI by coronary angiography, with clinical manifestations including severe angina, dizziness, dyspnea, and vomiting, and received first aid treatment within 12 h upon onset; (2) the patients who presented classic changes of myocardial enzymes of AMI (abnormal troponin, creatine kinase isoenzyme, and myoglobin levels); and (3) the patients who had good mental status and could cooperate with the treatment.

Exclusion criteria were defined as follows: (1) the patients who had chronic obstructive pulmonary disease (COPD) and severe mental diseases or were complicated with severe dysfunction in the liver, kidney, and other organs; (2) the patients who had a history of chronic heart disease or heart surgery; and (3) the patients who were complicated with cardiac insufficiency or language expressing difficulty.

2.3. First Aid Measures. The patients in the routine group accepted the traditional first aid mode. After admission, the blood test was performed on patients in time, two or three effective vein passages were opened as early as possible, patients were guided to rest in bed, and continuous electrocardiographic monitoring was conducted to closely monitor changes in various vital signs and carefully observe patients' condition. After the patients were diagnosed, the nurses prepared the patients for surgery and sent them to the catheterization room [11, 12].

The graded emergency nursing group mode under the assistance of multidisciplinary first aid knowledge Internet-based approach was conducted on patients in the observation group with the following specific steps. (1) An emergency nursing group consisting of 1 head nurse, 2 senior nurses, 5 nurses, and 2 specialist physicians was set up with the head nurse as the group leader. The emergency nurses were graded, to be specific, those with at least 5 years of working experience and obtained the professional title of above senior nurse were primary nurses; those with at least 3 years of working experience and obtained the professional title of nurse or senior nurse were secondary nurses; and the nurses, practice nurses, or senior nurses engaged in advanced studies with less than 3 years of working experience were tertiary nurses. (2) A regional Internet collaborative treatment mode for AMI was established. With the help of the "BianQueFeiJiu" remote emergency system and the AMI WeChat group, physicians of the community clinic, emergency clinic, and our hospital could quickly send patients' ECGs to our AMI emergency center and perform online communication, realizing disease recognition and consultation in a timely manner. The "BianQueFeiJiu" information-based system was equipped in ambulance that enabled the use of wireless 12-lead ECG monitor, oximetry, glucometer, etc., to monitor patients' various vital signs and transmit these data and site rescue video to our AMI emergency center via 4G satellite channel in real time so that the experts of the emergency center could carry out consultation on patients' sudden condition in advance based on the data and video and timely provide relatively reasonable guidance on first aid, and patients admitted to the primary-level medical unit of remote area or on the way to the hospital could receive treatment from our hospital in advance. (3) Weekly multidepartment assistance training was carried out to members of the group with the following contents. First, the group leader clarified the training key points and objectives; second, the director of the department of cardiology explained the clinical manifestations, diagnosis, and first aid key points of AMI with specific cases in detail, focusing on helping the emergency nurses to master relevant AMI knowledge; third, based on the selected cases, the director of emergency department explained the diagnosis, first aid, relevant examinations, escort, preoperative preparation, etc., in the first aid of AMI, nursing key points, and relevant precautions of various links and handing over to the catheterization room in detail; and finally, the head nurse of cardiac care unit explained the relevant nursing operation of patients in the unit by referring to classic cases and demonstrating on-site operation. Members of the group raised questions about the problems that occurred during first aid based on the explanation of each department. According to the training and possible problems, the group leader did in-depth organization and analysis, discussed with experts of other departments, optimized and improved various links of first aid in combination with the opinions of other group members, and established a new standardized first aid process.

2.4. Observation Indexes. Fast response indicators: the time from onset to admission, admission to the completion of first myocardial enzyme examination, first medical contact to vascular opening, and onset to calling 120 patients in the two groups was recorded.

After the patients' condition was stable, the satisfaction of the clinical care of AMI patients in our emergency center was investigated with the questionnaire made by our hospital, which contained 4 items, namely, reception operation, basic nursing, service attitude, and service quality. On a scale of 0–100 points, higher scores indicated higher patient satisfaction on clinical emergency care.

The quality of life of patients in the two groups was assessed by the myocardial infarction dimensional assessment scale (MIDAS) [13], which included 7 dimensions (emotional reaction, security, diet, physical activity, dependency, worry about medication, and adverse drug reactions) and 35 items. Each item was rated by the 5-grade scoring method (0–4 points), and higher scores indicated the worse quality of life.

Prognosis: the successful rescue rate, AMI recurrence rate, and PCI reuse rate of the two groups were observed and recorded.

The occurrence of complications of the two groups was recorded, which included arrhythmia, cardiogenic shock, chest pain, and hypotension.

2.5. Statistical Methods. In this study, the data were processed by the professional statistical software SPSS23.0, the picture drawing software was GraphPad Prism 7 (GraphPad Software, San Diego, USA), the enumeration data were examined by the X^2 test and expressed by (n(%)), the measurement data were examined by the t test and expressed by mean ± SD, and differences were considered statistically significant at $P < 0.05$.

3. Results

3.1. Comparison of Clinical Data. No statistical differences in general data including the mean age, blood pressure value, infarction site, and place of residence between the two groups were observed ($P > 0.05$) (see Table 1).

3.2. Comparison of Rapid Response Indicators. Various fast response indicators were significantly lower in the observation group than in the routine group ($P < 0.001$) (see Table 2).

3.3. Comparison of Nursing Satisfaction Scores. The nursing satisfaction score was significantly higher in the observation group than in the routine group ($P < 0.001$) (see Figure 1).

3.4. Comparison of Quality of Life Scores. The quality of life score was significantly lower in the observation group than in the routine group ($P < 0.001$) (see Figure 2).

3.5. Comparison of Prognosis. Compared with the routine group, the observation group obtained significantly higher successful rescue rate ($P < 0.05$) and significantly lower AMI recurrence rate and PCI reuse rate ($P < 0.05$) (see Table 3).

3.6. Comparison of Complication Rates. The total complication rate was significantly lower in the observation group than in the routine group ($P < 0.05$) (see Table 4).

4. Discussion

AMI is a symptom of myocardial necrosis due to acute, sustained ischemia and hypoxia in coronary arteries, which is often complicated by arrhythmias, heart failure, and other complications, seriously threatening the life health of patients [14]. Several studies have confirmed that, for AMI patients, the implementation of timely and effective care is a key to reducing mortality and improving the quality of survival [15–17]. Conventional first aid models are often less normative and methodical and tend to make mistakes in the actual on-site rescue process with low efficiency, resulting in poor patient outcomes. With the rapid development of Internet technology in recent years, the “Internet + smart first aid” mode has been established in hospitals, which integrates modern Internet communication technology into clinical first aid, breaks through the spatiotemporal limitations of traditional prehospital rescue medical activity, better achieves prehospital and in-hospital seamless docking, and greatly eliminates the rescue blind area [18]. AMI patients have an urgent and complex condition, which requires multiple departments to carry out a common rescue treatment by the way of consultation, which has achieved the expected effect in the first aid of AMI [19, 20]. The reasons are as follows: (1) In the rescue and treatment modes, the diagnosis and treatment of various departments are conducted independently, so the departments cannot timely communicate on the information of clinical diagnosis and understand the patients’ condition, often leading to missing the optimal treatment timing and extending the time of rescue treatment. (2) The multidepartment model of first aid has multiple roles from multiple departments and is able to ensure that, during the process of rescuing patients, the operation of the organization is not affected by external factors, thereby greatly enhancing the rescue effect [21]. Graded first aid triages patients separately from different grades of critical care such that nurses with different grades exert the greatest first aid efficiency, which has been proved in the first aid of patients with critical cardiovascular disease in the emergency department [22]. By reviewing relevant information and combining it with clinical first aid emergency, the study achieved better rescue outcomes by implementing graded acute care group rescue measures assisted by a multidisciplinary emergency knowledge Internet-based approach for AMI patients.

The comparison of various indices of rapid response between the two groups revealed that, compared with the routine group, the indices such as time from onset to admission and from first medical contact to vascular opening were significantly lower in the observation group, and the reason was that such care model well solved the problems such as delays in hospital care. This care model can connect emergency centers, clinics, medical service stations, ambulance, etc., into a single emergency network, which maximally extends advanced rescue technology to the front line and better achieves synergistic first aid of AMI, thus effectively avoiding under- or overtreatment, which has been confirmed in the rescue of patients with acute cerebral hemorrhage [23]. The study results showed that the nursing

Table 1: Comparison of clinical data.

Item	Observation group	Routine group	X^2/t	P
Gender			0.044	0.833
Male/female	23/22	22/23		
Body mass index (kg/m^2)	22.16 ± 5.38	22.21 ± 5.27	0.045	0.965
Mean age (mean ± SD, years)	61.26 ± 3.26	61.32 ± 3.31	0.087	0.931
Mean course of disease (mean ± SD, h)	3.02 ± 0.24	3.04 ± 0.31	0.342	0.733
Blood pressure value (mmHg)				
Systolic blood pressure	136.22 ± 8.25	136.31 ± 8.19	0.052	0.959
Diastolic blood pressure	82.15 ± 6.28	82.24 ± 6.24	0.068	0.946
Renal function indicator				
Urine nitrogen (mmol/L)	6.23 ± 0.73	6.27 ± 0.65	0.275	0.784
Creatinine (μmol/L)	82.16 ± 11.23	82.21 ± 11.18	0.021	0.983
Infarction site				
Inferior wall	14 (31.11%)	15 (33.33%)	0.051	0.822
Anterior wall	12 (26.67%)	14 (31.11%)	0.216	0.642
High lateral wall	19 (42.22%)	16 (35.56%)	0.421	0.517
Blood lipid (mmol/L)				
Triacylglycerol	1.46 ± 0.25	1.42 ± 0.28	0.715	0.477
Cholesterol	4.62 ± 0.41	4.71 ± 0.52	0.912	0.364
Educational degree				
College	3 (6.67%)	5 (11.11%)	0.549	0.459
High school	12 (26.67%)	13 (28.89%)	0.055	0.814
Primary school	30 (66.67%)	27 (60.00%)	0.431	0.512
Place of residence			0.180	0.671
Urban area	19 (42.22%)	21 (46.67%)		
Rural area	26 (57.78%)	24 (53.33%)		

Table 2: Comparison of rapid response indicators (mean ± SD, min).

Group	n	Time from onset to admission	Time from admission to the completion of first myocardial enzyme examination	Time from first medical contact to vascular opening	Time from onset to calling 120
Observation	45	54.27 ± 14.26	13.27 ± 3.26	89.46 ± 10.17	20.23 ± 5.26
Routine	45	66.23 ± 11.34	24.27 ± 3.31	117.23 ± 9.27	36.17 ± 5.18
t		4.404	15.883	13.537	14.484
P		<0.001	<0.001	<0.001	<0.001

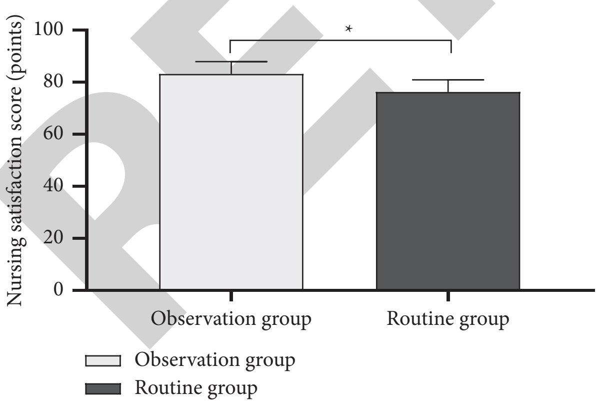

Figure 1: Comparison of nursing satisfaction scores between the two groups (mean ± SD). Note: the horizontal axis indicates the observation group and the routine group, and the vertical axis indicates the nursing satisfaction score in points; the nursing satisfaction scores of the observation group and the routine group were (83.16 ± 4.73) and (83.16 ± 4.73); * indicates a significant difference in the nursing satisfaction scores between the two groups ($t = 6.999$; $P < 0.001$).

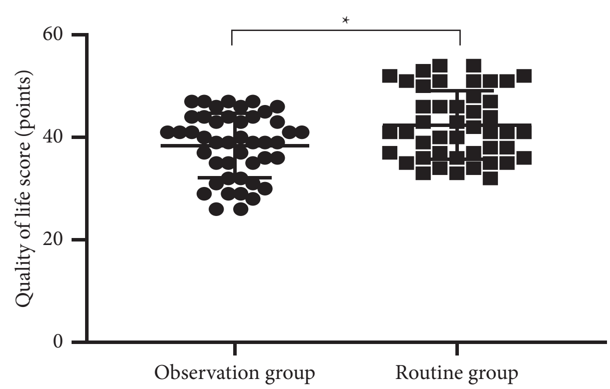

Figure 2: Comparison of the quality of life scores between the two groups (mean ± SD). Note: the horizontal axis indicates the observation group and the routine group, and the vertical axis indicates the quality of life score in points; the mean quality of life scores of the observation group and the routine group were (38.44 ± 6.28) and (42.44 ± 6.69); * indicates a significant difference in the mean quality of life scores between the two groups ($t = 2.924$; $P < 0.05$).

Table 3: Comparison of prognosis between the two groups (n(%)).

Group	n	Successful rescue rate	AMI recurrence rate	PCI reuse rate
Observation	45	100 (45/45)	2.22 (1/45)	0 (0.00)
Routine	45	91.11 (41/45)	13.33 (6/45)	8.89 (4/45)
X^2		4.186	3.873	4.186
P		<0.05	<0.05	<0.05

Table 4: Comparison of complication rates between the two groups (n(%)).

Group	n	Arrhythmia	Cardiogenic shock	Chest pain	Hypotension	Total incidence rate
Observation	45	0 (0.00)	1 (2.22)	0 (0.00)	1 (2.22)	4.44% (2/45)
Routine	45	1 (2.22)	2 (4.44)	2 (4.44)	3 (6.67)	17.78% (8/45)
t						4.050
P						<0.05

satisfaction score was significantly higher in the observation group than in the routine group, indicating that the graded emergency nursing group with the assistance of multidisciplinary emergency knowledge Internet-based approach could greatly improve patients' nursing satisfaction, and the reason was that group members performed their own tasks during the process of rescue, implemented comprehensive care to patients based on the first aid knowledge of AMI they had mastered, and obtained the recognition from patients and their family members because of their solid expertise and operational skills and high-efficient group care, thus enhancing the satisfaction [24, 25]. Shortcomings of the study are as follows: due to the limited study conditions, the study had a smaller sample size and single case source, and the effect of factors such as disease classification on study results was not considered, so the specific rescue plan should be constantly summarized and improved in future clinical practice.

Data Availability

The data used to support the findings of this study are available on reasonable request from the corresponding author.

Conflicts of Interest

The authors declare no conflicts of interest.

References

[1] W. Kim, K. Jin-Seok, J.-S. Kim et al., "Cilostazol-based triple versus potent P2Y12 inhibitor-based dual antiplatelet therapy in patients with acute myocardial infarction undergoing percutaneous coronary intervention," *Heart and Vessels*, vol. 35, no. 9, pp. 1181–1192, 2020.

[2] J. Yang, L. Wang, T. Sun, Q. Guo, F. Liu, and Y. Zhou, "Obesity is associated with worse long-term outcomes in hypertrophic cardiomyopathy patients with acute myocardial infarction," *Perfusion*, vol. 35, no. 5, pp. 384–392, 2020.

[3] H. Wada, M. Ogita, K. S. Nakao et al., "Guideline adherence and long-term clinical outcomes in patients with acute myocardial infarction: a Japanese Registry of Acute Myocardial Infarction Diagnosed by Universal Definition (J-MINUET) substudy," *European Heart Journal. Acute Cardiovascular Care*, vol. 9, no. 8, pp. 939–947, 2020.

[4] Y. Yang, Y. Cao, W. Huang, and W. Jiang, "Acute myocardial infarction after renal transplantation treated with percutaneous coronary intervention: a valuable lesson from a clinical case report," *Annals of Palliative Medicine*, vol. 10, no. 6, pp. 7028–7032, 2021.

[5] P. Ygal, G. S. Shiran Nili, G. Harel, and A. Shiyovich, "Potassium levels as a marker of imminent acute kidney injury among patients admitted with acute myocardial infarction. Soroka Acute Myocardial Infarction II (Sami-II) Project," *International Journal of Cardiology*, vol. 322, pp. 214–219, 2021.

[6] N. Kensaku, N. Watanabe, K. Nehiro, and S. Yoshisato, "Clinical outcomes of nonagenarians with acute myocardial infarction who undergo percutaneous coronary intervention." *Eur Heart J Acute Cardiovasc Care*, vol. 9, no. 5, pp. 488–495, 2020.

[7] O. J. Liakopoulos, I,D Slottosch, H. Welp et al., "Surgical revascularization for acute coronary syndromes: a report from the North Rhine-Westphalia surgical myocardial infarction registry," *European Journal of Cardio-Thoracic Surgery*, vol. 58, no. 6, pp. 1137–1144, 2020.

[8] K. Prabhakaran, A. Azim, M. Khan et al., "Predicting the need for tracheostomy in trauma patients without severe head injury," *The American Journal of Surgery*, vol. 220, pp. 495–498, 2020.

[9] S. Zhang, J. Yue, Z. Ge, Y. Xie, M. Zhang, and L. Jiang, "Activation of CXCR7 alleviates cardiac insufficiency after myocardial infarction by promoting angiogenesis and reducing apoptosis," *Biomedicine & Pharmacotherapy*, vol. 127, Article ID 110168, 2020.

[10] World Medical Association, "World Medical Association Declaration of Helsinki: ethical principles for medical research involving human subjects," *JAMA*, vol. 310, no. 20, pp. 2191–2194, 2013.

[11] W. Matthew, K. Hacer, and P. Anthony, "Evaluation of participant reluctance, confidence, and self-reported behaviors since being trained in a pharmacy Mental Health First Aid initiative," *PLoS One*, vol. 15, Article ID e0232627, 2020.

[12] R.-F. Guillermo, C.-R. Jaume, A.-B. Santiago, and G. D. David, "A novel clinical risk prediction model for myocardial infarction, coronary revascularization, and cardiac death according to clinical, exercise, and gated SPECT variables (VH-RS)," *Eur Heart J Cardiovasc Imaging*, vol. 21, pp. 210–221, 2020.

Hindawi
Journal of Healthcare Engineering
Volume 2022, Article ID 2116224, 8 pages
https://doi.org/10.1155/2022/2116224

Research Article

Subclinical Diabetic Peripheral Vascular Disease and Epidemiology Using Logistic Regression Mathematical Model and Medical Image Registration Algorithm

Nailong Jia, Long Fan, Chuizhi Wang, Qimao Fu, Yan Chen, Changkun Lin, and Yupeng Zhang

Department of Radiology, The Second Affiliated Hospital of Hainan Medical College, Haikou 570311, Hainan, China

Correspondence should be addressed to Yupeng Zhang; dbhui013@hainmc.edu.cn

Received 30 August 2021; Revised 11 December 2021; Accepted 14 December 2021; Published 17 January 2022

Academic Editor: Enas Abdulhay

The study aims to explore the effect of subclinical diabetic peripheral vascular disease and an epidemiological investigation of colour Doppler ultrasound images based on a logistic regression mathematical model and a medical image registration algorithm. Subclinical diabetes patients were selected as subjects, and after ultrasound colour Doppler ultrasonography of peripheral blood vessels, ultrasound images were taken. The experimental results show that the area under the curve (AUC) predicted by the model was 0.748, the sensitivity was 94.12%, and the specificity was 67.93%. All Δ were smaller than a single pixel. The detection rate of colour Doppler ultrasonography was 82.6%, which was significantly better than that of clinical examination ($P < 0.01$). The age, course of disease, SBP, low-density lipoprotein cholesterol (LDL-C), total cholesterol (TC), and triglyceride (TG) of the peripheral vascular disease group were significantly different from those of the no peripheral vascular disease group ($P < 0.05$). The incidence of peripheral vascular diseases and nonperipheral vascular diseases in male patients was remarkably higher than that in female patients ($P < 0.05$). Moreover, with the increase of age, the incidence of peripheral vascular disease and nonperipheral vascular disease in diabetic patients showed a trend of gradual increase ($P < 0.05$). In summary, the mathematical model and registration method have high accuracy for medical image registration of patients with the diabetes epidemic. In addition, the age, course of disease, SBP, LDL-C, TG, and TC of diabetic patients were significantly different from those of normal people, which can provide a reference for the development of later diabetes epidemiology.

1. Introduction

When doctors diagnose and treat patients' diseases, they often need to image patients with X-ray, CT, MRI, PET, SPECT, and other imaging modes to provide complementary information on patient anatomy and functional metabolism. Multimode medical image registration is to transform the spatial position of pixels in an image so that it is aligned with the pixels of other pattern images in spatial position, thereby merging image data of various imaging modes and utilizing respective image information [1]. The characteristic is to express information from many aspects of the human body on an image. The voxel similarity-based registration method is a method of high precision and robustness because it directly uses the statistical property of image pixel grayscale information, i.e., mutual information, as the basis for registration, without extracting the anatomical features of the image. Compared with the traditional method, this method has the advantages of high registration accuracy (reaching subturbulence level), good reliability, and no need for image presegmentation and feature extraction. The image after registration and fusion is more conducive to further clinical comprehensive diagnosis [2]. It has received widespread attention and has found wide application in the field of medical image registration.

The most used optimization algorithms in mutual information-based medical image registration are the simplex method and the Powell method, in addition to the simulated annealing algorithm and the genetic algorithm [3]. These optimization algorithms have their own advantages, but they all have shortcomings. The Powell method and the simplex method do not need to calculate the derivative, but the Powell method can easily fall into the local optimum in the registration process, while the simplex method converges too slowly; the simulated annealing algorithm can jump out of the local optimal trap. The time is long and sometimes enters the wrong search direction, so the optimal solution cannot be obtained, and the genetic algorithm is prone to the problem of "premature convergence" [4].

As China continues to age, the incidence of diabetes epidemiology is on the rise, and peripheral vascular disease is the main cause of disability in subclinical diabetes. Clinically, when there are obvious symptoms, it indicates that peripheral vascular lesions have occurred for macrovascular disease. 190 cases of subclinical diabetes epidemic patients in our hospital were examined by colour Doppler ultrasound. A binary logistic regression mathematical model was established to analyze the fitting effect, and a mutual information medical image registration algorithm was used for image analysis. The objective is to know the pathological changes and epidemiological characteristics of peripheral blood vessels more accurately in patients with diabetes mellitus and to explore the risk factors of pathological changes for early diagnosis and prevention.

2. Data and Methods

2.1. General Information. In this study, 190 cases of subclinical diabetes epidemic patients were selected from October 2017 to October 2020. The selected patients met the WHO criteria for diabetes diagnosis, including renal dysfunction, myocardial infarction, cerebral haemorrhage, and cerebral infarction. There were 130 males and 60 females, aged 38–79 years old, with an average of (58.9 ± 6.9) years. The course of disease was 1–28 years, with an average of (7.1 ± 3.4) years. Another 33 healthy subjects were selected as the group without peripheral vascular disease. The patients included had signed informed consent, and the study had been approved by the ethics committee of the hospital.

2.2. Research Methods

2.2.1. Laboratory Inspection. All patients were fasting venous blood on the 2nd day after admission and were checked for fasting blood glucose (FBG), glycosylated hemoglobin (HbAlc), low-density lipoprotein cholesterol (LDL-C), high-density lipoprotein cholesterol (HDL-C), total cholesterol (TC), and triglyceride (TG).

2.2.2. Colour Doppler Ultrasonography. Using the colour Doppler diagnostic instrument, the probe frequency was 7.5~10.0 MHz, the wall filter was 50~100 Hz, and the angle between the sound beam and the blood flow was <60°. The patient was placed in the supine or prone position, and the feet were straightened. The bilateral peripheral arterial vessels (femoral common femoral artery, superficial femoral artery, deep femoral artery, radial artery, dorsal artery, and anterior tibialis anterior artery) were examined to detect the diameter of the vessel. Intravascular wall plaque, observing vascular stenosis and colour flow filling, measuring intravascular-medial thickness (IMT). The diagnostic criteria for peripheral vascular disease are as follows: stenosis; plaque (single, multiple, and diffuse); intima is not thick, but echo is enhanced; femoral artery IMT ≥1 mm.

3. The Registration Method Based on Mutual Information and the Hybrid Optimization Algorithm

3.1. Image Registration Principle Based on Mutual Information. Mutual information is a basic concept in information theory. It is used to describe the statistical correlation between two random variables. It can be described by entropy as follows:

$$I(A, B) = H(A) + H(B) - H(A, B). \tag{1}$$

3.2. Registration Transformation Model. For the two images to be registered, a unified stereo coordinate system is first established. The coordinate origin is defined in the gravy centre of gravity of the image, and the two images are coarsely registered. Selecting one image as the reference image R and the other image as the floating image F, the rigid body transformation from the spatial coordinate PF of the floating image to the spatial coordinate PR of the reference image can be described by the following equation:

$$V_R \circ (P_R - C_R) = R_x(\Phi_x) \circ R_y(\Phi_y) \circ R_z(\Phi_z) \circ V_F \circ (P_F - C_F) + t(t_x, t_y, t_z). \tag{2}$$

3.3. Hybrid Optimization Algorithm. The genetic algorithm (GA) is an efficient parallel global search algorithm that simulates the principle of natural selection and genetic mechanism. The GA algorithm flow is shown in Figure 1. Unlike many traditional search algorithms, the search results are closely related to the initial point selection and are easy to fall into the local maximum excellent solution [5].

The SA starts from a higher initial temperature T, and with the continuous decrease of the temperature parameter, the probability of the jump feature is combined with the global optimal solution of the objective function in the solution space; that is, the local optimal solution jumps probabilistically and finally tends to be globally optimal [6]. The SA algorithm flow is shown in Figure 2.

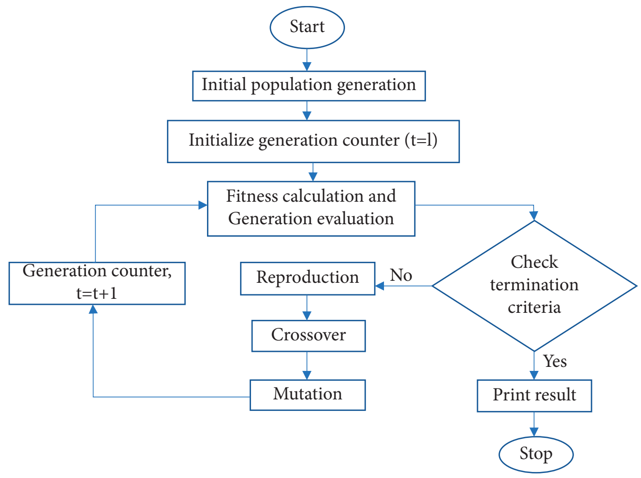

Figure 1: Genetic algorithm flow.

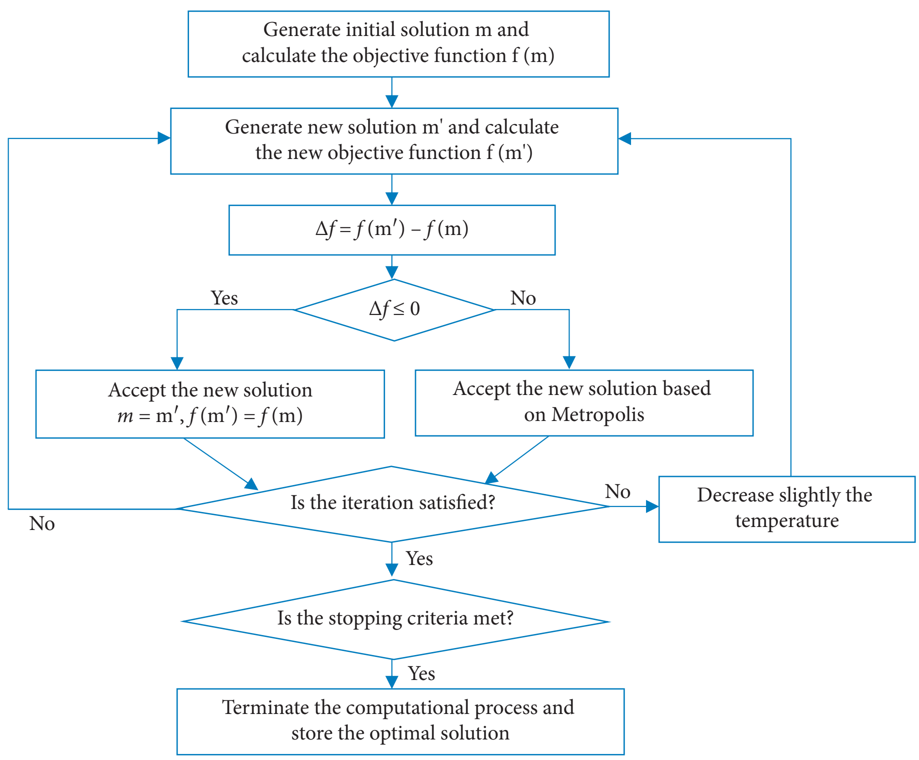

Figure 2: Simulated annealing algorithm (SA) process.

The scope of the search will be narrowed rapidly, but the rapidly converged group does not necessarily achieve the global optimal, which leads to the problem of "premature convergence" [7]. For this "premature convergence," a hybrid optimization algorithm combining the genetic algorithm and the simulated annealing algorithm is an effective solution to introduce Metropolis acceptance criteria in GA.

3.4. Hybrid Optimization Algorithm Parameter Determ ination

(1) In the implementation of the hybrid optimization algorithm, the gene population with the number of chromosomes $n = 50$ is selected, the gene string length is 57, the coding order is $(t_x, t_y, t_z, \Phi_x, \Phi_y, \Phi_z)$, the single-point crossover is adopted, the crossover probability is 0.6, and the mutation probability is 0.02.

Each parameter in the stiffness transformation parameter $(t_x, t_y, t_z, \Phi_x, \Phi_y, \Phi_z)$ is encoded. Since, the coordinate centre of the image is defined in the gravy centre of gravity of the image, which is equivalent to coarse registration of the two images, the amount of translation in the direction of the coordinate axis is generally not large, between −15 and 15 mm, each translation parameter uses 9-bit binary code, the rotation angle is between −10° and 10°, each translation parameter uses 10-bit binary code, so the resolution of the translation amount is about 0.06 mm/bit, and the resolution of the angle is about 0.02°/bit.

(2) In order for the algorithm to reach a quasiequilibrium state at the beginning, the initial acceptance rate should be made.

$$\chi_0 = \frac{M}{N} \approx 1. \tag{3}$$

In this study, it uses the method proposed in [8] to determine T_0 by calculating the average increment of the objective function of several random transformations:

$$T_0 = \frac{\overline{\overline{\Delta f^+}}}{\ln\left(\chi_0^{-1}\right)}. \tag{4}$$

The overall structure of mutual information hybrid algorithms is shown in Figure 3.

3.5. Applying a Hybrid Optimization Algorithm to Solve Spatial Transformation Parameters. The main steps of applying mutual information and hybrid optimization algorithms for image registration are as follows:

(1) Initialize the parameters of the algorithm, $T \longrightarrow T0$, randomly generate a group of initial individuals to form the initial population, and calculate the corresponding objective function value f of everyone in the population, called the fitness value. The individual fitness value of everyone in this study is individual. Mutual information minus the minimum mutual information in this generation of individuals;

(2) Determine whether the algorithm stops the criterion. If it is met, the algorithm ends and returns the optimal solution; otherwise, the following steps are performed;

(3) Using the roulette method to select n/2 pairs of individuals with large adaptation values from the population, as the parent, perform the following operations for each pair of parents:

 (a) Calculate the fitness value f_{C1}, f_{C2} of C1, C2 by the parent P1, P2 by crossing and mutating to generate the children C1, C2

 (b) If $f_{Ci}\,(f_{Pi}, (i = 1, 2))$, replace Pi with Ci; otherwise, accept Ci with probability $\exp[-(f_{Ci} - f_{Pi})/T]$

(4) $T = T \circ \alpha$, return 2.

4. CT-MR Registration

The Vanderbilt University "Review Image Registration Algorithm Evaluation" project has a set of subclinical diabetes patient data practice groups for researchers to conduct initial evaluation of the algorithm. The data set for CT-MR and PET-MR registration is also given. As a result, we applied this set of data and its standard results to evaluate the accuracy of the algorithm results.

The practice group includes a set of CT data and 6 sets of MR data for a subclinical diabetic patient. The 6 sets of MR data are PD, T1, T2, and PD-rectified, T1-rectified, and T2-rectified images, respectively. CT image resolution is $512 \times 512 \times 29$ and voxel size is $0.653595\,\text{mm} \times 0.653595\,\text{mm} \times 4\,\text{mm}$. MR image resolution is $256 \times 256 \times 26$, and voxel size is $(1.25\text{~}1.28\,\text{mm}) \times (1.25\text{~}1.28\,\text{mm}) \times (4\text{~}4.12\,\text{mm})$.

We use the registration method proposed in this study to register CT and MRI images, using MRI images as registration reference images, CT images as registration floating images, and the PV interpolation method for registration experiments. In the experiment, the image data is subsampled to speed up the calculation, and the sampling range on the XY plane is limited to the centre of gravity of the human brain, which reduces the influence of image background pixels on mutual information calculation. We evaluate the accuracy of the registration results by the following methods: 8 vertices qi, MI of the registered floating image, and 8 vertices $q_{i,\text{ref}}$ of the standard result:

$$\Delta = \frac{1}{8}\sum_{i=1}^{8}\left|q_{i,\text{ref}} - q_{i,\text{MI}}\right|, \tag{5}$$

$$\Delta k = \frac{1}{8}\sum_{i=1}^{8}\left|\sum_{i=1}^{8}\left|q_{i,\text{ref},k} - q_{i,\text{MI},k}\right|\right| k = x, y, z, \tag{6}$$

where Δ represents the average geometric distance of the eight corresponding vertices, representing the average absolute error along the coordinate axis, and the registration results are compared with the gold standard according to equations (5) and (6). The results are shown in Table 1.

The registration results of the first 4 behaviours in the table and the registration result of the 5th behaviour document are shown. The pixel diagonal distance in the M R image is taken as a pixel size, namely:

$$\sqrt{1.25^2 + 1.25^2 + 4.0^2} \approx 4.373\,\text{mm}. \tag{7}$$

It can be concluded from Table 1 that all Δ are smaller than a single pixel size, and our registration result meets the subpixel precision requirement. The characteristics of the data are used to set the transformation parameter search order in the Powell optimization process. However, the algorithm does not make any assumptions about the image data of the test. It is not necessary to modify the optimization process for the characteristics of the image. Overall, our algorithm's registration result is better, and the versatility is stronger.

Figure 4 shows the CT image and MR image of the patient in the practice group and the registration results. Comparing Figures 1(a) and 1(b), the original spatial

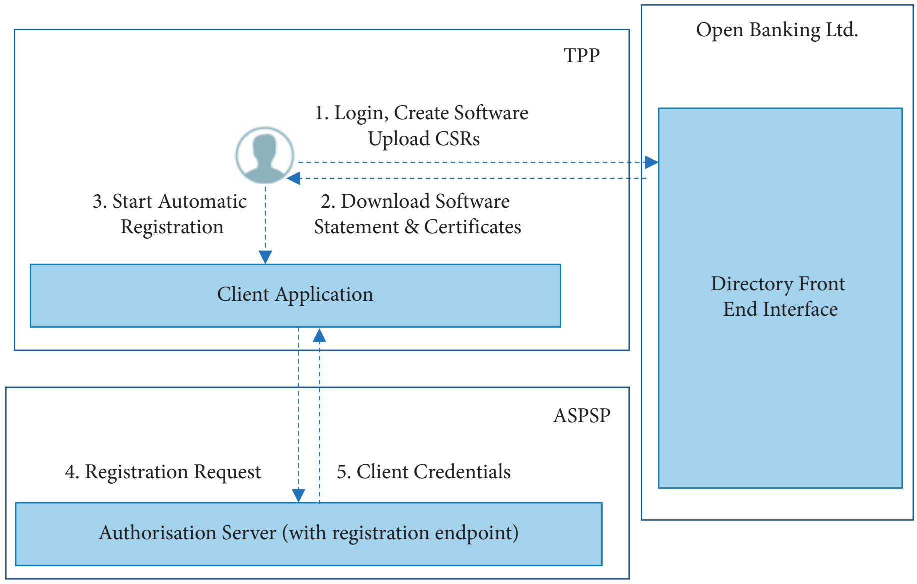

Figure 3: Mutual information hybrid algorithms.

Table 1: CT-MR registration results.

	CT-PD	CT-T1	CT-T2	CT-PDr	CT-T1r	CT-T2r
Δx	0.723	1.212	2.083	1.561	0.407	1.169
Δy	0.772	1.261	2.061	1.442	0.781	1.203
Δz	1.712	1.190	2.330	2.600	1.129	1.251
Δ	2.210	2.262	3.891	3.818	1.535	2.350
Δ [9]	2.561	1.698	2.899	3.144	1.873	3.712

positions of the two images differ greatly. From (d), after the transformation, the two images achieved a good registration result.

5. Statistical Analysis

The results were expressed as mean ± standard deviation ($x \pm s$), and SPSS25.0 statistical software was used for statistical analysis. The incidence rate of peripheral vascular disease and nonperipheral vascular disease was observed by the rank sum test. The results of two groups were compared by the t test and the x^2 test. $P < 0.05$ showed that there was statistical difference, and $P < 0.01$ indicated significant statistical difference. The binary logistic regression model was established according to the single factor. The Hosmer–Lemeshow goodness-of-fit test was used to evaluate the fitting degree of the model. The accuracy of the prediction model was evaluated by AUC (area under the curve).

6. Results

6.1. Colour Doppler Ultrasonography for Peripheral Vascular Disease. Among 190 patients, 157 cases of peripheral vasculopathy were detected by colour Doppler ultrasound, including 132 cases of plaque, accounting for 84.1%; 64 cases of intimal thickening, accounting for 40.8%; and 38 cases of arteriosclerosis, accounting for 24.2%. There were 32 cases of vascular stenosis, accounting for 20.4%, and 16 cases of vascular occlusion, accounting for 10.2%. 105 cases of the posterior tibial artery were involved, accounting for 66.9%; 90 cases of the dorsal artery, accounting for 57.3%; 65 cases of the femoral artery, accounting for 41.4%; 54 cases of the anterior tibial artery, accounting for 34.4%; and 40 cases of radial artery 6, accounting for 25.5% (Figures 5 and 6).

6.2. Comparison of Clinical Examination and Colour Doppler Ultrasonography. Among the 190 patients, 56 patients had symptoms (peripheral limb pain, numbness, peripheral cold sensation, foot ulcer, and dorsal artery pulsation disappeared). The detection rate was 29.5%; colour Doppler ultrasonography showed there were 157 cases of peripheral vascular disease, and the detection rate was 82.6%; the detection rate of the latter was significantly better than the former, and the difference was statistically significant ($P < 0.01$).

6.3. Analysis of Peripheral Vascular Disease Factors. The age, duration of disease, SBP, LDL-C, TG, and TC in the group with peripheral vascular disease were significantly different from those without peripheral vascular disease ($P < 0.05$ or < 0.01). There were no significant differences in gender, BMI, DBP, FBG, HbAlc, and HDL-C between the patients with peripheral vascular disease and those without peripheral vascular disease ($P > 0.05$) (Table 2).

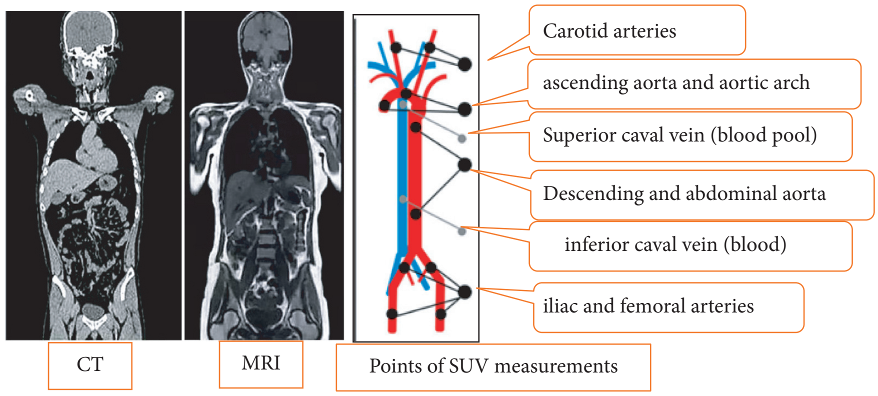

Figure 4: CT-MR image registration result.

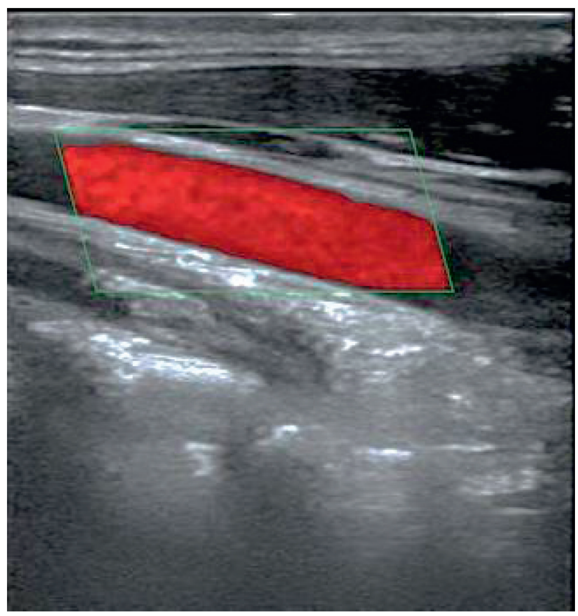

Figure 5: Colour Doppler image of the anterior tibial artery.

6.4. Epidemiological Analysis of Peripheral Vascular Diseases of Different Ages and Genders. The incidence of peripheral vascular disease and nonperipheral vascular disease was compared in diabetic patients of different ages and genders (Table 3). It was found that the incidence rate of peripheral vascular disease and nonperipheral vascular disease in male patients were higher than that in females, and the difference was statistically significant ($P < 0.05$). With the increase of age, the incidence rate of peripheral vascular disease and nonperipheral vascular disease in diabetes showed a gradual increase trend ($P < 0.05$).

6.5. Analysis of Prediction and Fitting Effects of the Mathematical Model. The meaningful independent variables were selected, and the ROC curve of the mathematical model constructed is shown in Figure 7. Through repeated calculation, the AUC value predicted by the model was 0.748, the sensitivity was 94.12%, and the specificity was 67.93%, which indicated that the logistic regression model had a good fitting effect.

7. Discussion

Subclinical diabetic peripheral vascular disease is a common complication of diabetes, and severe cases can cause gangrene in patients. According to statistics, the amputation rate of diabetic peripheral vascular disease is 5 to 10 times that of normal people, and the incidence of peripheral vascular disease with a diabetes duration of more than 5 years is more than 90%, while that of nondiabetics is 10%. The early clinical manifestations of peripheral vascular disease lack specificity. Once there is resting pain, intermittent claudication, ischemic gangrene, etc., trauma treatment or amputation is needed, which brings psychological and physiological relief to the patient. The pain also increases the pressure on the patient's life [10]. Diabetes epidemiology was investigated, and the results showed that the incidence rates of peripheral vascular disease and nonperipheral vascular disease in male diabetic patients were higher than those in females ($P < 0.05$), and the incidence rates of prediabetes and diabetes increased gradually

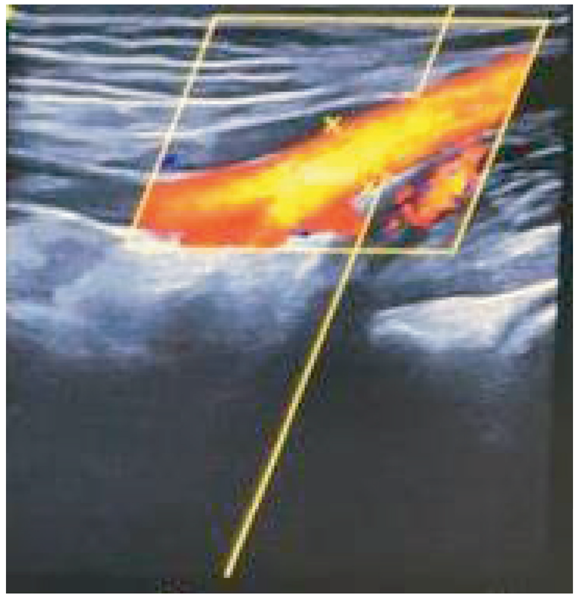

Figure 6: Brachial artery colour Doppler images.

Table 2: Analysis of related factors in the groups with peripheral vascular disease and without peripheral vascular disease.

Index	Peripheral vascular disease group ($n = 157$)	Without peripheral vascular disease group ($n = 33$)	χ^2/t	P
Gender (male or female)	108/49	20/13	0.363	0.125
Age (years)	66.2 ± 6.6	51.8 ± 5.4	7.791	0.000
Disease course (years)	9.1 ± 2.5	5.5 ± 1.6	6.772	0.000
BMI (kg/m^2)	24.1 ± 2.7	23.8 ± 2.2	0.547	0.120
SBP (mmHg)	160.4 ± 16.1	129.0 ± 14.9	7.039	0.000
DBP (mmHg)	78.2 ± 7.8	74.1 ± 6.2	0.993	0.088
FBG (mmol/L)	9.7 ± 2.5	9.6 ± 3.3	0.105	0.323
HbAlc (%)	8.2 ± 0.9	8.6 ± 1.0	1.326	0.072
HDL-C (mmol/L)	1.3 ± 0.5	1.4 ± 0.8	0.573	0.116
LDL-C (mmol/L)	2.9 ± 0.9	2.1 ± 1.0	2.674	0.063
TG (mmol/L)	2.6 ± 1.2	2.0 ± 1.8	2.558	0.069
TC (mmol/L)	5.6 ± 1.3	4.9 ± 0.7	2.373	0.072

Table 3: Comparison of the incidence of peripheral vascular disease and nonperipheral vascular disease in diabetic patients of different ages and genders (case (%)).

Age	Peripheral vascular disease ($n = 157$)			Nonperipheral vascular disease ($n = 33$)		
	Male	Female	Total	Male	Female	Total
30–40	8 (5.10)	7 (4.46)	15 (9.55)	3 (9.09)	1 (3.03)	4 (12.12)
40–50	12 (7.64)	10 (6.37)	22 (14.01)	3 (9.09)	2 (6.06)	5 (15.15)
50–60	18 (11.46)	13 (8.28)	31 (19.75)	4 (12.12)	2 (6.06)	6 (18.18)
60–70	24 (15.29)	16 (10.19)	40 (25.48)	5 (15.15)	3 (9.09)	8 (24.24)
70–80	29 (18.47)	20 (12.74)	49 (31.21)	7 (21.21)	3 (9.09)	10 (30.30)
P	0.001	0.002	0.001	0.01	0.03	0.001

with age, which was consistent with the results of [11]. Therefore, the early diagnosis and prevention of subclinical diabetes and peripheral vascular disease is particularly important.

Colour Doppler ultrasonography is characterized by simple operations and no trauma. It can detect arterial lesions early and make effective judgments on the severity of lesions and the location of lesions [12]. Research shows that colour Doppler ultrasound is the preferred method for peripheral vascular lesion examination in subclinical diabetes patients and has important clinical guiding significance for early diagnosis, prevention, and treatment. In this group of 190 patients with subclinical diabetes, the detection rate of peripheral vascular lesions was 29.5%, and colour Doppler ultrasonography was 82.6%. The detection rate of the latter was significantly better than the former. The difference was statistically significant ($P < 0.01$). Studies have shown that colour Doppler ultrasound examinations can be used as a

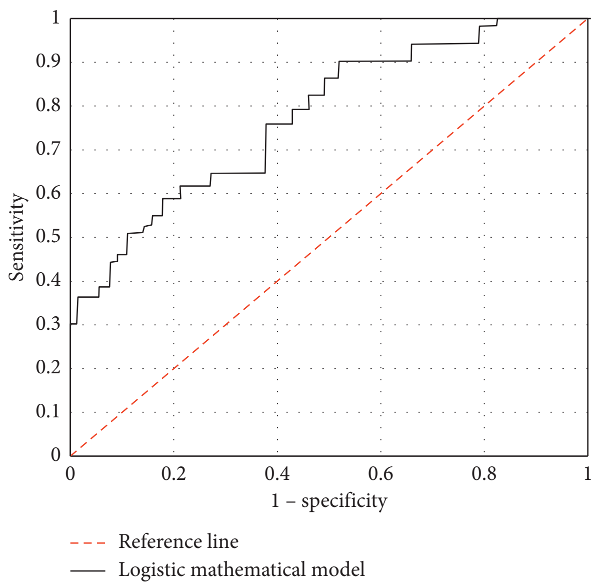

Figure 7: The ROC curve of the logistic regression mathematical model constructed.

routine examination of T2DM, which is conducive to the early detection of peripheral vascular lesions. Among the 157 patients with peripheral vascular disease, plaque accounted for 84.1%, followed by intima thickening in 64 cases. The cumulative posterior tibial artery was 66.9%, followed by the dorsal artery. Studies have shown that peripheral vascular lesions are mainly plaques, followed by intimal thickening, and cumulative after the posterior tibial artery. After the logistic regression mathematical model was constructed, the prediction fitting effect was good, which was consistent with the research of [13].

8. Conclusion

In this study, the hybrid optimization algorithm was used to register the multi-mode medical images. The genetic algorithm is a popular global optimization strategy with a wide application space. In addition, the algorithm also has good advancements, which can easily overcome the problem that the genetic algorithm is prone to early convergence, and it is not easy to fall into a local optimal state. The accuracy of the algorithm can reach subpixel levels, and the algorithm can be automatically implemented. This method is suitable for clinical application because it does not require manual intervention or more preprocessing of images. However, the theoretical derivation and model establishment need to be further discussed, and the registration accuracy also needs to be improved.

Data Availability

The data used to support the findings of this study are available from the corresponding author upon reasonable request.

Conflicts of Interest

The authors declare that they have no conflicts of interest.

Authors' Contributions

Nailong Jia and Long Fan contributed equally to this work.

References

[1] R. Popple, M. Bredel, I. Brezovich, M. Dobelbower, W. Fisher, and J. Fiveash, "Su-f-j-96: comparison of frame-based and mutual information registration techniques for ct and mr image sets," *Medical Physics*, vol. 43, no. 6, pp. 3428-3429, 2016.

[2] M. B. Skouson, Q. Quji Guo, and Z. P. Zhi-Pei Liang, "A bound on mutual information for image registration," *IEEE Transactions on Medical Imaging*, vol. 20, no. 8, pp. 843–846, 2001.

[3] S. Pradhan and D. Patra, "Enhanced mutual information based medical image registration," *IET Image Processing*, vol. 10, no. 5, pp. 418–427, 2016.

[4] Y. Zhuang, K. Gao, X. Miu, L. Han, and X. Gong, "Infrared and visual image registration based on mutual information with a combined particle swarm optimization - Powell search algorithm," *Optik*, vol. 127, no. 1, pp. 188–191, 2016.

[5] F. Zhu, J. Ren, M. Ding, and X. Zhang, "The spiking cortical model based structural representations for non-rigid multimodal medical image registration," *Journal of Medical Imaging and Health Informatics*, vol. 7, no. 5, pp. 1001–1004, 2017.

[6] J. Zhang, M. Zareapoor, X. He, D. Shen, D. Feng, and J. Yang, "Mutual information based multi-modal remote sensing image registration using adaptive feature weight," *Remote Sensing Letters*, vol. 9, no. 7, pp. 646–655, 2018.

[7] S. Reaungamornrat, T. De Silva, A. Uneri et al., "Mind demons: symmetric diffeomorphic deformable registration of mr and ct for image-guided spine surgery," *IEEE Transactions on Medical Imaging*, vol. 35, no. 11, pp. 2413–2424, 2016.

[8] Y. Wan, H. Hu, Y. Xu, Q. Chen, Y. Wang, and D. Gao, "A robust and accurate non-rigid medical image registration algorithm based on multi-level deformable model," *Iranian Journal of Public Health*, vol. 46, no. 12, pp. 1679–1689, 2017.

[9] G. Rabatel and S. Labbé, "Registration of visible and near infrared unmanned aerial vehicle images based on fourier-mellin transform," *Precision Agriculture*, vol. 17, no. 5, pp. 1–24, 2018.

[10] X. Wang, S. Wang, L. Sun, and G. Qin, "Prevalence of diabetes mellitus in 2019 novel coronavirus: a meta-analysis," *Diabetes Research and Clinical Practice*, vol. 164, Article ID 108200, 2020.

[11] H. Cao, J. Ou, L. Chen et al., "Dietary polyphenols and type 2 diabetes: human study and clinical trial," *Critical Reviews in Food Science and Nutrition*, vol. 59, no. 20, pp. 3371–3379, 2019.

[12] L. Shen, X. Huang, C. Fan, and Y. Li, "Enhanced mutual information-based medical image registration using a hybrid optimisation technique," *Electronics Letters*, vol. 54, no. 15, pp. 926–928, 2018.

[13] T. W. Ho, C. T. Huang, S. Y. Ruan, Y. J. Tsai, F. Lai, and C. J. Yu, "Diabetes mellitus in patients with chronic obstructive pulmonary disease-The impact on mortality," *PLoS One*, vol. 12, no. 4, Article ID e0175794, 2017.

Hindawi
Journal of Healthcare Engineering
Volume 2023, Article ID 9873529, 1 page
https://doi.org/10.1155/2023/9873529

Retraction

Retracted: MicroRNA-517c Functions as a Tumor Suppressor in Hepatocellular Carcinoma via Downregulation of KPNA2 and Inhibition of PI3K/AKT Pathway

Journal of Healthcare Engineering

Received 12 November 2022; Accepted 12 November 2022; Published 29 January 2023

Journal of Healthcare Engineering has retracted the article titled "MicroRNA-517c Functions as a Tumor Suppressor in Hepatocellular Carcinoma via Downregulation of KPNA2 and Inhibition of PI3K/AKT Pathway" [1] due to concerns that the peer review process has been compromised.

Following an investigation conducted by the Hindawi Research Integrity team [2], significant concerns were identified with the peer reviewers assigned to this article; the investigation has concluded that the peer review process was compromised. We therefore can no longer trust the peer review process, and the article is being retracted with the agreement of the Chief Editor.

References

[1] L. Ma, C. Tao, and Y. Zhang, "MicroRNA-517c Functions as a Tumor Suppressor in Hepatocellular Carcinoma via Downregulation of KPNA2 and Inhibition of PI3K/AKT Pathway," *Journal of Healthcare Engineering*, vol. 2022, Article ID 7026174, 9 pages, 2022.

[2] L. Ferguson, "Advancing Research Integrity Collaboratively and with Vigour," 2022, https://www.hindawi.com/post/advancing-research-integrity-collaboratively-and-vigour/.

Hindawi
Journal of Healthcare Engineering
Volume 2022, Article ID 7026174, 9 pages
https://doi.org/10.1155/2022/7026174

Research Article

MicroRNA-517c Functions as a Tumor Suppressor in Hepatocellular Carcinoma via Downregulation of KPNA2 and Inhibition of PI3K/AKT Pathway

Limin Ma, Changming Tao, and Yingying Zhang

Department of Infectious, Liaocheng People's Hospital, Liaocheng 252000, Shandong, China

Correspondence should be addressed to Yingying Zhang; zhangyingying@lchospital.org.cn

Received 2 December 2021; Revised 24 December 2021; Accepted 31 December 2021; Published 15 January 2022

Academic Editor: Enas Abdulhay

Objective. Hepatocellular carcinoma (HCC) is a kind of solid and highly aggressive malignant tumor with poor prognosis. MicroRNA (miRNA/miR) has been confirmed to be involved in HCC development. The current study focused on the functions and mechanisms of miR-517c in HCC. *Methods*. Expressions of miR-517c and Karyopherin $\alpha 2$ (KPNA2) mRNA in HCC cell lines and tissue samples were examined using quantitative real-time polymerase chain reaction (qRT-PCR). Western blot was conducted for detections of epithelial-to-mesenchymal transition (EMT) and PI3K/AKT markers. 3-(4,5-Dimethylthiazol-2-yl)-2,5-diphenyl tetrazolium bromide (MTT) and Transwell assays were utilized to investigate the influence of miR-517c on HCC cell proliferation, invasion, and migration. TargetScan and luciferase reporter assay were performed to search for the potential target gene of miR-517c. *Results*. We demonstrated that miR-517c expressions were decreased in HCC tissues and cells. Moreover, the clinical analysis showed that decreased miR-517c expressions in HCC tissues correlated with shorter overall survival and malignant clinicopathologic features of HCC patients. MTT assay showed that miR-517c upregulation prominently repressed HCC cell proliferation. In addition, miR-517c restoration could significantly suppress HCC cell invasion and migration as demonstrated by Transwell assays. We also found that miR-517c directly targeted KPNA2 and regulated the PI3K/AKT pathway and EMT, exerting prohibitory functions in HCC. *Conclusion*. Taken together, this study stated that miR-517c inhibited HCC progression via regulating the PI3K/AKT pathway and EMT and targeting KPNA2 in HCC, providing a novel insight into HCC treatment.

1. Introduction

Hepatocellular carcinoma (HCC) is one of the leading causes for tumor-related mortalities worldwide [1]. Deterioration of the original tumor, metastasis, and relapse have been identified as common factors for the high mortality rates of patients with HCC [2]. The current treatment strategies for HCC patients are mainly liver transplantation and tumor resection. However, advanced diagnoses of HCC patients are very common, and lacking specific biomarkers as well as high metastasis rates in advanced stages made tumor resection impracticable; as a result, only a few HCC patients are suitable for surgery [3, 4]. In addition, even in patients who had received the surgical treatment, the high metastatic and recurrent risks would limit the survival rates [5]. Therefore, it is emergent to unravel the mechanism of HCC metastasis and recurrence, to explore promising therapeutic approaches for HCC treatments.

MicroRNA (miRNA/miR) is a kind of small, noncoding single-stranded RNA, which regulates expressions of genes via interaction with mRNA 3′-UTRs, reducing the translation efficiencies and/or stabilities of target genes in sequence-specific manners [6]. Emerging evidence has indicated that miR is implicated in varieties of biological processes, including cell invasion, viability, and apoptosis [7, 8]. A number of known miRs have been confirmed to exert critical functions in tumorigenesis through regulating specific target genes. Recent studies have indicated that dysregulated miRs in HCC could be used as promising therapeutic and diagnostic targets [9]. Therefore, it is imperative to characterize novel miRs which participated in HCC metastasis and tumorigenesis, providing novel insights into HCC diagnosis, therapies, and prognosis.

miR-517c, a pivotal functional miR, has been recently identified as a tumor-related miR. Despite a previous study which indicated that downregulation of miR-517c promoted HCC proliferation [10], the clinical significance and potential mechanism of miR-517c in HCC need further elucidation. Therefore, we measured the expressions of miR-517c in HCC and searched for the effect of miR-517c on HCC. As demonstrated by the results of our study, we found that overexpression of miR-517c inhibited HCC cell proliferation, migration, and invasion. Moreover, we identified KPNA2 as a direct target of miR-517c in HCC. Consistent with our findings, studies by Lu et al. showed that miR-517c inhibited glioblastoma autophagy and EMT through disruptions of TP53 nuclear translocation via regulating KPNA2 [11]. Findings of our study indicated that miR-517c may act as a novel target in HCC therapies.

2. Materials and Methods

2.1. Tissue Specimens and Cell Cultures. Tissue samples were surgically resected from HCC patients with informed consent at Liaocheng People's Hospital. No patients had received any chemotherapy or radiotherapy treatment prior to the tissue collection. The tissues were frozen in liquid nitrogen immediately, followed by preservation at −80°C. The patients were divided into high and low miR-517c expression groups according to the median level of miR-517c. The present study was conducted in accordance with the Declaration of Helsinki.

The HCC cell lines (Huh7 and Hep3B) and normal liver cells LO2 were purchased from the Shanghai Cell Bank of Chinese Academy of Sciences (Shanghai, China). All cells were cultured in DMEM (Invitrogen, Carlsbad, CA, USA) including 10% FBS (Invitrogen) with 5% CO_2 at 37°C.

2.2. qRT-PCR. Total RNAs were isolated using TRIzol (Invitrogen) and reverse transcribed into cDNA using PrimeScript RT-PCR kit (Takara Biotechnology Co., Ltd., Dalian, China). The miR-517c and KPNA2 expressions were examined by RT-PCR analysis using the TaqMan miRNA assay (Applied Biosystems, Carlsbad, CA, USA) and One Step SYBR PrimeScript™ RT-PCR Kit (Takara) with U6 and GAPDH as internal controls on an ABI 7900 system (Applied Biosystems), respectively. The thermocycling conditions were as follows: pre-denaturation at 94°C for 5 min, followed by 40 cycles of denaturation at 94°C for 30 sec, annealing at 55°C for 30 sec, and extension at 72°C for 90 sec. The $2^{-\Delta\Delta Ct}$ method was utilized for the relative expression quantification. The primers were as follows: miR-517c forward, 5′-GCC ACA TCG TGC ATC CTT TT-3′, reverse, 5′-GTC GTA CCA GTG CAG GGT CC-3'; KPNA2 forward, 5′-ATT GCA GGT GAT GGC TCA GT-3′, reverse, 5′-CTG CTC AAC AGC ATC TAT CG-3′; GAPDH forward, 5′-GCA CCG TCA AGG CTG AGA AC-3′, reverse, 5′-TGG TGA AGA CGC CAG TGG A-3′; U6 forward, 5′- CTC GCT TCG GCA GCA CA-3′, reverse, 5′- AAC GCT TCA CGA ATT TGC GT-3′.

2.3. Cell Transfection. The HCC cells were transfected with miR-517c mimics, inhibitors, or the negative controls by Lipofectamine® 2000 (Invitrogen, Carlsbad, CA). 48 h after the transfections, cells were harvested for the subsequent experiments.

2.4. MTT Assay. The cell proliferation ability was detected by MTT assays. In brief, HCC cells with different transfections (miR-517c mimics/inhibitors) were plated into 96-well plates and incubated for 0, 24, 48, and 72 h. Then, MTT (5 mg/ml) solution was appended into each well and incubated for another 4 h. After that, 150 μl DMSO was added. The OD_{490} values were determined with a microplate (BioTek, Winooski, VT, USA).

2.5. Transwell Assays. Cell invasion and migration abilities were assessed by performing Transwell assays. 8 μm-pore-sized Transwell chambers (BD Biosciences, San Jose, CA, USA) coated with or without Matrigel were used for invasion and migration assays, respectively. The transfected cells maintained in the medium without serum were plated into the upper chambers. The medium containing 10% FBS was added into the lower chambers as a chemoattractant. After being incubated for 48 h at 37°C, the invasive or migratory cells in the bottom chamber were fixed with 95% ethyl alcohol for 15 min at room temperature and stained with 0.1% crystal violet for 10 min at room temperature. In the meantime, the noninvading or nonmigrating cells remaining on the top chambers were removed with cotton swabs. Finally, the results were photographed and quantified in five randomly selected fields under a microscope (Olympus, Japan).

2.6. Western Blotting. Total protein extractions were performed with lysis buffer (Thermo Fisher Scientific, Inc.). The BCA Protein Assay Kit (Thermo Scientific) was utilized to measure the protein concentrations. An equal amount of protein samples were subjected to 10% SDS-PAGE, followed by transfer onto PVDF membranes (Invitrogen). After being blocked with 5% skimmed milk, the membrane was then incubated at 4°C overnight with primary antibodies against E-cadherin (1 : 2000, Abcam), N-cadherin (1 : 2000, Abcam), vimentin (1 : 1000, Abcam), PI3K (1 : 1000, Abcam, Cambridge, MA, USA), p-PI3K (1 : 2000, Abcam), AKT (1 : 1000, Abcam), p-AKT (1 : 1000, Abcam), and GAPDH (1 : 1000, Abcam). After that, the membranes were probed with appropriate HRP-labeled secondary antibody (1 : 3,000, Abcam) for 2 h at room temperature. Finally, the protein band was visualized with ECL reagents (Millipore, USA). GAPDH was an internal control.

2.7. Bioinformatic Analysis. The putative human target genes of miR-517c were analyzed using TargetScan (version 6.0; targetscan.org/)

2.8. Luciferase Reporter Assay. Luciferase reporter plasmids containing wild-type (WT) or mutant (MUT) sequences of miR-517c in KPNA2 3′-UTR were chemically synthesized by GenePharma. For luciferase report assays, HCC cells were cotransfected with miR-517c mimics and KPNA2 3′-UTR-WT/MUT by Lipofectamine 2000 (Invitrogen) following the manufacturer's protocols. 48 h after the transfection, a Dual Luciferase Reporter Assay system (Promega, Fitchburg, WI, USA) was applied for the detection of the luciferase activity.

2.9. Statistical Analysis. All data in the current study were from at least three independent experiments. The statistical analysis was conducted using SPSS software version 17.0 (SPSS Inc., Chicago, IL). Comparisons between two groups were performed by Student's t test, while comparisons among multiple groups were conducted by ANOVA and Scheffe's post-hoc analysis. The Kaplan–Meier method with the log-rank test was utilized to estimate the survival rates. $P < 0.05$ indicated statistically significant differences.

3. Results

3.1. Lowered miR-517c Expressions in HCC Correlated with the Malignant Phenotypes of HCC Patients. miR-517c expressions in HCC tissues and cells were measured by qRT-PCR. The results indicated that that miR-517c was significantly downregulated in HCC tissues (Figure 1(a)). Similarly, the decreased miR-517c expression was also identified in HCC cells (Figure 1(b)). Furthermore, we sought for the clinical values of miR-517c in HCC progression. The HCC patients involved in the current study were divided into high and low miR-517c expression groups according to the median level of miR-517c. As shown in Table 1, patients with low miR-517c expressions exhibited more malignant clinicopathologic phenotypes than those with high miR-517c expressions. In addition, we also found that low miR-517c expression in HCC patients frequently led to shorter overall survival rates than high miR-517c levels (Figure 1(c)).

3.2. miR-517c Restoration Suppressed HCC Cell Proliferation. As we had confirmed the downregulation of miR-517c in HCC tissues and cells, the MTT assays were further conducted to assess the potential functions of miR-517c in HCC cell proliferation by performing gain or loss functions of miR-517c. In brief, Huh7 and Hep3B cells were transfected with miR-517c mimics or inhibitors to overexpress or inhibit miR-517c expressions. The transfection efficiencies were confirmed by qRT-PCR, and results revealed the successful overexpression or silence of miR-517c (Figures 2(a) and 2(b)). Then, results of MTT assays indicated that miR-517c overexpression in Huh7 cells significantly suppressed cell viability (Figure 2(c)). Moreover, miR-517c silence dramatically elevated the viability of Hep3B cells (Figure 2(d)).

3.3. miR-517c Inhibited Invasion and Migration of HCC Cells. To further confirm the biological effects of miR-517c on HCC progression, Transwell assays were performed. Results demonstrated that Huh7 cell invasion and migration were evidently inhibited by miR-517c overexpression (Figures 3(a) and 3(b)). Moreover, the promotion of cell invasion and migration was identified in Hep3B cells transfected with miR-517c inhibitor (Figures 3(c) and 3(d)). Therefore, we concluded that miR-517c exhibited prohibitory roles in HCC progression.

3.4. Overexpression of miR-517c Inhibited HCC EMT and Inactivated the PI3K/AKT Pathway in HCC Cells. To search for the mechanisms by which miR-517c inhibited HCC metastasis and tumorigenesis, we analyzed the influence of miR-517c on expression levels of proteins involved in the EMT and PI3K/AKT signaling pathway, which were related to tumorigenesis. Western blot results demonstrated obvious increase in E-cadherin and significant decrease in N-cadherin and vimentin in Huh7 cells transfected with miR-517c mimics (Figure 4(a)). In Hep3B cells, miR-517c silence dramatically downregulated the E-cadherin expressions and upregulated the N-cadherin and vimentin expressions (Figure 4(b)). Moreover, the phosphorylation of PI3K and AKT was evidently decreased by miR-517c overexpression and remarkably increased by miR-517c inhibition (Figures 4(c) and 4(d)). Collectively, all these findings showed that miR-517c exerted prohibitory functions in HCC cells via regulation of the EMT and PI3K/AKT signaling pathway.

3.5. KPNA2 Was Directly Targeted by miR-517c in HCC Cells. Finally, TargetScan was used to explore the potential targets of miR-517c for further discovery of the mechanisms by which miR-517c inhibited HCC progression. Results indicated that KPNA2 was a candidate target of miR-517c (Figure 5(a)). Thereafter, luciferase reporter assay was carried out to confirm the association between them. miR-517c mimics dramatically decreased the luciferase activity of HCC cells which were transfected with KPNA2-3′UTR-WT, while they did not prominently influence the luciferase activities of cells with transfection of KPNA2-3′UTR-MUT (Figure 5(b)). In addition, we also analyzed the effects of miR-517c on expressions of KPNA2. As demonstrated by the qRT-PCR analysis, we found that KPNA2 expressions presented significant decrease in Huh7 cells transfected with miR-517c mimics (Figure 5(c)). On the contrary, miR-517c inhibition increased the KPNA2 expressions in Hep3B cells (Figure 5(d)). Taken together, results suggested that KPNA2 was a target of miR-517c.

3.6. Increased KPNA2 in HCC Was Related to Shorter Survival Rate of HCC Patients. Subsequently, the expressions and clinical significance of KPNA2 in HCC patients were further investigated. qRT-PCR results indicated that KPNA2 was markedly upregulated in HCC tissues

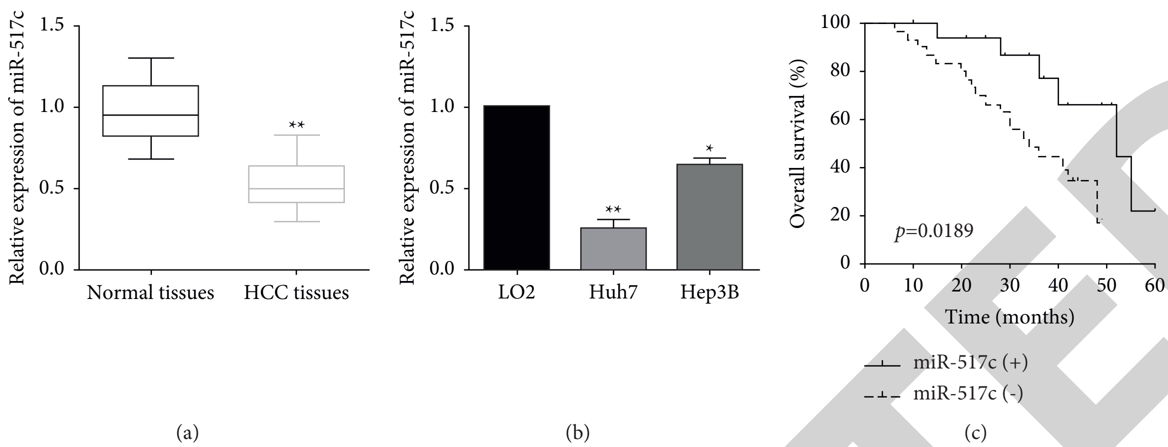

Figure 1: miR-517c was downregulated in HCC and correlated with the adverse clinicopathological features of HCC patients ($n = 47$). (a, b) miR-517c levels in HCC tissues or cells were detected by qRT-PCR. (c) Kaplan–Meier analysis of HCC patients with different miR-517c expressions. $^{*}p < 0.05$; $^{**}p < 0.01$.

Table 1: Correlation of miR-517c expression with the clinicopathological characteristics of the HCC patients.

Clinicopathological features	Cases ($n = 47$)	miR-517c[a] expression		p value
		High ($n = 19$)	Low ($n = 28$)	
Age (years)				0.2138
>60	24	10	14	
≤60	23	9	14	
Gender				0.3141
Male	24	8	16	
Female	23	11	12	
Tumor size (cm)				0.0124*
≥5.0	23	4	19	
<5.0	24	15	9	
TNM stage				0.0209*
I-II	25	15	10	
III	22	4	18	
AFP (ng/ml)				0.1620
<400	23	13	10	
>400	24	6	18	
HBV-negative	21	7	14	0.0958
HBV-positive	26	12	14	
Presence of venous invasion	23	3	20	0.0203*
Absence of venous invasion	24	16	8	
Cirrhosis				0.0687
Yes	29	12	17	
No	18	7	11	
BCLC stage				0.0105*
0-A	21	14	7	
B-C	26	5	21	

TNM: tumor-node-metastasis; AFP: alpha-fetoprotein; HBV: hepatitis B virus; BCLC: Barcelona Clinic liver cancer. [a]The mean expression level of miR-517c was used as the cutoff; *statistically significant.

(Figure 6(a)). Similarly, the increased KPNA2 expression was also found in HCC cells (Figure 6(b)). Thereafter, the Kaplan–Meier method was utilized to determine the influence of KPNA2 on the survival rate of HCC patients. As expected, we found that the overall survival of HCC patients with high KPNA2 expressions were significantly shorter than patients with low KPNA2 expressions (Figure 6(c)).

4. Discussion

Despite the improvements of the therapeutic methods in HCC treatments over the years, metastasis and relapse of HCC have recently compromised the efficiency of the novel therapies and the survival rates of patients with HCC remain dismal [12]. Hence, thorough understandings of the

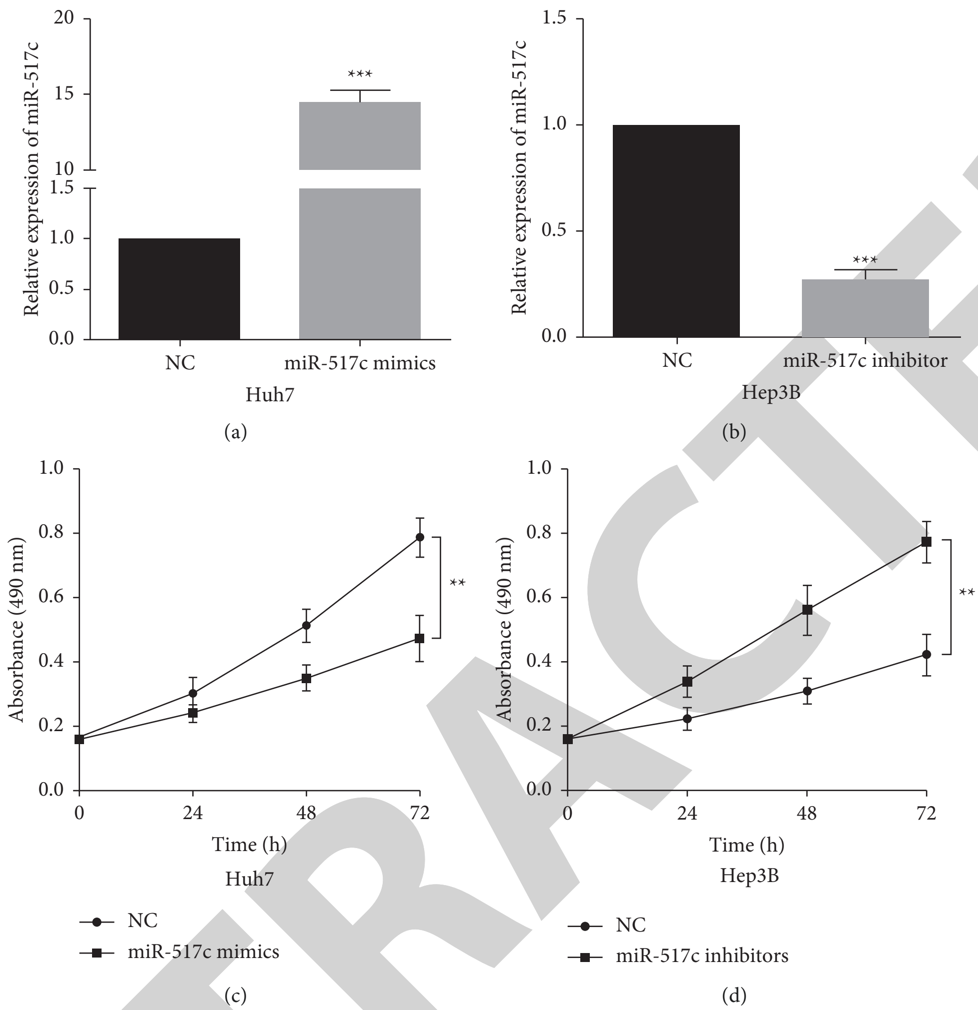

Figure 2: miR-517c overexpression inhibited HCC cell viability. (a, b) The transfection efficiencies of miR-517c mimics or inhibitors in Huh7 and Hep3B cells were examined by qRT-PCR. (c, d) MTT assays were performed to detect the influence of miR-517c on HCC cell viability. $^{**}p < 0.01$; $^{***}p < 0.001$.

mechanisms underlying HCC metastasis are imperative. Accumulating studies have shown that miRs are implicated in tumor development, serving as promising diagnosis biomarkers, effective prognosis factors, and novel therapy targets in numerous tumors, including HCC [13, 14]. Therefore, further study about the functional roles and responsible mechanisms of specific miRs in HCC may help to identify novel biomarkers. In our study, we identified the downregulated miR-517c in HCC and confirmed that decreased miR-517c indicated shorter survival rate and malignant clinical outcomes. Moreover, we also demonstrated that miR-517c upregulation inhibited HCC proliferation, invasion, and migration.

Epithelial-to-mesenchymal transition (EMT) plays a vital role in metastasis and invasion, which are the main causes of most tumor-related deaths, including deaths caused by HCC [15]. Therefore, metastasis and recurrence are mainly responsible for the lethal outcome of HCC patients [16]. It is of great importance to better understand the underlying mechanisms of HCC metastasis. During the typical EMT process, polarized and adherent epithelial cells would be transformed into invasive mesenchymal phenotypes [17]. In brief, the epithelial cell-cell adhesion molecules, such as E-cadherin, would be downregulated, whereas the mesenchymal markers, including vimentin and N-cadherin, are upregulated [18]. A growing number of studies have revealed that EMT served as a main cause for HCC metastasis. However, the association between miR-517c and EMT in HCC was poorly investigated. We found that miR-517c restoration significantly inhibited HCC cell EMT.

It is well known that the PI3K/Akt pathway plays important roles in cell differentiation, apoptosis, and proliferation and has been shown to be implicated in HCC development [19, 20]. Therefore, inhibition of the PI3K/Akt pathway is considered as a promising strategy in tumor therapies. We found that miR-517c upregulation deactivated this pathway in HCC cells. Karyopherin alpha 2 (KPNA2) belongs to the importin α family and participates in the regulation of nucleocytoplasmic transport [21]. It has been shown that KPNA2 is implicated in the pathogenesis of various cancers [22, 23]. Upregulated KPNA2 levels are

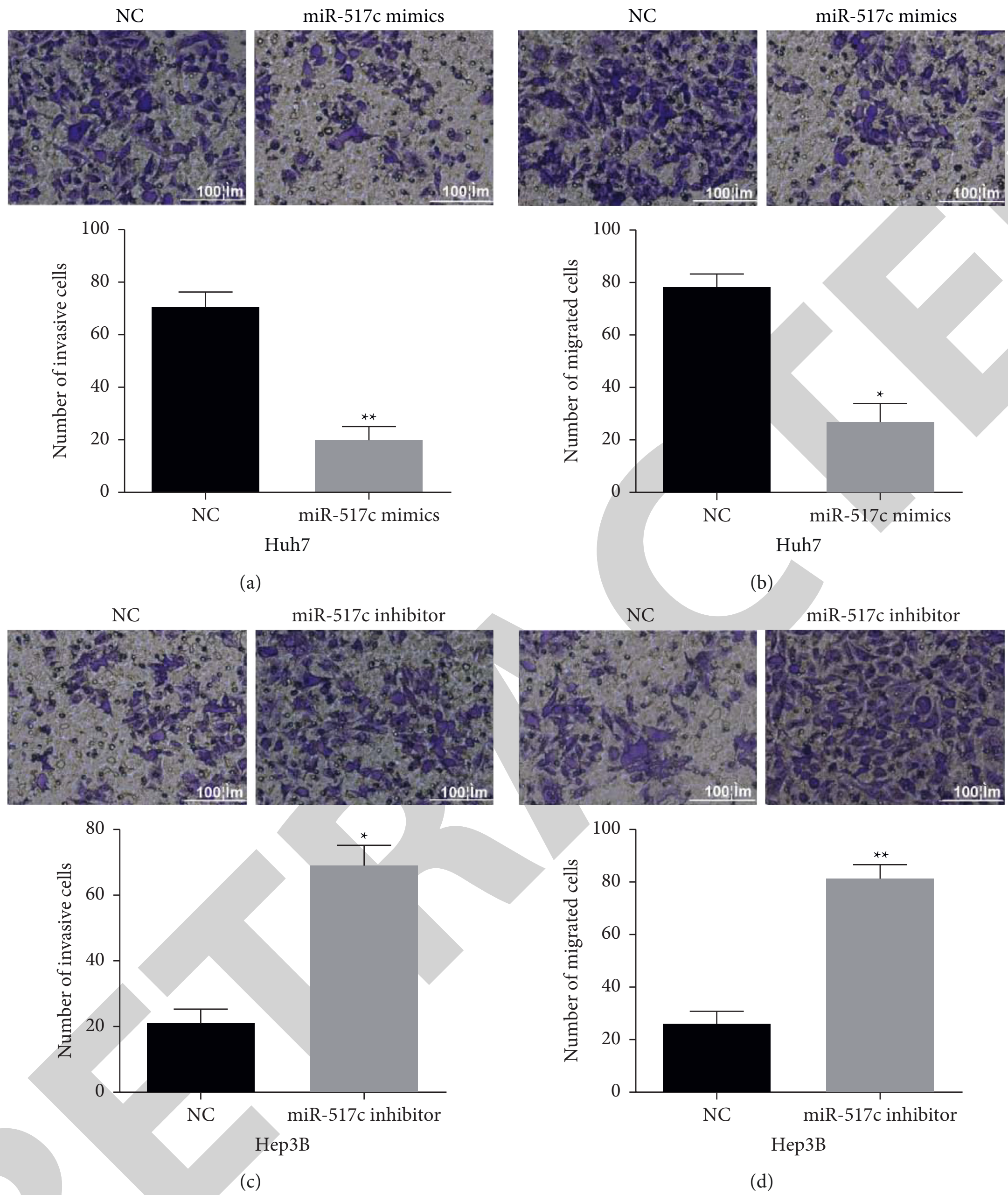

Figure 3: miR-517c upregulation suppressed HCC cell invasion and migration. (a, b) miR-517c upregulation inhibited Huh7 cell invasion and migration. (c, d) miR-517c inhibition facilitated Hep3B cell invasion and migration. $^{*}p < 0.05$; $^{**}p < 0.01$.

found to be correlated with adverse outcomes of patients with clear-cell and papillary renal-cell cancer [24], bladder cancer [25], epithelial ovarian cancer [26], and so forth. Regarding HCC, KPNA2 was confirmed to accelerate HCC progression, suggesting its oncogenic roles in HCC [27]. In the current study, we further explored the biological functions and clinical significance of KPNA2 in HCC. Results demonstrated that increased KPNA2 in HCC tissues correlated with the shorter survival rate of the HCC patients. Moreover, according to bioinformatic analysis, KPNA2 was a direct target of miR-517c. Furthermore, KPNA2 was also confirmed to partially participate in the functional roles of miR-517c in HCC progression.

In conclusion, results of our study demonstrated that miR-517c was downregulated in HCC. The decreased miR-517c expressions indicated adverse clinical outcomes of HCC patients. Moreover, we found that miR-517c inhibited HCC progression, such as viability, invasion, and migration, through regulating the EMT and PI3K/Akt pathway. In addition, the direct regulation of miR-517c on KPNA2 in HCC was also considered to be one of the mechanisms by which miR-517c exerted its inhibitory effects. Therefore, we draw the conclusion that the miR-517c/KPNA2 axis may be a novel treatment pathway of HCC. However, the functions of miR-517c in HCC should be further confirmed *in vivo* in future.

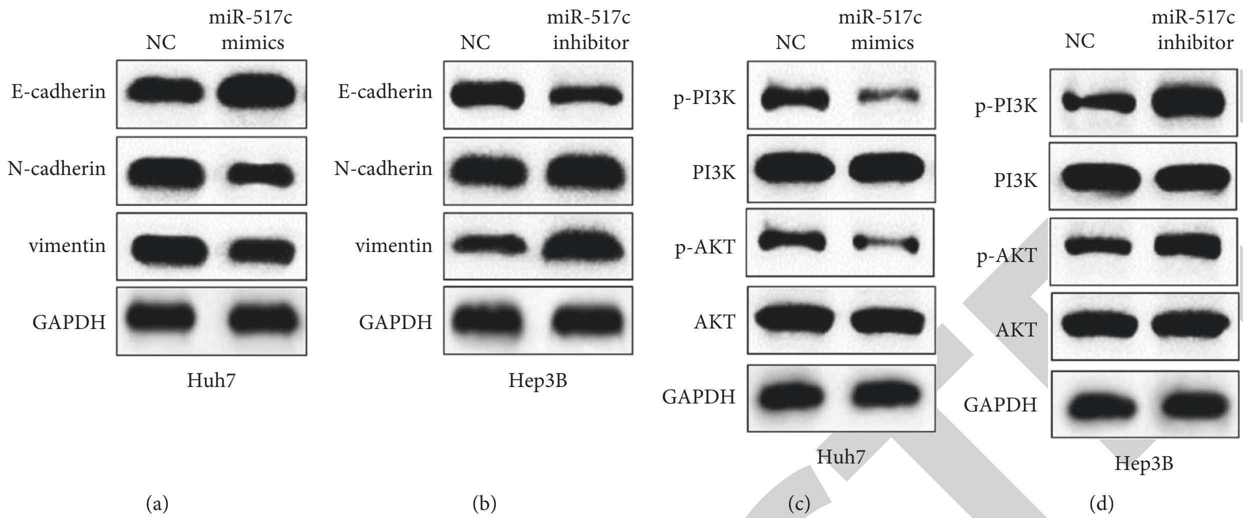

Figure 4: miR-517c regulated EMT and PI3K/AKT progress in HCC cell. (a, b) The influence of miR-517c on HCC cell EMT was analyzed by Western blot. (c, d) Western blot was used to detect the effects of miR-517c on PI3K/AKT in HCC cell.

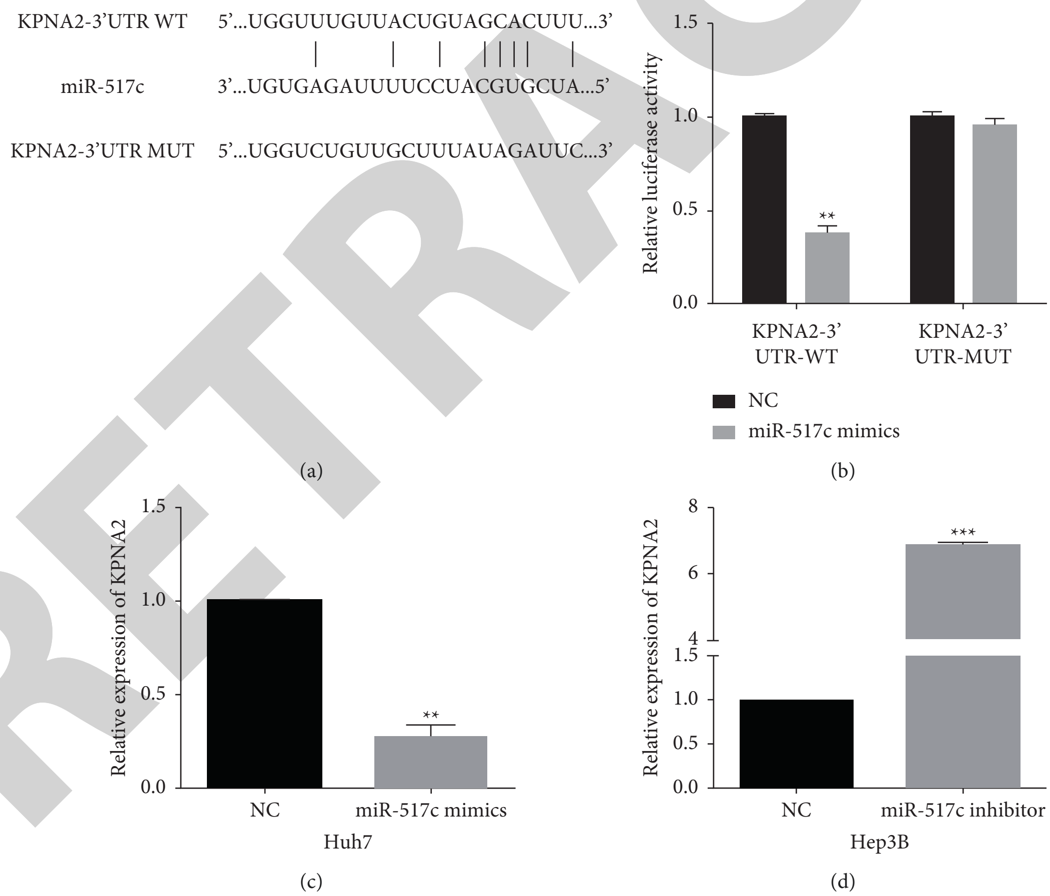

Figure 5: miR-517c regulated KPNA2 expression in HCC cells. (a) Potential binding sites of miR-517c in KPNA2-3′UTRs. (b) Luciferase activity of HCC cells cotransfected with miR-517c mimics and KPNA2-WT/MUT. (c, d) Regulatory roles of miR-517c in KPNA2 expressions were detected by qRT-PCR. $^{**}p < 0.01$; $^{***}p < 0.001$.

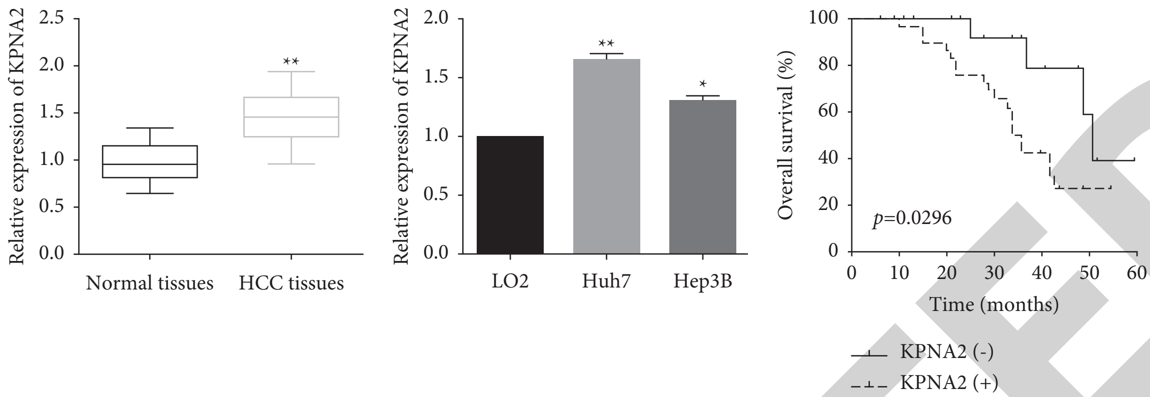

(a) (b) (c)

Figure 6: KPNA2 overexpression correlated with shorter overall survival of HCC patients ($n = 47$). (a, b) Increased KPNA2 expressions in HCC tissues and cell lines were identified by qRT-PCR. (c) The correlation between KPNA2 expressions and the survival rate of HCC patients were determined by Kaplan–Meier analysis. $^{*}p < 0.05$; $^{**}p < 0.01$.

Data Availability

Data to support the findings of this study are available on reasonable request to the corresponding author.

Conflicts of Interest

The authors declare no conflicts of interest.

Authors' Contributions

Limin Ma and Changming Tao contributed equally to this article.

References

[1] F. Bray, J. Ferlay, I. Soerjomataram, R. L. Siegel, L. A. Torre, and A. Jemal, "Global cancer statistics 2018: GLOBOCAN estimates of incidence and mortality worldwide for 36 cancers in 185 countries," *CA: A Cancer Journal for Clinicians*, vol. 68, no. 6, pp. 394–424, 2018.

[2] S. C. Lee, H. T. Tan, and M. C. Chung, "Prognostic biomarkers for prediction of recurrence of hepatocellular carcinoma: current status and future prospects," *World Journal of Gastroenterology*, vol. 20, no. 12, pp. 3112–3124, 2014.

[3] A. Budny, P. Kozlowski, M. Kaminska et al., "[Epidemiology and risk factors of hepatocellular carcinoma]," *Polski Merkuriusz Lekarski*, vol. 43, pp. 133–139, 2017.

[4] M. Li, Z. Wang, J. Cao et al., "Risk factors and prognosis of patients with recurrent hepatocellular carcinoma who undergo liver re-resections," *European Journal of Surgical Oncology*, vol. 45, no. 9, pp. 1684–1690, 2019.

[5] C. Yilmaz, C. A. Karaca, Z. Iakobadze et al., "Factors affecting recurrence and survival after liver transplantation for hepatocellular carcinoma," *Transplantation Proceedings*, vol. 50, no. 10, pp. 3571–3576, 2018.

[6] D. P. Bartel, "MicroRNAs," *Cell*, vol. 116, no. 2, pp. 281–297, 2004.

[7] M. A. Iqbal, S. Arora, G. Prakasam, G. A. Calin, and M. A. Syed, "MicroRNA in lung cancer: role, mechanisms, pathways and therapeutic relevance," *Molecular Aspects of Medicine*, vol. 70, pp. 3–20, 2018.

[8] S. L. Park, T.-M. Cho, S. Y. Won et al., "MicroRNA-20b inhibits the proliferation, migration and invasion of bladder cancer EJ cells via the targeting of cell cycle regulation and Sp-1-mediated MMP-2 expression," *Oncology Reports*, vol. 34, no. 3, pp. 1605–1612, 2015.

[9] S. Volinia, G. A. Calin, C.-G. Liu et al., "A microRNA expression signature of human solid tumors defines cancer gene targets," *Proceedings of the National Academy of Sciences*, vol. 103, no. 7, pp. 2257–2261, 2006.

[10] R.-F. Liu, X. Xu, J. Huang et al., "Down-regulation of miR-517a and miR-517c promotes proliferation of hepatocellular carcinoma cells via targeting Pyk2," *Cancer Letters*, vol. 329, no. 2, pp. 164–173, 2013.

[11] Y. Lu, L. Xiao, Y. Liu et al., "MIR517C inhibits autophagy and the epithelial-to-mesenchymal (-like) transition phenotype in human glioblastoma through KPNA2-dependent disruption of TP53 nuclear translocation," *Autophagy*, vol. 11, no. 12, pp. 2213–2232, 2015.

[12] Y. Sugino, K. Yamakado, T. Yamanaka et al., "Role of curative treatment in patients with intermediate-stage hepatocellular carcinoma," *Japanese Journal of Radiology*, vol. 35, no. 5, pp. 254–261, 2017.

[13] S. Giordano and A. Columbano, "MicroRNAs: new tools for diagnosis, prognosis, and therapy in hepatocellular carcinoma?" *Hepatology*, vol. 57, no. 2, pp. 840–847, 2013.

[14] W. C. S. Cho, "MicroRNAs: potential biomarkers for cancer diagnosis, prognosis and targets for therapy," *The International Journal of Biochemistry & Cell Biology*, vol. 42, no. 8, pp. 1273–1281, 2010.

[15] Y. Shi, N. Qin, Q. Zhou et al., "Role of IQGAP3 in metastasis and epithelial-mesenchymal transition in human hepatocellular carcinoma," *Journal of Translational Medicine*, vol. 15, no. 1, p. 176, 2017.

[16] J. Lin, L. Wu, X. Bai et al., "Combination treatment including targeted therapy for advanced hepatocellular carcinoma," *Oncotarget*, vol. 7, no. 43, pp. 71036–71051, 2016.

[17] N. M. Aiello and Y. Kang, "Context-dependent EMT programs in cancer metastasis," *Journal of Experimental Medicine*, vol. 216, no. 5, pp. 1016–1026, 2019.

[18] I. Pastushenko and C. Blanpain, "EMT transition states during tumor progression and metastasis," *Trends in Cell Biology*, vol. 29, no. 3, pp. 212–226, 2019.

Hindawi
Journal of Healthcare Engineering
Volume 2022, Article ID 9862727, 1 page
https://doi.org/10.1155/2022/9862727

Retraction

Retracted: Robotic-Assisted Laparoscopic Sacrocolpopexy for Pelvic Organ Prolapse: A Single Center Experience in China

Journal of Healthcare Engineering

Received 19 November 2022; Accepted 19 November 2022; Published 8 December 2022

Journal of Healthcare Engineering has retracted the article titled "Robotic-Assisted Laparoscopic Sacrocolpopexy for Pelvic Organ Prolapse: A Single Center Experience in China" [1] due to concerns that the peer review process has been compromised.

Following an investigation conducted by the Hindawi Research Integrity team [2], significant concerns were identified with the peer reviewers assigned to this article; the investigation has concluded that the peer review process was compromised. We therefore can no longer trust the peer review process, and the article is being retracted with the agreement of the Chief Editor.

The authors do not agree to the retraction.

References

[1] K. Niu, Q. Zhai, W. Fan et al., "Robotic-Assisted Laparoscopic Sacrocolpopexy for Pelvic Organ Prolapse: A Single Center Experience in China," *Journal of Healthcare Engineering*, vol. 2022, Article ID 6201098, 5 pages, 2022.

[2] L. Ferguson, "Advancing Research Integrity Collaboratively and with Vigour," 2022, https://www.hindawi.com/post/advancing-research-integrity-collaboratively-and-vigour/.

Hindawi
Journal of Healthcare Engineering
Volume 2022, Article ID 6201098, 5 pages
https://doi.org/10.1155/2022/6201098

Research Article

Robotic-Assisted Laparoscopic Sacrocolpopexy for Pelvic Organ Prolapse: A Single Center Experience in China

Ke Niu,[1,2] Qingzhi Zhai,[1] Wensheng Fan,[1] Li'an Li,[1] Wen Yang,[1] Mingxia Ye,[1] and Yuanguang Meng[1,2]

[1]*Senior Department of Gynecology and Obstetrics, First Medical Center, Chinese PLA General Hospital, Beijing, China*
[2]*Chinese PLA Medical College, Beijing, China*

Correspondence should be addressed to Yuanguang Meng; yuanguangmeng@st.btbu.edu.cn

Ke Niu and Qingzhi Zhai contributed equally to this work.

Received 24 November 2021; Revised 15 December 2021; Accepted 22 December 2021; Published 12 January 2022

Academic Editor: Enas Abdulhay

Objective. The aim is to investigate the efficiency and outcome of robotic-assisted sacrocolpopexy (RASC) in a cohort of patients with pelvic organ prolapse (POP) in our Gynecology Department. *Methods*. We performed a retrospective study of female patients who underwent RASC in Chinese PLA General Hospital from January 2013 to December 2020. Their clinical features included age, degree of prolapse, menopause time, body mass index, pregnancy, delivery, operation time, and bleeding volume. All patients were followed up for more than 6 months. POP-Q was recorded to evaluate the position of prolapsed organs. PFDI-20, PFIQ-7, and PGI-I were used to evaluate the life quality after surgery. *Results*. Twenty-four patients with POP received RASC in our center. The intraoperative bleeding was 86.9 ± 98.3 ml (20–300 ml). The operation time was 143.5 ± 47.3 min (60–240 minutes). The hospitalization time was 10.4 ± 2.1 days (8–16 days). And the follow-up time was 40.8 ± 22.0 months (6–72 months). In the POP-Q follow-up, postoperative Aa, Ba, Ap, Bp, and C were significantly improved than those before surgery ($P < 0.05$). The objective and subjective cure rate was 100%. PGI-I score was very good in 9 (9/24), very good in 10 (10/24), and good in 3 (3/24). Postoperative PFDI-20 and PFIQ-7 were 2.78 ± 3.82 and 1.57 ± 3.86, which decreased dramatically after surgery ($P < 0.05$). Mesh exposure occurred in 4 cases (16.7%) at 2–12 months. The exposed diameters were less than 1 cm in 3 cases (2 A/T3/S1) and 1-2 cm in 1 case (3 B/T3/S1). These mesh exposures healed after conservative observation or mesh excision. *Conclusion*. RASC for POP has the advantage of less bleeding and hospitalization time. It is a minimally invasive option for pelvic organ prolapse.

1. Introduction

Pelvic organ prolapse (POP) is a common disease which occurs in about 40–60% of parous women [1, 2]. It causes a variety of symptoms and decreased the life quality of old women [3]. Because the aging population in China increased gradually, the rates of POP surgery are predicted to grow [4]. Traditional vaginal surgery for POP has been plagued with high failure rates and complications after mesh-transplantation. Sacrocolpopexy has been the gold standard for the treatment of vaginal vault prolapse for decades [5]. It offers better postoperative results than vaginal surgical techniques [6].

With the application of robotic-assisted surgery in gynecologic surgery from 2005, researchers began to introduce this technology into POP surgery. Robotic technology can provide enhanced visualization and wristed instrumentation, enabling surgeons to perform minimally invasive operations [7]. Robotic-assisted sacrocolpopexy (RASC) has been developed as minimally invasive adaptations of sacrocolpopexy [7]. Chinese PLA General Hospital is the first hospital to use robotic-assisted technology in gynecologic surgery in China. RASC has been performed since June 2013. The primary objective of the present study was to report the surgical and patient-centered outcomes as well as adverse events in RASC surgery.

2. Material and Method

We performed a retrospective analysis of patients undergoing RASC for symptomatic apical POP from January 2013 to December 2020 at Chinese PLA General Hospital. Inclusion criteria for RASC were symptomatic apical and anterior prolapse stage ≥ III, negative cervical cytology, and no abnormal uterine bleeding. The concomitant presence of urinary incontinence was not considered an exclusion criterion. RASC was performed using the Da Vinci Robot (Intuitive, Sunnyvale, CA, USA). The clinical data of the patients were collected, including age, body mass index, menopause, pregnancy and delivery times, previous pelvic floor surgery history, internal medicine complications, operation time, bleeding, postoperative complication, and quality of life.

POP was defined according to the pelvic organ prolapse quantification (POP-Q) system. A POP-Q with nine points (points Aa, Ba, Ap, Bp, C, *D*, Gh, Pb, and TVL) was used. The patients were followed up for more than 6 months by the chief physician by gynecological physical examination and postoperative prolapse evaluation in outpatient. Scores from the Pelvic Floor Distress Inventory (PFDI-20) and Pelvic Floor Impact Questionnaire (PFIQ-7) surveys were used to evaluate preoperative and postoperative life quality outcomes.

The basic data of patients were collected by Microsoft Excel (Microsoft Corporation, Redmond, WA, USA) and statistically analyzed by using SPSS 26.0 software.

3. Results

Twenty-four patients were involved in our study, with a mean age of 63.3. They were all menopausal. Preoperative demographic characteristics are listed in Table 1.

3.1. Intraoperation Information. The mesh materials used for robot-assisted vaginal vault fixation are all Johnson and Johnson mesh. There were no conversions to laparotomy or intraoperative complications.

3.2. Postoperative Follow-Up. 24 patients received robotic-assisted operation, including 15 patients who received laparoscopic-assisted hysterectomy (LAH) and bilateral salpingo-oophorectomy (BSO). Mean operation time was 149 min and bleeding was 62.9 ml. Urinary catheter was placed before operation and was removed at 2–4 days after operation. Mean follow-up time was 58.9 months (as shown in Table 2).

All the patients were followed up for more than 6 months (40.8 ± 22.0 months (6–72 months)). Anatomic outcomes are listed in Table 3. The standard of postoperative objective cure was POP-Q stage I. In outpatient follow-up, stage I was found in all cases. The objective cure rate was 100%. No prolapse recurrence occurred. PGI-I score was very good in 9 (9/24), very good in 10 (10/24), and good in 3 (3/24). Postoperative PFDI-12 and PFIQ-7 decreased dramatically. The subjective cure rate was 100% (as shown in Table 4).

However, mesh exposure occurred in 4 cases (16.7%) at 2–12 month after surgery. The exposure diameter was less than 1 cm in 3 cases (2 A/T3/S1) and 1-2 cm in 1 case (3 B/T3/S1) (IUGA/ICS Prosthesis/Graft Complication Classification System). The adverse symptoms were increased vaginal secretions and bloody vaginal secretions. According to the guidelines proposed by the American Society of Obstetricians and Gynecologists (ACOG) and the Gynecological Urology Association (AUGS) in 2017, estrogen ointment and metronidazole suppository were used locally in 3 cases (2 A/T3/S1), and the exposed mesh was partially excised in 1 case (3 B/T3/S1). All patients healed in 3 months.

4. Discussion

Our prospective review shows that RASC is safe and highly effective in treating advanced apical and anterior prolapse at a midterm follow-up. It has obvious advantages in intraoperative bleeding (86.9 ml in average), operation time (149.0 min), and hospitalization time (8.5 days). Also, the urinary catheter can be removed in 3 days after operation. In our follow-up, a significant improvement in POP-Q score and QOL was found in all patients with an overall objective cure rate of 100%. These results indicated that it is a minimal invasive technique for POP.

In 2005, U.S. Food and Drug Administration (FDA) approved Da Vinci surgical system for gynecological surgery. In 2006, the Chinese PLA General Hospital introduced China's first Da Vinci robot operation system. Elliott reported the first series of robot-assisted laparoscopic sacrocolpopexy for high-grade vaginal vault prolapse [8]. The first robot-assisted gynecological operation in China was completed in our hospital in 2009. In 2013, we began to perform RASC for patients with POP. In our series, mean intraoperative bleeding was 86.9 ml and operation time was 149.0 min. Postoperative PFDI-20, PFIQ-7, and PGI-I were significantly improved than before surgery ($P < 0.05$). The objective and subjective success rate was 100% at more than 6-month follow-up. In previous research studies, Di Marco et al. reported that the average operation time was 210 minutes, and there was no recurrence after 4 months of follow-up [9]. Salamon et al. reported a series of 120 patients who underwent RASC [10]. The average operation time was 161 minutes, and the bleeding volume was the lowest (<100 ml). The cure rate was 89%. Serati et al. systematically reported that the objective cure rate was 84–100% in patients of all prolapses after RASC with an overall recurrence rate of 6.4% [7]. Culligan reported that 97% of the patients were satisfied, 95% of the patients were cured, and there was no prolapse symptom in the PDFI-20 questionnaire [11]. These data show that the RASC is a reliable and mature technique for POP.

The robot-assisted surgery is a dedicated technique, so the learning curve is also important for surgeons, especially for the beginners. In 2018, Carter-Brooks CM et al. found that the dedicated robotic team decreased operative time significantly by 26 minutes during robotic-assisted sacrocolpopexy with a 17.7% reduction [12]. Geller et al. believed that after 20 surgeries, the total time required for RASC surgery was significantly reduced [13]. Mourik et al. described a reduction in operative time after 12 sacral vaginal surgeries and 12 consecutive surgeries [14]. Germain et al.

Table 1: Preoperative demographic characteristics.

	Range (n)	Mean ± sd	95%CI
Age (years)	46–77	63.3 ± 11.7	
Pregnancy (times)			
<3	7 (29.2%)		
≥3	17 (70.8%)		
Delivery (times)			
<3	18 (75.0%)		
≥3	6 (25.0%)		
BMI	19–29	24.29 ± 2.87	23.2–25.4
Prior hysterectomy	2		
Prior POP surgery	0		
Prior stress urinary incontinence surgery	0		
POP-Q at baseline			
Point Ba ≥ − 1	16		
Point $C \geq -1$	18		
Point Bp ≥ −1	6		
Occult stress urinary incontinence	0		
Urinary urgency	0		
Fecal incontinence	0		
Vaginal bulge	24		

Table 2: Postoperative demographic characteristics.

	Range(n)	Mean ± sd	95% CI
Robotic-assisted operation			
RASC	9 (37.5%)		
LAH + BSO + RASC	15 (62.5%)		
Operation time (min)	60–240	149.0 ± 43.7	114.9–172.1
Bleeding (ml)	20–300	62.9 ± 77.5	27.5–146.3
Hospital stay (d)	8–16	8.5 ± 2.9	9.1–11.7
Postoperative catheter placement (d)	2–4	3.0 ± 0.7	2.8–3.3
Follow-up (month)	6–72	58.9 ± 22.5	27.6–54.1

LAH : laparoscopic-assisted hysterectomy; BSO: bilateral salpingo-oophorectomy.

Table 3: POP-Q characteristics of patients underwent RASC.

	Aa	Ba	Ap	Bp	C	Gh	Pb	TVL
Preoperative	0.90 ± 2.43	1.48 ± 2.54	−1.21 ± 2.08	−0.92 ± 2.39	1.52 ± 2.54	4.73 ± 0.44	2.94 ± 0.37	7.88 ± 0.30
Postoperative	−3.00 ± 0.00	−3.00 ± 0.00	−3.00 ± 0.00	−3.00 ± 0.00	−6.06 ± 0.52	4.39 ± 0.24	3.33 ± 0.24	7.67 ± 0.24
F	130.884	86.197	27.492	40.891	28.866	0.249	1.282	0.551
P	0.000	0.000	0.000	0.000	0.000	0.620	0.263	0.462

Table 4: Postoperative QOL of patients underwent RASC.

	PFDI-20	PFIQ-7	PGI-1
Preoperation	76.93 ± 25.31	65.17 ± 31.86	
Postoperation	2.78 ± 3.82	1.57 ± 3.86	1.71 ± 0.69
F	44.076	28.265	
P	0.000	0.000	

reported an 18% reduction in surgical time after 10 surgeries in 52 patients treated with the RSC over a seven-year period [15]. Similarly, Akl et al. also reported that the operation time was reduced by 25.4% based on the experience of the first 10 cases [16]. We divided 24 patients into two groups by the admission time (Group 1 : 2013.06–2016.06, $n = 12$; Group 2 : 2016.06–2020.12, $n = 12$). The mean bleeding and operation time were 92.5 ml and 164.0 min in Group 1 and 29.2 ml and 133.3 min in Group 2, suggesting a 68.0% and 18.7% reduction. The hospitalization decreased from 9.4 days to 7.7 days. These results confirmed that RASC is a feasible procedure with short learning curve. Yet, when we started adopting RASC in 2013, we had performed more than 1000 robot-assisted gynecological operations. For surgeons without any robot-assisted gynecological operation experience, more than 20 cases may be needed to gain enough experience for RASC.

The cost of robotic surgery is an important issue in choosing individual strategies. It includes the purchase and the maintenance of robot platform [17]. In addition, the robotic surgical instruments and the need for professional and special engineering assistance are key factors to be considered [17]. In 2011 Judd reported that the cost of robotic surgery was $8,508, 47% more than commitment

ASC ($5,792) and 15.7% more than laparoscopic surgery ($7,353) [18]. In China, the average cost of robotic surgery is $8,400, about 8 times of ASC ($1,000) and about 7 times of laparoscopic surgery ($1,200). Meanwhile the robot-assisted surgery has not been covered by social insurance. The high cost hindered the wide application in China. Therefore, the cost-efficiency analysis is needed to confirm which patients benefit more from robotic surgery.

Our study has some limitations. First, it was a single-center prospective study that did not allow comparing the possible efficacy of RASC with ASC or LASC. Furthermore, the sample size is small due to the high costs. Lastly, we lack the assessment of storage and voiding urinary symptoms before and after surgery.

5. Conclusions

The introduction of robotic technology has significantly improved the efficacy and safety of ASC by converting open surgical procedures to a minimally invasive approach. We think RASC can be recommended to patients with old age or with financial support. Due to the complex manipulation, the operators should have enough practice of laparoscopic surgery. Long-term follow-up is also necessary to help inform surgeons to build a shared decision-making model. The cost-efficiency evaluation is also needed due to the expensive cost of the surgery.

Data Availability

The datasets used and/or analyzed during the current study are available from the corresponding author on reasonable request.

Ethical Approval

All procedures performed in the studies involving human participants were in accordance with the ethical standards of the institutional research committee and with the 1964 Helsinki Declaration and its later amendments or comparable ethical standards.

Consent

Informed consent was obtained from all individual participants included in the study.

Conflicts of Interest

The authors declare that they have no conflicts of interest.

Authors' Contributions

Ke Niu and Qingzhi Zhai contributed equally to this work.

References

[1] V. L. Handa, E. Garrett, S. Hendrix, E. Gold, and J. Robbins, "Progression and remission of pelvic organ prolapse: a longitudinal study of menopausal women," *American Journal of Obstetrics and Gynecology*, vol. 190, no. 1, pp. 27–32, 2004.

[2] S. L. Hendrix, A. Clark, I. Nygaard, A. Aragaki, V. Barnabei, and A. McTiernan, "Pelvic organ prolapse in the Women's Health Initiative: gravity and gravidity," *American Journal of Obstetrics and Gynecology*, vol. 186, no. 6, pp. 1160–1166, 2002.

[3] I. Nygaard, L. Brubaker, H. M. Zyczynski et al., "Long-term outcomes following abdominal sacrocolpopexy for pelvic organ prolapse," *JAMA*, vol. 309, no. 19, pp. 2016–2024, 2013.

[4] Z. Li, T. Xu, Z. Li, J. Gong, Q. Liu, and L. Zhu, "An epidemiologic study of pelvic organ prolapse in rural Chinese women: a population-based sample in China," *International Urogynecology Journal*, vol. 30, no. 11, pp. 1925–1932, 2019.

[5] E. Illiano, K. Giannitsas, A. Zucchi et al., "Sacrocolpopexy for posthysterectomy vaginal vault prolapse: long-term follow-up," *International Urogynecology Journal*, vol. 27, no. 10, pp. 1563–1569, 2016.

[6] C. Maher, B. Feiner, K. Baessler, C. Christmann-Schmid, N. Haya, and J. Brown, "Surgery for women with apical vaginal prolapse," *Cochrane Database of Systematic Reviews*, vol. 10, no. 10, Article ID CD012376, 2016.

[7] M. Serati, G. Bogani, P. Sorice et al., "Robot-assisted sacrocolpopexy for pelvic organ prolapse: a systematic review and meta-analysis of comparative studies," *European Urology*, vol. 66, no. 2, pp. 303–318, 2014.

[8] D. S. Elliott, I. Frank, D. S. Dimarco, and G. K. Chow, "Gynecologic use of robotically assisted laparoscopy: sacrocolpopexy for the treatment of high-grade vaginal vault prolapse," *The American Journal of Surgery*, vol. 188, no. 4, pp. 52–56, 2004 Oct.

[9] D. S. Di Marco, G. K. Chow, M. T. Gettman, and D. S. Elliott, "Robotic-assisted laparoscopic sacrocolpopexy for treatment of vaginal vault prolapse," *Urology*, vol. 63, no. 2, pp. 373–376, 2004.

[10] C. G. Salamon and P. J. Culligan, "Subjective and objective outcomes 1 year after robotic-assisted laparoscopic sacrocolpopexy," *Journal of Robotic Surgery*, vol. 7, no. 1, pp. 35–38, 2013.

[11] P. J. Culligan, E. Gurshumov, C. Lewis et al., "Subjective and objective results 1 year after robotic sacrocolpopexy using a lightweight Y-mesh," *International Urogynecology Journal*, vol. 25, no. 6, pp. 731–735, 2014.

[12] C. M. Carter-Brooks, A. L. Du, M. J. Bonidie, and J. P. Shepherd, "The impact of a dedicated robotic team on robotic-assisted sacrocolpopexy outcomes," *Female Pelvic Medicine & Reconstructive Surgery*, vol. 24, no. 1, pp. 13–16, 2018.

[13] E. J. Geller, B. A. Parnell, and G. C. Dunivan, "Robotic vs abdominal sacrocolpopexy: 44-month pelvic floor outcomes," *Urology*, vol. 79, no. 3, pp. 532–536, 2012.

[14] S. L. Mourik, J. E. Martens, and M. Aktas, "Uterine preservation in pelvic organ prolapse using robot assisted laparoscopic sacrohysteropexy: quality of life and technique," *European Journal of Obstetrics & Gynecology and Reproductive Biology*, vol. 165, no. 1, pp. 122–127, 2012.

[15] A. Germain, F. Thibault, M. Galifet et al., "Long-term outcomes after totally robotic sacrocolpopexy for treatment of pelvic organ prolapse," *Surgical Endoscopy*, vol. 27, no. 2, pp. 525–529, 2013.

[16] M. N. Akl, J. B. Long, D. L. Giles et al., "Robotic-assisted sacrocolpopexy: technique and learning curve," *Surgical Endoscopy*, vol. 23, no. 10, pp. 2390–2394, 2009.

[17] A. Giannini, E. Russo, E. Malacarne, E. Cecchi, P. Mannella, and T. Simoncini, "Role of robotic surgery on pelvic floor reconstruction," *Minerva Ginecologica*, vol. 71, no. 1, pp. 4–17, 2019.

Hindawi
Journal of Healthcare Engineering
Volume 2022, Article ID 1272338, 10 pages
https://doi.org/10.1155/2022/1272338

Research Article

Identification of Hub Genes of Keloid Fibroblasts by Coexpression Network Analysis and Degree Algorithm

Xianglan Li,[1] Rihua Jiang ,[1] Haiguo Jin,[2] and Zhehao Huang [3]

[1]*Department of Dermatology, China-Japan Union Hospital of Jilin University, Changchun 130033, Jilin, China*
[2]*Department of Radiotherapy, Jilin Guowen Hospital, Changchun 130000, Jilin, China*
[3]*Department of Neurosurgery, China-Japan Union Hospital of Jilin University, Changchun 130033, Jilin, China*

Correspondence should be addressed to Zhehao Huang; ms005@jlu.edu.cn

Received 25 November 2021; Revised 13 December 2021; Accepted 15 December 2021; Published 8 January 2022

Academic Editor: Enas Abdulhay

Background. Keloid is a benign dermal tumor characterized by abnormal proliferation and invasion of fibroblasts. The establishment of biomarkers is essential for the diagnosis and treatment of keloids. *Methods*. We systematically identified coexpression modules using the weighted gene coexpression network analysis method (WGCNA). Differential expressed genes (DEGs) in GSE145725 and genes in significant modules were integrated to identify overlapping key genes. Gene Ontology (GO) and Kyoto Encyclopedia of Genes and Genomes (KEGG) enrichment analyses were then performed, as well as protein-protein interaction (PPI) network construction for hub gene screening. *Results*. Using the *R* package of WGCNA, 22 coexpression modules consisting of different genes were identified from the top 5,000 genes with maximum mean absolute deviation in 19 human fibroblast samples. Blue-green and yellow modules were identified as the most important modules, where genes overlapping with DEGs were identified as key genes. We identified the most critical functions and pathways as extracellular structure organization, vascular smooth muscle contraction, and the cGMP-PKG signaling pathway. Hub genes from key genes as BMP4, MSX1, HAND2, TBX2, SIX1, IRX1, EDN1, DLX5, MEF2C, and DLX2 were identified. *Conclusion*. The blue-green and yellow modules may play an important role in the pathogenesis of keloid. 10 hub genes were identified as potential biomarkers and therapeutic targets for keloid.

1. Introduction

Keloids are mainly associated with excessive proliferation of fibroblasts and massive deposition of the extracellular matrix following skin injury [1]. The clinical presentation of keloids is primarily a growth of scar tissue above the skin, usually accompanied by pruritus and pain [2]. Some studies have shown that keloid formation is closely related to genetic regulation, inflammatory factors, cytokines, and immune factors [3, 4]. The treatment of keloid is not ideal because of unclear pathogenesis and regulatory mechanisms underlying keloids [5]. For these reasons, the identification of hub genes involved in keloid is urgent and highly demanded for improving the clinical outcome.

Keloids have some similarities to tumors; in particular, the fibroblasts in keloids have unlimited proliferation and invasive growth [6]. Fibroblasts are the most abundant cells in the dermis and maintain dermal structure by producing an extracellular matrix (ECM) [7]. The ECM is in a constant state of synthesis, degradation, and remodeling, both under normal conditions and in the presence of disease or injury [8]. After a 2-3 d period of haemostasis and inflammation, the dermis undergoes a proliferative phase in which fibroblasts move from a homeostatic state to an activated state, where their ability to proliferate and migrate is significantly enhanced and they differentiate into a unique phenotype, myofibroblasts, which have stronger contractile properties and synthesized the ECM more rapidly, thereby accelerating wound closure [9]. Once the tissue is fully repaired, these myofibroblasts undergo apoptosis and senescence or revert to deactivated fibroblasts [10]. However, the persistence of active fibroblasts (including myofibroblasts) at the site of injury may lead to excessive deposition of the ECM and the formation of abnormal scarring. So, the thickness of the scar is usually positively correlated with the number of fibroblasts in the dermis and the density of collagen (the main component of the ECM). Therefore, inhibition of fibroblast proliferation has long been a hot topic in scar research.

Weighted gene coexpression network (WGCNA) analysis [11] first clusters genes with similar expression patterns into a module by calculating expression correlations between genes and then analyses the correlation between the module and the sample characteristics, such as clinicopathological parameters and treatments. WGCNA rapidly extracts modules and genes that correlate with sample characteristics from transcriptomic data and obtains biomarkers with better biological significance than differential expression analysis based on comparative intramodule connectivity and gene significance [12]. In this study, we constructed a WGCNA-based gene coexpression network, identifying 22 modules. We also performed GO and KEGG enrichment analysis of genes overlapping in 2 modules closely related to keloid fibroblast and DEGs. A PPI network was also constructed, and 10 hub genes were screened out, including BMP4, MSX1, HAND2, TBX2, SIX1, IRX1, EDN1, DLX5, MEF2C, and DLX2. These hub genes may be biomarkers for diagnosis and therapy of keloid.

2. Methods

2.1. Data Collection. The gene expression dataset GSE145725 (https://www.ncbi.nlm.nih.gov/geo/query/acc.cgi?acc=GSE145725) provided by Yuanyuan Kang et al. [13] was downloaded from the Gene Expression Omnibus (GEO) database [14]. 10 cell lines (5 normal fibroblast and 5 keloid fibroblast) were grown in replicate cultures and subjected to RNA extraction. One of the keloid samples was removed after QC. RNA samples with RNA integrity number (RIN) above 9.8 were hybridized to GeneChip PrimeView Human Gene Expression Arrays (Affymetrix).

2.2. Weighted Gene Correlation Network Analysis (WGCNA). WGCNA aims to identify coexpressed gene modules to explore the relationship between gene networks and phenotypes and to examine the core genes in the network [11]. Only top 5000 genes with maximum mean absolute deviation were selected, and abnormal samples were detected using the Z-score method, with Z-score value −2.5 as a cutoff for identifying outliers. According to the scale-free topology criterion, 22 was determined as the optimal soft threshold, with minimum module size 30 and the module detection sensitivity deep split 2. Based on the soft threshold, scale-free network and topology matrices were constructed. The gene modules were dynamically cut and eigengenes were calculated, with 30 as the minimum number of genes in the module. According to the module eigengenes, intermodule correlations were constructed and hierarchical clustering was performed. Finally, 22 modules were obtained and Pearson correlations between modules and clinical features were analyzed.

2.3. Differential Expression Analysis. The GSE145725 dataset was downloaded from the GEO database via the *R* (version 3.6.3) package of GEO query 2.54.1 [15]. The probes corresponding to more than one molecule were removed, and only the probe with the largest signal value was retained when probes correspond to the same molecule. Then, the samples were normalized by box plots, and the clustering between sample groups was demonstrated by PCA plots and UMAP plots. The limma 3.42.2 package was then used for the differential expression analysis between the keloid fibroblast group and normal fibroblast. The top 20 differentially expressed genes (DEGs) were visualized as heatmap using the ComplexHeatmap 2.2.0 package [16] with the clustering method of Euclidean distances.

2.4. Key Gene Identification and Enrichment Analysis. The green-yellow and blue modules are the modules most associated with the keloid fibroblast phenotype. The overlapped genes in the two modules and DEGs were identified as the key genes. Using the org.Hs.eg.db 3.10.0 package, the key gene symbols were converted into Entrez IDs and then subjected to Gene Ontology (GO) and Kyoto Encyclopedia of Genes and Genomes (KEGG) enrichment analysis through the cluster Profiler 3.14.3 package [17].

2.5. Protein-Protein Interaction (PPI) Network Construction. Key genes were uploaded to the STRING database (version 11.0) to construct the PPI network [18]. Interactions with a score above 0.4 were considered significant. The PPI network was visualized using Cytoscape software (version 3.8.3) [19]. Top 10 key genes with highest degree were detected as hub genes by CytoHubba plugin.

2.6. Correlation Analysis and Expression of Hub Genes. Correlations between hub genes were analyzed, and Spearman's correlation coefficients were calculated for variables that did not satisfy the normal distribution ($P < 0.05$). The correlation matrix and scatter plot were also plotted using the ggplot2 3.3.3 package.

The expression profiles of the hub genes were first subjected to the Shapiro–Wilk normality test. The Wilcoxon rank sum test was chosen when the gene expression values did not satisfy the normality test ($P < 0.05$).

3. Results

3.1. WGCNA. To identify significant modules, firstly, expression profile distribution of all samples was checked and abnormal samples were detected. The results showed that the median across the samples was essentially at one level, indicating good normalization between samples (Figure 1(a)). Besides, no outlier sample was found (Figure 1(b)). Then, all given soft powers were traversed to get the smallest one which can make the correlation network conform to non-scale network attributes, and a soft threshold of 22 was chosen (Figure 1(c)). Based on the soft threshold power and dynamic tree cut, 22 modules were identified (Figure 2(a)).

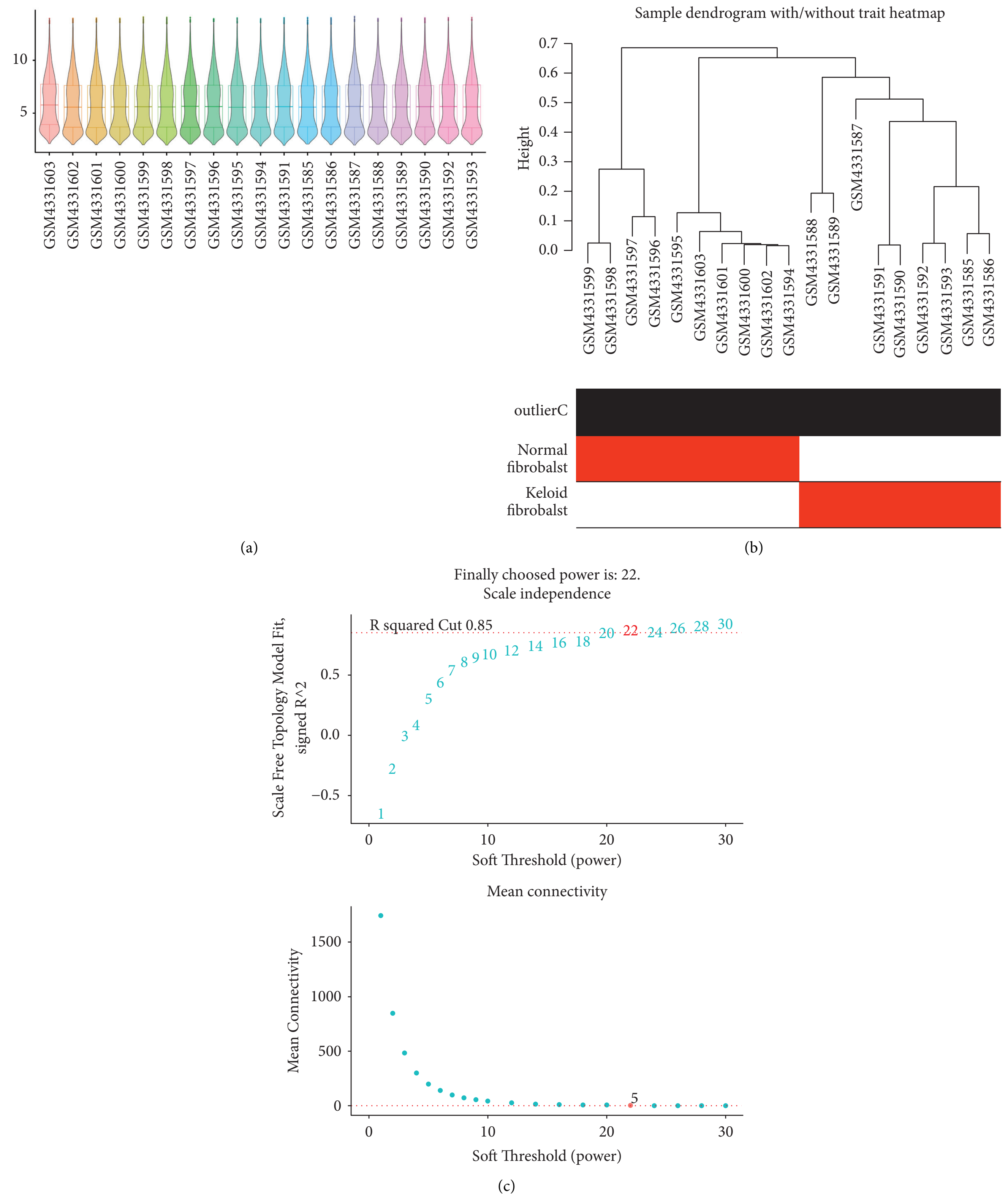

Figure 1: Expression data preprocess and soft power detection. (a) Boxplot plus violin plot showing the expression profile distribution of all keloid fibroblasts samples. (b) Hierarchical clustering showing sample correlations and outlier samples. Samples labeled with red bars in the outlier C row are detected potential outlier samples. (c) Network topology for different soft powers. The soft threshold power in the WGCNA was determined based on a scale-free R^2 ($R^2 = 0.85$).

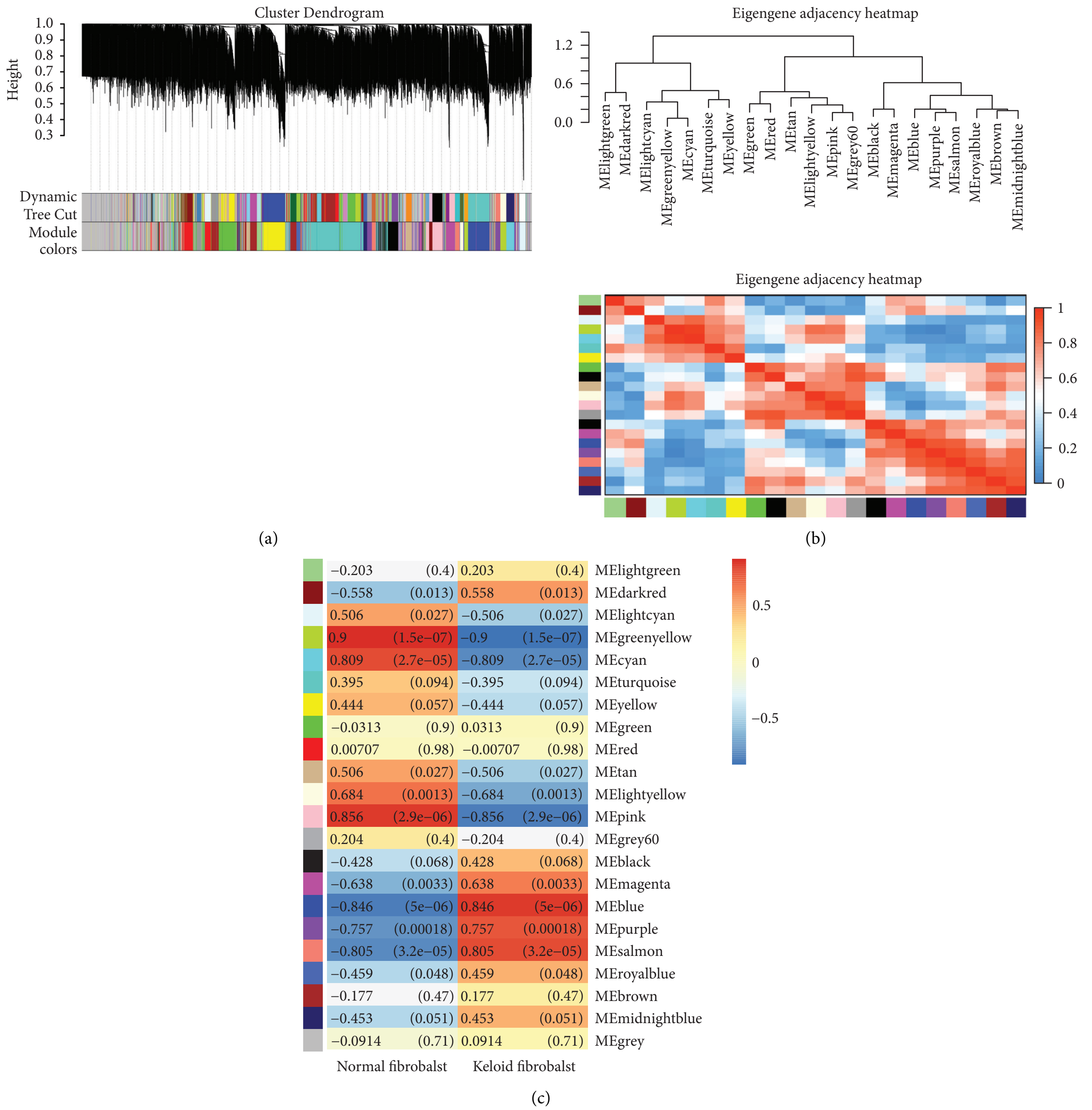

Figure 2: Construction of coexpression modules. (a), WGCNA module plot. Dynamic Tree Cut represents initial modules. Module colors represent final modules. Each branch in the hierarchical tree or each vertical line in color bars represents one gene. Genes not attributed to any module would be colored by grey. (b) Correlation of all identified modules. Each color represents one module. (c) WGCNA module trait correlation plot. Each row represents one module. Each column represents one trait attribute. Blue color represents negative correlation, and red color represents positive correlation.

To clarify the interrelationship between the 22 coexpression modules, we performed a cluster analysis (Figure 2(b)). 22 modules differed significantly from each other (Figure 2(c)). Several modules were associated with keloid fibroblasts. In particular, the blue module was most positively correlated with keloid fibroblasts, and the green-yellow module was the most negatively correlated with keloid fibroblasts.

3.2. Differential Expression Analysis. Meanwhile, we performed differential expression analysis on the GSE145725 dataset to identify aberrantly expressed genes in keloid fibroblasts. Principal component analysis (PCA) plots showed significant differences between the keloid fibroblast and normal fibroblast groups (Figure 3(a)). Subsequently, 19043 genes were filtered. Of these, 458 IDs met

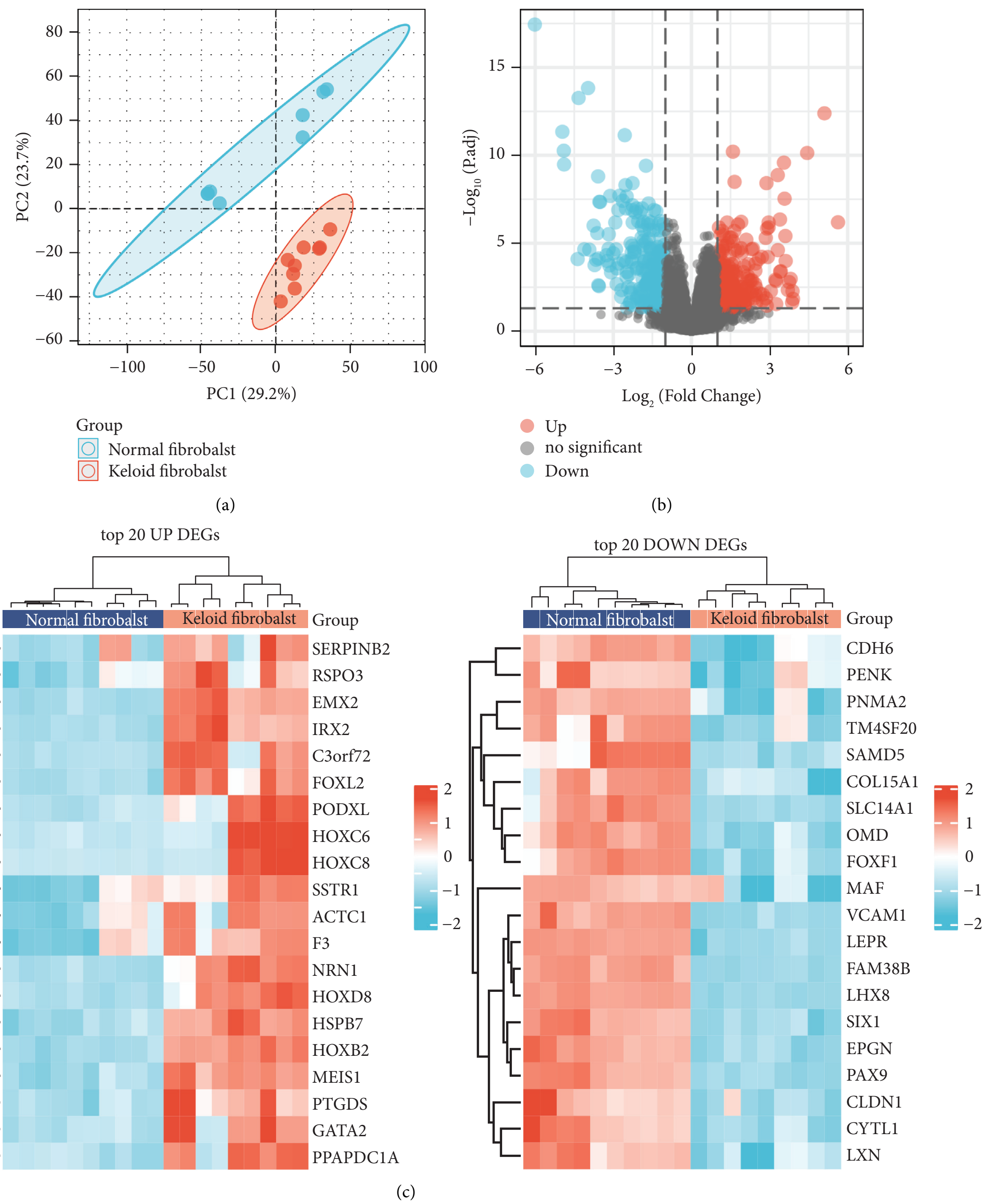

Figure 3: Differential genes' screening on the GSE145725 dataset. (a) PCA plot. (b) Volcano plot, with threshold as |logFC| > 1 & p.adj <0.05. (c) Heatmap visualizing the expression profile of top 20 genes with the highest or lowest expression.

the threshold of |log2(FC)| > 1 and p.adj<0.05, under which the number of upregulated gene in keloid fibroblasts was 215 and in normal fibroblasts was 243 (Figure 3(b)). In addition, we show the expression profile of top 20 genes with high and low expression in a heat map (Figure 3(c)).

3.3. Key Gene Screening and Enrichment Analysis. From WGCNA modules, we selected the blue module and green-yellow module as the important modules (Figure 4(a)). The genes in these modules were then intersected with DEGs, and the 186 overlapped genes were regarded as key genes (Figure 4(b)). To understanding the functions and pathways in

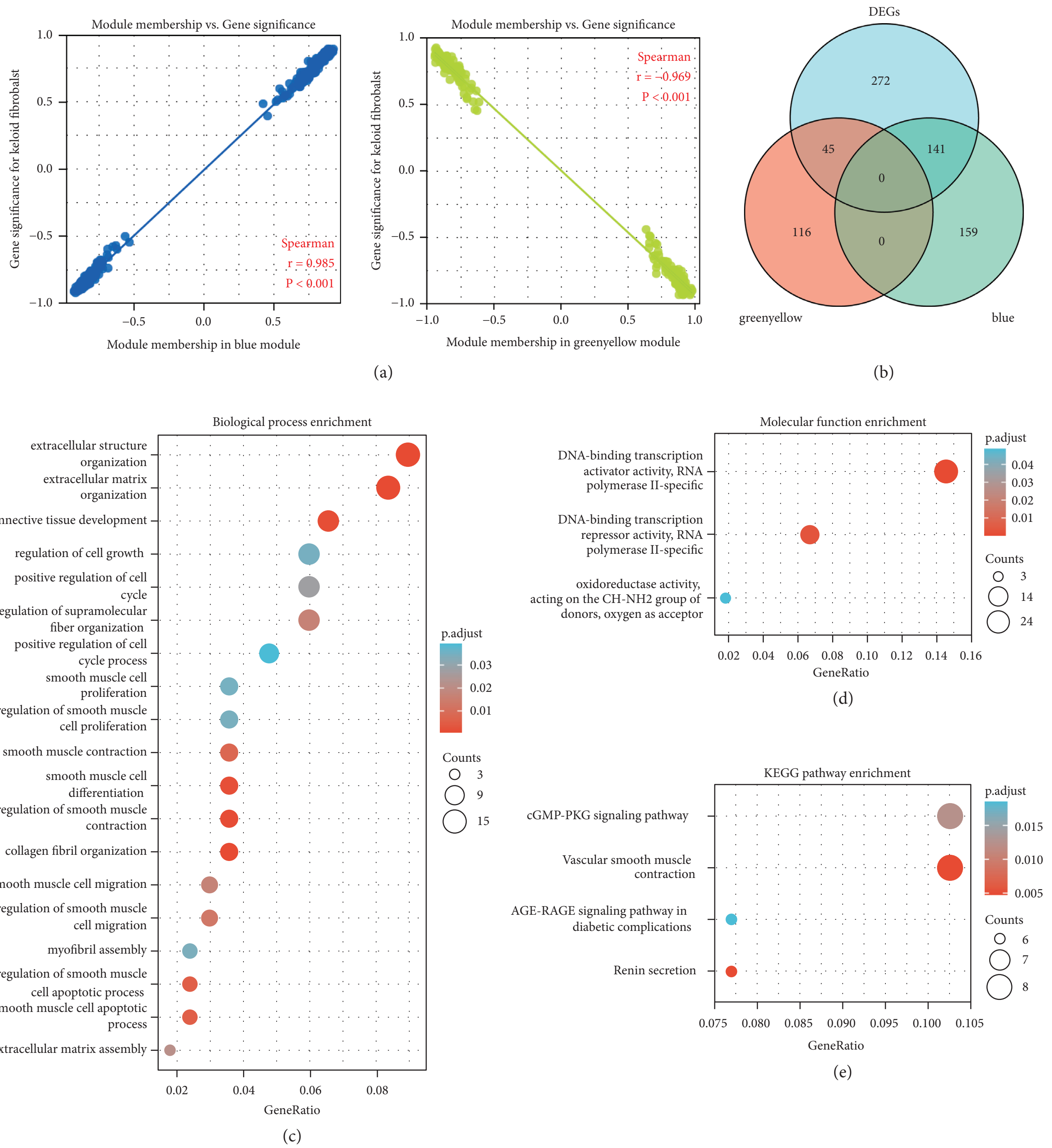

FIGURE 4: Key genes' screening and function prediction. (a) The scatterplot reveals a strong correlation between module membership (MM) and gene significance (GS) in the blue and green-yellow modules. The dot indicates all genes within the modules. (b) The Venn diagram showing key genes. (c) GO-BP enrichment analysis of key genes. (d) GO-MF enrichment analysis of key genes. (e) KEGG enrichment analysis of key genes.

which these genes are involved, GO and KEGG enrichment analysis were performed. Through ID conversion, 176 Entrez ID was filtered. Under the criterion of p.adj<0.05 and q value<0.2, there were 537 entries for biological process (BP), 3 entries for molecular function (MF), and 4 entries for KEGG. In GO-BP analysis, a bubble plot showed that key genes were significantly enriched in the regulation of supramolecular fiber organization, extracellular structure organization, extracellular matrix organization, regulation of cell growth, positive regulation of cell cycle, connective tissue development, and extracellular structure organization (Figure 4(c)). Oxidoreductase activity, acting on the CH-NH2 group of donors, oxygen as the acceptor, DNA-binding transcription activator activity, RNA polymerase II-specific, DNA-binding transcription repressor activity, and RNA polymerase II-specific were the significant MF entries (Figure 4(d)). Besides,

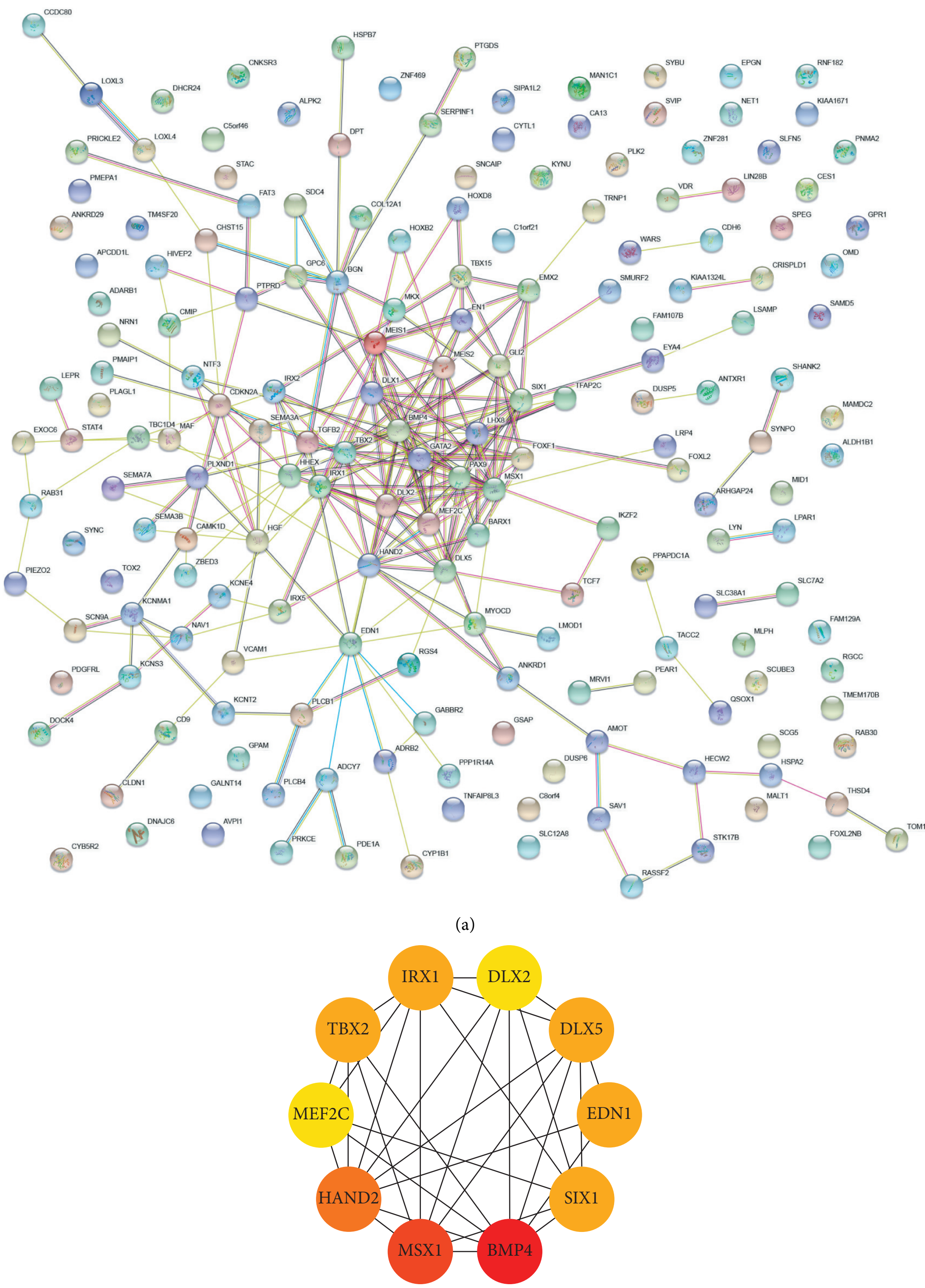

(a)

(b)

FIGURE 5: PPI network construction. (a) PPI network was constructed based on 186 key genes in the String website, with interaction score 0.4. (b) Top 10 hub genes were identified by degree algorithm in Cytoscape software.

key genes were involved in the vascular smooth muscle contraction, cGMP-PKG signaling pathway, renin secretion, and AGE-RAGE signaling pathway in diabetic complications (Figure 4(e)). There were no GO-CC enrichment terms.

3.4. Hub Gene Identification. To find the hub genes in keloid fibroblasts, we uploaded the 186 key genes to the String database. Under the threshold of 0.4 interaction score, a PPI network was constructed (Figure 5(a)). Then, the interaction

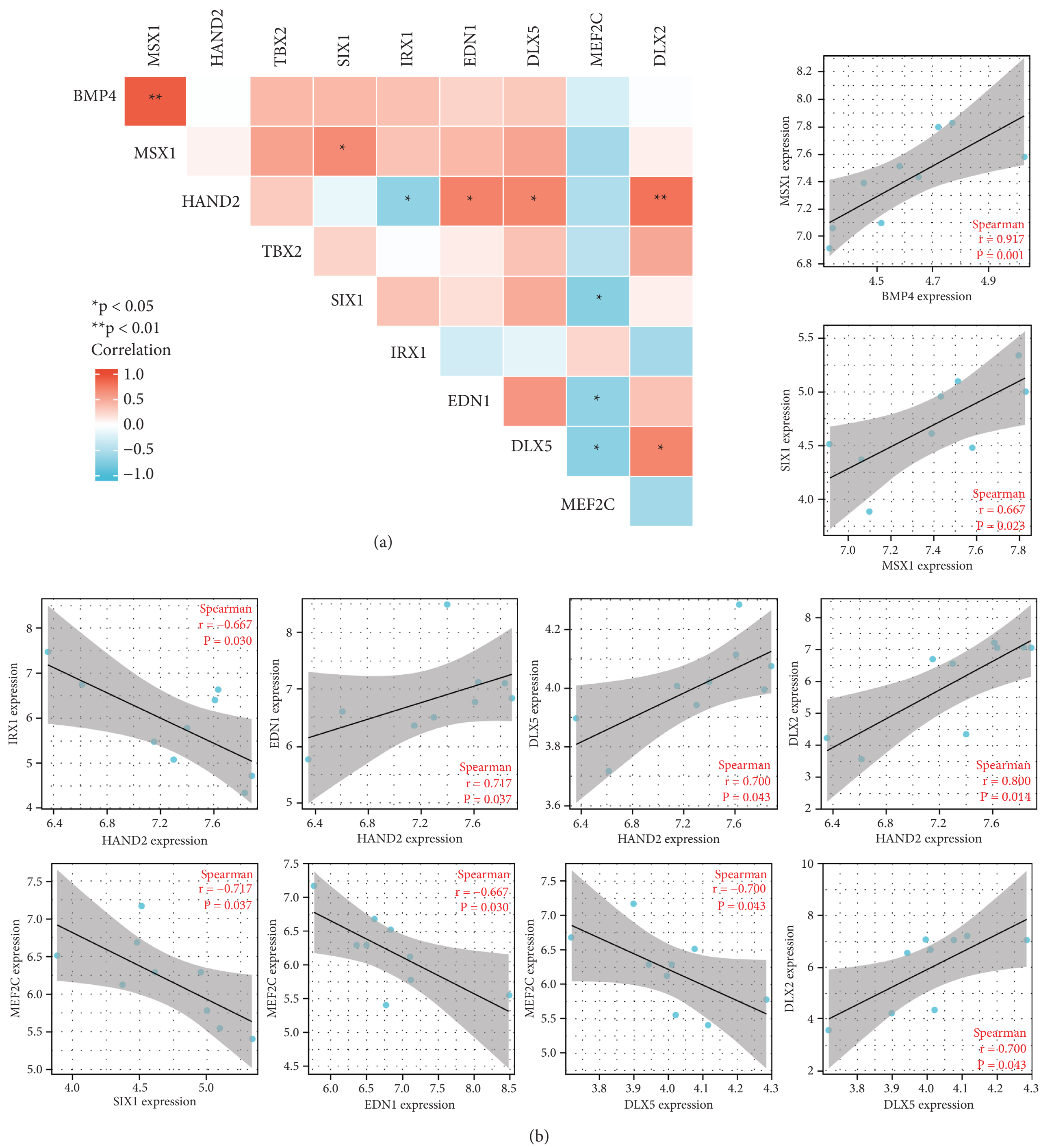

Figure 6: Hub gene correlation. Correlation among hub genes was calculated by Spearman's method and visualized as a matrix heat map (a) and scatter plot (b).

data were downloaded and imported into Cytoscape software. Filtered by CytoHubba calculation, the top 10 hub genes with highest degree were BMP4, MSX1, HAND2, TBX2, SIX1, IRX1, EDN1, DLX5, MEF2C, and DLX2 (Figure 5(b)). Then, we calculated the correlation of hub gene expression with Spearman's rank (rs) test. There was a positive correlation between BMP4 and MSX1, between MSX1 and SIX1, between HAND2 and EDN1, between HAND2 and DLX5, between HAND2 and DLX2, and between DLX5 and DLX2. Additionally, IRX1 was negatively correlated with HAND2. MEF2C was negatively correlated with SIX1, EDN1, and DLX5 (Figures 6(a) and 6(b)). In terms of expression level, BMP4, MSX1, TBX2, SIX1, DLX5, and DLX2 were lowly expressed, while HAND2, IRX1, EDN1, and MEF2C were highly expressed in keloid fibroblasts (Figure 7).

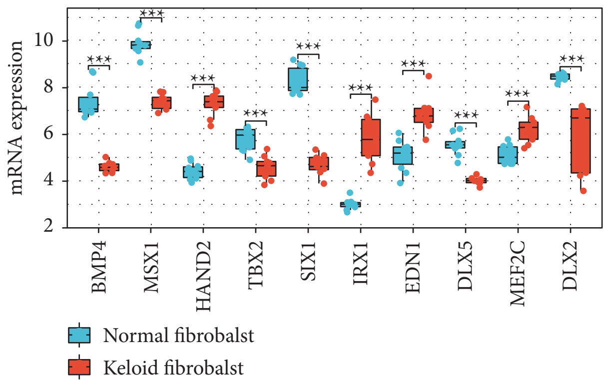

Figure 7: Hub gene expression. The difference of hub gene expression between the normal fibroblast group and keloid fibroblast group was calculated by the Wilcoxon rank sum test. $^{***}P < 0.001$.

4. Discussion

Despite different treatments such as compression therapy, corticosteroid injection, and surgical methods, the recurrence rate of keloids remains high [20]. To identify better treatment targets of keloid, this study used WGCNA analysis, differential expression analysis, and degree algorithm and screened out 10 hub genes associated with keloid fibroblast from the GSE145725 dataset, including BMP4, MSX1, HAND2, TBX2, SIX1, IRX1, EDN1, DLX5, MEF2C, and DLX2.

Among these hub genes, only BMP4 was reported in keloid. As we know, this gene encodes a secreted ligand of the transforming growth factor (TGF)-β superfamily of proteins. Ligands of this family bind various TGF-β receptors leading to recruitment and activation of SMAD family transcription factors that regulate gene expression [21]. According to the work of Xing Dai et al., activation of the BMP4/Smad signaling pathway may promote transdifferentiation of primary keloid myofibroblasts to adipocyte-like cells [22].

The emergence of myofibroblasts is an inevitable process of tissue repair, and this transdifferentiation process is dependent on signaling through the TGF-β1/Smads pathway, whose activation leads to the binding of Smad3 to Smad4 and the initiation of fibrotic genes expression such as ACTA2 [23, 24]. The TGF-β1/Smads signaling pathway runs through the entire process of wound healing from the inflammatory phase to the remodeling phase and is one of the major pathways regulating scar formation [25]. BMP4 could facilitate this pathway, thus suggesting the reliability of the results of this study.

In GO-BP-enriched terms shown in the bubble plot, BMP4 was enriched in terms including smooth muscle cell differentiation, regulation of smooth muscle cell proliferation, smooth muscle cell proliferation, and connective tissue development. These BPs were all related to keloid fibroblasts or keloid [26]. In addition to BMP4, other hub genes were also involved in many GO-BP. EDN1, in particular has a regulatory effect on many keloid-related BPs, including regulation of supramolecular fiber organization, myofibril assembly, regulation of smooth muscle contraction, smooth muscle cell differentiation, smooth muscle contraction, regulation of smooth muscle cell proliferation, smooth muscle cell proliferation, regulation of smooth muscle cell migration, smooth muscle cell migration, smooth muscle cell apoptotic process, regulation of smooth muscle cell apoptotic process, regulation of cell growth, positive regulation of cell cycle process, positive regulation of cell cycle, connective tissue development.

Besides, KEGG enrichment analysis showed that the cGMP-PKG signaling pathway was significantly enriched. As we know, this pathway mediates platelet activation, cardioprotection, smooth muscle relaxation, decrease in intracellular free calcium, and reduced cardiac hypertrophy [27]. Importantly, PKG is a protein kinase that when activated by the second messenger cGMP, phosphorylates VASP, thereby promoting cell growth and differentiation [28], and phosphorylates Bad [29] and CREB [30], thereby decreasing the activity of caspase-3 and inhibiting apoptosis.

Although the sample size of this study is not rich enough and there is no external dataset to validate the screening results, this study is still the first to identify key aberrant genes in keloid fibroblast based on the WGCNA algorithm, which provides therapeutic targets for keloid and reference for future research. The limit is that there are not enough solid foundation to support the opinion. Further experiments are still needed to confirm the study.

5. Conclusions

The blue-green and yellow modules may play an important role in the pathogenesis of keloid. 10 hub genes were identified as potential biomarkers and therapeutic targets for keloid.

Data Availability

The data used to support this study are available from the corresponding author upon request.

Conflicts of Interest

The authors declare no conflicts of interest.

Authors' Contributions

Xianglan Li and Rihua Jiang contributed equally to this study.

Acknowledgments

This work was funded by A novel Mechanism of TGF-β1 Promoting Keloid Derived Fibroblast Proliferation, Migration and ECM Synthesizing TGF-Beta1 (20170414058GH).

References

[1] A. Jfri, E. O'Brien, A. Alavi, and S. R. Goldberg, "Association of hidradenitis suppurativa and keloid formation: a therapeutic challenge," *JAAD Case Reports*, vol. 5, no. 8, pp. 675–678, 2019.

[2] J. Huang, T. Tu, W. Wang et al., "Aligned topography mediated cell elongation reverses pathological phenotype of

in vitro cultured keloid fibroblasts," *Journal of Biomedical Materials Research Part A*, vol. 107, no. 7, pp. 1366–1378, 2019.

[3] Y. Xin, P. Min, H. Xu, Z. Zhang, Y. Zhang, and Y. Zhang, "CD26 upregulates proliferation and invasion in keloid fibroblasts through an IGF-1-induced PI3K/AKT/mTOR pathway," *Burns & trauma*, vol. 8, 2020.

[4] H. D. Gamil, F. M. Khattab, M. M. El Fawal, and S. E. Eldeeb, "Comparison of intralesional triamcinolone acetonide, botulinum toxin type A, and their combination for the treatment of keloid lesions," *Journal of Dermatological Treatment*, vol. 31, no. 5, pp. 535–544, 2020.

[5] B. Chen, J. Ding, J. Jin, N. Song, and Y. Liu, "Continuous tension reduction to prevent keloid recurrence after surgical excision: preliminary experience in Asian patients," *Dermatologic Therapy*, vol. 33, Article ID e13553, 2020.

[6] C.-C. Deng, D.-H. Zhu, Y.-J. Chen et al., "TRAF4 promotes fibroblast proliferation in keloids by destabilizing p53 via interacting with the deubiquitinase USP10," *Journal of Investigative Dermatology*, vol. 139, no. 9, pp. 1925–1935, 2019.

[7] V. Haydont, V. Neiveyans, P. Perez et al., "Fibroblasts from the human skin dermo-hypodermal junction are distinct from dermal papillary and reticular fibroblasts and from mesenchymal stem cells and exhibit a specific molecular profile related to extracellular matrix organization and modeling," *Cells*, vol. 9, 2020.

[8] J. D. Humphrey, E. R. Dufresne, and M. A. Schwartz, "Mechanotransduction and extracellular matrix homeostasis," *Nature Reviews Molecular Cell Biology*, vol. 15, no. 12, pp. 802–812, 2014.

[9] H. J. Lee and Y. J. Jang, "Recent understandings of biology, prophylaxis and treatment strategies for hypertrophic scars and keloids," *International Journal of Molecular Sciences*, vol. 19, 2018.

[10] B. Hinz and D. Lagares, "Evasion of apoptosis by myofibroblasts: a hallmark of fibrotic diseases," *Nature Reviews Rheumatology*, vol. 16, no. 1, pp. 11–31, 2020.

[11] P. Langfelder and S. Horvath, "WGCNA: an R package for weighted correlation network analysis," *BMC Bioinformatics*, vol. 9, no. 1, p. 559, 2008.

[12] Z. Tian, W. He, J. Tang et al., "Identification of important modules and biomarkers in breast cancer based on WGCNA," *OncoTargets and Therapy*, pp. 6805–6817, 2020.

[13] Y. Kang, M. R. Roh, S. Rajadurai et al., "Hypoxia and HIF-1α regulate collagen production in keloids," *Journal of Investigative Dermatology*, vol. 140, no. 11, pp. 2157–2165, 2020.

[14] T. Barrett, S. E. Wilhite, P. Ledoux et al., "NCBI geo: archive for functional genomics data sets--update," *Nucleic Acids Research*, vol. 41, pp. D991–D995, 2013.

[15] S. Davis and P. S. Meltzer, "GEOquery: a bridge between the gene expression Omnibus (GEO) and BioConductor," *Bioinformatics*, vol. 23, no. 14, pp. 1846-1847, 2007.

[16] Z. Gu, R. Eils, and M. Schlesner, "Complex heatmaps reveal patterns and correlations in multidimensional genomic data," *Bioinformatics*, vol. 32, no. 18, pp. 2847–2849, 2016.

[17] G. Yu, L.-G. Wang, Y. Han, and Q.-Y. He, "clusterProfiler: an R Package for comparing biological themes among gene clusters," *OMICS: A Journal of Integrative Biology*, vol. 16, no. 5, pp. 284–287, 2012.

[18] D. Szklarczyk, A. L. Gable, K. C. Nastou et al., "The STRING database in 2021: customizable protein-protein networks, and functional characterization of user-uploaded gene/measurement sets," *Nucleic Acids Research*, vol. 49, no. D1, pp. D605–D612, 2021.

[19] G. Su, J. H. Morris, B. Demchak, and G. D. Bader, "Biological network exploration with Cytoscape 3," *Current protocols in bioinformatics*, vol. 47, pp. 8–24, 2014.

[20] R. Ogawa, "Keloid and hypertrophic scars are the result of chronic inflammation in the reticular dermis," *International Journal of Molecular Sciences*, vol. 18, 2017.

[21] A. Hanna and N. G. Frangogiannis, "The role of the TGF-β superfamily in myocardial infarction," *Frontiers in Cardiovascular Medicine*, vol. 6, p. 140, 2019.

[22] X. Dai and T. C. Lei, "Botulinum toxin A promotes the transdifferentiation of primary keloid myofibroblasts into adipocyte-like cells," *Basic and Clinical Pharmacology and Toxicology*, vol. 129, no. 6, pp. 462–469, 2021.

[23] J. T. Chi, E. H. Rodriguez, Z. Wang et al., "Gene expression programs of human smooth muscle cells: tissue-specific differentiation and prognostic significance in breast cancers," *PLoS Genetics*, vol. 3, pp. 1770–1784, 2007.

[24] G. K. Owens and G. Wise, "Regulation of differentiation/maturation in vascular smooth muscle cells by hormones and growth factors," *Agents Prostaglandins and Control of Vascular Smooth Muscle Cell Proliferation*, vol. 48, pp. 3–24, 1997.

[25] P.-H. Wang, B.-S. Huang, H.-C. Horng, C.-C. Yeh, and Y.-J. Chen, "Wound healing," *Journal of the Chinese Medical Association*, vol. 81, no. 2, pp. 94–101, 2018.

[26] A. L. Rippa, E. P. Kalabusheva, and E. A. Vorotelyak, "Regeneration of dermis: scarring and cells involved," *Cells*, vol. 8, 2019.

[27] J. Inserte and D. Garcia-Dorado, "The cGMP/PKG pathway as a common mediator of cardioprotection: translatability and mechanism," *British Journal of Pharmacology*, vol. 172, no. 8, pp. 1996–2009, 2015.

[28] J. C. Wong and R. R. Fiscus, "Essential roles of the nitric oxide (no)/cGMP/protein kinase G type-Iα (PKG-Iα) signaling pathway and the atrial natriuretic peptide (ANP)/cGMP/PKG-Iα autocrine loop in promoting proliferation and cell survival of OP9 bone marrow stromal cells," *Journal of Cellular Biochemistry*, vol. 112, no. 3, pp. 829–839, 2011.

[29] M. G. Johlfs and R. R. Fiscus, "Protein kinase G type-Iα phosphorylates the apoptosis-regulating protein Bad at serine 155 and protects against apoptosis in N1E-115 cells," *Neurochemistry International*, vol. 56, no. 4, pp. 546–553, 2010.

[30] J. C. Wong, M. Bathina, and R. R. Fiscus, "Cyclic GMP/protein kinase G type-Iα (PKG-Iα) signaling pathway promotes CREB phosphorylation and maintains higher c-IAP1, livin, survivin, and Mcl-1 expression and the inhibition of PKG-Iα kinase activity synergizes with cisplatin in non-small cell lung cancer cells," *Journal of Cellular Biochemistry*, vol. 113, no. 11, pp. 3587–3598, 2012.

Hindawi
Journal of Healthcare Engineering
Volume 2022, Article ID 5691203, 9 pages
https://doi.org/10.1155/2022/5691203

Research Article

Design of Resources Allocation in 6G Cybertwin Technology Using the Fuzzy Neuro Model in Healthcare Systems

Salman Ali Syed,[1] K. Sheela Sobana Rani,[2] Gouse Baig Mohammad,[3] G. Anil kumar,[4] Krishna Keerthi Chennam,[5] R. Jaikumar,[6] Yuvaraj Natarajan,[7] K. Srihari,[8] U. Barakkath Nisha,[9] and Venkatesa Prabhu Sundramurthy[10]

[1]*Department of Computer Science, College of Science and Arts, Jouf University, Tabarjal, Al Jouf Province, Saudi Arabia*
[2]*Electrical and Electronics Engineering, Sri Ramakrishna Institute of Technology, Coimbatore, India*
[3]*Department of Computer Science and Engineering, Vardhaman College of Engineering, Hyderabad, India*
[4]*Computer Science and Engineering, Scient Institute of Technology, Hyderabad, India*
[5]*G. Narayanamma Institute of Technology and Science, Hyderabad, India*
[6]*Department of Electronics and Communication Engineering, KGiSL Institute of Technology, Coimbatore, Tamil Nadu, India*
[7]*ICT Academy, Chennai, Tamil Nadu, India*
[8]*Department of Computer Science and Engineering, SNS College of Technology, Coimbatore, Tamil Nadu, India*
[9]*Department of Information Technology, Sri Krishna College of Engineering and Technology, Coimbatore, Tamil Nadu, India*
[10]*Department of Chemical Engineering, Addis Ababa Science and Technology University, Addis Ababa, Ethiopia*

Correspondence should be addressed to Venkatesa Prabhu Sundramurthy; venkatesa.prabhu@aastu.edu.et

Received 15 November 2021; Revised 1 December 2021; Accepted 18 December 2021; Published 10 January 2022

Academic Editor: Enas Abdulhay

In 6G edge communication networks, the machine learning models play a major role in enabling intelligent decision-making in case of optimal resource allocation in case of the healthcare system. However, it causes a bottleneck, in the form of sophisticated memory calculations, between the hidden layers and the cost of communication between the edge devices/edge nodes and the cloud centres, while transmitting the data from the healthcare management system to the cloud centre via edge nodes. In order to reduce these hurdles, it is important to share workloads to further eliminate the problems related to complicated memory calculations and transmission costs. The effort aims mainly to reduce storage costs and cloud computing associated with neural networks as the complexity of the computations increases with increasing numbers of hidden layers. This study modifies federated teaching to function with distributed assignment resource settings as a distributed deep learning model. It improves the capacity to learn from the data and assigns an ideal workload depending on the limited available resources, slow network connection, and more edge devices. Current network status can be sent to the cloud centre by the edge devices and edge nodes autonomously using cybertwin, meaning that local data are often updated to calculate global data. The simulation shows how effective resource management and allocation is better than standard approaches. It is seen from the results that the proposed method achieves higher resource utilization and success rate than existing methods. Index Terms are fuzzy, healthcare, bioinformatics, 6G wireless communication, cybertwin, machine learning, neural network, and edge.

1. Introduction

Since the development of edge computing [1], it has emerged as a key strategic approach in a variety of application areas, especially in the fields of data aggregation, network connectivity, and other industrial tasks. The edge is regarded as an open platform for storage and computing applications because it is situated near a data source or an object on the network side. Edge computing is placed between the cloud and end devices and uses a high-speed data communication channel with a local data processing capability between them to transfer data with processing power equivalent to that of the cloud [2].

There are some basic facilities in the current healthcare system, but time and space are the main obstacles. Because of the existing circumstances, this is unavoidable; nevertheless, in the near future, it will not be a hindrance to progress. It is also worth noting that an ambulance service is nothing more than a vehicle for transporting patients with oxygen and road traffic priority. In addition, the current state of aged care is woefully inadequate. There is a great deal of emphasis on medical staff in the care of the older population. However, it has not been made available yet. In ambulances, most patients die on the way to or from the hospital or even before the ambulance gets there. Current healthcare systems also lack an accident detection system [3].

Real-time accident detection is needed to ensure that medical services are available immediately and on the scene. Furthermore, outbreaks like COVID-19 cannot be handled due to a lack of technological infrastructure. This includes epidemics and pandemics. In the future, a virus identical to this one is likely to surface. As a result, creating an intelligent healthcare system is critical. The high data throughput and low delay needs of 6G technology for future healthcare necessitate the use of this technology. Telesurgery, in particular, necessitates instantaneous communication. Intelligent healthcare systems will also benefit from holographic communication and augmented or virtual reality. As a result, intelligent healthcare cannot make use of 5G and 5G B5G. In the 5G era, intelligent healthcare will be largely adopted, which will propel a significant amount of progress [4].

The virtual cyberspace in the edge cloud is where the virtual representation of the end (humans and things) resides, making it a critical part of the cybertwin communication model. Cybertwin can meet three distinct needs by supplying 3 different features: network communications assistant feature, network behaviour logger feature, and digital asset feature [5, 6]. It is crucial that an end device connect to the server offering the services. The cybertwin will access the network in order to provide the required service to the end, and once that service is completed, will return the service to the end. This is the most fundamental function of the cybertwin's communications assistant. Cybertwin can be thought of as the digital representation of the goals, which allows the system to collect and log all the data about the network behaviour of the user's system. After removing sensitive information, cybertwin converts the behaviour data of the users into a digital asset for sale [7].

Cybertwin on the boundary has been configured to meet the needs of various industries, such as rapid connection and strong security. Data are being gathered at the cloud centre, while, on the other hand, edge computing features device-based processing. As end-user resources get closer to users, latency between the cloud data centre and devices decreases. This, in turn, allows for slightly improved quality of service (QoS). Also, as the number of devices that will be able to connect to the internet increases, the network bandwidth or capacity will be a major constraint on cloud computing. Likewise, the complexity of end-user requirements raises the difficulty of service allocation. Above all, excellent resource selection is critical to meeting end-user needs [8–14].

During the onset of large-scale distributed neural network use, the limited computing resources found at the edge devices present several challenges. A shortage of resources limits storage. These limitations are the shortage of energy and defects in architecture. Despite their complementary relationship and the reduced latency that they enjoy, the edge did not have the necessary resources to make use of cloud computing. A significant influence on application performance, task scheduling, and end-user QoS is the allocation or prediction of available resources. Providing an estimate of the required resources for each end-user will produce an appropriate resource plan, which should use certain parameters to estimate the amount of resources consumed. Therefore, in order to meet the user's QoS, the resource estimation needs to incorporate a task allocation strategy that is optimised for edge computing.

Historical research has identified cloud, edge nodes, and end-user devices as the requirements for neural network deployment. Neural networks are less latency-sensitive when there is increased resource allocation, but they have the potential to pass on the original source in the event of latency-critical applications. Edge users are offered distributed services via multiple hidden layers of neural networks. The neural network model predicts and then allocates energy resources in a near real-time manner, with minimal delay [7]. The distributed neural network architecture can identify when tasks get allocated to different partitions at the edge and will always use a partition with fewer resources if distributed edge nodes are utilised.

The aim is to design and implement distributed neural networks (DNNs) on edge networks with better performance, so that devices at the edge are capable of intelligent workload prediction. A long-standing constraint on computation and resourcing, represented by the trade-off between the computational load and resourcing task, has to be maintained using distributed neural networks.

Here, we developed federated learning (FL) [15, 16] as a subset of cybertwin as a preliminary model to assist with decisions related to reresource allocation. Such constraints as memory and communication complexity are incorporated into the preliminary model.

The major contribution of the proposed work is stated as follows:

(i) To improve the effectiveness of resource allocation decisions, the author built a FL model. With the DNN serving as a secondary model, it is now possible to use the following rules: edge resources allow zero or multiple edge devices, resources available, memory requirements, and user quality of service requirements.

(ii) Decentralized training data distribution is a solution that optimises the reuse of valuable network resources, even in the event of an unreliable network. To distribute environments such as this, FL (each iteration) enables the edge node to compute updates to the cloud centre independent of system requirements, user cases, data size, and implementation effort.

(iii) Conceptually, it can be said that the model compares the total number of servers connected to the data centre, the number of servers on the edge that connect to the cloud, and the response time

This study is structured as follows: Section 2 provides the network model. Section 3 discusses the problem formulation, and Section 4 provides a detailed discussion on resource allocation using the FNN wireless healthcare model. Section 5 evaluates the entire work with existing resource allocation models. Section 6 concludes the entire work with possible directions for future scope.

2. Network Model

Edge computing fundamentals are discussed in this section, which finds it situated between the cloud and the edge devices. Storage, computation, and network services can benefit from edge computing. Edge computing has a distributed FNN wireless healthcare model that is utilised to make distributed computation possible with severely limited memory and processing power in the edge nodes and edge devices. Because edge devices are near the resources, real-time communication is possible.

The cyber twin aims to process data while providing the ability to communicate and perform computations freely. The present study uses a 3-tier architecture with an edge computing model, as shown in Figure 1.

The control BSs is responsible for data providing to the control plane that decides the required resources for the edge IoT devices. This resource allocation with uplink and downlink BSs enables user plane to allocate the resources for data communication from edge devices via edge IoT devices.

This edge device is made to generate data and make the client consume more of it. In particular, it urges clients to use more resources from the edge nodes rather than the cloud. Devices may range from smartphones to IoT sensor nodes, intelligent vehicles, and even smart cities. The edge devices collect data and communicate with each other using a sensor network. The cloud servers located in the cloud centre have significantly more energy and computing power than numerous edge devices [10].

Switches, routers, and local servers, which are typically deployed for special services, sit on the edge nodes. The compute, storage, processing, and data forwarding are all in place with these nodes. A single or multihop connection can be used to connect edge devices with edge nodes or edge servers. Computing, network, storage, and software resources are all available in the microdata centre (MDC). Cluster servers and data centres that act as storage and processing points for data received from edge devices are positioned at the top of the cloud layer.

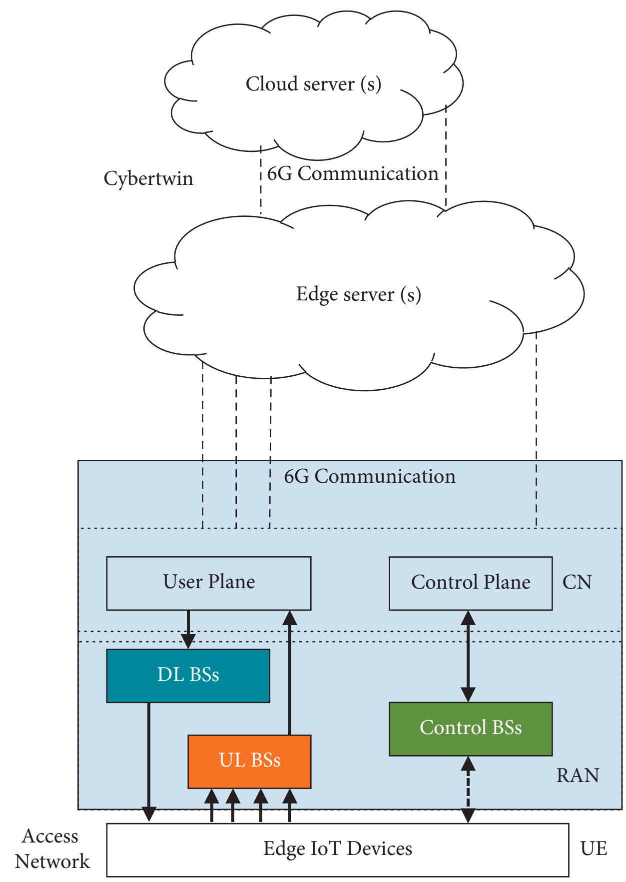

Figure 1: 6G edge computing framework.

Figure 2 shows the process of a service request when using edge computing. Users can submit requests to the administrator by using edge devices at the beginning. In order to meet the QoS user requirements, the query is stored in the edge nodes and is then passed on to the cloud centres through the edge nodes. Resources, sensor availability, service, and applications influence the statistics generated by the monitoring equipment. This equipment processes data that are sent to the edge nodes and QoS service levels for each user requirement, and these data are analysed to provide appropriate levels of service for each user. To allocate resources in an optimal manner, a FNN wireless healthcare model processes each service on an edge device locally to provide the optimal distribution of energy and bandwidth. A distributed FNN wireless healthcare model selects an existing resource and allocates it according to user QoS requirements.

3. Problem Formulation

The study aims to improve the allocation of energy considering all constraints for optimal consumption of energy at the IoT edge network. Furthermore, it considers various constraints including resource allocation constraints, computational resource constraints, radio resource constraints, radio resource allocation over IoT edge constraints, latency constraints, and task execution constraints. It is hence formulated as follows:

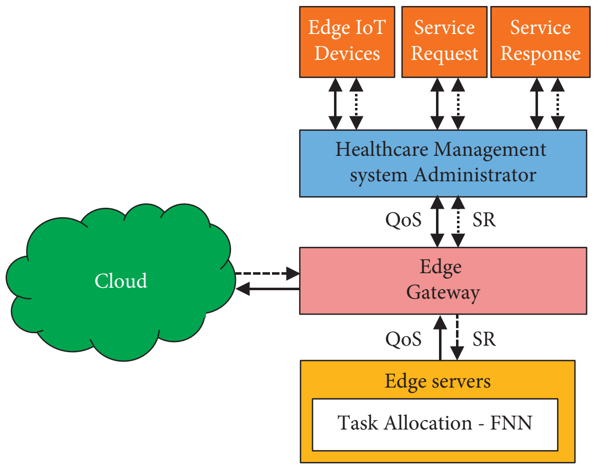

FIGURE 2: The service request in cybertwin for resource allocation.

$$
\begin{aligned}
&\min_{a,\theta,f} \sum_{i=1}^{N} a(i)\left(e_c(i)\right) + C(i)\Big(1 - k\big(f^2(i)\big)a(i)\Big),\\
&C_1\colon \sum_{i=1}^{N} f(i) \leq F,\\
&C_2\colon 0 \leq f_i \leq a_i * F,\\
&C_3\colon \sum_{i=1}^{N} \theta_i \leq L,\\
&C_4\colon 0 \leq \theta_i \leq a_i L,\\
&C_5\colon a_i \in \{0,1\},\\
&C_6\colon \frac{C(i)}{f(i)}(1 - a(i)) + a(i)\left(\frac{C(i)}{f(i)} + \frac{D(i)}{R(i)}\right) \leq T(i),
\end{aligned}
\tag{1}
$$

where α is the execution vector, θ is the allocation of radio resource by 6G network, and f is the resource allocated in servers.

Furthermore, the tasks are executed locally while considering all the constrains $\alpha(i) = 0$ [6], and the parameters are set as follows: $\alpha(i)t_c(i) = 0$ and $\alpha(i)e_c(i) = 0$ for local task execution.

(i) $C1$—resource allocation constraints
(ii) $C2$—computational resource constraints
(iii) $C3$—radio resource constraints
(iv) $C4$—radio resource allocation over IoT edge constraints
(v) $C5$—latency constraint
(vi) $C6$—task execution constraints

4. FNN Resource Allocation

A multinode FNN wireless healthcare model is often referred as the FNN wireless healthcare model that aims to improve the precision and performance and scales according to larger data size. The increasing size of input data learning for learning reduces significantly the training errors and enables error-free complex operations [8]. This allows the distributed FNN wireless healthcare model computing to draw significant decisions and conclusions over larger data sizes or in case of complex computing. The purpose-built distributed FNN wireless healthcare model operates in distributed edge computing environment that gains advantage in terms of its performance requirement, user cases, data size, and implementation effort.

The FNN wireless healthcare model learns the entire model with suitable parameters in the form of a matrix $W \in Rx \times y$ from the data stored across edge devices, where x and y represent the input and output dimensions. Consider a FL model at round $t \geq 0$, where the server is allowed to distribute the current FL $W(t)$ over the edge IoT devices. The edge devices update independently the FL model $W(t)$ in terms of its local data. The data model after update is considered as $W_1(t), W_2(t), \ldots, W_n(t)$, and hence, the update on the edge device say i is defined as $H_i(t) = W_i(t) - W(t)$, where the edge devices $i \in S(t)$. The edge device sends update to the edge node and then to the cloud centre, where it computes the global update based on the aggregation of edge device update.

$$
\begin{aligned}
W(t+1) &= W(t) + H(t)\,\eta(t),\\
H(t) &= n^{-1}(t)^{\sum_{i\in S(t)} H_i(t)}.
\end{aligned}
\tag{2}
$$

The edge node is allowed to select $\eta(t)$, the learning rate, and for faster computation, we have considered $\eta(t) = 1$. The FL is described for the DNN in next section, where it uses an individual matrix (W) in order of representing the parameters over each hidden layer. The parameters representing the full connected layers of the DNN in FL is hence described in the form of 2D matrix. On the other hand, the study aims to increase the efficiency of communication using the FNN wireless healthcare model that tends to reduce the communication and transmission cost of sending the updates $H_i(t)$ to the cloud centre. Whereas, the edge model considers learning the data from edge devices with constrained internet connectivity and its computational availability. To attain gradient computations, the loss function L with a parameter vector w is minimised using the learning problem to attain a closed form solution.

The study considers a simplest circulant matrix approach considering a vector r with viable error rates. Hence, the circulant matrix $R \in R^{x \times y}$ over a vector r is expressed as follows:

$$
\mathrm{Cir}(r) = R \coloneqq \begin{bmatrix} r_0 & r_{d-1} & \cdots & r_2 & r_1\\ r_1 & r_0 & r_{d-1} & \cdots & r_2\\ \vdots & r_1 & r_0 & \cdots & \vdots\\ r_{d-2} & \vdots & \vdots & \ddots & r_{d-1}\\ r_{d-1} & r_{d-2} & \cdots & r_1 & r_0 \end{bmatrix}. \tag{3}
$$

It has reduced the cost of storage to $O(d)$ instead of $O(d^2)$. The computations using the circulant matrix uses fast Fourier transform to increase the speed of computations.

Therefore, the computational complexity for a single-layered DNN (Figure 3) with a vector r having a dimension d is defined as $O(d\log d)$.

The modified circulant matrix $R \in R^{d\times n}$ is expressed as

$$R = SHG\Pi HB, \tag{4}$$

where G, S, and B are the diagonal matrices, H is the Walsh–Hadamard matrix, and $\Pi \in \{0, 1\}^{d\times d}$ is the permutation matrix.

At the edge IoT device, the resource allocation should meet the user needs, and it should satisfy the QoS needs. Therefore, the set of resources in the edge node with the same service is stated as follows:

$$R = \{r_1, r_2, \ldots, r_n\}. \tag{5}$$

Considering all the attributes for resource allocation, the resource allocation is carried out based on user requirement, and the resource set $q(i)$ is defined in terms of QoS attributes available for resource allocation.

$$q(i) = \{q_1, q_2, \ldots, q_n\}, \tag{6}$$

where n is the index resource with QoS attributes including response time, availability, cost, and reliability.

Here, the cost is estimated as follows:

$$p = UbD_{ed}\frac{\mu}{\varphi}, \tag{7}$$

where U is the basic service cost, μ is the total requests, φ is the total service requests, b is the cost regulation, and D_{ed} is the edge IoT device.

If the resource is similar to the QoS attributes as demanded by edge device, the attributes set is thus expressed as follows:

$$u = \{u_1, u_2, \ldots, u_m\}. \tag{8}$$

The attribute matrix for QoS with respect to the resources is defined in the form of a decision matrix.

$$\begin{aligned} R &= (r(ij))_{n\times m},\\ &= \begin{pmatrix} r_{11} & r_{12} & \cdots & r_{1m}\\ r_{21} & r_{22} & \cdots & r_{2m}\\ \vdots & \vdots & \ddots & \vdots\\ r_{n1} & r_{n2} & \cdots & r_{nm} \end{pmatrix}, \end{aligned} \tag{9}$$

where $r(ij)$ is the QoS attribute of j^{th} value over a resource (i).

The processing of the attribute matrix is considered meaningless if the units of measurement units are different for the QoS attributes. Hence, the relationship existing between user satisfaction and the QoS attributes is formulated as follows:

$$z(ij) = \begin{cases} \dfrac{r(ij) - \min r(j)}{\max r(j) - \min r(j)}, & q > 0,\\[2ex] \dfrac{\min r(j) - r(ij)}{\max r(j) - \min r(j)}, & q \le 0. \end{cases} \tag{10}$$

Here, an objective weight is set for each attribute, since the edge devices at the end-user have selected preference for a specific attribute that tends to affect the measurement directly, and it utilizes a weighted technique to estimate the preference.

$$\begin{aligned} d(u,i) &= \sum_{j=1}^{m} \sqrt{w(j) * (q(j) - u(j))^2},\\ \operatorname{sim} d(u,i) &= \frac{1}{1 + d(u,i)}, \end{aligned} \tag{11}$$

where $w(j)$ is the resource attribute weight, $d(u, i)$ is the distance from ideal to edge node (i), and sim$d$ (u, i) is the proximity degree [0, 1].

5. Performance Evaluation

In this section, the entire simulation is conducted in Matlab environment to study the effectiveness of the proposed model. This section focuses on the experimentation that has been conducted to verify the effectiveness of the FNN wireless healthcare model in helping resource allocation decisions regarding metrics like average success rate, job response time, and resource utilisation levels. Latency is calculated by finding the Euclidean distance between edge devices according to the distance model in [9]. Response time is a factor in resource allocation, and an edge device with a high-valued response time would be considered a failure-allocated task. The study uses three data centres with 100 servers, where each server consists of 6 cores with 5 hostings per server. The location of data centre is considered random with 30 ms response time and with 100 bytes low latency level.

FNN wireless healthcare model effectiveness is studied through 3 different performance metrics in this study. For the first time, the average response time of each allocated resource to the edge device is measured when computing the impact of cloud servers on the network node. Also, the average task utilisation is estimated at the node where the task is created, and third, the likelihood of tasks allocated per failure is calculated. Each of these 3 responses is analysed under consideration of response time constraints, and eventually, network throughput is estimated.

5.1. Influence of Data Centre with Core Server. According to estimations, the performance of three techniques on three different servers connected to a data centre is expected. This study will lead to the increase of between 200 and 2000 cloud servers. Careful consideration has been given to the servers, such that the total servers that are connected to the cloud data centre have the same number of servers as those connected to a microdata centre. Figure 4(a) shows the total servers connected to edge servers for each allocated task. The FNN wireless healthcare model improves the performance relative to the current FL and DNN when more resources are shared among the edge nodes. There is an optimum level of performance even if only a small number of servers are connected to the edge servers.

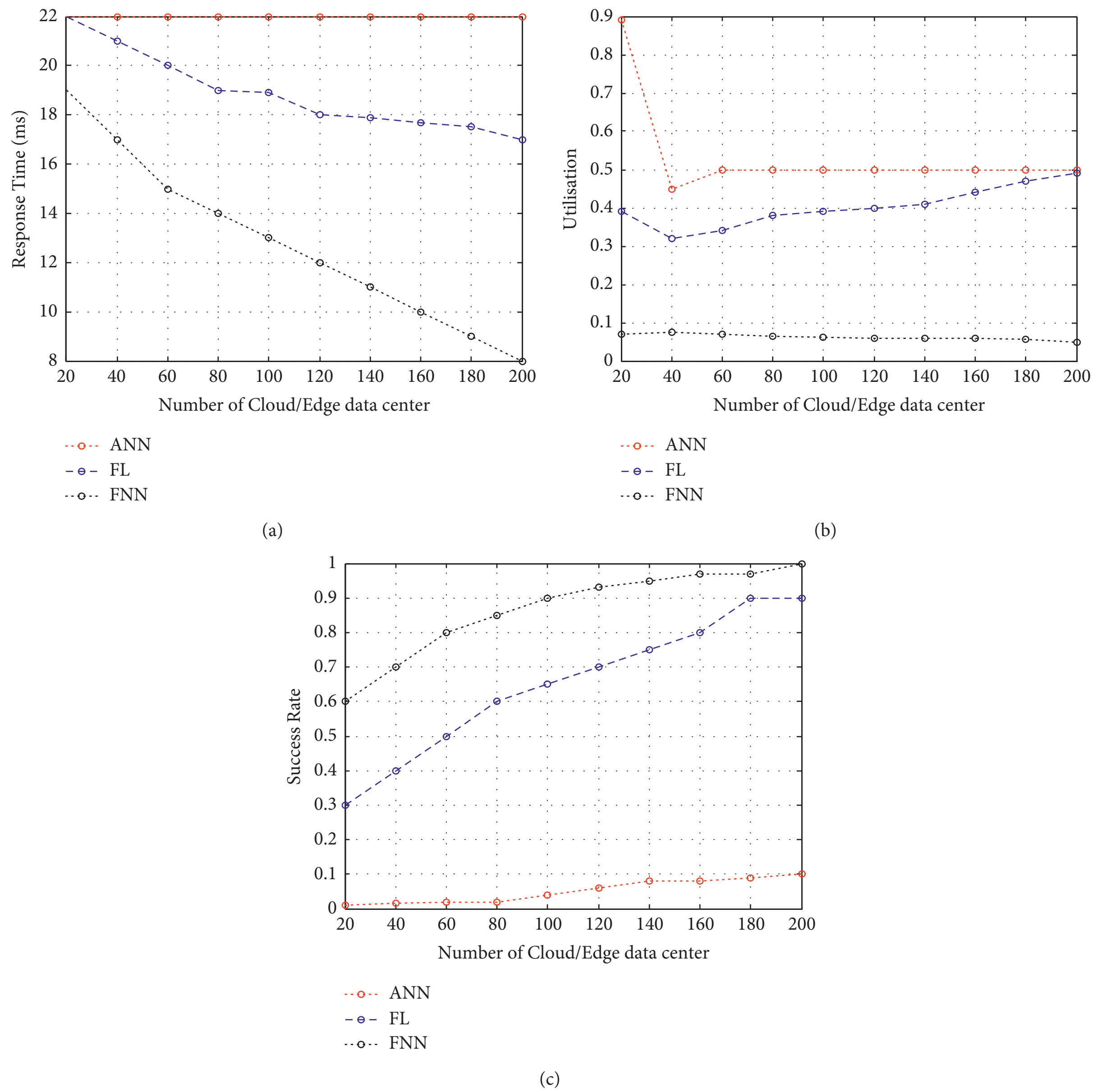

FIGURE 3: (a) Response time w.r.t the influence of data centre. (b) Resource utilisation w.r.t the influence of data centre. (c) Success rate w.r.t the influence of data centre.

In Figure 4(b), higher-order use of resources is illustrated. One microdata centre of edge handles over 150 cloud servers, allowing for greater overall resource utilisation than just the amount of time spent on scare resources. Additionally, as more servers are added, the resource utilisation success rate increases and never reaches 99.99%. The higher the burden, the less successful the existing FL and DNN methods are. As these methods have a harder time handling the increased burden, they have a negative impact on the success rate. However, missing the response time constraint (Figure 4(c)) is a significant barrier to making neighbourhood edge data centres a reality. Constrained response time, limited resource utilisation, and improved success rate were found to improve overall performance with the experimental results.

5.2. Influence of Data Centre on the Entire Network. This proposed study confirms that the FNN wireless healthcare model achieves the desired performance even when run on several edge nodes or in microdata centres. Here, we go from a state with around 200 edge nodes to around 20 edge nodes, and then, groups of 20 edge nodes are grouped together with each group assigned to a service provider. Figure 3(a) shows that as edge nodes increase, response time decreases from 20 to 10 ms. It is because the edge nodes and edge devices are farther apart today. Another feature that already exists functions with a similar range; response time grows from 18 ms to 21 ms. Since the cloud centre appears unaffected by available edge nodes, it can be concluded that the cloud centre does not rely on the availability of nodes on the edge. Figures 3(b) and 3(c) illustrate an increase in the amount of

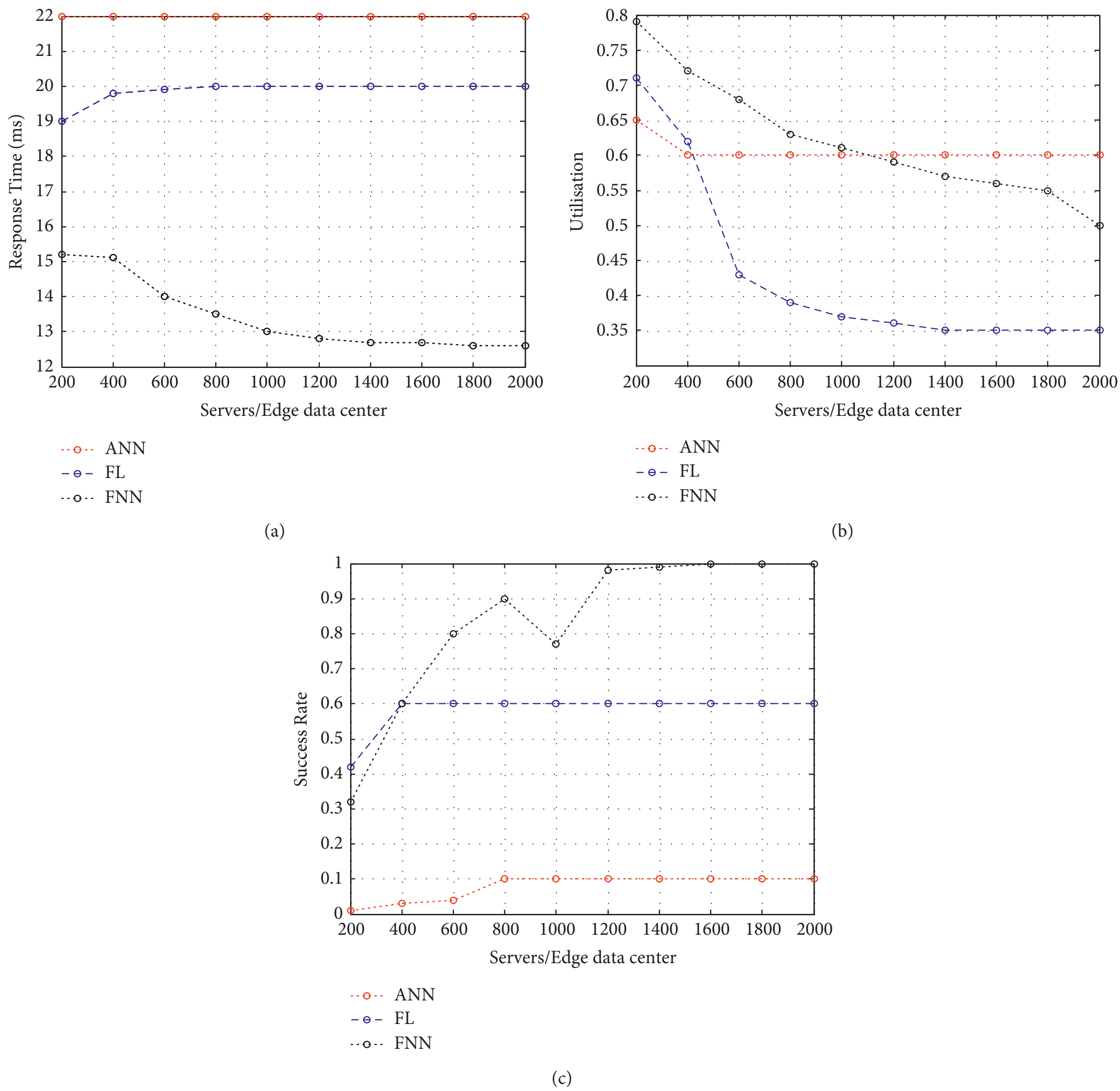

FIGURE 4: (a) Response time w.r.t the influence of connected data centre. (b) Resource utilisation w.r.t the influence of connected data centre. (c) Success rate w.r.t the influence of connected data centre.

resources used by the FNN wireless healthcare model compared to the existing FL and DNN. Additionally, the proposed mechanism has a higher success rate than in Figure 3(c). The findings demonstrate that the FL and DNN are better than other systems at significantly increasing performance.

5.3. Impact of Response Time Constraint. The average response time tends to increase as the response time constraint increases (Figure 5(a)). This increases scalability, as the workloads can be distributed fairly between edge devices and edge nodes. Because of their distance, their response time tends to be impacted. For example, in Figure 5(b), the resource utilisation is compared, and it is found that the increased response time constraint causes the utilisation to increase. Performance similar to the FNN wireless healthcare model can be achieved if the response time constraint at the edge nodes is increased. The edge node can provide a higher percentage of completed tasks in cloud locations because it has a lower response time constraint. Furthermore, as shown in Figure 5(c), the average success rate increases when reresponse time constraints are extended. When compared to other existing resource allocation methods, the proposed solution obtained an average success rate of 99.9%. According to the results, the FNN wireless healthcare model has an edge over other methods, even when response time limits are present.

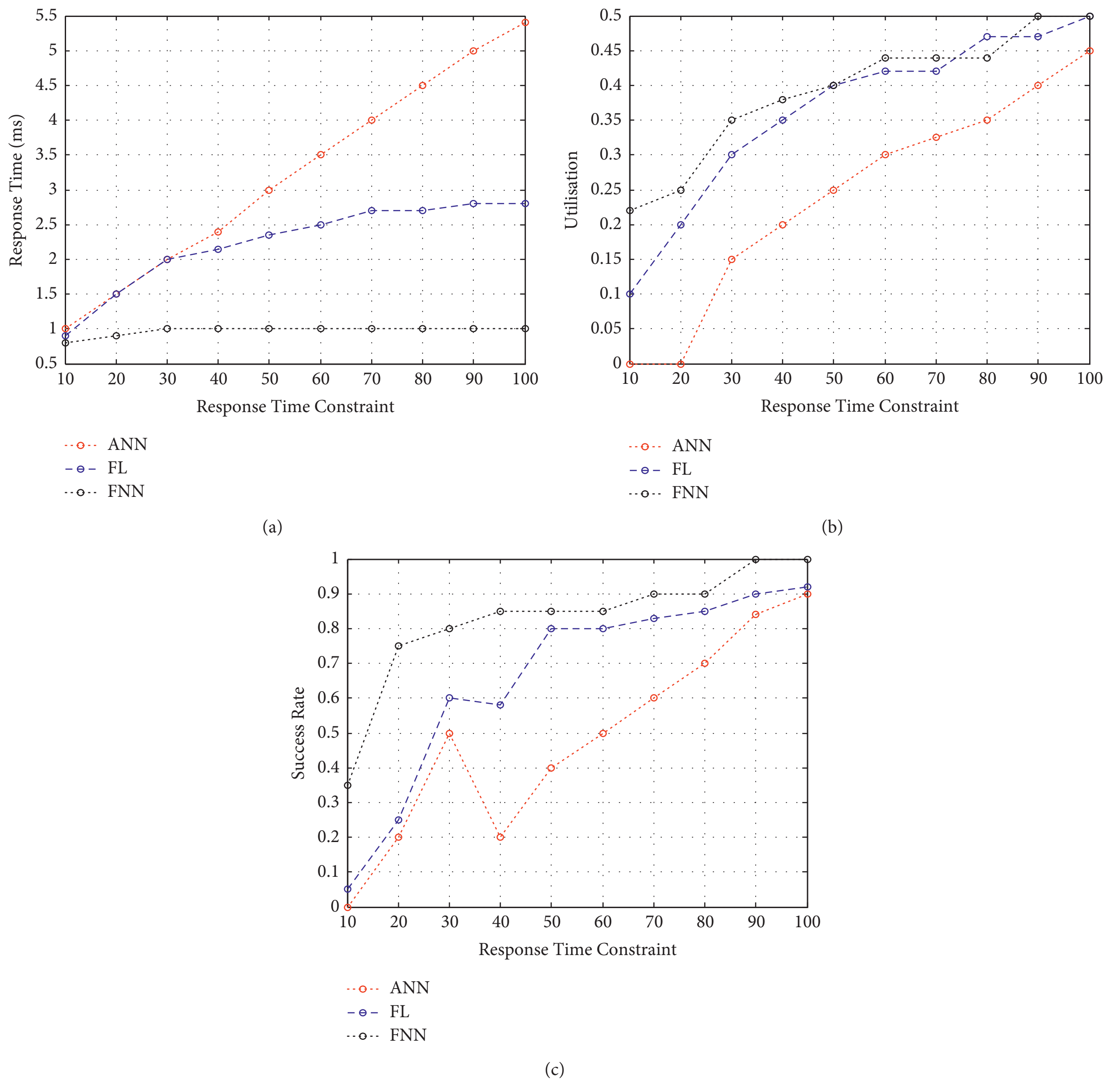

Figure 5: (a) Response time w.r.t response time constraints. (b) Resource utilisation w.r.t response time constraints. (c) Success rate w.r.t response time constraints.

6. Conclusion

In this study, the FNN wireless healthcare model applies its distributed resource allocation settings to allocate optimal resources to the edge devices. To support the distributed settings of edge intelligence, FL adjustments are implemented. In terms of improved average success rate, higher resource utilisation, and increased network throughput, the design of computational and storage cost reduction in the edge network and in hidden layers has been a big success. Conventional methods demonstrate higher scalability in distributed deep learning models compared to the FNN wireless healthcare model. In future, metaheuristic models can be deployed to create shear intelligence on detecting optimal resource allocation to edge devices.

Data Availability

The datasets used and/or analysed during the current study are available from the corresponding author upon request.

Conflicts of Interest

The authors declare that there are no conflicts of interest.

References

[1] S. Weisong, S. Hui, C. Jie, Z. Quan, and L. Wei, "Edge computing—an emerging computing model for the Internet of everything era," *Journal of Computer Research and Development*, vol. 54, no. 5, 907 pages, 2017.

[2] Q. Yu, J. Ren, Y. Fu, Y. Li, and W. Zhang, "Cybertwin: an origin of next generation network architecture," *IEEE Wireless Communications*, vol. 26, no. 6, pp. 111–117, 2019.

[3] S. Nayak and R. Patgiri, "6G communication technology: a vision on intelligent healthcare," in *Health Informatics: A Computational Perspective in Healthcare*, pp. 1–18, Springer, Singapore, 2021.

[4] M. S. Kaiser, N. Zenia, F. Tabassum et al., "6G access network for intelligent internet of healthcare things: opportunity, challenges, and research directions," in *Proceedings of the International Conference on Trends in Computational and Cognitive Engineering*, pp. 317–328, Springer, Singapore, December 2021.

[5] W. Shi, J. Cao, Q. Zhang, Y. Li, and L. Xu, "Edge computing: vision and challenges," *IEEE Internet of Things Journal*, vol. 3, no. 5, pp. 637–646, 2016.

[6] Y. Guan, R. Lu, Y. Zheng, S. Zhang, J. Shao, and G. Wei, "Toward privacy-preserving cybertwin-based spatio-temporal keyword query for ITS in 6G era," *IEEE Internet of Things Journal*, vol. 8, no. 22, pp. 16243–16255, 2021.

[7] S. Yan, Q. Ye, and W. Zhuang, "Learning-based transmission protocol customization for VoD streaming in cybertwin-enabled next generation core networks," *IEEE Internet of Things Journal*, vol. 8, no. 22, pp. 16326–16336, 2021.

[8] A. Halevy, P. Norvig, and F. Pereira, "The unreasonable effectiveness of data," *IEEE Intelligent Systems*, vol. 24, no. 2, pp. 8–12, 2009.

[9] R. Goonatilake and R. A. Bachnak, "Modeling latency in a network distribution," *Network and Communication Technologies*, vol. 1, no. 2, p. 1, 2012.

[10] M. Adhikari, A. Munusamy, N. Kumar, and S. N. Srirama, "Cybertwin-driven resource provisioning for IoE applications at 6G-enabled edge networks," *IEEE Transactions on Industrial Informatics*, p. 1, 2021.

[11] Y. Wang, M. Sheng, X. Wang, L. Wang, and J. Li, "Mobile-edge computing: partial computation offloading using dynamic voltage scaling," *IEEE Transactions on Communications*, vol. 64, no. 10, pp. 4268–4282, 2016.

[12] T. K. Rodrigues, J. Liu, and N. Kato, "Application of cybertwin for offloading in mobile multi-access edge computing for 6G networks," *IEEE Internet of Things Journal*, vol. 8, no. 22, pp. 16231–16242, 2021.

[13] H. Liang, H. Li, and W. Zhang, "A combinatorial auction resource trading mechanism for cybertwin based 6G network," *IEEE Internet of Things Journal*, vol. 8, no. 22, pp. 16349–16358, 2021.

[14] S. Juneja, M. Gahlan, G. Dhiman, and S. Kautish, "Futuristic cyber-twin architecture for 6g technology to support internet of everything," *Scientific Programming*, vol. 2021, Article ID 9101782, 2021.

[15] S. Wang, T. Tuor, T. Salonidis et al., "Adaptive federated learning in resource constrained edge computing systems," *IEEE Journal on Selected Areas in Communications*, vol. 37, no. 6, pp. 1205–1221, 2019.

[16] Q. Yang, Y. Liu, T. Chen, and Y. Tong, "Federated machine learning," *ACM Transactions on Intelligent Systems and Technology*, vol. 10, no. 2, pp. 1–19, 2019.

Hindawi
Journal of Healthcare Engineering
Volume 2022, Article ID 2500377, 8 pages
https://doi.org/10.1155/2022/2500377

Research Article

Improved Handover Authentication in Fifth-Generation Communication Networks Using Fuzzy Evolutionary Optimisation with Nanocore Elements in Mobile Healthcare Applications

J. Divakaran,[1] S. K. Prashanth,[2] Gouse Baig Mohammad,[3] Dr Shitharth,[4] Sachi Nandan Mohanty,[3] C. Arvind,[5] K. Srihari,[6] Yasir Abdullah R.,[7] and Venkatesa Prabhu Sundramurthy[8]

[1]*Department of Electronics and Communication Engineering, K S R Institute for Engineering and Technology, Tiruchengode, Tamilnadu, India*
[2]*Vardhaman College of Engineering, Hyderabad, India*
[3]*Department of Computer Science and Engineering, Vardhaman College of Engineering, Hyderabad, India*
[4]*Kebri Dehar University, Department of Computer Science and Engineering, Kebri Dehar, Ethiopia*
[5]*Department of Electronics and Communication Engineering, Karpagam College of Engineering, Coimbatore, India*
[6]*Department of Computer Science Engineering, SNS College of Technology, Coimbatore, India*
[7]*CSBS, Sri Krishna College of Engineering and Technology, Coimbatore, India*
[8]*Department of Chemical Engineering, Addis Abada Science and Technology University, Addis Ababa, Ethiopia*

Correspondence should be addressed to Venkatesa Prabhu Sundramurthy; venkatesa.prabhu@aastu.edu.et

Received 8 November 2021; Revised 15 December 2021; Accepted 20 December 2021; Published 7 January 2022

Academic Editor: Enas Abdulhay

Authentication is a suitable form of restricting the network from different types of attacks, especially in case of fifth-generation telecommunication networks, especially in healthcare applications. The handover and authentication mechanism are one such type that enables mitigation of attacks in health-related services. In this paper, we model an evolutionary model that uses a fuzzy evolutionary model in maintaining the handover and key management to improve the performance of authentication in nanocore technology-based 5G networks. The model is designed in such a way that it minimizes the delays and complexity while authenticating the networks in 5G networks. The attacks are mitigated using an evolutionary model when it is trained with the relevant attack datasets, and the model is validated to mitigate the attacks. The simulation is conducted to test the efficacy of the model, and the results of simulation show that the proposed method is effective in improving the handling and authentication and mitigation against various types of attacks in mobile health applications.

1. Introduction

In recent times, the mobile and telecommunication devices get faster and more functional with each wireless network applicable on mobile health programs in healthcare. The speeds we have today were made possible by 4G [1]. Nevertheless, 4G networks are nearing their capacity limit as more people get online and demand even more data from their gadgets and smartphones. The researchers are now on the verge of transitioning to 5G, the wireless technology.

The increased traffic can be handled on this network than on Long-Term Evolution (LTE) networks. The 5G mobile network concept is being discussed by both business and academia. Next-generation mobile networks should be in place by 2020, according to current estimates. With increasing data traffic, devices are being studied to see if it is possible to attain 1 ms latency [2]. There will also be new features in 5G, such as the heterogeneous network integration with the network security over reliability and provisioning [3, 4].

As a result of these performance requirements, various 5G network technology solutions have been implemented, including HetNets, software-defined networking (SDN), and more. SDN has gotten a lot of interest recently as a promising new technology for the next generation of wireless mobile networks [5–8]. Control plane and data forwarding are separated or decoupled in an SDN, allowing a centralised controller to take control of the network. The control plane of an SDN network is independent of data forwarding and programmable. This SDN functionality makes network configuration and reconfiguration much simpler [9].

Additionally, it offers excellent security management over network opportunities in terms of adaptability and programmability. In contrast, developing SDN and NFV technologies may run and instantiate networks and their services in order to minimise costs and improve performance [10]. The 5G heterogeneous networks are critical to achieving goals such as low energy consumption, low cost, and full coverage. HetNet heterogeneity allows for more coverage, higher capacity, and improved performance.

Different 5G cells, including relays, microcells, and femtocells are being proposed to support imminent coverage [11]. As a result, the next-generation network is expected to be significantly more heterogeneous, and because of the densified deployment of a small cell, users should expect to see more frequent handoffs [12–21].

Vertical handover is critical in such a heterogeneous environment because it allows different networks to be integrated with one another. As a result, the researchers will be able to take advantage of the best features of existing networks. For a registered and valid user to gain access to network resources, authentication is necessary. Furthermore, mutual authentication can maintain secrecy by protecting communication entities from diverse threats and ensuring the integrity of their data. Due to frequent user movement across multiple networks, a smooth and secure solution for handover authentication is required to protect against various attacks.

In order to provide secured access to users on a foreign network, a rapid and effective authentication mechanism must be designed. However, there are not many studies looking specifically at 5G mobile network architecture and security in mobile healthcare applications.

Due to certificate-based authentication high security and ability to provide authentication, a system based on shared key distribution for certificate authentication is proposed. Thus, users in the 5G network environment can be certified by other networks. It is intended that the effectiveness of security management techniques, as well as the overall network view, will be improved using an evolutionary model. Transport Layer Security (TLS) is used in the proposed approach, but it is enhanced with preinitial authentication, which gives a shared certificate to registered user equipment only. As a result, the suggested system incorporates mutual authentication, key exchange, and agreement components. Data integrity and privacy are also provided as well as resistance against many forms of attacks.

The main contributions are given as follows:

(i) Using the SDN for network management and security, as well as the HAU for seamless and effective handover, helps to create a global perspective of the network.

(ii) To provide great security and mutual authentication, the TLS protocol should be used.

(iii) This ensures that vertical handover processes are consistent and secure because the certificate authentication relies on key distribution that has a fuzzy evolutionary model. The evolutionary model maintains the handover and key management to improve the performance of authentication with nanocore elements in 5G networks.

2. Related Works

By extending the 3GPP LTE hierarchical architecture and integrating the SDN technology, they presented a 5G mobile network architecture that can leverage intelligence and programmable networking capabilities. An authentication handover [22] based on SDN functions is presented in the design, and this allows subscribers to track their movements and their next location to be monitored. As a result, AHM is able to recognise prospective target cells and begin the handover operation to minimise the associated signalling delay.

Symmetric key cryptography and Elliptic Curve Diffie–Hellman are used in [23] to propose an authentication mechanism for LTE networks. With the addition of a local authenticator, they fixed the flaws in the EAP-AKA protocol. As a result, this approach can safeguard user identification against a variety of attacks while also enabling data integrity and mutual authentication across users. In the context of 5G networks, the approach may not be efficient or scalable due to the high number of small cells and users.

He et al. [24] presented a technique based on binary pairing functions to secure the operation of handover and reduce the communication and computation costs as an alternative authentication scheme. The delay can be as high because the authentication server is normally placed remotely, which makes it unsuitable for 5G requirements due to frequent handovers between the authentication server and tiny cell access points.

An evolved packet system in LTE networks was proposed by in [25] to overcome numerous flaws of EAP by lowering computational overhead and authentication latency and satisfying security requirements. EPS uses simple password key exchange. With a secret key, the major goal is to keep the user UE private while also minimising the size of sent messages and speeding up the protocol. The authentication process gets more simplified, but there is a risk of increased delays in 5G small cell networks due to a higher frequency of enquiries.

3. System Model

In order to have robust security against multiple attacks, the heterogeneous 5G mobile network environment should match the criteria of secured data transmission from mobile health applications [26, 27].

The researchers also need to meet the following requirements: mutual authentication, data privacy and integrity, and protection from passive and active attacks such as DoS and Man in the Middle (MitM) attacks. Because millimetre waves have poor signal transmission characteristics and operate at very high frequencies, the 5G mobile network is more heterogeneous, with many tiny cells.

Network accessing over UE differs from that of access points (APs) and evolved network nodes (eNBs). Using 5G multilayer coverage, this heterogeneous paradigm not only keeps up with the progress of existing technologies but also meets the data traffic demand with small cells that provide extremely high throughput and underlying macrocells that provide ubiquitous coverage even with small cell deployment. Minimal power tiny cells are, therefore, expected to be a significant part of the 5G network, enabling users to communicate at low cost while also providing great capacity.

Figure 1 shows the handover authentication unit (HAU) installed in the 5G mobile network SDN controller, which underpins SDN technology.

All 5G access points, base station (BS), and switches are equipped with relevant SDN protocols to support SDN-enabled 5G networks. To ensure flawless handover authentication, the implemented HAU must keep tabs on and forecast the locations of registered mobile users and then prepare the necessary BS and APs before the users arrive. The HAU stores and analyses user data by employing a traffic flow filter to collect physical layer attributes from registered users. Once user equipment has been preauthenticated for the first time, data collection will begin.

The study uses a downlink LTE system, where the eNB is placed within the UE (u) set. It is then distributed inside the network coverage range. The eNBand UE is of a single SISO antenna type.

We consider the user set $S = \{1, 2, \ldots, S\}$ with the service set u_s, where $\cup_{s\in S} u_s = u$ and $s \in S$. Each individual user is allowed to authenticate the network for one time $\cap_{s\in S} u_s = \varnothing$.

While TDMA is employed in LTE, the OFDMA technology is used in the multiple access strategy. Due to signalling limits and the assignment of radio resource blocks, this is taken into account. The LTE system places the K RBs in k sets, which are then distributed. The TTI is the period of time during which the UE is given access to the RRA algorithm-allocated resources. The TTI here is the same as the RB timing duration, and each RB is assigned to a single UE for the period of a single TTI.

Each TTI complex channel coefficient $h_{u,k}$ contains the propagation effects over the LTE channel, such as shadowing, path loss, and small-scale fading UE ($u \in U$) and eNB over RB ($k \in K$). Channel response is referred to as a complex channel coefficient because coherence is greater than RB; hence, the channel fades flatly. Subcarrier and the 1st OFDM

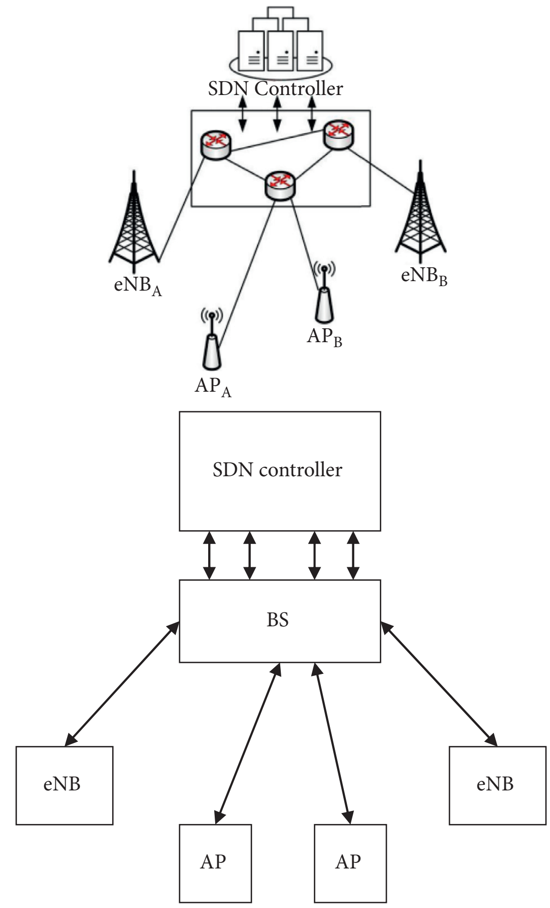

Figure 1: Simplified 5G network architecture with SDN for medical datasets.

symbol are the most common uses for this. In order to estimate the $h_{u,k}$, UE uses pilot symbols, and the data are transmitted via eNB for transmission. This estimates the channel $\widehat{h}_{u,k}$ to be as, and it is modelled as follows:

$$\widehat{h}_{u,k} = \sqrt{(1-\xi)h_{u,k}} + \sqrt{\xi_\eta}, \tag{1}$$

where $\xi \in (0, 1)$- channel estimation degradation and $\eta \in C$- channel estimation error.

The channel estimation error is modelled as a random variable as follows:

$$E\left\{|\eta|^2\right\} = E\left\{\left|h_{u,k}\right|^2\right\}. \tag{2}$$

The current research finds the authentication error linked to channel estimate errors, and the parameter ξ is assessed depending on the impact of those flaws. Finally, reports are taken into account at each TTI, and the eNB obtains measurements immediately.

Additionally, the estimated instantaneous SNR $\widehat{\gamma}_{u,k}$ for each TTI is determined as follows:

$$\widehat{\gamma}_{u,k} = \frac{p_{u,k}\left|\widehat{h}_{u,k}\right|^2}{\sigma^2}, \tag{3}$$

where $p_{u,k}$- eNB power and σ^2- AWGN power.

The link adaptation mechanism, which is employed in LTE as well, selects the MCS (m) from a list of MCSs using eNB (M).

When applied to the set, the MCS selection employs $\hat{\gamma}_{u,k}$ and considers $M = |M|$ with varying MCS, where $|\cdot|$ specifies the cardinality. The UE u in k-related MCS $m_{u,k}$ is determined as follows:

$$m_{u,k} = f\left(\hat{\gamma}_{u,k}\right), \tag{4}$$

where $f\,(\hat{\gamma}_{u,k})$- link adaptation function.

The eNB used in this study selects the superior MCS from among the available UE, resulting in a higher data rate per unit of network power consumed.

UE uses MCS to transmit information to the eNB, which assures the block error rate value. The needed block error rate value is utilised to acquire the link adaption curve with minimal SNR $\hat{\gamma}_{u,k,m}$, and it is evaluated as follows:

$$\hat{\gamma}_{u,k,m} = f^{-1}\left(m_{u,k}\right), \tag{5}$$

where $f^{-1}(\cdot)$- inverse link adaptation function.

The throughput rate $r_{u,k,m}$ over a user k of UE u through a multichannel system m is illustrated as follows:

$$R_u = \sum_{k=1}^{K=|K|} \sum_{m=1}^{M=|M|} r_{u,k,m} x_{u,k,m}, \tag{6}$$

where $x_{u,k,m}$- assignment allocation index.

The authentication τ_u for the UE u is obtained via R_u rate using $\varphi(\cdot)$ function as follows:

$$\tau_u = \phi\left(R_u\right). \tag{7}$$

4. Proposed Method

Because the 5G mobile network will be highly heterogeneous, mutual authentication between the users and server is one network criterion. The suggested system makes use of mutual authentication and FEA-TLS security capabilities. Apart from these characteristics, FEA-TLS comes with even more noteworthy ones, including fragmentation, key exchange and agreement, reauthentication, and resilience to MitM and replay attacks.

When it comes to the FEA-TLS protocol specification, the following shows the process of the proposed protocol:

(i) Public key infrastructure is used by FEA-TLS; therefore, certificates are required
(ii) The UE and the authentication server are the first points of contact
(iii) The certification authority issues certificates to authentication servers and user equipment
(iv) The user equipment certificate must be validated with a network server during the UE lifetime
(v) To verify a user certificate, the authentication server needs a certificate from a certification authority

4.1. Proposed FEA-TLS Protocol. According to the estimations, the suggested protocol is more efficient than other evolutionary TLS-based systems when it comes to handover authentication with the signed certificate. It also fits the 5G mobile network requirement for a heterogeneous environment. Key exchanges are made possible with the deployment of this FEA-TLS-based system for authenticating user equipment.

An initial authentication strategy using shared key cryptography is proposed for use in the new protocol, and this key will be utilised by the UE to obtain a certificate and gain access to resources on the foreign network during vertical handover. UE requests for the foreign network certificate rather than transferring it straight from that authority to UE, which is one of the key aspects of the proposed system.

Figure 2 shows the beginning of the handover authentication procedure. Figure 3 shows the process as it continues. As a result, the proposed technique protects the UE identity from being attacked.

4.1.1. Preinitial Authentication. The user equipment will transmit the handover request and physical layer attributes to the home network eNB. The HAU then verifies these data before distributing the symmetric keys. eNB on the home network then responds with symmetric keys from the home networks, as depicted in Figure 2.

4.1.2. FEA-TLS Authentication. Before the UE begins the authentication process, the eNB shares the identity of UE with the AP of a foreign network for the identification verification process that is provided by the UE during the handover request, as illustrated in Figure 3. The UE will now send the AP a start packet. It is common for this AP to send the UE a FEA-TLS request packet. The UE responds to the AP with a packet including identification information.

As soon as the AP receives the UE identification information, it compares it with the UE id received from the eNB in the home network and confirms the information. Additionally, the AP will need to send an empty FEA-TLS/start packet, which is an FEA-TLS-packet type with the start bit set, to the UE during this verification process. The UE will send a welcome message with a cipher message, packet type, a session Id, and a random number to begin the FEA-TLS interaction.

This will be followed by a response from the AP with an EAP request packet with the FEA-TLS packet type along with the hello message and version number along with an acknowledgement to begin key exchange with the AP settings. To verify the certificate, the UE will send an already shared symmetric key along with a signed response from it. This packet is subsequently forwarded to the AP, which verifies and responds with the completed message containing the signed certificate and key of the response of UE authentication to the AP. After receiving the completion handshake message, the UE responds using a null message if

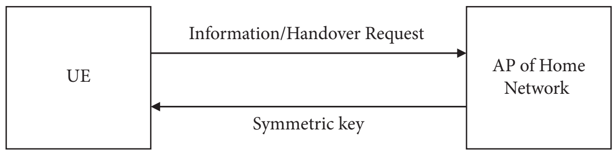

Figure 2: Healthcare security (initial authentication).

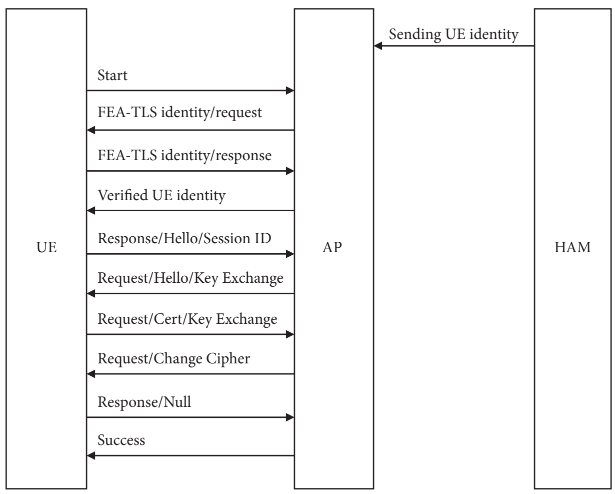

Figure 3: Flow of authentication for medical data.

the verification was successful. This session will come to an end when the AP responds with a success message.

Assume that the home network registers the UE with a SIM and a key is shared between the two networks. Therefore, when the UE leaves its home network and enters a foreign network, it must gain access to the foreign network. Both parties to the roaming agreement have signed it, as shown in Figure 3.

Public keys that are known by the UE, home network, and the foreign network tend to get shared between the networks via the proposed FEA-TLS authentication. A certificate issued by the certification body is also present on both networks. SDN controller HAU shares user identity with the foreign network AP prior authentication based on UE location.

By eliminating the need to communicate identity verification to the HAU, this AP can perform UE identity verification faster, allowing for seamless authentication handover for the UE. As soon as the UE returns to its home network, the HAU will see if the new UE it just added is in the list of previously registered ones. As long as the UE is on the list, HAU will have access to its own private network.

5. Security Verification

This section conducts both informal analyses as shown below.

5.1. Mutual Authentication. FEA-TLS provides mutual authentication between the HAU and UE. With a handover request, the UE challenges the HAU preinitial authentication. Only the HAU has access to UE secret key, which grants UE network access.

5.2. User Identity Protection. The UE will have access to foreign Aps, if it requests a certificate. By distributing certificates in a fresh order, random variable, time, and the UE location are obscured. Each time a new user registers, the generation of temporary Id is carried out using a randomly generated variable. Aside from that, this temporary identifier will be altered at random, making it impossible to track down the original registrant. HAU in SDN has access to the user current location. By doing this, the user equipment identity is protected.

5.3. Signaling Overhead. In the FEA-TLS approach, authentication takes place between an AP of a foreign network and a user. Due to the SDN-enabled 5G network, there are no additional user ID verification and round-trip delays, and it takes much less time.

5.4. Passive Attack. A valid request packet may be obtained with this technique, but the message cannot be decrypted without private key. The fact that SHA-1 features a mechanism for generating keys makes it difficult to decrypt without the private key. As a result, the study designed the evolutionary system to be resistant to a passive attack.

5.5. MitM Attack. MitM attacks will not be able to succeed against this model. When an identity of the user is secured by a temporary public key pair issued by the UE, attackers cannot get their hands on or change the key, and thus, it is useless to them. As a result, the HAU only shares the UE identification with the AP when the UE makes a handover request and finds the UE position. As a result, passive attacks are not a problem.

6. Results and Discussion

In this section, the performance evaluation is conducted on fuzzy evolutionary algorithm to control the HAU. The model is compared with existing methods in terms of various metrics including space complexity, communication overheads, executed handovers, and latency in handover.

6.1. Communication Overheads. Figure 4 shows the communication overhead between FEA-TLS on HAU with existing fuzzy and TLS methods. The results of communication overhead show that the proposed FEA-TLS achieves reduced communication overhead than the other methods.

6.2. Space Complexities. Figure 5 shows the space complexity between FEA-TLS on HAU with existing fuzzy and TLS methods. The results of space complexity show that the proposed FEA-TLS achieves reduced space complexity than the other methods.

6.3. Handover Latencies. Figure 6 shows the handover latencies between FEA-TLS on HAU with existing fuzzy and TLS methods. The results of handover latency show that the proposed FEA-TLS achieves reduced handover latency than the other methods.

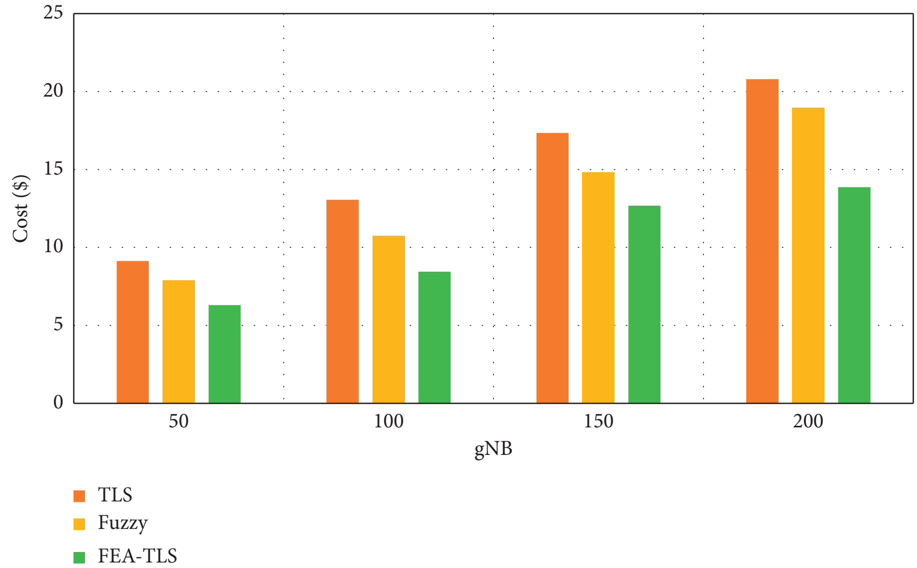

Figure 4: Communication overhead in the medical database.

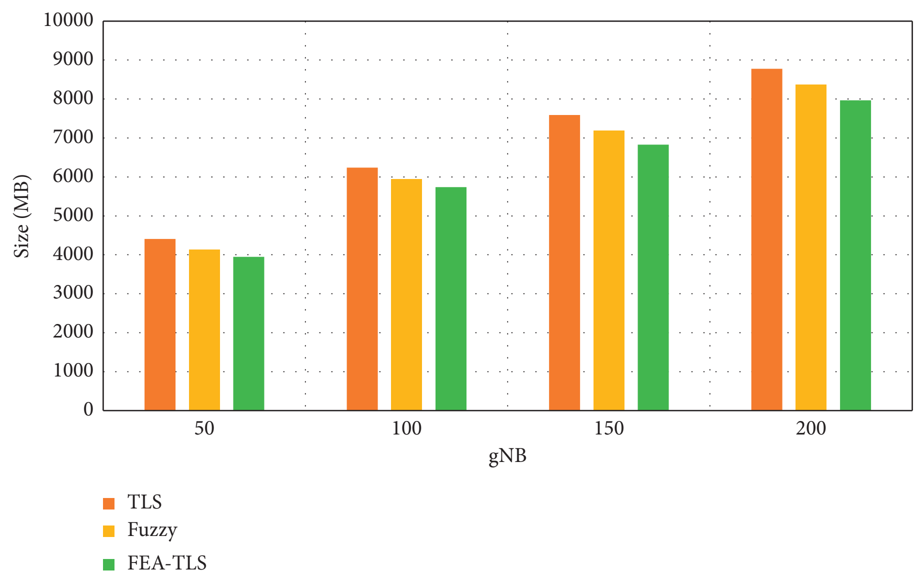

Figure 5: Space complexity for medical databases.

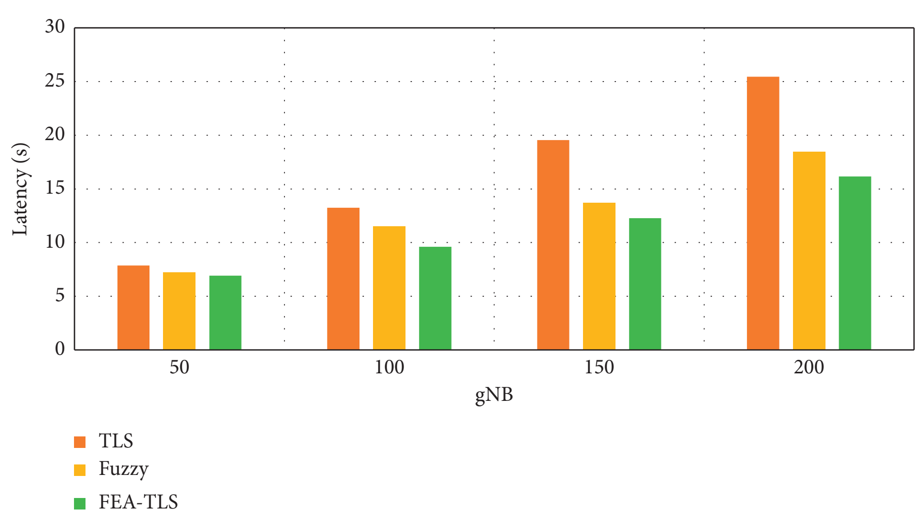

Figure 6: Handover latency in patients' history.

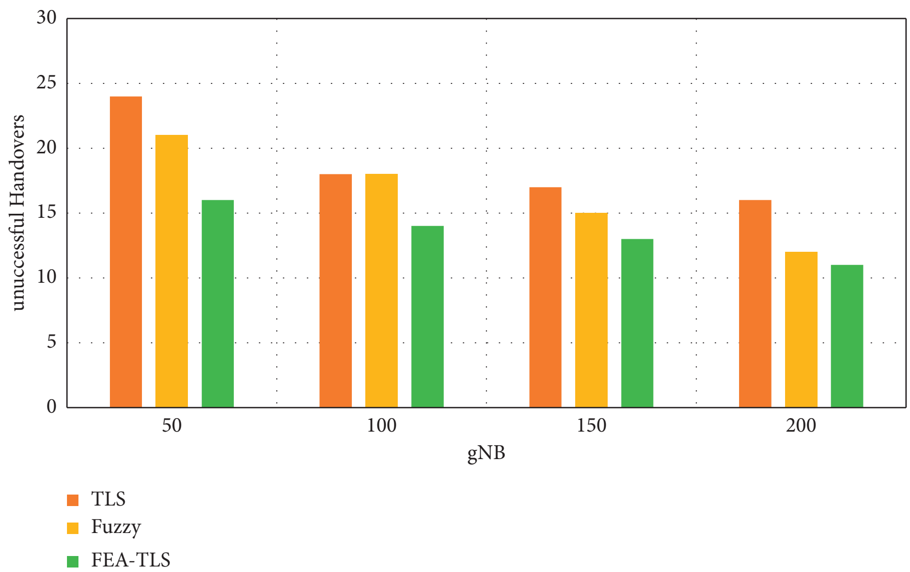

Figure 7: Executed handover security in the medical Mongo database.

6.4. Executed Handovers. Figure 7 shows the executed handover between FEA-TLS on HAU with existing fuzzy and TLS methods. The results of executed handover show that the proposed FEA-TLS achieves highly successful handover than the other methods.

From the results, it cloud be inferred that the proposed method achieves higher rate of accuracy in detecting the attacks while the data are transmitted from mobile health programs in healthcare. This shows higher efficacy in improving the mitigation of attacks in the healthcare field.

7. Conclusions

In this paper, we proposed the fuzzy evolutionary model for handover and key management in 5G networks for improving the network performance in terms of authentication in mobile health programs. The use of nanocore elements in 5G hardware with the fuzzy evolutionary model reduces the computational complexity and delays while authenticating the messages and users. The evolutionary model mitigates the attacks during the training process with relevant datasets, and the validation shows improved detection accuracy for the mitigation of the attacks. The simulation shows an improved efficacy of the fuzzy evolutionary model in terms of improved accuracy, and furthermore, it shows secured authentication of input messages and users into the network against various type of attacks in mobile health programs. The space complexity, handover latency, and executed handovers are minimal in the fuzzy evolutionary model than in other methods.

Data Availability

The datasets used and/or analyzed during the current study are available from the corresponding author on reasonable request.

Conflicts of Interest

There are no conflicts of interest.

References

[1] M. M. Aslam, L. Du, X. Zhang, Y. Chen, Z. Ahmed, and B. Qureshi, "Sixth generation (6G) cognitive radio network (CRN) application, requirements, security issues, and key challenges," *Wireless Communications and Mobile Computing*, vol. 2021, Article ID 1331428, 18 pages, 2021.

[2] Q. Wang, C. Cheng, and L. Zuo, "Analysis and improvement of a NTRU-based handover authentication scheme," *IEEE Communications Letters*, vol. 23, no. 10, pp. 1692–1695, 2019.

[3] S. A. H. Mohsan and H. Amjad, "A comprehensive survey on hybrid wireless networks: practical considerations, challenges, applications and research directions," *Optical and Quantum Electronics*, vol. 53, no. 9, pp. 1–56, 2021.

[4] P. Ranaweera, A. D. Jurcut, and M. Liyanage, "Survey on multi-access edge computing security and privacy," *IEEE Communications Surveys & Tutorials*, vol. 23, no. 2, pp. 1078–1124, 2021.

[5] Y. Zeng, H. Guang, and G. Li, "Attribute-based anonymous handover authentication protocol for wireless networks," *Security and Communication Networks*, vol. 2018, Article ID 8470949, 9 pages, 2018.

[6] K. V. Singh and M. Pandey, "SDN-based fast handover approach to improve the QoS of video streaming over Wi-Fi networks," in *Computing and Network Sustainability*, pp. 137–146, Springer, Singapore, 2019.

[7] J. Mo, Z. Hu, and Y. Lin, "An efficient privacy-preserving handover authentication scheme for mobile wireless network," in *Proceedings of the International Conference on Cloud Computing and Security*, pp. 490–505, Springer, Singapore, 2018, June.

[8] G. Li, W. Chen, B. Zhang, and S. Lu, "A fine-grained anonymous handover authentication protocol based on consortium blockchain for wireless networks," *Journal of Parallel and Distributed Computing*, vol. 157, pp. 157–167, 2021.

[9] P. Ranaweera, A. Jurcut, and M. Liyanage, “MEC-enabled 5G use cases: a survey on security vulnerabilities and countermeasures,” *ACM Computing Surveys*, vol. 54, no. 9, pp. 1–37, 2021.
[10] R. M. Abdullah, A. Z. Abualkishik, and A. A. Alwan, “Improved handover decision algorithm using multiple criteria,” *Procedia Computer Science*, vol. 141, pp. 32–39, 2018.
[11] H. Yu and M. Zhou, “Improved handover algorithm to avoid duplication AAA authentication in proxy MIPv6,” *International journal of Computer Networks & Communications*, vol. 10, pp. 75–85, 2018.
[12] M. Faheem, S. B. H. Shah, R. A. Butt et al., “Smart grid communication and information technologies in the perspective of Industry 4.0: opportunities and challenges,” *Computer Science Review*, vol. 30, pp. 1–30, 2018.
[13] F. Guo, F. R. Yu, H. Zhang, X. Li, H. Ji, and V. C. Leung, “Enabling massive IoT toward 6G: a comprehensive survey,” *IEEE Internet of Things Journal*, vol. 8, 2021.
[14] S. A. Chaudhry, M. S. Farash, H. Naqvi, S. H. Islam, and T. Shon, “A robust and efficient privacy aware handover authentication scheme for wireless networks,” *Wireless Personal Communications*, vol. 93, no. 2, pp. 311–335, 2017.
[15] Y. Xie, L. Wu, N. Kumar, and J. Shen, “Analysis and improvement of a privacy-aware handover authentication scheme for wireless network,” *Wireless Personal Communications*, vol. 93, no. 2, pp. 523–541, 2017.
[16] Z. Zhou, H. Zhang, and Z. Sun, “An improved privacy-aware handoff authentication protocol for VANETs,” *Wireless Personal Communications*, vol. 97, no. 3, pp. 3601–3618, 2017.
[17] P. Wang, Y. Liu, and S. Lv, “An improved lightweight identity authentication protocol for VANET,” *Journal of Internet Technology*, vol. 20, no. 5, pp. 1491–1504, 2019.
[18] S. O. Ogundoyin, “A provably secure pairing-free anonymous handover authentication protocol for mobile wireless networks,” *International Journal of Mobile Communications*, vol. 18, no. 5, pp. 509–539, 2020.
[19] Y. Wang, W. Zhang, X. Wang, W. Guo, M. K. Khan, and P. Fan, “Improving the security of LTE-R for high-speed railway: from the access authentication view,” *IEEE Transactions on Intelligent Transportation Systems*, 2020.
[20] D. He, S. Zeadally, L. Wu, and H. Wang, “Analysis of handover authentication protocols for mobile wireless networks using identity-based public key cryptography,” *Computer Networks*, vol. 128, pp. 154–163, 2017.
[21] Y. Guo and Y. Guo, “FogHA: an efficient handover authentication for mobile devices in fog computing,” *Computers & Security*, Article ID 102358, 2021.
[22] X. Duan and X. Wang, “Authentication handover and privacy protection in 5G hetnets using software-defined networking,” *IEEE Communications Magazine*, vol. 53, no. 4, pp. 28–35, 2015.
[23] Y. E. H. El Idrissi, N. Zahid, and M. Jedra, “Security analysis of 3GPP (LTE)—WLAN interworking and a new local authentication method based on EAP-AKA,” in *Proceedings of the First International Conference on Future Generation Communication Technologies*, pp. 137–142, IEEE, London UK, 2012 December.
[24] D. He, C. Chen, S. Chan, and J. Bu, “Secure and efficient handover authentication based on bilinear pairing functions,” *IEEE Transactions on Wireless Communications*, vol. 11, no. 1, pp. 48–53, 2011.
[25] K. A. Alezabi, F. Hashim, S. J. Hashim, and B. M. Ali, “An efficient authentication and key agreement protocol for 4G (LTE) networks,” in *Proceedings of the 2014 IEEE Region 10 Symposium*, pp. 502–507, IEEE, Kualumpur, Malaysia, 2014 April.
[26] X. Yan and X. Ren, “5G edge computing enabled directional data collection for medical community electronic health records,” *Journal of Healthcare Engineering*, vol. 2021, Article ID 5598077, 12 pages, 2021.
[27] K. Hameed, I. S. Bajwa, N. Sarwar, W. Anwar, Z. Mushtaq, and T. Rashid, “Integration of 5G and block-chain technologies in smart telemedicine using IoT,” *Journal of Healthcare Engineering*, vol. 2021, Article ID 8814364, 18 pages, 2021.

Hindawi
Journal of Healthcare Engineering
Volume 2022, Article ID 9048123, 9 pages
https://doi.org/10.1155/2022/9048123

Research Article

Multispectral Image under Tissue Classification Algorithm in Screening of Cervical Cancer

Pei Wang,[1] **Shuwei Wang**,[2] **Yuan Zhang**,[1] **and Xiaoyan Duan**[1]

[1]*Department of Gynaecology, Hebei Provincial People's Hospital, Shijiazhuang 050051, Hebei, China*
[2]*Department of Gynaecology, Chengde Hospital of Traditional Chinese Medicine, Chengde 067000, Hebei, China*

Correspondence should be addressed to Pei Wang; 06122311@cumt.edu.cn

Received 13 September 2021; Revised 6 December 2021; Accepted 10 December 2021; Published 7 January 2022

Academic Editor: Enas Abdulhay

The objectives of this study were to improve the efficiency and accuracy of early clinical diagnosis of cervical cancer and to explore the application of tissue classification algorithm combined with multispectral imaging in screening of cervical cancer. 50 patients with suspected cervical cancer were selected. Firstly, the multispectral imaging technology was used to collect the multispectral images of the cervical tissues of 50 patients under the conventional white light waveband, the narrowband green light waveband, and the narrowband blue light waveband. Secondly, the collected multispectral images were fused, and then the tissue classification algorithm was used to segment the diseased area according to the difference between the cervical tissues without lesions and the cervical tissues with lesions. The difference in the contrast and other characteristics of the multiband spectrum fusion image would segment the diseased area, which was compared with the results of the disease examination. The average gradient, standard deviation (SD), and image entropy were adopted to evaluate the image quality, and the sensitivity and specificity were selected to evaluate the clinical application value of discussed method. The fused spectral image was compared with the image without lesions, it was found that there was a clear difference, and the fused multispectral image showed a contrast of 0.7549, which was also higher than that before fusion (0.4716), showing statistical difference ($P < 0.05$). The average gradient, SD, and image entropy of the multispectral image assisted by the tissue classification algorithm were 2.0765, 65.2579, and 4.974, respectively, showing statistical difference ($P < 0.05$). Compared with the three reported indicators, the values of the algorithm in this study were higher. The sensitivity and specificity of the multispectral image with the tissue classification algorithm were 85.3% and 70.8%, respectively, which were both greater than those of the image without the algorithm. It showed that the multispectral image assisted by tissue classification algorithm can effectively screen the cervical cancer and can quickly, efficiently, and safely segment the cervical tissue from the lesion area and the nonlesion area. The segmentation result was the same as that of the doctor's disease examination, indicating that it showed high clinical application value. This provided an effective reference for the clinical application of multispectral imaging technology assisted by tissue classification algorithm in the early screening and diagnosis of cervical cancer.

1. Introduction

Cervical cancer is a common malignant tumor in women. Its incidence ranks third in the world and ranks among the top three fatal gynecological tumors in most developing countries. According to a report from the World Health Organization (WHO), approximately 550,000 women worldwide become patients with new cases of cervical cancer each year, and more than half of these patients die of cervical cancer. As a developing country, China has more than 150,000 new patients with cervical cancer each year, of which more than 60,000 fatal cases accounting for more than 30% of new female patients with cervical cancer in the world. In recent years, the number of young female patients has gradually increased [1]. The site of cervical cancer is in the female cervix, and the cause is the growth and proliferation of abnormal cells in the female body. Early cervical cancer generally has no special differential symptoms, and late cervical cancer can develop into cervical cancer in situ and cervical invasive cancer [2]. Some countries under development and with scarce medical resources lack advanced medical resources and inspection equipment, so that women cannot get timely early screening and diagnosis, leading to cervical cancer gradually becoming the death killer of women.

The early diagnosis and identification methods of cervical cancer mainly include cell smear, colposcopy, and biopsy [3]. These examination methods have different shortcomings. For example, the cell smear method can easily lead to missed diagnosis of cancer cells because of the limited available cell smears; and the colposcopy method is mainly the result of the subjective judgment of the colposcopy doctor, so it is highly subjective and cannot make individualized diagnosis of patients. For female patients, the biopsy method needs to bear a physical and psychological burden, the test results are usually not available in a short time, and it is easy to delay the patient's treatment opportunity [4,5]. Cervical cancerous tissue will undergo physiological and pathological changes, which will cause optical changes in the tissue. Optical pathological diagnosis can avoid the above defects and has the characteristics of noninvasive and rapid. Especially, multispectral imaging technology has been widely used in recent years. Multispectral imaging technology is a new photoelectric detection technology. As an analysis tool, it has been widely used in many fields including biomedicine due to its unique technical advantages of both spectral detection and imaging. The biggest difference between multispectral imaging technology and ordinary imaging technology is that it converts black and white imaging or red, blue, and green imaging with low color accuracy into spectral imaging with higher color dimensions. A set of image sequences collected at different band positions are used to accurately record the "color" information of the marker sample and to obtain a high-resolution spectrum of each pixel in the image, instead of the three primary color images seen by the naked eye. With the assistance of multispectral fluorescence microscopes, quantum dots can achieve high accuracy and sensitive quantitative detection of molecular information, in situ and real-time co-imaging, and multimolecule co-imaging and interaction. Multispectral fluorescence imaging based on quantum dots can help improve tumor classification and predict tumor prognosis. Hu and Ma [6] used the snapshot multispectral narrowband imaging technology to accelerate the spectral image acquisition process, improve the grayscale contrast between tissues of different disease levels, and realize the automatic classification of cervical tissue lesions with high frame rate.

In order to better screen for cervical cancer, it is necessary to identify and segment the image of the lesion. At present, the extraction of cervical cancer image lesions is generally performed by doctors for manual segmentation, which depends on the doctor's theoretical knowledge and experience, and is highly subjective. In addition, it is time-consuming and labor-intensive, more and more images need to be processed, and manual segmentation obviously cannot meet the demand. With the application of computer algorithms in medical imaging, the use of intelligent algorithms for automatic or semiautomatic segmentation of lesions can greatly reduce the workload of doctors. The tissue classification algorithm is through the aid of computer algorithms; all elements in the original image will be summarized into several clusters with different differences [7]. The elements in the cluster have similar elements, but there are big differences between clusters [8]. That is, after inputting the original feature map, it is a computer technology that divides the feature regions of different images. It includes several modules such as computer signal processing, image analysis, image fusion, segmentation, and recombination. The type, size, range, shape, and other information of the target are displayed in the figure in the form of division, and the final inspector will get the most intuitive image morphology [9]. At present, there have been research projects on applying tissue classification algorithm to the research of lung cancer, and there are very few research projects corresponding to cervical cancer. Therefore, the characteristic wavelength of whether the lesion occurs were adopted in this study, and the tissue classification algorithm-assisted multispectral imaging technology was applied to the screening and diagnosis of cervical cancer patients, so as to realize the early screening and discrimination of cervical cancer, providing theoretical reference for clinically rapid and efficient screening of cervical cancer.

2. Methods

2.1. Research Objects. In this study, 50 patients with suspected cervical cancer from October 2019 to October 2020 in the hospital were selected as the research objects. They were between 25 and 55 years old, with an average age of 40.2 ± 5.3 years.

The inclusion criteria were defined as follows: patients who were between 25 and 55 years old; patients with no pregnancy and no sexual history during the experimental study; patients with no symptoms of reproductive tract infections or bleeding; and patients without vagina operations such as lavage.

The exclusion criteria were defined as follows: patients with reproductive tract co-infected diseases or vaginal bleeding; women during pregnancy and menstrual period; patients who underwent cervical resection or took drugs to wash and treat the cervix within 48 hours; patients with mental or consciousness disorder and poor compliance; and patients who were allergic to alcohol.

All patients in this study and their authorized persons had signed the informed consent forms, and the study had been approved by the Medical Ethics Committee of the hospital.

2.2. Principle of Multispectral Imaging for Cervical Tissue Examination. The micro-snapshot narrowband multispectral imaging system was adopted in this study. Three narrowband multispectral images of 50 patients' cervical tissues were collected under conventional white light waveband, narrowband green light waveband, and narrowband blue light waveband, with the number of acquisition frames of about 25 fps. The specific details are shown in Figure 1.

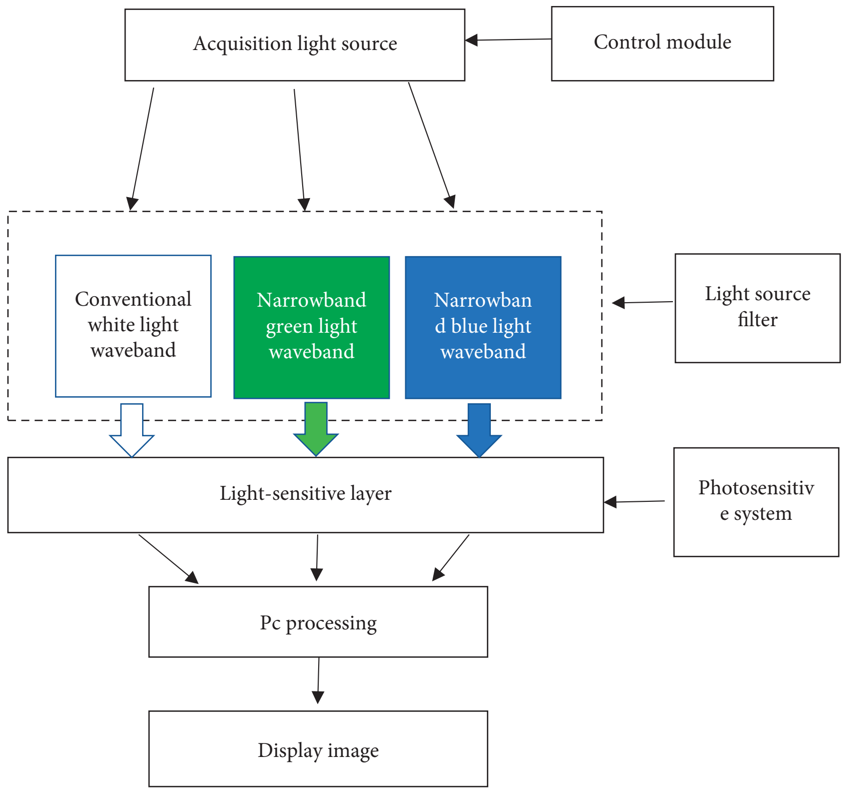

Figure 1: Schematic diagram of multispectral imaging system.

2.3. Multiband Image Fusion. Before the organization algorithm, the multispectral image was firstly fused to eliminate the influence of factors such as different wavebands, degree of filtering, and conversion rate with different wavebands [9]. In this study, contrast was used to measure image clarity, and the below equation is taken as the calculation standard:

$$\text{Contrast} = \sum_{\delta} \delta(i, j)^2 p_{\delta}(i, j). \tag{1}$$

In (1), $\delta(i,j) = |i - j|$ represents the difference in gray value between two adjacent image elements and $p_{\delta}(i,j)$ refers to the distribution probability of two image elements when the gray value between the two adjacent image elements was δ.

2.4. Multispectral Fusion Image Combined with Tissue Classification Algorithm. Due to the difference in the contrast of the multiband spectrum fusion image between the uninfected cervical tissue and the diseased cervical tissue, the gray value of the lesion area is generally slightly smaller than that of the normal tissue [10]. Therefore, the tissue classification algorithm was used to classify the spectra of different tissues in this study. The tissue classification algorithm is to use the band characteristics or spatial characteristics of the multispectral image as the boundary between normal and diseased, so that the elements on the spectrum are divided into different levels or categories, thereby realizing alternative subjective analysis [11]. The tissue classification algorithm used in this study was mainly to adopt the K-value clustering algorithm to summarize and analyze the physiological and pathological regional features of the cervical cancer site and then apply the corresponding regional features to analyze the cervical tissues of 50 patients with no lesions. The second step was to convert a monochrome black and white image into a distribution image of a given color. The algorithm principle is shown in Figure 2. The K-means clustering (KMC) algorithm was adopted to divide the lesion area and the nonlesion area, and then a single gray-scale image was stored into a multicolor image that can be intuitively distinguished. On the one hand, it improved the precise identification of the target area on multispectral imaging and increased the feature discrimination of the image and the features that can be easily distinguished; on the other hand, it can also make the clinical imaging physicians more acceptable when judging the multispectral imaging map intuitively [12]. Therefore, after the KMC algorithm obtained the gray image, the most classic Bayer image color array format interpolation algorithm was used. In this study, the diseased cervical tissue was marked in red, and the normal cervical tissue was marked in green.

2.5. Evaluation Indicators for Tissue Classification Algorithm-Assisted Multispectral Image. In order not to be affected by subjective evaluation, a quantitative evaluation equation was adopted to evaluate the image quality, so as to evaluate the restored color images through quantitative indicators to improve the accuracy of image discrimination. The average gradient, SD, and image entropy were selected as the evaluation indicators to restore the image results. The results

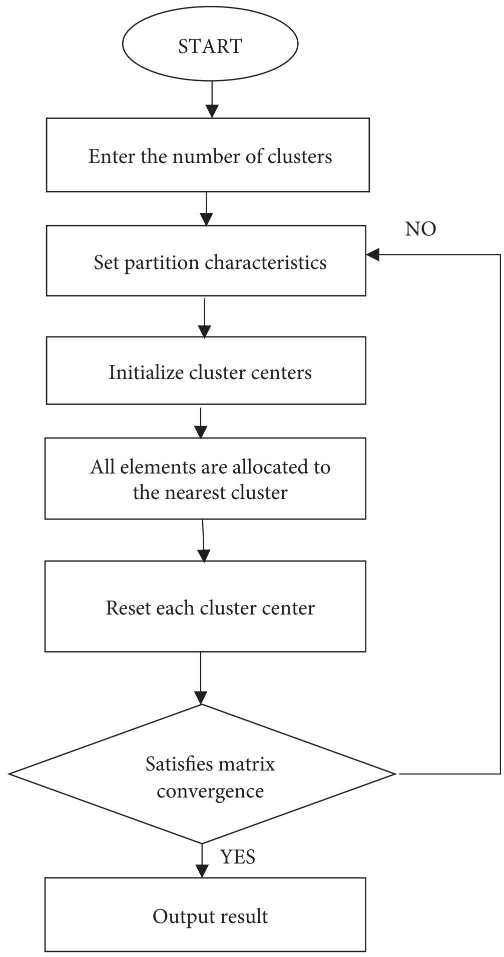

Figure 2: The algorithm principle.

of this study were compared with the reported International Commission on Illumination (CIE) color reduction method [13]. In the below equations, G represents the average gradient, which was the average of the image gray value change rate and used to reflect the sharpness of the image; and the larger the G, the better the image; SD represents the dispersion of the pixels and the average value in the image. Generally, the larger the SD value, the higher the image pixels and the better the quality; H is the image entropy, which represents the characteristics of all gray values of each image. The larger the value of G, the more average information the image contains and the better the image quality.

$$G = \frac{1}{M \times N} \sum_{i=1}^{M} \sum_{j=1}^{N} \sqrt{\frac{\Delta f/\Delta x^2 + \Delta f/\Delta y^2}{2}}, \quad (2)$$

$$SD = \sqrt{\frac{1}{M \times N} \sum_{i=1}^{M} \sum_{j=1}^{N} \left(p_{i,j} - \overline{x}\right)^2}, \quad (3)$$

$$H = -\sum_{i=0}^{n-1} p_i \log_2 p_i. \quad (4)$$

In (2) above, $M \times N$ represents the size of the image; i and j represent the pixel value of an element in the i-th row and j-th column, respectively; $\Delta f/\Delta x$ is the image on the X axis (horizontal direction); and $\Delta f/\Delta y$ is the gradient of the image on the Y axis (vertical direction). In (3), $P_{i,j}$ represents the pixel value of the i-th row and j column; and $\overline{x}$ represents the average value of the image. In the above equation (4), $n-1$ represents the $n-1$ gray levels of the image, and p_i refers to the probability of occurrence of the i-th gray value.

2.6. Indicators for Combination of Algorithm and Clinical Examination. The aforementioned tissue classification algorithm combined with multispectral imaging was used to systematically examine the cervical cancers of 50 patients. In order to prevent infection, in all patients were used disposable operating tools during the examination, and experienced imaging physicians and gynecologists perform biopsy sampling, detection, image collection, and analysis of results. At least 3 test points were collected for each patient. Sensitivity and specificity were selected as the indicators of the algorithm in clinical multispectral imaging.

$$Se = \frac{A}{A + C} \times 100\%. \quad (5)$$

$$Sp = \frac{B}{C + B} \times 100\%. \quad (6)$$

In equations (5) and (6) above, *Se* and *Sp* refer to the sensitivity and specificity, respectively; *A* means that the results of the disease examination and the algorithm check of this research were both positive (with disease); *B* means that the results of the disease examination and the algorithm check of this study were both negative (no disease); *C* means that the result of the disease examination was positive and the result of algorithm adopted in this study was negative; and *D* means that the side-by-side result was negative and the result of this algorithm was positive.

3. Results

3.1. Multiband Image Fusion Results. After all the cervical tissues were preprocessed, the images were fused and processed according to whether different cervical tissues had different characteristic bands and response to light. It was found that there was a great difference between the fused spectral image 3(b) and the image 3(a) without lesions. At the same time, it was found that the contrast of the fused spectral image was 0.7549, which was also higher than the contrast of 0.4716 after the fusion, showing statistical difference ($P < 0.05$). It indicated that the separation of the fused image was improved and the image was clearer, as shown in Figures 3 and 4.

3.2. Algorithm-Assisted Spectral Image Results. The histological algorithm and multispectral image were combined to perform K-means unsupervised classification processing and color restoration technology on the collected cervical tissue. Figure 5(a) shows the 3 detection points of the cervical tissue and whether there were lesions. Figure 5(b) shows the multispectral image after fusion processing and the location of the detection points on the image. Figure 5(c) shows the tissue classification algorithm-assisted fusion processing spectral cervical tissue and the results of segmentation in this image. The green mark in the figure is the area without lesions, while the red mark is the area with lesions. In the results of tissue classification diagnosis, Figure 5(c) is more intuitive than Figures 5(a) and 5(b) for whether the cervical tissue was cancerous or not and its scope, making it easier for clinicians to diagnose quickly.

3.3. Evaluation Indicators for Tissue Algorithm Image. The restored image was evaluated using three indicators. As given in Figure 6, the multispectral image average gradient, SD, and image entropy in this study based on the tissue classification algorithm were 2.0765, 65.2579, and 4.974, respectively, which were higher in contrast to the reported values (1.1777, 50.4657, and 3.9025, respectively), showing statistical difference ($P < 0.05$). It disclosed that the multispectral cervical tissue image based on the tissue classification algorithm was clearer, the segmentation of the lesion was clearer, and the overall quality of the image was better. Therefore, it could be applied in clinics to assist doctors in effectively completing the diagnosis of cervical cancer.

3.4. Results on Clinical Examination Indicators. To test the clinical performance of the tissue classification algorithm for cervical cancer tissue screening, the overall performance was evaluated by using two indicators (sensitivity and specificity). The multispectral image was compared with the tissue classification algorithm and the multispectral image without the algorithm. It was found (as illustrated in Figure 7) that the sensitivity and the specificity of the multispectral image with the tissue classification algorithm were 85.3% and 70.8%, respectively, both of which were larger than those of the images without the algorithm. Such results suggested that the use of tissue classification algorithm to assist multispectral imaging in screening cervical cancer showed higher accuracy and clinical application value.

4. Discussion

There are nearly 150,000 new cases of cervical cancer in China each year, and deaths due to cervical cancer account for nearly 20% of the female tumor deaths all over the world. The main cause of cervical cancer is that women are infected by human papillomavirus (HPV) [14]. Infection with high-risk HPV can cause abnormal cancer of the cervix and cause epithelial damage of the cervix. Women who are infected with high-risk HPV, without effective and timely treatment, will have a 10% chance of developing persistent HPV. Persistent HPV will continue to infect epithelial cells in the cervical tissue, causing heterogeneous proliferation of cervical epithelial cells, triggering cervical epithelial cancer, and greatly increasing the risk of eventually becoming cervical cancer [15]. Some researchers use HPV virus testing to screen cervical cancer to improve the screening and early diagnosis of cervical cancer. The detection method proposed by Digene has little specificity for HPV detection, the specificity for detecting all types of HPV viruses is not more than 10%, and the specificity for detecting high-risk HPV viruses that have been typed is only 30% [16]. Testing for HPV not only is low in specificity and produces unsatisfactory results but also causes physical and psychological distress to women. In recent years, some physicians have used multispectral imaging technology to assist in the screening of cervical cancer. Generally speaking, most new HPV infections do not cause symptoms or the disease can resolve spontaneously, but persistent infection with high-risk HPV (mainly types 16 and 18) may cause precancerous lesions. The high incidence of HPV infection is usually between 16 and 20 years old. It usually heals on its own but may also continue to be infected. If it is not treated in time, it may develop into cervical cancer after 10 to 20 years. Therefore, if cervical cancer can be detected early and treated early, most patients can be cured. Therefore, early screening and diagnosis of cervical cancer is of great significance for

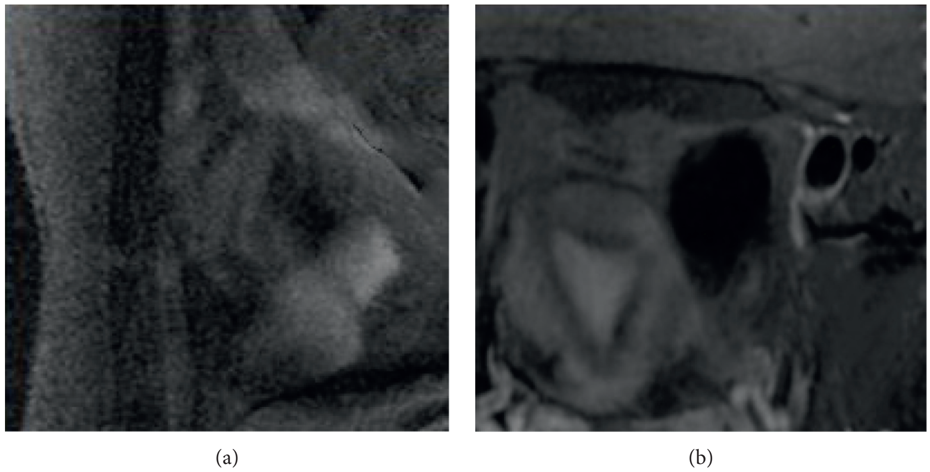

FIGURE 3: Processed images of normal tissue and fusion image: (a) image of the extracted cervical tissue (b) image for lesion area after multispectral fusion processing.

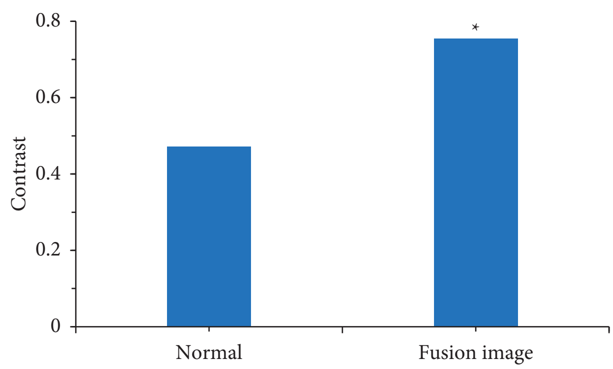

FIGURE 4: Contrast of two extracted images. *Note.* * means the difference was statistically great in contrast to the fusion image ($P < 0.05$).

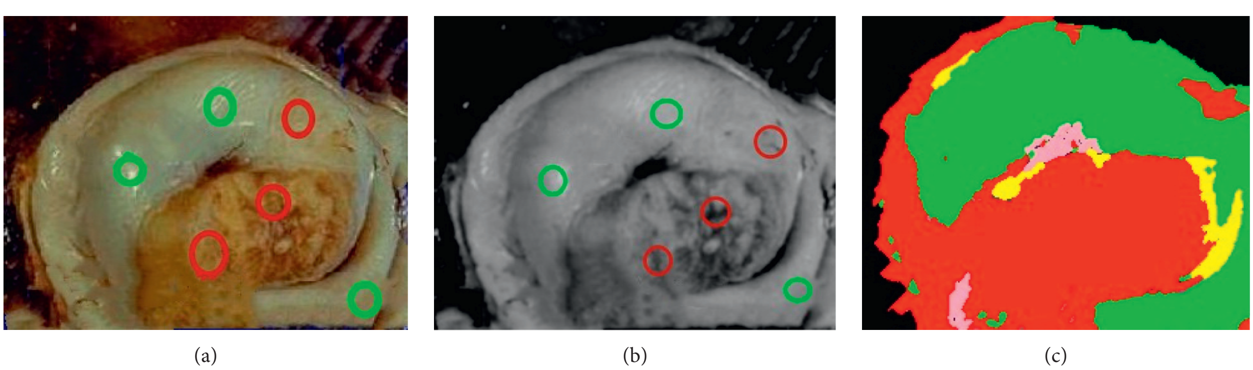

FIGURE 5: Classification and diagnosis results of tissues: (a) the 3 detection points of cervical tissue and whether there were lesions; (b) the multispectral image after fusion processing and the position of the detection points on the image; and (c) the tissue classification algorithm-assisted fusion processing spectral cervical tissue and the result of the segmentation.

reducing the morbidity and mortality of patients. Cervical cancer screening begins with the introduction of Hirsch cytology test into the clinic as a routine screening item. At present, the early diagnosis and identification methods for cervical cancer have different shortcomings. Multispectral imaging examination, as a way of using the optical changes of cervical cancerous tissue, is noninvasive and effective in the screening of cervical cancer.

Multispectral imaging generally refers to a type of spectrum with a narrowband and high resolution and does not specifically refer to a certain spectrum. Its imaging principle is a spatial three-dimensional cube image formed

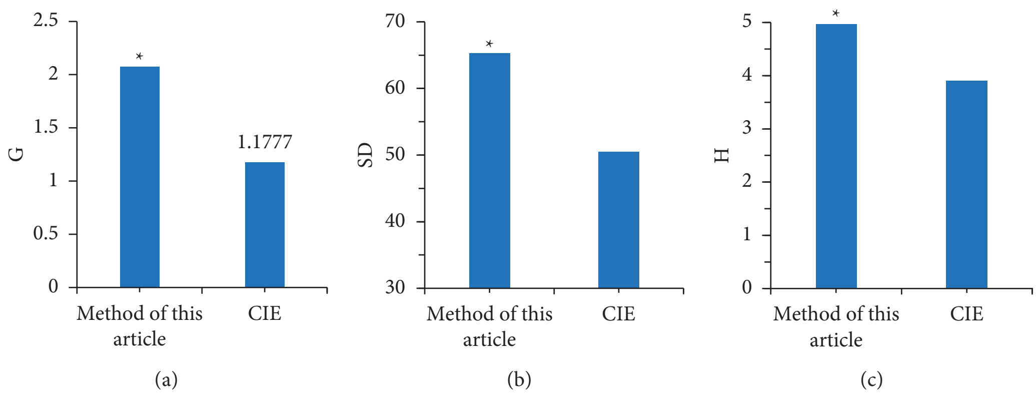

Figure 6: Comparison on evaluation indicators of restored color images: (a) the average gradient of the image; (b) the standard deviation of the image; and (c) the image entropy of the image. *Compared with the CIE algorithm, the difference was statistically significant ($P < 0.05$).

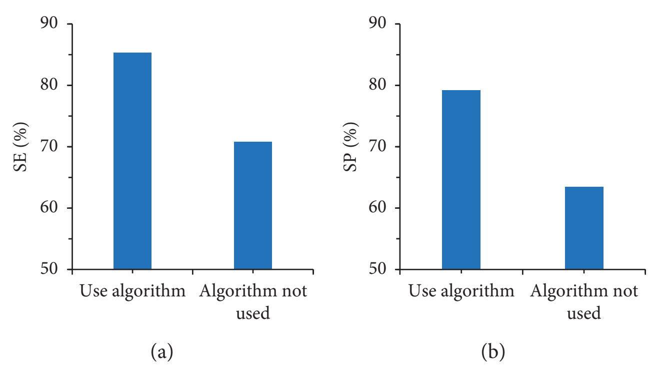

Figure 7: Comparison on sensitivity and specificity: (a) comparison results of sensitivity and (b) comparison results of specificity.

by an optical image at a certain wavelength. Through the multispectral image, not only the image data of the research target at a certain wavelength can be obtained, which is used to obtain the two-dimensional morphological data of the research object, but also the spectral data of a certain wavelength in the three-dimensional space can be used to obtain the research object information contained within the space. Therefore, multispectral imaging technology has been applied to various aspects [17]. Image fusion is also an important point in multispectral imaging technology. The definition of multispectral image fusion is to combine all the characteristic information of the multispectral image at the same wavelength through a specific combination. Relying on their spatial correlation and complementarity, it finally gets a clearer and higher resolution image than the original image [18]. In this study, it was found that after the cervical tissues of all patients were processed, the spectral image after image fusion processing and the image 3(a) without lesions were combined according to the characteristic wavelength band of different cervical tissues and the response to light. In addition, the contrast of the fused multispectral image was 0.7549, which was also higher than the fused contrast of 0.4716, indicating that the separation of the fused image was improved and the image was clearer.

At present, artificial intelligence algorithms have been widely used in the medical field. For example, Dorta-Estremera uses deep learning algorithms to identify unbalanced error reports in medical data [19]. The tissue classification algorithm uses the band characteristics or spatial characteristics of the multispectral image to classify it as the boundary between unoccurring lesions and suspected lesions, so that the elements on the spectrum are divided into different levels or categories, thereby realizing alternative subjective analysis [20]. In this study, the tissue classification algorithm was applied to analyze the multispectral image of cervical tissue. Comparison of unfused and fused multispectral images showed that after the tissue classification algorithm was used to process the fused cervical tissue image, the area and the range of the cervical tissue in the image were more intuitive so that it was easier for doctors to quickly screen out cancerous lesions by color classification. In addition, the restored image was evaluated using three indicators. The result revealed that the multispectral image average gradient, SD, and image entropy in this study based on the tissue classification algorithm were 2.0765, 65.2579, and 4.974, respectively, which were higher in contrast to the reported values (1.1777, 50.4657, and 3.9025, respectively). It suggests that the multispectral cervical tissue image based on the tissue classification algorithm is clearer, the segmentation of the lesion is clearer, and the overall quality of the image is better.

With the application of optical imaging and computer algorithm technology in medical treatment in recent years, multispectral imaging technology can present high-definition and high-resolution imaging and lesion screening of cervical tissue. Studies have found that the sensitivity of multispectral imaging technology can reach nearly 96% and the specificity can reach nearly 56% [21]. In this study, the multispectral image of the tissue classification algorithm was compared with the multispectral image of the nonapplied algorithm. It was found that the sensitivity and specificity of the multispectral image with the tissue classification algorithm were 85.3% and 70.8%, respectively, which were higher than those of the image without the algorithm. It indicates that the use of tissue classification algorithm to assist multispectral imaging shows higher accuracy and higher clinical application value in screening of the cervical cancer.

5. Conclusion

Multispectral imaging assisted by tissue classification algorithm can effectively screen for cervical cancer and can quickly, efficiently, and safely segment the cervical tissue from the lesion area and the no-lesion area. The segmentation result was the same as the result of the physician's medical examination, showing that its clinical application value was high. This study could provide a new idea for the clinical application of tissue classification algorithm-assisted multispectral imaging technology in the early screening and diagnosis of cervical cancer. However, there were still some shortcomings in this study. The included sample size was small. To obtain more detailed results, more sample studies are needed in the future.

Data Availability

The data used to support the findings of this study are available from the corresponding author upon request.

Conflicts of Interest

The authors declare no conflicts of interest.

Authors' Contributions

Pei Wang and Shuwei Wang contributed equally to this work.

References

[1] C. González de Villaumbrosia, J. Martínez Peromingo, J. Ortiz Imedio et al., "Implementation of an algorithm of cohort classification to prevent the spread of COVID-19 in nursing homes," *Journal of the American Medical Directors Association*, vol. 21, no. 12, pp. 1811–1814, 2020.

[2] C. E. da Silva and P. E. P. de Freitas, "Classification of meningiomas based on their surgical removal, world Health organization grade, and cytogenetic profile: a treatment algorithm," *World Neurosurgery*, vol. 105, pp. 289–293, 2017.

[3] C. A. Johnson, D. James, A. Marzan, and M. Armaos, "Cervical cancer: an overview of pathophysiology and management," *Seminars in Oncology Nursing*, vol. 35, no. 2, pp. 166–174, 2019.

[4] A. P. Twinanda, J. Marescaux, M. de Mathelin, and N. Padoy, "Classification approach for automatic laparoscopic video database organization," *International Journal of Computer Assisted Radiology and Surgery*, vol. 10, no. 9, pp. 1449–1460, 2015.

[5] N. Weixin, "A novel algorithm for ventricular arrhythmia classification using a fuzzy logic approach," *Australasian Physical & Engineering Sciences in Medicine*, vol. 39, no. 4, pp. 903–912, 2016.

[6] Z. Hu and D. Ma, "The precision prevention and therapy of HPV-related cervical cancer: new concepts and clinical implications," *Cancer Medicine*, vol. 7, no. 10, pp. 5217–5236, 2018.

[7] J.-H. Lee and S.-N. Jeong, "Efficacy of deep convolutional neural network algorithm for the identification and classification of dental implant systems, using panoramic and periapical radiographs," *Medicine*, vol. 99, no. 26, Article ID e20787, 2020.

[8] S. R. Piccolo, T. J. Lee, E. Suh, and K. Hill, "ShinyLearner: a containerized benchmarking tool for machine-learning classification of tabular data," *GigaScience*, vol. 9, no. 4, Article ID giaa026, 2020.

[9] H. R. Pugsley, "Quantifying autophagy: measuring LC3 puncta and autolysosome formation in cells using multispectral imaging flow cytometry," *Methods*, vol. 112, pp. 147–156, 2017.

[10] S. Cohen, A. M. Valm, and J. Lippincott-Schwartz, "Multispectral live-cell imaging," *Current Protocols in Cell Biology*, vol. 79, no. 1, p. e46, 2018.

[11] J. A. Shenson, G. S. Liu, J. Farrell, and N. H. Blevins, "Multispectral imaging for automated tissue identification of normal human surgical specimens," *Otolaryngology-Head and Neck Surgery*, vol. 164, no. 2, pp. 328–335, 2021.

[12] A. D. Griffiths, H. Chen, D. D.-U. Li et al., "Multispectral time-of-flight imaging using light-emitting diodes," *Optics Express*, vol. 27, no. 24, Article ID 35485, 2019.

[13] G. E. Jones, A. Yoo, V. A. King, M. Sowa, and D. M. Pinson, "Snapshot multispectral imaging is not inferior to SPY laser fluorescence imaging when predicting murine flap necrosis," *Plastic and Reconstructive Surgery*, vol. 145, no. 1, pp. 85e–93e, 2020.

[14] H. R. Pugsley, "Assessing autophagic flux by measuring LC3, p62, and LAMP1 Co-localization using multispectral imaging flow cytometry," *Journal of Visualized Experiments*, vol. 125, Article ID 55637, 2017.

[15] J. Spigulis, "Multispectral, fluorescent and photoplethysmographic imaging for remote skin assessment," *Sensors*, vol. 17, no. 5, p. 1165, 2017.

[16] G. Saiko and A. Betlen, "Optimization of band selection in multispectral and narrow-band imaging: an analytical approach," *Advances in Experimental Medicine & Biology*, vol. 1232, pp. 361–367, 2020.

[17] S.-J. Bae, D.-S. Lee, V. Berezin, U. Kang, and K.-H. Lee, "Multispectral autofluorescence imaging for detection of cervical lesions: a preclinical study," *Journal of Obstetrics and Gynaecology Research*, vol. 42, no. 12, pp. 1846–1853, 2016.

[18] J. H. Wang, Z. Wu, Q. S. Wu, and L. B. Zeng, "The study on combined screening method for TBS and cervical cancer cell's DNA quantitative analysis based on multi-spectral imaging technology," *Guang Pu Xue Yu Guang Pu Fen Xi*, vol. 37, no. 2, pp. 545–550, 2017.

[19] S. Dorta-Estremera, L. E. Colbert, S. S. Nookala et al., "Kinetics of intratumoral immune cell activation during chemoradiation for cervical cancer," *International Journal of*

Radiation Oncology, Biology, Physics, vol. 102, no. 3, pp. 593–600, 2018.

[20] R. Pratama, J. J. Hwang, J. H. Lee, G. Song, and H. R. Park, “Authentication of differential gene expression in oral squamous cell carcinoma using machine learning applications,” *BMC Oral Health*, vol. 21, no. 1, p. 281, 2021.

[21] Y. Liu, D. Gao, M. Xu, and Z. Yuan, “Multispectral photoacoustic imaging of cancer with broadband CuS nanoparticles covering both near-infrared I and II biological windows,” *Journal of Biophotonics*, vol. 12, no. 3, Article ID e201800237, 2019.

Hindawi
Journal of Healthcare Engineering
Volume 2023, Article ID 9860913, 1 page
https://doi.org/10.1155/2023/9860913

Retraction

Retracted: Study on Toll-Like Receptor 2-Mediated Inflammation-Induced Familial Hypertension Combined with Hyperlipemia and Its Mechanism

Journal of Healthcare Engineering

Received 11 February 2023; Accepted 11 February 2023; Published 18 February 2023

Journal of Healthcare Engineering has retracted the article titled "Study on Toll-Like Receptor 2-Mediated Inflammation-Induced Familial Hypertension Combined with Hyperlipemia and Its Mechanism" [1] due to concerns that the peer review process has been compromised.

Following an investigation conducted by the Hindawi Research Integrity team [2], significant concerns were identified with the peer reviewers assigned to this article; the investigation has concluded that the peer review process was compromised. We therefore can no longer trust the peer review process, and the article is being retracted with the agreement of the Chief Editor.

The authors disagree with the retraction.

References

[1] J. Liu, C. Li, Q. Wang, H. Hu, C. Li, and J. Qian, "Study on Toll-Like Receptor 2-Mediated Inflammation-Induced Familial Hypertension Combined with Hyperlipemia and Its Mechanism," *Journal of Healthcare Engineering*, vol. 2022, Article ID 1473597, 13 pages, 2022.

[2] L. Ferguson, "Advancing Research Integrity Collaboratively and with Vigour," 2022, https://www.hindawi.com/post/advancing-research-integrity-collaboratively-and-vigour/.

Hindawi
Journal of Healthcare Engineering
Volume 2022, Article ID 1473597, 13 pages
https://doi.org/10.1155/2022/1473597

Research Article

Study on Toll-Like Receptor 2-Mediated Inflammation-Induced Familial Hypertension Combined with Hyperlipemia and Its Mechanism

Jia Liu,[1] **Chunjing Li**,[1] **Qiuyang Wang**,[1] **Haiyan Hu**,[2] **Chunhong Li**,[1] **and Jiuguang Qian**[1]

[1]*Department of Cardiovascular Medicine, The First Affiliated Hospital of Qiqihar Medical University, Qiqihar 161041, China*
[2]*Department of General Practice, The First Affiliated Hospital of Qiqihar Medical University, Qiqihar 161041, China*

Correspondence should be addressed to Jiuguang Qian; xinneisanke0162@qmu.edu.cn

Received 27 November 2021; Revised 14 December 2021; Accepted 23 December 2021; Published 5 January 2022

Academic Editor: Enas Abdulhay

According to the latest clinical data, cardiovascular diseases have ranked first in prone diseases, causing 40% of the premature deaths of China's population. This study aimed to investigate the influence of Toll-like receptor 2- (TLR2-) mediated inflammation on the occurrence and development of familial hypertension combined with hyperlipemia and its related mechanism. Blood specimens from 66 patients undergoing coronary atherosclerosis were collected and grouped, including 22 patients into the control group, 25 into the familial hypertension group, and 19 into familial hypertension combined with hyperlipemia group. In this study, ELISA was conducted for determining the levels of four inflammatory factors of TLR2 and IL-1β, IL-6, TNF-ɑ, and CCL2 in serum and the levels of relevant indicators in mice. C57Bl/6j and genetically engineered *C.129(B6)-Tlr2tm1Kir/J* mice were given subcutaneous injection of normal saline (wild-saline group), 8-week 40% high-fat diet (wild-high-fat group), and subcutaneous Alzet-implanted angiotensin II micropump supplemented with the research diet (wild-high fat-Ang II group, *Tlr2*$^{-/-}$-high fat-Ang II group). Blood pressure in mice was recorded consecutively with a noninvasive hemopiezometer for eight weeks. TLR2 and IL-1β, IL-6, TNF-ɑ, and CCL2 in serum of patients with familial hypertension combined with hyperlipemia and the hypertension combined with hyperlipemia mouse model were higher than those in the normal group. Under combined intervention of Ang II and the research diet, mRNA expression related to blood pressure, blood lipid, and fat metabolism in *Tlr2*$^{-/-}$ genetically engineering mice was significantly lower than that in the wild-high fat-Ang II group. The phosphorylation levels of AKT, IKK, and p65 in mice with hypertension combined with hyperlipidemia were significantly higher than those in normal group. The levels of blood pressure and blood lipid in mice after blocking the AKT or NF-κB pathway were significantly downregulated compared with those in the wild-high fat-Ang II group, with statistically significant differences (both $P < 0.05$). In conclusion, TLR2 regulates inflammation through Akt-NF-κB pathway, thus inducing the occurrence and development of familial hypertension combined with hyperlipemia.

1. Introduction

According to the latest clinical data, cardiovascular diseases have ranked first in prone diseases, causing 40% of the premature deaths of China's population [1–3]. Among these, hypertension and hyperlipemia are the most common diseases. Patients with hypertension account for about 43% of the total patients with cardiovascular diseases [4, 5], and patients with dyslipidemia accounting for 40.4% [6]. With the improvement of quality of life, hypertension combined with hyperlipemia has become the normal state for patients with cardiovascular diseases. Long-term hypertension and hyperlipemia can result in malignant diseases, such as stroke, myocardial infarction, renal failure, congestive heart failure, progressive atherosclerosis, and dementia [7]. Gender, age, smoking, regulation of intestinal flora, lifestyle, and genetic determinism can all be taken as individual difference factors for the occurrence of hypertension combined with hyperlipemia. The complexity of influencing factors is one of the important reasons for its long-time treatment courses [8–11]. At present, the main means for regulating blood pressure and blood lipid is a drug intervention, with hypotensors (calcium-ion-channel antagonists, ACEI, ARB, etc.) combined with lipid-lowering drugs (HMG-CoA inhibitors) as a common strategy for early and long-term blood pressure and blood lipid control [12, 13].

Primary familial hypertension is a relatively special disease, which is mainly induced by the family inheritance as the disease factor, and acquired factors as the induction factor. A series of recent studies have shown that immune system disorders are closely linked to the occurrence of primary hypertension combined with hyperlipemia. T cells act with angiotensin II receptors to release TNF-α, IL-6, IL-17A, and other proinflammatory factors to regulate blood pressure [14]. HMBG1/TLRs and HMBG1/RAGE signaling pathways cause arterial spasm, inflammatory cell adhesion infiltration, and vascular injury, thereby leading to hypertension by acting vascular endothelium [15]. Infiltration and adhesion were also found in proinflammatory factors, such as IL-1β and CCL2 in lipid disorders [16, 17]. Therefore, we speculated that inflammation plays an important role in the occurrence and development of primary hypertension combined with hyperlipidemia.

TLR systems have been proven to play a key role in regulating the release, migration, and infiltration of inflammatory factors [18]; TLR2/TLR4 pathway interacts with NF-B, MAPK, PI3 K-Akt, mTOR, and other related pathways, regulating IL-1β, IL-6, TNF-α, CCL2, and other proinflammatory factors involved in a variety of physiological activities [19]. Recent research has shown that intestinal floras regulate inflammation on the occurrence and development of cardiovascular diseases through TLR2 [20], which can also promote the occurrence of thrombotic diseases combined with hyperlipemia [21]. Therefore, we speculated that TLR2-regulated inflammatory response also plays a role in primary hypertension combined with hyperlipemia.

On the basis of conventional medication treatment, the study on new pathological intervention targets for hypertension and hyperlipemia is still vacant. It is urgent to explore the pathogenesis of hypertension and hyperlipemia from the molecules and signaling pathways, providing a new treatment direction for clinical practice. For that, in this study, we explored the correlation between hypertension and hyperlipidemia and TLR2 level starting from the clinical blood specimen, and the specific role and molecular mechanism of TLR2 inducing the occurrence and development of hypertension and hyperlipidemia in the animal model. And we found that TLR2 can regulate inflammatory factor levels through Akt/NF-κB pathway, inducing the occurrence of hypertension combined with hyperlipemia, which may be a new clinical intervention target.

2. Methods

2.1. Collection and Grouping of Clinical Blood Specimen. Blood specimen was collected from 80 patients with atherosclerosis who underwent percutaneous coronary intervention (PCI) in the Cardiology Department during the time from August 2019 to December 2020. Among these, 14 were excluded due to blood test failure and incomplete patient information, and 66 were included in statistical analysis. According to blood pressure and blood lipid, the 66 samples were divided into three groups: (1) 22 into the control group (with normal levels of blood pressure and blood lipid); (2) 25 into the primary hypertension group (with higher systolic or diastolic pressure than normal, and normal blood lipid level); and (3) 19 into primary hypertension combined with hyperlipemia (with higher systolic or diastolic pressure than normal, as well as higher TC, triglyceride, and LDL). This study has been approved by the Ethics Committee of our hospital, and all patients have signed informed consent.

2.2. Animals and Construction of Animal Model. 4-week C57Bl/6j male mice (weight: 17.36 ± 0.82 g) and 4-week genetically engineered *C.129(B6)-Tlr2tm1Kir/J* male mice (i.e., *Tlr2*$^{-/-}$ mice, weight:18.55 ± 0.91 g) were all raised in Class SPF Animal Experimental Center, with the temperature of 21~25°C, the humidity of 40%~60%, breeding illumination degree of 20lx, and light and shade alternating of (12 h : 12 h), and were free of food and water. C57Bl/6j mice were purchased from Charles River Laboratories (Animal License No. SCXK (Shanghai) 2017–0011). *C.129(B6)-Tlr2tm1Kir/J* mice (Product No. 022507) were purchased from Jackson Laboratory, and all tests have been approved by the Animal Ethics.

Anesthesia in mice was abdominal injection of pentobarbital sodium (50 mg/kg), while euthanasia in mice was hypoxia to death with carbon dioxide.

2.2.1. Construction of Animal Model

(1) *Construction of Mice Model with Hypertension (22–23).* Angiotensin II (Ang II, MCE, 4474-91-3) was dissolved into dimethyl sulfoxide (DMSO, 10%) and corn oil (10%) successively into 5.23 mg/ml (5 mM) mother solution, which was poured into Alzet-implanted administration pump (US Alzet, 2006 micropump) capsule. After anaesthesia, 1 cm off the right of the back centerline of mice was cut into the skin parallel along the spine, isolated 2~3 cm length to the head bluntly; a micropump was implanted, with the release outlet toward the head, and finally, the cut was stitched. The drug pump released Ang II to the surrounding skin at 1000 ng/kg/min for 8 weeks, acting on AT1 receptor to induce the occurrence of hypertension.
(2) *Construction of Mice Model with Hyperlipemia.* From 4 weeks old, the mice were fed with research diets (D12492) for 8 weeks to induce the occurrence of hyperlipidemia.
(3) *Construction of Mice Model with Hypertension Combined with Hyperlipemia.* Ang II administration pump capsule was implanted combined with hyperlipemia feed as intervention to construct model

mice with hypertension combined with hyperlipemia.

(4) *Construction of Mice Model with Blocking Akt Pathway.* Akt pathway inhibitor CCT128930 (MCE, 885499-61-6) was dissolved into 2.75 mg/mL (8.04 mM) mother solution with dimethyl sulfoxide (DMSO, 10%), polyethylene glycol 300 (PEG300, 40%), and Tween-80 (Tween-80, 5%) successively. Mice were injected with CCT128930 5 mg/kg caudal vein 3 times a week from 4 weeks old for 8 weeks to block the Akt pathway.

(5) *Construction of Mice Model with Blocking NF-κB Pathway.* NF-κB pathway inhibitor BAY 11–7082 (MCE, 19542-67-7) was dissolved into 2.5 mg/mL (12.06 mM) mother solution with dimethyl sulfoxide (DMSO, 10%) and corn oil (10%) successively. Mice were intraperitoneally injected with 2.5 mg/kg BAY 11–7082 twice a week from 4 weeks old for 8 weeks to block the NF-κB pathway.

2.2.2. Mouse Grouping and Quantity

(1) Levels of TLR2, related proinflammatory factors, and lipid metabolism-related mRNAs in mice with hypertension combined with hyperlipidemia induced by Ang II combined with the research diet: in this section, the mice were divided into three groups ($n = 5$): (a) wild saline; (b) wild-high fat; and (c) wild-high fat Ang II.

(2) Levels of blood pressure and blood lipid and related inflammatory factors in mice knockout *Tlr2* genes: in this section, the mice were divided into three groups ($n = 5$): (a) wild saline; (b) wild-high fat-Ang II; and (c) $Tlr2^{-/-}$-high fat-Ang II.

(3) Akt, IKK, and p65 protein expressions and their phosphorylation levels in model mice with hypertension combined with hyperlipemia: in this section, the mice were divided into three groups ($n = 5$): (a) wild saline; (b) wild-high fat-Ang II; and (c) $Tlr2^{-/-}$-high fat-Ang II.

(4) Verification of Akt pathway in TLR2-induced hypertension combined with hyperlipemia: in this section, the mice were divided into four groups ($n = 5$): (a) wild saline; (b) wild-high fat-Ang II; and (c) $Tlr2^{-/-}$-high fat-Ang II; and (d) wild-high-fat-Ang II-CCT128930.

(5) Verification of NF-κB pathway in TLR2-induced hypertension combined with hyperlipemia: in this section, the mice were divided into four groups ($n = 5$): (a) wild saline; (b) wild-high fat-Ang II; (c) $Tlr2^{-/-}$-high fat-Ang II; and (d) wild-high fat-Ang II-BAY11-7082.

2.3. Blood Pressure Monitoring. A noninvasive hemopiezometer (Kent) was adopted to record diastolic and systolic pressure every Wednesday and calculate MAP (MAP = (systolic pressure + 2 × diastolic pressure/3).

2.4. Blood Lipid Test

2.4.1. Clinical Blood Specimen. Clinical blood specimen was collected into the procoagulant tube and centrifuged at 3500 rpm for 7 min after resting for 5 min. The upper serum was absorbed into the EP tube for measurement. TC detection kit (Nanjing Jiancheng Bio, A111-1-1), triglyceride detection kit (Nanjing Jiancheng Bio, A110-1-1), LDL cholesterol LDL-C detection kit (Nanjing Jiancheng Bio, A113-1-1), and HDL cholesterol HDL-C determination kit (Nanjing Jiancheng Bio, A112-1-1) were adopted for coloring. The absorbance value was measured with the enzyme plate analyzer to calculate the concentration of the four components.

2.4.2. Blood Specimen from Mice. After fasting overnight, 1 ml blood was collected from mouse eyeballs and placed into a coagulation procoagulant tube (BD) after fully anesthetized by intraperitoneal injection of pentobarbital sodium (80 mg/kg). After resting for 5 min, the mice were centrifuged at 3500 rpm for 7 min, and the upper serum was absorbed into the EP tube for measurement. The determination method was the same as above.

2.5. ELISA

2.5.1. Clinical Blood Specimen. The collection method for serum was the same as "4. Blood lipid detection of clinical blood specimen." Human TLR2 ELISA Kit (ABCAM, AB227897), human IL-1β ELISA Kit (ABCAM, AB100562), human IL-6 ELISA Kit (ABCAM, AB178013), human TNF-ɑ ELISA Kit (ABCAM, AB181412), and human CCl2 ELISA Kit (ABCAM, AB179886) were used to detect the levels of TLR2, IL-1β, IL-6, TNF-ɑ, and CCL2 in serum.

2.5.2. Blood Specimen of Mice. The collection method for serum was the same as "4. Blood lipid detection of clinical blood specimen." Mouse TLR2 ELISA Kit (ABCAM, AB224880), mouse IL-1β ELISA Kit (ABCAM, AB197742), mouse IL-6 ELISA Kit (ABCAM, AB100712), mouse-derived TNF-ɑ ELISA Kit (ABCAM, AB208348), and mouse-derived CCl2 ELISA Kit (ABCAM, AB208985) were used to detect the levels of TLR2, IL-1β, IL-6, TNF-ɑ, and CCL2 in serum.

2.6. Quantitative Real-Time PCR (qRT-PCR). After sacrificing mice with carbon dioxide, the liver was collected and washed for residual blood with 0.9% saline and stored at −80°C. 30 mg tissues was taken, fully broken on the ice in homogenate, with 1 ml TRIzol RNA separation reagent (Thermo Fisher, 10296010). After resting 5 min, the tissues were centrifuged at 12000 rpm for 15 min, and the upper clarification aqueous phase was taken. RNA was precipitated with isopropanol and washed with 75% ethanol solution. After the precipitation was air-dried, RNA concentration was determined with a microplate analyzer. After recording the RNA reversal to a cDNA template with the Reversal

Reagent (Takara, RR037Q), qRT-PCR (Applied Biosystems ABI 7500) was performed with TB Green qPCR reagent (Takara, RR82LR). Amplification conditions: (1) Phase I, 95°C for 30 s; (2) Phase II, 95°C for 5 s, 60°C for 30 s, for 40 cycles; (3) Phase III, 95°C for 15 s, 60°C for 60 s, and 95°C for 15 s. The amplification multiple of genes relative to the internal reference was calculated by $2^{-\Delta\Delta\ Ct}$ formula according to Ct value. The upstream and downstream primer sequences are shown in Table 1.

2.7. Western Blot. After intraperitoneal injection of pentobarbital sodium (80 mg/kg) anaesthesia in mice, the hearts were collected and the residual blood was washed with 0.9% saline and stored at −80°C. The total protein was extracted from 30 mg tissues, with a 600 ml protein cracking solution (Keyki, KGP702). The protein concentration was determined with a protein concentration determination kit (Beyotime, P0006), and SDS-PAGE protein upper-like buffer (Beyotime, P0015) was added to obtain the protein sample 5 min after 100°C degeneration. 50 μg proteins was sampled from each lane. After SDS-PAGE cataphoresis, the proteins were transferred to PVDF membrane and incubated overnight at 4°C, with primary antibodies at 1 : 1000 of p-Akt (Thermo Fisher, PA5-95669, 1 : 5000), t-Akt (Thermo Fisher, PA5-29169, 1 : 4000), p-IKK (Thermo Fisher, PA5-104696, 1 : 4000), t-IKK (Thermo Fisher, PA5-86059, 1 : 1000), p-p65 (Thermo Fisher, PA5-104961, 1 : 5000), t-p65 (Thermo Fisher, PA5-16545, 1 : 4000), and Gapdh (Thermo Fisher, AM4300, 1 : 8000). Secondary antibodies of HRP-labeled sheep anti-rabbit (ABCAM, AB205718, 1 : 10,000) and rabbit anti-mouse (ABCAM, AB6728, 1 : 10,000) were added after washing 3 times with TBST and incubated at room temperature for 2 h. After washing with TBST, a chemiluminescence system (Millipore Corporation, Billerica, MA, USA) was adopted for developing, and ImageJ (NIH, Bethesda, MD, USA) for Grayscale analysis of the strips.

2.8. Statistical Methods. SPSS 19.0 software and GraphPad Prism 8.0 software was employed as well. The count data were statistically analyzed with *t*-test (two sets of data) or one-factor ANOVA (three sets and above data). Data were represented by $x \pm s$. $P < 0.05$ was defined as the statistically significant difference.

3. Results

3.1. Levels of TLR2 and Related Proinflammatory Factors in Clinical Blood Specimen. The general conditions of three clinical patients' specimen were statistically analyzed, and the baseline was adjusted to the same level. Except for related indicators of hypertension, hyperlipemia and medication, there were no statistical differences in age, gender distribution, smoking, previous history, and medication in the subjects of control, familial hypertension, and familial hypertension combined with hyperlipidemia groups (all $P > 0.05$, Table 2). Both systolic and diastolic pressure were significantly higher in the primary hypertension group and primary hypertension combined with hyperlipidemia group than those in the control group (both $P < 0.001$, Table 2). TC, triglyceride, and LDL were significantly higher and lower HDL in the primary hypertension combined with hyperlipidemia group than those in the other two groups (both $P < 0.001$, Table 2). According to the results of ELISA for relevant indicators of blood specimen in serums, the levels of TLR2, IL1-β, IL-6, and TNF-ɑ were significantly higher in primary hypertension group and primary hypertension combined with hyperlipidemia group than those in the control group (all $P < 0.001$, Table 3), with no significant difference in CCL2 levels among three groups ($P = 0.805$, Table 3). ELISA for a clinical sample of serum showed that in primary hypertension and primary hypertension combined with hyperlipemia groups, TLR2 and the concentration of related inflammatory factors were above normal levels, suggesting that TLR2 may be related to the development of inflammation.

3.2. TLR2, Related Proinflammatory Factors, and Fat Metabolism-Related mRNA Levels in Mice with Hypertension Combined with Hyperlipidemia Induced Jointly by Ang II and Research Diet. In order to further explore the correlation between hypertension combined with hyperlipidemia and TLR2 in the animal model, the combined method of Ang II and research diet was adopted in this study. Significant changes in blood lipid and blood pressure levels were found in the wild-high fat group and wild-high fat-Ang II group in which TC and LDL levels were significantly elevated compared with those in the wild-saline group, with statistically significant difference ($n = 5$, all $P < 0.001$, Figure 1(a)). No significant differences were observed between HDL and triglyceride ($n = 5$, both $P > 0.05$, Figure 1(a)). MAP also increased significantly compared with that in the control group ($n = 5$, all of $P < 0.001$, Figure 1(b)), and the model of mice with hypertension combined with hyperlipidemia was successfully constructed. TLR2, IL1-β, IL-6, and TNF-ɑ levels in serum of mice with hypertension combined with hyperlipidemia also significantly increased ($n = 5$, all $P < 0.001$, Figure 1(c)), but there was no obvious difference in CCL2 ($n = 5$, $P > 0.05$, Figure 1(c)). In addition, in the qPCR detected lipid metabolism-related mRNAs, genes responsible for fatty acid oxidation, fat hydrolysis, and cholesterol hydrolysis were downregulated to varying degrees ($n = 5$, all $P < 0.001$, Figure 1(d)). In the model of mice with hypertension combined with hyperlipidemia constructed by hyperlipemia and Ang II, blood lipid and blood pressure levels and lipid metabolism functions have changed pathologically to different degrees. At the same time, TLR2 and related inflammatory factors also increased to varying degrees in serum, suggesting the occurrence and development of hypertension combined with hyperlipidemia.

3.3. Blood Pressure, Blood Lipid, and Related Inflammatory Factor Levels in Mice with Knockout Tlr2 Gene. To intuitively verify the influence of TLR2 on pathology processes, the study group purchased $Tlr2^{-/-}$ mice bred by the Jackson Laboratory. In mice, after knocking out of Tlr2 gene, MAP

Table 1: Upstream and downstream primer sequences of each gene.

Gene	Upstream primer (5'-3')	Downstream primer (5'-3')
Gapdh	AGG TCG GTG TGA ACG GAT TTG	TGT AGA CCA TGT AGT TGA GGT CA
mAcsm2	GCC AGA CAG AAA CGG GAC TT	ACA TGC CGA TAG GCC AGA TG
mAcad10	TGG CTG TGG GCT GGG AG	AAA TAG GAG CTG ACG GGC AC
mAcat3	TGG CCA CTT TGA CAA GGA GAT	CTG TTG CAT TAG CAG TTG TGA
mAcat2	GAC CCC GTG GTC ATC GTC	CCA CAA CCT GCC GTC AAG A
mAcsbg1	ACT CGC AAA CCA GCT CC	AGT ACA GAA AGG TTC CAG GCG
mAcox3	GGG TGA TGG TCG GTG ACA TT	CGG ACA TCC TTA AAG GGG CT
mAcsl1	ATC TGG TGG AAC GAG GCA AG	TCC TTT GGG GTT GCC TGT AG
mCpt1	CAG CTG CTG ACC TCT GAC C	AAA GTC ATT CCA GAC ACG CCA
mPparδ	GAA CAG CCA CAG GAG GAG AC	GAG GAA GGG GAG GAA TTC TG
mEI	CTA TCC CAA TGG CGG TGA CTT C	CGT GCT CGC ATT TCA CCA TC
mHL	CTA TGG CTG GAG GAA TCT G	TGG CAT CAT CAG GAG AAA G
mLipe	CTT CCA GTT ACC TGC CA	AAT CGG CCA CCG GTA AAG AG
mLpl	TGG ATG AGC GAC TCC TAC TTC A	CGG ATC CTC TCG ATG ACG AA
mGpat	GCT GCA ACT GAG ACG AAC CT	AAG CCC CCA AGC TTG TGA AT
mSqle	GCA ATC TAC GCC ACG TAT TTC T	GGG CCC GTG GTT TTG T
mMvd	GAG GGA GAC CTC TCC GAA GT	GTC TGC ARG CCC ACT GTA CT
mAbca1	GTT TTG GAG ATG GTT ATA CAA TAG TTG T	TTC CCG GAA ACG CAA GTC

Table 2: Sample baseline information: comparison of general data, disease history, and medication history of control group, familial hypertension group, and familial hypertension combined with hyperlipidemia group.

Baseline indicator		Control group	Familial hypertension	Familial hypertension combined with hyperlipemia	P
Natural properties	Number of cases (n)	22	25	19	
	Gender distribution (female cases/proportion (%))	6 (27.27)	8 (32)	6 (31.58)	0.930
	Age (years)	53.55 ± 15.02	52.92 ± 29.91	52.32 ± 21.12	0.701
	Smoking history (positive cases/proportion (%))	8 (36.36)	7 (28)	8 (42.10)	0.613
Disease history	Diabetes mellitus	10 (45.45)	12 (48)	9 (47.37)	0.984
	Type I diabetes mellitus	1 (4.54)	0 (0)	1 (5.26)	0.528
	Type II diabetes mellitus	9 (40.9)	12 (48)	7 (36.84)	0.748
	Hyperlipidemia	0 (0)	0 (0)	19 (100)	<0.001
	Atherosclerosis	19 (86.36)	22 (88)	16 (84.21)	0.936
	Heart failure	1 (4.54)	0 (0)	1 (5.26)	0.528
	Angina	2 (9.09)	2 (8)	2 (10.53)	0.959
	Stable	0 (0)	1 (4)	0 (0)	0.435
	Unstable	2 (9.09)	1 (4)	2 (10.53)	0.682
	Myocardial infarction	10 (45.45)	11 (44)	10 (52.63)	0.838
	STEMI	5 (22.73)	4 (16)	7 (36.84)	0.273
	NSTEMI	5 (22.73)	7 (28)	5 (26.32)	0.916
	Stroke	0 (0)	0 (0)	0 (0)	1.000
Drug use history	Aspirin	12 (54.54)	10 (40)	10 (52.63)	0.556
	Clopidogrel	10 (45.45)	10 (40)	9 (47.37)	0.874
	Insulin	10 (45.45)	11 (44)	9 (47.37)	0.976
	OHA	12 (54.54)	10 (40)	9 (47.37)	0.608
	Statins	0 (0)	0 (0)	19 (100)	<0.001
	β-Receptor blocking pharmacon	2 (9.09)	22 (88)	19 (100)	<0.001
	Diuretic	3 (13.64)	23 (92)	18 (94.7)	<0.001
	CCB	0 (0)	21 (84)	19 (100)	<0.001
	ACEI	2 (9.09)	20 (80	18 (94.7)	<0.001
	ARB	1 (4.54)	22 (88)	19 (100)	<0.001
Blood pressure level	Systolic pressure (mmHg)	129.82 ± 35.58	149.24 ± 94.023	155.42 ± 56.04	<0.001

was higher than that of the wild-saline group ($n = 5$, $P < 0.001$, Figure 2(a)) but significantly decreased compared with the wild-high fat-Ang II group ($n = 5$, $P < 0.001$, Figure 2(a)). The concentration levels of TC and LDL in serum of the wild-high fat-Ang II group increased but significantly decreased after knocking out Tlr2 gene ($n = 5$, all $P < 0.001$, Figure 2(b)). After knocking out, TLR2 was not detected in serum; the levels of IL-1β and TNF-α in serum

Table 3: Comparison of TLR2 and inflammatory factor expression levels in serum of control, familial hypertension, and familial hypertension combined with hyperlipemia groups.

Indicator	Control group	Familial hypertension	Familial hypertension combined with hyperlipemia	F	P
TLR2	41.26 ± 6.80	$58.89 \pm 11.33^{***}$	$63.39 \pm 9.95^{***}$	31.52	<0.001
IL-1β	4.31 ± 0.86	$24.74 \pm 5.56^{***}$	$32.00 \pm 7.57^{***\dagger\dagger\dagger}$	153.10	<0.001
IL-6	8.14 ± 3.53	$35.01 \pm 10.51^{***}$	$37.92 \pm 16.88^{***}$	45.46	<0.001
TNF-α	54.75 ± 18.01	$190.70 \pm 56.51^{***}$	$262.8 \pm 63.50^{***\dagger\dagger\dagger}$	94.29	<0.001
CCL2	153.60 ± 18.63	149.80 ± 19.99	151.40 ± 19.87	0.22	0.805

***Familial hypertension group versus control group, $P < 0.001$; †††familial hypertension compared with hyperlipemia versus control group, $P < 0.001$.

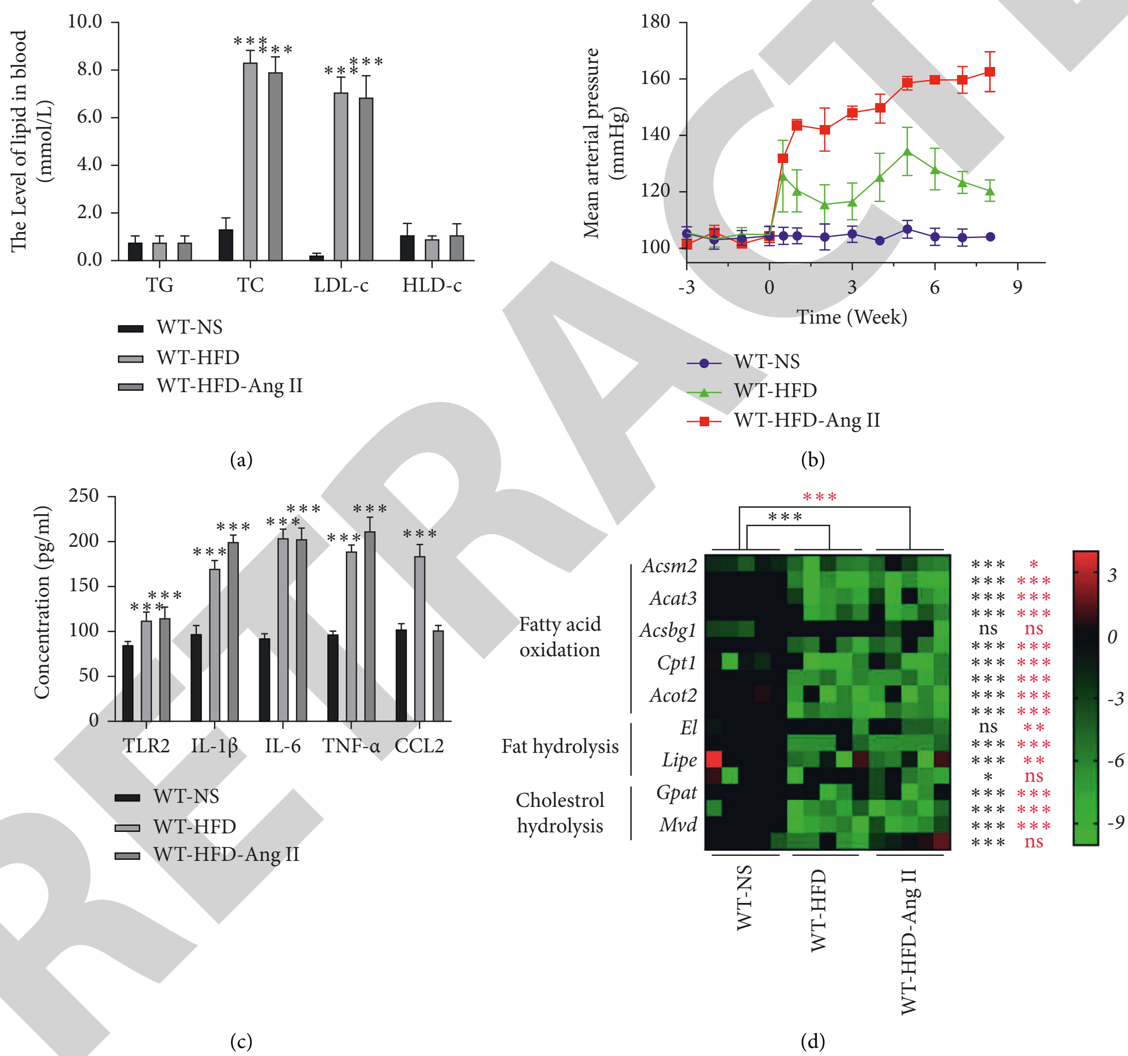

Figure 1: Comparison of blood lipid levels, MAP, TLR2 and expressions of inflammatory factors, and changes of gene expression in each group. (a) Comparison of blood lipid levels: the concentration of TC and LDL in serum was lower in high fat-Ang II group and high-fat group than that in the control group, and the difference in the concentration of triglyceride and HDL was not statistically significant compared to the control group. (b) Comparison of MAP levels in each group: high fat-Ang II group had significantly higher MAP than high-fat group after the construction of the model, and in the meantime, MAP in the two groups was significantly higher than that in the control group. (c) Comparison of TLR2 and proinflammatory factor levels in serum of each group: TLR2 and proinflammatory factor levels were significantly higher in high-fat group than those in the control group, and TLR2 and IL-1β, IL-6, TNF-α, and CCL2 levels did not significantly increase compared to the control group, while CCL2 levels were not statistically significant compared to the control groups. (d) Heat map of gene expression abundance detected by qPCR showed significantly lower genes related to fatty acid oxidation, fatty hydrolysis, and cholesterolosis in high fat-Ang II group and high-fat group compared with the control groups ($n = 5$; $^{***}P < 0.001$).

significantly decreased compared with those in the wild-high fat-Ang II group ($n = 5$, both $P < 0.001$, Figure 2(c)). The levels of IL-6 and CCL2 did not differ significantly among the groups ($n = 5$, all $P > 0.05$, Figure 2(c)). Lipid metabolism-related mRNAs increased in varying degrees in *Tlr2*$^{-/-}$-high fat-Ang II group compared with those in the wild-high fat-Ang II group ($n = 5$, both $P < 0.001$, Figure 2(d)), while there were no significant differences in the expressions of these genes in *Tlr2*$^{-/-}$-high fat-Ang II group and wild-saline group ($n = 5$, both $P > 0.05$, Figure 2(d)). After directly knocking out TLR2 gene to eliminate TLR2 function in model mice, the symptoms of hypertension and hyperlipemia were relieved in the knockout group compared with those in hypertension combined with hyperlipidemia group. It showed that TLR2 plays a role in the occurrence and development of hypertension combined with hyperlipidemia.

3.4. Akt, IKK, and p65 Protein Expressions and Phosphorylation Levels in Mice with Hypertension Combined with Hyperlipidemia. To explore the molecular mechanisms of occurrence and development of TLR2-induced hypertension combined with hyperlipidemia, the study group conducted a Western blot assay for proteins to explore the expressions of key proteins in TLR2-related inflammatory pathways in this case model. The phosphorylation levels of Akt, IKK, and p65 proteins in the wild-high fat-Ang II group were significantly increased ($n = 5$, all $P < 0.001$, Figure 3), which were significantly lower than in the wild-high fat-Ang II group after knocking out *Tlr2* gene ($n = 5$, all $P < 0.001$, Figure 3), with no significant difference from the wild-saline group ($n = 5$, mean $P > 0.05$, Figure 3). The protein results suggested that Akt and NF-κB pathways may participate in the occurrence and development of TLR2 regulatory disease.

3.5. Verification of Akt Pathway in TLR2-Induced Hypertension Combined with Hyperlipemia. To verify the apparent involvement of Akt in the process, the study group adopted the inhibitor to block the Akt pathway, and the phosphorylation level of Akt protein was significantly downregulated compared with that in the wild-high fat-Ang II group ($n = 5$, $P < 0.001$, Figure 4(a)). The mice model with inhibited Akt pathway was successfully constructed. After knocking out of Tlr2 gene, MAP in mice significantly decreased compared with that in the wild-high fat-Ang II group ($n = 5$, $P < 0.001$, Figure 4(b)). Similarly, after blocking the Akt pathway, MAP in the wild-high fat-Ang II group-CCT128930 group significantly decreased compared with that in the wild-high fat-Ang II group ($n = 5$, $P < 0.001$, Figure 4(b)), with no significant difference from the *Tlr2*$^{-/-}$-high fat-Ang II group ($n = 5$, $P > 0.05$, Figure 4(b)). The TC and LDL of wild-high fat-ANG II-CCT128930 group were significantly lower than those in the wild-high fat-ANG II group ($n = 5$, both $P > 0.05$, Figure 4(c)), with no significant difference from *Tlr2*$^{-/-}$-high fat-Ang II group ($n = 5$, all $P > 0.05$, Figure 4(c)). The levels of IL-1β and TNF-α in serum in the wild-high fat-Ang II-CCT128930 group were lower than those in the wild-high fat-Ang II group ($n = 5$, both $P < 0.001$, Figure 4(d)), with no significant difference from those in the *TLR2*$^{-/-}$-high fat-Ang II group ($n = 5$, both $P < 0.001$, Figure 4(d)). The CCL2 level was also lower than that in the wild-high fat-Ang II group and *Tlr2*$^{-/-}$-high fat-Ang II group ($n = 5$, both $P < 0.001$, Figure 4(d)). IL-6 level did not differ significantly in wild-high fat-Ang II-CCT128930 group and wild-high fat-Ang II group ($n = 5$, both $P < 0.001$, Figure 4(d)). *Tlr2* gene knockout improved the hypertension and hyperlipidemia symptoms, suggesting that TLR2 promotes inflammation by activating Akt pathway, thus inducing the occurrence and development of hypertension combined with hyperlipemia.

3.6. Verification of NF-κB Pathway Involved in TLR2-Induced Hypertension Combined with Hyperlipemia. To verify the involvement of NF-κB in the process, the study group employed the inhibitor to block the NF-κB pathway. The phosphorylation levels of NF-κB protein were significantly downregulated compared with that in the wild-high fat-Ang II group ($n = 5$, $P < 0.001$, Figure 5(a)). The mice model with inhibited NF-κB pathway was successfully constructed. After knocking out of *Tlr2* gene, MAP in mice significantly decreased compared with that in wild-high fat-Ang II group ($n = 5$, $P < 0.001$, Figure 5(b)). It was also lower in the wild-high fat-Ang II-BAY11-7082 group than that in the wild-high fat-Ang II group after blocking the NF-κB pathway ($n = 5$, $P < 0.001$, Figure 5(b)), with no significant difference from *Tlr2*$^{-/-}$-high fat-Ang II group ($n = 5$, $P > 0.05$, Figure 5(b)). The TC and LDL in wild-high fat-Ang II-BAY11-7082 group decreased significantly compared with the wild-high fat-Ang II group ($n = 5$, $P < 0.001$, Figure 5(c)), with no significant difference from *Tlr2*$^{-/-}$-high fat-Ang II group ($n = 5$, $P > 0.05$, Figure 5(c)). The levels of IL-1β and TNF-α in serum of the wild-high fat-Ang II-BAY11-7082 were lower than those of the wild-high fat-Ang II-BAY11-7082 group ($n = 5$, $P < 0.001$, Figure 5(d)), with no significant difference from *Tlr2*$^{-/-}$-high fat-Ang II group ($n = 5$, both $P > 0.05$, Figure 5(d)). IL-6 and CCL2 levels showed no significant difference in the wild-high fat-Ang II-BAY11-7082 group and wild-high fat-Ang II group ($n = 5$, both $P > 0.05$, Figure 5(d)). Inhibiting NF-κB pathway also improved hypertension and hyperlipemia symptoms, suggesting that TLR2 promotes inflammation through the activation of NF-κB pathway, thus inducing the occurrence and development of hypertension combined with hyperlipemia.

4. Discussion

With the development of society and the improvement of material levels, hypertension has become the most common cardiovascular disease [1, 2]. Among them, primary familial hypertension is a relatively special type. Although genetic factors are dominant in such patients, nongenetic factors still cannot be ignored. Relevant studies have shown that the degree and speed of nongenetic factors inducing hypertension is greater in patients with familial hypertension [2]. In recent years, there have been many studies on

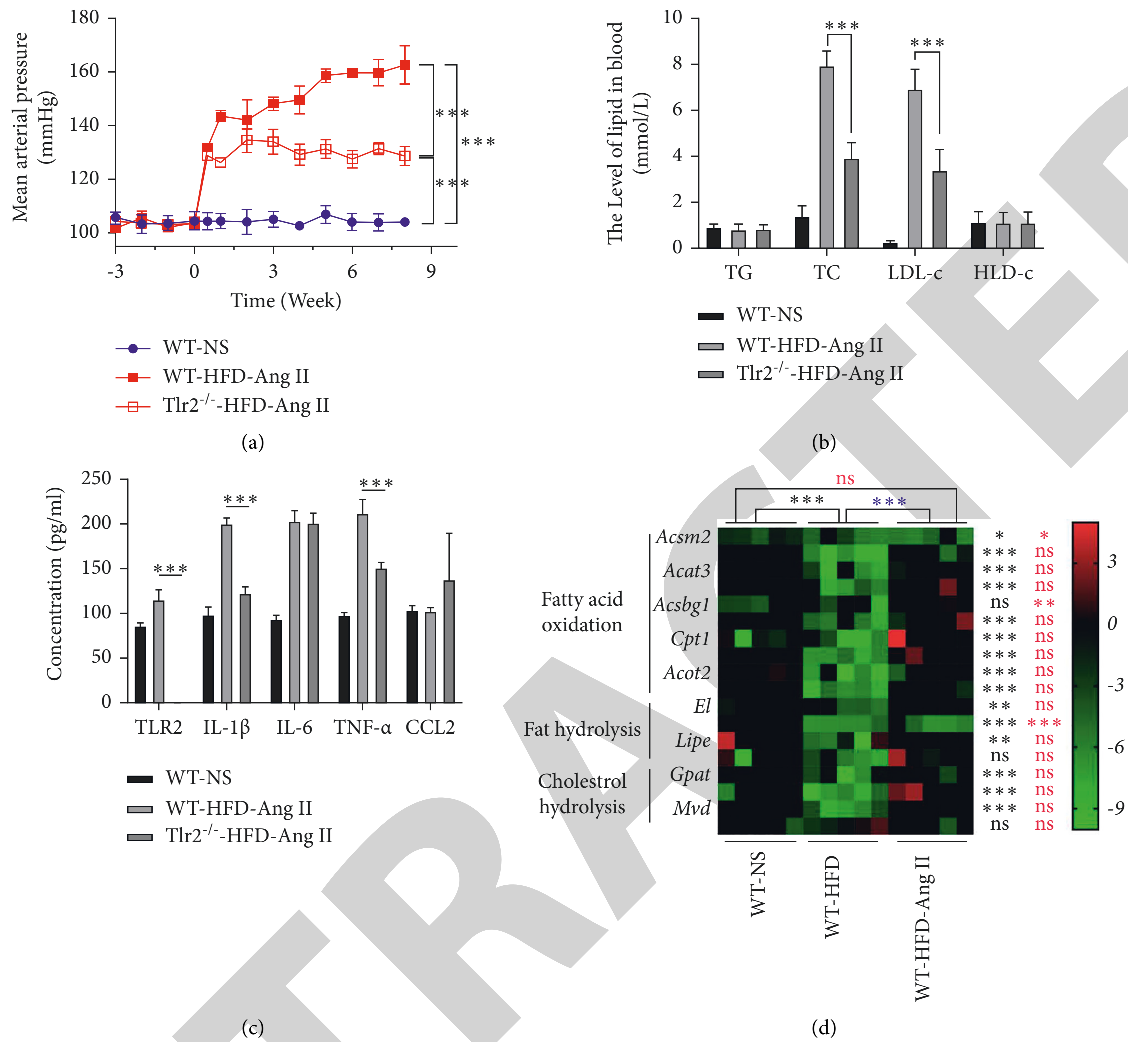

Figure 2: Changes of MAP, blood lipid levels, TLR2 in serum and inflammatory factor concentrations, and lipid metabolism-related gene expression between *Tlr2*$^{-/-}$-high fat-Ang II group and wild-high lipid-Ang II groups. (a) Comparison of MAP in *Tlr2*$^{-/-}$-high fat-Ang II group and wild-high fat-Ang II group, MAP after the construction of the model was significantly lower in the *Tlr2*$^{-/-}$-high fat-Ang II group than that in the wild-high fat-Ang II group. (b) Comparison of lipids and apolipoproteins in serum in *Tlr2*$^{-/-}$-high fat-Ang II group and wild-high fat-Ang II group, TC and LDL in serum significantly decreased in the *Tlr2*$^{-/-}$-high fat-Ang II group compared to the wild-high fat-Ang II group, while there was no significantly statistical difference between triglyceride and HDL between the two groups. (c) *Tlr2*$^{-/-}$-high fat-Ang II group was not detected TLR2 in serum; at the same time, the levels of IL-1β and TNF-α were significantly lower than those in wild-high fat-Ang II group, with no statistical difference in IL-6 and CCL2 concentrations in serum than those in the wild-high fat-Ang II group. (d) Heat map of gene expression abundance detected by qPCR showed significantly increased related gene expressions of fatty acid oxidation, fat hydrolysis, and cholesterol hydrolysis in the *Tlr2*$^{-/-}$-high fat-Ang II group compared to the wild-high fat-Ang II group ($n = 5$; $^{***}P < 0.001$).

hypertension combined with hyperlipemia from the perspective of immune function and related signaling pathways, with the increasing connection between cardiovascular diseases and inflammatory response. But the study of hypertension and hyperlipemia has no good target and inflammatory regulation methods [22–24]. The exploration of hypertension combined with hyperlipemia intervention target and its association with inflammatory response are the hot spots in recent years. Therefore, we expect to screen a protein target related to inflammation with a positive regulatory effect on primary hypertension combined with hyperlipemia.

First, we collected three clinical blood specimens: control, primary hypertension, and primary hypertension combined with hyperlipemia, and measured the levels of IL-1β, IL-6, TNF-ɑ, and CCL2 inflammatory factors in serum by ELISA. It was found that the four inflammatory factor levels in serum of primary hypertension group and primary hypertension combined with hyperlipidemia group were significantly higher than those in the control group, and the research conclusions of the correlation between inflammation and primary hypertension complicated with hyperlipidemia are consistent with the existing conclusions [25–27]. Inflammation is closely related to cardiovascular

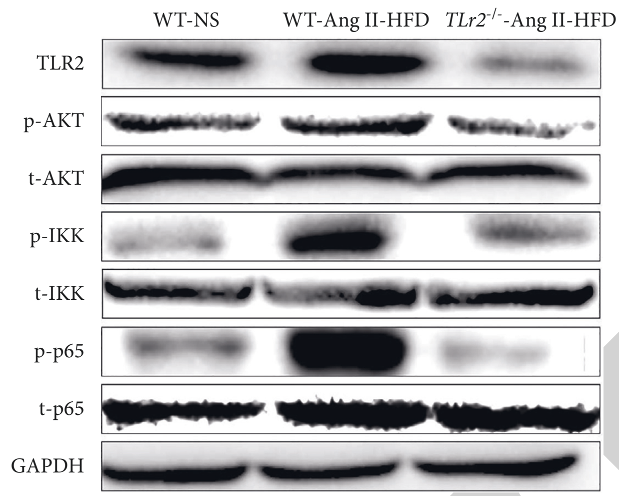

FIGURE 3: Detection of p-Akt, t-Akt, p-IKK, t-IKK, p-p65, and t-p65 protein levels in each group.

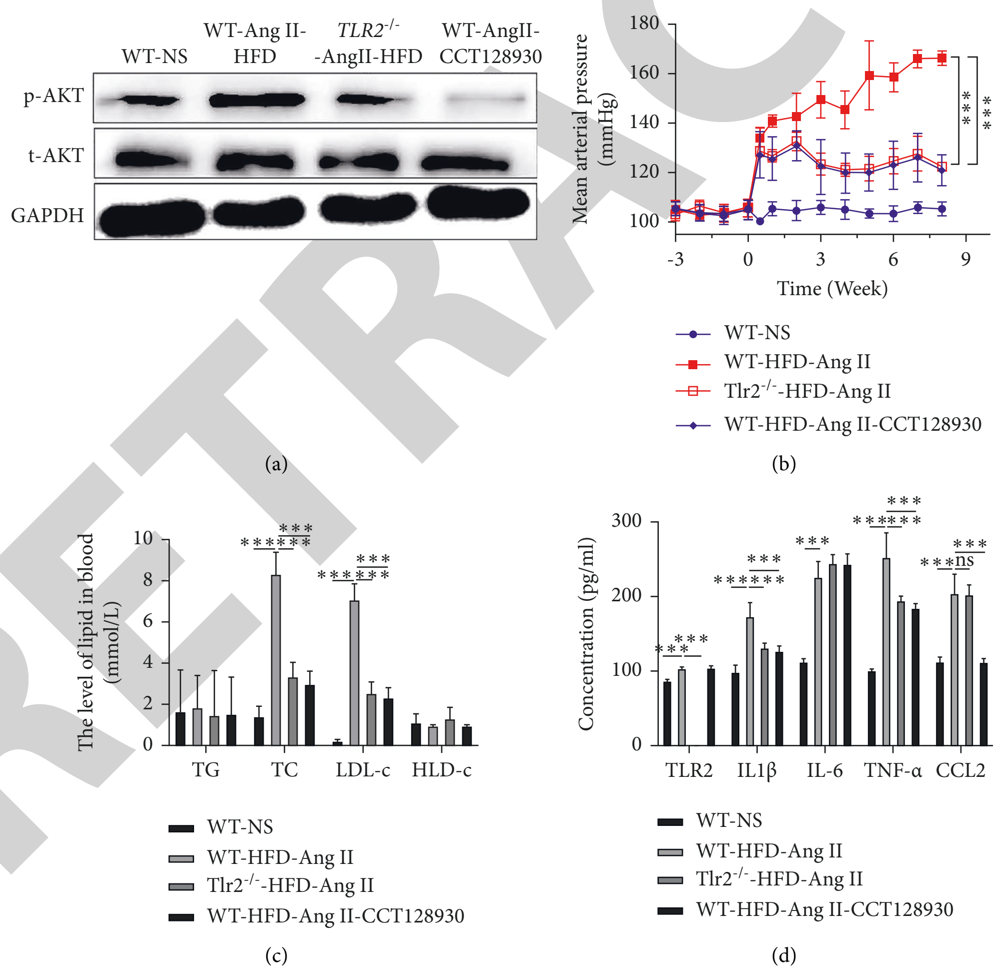

FIGURE 4: Changes of Akt pathway protein, MAP, lipid level, and apolipoprotein level, TLR2 and inflammatory factors compared those after blocking the Akt pathway. (a) The expression of p-Akt, t-Akt proteins in the wild-high fat-Ang II-CCT128930 group was significantly lower than that in wild-high fat-Ang II group. (b) After the construction of the model, MAP in the wild-high fat-Ang II-CCT128930 group significantly decreased compared with that in the wild-high fat-Ang II group. (c) The TC and LDL in serum decreased significantly in wild-high fat-Ang II-CCT128930 group and wild-high fat-Ang II group compared with those in the wild-high fat-Ang II group, but there was no significantly statistical difference in triglyceride and HDL between the two groups. (d) Comparison of serum levels of TLR2 and proinflammatory factor in each group. The concentration of IL-1β, TNF-α, and CCL2 in serum significantly decreased in the wild-high fat-Ang II-CCT128930 group compared with that in the wild-high fat-Ang II group, with no statistical difference in the concentration of TLR2 and IL-6 ($n = 5$; $^{***}P < 0.001$).

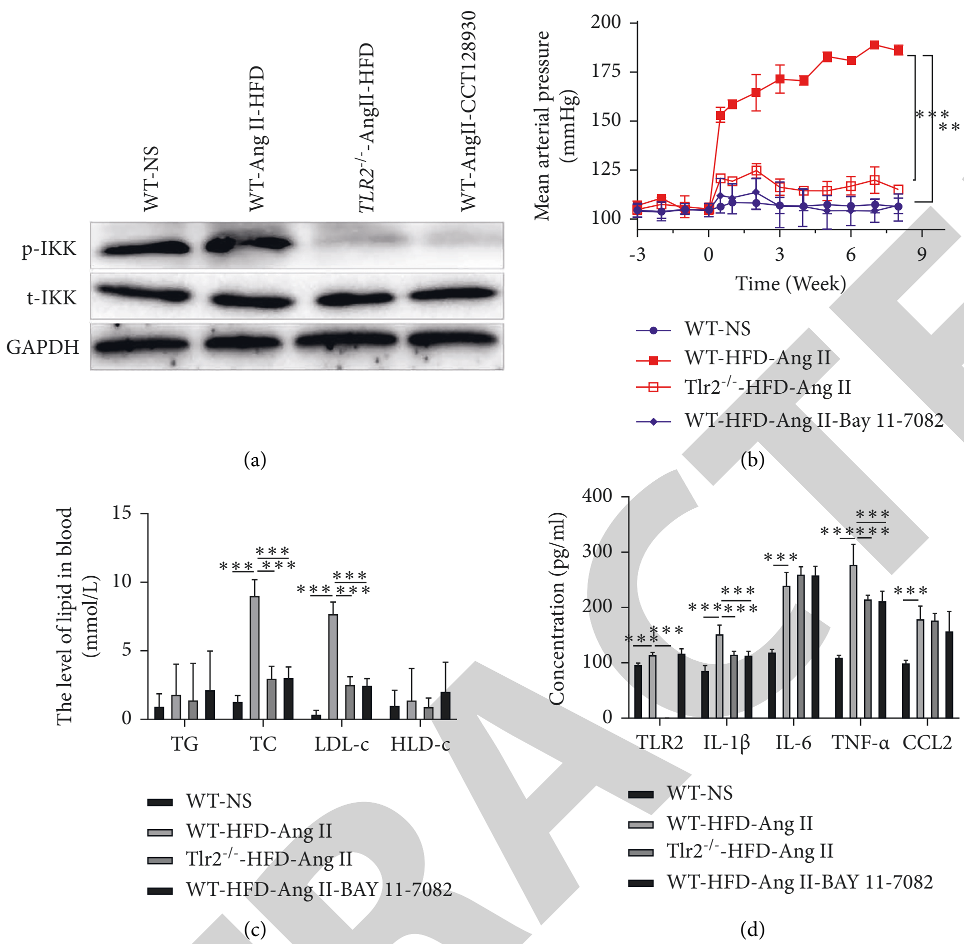

FIGURE 5: Changes in NF-κB pathway protein, MAP, lipid level, and apolipoprotein levels, TLR2, and inflammatory factors after blocking the NF-κB pathway. (a) IKK and protein expression levels of the wild-high fat-Ang II-BAY11-7082 group were significantly lower than those of the wild-high fat-Ang II group. (b) MAP in the wild-high fat-Ang II-BAY11-7082 group significantly decreased compared with the wild-high fat-Ang II group. (c) The TC and LDL in serum significantly decreased in the wild-high fat-Ang II group and wild-high fat-Ang II group, with no significant statistical difference between triglyceride and high-density lipoprotein in the two groups. (d) The concentrations of IL-1β and TNF-α in serum significantly decreased in the wild-high fat-Ang II-BAY11-7082 group compared with the wild-high fat-Ang II group, with no statistical difference in the concentrations of TLR2, IL-6, and CCL2 ($n = 5$; $^{***}P < 0.001$).

disease, and early inflammation infiltration is of important significance in cardiovascular pathogenesis. Regulation of inflammation is extremely extensive and involves complex signaling pathways [28]. Among these, NF-κB signaling pathway was studied deeply and thoroughly. We expected to investigate the effects of NF-κB signaling and hypertension with hyperlipemia, so we first assumed the inflammatory effects of TLR-related protein molecules upstream of NF-κB signaling pathway, measured TLR2 levels in the three clinical specimens by ELISA, and found a significant increase in TLR2 levels in familial hypertension group and familial hypertension combined with hyperlipidemia group compared with those in the control group. In conclusion, we assumed that TLR2-mediated inflammatory responses can play a role in primary hypertension combined with hyperlipemia.

This study is clinical problem-oriented, and after finding that TLR2 has a role in primary hypertension combined with hyperlipemia, we focused on the animal model. The specific effect of TLR2 on the occurrence and development of the diseases is highly controllable in the animal model, so we constructed the models of hypertension, hyperlipidemia, and hypertension combined with hyperlipidemia according to the relevant and reliable model-making methods [29–32]. Real-time monitoring of blood pressure of different models was given to the mice in different models to ensure the reliability of blood lipid levels in different mice for the occurrence of a lipid disorder. With high similarity to clinical blood specimens, some levels of inflammatory factors in pure hypertension were elevated. Despite irregular changes in IL-6 and CCL2, the overall inflammation remains elevated; also, TLR2 levels increased in serum. The conclusions as above obtained in the mouse model made us more convinced that TLR2 has great significance in the occurrence and development of hypertension combined with hyperlipemia. To provide a more direct verification of the role of the TLR2, we compared the degree of pathological changes of hypertension and hyperlipidemia in wild mice and gene knockout mice under the same modeling method with a *TLR*$^{2\ -/-}$ knockout mouse model. Compared with wild mice, the occurrence of hypertension and hyperlipidemia in mice after losing TLR2 gene function was more delayed, and the degree of pathological changes was less. Meanwhile, the related inflammatory factors were reduced to comparable levels in the control group after knocking out *Tlr2* gene. In conclusion, we can determine that TLR2-induced inflammation plays an important role in the disease process of hypertension combined with hyperlipemia.

In order to deeply reveal the molecular effect of TLR2-induced diseases, as well as add new cognition to the pathogenesis of hypertension and hyperlipidemia, we have conducted further studies on the signaling pathway. Recent literature reported that TLR2/4 has clear molecular interaction mechanisms with the downstream PI3K/Akt pathway and NF-κB pathway [33–35]. Therefore, we assumed that the presence of TLR2 activates these two signaling pathways, which are then activated for the transcription of downstream inflammatory factor encoding genes, resulting in increased release of inflammatory factors, creating a microenvironment of inflammatory infiltration, and ultimately inducing the occurrence of hypertension and hyperlipidemia. First, we tested the degree of activation of Akt and NF-κB signaling pathways in control, hypertensive combined with hyperlipemia and *Tlr2*$^{-/-}$ groups. Western blot essay found a significant increase in phosphorylation levels of Akt, IKK, and p68 proteins, meaning that Akt and NF-κB signaling pathways were activated in the model of hypertension combined with hyperlipemia. To elucidate the role of TLR2, we simultaneously detected the degree of activation of Akt and NF-κB signaling pathways in the *Tlr2*$^{-/-}$ model and found that the phosphorylation levels of Akt, IKK, and p68 proteins were recovered to comparable to controls in the gene knockout model. As in the above conclusion, it can be proved that Akt and NF-κB signaling pathways have a certain role in hypertension combined with hyperlipemia. To further confirm the role of the two signaling pathways in the occurrence and development of this disease, we blocked Akt and NF-κB signaling pathways with different inhibitors corresponding to the two pathways. As expected, we found that blood pressure and lipid levels were still higher than those in the wild-saline group (controls) regardless of which path was being knocked out. However, it significantly decreased in the wild hypertension combined with hyperlipemia model, even the pathological changes were comparable after knocking out *Tlr2* gene, with lower inflammatory factor levels. Therefore, we can confirm the positive effect of blocking Akt and NF-κB pathways on the improvement of hypertension combined with hyperlipemia.

5. Conclusion

According to our study, TLR2, inflammatory response, Akt pathway, and NF-κB pathway all contributed to the occurrence and development of hypertension combined with hyperlipemia, and previous literature have more or less reported the relationship between the four factors and hypertension combined with hyperlipidemia [36, 37]. However, there was almost no systematic research of the four on the occurrence and development of the disease. Our study systematically explained the induction of inflammation through Akt/NF-κB pathway and thus promoted the occurrence and development of hypertension combined with hyperlipemia. In addition, we removed the effects of TLR2, Akt, and NF-κB pathways, respectively, and found that the three were more or less effective in the occurrence and development of the disease. These findings added new cognition to gene-level research of cardiovascular disease. Although our research reveals the role of TLR2 on hypertension combined with hyperlipemia, it still lacks systematic verification for whether TLR2 is a good intervention target to control hypertension. We expect to continuously expand the subsequent protein interaction network with TLR2 as the center and finally screen the new target to intervene in primary familial hypertension combined with hyperlipemia to effectively control the occurrence and development of such cardiovascular diseases.

Data Availability

The datasets used and/or analyzed during the present study are available from the corresponding author upon reasonable request.

Ethical Approval

The study was approved by the Ethics Committee of The First Affiliated Hospital of Qiqihar Medical University.

Consent

Signed written informed consent was obtained from the patients and/or guardians.

Conflicts of Interest

The authors declare that they have no conflicts of interest.

Authors' Contributions

JL, CJL, and JQ conceived and designed the study. JL, QW, HH, CHL, and JQ were responsible for the collection, analysis and interpretation of the data. CJL drafted the manuscript. JQ revised the manuscript critically for important intellectual content. All authors read and approved the final manuscript.

Acknowledgments

This study was funded by the Fundamental Scientific Research Funds of Colleges and Universities in Heilongjiang Province (2020-KYYWF-0041).

References

[1] D. Zhao, J. Liu, M. Wang, X. Zhang, and M. Zhou, "Epidemiology of cardiovascular disease in China: current features and implications," *Nature Reviews Cardiology*, vol. 16, no. 4, pp. 203–212, 2019.

[2] M. Zhou, H. Wang, J. Zhu et al., “Cause-specific mortality for 240 causes in China during 1990-2013: a systematic subnational analysis for the Global Burden of Disease Study 2013,” *The Lancet*, vol. 387, no. 10015, pp. 251–272, 2016.

[3] G. Yang, Y. Wang, Y. Zeng et al., “Rapid health transition in China, 1990-2010: findings from the global burden of disease study 2010,” *The Lancet*, vol. 381, no. 9882, pp. 1987–2015, 2013.

[4] G. Zhang, C. Yu, M. Zhou, L. Wang, Y. Zhang, and L. Luo, “Burden of Ischaemic heart disease and attributable risk factors in China from 1990 to 2015: findings from the global burden of disease 2015 study,” *BMC Cardiovascular Disorders*, vol. 18, no. 1, p. 18, 2018.

[5] W. Wang, B. Jiang, H. Sun et al., “Prevalence, incidence, and mortality of stroke in China,” *Circulation*, vol. 135, no. 8, pp. 759–771, 2017.

[6] M. Zhang, Q. Deng, L. Wang et al., “Prevalence of dyslipidemia and achievement of low-density lipoprotein cholesterol targets in Chinese adults: a nationally representative survey of 163,641 adults,” *International Journal of Cardiology*, vol. 260, pp. 196–203, 2018.

[7] E. D. Michos, J. W. McEvoy, and R. S. Blumenthal, “Lipid management for the prevention of atherosclerotic cardiovascular disease,” *New England Journal of Medicine*, vol. 381, no. 16, pp. 1557–1567, 2019.

[8] A. C. Razavi, K. S. Potts, T. N. Kelly, and L. A. Bazzano, “Sex, gut microbiome, and cardiovascular disease risk,” *Biology of Sex Differences*, vol. 10, no. 1, p. 29, 2019.

[9] V. Adams and A. Linke, “Impact of exercise training on cardiovascular disease and risk,” *Biochimica et Biophysica Acta - Molecular Basis of Disease*, vol. 1865, no. 4, pp. 728–734, 2019.

[10] C. Fiuza-Luces, A. Santos-Lozano, M. Joyner et al., “Exercise benefits in cardiovascular disease: beyond attenuation of traditional risk factors,” *Nature Reviews Cardiology*, vol. 15, no. 12, pp. 731–743, 2018.

[11] M. R. Thomas and G. Y. H. Lip, “Novel risk markers and risk assessments for cardiovascular disease,” *Circulation Research*, vol. 120, no. 1, pp. 133–149, 2017.

[12] S. J. Taler, “Initial treatment of hypertension,” *New England Journal of Medicine*, vol. 378, no. 7, pp. 636–644, 2018.

[13] B. Bozkurt, D. Aguilar, A. Deswal et al., “Contributory risk and management of comorbidities of hypertension, obesity, diabetes mellitus, hyperlipidemia, and metabolic syndrome in chronic heart failure: a scientific statement from the American heart association,” *Circulation*, vol. 134, pp. e535–e578, 2016.

[14] T. P. Mikolajczyk and T. J. Guzik, “Adaptive immunity in hypertension,” *Current Hypertension Reports*, vol. 21, p. 68, 2019.

[15] M. Sakuma, S. Toyoda, T. Inoue, and K. Node, “Inflammation in pulmonary artery hypertension,” *Vascular Pharmacology*, vol. 118-119, Article ID 106562, 2019.

[16] P. Libby, J. E. Buring, L. Badimon et al., “Atherosclerosis,” *Nature Reviews Disease Primers*, vol. 5, no. 1, p. 56, 2019.

[17] S. Zhong, L. Li, X. Shen et al., “An update on lipid oxidation and inflammation in cardiovascular diseases,” *Free Radical Biology and Medicine*, vol. 144, pp. 266–278, 2019.

[18] J. Korbecki and K. Bajdak-Rusinek, “The effect of palmitic acid on inflammatory response in macrophages: an overview of molecular mechanisms,” *Inflammation Research*, vol. 68, no. 11, pp. 915–932, 2019.

[19] W. Xie, P. Zhou, Y. Sun et al., “Protective effects and target network analysis of ginsenoside Rg1 in cerebral ischemia and reperfusion injury: a comprehensive overview of experimental studies,” *Cells*, vol. 7, no. 12, p. 270, 2018.

[20] S. Ascher and C. Reinhardt, “The gut microbiota: an emerging risk factor for cardiovascular and cerebrovascular disease,” *European Journal of Immunology*, vol. 48, no. 4, pp. 564–575, 2018.

[21] S. Biswas, A. Zimman, D. Gao, T. V. Byzova, and E. A. Podrez, “TLR2 plays a key role in platelet hyperreactivity and accelerated thrombosis associated with hyperlipidemia,” *Circulation Research*, vol. 121, no. 8, pp. 951–962, 2017.

[22] Z.-L. Zhang, M.-M. Zhu, H.-L. Li et al., “Influence of PRKCH gene polymorphism on antihypertensive response to amlodipine and telmisartan,” *Clinical and Experimental Hypertension*, vol. 39, no. 8, pp. 726–731, 2017.

[23] C. R. Williamson, S. Khurana, P. Nguyen, C. J. Byrne, and T. C. Tai, “Comparative analysis of renin-angiotensin system (RAS)-Related gene expression between hypertensive and normotensive rats,” *Medical Science Monitor Basic Research*, vol. 23, pp. 20–24, 2017.

[24] W. Feng, L. Sun, and X. F. Qu, “Association of AGTR1 and ACE2 gene polymorphisms with structural atrial fibrillation in a Chinese Han population,” *Die Pharmazie*, vol. 72, pp. 17–21, 2017.

[25] G. Seravalle and G. Grassi, “Obesity and hypertension,” *Die Pharmazie*, vol. 72, pp. 17–21, 2017.

[26] A. R. Tall and L. Yvan-Charvet, “Cholesterol, inflammation and innate immunity,” *Nature Reviews Immunology*, vol. 15, no. 2, pp. 104–116, 2015.

[27] M. Haneklaus and L. A. J. O’Neill, “NLRP3 at the interface of metabolism and inflammation,” *Immunological Reviews*, vol. 265, no. 1, pp. 53–62, 2015.

[28] J. Ben, B. Jiang, D. Wang et al., “Major vault protein suppresses obesity and atherosclerosis through inhibiting IKK-NF-κB signaling mediated inflammation,” *Nature Communications*, vol. 10, no. 1, p. 1801, 2019.

[29] H. Ding, Y. Zhou, and H. Huang, “MiR-101a ameliorates AngII-mediated hypertensive nephropathy by blockade of TGFβ/Smad3 and NF-κB signalling in a mouse model of hypertension,” *Clinical and Experimental Pharmacology and Physiology*, vol. 46, no. 3, pp. 246–254, 2019.

[30] Y. T. Tung, H. L. Chen, H. S. Wu, M. H. Ho, K. Y. Chong, and C. M. Chen, “Kefir peptides prevent hyperlipidemia and obesity in high-fat-diet-induced obese rats via lipid metabolism modulation,” *Molecular Nutrition & Food Research*, vol. 62, 2018.

[31] P. Zhong, D. Quan, Y. Huang, and H. Huang, “CaMKII activation promotes cardiac electrical remodeling and increases the susceptibility to arrhythmia induction in high-fat diet-fed mice with hyperlipidemia conditions,” *Journal of Cardiovascular Pharmacology*, vol. 70, no. 4, pp. 245–254, 2017.

[32] Y.-R. Guo and S.-Y. Choung, “Germacrone attenuates hyperlipidemia and improves lipid metabolism in high-fat diet-induced obese C57bl/6J mice,” *Journal of Medicinal Food*, vol. 20, no. 1, pp. 46–55, 2017.

[33] X. Jiang, L. Fang, H. Wu et al., “TLR2 regulates allergic airway inflammation and autophagy through PI3K/Akt signaling pathway,” *Inflammation*, vol. 40, no. 4, pp. 1382–1392, 2017.

[34] N. Zhai, H. Li, H. Song et al., “Hepatitis C virus induces MDSCs-like monocytes through TLR2/PI3K/AKT/STAT3 signaling,” *PLoS One*, vol. 12, no. 1, Article ID e0170516, 2017.

[35] J.-A. Cho, T.-J. Kim, H.-J. Moon, Y.-J. Kim, H.-K. Yoon, and S.-Y. Seong, “Cardiolipin activates antigen-presenting cells via TLR2-PI3K-PKN1-AKT/p38-NF-kB signaling to prime

Hindawi
Journal of Healthcare Engineering
Volume 2022, Article ID 5914541, 10 pages
https://doi.org/10.1155/2022/5914541

Research Article

The Predictive Efficacy of Serum Exosomal microRNA-122 and microRNA-148a for Hepatocellular Carcinoma Based on Smart Healthcare

Peng Deng, Mi Li, and Yuni Wu

Department of Oncology, Chongqing General Hospital, Chongqing 610095, China

Correspondence should be addressed to Yuni Wu; yuniwu1985@163.com

Received 12 October 2021; Accepted 6 December 2021; Published 4 January 2022

Academic Editor: Enas Abdulhay

Objective. Hepatocellular carcinoma (HCC) remains a devastating tumor globally. Serum exosomes are reliable biomarkers for tumors, including HCC. Hence, this study explored the efficacy and mechanism of serum exosomes in HCC. *Methods*. microRNA (miR)-122 and miR-148a expressions in serum exosomes from HCC patients and healthy subjects and their predictive efficacy for HCC were detected. Correlation between serum exosomal miR-122/148a expressions with survival rate, clinical stage, lymph node metastasis, and tumor differentiation level and levels of HCC-related serum markers (CA199, FucAFP, ALD-A, and AFu) were detected. PAX2 staining intensity and expression in HCC were measured. PAX2 predictive efficacy for HCC and its correlation with clinical stage, lymph node metastasis, tumor differentiation level, and HCC-related serum marker levels were analyzed. The targeted binding relationship between miR-122 and miR-148a and PAX2 was predicted and verified. *Results*. Serum exosomal miR-122 and miR-148a expressions were downregulated in HCC, showing potent predictive efficacy for HCC, which was negatively related to clinical stage and lymph node metastasis and positively related to tumor differentiation level, patient survival rate, and HCC-related serum marker levels. PAX2 showed increased staining intensity and expression in HCC, together with high predictive efficacy for HCC. PAX2 expression showed a positive correlation with clinical stage and lymph node metastasis and a negative correlation with tumor differentiation level and HCC-related serum marker levels. miR-122 and miR-148a conjointly targeted PAX2 in HCC. *Conclusion*. We demonstrated that serum exosomal miR-122 and miR-148a played a predictive role and were linked to prognosis in HCC via interactions with PAX2.

1. Introduction

Hepatocellular carcinoma (HCC), as a frequent malignancy that usually occurs in the presence of chronic liver disease, accounts for 75–85% of primary liver cancers and contributes to the vast majority of cancer-related deaths [1, 2]. HCC develops mostly as a consequence of hepatitis B infection; in addition, other risk factors including genetic causes, excessive drinking, hepatitis C infection, and fatty liver disease also contribute to HCC initiation and progression [3, 4]. Due to insidious symptoms in the early stage and subsequent rapid tumor development, a majority of HCC patients are not diagnosed until the late stage, during which HCC is largely incurable due to the low therapeutic response rate and apparent drug resistance [5, 6]. Surgical resection and liver transplantation are still two standard methods for treating HCC; however, the recurrence rate after radical resection and transplantation remains high, notably reducing the long-term survival of HCC patients [7–9]. Therefore, novel predicative biomarkers are in urgent need for promoting HCC diagnosis as well as improving the prognosis.

Exosomes are characterized by small bilipid protein structures with a diameter of 30–150 nm and show the presence of almost all biological fluids including serum, which makes them recognized as reliable biomarkers for cancer prognosis and diagnosis [10]. Exosomes harbor abundant biological cargoes, such as DNA, microRNAs (miRs), and proteins, which underlie their potential to be biomarkers for diagnostic applications [11]. miRs, defined as a group of small endogenous noncoding RNAs, are potent regulators of posttranscriptional gene expression, promising to be candidates for developing biomarkers [12, 13]. Serum exosomal microRNAs (miRs) are very stable and can act as effective biomarkers for early cancer diagnosis [14]. Accumulating studies have demonstrated that serum exosomal miRs have great value in HCC diagnosis and therapy and can also be used as novel hallmarks for HCC recurrence prediction [6, 15].

Therefore, it was reasonable to hypothesize that serum exosomes may possess an underlying value in HCC prediction and prognosis via carrying miRs through possible mechanisms. Consequently, a series of predictions and experiments were performed to determine the role of HCC-related serum exosomal miRs and their related mechanisms in HCC prediction and prognostic evaluation with the purpose to provide some novel insights for HCC treatment.

2. Materials and Methods

2.1. Clinical Sample Collection. HCC serum samples were collected from Chongqing General Hospital. HCC patients had no history of acute, chronic, or malignant diseases or surgery in the previous 12 months based on the screening results of the physical examination center of Chongqing General Hospital. Histologically, HCC patients were confirmed with no radiotherapy and chemotherapy history and no acute/chronic inflammation signs. Normal subjects ($n = 31$) were matched with HCC patients ($n = 59$) by age and gender. This study got approval from the Ethics Committee of Chongqing General Hospital. All subjects signed informed consent. All experiments were performed following the guidelines and principles of the Declaration of Helsinki.

Peripheral blood samples were collected in the serum separation tube and treated within 2 h. After centrifugation (1200g, 4°C, and 10 min) of the blood samples, the supernatant was absorbed and centrifuged (3,000g, 4°C, and 15 min). Next, the supernatant was crushed into several equal parts and stored at −80°C.

2.2. Extraction of Serum Exosomes. The exosomes were separated using gradient centrifugation as previously described [16]. Specifically, serum samples were unfrozen on ice. Next, serum (1 mL) was diluted in phosphate-buffered saline (PBS, 11 mL) and then ultracentrifuged (150,000g, 4°C overnight). After discarding the supernatant, the precipitate was rinsed with PBS (11 mL), followed by centrifugation (150,000g, 4°C, and 2 h). Afterwards, after the supernatant was removed, the precipitate underwent a resuspension in PBS.

2.3. Transmission Electron Microscope (TEM) Analysis. Exosome samples were diluted using PBS at an appropriate volume. Next, the diluted exosomes (10 μL) were added to the copper mesh for 1 min with excess liquid absorbed using filter paper, followed by a 1min staining with 2% uranyl acetate (10 μL) with excess staining solution absorbed using filter paper. Next, the copper mesh underwent a 15-minute air-drying and was imaged on an FEI Tecnai G2 Spirit TEM (Thermo Fisher Scientific Inc., Waltham, MA, USA) at a voltage of 120 kV.

2.4. Nanoparticle Tracking Analysis (NTA). NTA was conducted for the determination of exosome size and distribution utilizing the NanoSight NS300 system and NTA 2.3 (Malvern Instruments Ltd., Malvern, UK) in compliance with the instructions of the manufacturer.

2.5. Flow Cytometry. Anti-CD63, anti-CD81, and anti-CD47 antibodies or PI were used to label the extracted exosomes. A flow cytometer was used to excitate 525/620 nm band-pass filters at 488 nm wavelength for detecting FITC/PI fluorescence to evaluate the positive rates of CD63, CD81, CD47, and PI in the extracted exosomes.

2.6. Detection of HCC-Related Serum Markers. Concentrations of cancer antigen 199 (CA199), fucosylated alpha-fetoprotein (FucAFP), aldolase A (ALD-A), and Alpha-L-fucosidase (AFU) were detected using enzyme-linked immunosorbent assay kits (Nanjing JianCheng Bioengineering Institute, Nanjing, Jiangsu, China). All operations were carried out as per the kit instructions.

2.7. Dual-Luciferase Reporter Gene Assay. The binding relationship of miR-122/148a and PAX2 was first predicted through StarBase (https://starbase.sysu.edu.cn/). The wild-type (WT) PAX2 3′UTR fragment containing miR-122/148a binding sites or mutant (MT) (in the absence of predicted miR target sequence) was inserted into pmirGLO (Shanghai Generay Biotech Co., Ltd., Shanghai, China) plasmid. The reporter plasmid (pmirGLO-PAX2-WT/MT) was cotransfected with miR-122/148a mimic or mimic NC into HEK293T cells. After 48 h of transfection, cell lysate was collected and luciferase activity was measured using Tecan Infinite M200 PRO instrument and Dual-Luciferase Reporter System (Promega Corp., Madison, Wisconsin, USA). The firefly luciferase fluorescence intensity was standardized using Renilla luciferase fluorescence intensity.

2.8. Bioinformatics Analysis. HCCGSE104251 and GSE138178 microarrays were obtained from the Gene Expression Omnibus (GEO) database (https://www.ncbi.nlm.nih.gov/geo/), which were then normalized using the R language limma package (https://cran.r-project.org/web/packages/pheatmap/) with $|\log FC| > 2$ and adj. $p < 0.05$ as the screening thresholds. The heatmaps were drawn. The targeted binding relationship between miR-122/148a and PAX2 was predicted through StarBase (https://starbase.sysu.edu.cn/). The relationship between miR-122 and miR-148a expressions and the survival rate of HCC patients was measured using the KM-Plotter website (https://kmplot.com/analysis/). The staining intensity of paired box (PAX) 2, cyclinD1 (CCND1), myelocytomatosis viral oncogene homolog (MYC), neural precursor cell expressed, developmentally downregulated 4 (NEDD4), and C-X-C motif chemokine ligand 5 (CXCL5) in normal liver tissues and HCC tissues was determined through the Human Protein Atlas website (https://www.proteinatlas.org/).

2.9. Reverse Transcription-Quantitative Polymerase Chain Reaction (RT-qPCR). cDNA synthesis was performed using the All-in-One™ miRNAFirst-Strand cDNA Synthesis Kit (GeneCopoeia, Rockville, MD, USA) as per the manufacturer's protocols. Reverse transcription was accomplished via a 60-minute incubation of the mixture at 37°C and then a 5-minute incubation at 85°C, followed by storage at 4°C. RT-qPCR was carried out utilizing ChamQ SYBR qPCR Master Mix (NanJing Vazyme Biotech Co., Ltd, Nanjing, Jiangsu, China) as per the instructions of the manufacturer. All reactions were checked three times. miRprimer2 software 32 was used for miRNA forward primer design, and its synthesis was finished by Nanjing Genscript Technology Co., Ltd. (Nanjing, Jiangsu, China). RT-qPCR was carried out on the StepOnePlus real-time PCR system (Applied Biosystems, Waltham, MA, USA) under the conditions of 3 min at 95°C, and then 40 cycles of 10 s at 95°C and 30 s at 60°C. The geometric mean of the internal reference was used for RT-qPCR value normalization, and the relative expression was determined using the $2^{-\Delta\Delta Ct}$ method.

2.10. Statistical Analysis. SPSS 21.0 (IBM Corp., Armonk, NY, USA) was utilized to analyze data. The Kolmogorov–Smirnov test confirmed that data were normally distributed. The results were represented as mean ± standard deviation. The comparison between the two groups was analyzed using a *t*-test. A comparison among multiple groups was analyzed using one-way and two-way analysis of variance (ANOVA) followed by Tukey's multiple comparison test. Fisher's exact test was utilized for measurement data. Correlation was analyzed utilizing Pearson's correlation coefficient test, and a receiver operating characteristic (ROC) curve was drawn to evaluate the predictive efficacy of miR-122/148a and PAX2 for HCC. The p value was gained from a two-sided test. $p < 0.05$ meant statistically significant.

3. Results

3.1. Serum Exosomes in HCC Patients Were Successfully Extracted. First, exosomes were extracted from the serum of 31 healthy subjects and 59 HCC patients using gradient centrifugation. The size of the extracted particles was analyzed using the NanoSight NS300 system and NTA 2.3 software, which was observed to be about 92.46 ± 2.41 nm (Figure 1(a)). In addition, the extracted particles were found to be barrel-shaped, ellipsoidal, or round, with a diameter of about 100 nm under a TEM (Figure 1(b)). To further exclude the influence of apoptotic bodies on the subsequent experimental results, we used PI staining and observed that the extracted exosomes were negative for PI staining, as shown by flow cytometry results (Figure 1(c)). Exosome specific surface markers (CD63, CD81, and CD47) were further determined using flow cytometry, and it was found that CD63, CD81, and CD47 showed positive expression in the extracted exosomes (Figure 1(d)). From all the above-mentioned, we confirmed that the extracted particles were in line with the characteristics of exosomes.

3.2. miR-122/148a Was Poorly Expressed in HCC Patient Serum Exosomes and Correlated with Prognosis. Firstly, differentially expressed miRs in serum exosomes of 5 HCC patients and 5 healthy subjects in the GSE104251 dataset from the GEO database (https://www.ncbi.nlm.nih.gov/geo/) were analyzed, and 179 differentially expressed miRs were screened (Figure 2(a)) based on the threshold of $|\log FC| > 2$ and $p < 0.05$. The first 50 miRs with differential expression were displayed on the heatmap (Figure 2(b)). Next, expressions of the first 6 differentially expressed miRs (miR-122, miR-239, miR-148a, miR-447, miR-681, and miR-581) in serum exosomes of 31 healthy subjects and 59 HCC patients were detected using RT-qPCR. miR-122 and miR-148a were found to be dramatically downregulated in serum exosomes of HCC patients (Figure 2(c)). Meanwhile, the predictive efficacy of the first 6 differentially expressed miRs (miR-122, miR-239, miR-148a, miR-447, miR-681, and miR-581) for HCC patients was measured using an ROC curve. miR-122 and miR-148a showed the largest area under the curve (Figure 2(d)). Subsequently, miR-122 and miR-148 effects on HCC patient survival rate were predicted through the KM-Plotter website (https://kmplot.com/analysis/), and it was found that HCC patients with low expression of miR-122/148a had a lower survival rate (Figure 2(e)). In addition, according to our findings, miR-122/148a expression was negatively correlated with the clinical stage and lymph node metastasis of HCC patients, while positively correlated with the tumor differentiation level (Figures 2(f)–2(h)).

3.3. miR-122/148a Expression Was Negatively Correlated with HCC-Related Serum Marker Levels. To further determine the role of miR-122/148a in HCC patients, we further analyzed the relationship between miR-122/148a expression in serum exosomes and the concentration of HCC-related serum markers (CA199, FucAFP, ALD-A, and AFu) in HCC patients. First, levels of CA199, FucAFP, ALD-A, and AFu in 59 HCC patients were found to show an obvious elevation relative to those in 31 healthy subjects (Figures 3(a)–3(d)). Next, as shown by our results, miR-122/148a expression was negatively related to HCC-associated serum marker concentrations (Figures 3(e)–3(h)).

3.4. PAX2 Was Highly Expressed in Serum of HCC Patients. Subsequently, we downloaded the HCC GSE138178 microarray (including HCC tissues and normal adjacent liver tissues of 49 HCC patients) from the GEO database (https://www.ncbi.nlm.nih.gov/geo/). By setting the threshold $|\log FC| > 2$ and $p < 0.05$, 539 differentially expressed genes were identified (Figure 4(a)). The first 50 differentially expressed mRNAs were displayed in the heatmap (Figure 4(b)). The staining intensity of PAX2, CCND1, MYC, NEDD4, and CXCL5 in normal liver tissues

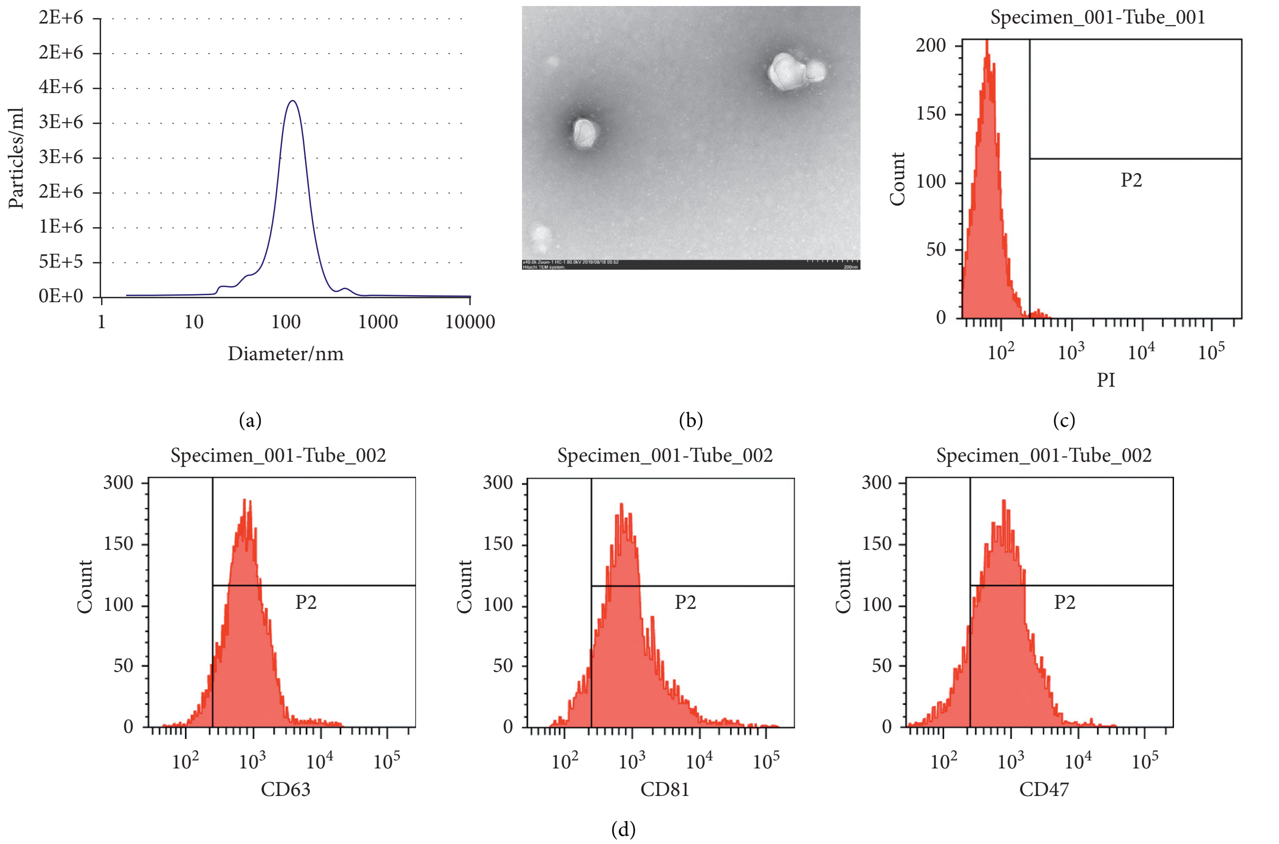

Figure 1: Serum exosomes in HCC patients are successfully extracted. (a) The size and distribution of exosomes was analyzed using NanoSight NS300 system and NTA 2.3 software; (b) the shape and size of exosomes were detected using a TEM; (c) the positive rate of exosomes was detected by PI staining; (d) the surface marker proteins CD63, CD81, and CD47 of exosomes were determined utilizing flow cytometry. All tests were repeated three times.

and HCC tissues was further determined through the Human Protein Atlas website (https://www.proteinatlas.org/), which was found to show a notable elevation in HCC tissues compared to that in normal liver tissues (Figures 4(c)–4(g)). Furthermore, PAX2, CCND1, MYC, NEDD4, and CXCL5 expressions in the serum of 31 healthy subjects and 59 HCC patients were detected using RT-qPCR, and they were found to be noticeably increased in the serum of HCC patients relative to those in normal subjects, among which PAX2 exhibited the most significant expression difference (Figure 4(h)).

3.5. PAX2 Expression Was Related to HCC Patient Prognosis. To further explore PAX2's role in HCC and its clinical-predictive efficacy, we first used a ROC curve to predict the predictive efficacy of PAX2, CCND1, MYC, NEDD4, and CXCL5 expressions for HCC. PAX2 showed the highest predictive efficacy for HCC (Figure 5(a)). The relationship between PAX2 expression and the clinical stage, lymph node metastasis, and tumor differentiation level of HCC patients was further analyzed. As shown by our results, PAX2 expression showed a positive correlation with clinical stage and lymph node metastasis, while a negative correlation with tumor differentiation level (Figures 5(b)–5(d)). Furthermore, levels of CA199, FucAFP, ALD-A, and AFu were found to be positively correlated with PAX2expression in the 59 HCC patients (Figures 5(e)–5(h)). From all of the abovementioned, PAX2 was crucial in the HCC occurrence and prediction.

3.6. miR-122 and miR-148a Conjointly Targeted PAX2. To further determine the regulatory mechanism of miR-122 and miR-148a in PAX2, we first predicted the targeted binding relationship between miR-122/148a and PAX2 via the StarBase website (https://starbase.sysu.edu.cn/), and it was observed that miR-122 and miR-148a could target PAX2 3′UTR sequence (Figures 6(a) and 6(b)). The dual-luciferase reporter gene assay was designed to further verify the above binding relationship. 293 T cells cotransfected with miR-122/148a mimic and PAX2-WT showed remarkably decreased luciferase activity, while those cotransfected with mimic NC and PAX2-MT exhibited no obvious change (Figures 6(c) and 6(d)). Subsequently, we verified that miR-122/148a expression showed a negative correlation with PAX2expression in HCC (Figures 6(e) and 6(f)).

4. Discussion

Globally, HCC still accounts largely for tumor-related death [17]. Exosomes, widely distributed in biological fluids including serum, are found to be implicated in

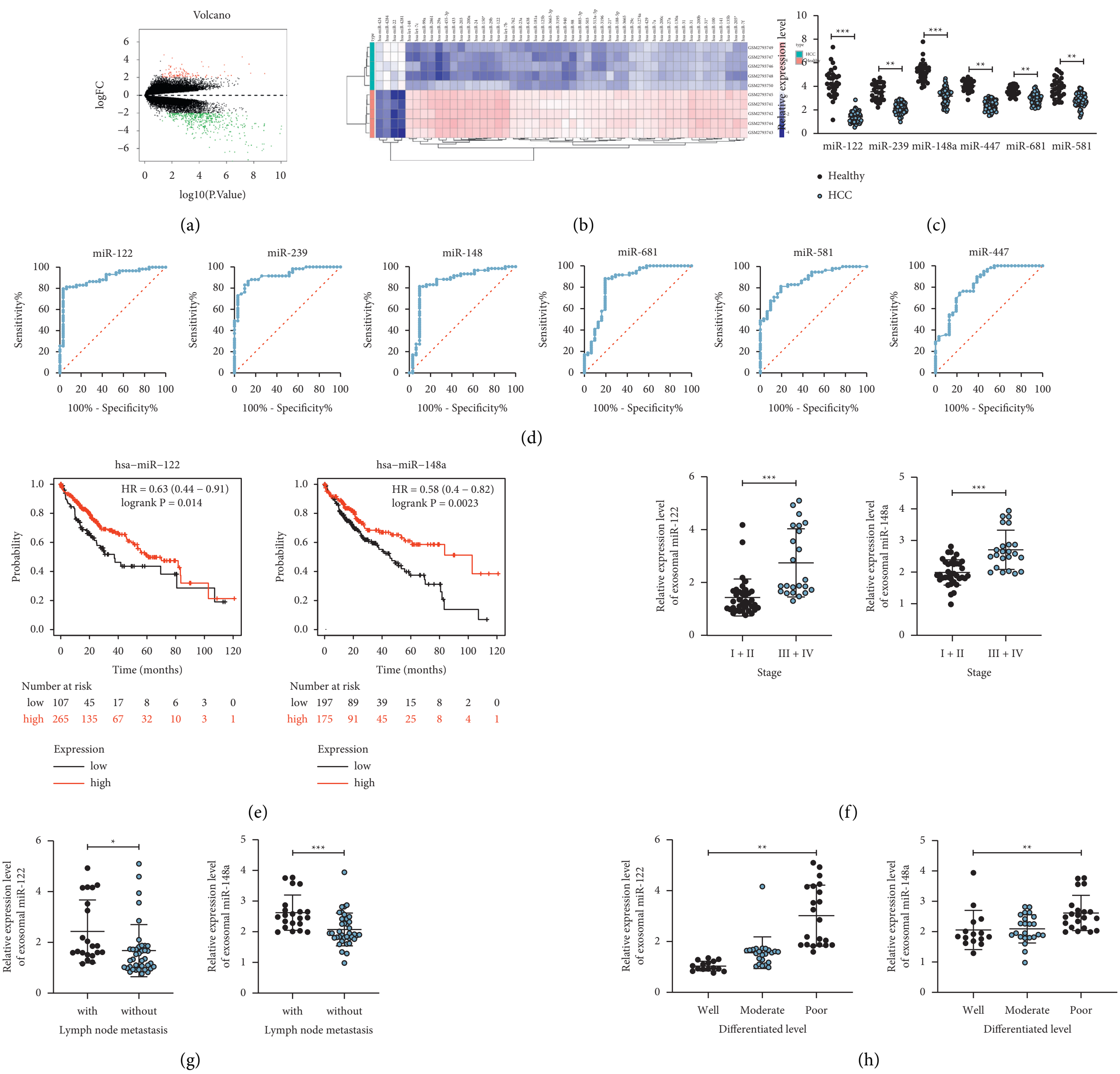

Figure 2: Serum exosomal miR-122 and miR-148a are poorly expressed in HCC and are correlated with prognosis. (a) Volcano plots for the differentially expressed miRs in serum exosome GSE104251 dataset; (b) a heatmap of the top 50 miRs with the highest degree of differential expression in GSE104251 microarray; (c) RT-qPCR was utilized to measure expressions of miR-122, miR-239, miR-148a, miR-447, miR-681, and miR-581 in serum exosomes of 31 healthy subjects and 59 HCC patients; (d) the predictive efficacy of miR-122, miR-239, miR-148a, miR-447, miR-681, and miR-581 for HCC patients was measured using ROC curves; (e) miR-122/148a effects on HCC patient survival rate were predicted using the KM-Plotter website (https://kmplot.com/analysis/); (f–h) the relationships between miR-122/148a expression and the clinical stage, lymph node metastasis, and tumor differentiation level of HCC patients. All experiments were repeated at least three times, and each point represented one subject. Data in panel C were analyzed utilizing the unpaired t-test. $^{*}p < 0.05$; $^{**}p < 0.01$; $^{***}p < 0.001$.

tumors via carrying their functional cargos, including miRs, thereby showing potential applications in the therapeutic interventions of tumors [18]. In the present study, we demonstrated that HCC patient serum exosomal miR-122 and miR-148a were predictive factors for HCC and related to HCC patient prognosis, which were mediated by their conjointly targeted PAX2 in HCC.

Serum exosomal miRs promise to be biomarkers for HCC prediction [6, 15]. In addition, as has been reported previously, miR-122 is abundant in the liver, and its reduction plays a pathogenic role in liver diseases [19]. Aberrantly decreased miR-148a expression has been described in multiple tumors, with its depletion frequently related to an advanced clinical stage and metastasis, as well as poor clinical

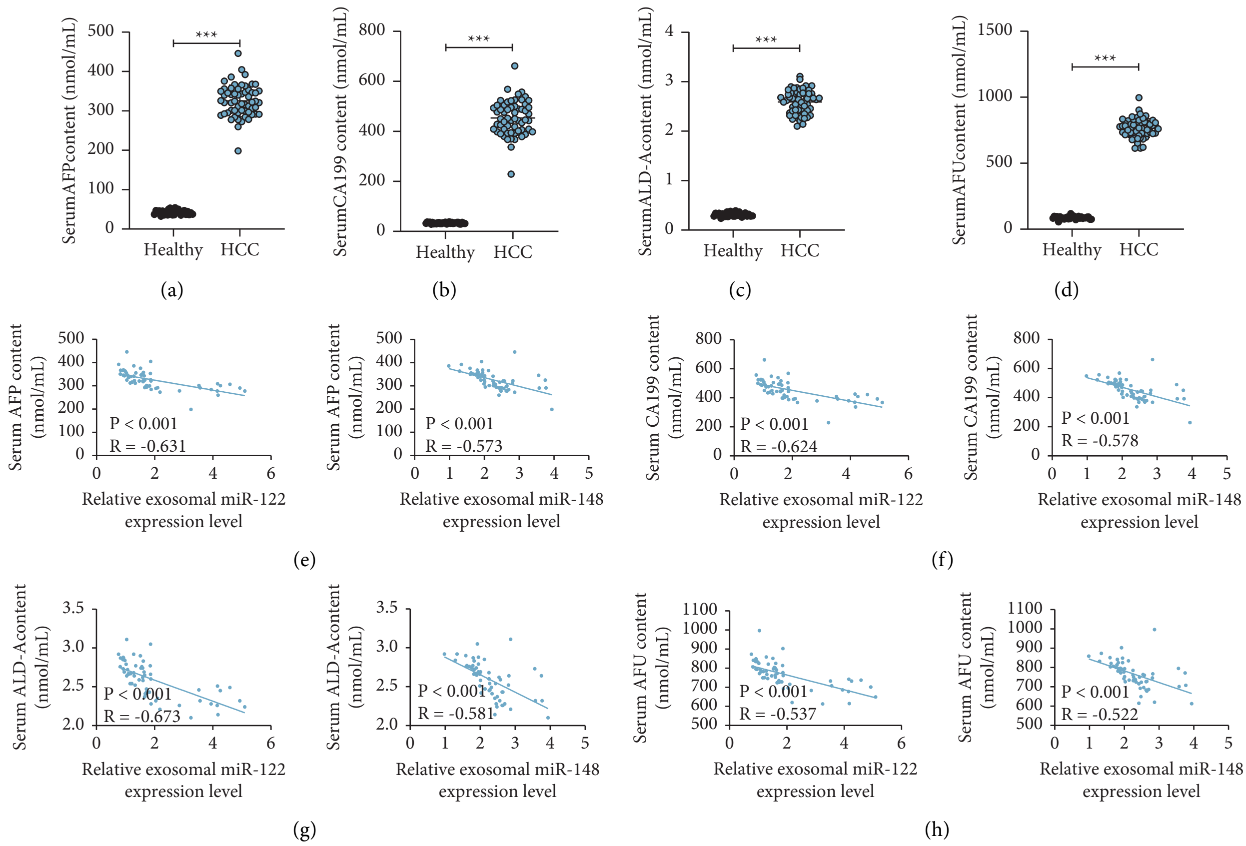

FIGURE 3: miR-122/148a expression is negatively related to levels of HCC-related serum markers. (a–d) Concentrations of CA199, FucAFP, ALD-A, and AFu in 59 HCC patients were detected; (e–h) the correlation of miR-122/148a expression with the serum levels of CA199, FucAFP, ALD-A, and AFu was analyzed. Data were analyzed using the unpaired t-test. $^{***}p < 0.001$.

outcome [20]. In the present study, differentially expressed miRs in serum exosomes of HCC patients and healthy subjects were first obtained using the GSE104251 microarray, and then we identified the first 6 differentially expressed miRs, among which miR-122 and miR-148a were the two most downregulated miRs in serum exosomes of HCC patients and showed potent predictive efficacy for HCC, and their expressions were negatively related to the clinical stage and lymph node metastasis, and positively correlated with the survival rate and the tumor differentiation level of HCC patients. Likewise, serum exosomal miR-122 shows an obvious downregulation in HCC patients, promising to be a reliable serological biomarker for HCC [21]. miR-122 expression is tightly linked to tumor size and tumor stage in HCC, and reduced miR-122 expression is associated with the short survival of HCC patients [22]. Numerous studies have demonstrated the abnormally reduced miR-148a expression in HCC [23, 24]. A previous work further pointed out that serum miR-148a expression strongly exhibits a negative correlation with tumor size and tumor-node-metastasis stage in HCC and a positive correlation with overall survival and prognosis of HCC patients [25].

As has been demonstrated previously, FucAFP, AFU, CA199, and ALD-A are effective HCC-specific indexes with their high levels correlated with a high risk of HCC [26–29]. According to our findings, levels of HCC-related serum markers (CA199, FucAFP, ALD-A, and AFu) were obviously elevated in HCC patients, and miR-122/148a expression showed a negative correlation with levels of these indexes. Consistently, downregulated miR-122 has been pointed out to be related to the deregulation of ALD-A in liver disease [30]. miR-122 is negatively linked to AFP, an independent risk factor, in HCC [31].

On the other hand, growing studies have shown that PAX2 acts as an oncogenic gene in diverse cancers, such as endometrial cancer and ovarian cancer [32, 33]. Differentially expressed genes in HCC were screened in this study, and we identified PAX2 as the most remarkably upregulated gene in HCC. In agreement with our observations, in prior work, PAX2 is found dramatically elevated in HCC [34]. PAX2 is proposed to possess a clinical-predictive role in endometrial endometrioid carcinoma [35]. As shown by our results, PAX2 showed strong predictive efficacy for HCC, with its expression positively correlated with clinical stage, lymph node metastasis, and HCC-related serum markers (CA199, FucAFP, ALD-A, and AFu), and negatively correlated with tumor differentiation level. Likewise, it has been shown that upregulated PAX2 is tightly related to HCC cell propagation [36].

To further determine the regulatory mechanism of miR-122/148a in PAX2, we first predicted and then verified that miR-122 and miR-148a conjointly targeted PAX2 in HCC.

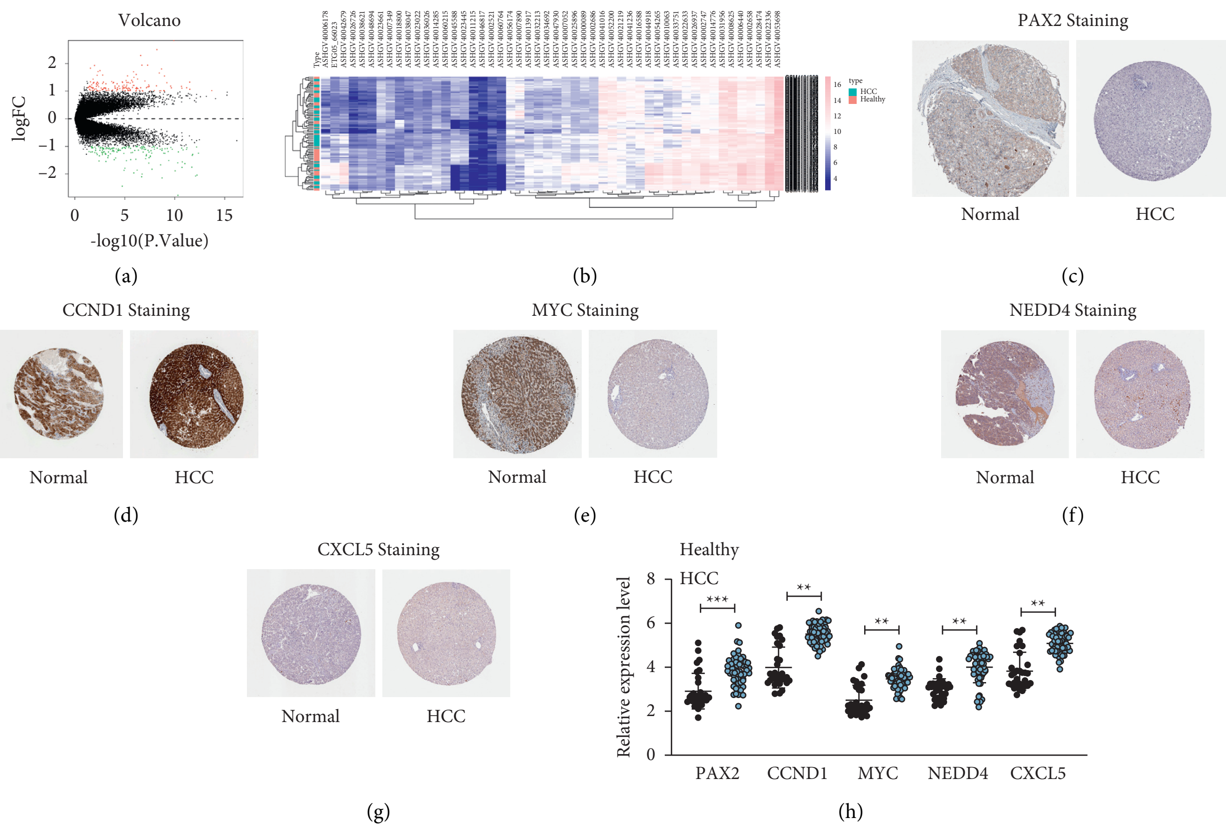

Figure 4: PAX2 is highly expressed in serum of HCC patients. (a) Volcano plots for the differentially expressed mRNAs in the GSE138178 dataset; (b) a heatmap of the top 50 differentially expressed mRNAs in the GSE138178 dataset; (c–g) the staining intensities of PAX2, CCND1, MYC, NEDD4, and CXCL5 in normal liver tissues and HCC tissues were determined through the Human Protein Atlas website (https://www.proteinatlas.org/); (h) PAX2, CCND1, MYC, NEDD4, and CXCL5 expressions in the serum of 31 healthy subjects and 59 HCC patients was detected using RT-qPCR. Data in panel H were analyzed utilizing the unpaired t-test. $^{**}p < 0.01$; $^{***}p < 0.001$.

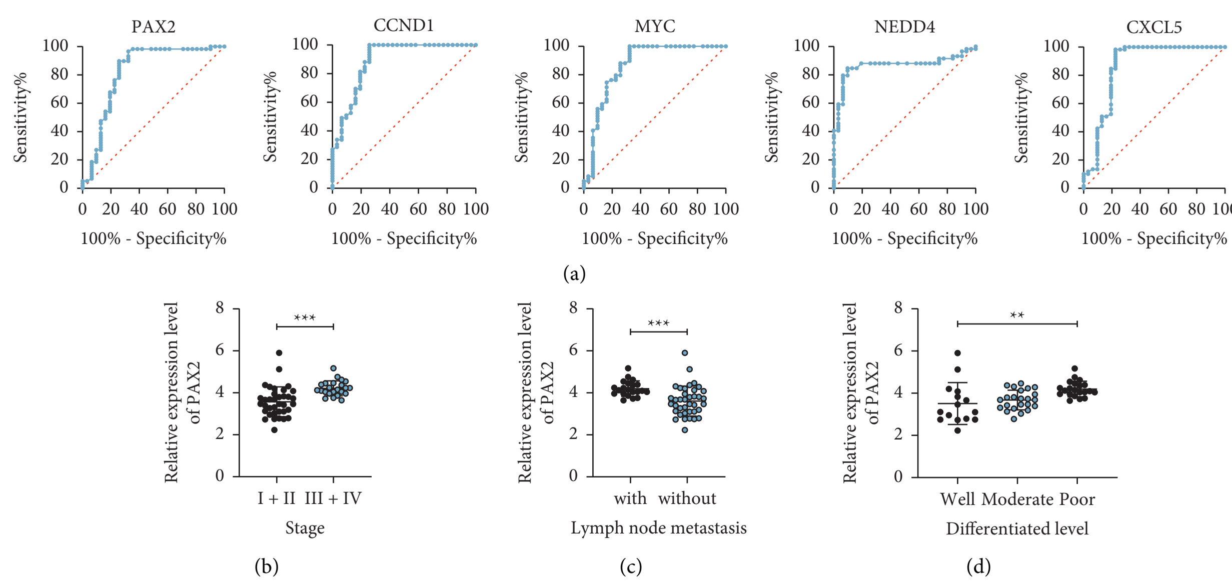

Figure 5: Continued.

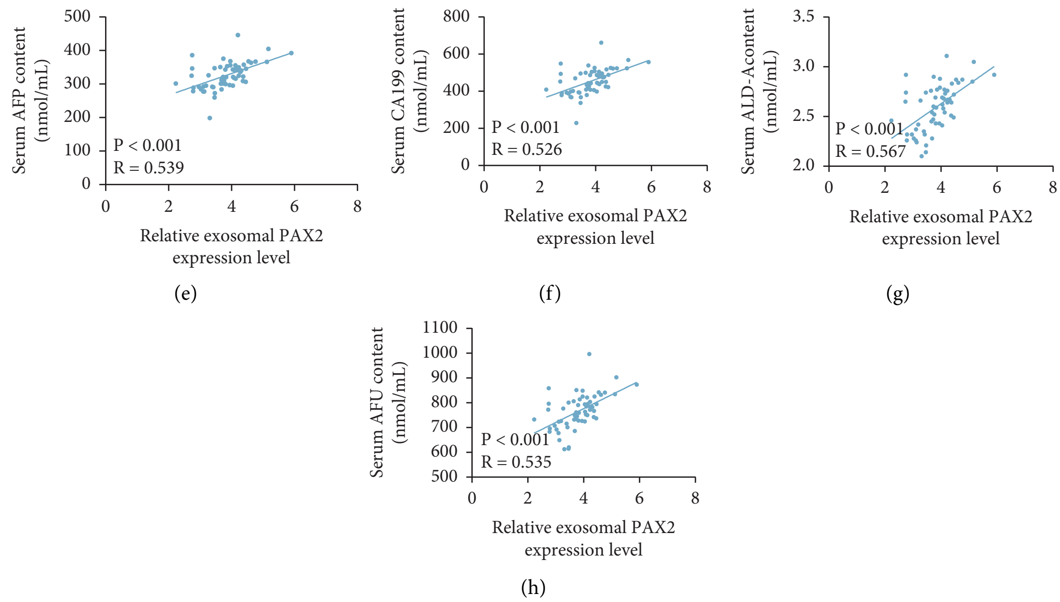

Figure 5: PAX2 expression is related to the prognosis of HCC patients. (a) The ROC curve was used to predict the predictive efficacy of PAX2, CCND1, MYC, NEDD4, and CXCL5 expressions in HCC patients; (b–d) the relationship between PAX2 expression and clinical stage, lymph node metastasis, and tumor differentiation level of HCC patients was analyzed; (e–h) the correlation between levels of CA199, FucAFP, ALD-A, and AFu and PAX2 expression in 59 HCC patients was analyzed. Each experiment was done three times repeatedly. $^{**}p < 0.01$; $^{***}p < 0.001$.

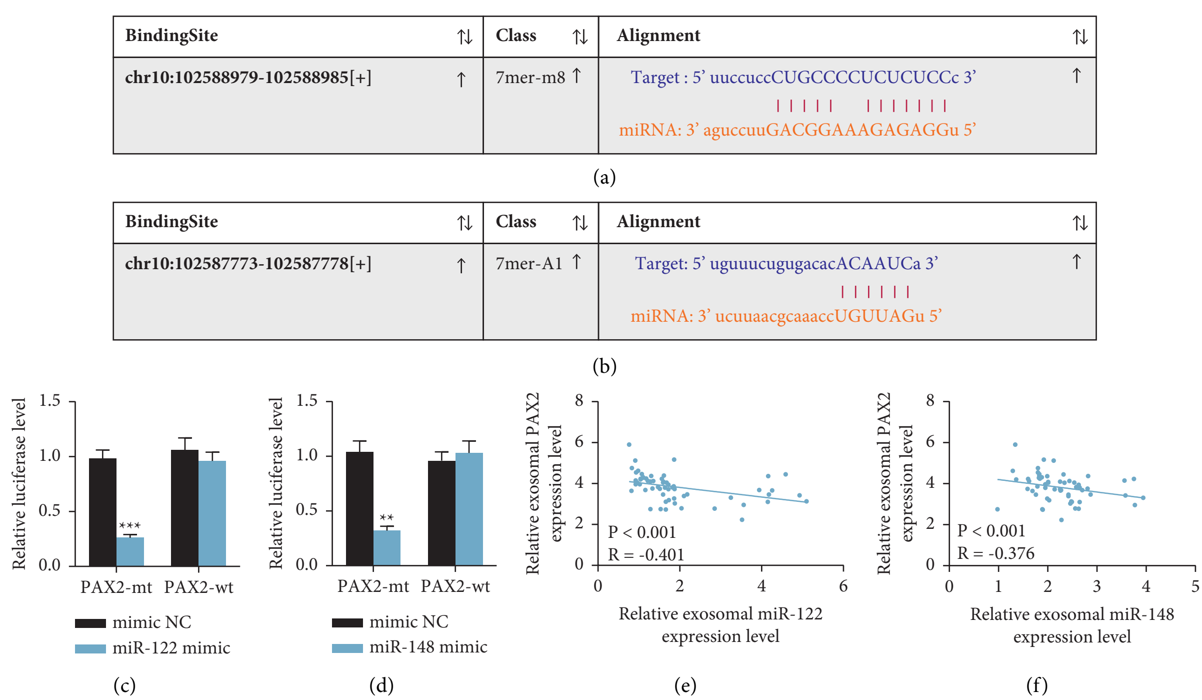

Figure 6: miR-122 and miR-148a jointly target PAX2. (a, b) The targeting binding sites between miR-122/148a and PAX2 were predicted through the StarBase website (https://starbase.sysu.edu.cn/); (c, d) The dual-luciferase reporter gene assay was designed to further verify the targeted binding relationships between miR-122/148a and PAX2; (e, f) Pearson's correlation coefficient test was used to analyze the correlation between miR-122/148a expression and PAX2 expression. Each experiment was done three times repeatedly. $^{**}p < 0.01$; $^{***}p < 0.001$.

Consistently, previous work has proposed that PAX2 functions as a serum exosomal miR-targeted gene in HCC [36]. miR-122 exhibits a negative correlation with PAX8 in H9C2 myocytes [37]. Nevertheless, little could be retrieved about PAX2's predictive efficacy in HCC and the interplay between miR-122/148a and PAX2 in HCC, which, on the other hand, demonstrated the novelty of this study.

5. Conclusion

All in all, this study supported that HCC patient serum exosomal miR-122 and miR-148a played predictive roles in HCC and were linked to patient prognosis via interactions with their conjointly targeted PAX2 in HCC. miR-122 seemed to have higher relevance to PAX2 expression than miR-148; however, more studies are required to draw a certain conclusion that miR-122 had a more important effect than miR-148. We would like to focus on this issue in our future studies, and we would like to investigate the involvement of other potential targets such as CCND1, MYC, NEDD4, and CXCL5 in the near future. Anyway, these results discovered a novel serum exosome-based therapy for HCC patients and provided therapeutic values for HCC treatment.

Data Availability

The datasets used and/or analyzed during the current study are available from the corresponding author on reasonable request.

Conflicts of Interest

The authors declare that they have no conflicts of interest.

Authors' Contributions

Peng Deng and Mi Li contributed equally to this work.

References

[1] P. S. Harris, R. M. Hansen, M. E. Gray, O. I. Massoud, B. M. McGuire, and M. G. Shoreibah, "Hepatocellular carcinoma surveillance: an evidence-based approach," *World Journal of Gastroenterology*, vol. 25, no. 13, pp. 1550–1559, 2019.

[2] H.-W. Sim and J. Knox, "Hepatocellular carcinoma in the era of immunotherapy," *Current Problems in Cancer*, vol. 42, no. 1, pp. 40–48, 2018.

[3] S. Caruso, D. R. O'Brien, S. P. Cleary, L. R. Roberts, and J. Zucman-Rossi, "Genetics of HCC: novel approaches to explore molecular diversity," *Hepatology*, vol. 73, no. S1, 2020.

[4] B. Zheng, Y.-J. Zhu, H.-Y. Wang, and L. Chen, "Gender disparity in hepatocellular carcinoma (HCC): multiple underlying mechanisms," *Science China Life Sciences*, vol. 60, no. 6, pp. 575–584, 2017.

[5] S. Chen, Q. Cao, W. Wen, and H. Wang, "Targeted therapy for hepatocellular carcinoma: challenges and opportunities," *Cancer Letters*, vol. 460, pp. 1–9, 2019.

[6] L. Jun, G. Yang, and L. Zhisu, "The utility of serum exosomal microRNAs in hepatocellular carcinoma," *Biomedicine & Pharmacotherapy*, vol. 111, pp. 1221–1227, 2019.

[7] S. Umeda, M. Kanda, and Y. Kodera, "Recent advances in molecular biomarkers for patients with hepatocellular carcinoma," *Expert Review of Molecular Diagnostics*, vol. 19, no. 8, pp. 725–738, 2019.

[8] Z.-Y. Wang, L. Geng, and S.-S. Zheng, "Current strategies for preventing the recurrence of hepatocellular carcinoma after liver transplantation," *Hepatobiliary & Pancreatic Diseases International*, vol. 14, no. 2, pp. 145–149, 2015.

[9] G. C. Wilson and D. A. Geller, "Evolving surgical options for hepatocellular carcinoma," *Surgical Oncology Clinics of North America*, vol. 28, no. 4, pp. 645–661, 2019.

[10] I.-M. Chung, G. Rajakumar, B. Venkidasamy, U. Subramanian, and M. Thiruvengadam, "Exosomes: current use and future applications," *Clinica Chimica Acta*, vol. 500, pp. 226–232, 2020.

[11] V. P. Jayaseelan, "Emerging role of exosomes as promising diagnostic tool for cancer," *Cancer Gene Therapy*, vol. 27, no. 6, pp. 395–398, 2020.

[12] T. X. Lu and M. E. Rothenberg, "MicroRNA," *Journal of Allergy and Clinical Immunology*, vol. 141, no. 4, pp. 1202–1207, 2018.

[13] K. Saliminejad, H. R. Khorram Khorshid, S. Soleymani Fard, and S. H. Ghaffari, "An overview of microRNAs: biology, functions, therapeutics, and analysis methods," *Journal of Cellular Physiology*, vol. 234, no. 5, pp. 5451–5465, 2019.

[14] M. Salehi and M. Sharifi, "Exosomal miRNAs as novel cancer biomarkers: challenges and opportunities," *Journal of Cellular Physiology*, vol. 233, no. 9, pp. 6370–6380, 2018.

[15] K. Sugimachi, T. Matsumura, H. Hirata et al., "Identification of a bona fide microRNA biomarker in serum exosomes that predicts hepatocellular carcinoma recurrence after liver transplantation," *British Journal of Cancer*, vol. 112, no. 3, pp. 532–538, 2015.

[16] S. A. Melo, L. B. Luecke, C. Kahlert et al., "Glypican-1 identifies cancer exosomes and detects early pancreatic cancer," *Nature*, vol. 523, no. 7559, pp. 177–182, 2015.

[17] T. Couri and A. Pillai, "Goals and targets for personalized therapy for HCC," *Hepatology International*, vol. 13, no. 2, pp. 125–137, 2019.

[18] W. Xu, Z. Yang, and N. Lu, "From pathogenesis to clinical application: insights into exosomes as transfer vectors in cancer," *Journal of Experimental & Clinical Cancer Research*, vol. 35, no. 1, p. 156, 2016.

[19] T. Csak, S. Bala, D. Lippai et al., "microRNA-122 regulates hypoxia-inducible factor-1 and vimentin in hepatocytes and correlates with fibrosis in diet-induced steatohepatitis," *Liver International*, vol. 35, no. 2, pp. 532–541, 2015.

[20] M. Friedrich, K. Pracht, M.-F. Mashreghi, H.-M. Jäck, A. Radbruch, and B. Seliger, "The role of the miR-148/-152 family in physiology and disease," *European Journal of Immunology*, vol. 47, no. 12, pp. 2026–2038, 2017.

[21] W. Sohn, J. Kim, S. H. Kang et al., "Serum exosomal microRNAs as novel biomarkers for hepatocellular carcinoma," *Experimental & Molecular Medicine*, vol. 47, no. 9, p. e184, 2015.

[22] Y. Jin, J. Wang, J. Han, D. Luo, and Z. Sun, "MiR-122 inhibits epithelial-mesenchymal transition in hepatocellular carcinoma by targeting Snail1 and Snail2 and suppressing WNT/β-cadherin signaling pathway," *Experimental Cell Research*, vol. 360, no. 2, pp. 210–217, 2017.

[23] K. R. Babu and M. U. Muckenthaler, "miR-148a regulates expression of the transferrin receptor 1 in hepatocellular carcinoma," *Scientific Reports*, vol. 9, no. 1, p. 1518, 2019.

[24] X.-R. Long, Y. He, C. Huang, and J. Li, "MicroRNA-148a is silenced by hypermethylation and interacts with DNA

methyltransferase 1 in hepatocellular carcinogenesis," *International Journal of Oncology*, vol. 44, no. 6, pp. 1915–1922, 2014.

[25] F. Wang, H. Ying, B. He, Y. Pan, H. Sun, and S. Wang, "Circulating miR-148/152 family as potential biomarkers in hepatocellular carcinoma," *Tumor Biology*, vol. 37, no. 4, pp. 4945–4953, 2016.

[26] Z. Junna, C. Gongde, X. Jinying, and Z. Xiu, "Serum AFU, 5'-NT and AFP as biomarkers for primary hepatocellular carcinoma diagnosis," *Open Medicine*, vol. 12, no. 1, pp. 354–358, 2017.

[27] N. C. W. Lee, M. A. Carella, S. Papa, and C. Bubici, "High expression of glycolytic genes in cirrhosis correlates with the risk of developing liver cancer," *Frontiers in Cell and Developmental Biology*, vol. 6, p. 138, 2018.

[28] M. Wu, Z. Liu, A. Zhang, and N. Li, "Associated measurement of fucosylated levels of AFP, DCP, and GPC3 for early diagnosis in hepatocellular carcinoma," *The International Journal of Biological Markers*, vol. 34, no. 1, pp. 20–26, 2019.

[29] L. Zhang, J. Chen, C. Gao, C. Liu, and K. Xu, "An efficient model for auxiliary diagnosis of hepatocellular carcinoma based on gene expression programming," *Medical & Biological Engineering & Computing*, vol. 56, no. 10, pp. 1771–1779, 2018.

[30] A. Alisi, L. Da Sacco, G. Bruscalupi et al., "Mirnome analysis reveals novel molecular determinants in the pathogenesis of diet-induced nonalcoholic fatty liver disease," *Laboratory Investigation*, vol. 91, no. 2, pp. 283–293, 2011.

[31] D. D. Qiao, J. Yang, X. F. Lei et al., "Expression of microRNA-122 and microRNA-22 in HBV-related liver cancer and the correlation with clinical features," *European Review for Medical and Pharmacological Sciences*, vol. 21, no. 4, pp. 742–747, 2017.

[32] S. Yang, R. Yang, R. Lin, and L. Si, "MicroRNA-375 inhibits the growth, drug sensitivity and metastasis of human ovarian cancer cells by targeting PAX2," *Journal of B.U.ON. : Official Journal of the Balkan Union of Oncology*, vol. 24, no. 6, pp. 2341–2346, 2019.

[33] K. Zeng, Y. Wu, C. Wang et al., "ASH2L is involved in promotion of endometrial cancer progression via upregulation of PAX2 transcription," *Cancer Science*, vol. 111, no. 6, pp. 2062–2077, 2020.

[34] Y. Lu and W. Li, "Functional characterization of E2F3b in human HepG2 liver cancer cell line," *Journal of Cellular Biochemistry*, vol. 119, no. 4, pp. 3429–3439, 2018.

[35] E. Rewcastle, A. E. Varhaugvik, E. Gudlaugsson et al., "Assessing the prognostic value of PAX2 and PTEN in endometrial carcinogenesis," *Endocrine-Related Cancer*, vol. 25, no. 12, pp. 981–991, 2018.

[36] G. Wang, W. Zhao, H. Wang et al., "Exosomal MiR-744 inhibits proliferation and sorafenib chemoresistance in hepatocellular carcinoma by targeting PAX2," *Medical Science Monitor*, vol. 25, pp. 7209–7217, 2019.

[37] X. Huang, F. Huang, D. Yang et al., "Expression of microRNA-122 contributes to apoptosis in H9C2 myocytes," *Journal of Cellular and Molecular Medicine*, vol. 16, no. 11, pp. 2637–2646, 2012.

Hindawi
Journal of Healthcare Engineering
Volume 2021, Article ID 6225403, 8 pages
https://doi.org/10.1155/2021/6225403

Research Article

Big Data Information under Proportional Hazard Mathematical Model in Analysis of Hepatitis B Virus Infection Data of Patients with Interventional Liver Cancer through Antiviral Therapy of Entecavir

Yichi Zhang,[1,2] **Shuai Zhao**,[1,2] **Han Ding**,[1,2] **Xiaoling Song**,[1] **Huijie Miao**,[1] **Xuya Cui**,[1] **Jian Wang**,[1,2] **and Bing Han**[1,2]

[1]*Department of Transplantation, Xinhua Hospital Affiliated to Shanghai Jiao Tong University School of Medicine, 1665 Kongjiang Road, Yangpu District, Shanghai 200092, China*
[2]*Department of General Surgery, Xinhua Hospital Affiliated to Shanghai Jiao Tong University School of Medicine, 1665 Kongjiang Road, Yangpu District, Shanghai 200092, China*

Correspondence should be addressed to Bing Han; 161604425@m.gduf.edu.cn

Received 29 August 2021; Revised 28 November 2021; Accepted 1 December 2021; Published 23 December 2021

Academic Editor: Enas Abdulhay

The objective of this study was to analyze the application of proportional hazard mathematical model (PHMM) in Hepatitis B Virus (HBV) infection analysis of interventional liver cancer patients treated with entecavir, so as to provide data support for clinical diagnosis and treatment. Based on the survival analysis, the treatment factor x was undertaken as an independent variable to perform linear regression. The regression model took the hazard rate function as the dependent variable to establish an exponential regression equation to construct a PHMM. 136 patients with primary liver cancer receiving interventional chemoembolization combined with the drug (entecavir) were selected as the experimental group, who were in the computer gene expression omnibus (GEO). 87 patients with primary liver cancer who underwent interventional chemoembolization therapy without antiviral treatment were taken as the control group. The PHMM was adopted for comprehensive analysis. In addition, the factors affecting the virological response to antiviral therapy were analyzed using the multiple logistic regression. The results revealed that HBV deoxyribonucleic acid (DNA) negative conversion rate, Hepatitis B e-Antigen (HBeAg) negative conversion rate, and HBeAg serological conversion rate in the experimental group were much higher than those in the control group ($P < 0.05$). HBV DNA level and proportion of HBsAg <100 IU/mL in the experimental group were much lower than those in the control group ($P < 0.05$). The virological breakthrough rate and incidence of adverse events at week 24 in the experimental group were greatly lower than those in the control group ($P < 0.05$). The adverse virological response of patient was positively correlated with HBV DNA load and HBeAg status and negatively correlated with alanine aminotransferase (ALT) level ($P < 0.05$). Therefore, entecavir can significantly inhibit HBV DNA replication in patients with liver cancer, showing high antiviral effect. High baseline HBV DNA load, positive HBeAg, and low baseline alanine aminotransferase levels were independent risk factors for adverse virology response to entecavir antiviral therapy, which provided a reference for the selection of antiviral drugs for HBV infection.

1. Introduction

Primary liver cancer is one of the most common malignant tumors in China [1, 2]. China is a major country in the incidence of hepatitis, and the main causes of morbidity and mortality include HBV, HCV, and aflatoxin [3, 4]. According to relevant research reports, the proportion of people carrying HBV virus in China is about 10%, and HBV usually acts together with other related factors to lead to the occurrence of cirrhosis, resulting in human hepatocellular carcinoma [5]. Considering that the early symptoms of liver cancer are relatively insidious and not typical enough, they often develop to middle to advanced stages when they are discovered. At this time, liver transplantation, liver resection, interventional therapy, radiotherapy, chemotherapy, and other methods should be selected [6]. Transcatheter arterial chemoembolization (TACE) is the most common surgical treatment for liver cancer, which has a strong inhibitory and killing effect on tumor. However, during the period, it will affect the transport of liver blood, cause damage to the normal liver tissues, and greatly reduce the antivirus effect, which will eventually lead to a large number of rapid replications of HBV, resulting in liver failure, hepatic encephalopathy, and other complications [7–9]. Therefore, antiviral therapy during surgery is crucial for the prognosis of patients.

There is also a lot of research on antiviral drugs. For example, Cho et al. [10] compared the efficacy of tenofovir and entecavir in antiviral therapy in 53 patients with chronic kidney disease and found that the safety of hepatic artery embolization in patients with chronic kidney disease was comparable between tenofovir and entecavir. Liao et al. [11] compared the roles of lamivudine and entecavir in the reactivation of HBV induced by chemotherapy and found that entecavir had better clinical observation effect than lamivudine. Entecavir is a guanine nucleoside analogue that can inhibit HBV activity through phosphorylation and competition with HBV polymerase deoxyguanosine triphosphate nucleoside [12]. In clinical follow-up studies for some malignant tumors, chronic diseases, and other diseases, it is not comprehensive enough to consider the outcome, and it is also necessary to consider the length of time the subject has experienced a certain outcome. At present, proportional hazard mathematical model (PHMM) is commonly used for multivariate analysis of survival data so that the survival outcome, survival time, and processing censored data can be handled synchronously. The advantage of PHMM analysis is that it can analyze categorical and numerical variables and expand the scope of survival analysis from single-factor to multifactor analysis. In addition, it can analyze the survival of several factors at the same time, and the statistical model provides the effect of each factor. PHMM takes the occurrence of end-point events and the time elapsed for the end-point events as dependent variables. It can analyze the impacts of multiple factors on survival time and analyze data with censored data and does not require estimation of the distribution type of data. During the observation, it is necessary to avoid the loss of follow-up of the observation object, the censorship ratio is too large, and the bias accelerates. However, the application of PHMM analysis has an important premise, which refers to the proportional hazard (the impact of a certain factor on survival is the same at any time and does not change with time). When the premise is met, the PHMM can be applied.

In summary, TACE has the side effects of destroying liver function, so it is particularly important to choose appropriate antiviral drugs for interventional therapy. Based on this, the clinical efficacy of entecavir was comprehensively evaluated by comparing the HBV deoxyribonucleic acid (DNA) conversion rate, HBV DNA infection level, HBeAg conversion rate, serum positive conversion rate, HBsAg <100 IU/mL ratio, and complications between the two groups of patients, to comprehensively evaluate the efficacy and safety of entecavir in the treatment of HBV infection in HCC patients.

2. Materials and Methods

2.1. Research Object and Basic Information. In this study, 136 patients with primary liver cancer who underwent interventional chemoembolization combined with antiviral therapy of entecavir in the computer gene expression omnibus (GEO) data library were selected as the experimental group, and 87 patients with primary hepatocellular carcinoma treated with interventional chemoembolization without antiviral drugs were taken as the control group. This study had been approved by the ethics committee of hospital, and patients and their families had been informed of the study and signed informed consent.

Inclusion criteria were as follows: patients aged 30–76 years, patients diagnosed with hepatocellular carcinoma by pathology, and patients without obvious diseases of heart, lung, kidney, and other organs. Exclusion criteria were as follows: patients with antiviral history before surgery, patients with cerebral renal syndrome before surgery, patients with other types of liver disease, and patients who have received liver surgery before.

2.2. PHMM Analysis. Kaplan-Meier curves and Logrank test tests were univariate analysis, which studied the relationship between a single variable and survival, and they were only applicable to categorical variables instead of numerical variables, such as gene expression in malignant tumors. In univariate analysis of survival, the survival function (or cumulative survival rate) was expressed as follows:

$$S(t, x), \tag{1}$$

where S represented the probability that the survival time T of the research object was greater than a certain time t and x represented the independent variable (a certain processing factor), whose assignment rules were given as follows:

$$x = \begin{cases} 0, \text{no treatment} \quad \text{factor} \\ 1, \text{ treatment} \quad \text{factor} \end{cases}. \tag{2}$$

Then, the risk of patients in a treatment group at time t was shown in (3); and the risk of patients in the control group at time t was shown in (4).

$$w(t) = w_0(t) \times \exp(\beta), \tag{3}$$

$$w(t) = w_0(t), \tag{4}$$

$$\begin{aligned} \text{relative risk degree} &= \frac{\text{handling group risks}}{\text{control group risk}} = \frac{w_0(t) \times \exp(\beta)}{w_0(t)} \\ &= \exp(\beta). \end{aligned} \tag{5}$$

The death function was written as

$$D(t,x) = 1 - S(t,x), \tag{6}$$

where D represented the cumulative mortality from the observation follow-up to time t. The death density function was $m(t,x) = D(t,x)$, where m referred to the death density function (the instantaneous death rate at time t). The risk function was shown as follows:

$$w(t,x) = \frac{m(t,x)}{S(t,x)}, \tag{7}$$

where w was the hazard rate function, which represented the ratio of the instantaneous death rate at time t to the number of survivors at time t (conditional instantaneous mortality rate).

The PHMM could be established as follows.

The data in survival analysis contained censored data, and the time variable t usually does not satisfy normal distribution and homogeneity of variance. Therefore, the PHMM could not take $S(t,x)$ as the dependent variable directly, and x was undertaken as the independent variable for linear regression. The regression model has taken $w(t,x)$ as the dependent variable, and an exponential regression equation was established as

$$w(t) = w_0(t)e^{(\beta_1 x_1+\beta_2 x_2+\beta_3 x_3+\cdots\beta_k x_k)}. \tag{8}$$

In equation (8), $w(0)$ was the hazard rate function of the baseline survival distribution, which referred to the hazard function when all accompanying variables were 0; $x = (x_1, x_2, x_3, \ldots x_k)$ was the prognostic variable (independent variable covariate, which could be continuous or discrete); $w_0(t)$ was the risk function when the covariate value was 0; and $\beta = (\beta_1, \beta_2, \beta_3, \ldots \beta_k)$ referred to the regression coefficient of the model, and the meaning of which was as follows:

$$\mathrm{In}\left(\frac{w(t)}{w_0(t)}\right) = \beta_1 x_1 + \beta_2 x_2 + \beta_3 x_3 + \cdots \beta_k x_k. \tag{9}$$

In the PHMM, survival time or recovery time was taken as the dependent variable, and a group of variables related to survival time were used as independent variables and prognostic variables or covariates. The assumption of the regression model was as follows:

$$\text{risk ratio} = \frac{w(t)}{w_0(t)}. \tag{10}$$

The hazard ratio was a fixed value, which meant that the impact of the covariate on the survival rate did not change with time.

2.3. PCR Detection of HBV DNA Levels and Drug Resistance Gene Mutations. HBV DNA level and drug-resistant gene mutation were detected by fluorescence quantitative polymerase chain reaction (PCR), which was carried out on the ABI7500 PCR instrument produced by Life Technology in the United States. The amplification degree was as follows: 2 minutes of incubation at 50°C, 4 minutes of predenaturation at 94°C, 50 seconds at 60°C, and 50 cycles. HBV DNA $<10^3$ copy/mL is considered negative. HBV serological marker HBsAg was detected by enzyme-linked immunosorbent assay with reagent from SYM-BIO LIFESCIENCE in Suzhou province. The patient's serum was dripped on the microporous plate, incubated at 37°C for 30 minutes, and OD value was determined by an enzyme marker after washing and color development. HBsAg <0.5 PEI U/mL was considered negative.

2.4. Observation Indicators. HBV DNA negative conversion rate, HBV DNA infection level, HBeAg negative conversion rate, serological conversion rate, and condition of HBsAg <100 IU/mL were compared between the two groups at weeks 10, 20, 30, 40, and 50. rtL180M variation, rtL180M + rtM204V/I + rtA181T variation, and rtL180M + rtM204V/I were recorded in the two groups. Virological breakthrough rate (virological breakthrough rate = number of patients with genetic mutations/total number of patients) and incidence of adverse events (HBV DNA $<10^3$ copy/mL indicates a good virological response) at week 24 were compared between the two groups. And postoperative complications were recorded in both groups.

2.5. Statistical Methods. In this study, SPSS19.0 statistical software was used for data processing, the measurement data was expressed as mean ± standard deviation ($\overline{x} \pm s$), and the counting data was expressed as percentage. Multivariate logistic regression was adopted to analyze the factors affecting the virological response to antiviral therapy. T test was conducted to compare the data of experimental group and control group. $P < 0.05$ indicated statistical significance, and Origin8.0 was used for plotting.

3. Results

3.1. Comparison of Basic Conditions before Surgery. As shown in Figure 1, there was no statistically significant difference in age, height, weight, tumor size, hemoglobin albumin, total bilirubin, ALT, positive rate of HBV infection, proportion of sclerosing hepatocellular carcinoma, and proportion of tumor thrombus between the two groups ($P > 0.05$). Figure 2 shows the preoperative CT diagnostic images of some patients. Figure 2(a) shows a 63-year-old male patient with low density shadow in the right lobe and the left lobe of the liver, pleural effusion on the right, and multiple metastases in both lungs, and space-occupying lesions are considered. Figure 2(b) shows a female patient aged 58 years old. Most of her liver is metastatic lesions, and the lesions on the medial segment of the left lobe of the liver and the upper part of the right anterior lobe of the liver are relatively large. Figure 2(c) shows a female patient aged 70 years with dotted high-density shadow in the right lobe of the liver and dilatation of the intrahepatic bile duct. The carcinoma of the bile duct cells in the right lobe of the liver with multiple intrahepatic metastases is considered.

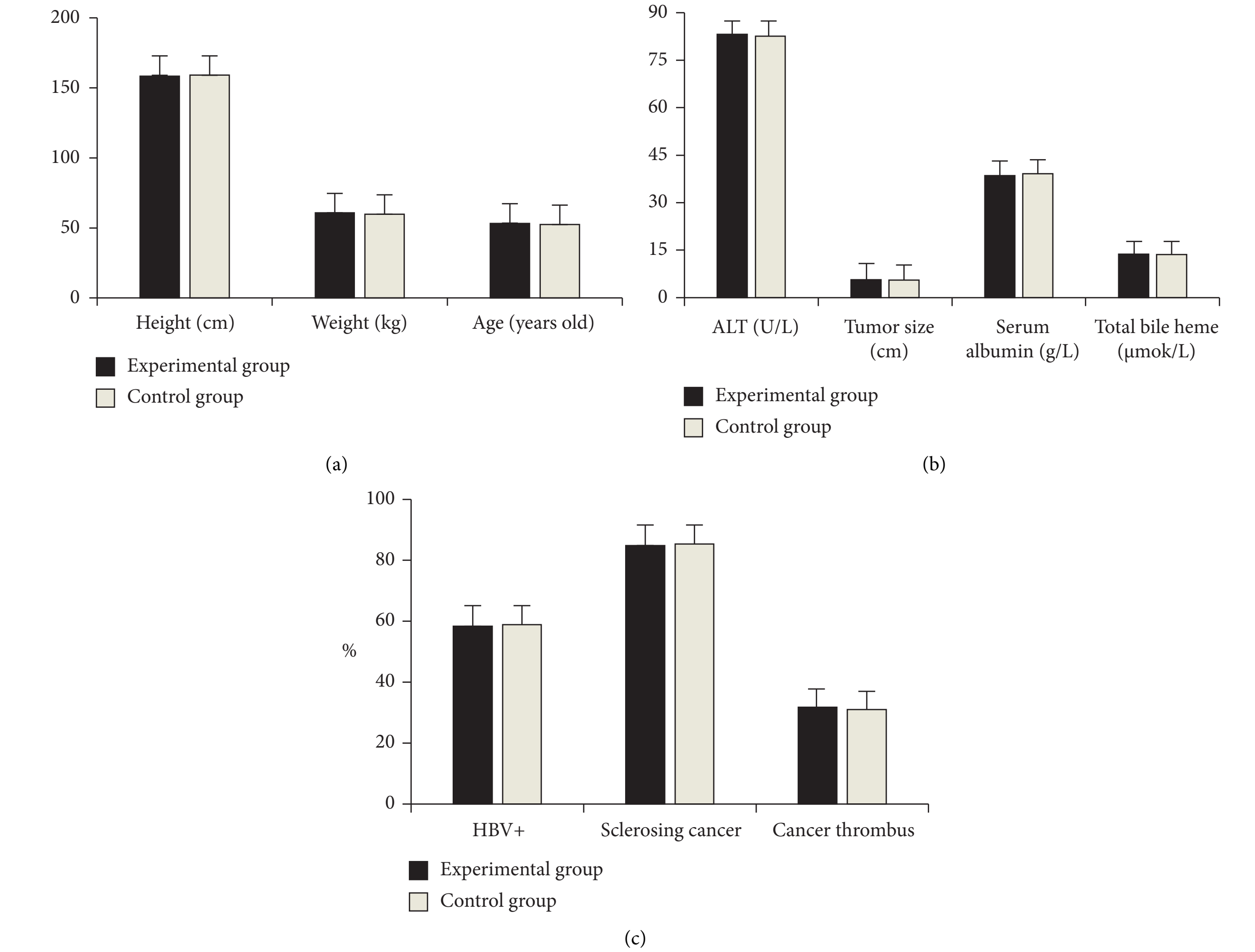

Figure 1: Comparison of basic conditions of the experimental group and the control group. (a) Age, height, and weight of the two groups. (b) Tumor size, hemoglobin albumin, total bilirubin, and ALT in the two groups. (c) The positive rate of HBV infection, the proportion of sclerosing hepatocellular carcinoma, and the proportion of tumor embolism in the two groups.

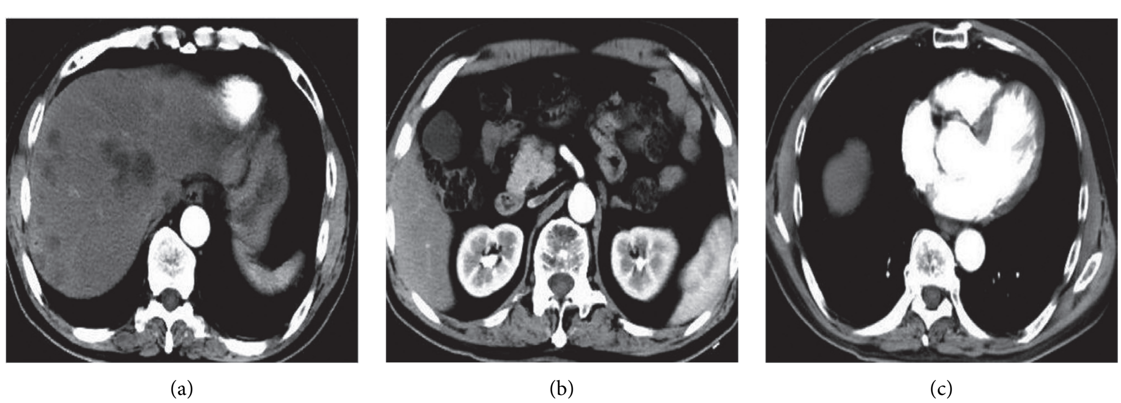

Figure 2: Preoperative CT diagnostic images of patients. (a) The image of a male patient aged 63 years. (b) The image of a female patient aged 58 years. (c) The image of a female patient aged 70 years.

3.2. Comparison of HBV DNA Level and Negative Conversion Rate between the Two Groups. As shown in Figure 3, in the experimental group, at weeks 10, 20, 30, 40, and 50, the HBV DNA negative conversion rates were 78.43%, 83.59%, 90.93%, 92.56%, and 94.83%, respectively, and the HBVDNA levels were 5.21 ± 1.75, 4.28 ± 1.16, 4.07 ± 0.86, 3.59 ± 1.42, and 3.51 ± 0.47, respectively. In the control group, at weeks 10, 20, 30, 40, and 50, HBV DNA negative

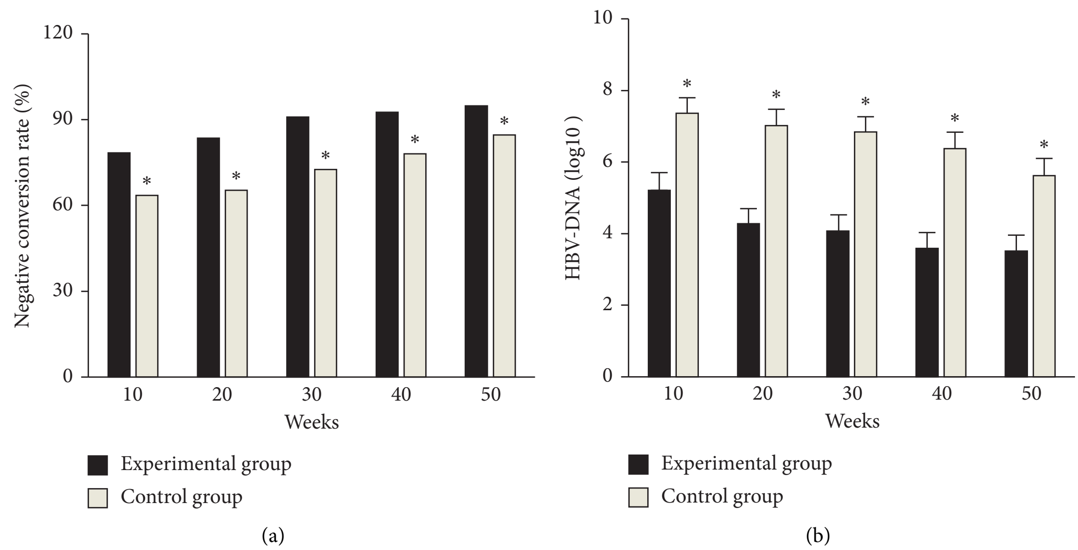

Figure 3: Comparison of HBV DNA level and negative conversion rate between the two groups in each period. (a) HBV DNA negative conversion rate of patients in the two groups. (b) HBV DNA level in both groups; ∗ indicates that the difference between the experimental group and the experimental group is statistically significant ($P < 0.05$).

conversion rate was 63.51%, 65.27%, 72.54%, 78.05%, and 84.62%, and HBV DNA levels were 7.36 ± 2.86, 7.02 ± 3.03, 6.84 ± 2.55, 6.37 ± 2.84, and 5.62 ± 1.93, respectively. Among them, the HBV DNA negative conversion rate in the experimental group was significantly higher than that in the control group at each time period, and the difference was statistically significant ($P < 0.05$). HBV DNA level in the experimental group was significantly lower than that in the control group at each time period, and the difference was statistically significant ($P < 0.05$).

3.3. The Change of HBeAg in the Two Groups. As shown in Figures 4 and 5, in the experimental group, at weeks 10, 20, 30, 40, and 50, the negative conversion ratios of HBeAg were 20.43%, 31.54%, 46.77%, 59.41%, and 71.53%, respectively, and the serological conversion rates of HBeAg were 4.66%, 7.83%, 15.92%, 28.71%, and 39.08%, respectively. In the control group, at weeks 10, 20, 30, 40, and 50, the patients' negative conversion ratios of HBeAg were 9.38%, 22.58%, 30.19%, 39.56%, and 54.28%, and the serological conversion rates of HBeAg were 2.96%, 4.22%, 7.17%, 12.04%, and 18.37%, respectively. Among them, the negative conversion rate of HBeAg in the experimental group was significantly higher than that in the control group at each time period, and the difference was statistically significant ($P < 0.05$). The serological conversion rate of HBeAg in the experimental group at each time period was significantly higher than that in the control group, and the difference was statistically significant ($P < 0.05$).

3.4. Virological Breakthrough Rate and Incidence of Adverse Events in the Two Groups. As shown in Figure 6, 8 patients with adverse virological response finally appeared in the experimental group at week 24, with an incidence of adverse events of 5.81%. rtL180M mutation was found in 4 patients, and rtL180M + rtM204V/I + rtA181T mutation was found in

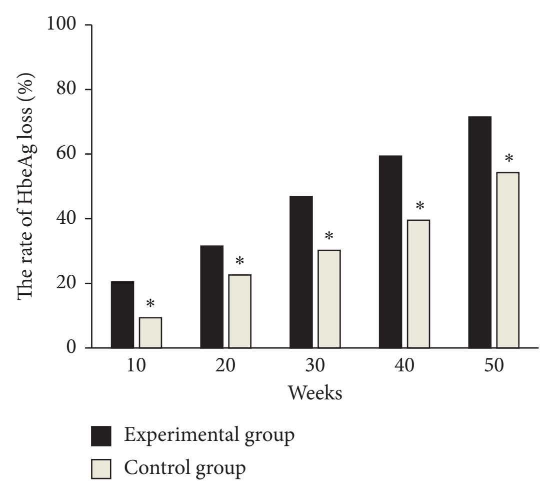

Figure 4: Comparison of negative conversion rate of HBeAg in each period between the two groups. * indicates that the difference between the experimental group and the experimental group is statistically significant ($P < 0.05$).

5 patients, and the virological breakthrough rate was 6.62%. In the control group, 9 patients with adverse virological response finally appeared at week 24, with an incidence of adverse events of 10.34%. There were 3 patients with rtL180M mutation, 5 patients with rtL180M + rtM204V/I mutation, and the virological breakthrough rate was 9.20%. Among them, the virological breakthrough rate and incidence of adverse events in the experimental group were significantly lower than those in the control group, and the differences were statistically significant ($P < 0.05$).

3.5. Condition of HBsAg <100 IU/mL in the Two Groups. As shown in Figure 7, at weeks 10, 20, 30, 40, and 50, the proportion of HBsAg <100 IU/mL in the experimental

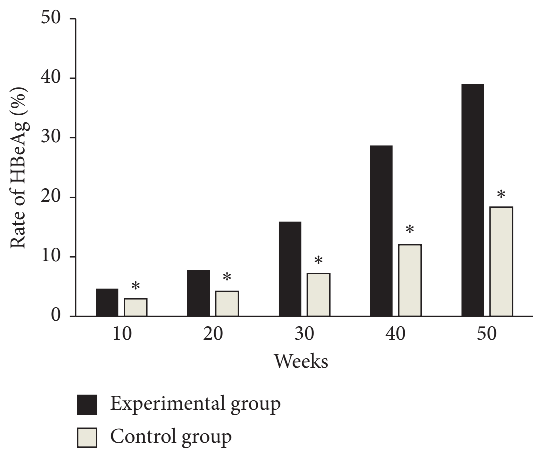

Figure 5: Serological conversion rate of HBeAg in two groups of patients in each period. * indicates that the difference between the experimental group and the experimental group is statistically significant ($P < 0.05$).

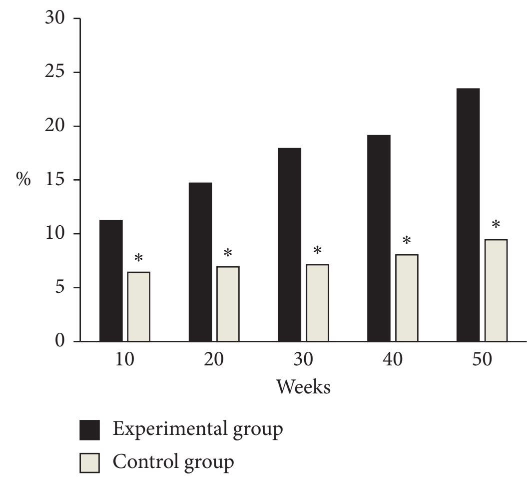

Figure 7: Condition of HBsAg <100 IU/ml in two groups of patients. * indicates that the difference between the experimental group and the experimental group is statistically significant ($P < 0.05$).

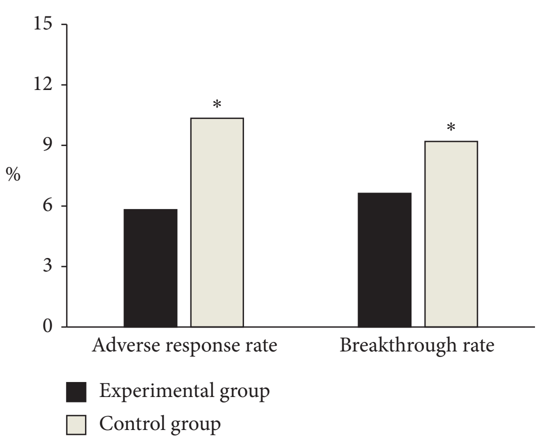

Figure 6: Virological breakthrough rate and incidence of adverse events of patients in the two groups. * indicates that the difference between the experimental group and the experimental group is statistically significant ($P < 0.05$).

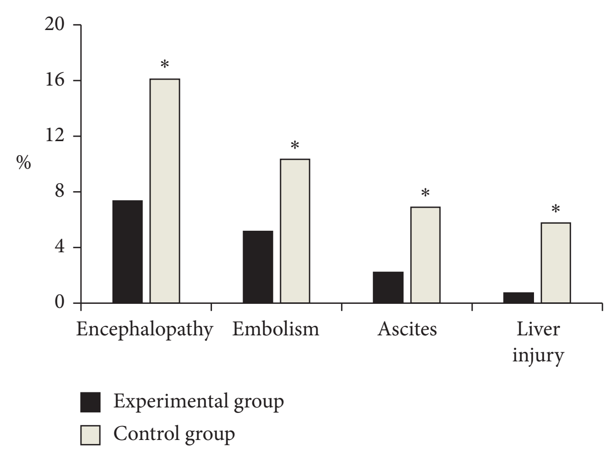

Figure 8: Postoperative complications of the two groups of patients. * indicates that the difference between the experimental group and the experimental group is statistically significant ($P < 0.05$).

group was 11.24%, 14.70%, 17.93%, 19.11%, and 23.46%, respectively. And the proportion of HBsAg <100 IU/mL at weeks 10, 20, 30, 40, and 50 in the control group was 6.42%, 6.93%, 7.14%, 8.05%, and 9.46%, respectively. Among them, the proportion of HBsAg <100 IU/mL in the experimental group was significantly lower than that in the control group at each time period, and the difference was statistically significant ($P < 0.05$).

3.6. Postoperative Complications of the Two Groups of Patients. As shown in Figure 8, in the experimental group, there were 10 cases of postoperative hepatic encephalopathy, with the complication rate of 7.35%; 7 cases with concurrent embolization, with the complication rate of 5.15%; 3 cases with concurrent ascites, with the complication rate of 2.21%; and 1 case with acute liver function injury, with the complication rate of 0.74%. In the control group, there were 14 cases of postoperative hepatic encephalopathy, with a complication rate of 16.09%; 9 cases of concurrent embolization, with a complication rate of 10.34%; 6 cases of concurrent ascites, with a complication rate of 6.90%; 5 cases of acute liver function injury, with a complication rate of 5.75%. Among them, the incidence of postoperative complications in the experimental group was significantly lower than that in the control group, and the difference was statistically significant ($P < 0.05$).

3.7. Regression Analysis of Human Papillomavirus (HPV) Infection and Clinical Pathological Characteristics of Patients. The PHMM analysis was performed to eliminate the impacts and effects of age, height, weight, baseline HBV DNA load, HBeAg status, ALT level, tumor size, proportion of sclerosing hepatocellular carcinoma, hemoglobin albumin level, and total bilirubin level. The variables with statistical significance for the virological adverse reactions of patients selected by the univariate analysis were analyzed by the proportional hazard function model, and the results were shown in Table 1. The analysis results suggested that the regression coefficients of the adverse virological response with age, HBV DNA load, and HBeAg state were 0.419, 0.593, and 0.473, respectively, showing significant positive correlation ($P < 0.05$); and the regression coefficient to the ALT level was −0.452, showing significant negative correlation ($P < 0.05$). There was no significant correlation between adverse virological response of patients and their height, weight, tumor size, proportion of sclerosing hepatocellular carcinoma, hemoglobin albumin level, and total bilirubin level ($P > 0.05$). Then, the age, HBV DNA load, HBeAg status, and ALT level of patients were undertaken as independent variables for multivariate logistic regression analysis, and the results were shown in Table 2. The results revealed that the regression coefficients of the adverse virological response of patient with HBV DNA load and HBeAg status were 0.631 and 0.569, respectively, showing significantly positive correlations ($P < 0.05$); the regression coefficient with ALT level was −0.583, showing an obviously negative correlation ($P < 0.05$); and there was no visible correlation between age and adverse virological response of patients ($P > 0.05$).

Table 1: Univariate regression analysis of virological responses to antiviral therapy.

Independent variables	Regression coefficients	t	P
Age	0.419	4.642	0.048
Height	0.246	2.115	0.087
Weight	0.218	2.074	0.070
HBV DNA load	0.593	5.116	0.005
HBeAg status	0.473	5.025	0.008
ALT level	−0.452	4.957	0.014
Tumor size	0.327	3.116	0.053
The proportion of sclerosing hepatocellular carcinoma	0.253	1.528	0.071
Hemoglobin albumin level	0.166	1.395	0.054
Total bilirubin level	0.280	1.507	0.062

Table 2: Multivariate regression analysis of virological responses to antiviral therapy.

Independent variables	Regression coefficients	t	P
Age	0.270	3.127	0.056
HBeAg status	0.569	5.731	0.014
ALT level	−0.583	5.114	0.017
HBV DNA load	0.631	6.427	0.006

4. Discussion

In the era of computer big data, how to effectively mine the value of data has become one of the key issues concerned by all walks of life. In particular, data information in the medical field is complex and has many categories. Only by filtering and integrating with computers can the value of data be maximized, and the database is the representative of this means [13]. Therefore, the treatment factor x was undertaken as an independent variable to perform linear regression based on the survival analysis. The regression model took the hazard rate function as the dependent variable to establish an exponential regression equation to construct a PHMM. The data of the first-line liver cancer patients in the GEO database were collected for multiple logistic regression to analyze the factors that affect the virological response to antiviral therapy. The results showed that the negative rates of HBV DNA of the experimental group at weeks 10, 20, 30, 40, and 50 were greatly higher than those of the control group ($P < 0.05$), and the HBV DNA level was observably lower in contrast to the control group ($P < 0.05$). Such results were consistent with the research results of Kim et al. [14], showing that entecavir could effectively reduce the HBV DNA level of patients undergoing surgical treatment and maintain the long-term inhibition. Hepatitis B surface antigen is an indicator of HBV infection. The seroconversion of hepatitis B surface antigen shows that the host immune system has an overwhelming advantage over the virus and is used as a sign of recovery from HBV infection. It was found in this study that the HBeAg negative conversion rate and serum conversion rate of the experimental group at weeks 10, 20, 30, 40, and 50 were remarkably higher in contrast to those of the control group ($P < 0.05$), which was consistent with the long-term follow-up results of Mücke et al. [15]. This may be because entecavir can directly act on transcription and replication of ccc DNA and subgenomic mRNA related to HBsAg expression, thus improving the negative conversion ratio and serological conversion rate of HBeAg [16]. In this study, it was found that the probability of postoperative hepatic encephalopathy, embolism, ascites, and acute liver function injury in the experimental group was significantly lower than that in the control group ($P < 0.05$), indicating that entecavir could reduce the risk of postoperative complications and was safe and feasible.

At present, it is generally believed that virological response evaluation should be carried out in the 24th week of antiviral therapy, and targeted treatment can be carried out according to the virological response. In this research, it was found that the virological breakthrough rate and incidence of adverse events of patients in the experimental group at week 24 were significantly lower than those in the control group ($P < 0.05$), which was similar to the study results of Zhu et al. [17], indicating that entecavir had higher antiviral intensity. In addition to that, the PHMM was also used to analyze the relevant factors that affect the virological response of antiviral therapy. It was found that there was an observably positive correlation between the adverse virological response, HBV DNA load, and HBeAg status of patients ($P < 0.05$). Such results indicated that the high baseline HBV DNA load is a risk factor for the adverse virological response to entecavir treatment. The higher the load, the greater the likelihood of adverse virological reactions. The positive HBeAg is more likely to cause adverse reactions. ALT is an evaluation index of liver inflammation, and its level also reflects the degree of immune clearance of patients. In this research, it was found that there was a significant negative correlation between adverse virological response and ALT level ($P < 0.05$), which was similar to the result of Mak et al. [18] who found a higher rate of adverse virological response when baseline ALT level < 5ULN. The lower the ALT level, the better the virological response, and the better the antiviral effect of entecavir.

5. Conclusion

Based on the computer GEO database under the PHMM, the clinical efficacy of entecavir antiviral therapy in patients undergoing interventional surgery for liver cancer was analyzed, which provided a reference for the future application of entecavir in malignant tumors. However, there were many shortcomings for this study. The sample size of the selected patients was small and the follow-up time was short, lasting only 50 weeks, which was not clear enough for the patients after half a year. The samples with longer follow-up time could be selected accordingly. In summary, entecavir could greatly reduce the HBV DNA levels and ALT levels, increase the HBeAg negative conversion rate, and exert a good antiviral effect compared with the seropositive conversion rate of interventional therapy for liver cancer patients. The PHMM analysis revealed that high baseline HBV DNA load, positive HBeAg, and low baseline ALT levels were independent risk factors for poor virological response to entecavir antiviral therapy.

Data Availability

The data used to support the findings of this study are available from the corresponding author upon request.

Conflicts of Interest

The authors declare no conflicts of interest.

Authors' Contributions

Y. Zhang and S. Zhao contributed equally to this work.

References

[1] H.-I. Yang, M.-L. Yeh, G. L. Wong et al., "Real-world effectiveness from the asia pacific rim liver consortium for HBV risk score for the prediction of hepatocellular carcinoma in chronic hepatitis B patients treated with oral antiviral therapy," *The Journal of Infectious Diseases*, vol. 221, no. 3, pp. 389–399, 2020.

[2] M. Hu, Y. Zhong, S. Xie, H. Lv, and Z. Lv, "Fuzzy system based medical image processing for brain disease prediction," *Frontiers in Neuroscience*, vol. 15, Article ID 714318, 2021.

[3] T. Mercier, G. Deslypere, and K. Nackaerts, "Ramsay Hunt syndrome: a rare complication of herpes zoster infection in a lung cancer patient," *Acta Clinica Belgica*, vol. 74, no. 5, pp. 355–358, 2019.

[4] A. Kothapalli and M. A. Khattak, "Safety and efficacy of anti-PD-1 therapy for metastatic melanoma and non-small-cell lung cancer in patients with viral hepatitis: a case series," *Melanoma Research*, vol. 28, no. 2, pp. 155–158, 2018.

[5] Z.-H. Yao, W.-Y. Liao, C.-C. Ho et al., "Incidence of hepatitis B reactivation during epidermal growth factor receptor tyrosine kinase inhibitor treatment in non-small-cell lung cancer patients," *European Journal of Cancer*, vol. 117, pp. 107–115, 2019.

[6] F. Al-Ani, A. Kalra, D. Yeoun et al., "The impact of hepatitis C anti viral therapy initiative on overall health maintenance," *American Journal of Gastroenterology*, vol. 113, pp. S559–S560, 2018.

[7] M. Mott and H. Richard, "Tumor-infiltrating lymphocytes in metastatic lung cancer to the brain," *American Journal of Clinical Pathology*, vol. 150, no. 1, pp. S38–S39, 2018.

[8] R. Califano, F. Gomes, C. J. Ackermann, S. Rafee, G. Tsakonas, and S. Ekman, "Immune checkpoint blockade for non-small cell lung cancer: what is the role in the special populations?" *European Journal of Cancer*, vol. 125, pp. 1–11, 2020.

[9] M. Visentini, L. Quartuccio, M. Del Padre et al., "Late relapses of hepatitis C virus-cured mixed cryoglobulinaemia associated with infection or cancer," *Rheumatology*, vol. 57, no. 10, pp. 1870-1871, 2018.

[10] Y. Y. Cho, Y. H. Choi, S. J. Yu et al., "Tenofovir and entecavir have similar renal adverse events on hepatocellular carcinoma patients treated with transarterial chemoembolization," *Journal of Liver Cancer*, vol. 19, no. 2, pp. 128–135, 2019.

[11] Y.-J. Liao, Y.-C. Li, S.-W. Lee et al., "Lamivudine versus entecavir in the rescue of chemotherapy-induced hepatitis B flare-up," *Journal of the Chinese Medical Association*, vol. 80, no. 12, pp. 758–765, 2017.

[12] L. Y. Mak, M. Ko, E. To et al., "Serum Mac-2-binding protein glycosylation isomer and risk of hepatocellular carcinoma in entecavir-treated chronic hepatitis B patients," *Journal of Gastroenterology and Hepatology*, vol. 34, no. 10, pp. 1817–1823, 2019.

[13] Y. C. Hsu, G. L. H. Wong, C. H. Chen et al., "Tenofovir versus entecavir for hepatocellular carcinoma prevention in an international Consortium of chronic hepatitis B," *American Journal of Gastroenterology*, vol. 115, no. 2, pp. 271–280, 2020.

[14] S. U. Kim, Y. S. Seo, H. A. Lee et al., "A multicenter study of entecavir vs. tenofovir on prognosis of treatment-naïve chronic hepatitis B in South Korea," *Journal of Hepatology*, vol. 71, no. 3, pp. 456–464, 2019.

[15] M. M. Mücke, L. I. Backus, V. T. Mücke et al., "Hepatitis B virus reactivation during direct-acting antiviral therapy for hepatitis C: a systematic review and meta-analysis," *The lancet. Gastroenterology & hepatology*, vol. 3, no. 3, pp. 172–180, 2018.

[16] L.-Y. Mak, V. Cruz-Ramón, P. Chinchilla-López et al., "Global epidemiology, prevention, and management of hepatocellular carcinoma," *American Society of Clinical Oncology Educational Book*, vol. 38, no. 38, pp. 262–279, 2018.

[17] R. Zhu, "Effect of kushenin combined with entecavir therapy on hepatic fibrosis and immune response in patients with chronic hepatitis B," *Journal of Hainan Medical University*, vol. 24, no. 11, pp. 13–16, 2018.

[18] F. Carrat, H. Fontaine, C. Dorival et al., "Clinical outcomes in patients with chronic hepatitis C after direct-acting antiviral treatment: a prospective cohort study," *The Lancet*, vol. 393, no. 10179, pp. 1453–1464, 2019.

Hindawi
Journal of Healthcare Engineering
Volume 2021, Article ID 2819986, 9 pages
https://doi.org/10.1155/2021/2819986

Research Article

Segnet Network Algorithm-Based Ultrasound Images in the Diagnosis of Gallbladder Stones Complicated with Gallbladder Carcinoma and the Relationship between P16 Expression with Gallbladder Carcinoma

Liang Xue ,[1] Xiaohui Wang ,[1] Yong Yang ,[1] Guodong Zhao ,[1] Yanzhen Han ,[1] Zexian Fu ,[1] Guangxin Sun ,[1] and Jie Yang [2]

[1]*Department V of General Surgery, Affiliated Hospital of Hebei Engineering University, Handan 056002, Hebei, China*
[2]*Endocrine Department, Affiliated Hospital of Hebei Engineering University, Handan 056002, Hebei, China*

Correspondence should be addressed to Jie Yang; xueliang@hdc.edu.cn

Received 15 September 2021; Revised 28 November 2021; Accepted 1 December 2021; Published 21 December 2021

Academic Editor: Enas Abdulhay

The study focused on how to improve the diagnostic coincidence rate of patients with gallbladder stones and gallbladder cancer based on an optimized Segnet network algorithm and the relationship of gallbladder cancer with multiple tumor suppressor 1 (P16). 300 patients diagnosed with gallbladder cancer in the hospital were selected as the research subjects. The pyramid pooling operation was incorporated into the original Segnet network algorithm, and its performance was evaluated, factoring into the intersection of union (IoU), algorithm precision (Pre), and recall rate (Recall). After 8 hours of fasting, conventional ultrasound and contrast-enhanced ultrasound examinations were performed, and the images were evaluated by three experienced ultrasound diagnosticians. The positive signal of P16 immunohistochemical staining was brownish yellow, which was generally concentrated in the nucleus, and a small part was located in the cytoplasm. In each slice, ten visual fields were selected. Then, they were observed under a high-power mirror, and the number was counted. It was found that the optimized Segnet network algorithm increased the IoU by 7.3%, the precision by 8.2%, and the recall rate by 11.1%. The diagnostic coincidence rates of conventional ultrasound and contrast-enhanced ultrasound examinations for gallbladder cancer were 78.13% (25/32) and 87.5% (25/32), respectively. The positive expression rate of P16 in gallbladder adenocarcinoma (47.06%) was significantly lower than that of acute cholecystitis with gallbladder stones (84.38%) and gallbladder polyps (67.16%) ($P < 0.05$). The positive expression rate of P16 in patients with stage III and stage IV (33.33% and 40%) was significantly lower than that in patients with stages I and II (87.5% and 80%) ($P < 0.05$). The positive expression rate of P16 in high differentiation (86.67%) was significantly higher than that of moderate differentiation (40%) and poor differentiation (28.57%) ($P < 0.05$). In short, contrast-enhanced ultrasound can effectively improve the diagnostic coincidence rate of gallbladder cancer, and the expression of P16 in gallbladder cancer is closely related to tumor staging and differentiation.

1. Introduction

Gallbladder carcinoma, mainly adenocarcinoma, is a common malignant tumor in the extrahepatic biliary system [1]. In China, the average age of the onset of gallbladder cancer is approximately 56 years. Generally speaking, gallbladder cancer is more common in women. In addition, more than 85% of clinical gallbladder cancer patients have gallbladder stones [2]. The incidence of gallbladder cancer in patients with gallbladder stones is about 7 times higher than that of people without gallbladder stones. Among patients with gallbladder stones, the risk of gallbladder cancer in patients with a single gallbladder stone greater than 3 cm in diameter is 10 times that of patients with a gallbladder stone less than 1 cm in diameter. Therefore, the cause of gallbladder cancer may be related to gallbladder stones [3]. The P16 gene, also known as multiple tumor suppressor 1 (MTS-1) gene, is a new type of tumor suppressor gene located on human chromosome 92P1. When the P16 protein is expressed at a low level, it will cause cell disorders and abnormal cell growth, and ultimately, it will lead to the formation of tumors [4].

For a long time, the main methods to diagnose gallbladder cancer included conventional ultrasound, computerized tomography (CT), endoscopic ultrasound, and magnetic resonance imaging (MRI) [5]. Conventional ultrasound can make accurate judgments on the morphological changes of gallbladder cancer, such as whether the size, location, and shape are regular, whether the bile duct is dilated, the degree of dilation, and the invasion of the adjacent tissue and lymph node metastasis, and it is recognized as the first choice to diagnose malignant tumors of the biliary system. Its diagnostic coincidence rate is approximately 80% [6]. Contrast-enhanced ultrasound can specifically diagnose tumors with rich and poor blood supply, and especially in the parenchymal stage, it can comprehensively scan the surrounding tissue of gallbladder cancer and detect lesions that conventional ultrasound cannot find [7]. Contrast-enhanced ultrasound uses a contrast agent to perfuse the tissue. The peak time (TTP), peak intensity (PI), contrast agent perfusion rate, and other related parameters are recorded to determine the benign and malignant tumors. It significantly improves the diagnostic coincidence rate [8].

Deep learning can extract the essential features of the target by network training on a large amount to elevate the classification accuracy. During the training, it can not only automatically learn but also automatically modify the learning parameters [9]. In this research, a Segnet algorithm was proposed that can reduce the running time of the model while keeping the detection accuracy unchanged. The Segnet algorithm can store the pooled index, avoid saving the feature map of the decoded part, and save memory [10].

The innovation of this study was to propose a new Segnet algorithm to process the conventional two-dimensional ultrasound image of 300 patients with gallbladder stones and gallbladder cancer. The immunohistochemical method was used to detect the expression level of the P16 protein in the cancer tissue. The primary objective of the study was to explore the accuracy, specificity, and sensitivity of contrast-enhanced ultrasound in the diagnosis of gallbladder cancer, as well as the relationship between the P16 protein expression and the tumor to fully understand the mechanism of gallbladder cancer and provide an evidence-based basis for the clinical diagnosis and treatment of gallbladder cancer.

2. Materials and Methods

2.1. Research Subjects. In the study, 300 patients diagnosed with gallbladder cancer in the hospital from October 15, 2017, to April 25, 2021, were selected as the research subjects, including 135 males and 165 females, with an average age of (56.82 ± 12.74) years. Inclusion criteria include those (I) aged over 50, (II) suffering from gallbladder stones for more than five years, (III) with the diameter of stones greater than 2 cm, (IV) with the local gallbladder wall thickened, and (V) with gallbladder polyps greater than 1 cm. The clinical symptoms included dull pain, abdominal distension, indigestion, nausea, and vomiting. The experiment has been approved by the ethics committee of the hospital. The patients and their families understood the research and signed an informed consent form.

2.2. Segnet Network Algorithm. The Segnet network algorithm mainly includes an encoding network and a decoding network. It can completely retain the feature information of the image, reduce the number of training parameters, shorten the training time, and display high-precision semantic segmentation images. The Segnet network algorithm comprises the convolutional layer, the normalization layer, the activation function, and the pooling layer (Figure 1).

The Segnet network algorithm structure has a symmetrical structure, with the left side of the network representing the encoding network and the right side representing the decoding network [11]. In the Segnet network, the pooling layer and the upsampling layer are used for image segmentation. The feature extraction of the target is completed by the left convolution layer, i.e., the encoding network. The pooling layer is used mainly to shrink the picture and perform deconvolution and upsampling operations [12]. Deconvolution is to make the classification features of the image more obvious. Upsampling is to restore the image to the same size as the input image. The encoding network extracts the features of the segmented image, transmits it to the decoding network, and outputs the semantic segmentation image (Figure 2).

In the training process, the linear expression cannot fully meet the actual needs, and the Relu function is often used for fitting. The Relu function is easy to calculate and fast to converge, and it is expressed as follows:

$$\mathrm{f}(\mathrm{x}) = \begin{cases} x, & x > 0, \\ 0, & x \leq 0. \end{cases} \quad (1)$$

When the input signal ≤ 0, the output is 0. When the input signal $x > 0$, the output is equal to the input.

2.3. Pyramid Pooling Operation. In the original segnet network, the pooling operation will cause the loss of some high-frequency components in the image, produce a purification module, and lose the pixel position and spatial information (Figure 3). To avoid this problem, the pyramid pooling operation is introduced. The pyramid pooling module uses different coarse and fine scales to fuse features, and the output of different scales includes feature maps of various sizes. It avoids producing fuzzy blocks as much as possible and retains the original features extracted by the convolutional neural network (CNN) (Figure 4).

2.4. Evaluation Indicators of Experimental Results. There are three evaluation indicators to determine the accuracy of feature extraction. The first is the intersection of union (IoU). It represents the degree of overlap between the candidate area generated when detecting the target and the original marked area, and it is expressed as follows:

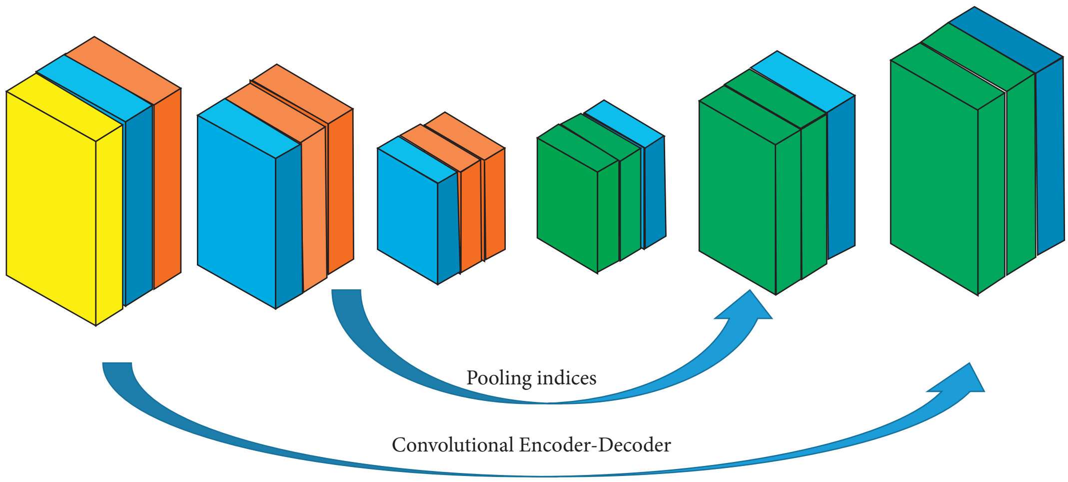

Figure 1: Structure of the Segnet network algorithm.

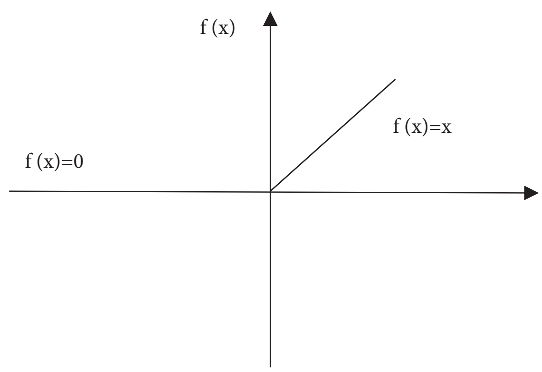

Figure 2: Relu function.

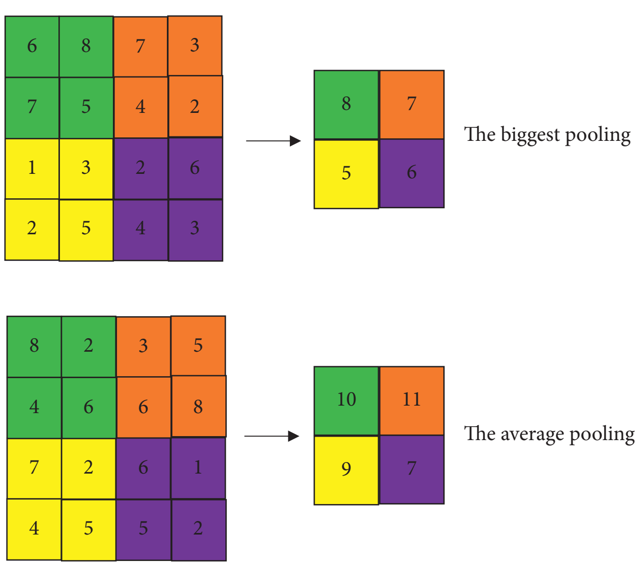

Figure 3: Original pooling operation.

$$\mathrm{IoU} = \frac{T1}{T1 + S1 + S2}, \tag{2}$$

where T1 represents a correctly detected nontarget feature, S1 represents a nontarget feature that is erroneously detected as a target feature, and S2 represents a target feature that is erroneously detected as a nontarget feature.

The second is the precision (Pre), which is the percentage of real target pixels in the detected target features, and it is expressed as follows:

$$\mathrm{Pre} = \frac{T1}{T1 + S2}, \tag{3}$$

where $T1$ represents a correctly detected nontarget feature, and S2 represents a target feature that is incorrectly detected as a nontarget feature.

The third is the recall rate (Recall). It is the ratio of the detected real target pixels to all the ultrasound samples of the test set and is expressed as follows:

$$\mathrm{Recall} = \frac{T1}{T1 + T2}, \tag{4}$$

where $T1$ represents the nontarget feature that is correctly detected, and $T2$ represents the target feature that is correctly detected.

2.5. Ultrasonic Diagnostic Equipment. After 8 hours of fasting, patients with gallbladder cancer underwent a routine ultrasound examination. The patient was in a supine position to have the multisection examination of the upper abdomen, and

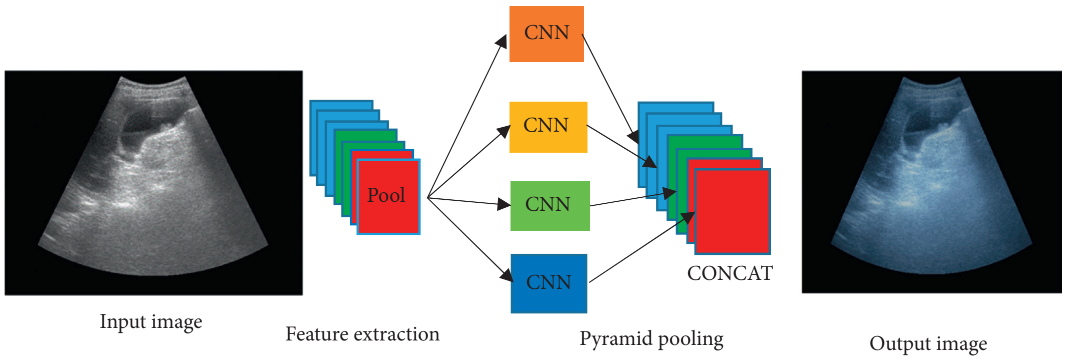

Figure 4: Pyramid pooling module.

the location, number, size, shape, boundary, and thickness of the gallbladder wall were recorded. Color ultrasound diagnostic apparatus was used for contrast-enhanced ultrasound, and an abdominal probe with a frequency of 3.5 MHz was used to detect the blood flow signal and shape of the lesion and determine the blood flow velocity. After angiography, three experienced ultrasound diagnosticians evaluated the images independently.

2.6. Immunohistochemical Staining Procedure and Result Judgment. The P16-positive gastric cancer tissue was used as a positive control, and the phosphate buffered saline (PBS) instead of P16 primary antibody was used as a negative control. The specific steps were as follows:

Firstly, after being dewaxed and hydrated, the paraffin sections were rinsed with PBS (PH = 7.4) three times for 3 minutes each time. Then, according to the requirements of each antibody, the tissue antigen was repaired accordingly. Each slice was immersed in 50uL peroxidase blocking solution to incubate for 10 minutes at room temperature to block the activity of endogenous peroxidase. Then, it was rinsed with PBS three times for 3 minutes each time. Next, each slice was immersed in 50uL normal nonimmune animal serum to incubate for 10 minutes at room temperature. Subsequently, the serum was removed, and each slice was immersed in 50uL of the primary antibody to incubate for 60 minutes at room temperature. Again, it was rinsed with PBS three times for 3 to 5 minutes each time. After the PBS solution was removed, each slice was immersed in 50uL biotin-labeled secondary antibody to incubate for 10 minutes at room temperature. Then, it was rinsed with PBS three times for 3 minutes each time. After the PBS solution was removed, each slice was immersed in 50uL streptavidin-peroxidase solution to incubate for 10 minutes at room temperature. Then, it was rinsed with PBS three times for 3 minutes each time. After the PBS solution was removed, each slice was immersed in 100uL of freshly prepared diaminobenzidine (DAB) solution and observed under a microscope for 3 to 10 minutes. Next, it was rinsed with tap water and stained with hematoxylin, followed by rinsing with PBS or tap water to return to blue. DAB was used for color development. The slices were dehydrated and dried with gradient alcohol, cleared with xylene, and mounted with neutral gum.

The positive signal of P16 immunohistochemical staining was brownish-yellow, generally concentrated in the nucleus, with a small part in the cytoplasm. In each slice, 10 fields of view were selected, which were then observed under a high-power mirror to count the number. More than 60% of the cells in the field of view with brown-yellow particles was defined as strong positive (+++), 30% to 60% of the cells with brown-yellow particles was defined as positive (++), 5% to 30% of cells with brown-yellow particles was defined as weakly positive (+), and no obvious brown particles in the cell were defined as negative (-). A weak positive expression or above was considered a positive expression.

2.7. Statistical Methods. In this study, SPSS21.0 statistical software was used for statistical analysis of the result data. The calculated data that conformed to the normal distribution were represented by the mean standard deviation ($\overline{x} \pm s$), and the calculated data that did not conform were represented by the percentage (%). The comparison of counting data adopts χ^2 test. $P < 0.05$ indicated that the difference was significant.

3. Results

3.1. Performance of the Segnet Network Algorithm. The Segnet and the optimized Segnet with the pyramid model were trained separately. Figure 5 shows the loss value/accuracy change curve of the training set and the validation set. Figure 6 shows the semantic segmentation network. According to the result data, the optimized Segnet network algorithm of the pyramid pooling operation increased the IoU by 7.3%, the precise (Pre) by 8.2%, and the recall rate (Recall) by 11.1%. It suggested that the semantic segmentation model with pyramid pooling elevated the accuracy and speed of target extraction.

3.2. General Information of the Subjects. There were 300 patients with gallbladder cancer, including 135 males and 165 females, ranging in age from 50 to 75 years. Pathological examination showed 32 cases of gallbladder malignant tumors, of which gallbladder adenocarcinoma accounted for 53.12% (17 cases), gallbladder squamous cell carcinoma accounted for 25% (8 cases), gallbladder adenosquamous

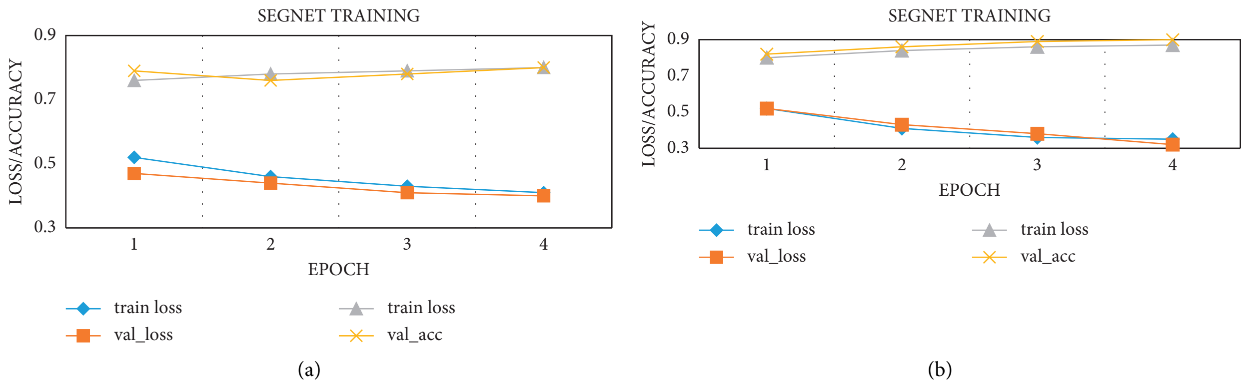

Figure 5: Loss value/accuracy curve of training set and validation set. (a) Segnet network algorithm. (b) Optimized Segnet network algorithm.

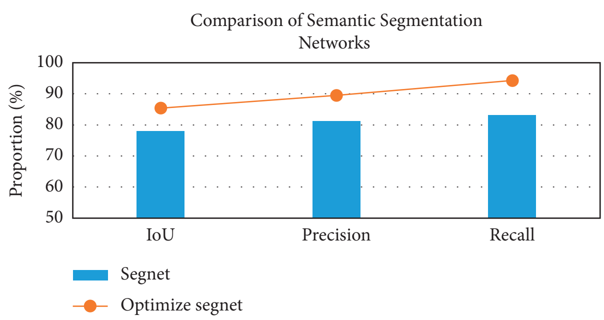

Figure 6: Comparison of semantic segmentation networks.

carcinoma accounted for 15.63% (5 cases), and gallbladder villous cystic glands tumor accounted for 6.25% (2 cases). There were 168 cases of benign gallbladder lesions, including 40% (67 cases) of gallbladder polyps, 11.31% (19 cases) of gallbladder adenoma, 8.33% (14 cases) of biliary sludge, 19.04% (32 cases) of acute cholecystitis with gallbladder stones, and 21.43% (36 cases) of chronic cholecystitis with gallbladder stones (Figure 7).

3.3. Results of Conventional Ultrasound Examination. 25 cases of gallbladder cancer were detected by conventional ultrasound examination. The diagnosis coincidence rate was 78.13% (25/32). 4 cases of nodular gallbladder carcinoma had nodular protrusions in the gallbladder cavity, wide basement, irregular edges, and heterogeneous internal echoes. The abnormal central echoes caused by stones, air, or necrosis were noted (Table 1). In 5 cases of thick-walled gallbladder carcinoma, the gallbladder wall was locally thickened or diffusely unevenly thickened, showing hyperechoic (more common) or hypoechoic signals, and the entire gallbladder was stiff, deformed, and the wall was rough or irregular. In 5 cases of solid gallbladder carcinoma, the entire gallbladder showed disordered low-echo or medium-echo solid masses, and the dark areas in the gallbladder cavity disappeared, often accompanied by gallbladder stones. There were 6 cases of mixed gallbladder carcinoma, and both thick-walled and nodular types were noted (Figure 8).

3.4. Results of Contrast-Enhanced Ultrasound Examination. 28 cases of gallbladder cancer were examined by contrast-enhanced ultrasound, and the diagnosis coincidence rate was 87.5% (25/32). For patients with gallbladder stones combined with gallbladder cancer, the mass was large, the boundary was not clear, and the surrounding halo was visible. There were irregular liquid dark areas inside, the mass was adjacent to the gallbladder, and the boundary with the gallbladder was not clear (Figure 9; Table 2).

3.5. Immunohistochemical Staining Results of P16. The positive expression of P16 was mainly concentrated in the nucleus and cytoplasm, with brownish-yellow particles, and some cell membranes were also stained (Figure 10).

3.6. Expression of P16 in Lesions of Gallbladder Carcinoma. In 17 cases of gallbladder adenocarcinoma, the positive expression rate of P16 was 47.06%. In 67 cases of gallbladder polyps, the positive expression rate of P16 was 67.16%. In 32 cases of acute cholecystitis with gallbladder stones, the positive expression rate of P16 was 84.38%. In 36 cases of chronic cholecystitis with gallbladder stones, the positive expression rate of P16 was 81.56%. The positive expression rate of P16 in gallbladder adenocarcinoma was significantly lower than that in patients with other gallbladder lesions, and the difference was significant ($P < 0.05$) (Figure 11).

3.7. The Relationship between the Positive Expression of P16 and Pathological Features. As per the clinical staging of gallbladder cancer, there are 8 cases in stage I, 5 cases in stage II, 9 cases in stage III, and 10 cases in stage IV. The positive expression rate of P16 in the patients of stages III and IV (33.33% and 40%) was significantly lower than that of the patients of stages I and II (87.5% and 80%), and the difference is significant ($P < 0.05$) (Figure 12).

According to the results of tumor differentiation, 7 cases were poorly differentiated, 10 cases were moderately differentiated, and 15 cases were highly differentiated. The positive expression rate of P16 in the high differentiation (86.67%) was significantly higher than that of moderate

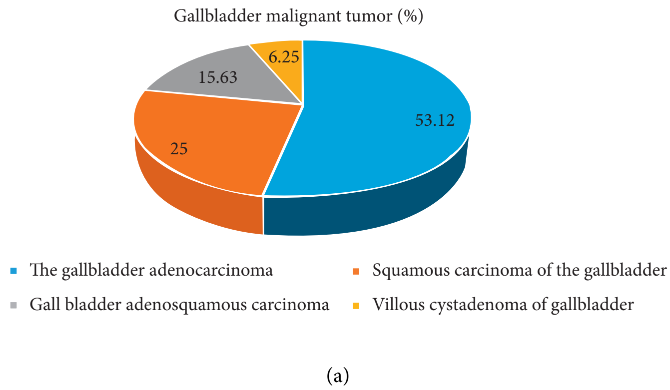

Figure 7: The pathological examination results. (a) Malignant tumor of the gallbladder. (b) Benign lesions of the gallbladder.

Table 1: Conventional ultrasound examination results.

	Gallbladder malignant tumor	Benign gallbladder disease
Pathological diagnosis (case)	32	168
Conventional ultrasound diagnosis (case)	25	161
Diagnosis coincidence rate (%)	78.13	95.83

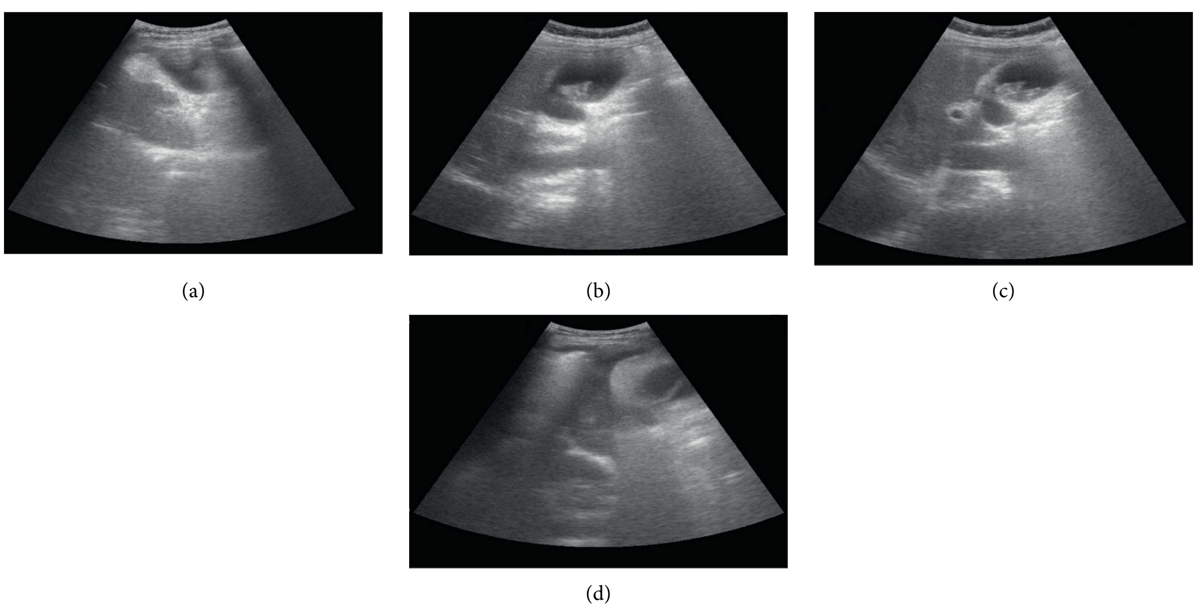

Figure 8: Conventional ultrasound examination results. (a) Nodular type, with moderate and weak echoes. (b) Thick-walled type, with diffuse and uneven thickening of the gallbladder wall. (c) Solid type, with an enlarged gallbladder, strong echo group with sound shadow. (d) Mixed type, the gallbladder wall was thickened regularly with papillary protrusions.

differentiation (40%) and poor differentiation (28.57%), and the difference was significant ($P < 0.05$) (Figure 13).

4. Discussion

Gallbladder cancer is a common malignant tumor of the biliary system, and its incidence has been increasing in recent years. Gallbladder cancer combined with gallbladder stones continuously stimulates the gallbladder wall mucosa, causing the abnormal proliferation of mucosal epithelial cells and cholestasis. Gallbladder cancer lacks specific clinical manifestations in the early stage and has similar symptoms of gallbladder stones. Therefore, when it is discovered, it is already in the middle and late stages when the best treatment opportunity has been lost [13,14]. At present, the early diagnosis of gallbladder cancer combined with gallbladder stones is a clinical problem that needs to be solved urgently.

Conventional ultrasound examination is easy to operate, noninvasive, low in price, and easy to be accepted by patients. It is recognized as the first choice for the diagnosis of gallbladder cancer [15]. However, because of the limitations

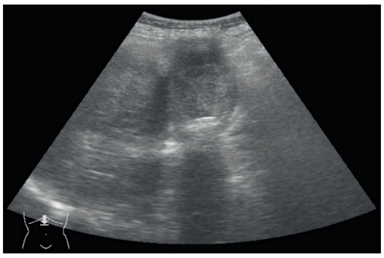

(a)

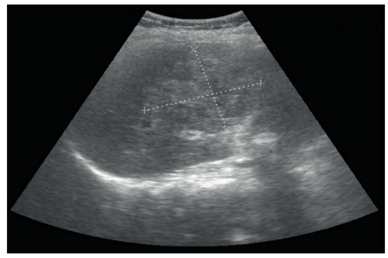

(b)

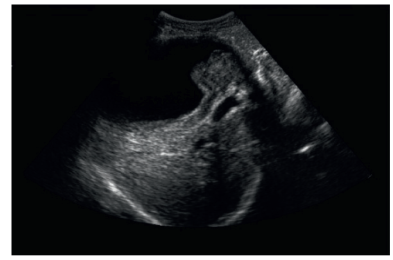

(c)

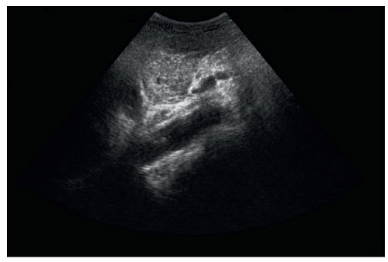

(d)

Figure 9: Contrast-enhanced ultrasound examination. (a) The patient was a 62-year-old male with a history of gallbladder stones for 5 years and epigastric pain for 5 days. Contrast-enhanced ultrasound examination of the abdomen showed that the continuity of the gallbladder wall was locally interrupted, and a slightly strong echogenic nodule protruding into the cavity was seen near the bottom. (b) The patient was a 55-year-old female with dull pain in the upper abdomen for half a year. Contrast-enhanced ultrasound examination of the abdomen showed the thickening of the gallbladder wall, and a moderate echogenic mass filled the cyst cavity at the bottom of the gallbladder. (c) The patient was a 53-year-old female with abdominal pain for 3 days. Contrast-enhanced ultrasound examination of the abdomen showed that the gallbladder volume increased significantly, and a solid mass with irregular shape was seen in the cyst cavity. (d) The patient was a 64-year-old female with a history of gallbladder stones for 5 years and epigastric pain for 5 days. Contrast-enhanced ultrasound examination of the abdomen showed clear boundaries of gallbladder lesions and irregular thickening of the cyst wall.

Table 2: Results of contrast-enhanced ultrasound examination.

	Gallbladder malignant tumor	Benign gallbladder disease
Pathological diagnosis (case)	32	168
Contrast ultrasound diagnosis (case)	28	166
Diagnosis coincidence rate (%)	87.5	98.8

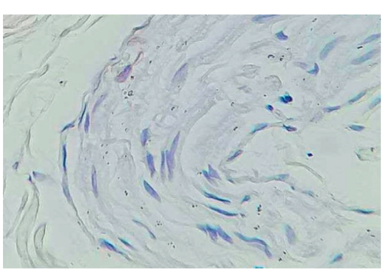

(a)

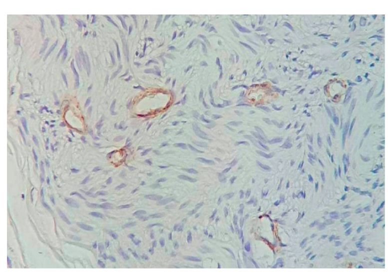

(b)

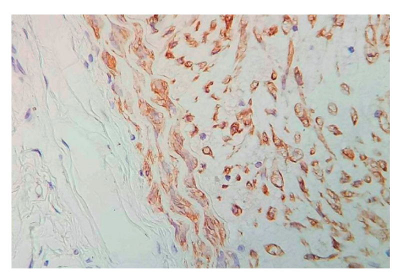

(c)

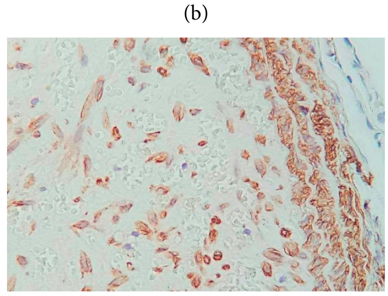

(d)

Figure 10: Results of immunohistochemical staining. (a) P16 was negatively expressed (×200). (b) P16 was weakly expressed (×200). (c) P16 was positively expressed (×200). (d) P16 was strongly positively expressed (×200).

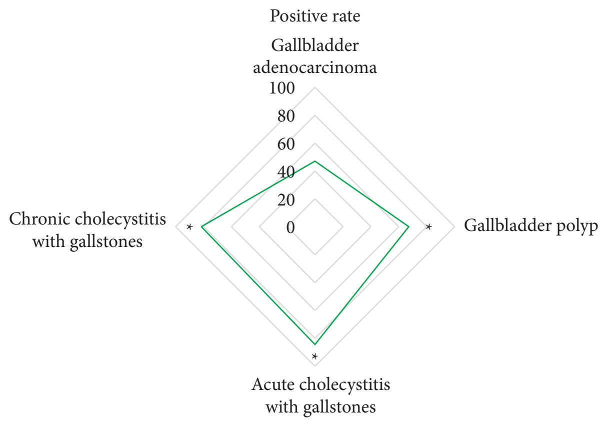

Figure 11: Positive expression of P16 in the lesions of gallbladder cancer. *indicates that compared with gallbladder adenocarcinoma, the difference was significant, i.e., $P < 0.05$.

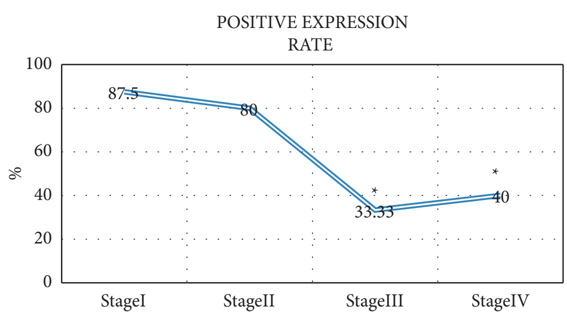

Figure 12: The relationship between the positive expression of P16 and tumor stage. *means that compared with stage (I), the difference was significant, i.e., $P < 0.05$.

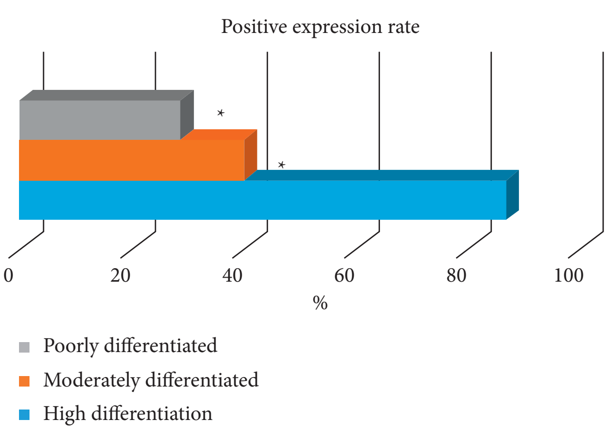

Figure 13: The relationship between the positive expression of P16 and the degree of differentiation. *indicates that compared with high differentiation, the difference was significant, i.e., $P < 0.05$.

of the technology itself, the microvessels of the lesion cannot be well-evaluated. In this study, 25 cases of gallbladder cancer were detected by conventional ultrasound, and the diagnosis coincidence rate was 78.13% (25/32), which was consistent with the research results of Rana et al. (2016) [16]. There were a total of 7 cases of missed and misdiagnosed cases. The main reasons were as follows: firstly, there is a certain amount of bile mud and viscous bile deposited in the gallbladder, and they do not move when the body position changes. Secondly, the thickness of the normal gallbladder wall is approximately 2 mm. When it is greater than 4 mm, the stone has an arc shape, and it is easy to misdiagnose the gallbladder with a thickened gallbladder wall and gallbladder cancer as chronic cholecystitis and gallstone disease. Thirdly, there are many organs around the gallbladder and abundant vessels. After gallbladder cancer has infiltrated, the outline of the gallbladder is unclear, and it is easy to be misdiagnosed as a tumor in the surrounding tissue.

Contrast-enhanced ultrasound technology is an imaging technology to understand the anatomy of tumor blood vessels. It can enhance the backscattered echo of the cells and improve the diagnostic coincidence rate. However, the low-resolution results in the unclear intima of large blood vessels, and it is unable to identify tiny blood vessels [17]. In this study, 28 cases of gallbladder cancer were detected by contrast-enhanced ultrasound, and the diagnosis coincidence rate was 87.5% (25/32). Contrast-enhanced ultrasound can observe the blood flow characteristics of the lesions of gallbladder cancer patients in real time, accurately display the spatial distribution of vascular perfusion, and significantly improve the signal ratio of detection. In this study, it can accurately detect the invasive growth of gallbladder tumors, providing a theoretical basis for the diagnosis of gallbladder cancer.

The P16 gene is a tumor suppressor gene directly involved in the negative feedback regulation of the cell cycle, and its level is closely related to the cell cycle [18,19]. When the P16 gene has mutations or deletions, it will lead to a low expression or the inactivation of the P16 protein, leading to cell cycle disorders [20]. In this study, the positive expression rate of P16 in gallbladder adenocarcinoma (47.06%) was significantly lower than that of acute cholecystitis with gallbladder stones (84.38%) and gallbladder polyps (67.16%) ($P < 0.05$). It showed that P16 was obviously missing in gallbladder cancer tissue, and the deletion and mutation of the P16 gene would lead to the occurrence of gallbladder cancer. The positive expression rate of P16 in the high differentiation (86.67%) was significantly higher than that in the middle differentiation (40%) and poor differentiation (28.57%) ($P < 0.05$), indicating that the positive expression of P16 protein in the gallbladder cancer tissue was related to the degree of tissue differentiation.

5. Conclusion

In this study, the ultrasound images based on the optimized Segnet network algorithm were used to diagnose 300 patients with gallbladder stones and gallbladder cancer. It was found that contrast-enhanced ultrasound can effectively improve the diagnostic coincidence rate of gallbladder cancer, and the expression of P16 in gallbladder cancer was closely related to tumor staging and differentiation. However, some limitations in the study should be noted. The sample size is small, which will reduce the power of the study. In the follow-up, an expanded sample size is necessary to strengthen the findings of the study. In conclusion, ultrasound imaging as a new imaging technology has guiding significance in the early diagnosis and identification of gallbladder cancer.

Data Availability

The data used to support the findings of this study are available from the corresponding author upon request.

Conflicts of Interest

The authors declare no conflicts of interest.

References

[1] X. Hu, W. Luo, J. Hu et al., "Brain SegNet: 3D local refinement network for brain lesion segmentation," *BMC Medical Imaging*, vol. 20, no. 1, p. 17, 2020.

[2] S. Almotairi, G. Kareem, M. Aouf, B. Almutairi, and M. A.-M. Salem, "Liver tumor segmentation in CT scans using modified SegNet," *Sensors*, vol. 20, no. 5, p. 1516.

[3] H. Wang, W. Ling, and Y. Luo, "Contrast-enhanced ultrasound findings of gallbladder adenocarcinoma with sarcomatoid carcinoma accompanied by intrahepatic metastasis," *Medicine*, vol. 97, no. 21, Article ID e10773, 2018.

[4] F. Zhang, W. Chen, L. Zhang, C. Hou, and M. Zhang, "Usefulness of ultrasound in differentiating xanthogranulomatous cholecystitis from gallbladder carcinoma," *Ultrasound in Medicine and Biology*, vol. 45, no. 11, pp. 2925–2931, 2019.

[5] N. Kalra, P. Gupta, M. Singhal et al., "Cross-sectional imaging of gallbladder carcinoma: an update," *Journal of Clinical and Experimental Hepatology*, vol. 9, no. 3, pp. 334–344, 2019.

[6] S. Z. Wennmacker, M. P. Lamberts, M. Di Martino, J. P. Drenth, K. S. Gurusamy, and C. J. van Laarhoven, "Transabdominal ultrasound and endoscopic ultrasound for diagnosis of gallbladder polyps," *Cochrane Database of Systematic Reviews*, vol. 2018, no. 8, Article ID CD012233, 2018.

[7] D. E. Bosch, M. M. Yeh, R. A. Schmidt, P. E. Swanson, and C. D. Truong, "Gallbladder carcinoma and epithelial dysplasia: appropriate sampling for histopathology," *Annals of Diagnostic Pathology*, vol. 37, pp. 7–11, 2018.

[8] T. Furuhashi, T. Abe, K. Sakata et al., "Extremely rare case of H-type gallbladder duplication coexistent with carcinoma: a case report and review of the literature," *Surgical Case Reports*, vol. 6, no. 1, p. 193, 2020.

[9] K. Abbasi, P. Razzaghi, A. Poso, S. Ghanbari-Ara, and A. Masoudi-Nejad, "Deep learning in drug target interaction prediction: current and future perspectives," *Current Medicinal Chemistry*, vol. 28, no. 11, pp. 2100–2113, 2021.

[10] M. Hu, Y. Zhong, S. Xie, H. Lv, and Z. Lv, "Fuzzy system based medical image processing for brain disease prediction," *Frontiers in Neuroscience*, vol. 15, Article ID 714318, 2021.

[11] Z. Wan, Y. Dong, Z. Yu, H. Lv, and Z. Lv, "Semi-supervised support vector machine for digital twins based brain image fusion," *Frontiers in Neuroscience*, vol. 15, Article ID 705323, 2021.

[12] Z. Lv, L. Qiao, Q. Wang, and F. Piccialli, "Advanced machine-learning methods for brain-computer interfacing," *IEEE/ACM Transactions on Computational Biology and Bioinformatics*, vol. 18, no. 5, pp. 1688–1698, 2021.

[13] K. Mochizuki, H. Hata, K. Naitou, U. Motosugi, and T. Kondo, "Carcinosarcoma (adenocarcinoma, neuroendocrine carcinoma, undifferentiated carcinoma and chondrosarcoma) of the gallbladder," *Clinical Journal of Gastroenterology*, vol. 13, no. 1, pp. 110–115, 2020.

[14] V. Jha, P. Sharma, and K. A. Mandal, "Incidental gallbladder carcinoma: utility of histopathological evaluation of routine cholecystectomy specimens," *South Asian journal of cancer*, vol. 7, no. 1, pp. 21–23, 2018.

[15] K. Suzuki, K. Abe, and M. Ohbu, "A resected gallbladder carcinoma coexisting with adenomyomatosis involving varied degrees of intraepithelial dysplasia: a case report and literature review," *Surgical Laparoscopy Endoscopy & Percutaneous Techniques*, vol. 29, no. 4, pp. 290–296, 2019.

[16] C. Rana, N. Krishnani, and N. Kumari, "Ultrasound-guided fine needle aspiration cytology of gallbladder lesions: a study of 596 cases," *Cytopathology*, vol. 27, no. 6, pp. 398–406, 2016.

[17] A. Al Khader, E. Nsour, A. Alrubaye, and M. Al-Saghbini, "Poorly cohesive cell carcinoma of the gallbladder with signet rings and neuroendocrine-like morphology: a rare incidental histopathological diagnosis with lessons to learn," *American Journal of Case Reports*, vol. 20, pp. 1558–1561, 2019.

[18] S. Y. Cha, Y. K. Kim, J. H. Min, J. Lee, D. I. Cha, and S. J. Lee, "Usefulness of noncontrast MRI in differentiation between gallbladder carcinoma and benign conditions manifesting as focal mild wall thickening," *Clinical Imaging*, vol. 54, pp. 63–70, 2019.

[19] T. Fujimoto and Y. Kato, "Polypoid gallbladder tumors with a deep hypoechoic area and a conically thickened outermost hyperechoic layer suggest shallow T2 carcinoma," *Acta Radiologica Open*, vol. 8, no. 5, Article ID 2058460119847995, 2019.

[20] Y. Xu, Q.-N. Chen, H. Wang, N.-B. Liu, and B.-M. Shi, "Synchronous hepatocellular carcinoma and gallbladder adenocarcinoma with neuroendocrine differentiation: a case report and literature review," *BMC Surgery*, vol. 20, no. 1, p. 246, 2020.

Hindawi
Journal of Healthcare Engineering
Volume 2021, Article ID 4272411, 9 pages
https://doi.org/10.1155/2021/4272411

Research Article

Clone Selection Artificial Intelligence Algorithm-Based Positron Emission Tomography-Computed Tomography Image Information Data Analysis for the Qualitative Diagnosis of Serous Cavity Effusion in Patients with Malignant Tumors

Jing Wei, [1] **Pingwei Li**, [2] **Huai Zhang**, [1] **and Ronghua Zhu** [1]

[1] *Department of Nuclear Medicine, Huai'an First People's Hospital, 6 Beijing West Road, Huaiyin District, Huai'an 223300, Jiangsu, China*
[2] *Department of Radiotherapy, Huai'an First People's Hospital, 6 Beijing West Road, Huaiyin District, Huai'an 223300, Jiangsu, China*

Correspondence should be addressed to Jing Wei; 2018040700019@jlxy.nju.edu.cn

Received 29 August 2021; Revised 28 November 2021; Accepted 1 December 2021; Published 18 December 2021

Academic Editor: Enas Abdulhay

This study aimed to investigate the application of positron emission tomography- (PET-) computed tomography (CT) image information data combined with serous cavity effusion based on clone selection artificial intelligence algorithm in the diagnosis of patients with malignant tumors. A total of 97 patients with PET-CT scanning and empirically confirmed as serous cavity effusion were retrospectively analyzed in this study. The clone selection artificial intelligence algorithm was applied to register the PET-CT images, and the patients were rolled into a benign effusion group and a malignant effusion group according to the benign and malignant conditions of the serous cavity effusion. Besides, the causes of patients from the two groups were analyzed, and there was a comparison of their physiological conditions. Subsequently, CT values of different KeV, lipid/water, water/iodine, and water/calcium concentrations were measured, and the differences of the above quantitative parameters between benign and malignant serous cavity effusion were compared, as well as the registration results of the clone algorithm. The results showed that the registration time and misalignment times of clonal selection algorithm (13.88, 0) were lower than those of genetic algorithm (18.72, 8). There were marked differences in CT values of 40–60 keV and 130–140 keV between the two groups. The concentrations of lipid/water, water/iodine, and water/calcium in basal substances of the malignant effusion group were obviously higher than the concentrations of the benign effusion group ($P < 0.05$). Benign and malignant effusions presented different manifestations in PET-CT, which was conducive to the further diagnosis of malignant tumors. Based on clone selection artificial intelligence algorithm, PET-CT could provide a new multiparameter method for the identification of benign and malignant serous cavity effusions and benign and malignant tumors.

1. Introduction

Serous cavity effusion (SCE) is a common symptom and sign in clinical work, which is divided into pleural effusion, ascites, and pericardial effusion [1, 2]. When the effusions occur in two or more parts of the patient's body simultaneously or successively during the course of the disease, they are called polyserositis. The causes of SCE are often complicated, and the common causes include malignant tumor, tuberculosis, hypoproteinemia, and hepatogenic, nephrogenic, cardiogenic, and autoimmune diseases [3–5]. At present, there are various methods for detection of SCE. The frequently used methods contain biochemical examination, tumor marker, exfoliated cell detection, flow cytometry, and telomerase activity assay. However, the detection rates of these methods are generally low, so it is often necessary to carry out repeated tests to get more accurate results [6]. Moreover, the traditional imaging detections such as X-ray, ultrasound, and computed tomography (CT) can only detect diseases by relying on morphological changes, and it is impossible to achieve more effective inspections for early disease [7, 8]. At this stage, medical diagnosis and treatment capabilities with the further advancement of E-health have been improved directly or indirectly from digital medical equipment to high-level information and knowledge sharing, and various digital imaging and postprocessing technologies make disease diagnosis more intuitive and accurate. Under this background, positron emission tomography-(PET-) CT has gradually been applied in the detection of SCE. The PET-CT imaging is a method combining molecular metabolism with anatomical structure images. It has obvious advantages in early identification and diagnosis of most diseases [9]. The detection method is easy to operate and noninvasive and lets patients suffer little pain. After long-term clinical application, it has been proved to have obvious advantages in the differential diagnosis of various diseases. Above all, it has been applied better in identifying the nature of effusion and finding the primary lesion of malignant effusion [10, 11]. In addition, the registration based on the shape feature points of the PET-CT image is difficult and requires the application of external reference point features for registration. However, due to the characteristics of mutual information function and multiple extreme values, there are usually multiple local extreme values, so that the optimization process may converge to the local extreme value and get wrong registration parameters, resulting in mismatching of image registration. In recent years, clonal selection algorithm is widely used in pattern recognition and combinatorial optimization. Its core is to multiply replication operator and mutation operator, retain the best individual, and improve the poor individual. It is an efficient and fast convergence algorithm. Therefore, the patients were detected by PET-CT using clone selection artificial intelligence algorithm in this study, and patients with benign and malignant effusions were evaluated, thereby providing new ideas for clinical treatment of peripheral facial paralysis and pointing out new directions.

2. Methods

2.1. Subjects Investigated and Grouping. 97 patients who underwent PET-CT scanning in hospital from June in 2017 to June 2019 and were empirically diagnosed as SCE were retrospectively analyzed. In the patients with malignant effusion, the primary lesions of some with malignant tumors have been confirmed by pathology, except for others with liver cirrhosis and primary liver cancer. According to the nature of effusion, 97 patients were divided into benign and malignant effusion, including 25 benign and 72 malignant. All the patients participating in the experiment had signed informed consent forms, and this study had been approved by ethics committee of hospital.

2.2. Inclusion and Exclusion Criteria. The inclusion criteria for the patients participating in the experiment were as follows: the patients met the diagnostic criteria of Western medicine, were above 20 years and below 65 years of age, had no other acute diseases or severe complications during the period of developing SCE, and were under no other treatment.

The exclusion criteria of patients participating in the experiment were as follows: patients in pregnancy or early pregnancy, having severe cardiovascular and cerebrovascular diseases, liver and kidney function disease, and hematopoietic failure, having cerebral infarction, cerebral hemorrhage, or other brain diseases, having participated in other clinical experiments, not developing SCE for the first time, and having the disease again after receiving treatments on the first onset.

2.3. Immunohistochemical Staining Reaction. The SCE was made into a smear and rinsed; after that, the smear was soaked in the permeable solution for 5 minutes, and then phosphate buffer solution (PBS) was applied to rinse the soaked smear. The rinsed section was added with PBS to be incubated in an incubator at 37°C for 30 minutes. After the incubation, the enzyme reaction solution was added to the incubated section for light avoidance reaction, and it was rinsed after 1 hour of the light avoidance reaction. Then, fluorescein isothiocyanate (FITC) working solution was added to continue the reaction for 30 minutes in the dark; and the section was rinsed after the reaction finished. Finally, 4′,6-diamidino-2-phenylindole (DAPI) working solution was dropped on the surface of the section, which was observed with a computer fluorescence microscope.

2.4. Positron Emission Tomography-Computed Tomography Scanning Detection Method. The Discovery ST 4 PET-CT instrument was for PET-CT scanning, and Advanced PET and Lightspeed 4-slice spiral computed tomography (CT) were combined on the same machine rack. Before the detection, the patient should fast for 4–6 hours in advance, and the fasting blood glucose of the patient had to be less than 7 mmol/L. If the patient's blood glucose was too high before the detection, the insulin should be injected appropriately to control the blood glucose within the normal range. After the patient stayed at rest for 15 minutes, the patient was given an intravenous injection of imaging agent with the amount of 3.71–4.82 MBq/kg. After the injection, the patient would continue to maintain a resting state for 45–60 minutes. Moreover, PET-CT scanning was applied immediately after the patient urinated. During the detection, the patient was placed in a supine position, held his head with his hands, kept breathing calm, and was scanned from the top of the skull to the upper femur on both sides. Gemstone spectral imaging (GSI) mode was used for CT scanning, with a spiral scanning speed of 0.6 s/ week, a detector width of 4 cm, a voltage of instantaneous switching between high and low energy (140 kVp and 80 kVp), and a tube current of about 600 mA. The first group of image reconstruction was the common 140 kVp image, which was used for real-time observation during the detection process, with a layer thickness/layer interval of 5 mm. The second group was a single energy (70 keV) image with a layer thickness/layer interval of 1.25 mm. In addition, standard algorithms were employed for image reconstruction.

2.5. PET-CT Image Registration Based on Clone Selection Algorithm. The clone selection process is a positive feedback process, and the clone selection algorithm is employed to find the maximum value of normalized mutual information and its corresponding registration parameters. The specific steps are as follows.

The first step is initialization. The PET-CT image is used as the initial research object, corresponding to the possible solutions of registration parameters. The floating-point number is encoded, and the base number is 19, in which the first 10 bits correspond to the rotation parameters of the image space transformation, and the last 9 bits correspond to the scale parameters of the image transformation. The probability of crossover is set as $Yi = 0.7$ and the probability of mutation as $Yt = 0.02$. The second step is evaluation and selection. The normalized mutual information value is calculated; the larger 30 of them are selected to enter the memory set Pn and the remaining Pm. The third step is clone. In the memory set Pn, K with higher normalized mutual information value are selected for cloning, and the number of clones is proportional to the fitness. It is ensured that the selection of registration parameters develops towards the optimization direction.

The fourth step is crossover and mutation. The supermutation process in biological clone selection is simulated, and the cross-mutation operation is carried out on the results after clone, so the mutation rate is inversely proportional to the fitness, thus enlarging the search range of registration parameters. The fifth step is the second evaluation and selection. The affinity of the mutated antibodies is recalculated. If the affinity of some clone results is higher than that of the highest Pn, the body with the lowest affinity in Pn is replaced with these antibodies to form a new memory set. The sixth step is extinction. The process of natural cell extinction in biological clonal selection is simulated. In Pm, d results with the lowest affinity are selected to reinitialize, which can ensure the speed of convergence. The seventh step is to check whether the termination conditions are met. If they are met, terminate; otherwise, go to the second step and enter the next generation avoidance.

The clone algorithm can realize the diversity of the search space and optimize the objective function of medical image registration, with good performance.

2.6. Image Processing, Analysis, and Measurement. The image analysis and measurement were on the professional workstation AW4.5. Three radiologists with ten years of work experience carried out the measurement independently, and they did not know the final results of the subjects investigated. On the mixed energy 140 kVp imaging image, the most obvious layer of the effusion in the image was selected to measure the CT value. Besides, circular reactive oxygen intermediate (ROI) with a diameter of 5–10 mm was selected, and three-point measurement was carried out, and the average value was selected. The single energy image (70 keV, and 5 mm) was loaded into spectrum imaging analysis software GSI viewer for analysis. The ROI of the same patient was measured against the corresponding region of the mixed energy, and the ROI data file was saved. The data file was an Excel spreadsheet file, containing the CT value (HU) of each single energy level 40–140 keV (the interval for 10 keV) and effective atomic number; the statistical software was employed to calculate the peak of effective atomic number distribution; and lipid (water), water (iodine), and water (calcium) were selected as the paired base substances, and their concentrations were generated by the data file.

2.7. Statistical Analysis. SPSS 17.0 statistical analysis software was used for the statistical methods. The results of counting were expressed as mean ± standard deviation ($\overline{x} \pm s$), and t-test was applied for comparison between the two groups. The receiver operating characteristic curve (ROC) was employed to evaluate the value of paired base substances in the diagnosis of malignant effusion, and AUC was applied to determine the accuracy of base substance concentration in the diagnosis of malignant effusion. What is more, the threshold value, sensitivity, and specificity for the diagnosis of malignant effusion were calculated, and $P < 0.05$ was considered to represent statistically significant difference.

3. Results

3.1. Comparison of the Basic Data of Patients. Based on the nature of the effusion, 97 patients were classified into benign and malignant effusion, respectively. There were 25 patients with benign effusion including 11 males and 14 females, the average age was 62.17 ± 6.33 years, and the course of disease was 2.57 ± 0.24 years. What is more, 72 patients were malignant effusion including 33 males and 39 females, with an average age of 63.74 ± 4.76 years and the disease course of 3.57 ± 1.24 years. The results in Figure 1 show that the difference in general data between the two groups of patients was not statistically remarkably significant ($P > 0.05$).

3.2. Analysis of the Causes of the Patients in the Two Groups. There were 25 patients in the benign effusion group, and their specific causes are shown in Figure 2. The benign effusion group included 8 patients of liver cirrhosis with ascites, 2 patients of heart failure with pleural effusion, 13 patients of pneumonia with pleural effusion, and 2 patients of tuberculous pneumonitis with ascites. Figure 3 shows the specific causes of 72 patients in the malignant effusion group. Besides, there were 14 patients of gastrointestinal malignant tumors with ascites, 44 patients of lung cancer with pleural effusion, 9 patients of breast cancer with multiple metastases and pleural effusion, 3 patients of ovarian cancer with ascites, and 2 patients of esophageal cancer with pleural effusion in the malignant effusion group. There was no statistical difference in the number of cases of each cause of the above patients ($P > 0.05$).

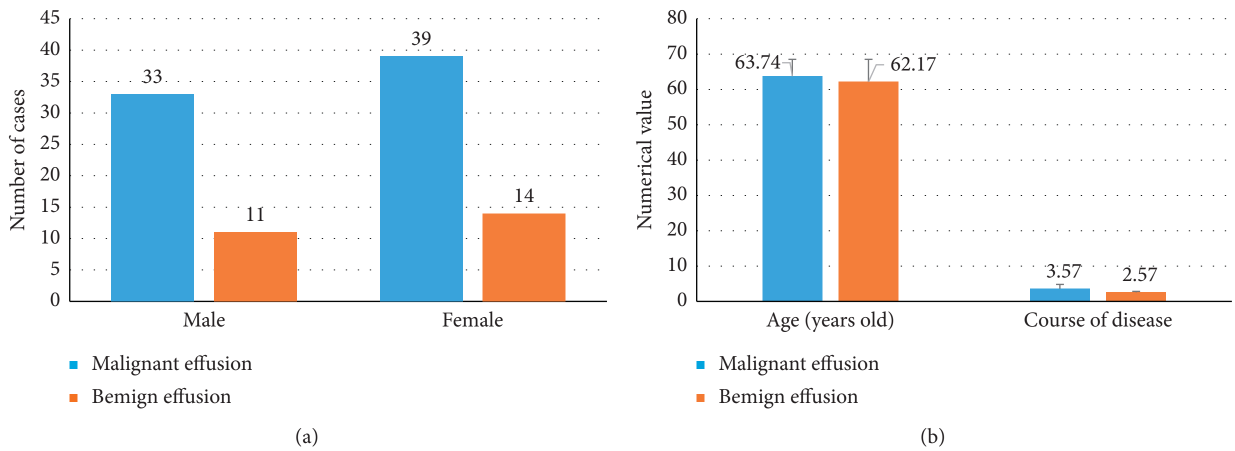

Figure 1: Comparison of the basic data of the patients in the two groups. (a) Comparison of the gender among the patients in the two groups; (b) comparison of the age and course of disease among the patients in the two groups.

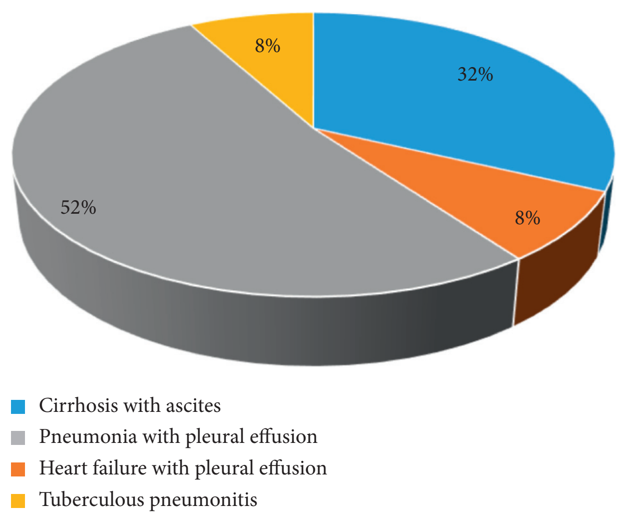

Figure 2: The disease causes of the patients with benign effusion.

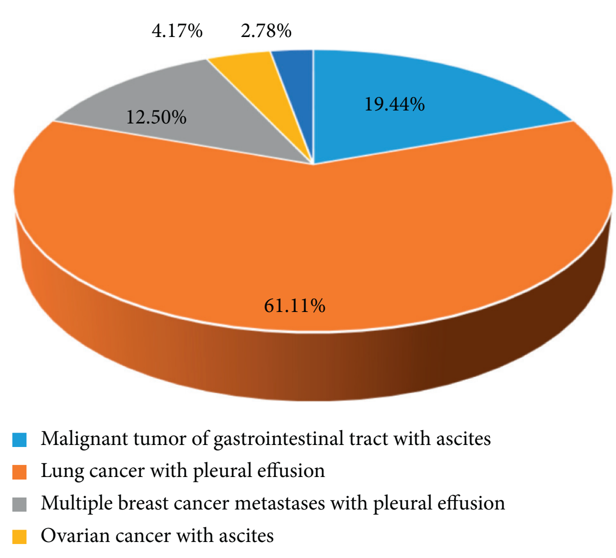

Figure 3: The disease causes of the patients with malignant effusion.

3.3. Comparison of the Physiological Conditions of the Patients in the Two Groups. The two groups of patients were subjected to immunohistochemical tests, and the representative results were selected for display shown in Figure 4. In addition, the immunohistochemical results of the benign effusion group showed that there was a small amount of positive cells; namely, the overall degree of cell malignancy was not high; meanwhile the immunohistochemical results of the malignant effusion group indicated that the positive cells were abundant in the effusion; namely, the whole cells had the high degree of malignancy.

3.4. Comparison of PET-CT Image Registration Values between Clone Selection Algorithm and Genetic Algorithm. Figure 5 discloses that the average difference of the maximum value of the normalized mutual information of PET-CT image registration of the clone selection algorithm is small, with no statistically huge difference ($P > 0.05$). Furthermore, the registration time and mismatching times were lower than those of genetic algorithm, and the differences were statistically substantial ($P < 0.05$).

The lungs were further taken as the comparison objects. The pneumonia with pleural effusion and lung cancer with pleural effusion were selected as the examples of the benign and malignant effusion group, respectively, as shown in Figure 6. In the PET-CT image of benign effusion, it is shown that there were concentrated shadows of radioactive distribution in lymph nodes and the larger range of lesion, so that they were presumed to be infectious lesions, and pneumonia was diagnosed based on medical history. There was no obvious radioactive concentrated area in the PET-CT image of malignant effusion, so as to speculate to be lung cancer with lymph node metastasis and diagnose lung cancer combined with medical history.

3.5. The CT Values of the Patients in the Two Groups under Different Energies. The differences in CT of the patients from the two groups were compared under different energies, and the results are expressed in Figure 7. Under the low energy (40–60 keV), the CT values of the benign effusion group were 41.24 ± 18.45 HU, 31.75 ± 12.8 HU, and 25.78 ± 11.12 HU; and the CT values of the malignant effusion group were 0.96 ± 19.45 HU, 7.99 ± 12.48 HU, and 12.57 ± 11.22 HU, with a statistical difference between the two groups ($P < 0.05$). Under 70–120 keV, the CT values of the benign effusion group were 21.15 ± 6.27 HU, 18.11 ± 6.33HU, 15.99 ± 5.24 HU, 15.24 ± 8.45 HU, 15.02 ± 4.21 HU, and 14.71 ± 6.66 HU; the CT values of malignant effusion group were 15.82 ± 7.67 HU, 17.55 ± 10.63 HU, 19.33 ± 11.27 HU, 20.01 ± 9.67 HU, 20.14 ± 10.44 HU, and 21.98 ± 10.57 HU, and the difference between the two groups was not statistically dramatic ($P > 0.05$). Under 130–140 keV, the CT values of the benign effusion group were 14.11 ± 6.17 HU and 13.56 ± 6.54 HU, while the CT values of the malignant effusion group were 21.44 ± 11.66 HU and 21.97 ± 12.57 HU; thus, there was a statistical difference in the two groups ($P < 0.05$).

3.6. The Paired Base Substances of the Patients in the Two Groups. Figure 8 illustrates that the contents of lipid/water, water/iodine, and water/calcium in malignant effusion were sharply higher than the contents of benign effusion. What is more, the content of lipid/water in malignant effusion was 221.44 ± 189.45 g/L, while its content in the benign effusion was 201.45 ± 197.56 g/L; the contents of water/iodine in the malignant and benign effusion were 1024.69 ± 19.48 g/L and 1008.48 ± 18.27 g/L, respectively; and the contents of water/calcium in the malignant and benign effusion were 1027.87 ± 11.66 g/L and 1009.48 ± 9.21 g/L, respectively. Therefore, there was a statistical difference between the two groups ($P < 0.05$).

Figure 9 demonstrates that the diagnostic sensitivity, specificity, and AUC of malignant effusion were 95.5%, 92.6%, and 97.7%, respectively, when the lipid/water concentration was over 104.34 g/L; when the water/iodine concentration was more than 1024.22 g/L, the diagnostic sensitivity, specificity, and AUC of malignant effusion were 86.4%, 77.8%, and 79.8%, respectively; and the diagnostic sensitivity, specificity, and AUC of malignant effusion were 86.4%, 92.6%, and 86.7%, respectively, when the water/calcium concentration was greater than 1028.44 g/L.

4. Discussion

Serous cavity refers to the human chest, abdominal cavity, pericardial cavity, and so forth. Under normal conditions, only a small amount of fluid in the serous cavity provides lubrication and protection (the fluid in the pleural cavity <20 mL, the fluid in the peritoneal cavity <50 mL, and the fluid in the pericardial cavity 10–50 mL). However, the increased volume of fluid in the cavity leads to the occurrence of effusion under pathological conditions, which is called SCE. Once the disease is complicated by SCE, it often indicates the severity of the disease [12, 13]. Based on the causes of the effusion, the effusion can be divided into benign and malignant. The study of Sherman-Samis et al. (2019) showed that many common causes of benign SCE were decompensation of liver cirrhosis, cardiac insufficiency, renal function failure, tuberculosis, and nonspecific inflammation. However, malignant SCE often existed in the late stages of various malignant tumors. This was because the blood vessels and lymph vessels were invaded by malignant tumor, or lymph nodes metastasis was to hinder the backflow and absorption of SCE; or tumor cells directly invaded blood vessels to increase the capillary permeability [14]. It was consistent with the pathological detection results of the study. The gold standard for diagnosing malignant effusion is to find tumor cells in SCE, but only when the malignant tumor invades the pleura or peritoneum or directly falls off in the effusion will a positive result be obtained. Moreover, its specificity is high, but the positive rate is low [15]. Das proved in a study that 58% was the positive rate of a single test in the pleural effusion. In addition, there was a false negative rate in the detection of malignant exfoliative cytology, and its sensitivity was only 40–60% [16]. Therefore, the PET-CT scanning detection proposed in the experiment plays an important role in assisting the diagnosis

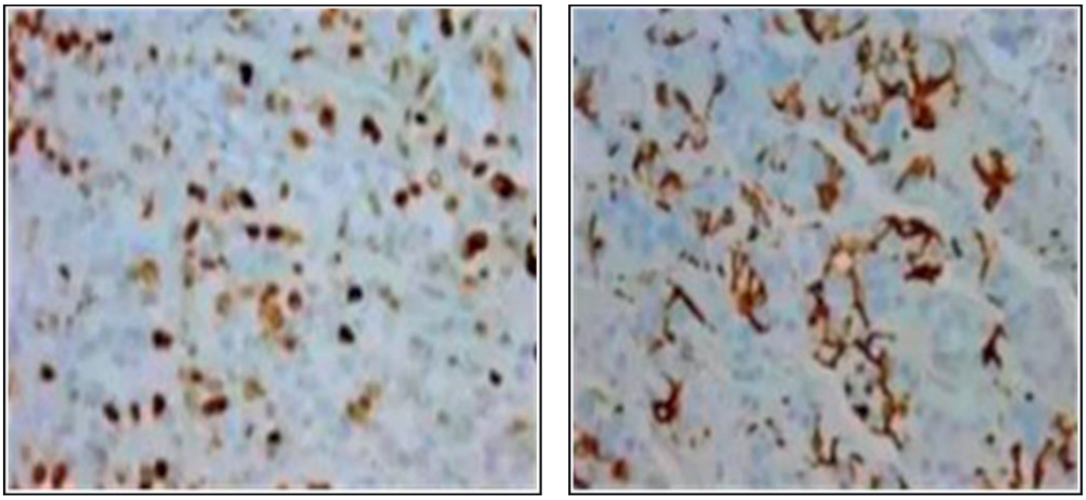

(a) (b)

Figure 4: The immunohistochemical results of the patients in the two groups. (a) The results of benign effusion group; (b) the results of malignant effusion group.

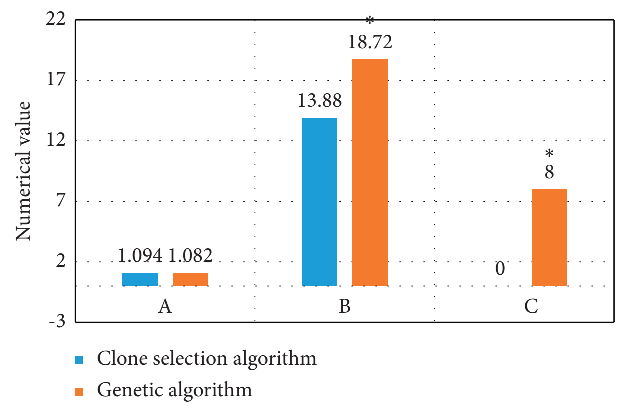

Figure 5: PET-CT image registration values. Note. (a) The average value of the maximum normalized mutual information; (b) registration time; (c) the times of mismatching. * indicates that the difference compared with clone selection algorithm is statistically significant.

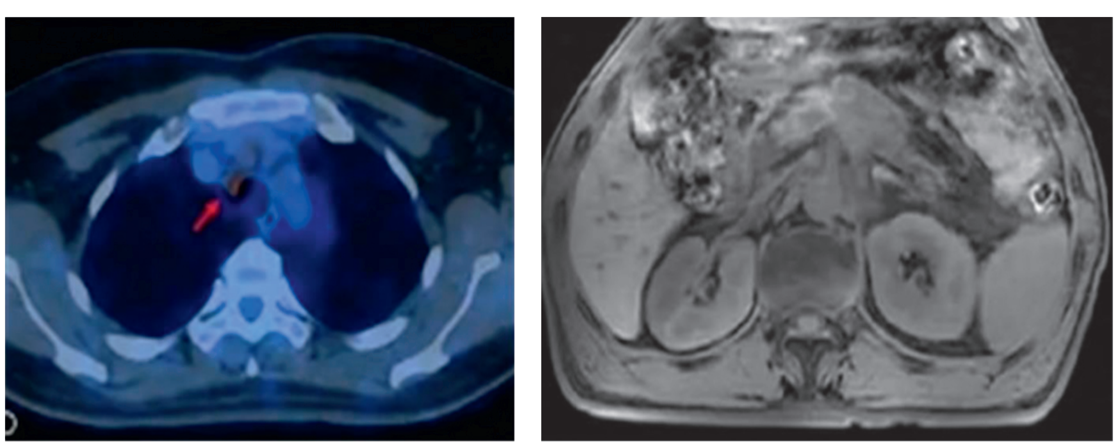

(a) (b)

Figure 6: The PET-CT images of two patients. (a) PET-CT image of the pneumonia with pleural effusion patient; (b) PET-CT image of the lung cancer with pleural effusion patient.

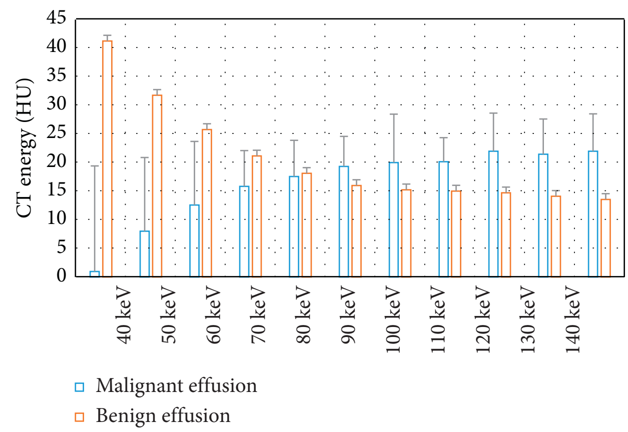

Figure 7: The CT values of benign and malignant effusion under different energies.

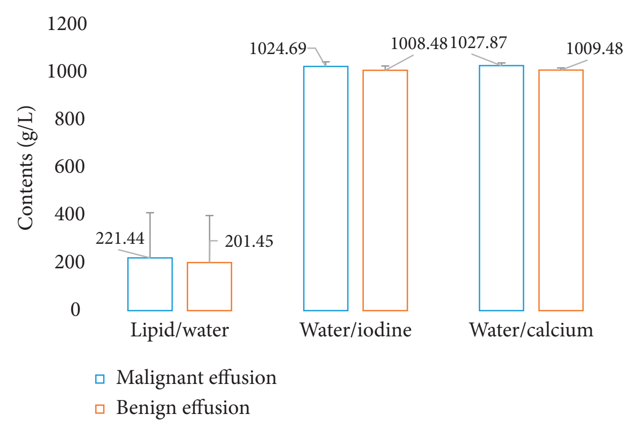

Figure 8: Comparison of the concentrations of paired base substances in the benign and malignant effusion.

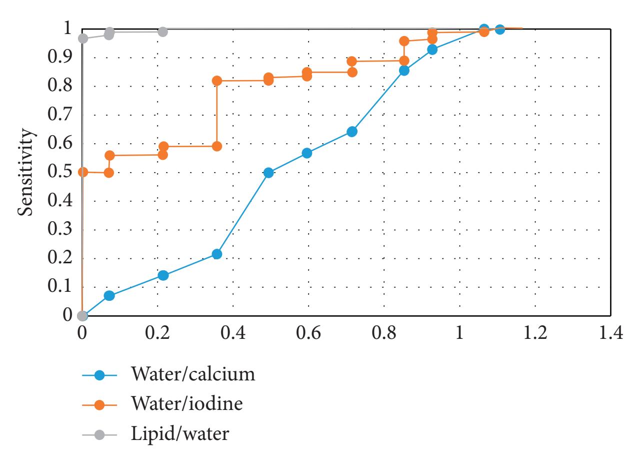

Figure 9: The ROC curve of paired base substances for diagnosis of malignant effusion.

of malignant effusion. It has great advantages in the diagnosis of tumors, and it can diagnose most tumors on the double-layer structure and functional metabolism through whole body imaging. What is more, it has very critical significance in finding the primary tumor lesion, and the nature diagnosis of patients with pleural and abdominal effusion is also relatively clear [17–19].

Harrison et al. summarized and sorted out the diseases that produced serous cavity effusion. The results illustrated that the main cause was malignant tumors in the chest and abdominal cavity, and pericardial effusion and tuberculosis also accounted for a large proportion, followed by connective tissue diseases, inflammatory infection, liver cirrhosis, heart function failure, hypothyroidism, and nephrotic syndrome [20]. The results were similar to the results of the study. However, there are certain differences in details, which may be caused by too few samples in the study. The PET-CT imaging based on the artificial intelligence algorithm of clone selection injects a small amount of positron nuclide tracer into the human body. The commonly used tracer is PF-FDG, which is adopted to detect the distribution of these positron nuclides in various organs of the human body. CT is employed to display the physiological metabolism of the main organs of the human body and to accurately locate, thereby fusing images. In this study, the clone selection algorithm was used to find that the registration time and mismatching times were both low, which achieved the optimal registration of PET-CT images and improved the accuracy of imaging results [21–23]. Zaucha et al. [24] stated that PET-CT was of great significance in finding primary tumor lesions and was more accurate in the diagnosis of patients with pleural and ascites effusion. It was also consistent with the experimental results of the study, showing that it is more sensitive to the diagnosis of malignant tumors. The paired base substances of lipid (water), water (iodine), and water (calcium) contents were selected for analysis, because the range of substances commonly used in medicine from fat to iodine contrast agents was included [25]. Knorr et al. have proved that free fatty acids in malignant ascites were 3 times higher than those in liver cirrhosis, and both saturated and unsaturated fatty acids in malignant ascites were higher than those in liver cirrhosis [26]. This is because fatty acids are the energy substrate for tumor cell metabolism, and malignant effusion contains dense and abundant tumor cells, which grow and metabolize vigorously, so lipids increase in malignant ascites [27–30]. It was reflected in the results of the study, indicating that the liquid concentration of the malignant effusion was higher than that of the benign effusion.

5. Conclusion

In this study, there was an investigation on the effect of PET-CT imaging detection image information and data information based on clone selection artificial intelligence algorithm in the diagnosis of serous cavity effusion in patients with different types of tumors. Besides, it was analyzed according to benign effusion and malignant effusion. It was found that the registration time and the times of mismatching of PET-CT images under the clone selection algorithm were both low, and the optimal registration of PET-CT images was realized. The image results indicated that benign and malignant serous cavity effusion could not be distinguished by CT values of routine mixed energy and 70–80 keV single energy (equivalent to mixed energy), while the CT value of low energy (40–60 keV) image played a critical role in the identification of benign and malignant effusions. However, the overall sample size of this study is small, and only relevant analysis for benign effusion and malignant effusion does not analyze many other clinical factors and the prognosis of patients. In the future, the sample size will be expanded to conduct more in-depth and comprehensive research and exploration in this direction. In short, PET-CT based on the artificial intelligence algorithm of clone selection has important diagnostic value in unexplained serous cavity effusion and has high sensitivity, specificity, and accuracy in the diagnosis of malignant pleural effusion.

Data Availability

The data used to support the findings of this study are available from the corresponding author upon request.

Conflicts of Interest

The authors declare no conflicts of interest.

References

[1] H. Lan and W. Song-Ping, "Clinical analysis of 50 cases of serous cavity effusion related with paragonimiasis," *Zhongguo Xue Xi Chong Bing Fang Zhi Za Zhi*, vol. 30, no. 4, pp. 452–454, 2018.

[2] L. Nicolè, F. Cappello, R. Cappellesso, C. J VandenBussche, and A Fassina, "MicroRNA profiling in serous cavity specimens: diagnostic challenges and new opportunities," *Cancer cytopathology*, vol. 127, no. 8, pp. 493–500, 2019.

[3] P. Jangsiriwitayakorn, N. Patarapadungkit, S. Chaiwiriyakul, T. Ratchaneekorn, S. Phannatorn, and N. Luxkana, "Comparative analysis of modified liquid-based cytology and cytorich red preparation in assessment of serous cavity effusion for cancer diagnosis," *Asian Pacific Journal of Cancer Prevention*, vol. 19, no. 6, pp. 1571–1575, 2018.

[4] T. Patel, P. Patel, S. Mehta, S. Majal, J. Dhaval, and K. Nisha, "The value of cytology in diagnosis of serous cavity effusions in malignant lymphomas: an experience of a tertiary care center," *Diagnostic Cytopathology*, vol. 47, no. 8, pp. 776–782, 2019.

[5] N. Filippov-Levy, H. Cohen-Schussheim, C. G. Tropé et al., "Expression and clinical role of long non-coding RNA in high-grade serous carcinoma," *Gynecologic Oncology*, vol. 148, no. 3, pp. 559–566, 2018.

[6] M. Kishore, P. Gupta, A. K. Malhotra, V. Kumar, S. Singh, and M. Bhardwaj, "Cytodiagnosis of extramedullary hematopoiesis in serous effusion: a rare presentation unfolding the underlying etiology," *CytoJournal*, vol. 15, p. 18, 2018.

[7] A. Raatz, M. Schöber, R. Zant et al., "Risk factors for chylothorax and persistent serous effusions after congenital heart surgery," *European Journal of Cardio-Thoracic Surgery*, vol. 56, no. 6, pp. 1162–1169, 2019.

[8] A. Harbhajanka, A. Brickman, J.-W. Park, V. B. Reddy, P. Bitterman, and P. Gattuso, "Cytomorphology, clinicopathologic, and cytogenetics correlation of myelomatous effusion of serous cavities: a retrospective review," *Diagnostic Cytopathology*, vol. 44, no. 9, pp. 742–747, 2016.

[9] H. J. Min, J. W. Choe, M. Y. Chang, K. S. Kim, S. Y. Lee, and S.-K. Mun, "The expression and correlation of Hsp 70 and Hsp 27 in serous middle ear effusion fluids of pediatric patients-a preliminary study," *International Journal of Pediatric Otorhinolaryngology*, vol. 101, pp. 145–149, 2017.

[10] W. B. Peng, X. Sun, M. Zhou et al., "Value of PET/MRI in the diagnosis of malignant pleural effusion in comparison with PET/CT," *Zhonghua Yixue Zazhi*, vol. 101, no. 30, pp. 2363–2369, 2021.

[11] D. Chen, X. Song, F. Shi et al., "Greater efficacy of intracavitary infusion of bevacizumab compared to traditional local treatments for patients with malignant cavity serous effusion," *Oncotarget*, vol. 8, no. 21, pp. 35262–35271, 2017.

[12] M. T. Siddiqui, F. Schmitt, and A. Churg, "Proceedings of the American Society of Cytopathology companion session at the 2019 United States and Canadian Academy of Pathology Annual meeting, part 2: effusion cytology with focus on theranostics and diagnosis of malignant mesothelioma," *Journal of the American Society of Cytopathology*, vol. 8, no. 6, pp. 352–361, 2019.

[13] S. Val, M. Poley, K. Anna et al., "Characterization of mucoid and serous middle ear effusions from patients with chronic otitis media: implication of different biological mechanisms?" *Pediatric Research*, vol. 84, no. 2, pp. 296–305, 2018.

[14] M. Sherman-Samis, H. Onallah, A. Holth, R. Reich, and B. Davidson, "SOX2 and SOX9 are markers of clinically aggressive disease in metastatic high-grade serous carcinoma," *Gynecologic Oncology*, vol. 153, no. 3, pp. 651–660, 2019.

[15] L.-Y. Xing, J. Yin, M. Shao et al., "Clinical characteristics and prognosis of serous body cavity effusions in patients with sepsis: a retrospective observational study," *BMC Anesthesiology*, vol. 18, no. 1, p. 169, 2018.

[16] D. K. Das, "Age and sex distribution in malignant and tuberculous serous effusions: a study of 127 patients and review of the literature," *Geriatrics and Gerontology International*, vol. 15, no. 9, pp. 1143–1150, 2015.

[17] N. Patarapadungkit, P. Jangsiriwitayakorn, S. Chaiwiriyakul et al., "Modified liquid-based cytology technique for immunocytochemistry in effusion specimen," *Asian Pacific Journal of Cancer Prevention*, vol. 20, no. 9, pp. 2611–2617, 2019.

[18] G. Akaike, M. Itani, H. Shah et al., "PET/CT in the diagnosis and workup of sarcoidosis: focus on Atypical Manifestations," *RadioGraphics*, vol. 38, no. 5, pp. 1536–1549, 2018.

[19] R. Fonti, M. Conson, and S. Del Vecchio, "PET/CT in radiation oncology," *Seminars in Oncology*, vol. 46, no. 3, pp. 202–209, 2019.

[20] D. J. Harrison, M. T. Parisi, and B. L. Shulkin, "The role of 18 F-FDG-PET/CT in pediatric sarcoma," *Seminars in Nuclear Medicine*, vol. 47, no. 3, pp. 229–241, 2017.

[21] J. P. Bois, D. Muser, and P. Chareonthaitawee, "PET/CT evaluation of cardiac sarcoidosis," *PET Clinics*, vol. 14, no. 2, pp. 223–232, 2019.

[22] X. Zhang and Z. Guan, "PET/CT in the diagnosis and prognosis of osteosarcoma," *Frontiers in Bioscience*, vol. 23, pp. 2157–2165, 2018.

[23] G. S. Shroff, B. S. Sabloff, M. T. Truong, B. W. Carter, and C. Viswanathan, "PET/CT interpretative pitfalls in thoracic malignancies," *Seminars in Ultrasound, CT and MRI*, vol. 39, no. 3, pp. 282–288, 2018.

[24] J. M. Zaucha, S. Chauvie, R. Zaucha, A. Biggii, and A. Gallamini, "The role of PET/CT in the modern treatment of Hodgkin lymphoma," *Cancer Treatment Reviews*, vol. 77, pp. 44–56, 2019.

[25] W. Chen and J. Jeudy, "Assessment of myocarditis: cardiac MR, PET/CT, or PET/MR?" *Current Cardiology Reports*, vol. 21, no. 8, p. 76, 2019.

[26] K. Knorr, M. Eiber, T. Maurer, H.-J. Wester, and K. Scheidhauer, "PET-CT/-MRT der Prostata," *Radiologe, Der*, vol. 57, no. 8, pp. 631–636, 2017.

[27] G. Giovacchini, E. Giovannini, M. Riondato, and A. Ciarmiello, "PET/CT with 68Ga-PSMA in prostate cancer: radiopharmaceutical background and clinical implications," *Current Radiopharmaceuticals*, vol. 11, no. 1, pp. 4–13, 2018.

[28] M. Tana, S. di Carlo, M. Romano, M Alessandri, C Schiavone, and A Montagnani, "FDG-PET/CT assessment of pulmonary sarcoidosis: a guide for internists," *Current Medical Imaging Reviews*, vol. 15, no. 1, pp. 21–25, 2019.

[29] N. Aide, R. J. Hicks, C. Le Tourneau, S. Lheureux, S. Fanti, and E. Lopci, "FDG PET/CT for assessing tumour response to immunotherapy," *European Journal of Nuclear Medicine and Molecular Imaging*, vol. 46, no. 1, pp. 238–250, 2019.

[30] J. van Sluis, J. de Jong, J. Schaar et al., "Performance characteristics of the digital biograph vision PET/CT system," *Journal of Nuclear Medicine*, vol. 60, no. 7, pp. 1031–1036, 2019.

Hindawi
Journal of Healthcare Engineering
Volume 2023, Article ID 9827564, 1 page
https://doi.org/10.1155/2023/9827564

Retraction

Retracted: Application of Clavien–Dindo Classification System for Complications of Minimally Invasive Percutaneous Nephrolithotomy

Journal of Healthcare Engineering

Received 8 August 2023; Accepted 8 August 2023; Published 9 August 2023

This article has been retracted by Hindawi following an investigation undertaken by the publisher [1]. This investigation has uncovered evidence of one or more of the following indicators of systematic manipulation of the publication process:

(1) Discrepancies in scope
(2) Discrepancies in the description of the research reported
(3) Discrepancies between the availability of data and the research described
(4) Inappropriate citations
(5) Incoherent, meaningless and/or irrelevant content included in the article
(6) Peer-review manipulation

The presence of these indicators undermines our confidence in the integrity of the article's content and we cannot, therefore, vouch for its reliability. Please note that this notice is intended solely to alert readers that the content of this article is unreliable. We have not investigated whether authors were aware of or involved in the systematic manipulation of the publication process.

In addition, our investigation has also shown that one or more of the following human-subject reporting requirements has not been met in this article: ethical approval by an Institutional Review Board (IRB) committee or equivalent, patient/participant consent to participate, and/or agreement to publish patient/participant details (where relevant).

Wiley and Hindawi regrets that the usual quality checks did not identify these issues before publication and have since put additional measures in place to safeguard research integrity.

We wish to credit our own Research Integrity and Research Publishing teams and anonymous and named external researchers and research integrity experts for contributing to this investigation.

The corresponding author, as the representative of all authors, has been given the opportunity to register their agreement or disagreement to this retraction. We have kept a record of any response received.

References

[1] X. Zhang, Z. Zhu, and J. Wu, "Application of Clavien–Dindo Classification System for Complications of Minimally Invasive Percutaneous Nephrolithotomy," *Journal of Healthcare Engineering*, vol. 2021, Article ID 5361415, 5 pages, 2021.

Hindawi
Journal of Healthcare Engineering
Volume 2021, Article ID 5361415, 5 pages
https://doi.org/10.1155/2021/5361415

Research Article

Application of Clavien–Dindo Classification System for Complications of Minimally Invasive Percutaneous Nephrolithotomy

Xiao-Jun Zhang, Zheng-Jie Zhu, and Jun-Jie Wu

Department of Urology Surgery, The Affiliated Xiangshan Hospital of Wenzhou Medical University, Ningbo, Zhejiang Province 315700, China

Correspondence should be addressed to Jun-Jie Wu; junjiewu2021@163.com

Received 17 July 2021; Accepted 22 November 2021; Published 15 December 2021

Academic Editor: Enas Abdulhay

Objective. To investigate the clinical applications of the Clavien–Dindo classification system (CDCS) in the assessment of perioperative complications in minimally invasive percutaneous nephrolithotomy (MPCNL). *Methods*. Totally, 390 patients with renal stones in our hospital from March 2015 to March 2020 were included for this study and then were divided into observation group (complication group, 78 cases) and control group (noncomplication group, 312 cases) according to the incidence of perioperative complications in CDCS. Single factor analysis and multivariate logistic regression analysis were used to analyze the risk factors of the perioperative complications of MPCNL. *Results*. The total incidence of complication in the 390 cases with MPCNL was 20.00% (78 cases) according to CDCS, among which the incidence of complications at grades I, II, III, IV, and V was 6.92% (27 cases), 8.21% (32 cases), 2.82% (11 cases), 1.79% (7 cases), and 0.26% (1 case), respectively. The proportion of patients, that aged >60 years, complicated with comorbidities, sophisticated calculi, the preoperative albumin level (<35 g/L), the operation time (>180 minutes), intraoperative bleeding volume (>300 mL), and hospitalization time (>7 days) in the observation group was significantly higher than that in the control group ((75.64% vs. 61.86%, 38.46% vs. 24.36%, 83.33% vs. 69.55%, 83.33% vs. 69.55%, 70.51% vs. 30.76%, 53.85% vs. 36.54%, and 60.26% vs. 43.27%), all $P < 0.05$). Multivariate logistic regression analysis showed that gender, associated comorbidities, preoperative albumin level, calculus complexity, operation time, and intraoperative bleeding volume (>300 mL) were correlated with the occurrence of complications ($P \leq 0.001$, 0.001, 0.001, 0.001, 0.003, and 0.001 respectively). *Conclusion*. The CDCS can give standard and more comparative criteria for the assessment of perioperative complications, which will provide reference data for reducing complications and ensuring safety profiles in these high-risk patients.

1. Introduction

Renal stones were one of the most common diseases in the urinary system, and it often occurs in the young and the middle-aged people; the morbidity was higher in males than females [1, 2]. Studies showed that, about 40% to 75% of patients with renal stones underwent different degrees of back pain, which is often taken as the primary clinical manifestation to visit doctors [3]. At the early stage, patients with small diameter stones and mild symptoms can alleviate the illness by drinking lots of water and physical exercises or other conservative treatments [4, 5]. However, with the influence of the patient's diets, environmental conditions, and other factors, the diameter of renal stones will be gradually enlarged in some people; consequently, the frequency and duration time of pain will increase, and hematuresis, hydronephrosis, or urinary tract obstruction would be found in some serious patients [6, 7]. When conservative treatment does not work for kidney stones, procedures such as transurethral ureteroscopic lithotripsy, percutaneous nephrolithotripsy, and laparoscopic ureterolithotripsy are often considered alternatives to conservative treatment. [8, 9].

Minimally invasive percutaneous nephrolithotomy (MPCNL) is a most common operation in urology, which was modified on the basis of percutaneous nephrolithotomy.

MPCNL had the advantage of small trauma, high discharging rate, rapid recovering course, and so on. MPCNL was effective for renal stones, but the complications in the perioperative period did not receive enough attention compared with its clinical efficacy. And, the evaluation of complications was usually based on operator's experience, but lacked consistent criteria [10]. How to carry out quantitative evaluation and reduce the incidence of perioperative complications in MPCNL are becoming surgical hotspots. In order to investigate the criteria of standardized assessment and the risk factors of the complications of MPCNL, 390 patients with renal stones from March 2015 to March 2020 in our hospital were collected in the study, and the Clavien–Dindo classification system (CDCS) was adopted to analyze the perioperative complications.

2. Patients and Methods

2.1. Patient Data. Totally, 390 patients with renal stones who underwent MPCNL from March 2015 to March 2020 in our hospital were collected, including 254 males and 136 females; aged from 40 to 70 years; 274 urban patients and 116 rural patients; 156 patients with diabetes, hypertension, chronic bronchitis, or other general comorbidities, and 234 patients without comorbidity; and 255 patients with simple renal stones and 135 patients with complex renal stones [11] (including stone diameter >25 mm, horn-like or multiple renal stones, stones that are difficult to remove caused by abnormal anatomy, etc.).

2.2. Surgical Methods. Epidural anesthesia or general anesthesia with endotracheal intubation were performed in operation, these patients were performed or supervised by a single surgeon who had previous experience of MPCNL. All patients were placed in the lithotomy position with conventional sterilization of surgery area, and the surgical towels were placed. The 5 Fr or 6 Fr ureteral catheter was inserted to the target ureter directed by ureteroscopic vision. After uretheral catheter insertion, the patients were replaced in a prone position, and percutaneous access was achieved by fluoroscopic guidance using an 18–20-gauge needle. Patients were punctured under the direction of B ultrasound. Then, the ureteroscope (Richard wolf, Germany) was placed in the renal pelvis, and the holmium laser (Litho, Italy) was used to fragment renal stones. The stones were discharged under the pressure of the irrigation solution or were taken out with basket catheter. At the end of surgery, a nephrostomy tube was inserted and removed 1 week after surgery, the double *J* ureteral catheter was inserted into the renal pelvis and removed 1 month after surgery, and the operation time was calculated from the insertion of ureteral catheter to the placement of nephrostomy tube.

2.3. Classification Standards and Evaluation Methods. Perioperative complications were divided into grade I, II, III, IV, and V according to CDCS [12]. Grade I: the complications had mild impacts on patients' recovery, but there is no threat to the life of patients, and these antipyretics, analgesics, antiemetics, diuretics, and physical therapy were allowed to application. Grade II: on the basis of grade I, other kinds of drugs, blood infusion, or total intravenous nutrition were required. Grade III: surgery, endoscope, or radiotherapy were required, including grade IIIa and grade IIIb; grade IIIa did not require general anesthesia, which could be performed by surgical intervention directly; grade IIIb required to carry out general anesthesia. Grade IV: it includes grade IVa and grade IVb; the former one's complications having life threats to the patients, who showed single organ failure and needed ICU care, and the latter one manifested as multiple organ failure. Grade V: patients' death was caused by complications. The incidence of perioperative complications in patients was observed and recorded.

2.4. Statistical Analysis. The data were analyzed with SPSS22.0 statistical software; the measurement data was expressed as mean ± standard deviation ($\bar{x} \pm SD$) and analyzed by the *t*-test; the numerical data were expressed as n (%) and analyzed by chi-square (χ^2) test; the single factor analysis and multivariate logistic regression analysis were used to analyze the risk factors of MPCNL complications; and P value <0.05 was considered to be statistically significant.

3. Result

3.1. Comparison of the Incidence of Complications of CDCS in MPCNL. According to CDCS, totally there were 390 cases in MPCNL complications; the cases of grade I, II, III, IV, and V complications were 6.92% (27 cases), 8.21% (32 cases), 2.82% (11 cases), 1.79% (7 cases), and 0.26% (1 case), respectively. Among these complications, the proportion of cases with fever (body temperature ≧ 39°C) was the largest (4.87%), the complications within grade III were 70 cases (89.74%), mainly including urinary infections and blood transfusion caused by intraoperative bleeding, and the proportion of infection and blood transfusion was 4.10% and 3.08%, respectively; there was 1 patient who died of acute myocardial infarction. The results are shown in Table 1.

3.2. Comparison and Analysis of Clinical Data in Two Groups. There were no significant differences in gender, BMI, demographic characteristics, and anesthesia between the two groups ($P > 0.05$). Age (>60 years), associated comorbidities, preoperative albumin level (<35 g/L), stone complexity, operation time (>180 min), intraoperative bleeding volume (>300 ml), and hospital stays (>7 days) of the observation group (complication group) were significantly higher than that of the control group (noncomplication group). The results are shown in Table 2.

3.3. Multivariate Logistic Regression Analysis of Complications. 78 patients with complications of MPCNL in perioperation were analyzed by multivariate logistic regression analysis, the results demonstrated that age (>60 years), associated comorbidities, preoperative albumin levels

Table 1: Comparison of CDCS of MPCNL complication in 390 patients (n (%)).

Grade	Complications	Incidence rate
Grade I		27 (6.92%)
	Body temperature ≧39°C	19 (4.87%)
	Increase of CCR, (alanine aminotransferase) ALT	5 (1.28%)
	Application of analgesic drugs	3 (0.77%)
Grade II		32 (8.21%)
	Blood transfusion caused by intraoperative bleeding	12 (3.08%)
	Urinary infections	16 (4.10%)
	Perirenal effusion	4 (1.03%)
Grade IIIa		8 (2.05%)
	Urinary tract obstruction	3 (0.77%)
	Closed drainage of thoracic cavity	2 (0.51%)
	Embolization of renal artery caused by bleeding	1 (0.26%)
	Renal pelvis perforation	1 (0.26%)
Grade IIIb		3 (0.77%)
	Renal abscess	2 (0.51%)
	Unilateral nephrectomy	1 (0.26%)
Grade IVa		6 (1.54%)
	Myocardial infarction	2 (0.51%)
	Cerebral stroke	2 (0.51%)
	Colonic injury	1 (0.26%)
	Acute renal failure	1 (0.26%)
Grade IVb		1 (0.26%)
	Shock	1 (0.26%)
Grade V		1 (0.26%)
	Death	1 (0.26%)

Table 2: Comparison of complications in two groups (n (%)).

Items		Observation group (78)	Control group (312)	χ^2	P
Gender					
	Male	52 (66.67%)	207 (66.35%)	0.052	0.820
	Female	26 (33.33%)	110 (33.65%)		
Age (years)					
	>60	59 (75.64%)	193 (61.86%)	5.184	0.023
	≦60	19 (24.36%)	119 (38.14%)		
BMI (body mass index) (kg/m^2)					
	>23	46 (58.97%)	190 (60.90%)	0.097	0.756
	≦23	32 (41.03%)	122 (39.10%)		
Demographic characteristics					
	Urban	55 (70.51%)	219 (70.19%)	0.003	0.956
	Rural	23 (29.49%)	93 (29.81%)		
Associated comorbidities					
	Yes	30 (38.46%)	136 (24.36%)	6.270	0.012
	No	48 (61.54%)	176 (75.64%)		
Preoperative albumin (g/L)					
	≧35	65 (83.33%)	217 (69.55%)	6.843	0.009
	<35	12 (16.67%)	95 (30.45%)		
Stone complexity					
	Simple	39 (50.00%)	216 (69.23%)	10.196	0.001
	Complex	39 (50.00%)	96 (30.77%)		
Operation time (min)					
	>180	55 (70.51%)	96 (30.76%)	41.541	≤0.001
	≦180	23 (29.49%)	216 (69.23%)		
Intraoperative bleeding volume (mL)					
	>300	42 (53.85%)	114 (36.54%)	8.337	0.004
	≦300	35 (46.15%)	198 (63.46%)		
Hospital stays (d)					
	>7	47 (60.26%)	135 (43.27%)	7.235	0.007
	≦7	31 (39.74%)	177 (56.73%)		
Anesthesia methods					
	Epidural anesthesia	54 (69.23%)	201 (64.42%)	0.637	0.425
	General anesthesia	24 (30.77%)	111 (35.58%)		

Table 3: Results of multivariate logistic regression analysis of Clavien–Dindo classification of complications in perioperation.

Items	B	Sb	Wald	P	OR	95%CI
Age	1.082	0.075	205.618	≤0.001	1.142	0.985–3.420
Associated comorbidities	0.983	0.185	28.264	≤0.001	1.125	0.783–3.8404
Preoperative albumin levels	2.465	0.317	60.279	≤0.001	4.412	2.398–21.917
Stone complexity	2.146	0.224	92.159	≤0.001	3.126	2.017–13.252
Operation time	1.017	0.126	65.052	0.003	2.562	2.001–3.540
Intraoperative bleeding volume	2.016	0.220	83.936	≤0.001	3.765	2.446–11.557

(<35 g/L), the stone complexity, the operation time (>180 min), and intraoperative bleeding volume (>300 ml) were associated with complications in patients by Claivien–Dindo classification. The results are shown in Table 3.

4. Discussion

Currently, MPCNL is one of the most common clinical treatments for renal stones. Percutaneous renal channel is F16 ~ F20, which is far less than the traditional Fr 24 ~ Fr 34. Thus, MPCNL can greatly shorten the area of the incision, reduce surgical injury, and increase the stone discharging rate. Some previous studies have reported that MPCNL promoted clinical efficacy, while some new complications appeared, which can lead to the increasing trend of total incidence rate of complications [13, 14]. CDCS began to be applied for clinical assessment of complications, with the improvement and update of CDCS in past decades, and surgical complications can be more detailed, reasonable, and objective to evaluate [15].

One researcher [16] analyzed the perioperative complications of 172 stone patients undergoing MPCNL using CDCS and showed that the overall incidence of complications was almost as high as 30%, with 9.88%, 6.98%, 7.56%, 3.49%, and 0.58% of class I, II, III, IV, and V complications, respectively. Nevertheless, the total incidence of complication of this study was 20.00% (78/390), and the incidence of complication of grade I, II, III, IV, and V were 6.92% (27/390), 8.21% (32/390), 2.82% (11/390), 1.79% (7/390), and 0.26% (1/390), respectively. The total incidence of complications and the complications of grade III and IV were reduced, and the possible explanations may be related to the differences of surgeons' experience and improvements in technology and equipments. Zeng et al. [17] adopted the CDCS to classify the perioperative complications of 377 patients in MPCNL, and the results showed that the associated comorbidities, stone complexity, and urinary abnormal anatomy were closely correlated with occurrence of perioperative complications. In this study, part of the results was similar as the results of Zeng et al [17]; moreover, our results agreed that the age, preoperative albumin levels, operation time, and intraoperative bleeding volume were the risk factors of perioperative complications of stones in patients.

In this study, the major complications in MPCNL were fever, infections, and bleeding within grade III of CDCS, which were the most common three adverse reactions, but grade IV~V of CDCS were major threats to the life security of patients. Therefore, the analysis of factors related to the occurrence of complications of CDCS can provide reference data for the managements of preoperative assessment and surgical scheme. According to the results of multivariate logistic regression analysis, the possible reasons may be explained in terms of these risk factors. Firstly, patients with age >60 years were often complicated with one or more comorbidities, and this will result in the decrease of coagulation function, body organic function, and surgical tolerance [18, 19]. Secondly, albumin is the common protein in plasma, which can reflect the condition of liver function and body immunity at a certain extent [20], and once the liver function was impaired, albumin levels were also reduced; meanwhile, there were obstacles in coagulation function and body immunity. Thirdly, urinary abnormal anatomy, large size stones, and complex location stones will increase the difficulties of fragmenting and discharging of stones [21, 22]. Lastly, the longer operation time and wound exposure time will increase the risk of bacterial infections and the volume of bleeding, and these risk factors mentioned above were influenced each other and increased the probability of complications, and made an interactive effect to deteriorate the safety profiles on patients [23].

In this study, several viewpoints must be presented for prevention and management of complications in MPCNL. If severe skeletal deformities, urinary abnormal anatomy, or hydronephrosis were not obvious, puncture should be performed under the B ultrasonic or C-arm on necessity of avoiding the main blood vessels. Once the main renal blood vessels injured and large bleeding appeared, nephrostomy tube should be immediately closed, and immediate hemostasis must be taken [24, 25]. Referring to elderly patients with poor nutritional status or complicated with several comorbidities, the related examinations and preassessment should be well performed before operation [18]. In this study, one patient died of acute myocardial infarction, which reminded urologists that they must carry out more rigorous preoperative assessment for these elderly patients complicated with comorbidities.

In conclusion, the CDCS can give standard and more comparative criteria for the assessment of perioperative complications in MPCNL, and the urologists should pay more attention to these high-risk factors, which will provide reference data to ensure surgical safety and promote the clinical efficacy.

Data Availability

The simulation experiment data used to support the findings of this study are available from the corresponding author upon request.

Hindawi
Journal of Healthcare Engineering
Volume 2021, Article ID 7538984, 8 pages
https://doi.org/10.1155/2021/7538984

Research Article

Ultrasound Elastography under Deep Learning Algorithm to Analyze the Therapeutic Effect of Clustered Regularly Interspaced Short Palindromic Repeats Short Hairpin Ribonucleic Acid Nanoparticles on Cervical Cancer

Minghui Li, Weiwei Li, and Liang Zhao

Department of Ultrasound Diagnosis, Affiliated Tumor Hospital of Xinjiang Medical University, Urumqi 830011, Xinjiang, China

Correspondence should be addressed to Minghui Li; 182060033@stu.just.edu.cn

Received 28 August 2021; Revised 31 October 2021; Accepted 5 November 2021; Published 29 November 2021

Academic Editor: Enas Abdulhay

This study aimed to analyze the effect of the deep learning algorithm on ultrasound elastography on the treatment of cervical cancer with clustered regularly interspaced short palindromic repeats (CRISPR) short hairpin ribonucleic acid (shRNA) nanoparticles, aiming to provide a reference for the clinical application of deep learning to analyze the therapeutic effect of the disease. In this study, CRISPR and shRNA plasmid nanoparticle drugs were used to treat 55 patients with cervical cancer in the experimental group, and normal saline was injected to another 53 patients in the control group, so compare the effect of nanoparticles in the treatment of cervical cancer. Professional doctors and the recurrent neural network (RNN) intelligent algorithm were used to score cervical cancer based on the ultrasound elastograph images by taking blue, green, and red (BGR) as diagnosis criteria. As a result, the experimental group had a total of 217 points before drug administration and a total of 224 points after drug administration. Each patient had an average increase of 0.13 points. The control group had a total of 200 points before drug administration and a total of 223 points after drug administration, and each patient had an average increase of 0.43 points. The experimental group was obviously different from the control group ($P < 0.05$). Each tissue image output by the RNN was clearer than the original image, and the score given by intelligent calculation was faster than that of professional doctors. The monitoring effect of the deep learning RNN intelligent algorithm on the therapeutic effect of nanomedicine was analyzed. It was found that the average accuracy of the experimental group and the control group was 98.95% and 90.34%, respectively; and the experimental group was greatly different from the control group ($P < 0.05$). In short, nano-CRISPR and shRNA drugs had remarkable effects on the treatment of cervical cancer, and the scores given by the deep learning intelligent algorithm were faster and more accurate, which provided theoretical guidance for the clinical application of deep learning algorithms to analyze the treatment effects of diseases.

1. Introduction

Cervical cancer is a common gynecological malignant tumor [1]. Carcinoma in situ is concentrated in the age of 30–35, and invasive cancer is concentrated in the age of 45–55. There is a trend of younger generation. With the development of imaging, examinations are becoming more and more common, enabling early detection and early treatment of cervical cancer, and its mortality significantly decline [2]. The etiology is related to viral infection, sexual behavior, number of childbirths, and other factors. Cervical smear cytology is the main method of cervical cancer screening. Others include the cervical iodine test and colposcopy. However, in some economically underdeveloped areas, early screening for cervical cancer is not universal, and women who have been vaccinated against human papillomavirus (HPV) are still at risk of getting the disease. Therefore, it is necessary to study a new type of drug to treat HPV to achieve the purpose of reversing cervical tissue lesions.

In recent years, with the development of the material field, nanomedicine has been widely reported in the treatment of cervical cancer. CRISPR is a repetitive sequence in the genome of prokaryotes, which can integrate its own genes into the genes of bacteria, and bacteria have evolved the CRISPR-Cas9 system to understand foreign genes [3]. It can make the genome more effective to produce changes or mutations, and the efficiency is higher than other gene editing techniques, but it may produce a large number of accidental targets in human cancer cells [4]. shRNA has two short inverted repeats, separated by a stem-loop sequence to form a hairpin structure [5]. When small interfering RNA is delivered in vivo, the siRNA sequence is cloned into a plasmid vector as a short hairpin; when it is delivered to an animal body, the hairpin sequence is expressed to form double-stranded RNA and processed by the RNAi channel. Transfection of cervical cancer tissue with nanoparticles containing clustered regularly interspaced short palindromic repeats (CRISPR) and short hairpin RNA (shRNA) plasmids can effectively inhibit the growth of cervical cancer cells [6].

Ultrasound-assisted elastography (ETE) can be roughly divided into two categories: intravascular elastography and tissue elastography, which can be used to analyze the therapeutic effect of cervical cancer [7]. Deep learning is a new research direction in the field of machine learning; it has achieved results in speech and image recognition, search technology, data mining, machine learning translation, and other related fields and has solved many complex pattern recognition problems and made great progress in artificial intelligence-related technologies [8]. The recurrent neural network (RNN) is one of the common deep learning algorithms. The RNN takes sequence data as input, recursively in the evolution direction of the sequence, and all nodes (cyclic units) are connected in a chain [9]. In this study, 108 patients with cervical cancer were randomly divided into an experimental group with 55 patents treated with CRISPR and shRNA plasmid nanoparticle drugs and a control group with 53 patients treated with the same amount of normal saline. The ultrasound elasticity of the two groups before and after administration was collected. In addition, the imaging results were compared to analyze the effect of CRISPR shRNA nanoparticles in the treatment of cervical cancer, aiming to provide data support and theoretical guidance for the clinical diagnosis and treatment of cervical cancer.

2. Materials and Methods

2.1. Research Objects and Their Grouping. In this study, 108 cervical cancer patients diagnosed by colposcopy biopsy in the hospital from January 2018 to January 2020 were selected as the research objects, with an average age of 43.2 ± 8.9 years old. 55 cases were randomly selected as the experimental group, and the remaining 53 cases were undertaken as controls. This study had been approved by the ethics committee of the hospital, and the patients and their families had understood the content and methods of the study and agreed to sign the corresponding informed consents.

The inclusion criteria were defined as follows: patients whose age was between 18 and 65, patients who were diagnosed with cervical cancer after clinical diagnosis, patients who had not received other drug treatment recently, patients had not received chemotherapy and radiotherapy, and patients who had no history of other treatments in the reproductive system.

The exclusion criteria were defined as follows: patients who had undergone tumor resection, patients with incomplete clinical data, and patients who did not cooperate with doctors throughout the treatment.

2.2. Nanoparticle Preparation and Drug Administration of CRISPR and shRNA. The poly β-amino ester (PBAE) and CRISPR/shRNA plasmid DNA were diluted in 25 mM of (pH = 5) sodium acetate solution. According to the different mass ratio (PBAE to plasmid), the PBAE solution was added dropwise to the same volume of the plasmid-containing solution and mixed gently for 30 seconds. The mixture was allowed to stand at room temperature for 15 minutes to completely synthesize PBAE/nanoparticles of plasmid deoxyribonucleic acid (DNA). 1% pentobarbital solution was intraperitoneally injected. The synthesized nanoparticles (containing 10 ug of plasmid) were injected into the vagina of patients with cervical cancer in the experimental group. Among the 55 cases in the experimental group, 25 cases were injected with PBAE/CRISPR plasmid DNA nanoparticle drugs, and 30 cases were injected with PBAE/shRNA plasmid DNA nanoparticle drugs, once a day for 20 days. The control group was injected with the same amount of normal saline, and then, the changes in the ultrasound elastography scores of the experimental group were observed.

2.3. Ultrasound Elastography. All patients underwent ultrasound elastography examination after vaginal ultrasound examination. The probe was moved to the cervix to observe the size of the cervix, the capsule, the characteristics of the gray-scale ultrasound, and the blood flow velocity of the cervix. Then, the probe was moved to the vaginal fornix and lightly attached to the external cervix for testing, the duration was 3–5 s, and the color coding ranged 0–180 kPa. The measurement should be repeated for 3 times to record and calculate the average of each group of data. All images were completed by an experienced professional imaging physician.

2.4. RNN under Deep Learning Algorithm. Convolutional neural network (CNN) models are widely used in image classification. Among them, the network neurons in the same layer are not independent of each other, but have a certain correlation. In the RNN model, the convolutional layer is built by combining the single-loop neural network and the convolutional layer, and the sampling layer is consistent with the same output layer. A simple RNN consisted of an input layer, a hidden layer, and an output layer. Its dynamic system had an input dynamic system and an input dynamic system, as shown in Figure 1. The equations of the dynamic system without input are (1) and

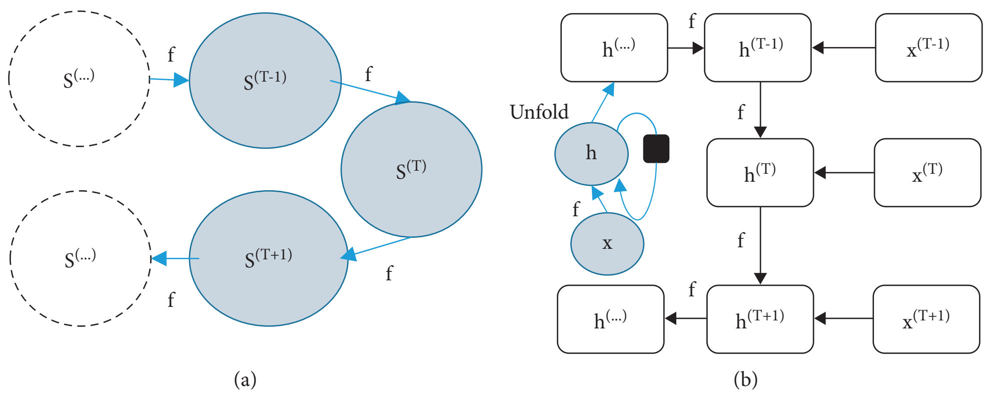

Figure 1: Dynamic system diagram. (a) A dynamic system without input. (b) A dynamic system with input.

(2); the equations for the dynamic system with input are (3) and (4). f represents the unit operation, the final state of the dynamic system with input is represented as h, the final state of the dynamic system without input is represented as S, X represents the input, T represents the state of the unit, T+1 and T–1 represent the increase or decrease of the unit state, and the ellipsis indicates the follow-up process can continue to run as such.

$$\begin{aligned} S^{(T)} &= f\left(S^{(T-1)};\theta\right),\\ S^{(3)} &= f\left(S^{(2)};\theta\right) = f\left(f\left(S^{(1)};\theta\right);\theta\right),\\ h^{(T)} &= f\left(h^{(T-1)}, X^{(T)};\theta\right),\\ h^{(T)} &= g^{(T)}\left(X^{(T)}, X^{(T-1)}, X^{(T-2)},\ldots, X^{(2)}, X^{(1)}\right)\\ &= f\left(h^{(T-1)}, X^{(T)};\theta\right). \end{aligned} \tag{1}$$

The following RNN algorithm was proposed by Hinton in 2015 [10], which uses ReLU to activate neurons and initializes the weights of the entire network to make the final model effect better than most existing algorithms. The location of the forget gate in the algorithm flowchart is shown in Figure 2, and the red circle area is shown in equation (2). f represents the internal unit operation, t represents the state of the unit, the unit operation on the state is defined as function f_t, A and Tanc represent the inputs of the vector, the final state of the forget gate is represented as h, the final state of the input gate is expressed as i, the final state of the total input is represented as C, O refers to the final state of the output gate, and T-1 represents the reduction of the unit state.

$$f_t = A\left(W_{fx}x_t + W_{Th}h_{t-1} + b_f\right). \tag{2}$$

The input gate positioning in the algorithm flowchart is shown in Figure 3 (the red circle area), and the equations are given as follows:

$$\begin{aligned} C'_t &= Tanh\left(W_{cx}x_t + W_{ch}h_{t-1} + b_c\right),\\ i_t &= A\left(W_{ix}x_t + W_{Th}h_{t-1} + b_i\right). \end{aligned} \tag{3}$$

The total input positioning in the algorithm flowchart is shown in Figure 4 (the red circle area) and equation (4).

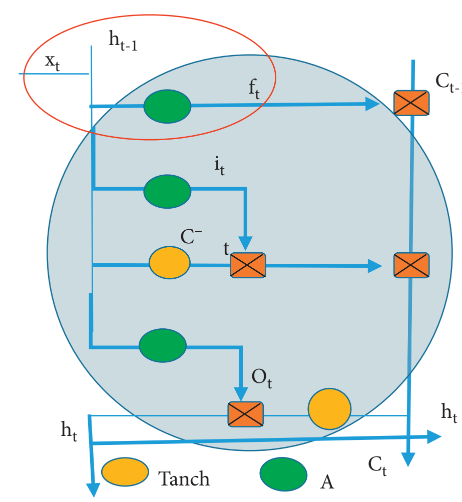

Figure 2: Diagram for location of the forgotten gate.

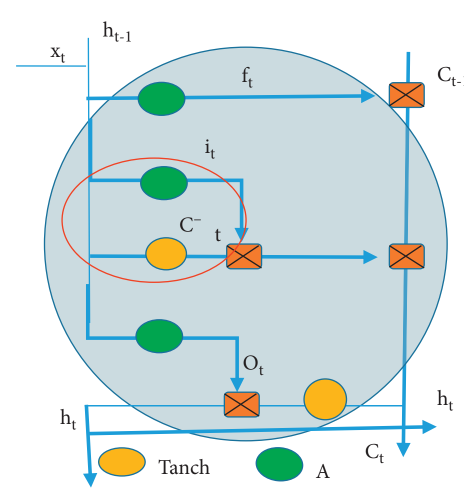

Figure 3: Diagram for location of the input gate.

$$C_t = f_t * C_{t-1} + i_t * C'. \tag{4}$$

The location of the output gate in the algorithm flowchart is shown in Figure 5 (the red circle area) and equations (5) and (6).

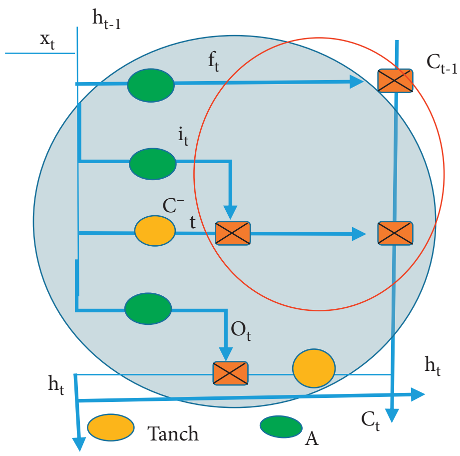

Figure 4: Diagram for location of the total input.

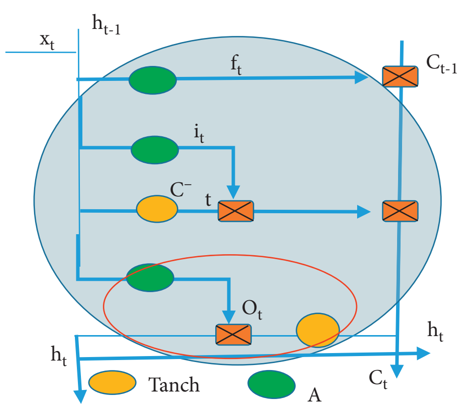

Figure 5: The location of the output gate in the algorithm flowchart.

$$o_t = A\left(W_{ox}x_t + W_{oh}h_{t-1} + b_o\right), \tag{5}$$

$$h_t = o_t * \mathrm{Tanh}\left(C_t\right)(f). \tag{6}$$

2.5. The Treatment and Efficacy Evaluation. ETE image evaluation was given as follows. The elasticity diagram used different colors to represent the hardness of different tissues, in which red indicates the average hardness was softer and the tissue was softer, green indicates the average elasticity of the tissue, and blue indicates the average hardness was harder. Generally, in normal cervical imaging, the display is mostly blue and green, and a small part of it is red. The specific scoring method studied in this study was defined as follows. If blue, green, and red were visible and blue area was ≤50%, the score was 1 point; if blue and green alternated without red and the blue area was ≤50%, the score was 2 points; if blue and green were visible with no red and the blue area was 50%–70%, the score was 3 points; if the image display was mainly blue, with a small part of green and no red and the blue area was more than 70%, the score was 4 points; and if the entire area of the cervix was shown in uniform blue, the score was 5 points.

In order to quantitatively evaluate the performance of the algorithm in this study, three commonly used evaluation indicators in medical image segmentation were used as the standard to measure the results of this experiment. Accuracy represented the ratio of all correctly predicted pixels to the total number of pixels. The specific calculation method is shown in equation (7), where TP represents the number of true positive, FP represents the number of false positive, FN represents the number of false negative, and TN represents the number of true negative.

$$A = \frac{\mathrm{TP} + \mathrm{TN}}{\mathrm{TN} + \mathrm{TP} + \mathrm{FP} + \mathrm{FN}}. \tag{7}$$

2.6. Statistical Methods. The software used for data processing in this study was SPSS 19.0. For statistical analysis, measurement data were expressed as mean ± standard deviation ($\overline{x} \pm s$), and count data were expressed as percentage (%). Pairwise comparison used analysis of variance. $P < 0.05$ means the difference was statistically significant.

3. Results

3.1. The Therapeutic Effect of CRISPR and shRNA Plasmid Nanoparticles on Cervical Cancer. As shown in Figure 6, 25 image scores of CRISPR nanoparticles before the drug administration were randomly selected, including 1 patient with 1 point, 2 patients with 2 points, 3 patients with 3 points, 12 patients with 4 points, and 7 patients with 5 points. After drug administration, there were 0 patient at 1 point, 1 patient at 2 points, 2 patients at 3 points, 13 patients at 4 points, and 9 patients at 5 points.

As shown in Figure 7, 30 cases of imaging scores before shRNA nanoparticle drug administration were randomly selected from the experimental group; there were 1 patient with 1 point, 3 patients with 2 points, 4 patients with 3 points, 14 patients with 4 points, and 8 patients with 5 points; after drug administration, there was 1 patient at 1 point, 2 patients at 2 points, 3 patients at 3 points, 15 patients at 4 points, and 9 patients at 5 points.

As shown in Figure 8, the image scores of the control group before drug administration were 3 patients at 1 point, 6 patients at 2 points, 5 patients at 3 points, 25 patients at 4 points, and 14 patients at 5 points. After drug administration, there were 2 patients at 1 point, 1 patient at 2 points, 2 patients at 3 points, 27 patients at 4 points, and 21 patients at 5 points.

As shown in Figure 9, the experimental group had a total of 217 points before drug administration and a total of 224 points after drug administration, with an average increase of 0.13 points per patient, and the control group had a total of 200 points before drug administration and a total of 223 points after drug administration, with each patient having an average increase of 0.43 points. Therefore, the experimental group was greatly different from the control group ($P < 0.05$).

3.2. Image Analysis of Ultrasound Elastography under RNN. Figure 10 shows a traditional ultrasound image of three random patients. The image was not in color. It can roughly

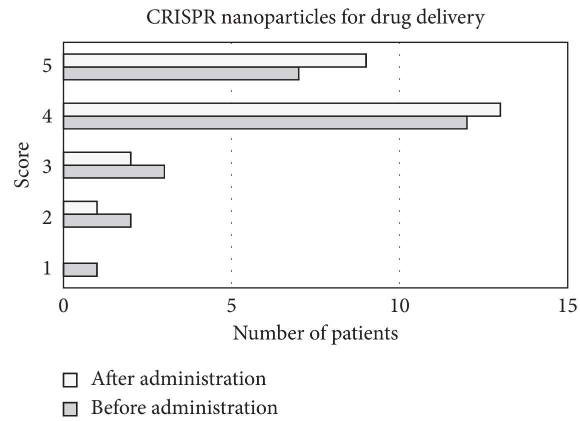

Figure 6: The CRISPR nanoparticles drug administration score for patients in the experimental group.

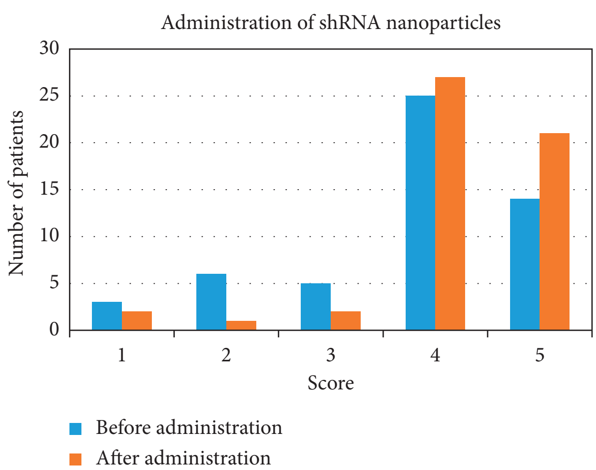

Figure 7: The drug administration score of shRNA nanoparticle of the experimental group.

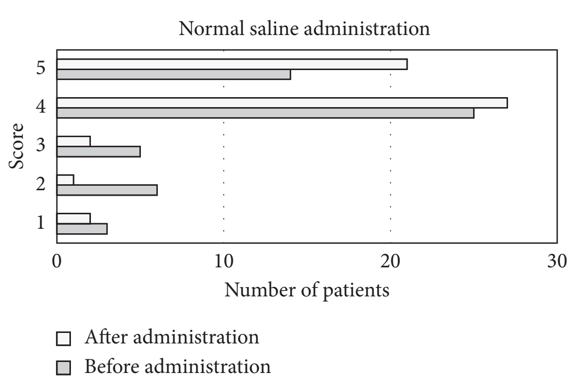

Figure 8: The scoring of drug administration with normal saline in the control group.

analyze cervical cancer qualitatively, but it was difficult to analyze cervical cancer quantitatively. With the development of technology, ultrasonic elastic imaging can simultaneously perform qualitative and quantitative analyses of cervical cancer.

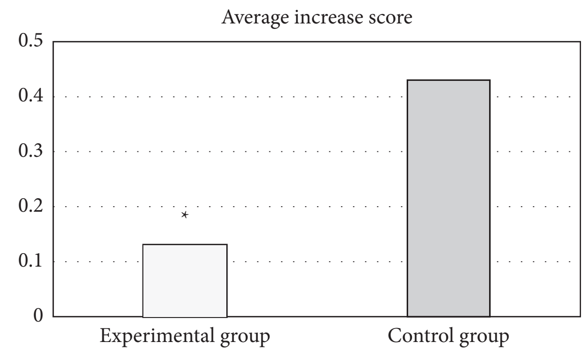

Figure 9: The scoring of drug administration with normal saline in the control group. *The difference was statistically great in contrast to the control group ($P < 0.05$).

Figure 11 shows the analysis process of the algorithm's influence on ultrasound elastography. The following figure is the image of five random patients, and A, B, C, D, and E in the figure refer to five different scores of 1–5, respectively. Figures A1, B1, and C1 are the original images of ultrasonic elastic imaging, and different colors represent tissues of different hardness. Figures A2, B2, and C2 show tissue images output by the deep learning algorithm based on the original ultrasound elastography image. Compared with the original image, the hardness of the tissue can be clearly distinguished. Figures A3, B3, and C3 show the blue area of the hardness output by the deep learning algorithm. The score was given through the calculation of the intelligent algorithm. Compared with professional doctors, this method was faster and more accurate.

The scores given by professional doctors and RNN intelligent algorithms were compared to analyze the monitoring effect of deep learning on the therapeutic effect of nanomedicine. Each test was performed three times, as shown in Figure 12. The data showed that the accuracy of the experimental group was 98.76%, 99.13%, and 98.96% for three times, respectively, and that for the control group was 89.43%, 91.15%, and 90.45%, respectively.

As shown in Figure 13, the average accuracy of the experimental group was 98.95%; the average accuracy of the control group was 90.34% and that in the experimental group was greatly different from that in the control group ($P < 0.05$).

4. Discussion

Persistent high-risk HPV infection is the main risk factor for cervical cancer. Even if the HPV vaccine has been vaccinated, the risk of other high-risk HPV infections faced by women still exists. Although the HPV vaccine can stimulate the body to produce antibodies to avoid infection, its therapeutic effect is minimal for women who already have cervical disease. Cervical screening can also be done on a regular basis, but in some economically underdeveloped areas, this type of examination is not universal and easy to achieve. Therefore, considering the actual needs of patients threatened by the HPV virus, this study combined PBAE and

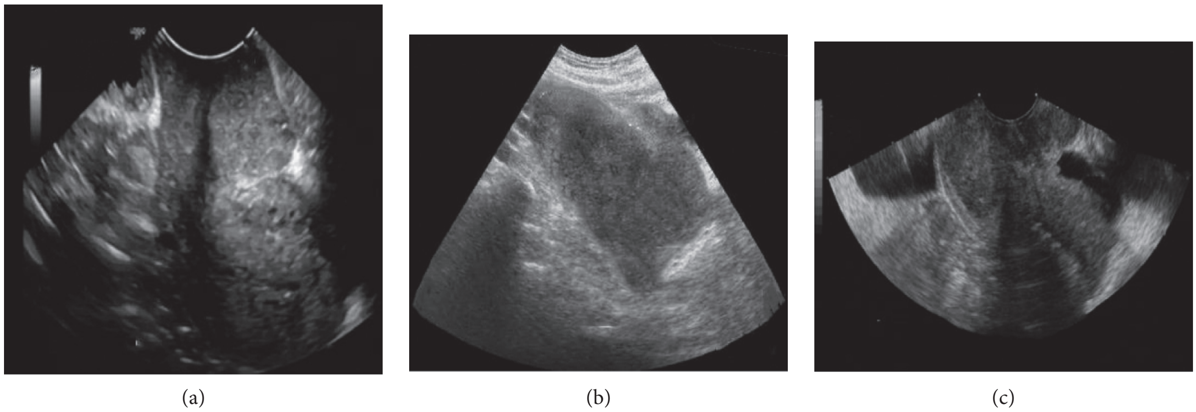

Figure 10: Traditional ultrasound image of cervical cancer. (a) An image of the early symptoms of cervical cancer. (b) The uterine cavity is closed and the periphery of the cervical lesion is blurred. (c) The cervical lesions are visible.

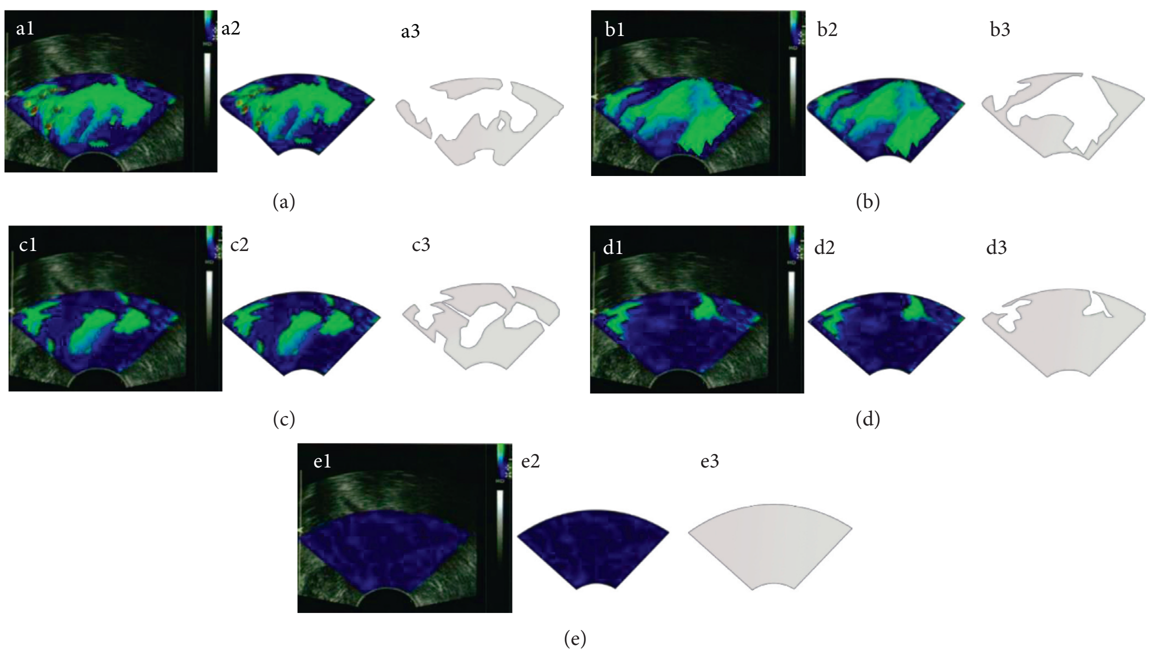

Figure 11: Diagram of ultrasonic elastic imaging analysis under the deep learning algorithm.

CRISPR shRNA to design a nanoparticle drug. In the field of molecular biology today, the silencing technology represented by shRNA can bind to mRNA encoding the protein at the mRNA level, so that the gene can be specifically degraded [11]. Knockout technology represented by CRISPR uses double-stranded DNA cutting and mismatch repair to prevent specific genes from achieving normal transcription and translation at the DNA level [12, 13]. Since these functional plasmids cannot penetrate the body's organs and tissues by themselves, an appropriate carrier system is needed [14]. In this study, PBAE with low toxicity, good degradability, high transfection efficiency, and excellent stability was used to complete plasmid delivery. It has currently shown good efficacy in the clinical treatment of some cancers.

Ultrasound-assisted elastography technology can detect tumors and spreading diseases that cannot be detected by traditional ultrasound and is an important imaging method to analyze and detect the therapeutic effect of cervical cancer [15, 16]. The RNN is one of the common deep learning algorithms. It is a type of algorithm that takes sequence data as input and recursively in the direction of sequence evolution, its nodes are connected in a chain, and it is featured with memory, parameter sharing, and Turing completeness [17, 18]. It has great advantages when learning the nonlinear features of the sequence. Under its optimization, ultrasound elastography can monitor the effect of disease treatment more accurately [19]. In this study, 108 patients with cervical cancer were selected and randomly divided into an experimental group with 55 patients treated with CRISPR and

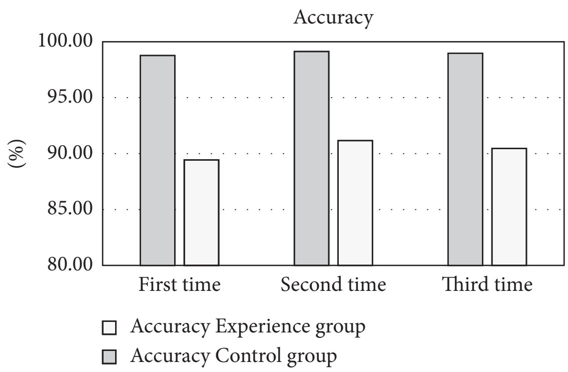

Figure 12: The comparison on accuracy in the experimental group and the control group.

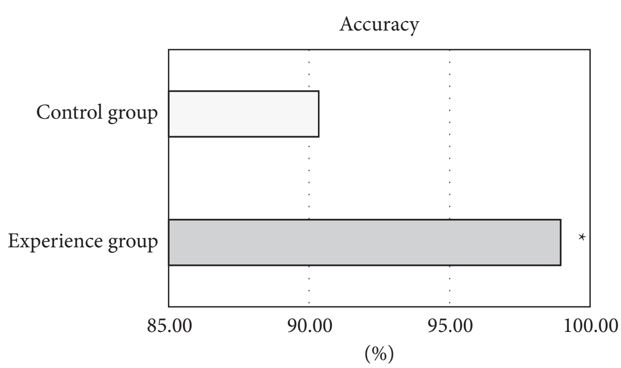

Figure 13: Comparison on average accuracy between the experimental group and the control group. *The difference was statistically great in contrast to the control group ($P < 0.05$).

shRNA plasmid nanoparticle drugs and a control groups (53 patients) treated with the same amount of normal saline. The ultrasound elastography image results before and after the administration of the two groups were collected and compared to analyze the effect of CRISPR shRNA nanoparticles in the treatment of cervical cancer, aiming to provide data support and theoretical guidance for the clinical diagnosis and treatment of cervical cancer. The results showed that the experimental group had a total of 217 points before drug administration and a total of 224 points after drug administration. Each patient had an average increase of 0.13 points. The control group had a total of 200 points before drug administration and a total of 223 points after drug administration. Each patient had an average increase of 0.43 points. Therefore, the experimental group was significantly different from the control group ($P < 0.05$). Each organization chart output by the RNN algorithm was clearer than the original image, and the score given by intelligent calculation was faster than that of professional doctors. The monitoring effect of the deep learning RNN intelligent algorithm on the therapeutic effect of nanomedicine was analyzed, it was found that the average accuracy of the experimental group and control group was 98.95% and 90.34%, respectively, and the experimental group was significantly different from the control group ($P < 0.05$). Such results were consistent with the research conclusions of Zhu et al. [20]. Nano-CRISPR and shRNA drugs are effective in the treatment of cervical cancer. Nano-CRISPR and shRNA drugs have significant effects on the treatment of cervical cancer, and the scores given by the deep learning intelligent algorithm are faster and more accurate, which can provide theoretical guidance for the clinical application of deep learning algorithms to analyze the treatment effects of diseases.

5. Conclusion

In this study, CRISPR and shRNA plasmid nanoparticle drugs were used to treat patients with cervical cancer, and the effects of nanoparticle treatment on cervical cancer were compared with those without drug treatment. In addition, the scores for cervical cancer were given by doctors and RNN intelligent algorithms to compare and analyze the monitoring effect of deep learning on the therapeutic effect of nanomedicine. The results suggested that nano-CRISPR and shRNA drugs can effectively inhibit the growth of cervical cancer cells and had a significant effect on the treatment of cervical cancer; each tissue image output by the deep learning algorithm was clearer and more identifiable, and the score given by the intelligent algorithm calculation was faster and more accurate. However, the sample size selected in this study was relatively small, which may have a certain impact on the final results of the experiment. Therefore, in future experiments, it is necessary to expand the sample size and further analyze and compare the effects of ultrasound elastography of deep learning algorithms on the treatment of cervical cancer with CRISPR shRNA nanoparticles. In short, it provided theoretical guidance for the clinical application of deep learning to analyze the therapeutic effect of diseases.

Data Availability

The data used to support the findings of this study are available from the corresponding author upon request.

Conflicts of Interest

The authors declare that they have no conflicts of interest.

Acknowledgments

This work was supported by the Natural Science Foundation of Xinjiang Uygur Autonomous Region (2017D01C406).

References

[1] E. Moen, D. Bannon, T. Kudo, W. Graf, M. Covert, and D. Van Valen, "Deep learning for cellular image analysis," *Nature Methods*, vol. 16, no. 12, pp. 1233–1246, 2019.

[2] J.-H. Lee, D.-H. Kim, S.-N. Jeong, and S.-H. Choi, "Detection and diagnosis of dental caries using a deep learning-based convolutional neural network algorithm," *Journal of Dentistry*, vol. 77, pp. 106–111, 2018.

[3] R. Forghani, A. Chatterjee, C. Reinhold et al., "Head and neck squamous cell carcinoma: prediction of cervical lymph node metastasis by dual-energy CT texture analysis with machine

learning," *European Radiology*, vol. 29, no. 11, pp. 6172–6181, 2019.

[4] S. M. Dadfar, K. Roemhild, N. I. Drude et al., "Iron oxide nanoparticles: diagnostic, therapeutic and theranostic applications," *Advanced Drug Delivery Reviews*, vol. 138, pp. 302–325, 2019.

[5] M. Li, P. Zou, K. Tyner, and S. Lee, "Physiologically based pharmacokinetic (PBPK) modeling of pharmaceutical nanoparticles," *The AAPS Journal*, vol. 19, no. 1, pp. 26–42, 2017.

[6] C. Liu, C. Xiao, J. Chen et al., "Risk factor analysis for predicting cervical lymph node metastasis in papillary thyroid carcinoma: a study of 966 patients," *BMC Cancer*, vol. 19, no. 1, p. 622, 2019.

[7] X. Q. Wang, X. Wei, Y. Xu, H. L. Wang, X. J. Xin, and S. Zhang, "Analysis of the relationship between ultrasonographic features and cervical lymph node skip metastasis of papillary thyroid micro-carcinoma," *Zhonghua Zhongliu Zazhi*, vol. 41, no. 5, pp. 373–377, 2019, in Chinese.

[8] J. Xu, P. Wang, W. Yue, Y. Luo, and Z. Li, "Application of ultrasonic shear wave elastography and contrast-enhanced ultrasound in the differential diagnosis of patients with benign and malignant thyroid lesions," *Gland Surgery*, vol. 9, no. 6, pp. 2136–2143, 2020 Dec.

[9] K. Brage, J. Hjarbaek, P. Kjaer, K. G. Ingwersen, and B. Juul-Kristensen, "Ultrasonic strain elastography for detecting abnormalities in the supraspinatus tendon: an intra- and inter-rater reliability study," *BMJ Open*, vol. 9, no. 5, Article ID e027725, 2019.

[10] R. Venkatesan and S. Prabu, "Hyperspectral image features classification using deep learning recurrent neural networks," *Journal of Medical Systems*, vol. 43, no. 7, p. 216, 2019.

[11] F. Barbero, L. Russo, M. Vitali et al., "Formation of the protein corona: the interface between nanoparticles and the immune system," *Seminars in Immunology*, vol. 34, pp. 52–60, 2017.

[12] J. Wang, W. Wei, and R. Guo, "Ultrasonic elastography and conventional ultrasound in the diagnosis of thyroid micronodules," *Pakistan journal of medical sciences*, vol. 35, no. 6, pp. 1526–1531, 2019.

[13] H. Kang, X. Qian, R. Chen et al., "2-D ultrasonic array-based optical coherence elastography," *IEEE Transactions on Ultrasonics, Ferroelectrics, and Frequency Control*, vol. 68, no. 4, pp. 1096–1104, 2021.

[14] X. Q. Wang, W. Wei, X. Wei et al., "Study on the relationship between ultrasonographic features of papillary thyroid carcinoma and central cervical lymph node metastasis," *Zhonghua Zhongliu Zazhi*, vol. 40, no. 3, pp. 196–200, 2018, in Chinese.

[15] R. Cui, W. L. Yang, W. Chen et al., "The value of ultrasonic elastography in the differential diagnosis of choroidal melanoma and choroidal hemangioma," *Zhonghua Yan Ke Za Zhi*, vol. 56, no. 9, pp. 676–680, 2020, in Chinese.

[16] Y. Zhu, S. Deng, Y. Zhang, and Q Jiang, "Comparative study of ultrasonic elastography and conventional ultrasound in diagnosis of malignant anus neoplasm," *Experimental and therapeutic medicine*, vol. 15, no. 3, pp. 2343–2346, 2018.

[17] F. Zvietcovich, A. Nair, Y. S. Ambekar et al., "Confocal air-coupled ultrasonic optical coherence elastography probe for quantitative biomechanics," *Optics Letters*, vol. 45, no. 23, pp. 6567–6570, 2020.

[18] S. H. Baik, J. W. Seo, J.-H. Kim, S.-K. Lee, E. C. Choi, and J. Kim, "Prognostic value of cervical nodal necrosis observed in preoperative ct and MRI of patients with tongue squamous cell carcinoma and cervical node metastases: a retrospective study," *American Journal of Roentgenology*, vol. 213, no. 2, pp. 437–443, 2019.

[19] K. Wang, X. Lu, H. Zhou et al., "Deep learning Radiomics of shear wave elastography significantly improved diagnostic performance for assessing liver fibrosis in chronic hepatitis B: a prospective multicentre study," *Gut*, vol. 68, no. 4, pp. 729–741, 2019.

[20] D. Zhu, H. Shen, S. Tan et al., "Nanoparticles based on poly (β-Amino ester) and HPV16-targeting CRISPR/shRNA as potential drugs for HPV16-related cervical malignancy," *Molecular Therapy*, vol. 26, no. 10, pp. 2443–2455, 2018.

Hindawi
Journal of Healthcare Engineering
Volume 2021, Article ID 9734612, 7 pages
https://doi.org/10.1155/2021/9734612

Research Article

CT Image Feature Diagnosis on the Basis of Deep Learning Algorithm for Preoperative Patients and Complications of Transcatheter Aortic Valve Implantation

Xiong Zheng,[1] **Zhang Qian**,[2] **Xiaofang Wang**,[1] **Zhen Zhang**,[1] **and Lei Liu**[1]

[1]*Cardiovascular Surgery, Fuyang People's Hospital, Fuyang 236000, Anhui, China*
[2]*Structure I Ward, Fuwai Hospital, Chinese Academy of Medical Sciences, Beijing 100037, China*

Correspondence should be addressed to Lei Liu; 20132524@stu.nmu.edu.cn

Received 11 September 2021; Revised 3 November 2021; Accepted 8 November 2021; Published 29 November 2021

Academic Editor: Enas Abdulhay

This work was aimed to explore the role of CT angiography information provided by deep learning algorithm in the diagnosis and complications of the disease focusing on congenital aortic valve disease and severe aortic valve stenosis. 120 patients who underwent ultrasound cardiography for aortic stenosis and underwent transcatheter aortic valve implantation (TAVI) in hospital were selected as the research objects. Patients received CT examination of deep learning algorithm within one week. The measurement methods were long and short diameter method, area method, and perimeter method. The deep learning algorithm was used to measure the long and short diameter, area, and perimeter of the target area before CT image processing. The results showed that the average diameter of long and short diameter measurement was 95% CI (0.84, 0.92), the average diameter of perimeter measurement was 95% CI (0.68, 0.87), and the average diameter of area measurement was 95% CI (0.72, 0.91). Among the 52 patients, 35 cases were hypertension (67%), 13 cases were diabetes (25%), 6 cases were chronic renal insufficiency ($Cr > 2$ mg/dL) (11%) (2 cases were treated with hemodialysis, 3.8%), 11 patients had chronic pulmonary disease (21%), 9 patients had cerebrovascular disease (17.3%) and atrial flutter and atrial fibrillation. Deep learning can achieve excellent results in CT image processing, and it was of great significance for the diagnosis of TAVI patients, improving the success rate of treatment and the prognosis of patients.

1. Introduction

Aortic valve stenosis is a common cardiovascular disease. Once clinical symptoms occurs, it develops rapidly, and the prognosis is extremely poor [1]. Current guidelines suggest that severe aortic stenosis patients with clinical symptoms should be treated as soon as possible. However, for elderly patients with multiple serious complications, postoperative mortality and incidence of complications increased significantly [2]. On this background, transcatheter aortic valve implantation (TAVI) came into being. The advantage of surgery is that there is no need to open the chest, so the trauma is small, and the postoperative recovery is quick. At present, China's TAVI is still in the primary stage and lacks experience [3]. Based on the particularity of TAVI surgery "high-risk requirements" and "nonvisualization," the clinical complications and aortic root anatomy of Chinese patients are different from those of western studies, but there is no systematic summary [4]. In recent years, TAVI became a new treatment method. Many studies reported that the annulus size measured by CT is the "gold" standard for the selection of valve rings, and the existing studies have confirmed that the use of CT in the diagnosis of TAVI disease can achieve excellent results [5]. CT angiography with deep learning algorithm can provide detailed anatomical image data of aortic root sinus and become a routine examination before operation for severe aortic stenosis [6]. In recent years, many studies showed that CT angiography based on deep learning algorithm is more accurate in the diagnosis of bicuspid aortic valve. In addition, it can also clarify the injury of ascending aorta [7]. For patients with aortic valve disease, CT angiography with deep learning algorithm can not only provide anatomical information but also quantitatively analyze aortic valve calcification [8]. The important role of deep learning algorithm CT angiography in aortic valve disease diagnosis and preoperative risk assessment sounded the clinical alarm for these patients in advance. Aortic valve interventional therapy became a research hotspot and direction of interventional therapy for structural heart disease [8].

These patients are mostly elderly, serious complications and cannot tolerate valve implantation surgery [9]. Studies indicated that TAVI can not only reduce aortic cross-valvular pressure in patients with aortic valve stenosis but also improve myocardial function and reduce mortality [10, 11]. China is rapidly entering an aging society, and patients with calcified aortic stenosis are increasing year by year [12]. TAVI has broad development prospects. Based on the particularity of surgery "high-risk requirements" and "nonvisualization" of TAVI, the preoperative clinical evaluation and imaging evaluation are to screen suitable patients and prevent intraoperative complications [13]. The purpose of this study was to investigate the role of CT angiography information provided by the deep learning algorithm in the diagnosis and complications of congenital aortic valve disease and severe aortic valve stenosis. The purpose of optimizing and improving CT scanning mode evaluation of deep learning algorithm before TAVI was to provide more safe and effective scanning methods for surgical patients.

2. Materials and Methods

2.1. Research Objects. 120 patients underwent ultrasound cardiography of aortic stenosis in the hospital from February 2018 to December 2020. The average age of them was 72.46 ± 6.75 years old, and there were 67 males. According to the comprehensive evaluation, the risk of surgery was too high to tolerate surgical valve ring replacement. Therefore, it was recommended that patients with severe aortic stenosis who had percutaneous main valve replacement and arterial replacement received cardiac enhanced CT examination within one week could be included. Patients with rheumatic heart disease who had undergone aortic valve replacement or the patients with infective endocarditis were excluded. A total of 120 patients were selected. General information, traditional risk factors, and other information of patients were collected by consulting medical records and telephone follow-up. The study was approved by the medical ethics committee, and patients signed informed consent.

2.2. CT Scanning. All patients who underwent cardiac scanning signed informed consent for scanning. The patient sat for 30 minutes before the examination, and the professional staff explained the precautions of the examination. CT scan included plain cardiac scan and prospective electrocardiogram-gated coronary spiral scan (anterior) (35–73% cardiac cycle) and dynamic large-pitch scan. The prospective electrocardiogram-gated trigger technique was used to scan the supine position of calcification, and the electrocardiogram-gated device was connected. The width of the collimator was 0.733 mm, the matrix was 500 × 500, and the thickness was 2.6 mm. The scanning range was from tracheal bulge to apex. After inhalation, breath hold twice had completed the scan, and the scan time was 7 s. The enhanced CT scan was performed with prospective electrocardiogram-gated (60% cardiac cycle) and dynamic large-pitch scanning. The scanning range was from the apex to the diaphragm. Onepak 370 (370 mg/mL, OP) was used as thw contrast agent. Dual-tube high pressure injection was used to connect the automatic injector to the elbow vein and measure the circulation time. The method was to select the level of aortic root, embed 17 cannula needles into the vein before scanning the elbow, inject 16 mL Onepak 370, with a flow rate of 6 mL/*s*, delay scanning of 7 s, and scan one layer with a thickness of 6 mm. The rotation time of the spherical tube was 1.3 s/circle. The scanning can be stopped when the density of the ascending aortic root changed from high to low. In the time-density curve obtained by dynamic analysis software, the actual delay time was obtained 5 s after the peak attenuation delay of contrast agent in the region of interest of ascending aorta. Two injection stages were conducted.

2.3. CT Images of Deep Learning Algorithm. In the Caffe environment, according to the existing experience and knowledge, combined with the CT image characteristics of aortic aneurysm, the CT performance of the aorta was analyzed (TJ-2 fully convolutional network model suitable for experiments was analyzed. The model structure was shown in Figure 1.). The TJ-2 fully convolutional network model can theoretically enter any size of the graph, for example, and generate the corresponding image output after calculation. The network model had good fault tolerance. The experimental data set was divided into training set and verification set, and these data were applied to the designed model for training in TJ-2. After training, the accuracy of the training results and other information can be obtained, and the problems in the experiment can be found by comparison. Image transmission to postprocessing workstations (syngo Imaging, Siemens, medical solution systems, Forchheim) was analyzed using three-dimensional software. Parameters were as follows: reconstruction layer thickness, 1.2 mm; reconstruction interval, 0.8 m; and convolution kernel, d32f. Image postprocessing techniques were intensity projection, multiplanar reconstruction, and surface reconstruction. Two experienced radiologists worked together to complete image analysis, discuss, and deal with different problems.

x samples $n_{\mathrm{i}} \in \mathrm{DX}$ ($i = 1, 2, \ldots,$ x) are controlled into q:

$$U_{I1} = \left\{ 1^{1st} 2^{\text{other}} \right. . \tag{1}$$

The property of matrix U is $U = (U_{il})$.

$$\begin{gathered} U_{i1} \varepsilon (1, 2), \\ \sum_{i=1}^{e} U_{I1} = 2 (1 = 2, 3, \ldots X). \end{gathered} \tag{2}$$

The overall difference is as follows.

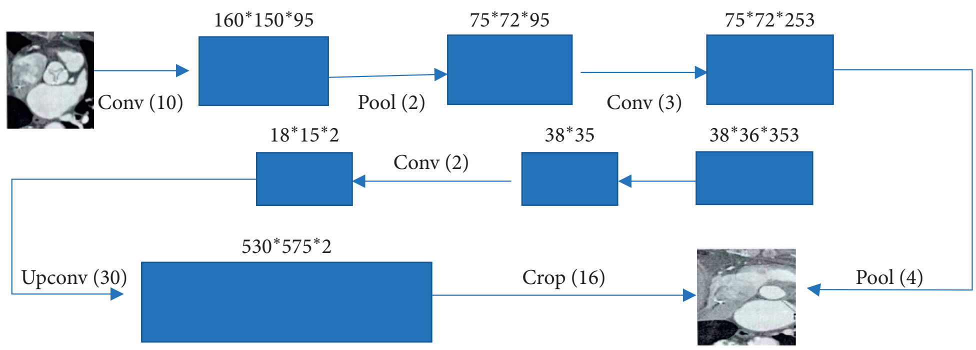

Figure 1: TJ-2 fully convolutional network model.

$$P(U) = \sum_{i=1}^{e} P(1)(u) = \sum_{i=1}^{e}\sum_{1=1}^{e} Uil\|n1 - \overline{ni}\|. \quad (3)$$

The TJ-2 deep learning piecewise network model is shown in Figure 1. The whole network structure experienced four convolution operations, two convolution pool operations, and one deconvolution operation. After this processing, the output image was the same size as the input image. The location of the aorta and aortic aneurysm was marked on the output image. TJ-1 full convolution network was mainly used for optimizing the experimental data, which greatly improved the computational efficiency. Although the TJ-1 full convolution network design was not as complex as the classical deep learning network, such as AlexNet and VGg segmentation network, the TJ-2 network can also complete the segmentation task well and had high operation efficiency and energy saving effect.

Obviously, such a small amount of data cannot be applied to deep learning algorithms. The square equation of translation and rotation was used to expand the dataset. The obtained original data were moved three times to the left and right, and the unit of each second translation was 20 pixels. On the basis of the obtained image, original data were moved three times to the up and down, and each translation was 15 pixels. After left and right translation and up and down translation, 1,617 slices were obtained. Next, the rotation operation was carried out. Each rotated 45° clockwise, a total of 7cycles. The dataset was expanded to 12,936 slices.

After 28 iterations, the trained TJ-2 full convolution network model was obtained. The trained TJ-21 model can be directly used for aortic image segmentation test. The specific experimental results can be explained as follows. GPU used NVIDIA GTX 1170 to conduct experiments in the Cafe environment of Ubuntu 13.02.

2.4. Image Measurement and Analysis. The acquisition phase of CT cardiac image was cardiac cycle, which was about 28%–71%. When the coronary image of the patient was recorded, in the case of arterial stenosis, as long as the stenosis rate of one coronary artery was >51%, the patient was defined as coronary heart disease. The two valves and two sinuses of the aortic valve were measured, and disappeared plane was measured simultaneously in the test. The long and short diameter measurement method was used to calculate the average diameter of the valve ring according to long diameter + short diameter. Ellipticity index (EI) was used to evaluate the ellipticity of the petal ring. EI was the maximum long diameter of ellipse divided by its minimum diameter. When EI ≤1, the measured plane was defined as a circle, the difference between the maximum diameter and the minimum diameter was less than 11% of the minimum diameter, and if EI > 1, the measured plane was defined as an ellipse (Figure 2 shows the measurement process).

As shown in Figure 2, the enhanced cardiac contraction image was selected for processing. In the coronal position, the long axis (a) of the ventricle was cut along the left side, and the sagittal oblique position (b) perpendicular to the long axis of the left ventricle was reconstructed to obtain the double oblique figure by axial cutting. The double oblique figure was obtained by axial cutting, and short axis of the aortic sinus was roughly flat (c). The lowest point of the adjusted cardiac sinus and the lowest point of the left sinus were determined by the whole tangent on the coronal line (the dotted line in (a) and (b)), respectively. The lowest point of the solid-free square sinus was determined at the sagittal oblique point, so that the lowest point of each valve in the triple aortic valve was flat ((e)–(g)). (g) showed the aortic valve ring on the double oblique transverse axis.

Figure 3 shows different measurement methods. Aortic rings were measured by long and short diameter method (a), perimeter method (b), and area method (c). All measurements were performed by two experienced doctors according to the blind method. Each observer measured the size according to the three methods shown in the diagram. In order to assess the observer's inherent reliability, at least one month later, the observer reconstructed and defined the measurement plane according to the original image. The size of the valve ring was measured, and then a second measurement was conducted.

2.5. Statistical Analysis. The general situation of the selected patients was classified and analyzed. Results were based on the mean, standard deviation, or frequency and percentage ratio representation, and the normal distribution was tested by continuous variables. Chi-square test or accurate test was used to compare the classification variables. The difference in

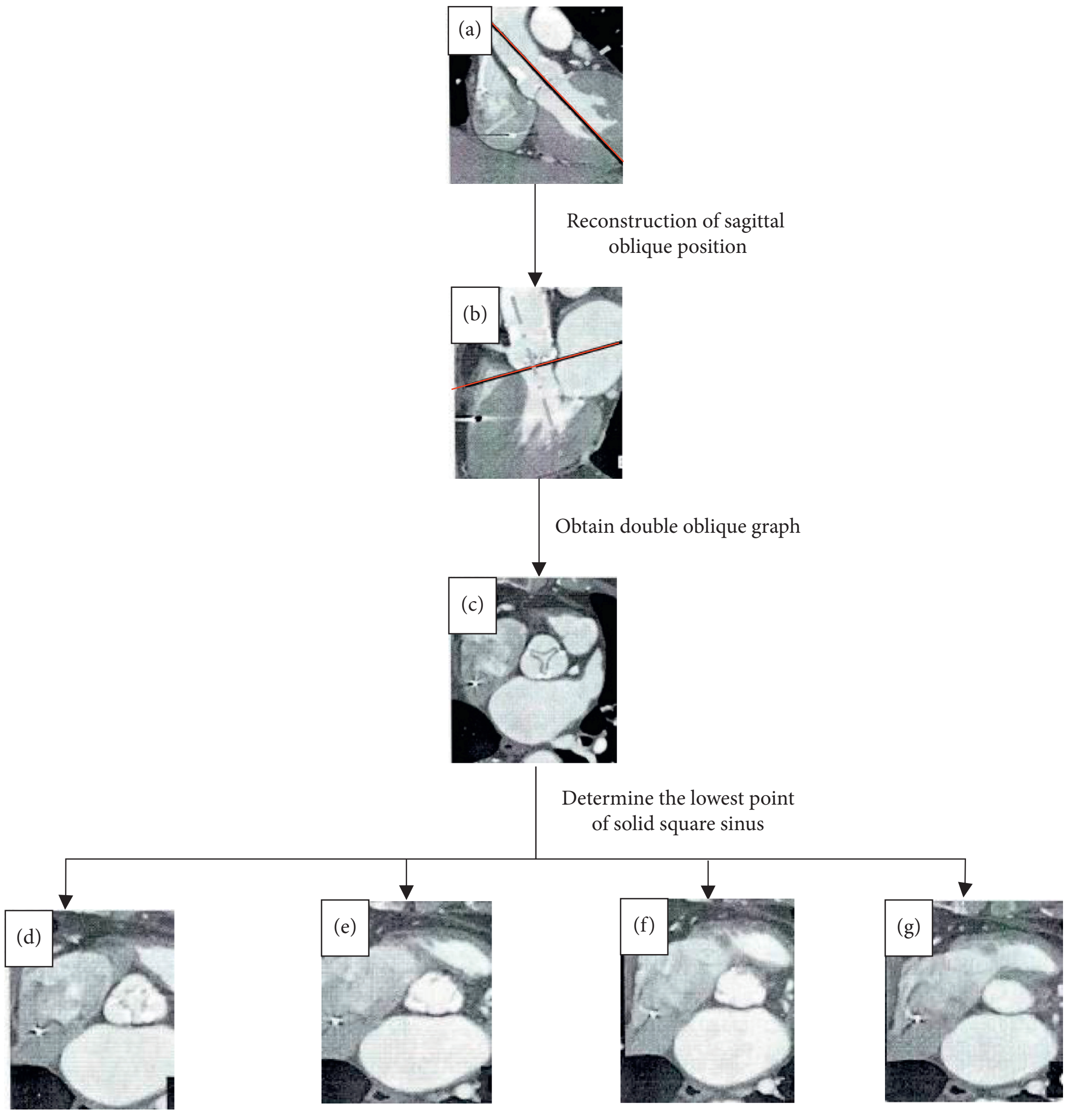

Figure 2: Measurement process.

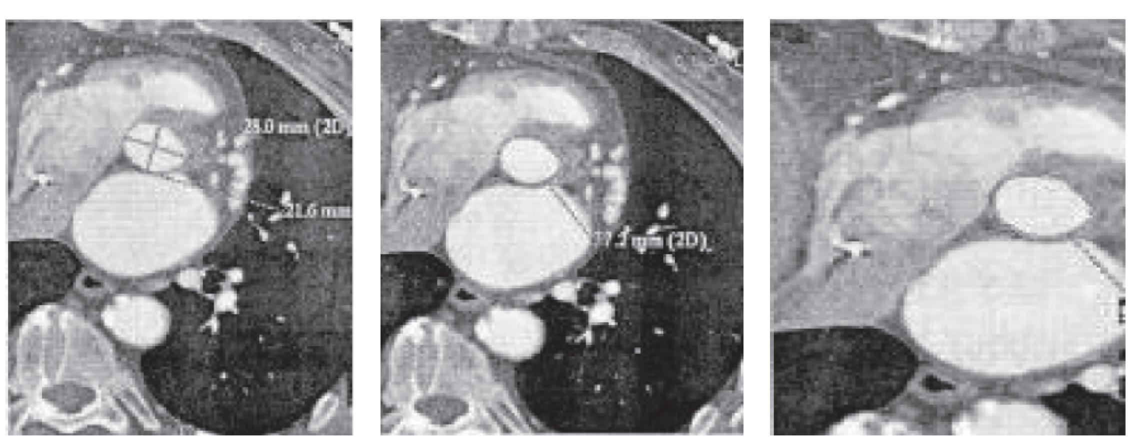

Figure 3: Results of three methods for measuring aortic valve ring.

average diameter measured by different methods was compared, and the paired test was adopted. Interclass correlation coefficient was defined as interobserver or the ratio intraobserver variability to overall variability. The 95% confidence interval was calculated by the data analysis method. Statistical analysis was performed in SPSS19, and $P < 0.05$ was considered statistically significant.

3. Results

3.1. Basic Data of Patients. 120 patients underwent CT examination. The average age was 72.46 ± 6.75 years. Male patients accounted for about 58%. 52 patients received TAVI eventually. All patients were successfully treated with TAVI after operation and had no valve ring rupture, leaflet embolism, or coronary artery occlusion (Table 1).

Table 1: HEBIN basic data of patients.

Variable	Patient ($n = 120$)
Mean transvalvular pressure gradient (mm/hg)	57.65 ± 15.3
Gender (male)	67 (58%)
Height (cm)	164 ± 8.2
Body surface area (m^2)	1.73 ± 0.15
Hypertension (%)	58 (48.3%)
Diabetes (%)	30 (25%)
Coronary heart disease (%)	32 (26.7%)
Peak velocity of aortic valve (m/s)	5.133 ± 0.65
Left ventricular ejection fraction (%)	54.3 ± 15.4

3.2. Effect Evaluation of Deep Learning Algorithm in CT Image Processing. In the training process, the convergence change of the loss function can be obtained. With the increase of training times, the accuracy of the verification data obtained by the entire TJ-2 network was getting higher and higher. However, when the accuracy reached 80%, the accuracy can increase little. Until the end of the training, the loss function also gradually converged and showed a constant trend. The final accuracy was 82%. The training process of the TJ-2 full convolution network was completed. The learning changes of training the TJ-2 full convolution network indicated changes of three kinds of learning in TJ-2 network during training. The learning rate can control the loss function of the whole TJ-2 volume product neural network to decrease smoothly (Figure 4). The following image was about the aortic valve CT image and algorithm for CT image target region segmentation results. It revealed that the application of deep learning to calculate and process can clearly show the specific area of the lesion (Figure 5).

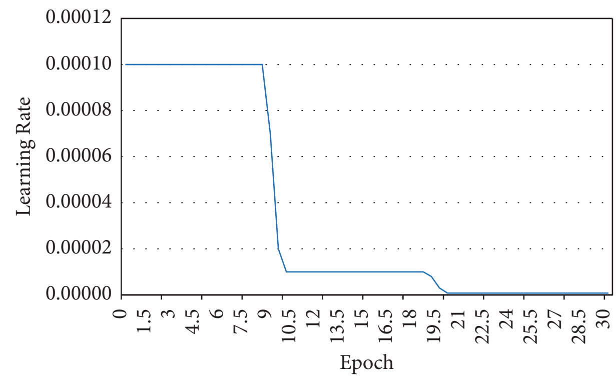

Figure 4: Training TJ-2 full convolution network learning rate changes.

3.3. Measurement of Aortic Root Anatomy Using CT Images of Deep Learning Algorithm. The mean diameter calculated by the long and short diameter, the mean diameter calculated by the perimeter, and the mean diameter calculated by the area were used for paired test in CT. The results showed that the size of annulus in CT was larger, and there was no significant difference in the average diameter measured by three CT methods (23.2 ± 3.85, 24.12 ± 3.52, and 23.74 ± 2.25, $P > 0.05$) (Figure 6).

The diameter results calculated by the CT of the deep learning algorithm according to the measurement methods such as long-short diameter, area, and perimeter are shown in Table 2.

3.4. Complications. Among the 52 patients, there were 35 cases of hypertension, accounting for 67%, 13 cases of diabetes, accounting for 25%, 6 cases of chronic renal insufficiency (Cr > 2 mg/dL), accounting for 11% (including 2 cases of hemodialysis maintenance, accounting for 3.8%), 11 cases of chronic lung disease, accounting for 21%, 9 cases of cerebrovascular disease, accounting for 17.3%, and atrial flutter and atrial fibrillation. There were no patients with infective endocarditis (Table 3).

4. Discussion

At present, the preoperative screening of patients to undergo CT plays an important role, which can be used to provide important information for clinical sheath approach. It also provides anatomical information for the weight of ascending aorta, the size of aortic root, and aortic ring [14]. TAVI requires preoperative examination to assess the size of aortic rings noninvasively and accurately, which is of great significance for the size selection of TAVI valve rings. If the size of the valve ring is not good, it will cause complications around the ring, such as aortic regurgitation, valve embolism, and ring tearing. Computer tomography can provide accurate anatomical shape and size of aortic rings [15]. Previous studies suggested that the valve diameter selected by CT and two-dimensional ultrasound is larger than the ring diameter measured by ECG, which reduces aortic regurgitation [16]. Deep learning was widely used in medical fields, such as image or data processing, and achieved excellent processing results [17]. In this study, the TJ-2 full convolution network in deep learning was used to process CT images of patients. The results showed that the lesions in CT images can be effectively identified, which laid a foundation for subsequent research. Such results were consistent with the excellent results obtained by Guo et al. [18] who

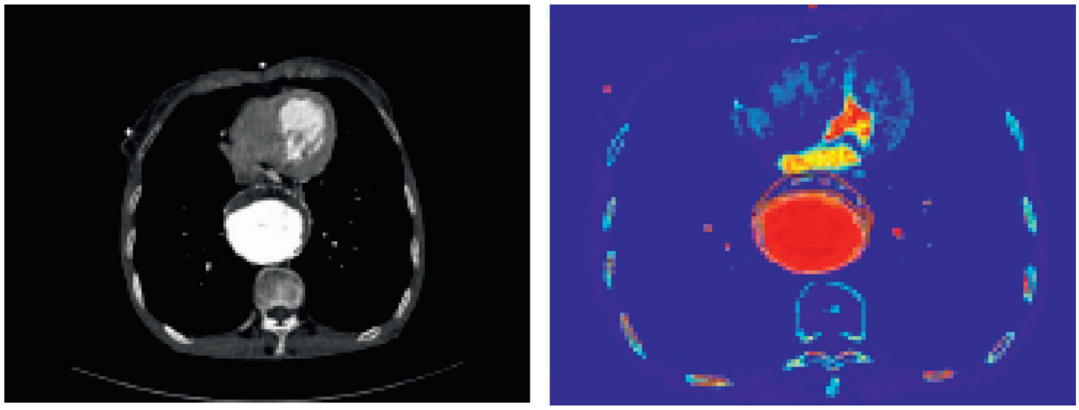

Figure 5: The CT images of aortic valves and the results of target region segmentation in CT images by the algorithm.

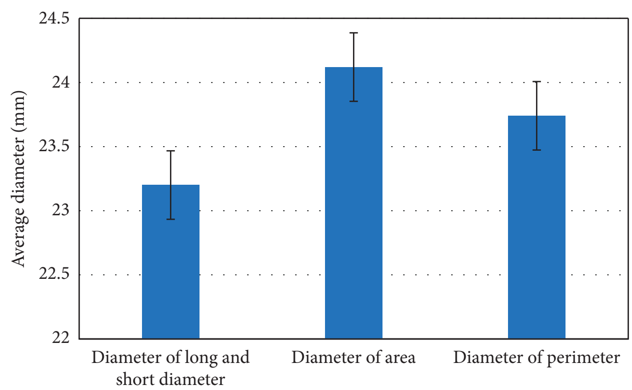

Figure 6: Average diameters measured by three CT methods.

Table 2: Measurement of aortic root anatomy using CT images of the deep learning algorithm.

Measurement	95% CI (lower limit, upper limit)
Mean diameter calculated by the long and short diameter (mm)	0.88 (0.84, 0.92)
Mean diameter calculated by the perimeter (mm)	0.76 (0.68, 0.87)
Mean diameter calculated by the area (mm)	0.85 (0.72, 0.91)

Table 3: Complication information.

Item	Cases ($n = 52$)
Hypertension (%)	35 (67.3)
Diabetes (%)	13 (25.0)
Chronic renal insufficiency (Cr > 2 mg/dL) (%)	6 (11.5)
Hemodialysis maintenance (%)	2 (3.8)
Chronic lung disease (%)	11 (21.2)
Cerebrovascular disease (%)	9 (17.3)

adopted the Elman neural network model in deep learning for image processing.

The repeatability of the diameter of the measured ring measured by the perimeter of scientific research evaluation is lower than that of the average diameter method and the area method. The average diameter measured by the area method is generally larger than that measured by the perimeter method in different cardiac cycles. In the contraction period, the elliptic index of the ring is minimal, which is closer to the circle than other cardiac cycles [19]. However, the diameter difference between the two calculated by the perimeter method and area method in the diastolic period is greater than that in the contraction period [20]. After stent implantation, especially after balloon implantation, the shape of the stent is round, and the same situation before and after surgery is the circumference of the ring. The ring diameter measured by the circle method may be more suitable for ring selection. The results of this study used the long-short diameter calculation, perimeter calculation, and area calculation in CT images to obtain the average diameter. The results represented that there was no significant difference in the average diameter measured by the three CT methods.

5. Conclusion

This study was to explore the use of deep learning in the measurement of information in CT images and its impact on surgical results. Of the 120 patients in this study, 52 eventually received TAVI treatment. The aortic ring diameter measured by three CT methods of deep learning algorithm is larger than that measured by CT, but there is no significant difference in the aortic ring diameter measured by their diameter measurement methods, and the area method and the long and short diameter method have high repeatability. Limitations are that although the size of the ring was chosen according to the different methods of measuring the ring, the most important thing is whether the final patient can undergo surgery, which is affected by many factors, including the vascular condition of the approach and the distortion angle of the blood vessel to the aorta, the diameter of the sinus orifice, and the width of the sinus orifice. This study summarizes and analyzes the characteristics of clinical complications and main influencing factors in patients with high-risk aortic valve stenosis and the preliminary experience according to moving root and anatomical data measurement. In the future, the sample size will be further expanded to integrate clinical data combined with intraoperative and clinical conditions, so that the preoperative evaluation results can better guide the screening of TAVI patients and standardize the success rate and prognosis of TAVI.

Data Availability

The data used to support the findings of this study are available from the corresponding author upon request.

Conflicts of Interest

The authors declare no conflicts of interest.

References

[1] R. F. Gohmann, P. Lauten, P. Seitz et al., "Combined coronary CT-angiography and TAVI-planning: a contrast-neutral routine approach for ruling-out significant coronary artery disease," *Journal of Clinical Medicine*, vol. 9, no. 6, p. 1623, 2020.

[2] S. Shnayien, K. K. Bressem, N. L. Beetz, P. Asbach, B. Hamm, and S. M. Niehues, "Radiation dose reduction in preprocedural CT imaging for TAVI/TAVR using a novel 3-phase protocol: a single institution's experience," *RöFo - Fortschritte auf dem Gebiet der Röntgenstrahlen und der bildgebenden Verfahren*, vol. 192, no. 12, pp. 1174–1182, 2020, Epub 2020 Apr 16. PMID: 32299112.

[3] G. Latsios, T. N. Spyridopoulos, K. Toutouzas et al., "Multislice CT (MSCT) imaging in pretrans-catheter aortic valve implantation (TAVI) screening. How to perform and how to interpret," *Hellenic Journal of Cardiology*, vol. 59, no. 1, pp. 3–7, 2018, Epub 2017 Oct 28. PMID: 29111398.

[4] M. Soschynski, F. Capilli, P. Ruile, F.-J. Neumann, M. Langer, and T. Krauss, "Post-TAVI follow-up with MDCT of the valve prosthesis: technical application, regular findings and typical local post-interventional complications," *RöFo - Fortschritte auf dem Gebiet der Röntgenstrahlen und der bildgebenden Verfahren*, vol. 190, no. 06, pp. 521–530, 2018, Epub 2017 Dec 28. PMID: 29284171.

[5] L. La Grutta, P. Toia, E. Grassedonio et al., "TAVI imaging: over the echocardiography," *La radiologia medica*, vol. 125, no. 11, pp. 1148–1166, 2020, Epub 2020 Sep 18. PMID: 32948928.

[6] A. M. Bucher, M. H. Albrecht, J. E. Scholtz et al., "High-pitch dual-source CT angiography before TAVI - the value of ECG gating," *Current Medical Imaging Formerly Current Medical Imaging Reviews*, vol. 15, no. 4, pp. 373–379, 2019.

[7] H. Jilaihawi, F. M. Asch, E. Manasse et al., "Systematic CT methodology for the evaluation of subclinical leaflet thrombosis," *Journal of the American College of Cardiology: Cardiovascular Imaging*, vol. 10, no. 4, pp. 461–470, 2017.

[8] A. D. Annoni, D. Andreini, G. Pontone et al., "CT angiography prior to TAVI procedure using third-generation scanner with wide volume coverage: feasibility, renal safety and diagnostic accuracy for coronary tree," *British Journal of Radiology*, vol. 91, no. 1090, Article ID 20180196, 2018.

[9] M. Marwan and S. Achenbach, "Role of cardiac CT before transcatheter aortic valve implantation (TAVI)," *Current Cardiology Reports*, vol. 18, no. 2, p. 21, 2016.

[10] N. Schicchi, M. Fogante, P. E. Pirani et al., "Third generation dual source CT with ultra-high pitch protocol for TAVI planning and coronary tree assessment: feasibility, image quality and diagnostic performance," *European Journal of Radiology*, vol. 122, 2020 Epub 2019 Nov 13. PMID: 31759224, Article ID 108749.

[11] I. Harries, J. R. Weir-McCall, M. C. Williams et al., "CT imaging prior to transcatheter aortic valve implantation in the UK," *Open Heart*, vol. 7, no. 1, PMID: 32518659; PMCID: PMC7254150, Article ID e001233, 2020.

[12] S. Achenbach, V. Delgado, J. Hausleiter, P. Schoenhagen, J. K. Min, and J. A. Leipsic, "SCCT expert consensus document on computed tomography imaging before transcatheter aortic valve implantation (TAVI)/transcatheter aortic valve replacement (TAVR)," *Journal of Cardiovascular Computed Tomography*, vol. 6, no. 6, pp. 366–380, 2012, Epub 2012 Nov 14. PMID: 23217460.

[13] P. Lantelme and B. Harbaoui, "Le bilan optimal avant TAVI," *Annales de Cardiologie et d'Angeiologie*, vol. 68, no. 6, pp. 410–414, 2019, Epub 2019 Oct 21. PMID: 31648795.

[14] M. Pamminger, G. Klug, C. Kranewitter et al., "Non-contrast MRI protocol for TAVI guidance: quiescent-interval single-shot angiography in comparison with contrast-enhanced CT," *European Radiology*, vol. 30, no. 9, pp. 4847–4856, 2020, Epub 2020 Apr 22. PMID: 32318849.

[15] H. Benamer, B. Chevalier, A. Roy et al., "Procédure de TAVI par voie fémorale chez la femme: technique minimaliste," *Annales de Cardiologie et d'Angeiologie*, vol. 65, no. 6, pp. 425–432, 2016, Epub 2016 Nov 2. PMID: 27816175.

[16] A. R. Wahadat, W. Tanis, L. E. Swart et al., "Added value of 18F-FDG-PET/CT and cardiac CTA in suspected transcatheter aortic valve endocarditis," *Journal of Nuclear Cardiology*, vol. 26, 2019 Epub ahead of print. PMID: 31792918.

[17] S. Guo, R. Chen, H. Li, T. Zhang, and Y. Liu, "Identify severity bug report with distribution imbalance by CR-SMOTE and ELM," *International Journal of Software Engineering and Knowledge Engineering*, vol. 29, no. 2, pp. 139–175, 2019.

[18] C. Guo, J. Lu, Z. Tian, W. Guo, and A. Darvishan, "Optimization of critical parameters of PEM fuel cell using TLBO-DE based on Elman neural network," *Energy Conversion and Management*, vol. 183, pp. 149–158, 2019.

[19] S. Matsumoto, Y. Yamada, M. Hashimoto et al., "CT imaging before transcatheter aortic valve implantation (TAVI) using variable helical pitch scanning and its diagnostic performance for coronary artery disease," *European Radiology*, vol. 27, no. 5, pp. 1963–1970, 2017, Epub 2016 Aug 25. PMID: 27562479.

[20] F. Ammon, D. Bittner, M. Hell et al., "CT-derived left ventricular global strain: a head-to-head comparison with speckle tracking echocardiography," *The International Journal of Cardiovascular Imaging*, vol. 35, no. 9, pp. 1701–1707, 2019, Epub 2019 Apr 5. PMID: 30953252.

Hindawi
Journal of Healthcare Engineering
Volume 2021, Article ID 9886521, 9 pages
https://doi.org/10.1155/2021/9886521

Research Article

Intelligent Recognition Algorithm-Based Color Doppler Ultrasound in the Treatment of Dangerous Placenta Previa

Xiaoxiao Zheng, Xiaoqiong Li, Jinxia Xu, and Yunbo Wei

Department of Obstetrics, Huai'an Maternal and Child Health Hospital, No. 104 Renmin South Road, Huai'an 223001, Jiangsu, China

Correspondence should be addressed to Yunbo Wei; 2017041011@stu.gzucm.edu.cn

Received 24 August 2021; Accepted 28 September 2021; Published 29 November 2021

Academic Editor: Enas Abdulhay

The study focused on the clinical diagnostic value of color Doppler ultrasound of dangerous placenta previa patients under the guidance of intelligent recognition algorithms. 58 patients with placenta previa and placenta accreta admitted to the hospital for treatment were selected as research subjects. The color Doppler ultrasound under the guidance of intelligent recognition algorithm was compared with the two-dimensional ultrasound for specificity, sensitivity, and accuracy. The color Doppler ultrasound results showed that, of the 58 patients, there were 32 cases of complete placenta previa and 26 cases of incomplete placenta previa, which were consistent with the surgical pathology results. It was found that patients with malignant placenta previa and placenta accreta had thickened placenta, disappeared posterior placental space, myometrium <2 mm, and increased incidence of cervical enlargement ($P < 0.05$). In conclusion, the recognition accuracy of color Doppler ultrasound under the guidance of the intelligent recognition algorithm is more than 90%, and it can effectively identify dangerous placenta previa, assisting doctors in diagnosis and treatment of dangerous placenta previa.

1. Introduction

Dangerous placenta previa may cause severe trauma, postpartum hemorrhage, blood clotting, etc., endangering the life of pregnant women [1]. Studies have shown that trophoblast cell invasion and dysplasia of uterine exfoliated tissue are serious causes of dangerous placenta. With the implementation of the second child policy, the number of patients with dangerous placenta previa has increased year by year [2, 3]. The maternal mortality rate is 7%, and the dangerous placenta previa is common in women with a cesarean section. There is likely to be placental implantation at the scar site of the last cesarean section. That is to say, placental villi have invaded part of the myometrium [4]. When women are at risk of dangerous placenta previa and placenta accreta, the placenta needs to be removed manually. It is the most serious complication of pregnancy, causing massive bleeding, uterine perforation, infection, and even death. Hence, early diagnosis and timely treatment are the key to improving the quality of delivery [5, 6].

Artificial intelligence [3] is a comprehensive discipline concerning control theory science, neuroscience, mathematics, information theory science, and game theory science. It is characterized by machines that can be as smart as human minds and can think and perceive like humans. Color Doppler ultrasound is a noninvasive diagnostic method. Under the guidance of electronic technology, it can detect the spatial information of the blood flow in the tested part in real time, and it can provide abundant blood circulation information. Therefore, it is highly valued clinically [7, 8]. Doppler color ultrasound has no radiation and minimizes the damage to pregnant women and fetuses. It is highly-safe, reliable, comfortable, and is easy to perform. The operator can see clear images and diagnose uterine differentiation, placenta, abnormalities, and the blood flow of pregnant women in time. Therefore, it is often used for early diagnosis of dangerous placenta previa. Malignant placenta can be detected by ultrasound in the middle and late stages of pregnancy, and active clinical treatment can reduce the risk of postpartum hemorrhage.

Two-dimensional ultrasound can directly observe the shape and thickness of the placenta, the space behind the placenta, and the condition of the myometrium, and Doppler ultrasound can be used to detect blood flow signals. The main content of ultrasound diagnosis [9–11] includes (i) placenta previa; (ii) a lacuna is formed in the placenta; (iii) the placenta attaches to the thin muscle layer and disappears; (iv) placenta partly or completely disappears from the posterior placenta space; and (v) the interface between the front wall of the uterus and the back wall of the bladder. Doppler ultrasound image of malignant placenta shows (i) vortex of blood flow in the placental blood pool; (ii) turbulent flow in the blood pool; (iii) rich blood flow at the interface between the uterus and bladder; and (iv) increased blood vessels around the placenta. The Doppler color ultrasound can monitor blood flow and is sensitive to placental accreta. Su Jilian et al. reported that the sensitivity of Doppler color ultrasound for placenta was 98%, and the negative predictive value was 100%, meeting the best classification and exclusion criteria.

When it comes to ultrasonic images, great progress has been made from the manual identification of the indicator diagram to the use of computer identification and diagnosis. Traditional machine learning models can be divided into shallow learning and deep learning according to their structural levels. Most machine learning models are shallow learning, which are only effective for some simple or limited problems but are obviously at a disadvantage in the face of complex problems with large data scale. Deep learning network, with multiple hidden layers, can realize mapping transformation from low-dimensional space to high-dimensional space through multilayer nonlinear transformation and to distinguish and classify complex input data features in high-dimensional space. The intelligent recognition algorithm based on deep learning has a good clinical application effect for dealing with a large number of complex and numerous medical images.

In the study, 58 patients with severe placenta previa were selected as research subjects, and they all accepted the Doppler color ultrasound examination under the guidance of an intelligent recognition algorithm. Then, the diagnosis accuracy and sensitivity of the intelligent algorithm were investigated.

2. Materials and Methods

2.1. Research Subjects. In the study, 58 patients with dangerous placenta previa admitted to a tertiary hospital from March 2019 to September 2020 were selected as research subjects. They were aged between 30 and 46 years old, with an average of 38.29 ± 2.59 years old. The gestational period was between 34 and 40 weeks, with an average of 36.62 ± 3.11 weeks. The number of cesarean sections was 1–3, and the lower uterine incision was a transverse incision. The number of pregnancies was between 1 and 4. The diagnostic criteria for dangerous placenta previa were as follows: with a history of cesarean section and placenta previa was diagnosed prenatally.

Inclusion criteria: (i) diagnosed with dangerous placenta previa as per *Obstetrics and Gynecology*; (ii) all underwent surgical delivery and pathological examination, of singleton pregnancy; (iii) patients and their families were aware of and voluntarily joined this study and signed informed consent form.

Exclusion criteria: (i) not undergoing surgical pathological examination; (ii) cooperating with the doctor in the study. Additionally, patients with coagulation dysfunction and incomplete data were excluded.

2.2. Intelligent Recognition SVM Algorithm. SVM classification method is to maximize the classification margin by discovering the hyperplane in the space. However, practical problems are often nonlinear, and it is very difficult to find a hyperplane in the spatial dimension to separate data. SVM can construct the optimal classification structure hyperplane through the core function, so as to realize the linear global optimal solution.

In the study, the SVM classifier is used, and the icons extracted from the self-encoding decomposition group represent different classifications. For example, if there are n categories, n SVM classifiers can be built. For example, x_i represents the sample, w represents the weight matrix, wj represents the weight vector of the jth classifier, b represents the bias matrix, bj is the bias term of the jth classifier, C represents the penalty factor, ξij is the slack variable, $\varphi(xi)$ has the nonlinear mapping function, and commonly, the kernel function $k(x)$ replaces the mapping function $\varphi(x)$ to simplify the mapping from the low-dimensional space to high-dimensional space. The ideal objective function can be expressed as follows.

$$
\begin{aligned}
& min\frac{1}{2}\left\|w_j\right\|^2 + C\sum_{i=1}^{l}\xi_i^j, \\
& s.t.\left(w_j\right)T\dot{\oint}\left(x_i\right) + b_j \geq 1 - \xi_i^j, if\, y_{i=}j, \\
& \left(w_j\right)\dot{T}\oint\left(x_i\right) + b_j \leq -1 + \xi_i^j, if\, y_i \neq j, \quad \xi_i^j \geq 0, \quad i = 1, 2, \cdots, l.
\end{aligned} \tag{1}
$$

By solving N optimization problems as equation (1), N decision functions are obtained, and f is the decision function as follows.

$$
\begin{cases}
f_1(x) = (w_1)T\dot{\oint}(x) + b_1 \\
\cdots \\
f_n(x) = (w_n)\dot{T}\oint(x) + b_n
\end{cases} \tag{2}
$$

Substituting the test sample iX into equation (2) can obtain the sample value belonging to the decision function of each classifier. By selecting the classifier represented by the largest decision function value, the classification category of the sample can be identified calculated as follows:

$$
class(x) = arg\,max\left(w_j\right)\dot{T}k(x) + b_j\big). \tag{3}
$$

2.3. Intelligent Identification Process. Pattern recognition is the scientific identification to describe and classify research subjects. A pattern is to quantitatively and structurally describe an entity object, and a set of similar things is called a pattern class. Through pattern recognition, data are processed and analyzed in various ways and then described and classified. This recognition and classification technology transfers various feature description information of objects to the machine and automatically classifies various objects to their pattern classes.

Traditional pattern recognition methods include linear regression, nearest neighbor classification, and principal component analysis clustering algorithms. In recent years, with the development of machine learning technologies such as artificial neural networks (ANN), ANN-based learning technologies have become a worldwide research hotspot. Figure 1 is the pattern recognition flow chart.

2.4. Ultrasound Examination. Color Doppler Ultrasound uses the top color Doppler ultrasound diagnosis system of Germany Siemens ACUSON Oxana series. Examination: the bladder of the patient should be full before the examination. The patient was in a supine position. The frequency of the probe for transabdominal examination is 2.5–5 MHz, and the frequency of the probe for transvaginal examination is 7–12 MHz. The patient was scanned for the position and thickness of the placenta, the echo of the placenta, the edges, borders, and thickness of the placenta, and the uterus. For patients whose placenta was at the bottom of the anterior wall, special attention should be paid to the continuity of the posterior wall and the correlation between the posterior bladder wall and the anterior uterine wall. The color ultrasound images of the placental substance and the posterior placenta were then analyzed.

Two-dimensional ultrasound examination: a two-dimensional ultrasound diagnosis and treatment instrument is used, and the frequency of the abdominal probe is set at 3.5 MHz. Before the examination, the patient was asked to drink water to keep the bladder full. The position of the placenta was determined by moving the probe to examine the fetus and its surrounding conditions and detect the distance between the placenta and the cervix, the uterine wall, the posterior wall of the bladder, the muscle layer, and the thickness of the placental implant.

2.5. Evaluation Index. The two-dimensional ultrasound and color Doppler ultrasound results were analyzed under the guidance of intelligent recognition algorithms. With the results of surgical examination as the "gold standard," the sensitivity, accuracy, and specificity of two-dimensional ultrasound and color Doppler ultrasound were evaluated.

2.6. Statistical Methods. The data in this study were processed by SPSS21.0 software, and $(x(-) \pm s)$ and n (%) were used to represent measurement data (t-test) and count data ($\chi 2$), respectively. $P < 0.05$ indicated that the difference was statistically significant.

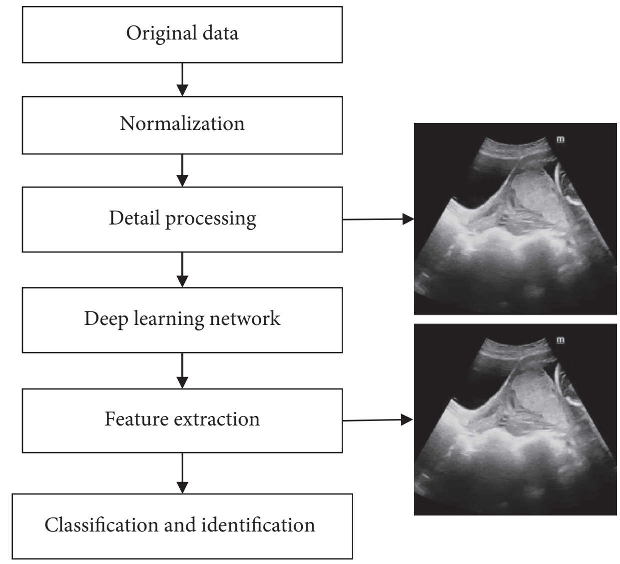

Figure 1: Intelligent recognition process.

3. Results

3.1. Routine Placenta Data. All the cases were confirmed by surgery, including 15 cases of marginal placenta previa, 11 cases of partial placenta previa, and 32 cases of central placenta previa. The placenta was attached to the anterior wall in 20 cases, the posterior wall in 8 cases, the anterior and right wall in 2 cases, and the anterior and left wall in 1 case. Ultrasound showed 15 cases of marginal placenta previa, 12 cases of partial placenta previa, and 31 cases of central placenta previa, as shown in Figure 2.

3.2. Color Doppler Ultrasound in the Examination of Dangerous Placenta Previa. Of the 58 patients, 32 had complete placenta previa, 11 had partial placenta, and 15 had marginal placenta. 47 cases were detected by color Doppler ultrasound, and the correct rate was 81.03%. There were 41 cases correctly detected by both of the two-dimensional and Doppler color ultrasound and 5 cases incorrectly detected by both of the two methods, as shown in Figures 3 and 4.

3.3. Abnormal Results of Placental Attachment Examined by Color Doppler Ultrasound. Of the 58 patients, there were 27 cases of abnormal placental attachment, and color Doppler ultrasound detected 30 cases of abnormal placental attachment. The detection rate of various abnormal placental attachments using Doppler color ultrasound and two-dimensional ultrasound showed $^{*}P > 0.05$, and there was no statistically significant difference, as shown in Figure 5.

3.4. Examination Results of Dangerous Placenta Previa by Color Doppler Ultrasound under the Guidance of Intelligent Recognition Algorithm. The ultrasound examination results were compared with the surgical pathology results. The ultrasound examination results showed that, of 58 patients, there were 52 cases of complete placenta previa and 6 cases

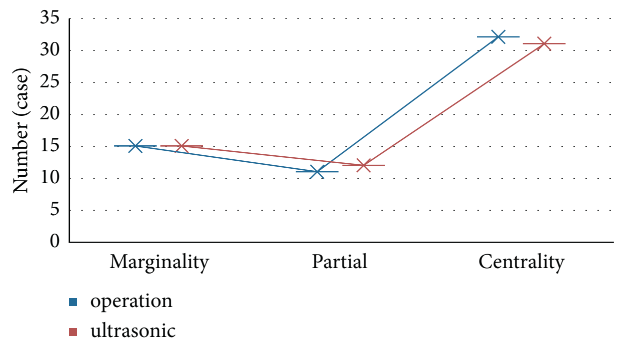

Figure 2: Placenta data of the subjects.

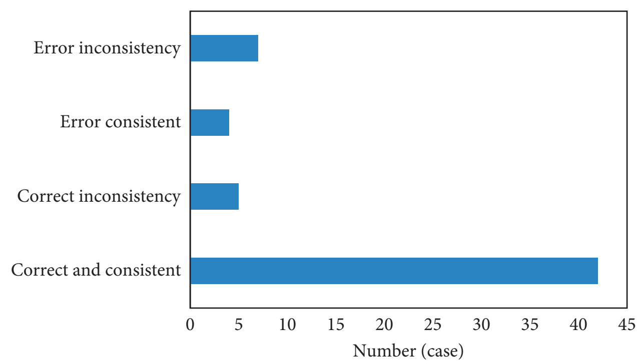

Figure 3: Color Doppler ultrasound in the diagnosis of malignant placenta previa.

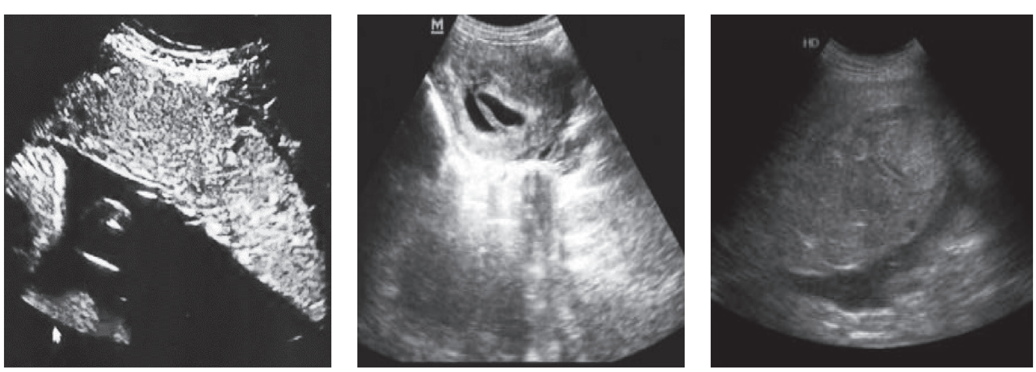

(a) (b) (c)

Figure 4: Ultrasound image characteristics of dangerous placenta previa.

of incomplete placenta previa, which were consistent with the surgical pathological results. Ultrasound diagnosis detected 54 cases of placenta accreta and 4 cases without placental accreta. The specific results of the ultrasound examination are shown in Figure 6.

3.5. Comparison of Results of Placenta Previa of Surgical Pathological Examination and Ultrasound Examination under the Guidance of Intelligent Recognition Algorithms. Figure 7 shows the results detected by the intelligent recognition algorithm. It was noted that the intelligent recognition algorithm proposed in this study can locate the placenta previa position accurately, and the positioning result was basically similar to the manual positioning result of the doctor.

The white dotted line represented the manual positioning result of the doctor, and the red dotted line represented the positioning result of the intelligent recognition algorithm.

The results of the ultrasound examination were then compared with the postoperative pathological results. The ultrasound examination detected 38 cases of complete placenta previa and 10 cases of incomplete placenta previa, in line with surgical pathology. The ultrasound examination results showed that 39 cases had placenta accreta and 9 cases

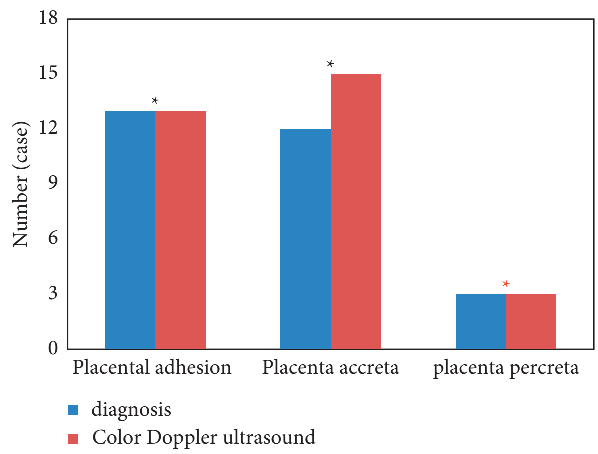

FIGURE 5: Abnormal results of placental attachment examined by color Doppler ultrasound ($^*P > 0.05$ indicated statistically significant difference between groups).

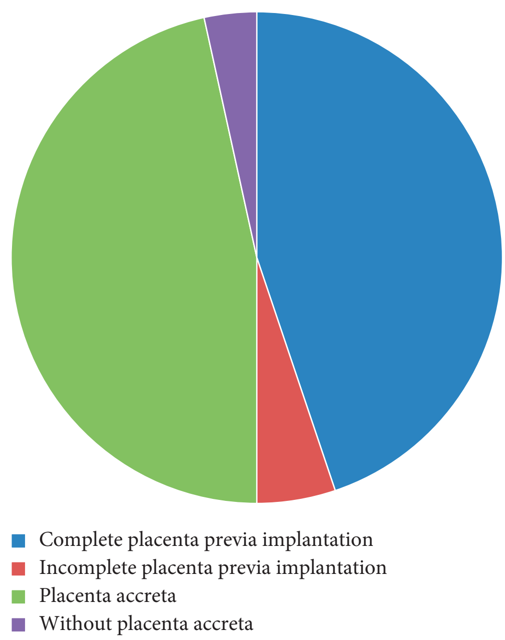

FIGURE 6: Ultrasound examination results.

FIGURE 7: Ultrasonic positioning of placenta previa based on the intelligent recognition algorithm.

had no placenta accreta. Compared with surgical pathology results, 2 cases were missed and 2 cases were misdiagnosed (Figure 8).

3.6. Application of Color Doppler Ultrasound in the Diagnosis of Cicatricial Placenta Previa. Surgical results showed that, of 58 suspected patients, 50 cases had placenta previa and

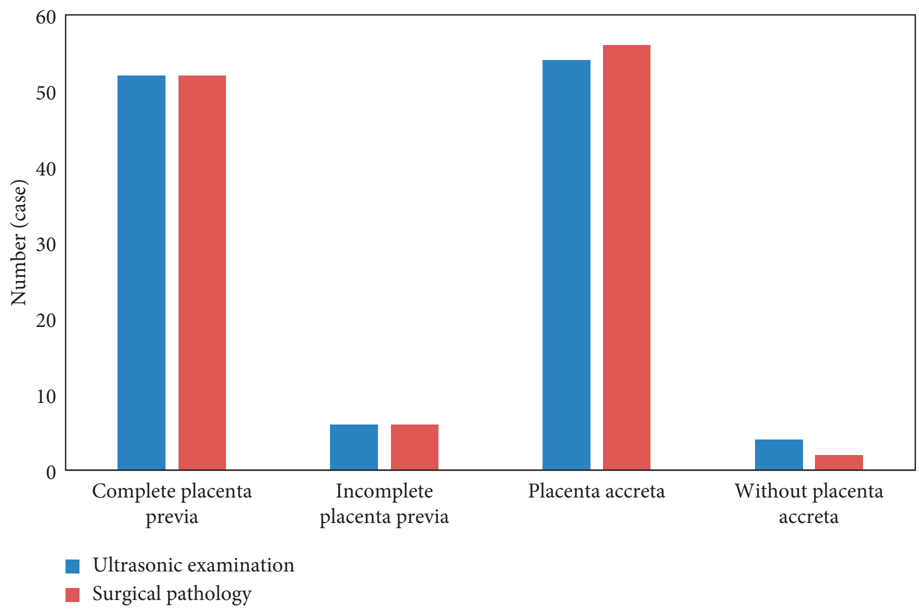

Figure 8: Comparison of ultrasound results and surgical pathology results for placenta previa.

placenta accreta. The diagnostic accuracy rate of two-dimensional ultrasound for placenta previa and placenta accreta was 78.57% (43/58), which was lower than 94.29% (54/58) of color Doppler ultrasound, and the difference was statistically significant ($X^2 = 7.368$, $P = 0.007$) (Figure 9).

3.7. Comparison of Conventional Two-Dimensional Ultrasound and Color Doppler Ultrasound Results. ROC curve analysis showed that the sensitivity and AUC of color Doppler ultrasound diagnosis were higher than those of conventional two-dimensional ultrasound, and the difference was statistically significant ($^{\theta}P < 0.05$) (Figure 10).

3.8. Features of Color Doppler Ultrasound with and without Placenta Implantation. Color Doppler ultrasound showed that dangerous placenta with placenta implantation has higher incidence of thickened placenta and loss of posterior placental space and significantly higher incidence of myometrium <2 mm and expanded cervical expanded than that without placenta implantation ($^{*}P < 0.05$), as shown in Figure 11.

3.9. Pregnancy Outcome. The amount of postpartum blood loss in pregnant women with placenta implantation was significantly higher than that in pregnant women without placenta implantation, with statistical significance ($^{*}P < 0.05$), as shown in Figure 12.

4. Discussion

Dangerous placenta previa refers to the presence or absence of placenta accreta on the basis of placenta previa. Placenta previa refers to the lower edge of the placenta away from the cervix, attached to the lower part of the uterus, or covering the cervix after 28 weeks of pregnancy [12]. According to the relationship between the placenta and the cervical foramen, placenta previa can be divided into 3 types: complete, partial, and marginal [13]. Studies have shown that compared with pregnant women without a history of cesarean section, the incidence of placenta previa in pregnant women with a history of cesarean section can increase by 5 times. Statistics show that the mortality rate of patients with malignant placenta previa can reach as high as 10%, seriously threatening the lives of pregnant women [14]. In order to reduce the mortality rate of pregnant women and improve their health, it is important to diagnose placenta previa and placenta accreta as soon as possible, so as to take timely measures to terminate the pregnancy.

For dangerous placenta previa, to diagnose placenta accreta or not before surgery has a great influence on the treatment effect [15]. Ultrasound is an economical and effective prenatal diagnosis method for malignant placenta previa. It can perform noninvasive multiangle examination and clearly show the relationship between placental thickness, fetal manifestations, and cervical and subuterine scars [5]. Furthermore, with the development of power Doppler and three-dimensional ultrasound technology, its sensitivity and specificity have been elevated. However, ultrasound cannot accurately assess the depth of placental accreta in patients with abnormal placental attachment.

At present, artificial intelligence algorithms have been widely used in the medical field [16]. Under the guidance of intelligent recognition algorithms, color Doppler ultrasound is used to detect malignant placenta previa. It is noninvasive, with high reproducibility and low cost [17–19]. Color Doppler ultrasound can be divided into transabdominal ultrasound and transperineal ultrasound. Transabdominal ultrasound is the simplest and a commonly used method. Color Doppler ultrasound images show that the posterior placenta space disappears, the placenta is thickened, and the myometrium at the placental attachment is significantly

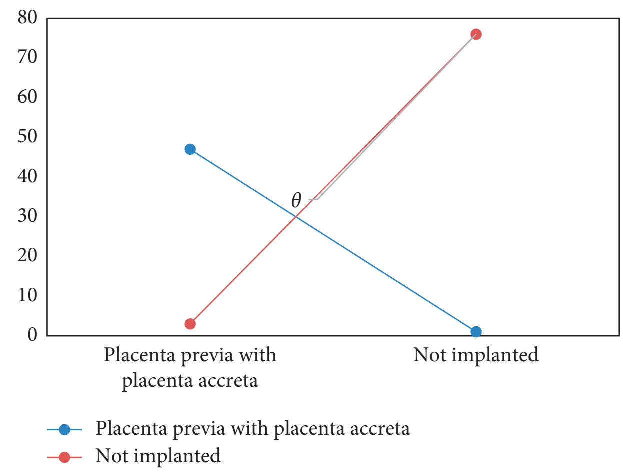

FIGURE 9: Application of color Doppler ultrasound in the diagnosis of placenta previa with placenta previa ($^{\theta}P < 0.05$ indicated that the difference between groups was statistically significant).

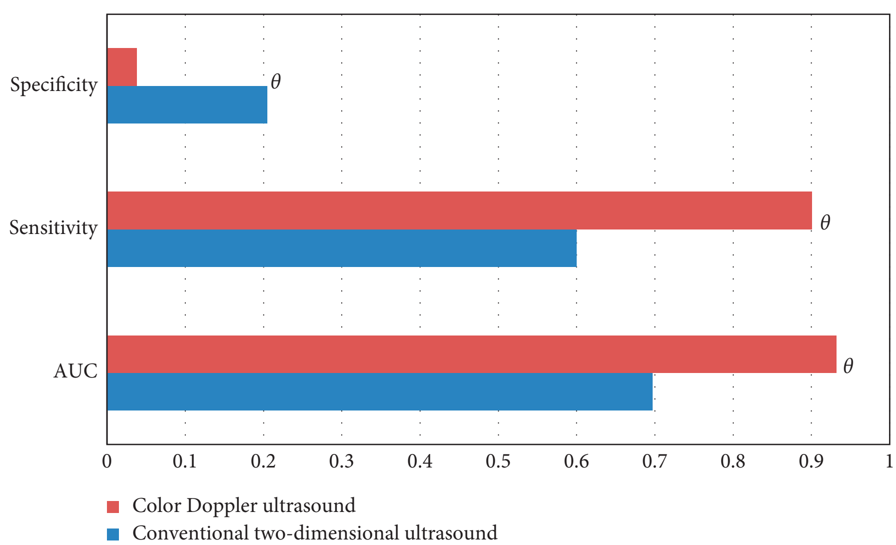

FIGURE 10: ROC curve analysis results of two-dimensional conventional ultrasound and color Doppler ultrasound ($^{\theta}P < 0.05$ indicated that the difference between groups was statistically significant).

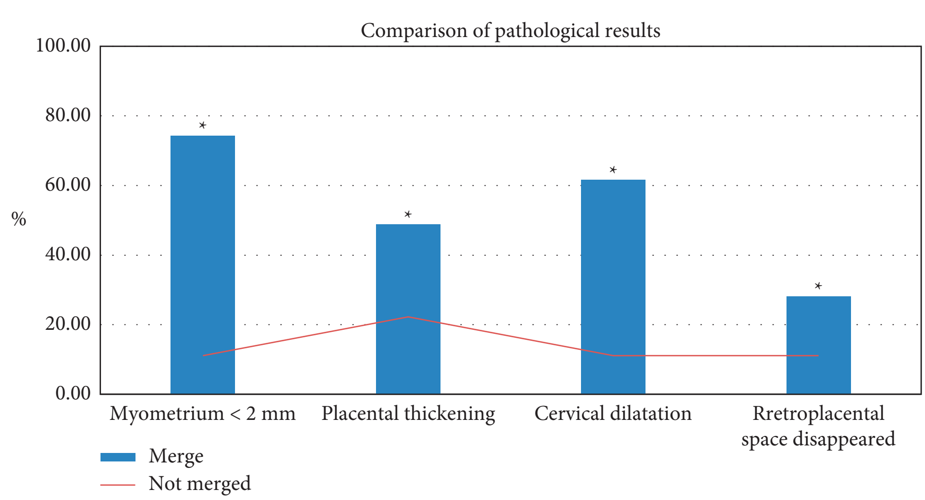

FIGURE 11: Characteristics of color Doppler ultrasound with and without placenta implantation ($^{*}P < 0.05$).

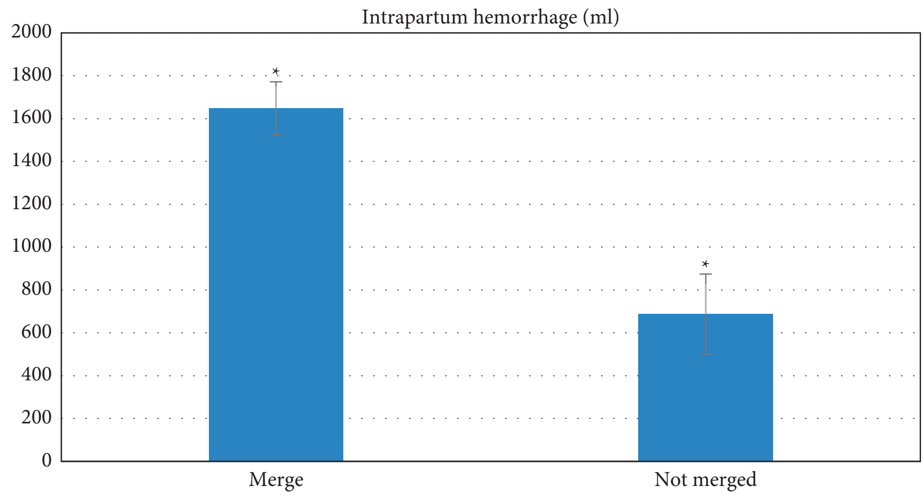

Figure 12: Pregnancy outcomes ($^*P < 0.05$).

thinned. The images can effectively determine whether there is a placenta accreta, which facilitates the diagnosis of the doctor [20–22]. For those with a thick abdominal fat layer, the accuracy of abdominal ultrasound is reduced, consistent with results of Guo et al. [23]. At this time, the perineum multisection examination can fully make up for the missed detection of the cervix and lower uterus. Transperineal ultrasound can effectively identify the relationship between the placenta and myometrium. Most ultrasound images show swelling of the lower part of the uterus, enlarged cervix, placenta coverage, and abundant blood flow in the lower part of the uterus.

The combination of abdominal examination and perineal examination can complement each other to improve the accuracy of the detection of malignant placenta previa with placenta accreta [24, 25]. In patients with malignant placenta previa and placenta accreta, ultrasound can display obvious blood flow changes, such as abnormal blood flow in the placental cavity, abundant blood flow signals, placenta accreta, thinned echo zone between the uterus and placenta, the enlarged cervix, and the thinned myometrium. Color Doppler ultrasound can accurately identify whether it is complete placenta previa. Compared with the postoperative pathological results, there are a few missed and misdiagnosed cases of placenta accrete, consistent with results of Yuwen et al. [26]. For pregnant women with placental accreta, the hysterectomy rate and blood loss are higher, indicating a great impact of placental accreta on mothers. Timely prenatal ultrasound examination can quickly screen the lesions in the early stage, which assists doctors in judging the severity of the disease in a timely manner, and can provide an accurate basis for further treatment.

Limitations: this article does not discuss the situation of patients with malignant placenta previa combined with placenta accreta, which needs to be continuously explored in the clinic. Despite the high accuracy of color Doppler ultrasound, it cannot completely replace ultrasound due to the high cost. Hence, an appropriate examination method is required according to the patient's specific condition.

In conclusion, under the guidance of intelligent recognition algorithms, color Doppler ultrasound has high accuracy in the detection of malignant placenta previa and can correctly assess the severity of malignant placenta previa and placenta accreta. This study is of great significance for improving the quality of pregnancy and ensuring the safety of mothers and babies.

Data Availability

The data used to support the findings of this study are available from the corresponding author upon request.

Conflicts of Interest

The authors declare no conflicts of interest.

References

[1] A. Winnie and S. Berggruen, "Ultrasound imaging of placenta accreta with MRI correlation," *Ultrasound Quarterly*, vol. 31, no. 1, pp. 23–33, 2015.

[2] L. K. Perriera, A. A. Arslan, and R. Masch, "Placenta praevia and the risk of adverse outcomes during second trimester abortion: a retrospective cohort study," *The Australian and New Zealand Journal of Obstetrics and Gynaecology*, vol. 57, no. 1, pp. 99–104, 2017.

[3] W. A. Mar, S. Berggruen, and U. Atueyi, "Ultrasound imaging of placenta accreta with MR correlation," *Ultrasound Quarterly*, vol. 31, no. 1, pp. 23–33, 2015.

[4] S. Mastubara, H. Takahashi, and Y. Baba, "Aortic balloon occlusion for placenta previa accreta: surgical details are important," *CardioVascular and Interventional Radiology*, vol. 40, no. 3, pp. 478-479, 2017.

[5] Y. L. Wang, F. M. Su, and H. Y. Zhang, "Aortic balloon occlusion for controlling intraoperati- ve hemorrhage in patients with placenta previa increta/percreta. Matern Fetal," *Neonatal Med*, vol. 30, no. 21, pp. 2564–2568, 2017.

[6] E. Jauniaux, S. L. Colins, and D. Jurkovic, "Accreta placentation: a systematic review of prenatal ultrasound imaging and

grading of villous invasiveness," *American Journal of Obstetrics and Gynecology*, vol. 215, no. 6, pp. 712–721, 2016.
[7] Y. Ono, Y. Murayama, and S. Era, "Study of the utility and problems of common iliac artery balloon occlusion for placenta previa with accrete," *Obstet Gynaecol Res*, vol. 44, no. 3, pp. 456–462, 2018.
[8] N. E. Budorick, R. Figueroa, and M. Vizcarra, "Another look at ultrasound and magnetic resonance imaging for diagnosis of placenta accrete," *Matern Fetal Neonatal Med*, vol. 30, no. 20, pp. 2422–2427, 2017.
[9] A. L. Valentini, B. Gui, and V. Ninivaggi, "The morbidly adherent placenta: when and what association of signs can improve MRI diagnosis," *Our experienceDiagn Interv Radiol*, vol. 23, no. 3, pp. 180–186, 2017.
[10] B. Satija, S. Kumar, and L. Wadhwa, "Utility of ultrasound and magnetic resonance imaging in prenatal diagnosis of placenta accrete:A prospective study," *Indian Radiol Imaging*, vol. 25, no. 4, pp. 464–470, 2015.
[11] F. Luo, L. Xie, and P. Xie, "Intraoperative aortic balloon occlusion in patients with placenta previa and/or placenta accrete: a retrospective study," *Taiwanese Journal of Obstetrics & Gynecology*, vol. 56, no. 2, pp. 147–152, 2017.
[12] X. H. Duan, Y. L. Wang, and X. W. Han, "Caesarean section combined with temporary aortic balloon occlusion followed by uterine artery embolisation for the management of placenta accrete," *Clinical Radiology*, vol. 70, no. 9, pp. 932–937, 2015.
[13] Y. L. Wang, X. H. Duan, and X. W. Han, "Comparison of temporary abdominal aortic occlusion with internal iliac artery occlusion for patients with placenta accreta-a non-randomised prospective study," *Vasa*, vol. 46, no. 1, pp. 53–77, 2017.
[14] R. M. Silver, "Abnormal placentation placenta previa vasa previa and placenta accrete," *ObObstet Gynecol*, vol. 126, no. 3, pp. 654–668, 20l5.
[15] W. P. Hu and H. F. Hu, "Heterogeneous face recognition based on modality-independent Kernel Fisher discriminant analysis joint sparse auto-encoder," *Electronics Letters*, vol. 52, no. 21, pp. 1753–1755, 2016.
[16] S. Guo, R. Chen, H. Li, T. Zhang, and Y. Liu, "Identify severity bug report with distribution imbalance by CR-SMOTE and ELM," *International Journal of Software Engineering and Knowledge Engineering*, vol. 29, no. 2, pp. 136–175, 2019.
[17] J. Xu, L. Xiang, and Q. S. Liu, "Stacked sparse autoencoder (SSAE) for nuclei detection on breast cancer histopathology images," *IEEE Transactions on Medical Imaging*, vol. 35, no. 1, pp. 119–130, 2016.
[18] A. Alotaibi and A. Mahmood, "Deep face liveness detection based on nonlinear diffusion using convolution neural network," *Signal Image & Video Processing* .vol. 11, no. 4, pp. 1–8, 2017.
[19] G. Pagani, G. Cali, and G. Acharya, "Diagnostic accuracy of ultrasound in detecting the severity of abnormally invasive placentation a systematic review and meta-analysis," *Acta Obstetricia et Gynecologica Scandinavica*, vol. 97, no. 1, pp. 25–37, 2018.
[20] E. Jauniaux, A. Bhide, and A. Kennedy, "FIGO consensus guidelines on placenta accreta spectrum disorders Prenatal diagnosis and screening," *Int Gynecol Obstet*, vol. 140, no. 3, pp. 274–280, 2018.
[21] K. L. Downes, S. N. Hinkle, and L. A. Sjaarda, "Previous prelabor or intrapartum cesarean delivery and risk of placenta previa," *Am Obst Gynecol*, vol. 212, no. 5, p. 669, 2015.
[22] K. A. Robinson, J. S. Kriegshauser, and N. Dahiya, "Detection of transplant renal artery stenosis determining normal velocities at the renal artery anastomosis," *Abdom Radiol (NY)*, vol. 42, no. 1, pp. 254–259, 2017.
[23] P. Guo, Y. Wu, X. Yuan, and Z. Wan, "Clinical diagnostic value and analysis of MRI combined with ultrasound in prenatal pernicious placenta previa with placenta accreta," *Annals of Palliative Medicine*, vol. 10, no. 6, pp. 6753–6759, 2021 Jun.
[24] S. P. Rajamohana and K. Umamaheswari, "Hybrid approach of improved binary particle swarm optimization and shuffled frog leaping for feature selection," *Computers & Electrical Engineering*, vol. 67, pp. 497–508, 2018.
[25] X. H. Liang, M. J. Zuo, and Z. P. Feng, "Dynamic modeling of gearbox faults: a review," *Mechanical Systems and Signal Processing*, vol. 98, pp. 852–876, 2018.
[26] H. A. N. Yuwen, Z. Yanli, C. Liping et al., "Diagnostic effect of transabdominal ultrasound combined with magnetic resonance imaging on pernicious placenta previa and pregnancy outcome," *IMAGING SCIENCE AND PHOTOCHEMISTRY*, vol. 38, no. 4, p. 657, 2020.

Hindawi
Journal of Healthcare Engineering
Volume 2021, Article ID 5359084, 11 pages
https://doi.org/10.1155/2021/5359084

Research Article

Diagnostic Value of Deep Learning-Based CT Feature for Severe Pulmonary Infection

Tinglong Huang, Xuelan Zheng, Lisui He, and Zhiliang Chen

Department of Critical Care Medicine, The Second Affiliated Hospital of Fujian Medical University, Quanzhou 362000, Fujian, China

Correspondence should be addressed to Tinglong Huang; huangtinglong@fjmu.edu.cn

Received 13 September 2021; Revised 22 October 2021; Accepted 25 October 2021; Published 26 November 2021

Academic Editor: Enas Abdulhay

The study aimed to explore the diagnostic value of computed tomography (CT) images based on cavity convolution U-Net algorithm for patients with severe pulmonary infection. A new lung CT image segmentation algorithm (U-Net+ deep convolution (DC)) was proposed based on U-Net network and compared with convolutional neural network (CNN) algorithm. Then, it was applied to CT image diagnosis of 100 patients with severe lung infection in The Second Affiliated Hospital of Fujian Medical University hospital and compared with traditional methods, and its sensitivity, specificity, and accuracy were compared. It was found that the single training time and loss of U-Net + DC algorithm were reduced by 59.4% and 9.8%, respectively, compared with CNN algorithm, while Dice increased by 3.6%. The lung contour segmented by the proposed model was smooth, which was the closest to the gold standard. Fungal infection, bacterial infection, viral infection, tuberculosis infection, and mixed infection accounted for 28%, 18%, 7%, 7%, and 40%, respectively. 36%, 38%, 26%, 17%, and 20% of the patients had ground-glass shadow, solid shadow, nodule or mass shadow, reticular or linear shadow, and hollow shadow in CT, respectively. The incidence of various CT characteristics in patients with fungal and bacterial infections was statistically significant ($P < 0.05$). The specificity (94.32%) and accuracy (97.22%) of CT image diagnosis based on U-Net + DC algorithm were significantly higher than traditional diagnostic method (75.74% and 74.23%), and the differences were statistically significant ($P < 0.05$). The network of the algorithm in this study demonstrated excellent image segmentation effect. The CT image based on the U-Net + DC algorithm can be used for the diagnosis of patients with severe pulmonary infection, with high diagnostic value.

1. Introduction

At present, the incidence of postoperative pulmonary infection is very high [1]. If the diagnosis is not timely, it is easy to miss the best treatment time. Studies have shown that if the diagnosis can be made in advance, the survival rate of patients with pulmonary infection can be increased by about 40% [2, 3]. Therefore, early and accurate diagnosis of pulmonary infection has become a key issue to improve the cure rate [4, 5]. The main pathogens are bacteria, fungi, viruses, parasites, etc. In addition to pathogen testing, computed tomography (CT) imaging diagnosis has become a common and important method for medical diagnosis. However, as the main feature of judging pulmonary infection, lung CT signs are particularly important from the clarity of lung images and the accurate expression of lung information. Traditional medical image segmentation extracts lung information according to the shallow features of the image and depends on the judgment of the doctor [6]. The addition of subjective factors leads to inaccurate segmentation. Lu et al. [7] proposed a fuzzy logic technology to determine the threshold to achieve accurate segmentation of melanin, but the segmentation effect is poor and inefficient.

With the development of artificial intelligence and information, convolution neural network is introduced into the segmentation of medical images. Nasrullah et al. [8] proposed and used it in the semantic segmentation of natural images and made great progress at that time. In the past segmentation experience, it has exceeded the traditional segmentation method, but its shortcomings cannot be ignored. The excessive multiples adopted in the upsampling operation cause the segmentation accuracy to be not high enough, and the context information is not fully integrated, resulting in low accuracy and precision, which will have a great impact on the survival rate of subsequent diagnosis and posttreatment [9, 10]. The fully convolutional neural network has made great contributions to this problem. As a representative of fully convolutional neural networks, U-Net network can make good use of lower-level information and fuse high-level information when sampling operations [11]. In the following studies, some network structures with better performance are combined with the U-Net network. Baek et al. [12] modified the U-Net to strengthen the position of the feature map, so as to improve the accuracy of extracting the segmentation contour. The 3DU-Net model improves the segmentation performance again by learning the spatial information of the image [13]. In this work, a new lung CT image segmentation algorithm was proposed by adding cavity convolution on the basis of U-Net network. Compared with CNN algorithm, it is applied to the diagnosis of 100 patients with severe pulmonary infection. The sensitivity, specificity, and accuracy of diagnosis are compared with the traditional diagnostic method. It is hoped to provide some theoretical reference for the diagnosis of CT images based on cavity convolution U-Net algorithm in patients with severe pulmonary infection.

2. Materials and Methods

2.1. Research Objects. In this study, 100 patients with severe pulmonary infection in hospital from July 2019 to July 2021 were enrolled. There were 46 males and 54 females, aged 20–66 years. CT image features based on U-Net + DC algorithm were used to diagnose patients with severe pulmonary infection, which was compared with those of traditional diagnostic methods. The study was approved by the Medical Ethics Committee of Hospital. Patients and their families were informed of the study and signed informed consent.

Inclusion criteria were as follows: (1) separate the same pathogen twice in succession from patient sputum; (2) patients with lung invasive lesions showed by chest X-ray; (3) patients with cough, expectoration, and rales; (4) patients with pathogens isolated from blood or pleural effusion.

Exclusion criteria were as follows: (1) patients who did not sign the informed consent; (2) patients with incomplete clinical data; (3) patients who dropped out of the experiment for personal reasons.

2.2. Lung CT Image Segmentation Based on U-Net and Cavity Convolution. The ability of deep learning to extract features is beyond reach of previous machine learning. On account of the fact that the ability of U-Net network to process and integrate high-level and low-level information is better than that of CNN, it is widely used in medical image segmentation. In order to achieve the segmentation of lung CT images, this paper adds cavity deep convolution (DC) on the basis of U-Net network, simplifies and improves the U-Net network, and adds an activation function to increase the nonlinearity of the model. A new lung CT image segmentation algorithm (U-Net + DC) is proposed. The U-Net network is different from the convolution block of the network model proposed in this paper as shown in Figure 1. The convolution block of the network model proposed in this paper is less than the convolution block of the U-Net network by one convolution and an activation function, and the convolution block uses an empty convolution, which can simplify the structure, increase the receptive field, and improve the ability to extract information.

The convolution process of a two-dimensional image can be represented as

$$o(a,b) = (i \times k)(a,b) = \sum_{c}\sum_{d} i(c+a, d+b) \times k(c,d). \tag{1}$$

In equation (1), i is input, k is convolution kernel, and o is output. When (a, b), (c, d) is the size of the input image to select the convolution kernel, a smaller convolution kernel is usually selected, which can not only reduce the number of parameters but also increase nonlinearity. The total parameters p are as follows:

$$P = \omega + B = k^2 \times C \times N + N. \tag{2}$$

In equation (2), ω is the weight, B is the partial value, C is the number of characteristic channels, and N is feature mapping. As a special convolution, cavity convolution can increase the nonlinearity of the model. The essence is to add holes in the convolution and increase the receptive field under the condition of keeping the number of parameters unchanged, which is of great significance to improve the accuracy of image segmentation. Figure 2 shows the schematic diagram of cavity convolution [14].

Because of the interval of empty convolution, it may cause information discontinuity in practical applications, especially when the image is small and the interval is too large. To solve this problem, this paper designs the cavity size according to Hybrid Dilated Convolution (HDC) standard, which needs to meet the following equation:

$$m_n = mix\left[m_{n+1} - 2r_n, m_n - 2\left(m_{n+1} - r_n\right), r_n\right]. \tag{3}$$

In equation (3), m_n is the largest void spacing before the n layer and r_n is the void interval of the n layer. The last layer the void spacing selected in this article is (1,2,5).

The pooling layer is downsampling, and the reverse pooling layer is upsampling on the contrary. If it is the maximum pooling $m_n = r_n$ in the network transformation process, the location of the activation value is recorded. On the contrary, the location of the nonmaximum is set to 0. Maximum pooling and antipooling are shown in Figure 3.

In this study, the classification output uses *sigmoid* function, which is very sensitive between [−4,4], especially for subtle changes in data that feel very strong. It can be expressed as follows:

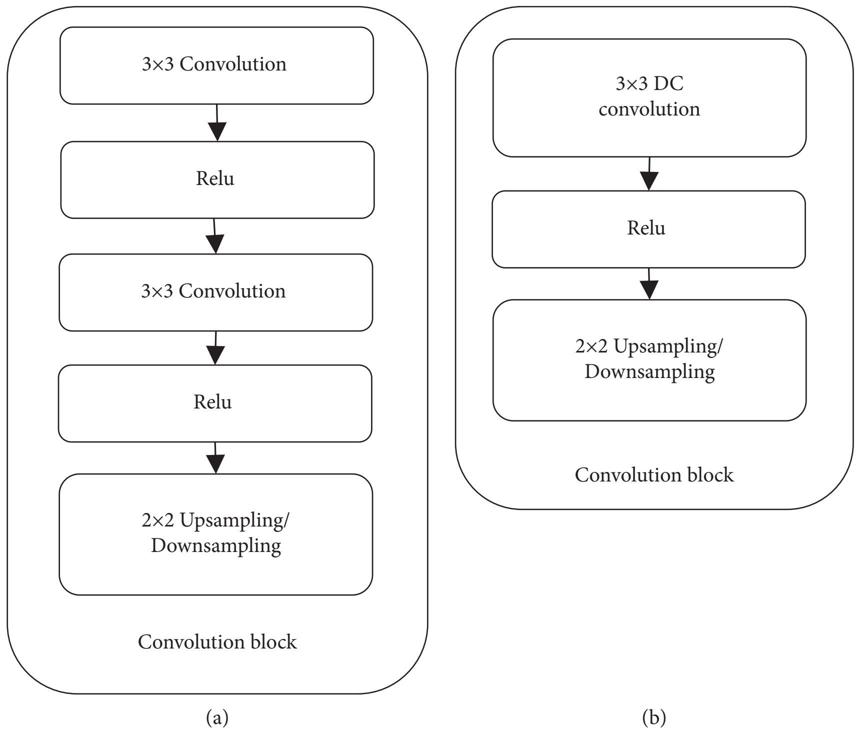

Figure 1: Comparison of two network convolution blocks. (a) U-Net network convolution blocks. (b) U-Net + DC model convolution block proposed in this paper.

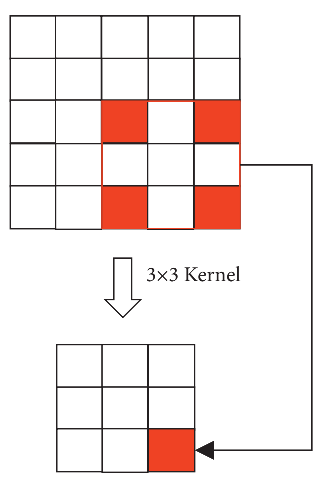

Figure 2: Schematic of cavity convolution.

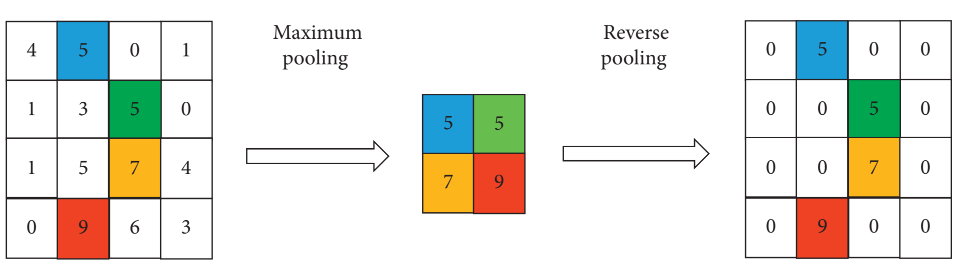

Figure 3: Maximum pooling and reverse pooling.

$$Sigmoid = \frac{1}{e^{-a}} = \frac{1}{1 + e^{-(\omega x + c)}},$$
$$Sigmoid'(a) = \frac{e^{-a}}{(1 + e^{-a})^2}. \tag{4}$$

There are also some problems in the *sidmoid* function. When the number of layers increases, the gradient disappears. The reverse transfer process is as follows:

$$\frac{\partial c}{\partial f_k} = Sigmoid'(a_k)\omega_{k+1} Sigmoid'(a_{k+1})\omega_{k+2} \ldots Sigmoid'(a_n)\frac{\partial c}{\partial h_k}, \tag{5}$$

$$h_k = Sigmoid(a_n) = Sigmoid(\omega_n a_{n-1} + f_n). \tag{6}$$

In equation (5), $\partial c/\partial f_k$ is the gradient of the function to the bias term and a_n is the output.

The Relu function can solve the problem of gradient disappearance, and the convergence rate is fast. The expression is as follows:

$$\mathrm{Relu}(x) = \max(0, x),$$
$$\mathrm{Relu}'(x) = \begin{cases} 0, x < 0 \\ 1, x > 0 \end{cases} \tag{7}$$

The loss function can increase the robustness of the model, which is crucial to the optimization of the model. The expression of mean square error loss D function is shown in the following equation:

$$D = \frac{1}{2n}\sum (y - F(i))^2. \tag{8}$$

In equation (8), $F(i)$ is the output of the model. Then, activation function is as follows:

$$Sigmoid(Z) = Sigmoid(\omega A + b). \tag{9}$$

In equation (9), A and Z are the input and output of the last layer and b is the offset. However, compared with the mean square error loss function, the cross entropy loss function and the Sigmoid function are better. So this paper selects the cross entropy loss function, and its expression is shown in the following equation:

$$D = \frac{1}{n}\sum [y \log(F(i)) + (1 - y)\log(1 - F(i))]. \tag{10}$$

Image denoising and data enhancement are needed before training. Curvature-driven denoising method is used in this paper. Curvature-driven minimization energy function is as follows:

$$G(v) = \lambda \int_\Omega |h_v| \mathrm{d}x + \int_\Omega (F - v)^2 \mathrm{d}x. \tag{11}$$

In equation (11), $(x, y, v(x, y))$ is a surface, $(x, y, F(x, y))$ is the input image, and λ is the parameter. The regularization h_v is expressed as follows:

$$h_v = \frac{1}{2}\nabla\left(\frac{\nabla v}{\sqrt{1 + |\nabla v|^2}}\right). \tag{12}$$

According to the corresponding Euler-Lagrange function, curvature smoothing is realized. In order to improve the convergence speed, we choose Z-score standardized processing:

$$x_1 = \frac{x_2 - \overline{x}}{\sigma}. \tag{13}$$

In equation (13), $\overline{x}$ is the mean and σ is the standard deviation. The data enhancement increases the robustness and generalization ability of the model to prevent the occurrence of overfitting. The enhancement methods selected in this paper are rotation, flip, offset, scaling, elastic transformation, and so on. The original data is extended to about 20,000, and it is trained. The image segmentation process constructed in this paper is shown in Figure 4.

2.3. Simulation Experiment. Simulation environment: the operating system is Windows 10 on LINUX, the processor is Xeon CPU E5-2630, the display card is NVIDIA Quadro K2200, the framework is TensorFlow and Keras, the language is Python 3.5, and the visual library is OpenCV, SimpleITK, CUDA9.0, cudnn, etc.

Network parameters: input image resolution is 256256, convolution block is a hole convolution and activation function, convolution kernel size is 33, according to HDC principle, hole interval is (1,2,5), activation function is Relu function, with 2×2 maximum pooling downsampling, 1×1 convolution layer for multichannel feature fusion, 3×3 convolution upsampling, and the number of training in this paper is 60.

In this study, the lung CT image data is used as the simulation object, and the CNN algorithm is introduced to compare with the algorithm in this paper. The measurement index is Dice coefficient [15].

$$\mathrm{Dice} = \frac{2|E \cap F|}{|E| + |F|}. \tag{14}$$

In equation (14), E is the gold standard for the segmentation of pulmonary nodules, F is the segmentation

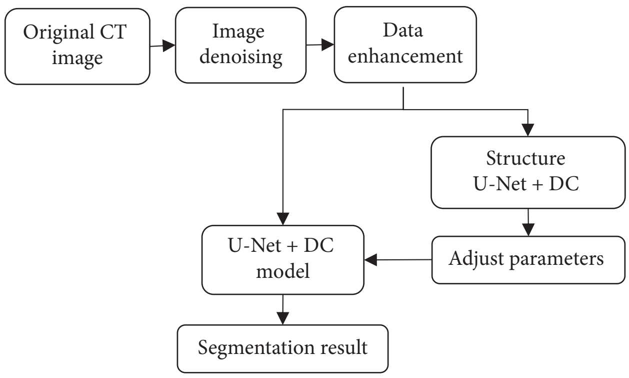

Figure 4: Construction of algorithm segmentation flow.

result, and the range of Dice coefficient is [0,1]. The larger the value is, the better the algorithm performance is.

2.4. CT Examination and Radiofrequency Ablation. At the beginning of scanning, the patient was supine in the center of the CT examination bed. The patient should maintain a peaceful state of mind, not move the body, and routinely inhale. Scanning ranges from chest entrance to diaphragm. Scanning parameters: CT tube voltage is 120 kV, tube current is 300 mAs, scanning field is 260~360 mm, matrix is 512512, layer thickness is 4 mm, and layer spacing is 4 mm. Siemens CT tube voltage is 120 kV, tube current is 380 mAs, scanning field is 220~280 mm, matrix is 512512, layer thickness is 2 mm, and layer spacing is 2 mm. All patients underwent plain scan. CT image is uploaded to Siemens for readings, window width of lung window is 1 600, window level of lung window is 400, and window width of Mediastinal window is 350. The CT images were reviewed by two experienced physicians respectively, and conclusions were reached through discussion in case of disagreement.

2.5. Observation Indicators. The types of pathogens, morphological characteristics of CT manifestations, and lesion distribution of patients with severe pulmonary infection were recorded, and the incidence of morphological characteristics of CT manifestations of pulmonary infection with different pathogens was compared. The sensitivity, specificity, and accuracy of traditional method diagnosis and CT image diagnosis based on U-Net + DC algorithm were compared and calculated.

$$\text{sensitivity} = \frac{\text{TP}}{\text{TP} + \text{FN}} \times 100\%, \tag{15}$$

$$\text{specificity} = \frac{\text{TN}}{\text{TN} + \text{FN}} \times 100\%, \tag{16}$$

$$\text{accuracy rate} = \frac{\text{TP} + \text{TN}}{\text{Total}} \times 100\%. \tag{17}$$

In equations (15), (16), and (17), TP represents true positive, TN represents true negative, FP represents false positive, and FN represents false negative.

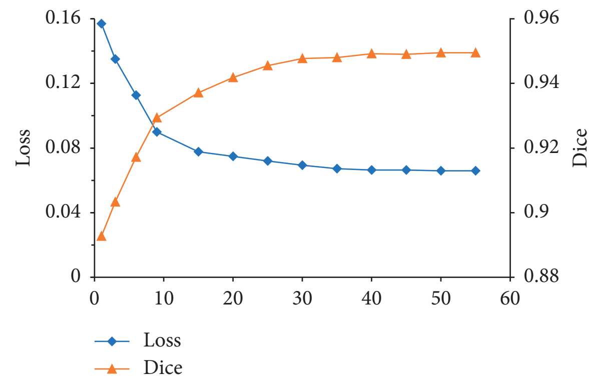

Figure 5: Changes in Loss value and Dice coefficient of U-Net + DC model under different iterations.

2.6. Statistical Methods. The data in this study were analyzed by SPSS 22.0 statistical software. The measurement data were expressed as mean ± standard deviation ($\overline{x} \pm s$), and the count data were expressed as percentage (%). The difference was statistically significant with $P < 0.05$.

3. Results

3.1. Algorithm Simulation Effects. Figure 5 shows the changes in the Loss value and Dice of the U-Net + DC model as the number of iterations increased. It was noted that when the number of iterations was 30, the Loss value tended to be stable, and finally, the Loss value reached 0.0659, and Dice increased with the number of iterations and, finally, reached 0.9495.

Figure 6 shows the single training time of the two algorithms. It was noted that the single training time of the CNN algorithm was 690 s, and the single training time of the U-Net + DC algorithm was 280 s. The single training time of the U-Net + DC algorithm was significantly less than the single training time of the CNN algorithm by 59.4%, and the difference was statistically significant ($P < 0.05$).

Figure 7 shows the Loss value and Dice coefficient of the two algorithms. It was noted that the Loss value and Dice of the CNN algorithm were 0.0731 and 0.9387, respectively, and the Loss value and Dice of the U-Net + DC algorithm were 0.0659 and 0.9495, respectively. The Loss value of the U-Net + DC algorithm was smaller than the Loss value of the CNN algorithm by 9.8%, and the difference was statistically significant ($P < 0.05$). The Dice of the U-Net + DC algorithm was larger than the Dice of the CNN algorithm by 3.6%, and the difference was statistically significant ($P < 0.05$). It showed that, with the gold standard as a reference, the Loss value and Dice of the U-Net + DC algorithm were improved versus the CNN algorithm, and its segmentation effect was better than that of the CNN algorithm.

3.2. Comparison of Lung CT Image Segmentation Effects of the Two Algorithms. Figure 8 shows the lung CT image segmentation effects of the two algorithms. It was noted that, with the gold standard as a reference, the edges segmented by the CNN algorithm were blurred, and the segmentation

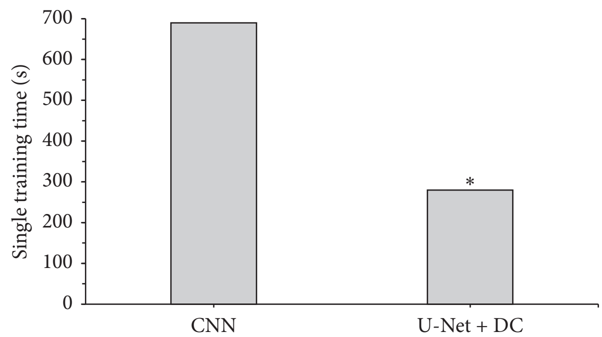

Figure 6: Comparison of single training time of the two algorithms. *Note.* * indicates that the difference was statistically significant compared to the CNN algorithm ($P < 0.05$).

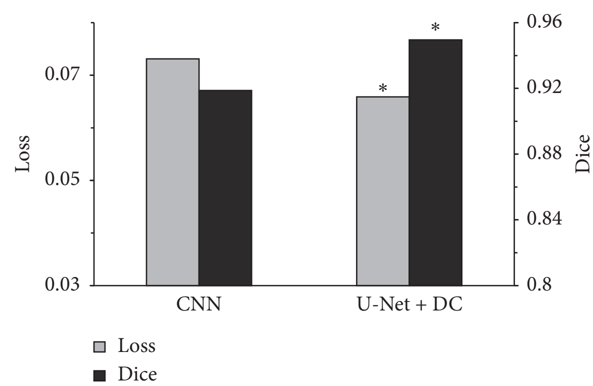

Figure 7: Comparison of Loss value and Dice of the two algorithms. *Note.* * indicates that the difference was statistically significant compared to the CNN algorithm ($P < 0.05$).

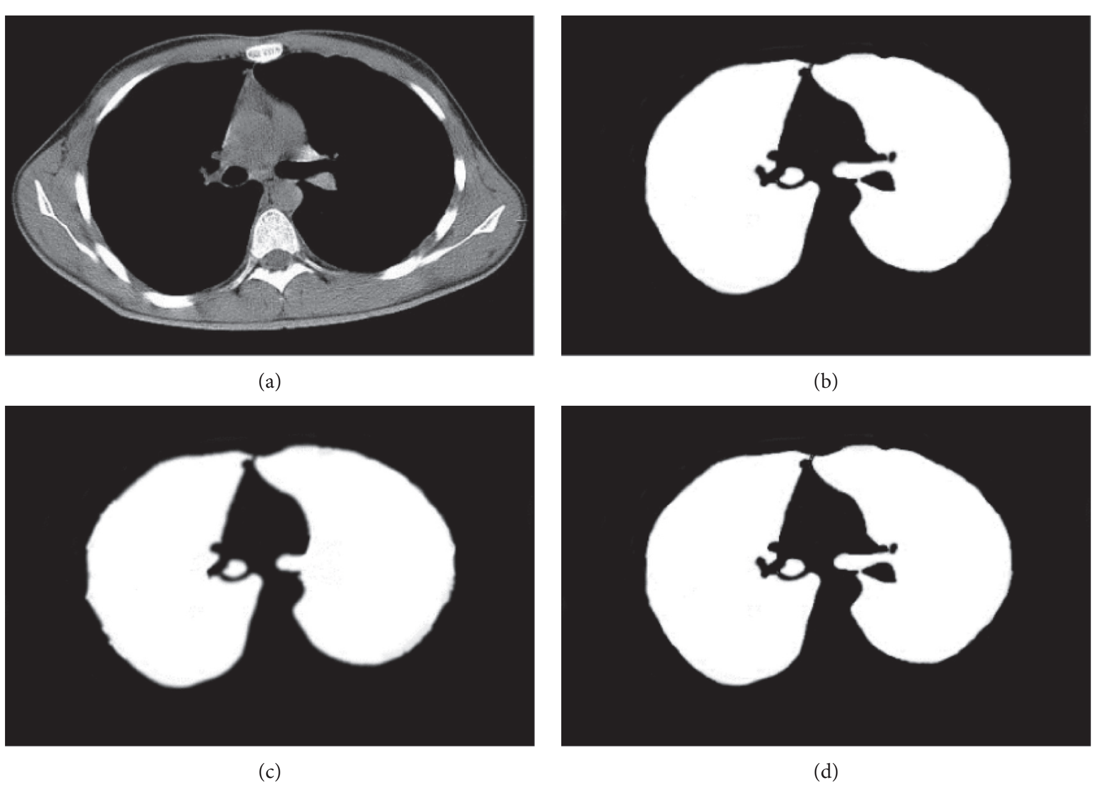

Figure 8: Comparison of lung CT image segmentation results of the two algorithms. (a) The original image, (b) the gold standard, (c) the CNN segmentation result, and (d) the U-Net + DC segmentation result.

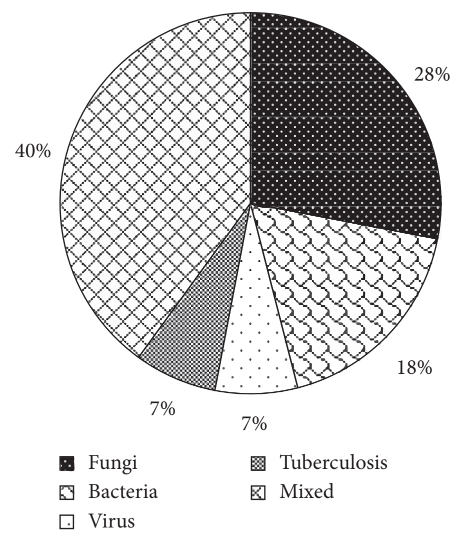

Figure 9: The types of pathogens in patients with severe lung infections.

was affected by the fine blood vessels of the lung organs and other tissue, while the outline of the lungs segmented by the U-Net + DC algorithm was more accurate, and the edges were smoother, which was closer to the gold standard.

3.3. Types and Morphological Characteristics of Pathogens in Patients with Severe Lung Infections. Figure 9 shows the pathogens in patients with severe lung infections. Of the 100 patients with severe lung infections, 28% (28 cases) had fungal infections, 18% (18 cases) had bacterial infections, 7% (7 cases) had viral infections, 7% (7 cases) had tuberculosis infections, and 40% (40 cases) had mixed infections, accounting for the highest proportion.

Figure 10 shows the CT morphological characteristics of severe lung infections. Of the 100 patients with severe pulmonary infections, 36% (36 cases) had ground-glass shadows, 38% (38 cases) had consolidation shadows, 26% (26 cases) had nodules or masses, 17% (17 cases) had reticulated or linear shadows, and 20% (20 cases) had hollow shadows.

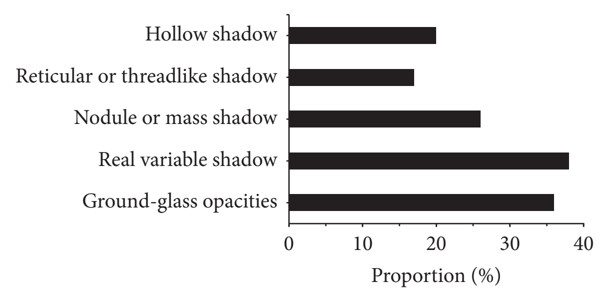

Figure 10: CT morphological characteristics of patients with severe lung infections.

3.4. Images of Various Morphological Features of Patients with Severe Lung Infections. Figure 11 shows images of various morphological features of patients with severe lung infections. Figure 11(a) shows the ground-glass shadow of the right lung. Figure 11(b) shows the large consolidation shadows of the lungs. Figure 11(c) shows the mass-like high-density shadows of the upper lobe of the left lung, and the lungs had multiple small nodules with clear boundaries. Figure 11(d) shows ground-glass shadows and fine mesh shadows. Figure 11(e) shows a hollow shadow in the upper right lung, with patches of increased density around it.

3.5. The Distribution of Lesions in Patients with Severe Lung Infections. Figure 12 shows the lesion distribution of patients with severe lung infections. It was noted that there were 20 cases, 10 cases, 3 cases, and 3 cases with subpleural distribution, middle internal zone distribution, diffuse distribution, and irregular distribution in patients with ground-glass shadows in CT; of the patients with consolidation shadows in CT, there were 21, 8, 5, and 4 cases with subpleural distribution, midinternal zone distribution, diffuse distribution, and irregular distribution, respectively; of the patients with nodules or masses in CT, there were 10 cases, 3 cases, 12 cases, and 1 case with the subpleural distribution, the middle and inner zone distribution, the diffuse distribution, and the irregular distribution, respectively; of the patients with network or line-like shadows in CT, there were 12 cases, 1 case, 3 cases, and 2 cases with the subpleural distribution, the middle inner zone distribution, the diffuse distribution, and irregular distribution, respectively; of the patients with hollow shadows in CT, there were 13 cases, 1 case, 4 cases, and 3 cases with subpleural distribution, midinternal zone distribution, diffuse distribution, and irregular distribution, respectively.

3.6. Comparison of the Incidence of Different CT Morphological Characteristics of Lung Infections with Different Pathogens. Figure 13 shows the incidence of different CT morphological characteristics lung infections with different

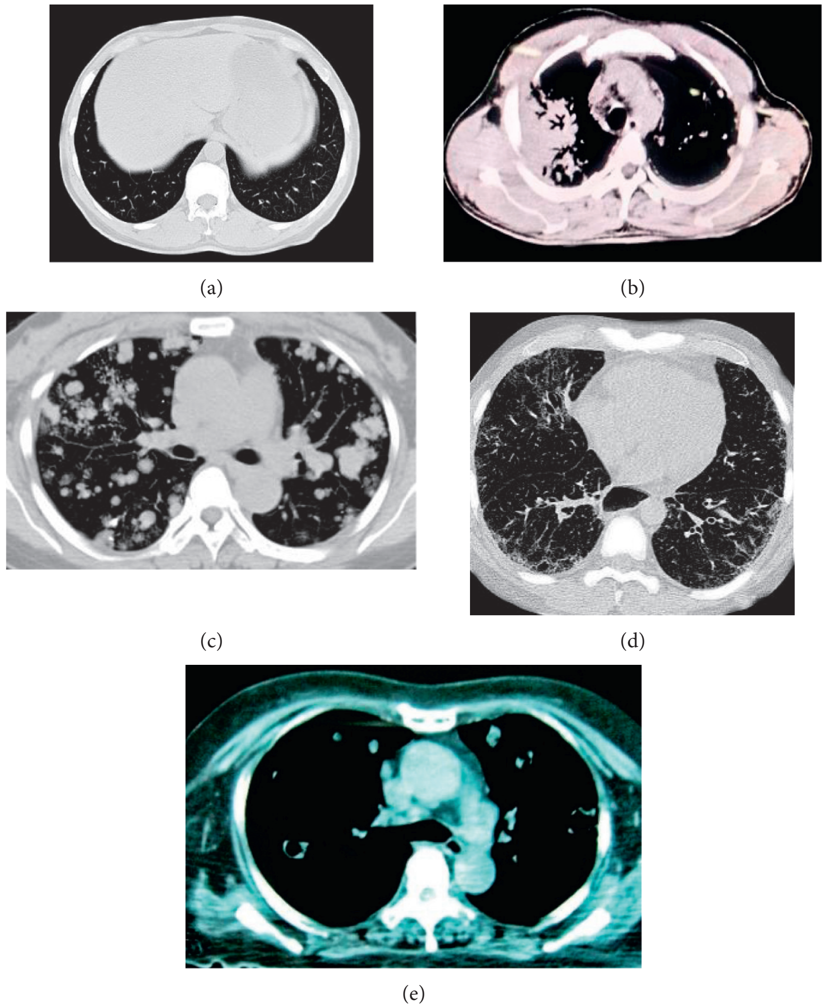

Figure 11: Various morphological feature images of patients with severe lung infections. (a) Ground-glass shadow, (b) consolidation shadow, (c) nodule or mass shadow, (d) network or line-like shadow, and (e) hollow shadow.

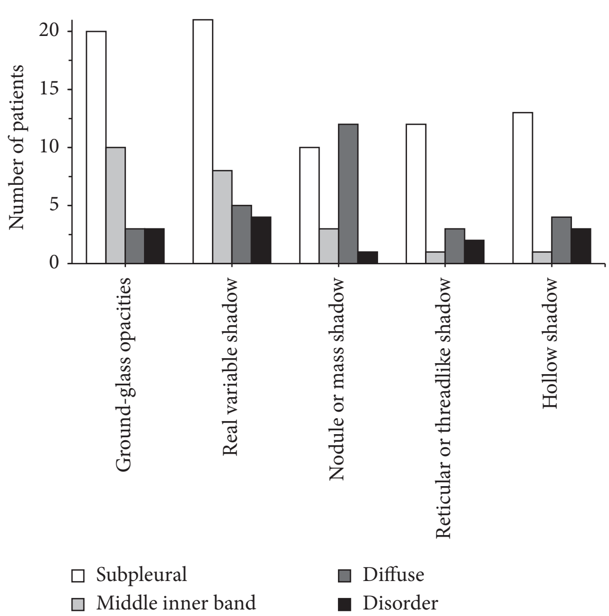

Figure 12: The distribution of lesions in patients with severe lung infections.

pathogens. It was noted that the incidence of ground-glass shadows, consolidation shadows, nodules or mass shadows, network or line-like shadows, and hollow shadows in patients with fungal infections was 25%, 25%, 14.3%, 7.1%, and 28.6, respectively; the incidence of ground-glass shadow, consolidation shadow, nodule or mass shadow, network or linear shadow, and hollow shadow in patients with bacterial infections was 16.7%, 5.6%, 44.4%, 22.2%, and 11.1%, respectively. There were statistically significant differences in the incidence of ground-glass shadows, consolidation shadows, nodules or mass shadows, network or line-like shadows, and hollow shadows in patients with fungal and bacterial infections ($P < 0.05$).

3.7. Diagnosis Accuracy of Patients with Severe Lung Infection in Two Ways. Figure 14 shows the sensitivity, specificity, and accuracy of the two methods of diagnosis. It was noted that the sensitivity of the traditional method was 88.31%, the specificity was 75.74%, and the accuracy was 74.23%; the sensitivity of CT image diagnosis based on the U-Net + DC algorithm was 98.13%, the specificity was 94.32%, and the

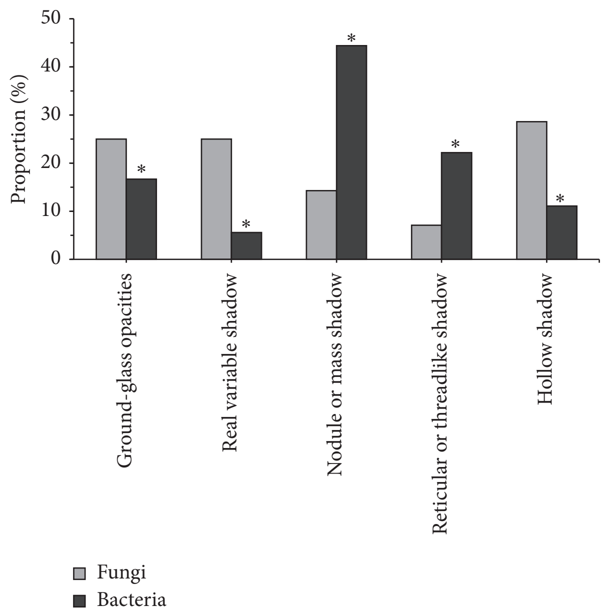

FIGURE 13: Comparison of the incidence of different CT morphological characteristics of lung infections with different pathogens. *Note.* * means the difference was statistically significant compared to fungal infections ($P < 0.05$).

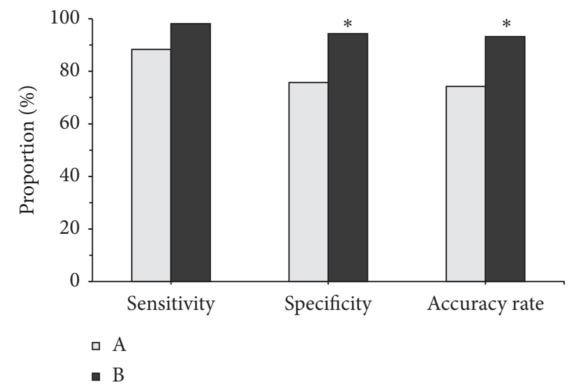

FIGURE 14: Comparison of the sensitivity, specificity, and accuracy of the two diagnosis methods. (a) Traditional method diagnosis. (b) CT image diagnosis based on U-Net + DC algorithm. *Note.* * indicates that, compared with the traditional method, the difference was statistically significant ($P < 0.05$).

accuracy was 97.22%; the specificity and accuracy of CT image diagnosis based on U-Net + DC algorithm were significantly higher than those of traditional method, and the difference was *statistically* significant ($P < 0.05$).

4. Discussion

At present, the morbidity and mortality of patients after the surgery are extremely high due to severe lung infections [16]. CT imaging plays an important role in the diagnosis of severe pulmonary infections and there are high requirements on the accuracy and resolution of the images. With the rapid development of artificial intelligence and information technology, the application of deep learning in medical imaging has made great contributions to the segmentation and diagnosis of medical images [17, 18]. In this study, DC was incorporated into the U-Net network to simplify and improve the U-Net network, and then the improved one was used to process the lung CT images, and its segmentation effect was compared with that of the CNN algorithm. The results showed that the U-Net + DC algorithm had shorter single training time and a lower Loss value than the CNN algorithm, and the difference was statistically significant ($P < 0.05$). Specifically, the single training time was reduced by 59.4% and the Loss value was reduced by 9.8%. The Dice of the U-Net + DC algorithm was larger than the Dice of the CNN algorithm by 3.6%, and the difference was statistically significant ($P < 0.05$). It showed that, with the gold standard as a reference, the U-Net + DC algorithm's various indicators were improved versus the CNN algorithm. It can segment the contours of the lungs more accurately, and the edges were smoother, which was closer to the gold standard.

After that, it was applied to the diagnosis of 100 patients with severe lung infections, and it was compared with the traditional method for the sensitivity, specificity, and accuracy of the diagnosis. The results found that, of the 100 patients with severe lung infections, 28% (28 cases) had fungal infections, 18% (18 cases) had bacterial infections, 7% (7 cases) had viral infections, 7% (7 cases) had tuberculosis infections, and 40% (40 cases) had mixed infections, accounting for the highest proportion. This was in line with the results of Suleyman et al. [19] that, of the 88 patients with lung infections after hematopoietic stem cell transplantation, 27 cases had fungal infections, 12 cases had bacterial infections, and 88 cases had viral infections. Of the 36 patients with ground-glass shadows in CT, there were 20 cases, 10 cases, 3 cases, and 3 cases with subpleural distribution, middle internal zone distribution, diffuse distribution, and irregular distribution; of the 38 patients with consolidation shadows in CT, there were 21, 8, 5, and 4 cases with subpleural distribution, midinternal zone distribution, diffuse distribution, and irregular distribution, respectively; of the 26 patients with nodules or masses in CT, there were 10 cases, 3 cases, 12 cases, and 1 case with the subpleural distribution, the middle and inner zone distribution, the diffuse distribution, and the irregular distribution, respectively; of the 17 patients with network or line-like shadows in CT, there were 12 cases, 1 case, 3 cases, and 2 cases with the subpleural distribution, the middle inner zone distribution, the diffuse distribution, and irregular distribution, respectively; of the 20 patients with hollow shadows in CT, there were 13 cases, 1 case, 4 cases, and 3 cases with subpleural distribution, midinternal zone distribution, diffuse distribution, and irregular distribution, respectively. This was consistent with the results of Ioannou et al. [20] that 4 out of 10 cases of *Aspergillus* infection had subpleural wedge-shaped consolidation shadows. The incidence of ground-glass shadows, consolidation shadows, nodules or mass shadows, network or line-like shadows, and hollow shadows in patients with fungal infections was 25%, 25%, 14.3%, 7.1%, and 28.6, respectively; the incidence of ground-glass shadow, consolidation shadow, nodule or mass shadow, network or linear shadow, and hollow shadow in patients with bacterial infections was 16.7%, 5.6%, 44.4%, 22.2%, and 11.1%, respectively. There were statistically significant differences in the incidence of ground-glass shadows, consolidation shadows, nodules or mass shadows, network or line-like shadows, and hollow shadows in patients with fungal and bacterial infections ($P < 0.05$). The specificity (94.32%) and accuracy (97.22%) of CT image diagnosis based on U-Net + DC algorithm were significantly higher than those of traditional method (75.74% and 74.23%), and the differences were statistically significant ($P < 0.05$). This is better than Chung et al. [21]. The addition of deep learning algorithm makes the diagnosis and segmentation of severe lung patients more accurate and helps medical staff to control the disease more effectively, so as to better treat it.

5. Conclusion

In this study, the DC was incorporated into the U-Net network to simplify and improve the U-Net network, and the improved algorithm was used to process lung CT images, and then it was compared with the CNN algorithm for the sensitivity, specificity, and accuracy of diagnosis. The results showed that the network of the algorithm in this study had better image segmentation effects; in medical diagnosis, CT images based on U-Net + DC algorithm can be used to diagnose severely infected patients, demonstrating high diagnostic value. However, some limitations in the study should be noted. The sample size is small, which will reduce the power of the study. In the followup, expanded sample size is necessary to strengthen the findings of the study. In conclusion, CT images based on hollow convolution U-Net algorithm are analyzed, which improves the segmentation effect of images and provides a new direction for the diagnosis of patients with severe pulmonary infection.

Data Availability

The data used to support the findings of this study are available from the corresponding author upon request.

Conflicts of Interest

The authors declare no conflicts of interest.

Authors' Contributions

T. Huang and X. Zheng contributed equally to this work.

References

[1] J. Shen, L. Huang, and C. Hao, "Value of multi-slice spiral computed tomography for diagnosis of tracheobronchial foreign body aspiration in children: 5-year retrospective study," *Pediatrics International*, vol. 62, no. 10, pp. 1184–1188, 2020 Oct.

[2] C. Huang, L. Huang, Y. Wang et al., "6-month consequences of COVID-19 in patients discharged from hospital: a cohort study," *The Lancet*, vol. 397, no. 10270, pp. 220–232, 2021 Jan 16.

[3] L. Jin and K. Chang, "Optimized fuzzy C-means algorithm-based coronal magnetic resonance imaging scanning in tracheal foreign bodies of children," *J Healthc Eng*, vol. 2021, Article ID 5678994, 2021 Jul 7.

[4] C. Fernández-de-las-Peñas, V. Gómez-Mayordomo, D. García-Azorín et al., "Previous history of migraine is associated with fatigue, but not headache, as long-term post-COVID symptom after severe acute respiratory SARS-CoV-2 infection: a case-control study," *Frontiers in Human Neuroscience*, vol. 15, Article ID 678472, 2021 Jun 28.

[5] X. Xu, C. Yu, J. Qu et al., "Imaging and clinical features of patients with 2019 novel coronavirus SARS-CoV-2," *European Journal of Nuclear Medicine and Molecular Imaging*, vol. 47, no. 5, pp. 1275–1280, 2020 May.

[6] B. Shaw, M. Daskareh, and A. Gholamrezanezhad, "The lingering manifestations of COVID-19 during and after convalescence: update on long-term pulmonary consequences of coronavirus disease 2019 (COVID-19)," *La radiologia medica*, vol. 126, no. 1, pp. 40–46, 2021 Jan.

[7] M. T. Lu, V. K. Raghu, T. Mayrhofer, H. J. W. L. Aerts, and U. Hoffmann, "Deep learning using chest radiographs to identify high-risk smokers for lung cancer screening computed tomography: development and validation of a prediction model," *Annals of Internal Medicine*, vol. 173, no. 9, pp. 704–713, 2020 Nov 3.

[8] N. Nasrullah, J. Sang, M. S. Alam, M. Mateen, B. Cai, and H. Hu, "Automated lung nodule detection and classification using deep learning combined with multiple strategies," *Sensors*, vol. 19, no. 17, p. 3722, 2019 Aug 28.

[9] J. Kottlors, S. Geissen, H. Jendreizik et al., "Contrast-enhanced black blood MRI sequence is superior to conventional T1 sequence in automated detection of brain metastases by convolutional neural networks," *Diagnostics*, vol. 11, no. 6, p. 1016, 2021 Jun 1.

[10] S.-A. Lee, S.-W. Jo, S.-K. Chang, and K.-H. Kwon, "Improvement of the diagnostic performance of facial neuritis using contrast-enhanced 3D T1 black-blood imaging: comparison with contrast-enhanced 3D T1-spoiled gradient-echo imaging," *Journal of Clinical Medicine*, vol. 10, no. 9, p. 1850, 2021 Apr 24.

[11] Z. Wan, Y. Dong, Z. Yu, H. Lv, and Z. Lv, "Semi-supervised support vector machine for digital twins based brain image fusion," *Frontiers in Neuroscience*, vol. 15, Article ID 705323, 2021 Jul 9.

[12] S. Baek, Y. He, B. G. Allen et al., "Deep segmentation networks predict survival of non-small cell lung cancer," *Scientific Reports*, vol. 9, no. 1, Article ID 17286, 2019 Nov 21.

[13] Z. Lv, L. Qiao, Q. Wang, and F. Piccialli, "Advanced machine-learning methods for brain-computer interfacing," *IEEE/ACM Transactions on Computational Biology and Bioinformatics*, vol. 18, pp. 1688–1698, 2020 Jul 17.

[14] S. A. Mattonen, G. A. Davidzon, S. Bakr et al., "[18F] FDG positron emission tomography (PET) tumor and penumbra imaging features predict recurrence in non-small cell lung cancer," *Tomography*, vol. 5, no. 1, pp. 145–153, 2019 Mar.

[15] M. Hu, Y. Zhong, S. Xie, H. Lv, and Z. Lv, "Fuzzy system based medical image processing for brain disease prediction," *Frontiers in Neuroscience*, vol. 15, Article ID 714318, 2021 Jul 30.

[16] Y. Chen and J. Bai, "Maternal and infant outcomes of full-term pregnancy combined with COVID-2019 in Wuhan, China: retrospective case series," *Archives of Gynecology and Obstetrics*, vol. 302, no. 3, pp. 545–551, 2020 Sep.

[17] S. Ather, T. Kadir, and F. Gleeson, "Artificial intelligence and radiomics in pulmonary nodule management: current status and future applications," *Clinical Radiology*, vol. 75, no. 1, pp. 13–19, 2020 Jan.

[18] R. Chrzan, M. Bociąga-Jasik, A. Bryll, A. Grochowska, and T. Popiela, "Differences among COVID-19, bronchopneumonia and atypical pneumonia in chest high resolution computed tomography assessed by artificial intelligence technology," *Journal of Personalized Medicine*, vol. 11, no. 5, p. 391, 2021 May 10.

[19] G. Suleyman, R. A. Fadel, K. M. Malette et al., "Clinical characteristics and morbidity associated with coronavirus disease 2019 in a series of patients in metropolitan detroit," *JAMA Network Open*, vol. 3, no. 6, Article ID e2012270, 2020 Jun 1.

[20] G. N. Ioannou, E. Locke, P. Green et al., "Risk factors for hospitalization, mechanical ventilation, or death among 10 131 US veterans with SARS-CoV-2 infection," *JAMA Network Open*, vol. 3, no. 9, Article ID e2022310, 2020 Sep 1.

[21] M. Chung, A. Bernheim, X. Mei et al., "CT imaging features of 2019 novel coronavirus (2019-nCoV)," *Radiology*, vol. 295, no. 1, pp. 202–207, 2020 Apr.

Hindawi
Journal of Healthcare Engineering
Volume 2021, Article ID 8201363, 9 pages
https://doi.org/10.1155/2021/8201363

Research Article

Children's Neurological Status Epilepticus and Poor Prognostic Factors through Electroencephalogram Image under Composite Domain Analysis Algorithm

Runhan Zhang, Chao Gao, Junting Liu, Manting Zhao, and Yongli Wu

Department of Child Healthcare, Cangzhou Central Hospital, Cangzhou 061000, Hebei, China

Correspondence should be addressed to Yongli Wu; wuyongli@stu.cpu.edu.cn

Received 25 August 2021; Revised 29 September 2021; Accepted 30 September 2021; Published 25 November 2021

Academic Editor: Enas Abdulhay

This study aimed to analyze the application of composite domain analysis algorithm for electroencephalogram (EEG) images of children with epilepsy and to investigate the risk factors related to poor prognosis. 70 children with neurological epilepsy admitted to the hospital were selected as the research objects. Besides, the EEG of the children during the intermittent and seizure phases of epilepsy were collected, so as to establish a composite domain analysis algorithm model. Then, the model was applied in EEG analysis. The clinical disease type and prognosis of children were statistically analyzed, and the risk factors that affected the prognosis of children were investigated. The results showed that the EEG signal values of the detail coefficients (d51 and d52) and the approximate coefficient (c5) during the epileptic seizure period were higher markedly than the signal values of the epileptic intermittent period; the EEG signal of the epileptic intermittent period was a transient waveform, which appeared as sharp waves or spikes. The EEG signal of epileptic seizures was continuous, with a composite waveform of sharp waves and spikes, and the change amplitude of the wavelet envelope spectrum during epileptic seizures was also higher hugely than that of intermittent epilepsy. The accurate identification rate, specificity, and sensitivity of EEG analysis with the composite domain algorithm were higher than those without the algorithm. Among the five types of epileptic seizures in children, the proportion of systemic tonic-clonic status was the largest, and the proportion of myoclonic status was equal to that of complex partial epileptic status, both of which were relatively small. The proportion of children with a better prognosis was 75.71% (53/70), which was higher than those with a poor prognosis 24.29% (17/70). Abnormal imaging examination (odds ratio (OR) = 3.823 and 95% confidence interval (CI) = 1.643–8.897); seizure duration greater than 1 hour (OR = 1.855 and 95% CI = 1.076–3.199); C-reactive protein (CRP) (OR = 5.089 and 95% CI = 1.507–17.187); and abnormal blood glucose (OR = 3.077, 95%CI = 1.640–5.773) were all independent risk factors for poor prognosis (all $P < 0.05$). The composite domain analysis algorithm was helpful for clinicians to find the difference in the EEG signals between the epileptic seizure period and the epileptic intermittent period in a short time, thereby improving the doctor's analysis of the results, which could reflect its marked superiority. In addition, abnormal imaging examinations, convulsion duration greater than 1 hour, CRP, and abnormal blood glucose were independent risk factors for poor prognosis in children. Therefore, the invasion of related risk factors could be reduced clinically by prognostic review with medical advice, attention to food safety and hygiene, and improvement of children's immunity.

1. Introduction

Children's neurological epilepsy is a common neurological syndrome caused by complex, recurrent, paroxysmal, and temporary brain dysfunction in children (0–18 years old). It is characterized by transient, rigid, paroxysmal, and repetitive central nervous system dysfunction. Its causes are mainly perinatal ischemia and hypoxia, cortical dysplasia, low-grade glioma, encephalitis, trauma, and so on, and it is a relatively common disease of children's nervous system [1]. Children can show sweating, convulsions, frequent convulsions, and even suffocation during the onset of the disease, which can easily cause loss of consciousness [2]. According to relevant epidemiological data, the prevalence of neurogenic epilepsy in children is about 6%, and there are at least 8.5 million children with epilepsy in China [3–5].

However, according to reports, the probability of intellectual impairment and structural abnormalities in epilepsy patients is about 20%–65%. Most of the patients have a chronic recurrent disease due to failure to detect and receive the appropriate treatment as early as possible and are accompanied by cognitive dysfunction, which seriously affects the healthy growth of children [6].

At present, the methods for detecting epilepsy in the clinic include computerized tomography (CT), magnetic resonance imaging (MRI), and EEG. What is more, EEG, the most commonly used technique in the clinic, uses electrical signals to record the activity of clusters of brain cells [7]. This examination technique appeared early in the 1970s, and a German professor named Hans Berger first recorded active currents from the human cerebral cortex in the 1990s. In 1935, researchers recorded 3 Hz pulses and ware complexes in the brains of epileptic patients such that slow comprehensive wave can further promote the application progress of EEG in clinical medicine [8]. Seizures will have physiological reactions similar to those of hysteria, syncope, migraine, and other diseases, which are easily confused [9]. Thus, it was necessary to use EEG inspection. According to relevant statistics, 83% of children with epilepsy have abnormal EEG. If proper EEG induction is performed, more patients will have abnormal EEG [10]. Epilepsy will not only damage the body of children but also leave children with sequelae and bring some social discrimination. Therefore, early detection and timely treatment are key to reducing children's neurological epileptic seizures [11].

The composite domain analysis algorithm was a multilead algorithm model that combined time-domain analysis, frequency-domain analysis, and time-frequency analysis. It can improve the efficiency of EEG data analysis and highlight its clinical application potential. In this study, 70 children with neurological epilepsy were selected, followed by EEG tracking. Then, the composite domain analysis algorithm was adopted to explore the clinical characteristics and prognostic factors of children with neurological epilepsy to provide a valuable reference for clinical treatment.

2. Materials and Methods

2.1. General Data. A total of 70 children with neurogenic epilepsy admitted to the hospital from June 2017 to March 2019 were selected as the research objects, including 38 male and 32 female children. Besides, they were from 1 month old to 17 years old, with an average age of 5.02 ± 1.24 years. There were 18 cases under 1 year, 20 cases between 1 and 3 years, 5 cases between 3 and 6 years, and 27 cases between 6 and 17 years. Based on the cause of the children, 23 cases suffered from central nervous system infection, 18 cases had hypoxic-ischemic encephalopathy, 14 cases had intracranial hemorrhage, and 15 cases suffered from head trauma. The diagnostic criteria were referred to the relevant diagnostic criteria in the 2006 International Anti-Epilepsy League Epilepsy Guidelines [12]. The inclusion criteria were defined to include children patients who met the above diagnostic criteria, did not take relevant antiepileptic drugs 3 months before treatment, were not contraindicated with antiepileptic drugs, were not allergic to the relevant treatment and examination drugs used in the treatment or examination in this study, and knew and signed the informed consent (their family members were aware of this study and also signed the informed consent). The exclusion criteria were defined to include children patients who were combined with cognitive impairment; had poor compliance and were unable to cooperate with the researchers; were accompanied by congenital heart disease, meningitis, and cerebrovascular malformations; suffered from abnormal liver and kidney function or were in a stressful state, and switched to other antiepileptic drugs during this study.

2.2. Research Methods

2.2.1. EEG Collection. Before the examination, the children needed to remove their hair and wash their scalp, which should be kept clean and dry. The 16-lead video EEG system produced by Siemens, Germany, was used for examination. The electrodes, 2 reference electrodes, and the anti-interference ground wire were placed in 19 recording electrodes according to the l0–20 system. The scalp resistance of each electrode should be lower than 4.5 kW, the amplitude was 100 uV/cm, the speed of paper skip was 11 mm/s, and there was the routine unipolar lead tracing and the routine flash stimulation test. The monitoring should be continued for 18 hours, and one complete sleep cycle should be recorded at least. Then, the method of continuous playback was employed to intercept the complete EEG during the awake, sleepy, and nonrapid eye movement (NREM) phases. The videos of EEG after 3 months and 6 months of treatment of all children were rechecked to observe the change of EEG discharge frequency.

2.2.2. Composite Domain Analysis Algorithm Model. Based on the children's EEG data, an epileptic EEG signal analysis algorithm of wavelet envelope spectrum was designed under composite domain analysis to better record and analyze the children's EEG data, and the valuable information could be extracted as the basis of clinical treatment.

First, the double-density discrete wavelet transform function was established, and the specific equation was as follows:

$$W(i) = \sqrt{2}\sum_{n} l_0(n)W(2i-n), \tag{1}$$

$$P(i) = \sqrt{2}\sum_{n} l_1(n)W(2i-n). \tag{2}$$

$W(i)$ represented the scale function, l_0 expressed the low-pass filter, l_1 stood for the high-pass filter, and $P(i)$ meant the wavelet number. $ls(n)$, $s = 0, 1, 2$ should meet the following reconstruction conditions, which were presented as follows:.

$$L_0(t)L_0\left(\frac{1}{t}\right) + L_1(t)L_1\left(\frac{1}{t}\right) + L_2(t)L_2\left(\frac{1}{t}\right) = 2, \quad (3)$$

$$L_0(t)L_0\left(-\frac{1}{t}\right) + L_1(t)L_1\left(-\frac{1}{t}\right) + L_2(t)L_2\left(-\frac{1}{t}\right) = 2. \quad (4)$$

Thus, the following equations could be obtained:

$$W_r = W(i-r), \quad (5)$$

$$P_{1,z,r}(i) = P_1\left(2^z i - r\right), \quad (6)$$

$$P_{2,z,r}(i) = P_2\left(2^z i - r\right). \quad (7)$$

Among them, there was $\{z, r \in a, z \geq 0\}$, so the signal to be processed $y(i)$ could be expressed as follows:

$$y(i) = \sum_{r=-\infty} f(r)W_r(i) + \sum_{s=1}^{2}\sum_{z=0}^{\infty}\sum_{r=-\infty}^{\infty} q_s(z,r)P_{s,z,r}(i). \quad (8)$$

In the following equations, f and q stood for the low-frequency coefficient and the high-frequency coefficient, respectively:

$$f(r) = \int v(i)W_r(i)qi, \quad (9)$$

$$q_s(z,r) = \int v(i)P_{s,r,z}(i)qi, \quad s = 1,2. \quad (10)$$

Envelope spectrum analysis, also known as envelope demodulation analysis, is a very effective method for detecting periodic effects of signals, which is extensively used in mechanical fault diagnosis. In order to obtain a clearer and smoother envelope curve, the Hilbert transform formula was required as follows:

$$\begin{aligned}\overline{y}(i) &= y(i) * \frac{1}{\Pi\Gamma} \\ &= \frac{1}{\Pi}\int_{-\infty}^{\infty}\frac{y(\Gamma)}{i-\Gamma}a\Gamma.\end{aligned} \quad (11)$$

$y(i)$ indicated the continuous-time signal, and Γ represented the transformation parameter. Moreover, an analytical signal was constructed by $\overline{y}(i)$ and $y(i)$ in the above equation, as follows:

$$F(i) = y(i) + z\overline{y}(i). \quad (12)$$

Then, the amplitude function could be obtained by taking the modulus value of $F(i)$, which was expressed as follows:

$$O(i) = \lfloor F(i) \rfloor = \sqrt{[y(i)]^2 + [\overline{y}(i)]^2}. \quad (13)$$

The two were combined to analyze the wavelet envelope spectrum of epileptic brain signals, to effectively demodulate the low-frequency signal of each subband from the high-frequency signal in the wavelet domain.

2.2.3. Algorithm Index. The commonly used indexes to evaluate the accuracy of the algorithm are accuracy (Acc), sensitivity (Sen), and specificity (Spe):

$$\begin{aligned}\mathrm{Acc} &= \frac{\mathrm{TP}+\mathrm{TN}}{\mathrm{TP}+\mathrm{TN}+\mathrm{FP}+\mathrm{FN}} \times 100\%, \\ \mathrm{Sen} &= \frac{\mathrm{TP}}{\mathrm{TP}+\mathrm{FN}} \times 100\%, \\ \mathrm{Spe} &= \frac{\mathrm{TN}}{\mathrm{TN}+\mathrm{FP}} \times 100\%.\end{aligned} \quad (14)$$

TP is the amount of positive data predicted as positive data, TV is the amount of negative data predicted as negative data, FP is the amount of negative data predicted as positive data, and FN is the amount of positive data predicted as negative data.

The double-density discrete wavelet transform decomposition coefficients and the corresponding coefficient envelope spectrum of the EEG signals in children patients were recorded during the intermittent and seizure periods of epilepsy. Since frequency components higher than 70 Hz lacked application value in research and analysis, the Butterworth low-pass filter was adopted to filter EEG signals to remove high-frequency interference. The EEG signals could be decomposed into several different frequency segments by using the compound domain analysis algorithm. These segments could not only separate the mutation signals of the EEG signals but also retain the time information of each segment, which can provide reference materials for the follow-up research. The wavelet envelope spectrum obtained in this study contained not only time-frequency information but also frequency-modulation and amplitude-modulation information, which better revealed the frequency and variation law of the mutation signal in the time-frequency domain. Moreover, the application of dual-density discrete wavelet transform also increased the ability to capture the signal details.

2.2.4. Simulation Algorithm Flow. First, the epileptic EEG signal is processed, and the processing flow is shown in Figure 1.

Epilepsy EEG detection can be formalized as EEG signal classification. The classifiers used in this study are SVM, KNN, LDA, and DT. The four classifiers are introduced as follows.

SVM: Map the data to a higher dimensional feature space, and then determine a hyperplane in this projection space to maximize the classification interval.

KNN: The test sample category is determined based on the category of the K samples closest to it in the feature space; that is, the sample category belongs to most of the k nearest neighbor samples. The number of nearest neighbors K is the only parameter in the KNN model. If $k = 1$, the test sample category will be marked as the nearest neighbor sample category.

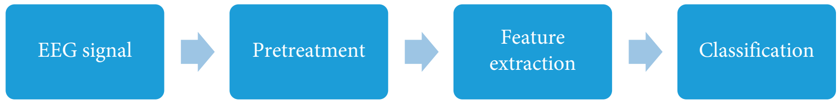

Figure 1: Algorithm flow of epileptic EEG signal analysis.

LDA: It is a classical linear learning method, which projects historical data onto a straight line. After projection, it ensures that the distance between similar data is as close as possible and the distance between different types of data is as far as possible.

DT: It is a nonparametric classifier, which derives decision rules according to the characteristics of training data. Its structure is similar to the flow chart, which is a directed tree composed of root nodes, internal nodes, and leaf nodes. Branching starts from the root node, where each internal node represents the test of a certain attribute of the data, and each leaf node represents the class or its distribution. Once the decision rules are generated and the tree structure is formed, the test data can be input into the tree and divided into different categories.

2.3. Statistical Processing. The collected data were sorted, summarized, and analyzed by SPSS 23.0. Measurement data were expressed as mean ± standard deviation ($\pm s$), and single sample data were represented by t test. In addition, $P < 0.05$ indicated that the difference was statistically substantial.

3. Results

3.1. Double-Density Discrete Wavelet Transform Decomposition Coefficients of EEG Signals and the Corresponding Coefficient Envelope Spectrum. Figures 2 and 3 show that the EEG signal values of the detail coefficients (d51 and d52) and the approximate coefficient (c5) of the epileptic period rose obviously in contrast to the signal values of the epileptic intermittent period. The interphase EEG signal was a transient waveform, which appeared as sharp waves. Besides, the EEG signal of epileptic seizures was continuous, with a composite waveform of sharp waves and spikes, and the change amplitude of the wavelet envelope spectrum in the seizure period was also greatly higher than that in the epileptic intermittent period.

3.2. Recognition Performance of the Composite Domain Analysis Algorithm. Figure 4 indicates that the correct recognition rate, specificity, and sensitivity of EEG analysis after using the algorithm were greater than the analysis value without using the algorithm, and the difference was statistically remarkable ($^*P < 0.05$).

3.3. Statistics of Types of Epileptic Seizures in Children. Among the five types of epileptic seizures in children, the proportion of systemic tonic-clonic status was the largest, the proportion of myoclonic status and complex partial status of epileptic status was equal to each other, and the difference was statistically obvious after comparison ($^*P < 0.05$) (Figure 5).

3.4. The Prognosis of all the Child Patients. Figure 6 reveals that the proportion of children with a good prognosis was 75.71% (53/70), which was higher than that of patients with a poor prognosis 24.29% (17/70), with a statistically marked difference ($^*P < 0.05$).

3.5. Single-Factor Analysis on the Prognosis of Children Patients. The single factor analysis showed that the proportion of imaging examination, convulsion duration, CRP, and blood glucose in children with good prognosis was statistically significant compared with the proportion of children with poor prognosis ($P < 0.05$), as shown in Table 1.

3.6. Multiple-Factor Analysis and Logistic Multiple-Factor Regression Analysis on Middle-Aged and Elderly Bronchial Asthma. The independent risk factors for poor prognosis in children included abnormal imaging examination, convulsion duration greater than 1 hour, CRP, and abnormal blood glucose (Table 2).

3.7. Comparison of EEG and Discharge Index in Children with Epilepsy before and after Treatment. The EEG discharge index of 70 children with epilepsy was 62.8 ± 12.567 before treatment and decreased significantly after treatment. There was a significant difference before and after treatment, $t = 5.766$, $P = 0.000$ ($^*P < 0.005$). Figures 7 and 8 and Table 3 show the details.

4. Discussion

The clinical pathogenesis of epilepsy is relatively complicated, and a clear conclusion has not yet been obtained. Some studies believe that the disease is mainly caused by neurotoxicity, which leads to disorders of intracellular energy, thereby triggering the functions of breathing, liver, and kidney innervated by nerves. Obstacles cause the patients to have cognitive, behavioral, and local neurological deficits, which reduce the quality of life of the children and shorten the survival time of the child patients [13, 14]. Special examinations for children in the clinic include EEG and MRI, and EEG is critical evidence for the diagnosis of epilepsy. Therefore, most clinical doctors recommend that children's family members receive this examination, and the examination process will not make the child patient feel pain. Moreover, the clinical use rate is relatively high [15–17].

In order to improve the accuracy of the EEG examination results, the composite domain analysis algorithm was adopted in this study, the algorithm idea of wavelet envelope analysis

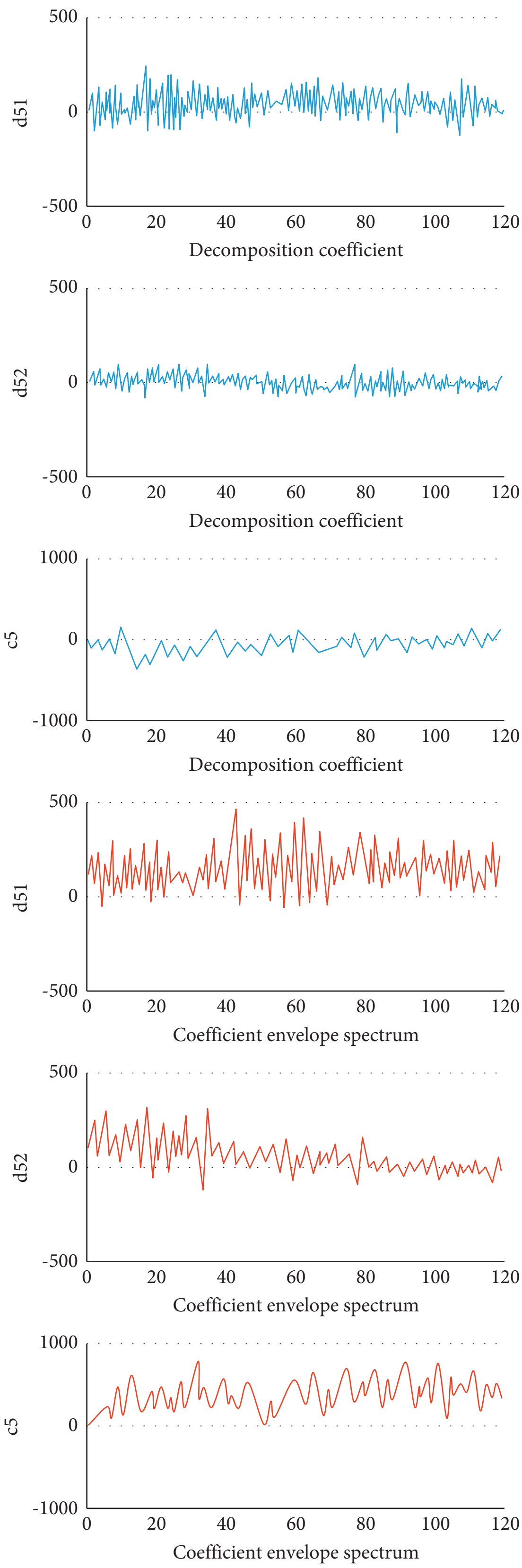

FIGURE 2: Double-density discrete wavelet transform decomposition coefficients of EEG signals during intermittent epilepsy and the corresponding coefficient envelope spectrum.

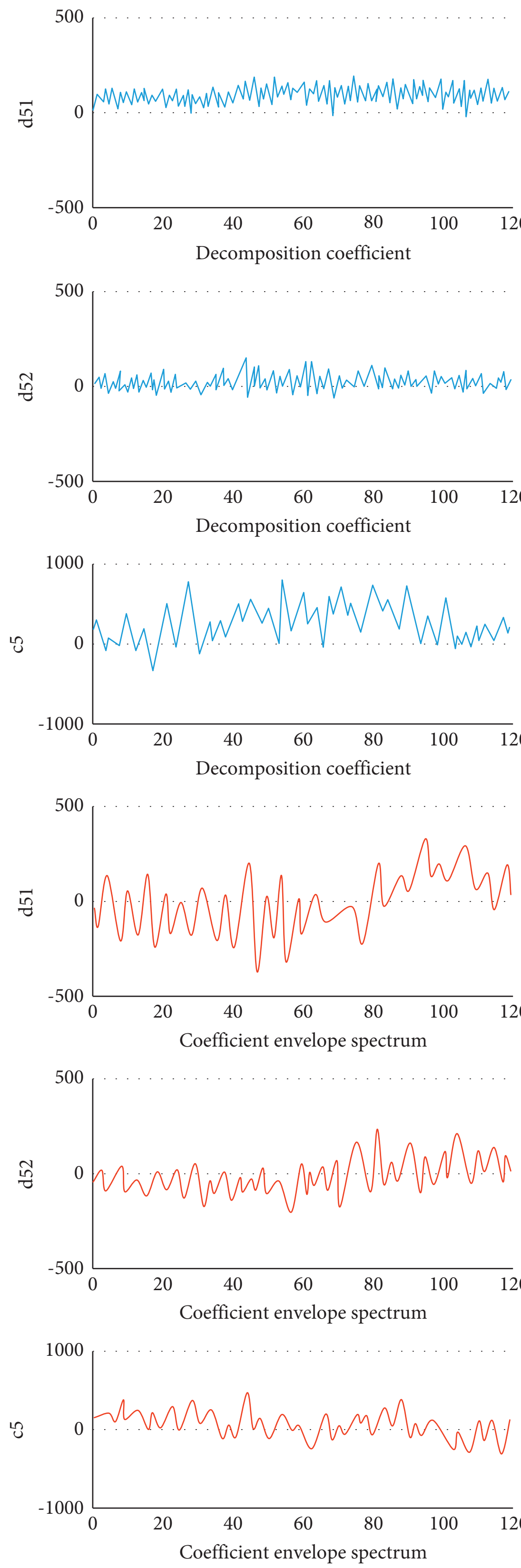

FIGURE 3: Double-density discrete wavelet transform decomposition coefficients of EEG signals during epileptic seizures and the corresponding coefficient envelope spectrum.

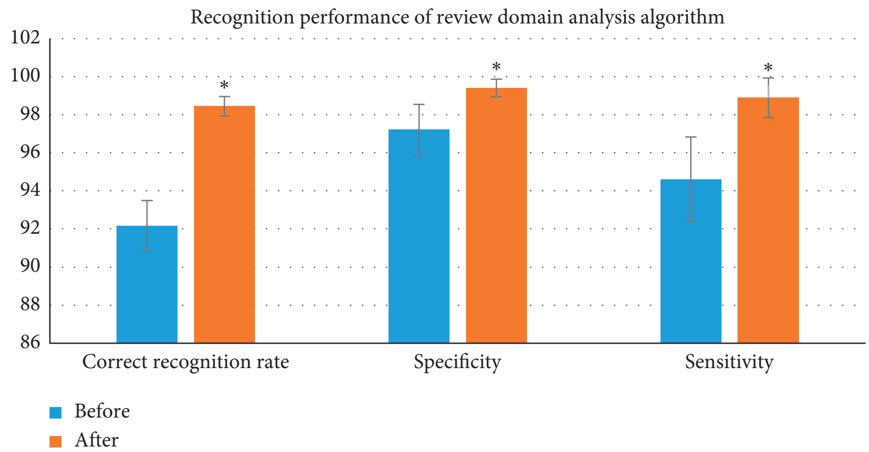

FIGURE 4: Recognition performance of the composite domain analysis algorithm (compared with EEG analysis using the algorithm, $^{*}P < 0.05$).

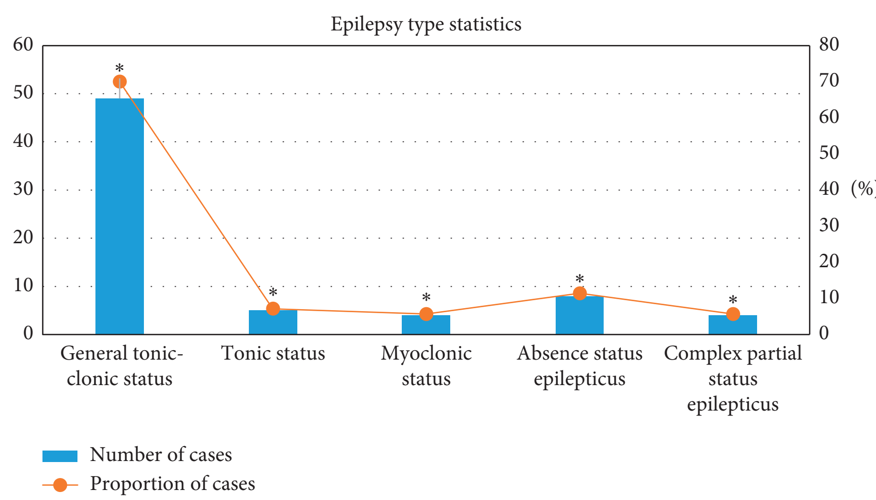

FIGURE 5: Statistics of epileptic seizure types in children ($^{*}P < 0.05$).

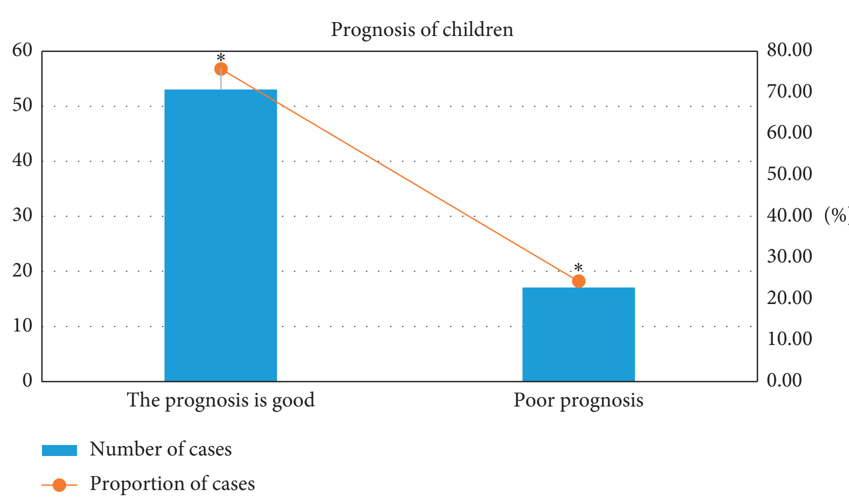

FIGURE 6: Comparison of the prognosis of the children patients ($^{*}P < 0.05$).

was introduced into the field of epilepsy identification to reduce the influence of excessive fluctuation between single recognition data when the EEG signal analysis algorithm processed fixed classification tasks. Through systematic analysis of formic acid, the results of this study found that the interphase signal was a transient waveform, manifested as

Table 1: Single factor analysis on prognosis of children (cases (%)).

Relevant factors		Good prognosis ($n = 53$)	Poor prognosis ($n = 17$)	P value
Gender	Male	25 (47.17)	9 (52.94)	>0.05
	Female	28 (52.83)	8 (47.06)	
Age (years old)	<6 years old	32 (60.38)	11 (64.71)	>0.05
	≥6 years old	21 (39.62)	6 (35.29)	
Imaging examination	Abnormal	45 (84.91)	14 (82.35)	<0.05
	Normal	8 (15.09)	3 (17.65)	
Past medical history	Yes	17 (32.08)	5 (29.41)	>0.05
	No	36 (67.92)	12 (70.59)	
Duration of convulsion (hour)	<1 hour	45 (84.91)	15 (88.24)	<0.05
	>1 hour	8 (15.09)	2 (11.76)	
CRP (mg/dL)	Abnormal	46 (86.79)	11 (64.71)	<0.05
	Normal	7 (13.21)	6 (35.29)	
Blood glucose (mmol/L)	Normal	47 (88.68)	7 (41.18)	<0.05
	Abnormal	6 (11.32)	10 (58.82)	

Table 2: Multiple-factor analysis on affecting the prognosis of children patients.

Factors	β	SE	Wald χ^2 value	P	OR	95% CI
Abnormal imaging examination	1.341	0.431	5.024	0.002	3.823	1.643–8.897
Convulsion duration >1 hour	0.618	0.278	4.048	0.026	1.855	1.076–3.199
CRP	1.627	0.621	7.055	0.009	5.089	1.507–17.187
Abnormal blood glucose	1.124	0.321	4.353	≤0.001	3.077	1.640–5.773

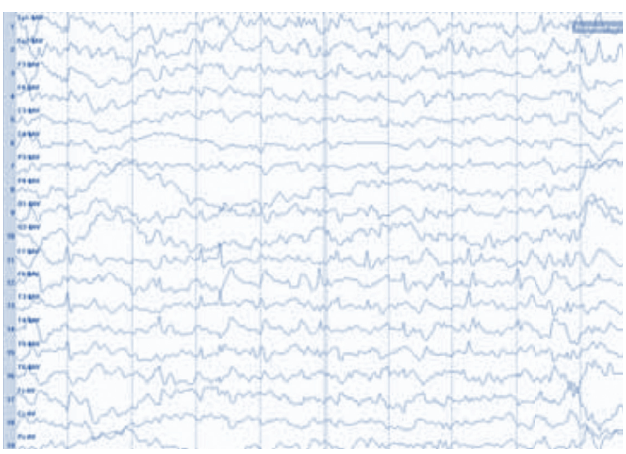

Figure 7: EEG after three months of treatment.

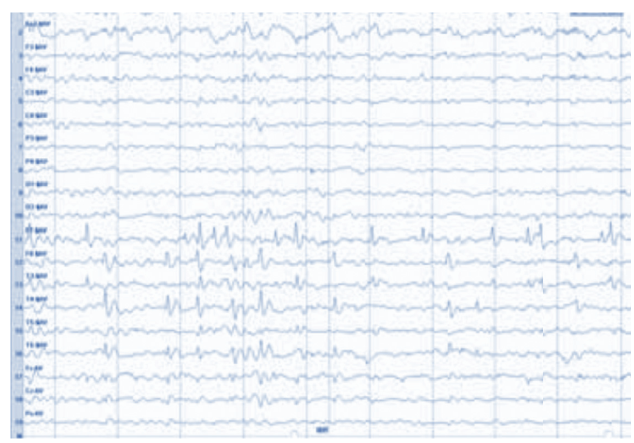

Figure 8: EEG after six months of treatment.

sharp waves or spikes, and the EEG signal of epileptic seizures is continuous, with a composite waveform consisting of sharp waves and spikes. Besides, the latter was brain waves to move more than the former, indicating that brain activity was relatively active in children with epilepsy. However, there were still differences between the intermittent EEG of epilepsy and the normal EEG because the intermittent EEG signal of epilepsy and the EEG signal of epilepsy were abnormal EEG. In this study, algorithm analysis was used, so that persevering clinicians could quickly differentiate and draw conclusions, which shortened the time of clinical diagnosis and promoted the treatment efficiency.

In this study, the clinical data and prognosis of the children were also analyzed. It was found that the generalized tonic-clonic status accounted for the largest proportion among the five types of epileptic seizures in children. Myoclonic status and complex partial status epilepticus accounted for the same proportion, and both had a smaller proportion. Furthermore, the proportion of children with a good prognosis was 75.71% (53/70), higher than that of patients with a poor prognosis (24.29%) (17/70). Statistical analysis of factors affecting the prognosis revealed that abnormal imaging examination, convulsion duration >1

Table 3: Changes of the EEG discharge index before and after treatment in 70 cases of children with epilepsy.

	Before treatment	After treatment	t	P
Discharge index	62.8 + 12.567	< 50	5.766	0.000

hour, CRP, and abnormal blood glucose were all independent risk factors for poor prognosis in children patients.

According to a study by Hamano et al. [18], children with epilepsy with abnormal brain CT had a higher risk of poor prognosis, which corresponded to the results of this study. It might be because epilepsy was in a dynamic and constantly changing development process, so abnormalities occurred in daily cranial imaging examinations. According to the results of neuropathological studies, the continuous point activity abnormality of the central nervous system might result in irreversible neuronal damage and even death [19]. Children with recurrent clinical manifestations such as vomiting, nausea, vertigo, limb pain, headache, and abdominal pain, especially school-age patients, should be questioned on medical history in detail. If necessary, the corresponding auxiliary examination should be given. On the basis of excluding common diseases such as pediatric surgery, the disease should be highly suspected. Children should be treated immediately after their diagnosis, followed up, and observed, with paying attention to the toxic and side effects of drugs. They should be given early intervention and treatment in time, and their dose should be mastered. Half an hour after the onset of epilepsy, the child patient had brain hypoxia and decreased metabolic rate, and more than 1 hour could lead to permanent and irreversible brain damage. Therefore, the duration of convulsions longer than 1 hour was also one of the risk factors affecting the prognosis of children. Seizures can trigger a rapid stress response in the body, which increases the possibility of infection. What is more, CRP abnormalities are more common in infections, such as bacterial meningitis, sepsis, and other related encephalopathy. At the same time, studies have pointed out that blood glucose levels are not normal. The prognosis of children within the range is poor, and previous studies have confirmed that hypoglycemia can lead to brain damage [20]. Some children with poor prognosis in this study also suffered from hypoglycemia. Relevant researchers have also found that hyperglycemia is associated with the poor prognosis of patients with epilepsy. Therefore, it is necessary to understand whether children have the above risk factors during treatment and to diagnose and treat them in time [21].

5. Conclusion

To sum up, the composite domain analysis algorithm was applied in this study to analyze the EEG images of 70 children with neurogenic epilepsy, suggesting the difference between the EEG signals in the epileptic intermittent period and the epileptic period, which improved the doctor's understanding of the results. It also reflected the significant superiority of the composite domain analysis algorithm. In this study, the influencing factors of the patient's poor prognosis were also analyzed and sorted out, indicating that abnormal imaging examination, convulsion duration >1 hour, CRP, and abnormal blood glucose were independent risk factors for the poor prognosis of children patients. Therefore, the invasion of related risk factors could be reduced clinically through the prognostic review with medical advice, attention to food safety and hygiene, and improvement of children's immunity. In addition, researchers should continue to investigate the risk factors of poor prognosis in children patients with epilepsy and introduce them into the preventive treatment process to enhance rapid recovery of children patients.

The shortcomings of this study are that the description of the EEG research process is simple, and no more in-depth analysis has been carried out. Therefore, further in-depth discussions are needed in future research to better provide a clinical reference.

Data Availability

The data used to support the findings of this study are available from the corresponding author upon request.

Conflicts of Interest

The authors declare no conflicts of interest.

References

[1] B. Deng and Y. Shi, "Modeling and optimizing the composite prepreg tape winding process based on grey relational analysis coupled with BP neural network and bat algorithm," *Nanoscale Research Letters*, vol. 14, no. 1, p. 296, 2019.

[2] A. B. Rosenfeldt, S. M. Linder, S. Davidson et al., "Combined aerobic exercise and task practice improve health-related quality of life poststroke: a preliminary analysis," *Archives of Physical Medicine and Rehabilitation*, vol. 100, no. 5, pp. 923–930, 2019.

[3] P. Huang, Z. Huang, X. Lu et al., "Study on glycoprotein terahertz time-domain spectroscopy based on composite multiscale entropy feature extraction method," *Spectrochimica Acta Part A: Molecular and Biomolecular Spectroscopy*, vol. 229, Article ID 117948, 2020.

[4] J. G. Lees, D. Lee, R. A. Studer et al., "Gene3D: multi-domain annotations for protein sequence and comparative genome analysis," *Nucleic Acids Research*, vol. 42, no. D1, pp. D240–D245, 2014.

[5] X. Jin, "Iterative learning control for MIMO nonlinear systems with iteration-varying trial lengths using modified composite energy function analysis," *IEEE Transactions on Cybernetics*, vol. 99, pp. 1–11, 2020.

[6] J. Musuuza, B. L. Sutherland, S. Kurter, P. Balasubramanian, C. M. Bartels, and M. B. Brennan, "A systematic review of multidisciplinary teams to reduce major amputations for patients with diabetic foot ulcers," *Journal of Vascular Surgery*, vol. 71, no. 4, pp. 1433–1446, 2020.

[7] Y. Zhang, M. L. N. Chen, and L. Jun Jiang, "Analysis of electromagnetic vortex beams using modified dynamic mode decomposition in spatial angular domain," *Optics Express*, vol. 27, no. 20, pp. 27702–27711, 2019.

[8] K. K. Ray, S. J. Nicholls, K. A. Buhr, H. N. Ginsberg, J. O. Johansson, and K. Kalantar-Zadeh, "Effect of apabetalone added to standard therapy on major adverse cardiovascular events in patients with recent acute coronary syndrome and type 2 diabetes: a randomized clinical trial," *Journal of the American Medical Association*, vol. 323, no. 16, pp. 1565–1573, 2020.

[9] S. W. Long, R. J. Olsen, P. A. Christensen et al., "Molecular architecture of early dissemination and massive second wave

of the SARS-CoV-2 virus in a major metropolitan area," *mBio*, vol. 11, no. 6, pp. e02707–20, 2020.
[10] G. Ispirova, T. Eftimov, and B. K. Seljak, "Evaluating missing value imputation methods for food composition databases," *Food and Cosmetics Toxicology*, vol. 141, Article ID 111368, 2020.
[11] Z. Tang, H. Deng, Q. Liu, J. Guo, and L. Shang, "Quantitative analysis of low-concentration α-HMX based on terahertz spectroscopy," *Analytical Methods*, vol. 12, no. 47, pp. 5684–5690, 2020.
[12] O. Yu, R. Schulze-Rath, J. Grafton, K. Hansen, D. Scholes, and S. D. Reed, "Adenomyosis incidence, prevalence and treatment: United States population-based study 2006-2015," *American Journal of Obstetrics and Gynecology*, vol. 223, no. 1, pp. 94–e10, 2020.
[13] B. van den Munckhof, C. Alderweireld, S. Davelaar et al., "Treatment of electrical status epilepticus in sleep: clinical and EEG characteristics and response to 147 treatments in 47 patients," *European Journal of Paediatric Neurology*, vol. 22, no. 1, pp. 64–71, 2018.
[14] X. F. Li, B. Ai, J. W. Ye et al., "[Clinical analysis of seven cases of H1N1 influenza-associated encephalopathy in children]," *Zhonghua Er Ke Za Zhi*, vol. 57, no. 7, pp. 538–542, 2019, Chinese.
[15] A. Jeong, J. Strahle, A. K. Vellimana, D. D. Limbrick, M. D. Smyth, and M. Bertrand, "Hemispherotomy in children with electrical status epilepticus of sleep," *Journal of Neurosurgery: Pediatrics*, vol. 19, no. 1, pp. 56–62, 2017.
[16] R. H. Hommady, M. T. Alrifai, O. K. Mubayrik et al., "Retrospective review of pediatric status epilepticus in 116 Saudi patients: predictors of outcome," *Annals of Saudi Medicine*, vol. 37, no. 6, pp. 455–460, 2017.
[17] D. R. Nordli, S. L. Moshé, S. Shinnar et al., "FEBSTAT study team. acute EEG findings in children with febrile status epilepticus: results of the FEBSTAT study," *Neurology*, vol. 79, no. 22, pp. 2180–2186, 2012.
[18] S. I. Hamano, K. Sugai, M. Miki, T. Tabata, T. Fukuyama, and M. Osawa, "Efficacy, safety, and pharmacokinetics of intravenous midazolam in Japanese children with status epilepticus," *Journal of Neurological Sciences*, vol. 396, pp. 150–158, 2019.
[19] S. Kanmaz, E. Simsek, H. M. Serin et al., "Sulthiame add-on treatment in children with epileptic encephalopathy with status epilepticus: an efficacy analysis in etiologic subgroups," *Neurological Sciences*, vol. 42, no. 1, pp. 183–191, 2021.
[20] M. K. Goyal, S. Sinha, S. Ravishankar, and J. J. Shivshankar, "Role of MR imaging in the evaluation of etiology of status epilepticus," *Journal of Neurological Sciences*, vol. 272, no. 1-2, pp. 143–150, 2008.
[21] K. L. Wagenman, T. P. Blake, S. M. Sanchez et al., "Electrographic status epilepticus and long-term outcome in critically ill children," *Neurology*, vol. 82, no. 5, pp. 396–404, 2014.

Hindawi
Journal of Healthcare Engineering
Volume 2021, Article ID 9510783, 9 pages
https://doi.org/10.1155/2021/9510783

Research Article

Internet of Things-Based Ultrasound-Guided Erector Spinae Plane Block Combined with Edaravone Anesthesia in Thoracoscopic Lobectomy

Xiuyan Wang, Xuan Zhou, Lin Li, and Cuijie Liu

Department of Anesthesiology, Affiliated Hongqi Hospital of Mudanjiang Medical University, Mudanjiang 157011, Heilongjiang, China

Correspondence should be addressed to Cuijie Liu; 1751060274@xzyz.edu.cn

Received 11 September 2021; Revised 22 October 2021; Accepted 25 October 2021; Published 13 November 2021

Academic Editor: Enas Abdulhay

This paper aimed to study the application value of Internet of Things (IoT) edge computing algorithm-based ultrasound-guided erector spinae plane block combined with edaravone anesthesia in thoracoscopic lobectomy. A total of 110 patients undergoing thoracoscopic resection were selected as subjects. The patients were anesthetized with erector spinae plane block combined with edaravone before surgery and underwent chest ultrasound scan. IoT edge computing algorithm was constructed and applied to ultrasound images of patients to enhance and denoise the images. It was found that, in different mixed noise mixtures (Gaussian noise 10% + speckle noise 90%; Gaussian noise 30% + speckle noise 70%), the edge computing algorithm can still maintain the edge information of the output image, showing better performance on edge information detection and denoising compared with the Prewitt and Canny operator. In addition, visual analog scale (VAS) scores decreased with postoperative time after edaravone anesthesia induction and erector spinae plane block lobectomy and reached the lowest level after five days. In short, erector spinae plane block combined with edaravone showed good sedative and analgesic effects on patients undergoing thoracoscopic lobectomy. Ultrasound images processed by IoT edge computing algorithm showed high accuracy in the identification of lung lesions, which was worth applying to clinical diagnosis.

1. Introduction

Lobectomy is mainly used for lobectomy of malignant tumors limited to the lung, pulmonary damage caused by tuberculosis, severe bullae, bronchiectasis, interstitial lesions, trauma, and dysplasia. Lobectomy is a kind of routine pulmonary resection [1]. The human body has five lobes in the chest cavity. The right lung is made up of the upper lobe, the middle lobe, and the lower lobe. The left lung is made up of two lobes, the upper lobe and the lower lobe. Lobectomy is suitable for lung cancer and irreversible lesions confined to the lung lobe. It mainly includes right upper lobectomy, right middle lobe lobectomy, right lower lobectomy, left upper lobectomy, and left lower lobectomy. If the lesion involves two lobes or the middle bronchus, upper-middle or lower-middle lobe, two-lobe lung resection is feasible [2]. In general, the quality of life of patients after surgery is good. In normal survival, postoperative patients need to pay attention to climate changes, keep warm, pay attention to diet, and avoid irritating gases [3]. In addition, patients need to exercise properly to enhance their resistance, closely observe their symptoms and signs, and go to the hospital for comprehensive examination and treatment as soon as possible if there is an abnormality [4, 5]. Thoracoscopic lobectomy means that, with the assistance of thoracoscopy, the surgeon only observes the situation in the thoracic cavity in real time through a TV screen and completes the operation through one to four hole-like incisions (without spreading the ribs) with the longest length not exceeding 5 cm. The veins, arteries, and bronchi are cut off anatomically to completely remove the lung lobes. At present, video-assisted thoracic surgery (VATS) lobectomy has basically matured and gained wide acceptance. The surgical technique is also gradually refined and perfected day by day [6, 7]. The

National Comprehensive Cancer Network (NCCN) lung cancer treatment guidelines clearly point out that "VATS lobectomy is a viable option for resectable lung cancer," which means that the role of thoracoscopic lobectomy for the treatment of benign lung lesions or early malignant lesions has been confirmed [8].

However, the postoperative pain of this type of surgery is relatively strong. Insufficient intraoperative anesthesia or insufficient postoperative analgesia will affect the patient's cough, sputum, and so on, which may easily lead to adverse events and affect the patient's recovery process. Edaravone is a new type of free radical scavenger, which can scavenge oxygen-free radicals, inhibit lipid peroxidation of cell membranes, and reduce tissue edema and damage. Studies have shown that edaravone can reduce the production of inflammatory factors in the human body and has a protective effect on the lungs of patients [9]. In recent years, an interfascial plane block technique has gradually been used clinically, that is, ultrasound-guided erector spinae plane block (ESPB). It was first applied to severe acute postoperative pain and neuropathic pain in 2016, and it was successful. Studies have shown that ESPB is easy to operate, has high safety, low error rate, good analgesic effect, and few adverse reactions, and shows broad clinical application prospects [10].

With the full integration and adoption of cutting-edge technologies such as big data, Internet+, AI, and Internet of Things (IoT), AI-assisted medicine has shown strong influence and vitality. It plays an important supporting role in deepening the reform of the medical and health system, accelerating the construction of "healthy China," and promoting the development of the medical and health industry [11]. At present, medical imaging such as ultrasound (scanning the human body with ultrasound beam and obtaining images of internal organs by receiving and processing reflected signals) and magnetic resonance have gradually developed from auxiliary examination methods into the most important clinical diagnosis and differential diagnosis methods in modern medicine [12, 13]. Through big data plus artificial intelligence technology solutions, AI-assisted diagnosis and treatment adoptions are built, medical imaging data are modeled and analyzed, and conditions and lesions are analyzed to provide decision support for doctors and improve medical efficiency and quality [14, 15]. In this way, the high rate of misdiagnosis and missed diagnosis due to the limitation of doctors' experience in the field of medical imaging can be better solved, so did the long reading time, slow speed, and many other problems [16].

In the process of thoracoscopic lobectomy, some small pulmonary nodules cannot be accurately located during thoracoscopic surgery, and the boundary of pulmonary nodules is not easy to be identified. Ultrasonic guidance based on IoT edge detection algorithm was used to identify and locate hilar vessels and to surround small nodules in thoracoscopic lobotomy, to study the adoption value of the intelligent algorithm and ultrasound image in thoracoscopic lobectomy, aiming to provide more reference for the diagnosis and treatment of lobectomy and the sedation and analgesia methods of postoperative patients.

2. Materials and Methods

2.1. General Information. In this study, 110 patients who received thoracoscopic lobotomy in hospital from September 2019 to September 2020 were collected as subjects, including 58 male patients and 52 female patients aged 25~68 years (43.7 ± 5.2 years on average). This study had been approved by the Medical Ethics Committee. The patients and their families understood the content and methods of the study and agreed to sign the corresponding informed consent.

Inclusion criteria were as follows: (i) patients who underwent lobectomy after prepathological and imaging diagnosis of lobectomy; (ii) patients aged between 45 and 65 years; (iii) patients with no pulmonary metastasis, mediastinal lymph node enlargement, or pleural hypertrophy; (iv) patients who had not received any other drugs or antibiotics recently; (v) patients with normal coagulation function and platelets.

Exclusion criteria were as follows: (i) patients with other system or organ lesions; (ii) patients who did not cooperate with treatment due to personal or other factors; (iii) patients with incomplete clinical data and medical history.

2.2. Patient Anesthesia and Surgical Methods. All patients were fasting and abstaining from drinking 6 h before anesthesia induction, and all vital signs were monitored before surgery, including heart rate, diastolic blood pressure, systolic blood pressure, pulse oxygen saturation, and mean arterial pressure. 0.5 mg/Kg edaravone was added to 100 mL normal saline, and the infusion was completed within 30 min. A conventional disinfection towel was taken from the surgical position, and an erector spinae plane block was performed under the guidance of ultrasound. The puncture was performed after local anesthesia with 1% lidocaine at the puncture site. Local anesthetic drugs were injected after a puncture to the designated location, and a two-point block was selected according to the intercostal incision. Each puncture site was injected with 10 mL of drugs, and 0.5 mg/Kg edaravone was used as an anesthetic. The results of nerve block were tested by alcohol cotton ball 10 minutes after injection.

In lobotomy, an incision was made in the fifth intercostal area between the midaxillary line and the anterior axillary line, approaching the hilum at a small angle to facilitate the operation of hand instruments along the longitudinal axis. During the operation, the hemodynamic indexes of patients were monitored in real time, and the corresponding vasoactive drugs were timely corrected in case of intraoperative hemodynamic instability.

All patients included in the study underwent lung ultrasound examination. The patient was placed in a lateral position, and a high-frequency linear array probe was used for sagittal scanning. After the T4 spinous process was positioned, the probe was moved 3–5 cm to the outside to show the T5 transverse process, pleura, and transverse costal ligament. The ultrasound images were interpreted by two attending physicians or imaging physicians with rich clinical experience. The specific location of pulmonary lesions, the maximum diameter of the lesion site, and hilar and mediastinal lymph node enlargement were mainly observed and analyzed by ultrasound.

2.3. IoT Edge Computing. The image edge generally refers to the position where the grayscale change rate of the image is the largest. Edge detection refers to the process of detecting edge points and edge segments from the image and describing the edge direction. The image is regarded as a binary function $f(x, y)$, (x, y) is the position of the pixel, and $f(x, y)$ is the gray value at that point so that the image is regarded as a curved surface. The edge of the image is the most drastically changing position on the curved surface, and this position is also the position of the local extreme point of the curved surface. The basic idea of the image segmentation method based on edge detection is determining the edge pixels in the image first. Then, these pixels are connected together to form the required area boundary. Figure 1 shows the image edge type and its derivative curve law.

The brightness change of the image can be processed and enhanced by the difference between adjacent points. Differential processing of adjacent points in the horizontal direction can detect the brightness change in the vertical direction, that is, the horizontal edge detector (horizontal edge detector). Differential processing of adjacent points in the vertical direction can detect the brightness change in the horizontal direction, that is, the vertical edge detector (vertical edge detector). The expressions are shown in

$$E_x = \left|P_{x,y} - P_{x+1,y}\right|, \tag{1}$$

$$E_y = \left|P_{x,y} - P_{x,y+1}\right|. \tag{2}$$

Among them, E_x represents the vertical edge and E_y represents the horizontal edge. The horizontal edge detection operator and the vertical edge detection operator are combined, and the vertical edge and the horizontal edge can be detected at the same time, as shown in

$$E_{x,y} = \left|P_{x,y} - P_{x+1,y} + P_{x,y} - P_{x,y+1}\right|. \tag{3}$$

From the above equation, equation (4) is obtained:

$$E_{x,y} = \left|2 \times P_{x,y} - P_{x+1,y} - P_{x,y+1}\right|. \tag{4}$$

If a pixel is inserted between two adjacent difference points to achieve this, it is equivalent to using two adjacent first-order differences as the new horizontal difference, as in

$$\begin{aligned} E_{xxx,y} &= E_{xx+1,y} + E_{xx,y} = \left|P_{x+1,y} - P_{x,y} + P_{x,y} - P_{x-1,y}\right| \\ &= \left|P_{x+1,y} - P_{x-1,y}\right|. \end{aligned} \tag{5}$$

Here, E_{xx} represents the new level difference.

A gradient operator is defined by the method of first-order differentiation. The gradient is a vector, which indicates the direction of the most dramatic change in the gray level of the image.

$$\nabla f = \left(\frac{\partial f}{\partial x}, \frac{\partial f}{\partial y}\right). \tag{6}$$

The gradient can be expressed as

$$\|\nabla f\| = \sqrt{\left(\frac{\partial f}{\partial x}\right)^2 + \left(\frac{\partial f}{\partial y}\right)^2}. \tag{7}$$

The direction of the gradient is shown in

$$\theta = \left(\frac{\partial f/\partial y}{\partial f/\partial x}\right). \tag{8}$$

In actual image processing, the difference method is used for calculation. However, the use of the differential method for edge detection must make the direction of the difference perpendicular to the direction of the edge. Therefore, it is necessary to perform difference calculations in different directions of the image, which increases the amount of calculation. Generally, the edges are divided into horizontal edges, vertical edges, and diagonal edges.

2.3.1. Roberts Operator. The Roberts gradient operator uses the difference between the values of two adjacent pixels in the diagonal direction as a measurement standard, and its calculation method is shown in

$$G_x = f(i, j) - f(i-1, j-1), \tag{9}$$

$$G_y = f(i-1, j) - f(i, j-1), \tag{10}$$

$$|G(x, y)| = \sqrt{G_x^2 + G_y^2}. \tag{11}$$

Equation (11) is written in the form of convolution operation, and the convolution kernels are the following equations:

$$G_x = \begin{bmatrix} -1 & 0 \\ 0 & 1 \end{bmatrix}, \tag{12}$$

$$G_y = \begin{bmatrix} 0 & 11 \\ 1 & 0 \end{bmatrix}. \tag{13}$$

2.3.2. Prewitt Operator. The Prewitt operator combines the method of difference operation and neighborhood averaging, and its convolution template is shown in

$$G_x = \begin{bmatrix} -1 & 0 & 1 \\ -1 & 0 & 1 \\ -1 & 0 & 1 \end{bmatrix}, \tag{14}$$

$$G_y = \begin{bmatrix} -1 & -1 & -1 \\ 0 & 0 & 0 \\ 1 & 1 & 1 \end{bmatrix}. \tag{15}$$

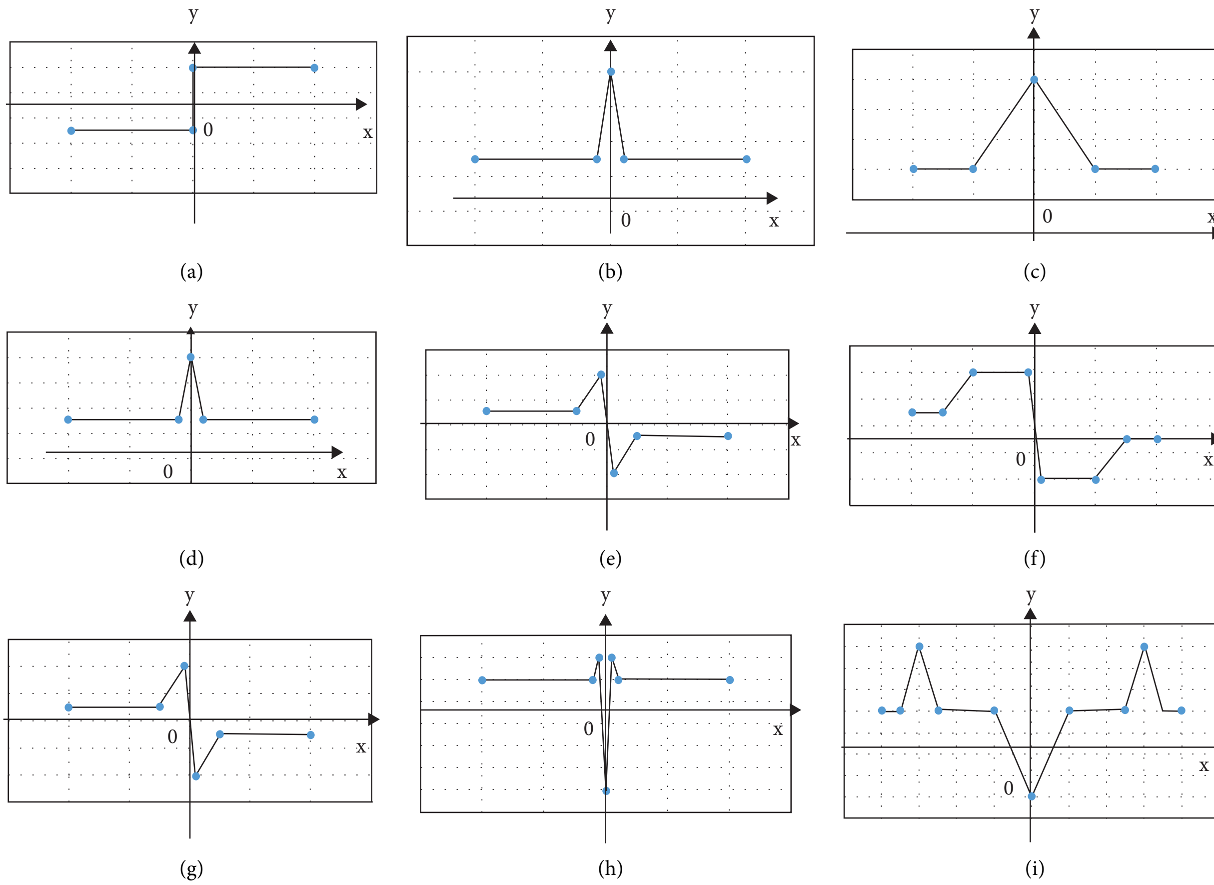

Figure 1: Image edge type and its derivative curve law. (a) Gray cross section-step shape; (b) gray cross section-thin line shape; (c) gray cross section slope gradient; (d) first-order differential-step shape; (e) first-order differential-thin line shape; (f) first-order differential-slope gradient shape; (g) second-order differential-step shape; (h) second-order differential-thin line shape; (i) second-order differential-slope gradient shape.

2.3.3. Soble Operator. The two Soble operators are for detecting horizontal edges and detecting vertical edges. It weighs the influence of the position of the pixel, which can reduce the degree of edge blur. Since the Soble operator is a form of filter operator, it is used to extract the edge and can use the fast convolution function, which is simple and effective. However, the Soble operator does not strictly distinguish the main body of the image from the background; that is, it is not based on image grayscale processing. Figure 2 shows the template of the Soble operator.

2.3.4. Prewitt Edge Detection Operator. If the weights of the center pixels of the two Prewitt template operators are doubled, the well-known Soble edge detection operator is obtained. It is composed of two masks that determine the edge in a vector manner. Soble has better performance than other edge detection operators in the same period as the Prewitt operator (Figure 3).

2.4. Evaluation of Edge Detection Effect of Ultrasonic Images. Ultrasound uses the difference between echo and original sound waves to produce images. The ultrasonic wave will change after being reflected by the object. The change is related to the shape characteristics of the object, and the shape of the object is determined according to the reflected wave. Ultrasound is injected into the body through the organs and tissues with different acoustic impedance and different attenuation characteristics from the surface to the deep, resulting in different reflections and attenuations. However, the existing ultrasound imaging technology is susceptible to interference from image noise, and the detection effect of blur and discontinuous edges is not good. Therefore, the IoT edge detection algorithm processes the ultrasound image and then judges its blur and discontinuous edge detection effect on the ultrasound image by setting the direction of the edge detection and the edge gray threshold.

2.5. VAS Evaluation Criteria. VAS is used for pain assessment and is widely used in clinical practice. The basic method is to use a moving ruler about 10 cm long with 10 scales on one side, and the two ends are "0" and "10" points, respectively. 0 points mean no pain, and 10 points mean the most severe pain that is unbearable [17].

2.6. Statistical Methods. The data processing in this study was analyzed by SPSS 19.0 version statistical software, some

-1	0	+1
-2	0	+2
-1	0	+1

(a)

+1	+2	+1
0	0	0
-1	-2	-1

(b)

FIGURE 2: The template of the Soble operator. (a)G_x; (b)G_y.

1	0	-1
1	0	-1
1	0	-1

(a)

1	1	1
0	0	0
-1	-1	-1

(b)

FIGURE 3: Template of Prewitt operator. (a) The Prewitt operator template Mx; (b) the Prewitt operator template My.

measurement data were expressed by the mean ± standard deviation ($\overline{x} \pm s$), and the count data were expressed by the percentage (%). Pairwise comparison used analysis of variance. $P < 0.05$ indicated that the difference was significant.

3. Results

3.1. Lung Ultrasound Signs. Figure 4 shows the ultrasound signs of the lungs. In a normal lung ultrasound image, a hyperechoic line that slid back and forth with breathing motion was seen on the deep surface of the rib line, which was called the "pleural line." When the ultrasound was projected perpendicularly to the pleura-lung surface, reverberation artifacts may appear, which were manifested as multiple echoes arranged at equal distances. Its intensity decreased successively, called "A line," so the normal lung ultrasound image features were "slip sign" and "A line."

3.2. Signal-to-Noise Ratio of the Output Image. The signal-to-noise ratio of the filtered image can represent the denoising effect of the algorithm on the image with noise. Figures 5 and 6 show the signal-to-noise ratio (SNR) of the output image processed by different filters under Gaussian noise 10% and speckle noise 90% and Gaussian noise 30% and speckle noise 70% of the noise mixed conditions, respectively. Under different mixed noise conditions and signal-to-noise ratio conditions, the edge detection algorithm can still better maintain the edge information of the output image, and the image enhancement effect was ideal.

3.3. Lung Ultrasound Edge Detection. Figure 7 shows the ultrasound images of the lung and the image after image enhancement and noise processing were performed by the edge detection algorithms of the Canny operator, Prewitt operator, and Soble operator. The improved filter of the edge detection algorithm can not only maintain the original texture details and edge information of the input and output images in the image processing process but also process and suppress the noise pollution of the background of the image and the internal noise of the organization to a higher degree. Moreover, the Soble operator had better edge detection performance than the Prewitt operator and Canny operator in the same period and had better edge information detection and denoising performance for ultrasound images.

3.4. Detection Rate of Lung Nodules by Three Edge Detection Operators. Figure 8 shows the comparison results of the detection rates of lung nodules of different sizes after the Canny operator, Prewitt operator, and Soble operator edge

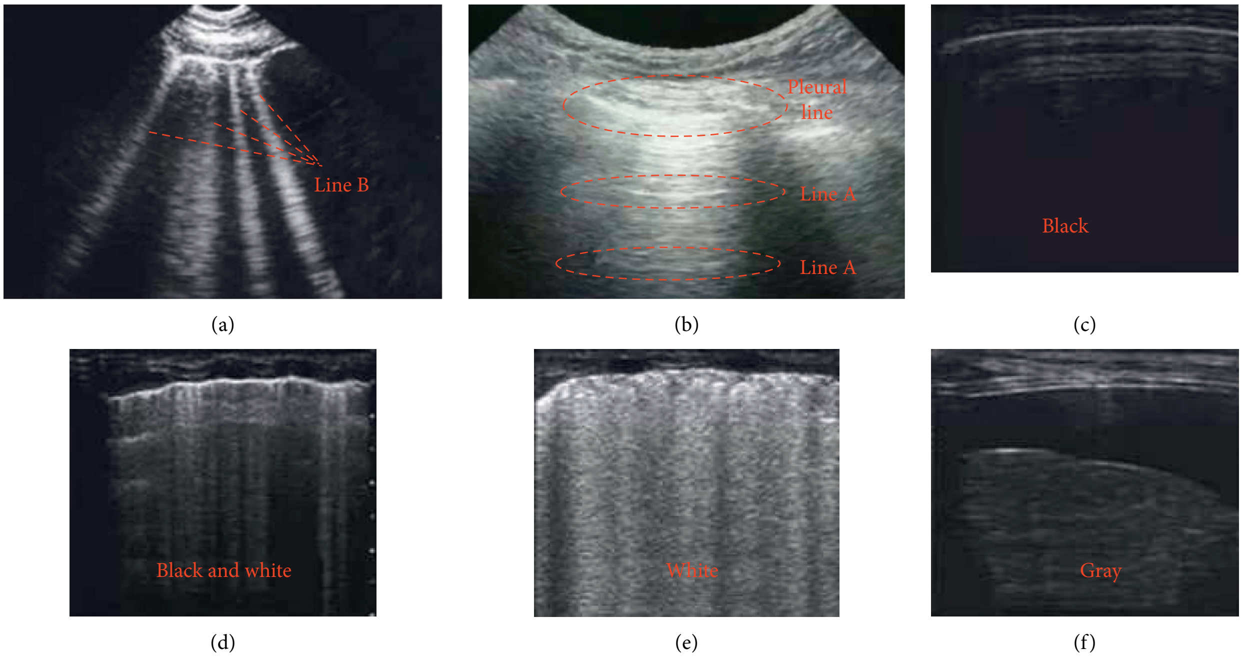

FIGURE 4: Ultrasound signs of the lungs. (a) A line; (b) B line; (c) normal; (d) mild-to-moderate interstitial edema; (e) severe interstitial edema and alveolar edema; (f) lung consolidation.

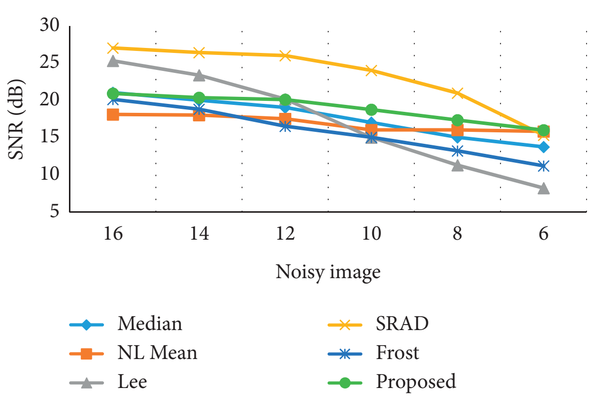

FIGURE 5: Signal-to-noise ratio of the output image of the edge detection filter (Gaussian noise 10%; speckle noise 90%).

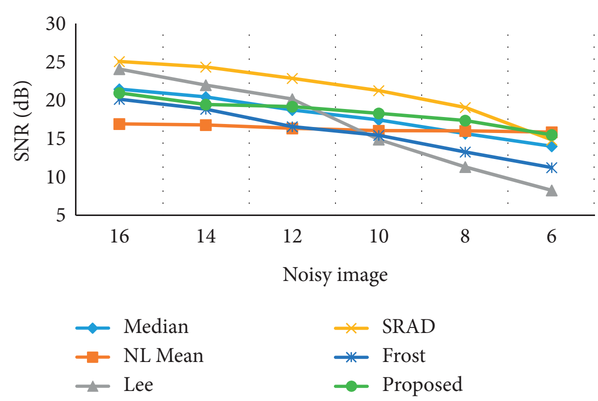

FIGURE 6: Signal-to-noise ratio of the output image of the edge detection filter (Gaussian noise 30%; speckle noise 70%).

detection algorithms processed lung ultrasound images. For lung nodules smaller than 6 mm, the detection rates of the three edge detection operators were 90.98%, 87.53%, and 92.35%, respectively. For lung nodules from 6 to 30 mm, the detection rates of the three edge detection operators were 88.32%, 90.87%, and 95.44%, respectively. The detection rate of the Soble operator for lung nodules of different sizes was significantly higher than that of the Canny operator and Prewitt operator edge detection algorithm ($P < 0.05$).

3.5. VAS Score after the Patient's Operation. Figure 9 shows the visual analog score (VAS) of patients in different periods after thoracoscopic lobectomy. Figure 9(a) shows the VAS score result in the resting state, and Figure 9(b) shows the VAS score result in the patient's exercise state. After edaravone was used for induction of anesthesia and lobectomy after erector spinae plane block, the patient's VAS score decreased with the prolongation of postoperative time. After five days, the patient's VAS score was reduced to a lower level.

4. Discussion

Edge detection of medical image is an important basis for image segmentation, object recognition, region shape extraction, and other image processing fields. In the process of image understanding and analysis, the first step is often edge detection to identify the points with obvious brightness changes in digital images [18]. The so-called edge refers to the set of pixels with sharp changes in the gray level of the surrounding pixels, which is the basic feature of the image. Edge exists between target, background, and region, which is

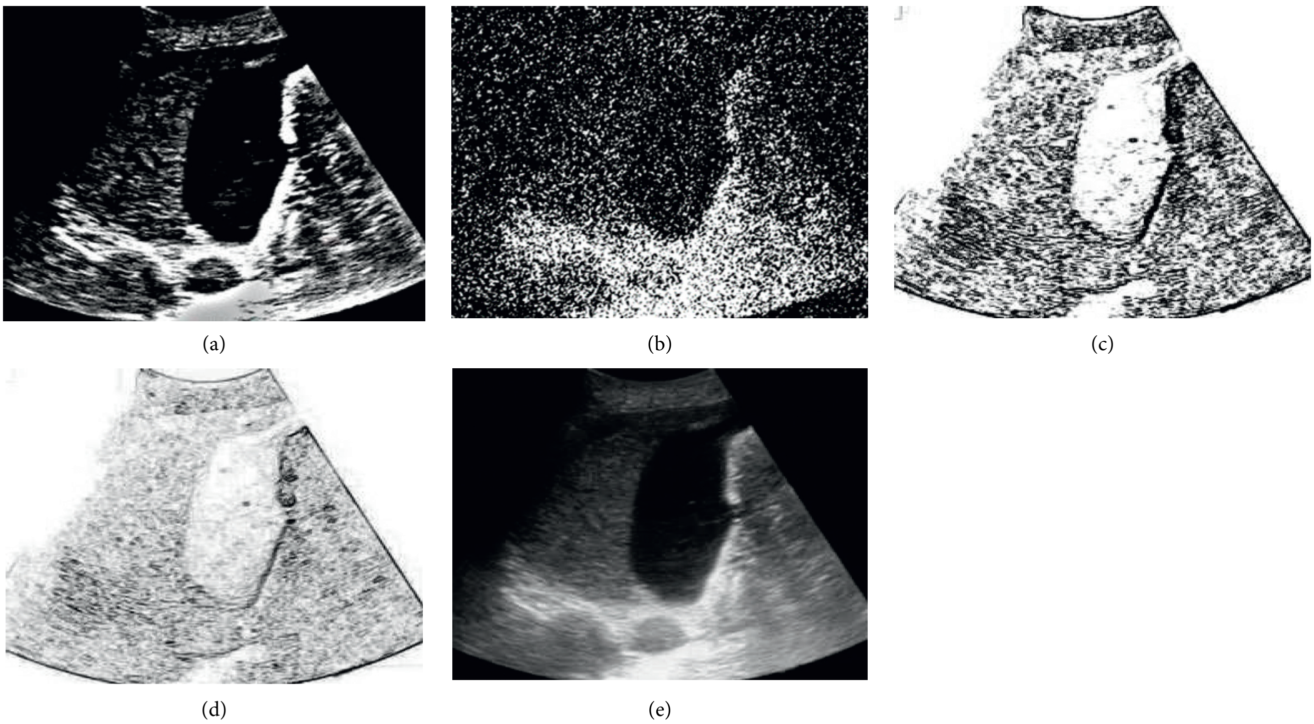

Figure 7: Ultrasonic edge detection of lungs. (a) The original image; (b) the image contaminated by noise; (c–e) edge detection and image processing of Canny operator, Prewitt operator, and Soble operator, respectively.

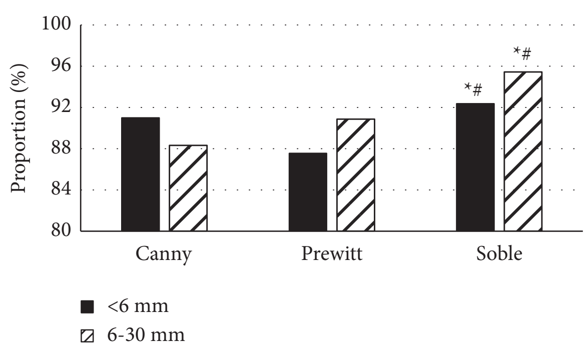

Figure 8: Detection rate of lung nodules by three edge detection operators. Note: * means significant difference compared to Canny operator ($P < 0.05$); # means significant difference compared to Prewitt operator ($P < 0.05$).

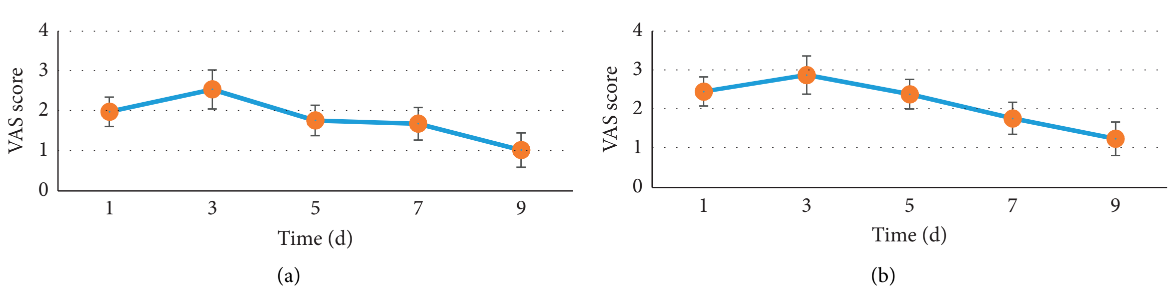

Figure 9: Postoperative VAS score of patients. (a) The VAS score in the resting state; (b) the VAS score in the exercise state.

the most important basis for image segmentation. As an indicator of position, edge is insensitive to changes in gray level, so it is an important feature of image matching [19]. Image edge contains the useful information used for identification in the image, which greatly reduces the amount of data, eliminates the irrelevant information, and retains the important structural attributes of the image. The use of edge detection technology for visual detection has become the latest trend in image sensor adoptions. In addition, as edge detection plays an important role in image analysis such as computer vision and ultrasound, it provides valuable feature parameters for people to describe or identify objects and to interpret images. Cao et al. [20] found that ultrasound-guided erector spinae plane block technology had the advantages of simple operation and high safety factor. In addition, ultrasound-guided erector spinae plane block lobectomy was performed with high recognition of intermuscular images and no risk of spinal cord injury compared with other blocking methods. Erector spinae plane block has a long duration of action and a wide range of action. To a certain extent, it can effectively shorten the hospital stay of patients undergoing lobectomy and accelerate the postoperative recovery speed, which has a high adoption value.

In this study, patients undergoing laparoscopic lobectomy were selected as subjects, and lung ultrasound examination was performed on the included patients. The ultrasonic image was filtered, enhanced, and denoised by IoT edge detection algorithm. Ultrasound images were processed and used in erector spinae plane block combined with edaravone anesthesia-induced lobectomy. It was found that, under different mixed noise conditions and SNR conditions, the edge detection algorithm can still maintain the edge information of the output image well and the image enhancement effect was good. The Soble operator had better edge detection performance than the Prewitt operator and Canny operator at the same period and had better edge information detection performance for ultrasonic images. Edge detection and filtering had a good effect on noise removal of ultrasonic images. The detection rate of the Soble operator for pulmonary nodules of different sizes was significantly higher than that of the Canny operator and Prewitt operator ($P < 0.05$). VAS scores decreased with postoperative time after edaravone anesthesia induction and erector spinae plane block lobectomy. After five days, the VAS score of the patients was reduced to a low level. The results of this study were in line with expectations. A number of previous studies have shown that erector spinal muscle plane block combined with edaravone has a positive sedative and analgesic effect on patients undergoing thoracoscopic lobectomy. Ultrasound images based on IoT edge computing algorithm are more accurate in the identification of lung lesions. This was similar to the results of Williams et al. [21], indicating that erector spinae plane block combined with edaravone anesthesia induction had good sedative and analgesic effects on patients undergoing thoracoscopic lobectomy, which also improved the prognosis of patients.

5. Conclusion

In this study, three edge detection algorithm models were constructed and applied in the ultrasound images of 110 patients with lung disease. The results found that the erector spinal muscle plane block combined with edaravone had a better sedative and analgesic effect on patients undergoing thoracoscopic lobectomy. The ultrasound image based on the IoT edge computing algorithm showed higher accuracy in identifying lung lesions, and it was worth applying to clinical diagnosis. The disadvantage was that it lacked comparison with other intelligent algorithms, and the representativeness was low. Therefore, in subsequent experiments, an improvement and optimization would be made in this area, and more in-depth exploration of this direction would be carried out. In summary, this study provided a reference for the application of intelligent algorithms such as edge detection in medical imaging.

Data Availability

The data used to support the findings of this study are available from the corresponding author upon request.

Conflicts of Interest

The authors declare no conflicts of interest.

References

[1] R. M. Reddy, M. L. Gorrepati, D. S. Oh, S. Mehendale, and M. F. Reed, "Robotic-assisted versus thoracoscopic lobectomy outcomes from high-volume thoracic surgeons," *Ann Thorac Surg*, vol. 106, no. 3, pp. 902–908, 2018, Epub 2018 Apr 25. PMID: 29704479.

[2] Z. Wan, Y. Dong, Z. Yu, H. Lv, and Z. Lv, "Semi-supervised support vector machine for digital twins based brain image fusion," *Frontiers in Neuroscience*, vol. 15, 2021 PMID: 34305523, Article ID 705323.

[3] D. S. Oh, R. M. Reddy, M. L. Gorrepati, S. Mehendale, and M. F. Reed, "Robotic-assisted, video-assisted thoracoscopic and open lobectomy: propensity-matched analysis of recent premier data," *Ann Thorac Surg*, vol. 104, no. 5, pp. 1733–1740, 2017, PMID: 29054214.

[4] Y. Zheng, Y. Zhou, H. Zhou, and X. Gong, "Ultrasound image edge detection based on a novel multiplicative gradient and Canny operator," *Ultrasonic Imaging*, vol. 37, no. 3, pp. 238–250, 2015, PMID: 25315657.

[5] C. Lee, A. Zhang, B. Yu, and S. Park, "Comparison study between RMS and edge detection image processing algorithms for a pulsed laser UWPI (ultrasonic wave propagation imaging)-based NDT technique," *Sensors*, vol. 17, no. 6, p. 1224, 2017.

[6] Y. Li, J. L. Zhao, Z. H. Lv, and J. H. Li, "Medical image fusion method by deep learning," *International Journal of Cognitive Computing in Engineering*, vol. 2, pp. 21–29, 2021.

[7] D. Shao, Y. Yuan, Y. Xiang, Z. Yu, P. Liu, and D. C. Liu, "Artifacts detection-based adaptive filtering to noise reduction of strain imaging," *Ultrasonics*, vol. 98, pp. 99–107, 2019, Epub 2019 May 23. PMID: 31238255.

[8] H. Du, R. Ma, X. Wang, J. Zhang, and J. Fang, "Bas-relief map using texture analysis with application to live enhancement of ultrasound images," *Ultrasound in Medicine and Biology*, vol. 41, no. 5, pp. 1446–1460, 2015, Epub 2015 Jan 29. PMID: 25641600.

[9] Z. Zhang, Z. Luo, A. Bi et al., "Compound edaravone alleviates lipopolysaccharide (LPS)-induced acute lung injury in mice," *European Journal of Pharmacology*, vol. 811, pp. 1–11, 2017, Epub 2017 May 25. PMID: 28552343.

[10] S. Tulgar, M. E. Aydin, A. Ahiskalioglu, A. De Cassai, and Y. Gurkan, "Anesthetic techniques: focus on lumbar erector spinae plane block," *Local and Regional Anesthesia*, vol. 13, pp. 121–133, 2020, PMID: 33061562; PMCID: PMC7532310.
[11] Z. H. Lv, H. Yang, A. K. Singh, G. Manogaran, and H. B. Lv, "Trustworthiness in industrial IoT systems based on artificial intelligence," *IEEE Transactions on Industrial Informatics*, vol. 17, no. 99, p. 1, 2020.
[12] C. Menna, M. Ibrahim, E. A. Rendina, F. Venuta, and C. Andreetti, "Cost/efficacy evaluation of the technologies applied to video-assisted thoracoscopic surgery lobectomy," *The Journal of Visualized Surgery*, vol. 3, p. 152, 2017 PMID: 29302428.
[13] J. E. Scott, A. Singh, J. B. Case, P. D. Mayhew, and J. J. Runge, "Determination of optimal location for thoracoscopic-assisted pulmonary surgery for lung lobectomy in cats," *American Journal of Veterinary Research*, vol. 80, no. 11, pp. 1050–1054, 2019.
[14] X. Yang, L. Wang, C. Zhang, D. Zhao, Y. Lu, and Z. Wang, "The feasibility and advantages of subxiphoid uniportal video-assisted thoracoscopic surgery in pulmonary lobectomy," *World Journal of Surgery*, vol. 43, no. 7, pp. 1841–1849, 2019, PMID.
[15] J. L. Tang, Y. Wang, C. R. Huang, H. Liu, and N. Al-Nabhan, "Image edge detection based on singular value feature vector and gradient operator," *Mathematical Biosciences and Engineering*, vol. 17, no. 4, pp. 3721–3735, 2020.
[16] J. H. Woo, Y. J. Kim, K. C. Kim, C. H. Kim, and J. Jun, "The effect of interscalene block on ipsilateral shoulder pain and pulmonary function in patients undergoing lung lobectomy: a randomized controlled trial," *Medicine (Baltimore)*, vol. 97, no. 24, PMID: 29901598, Article ID e11034, 2018.
[17] T. S. Shafshak and R. Elnemr, "The visual analogue scale versus numerical rating scale in measuring pain severity and predicting disability in low back pain," *Journal of Clinical Rheumatology*, vol. 27, no. 7, pp. 282–285, 2021, PMID: 31985722.
[18] A. Azeroual and K. Afdel, "Fast image edge detection based on faber schauder wavelet and otsu threshold," *Heliyon*, vol. 3, no. 12, PMID: 29387817, Article ID e00485, 2018.
[19] Y. Pan, T. Zhou, and Y. Xia, "Bacterial foraging based edge detection for cell image segmentation," *Annu Int Conf IEEE Eng Med Biol Soc*, vol. 2015, pp. 3873–3876, 2015, PMID: 26737139.
[20] J. Cao, L. Chen, M. Wang, and Y. Tian, "Implementing a parallel image edge detection algorithm based on the otsu-canny operator on the hadoop platform," *Computational Intelligence and Neuroscience*, vol. 2018, 2018 PMID: 29861711, Article ID 3598284.
[21] A. M. Williams, L. Zhao, T. R. Grenda et al., "Higher long-term quality of life metrics after VATS lobectomy compared to robotic-assisted lobectomy," *Ann Thorac Surg*, vol. 19, no. 20, pp. S0003–S4975, 2020, Epub ahead of print. PMID: 32599037.

Hindawi
Journal of Healthcare Engineering
Volume 2021, Article ID 3631208, 12 pages
https://doi.org/10.1155/2021/3631208

Research Article

OS-LALM-OGM Algorithm-Based Computed Tomography Image for Characteristics and Comorbidities of Patients before Transcatheter Aortic Valve Implantation

Wenjie Sun,[1] **Jin He**,[2] **Xianzhen Tan**,[1] **Yi Wang**,[3] **Fei Chen**,[4] **Dan Xu**,[1] **and An Xie**[1]

[1]*Department of Radiology, Hunan Provincial People's Hospital, First Affiliated Hospital of Hunan Normal University, Changsha 410002, Hunan, China*
[2]*Department of Cardiology, Hunan Provincial People's Hospital, First Affiliated Hospital of Hunan Normal University, Changsha 410002, Hunan, China*
[3]*Department of General Surgery, Hunan Provincial People's Hospital, First Affiliated Hospital of Hunan Normal University, Changsha 410002, Hunan, China*
[4]*Department of Cardio-Thoracic Surgery, Hunan Provincial People's Hospital, First Affiliated Hospital of Hunan Normal University, Changsha 410002, Hunan, China*

Correspondence should be addressed to An Xie; 1502024342@st.nuc.edu.cn

Received 22 August 2021; Revised 26 September 2021; Accepted 27 September 2021; Published 11 November 2021

Academic Editor: Enas Abdulhay

Based on the ordered subsets (OS), a linear augmentation Lagrangian method (OS-LALM) was constructed, which was then combined with the optimized gradient method (OGM) to construct the OS-LALM-OGM, so as to discuss application of the computed tomography (CT) images based on OS-LALM-OGM in evaluation of clinical manifestations and complications of patients before transcatheter aortic valve implantation (TAVI). The OS-LALM-OGM was compared with the filtered back projection (FBP) and OS-LALM. In addition, it was applied to evaluate the conditions of 128 patients before TAVI. It was found that the peak signal-to-noise ratio (PSNR) of OS-LALM-OGM was greater than that of the FBP and OS-LALM when the number of iterations was 5, 20, and 40, while the root mean square error (RMSD) was the opposite ($P < 0.05$). The proportion of dyspnea was the highest, 38.28%, followed by angina (19.53%) and fainting (21.09%). The long diameter of the annulus and the average inner diameter of the annulus measured by the CT image based on the OS-LALM-OGM algorithm were greatly larger than the inner diameter of the aortic annulus measured by the CT based on the FBP algorithm ($P < 0.05$); the evaluation sensitivity (95.24%) and specificity (85.85%) of CT based on the OS-LALM-OGM algorithm were obviously greater than those of X-ray, which were 84.43% and 76.77%, respectively ($P < 0.05$). In short, the OS-LALM-OGM proposed had a relatively excellent effect on CT image reconstruction. The CT image based on the OS-LALM-OGM algorithm showed a better evaluation performance for patients before TAVI than the traditional FBP algorithm, showing higher sensitivity and specificity.

1. Introduction

The aortic valve is a "valve" located between the left ventricle and the aorta. When the ventricles contract, the aortic valve opens and blood flows into the aorta. Aortic valve stenosis refers to the abnormality of the aortic valve structure or function caused by rheumatic fever, congenital malformations, and valve calcification, which causes restricted aortic valve opening and causes left ventricular ejection disorders [1, 2]. The disease progresses slowly, and there may be no obvious symptoms for a long time. As the disease worsens, symptoms such as angina and dizziness may appear [3]. If aortic valve stenosis cannot be treated in time, it can also lead to complications such as heart failure, arrhythmia, congestive heart failure, infective endocarditis, systemic embolism, and gastrointestinal bleeding [4]. TAVI is an interventional therapy that has emerged in recent years to treat aortic valve stenosis. It can deliver an interventional catheter through the femoral artery to deliver the artificial heart valve to the aortic valve. The area is opened to complete the implantation of the artificial valve and restore the valve function. This operation does not require thoracotomy and has the advantages of less trauma to the patient and quick recovery after surgery [5, 6]. The current clinical preoperative evaluation of TAVI patients includes clinical and aortic root anatomical indication evaluation. Imaging examinations can be used to assess the aortic root morphology and anatomical adjacency, locate the aortic valve annulus, and help doctors select patients for surgery.

CT mainly uses precisely collimated X-ray beams, gamma rays, and ultrasound together with extremely sensitive detectors to scan a certain part of the human body one by one, with fast scanning time, clear image, and other characteristics [7, 8]. The clinical use of CT will use high radiation doses to obtain high-quality images with higher resolution and better display effects, but high radiation can cause damage to the patient's body, causing cancer, gene mutations, leukemia, and other diseases [9]. Therefore, how to use the obtained noise image and incomplete projection data to reconstruct a higher-quality CT image is a hot topic for current scholars. OS is a method that uses only a subset of observation data to perform gradient calculations. Momentum terms can be introduced to speed up the convergence of the algorithm and improve system performance [10]. Gradient algorithm is a kind of momentum technology, which can solve large-scale optimization, including signal and image processing, machine learning, and communication. LALM is generally used to solve compound convex optimization, but it has the disadvantages of difficult reference selection and slow convergence [11, 12]. Therefore, the OS was adopted to optimize the LALM and then combined the OGM to construct a CT image reconstruction algorithm, so as to provide help for patient evaluation before TAVI.

In summary, CT imaging has a wide range of applications in the field of medical screening, but there are also some urgent problems to be solved. Based on this, the ordered subset (OS) was adopted to optimize the linear augmentation Lagrangian iterative algorithm into OS-LALM, which was then combined with the optimized gradient method (OGM) to construct the OS-LALM-OGM. The OS-LALM-OGM was compared with the filtered back projection (FBP) and OS-LALM and applied to evaluate the 128 patients before TAVI. The application of CT images in the evaluation of clinical manifestations and complications of patients before TAVI was comprehensively evaluated, so as to provide a good theoretical basis for imaging detection of patients before TAVI.

2. Materials and Methods

2.1. Research Objects. 128 high-risk patients with severe aortic valve stenosis who were admitted to the hospital from May 2018 to March 5, 2021, were selected as the research objects, including 91 males and 59 females, aged 60–90 years old. The study had been approved by the Ethics Committee of Hospital, and the patients and their families had understood the situation of the study and signed the informed consent forms.

The inclusion criteria were defined as follows: patients with area of arterial valve less than 0.8 cm2, patients with transvalvular pressure difference of aortic valve greater than 40 mmHg, and patients with surgical contraindications.

The exclusion criteria were defined as follows: patients with incomplete clinical data, patients with psychiatric diseases, patients with transvalvular peak flow rate less than 4 m/s, and patients who withdrew from the experiment due to personal reasons.

2.2. CT Examination. In this study, the third-generation 192-slice force dual-source spiral CT scanner produced by Siemens (Germany) was used for retrospective ECG-gated coronary scans and large-pitch total aortic scans. The contrast agent was 370 mgI/mL iopromide. The contrast agent and saline were injected into the vein sequentially, and then the dynamic continuous same-layer monitoring scan was performed. The monitoring level was 1 cm below the tracheal bifurcation. The region of interest (ROI) was selected in the ascending aorta for CT value monitoring, and the scan was automatically triggered when the 100 HU threshold was reached. The scanning range was defined as follows: the aortic root scan covered the entire heart, and the full aortic scan extended from the entrance of the thorax to the lesser trochanter of the femur. The scanning parameters were as follows: the matrix was 512×512, the tube voltage was 110 kV, the tube current was 60 mAs, the CARE Dose4D automatic current was used, the layer spacing was 0.75 mm, and the layer thickness was 0.75 mm. The original images obtained were sent to the workstation for image reconstruction processing, and two senior physicians were selected for evaluation. The ALD and the annulus short diameter (ASD) of annulus were recorded, and the calculated averages of ALD and ASD can represent the AID of annulus. The diameters of the sinus and sinus tube junction, the diameter of the ascending aorta, and the height of the coronary artery opening were measured and recorded.

2.3. Construction of OS-LALM-OGM. Firstly, the CT image was set to the following model:

$$y = Mx + \theta. \tag{1}$$

In equation (1), y represents the measurement data, M represents the forward projection operator, x represents the image to be reconstructed, and θ referrs to the noise. The penalty weighted least squares (PLWS) were incorporated to reconstruct image x; then, the following equation could be obtained:

$$\overline{\overline{x}} = \arg\min_{x \geq 0} \left\{ \varphi(x) \triangleq \frac{\|\overline{\overline{y}} - Nx\|_P^2 + Q(x)}{2} \right\}. \tag{2}$$

In the above equation, N represents the system matrix, $\overline{\overline{y}}$ represents the sine graph with noise, P refers to the statistical weight matrix, and Q means the regular term retaining the edges. Then, the edge preservation regularization function can be expressed as follows:

$$Q(x) \triangleq \sum_i \lambda_i \sum_n u_r u_{r+e_i} \eta_i [(B_i x)_r]. \quad (3)$$

In equation (3), λ_i, e_i, and η_i refer to the regularization parameter, the corresponding offset, and the potential function, respectively; B_i is the finite difference matrix in the ith direction, and u_r represents the voxel-related weight. The following equation could be obtained by converting it into a compound convex optimization:

$$(\overline{\overline{x}}, \overline{\overline{t}}) \in \arg\min_{x,t} \{p(t) + q(x)\}. \quad (4)$$

In the above equation, $p()$ and $q()$ are convex functions, p represents the weighted quadratic data fitting term, and q represents the edge retention regularization term. Then, the LALM was incorporated [13] for solution; then the following equations could be obtained:

$$x^{(u+1)} \in \arg\min_x \left\{ q(x) + \vartheta_u(x) + \frac{\rho \left\| x - x^u \right\|_R^2}{2} \right\}, \quad (5)$$

$$k^{(u+1)} \in \arg\min_x \left\{ p(t) + \frac{\rho \left\| Mx^{(u+1)} - k - d^{(u)} \right\|_2^2}{2} \right\}, \quad (6)$$

$$d^{(u+1)} = d^{(u)} - Mx^{(u+1)} + t^{(u+1)}. \quad (7)$$

In equations (5)–(7), R represents the diagonal optimization matrix, $p()$ is set as a quadratic loss function, and ρ represents the penalty parameter; then the previous equation could be transformed into a least squares regularization matter as follows:

$$\overline{\overline{x}} = \arg\min_x \left\{ \varphi(x) \triangleq \frac{\rho \| y - Mx \|_2^2}{2} + q(x) \right\}. \quad (8)$$

If $T(x) \triangleq p(Mx)$ was defined as a quadratic data fitting term and can be accelerated by an OS, then the following could be obtained:

$$\Delta T(x) \approx W \Delta T_W(x). \quad (9)$$

In equation (9), W represents the number of quadratic functions and $\Delta T(x)$ represents the gradient of the subset. In consideration that that the near-end mapping of the quadratic function was linear, the update of k can have a closed solution, which was written as follows:

$$t^{(u+1)} = \frac{\rho \left(Mx^{(u+1)} - d^{(u)} \right) + y}{\rho + 1}. \quad (10)$$

The following equation could be obtained by combining equations (7) and (10):

$$t^{(u+1)} + \rho d^{(u+1)} = y. \quad (11)$$

Then, new equations could be found after d was initialized:

$$d_{(o)} = \frac{y - t_{(0)}}{\rho}, \quad (12)$$

$$\overline{\overline{t}} \triangleq t - y. \quad (13)$$

In equations (12) and (13), $\overline{\overline{t}}$ represents the split residual; then the initial LALM can be obtained:

$$\begin{aligned} e^{(u+1)} &= M' \left(\rho \left(Mx^{(u)} - y \right) + (1 - \rho) \overline{\overline{t}}^{(u)} \right), \\ x^{(u+1)} &\in \operatorname{prox}_{(l/\rho)q} \left(x^u - \left(\frac{l}{\rho} \right) r^{(u+1)} \right), \\ \overline{\overline{t}}^{(u+1)} &= \frac{\rho \left(Mx^{(u+1)} - y \right) + \overline{\overline{t}}^{(u)}}{\rho + 1}. \end{aligned} \quad (14)$$

Then, $p \triangleq M\imath(t)$ was set as the split gradient; it can be optimized as follows:

$$\begin{aligned} e^{(u+1)} &= \rho \Delta T\left(x^{(u)} \right) + (1 - \rho) p^{(u)}, \\ x^{(u+1)} &\in \operatorname{prox}_{(l/\rho)q} \left(x^u - \left(\frac{l}{\rho} \right) e^{(u+1)} \right), \\ p^{(u+1)} &= \frac{\rho \Delta T\left(x^{(u+1)} \right) + p^{(u)}}{\rho + 1}. \end{aligned} \quad (15)$$

The previous process was the OS-based LALM, which only needed the gradient of T to be updated to accelerate the ordered subset. However, there was still a problem with this algorithm; that is, the penalty parameter ρ value was not fixed. The deterministic downward continuation technique was applied to determine the optimal size of the parameter ρ value, so it could be written as follows:

$$\varpi(u) \triangleq \left(p^{(u)} - \Delta T\left(x^{(u+1)} \right) \right) \left(\Delta T\left(x^{(u+1)} \right) - \Delta T\left(x^{(u)} \right) \right). \quad (16)$$

It was assumed the iteration was restarted at the z^{th} iteration, and then the optimal penalty parameter ρ can be expressed as follows:

$$\rho_i = \begin{bmatrix} 1, & g = 0 \\ \max\left[\dfrac{\pi}{g+1}\sqrt{1-\left(\dfrac{\pi}{2g+2}\right)^2}, \rho_{\min}\right], & \text{otherwise} \end{bmatrix}. \tag{17}$$

In equation (17), g represents the number of iterations. This method can effectively solve the regularized least squares and simplify the selection of parameters through the deterministic downward continuation method based on the second-order damping system. However, it only used the current gradient to estimate the search direction will accumulate gradient errors, so that the reconstructed images were unstable. Based on this, the OGM was incorporated; then the CT image reconstruction can be expressed as follows:

$$\begin{cases} M \leftarrow E^{1/2} M \\ y \leftarrow E^{1/2} y \\ p \leftarrow Q + \kappa_\Omega \end{cases} \tag{18}$$

In equation (18), κ_Ω was the characteristic function of the convex set Ω. The above process was the constructed OS-LALM-OGM.

2.4. Design of Simulation Experiment. This experiment run on a real data platform. The operating environment was defined as follows: Virtual Box centos 6.6–32 bit system was installed, central processing unit (CPU) was AMD Athlon 2.99 GHz, memory was 1.75 GB, and the video resolution was 480 × 320. The (FBP) [14] and OS-LALM [15] were compared with the OS-LALM-OGM algorithm constructed. The number of OS was 40, and the PSNR and RMSD of the three algorithms under different function iteration times (5, 20, and 40) were recorded and compared:

$$\text{PSNR} = 10\log_{10}\frac{255 * 255}{\left[\sum_{i=1}^{A}\sum_{j=1}^{N}\left(x(i,j) - y(i,j)\right)^2 / A * C\right]}, \tag{19}$$

$$\text{RMSD} = \frac{\left\| x^{v} - \overleftarrow{x} \right\|}{\sqrt{O_\alpha}}. \tag{20}$$

In equations (19) and (20), $A * C$ represents the image size and x, y, and A refer to the original image, the noisy image, and the number of iterations, respectively. The larger the PSNR value meant the better the image reconstruction effect, and the smaller the RMSD value meant the better the image reconstruction effect.

2.5. Observation Indicators. The observation indicators included the clinical manifestations (angina, fainting, and dyspnea), complications (hypertension, diabetes, renal insufficiency, cerebrovascular disease, atrial flutter, and atrial fibrillation), CT image data, and the anatomical data of the aortic root of patients with bicuspid and tricuspid valve (ALD, ASD, AID, sinus inner diameter (SID), sinus junction inner diameter (SJID), ascending aorta inner diameter (AAID), left coronary opening height (LCOH), and the right coronary opening height (RCOH)) of the patients. In addition, the evaluation sensitivity and specificity of CTs under different algorithms were calculated, respectively.

2.6. Statistical Methods. The data processing was analyzed by SPSS19.0 version statistical software. The measurement data was indicated as mean ± standard deviation ($\overline{x} \pm s$), and the count data was displayed as percentage (%). The PSNR and RMSD of OS-LALM-OGM, FBP, and OS-LALM were compared in pairwise with single-factor analysis of variance. The difference was statistically significant at $P < 0.05$.

3. Results

3.1. Comparison on Image Reconstruction Effects of Three Algorithms. Figure 1 and 2 show the PSNR and RMSD comparisons of the three algorithms under different iteration times. The PSNR of the OS-LALM-OGM algorithm was much greater than that of the FBP and OS-LALM algorithms, and the differences was statistically obvious ($P < 0.05$), while the RMSD of the OS-LALM-OGM algorithm was smaller greatly than that of the FBP and OS-LALM algorithms, showing remarkable different in statistics ($P < 0.05$). In addition, the PSNR and RMSD of FBP and OS-LALM algorithms showed no statistical difference ($P > 0.05$).

3.2. Image of a Patient with Aortic Valve Stenosis. Figures 3–6 and Table 1 show the analysis of a patient with aortic valve stenosis. The diagnosis was a TYPE0 bicuspid valve, the leaflets were significantly thickened and severely calcified, the size of the French sinus was reasonable, the ascending aorta was slightly wider, the heart was horizontal, double crown height was normal, the left ventricle was small, and the myocardium was thickened, so it was determined as right femoral artery was clinically recommended as the main approach.

3.3. The Clinical Manifestations and Complications of Patients. Figure 7 illustrates the clinical manifestations of patients, in which 1 refers to angina, 2 refers to fainting, and 3 refers to dyspnea. It can be seen that there were 25 cases of angina in 128 patients, accounting for 19.53%, 27 cases of fainting (accounting for 21.09%), and 49 cases of dyspnea (accounting for 38.28%). Among them, the proportion of patients with dyspnea was much more than the proportions of patients with angina and fainting ($P < 0.05$).

Figure 8 illustrates the complications of patients, in which 1 indicates hypertension, 2 indicates diabetes, 3 refers

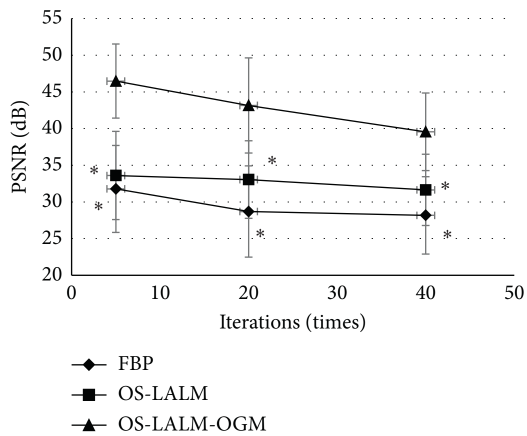

FIGURE 1: Comparison on PSNR of three algorithms under different iteration times. * indicates that the difference was remarkable in statistics in contrast to OS-LALM-OGM ($P < 0.05$).

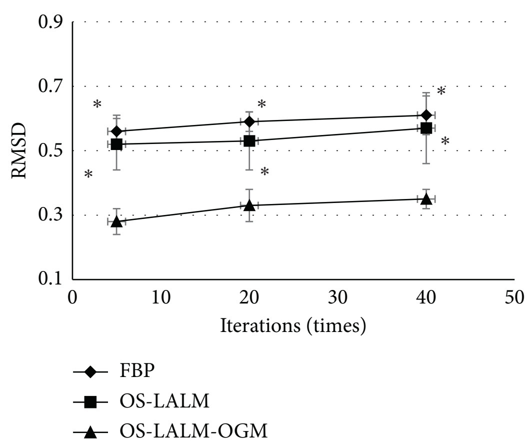

FIGURE 2: Comparison on RMSD of three algorithms under different iteration times. * indicates that the difference was remarkable in statistics in contrast to OS-LALM-OGM ($P < 0.05$).

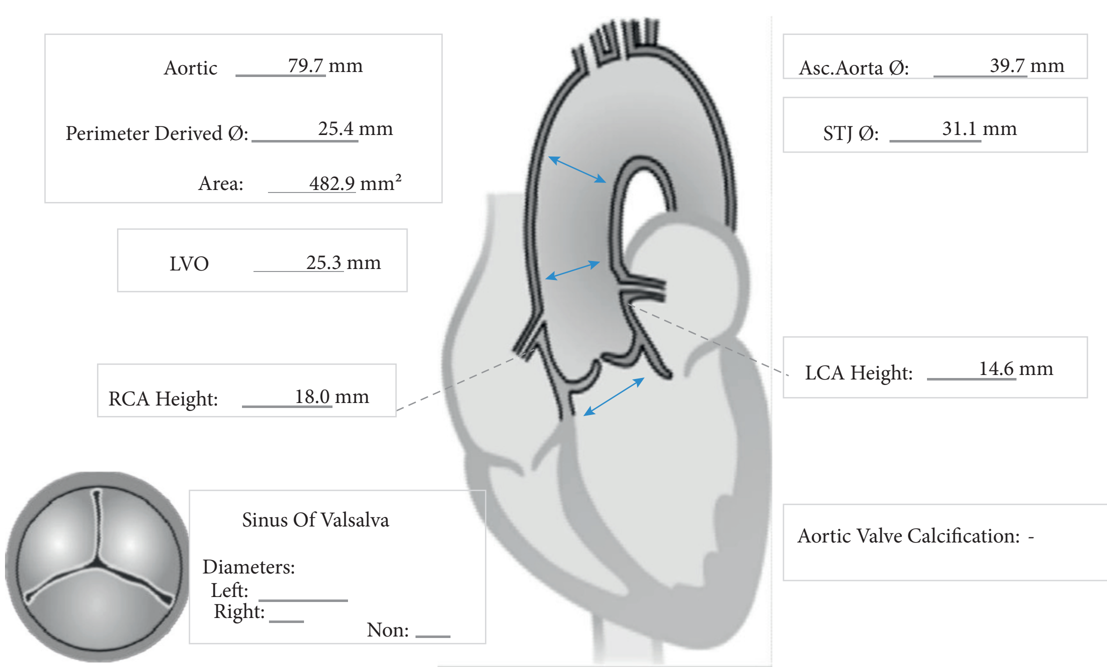

FIGURE 3: The aortic valve and measurement results of various indicators of patients.

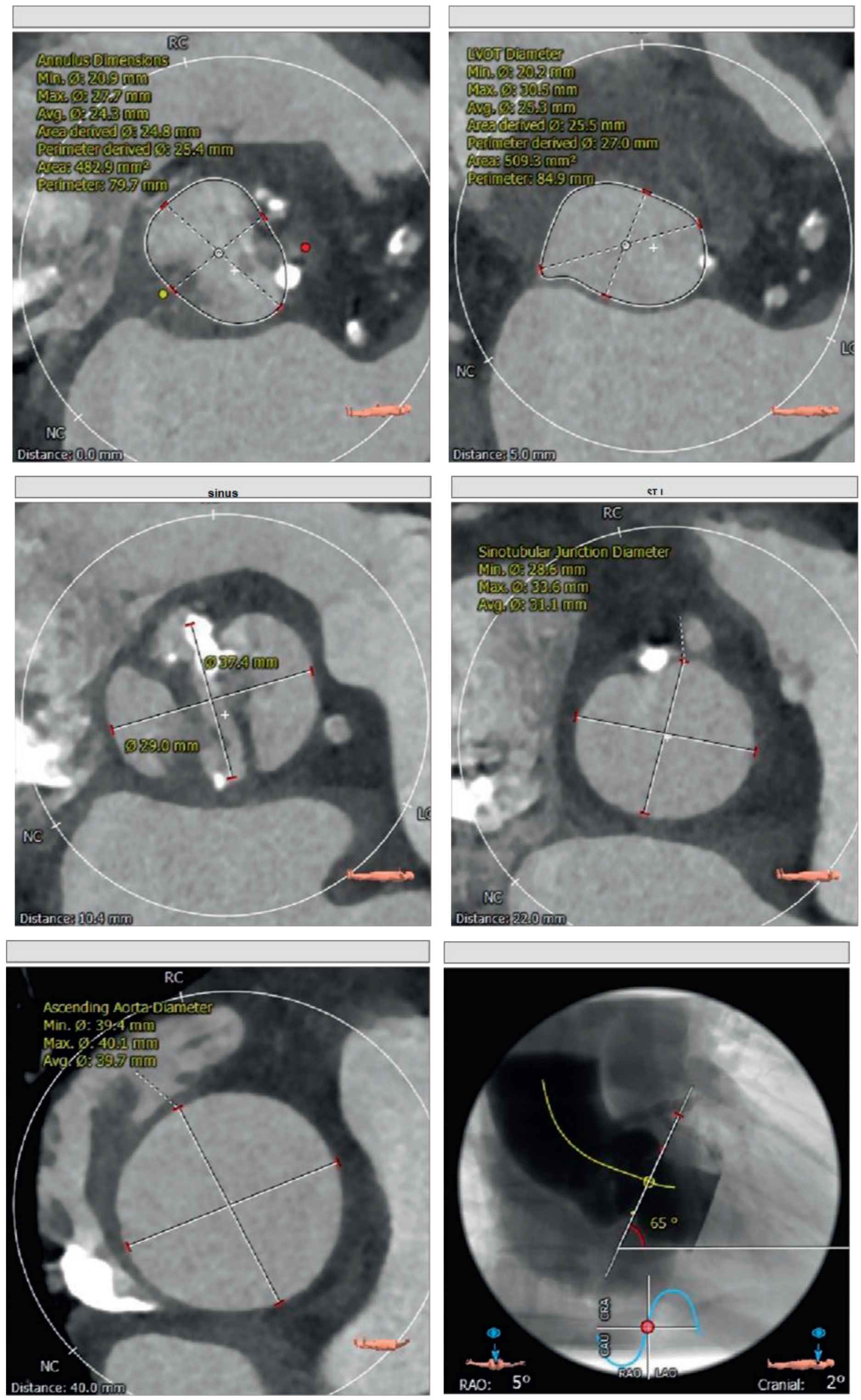

Figure 4: CT image and index measurement of patients.

to renal insufficiency, 4 refers to cerebrovascular disease, and 5 represents atrial flutter and atrial fibrillation. It revealed that 59 of 128 patients had hypertension (accounting for 46.1%), 26 had diabetes (accounting for 20.31%), 9 had renal insufficiency (accounting for 7.03%), 21 cases had cerebrovascular disease (accounting for 16.41%), and 19 cases had atrial flutter and atrial fibrillation (accounting for 14.84%). Thus, the proportion of patients with hypertension was much higher in contrast to that of patients with diabetes, renal insufficiency, cerebrovascular disease, and atrial flutter

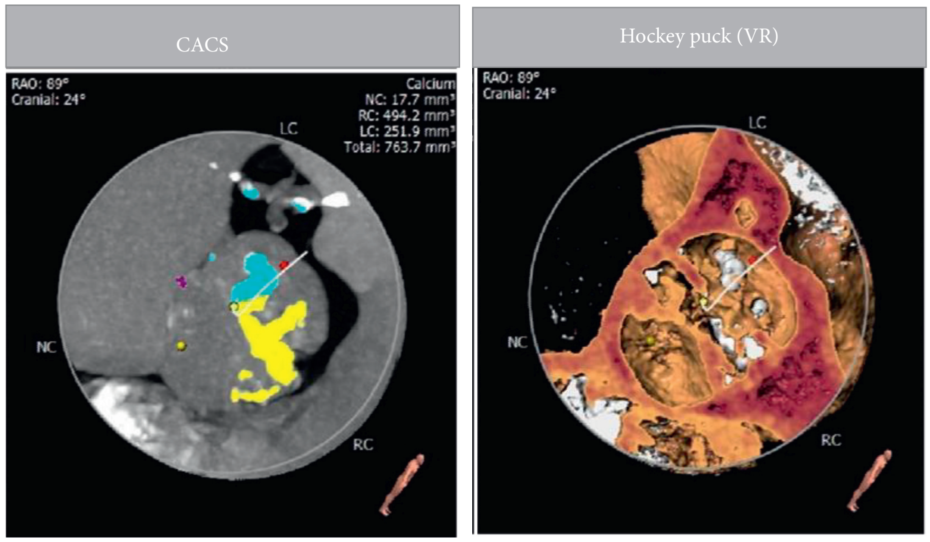

FIGURE 5: The coronary artery calcification score of patients.

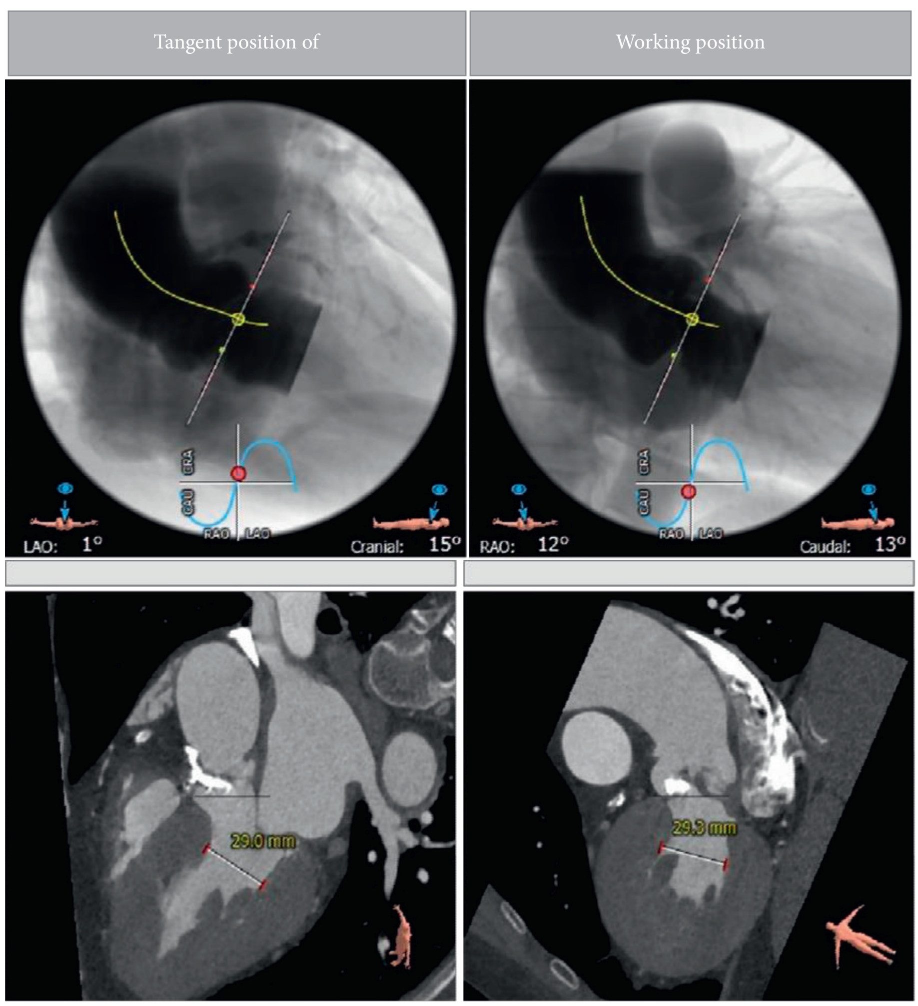

FIGURE 6: The angiographic position display (left coronary tangential position) of a patient.

Table 1: The maximum, minimum, and average values of each structure of the aortic valve.

Ascending aorta Ø	Min: 39.4 mm max: 40.1 mm average: 39.7 mm
Sinotubular junction Ø	Min: 28.6 mm max: 33.6 mm average: 31.1 mm
Aortic annulus	Min Ø: 20.9 mm max Ø: 27.7 mm average Ø: 24.3 mm eccentricity: 0.24
LVOT Ø	Min: 20.2 mm max: 30.5 mm average: 25.3 mm
Sinus of valsalva height	
Aortomitral continuity length	
Annulus to apex	

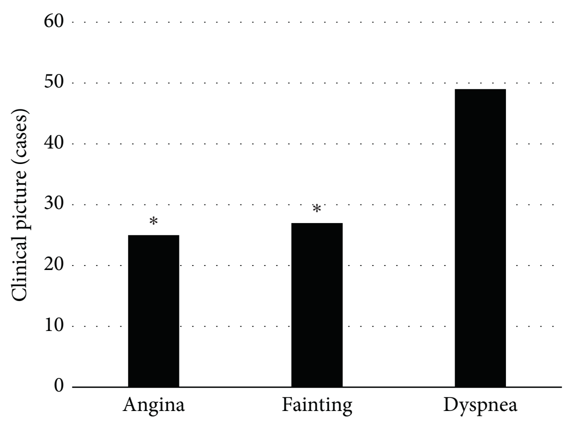

Figure 7: The clinical manifestations of patients. * suggests that the difference was obvious in statistics in contrast to dyspnea ($P < 0.05$).

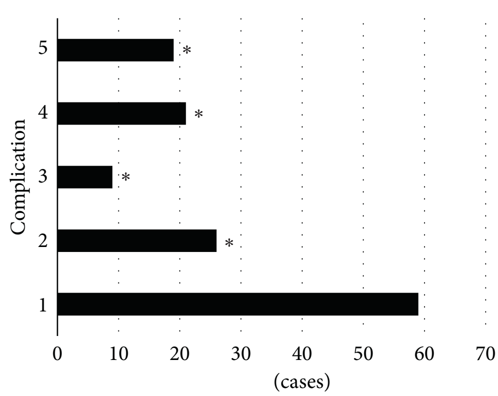

Figure 8: The complications of patients (1: hypertension; 2: diabetes; 3: renal insufficiency; 4: cerebrovascular disease; 5: atrial flutter and atrial fibrillation). * suggests that the difference was obvious in statistics in contrast to hypertension ($P < 0.05$).

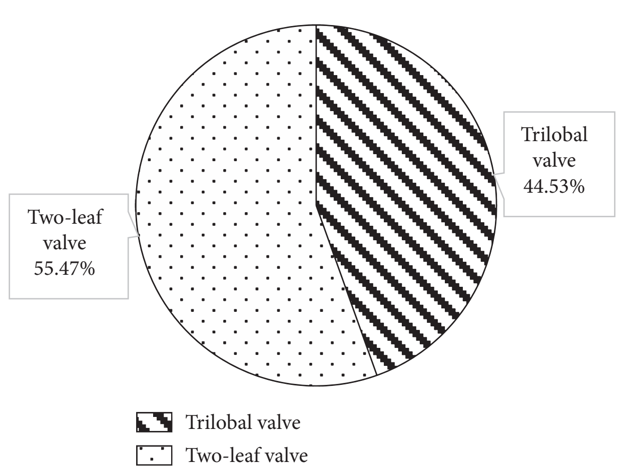

Figure 9: CT measurement results of the aortic root of the patient.

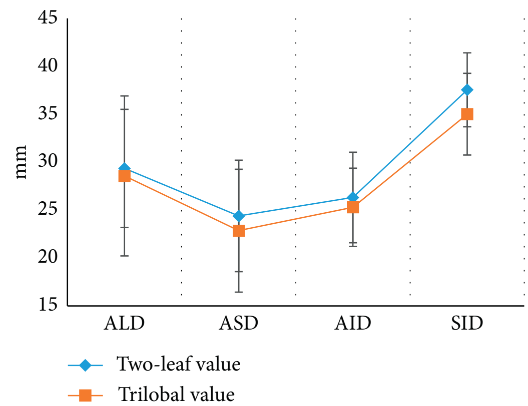

Figure 10: Comparison on ALD, ASD, AID, and SID of patients with bicuspid valves and trilobular valves.

and atrial fibrillation, showing observable and meaningful differences ($P < 0.05$).

3.4. CT Measurement Results of the Aortic Root of the Patient. Figure 9 shows the CT measurement results of the aortic root of the patient. It discloses that among the 128 patients, 71 were bicuspid valves (accounting for 55.47%) and 57 cases were trilobular valves (accounting for 44.53%).

3.5. The Anatomical Data of the Aortic Roots of Bicuspid Valves and Trilobular Valves of the Patients. The anatomical data of the aortic roots of the patient's bicuspid valves and trilobular valves were shown in Figures 10 and 11. It was clear that the ALD was 29.35 ± 6.17 mm, ASD was 24.38 ± 5.82 mm, AID was 26.31 ± 4.71 mm, SID was 37.55 ± 3.86 mm, SJID was 36.24 ± 5.11 mm, AAID was 41.49 ± 4.02 mm, LCOH was 17.46 ± 3.82 mm, and RCOH was 16.37 ± 3.51 mm for patients with bicuspid valves. The ALD, ASD, AID, SID, SJID, AAID, LCOH, and RCOH of patients with trilobular valves were 28.56 ± 8.34 mm, 22.86 ± 6.41 mm, 25.29 ± 4.08 mm, 35.01 ± 4.26 mm, 32.86 ± 4.27 mm, 38.35 ± 5.21 mm, 12.85 ± 4.24 mm, and 16.02 ± 4.05 mm. The data here indicated that the patients with bicuspid valve showed no great differences in ALD, ASD, AID, SID, SJID, AAID, and RCOH ($P > 0.05$) but great difference in LCOH ($P < 0.05$) in contrast to the patients with trilobular valves.

3.6. Comparison on CT Image of Aortic Valve Annulus Measurement Results Based on OS-LALM-OGM Algorithm and FBP Algorithm. Figure 12 shows a comparison of CT image aortic valve annulus measurement results based on OS-LALM-OGM algorithm and FBP algorithm. It could be observed that the annulus long diameter and the average inner diameter of the annulus measured by the CT image based on the OS-LALM-OGM algorithm were significantly larger than the aortic annulus inner diameter measured by the CT based on the FBP algorithm, and the difference was statistically obvious ($P < 0.05$), while the difference between the short diameter of the valve annulus and the inner diameter of the aortic annulus measured by CT based on the OS-LALM-OGM algorithm and the inner diameter of the aortic annulus measured by CT based on the FBP algorithm was not statistically observable ($P > 0.05$).

3.7. Comparison on the Evaluation Performance of CT Images for Patients Based on OS-LALM-OGM Algorithm and FBP Algorithm. Figures 13 and 14 show the comparisons on the evaluation performance of CT images based on OS-LALM-OGM algorithm and FBP algorithm for patients. The sensitivity and specificity of CT evaluation based on OS-LALM-OGM algorithm were 95.24% and 85.85%, respectively, and those for CT evaluation based on FBP algorithm were 84.43% and 76.77%, respectively. Thus, the sensitivity and specificity of CT evaluation based on OS-LALM-OGM algorithm were dramatically greater than those based on FBP algorithm, and the differences were statistically great ($P < 0.05$).

4. Discussion

The evaluation of preoperative clinical conditions and comorbidities of TAVI has always been an important reference for clinical judgment of surgical indications. The aortic valve annulus is the key to the parameters of the aortic root. Excessive aortic diameter can cause aortic root rupture and coronary ostia, while stenosis or too small aortic diameter can cause severe valve regurgitation. As a commonly used clinical examination method, CT also plays a crucial role in the evaluation of patients before TAVI [16]. Therefore, the LALM was optimized based on OS and then combined the OGM to construct the CT image reconstruction algorithm OS-LALM-OGM, which was applied in evaluation of 128 patients with severe aortic valve stenosis. Simulation experiments found that the PSNR of the OS-LALM-OGM algorithm was much greater in contrast to that of the FBP and OS-LALM algorithms, while the RMSD was much smaller, and the differences were statistically meaningful ($P < 0.05$). Such results were similar to Østergaard et al. [17], indicating that the OS-LALM-OGM algorithm proposed had a relatively excellent effect on CT image reconstruction, so it can be used as one of the algorithms that can effectively improve the quality of CT images in the future.

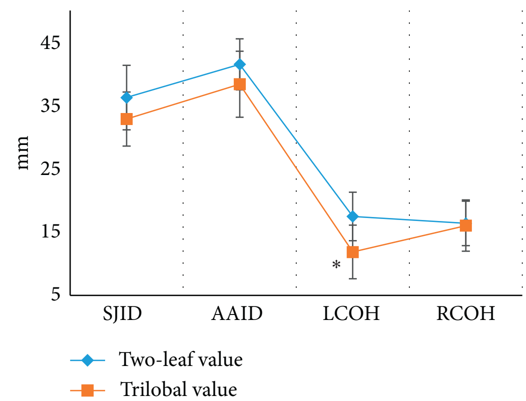

Figure 11: Comparison on SJID, AAID, LCOH, and RCOH of patients with bicuspid valves and trilobular valves. * indicates that obvious difference can be found in contrast to patients with bicuspid valves ($P < 0.05$).

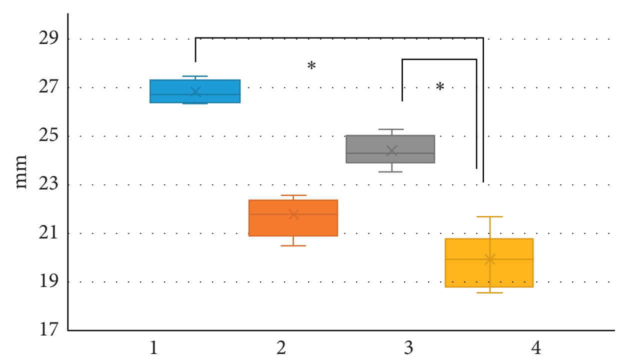

Figure 12: Comparison on CT image aortic annulus measurement results based on OS-LALM-OGM algorithm and FBP algorithm. *Note.* 1, 2, and 3 in the figure refers to the annulus long diameter, annulus short diameter, and average inner diameter of annulus measured by CT based on the OS-LALM-OGM algorithm, respectively, and 4 represents the inner diameter of the aortic annulus measured by CT based on the FBP algorithm. * indicates that visible difference could be found in contrast to 4 ($P < 0.05$).

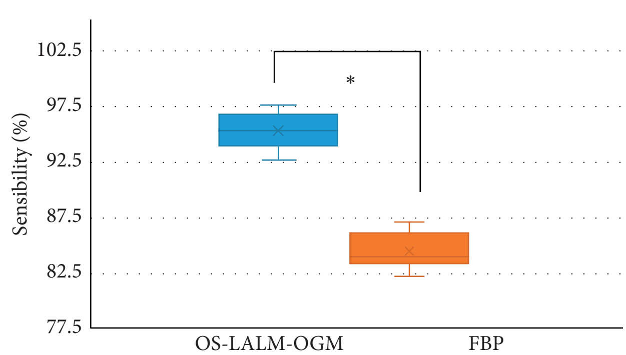

Figure 13: Comparison on the sensitivity of CT images to patients based on OS-LALM-OGM algorithm and FBP algorithm. * indicates that the different in contrast to CT results under FBP algorithm was meaningful in statistics ($P < 0.05$).

Of the 128 patients, 49 had dyspnea, accounting for the highest proportion (38.28%), followed by angina (19.53%) and fainting (21.09%). This suggested that CT and ultrasound screening should be performed as soon as possible for patients with related symptoms, so as to accurately diagnose the aortic valve stenosis. Among the 128 patients, 71 cases had bicuspid valves (accounting for 55.47%) and 57 cases had tricuspid valves (accounting for 44.53%). This indicated that the proportion of severe aortic valve stenosis caused by the bivalve deformity was higher, which may be due to the difficulty of intraoperative valve release caused by calcification of the valve leaflets and uneven leaflet force in patients with bicuspid valve, and the incidence of paravalvular leakage after release was higher than that of patients with tricuspid valve [18]. The height of the left coronary opening of the bicuspid valve was greater obviously than that of the

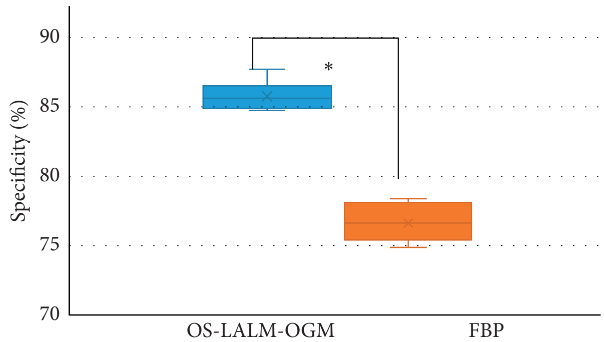

Figure 14: Comparison on the specificity of CT images to patients based on OS-LALM-OGM algorithm and FBP algorithm. * indicates that the different in contrast to CT results under FBP algorithm was meaningful in statistics ($P < 0.05$).

tricuspid valve ($P < 0.05$), which was different from the results of Singh et al. [19]. The reason of such difference may be that abnormal development of the left main stem may aggravate the degree of coronary artery obstruction during the operation, and the widening of the ascending aorta could lead to the occurrence of intraoperative dissection. The ALD and annulus AID of measured by CT image based on OS-LALM-OGM algorithm were significantly larger than the aortic annulus diameter measured by CT based on FBP algorithm, and the difference was statistically significant ($P < 0.05$), which may be due to the three-dimensional shape of the aortic root and the oval shape of aortic valve, and measuring the ALD and ASD separately could more closely reflect the actual inner diameter of the aortic annulus [20]. The sensitivity and specificity of CT evaluation based on the OS-LALM-OGM algorithm were significantly greater than those based on the FBP algorithm, and the differences were statistically significant ($P < 0.05$), which suggested that CT images based on the OS-LALM-OGM algorithm had better evaluation performance for patients before TAVI than CT based on the FBP.

5. Conclusion

Based on the OS, OS-LALM was constructed, which was then combined with the OGM to construct the OS-LALM-OGM. The OS-LALM-OGM was compared with the FBP and OS-LALM and applied to evaluate the 128 patients before TAVI. It was found that the OS-LALM-OGM algorithm proposed had a relatively excellent effect in CT image reconstruction. The CT image based on the OS-LALM-OGM algorithm showed better evaluation performance for patients before TAVI than the traditional FBP and OS-LALM algorithms, showing higher sensitivity and specificity. However, the sample size for the study was small, and there was a lack of relevant registration data for patients with severe aortic stenosis. In the future, the selection of patient samples will be increased to further explore the reconstruction effect of OS-LALM-OGM on CT images. In short, the results of this study could provide a good theoretical basis for imaging detection of patients before TAVI.

Data Availability

The data used to support the findings of this study are available from the corresponding author upon request.

Conflicts of Interest

The authors declare no conflicts of interest.

Acknowledgments

This work was supported by Scientific Research Project of Hunan Health Committee (no. B20200059), Clinical Medical Technology Innovation Guidance Project in Hunan Province (no. 2020SK50925), Youth Program of Hunan Natural Science Foundation (no. 2020JJ5306), and Class B Project of Hunan Health Committee (no. B2019071).

References

[1] N. Nalluri, V. Atti, A. B. Munir et al., "Valve in valve transcatheter aortic valve implantation (ViV-TAVI) versus redo-Surgical aortic valve replacement (redo-SAVR): a systematic review and meta-analysis," *Journal of Interventional Cardiology*, vol. 31, no. 5, pp. 661–671, 2018 Oct.

[2] A. B. Freitas-Ferraz, J. Rodés-Cabau, L. Junquera Vega et al., "Transesophageal echocardiography complications associated with interventional cardiology procedures," *American Heart Journal*, vol. 221, pp. 19–28, 2020 Mar.

[3] M. Soschynski, F. Capilli, P. Ruile, F.-J. Neumann, M. Langer, and T. Krauss, "Post-TAVI follow-up with MDCT of the valve prosthesis: technical application, regular findings and typical local post-interventional complications," *RöFo - Fortschritte auf dem Gebiet der Röntgenstrahlen und der bildgebenden Verfahren*, vol. 190, no. 06, pp. 521–530, 2018 Jun, English.

[4] R. L. Walas, L. Kukulski, J. Rychter et al., "Vascular access site complications after transfemoral transcatheter aortic valve implantation in the POL-TAVI Registry: surgical versus percutaneous approach," *The Journal of Cardiovascular Surgery*, vol. 61, no. 1, pp. 117–122, 2020 Feb.

[5] S. C. Vipparthy, V. Ravi, S. Avula et al., "Meta-analysis of transcatheter aortic valve implantation versus surgical aortic valve replacement in patients with low surgical risk," *The American Journal of Cardiology*, vol. 125, no. 3, pp. 459–468, 2020 Feb 1.

[6] A. Khan, A. Aslam, K. N. Satti, and S. Ashiq, “Infective endocarditis post-transcatheter aortic valve implantation (TAVI), microbiological profile and clinical outcomes: a systematic review,” *PLoS One*, vol. 15, no. 1, Article ID e0225077, 2020 Jan 17.

[7] M. Ranasinghe, K. Peter, and J. McFadyen, “Thromboembolic and bleeding complications in transcatheter aortic valve implantation: insights on mechanisms, prophylaxis and therapy,” *Journal of Clinical Medicine*, vol. 8, no. 2, p. 280, 2019 Feb 25.

[8] L. Yi, Z. Junli, L. Zhihan, and L. Jinhua, “Medical image fusion method by deep learning,” *International Journal of Cognitive Computing in Engineering*, vol. 2, pp. 21–29, 2021.

[9] M. K. Murray, E. Hofmann, R. De Rosa et al., “Life beyond 5 Years after TAVI: patients’ perceived Health status and long-term outcome after transcatheter aortic valve implantation,” *Journal of Interventional Cardiology*, vol. 2019, Article ID 4292987, 7 pages, 2019 Oct 1.

[10] H. Benamer, B. Chevalier, A. Roy et al., “Procédure de TAVI par voie fémorale chez la femme: technique minimaliste,” *Annales de Cardiologie et d’Angeiologie*, vol. 65, no. 6, pp. 425–432, 2016 Dec, French.

[11] M. Abdelghani and P. W. Serruys, “Patient selection for TAVI in 2016: should we break through the low-risk barrier?” *EuroIntervention*, vol. 12, no. Y, pp. Y46–Y50, 2016 Sep 18.

[12] A. Lansky, M. I. Ghare, D. Tchétché, and A. Baumbach, “TAVI and the brain: update on definitions, evidence of neuroprotection and adjunctive pharmacotherapy,” *EuroIntervention*, vol. 14, no. AB, pp. AB53–AB63, 2018 Aug 31.

[13] Z. Liu, E. Kidney, D. Bem et al., “Transcatheter aortic valve implantation for aortic stenosis in high surgical risk patients: a systematic review and meta-analysis,” *PLoS One*, vol. 13, no. 5, Article ID e0196877, 2018 May 10.

[14] G. Witberg, U. Landes, A. Lador, D. Yahav, and R. Kornowski, “Meta-analysis of transcatheter aortic valve implantation versus surgical aortic valve replacement in patients at low surgical risk,” *EuroIntervention*, vol. 15, no. 12, pp. e1047–e1056, 2019 Dec 20.

[15] G. Lanzillo, A. Mangieri, M. Pagnesi et al., “Pacemaker-related complications in patients undergoing transcatheter aortic valve implantation: a single-center experience,” *Journal of Invasive Cardiology*, vol. 32, no. 12, pp. E362–E369, 2020 Dec.

[16] S. Zhang and P. L. Kolominsky-Rabas, “How TAVI registries report clinical outcomes-A systematic review of endpoints based on VARC-2 definitions,” *PLoS One*, vol. 12, no. 9, Article ID e0180815, 2017 Sep 14.

[17] L. Østergaard, T. K. Lauridsen, K. Iversen et al., “Infective endocarditis in patients who have undergone transcatheter aortic valve implantation: a review,” *Clinical Microbiology and Infections*, vol. 26, no. 8, pp. 999–1007, 2020 Aug.

[18] M. J. A. G. De Ronde-Tillmans, J. A. Goudzwaard, N. El Faquir et al., “TAVI Care and Cure, the Rotterdam multidisciplinary program for patients undergoing transcatheter aortic valve implantation: design and rationale,” *International Journal of Cardiology*, vol. 302, pp. 36–41, 2020 Mar 1.

[19] K. Singh, K. Carson, O. Akbar Ali et al., “Efficacy and complications of transcatheter aortic valve implantation with and without balloon aortic valvuloplasty,” *Journal of Heart Valve Disease*, vol. 26, no. 2, pp. 139–145, 2017 Mar.

[20] S. P. Potluri, M. Hamandi, S. S. Basra et al., “Comparison of frequency of vascular complications with ultrasound-guided versus fluroscopic roadmap-guided femoral arterial access in patients who underwent transcatheter aortic valve implantation,” *The American Journal of Cardiology*, vol. 132, pp. 93–99, 2020 Oct 1.

Hindawi
Journal of Healthcare Engineering
Volume 2021, Article ID 4658398, 9 pages
https://doi.org/10.1155/2021/4658398

Research Article

Computerized Tomography Image Features under the Reconstruction Algorithm in the Evaluation of the Effect of Ropivacaine Combined with Dexamethasone and Dexmedetomidine on Assisted Thoracoscopic Lobectomy

Yan Cui[1,2] **Yang Sun**[1,2] **Meng Xia**[1,2] **Dan Yao**[1,2] **and Jun Lei**[1,2]

[1]*Department of Anaesthesia, Affiliated Nanjing Brain Hospital, Nanjing Medical University, Nanjing 210029, China*
[2]*Department of Anaesthesia, Nanjing Chest Hospital, Nanjing 210029, China*

Correspondence should be addressed to Jun Lei; 101011993@seu.edu.cn

Received 28 August 2021; Accepted 25 October 2021; Published 10 November 2021

Academic Editor: Enas Abdulhay

This research was aimed to study CT image features based on the backprojection filtering reconstruction algorithm and evaluate the effect of ropivacaine combined with dexamethasone and dexmedetomidine on assisted thoracoscopic lobectomy to provide reference for clinical diagnosis. A total of 110 patients undergoing laparoscopic resection were selected as the study subjects. Anesthesia induction and nerve block were performed with ropivacaine combined with dexamethasone and dexmedetomidine before surgery, and chest CT scan was performed. The backprojection image reconstruction algorithm was constructed and applied to patient CT images for reconstruction processing. The results showed that when the overlapping step size was 16 and the block size was 32×32, the running time of the algorithm was the shortest. The resolution and sharpness of reconstructed images were better than the Fourier transform analytical method and iterative reconstruction algorithm. The detection rates of lung nodules smaller than 6 mm and 6–30 mm (92.35% and 95.44%) were significantly higher than those of the Fourier transform analytical method and iterative reconstruction algorithm (90.98% and 87.53%; 88.32% and 90.87%) ($P < 0.05$). After anesthesia induction and lobectomy with ropivacaine combined with dexamethasone and dexmedetomidine, the visual analogue scale (VAS) decreased with postoperative time. The VAS score decreased to a lower level (1.76 ± 0.54) after five days. In summary, ropivacaine combined with dexamethasone and dexmedetomidine had better sedation and analgesia effects in patients with thoracoscopic lobectomy. CT images based on backprojection reconstruction algorithm had a high recognition accuracy for lung lesions.

1. Introduction

Lobectomy is mainly used for malignancies confined to the lobes, lung damage caused by tuberculosis, severe bullae, bronchiectasis, interstitial lesions, trauma, and dysplasia, which refers to routine removal of the lungs [1]. There are five lobes in the chest. The right lung is made up of the upper, middle, and lower lobes. The left lung is made up of two lobes, the upper and lower lobes. Lobectomy is used for lung cancer and irreversible disease confined to the lung lobe. It mainly includes right upper lobe resection, right middle lobe resection, right lower lobe resection, left upper lobe resection, and left lower lobe resection. If the lesion involves both lobes or intermediate bronchial tubes, upper middle or lower middle lobe pneumonectomy is feasible [2]. In general, the postoperative quality of life of patients is not bad. Postoperative patients need to pay attention to the change of climate and pay attention to diet and avoid irritant gases in normal survival [3]. In addition, it is necessary to take proper exercise to strengthen resistance and closely observe the symptoms and signs of oneself. If abnormal, it is necessary to go to the hospital for comprehensive examination and treatment as soon as possible [4, 5]. Thoracoscopic lobectomy is a kind of lobectomy in which the thoracoscopic surgeon only watches the thoracoscopic situation through the TV screen in real time and performs the operation through one to four hole-like incisions no longer than 5 cm (without repositioning the ribs). Veins, arteries, and bronchial tubes were dissected anatomically, and the lung lobe was completely removed. At present, video-assisted thoracic surgery (VATS) lobectomy is basically mature and widely accepted. Its surgical techniques are also gradually refined and improved [6, 7]. The National Comprehensive Cancer Network (NCCN) guidelines for the treatment of lung cancer clearly state that "VATS lobectomy is a viable option for resectable lung cancer," which means that the role of thoracoscopic lobectomy in the treatment of benign or early malignant lung lesions has been confirmed [8, 9].

With the continuous breakthrough of medical imaging technology, the revolution of life science is promoted, such as CT, which provides great help for doctors' clinical diagnosis and treatment [10]. CT is widely used in the diagnosis of lung and other lesions due to its advantages of nonoverlapping cross-sectional imaging, high density resolution, and easy detection of small lesions, as well as energy spectrum and perfusion functional imaging [11, 12]. However, the current segmentation of conventional CT images has great limitations and challenges, and there are problems such as blurred boundary of lesions and insignificant brightness difference [13, 14]. Image reconstruction technology plays an important role in many fields. In the research and implementation of reconstruction algorithms, there are a series of extremely complex image processing and mathematical calculation problems [15, 16]. The essence of backprojection reconstruction refers to evenly erasing (backprojection) the ray projection from the finite object space onto all points in the infinite space reached by the ray, including the original pixel value of 0 points. At present, algorithms such as image reconstruction and computer-assisted medical image analysis have obvious advantages in major breakthroughs in technology and improvement of the medical level and have also become an effective way to solve medical image problems [17].

Therefore, it was attempted to construct a filtering backprojection reconstruction algorithm. The ramp-Lak filter was convolved with $\sin(x)/x$ to obtain the Shepp-Logan filter. Reconstruction of CT images and noisy data was carried out through the sheep-Logan filter to evaluate the effect of ropivacaine combined with dexamethasone and dexmedetomidine on assisted thoracoscopic lobectomy using CT image features based on reconstruction algorithm.

2. Materials and Methods

2.1. The General Information. In this study, 110 patients undergoing laparoscopy-guided lobectomy admitted to the hospital from January 2019 to September 2020 were collected as the research objects. There were 58 male patients and 52 female patients, aged 52.37 ± 5.68 years. The study had been approved by the Ethics Committee of the hospital. Patients and their families understood the content and methods of the study and signed corresponding informed consent forms.

The inclusion criteria were as follows: (i) patients who underwent lobectomy after prepathological and imaging diagnosis of lobectomy; (ii) patients aged between 45 and 65 years old; (iii) patients without metastasis of lung lesions, mediastinal lymph node enlargement, or pleural hypertrophy occurred; (iv) patients who were not recently treated with other drugs or antibiotics in the study; (v) patients with normal coagulation function and platelets.

The exclusion criteria were as follows: (i) patients with other systemic or organ lesions; (ii) patients who did not cooperate with treatment due to personal or other factors; (iii) patients with incomplete clinical data and medical history.

2.2. Anesthesia and Surgical Methods of Patients. All patients were fasting and abstaining from drinking six hours before anesthesia induction, and all vital signs including heart rate, diastolic blood pressure, systolic blood pressure, pulse oxygen saturation, and mean arterial pressure were monitored before surgery. 0.5% ropivacaine combined with 30 mL 1 μg/Kg DEX was used. Routine disinfection and towel laying were performed on the surgical position, nerve block was performed under ultrasound guidance, and puncture was performed after local anesthesia with 1% lidocaine at the puncture site. After puncture to the specified location, local anesthesia was injected, and two-point blocking method was adopted according to the intercostal space of the surgical incision.

10 mL of drugs was injected into each puncture site, and a mixture of 0.5% ropivacaine and 1 μg/Kg DEX was used as an anesthetic. The nerve block results were tested with alcohol cotton balls ten minutes after the injection.

The lobectomy incision was made between the mid-axillary line and the front of the axillary line in the fifth intercostal area, which was close to the hilum at a small angle to facilitate the operation of hand instruments along the longitudinal axis. Hemodynamic indexes of patients were monitored in real time during surgery, and corresponding vasoactive drugs were used to correct intraoperative hemodynamic instability.

All patients enrolled in the study underwent chest enhanced CT scans, which were interpreted by two attending physicians or radiologists with extensive clinical experience. If there was a difference between the two, a third physician should be asked to interpret. CT was used to observe and analyze the specific location of lung lesions, the maximum diameter of the lesion site, and hilar and mediastinal lymph node enlargement.

2.3. Backprojection Reconstruction Algorithm. When the backprojection reconstruction algorithm processes medical image data, the processed image is regarded as a two-dimensional matrix x. The image reconstruction process is as shown in the following equation:

$$T_{(x)} = d\left(\sum_{n=1}^{y} H_x + p\right). \tag{1}$$

In equation (1), $T_{(x)}$ is the feature map obtained by weighting the image matrix by the convolution kernel, H

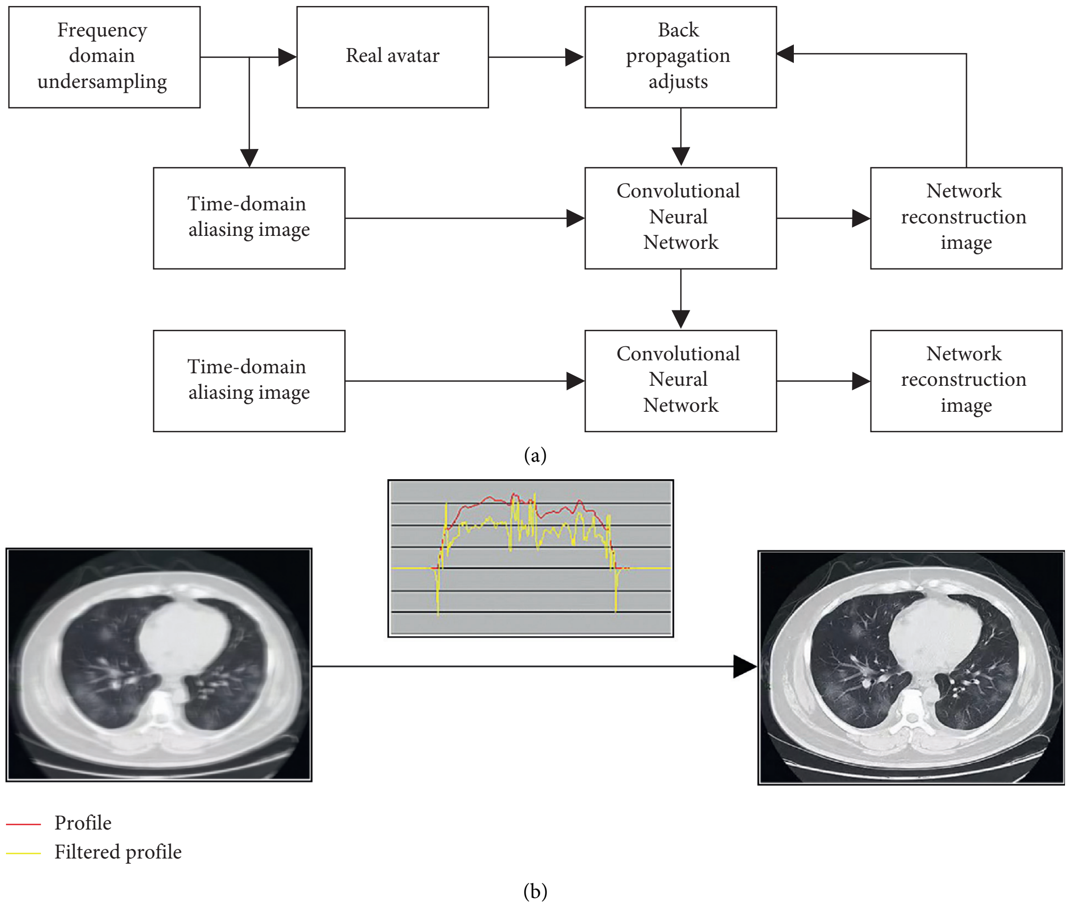

FIGURE 1: Medical image reconstruction (a) and reconstruction effect (b) based on backprojection.

represents the convolution kernel, p is the bias, n is the square of the size of the convolution kernel, and d represents the activation function. The backpropagation algorithm can accurately identify the optimal parameters in the network during the process of training the neural network. It is currently commonly used and effective. The update rule of each layer of convolution kernel H is as shown in the following equation:

$$H_{\alpha+1} = H_{\alpha} + \Delta H_{\alpha+1}, \tag{2}$$

$$\Delta H_{\alpha+1} = \beta H_{\alpha} - \theta\sigma\nabla a H_{\alpha}. \tag{3}$$

In equations (2) and (3), H is the convolution kernel, α is the number of layers, β is the weight of the gradient value of the previous layer, δ is the learning factor, θ is the momentum, and a is the loss function. The medical image reconstruction process based on backprojection is shown in Figure 1.

The network parameters are adjusted by backpropagation by minimizing the residuals of the reconstructed image and the corresponding real image, as shown in Figure 1, which is the network training process. The optimized network is obtained by training, and the aliased image is input in it to perform image reconstruction so that the obtained high-quality images can be used in clinical medical diagnosis.

Neural networks have independent connection and calculation methods, but they are all based on backpropagation algorithms, on which network parameters are adjusted and optimized.

$$T(n) = \int_{-\infty}^{+\infty} I(x)O(n-x)Y_x. \tag{4}$$

It is supposed that $f(a, b)$ is the image to be reconstructed, $T(s, \alpha)$ denotes a parallel projection of $f(a, b)$ acquired at an angle, and c is the coordinate axis of the projected X-ray parallel to the angle α. The coordinate axis is perpendicular to the coordinate axis where S is located; then, there is the following equation:

$$T(s, \alpha) = \int_{-\infty}^{+\infty} f(s, c)\mathrm{d}s. \tag{5}$$

In equation (5), s represents the distance from the projected ray to the center of symmetry (i.e., the center of rotation). One-dimensional Fourier transform is performed on $T(s, \alpha)$ of equation (5).

$$T(\varpi, \alpha) = \int_{-\infty}^{+\infty} T(s, \alpha)e^{-2jn\varpi s}\mathrm{d}t. \tag{6}$$

Equation (1) is substituted into equation (2) to get the following equation:

$$T(\varpi, \alpha) = \int_{-\infty}^{+\infty}\int_{-\infty}^{+\infty} f(s, c)e^{-2jn\varpi s}\mathrm{d}t\mathrm{d}s. \quad (7)$$

In equation (7), ω represents the filter function, c is the coordinate axis parallel to the projected X-ray under the angle α, and s represents the distance from the projected ray to the center of symmetry (i.e., the center of rotation). Figure 2 shows the reconstructed image space coordinate system and projection space coordinate system.

In Figure 2, the coordinates of point n in the a-o-b coordinate system are shown in equations (8) and (9).

$$a = R\cos\beta, \quad (8)$$

$$b = R\sin\beta. \quad (9)$$

In the equations, R represents the distance between the point n and the origin in Figure 2. Similarly, the coordinates of point n in s-o-c are shown in equations (10)–(13).

$$s = R\ \cos(\beta - \alpha), \quad (10)$$

$$R\ \cos(\beta - \alpha) = a\ \cos\ \alpha + b\ \sin\ \alpha, \quad (11)$$

$$c = R\ \sin(\beta - \alpha), \quad (12)$$

$$R\ \sin(\beta - \alpha) = b\ \cos\ \alpha + a\ \sin\ \alpha. \quad (13)$$

R represents the distance between the point n and the origin in Figure 2. The above equations are substituted into equation (7) to get the following equation:

$$T(\varpi, \alpha) = \int_{-\infty}^{+\infty}\int_{-\infty}^{+\infty} f(a, b)e^{-2jn\varpi(a\ \cos\ \alpha + b\ \sin\ \alpha)}\mathrm{d}a\mathrm{d}b. \quad (14)$$

The two-dimensional Fourier transform of the image $f(a, b)$ to be reconstructed is set as $F(i, j)$; then, $F(i, j)$ is expressed as follows:

$$F(i, j) = \int_{-\infty}^{+\infty}\int_{-\infty}^{+\infty} f(a, b)e^{-2jn(ia + jb)}\mathrm{d}a\mathrm{d}b. \quad (15)$$

It is supposed that equations (16) and (17) are true.

$$i = \varpi\ \cos\ \alpha, \quad (16)$$

$$j = \varpi\ \sin\ \alpha. \quad (17)$$

Then, there is the following equation:

$$F(\varpi\ \cos\ a, \varpi\ \sin\ a) = T(\varpi, a). \quad (18)$$

According to the Fourier transform, the image function $f(a, b)$ can be restored by its inverse Fourier transform $F(i, j)$.

$$f(a, b) = \int_{-\infty}^{+\infty}\int_{-\infty}^{+\infty} F(i, j)e^{2jn(ia + jb)}\mathrm{d}i\mathrm{d}j. \quad (19)$$

$i = \varpi\ \cos\ \alpha$ and $j = \varpi\ \sin\ \alpha$; then, there is equation (20) after the calculation of equation (18).

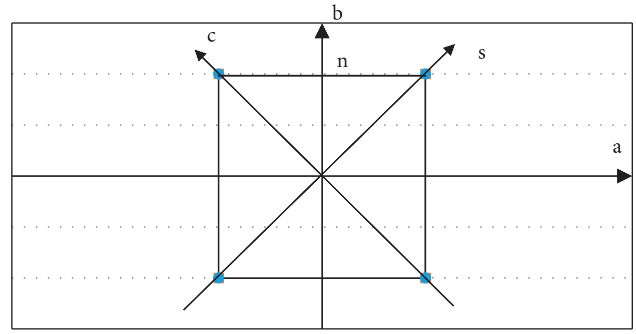

Figure 2: Image space coordinate system and projection space coordinate system.

$$f(a, b) = \int_{0}^{2n}\int_{-\infty}^{+\infty} T(\varpi, a)e^{j2n\varpi(a\ \cos\ \alpha + b\ \sin\ \alpha)}\varpi\mathrm{d}\varpi\mathrm{d}\theta. \quad (20)$$

Equation (19) is transformed into the following form using symmetric relationship (21), as shown in equation (22).

$$T(\varpi, \alpha + \pi) = T(-\varpi, \alpha), \quad (21)$$

$$f(a, b) = \int_{0}^{\pi}\mathrm{d}\alpha\int_{-\infty}^{+\infty} T(\varpi, a)|\varpi|e^{j2n\varpi(a\ \cos\ \alpha + b\ \sin\ \alpha)}\mathrm{d}\varpi, \quad (22)$$

$$g(a\ \cos\ \alpha + b\ \sin\ \alpha) = \int_{-\infty}^{+\infty} T(\varpi, a)|\varpi|e^{j2n\varpi(a\ \cos\ \alpha + b\ \sin\ \alpha)}\mathrm{d}\varpi, \quad (23)$$

$$f(a, b) = \int_{0}^{\pi} g(a\ \cos\ \alpha + b\ \sin\ \alpha)\mathrm{d}\alpha. \quad (24)$$

Equations (23) and (24) are the main equations for filtering backprojection, $|\omega|$ in (22) represents the filter function, and $f(a, b)$ is the reconstructed image.

2.4. Image Reconstruction and Effect Evaluation. In this study, a backprojection image reconstruction algorithm was used to reconstruct the lung lesions of patients undergoing lobectomy, and filtering function was added to solve the problem of image sharpness. In addition, the iterative reconstruction algorithm (using the method of solving linear equations to reconstruct the image) and Fourier transform analytical method were introduced. In the arterial phase of chest enhanced CT, the pulmonary artery, pulmonary vein, lesion, and blood-supplying artery were reconstructed. Through the reconstruction of 3D images, the lesions were presented more clearly in the form of three dimensions and visualization, so as to realize the simulation effect.

2.5. Statistical Methods. SPSS 19.0 was employed for data statistics and analysis. Mean ± standard deviation (□$x \pm s$) was how measurement data were expressed, and percentage was how count data were expressed. The pairwise comparison was performed by analysis of variance. The difference was statistically considerable with $P < 0.05$.

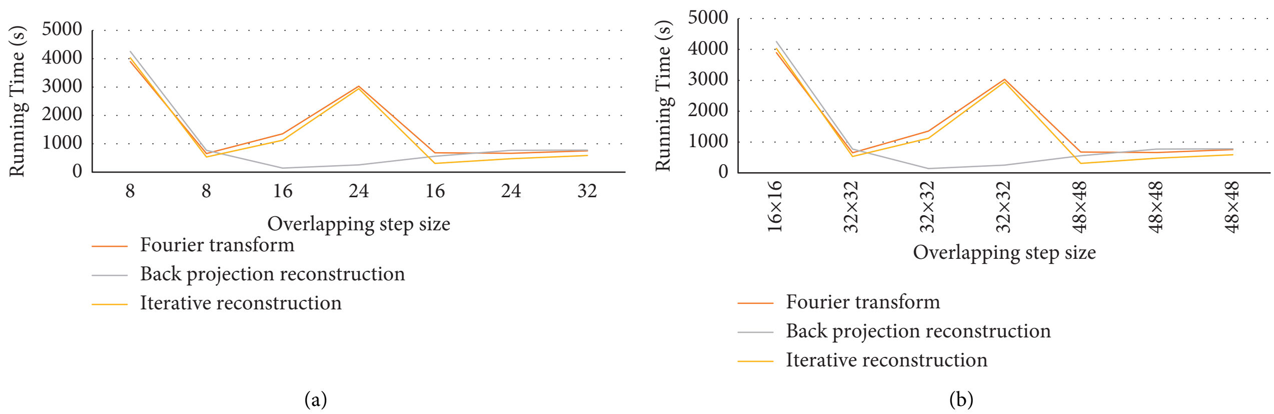

FIGURE 3: Image reconstruction running time. (a) The running time of different overlapping steps. (b) The running time of different block sizes.

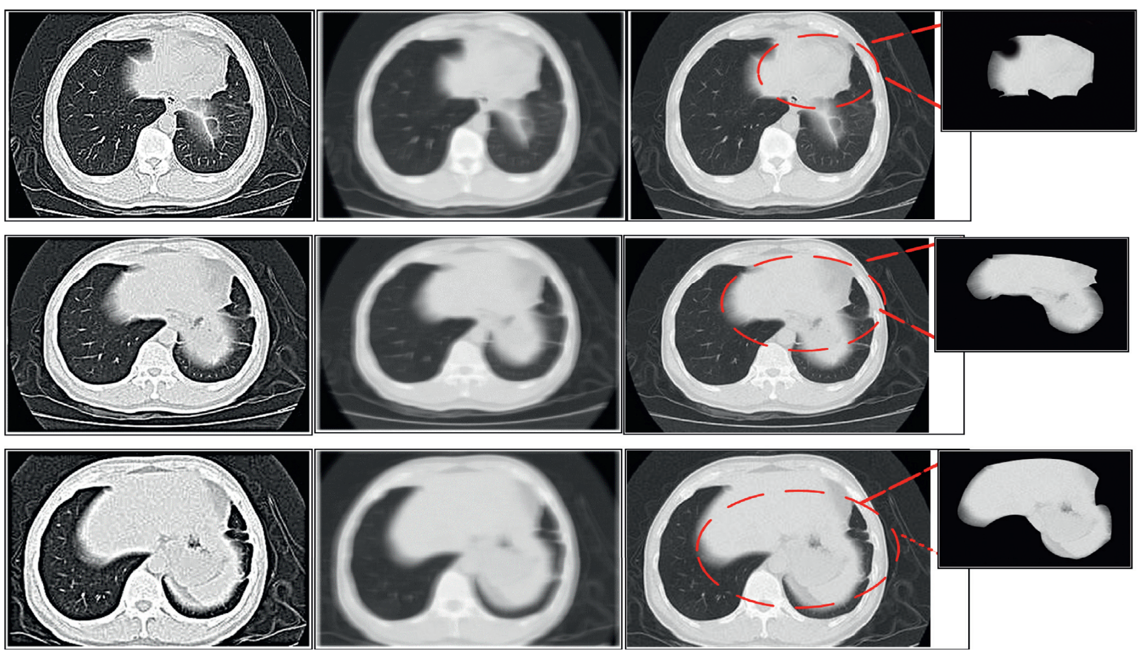

FIGURE 4: Reconstruction of CT images of lungs by backprojection.

3. Results

3.1. Running Time of the CT Image Reconstruction Algorithm. Figure 3 shows the running time of CT image reconstruction by Fourier transform analysis, iterative reconstruction algorithm, and backprojection image reconstruction algorithm. Figures 3(a) and 3(b) show the calculation time under different block and different overlap step parameter settings, respectively. The Fourier transform analysis had the shortest running time when the overlap step was 8, the block size was 32×32, and the overlap step was 16. The iterative reconstruction algorithm had the shortest running time when the overlap step was 16 and the block size was 48×48. When the overlap step was 16 and the block size was 32×32, the backprojection image reconstruction algorithm had the shortest running time.

3.2. Analysis of the Effect of CT Image Reconstruction. According to the noise characteristics in the data, the filtering function was applied to the original data, and the signal in the image was filtered, removing noise and artifacts to reconstruct the image. In Figure 4, there were patchy, subsegmental, and segmental ground-glass density shadows in the CT images of pulmonary lesions, which were separated into paving stone-like changes by the thickening of small honeycomb-like interlobular septa. In addition, large consolidation in the middle lobe of the right lung and patchy consolidation in the posterior basal segment of the lower lobe were observed. The density shadow of ground glass and the thickening of interlobular interval were seen obviously after image removal and processing by the backprojection filter reconstruction algorithm.

3.3. Analysis of the Reconstruction Effect of Three Algorithms. Figure 5 shows the CT images of a central lung cancer patient and a right upper lobe lung cancer patient, as well as the results of reconstruction by Fourier transform analysis, iterative reconstruction algorithm, and backprojection image reconstruction algorithm. Through adaptive image selection and super-resolution reconstruction, the backprojection reconstruction algorithm continuously corrected the structural information of the target image block, so as to obtain high definition and clear image edge. High-resolution images with dramatically enhanced details can eliminate the interference of image noise and artifacts and reconstruct clear CT images. The image clarity and resolution obtained by the backprojection reconstruction algorithm were superior to those of Fourier transform analysis and iterative reconstruction algorithm.

3.4. Detection Rate of Pulmonary Nodules by Three Reconstruction Algorithms. Figure 6 shows the comparison of the detection rates of pulmonary nodules of different sizes after the three algorithms, namely, Fourier transform analysis method, iterative reconstruction algorithm, and backprojection image reconstruction, processed the lung CT images. For pulmonary nodules smaller than 6 mm, the detection rates of the three algorithms were 90.98%, 87.53%, and 92.35%, respectively. For 6–30 mm lung nodules, the detection rates of the three algorithms were 88.32%, 90.87%, and 95.44%, respectively. The detection rate of pulmonary nodules of different sizes by backprojection image reconstruction algorithm was significantly higher than that by the Fourier transform analytical method and iterative reconstruction algorithm ($P < 0.05$).

3.5. Patient's Lung Disease Types. Figure 7 shows the types of lung lesions and their proportion in patients undergoing lobectomy. Patients with central lung tumors and right upper lobe tumors accounted for a relatively high proportion of 43.21% and 29.54%, respectively, followed by tuberculosis, severe lung infection, and pulmonary fibrosis, accounting for 8.11%, 8.93%, and 10.21%, respectively.

3.6. VAS Scores of Patients at Different Postoperative Periods. Figure 8 shows the VAS scores at different periods after thoracoscopic lobectomy. Figure 8(a) shows the VAS score under the resting state, and Figure 8(b) shows the VAS score under the exercise state. Ropivacaine combined with dexamethasone and dexmedetomidine was used for anesthesia induction and lobectomy after nerve block, and VAS scores decreased with the extension of postoperative time. The VAS score decreased to a low level after five days.

4. Discussion

The basis of CT image reconstruction is as follows. The same X-ray intensity passes through different substances, and different substances in the human body are distinguished by using this law [18, 19]. The structures that X-rays pass through each layer of the body in a CT scan are broken up into small cubes called voxels. Each cube corresponds to a separate attenuation signal, and this signal is fed into the corresponding cell in the image plane matrix called pixel. The attenuation signal of each voxel is input into the corresponding pixel and then reflected in different gray scales, which is the process of CT image reconstruction [20, 21]. For the backprojection image reconstruction algorithm, the problem of image sharpness is solved by adding a filter function. The reconstructed image is blurred when the filter function is not added, and the reconstructed image after the filter function is added can make it clear. Due to the fast reconstruction speed and high image quality of the backprojection filter, it has become the most commonly used CT image reconstruction method. Although the iterative reconstruction algorithm has been proposed very early, due to its large amount of calculation and slow reconstruction speed, it depends on the breakthrough of computer performance. Therefore, the backprojection reconstruction algorithm is widely used in current applications [22, 23]. In this study, a backprojection image reconstruction algorithm was used to reconstruct the lung lesions of patients undergoing lobectomy by CT three-dimensional reconstruction, and a filter function was added to solve the problem of image sharpness. In addition, iterative reconstruction algorithm and Fourier transform analysis method were introduced. Aiming at the arterial phase of enhanced CT of the patient's chest, the pulmonary artery, pulmonary vein, lesion, and blood supply artery were reconstructed, and the lesion was visualized more clearly through the reconstructed three-dimensional image, achieving the effect of simulation.

Through the backprojection reconstruction algorithm to process the CT image, it was found that when the overlap step was 16 and the block size was 32×32, the backprojection image reconstruction algorithm had the shortest running time. Therefore, to ensure that a higher-quality image was obtained after reconstruction, the setting of image block parameters should not affect the reconstruction result. The image separation parameters of this study were set as follows. The block size was 32×32, and the overlap step length was 16 pixels. The detection rate of backprojection image reconstruction algorithm for lung nodules smaller than 6 mm and 6–30 mm was significantly higher than that of the Fourier transform analytical method and iterative reconstruction algorithm ($P < 0.05$). The results were similar to those of Yoshida et al. [24], which showed that the backprojection image reconstruction algorithm can continuously modify the structure information of the target image through super-resolution reconstruction, make the image clear, and facilitate the identification of the lesion. The patients included in this study were treated with ropivacaine combined with dexamethasone and dexmedetomidine for induction of anesthesia and lobectomy for nerve block. The patient's VAS score decreased with the extension of postoperative time. After five days, the patient's VAS score can be reduced to a lower level. This was similar to the results of Williams et al. [25]. It was verified that combined induction of anesthesia and nerve block had a positive effect on postoperative pain and postoperative recovery.

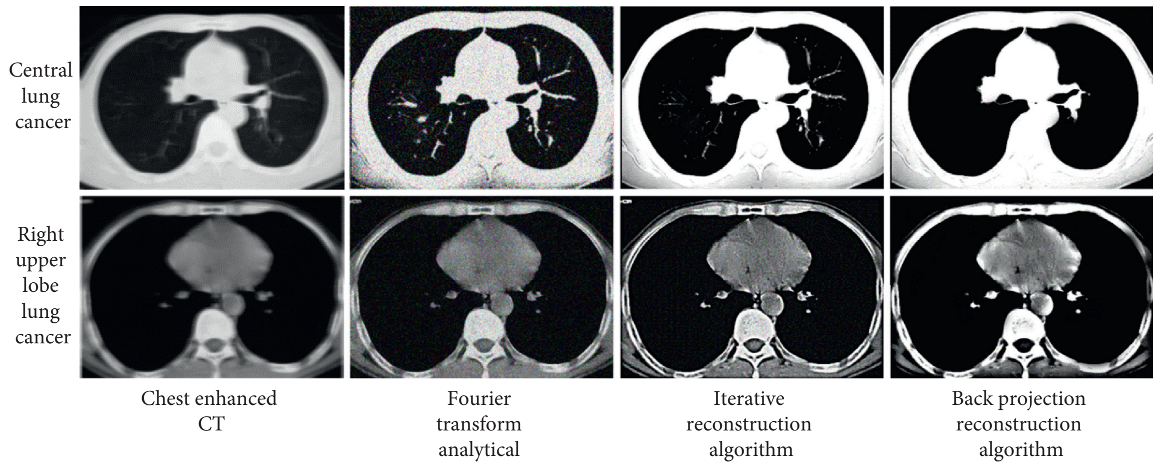

Figure 5: Analysis of the reconstruction effect of the three algorithms.

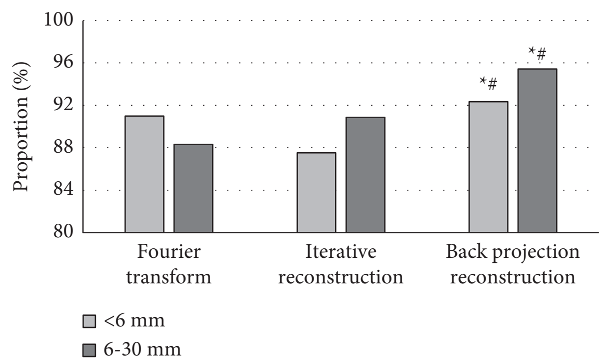

Figure 6: Detection rates of pulmonary nodules by three reconstruction algorithms.

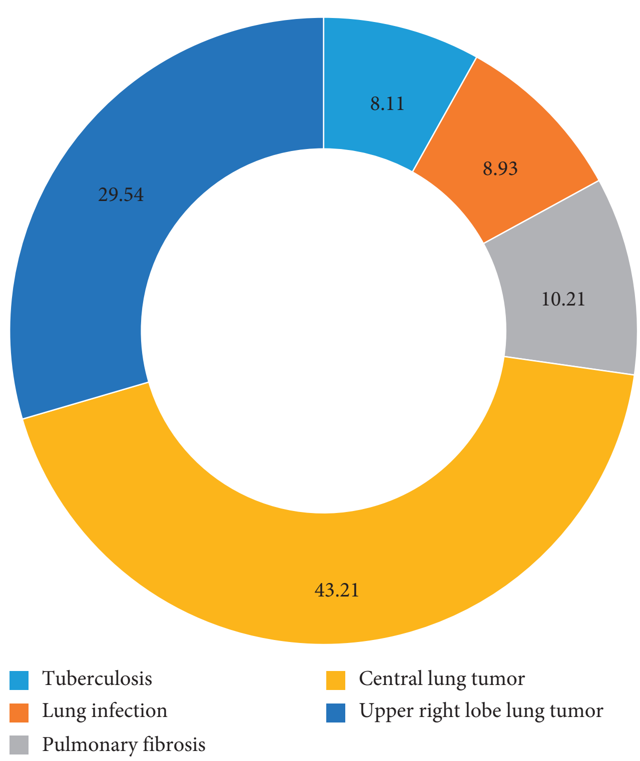

Figure 7: Types of lung lesions in the patients.

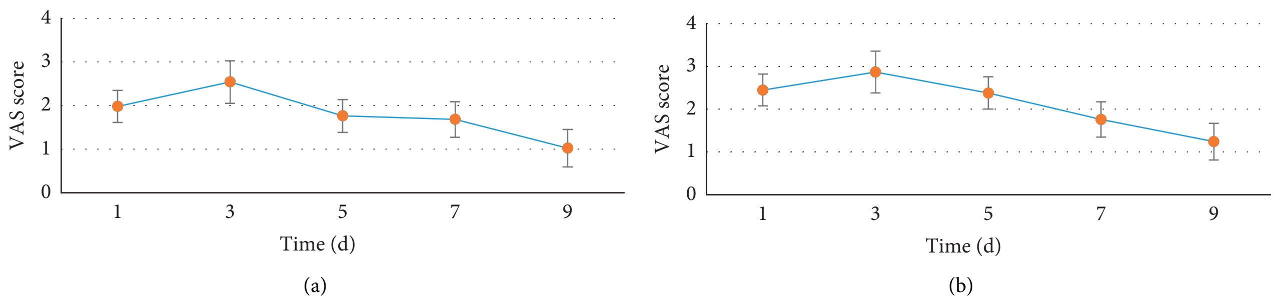

Figure 8: VAS score of patients after operation. (a) The VAS score in the resting state. (b) The VAS score in the exercise state.

5. Conclusion

In this study, a backprojection image reconstruction algorithm was established and applied to CT images of patients undergoing thoracoscopic lobectomy. The image was reconstructed to remove noise and artifacts to obtain a clear image and identify lesions. Then, the effect of ropivacaine combined with DXM and DEX in blocking thoracoscopic lobectomy was studied by evaluating CT image features based on reconstruction algorithm. The results showed that ropivacaine combined with dexamethasone and dexmedetomidine had ideal sedation and analgesia effects in patients with thoracoscopic lobectomy. The CT image based on the backprojection reconstruction algorithm had a high recognition accuracy for lung lesions, which was worth applying to clinical diagnosis. However, this study lacked comparison with other intelligent algorithms and was less representative. Therefore, this aspect will be improved and optimized in the subsequent experiments, and the CT image features based on reconstruction algorithm will be further analyzed to evaluate the effect of ropivacaine combined with dexamethasone and dexmedetomidine in the treatment of video-assisted thoracoscopic lobectomy. In conclusion, this study provides a reference for the application of intelligent reconstruction algorithms such as backprojection filtering in medical images.

Data Availability

The data used to support the findings of this study are available from the corresponding author upon request.

Conflicts of Interest

The authors declare no conflicts of interest.

Authors' Contributions

Yan Cui and Yang Sun contributed equally to this work.

References

[1] S. X. Sun, T. W. Moseley, H. M. Kuerer, and W. T. Yang, "Imaging-based approach to axillary lymph node staging and sentinel lymph node biopsy in patients with breast cancer," *American Journal of Roentgenology*, vol. 214, no. 2, pp. 249–258, 2020, Epub 2019 Nov 12. PMID: 31714846.

[2] R. M. Reddy, M. L. Gorrepati, D. S. Oh, S. Mehendale, and M. F. Reed, "Robotic-assisted versus thoracoscopic lobectomy outcomes from high-volume thoracic surgeons," *The Annals of Thoracic Surgery*, vol. 106, no. 3, pp. 902–908, 2018, Epub 2018 Apr 25. PMID: 29704479.

[3] S. Tane, W. Nishio, Y. Nishioka et al., "Evaluation of the residual lung function after thoracoscopic segmentectomy compared with lobectomy," *The Annals of Thoracic Surgery*, vol. 108, no. 5, pp. 1543–1550, 2019, Epub 2019 Jul 11. PMID: 31302085.

[4] D. S. Oh, R. M. Reddy, M. L. Gorrepati, S. Mehendale, and M. F. Reed, "Robotic-assisted, video-assisted thoracoscopic and open lobectomy: propensity-matched analysis of recent premier data," *The Annals of Thoracic Surgery*, vol. 104, no. 5, pp. 1733–1740, 2017, PMID: 29054214.

[5] T. Humphries, J. Winn, and A. Faridani, "Superiorized algorithm for reconstruction of CT images from sparse-view and limited-angle polyenergetic data," *Physics in Medicine and Biology*, vol. 62, no. 16, pp. 6762–6783, 2017.

[6] X. Tao, H. Zhang, Y. Wang et al., "VVBP-tensor in the FBP algorithm: its properties and application in low-dose CT reconstruction," *IEEE Transactions on Medical Imaging*, vol. 39, no. 3, pp. 764–776, 2020, Epub 2019 Aug 13. PMID: 31425024.

[7] C.-J. Hsieh, T.-K. Huang, T.-H. Hsieh et al., "Compressed sensing based CT reconstruction algorithm combined with modified Canny edge detection," *Physics in Medicine and Biology*, vol. 63, no. 15, Article ID 155011, 2018.

[8] J. Wang, J. Liang, J. Cheng, Y. Guo, and L. Zeng, "Deep learning based image reconstruction algorithm for limited-angle translational computed tomography," *PLoS One*, vol. 15, no. 1, PMID: 31905225, Article ID e0226963, 2020.

[9] M. Wang, Y. Zhang, R. Liu, S. Guo, and H. Yu, "An adaptive reconstruction algorithm for spectral CT regularized by a reference image," *Physics in Medicine and Biology*, vol. 61, no. 24, pp. 8699–8719, 2016, PMID: 27880738.

[10] J. Guo, L. Zeng, and X. Zou, "An improved half-covered helical cone-beam CT reconstruction algorithm based on localized reconstruction filter," *Journal of X-Ray Science and Technology*, vol. 19, no. 3, pp. 293–312, 2011, PMID: 21876280.

[11] L. Bertolaccini, F. Calabrese, K. Kawamukai, J. Brandolini, and P. Solli, "The relativity of operative time on the outcomes of the video-assisted thoracoscopic lobectomies," *Journal of Thoracic Disease*, vol. 11, no. S3, pp. S354–S355, 2019, PMID: 30997219.

[12] W.-T. Hung, Y.-J. Cheng, and J.-S. Chen, "Video-assisted thoracoscopic surgery lobectomy for lung cancer in non-intubated anesthesia," *Thoracic Surgery Clinics*, vol. 30, no. 1, pp. 73–82, 2020, PMID: 31761286.

[13] R. E. Merritt, P. J. Kneuertz, and D. M. D'Souza, "Successful transition to robotic-assisted lobectomy with previous proficiency in thoracoscopic lobectomy," *Innovations: Technology and Techniques in Cardiothoracic and Vascular Surgery*, vol. 14, no. 3, pp. 263–271, 2019, PMID: 31050320.

[14] Y. Li, J. Zhao, Z. Lv, and J. Li, "Medical image fusion method by deep learning," *International Journal of Cognitive Computing in Engineering*, vol. 2, pp. 21–29, 2021.

[15] J. E. Scott, A. Singh, J. B. Case, P. D. Mayhew, and J. J. Runge, "Determination of optimal location for thoracoscopic-assisted pulmonary surgery for lung lobectomy in cats," *American Journal of Veterinary Research*, vol. 80, no. 11, pp. 1050–1054, 2019.

[16] X. Yang, L. Wang, C. Zhang, D. Zhao, Y. Lu, and Z. Wang, "The feasibility and advantages of subxiphoid uniportal video-assisted thoracoscopic surgery in pulmonary lobectomy," *World Journal of Surgery*, vol. 43, no. 7, pp. 1841–1849, 2019.

[17] M. Hu, Y. Zhong, S. Xie, H. Lv, and Z. Lv, "Fuzzy system based medical image processing for brain disease prediction," *Frontiers in Neuroscience*, vol. 15, Article ID 714318, 2021.

[18] I. S. Sarkaria, M. L. Gorrepati, S. Mehendale, and D. S. Oh, "Lobectomy in octogenarians: real world outcomes for robotic-assisted, video-assisted thoracoscopic, and open approaches," *Journal of Thoracic Disease*, vol. 11, no. 6, pp. 2420–2430, 2019.

[19] D. M. Nguyen, I. S. Sarkaria, C. Song et al., "Clinical and economic comparative effectiveness of robotic-assisted, video-assisted thoracoscopic, and open lobectomy," *Journal of Thoracic Disease*, vol. 12, no. 3, pp. 296–306, 2020.

[20] J. Gou, X. Wu, and H. Dong, "Reduced iteration image reconstruction of incomplete projection CT using regularization strategy through Lp norm dictionary learning," *Journal of X-Ray Science and Technology*, vol. 27, no. 3, pp. 559–572, 2019.

[21] L. H. Hu, X. Xu, W. Y. Shen, Y. Qi, H. Tian, and J. X. He, "[Application of thoracoscopy-guided thoracic paravertebral block for analgesia after single-port video-assisted pulmonary lobectomy]," *Zhonghua Yixue Zazhi*, vol. 100, no. 33, pp. 2596–2600, 2020, Chinese.

[22] J. H. Woo, Y. J. Kim, K. C. Kim, C. H. Kim, and J. Jun, "The effect of interscalene block on ipsilateral shoulder pain and pulmonary function in patients undergoing lung lobectomy," *Medicine (Baltimore)*, vol. 97, no. 24, PMID: 29901598, Article ID e11034, 2018.

[23] N. J. Vennart, N. Bird, J. Buscombe, H. K. Cheow, E. Nowosinska, and S. Heard, "Optimization of PET/CT image quality using the GE 'Sharp IR' point-spread function reconstruction algorithm," *Nuclear Medicine Communications*, vol. 38, no. 6, pp. 471–479, 2017, PMID: 28394818.

[24] T. Yoshida, T. Fujiwara, K. Furutani, N. Ohashi, and H. Baba, "Effects of ropivacaine concentration on the spread of sensory block produced by continuous thoracic paravertebral block: a prospective, randomised, controlled, double-blind study," *Anaesthesia*, vol. 69, no. 3, pp. 231–239, 2014, Epub 2014 Jan 21. PMID: 24447266.

[25] A. M. Williams, L. Zhao, T. R. Grenda et al., "Higher long-term quality of life metrics after video-assisted thoracoscopic surgery lobectomy compared with robotic-assisted lobectomy," *The Annals of Thoracic Surgery*, vol. S0003–S4975, no. 20, Epub ahead of print. PMID: 32599037, 2020.

Hindawi
Journal of Healthcare Engineering
Volume 2021, Article ID 2110612, 9 pages
https://doi.org/10.1155/2021/2110612

Research Article

Computed Tomography Image Features under Convolutional Neural Network Algorithm in Analysis of Inflammatory Factor Level and Prognosis of Patients with Hepatitis B Virus-Associated Acute-on-Chronic Liver Failure

Zhibing Xie [1], **Li Ding** [2], **and Yongzhong Li** [1]

[1] *Infectious Disease Center, Huaihua First People's Hospital, Huaihua 418000, Hunan, China*
[2] *Breast and Thyroid Surgery, Huaihua First People's Hospital, Huaihua 418000, Hunan, China*

Correspondence should be addressed to Zhibing Xie; 1410601320@stu.cque.edu.cn

Received 30 August 2021; Revised 18 October 2021; Accepted 20 October 2021; Published 8 November 2021

Academic Editor: Enas Abdulhay

This study aimed to explore the application value of three-dimensional (3D) convolutional neural networks (3D-CNN)-based computed tomography (CT) image intelligent segmentation model in the identification of lesions of patients with hepatitis B virus-associated acute-on-chronic liver failure (HBV-ACLF). A total of 30 patients with HBV-ACLF, 30 patients with chronic HBV hospitalized in hospital, and 30 healthy volunteers were selected as subjects. Liver function and serum inflammatory factors were measured in each group, and the 3D-CNN algorithm model was applied to CT imaging. The results showed that the levels of interleukin (IL)-6, IL-26, and IL-37 in the HBV-ACLF group were the highest, which were 128.43 ± 45.16 pg/mL, 1237.47 ± 536.22 pg/mL, and 50.83 ± 7.62 pg/mL, respectively. Total bilirubin (TBIL) ($P = 0.035$) and IL-26 ($P = 0.013$) were independent predictors that affected the prognosis of HBV-ACLF patients. The results of lesion segmentation showed that the Dice coefficient of 3D-CNN low-density focus and enhanced focus segmentation was the highest (0.821 ± 0.07 and 0.773 ± 0.071), and the marked area was close to the area manually drawn by the doctor. 3D CNN was superior to other algorithms in the number of nodular lesions detected (533), sensitivity (97.5%), and missed detection rate (0.52%) ($P < 0.05$). In short, IL-26 may become a useful biomarker in the treatment of HBV-ACLF. The 3D-CNN model improved the segmentation performance of lesions in CT images of HBV-ACLF patients, which provided a reference for the diagnosis and prognosis of HBV-ACLF.

1. Introduction

Acute-on-chronic liver failure (ACLF) refers to the acute deterioration of liver failure syndrome in patients with chronic liver disease whose liver function is originally stable under the action of various acute injury factors [1, 2]. Related research pointed out that more than 30% of ACLF patients are caused by infection, and the main cause of ACLF in China is hepatitis B virus (HBV) infection [3]. The patient's infection index has risen greatly, which is directly proportional to the severity of the disease and the mortality rate. This type of infection is mainly caused by bacteria such as Gram-negative bacilli. However, in recent years, with the abuse of antibiotics and the increase in the types of multidrug resistant bacteria, the infection range of HBV-ACLF patients is gradually expanding [4]. Bacteria generally induce inflammation through pathogen-associated molecular patterns (PAMPs) and virulent factors [5]. Studies found that the possible involvement in the pathogenesis of HBV-ACLF includes immune damage, inflammation, and cell apoptosis. It shows that the level of inflammatory factors in serum will change when HBV-ACLF occurs [6, 7], and its expression has potential clinical treatment and prognostic evaluation value.

Image omics is a technology that deeply mines data features from medical images through high-throughput multidimensional analysis [8]. The use of advanced image analysis tools and various data statistics and analysis tools for accurate diagnosis provides a powerful tool for modern medicine [9, 10]. In recent years, with the development of big data and medical imaging, imaging omics has been widely used in the prediction of the internal microscopic manifestations, pathological manifestations, and gene expression of clinical lesions [11]. Among them, computed tomography (CT) is the most valuable examination method at present. CT plain scan can describe the morphological characteristics of the lesion and clarify the status of the lesion, while the enhanced CT scan can reflect the characteristics of the blood supply of the lesion and the relationship with the surrounding tissue structure [12]. However, it is not ideal for the segmentation of low-density or nodular lesions in the liver of HBV-associated ACLF patients. CT images have many slices, and the size, location, and shape of low-density lesions are inconsistent. Manual reading is time-consuming and laborious, and there is no uniform standard for segmentation results. It is easy to have inconsistent diagnosis results from different doctors [13, 14]. Therefore, more intelligent algorithms are needed for image segmentation.

Convolutional neural network (CNN) has demonstrated more substantial effects and better clinical application prospects than traditional shallow learning methods in image segmentation and classification [15]. However, most of them are based on 2D cross section for feature extraction, and it is difficult to make full use of the data correlation in the vertical axis [16]. On this basis, an automatic segmentation algorithm based on 3D CNN for dual-channel 3D dense connection network is proposed. Convolution kernels of different sizes are used to extract multiscale features under different scale receptive fields. Then, the densely connected blocks of each channel were used for feature learning and transmission. After the features were connected, they were input to the classification layer to classify the target volume element [17, 18], and finally the automatic segmentation of the lesion was realized.

To sum up, the use of 3D-CNN model to optimize medical CT images to assist physicians in detecting low-density foci or nodular lesions in the liver of patients with HBV-associated ACLF has become a hot topic of current research by scholars. In this study, liver function and serum inflammatory cytokine levels were detected in 30 HBV-associated ACLF patients, 30 CHB patients, and 30 healthy volunteers. The end-to-end neural network architecture was designed based on 3D-CNN and applied to CT image analysis, to comprehensively evaluate the application value of 3D-CNN algorithm combined with CT imaging in the level of inflammatory factors and prognosis of HBV-associated ACLF patients.

2. Materials and Methods

2.1. Research Objects. A total of 30 patients with HBV-associated ACLF hospitalized in hospital from May 2019 to May 2020 were collected, with an age range of 30–80 years. Chronic active hepatitis B (CHB) patients were 30 cases, aged 31–77 years. Thirty healthy volunteers who underwent physical examination in this hospital during the same period were selected as healthy control group, aged 20–67 years.

Inclusion criteria for HBV-associated ACLF were as follows: patients who were in line with the diagnostic criteria of Guidelines for Diagnosis and Treatment of Liver Failure published by Liver Failure and Artificial Liver Research Group of Chinese Association of Infectious Diseases in 2018 [19] and serum total bilirubin in patients being 10 times or more than the normal value or increased by 17.1 μmol/L/day. Exclusion criteria were as follows: patients who had coinfection with other hepatitis viruses or immunodeficiency viruses, patients with drug-induced hepatitis and alcoholic liver, patients who had liver disease caused by parasitic infection, patients with hyperthyroidism, women in pregnancy or lactating period, and patients with liver metastasis of primary liver cancer or malignant tumor.

Inclusion criteria for CHB patients were the following: patients who were in line with the diagnostic criteria of Guidelines for Prevention and Treatment of chronic hepatitis B published by the Chinese Society of Liver Diseases and the Chinese Society of Infectious Diseases in 2015 [20] and the history of infection being more than six months. Exclusion criteria were the following: patients complicated with other viral hepatitis; patients with alcoholic liver, cirrhosis, drug-induced hepatitis, or fatty liver; patients with genetic metabolic liver disease; patients with autoimmune liver disease or parasitic liver disease; and patients with liver metastasis of primary liver cancer or malignant tumor.

Inclusion criteria of healthy volunteers were the following: all examination indexes and biochemical indexes being normal, and the patients not taking any drugs in the past week. Exclusion criteria were the following: those with organic diseases.

This experiment had been approved by the ethics committee of the hospital. All the experimental matters had been informed to the subjects and their families, who had signed informed consent.

2.2. Main Instruments and Reagents. Automatic blood coagulation analyzer was from Nanjing VEDENG Medical Co., Ltd. Centrifuge was from Nanjing Yiruoda Instrument Equipment Co., Ltd. Low-temperature refrigerator was from Jinan OLABO Instrument Equipment Co., Ltd. Microplate reader was from Jinan Laobao Medical Equipment Co., Ltd. Interleukin- (IL-) 26 kit was from Shanghai Yiyan Biotechnology Co., Ltd. IL-6 kit was from Shanghai Tongwei Industrial Co., Ltd. IL-27 kit was from Shanghai Jichun Industrial Co., Ltd. Enzyme conjugate was from Shanghai Rayzbio Biotechnology Co., Ltd. Termination fluid was from Shanghai Acmec Biochemical Co., Ltd.

2.3. Liver Function and Inflammatory Factor Detection. 5 mL of fasting venous blood was collected from all participants in the morning. After the blood sample was coagulated, it was centrifuged at a frequency of 3,500 rpm for 10 minutes. If the sample did not show hemolysis or lipemia, the upper serum was taken and stored in a refrigerator at −80°C. Routine detections were implemented for alanine aminotransferase (ALT), aspartate aminotransferase (AST), serum total bilirubin (TBIL), prothrombin time (PT), and activated partial thromboplastin time (APTT) using automatic serum coagulation analyzer. IL-26 was measured by double-antibody sandwich enzyme-linked immunosorbent assay (ELISA). The kit was taken out from the 4°C refrigerator and cooled to room temperature. The distilled water was diluted in a ratio of 1 : 20, and washing solution was prepared. The standard material was diluted to different concentrations, and 100 μL of the tested serum sample was injected into the well of the ELISA plate. The plate was sealed and left standing at 37°C for 1 hour; then, the plate was thoroughly cleaned for five times and dried. 100 μL biotinylated antibody was injected into each well, and the sealed plates were stood at 37°C for 1 hour. The plate was cleaned five times and dried. 100 μL enzymatic conjugate was added into each well, standing at 37°C for 15 min. The plate was cleaned five times and dried. Then, 50 μL of substrates A and B was added into each well, standing for 15 minutes at 37°C in dark. One drop of terminating solution was added to each well to terminate the experimental reaction. The absorbance was measured at 450 nm using a microplate analyzer. The operation for the determination of IL-6 and IL-27 was the same as above.

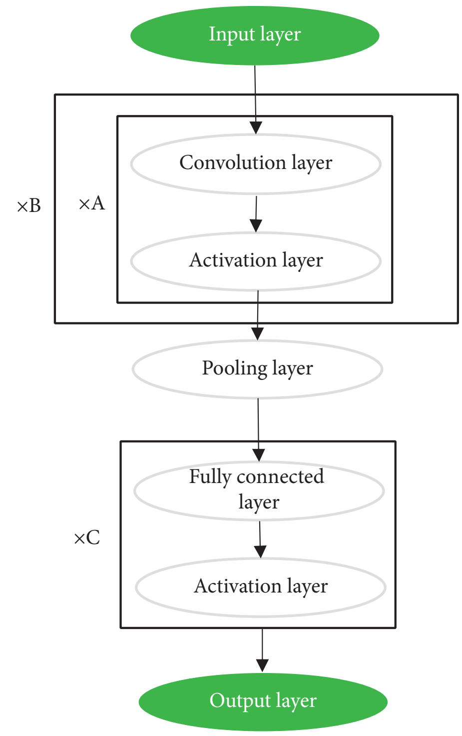

Figure 1: Structure diagram of CNN.

2.4. CNN Algorithm. Convolutional network is a kind of neural network structure, which is regarded as a special artificial neural network. The input data is calculated through the multilayer nonlinear mapping, and the prediction result is output. Its essence is a regression optimization calculation, which introduces a feedback layer into the traditional multilayer perception network structure to optimize the prediction results. It mixes A convolutional layer-activation layer, extracts image feature information, connects a pooling layer for downsampling, and repeats it many times until the image is minimized. Then, it connects a fully connected layer to convert all feature images into feature vectors. Finally, the result is obtained through the output layer. The basic network structure is shown in Figure 1.

The convolutional layer extracts the feature information of a certain area, and the image obtained after convolution is the feature map. In the CNN, the convolutional layer has two key characteristics of local connection and weight sharing. The meaning of local connection is that each point in the back layer only connects the corresponding area in the front layer. Weight sharing means that it inputs a picture and scans it with a convolution kernel. The number in the convolution kernel is called the weight. Each position in this picture is scanned by the same convolution kernel, so the weight is the same; that is, it is shared. The structure diagram is roughly as shown in Figure 2.

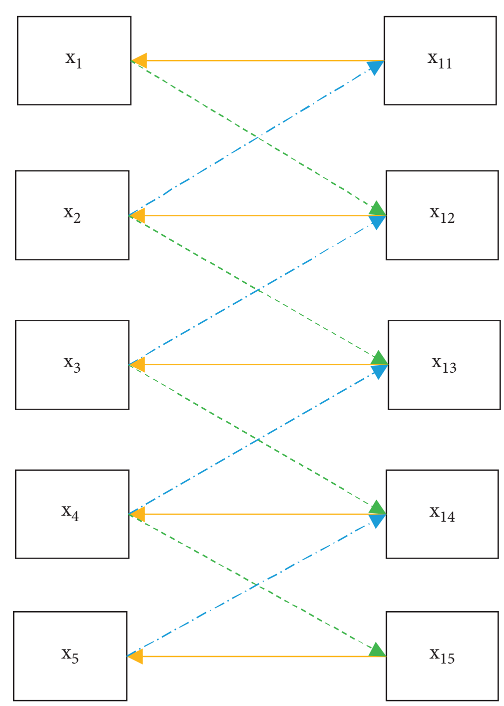

Figure 2: Local connection and weight sharing.

In the CNN, the definition of the 3D convolutional layer is as follows:

$$I_n^j(a,b,c) = \sum_h \sum_{e,f,g} I_h^{j-1}(a-e, b-f, c-g) M_{\mathrm{hn}}^j(e,f,g) + p_n^j. \tag{1}$$

Here, $I_n^j \in \theta^3$ is the nth feature image representing the jth layer, $M_{\mathrm{hn}}^j \in \theta^3$ is the 3D convolution kernel connecting I_h^{j-1} and I_n^j, and $p_n^j \in \theta^3$ is the offset of connecting $_I^{j-1}$ and I_n^j. A convolution kernel moves in the layer of the neural network, thereby obtaining a feature image of the next layer. The expression of the size of the image is as follows:

$$O_{\text{out}} = \frac{O_{\text{in}} - Q + 2R}{T} + 1. \tag{2}$$

Here, O_{in} is the size of the input feature image, Q is the size of the corresponding convolution kernel, R is the number of boundary zero padding, and T represents the length of the convolution kernel when it moves. In the neural network, there are two main types of pooling layers, the largest pool and the average pool. The calculation method of the maximum pool is as follows:

$$I_n^j(a,b,c) = \max_{0\le e,f,g\le w}\left\{I_n^{j-1}(a\cdot w+e, b\cdot w+f, c\cdot w+g)\right\}. \tag{3}$$

The average pool is expressed as follows:

$$I_n^j(a,b,c) = \frac{1}{w^3}\sum_{e=0}^{w}\sum_{f=0}^{w}\sum_{g=0}^{w} I_n^{j-1}(a\cdot w+e, b\cdot w+f, c\cdot w+g). \tag{4}$$

Here, w is the size of pooling. After passing through the pooling layer, the number of feature maps does not change, and the size of the image is calculated by the following equation:

$$O_{\text{out}} = \frac{O_{\text{in}} - w}{T} + 1. \tag{5}$$

Here, O_{in} is the size of the input feature image, w is the pooling size, and T is the pooling step size. For the fully connected layer, each neuron in it will be connected to the previous layer, and the Softmax layer is often used as the output layer of the CNN. Its expression is as follows:

$$I_u^N = \frac{x^{I_u^{N-1}}}{\sum_{v=1}^{v} x^{I_v^{N-1}}} \text{ for } u = 1,\cdots,V. \tag{6}$$

Here, V represents the total number of categories, N is the total number of layers of the neural network, I_V^{N-1} is the v th node in the $N-1$ th layer (usually a fully connected layer), and I_u^N represents the uth node in the Nth layer (i.e., the output layer). The sum of the probabilities of all categories is 1.

Since most of the low-density areas of the liver occupy a small area in the image, the channels in the network are usually used to sample under the pooling layer to avoid excessive loss of small information. The convolution module is employed to extract the information of this layer, and then deconvolution is performed to generate cascade with the feature image, which enables multilevel feature learning, thereby helping to detect low-density areas of different sizes.

2.5. 3D-CNN. 2D-CNNs mainly focus on 2D neighborhood information, while 3D-CNN is calculated through three dimensions and extracts features in 3D space. The main content of this study is applying 3D-CNN to the segmentation of low-density lesions in the liver area.

CNNs are individually estimated according to the neighborhood and context of each volume element in the image, and feature extraction is completed by cascading a series of convolution operations. 3D-CNN uses a 3D convolution kernel, facing the initial 3D data, which completes the convolution calculation through the input layer and the convolution kernel. After addition of the bias term, the nonlinear excitation function is used to obtain the output characteristic image. The basic network structure is shown in Figure 3.

The calculation method is expressed as follows:

$$y_{z-1}^u = g\left(\sum q_z^{u,v} \otimes y_{z-1}^v + d_z^u\right). \tag{7}$$

Here, each $q_z^{u,v}$ is the learned hidden weight, u represents the number of convolution kernels (the dimension of the output feature), v represents the dimension of the input feature, y_{z-1}^v represents the output 3D feature map, d_z^u represents the bias term, $\otimes$ is the convolution calculation, and g represents the nonlinear activation function. In 3D-CNN, if features are input to the network layer with a higher level, complex features will appear, which are used for classification. The end of the CNN is the classification layer, which is compared with the labels used for classification. This layer generally uses a normalized exponential function, which is defined and expressed as follows:

$$x_s = \frac{r^{O_s}}{\sum_s^N r^{O_s}}. \tag{8}$$

Here, O_s represents the output of the previous layer, s represents the index number of the estimated category, N is the number of categories in the layer, and x_s represents the ratio of the index of the estimated category at this time to the sum of all category factors. With the help of Softmax, the output value of each category is adjusted to the estimated probability compared with it.

2.6. Low-Density Foci Segmentation Based on 3D-CNN. The low-density stove segmentation process based on 3D-CNN is shown in Figure 4. In the training stage, the training set image is input, and the volume elements are normalized through preprocessing. Then, the features of each dimension are learned and extracted. According to the estimated conclusion and classification label, the patches generated by the loss function in the training and test set images are counted and then normalized. The categories of the volume elements are calculated through the network model one by one, and the segmentation result image is output.

2.7. CT Examination. A Brilliance 64-row helical scanner (GE Company, USA) was employed for inspection. The layer thickness was 5 mm, the spacing was 5 mm, and the reconstruction layer thickness was 0.625 mm. The tube current was 380 mA, the tube voltage was 125 kV, and the collimator width was 0.625 mm. In the enhanced scan, 80–100 mL (350 mg/100 mL) of the contrast agent iohexol

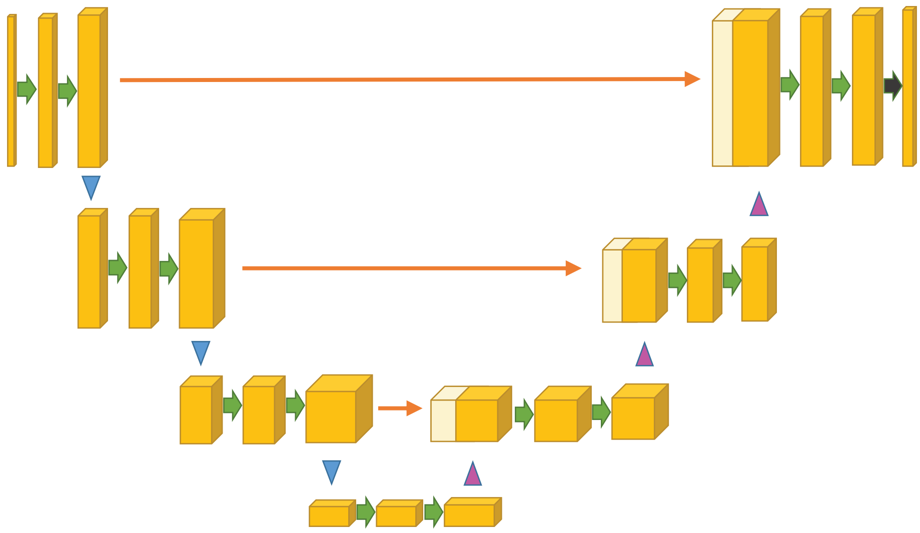

Figure 3: Basic network structures of 3D-CNN.

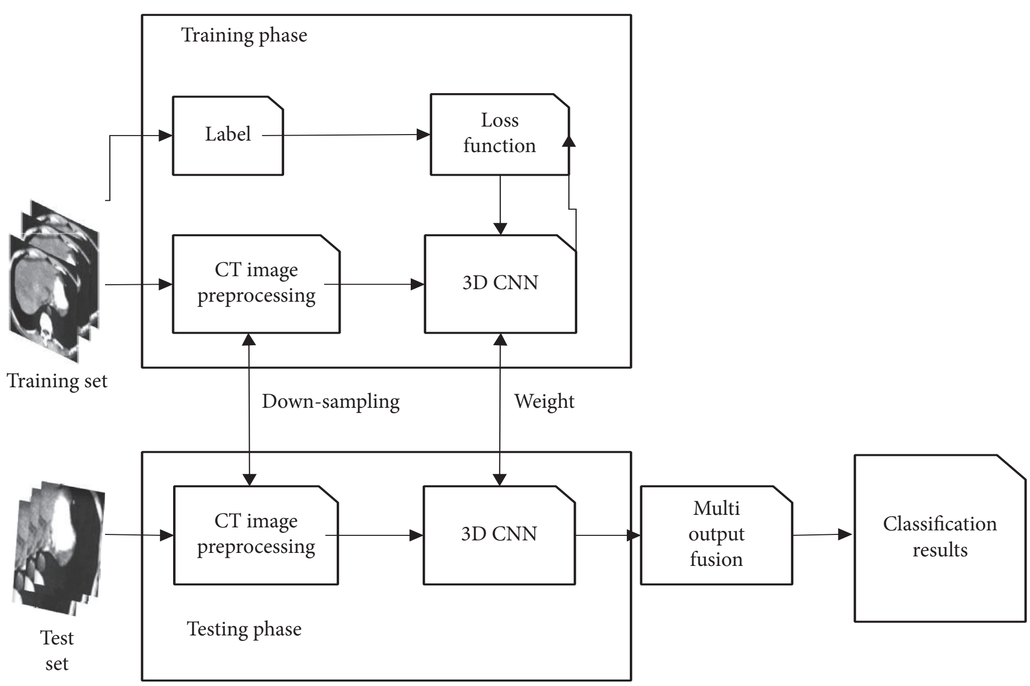

Figure 4: 3D-CNN's low-density foci segmentation process.

was injected at a flow rate of 3-4 mL/s. Scanning phases were 20–25 s in the arterial phase, 65–70 s in the venous phase, and 180 s in the delayed phase. The image data was processed by the system's own imaging workstation.

2.8. Statistical Analysis. SPSS 24.0 was used for statistical analysis of all experimental data. The continuous variables conforming to normal distribution were represented as mean ± standard deviation ($\overline{x} \pm s$), and the t-test was used for comparison between groups. One-way analysis of variance was used for comparison between multiple groups. Multivariate analysis was performed using logistic regression equation analysis. The correlation was assessed by Pearson test. $P < 0.05$ was considered statistically considerable.

3. Results

3.1. Comparison of the Levels of Inflammatory Factors among the Three Groups of Objects. In Figure 5, IL-6, IL-26, and IL-37 in the HBV-ACLF group were 128.43 ± 45.16 pg/mL, 1237.47 ± 536.22 pg/mL, and 50.83 ± 7.62 pg/mL, respectively, which were higher than those of 89.17 ± 28.39 pg/mL, 689.14 ± 351.7 pg/mL, and 31.19 ± 5.82 pg/mL in CHB group and those of the healthy group 58.45 ± 13.22 pg/mL,

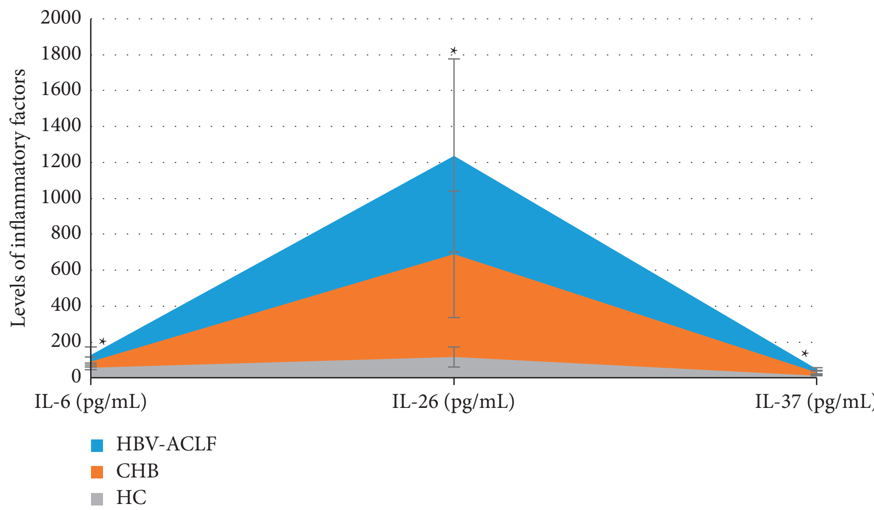

Figure 5: Comparison of the levels of inflammatory factors among the three groups of objects. Note: * indicates that the level of inflammatory factors in the HBV-ACLF group had a considerable difference compared with the CHB group and the HC group ($P < 0.05$).

Table 1: Prognostic risk factors of HBV-associated ACLF patients.

	P	Univariate analysis OR	95% CI	P	Multifactor analysis OR	95% CI
ALT (U/L)	0.291	1.000	0.987–1.000			
AST (U/L)	0.698	1.000	0.995–1.000			
TBIL (μmol/L)	0.004	1.0078	1.004–1.021	0.035	1.015	1.000–1.026
PT (s)	0.012	1.136	1.031–1.215	0.388	1.356	0.682–2.521
APTT (s)	0.005	1.043	1.008–1.098	0.891	1.002	0.936–1.054
IL-6 (pg/mL)	0.077	1.253	0.998–1.561	0.605	0.187	0.001–1.298
IL-26 (pg/mL)	≤0.001	1.004	0.936–1.006	0.013	1.005	1.000–1.006
IL-37 (pg/mL)	0.340	0.991	0.972–1.008	0.072	1.015	0.993–1.066

116.43 ± 56.29 pg/mL, and 14.14 ± 2.18 pg/mL, respectively. The differences were considerable ($P < 0.05$).

3.2. Prognostic Risk Factors of HBV-Associated ACLF Patients. Table 1 shows the single-factor and multifactor logistic regression analysis. In the univariate analysis of the prognosis of HBV-associated ACLF patients, TBIL ($P = 0.004$), PT ($P = 0.012$), APTT ($P = 0.005$), and IL-26 ($P < 0.001$) were considerable. In the multivariate analysis, TBIL ($P = 0.035$) and IL-26 ($P = 0.013$) were independent predictors of the prognosis of patients with HBV-associated ACLF.

3.3. Analysis of CT Image Low-Density Foci Segmentation Results Based on Three Algorithms. In Figure 6, the machine learning-based algorithms Deep Medic and Seg Net were compared with the 3D-CNN model. According to the Dice coefficient of the segmentation results, the Dice coefficient of 3D-CNN (0.884 ± 0.068) in the overall segmentation of low-density stoves was slightly lower than Deep Medic algorithm (0.900 ± 0.077) and higher than Seg Net algorithm (0.846 ± 0.072). In the core segmentation of low-density foci, the Dice coefficient of 3D-CNN was 0.821 ± 0.07, which was higher than Deep Medic algorithm (0.763 ± 0.069) and Seg Net algorithm (0.754 ± 0.076). In the segmentation of enhanced lesions, the Dice coefficient of 3D-CNN (0.773 ± 0.071) was higher than that of Deep Medic algorithm (0.731 ± 0.074) and Seg Net algorithm (0.694 ± 0.078), and the difference was considerable ($P < 0.05$).

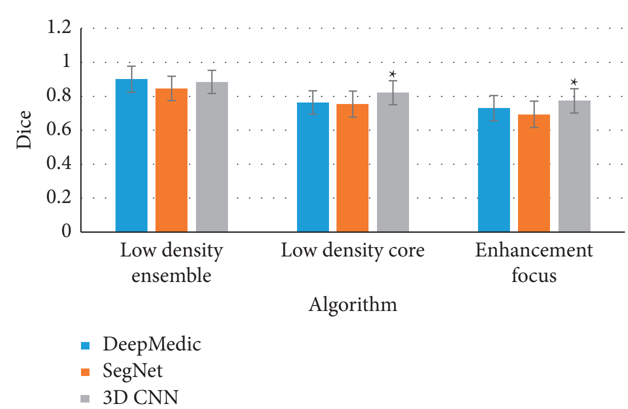

Figure 6: Analysis of CT image low-density lesion segmentation results based on three algorithms. Note: * indicates that the Dice coefficient of the 3D-CNN model was considerable compared to the other two algorithms ($P < 0.05$).

A 53-year-old male patient presented with intermittent abdominal distension for two years with exacerbation and yellowing of eyes and skin for two weeks. CT examination two years ago showed cirrhosis. That time, the patient visited the hospital due to abdominal distension and fatigue. HBsAg (+),

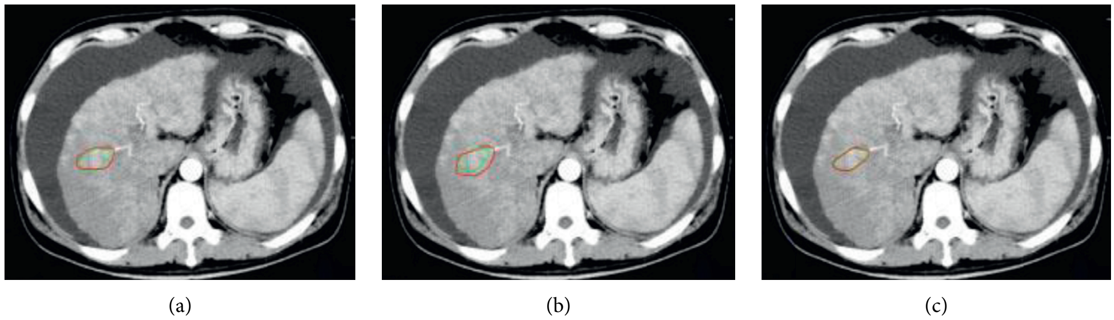

FIGURE 7: Different algorithm models segmentation results of low-density foci. (a) The CT image marked by the Deep Medic algorithm model, (b) the CT image marked by the Seg Net algorithm model, and (c) the CT image marked by the 3D-CNN model.

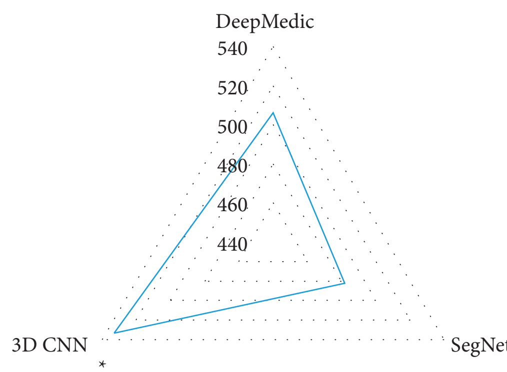

(a)

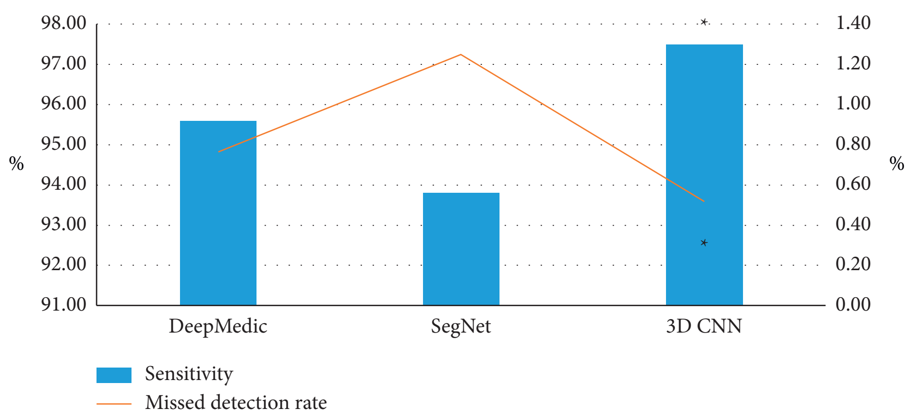

(b)

FIGURE 8: Comparison of CT image candidate detection results based on three algorithms. (a) The comparison of the number of nodular lesions detected by the three algorithms. (b) The comparison of the sensitivity and missed detection rate of the three algorithms. Note: *indicates that the detection performance of the 3D-CNN model was considerable compared to the other two algorithms ($P < 0.05$).

HBeAg (−), and HBV DNA 2.46×10^5 IU/mL were examined. Figure 7 shows the results of segmentation of low-density foci by different algorithm models. Green was the lesion area marked by the doctor, and red was the lesion area automatically marked by the three algorithm models. The 3D-CNN marked the area more closely to the area the doctor had sketched by hand.

3.4. Comparison of CT Image Candidate Detection Results Based on Three Algorithms. The results of candidate detection of nodular lesions using different algorithms are shown in Figure 8. The number of nodular lesions detected by 3D-CNN was 533, which was higher than that of Deep Medic algorithm (506) and Seg Net algorithm (482). Sensitivity (97.5%) of 3D-CNN was higher than that of Deep Medic algorithm (95.6%) and Seg Net algorithm (93.8%). The missed detection rate (0.52%) of 3D-CNN was lower than that of Deep Medic algorithm (0.76%) and the Seg Net algorithm (1.25%), and the difference was considerable ($P < 0.05$).

4. Discussion

HBV-associated ACLF is a reaction after a series of injuries, such as systemic immune disorders due to various inducements of acute liver injury based on chronic liver disease [21, 22]. It causes severe liver damage or failure. HBV-ACLF can lead to rapid deterioration of liver function, circulatory system, and organ dysfunction in the course of disease development, which is of high mortality and poor prognosis [23]. Many studies deemed that immune dysfunction is the main cause of ACLF. In the early stage, immune overexcitation and continuous inflammatory response cause a large number of liver cell necrosis [24, 25], while inflammatory cell infiltration and microcirculation disorder also exist. With the progress of the disease, liver failure, toxin accumulation in the body, internal environment disorder, and other consequences gradually appear [26]. In clinical practice, experts usually segment lesions manually based on their professional knowledge and work experience. The method based on computer automatic segmentation can effectively help doctors relieve working pressure and quickly and accurately obtain the feedback of the lesion area to doctors [27], which provides good diagnostic conditions and recommendations for treatment options. In clinical practice, CNN is usually used to build a medical image segmentation algorithm model to assist physicians to greatly improve the analysis effect of imaging features [28]. In this study, liver function and serum inflammatory cytokine levels were detected in 30 HBV-ACLF patients, 30 CHB patients, and 30 healthy volunteers. The end-to-end neural network architecture based on 3D-CNN was designed and applied to CT image analysis.

The results showed that the levels of IL-6, IL-26, and IL-37 were the highest in HBV-ACLF group, and TBIL and IL-26 were independent predictors of the prognosis of HBV-ACLF patients. The results of focal segmentation showed that the Dice coefficient of low-density focal core and enhanced focal segmentation was the highest in 3D CNN, and the labeled regions were closer to the regions delineated manually by doctors. Moreover, 3D CNN was superior to other algorithms in the number, sensitivity, and missed detection rate of nodular lesions detected ($P < 0.05$). In short, IL-26 may be a useful biomarker in the treatment of HBV-ACLF. The 3D-CNN model improved the segmentation performance of lesions in CT images of patients with HBV-ACLF, providing a reference for the diagnosis and prognosis of HBV-ACLF. This is consistent with the research results of Osuna-Coutiño and Martinez-Carranza [29]. 3D-CNN model makes full use of the interlayer information of CT images to improve the continuity of CT image segmentation. Hamidian et al. [30] pointed out that 3D-CNN combined the advantages of 2D and 3D models and significantly improved the segmentation performance of the model. It was found that TBIL and IL-26 were independent predictors of prognosis in patients with HBV-ACLF, and IL-26 may be a useful biomarker in the treatment of HBV-ACLF.

5. Conclusion

In this study, an intelligent CT image segmentation model based on 3D-CNN algorithm was established to integrate 2D and 3D models, which was applied to CT images of HBV-ACLF patients. The results showed that the 3D-CNN algorithm model had ideal performance in CT image segmentation of HBV-ACLF patients. However, there are still some shortcomings in this study. The experimental results have certain limitations and one-sidedness, so it is necessary to increase the sample size in the future and conduct further exploration in this direction. In conclusion, 3D-CNN model greatly improves the segmentation performance of CT images of patients with HBV-ACLF, which provides a reference for the diagnosis and prognosis of HBV-ACLF.

Data Availability

The data used to support the findings of this study are available from the corresponding author upon request.

Conflicts of Interest

The authors declare that they have no conflicts of interest.

Authors' Contributions

Zhibing Xie and Li Ding authors contributed equally to this work.

References

[1] C. Solé and E. Solà, "Update on acute-on-chronic liver failure," *Gastroenterología Y Hepatología (English Edition)*, vol. 41, no. 1, pp. 43–53, 2018, Epub 2017 Jun 24. PMID: 28655410.

[2] T. Gustot and R. Jalan, "Acute-on-chronic liver failure in patients with alcohol-related liver disease," *Journal of Hepatology*, vol. 70, no. 2, pp. 319–327, 2019, PMID: 30658733.

[3] D. Wu, S. Zhang, Z. Xie et al., "Plasminogen as a prognostic biomarker for HBV-related acute-on-chronic liver failure," *Journal of Clinical Investigation*, vol. 130, no. 4, pp. 2069–2080, 2020, PMID: 32175919; PMCID: PMC7108894.

[4] C. Li, H.-B. Su, X.-Y. Liu, and J.-H. Hu, "Clinical characteristics and 28-d outcomes of bacterial infections in patients with hepatitis B virus-related acute-on-chronic liver failure," *World Journal of Clinical Cases*, vol. 8, no. 6, pp. 1042–1055, 2020, PMID: 32258075; PMCID: PMC7103966.

[5] H. Liu, Q. Zhang, L. Liu et al., "Effect of artificial liver support system on short-term prognosis of patients with hepatitis B virus-related acute-on-chronic liver failure," *Artificial Organs*, vol. 44, no. 10, pp. E434–E447, 2020, Epub 2020 May 12. PMID: 32320491.

[6] Y. Jia, L. Ma, Y. Wang et al., "NLRP3 inflammasome and related cytokines reflect the immune status of patients with HBV-ACLF," *Molecular Immunology*, vol. 120, pp. 179–186, 2020, Epub 2020 Mar 10. PMID: 32169738.

[7] G. Shen, S. Sun, J. Huang et al., "Dynamic changes of T cell receptor repertoires in patients with hepatitis B virus-related acute-on-chronic liver failure," *Hepatology International*, vol. 14, no. 1, pp. 47–56, 2020, Epub 2019 Dec 23. PMID: 31872330.

[8] E. Schmid, K. Leeson, K. T. Xu, P. Richman, C. Nwosu, and L. Carrasco, "CT imaging history for patients presenting to the ED with renal colic--evidence from a multi-hospital database," *BMC Emergency Medicine*, vol. 19, no. 1, p. 24, 2019, PMID: 30823896; PMCID: PMC6397471.

[9] M. Matthews, P. Richman, S. Krall et al., "Prior CT imaging history for patients who undergo whole-body CT for acute traumatic injury and are discharged home from the emergency department," *BMC Emergency Medicine*, vol. 18, no. 1, p. 34, 2018, PMID: 30326855; PMCID: PMC6192200.

[10] S. Jha, "Coronary computed tomography," *PET Clinics*, vol. 14, no. 2, pp. 193–195, 2019, Epub 2019 Feb 1. PMID: 30826017.

[11] V. Desai, M. Cox, S. Deshmukh, and C. G. Roth, "Contrast-enhanced or noncontrast CT for renal colic: utilizing urinalysis and patient history of urolithiasis to decide," *Emergency Radiology*, vol. 25, no. 5, pp. 455–460, 2018, Epub 2018 Apr 20. PMID: 29675722.

[12] Y. Fukukura, Y. Kumagae, R. Higashi et al., "Visual enhancement pattern during the delayed phase of enhanced CT as an independent prognostic factor in stage IV pancreatic ductal adenocarcinoma," *Pancreatology*, vol. 20, no. 6, pp. 1155–1163, 2020, Epub 2020 Jul 28. PMID: 32800574.

[13] M. J. Willemink and P. B. Noël, "The evolution of image reconstruction for CT-from filtered back projection to artificial intelligence," *European Radiology*, vol. 29, no. 5, pp. 2185–2195, 2019, Epub 2018 Oct 30. PMID: 30377791; PMCID: PMC6443602.

[14] A. Kambadakone, "Artificial Intelligence and CT image reconstruction: potential of a new era in radiation dose reduction," *Journal of the American College of Radiology*, vol. 17, no. 5, pp. 649–651, 2020, Epub 2020 Jan 28. PMID: 32004484.

[15] X. Yang, N. Wang, B. Song, and X. Gao, "BoSR: a CNN-based aurora image retrieval method," *Neural Networks*, vol. 116, pp. 188–197, 2019, Epub 2019 May 2. PMID: 31121417.

[16] T.-H. Hsieh and J.-F. Kiang, "Comparison of CNN algorithms on hyperspectral image classification in agricultural lands," *Sensors*, vol. 20, no. 6, p. 1734, 2020, PMID: 32244929; PMCID: PMC7146316.

[17] F. Feng, S. Wang, C. Wang, and J. Zhang, "Learning deep hierarchical spatial-spectral features for hyperspectral image classification based on residual 3D-2D CNN," *Sensors*, vol. 19, no. 23, p. 5276, 2019, PMID: 31795511; PMCID: PMC6928880.

[18] J. Yu, B. Yang, J. Wang, J. Leader, D. Wilson, and J. Pu, "2D CNN versus 3D CNN for false-positive reduction in lung cancer screening," *Journal of Medical Imaging*, vol. 7, no. 5, Article ID 051202, Epub 2020 Oct 13. PMID: 33062802; PMCID: PMC7550796, 2020.

[19] S. K. Sarin, A. Choudhury, A. Choudhury et al., "Acute-on-chronic liver failure: consensus recommendations of the Asian Pacific association for the study of the liver (APASL): an update," *Hepatology International*, vol. 13, no. 4, pp. 353–390, 2019, Epub 2019 Jun 6. Erratum in: Hepatol Int. 2019 Nov; 13(6):826-828. PMID: 31172417; PMCID: PMC6728300.

[20] Chinese Society of Hepatology, "Chinese medical association; Chinese society of infectious diseases, Chinese medical association. [the guidelines of prevention and treatment for chronic hepatitis B]," *Zhonghua Gan Zang Bing Za Zhi*, vol. 13, no. 12, pp. 881–891, 2005, Chinese. PMID: 16491521.

[21] Z. Sun, X. Liu, D. Wu et al., "Circulating proteomic panels for diagnosis and risk stratification of acute-on-chronic liver failure in patients with viral hepatitis B," *Theranostics*, vol. 9, no. 4, pp. 1200–1214, 2019, PMID: 30867825; PMCID: PMC6401414.

[22] J. Yao, S. Li, L. Zhou et al., "Therapeutic effect of double plasma molecular adsorption system and sequential half-dose plasma exchange in patients with HBV-related acute-on-chronic liver failure," *Journal of Clinical Apheresis*, vol. 34, no. 4, pp. 392–398, 2019, Epub 2019 Feb 13. PMID: 30758886; PMCID: PMC6767528.

[23] X. Pang, X. Li, Z. Mo et al., "IFI16 is involved in HBV-associated acute-on-chronic liver failure inflammation," *BMC Gastroenterology*, vol. 18, no. 1, p. 61, 2018, PMID: 29743020; PMCID: PMC5944170.

[24] Q. Yan, L. Wang, L. Lai et al., "Next generation sequencing reveals novel alterations in B-cell heavy chain receptor repertoires associated with acute-on-chronic liver failure," *International Journal of Molecular Medicine*, vol. 43, no. 1, pp. 243–255, 2019, Epub 2018 Oct 22. PMID: 30365073; PMCID: PMC6257861.

[25] F. Liu, X. Duan, Z. Wan et al., "Lower number and decreased function of natural killer cells in hepatitis B virus related acute-on-chronic liver failure," *Clinics and Research in Hepatology and Gastroenterology*, vol. 40, no. 5, pp. 605–613, 2016, Epub 2016 Apr 1. PMID: 27053076.

[26] D.-N. Zhang, Y. Liu, X. Li et al., "Imbalance between soluble and membrane-bound CD100 regulates monocytes activity in hepatitis B virus-associated acute-on-chronic liver failure," *Viral Immunology*, vol. 34, no. 4, pp. 273–283, 2021, Epub 2021 Feb 26. PMID: 33646067.

[27] X. Dong, Y. Lei, T. Wang et al., "Automatic multiorgan segmentation in thoraxCTimages using U-net-GAN," *Medical Physics*, vol. 46, no. 5, pp. 2157–2168, 2019, Epub 2019 Mar 22. PMID: 30810231; PMCID: PMC6510589.

[28] X. Zhou, "Automatic segmentation of multiple organs on 3D CT images by using deep learning approaches," *Advances in Experimental Medicine and Biology*, vol. 1213, pp. 135–147, 2020, PMID: 32030668.

[29] J. Osuna-Coutiño and J. Martinez-Carranza, "High level 3D structure extraction from a single image using a CNN-based approach," *Sensors*, vol. 19, no. 3, p. 563, 2019, PMID: 30700031; PMCID: PMC6386827.

[30] S. Hamidian, B. Sahiner, N. Petrick, and A. Pezeshk, "3D convolutional neural network for automatic detection of lung nodules in chest CT," *Medical Imaging 2017: Computer-Aided Diagnosis*, vol. 10134, Article ID 1013409, 2017 Epub 2017 Mar 3. PMID: 28845077; PMCID: PMC5568782.

Hindawi
Journal of Healthcare Engineering
Volume 2021, Article ID 4360122, 19 pages
https://doi.org/10.1155/2021/4360122

Review Article

A Review on the Use of Microsoft Kinect for Gait Abnormality and Postural Disorder Assessment

Anthony Bawa, Konstantinos Banitsas, and Maysam Abbod

Department of Electronic and Electrical Engineering, College of Engineering, Design and Physical Sciences, Brunel University, UB8 3PH, Uxbridge, UK

Correspondence should be addressed to Anthony Bawa; 2034163@brunel.ac.uk

Received 29 July 2021; Accepted 16 October 2021; Published 1 November 2021

Academic Editor: Daniel Espino

Gait and posture studies have gained much prominence among researchers and have attracted the interest of clinicians. The ability to detect gait abnormality and posture disorder plays a crucial role in the diagnosis and treatment of some diseases. Microsoft Kinect is presented as a noninvasive sensor essential for medical diagnostic and therapeutic purposes. There are currently no relevant studies that attempt to summarise the existing literature on gait and posture abnormalities using Kinect technology. The purpose of this study is to critically evaluate the existing research on gait and posture abnormalities using the Kinect sensor as the main diagnostic tool. Our studies search identified 458 for gait abnormality, 283 for posture disorder of which 26 studies were included for gait abnormality, and 13 for posture. The results indicate that Kinect sensor is a useful tool for the assessment of kinematic features. In conclusion, Microsoft Kinect sensor is presented as a useful tool for gait abnormality, postural disorder analysis, and physiotherapy. It can also help track the progress of patients who are undergoing rehabilitation.

1. Introduction

Microsoft's Kinect sensor is a motion-sensing device that gives users the features to interact with game consoles and computers via ways such as gestures, spoken commands, or movement [1]. Kinect sensors provide new and enhanced features for motion detection and 3D reconstruction. Kinect sensors also introduce many features that allow for more accurate research into the movement of the human body and its gestures. The sensors allow for interaction through voice commands that is a unique component of the technology. It has detectors and infrared emitters to capture human physical activities.

The key components of Microsoft Kinect sensors are the RGB cameras, IR depth sensors, and the multiple microphone array. The second version of Kinect has some enhanced features compared to earlier Kinect [2]. The colour camera of Kinect v2 has $1{,}920 \times 1{,}080$ @30fps while that of Kinect v1 has 640×480 @30fps. In terms of the depth camera capabilities, Kinect v2 uses 512×424 pixels, while Kinect v1 uses 320×240 pixels, and as a result, Kinect v2 has better image recognition compared to the earlier version. Kinect v2 is noted to have a wider area view compared to Kinect v1. Another key feature is that Kinect v2 has better skeletal joint tracking where it is able to capture 26 joints, whereas Kinect v1 can only capture 20 joints. The unique feature of Kinect sensors can be applied to the medical field for the purposes of diagnosing diseases and physiotherapy rehabilitation of people who may have walking disabilities due to physical injury or related diseases.

As stated above, Kinect has found application in many areas related to posture and motion capturing. The major bulk of studies are related to Kinect research in the areas of motion tracking, monitoring, diagnosis, and rehabilitation. Some representative studies with Kinect technology include: Lavanya et al. [3] presented dynamic finger gestures with skeletal data extracted from the depth sensor. A unique technique was designed for the recognition of dynamic gestures that can be used in auditoriums and classrooms. This approach allowed for more dynamic hand gestures to be developed that can be used in different environments. An example is a tutor using this technique to instruct students in a classroom who have speech problems to assist in their studies.

The use of Kinect for medical monitoring and diagnosis has also been trialed by researchers. Ales Prochazka et al. [4] presented a novel technique of using Kinect for heart rate estimation and breath monitoring to determine the likelihood of any medical condition. The mean thorax movement was monitored within a selected area to estimate the breathing of patients. Huy-Hieu et al. [5] presented a real-time system for the detection of objects for patients who are visually impaired. A unique system was designed that allowed visually impaired people to move freely and to detect any obstructions. Object detection was based on the 3D information captured with a depth sensor. However, the designed system was limited to only indoor use. Xin Dang et al. [6] presented a novel interactive system with an electroencephalogram and depth sensor for people with dementia. Skeletal data captured from the depth sensor were extracted to determine the motion of a user and their mental state. The designed system using a deep neural network can be used to aid patients with dementia. Torres et al. [7] provided a novel approach to assist physicians in the diagnosis of Parkinson's disease using posture and movement captured with Kinect. The characteristics of movements such as frequency and amplitude were essential to study tremors in people with Parkinson's. The results achieved in the study can assist clinicians to diagnose Parkinson's based on the tremors intensity and the postural changes.

Kinect sensors are also widely used for the purposes of rehabilitation. Capecci et al. [8] demonstrated an innovative approach in the evaluation of dynamic movement in a rehabilitation scenario. They were able to track skeletal joints in evaluating the performance of patients during a low back pain physiotherapy exercise. Postolache et al. [9] developed a unique framework for physiotherapy assessment based on a mobile application using skeletal data. The designed system assists physiotherapists to improve the effectiveness of the training sessions for patients undergoing rehabilitation. Monique Wochatz et al. [10] illustrated a reliable and valid assessment of the lower extremity rehabilitation of exercises using Kinect v2 sensors. The authors demonstrated the Kinect sensor as a reliable tool in assessing the lower limb position and the joint angles during exercises. Sanjay et al. [11] developed a unique framework for stroke rehabilitation of patients in a home environment. A framework was designed to aid patients who have suffered a stroke in their treatment process. The designed system can be used indoors to help patients who have difficulty in movement.

Abnormal gait is the asymmetric movement of a person that is most likely to be caused by disease or physical injuries. This could be a result of nerves damage, injuries, weakness of muscles, or joint problems. The detection of gait abnormalities at an early stage can help prevent other complications. There are traditional wearable sensors for gait abnormal detection; however, these conventional methods are quite cumbersome to use. Kinect is seen as a better alternative to wearable sensors in gait abnormal detection.

As such, gait analysis has also received wide interest among researchers [12–14]. Kinematic features such as the step length, walking speed, and cadence are useful to determine the gait of an individual. This will normally be cyclical and symmetric unless there are some forms of abnormalities. The human gait could be affected by the musculosketal and neurological systems as well as the motions habits [15]. Hassain Bari et al. [16] presented a novel method by designing a deep neural network for gait recognition. This was then evaluated with a 3D skeletal gait data set. Another study by Wan Zharfan et al. [17] illustrated an economic technique of gait analysis based on pixel coordinates of body joints. The technique served as an alternative method to determine gait parameters in a Vicon motion analysis.

The human posture is the physical positioning by which the body takes at a particular time. Posture is the arrangement of the structure of the human body and its position. Correct body posture can help reduce pressure on the human body by keeping it balanced. The human body posture may be intentional or unintentional due to natural causes. There are several techniques for postures recognition with skeletal data. Samiul Monir et al. [18] presented a novel technique with a rotation and scale-invariant for posture recognition from skeletal features. This technique for posture recognition used skeletal data and angle rotation of an individual. A set of vectors and manipulation of angles were used to determine the posture. Zequn et al. [19] developed a novel posture recognition model that can be used to identify different postures captured. The depth sensor was used to generate features of different body parts of an individual. The captured features were then fed into the support vector machine (SVM) to identify the posture.

Although there are quite a number of studies available using Kinect for the assessment of gait and posture abnormalities, to the best of our knowledge, there is no overall review study that attempts to summarise articles on the use of the Kinect sensor for gait abnormality and posture disorder assessment. Our review adopts a systematic approach similarly used by Shmuel Springer et al. [20]. The study provides up-to-date review of the articles for analysis and discussion.

2. Methods

In this section, we retrieve articles that meet the inclusion criteria for our study. The existing articles identified were summarised into tables indicating the methods used and the sampling area. The sample area stated the source from which the article was retrieved, the authors of the article, and the year it was published. Our focus was on articles that used Kinect sensors for assessing gait and posture abnormalities.

2.1. Search and Identification of Articles. The scholarly database used to identify the articles were: IEEE Xplore, ScienceDirect, CINAHL plus, and PubMed. The search was done in two different parts as follows:

(i) Part 1: the use of Kinect sensors for the detection of gait abnormality or disorder

(ii) Part 2: the use of Kinect sensors for detection posture disorder or instability

The key terms used in part 1 of the search were: "Kinect sensor," "gait abnormality," "gait disorder," and "walking abnormality." In the second part, the key terms used were: "Kinect sensor," "posture disorder," "posture abnormality," and "posture instability." The search was conducted between January and May 2021 to retrieve the most recent articles.

2.2. Eligibility Criteria of the Identified Articles. In identifying the articles for the study, we conducted two different searches for the database by two independent authors. The authors were able to identify and remove duplicate articles from the various database. The elimination of irrelevant articles was done without bias or oversight in order to get all relevant articles that meet the inclusion criteria. A number of diseases that could affect gait and posture abnormalities were included. They were: Parkinson's, ataxia, multiple scoliosis, stroke, and depression.

The exclusion criteria were for articles that only discussed gait detection and postures without considering abnormality. In the second part, articles that only discuss posture assessments without examining posture disorder or deformity were also not included. Articles that used wearable sensors for gait abnormality and posture disorder detection were not included. Figure 1 is a flowchart diagram of the search methodology.

3. Results

The initial search and retrieval of all articles from the various database were 458 for gait and 283 for posture, all using Kinect technology. The articles were further screened to ensure they meet the eligibility criteria for this study. In the end, a total of 26 articles were included for gait abnormality and 13 articles for posture disorders.

Table 1 summarises all the studies that were included for the review for gait abnormality, the journals where the articles were retrieved and the year of publications. In Table 1, the methodology describes the sampling method applied, the statistical method, and the descriptive approach used. That sampling method describes the number of participants in the study, gender, and age distribution. The disease associated with the abnormality was stated. The sampling methods from the reviewed articles were categorised as fully stated, partially, or not stated. The statistical method describes the statistical techniques that were used in the analysis of the data. The statistical methods were either sufficiently used or partially used. It describes the models and mathematical equations that were used in the analysis of skeletal data. The description method used refers to capturing of the skeletal data, processing of data, algorithms used, and the analysis of the results. It also includes the tools used in the analysis of results and a detailed discussion of the findings. Finally, the description method was either adequate or partial description.

The approach used in Table 1 was also similarly adopted in Table 2 except that it summarised the various articles for identifying posture disorders using Kinect. The sampling methods, statistical methods, and the description method are also indicated in this table.

In Table 3, the details of each article included in the study were categorised into two major phases. The first phase deals with the sampling technique used in each study while the second phase describes the key gait features captured with the major findings of each study. The limitations for each study were also included in the table.

A total number of 26 articles were reviewed. Most of the articles stated the number of participants in the study except in [26,28,37,42,43,45]. The majority of the studies used Kinect v2 as the main tool for capturing skeletal data for gait abnormality assessment, while a few articles used the older Kinect v1. In [37,44], the Asus Xtion PRO was used as a gold standard with a Kinect sensor for capturing skeletal data. Most of the reviewed articles did not state the data analysis tool. However, in [22,25,29,31,35,39,40], MATLAB was explicitly stated as the main tool for data analysis. In [23], the SPSS package was used as the data analysis tool. The gait features captured were mainly the step/stride length (m), stride time (s), gait speed (m/s), gait cycle (deg), gait rhythm (m/s), and step time (s). Some of the key joint angles measured were the hip, knee, and the ankle. Various algorithms were used to train the models for gait abnormality detection.

A total number of 13 articles were included for the assessment of posture abnormality or disorder. Some of the reviewed articles [42,46,50,51] did not state the participants in the studies. In Table 4, Kinect v2 was mostly used for skeletal data capturing, except in a few studies that used Kinect v1. Nine of the reviewed articles used Kinect v2 while four used Kinect v1. Most of the studies did not state any medical condition that resulted in posture abnormality. However, in [47], Parkinson's disease was stated, and in [56], a case of chronic traumatic brain injury was present. In [50,58], patients with suspected multiple scoliosis were also assessed for posture abnormality. The majority of the reviewed articles did not state the data analysis tool except in [47,48,50] that stated MATLAB. In [58], the IBM Watson Analytics was used to analyse the data for posture abnormality for patients with suspected cases of multiple scoliosis.

4. Discussion

4.1. Gait Abnormality or Disorder. The purpose of this study is to review the available studies using Microsoft Kinect for the assessment of gait and posture abnormalities. The key features measured included the angles formed by leg swing, speed, and distance of each gait step. These parameters were useful in detecting gait asymmetry in order to distinguish normal from abnormal gait. Some other components from the summarised studies were the algorithms used, the major findings of each study, and limitations.

From the reviewed articles, various methods were employed in assessing and detecting gait abnormality. The gait features captured were mainly the step/stride length (m), gait speed (m/s), gait cycle (deg), and step time (s). Some other gait features captured from the studies were angles of knee joints, ankle joints, and hip angles joints. The measured

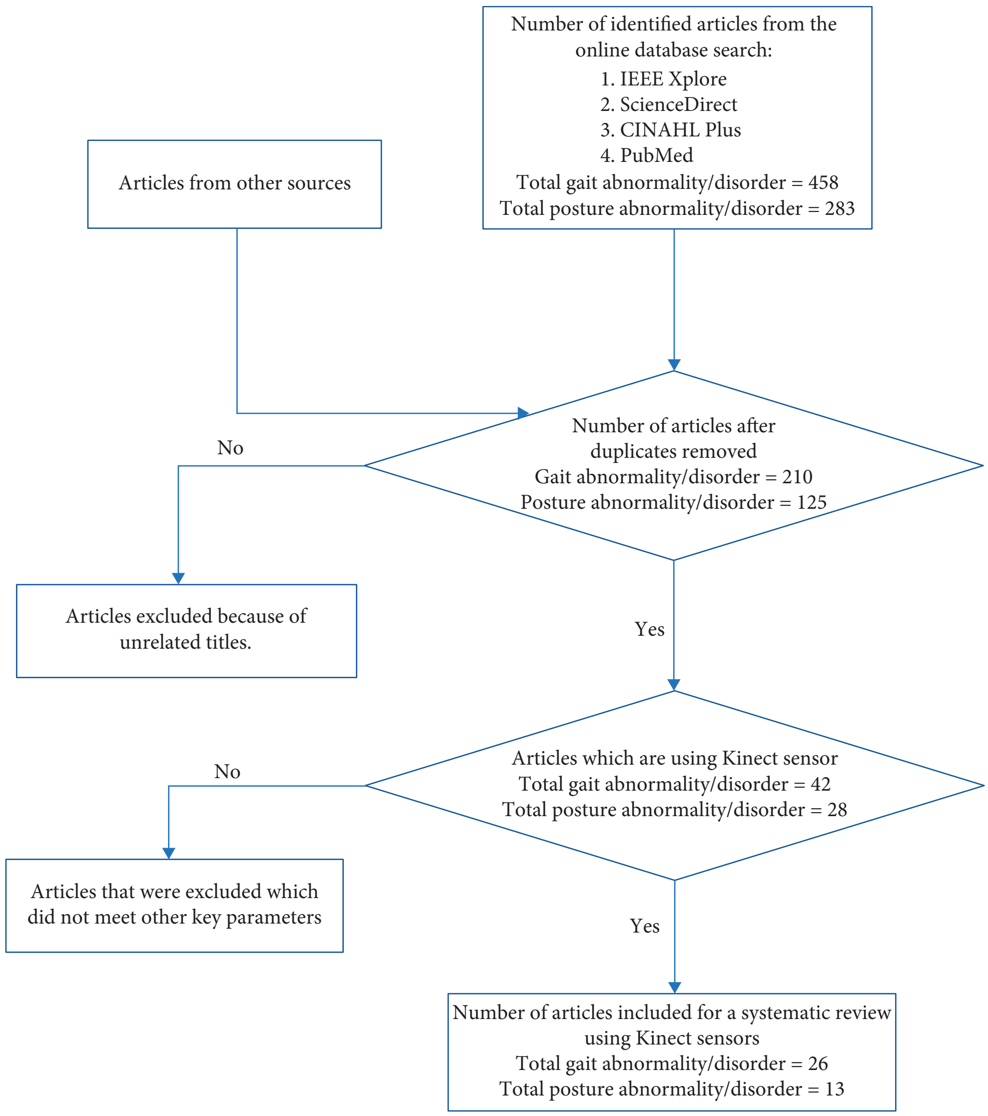

Figure 1: Flowchart for the search methodology of articles included.

joint angles were used to train the models in detecting gait abnormalities. The measurement of joint angles helped improve the efficiency and robustness of the trained models to detect gait abnormality.

They were various algorithms used to train the models for gaits abnormality detection. Some of the algorithms used in Table 3 were machine learning algorithms. The machine learning algorithms were either supervised or unsupervised, depending on the approach used. Supervised machine learning algorithms use classifications and regressions, while unsupervised use clustering and associations to determine outliers in the data. Algorithms that were used in the designed models for gait abnormality were: Bayesian algorithm, K-nearest neighbors algorithm (KNN), convolutional neural network (CNN), recurrent neural network (RNN), long short-term memory (RNN-LSTM), isolated forest (IF) algorithm, and one-class support vector machine (OC-SVM) algorithm. Depending on the algorithm that was used and the mythological approach, different accuracy were achieved. The Bayesian algorithm was commonly used in [15, 19, 23, 33] for the assessment of gait abnormalities. RNN-LSTN algorithm was used in three of the studies [20, 36, 37, 40]. Amr Elkholy et al. used unsupervised one-class support vector machine (OC-SVM) and isolated forest algorithms for abnormal detection in [31, 33]. Some other algorithms such as the EDSS and MSWS were also applied in [27]. The algorithms used in the various studies cannot be compared to determine which is more efficient and robust. This is because different methods and data sets were used to achieve the desired accuracy.

The general limitation of the summarised studies has to do with the relatively small data set used. Most of the studies did not use a large data set to test the robustness of the trained model except in [21, 22, 25, 29, 33, 34, 44] that used large data sets. Another limitation was some gait parameters were not used in training the models for abnormal gait assessment. Some studies did not also include key joint angles in the trained model. Therefore, some of the models

Table 1: Reviewed articles on gait abnormality or disorder.

Sample study area			Methodology used for the reviewed articles		
Authors	Journal/conference paper	Year of publication	Sampling method in study	Statistical method	Description method
Bei et al. [21]	IEEE sensors journal	2018	Partially stated	Sufficiently used	Adequate description
Wang et al. [22]	IEEE sensors journal	2019	Fully stated	Sufficiently used	Adequate description
Tsukagoshi et al. [23]	Journal of clinical neuroscience	2019	Fully stated	Sufficiently used	Partial description
Amin amini et al. [24]	Journal of healthcare engineering	2019	Fully stated	Sufficiently used	Adequate description
Prochazka et al. [25]	Elsevier – digital signal processing	2015	Partially stated	Partially used	Partial description
Pachón-Suescún et al. [26]	International journal of electrical and computer engineering (IJECE)	2020	Partially stated	Partially used	Partial description
Gholami et al. [27]	IEEE journal of biomedical and health informatics	2016	Fully stated	Partially used	Adequate description
Maxime devanne et al. [28]	International conference on pattern recognition (ICPR)	2016	Not stated	Not used	Adequate description
Latorre et al. [29]	Elsevier – journal of biomechanics	2018	Fully stated	Partially used	Adequate description
Prakash et al. [30]	IEEE transactions on instrumentation and measurements	2021	Fully stated	Partially used	Adequate description
Nguyen et al. [31]	Sensors, MDPI	2016	Partially stated	Sufficiently used	Adequate description
Shrivastava et al. [32]	Elsevier – materials today: Proceedings	2020	Partially stated	Partially used	Partial description
Prochazka et al. [33]	IEEE international conference on image processing (ICIP)	2014	Partially stated	Partially used	Partial description
Fang et al. [34]	IEEE access on multiphysics	2019	Fully stated	Sufficiently used	Adequate description
Ismail et al. [35]	IEEE international conference on advances in biomedical engineering (ICABME)	2017	Partially stated	Not used	Partial description
Amini et al. [36]	Disability and rehabilitation: Assistive technology	2018	Fully stated	Sufficiently used	Adequate description
Elkholy et al. [37]	IEEE journal of biomedical and health informatics	2019	Not stated	Partially used	Partial description
Soltaninejad et al. [38]	Sensors, MDPI	2019	Fully stated	Partially used	Adequate description
Kozlow et al. [39]	Sensors, MDPI	2018	Fully stated	Sufficiently used	Adequate description
Chakraborty et al. [40]	International conference on computational science	2020	Partially stated	Partially used	Partial description
Jyothsna et al. [41]	IEEE engineering in medicine and biology society (EMBC)	2020	Partially stated	Not used	Partial description
Won et al. [42]	IEEE engineering in medicine and biology society (EMBC)	2019	Not stated	Not used	Partial description
Jinnovart et al. [43]	IEEE conference on decision and control (CDC)	2020	Not stated	Not used	Partial description
Elkholy et al. [44]	International conference of the IEEE engineering in medicine and biology society (EMBC)	2020	Fully stated	Not used	Adequate description
Meng et al. [45]	Joint conference on computer vision, imaging and computer graphics theory and applications	2016	Not stated	Not used	Partial description
Jun et al. [46]	IEEE access	2020	Not stated	Not used	Partial description

did not give high precision and robustness in assessing gait abnormalities. Also, the use of Kinect v1 has limited capabilities compared to Kinect v2 that has more enhanced 3D skeletal tracking capabilities.

4.2. Posture Abnormality or Disorder. From Table 4, some body features were measured to determine the posture abnormality of a person. They were the body center mass position and the shoulder position angulation. The head

Table 2: Reviewed articles on posture abnormality or disorder.

Sample study area		Methodology used for the reviewed articles			
Authors	Journal/Conference	Year of publication	Sampling method in study	Statistical methods	Description of model used
Ferrais et al. [47]	Sensors, MDPI	2019	Fully stated	Sufficiently used	Adequate description
Jawed et al. [48]	IEEE international conference on emerging trends in engineering, sciences and technology	2019	Not stated	Not used	Partial description
Yang et al. [49]	IEEE sensors	2014	Fully stated	Sufficiently used	Partial description
Castroa et al. [50]	Elsevier porto biomedical journal	2016	Fully stated	Partially used	Adequate description
Chin-hsuan et al. [51]	Sensors, MDPI	2020	Fully stated	Sufficiently used	Adequate description
Abobakr et al. [52]	IEEE international conference on systems, man, and cybernetics	2017	Partially stated	Not used	Partial description
Napoli et al. [53]	Biomedical engineering society	2017	Partially stated	Partially used	Partial description
Meng-Che shih et al. [54]	Journal of neuro engineering and rehabilitation	2016	Fully stated	Sufficiently used	Adequate description
Chanpimol et al. [55]	Archives of physiotherapy	2017	Partially stated	Partially used	Partial description
Bortone et al. [56]	IEEE-EMBS international conference on biomedical and health informatics	2014	Not stated	Not used	Partial description
Modesto et al. [57]	Elsevier applied ergonomics	2017	Partially stated	Not stated	Partial description
Norbert et al. [58]	Health informatics meets eHealth	2017	Fully stated	Fully stated	Adequate description
Rose et al. [59]	Elsevier: gait and posture	2012	Partially stated	Not stated	Partial description

position and the neck angles were also essential to detect postural instability. In [47,49], the center of body mass was used to determine the postural instability. The rapid upper limb assessment (RULA) method was commonly used to assess postural instability in [52,57]. The distance between the neck, shoulder blade, and angles was very essential in determining the abnormal posture of a person. In [52], the height, hips, and shoulder position were measured as well as the shoulder angles. In [53], the knee joints, ankle joints, the lateral joints, and interior joints were computed. The spine angle was also used in [47] to determine the abnormal posture of an individual.

Different algorithms were used to determine postural disorder from the summarised studies. The algorithms that were used included pattern recognition neural algorithm, CoVNet model, Berg balance scale (BBS) method, and the RULA technique. These algorithms were used to track the static body position features and key joint angles to determine the postural instability of a person. The accuracy in the detection of posture disorder was not considered because the studies focused only on determining if there was posture abnormality.

The limitations of the various summarised studies largely depended on the small data set used in the various studies.

4.3. Mathematical Analysis of Gait Abnormality. In Sun Bie et al. [21], the spatial position was used with the associated joints for each subject walking. The extracted joint angle formed were then calculated. The equations used in the joint angle computation were given by the following equation:

$$\begin{aligned} \mathrm{len}(i,k) &= \|J[i]-J[k]\|, \\ \theta(i,k,j) &= \cos^{-1}\frac{(J[i]-J[k])*(J[j]-J[k])}{\|J[i]-J[k]-J[j]-J[k]\|}, \end{aligned} \tag{1}$$

where *J[i]* represents the joints, *len (i,k)* represents the distance between joint *i*, and *k* θ *(i, k, j)* describes the angle formed by joint *i*, *k*, and *j*. Therefore, the angles formed by the left leg and the right leg were calculated by the following equation:

$$\begin{aligned} R_s &= \rho(\theta_l,\theta_r) \\ &= \frac{\mathrm{E}[(\theta_l-m_{\theta l})*(\theta_r-m_{\theta r})]}{\sqrt{\mathrm{E}(\theta_l-m_{\theta l})*\mathrm{E}(\theta_r-m_{\theta r})}}, \end{aligned} \tag{2}$$

where θ_l and θ_r represents the angles formed on the left and right leg, respectively, of a subject walking and E(∗) represents the expected value of the operation for the simulation. The equations were used in computing the key joint angles to determine gait asymmetry. The angles calculated were the hip angle, knee angle, and the ankle angle. The challenge with this technique is that there may be some difficulties in measuring the inner joint angles of subjects. The gait cycles were computed and given by the following equation:

Table 3: Detailed features of articles on gait abnormality or disorder.

Sampling techniques			Key gait features and aims of the identified articles							
Authors	Gender and age range of participants	Abnormality or disease	Kinect sensor version	Data type capture	Gait parameters measured	Data analysis tool	Algorithm used	Accuracy achieved (%)	Major findings	Limitations of study
Bei et al. [21]	Gender and age not stated	70 normal walking and 50 walking disorder	Kinect v2	Skeletal data	Leg swing angle (deg), knee and ankle joint angle (deg), step length (m), gait cycle (deg)	Not stated	K-means algorithms, Bayesian algorithms	Not stated	A novel technique was designed to demonstrate movement disorder through gait symmetry analysis	Some key gait parameters and joint angle were not considered. Only a small data set was used to test the model
Wang et al. [22]	98 individuals; gender and age not stated	Depression	Kinect v2	Skeletal data	Gait velocity (m/s), *Joint angles (deg)*	MATLAB	t-SNE algorithm	93.75	A nonintrusive framework was designed to detect depression	Some gait features are required to improve the robustness of the model in a real environment
Tsukagoshi et al. [23]	Ataxia (male = 14 female = 11); age 54.1 ± 14.6 years. Parkinson's (male = 10 female = 15); age 68.4 ± 8.1 years. Healthy people (male = 13 female = 12), age 62.0 ± 13.9 years	25 Patients with ataxia, 25 patients with Parkinson's, and 25 health people	Kinect v2	Skeletal data	Stride length (m), feet length (m), gait rhythm, (m/s)	SPSS package suit	Clinical scale	Not stated	Kinect depth sensor to quantitatively evaluate gait interference for patients who have a movement disorder	Body joint gaits angulation were not considered and thus there may be less precision with this model
Amini et al. [24]	15 participants (12 male and 3 female); average age 54–92 years	People with Parkinson's	Kinect v2	Skeletal data	Gait cycle (deg), knee angle (deg), number of footsteps (m)	Not stated	Heuristic fall detection algorithm	Not stated	A unique model was designed to detect freeze of gait for people with Parkinson's	The developed system is limited to only the x-axis for the freeze of gait detection
Aleš prochazka et al. [25]	51 individuals; gender not stated; age: Parkinson's, 52–87 years, healthy mature: 32–81 years, young: 23–25 years	18 Individuals with Parkinson's, 18 healthy matured, and 15young ones	Kinect v1	Not stated	Step length (m), gait length (m/s), stride length (m)	MATLAB	Bayesian algorithm	94.1	A novel technique was developed using Bayesian classification algorithm to recognise gaits disorder for people with Parkinson's disease	Some key joint angles were excluded in developing an abnormal gait recognition model and thus not so efficient

Table 3: Continued.

Sampling techniques			Key gait features and aims of the identified articles							
Authors	Gender and age range of participants	Abnormality or disease	Kinect sensor version	Data type capture	Gait parameters measured	Data analysis tool	Algorithm used	Accuracy achieved (%)	Major findings	Limitations of study
Cesar et al. [26]	Gender and age not stated	Not stated	Kinect v2	Skeletal data	Step speed (m/s), stride speed	MATLAB	LSTM algorithm	98.1	A model was designed to detect gait abnormality using the LSTM algorithm	Body joint angles are required to test and improve the accuracy of the model
Gholami et al. [27]	MS (male = 1, female = 9); age = 41–79 years. NP (male = 1, female = 9); age 36–80 years	10 multiple scoliosis and 10 normal people	Kinect v2	Skeletal data	Gait velocity (m/s), stride length (m), stride time (s), step time (s)	Not stated	EDSS algorithm and MSWS algorithm	Not stated	A novel framework was designed to evaluate the gaits abnormality of people with multiple scoliosis	The designed framework does not provide enough reliability to detect the disease. There is less accuracy with the designed model.
Devanne et al. [28]	Gender and age not stated	Not stated	Kinect v2	Skeletal data	Step length (m), body joint angles (deg)	Not stated	Riemannian manifold algorithm	Not stated	A model is designed to detect gait abnormality using motion trajectories	The method is not able to identify static gait abnormality such as a freeze of gait
Latorre et al. [29]	45 healthy individuals (men = 31, women = 14); age 30.6 ± 7.6 years. 38 stroke survived people (men = 22, women = 16); age = 56.1 ± 13.2 years	45 Healthy individuals and 38 stroke surviving people	Kinect v2	Skeletal data	Gait speed (m/s), stride length (m), stride time (s), swing time (s), step time (s), step asymmetry	MATLAB	Bayesian algorithm	Not stated	The authors illustrated the reliability of using Kinect-based methods to estimate gait disorder for poststroke adult individuals	The method used in the study were limited which influenced some errors with the gait parameters measured
Prakash et al. [30]	24 individuals (13 males and 11 females); age not stated	Not stated	Kinect v2	Skeletal data	Left knee angle (deg), right knee angle (deg)	Not stated	IR-UMB algorithm	Not stated	A model was developed to detect gait abnormality using contactless IR-UWB	Only the knee angle was considered and this may not give accuracy of the designed model

Table 3: Continued.

Sampling techniques					Key gait features and aims of the identified articles					
Authors	Gender and age range of participants	Abnormality or disease	Kinect sensor version	Data type capture	Gait parameters measured	Data analysis tool	Algorithm used	Accuracy achieved (%)	Major findings	Limitations of study
Nguyen et al. [31]	20 individuals; gender and age not stated	10 healthy people and 10 abnormal (Parkinson's/stroke)	Kinect v2	Skeletal data	Left hip angle (deg), right hip angle (deg), left knee angle (deg), right knee (deg), left ankle (deg), right ankle (deg)	MATLAB	HMM algorithm	90.12	A novel approach was designed for gait abnormality detection using skeletal-based data with no prior knowledge of individual gait	The method used in the study provided enough precision of the results achieved
Shrivastava et al. [32]	24 individuals; gender and age not stated	12 Normal walking and 12 abnormal walking	Kinect v1	Skeletal data	Step length (m), gait cycle (s), hip left foot angle (deg), right foot angle (deg)	MATLAB	KNN algorithm, SVM algorithm, and decision tree algorithm	83.33	The authors developed a model using machine learning for gaits abnormality detection using data from Kinect	The model used does not provide high precision and efficiency for detecting gait abnormality
Prochazka et. Al [33]	36 individuals; gender not stated; people with Parkinson's: age = 52–87 years, healthy control: age = 32–81 years	18 Individuals with Parkinson's. 18 healthy control	Kinect v1	Skeletal data	Stride length (m),	MATLAB	Skeletal tracking algorithm	90	A system was designed to detect Parkinson's disease based on the gaits features. This could be used for early detection of Parkinson's.	Only a few parameters such as stride length were used and this does not provide enough efficiency and reliability of the model
Fang et al. [34]	3,669 individuals (1555 males and 2114 females); age range 22–28 years	Suspected cases of depression	Kinect v2	Skeletal data	Walking speed (m/s), arm swing (mm), stride length (m), vertical head position (deg)	MATLAB	SVM algorithm; KNN, RF, and LR algorithms; linear discriminant analysis (LDA)	91.58	A novel model was designed using different ML to detect depression prevalence among students	Different viewing points were not considered in developing a model to detect depression
Ismail et al. [35]	11 individuals; gender not stated; age = 21–25 years	11 healthy control individuals	Kinect v2	Skeletal data	Gait speed (m/s), stride length (m), right knee angle (deg), left knee angle (deg), right ankle (deg), left ankle (deg), hip angle (deg)	MATLAB	Angle average algorithm	Not stated	A novel system is developed to determine gait abnormalities using gait cycle	There were some marginal errors in the data set used that does not provide enough efficiency of the model used in detecting abnormality

Table 3: Continued.

Sampling techniques		Key gait features and aims of the identified articles								
Authors	Gender and age range of participants	Abnormality or disease	Kinect sensor version	Data type capture	Gait parameters measured	Data analysis tool	Algorithm used	Accuracy achieved (%)	Major findings	Limitations of study
Amin amini et al. [36]	11 healthy subjects; age range 24–31 years	Not stated	Kinect v2	Skeletal data	Body angle (deg), feet/joint distance	Not stated	Pythagorean theorem	Not stated	A unique model is designed for casting automatic/ dynamic visuals for people with Parkinson's disease	The designed model is limited to indoor environment use
Elkholy et al. [37]	Gender and age not stated	Not stated	Kinect v2, Asus Xtion PRO	Skeletal data	Gait speed (m/s), gait cycle (deg), stride length (m)	Not stated	OC-SVM algorithm and IF algorithm	Not stated	A new approach was designed to detect gait abnormality based on unsupervised gait energy image (GEI)	Some factors that could affect the accuracy of abnormal gaits detection based on the GEI were not considered
Saltaninejad et al. [38]	5 individuals (4 males and 1 female); average age = 30.8 years	Not stated	Kinect v2	Skeletal data	Gait speed (m/s), hip angle (deg), knee angle (deg)	Not stated	Best removal algorithm for FOG	90	An automatic and fast assessment for FOG was designed	The model needs to be tested with real P.D patients to improve its reliability
Kozlow et al. [39]	21 Males and 9 females; age = 25 ± 5.2 years	28 Healthy individuals	Kinect v2	Skeletal data	Cadence (step/ min), left angle joint angle (deg), left knee joint angle (deg), right angle joint angle (deg), right knee joint angle (deg), left stride (deg), right stride length (deg)	MATLAB	Bayesian algorithm	88.68	The authors demonstrated the use of Bayesian network algorithm to classify gait abnormality	There are some limitations to the robustness and accuracy of this framework in detecting gait abnormality
Chakraborty et al. [40]	15 individuals; gender and age not stated	Patients with cerebral palsy	Kinect v2	Skeletal data	Gait cycle (deg), left ankle (deg), right ankle (deg)	MATLAB	Dempster shafer classifier	87.5	A novel technique is designed based on automated gait to detect gait abnormality for patients with cerebral palsy	This technique could be challenging in a real environment

Table 3: Continued.

Sampling techniques					Key gait features and aims of the identified articles					
Authors	Gender and age range of participants	Abnormality or disease	Kinect sensor version	Data type capture	Gait parameters measured	Data analysis tool	Algorithm used	Accuracy achieved (%)	Major findings	Limitations of study
Jyothsna et al. [41]	20 individuals; gender not stated; age = 80 years and above	20 people making up the various group, cognitive healthy individuals (CHI), subject cognitive impaired (SCI), and possible mildly cognitive person (pMCI)	Kinect v2	Skeletal data	Stride length (m), mean stride (m), step time (min), cadence (m), gait velocity (m/s)	Not stated	Convolutional neural network algorithm	Note stated	A framework was designed to detect the gait abnormality for patients with dementia	More gaits parameters need to be extracted to test the model on a large data set for dementia patients to improve the efficiency
Deok-won et al. [42]	Gender and age not stated	Not stated	Kinect v2	Skeletal data	Stride length (m), lower limbs body joint angles (deg)	Not stated	RNN-LSTM algorithm	97	The abnormal gait recognition model was designed that is capable of recognising five different abnormal gaits patterns using multiple Kinect sensors	The challenge with this model is that it can only recognise abnormal gait that were used in the training of the RNN-LSTM model. Some abnormal gaits may not be recognised.
Jinnovart et al. [43]	Gender and age not stated	Not stated	Kinect v2	Skeletal data	Stride length (m), body joint angles	Not stated	RNN algorithm, LSTM algorithm, and GRU algorithm	RNN = 73.4, LSTM = 82.8, and GRU = 81.6	A real-time recognition of abnormal gait was presented using recurrent neural network	Some abnormal gait may not be recognised with the designed model
Amr et al. [44]	43 individuals; gender for abnormal gait: male = 19 and female = 13; age = 18–85 years. Healthy control people (male = 8 and female = 3); age = 27–64 years	32 Patients with gait abnormality and 11 healthy control people	Kinect v2, Asus Xtion PRO	Skeletal data	Gait cycle (deg), swing phase(deg), step length (deg)	Not stated	OC-SVM algorithm and IF algorithm	Not stated	A robust and efficient skeletal system was developed to detect abnormal activities performed by a person	The model will require a large data set to test the efficiency of the designed model

Table 3: Continued.

Sampling techniques			Key gait features and aims of the identified articles							
Authors	Gender and age range of participants	Abnormality or disease	Kinect sensor version	Data type capture	Gait parameters measured	Data analysis tool	Algorithm used	Accuracy achieved (%)	Major findings	Limitations of study
Menget al. [45]	Gender and age not stated	Not stated	Kinect v2	Skeletal data	Interskeletal joint distance	Not stated	Random forest classifier	Not stated	A system was developed using a skeletal inter-joint distance to detect abnormal gait and normal gait	The developed system may not be robust because only a few gait features were used on small data sets for abnormal gait detection
Jun et al. [46]	9 individuals; gender and age not stated	1 normal person and 8 abnormal gait	Kinect v2	Skeletal data	Left hip angle (deg), right hip angle (deg), left knee angle (deg), right knee (deg), left ankle (deg), right ankle (deg)	Not stated	RNN algorithm and LSTM algorithm	Not stated	An extraction method feature was developed using RNN to increase the performance of gait abnormality from a skeletal base system	A small data set was used to test the model, and this does not provide high efficiency for gait abnormal detection

RNN: recurrent neural network; LSTM: long short-term memory; GRU: gated recurrent units; OC-SVM: one-class support vector machine; IF: isolation forest; HMM: hidden Markov model; and KNN: k-nearest neighbors.

Table 4: Detailed features of articles on posture abnormality or disorder.

	Sampling techniques				Key body features and aims of the identified articles				
Authors	Gender and age of participants	Abnormality/ disease	Kinect sensor version	Data type capture	Body features measured	Data analysis tool	Algorithm used	Major findings	Limitations of the study
Ferrais et al. [47]	14 individuals (8 male and 6 female); age = 53–80 years	Parkinson's disease	Kinect v2	Skeletal data	Centre of body mass (m)	MATLAB	KNN algorithm	A system is designed for the automatic posture analysis of people with Parkinson's to determine postural instability	More subjects are required to test the model to improve its reliability and efficiency
Jawed et al. [48]	Gender and age not stated	Not stated	Kinect v1	Skeletal data	Body joint angles (deg), body position (m)	MATLAB	Pattern recognition neural algorithm	A system was developed using pattern recognition neural network model that is capable of analysing the whole body of a patient to determine if there is any postural disorder	Not much efficiency with this model in detecting postural disorder with high accuracy
Yang et al. [49]	18 individuals, 9 males and 9 females; age = 24.0 ± 0.7 years	Not stated	Kinect v2	Skeletal data	Centre of body mass (m)	Not stated	RSM algorithm	A system was designed to evaluate the standing balance to determine posture instability	There may be some variations in the calibration to measure the COM
Castroa et al. [50]	98 individuals (males = 50 and females = 48) average; age 24.7 years	Suspected scoliosis disease	Kinect v2	Skeletal data	Shoulder angulations (deg)	MATLAB	SA method	The Kinect sensor was used to quantitatively evaluate the posture of the spine to determine if there is any posture instability	The challenge was that the S2's spinal exposition process was unassured
Chin-Hsuan Liu et al. [51]	45 individuals (15 youth and 30 elderly); age of youth = 24.06 ± 2.02 years; age of elderly = 71.13 ± 4.56 years	Not stated	Kinect v2	Skeletal data	Body joint angles (deg), center of body mass (m)	Not stated	Mediolateral (ML) algorithm	A system was designed to investigate the postural instability using the body joint coordination patterns	Only the mediolateral (ML) motion direction is considered in determining impairments of an individual

Table 4: Continued.

	Sampling techniques		Key body features and aims of the identified articles						
Authors	Gender and age of participants	Abnormality/ disease	Kinect sensor version	Data type capture	Body features measured	Data analysis tool	Algorithm used	Major findings	Limitations of the study
Abobakr et al. [52]	Gender and age not stated	Not stated	Kinect v2	Skeletal data	Body joint angles (deg)	Not stated	ConVnet algorithm, AlexNet CNN algorithm, and RULA method	A system was developed using Kinect and for the early detection of postural work-related disorders for people in a manufacturing industry	The methods used only considered the joint angles in designing the model and thus the may not be enough precision
Alessandro Napoli et al. [53]	15 individuals (7 male and 8 female); age not stated	Not stated	Kinect v2	Skeletal data	3D position of body distance (m), spine angle (deg)	Not stated	Balance detection algorithm	A system was designed to determine balancing deficits and postural instability of individuals	There should be an expansion of the features of automatic assessment of postural stability in determining the postural instability
Meng-Che shih. Et l. [54]	Gender BBE (male = 9 and female = 1); gender BT (male = 7 and female = 3); age BBE group 67.5 ± 9.96 years; age BT group 68.8 ± 9.67	Individuals with Parkinson's disease balance-based exergaming group ($N = 10$), balance training group ($N = 10$)	Kinect v2	Skeletal data	Limit of stability (LOS), one leg stance (OLS)	Not stated	BBS method	The authors used a novel technique to assess the postural stability of individuals with Parkinson's disease	The sample size was small, and calibration variability was observed in the exergaming session
Chanpimol et al. [55]	1 individual (1 male); age = 37 years	Chronic traumatic brain injury (TBI)	Kinect v2	Skeletal data	Body position distance (m)	Not stated	Limits of stability (LOS) algorithm	A study to improve the dynamic balance of an individual with TBI and improve the postural instability.	The designed system is limited to a single individual with TBI
Bortone et al. [56]	Gender and age not stated	Not stated	Kinect v1	Skeletal data	Joint angles (deg)	Not stated	Nonasymmetric pattern	An innovative system was designed to identify postural abnormalities using a two-stage approach	The body features measured do provide enough reliability and precision in detecting postural abnormality

Table 4: Continued.

	Sampling techniques		Key body features and aims of the identified articles						
Authors	Gender and age of participants	Abnormality/disease	Kinect sensor version	Data type capture	Body features measured	Data analysis tool	Algorithm used	Major findings	Limitations of the study
Modesto et al. [57]	Gender and age not stated	Not stated	Kinect v2	Skeletal data	Body position (m), joint angles (deg), motion sequence (deg)	Not stated	RULA method	A system was developed using Kinect v2 to detect awkward postures in real time	This designed model needs further investigation to determine its behaviour in a real working environment
Norbert et al. [58]	30 individuals (male = 18 and Female = 12); average age = 16 years	30 students suspected of scoliosis	Kinect v1	Skeletal data	Height measurement of hips and shoulders, angle of hips and shoulder (deg)	IBM Watson analytics	Nonirradiate body tracking method	The detection of scoliosis from students due to their incorrect posture	The confusion matrix used showed Kinect sensor may not provide accurate screening of data captured
Rose A. et al. [59]	20 individuals; gender and age not stated	20 healthy subjects	Kinect v1	Skeletal data	Body joint angles, knee joint, ankle joint, lateral/anterior joint angles	Not stated	Regression algorithm	A postural control assessment to determine those with postural control and those with postural imbalance	Measuring the internal and external joints rotations had limitations, and thus, there are some variations of the results

BBS: Berg balance scale; CNN: convolutional neural networks; RULA = rapid upper limb assessment; and SA: shoulder angulation.

$$T_s = \frac{1}{n-1}\sum_{i=2}^{i=n}\left|x_i - x_i - 1\right| * 0.0333, \tag{3}$$

where $|*|$ is the absolute value from the operation and 0.0333 is the conversion factor from the Kinect sensor.

In [37], the gait energy image (GEI) was used based on the Gaussian mixture model (GMM) for each pixel in the simulation. The GEI was the image captured with the Kinect sensor of an individual in a walkway. It can be used to determine the dynamic information of a gait sequence. The gait cycle was then extracted and computed at the point where a normalised autocorrelation from the silhouette image was high in the GEI.

$$C(N) = \frac{\sum_{x,y}\sum_{n=0}^{k} S(x,y,n)S(x,y,n+N)}{\sqrt{\sum_{x,y}\sum_{n=0}^{k} S(x,y,n)^2}\sqrt{\sum_{x,y}\sum_{n=0}^{k}(x,y,n+N)^2}}, \tag{4}$$

where *C(N)* represents the autocorrelation for *N* frameshift, and the *N* value is chosen to empirically represent all the abnormal gait cycles that exist in the tested data sets; $K = N_{Total}-N-1$ where N_{Total} represents the total number of frames sequence. *S(x, y, n)* indicates the pixel values at a position *(x,y)* in the silhouette frame *n*. The GEI was then computed as an average of the normalised and aligned silhouette over the gait cycle in the following equation:

$$G(x,y) = \frac{1}{n_{\text{cycle}}}\sum_{i=1}^{n_{\text{cycle}}} S_i(x,y), \tag{5}$$

where n_{cycle} represents the frame of the gait cycle while S_i is the silhouette frame of *x*, y pixel coordinates of the image captured. The extracted gait energy image (GEI) and the gait cycle were used to determine gait abnormality from different viewing points based on the colour image sequence. However, this technique does not consider factors that may affect the colour image sequence such as clothes variations.

In [32], the Euclidian distance was used to compute the joints and dynamic body parts for a subject to determine gait abnormality. The Euclidian distance is defined in the following equation, where the distance *r* and *s* are the shortest distance between the line segment *rs*:

$$\begin{aligned} d(r,s) &= d(s,r) \\ &= \sqrt{(r_x - s_x)^2 + (r_y - s_y)^2 + (r_z - s_z)^2}. \end{aligned} \tag{6}$$

Hero's formula was then used to calculate the triangular area of the gait cycle. The area obtained by Hero's formula is given by the following equation:

$$\text{Area\_of\_triangle} = \sqrt{(r_x - s_x)^2 + (r_y - s_y)^2 + (r_z - s_z)^2}. \tag{7}$$

The step length was then calculated between the right foot from left foot in the Euclidian distance as follows:

$$\text{step\_length} = \sum_{i=1}^{n}\sqrt{A+B}, \tag{8}$$

where *A* and *B* are defined as the area formed by the joint angles.

The areas and angles were formed between the hip right foot and the left foot. A triangle was generated to get the area and angle between the right foot. Therefore, the Euclidean distance to compute for the maximum foot distance lifted from the ground is given by the following equation:

$$\text{Ground}_{\text{clearance}} = \max\left(\text{right\_foot}_y\right) - \min\left(\text{right\_foot}_y\right). \tag{9}$$

The limitations in using the Euclidean distance for computation has to do with the multiple dimensions and the sparse nature of data. This presents some variations in trying to measure the gait distances for subjects in a walkway.

In [44], asymmetry features were used to detect walking abnormality in a subject. The motion asymmetry between the right body parts and the left body parts of the skeletal data was extracted. The average distance extracted from the skeletal data for a pair of joint angles was then computed. The Euclidean distance used to represent the asymmetry feature was calculated from the following equation:

$$D_{ij}^{p} = \frac{\sum_{t=1}^{n}\sqrt{\left(x_{it} - x_{jt}\right)^2 + \left(y_{it} - y_{jt}\right)^2 + \left(z_{it} - z_{it}\right)^2}}{n}, \tag{10}$$

where D^{ρ} represents the left and right of the average distance of a subject while x_{it}, y_{it}, and z_{it} represents the 3D coordinates of the joint *i* of a subject of frame *t* and *n* is the number of frames of action sequence. N_p is the set of joints for the left and right body parts of an individual. The velocity magnitude feature was computed in the study to detect slow action performed by the subject. The equation used to calculate is as follows:

$$V = \frac{\sum_{t=1}^{n-1}\sum_{i=1}^{N}\sqrt{\left(x_{i(t+1)} - x_{it}\right)^2 + \left(y_{i(t+1)} - yit\right)^2 + \left(z_{i(t+1)} - z_{it}\right)^2}}{(n-1)N}. \tag{11}$$

Equation (11) is essential in computing the displacement magnitude for each body joint between two successive frames where *N* represents the number of joints and *n* represents the number of frames.

In [27], gait assessment of a patient was evaluated by extracting the time series for the knee angles and the gait cycle of dynamic time warping (DTW). The knee DTW distance and the hip were then calculated and averaged to get the mean DTW distance of individual patients. The mean DTW distance for the hip joints and the knee that are denoted by D_{HP} and D_{KP} are defined by the following equations:

$$D_{KP} := \frac{1}{2}\left[\frac{1}{m_p n_c m_c}\sum_{j=1}^{m_p}\sum_{q=1}^{n_c}\sum_{r=1}^{m_c}\mathrm{DTW}\left(\theta_{LK_{i,t}}, \phi_{LK_{q,r}}\right) + \frac{1}{m_p n_c m_c}\sum_{j=1}^{m_p}\sum_{q=1}^{n_c}\sum_{r=1}^{m_c}\mathrm{DTW}\left(\theta_{RK_{i,t}}, \phi_{RK_{q,r}}\right)\right], \tag{12}$$

$$D_{HP} := \frac{1}{2}\left[\frac{1}{m_p n_c m_c}\sum_{j=1}^{m_p}\sum_{q=1}^{n_c}\sum_{r=1}^{m_c}\mathrm{DTW}\left(\theta_{LH_{i,t}}, \phi_{LH_{q,r}}\right) + \frac{1}{m_p n_c m_c}\sum_{j=1}^{m_p}\sum_{q=1}^{n_c}\sum_{r=1}^{m_c}\mathrm{DTW}\left(\theta_{RH_{i,t}}, \phi_{RH_{q,r}}\right)\right]. \tag{13}$$

4.4. Equations for Postural Abnormality Assessment. Several researchers have proposed different techniques for the recognition of the human posture and 3D human reconstruction. The posture probability density is used to reconstruct the posture of human beings [60]. It is based on human body measurement that can be used to determine posture. This is used as a density estimator in the following equation:

$$\widehat{p}(x; h, \gamma) = \sum_{n=1}^{N} \gamma_n \kappa\left(\frac{x - x_n}{h}\right), \tag{14}$$

where *K(.)* is the kernel, *h* is the bandwidth of the kernel, and *d* is the degree of freedom of the data. The probability density estimate is then given by the function where the weights γ in each kernel are based on the reduced set density estimation (RSDE).

The RULA-based method is a common technique for posture assessment of an individual. This technique can be used to determine the postural abnormality of an individual. Two techniques are used to calculate the joint angles, which are input from a module score. These techniques use a voxel-based angle estimation in which the RULA score for the upper joints is computed based on their location. The joint angles are computed using vectors that are dependable on the location of each joint with correspondence to the parent joint location. This is given by the angle between two vectors of the parents' joints and the child's joints in the following equation:

$$\theta = \cos^{-1}\frac{p_1 \cdot p_2}{\|p_1\| \cdot \|p_2\|}. \tag{15}$$

The magnitude of the two vectors P_1 and P_2 are calculated by:

$\|p_1\| = \sqrt{p_1 \cdot p_1}$ and $\|p_2\| = \sqrt{p_2 \cdot p_2}$, where the computed value is then submitted into equation (15). The RULA method is a good technique for posture assessment because it is easy and fast to use. This can be used in the evaluation of posture disorder without the need to conduct any experimental measurements. This technique is, therefore, significant to conduct risks of musculoskeletal disease with regard to the posture of an individual.

5. Conclusion

In this study, we presented Microsoft Kinect as a noncontact tool for the assessment of gait abnormality and posture disorder. While there are several studies on gait recognition, only a few have dealt with the assessment of gait and posture abnormalities. Early detection of gaits and posture abnormalities plays a significant role for clinicians to provide corrective rehabilitation measures. Even though this is a comprehensive study, there may be some articles that are not included.

In our study, we presented 26 studies for gait abnormality assessment and 13 articles for posture disorder. The summarised studies differ by the methodology used, the gait features extracted, and the analytical tools used to process the skeletal data. Different algorithms were applied in the summarised studies, and some of them made use of machine learning algorithms. The results showed what has been done so far in the area of gait and posture abnormality assessment.

From our analysis, Kinect sensors have a high success rate of approximately 87% in abnormalities assessment. It has an accuracy ranging between 83% and 98.1% from the summarised articles for gait abnormality. This is quite acceptable in the clinical settings for the purposes of diagnosis of diseases associated with gait and posture disorders. Although Microsoft has stopped the release of Kinect sensors, it is still an important tool for diagnostic purposes. It can be concluded that Kinect sensor is an essential monitoring tool for use in medical diagnostics and can also help track the progress of patients who are undergoing rehabilitation.

Data Availability

The data that support the findings of this review paper can be sourced from the summarised table in the study and the references provided.

Conflicts of Interest

The authors declare that there are no conflicts of interest in this paper.

References

[1] H. Alabbasi, A. Gradinaru, F. Moldoveanu, and A. Moldoveanu, "Human motion tracking & evaluation using k," in *Proceedings of the 2015 E-Health and Bioengineering Conference (EHB)*, pp. 1–4, Iasi, Romania, November 2015.

[2] The difference between Kinect v2 and v1-the Ghost Howls (skarredghost.com), 2021, https://skarredghost.com/2016/12/02/the-difference-between-kinect-v2-and-v1/.

[3] M. R. L. Varshini and C. M. Vidhyapathi, "Dynamic fingure gesture recognition using KINECT," in *Proceedings of the 2016 International Conference on Advanced Communication Control and Computing Technologies (ICACCCT)*.

[4] A. Procházka, M. Schätz, O. Vyšata, and M. Vališ, "Microsoft kinect visual and depth sensors for breathing and heart rate analysis," *Sensors*, vol. 16, no. 7, p. 996, 2016.

[5] T.-L. Huy-Hieu Pham and N. Vuillerme, "Real-time obstacle detection system in indoor environment for the visually impaired using microsoft kinect sensor," *Journal of Sensors*, vol. 2016, Article ID 3754918, 13 pages, 2016.

[6] X. Dang, B. Kang, X. Liu, and G. Cui, "An interactive care system based on a depth image and EEG for aged patients with dementia," *Journal of Healthcare Engineering*, vol. 2017, Article ID 4128183, 8 pages, 2017.

[7] R. Torres, M. Huerta, R. Clotet et al., "Diagnosis of the corporal movement in Parkinson's disease using kinect sensors," in *Proceedings of the World Congress on Medical Physics and Biomedical Engineering*, D. Jaffray, Ed., Toronto, Canada, June 2015.

[8] M. Capecci, M. Ceravolo, F. Ferracuti et al., "Accuracy evaluation of the kinect v2 sensor during dynamic movements in a rehabilitation scenario," in *Proceedings of the 2016 38th Annual International Conference of the IEEE Engineering in Medicine and Biology Society (EMBC)*, pp. 5409–5412.

[9] O. Postolache, F. Cary, P. S. Girão, and N. Duarte, "Physiotherapy assessment based on kinect and mobile APPs," in *Proceedings of the 2015 6th International Conference on Information, Intelligence, Systems and Applications (IISA)*, pp. 1–6, Corfu, Greece, January 2015.

[10] M. Wochatz, N. Tilgner, S. Mueller et al., "Reliability and validity of the kinect V2 for the assessment of lower extremity rehabilitation exercises," *Gait & Posture*, vol. 70, pp. 330–335, 2019.

[11] S. Saini, D. R. Awang Rambli, S. Sulaiman, M. Nordin Zakaria, and S. Rohkmah Mohd Shukri, "A low-cost game framework for a home-based stroke rehabilitation system," in *Proceedings of the 2012 International Conference on Computer & Information Science (ICCIS)*, IEEE, 2012.

[12] M. Nixon, T. Tan, and R. Chellappa, "Human identification based on gait," *Majlesi Journal of Electric. Engineering*, vol. 2, no. 3, pp. 15–23, 2008.

[13] M. S. Nixon and J. N. Carter, "Automatic recognition by gait," *Proceedings of the IEEE*, vol. 94, no. 11, pp. 2013–2024, 2006.

[14] M. Aqmar, Y. Fujihara, Y. Makihara, and Y. Yagi, "Gait recognition by fluctuations," *Computer Vision and Image Understanding*, vol. 126, pp. 38–52, 2014.

[15] G. Johansson, "Visual perception of biological motion and a model for its analysis," *Perception & Psychophysics*, vol. 14, no. 2, pp. 201–211, 1973.

[16] A. S. M. H. Bari and M. L. Gavrilova, "Artificial neural network based gait recognition using kinect sensor," *IEEE Access*, vol. 7, pp. 162708–162722, 2019.

[17] W. Z. Abiddin, R. Jailani, A. R. Omar, and I. M. Yassin, "Development of MATLAB kinect skeletal tracking system (MKSTS) for gait analysis," in *Proceedings of the 2016 IEEE Symposium on Computer Applications & Industrial Electronics (ISCAIE)*, pp. 216–220, Penang, Malaysia, May 2016.

[18] S. Monir, S. Rubya, and H. S. Ferdous, "Rotation and scale invariant posture recognition using microsoft kinect skeletal tracking feature," in *Proceedings of the 2012 12th International Conference on Intelligent Systems Design and Applications (ISDA)*, pp. 404–409, Kochi, India, January 2012.

[19] Z. Zhang, Y. Liu, A. Li, and M. Wang, "A novel method for user-defined human posture recognition using kinect," in *Proceedings of the 2014 7th International Congress on Image and Signal Processing*, pp. 736–740, Dalian, China, October 2014.

[20] S. Springer and G. Y. Seligmann, "Validity of the kinect for gait assessment: a focused review," *Sensors*, vol. 16, no. 2, p. 194, 2016.

[21] S. Bei, Z. Zhen, Z. Xing, L. Taocheng, and L. Qin, "Movement disorder detection via adaptively fused gait analysis based on kinect sensors," *IEEE Sensors Journal*, vol. 18, no. 17, pp. 7305–7314, 2018.

[22] T. Wang, C. Li, C. Wu et al., "A gait assessment framework for depression detection using kinect sensors," *IEEE Sensors Journal*, vol. 21, no. 3, pp. 3260–3270, 2021.

[23] S. Tsukagoshi, M. Furuta, K. Hirayanagi et al., "Noninvasive and quantitative evaluation of movement disorder disability using an infrared depth sensor," *Journal of Clinical Neuroscience*, vol. 71, pp. 135–140, 2020.

[24] A. Amini and K. Banitsas, "Using kinect v2 to control a laser visual cue system to improve the mobility during freezing of gait in Parkinson's disease," *Journal of healthcare engineering*, vol. 2019, Article ID 3845462, 8 pages, 2019.

[25] A. Procházka, O. Vyšata, M. Vališ, O. Ťupa, M. Schätz, and V. Mařík, "Bayesian classification and analysis of gait disorders using image and depth sensors of Microsoft Kinect," *Digital Signal Processing*, vol. 47, pp. 169–177, 2015.

[26] C. G. Pachón-Suescún, J. O. Pinzón-Arenas, and R. Jiménez-Moreno, "Abnormal gait detection by means of LSTM," *International Journal of Electrical and Computer Engineering*, vol. 10, no. 2, pp. 2088–8708, 2020.

[27] F. Gholami, D. A. Trojan, J. Kövecses, W. M. Haddad, and B. Gholami, "A Microsoft kinect-based point-of-care gait assessment framework for multiple sclerosis patients," *IEEE Journal of Biomedical and Health Informatics*, vol. 21, no. 5, pp. 1376–1385, 2017.

[28] M. Devanne, H. Wannous, S. Berretti, P. Pala, M. Daoudi, and A. Bimbo, "Learning shape variations of motion trajectories for gait analysis," in *Proceedings of the 2016 23rd International Conference on Pattern Recognition (ICPR). IEEE*, 2016.

[29] J. Latorre, C. Colomer, M. Alcañiz, and R. Llorens, "Gait analysis with the kinect v2: normative study with healthy individuals and comprehensive study of its sensitivity, validity, and reliability in individuals with stroke," *Journal of NeuroEngineering and Rehabilitation*, vol. 16, p. 97, 2019.

[30] S. P. Rana, M. Dey, M. Ghavami, and S. Dudley, "3-D gait abnormality detection employing contactless IR-UWB sensing phenomenon," *IEEE Transactions on Instrumentation and Measurement*, vol. 70, pp. 1–10, Article ID 6006510, 2021.

[31] T.-N. Nguyen, H.-H. Huynh, and J. Meunier, "Skeleton-based abnormal gait detection," *Sensors*, vol. 16, no. 11, p. 1792, 2016.

[32] S. Shrivastava, J. Bharti, and R. K. Pateriya, "Machine learning based gait abnormality detection using microsoft kinect sensor," *Materials Today: Proceedings*, 2021.

[33] A. Procházka, M. Schätz, O. Ťupa, M. Yadollahi, O. Vyšata, and M. Walls, "The MS kinect image and depth sensors use for gait features detection," in *Proceedings of the 2014 IEEE International Conference on Image Processing (ICIP)*, pp. 2271–2274, Paris, France, October 2014.

[34] J. Fang, T. Wang, C. Li et al., "Depression prevalence in postgraduate students and its association with gait abnormality," *IEEE Access*, vol. 7, pp. 174425–174437, 2019.

[35] A. Ismail, H. Shouman, A. Cherry, and M. Hajj-Hassan, "Torwads real time kinect anlysis system for early diagnosis of gait cycle abnormalities," in *Proceedings of the 2017 Fourth International Conference on Advances in Biomedical Engineering (ICABME)*, pp. 1–4, Beirut, Lebanon, October 2017.

[36] A. Amin, K. Banitsas, and W. R. Young, "Kinect4FOG: monitoring and improving mobility in people with Parkinson's using a novel system incorporating the microsoft kinect v2," *Disability and Rehabilitation: Assistive Technology*, vol. 14, no. 6, pp. 566–573, 2019.

[37] A. Elkholy, Y. Makihara, W. Gomaa, M. A. Rahman Ahad, and Y. Yagi, "Unsupervised GEI-based gait disorders detection from different views," in *Proceedings of the 2019 41st Annual International Conference of the IEEE Engineering in Medicine and Biology Society (EMBC)*, pp. 5423–5426, Berlin, Germany, July 2019.

[38] S. Soltaninejad, I. Cheng, and A. Basu, "Kin-FOG: automatic simulated freezing of gait (FOG) assessment system for Parkinson's disease," *Sensors*, vol. 19, p. 2416, 2019.

[39] P. Kozlow, N. Abid, and S. Yanushkevich, "Gait type Analysis using dynamic Bayesian networks," *Sensors*, vol. 18, no. 10, p. 3329, 2018.

[40] S. Chakraborty, T. Noble, and A. Nandy, "Gait abnormality detection in people with cerebral palsy using an uncertainty-based state-space model," in *Proceedings of the International Conference on Computational Science*, Faro, Portugal, June 2020.

[41] J. Kondragunta and G. Hirtz, "Gait parameter estimation of elderly people using 3D human pose estimation in early detection of dementia," in *Proceedings of the 2020 42nd Annual International Conference of the IEEE Engineering in Medicine & Biology Society (EMBC)*, pp. 5798–5801, Montreal, Canada, July 2020.

[42] D.-W. Lee, K. Jun, S. Lee, J.-K. Ko, and M. S. Kim, "Abnormal gait recognition using 3D joint information of multiple kinects system and RNN-LSTM," in *Proceedings o f the 2019 41st Annual International Conference of the IEEE Engineering in Medicine and Biology Society (EMBC)*, pp. 542–545, Berlin, Germany, July 2019.

[43] T. Jinnovart, X. Cai, and K. Thonglek, "Abnormal gait recognition in real-time using recurrent neural networks," in *Proceedings of the 2020 59th IEEE Conference on Decision and Control (CDC)*, pp. 972–977, Jeju, Korea (South), December 2020.

[44] A. Elkholy, M. E. Hussein, W. Gomaa, D. Damen, and E. Saba, "Efficient and robust skeleton-based quality assessment and abnormality detection in human action performance," *IEEE Journal of Biomedical and Health Informatics*, vol. 24, no. 1, pp. 280–291, 2020.

[45] M. Meng, H. Drira, D. Mohamed, and J. Boonaert, "Detection of abnormal gait from skeleton data," in *Proceedings of the VISIGRAPP Conference*, Rome, Italy, February 2016.

[46] K. Jun, D. Lee, K. Lee, S. Lee, and M. S. Kim, "Feature extraction using an RNN autoencoder for skeleton-based abnormal gait recognition," *IEEE Access*, vol. 8, pp. 19196–19207, 2020.

[47] C. Ferraris, R. Nerino, A. Chimienti et al., "feasibility of home-based automated assessment of postural instability and lower limb impairments in Parkinson's disease," *Sensors*, vol. 19, no. 5, p. 1129, 2019.

[48] U. Jawed, A. Mazhar, F. Altaf, A. Rehman, S. Shams, and A. Asghar, "Rehabilitation posture correction using neural network," in *Proceedings of the 2019 4th International Conference on Emerging Trends in Engineering, Sciences and Technology (ICEEST)*, Karachi, Pakistan, December 2019.

[49] Y. Yang, F. Pu, Y. Li, S. Li, Y. Fan, and D. Li, "Reliability and validity of kinect RGB-D sensor for assessing standing balance," *IEEE Sensors Journal*, vol. 14, no. 5, pp. 1633–1638, 2014.

[50] A. P. G. Castro, J. D. Pacheco, C. Lourenço et al., "Evaluation of spinal posture using microsoft kinect™: a preliminary case-study with 98 volunteers," *Porto Biomedical Journal*, vol. 2, no. 1, pp. 18–22, 2017.

[51] C.-H. Liu, P. Lee, Y.-L. Chen, C.-W. Yen, and C.-W. Yu, "Study of postural stability features by using kinect depth sensors to assess body joint coordination patterns," *Sensors*, vol. 20, no. 5, p. 1291, 2020.

[52] A. Abobakr, D. Nahavandi, J. Iskander, M. Hossny, S. Nahavandi, and M. Smets, "RGB-D human posture analysis for ergonomie studies using deep convolutional neural network," in *Proceedings of the 2017 IEEE International Conference on Systems, Man, and Cybernetics (SMC)*, pp. 2885–2890, Banff, Canada, October 2017.

[53] A. Napoli, S. M. Glass, C. Tucker, and I. Obeid, "The automated assessment of postural stability: balance detection algorithm," *Annals of Biomedical Engineering*, vol. 45, pp. 2784–2793, 2017.

[54] M. C. Shih, R. Y. Wang, S. J. Cheng, and Y. R. Yang, "Effects of a balance-based exergaming intervention using the kinect sensor on posture stability in individuals with Parkinson's disease: a single-blinded randomized controlled trial," *Journal of NeuroEngineering and Rehabilitation*, vol. 13, p. 78, 2016.

[55] S. Chanpimol, B. Seamon, H. Hernandez, M. Harris-Love, and M. R. Blackman, "Using Xbox kinect motion capture technology to improve clinical rehabilitation outcomes for balance and cardiovascular health in an individual with chronic TBI," *Arch Physiother*, vol. 7, p. 6, 2017.

[56] I. Bortone, A. Argentiero, N. Agnello, S. S. Sabato, and A. Bucciero, "A two-stage approach to bring the postural assessment to masses: the KISS-health project," in *Proceedings of the IEEE-EMBS International Conference on Biomedical and Health Informatics (BHI)*, pp. 371–374, Valencia, Spain, June 2014.

[57] V. M. Manghisi, A. Emmanuele Uva, M. Fiorentino, V. Bevilacqua, G. Francesco Trotta, and G. Monno, "Real time RULA assessment using kinect v2 sensor," *Applied Ergonomics*, vol. 65, pp. 481–491, 2017, ISSN 0003-6870.

[58] N. Gal-Nadasan, E. G. Gal-Nadasan, V. Stoicu-Tivadar, D. V. Poenaru, and D. Popa-Andrei, "Measuring the negative impact of long sitting hours at high school students using the microsoft kinect," *Health Informatics Meets eHealth*, vol. 236, pp. 383–388, 2017.

[59] R. A. Clark, Y.-H. Pua, K. Fortin et al., "Validity of the microsoft kinect for assessment of postural control," *Gait & Posture*, vol. 36, no. 3, pp. 372–377, 2012, ISSN 0966-6362.

[60] T. Harada, T. Sato, and T. Mori, "Human posture reconstruction based on posture probability density," in *Proceedings of the 2005 IEEE/RSJ International Conference on Intelligent Robots and Systems*, pp. 4063–4070, Edmonton, Canada, August 2005.

Hindawi
Journal of Healthcare Engineering
Volume 2021, Article ID 1709793, 9 pages
https://doi.org/10.1155/2021/1709793

Research Article

CT Image Features under Reconstruction Algorithm in Analysis of the Effect of Probiotics Combined with Ursodeoxycholic Acid in Treatment of Intrahepatic Cholestasis of Pregnancy

Hongxue Liu, Haidong Wang, and Muling Zhang

Department of Obstetrics, The Affiliated Huaian No. 1 People's Hospital of Nanjing Medical University, Huai'an 223300, Jiangsu, China

Correspondence should be addressed to Muling Zhang; hayyliuhx@njmu.edu.cn

Received 28 August 2021; Revised 12 October 2021; Accepted 15 October 2021; Published 31 October 2021

Academic Editor: Enas Abdulhay

This research was to explore the adoption value of computed tomography (CT) images based on adaptive statistical iterative reconstruction (ASIR) algorithm in the evaluation of probiotics combined with ursodeoxycholic acid in the treatment of intrahepatic cholestasis of pregnancy (ICP). A total of 82 patients with ICP were selected as the research subjects and they were randomly rolled into experimental group (380 mg probiotics enteric-soluble capsule twice a day, combined with 90 mg ursodeoxycholic acid soft capsule three times a day) and control group (90 mg ursodeoxycholic acid soft capsule three times a day), with 41 cases in each. The treatment course was four months. The ASIR algorithm was constructed and applied to the CT image analysis and diagnosis of ICP patients. The effects of filtering back projection (FBP) reconstruction and ASIR algorithm on CT image quality, denoising degree, and artifacts of ICP patients were compared. Moreover, blood indicator levels of ICP patients before and after treatment were assessed. The results showed that the SD values of liver and gallbladder (20.77 Hu and 27.58 Hu) in the reconstructed image of the ASIR algorithm were significantly lower than those of the FBP algorithm (40.58 Hu and 45.63 Hu) ($P < 0.05$). The SNR values of the liver and gallbladder (3.68 and 2.05) of the reconstructed image were significantly higher than those of the FBP algorithm (1.91 and 1.19) ($P < 0.05$). The overall image quality after ASIR reconstruction (3.92 points) was significantly better than that of the FBP algorithm (2.36 points), and the image noise score (3.21 points) reconstructed by the FBP algorithm was higher than that by the ASIR algorithm (1.83 points). The artifact score of FBP reconstructed image (4.47 points) was greatly higher than that of ASIR algorithm (2.26 points) ($P < 0.05$). Before treatment, there was no remarkable difference in the indexes between the two groups of patients ($P > 0.05$). After treatment, the γ-glutamyltransferase (γ-GT) and alkaline phosphatase (ALP) levels (327.55 U/L and 778.15 μmol/L) of the experimental group of ICP patients were higher than those of the control group (248.63 U/L and 668.43 μmol/L), with substantial difference between the two groups ($P < 0.05$). The blood ammonia (BA) level (151.09 μmol/L) of the experimental group was lower than that of the control group (178.46 μmol/L), and the difference between the two groups was remarkable ($P < 0.05$). To sum up, the CT image denoising degree based on ASIR algorithm was high, with few artifacts and good overall quality. Probiotics combined with ursodeoxycholic acid in the treatment of ICP can effectively improve the liver function and intestinal flora of patients, which was of great significance in the clinical diagnosis and treatment of the disease.

1. Introduction

Intrahepatic cholestasis of pregnancy (ICP) is a female disease occurring during pregnancy, which will endanger the fetus and lead to the increase of neonatal morbidity and mortality [1]. Patients with ICP typically experience problems such as elevated blood and bile acids and abnormal liver function. For pregnant women, these symptoms usually disappear immediately after delivery, but they are harmful to the fetus, and fetal intrauterine compression causes premature delivery, leading to neonatal asphyxia or death [2]. The incidence of this disease is up to 0.8%–12.0%, and it disappears immediately after delivery. However, the recurrence rate is high, and the patients will relapse again when they become pregnant again or take contraceptive drugs [3]. The pathogenesis of ICP is complex and not yet clear. Treatment is mainly through choleretics and hepatoprotective drugs, such as ursodeoxycholic acid and choline [4]. At present, researchers usually combine adenosylmethionine with ursodeoxycholic acid for research, but there are some shortcomings such as small sample size and complex control. Studies pointed out that probiotics can improve the microecological environment in vivo, with low cost and no invasion, which can prevent and cure hepatobiliary diseases and reduce the harm [5]. At present, there are few studies combining ursodeoxycholic acid and probiotics to treat IPC.

Nowadays, computed tomography (CT) is widely utilized in clinical medicine. Because of its fast scanning speed and clear images, it has become the main imaging tool for medical auxiliary diagnosis and scientific research. CT liver scan can choose any time phase for continuous scan. After a lot of clinical practice, CT scan has become a routine method for examination of liver and gallbladder diseases, and it has played an important role in the diagnosis and treatment of IPC [6]. The CT image reconstruction method is an important technology in the image imaging process, and the optimization of the image is particularly important. At present, the filtered back projection (FBP) method is the main algorithm for CT image reconstruction. The algorithm reconstructs quickly, but the noise is obvious, the imaging is not detailed enough, and it will aggravate the patient's radiation. The iterative reconstruction (IR) algorithm also has problems such as noise and artifacts [7]. Adaptive statistical iterative reconstruction (ASIR) can improve imaging quality, reduce radiation dose, and overcome the shortcomings of the above technologies, which is the most widely utilized iterative reconstruction technology at present [8]. ASIR image reconstruction algorithm can reduce imaging noise and artifact, improve image quality without interfering with clinical diagnosis, and is utilized for clinical treatment, which has been approved by the American medical management system [9]. In this study, ICP patients were taken as the research object, and the ASIR algorithm was applied to the CT image analysis and diagnosis of ICP patients by constructing the ASIR algorithm. The effects of filtering back projection (FBP) reconstruction and ASIR algorithm on CT image quality, denoising degree, and artifacts of ICP patients were compared. Blood indicator levels of ICP patients before and after treatment were detected to evaluate the clinical effect of probiotics combined with ursodeoxycholic acid in ICP treatment. It was hoped to provide a reliable basis for the application of ASIR based CT imaging in clinical diagnosis and treatment.

2. Materials and Methods

2.1. Research Objects. A total of 82 patients, ranging in age from 24 to 36 years, with an average age of 26 years, who underwent ICP specific detection in our hospital from July 2019 to May 2020, were selected for CT imaging examination. They were randomly divided into experimental group and control group, with 41 patients in each group. There was no statistical difference in general information between the two groups ($P > 0.05$). This study had been approved by the Ethics Committee of the Hospital, and informed consent was signed by the patients and their families.

Inclusion criteria were as follows: (i) clinically confirmed ICP patients (the ICP diagnostic criteria of *Chinese Journal of Obstetrics and Gynecology* edited by Cao [10]); (ii) skin pruritus being the main symptom during pregnancy; (iii) abnormal liver function, mainly slightly increased serum transaminase; (iv) the patient being in good general condition without obvious vomiting, weakness, or other diseases; (v) pruritus quickly subsiding after delivery, and liver function quickly returning to normal; and (vi) patients with elevated bile acid level.

Exclusion criteria for subjects were as follows: (i) those who had liver or gallbladder disease, or skin diseases before pregnancy which affected the observation indicators; (ii) patients who had received treatment that affected the observation indicators before inclusion; (iii) only statistical results without specific data listed; (iv) those who utilized the combination of drugs which affected the judgment of the results and could not be excluded by the control.

2.2. Grouping. The included IPC patients were randomly divided into experimental group and control group, with 41 patients in each group. Patients in the experimental group were given probiotic enteric-coated capsules 380 mg twice a day, combined with ursodeoxycholic acid soft capsules 90 mg three times a day for four months. Patients in the control group were given ursodeoxycholic acid soft capsule 90 mg three times a day for four months. During the treatment, neither group of patients took other drugs.

2.3. Observation Indicators and Detection. The blood sample test was as follows: 5 mL of venous blood was extracted from the patients on an empty stomach in the morning and placed in an anticoagulant tube. Levels of γ-glutamyl transferase (γ-GT), blood ammonia (BA), alkaline phosphatase (ALP), and total cholesterol (TC) were detected by Hitachi automatic biochemical analyzer.

2.4. Inspection Method and Reconstruction Method. All patients were scanned using a General Electric 256-bar widebody detector CT (Revolution, General Engine, GE, USA). Prior to the CT scan, the patients underwent inhalation and breath-holding training to reduce breathing movements and removed clothing at the site of examination, including various items with metallic substances, such as earrings and keys. During the examination, the patients were supine with their arms raised above their heads, and they were required not to move freely to avoid artifacts. Patients were first examined with a conventional dose scan, with a preset noise index (NI) of 14. FBP was utilized for image reconstruction. The NI was set at 24, and the image was reconstructed by ASIR. Scanning was under 120 KV and 150 mAs, reconstruction layer thickness was 0.625 mm, field of view was 220 mm, scanning time was 0.5 s, cycle time was 1 s, and matrix was 512 × 512.

2.5. CT Image Reconstruction Based on ASIR Algorithm. The main idea of the ASIR iterative reconstruction algorithm is making all currently estimated images satisfy an equation in each update. In the iterative correction process, only the projection value of one projection unit is considered at a time. The calculation process of the reconstruction algorithm is shown in Figure 1.

The specific reconstruction steps of the ASIR algorithm are as follows:

(I) Assign an unknown image vector, and k is a constant.

$$R_k = R_k^{(0)} \, (k = 1, 2, 3 \ldots n). \tag{1}$$

(II) The estimated projection values of all equations are calculated, where Z_{kc} is the relaxation parameter.

$$Y_c^* = \sum_{k=1}^{n} Z_{kc} R_k^{(0)} \, (k = 1, 2, 3 \ldots n). \tag{2}$$

(III) The error is calculated, and $\boldsymbol{\Phi}$ is the error parameter.

$$\Phi_c = Y_c - Y_c^* \, (k = 1, 2, 3, \ldots n). \tag{3}$$

(IV) The correction value of the k-th pixel is calculated.

$$E_k = \frac{1}{Z_{kc}} \sum_{k=1}^{N} \Phi_c \frac{1}{Z_{ik}}. \tag{4}$$

Among them, i is the ray passing through pixel k, and all rays passing through the pixel are summed at the same time.

(V) The k-th pixel value is corrected.

$$R_k = E_k + R_k^{(0)}. \tag{5}$$

To sum up, all rays passing through the pixel are utilized to correct it to complete the first iteration. The average value of each projection band can reduce the error, thereby avoiding the influence caused by the reconstruction result, which has a noise reduction effect in the image reconstruction process.

2.6. Image Objective and Subjective Evaluation Indicators. After reconstruction, two kinds of noise reduction images of each patient were obtained, and all the images were transmitted to GE workstation (General Engine Advantage Workstation 4.7). The patient's personal information and scan and reconstruction information were hidden. The patient's CT value (the relative density of tissue structure on the CT image, in Hu) and the SD value (the background noise value of the abdominal fat on the same plane) were

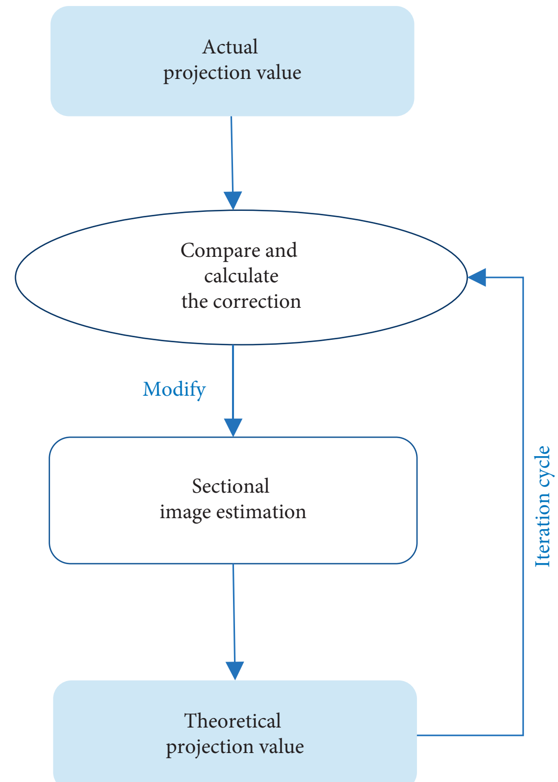

Figure 1: Schematic diagram of the calculation process of ASIR iterative reconstruction algorithm.

measured. The signal-to-noise ratio (SNR) was calculated. SNR = CT value/SD value. All data were measured three times, and the average value was taken as the final statistical result.

Subjective evaluation was performed by radiologists using a double-blind method to evaluate all images. A 5-point system was adopted to evaluate the overall image quality (unclear texture, blurred contrast, and unclear image indicated 1 point; the texture was fuzzy, the contrast was fuzzy, and the image roughly indicated 2 points; the texture was not clear, the contrast was not clear, and the image was not fine, indicating 3 points; the texture was clear, the contrast was clear, and the image was delicate, indicating 4 points; clear texture, clear contrast, and fine image indicated 5 points). A 5-point Likert method [11] was adopted to evaluate image noise (image noise was completely acceptable, 1 point; less than average noise, 2 points; average noise, 3 points; above average noise, 4 points; unacceptable image noise, 5 points). Each artifact was also scored by a 5-point method (no artifact, 1 point; small artifacts did not affect the organizational structure, 2 points; slight effects on the structure, 3 points; the artifact was large, affecting the main structure, 4 points; the artifact was extremely heavy, and the image was unacceptable, 5 points).

2.7. Statistical Analysis. SPSS 24.0 was utilized for statistical analysis. All experimental data were represented as mean ± standard deviation ($\overline{x} \pm s$). One-way analysis of variance was utilized for statistical data. Friedman rank-sum test was utilized to compare the subjective scores of overall image quality, noise, and artifacts, and the test level was $\alpha = 0.05$. $P < 0.05$ was statistically remarkable.

3. Results

3.1. Abdominal CT Images of ICP Patients with Different Reconstruction Algorithms. Figure 2 shows a 28-year-old ICP patient with a thin-slice CT scan of the lower abdomen with two reconstruction algorithms. A, B, and C represent the plain scan phase, arterial phase, and portal phase, respectively, and A1, B1, and C1 represent FBP, while A2, B2, and C2 represent ASIR. Observed from the CT image, the image reconstructed by the ASIR algorithm shows that the lesion area is relatively clear, and the edge contrast is high. The FBP reconstructed image has blurry edges and poor contrast. The overall quality of the FBP reconstructed image is worse than that of ASIR, the image noise is high, and the artifacts are obvious.

3.2. Objective Indicator Analysis of CT Image Based on Reconstruction Algorithm. Routine CT scans of the abdomen of 30 ICP patients were performed, and the initial images were reconstructed by two reconstruction algorithms, FBP and ASIR. The unreconstituted images with a thickness of 0.625 mm were obtained. According to the obtained images, the data of different organs in the abdomen of ICP patients were measured and analyzed, and the CT, SD, and SNR values of the reconstructed image under different reconstruction algorithms were obtained.

3.2.1. CT Value Analysis of Reconstructed Image. The CT value analysis results are shown in Figure 3. For the CT value of the liver, the CT values of the reconstructed image of FBP and ASIR were 77.43 Hu and 76.51 Hu, respectively, and there was no considerable difference between the two ($P > 0.05$). For the CT value of the gallbladder, the CT values of the reconstructed images of FBP and ASIR were 54.37 Hu and 56.58 Hu, respectively, and the difference between the two was not remarkable ($P > 0.05$).

3.2.2. SD Value Analysis of Reconstructed Image. The SD value analysis results are shown in Figure 4. The SD value of the liver was analyzed. The SD values of the reconstructed image of the FBP and ASIR algorithms were 40.58 Hu and 20.77 Hu, respectively. The SD value of the reconstructed image of the ASIR algorithm was notably lower than that of the FBP algorithm ($P < 0.05$). The SD value of the gallbladder was analyzed. The SD values of the reconstructed image of FBP and ASIR were 45.63 Hu and 27.58 Hu, respectively. The SD value of the reconstructed image of the ASIR algorithm was notably lower than that of the FBP algorithm ($P < 0.05$).

3.2.3. SNR Value Analysis of Reconstructed Image. The SNR value analysis results are shown in Figure 5. The SNR value of the liver was analyzed. The SNR values of the reconstructed image of the FBP and ASIR algorithms were 1.91 and 3.68, respectively. The SNR value of the reconstructed image of the ASIR algorithm was notably lower than that of the FBP algorithm ($P < 0.05$). The SNR value of the gallbladder was analyzed. The SNR values of the reconstructed image of the FBP and ASIR algorithms were 1.19 and 2.05, respectively. The SNR value of the reconstructed image of the ASIR algorithm was notably lower than that of the FBP algorithm ($P < 0.05$).

In summary, in the CT image of the ASIR algorithm, the noise value (SD value) of the abdominal liver and gallbladder of ICP patients was notably lower than that of the FBP reconstruction algorithm, while the signal-to-noise ratio (SNR) was considerably higher than that of the FBP reconstruction image. There was no considerable difference in the CT value of the reconstructed image between the two algorithms.

3.3. Subjective Evaluation of CT Images Based on Reconstruction Algorithm. Figures 6 and 7 show partially enlarged views of CT images of a certain ICP patient's abdominal CT reconstructed by FBP and ASIR, respectively.

Figure 8 shows the mean statistical graph of the overall quality, noise, and artifacts of the reconstructed CT image scored by the radiologist. The scoring results showed that the image quality scores of the FBP and ASIR algorithms were 2.36 and 3.92, respectively. The overall image quality after ASIR reconstruction was substantially better than that of the FBP algorithm ($P < 0.05$). In the evaluation of image noise, the scores of FBP and ASIR were 3.21 and 1.83, respectively. Compared with the ASIR algorithm, the FBP reconstructed image had higher noise, and the difference was remarkable ($P < 0.05$). The evaluation of image artifacts showed that FBP had more image artifacts than the ASIR algorithm, and the difference was remarkable ($P < 0.05$).

3.4. Observation Indicators of Experimental Group and Control Group before and after Treatment. The ICP patients in the experimental group were treated with probiotics combined with ursodeoxycholic acid, and the ICP patients in the control group were treated with ursodeoxycholic acid. The blood indicators of the two groups of patients before and after treatment were recorded, including γ-glutamyl transferase (γ-GT), blood ammonia (BA), alkaline phosphatase (ALP) levels, and total cholesterol (TC). The changes of these indicators were analyzed to draw a graph of the changes of blood indicators in each group before and after treatment. The results showed that, before treatment, there was no statistical difference in each indicator between the two groups of patients ($P > 0.05$). After treatment, the γ-GT and ALP levels of ICP patients in the experimental group were higher than those in the control group, and the difference was remarkable ($P < 0.05$). The BA level of the experimental group greatly was lower than that of the control group ($P < 0.05$). The difference in TC values between the two groups after treatment was not remarkable ($P > 0.05$). Figure 9 shows a graph of the changes of blood indicator levels before and after treatment in the experimental group and the control group.

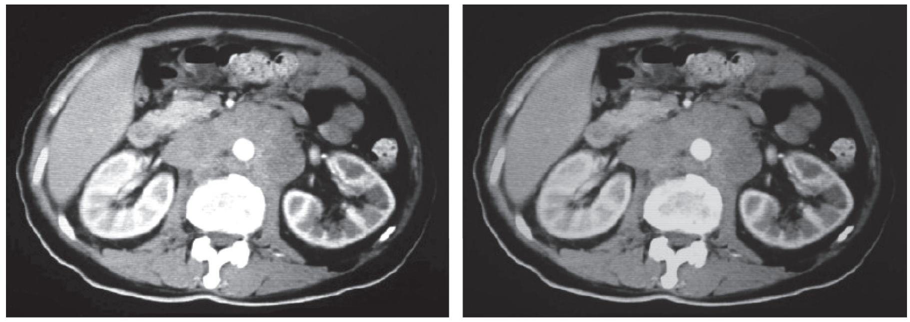

(a)

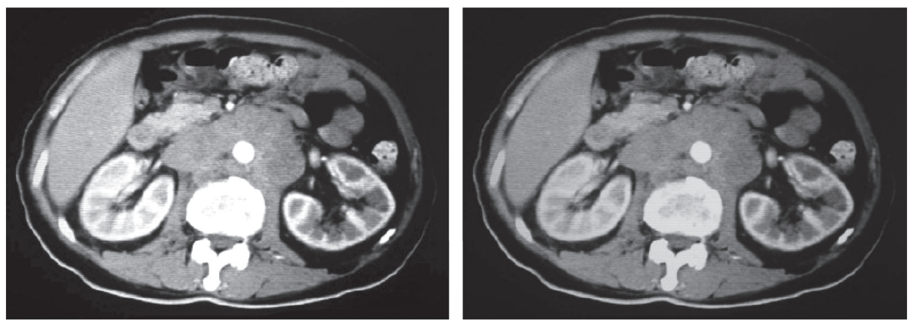

(b)

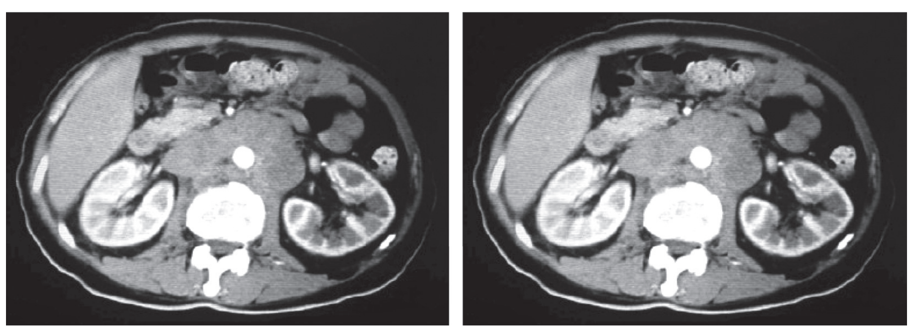

(c)

Figure 2: FBP and ASIR reconstruction of the CT scan of the abdomen of ICP patients. A, B, and C represent the plain scan phase, arterial phase, and portal phase, respectively, and A1, B1, and C1 represent FBP, while A2, B2, and C2 represent ASIR.

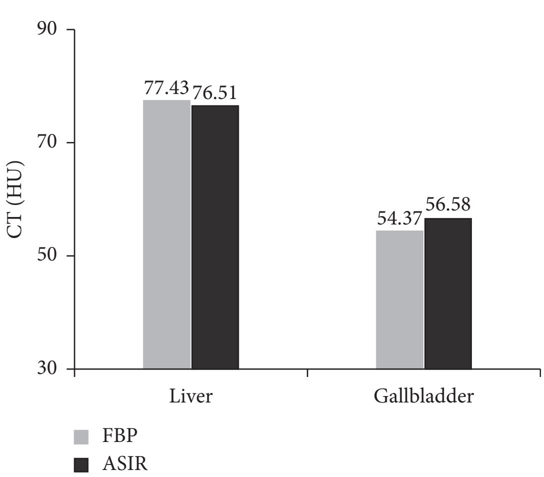

Figure 3: CT values of reconstructed images.

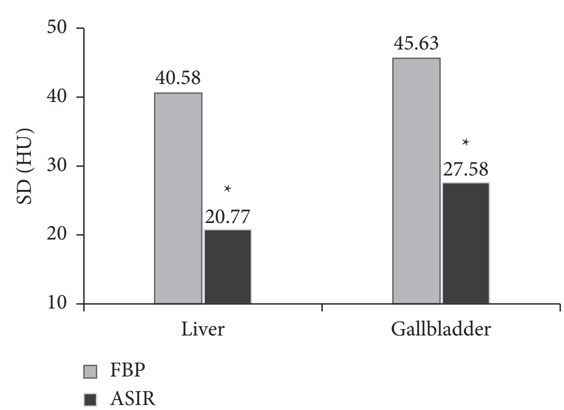

Figure 4: SD values of reconstructed images. *indicates that the SD value of the reconstructed image of FBP and ASIR algorithm is substantially different ($P < 0.05$).

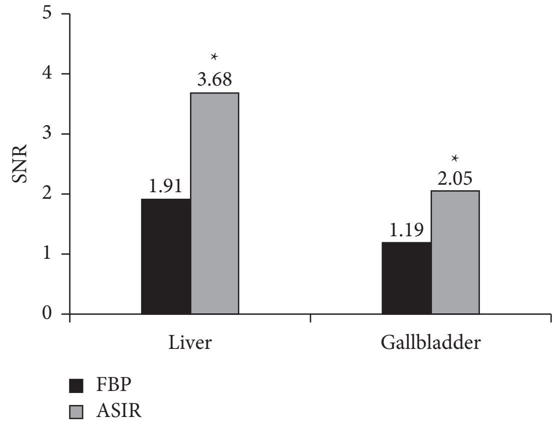

FIGURE 5: SNR values of reconstructed images. *indicates that the SNR value of the reconstructed image of FBP and ASIR algorithm is substantially different ($P < 0.05$).

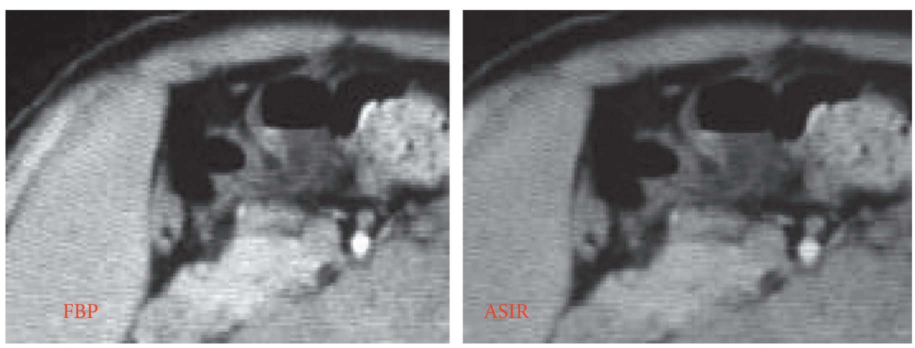

FIGURE 6: The partially enlarged views of liver imaging after reconstruction of the abdominal CT image of an ICP patient in two ways. *Note.* The average scores of subjective evaluations of FBP reconstructed images show image quality of 2.34 points, noise of 2.33 points, and artifacts of 4.45 points; the average scores of subjective evaluations of ASIR reconstructed images show image quality of 3.9 points, noise of 1.85 points, and artifacts of 2.34 points.

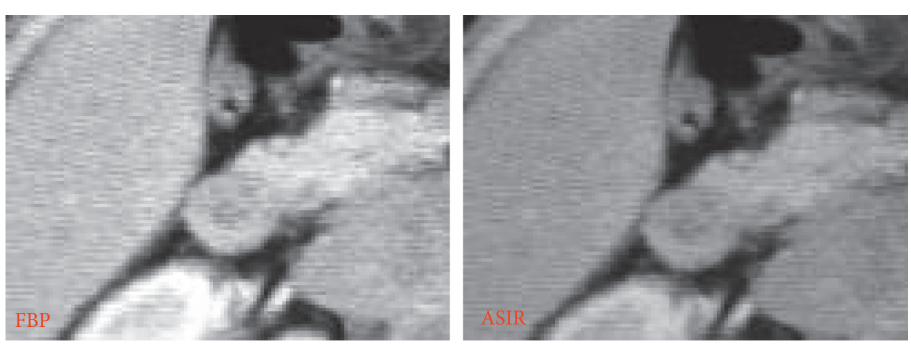

FIGURE 7: The partially enlarged views of gallbladder imaging after reconstruction of the abdominal CT image of an ICP patient in two ways. *Note.* The average scores of subjective evaluations of FBP reconstructed images show image quality of 2.38 points, noise of 2.29 points, and artifacts of 4.49 points; the average scores of subjective evaluations of ASIR reconstructed images show image quality of 3.94 points, noise of 1.81 points, and artifacts of 2.38 points.

4. Discussion

ICP generally has familial clusters, and the rate of recurrence is high. Medically, it is generally treated with liver protection and choleretic treatment [1]. The liver and gallbladder in the human body and the gastrointestinal system have the same embryonic origin, so there is a close relationship between tissue composition and organic function [12]. Probiotics can improve the microecological environment in the body, are cheap and noninvasive, which can prevent and treat liver and gallbladder diseases, reduce harm, and are nonpathogenic. Ursodeoxycholic acid can induce the massive secretion of endogenous bile acid in the treatment of IPC, regulate the concentration of hydrophilic bile acid, and prevent the functional damage of liver cells in the body. In this way, the liver's blocking structure is adjusted to alleviate the degree and progression of IPC patients [13].

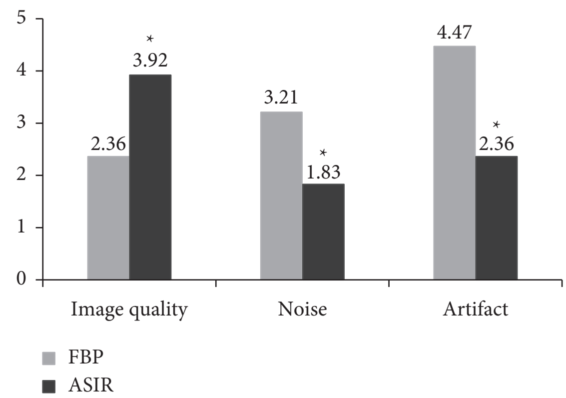

Figure 8: Subjective scoring results of reconstructed images. *Note.* * indicates that the subjective scores of the reconstructed images of FBP and ASIR algorithms are substantially different ($P < 0.05$).

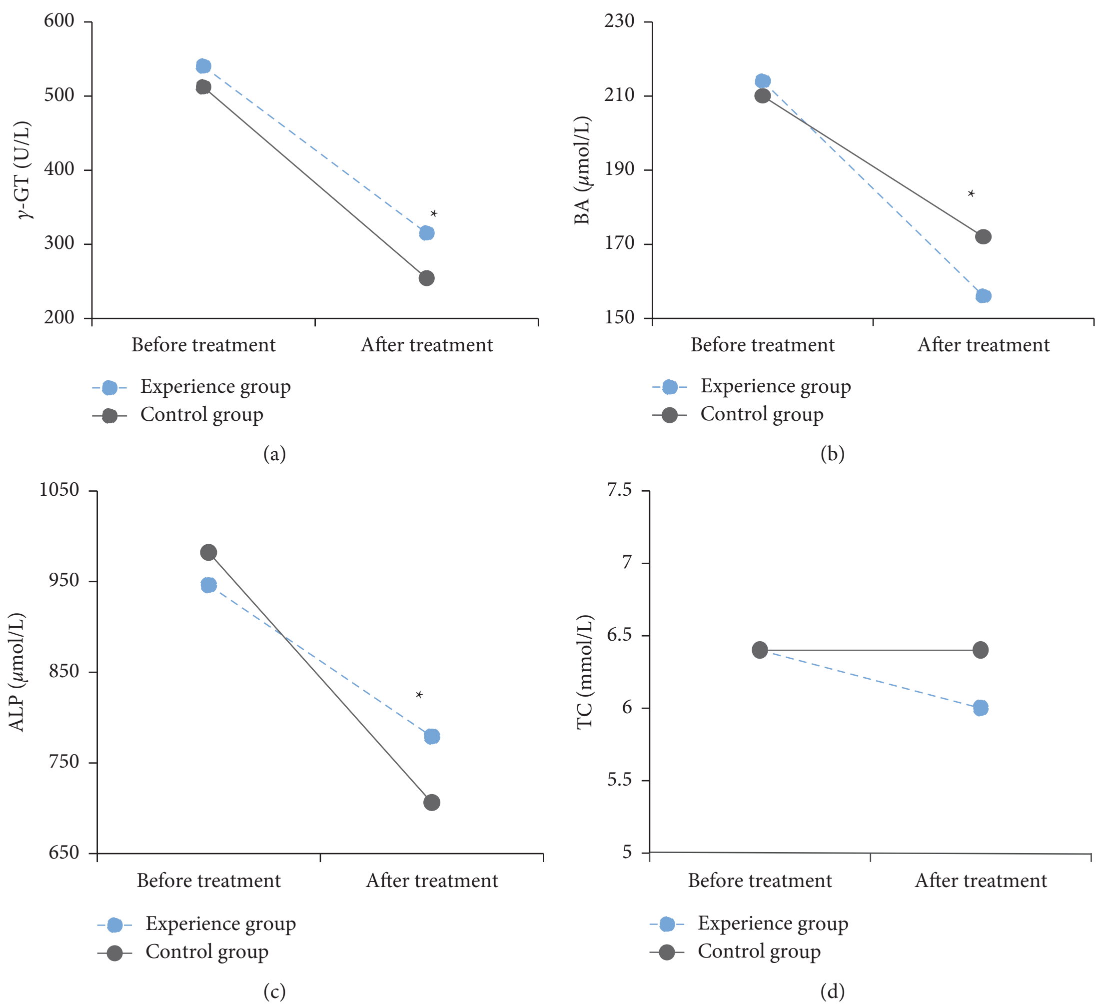

Figure 9: Changes of blood indicators in the experimental group and the control group before and after treatment. (a) The changes of γ-GT in the two groups of patients, (b) the changes in BA of the two groups of patients, (c) the changes in ALP of the two groups of patients, and (d) the changes in TC of the two groups of patients. *indicates considerable differences in blood indicators between the experimental group and the control group ($P < 0.05$).

This study combined probiotics and ursodeoxycholic acid to treat IPC. The results showed that, before treatment, there was no statistical difference in each indicator between the two groups of patients ($P > 0.05$). After treatment, the γ-GT and ALP levels of ICP patients in the experimental group were greatly higher than those in the control group ($P < 0.05$). The BA level of the experimental group was lower than that of the control group, and the difference was remarkable ($P < 0.05$). There was no considerable difference in TC values between the two groups after treatment ($P > 0.05$). It was proved that the combined application of ursodeoxycholic acid and probiotics was effective in improving liver function in patients with ICP, which may be related to the antioxidant and antiapoptotic effects of ursodeoxycholic acid in the above-mentioned mechanism [14]. Probiotics can regulate the intestinal flora, avoid excessive growth of small intestinal bacteria, and reduce intestinal endotoxemia and BA levels. They can also improve the liver function of patients and reduce the occurrence of mild HE and the possibility of mild HE progressing to clinical symptoms of HE [15]. There were no adverse reactions in all cases in this study, which also suggested that the drug had good safety.

Nowadays, CT is widely utilized in clinical medicine. Because of its advantages such as fast scanning speed and clear images, it has become the main imaging tool for medical auxiliary diagnosis and scientific research, which has played an important role in the diagnosis and treatment of IPC [16]. FBP, which is often utilized in image inspection, has heavy artifacts, great noise, and insufficient image quality [17]. ASIR can improve the image quality, reduce the radiation dose, and overcome the shortcomings of the above technologies and is currently the most widely utilized iterative reconstruction [18]. ASIR uses the resources obtained by FBR as the initial image for reconstruction, changes the measured values of different pixels into new estimated values, and then compares the target value with the new value. In the subsequent iterative reconstruction, the process is repeated until the new pixel value is wirelessly close to the expected value [19]. In recent years, iterative reconstruction has gradually been introduced into the field of image noise reduction. A series of current studies have also observed that ASIR has better image quality than FBP [20]. In this study, the subjective evaluation results of CT images showed that, in terms of image quality, the scores of FBP and ASIR were 2.36 and 3.92, respectively. The overall image quality after ASIR reconstruction was substantially better than that of the FBP algorithm ($P < 0.05$). In the evaluation of image noise, the scores of FBP and ASIR were 3.21 and 1.83, respectively. Compared with the ASIR algorithm, the FBP reconstructed image had higher noise, and the difference between the two was remarkable ($P < 0.05$). In the evaluation of image artifacts, FBP had more image artifacts than ASIR algorithm reconstruction, and the difference was remarkable ($P < 0.05$). It was shown that the image noise of ASIR at the aorta and skeletal muscle was notably lower than that of traditional FBP and ASIR, and the image quality can meet clinical needs. The objective indicator analysis results of the CT image showed that, in the CT image of the ASIR algorithm, the noise value (SD value) of the abdominal liver and gallbladder of ICP patients was notably lower than that of the FBP reconstruction algorithm ($P < 0.05$). However, the SNR was considerably higher than the FBP reconstructed image ($P < 0.05$). These results were consistent with the research conclusions of Dimmitt et al. (2019) [21]. It was proved that the noise of the CT image reconstructed by the ASIR model was considerably reduced, the image quality was improved, and the advantages of image quality and lesion detection were obvious.

5. Conclusion

In this study, patients with intrahepatic cholestasis of pregnancy (ICP) were selected as the research objects. ASIR reconstruction algorithm was established, which was applied to the CT image analysis and diagnosis of ICP patients, and the influence of the reconstruction algorithm on the CT image of ICP patients was discussed. Then, the clinical effect of probiotics combined with ursodeoxycholic acid in the treatment of ICP was evaluated. The results showed that SD and SNR values of liver and gallbladder reconstructed by ASIR algorithm were significantly lower than those of FBP algorithm. The overall image quality, image noise score, and pseudofilm review score after ASIR reconstruction were significantly better than those of FBP algorithm ($P < 0.05$). Before treatment, there was no statistical difference in all indicators between the two groups ($P > 0.05$). After treatment, the levels of γ -glutamyl transferase (γ-GT) and alkaline phosphatase (ALP) in the experimental group were higher than those in the control group, while the level of serum ammonia (BA) in the experimental group was lower than that in the control group, both with substantial differences ($P < 0.05$). It was proved that CT images based on ASIR reconstruction algorithm had high denoising degree, fewer artifacts, and good overall quality. Probiotics combined with ursodeoxycholic acid in the treatment of ICP can effectively improve the liver function and intestinal flora of patients. This study can provide a reliable basis for the adoption of CT imaging technology based on ASIR reconstruction algorithm in the diagnosis and treatment of ICP. However, the deficiency is that only abdominal CT images based on ASRI reconstruction algorithm at conventional doses are discussed. In future clinical studies, the influence of ASRI reconstruction algorithm on low-dose CT images needs to be discussed, so as to further illustrate its noise reduction efficiency in CT images.

Data Availability

The data used to support the findings of this study are available from the corresponding author upon request.

Conflicts of Interest

The authors declare no conflicts of interest.

References

[1] D. D. Smith and K. M. Rood, "Intrahepatic cholestasis of pregnancy," *Clinical Obstetrics and Gynecology*, vol. 63, no. 1, pp. 134–151, 2020.

[2] L. C. Chappell, J. L. Bell, A. Smith et al., "Ursodeoxycholic acid versus placebo in women with intrahepatic cholestasis of pregnancy (PITCHES): a randomised controlled trial," *The Lancet (North American Edition)*, vol. 394, no. 10201, pp. 849–860, 2019.

[3] A. M. Wood, E. G. Livingston, B. L. Hughes, and J. A. Kuller, "Intrahepatic cholestasis of pregnancy: a review of diagnosis and management," *Obstetrical and Gynecological Survey*, vol. 73, no. 2, pp. 103–109, 2018.

[4] K. R. Palmer, L. Xiaohua, and B. W. Mol, "Management of intrahepatic cholestasis in pregnancy," *The Lancet*, vol. 393, no. 10174, pp. 853-854, 2019.

[5] K. F. Walker, L. C. Chappell, W. M. Hague, P. Middleton, and J. G. Thornton, "Pharmacological interventions for treating intrahepatic cholestasis of pregnancy," *Cochrane Database of Systematic Reviews*, vol. 2020, no. 7, Article ID CD000493, 2020.

[6] S. D. Rawson, J. Maksimcuka, P. J. Withers, and S. H. Cartmell, "X-ray computed tomography in life sciences," *BMC Biology*, vol. 18, no. 1, p. 21, 2020.

[7] R. Singh, S. R. Digumarthy, V. V. Muse et al., "Image quality and lesion detection on deep learning reconstruction and iterative reconstruction of submillisievert chest and abdominal CT," *American Journal of Roentgenology*, vol. 214, no. 3, pp. 566–573, 2020.

[8] D. Prezzi, K. Owczarczyk, P. Bassett et al., "Adaptive statistical iterative reconstruction (ASIR) affects CT radiomics quantification in primary colorectal cancer," *European Radiology*, vol. 29, no. 10, pp. 5227–5235, 2019.

[9] X. Li, H. Shu, Y. Zhang et al., "Low-dose CT with adaptive statistical iterative reconstruction for evaluation of urinary stone," *Oncotarget*, vol. 9, no. 28, pp. 20103–20111, 2018.

[10] M. J. Bicocca, J. D. Sperling, and S. P. Chauhan, "Intrahepatic cholestasis of pregnancy: review of six national and regional guidelines," *European Journal of Obstetrics & Gynecology and Reproductive Biology*, vol. 231, pp. 180–187, 2018.

[11] A. Örgel, G. Bier, F. Hennersdorf, H. Richter, U. Ernemann, and T.-K. Hauser, "Image quality of CT angiography of supra-aortic arteries," *Clinical Neuroradiology*, vol. 30, no. 1, pp. 101–107, 2020.

[12] A. E. Kremer, K. Wolf, and S. Ständer, "Intrahepatische s," *Hautarzt, Der*, vol. 68, no. 2, pp. 95–102, 2017.

[13] C. C. Oh and H. Oon, "Intrahepatic cholestasis of pregnancy," *Cutis*, vol. 102, no. 3, pp. E26–E27, 2018.

[14] H.-U. Marschall, "Ursodeoxycholic acid for intrahepatic cholestasis in pregnancy," *The Lancet*, vol. 394, no. 10201, pp. 810–812, 2019.

[15] K. Halloran and M. A. Underwood, "Probiotic mechanisms of action," *Early Human Development*, vol. 135, pp. 58–65, 2019.

[16] T. Odle, "Emergency computed tomography," *Radiologic Technology*, vol. 91, no. 3, pp. 267CT–287CT, 2020.

[17] M. Tozakidou, I. Apine, K. U. Petersen et al., "Comparison of different iterative CT reconstruction techniques and filtered back projection for assessment of the medial clavicular epiphysis in forensic age estimation," *International Journal of Legal Medicine*, vol. 134, no. 1, pp. 355–361, 2020.

[18] A. Shah, M. Rees, E. Kar, K. Bolton, V. Lee, and A. Panigrahy, "Adaptive statistical iterative reconstruction use for radiation dose reduction in pediatric lower-extremity CT: impact on diagnostic image quality," *Skeletal Radiology*, vol. 47, no. 6, pp. 785–793, 2018.

[19] C. Park, K. S. Choo, J. H. Kim, K. J. Nam, J. W. Lee, and J. Y. Kim, "Image quality and radiation dose in CT venography using model-based iterative reconstruction at 80 kVp versus adaptive statistical iterative reconstruction-V at 70 kVp," *Korean Journal of Radiology*, vol. 20, no. 7, pp. 1167–1175, 2019.

[20] M. H. Goodenberger, N. A. Wagner-Bartak, S. Gupta et al., "Computed tomography image quality evaluation of a new iterative reconstruction algorithm in the abdomen (adaptive statistical iterative reconstruction-V) a comparison with model-based iterative reconstruction, adaptive statistical iterative reconstruction, and filtered back projection reconstructions," *Journal of Computer Assisted Tomography*, vol. 42, no. 2, pp. 184–190, 2018.

[21] A. M. Dimmitt, J. A. Pelz, M. E. Albertson et al., "Evaluation of adaptive statistical iterative reconstruction-V reconstruction algorithm vs. filtered back projection in the detection of h liver lesions," *Journal of Computer Assisted Tomography*, vol. 43, no. 2, pp. 200–205, 2019.

Hindawi
Journal of Healthcare Engineering
Volume 2021, Article ID 3774423, 9 pages
https://doi.org/10.1155/2021/3774423

Research Article

Deep-Learning-Based CT Imaging in the Quantitative Evaluation of Chronic Kidney Diseases

Xu Fu,[1] **Huaiqin Liu**,[2] **Xiaowang Bi**,[2] **and Xiao Gong**[2]

[1]*Second Department of Nephrology, Zibo Central Hospital, Zibo 255000, Shandong, China*
[2]*Department of Radiology, Zibo Central Hospital, Zibo 255000, Shandong, China*

Correspondence should be addressed to Xiao Gong; 20181510078@stu.sspu.edu.cn

Received 24 August 2021; Revised 29 September 2021; Accepted 1 October 2021; Published 28 October 2021

Academic Editor: Enas Abdulhay

This study focused on the application of deep learning algorithms in the segmentation of CT images, so as to diagnose chronic kidney diseases accurately and quantitatively. First, the residual dual-attention module (RDA module) was used for automatic segmentation of renal cysts in CT images. 79 patients with renal cysts were selected as research subjects, of whom 27 cases were defined as the test group and 52 cases were defined as the training group. The segmentation results of the test group were evaluated factoring into the Dice similarity coefficient (DSC), precision, and recall. The experimental results showed that the loss function value of the RDA-UNET model rapidly decayed and converged, and the segmentation results of the model in the study were roughly the same as those of manual labeling, indicating that the model had high accuracy in image segmentation, and the contour of the kidney can be segmented accurately. Next, the RDA-UNET model achieved 96.25% DSC, 96.34% precision, and 96.88% recall for the left kidney and 94.22% DSC, 95.34% precision, and 94.61% recall for the right kidney, which were better than other algorithms. The results showed that the algorithm model in this study was superior to other algorithms in each evaluation index. It explained the advantages of this model compared with other algorithm models. In conclusion, the RDA-UNET model can effectively improve the accuracy of CT image segmentation, and it is worth of promotion in the quantitative assessment of chronic kidney diseases through CT imaging.

1. Introduction

At present, chronic kidney disease has affected approximately 10% of the world's population, killing millions of people every year, and hundreds of thousands of people undergo dialysis to maintain their lives [1]. Chronic kidney disease refers to changes in the structure and function of the kidney that have occurred for more than three months. Renal cysts are one of them, but renal cysts are benign structural changes. Renal cysts grow slowly and will not have an impact on patients in the short term. However, as the cysts increase, they will compress the gastrointestinal tract. As a result, the volumes of the stomach and intestine shrink, and the patient will feel full all the time. Some patients also have symptoms of fever, vomiting, and abdominal pain, so they will have a negative impact on the patient's psychology and physiology [2–4]. During treatment, it is difficult to accurately distinguish renal cysts from small cystic renal cell carcinoma, which affects the formulation of appropriate treatment plans for patients [5]. Hence, finding a safe and reliable way to detect renal cysts is important for the treatment of patients. In clinical practice, X-rays, CT, and B-ultrasound are commonly used to diagnose patients with the kidney disease. CT scans a part of the human body with X-ray beams to obtain a cross-section or stereo image of the part being examined. It can provide complete three-dimensional information of the part of the body being examined, clearly displaying the organs and structures, as well as the lesions. The biggest advantage is that it can be viewed in layers so that more organizational information can be displayed after calculation [6]. Therefore, the application of CT in kidney examination is a hotspot of current research.

Deep learning is the core of artificial intelligence technology, and it is a research hotspot in recent years. In 2006, Dong first proposed the concept of deep learning. In order to optimize the deep structure, they proposed a greedy layer-by-layer training algorithm on the basis of the deep belief network [7]. Deep learning algorithms have also been widely used in medical image segmentation. Song et al. used the kernel fuzzy C-means algorithm and the improved GrowCut algorithm to segment kidney images, and the automatically generated seed labels heightened the segmentation efficiency [8]. Xiang et al. used cortical models and nonuniform maps to depict the kidney structure in CT images [9]. Xiong et al. proposed a tumor segmentation method based on adaptive partitioned firework level sets, which effectively segmented kidney tumors in ultrasound images [10]. Gao incorporated the level set into image segmentation to process images with uneven gray values and achieved good segmentation results [11]. Hu introduced the target tracking mechanism into the traditional image segmentation and achieved good segmentation results [12].

In this study, the U-shaped fully convolutional neural network (CNN) segmentation model was optimized by incorporating a residual dual-attention module to the model to elevate the accuracy of locating the edge of the cyst, thus to accurately and quantitatively assess chronic kidney diseases.

2. Experimental Principles and Methods

2.1. UNET Segmentation Model Based on the RDA Module. The RDA module is incorporated into the UNET model, so the optimized one is called RDA-UNET, and the structure is shown in Figure 1.

2.1.1. RDA Module. Heet al. deepened the network by stacking residual units to ensure the integrity and safety of the information and reduce the learning difficulty [13]. Woo et al. proposed a convolution algorithm that combines the channel with spatial information to extract information features, but the convolutional features are messy, so the attention mechanism can only focus on meaningful features extracted from a certain dimension [14]. In this study, a residual attention module is proposed based on the residual unit structure and attention mechanism, as shown in Figure 2.

For the input image, after going through the convolutional operation twice in the RDA module, it is processed by the channel and spatial attention mechanism, and then elements are added to it, followed by the residual connection with the original image, and finally, it is processed by the ReLU function. The original image is $Y \in Ww \times w \times c$, y is the size of the image, and C is the number of channels. The specific process of the dual-attention mechanism is as follows. According to the position of the pixel, the spatial attention mechanism identifies its contribution, and then the 1×1 convolution and sigmoid activation function are used to calculate the single-channel spatial attention mask $Q \in Ww \times w \times 1$ of each position pixel. Then, the original image Y is multiplied with the single-channel spatial attention mask Q. For the channel spatial attention mechanism, the contribution of each channel is firstly identified, and then 1×1 convolution and sigmoid activation function are used to calculate out-channel attention code $P \in W1 \times 1 \times c$, and finally, the original image is multiplied by the channel attention code. The steps of the dual-attention mechanism can be expressed as follows:

$$Y' = Q(Y) \otimes Y + P(Y) \otimes Y, \tag{1}$$

where Y' represents the output image, $\otimes$ represents element-wise multiplication, and $Q(Y)$ and $P(Y)$ represent the size same as Y in the channel and space, respectively. The RDA module has two advantages. One is to repeatedly use the features, and the other is the adaptive learning feature table. Hence, the module can learn the features of the image more effectively.

2.1.2. RDA-UNET Network Structure. According to the structural characteristics of UNET, the RDA module is introduced to design a new deep segmentation model, and its network structure is shown in Figure 1. It is mainly composed of four parts of encoder, bottleneck layer, decoder, and classifier. The encoder mainly includes the RDA module and the maximum pooling layer. The main function is to extract the semantic features of the original image. The pooling layer is mainly used for image downsampling, so as to increase the neuron sensor to obtain more detailed semantic feature information. The bottleneck layer is mainly composed of two convolutional layers, which are mainly used during the transition from the encoder to the decoder. Two deconvolutional layers and an RDA template form the decoder part, which is mainly used for image feature reconstruction, and the deconvolution layer is used for upsampling to improve the resolution of the image. The classifier is composed of a convolution layer and a softmax layer. This part can be used to estimate the background image before and after. In this part, the convolution layer can reduce the number of channels. Softmax is used to calculate the probability of the pixel belonging to a certain category. In the decoder and encoder, images of the same level can be jump-connected, thus providing rich pixel-level information for feature reconstruction. In addition, zero-filling convolution is used in each convolutional layer to obtain feature maps of the same size. In order to prevent the gradient from rising and disappearing, BN is used for all convolutional layers (the parameter settings used by the encoder and decoder are similar).

The probability map is the ratio of each pixel on the kidney and not on the kidney. The loss function is obtained by manually labeling the mask and the probability map. In this study, Dice loss is used to optimize training [15]. Dice coefficient is to evaluate the similarity, which can be expressed as follows.

$$\text{Loss} = 1 - \frac{2\sum_y^N h_i(y)k_i(y)}{\sum_y^N h_i^2(y) + \sum_y^N k_i^2(y)}, \tag{2}$$

where N represents the number of pixels, $h_i(y)$ represents the estimated probability that the yth pixel belongs to category i, and $k_i(y)$ represents the probability that the true yth pixel belongs to category i.

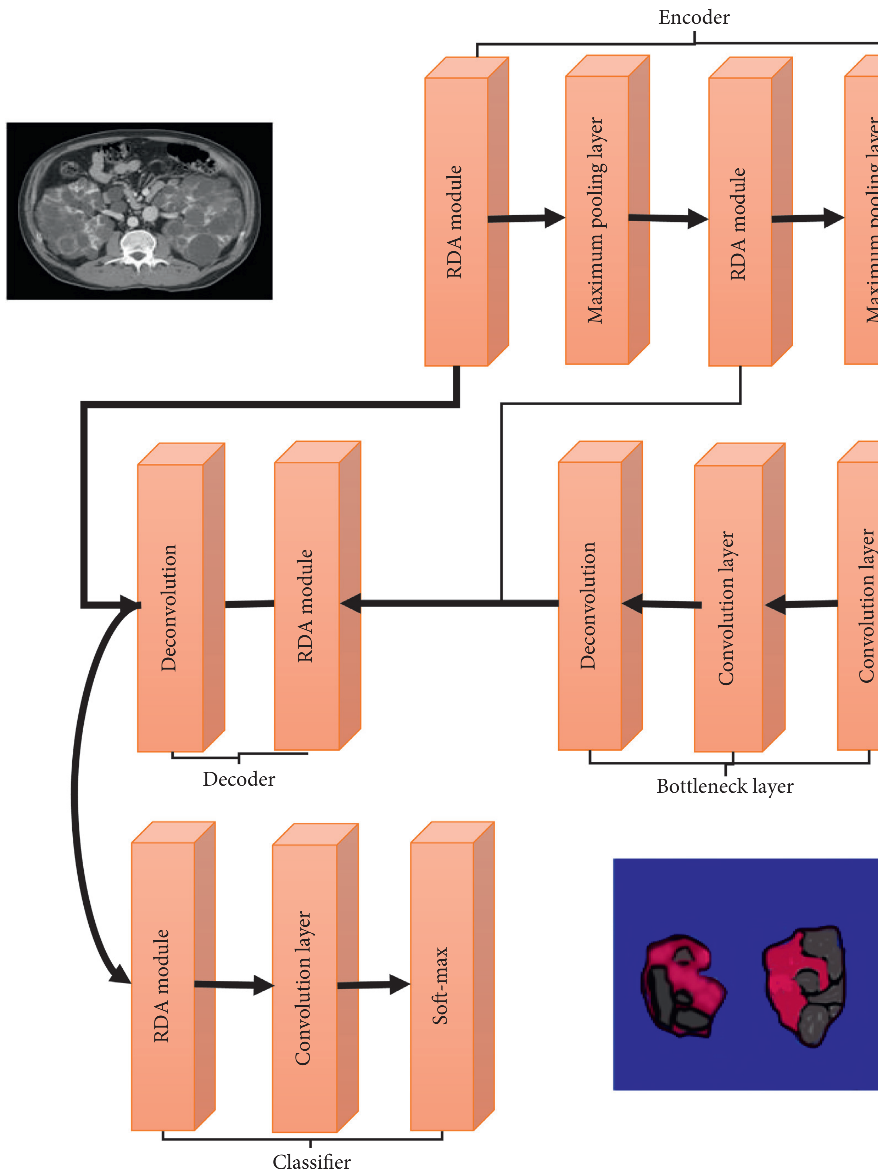

Figure 1: RDA-UNET network structure.

2.2. Experimental Settings. Dataset: the clinical abdominal plain CT images of patients with renal cysts were collected, and the images with obvious renal cyst lesions were manually marked by experienced experts. The data format is set to DICOM format, the distance between pixels is 0.625 mm, the thickness of image slices is generally 1.0 mm, and the distance between slices is about 0.5 mm. The resolution of Tuqiang is set to 512×512. A total of 79 patients with renal cysts were selected, and 6000 slice images were obtained. 27 cases were defined as the test group, and 52 cases were defined as the training group.

Preprocessing: the image needs to be processed before the experiment. First, the window width and window position of the image are adjusted to 420 hu and 60 hu, and then the size of the image is reduced to increase the number of images for each training. The image size is adjusted to 256×256. In order to make the network training more adequate, it is necessary to double the training set data by horizontal flipping. Finally, the image is normalized.

Hardware configuration and development environment: processor: Intel (R) Core(TM) i7-4790 CPU @ 3.60 GHz; discrete graphics card: Ge Force GTX Titan X; memory (RAM): 32.0 GB; system type: Ubuntu 16.04; development language: Python; deep learning framework: PyTorch [16]; image reading software: ITK-SNAP [17].

Parameter settings: batch size is set to 16; the initial learning rate is set to 10^{-3}, and it is automatically set to 10^{-4} when 30 epochs are completed; the momentum is set to 0.95,

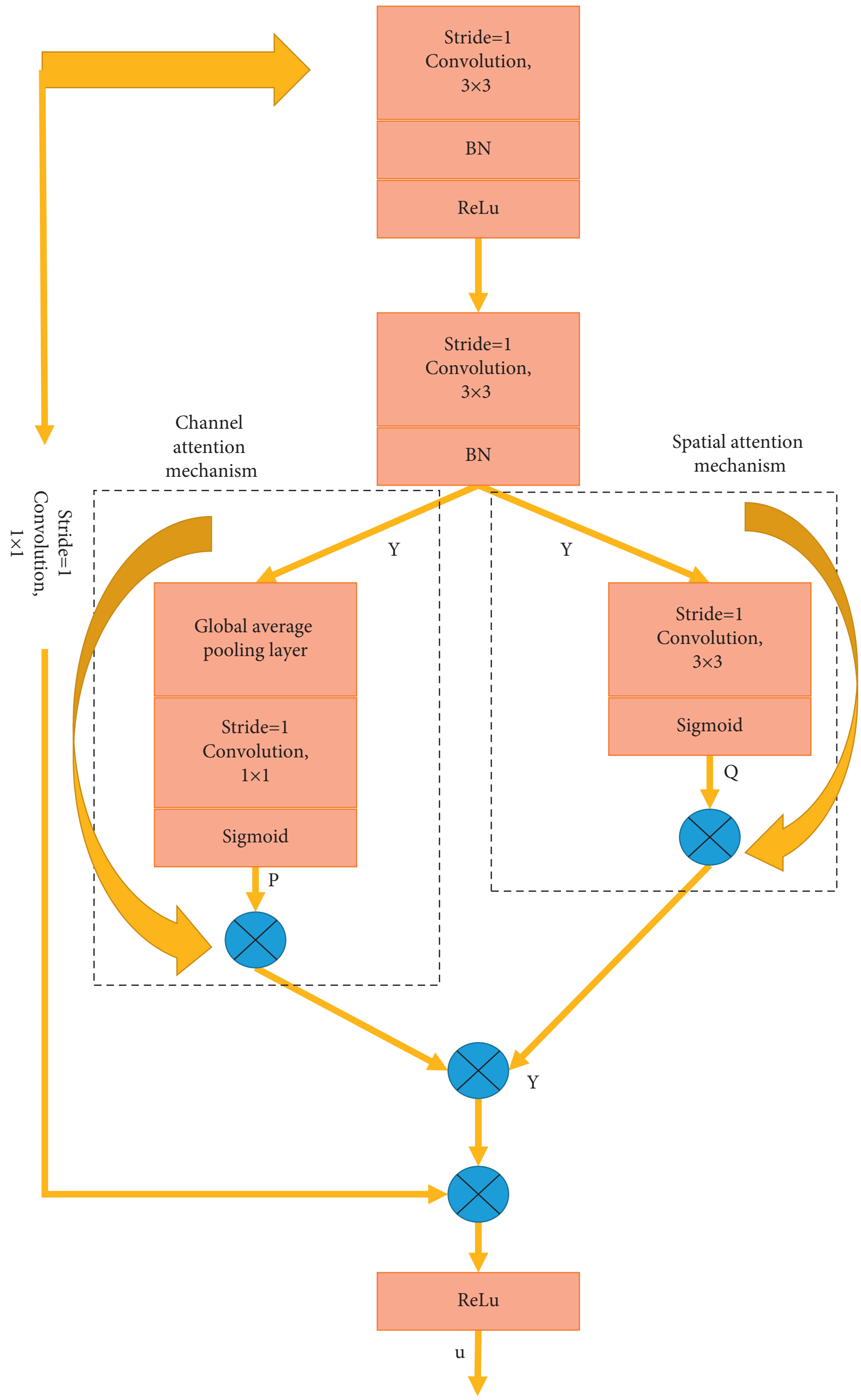

Figure 2: RDA module structure.

and the weight attenuation coefficient is constant 10^{-4}. The Adam optimizer is used for training, the training stops automatically after 50 epochs, and the test selects the parameter with the smallest loss value.

2.3. Evaluation Index. According to Figure 3, the kidneys are located on both sides of the spine. In this study, the spine was regarded as the dividing line, and the method of artificially annotating images and the method of network prediction

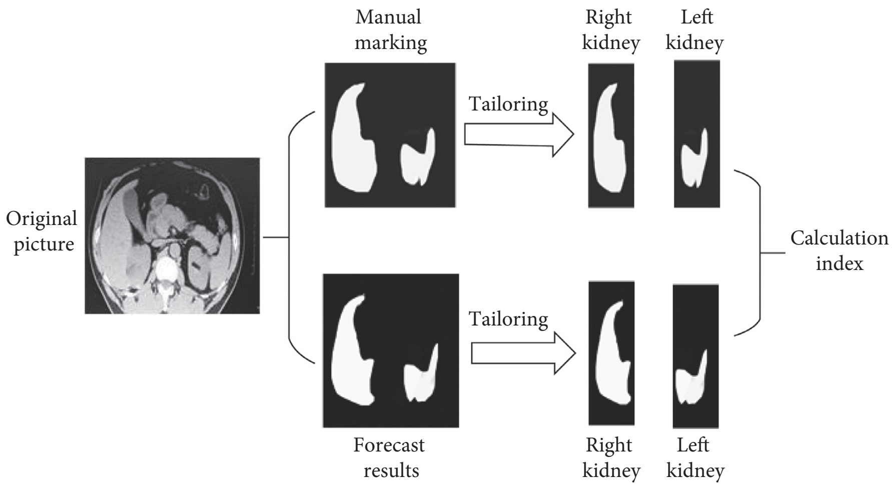

Figure 3: Evaluation method.

were used to segment the left and right kidneys. Since the left and right kidneys are not at the same height, the image will display other parts except the kidneys. The parts will be deleted during manual labeling and grid prediction. The segmentation accuracy was evaluated factoring into DSC, recall, and precision, defined as follows.

$$\mathrm{DSC} = \frac{2|E \cap F|}{|E| + |F|}, \tag{3}$$

$$\mathrm{precision} = \frac{SQ}{SQ + HQ}, \tag{4}$$

$$\mathrm{recall} = \frac{SQ}{SQ + HM}. \tag{5}$$

In equation (3), the model prediction result is E, F is the corresponding manual labeling result, and $E \cap F$ represents the foreground part in the segmentation image. In equations (4) and (5), SQ represents the part of the kidney that is correctly predicted, HQ represents that the background is predicted as the kidney, and HM represents that the kidney is predicted as the background.

2.4. User Interface. In order to facilitate operations, a simple user interface was designed using the Tkinter module based on the RDA-UNET model. This interface can accurately infer the edge contour, assisting users in segmentation.

2.5. Principles of 3D Reconstruction. CT imaging can reconstruct the three-dimensional image of the kidney. The three-dimensional image can accurately locate the area where the kidney is located to extract effective information. Doctors can preliminarily diagnose the type, the size, and the area of the renal cysts through the three-dimensional image. In addition, studies [18] have shown that the total kidney volume (TKV) is associated with the renal function to a certain extent. The TKV can be estimated by reconstructing the three-dimensional image of the kidney, and then the severity of the disease is evaluated. Therefore, the three-dimensional image of the kidney is reconstructed in the study.

3. Results

3.1. Comparison of Segmentation Effects. Figure 4 shows the relationship between the loss function of the network model in this study and the number of iterations in the training process. It was noted that the value of loss function can quickly decay and converge when the Adam optimizer was used.

Figure 5 shows the segmentation results of some images and their visualization during the training process. It was noted that the segmentation results of the algorithm proposed in this study were roughly similar to the results of manual labeling, and the spatial attention mechanism effectively and adaptively learned the spatial features. On the test set, the evaluation indicators of network models of different depths are shown in Table 1. The original models mainly included FCN-8S, FCN-16S, U-Net, and FCN-VGG10. On the basis of U-Net, U-Net (+BN) model was obtained, and UNet++ was further obtained on the basis of U-Net (+BN). In order to ensure the fairness of the experiment, no in-depth monitoring strategy was used throughout the process, and all models were trained from scratch and shared the same parameter value and Dice loss optimization. It was noted from Table 1 that the RDA-UNET model achieved 96.25% DSC, 96.34% precision, and 96.88% recall for the left kidney and 94.22% DSC, 95.34% precision, and 94.61% recall for the right kidney, which were better than other algorithms. The comparison between U-Net revealed that the use of BN greatly improved the segmentation performance.

The segmentation results of different models are shown in Figure 6. It was noted that compared with other algorithms, the RDA-UNET can segment the image more accurately and can effectively cope with changes in the shape of the kidney cysts.

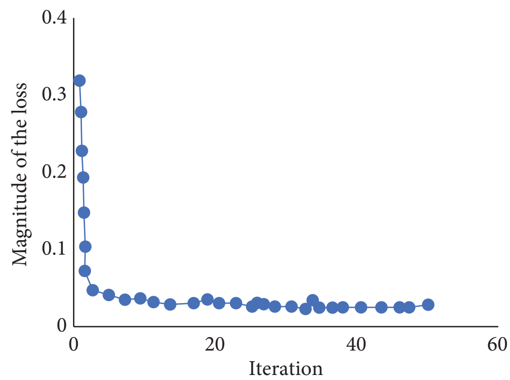

Figure 4: The decay curve of the loss function.

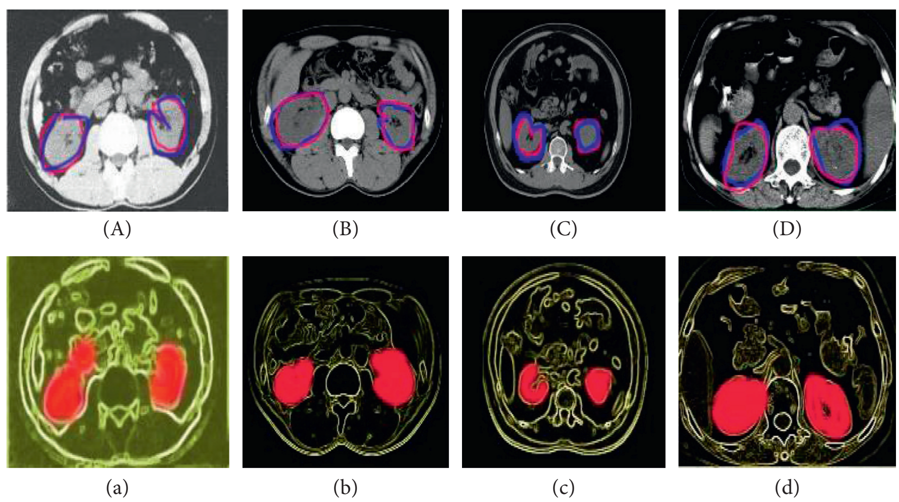

Figure 5: Segmentation effect and the visualization (the first line is the segmentation result, the red line is manual labeling, and the blue line is the network segmentation result. The second line is the spatial attention mask generated by the last RDA module).

Table 1: Average value of the evaluation index of different deep network models on the test set (%).

Model		FCN-8S[24]	FCN-16S[24]	FCN-VGG10[19]	U-Net[27]	U-Net (+BN)	UNet++[32]	RDA-UNET
Left kidney	DSC	88.12	87.53	95.23	92.65	95.09	94.88	96.25
	Precision	89.25	87.22	96.45	92.48	95.67	95.22	96.34
	Recall	89.88	87.43	95.55	93.66	96.45	95.88	96.88
Right kidney	DSC	85.34	84.13	92.23	90.44	93.79	93.32	94.22
	Precision	87.83	84.23	95.88	91.67	94.67	95.11	95.34
	Recall	87.03	88.46	91.19	92.57	94.65	94.45	94.61

3.2. Visualization of Results

3.2.1. The User Interface. Figure 7 shows the user operation interface. Figure 7(a) is the initial interface, which was mainly composed of three parts of the button for selecting the image, the button for segmenting, and the image display container. Clicking the button to select the image can load the image from the catalog to the interface. Figure 7(b) is the screen displayed on the interface after the original CT image was loaded. To click the segmentation button, the system would automatically start the image segmentation, and the segmentation results were then displayed and saved. Figure 7(c) shows the final segmentation results. When the segmentation was completed, the resulting image would be displayed. The red solid line is the contour of the kidney cyst depicted.

3.2.2. Three-Dimensional Reconstruction Results. As shown in Figure 8, the CT image of a patient was segmented first, and then the segmentation results were fused. ITK-SNAP software was used to construct a three-dimensional image.

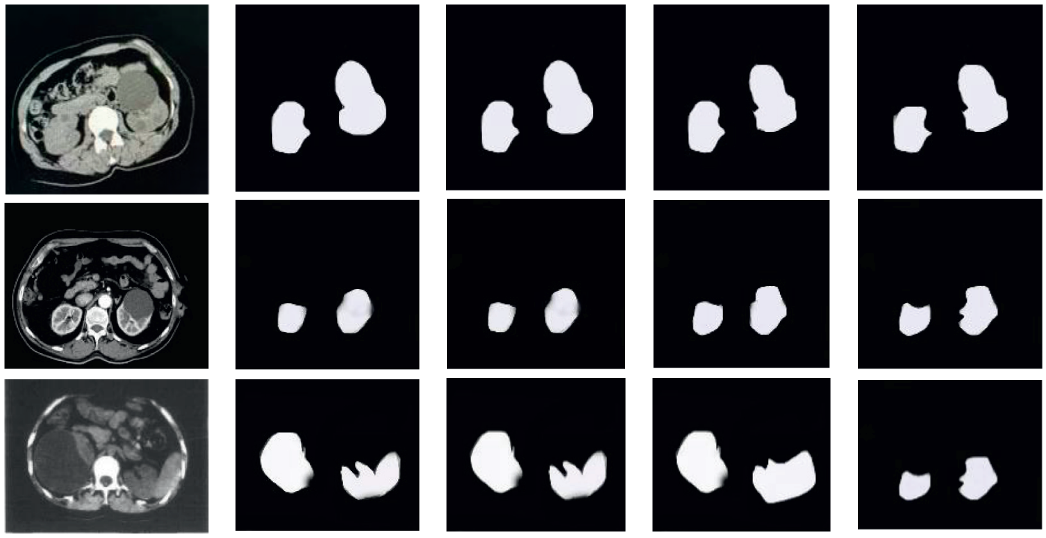

(a) (b) (c) (d) (e)

Figure 6: Segmentation results of different models. (a) Original image. (b) Manually annotated result. (c) RDA-UNET. (d) FCN-VGG10. (e) U-Net.

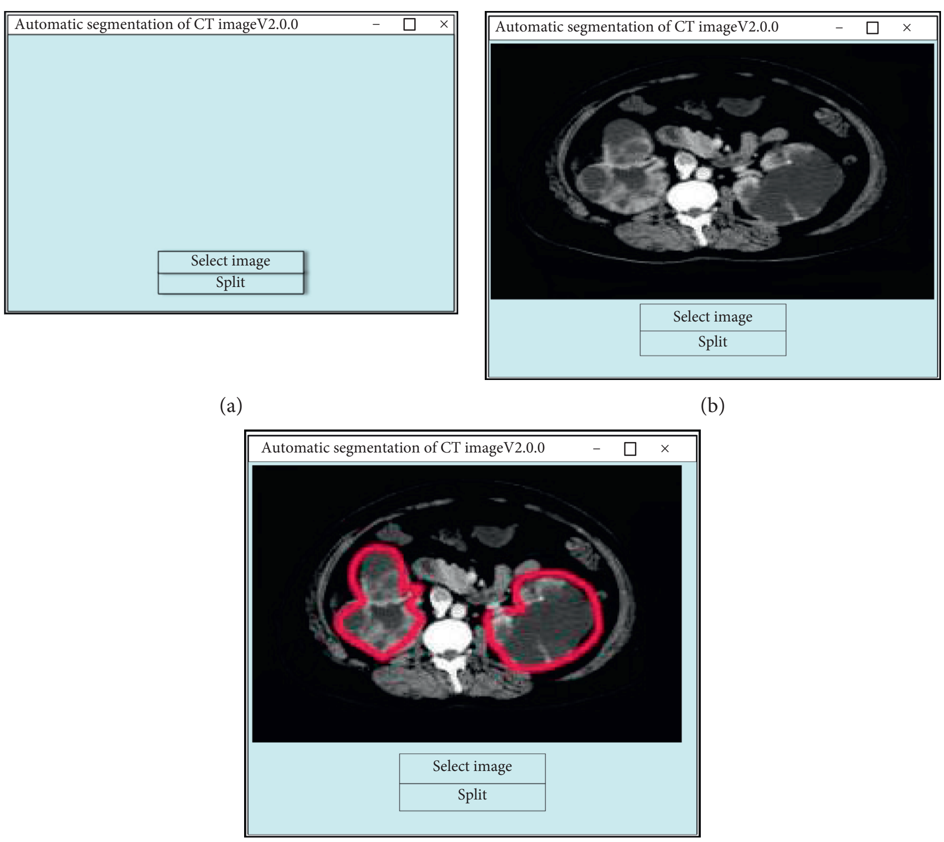

(a) (b)

(c)

Figure 7: Schematic diagram of the user operation interface. (a) Initial interface. (b) Image loaded. (c) The result displayed.

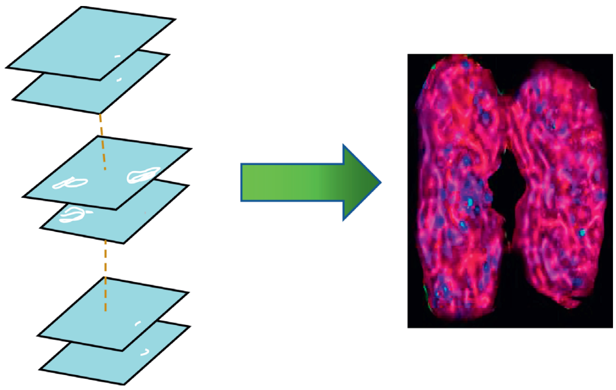

Figure 8: Three-dimensional reconstruction of a CT image of renal cysts.

4. Discussion

The constantly accelerated life rhythm resulting from the development of the economy results in constantly increasing pressure, so more and more diseases occur, threatening the health of people. The kidney disease is a representative one and attracts more and more attention. With the widespread application of artificial intelligence technology in medical imaging, image segmentation technology based on deep learning has become a focus. Intelligent algorithm can effectively segment images to obtain detailed image data, providing reference for the clinical diagnosis and treatment. In this study, a deep-learning-based segmentation model, RDA-UNET, was designed based on the residual dual-attention module, and its performance was compared with FCN-8S, FCN-16S, U-Net, FCN-VGG10, and U-Net (+BN). The results showed that the loss function value of the RDA-UNET model attenuated and tended to converge in a short time, in line with the research results of Zheng et al. [19], who combined deep learning with marginal space learning (MSL) to construct a renal segmentation algorithm and found that the segmentation accuracy of the RDA-UNET model was higher than that of other traditional algorithms.

Finally, RDA-UNET was compared with FCN-8S, FCN-16S, U-Net, FCN-VGG10, and U-Net (+BN) models, factoring into different evaluation indicators. The results showed that the RDA-UNET model achieved 96.25% DSC, 96.34% precision, and 96.88% recall for the left kidney and 94.22% DSC, 95.34% precision, and 94.61% recall for the right kidney, which were better than other algorithms. Thong et al. introduced two transformation methods and proposed a simple depth segmentation model, which can enhance the segmentation of renal CT images [20]. Xia et al. designed a semantic segmentation model based on the SCNN and ResNet combined with SIFT flow transform, which achieved a good segmentation effect with a small proportion of detailed information [21]. Sharma et al. proposed a neural network model for the segmentation of multiple renal cysts based on the structure of the VGG network. However, the morphology of renal cysts would change greatly with renal disease, so the edge contour of renal cysts could not be well located [22]. The results confirmed that the RDA-UNET model constructed in this study had good application feasibility in intelligent segmentation of renal organs and quantitative evaluation of nephropathy.

5. Conclusion

In this study, RDA-UNET, a new segmentation model based on deep learning, was proposed to segment CT images of renal cysts. Through comparison with other kidney segmentation models in terms of Dice, precision, and recall, it proved that this model had obvious advantages in the segmentation of CT slice images of renal cysts. However, some limitations in the study should be noted. The sample size is small, which will reduce the power of the study. In the follow-up, an expanded sample size is necessary to strengthen the findings of the study. In conclusion, the RDA-UNET model has high accuracy in the segmentation of CT images of renal cysts, and the study provides a reference for the diagnosis and treatment of kidney diseases.

Data Availability

The data used to support the findings of this study are available from the corresponding author upon request.

Conflicts of Interest

The authors declare no conflicts of interest.

References

[1] R. L. Chevalier, "Evolutionary nephrology," *Kidney International Reports*, vol. 2, no. 3, pp. 302–317, 2017.

[2] Z. Wan, Y. Dong, Z. Yu, H. Lv, and Z. Lv, "Semi-supervised support vector machine for digital twins based brain image fusion," *Frontiers in Neuroscience*, vol. 15, Article ID 705323, 2021.

[3] X. F. Chen, "Injection of ultrasonic interventional puncture is the clinical effect in the treatment of patients with liver cyst," *Journal of Clinical Medical Literature*, vol. 5, no. 6, pp. 142-143, 2018.

[4] D. Y. Chen, "Observation of the treatment of simple liver cyst under the ultrasound guidance of different drugs," *Northern Pharmacy*, vol. 10, no. 4, pp. 122-123, 2017.

[5] J. L. Zhang, M. Wu, and J. W. Xia, "CT imaging differential diagnostic analysis of cystic small renal cancer and complex renal cyst," *Modern Hospital*, vol. 17, no. 10, pp. 1549–1551, 2017.

[6] M. Hu, Y. Zhong, S. Xie, H. Lv, and Z. Lv, "Fuzzy system based medical image processing for brain disease prediction," *Frontiers in Neuroscience*, vol. 15, Article ID 714318, 2021.

[7] H. H. Dong, "Research and review of deep learning in artificial intelligence," *Computer programming skills and maintenance*, vol. 18, no. 8, pp. 153–155, 2018.

[8] H. Song, W. Kang, Q. Zhang, and S. Wang, "Kidney segmentation in CT sequences using SKFCM and improved GrowCut algorithm," *BMC Systems Biology*, vol. 9, no. Suppl 5, p. S5, 2015.

[9] D. Xiang, U. Bagci, C. Jin et al., "CorteXpert: a model-based method for automatic renal cortex segmentation," *Medical Image Analysis*, vol. 42, pp. 257–273, 2017.

[10] X. L. Xiong, Y. Guo, Y. Y. Wang et al., “Ultrasonic image segmentation of kidney tumors based on adaptive partition evolution level sets,” *Journal of Biomedical Engineering*, vol. 36, no. 6, pp. 945–956, 2019.

[11] Y. Gao, *RenMR Image Segmentation Methods Based on Graph Cutting and Horizontal Sets*, Maritime Affairs University of Dalian, Dalian, China, 2014.

[12] F. Z. Hu, *Study on the Renal CT Sequence Image Segmentation Method*, Harbin University of Technology, Heilongjiang Sheng China, 2015.

[13] K. He, X. Zhang, S. Ren, and J. Sun, “Deep residual learning for image recognition,” in *Proceedings of the IEEE conference on computer vision and pattern recognition*, pp. 770–778, Las Vegas, NV, USA, June 2016.

[14] S. Woo, J. Park, and J.-Y. Lee, “CBAM: convolutional block attention module,” in *Proceedings of the European Conference on Computer Vision (ECCV)*, pp. 3–19, Munich, Germany, September 2018.

[15] F. Milletari, N. Navab, and S. A. Ahmadi, “V-net: fully convolutional neural networks for volumetric medical image segmentation,” in *Proceedings of the 2016 Fourth International Conference on 3D Vision (3DV)*, pp. 565–571, IEEE, Stanford, CA, USA, October 2016.

[16] A. Paszke, S. Gross, S. Chintala et al., “Automatic differentiation in Pytorch,” in *Proceedings of the NIPS 2017 Workshop on Autodiff*, Long Beach, CA, USA, December 2017.

[17] P. A. Yushkevich and G. Gerig, “ITK-SNAP: an intractive medical image segmentation tool to meet the need for expert-guided segmentation of complex medical images,” *IEEE Pulse*, vol. 8, no. 4, pp. 54–57, 2017.

[18] A. B. Chapman, J. E. Bost, V. E. Torres et al., “Kidney volume and functional outcomes in autosomal dominant polycystic kidney disease,” *Clinical Journal of the American Society of Nephrology*, vol. 7, no. 3, pp. 479–486, 2012.

[19] Y. Zheng, D. Liu, B. Georgescu, and D. Xu, *Deep Learning and Convolutional Neural Networks for Medical Image Computing*, Springer, Berlin, Germany, 2017.

[20] W. Thong, S. Kadoury, N. Piché, and C. J. Pal, “Convolutional networks for kidney segmentation in contrast-enhanced CT scans,” *Computer Methods in Biomechanics and Biomedical Engineering: Imaging & Visualization*, vol. 6, no. 3, 2018.

[21] K. J. Xia, H. S. Yin, and Y. D. Zhang, “Deep semantic segmentation of kidney and space-occupying lesion area based on SCNN and ResNet models combined with SIFT-flow algorithm,” *Journal of Medical Systems*, vol. 43, no. 1, p. 2, 2018.

[22] K. Sharma, C. Rupprecht, A. Caroli et al., “Automatic segmentation of kidneys using deep learning for total kidney volume quantification in autosomal dominant polycystic kidney disease,” *Scientific Reports*, vol. 7, no. 1, p. 2049, 2017.

Hindawi
Journal of Healthcare Engineering
Volume 2021, Article ID 6183946, 11 pages
https://doi.org/10.1155/2021/6183946

Research Article

Chest Computed Tomography Images in Neonatal Bronchial Pneumonia under the Adaptive Statistical Iterative Reconstruction Algorithm

Ying Sun, [1] **Liao Wu**, [2] **Zhaofang Tian**, [1] **and Tianping Bao** [1]

[1]*Department of Neonatology, The Affiliated Huai'an No. 1 People's Hospital of Nanjing Medical University, Huai'an 223300, Jiangsu, China*
[2]*Department of Neurology, The Affiliated Huai'an No. 1 People's Hospital of Nanjing Medical University, Huai'an 223300, Jiangsu, China*

Correspondence should be addressed to Ying Sun; 1400540135@xs.hnit.edu.cn

Received 28 August 2021; Revised 30 September 2021; Accepted 4 October 2021; Published 27 October 2021

Academic Editor: Enas Abdulhay

This study was to explore the application value of chest computed tomography (CT) images processed by artificial intelligence (AI) algorithms in the diagnosis of neonatal bronchial pneumonia (NBP). The AI adaptive statistical iterative reconstruction (ASiR) algorithm was adopted to reconstruct the chest CT image to compare and analyze the effect of the reconstruction of CT image under the ASiR algorithm under different preweight and postweight values based on the objective measurement and subjective evaluation. 85 neonates with pneumonia treated in hospital from September 1, 2015, to July 1, 2020, were selected as the research objects to analyze their CT imaging characteristics. Subsequently, the peripheral blood of healthy neonates during the same period was collected, and the levels of C-reactive protein (CRP) and erythrocyte sedimentation rate (ESR) were detected. The efficiency of CT examination, CRP, ESR, and combined examination in the diagnosis of NBP was analyzed. The results showed that the subjective quality score, lung window subjective score, and mediastinal window subjective score were the highest after CT image reconstruction when the preweight value of the ASiR algorithm was 50%. After treatment, 79 NBP cases (92.9%) showed ground-glass features in CT images. Compared with the healthy neonates, the levels of CRP and ESR in the peripheral blood of neonates with bronchial pneumonia were much lower ($P < 0.05$). The accuracy rates of CT examination, CRP examination, ESR examination, CRP + ESR examination, and CRP + ESR + CT examination for the diagnosis of NBP were 80.7%, 75.3%, 75.1%, 80.3%, and 98.6%, respectively. CT technology based on AI algorithm showed high clinical application value in the feature analysis of NBP.

1. Introduction

Neonatal bronchial pneumonia (NBP) is the most common pediatric pneumonia disease caused by mycoplasma infection, accounting for about 10% of neonatal pneumonia. Because of the anatomical and physiological characteristics of the neonatal respiratory tract and the immune characteristics of the body, the morbidity and mortality of bronchial pneumonia in children are significantly increased compared with adults, and its clinical symptoms are different. It is still one of the important diseases threatening the health of newborns [1]. According to the statistics of the causes of neonatal death of the World Health Organization (WHO) from 2000 to 2003, bronchopneumonia accounted for 19%, which is the first cause of neonatal death; the incidence of NBP in developed countries is 0.05 times/person/year. In developing countries, the incidence of NBP is 6 times that of developed countries, and the anatomical characteristics of children and the sensitivity of individuals to drugs are different. Approximately 2.4 million children die every year. NBP caused by multiple pathogens and physical and chemical factors is still threatening the health and life of newborns [2]. At present, pneumonia still ranks first in the neonatal prevalence and mortality in our country.

Therefore, it is necessary to explore the diagnosis and treatment methods of NBP, further improve the diagnosis and treatment of NBP, promote the early recovery of children, and reduce the pain of children. Most of the NBP treated with regular drugs have good results, but some children with pneumonia only rely on conventional drugs to treat the results poorly. Therefore, the diagnosis and treatment of neonatal pneumonia still need to be further explored [3]. There are many diagnostic methods for NBP, such as fiberoptic bronchoscopy and bronchography. CT imaging has also been used in the diagnosis of NBP and has a certain diagnostic value [4] with the rapid development of imaging technology. However, CT scan is highly radioactive. In order to reduce its impact on neonates' health, low-dose CT is often used clinically to diagnose pediatric diseases. Low-dose CT scanning reduces the radiation while increasing the noise in the image, which affects the diagnosis accuracy of the disease to a certain extent [5, 6].

The ASiR (an AI algorithm) has been introduced in recent years to balance the quality of CT image and radiation dose, and it has been proven to significantly improve the image quality and reduce the radiation dose of CT scans [7–9]. Compared with the filtered back projection (FBP) algorithm, the ASiR algorithm can reconstruct high-quality CT images with low noise and less artifacts [10], because the traditional iterative reconstruction algorithm runs slowly and the modified ASiR algorithm can effectively weight FBP data and ASiR data to fuse, while reducing the image noise and increasing the processing speed [11].

Based on this, the AI ASiR algorithm was introduced firstly in this study to reconstruct the low-dose chest CT images of neonates, and then the CT characteristics and clinical features of neonates with bronchial pneumonia were analyzed. In addition, the accuracy of different methods for the diagnosis of bronchial pneumonia was analyzed and compared. This study was intended to provide a reference for improving the clinical diagnosis rate of NBP.

2. Basic Theories of CT Reconstruction

2.1. Physical Basis of CT Reconstruction. The CT imaging process mainly used different energy waves as radiation sources to perform projection of the object after irradiation, so as to obtain the reconstructed object [12]. The radiation source of CT imaging was mostly X-ray or γ-ray. X-ray was selected as an example to explain the principle of CT image reconstruction. When X-rays passed through an object, they would gradually attenuate in the body of the object. The density of the constructed object was different, so the attenuation speed of X-ray was also different. For objects with a more homogeneous medium, the attenuation of X-rays obeyed the Lambert–Beer theorem [13]:

$$I = I_0 e^{-\mu x}, \tag{1}$$

where I refers to the intensity after the attenuation of the ray through the object, I_0 represents the intensity when the ray was incident, μ is the attenuation coefficient, and x refers to the transmission length.

For inhomogeneous object, the attenuation coefficient μ could be regarded as a function of x and y; that is, $\mu = \mu(x, y)$. Therefore, the total attenuation of the ray that can pass through the object along path L in a certain direction i could be expressed as follows:

$$\int_L \mu di = \ln\left(\frac{I_0}{I}\right). \tag{2}$$

2.2. Mathematical Basis of CT Reconstruction. The mathematical basis of CT image reconstruction was the Radon transformation (as shown in Figure 1) and the inverse transform theory proposed by the Austrian Mathematician Radon in 1917 [14].

As given in Figure 1, the calculation equation of straight line L in the plane xoy could be written as follows:

$$L: s = x\cos\varphi + y\sin\varphi, \tag{3}$$

where s represents the distance from origin O to straight line L, and φ represents the angle between the normal of straight line L and the x-axis (positive direction).

The mathematical expression of the line integral value of the attenuation function $f(x, y)$ along straight line L could be written as follows:

$$R_f(s, \varphi) = \int_L f(x, y)\mathrm{d}l, \tag{4}$$

where R refers to the Radon transformation of the attenuation function, which could be expressed as R_f.

The coordinate system xoy was rotated counterclockwise by φ degrees along origin O to obtain a new coordinate system $x'oy'$. Then, the parameter equations of x and y of straight line L in this coordinate system are given as follows:

$$\begin{cases} x = x'\cos\varphi - y'\sin\varphi, \\ y = x'\sin\varphi + y'\cos\varphi. \end{cases} \tag{5}$$

After equation (5) was incorporated into equation (4), the Radon transformation of the attenuation function could be performed in a rotating coordinate system, which could be written as follows:

$$R_f(s, \varphi) = \int_{-\infty}^{\infty} (x'\cos\varphi - y'\sin\varphi, x'\sin\varphi + y'\cos\varphi)dy'. \tag{6}$$

The process of Radon inverse transformation was the process of CT image reconstruction, which required to calculate the target object density based on projection data. The specific calculation equation of Radon inverse transformation is shown as follows:

$$f(r, \theta) = \frac{1}{2\pi^2}\int_0^{\pi}\int_{-\infty}^{\infty} \frac{1}{r\cos(\theta - \varphi) - s}\frac{\partial R_f(s, \varphi)}{\partial s}\mathrm{d}s\mathrm{d}\varphi. \tag{7}$$

where $f(r, \theta)$ is the polar coordinate representation of the attenuation function.

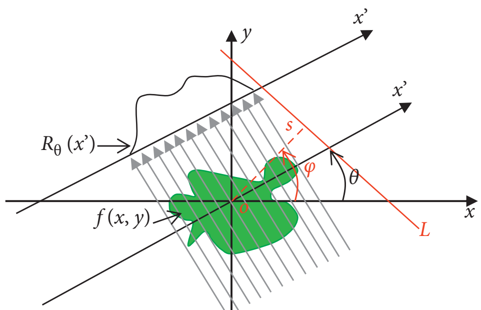

Figure 1: Radon transformation.

Equation (7) was conversed to obtain the convolution form. The polar coordinate representation of the converted attenuation function could be written as $f(r,\theta) = (1/2\pi)\int_0^\pi d\varphi\ (R_f'(s,\varphi) * (1/\pi x_r))_{x_r = r\cos(\theta-\varphi)}$, where $*$ is convolution and $(1/\pi x_r)$ refers to the convolution factor of Hilbert transform.

3. Methods

In this study, 85 NBP patients treated in our hospital from September 1, 2015, to July 1, 2020, were selected as the research objects. Firstly, all children underwent a CT imaging examination. After the examination, the CT images were processed using AI algorithms, and the quality of the processed CT images would be independently evaluated by two radiologists with at least 5 years of work experience. After that, 85 newborn children with pneumonia and 95 healthy children were checked for biochemical indicators, and the biochemical indicators of the two groups of children were compared. Finally, all research data were collected, and the biochemical indicators of the two groups of children were statistically analyzed. The sensitivity, specificity, and accuracy of CT diagnosis were analyzed and compared. The detailed research methods were as follows.

3.1. Research Objects. 85 cases of pneumonia neonates treated in hospital from September 1, 2015, to July 1, 2020, were selected as the research objects: 48 males and 37 females. 95 healthy children who underwent physical examination at the hospital during the same period served as the control group. The families of all had been clarified about the radioactivity of CT examination and the risks of enhanced examinations before the examination and had signed the informed consent forms. All examinations in this trial had been approved by the Medical Ethics Committee of the hospital.

3.2. Imaging Examination. The scan range of the image was strictly set. Brilliance 64-slice spiral CT (128 slices) was used to scan from the top to the bottom of the child's chest to the diaphragmatic level of the lung base. After the consent of neonates' family members, CT scan was performed in neonates' quiet state to remove the metal material on the chest to avoid the appearance of image artifacts. 0.5 mmBp lead clothing was adopted to cover the lower abdomen and pelvic cavity of the neonate, and the neonate was required to keep a supine position for chest CT scan. During the scanning, the specific parameters of the CT scan were set according to the requirements for chest low-dose scan of neonates. The tube voltage was 100~120 kV, the tube current was 50 mA, the speed was 0.8 s/rot, the pitch was 1.375 : 1.000, the noise index was 12, the layer thickness was 5 mm, and the spacing was 5 mm.

3.3. CT Images Process Based on AI Algorithm. The CT images obtained from low-dose scans were reconstructed using the AI ASiR and FBP algorithms. The preweight value of ASiR was set to 0%, 10%, 20%, 30%, 40%, 50%, 60%, 70%, 80%, 90%, and 100% to evaluate the reconstructed image with the ASiR algorithms. The preweight value was turned off to optimize the subjective scores of the mediastinal window and lung window so that they both could reach the highest preweight values, based on which the postweight value interval of the ASiR algorithm was set in turn. The percentage indicated the proportion of iterative reconstruction. When the proportion was 0%, it meant that the FBP algorithm was used for image reconstruction, and when the proportion was 100%, it meant that the ASiR algorithm was used for image reconstruction. The type of image reconstruction had to select a standard algorithm, and the reconstructed layer thickness was set to 1.25 mm.

3.4. Quality Evaluation of Reconstructed CT Image. The chest CT image was uploaded to the workstation for observation. The region of interest (ROI) was selected in the lung field, aorta, paraspinal soft tissue, and vertebral body in the upper (sternoclavicular joint layer), middle (pulmonary vein layer), and lower (near diaphragmatic muscle layer) parts of the axial CT image, and the ROI = 100 mm^2. The CT values (represented by ROIa and ROIm) and the density standard deviations (SD) of different ROI regions were recorded, and the average of the CT values of the 3 slices was calculated and adopted. The noise and contrast-to-noise ratio (CNR) in the reconstructed image were detected and calculated, respectively, of which CNR could be calculated with CNR = (ROIa/ROIm)/SD. When it was required to extract ROI regions in images of different levels, it was necessary to ensure that the position, size, and shape of the ROI were consistent.

2 radiologists with at least 5 years of work experience were selected for independent subjective evaluation of CT images. The mediastinal window and lung window were observed and scored. The scoring criteria were defined as follows. If the image reconstruction quality was very poor so that it could not be used for the clinical diagnosis of the disease, 1 point was scored; 2 points meant that the image reconstruction quality was relatively poor and could not meet the basic requirements of clinical disease diagnosis; 3 points indicated that image reconstruction quality was relatively average and basically could meet the requirements of clinical disease diagnosis; 4 points indicated that the image reconstruction quality was good and could meet the clinical requirements for the diagnosis requirements of the

above diseases; and 5 points were awarded for the good image reconstruction quality, which could fully meet the diagnosis requirements of the clinical diseases. When the total score of the image evaluation exceeded 3 points, the image could be used in the clinical diagnosis of the disease. If there were any different opinions between the 2 radiologists, this could be solved by negotiation.

3.5. Biochemical Indicators Examinations of Neonates. The venous blood had to be collected from all neonates. The neonate was required to fast with water 10 hours before blood collection. After 10 mL of venous blood was collected, the ESR level was detected according to Widman's method, and the CRP level was detected using an automatic biochemical analyzer. The normal level of ESR was 0~10 mm/h, and the normal level of CRP was >10 mg/L.

3.6. Statistical Analysis. The SPSS 22.0 statistical software package was adopted to process and analyze the test result data. The Kappa test was used to detect the consistency of the subjective scoring results of CT images. Kappa ≤0.4 was regarded as poor consistency, Kappa = 0.4–0.75 was regarded as good consistency, and Kappa ≥0.75 was regarded as excellent consistency. The single-factor ANOVA was applied to compare the image score results after reconstruction with different weights of the ASiR algorithm, and the LSD method was selected for pairwise comparison. The differences in the basic data and biochemical indicators of the two groups of neonates were compared using the independent-samples *t*-test, and the differences in the basic data and diagnosis accuracy of CT, biochemical indicators, and CT combined biochemical indicators of the two groups of neonates were compared using the chi-square test. When $P < 0.05$, the difference was statistically significant.

4. Results

4.1. Impacts of Preweight Value on Reconstructed Image Quality Based on ASiR Algorithm. The image noise and CNR changes after reconstruction of chest CT images using different preweight values (0%, 10%, 20%, 30%, 40%, 50%, 60%, 70%, 80%, 90%, and 100%) of ASiR algorithm were analyzed firstly (as shown in Figure 2). With the gradual increase of the preweight value, the noise value in the CT image showed a gradually decreasing trend, while the CNR value showed a gradually increasing trend.

Secondly, the differences between the subjective noise and subjective quality score of the image were compared after the chest CT image was reconstructed with the ASiR algorithm with different preweight values (0%, 10%, 20%, 30%, 40%, 50%, 60%, 70%, 80%, 90%, and 100%), and the results are illustrated in Figure 3. With the gradual increase of the preweight value of the ASiR algorithm, the subjective noise score in the reconstructed CT image showed a gradual decline, indicating that the noise in the reconstructed CT image was gradually reduced during the operation of the ASiR algorithm. With the gradual increase of the preweight value of the ASiR algorithm, the subjective quality score of the reconstructed CT image did not show a gradual upward trend. When the preweight value was 0%~50%, the subjective quality score increased gradually; the subjective quality score showed a gradual decline trend when the preweight value was 50%~100%. Among them, the subjective quality score of the CT image was the highest after reconstruction with the ASiR algorithm with 50% preweight value.

Then, the difference between the mediastinal window subjective score and lung window subjective score was compared when the chest CT image was reconstructed using the ASiR algorithm with different preweight values (0%, 10%, 20%, 30%, 40%, 50%, 60%, 70%, 80%, 90%, and 100%), and the analysis results are revealed in Figures 4 and 5, respectively. The changes in the mediastinal window and lung window subjective scores of the CT images after reconstruction were basically the same as the changes in the subjective quality score. When the preweight value was 40%~60%, the mediastinal window and lung window subjective scores of the CT images reconstructed by the ASiR algorithm were obviously higher. Among them, the mediastinal window and lung window subjective scores of the CT image after reconstruction by the ASiR algorithm with a preweight value of 50% were the highest.

4.2. Impacts of Postweight Value on Reconstructed Image Quality Based on ASiR Algorithm. The above results revealed that the reconstructed CT image quality was the best when the preweight value in the ASiR algorithm was 50%. Therefore, the preweight value in the ASiR algorithm was set to 0% and 50% to compare and analyze the impacts of different postweight values on the CT value of different positions after CT image reconstruction. As shown in Figure 6, the CT value of lung tissue after reconstruction using the ASiR algorithm under different preweight values showed a gradual downward trend with the increase of postweight value. The CT value of lung tissue under 50% of preweight value was obviously lower than that under the 0% of the preweight value when the postweight value was 50%~100%, as illustrated in Figure 6(a). With the increase of postweight value, the CT value of the vertebral body and aorta after reconstruction of the ASiR algorithm under different preweight values showed a gradual decrease, but the CT value of paraspine soft tissue was not changed greatly. The CT values of the vertebral body, aorta, and paraspine soft tissue under the preweight value of 50% were all less than those under the preweight value of 0% (as shown in Figures 6(b)–6(d)).

The impacts of ASiR algorithm on the SD value of the target position after reconstruction of the CT image under different postweight values were analyzed and compared, and the results are given in Figure 7. With the increase of postweight value, the SD value of lung tissue after reconstruction with ASiR algorithm at 0% preweight value was not obvious, while that after reconstruction with ASiR algorithm at 50% preweight value showed a trend of first increasing and then decreasing. Among them, the SD value of lung tissue under 70% postweight value was the largest (as disclosed in Figure 7(a)). As the postweight value increased, the SD values of the vertebral body, aorta, and paraspine soft tissue in CT images after reconstruction with

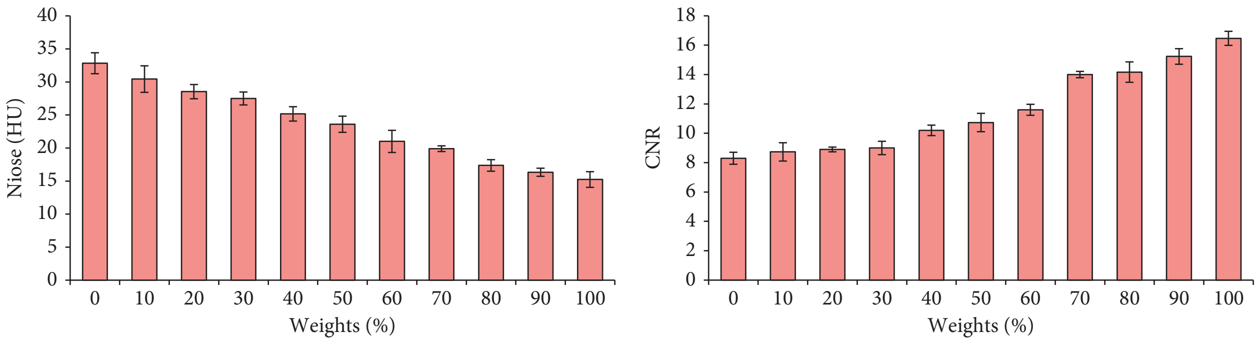

(a) (b)

Figure 2: Objective evaluation results of CT images after reconstruction using the ASiR algorithm with different preweight values. (a) Noise (HU); (b) CNR.

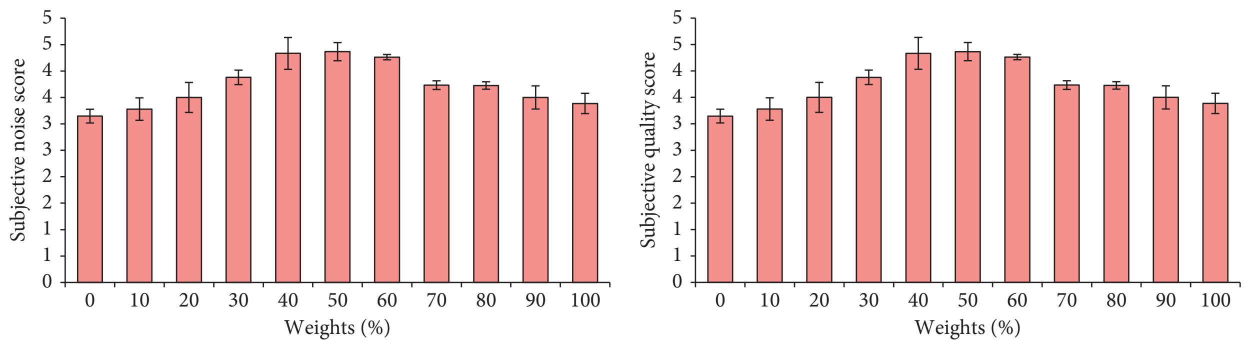

(a) (b)

Figure 3: Comparison of subjective noise and quality score of CT images reconstructed by ASiR algorithm with different preweight values. (a) Subjective noise score; (b) subjective quality score.

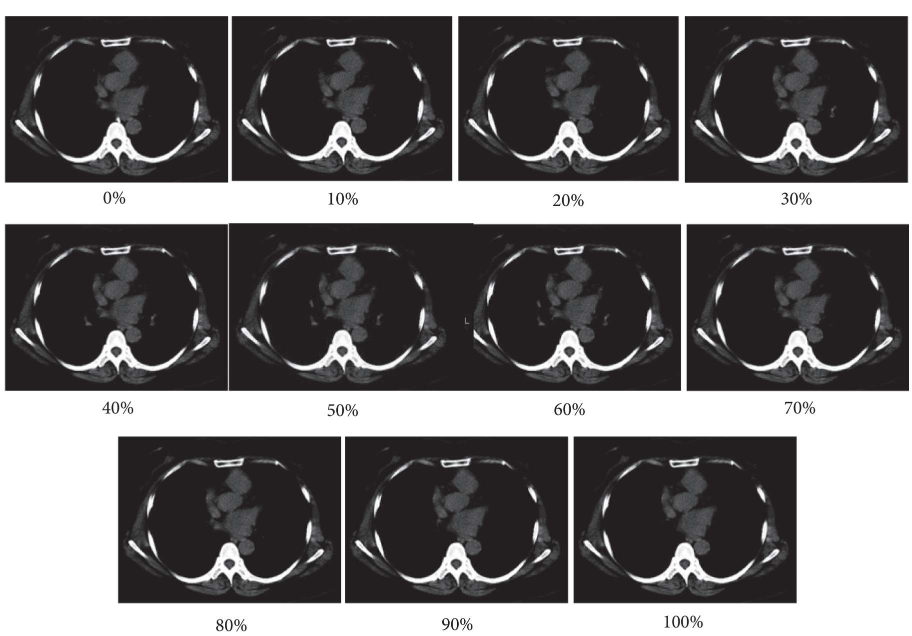

(a)

Figure 4: Continued.

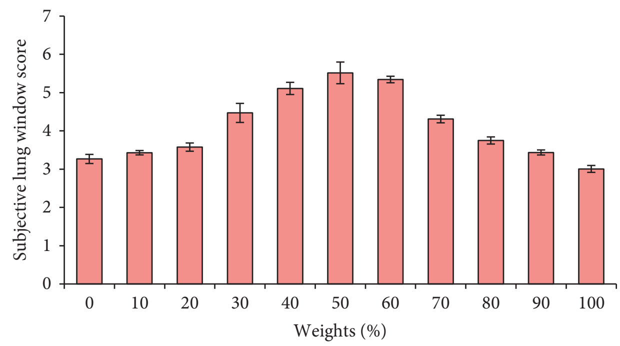

(b)

Figure 4: Comparison of the mediastinal window subjective scores of CT images after reconstruction of the ASiR algorithm with different preweight values. (a) CT image; (b) subjective lung window score.

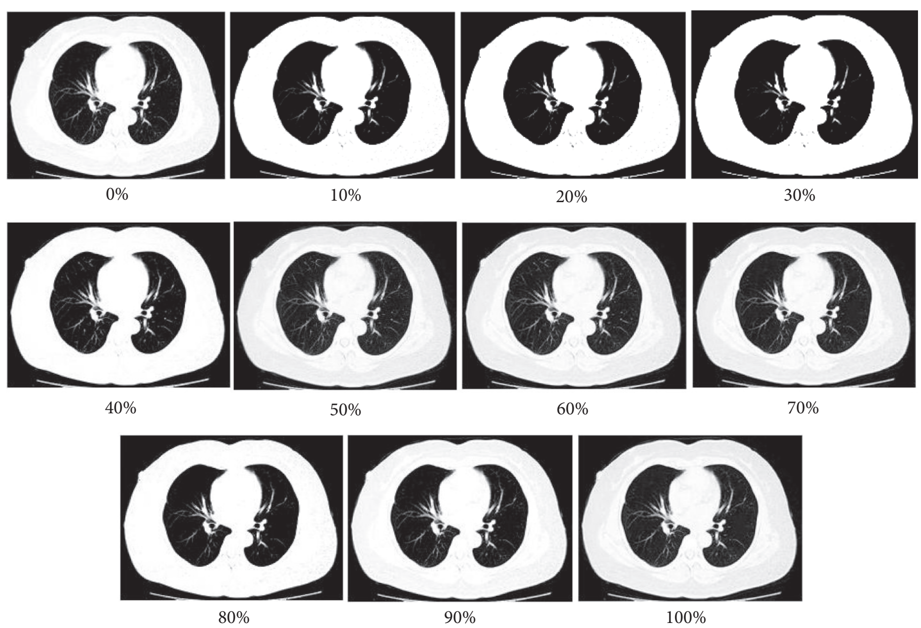

(a)

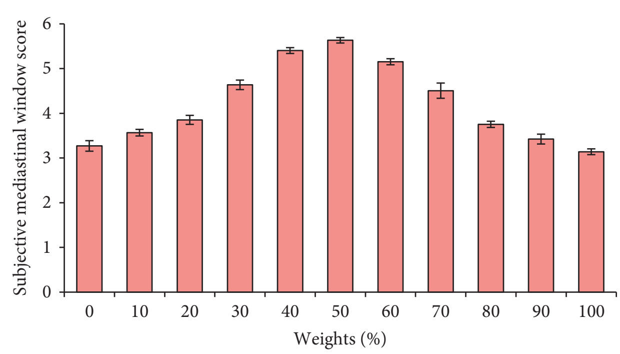

(b)

Figure 5: Comparison of subjective mediastinal window scores of CT images reconstructed by ASiR algorithm with different preweight values. (a) CT image; (b) subjective mediastinal window score.

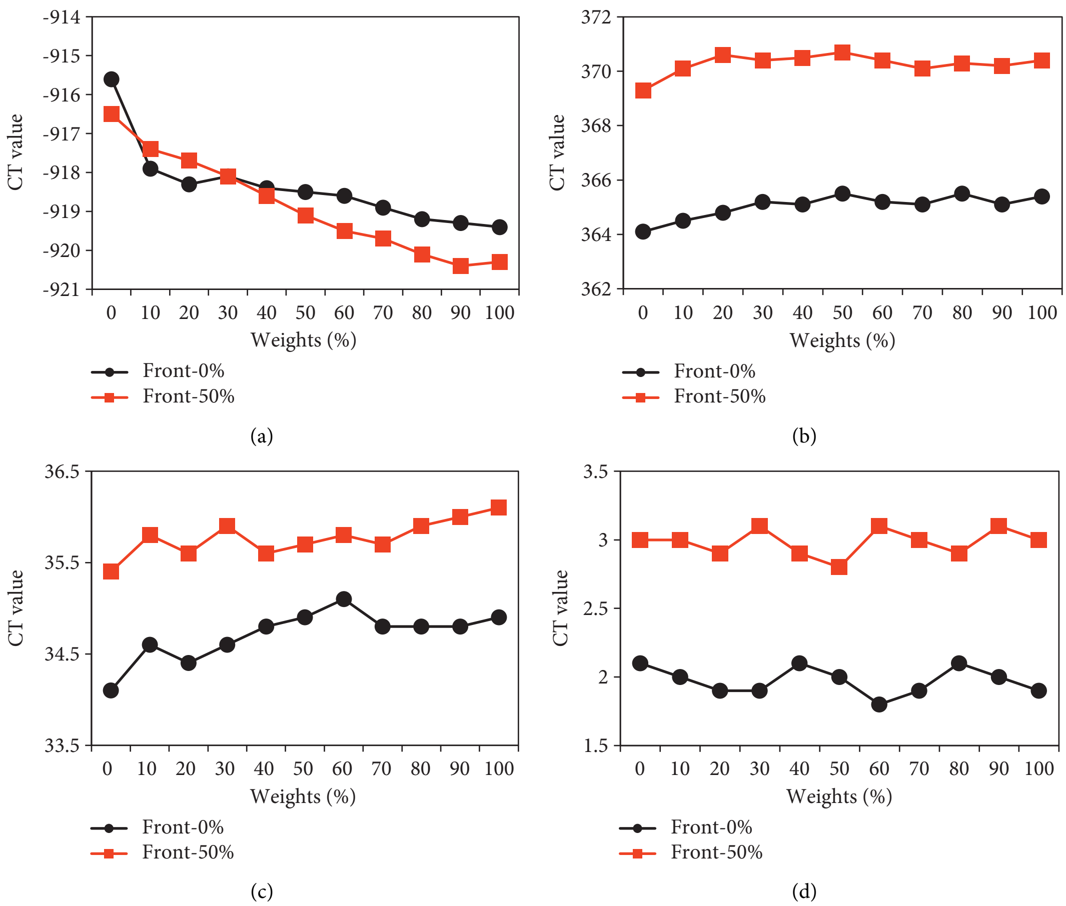

Figure 6: Changes in CT values of various tissues after reconstruction of the ASiR algorithm under different postweight values.

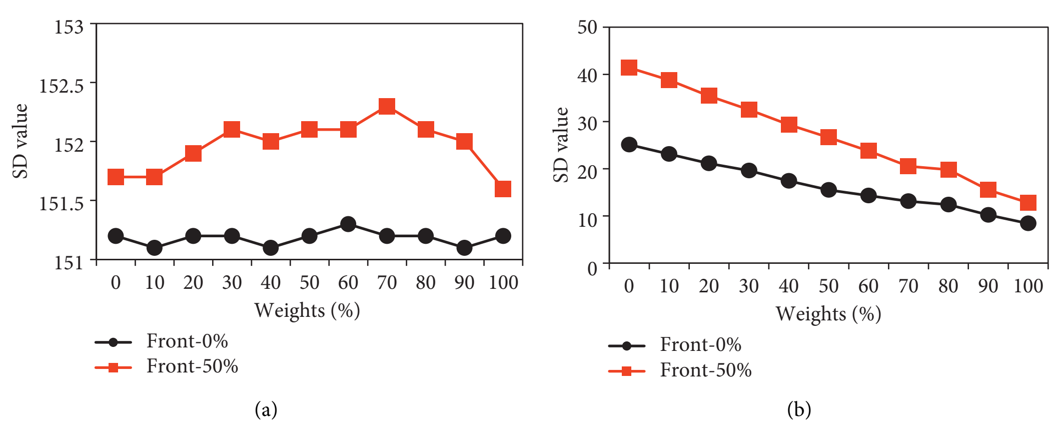

Figure 7: Continued.

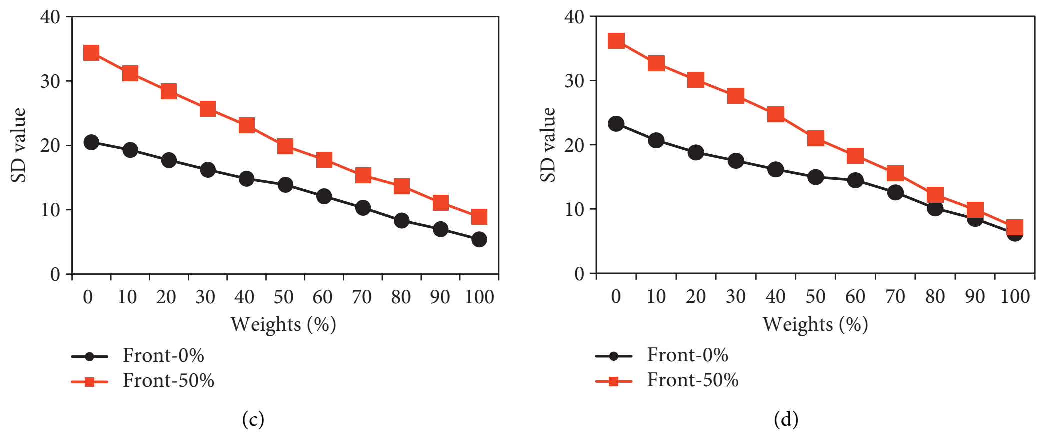

Figure 7: Changes in SD values of each tissue after reconstruction of the ASiR algorithm under different postweight values.

different preweight values of the ASiR algorithm showed gradual declines. The SD values of the vertebral body, aorta, and paraspine soft tissue after reconstruction with the ASiR algorithm under 0% preweight value were much lower than those under the 50% preweight value (as shown in Figures 7(b)–7(d)).

4.3. CT Characteristics of NBP. The CT images of 2 neonates were undertaken as examples to analyze the characteristics of CT images (Figure 8). In the CT image of neonate A, a large area of increased density shadow could be clearly observed in the lower right lobe of the lung, the internal density was not uniform, and the air shadow of the bronchus could be clearly observed. In the CT image of neonate B, patchy and ground-glass shadows could be clearly observed in the left lower lobe of the lung, and the characteristics of bronchial inflation could be seen.

The characteristics of CT images of 85 neonates with bronchial pneumonia were analyzed (as shown in Table 1). The ground-glass CT imaging characteristic accounted for the highest proportion, followed by nodular/small air cavity consolidation, and the vascular bundle thickening also accounted for more than 50%.

4.4. Characteristics of Biochemical Indicators of NBP. The differences between the levels of CRP and ESR in peripheral blood of healthy neonates and neonates with bronchial pneumonia were compared, and the results are illustrated in Figure 9. The levels of CRP and ESR in peripheral blood of neonates with bronchial pneumonia were 27.3 ± 3.5 mg/L and 19.1 ± 3.7 mm/h, respectively. The levels of CRP and ESR in peripheral blood of healthy neonates were 2.7 ± 2.4 mg/L and 6.1 ± 4.8 mm/h, respectively. After comparison, it was found that the CRP and ESR levels in peripheral blood of neonates with bronchial pneumonia were remarkably lower in contrast to the healthy neonates ($P < 0.05$).

4.5. Analysis of the CT Value and Biochemical Indicators in the Diagnosis of Bronchial Pneumonia. The specificity, sensitivity, and accuracy of CT examination, CRP examination, ESR examination, CRP + ESR examination, and CRP + ESR + CT examination in the diagnosis of NBP were analyzed and compared. As suggested in Figure 10, the accuracies of CT examination, CRP examination, ESR examination, CRP + ESR examination, and CRP + ESR + CT examination to diagnose the NBP were 80.7%, 75.3%, 75.1%, 80.3%, and 98.6%, respectively.

5. Discussion

Bronchial pneumonia is the most common infectious disease in infants and young children, caused by bacteria, viral infection, or colds [15]. Due to the gradual deepening of air pollution, there are more and more pathogenic bacteria that cause diseases, and the resistance of infants and young children is lower, so the younger neonates are more susceptible to bronchial pneumonia. The main clinical manifestations of the disease are mostly fever, chills, cough, headache and general malaise, fatigue, loss of appetite, nausea, vomiting, and diarrhea. The symptoms are not serious, but they are more common. However, as the symptoms worsen, there will be symptoms such as coughing, and, in infants and young children, there are symptoms such as wheezing or difficulty breathing. In severe cases, there will be extrapulmonary manifestations, such as the nervous system, digestive system, blood system, muscles, and bones. Such abnormalities are more common in mycoplasma pneumonia. The pathogenesis of *mycoplasma pneumonia* is not very clear, mainly including respiratory epithelial adsorption, direct invasion of *Mycoplasma pneumoniae*, and the theory of immunological disorders [16, 17].

At present, imaging methods such as X-ray, chest CT, and bronchography are clinically used in the diagnosis of bronchial pneumonia [18]. As a kind of invasive examination, bronchography is of little value in newborn children. Therefore, X-ray and chest CT are often used in newborns. In previous studies of *Mycoplasma pneumoniae* lung X-ray results, only the consolidation of lung lobes/pulmonary segments and diffusely infiltrated mesh nodules can be clearly distinguished. The current study found that the results of pathological slices showed changes in bronchial

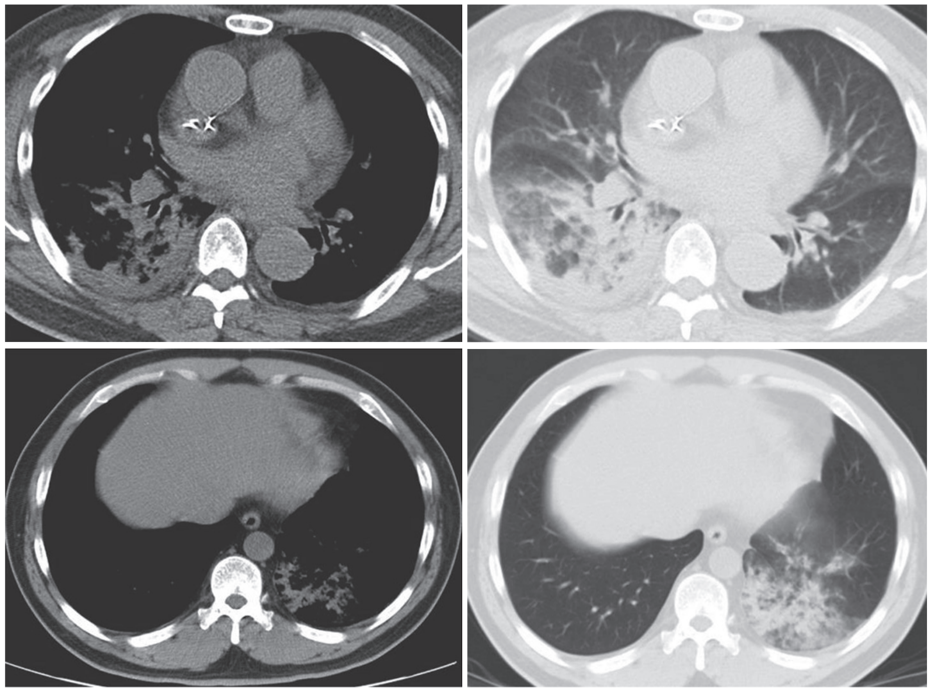

Figure 8: CT images of 2 neonates with NBP.

Table 1: The characteristic distribution of CT images of neonates with bronchial pneumonia.

CT characteristics	Cases ($n = 85$)	Percentage
Ground-glass	79	92.9
Nodular/small air cavity consolidation	74	87.1
Vascular bundle thickening	56	65.9
Atelectasis	34	40.0
Pleural effusion	27	31.8
Swollen lymph nodes	22	25.9
Large sheet consolidation	21	24.7

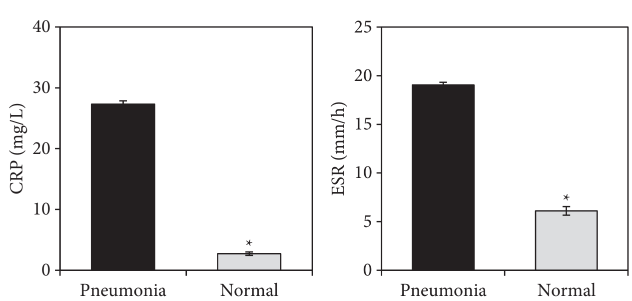

Figure 9: Comparison of (a) CRP and (b) ESR levels in peripheral blood between the two groups of neonates.

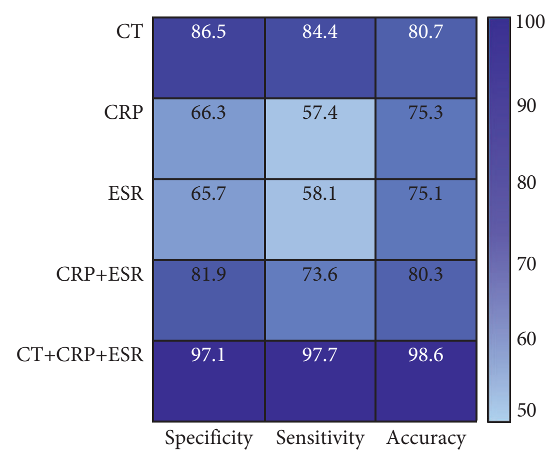

Figure 10: Comparison of the efficiency of different methods for diagnosing NBP.

inflammation and lobular consolidation, and chest X-rays could not show corresponding image changes. In the lung CT scan, the changes in bronchial inflammation such as the central nodules of the lobules can be clearly distinguished, and the patchy shadows and the pneumonia images with ground-glass changes can also be seen. Based on the lung CT thin-slice plain scan, it was known that more than two images presented in the above X-rays. At the same time, the “tree bud sign” and “tree fog sign” formed by the point and sheet infiltration formed in the early stage of the disease and the “double track sign” formed by the thickening and inflation of the bronchial wall formed by airway mucosal damage can also be affected. It can be clearly observed that uniform ground-glass changes can be clearly distributed in lung CT images. In summary, chest CT is the best examination method among neonatal pneumonia bronchial examinations. However, CT scan has high radiation. In order to reduce its impact on children’s health, low-dose CT is often used clinically to diagnose pediatric diseases. Low-dose CT scanning reduces the radiation but at the same time increases the noise in the image, which affects the diagnosis accuracy of the disease to a certain extent. With the continuous update and iteration of computer network technology, various image processing technologies have also been rapidly developed and penetrated into all walks of life. Various AI algorithms have also been applied and developed in the field of medical imaging. The iterative reconstruction algorithm under AI can achieve noise control through the description and expression of noise characteristics, so it has been widely used in the reconstruction of low-dose CT imaging, of which the ASiR algorithm is the most widely used [19–22]. Therefore, the effect of CT image reconstruction using the ASiR algorithm under AI was evaluated through subjective evaluation and objective measurement firstly. The results showed that, compared with the FBP algorithm, the noise of the CT image after reconstruction by the ASiR algorithm was dramatically reduced and the quality score was improved greatly. When the preweight value was 50%, the reconstruction of the CT image by the ASiR algorithm showed the best effect. When the preconditions of the ASiR algorithm are determined, the postweight value can affect the objective indicators of the image and the supervisor's score. It was found in this study that, with the increase of postweight value, the SD values of the vertebral body, aorta, and paraspine soft tissue decreased obviously, while the SD value of lung tissue did not change much. This may be due to the heterogeneity of the lung tissue itself.

Subsequently, the CT characteristics of neonates with bronchial pneumonia were analyzed, and the results showed that ground-glass features accounted for the largest proportion, followed by nodular/small patchy air cavity consolidation and vascular bundle thickening. Ground-glass can show increased lung density and blurred edges; part of it shows the distribution of full title pages; and the pathological basis is the appearance of a small amount of serous and inflammatory exudate in the alveoli [23]. The nodular/small patchy air cavity consolidation mainly shows small patches of increased density, occupying almost all acinars and lobules [24]. In addition, the changes in serum CRP and ESR levels of neonates were detected in this study. Serum CRP is a systemic inflammatory response protein, which can reflect the infection status of neonates [25]. ESR is a nonspecific marker for the evaluation of tissue inflammation and destruction, which can reflect the aggregation state of the fibrinogen and immunoglobulin of patients [26]. The results of this study revealed that neonates with bronchial pneumonia showed greatly increased CRP and ESR levels, indicating that they suffered from systemic inflammatory response. In addition, the diagnostic accuracy on neonates with bronchial pneumonia using only CRP or ESR levels was only about 75%, while that of CRP + ESR + CT examination could be as high as 98.6%.

6. Conclusion

In this study, the CT images of NBP patients were reconstructed based on the AI ASiR algorithm, and it was applied in combination with the detection of serum CRP and ESR levels in the diagnosis of NBP. It was found in this study that the AI ASiR algorithm can significantly improve the quality of CT images of NBP, and CT technology based on the AI ASiR algorithm can be used in the clinical diagnosis of bronchial pneumonia in children, but the efficiency of identifying bacterial and viral pneumonia was still low and had to be improved. The diagnostic method combining CT scan and serum CRP and ESR level detection had significantly improved the sensitivity, specificity, and accuracy of disease diagnosis. This study provided reference and basis for the early diagnosis and treatment of NBP in children. However, there were still some shortcomings in this study. For example, it only analyzed the influence of the preweight and postweight values on the reconstruction effect of the AI ASiR algorithm, and the influence of other parameters on the image quality needed to be considered in the follow-up. In addition, it only analyzed the CT characteristics of NBP in children. In the follow-up, the sample size needed to be further expanded to explore the differences and diagnostic efficiency in CT characteristics of bacterial and viral NBP.

Data Availability

The data used to support the findings of this study are available from the corresponding author upon request.

Conflicts of Interest

The authors declare no conflicts of interest.

References

[1] G. Malkoçoğlu, H. Gencer, A. Kaya, N. Dalgıç, M. E. Bulut, and E. Aktaş, "Corynebacterium propinquum bronchopneumonia in a child with ataxia telangiectasia," *Turkish Journal of Pediatrics*, vol. 58, no. 5, pp. 558–561, 2016.

[2] F. Lupariello, G. Di Vella, and G. Botta, "Infantile hypertrophic cardiomyopathy and bronchopneumonia as causes of an unexpected death in an 11-month-old child," *Fetal and Pediatric Pathology*, vol. 39, no. 5, pp. 452–454, 2020.

[3] P. Fernández-Rodríguez, R. Fernández López, I. Acevedo Báñez, J. Mohigefer Barrera, and J. M. Jiménez-Hoyuela García, "18F-FDG PET/CT in lung B lymphoid hyperplasia-type Castleman disease," *European Journal of Nuclear Medicine and Molecular Imaging*, vol. 47, no. 1, pp. 222-223, 2020.

[4] D. M. Libby, N. Wu, I.-J. Lee et al., "CT screening for lung cancer," *Chest*, vol. 129, no. 4, pp. 1039–1042, 2006.

[5] J. M. Wolterink, T. Leiner, M. A. Viergever, and I. Isgum, "Generative adversarial networks for noise reduction in low-dose CT," *IEEE Transactions on Medical Imaging*, vol. 36, no. 12, pp. 2536–2545, 2017.

[6] Q. Xie, D. Zeng, Q. Zhao et al., "Robust low-dose CT sinogram preprocessing via exploiting noise-generating mechanism," *IEEE Transactions on Medical Imaging*, vol. 36, no. 12, pp. 2487–2498, 2017.

[7] M. Tsuda, H. Yunaga, A. Murakami, and S. Yata, "Adaptive statistical iterative reconstruction for computed tomography of the spine," *Radiography*, vol. 27, no. 3, pp. 768–772, 2021.

[8] D. Prezzi, K. Owczarczyk, P. Bassett et al., "Adaptive statistical iterative reconstruction (ASIR) affects CT radiomics quantification in primary colorectal cancer," *European Radiology*, vol. 29, no. 10, pp. 5227–5235, 2019.

[9] Z. Ren, X. Zhang, Z. Hu et al., "Application of adaptive statistical iterative reconstruction-V with combination of 80

kV for reducing radiation dose and improving image quality in renal computed tomography angiography for slim patients," *Academic Radiology*, vol. 26, no. 11, pp. e324–e332, 2019.

[10] R. N. Southard, D. M. E. Bardo, M. H. Temkit, M. A. Thorkelson, R. A. Augustyn, and C. A. Martinot, "Comparison of iterative model reconstruction versus filtered back-projection in pediatric emergency head CT: dose, image quality, and image-reconstruction times," *American Journal of Neuroradiology*, vol. 40, no. 5, pp. 866–871, 2019.

[11] M. Gatti, F. Marchisio, M. Fronda et al., "Adaptive statistical iterative reconstruction-V versus adaptive statistical iterative reconstruction," *Journal of Computer Assisted Tomography*, vol. 42, no. 2, pp. 191–196, 2018.

[12] M. Karcaaltincaba and A. Aykut, "Dual-energy CT revisited by multidetector ct: review of principles and clinical applications," *Diagnostic and interventional radiology*, vol. 17, no. 3, pp. 181–194, 2010.

[13] H. Shi, Z. Yang, and S. Luo, "Reduce beam hardening artifacts of polychromatic X-ray computed tomography by an iterative approximation approach," *Journal of X-Ray Science and Technology*, vol. 25, no. 3, pp. 417–428, 2017.

[14] A. Averbuch, I. Sedelnikov, and Y. Shkolnisky, "CT reconstruction from parallel and fan-beam projections by a 2-D discrete radon transform," *IEEE Transactions on Image Processing*, vol. 21, no. 2, pp. 733–741, 2012.

[15] Y.-p. Tan, B.-y. Tan, J. Pan, J. Wu, S.-z. Zeng, and H.-y. Wei, "Epidemiologic and clinical characteristics of 10 children with coronavirus disease 2019 in Changsha, China," *Journal of Clinical Virology*, vol. 127, Article ID 104353, 2020.

[16] H. Liu, W. Wang, and X. Gao, "Comparison of the efficacy of ambroxol hydrochloride and N-acetylcysteine in the treatment of children with bronchopneumonia and their influence on prognosis," *Experimental and therapeutic medicine*, vol. 20, no. 6, p. 130, 2020.

[17] S. H. Mahmood, M. Khan, L. T. Qadar, F. Yousuf, and M. Hasan, "A unique manifestation of bardet-biedl syndrome with otolaryngologic symptoms and bronchopneumonia in a one-year-old girl," *Cureus*, vol. 11, no. 9, Article ID e5717, 2019.

[18] B. De Escalante Yangüela, A. Gracia Gutiérrez, B. Gracia Tello, V. Alastrué Del Castaño, E. Bueno Juana, and S. Algárate Cajo, "Bilateral bronchopneumonia due to Rothia mucilaginosa," *Anales del Sistema Sanitario de Navarra*, vol. 40, no. 3, pp. 479–483, 2017, PM.

[19] Y. Chen, W. Li, and S. Liu, "Quantitative influence of adaptive statistical iterative reconstruction on CT image histology of patients with primary colorectal cancer," *Journal of Pakistan Medical Association*, vol. 70, no. 9, pp. 78–83, 2020.

[20] Y. Noda, S. Goshima, H. Koyasu et al., "Renovascular CT: comparison between adaptive statistical iterative reconstruction and model-based iterative reconstruction," *Clinical Radiology*, vol. 72, no. 10, pp. e13–e19, 2017.

[21] A. Shah, M. Rees, E. Kar, K. Bolton, V. Lee, and A. Panigrahy, "Adaptive statistical iterative reconstruction use for radiation dose reduction in pediatric lower-extremity CT: impact on diagnostic image quality," *Skeletal Radiology*, vol. 47, no. 6, pp. 785–793, 2018.

[22] N. K. Lee, S. Kim, S. B. Hong et al., "Low-dose CT with the adaptive statistical iterative reconstruction V technique in abdominal organ injury: comparison with routine-dose CT with filtered back projection," *American Journal of Roentgenology*, vol. 213, no. 3, pp. 659–666, 2019.

[23] X. Zhang, W. Song, X. Liu, and L. Lyu, "CT image of novel coronavirus pneumonia: a case report," *Japanese Journal of Radiology*, vol. 38, no. 5, pp. 407-408, 2020.

[24] C. P. Upchurch, C. G. Grijalva, R. G. Wunderink et al., "Community-Acquired pneumonia visualized on CT scans but not chest radiographs," *Chest*, vol. 153, no. 3, pp. 601–610, 2018.

[25] D. Wussler, N. Kozhuharov, M. Tavares Oliveira et al., "Clinical utility of procalcitonin in the diagnosis of pneumonia," *Clinical Chemistry*, vol. 65, no. 12, pp. 1532–1542, 2019.

[26] Y. Huang, A. Liu, L. Liang et al., "Diagnostic value of blood parameters for community-acquired pneumonia," *International Immunopharmacology*, vol. 64, pp. 10–15, 2018.

Hindawi
Journal of Healthcare Engineering
Volume 2021, Article ID 1535046, 11 pages
https://doi.org/10.1155/2021/1535046

Research Article

Susceptible-Infected-Removed Mathematical Model under Deep Learning in Hospital Infection Control of Novel Coronavirus Pneumonia

Ting Liu,[1] **Yanling Bai**,[2] **Mingmei Du**,[2] **Yueming Gao**,[3] **and Yunxi Liu**[2]

[1]*First Department of Health Care, The Second Medical Center and National Clinical Research Center for Geriatric Diseases, Chinese PLA General Hospital, Beijing 100853, China*
[2]*Department of Disease Control and Prevention, The First Medical Center of Chinese PLA General Hospital, Beijing 100853, China*
[3]*Department of Rehabilitation Medicine, The Second Medical Center and National Clinical Research Center for Geriatric Diseases, Chinese PLA General Hospital, Beijing 100853, China*

Correspondence should be addressed to Yunxi Liu; 201801010518@stu.hnie.edu.cn

Received 28 August 2021; Revised 25 September 2021; Accepted 29 September 2021; Published 27 October 2021

Academic Editor: Enas Abdulhay

Objective. This research aimed to explore the application of a mathematical model based on deep learning in hospital infection control of novel coronavirus (COVID-19) pneumonia. *Methods*. First, the epidemic data of Beijing, China, were utilized to make a definite susceptible-infected-removed (SIR) model fitting to determine the estimated value of the COVID-19 removal intensity β, which was then used to do a determined SIR model and a stochastic SIR model fitting for the hospital. In addition, the reasonable β and γ estimates of the hospital were determined, and the spread of the epidemic in hospital was simulated, to discuss the impact of basal reproductive number changes, isolation, vaccination, and so forth on COVID-19. *Results*. There was a certain gap between the fitting of SIR to the remover and the actual data. The fitting of the number of infections was accurate. The growth rate of the number of infections decreased after measures, such as isolation, were taken. The effect of herd immunity was achieved after the overall immunity reached 70.9%. *Conclusion*. The SIR model based on deep learning and the stochastic SIR fitting model were accurate in judging the development trend of the epidemic, which can provide basis and reference for hospital epidemic infection control.

1. Introduction

Novel coronavirus (COVID-19) is one of the current coronaviruses that can infect humans. On December 1, 2019, the first suspected case of COVID-19 was admitted to Jinyintan Hospital in Wuhan. After that, major hospitals in Wuhan received similar unidentified pneumonia patients one after another. The Wuhan Municipal Health Commission started an epidemiological investigation on December 29. On January 8, 2020, experts from the National Health Commission of China announced that the pathogen was a novel coronavirus [1]. According to the report of the Wuhan Health Commission on January 16, 41 new patients were reported in Wuhan, and 19 new cases were reported on January 19. Zhong Nanshan, head of the national expert team, said on January 20 that the disease was "human-to-human infectious" and that 217 new cases had been reported in Wuhan that day. The first cases were reported in Tianjin, Jiangxi, Zhejiang, and Henan provinces on January 21, marking the start of a full-scale outbreak of COVID-19 in China. As of March 1, the total number of confirmed cases in China has reached 80,000. Meanwhile, other countries have also reported the emergence of novel coronavirus infections. At present, the epidemic in China has been basically brought under control through continuous efforts. However, the epidemic continues to spread in other countries and the international situation is still grim. Against the background of global economic integration, the prevention and control of the epidemic must not be slackened. Currently, research on the COVID-19 model is mostly focused on the whole region [2]. There have been very few studies on hospitals. However, as the main battlefield of antiepidemic, it is very necessary to study the law of epidemic transmission and its control transmission. Specifically, health care workers are more likely to come into contact with patients and get sick. When health care workers get sick, it is not only a major blow to the health care system, but it also increases the risk to the general population. This is extremely detrimental to the prevention and control of the epidemic [3].

The use of models to study infection began as early as the 18th century. The concept of establishing a model to solve the spread of infectious diseases was first proposed by Bernoulli when he studied the smallpox virus. By the middle of the 20th century, scientists began systematic research on it. In 1926, Kermack and Mckendrick proposed the classic susceptible-infected-removed (SIR) warehouse model [4]. Various subsequent models were proposed based on that. Later, as the research on infectious disease models continues to deepen, scientists have further subdivided and characterized different infectious diseases, such as SIR and SIES models. In recent years, infectious disease models have developed rapidly with the development of computing power and big data. Many scientists modeled various infectious diseases. For example, some scientists established an SIR model with H1N1 as the research object and conducted a simulation study on it. There were many similar examples [5]. A large amount of research data showed that the establishment of infectious disease research models can effectively predict the development trend of infectious diseases, which was extremely important for the treatment and control of infectious diseases. The establishment of infectious disease models has occupied an irreplaceable and important position in modern infectious disease research.

Therefore, a SIR and stochastic model was established based on the data of the whole area of Beijing. Then, the data of the hospital was used as the research data to carry out empirical analysis on the model. It was expected to provide a basis for epidemic control and subsequent similar events.

2. Research Methods

2.1. Determination of SIR Model. Based on a set of ordinary differential equations, the population was divided into three types: susceptible, infected, and evacuated to establish the SIR model. Susceptible persons were represented by S_t, which meant the number of susceptible persons, and the susceptible persons were defined as healthy people who had not yet been infected with the disease. Infected people were expressed by I_t, which meant the number of people infected at time t, which was defined as a group that had been infected and could transmit from person to person. The migrants were represented by R_t, which meant the number of migrants at time t, which was defined as the people who had been isolated, passed away, or recovered from immunity. Assuming that an epidemic occurred in a closed environment, the effects of normal birth rate and death rate were excluded, while population dynamics were ignored, and the total population was counted as N. Then,

$$S_t + I_t + R_t = N. \tag{1}$$

In a unit of time at time t, if the infection intensity was β, the number of new infections was $\beta S_t l_t$. At time t, the number of people who were evacuated due to death and recovery was proportional to the number of infections. If the intensity of removal was calculated as r, the number of people who were evacuated was rI_t. The specific SIR model with different parameters is shown in Figure 1.

2.2. Stochastic SIR Model. For the stochastic SIR model, the stochastic process is as follows: for a given probability space $(\Omega, \wp, P)$ and a given parameter set T, each parameter satisfies $t \in T$. Then, $X_T = \{X(t, w), t \in T\}$ is the random variable defined in the probability space $(\Omega, \wp, P)$, and the corresponding random process $X_T = \{X(t, w), t \in T\}$ in the probability space $(\Omega, \wp, P)$ is denoted as $\{X(t), t \in T\}$ or $X(t)$. The discrete state continuous-time Markov process is as follows: in a random process $\{X(t), t \in T\}$, if there are any integer n and space states I, $0 \leq t_0 < t_1 < t_2 < \ldots < t_{n+1}$, $t_k \in T$, $k = 0, 1, 2, \ldots, n+1$, and their states meet the following conditions:

$$\begin{aligned} &P\{X(t_{n+1}) \leq i_{n+1} | X(t_n) = i_n, \ldots, X(t_0) = i_0\} \\ &= P\{X(t_{n+1}) \leq i_{n+1} | X(t_n) = i_n\}. \end{aligned} \tag{2}$$

Then, the stochastic process $\{X(t), t \in T\}$ is a discrete state continuous Markov process. Continuous-time Markov chain: for the random process $\{X(t), t \in T\}$, if there are any integers n and state space I, I, $0 \leq t_0 < t_1 < t_2 < \ldots < t_{n+1}$, $t_k \in T$, $k = 0, 1, 2, \ldots, n+1$, and the state satisfies the following conditions:

$$\begin{aligned} &P\{X(t_{n+1}) = i_{n+1} | X(t_n) = i_n, \ldots, X(t_0) = i_0\} \\ &= P\{X(t_{n+1}) = i_{n+1} | X(t_n) = i_n\}. \end{aligned} \tag{3}$$

Then, the stochastic process $\{X(t), t \in T\}$ is called the continuous-time Markov process, also known as the process $Q-$. The transition probability function: let $\{X(t), t \in T\}$ be a continuous countable Marko chain; then, for any i, the transition probability $j \in E$ is as follows:

$$pij(s, t) = P\{X(t) = j | X(S) = i\}, \quad s \leq t;\ i,\ j \in E. \tag{4}$$

The above Markov chain is called the time homogenous Markov chain, and its transition probability is only related to the time interval and has nothing to do with the time selection. Therefore, when only the time homogenous Markov chain was considered, the above formula can be rewritten as follows:

$$\begin{aligned} p_{\mathrm{ij}}(t-s) &= P\{X(t) = j | X(s) = i\} \\ &= P\{X(t-s) = j | X(0) = i\}, \quad s \leq t;\ i,\ j \in I. \end{aligned} \tag{5}$$

The transition probability matrix is defined as follows:

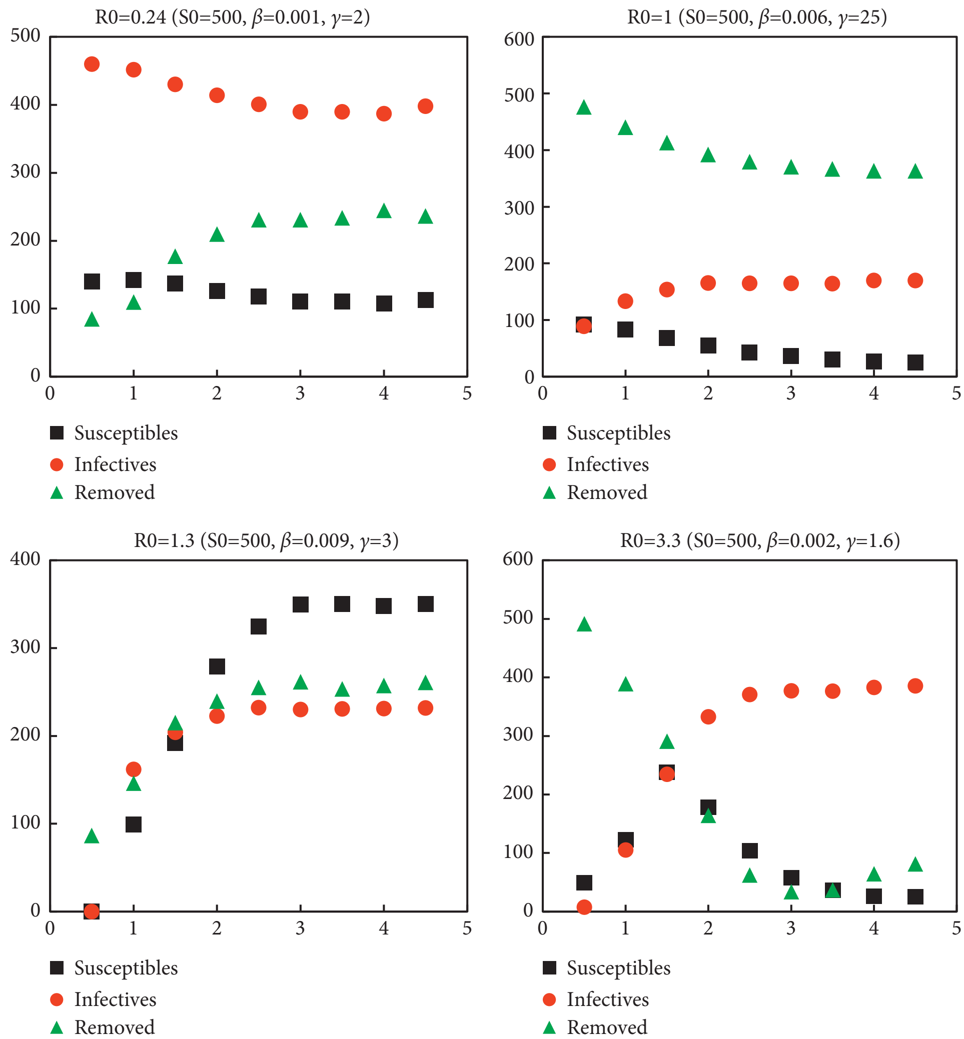

Figure 1: SIR epidemic model with different parameters.

$$P(t) = (pij(t))i, \quad j \in l. \tag{6}$$

Chapman–Kolmogorov equation: for any $s, t \geq 0$, i, $j \in I$, there is the following equation:

$$p_{ij}(s+t) = \sum_{k \in I} p_{ik}(s) p_{kj}(t). \tag{7}$$

Its matrix form is as follows:

$$P(s+t) = P(s)P(t), \quad \forall s, t \in [0, \infty). \tag{8}$$

The transition rate matrix is defined as follows:

$$A = \begin{pmatrix} a_{00} & a_{01} & a_{02} & \dots a_{0n} \\ a_{10} & a_{11} & a_{12} & \dots a_{1n} \\ a_{20} & a_{21} & a_{22} & \cdots a_{2n} \\ \vdots & \vdots & \vdots & \ddots \vdots \\ a_{n0} & a_{n1} & a_{n2} & \cdots a_{nn} \end{pmatrix},$$

$$a_{ij} = \lim_{\Delta t \longrightarrow 0^+} \frac{p_{ij}(\Delta t) - p_{ij}(0)}{\Delta t} = \left\{ \begin{matrix} \lim_{\Delta t \longrightarrow 0} \dfrac{p_{ij}(\Delta t)}{\Delta t}, & i \neq j \\ \lim_{\Delta t \longrightarrow 0} + \dfrac{p_{ij}(\Delta t)}{\Delta t}, & i = j \end{matrix} \right\}. \tag{9}$$

According to $\sum_{j=0}^{\infty} p_{ij}(\Delta t) = 1$, the following equation is acquired:

$$1 - p_{ij}(\Delta t) = \sum_{j=0, j \neq i}^{\infty} p_{ij}(\Delta t) = \sum_{j=0, j \neq i}^{\infty} \left[a_{ij} \Delta t + o(\Delta t) \right]. \tag{10}$$

Further, equation (11) is acquired:

$$a_{ii} = \lim_{\Delta t \longrightarrow 0^+} \frac{-\sum_{j=0, j \neq 1}^{\infty} \left[a_{ij} \Delta t + o(\Delta t) \right]}{\Delta t} = -\sum_{j=0, j \neq i}^{\infty} a_{ij}. \tag{11}$$

Then, the following equation is obtained:

$$\sum_{j=0}^{\infty} a_{ij} = a_{ii} + \sum_{j=0, j\neq i}^{\infty} a_{ij} = 0. \tag{12}$$

The pure generative process is defined as follows:

$$P\{X_{t+dt} = j|X_t = i\} = \begin{cases} \eta_i dt + o(dt), & j = i-1, \\ 1-\eta_i dt + o(dt), & j = i, \\ o(dt), & \text{others}. \end{cases} \tag{13}$$

The birth and death processes are shown as follows:

$$P\{Xt + dt = j|Xt = i\} = \begin{cases} \varsigma i dt + o(dt), & j = i+1, \\ \eta i dt + o(dt), & i = i-1, \\ 1-(\varsigma i + \eta i)dt + o(dt), & j = i, \\ o(dt), & \text{others}. \end{cases} \tag{14}$$

A susceptible person was likely to become infected with a probability of $\beta S_t I_t dt$. The probability that an infected person would recover or die and become a remover is $\gamma I_t dt$. The probability of the above two occurrences is $1-(\beta S_t + \gamma)I_t dt$. Therefore, the transition probability of a binary random process $\{S_t, I_t, t \geq 0\}$ is as follows:

$$P\{(S,I)_{t+dt} = (i,j)|(S,I)_t = (m,n)\}. \tag{15}$$

β and γ are removal coefficients. Specific infectious disease random models and least square cases under different coefficients are shown in Figures 2 and 3.

2.3. Parameter Estimation

Least square method: assuming unknown parameters $\theta = (\beta, \gamma)$, then the number of infected persons is $I = \{I_i, 1 \leq i \leq N\}$, the simulated value of the number of infected persons is $Y(\theta) = \{y_i(\theta), 1 \leq i \leq N\}$, and the residual is $V = Y(\theta) - 1$ and the sum of squares $\mathrm{SSE}(\theta)$ of the residual is as follows:

$$\begin{aligned} \mathrm{SSE}(\theta) &= \|V\|^2 \\ &= \sum_{i=1}^{N} [y_i(\theta) - I_i]^2, \end{aligned}$$

$$\begin{cases} \dfrac{\partial \mathrm{SSE}(\theta)}{\partial \beta} = 2\sum_{i=1}^{N} [y_i(\theta) - I_i] \dfrac{\partial y_i(\theta)}{\partial \beta}, \\ \dfrac{\partial \mathrm{SSE}(\theta)}{\partial \beta} = 2\sum_{i=1}^{N} [y_i(\theta) - I_i] \dfrac{\partial y_i(\theta)}{\partial \gamma}. \end{cases} \tag{16}$$

Weighted least square method: the recent data was given a large weight, while the long-term data was given a smaller weight, $w^{N-i}, 0 < w < 1$, so the sum of squares $\mathrm{SSE}(\theta)$ of the residual is as follows:

$$\mathrm{SSE}(\theta) = \|V\|^2 = \sum_{i=1}^{N} w^{N-i} [y_i(\theta) - I_i]^2 + \sum_{i=N+1}^{M} [y_i(\theta) - I_i]^2. \tag{17}$$

2.4. Empirical Study on COVID-19 in Hospital.

Firstly, the SIR model was used to fit the epidemic situation of the hospital. In the SIR model, the whole population was classified into susceptible persons (S_t), infected persons (I_t), and displaced persons (R_t). New diagnoses in hospital every day are shown in Figure 4. The number of newly diagnosed patients in hospital on a daily basis was consistent with the basic trend (I_t) in the SIR model, so the SIR model can be used for fitting.

The parameter estimation of the SIR model was determined. The number of communicators was taken as the number of confirmed cases on the day minus the number of deaths and ceases on the day, and the cumulative number of deaths and ceases R_t was obtained as follows:

I_t = number confirmed on a day − cumulative number of deaths and cures.

R_t = cumulative number of deaths and cures

The number of persons hospitalized with the virus per day and the cumulative number of deaths and discharges are the number of evacuees. Then, the differential equation of SIR model is determined as follows:

$$\begin{cases} \dfrac{\mathrm{d}s_t}{\mathrm{d}t} = -\beta S_t I_t, \\ \dfrac{\mathrm{d}I_t}{\mathrm{d}t} = \beta S_t I_t - \gamma I_t, \\ \dfrac{\mathrm{d}R_t}{\mathrm{d}t} = \gamma I_t. \end{cases} \tag{18}$$

The initial value was $I_0 = 241, R_0 = 5$, and the parameters to be evaluated were S_0, β, and γ. The least square method was used to estimate the unknown parameters. First, the following definition is made to estimate γ:

$$\gamma(t) = \frac{R(t) - R(t-1)}{I(t-1)}. \tag{19}$$

Thus, an estimate of 0.071 for γ is obtained, representing a recovery time of approximately 14 days per patient. Then, the least square estimation of S_0 and β is carried out by using the estimated value of the obtained γ. The parameter domain of unknown parameters is $[1.6 \times 10^{-4}, 1.8 \times 10^{-4}] \times [1600, 1800]$, and the minimum value SSE is found to obtain the 3D stereogram and contour map. The least square estimate of S_0 and β is as follows:

$$\widehat{\beta} = 1.68 \times 10^{-4} \widehat{S}_0 = 1672. \tag{20}$$

The sum of squares of the residuals is as follows:

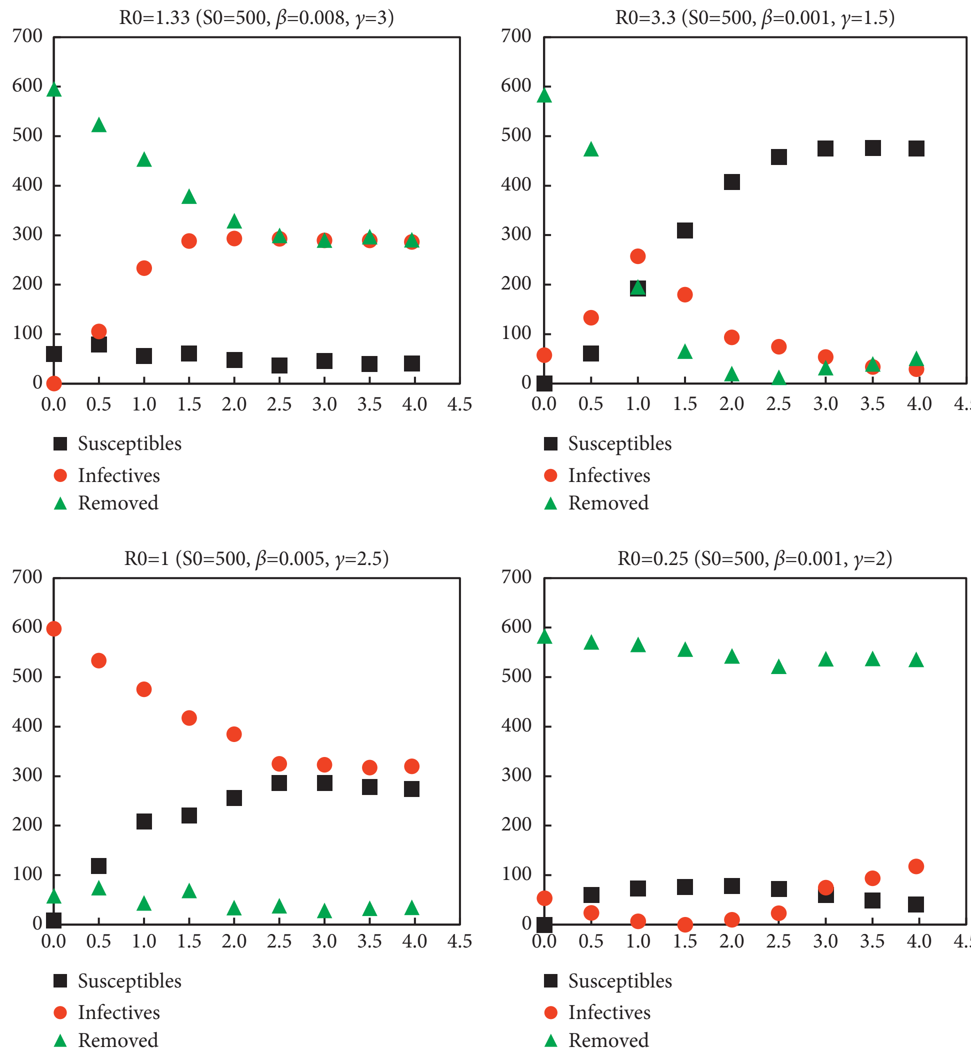

FIGURE 2: Random SIR epidemic model under different parameters.

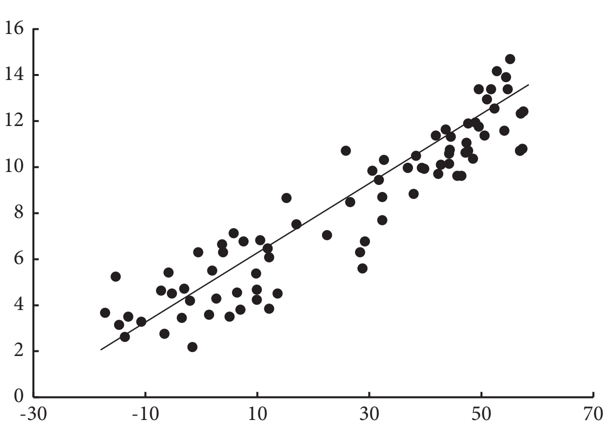

FIGURE 3: Least square case.

$$\mathrm{SSE} = 1.277 \times 10^{5}. \tag{21}$$

Then, the obtained $S_0 = 1672$ is used for the least square estimation of β and γ. The parameter domain of unknown parameters is $[1.6 \times 10^{-4}, 1.8 \times 10^{-4}] \times [0.068, 0.076]$, the minimum value SSE within the range is found, and the 3D stereogram and contour map are obtained. The least squares estimate is as follows:

$$\begin{aligned} \hat{\beta} &= 1.684 \times 10^{-4}, \\ \hat{\gamma} &= 0.072. \end{aligned} \tag{22}$$

The corresponding residual peace is as follows:

$$\mathrm{SSE} = 1.2633 \times 10^{5}. \tag{23}$$

Parameter estimation of stochastic SIR model was as follows. Simulation steps of the stochastic process are as follows: (i) when $t = 0$, the initial value is set as $(S_0, I_0), \beta, \gamma$. (ii) Random numbers with exponential distribution parameter $\beta S_t I_t + \gamma I_t$ are generated. (iii) Random number k that obeys uniform distribution $U(0, 1)$ is generated. Let $p = \beta S_t / \beta S_t + \gamma$, if $r \leq p$, then $(S_{t+dt}, I_{t+dt}) = (S_t - 1, I_t + 1)$. If $r > p$, then $(S_{t+dt}, I_{t+dt}) = (S_t, I_t - 1)$. (iv) The pretransfer state (S_t, I_t) is replaced with the posttransfer state (S_{t+dt}, I_{t+dt}); the previous process is repeated, and the process is terminated when $S_t = 0$ or when $I_t = 0$. The initial

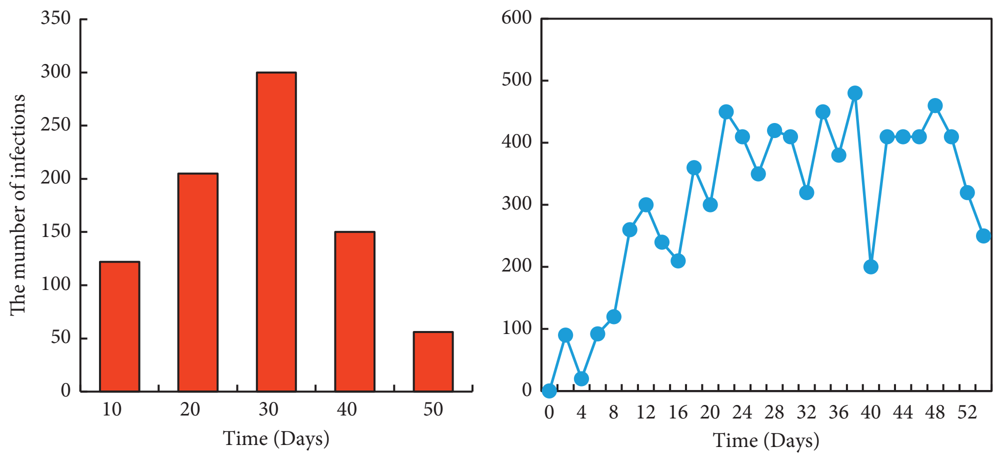

Figure 4: New diagnoses and statistics in hospital every day. (a) Newly diagnosed infections per day. (b) The number of new infections per day.

value is the same as that of the determined SIR model. The 25×25 grid is taken and the parameter domain is set as $[2.5 \times 10^{-6}, 2.7 \times 10^{-6}] \times [0.06, 0.08]$. The minimum value of SSE is obtained via MATLAB, to draw the 3D stereogram and contour diagram. The least square estimate of the position parameter is as follows:

$$\begin{aligned} \widehat{\beta} &= 2.588 \times 10^{-6}, \\ \widehat{\gamma} &= 0.073. \end{aligned} \tag{24}$$

For the determined SIR model, the parameter fitting is substituted to extract the I change image. For the stochastic SIR model, the $I1$ change image is also obtained by fitting its 10,000 orbits and averaging the values of the orbits on the whole point (Figure 5).

Although there is a certain gap in the image, considering the error that may occur in the operation is acceptable, the previous view is confirmed. The determined SIR model is regarded as the value of the whole point of the stochastic SIR model. When the stochastic SIR model has enough orbits to eliminate its random interference, the average value of the two is converged. The results of the two are similar, but the process is opposite. The determined SIR model is regarded as a macroscopic change. The stochastic SIR model is a microscopic action, which determines the change of a single person each time, which is more in line with objective changes. The changes in the three types of populations in the SIR model are not achieved overnight, so the stochastic SIR model is more convincing and more reasonable than the determined SIR model.

2.5. Statistical Methods. SPSS 22.0 data analysis software was used to analyze the data. The counting data were expressed as a percentage, and the measurement data were expressed as mean ± standard deviation. Analysis of variance was used to compare the data between groups, and $P < 0.05$ was considered statistically significant.

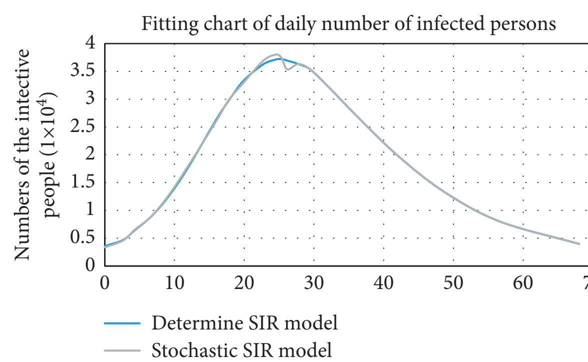

Figure 5: Fitting graph of the number of daily infected persons of determined SIR model and stochastic SIR model.

3. Results

3.1. Results Comparisons. The percentage error between the daily number of infected people and the actual number after February 12, the comparison between the fitting number of infected people and the real number, and the comparison of the number of displaced people are shown in Figure 6. For accurate data, the error control was better. There was not much difference between the fit number and the real number of infected people. There was a certain error in the fitting of the number of patients removed, which may be caused by a large number of patients during the epidemic and the failure of timely treatment and death of some patients or their self-healing.

3.2. Estimation of the Basic Regeneration Number. The variation of effective regenerative number and the relationship between basal regenerative number and herd immunity are shown in Figure 7. The effective number of regenerations in the first day was the basic number of regenerations, and the effective number of regenerations decreased as the susceptible person became infected. After the isolation of infected

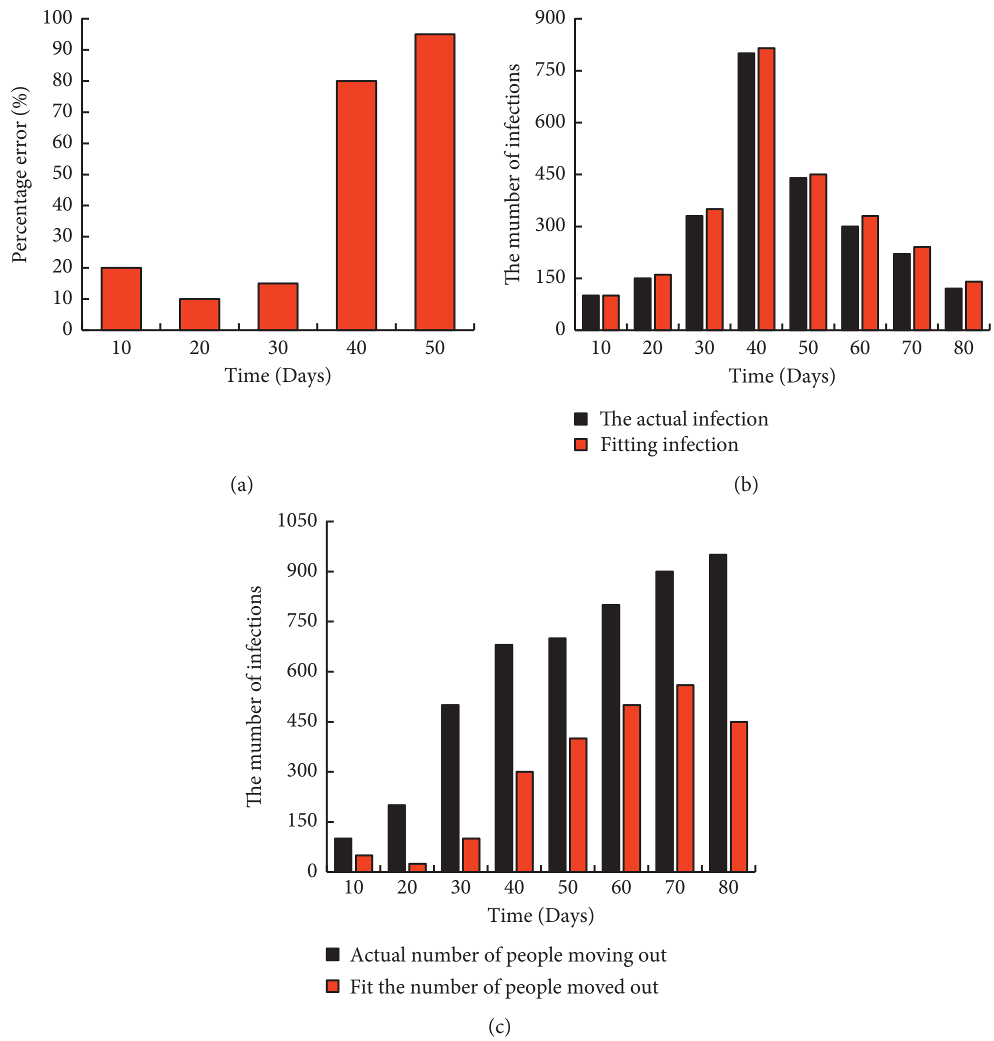

Figure 6: Comparison of fitting results. (a) Percentage of error between the daily infected number and the actual number. (b) Comparison between the actual number of people and the fitted number. (c) Comparison of the number of migrants.

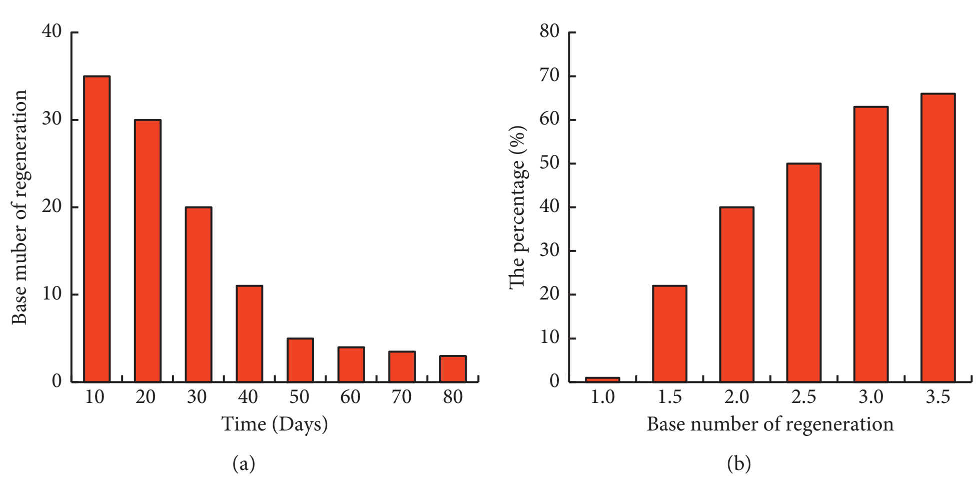

Figure 7: Analysis of basic regenerative number. (a) The variation of the base regeneration number. (b) Relationship between basal regenerative number and the proportion of herd immunity.

people and other measures, the susceptible group continued to shrink. The effect of herd immunity was achieved when the immune population reached 70.9% in the population, that is, when the basic regeneration number was less than or equal to 1. When the base regeneration number was less than or equal to 1, the outbreak would only occur in a small area and ended quickly.

3.3. Influences of Infection Intensity on the Development of the Epidemic. The number of people infected under different infection intensities is shown in Figure 8. When β decreased to 30%, the peak number of infections decreased significantly, and when β decreased to 50%, the peak number of infections decreased further. As β went down, the ability of the new coronet to infect went down, so did the peak number of infections. Although it had a small effect on the total number of people infected, it can slow the progression of the epidemic and reduce the pressure on medical care by delaying the peak.

3.4. The Impact of Vaccines and Other Measures on the Outbreak. Figures 9 and 10 show the comparison of 30% vaccine-covered and 30% vaccine-covered and quarantined with no measures of infection. When vaccine coverage reached 30 percent, both the peak daily patient count and the cumulative number of patients declined by 34 percent. When the vaccine was covered by 30% and the isolation measures were taken, the peak daily cumulative number of patients and the total cumulative number of patients decreased further, by 70%. Vaccine coverage and isolation control were proven effective.

4. Discussion

Infectious diseases have always been one of the common and dangerous factors threatening human life and health. Because of their tendency to spread on a large scale, they lead to not only the demise of individuals but also the demise of species, nations, and even civilizations. Civilizations have been wiped out by infectious diseases throughout human history. Early Spanish explorers to Latin America, for example, discovered that the Mayas and Incas who had lived there for generations were wiped out by smallpox [6]. In addition to that, there have been a number of similar epidemics in human history, such as the plague in the heartland of Mongolia in the east and the Black Death in the west. These have caused great disasters to human society. There were many similar cases. In ancient China, there were 261 plague cases recorded, and some scholars even found records of plague in oracle bones. To sum up, infectious diseases have a huge impact on human society [7]. Human beings have never stopped fighting against infectious diseases. As early as the pre-Qin period, China cut off the source of infection through isolation and other means. Modern western scholars performed smallpox virus research, and the smallpox virus has been eliminated. Another example is the outbreak of plague in Northeast China during the period of the Republic of China. Liande Wu, a medical doctor, was ordered to stop a deadly infectious disease [8].

With the continuous development of modern science and technology and medical treatment, the medical level has improved a lot. Human research on infectious diseases is deepening, but bacteria and viruses are also constantly mutating and evolving. All kinds of new pathogens emerge in an endless stream. For example, there was the outbreak of hepatitis C in China in 1989 and the middle east respiratory syndrome (MERS), which was prevalent in a small area in the Middle East a few years ago, and SARS which was prevalent in a large area in the world in 2003. In recent years, as the range of human activities continues to expand, the boundary between human beings and nature is getting lower and lower, which leads to the increasing probability of human being being infected with infectious diseases [9]. For example, the H1NI virus which emerged in 2009 originally appeared in birds. After continuous mutation, it eventually became parasitic on people. It took the lives of tens of thousands of people in the United States and caused a huge burden to the American society. There are more than 3,000 known viruses, and this is just the tip of the iceberg. Human beings have a long way to go in the prevention and treatment of infectious diseases [10].

Using models to study infection began as early as the 18th century. The concept of establishing a model to solve the spread of infectious diseases was first proposed by Bernoulli when he studied the smallpox virus. By the middle of the 20th century, scientists began systematic research on it. In 1926, Kermack and Mckendrick proposed the classic susceptible-infected-removed (SIR) warehouse model [11]. Various subsequent models were proposed based on that. Later, as the research on infectious disease models continues to deepen, scientists have further subdivided and characterized different infectious diseases, such as SIR and SIES models. In recent years, infectious disease models have developed rapidly with the development of computing power and big data. Many scientists modeled various infectious diseases [12]. For example, some scientists established an SIR model with H1N1 as the research object and conducted a simulation study on it [13]. There were many similar examples. A large amount of research data showed that the establishment of infectious disease research models can effectively predict the development trend of infectious diseases, which was extremely important for the treatment and control of infectious diseases. The establishment of infectious disease models has occupied an irreplaceable and important position in modern infectious disease research. Therefore, the SIR model and SIR stochastic model based on deep learning were established in this work to explore the development law of the COVID-19.

COVID-19 is one of the current coronaviruses that can infect humans. On December 1, 2019, the first suspected case of COVID-19 was admitted to Jinyintan Hospital in Wuhan. After that, major hospitals in Wuhan received similar unidentified pneumonia patients one after another. The Wuhan Municipal Health Commission started an epidemiological investigation on December 29. On January 8, 2020, experts from the National Health Commission of China announced that the pathogen was

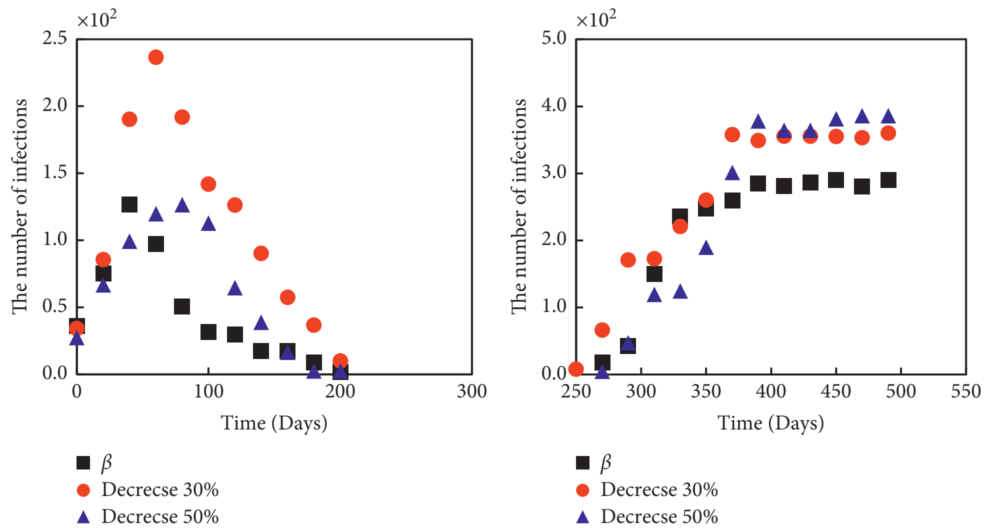

Figure 8: Number of infected persons under different infection intensities.

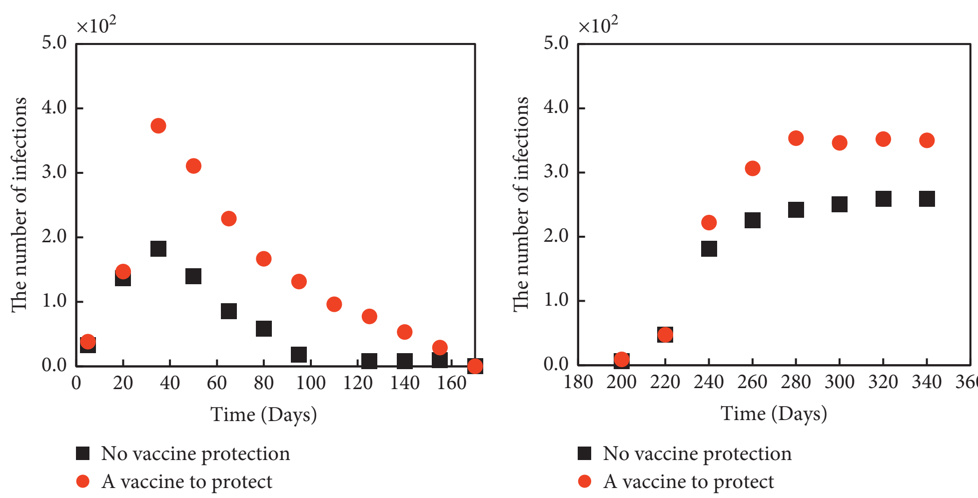

Figure 9: Comparison of the number of infected persons with vaccine coverage and those without vaccine coverage.

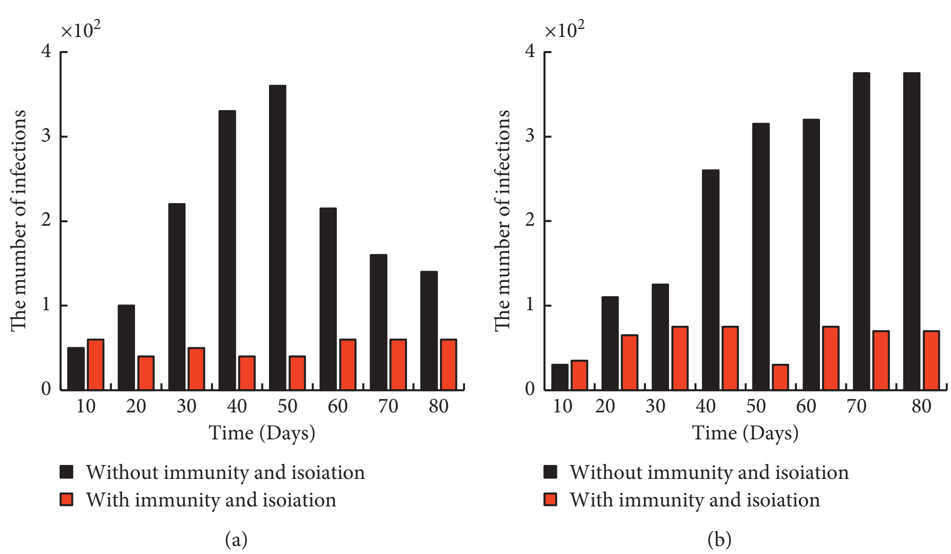

Figure 10: Comparison of 30% vaccine coverage plus isolation and no measures.

a novel coronavirus. According to the report of the Wuhan Health Commission on January 16, 41 new patients were reported in Wuhan, and 19 new cases were reported on January 19. Zhong Nanshan, head of the national expert team, said on January 20 that the disease was "human-to-human infectious" and that 217 new cases had been reported in Wuhan that day [14]. The first cases were reported in Tianjin, Jiangxi, Zhejiang, and Henan provinces on January 21, marking the start of a full-scale outbreak of COVID-19 in China. As of March 1, the total number of confirmed cases in China has reached 80,000. Meanwhile, other countries have also reported the emergence of novel coronavirus infection. At present, the epidemic in China has been basically brought under control through continuous efforts. However, the epidemic continues to spread in other countries and the international situation is still grim. Against the background of global economic integration, the prevention and control of the epidemic must not be slackened. Currently, research on the COVID-19 model is mostly focused on the whole region. There have been very few studies on hospitals. However, as the main battlefield of antiepidemic, it is very necessary to study the law of epidemic transmission and its control transmission. Specifically, health care workers are more likely to come into contact with patients and get sick. When health care workers get sick, it not only is a major blow to the health care system but also increases the risk to the general population this is extremely detrimental to the prevention and control of the epidemic [15].

Therefore, a retrospective analysis of the occurrence of COVID-19 in hospital was performed by using the SIR model based on deep learning and the SIR stochastic model. Based on the SIR model, the COVID-19 epidemic situation in Wuhan was studied, and the research time was from January 23, 2020, to March 31, 2020. The law of the spread of the epidemic was discovered through daily epidemic information and restoring of its development process. Finally, some valuable information was obtained through the model, which had positive significance for potential prevention and control work in the future. The determined SIR model and stochastic SIR model were taken as the core, and then the Wuhan area was modeled. First, S_0 was used as the parameter to be estimated, and its range was determined by MATLAB to find a better fitting effect. Then, the obtained o value was used to find β and Y suitable for the Wuhan area. In the stochastic SIR model, the continuous-time Markov Chain was used to fit S_0, B, and y again. The residual square SSE chart of the daily number of infected persons was plotted through the computer running 5,000 orbits, and the extreme points of the infection intensity B and the recovery intensity were found, which were compared with the determination of the SIR equation, and the error was within a reasonable range. Then, a simulation of 10,000 orbits was implemented to draw a simulation diagram of the three groups of people, which showed that the determined SIR model was the mean process of the stochastic SIR model without considering the covariance. Finally, the different results of changing the intensity of infection and the intensity of removal on the development of the epidemic were discussed. It was found that quarantine, vaccine, and other measures had an impact on the development of the epidemic. The intensity of infection was a key factor affecting the outbreak. It was also found that the SIR model and stochastic model based on deep learning had an ideal prediction effect on the development trend of the epidemic.

5. Conclusion

The deep learning SIR model and stochastic SIR model were used to retrospectively study the occurrence of COVID-19 in hospital. It was found that the above two models were accurate in predicting the development trend of the epidemic and had a high prospect in hospital epidemic control. In addition, vaccine, isolation, and infection intensity had a great impact on the development of the epidemic, and the epidemic can be controlled from these three aspects when similar situations occur in the future. However, due to the limited sample and space, the study on this issue is not comprehensive and in-depth enough. In future study and work, it will expand the sample for further study.

This work was developed based on the determined SIR model and stochastic SIR model. Although some effects were achieved in predictive analysis, there are many shortcomings. First, the variability of B and y is not fully considered, which are set as a constant. From the beginning to the end of the epidemic, B and y may change due to various reasons such as the government's control and the update of medical resources, so the patient's ability to get infected should go down, and the level of recovery should go up as various drugs are tested, In the future, we can consider its time-varying function to conform to objective facts. Secondly, the description index of the model is too single. For the most critical infection intensity and recovery intensity, population mobility, medical resource level, and aging rate in each region are different, which are all important parameters affecting the accuracy of the model. In the future, it can be considered as a breakthrough to continuously optimize model equations and parameters to achieve more accurate results.

Data Availability

The data used to support the findings of this study are available from the corresponding author upon request.

Conflicts of Interest

The authors declare no conflicts of interest.

Authors' Contributions

Ting Liu and Yanling Bai contributed equally to this work.

References

[1] S. Wicker, "BK 3101 - i," *Internist*, vol. 60, no. 6, pp. 661–666, 2019.

[2] H. Li, R. Bai, Z. Zhao et al., "Application of droplet digital PCR to detect the pathogens of infectious diseases," *Bioscience Reports*, vol. 38, no. 6, Article ID BSR20181170, 2018.

[3] M. Lounis and D. K. Bagal, "Estimation of SIR model's parameters of COVID-19 in Algeria," *Bulletin of the National Research Centre*, vol. 44, no. 1, 2020.

[4] Z. Lv, X. Li, and W. Li, "Virtual reality geographical interactive scene semantics research for immersive geography learning," *Neurocomputing*, vol. 254, no. 6, pp. 71–78, 2017.

[5] L. Zhihan, L. Xiaoming, W. Weixi, Z. Baoyun, H. Jinxing, and F. Shengzhong, "Government affairs service platform for smart city," *Future Generation Computer Systems: FGCS*, vol. 81, pp. 443–451, 2018.

[6] I. Cooper, A. Mondal, and C. G. Antonopoulos, "A SIR model assumption for the spread of COVID-19 in different communities," *Chaos, Solitons & Fractals*, vol. 139, Article ID 110057, 2020.

[7] F. Ball, T. Britton, K. Y. Leung, and D. Sirl, "A stochastic SIR network epidemic model with preventive dropping of edges," *Journal of Mathematical Biology*, vol. 78, no. 6, pp. 1875–1951, 2019.

[8] Z. Chladná, J. Kopfová, D. Rachinskii, and S. C. Rouf, "Global dynamics of SIR model with switched transmission rate," *Journal of Mathematical Biology*, vol. 80, no. 4, pp. 1209–1233, 2020.

[9] J. Libertucci and V. B. Young, "The role of the microbiota in infectious diseases," *Nature Microbiology*, vol. 4, no. 1, pp. 35–45, 2019.

[10] G. Kak, M. Raza, and B. K. Tiwari, "Interferon-gamma (IFN-γ): e," *Biomolecular Concepts*, vol. 9, no. 1, pp. 64–79, 2018.

[11] D. Prodanov, "Analytical parameter estimation of the SIR epidemic model. Applications to the COVID-19 pandemic," *Entropy*, vol. 23, no. 1, p. 59, 2020.

[12] A. Comunian, R. Gaburro, and M. Giudici, "Inversion of a SIR-based model: a critical analysis about the application to COVID-19 epidemic," *Physica D: Nonlinear Phenomena*, vol. 413, Article ID 132674, 2020.

[13] J. Y. Chung, M. N. Thone, and Y. J. Kwon, "COVID-19 vaccines: the status and perspectives in delivery points of view," *Advanced Drug Delivery Reviews*, vol. 170, pp. 1–25, 2021.

[14] H. J. Han, C. Nwagwu, O. Anyim, C. Ekweremadu, and S. Kim, "COVID-19 and cancer: from basic mechanisms to vaccine development using nanotechnology," *International Immunopharmacology*, vol. 90, Article ID 107247, 2021.

[15] N. Taleghani and F. Taghipour, "Diagnosis of COVID-19 for controlling the pandemic: a review of the state-of-the-art," *Biosensors and Bioelectronics*, vol. 174, Article ID 112830, 2021.

Hindawi
Journal of Healthcare Engineering
Volume 2021, Article ID 7036863, 9 pages
https://doi.org/10.1155/2021/7036863

Research Article

Diffusion Tensor Imaging Features of Watershed Segmentation Algorithm for Analysis of the Relationship between Depression and Brain Nerve Function of Patients with End-Stage Renal Disease

Feng Zhu,[1] **Jiao Xu**,[2] **Mei Yang**,[1] **and Haitao Chi**[3]

[1]*Department of Nephrology, Dalian University Affiliated Xinhua Hospital, Dalian 116021, Liaoning, China*
[2]*Department of Liver Diseases, Dalian Sixth People's Hospital, Dalian 116001, Liaoning, China*
[3]*Department of Neurology, Dalian University Affiliated Xinhua Hospital, Dalian 116021, Liaoning, China*

Correspondence should be addressed to Haitao Chi; 20150401111@m.scnu.edu.cn

Received 22 August 2021; Revised 26 September 2021; Accepted 28 September 2021; Published 25 October 2021

Academic Editor: Enas Abdulhay

The aim of this research was to explore the relationship between depression and brain nerve function in patients with end-stage renal disease (ESRD) and long-term maintenance hemodialysis (MHD) based on watershed segmentation algorithm using diffusion tensor imaging (DTI) technology. A total of 29 ESRD patients with depression who received MHD treatment in the hemodialysis center of hospital were included as the research subjects (case group). A total of 29 healthy volunteers were recruited as the control group, and a total of 29 ESRD patients with depression and brain lesions were recruited as the control group (HC group). Within 24 h after hemodialysis, the blood biochemical indexes were collected before this DTI examination. All participants completed the neuropsychological scale (MoCA, TMT A, DST, SAS, and SDS) test. The original DTI data of all subjects were collected and processed based on watershed segmentation algorithm, and the results of automatic segmentation according to the image were evaluated as DSC = 0.9446, MPA = 0.9352, and IOU = 0.8911. Finally, the average value of imaging brain neuropathy in patients with depression in the department of nephrology was obtained. The differences in neuropsychological scale scores (PSQI, MoCA, TMTA, DST, SAS, and SDS) between the two groups were statistically significant ($P < 0.05$). The differences of FA values in all the white matter partitions of Fu organs, except the cingulum of hippocampus (CgH) between the two groups, were statistically significant ($P < 0.05$). ESRD and DTI quantitative detection under the guidance of watershed segmentation algorithm in MHD patients showed that ESRD patients can be early identified, so as to carry out psychological nursing as soon as possible to reduce the occurrence of depression, and then protect the brain nerve to reduce brain neuropathy.

1. Introduction

End-stage renal disease (ESRD) [1] is a worldwide public health problem. It generally refers to the middle and late stages of various types of chronic kidney diseases and has a certain degree of similarity with the concept of uremia. However, there are still some differences in diagnostic criteria. Generally, ESRD can be diagnosed when the glomerular filtration rate is low to a certain standard. This standard is generally recognized as 15 mL (min.1.73 m^2) as the standard line. When the chronic kidney disease reaches the fifth stage, it enters the ESRD. At this stage, with the further decline of renal function, toxins continue to accumulate in the body, which may cause various symptoms of uremia. Generally, it relies on continuous maintenance dialysis or looking for appropriate renal sources for transplantation replacement therapy [2, 3]. In the ESRD for a long time, a large number of toxins accumulated in the body may cause damage to multiple important organs in the body. The central nervous system is the most likely to be affected. The central nervous system may cause many complications after injury, such as cerebrovascular injury, behavioral cognitive impairment, brain atrophy, cerebral infarction, and depression. According to relevant data, about 60% of ESRD patients have cognitive impairment, so it is of great significance to diagnose and intervene the brain structure changes of renal disease patients as soon as possible [4, 5]. However, the exact pathogenesis of cognitive impairment in ESRD patients is still unclear. Diffusion tensor imaging (DTI) can quantitatively display the abnormal pathological changes of white matter microstructure [6], and tract-based spatial statistics (TBSS) is a more ideal imaging method for automatic and efficient evaluation of white matter fiber integrity [7].

Watershed algorithm is a kind of algorithm technology derived from geodesy topology. It has many advantages, and the logical ideas in the algorithm are easy to understand. Therefore, it is widely used in various fields. Now, it is mainly used in image segmentation [8, 9]. The gradient map of the image to be segmented is regarded as the topology in geodesy [10, 11]. Watershed algorithm is a kind of applied morphology in general. Its main idea is to analogize the selected target image to topography. The gray value of the image represents the altitude of the terrain, and the gray pixels in the image represent the valleys and peaks in the terrain. It is assumed that a hole is placed on each extreme point of the gray pixel, and the analogy model is put into the water. At this moment, the terrain and area formed by the process of water rising from the extreme point are basins. Different catchment basins in the image are about to converge, and the junction of its convergence becomes a watershed [12]. The watershed algorithm is a mathematical morphological method, which belongs to a region segmentation technology, and is an effective image segmentation method. In addition, it is featured with fast calculation speed and more accurate positioning, so it has many applications in the field of image analysis. Marking extraction in an image is a method of controlling oversegmentation. The minimum value area of the original gradient image is forcibly modified by the previously mentioned marking, and irrelevant minimum values in the original gradient image are shielded, showing very good segmentation effect. DTI is currently the only noninvasive examination method that can track white matter fiber tracts in vivo and effectively observe it. It can directly show the spatial relationship between acute cerebral infarction lesions and fiber tract, so as to judge the severity of brain injury. At this stage, there are relatively few studies on the watershed algorithm in MRI DTT imaging on depression and brain nerve function in patients with ESRD. Therefore, in this study, the watershed algorithm was adopted to the image processing network, the DTI technology was applied to image the patient's CST, and the DTI images of brain injury were collected to understand the sleep, anxiety, and depression of patients in time and develop treatment plans for the patient as soon as possible to improve prognosis, so as to provide help for clinical diagnosis and treatment.

2. Methods

2.1. Research Objects. Twenty-nine ESRD patients who underwent hemodialysis in the hemodialysis center of the department of nephrology at a tertiary hospital from October 2018 to November 2019 were enrolled as the case group. Twenty-nine local healthy volunteers matched with the case group in age, gender, years of education, anxiety, depression, and sleep quality scores were enrolled. All subjects were educated for ≥6 years and were right-handed (Figure 1).

2.2. Inclusion and Exclusion Criteria. The inclusion criteria were as follows: (1) patients diagnosed with ESRD, according to K/DOQI chronic kidney disease classification criteria; (2) patients who underwent regular dialysis for three months; (3) patients with no history of renal transplantation or acute renal failure; (4) patients without previous headless trauma, intracranial occupation, stroke, mental and neurological diseases, metabolic diseases, and other diseases that may affect the nervous system; (5) patients with no history of smoking, drug addiction, or alcoholism; and (6) patients without MRI contraindications. This study was a prospective study and was approved by the hospital ethics committee. All subjects signed informed consent. The participants' general demographic information, conducted neuropsychological tests and MR scans, and relevant blood biochemical indexes were collected.

The exclusion criteria were as follows: (1) patients with lesions >1.0 cm in the brain confirmed by clinical history and conventional MRI examination, such as cerebral hemorrhage, cerebral infarction, and brain tumors; (2) patients who cannot complete the neuropsychological scale test; and (3) patients with MRI contraindications.

2.3. Watershed Segmentation Algorithm. Watershed algorithm is a kind of algorithm technology derived from geodesic topology. It has many advantages, and the logical ideas in the algorithm are easy to understand. Therefore, it is widely used in various fields. Now, it is mainly used in image segmentation [13, 14]. By applying this method to the field of image segmentation, it has made a significant contribution to optimizing the segmentation effect of the image. With further research on the watershed algorithm, the mathematical morphology technology was added to the segmentation field. Therefore, the complexity of the watershed algorithm is gradually improved, and the effect of the segmentation image is further improved. In different scenes and fields, the label and segmentation of the target image are realized at different levels, and the outline of the label parts after segmentation is clear.

The basic definition of watershed algorithm is as follows: the two-dimensional image N to be segmented is selected to set the discrete value in the interval of [0, M]. The image is defined as a gray image, where M is a positive number, and the following conditions need to be met:

$$D_N \varepsilon R^2 \longrightarrow \{0, 1, \ldots, M\}, \quad (1)$$

$$F \longrightarrow N(F). \quad (2)$$

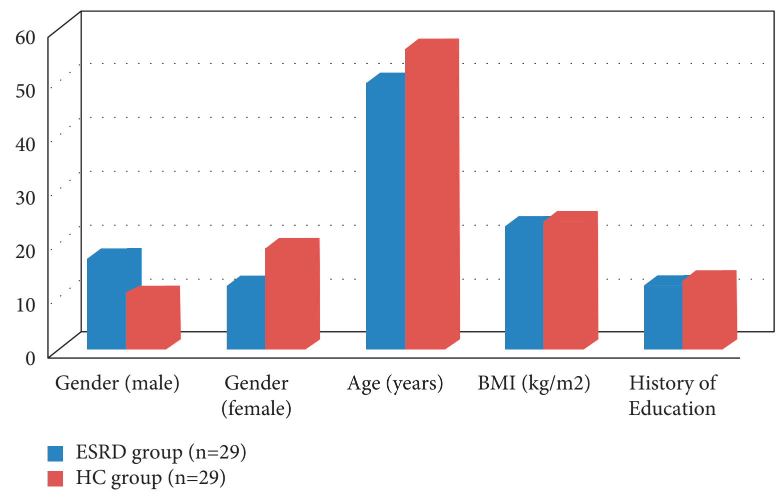

Figure 1: Comparison of differences in population data of subjects.

Let U be a grid, which represents a subset of the set $R^2 \times R^2$. Each grid has different names according to the number of grids contained in it.

Definition 1. Pixel set with height of H is selected from the selected image N.

$$T_H = \{F \in D \mid N(F) \leq H\}. \tag{3}$$

H represents the threshold, and n_A (α, B) geodesic distance is used to represent the distance between two points. The selection of these two points needs to satisfy a, $b \in A$. If $B \subseteq A$ appears, region B is divided into random G regions, and G regions are connected with each other, denoted as B_i, where $i = 1,\ldots,G$.

Definition 2. In set A, B_i divided into random regions is selected, and the solution equation of the influence region corresponding to this part is as follows:

$$\mathrm{NR}_A(B_i, B) = \left\{F \in A \mid (F, B_i) < N_A\left(F, \frac{B}{B_i}\right)\right\}. \tag{4}$$

Definition 3. Connect B and B_i to form a collection NR_A (B).

$$\mathrm{NR}_A(B) = \bigcup_{i=1}^{G} iR_A(B_i, B). \tag{5}$$

Definition 4. In set A, the absolute complement SKIZ of $\mathrm{NR}_A(B)$ is considered to be the skeleton affecting some regions.

$$\mathrm{SKIZ}_A(B) = \frac{A}{NR_A(B)}. \tag{6}$$

After the pixels in the foreground part are concentrated, the SKIZ is obtained, and the following equations are derived:

$$z_{h_{\min}} = \{F \in D \mid N(F) = h_{\min}\} = T_{h_{\min}}, \tag{7}$$

$$z_{G+1} = \mathrm{MIN}_{h+1} \cup NR_{T_{h+1}}(z_h), \quad h \in [h_{\min} - h_{\max}]. \tag{8}$$

Definition 5. In D, the watershed region Wshed (f) is the absolute complement set corresponding to $z_{h_{\max}}$.

$$\mathrm{Wshed}(\mathrm{f}) = \frac{D}{Z_{h_{\max}}}. \tag{9}$$

If there is a big difference in the gray value between the selected image and the target image background, then it is believed that the segmentation effect is better. If the difference between the both is not obvious, the phenomenon of "undersegmentation" easily appears. Therefore, the contrast of the image is enhanced to a certain extent, and the mathematical morphology technology is added into the segmentation field, so that the gray value between the selected image and the background of the target image is greatly different. Let ut (x, y) and $f(x, y)$ denote the denoised image and the gray image, respectively, and carry out the top-cap transformation on $f(x, y)$ to retain the region with large brightness in the original image. The top-hat transformation result is as follows:

$$h = f - (f \circ b). \tag{10}$$

b represents the structural element. $f \circ b$ represents the opening operation of b to f. The bottom-cap transformation is performed on $f(x, y)$ to save the dark details in the image. The bottom-cap transformation result is as follows:

$$j = (f \bullet b) - f. \tag{11}$$

$f{\cdot}b$ denotes closed operation b to f. $h(x, y)$ and $j(x, y)$ are added to get contrast enhanced gray image.

$$i(x, y) = h(x, y) + j(x, y). \tag{12}$$

$i \oplus b$ and $i \Theta b$ represent the expansion operation and corrosion operation of b to i, respectively, and the gradient of morphological image is as follows:

$$g = (i \oplus b) - (i \Theta b). \tag{13}$$

The flowchart of improved watershed segmentation algorithm is shown in Figure 2.

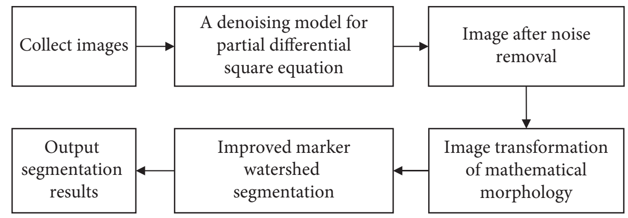

Figure 2: Image segmentation process based on improved watershed algorithm.

2.4. Assessment of Depression. Center for Epidemiological Survey, Depression (CES-D) was used to evaluate depression. One-way analysis of variance (ANOVA) was used to compare the differences among the three groups in terms of age, years of education, neuropsychological scale score, and DTI parameters (FA, MD, AD, and RD values) between the two groups. CES-D was designed to evaluate the frequency of current depressive symptoms, focusing on depression emotion or mood. CES-D, also known as the self-rating depression scale of stream invocation, was prepared by Sirodff at the National Institutes of Mental Health in 1997, known as the center for epidemiological studies depression scale. It is widely used in the field of depression diagnosis and is used in the clinical screening of patients with depressive symptoms in order to further check and diagnose them. Some also used an individual emotional examination to assess the severity of depressive symptoms. Compared with other self-rating depression scales, CES-D focuses more on the individual emotional experience and less on the somatic symptoms in depression. The minimum score of depression was 0, and the maximum score was 60. Psychologists set the 16 points as the dividing point. Those who scored above 16 points belonged to the depressed group, and those who scored below 16 points belonged to the nondepressed group. Sixteen to twenty points indicated mild depression, 21–25 points indicated moderate depression, and 26–60 points indicated severe depression. The degree of depression is easily affected by mood and mental state, so the measurement results may be different at different times, which is normal.

2.5. Inspection Equipment

2.5.1. DTI Examination. All subjects underwent examination and data acquisition using Siemens Verio 3.0T superconducting magnetic resonance imaging (Magnetom Verio 3.0T) and used 12-channel standard head coil. The specific process and DTI parameters were as follows. Single excitation white-spin plane echo sequence was used. Specific parameters are as follows: echo time (TE) = 86 ms, repeat time (TR) = 11908 ms, slice number (slice) = 65, slice thickness (ST) = 2 mm, matrix size (MS) = 128 x 128, field of view (FOV) = 244 mm × 244 mm, voxel size (VS) = 2 mm × 2 mm × 2 mm, diffusion weighted directions = 30, and b value = 0s/mm^2, 1000s/ram^2. The total examination time was 12 min and 56 s.

2.5.2. Blood Biochemical Examination Information. Before this MRI examination and within 24 h after hemodialysis, the patient group was tested for the following clinical biochemical indicators: serum creatinine (Scr), blood urea nitrogen (BUN), blood kalium (K), blood calcium (Ca), and blood phosphorus (P).

2.5.3. MRI Examination. The nuclear magnetic resonance (NMR) scanning equipment, 1.5 T HDC nuclear magnetic superconducting magnetic resonance scanner of the United States, with 8-channel head coil, was used. The patients were allowed to maintain supine posture on the check bed. The head and neck joint coil was used to fix the head of the patients. The quality of the head coil was tested before routine scanning to ensure that the 12 channels of the coil were all working properly. Subjects wore earplugs to avoid excessive noise affecting the tester' s state, and then, all the MRI scan lights were turned off to avoid unnecessary light interference.

2.6. Statistical Method. SPSS19.0 software was used for statistical analysis. Measurement data conforming to normal distribution were expressed as mean ± standard deviation, and the difference between groups was analyzed by independent sample t-test. The measurement data that did not conform to the normal distribution were represented by median and quarter position, and the difference between groups was analyzed by nonparametric rank sum test. Count data were expressed as n (%). Differences between groups were analyzed by chi-square test. Pearson correlation analysis was performed for DTI diffusion index, depression score, and clinical biochemical index. $P < 0.05$ was considered statistically significant.

3. Results

3.1. Correlation Analysis of DTI Diffusion Indexes with Depression Score and Clinical Biochemical Indexes Based on Segmentation Algorithm. The correlation analysis in this study showed that the FA value in the anterior part of the left corona was positively correlated with the DST score ($r = 0.586$, $P = 0.007$). The FA value of the right hook was positively correlated with MoCA score and negatively correlated with TMTA ($r = 0.545$, $P = 0.013$; $r = .0.464$, $P = 0.039$). Left Nd and subiculum MD values were negatively correlated with depression score ($r = -0.463$, $P = 0.040$). There was no correlation between the values of FA, MD, AD, and RD in all the different brain regions and PSQI scores ($P > 0.05$). In addition, there was no significant correlation between the results of DTI dispersion indexes and the blood biochemical indexes of the subjects ($P > 0.05$) (Figure 3).

The segmentation results of the target image based on the watershed algorithm model are shown in Figure 4. The results of automatic segmentation based on the image were evaluated as $DSC = 0.9152$, $MPA = 0.9229$, and $IOU = 0.8450$. In order to improve the segmentation accuracy of the watershed model, the watershed algorithm with fine-tuning weight was tested to segment the target image. The image was processed independently under the algorithm processing, but the processing results were continuous and stable in time. The results are shown in Figure 4. The evaluation of the automatic segmentation results based on the image was $DSC = 0.9446$, $MPA = 0.9352$, and $IOU = 0.8911$.

3.2. Comparison of Neuropsychological Cognitive Scores among Subjects. The differences in MoCA score and TMT_A score between the ESRD group and the HC group were statistically significant (Figure 5).

3.3. Comparison of Difference Values in DIC Measurement of Brain Volume by ESRD. Compared with the HC group, almost all white matter areas of ESRD maintenance hemodialysis patients had decreased FA value and increased MD value and RD value. Only in the right superior corona radiata, left superior corona radiata, right superior longitudinal bundle, the difference was statistically significant ($P < 0.05$) (Figure 6).

3.4. Comparison of General Condition between Depression Group and Nondepression Group. A total of 176 questionnaires were distributed to patients with regular hemodialysis for more than half a year in the hemodialysis room and were distributed and recovered by the competent nurses in the dialysis room. The recovery rate was 100%. There were 103 males and 73 females, with an average age of 61.24 ± 12.08 years. There were 58 cases in depression group and 29 cases in nondepression group. The number of depression accounts for 66% of the total. The general status of the two groups was significantly different in personal monthly income and working status ($P > 0.05$) (Figure 7).

3.5. Analysis of Brain Neuropathy Caused by Depression in Patients with ESRD. Depression often leads to the expansion of physical symptoms in patients with cerebral stroke, which generally causes double damage to the normal physical and social functions of patients, and at the same time seriously affects the self-psychological adjustment function of patients. The impact of psychological problems often leads to patients giving up or interrupting treatment, and then, they lose hope for subsequent life and recovery, which directly or indirectly affects the positive cooperation of patients in clinical treatment, thus affecting the best time for rehabilitation of patients and causing serious burdens on families and society (Figure 8). After stimulation of the vagus nerve, the brain activity of patients increased significantly. Patients with severe depression should communicate effectively with the attending physician timely and relieve anxiety and depression as much as possible after using certain antidepressant drugs. Then, further psychological treatment and psychological care were conducted. Figure 8 is a DWI image of the patient's skull. Both T2 and diffusion effects can cause DWI signal enhancement, and lesions with reduced or limited diffusion had higher signals on DWI images. In the imaging process, there was false positive performance with reduced dispersion due to the residual T2 component. Figures 8(a)–8(d) all show the characteristics of clear imaging and high resolution.

4. Discussion

ESRD is the end stage of chronic renal failure [15]. It generally refers to the middle and late stages of various types of chronic renal diseases, which is somewhat similar to the concept of uremia, but there are still some differences in the diagnostic criteria. When the chronic renal disease reaches the fifth stage, it enters the end stage of renal disease. At this time, with the further decline of renal function, the patients continue to accumulate toxins in the body, which may cause various symptoms of uremia. The patients generally maintain their normal life through hemodialysis. In addition, if the appropriate renal source can be found for transplantation and replacement, it can be treated. However, the psychological state of patients with such diseases often has various problems, among which depression is the most common [16, 17]. Studies showed that the incidence of depression in ESRD hemodialysis patients is much higher than that in the general population of 20%–30%. Depression is very harmful to hemodialysis patients. Studies indicated that depression in patients before dialysis treatment can produce a series of psychosomatic reactions, increasing the incidence and mortality of cardiovascular diseases [18]. The incidence of depression in ESRD hemodialysis patients was 42.2%, higher than foreign reports. The reasons may be related to the personality and mental stress of Chinese people and factors such as personal tolerance and economic level [19]. The study of Yoong et al. [20] showed that 49.9% of ESRD patients experienced increased depression, and 45.4% of ESRD patients experienced increased anxiety during treatment. The high proportion of anxiety and depression emphasizes the importance of testing and nursing care for ESRD patients during dialysis care. Mu et al. [21] segmented rough semantics in DTI images based on the feature extraction of deep learning, realized super pixel segmentation algorithm, used boundary optimization algorithm to optimize the segmentation accuracy of image edges, and improved the accuracy of image segmentation. In this study, the watershed algorithm was applied to the DWI imaging of patients with brain diseases, which had significant value for the early diagnosis of ESRD patients and psychological care. The correlation analysis of the DTI diffusion index of the segmentation algorithm in the image with the depression score and clinical biochemical indicators. The results showed that the FA value of the anterior left crown was positively correlated with the DST score

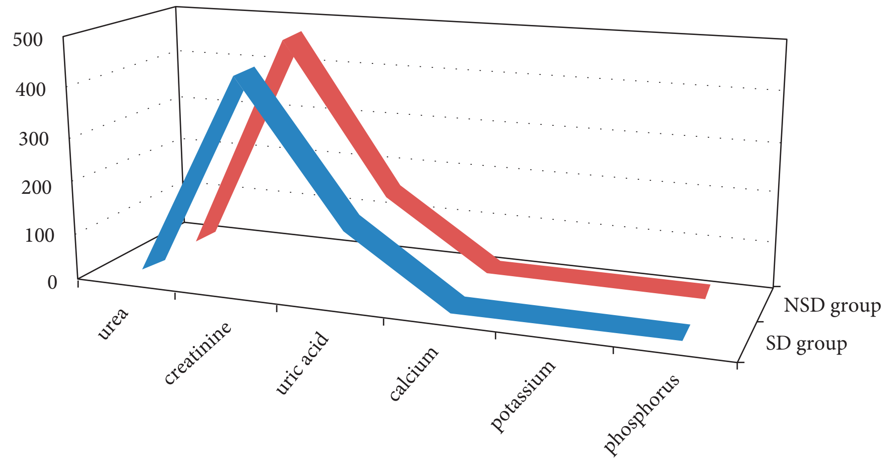

Figure 3: Comparison of blood biochemical indexes between SD group and NSD group of patients.

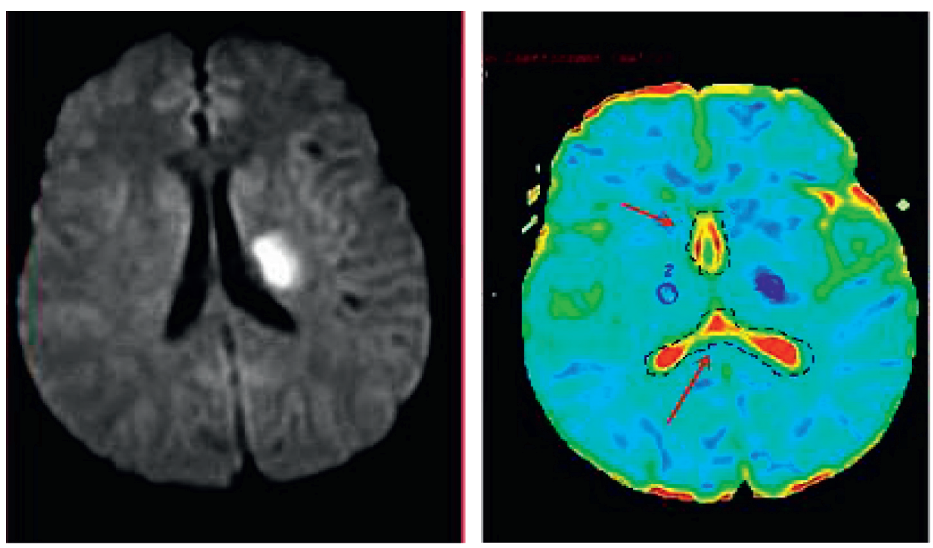

Figure 4: Comparison of watershed segmentation graph and original graph.

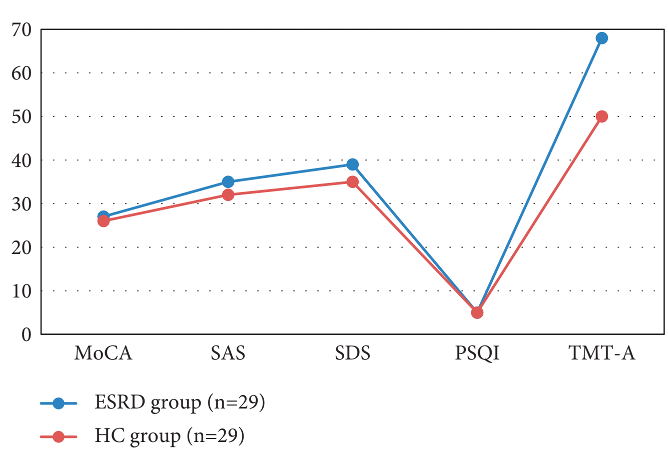

Figure 5: Comparison of neuropsychological cognitive scores among subjects.

($r = 0.586$, $P = 0.007$). The FA value of right uppercut was positively correlated with MoCA score ($r = 0.545$, $P = 0.013$) and negatively correlated with TMTA ($r = 0.464$, $P = 0.039$). The correlation between the results of DTI dispersion index and the blood biochemical indexes of subjects was not significant. The left Nd and subiculum MD values were

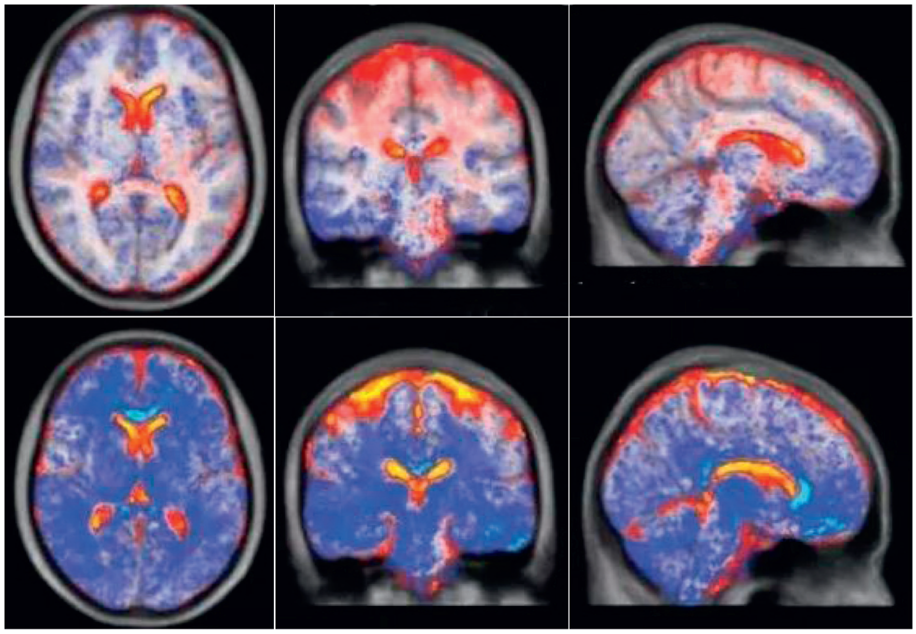

Figure 6: Comparison of difference values in DIC measurement of brain volume by ESRD based on voxel brain volume measurement. Red: atrophy; yellow: more severe atrophy.

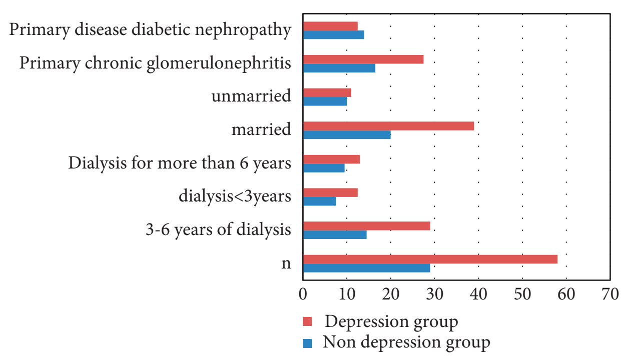

Figure 7: Comparison of condition between depression group and nondepression group.

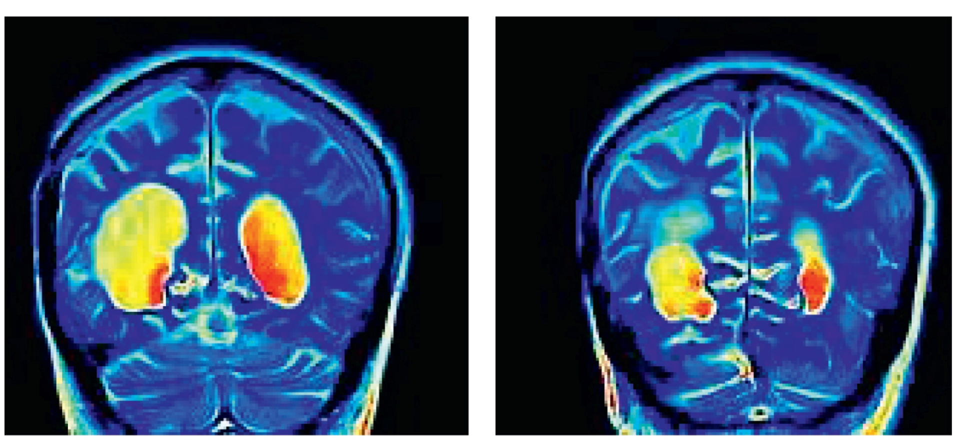

(a)

(b)

Figure 8: Continued.

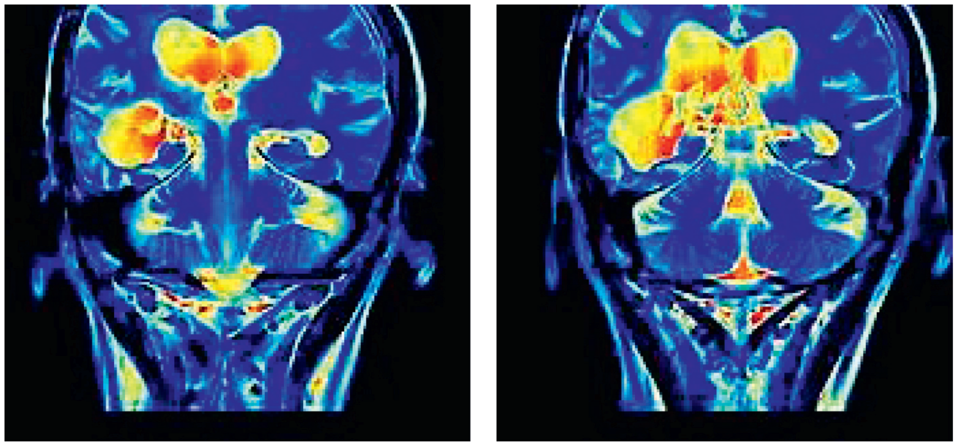

(c) (d)

Figure 8: Depression causing brain lesions in patients.

negatively correlated with depression scores ($r = -0.463$, $P = 0.040$).

DTI technology is one of the most effective tools for noninvasively studying the structural and pathological changes of white matter (WM) at the microstructure level. It uses the diffusion anisotropy of water molecules in human tissues, uses various parameters to reflect the direction and degree of water molecule movement in fiber bundles, and visualizes the changes of WM microstructure. The main parameters include the following [22]: fractional anisotropy (FA), axial diffusion coefficient (AD), radial diffusion coefficient (RD), and mean diffusion rate (MD). Moreover, based on the imaging features of watershed segmentation algorithm, ESRD can be diagnosed early. Early treatment can reduce the medical costs, relieve economic pressure, and reduce depression complicated with brain lesions. Asman et al. [23] segmented the medical images and converted the TI-weighted DTI imaging data of the label information of the multiatlas segmentation into fully automated. The segmentation method constructed in the article showed a good effect on the FA of the measured image.

In this study, DTI technology is used to explore the correlation between depression and brain neuropathy in ESRD patients based on methods. The following conclusions are drawn: early diagnosis of ESRD based on watershed segmentation algorithm is conducive to early treatment and reduce depression and brain lesions in ESRD patients.

5. Conclusion

The purpose of this study is to use the watershed algorithm to segment the DTI image of the brain of ESRD patients and further analyze and explore the relationship between depression and brain nerve function of ESRD patients. The original DTI data of all subjects were collected and processed based on the watershed segmentation algorithm, and the results of automatic segmentation were evaluated as $DSC = 0.9446$, $MPA = 0.9352$, and $IOU = 0.8911$. The analysis of DTI images after watershed algorithm segmentation suggested that the WM microstructure of patients had undergone a certain degree of change and atrophy, and three main WM fibers had undergone lesions. However, the research content still has some limitations. This study only focuses on a single imaging diagnosis method, and the number of samples is not large enough. Therefore, it is necessary to increase the number of samples and deepen the further exploration of watershed algorithm. In conclusion, this study can analyze and judge the relationship between depression and brain nerve function in ESRD patients through watershed algorithm, which provides certain data support and theoretical basis for the diagnosis and treatment of depression in ESRD patients. The only shortcoming of this study was that the number of cases was not large and the number of subjects included in the experiment was limited. At a certain time, multiple centers can be used to conduct experiments, and the algorithm dataset training required a lot of data, so follow-up work needed to increase the training dataset and increase the accuracy.

Data Availability

The data used to support the findings of this study are available from the corresponding author upon request.

Conflicts of Interest

The authors declare no conflicts of interest.

References

[1] J. Tangren, M. Nadel, and M. A. Hladunewich, "Pregnancy and end-stage renal disease," *Blood Purification*, vol. 45, no. 1-3, pp. 194–200, 2018.

[2] T. Tsuzuki, H. Iwata, Y. Murase, T. Takahara, and A. Ohashi, "Renal tumors in end-stage renal disease: a comprehensive review," *International Journal of Urology*, vol. 25, no. 9, pp. 780–786, 2018.

[3] G. Cobo, B. Lindholm, and P. Stenvinkel, "Chronic inflammation in end-stage renal disease and dialysis," *Nephrology Dialysis Transplantation*, vol. 33, 2018.

[4] N. M. Chu and M. A. McAdams-DeMarco, “Exercise and cognitive function in patients with end-stage kidney disease,” *Seminars in Dialysis*, vol. 32, no. 4, pp. 283–290, 2019.
[5] D. A. Drew, D. E. Weiner, and M. J. Sarnak, “Cognitive impairment in CKD: pathophysiology, management, and prevention,” *American Journal of Kidney Diseases*, vol. 74, no. 6, pp. 782–790, 2019.
[6] B. S. Park, S. E. Kim, H. J. Lee et al., “Alterations in structural and functional connectivities in patients with end-stage renal disease,” *Journal of Clinical Neurology*, vol. 16, no. 3, pp. 390–400, 2020.
[7] M. C. Chou, C. H. Ko, T. J. Hsieh, J. M. Chang, and W. S. Chung, “A preliminary report of longitudinal white matter alterations in patients with end-stage renal disease: a three-year diffusion tensor imaging study,” *PLoS One*, vol. 14, no. 4, Article ID e0215942, 2019.
[8] S. M. K. Hasan, M. Ahmad, and M. Ahmad, “Two-step verification of brain tumor segmentation using watershed-matching algorithm,” *Brain Inform*, vol. 5, no. 2, p. 8, 2018 Aug 14.
[9] L. Bonanno, N. Mammone, S. De Salvo et al., “Multiple Sclerosis lesions detection by a hybrid Watershed-Clustering algorithm,” *Clinical Imaging*, vol. 72, pp. 162–167, 2021.
[10] X. Shen, Y. Qi, T. Ma, and Z. Zhou, “A dicentric chromosome identification method based on clustering and watershed algorithm,” *Scientific Reports*, vol. 9, no. 1, p. 2285, 2019.
[11] X. Zhu, S. Su, M. Fu et al., “A density-watershed algorithm (DWA) method for robust, accurate and automatic classification of dual-fluorescence and four-cluster droplet digital PCR data,” *Analyst*, vol. 144, no. 16, pp. 4757–4771, 2019.
[12] M. Kowal, M. Żejmo, M. Skobel, J. Korbicz, and R. Monczak, “Cell nuclei segmentation in cytological images using convolutional neural network and seeded watershed algorithm,” *Journal of Digital Imaging*, vol. 33, no. 1, pp. 231–242, 2020.
[13] M. A. Khan, I. U. Lali, A. Rehman et al., “Brain tumor detection and classification: a framework of marker-based watershed algorithm and multilevel priority features selection,” *Microscopy Research and Technique*, vol. 82, no. 6, pp. 909–922, 2019.
[14] V. Sivakumar and N. Janakiraman, “A novel method for segmenting brain tumor using modified watershed algorithm in MRI image with FPGA,” *Biosystems*, vol. 198, Article ID 104226, 2020.
[15] E. I. Mandel, R. E. Bernacki, and S. D. Block, “Serious illness conversations in ESRD,” *Clinical Journal of the American Society of Nephrology*, vol. 12, no. 5, pp. 854–863, 2017.
[16] T. King-Wing Ma and P. Kam-Tao Li, “Depression in dialysis patients,” *Nephrology*, vol. 21, no. 8, pp. 639–646, 2016.
[17] V. Wang, H. Vilme, M. L. Maciejewski, and L. E. Boulware, “The economic burden of chronic kidney disease and end-stage renal disease,” *Seminars in Nephrology*, vol. 36, no. 4, pp. 319–330, 2016.
[18] H. Moradi, E. Streja, and N. D. Vaziri, “ESRD-induced dyslipidemia-Should management of lipid disorders differ in dialysis patients?” *Seminars in Dialysis*, vol. 31, no. 4, pp. 398–405, 2018.
[19] S. D. Cohen, D. Cukor, and P. L. Kimmel, “Anxiety in patients treated with hemodialysis,” *Clinical Journal of the American Society of Nephrology*, vol. 11, no. 12, pp. 2250–2255, 2016.
[20] R. K. Yoong, N. Mooppil, E. Y. Khoo et al., “Prevalence and determinants of anxiety and depression in end stage renal disease (ESRD). A comparison between ESRD patients with and without coexisting diabetes mellitus,” *Journal of Psychosomatic Research*, vol. 94, pp. 68–72, 2017.
[21] Y. Mu, Q. Li, and Y. Zhang, “White matter segmentation algorithm for DTI images based on super-pixel full convolutional network,” *Journal of Medical Systems*, vol. 43, no. 9, p. 303, 2019.
[22] Y. Zhao, Y. Zhang, Z. Yang et al., “Sleep disorders and cognitive impairment in peritoneal dialysis: a multicenter prospective cohort study,” *Kidney & Blood Pressure Research*, vol. 44, no. 5, pp. 1115–1127, 2019.
[23] A. J. Asman, C. B. Lauzon, and B. A. Landman, “Robust intermodality multi-atlas segmentation for PACS-based DTI quality control,” *Proceedings of SPIE-The International Society for Optical Engineering*, p. 8674, 2013.

Hindawi
Journal of Healthcare Engineering
Volume 2021, Article ID 9026223, 9 pages
https://doi.org/10.1155/2021/9026223

Research Article

Effects of Compound Danshen Injection Combined with Magnesium Sulfate on Pregnancy-Induced Hypertension Syndrome under the Guidance of Empirical Mode Decomposition Algorithm-Based Ultrasound Image

Xia Zhao , Hongbin Wang , Yanan Gao , and Yanan Wang

Department of Obstetrics and Gynecology, The Fourth Hospital of Shijiazhuang, Shijiazhuang 050011, China

Correspondence should be addressed to Yanan Wang; 06122448@cumt.edu.cn

Received 22 August 2021; Revised 26 September 2021; Accepted 29 September 2021; Published 25 October 2021

Academic Editor: Enas Abdulhay

Objective. The study focused on the separation effects of ultrasound blood flow signal detection, based on empirical mode decomposition (EMD) algorithm, and the clinical efficacy of Compound Danshen injection and magnesium sulfate in the treatment of pregnancy-induced hypertension (PIH) syndrome. *Methods*. The empirical mode decomposition (EMD) algorithm was optimized first and compared with other algorithms for the accuracy and stability in separation of blood flow signals. 80 patients with PIH syndrome undergoing ultrasound examination were selected as the research subjects and randomly divided into control group and observation group according to the actual treatment methods. 40 cases in the observation group were treated with Compound Danshen injection + magnesium sulfate, and 40 cases in the control group were treated with magnesium sulfate. After the treatment, the clinical indicators of the two groups of patients were analyzed. *Results*. The accuracy and stability in separating blood flow signal of the optimized EMD algorithm were better than those of other algorithms. After treatment, the total effective rate and blood pressure control of the observation group were significantly better than those of the control group, and the incidence of adverse maternal and infant outcomes was significantly lower than that of the control group. After treatment, the endothelin-1 (ET-1), C-reactive protein (CRP), and homocysteine (Hcy) indexes of the two groups of patients decreased significantly, and the decrease level of the observation group was significantly greater than that of the control group ($P < 0.05$). The prothrombin time (PT), fibrinogen (FIB), activated partial thromboplastin time (APTT), and plasma thrombin time (TT) levels of the two groups after treatment were better than those before treatment, and the observation group was better than the control group ($P < 0.05$). *Conclusion*. The optimized EMD algorithm is of great value for the separation of ultrasound blood flow signals. For patients with PIH syndrome, Compound Danshen injection combined with magnesium sulfate can be used as a treatment plan, which can improve maternal and infant outcomes; control blood pressure; reduce 24 h urine protein and serum ET-1, Hcy, and CRP levels; and improve coagulation function. It is worthy of promotion.

1. Introduction

Usually, pregnancy-induced hypertension (PIH) syndrome occurs in women with more than 20 weeks of pregnancy. Clinically, it mainly manifests itself as hypertension, proteinuria, and edema of limbs [1, 2]. PIH syndrome threatens maternal and infant health and can easily cause adverse events such as premature delivery, eclampsia, postpartum infection, or hemorrhage, which is not conducive to pregnancy outcome [3, 4]. Currently, the etiology of hypertension in pregnant women is mainly summarized as systemic small vasospasm [5]. Therefore, in practice, it is necessary to relieve systemic small vasospasm, and this strategy has been proved to have a significant effect [6]. Magnesium sulfate is a clinically effective drug for relieving systemic small vasospasm, and it is found to be effective in the treatment of hypertension in pregnancy [7]. However, the use of magnesium sulfate alone cannot achieve satisfactory results. Compound Danshen injection is a Chinese patent medicine mainly composed of Danshen (a traditional

Chinese medicine to promote blood circulation and dredge meridians) and Jiangxiang (a traditional Chinese medicine to remove stasis and stop bleeding) [8]. Compound Danshen injection has a variety of pharmacological effects, such as expanding blood vessels, improving microcirculation, scavenging oxygen free radical, protecting liver function, and sedating the mind [9], which can effectively lower blood pressure, thereby alleviating vascular endothelial injury [10]. Generally speaking, to treat small vasospasm in patients is to restore the secretion function of nitric oxide and vascular endothelin [11]. Research has found that Danshen has a good effect on improving this function [12].

Ultrasound Doppler technology has become an important method for the diagnosis and efficacy evaluation of diseases of the blood circulatory system, especially cardiovascular diseases, because of its ability to measure blood flow nondestructively. Due to the simplicity and noninvasiveness of ultrasound diagnosis technology, in recent years, ultrasound examination has gradually been used in the functional and morphological evaluation of PIH. Studies have shown that functional and morphological changes (such as endothelial diastolic function and vascular stiffness) are related to the occurrence and development of PIH. However, the blood flow signal detected by traditional ultrasound often contains the signal of the tube wall, which will interfere with the blood flow speed to a certain extent, leading to deviations in the diagnosis and evaluation of the disease. Empirical mode decomposition (EMD) has significant advantages in the processing of nonlinear and nonstationary signals. However, it adds the first few layers as the blood flow signal during the separation process, which leads to a certain deviation in the separation results. Hence, it needs to be further optimized.

In this study, the EMD algorithm was optimized to separate ultrasound Doppler blood flow and vessel wall signals. 80 patients with PIH syndrome were taken as the research subjects to explore the effect of the combined therapy of Compound Danshen injection and magnesium sulfate on PIH, expected to provide reference value for its clinical application.

2. Research Methods

2.1. Research Subjects and Grouping. 80 patients with PIH syndrome admitted to the hospital from July 2019 to August 2020 were selected as research subjects, and they were divided into a control group and an observation group according to different treatments. There were 40 cases in the control group, aged 23–40 years, with an average age of 29.34 ± 7.56 years. The gestational age was 31–41 weeks, with an average gestational age of 34.86 ± 3.95 weeks. There were 31 primiparous women and 9 postpartum women. There were also 40 cases in the observation group, aged 22–40 years, with an average age of 28.55 ± 6.94 years. The gestational age was between 32–41 weeks, with an average gestational age of 35.62 ± 3.80 weeks. There were 32 primiparous women and 8 postpartum women. The inclusion criteria of this study were as follows: (1) meeting the diagnosis criteria for the pregnancy-induced hypertension syndrome; (2) single pregnancy. Patients with other serious gynecological diseases were excluded. The experimental procedure of this study has been approved by the ethics committee of the hospital, and all the subjects included in the study have signed informed consent form. The two groups were compared for the age, gestational age, number of pregnancies, and other data. A P value greater than 0.05 was considered comparable.

2.2. The Separation Method of Blood Flow and Tube Wall Signals Based on EMD Algorithm. The blood flow is the integration of multiple moving blood cells, and the ultrasound Doppler signal scattered back by a single blood particle can be expressed as follows:

$$S_i(t) = A_i B_i \cos[\varphi(t) + \psi_i] C_i^t(t) C_i^r(t), \tag{1}$$

where i represents the number of the particle; A_i indicates the acoustic field characteristics of the particle's location; B_i is the scattering coefficient of the particle.

$C_i^t(t)$ and $C_i^r(t)$ represent the shapes of the ultrasound transmitting gate and receiving gate, respectively; and $\varphi(t)$ is the particle motion coefficient, $\varphi(t) = \omega_0 t + \varphi_d(t)$, where ω_0 is the angular frequency of ultrasonic emission and $\varphi_d(t)$ represents the phase change caused by the motion of the particle.

Assuming that the blood vessel is a straight round tube, the radial distribution of blood flow velocity can be expressed as follows.

$$s(y,t) = 2v_0\left(1 - y^2\right) + \sum_P v_p|\psi|_p \cos\left(\mathrm{pwt} + \varepsilon_p + \chi_p\right), \tag{2}$$

where

$$\psi = \alpha i^{3/2} \frac{J_0\left(\alpha i^{3/2}\right) - J_0\left(y\alpha i^{3/2}\right)}{\alpha i^{3/2} J_0\left(\alpha i^{3/2}\right) - 2J_1\left(\alpha i^{3/2}\right)}, \tag{3}$$

where y is the ratio of the distance from the center of the blood vessel to the radius of the blood vessel; J_0 and J_1 represent the Bessel function of the orders of 0 and 1, respectively; $v_p$represents the magnitude of the p-order Fourier coefficient of the average blood flow velocity curve; ε_p represents the phase of the p-order Fourier coefficient of the average blood flow velocity curve; w is the angular frequency of the heart beat; χ is the phase of ψ; and v_0 is the initial blood flow velocity.

The pulsation of the blood vessel wall can be analyzed by the curve of blood pressure over time. Assuming that the cross-sectional area of the blood vessel is S and the blood pressure is P, the characteristic function of the blood vessel wall can be expressed as follows:

$$S(t) = ae^{bP(t)} + c, \tag{4}$$

where a, b, e are constants related to the physiological characteristics of the blood vessel wall: $a = 3.6\,cm^2$, $b = -0.0119\,mmHg$, $c = 3.05\,cm^2$.

Then, the pulsation velocity curve of the blood vessel wall can be expressed as follows:

$$v(t) = \frac{dr(t)}{dt}, \tag{5}$$

where $r(t)$ is the radius of the blood vessel, $r(t) = \sqrt{S(t)/\pi}$.

According to the Doppler frequency shift formula, the ultrasonic Doppler tube wall signal is calculated as follows:

$$x_w = a_w \exp[i\phi_d(t)], \tag{6}$$

where a_w represents the constant of the signal amplitude of the tube wall.

The original signal is decomposed into the eigenmode function (IMF) of each layer through the EMD algorithm, and the original signal is finally $N-1$ decomposed into $N-1$ IMF and a residual component.

$$s(t) = \sum_{t=1}^{N-1} x_i(t) + r(t), \tag{7}$$

where $r(t)$ is the residual component.

For further time-frequency analysis of the original signal, the Hilbert transform needs to be performed on the IMF decomposed by the EMD algorithm. Then, the Hilbert transform of $x_i(t)$ can be expressed as follows:

$$y_i(t) = \frac{1}{\pi}\int_{-\infty}^{+\infty} \frac{x_i(\tau)}{t-\tau} d\tau. \tag{8}$$

The analytical signal $z_i(t)$ of $x_i(t)$ can be expressed as follows:

$$z_i(t) = x_i(t) + iy_i(t) = a_i(t)e^{\beta_i(t)}, \tag{9}$$

where $a_i(t)$ represents the amplitude of the analytical signal, $a_i(t) = \sqrt{x_i^2(t) - y_i^2(t)}$; and $\beta_i(t)$ represents the phase angle of the analytical signal, $\beta_i(t) = \arctan[y_i(t)/x_i(t)]$.

The instantaneous frequency is calculated as follows:

$$w_i(t) = \frac{d\beta_i(t)}{dt}. \tag{10}$$

Then, the original blood flow signal can be expressed as follows:

$$s(t) = \mathrm{Re}\left\{\sum_{i=1}^{n} a_i(t)\exp\left[i\int w_i(t)dt\right]\right\}. \tag{11}$$

In order to improve the accuracy of extracting pipe wall signals, an adaptive wavelet threshold algorithm is introduced to optimize the EMD algorithm. The i-th layer IMF component $x_i(t)$ can be expressed as follows:

$$x_i(t) = \begin{cases} b_i(t) & 1 \le i \le k-1 \\ b_i(t) + w_i(t) & k \le i \le M-1, \\ w_i(t) & M \le i \le N \end{cases} \tag{12}$$

where $b_i(t)$ is the blood flow signal; $w_i(t)$ is the wall signal; and k, M, and N are the numbers of different layers of the IMF component: k is the number of the blood flow signal layers, M is the number of layers of IMF component containing both the tube wall and the blood flow signal, and N is the number of IMF component layers of the tube wall signal.

According to the noise power estimation algorithm in wavelet decomposition and the characteristics of EMD decomposition, the power of the first layer blood flow signal IMF is expressed as follows:

$$\sigma_1 = \frac{\mathrm{median}\{|x_1(t) - \mathrm{median}\, x_1(t)|\}}{0.6745}. \tag{13}$$

The power of the blood flow signal IMF in the i-th layer can be expressed as follows.

$$\sigma_i = \frac{\sigma_1}{\sqrt{2}^{i-1}}. \tag{14}$$

The threshold denoising method is used to remove the blood flow signal in the tube wall signal, and the tube wall signal can be expressed as follows:

$$w_i = \begin{cases} \mathrm{sgn}[x_i(t)]\left\{|x_i(t)| - \dfrac{2\sigma_i}{1+\exp\{L[x_i^2(t) - \sigma_i^2]\}}\right\} & |x_i(t)| > \sigma_i \\ 0 & |x_i(t)| \le \sigma_i. \end{cases} \tag{15}$$

Finally, the signal is reconstructed, and the signal calculation method of the original pipe wall is as follows:

$$w(t) = \sum_{i=k}^{M-1} w_i(t) + \sum_{i=M}^{n} x_i(t). \tag{16}$$

Then, the extreme values of the original ultrasonic blood flow signal are solved, then the upper and lower envelopes are obtained, and the average value of the upper and lower envelopes is subtracted from the initial signal to obtain the optimized signal, which is regarded as the first layer of the IMF. Next, the remaining signals are calculated and used as a new signal. After the signal decomposition termination condition is met, the separation of the blood flow signal is completed. The specific flow to separate the blood flow signal by the optimized EMD algorithm is shown in Figure 1.

2.3. Separation Effect of Blood Flow and Tube Wall Signals by Doppler Ultrasound. In this study, the separation effects of blood flow and vessel wall signals by Doppler ultrasound are evaluated factored into the relative error of the average frequency curve of the blood flow signal (E_f) and the mean relative error (MRE) of the power spectrum of the blood flow signal. They are commonly used blood flow evaluation parameters, expressed as follows:

$$E_f = \sqrt{\frac{\sum_t [F(t) - F_s(t)]^2}{\sum_t F_s(t)^2}}, \tag{17}$$

where $F_s(t)$ is the average frequency of the standard pure blood flow signal and $F(t)$ is the average frequency of the blood flow signal extracted by the separation algorithm.

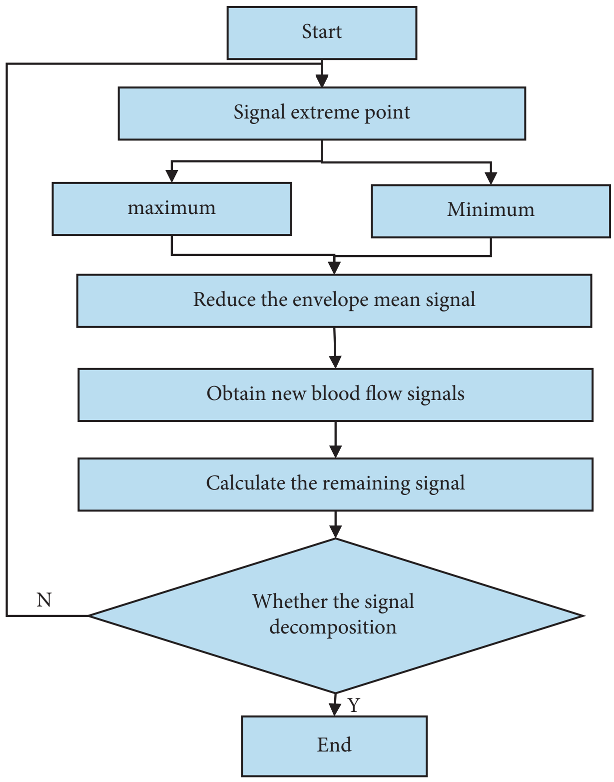

Figure 1: Flow chart of blood flow signal separation by the optimized EMD algorithm.

$$\text{MRE} = \frac{1}{M}\sum_{i=1}^{M}\frac{\sum_f \left|P_1(f,i) - P_2(f,i)\right|}{\sum_f P_2(f,i)}, \tag{18}$$

where f represents the frequency; M is the total number of blood flow signal segments; and P_1 and P_2, respectively, represent the power spectral density of the initial blood flow signal and the separated blood flow signal in the i-th time period.

2.4. Treatment Plans and Observation Indicators for Different Groups. Patients in both groups were examined by the ultrasonic diagnostic instrument produced by Philips, and the probe frequency was adjusted to 2.0–5.0 mhz. At the beginning of the examination, the position of the umbilical cord was first determined, and the placental umbilical artery was sampled with a volume of 2 mL to ensure that the arterial vasculature angle and pulse Doppler sampling should be below 30°. Then, the blood flow spectrum was determined.

The control group was treated with magnesium sulfate alone, and the observation group was treated with Compound Danshen injection and magnesium sulfate. The specific scheme was as follows.

Control group used magnesium sulfate alone. The dosage of the drug was 4~10 mL/time, mixed and diluted with 5% glucose injection and then intravenously infused, once a day on average, for a total of 10 days.

Observation group used Compound Danshen injection and magnesium sulfate. The dosage and method of magnesium sulfate were the same as the control group. The dosage of Compound Danshen injection was 10–20 mL/time, and it was diluted with 100–500 mL glucose injection with a concentration of 5%. Intravenous infusion was carried out once a day on average. The treatment also lasted 10 days.

The two groups were compared for the blood pressure and 24 h urine protein before and after treatment; the levels of serum endothelin-1 (ET-1), homocysteine (Hcy), and C-reactive protein (CRP) before and after treatment; the changes of blood coagulation function indexes, such as plasma prothrombin time (PT), fibrinogen (FIB), activated partial thromboplastin time (APTT), and plasma thrombin time (TT) before and after treatment; and the outcome of pregnancy.

2.5. Efficacy Evaluation. After the treatment, if the relevant clinical symptoms (such as edema, urine protein) basically disappear and the fetus is delivered smoothly, it is considered markedly effective; if the relevant clinical symptoms have been greatly reduced and, although the fetus can be delivered naturally, there are different degrees of suffocation, it is considered effective; if the relevant clinical symptoms of the patient are not significantly reduced and the pregnancy is forced to terminate, it is considered ineffective. Total effective rate = (markedly effective + effective)/number of cases × 100%.

2.6. Statistical Analysis. In this study, SPSS 22.0 was used for data processing and analysis, measurement data was expressed in the form of "$\bar{x} \pm s$," and t-test was used for comparison between groups. Count data were expressed by "n" (%), and chi-square test was used for comparison between groups. $P < 0.05$ indicated that the difference was statistically significant.

3. Results

3.1. Separation Results of Blood Flow Signal Based on Optimized EMD Algorithm. The ultrasound Doppler blood flow signal was separated using the optimized EMD algorithm, and the result is shown in Figure 2. It was noted that the optimized EMD algorithm can separate the blood flow signal and the tube wall signal.

The optimized EMD algorithm was used to decompose the ultrasound Doppler blood flow signal into multiple instantaneous frequencies. Here, the instantaneous frequencies of the 1st to 6th layers were analyzed (Figure 3). With the continuous increase of the number of layers, the instantaneous frequency corresponding to the IMF lowered continuously.

Then, the changes of instantaneous frequency over the amplitude were further analyzed (Figure 4). It was found that as the instantaneous frequency continued to increase, its corresponding amplitude gradually decreased.

The traditional EMD algorithm, the optimized EMD algorithm, and the high-pass filter method (HPF) were compared for the power spectral density after the ultrasound Doppler blood flow signal was separated (Figure 5). The

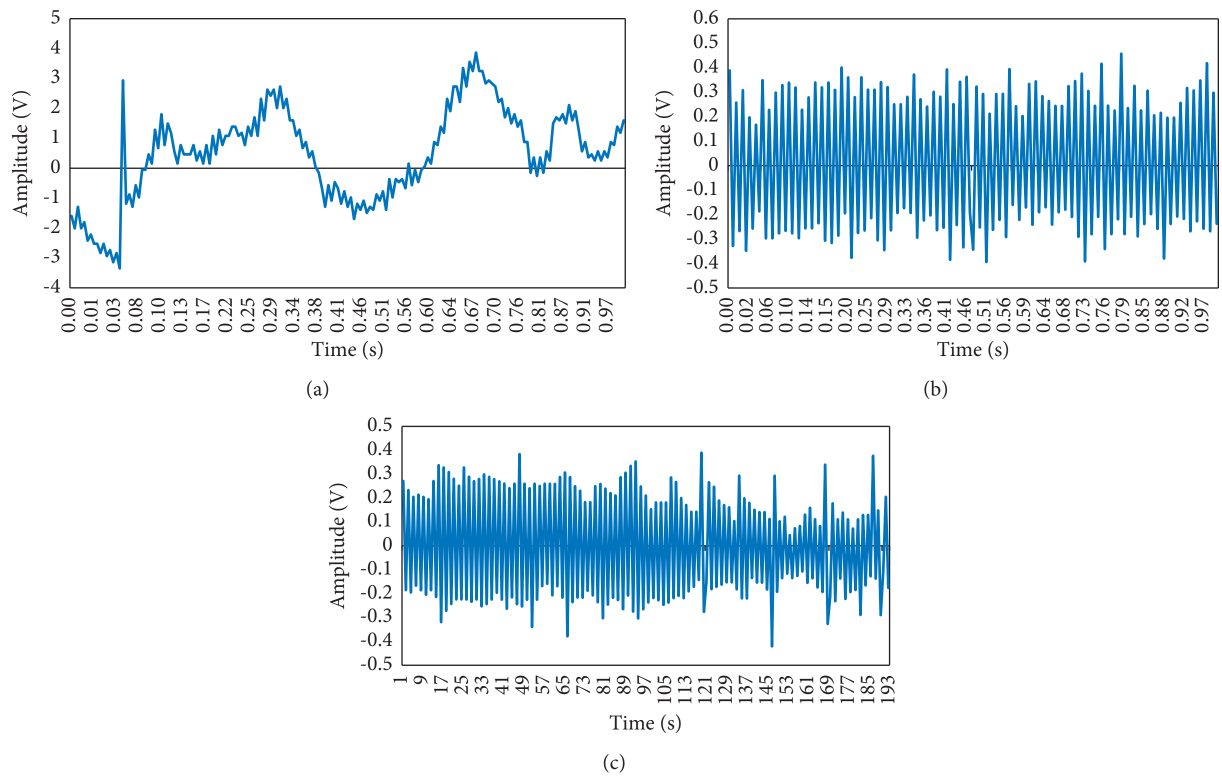

Figure 2: The separation effects of blood flow signal based on EMD optimization algorithm: (a) original blood flow signal diagram with tube wall; (b) blood flow signal separated by EMD algorithm; (c) blood flow signal separated by the optimized EMD algorithm.

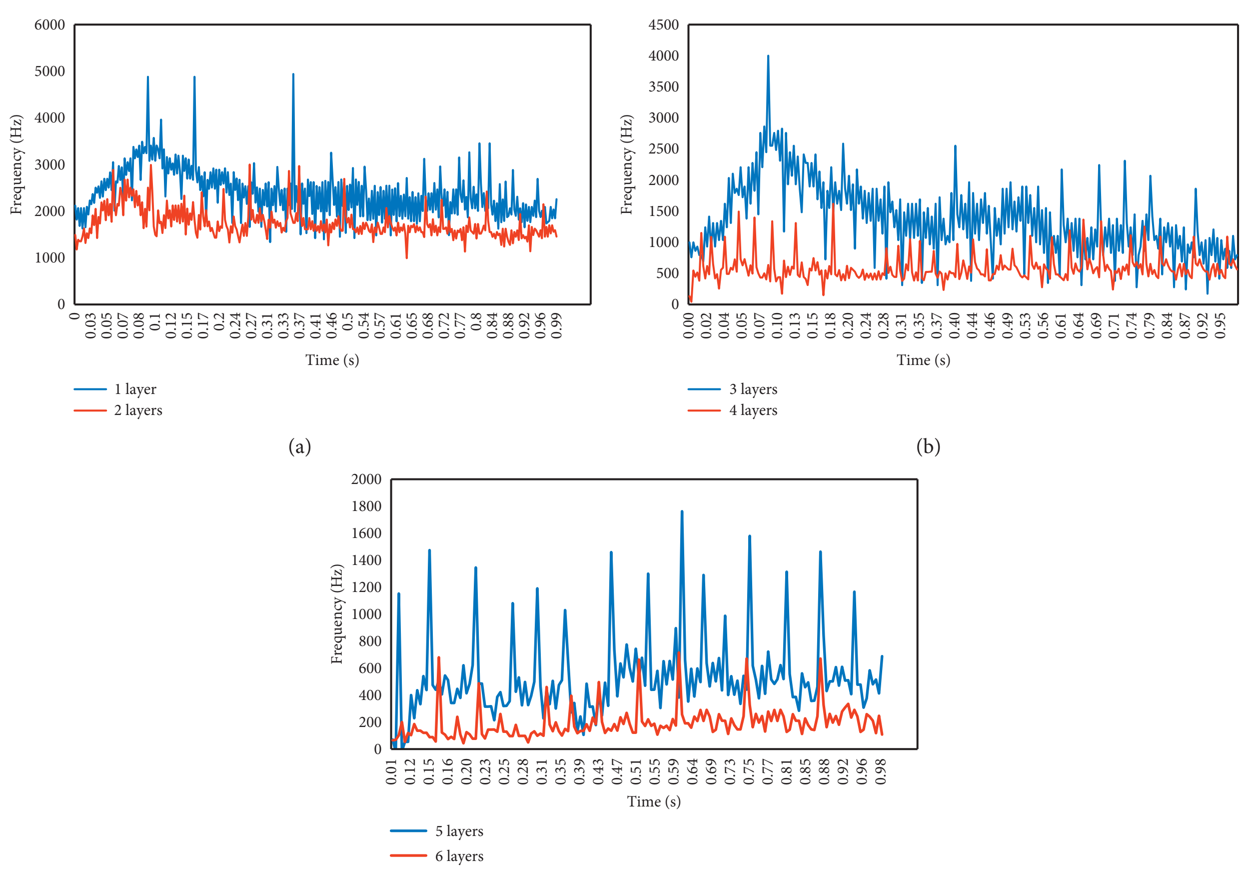

Figure 3: Multilayer instantaneous frequencies of blood flow signal decomposed by the optimized EMD algorithm: (a) 1~2 layers; (b) 3~4 layers; (c) 5~6 layers.

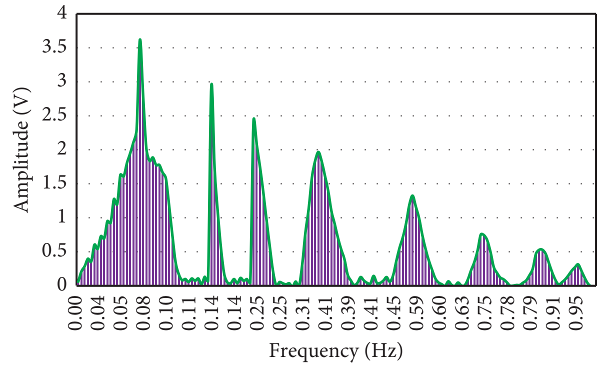

Figure 4: Changes of blood flow signal amplitude at different frequencies.

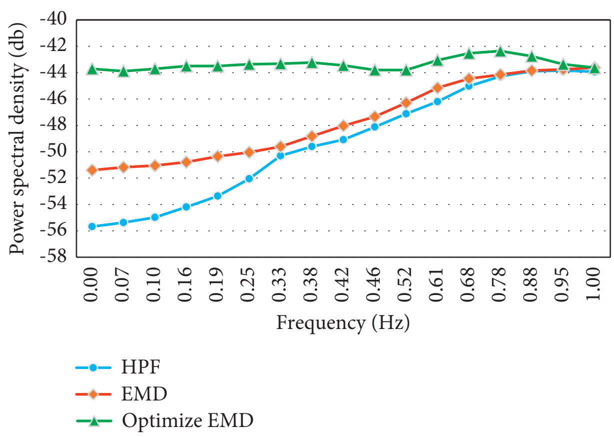

Figure 5: The power spectral density curves of blood flow signals separated by different algorithms.

power spectral density of blood signals separated by the optimized EMD algorithm was greater than those of the other two algorithms under different frequencies.

3.2. Separation Effects of Blood Flow and Tube Wall Signal by Optimized EMD Algorithm. Different algorithms were compared for the Ef and MRE values (Figures 6 and 7). It was found that the Ef and MRE values of the optimized EMD algorithm at different frequencies were significantly higher than those of the other two algorithms, and the optimized EMD algorithm showed statistically significant differences from the traditional EMD algorithm in Ef and MRE values ($P < 0.05$).

3.3. Clinical Efficacy. As for the total effective rate of the two groups of patients in this study, the total effective rate of the observation group was significantly better, and the difference compared with the control group was statistically significant ($P < 0.05$) (Table 1).

3.4. Blood Pressure. In this study, there was no significant difference in various indicators between the two groups of patients before treatment ($P > 0.05$). After treatment, from the perspective of blood pressure control, the observation group's SBP, DBP, and 24 h urine protein indexes were significantly better, and the difference was statistically

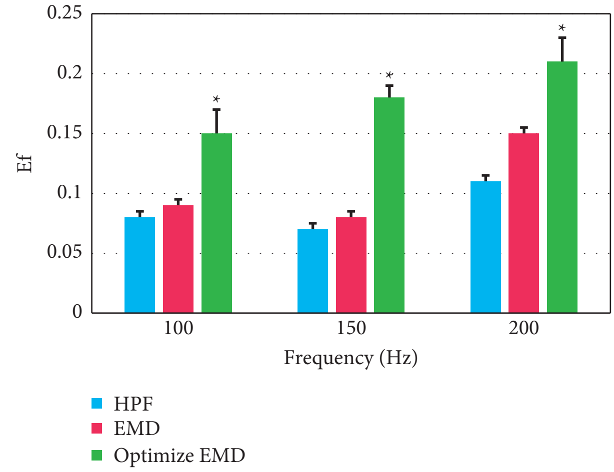

Figure 6: Comparison of Ef values of different algorithms under different frequencies (*indicates statistical difference compared with traditional EMD algorithm).

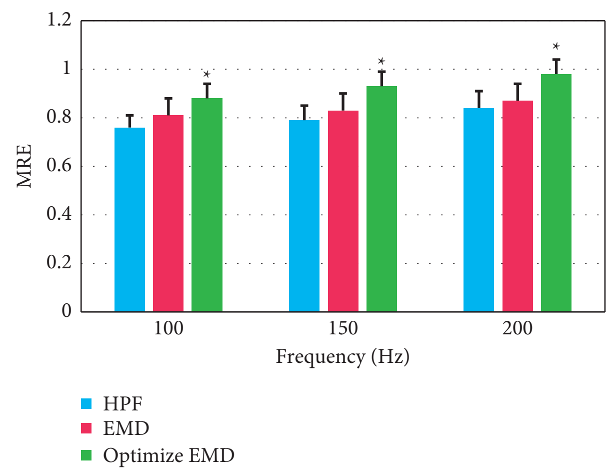

Figure 7: Comparison of MRE values of different algorithms under different frequencies (*indicates statistical difference compared with traditional EMD algorithm).

Table 1: Comparison of the total effective rate of the two groups of patients after treatment.

Index	Observation group	Control group	P value
Markedly effective (n)	23	18	0.031*
Effective (n)	14	11	0.048*
Ineffective (n)	3	11	0.003**
Total effective rate (%)	92.50	72.50	0.016*

*represents a statistical difference compared with the control group, $P < 0.05$; **represents a significant difference compared with the control group, $P < 0.01$.

Table 2: Comparison of blood pressure control between the two groups of patients after treatment.

Index	Time	Observation group	Control group	P value
SBP (mmHg)	Before treatment	158.32 ± 11.86	159.33 ± 11.90	0.913
	After treatment	127.85 ± 9.34	138.49 ± 9.11	0.021^*
DBP (mmHg)	Before treatment	117.09 ± 11.56	119.13 ± 10.97	0.861
	After treatment	78.35 ± 9.77	85.84 ± 8.71	0.032^*
24 h urine protein (g)	Before treatment	4.19 ± 1.36	4.17 ± 1.29	0.953
	After treatment	1.36 ± 0.24	2.25 ± 0.26	0.016^*

*represents a statistical difference compared with the control group, $P < 0.05$.

significant compared with the control group ($P < 0.05$) (Table 2).

3.5. Expression of ET-1, CRP, and Hcy. In this study, there was no significant difference in the expression of ET-1, CRP, and Hcy between the two groups of patients before treatment ($P > 0.05$). After treatment, the ET-1, CRP, and Hcy indexes of the two groups of patients decreased significantly, and the decrease in the observation group was more obvious than that in the control group ($P < 0.05$) (Table 3).

3.6. Coagulation Function. Before treatment, there was no significant difference in the levels of PT, APTT, TT, and FIB between the two groups ($P > 0.05$); after treatment, the levels of PT, APTT, TT, and FIB in the two groups were better than those before treatment, and the observation group was better than the control group. The difference was statistically significant ($P < 0.05$) (Table 4).

3.7. Maternal and Infant Outcome. As shown in Table 5, the incidence of adverse maternal and infant outcomes in the observation group was significantly lower than that in the control group ($P < 0.05$).

4. Discussion

Compound Danshen injection can prevent coagulation dysfunction, cerebrovascular accidents, and other complications. Combined with magnesium sulfate, it can not only effectively alleviate PIH syndrome, but also improve blood circulation and immunity [13, 14]. In this study, it was found that the blood pressure and 24 h urine protein of the observation group after treatment were significantly better than those in the control group ($P < 0.05$). It can be inferred that the treatment plan of Compound Danshen injection combined with magnesium sulfate is helpful to optimize the blood pressure control of patients with PIH syndrome. In addition, the total effective rate in the observation group was significantly higher than that of the control group ($P < 0.05$). It can be inferred that the treatment plan of Compound Danshen injection combined with magnesium sulfate can improve the maternal and infant outcomes.

Hcy is an important intermediate product in the process of methionine metabolism. The increase of serum Hcy level in pregnant women is closely related to the occurrence and development of HDP [15]. CRP is one of the important indicators that reflect the body's inflammatory response. The increase in serum CRP concentration in HDP patients has a certain correlation with vascular endothelial damage [16]. The results of this study showed that, after treatment, the serum Hcy and CRP levels of the observation group were significantly lower than those of the control group, suggesting that the combination of Compound Danshen injection and magnesium sulfate can significantly reduce the serum Hcy and CRP levels of HDP patients.

From the perspective of traditional Chinese medicine, hypertension during pregnancy belongs to the category of "blood stasis," and its occurrence is related to the blood stasis, deficiency of qi and blood, and obstruction of blood circulation. Therefore, the treatment aims to promote blood circulation, remove blood stasis, and dredge the meridians. Compound Danshen injection is a Chinese patent medicine composed of traditional Chinese medicine Danshen and Jiangxiang. Danshen is slightly cold and bitter, and it has the effects of calming the mind, removing blood stasis, and promoting blood circulation [17, 18]. Jiangxiang is known for nourishing the heart, dredging the meridians, relieving pain, stopping bleeding, and removing blood stasis [19]. The combination of the two has the effect of calming the mind, promoting blood circulation, and removing blood stasis [20]. It has been found that the polyphenols in Danshen can inhibit the release of a variety of coagulation factors [21]. By inhibiting the release of the α receptor, the aggregation of platelets is greatly reduced, so as to relax the capillaries and increase the secretion of nitric oxide (NO) in endothelial cells, to reduce the oxygen consumption of the myocardium, improve microcirculation, and effectively control the blood pressure [22]. At the same time, Danshen can positively affect the blood rheology and increase the perfusion flow of the placenta, so that the placenta can get sufficient blood supply and the occurrence of adverse pregnancy outcomes is greatly reduced [23]. Dalbergin and volatile oil in Jiangxiang can regulate the balance between ET and NO and antagonize thrombosis [24, 25], thereby improving the patient's oxidative stress and blood hypercoagulability and reducing the incidence of adverse pregnancy outcomes.

In conclusion, the treatment of PIH syndrome patients with Compound Danshen injection combined with magnesium sulfate proved to be effective and can improve maternal and infant outcomes; control blood pressure; and reduce 24 h urine protein and serum ET-1, Hcy, and CRP. Additionally, it can improve the blood coagulation function, and thus the treatment plan can be widely promoted in the clinic.

Table 3: The expression of CRP and Hcy in the two groups of patients before and after treatment.

Index	Time	Observation group	Control group	P value
ET-1 (mg/L)	Before treatment	52.41 ± 5.73	52.97 ± 6.04	0.864
	After treatment	43.11 ± 4.28	49.88 ± 5.03	0.023^{*}
CRP (mg/L)	Before treatment	16.24 ± 1.87	16.28 ± 1.93	0.904
	After treatment	3.61 ± 0.54	9.28 ± 0.93	0.008^{**}
Hcy (μmol/L)	Before treatment	23.11 ± 2.97	23.24 ± 3.05	0.895
	After treatment	12.56 ± 1.74	19.15 ± 1.86	0.009^{**}

*represents a statistical difference compared with the control group, $P < 0.05$; **represents a significant difference compared with the control group, $P < 0.01$.

Table 4: The coagulation function indexes of the two groups before and after treatment.

Index	Time	Observation group	Control group	P value
PT (s)	Before treatment	10.16 ± 1.01	10.18 ± 0.89	0.693
	After treatment	12.98 ± 1.25	11.01 ± 0.94	0.041
APTT (s)	Before treatment	21.41 ± 2.15	21.36 ± 2.21	0.572
	After treatment	29.85 ± 2.43	25.07 ± 2.11	0.032^{*}
TT (s)	Before treatment	16.12 ± 0.49	16.16 ± 0.55	0.610
	After treatment	17.85 ± 0.27	16.86 ± 0.28	0.038^{*}
FIB (g/L)	Before treatment	5.06 ± 0.46	5.04 ± 0.47	0.566
	After treatment	3.12 ± 0.52	4.32 ± 0.64	0.021^{*}

*represents a statistical difference compared with the control group, $P < 0.05$.

Table 5: The incidence of adverse maternal and infant outcomes in the two groups.

Index	Observation group	Control group	P value
Premature delivery (n)	1	2	
Placental abruption (n)	0	1	
Eclampsia (n)	0	1	
Postpartum hemorrhage (n)	1	2	-
Weak contractions (n)	0	1	
Neonatal asphyxia (n)	1	2	
Incidence (n (%))	3 [7.50]	9 [22.50]	0.017^{*}

*represents a statistical difference compared with the control group, $P < 0.05$.

5. Conclusion

Based on the EMD algorithm, this study established a separation method of ultrasound blood flow signal, which was then applied to the diagnosis of patients with pregnancy-induced hypertension syndrome. Compound Danshen injection combined with magnesium sulfate was used to treat patients with pregnancy-induced hypertension syndrome. EMD algorithm can improve the accuracy of blood flow signal separation in ultrasonic images. Treatment of pregnancy-induced hypertension syndrome by Compound Danshen injection combined with magnesium sulfate can improve maternal and infant outcomes; control blood pressure; reduce 24 h urinary protein and serum ET-1, Hcy, and CRP levels; and improve coagulation function. However, the study still has the following disadvantages. It only analyzes the strain curve of the ultrasonic imaging blood flow signal. In future work, on the basis of ultrasonic imaging blood flow signal strain curve, the peak strain, negative peak strain, and positive peak strain rate should be evaluated, to evaluate the value of blood flow signal decomposition based on EMD algorithm in the diagnosis of pregnancy-induced hypertension syndrome. In conclusion, the EMD algorithm optimized in this study is of great significance for the diagnosis based on ultrasonic blood flow signals. Compound Danshen injection combined with magnesium sulfate can improve clinical indicators of pregnancy-induced hypertension syndrome, providing a reference basis for the clinical diagnosis and treatment of pregnancy-induced hypertension syndrome.

Data Availability

The data used to support the findings of this study are available from the corresponding author upon request.

Conflicts of Interest

The authors declare no conflicts of interest.

Authors' Contributions

Xia Zhao and Hongbin Wang contributed equally to this work.

References

[1] S. T. Younes and M. J. Ryan, "Pathophysiology of cerebral vascular dysfunction in pregnancy-induced hypertension," *Current Hypertension Reports*, vol. 21, no. 7, p. 52, 2019.

[2] J. Y. Li, P. H. Wang, S. G. Vitale et al., "Pregnancy-induced hypertension is an independent risk factor for meconium aspiration syndrome: a retrospective population based cohort study," *Taiwanese Journal of Obstetrics & Gynecology*, vol. 58, no. 3, pp. 396–400, 2019.

[3] K. E. Innes, S. Kandati, K. L. Flack, P. Agarwal, and T. K. Selfe, "The relationship of restless legs syndrome to history of pregnancy-induced hypertension," *Journal of Women's Health*, vol. 25, no. 4, pp. 397–408, 2016.

[4] X. Y. Gao, "Analysis of related risk factors of retinopathy in pregnancy induced hypertension syndrome," *International Journal of Ophthalmology*, vol. 15, no. 5, pp. 904-905, 2015.

[5] L. Zeng, K. Yang, and J. Ge, "Uncovering the pharmacological mechanism of astragalus salvia compound on pregnancy-induced hypertension syndrome by a network pharmacology approach," *Scientific Reports*, vol. 7, no. 1, Article ID 16849, 2017.

[6] E. P. Reddy, B. Muthukumaraswamy, and Yasodha, "Magnesium levels in pregnancy induced hypertension," *International Journal of Research in Pharmaceutical ences*, vol. 8, no. 3, pp. 463–466, 2017.

[7] T. Yamamoto, K. Mori, T. Esaki, Y. Nakao, J. Tokugawa, and M. Watanabe, "Preventive effect of continuous cisternal irrigation with magnesium sulfate solution on angiographic cerebral vasospasms associated with aneurysmal subarachnoid hemorrhages: a randomized controlled trial," *Journal of Neurosurgery*, vol. 124, no. 1, pp. 18–26, 2016.

[8] L. Fen, M. Y. Yan, and Jinan, "Analysis of the perinatal outcome of the early severe preeclampsia women treated with compound danshen injection and low molecular weight heparin," *Chinese Journal of Integrated Traditional and Western Medicine*, vol. 32, no. 1, p. 13, 2012.

[9] W. Jianmin, "Meta-analysis on effect of compound Danshen injection in treating neonatal hypoxic-ischemic encephalopathy," *China Journal of Chinese Materia Medica*, vol. 40, no. 1, p. 141, 2015.

[10] C. Jia, S. Han, L. Wei et al., "Protective effect of compound Danshen (Salvia miltiorrhiza) dripping pills alone and in combination with carbamazepine on kainic acid-induced temporal lobe epilepsy and cognitive impairment in rats," *Pharmaceutical Biology*, vol. 56, no. 1, pp. 217–224, 2018.

[11] Y. Wang, R. X. Liu, and H. Liu, "Association of adiponectin gene polymorphisms with hypertensive disorder complicating pregnancy and disorders of lipid metabolism," *Genetics and Molecular Research*, vol. 14, no. 4, pp. 15213–15223, 2015.

[12] J. Zhang, R. Liang, L. Wang, and B Yang, "Effects and mechanisms of Danshen-Shanzha herb-pair for atherosclerosis treatment using network pharmacology and experimental pharmacology," *Journal of Ethnopharmacology*, vol. 229, pp. 104–114, 2019.

[13] K. Yang, G. Dong, Y. Tian, and J Li, "Effects of compound Danshen injection combined with magnesium sulfate on serum MPO and hs-CRP in patients with severe preeclampsia," *Experimental and therapeutic medicine*, vol. 16, pp. 167–170, 2018.

[14] Z. Li, P. Yuan, and C. Zhu, "Effect of the mixed liquor of danshen and magnesium sulfate injection on IgG and IgM in serum of rabbits with lumbar intervertebral disc herniation," *Zhongguo gu shang = China journal of orthopaedics and traumatology*, vol. 22, no. 10, p. 773, 2009.

[15] X. Yuan, T. Wang, J. Gao et al., "Associations of homocysteine status and homocysteine metabolism enzyme polymorphisms with hypertension and dyslipidemia in a Chinese hypertensive population," *Clinical and Experimental Hypertension*, vol. 2019, Article ID 1571599, 9 pages, 2019.

[16] L. Wang, Z. Q. Liu, Y. Q. Huo, L. J. Yao, X. G. Wei, and Y. F. Wang, "Change of hs-CRP, sVCAM-1, NT-proBNP levels in patients with pregnancy-induced hypertension after therapy with magnesium sulfate and nifudipine," *Asian Pacific Journal of Tropical Medicine*, vol. 6, no. 11, pp. 897–901, 2013.

[17] S. W. S. Leung, D.-Y. Zhu, and R. Y. K. Man, "Effects of the aqueous extract of Salvia Miltiorrhiza (danshen) and its magnesium tanshinoate B-enriched form on blood pressure," *Phytotherapy Research*, vol. 24, no. 5, pp. 769–774, 2010.

[18] D. H. Yang, Z. Y. Ye, B Jin et al., "Salvianolate inhibits cytokine gene expression in small intestine of cirrhotic rats," *World Journal of Gastroenterology*, vol. 17, no. 14, pp. 1903–1909, 2011.

[19] L. Xiang, W. Leihong, L. Wei et al., "A network pharmacology study of Chinese medicine qishenyiqi to reveal its underlying multi-compound, multi-target, multi-pathway mode of action," *PLoS One*, vol. 9, no. 5, Article ID e95004, 2014.

[20] Z.-Z. Wang, W.-J. Ying, and X.-D. Meng, "Compound Danshen injection combined with somatostatin for treatment of patients with severe acute pancreatitis: effect on gastrointestinal function and serum tumor necrosis factor-α and interleukin-6 levels," *World Chinese Journal of Digestology*, vol. 24, no. 15, Article ID 2394, 2016.

[21] B. Han, X. Zhang, Q. Zhang et al., "Protective effects of salvianolate on microvascular flow in a porcine model of myocardial ischaemia and reperfusion," *Archives of Cardiovascular Diseases*, vol. 104, no. 5, pp. 313–324, 2011.

[22] Q. He, S. Wang, X. Liu et al., "Salvianolate lyophilized injection promotes post-stroke functional recovery via the activation of VEGF and BDNF-TrkB-CREB signaling pathway," *International Journal of Clinical and Experimental Medicine*, vol. 8, no. 1, pp. 108–22, 2015.

[23] C. X. Tong, X. F. Xing, and S. H. Qiao, "Clinical effectiveness assessment of compound danshen injection on early onset severe preeclampsia patients," *Chinese Journal of Integrated Traditional and Western Medicine*, vol. 32, no. 4, p. 482, 2012.

[24] D. Choudhary, P. Kushwaha, J. Gautam et al., "Fast and long acting neoflavonoids dalbergin isolated from Dalbergia sissoo heartwood is osteoprotective in ovariectomized model of osteoporosis: osteoprotective effect of Dalbergin," *Biomedicine & Pharmacotherapy*, vol. 83, pp. 942–957, 2016.

[25] P. Kumar, P. Kushwaha, N. Ahmad et al., "Design and synthesis of dalbergin analogues and evaluation of anti-osteoporotic activity," *Bioorganic & Medicinal Chemistry Letters*, vol. 27, no. 8, pp. 1765–1775, 2017.

Hindawi
Journal of Healthcare Engineering
Volume 2021, Article ID 3417285, 9 pages
https://doi.org/10.1155/2021/3417285

Research Article

Computed Tomography Image under Convolutional Neural Network Deep Learning Algorithm in Pulmonary Nodule Detection and Lung Function Examination

Chan Zhang,[1] **Jing Li**,[2] **Jian Huang**,[2] **and Shangjie Wu**[1]

[1]*Department of Respiratory Medicine, Xiangya Second Hospital of Central South University, Changsha 410006, Hunan, China*
[2]*Department of Imaging, Changsha Fourth Hospital (Changsha Hospital Affiliated to Hunan Normal University), Changsha 410006, Hunan, China*

Correspondence should be addressed to Shangjie Wu; wushangjie@csu.edu.cn

Received 25 August 2021; Revised 20 September 2021; Accepted 24 September 2021; Published 22 October 2021

Academic Editor: Enas Abdulhay

The objective of this study was to perform segmentation and extraction of CT images of pulmonary nodules based on convolutional neural networks (CNNs). The Mask-RCNN algorithm model is a typical end-to-end image segmentation model, which uses the R-FCN structure for nodule detection. The effect of applying the two algorithm models to the computed tomography (CT) diagnosis of pulmonary nodules was analyzed, and different indexes of pulmonary nodule CT images in lung function examination after algorithm optimization were compared. A total of 56 patients diagnosed with pulmonary nodules by surgery or puncture were taken as the research objects. Based on the Mask-RCNN algorithm, a model for CT image segmentation processing of pulmonary nodules was proposed. Subsequently, the 3D Faster-RCNN model was used to label the nodules in the pulmonary nodules. The experimental results showed that the trained Mask-RCNN algorithm model can effectively complete the segmentation task of lung CT images, but there was a little jitter at the boundary. The speed of R-FCN algorithm for nodular detection was 0.172 seconds/picture, and the accuracy was 88.9%. CT scans were performed on the 56 patients based on a deep learning algorithm. The results showed that 30 cases of malignant pulmonary nodules were confirmed, and the diagnostic accuracy was 93.75%. There were 22 benign lesions, the diagnostic accuracy was 91.67%, and the overall diagnostic accuracy was 92.85%. This study effectively improved the diagnostic efficiency of CT images of pulmonary nodules, and the accuracy of CT images in the diagnosis of pulmonary nodules was analyzed and evaluated. It provided theoretical support for the follow-up diagnosis of pulmonary nodules and the treatment of lung cancer. It also significantly improved the diagnostic effect and detection efficiency of pulmonary nodules.

1. Introduction

Pulmonary nodules are considered to be a multi-system and multi-organ granulomatous disease with unknown etiology at present, which often occurs in the lungs, bilateral hilar lymph nodes, eyes, skin, and other organs, and the incidence in the chest is as high as 80%–90% [1]. At present, there have been many studies on the pathogenic causes of pulmonary nodules, including observation and study on bacteria, viruses, mycoplasma, fungi, and other infectious factors, but the exact pathogenic causes have not been obtained. According to relevant studies, most people currently believe that the important pathogenesis of pulmonary sarcoidosis is the disorder of cellular immune function and humoral immune function, which is the result of the interaction between cellular immunity and humoral function of the body caused by unknown antigens [2, 3]. In recent years, with the development of society and changes of environment, the incidence of various lung diseases in China has been on the rise, among which lung cancer has become the cancer with the highest incidence in China. According to relevant data [4], in 2015 alone, the number of deaths due to lung cancer in China reached more than 700,000. Lung cancer was the leading cause of cancer deaths in 2018, accounting for 20 percent of all cancer deaths. By the end of 2017, the number of lung cancer patients and deaths in China had reached 800,000 and 700,000. The incidence of lung cancer is increasing at an annual rate of 27%, based on which the mortality rate of lung cancer patients in China will increase to 40% in the next 20 years [5].

The manifestations of early lung cancer are mainly pulmonary nodules, and there are generally no other specific symptoms in clinical practice. Lung cancer usually goes undetected by patients until they have obvious symptoms. Such symptoms include fever caused by repeated infection, inflammation of the lungs, chest tightness and shortness of breath, persistent coughing and hemoptysis, and excessive fatigue. At that time, lung cancer has generally entered the middle and late stages, and the best treatment period has been missed. At this time, the optimal treatment period has been missed, so the early diagnosis of lung cancer is extremely important. One of the key factors determining the survival rate of patients with lung cancer is the early accurate diagnosis of pulmonary nodules [6, 7]. If early pulmonary nodules are diagnosed and treated in advance and its early symptoms and related indicators are studied, it can effectively improve the early diagnosis rate and survival rate of lung cancer patients.

Currently, the main detection methods for lung cancer include computed tomography (CT) [1, 8]. CT is based on X-ray technology. The X-ray is sent out by the scanner in a fan-shaped wire bundle of a certain thickness to illuminate the patient at different angles. Then, the collected data are converted into current intensity signals in and out of the computer through the scanner and finally converted into three-dimensional images through the algorithm. CT detection is very important in the examination of lung function, but the analysis and diagnosis of lung CT images are often affected by doctors' experience and other subjective reasons. The diagnosis of the same CT image varies greatly among doctors of different skills, and a large number of CT images also produce excessive burden on radiologists. Therefore, algorithm-assisted processing of CT images based on convolutional neural network (CNN) is extremely important. Generally, there are two important methods for the algorithm-assisted CT diagnosis of pulmonary nodules [9, 10]. The first is the segmentation of lung CT images. To ensure that doctors can observe the nodules in the three-dimensional images carefully, the lung parenchyma needs to be segmented to remove the irrelevant data in the CT images. The second is adopting the algorithm to automate the detection of pulmonary nodules in CT images, which can not only effectively improve the diagnostic efficiency of radiologists but also improve the poor diagnostic effect caused by subjective differences.

Therefore, a model for CT image analysis of pulmonary nodules was proposed based on CNN deep learning technology, and then a comparison of different indexes of lung function examination of pulmonary nodules CT images was conducted after the optimization of the algorithm. The results of this study were intended to provide reference for the improvement of clinical diagnosis and treatment of patients with pulmonary nodules.

2. Methods

2.1. Research Objects. Fifty-six patients with pulmonary nodules confirmed by surgery or puncture in the hospital from May 2018 to May 2020 were selected as the research subjects. All patients received CT and MRI examination at admission and had complete clinical diagnosis records and imaging data. Among the 56 patients, 34 were males and 22 were females. Patients ranged in age from 30 to 77 years, with a mean age of (56.8 ± 4.7) years. The diameter of nodules in all patients ranged from 1.1 cm to 2.8 cm, with an average diameter of (2.0 ± 0.4) cm. There were 28 cases of right pulmonary nodules and 27 cases of left pulmonary nodules. All patients had signed informed consent, and this study had been approved by the Ethics Committee of the hospital.

Inclusion criteria were as follows: (i) those who met the diagnostic criteria of pulmonary nodules; (ii) patients who did not receive any radiotherapy, chemotherapy, or other treatment before treatment; (iii) patients who had no other serious heart, liver, kidney, and brain diseases or malignant tumors; (iv) patients who agreed and accepted the research; and (v) patients who were not allergic to contrast agents.

Exclusion criteria were as follows: (i) patients with imperfect imaging data; (ii) patients who were unable to cooperate with the completion of imaging examination; (iii) patients who were allergic to contrast agents; and (iv) patients with other serious heart, liver, kidney, and brain diseases or malignant tumors.

2.2. CT Examination. Whole-body low-dose CT was performed using a Siemens Somatom Emotion 16-slice spiral CT scanner. Patients were trained to hold their breath before the scan, and the whole lung scan was performed. Voltage and current were set as 120 kV and 100 mAs, respectively. The layer thickness was 8.0 mm, layer spacing was 1 mm, reconstruction interval was 8.0 mm, pitch was 0.811, and collimation was 16×0.75. For a CT scan, the patient was supine with arms crossed and placed in the lower abdomen. During scanning, the maximum layer of pulmonary nodules was selected for dynamic enhanced scanning. After the scanning range was reduced, the nonionic contrast agent ioversol (320 mgl/mL) was injected through cubital vein with high pressure, the dose was 90 mL, and the rate was 4.0 mL/s.

2.3. CT Image Segmentation Based on Mask-RCNN Algorithm Model. The Mask-RCNN algorithm model is a type of algorithm that combines detection and classification based on the Faster-RCNN algorithm. It is a convolutional neural network model that combines object detection and image segmentation [11]. Under the interaction of the target detection algorithm and the segmentation algorithm, the pixel-level segmentation effect is achieved, and the segmentation of the CT image is completed efficiently and quickly. Unlike the Faster-RCNN algorithm, the Mask-RCNN algorithm replaces the ROI pooling layer in the original algorithm with a better ROI alignment layer, which effectively improves the accuracy of the image segmentation boundary [12]. Based on the new network model, a fully convolutional network is used for image segmentation. The structure diagram is shown in Figure 1.

The change of the ROI alignment layer is the most important update implemented on the Mask-RCNN algorithm repooling layer, which realizes the mutual correspondence between output pixels and input pixels and effectively retains the spatial data contained in the image. The target pixel position in the original CT image in the image processing process is calculated by the following equations.

$$\begin{aligned} \mathrm{Src}M &= \mathrm{dst}\,M\left(\frac{\mathrm{src\ Width}}{\mathrm{dst\ Width}}\right),\\ \mathrm{Src}N &= \mathrm{dst}\,N\left(\frac{\mathrm{src\ Height}}{\mathrm{dst\ Height}}\right), \end{aligned} \tag{1}$$

where dstM and dstN represent the pixel coordinates in the area suggestion box, srcM and srcN represent the coordinates of the target pixel in the original CT image, srcWidth and srcHeight represent the width and height of the original image, respectively, and dstWidth and dstHeight are the width and height of the regional suggestion box, respectively. The following equation is used to calculate the pixel value of the sampling point of each unit through the bilinear interpolation method, and then the maximum pooling operation is implemented.

$$t(e+f, g+h) = (1-f)(1-h)t(e,g) + (1-f)ht(e,g+1) + f(1-h) + (e+1,g) + fht(e+1,g+1). \tag{2}$$

In the equation, there are four coordinate points to interpolate the M and N directions.

The loss function is used to train the model, which includes the bounding box regression loss and the target classification loss. The overall loss function expression equation is as follows.

$$k = k_{clS} + k_{\mathrm{box}} + k_{\mathrm{mask}}, \tag{3}$$

where k_{mask} refers to the average binary cross-entropy loss, and its expression is as follows.

$$\mathrm{Crossentropy}(t,0) = -(t,\ \log(v) + (1-t)\log(1-v)), \tag{4}$$

where t represents the target and v represents the output of the network model. The processing of the loss function generates labels of different category attributes for objects of different categories so that the interaction between the same categories will not occur.

2.4. Pulmonary Nodule Detection Algorithm Based on R-FCN. The CT image of the lungs segmented by the Mask-RCNN algorithm was used as the input of CNN for feature extraction. Subsequently, the fully convolutional network R-FCN was used as the detection algorithm model for pulmonary nodules, which is an end-to-end network model [13]. Similar to Faster-RCNN, R-FCN also performs network extraction of ROI, but Faster-RCNN loses certain characteristics after the extraction process. To retain some of the missing features, Faster-RCNN uses a deeper network model, but it undoubtedly sacrifices the training and testing efficiency of the model. The R-FCN used encodes location information by creating a location-sensitive feature map to retain the relevant features of the data, and there is no convolutional layer behind the pooling layer. The model's structure and location-sensitive features are shown in Figures 2 and 3.

For the grid of the mth row and nth column of the target object F, the expression of the position-sensitive pooling layer is as follows.

$$r_F(m,n\,|\,\theta) = \sum_{(x,y)\varepsilon\mathrm{bin}(m,n)} \frac{z_{m,n,F}(x+x_0, y+y_0\,|_{\theta})}{n}, \tag{5}$$

where $r_F(m,n)$ represents the average score of the (m, n) th network in the F target after passing through the pooling layer, $z_{m,n,F}$ is an output of the sensitive feature map at the $k^2(F{+}1)$th position, (x_0, y_0) represents the coordinates of the ROI, n means the number of all pixels in the model, and θ represents the parameters in the network; the score expression of the target F object is as follows.

$$r_F(\theta) = \sum_{m,n} r_F(m,n\,|\,\theta). \tag{6}$$

Then, the loss function of each target object consisting of cross-entropy loss and boundary regression loss is calculated.

$$k\left(r, v_{x,y,w,h}\right) = K_{c_l s}(r_{c^*}) + \phi[c^* > 0]k_{\mathrm{reg}}(v, v^*), \tag{7}$$

where c^* represents the true calibration value of ROI, $K_{c_l s}(r_{c^*})$ represents the cross-entropy loss function, $k_{\mathrm{reg}}(v, v^*)$ represents the boundary loss function, and v^* represents the real border of the ROI.

2.5. Statistical Mathematical Processing. SPSS 19.0 was used for statistical analysis. The measurement data conforming to normal distribution were expressed as mean ± standard deviation, and the difference between groups was analyzed

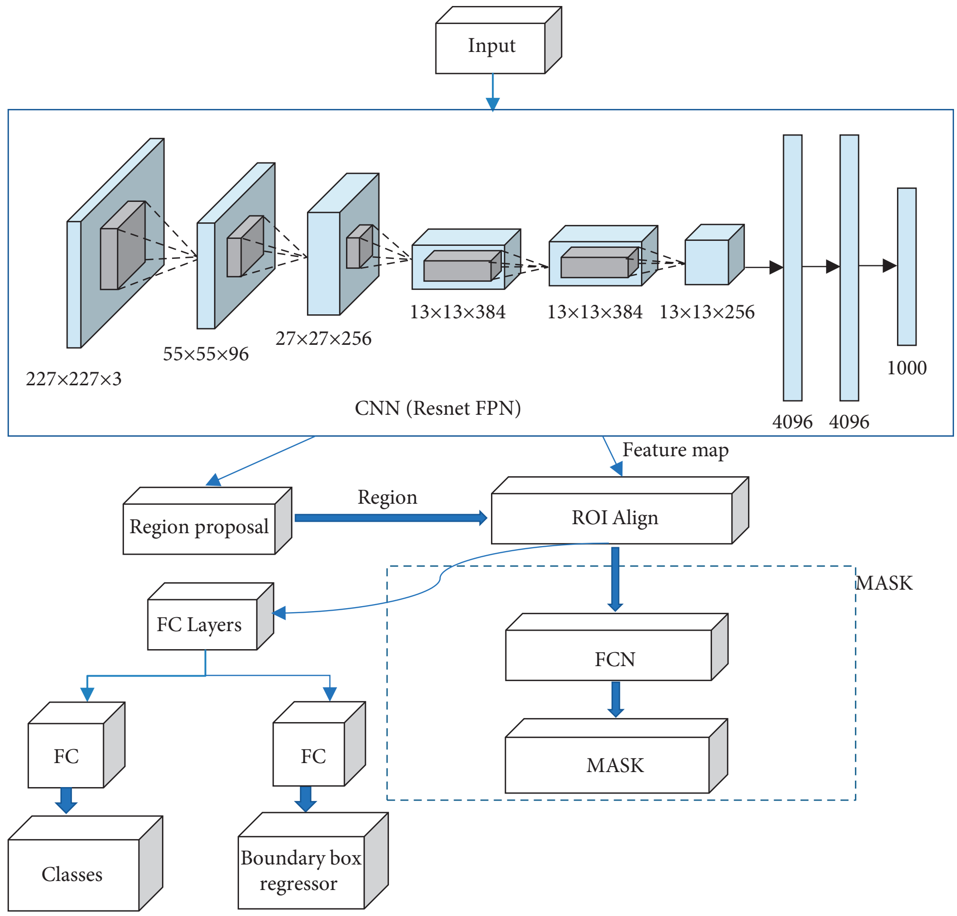

Figure 1: Schematic diagram of Mask-RCNN algorithm segmentation.

by independent sample t-test. The measurement data that did not conform to normal distribution were represented by median value and quad position, and the comparison between groups was analyzed by nonparametric rank sum test. N (%) was used to represent the count data, and chi-square test was used to analyze the difference between groups. The p value was calculated according to the variance value, and $p < 0.05$ was considered statistically significant.

3. Results

3.1. Image Segmentation Results Based on Mask-RCNN Algorithm Model. The deep learning framework for algorithm models was TensorFlow. This learning framework has a high degree of flexibility and strong portability, which supports multi-language and automatic differentiation. Regarding the training of the algorithm model, the CT image data used in this study were all the medical image data of the observation objects selected.

The training of the Mask-RCNN algorithm model used a stochastic gradient descent training network (SGD), the number of iterations (epoch) was 500, the momentum was 0.8, the learning rate was 0.0001, the batch size was 4, and the weight attenuation was 0.0001. After 400 iterations of the network model, the loss started to converge. Therefore, it was decided to use the training model after 450 iterations to segment the lung CT image. The comparison chart of the effect before and after segmentation is shown in Figure 4.

From the before and after comparison of the segmentation effect of the Mask-RCNN algorithm model on the lung CT image, the trained Mask-RCNN algorithm model can effectively complete the segmentation task of the lung CT image, but there was a slight jitter at the boundary. Therefore, the Mask-RCNN algorithm model cannot fully learn the boundary features of the image, but the segmentation of the lung parenchyma fully met the requirements.

3.2. Comparison of Results of Pulmonary Nodule Detection Algorithms Based on R-FCN. The CT image data used in this section were all the medical image data of the observed objects selected in this study. Each lung CT image contained pulmonary nodules with a diameter range of approximately 1.1 cm–2.8 cm, with an average diameter of (2.0 ± 0.4) cm. The position and shape of nodules in all CT images were not fixed. Randomly assigned according to a 2 : 1 ratio, the datasets were divided into training set and verification set. Nodules on all CT images contained both benign and malignant lesions. Malignant lesions were characterized by irregular and burr-like edges and exponential growth rate. Benign lesions were characterized by nodules with relatively smooth edges and slow growth.

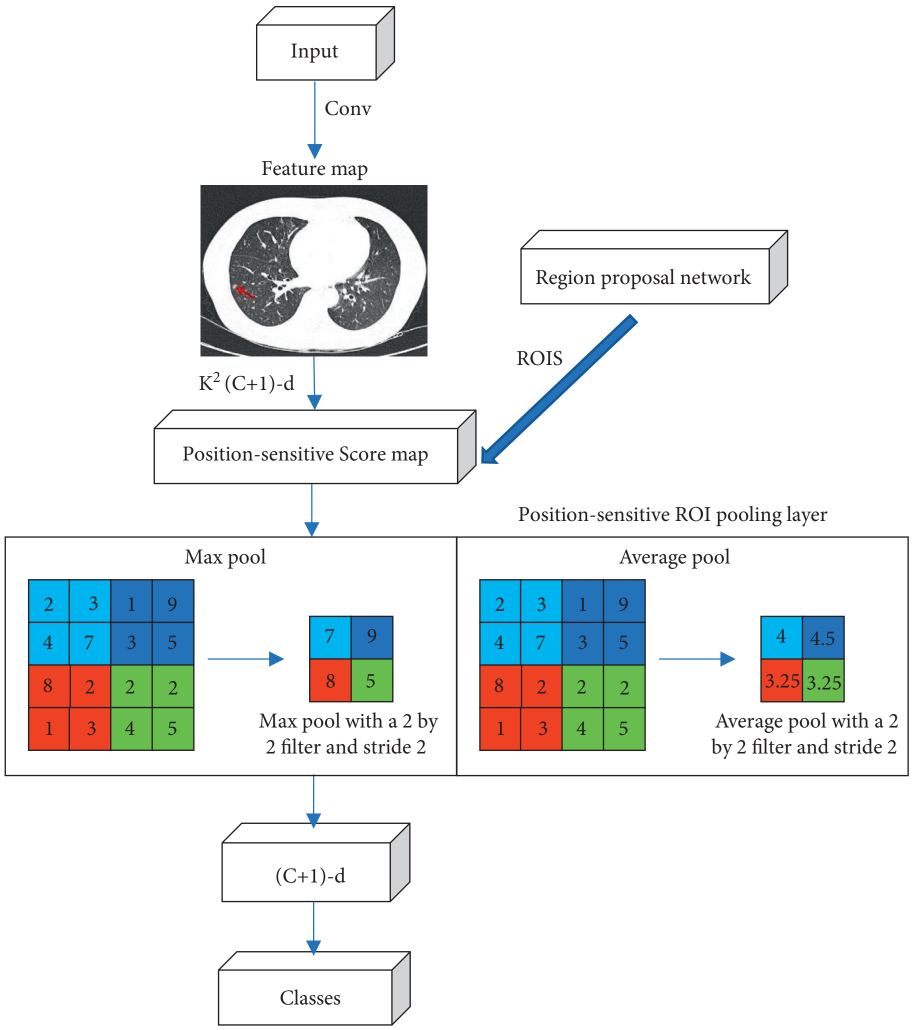

Figure 2: Schematic diagram of R-FCN model structure.

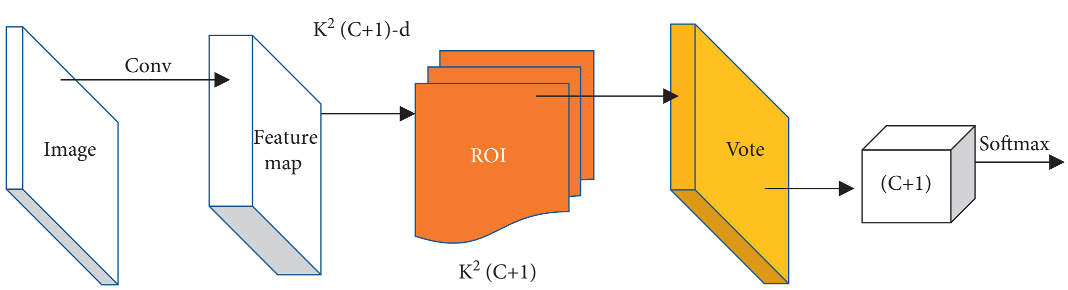

Figure 3: Location-sensitive feature map of R-FCN.

The training of the R-FCN algorithm model used a stochastic gradient descent training network (SGD), the number of iterations (epoch) was 500, the momentum was 0.8, the learning rate was 0.0001, the batch size was 4, and the weight decay was 0.0001. According to the experimental results, the speed of R-FCN algorithm for nodule detection was 0.172 seconds/frame, and the accuracy was 88.9%. The results before and after the test are shown in Figure 5.

3.3. CT Image Performance of Different Pulmonary Nodules Based on Deep Learning. Fifty-six patients who were diagnosed with pulmonary nodules by surgery or puncture in the hospital in a certain area were the research objects. Among 56 cases of pulmonary nodules diagnosed after surgery or pathological examination, 32 cases were malignant lesions and 24 cases were benign lesions. CT scans based on deep learning algorithms were performed on

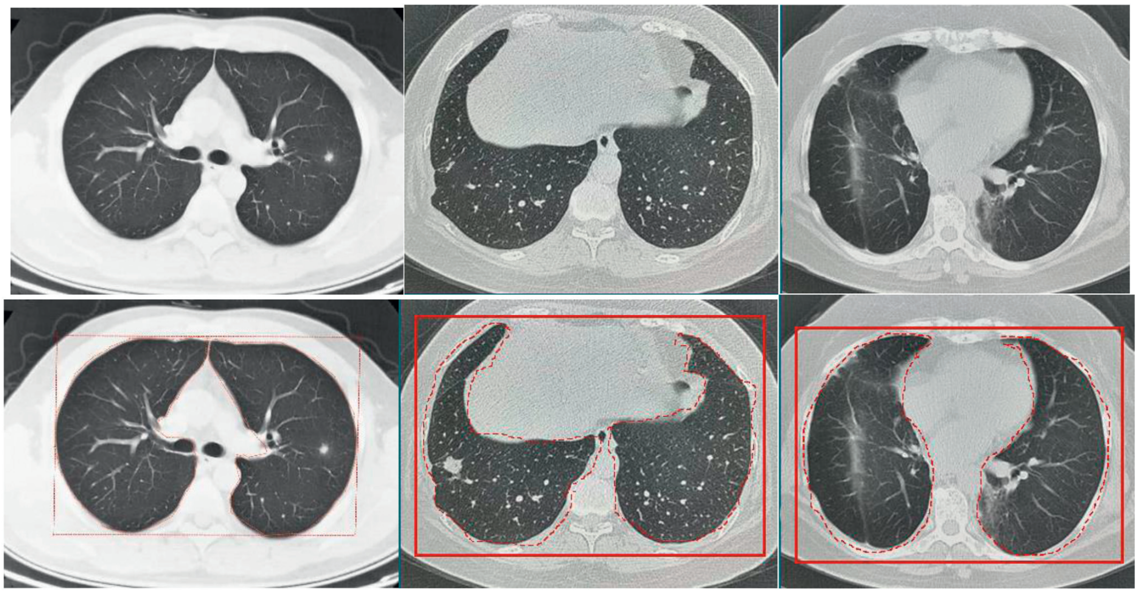

Figure 4: Comparison of the segmentation effect of Mask-RCNN algorithm on lung CT images (the box represents the automatic selection and labeling of lung parenchyma by Mask-RCNN algorithm, and the dotted line represents the further automatic segmentation of lung parenchyma).

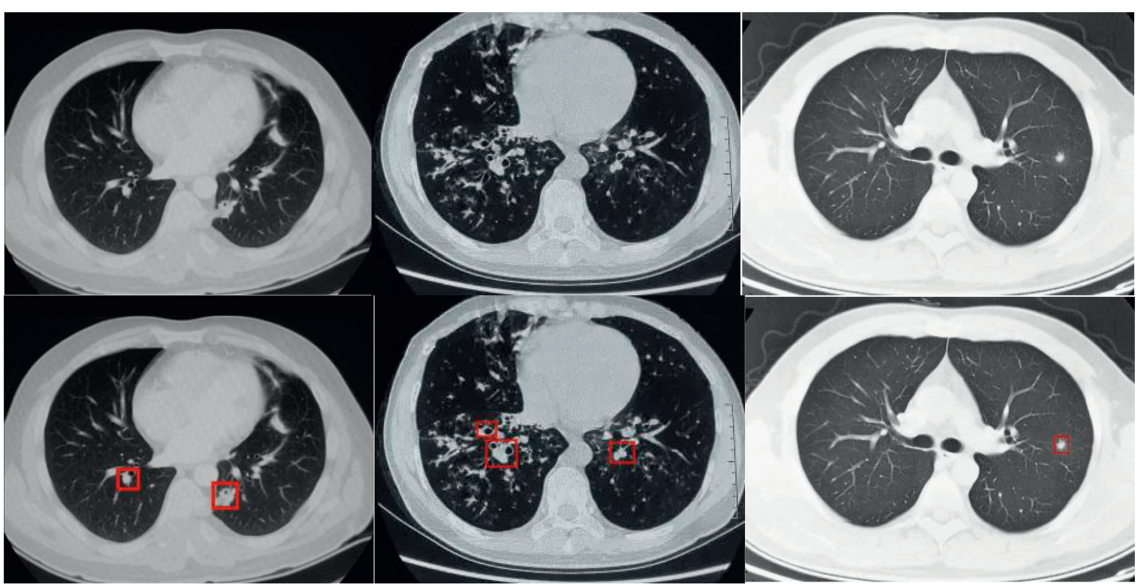

Figure 5: Comparison of the detection effect of R-FCN algorithm on CT images of pulmonary nodules (the box represents the automatic segmentation labeling of pulmonary nodules by R-FCN algorithm).

these 56 patients, 30 cases of malignant lesions of pulmonary nodules were confirmed, and the diagnosis accuracy was 93.75%. There were 22 cases of benign lesions, the diagnostic accuracy was 91.67%, and the overall diagnostic accuracy was 92.85%. At the same time, MRI scan diagnosis was performed, 27 cases of malignant lesions were detected, and the diagnosis accuracy was 84.38%. 16 cases of benign lesions were detected, the diagnostic accuracy was 66.66%, and the overall diagnostic accuracy was 76.78%. In Figure 6, the accuracy of CT scan based on deep learning for the diagnosis of pulmonary nodules was higher than that of MRI.

The CT scan parameters of different pulmonary nodules were recorded. The peak enhancement (PH) and the ratio of aortic enhancement (SPH/PPH) of malignant nodules and inflammatory nodules were higher than those of benign nodules. The detailed values are shown in Figures 7–8.

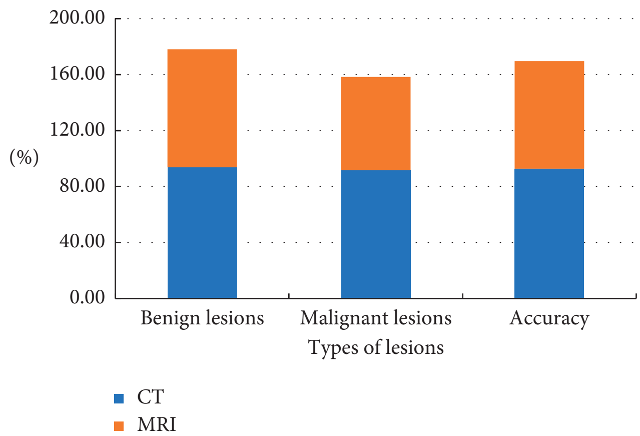

Figure 6: Comparison of the diagnostic accuracy of CT and MRI on CT images of pulmonary nodules.

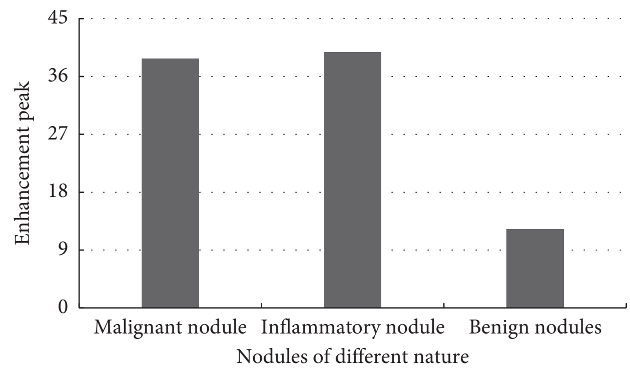

Figure 7: Enhanced peak CT scan parameters of different types of pulmonary nodules.

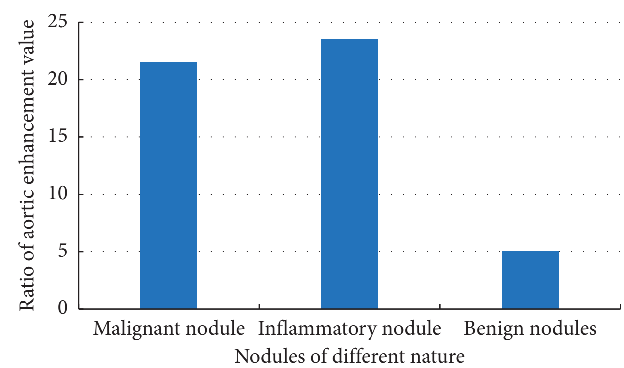

Figure 8: CT scan parameters of the ratio of aortic enhancement value of different pulmonary nodules.

4. Discussion

The incidence of lung diseases has been increasing year by year, and lung cancer has become the number one enemy affecting the health of Chinese people in recent years. As an important feature of early lung cancer, pulmonary nodules are of great significance for the medical diagnosis and observation analysis of lung cancer. Rapid and effective diagnosis of pulmonary nodules can effectively improve the survival rate of patients with pulmonary diseases.

In the current clinical diagnosis of pulmonary nodules, it is generally believed that benign pulmonary nodules mainly occur in the posterior part of the upper lobe and the dorsal part of the lower lobe of the lung [14–16]. Most of the inflammatory nodules were found in the dorsal and inferior lobes of the lungs. The common sites of malignant nodules are mainly the upper lobe, lingual lobe, and middle lobe of the lung. The morphology of pulmonary nodules is classified into lobular, quasi-circular, and irregular shapes. The quasi-round shape is mainly manifested by the accumulation of nodular masses, usually with expansible growth, and malignant and benign can occur. The irregularity is usually seen in inflammatory nodules. The lobulated nodules are characterized by oval or round mass with uneven surface. According to relevant data, lobulated nodules are present in more than 70% of lung cancer patients [17]. Malicious nodules often have lobulated contours or irregular nodular edges. Almost 90% of lobulated nodules are malignant lesions. Malignant nodules also have features other than lobulated nodules, such as burr-like features, pleural depression, and obvious fibrous tissue proliferation in and around the nodules.

At the present stage of clinical treatment, fiberoptic bronchoscopy, CT, MRI, and needle biopsy are all conventional methods for the diagnosis of pulmonary nodules. However, due to the low sensitivity and limited value of chest radiograph, fiberoptic bronchoscopy has been gradually phased out in the diagnosis of early lung cancer [18]. In addition, puncture biopsy is an invasive operation for tumor detection, which will cause certain physical and mental damage to patients and has poor tolerance. The spatial resolution of MRI imaging examination is low [19], and the morphological characteristics of small and medium-sized pulmonary nodules are not obvious. Moreover, the price is relatively high. CT is currently a research hotspot in the examination of pulmonary nodules, with its remarkable advantages of fast and efficient scanning, small noninvasive radiation, and high tissue resolution. It can not only provide the morphological information of pulmonary nodules but also have a good display rate of the subtle signs of pulmonary nodules.

At present, CT images have become one of the procedures of routine clinical examination, and the number of CT images has increased greatly in recent years, which has certain requirements on the diagnostic accuracy and efficiency of radiologists. Therefore, it is of great significance to help radiologists effectively improve the diagnostic efficiency. Nowadays, CT scanning equipment has high spatial resolution [20, 21]. With the gradual development of computer and artificial intelligence algorithms, the automation engineering in the field of medical imaging has become increasingly important. Deep learning algorithms have been widely used in image processing, such as image segmentation, target selection, and image enhancement [22, 23]. In today's environment of significantly enhanced server computing capacity, richer datasets, and perfect network training technology, many algorithm models have been proposed. The recognition ability and precision of medical images are also gradually improving. When applied to the processing of medical images, it can completely replace doctors' preliminary subjective diagnosis of diseases in some cases.

5. Conclusion

This study aimed to use deep learning technology to segment and extract the CT images of pulmonary nodules, so as to further improve the clinical diagnosis effect of pulmonary nodules. The results showed that the speed of R-FCN algorithm for nodule detection was 0.172 seconds/piece, and the accuracy was 88.9%. By comparing the CT image effects after segmentation detection, the diagnostic accuracy of CT scan based on deep learning for pulmonary nodules was 91.67%, and the overall diagnostic accuracy was 92.85%. CT scan parameters of pulmonary nodules with different properties were recorded. The enhancement peak value (PH) and aortic enhancement value ratio (SPH/PPH) of malignant and inflammatory nodules were higher than those of benign nodules, and the data showed good consistency with the results of surgical examination. Moreover, the data showed a good agreement with the results of surgical examination. These results indicated that CT images based on deep learning were efficient and accurate in the diagnosis of pulmonary nodules. However, the research content of this work still has some limitations. Only a single imaging diagnosis method was studied, and the sample size was not large enough. At present, only automatic detection and labeling of pulmonary nodules can be achieved, but the nature of nodules cannot be distinguished, and artificial diagnosis is still needed. Therefore, it is necessary to increase the number of samples and further explore the deep learning algorithm in the future. In conclusion, this study can effectively improve the diagnostic efficiency of CT images for pulmonary nodules, and analyze and evaluate the accuracy of CT images for pulmonary nodules. In addition, it provides theoretical support for the follow-up diagnosis of pulmonary nodules and the treatment of lung cancer and also significantly improves the diagnostic effect and detection efficiency of pulmonary nodules.

Data Availability

The data used to support the findings of this study are available from the corresponding author upon request.

Conflicts of Interest

The authors declare that they have no conflicts of interest.

References

[1] D. Groheux, G. Quere, E. Blanc et al., "FDG PET-CT for solitary pulmonary nodule and lung cancer: literature review," *Diagnostic and Interventional Imaging*, vol. 97, no. 10, pp. 1003–1017, 2016, Epub 2016 Aug 24. PMID: 27567555.

[2] M. Casal Moura, P. J. Navin, G. B. Johnson et al., "Pulmonary nodules in patients with primary Sjögren's syndrome: causes, clinico-radiologic features, and outcomes," *Respiratory Medicine*, vol. 174, Article ID 106200, 2020, Epub 2020 Oct 22. PMID: 33147563.

[3] F. Setianingrum, R. Rautemaa-Richardson, and D. W. Denning, "Pulmonary cryptococcosis: a review of pathobiology and clinical aspects," *Medical Mycology*, vol. 57, no. 2, pp. 133–150, 2019.

[4] J. A. Barta, C. A. Powell, and J. P. Wisnivesky, "Global epidemiology of lung cancer," *Annals of Global Health*, vol. 85, no. 1, p. 8, 2019, PMID: 30741509; PMCID: PMC6724220.

[5] M. Cao and W. Chen, "Epidemiology of lung cancer in China," *Thoracic Cancer*, vol. 10, no. 1, pp. 3–7, 2019, Epub 2018 Nov 28. PMID: 30485694.

[6] K. Martini, M. Eberhard, and T. Frauenfelder, "Lungenrundherde - eü," *Therapeutische Umschau*, vol. 77, no. 2, pp. 75–80, 2020, German.

[7] C. Trinidad López, C. Delgado Sánchez-Gracián, E. Utrera Pérez, C. Jurado Basildo, and C. A. Sepúlveda Villegas, "Incidental pulmonary nodules: characterization and management," *Radiología (English Edition)*, vol. 61, no. 5, pp. 357–369, 2019, English, Spanish, Epub 2019 May 6. PMID: 31072604.

[8] M. Oudkerk, S. Liu, M. A. Heuvelmans, J. E. Walter, and J. K. Field, "Lung cancer LDCT screening and mortality reduction - evidence, pitfalls and future perspectives," *Nature Reviews Clinical Oncology*, vol. 18, no. 3, pp. 135–151, 2021, Epub 2020 Oct 12. PMID: 33046839.

[9] S. Ather, T. Kadir, and F. Gleeson, "Artificial intelligence and radiomics in pulmonary nodule management: current status and future applications," *Clinical Radiology*, vol. 75, no. 1, pp. 13–19, 2020, Epub 2019 Jun 12. PMID: 31202567.

[10] S. Raoof, P. Bondalapati, R. Vydyula et al., "Cystic lung diseases," *Chest*, vol. 150, no. 4, pp. 945–965, 2016, Epub 2016 May 13. PMID: 27180915.

[11] N. Kumar, R. Verma, D. Anand et al., "A multi-organ nucleus segmentation challenge," *IEEE Transactions on Medical Imaging*, vol. 39, no. 5, pp. 1380–1391, 2020, Epub 2019 Oct 23. PMID: 31647422.

[12] M. Fan, H. Zheng, S. Zheng et al., "Mass detection and segmentation in digital breast tomosynthesis using 3D-mask region-based convolutional neural network: a comparative analysis," *Frontiers in Molecular Biosciences*, vol. 7, Article ID 599333, 2020.

[13] A. Nasirahmadi, B. Sturm, S. Edwards et al., "Deep learning and machine vision approaches for posture detection of individual pigs," *Sensors*, vol. 19, no. 17, Article ID 3738, 2019.

[14] Z. K. Jiang, Y. K. Xie, J. Q. Huang, and J. S. Chen, "Colorectal cancer with indeterminate pulmonary nodules," *Neoplasma*, vol. 67, no. 03, pp. 439–449, 2020, Epub 2020 Feb 28. PMID: 32122141.

[15] G. Sommer, M. Koenigkam-Santos, J. Biederer, and M. Puderbach, "Rolle der MRT zur Detektion und Abklärung pulmonaler Rundherde," *Radiologe, Der*, vol. 54, no. 5, pp. 470–477, 2014 May, German.

[16] N. Nasrullah, J. Sang, M. S. Alam, M. Mateen, B. Cai, and H. Hu, "Automated lung nodule detection and classification using deep learning combined with multiple strategies," *Sensors*, vol. 19, no. 17, Article ID 3722, 2019.

[17] J. E. Walter, M. A. Heuvelmans, G. H. de Bock et al., "Relationship between the number of new nodules and lung cancer probability in incidence screening rounds of CT lung cancer screening: the NELSON study," *Lung Cancer*, vol. 125, pp. 103–108, 2018, Epub 2018 May 14. PMID: 30429006.

[18] D. C. Murphy, K. Jackson, R. Johnston et al., "The value of bronchoscopy in patients with non-massive haemoptysis and

a clear or benign computer tomogram scan," *The Clinical Respiratory Journal*, vol. 15, no. 4, pp. 430–436, 2021, Epub 2020 Dec 26. PMID: 33301639.

[19] J. Biederer, Y. Ohno, H. Hatabu et al., "Screening for lung cancer: does MRI have a role?" *European Journal of Radiology*, vol. 86, pp. 353–360, 2017, Epub 2016 Sep 16. PMID: 27665148.

[20] D. M. Yuan, Y. L. Lü, Y. W. Yao et al., "Diagnostic efficiency and complication rate of CT-guided lung biopsy: a single center experience of the procedures conducted over a 10-year period," *Chinese Medical Journal*, vol. 124, no. 20, pp. 3227–3231, 2011, PMID: 22088512.

[21] T. F. Peng, T. Ren, H. S. Wang, Z. X. Feng, and M. F. Wang, "Diagnostic value of rapid on-site evaluation for CT-guided percutaneous fine needle aspiration in the diagnosis of pulmonary occupying lesions," *BioMed Research International*, vol. 2020, Article ID 9842768, 8 pages, 2020.

[22] S. Guo, R. Chen, H. Li, T. Zhang, and Y. Liu, "Identify severity bug report with distribution imbalance by CR-SMOTE and ELM," *International Journal of Software Engineering and Knowledge Engineering*, vol. 29, no. 2, pp. 136–175, 2019.

[23] J. C. Gore, "Artificial intelligence in medical imaging," *Magnetic Resonance Imaging*, vol. 68, pp. A1–A4, 2020, Epub 2019 Dec 16. PMID: 31857130.

Hindawi
Journal of Healthcare Engineering
Volume 2021, Article ID 6844549, 10 pages
https://doi.org/10.1155/2021/6844549

Research Article

Diagnosis of Cardiac Rehabilitation after Percutaneous Coronary Intervention in Acute Myocardial Infarction Patients by Emission Computed Tomography Image Features under Filtered Back Projection Reconstruction Algorithm

Yuan Lv and Suyu Zhao

Department of Cardiology, Lishui People's Hospital, Lishui 323000, Zhejiang, China

Correspondence should be addressed to Suyu Zhao; 1923011109@siit.edu.cn

Received 22 August 2021; Revised 29 September 2021; Accepted 30 September 2021; Published 22 October 2021

Academic Editor: Enas Abdulhay

This study aimed to explore the application value of emission computed tomography (ECT) imaging technology based on filtered back projection reconstruction algorithm (FBP) in cardiac function examination after percutaneous coronary intervention (PCI) in patients with acute myocardial infarction (AMI). Eighty patients with myocardial infarction diagnosed by medical history, electrocardiograph (ECG), and myocardial enzyme admitted to hospital from February 2018 to February 2019 were selected as the research objects. All patients underwent PCI seven days after the onset of myocardial infarction. ECT was performed for all patients before and after surgery. In addition, all ECT images were processed by the FBP reconstruction algorithm. On this basis, preoperative and postoperative cardiac surgery function and ischemia of the patients were diagnosed. Then, the diagnostic results were compared with the results of coronary angiography and echocardiogram. The results showed that all patients had a total of 541 segments before PCI surgery. ECT examination revealed 294 abnormal segments of the ventricular wall, with a total score of 585 points. A total of 100 segments were scored with 1 point, a total of 194 segments were scored with 2 points, and a total of 50 segments were scored with 3 points. After PCI, the number of abnormal segments was reduced to 58, with a total score of 193. There were 6 segments with a score of 1, 44 segments with a score of 2, and 5 segments with a score of 3. The left ventricular diastolic volume (EDV), left ventricular systolic volume (ESV), stroke volume (CO), and ejection fraction (EF) of the patients before the operation were 148 ± 16 mL, 77 ± 14.5 mL, 4.29 ± 0.37 L/min, and $41.9 \pm 8\%$, respectively. The EDV, ESV, CO, and EF of the patients after surgery were 132 ± 16 mL, 62 ± 13 mL, 4.89 ± 0.71, and $53 \pm 6\%$, respectively. Significant changes occurred in various systolic function parameters before and after surgery, $P < 0.05$. The standardized regression coefficients of the three groups were 0.32, 0.41, and 0.47, respectively, $P < 0.05$, which indicated that the greater the coronary artery stenosis rate, the higher the diagnostic coincidence rate of left anterior descending limb (LAD), left circumflex branch (LCX), and left coronary artery (RCA). The conformity of ECT imaging in the LCX group for diagnosis of myocardial ischemia was higher than that of UCG, $P < 0.05$. To sum up, the ECT technology based on the FBP reconstruction algorithm had a good application prospect in the diagnosis of cardiac function recovery in AMI patients after PCI.

1. Introduction

In recent years, with the aggravation of the aging of the population in China and the increasing pressure on people's life, the prevalence and mortality of cardiovascular diseases are rising. Among them, coronary atherosclerotic heart disease (CAD) has become one of the primary cardiovascular diseases threatening the life and health of Chinese people [1]. Coronary heart disease (CHD) is defined as a narrowing or obstruction of the lumen caused by atherosclerosis of the coronary artery, or a functional change in the coronary artery that leads to myocardial ischemia, hypoxia, or necrosis that further leads to heart disease. Clinically, CHD is generally classified into five types: (i) asymptomatic myocardial ischemia, (ii) angina pectoris, (iii) acute myocardial infarction (AMI), (iv) ischemic cardiomyopathy, and (v) sudden death. Among them, AMI is the most common and serious [2]. AMI is defined as the rapid reduction or interruption of the blood supply of the coronary artery based on coronary artery disease, resulting in severe and persistent acute ischemia of the corresponding myocardium leading to myocardial necrosis. Once myocardial infarction occurs, ventricular remodeling will occur, which will further lead to complications such as left ventricular dysfunction and congestive heart failure. They will seriously affect the long-term prognosis of patients and reduce the quality of life of patients [3]. Effective and timely reperfusion is the key to the early treatment of AMI. Clinical data showed that percutaneous coronary intervention (PCI) has a good therapeutic effect on AMI. However, recent studies pointed out that PCI has time compliance in the treatment of AMI. Direct PCI within twelve hours of acute myocardial infarction can effectively save the myocardium, reduce the size of myocardial infarction, and improve left ventricular remodeling. However, PCI was less effective in saving dying cardiomyocytes after seven days of acute myocardial infarction. Its effects on improving the blood flow of the left ventricular remodeling, resting or hibernating myocardium, and preventing the expansion and extension of the infarct area remain controversial. In addition, many studies revealed that about 30%~40% of AMI patients will have no-reflow after PCI, which seriously affects the therapeutic effect and leads to the prognosis of patients. Therefore, there is an urgent need for an effective method to examine and evaluate the cardiac function recovery of AMI patients after PCI [4–6].

Radionuclide emission computed tomography (ECT) is a computer aided technique, which uses isotopes to label drugs, thereby measuring the concentration intensity of isotopes in various organs in the body and its change with time based on the principle of human body synthesis. In this way, the visual shape of the organs is displayed, and the functional image information of their physiological process and metabolism is reflected [7]. ECT technology develops rapidly and has become one of the markers of nuclear medicine modernization at present [8]. It has been widely used in the diagnosis of tumors, bone diseases, and cerebrovascular diseases because it can well combine functional images with anatomical images. It is also the main means of heart disease diagnosis, especially in the diagnosis of coronary heart disease, which shows a good diagnostic efficiency and has become one of the recognized methods to detect coronary heart disease. When radiopharmaceuticals enter the coronary arteries, they are selectively ingested by normal cardiomyocytes, and the amount ingested is proportional to the coronary blood flow. When a coronary artery is narrowed or blocked, blood flow in the coronary arteries is reduced, and heart muscle cells are damaged. At that point, the ability of the heart muscle to absorb radioactive drugs is reduced or even unable to absorb them. Therefore, ECT can accurately display the metabolism and blood flow of the myocardium, so as to further determine whether the myocardium is ischemic, ischemic site, and ischemic area. Compared with coronary angiography, exercise plate, and other examination methods, it has the advantages of noninvasive and no exercise load, so it is a relatively safe and effective examination method in clinical practice [9]. Patients with negative ECT examinations can basically exclude coronary heart disease. For patients with positive ECT examination, the specific coronary artery lesions are further inferred according to the abnormal blood flow distribution and perfusion volume.

ECT examination is mainly classified into functional image examination and anatomical structure image examination, but the image resolution collected by functional image examination is very low and lacks anatomical information. To solve this problem, image fusion is proposed. At present, CET and CT can be organically combined to provide high-quality images with anatomical localization. To a certain extent, the quality of ECT images is provided [10]. However, there are still many problems such as image quality distortion caused by attenuation factors such as the Compton effect and scattering on image fusion. Image reconstruction technology has developed rapidly in recent years. According to the collected data, the image is reconstructed by computing the pixels in the image matrix. FBP is the most widely used algorithm in image reconstruction at present. At present, it mainly exists in the X-ray CT system, but there are few studies on its application in CET [11].

In this study, patients with acute heart infarction were taken as the research objects. ECT examination was performed before and after PCI. FBP algorithm was used to process the obtained images, and on this basis, the efficacy of PCI in MAI was evaluated, to provide reference and basis for clinical use of ECT, PCI, and FBP algorithm in treatment and diagnosis of AMI.

2. Materials and Methods

2.1. Research Objects. A total of 80 patients admitted to the hospital from February 2018 to February 2019 who were diagnosed with AMI by medical history, ECG, and myocardial enzyme were selected. There were 55 male patients and 25 female patients, with an average age of 61.6 ± 11.2 years. Exclusion criteria are as follows: patients with onset less than twelve hours or longer than one month; patients suffering from cerebrovascular diseases or severe liver and kidney dysfunction or hyperthyroidism; patients suffering from malignant arrhythmia, congenital heart disease, cardiac hypertrophy, and myocarditis resulting in cardiac insufficiency; patients with a history of respiratory dysfunction, malignant tumor, or active bleeding; and patients who were long-term bedridden and unable to perform ECT examination. All studies had obtained patients' informed consent and met the requirements of medical ethics.

2.2. Overview of Research Methods. All the subjects underwent percutaneous coronary intervention (PCI) seven days after myocardial infarction. All patients were examined with radionuclide emission computed tomography (ECT) before and after surgery. All ECT images are processed by filtering back projection reconstruction algorithm. On this basis, the preoperative and postoperative cardiac operation function and ischemia were diagnosed. The diagnostic results were compared with coronary angiography and ultrasound ECG.

2.3. ECT Inspection Method. The inspection instrument was Siemens symbia-1, the imaging agent was 9mTc-MIBI, and the radiochemical purity was >95%. All patients were routinely given antiplatelet aggregation, anticoagulants, beta-blockers, nitrates, ACEI drugs, and statins after admission. 99mTc-MIBI was intravenously injected on the morning of the 7th day of admission, in the fasting and resting state, with a dose of 925~1110 MBq (25~30 mCi). Half an hour later, the patient was fed a fried egg or 250 mL of pure milk. Resting-gated myocardial perfusion imaging was performed 1.5 to 2 hours later. ECT was equipped with a parallel hole low energy and high-resolution collimator. The R wave of ECG was the trigger wave. The patient lied on the examination bed with his head outwards. ECG gating device was opened, and the ECG electrodes were connected correctly. The starting angle of probe 1 was −45°, and the starting angle of probe 2 was 56°. The angle between probes was 101°, one position per 3D, running 1050 in total, and 36 individual positions were collected. Eight frames were collected per cardiac cycle, and the acceptable heart rate range was ±20% of the mean heart rate. The matrix was 64 × 64, and the acquisition time was 30 seconds/section. The energy peak was 140, and the magnification (ZOOM) was 1.33.

ECT results were classified into four grades: normal (grade 0), decreased perfusion (grade 1), substantially decreased perfusion (grade 2), and perfusion defect (grade 3). The calculation of wall thickening rate was automatically graded into normal wall thickening rate (>25%, grade 0), reduced (10~24%, grade 1), substantially reduced (10% to 9%, grade 2), and substantially reduced or no exercise (<9%, grade 3).

2.4. Image Processing Method. The back projection reconstruction algorithm usually introduces star artifacts, which will lead to image distortion after reconstruction. This problem can be solved by rate-wave processing of the image before reconstruction.

The projection theorem is the basis of image reconstruction. The specific content is as follows. A slice of the 2D Fourier transform $F(w_1, w_2) = \widehat{F}(\rho, \phi)$ of $f(x, y)$ is given by the 1D Fourier transform of an image $p_\phi(x_r)$ projected at the angle ϕ of view $f(x, y)$. The slice and the axis w_1 intersect at an angle ϕ and pass through the origin of the coordinate. The specific schematic diagram is shown in Figure 1. It is further explained that the 1D Fourier transform of the projection of the image $f(x, y)$ in the direction ϕ gives a slice of the 2D Fourier transform of $f(x, y)$, and the position of the slice passes through the origin and forms an angle ϕ with w_1.

$$\zeta_1\left[p_\phi(x_r)\right] = \widehat{F}(\rho, \phi)|_{\phi=arctg w_2/w_1}. \tag{1}$$

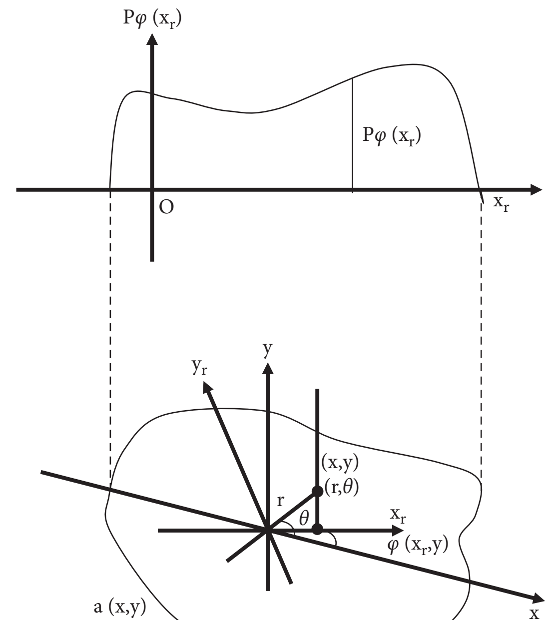

Figure 1: Coordinate system used for FBP.

The relationship between the projection angle ϕ of view and the rotation coordinates (x_r, y_r) and (x, y) is as follows.

$$\begin{cases} x_r = x \cos \phi + y \sin \phi, \\ y_r = -x \sin \phi + y \cos \phi. \end{cases} \tag{2}$$

w_1, w_2 are not independent but bound by

$$\begin{cases} w_1 = 2\pi\rho \cos \phi, \\ w_2 = 2\pi\rho \sin \phi. \end{cases} \tag{3}$$

FBP reconstruction is as follows. The image to be built is $a(x, y)$; then, its 2D Fourier transform is $A(w_1, w_2) = \widehat{A}(\rho, \theta)$. According to the central slice theorem, $\widehat{A}(\rho, \theta)$ is obtained by 1D Fourier transform of $p_\phi(x_r)$ of the projection of $a(x, y)$ under different viewing angles, which is expressed as follows.

$$A(w_1, w_2) = \widehat{A}(\rho, \theta) = \xi_1\left[p_\phi(x_r)\right] = P_\phi(\rho) = P(\rho, \phi). \tag{4}$$

The image to be built is as follows.

$$\overset{\Delta}{a}(r, \theta) = a(x, y) = \xi_2^{-1}\left[A(w_1, w_2)\right]. \tag{5}$$

Then, there is

$$\overset{\Delta}{a}(r, \theta) = \int_0^X d\phi \int_{-\infty}^{\infty} |\rho| P(\rho, \phi) e^{J\pi\rho r \cos(\theta-\phi)} d\rho. \tag{6}$$

The second integral of equation (6) is as follows.

$$\int_{-\infty}^{\infty} |\rho| P(\rho, \phi) e^{J2\pi\rho r \cos(\theta-\phi)} d\rho. \tag{7}$$

The above equation is rewritten as the inverse Fourier variant with the spatial variable x_r as follows.

$$\int_{-\infty}^{\infty} |\rho| P(\rho,\phi) e^{J2\pi \rho r \cos(\theta-\phi)} d\rho = \int_{-\infty}^{\infty} |\rho| P(\rho,\phi) e^{J2\pi \rho r \cos(\theta-\phi)} |_{xr=r\cos(\theta-\phi)}, \\ = g(x_r,\phi)|_{x_r=r\cos(\theta-\phi)} \\ = g[r\cos(\theta-\phi),\phi] \tag{8}$$

$$g(x_r,\phi) = p(x,\phi) * h(x_r). \tag{9}$$

Equation (9) is substituted in equation (5), and then, equation (10) is obtained.

$$\overset{\Delta}{a}(r,\theta) = \int_0^X g[r\cos(\theta-\phi),\phi]\mathrm{d}\phi. \tag{10}$$

Equation (10) is the filter back projection equation, which can reflect the various steps of the filter back projection algorithm. The schematic block diagram of the specific filtering back projection reconstruction process is shown in Figure 2. Generally speaking, it has three major steps:

(I) The projection $p(x_r,\phi_i)$ measured under the fixed viewing angle ϕ_1 is filtered to obtain the filtered projection $g(x_r,\phi_i)$

(II) For each ϕ_i, $g(x_r,\phi_i)$ is projected back on all points (r,θ) on the ray satisfying $x_r = r\cos(\theta-\phi_i)$

(III) All the back projection values $(0<\phi<\pi)$ in the second step are integrated to get the reconstructed image

2.5. Image Reconstruction Effect Evaluation. The required calculation is used to evaluate the reconstruction effect of the algorithm proposed in this study and the traditional algorithm. The lower the amount of calculation, the better the reconstruction effect. The specific calculation process is as follows. It is supposed that the one-dimensional calculation of N points in the algorithm proposed in this study is a function of the transformation length IV, denoted by $A(N)$, and $A(N) = O(N\log_2 N)$. The calculation amount of the first step of filtering is real number multiplication and addition of $A(2N)$ times. The calculation amount of the second step is real number multiplication of $2N$ times. The calculation amount of the third step is the same as that of the first step. Therefore, to complete the filtering of azimuth projection data, the amount of calculation required is expressed as follows.

$$\begin{cases} \text{Real number multiplication}: 2A(2N) + 2N, \\ \text{Real number addition}: 2A(2N). \end{cases} \tag{11}$$

The calculation steps required by the traditional algorithm are the same as those of the new method as follows.

$$\begin{cases} \text{Real number multiplication}: 5A(2N) + 4N, \\ \text{Real number addition}: 5A(2N). \end{cases} \tag{12}$$

2.6. Treatment Methods. All patients underwent PCI seven days after AMI. 6F guiding catheter was placed at the opening of the diseased vessel. The guidewire was inserted to the distal end of the stenosis and the occlusion. Balloon angioplasty was performed on the lesion site through balloon insertion along the guidewire. Then, according to the diameter and length of the lesion, the appropriate stent was selected for intracoronary stent implantation, and the balloon pressure of the stent was preexpanded and the balloon pressure of the stent was released regarding the characteristics of the lesion. All patients received 9mTc-MIBI resting-gated myocardial perfusion two days after PCI, using the same method as before. The myocardial perfusion and cardiac function improvement were evaluated. The imaging method was the same as before. To ensure the comparability of myocardial images, the activity of the imaging agent, the instrument, and the position of the patient were as consistent as possible before and after stent implantation in the same patient.

2.7. Statistical Methods. SPSS 11.0 was employed for data statistics and analysis. Mean ± standard deviation ($\square x \pm s$) was how measurement data were expressed, and the t-test was used to test the significance of patients' data before and after the operation. Percentage (%) was how count data were expressed, and the χ^2 test was used to test the significance. The pairwise comparison was performed by analysis of variance. The difference was statistically considerable with $P < 0.05$.

3. Results

3.1. General Patient Information. General information of the patient's age and sex, smoking history, number of diseased blood vessels, coronary artery branches, and ECG are shown in Tables 1 and 2. The average age of the patients was 59.1 ± 12.33. There were 55 male patients, accounting for 68.7%. The number of patients with diseased blood vessels of 1 and 2 was 37 and 38, respectively. The numbers of patients with the three types of coronary artery branch lesions were basically the same, which were 36, 27, and 31, respectively. Most of the patients showed AMI and myocardial ischemia.

3.2. Patient ECT Examination Results. The ECT examination results before and after the operation and the comparison of ECT before and after processing by the FBP reconstruction algorithm are shown in Figures 3 and 4. The results of ECT examination before PCI operation indicated that the left ventricular apex, anterior wall, and septal segment were almost defective in resting state, and the inferior wall partial septal segment was obviously sparse or defective. Cardiac perfusion and filling gradually recovered over time after PCI

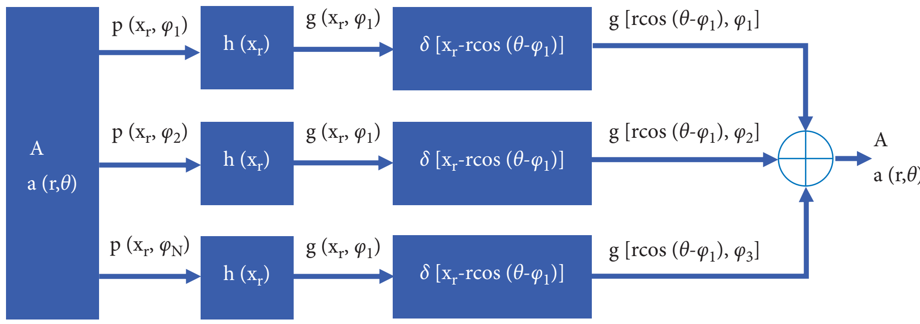

Figure 2: Schematic diagram of FBP reconstruction.

Table 1: Patient age and underlying disease data.

Index	$N = 80$
Age (years)	59.1 ± 12.33
Gender (male, n (%))	55 (68.7%)
Smoking history (n (%))	53 (66%)
Hypertension (n (%))	44 (55%)
Diabetes mellitus (n (%))	77 (96.2%)
Dyslipidemia (n (%))	61 (76.25%)

Table 2: UCG examination and coronary artery lesions of patients.

Item		Case number
Number of diseased vessels	0	9
	1	37
	2	38
	3	11
Types of coronary artery branch lesions	LAD	37 (46%)
	LCX	26 (32.5%)
	RCA	31 (38.7%)
Echocardiographic test results	Normal	2 (2.5%)
	Myocardial ischemia	39 (48.75%)
	Myocardial infarction	39 (48.75%)

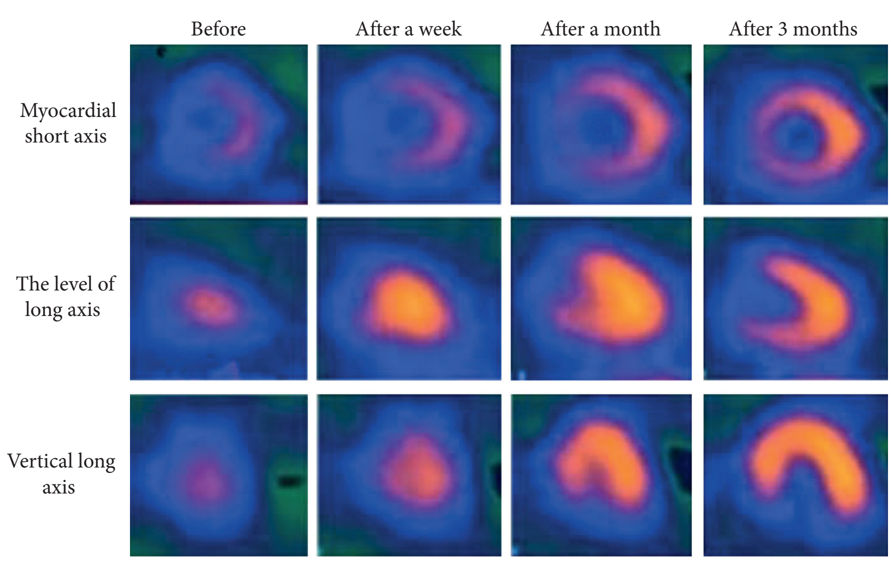

Figure 3: ECT images of patients at various stages before processing by the FBP reconstruction algorithm.

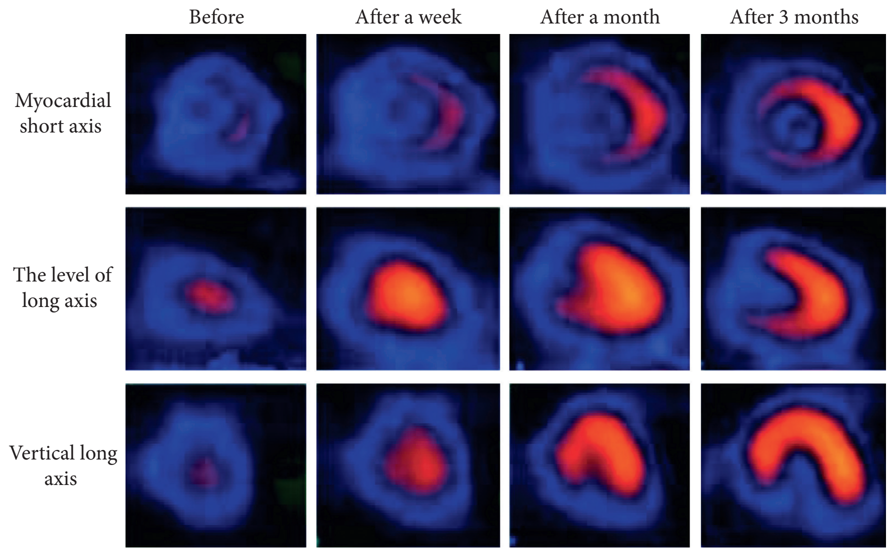

Figure 4: ECT images of patients at various stages after processing by the FBP reconstruction algorithm.

surgery. Figures 3 and 4 were compared, the quality of the ECT image processed by the unfiltered back projection reconstruction algorithm was poor, and the image was blurry. After being processed by the FBP reconstruction algorithm, the image quality was substantially improved, and the contour and edge of the target observation part became clearer.

3.3. Comparison of the Amount of Calculation Required for Image Reconstruction of the Two Algorithms. Table 3 shows the comparison results of the calculation amount required for image reconstruction under different algorithms. In the new method, since only $[M/4]$ back projection calculations of azimuths require positioning operations $[X]$ (representing the smallest integer greater than X), and in each direction, only the pixels in the positioning part need positioning operations, the calculation amount of multiplication in the new method operation is $3N[M/4]/2$ approximately, and the calculation amount of other operations can be deduced by analogy. Therefore, the required calculation of the new method is only 1/8 of the traditional method.

3.4. Comparison of Myocardial Perfusion before and after PCI. The comparison of myocardial perfusion in patients before and after PCI operation is shown in Figure 5. All patients had a total of 541 segments before PCI. ECT examination revealed 294 abnormal segments of the ventricular wall, with a total score of 585 points. A total of 100 segments were scored with 1 point, a total of 194 segments were scored with 2 points, and a total of 50 segments were scored with 3 points. After PCI, the number of abnormal segments was reduced to 58, with a total score of 193. There were 6 segments with a score of 1, 44 segments with a score of 2, and 5 segments with a score of 3. The decrease in blood perfusion of patients after PCI surgery was considerable.

Table 3: The amount of calculation required for reconstruction under different algorithms.

Operation Algorithm	Multiplication	Addition	Rounding
Traditional algorithm	$3MN$	$2MN^2$	MN^2
New method	$3N[M/4]/2$	$N^2[M/4]$	$N^2[M/4]/2$

3.5. Comparison of Systolic Function Parameters of Patients before and after PCI. The comparison of the cardiac function parameters of the patients before and after PCI is shown in Figure 6. The EDV, ESV, CO, and EF of the patients before the operation were 148 ± 16 mL, 77 ± 14.5 mL, 4.29 ± 0.37 L/min, and $41.9 \pm 8\%$, respectively. The EDV, ESV, CO, and EF of the patients after surgery were 132 ± 16 mL, 62 ± 13 mL, 4.89 ± 0.71, and $53 \pm 6\%$, respectively. Various parameters of cardiac systolic function changed substantially before and after the operation, and the difference was considerable, $P < 0.05$.

3.6. Comparison of ECT Imaging and CAG Results Based on FBP Reconstruction Algorithm. According to the classification of coronary artery disease, the patients were rolled into three groups of left anterior descending limb (LAD), left circumflex artery (LCX), and left coronary artery (RCA), to perform regression analysis of ECT diagnosis coincidence rate and coronary artery stenosis rate. From Figure 7, in the LAD group, $F = 4.39$, $P < 0.05$, which was statistically considerable. In the LCX group, $F = 8.21$, $P < 0.05$, which was statistically considerable. In the RCA group, $F = 11.36$, $P < 0.05$, which was statistically considerable. The standardized regression coefficients of the three groups were 0.29, 0.42, and 0.48, respectively, and the significance of the three groups was $P < 0.05$, which indicated that the greater the coronary artery stenosis rate, the higher the diagnostic coincidence rate of the three groups of LAD, LAD, and RCA.

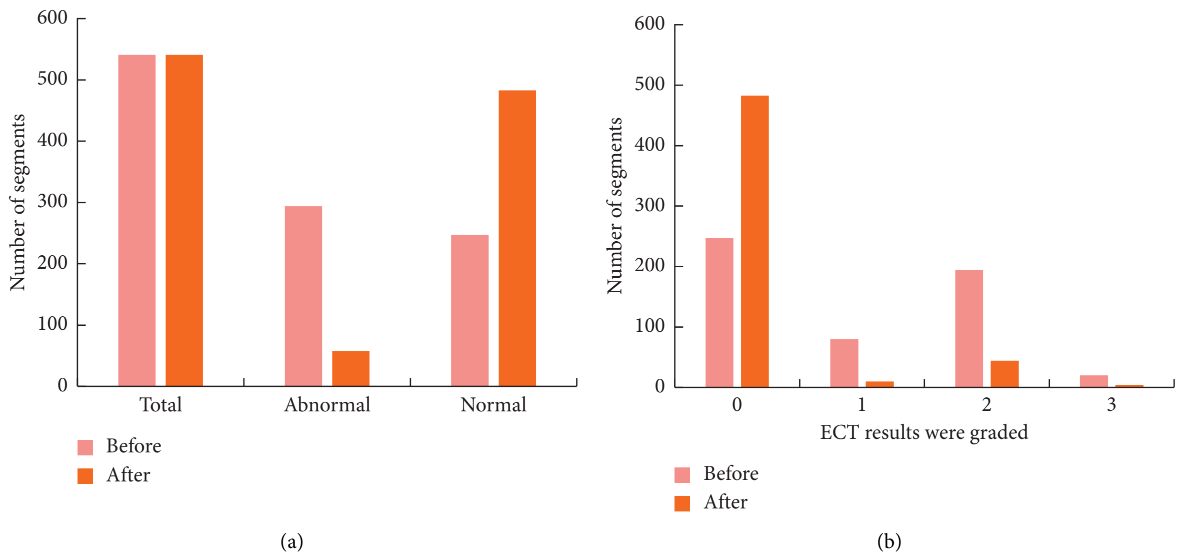

Figure 5: Classification of ECT examination results before and after surgery.

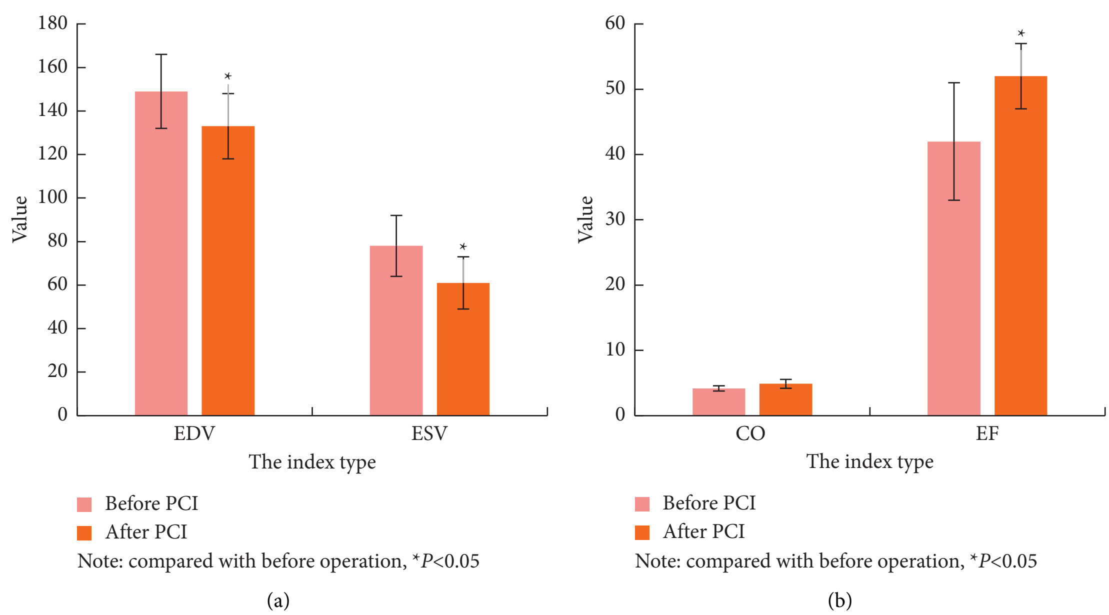

Figure 6: Comparison of patient's systolic function before and after surgery, compared with before operation, $^*P < 0.05$.

3.7. Comparison of Diagnosis Coincidence between Myocardial ECT Imaging and UCG. The comparison results of myocardial ECT imaging and UCG diagnosis are shown in Figure 8. There was no difference between the LAD group's myocardial ECT imaging in the diagnosis of myocardial ischemia and UCG, $P = 1$. The conformity of ECT imaging in the LCX group for diagnosis of myocardial ischemia was higher than that of UCG, and the difference was considerable, $P < 0.05$. The conformity of ECT imaging in the RCA group for diagnosis of myocardial ischemia was higher than that of UCG, but the difference was not considerable, $P > 0.05$.

4. Discussion

AMI refers to the rapid reduction and interruption of the blood supply of the coronary artery when the coronary artery disease occurs, and then, the relevant myocardium presents continuous ischemia and then leads to myocardial necrosis [12]. As the most serious coronary heart disease, acute attack infarction seriously threatens people's life and health. In addition, the aging of our population is becoming more and more serious. AMI has become one of the major causes of death in China. Currently, the most effective treatment for AMI is PCI [13]. All the patients in this study

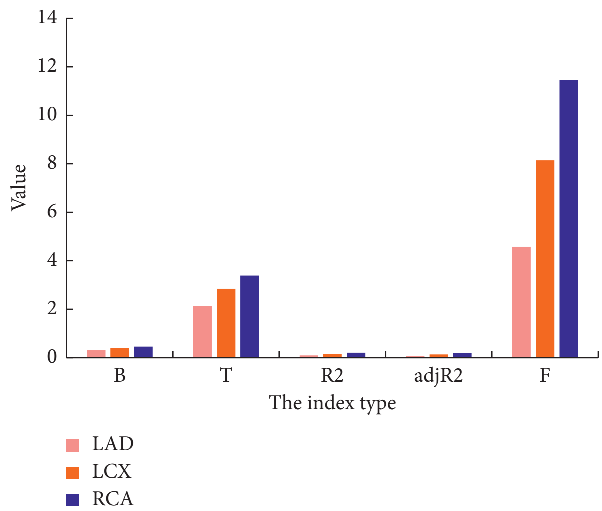

Figure 7: Regression analysis of ECT diagnosis coincidence rate and coronary artery stenosis rate.

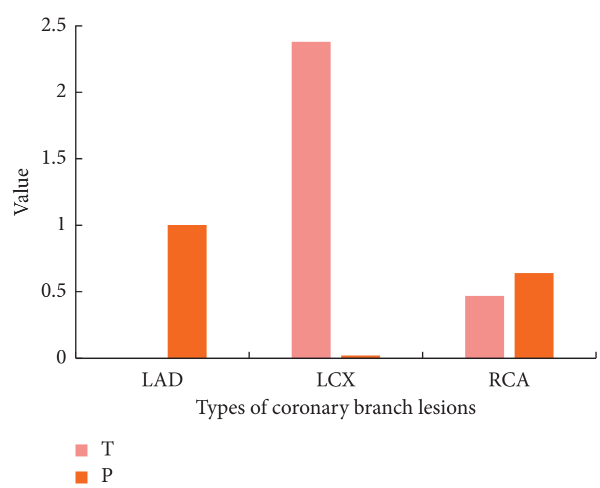

Figure 8: Comparison of the diagnosis coincidence between myocardial ECT imaging and UCG.

underwent PCI seven days after the occurrence of AMI, and the cardiac perfusion function of most patients was improved after the operation. Then, the parameters of cardiac systolic function all changed greatly compared with those before the operation, which suggested that PCI had a good effect on cardiac perfusion and systolic function in patients with AMI.

At present, coronary angiography is still the gold standard for the diagnosis of AMI. With the continuous development of nuclear medicine and imaging technology, radionuclide ECT has also been applied in the diagnosis of heart diseases [14]. ECT is defined as a computer aided technology that uses isotopes to label drugs. Using the principle of human body synthesis, it measures the concentration intensity of isotopes in various organs of the body and its change with time. In this way, the visual shape of the organs is displayed and the functional image information of their physiological process and metabolism is reflected [15]. Clinical data showed that ECT can well reflect myocardial metabolism and blood flow. ECT can also judge the bleeding site, whether bleeding or not, and bleeding area. Compared with coronary angiography, exercise plate, and other examination methods, it has the advantages of noninvasive and no exercise load, which is a noninvasive examination method with good clinical application prospects at present. However, there is currently no consensus on the accuracy, sensitivity, and specificity of ECT in the diagnosis of AMI [16].

Image reconstruction is an important research branch in image processing. It refers to the reconstruction of images based on the data obtained from object detection. Its significance lies in obtaining the image of the internal structure of the detected object without causing any physical damage to the object. Due to its considerable advantages, it has shown unique importance in various application fields [17–19]. For example, it has many applications in medical radiology, nuclear medicine, electron microscopy, radio radar astronomy, light microscopy, holographic imaging, and theoretical vision. FBP algorithm is one of the most widely used algorithms in medical image reconstruction. At present, it is widely used in the generation X-ray CT system [20–22]. CT examination is an important part of the ECT examination. In addition, the images obtained by CT examination are generally of poor quality and low resolution, which seriously affects the quality of the final ECT image fusion. In addition, the images obtained by ECT examination are all the images obtained by the fusion of CT examination and radiological examination, which is also one of the reasons that affect the image quality of ECT examination. At present, the application research of the FBP reconstruction algorithm is basically focused on CT and X-ray image processing, while the application research of ECT image processing is almost absent [23–26].

In this study, the diagnostic effect of ECT image features based on the FBP reconstruction algorithm on the recovery of cardiac function in patients with AMI after PCI surgery was explored. The results showed that all patients had a total of 541 segments before PCI. ECT examination showed 294 abnormal segments of the ventricular wall, with a total score of 585. A total of 100 segments were scored as 1 point, a total of 194 segments were scored as 2 points, and a total of 50 segments were scored as 3 points. After PCI, the abnormal segments were reduced to 58 segments, with a total score of 193. Six segments scored 1 point, 44 segments scored 2 points, and 5 segments scored 3 points. The preoperative EDV, ESV, CO, and EF were 148 ± 16 mL, 77 ± 14.5 mL, 4.29 ± 0.37 L/min, and $41.9 \pm 8\%$, respectively. The EDV, ESV, CO, and EF of the postoperative patients were 132 ± 16 mL, 62 ± 13 mL, 4.89 ± 0.71, and $53 \pm 6\%$, respectively. All systolic function parameters changed significantly after the operation, $P < 0.05$. The standardized regression coefficients of the three groups were 0.32, 0.41, and 0.47, respectively, $P = 0.05$, indicating that the greater the coronary stenosis rate, the higher the diagnostic coincidence rate of LAD, LAD, and RCA. The diagnostic conformity of ECT images in the LCX group for myocardial ischemia was higher than that of UCG, $P < 0.05$, which showed that the results of

ECT examination after PCI showed that the patient's cardiac perfusion and cardiac systolic function were greatly improved. The coincidence rate of the ECT examination based on the filtered back projection reconstruction algorithm for the cardiac function examination results and the coronary angiography examination results increased with the increase of the coronary artery stenosis rate. Compared with cardiac ultrasound, the ECT examination based on the filtered back projection reconstruction algorithm had a higher degree of agreement between the results of the cardiac function examination and the results of coronary angiography. In summary, the ECT technology based on the filtered back projection reconstruction algorithm had a good application prospect in the examination of cardiac function after PCI in AMI patients. However, due to the limited sample size and space, the study was not comprehensive and in-depth enough. In future studies and work, the sample will be further expanded and further studied.

5. Conclusion

This study investigated the diagnostic effect of ECT image features based on the FBP reconstruction algorithm on cardiac recovery after PCI in AMI patients. The results showed that the patients' visceral function recovered significantly after PCI, and ECT based on the FBP reconstruction algorithm had better performance in cardiac function examination than cardiac ultrasound. This study provides a reference and basis for the application of PCI, FBP reconstruction algorithm, and ECT in the diagnosis and treatment of AMI patients. However, due to the limited sample size and space, this study still has some limitations and deficiencies. In future studies and work, we will expand the sample size to further study this problem.

Data Availability

The data used to support the findings of this study are available from the corresponding author upon request.

Conflicts of Interest

The authors declare no conflicts of interest.

References

[1] S. Dorbala, K. Ananthasubramaniam, I. S. Armstrong et al., "Single photon emission computed tomography (SPECT) myocardial perfusion imaging guidelines: instrumentation, acquisition, processing, and interpretation," *Journal of Nuclear Cardiology*, vol. 25, no. 5, pp. 1784–1846, 2018.

[2] H.-J. Pietzsch, C. Mamat, C. Müller, and R. Schibli, "Single photon emission computed tomography tracer," *Molecular Imaging in Oncology*, vol. 216, pp. 227–282, 2020.

[3] N.-T. Yao, Q. Zheng, Z.-Q. Xu et al., "Positron emission computed tomography/single photon emission computed tomography in Parkinson disease," *Chinese Medical Journal*, vol. 133, no. 12, pp. 1448–1455, 2020.

[4] U. Bhure, J. E. Roos, M. d. S. Perez-Lago, and K. Strobel, "Single-photon emission computed tomography/computed tomography arthrography of wrist, ankle, and knee joints," *Nuclear Medicine Communications*, vol. 41, no. 3, pp. 182–188, 2020.

[5] C. A. Raji and T. A. Henderson, "PET and single-photon emission computed tomography in brain concussion," *Neuroimaging Clinics of North America*, vol. 28, no. 1, pp. 67–82, 2018.

[6] Y. Chen, Y. Tao, L. Zhang, W. Xu, and X. Zhou, "Diagnostic and prognostic value of biomarkers in acute myocardial infarction," *Postgraduate Medical Journal*, vol. 95, no. 1122, pp. 210–216, 2019.

[7] J. Chandrasekhar, A. Gill, and R. Mehran, "Acute myocardial infarction in young women: current perspectives," *International Journal of Women's Health*, vol. 10, pp. 267–284, 2018.

[8] J. McCord, L. Aurora, B. Lindahl et al., "Symptoms predictive of acute myocardial infarction in the troponin era: analysis from the TRAPID-AMI study," *Critical Pathways in Cardiology: Journal of Evidence-Based Medicine*, vol. 18, no. 1, pp. 10–15, 2019.

[9] H. Akioka, K. Yufu, Y. Teshima et al., "Seasonal variations of weather conditions on acute myocardial infarction onset: oita AMI Registry," *Heart and Vessels*, vol. 34, no. 1, pp. 9–18, 2019.

[10] H. Ranjbaran, S. Abediankenari, M. Mohammadi et al., "Wharton's jelly derived-mesenchymal stem cells: isolation and characterization," *Acta Medica Iranica*, vol. 56, no. 1, pp. 28–33, 2018.

[11] M. M. Monita and L. Gonzalez, "Acute Mesenteric Ischemia," in *StatPearls*StatPearls Publishing, Treasure Island, FL, USA, 2020.

[12] M. Bahall and K. Khan, "Quality of life of patients with first-time AMI: a descriptive study," *Health and Quality of Life Outcomes*, vol. 16, no. 1, p. 32, 2018.

[13] K. Wita, A. Kułach, J. Sikora et al., "Managed care after acute myocardial infarction (MC-AMI) reduces total mortality in 12-month follow-up-results from a Poland's national health fund program of comprehensive post-MI care-a population-wide analysis," *Journal of Clinical Medicine*, vol. 9, no. 10, p. 3178, 2020.

[14] Q. Wang, B. Liu, Y. Wang, B. Bai, T. Yu, and X. m. Chu, "The biomarkers of key miRNAs and target genes associated with acute myocardial infarction," *PeerJ*, vol. 8, Article ID e9129, 2020.

[15] M. J. Willemink and P. B. Noël, "The evolution of image reconstruction for CT-from filtered back projection to artificial intelligence," *European Radiology*, vol. 29, no. 5, pp. 2185–2195, 2019.

[16] M. H. Goodenberger, N. A. Wagner-Bartak, S. Gupta et al., "Computed tomography image quality evaluation of a new iterative reconstruction algorithm in the abdomen (adaptive statistical iterative reconstruction-V) a comparison with model-based iterative reconstruction, adaptive statistical iterative reconstruction, and filtered back projection reconstructions," *Journal of Computer Assisted Tomography*, vol. 42, no. 2, pp. 184–190, 2018.

[17] A. M. Dimmitt, J. A. Pelz, M. E. Albertson et al., "Evaluation of adaptive statistical iterative reconstruction-V reconstruction algorithm vs filtered back projection in the detection of hypodense liver lesions," *Journal of Computer Assisted Tomography*, vol. 43, no. 2, pp. 200–205, 2019.

[18] Z. Lv, X. Li, and W. Li, "Virtual reality geographical interactive scene semantics research for immersive geography learning," *Neurocomputing*, vol. 254, pp. 71–78, 2017.

[19] Z. Lv, X. Li, W. Wang, B. Zhang, J. Hu, and S. Feng, "Government affairs service platform for smart city," *Future Generation Computer Systems*, vol. 81, pp. 443–451, 2018.

[20] Y. J. Shin, W. Chang, J. C. Ye et al., "Low-dose abdominal CT using a deep learning-based denoising algorithm: a comparison with CT reconstructed with filtered back projection or iterative reconstruction algorithm," *Korean Journal of Radiology*, vol. 21, no. 3, pp. 356–364, 2020.
[21] W. Stiller, "Basics of iterative reconstruction methods in computed tomography: a vendor-independent overview," *European Journal of Radiology*, vol. 109, pp. 147–154, 2018.
[22] T. Higaki, Y. Nakamura, J. Zhou et al., "Deep learning reconstruction at CT: phantom study of the image characteristics," *Academic Radiology*, vol. 27, no. 1, pp. 82–87, 2020.
[23] T. Wang, H. Kudo, F. Yamazaki, and H. Liu, "A fast regularized iterative algorithm for fan-beam CT reconstruction," *Physics in Medicine and Biology*, vol. 64, no. 14, Article ID 145006, 2019.
[24] J. Greffier, A. Hamard, F. Pereira et al., "Image quality and dose reduction opportunity of deep learning image reconstruction algorithm for CT: a phantom study," *European Radiology*, vol. 30, no. 7, pp. 3951–3959, 2020.
[25] S. Ozaki, A. Haga, E. Chao et al., "Fast statistical iterative reconstruction for mega-voltage computed tomography," *Journal of Medical Investigation*, vol. 67, no. 1, pp. 30–39, 2020.
[26] K. Sato, Y. Tomita, R. Kageyama, Y. Takane, S. Kayano, and H. Saito, "Method to calculate frequency characteristics of reconstruction filter kernel in X-ray computed tomography," *Physical and Engineering Sciences in Medicine*, vol. 43, no. 1, pp. 69–78, 2019.

Hindawi
Journal of Healthcare Engineering
Volume 2021, Article ID 5317403, 12 pages
https://doi.org/10.1155/2021/5317403

Research Article

Deep Learning Algorithms-Based CT Images in Glucocorticoid Therapy in Asthma Children with Small Airway Obstruction

Yu Qin,[1] **Jing Wang**,[2] **Yanjun Han**,[1] **and Ling Lu**[3]

[1]*Department of Pediatrics, Xingtai People's Hospital, Xingtai 054001, Hebei, China*
[2]*Department of Endocrinology, Xingtai People's Hospital, Xingtai 054001, Hebei, China*
[3]*Department of Pediatrics, Zaozhuang Municipal Hospital, Zaozhuang, Shandong 277100, China*

Correspondence should be addressed to Ling Lu; 3160200102@caa.edu.cn

Received 28 August 2021; Revised 29 September 2021; Accepted 1 October 2021; Published 21 October 2021

Academic Editor: Enas Abdulhay

CT image information data under deep learning algorithms was adopted to evaluate small airway function and analyze the clinical efficacy of different glucocorticoid administration ways in asthmatic children with small airway obstruction. The Res-NET in the deep learning algorithm was used to perform feature extraction, summary classification, and other reconstruction of CT images. A deep learning network model Mask-R-CNN was constructed to enhance the ability of image reconstruction. A total of 118 children hospitalized with acute exacerbation of asthma in the hospital were recruited. After acute exacerbation treatment, 96 children with asthma were screened out for small airway obstruction, which were divided into glucocorticoid aerosol inhalation group (group A, 32 cases), glucocorticoid combined with bronchodilator aerosol inhalation group (group B, 32 cases), and oral hormone therapy group (group C, 32 cases). Asthmatic children with small airway obstruction were screened after acute exacerbation treatment and were rolled into glucocorticoid aerosol inhalation group (group A), glucocorticoid combined with bronchodilators aerosol inhalation group (group B), and oral hormone therapy group (group C). Lung function indicators (maximal mid-expiratory flow (MMEF75 and 25), 50% forced expiratory flow (FEF50), and 75% forced expiratory flow (FEF75)), FeNO level, and airway inflammation indicators (IL-6, IL-35, and eosinophilic (EOS)) were compared before and one month after treatment. The ratio of airway wall thickness to outer diameter (T/D) and the percentage of airway wall area to total airway area (WA%) were measured by e-Health high-resolution CT (HRCT). The constructed network model was used to measure the patient's coronary artery plaque and blood vessel volume, and the image was reconstructed on the Res-Net network. It was found that the MSE value of the Res-Net network was the lowest, and the efficiency was very high during the training process. T/D and WA (%) of asthmatic children with small airway obstruction after treatment were significantly lower than those before treatment ($P < 0.01$). After treatment, MMEF75/25 and FEF75 were significantly higher than those before treatment ($P < 0.05$). Lung function-related indicator FEF50 was significantly higher than that before treatment ($P < 0.01$). FeNO level after treatment was remarkably lower than that before treatment ($P < 0.01$). In addition, lung function-related indicators, airway inflammation indicators, and FeNO level improved the most in group C, followed by group B, and those improvements in group A were the least obvious, with great differences among groups ($P < 0.05$). In summary, the Res-Net model proposed was of certain feasibility and effectiveness for CT image segmentation and can effectively improve the clinical evaluation of patient CT image information. Glucocorticoids could improve small airway function and airway inflammation in asthmatic children with small airway obstruction, and oral corticosteroids were more effective than aerosol inhalation therapy.

1. Introduction

Bronchial asthma, referred to as asthma, is a relatively common small airway disease, which is the chronic inflammation of the airway involving a variety of cells such as eosinophils and lymphocytes [1]. The incidence of asthma occurs in all ages, especially in children [2]. Studies have shown that children under the age of 14 suffer the most severe damage from asthma [3]. With the acceleration of urbanization and the increase of air pollution, the prevalence of childhood asthma in China is increasing year by year, which poses a serious threat to children's physical and mental health [4]. Glucocorticoids are the basic drugs for clinical treatment of asthma, which can not only participate in the multiple processes of airway inflammation, but also affect the permeability of capillaries. Moreover, it has a significant effect on alleviating bronchospasm and preventing pulmonary edema. As a result, the lung function is improved, and finally the onset of asthma is inhibited [5, 6]. There are many ways of drug treatment; systemic administration takes effect quickly, yet there are many adverse reactions; thus, it is restricted in clinical use. Local treatments are usually susceptible to drug particle size restrictions. However, the drug directly acts on the target organs, which is safe and effective. Studies have shown that glucocorticoid combined with bronchodilators can improve the clinical symptoms and pulmonary airway function of asthma patients, and the clinical efficacy is better than single administration. Whether the combination of drugs has the same effect on asthmatic children with small airway obstruction is still not clear. Therefore, exploring the different ways of administration of glucocorticoids is of great significance for the clinical treatment of asthmatic children with small airway obstruction.

The small airway is the most important part of asthma and chronic obstructive pulmonary disease. The onset of asthma is characterized by irreversible obstruction of the patient's airway. Therefore, small airways play a key role in the control and management of asthma diseases [7].

Medical image analysis is greatly influenced by subjective experience. The use of CT for auxiliary diagnosis of diseases can quickly and accurately judge diseases and reduce the rate of missed diagnosis and misdiagnosis in clinical diagnosis. It can improve the diagnosis rate of clinical lung cancer, thereby improving the quality of life of patients after surgery. The application of deep learning methods in images can assist physicians to make early disease diagnosis, positive treatment plans, and effective clinical decisions through measurement, evaluation, classification, diagnosis, and assisting preoperative design, which can effectively improve the efficiency of medical imaging for disease detection, recognition, and diagnosis and then promote and realize computer assisted treatment in the field of medical and health. Deep learning can realize image translation and other operations through weight sharing and other methods, optimize complex operations of image preprocessing, and achieve target detection and image classification [8]. With the rapid development of the e-health field, a variety of medical electronic products such as lung function instruments [9], spiral CT [10], and high-resolution CT (HRCT) [11] can be adopted in the detection of small airway diseases. Among them, high-resolution CT is the preferred method for evaluating small airway function, and it is also a hot spot in the field of imaging [12]. Dual-source computed tomography is a new device based on mature 64-slice CT technology. It has a great breakthrough in time resolution. The system imaging time resolution reaches 83 ms, which is 0.1 s less than the time required for cardiac imaging. The speed of each heartbeat is fast, which effectively improves the time resolution and has become the main method for noninvasive diagnosis of coronary heart disease. Dual-source CT has the characteristics of thin layer thickness, small pitch, small collimation, etc. The whole heart cycle exposure scanning method has a large radiation dose to the patient's blood vessels.

HRCT is of high sensitivity and specificity for the detection of small airway diseases, which can quickly collect the information of the lesion area and accurately identify the small structural changes of the airway. It is a safe, noninvasive, and easy-to-operate inspection method, which is widely used in clinical practice. Deep learning networks are often used in medicine to learn original images and are widely used in image segmentation, image classification, and target image positioning. Some scholars have proposed in research that combining pixel information of different scales can extract the best size information; some researchers believe that reducing the size of the convolution kernel can increase the running speed of the neural network. At present, there are few reports on the diagnosis of glucocorticoid in the treatment of children with asthma with small airway function obstruction by high-resolution CT image information data, and the study of deep learning method in this aspect is still insufficient. On the basis of the above research, this research further optimizes the convolutional neural network. The Res-Net network is used to reconstruct CT images, and a deep learning network model is constructed to enhance the ability of image reconstruction. By measuring lung function, airway inflammation indicator, and FeNO level, the clinical efficacy of glucocorticoid therapy was explored, to provide a theoretical basis for the assessment of asthma and the exploration of treatments.

2. Materials and Methods

2.1. Research Subjects. A total of 118 children who were hospitalized with acute exacerbation of asthma from October 2017 to October 2019 were selected, including 72 males and 46 females (6.86 ± 2.31 years). Inclusion criteria: I, patients aged 1–14 years; II, patients who met the diagnostic criteria for childhood asthma [13]; III, patients who could receive FeNO and lung function tests. Exclusion criteria: I, patients received glucocorticoid therapy in the past month; II, patients with antihistamine treatment history; III, patients with lung tissue fibrosis; IV, patients with pneumonia, chronic obstructive pulmonary disease, or malignant tumor; V, patients with poor compliance. This experiment had been approved by the ethics committee of the hospital, and the children and their families included in the study had signed an informed consent.

2.2. Grouping and Treatments. All patients received treatments of anti-inflammatory, anti-asthma, and phlegm, and the course of treatment was 7–12 days. Lung function indicators and FeNO levels were measured after symptom improvement. During this period, 2 children with respiratory failure were excluded. Then, according to the lung function test results, 8 patients with normal small airway function and 12 patients with obstructed atmospheric airway function were excluded. A total of 96 patients with small airway obstruction were screened, and the basic data of patients with mild obstruction (MMEF75/25 ≥ 50%) and patients with severe obstruction (MMEF75/25 < 50%) were compared.

Exclusion criteria for normal small airway function: FEV1/FVC > 70%, FEV1, FVC, and PEF were all greater than 80% of predicted values; there were no more than 2 indicators lower than 65% of predicted values among FEF50%, FEF75%, and MMEF75/25.

Exclusion criteria for atmospheric channel functional obstruction: FEV1/FVC < 70%, FEV1, FVC, and PEF were all less than 80% of predicted values.

Inclusion criteria for small airway obstruction: FEV1/FVC > 70%, FEV1, FVC, and PEF were all greater than 80% of predicted values; there were no less than 2 indicators lower than 65% of predicted values among FEF50%, FEF75%, and MMEF75/25.

A total of 96 small airway obstruction children were randomly divided into group A, group B, and group C. Patients in group A were treated with glucocorticoid aerosol inhalation (local administration), namely, budesonide suspension, twice per day. The children in group B were treated with glucocorticoid combined with bronchodilator aerosol inhalation (local administration), namely, budesonide suspension combined with terbutaline sulfate atomization solution, twice per day. Group C were treated with systemic drug administration, namely, oral methylprednisolone at 8 mg/day.

2.3. HRCT Detection. Patients were examined using Siemens Somatom Definition DSCT, Germany. The e-health equipment HRCT was adopted to examine asthmatic children with small airway obstruction. Target scanning technology was adopted, and scanning was performed when patients were peacefully breathing. The scanning range included the aortic arch, tracheal bifurcation and 2 cm below the bifurcation, 2 cm above the top of the pulmonary diaphragm, and the inferior pulmonary vein trunk, with a total of 5 layers. Scanning parameters: 120 kV, 200 mA; reconstruction parameters: 1200–1500 Hu window width, −500 window level, 3 mm layer thickness, and 2 mm layer spacing. Two or more experienced pediatric imaging physicians selected all levels of airway on the cross-sectional image for measurement. The measurement diagram of the airway wall inner diameter L and the airway wall outer diameter D is shown in Figure 1, and the average value was taken.

The ratio of airway wall thickness to outer diameter (T/D) was calculated according to the following equation, and the percentage of airway wall area accounting for airway cross-sectional area (WA%) was calculated via equation (2).

$$\frac{T}{D} = \frac{D - L}{2D}, \tag{1}$$

$$\text{WA\%} = \frac{\pi (D/2)^2 - \pi (L/2)^2}{\pi (D/2)^2} \times 100\%. \tag{2}$$

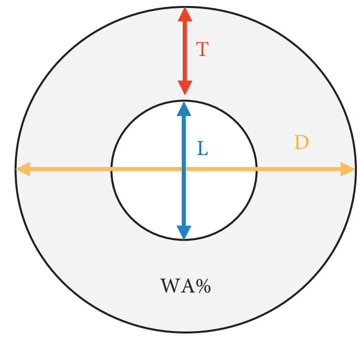

Figure 1: Schematic diagram of measurement of the inner and outer diameter of airway wall.

2.4. Deep Learning Reconstruction Algorithm. There are many algorithms for CT image reconstruction using deep learning, and the filtered backprojection algorithm can reconstruct CT images with better quality. The research on the network structure of deep learning is getting more and more in-depth, and the deep abstract semantic information of the image can also be extracted. As the number of layers increases, different neural networks have different trends in the classification of accuracy in the model. Networks such as AlexNet, GoogLeNet, and Res-Net are gradually decreasing in classification accuracy. The network depth keeps increasing, and the accuracy will increase to a certain extent, but beyond this level, there will be a gradient explosion problem, so the accuracy of the model training will decrease. In the NesNet network, there are residual errors and the results of the remaining modules, and its accuracy is better than that of networks such as AlexNet and GoogLeNet. As shown in Figure 2, the module connects the output to the input through skip connect. In the convolution calculation, a lot of image information corresponding to the input feature mapping of the residual module can be retained. This realizes that the NesNet network effectively improves the model when it is added in-depth.

2.5. Design of the Network Model. The R-CNN in the deep learning model follows the traditional target detection idea, first extracting candidate frames, and then extracting features for each frame. In the Fast-R-CNN network structure, classification, feature extraction, proposal extraction, and border regression are integrated into one network, which is conducive to the deep learning network to complete multiple tasks at the same time, and the detection speed is significantly improved. As shown in Figure 3, Mask-R-CNN adds a branch to Fast-R-CNN to obtain a new network framework. This new mask branch is applied to each RoI (Region of Interest). The small-scale fully convolutional neural network predicts the segmentation mask in a pixel-to-pixel manner, and a variety of flexible architecture designs are also added to the training. Mask-R-CNN uses bilinear interpolation to obtain the key coordinates of the small unit and performs the maximum pooling operation internally.

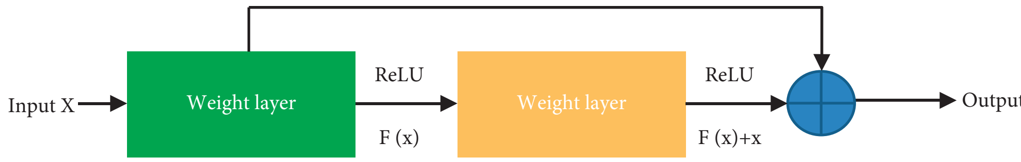

Figure 2: ResNet.

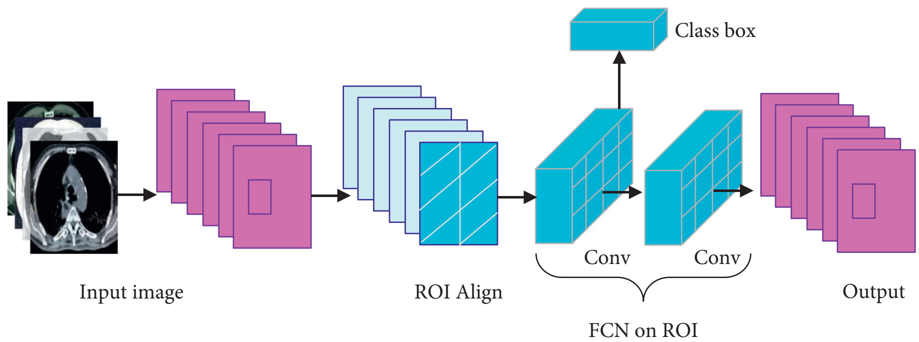

Figure 3: Structure of mask-R-CNN.

2.6. Model Improvement. The neural network trains the initial weight file on the MSCOCO data set in advance and trains it in the subsequent training process. The neural network of the multilayer residual block constitutes a semantic feature extraction module. The information after the module convolution operation and the input information are connected by the residual block through Skip connect to ensure the integrity of the information flow. The residual equation is as follows:

$$H(x) = F(x) + X. \tag{3}$$

In equation (3), $F(x)$ is the result of the convolution operation of the current residual block of the input information X. The upsampling function enables the input image to obtain deep abstract semantic information and restore feature maps of different sizes. When predicting the candidate frame, the feature map generated in the first step needs to have anchor boxes with different aspect ratios. If the size of the i-layer image is (H, W), and n is the number of candidate frame aspect ratios, then the aspect ratio $R = [R1, R2, R3, \ldots, Rn]$, H means height, and W means width; then, the equation for the total number of anchor boxes in this layer is expressed as

$$N = H \times W \times n. \tag{4}$$

Anchor boxes of different specifications slide on the feature map, and the target area is not necessarily within the frame selection area. The selection of the candidate frame in the algorithm is based on the degree of overlap (IOU) between the content of the candidate frame and the gold standard. If C is the candidate frame area, and D is the gold standard area, then equation (4) indicates that the coincidence degree of the two areas is

$$\mathrm{IOU} = \frac{(C \cap D)}{(C \cup D)}. \tag{5}$$

Let β be the threshold; if IOU $<\beta$, the candidate region is considered as a positive sample; if IOU $>\beta$, the candidate region is considered as a negative sample. After the Anchor box detection is valid, the offset between the candidate box and the gold standard is calculated. Let the height and width of the candidate box be (H, W), the center coordinates of the Anchor box (a, b), the height and width of the image (H_1, W_1), and the target coordinates (a_1, b_1), and then the offset is

$$\begin{aligned}
\Delta a &= \frac{a_1 - a}{W},\\
\Delta b &= \frac{b_1 - b}{h},\\
\Delta w &= \log \frac{w_1}{W},\\
\Delta h &= \frac{h_1}{h}.
\end{aligned} \tag{6}$$

After the prediction of the candidate box, enter the Anchor box in the RPN network example for classification and regression. First, the gold standard corresponding to the positive sample and the screening are performed to obtain the score of the Anchor box. Calculate the cross entropy function. The cross entropy function can adjust the backpropagation and classification. The function equation is as follows:

$$\mathrm{LOSS}_C = \sum_{j=1}^{T} y_j \log \frac{e^{aj}}{\sum_{K=1}^{T} e^{ak}}. \tag{7}$$

In the equation, y_j represents the probability value of the gold standard corresponding to the positive sample, and a_j represents the predicted probability of the sample before normalization. The loss function calculation is performed according to the offset calculated when the anchor box is generated and the offset between the positive sample and the gold standard. The equation is as follows:

$$\text{smooth}\,L(x) = \begin{cases} 0.5\,(x)^2, & if\ |x| < 1, \\ |x| - 0.5, & \text{otherwise}, \end{cases} \qquad (8)$$
$$L = \sum \text{smooth}_L\,(t - t^*).$$

The target area scores are obtained for sorting, and the candidate frames with high scores are normalized by bilinear interpolation.

2.7. Detection Indicators

2.7.1. FeNO. FeNO levels of children in each group were measured before and 1 month after treatment. Preparation before the test was as follows. Fasting food with high nitrogen content was conducted 10 hours before the test, and the consumption of stimulants drinks such as caffeine was prohibited. The strenuous activities were avoided, and the child was kept calm. Specific detection method: the nose clip was used to gently clip the patient's nose, and the filter was held by the mouth. Children breathed the air in lung out, then breathed normally, and kept the uniform speed of breath about 5 s.

2.7.2. Pulmonary function. Pulmonary ventilatory function was measured before and 1 month after treatment in each group with the Jaeger Master Screen. Children should not take hormones, bronchodilators, and other drugs one day before the test. Two hours before the test, children should fast for solids and liquids, avoid strenuous exercise, and remain calm. Specific test method: children should sit and then close the nasal cavity and mouth with a nasal clip to completely contain the filter. After breathing normally several times, children should try their best to exhale the air in the lungs quickly. The test was repeated for several times, the three test values conforming to the quality control standard were taken, and the maximum value was taken as the final test result. The indicators of small airway were as follows: MMEF75/25, FEF50%, FEF75%, FEV1, PEF, and FVC. The improvement rate = (Posttreatment − pretreatment)/pretreatment × 100%.

Serum airway inflammation indicators: IL-35 and IL-6 levels were detected by ELISA, and EOS was determined by automatic blood count.

2.8. Statistical Analysis. SPSS22.0 statistical software was used for analysis. Normally distributed measurement data were expressed as mean plus or minus standard deviation ($\overline{x} \pm s$), and differences between groups were analyzed by variance analysis. If $P < 0.05$, the difference was statistically significant.

3. Results

3.1. Comparison of Clinical Data. A total of 118 children with bronchial asthma were treated in the acute exacerbation period, after which 12 cases of children with large airway injury were excluded, 8 cases of small airway function were normal, and 2 cases of respiratory failure were also excluded. Table 1 shows comparison of basic data of children with different degrees of small airway obstruction. There was no significant difference in age, gender, and BMI between children with mild obstruction and children with severe obstruction ($P > 0.05$). The course of children with mild obstruction was 18.56 ± 8.69 (months), and the interval of medication was 7.36 ± 5.47 (h). The course of the children with severe obstruction was 20.26 ± 5.38 (months), and the interval of medication was 9.76 ± 6.59 (h). The duration of the disease in children with severe obstruction was longer than that in children with mild obstruction, and the time interval from onset to regular medication was longer than that of children with mild obstruction ($P < 0.05$).

Table 2 shows the comparison of baseline data of the three groups of asthmatic children with small airway obstruction. There were no statistically significant differences in age, gender, BMI, lung function-related indicators (MMEF75/25, FEF50, and FEF75), and FeNO levels between group A, group B, and group C ($P > 0.05$). However, the three groups had statistically significant differences in the course of disease and interval between medications ($P < 0.05$).

3.2. Imaging Characteristics of Asthmatic Children with Small Airway Obstruction. The HRCT of e-health equipment was adopted to examine the characteristics of small airway lesions in asthmatic children with small airway obstruction, as shown in Figure 4. In some patients, the wall of the bronchioles had thickened, with small nodules, branch shadows, or ring shadows (Figure 4(a)). About 3–5 mm below the pleura, there were multiple small nodules and branch-like dense shadows distributed in the center of the leaflets, which looked like branch buds (Figure 4(b)). The lungs had limited low-density shadows and clear edges (Figure 4(c)). Irregular patterns or patches appeared in areas with increased lung density and areas with decreased lung density, but the edges were very clear (Figure 4(d)). The red box in the images indicated the location of the lesion.

3.3. Comparison of HRCT Test Results and Small Airway Function before and after Treatment. HRCT was used to detect changes in T/D and WA (%) in asthmatic children with small airway obstruction in asthma before and after treatment. In Figure 5, before treatment, T/D and WA (%) were 34.65 ± 3.86 (%) and 85.29 ± 12.54 (%), respectively. After one month of treatment, the T/D and WA (%) of asthmatic children with small airway obstruction were 23.38 ± 3.27 (%) and 78.65 ± 13.45 (%), respectively. The T/D and WA (%) of asthmatic children with small airway obstruction after treatment were significantly lower than those before treatment ($P < 0.01$).

Before treatment, the MMEF75/25, FEF50, and FEF75 of asthmatic children with small airway obstruction were 2.08 ± 0.52, 2.38 ± 0.48, and 1.25 ± 0.32, respectively. After one month of treatment, the MMEF75/25, FEF50, and

Table 1: Basic conditions of children with different degrees small airway obstruction.

Item	Children with mild obstruction	Children with severe obstruction	F	P
Age (year)	6.38 ± 1.16	6.65 ± 0.98	0.103	0.747
Gender (male/female)	0.54 ± 0.52	0.49 ± 0.53	0.24	0.643
BMI (kg/m^2)	24.01 ± 3.20	22.76 ± 3.37	0.421	0.527
Course (month)	18.56 ± 8.69	20.26 ± 5.38	3.853	0.049
Interval of medication (h)	7.36 ± 5.47	$9.76 \pm 6.59^*$	9.763	0.001

Note. *The difference was significant.

Table 2: Basic data of asthmatic children with small airway obstruction in each group.

Item	Group A	Group B	Group C	F	P
Age (year)	6.43 ± 1.25	6.58 ± 1.05	6.63 ± 1.02	−2.650	0.674
Gender (male/female)	0.54 ± 0.52	0.49 ± 0.53	0.52 ± 0.50	0.421	0.643
BMI (kg/m^2)	24.07 ± 3.24	23.97 ± 3.36	24.28 ± 3.12	0.088	0.765
Course (month)	21.37 ± 8.95	19.48 ± 9.88	20.64 ± 10.03	1.265	0.279
Interval of medication (h)	9.65 ± 6.91	6.97 ± 5.65	8.62 ± 7.84	0.786	0.426
MMEF75/25	2.12 ± 0.59	2.13 ± 0.48	1.97 ± 0.53	0.71	0.456
FEF50	2.36 ± 0.56	2.27 ± 0.43	2.40 ± 0.46	0.581	0.534
FEF75	1.28 ± 0.19	1.27 ± 0.26	1.18 ± 0.22	2.282	0.102
FeNO (ppb)	34.78 ± 1.98	35.01 ± 2.21	34.78 ± 2.04	0.289	0.732

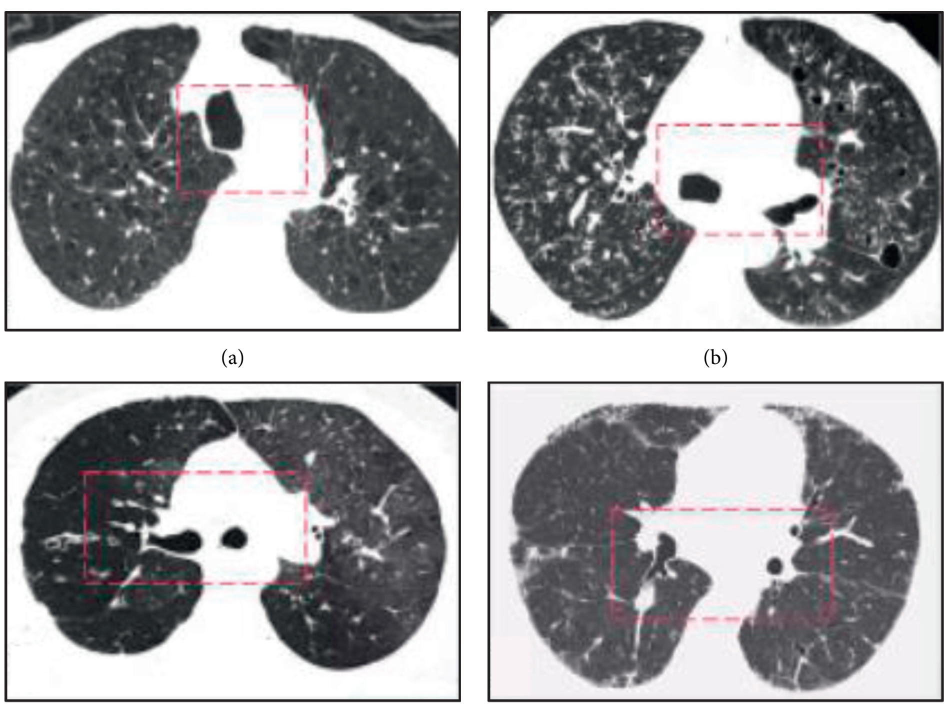

(a) (b) (c) (d)

Figure 4: HRCT images of asthmatic children with small airway obstruction. (a) Bronchiolar wall thickening; (b) tree-in-bud; (c) air trapping; (d) mosaic sign.

FEF75 of asthmatic children with small airway obstruction were 2.88 ± 0.84, 3.24 ± 0.79, and 1.68 ± 0.39, respectively. After treatment, the pulmonary function-related indicators MMEF75/25 and FEF75 were significantly higher than those before treatment ($P < 0.05$). After treatment, FEF50, a related indicator of lung function, was extremely significantly higher than that before treatment ($P < 0.01$) (Figure 6(a)). The FeNO level of asthmatic children with small airway obstruction was 35.00 ± 2.11 (ppb) before treatment and 34.12 ± 2.16 (ppb) after treatment. The FeNO level after treatment was lower than that before treatment ($P < 0.01$), as shown in Figure 6(b).

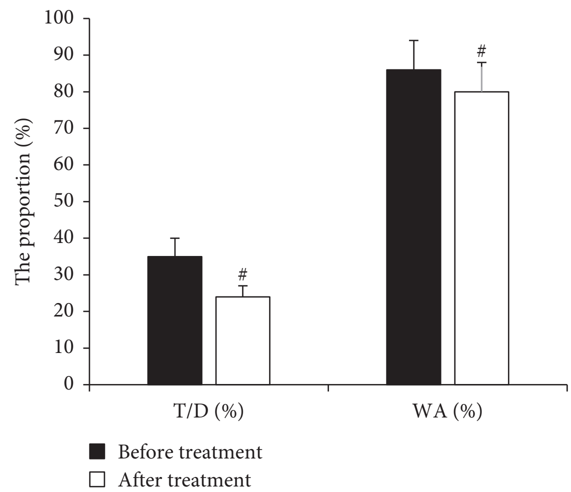

Figure 5: Comparison of T/D and WA (%) before and after treatment ($^{\#}P < 0.01$ as compared to that before treatment).

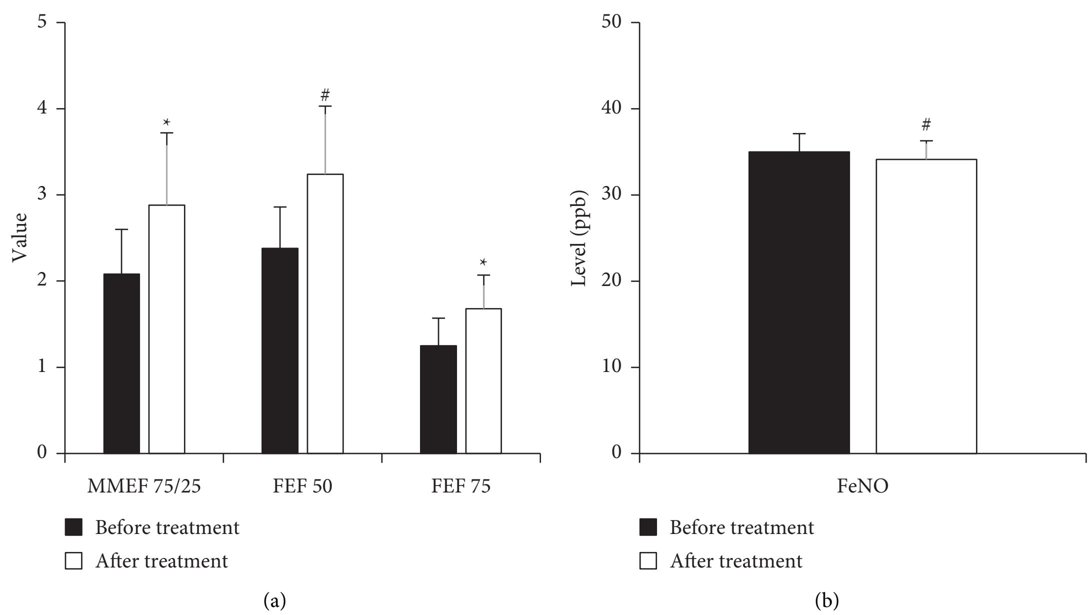

Figure 6: Comparison of lung function-related indicator and FeNO level before and after treatment. (a) Lung function-related indicator; (b) FeNO; $^{*}P < 0.05$ as compared to that before treatment; $^{\#}P < 0.01$ as compared to that before treatment.

3.4. Comparison of Improvement of Small Airway Function in Each Group. Figure 7 shows the changes in lung function of children in each group after treatment. The MMEF75/25 values of group A, group B, and group C were 2.55 ± 0.68, 2.92 ± 0.76, and 3.13 ± 0.92, respectively; FEF50 values were 2.82 ± 0.68, 3.03 ± 0.70, and 3.78 ± 0.74, respectively; FEF75 values were 1.50 ± 0.21, 1.71 ± 0.39, and 1.76 ± 0.46, respectively. The improvement rates were 17.32 ± 5.87 (%), 34.36 ± 4.98 (%), and 56.12 ± 9.54 (%), respectively. The MMEF75/25, FEF50, and FEF75 values and improvement rate of children in group B were significantly higher than those in group A ($P < 0.05$). The values of MMEF75/25, FEF50, FEF75, and improvement rate of children in group C were significantly higher than those in groups A and B ($P < 0.05$).

Figure 8 shows the comparison of FeNO levels of children in each group after treatment. FeNO levels of group A, group B, and group C were 34.76 ± 2.07 (ppb), 34.12 ± 2.18 (ppb), and 33.28 ± 2.16 (ppb), respectively. The FeNO level of children in group B was lower than that of group A ($P < 0.05$), and the level of FeNO of children in group C was lower than that of groups A and B ($P < 0.05$).

3.5. Comparison of Airway Inflammation Indicators in Each Group. The comparison of IL-6 and IL-35 levels of children in each group before and after treatment is shown in Figure 9. In Figure 9(a), the IL-6 levels (ng/mL) before treatment in group A, group B, and group C were 6.24 ± 1.54,

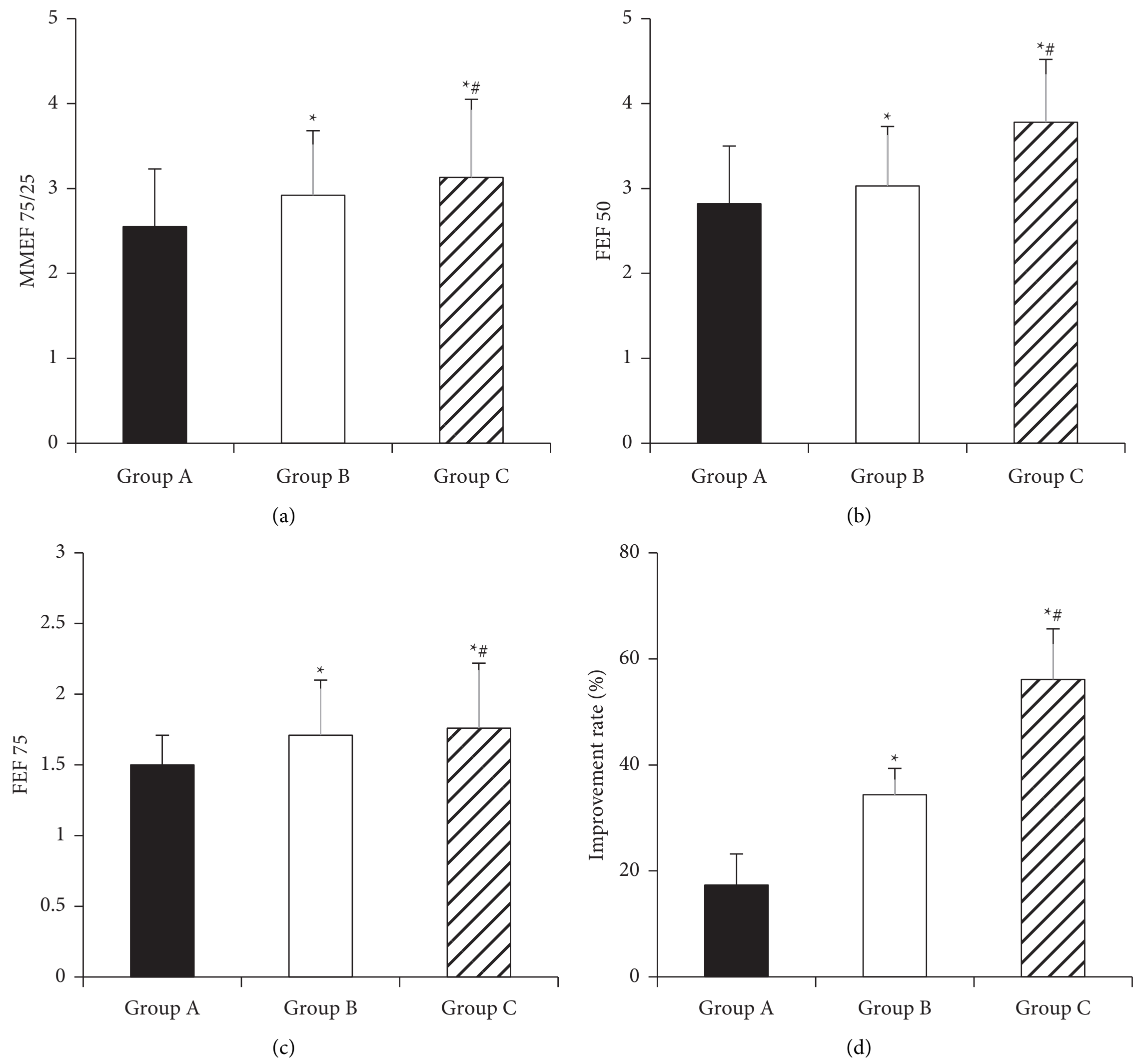

Figure 7: Comparison of lung function-related indicator after treatment in each group. (a) MMEF75/25; (b) FEF50; (c) FEF75; (d) improvement rate; *compared with group A $P < 0.05$; #compared with group B $P < 0.05$).

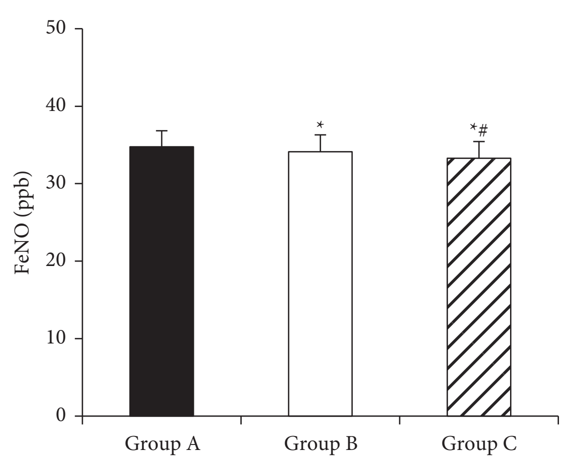

Figure 8: Comparison of FeNO levels after treatment in each group (*compared to group A ($P < 0.05$; #compared to group B $P < 0.05$).

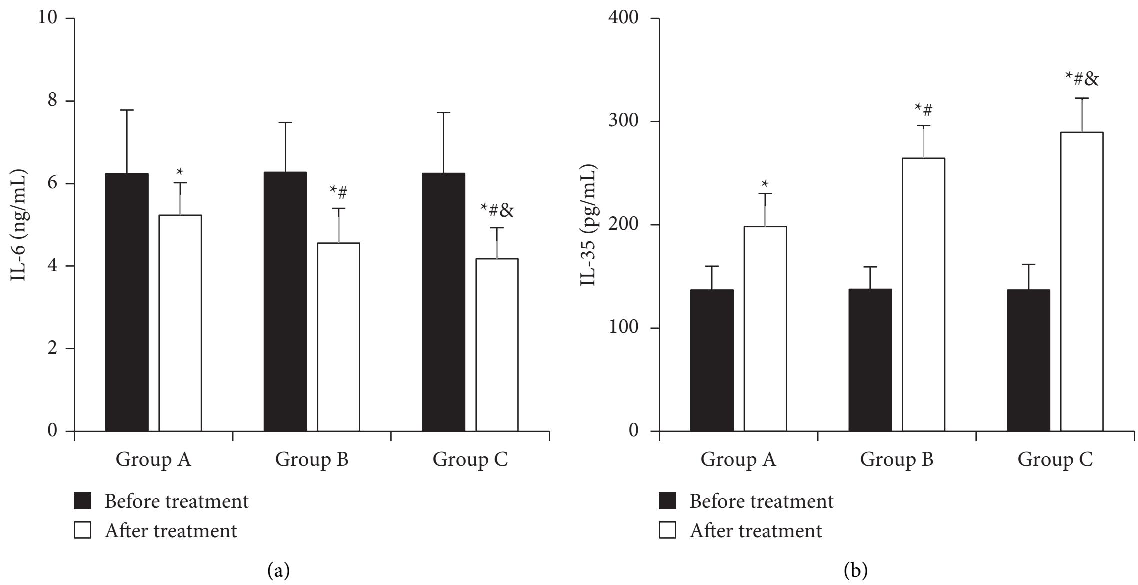

Figure 9: Comparison of IL-6 and IL-35 levels before and after treatment in each group. (a) IL-6; (b) IL-35; $^*P < 0.05$, compared to that before treatment; $^\#P < 0.05$, compared to that in group A; $^\&P < 0.05$, compared to that in group B.

6.27 ± 1.21, and 6.25 ± 1.47, respectively. The levels of IL-6 (ng/mL) after treatment were 5.23 ± 0.79, 4.56 ± 0.84, and 4.18 ± 0.75, respectively. After treatment, the IL-6 level of children in each group was significantly lower than that before treatment ($P < 0.05$), that of children in group B was lower than that of group A ($P < 0.05$), and that of children in group C was lower than that in group A and group B ($P < 0.05$). In Figure 7(b), the IL-35 levels (Pg/mL) of group A, group B, and group C before treatment were 136.67 ± 23.26, 137.56 ± 21.67, and 136.96 ± 24.72, respectively. The levels of IL-35 (Pg/mL) after treatment were 198.25 ± 32.02, 264.59 ± 31.64, and 289.65 ± 33.12, respectively. The levels of IL-35 in children in each group were significantly higher than those before treatment ($P < 0.05$), those in group B were higher than those in group A ($P < 0.05$), and those in group C were higher than those in group A and group B ($P < 0.05$).

The comparison of EOS values before and after treatment in each group is shown in Figure 10. The EOS ($\times 10^6$/L) before treatment in group A, group B, and group C was 685.28 ± 86.26, 692.54 ± 76.78, and 689.62 ± 79.94, respectively. EOS ($\times 10^6$/L) after treatment was 264.27 ± 42.65, 225.62 ± 40.37, and 201.35 ± 42.19, respectively. After treatment, the EOS of children in each group was significantly lower than that before treatment ($P < 0.05$), that of group B was lower than that of group A ($P < 0.05$), and that of group C was lower than that of group A and group B ($P < 0.05$).

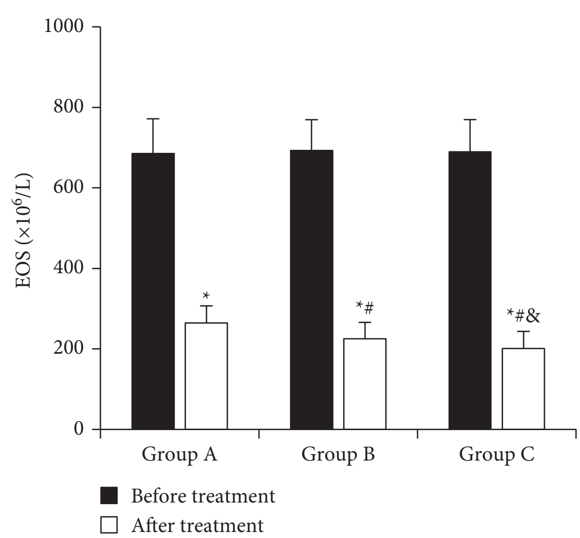

Figure 10: Comparison of EOS values before and after treatment in each group. $^*P < 0.05$, compared to that before treatment; # $P < 0.05$, compared to that in group A; & $P < 0.05$, compared to that in group B.

3.6. MSE Curve. The smaller the MSE, the better the accuracy of the prediction model to describe the experimental data. In Figure 11, the Res-Net network has a smaller MSE than the other two networks, and the effect is extremely fast during the training process, indicating the improvement. The network effect is remarkable.

3.7. CT Image. Figure 12(b) shows a CT image of the lungs. The patient was a male 52-year-old patient. Compared with the right lung, the left lung is obviously branched. In Figure 12(a), the patient's lungs show that the bronchial tubes are not thinned but widened, which is a typical branch expansion. The red box in the figure shows the characteristics of the lesion CT.

4. Discussion

Asthma is a heterogeneous disease of the airways, whose attacks usually involve the air passages and can also cause

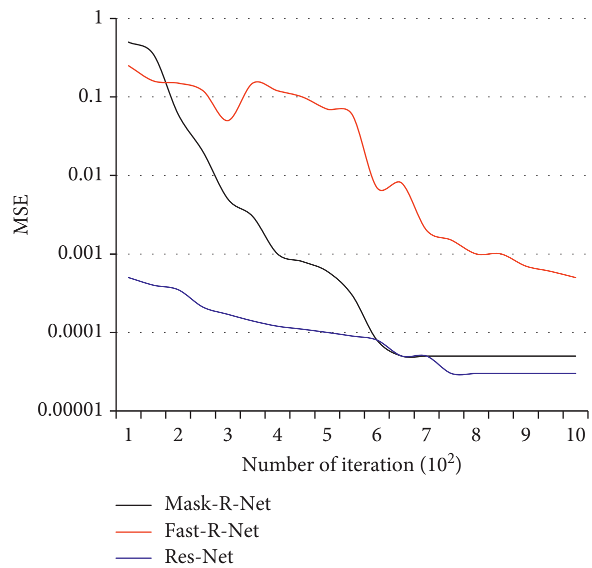

Figure 11: MSE curve diagram.

Figure 12: CT image of the patient's lungs.

obstruction or airflow limitation of small airways. e-health HRCT is an effective method to detect changes in airway structure. e-health HRCT was used to evaluate imaging changes in asthmatic children with small airway obstruction, and features such as thickening of bronchial wall, tree-in-bud, air trapping, and mosaic sign were found. It was almost consistent with the findings of Garcia-Clemente et al. [14]. In the research of Jiang et al. [15], 9 patients with small airway asthma and 20 healthy controls underwent HRCT with e-Health equipment, and the results showed that WA% in patients with small airway asthma was higher than that in healthy controls. In this research, T/D and WA (%) after glucocorticoid treatment were significantly lower than those before treatment ($P < 0.01$), which demonstrated the effectiveness of glucocorticoids in the treatment of asthma with small airway obstruction from the perspective of imaging.

FEEF50%, FEF75%, and MMEF75/25 are important clinical indicators for the evaluation of small airway function [16], and glucocorticoid is an effective method in preventing and treating asthma. FEEF50%, FEF75%, and MMEF75/25 were measured to evaluate the pulmonary function of asthmatic children with small airway obstruction before and after treatment. It was found that MMEF75/25 and FEF75 were significantly higher than those before treatment ($P < 0.05$), and FEF50 was significantly higher than that before treatment ($P < 0.01$). It suggested that, after glucocorticoid treatment, the pulmonary function of asthmatic children with small airway obstruction was effectively improved, which was consistent with the research results of Licari et al. [17]. FeNO is a marker of airway inflammation, and the greater the value, the more serious the airway obstruction [13]. It was found that FeNO level after treatment was lower than that before treatment ($P < 0.01$), indicating that glucocorticoid had alleviative effect on airway inflammation. Inflammatory cells in asthmatic children were activated, and there were more EOS in the airway epithelium, secreting a large amount of eosinophil basic protein, thus inducing the inflammatory damage of airway epithelium. The results showed that IL-6 and IL-35 played an important role in inflammatory response and airway hyper-responsiveness. It was found that IL-6, IL-35, and EOS of the children in each group were significantly improved after treatment compared with those before treatment, and the improvement was more obvious in group C compared with the other two groups. It suggested that glucocorticoids could relieve airway inflammation, and systemic administration was superior to local treatment. The results showed that aerosol therapy was superior to oral therapy. The atomizing device can disperse drugs into tiny droplets or particles, so that they are suspended in the gas, enter the respiratory tract or lung, and directly affect the drug on the lesion site, which can then wet the airway, clean the airway, and realize treatment effect.

Deep learning continues to develop rapidly. Researchers use repetitive programming of related programs to achieve effective deep learning algorithms. In deep learning, only the appropriate model needs to be selected, and the weight parameters of the model area are optimized after training. Chen et al. [18] simulated the evacuation design of buildings in the network model based on deep learning, introduced auxiliary image data prediction training algorithm, tracking sequence prediction training algorithm, and verified that the convolutional neural network model can predict data accuracy of the set. After the image is classified by deep learning, the location of the lesion can be displayed more clearly, and the characteristics of the lesion can be clearly classified. The image segmentation for deep learning in medicine includes convolutional neural network image segmentation and full convolutional neural network image segmentation. Frikel et al. [19] used microburst analysis to illustrate the appearance of artifacts in CT reconstruction images, which proved that deep learning algorithms can reconstruct the structure information of the scan target, and deep learning algorithms can achieve the effect of noise reduction.

5. Conclusion

The e-health equipment HRCT was adopted to diagnose childhood asthma with small airway obstruction. In this study, it was found that, after one month of treatment for children with asthma with small airway obstruction, the indexes related to lung function were significantly higher than those before treatment ($P < 0.05$), and the FeNO level of children with asthma with small airway obstruction was 35.00 ± 2.11 (ppb) before treatment and 34.12 ± 2.16 (ppb) after treatment. One month after treatment, T/D and WA were 23.38 ± 3.27 (%) and 78.65 ± 13.45 (%), respectively. Overall results showed that oral treatment was superior to aerosol inhalation. However, there are still some shortcomings in this research. For example, the number of samples is limited, and the clinic time and hospital are limited. Only the small airway function in one month after treatment is analyzed, but the long-term efficacy and possible side effects of the drug are not discussed. In the future, it needs to increase the diversity of sample regions and time, and further research on the effect of improving small airway function will be conducted. In short, the results of this study can provide a theoretical basis for the diagnosis and clinical treatment of asthma patients with small airway obstruction.

Data Availability

The data used to support the findings of this study are available from the corresponding author upon request.

Conflicts of Interest

The authors declare no conflicts of interest.

References

[1] J. R. Castillo, S. P. Peters, and W. W. Busse, "Asthma exacerbations: pathogenesis, prevention, and treatment," *The Journal of Allergy and Clinical Immunology: In Practice*, vol. 5, no. 4, pp. 918–927, 2017.

[2] H. E. Hoch, P. R. Houin, and P. C. Stillwell, "Asthma in children: a brief review for primary care providers," *Pediatric Annals*, vol. 48, no. 3, pp. e103–e109, 2019.

[3] C. Suárez-Castañón, G. Modroño-Riaño, and G. Solís-Sánchez, "Variabilidad e idoneidad del tratamiento antiasmático en pediatría de atención primaria," *Atención Primaria*, vol. 49, no. 5, pp. 263–270, 2017.

[4] P. Poowuttikul, S. Saini, and D. Seth, "Inner-city asthma in children," *Clinical Reviews in Allergy and Immunology*, vol. 56, no. 2, pp. 248–268, 2019.

[5] A. Grey and C. H. Katelaris, "Dupilumab in the treatment of asthma," *Immunotherapy*, vol. 11, no. 10, pp. 859–872, 2019.

[6] K. F. Rabe, P. Nair, G. Brusselle et al., "Efficacy and safety of dupilumab in glucocorticoid-dependent severe asthma," *New England Journal of Medicine*, vol. 378, no. 26, pp. 2475–2485, 2018.

[7] G. Azaldegi, J. Korta, O. Sardón, P. Corcuera, and E. G. Pérez-Yarza, "Disfunción de la pequeña vía aérea en niños con asma controlada," *Archivos de Bronconeumología*, vol. 55, no. 4, pp. 208–213, 2019.

[8] D. P. Clark, F. R. Schwartz, D. Marin, J. C. Ramirez-Giraldo, and C. T. Badea, "Deep learning based spectral extrapolation for dual-source, dual-energy x-ray computed tomography," *Medical Physics*, vol. 47, no. 9, pp. 4150–4163, 2020.

[9] L. Calciano, L. Portas, A. G. Corsico et al., "Biomarkers related to respiratory symptoms and lung function in adults with asthma," *Journal of Breath Research*, vol. 12, no. 2, Article ID 026012, 2018.

[10] S. Svenningsen, E. Haider, C. Boylan et al., "CT and functional MRI to evaluate airway mucus in severe asthma," *Chest*, vol. 155, no. 6, pp. 1178–1189, 2019.

[11] T. Tamada, H. Sugiura, T. Takahashi et al., "Coexisting COPD in elderly asthma with fixed airflow limitation: assessment by DLco% predicted and HRCT," *Journal of Asthma: Official Journal of the Association for the Care of Asthma*, vol. 54, no. 6, pp. 606–615, 2017.

[12] K. Dimakou, A. Gousiou, M. Toumbis et al., "Investigation of bronchiectasis in severe uncontrolled asthma," *The Clinical Respiratory Journal*, vol. 12, no. 3, pp. 1212–1218, 2018.

[13] S. Tang, Y. Xie, C. Yuan, X. Sun, and Y. Cui, "Fractional exhaled nitric oxide for the diagnosis of childhood asthma: a systematic review and meta-analysis," *Clinical Reviews in Allergy and Immunology*, vol. 56, no. 2, pp. 129–138, 2019.

[14] M. García-Clemente, A. I. Enríquez-Rodríguez, M. Iscar-Urrutia et al., "Severe asthma and bronchiectasis," *Journal of Asthma*, vol. 57, no. 5, pp. 505–509, 2020.
[15] D. Jiang, Z. Wang, C. Shen et al., "Small airway dysfunction may be an indicator of early asthma: findings from high-resolution CT," *Annals of Allergy, Asthma, & Immunology*, vol. 122, no. 5, pp. 498–501, 2019.
[16] M. F. Lutfi, "Patterns of changes and diagnostic values of FEF50%, FEF25%–75% and FEF50%/FEF25%–75% ratio in patients with varying control of bronchial asthma," *International Journal of Health Sciences*, vol. 10, no. 1, pp. 3–11, 2016.
[17] A. Licari, I. Brambilla, L. Sacchi, G. Marseglia, and G. Ciprandi, "Periostin, type 2 biomarker, is not associated with asthma control grade in asthmatic allergic children," *Respiratory Medicine*, vol. 151, pp. 118–120, 2019.
[18] Y. Chen, S. Hu, H. Mao, W. Deng, and X. Gao, "Application of the best evacuation model of deep learning in the design of public structures," *Image and Vision Computing*, vol. 102, Article ID 103975, 2020.
[19] J. Frikel, E. T. Quinto, and E. T. Quinto, "Characterization and reduction of artifacts in limited angle tomography," *Inverse Problems*, vol. 29, no. 12, Article ID 125007, 2013.

Hindawi
Journal of Healthcare Engineering
Volume 2021, Article ID 8198552, 7 pages
https://doi.org/10.1155/2021/8198552

Research Article

Artificial Intelligence-based MRI Images for Brain in Prediction of Alzheimer's Disease

Xiaowang Bi,[1] **Wei Liu**,[1] **Huaiqin Liu**,[1] **and Qun Shang**[1,2]

[1]*Department of Radiology, Zibo Central Hospital, Zibo 255000, Shandong, China*
[2]*China-Israel fMRI Precision Neuroimaging Joint Laboratory, Zibo 255000, Shandong, China*

Correspondence should be addressed to Qun Shang; 1400540124@xs.hnit.edu.cn

Received 24 August 2021; Revised 29 September 2021; Accepted 1 October 2021; Published 19 October 2021

Academic Editor: Enas Abdulhay

The study aimed to explore the accuracy and stability of Deep metric learning (DML) algorithm in Magnetic Resonance Imaging (MRI) examination of Alzheimer's Disease (AD) patients. In this study, MRI data of patients obtained were from Alzheimer's Disease Neuroimaging Initiative (ADNI) database (A total of 180 AD cases, 88 women, 92 men; 188 samples in healthy conditions (HC), including 90 females and 98 males. 210 samples of mild cognitive impairment (MCI), 104 females and 106 males). On the basis of deep learning, an early AD diagnosis system was constructed using CNN (Convolutional Neural Network) and DML algorithms. Then, the system was used to classify AD, HC, and MCI, and the two algorithms were compared for the accuracy and stability of in classification of MRI images. It was found that in the classification of AD and HC, the classification accuracy and sensitivity of the deep measurement learning model are both 0.83, superior to the CNN model; in terms of specificity, the classification specificity of the DML model was 0.82, slightly lower than that of the CNN model; and that in the classification of MCI and HC, the classification accuracy and sensitivity of the DML model was 0.65, superior to the CNN model; and in terms of specificity, the classification specificity of the DML model was 0.66, slightly lower than that of the CNN model. It suggested that the DML model demonstrated better classification effects on early AD patients. The loss curve analysis results showed that, for classification of AD and HC or MCI and HC, the DML algorithm can improve the convergence speed of the AD early prediction model. Therefore, the DML algorithm can significantly improve the clarity and quality of MRI images, elevate the classification accuracy and stability of early AD patients, and accelerate the convergence of the model, providing a new way for early prediction of AD.

1. Introduction

Alzheimer's Disease (AD) is a chronic neurodegenerative cognitive disease. At the onset of the disease, patients will suffer from cognitive dysfunction such as memory loss and language function loss [1]. Nowadays, with the aging of the population, the AD population is increasing rapidly, and it has become a major disease threatening the health of the elderly, which seriously affects the quality of life of the elderly, and the need for nursing and care brings about heavy burdens to the patient's family and society [2]. Clinically, the cause of Alzheimer's disease is still unclear, and the condition is irreversible, and a thorough treatment of the disease has not yet been developed [3]. Only when AD is diagnosed in the early stage can it be possible to slow down or inhibit the progression. Thus, early prediction and diagnosis of AD is very important and meaningful in clinical treatment. Mild Cognitive Impairment (MCI) is a cognitive dysfunction between Alzheimer's disease (AD) and Healthy Controls (HC) [4]. Studies have found that, most patients with MCI have developed AD [5].

At present, Magnetic Resonance Imaging (MRI) technology is a main method to diagnose AD. Studies have discovered that, there are prominent biological signs in the brains of AD patients, which is conducive to the early prediction and diagnosis of AD [6]. In-depth clinical research on AD has revealed that, family inheritance is an important cause of AD [7].

Artificial intelligence (AI) has developed rapidly in recent years, and AI technology has been widely used in the medical field [8]. Nowadays, machine learning (ML) or Deep Learning (DL) algorithms are always incorporated into MRI imaging [9], but the above methods all have limitations [10]. The machine learning algorithm analyzes the MRI image only after manually determining the area, but subjective factors will affect the subjectivity of the results [11]. Deep learning algorithms can automatically extract features of MRI images, but fails to interpret these features. As a result, it is difficult to identify biological features of AD [3]. Convolutional Neural Networks (CNN) is a kind of Feedforward Neural Networks with deep structure and convolution computation, which is one of the representative algorithms of deep learning and has the ability of representation learning. It can effectively reduce the dimension of a large amount of data into a small amount of data, while retaining image features, in line with the principle of image processing. Deep metric learning (DML) is a metric learning method. It is to learn a mapping from the original feature to the low-dimensional and dense vector space, so that the distance between objects of the same class is relatively close by using the commonly used distance function in the embedding space, while the distance between objects of different classes is relatively far.

In the study, the MRI data (There were 180 cases of AD, including 88 women and 92 men. There were 188 HC samples, including 90 females and 98 males. There were 210 samples of mild MCI, 104 females and 106 males) of patients were from the Alzheimer's Disease Neuroimaging Initiative (ADNI) database. The traditional machine learning algorithms and Convolutional Neural Networks (CNNs) were optimized by deep learning to construct an early diagnosis system of AD based on Depth metric learning (DML) algorithm. The system was used to classify AD, MCI, and HC, and different algorithms were compared for the clarity and specificity of MRI images.

2. Materials and methods

2.1. Experimental data. The experimental data of this study were from the ADNI database [12]. The MRI image data used in this article were divided into 3 categories, namely: 180 cases of AD, including 88 cases of females, and 92 cases of males; 188 samples of HC, including 90 cases of females and 98 cases of males; and 210 samples of MCI, including 104 females and 106 males. There was no significant difference in age and gender of the three types of subjects, and the average age was approximately 74 years old.

2.2. Pre-processing of MRI images. Figure 1 showed the preprocessing of the MRI image, including correction, segmentation, template formation, and skull removal. The MRI images were obtained at various angles due to the head movement during MRI scan. Generally, the brain MRI image includes the skull and neck bones, and the skulls and neck bones are different in size, thickness, and length between individuals. The classification of AD is mainly to analyze the internal tissue structure of the brain, and thus the skull and neck bones in the MRI image are all noise signals.

2.3. CNN model and parameters. CNN is extensively used in the field of image recognition for its unique structure [13]. To use deep learning technology to automatically segment MRI images can greatly reduce the dependence on the subjective judgment of doctors. The traditional CNN structure mainly includes the convolutional layer, the pooling layer, and the fully connected layer. The neural unit layers of various functions are stacked to form a deep CNN, as shown in Figure 2. There are a total of 8 convolutional layers, and the size of the convolution kernel used by each convolutional layer is 3×3×3, and the step size is 1×1×1. There are 5 pooling layers, all pooling layers use Maximum pooling, and the core size and step size of the first pooling layer are 1×2×2, that is, the time dimension is not pooled, and the core size and step size of the remaining pooling layers are 2×2×2. There are two fully connected layers, and the length of the output column vector is 4096. There is a softmax layer. The convolutional pooling layer aims to reduce the size of the feature map by half and double the number of channels.

2.4. DML loss function. The classification data used in this study contained data of AD, HC, and MCI. They were classified into two categories, namely AD and HC, MCI and HC. In the classification of AD and HC, the category label of AD is 0 and the category label of HC is 1. In MCI and HC, the category label of MCI is 0 and the category label of HC is 1.

2.4.1. Cross entropy loss function. This study uses the cross-entropy loss function, and the two-category cross-entropy loss function is adjusted to the following equation (1).

$$\text{cross\_entropy} = \frac{1}{N}\sum_{k=1}^{N} -\left[w_k \ln x_k + (1-w_k)\ln(1-x_k)\right], \tag{1}$$

Where N refers to the batch size, w_k represents the category of the Kth subject, and x_k refers to the probability that the Kth category label predicted by the detection system is 1, calculated as follows.

$$x_k = \text{Softmax}(w_k) = \frac{\exp(w_k^1)}{\exp(w_k^0) + \exp(w_k^1)}, \tag{2}$$

Where w_k refers to Kth classification vector, w_k^0 represents the first w_k value, and w_k^1 refers to the second w_k value.

2.4.2. Loss function based on metric learning. The loss function of metric learning is expressed as equation (3).

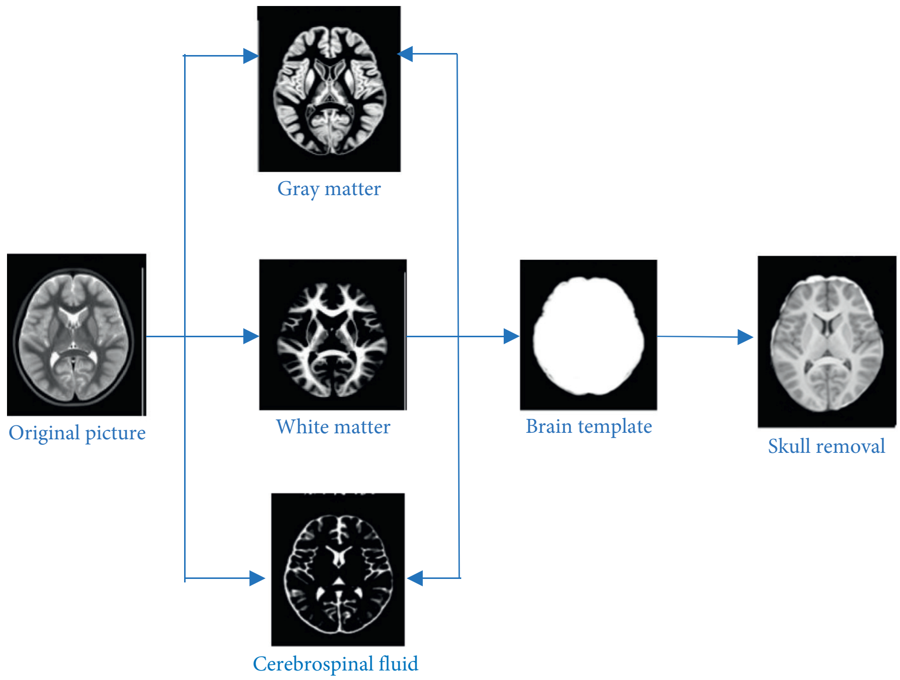

Figure 1: Preprocessing of MRI images.

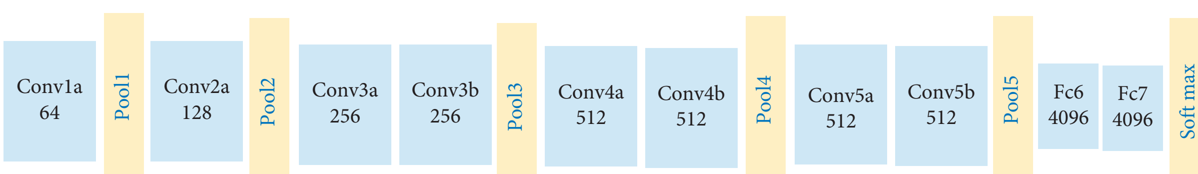

Figure 2: CNN structure.

$$\text{loss}_{\text{contrastive}} = \frac{2}{N(N+1)} \sum_{h=1} \sum_{g=h} \left[w_{hg} m\left(x_h, x_g\right) + \left(1 - w_{hg} \max\left(a - D\left(x_h, x_g\right), 0\right)\right) \right], \tag{3}$$

Where N refers to the batch size, a refers to the interval, x_h is the hth sample and x_g is the g th sample. When x_h and x_g belong to different categories, w_{hg} is 0; and when x_h and x_g belong to the same category, w_{hg} is 1. $D(x_h, x_g)$ is calculated as equation (4), and $f(x)$ represents the output vector.

$$D(x, y) = f(x) - f(y)_2. \tag{4}$$

2.4.3. Overall loss function. This research combines AD classification and DML to construct a DML loss function, expressed as follows.

$$\text{loss} = \text{cross}_{\text{entropy}} + q\,\text{loss}_{\text{conrastive}}, \tag{5}$$

Where $\text{cross}_{\text{entropy}}$ is calculated by equation (1); and $\text{loss}_{\text{conrastive}}$ is calculated by equation (3). The value of q is greater than 0, and it refers to the adjustment coefficient of classification and measurement loss.

2.5. Evaluation Index. The performance of predictive classification algorithms of early AD was evaluated factoring into Accuracy (Acc), Sensitivity (Sens), and Specificity (Spec). The number of patients accurately diagnosed is represented by the letter A, the number of normal subjects diagnosed as normal is represented by the letter B, the number of normal subjects who are incorrectly diagnosed as patients is represented by the letter C, and the number of patients who are mistakenly diagnosed as normal people is represented by the letter D. The involved indexes are calculated as follows.

Acc refers to the proportion of the number of people who can be correctly predicted and classified, calculated as equation (6).

$$Acc = \frac{A + B}{A + B + C + D}. \tag{6}$$

Sens refers to the ratio of the patients who are correctly detected to the total number of patients, calculated as equation (7).

$$\text{Sens} = \frac{A}{A + D}. \tag{7}$$

Spec refers to the ratio of the correctly detected normal samples to the total number of normal people, calculated as equation (8).

$$\text{Spec} = \frac{B}{B + C}. \tag{8}$$

2.6. Statistical analysis. Statistical analysis was performed using SPSS 24.0 software, expressed as mean ± standard deviation ($\bar{x} \pm s$). The count data were analyzed by t test, and α=0.05. $P < 0.05$ was the threshold for significance.

3. Results

3.1. Brain MRI features of AD patients. Figure 3 below showed MRI images of the brain of AD patients and normal people. In the MRI images of the brain of AD patients, brain atrophy was observed, which mainly occurred in the hippocampus, parahippocampal gyrus, and medial temporal lobes. At the same time, ventricles were dilated.

3.2. MRI images of AD patients based on CNN and DML algorithms. Figure 4 showed the MRI images of AD patients after processed by CNN and DML algorithms. Compared with MRI images processed by the CNN algorithm, MRI images processed by DML algorithm had clearer texture and better imaging effects on cerebral blood vessels. Further, the sharpness was higher, so DML can greatly improve the visual sharpness of MRI images.

3.3. Comparison of classification results. CNN and DML models classified the patients separately, and they were compared for the classification accuracy, sensitivity, and specificity. The specific classification effects of AD and HC, MCI and HC were shown as below.

3.3.1. Classification of AD and HC. Figure 5 below showed the classification results of AD and HC. It was noted that the classification accuracy and sensitivity of the deep measurement learning model are both 0.83, superior to the CNN model. In terms of specificity, the classification specificity of the DML model was 0.82, slightly lower than that of the CNN model.

3.3.2. Classification results of MCI and HC. Figure 6 showed the classification effects of MCI and HC. It was noted that in terms of accuracy and sensitivity, the classification accuracy and sensitivity of the DML model was 0.65, superior to the CNN model; and in terms of specificity, the classification specificity of the DML model was 0.66, slightly lower than that of the CNN model.

3.4. Loss curve analysis. The convergence curves of the CNN model and the MDL model were analyzed, and the loss curves of AD and HC, MCI and HC were shown below.

3.4.1. Classification of AD and HC. Figure 7 showed the loss curves of the classification of AD and HC when the CNN model and the DML model were used for training. It was noted that when the CNN model was used for training, as the number of iterations increased, the training loss decreased. At the beginning, the training loss decreased rapidly, but after 3000 iterations, the training loss decreased slowly, and the training loss tended to be stable and the model fully converged after 6000 iterations. When the DML model was used for training, the training loss decreased as the number of iterations increased. At the beginning, the training loss dropped quickly. After 2000 iterations, the training loss decreased slowly. The training loss tended to be stable and the model fully converged after 4500 iterations. Taken together, the DML model can improve the convergence speed of the model.

3.4.2. Classification results of MCI and HC. Figure 8 showed the loss curves of the classification of MCI and HC when the CNN model and the DML model were used for training. It was noted that when the CNN model was used for training, as the number of iterations increased, the training loss decreased. At the beginning, the training loss decreased rapidly, but after 4000 iterations, the training loss decreased slowly, and the training loss tended to be stable and the model fully converged after 7000 iterations. When the DML model was used for training, the training loss decreased as the number of iterations increased. At the beginning, the training loss dropped quickly. After 3000 iterations, the training loss decreased slowly. The training loss tended to be stable and the model fully converged after 4500 iterations. Taken together, the DML model can improve the convergence speed of the model.

4. Discussion

AD is a chronic degenerative cognitive disease of the nervous system. At the onset of the disease, patients will suffer from cognitive dysfunction such as memory loss and language function loss. The disease has a long incubation period and will worsen with time [14]. The pathogenesis of AD still remains unclear, and it cannot be cured once diagnosed. Therefore, early diagnosis and prediction become particularly important. Only when AD is diagnosed in the early stage can it be possible to slow down or inhibit the progression [15]. In recent years, there is a large amount of research on the classification and prediction of early AD using traditional machine learning methods [16], and the classification and prediction of early AD using deep learning technology is a common occurrence [17]. For example, Folego et al. (2020) [18] used CNNs to process MRI images, and the classification accuracy of AD and HC reached 0.97. Perezn et al. (2019) [19] connected multiple image blocks to classify the MRI samples in the ADNI database, and the

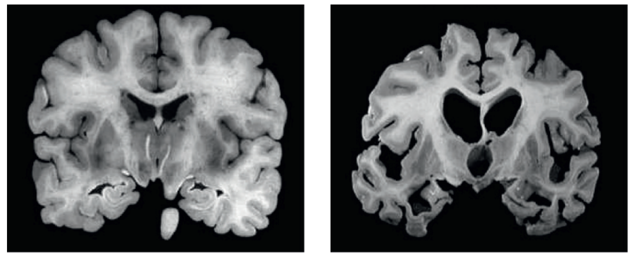

(a) (b)

Figure 3: MRI images of normal people and AD patients.

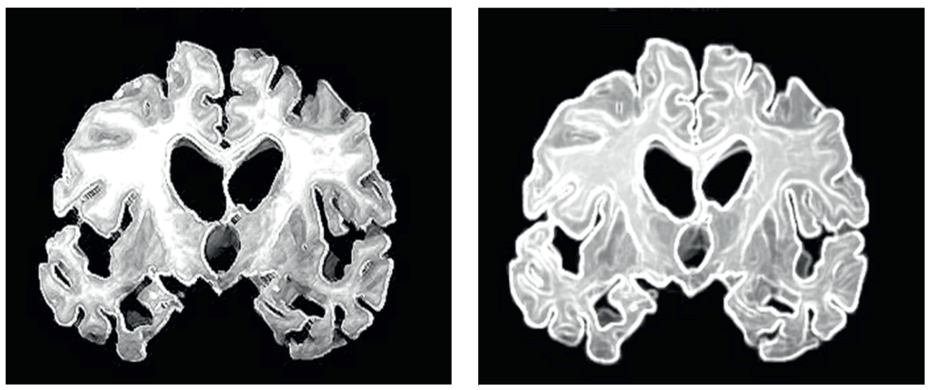

(a) (b)

Figure 4: MRI images of AD patients processed by CNN and DML algorithms. *Note.* Figure 4A was an MRI image of AD patients based on CNN algorithm; and Figure 4B was an MRI image of AD patients based on DML algorithm.

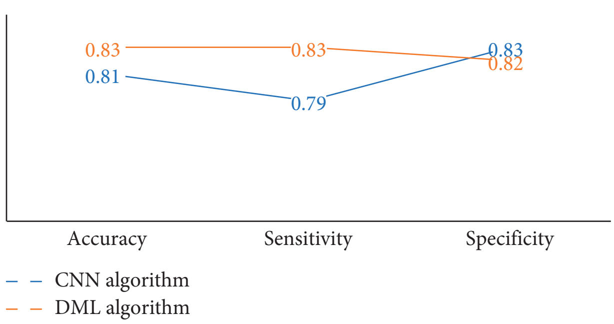

Figure 5: Classification effects of AD and HC.

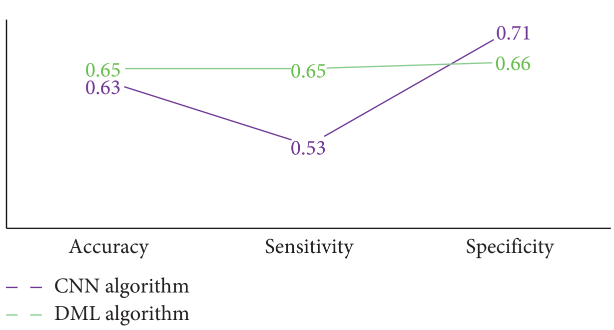

Figure 6: Comparison of classification effects between MCI and HC.

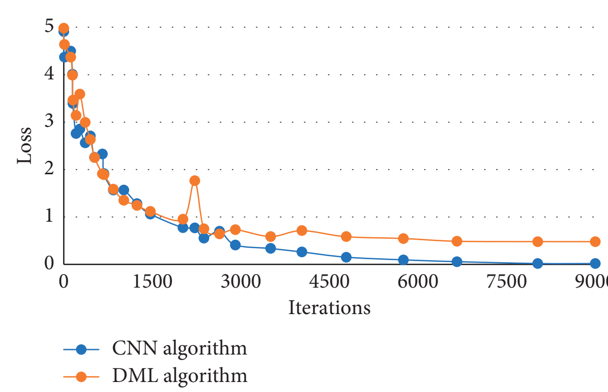

Figure 7: Loss curves of classification of AD and HC.

accuracy rate can reach 0.95. Therefore, to construct a simple, stable, and accurate early diagnosis system for AD is important for early intervention and treatment of AD. In order to explore the role of artificial intelligence in the prediction of early AD from MRI images, the CNN model and the DML model were used to classify AD, HC, and MCI.

Takenoshita et al. (2019) [20] extracted features of MRI samples in the ADNI database to classify AD, MCI, and HC, and the effect was very good. MRI of healthy persons and AD patients were compared, and it was found that brain atrophy occurred in AD patients, mainly in the hippocampus, parahippocampal gyrus, medial temporal lobe, and other

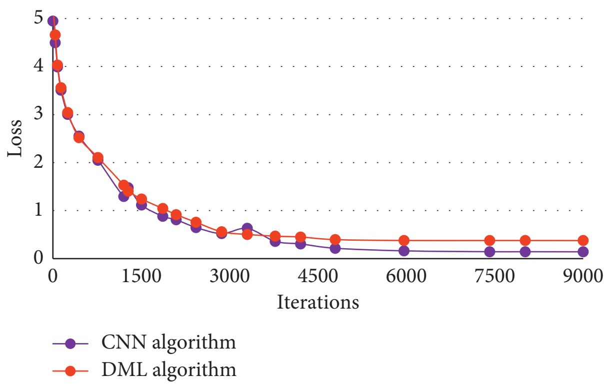

Figure 8: Loss curves of classification of MCI and HC.

brain regions, and ventricular dilation was also observed, which indicated that MRI images could clearly show the lesions in the brain domain of patients, and had diagnostic value. The classification accuracy and sensitivity of DML model were both 0.83, higher than those of CNN model. The classification specificity of DML model was 0.82, slightly lower than that of CNN model. Usually, sensitivity refers to the proportion of patients who are correctly diagnosed. If an AD patient is mistakenly diagnosed as a normal person, the opportunity for treatment will be missed and it will lead to serious consequences; if a normal person is mistakenly diagnosed as an AD patient, usually, he will be diagnosed again. Therefore, in clinical practice, specificity can be appropriately reduced to improve the sensitivity of prediction. Above, the DML model demonstrated better classification effects on early AD patients.

The training loss of CNN model decreased with the increase of iterations. After 3000 iterations, the decline rate of training loss tended to be gentle, and converged completely after 6000 iterations. The DML model also saw a decline in training loss with the increase of iterations. After 2000 iterations, the decline rate of training loss tended to be stable, and it completely converged after 4500 iterations. This showed that compared with the CNN model, the DML model in this study had a faster convergence speed and better computing performance. Figure 8 showed the loss curves of the classification of MCI and HC when the CNN model and the DML model were used for training. It was noted that when the CNN model was used for training, as the number of iterations increased, the training loss decreased. At the beginning, the training loss decreased rapidly, but after 4000 iterations, the training loss decreased slowly, and the training loss tended to be stable and the model fully converged after 7000 iterations. When the DML model was used for training, the training loss decreased as the number of iterations increased. At the beginning, the training loss dropped quickly. After 3000 iterations Whitwell, the training loss decreased slowly. The training loss tended to be stable and the model fully converged after 4500 iterations. Taken together, the DML model can improve the convergence speed of the model. Hence, the DML model can speed up the convergence for the classification of the both categories, which was in line with the research results of Vaithinathan et al. (2019) [21].

5. Conclusion

In the study, the MRI data used were from the ADNI database. On the basis of deep learning, an early diagnosis system for AD was constructed using CNN and DML algorithms. Then, the system was used to classify AD, HC, and MCI, and the two algorithms were compared for the accuracy and stability of in classification of MRI images. It was found that the DML algorithm can significantly improve the clarity and quality of MRI images, elevate the classification accuracy and stability of early AD patients, and accelerate the convergence of the model, providing a new way for early prediction of AD. However, some limitations in the study should be noted. The sample size is small, which will reduce the power of the study. In the follow-up, an expanded sample size is necessary to strengthen the findings of the study.

Data Availability

The data used to support the findings of this study are available from the corresponding author upon request.

Conflicts of Interest

The authors declare no conflicts of interest.

References

[1] V. Mantzavinos and A. Alexiou, "Biomarkers for Alzheimer's disease diagnosis," *Current Alzheimer Research*, vol. 14, no. 11, pp. 1149–1154, 2017.

[2] M. Hu, Y. Zhong, S. Xie, H. Lv, and Z. Lv, "Fuzzy system based medical image processing for brain disease prediction," *Frontiers in Neuroscience*, vol. 15, Article ID 714318, 2021 Jul 30.

[3] S. Basaia, F. Agosta, L. Wagner et al., "Automated classification of Alzheimer's disease and mild cognitive impairment using a single MRI and deep neural networks," *NeuroImage: Clinic*, vol. 21, Article ID 101645, 2019.

[4] S. Qiu, P. S. Joshi, M. I. Miller et al., "Development and validation of an interpretable deep learning framework for Alzheimer's disease classification," *Brain*, vol. 143, no. 6, pp. 1920–1933, 2020 Jun 1.

[5] K. McRae-McKee, C. T. Udeh-Momoh, G. Price et al., "Perspective: clinical relevance of the dichotomous classification of Alzheimer's disease biomarkers: should there be a "gray zone"?" *Alzheimer's and Dementia*, vol. 15, no. 10, pp. 1348–1356, 2019 Oct.

[6] Z. Wan, Y. Dong, Z. Yu, H. Lv, and Z. Lv, "Semi-supervised support vector machine for digital twins based brain image fusion," *Frontiers in Neuroscience*, vol. 15, Article ID 705323, 2021 Jul 9.

[7] J. L. Whitwell, "Alzheimer's disease neuroimaging," *Current Opinion in Neurology*, vol. 31, no. 4, pp. 396–404, 2018.

[8] X. Liu, K. Chen, T. Wu, D. Weidman, F. Lure, and J. Li, "Use of multimodality imaging and artificial intelligence for diagnosis and prognosis of early stages of Alzheimer's disease," *Translational Research*, vol. 194, pp. 56–67, 2018 Apr.

[9] D. Chen, P. Wawrzynski, and Z. Lv, "Cyber security in smart cities: a review of deep learning-based applications and case studies," *Sustainable Cities and Society*, vol. 66, Article ID 102655, 2020.

[10] N. An, H. Ding, J. Yang, R. Au, and T. F. A. Ang, “Deep ensemble learning for Alzheimer’s disease classification,” *Journal of Biomedical Informatics*, vol. 105, Article ID 103411, 2020 May.

[11] S. Spasov, L. Passamonti, A. Duggento, P. Liò, and N. Toschi, “A parameter-efficient deep learning approach to predict conversion from mild cognitive impairment to Alzheimer’s disease,” *NeuroImage*, vol. 189, pp. 276–287, 2019 Apr 1.

[12] H. Karcher, M. Savelieva, L. Qi et al., “Modelling decline in cognition to decline in function in Alzheimer’s disease,” *Current Alzheimer Research*, vol. 17, no. 7, pp. 635–657, 2020.

[13] Q. Li, X. Xing, and Q. Feng, “[Coupled convolutional and graph network-based diagnosis of Alzheimer’s disease using MRI],” *Nan Fang Yi Ke Da Xue Xue Bao*, vol. 40, no. 4, pp. 531–537, 2020 Apr 30, Chinese.

[14] L. Bloch and C. M. Friedrich, “Classification of Alzheimer’s Disease using volumetric features of multiple MRI scans,” in *Proceedings of the 2019 41st Annual International Conference of the IEEE Engineering in Medicine and Biology Society (EMBC)*, pp. 2396–2401, Berlin, Germany, 2019 July.

[15] C. R. Jack, D. A. Bennett, K. Blennow et al., “A/T/N: an unbiased descriptive classification scheme for Alzheimer disease biomarkers,” *Neurology*, vol. 87, no. 5, pp. 539–547, 2016 Aug 2.

[16] N. Madusanka, H.-K. Choi, J.-H. So, and B.-K. Choi, “Alzheimer’s disease classification based on multi-feature fusion,” *Current Medical Imaging Formerly Current Medical Imaging Reviews*, vol. 15, no. 2, pp. 161–169, 2019.

[17] N. Yamanakkanavar, J. Y. Choi, and B. Lee, “MRI segmentation and classification of human brain using deep learning for diagnosis of Alzheimer’s disease: a survey,” *Sensors*, vol. 20, no. 11, p. 3243, 2020 Jun 7.

[18] G. Folego, M. Weiler, R. F. Casseb, R. Pires, and A. Rocha, “Alzheimer’s disease detection through whole-brain 3D-CNN MRI,” *Frontiers in Bioengineering and Biotechnology*, vol. 8, Article ID 534592, 2020 Oct 30.

[19] J. PereznGonzalez, C. Azamar, and O. PinanRamirez, “Automatic classification of Alzheimer’s disease based on CPD brain point cloud registration for feature extraction,” in *Proceedings of the 2019 41st Annual International Conference of the IEEE Engineering in Medicine and Biology Society (EMBC)*, pp. 812–815, Berlin, Germany, 2019 July.

[20] N. Takenoshita, S. Shimizu, H. Kanetaka et al., “Classification of clinically diagnosed Alzheimer’s disease associated with diabetes based on amyloid and tau PET results,” *Journal of Alzheimer’s Disease*, vol. 71, no. 1, pp. 261–271, 2019.

[21] K. Vaithinathan and L. Parthiban, “A novel texture extraction technique with T1 weighted MRI for the classification of Alzheimer’s disease,” *Journal of Neuroscience Methods*, vol. 318, pp. 84–99, 2019 Apr 15.

Hindawi
Journal of Healthcare Engineering
Volume 2021, Article ID 4634659, 7 pages
https://doi.org/10.1155/2021/4634659

Research Article

Risk Factors of Enterostomy Infection Caused by Bacterial Infection through Mathematical Modelling-Based Information Data Analysis

Jing Li, Xiaoyu Liu, and Jun Chen

Gastrointestinal Surgery, Chongqing University Cancer Hospital, No. 181 Hanyu Road, Shapingba District, Chongqing 400030, China

Correspondence should be addressed to Jun Chen; lijing303300@cqu.edu.cn

Received 25 August 2021; Revised 20 September 2021; Accepted 24 September 2021; Published 16 October 2021

Academic Editor: Enas Abdulhay

Objective. The study aimed to explore the risk factors of infections after enterostomy through the information data analysis method based on a mathematical model. *Methods*. 156 cases of enterostomy patients admitted to the hospital were retrospectively selected as the study subjects and were divided into the infection group (17 cases) and normal group (139 cases) according to whether they were complicated with infections. Then, the factors of infection and related indexes before and after surgery were analyzed, and the data of the whole hospital were estimated by mathematical modelling. *Results*. The length of hospital stay in the infection group was 21 ± 11.2 days, which is longer than 10.1 ± 7.1 days in the normal group ($P < 0.05$). The incidence of anastomotic fistula in the infection group was 14%, which is higher than 2% in the normal group. The mortality rate of infection group (44%) was higher than that of normal group (5%). In the infection group, the incidence of single-cavity stoma (69%) was higher than that of double-cavity stoma (31%), the nosocomial infection rate (11%) was significantly higher compared with out of hospital (2%), and there were significant differences ($P < 0.05$). *Conclusions*. Patients with malnutrition and hypoproteinemia before enterostomy, the use of gastric tube and ventilator in the treatment, single lumen stomy in the operation, and the occurrence of anastomotic fistula were more likely to have concurrent infections.

1. Introduction

Enterostomy is a common surgical treatment for certain gastrointestinal diseases, which can effectively improve the quality of life of patients [1]. The specific operations of this method are to make an artificial wound in the abdomen of the human body and then suture the opening of the digestive tract so that the patient can excrete waste from the human body through this opening [2]. Patients who undergo the enterostomy often need to have their original diseases treated before permanent or temporary enterostomy, which will change the fecal excretion mode [3]. However, the waste discharged from the stoma cannot be controlled and often flows out involuntarily, soaking the abdominal skin around the stoma. Moreover, the excrement contains many bacteria, which often infect the stoma and surrounding tissues to cause complications, so that the quality of life of patients will be affected [4]. According to reports, the number of patients undergoing ostomy in Taiwan has increased by about 100,000 each year and the number of patients with early complications is about 6.3%–53.8% [5].

Among the many complications, the incidence of stoma infection is higher [6]. The common complications of ostomy include wound infections near the stoma, infections caused by sutures, detachment of the stoma mucosa, and complications caused by the patient's own factors. The above complications will have a serious impact on the patient's postoperative physiology and psychology, which also indirectly lead to unsatisfactory postoperative recovery [7]. In addition, the body's immunity will decrease after surgery and the integrity of the skin and mucous membranes will be destroyed, resulting in open wounds, especially the excretion of feces. Worse still, the stoma and surrounding tissues are prone to bacterial infections, and severe cases may even cause systemic acute infections due to local infections [8].

As its name suggests, mathematical modelling is the process to establish a mathematical model based on actual data information to deal with the problems in reality [9]. Specifically, information data are transformed from basic to in-depth and from rough adjustment to high precision so that more meaningful and usable information can be obtained from simple numbers to solve practical problems in life. It is also a process of integrating theory with practice [10, 11]. The establishment of mathematical models is diverse, and it has been extensively used in various industries, such as medicine and education [12, 13].

In this study, mathematical modelling was introduced to analyse the possible risk factors of bacterial infections after enterostomy, and the obtained data information was adopted in medical practice, which is expected to provide a certain theoretical basis for the prevention of complications caused by enterostomy.

2. Experimental Methods

2.1. Research Objects. 156 patients admitted to hospital for acute enterostomy from September 2018 to January 2021 were taken as the research subjects, including 89 male patients and 67 female patients, aged 54–89 years, with an average age of 56 ± 9 years, and they were rolled into the infection group ($n = 17$) and the normal group ($n = 139$) based on whether they had complicated infections. The criteria for infection were the white blood cell (WBC) count greater than 10×10^9/L, neutrophils greater than 80%, or were accompanied by cough, chest tightness, dyspnea, and other symptoms. One patient with 4 or more of the above could be diagnosed. The study had been approved by the ethics committee of hospital, and the patients and their family members understood the content and methods of this study and agreed to sign the corresponding informed consent.

Inclusion criteria: (1) all patients were between 50 and 90 years old, (2) patients and their families signed the informed consent, (3) patients were conscious during the study, and (4) the general clinical data of the patients were complete.

Exclusion criteria: (1) patients with heart, liver, and kidney dysfunction and (2) women in pregnancy.

2.2. Research Methods. In this study, a retrospective analysis was conducted on the postoperative development of the enterostomy in hospital, and the general data and clinical treatment data of the research subjects were sorted out for comparative analysis. Besides, the conditions of all patients in the hospital were explored on the basis of mathematical modelling.

2.3. Observation Indicators. The etiology of enterostomy in patients was analyzed, and the probability of infections in patients with different variables was compared. Different variables included factors such as stoma intestinal segment, anastomosis method, age, stoma-reduction interval, surgical time, postoperative hospital stay, postoperative anastomotic fistula, postoperative intestinal obstruction, and other factors.

The general information status of patients was compared for statistical significance, including gender, age, and etiology of the stoma.

According to the infection of enterostomy, the patients were divided into groups and compared for hypoproteinemia, the use history of gastric tube and ventilator, the postoperative malnutrition, and the stoma method. Besides, the mortality rate of the infected patients was also counted.

2.4. Analysis Method Based on Mathematical Modelling. The mathematical modelling was constructed based on randomly selected patients undergoing enterostomy, so as to estimate the conditions of all patients in the entire hospital.

In order to estimate the number of enterostomy patients with concurrent infection in the whole hospital, the number of enterostomy patients with concurrent infection in the hospital was set as $f(x)$, the number of randomly selected patients who underwent enterostomy was set as y, the number of infected cases was set as x, and the total number of patients undergoing enterostomy in the whole hospital was set as $f(y)$. Then, equation (1) could be obtained:

$$f(x) = f(y) \times \frac{x}{y}. \tag{1}$$

Thus, the number of patients without concurrent infection in the whole hospital $f(x')$ could be expressed in equations (2) and (3):

$$f(x') = f(y) - f(x), \tag{2}$$

$$f(x') = f(y) - \left(f(y) \times \frac{x}{y} \right). \tag{3}$$

The number of patients with concurrent infections caused by this factor in the whole hospital could be set as M to understand the proportion of concurrent infections after surgery caused by different factors in the whole hospital, and the number of cases with this cause in the randomly selected patients was set as M'. The calculation is shown in equations (4) and (5):

$$\frac{M}{f(x)} = \frac{M'}{x}, \tag{4}$$

$$M = \frac{M'}{x} \times \left(f(y) \times \frac{x}{y} \right). \tag{5}$$

Among them, the number of randomly selected patients who underwent enterostomy (y), the number of the infected patients (x), and the total number of patients who received enterostomy in the hospital ($f(y)$) were all the known quantity.

2.5. Statistical Methods. SPSS19.0 software was used for statistical analysis of the data, and the measurement data were expressed as mean ± standard deviation. One-way analysis was adopted for analysis. The Wilcoxon rank-sum test or *t*-test was used for measurement data, and count data were detected by the chi-square test or Fisher's exact test. In addition, $P < 0.05$ meant that the difference was statistically substantial.

3. Results

3.1. Comparison on the Incidence of Infection Caused by Different Factors. Table 1 shows the relationship between the occurrence of incision infection and gender and age. In the infection group, there were 11 males and 6 females. In the normal group, there were 78 males and 61 females. The average age of infected patients was 54 ± 7 years, and the average age of the uninfected was 57 ± 6 years, with no statistical significance ($P > 0.05$). Table 2 shows the relationship of the ostomy-reduction interval, operation time, and postoperative hospital stay with the incidence of infection. The length of stay in the infection group was 21 ± 11.2 days, which is longer than 10.1 ± 7.1 days in the normal group ($P < 0.05$). Figure 1 shows different intestinal sites for ostomy. It was found that there was no significant relationship between the intestinal site of ostomy and the incidence of infection ($P > 0.05$). Figure 2 shows the relationship between anastomotic fistula and the incision infection. The analysis showed that the incidence of anastomotic fistula in the infection group (14%) was higher than that in the normal group (2%) ($P < 0.05$). It can be concluded that there is a certain relationship between the postoperative hospital stay and postoperative anastomotic fistula with the incidence of infection.

There were a total of 350 patients undergoing enterostomy between September 2020 and March 2021 in this hospital. The etiology was then statistically analyzed, and the etiology distribution of patients with enterostomy in the whole hospital was estimated using the analytical method based on mathematical modelling, as shown in Figure 3. Among them, 122 cases were caused by colorectal cancer and obstruction, accounting for 34.8% of the number of enterostomy cases; 88 cases with colorectal trauma accounted for 25%; 35 cases with anastomotic fistula after colorectal cancer surgery accounted for 10%; 21 cases with colorectal perforation accounted for 6%; 17 cases suffered from intestinal obstruction (5%); 21 cases (6%) suffered from surgery/colonoscopy side injury; 12 patients had intestinal strangulation due to volvulus, accounting for 3.4%; and 13 cases had congenital megacolon, accounting for 3.7%. In addition, there were 21 patients with other etiologies, accounting for 6%.

3.2. Age and Gender Distribution of the Two Groups of Patients. After grouping, the general data of patients from the two groups were compared and evaluated (Table 3). It was found that there were no significant differences between the basic information of the two groups of patients ($P > 0.05$).

Table 1: The relationship of the incidence of incision infection with gender and age.

	Male	Female	Age (years)
The total number of cases	89	67	56 ± 9
The number of infected cases	11	6	54 ± 7
The number of noninfected cases	78	61	57 ± 6

3.3. Comparison on the Typical Stoma Status between the Normal Group and the Infection Group

3.3.1. Comparison on the Dermatitis around the Stoma. Figure 4(a) indicates that the patient's intestinal stoma was in a good state. There was no atrophy of the stoma, and there was no separation between the stoma and the surrounding skin tissue. Besides, the skin tissue around the stoma showed a normal state, without obvious redness, depression, and other symptoms. Figure 4(b) presents the stoma with poor healing after complicated infection. It was found that the stoma was in a shrinking state, and it was separated from the surrounding skin tissue. Moreover, the skin around the stoma had obvious redness, swelling, and depression symptoms.

3.3.2. Comparison on the Separation of the Stoma Mucosa. The intestinal stoma of one patient was in a good state after the surgery (Figure 5(a)), showing that there was no separation of the skin and mucosal tissue around the stoma. In Figure 5(b), the separation of the intestinal stoma and mucosal tissue could be clearly observed, and the surrounding skin had slight redness. Furthermore, it mainly occurred in the early stage after the surgery.

3.4. Comparison on Relevant Indicators of Patients from the Two Groups. The two groups were compared for relevant indexes, such as the history of gastric tube application, history of ventilator application, malnutrition, and hypoproteinemia. It was found that the proportion of these cases in the normal group was lower than that of the infection group. The mortality rate of the infection group was as high as 44%, while the mortality rate of patients in the normal group was only 5%, with obvious statistical significance ($P < 0.05$), as shown in Figure 6. In terms of the stoma methods, 69% of patients in the infection group had single-cavity stoma and 31% of patients had double-cavity stoma. Besides, 40% of patients had single-cavity stoma and 60% had double-cavity stoma in the normal group, suggesting that the single-cavity stoma would increase the chance of infection (Figure 7).

3.5. Comparison on the Conditions of Infection between In-Hospital and Out-of-Hospital Patients. Based on the results in Section 3.1, the infection rate of the hospitalized patients and out-of-hospital patients was further compared. It was found that the incidence of concurrent infections in hospitalized patients (11%) was higher than that of discharged patients at home (5%), with significant statistical differences ($P < 0.05$), as shown in Figure 8.

Table 2: The relationship of the stoma-reduction interval, the surgical time, and the number of days of hospitalization after surgery with the incidence of infection.

	Stoma-reduction interval (M)	Surgical time (min)	Number of days in hospital after surgery (D)
Total average time	7.9 ± 17.9	166.2 ± 80.5	13.2 ± 6.9
Time of infection	15.5 ± 43.9	140.9 ± 56.8	21 ± 11.2
Time of noninfection	7.1 ± 10.9	169.1 ± 83.0	10.1 ± 7.1

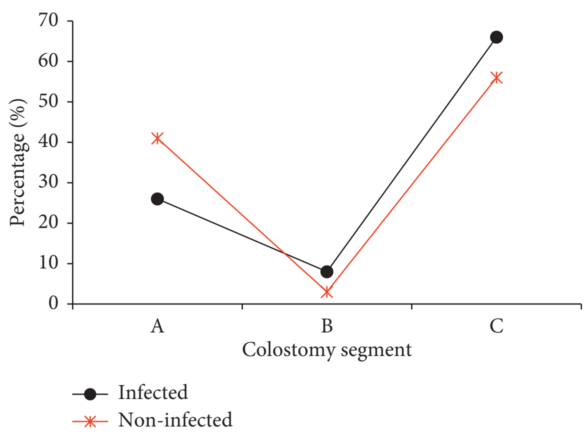

Figure 1: Comparison on infection rates of different stoma intestinal segments (*Note.* A: transverse colon; B: ascending colon; C: sigmoid colon).

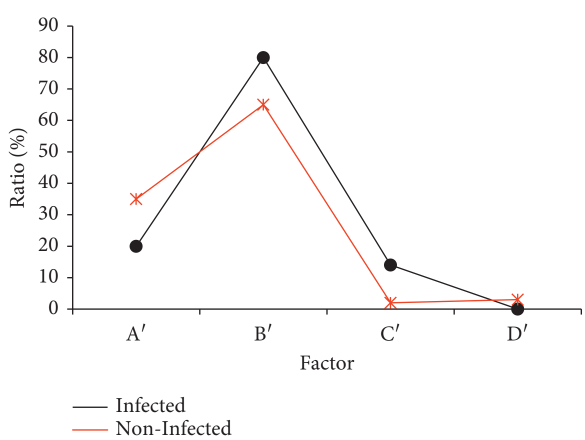

Figure 2: Data results of the anastomotic method, the occurrence of anastomotic fistula, and intestinal obstruction after infection (*Note.* A′: manual suture; B′: instrument anastomosis; C′: anastomotic fistula; D′: intestinal obstruction).

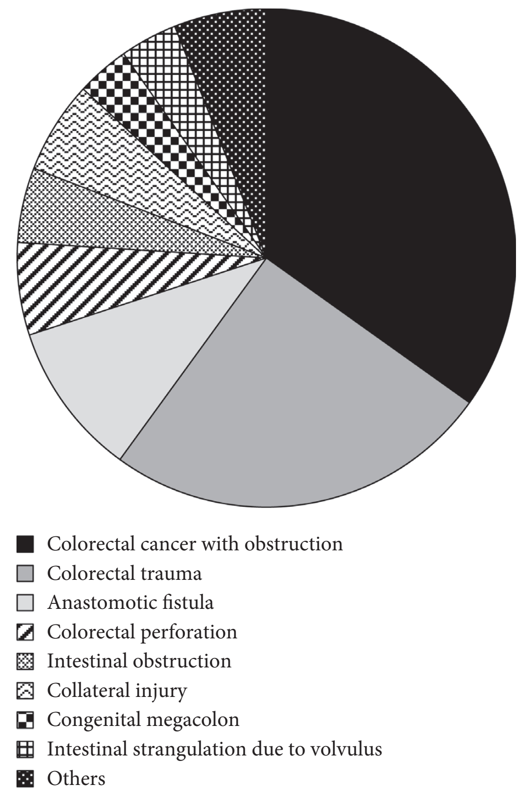

Figure 3: Prediction of the distribution of causes of enterostomy in the hospital based on data analysis of mathematical modelling.

4. Discussion

According to statistics, postoperative infection types mainly includes infections at the surgical site, lung, and urinary system, and about 3%–44% of colorectal cancer patients develop surgical site infection after surgery [14]. Moreover, postoperative infection seriously affects the prognosis of patients after surgical treatment. The study showed that the number of patients with colorectal cancer complicated with obstruction was the largest, accounting for 34.8% of the total number of colorectal cancer cases, indicating that most patients with colorectal cancer required enterostomy, but there were differences between patients in different countries. Carlsson et al. [15] concluded that colonic diverticulitis was the second cause of colorectostomy in that region, which was different from colorectal trauma ranking second in this study. Roque-castellano et al. [16] found that most of the patients requiring this operation suffered from nontumor diseases. The study results of Desay et al. [17] showed that the probability of tumor patients requiring ostomy and reductive surgery was only 13%, and the effective rate of this method reached 70%. The above study results clearly show the individual differences between patients in China and those in Western countries.

Some studies have suggested that old age seems to be a risk factor [18]. However, the results of this study showed that the incidence of postoperative complications after enterostomy was not significantly related to age ($P > 0.05$). It was found that postoperative coinfection was significantly related to postoperative hospital stay and whether postoperative anastomotic fistula occurred ($P < 0.05$). A longer postoperative hospital stay will lead to a higher infection rate. Based on this, the infection rate of hospitalized patients

Table 3: Comparison on general clinical data of patients from the two groups.

	The number of males	The number of females	Age (years)
Infection group	11	6	54 ± 7
Normal group	78	61	57 ± 6

Figure 4: Comparison between a normal stoma and a stoma with infectious dermatitis. (a) Normal stoma, female, 56 years old. (b) Infectious dermatitis, female, 54 years old.

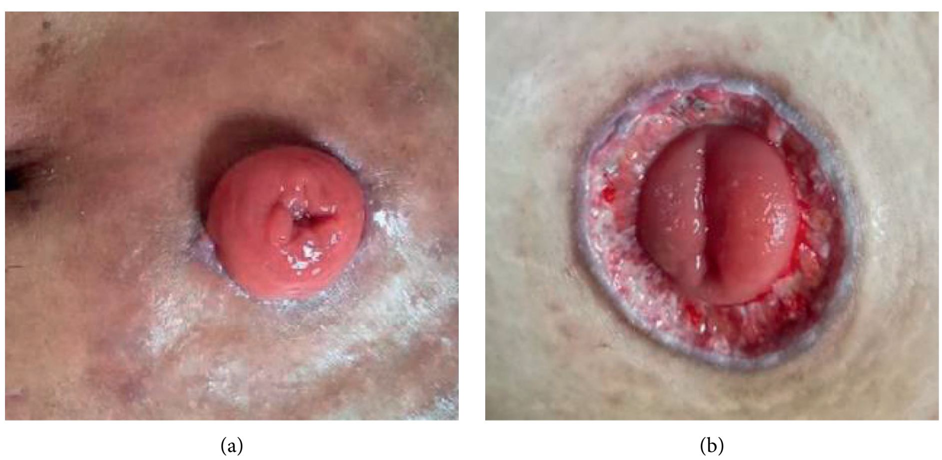

Figure 5: Comparison on mucosal separation between normal stoma and stove mouth. (a) Normal stoma, male, 58 years old. (b) Mucosal separation, male, 57 years old.

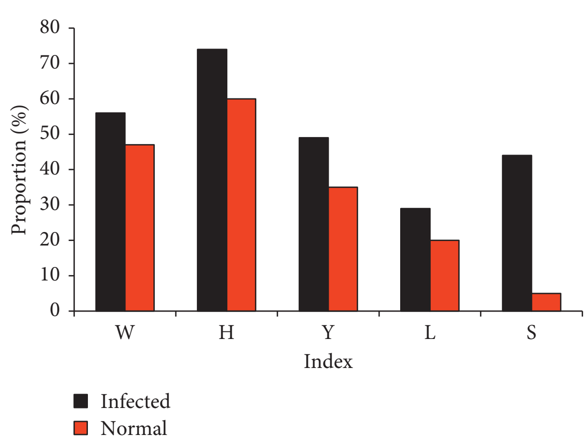

Figure 6: Comparison on relevant indicators between the two groups of patients (*Note*. W: history of gastric tube application; H: history of ventilator application; Y: preoperative malnutrition; L: hypoproteinemia; S: mortality rate).

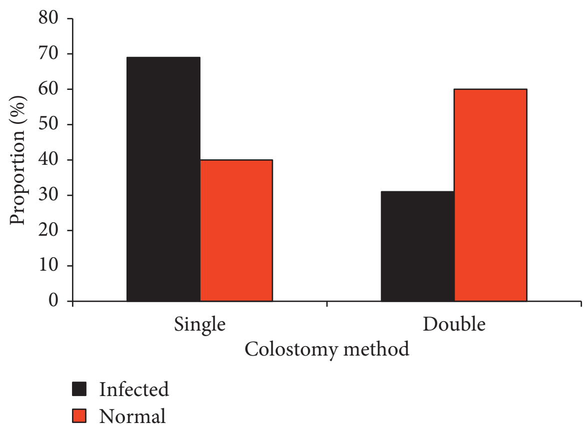

Figure 7: Comparison on the relationship between two groups of ostomy methods and concurrent infections.

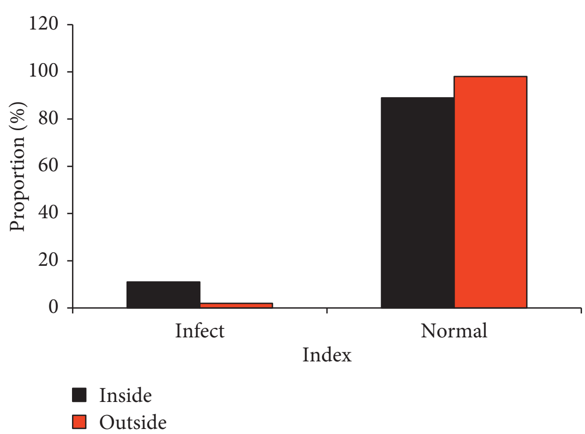

Figure 8: Comparison on the conditions of hospital infection and out-of-hospital infection.

and out-of-hospital patients was analyzed, and it was found that the nosocomial infection rate was higher compared with the out of hospital. Hospitalized patients have to have tests for postoperative efficacy and physical indicators of detection, which to a certain extent can reduce the body resistance and immune suppression and increase the vulnerability to infection. Moreover, there are so many people in hospital, including the patients, ward staff, the patient's family and friends, and health care workers, and they can all be regarded as carriers of the bacteria [19]. At home, although the nursing is not so professional as that in hospital, but there are few people around, so the probability of infection is lower in a certain extent.

In this study, the patients in the hospital were sampled randomly. The mathematical model established in Section 2.4 was employed to calculate, and then, the concurrent infections of all the patients in the hospital could be estimated. If a nationwide sampling survey is conducted, the mathematical modelling algorithm can also be adopted to estimate the postoperative infections after enterostomy in Taiwan. Mathematical modelling is to solve and optimize actual problems by calculations in the computer. After the data and information are processed, variables are introduced through abstract hypotheses and actual problems are expressed through mathematical theoretical knowledge to deal with actual problems. Wang et al. [20] applied mathematical modelling to analyse the data of traditional Chinese medicine and concluded that the modelling had good data analysis capabilities. Thus, it had certain guiding significance for the synthesis of Chinese patent medicines.

5. Conclusion

In the study, 156 cases of enterostomy patients were retrospectively selected as the study subjects and were divided into the infection group (17 cases) and normal group (139 cases) according to whether they were complicated with infections. The factors of infection and related indexes before and after surgery were analyzed, and the data of the whole hospital were estimated by mathematical modelling. In conclusion, patients with malnutrition and hypoproteinemia before enterostomy, the use of gastric tube and ventilator in the treatment, single lumen ostomy in the operation, and the occurrence of anastomotic fistula were more likely to have concurrent infections. However, some limitations in the study should be noted. The sample size is small, which will reduce the power of the study. In the follow-up, an expanded sample size is necessary to strengthen the findings of the study. It is hoped that this study can provide a reasonable theoretical basis for the prevention and treatment of postoperative infection after enterostomy to reduce the postoperative pain of patients and improve the quality of life of patients to a certain extent.

Data Availability

The data used to support the findings of this study are available from the corresponding author upon request.

Conflicts of Interest

The authors declare no conflicts of interest.

Authors' Contributions

Jing Li and Xiaoyu Liu contributed equally to this work.

References

[1] X. Zhang, R. Gao, J. L. Lin et al., "Effects of hospital-family holistic care model on the health outcome of patients with permanent enterostomy based on the theory of 'Timing it Righ'," *Journal of Clinical Nursing*, vol. 29, no. 13-14, pp. 2196–2208, 2020.

[2] P.-P. Xu, X.-P. Chang, X. Zhang et al., "Transumbilical enterostomy for Hirschsprung's disease with a two-stage laparoscopy-assisted pull-through procedure," *World Journal of Gastroenterology*, vol. 25, no. 46, pp. 6781–6789, 2019.

[3] G. Roveron, M. Antonini, M. Barbierato et al., "Clinical practice guidelines for the nursing management of percutaneous endoscopic gastrostomy and jejunostomy (PEG/PEJ) in adult patients," *The Journal of Wound, Ostomy and Continence Nursing*, vol. 45, no. 4, pp. 326–334, 2018, PMID: 29994859.

[4] U. Koc, K. Karaman, I. Gomceli et al., “A retrospective analysis of factors affecting early stoma complications,” *Ostomy/Wound Management*, vol. 63, no. 1, pp. 28–32, 2017, PMID: 28112647.

[5] F. Wang, L. Huang, H. Zhang, H. Jiang, X. Chang, and Y. Chu, “The mediating role of perceived stress on the relationship between perceived social support and self-care ability among Chinese enterostomy patients,” *Supportive Care in Cancer*, vol. 29, no. 6, pp. 3155–3162, 2020 Oct 19, Epub ahead of print. PMID: 33074359.

[6] Z. Tang, Z. Huang, W. Yan et al., “Complications of enterostomy and related risk factor analysis of very early onset inflammatory bowel disease with interleukin-10 signalling deficiency: a single-centre retrospective analysis,” *BMC Gastroenterology*, vol. 20, no. 1, p. 8, 2020.

[7] S. Ayaz-Alkaya, “Overview of psychosocial problems in individuals with stoma: a review of literature,” *International Wound Journal*, vol. 16, no. 1, pp. 243–249, 2019, Epub 2018 Nov 4. PMID: 30392194.

[8] D. P. V. Lambrichts, S. Vennix, G. D. Musters et al., “Hartmann’s procedure versus sigmoidectomy with primary anastomosis for perforated diverticulitis with purulent or faecal peritonitis (LADIES): a multicentre, parallel-group, randomised, open-label, superiority trial,” *The Lancet Gastroenterology & Hepatology*, vol. 4, no. 8, pp. 599–610, 2019 Aug, Epub 2019 Jun 6. PMID: 31178342.

[9] S. Q. Du and W. Yuan, “Mathematical modeling of interaction between innate and adaptive immune responses in COVID-19 and implications for viral pathogenesis,” *Journal of Medical Virology*, vol. 92, no. 9, pp. 1615–1628, 2020, Epub 2020 May 13. PMID: 32356908.

[10] H. A. Elkaranshawy, A. M. Makhlouf, and Y. Abouelseoud, “Using padé approximant method to solve the mathematical model of tumor-immune interactions,” in *Proceedings of the 2020 42nd Annual International Conference of the IEEE Engineering in Medicine & Biology Society (EMBC)*, pp. 2467–2470, Montreal, Canada, July 2020, PMID: 33018506.

[11] A. A. Viktorov, V. A. Kholodnov, V. D. Gladkikh, and A. V. Alekhnovich, “[Mathematical model of the influence of the environment on the aging of living systems],” *Advances in Gerontology*, vol. 26, no. 1, pp. 52–57, 2013, Russian. PMID: 24003728.

[12] S. M. Clifton, K. Hill, A. J. Karamchandani, E. A. Autry, P. McMahon, and G. Sun, “Mathematical model of gender bias and homophily in professional hierarchies,” *Chaos: An Interdisciplinary Journal of Nonlinear Science*, vol. 29, no. 2, Article ID 023135, 2019.

[13] D. Rudrauf, D. Bennequin, I. Granic, G. Landini, K. Friston, and K. Williford, “A mathematical model of embodied consciousness,” *Journal of Theoretical Biology*, vol. 428, pp. 106–131, 2017, Epub 2017 May 26. PMID: 28554611.

[14] J. Li, X. Liu, and J. Chen, “WITHDRAWN: analyzing risk factors for enterostomy infection and neuropsychology of patients by computer information data regression under endoscopic image guidance,” *Neuroscience Letters*, Article ID 135223, 2020, Epub ahead of print. PMID: 32619651.

[15] E. Carlsson, J. Fingren, A. M. Hallén, C. Petersén, and E. Lindholm, “The prevalence of ostomy-related complications 1 Year after ostomy surgery: a prospective, descriptive, clinical study,” *Ostomy/Wound Management*, vol. 62, no. 10, pp. 34–48, 2016, PMID: 27768579.

[16] K. Hida, R. Okamura, Y. Sakai et al., “Open versus laparoscopic surgery for advanced low rectal cancer,” *Annals of Surgery*, vol. 268, no. 2, pp. 318–324, 2018, PMID: 28628565.

[17] P. M. Polanco, A. A. Mokdad, H. Zhu, M. A. Choti, and S. Huerta, “Association of adjuvant chemotherapy with overall survival in patients with rectal cancer and pathologic complete response following neoadjuvant chemotherapy and resection,” *JAMA Oncology*, vol. 4, no. 7, pp. 938–943, 2018, PMID: 29710272.

[18] G. Bethell, S. Kenny, and H. Corbett, “Enterostomy-related complications and growth following reversal in infants,” *Archives of Disease in Childhood - Fetal and Neonatal Edition*, vol. 102, no. 3, pp. F230–F234, 2017, Epub 2016 Sep 26. PMID: 27671835.

[19] R. L. Harries, J. Ansell, R. J. Codd, and G. L. Williams, “A systematic review ofClostridium difficileinfection following reversal of ileostomy,” *Colorectal Disease*, vol. 19, no. 10, pp. 881–887, 2017, PMID: 28872758.

[20] P. Wang, K. Li, Y. Tao et al., “TCM-ADMEpred: a novel strategy for poly-pharmacokinetics prediction of traditional Chinese medicine based on single constituent pharmacokinetics, structural similarity, and mathematical modeling,” *Journal of Ethnopharmacology*, vol. 236, pp. 277–287, 2019, Epub 2019 Feb 28. PMID: 30826421.

Hindawi
Journal of Healthcare Engineering
Volume 2021, Article ID 6034180, 13 pages
https://doi.org/10.1155/2021/6034180

Research Article

Dynamic Electrocardiogram under P Wave Detection Algorithm Combined with Low-Dose Betaloc in Diagnosis and Treatment of Patients with Arrhythmia after Hepatocarcinoma Resection

Fenfen Jiang [1], Haokai Xu [2], Xiaowen Shi [1], Bingjiang Han [1], Zhenliang Chu [1], Bin Xu [1], and Xiaorong Liu [3]

[1] *Department of Cardiology, The Second Affiliated Hospital of Jiaxing University, Jiaxing 314000, Zhejiang, China*
[2] *Department of Surgery, Ningbo Yinzhou No. 2 Hospital, Ningbo 315199, Zhejiang, China*
[3] *Department of Surgery, The Second Affiliated Hospital of Jiaxing University, Jiaxing 314000, Zhejiang, China*

Correspondence should be addressed to Xiaorong Liu; 20161101012057@stu.hznu.edu.cn

Received 15 August 2021; Revised 23 September 2021; Accepted 28 September 2021; Published 16 October 2021

Academic Editor: Enas Abdulhay

This work aimed to study the diagnostic value of dynamic electrocardiogram (ECG) based on P wave detection algorithm for arrhythmia after hepatectomy in patients with primary liver cancer, and to compare the therapeutic effect of different doses of Betaloc. P wave detection algorithm was introduced for ECG automatic detection and analysis, which can be used for early diagnosis of arrhythmia. Sixty patients with arrhythmia after hepatectomy for primary liver cancer were selected as the research objects. They were randomly divided into control group, SD group, MD group, and HD group, with 15 cases in each group. No Betaloc, low-dose (≤47.5 mg), medium-dose (47.5–95 mg), and high-dose (142.5–190 mg) Betaloc were used for treatment. As a result, P wave detection algorithms can mark P waves that may be submerged in strong interference. P waves from arrhythmia database were used to verify the performance of the proposed algorithm. The prediction precision (Pp) of ventricular arrhythmia and atrial arrhythmia was 98.53% and 98.76%, respectively. Systolic blood pressure (117.35 ± 7.33, 126.44 ± 9.38, and 116.02 ± 8.2) mmHg in SD group, MD group, and HD group was significantly lower than that in control group (140.3 ± 7.21) mmHg after two weeks of treatment. Moreover, those of SD group and HD group were significantly lower than MD group ($P < 0.05$). The effective rate of cardiac function improvement in SD group ($72.35 \pm 1.21\%$) was significantly higher than that in control group, MD group, and HD group ($38.2 \pm 0.98\%$, $65.12 \pm 1.33\%$, and $60.43 \pm 1.25\%$; $P < 0.05$). In short, dynamic ECG based on P wave detection algorithm had high diagnostic value for arrhythmia after hepatectomy in patients with primary liver cancer. It was safe and effective for patients to choose small dose of Betaloc.

1. Introduction

Liver cancer is a malignant tumor that occurs in the liver, the largest organ of the human body. It is generally classified into PHC and secondary liver cancer according to its etiology and other factors [1, 2]. PHC mainly includes hepatocellular carcinoma, intrahepatic cholangiocarcinoma, cholangiocarcinoma, angiosarcoma, hemangioendothelioma, and hepatoblastoma [3, 4]. At present, the preferred clinical treatment for liver cancer is hepatectomy, which is the traditional radical treatment for liver cancer, and the five-year survival rate of patients after surgery is greater than 50% [5, 6]. However, this surgery has certain limitations and is only suitable for patients with good liver function and complete tumor resection. In addition, it can lead to serious complications, such as liver failure and bleeding [7, 8]. Arrhythmia refers to when the origin of heartbeat excitement is abnormal or the conduction pathway is abnormal, and the sequence of excitement is disordered, which changes the heartbeat rate or rhythm [9, 10]. Arrhythmia is caused by a variety of triggers, and different clinical symptoms can occur due to different causes and types. In severe cases, syncope and sudden death can occur [11, 12]. In addition, a variety of treatments or antiarrhythmic drugs will have different degrees of side effects on patients. Therefore, when a drug is choosing for treatment, it is necessary to have a certain understanding of the pharmacokinetics and pharmacodynamics of the drug to prevent it from causing adverse reactions and complications to patients [13–15].

The ECG of arrhythmia shows that P wave appears in advance, and the shape is different from that of sinus P wave. PR interval is greater than 0.12 s. The QRS pattern is the same as that of sinus rhythm. In addition to accompanied by ventricle difference, conduction can appear inconsistent. There are usually incomplete compensatory intervals after pre-phase contraction of room type [16–18]. Detection of P wave is of great significance to ECG analysis of arrhythmia and analysis of characteristic points of ECG signal. Therefore, a P wave detection algorithm was proposed in this study to perform automatic detection and analysis of ECG and locate the P wave starting point, so as to achieve accurate and effective prediction and diagnosis of arrhythmia [19, 20]. At present, β-blocker drugs are gradually widely used in arrhythmia, especially in patients with primary liver cancer after hepatectomy, such as β-blocker metoprolol succinate sustained-release tablets (Betaloc) [21, 22]. However, because β-blockers have a certain blocking effect on β-receptors, there are certain limitations in clinical application [23, 24]. In addition, there is still a lack of relevant studies on the effect of dosage of β-blocker metoprolol succinate sustained-release tablets (Betaloc) on arrhythmia and its therapeutic effect [25, 26].

Therefore, in this study, patients with arrhythmia after hepatectomy for primary liver cancer were selected as the research objects, and no Betaloc, low-dose Betaloc, medium-dose Betaloc, and high-dose Betaloc were used for patients. By studying the cardiac function indexes, blood lipid indexes, and liver function indexes of different patients in different treatment periods, the therapeutic effect of low-dose Betaloc on arrhythmia after hepatectomy in patients with primary liver cancer was analyzed.

2. Materials and Methods

2.1. Basic Information. In this study, 60 patients with arrhythmia after hepatectomy for primary liver cancer who were hospitalized in hospital from September 2018 to October 2020 were selected as the research objects. Among them, 30 were male and 30 were female. They were randomly divided into control group, SD group, MD group, and HD group, with 15 cases in each group. No Betaloc, low-dose (≤47.5 mg), medium-dose (47.5–95 mg), and high-dose (142.5–190 mg) Betaloc were used for treatment. This study had been approved by the Ethics Committee of hospital, and patients and their families understood the study content and methods and agreed to sign corresponding informed consent forms.

Inclusion criteria were as follows: (i) patients aged between 40 and 65 years old; (ii) patients who were emotionally stable and can cooperate with treatment and sample collection; (iii) patients with arrhythmia after hepatectomy; (iv) patients with complete clinical data and information; (v) patients who had no history of mental illness and were emotionally stable; (vi) the left ventricular ejection fraction (LVEF) was less than 45%, and the left ventricular short axis fractional shortening (FS) was less than 25%; and (vii) patients with cardiac function grades III and IIII.

Exclusion criteria were as follows: (i) patients who withdrew and transferred for treatment due to personal reasons; (ii) patients with other serious diseases or infectious diseases; (iii) patients with diseases, such as hypertension and coronary heart disease, or similar surgical treatment experience; (iv) patients whose tumors had metastasized; and (v) patients who had not undergone cooperative treatment due to personal or other factors.

2.2. Required Sample Size Calculation. The required sample size is calculated as follows:

$$N = \frac{Z^2 \times (P \times (1 - P))}{E^2}, \tag{1}$$

$$n = \frac{Z^2 \sigma^2}{d^2}. \tag{2}$$

In equation (1), N is the total number of samples required in the experiment and Z is the statistic. When the confidence level is 95%, $Z = 1.96$. When the confidence is 90%, $Z = 1.64\%$. E represents the error and P is the probability. In equation (2), n represents the required sample size for each group, d represents the sampling error range, and σ represents the standard deviation, which is generally 0.5. Through the above equations, it is calculated that n is 10, and the total number of samples required is 40 cases. In this study, 60 cases were selected, and there were 15 cases in each group.

2.3. ECG P Wave Detection Algorithm. The patient was placed in horizontal supine position with chest, wrist, and ankle exposed. The skin was cleaned with alcohol, and lead electrodes were placed to collect the electrocardiogram. Normal ECG signals are composed of P wave (from the point change of atrial depolarization before atrial contraction), QRS wave (from the change of ventricular depolarization before ventricular contraction), T wave (potential change during ventricular repolarization), PR segment, PR interval, ST segment, QT interval, and U wave with certain sequence (Figure 1).

The characteristic parameters related to P wave in ECG include P wave amplitude, PR interval, P wave duration, P wave dispersion, and atrial rate. P wave represents atrial depolarization, QRS wave represents ventricular depolarization, and T wave represents ventricular repolarization. In the actual ECG computer automatic analysis, the detected ECG signals are preprocessed first. The P wave amplitude is taken by the amplitude of the P-value. The PR interval refers to the beginning of the P wave to the beginning of the QRS wave, representing the time that the heart excited from the atria to the ventricles. The PR interval is divided into PA interval, AH interval, and HV interval, which is normally in the range of 120~200 ms. PR interval is obtained according to the following equation:

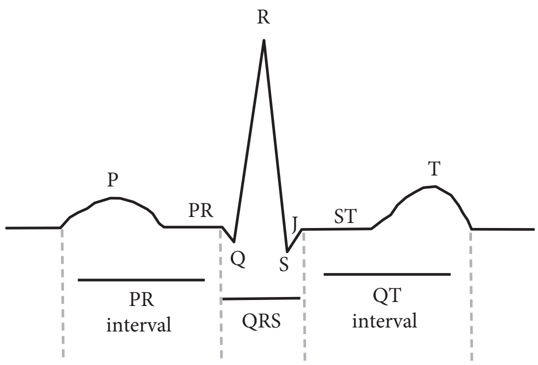

Figure 1: Waveform diagram of ECG signal.

$$\overline{PR} = \frac{(S_Q - S_P)}{t}. \tag{3}$$

In equation (3), S_Q represents the starting point of QRS wave, S_P represents the starting point of P wave, and t represents the sampling rate. The P wave time limit refers to the process of left and right atrium depolarization and repolarization, with the general time (width) less than 0.12 s and the voltage (amplitude) less than 0.25 mV. In the analysis of electrical signals, the P wave time limit is calculated by the following equation:

$$\text{P wave duration} = \frac{(S_P - E_P)}{t}. \tag{4}$$

In equation (4), S_P represents the starting point of P wave, E_P represents the end point of P wave, and T represents the sampling rate. P wave dispersion (PWD) refers to the difference between the maximum time (*Pm*) and the minimum time (*Pn*) measured in different leads of a 12-lead ECG recorded synchronically. The P wave dispersion of normal subjects is less than 40 ms, and the BBB 0 50 ms suggests the presence of heterogeneous electrical activity in different parts of the atrium P wave dispersion is a new index of body surface ECG in predicting atrial tachycardia and paroxysmal atrial fibrillation. The calculation method is shown in the following equation:

$$\text{P wave dispersion} = Pm - Pn. \tag{5}$$

In equation (5), *Pm* represents the maximum time limit of P wave, and *Pn* represents the minimum time limit of P wave. The calculation method of heart rate is shown in the following equation:

$$\text{HR} = \frac{60\,(s)}{\overline{\text{PP}} or \overline{\text{RR}}\,(s)}. \tag{6}$$

In equation (6), $\overline{\text{PP}}$ represents the average P-P interval and $\overline{\text{RR}}$ represents the average R-R interval. Figure 2 shows the flow of P wave detection algorithm.

After the QRS is detected, the P wave search segment is determined, and the zero crossing between the mode extremum pairs in this segment is the P wave. The method to determine the mode extremum pair is shown in the following equations:

$$P_x = \frac{2}{5} \times \left(\frac{1}{10} \sum_{i=1}^{10} X_i \right), \tag{7}$$

$$P_y = \frac{1}{3} \times \left(\frac{1}{10} \sum_{i=1}^{10} Y_i \right). \tag{8}$$

In equations (7) and (8), P represents the amplitude, X_i represents the positive maximum value of the P wave search segment, and Y_i represents the negative maximum value of the P wave search segment. The local modulus maximum pairs are determined by screening the modulus extreme value pairs whose amplitude of point A was greater than P_x and that of point B less than P_y, and the time interval was less than 100 ms. The detection of modulus extremum against slope is shown in the following equation:

$$K = \left| \frac{P_A - P_B}{P_A - P_B} \right|. \tag{9}$$

In this study, the search criteria for P wave were as follows. The maximum value of the scale coefficient in the window was the modulus maximum point, the minimum value of the scale coefficient was the modulus minimum point, and the zero crossing between them was the P wave.

2.4. Drug Therapy for Patients. The patients in the control group, SD group, MD group, and HD group were guided and managed in the course of medication and diet after surgery. In addition, the real-time monitoring was performed on the heart and lung function indexes, blood gas analysis indexes, and psychological status of each group of patients. The four groups of patients were treated with different doses of beta-blocker metoprolol succinate sustained-release tablets (Betaloc) after surgery.

No Betaloc was adopted by patients in control group. SD group: initial dose of Betaloc was 12 to 24 mg once a day, and the patient's tolerance was observed the next day. If the patient could tolerate the previous daily dose, the dose was doubled three weeks later and increased to the target dose of 47.5 mg in SD group. If the patient had adverse reactions or drug intolerance, it was necessary to reduce the drug dose and stop using it in severe cases. In addition, other agents were used or the Betaloc dosage was gradually restored after the patient's condition became stable. MD group: the initial dose of Betaloc was 12 to 24 mg once a day, and the patient tolerance was observed the next day. If the patient could tolerate the previous daily dose, the dose was doubled three weeks later and increased to the target dose of 47.5–95 mg in the MD group. If the patient had adverse reactions or drug intolerance, it was necessary to reduce the drug dose and stop using it in severe cases. In addition, other agents were used or Betaloc dosage was gradually restored after the patient's condition became stable. In the HD group, the initial dose of Betaloc was 12 to 24 mg once a day, and the patient's tolerance was observed the next day. If the patient could tolerate the previous daily dose, the dose was doubled three weeks later, and the target dose was successively

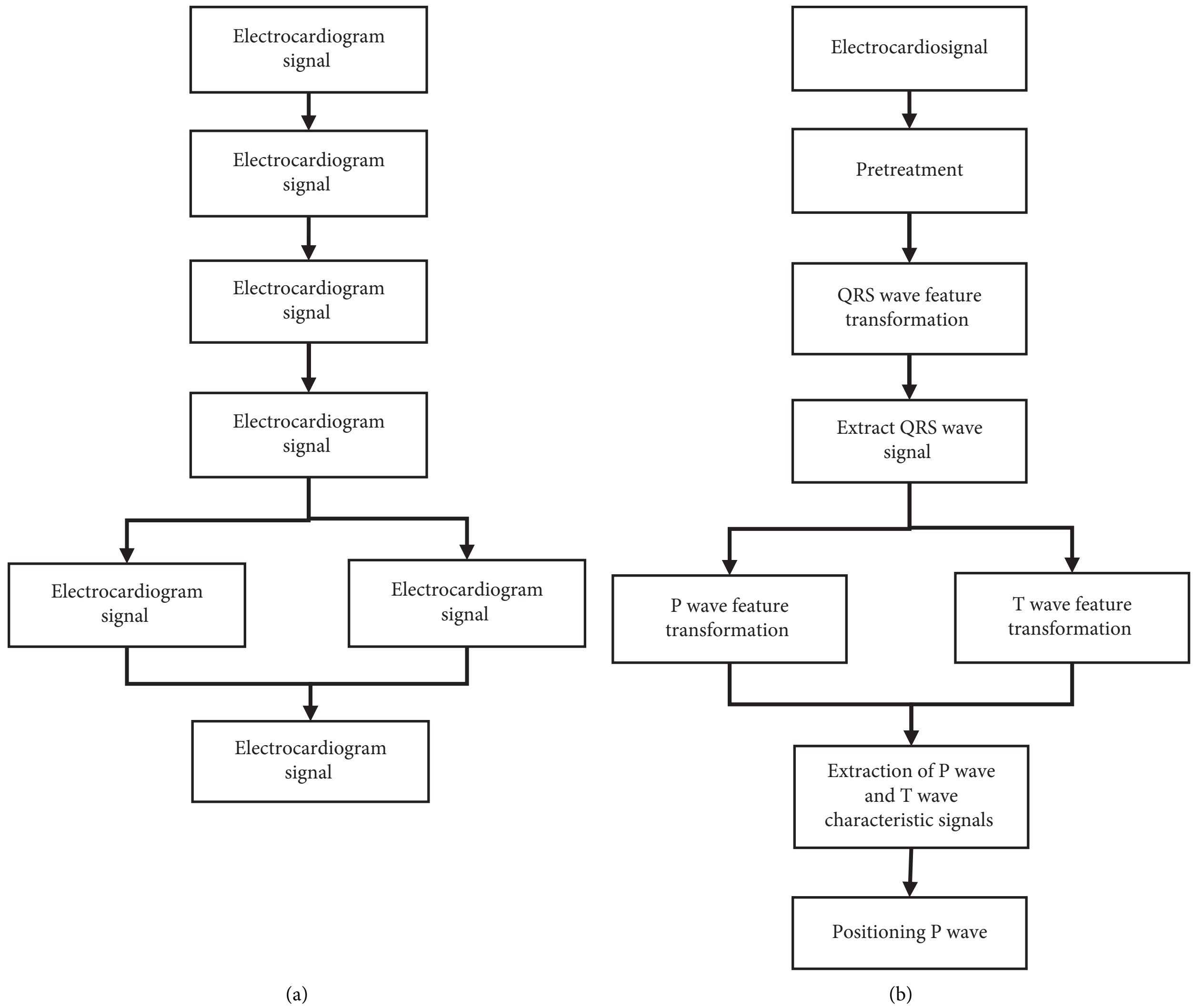

Figure 2: ECG detection process (a) and P wave detection process (b).

increased to 142.5–190 mg as that of the HD group. In the case of adverse reactions or drug intolerance in patients, the drug dose should be reduced and discontinued in severe cases, and the dosage of Betaloc should be gradually resumed after the patient's condition became stable.

2.5. Evaluation Indexes. The four groups of patients were treated with different treatment methods and doses. In addition, the patients' heart function indexes, blood lipid indexes, liver function indexes, and ECG signal were detected before and at different periods after treatment, including diastolic blood pressure, systolic blood pressure, heart rate, B-type natriuretic peptide precursor (pre-proBNP), blood sugar (GLU), cholesterol (TC), triglycerides (TG), alanine aminotransferase (ALT), aspartate aminotransferase (AST), and types and incidence of complications.

2.6. Statistical Methods. SPSS 19.0 was employed for data statistics and analysis. Mean ± standard deviation ($\overline{x} \pm s$) was how measurement data were expressed, and percentage (%) was how count data were expressed. Pairwise comparison adopted analysis of variance. The difference was statistically considerable with $P < 0.05$.

3. Results

3.1. ECG Signal Monitoring in Patients with Arrhythmia. Figure 3 shows the ECG signal monitoring record of patients with arrhythmia. In Figure 3(a), there was no relationship between the central atrial wave and the ventricular wave, showing a complete disconnection. The atrial rate was 88 bpm, the ventricular rate was 30 bpm, the atrial rate was greater than the ventricular rate, and the Q-T interval was 0.68 s. In Figure 3(b), the P wave appeared regularly, with a frequency of 62 bpm. After the first, third, and fourth P waves, there were downstream QRS-T complexes. QRS-T complexes without downcoming after the 5th wave were type I atrioventricular block.

Figure 4 shows the detection results of ECG signal. It was found that the P wave detection algorithm can mark the P wave, which may be submerged in strong interference,

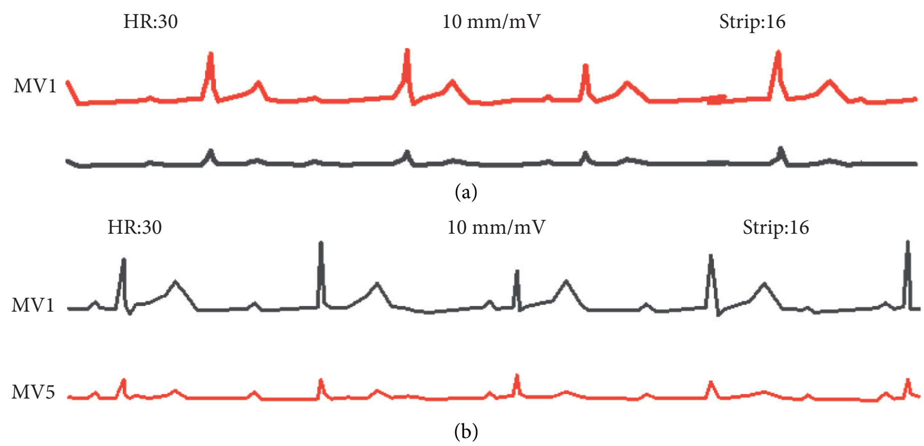

Figure 3: Patient's ECG signal monitoring chart. (a) ECG signal monitoring chart of a patient with arrhythmia. (b) ECG signal monitoring chart of patient with arrhythmia combined with atrioventricular block.

accurately locate the P wave and T wave peaks of ECG signal, and detect the P wave and T wave singularity. The diagnostic error rate (Er), sensitivity (Se), and prediction precision (Pp) of P wave detection algorithm for ventricular arrhythmia were 0.24%, 99.23%, and 98.53%, respectively. Er, Se, and Pp of atrial arrhythmia were 0.28%, 99.45%, and 98.76%, respectively.

3.2. Basic Patient Information. Figure 5 shows the comparison results of the basic information of the four groups of patients before treatment. Figure 5(c) shows the number of patients with cardiac function grades of grade III and IIII. Figure 5(d) shows the number of patients with mild heart failure, moderate heart failure, and no heart failure. There was no considerable difference in the proportion of patients with different ages, genders, heart function grades, and combined heart failure in each group ($P > 0.05$).

3.3. Changes of Diastolic Blood Pressure, Systolic Blood Pressure, and Heart Rate before and after Treatment. Figure 6(a) shows the changes in systolic blood pressure of the four groups of patients before treatment, one week after treatment, and two weeks after treatment. With the treatment time, the systolic blood pressure of the four groups of patients gradually decreased. After one week of treatment, patients in the SD group and HD group had lower systolic blood pressure, while the control group had higher systolic blood pressure. The systolic blood pressure of the SD group, MD group, and HD group after two weeks of treatment (117.35 ± 7.33 mmHg, 126.44 ± 9.38 mmHg, and 116.02 ± 8.2 mmHg) were significantly lower versus that of control group (140.3 ± 7.21 mmHg), and that of SD group and HD group was greatly inferior to the MD group ($P < 0.05$). Figure 6(b) shows the changes in diastolic blood pressure of the four groups of patients before treatment, one week after treatment, and two weeks after treatment. The diastolic blood pressure of the SD group was considerably inferior to that of the control group one week after treatment ($P < 0.05$). After two weeks of treatment, the diastolic blood pressure (74.12 ± 9.38 mmHg, 88.15 ± 8.2 mmHg, and 84.33 ± 7.21 mmHg) of the SD group, MD group, and HD group was substantially lower relative to that of control group (95.38 ± 7.33 mmHg), and that of SD group was evidently lower versus that of MD group and HD group ($P < 0.05$). Figure 6(c) shows the heart rate changes of the four groups of patients before treatment, one week after treatment, and two weeks after treatment. The heart rate of the SD group after two weeks of treatment was obviously inferior to that of the control group and the HD group ($P < 0.05$). Figure 6(d) shows the comparison results of the pre-proBNP content of type B natriuretic peptide of the four groups of patients. The pre-proBNP of SD group was notably lower versus that of control group, MD group, and HD group, and MD group was lower than HD group ($P < 0.05$).

3.4. Comparison on the Effective Rate of the Improvement of the Heart Function. Figure 7 shows the comparison results of the changes in the effective rate of cardiac function improvement after the four groups of patients were treated with different doses of Betaloc for 1, 2, and 3 weeks. After one week of treatment, patients in the MD and HD groups had a relatively higher effective rate of improvement in heart function. With the treatment time, the effective rate of cardiac function improvement of the four groups of patients gradually increased. After three weeks of treatment, the effective rate of cardiac function improvement ($72.35 \pm 1.21\%$) in the SD group was notably superior to that of the control, MD, and HD groups ($38.2 \pm 0.98\%$, $65.12 \pm 1.33\%$, and $60.43 \pm 1.25\%$) ($P < 0.05$).

3.5. Analysis of Blood Lipid Indexes before and after Treatment. Figure 8(a) shows the comparison results of the GLU content of the four groups of patients before and after treatment. There was no remarkable difference in the GLU content among the control group, SD group, MD group, and HD group before treatment ($P > 0.05$). After treatment, the GLU content of the SD group (5.84 ± 0.62 mmol/L) was greatly higher than that of the control group, MD group, and HD

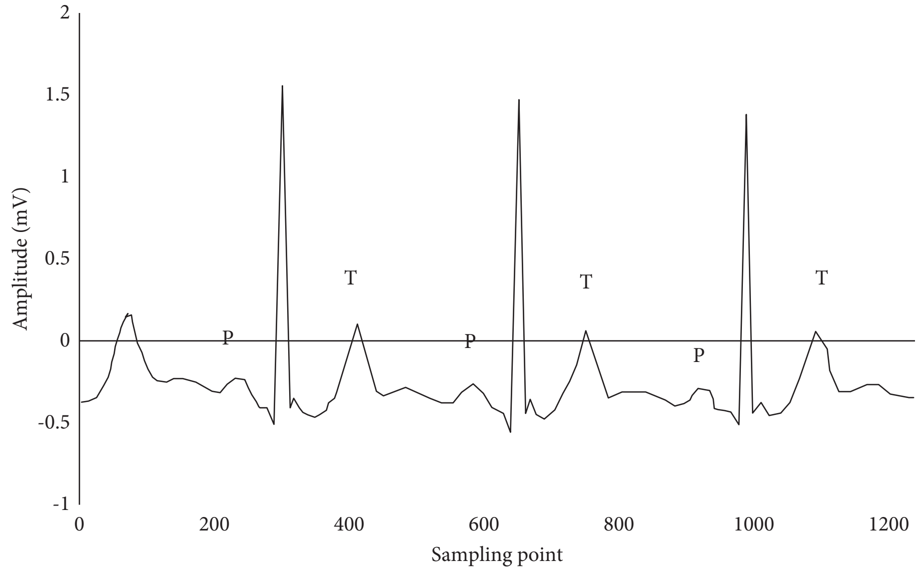

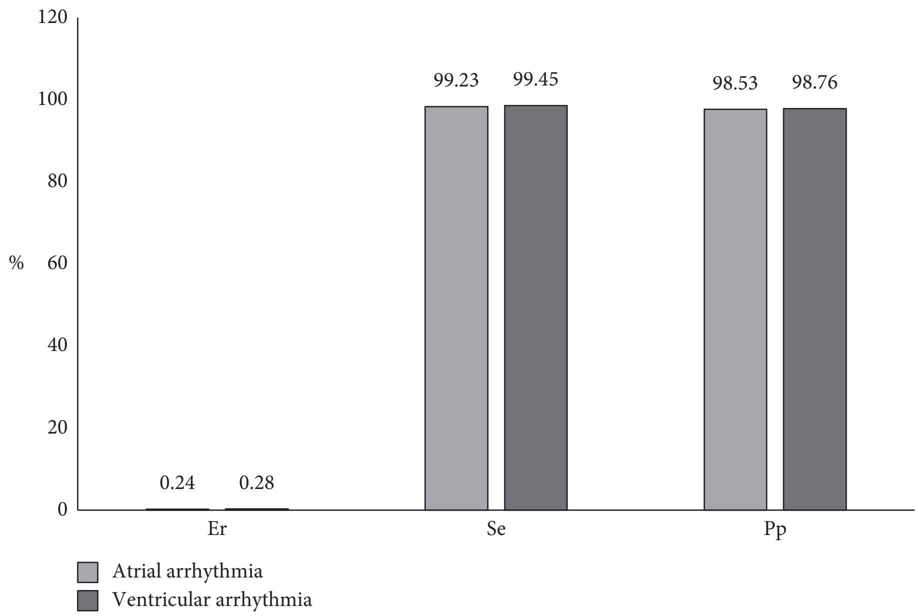

FIGURE 4: ECG signal detection results. (a) P and T wave detection results (P means P wave and T means T wave). (b) Arrhythmia diagnosis results.

group (4.56 ± 0.58 mmol/L, 4.97 ± 0.49 mmol/L, and 5.09 ± 0.54 mmol/L) ($P < 0.05$). Figures 8(b) and 8(c) present the comparison results of the TC content and TG content of the four groups of patients before and after treatment, respectively. There was no considerable difference in TC content and TG content among the control group, SD group, MD group, and HD group before treatment ($P > 0.05$). After treatment, the TC content and TG content of the SD group were dramatically superior to those of the control group, MD group, and HD group ($P < 0.05$).

Figure 9 shows the comparison results of the changes in liver function indexes ALT and AST content of the four groups of patients. From Figure 9(a), there was no substantial difference in ALT content among the four groups of patients after one week of treatment ($P > 0.05$). After two weeks and three weeks of treatment, the ALT content of the SD group was remarkably inferior to that of the control group, MD group, and HD group, and that of MD group and HD group was greatly lower versus control group ($P < 0.05$). From Figure 9(b), the AST content of the SD group and the HD group was notably lower than that of the control group and the MD group after two weeks of treatment, and that of MD group was dramatically lower relative to control group ($P < 0.05$). After three weeks of treatment, the content of SD group was substantially lower than that of control group, MD group, and HD group ($P < 0.05$).

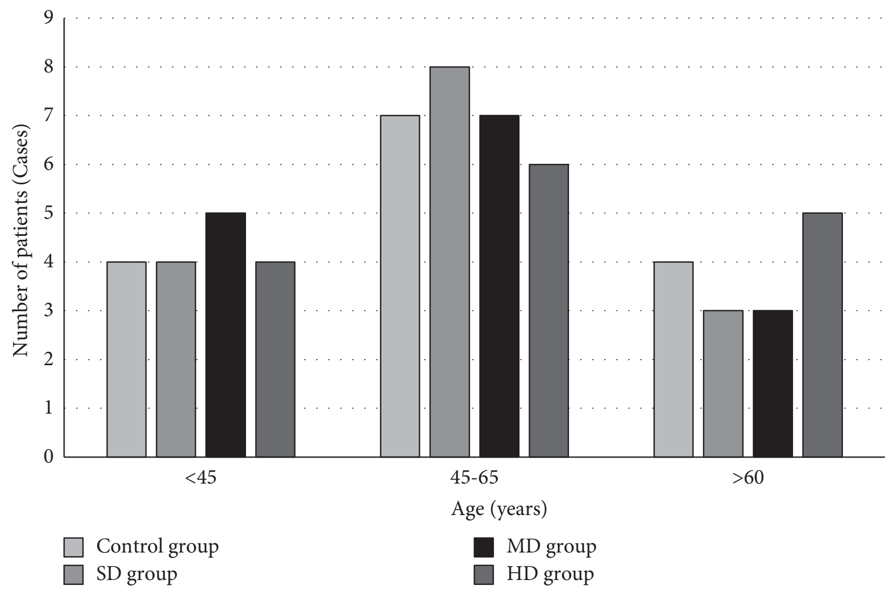

(a)

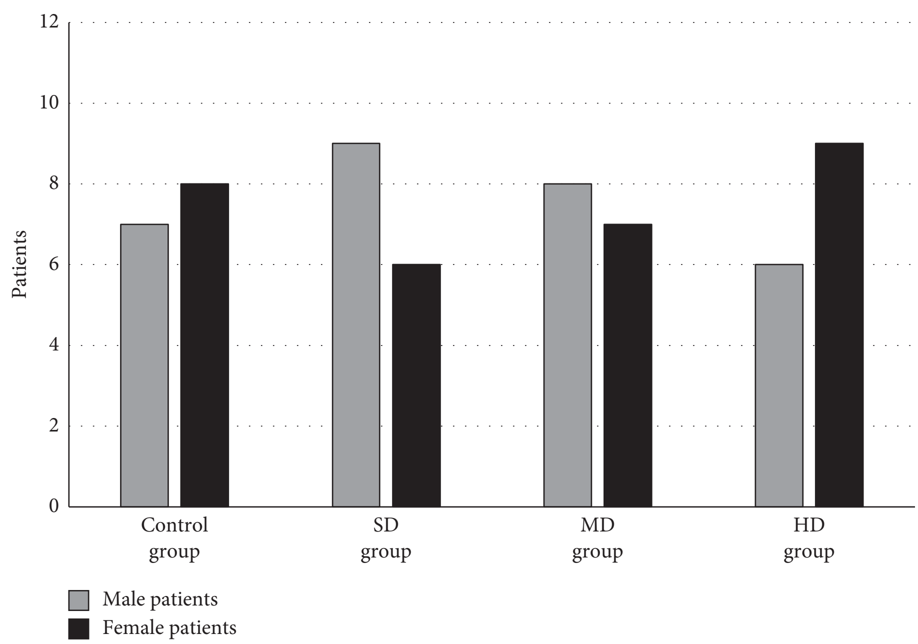

(b)

Figure 5: Continued.

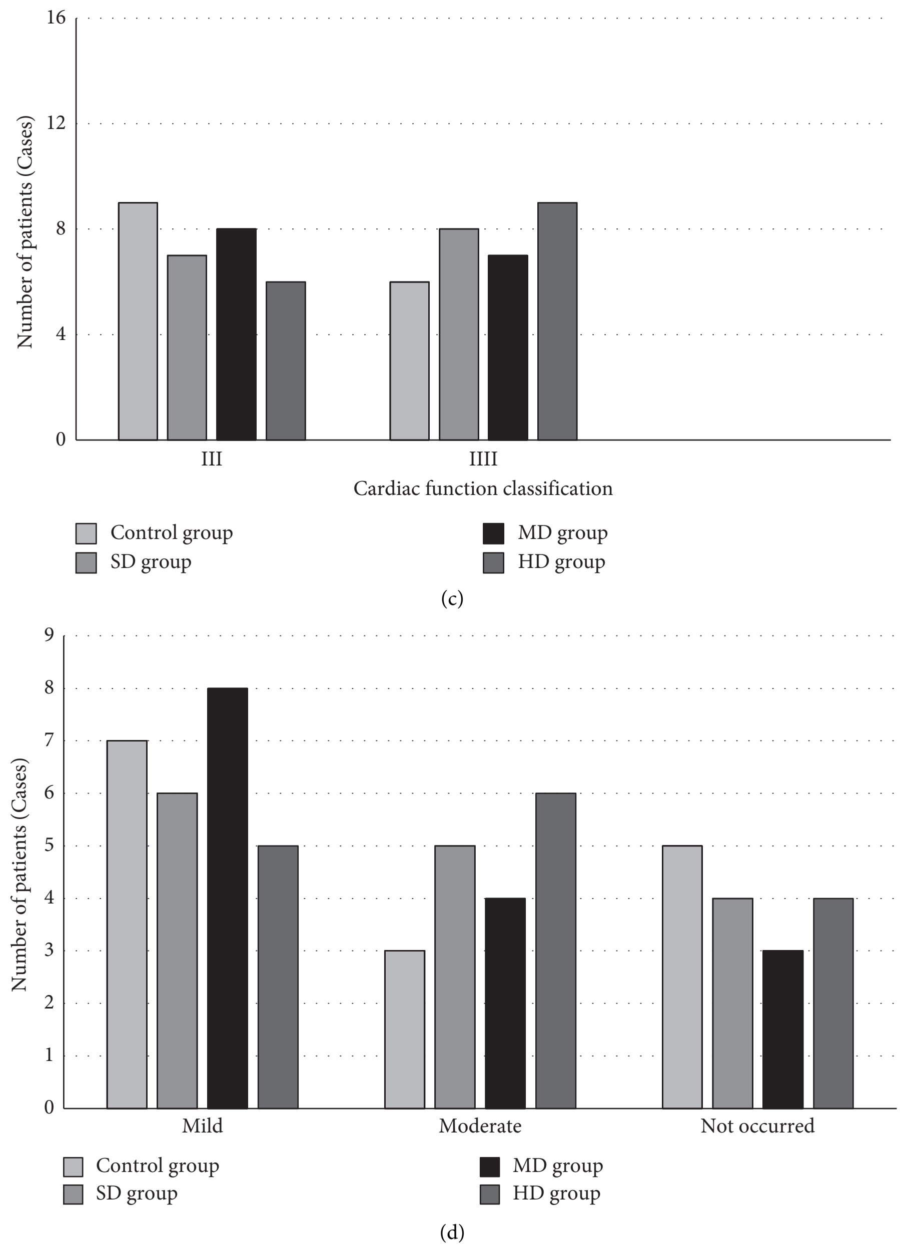

Figure 5: Comparison of the basic information of the four groups of patients. (a) Age. (b) Gender ratio. (c) Heart function level before treatment. (d) Patients complicated with heart failure.

3.6. Complications in the Four Groups. Figure 10 shows the types and incidence of complications in the four groups of patients before and during treatment. From Figures 10(a) and 10(b), patients with PHC undergoing hepatectomy for arrhythmia were prone to hypertension, diabetes, atrial fibrillation, postoperative arrhythmia, atrioventricular block, sinus bradycardia, hypotension, nausea and vomiting, headache, dizziness, etc. From Figure 10(c), the incidence of the above complications in the control group, SD group, MD group, and HD group was 34.6%, 12.4%, 20.5%, and 32.5%, respectively. The incidence of the above complications was the lowest in the SD group, followed by the MD group and the HD group.

4. Discussion

ECG records at the onset of arrhythmias are important evidence for the diagnosis of arrhythmias. During diagnosis, emphasis should be placed on checking whether the patient has organic heart disease such as hypertension, coronary heart disease, and myocarditis, and some physiological and pathological factors can cause arrhythmias [27, 28]. Physiological factors include exercise and emotional excitement, while pathological factors include cardiovascular diseases and endocrine diseases [29, 30]. Studies found that Betaloc is the drug with the lowest side effects among all drugs for the treatment of arrhythmia, and the only drug that can reduce

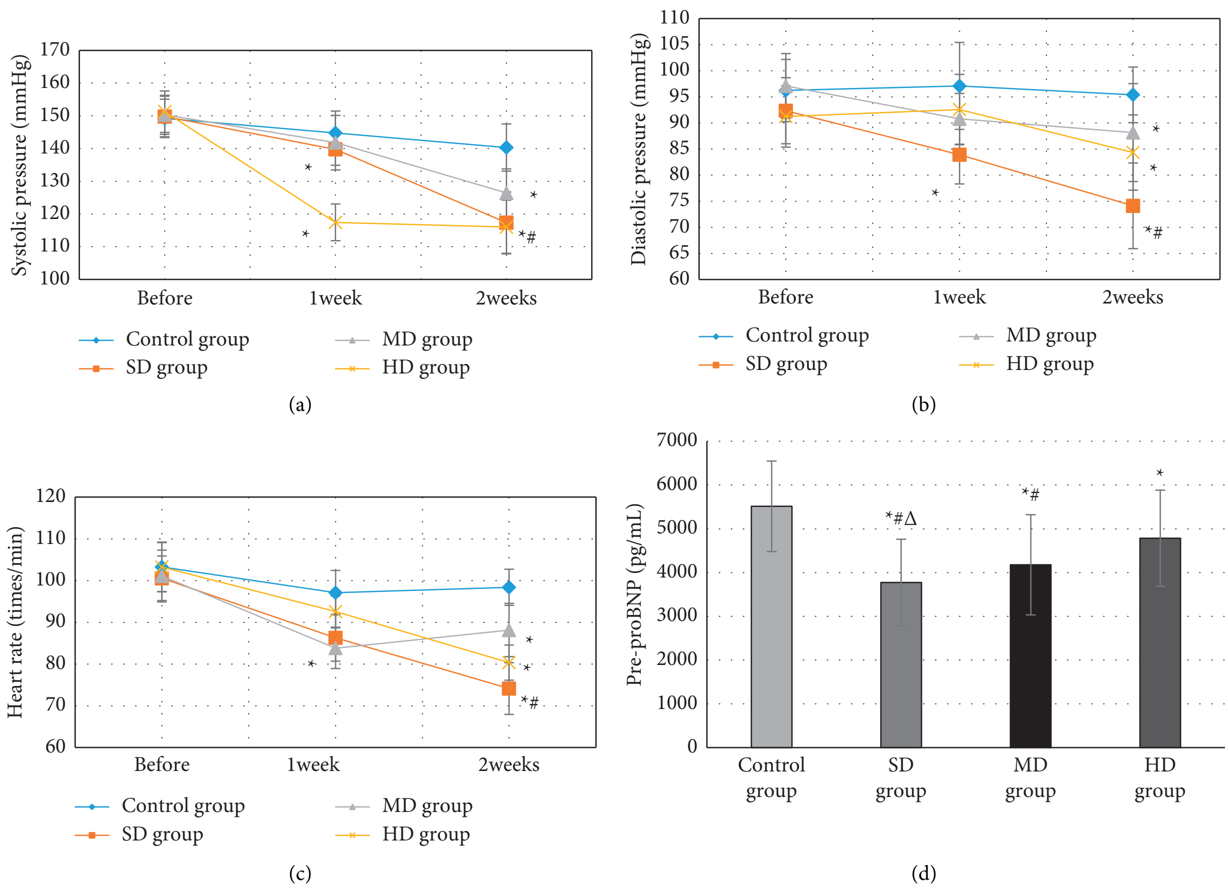

Figure 6: Changes of cardiac function indexes in the four groups. (a) Systolic blood pressure; (b) diastolic blood pressure; (c) changes in heart rate; (d) the pre-proBNP. * represents significant difference compared with control group ($P < 0.05$); # represents significant difference compared with HD group ($P < 0.05$); Δ represents significant difference compared with MD group ($P < 0.05$).

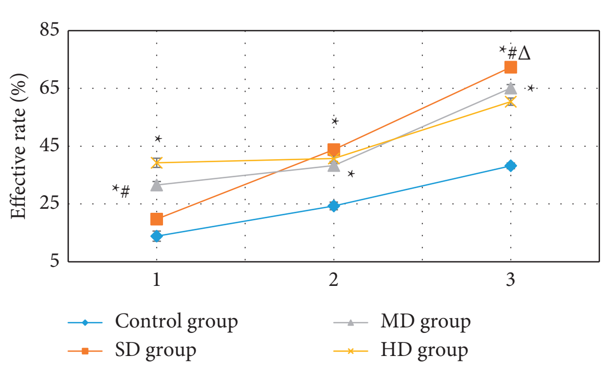

Figure 7: Comparison of the effective rate of cardiac function improvement in the four groups of patients. * indicates considerable differences versus control group ($P < 0.05$); # indicates considerable differences versus HD group ($P < 0.05$); Δ indicates considerable differences versus MD group ($P < 0.05$).

the mortality rate of the disease. It can not only be applied to angina pectoris and myocardial infarction, but also can effectively reduce myocardial oxygen consumption, slows heart rate, reduces angina pectoris, and effectively prevents arrhythmia after myocardial infarction [31–33]. Kotecha et al. [34] found that due to differences in physique and drug response of different patients, whether it is angina pectoris, arrhythmia, or heart failure, if Betaloc is selected as a therapeutic drug, it is necessary to start taking a small dose. If adverse reactions such as drug intolerance occur, it is necessary to stop taking it. The study of Blessberger et al. [35] found that Betaloc, as a beta-blocker, can slow down heart rate, reduce myocardial contractility, and thereby lower blood pressure. It mainly acts on the heart and has certain effects on bronchial smooth muscle. Although drugs such as Betaloc can reduce the heart rate and protect the heart, if the condition is unstable (when the condition is severe or acute left heart failure) for patients with arrhythmia or heart failure, they should avoid taking such drugs without authorization [36]. When heart failure worsens, fast heart rate is also a kind of self-protection. It is necessary to control the heart failure to a stable state before using Betaloc to lower the heart rate. Forcibly suppressing the heart rate when heart failure worsens will have a greater impact on the patient, and even life-threatening [37–39].

The P wave detection algorithm was introduced to detect and analyze the ECG automatically, and it was used in the early diagnosis of arrhythmia. Patients with arrhythmias after hepatectomy for PHC were selected as subjects and treated with different doses of Betaloc. The cardiac function indexes,

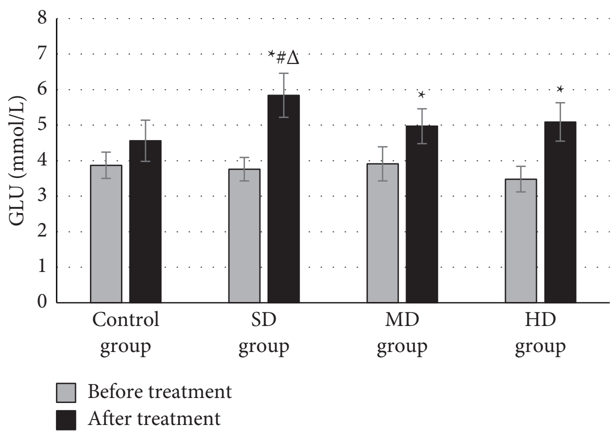

(a)

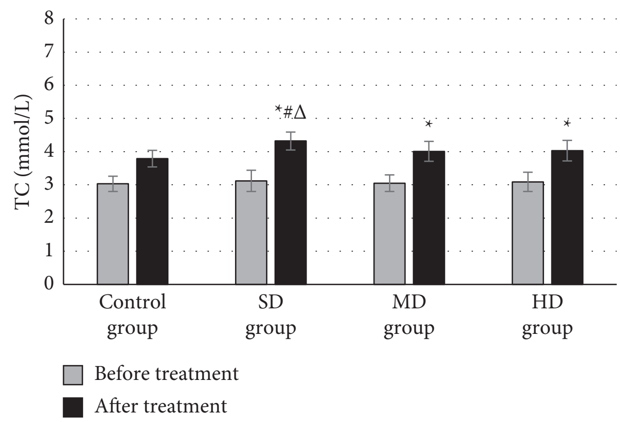

(b)

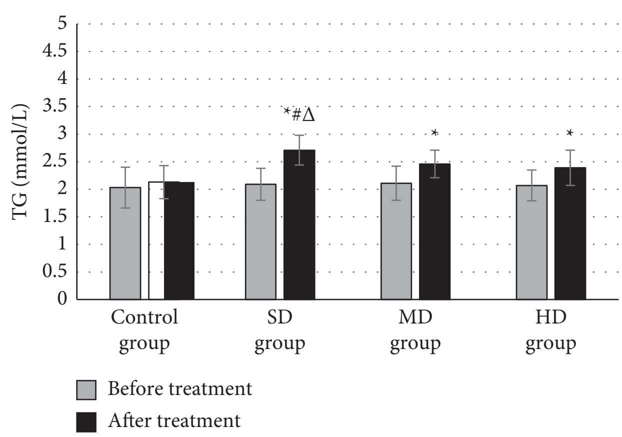

(c)

Figure 8: Comparison of blood lipid indexes of the four groups of patients before and after treatment. (a) GLU comparison before and after treatment. (b) TC comparison. (c) TG comparison. * indicates considerable differences versus control group ($P < 0.05$); # indicates considerable differences versus HD group ($P < 0.05$); and Δ indicates considerable differences versus MD group ($P < 0.05$).

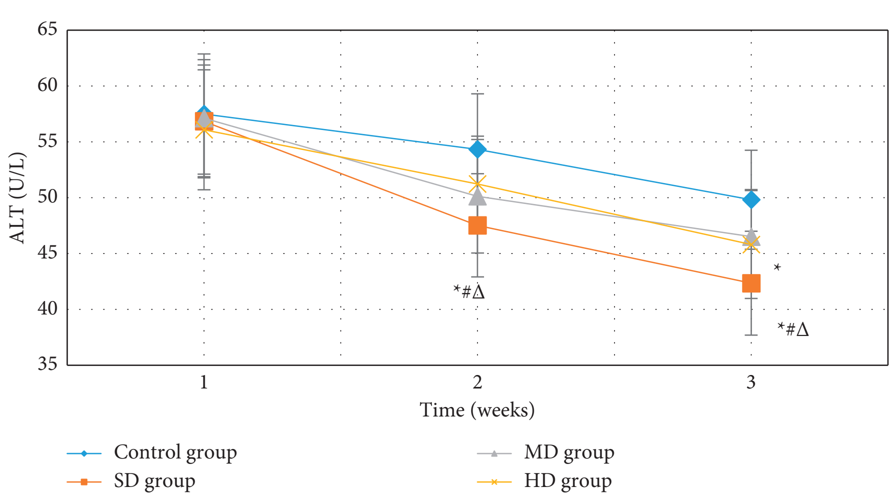

(a)

Figure 9: Continued.

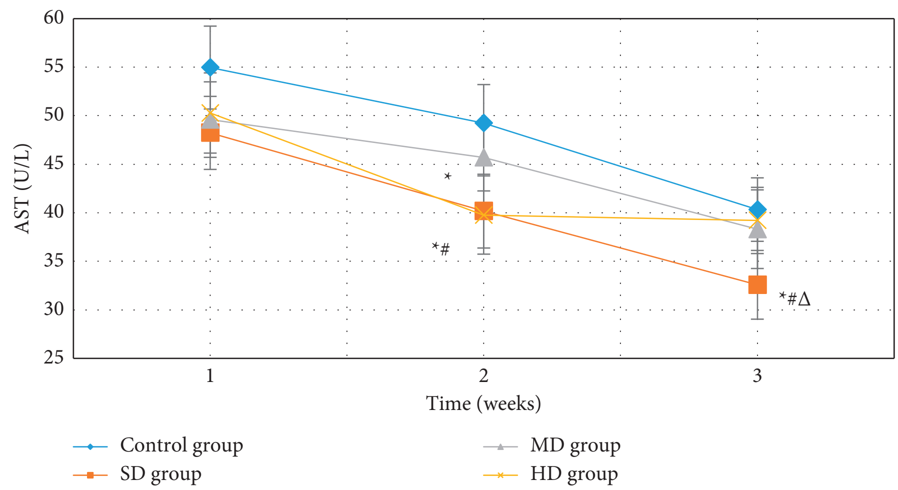

(b)

Figure 9: Analysis of liver function indexes of four groups of patients. (a) Changes in ALT content. (b) Changes in AST content. * represents remarkable versus control group ($P < 0.05$).

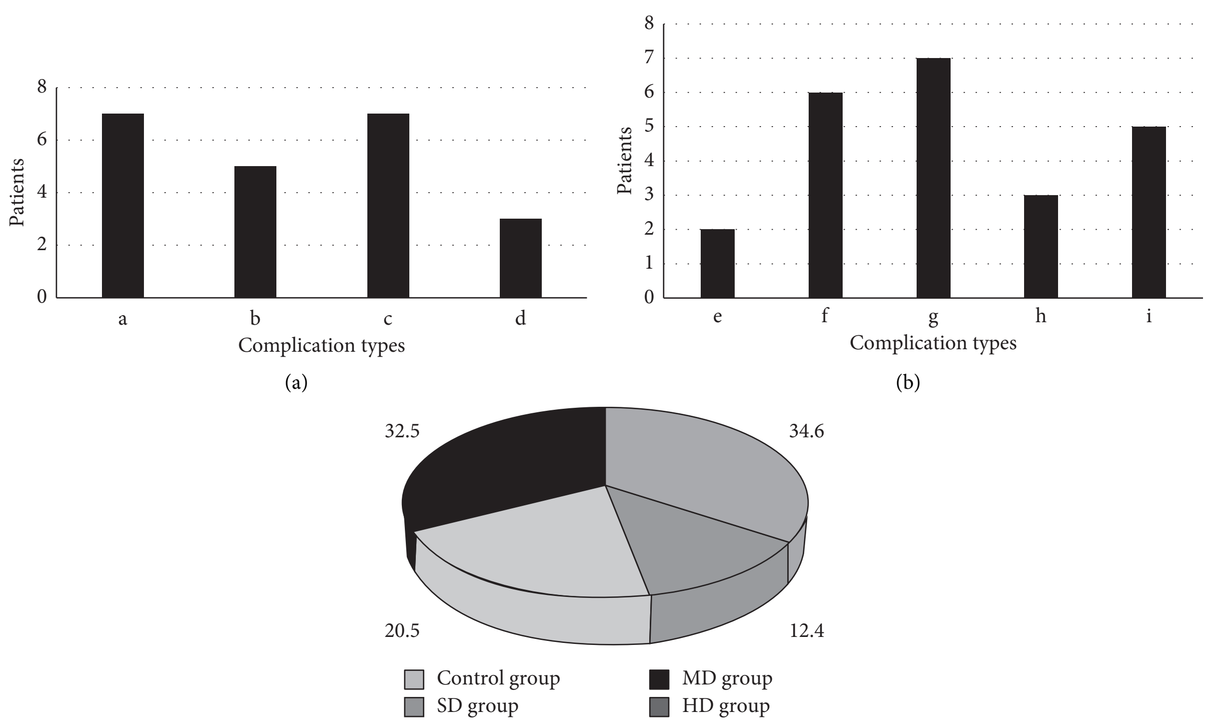

(c)

Figure 10: Complications occurred in the four groups of patients. (a, b) The types of complications in the four groups of patients. (a, b, c, d, e, f, g, h, and i indicate hypertension, diabetes, atrial fibrillation, atrioventricular block, sinus bradycardia, hypotension, nausea and vomiting, headache, and dizziness, respectively). (c) The complication rate.

blood lipid indexes, and liver function indexes of patients at different stages of treatment were analyzed; the therapeutic effect of low-dose Betaloc on arrhythmia after hepatectomy in patients with PHC was analyzed. As a result, the P wave detection algorithm can accurately locate the P wave and T wave peaks of the ECG signal. The diagnostic error rate, sensitivity, and correct prediction of ventricular arrhythmia were 0.24%, 99.23%, and 98.53%, respectively. The diagnostic error rate, sensitivity, and correct prediction of atrial arrhythmia were 0.28%, 99.45%, and 98.76%, respectively. Therefore, the proposed P wave detection algorithm had high application value for the diagnosis and early prediction of arrhythmia. The heart rate of the SD group after two weeks of treatment was obviously lower versus control group and the HD group ($P < 0.05$), which suggested that Betaloc can reduce the heart rate of patients with arrhythmia, and the effect of low-dose Betaloc in reducing the heart rate was the most obvious. The effective rate of cardiac function improvement in SD group (72.35 ± 1.21 mmHg) was remarkably superior to that of control group, MD group, and HD group (38.2 ± 0.98 mmHg, 65.12 ± 1.33 mmHg, and 60.43 ± 1.25 mmHg) ($P < 0.05$), which suggested that a small dose of Betaloc can significantly improve the cardiac function of patients with arrhythmia. After two weeks and three weeks of treatment, the ALT content of the SD group was substantially inferior to that of the control group, MD group, and HD group, and that of MD group and HD group was greatly lower versus control group ($P < 0.05$). After two weeks of treatment, the AST content of the SD group and the HD group was considerably lower versus control group and the MD group, and that of MD group was notably lower versus control group ($P < 0.05$). After three weeks of treatment, the content of SD group was evidently lower than that of control group, MD group, and HD group ($P < 0.05$), which was consistent with the results of Irizarry-Alvarado [40], indicating that patients with arrhythmia after PHC hepatectomy were safer to choose low-dose Betaloc, which had a good curative effect, can effectively reduce the heart rate, reduced the occurrence of complications, and improved heart function.

5. Conclusion

In this study, the automatic detection and analysis of ECG was carried out by introducing the P wave detection algorithm, and it was used for the early diagnosis of arrhythmia. Different doses of Betaloc were used to treat arrhythmia, so as to study the therapeutic effect of low-dose Betaloc on the complications of arrhythmia after hepatectomy in patients with primary liver cancer. The results suggested that dynamic ECG based on P wave detection algorithm had high diagnostic value for arrhythmia after hepatectomy in patients with primary liver cancer. The low-dose Betaloc used by patients was safer and had relatively better curative effect. However, the sample size selected in this study is small, which may have a certain impact on the experimental results, and the representativeness is low. Therefore, in the follow-up experiments, the sample size will be increased, and the application of Holter based on P wave detection algorithm combined with low-dose Betaloc in the diagnosis and treatment of arrhythmia after liver cancer resection will be further studied.

Data Availability

The data used to support the findings of this study are available from the corresponding author upon request.

Conflicts of Interest

The authors declare that they have no conflicts of interest.

Authors' Contributions

Fenfen Jiang and Haokai Xu contributed equally to this work.

Acknowledgments

This work was supported by Jiaxing Science and Technology Plan of China (2020AD30101 and 2021AD30103).

References

[1] J. A. Marrero, L. M. Kulik, and C. B. Sirlin, "Diagnosis, staging, and management of hepatocellular carcinoma: 2018 practice guidance by the American association for the study of liver diseases," *Hepatology*, vol. 68, no. 2, pp. 723–750, 2018.
[2] S. T. Orcutt and D. A. Anaya, "Liver resection and surgical strategies for management of primary liver cancer," *Cancer Control*, vol. 25, no. 1, Article ID 1073274817744621, 2018.
[3] X. L. Xu, X. D. Liu, M. Liang, and M. L. Bao, "Radiofrequency ablation versus hepatic resection for small hepatocellular carcinoma: systematic review of randomized controlled trials with meta-analysis and trial sequential analysis," *Radiology*, vol. 287, no. 2, pp. 461–472, 2018.
[4] R. E. Beard and A. Tsung, "Minimally invasive approaches for surgical management of primary liver cancers," *Cancer Control*, vol. 24, no. 3, Article ID 1073274817729234, 2017.
[5] S. D. Lu, L. Li, and X. M. Liang, "Updates and advancements in the management of hepatocellular carcinoma patients after hepatectomy," *Expert Review of Gastroenterology & Hepatology*, vol. 13, no. 11, pp. 1077–1088, 2019.
[6] C. Manterola, L. Grande, and T. Otzen, "Surgical treatment results of hepatocellular carcinoma in non-cirrhotic liver in southern Chile: case series with follow-up," *ANZ Journal of Surgery*, vol. 90, no. 1-2, pp. 92–96, 2020.
[7] L. Zeng, M. Tian, S. S. Chen et al., "Short-term outcomes of laparoscopic vs. Open hepatectomy for primary hepatocellular carcinoma: a prospective comparative study," *Curr Med Sci*, vol. 39, no. 5, pp. 778–783, 2019.
[8] Z. Morise, "Developments and perspectives of laparoscopic liver resection in the treatment of hepatocellular carcinoma," *Surgery Today*, vol. 49, no. 8, pp. 649–655, 2019.
[9] G. Yang, Y. Xiong, J. Sun, and W. Guan, "The efficacy of microwave ablation versus liver resection in the treatment of hepatocellular carcinoma and liver metastases: a systematic review and meta-analysis," *International Journal of Surgery*, vol. 77, pp. 85–93, 2020.
[10] Y. Li, J. L. Zhao, Z. H. Lv, and L. Jinhua, "Medical image fusion method by deep learning," *International Journal of Cognitive Computing in Engineering*, vol. 2, pp. 21–29, 2021.
[11] M. Hu, Y. Zhong, and S. Xie, "Fuzzy system based medical image processing for brain disease prediction," *Frontiers in Neuroscience*, vol. 15, Article ID 714318, 2021.
[12] K. Arima, H. Nitta, T. Beppu, and S. Nakagawa, "Impact of repeated hepatectomy on liver regeneration in hepatocellular carcinoma: a propensity score-based analysis," *Anticancer Research*, vol. 39, no. 2, pp. 965–970, 2019.
[13] S. G. Priori, A. A. Wilde, M. Horie et al., "HRS/EHRA/APHRS expert consensus statement on the diagnosis and management of patients with inherited primary arrhythmia syndromes: document endorsed by HRS, EHRA, and APHRS in May 2013 and by ACCF, AHA, PACES, and AEPC in June 2013," *Heart Rhythm*, vol. 10, no. 12, pp. 1932–1963, 2013.
[14] Q. Zhang, J. Chen, Y. Qin, W. Juejin, and Z. Lei, "Mutations in voltage-gated L-type calcium channel: implications in cardiac arrhythmia," *Channels*, vol. 12, no. 1, pp. 201–218, 2018.
[15] Z. Laksman, S. Barichello, T. M. Roston, W. D. Marc, and D. K. Andrew, "Acute management of ventricular arrhythmia

in patients with suspected inherited heart rhythm disorders," *JACC Clin Electrophysiol*, vol. 5, no. 3, pp. 267–283, 2019.

[16] S. G. Priori, A. A. Wilde, M. Horie et al., "Executive summary: HRS/EHRA/APHRS expert consensus statement on the diagnosis and management of patients with inherited primary arrhythmia syndromes," *Europace*, vol. 15, no. 10, pp. 1389–1406, 2013.

[17] B. Asatryan and A. Medeiros-Domingo, "Emerging implications of genetic testing in inherited primary arrhythmia syndromes," *Cardiology in Review*, vol. 27, no. 1, pp. 23–33, 2019.

[18] S. Ortmans, C. Daval, M. Aguilar et al., "Pharmacotherapy in inherited and acquired ventricular arrhythmia in structurally normal adult hearts," *Expert Opinion on Pharmacotherapy*, vol. 20, no. 17, pp. 2101–2114, 2019.

[19] J. Brouillette, S. Cyr, and C. Fiset, "Mechanisms of arrhythmia and sudden cardiac death in patients with HIV infection," *Canadian Journal of Cardiology*, vol. 35, no. 3, pp. 310–319, 2019.

[20] A. Pfenniger and R. Arora, "Beyond beta-blockers: targeting the sympathetic nervous system for the prevention and treatment of atrial fibrillation," *Cardiovascular Research*, vol. 115, no. 14, pp. 1940–1942, 2019.

[21] M. Ladouceur, "Arrhythmia and advanced heart failure in complex congenital heart diseases: what should we do?" *International Journal of Cardiology*, vol. 310, pp. 94-95, 2020.

[22] B. C. Clark and C. I. Berul, "Arrhythmia diagnosis and management throughout life in congenital heart disease," *Expert Rev Cardiovasc Ther*, vol. 14, no. 3, pp. 301–320, 2016.

[23] J. P. Moore, "Arrhythmia management for the adult patient with congenital heart disease: an update and analytical review," *Minerva Pediatrica*, vol. 66, no. 5, pp. 415–439, 2014.

[24] P. E. Longmuir, M. Sampson, J. Ham, W. Makenzie, J. P. Bhavika, and M. G. Robert, "The mental health of adolescents and pre-adolescents living with inherited arrhythmia syndromes: a systematic review of the literature," *Cardiology in the Young*, vol. 28, no. 5, pp. 621–631, 2018 May.

[25] M. Aoun and R. Tabbah, "Beta-blockers use from the general to the hemodialysis population," *Néphrologie & Thérapeutique*, vol. 15, no. 2, pp. 71–76, 2019.

[26] H. Blessberger, J. Kammler, H. Domanovits et al., "Perioperative beta-blockers for preventing surgery-related mortality and morbidity," *Cochrane Database of Systematic Reviews*, vol. 3, no. 3, Article ID CD004476, 2018.

[27] J. G. F. Cleland, K. V. Bunting, M. D. Flather et al., "Beta-blockers in Heart Failure Collaborative Group. Beta-blockers for heart failure with reduced, mid-range, and preserved ejection fraction: an individual patient-level analysis of double-blind randomized trials," *European Heart Journal*, vol. 39, no. 1, pp. 26–35, 2018.

[28] S. Prijic and R. Buchhorn, "Mechanisms of beta-blockers action in patients with heart failure," *Reviews on Recent Clinical Trials*, vol. 9, no. 2, pp. 58–60, 2014.

[29] M. J. Ackerman, S. G. Priori, A. M. Dubin et al., "Beta-blocker therapy for long QT syndrome and catecholaminergic polymorphic ventricular tachycardia: are all beta-blockers equivalent?" *Heart Rhythm*, vol. 14, no. 1, pp. e41–e44, 2017.

[30] H. Blessberger, S. R. Lewis, M. W. Pritchard et al., "Perioperative beta-blockers for preventing surgery-related mortality and morbidity in adults undergoing non-cardiac surgery," *Cochrane Database of Systematic Reviews*, vol. 9, no. 9, Article ID CD013438, 2019.

[31] E. Grandi and C. M. Ripplinger, "Antiarrhythmic mechanisms of beta blocker therapy," *Pharmacological Research*, vol. 146, p. 104274, 2019 Aug.

[32] F. M. Kusumoto, M. H. Schoenfeld, C. Barrett et al., "ACC/AHA/HRS guideline on the evaluation and management of patients with bradycardia and cardiac conduction delay: a report of the American college of cardiology/American heart association task force on clinical practice guidelines and the heart rhythm society," *Circulation*, vol. 140, no. 8, pp. e382–e482, 2018.

[33] R. M. John and S. Kumar, "Sinus node and atrial arrhythmias," *Circulation*, vol. 133, no. 19, pp. 1892–1900, 2016.

[34] D. Kotecha, J. Holmes, H. Krum et al., "Beta-Blockers in Heart Failure Collaborative Group. Efficacy of β blockers in patients with heart failure plus atrial fibrillation: an individual-patient data meta-analysis," *Lancet*, vol. 384, no. 9961, pp. 2235–2243, 2014.

[35] H. Blessberger, S. R. Lewis, M. W. Pritchard et al., "Perioperative beta-blockers for preventing surgery-related mortality and morbidity in adults undergoing cardiac surgery," *Cochrane Database of Systematic Reviews*, vol. 9, no. 9, Article ID CD013435, 2019.

[36] Y. Mareev and J. G. Cleland, "Should β-blockers be used in patients with heart failure and atrial fibrillation?" *Clinical Therapeutics*, vol. 37, no. 10, pp. 2215–2224, 2015.

[37] J. L. Martindale, I. S. deSouza, M. Silverberg, F. Joseph, and S. Richard, "β-Blockers versus calcium channel blockers for acute rate control of atrial fibrillation with rapid ventricular response: a systematic review," *European Journal of Emergency Medicine*, vol. 22, no. 3, pp. 150–154, 2015.

[38] S. Alegria, J. Costa, A. Vaz-Carneiro, and C. Daniel, "Cochrane Corner: perioperative beta-blockers for preventing surgery-related mortality and morbidity," *Revista Portuguesa de Cardiologia*, vol. 38, no. 10, pp. 691–694, 2019.

[39] R. Lampert, M. M. Burg, L. D. Jamner et al., "Effect of β-blockers on triggering of symptomatic atrial fibrillation by anger or stress," *Heart Rhythm*, vol. 16, no. 8, pp. 1167–1173, 2019.

[40] J. M. Irizarry-Alvarado, "Perioperative management of beta blockers and other antiarrhythmic medications," *Current Clinical Pharmacology*, vol. 12, no. 3, pp. 141–144, 2017.

Hindawi
Journal of Healthcare Engineering
Volume 2021, Article ID 6059060, 10 pages
https://doi.org/10.1155/2021/6059060

Research Article

Computed Tomography Image Texture under Feature Extraction Algorithm in the Diagnosis of Effect of Specific Nursing Intervention on Mycoplasma Pneumonia in Children

Yuyan Bi,[1] Cuifeng Jiang,[2] Hua Qi,[1] Haiwei Zhou,[1] and Lixia Sun[3]

[1]*Department of Pediatric Ward, Jinan City People's Hospital, Jinan 271199, Shandong Province, China*
[2]*Department of Pediatric Surgery, Jinan City People's Hospital, Jinan 271199, Shandong Province, China*
[3]*Department of Nursing, Jinan City People's Hospital, Jinan 271199, Shandong Province, China*

Correspondence should be addressed to Lixia Sun; 1811031053@nbu.edu.cn

Received 22 August 2021; Revised 25 September 2021; Accepted 27 September 2021; Published 16 October 2021

Academic Editor: Enas Abdulhay

To evaluate the effect of specific nursing intervention in children with mycoplasma pneumonia (MP), a feature extraction algorithm based on gray level co-occurrence matrix (GLCM) was proposed and combined with computed tomography (CT) image texture features. Then, 98 children with MP were rolled into the observation group with 49 cases (specific nursing) and the control group with 49 cases (routine nursing). CT images based on feature extraction algorithm of optimized GLCM were used to examine the children before and after nursing intervention, and the recovery of the two groups of children was discussed. The results showed that the proportion of lung texture increase, rope shadow, ground glass shadow, atelectasis, and pleural effusion in the observation group (24.11%, 3.86%, 8.53%, 15.03%, and 3.74%) was significantly lower than that in the control group (28.53%, 10.23%, 13.34%, 21.15%, and 8.13%) after nursing ($P < 0.05$). There were no significant differences in the proportion of small patchy shadows, large patchy consolidation shadows, and bronchiectasis between the observation group and the control group ($P > 0.05$). In the course of nursing intervention, in the observation group, the disappearance time of cough, normal temperature, disappearance time of lung rales, and absorption time of lung shadow (2.15 ± 0.86 days, 4.81 ± 1.14 days, 3.64 ± 0.55 days, and 5.96 ± 0.62 days) were significantly shorter than those in the control group (2.87 ± 0.95 days, 3.95 ± 1.06 days, 4.51 ± 1.02 days, and 8.14 ± 1.35 days) ($P < 0.05$). After nursing intervention, the proportion of satisfaction and total satisfaction in the experimental group (67.08% and 28.66%) was significantly higher than that in the control group (40.21% and 47.39%), while the proportion of dissatisfaction (4.26%) was significantly lower than that in the control group (12.4%) ($P < 0.05$). To sum up, specific nursing intervention was more beneficial to improve the progress of characterization recovery and the overall recovery effect of children with MP relative to conventional nursing. CT image based on feature extraction algorithm of optimized GLCM was of good adoption value in the diagnosis and treatment of MP in children.

1. Introduction

Mycoplasma pneumonia (MP) is a common respiratory disease in children. It is caused by mycoplasma pneumoniae infection and is often associated with atelectasis and large lung infiltration. It can cause extrapulmonary multisystem complications [1, 2]. Mycoplasma pneumonia in children is mainly transmitted by respiratory droplets, which then invades the respiratory mucosa. Through its special structure, it is closely adsorbed on the receptor of the cell membrane. It can then multiply and release toxic substances, which can trigger a cascade of symptoms. The prevalence rate of this disease is very high throughout the year, especially in winter. Mycoplasma pneumonia in children generally presents a subacute onset, and the clinical symptoms are usually dry cough, sore throat, headache, and unsteady fever. Sometimes, a severe cough with normal body temperature may be present [3]. If not treated in time, it will bring multisystem and organ damage to the children, and the skin will appear measles-like changes [4]. Specific nursing is a targeted approach to quality care, whose core is people-oriented. It embodies the humanistic spirit and respects the life value, personal dignity, and personal privacy of patients. Patients are greatly helped in rehabilitation treatment by advocating humanized service concept, paying attention to humanized nursing management, and creating humanized service environment [5, 6].

Relevant studies showed that MP is often manifested as the separation of clinical symptoms, signs, and imaging features, and the abnormal rate of pulmonary imaging is substantially higher than the positive rate of pulmonary signs [7]. Clinical examination of MP mainly adopts imaging methods, among which chest X-ray has a high spatial resolution for patient scan. It can reflect the overall condition of the lung, showing interstitial infiltration, lobular, lobular consolidation, and hilar lymph node enlargement. However, due to the overlapping relationship between the front and the rear, the resolution of pulmonary fine lesions is limited to a certain extent, so it is relatively difficult to detect early or ultraearly lesions [8, 9]. High-resolution CT scan can display patients' pulmonary lesions on multiple levels, which is conducive to accurate positioning and clear extent and range of lesions [10, 11]. Feature information extraction is an important work in medical image processing. Different image data need to be processed by different methods, such as the texture feature extraction method based on statistics, the feature extraction method based on frequency, and the feature extraction method based on model [12, 13]. Gray level co-occurrence matrix (GLCM) is the data used to describe the texture related information among image pixels. It can calculate the similarity of gray levels between different pixel points in a specific distance and direction to describe the overall texture information of the image [14] and effectively reduce the time of texture feature calculation and improve the efficiency of the algorithm. Therefore, a novel feature extraction algorithm based on GLCM was proposed and applied to the CT image evaluation of MP in children.

To sum up, the analysis of image texture features is an important work in clinical diagnosis and treatment. Therefore, 98 children with MP were rolled into the observation group with 49 cases (specific nursing) and the control group with 49 cases (routine nursing). CT images based on feature extraction algorithm of optimized GLCM were used to examine the children before and after nursing intervention, and the recovery of the two groups of children was discussed. This research was developed to comprehensively analyze the adoption of CT image texture feature based on GLCM feature extraction algorithm in evaluating the effect of specific nursing intervention in children with MP.

2. Materials and Methods

2.1. Research Objects. A total of 98 children with MP who were hospitalized in the hospital from June 15, 2019, to April 3, 2021, were selected as the study subjects, including 42 males and 56 females. All the children were divided into the experimental group (49 cases) and the control group (49 cases) according to different nursing plans. This study had been approved by the medical ethics committee of the hospital. The patients and their family members knew about this study and signed the informed consent.

Inclusion criteria: (I) school-age children, (II) children with acute onset, (III) children with fever and respiratory symptoms, (IV) chest X-ray showed patchy infiltrating opacity, (V) children with complete clinical data, and (VI) the family members signed the informed consent.

Exclusion criteria: (I) children unwilling to cooperate with the examination, (II) children with autoimmune diseases, (III) children who had received medical treatment, (IV) children with mixed pulmonary and extrapulmonary infections found by virus examination, and (V) children who quitted the experiment.

2.2. Imaging Examination. Philips Brilliance iCT 256-slice spiral extremely fast CT was used to perform high-resolution CT examination of the patient's lungs. The scan range was from the tip of the lung to the diaphragm. The scanning parameters were tube voltage of 120 kV, tube current of 30 mA, and fault of 1-2 mm.

Results judgment was as follows. The distribution, morphological characteristics, and the condition of lung, pleura, and mediastinum were evaluated by professional imaging physicians. The lesion involved sites were left (upper, middle, and lower) and right (upper, middle, and lower) lung field. A mediastinal window scan was also performed to evaluate lymph nodes and pleural cavities, such as pleural effusion. The lung features of HRCT mainly included increased lung texture, cord-like shadow, ground glass shadow, small patchy shadow, large patchy consolidation shadow, atelectasis, bronchiole dilatation, pleural effusion, and hilar mediastinal lymph node enlargement.

2.3. Feature Extraction Algorithm Based on Optimized GLCM. The GLCM can calculate the similarity between different pixels at a specific distance and gray level in a specific direction to describe the overall texture information of the image [15]. It is supposed that an image is Q and the gray level is z; then, the GLCM of the image is $z * z$. From a pixel point C with a gray level of c to a pixel point D that is e pixels away, the corresponding pixel points generated by the two points C and D are (c, d). Then, the number of all pixels appearing in the image can constitute the elements of the GLCM. In different directions (0°, 45°, 90°, 135°), the GLCM calculation equation is as follows:

$$
\begin{aligned}
F_0(c,d) &= [u-i=e, v-j=0, f(i,j)=c, f(u,v)=d \mid [(i,j),(u,v)\in Q]],\\
F_{45}(c,d) &= [u-i=e, v-j=e, f(i,j)=c, f(u,v)=d \mid [(i,j),(u,v)\in Q]],\\
F_{90}(c,d) &= [u-i=0, v-j=e, f(i,j)=c, f(u,v)=d \mid [(i,j),(u,v)\in Q]],\\
F_{135}(c,d) &= [u-i=-e, v-j=e, f(i,j)=c, f(u,v)=d \mid [(i,j),(u,v)\in Q]],
\end{aligned}
\tag{1}
$$

where $f(i,j)=c$ represents the pixel point with the coordinate (i,j) in the image and the gray value of c, $f(u,v)=d$ represents the pixel point with the coordinate (u,v) in the figure and the gray value of d, and $F_0(c,d)$, $F_{45}(c,d)$, $F_{90}(c,d)$, and $F_{135}(c,d)$ represent the number of pixel pairs appearing in the image at a distance of e and in the direction of 0°, 45°, 90°, and 135°, respectively.

Figure 1 graphically shows the specific definitions in the directions of 0°, 45°, 90°, and 135°.

To better understand the calculation method of the GLCM, a binary image with a gray level of 8 and a size of 5×4 (Figure 2(a)) is taken as an example. Figure 2(b) shows that the number of occurrences of the element $(1,1)$ in the 0° direction is 1, the number of occurrences of the element $(1,2)$ is 0, and the number of $(1,3)$ occurrences is 1. By analogy, the GLCM in the 0° direction is finally obtained. Figure 2(c) shows that the number of occurrences of element $(1,1)$ in the 90° direction is 0, the number of occurrences of element $(1,2)$ is 1, and the number of occurrences of $(1,3)$ is 1. Then, the final GLCM in the 90° direction is obtained.

However, the GLCM has a large amount of data, which is not conducive to the extraction of image features and the classification and recognition of images. Therefore, four statistical indicators of energy (Energy), moment of inertia (Contrast), correlation (Correlation), and entropy (Entropy) were redefined to summarize the characteristic information in the GLCM [16, 17].

Energy reflects the correlation between the distribution of image grayscale and image texture, and the size of the energy is directly proportional to the size of the texture. The larger the value of the moment of inertia, the clearer the image texture. Correlation reflects the correlation of the local pixel distribution of the image. Entropy reflects the texture complexity of the target image. The higher the texture complexity, the higher the entropy value, and vice versa, the lower the entropy.

The equations are as follows:

$$
\begin{aligned}
\text{Energy} &= \sum_i \sum_j F(i,j)^2,\\
\text{Contrast} &= \sum_{v=0}^{V_{g1}} v^2 \sum_{i=1}^{V_g} \sum_{j=1}^{V_g} F(i,j),\\
v &= |i-j|,\\
\text{Correlation} &= \frac{\left[\sum_i \sum_j (i,j)F(i,j) - \alpha_x \alpha_y\right]}{\beta_x \beta_y},\\
\text{Entropy} &= \sum_{i=2}^{2V_g} \log(F(i,j)) * F(i,j).
\end{aligned}
\tag{2}
$$

Among them, $P(i,j)$ represents the element value at the coordinate (i,j) in the GLCM, $i,j\in[0,z]$. z represents the gray level of the image. Then, the average value of the four directions of the special parameter is used as the final parameter value:

$$
\begin{aligned}
\text{Energy} &= \frac{(\text{Energy}_0 + \text{Energy}_{45} + \text{Energy}_{90} + \text{Energy}_{135})}{4},\\
\text{Contrast} &= \frac{(\text{Contrast}_0 + \text{Contrast}_{45} + \text{Contrast}_{90} + \text{Contrast}_{135})}{4},\\
\text{Correlation} &= \frac{(\text{Correlation}_0 + \text{Correlation}_{45} + \text{Correlation}_{90} + \text{Correlation}_{135})}{4},\\
\text{Entropy} &= \frac{(\text{Entropy}_0 + \text{Entropy}_{45} + \text{Entropy}_{90} + \text{Entropy}_{135})}{4}.
\end{aligned}
\tag{3}
$$

Eight lung cancer CT images, eight lung benign lesion CT images, and eight healthy adult lung CT images were selected, and the energy, moment of inertia, correlation, and entropy parameters of different types of CT images were calculated. The results were shown in Figure 3. When the feature parameters of the image were calculated by energy, entropy, correlation, and moment of inertia, the features of different types of samples were not obvious. Therefore, although the four parameters can describe the texture information of the image, there was no clear distinction between the feature information of different categories, which misled the image classification work.

To solve these problems, vector fitting [18] is proposed to optimize the GLCM, and the four directions of each feature

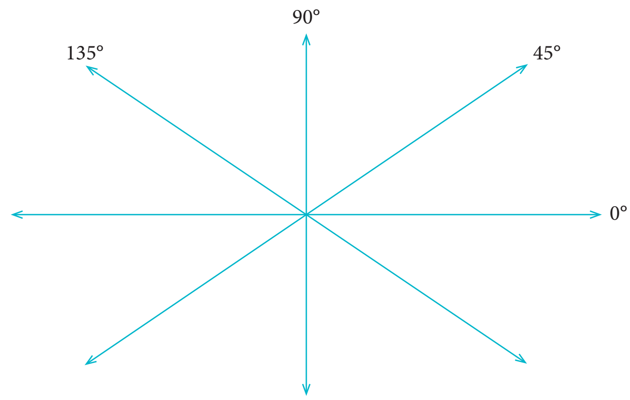

Figure 1: Calculation direction of GLCM.

(a)

1	2	3	6
1	4	4	5
5	3	6	1
6	5	1	3

(b)

	1	2	3	4	5	6
1	1	0	1	0	1	0
2	0	0	0	1	0	0
3	0	0	0	1	1	0
4	0	0	1	0	0	1
5	1	0	0	0	0	1
6	1	0	0	0	1	0

(c)

	1	2	3	4	5	6
1	0	1	1	1	0	0
2	0	0	1	0	0	0
3	0	0	0	0	0	2
4	0	0	0	1	1	0
5	1	0	1	0	0	0
6	1	0	0	0	1	0

Figure 2: Calculation of GLCM: (a) a binary image; (b) a GLCM in the 0° direction; (c) a GLCM in the 90° direction.

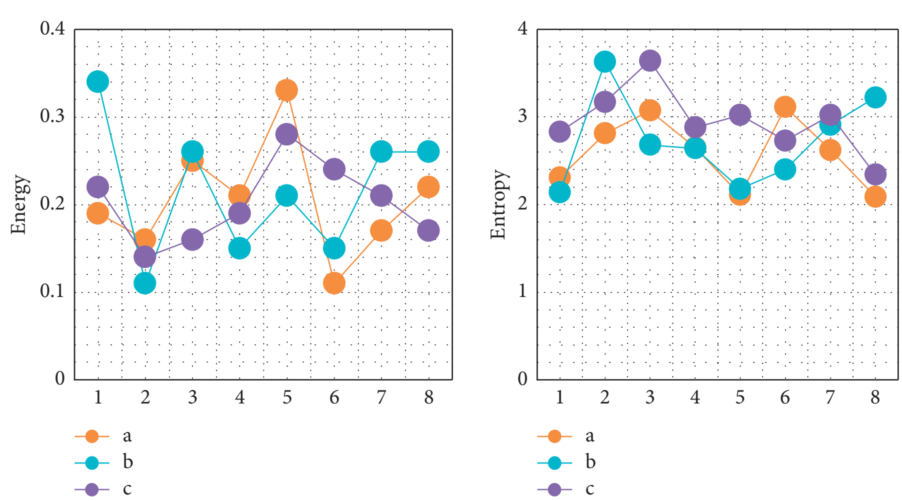

(a) (b)

Figure 3: Continued.

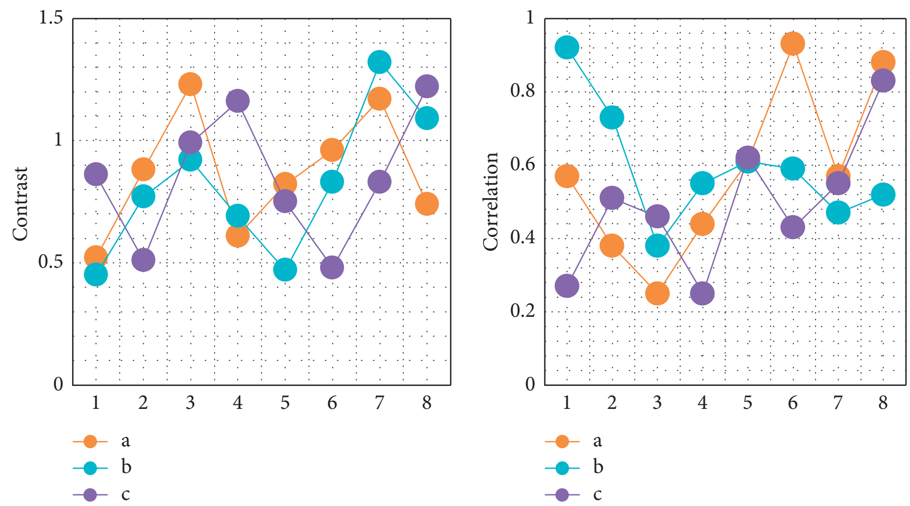

(c) (d)

FIGURE 3: Energy, moment of inertia, correlation, and entropy parameters of different types of CT images (a–c were CT images of lung cancer, CT of benign lung lesions, and CT of healthy adult lungs, respectively): (a) energy; (b) entropy; (c) moment of inertia; (d) correlation.

parameter are vectorized. The vector and modulus of these four vectors are regarded as new feature parameters, and they are expressed as follows:

$$\begin{aligned}
\text{Energy} &= \overrightarrow{\text{Energy}_0} + \overrightarrow{\text{Energy}_{45}} + \overrightarrow{\text{Energy}_{90}} + \overrightarrow{\text{Energy}_{135}},\\
\text{Contrast} &= \overrightarrow{\text{Contrast}_0} + \overrightarrow{\text{Contrast}_{45}} + \overrightarrow{\text{Contrast}_{90}} + \overrightarrow{\text{Contrast}_{135}},\\
\text{Correlation} &= \overrightarrow{\text{Correlation}_0} + \overrightarrow{\text{Correlation}_{45}} + \overrightarrow{\text{Correlation}_{90}} + \overrightarrow{\text{Correlation}_{135}},\\
\text{Entropy} &= \overrightarrow{\text{Entropy}_0} + \overrightarrow{\text{Entropy}_{45}} + \overrightarrow{\text{Entropy}_{90}} + \overrightarrow{\text{Entropy}_{135}}.
\end{aligned} \tag{4}$$

The optimized GLCM is applied to the above different categories of CT images (Figure 4). After the characteristic parameter vector fitting, the information difference of energy value, correlation, moment of inertia, and similarity of different categories of CT images are greatly improved. In general, the improved GLCM parameters based on vector fitting solve the problem that the difference of feature information is not obvious.

2.4. Nursing Methods. For the control group, routine treatment of anti-infection, physical cooling, antiasthmatic, sedation, oxygen inhalation, and other nursing treatment was performed. Nursing staff should understand the basic situation of children and the history of allergy through asking the children's parents. Appropriate psychological comfort was made to reduce children's fear of emotion.

Observation group nursing was as follows. (I) Physical sign nursing: the heart rate, respiration, pulse, and so on were observed during admission. If the child's temperature was unstable, it should be measured every two hours, and every five hours when the temperature was stable. For children with high fever, physical cooling and drug intervention can be used, while keeping their skin clean. (II) Psychological care: whether children had negative emotions such as irritability and anxiety were timely observed, and children's treatment compliance should be enhanced through language communication and interaction. At the same time, communicate was made with the families of the children, so did the targeted guidance. (III) Nutrition care: high-protein food was added in the diet of children to ensure adequate nutrition of children. (IV) Environmental care: nurse should pay attention to keep the ward clean and hygienic, fresh air, regular cleaning, and disinfection. (V) Propaganda and nursing: nurse should educate family members about disease prevention and control and conduct propaganda brochures, verbal education, and other methods to popularize knowledge about the disease. Nursing staff should closely observe the vital indicators and clinical signs of the children during treatment to avoid the occurrence of acute sudden symptoms.

2.5. Curative Effect Indexes. The improvement of clinical symptoms (the cough disappearance time, the time for returning to normal temperature, the disappearance time of

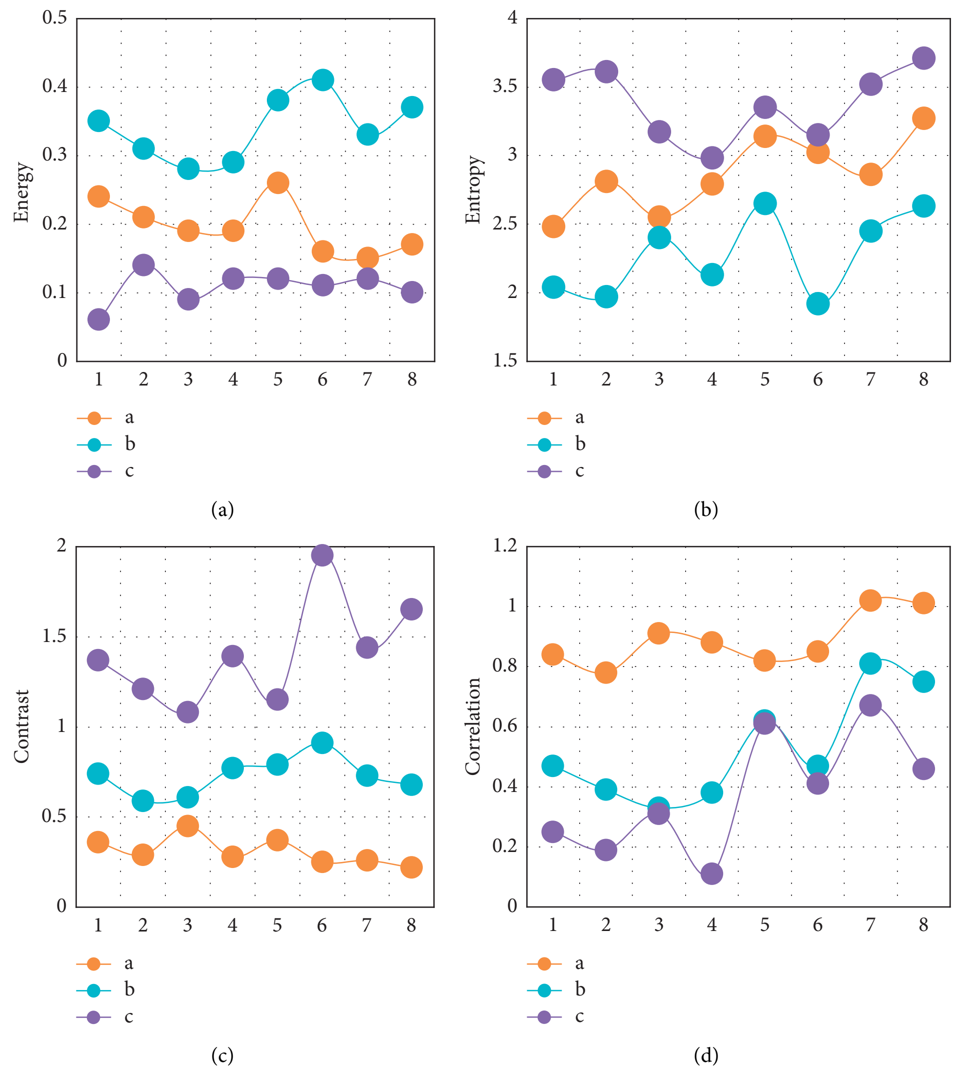

Figure 4: Energy, moment of inertia, correlation, and entropy parameters of different types of CT images after optimization (a–c were CT images of lung cancer, CT of benign lung lesions, and CT of healthy adult lungs, respectively): (a) energy; (b) entropy; (c) moment of inertia; (d) correlation.

lung rales, and the lung shadow absorption time) was recorded during treatment. The recovery of the two groups of children after half a month of treatment was compared and analyzed. The effects of different nursing interventions are shown in Table 1.

2.6. Statistical Analysis. SPSS 19.0 was employed for data statistics and analysis. Mean ± standard deviation ($\overline{x} \pm s$) was how measurement data were expressed, and percentage (%) was how count data were expressed. The pairwise comparison was performed by analysis of variance. The difference was statistically considerable with $P < 0.05$.

3. Results

3.1. Summary of Clinical Manifestations of Children. In Figure 5, the clinical symptoms of 98 children included fever, cough, sore throat, headache, fatigue, wheezing, and kicking sound. The cases of fever, cough, and sore throat were 86, 72, and 59, respectively. The onset time of fever was the earliest (1.24 ± 0.66 days), followed by cough (1.86 ± 1.13 days) and sore throat (1.94 ± 0.58 days). Cough lasted the longest (14.12 ± 3.02 days), followed by fever (8.27 ± 2.85 days).

3.2. CT Image of MP. Figure 6 shows chest CT images of a 6-year-old female child with no previous history of hypertension, diabetes, infectious disease, or family history (parents were healthy). Physical examination showed that the child was clear with no deformity of the chest, clear sound on percussion of both lungs, clear breath sound on auscultation of both lungs, no rales were heard, the heart rhythm was uniform, no deformity of the limbs and spine, and the movement was free. CT images showed consolidation of the right upper lobe with air bronchial sign. The lesion distribution was wedge-shaped, ground glass shadow around consolidation, interstitial change, and interlobular interstitial thickening was obvious.

Table 1: Curative effect indexes of nursing intervention.

Nursing effect	Standard
Satisfied	The child's symptoms improved substantially, and the clinical symptoms were relieved
Generally satisfied	The child's symptoms were slightly improved, and other clinical symptoms were partially relieved
Dissatisfied	The child's symptoms did not improve or worsen

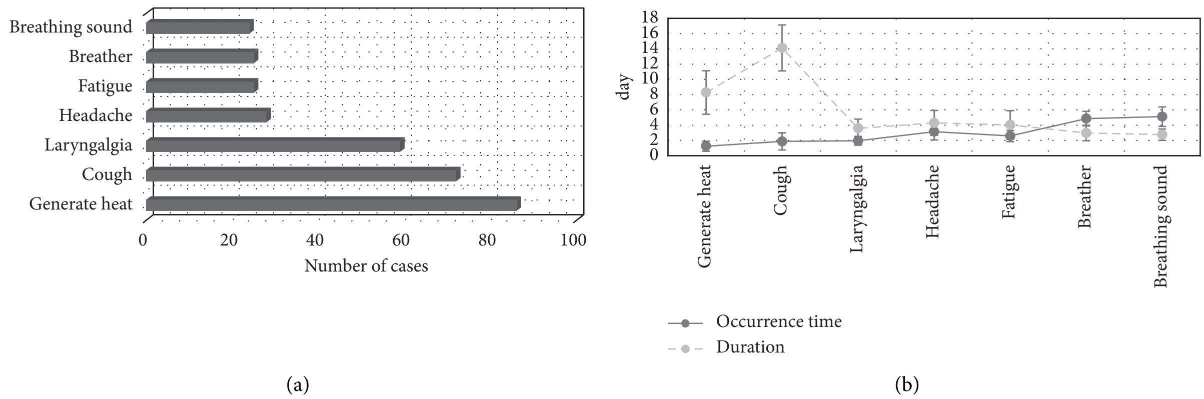

Figure 5: Summary of clinical manifestations of children: (a) the number of patients; (b) the time and duration of symptoms.

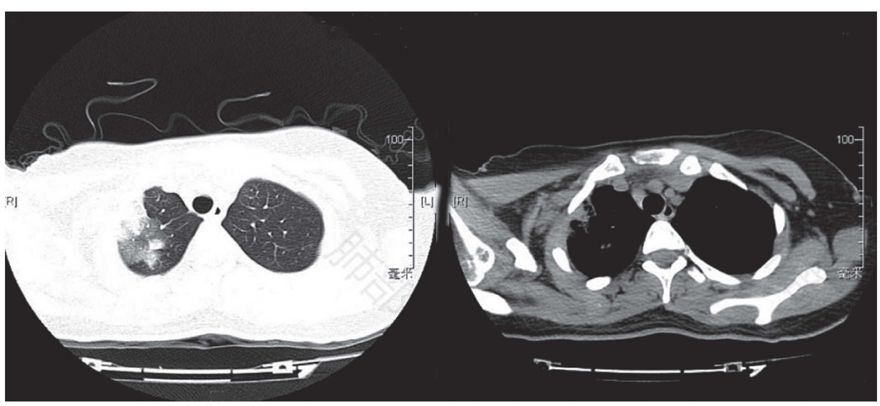

Figure 6: A 6-year-old female child's lung CT image.

3.3. CT Image Characteristics of Two Groups of Children after Nursing Intervention. Figure 7 shows the comparison of CT image features between the two groups after nursing intervention. After nursing, the proportion of increased lung texture, stripe shadow, ground glass shadow, atelectasis, and pleural effusion in the observation group was substantially lower than that in the control group ($P < 0.05$). There was no considerable difference in the proportion of small patchy shadow, large patchy consolidation shadow, and bronchiole dilation between the observation group and the control group ($P > 0.05$).

Figure 8 shows CT images of a 7-year-old male child in the experimental group before and after treatment. Contrast-enhanced CT scan before treatment revealed a distinctly unenhanced low-density area with compartments in the right lung consolidation, marked pleural thickening, and enlarged and uniformly marked lymph nodes behind the anterior tracheal vena cava. After three months of treatment, the review found that the general condition was good, with enlarged anterior mediastinum.

3.4. Comparison of Symptom Improvement of Two Groups of Children during Nursing. In Figure 9, the cough disappearance time, the time for returning to normal temperature, the disappearance time of lung rales, and the lung shadow absorption time of the observation group were substantially shorter than those of the control group, and the differences were great ($P < 0.05$).

3.5. Comparison of Satisfaction after Nursing Intervention between the Two Groups. Figure 10 shows that the proportion of satisfaction and total satisfaction of children in the experimental group after nursing intervention was substantially higher than that in the control group, and the difference was notable ($P < 0.05$). The proportion of

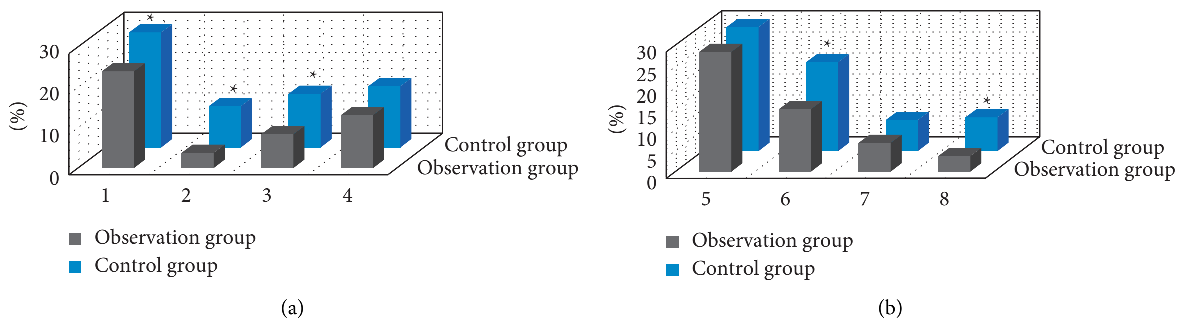

Figure 7: CT image characteristics of the two groups of children after nursing intervention: (a) increased lung texture, cable-like shadow, ground glass shadow, and small patchy shadow; (b) large sheet consolidation, atelectasis, bronchiectasis, and pleural effusion. *Note.* * indicated considerable difference compared with the observation group ($P < 0.05$).

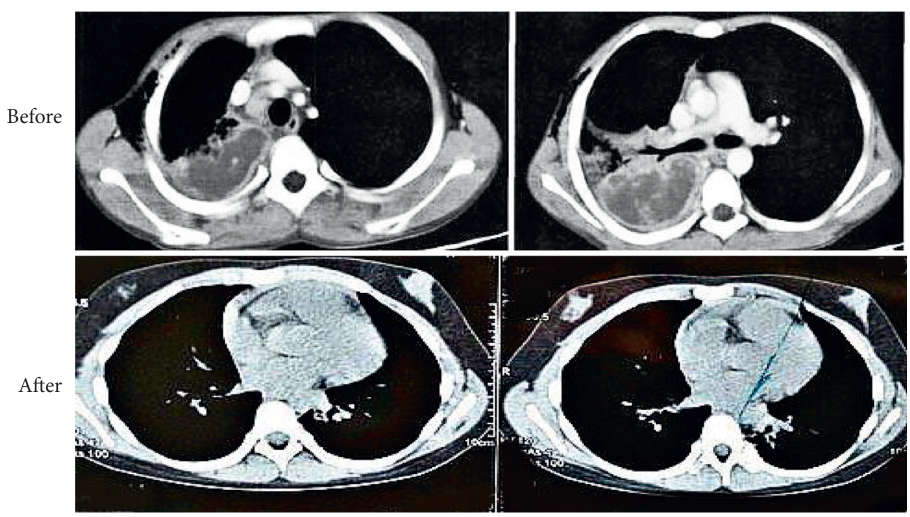

Figure 8: CT images of one child in the experimental group before and after nursing.

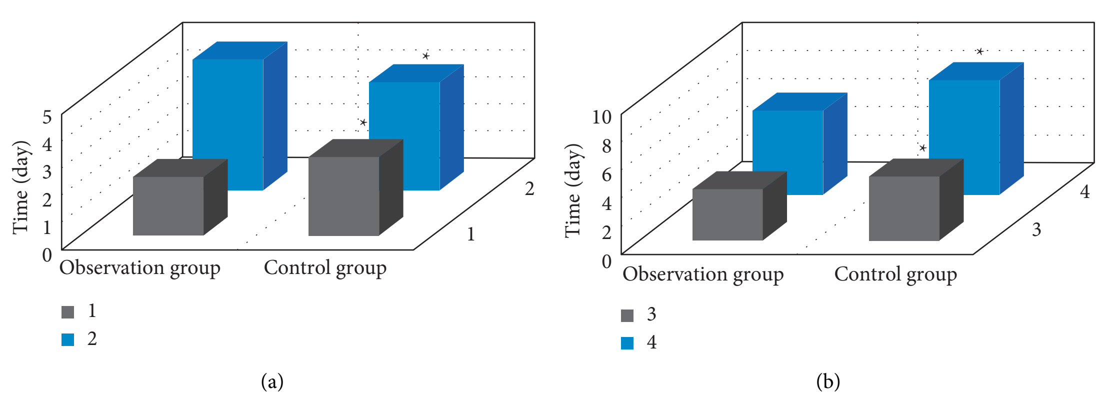

Figure 9: Comparison of symptoms improvement between the two groups during the nursing process: (a) 1 was the time when cough disappeared, and 2 was the time when body temperature was normal; (b) 3 was the disappearance time of lung rales, and 4 was the absorption time of lung shadows. Note: * indicated considerable difference compared with the observation group ($P < 0.05$).

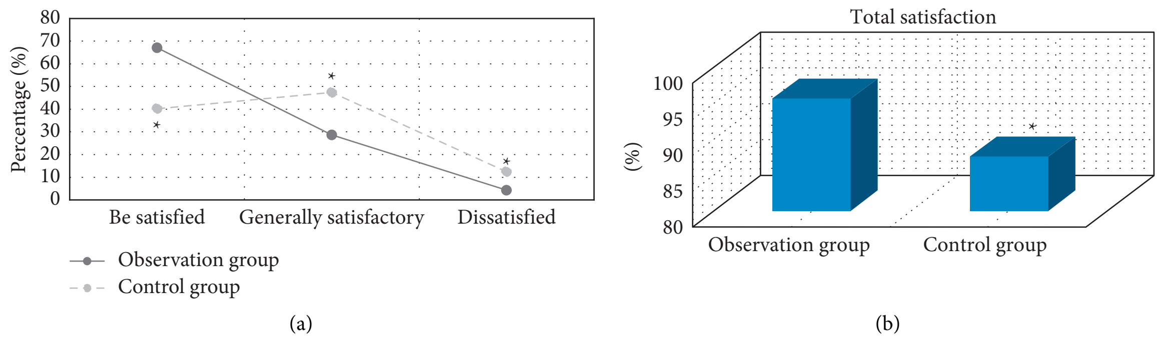

Figure 10: Comparison of satisfaction between the two groups after nursing intervention: (a) the proportion of satisfied, generally satisfied, and dissatisfied; (b) the proportion of total satisfaction. Note: * indicated considerable difference compared with the observation group ($P < 0.05$).

unsatisfied children in the experimental group after nursing intervention was substantially lower than that in the control group, and the difference was great ($P < 0.05$).

4. Discussion

Mycoplasma pneumonia is one of the common diseases in children, with a high incidence, which is extremely detrimental to children's physical and mental health development. In addition, due to the particularity of the body structure of children, treatment will bring some difficulties, so it is critical to choose reasonable and effective nursing treatment in clinical practice [19, 20]. Moreover, the infection of mycoplasma pneumoniae has a common antigen with the tissues in the body, so the infection will have a chain reaction with the corresponding tissues. Therefore, it is very necessary to clinically treat the disease and provide care for the disease [21]. According to this particularity, 98 children with MP were divided into 49 cases of the observation group (specific nursing) and 49 cases of the control group (routine nursing). Then, CT images based on the optimized GLCM feature extraction algorithm were used to examine the children before and after nursing intervention, and the recovery of the two groups of children was discussed. The clinical manifestations of the children were summarized, and it was found that the clinical manifestations of the 98 children included fever, cough, sore throat, headache, fatigue, and wheezing. The cases of fever, cough, and sore throat were 86, 72, and 59, respectively. The onset time of fever was the earliest (1.24 ± 0.66 days), and the duration of cough was the longest (14.12 ± 3.02 days).

The CT image characteristics of the two groups of children after nursing intervention were analyzed. It was found that the proportion of increased lung texture, stripe shadow, ground glass shadow, atelectasis, and pleural effusion in the observation group was substantially lower than that in the control group after nursing, and the difference was great ($P < 0.05$). This was similar to the findings of Hata et al. [22], indicating that specific nursing intervention can more effectively promote the recovery of children with MP compared with routine nursing. In addition, there was no considerable difference between the observation group and the control group in the proportion of small patchy shadow, large patchy consolidation shadow, and bronchiole dilation ($P > 0.05$), which was different from the research of Branco et al. [23]. The reason may be that the time of review in this study was relatively short and there was not a considerable difference in long-term outcomes in children. In the process of nursing intervention, the cough disappearance time, the time for returning to normal temperature, the disappearance time of lung rales, and the lung shadow absorption time in the observation group were substantially shorter than those in the control group ($P < 0.05$). It was proved that specific nursing measures for children with MP were conducive to improving the progress of children's characterization recovery [24]. After nursing intervention, the proportion of satisfaction and total satisfaction in the experimental group was substantially higher than that in the control group, while the proportion of dissatisfaction was substantially lower than that in the control group ($P < 0.05$), which indicated that the total nursing effect of specific nursing measures on children was substantially better than that of conventional nursing, which improved the satisfaction of children and their families [25].

5. Conclusion

In this study, CT images based on optimized co-occurrence matrix feature extraction algorithm were used to examine 98 children with mycoplasma pneumonia before and after nursing intervention and to explore the rehabilitation of the two groups of children. The results showed that, compared with conventional nursing, specific nursing intervention was beneficial to improve the progress of characterization recovery and the overall recovery effect of children with MP. Therefore, CT image based on feature extraction algorithm of optimized GLCM was of good adoption value in the diagnosis and treatment of MP in children. However, the optimized GLCM feature extraction algorithm designed was not trained and learned enough samples, so it is necessary to do further research on its image processing performance in the future. In conclusion, this study provides data support for clinical nursing intervention in children with MP.

Data Availability

The data used to support the findings of this study are available from the corresponding author upon request.

Conflicts of Interest

The authors declare no conflicts of interest.

References

[1] D. T. Huang, D. M. Yealy, M. R. Filbin et al., "Procalcitonin-guided use of antibiotics for lower respiratory tract infection," *New England Journal of Medicine*, vol. 379, no. 3, pp. 236–249, 2018.

[2] H. Lee, K. W. Yun, H. J. Lee, and E. H. Choi, "Antimicrobial therapy of macrolide-resistantMycoplasma pneumoniaepneumonia in children," *Expert Review of Anti-infective Therapy*, vol. 16, no. 1, pp. 23–34, 2018.

[3] P. K. Kutty, S. Jain, T. H. Taylor et al., "Mycoplasma pneumoniae among children hospitalized with community-acquired pneumonia," *Clinical Infectious Diseases*, vol. 68, no. 1, pp. 5–12, 2019.

[4] C. Krafft and C. Christy, "MycoplasmaPneumonia in children and adolescents," *Pediatrics in Review*, vol. 41, no. 1, pp. 12–19, 2020.

[5] R. Garza-Hernández, C. Melendez-Méndez, G. Castillo-Martínez, F. González-Salinas, M. d. l. Á. Fang-Huerta, and H. C. Hidalgo, "Surgical patients' perception about behaviors of humanized nursing care," *Hispanic Health Care International*, vol. 18, no. 1, pp. 27–31, 2020.

[6] S. Gómez-Cantarino, I. García-Valdivieso, E. Moncunill-Martínez, B. Yáñez-Araque, and M. I. Ugarte Gurrutxaga, "Developing a family-centered care model in the neonatal intensive care unit (NICU): a new vision to manage healthcare," *International Journal of Environmental Research and Public Health*, vol. 17, no. 19, p. 7197, 2020.

[7] S. R. Digumarthy, A. M. Padole, R. Lo Gullo, R. Singh, J.-A. O. Shepard, and M. K. Kalra, "CT texture analysis of histologically proven benign and malignant lung lesions," *Medicine*, vol. 97, no. 26, Article ID e11172, 2018.

[8] G.-M.-Y. Zhang, H. Sun, B. Shi, Z.-Y. Jin, and H.-D. Xue, "Quantitative CT texture analysis for evaluating histologic grade of urothelial carcinoma," *Abdominal Radiology*, vol. 42, no. 2, pp. 561–568, 2017.

[9] S. Ytre-Hauge, Ø. O. Salvesen, C. Krakstad, J. Trovik, and I. S. Haldorsen, "Tumour texture features from preoperative CT predict high-risk disease in endometrial cancer," *Clinical Radiology*, vol. 76, no. 1, pp. e13–e79, 2021.

[10] G.-M.-Y. Zhang, B. Shi, H.-D. Xue, B. Ganeshan, H. Sun, and Z.-Y. Jin, "Can quantitative CT texture analysis be used to differentiate subtypes of renal cell carcinoma?" *Clinical Radiology*, vol. 74, no. 4, pp. 287–294, 2019.

[11] A. Tabari, M. Torriani, K. K. Miller, A. Klibanski, M. K. Kalra, and M. A. Bredella, "Anorexia nervosa: analysis of trabecular texture with CT," *Radiology*, vol. 283, no. 1, pp. 178–185, 2017.

[12] R. Cannella, A. A. Borhani, M. I. Minervini, A. Tsung, and A. Furlan, "Evaluation of texture analysis for the differential diagnosis of focal nodular hyperplasia from hepatocellular adenoma on contrast-enhanced CT images," *Abdominal Radiology*, vol. 44, no. 4, pp. 1323–1330, 2019.

[13] S. Xie, Z. Yu, and Z. Lv, "Multi-disease prediction based on deep learning: a survey," *Computer Modeling in Engineering and Sciences*, vol. 128, no. 2, pp. 489–522, 2021.

[14] V. Baliyan, H. Kordbacheh, B. Parameswaran, B. Ganeshan, D. Sahani, and A. Kambadakone, "Virtual monoenergetic imaging in rapid kVp-switching dual-energy CT (DECT) of the abdomen: impact on CT texture analysis," *Abdominal Radiology*, vol. 43, no. 10, pp. 2693–2701, 2018.

[15] H. Park, L. Qin, P. Guerra, C. P. Bay, and A. B. Shinagare, "Decoding incidental ovarian lesions: use of texture analysis and machine learning for characterization and detection of malignancy," *Abdominal Radiology*, vol. 46, no. 6, pp. 2376–2383, 2021.

[16] S. Sacco, S. Benemei, S. Cevoli et al., "Development and validation of the ID-EC - the Italian version of the identify chronic migraine," *The Journal of Headache and Pain*, vol. 20, no. 1, p. 15, 2019.

[17] J. Greffier, A. Hamard, F. Pereira et al., "Image quality and dose reduction opportunity of deep learning image reconstruction algorithm for CT: a phantom study," *European Radiology*, vol. 30, no. 7, pp. 3951–3959, 2020.

[18] S. A. Nadeem, E. A. Hoffman, J. C. Sieren et al., "A CT-based automated algorithm for airway segmentation using freeze-and-grow propagation and deep learning," *IEEE Transactions on Medical Imaging*, vol. 40, no. 1, pp. 405–418, 2021.

[19] T. Weikert, D. J. Winkel, J. Bremerich et al., "Automated detection of pulmonary embolism in CT pulmonary angiograms using an AI-powered algorithm," *European Radiology*, vol. 30, no. 12, pp. 6545–6553, 2020.

[20] C. Chen and W. K. Kim, "The application of micro-CT in egg-laying hen bone analysis: introducing an automated bone separation algorithm," *Poultry Science*, vol. 99, no. 11, pp. 5175–5183, 2020.

[21] M. D. Patel, S. M. Ascher, M. M. Horrow et al., "Management of incidental adnexal findings on CT and mri: a white paper of the acr incidental findings committee," *Journal of the American College of Radiology*, vol. 17, no. 2, pp. 248–254, 2020.

[22] A. Hata, M. Yanagawa, K. Yamagata et al., "Deep learning algorithm for detection of aortic dissection on non-contrast-enhanced CT," *European Radiology*, vol. 31, no. 2, pp. 1151–1159, 2021.

[23] D. Branco, S. Kry, P. Taylor et al., "Development of a stereoscopic CT metal artifact management algorithm using gantry angle tilts for head and neck patients," *Journal of Applied Clinical Medical Physics*, vol. 21, no. 8, pp. 120–130, 2020.

[24] H. Zhang, D. Zeng, H. Zhang, J. Wang, Z. Liang, and J. Ma, "Applications of nonlocal means algorithm in low-dose X-ray CT image processing and reconstruction: a review," *Medical Physics*, vol. 44, no. 3, pp. 1168–1185, 2017.

[25] B. J. Shin and J. P. Earls, "Correspondence: submillisievert CT angiography for carotid arteries using wide array CT scanner and latest iterative reconstruction algorithm in comparison with previous generations technologies: feasibility and diagnostic accuracy," *Journal of Cardiovascular Computed Tomography*, vol. 13, no. 6, pp. 299-300, 2019.

Hindawi
Journal of Healthcare Engineering
Volume 2021, Article ID 3959844, 6 pages
https://doi.org/10.1155/2021/3959844

Research Article

An Artificial Neural Network Algorithm for the Evaluation of Postoperative Rehabilitation of Patients

Kunhao Tang, Ruogu Luo, and Sanhua Zhang

Department of Computer and Engineering, Hunan Institute of Technology, HengYang 421002, China

Correspondence should be addressed to Kunhao Tang; tangkh@hnit.edu.cn

Received 16 July 2021; Accepted 17 September 2021; Published 11 October 2021

Academic Editor: Enas Abdulhay

In order to explore the application of artificial neural network in rehabilitation evaluation, a kind of ANN stable and reliable artificial intelligence algorithm is proposed. By learning the existing clinical gait data, this method extracted the gait characteristic parameters of patients with different ages, disease types and course of disease, and repeated data iteration and finally simulated the corresponding gait parameters of patients. Experiments showed that the trained ANN had the same score as the human for most of the data (82.2%, Cohen's kappa = 0.743). There was a strong correlation between ANN and improved Ashworth scores as assessed by human raters ($r = 0.825$, $P < 0.01$). As a stable and reliable artificial intelligence algorithm, ANN can provide new ideas and methods for clinical rehabilitation evaluation.

1. Introduction

Artificial intelligence (AI) has become a neighborhood with many practical applications and active research topics. Artificial neural network (ANN), as an important branch of modern artificial intelligence technology, has been widely and deeply applied to modern medical activities due to its powerful learning ability and stable feature recognition and prediction functions [1]. Rehabilitation assessment is mainly a quantitative or qualitative description of patients' functional status, including physical motor function assessment, balance assessment, and other dimensions. However, at present, many rehabilitation assessment methods are time-consuming and laborious and difficult to accurately quantify [2]. Therefore, in recent years, artificial intelligence experts have designed and developed a variety of ANN algorithms, and in the real clinical environment to evaluate the rehabilitation of patients, they have achieved satisfactory results. As an artificial intelligence tool, the artificial neural network has been widely used in the clinical diagnosis of diseases such as tumor and pulmonary embolism since the 1990s. Dr. Robert H. Nielsen, the inventor of the neural computer, defined the neural network as a computing system composed of many simple and highly interconnected processing elements, which can deal with real problems by dynamically reacting to external input information [3]. Stroke has become a common disease in clinical practice due to its high morbidity and disability rate. It is often accompanied by a variety of functional disorders, among which the upper limb motor dysfunction is the most widely affecting limb dysfunction. Recently, rehabilitation medicine is gradually developing towards the direction of precision, long-distance, intelligence, and individuation, among which precise evaluation is an important direction. Based on the fusion of sensor technology and artificial intelligence theory, the automatic evaluation of upper limb motor function is deeply studied, and the motion measurement system is designed from the motor dysfunction of arm, hand, and upper limb activity function. Three different depth learning methods based on sensor data are proposed to realize the feature extraction of clinical scale [4].

Pryor et al. proposed a body evaluation model based on the mixed density neural network. The movement sequences of patients were collected by the Microsoft Kinect sensor as the input of the neural network. The neural network consists of two layers: self-coding layer and mixed density layer. The former is used to reduce the dimension of the motion sequence and extract the features, while the latter is used to express the patient's motion sequence as a Gaussian density function and compare it with the preset motion to evaluate the patient's body function. This model can be applied to the rehabilitation evaluation and training guidance of stroke rehabilitation patients in the family environment [5]. Wilkinson et al. used clustering analysis and artificial neural network to analyze the gait data of 74 stroke patients obtained by the three-dimensional motion analysis system. First, they performed clustering analysis on the gait patterns of patients through K-means algorithm, the characteristics used included 14 parameters such as the landing position of the patient's foot, and three patient clusters were obtained. The first touching position of the foot was found to correspond to the forefoot, foot base, and heel, respectively; then, the angle change of the knee joint was used as the input of the multilayer perceptron to classify the first touching position of the patient's foot, with a classification accuracy of 100% [6]. Based on the research results of this paper, it can be found that using sensor sensing technology and deep learning artificial intelligence analysis method can realize the accurate measurement and quantitative evaluation of the motor function of stroke patients, make up for the lack of traditional evaluation methods, and facilitate the development of rehabilitation evaluation in the family and community environment.

Building a virtual mechanical model or learning and forecasting existing data through neural network algorithm can better reflect the balance ability of the target population. However, the main problem at present is the lack of large sample and multidisease clinical evaluation model and its clinical feasibility needs further study.

2. Materials and Methods

Artificial intelligence is an important branch of computer science, which includes many application fields such as machine learning, machine vision, and intelligent search. Machine learning (ML) is the fundamental way to make computers intelligent, to put it simply. ML can be understood as enabling the computer to discover and mine deep rules from massive data and then carry out data classification and prediction, which is similar to the functional model in mathematics. The data sample is taken as the input variable, and the output is the expected result of simulation. ML can be further divided into supervised and unsupervised learning modes [7]. Unsupervised learning is to directly model the data without providing the data samples for training in advance. The ANN to be discussed is a supervised machine learning category requiring data training. See Figure 1 for the specific machine learning classification. Figure 2 provides a visual explanation of these two concepts through the function image.

2.1. Evaluation of Rehabilitation. Rehabilitation assessment is a process of collecting patient history and related data; putting forward hypotheses; carrying out inspection and measurement; comparing, synthesizing, analyzing, and interpreting the results; and finally forming a conclusion and diagnosis of obstacles. Rehabilitation assessment includes all functional or ability disabilities requiring rehabilitation treatment. Through rehabilitation assessment, the location, scope, type, nature, characteristics, degree, causes, and prognosis of obstacles can be found and determined, so as to provide the basis for the formulation of clear rehabilitation goals and rehabilitation treatment plans. Correct and accurate evaluation of rehabilitation is the premise and basis for formulating correct principles, plans, and specific implementation programs of rehabilitation treatment. In addition, the effect of patients' rehabilitation treatment also needs to be reflected by the change of rehabilitation evaluation results [8–10].

The whole process of rehabilitation treatment must rely on rehabilitation assessment. Generally speaking, rehabilitation assessment mainly has the following functions: (1) seek and determine the type, degree, and cause of obstacles; (2) guide the formulation of rehabilitation treatment plan; (3) determine rehabilitation treatment programs; (4) judge the rehabilitation effect; (5) prognostic analysis; and (6) prevent the occurrence and development of obstacles. In the process of assessing various functional disorders, the commonly used rehabilitation evaluation methods include observation method, investigation method, scale method, and instrument measurement method; among them, scale method is the most commonly used evaluation method in clinical practice at present, and it is a method to use standardized scale to classify the severity of dysfunction of patients or to summarize the score.

2.2. Circulating Neural Network. Recurring neural network (RNN), also known as automatic association network or feedback network, is one of the most popular deep learning algorithms at present. RNN units are connected to each other in turn to form a directed cycle, and the internal state of the units makes the network show dynamic temporal behavior. They are particularly powerful in tasks where context is crucial for predicting results and are often applied to solve problems in areas such as speech recognition and natural language processing. The RNN can use its internal memory to process any input sequence. In RNN, signals propagate forward and backward by introducing a loop in the network.

The forward propagation formula of RNN is shown as follows:

$$z_h^t = \sum_{i=1}^{I} wihx_i^t + \sum_{h'}^{H} wh'h^{a_{h'}{}^{t-1}}, \tag{1}$$

$$a_h^t = f_h\left(z_h^t\right), \tag{2}$$

$$y_k^t = \sum_{h=1}^{H} w_{hk}a_h^t, \tag{3}$$

where lining is the input vector of neuron I in the input layer at time t, a_h^{t-1} is 1 moment h' neurons' hidden state vectors,

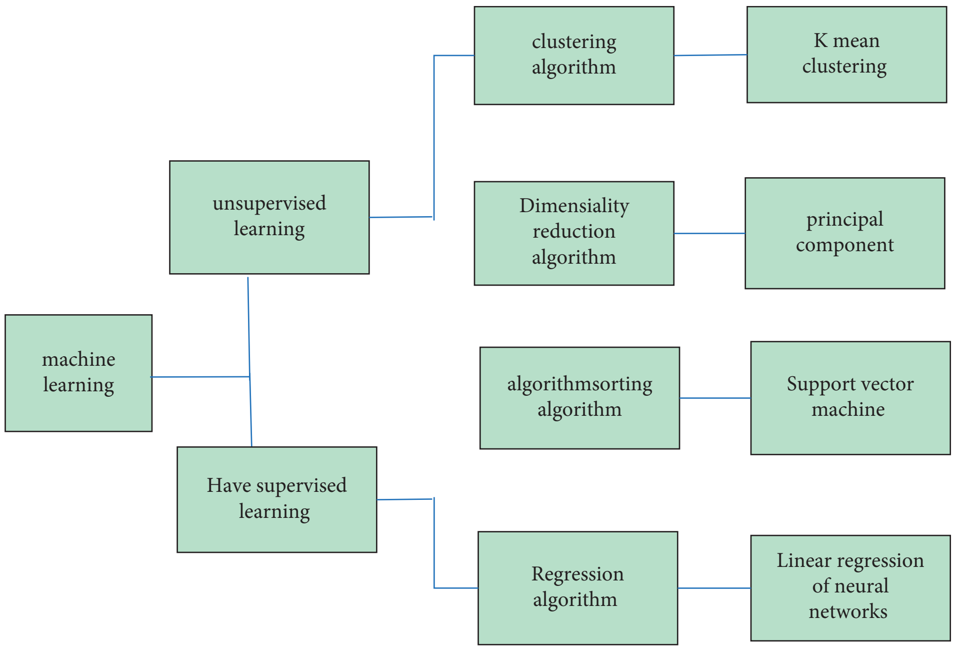

Figure 1: Machine learning classification.The ANN to be discussed is a supervised machine learning category requiring data training.

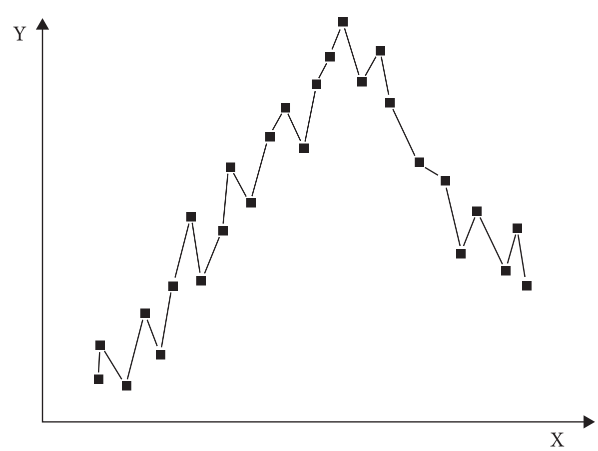

Figure 2: Fitting function simulation provides a visual explanation of these two concepts through the function image.

which are information from memory units at the previous moment, z_h^t is the input information at time t and the memory unit information at the previous time obtained by weighted product and sum, after nonlinear transformation of the activation function $f_h(\cdot)$. It becomes the information spit of the memory unit at the current moment. Common activation functions include Softmax, ReLU, and Tanh. y_h^t is the output vector of K neuron in the output layer at time t. $w_{ih}, w_{h'h}$, and w_{hk} are, respectively, the connection weights between the input layer and hidden layer, hidden layer and hidden layer, and hidden layer and output layer.

Accuracy: accurate rate can be used to represent the ability of the classifier to correctly classify samples in the whole sample set, that is, the ratio of all correctly classified samples to the total number of samples, including true positive and true negative samples, and their calculation is shown as follows:

$$\text{accuracy} = \frac{\text{TP} + \text{TN}}{\text{TP} + \text{FN} + \text{FP} + \text{TN}}. \tag{4}$$

Precision: accuracy is the percentage of samples that are predicted to be positive where the true value is also positive. It is the degree to which the predicted sample is close to the true value, and its calculation is shown in the following formula:

$$\text{precision} = \frac{\text{TP}}{\text{TP} + \text{FP}}. \tag{5}$$

False positive rate (FPR) represents how many negative samples were wrongly classified as positive, calculated as follows.

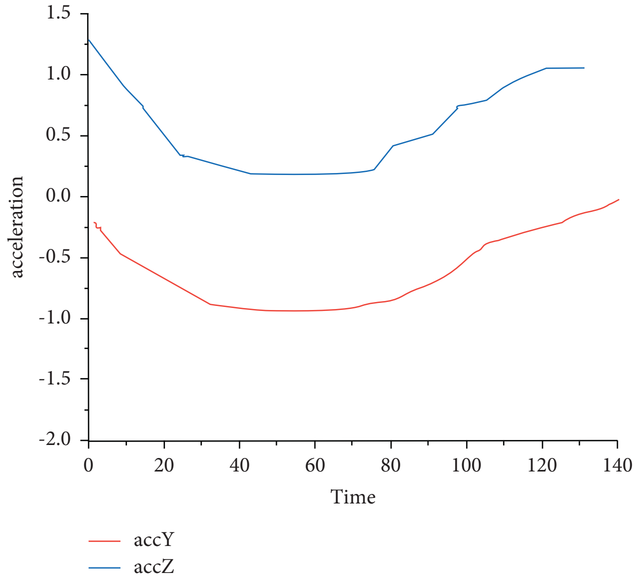

FIGURE 3: Sample IMU acceleration data of subjects at different stages. Due to the different severity, the patient's arm presents different distribution rules in the process of performing the same activity.

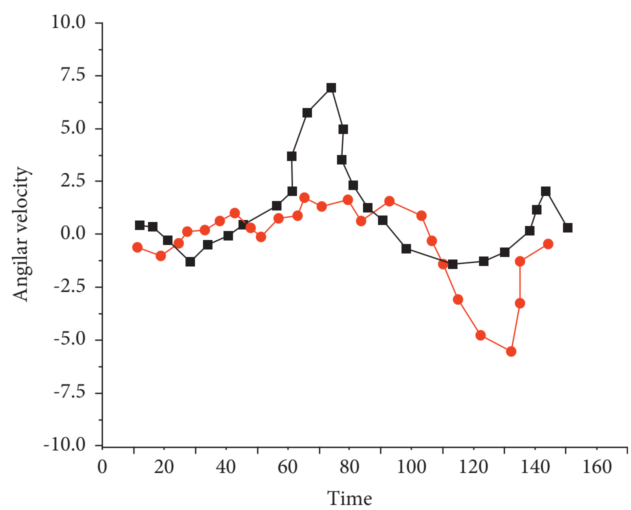

FIGURE 4: Sample data of subject's forearm IMU sensor. As for the logistic regression model, its average accuracy in 5 categories was 27.80%, with an average AUROC of 0.53 and AUPRC of 0.35.

TABLE 1: Brunnstrom staging confusion matrix (TARM).

		Ground truth					Classified sum
Prediction	Stage II	Stage II	Stage III	Stage IV	Stage V	Stage VI	
	Stage III	7	0	0	0	0	7
	Stage IV	0	9	0	0	0	9
	Stage V	0	3	0	0	0	9
	Stage VI	0	0	0	0	6	6
No. of samples		7	9	9	6	5	5
Accuracy		100%	100%	100%	100%	100%	

$$\mathrm{FRP} = \frac{\mathrm{FP}}{\mathrm{FP} + \mathrm{TN}}. \tag{6}$$

The mean square error can be understood as the Euclidean distance between the true value of the sample and the predicted value as follows:

$$\mathrm{MSE} = \frac{1}{N}\sum_{i=1}^{N}\left(y_i - \hat{y}_i\right)^2. \tag{7}$$

Since MSE contains square operation, the value of the calculated result is very large, which is not conducive to comparative analysis. Therefore, RMSE is born, that is, the square sign of MSE is taken to make the order of magnitude of the error result consistent with the order of magnitude of the sample data as follows:

$$\mathrm{RMSE} = \sqrt{\frac{1}{N}\sum_{i=1}^{N}\left(y_i - \hat{y}_i\right)^2}. \tag{8}$$

3. Results and Discussion

This data collection experiment was carried out in the Chinese Medicine Knowledge and Data Engineering Experiment of University of Electronic Science and Technology of China. The actions of the experiment were conducted under the guidance of clinical professionals, and all of them came from rehabilitation doctors with rich experience in the rehabilitation research of stroke patients and stroke rehabilitation treatment. According to the results of existing studies, at least 20 subjects (5 in each group) are required to achieve a statistical power of 0.95 in the test to detect differences in limb mobility among patients with different degrees of impairment. Therefore, a total of 36 healthy subjects (20 males, 16 females, mean age 23 ± 1.5 years) were enrolled in this study, and each participant was subjected to a Brunnstrom II–VI simulation of upper limb motor dysfunction in stroke patients.

The shoulder touch exercise was used as arm activity assessment, and the motor ability of the subjects' upper limbs was observed. Under normal circumstances, a complete movement process includes the following four steps:

(1) Starting position: the subject is comfortably seated on the chair, with the torso straight, head straight, neck straight, upper limbs hanging naturally on both sides of the body (neutral position), lower limbs naturally relaxed, and knees bent 90°

(2) Lift the hemiplegic arm on the sagittal plane to horizontal height (shoulder flexion 90°)

(3) Bend the elbow and touch the opposite shoulder with the palm of your hand (elbow flexion and forearm pronation)

(4) The upper limbs naturally return to the starting position (shoulder extension, elbow extension, and forearm pronation); therefore, the number of data samples in each period is equal to 36; a total of 180 samples were identified

In the simulation data collection stage, Figure 3 shows the sample triaxial acceleration data collected by two IMU of forearm and upper arm during the Brunnstrom II–VI simulation of movement disorders of the same subject. The solid line is the triaxial acceleration data collected by the IMU at the forearm position, while the dashed line is the triaxial acceleration data of the IMU at the forearm position. As can be seen from Figure 3, due to the different severity, the patient's arm presents different distribution rules in the process of performing the same activity. Stage II patients have higher severity, and the upper limb joints cannot realize a full range of activities.

From Figure 4, we first observe that the deep learning model based on the cyclic neural network has better performance than the linear model in all indicators. As for the logistic regression model, its average accuracy in 5 categories was 27.80%, with an average AUROC of 0.53 and AUPRC of 0.35, which was the worst performance among all models. This is consistent with previous research results that compared the neural network with linear model of time series data. Deep learning method has more and more complex parameters than the traditional learning method and can extract richer and more accurate features by itself.

In order to further prove the performance effect of the proposed method, we analyze the confusion matrix on the test set of all the methods. Table 1 denotes the confusion matrix of TARM and LR classification results on the test set. The TARM was consistent in classifying data for each Brunnstrom stage, and patients with stage III and IV injuries, depending on the location of the injury. The upper limb movements are more complex than those of other stage patients, leading to unstable data classification of these stages in the LR model.

4. Conclusions

Evaluation of rehabilitation is an important link in the process of rehabilitation treatment, which is the basis for the establishment of rehabilitation program and the evaluation of rehabilitation effect. In view of the upper limb motor dysfunction that often occurs after stroke, based on the objectivity and performance defects of the existing clinical rehabilitation evaluation methods and automatic evaluation research, deep learning technology was first applied to the automatic evaluation research of stroke rehabilitation. Firstly, the commonly used clinical scales are analyzed, and the motion measurement system is designed according to the evaluation project content and scoring requirements. Then, different depth learning algorithm models are output according to the data characteristics and expected output. Finally, this automatic evaluation research is compared with relevant depth learning algorithms to verify that the proposed method is a better method for realizing the automatic evaluation task of upper limb motor function. Experiments showed that the trained ANN had the same score as human for most of the data (82.2%, Cohen's kappa = 0.743). There was a strong correlation between ANN and improved Ashworth scores as assessed by human raters ($r = 0.825$, $p < 0.01$). These characteristics of ANN can help it to learn a large number of clinical data and then generate a stable clinical evaluation model, improve the accuracy and efficiency of rehabilitation evaluation, reduce the work intensity of rehabilitation physicians and therapists, and alleviate the current shortage of rehabilitation resources. Using measurement methods, although the degree of interference is low, it is easy to produce measurement error, affect the quality of the data, missing values, and other problems. In terms of data analysis, the data collected by neural network lack missing processing.

Data Availability

The data used to support the findings of this study are available from the corresponding author upon request.

Conflicts of Interest

The authors declare that there are no conflicts of interest.

Acknowledgments

This work was supported in part by the Education Bureau of Hunan Province of China (no. 15B061).

References

[1] K. Min, J. Beom, and B. R. Kim, "Clinical practice guideline for postoperative rehabilitation in older patients with hip fractures," *Annals of Rehabilitation Medicine*, vol. 45, no. 3, pp. 225–259, 2021.

[2] S. Suwarno, "Performance evaluation of artificial neural network classifiers for predicting cesarean sections," *International Journal of Scientific & Technology Research*, vol. 8, no. 9, pp. 1843–1846, 2019.

[3] A. M. Vukicevic, G. R. Jovicic, M. N. Jovicic, V. L. Milicevic, and N. D. Filipovic, "Assessment of cortical bone fracture resistance curves by fusing artificial neural networks and linear regression," *Computer Methods in Biomechanics and Biomedical Engineering*, vol. 21, no. 2, pp. 169–176, 2018.

[4] J. V. Papathanasiou and U. Carraro, "Postoperative rehabilitation of elderly patients," *Practical Issues in Geriatrics*, vol. 47, pp. 469–475, 2018.

[5] M. Pryor, R. Carrion, R. Wang, and G. Henry, "066 prospective evaluation of postoperative penile rehabilitation: penile morphology and patient satisfaction 2 Years following coloplast titan inflatable penile prosthesis," *The Journal of Sexual Medicine*, vol. 13, no. 5, p. S32, 2016.

[6] B. G. Wilkinson, J. J. Donnenwerth, and A. R. Peterson, "Use of blood flow restriction training for postoperative rehabilitation," *Current Sports Medicine Reports*, vol. 18, no. 6, pp. 224–228, 2019.

[7] A. F. Morey and F. Allen, "Re: prospective evaluation of postoperative penile rehabilitation: penile length/girth maintenance 1 year following coloplast titan inflatable penile prosthesis," *The Journal of Urology*, vol. 195, no. 2, 2016.

[8] M. W. Dusenberry, C. K. Brown, and K. L. Brewer, "Artificial neural networks: predicting head ct findings in elderly patients presenting with minor head injury after a fall," *The American Journal of Emergency Medicine*, vol. 35, no. 2, pp. 260–267, 2017.

[9] O. Ilves, A. HKkinen, and J. Dekker, "Quality of life and disability: can they be improved by active postoperative rehabilitation after spinal fusion surgery in patients with spondylolisthesis? a randomised controlled trial with 12-month follow-up," *European Spine Journal*, vol. 26, no. 3, pp. 1–8, 2017.

[10] O. Ilves, A. Hakkinen, J. Dekker et al., "Quality of life and disability: can they be improved by active postoperative rehabilitation after spinal fusion surgery in patients with spondylolisthesis? A randomised controlled trial with 12-month follow-up," *European Spine Journal*, vol. 26, no. 3, pp. 1–8, 2017.

Hindawi
Journal of Healthcare Engineering
Volume 2021, Article ID 6231116, 10 pages
https://doi.org/10.1155/2021/6231116

Research Article

Ultrasound Images Guided under Deep Learning in the Anesthesia Effect of the Regional Nerve Block on Scapular Fracture Surgery

Yubo Liu [1] and Liangzhen Cheng [2]

[1]*Department of Anesthesiology, Jiangxi Armed Police Corps Hospital, Nanchang 330000, Jiangxi, China*
[2]*Second Department of Surgery, Jiangxi Armed Police Corps Hospital, Nanchang 330000, Jiangxi, China*

Correspondence should be addressed to Yubo Liu; 32315305@njau.edu.cn

Received 29 June 2021; Revised 1 September 2021; Accepted 4 September 2021; Published 7 October 2021

Academic Editor: Enas Abdulhay

In order to discuss the clinical characteristics of patients with scapular fracture, deep learning model was adopted in ultrasound images of patients to locate the anesthesia point of patients during scapular fracture surgery treated with the regional nerve block. 100 patients with scapular fracture who were hospitalized for emergency treatment in the hospital were recruited. Patients in the algorithm group used ultrasound-guided regional nerve block puncture, and patients in the control group used traditional body surface anatomy for anesthesia positioning. The ultrasound images of the scapula of the contrast group were used for the identification of the deep learning model and analysis of anesthesia acupuncture sites. The ultrasound images of the scapula anatomy of the patients in the contrast group were extracted, and the convolutional neural network model was employed for training and test. Moreover, the model performance was evaluated. It was found that the adoption of deep learning greatly improved the accuracy of the image. It took an average of 7.5 ± 2.07 minutes from the time the puncture needle touched the skin to the completion of the injection in the algorithm group (treated with artificial intelligence ultrasound positioning). The operation time of the control group (anatomical positioning) averaged 10.2 ± 2.62 min. Moreover, there was a significant difference between the two groups ($p < 0.05$). The method adopted in the contrast group had high positioning accuracy and good anesthesia effect, and the patients had reduced postoperative complications of patients (all $P < 0.005$). The deep learning model can effectively improve the accuracy of ultrasound images and measure and assist the treatment of future clinical cases of scapular fractures. While improving medical efficiency, it can also accurately identify patient fractures, which has great adoption potential in improving the effect of surgical anesthesia.

1. Introduction

Scapular fracture was first described by Desault in 1805, who studied the characteristics of scapular fracture. Scapular fracture accounts for 1% of total body fractures and 5% of total shoulder fractures [1]. It is usually caused by accidents such as car accidents or falling from heights. The majority of young men and middle-aged men account for 64% to 90% [2]. Scapular fractures such as painful fractures and fall fractures (fatigue injuries) are rare. Scapular fracture is often part of multiple traumas and is often overlooked. With the development of society, science and technology, and transportation, its incidence is gradually increasing [3]. A combination of physical examination, x-ray, or CT examination can usually make a definitive diagnosis of shoulder and foot fractures. At present, most of the surgical treatments for scapular fractures focus on the shoulders, kidneys, and neck, including the articular surfaces, which need to be reduced anatomically as much as possible. However, the incidence of postoperative complications such as joint pain, instability, and shock is relatively high [4].

The local nerve block is mainly used for surgical anesthesia of the shoulder and wrist area. The requirements of local nerve block for patient's systemic physiological functions and hardware equipment are lower compared with general anesthesia, and postoperative pain relief is relatively less [5]. In addition, the local nerve block can reduce general anesthesia. In areas where the local nerve distribution is relatively concentrated, the local nerve block mainly forms various block paths, including muscle groove, subclavian, subclavian longitudinal penetration, subclavian polymorphic process, and axillary path [6]. The operation of traditional nerve fracture surgery requires that the patient should be awake and can assist to report feelings, and the puncture needle of the nerve trunk is contacted within a short period of time, which will cause the patient's subjective discomfort and may cause nerve damage during the puncture process [7]. The key to the success of nerve fracture surgery is the correctness of the position of the peripheral nerve. It requires the surgeon's high clinical experience, which has a great impact on the patient's various anatomical changes, so the success rate is not high. Nerve fracture surgery is often accompanied by lesions of blood vessels or important tissues and organs, which may cause serious complications or sequelae. The development and application of nerve stimulation devices have increased the success rate of nerve fracture surgery. However, puncture increases the discomfort of patients, and the use of intravenous analgesics and sedatives is gradually increasing [8]. In recent years, with the advancement of medical technology and the improvement of human medical treatment, the demand for rapid onset, long-term maintenance, high success rate, and uncomplicated nerve fracture surgery has also increased. With the help of the anatomical positioning of the nerve stimulator, the peripheral nerve block becomes wider and wider. In recent decades, the emergence of ultrasonic technology has made scapular fracture surgery safer and more effective and further expanded the scope of application [9]. This technology rapidly changed the way of clinical anesthesia, and local anesthesia can be performed in a visualized manner. Ultrasound is dynamic, real-time, recordable, and radiation-free, and ultrasound-guided nerve block technology has been developing and maturing in the past decade [10]. Ultrasound-guided nerve block is different from conventional techniques. Traditional methods identify target nerves by looking for paresthesia methods through body surface anatomical location or inducing neuromuscular contraction by nerve stimulator, but traditional methods cannot achieve visualization of puncture points [11]. Ultrasound imaging can visualize the nerve that needs to be blocked, as well as the accompanying blood vessels and important tissues around the nerve. By visualizing the nerve and the important structures surrounding the nerve, it is possible to ensure accurate diffusion of anesthetic drugs around the target nerve during nerve block. It also avoids damage to blood vessels and surrounding important tissue structures and reduces the incidence of adverse events such as intrathecal injection and intravascular injection [12].

Deep learning is a new research direction in the field of machine learning. Unlike traditional machine learning, deep learning neural networks include many hidden layers. The machine can automatically learn the characteristics of each level of the data and completely analyze and process the data information. The excellent results of deep learning technology in the medical field are mainly reflected in the processing and analysis of medical images [13]. It does not need to manually extract the function or preprocess the image. It can extract the information in the image and the depth features of the image, thus contributing to disease diagnosis and diagnosis. At present, the research and application of in-depth learning in the field of anesthesia are relatively rare, and the risk of death of patients after general anesthesia can be predicted based on the data extracted during surgery. In addition, deep learning has broad application prospects for its performance and scalability in anesthesia research.

The purpose of this research was discussing the following three issues: first, the difference in image accuracy between deep learning ultrasound images and ordinary ultrasound images; second, the adoption of artificial intelligence ultrasound to optimize anesthesia puncture path; third, the effectiveness of ultrasonographic imaging guided scapular regional nerve block in the treatment of surgical pain of fracture. It was hoped to provide reference for other regional nerve block anesthesia operations.

2. Methods

2.1. Research Objects. In this study, a total of 100 patients with scapula surgery who underwent surgery from July 2017 to July 2019 were recruited. This study had been approved by the Medical Ethics Committee of the Hospital, and the family members of the patients included in the study had signed the informed consent form.

Inclusion criteria were as follows: (i) patients with diseases such as hypertension, diabetes, and respiratory insufficiency according to the standards of the *American Society of Anesthesiology (ASA)*; (ii) scapular fracture surgery not exceeding four hours

Exclusion criteria were as follows: (i) patients with paralysis; (ii) patients with speech dysfunction; (iii) patients with skin infection at the puncture site; (iv) patients with arm nerve plexus injury; (v) patients with previous clavicle surgery experience; (vi) patients with pleural fluid or ascites

In 100 patients undergoing scapular surgery, 1% of the local anesthetic concentration and 7% of Lopimaran were injected into the area to be anesthetized. Patients were randomly rolled into control group (traditional body surface positioning) and algorithm group (ultrasound-guided positioning).

2.2. Experimental Environment

2.2.1. Construction of the Deep Learning Segmentation Model. Convolutional neural network is a commonly used deep learning algorithm [14]. The process is as follows. Triggered by the human visual system, the continuous modification is formed in a multilayer neural network suitable for processing and recognizing images. A classic convolutional neural network is composed of a convolutional neural layer and a normalization layer, and its structure is shown in Figure 1.

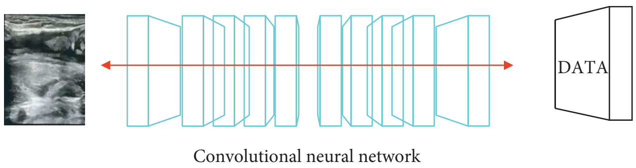

FIGURE 1: Convolutional neural network data analysis model.

3. SegNet Model

Seg is a brand-new deep fully convolutional neural network model (semantic pixel-wise neural network model) proposed by three deep learning experts (Yadri-narayanan, Kcndall, and Cipolla) from the University of Cambridge in 2010 that can perform image pixel-wise semantic division and image labeling [15]. The SegNet model is mainly composed of encoder, decoder, and oft-max layer. The encoder and decoder appear in pairs for image feature extraction and optimization. Its structure is shown in Figure 2.

The SegNet model divides an image into low-frequency part, which is obtained by low-pass filtering (smoothing and blurring) of the image, and high-frequency part, which is obtained by subtracting the low-frequency part from the original image [16]. The goal of the algorithm is enhancing the high-frequency parts that represent details, that is, multiplying the high-frequency parts by a certain gain value and then recombining them to obtain an enhanced image. Therefore, the core of the SegNet model is the calculation of the high-frequency part of the gain coefficient. One solution is setting the gain to a fixed value, and the other solution is expressing the gain value as a quantity related to the variance, which will be explained in the additional equation later.

It is assumed that the pixels in an image are represented as $x(i, j)$; then with (i, j) as the center, in the area where the window size is $(2n+1) * (2n+1)$, its local mean sum and variance can be expressed as the following equations:

$$m_x(i, j) = \frac{1}{(2n+1)^2} \sum_{k=i-n}^{i+n} \sum_{l=j-n}^{j+n} x(k, l),$$
$$\sigma_X^2(i, j) = \frac{1}{(2n+1)^2} \sum_{k=i-n}^{i+n} \sum_{i=j-n}^{j+n} \left[x(k, l) - m_x(i, j)\right]^2. \tag{1}$$

The mean value *mx* can be approximately regarded as the background part, at this time *x-m* is the high-frequency detail part, and the gain product for the high frequency is the following equation:

$$f(i, j) = m_x(i, j) + G(i, j)\left[x(i, j) - m_x(i, j)\right]. \tag{2}$$

For the gain G, the first option is taking a constant greater than 1 to achieve the enhanced effect, which is the following equation:

$$f(i, j) = m_x(i, j) + C\left[x(i, j) - m_x(i, j)\right]. \tag{3}$$

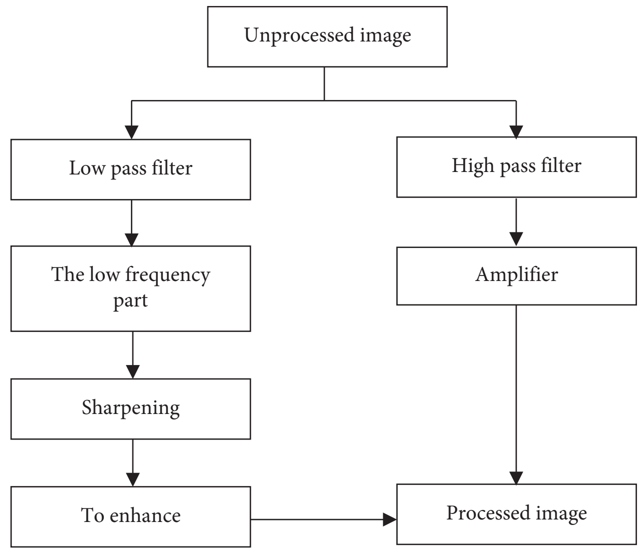

FIGURE 2: Image quality gain model.

Option two is that it is expressed as a change value inversely proportional to the local mean square error, which is the following equation:

$$f(i, j) = m_x(i, j) + \frac{D}{\sigma_x(i, j)}\left[x(i, j) - m_x(i, j)\right]. \tag{4}$$

The local mean square error is large in the high-frequency area of the image, and the gain value is small at this time, so that the result will not be too bright. However, the local mean square error is very small in the smooth area of the image, and the gain value is large at this time, which may amplify the noise signal. Therefore, it is necessary to limit the maximum gain to get better results.

3.1. Adaptive Contrast Enhancement.

3.1. Adaptive Contrast Enhancement. The principle of this network is classifying the image into two parts. The low-frequency part can be obtained by low-pass filtering of the image. The high-frequency part is obtained by subtracting the low-frequency part from the original image. The purpose of this algorithm is visualizing the image in detail, that is, multiplying the high-frequency part by a certain gain value to reconstruct the emphasized image. The core of enhancing image accuracy is repeatedly enlarging clear images in order to improve image quality.

Nowadays, medically generated images are mainly concentrated on low-frequency components, while noise and image details are concentrated on high-frequency components. The two components are separated in image processing, and different operations and processing are performed, which can avoid image detail loss and noise amplification when the histogram equalization algorithm is used. It aims to separate the high-frequency and low-frequency components of the input image. Medical ultrasound images have detailed and strict requirements, and blurring is not allowed, so Gaussian low-frequency filters were used in this study.

3.2. Anesthesia Methods. 4-5 μg/kg fentanyl, 1.5–2 mg/kg propofol, and 0.1 mg/kg vecuronium were used. After successful tracheal intubation, the anesthesia machine was connected to mechanical ventilation, the tidal volume was 8–10 mL/kg, and the respiratory rate was 8–12 times/min. During the operation, 0.06–0.1 μg/kg/min remifentanil was used for continuous intravenous pump injection, Sevoflurane 1.0–1.3 MAC inhalation maintained the depth of anesthesia within 40–60 BIS value, and intermittent intravenous injection of vecuronium was made to maintain muscle relaxation. If the heart rate was lower than 55 beats/min, 0.3 mg atropine was given, and when the systolic blood pressure was lower than 25% of the preoperative base value, 10 mg ephedrine was given to increase blood pressure.

3.3. Traditional Body Surface Localization of the Scapula Regional Nerve Block. The patient was anesthetized on the inner side and 1/3 of the unaffected side of the site to be anesthetized. The patient was supine with the head tilted to about 1.5–2.0 cm. After disinfection of the scapular fracture site, a 20 g puncture needle was inserted along the muscularly groove, and the needle was slowly inserted in the lower and lateral directions. The needle was inserted 1.5 to 2.0 cm, and the patient can feel the pain and location of the puncture, so that the physician was informed. 20 mL local anesthetic was injected into the muscle, and a 5-minute massage was made to spread the anesthetic fluid further away.

3.4. Artificial Intelligence Ultrasound-Guided Scapula Regional Nerve Block. The patient was anesthetized on the inner side and 1/3 of the unaffected side of the site to be anesthetized. The head should be tilted to about 1.5–2.0 cm and the patient should be supine with the scapula fracture in contact. After disinfection, ultrasound was used to detect the nerves that needed to be anesthetized. It was relatively more pronounced by detecting the neural structure at the margin lateral margin of the scapula. After the ultrasound showed the nerves at the anesthetic site, the location of the puncture should be determined and a local anesthetic of 20 mL was injected into the muscle. After 5 minutes of massage, the anesthetic fluid spread further.

3.5. Observation Indexes. The operative time, puncture depth, puncture adjustment time, time to start anesthesia, rate of good anesthesia, complication rate, and other indicators of the two localized nerve area approaches were shown. (I) The time of blocking action referred to the time from the contact with the skin of the puncture needle to the completion of the injection. The measuring tool of the ultrasonic device was used to measure the distance from the puncture point to the target, and the actual puncture depth was measured with a carrier. (II) The needle adjustment times during the puncture process were recorded, so did the occurrence of bone, needle head, and needle body defects during the puncture process. In addition, the number of cases of loss of electrical resistance when the transverse ligament of the upper arm was breached was also recorded. (III) The anesthetic effect was evaluated by other anesthesiologists, and the anesthetic level and effect were measured within 30 minutes after injection. The standard was as follows: excellent: completely painless; good: reduced sensation and mild pain; poor: normal feel and excruciating pain. (IV) The incidence of complications such as perceptual disturbance, vascular puncture injury, hematoma, puncture site pain, pneumothorax, and local anesthesia intoxication during the puncture process was recorded.

3.6. Statistical Methods. SPSS 16.0 was employed for analysis and statistics. Normally distributed measurement data were expressed as mean plus or minus standard deviation, and single-factor analysis of variance was used for comparison between groups. Nonnormally distributed measurement data were expressed as median and interquartile range, rank sum test rate was expressed as percentage (%), and Chi-square test was used. Chi-square test was also used for grade data. $P < 0.05$ suggested that the difference was statistically significant.

4. Results

4.1. Visual Evaluation of the Accuracy of Deep Learning Model Images and Non-AI Images. The prototype of the scanned object with "tomography" was shown clearly, so that the doctor can identify it. In Figure 3, the scapula reached the cutoff frequency after being filtered by Gaussian low-pass. When the filter dropped to a certain value, the boundary was clearly demarcated, leaving a clear barrier between it and its surroundings.

In Figure 4, the second enhancement made the dark part of the scanned object and the background next to it have better contrast, and the color layering was obvious, which can clearly highlight the characteristics of the main part.

Figure 5 shows a group of images of patients with fractures. In the image before enhancement and optimization, the fracture at the bottom right of Figure 5 does not seem to be obvious. If it was not enhanced, it was easy to be misjudged as a nonfracture site and affect the doctor's judgment, while the enhanced ultrasound image can clearly show the location of the fracture.

The second boundary enhancement focused on the optimization of some edge contours and the increase of contrast, which further brought the segmented image closer to the real value. Figure 6 shows the enhancement curve of accuracy.

4.2. The Relationship between the Location of the Traditional Nerve Block in the Scapula Region and the Actual Surface Location of the Ultrasound Scapula Region. The location of the traditional nerve in the scapula region overlapped with the actual body surface location of the nerve in the scapula region under ultrasound, accounting for 60%. The traditional location of the nerve in the scapula region was 38% outside the actual body surface position of the nerve in the scapula region under ultrasound. The traditional location of

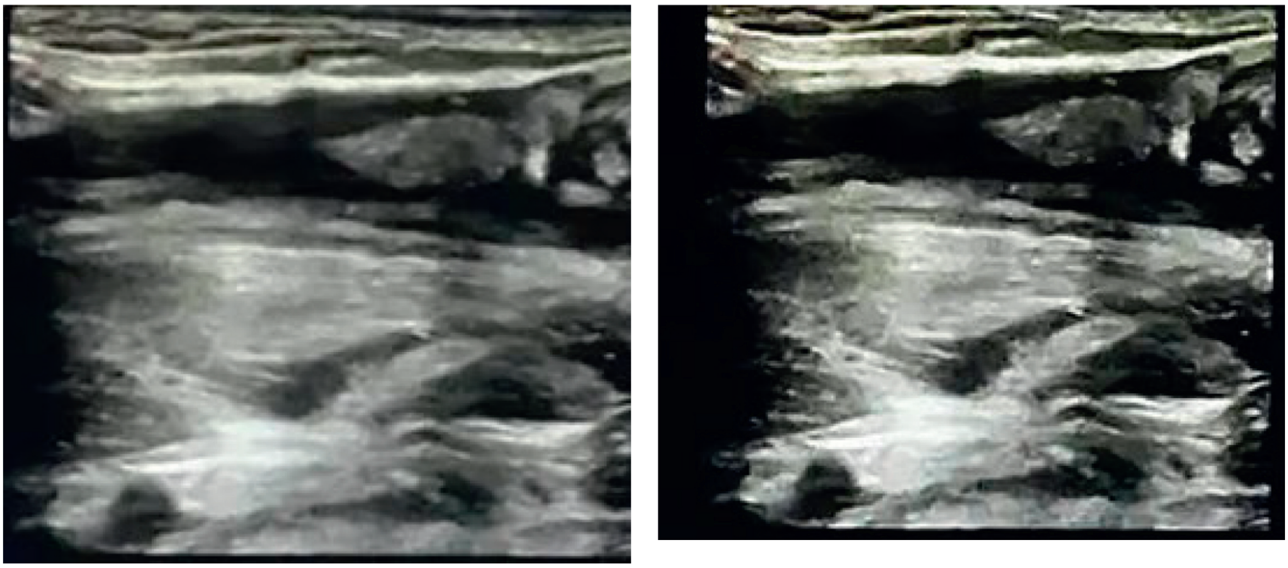

(a) (b)

Figure 3: Comparison of the effect of scapula ultrasound before and after the artificial intelligence enhancement. (a) Unenhanced ultrasound image of the scapula. (b) Enhanced ultrasound image of the scapula.

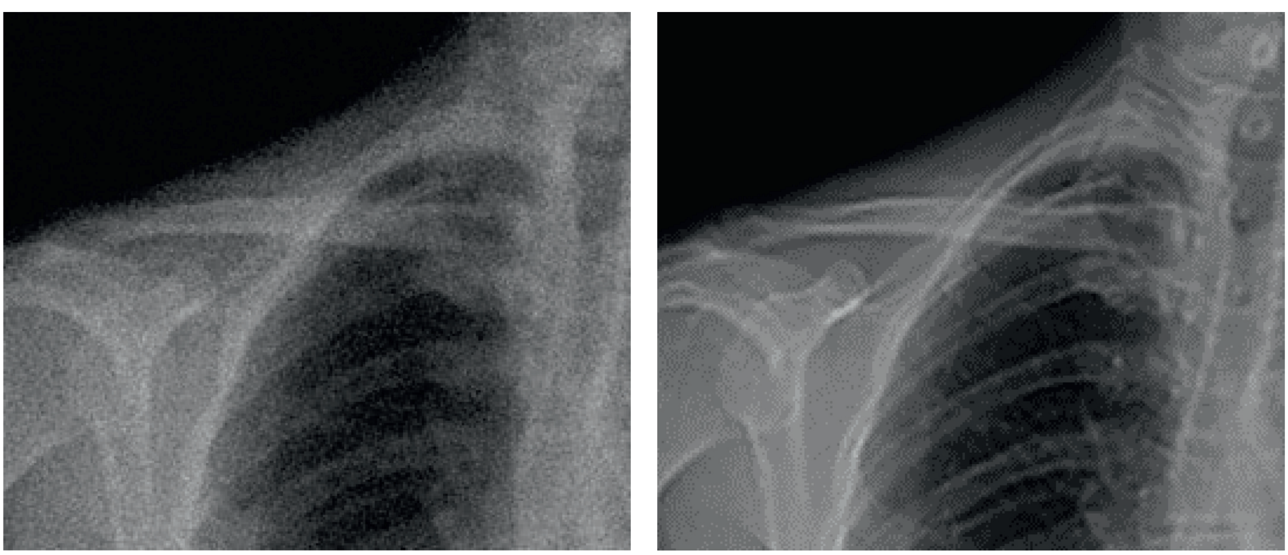

(a) (b)

Figure 4: Comparison of the effect of scapula CT before and after artificial intelligence enhancement. (a) Unenhanced CT image of the scapula. (b) Enhanced CT image of the scapula.

the nerve in the scapula region was 2% inside the actual body surface position of the nerve in the scapula region under ultrasound (Figure 7). The traditional positioning of the body surface of the scapula region was 0.63 cm away from the actual body surface of the scapula region under ultrasound. The location area of traditional and artificial intelligence ultrasound overlapped greatly, and the location area of artificial intelligence outside is about 36% more than that of the inside.

4.3. Comparisons of Injection Time and the Distance between the Puncture Point and the Scapula between the Two Groups. In the contrast group (artificial intelligence ultrasound positioning), it took an average of 7.7 ± 2.1 min from the time the puncture needle touched the skin to the completion of the injection. The operation time of the control group (anatomical positioning) averaged 10.7 ± 2.4 min, and there was a significant difference between the two groups ($p < 0.05$). The actual puncture depth of the contrast group

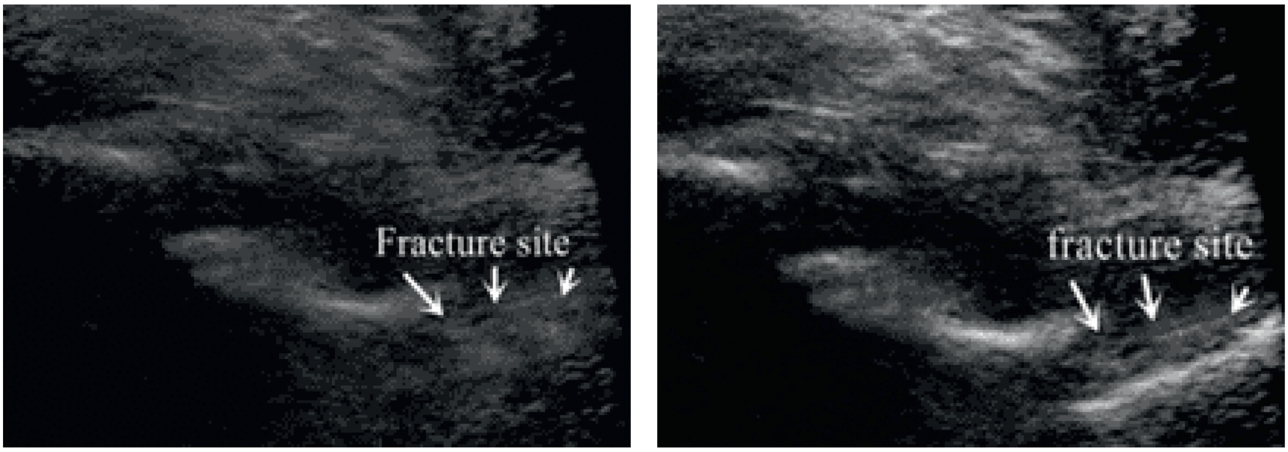

(a) (b)

Figure 5: Comparison of scapula fracture before and after ultrasound artificial intelligence enhancement. (a) Unenhanced ultrasound image of the scapula. (b) Enhanced ultrasound image of the scapula.

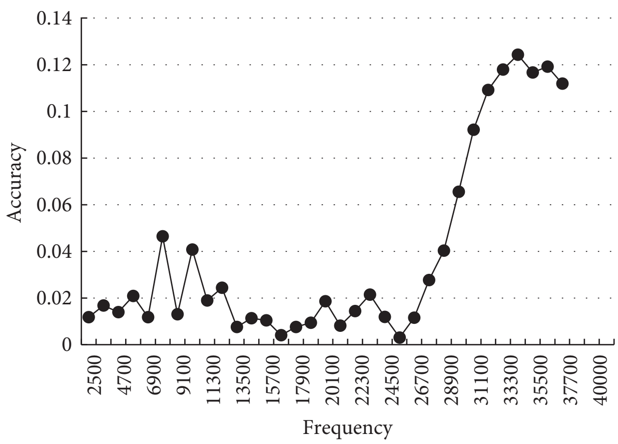

Figure 6: Accuracy enhancement curve.

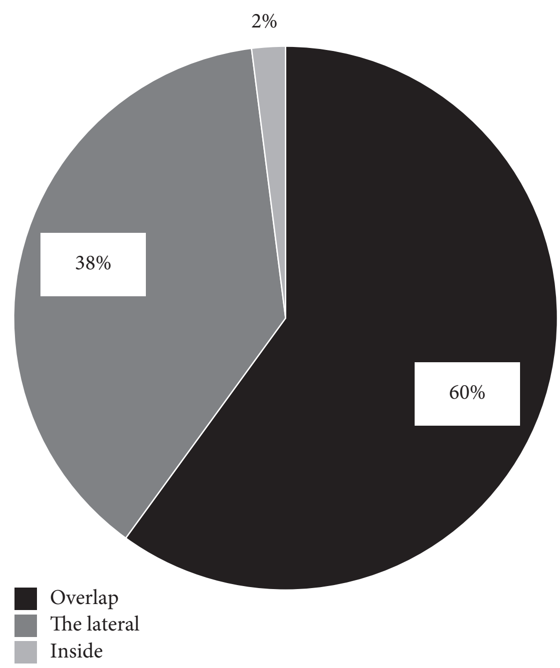

Figure 7: The proportion of the nerve location on the body surface in the scapula region of the traditional method and that under ultrasound.

was 62.5 ± 7.2 mm, and that of control group was 79.8 ± 8.9 mm. The difference between the two groups was significant ($p < 0.05$) (Figure 8).

4.4. Comparison of the Effects of the Motion Block between the Two Groups. The score of motion block effect in the contrast group and the control group is shown in Figure 9. The scores of clenched fist, elbow flexion, wrist extension, and arm lift were significantly different between the contrast group and the control group, and the motion block effect of the contrast group was better, with statistical difference ($P < 0.05$).

4.5. Comparison of Adverse Events during Puncture between the Two Groups. The number of needle tracks needed to be adjusted during puncture in the control group was 3.25 ± 1.36 times, and that in the contrast group was 2.11 ± 1.31 times. $P = 0.009$, with statistical difference. The times of encountering bone during puncture were 1.91 ± 1.34 times and 0.68 ± 0.73 times in the two groups, respectively, $P = 0.002$, with a statistical difference (Figure 10).

4.6. Evaluation of the Anesthesia Effect of the Two Groups. In the contrast group, there were 11 cases with excellent anesthesia effect and 9 cases with good anesthesia. There were 13 cases with excellent anesthesia effect and 7 cases with good anesthesia in the control group (Figure 11). The results showed that the anesthesia effect score of the contrast group was high and the anesthesia effect was good.

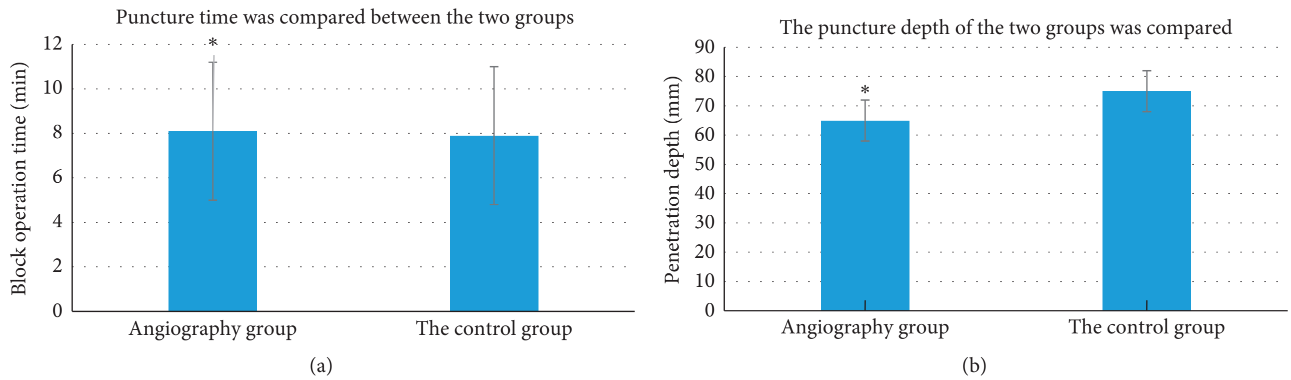

Figure 8: Comparison of puncture time and actual puncture depth between the two groups ($P < 0.05$). (a) Puncture time was compared between the two groups. (b) The puncture depth of the two groups was compared (*a considerable difference between groups).

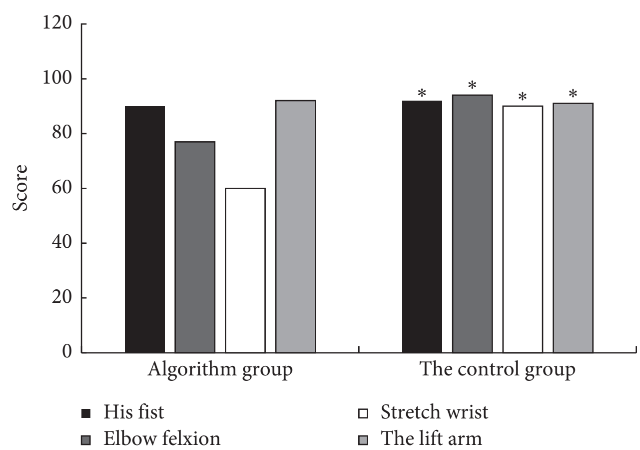

Figure 9: The score of motion block effect between the contrast group and the control group ($P < 0.05$) (*a considerable difference between groups).

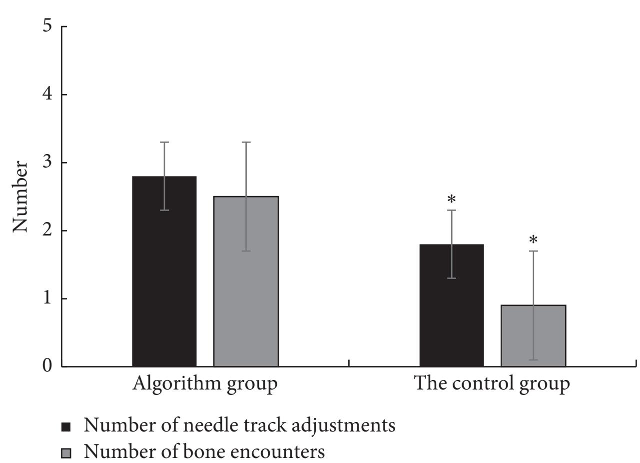

Figure 10: Adjustment of the number of needle tracks and the number of bone encounters between the two groups ($P < 0.05$) (*a considerable difference between groups).

4.7. Comparison of Puncture Sites and Puncture Adverse Reactions between the Two Groups of the Regional Nerve Block. In Figures 12 and 13, one patient in the control group had a transient abnormal sensation during puncture, while the contrast group did not show transient abnormal sensation. One case in the contrast group was found to have vascular injury, and hematomas were formed during the puncture of the injured blood vessel in the control group. The main

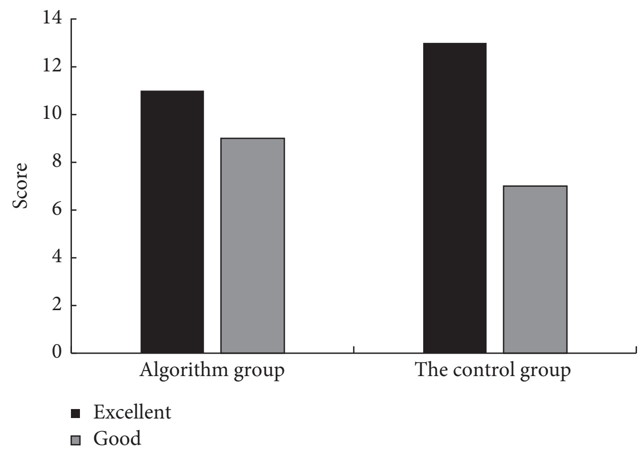

Figure 11: Comparison of anesthesia effect evaluation between the two groups.

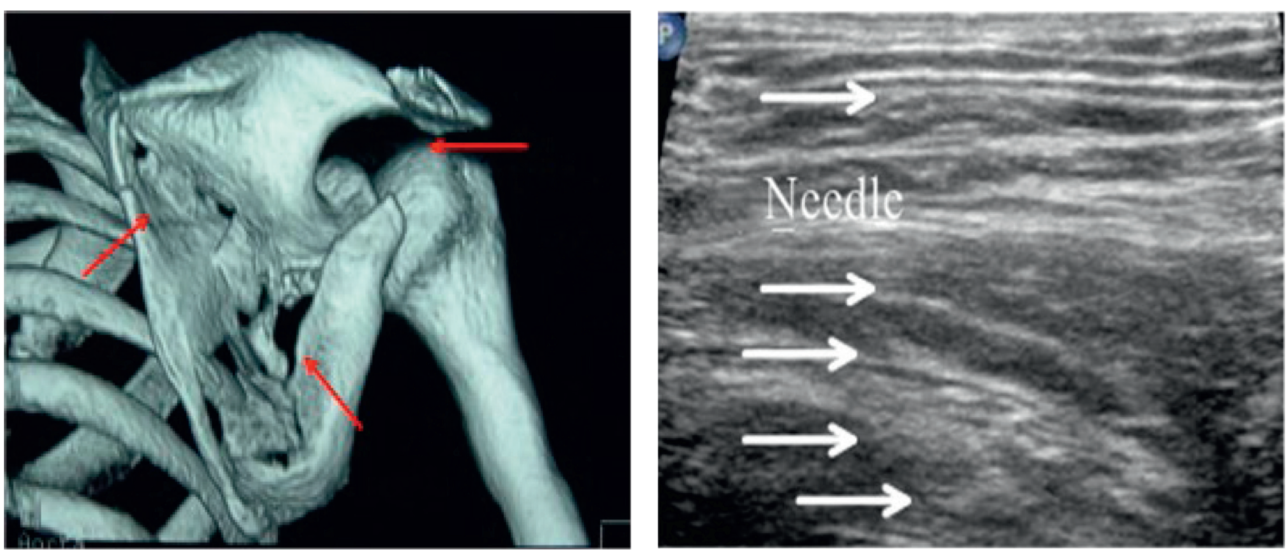

(a) (b)

Figure 12: The puncture site of the regional nerve block in the algorithm group (a) and the ultrasound anatomical diagram after puncture (b).

complaint of pain during puncture was obvious in the two groups, and there were six patients in the control group, which accounted for 30%. Patients in the contrast group did not have complain of significant pain, and there was a difference between the two groups ($p < 0.05$). There was no pneumothorax and local anesthetic poisoning in the two groups.

5. Discussion

The adoption of ultrasonic technology in regional nerve block has become a research hot issue in recent years. Ultrasound technology has produced revolutionary advances in nerve blocks, including the development of spinal regional nerve block [17]. However, there are few reports of the use of ultrasound for nerve block in thoracic paravertebral area. Nowadays, the application of ultrasound technology in clinical regional nerve block has harvested good results and accumulated experience related to real-time guidance of parathoracic region nerve block [18]. In ultrasound, the sagittal section scan block and the oblique section scan block use two modes. The patient can choose the position of the seated side and the position of the decubitus side, as well as the clinical anesthesia area or sitting position. The selection of ultrasonic detection mainly depends on the depth of puncture target and the body shape of the patient, and the weight of the patient has been shown in many studies to be an important factor affecting the depth of thoracic puncture [19]. An ultrasonic probe with the appropriate frequency must be selected by the scanning site. High-frequency linear detection was used for thoracic lateral spinal region nerve block [20]. Ultrasonic imaging is determined by the physical properties of the frequency and wavelength of the ultrasonic wave that detects radiation. Ultrasonic frequency units are related to resolution. The human ear can sense the frequency of sound waves within 20 Hz–20 kHz, and the medical

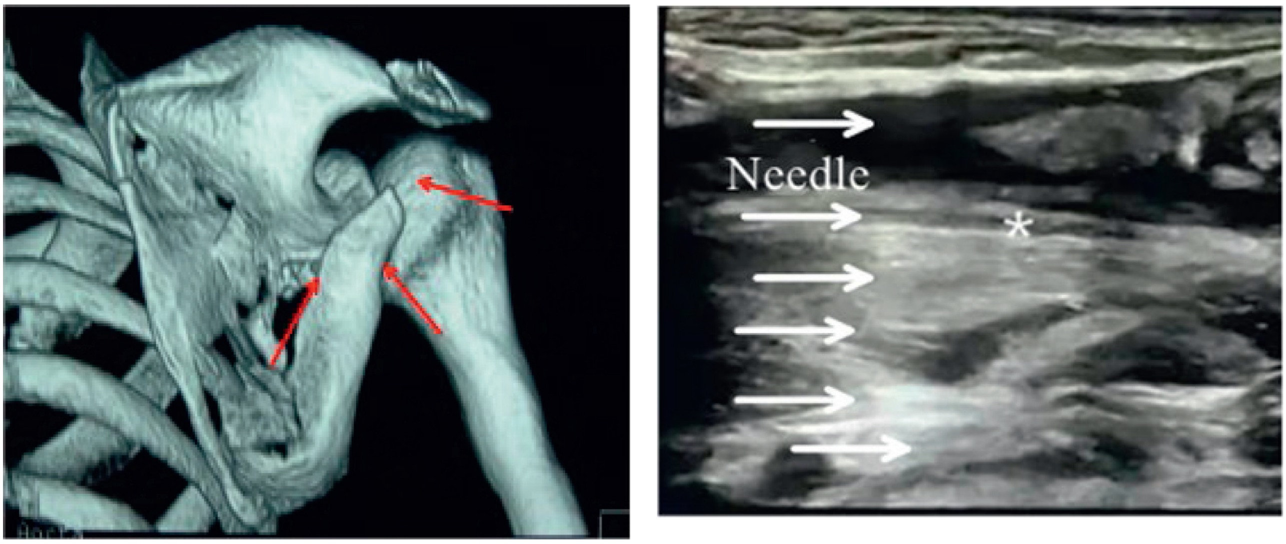

(a) (b)

Figure 13: The puncture site (a) of the regional nerve block and the ultrasound anatomy after puncture (b) in the control group. *The bleeding point.

diagnostic frequency of ultrasonic waves is 1–30 MHz. The higher the frequency of ultrasonic detection, the better the transverse resolution. Ultrasound wavelengths mean the distance between adjacent particles in two vibrating regions, allowing a clearer distinction between nerves and surrounding tissue. The longer the wavelength, the higher the transmittance. The frequency of the linear probe is 6–13 MHz, which is suitable for photographing the tissue structure of the body surface. Most of the detection frequencies are 2–7 MHz, which can be used for deep tissue structure imaging [21]. Therefore, the appropriate probe is selected according to the body type of the patient and the depth of the site to be anesthetized. In this study, the body mass of patients was less than 30 kg/m^2 and good imaging results were obtained using a high-frequency linear probe. The ultrasonic waves emitted by the probes penetrated the surface and propagated into the interior, reflecting the reactions that arouse when obstacles were encountered. Various obstacles can produce different echoes, which are collected and displayed on the screen to get a real-time view of the various parts of the internal organs. In addition, the color Doppler model was combined, which is particularly sensitive to the flow of fluids. Therefore, the blood vessels can be better observed by color Doppler spectroscopy and the flow and diffusion of local anesthesia injection can be observed, which can enable physicians to better conduct the next operation [22].

On the whole, traditional puncture anesthesia lacks the sense of breakthrough during epidural puncture, so the success rate is low and complications are high. A safe and effective guiding puncture method is urgently needed in clinic. The results showed that the fracture site was not obvious in the image before enhancement and optimization, and it was easy to be misjudged as a nonfracture site, affecting the judgment of doctors. The enhanced sonogram clearly showed the fracture location. The localization area of traditional ultrasound and artificial intelligence ultrasound overlapped greatly, and the area of artificial intelligence localization was 36% more than that of inner ultrasound. The algorithm group had fewer puncture needle channels, fewer adverse reactions, and broken operation time, indicating that the ultrasonic positioning effect of the algorithm was better than that of traditional puncture. After the visualization and real-time properties of artificial intelligence ultrasound were used for two control groups, the feasibility of applying ultrasonic image-guided regional nerve block based on deep learning to scapula fracture anesthesia was demonstrated.

6. Conclusion

The deep learning-based ultrasound image-guided imaging during scapular fracture surgery with regional nerve block anesthesia was compared with the use of traditional puncture anesthetics. It was proved that the method proposed in this study was more efficient than the traditional method, regardless of whether the method of puncture accuracy evaluation or evaluation of anesthesia effect was used. This method significantly shortened the time required for puncture and reduced complications compared with traditional puncture. In the future, we need to verify the performance of our constructed model in more cases and more disease types. In addition, based on the statistics of various parameters formed by patients using this method, its clinical diagnosis and prognostic predictive effects need to be further studied.

Data Availability

The data used to support the findings of this study are available from the corresponding author upon request.

Conflicts of Interest

The authors declare no conflicts of interest.

Authors' Contributions

Yubo Liu and Liangzhen Cheng contributed equally to this work.

References

[1] P. L. Gambus and S. Jaramillo, "Machine learning in anaesthesia: reactive, proactive. . . predictive!" *British Journal of Anaesthesia*, vol. 123, no. 4, pp. 401–403, 2019 Oct.

[2] S. Lee, N. Mohr, N. Street, and P. Nadkarni, "Machine learning in relation to emergency medicine clinical and operational scenarios: an overview," *Western Journal of Emergency Medicine*, vol. 20, no. 2, pp. 219–227, 2019 Mar.

[3] J. He, S. L. Baxter, J. Xu, J. Xu, X. Zhou, and K. Zhang, "The practical implementation of artificial intelligence technologies in medicine," *Nature Medicine*, vol. 25, no. 1, pp. 30–36, 2019 Jan.

[4] W. L. Bi, A. Hosny, M. B. Schabath et al., "Artificial intelligence in cancer imaging: clinical challenges and applications," *CA: A Cancer Journal for Clinicians*, Wiley Online Library, vol. 69, no. 2, pp. 127–157, 2019.

[5] Y. Song, S. Gao, W. Tan, Z. Qiu, H. Zhou, and Y. Zhao, "Multiple machine learnings revealed similar predictive accuracy for prognosis of PNETs from the surveillance, epidemiology, and end result database," *Journal of Cancer*, vol. 9, no. 21, pp. 3971–3978, 2018 Oct 10.

[6] R. Pirracchio, M. J. Cohen, I. Malenica et al., "Big data and targeted machine learning in action to assist medical decision in the ICU," *Anaesthesia Critical Care & Pain Medicine*, vol. 38, no. 4, pp. 377–384, 2019 Aug.

[7] Z. Lv, X. Li, and W. Li, "Virtual reality geographical interactive scene semantics research for immersive geography learning," *Neurocomputing*, vol. 254, no. 6, pp. 71–78, 2017.

[8] G. Wang, W. Li, S. Ourselin, and T. Vercauteren, "Automatic brAIn tumor segmentation using cascaded anisotropic convolutional neura networks," in *Proceedings Of the International MICCAI brAInlesion workshop*, pp. 178–190, Springer, Quebec City, Canada, September 2017.

[9] Y. Yuan, M. Chao, and Y.-C. Lo, "Automatic skin lesion segmentation using deep fully convolutional networks with jaccard distance," *IEEE Transactions on Medical Imaging*, vol. 36, no. 9, pp. 1876–1886, 2017 Sep.

[10] I. Gaudet-Ferrand, P. De La Arena, S. Bringuier et al., "Ultrasound-guided pudendal nerve block in children: a new technique of ultrasound-guided transperineal approach," *Pediatric Anesthesia*, vol. 28, no. 1, pp. 53–58, 2018 Jan.

[11] L. M. Smith and M. J. Barrington, "Ultrasound-guided blocks for cardiovascular surgery: which block for which patient?" *Current Opinion in Anaesthesiology*, vol. 33, no. 1, pp. 64–70, 2020 Feb.

[12] S. Singh, N. K. Choudhary, D. Lalin, and V. K. Verma, "Bilateral ultrasound-guided erector spinae plane block for postoperative analgesia in lumbar spine surgery: a randomized control trial," *Journal of Neurosurgical Anesthesiology*, vol. 32, no. 4, pp. 330–334, 2020 Oct.

[13] S. Ren, K. He, R. Girshick, and J. Sun, "Faster R-CNN: towards real-time object detection with region proposal networks," *IEEE Transactions on Pattern Analysis and Machine Intelligence*, vol. 39, no. 6, pp. 1137–1149, 2017 Jun.

[14] Q. Zhan, W. Wang, and G. de Haan, "Analysis of CNN-based remote-PPG to understand limitations and sensitivities," *Biomedical Optics Express*, vol. 11, no. 3, pp. 1268–1283, 2020 Feb 7.

[15] X. Hu, W. Luo, J. Hu et al., "Brain SegNet: 3D local refinement network for brain lesion segmentation," *BMC Medical Imaging*, vol. 20, no. 1, p. 17, 2020 Feb 11.

[16] H. Liang, B. Y. Tsui, H. Ni et al., "Evaluation and accurate diagnoses of pediatric diseases using artificial intelligence," *Nature Medicine*, vol. 25, no. 3, pp. 433–438, 2019 Mar.

[17] X. Fave, L. Zhang, J. Yang et al., "Delta-radiomics features for the prediction of patient outcomes in non-small cell lung cancer," *Scientific Reports*, vol. 7, no. 1, p. 588, 2017 Apr 3.

[18] S. Rizzo, F. Botta, S. Raimondi et al., "Radiomics: the facts and the challenges of image analysis," *European Radiology Experimental*, vol. 2, no. 1, p. 36, 2018 Nov 14.

[19] T. Kagawa, S. Yoshida, T. ShirAIshi et al., "Basic principles of magnetic resonance imaging for beginner oral and maxillofacial radiologists," *Oral Radiology*, Springer, vol. 33, no. 2, pp. 92–100, 2017.

[20] Z. Lv, X. Li, H. Lv, and W. Xiu, "BIM big data storage in WebVRGIS," *IEEE Transactions on Industrial Informatics*, vol. 16, no. 4, pp. 2566–2573, 2020.

[21] Q. R. Chen and S. P. Xie, "Lung cancer detection method based on deep learning," *Computer Technology and Development*, vol. 28, 2018.

[22] H. Seo, M. Badiei Khuzani, V. Vasudevan et al., "Machine learning techniques for biomedical image segmentation: an overview of technical aspects and introduction to state-of-art applications," *Medical Physics*, vol. 47, no. 5, pp. e148–e167, 2020 Jun.

Hindawi
Journal of Healthcare Engineering
Volume 2023, Article ID 9873058, 1 page
https://doi.org/10.1155/2023/9873058

Retraction

Retracted: Effect Analysis of Epidural Anesthesia with 0.4% Ropivacaine in Transforaminal Endoscopic Surgery

Journal of Healthcare Engineering

Received 8 August 2023; Accepted 8 August 2023; Published 9 August 2023

This article has been retracted by Hindawi following an investigation undertaken by the publisher [1]. This investigation has uncovered evidence of one or more of the following indicators of systematic manipulation of the publication process:

(1) Discrepancies in scope
(2) Discrepancies in the description of the research reported
(3) Discrepancies between the availability of data and the research described
(4) Inappropriate citations
(5) Incoherent, meaningless and/or irrelevant content included in the article
(6) Peer-review manipulation

The presence of these indicators undermines our confidence in the integrity of the article's content and we cannot, therefore, vouch for its reliability. Please note that this notice is intended solely to alert readers that the content of this article is unreliable. We have not investigated whether authors were aware of or involved in the systematic manipulation of the publication process.

In addition, our investigation has also shown that one or more of the following human-subject reporting requirements has not been met in this article: ethical approval by an Institutional Review Board (IRB) committee or equivalent, patient/participant consent to participate, and/or agreement to publish patient/participant details (where relevant).

Wiley and Hindawi regrets that the usual quality checks did not identify these issues before publication and have since put additional measures in place to safeguard research integrity.

We wish to credit our own Research Integrity and Research Publishing teams and anonymous and named external researchers and research integrity experts for contributing to this investigation.

The corresponding author, as the representative of all authors, has been given the opportunity to register their agreement or disagreement to this retraction. We have kept a record of any response received.

References

[1] B. Hu, H. Wang, T. Ma, Z. Fu, and Z. Feng, "Effect Analysis of Epidural Anesthesia with 0.4% Ropivacaine in Transforaminal Endoscopic Surgery," *Journal of Healthcare Engineering*, vol. 2021, Article ID 2929843, 6 pages, 2021.

Hindawi
Journal of Healthcare Engineering
Volume 2021, Article ID 2929843, 6 pages
https://doi.org/10.1155/2021/2929843

Research Article

Effect Analysis of Epidural Anesthesia with 0.4% Ropivacaine in Transforaminal Endoscopic Surgery

Bingwei Hu[1,2] **Hongwei Wang**[2] **Tingting Ma**[2] **Zhimei Fu**[2] **and Zhiying Feng**[1]

[1]*Department of Pain, The First Affiliated Hospital, Zhejiang University School of Medicine, Hangzhou 310003, China*
[2]*Department of Anesthesiology, Tongde Hospital of Zhejiang Province, Hangzhou 310012, China*

Correspondence should be addressed to Zhiying Feng; fzy1972@zju.edu.cn

Received 15 July 2021; Revised 15 August 2021; Accepted 13 September 2021; Published 6 October 2021

Academic Editor: Enas Abdulhay

Background. Epidural anesthesia used in percutaneous endoscopic lumbar discectomy (PELD) has the risk of complete neurotactile block. Patients cannot timely respond to the operator when the nerve is touched by mistake, so the potential risk of nerve injury cannot be avoided. According to pharmacodynamics, with the decrease of local anesthetic concentration, the nerve tactile gradually recovered; however, the analgesic effect also gradually weakened. Therefore, it is necessary to explore an appropriate concentration of local anesthetics that can keep the patients' nerve touch without pain. By comparing the advantages and disadvantages of 0.4% ropivacaine epidural anesthesia, local anesthesia and intravenous anesthesia on intraoperative circulation fluctuation, the incidence of salvage analgesia and the incidence of nerve non-touch, the feasibility of using low concentration epidural anesthesia in PELD to obtain enough analgesia and avoid the risk of nerve injury was confirmed. *Methods*. 153 cases of intervertebral foramen surgery from October 2017 to January 2020 were selected and divided into local anesthesia group (LA group), 0.4% ropivacaine epidural anesthesia group (EA group), and intravenous anesthesia group (IVA group) according to different anesthesia methods. The changes of blood pressure and heart rate, the incidence of rescue analgesia and nerve root non-touch were compared among the three groups. *Results*. The difference of map peak value among the three groups was statistically significant ($P < 0.001$); pairwise comparison showed that the map peak value of the LA group was higher than that of the EA group ($P < 0.001$) and IVA group ($P < 0.001$), but there was no statistical significance between the EA group and IVA group. The difference of HR peak value among the three groups was statistically significant; pairwise comparison showed that the HR peak value of the LA group was higher than that of the EA group ($P < 0.001$) and IVA group ($P < 0.001$), but there was no statistical significance between the EA group and IVA group. There was significant difference in the incidence of intraoperative hypertension among the three groups ($P < 0.05$); pairwise comparison showed that the incidence of intraoperative hypertension in the EA group was lower than that in the LA group ($P < 0.05$), while there was no significant difference between the IVA group, EA group, and LA group. There was significant difference in the incidence of rescue analgesia among the three groups ($P < 0.01$); pairwise comparison showed that the incidence of rescue analgesia in the EA group was lower than that in the LA group ($P < 0.05$) and IVA group ($P < 0.05$), but there was no significant difference between the LA group and IVA group. Due to the different analgesic mechanisms of the three anesthesia methods, local anesthesia and intravenous anesthesia do not cause the loss of nerve tactile, while the incidence of nerve tactile in 0.4% ropivacaine epidural anesthesia is only 2.4%, which is still satisfactory. *Conclusion*. Epidural anesthesia with 0.4% ropivacaine is a better anesthesia method for PELD. It not only has a low incidence of non-tactile nerve, but also has perfect analgesia and more stable intraoperative circulation.

1. Introduction

Percutaneous endoscopic transforaminal lumbar discectomy (PELD) is easy to touch or injure the spinal cord and nerve due to its close proximity to the spinal cord and dural sac. In order to avoid nerve injury, PELD is mainly local anesthesia, or intravenous anesthesia, general anesthesia or epidural anesthesia by anesthesiologists [1, 2]. General anesthesia can provide perfect analgesia, but it is difficult to find nerve injury due to unconsciousness of patients [3–5]. Spinal nerve function monitoring [6, 7] can provide protection for avoiding nerve injury under general anesthesia. However, additional equipment, personnel, and medical costs limit the popularization of the technology. Although patients with local anesthesia retain consciousness, previous studies have shown that analgesia is insufficient [8], and various analgesic drugs are needed to remedy [9, 10]. Epidural anesthesia can also retain the consciousness of patients and provide perfect analgesia. The other advantage is that the motor function of the lower limbs of the patients remains when the concentration of local anesthetics is low. The surgeon can detect the nerve injury by observing the movement of the toes of the patients [5, 11]. However, this is not the indicator that the surgeon really wants. Because of the sensory motor separation characteristics of ropivacaine, although a certain concentration of ropivacaine retains the motor function, the sensory fibers are completely blocked (including pain and touch), and the patients cannot perceive that the nerve tissue is touched by mistake during the operation. Therefore, in theory, blocking pain and retaining touch is a reliable index to avoid nerve injury. Pain was mainly transmitted by myelinated a δ fibers (2–6 μm) and unmyelinated C fibers (0.3–3 μm), while touch was mainly transmitted by myelinated a β fibers (6–12 μm). Different nerve fibers have different susceptibilities to local anesthetics. A δ nerve fiber is more susceptible to local anesthetics than a β nerve fiber, which leads to more pain block than touch [12]. Therefore, local anesthetics at appropriate concentrations can produce pain tactile separation block. Although some anesthesiologists [13] also recognize that low concentration of local anesthetics can retain the tactile sensation of nerve, there is no study to provide reference concentration of local anesthetics. Routine epidural anesthesia often uses 0.5% ropivacaine; although the analgesia is perfect, the nerve root tactile and lower limb motor function of patients are completely lost. Ren et al. [11] found that the analgesic effect of epidural anesthesia was satisfactory even when the concentration of ropivacaine was reduced to 0.375%. Therefore, when the concentration of ropivacaine is between 0.375% and 0.5%, there is an appropriate concentration, which can not only provide enough analgesia for patients but also retain nerve root tactile sensation. At this concentration, the patient's nerve root can be timely feedback when touched by mistake, and the operator can stop the operation in time to terminate the occurrence of nerve injury. Since October 2017, some patients with PELD in Zhejiang Litongde Hospital were treated with 0.4% ropivacaine epidural anesthesia, and the loss of nerve root tactile sensation was recorded in the electronic medical record.

2. Materials and Methods

2.1. Case Selection and Data Collection. Medical records of patients scheduled for PELD from October 2017 to January 2020 were collected from electronic medical record database (docare clinical anesthesia information system V5.0, madiston medical technology) of Zhejiang Litongde Hospital. Inclusion criteria were as follows: ASA grade I-II and patients scheduled for percutaneous transforaminal endoscopic discectomy. Exclusion criteria were as follows: age less than 18 or more than 80 years old; previous history of lumbar surgery; heart disease or cardiac insufficiency; liver and kidney dysfunction; patients with severe arrhythmia; patients with previous or current history of nervous system and mental disease; patients with abnormal coagulation function or platelet count; patients with other operations at the same time; and 2 or more segments of intervertebral disc nucleus pulposus removal. According to different anesthesia methods, they were divided into local anesthesia group (LA group), epidural anesthesia group (EA group), and intravenous anesthesia group (IVA group).

① Local anesthesia: 1% lidocaine infiltration anesthesia layer by layer. ② Epidural anesthesia with 0.4% ropivacaine: two segments of the lumbar spine were used as epidural puncture points on the cephalic side of the operation, and the epidural catheter was indwelled and placed toward the caudal side. After 5 minutes of 1% lidocaine test dose, 0.4% ropivacaine was given in batches until the anesthesia plane covered the operation area. ③ Intravenous anesthesia: 1 μg/kg fentanyl was slowly injected after prone position, and dexmedetomidine loading dose was 1 μg/kg (infusion time was 10 min), and then it was maintained at 0.3–0.5 $\mu g \cdot kg^{-1} \cdot H^{-1}$ for no more than 30 min. ④ Remedial analgesia: simple use of opioid remedy can obtain enough analgesic effect, but there is a risk of respiratory depression; especially in prone position, it will greatly increase the difficulty of rescue. Therefore, according to the patient's pain performance, anesthesiologists implement individualized multimodal analgesia (non-steroidal, weak opioid, and strong opioid analgesics) to remedy the pain, so as to minimize the occurrence of drug side effects.

2.2. Evaluating Indicator. Eneral information of patients enrolled in the study in the database, including gender, age, hypertension, height, weight, body mass index, basic mean arterial pressure (basicmap) and basic heart rate (basichr) at admission. The historical records of intraoperative vital signs were displayed intensively (data collection interval was 1 min), the mean arterial pressure (premap, postmap) and heart rate (prehr, posthr) at the moment of entering the operating room and at the end of the operation, the peak intraoperative mean arterial pressure (intramap) and the peak intraoperative heart rate (intrahr), the incidence of additional analgesics due to intolerance of pain, and the time of operation were registered the amount of transfusion during operation. Intraoperative hypertension was defined as a 20% or more increase in peak mean arterial pressure (figure) compared with baseline map. The presence of nerve root sensation was recorded (whether there was radiating pain or swelling sensation in the innervated area when the operator touched the nerve root consciously).

2.3. Statistical Analysis. SPSS 25.0 was used for statistical analysis and Graphpad Prism 8 was used for mapping. For continuous data, the Shapiro–Wilk test was used to test the normality. The measurement data conforming to the normal distribution were described by means and standard deviation (mean ± SD), and one-way ANOVA was used; the measurement data not conforming to the normal distribution were described by median (M) and interquartile (Q), and Kruskal–Wallis *h* test of independent samples was used. The counting data were described as percentages, and the χ^2 test was used. The Bonferroni method was used to correct the level of α. All tests were bilateral tests, and $P < 0.05$ indicated that the difference was statistically significant.

3. Result

In this study, 138 patients met the inclusion criteria, 15 patients met the exclusion criteria, and finally 123 patients were included in the study (Figure 1). There were 44 cases in the LA group, 41 cases in the EA group, and 38 cases in the IVA group. By the Shapiro–Wilk test, height, weight, BMI, basic map, basic HR, preoperative map, preoperative HR, intraoperative map peak, intraoperative HR peak, postoperative map, postoperative HR, and operation time were in normal distribution, and the data were analyzed by means of mean and standard deviation (mean ± SD). According to Levene's test of homogeneity of variance, the data were consistent with the homogeneity of variance; the age and infusion volume of patients in each group did not completely conform to the normal distribution, and the data were described by median (M) and interquartile (Q).

3.1. General Information. The height, weight, BMI, basic map, basic HR, and operation time of the patients were analyzed by one-way ANOVA. The Kruskal–Wallis *h* test of independent samples was used for age and infusion volume, and χ^2 test was used for gender and history of hypertension. The results showed that there was no significant difference among the groups (Table 1).

3.2. Comparison of Mean Arterial Pressure of Three Anesthesia Methods during Perioperative Period. One-way ANOVA showed that there was no significant difference in map before and after operation, but there was significant difference in map peak value during operation (Welch ANOVA was used for uneven variance; Welch $F = 9.828$, $P < 0.001$). The Games–Howell test showed that the peak value of intraoperative map in the LA group was 18.4 mmHg higher than that in the EA group (95% CI: 8.5–28.3 mmHg), and the difference was statistically significant ($P < 0.001$); the peak value of intraoperative map in the LA group was 13.3 mmHg higher than that in the IVA group (95% CI: 2.3–24.0 mmHg), and the difference was statistically significant ($P < 0.05$); there was no statistical significance between the EA group and IVA group (Figure 2).

3.3. Comparison of Perioperative Heart Rate among Three Anesthesia Methods. There was no significant difference in HR before and after operation in each group by one-way ANOVA, but there was significant difference in HR peak during operation between groups (uneven variance, Welch ANOVA; Welch $f = 24.166$, $P < 0.001$). The Games–Howell test showed that the peak value of intraoperative HR in the LA group was 17.7 bpm higher than that in the EA group (95% CI: 11.6–23.7 bpm), and the difference was statistically significant ($P < 0.001$); the peak value of intraoperative HR in the LA group was 14.30 bpm higher than that in the IVA group (95% CI: 5.9–22.2 bpm), and the difference was statistically significant ($P < 0.001$); there was no statistical significance between the EA group and IVA group (Figure 3).

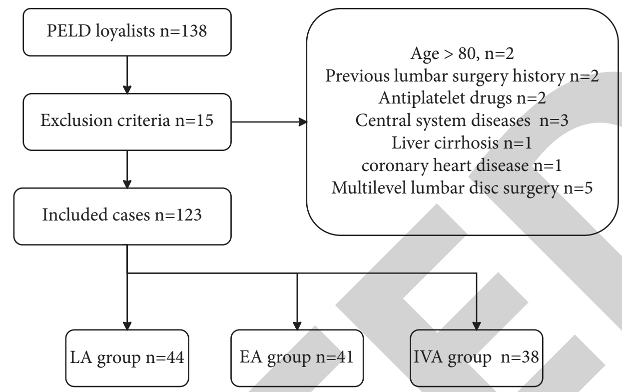

Figure 1: Patient flow diagram.

3.4. Comparison of the Incidence of Intraoperative Hypertension among Three Anesthesia Methods. The incidence of intraoperative hypertension in the LA group, EA group, and IVA group was 36.4%, 9.8%, and 18.4%, respectively. χ^2 test showed that there was significant difference in the incidence of intraoperative hypertension among the three groups ($\chi^2 = 9.175$, $P < 0.05$). Pairwise comparison showed that there was significant difference between the LA group and EA group ($P < 0.05$), but there was no significant difference between the LA group and IVA group and EA group and IVA group (Table 2).

3.5. Comparison of the Incidence of Intraoperative Salvage Analgesia among Three Anesthesia Methods. The incidence of intraoperative salvage analgesia in the LA group, EA group, and IVA group was 43.2%, 12.2%, and 36.8%, respectively. χ^2 test showed that there was significant difference in the incidence of intraoperative salvage analgesia among the three groups ($\chi^2 = 10.456$, $P < 0.01$) (Table 3). Pairwise comparison showed that there were significant differences between the EA group and LA group ($P < 0.05$) and EA group and IVA group ($P < 0.05$), but there was no significant difference between the LA group and IVA group (Table 3).

3.6. The Incidence of Non-Tactile Nerve Root in Three Anesthesia Methods. Because local anesthetics of LA mainly act on nerve endings to block the transmission of pain, while opioids of IVA mainly act on central opioid receptors to produce analgesic effect, neither of them can significantly affect the tactile sensation of nerve roots. EA not only blocked the pain fibers but also blocked the tactile fibers and motor nerves because of the action of local anesthetics on

Table 1: Information of patients.

Index	Group			Statistics	P value
	LA group	EA group	IVA group		
Sample size	44	41	38	—	—
Gender (example, %)					
Male	21 (7.7)	27 (53.7)	20 (52.6)	$\chi^2 = 2.977$	0.226
Age (years, M (Q))	52.5 (26)	58 (24)	54.5 (13)	$H = 2.199$	0.333
Height (cm, $\bar{x} \pm s$)	164.1 ± 7.6	166.8 ± 8.5	164.4 ± 7.0	$F = 1.533$	0.220
Body weight (kg, $\bar{x} \pm s$)	63.3 ± 10.6	65.1 ± 12.9	63.0 ± 9.8	$F = 0.432$	0.650
BMI (kg/m^2, $\bar{x} \pm s$)	23.4 ± 2.4	23.2 ± 3.2	23.2 ± 2.6	$F = 0.020$	0.980
Previous hypertension (cases, %)					
Yes	9 (20.5)	10 (24.4)	9 (23.7)	$\chi^2 = 0.479$	0.787
BasicHR (times/min, $\bar{x} \pm s$)	73.2 ± 11.2	74.4 ± 9.1	75.4 ± 11.3	$F = 0.458$	0.634
BasicMAP (mmHg, $\bar{x} \pm s$)	93.5 ± 11.3	93.1 ± 11.6	97.0 ± 13.6	$F = 1.262$	0.287
Infusion volume (ml, M (Q))	725 (200)	700 (200)	700 (250)	$H = 0.336$	0.845
Operation time (min, $\bar{x} \pm s$)	93.4 ± 19.9	93.1 ± 17.0	94.0 ± 23.4	$F = 0.023$	0.980

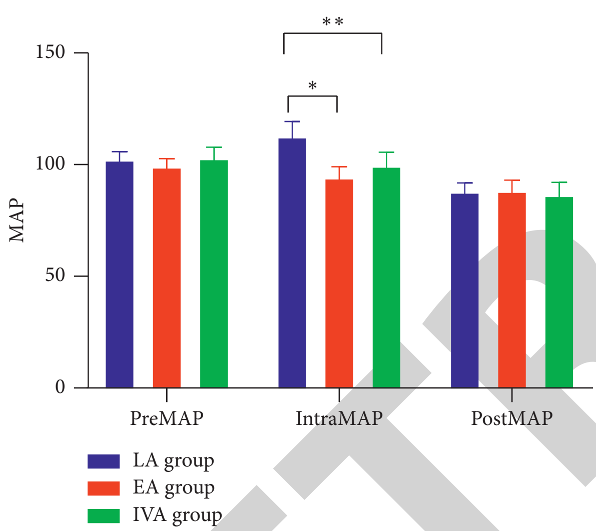

Figure 2: *The peak value of map in the LA group was significantly higher than that in the EA group ($P < 0.001$). **The peak value of map in the LA group was significantly higher than that in the IVA group ($P < 0.05$).

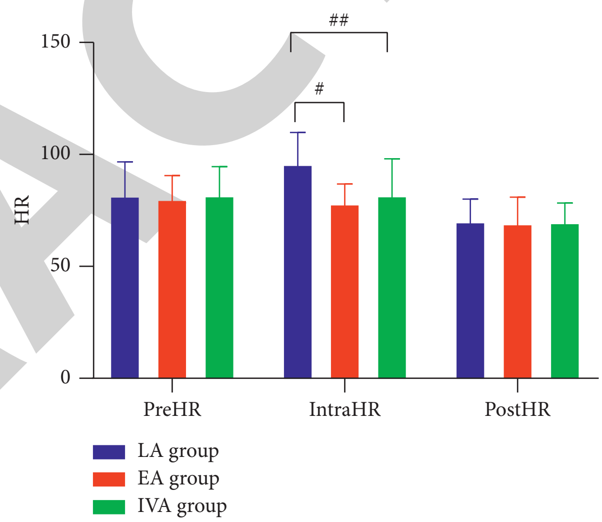

Figure 3: #The peak value of intraoperative HR in LA group was significantly different from that in EA group ($P < 0.001$); ##the peak value of intraoperative HR in LA group was significantly different from that in IVA group.

nerve roots and spinal cord. The degree of EA was positively correlated with the concentration of local anesthetics. In 41 patients undergoing epidural anesthesia with 0.4% ropivacaine, only one patient (2.4%) lost nerve root tactile sensation.

4. Discussion

To avoid nerve injury, local anesthesia with a low incidence of nerve root injury is usually recommended for PELD [14]. When a nerve is mistakenly touched, the patient can provide timely feedback. A study [3] showed that most patients with local anesthesia had moderate or severe pain when their nerve roots were stimulated, and 15 of 30 patients had fear of surgery. Therefore, anesthesiologists need to explore anesthesia methods that can not only provide effective analgesia, but also make the patient's feedback nerve be touched by mistake. Low-concentration ropivacaine epidural anesthesia is the most common research at present. It not only has good analgesic effect but also can preserve the motor function of patients' lower limbs. The operator can detect the nerve injury by observing the movement of patients' toes during the operation [5, 11]. But this method has a lag, and once the motor function is damaged, nerve damage occurs. Therefore, we need to find the local anesthetic concentration that can make the patient feedback the nerve touched immediately. 0.4% ropivacaine epidural anesthesia is a better choice, and only one of 41 patients in this study had complete loss of nerve root tactile. Because of the different mechanisms of action of drugs, 0.4% ropivacaine epidural anesthesia cannot completely retain the patient's nerve tactile, and only 2.4% of the incidence of nerve non-tactile is still satisfactory. The analgesic effect of epidural anesthesia is better than that of local anesthesia [15–18]. The analgesic effect of epidural anesthesia with 0.25% ropivacaine is close to that of local

Table 2: Comparison of the incidence of intraoperative hypertension among three groups.

Intraoperative hypertension	Grouping			Total	Statistic	P value
	LA group	EA group	IVA group			
Yes	16[a]	4[b]	7[a,b]	27		
Nothing	28	37	31	96	$\chi^2 = 9.175$	0.010
Total	44	41	38	123		

There was significant difference in the incidence of hypertension among the three groups ($P < 0.05$); the Bonferroni method was used to correct the level of blood pressure between two groups, and there was significant difference between the EA group and LA group ($P < 0.05$).

Table 3: Comparison of the incidence of analgesic rescue.

Remedial analgesia	Grouping			Total	Statistic	P value
	LA group	EA group	IVA group			
Yes	19[a]	5[b]	14[a]	33		
Nothing	25	36	29	90	$\chi^2 = 10.456$	0.005
Total	44	41	38	123		

There was significant difference in the incidence of intraoperative rescue among the three groups ($P < 0.01$); the Bonferroni method was used to correct the level of α, the difference was statistically significant between the EA group and LA group ($P < 0.05$), and the difference was statistically significant between the EA group and IVA group ($P < 0.05$).

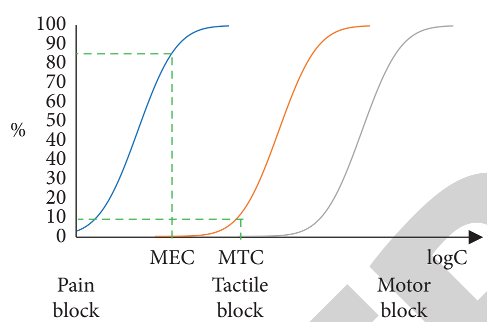

Figure 4: Dose effect curve of local anesthetics on pain, touch, and motor function.

anesthesia [18]. In this study, the incidence of rescue analgesia in 0.4% ropivacaine epidural anesthesia was significantly lower than that in local anesthesia, which indicated that the analgesic effect of 0.4% ropivacaine epidural anesthesia was better than that of local anesthesia, which was consistent with previous studies. Moreover, pain often leads to cardiovascular events. However, the peak value of mean arterial pressure, peak value of intraoperative heart rate, and incidence of intraoperative hypertension in 0.4% ropivacaine epidural anesthesia were significantly lower than those in local anesthesia, and the probability of cardiovascular events was lower. Therefore, epidural anesthesia has advantages over local anesthesia in reducing intraoperative salvage analgesia and stabilizing circulation. Compared with intravenous anesthesia, the incidence of rescue analgesia in 0.4% ropivacaine epidural anesthesia is much lower. However, this does not mean that its analgesic effect is better than intravenous anesthesia. Because the analgesic effect of intravenous anesthesia depends on the dose of opioids, the analgesic effect of intravenous anesthesia in this study can be improved by increasing the dose of opioids, but in the case of patients with PELD in prone position, adverse reactions such as respiratory depression caused by excessive dose are often more difficult to deal with. Therefore, the analgesic effect of 0.4% ropivacaine epidural anesthesia is better when the dosage of intravenous anesthesia is lower, and the safety of 0.4% ropivacaine epidural anesthesia is higher when the dosage of intravenous anesthesia is higher.

In summary, PELD with 0.4% ropivacaine epidural anesthesia can retain the nerve touch to a large extent to avoid nerve injury. At the same time, its analgesic efficacy and safety are better than local anesthesia and intravenous anesthesia. However, the choice of local anesthetic concentration in the study is based on the clinical experience of anesthesiologists, and it is not clear whether epidural anesthesia can reach the lower limit of effective analgesia concentration and the upper limit of nerve root tactile retention concentration. According to pharmacodynamics, for patients, the local anesthetic concentration just reached the pain disappeared, that is, the minimum effective concentration (MEC); with the increase of local anesthetic concentration, there is a suitable concentration, the patient's nerve tactile just disappeared, that is, the maximum tolerable concentration (MTC) of the patient's nerve tissue tactile is retained (Figure 4). The concentration of anesthetics is in the effective range between MEC and MTC. When the operation touches the nerve, the innervated area often shows slight radiation pain or acid swelling. When the operator receives feedback from the patient, the operation is terminated in time to avoid nerve injury. Therefore, the following study will apply biased coin design (BCD) to explore MEC and MTC of ropivacaine in PELD.

Data Availability

The simulation experiment data used to support the findings of this study are available from the corresponding author upon request.

Conflicts of Interest

The authors declare that there are no conflicts of interest regarding the publication of this paper.

Hindawi
Journal of Healthcare Engineering
Volume 2021, Article ID 3066930, 9 pages
https://doi.org/10.1155/2021/3066930

Research Article

Computed Tomography Image under Three-Dimensional Reconstruction Algorithm Based in Diagnosis of Renal Tumors and Retroperitoneal Laparoscopic Partial Nephrectomy

Haijie Zhang,[1,2] **Fu Yin**,[3] **Liyang Yang**,[1] **Anqi Qi**,[1] **Weiwei Cui**,[1] **Shanshan Yang**,[1] **and Ge Wen**[1]

[1]*Department of Imaging, Nanfang Hospital, Southern Medical University, Guangzhou 510515, China*
[2]*PET/CT Center, Department of Nuclear Medicine, The First Affiliated Hospital of Shenzhen University, Shenzhen 518000, China*
[3]*School of Information Engineering, Shenzhen University, Shenzhen 518000, China*

Correspondence should be addressed to Ge Wen; clym@ecupl.edu.cn

Received 29 June 2021; Revised 28 August 2021; Accepted 31 August 2021; Published 6 October 2021

Academic Editor: Enas Abdulhay

This study was to explore the clinical application value of computed tomography (CT) images based on a three-dimensional (3D) reconstruction algorithm for laparoscopic partial nephrectomy (LPN) in patients with renal tumors. 30 cases of renal cell carcinoma (RCC) patients admitted to the hospital were selected as the research objects and were rolled into two groups using a random table method. The patients who received PLN under the three-dimensional reconstruction and laparoscopic technique were included in the experimental group (group A), and the patients who received LPN using CT images only were included in the control group (group B). In addition, the treatment results of the two groups of patients were compared and analyzed. *Results*. The effective rate of the established model was 93.3%; the total renal arteriovenous variability of group A (13.3%) was higher than that of group B (6.7%), and the operation time (131.5 ± 32.1 minutes) was much lower than that of group B (158.7 ± 36.2 minutes), showing statistical significance ($P < 0.05$). *Conclusion*. CT images based on 3D reconstruction algorithms had high clinical application value for LPN in patients with renal tumors, which could improve the efficiency and safety of LPN.

1. Introduction

For early renal cell carcinoma (RCC), especially small RCC with a tumor diameter of less than 4 cm, the therapeutic effects of LPN and laparoscopic radical nephrectomy (LRN) are basically the same [1]. Because LPN only removes the tumor and part of the kidney tissue, the overall renal function after surgery is better than LRN [2]. Existing studies believe that LPN should be selected for isolated patients or patients with other diseases in the contralateral kidney. Compared with traditional open surgery, LPN not only greatly shortens the prognosis and hospitalization time of the patient but also reduces the economic burden of treatment for the patient and relieves the prognosis pain of patients due to surgery greatly [3, 4]. There are two approaches for LPN, namely, transabdominal and retroperitoneal. With the continuous updating of surgical instruments and the development of laparoscopic surgery technology in recent years, the retroperitoneal approach has gradually become a hot spot for scholars. In the past, conventional laparoscopy showed in two-dimensional (2D), which was difficult to achieve the ideal diagnosis and treatment effect. Moreover, in traditional medical imaging inspections, doctors mainly use tomographic images of a certain part of the human body and usually present the imaging results in two-dimensional images such as films or display screens. The result of this method is that the image results obtained are only judged by the personal subjective experience of the doctor. The doctor can only observe the subtleties of the image with the naked eye and the lack of objective evidence to support it, which may delay the condition of the patient [5].

With the continuous development of science and technology, medical imaging technology is also being updated simultaneously, making it possible to make up for the shortcomings in traditional imaging. In recent years, reports on three-dimensional (3D) reconstruction medical imaging technology are not uncommon, which have attracted widespread attention [6]. It uses visualization technology to provide greater assistance for the optimization of imaging effects, and the resulting images have a strong sense of reality, allowing doctors to observe and analyze images from multiple angles and levels. Studies have found that the use of the built-in software of the CT equipment can generate 3D reconstruction images, such as CT angiography (CTA) and CT urography (CTU), and obtain some reference information of the 3D anatomical structure with renal tumor and renal pedicle blood vessels (RPBV) [7]. However, this method does not use 3D image segmentation technology, so it is impossible to obtain a transparent and clear display of the organ structure image. In addition, the method does not use image fusion technology, so it cannot fuse the reconstructed model data information of multiple phases. The image information obtained is relatively scattered. Although it can provide valuable reference information for disease diagnosis, it cannot provide assistance for surgical planning, so the image obtained by this method cannot be called a true 3D reconstruction image [8].

Therefore, the study intended to explore the clinical application value of CT images based on a 3D reconstruction algorithm for LPN of patients with renal tumors by constructing a 3D reconstruction model of the kidney, so as to improve the efficiency and safety of LPN.

2. Materials and Methods

2.1. Research Objects. Thirty cases of renal cell carcinoma (RCC) patients admitted to the hospital from September 2018 to September 2019 were selected as the research objects and were rolled into two groups using a random table method. The patients who received PLN under the three-dimensional reconstruction and laparoscopic technique were included in the experimental group (group A), and the patients who received LPN using CT images only were included in the control group (group B). In addition, the treatment results of the two groups of patients were compared and analyzed. There were 15 cases in group A, including 8 males and 7 females, and they were 26~69 years old (with an average age of 52.40 ± 11.8 years). There were 15 cases in group B, including 9 males and 6 females, and they were 24~70 years old (with an average age of 50.5 ± 10.2 years). None of the selected patients had a previous medical history of contraindications for surgery, and none of them had any hypersensitivity to contrast agents. This study was approved by the hospital ethics committee, and all selected patients had signed the informed consent.

2.2. Variant Type of RPBV. Classification criteria of the renal artery were defined as follows: multiple renal arteries: there were other renal artery branches in addition to the main renal artery; premature renal artery branches: renal artery branches located at a distance ≤20 mm from the opening of the renal artery; and mixed type: a combination of above conditions.

Classification criteria of renal veins were defined as follows: multiple renal veins: the main branches of the renal veins could not merge into one branch before entering the kidney but still presented as branches; abnormal renal veins: the left renal vein run behind the left renal artery, the right renal artery run in front of the inferior vena cava, and there were 2 inferior vena cava; renal veins are abnormal: renal veins were anastomosed with reproductive veins and lumbar veins, respectively; others: renal tumor compressed the renal veins, causing deformation, and so on.

2.3. CT Scanning. A 64-slice spiral CT (Philips, Brilliance 64, Netherlands) was used for CT scanning. Before the scan, the patient was required to fast for 3 hours and drink 500 mL of water to fill the gastrointestinal tract, so as to enhance the contrast with the kidney tissue. In addition, the breathing exercises of patients had to be trained to minimize the artifacts caused by the breathing exercises on the CT scan, so as to ensure the reliability of collected data. The standard parameters of kidney CT scan were set to the following: the tube voltage was 120 kv, the tube current was 300 mA, the time per rotation was 0.5 s, the pitch was 0.984, the layer thickness was 5 mm, and the time for the tube to rotate a cycle was 0.5 s.

At the beginning of the scan, the patient was required to maintain a supine position and performed with CT plain scan and enhanced scan sequentially from the cartilage at the xiphoid process to the plane of the pubic symphysis. During the scanning, the patient was instructed to exhale and hold to the fullest body. When the contrast agent was not injected, a plain scan was performed. Then, the MEDRAD double-barreled high-pressure syringe (US) was adopted to inject the contrast agent (iopamidol solvent 370 in high concentration) intravenously at an injection rate of 5 mL/s, and the injection dose was 1.5 mL/Kg. After all the contrast agent was injected, the injection tube was flushed with a proper amount of saline, and the enhanced scan was started. The arterial phase scan setting was set as follows: the trigger threshold was set to 200 Hu, the contrast agent was injected, and the scan was performed by taking the abdominal aorta section as the region of interest (ROI). The scan in the venous phase was started from the intravenous injection of contrast agent until the delay 65 s. The scan in the excretory phase was started from the intravenous injection of contrast agent until the delay 600 s. After the scans in the above four phases were all completed, the original image with a thickness of 5 mm was thinned, and then all image data was imported into the MxView workstation equipped for the CT. Finally, all image data were recorded to a DVD disc.

2.4. Construction of 3D Reconstruction Model of Kidney. The key step of 3D reconstruction was image segmentation using RGM. The characteristic of RGM was to gather similar pixels to form a ROI. The specific operation method was given as follows: the data obtained from the arterial phase and venous phase scans were entered into mimics 17.0 (Materialise, Belgium), and the upper and lower threshold range was set to 210–1,615 Hu. The renal tumor, renal artery, and renal vein tissue structure were segmented with the RGM, and the other renal artery and renal vein branches outside the ROI were eliminated with artificial auxiliary software. Finally, an ideal 3D reconstruction model of the kidney was constructed. The flowchart of 3D reconstruction of medical images is in Figure 1.

After X-ray passed through the substance, the relationship between output intensity and input intensity was expressed as the following equation:

$$I_b = I_a e^{-\mu\triangle d}, \tag{1}$$

where Δd referred to the propagation distance of X-ray and μ was the X-ray attenuation coefficient of the substance. I_b referred to the output intensity, I_a represented the input intensity, and e referred to the input parameter.

When the X-ray passed through different tissue structures of the human body, the relationship between output intensity and input intensity was given as follows:

$$I_b = I_a\left(e^{-\mu_1\triangle d_1}e^{-\mu_2\triangle d_2}e^{-\mu_3\triangle d_3}\ldots\right). \tag{2}$$

The above equation could be converted into integral form as follows:

$$I_b = I_a e^{-\int \mu \mathrm{d}x}, \tag{3}$$

where x refers to the propagation distance.

CT was developed on the basis of Wratten transformation, the equation of which was as below.

It was known that the integral of a certain function $(x, y) = \hat{f}(r, \theta)$ along the straight line Z was as follows:

$$\begin{aligned} p &= \int_{-\infty}^{+\infty} f(x, y)\mathrm{d}z \\ &= \int_{-\infty}^{+\infty} \hat{f}(r, \theta)\mathrm{d}z, \\ &= \int_{-\infty}^{+\infty} \hat{f}\left(\sqrt{\sqrt{l^2 + z^2}}, \varnothing + \tan^{-1}\frac{z}{l}\right)\mathrm{d}z. \end{aligned} \tag{4}$$

Then, the Wratten equation could be inversely transformed into $\hat{f}(r, \theta) = 1/2\pi^2 \int_0^\pi \int_{-\infty}^{+\infty} (1/r\cos(\theta - \varnothing) - l)(\partial p/\partial l)\mathrm{d}l\mathrm{d}\varnothing$.

The pixel color values of the image were collected from back to front and from front to back, and the synthesis algorithm of which from back to front was given as follows:

$$\begin{aligned} C_b &= C_a(1 - \alpha_i) + C_i\alpha_i, \\ \alpha_b &= \alpha_a(1 - \alpha_i) + \alpha_i, \end{aligned} \tag{5}$$

where C_a represents the initial color, C_b represents the final color, and α_i refers to the opacity.

The synthesis algorithm from front to back was given as follows:

$$\begin{aligned} C_b\alpha_b &= C_a\alpha_a + C_i\alpha_i(1 - \alpha_a), \\ \alpha_b &= \alpha_i(1 - \alpha_a) + \alpha_a. \end{aligned} \tag{6}$$

During the image synthesis, α could continue to increase, the threshold was 1, and the transparency of the image was close to zero at this moment.

2.5. Evaluation of the Image Quality of 3D Reconstruction Model of the Kidney. The quality of the 3D reconstruction image was evaluated by a senior urologist and a senior imaging physician. Before the evaluation, the 3D reconstruction CT image quality scoring standard was developed according to the renal artery scoring standard of Sahani et al. [9], which was to record the branches of renal arteries and renal veins in detail. The evaluation had to be carried out in strict accordance with this standard. If the scores of individual images were different, the final score can be determined by researching relevant information and discussion of the two physicians. The specific criteria were given as follows: 1 point meant that the main renal artery (renal vein) and its first-level branches showed blurred blood vessel edges, with or without respiratory movement artifacts; 2 points meant that the main renal artery and its first- or second-level branches could be visible clearly, with smooth blood vessel edges and without respiratory movement artifacts, and the secondary branches were less than 4; 3 points meant that the main renal artery and its first, secondary, and tertiary branches were visible clearly, with smooth blood vessel edges, without respiratory movement artifacts, and the tertiary branches were less than 5; 4 points represented that the main renal artery and its first, secondary, and tertiary branches could be seen clearly, with smooth blood vessel edges, without respiratory motion artifacts, and the tertiary branches were greater than or equal to 5; and 5 points represented that the main trunk of the renal artery and its first, secondary, tertiary, and forth branches could be showed clearly, with smooth blood vessel edges and no artifacts of respiratory movement.

In this study, the standard for 3D reconstruction CT image of the kidney was set as follows: the renal vein score was greater than or equal to 4 points, which meant that 3 to 4 renal arteries could be distinguished from the reconstructed image; the renal vein score was greater than or equal to 2 points, which meant that 1~2 renal veins could be identified based on the reconstructed image.

2.6. Preparation before LPN. LPN was performed using the 2D laparoscopic equipment (KARL STORZ, Germany). First, the 3D reconstruction model of renal tumor prepared above was incorporated into mimics 17.0 software, the simulated surgery function of which was adopted to observe the operation of the model in all directions, realize the surgical demonstrations, and formulate scientific and effective surgical plans. During the surgery, the surgeon was in charge of the model magnification and rotation, and the assistant took the specific operations. During this period, the image of the renal cortex was reconstructed by moderately

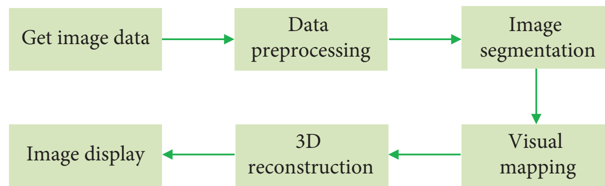

Figure 1: The flowchart of 3D reconstruction of medical images.

transparent processing so that the surgeon can clearly observe the structure of the RPBV and assist in the completion of the operation.

2.7. Application of 3D Reconstruction Model of Kidney in LRN. The practical application of the 3D model in LRN was to guide the operation through the artificial image fusion method; that is, the 3D reconstruction model image was fused and superimposed on the 2D laparoscopic image, and the fused image was displayed on a separate screen. Based on the results of the image fusion, the LRN was performed synchronously. The whole process was led by the surgeon and the surgical assistant performed the actual operation. Renal artery and renal vein can be clearly distinguished due to the different intensity of vascular pulsation, and operations such as ligation and disconnection were adopted accordingly. In group A, the 3D reconstruction model and artificial fusion image method were applied for preoperative guidance and intraoperative RPBV positioning and ligation. After the blood vessel and ureter were separated and cut, the patient's kidneys were freed and the kidney lesions were carefully removed, and then a drainage tube was placed between the peritoneum of the posterior abdominal wall and the intra-abdominal fascia. In group B, the CTA combined with CTU images were applied to guide the operation and to locate and ligate the renal artery and renal vein. After the blood vessel and ureter were separated and cut, the patient's kidney was freed and the renal lesion tissue was carefully removed. A drainage tube was placed between the peritoneum and the intra-abdominal fascia on the posterior wall of the abdomen. All patients underwent the surgery successfully without any accidental interruption.

2.8. Statistical Methods. The data were processed with SPSS 20.0 software for statistical analysis. The measurement data were indicated as mean ± standard deviation ($\overline{x} \pm s$), and an independent sample t-test was used; the count data was displayed as a percentage (%), and the X2 test was used for analysis. All data were considered statistically significant with $P < 0.05$, and there was no statistical difference when $P > 0.05$.

3. Results

3.1. Basic Information. There were 8 males and 7 females in group A, with an average age of 52.40 ± 11.8 years; there were 9 males and 6 females in group B with an average age of 50.5 ± 10.2 years old. As illustrated in Figure 2, there was no obvious difference between the two groups of patients in indicators such as age, gender, tumor distribution, body mass index (BMI), tumor maximum diameter (TMD), hemoglobin value, and the number of adrenal artery branches ($P > 0.05$). All selected patients did not withdraw due to accident event.

3.2. Visualization Results of the 3D Reconstruction Model of the Kidney. A 3D reconstruction model of the kidney of 15 patients in group A was successfully constructed. This model can clearly show the main renal artery and its fourth-level branches and the main renal vein and its second-level branches. The renal can be visually observed through this model. The outline of the tumor more objectively and effectively reflects the size of the renal tumor and its spatial distribution with other tissue structures; the kidney collecting system showed a clear structure and natural connections; the entire kidney system structure was clearly displayed with anatomical details. Figure 3 shows the images of image of renal tumor based on 2D CT and 3D reconstruction model for better comparison.

The use of a 3D reconstruction model of the kidney can clearly reflect the anatomical characteristics of RPBV. In Figure 4, the characteristics of renal artery variation were observed from the ventral and dorsal sides, so that the variation of the renal artery could be intuitively understood.

3.3. Image Quality Results of the 3D Reconstruction Model of the Kidney. Of the 15 kidney 3D reconstruction models prepared in this study, 14 cases met the standard, and the effective rate of the built model was 93.3% (as Figure 5). One case was unqualified because the patient's kidney was not filled with contrast medium enough, which resulted in fewer main branches of the renal artery in the 3D reconstruction model and incomplete display of the renal calyces in the renal collection system. Although the 3D reconstruction model of the kidney in this case was incomplete, it could still show the anatomical details of the renal artery and renal vein, so it had no effect on the LPN.

3.4. Classification on Variety of RPBV. Figures 6 and 7 show the comparisons on variations of renal artery vascular and variations on renal vein vascular in two groups, respectively. Most of the cases in both groups suffered from mixed renal artery variation, with 6 cases in group A and 7 cases in group B. The type of renal vein variation in group A was abnormal renal vein progression and other types, and there were only multiple vessels type renal vein variation in group B. There was no remarkable difference

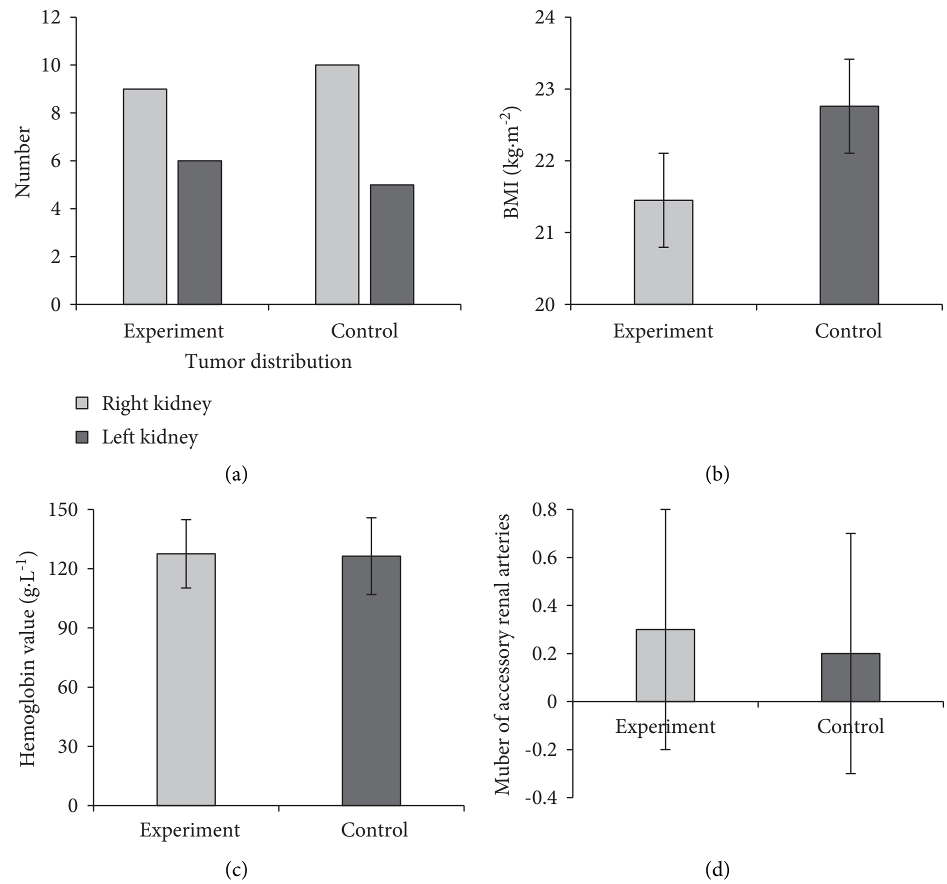

Figure 2: Basic information of patients in two groups.

between the two groups in the total renal artery variation rate and renal vein total variation rate ($P > 0.05$).

3.5. LPN Results. All the enrolled patients were diagnosed as RCC before surgery, followed by LPN, and there were no serious complications such as conversion to open surgery and major bleeding that occurred during the surgery. The 3D reconstruction model of the kidney used in group A could objectively and truly reflect the structural characteristics of the kidney, the type of RPBV variation, and the spatial position relationship of kidney tumors. The constructed 3D reconstruction model was adopted for preoperative scientific planning, and it was fused and superimposed with the 2D laparoscopic images during the surgery. The surgery of the patients in group A was successful. As shown in Figure 8, the RPBV variant type was that the left renal vein run behind the left renal artery. The 3D model showed that it was safer and more effective to ligate and cut the renal artery running forward.

The scan data obtained from CTA combined with CTU images were applied in group B for preoperative planning. The patients in group B had successful surgeries.

3.6. Analysis on Efficacy. The operation time, estimated blood loss, intraoperative blood transfusion number/rate, incidence of complication, postoperative hemoglobin value, tumor recurrence number/rate, and other index values were analyzed for the two groups of patients. The results given in Figure 9 revealed that the operation time of group A was visibly lower than that of group B, and the difference was great in statistics ($P < 0.05$), while the differences in other indicators were not extreme ($P > 0.05$). In addition, there was no tumor recurrence in the two groups.

4. Discussion

The clinical application value of CT images based on the 3D reconstruction algorithm for LPN in patients with renal tumors was discussed in this study, so as to improve the efficiency and safety of LPN. A 3D reconstruction model of the kidney was constructed, the image quality was evaluated, and the RPBV mutation of the patient was classified according to the kidney mutation classification standard. Then, the 3D reconstruction model of the kidney was applied to LPN, and the curative effect of two groups of patients was analyzed and compared. The results revealed that the constructed 3D reconstruction model of the kidney could objectively and truly reflect the structural characteristics of the kidney, the variant type of RPBV, and the spatial position relationship of the renal tumors, which was helpful for the rational planning and design of LPN before surgery. Applying the 3D reconstruction model of the kidney in LPN could greatly shorten the operation time without

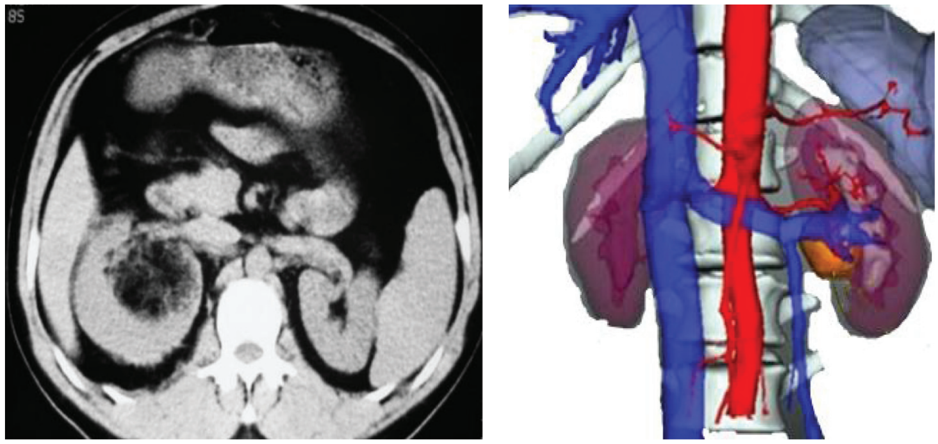

(a) (b)

Figure 3: Images of renal tumor (male patient aged 48 years; the tumor was in the right kidney with the size of 4.7 cm). (a) 2D CT image of renal tumor. (b) CT image of renal tumor based on the 3D reconstruction algorithm.

(a) (b)

Figure 4: 3D reconstruction model image of the renal artery. Variation type was premature renal artery branch A and B referred to the ventral renal artery and dorsal renal artery, respectively.

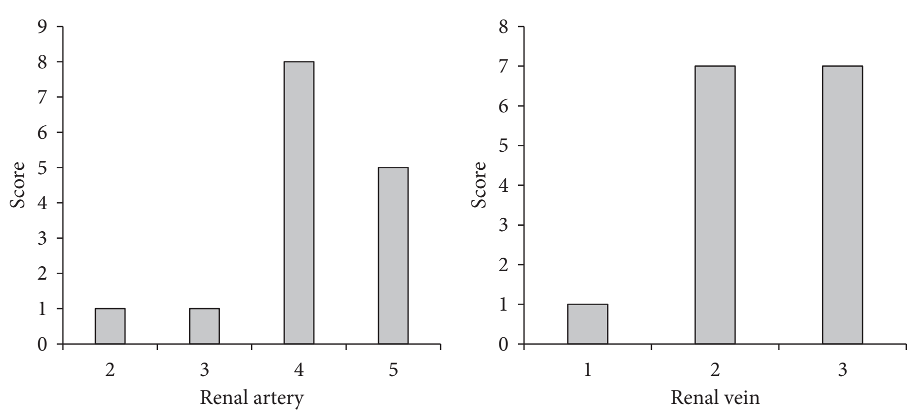

(a) (b)

Figure 5: Image quality of the 3D reconstruction model of the kidney. (a) Abscissa showed the quality evaluation score of renal artery image; (b) abscissa showed the quality evaluation score of renal vein image.

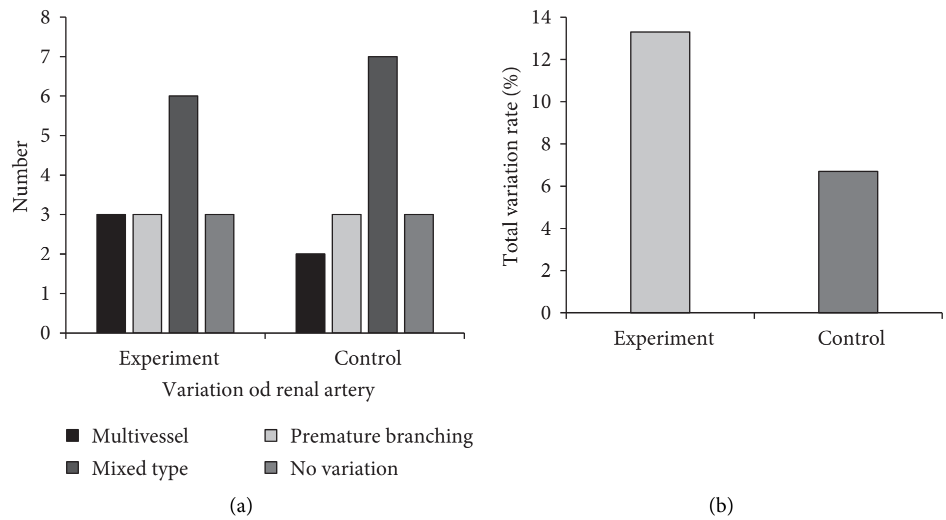

Figure 6: Variations of renal artery vascular in the two groups.

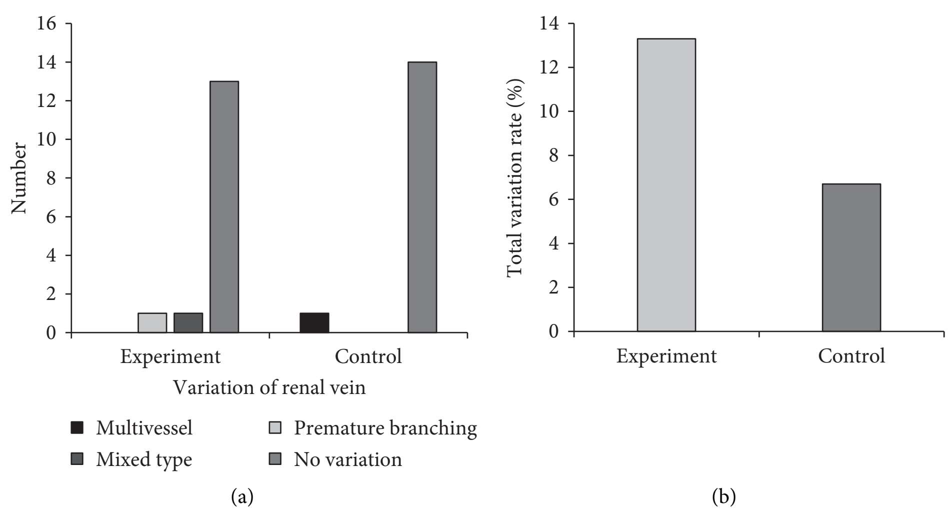

Figure 7: Variations on renal vein vascular in the two groups. "Other" refers to the deformation and variation of the renal vein on the affected side of the kidney due to compression by a larger tumor.

complications. Such a result was basically consistent with the research results of other scholars.

Malignant renal tumors mostly occur in the renal parenchyma, accounting for more than 80%, including RCC, renal sarcoma, renal metastases, Wilms tumor, and transitional cell carcinoma that occurs in the renal pelvis and calyx [10]. The adult renal tumor has the highest incidence rate of RCC, followed by transitional cell carcinoma originating from the collecting system of the kidney, so the renal tumor is also known as RCC. The human body is most likely to develop RCC when it is over 50 years old [11]. Compared with the transperitoneal approach, the surgeon can reach the kidney faster through the retroperitoneal laparoscopic approach and hardly interfere with other organs in the abdominal cavity. In addition, the renal arteries are mostly behind the renal veins, and the retroperitoneal approach facilitates direct exposure and treatment of the renal arteries [12]. However, because the target kidney is tightly connected with adjacent organs in the operation of the retroperitoneal approach, the operation space is narrow, and improper operation may cause damage to other organs of the patient. How to locate RPBV quickly and accurately and deal with it effectively has become a difficult topic for many scholars, and a comprehensive and accurate understanding of the anatomical characteristics of RPBV before surgery has become the key [13].

Huang et al. [14] used the 3D reconstruction model of the kidney to successfully implement the "zero ischemia partial nephrectomy," which not only effectively reduced the ischemic damage to the normal kidney during the operation but also promoted the research and development of partial nephrectomy with superselective renal artery occlusion. Xia et al. [15] reconstructed a digital 3D model of the kidney with clear blood vessel structure and strong stereo perception

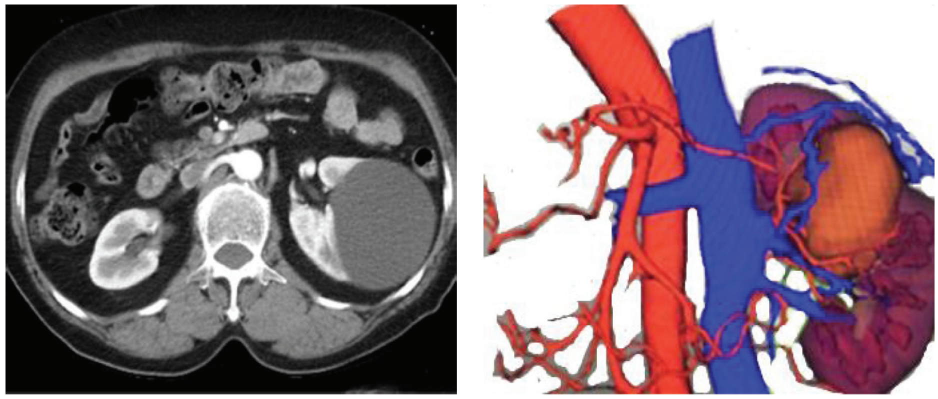

Figure 8: Images of RPBV laparoscopy and 3D reconstruction model of the kidney.

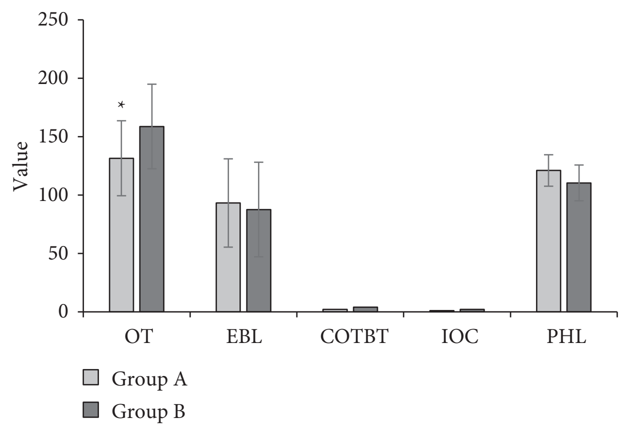

Figure 9: Comparison of the curative effect of patients in the two groups. ∗ indicates that group A is observably different from group B ($P < 0.05$); OT represents the operation time, EBL represents the estimated blood loss, COIBT represents the case of intraoperative blood transfusions, IOC represents the incidence of complication, and PHL represents postoperative hemoglobin value.

based on the CT scan data of preoperative patients and formulated a more reasonable surgical plan with the aid of simulated surgery; it was found that the actual operation was highly consistent with the 3D reconstruction; and based on this 3D model, clinical living kidney transplantation was successfully implemented, the prognosis was good, and there were no obvious surgical complications.

5. Conclusion

The conclusions of this study were summarized as follows: CT images based on the 3D reconstruction algorithm had high clinical application value for LPN in patients with renal tumors and could improve the efficiency and safety of LPN. It was necessary to further promote the application. However, there were still many shortcomings of this study. For example, the number of study subjects was small due to time and conditions, and the data results obtained had to be further researched. In future research, the number of samples had to be expanded to increase the persuasiveness of the data, so as to provide reliable reference information for clinical applications. The results of this study provided a reliable research basis for the clinical application of 3D technology and further demonstrated the good development prospects of 3D reconstruction technology in the medical field.

Data Availability

The data used to support the findings of this study are available from the corresponding author upon request.

Conflicts of Interest

The authors declare no conflicts of interest.

Authors' Contributions

Haijie Zhang and Fu Yin contributed equally to this work.

References

[1] R. V. Clayman, L. R. Kavoussi, R. S. Figenshau, P. S. Chandhoke, and D. M. Albala, "Laparoscopic nephroureterectomy: initial clinical case report," *Journal of Laparoendoscopic Surgery*, vol. 1, no. 6, pp. 343–349, 1991.

[2] J. Fu, S. Ye, and H.-j. Ye, "Retroperitoneal versus transperitoneal laparoscopic partial nephrectomy: a systematic review and meta-analysis," *Chinese Medical Sciences Journal*, vol. 30, no. 4, pp. 239–244, 2015.

[3] N. Torkamani, G. Jerums, P. Crammer et al., "Three dimensional glomerular reconstruction: a novel approach to evaluate renal microanatomy in diabetic kidney disease," *Scientific Reports*, vol. 9, no. 1, p. 1829, 2019.

[4] T. A. Durso, J. Carnell, T. T. Turk, and G. N. Gupta, "Three-dimensional reconstruction volume: a novel method for volume measurement in kidney cancer," *Journal of Endourology*, vol. 28, no. 6, pp. 745–750, 2014.

[5] J. O. Herrera-Caceres, A. Finelli, and M. A. S. Jewett, "Renal tumor biopsy: indicators, technique, safety, accuracy results, and impact on treatment decision management," *World Journal of Urology*, vol. 37, no. 3, pp. 437–443, 2019.

[6] C. Berczi and T. Flasko, "Renal tumor in pregnancy: a case report and review of the literature," *Urologia Internationalis*, vol. 99, no. 3, pp. 367–369, 2017.

[7] H. Ren, L. Gu, A. Andreasen et al., "Spatial organization of the vascular bundle and the interbundle region: three-dimensional reconstruction at the inner stripe of the outer medulla in the mouse kidney," *American Journal of Physiology—Renal Physiology*, vol. 306, no. 3, pp. F321–F326, 2014.

[8] J. Neuhaus, L. Blachut, R. Rabenalt et al., "Efficiency analysis of bipolar and multipolar radiofrequency ablation in an in vivo porcine kidney model using three-dimensional reconstruction of histologic section series," *Journal of Endourology*, vol. 25, no. 5, pp. 859–867, 2011.

[9] D. V. Sahani, S. P. Kalva, P. F. Hahn, and S. Saini, "16-MDCT angiography in living kidney donors at various tube potentials: impact on image quality and radiation dose," *American Journal of Roentgenology*, vol. 188, no. 1, pp. 115–120, 2007.

[10] A. S. Taylor, D. E. Spratt, S. M. Dhanasekaran, and R. Mehra, "Contemporary renal tumor categorization with biomarker and translational updates: a practical review," *Archives of Pathology & Laboratory Medicine*, vol. 143, no. 12, pp. 1477–1491, 2019.

[11] T. Yamagami, R. Yoshimatsu, K. Kajiwara et al., "Protection from injury of organs adjacent to a renal tumor during percutaneous cryoablation," *International Journal of Urology*, vol. 26, no. 8, pp. 785–790, 2019.

[12] W. Deng, Z. Zhou, J. Zhong et al., "Retroperitoneal laparoscopic partial versus radical nephrectomy for large (≥ 4 cm) and anatomically complex renal tumors: a propensity score matching study," *European Journal of Surgical Oncology*, vol. 46, no. 7, pp. 1360–1365, 2020.

[13] T. A. Durso, J. Carnell, T. T. Turk, and G. N. Gupta, "Three-dimensional reconstruction volume: a novel method for volume measurement in kidney cancer," *Journal of Endourology*, vol. 28, no. 6, pp. 745–750, 2014.

[14] J. Huang, S. Lü, Z. Hu, C. Huang, Y. Li, and Q. Wei, "Three-dimensional reconstruction of human kidney based on UroMedix-3D system and its application in kidney surgery," *Nan Fang Yi Ke Da Xue Xue Bao*, vol. 39, no. 5, pp. 614–620, 2019, Chinese.

[15] L. Xia, X. Zhang, X. Wang et al., "Transperitoneal versus retroperitoneal robot-assisted partial nephrectomy: a systematic review and meta-analysis," *International Journal of Surgery*, vol. 30, pp. 109–115, 2016.

Hindawi
Journal of Healthcare Engineering
Volume 2023, Article ID 9878935, 1 page
https://doi.org/10.1155/2023/9878935

Retraction

Retracted: Prescription of *Sageretia hamosa Brongn* Relieved Goiter through Promoted Apoptosis of Thyroid Cells via miR-511-3p and PTEN/PI3K/Akt Pathway

Journal of Healthcare Engineering

Received 1 August 2023; Accepted 1 August 2023; Published 2 August 2023

This article has been retracted by Hindawi following an investigation undertaken by the publisher [1]. This investigation has uncovered evidence of one or more of the following indicators of systematic manipulation of the publication process:

(1) Discrepancies in scope
(2) Discrepancies in the description of the research reported
(3) Discrepancies between the availability of data and the research described
(4) Inappropriate citations
(5) Incoherent, meaningless and/or irrelevant content included in the article
(6) Peer-review manipulation

The presence of these indicators undermines our confidence in the integrity of the article's content and we cannot, therefore, vouch for its reliability. Please note that this notice is intended solely to alert readers that the content of this article is unreliable. We have not investigated whether authors were aware of or involved in the systematic manipulation of the publication process.

Wiley and Hindawi regrets that the usual quality checks did not identify these issues before publication and have since put additional measures in place to safeguard research integrity.

We wish to credit our own Research Integrity and Research Publishing teams and anonymous and named external researchers and research integrity experts for contributing to this investigation.

The corresponding author, as the representative of all authors, has been given the opportunity to register their agreement or disagreement to this retraction. We have kept a record of any response received.

References

[1] Y. Deng, S. Chen, H. Wang, B. Wang, and K. Xiao, "Prescription of *Sageretia hamosa Brongn* Relieved Goiter through Promoted Apoptosis of Thyroid Cells via miR-511-3p and PTEN/PI3K/Akt Pathway," *Journal of Healthcare Engineering*, vol. 2021, Article ID 3506559, 13 pages, 2021.

Hindawi
Journal of Healthcare Engineering
Volume 2021, Article ID 3506559, 13 pages
https://doi.org/10.1155/2021/3506559

Research Article

Prescription of *Sageretia hamosa Brongn* Relieved Goiter through Promoted Apoptosis of Thyroid Cells via miR-511-3p and PTEN/PI3K/Akt Pathway

Yang-lin Deng,[1,2,3] Su Chen,[4] Hong-tu Wang,[5] Bo Wang,[6] and Kai Xiao [1,2]

[1]*Precision Medicine Research Center and National Clinical Research Center for Geriatrics, West China Hospital, Sichuan University, Chengdu 610041, China*
[2]*National Chengdu Center for Safety Evaluation of Drugs, West China Hospital, Sichuan University, Chengdu 610041, China*
[3]*Department of Pharmacy, First Affiliated Hospital of Kunming Medical University, Kunming 650032, China*
[4]*Department of Outpatient, First Affiliated Hospital of Kunming Medical University, Kunming 650032, China*
[5]*Department of Infections Disease, First Affiliated Hospital of Kunming Medical University, Kunming 650032, China*
[6]*Department of Neurosurgery, First Affiliated Hospital of Kunming Medical University, Kunming 650032, China*

Correspondence should be addressed to Kai Xiao; 2017324020105@stu.scu.edu.cn

Received 16 July 2021; Revised 5 August 2021; Accepted 8 September 2021; Published 29 September 2021

Academic Editor: Enas Abdulhay

Goiter is thyroid enlargement, in China, *Sageretia hamosa Brongn* (SHB) can be used to treat goiter, but it has not been reported. Therefore, data analytics of SHB prescription on thyroid were explored in this study to provide a theoretical support for SHB in the treatment of goiter. In this study, rat in goiter model was constructed by using propylthiouracil (PTU) and treated with SHB prescription. Thyroid function about the triiodothyronine (T3), free thyroxine (T4), free triiodothyronine (FT3), free thyroxine (FT4), and thyroid-stimulating hormone (TSH) were measured by ELISA; thyroid coefficient was calculated after weighed thyroid; and HE staining was applied to assess the morphology of thyroid tissue. miRNA microarrays were employed to detect miRNA expression in thyroid tissue of rats. Expression of miR-511-3p was measured by RT-qPCR; expression of proteins (PTEN and apoptosis-related proteins) was tested by western blotting; relationship between miR-511-3p and PTEN was investigated by dual luciferase reporter gene assay; cell viability rate was determined by CCK-8; and cell cycle distribution and apoptosis rate were detected by flow cytometry. The results showed that SHB prescription ameliorated goiter and downregulated miR-511-3p. miR-511-3p targeted PTEN in thyroid cells and PTEN negatively regulated the activation of PI3K/Akt pathway. Furthermore, the inhibition of apoptosis in thyroid cells caused by the overexpression of miR-511-3p or the activation of PI3K/Akt pathway was reversed by treatment of SHB prescription, inhibition of miR-511-3p, or overexpression of PTEN. In conclusion, SHB prescription promoted apoptosis of thyroid through decreased miR-511-3p and regulated PTEN/PI3K/Akt pathway, it might suggest possible medical applications.

1. Introduction

Goiter is thyroid enlargement, which is caused by a large number of agents in the environment or medication, some kinds of goiter with obvious hyperthyroidism or hypothyroidism [1]. Most patients present with benign disease and are euthyroid at presentation, but without effective treatment in time, and it will lead to more serious thyroid pathological changes [2]. Nowadays, the main treatments are thyroidectomy, partial resection, and single or repeated radioiodine therapy [3]. Thyroidectomy is a standard therapy for young and otherwise healthy patients, radioiodine therapy is an attractive alternative to surgery in older patients with cardiopulmonary disease, and thyroxin therapy may be tried in young patients with small diffuse goiters [4], and all have their limitations. In addition, goiter can be cured by many kinds of traditional Chinese medicine (TCM) as well [5].

In many regions of China, a lot of TCM show great curative effect on goiter [6]. For example, Xing Qi Hua Ying Tang ameliorated clinical symptoms of patients that were accompanied with reduction in the size of goiter [7]; besides, Haizao Yuhu Decoction alleviated iodine-deficient goiter via regulating thyroid hormone synthesis [8, 9]. *Sageretia hamosa Brongn* (SHB) is one of the TCM [10], it is known as Que Mei Teng in China, which has been used to treat many different kinds of disease among the people in Yunnan for a long time. According to folk processing methods and purposes, SHB can be used to treat goiter as well, but it has not been reported. Therefore, in this study, the function of SHB prescription on thyroid and its mechanism were explored.

The study found that the proliferation and apoptosis of thyroid cells are involved in the development of goiter [11, 12]. There was also a study that found that TCM named Kang-Jia-Wan played a therapeutic role via apoptosis induction in the goitrous glands [13]. The research found that TCM take effect through microRNA (miRNA)-target network [14, 15]. Moreover, miRNA deregulation observed in human goiter influences thyroid diseases [16]. All of those reports inspired us to focus on the miRNA that SHB regulated in thyroid cells, we used to figure out whether SHB prescription affects the proliferation and apoptosis of thyroid cells through miRNA, in order to explore a possible mechanism.

Here, we aimed to explore the underlying mechanism that SHB prescription promotes apoptosis and inhibits proliferation of thyroid cells in goiter, provided theoretical support for SHB in the treatment of goiter.

2. Materials and Methods

2.1. Construction of Rat in Goiter Model. 48 SD rats (weigh 250–300 g, half male, healthy) were randomly classified into six groups (8 rats in each group), Group 1 was the normal group without any disposal. Groups 2–6 were administered intragastrically by of propylthiouracil (PTU, #Js30643-5g; YOYOBIO, Shanghai, China) $1\,mL\cdot 100\,g^{-1}$ one day for 28 days in order to induce goiter. Each rat was fed with 20 g one day and drank freely during the experiment. The behavior and hair color of rats were observed, and each of them was weighed once a week. Animal Care and Use Committee approved this study.

2.2. Prescription of Sageretia hamosa Brongn. Prescription of SHB was a compatibility agent including *Sageretia hamosa Brongn* （SHB）, *Scutellaria barbata* D. Don （SBD）, and *Hedyotis diffusa* Willd. （HDW） (purchased from Kunming traditional Chinese Medicine Factory Co., Ltd.), abbreviated as SHB prescription in this study. Soaked 30 g SHB, 10 g SBD, and 10 g HDW into 750 g water for 30 min and then boiling for 1 h, extracted twice and combined all the extracts, subsequently, filtered with 200 mesh, concentrated the filtrate, then collected the extract (55–60°C, specific gravity of 1.058–1.06), granulating and drying, respectively.

2.3. Treatment. Two days after discontinuation of construction of rat in goiter model, Group 2–6 were treatment with Levothyroxin Sodium Tablets (LST, #B14202007312; Merck KGaA, Germany) or SHB prescription for 28 d. Blank control group, rats in goiter model without any treatment; LST group, rats in goiter model treated with LST $0.07\,mg\,kg^{-1}$ one day; light concentration of SHB prescription, rats in goiter model treated with SHB prescription in $63\,mg\cdot 100\,ml^{-1}\cdot 100\,g^{-1}$; moderate of SHB prescription, rats in goiter model treated with SHB prescription in $126\,mg\cdot 100\,ml^{-1}\cdot 100\,g^{-1}$; high concentration of SHB prescription, rats in goiter model treated with SHB prescription in $252\,mg\cdot 100\,ml^{-1}\cdot 100\,g^{-1}$.

2.4. Thyroid Function Observation. Serum samples of rat in each group were collected to measure the triiodothyronine (T3, # KL-E12896; Kanglang), thyroxine (T4, # KL-E1937 R; Kanglang), free triiodothyronine (FT3, #KL-E1640 R; Kanglang), free thyroxine (FT4, #KL-E1006 R; Kanglang), and thyroid-stimulating hormone (TSH, #KL16995; Kanglang) by using ELISA purchased from Shanghai Kanglang Biotechnology Co., Ltd according to the manufacturer's instructions.

2.5. Thyroid Coefficient Calculation. Thyroid of rats in each group was taken and weighed, and the thyroid coefficient was calculated by the formula (weight of thyroid/body weight of rat) × 100%.

2.6. Hematoxylin-Eosin (HE) Staining. After weighed, thyroid of rats in each group was used for hematoxylin-eosin (HE) staining to observe morphology of thyroid. To be brief, thyroid tissues in each group were embedded in paraffin wax to prepare 5 μm wax pieces, followed by HE staining. Tissue sections were stained by using hematoxylin and eosin staining kit (#GV358430; Yiji, Shanghai, China) according to the manufacturer's instructions. After washed for 10 min, stained slices were checked and photographed under a 200-fold light microscope.

2.7. RNA Extraction and miRNA Microarrays. Total RNA in rat thyroid sample of each group was extracted by using Trizol Total RNA Extractor (#KL-14770; Kanglang) according to the manufacturer's instructions. Then, the extracted RNA was further purified by ammonium acetate/ethanol precipitation. Reverse transcription followed by PCR is used to create cDNA constructs. Subsequently, PCR is performed with two primers that anneal to the ends of the adapters. TruSeq Small RNA Sample Preparation Kits (#RS-122-2001; Illumina, San Diego, USA) were used according to the manufacturer's instructions.

2.8. Cell Culture. Rat thyroid cells (FRTL-5) (#FE325; ATCC, USA) and human thyroid cells (Htori-3) (#FE744; ATCC, USA) were purchased from Shanghai Qiming Biotechnology Co., Ltd. and cultured in Dulbecco's Modified

Eagle Medium/Nutrient Mixture F-12 (DMEM-F12, #SH30023.01; YOYOBIO, Shanghai, China) containing 5% fetal bovine serum (FBS, #12657-029-OJN; Gibco, USA), 100 U/ml penicillin, 100 mg/ml streptomycin, and 2 mM L-glutamine at 37°C and 5% CO_2. When the thyroid cells reached 70–80% confluence, they were passaged in accordance with standard procedures.

2.9. Drug-Contained Serum. 30 SD rats (weigh 250–300 g, half male, healthy) were randomly divided into two groups, 15 rats which used to produce drug-contained serum were treated with SHB prescription in 252 mg,·100 ml^{-1}, 100 g^{-1}, and the other 15 rats which used to produce blank serum received the same dose of normal saline for 10 d. After the last gastrogavage for 1 h, blood samples from femoral artery were collected, then coagulation for 2 h, and carefully collected the supernatant after centrifugation at 1500 rpm for 10 min, and placed in −80°C refrigerator. The samples were filtered through 0.22 μm membrane before being used, filtrates were drug-contained serum and blank serum, respectively.

2.10. Cell Transfection and Treatment. miR-511-3p mimics, miR-511-3p inhibitor, si-PTEN, and pcDNA-PTEN were designed and produced by Guangzhou Ruibo Biotechnology Co., Ltd. (China). Invitrogen™ Lipofectamine™ 2000 Transfection Reagent (#11668027; Invitrogen, USA) was used to perform FRTL-5 and Htori-3 transfection according to the manufacturer's instructions. After transfected with miR-511-3p mimics, FRTL-5 and Htori-3 cultured with 1% blank serum as blank group, and 1%, 5%, and 10% drug-contained serum as SHB prescription light, moderate, and high dose groups, respectively. According to the experiment, 50 μg/mL 740 Y–P (#TQ0003; TargetMo, USA) was used to treat FRTL-5 and Htori-3, and FRTL-5 and Htori-3 which cultured with 10% drug-contained serum or transfected with miR-511-3p inhibitor/pcDNA-PTEN for 48 h.

2.11. Quantitative Reverse Transcription Polymerase Chain Reaction (RT-qPCR). Total RNA was extracted from FRTL-5 and Htori-3 in each group by using TRIzol reagent (#ZC-0021A; ZCIBIO, Shanghai, China). After reversed extracted total RNA into cDNA by using reverse transcription kit (#DXT-218061; Qiagen, USA), RT-qPCR was performed by using SYBR® Premix Ex Taq™ II (#HRR820A-1; Takara, Japan). The reaction conditions were as follows: 95°C for 7 min, *f* 45 cycles of 95°C for 1 min, 60°C for 35 s, and 72°C for 30 s, and finally at 72°C for 2 min. The forward and reverse primers were as follows: miR-511-3p F: 5′-ACACCCATCGTGTCTTTTGC-3′ and *R* 5′-CAATG-GACCACCATTCTGTCT-3'; U6 F: 5′-CTCGCTTCGGCA GCACA-3′ and *R* 5′-AACGCTTCACGAATTTGCGT-3'. Expression of miR-511-3p was determined by using the $2^{-\Delta\Delta Ct}$ method.

2.12. Western Blotting. Total protein was isolated from FRTL-5 and Htori-3 in each group by using total protein extraction kit (#2140; Millipore, USA), after measuring the concentration of isolated total protein by using BCA protein quantification kit (#GV357593; Yiji), they were separated by 10% sodium dodecyl sulfate polyacrylamide gel electrophoresis (SDS-PAGE), subsequently, transferred onto polyvinylidene difluoride (PVDF) membrane and blocked with 5% skim milk, then incubated with primary antibodies against Bcl-2 (1 : 1000, #ER1802-97; HUABIO, Hangzhou, China), anti-Bax (1 : 1000, #ER0907; HUABIO), anti-caspase-3 (1 : 1000, #ET1602-39; HUABIO), anti-PTEN (1 : 1000, #RT1519; HUABIO), anti-PI3K (1 : 1000, #bs-0128R; Bioss, Beijing, China), anti-p-PI3K (1 : 1000, #bs-5587R; Bioss), anti-Akt (1 : 1000, #bs-2056R; Bioss), anti-p-Akt (1 : 1000, # bs-5188R; Bioss), and anti-GAPDH (1 : 1000, #ER1901-65; HUABIO) overnight. The next day, the PVDF membrane was treated with secondary antibody (1 : 1000, #HA1024; HUABIO) and visualized by using SuperBrite™ ECL Western Blot Substrate/Detection Kit (#BIV-K823-200; BioVision, USA). The gray values of bands were analyzed by using ImageJ used to software.

2.13. Cell Count Kit-8 (CCK-8). Cell Count Kit-8 (CCK-8, #BA00208; Bioss) was used to detect cell viability of FRTL-5 and Htori-3 in each group according to the manufacturer's instructions. Then, the absorbance value was detected at a wavelength of 450 nm by using microplate reader.

2.14. Flow Cytometry. Flow cytometry was employed to measure cell cycle distribution and cell apoptosis rate. In order to measured cell cycle distribution, FRTL-5 and Htori-3 were stained with 50 mg/mL propidium iodide (PI) and RNase at 37°C for 30 min and then analyzed by flow cytometry. In order to measure cell apoptosis rate, FRTL-5 and Htori-3 were treated with 10 μL Annexin-V–Fluorescein Isothiocyanate (FITC) and PI at 4°C for 30 min in the dark, and analyzed by flow cytometry.

2.15. Dual Luciferase Reporter Genes Gene Assay. Dual luciferase reporter gene assay kit (#GV357366; Yiji) was used to verify relationship between miR-511-3p and PTEN. In brief, the 3′-Untranslated Regions (UTR) of PTEN wild type (WT) or mutant type (MUT) was cloned into the pGLO luciferase vector and transfected them with or without miR-511-3p mimics into 293T by using Invitrogen™ Lipofectamine™ 2000 Transfection Reagent. After 48 h, the luciferase activity was detected by using dual luciferase reporter assay system.

2.16. Statistical Analysis. Data are expressed as means ± standard error of the mean (SEM). Statistical analysis was performed by using a Student's *t*-test between two groups and one-way analysis of variance (ANOVA) among groups with GraphPad Prism 7.0 software. *P* values < 0.05 were considered statistically significant.

3. Results

3.1. Effect of SHB Prescription on Rat in Goiter Model. To verify the function of SHB prescription in goiter rat, first, the goiter model rat was established by using PTU, after PTU applied for 28 d, rats showed rough fur, loose skin, and slow reaction, and as Table 1 showed, the body weight of rat in the goiter group is less than the normal group. Then, we treated goiter rat with light, moderate, and high concentration of SHB prescription, and the LST treatment was the positive medicinal control group, after treatment for 28 d, their body weight increased compared with goiter rat without any treatment (Table 1); besides, the rats showed smooth fur, tight skin, and faster reaction. Besides, both SHB prescription and LST treatment reduced the thyroid coefficient ($P < 0.05$) (Table 2 and Figure 1(a)) and improved thyroid function ($P < 0.05$; Figure 1(b)). Moreover, HE staining results also indicated that high concentration of SHB prescription promoted morphology of thyroid tissue return to normal as LST done (Figure 1(c)). These results suggested that SHB prescription ameliorated goiter in concentration-dependent manner.

3.2. Regulation of SHB Prescription on Expression of miRNAs in Goiter Rat. In order to further explore the underlying mechanism of therapeutic effect of SHB prescription on goiter, we employed miRNA microarrays to detect the relative miRNA expression levels in thyroid tissue of rats in the above experimental groups. From this analysis, there were many differentials expressed miRNAs in the normal, goiter, LST, and SHB prescription groups (Figure 2(a)). We identified the top 10 miRNAs whose expression was upregulated in the goiter group compared with normal and decreased with LST and SHB prescription treatment, besides there were also the top 10 miRNAs whose expression was downregulated in the goiter group, and increased after LST and SHB prescription treatment (Table 3 and Figure 2(b)). Finally, miR-511-3p was chose for further experiments. As a first step in confirming the validity of the array data, we performed RT-qPCR on miR-511-3p, as shown in Figure 2(c) ($P < 0.05$), these it was overexpressed in the goiter group compared with the normal group, while its expression decreased after LST or SHB prescription treatment, and this was statistically significant, consistent with the microarray experiments. Therefore, we speculated that one of the ways that SHB prescription might improve goiter was through downregulation of miR-511-3p.

3.3. SHB Prescription Effected Proliferation and Apoptosis of Thyroid Cells through miR-511-3p. miRNAs participate in the regulation of cell physiological process and can be regulated by TCM, based on the miRNA microarrays results, miR-511-3p mimics was transfected into thyroid cell lines FRTL-5 and Htori-3, after treated with SHB prescription in different concentration, cell cycle, viability, and apoptosis ability were measured. First, RT-qPCR results showed that compared with the normal and the blank group, expression of miR-511-3p significantly increased in miR-511-3p mimics group, while it decreased with the increase of SHB prescription concentration ($P < 0.05$; Figure 3(a)). Moreover, flow cytometry, CCK-8, and western blotting results indicated that the overexpression of miR-511-3p accelerated cell cycle, promoted proliferation, and inhibited apoptosis of FRTL-5 and Htori-3, but SHB prescription reversed it in concentration-dependent manner ($P < 0.05$; Figures 3(b)–3(e)). Hence, SHB prescription suppressed proliferation and promoted apoptosis of thyroid cells as observations in more cells in G_1 phase and less cells in G_2/M phase through downregulated expression of miR-511-3p.

3.4. Relationship between miR-511-3p, PTEN, and PI3K/Akt Pathway. The target genes of miR-511-3p have predicted by using bioinformatics. PTEN aroused our great interest, and the binding sites are shown in Figure 4(a). In order to confirm the relationship between miR-511-3P and PTEN, a dual luciferase reporter gene assay was carried out, and the results revealed that the luciferase activity of PTEN-WT was markedly reduced in miR-511-3p mimics ($P < 0.05$), but the luciferase activity of PTEN-MUT had no significant different between NC and miR-511-3p mimics group ($P > 0.05$; Figure 4(b)). Besides, western blotting indicated that the overexpression of miR-511-3p significantly reduced the expression of PTEN protein ($P < 0.05$; Figure 4(c)), in addition, both overexpression of miR-511-3p and knockdown of PTEN activated PI3K/Akt pathway, while overexpression of PTEN inhibited PI3K/Akt pathway and relaxed the activation of PI3K/Akt pathway caused by overexpression of miR-511-3p ($P < 0.05$; Figure 4(d)). These results indicated that miR-511-3p targeted PTEN and regulated PI3K/Akt pathway in thyroid cells.

3.5. SHB Prescription Effected Proliferation and Apoptosis of Thyroid Cells through Regulated miR-511-3p/PTEN/PI3K/Akt Pathway. Aimed to clarify whether SHB prescription regulated proliferation and apoptosis of thyroid cells through miR-511-3p/PTEN/PI3K/Akt pathway, we first activated PI3K/Akt pathway by using 740 Y–P and then treated with SHB prescription, transfected miR-511-3p inhibitor or pcDNA-PTEN into FRTL-5 and Htori-3 and then measured the expression of protein related to PI3K/Akt pathway ($P < 0.05$; Figure 5(a)) and apoptosis ($P < 0.05$; Figure 5(e)) by western blotting, detected cell viability by CCK-8 ($P < 0.05$; Figure 5(c)), and measured cell cycle ($P < 0.05$; Figure 5(b)) and apoptosis rate ($P < 0.05$; Figure 5(d)) by flow cytometry. The results showed that 740 Y–P activated PI3K/Akt pathway in thyroid cells, enhanced cell viability ability, and suppressed cell apoptosis through increased cell in G_2/M phase. However, treatment of SHB prescription, inhibition of miR-511-3p, or overexpression of PTEN reverted these functions. These results indicated that SHB prescription inhibited proliferation and promoted apoptosis of thyroid cells through regulated miR-511-3p/PTEN/PI3K/Akt pathway.

Table 1: Weight changes of rats ($\overline{x} \pm s$, $n = 8$, g).

	Treatment	Concentration	Goiter 1 d	Goiter 14 d	Goiter 28 d	Treatment 28 d
Normal	—	—	188.58 ± 13.5	231.67 ± 21.5	248.67 ± 27.4	297.75 ± 48.4
	Blank	—	200.75 ± 22.7	229.67 ± 30.7	224.67 ± 30.0*	270.42 ± 38.9#
	LST		201.56 ± 13.7	224.33 ± 24.5	235.83 ± 27.6*	287.00 ± 48.7#
Goiter		Light	200.75 ± 16.3	236.17 ± 34.4	227.25 ± 36.8*	276.17 ± 57.4#
	SHB prescription	Moderate	200.42 ± 15.9	235.33 ± 26.4	228.83 ± 27.2*	277.00 ± 41.5#
		High	200.75 ± 19.5	230.17 ± 16.8	228.33 ± 16.7*	280.42 ± 40.4#

*$P < 0.05$ vs. normal group; #$P < 0.05$ vs. Goiter 28 d group.

Table 2: The weight of thyroid and body of rat after treatment ($\overline{x} \pm s$, $n = 8$).

	Treatment	Concentration	Body weight (g)	Thyroid weight (g)	Thyroid coefficient (%)
Normal	—	—	300.88 ± 49.6	0.0496 ± 0.00596	0.0169 ± 0.00362
	Blank	—	281.25 ± 44.2	0.0848 ± 0.01694	0.0306 ± 0.00631***
	LST		287.00 ± 48.79	0.0592 ± 0.0087	0.0207 ± 0.00187*###
Goiter		Light	258.25 ± 45.86	0.0681 ± 0.01069	0.0268 ± 0.00409***ΔΔ
	SHB prescription	Moderate	269.75 ± 41.55	0.0495 ± 0.00751	0.0184 ± 0.00183###Δ
		High	280.25 ± 46.63	0.0522 ± 0.00864	0.0192 ± 0.00472##

*$P < 0.05$ vs. normal group; ***$P < 0.001$ vs. normal group; ##$P < 0.01$ vs. blank group; ###$P < 0.001$ vs. blank group; Δ$P < 0.05$ vs. Goiter + LST group; ΔΔ$P < 0.01$ vs. Goiter + LST group.

4. Discussion

In this study, we found that rat in goiter model could be cured by SHB prescription, and then we explored the molecular mechanism via which SHB prescription promotes apoptosis of thyroid cells. We confirmed that SHB prescription induced downregulation of miR-511-3p and promoted apoptosis of thyroid cells through PTEN/PI3K/Akt pathway. The results suggested that SHB prescription was shown to be a promising therapeutic regimen for the treatment of goiter.

Although, it has been used as a folk medicine for goiter by local people in Yunnan, regrettably, we did not collect enough and complete information about patients in goiter treated with SHB for the report. While, in our study, the results showed that SHB prescription decreased thyroid coefficient, improved thyroid function, and relieved goiter in rat as LST worked. As a synthetic thyroxine, LST is the treatment of choice for hypothyroidism, it also could be used to treat goiter; however, goiter patient treated with LST was diagnosed levothyroxine-induced liver injury, after cessation of LST, liver enzymes gradually returned to normal [17, 18]. Despite a few study found that SHB scavenges reactive oxygen radical species and increases the resistance of low-density lipoprotein to oxidation [19, 20], and there is no any other research on pharmacology of SHB up to now. While, TCM is relatively benign, that suggested SHB prescription might has advantages to goiter patient.

In our study, besides SHB, SHB prescription also included *Scutellaria barbata* D. Don (SBD) and *Hedyotis diffusa* Willd. (HDW). SBD is used in traditional Chinese and Korean medicine as a perennial herb, which has heat-clearing and detoxifying properties [21]. Recent studies have shown that SBD protects oxygen glucose deprivation/reperfusion-induced injuries of PC12 cells [22]. Besides, SBD has shown impressive antitumour activity in cancer [23]. HDW is also a well-known TMC with a variety of activities, especially its anticancer effect in the clinic [24]. The latest study demonstrated that HDW significantly reduced inflammatory lesion and inflammatory cell infiltration in a mouse model of experimental autoimmune prostatitis [25]. In addition, HDW as a complementary therapy is important for the treatment of advanced nasopharyngeal carcinoma patients [26]. Fortunately, our results suggested that SHB prescription effectively inhibited proliferation and promoted apoptosis of thyroid cells by arresting the cell cycle at G_1 phase. As a disease with thyroid enlargement, abnormal proliferation and apoptosis of thyroid cell exist in goiter. Thus, promoting apoptosis and inhibiting proliferation of thyroid cells are an effective method for the treatment of goiter. Therefore, our work further demonstrated that SHB prescription was an ideal technique for the treatment of goiter.

TCMs have been widely used against a broad spectrum of biological activities, and a kind of the underlying mechanism is the regulation of miRNA. Such as downregulation of miR-294 by Baicalin was its key mechanism of action in decreasing embryonic stem cells proliferation [27]. In our study, the overexpression of miR-511-3p in thyroid cells significantly stimulated cell proliferation and restrained cell apoptosis, while SHB prescription reversed it through downregulated expression of miR-511-3p in concentration-dependent manners. Although there was some study reported miR-511-3p involved in regulation of inflammation or progression of cancer [28], it is seldom reported miR-511-3p play a role in thyroid disease. Our study has demonstrated that miR-511-3p promoted proliferation, effected cell cycle, and inhibited apoptosis of thyroid cells, it might a prospective marker of goiter, while the newest research indicated that miR-511-3p is involved in cell cycle, proliferation, and metastasis through regulated AKT3 [29].

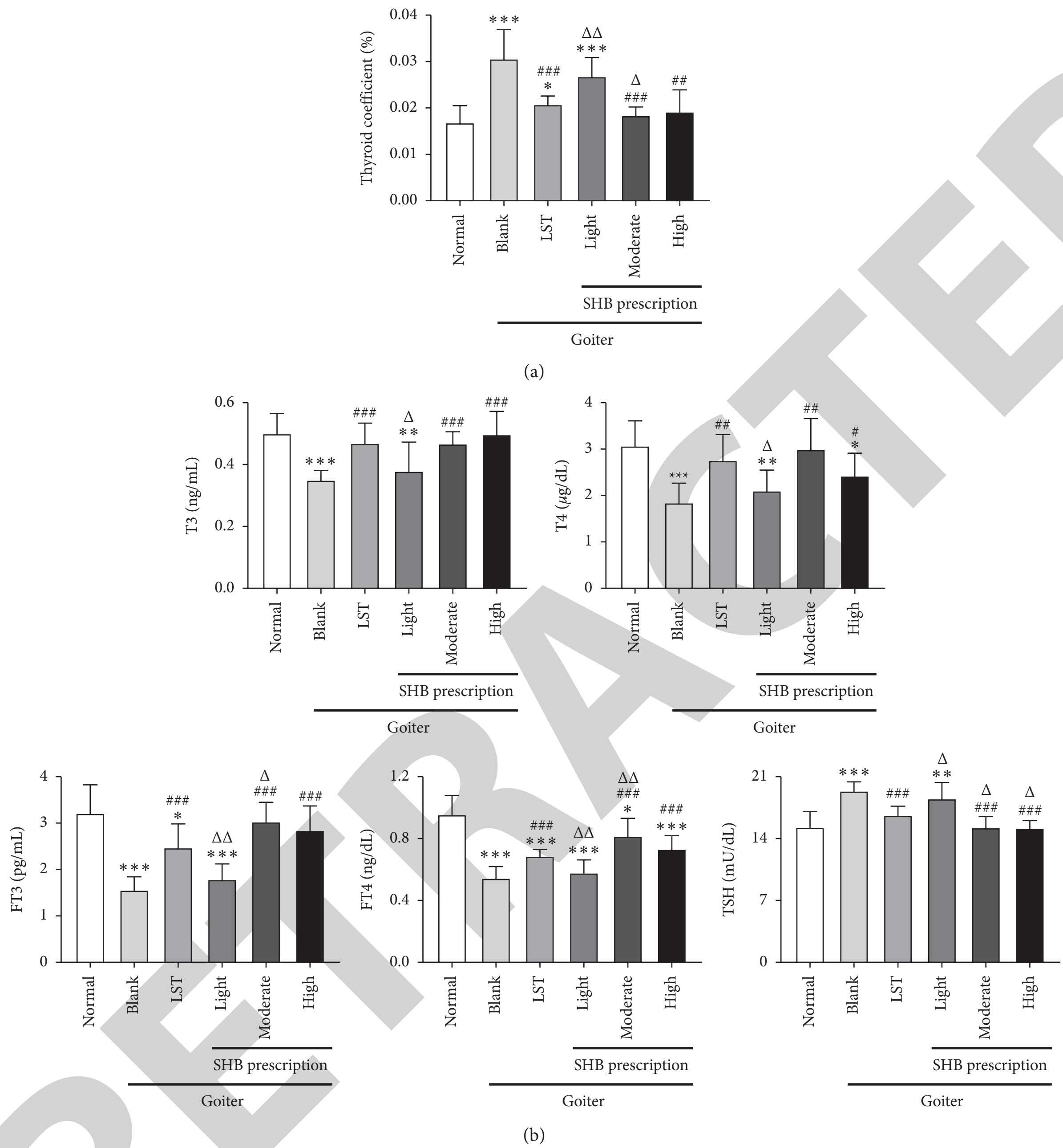

Figure 1: Continued.

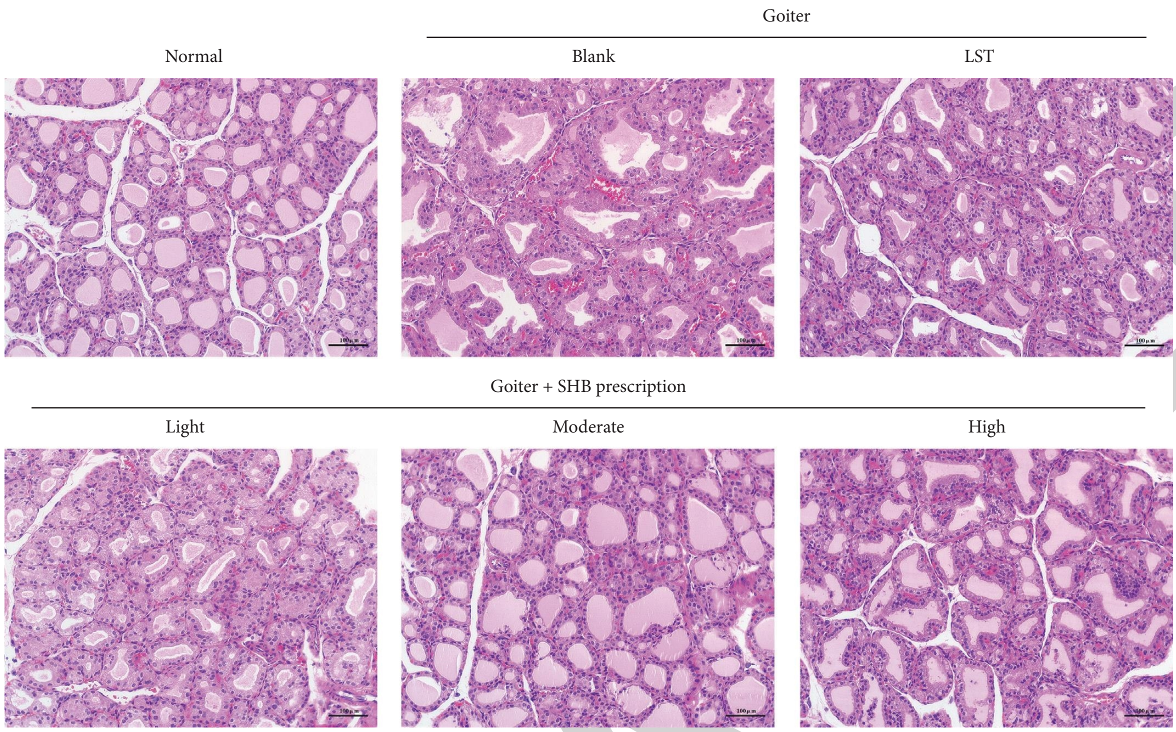

(c)

Figure 1: Effect of SHB prescription on rat in goiter model. (a) Thyroid coefficient of rat. (b) Thyroid function about triiodothyronine (T3), free thyroxine (T4), free triiodothyronine (FT3), free thyroxine (FT4), and thyroid-stimulating hormone (TSH) measured by ELISA. (c) HE staining of thyroid tissues (scale bar = 100 μm). $^{*}P < 0.05$ vs. normal group; $^{**}P < 0.01$ vs. normal group; $^{***}P < 0.001$ vs. normal group; $\#P < 0.05$ vs. blank group; $\#\#P < 0.01$ vs. blank group; $\#\#\#P < 0.001$ vs. blank group; $\Delta P < 0.05$ vs. Goiter + LST group; $\Delta\Delta P < 0.01$ vs. Goiter + LST group.

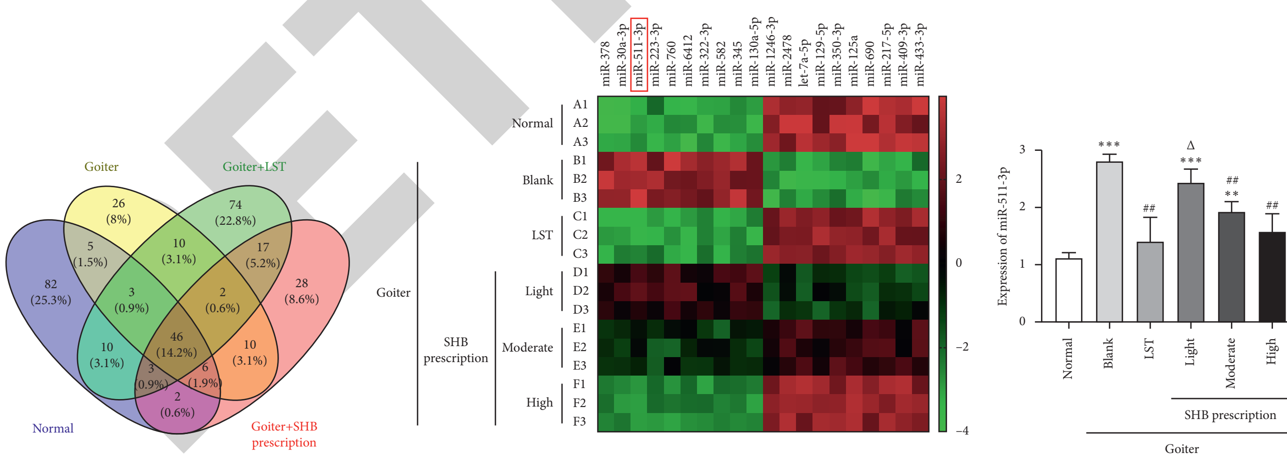

(a) (b) (c)

Figure 2: Regulation of SHB prescription on expression of miRNAs in goiter rat. (a) Venn diagram and (b) Heat map showing abnormally expressed miRNAs. (c) Expression of miR-511-3p measured by RT-qPCT. $^{**}P < 0.01$ vs. normal group; $^{***}P < 0.001$ vs. normal group; $\#\#P < 0.01$ vs. blank group; $\Delta P < 0.05$ vs. Goiter + LST group.

miRNAs take part in the regulation of cell physiological processes through binding its target genes. In our study, miR-511-3p targeting and downregulated the expression of phosphatase and tensin homolog deleted on chromosome ten (PTEN), which is a phosphatase, regulated cell cycle, migration, growth, DNA repair, and survival signaling [30]. It has been found that PTEN plays an important role in thyroid function and disease, and the loss of PTEN resulted in a

Table 3: Selected significantly different miRNAs in SHB prescription treatment compared to other groups.

miRNA	Regulation	Fold change	P value
miR-378	Down	−2.45	0.003
miR-30a-3p	Down	−0.58	0.014
miR-511-3p	Down	−0.25	0.008
miR-223-3p	Down	−0.35	0.021
miR-760	Down	−0.63	0.023
miR-6412	Down	−0.31	0.025
miR-322-3p	Down	−0.34	0.028
miR-582	Down	−0.76	0.022
miR-345	Down	−0.97	0.039
miR-130a-5p	Down	−1.48	0.004
Mir-1246-3p	Up	1.11	0.016
miR-2478	Up	2.05	0.023
Let-7a-5p	Up	0.27	0.039
miR-129-5p	Up	1.51	0.005
miR-350-3p	Up	0.74	0.014
miR-125a	Up	1.12	0.014
miR-690	Up	2.70	0.014
miR-217-5p	Up	1.92	0.020
miR-409-3p	Up	0.73	0.021
miR-433-3p	Up	1.10	0.023

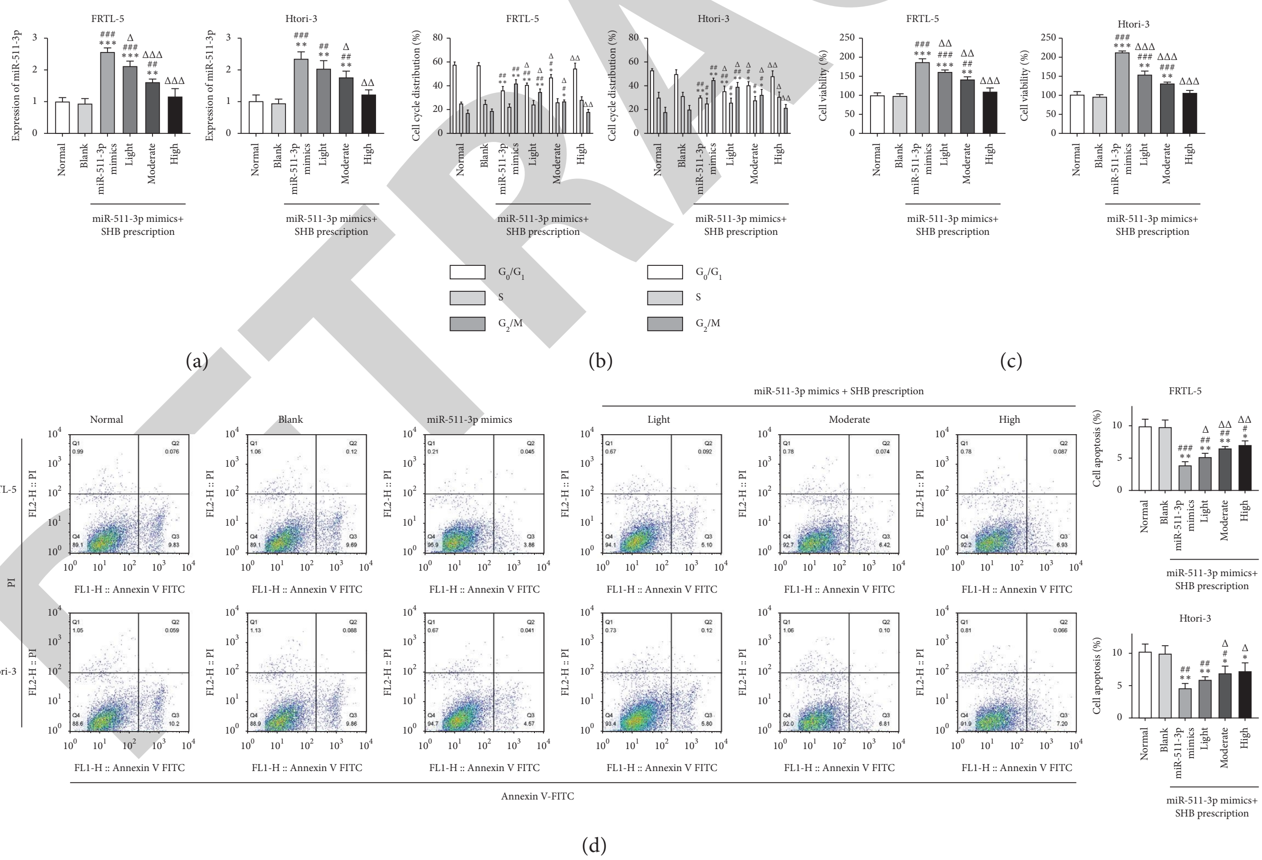

Figure 3: Continued.

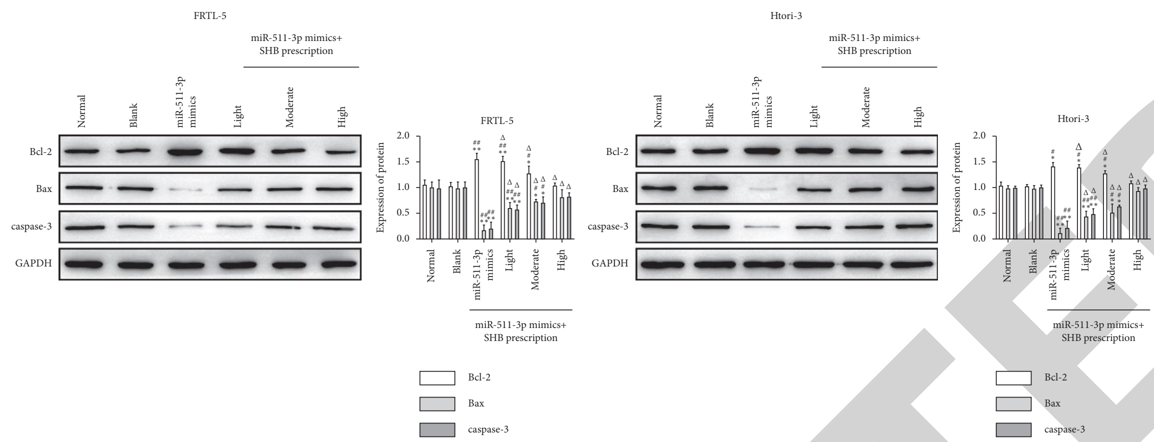

(e)

Figure 3: SHB prescription effected proliferation and apoptosis of thyroid cells through miR-511-3p. (a) Expression of miR-511-3p measured by RT-qPCT. (b) Cell cycle distribution of FRTL-5 and Htori-3 measured by flow cytometry. (c) Cell viability rate of FRTL-5 and Htori-3 measured by CCK-8. (d) Cell apoptosis rate of FRTL-5 and Htori-3 measured by flow cytometry. (e) Expression of apoptosis-related proteins Bcl-2, Bax, and caspase-3 measured by western blotting. $^{*}P < 0.05$ vs. normal group; $^{**}P < 0.01$ vs. normal group; $^{***}P < 0.001$ vs. normal group; $\#P < 0.05$ vs. blank group; $\#\#P < 0.01$ vs. blank group; $\#\#\#P < 0.001$ vs. blank group; $\Delta P < 0.05$ vs. miR-511-3p mimics group; $\Delta\Delta P < 0.01$ vs. miR-511-3p mimics group; $\Delta\Delta\Delta P < 0.001$ vs. miR-511-3p mimics group.

(a)

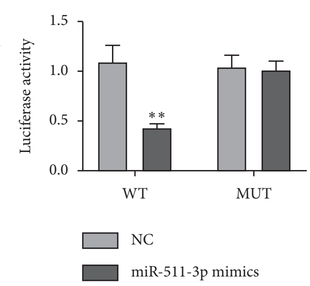

(b)

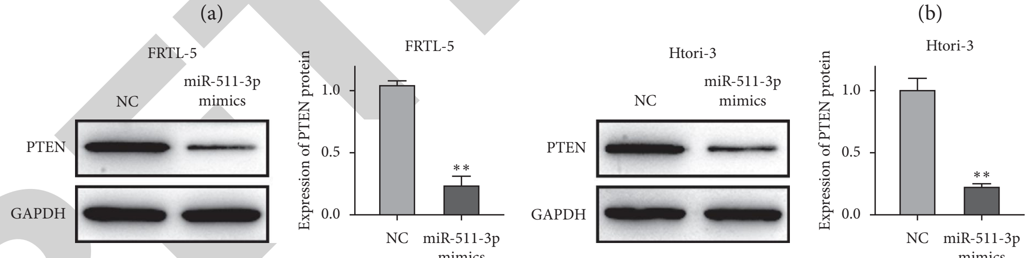

(c)

Figure 4: Continued.

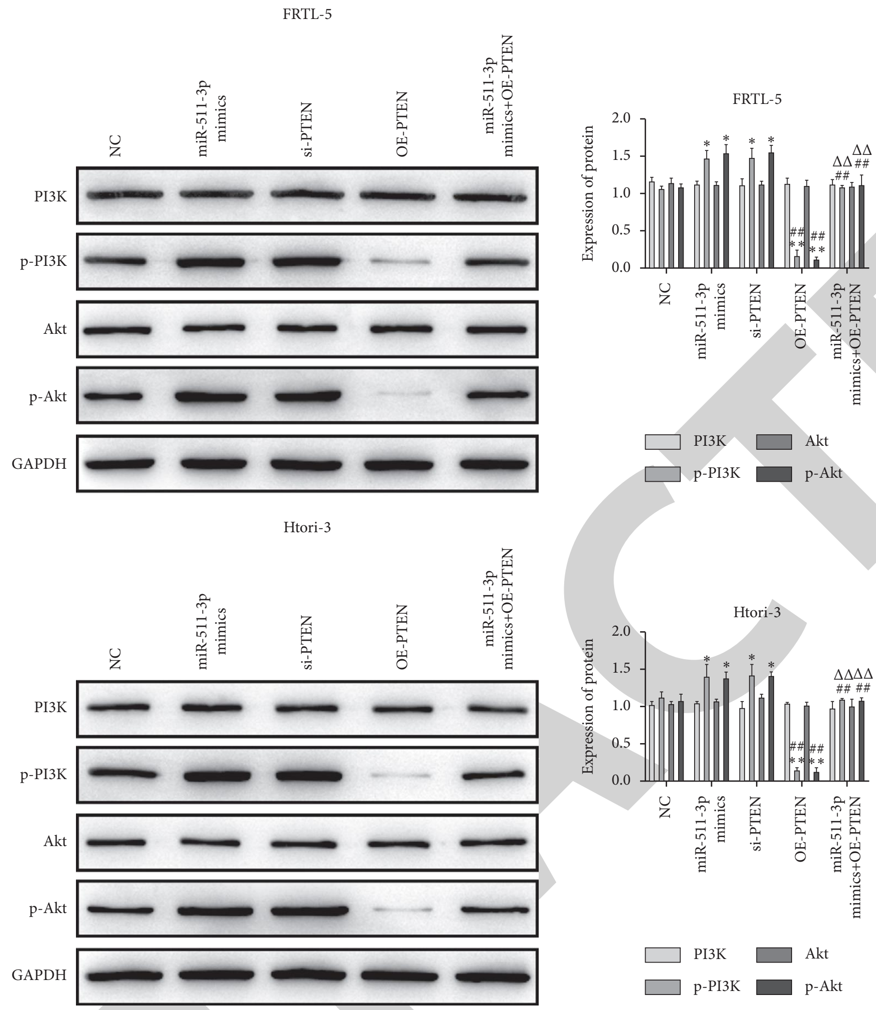

(d)

Figure 4: Relationship between miR-511-3p, PTEN, and PI3K/Akt pathway. (a) Binding sites between miR-511-3p and PTEN. (b) Relationship between miR-511-3p and PTEN verified by dual luciferase reporter gene assay. $^{**}P < 0.01$ vs. NC group. (c) Expression of PTEN protein measured by western blotting. $^{**}P < 0.01$ vs. NC group. (d) Expression of protein in PI3K/Akt pathway.$^{*}P < 0.05$ vs. NC group; $^{**}P < 0.01$ vs. NC group; $\#\#P < 0.01$ vs. miR-511-3p mimics group; $\Delta\Delta P < 0.01$ vs. OE-PTEN group.

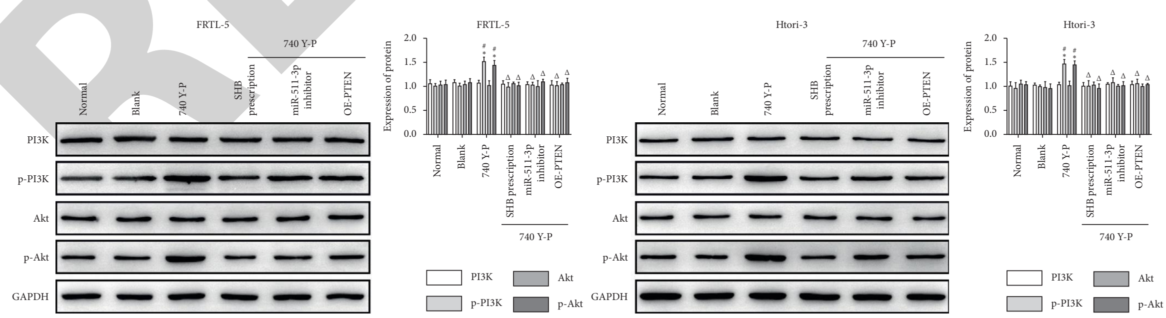

(a)

Figure 5: Continued.

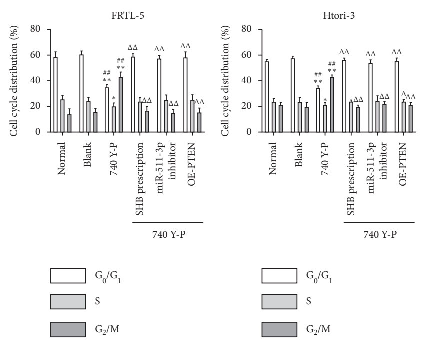

(b)

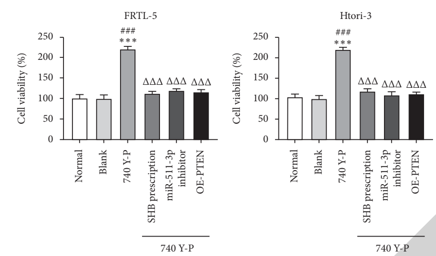

(c)

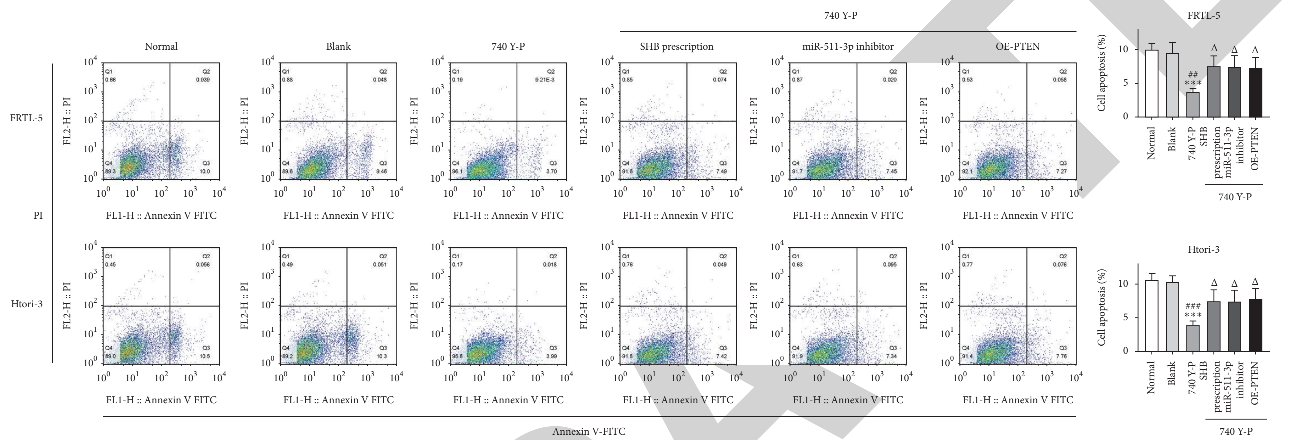

(d)

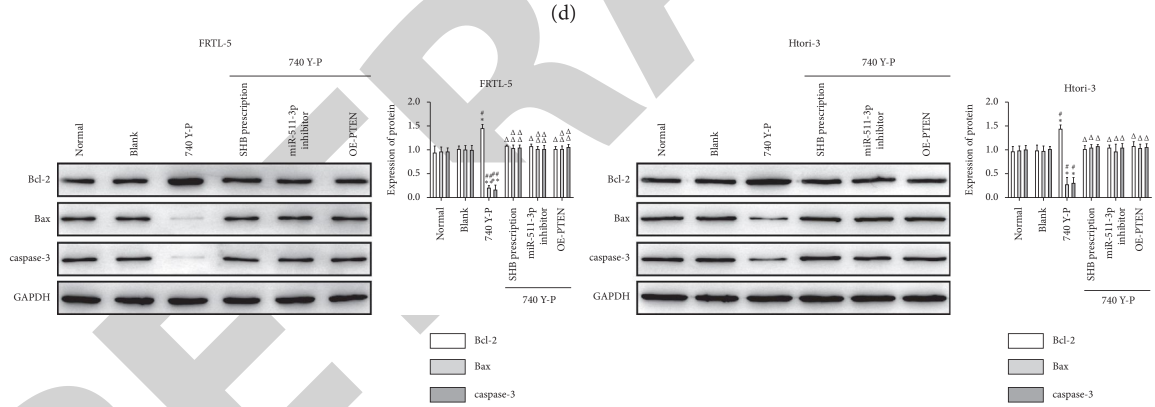

(e)

Figure 5: SHB prescription effected proliferation and apoptosis of thyroid cells through regulated miR-511-3p/PTEN/PI3K/Akt pathway. (a) Protein expression of PTEN measured by western blotting. (b) Cell cycle distribution of FRTL-5 and Htori-3 measured by flow cytometry. (c) Cell viability rate of FRTL-5 and Htori-3 measured by CCK-8. (d) Cell apoptosis rate of FRTL-5 and Htori-3 measured by flow cytometry. (e) Expression of apoptosis-related proteins Bcl-2, Bax, and caspase-3 measured by western blotting. $^*P < 0.05$ vs. normal group; $^{**}P < 0.01$ vs. normal group; $^{***}P < 0.001$ vs. normal group; $\#P < 0.05$ vs. blank group; $\#\#P < 0.01$ vs. blank group; $\#\#\#P < 0.001$ vs. blank group; $\Delta P < 0.05$ vs. 740 Y–P group; $\Delta\Delta P < 0.01$ vs. 740 Y–P group; $\Delta\Delta\Delta P < 0.001$ vs. 740 Y–P group.

significant increase in the thyrocyte proliferative index [31]. PTEN serves as a negative regulator of phosphatidylinositol-3-kinase (PI3K)/Akt signaling pathway, which is an important regulator of many cellular events, including apoptosis, proliferation, and motility [32]. Our results fund that the activation of PI3K/Akt signaling pathway enhanced proliferation and inhibited apoptosis of thyroid cells, while SHB prescription treatment, miR-511-3p inhibition, or PTEN overexpression reversed these effects. Interestingly, PTEN is a tumor suppressor gene mutated in many human cancers [33], and the loss of PTEN function leads to activation of PI3K/Akt signaling pathway and is strongly associated with progression of cancer [34]. Therefore, our result might suggest that SHB prescription not only help to treat goiter but also may have the effect of preventing thyroid cancer.

In summary, our results showed that were found to cure rat in goiter model and downregulated miR-511-3p in thyroid tissues and cells in concentration-dependent manner. Besides, there was a target relationship between miR-511-3p and PTEN in thyroid cells, and PTEN negatively regulated the activation of PI3K/Akt signaling pathway. Furthermore, the inhibition of apoptosis in thyroid cells caused by overexpression of miR-511-3p or activation of PI3K/Akt signaling pathway was reversed by treatment of SHB prescription, inhibition of miR-511-3p, or overexpression of PTEN. Therefore, our results indicated that SHB prescription promoted apoptosis of thyroid through decreased miR-511-3p and regulated PTEN/PI3K/Akt pathway.

The greatest regret of this study is that not enough and complete data of SHB prescription treated goiter patient were collected. Besides, the function of miR-511-3p and PTEN/PI3K/Akt pathway in the treatment of SHB prescription in goiter rat are performing now. Importantly, our study confirmed that SHB prescription not only help to treat goiter but also may prevent thyroid cancer; thus, research on SHB is warranted.

5. Conclusion

This study demonstrated that SHB prescription relieved goiter through inhibited proliferation and promoted apoptosis of thyroid cells via downregulated miR-511-3p and PTEN/PI3K/Akt pathway.

Abbreviations

SHB: *Sageretia hamosa brongn*
PTU: Propylthiouracil
T3: Triiodothyronine
T4: Free thyroxine
FT3: Free triiodothyronine
FT4: Free thyroxine
TSH: Thyroid-stimulating hormone
TCM: Traditional Chinese medicine
miRNA: MicroRNA
LST: Levothyroxin sodium tablets
HE: Hematoxylin-eosin
RT-qPCR: Reverse transcription-quantitative polymerase chain reaction
CCK-8: Cell Count Kit-8
FITC: Fluorescein isothiocyanate
UTR: Untranslated regions
WT: Wild type
MUT: Mutant type
PTEN: Phosphatase and tensin homolog deleted on chromosome ten
PI3K: Phosphatidylinositol-3-kinase
SBD: *Scutellaria barbata* D. Don
HDW: *Hedyotis diffusa* willd.

Data Availability

The simulation experiment data used to support the findings of this study are available from the corresponding author upon request.

Conflicts of Interest

The authors declare that there are no conflicts of interest regarding the publication of this paper.

Authors' Contributions

Yang-lin Deng and Su Chen contributed equally to this work.

Acknowledgments

This work was supported in part by the National Natural Science Foundation of China (Grant no. 41964007).

References

[1] J.-L. Wémeau, "Prise en charge thérapeutique des goitres," *La Presse Médicale*, vol. 40, no. 12, pp. 1147–1154, 2011.
[2] L. J. Hofland and S. W. J. Lamberts, "Somatostatin receptors and disease: role of receptor subtypes," *Baillière's Clinical Endocrinology and Metabolism*, vol. 10, no. 1, pp. 163–176, 1996.
[3] P. Bel Lassen, A. Kyrilli, M. Lytrivi, and B. Corvilain, "Graves' disease, multinodular goiter and subclinical hyperthyroidism," *Annales d'Endocrinologie*, vol. 80, no. 4, pp. 240–249, 2019.
[4] G. W. Randolph, J. J. Shin, H. C. Grillo et al., "The surgical management of goiter: part II. surgical treatment and results," *The Laryngoscope*, vol. 121, no. 1, pp. 68–76, 2011.
[5] H. Luo, M. Lü, X. Pei, and Z. Xia, "Chinese herbal medicine for subacute thyroiditis: a systematic review of randomized controlled trials," *Journal of Traditional Chinese Medicine*, vol. 34, no. 3, pp. 243–253, 2014.
[6] L. Liu, M. Heinrich, S. Myers, and S. A. Dworjanyn, "Towards a better understanding of medicinal uses of the brown seaweed Sargassum in Traditional Chinese Medicine: a phytochemical and pharmacological review," *Journal of Ethnopharmacology*, vol. 142, no. 3, pp. 591–619, 2012.
[7] M. L. Yang and B. Lu, "Treatment of goiter with traditional Chinese medicine regimen xing Qi Hua ying Tang: a clinical study on 72 patients with multinodular and diffuse goiter," *Journal of Alternative and Complementary Medicine (New York, N.Y.)*, vol. 24, no. 1, pp. 374–377, 2018.
[8] Y. Zhang, Y. Li, X. Mao et al., "Thyroid hormone synthesis: a potential target of a Chinese herbal formula Haizao Yuhu Decoction acting on iodine-deficient goiter," *Oncotarget*, vol. 7, no. 32, pp. 51699–51712, 2016.
[9] D. Liu, F. Chen, X. Yu et al., "Do different species of sargassum in Haizao Yuhu decoction cause different effects in a rat goiter model?" *Evidence-Based Complementary and Alternative Medicine*, vol. 2019, Article ID 5645620, 19 pages, 2019.
[10] T. K. Hyun, S. C. Song, C.-K. Song, and J.-S. Kim, "Nutritional and nutraceutical characteristics of Sageretia theezans fruit," *Journal of Food and Drug Analysis*, vol. 23, no. 4, pp. 742–749, 2015.
[11] J. M. Riesco, J. A. Juanes, J. Carretero et al., "Cell proliferation and apoptosis of thyroid follicular cells are involved in the involution of experimental non-tumoral hyperplastic goiter," *Anatomy and Embryology*, vol. 198, no. 6, pp. 439–450, 1998.
[12] H. Undeutsch, C. Löf, P. Pakarinen, M. Poutanen, and J. Kero, "Thyrocyte-specific Dicer1 deficiency alters thyroid follicular organization and prevents goiter development," *Endocrinology*, vol. 156, no. 4, pp. 1590–1601, 2015.

Hindawi
Journal of Healthcare Engineering
Volume 2021, Article ID 9577440, 10 pages
https://doi.org/10.1155/2021/9577440

Research Article

Values of Contrast-Enhanced Ultrasound in Classification and Diagnosis of Common Bile Duct and Superficial Organ Lesions under Compression Algorithm

Yezhao Li, Caihong Zhao, Minpei Qin, Xia Zhang, Haizhen Liao, and Haiqing Su

Department of Ultrasound, Minzu Hospital of Guangxi Zhuang Autonomous Region, Affiliated Minzu Hospital of Guangxi Medical University, Nanning 530001, China

Correspondence should be addressed to Haizhen Liao; 1807400101@e.gzhu.edu.cn

Received 27 June 2021; Accepted 8 September 2021; Published 29 September 2021

Academic Editor: Enas Abdulhay

This work aimed to investigate values of contrast-enhanced ultrasound (CEUS) under DEFLATE in the classification and diagnosis of the common bile duct and superficial lymphoid lesions. 88 patients with lower common bile duct lesions and 126 patients with superficial lymphoid lesions were selected as the subjects investigated and examined by CEUS under DEFLATE to compare characteristics and diagnostic efficiency of CEUS in different types of lesions. The time-intensity curve (TIC) was for quantitative analysis on CEUS results. The results showed that there were statistically significant differences in the comparison of time to peak (TTP), area under the curve (AUC), and gradient (Grad) of common bile duct walls in patients from the malignant group ($P < 0.05$), while the comparison of three indicators of patients in the benign group was not statistically remarkable ($P > 0.05$). In addition, there were statistically great differences in TTP, AUC, and Grad among patients in the benign and malignant groups ($P < 0.05$). The sensitivity, specificity, accuracy, and positive/negative predictive value of CEUS + ultrasound (US) in the diagnosis of benign and malignant lymph nodes were 92.83%, 87.14%, 89.54%, 91.23%, and 86.43%, respectively. The values of maximal intensity ($I_{\max}$) in the reactive hyperplasia group (group A), lymphoma group (group B), and metastatic lymph nodes group (group C) were compared, showing statistical differences ($P < 0.05$). The TTP and AUC of group B were higher than those of groups A and C, respectively ($P < 0.05$), and the base-to-peak ascending slope (K_{UP}) and the absolute value of the semidescending slope (K_{DOWN}) in group C increased hugely compared to group A ($P < 0.05$). It indicated that CEUS examination under DEFLATE could be applied in the qualitative diagnosis of lower common bile duct lesions and superficial lymphoid lesions, which was worthy of clinical application.

1. Introduction

The lesions located in the lower common bile duct usually include a variety of lesions such as stone inflammatory stenosis and tumor, which often cause biliary obstruction [1]. Compared with other imaging diagnostic methods, US examination has become the preferred method for obstruction lesions due to its convenient operation and low cost. Although the conventional US can also play an important role in the diagnosis of lower common bile duct lesions, it is easy to be affected by gastrointestinal gas; thus, it is difficult to give an accurate assessment of lower common bile duct lesions. Contrast-enhanced ultrasound (CEUS) is a new examination technology developed based on US technology, which is a major innovation of US technology [2]. With the rapid development of US contrast agents, liver, kidney, and bile duct imaging has been greatly enhanced by CEUS, and CEUS is now widely applied in abdominal and small organ diseases [3, 4]. CEUS technology can not only increase the display rate of lower common bile duct lesions but also clearly observe the enhancement speed and intensity of tissues or tumors. It is a critical tool to assist doctors in the diagnosis of lower common bile duct lesions. Therefore, the identification of lower common bile duct lesions with CEUS technology can provide more accurate and valuable information for subsequent clinical treatment and survival prognosis assessment. CEUS was first used for the diagnosis and differentiation of liver or heart diseases. Due to its continuous development and maturity, CEUS is gradually applied to the diagnosis of superficial organ lesions, such as thyroid, breast, and lymph node [5, 6]. There are differences in pathophysiological basis on different types of lymphoid lesions, the differentiation of benign and malignant lymph nodes is of great significance for the diagnosis and prognosis analysis of tumor diseases, and US examination is the preferred diagnostic method for superficial lymphoid lesions [7]. CEUS has a marked advantage in the qualitative study of benign and malignant enlarged lymph nodes in contrast to the conventional US and Doppler US imaging. The blood perfusion and microvascular distribution in lymph nodes can be observed clearly and in real time through CEUS, which provides more abundant information for doctors' subsequent diagnosis [8]. Thus, the classification and differentiation of lower common bile duct lesions and superficial lymphoid lesions by CEUS have great meanings for the clinical diagnosis of this disease and the selection of subsequent treatment options.

Data compression refers to the application of an appropriate data compression algorithm to process redundant data, so as to achieve data compression, which can not only increase the internal storage space of the device but also extend the working time to effectively improve the detection efficiency of the device [9]. Therefore, US data compression is one of the key links to promote the working efficiency of US equipment. Lossless compression means that complete original data information is retained during data compression without loss of information, and the decompression algorithm can be adopted to recover the original data, which is suitable for all kinds of scenarios requiring the retention of ultrasonic detailed data [10]. As a lossless compression algorithm, DEFLATE is an improved version of Lempel-Ziv 1977 compression format (LZ77), which is widely applied in a variety of real-time compression scenarios.

Therefore, DEFLATE was employed to compress CEUS data and analyze its compression performance and speed. Moreover, patients with lower common bile duct lesions and superficial lymphoid lesions were selected as the subjects investigated, respectively. By analyzing characteristics and diagnosis efficiency of different pathological types in CEUS, the application value of classification and diagnosis for abdominal and superficial organs were further discussed under DEFLATE of CEUS.

2. Materials and Methods

2.1. Contrast-Enhanced Ultrasound Diagnosis of Lower Common Bile Duct Lesions. A total of 88 patients with lower common bile duct lesions, admitted to the hospital from October 2018 to October 2019, were selected and grouped into a benign group (32 patients) and a malignant group (56 patients) based on the pathological results. Meanwhile, 30 healthy volunteers were selected and grouped into a control group. The criteria for inclusion were defined to include patients who had more than 5 mm maximum diameter of lesion, had received US examination, had good image quality, and were able to cooperate with doctors to complete the examination of respiration, posture, and so on. The criteria for exclusion were defined to include patients younger than 18 years or older than 80 years, suffering from pulmonary insufficiency, in pregnancy or lactation period, and allergic to the contrast agent. This experiment had been approved by the Ethics Committee of the hospital, and all the patients contained in the experiment had known about the experiment and agreed to it.

Patients drank 1,000 mL of water before the examination. Their lesion sites were scanned by conventional US and color Doppler US to observe the morphology, size, echo characteristics, and surrounding tissues of lesion sites. After that, CEUS mode was activated, and patients were instructed to breathe calmly to ensure the quality of the obtained best sections of contrast-enhanced imaging. Sulfur hexafluoride was selected as the contrast agent, and 0.9% sodium chloride (NaCl) was added into it to prepare suspension that was extracted 1.5 mL each time. When the timing of the instrument was started, an appropriate amount of contrast agent was quickly injected into the peripheral vein. Patients held their breath for 10 seconds before the arterial phase and breathed calmly for 10 seconds after the arterial phase. When the contrast agent completely subsided, the observation was stopped and the dynamic graphs within 120 seconds were stored.

TIC was used for the quantitative analysis of CEUS in and around the lesions. The region of interest (ROI) was selected and delineated based on lesion size. TIC were drawn to record various indicators by the instrument's own CEUS software. Three indicators, namely, TTP, AUC, and Grad, were selected for subsequent analysis.

2.2. Superficial Lymphoid Lesions Diagnosed by Contrast-Enhanced Ultrasound. 126 patients with superficial lymphoid lesions, admitted to the hospital from October 2018 to October 2019, were selected to undergo US examination. There were 72 males and 54 females with an average age of 51.25 ± 15.26 years. The experiment had been approved by the Ethics Committee of the hospital, and all patients included in the study had signed informed consent. The criteria for inclusion were patients who were over 18 years old, had contraindication of CEUS, and had pathological results that were obtained by a needle biopsy or surgery. The criteria for exclusion were patients who had poor-quality CEUS images, were observed for less than 90 seconds through CEUS, had incomplete pathological results, and did not suffer from tuberculosis in TIC analysis.

All the patients had conventional US examination in advance, to mainly observe the grayscale of the target lymph nodes and color Doppler ultrasonic characteristics. After that, the patients had a CEUS examination combined with low mechanical index imaging technology. Besides, the mechanical index was set within the range of 0.03–0.07, and posterior lymph nodes were regarded as the focus of the image. Contrast agent SonoVue was selected, which had a white freeze-drier power shape, to be added with normal saline for adequate dissolution, to prepare emulsion microbubble suspension. 2.5 mL of the contrast agent was injected into the median vein of a patient, and then, 10 mL of normal saline was applied to rapidly wash pipe. A timer was started as soon as the beginning of contrast agent injection, dynamic image with the length of about 3 minutes was obtained and stored. Two experienced sonographers were selected to diagnose lymph nodes as benign or malignant based on the ultrasonic image. The patients were divided into a benign group (including group A and a tuberculous lymphadenitis group (group D)) and a malignant group (including groups B and C) based on the criteria of US-mediated puncture or surgery, to calculate their sensitivity, specificity, accuracy, and positive/negative predictive values.

SonoLiver software was applied to analyze the CEUS images, and lymph nodes were regarded as ROI to draw TIC, to obtain indexes such as RT, TTP, mean transit time (mTT), and $I_{\max}$. In addition, K_{UP} and K_{DOWN} were calculated, and AUC was obtained by Qontra Xt software.

2.3. Lossless Compression Algorithm of Ultrasonic Data. Ultrasonic data should be preprocessed before compression. According to different classification characteristics of ultrasonic data, preprocessing methods were also different. The grass wave data were preprocessed with smooth processing, and the defect wave data were preprocessed with differential processing. After the grass wave data were smoothed, the signal became smoother, the burr decreased, and the information entropy of the grass wave signal decreased accordingly, to facilitate the subsequent compression processing operation. If two peaks met the requirements and the directions of two adjacent peaks were opposite, the principle of "appear first, process first" was followed. After the first peak was smoothed, the second peak would disappear. The method of differential processing was for the defect wave. The amplitude value range of defect wave was relatively wide and the data information entropy was relatively large. After differential processing, the signal amplitude information was converted into the amplitude change information, as shown in

$$M(i) = \begin{cases} A(i) - A(i-1), & i > 1, \\ A(i), & i = 1. \end{cases} \tag{1}$$

In equation (1), A represents the original signal, M stands for the processed signal, and i expresses the signal number.

The calculation method of data information entropy is shown as follows:

$$S(i) = -\sum_{i} P(X_i)\log_2 P(X_i). \tag{2}$$

In equation (2), S stands for the information entropy and P and $-\log_2 P(X_i)$ express probability and self-information of X_i, respectively.

DEFLATE was mainly composed of two coding methods (Huffman and LZ77), and the coding process is shown in Figure 1. After the raw data was entered, LZ77 encoding was first applied to generate Literal, Distance, and Length. Then, Huffman coding was employed to compress and process Distance elements to obtain DIST data rate and corresponding Huffman code table. Literal and Distance elements were combined to adopt the same operation as Distance elements to obtain LIT data rate and corresponding Huffman data table. After that, the Huffman data table was compressed, CL sequence was adopted, and SQ sequence was obtained after CL run-length coding. After its coding was compressed, the SQ data rate and the corresponding Huffman code table were obtained, and the CCL data rate was obtained after further processing.

The evaluation criteria for compression algorithms included compression ratio (CR), relative root mean squared error (R^2MSE), algorithm complexity, and correlation coefficient r. CR referred to the proportion of the number of bytes after compression in the number of bytes of raw data, and the following equation could be adopted to calculate CR:

$$\mathrm{CR} = \frac{N_{\text{after}}}{N_{\text{before}}} \times 100\%. \tag{3}$$

R^2MSE represents that the difference between compressed restored data and raw data, as shown in the following equation:

$$\mathrm{R}^2\mathrm{MSE} = \sqrt{\frac{\sum_{i=0}^{N} \left(X(i) - X'(i)\right)^2}{\sum_{i=1}^{N} X^2(i)}} \times 100\%. \tag{4}$$

In equation (4), $X(i)$ and $X'(i)$ stand for the raw restored data and compressed restored data, respectively.

r expresses the correlation between the restored data and raw data after compression, which is represented as follows:

$$r = \frac{E\left(X(i)X'(i)\right) - E\left(X(N)X'(i)\right)}{\sqrt{D\left(X(i)\right)}\sqrt{D\left(X'(i)\right)}}. \tag{5}$$

In equation (5), $E(X)$ and $D(X)$ represent mathematical expectation and variance, respectively.

CR, R^2MSE, and r are all evaluation indexes at the mathematical level. However, the evaluation of compression algorithm complexity was indispensable in practical application, and indirect quantization representation was usually expressed by compression speed and decompression speed.

2.4. Statistical Analysis. SPSS20.0 software was used for statistical analysis. The measurement data were expressed as mean ± standard deviation, and t-test was adopted to compare the differences among the groups. Besides, the measurement data were represented as percentage, and the χ^2 test was applied to compare the differences among the groups. If $P < 0.05$, the difference was statistically significant.

3. Results

3.1. Results of Data Compression Examined by Ultrasound under Compression Algorithm. The run-length encoding (RLE) [11], Huffman [12], and DEFLATE were employed to

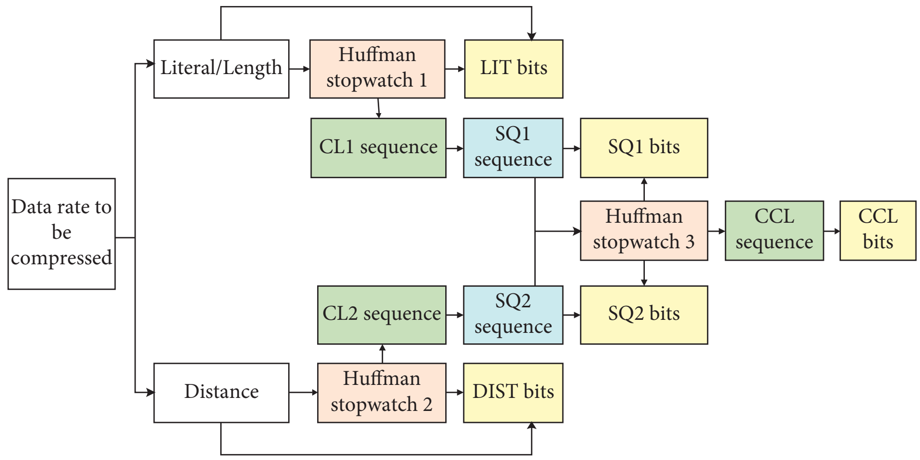

Figure 1: Flowchart of DEFLATE.

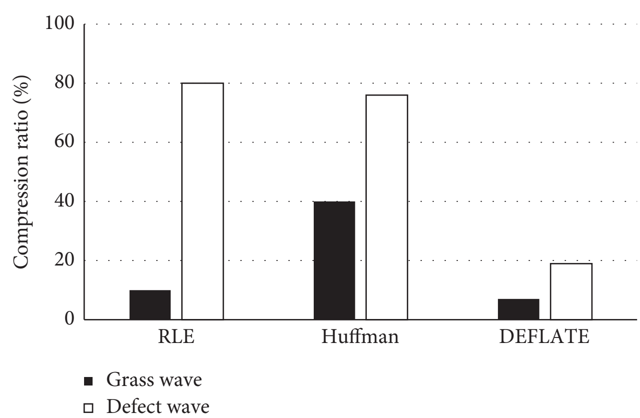

Figure 2: Comparison of compression performance of different algorithms.

compress grass wave and defect wave data. Figure 2 shows that CR of defect wave data obtained by different algorithms was higher than the ratio of grass wave data. The CR of grass wave data processed by RLE was markedly better than the ratio of defect wave data; CR of defect wave data processed by DEFLATE was the lowest; and CR of grass wave data processed by Huffman was the highest. Based on the above results, the compression effect of DEFLATE was better than the other two algorithms.

Under the two different platforms, the compression speed of each algorithm was lower than its decompression speed, and both the compression and decompression speed of RLE were the highest, while both the compression and decompression speed of DEFLATE were the lowest, as shown in Figure 3.

To sum up the above results, the speed of RLE, Huffman, and DEFLATE could all meet the real-time compression requirements in the personal computer (PC) platform, so DEFLATE with the best CR was selected. For the embedded platform, the compression speed of DEFLATE was too low to meet the requirements of real-time compression. Therefore, a balanced algorithm combination was selected; namely, RLE and DEFLATE were applied to compress grass wave and defect wave data, respectively.

3.2. The Contrast-Enhanced Ultrasound + Ultrasound Diagnosis of Lower Common Bile Duct Lesions. The results of patients' conventional US examination revealed that the lesions were located in the lower segment of the common bile duct, and lesions were $8 \times 8 \times 8\,mm^3$–$30 \times 32 \times 32\,mm^3$ with an average size of 15.6 ± 6.4 mm and a maximum diameter of 10–32 mm. The average maximum diameter of lesions was 22.3 ± 8.5 mm in patients from the malignant group, and there were 12 patients with isoechoic or hyperechoic and 44 patients with hypoechoic. The average maximum diameter of lesions in patients from the benign group was 13.8 ± 8.3 mm with 8 patients of hyper echo and 24 patients of hypo echo.

In the benign group, the lesions of 5 patients showed high enhancement in the arterial phase, among which lesions of 4 patients expressed synchronous regression in the venous phase compared with the bile duct wall and the lesion of 1 patient had a faster clearance rate compared to the bile duct wall and showed low enhancement. There were lesions of 23 patients representing isoenhancement in the arterial

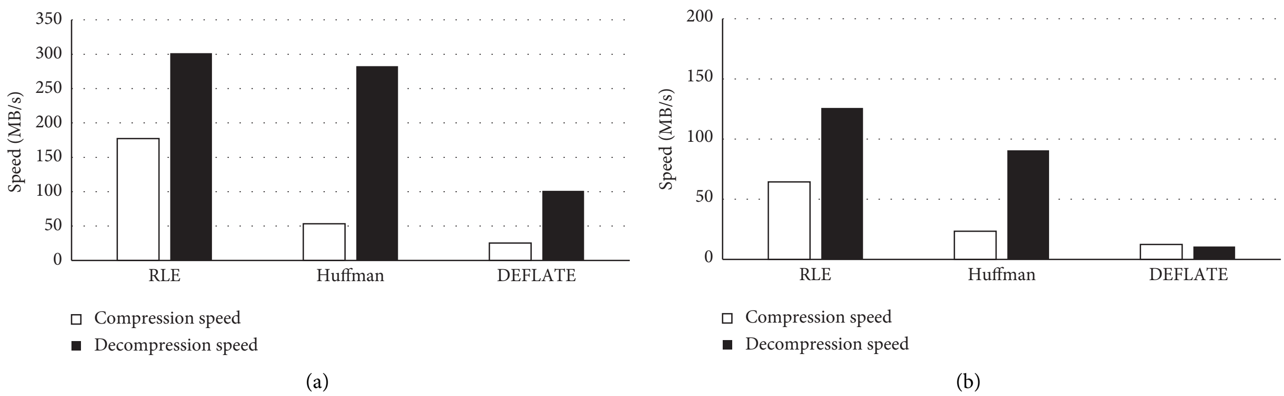

Figure 3: Comparison of the performance of different compression algorithms in the two different platforms. (a, b) The comparison of the performance of 3 compression algorithms in the PC and embedded platform.

phase, among which lesions of 19 patients had the clearance rate synchronized with the bile duct wall and expressed isoenhancement, and lesions of 4 patients had faster clearance rate compared with the bile duct wall in the venous phase and showed low enhancement, as shown in Figure 4(a).

In the malignant group, the lesions of 26 patients presented high enhancement in the arterial phase, among which lesions of 24 patients presented low enhancement in the venous phase and showed faster clearance in contrast to the bile duct wall, and lesions of 2 patients presented isoenhancement and had clearance synchronized with the common bile duct wall. There were lesions of 4 patients with isoenhancement in the arterial phase, lesions of 2 patients with low enhancement in the venous phase, and lesions of 2 patients with isoenhancement in the venous phase. In both phases, lesions of 3 patients showed low enhancement (Figure 4(b)).

The comparison results of CEUS indicators (TTP, AUC, and Grad) between lesions of patients in the benign group and surrounding bile duct walls are shown in Figure 5. The differences in CEUS indicators (TTP, AUC, and Grad) between lesions of patients in the benign group and surrounding bile duct walls were not marked with statistically obvious meanings ($P > 0.05$). Figure 6 indicates the comparison results of CEUS indicators (TTP, AUC, and Grad) between lesions in the malignant group and surrounding bile duct walls. The TTP of lesions in the malignant group was remarkably lower than that of the surrounding bile duct walls ($P < 0.05$), while AUC and Grad of lesions in the malignant group were greatly higher than those of the surrounding bile duct wall ($P < 0.05$).

The comparison of CEUS indicators (TTP, AUC, and Grad) among patients in the benign and malignant group is shown in Figure 7. TTP of patients in the malignant group was sharply lower than that of the benign group ($P < 0.05$), while AUC and Grad of patients in the malignant group were dramatically higher than those of the benign group ($P < 0.05$). Figure 8 illustrates the results of comparison of CEUS indicators (TTP, AUC, and Grad) of surrounding bile duct walls in patients from the control, benign, and malignant group. Besides, the comparison of TTP, AUC, and Grad of surrounding bile duct walls in patients from the three groups was not statistically substantial ($P > 0.05$).

3.3. Superficial Lymphoid Lesions Diagnosed by Contrast-Enhanced Ultrasound + Ultrasound. Pathological results demonstrated 126 patients with superficial lymphoid lesions including 52 patients in the benign group (18 patients with tuberculous lymphadenitis and 34 patients with reactive hyperplasia) and 74 patients in the malignant group (23 patients with lymphoma and 51 patients with metastatic lymph nodes). Table 1 shows the sensitivity, specificity, accuracy, and positive/negative predictive values diagnosed by CEUS. Moreover, the CEUS images of superficial lymphoid lesions are shown in Figure 9. In the benign group, the image of a patient with reactive hyperplasia shows uniform enhancement (Figure 9(a)) from center to periphery (Figure 9(b)). Figure 9(f) indicates that the image of a patient with tuberculous lymphadenitis presents uneven circular enhancement. In the malignant group, the image of a patient with metastatic lymph nodes shows the enhancement from periphery to center (Figure 9(c)) and manifested as a nonhomogeneous enhancement (Figure 9(d)), while the image of a patient with lymphoma presents as mixed enhancement with snowstorm shape (Figure 9(e)).

Figure 10 demonstrates that the RT and mTT of patients in groups A, B, and C were not extremely different ($P > 0.05$), while there was statistical meaning in I_{max} of the three groups ($P < 0.05$). TTP of patients in group B was higher than that of group C ($P < 0.05$). K_{UP} and K_{DOWN} of the patients in group C increased obviously in contrast to group A ($P < 0.05$), and AUC of the patients in group C was significantly higher than the value of groups A and B ($P < 0.05$), as shown in Figure 11.

4. Discussion

DEFLATE was applied to CEUS image processing and the results showed that the compression effect of DEFLATE was superior to that of RLE and Huffman, which was consistent with the research results of Bras and Velden [13],

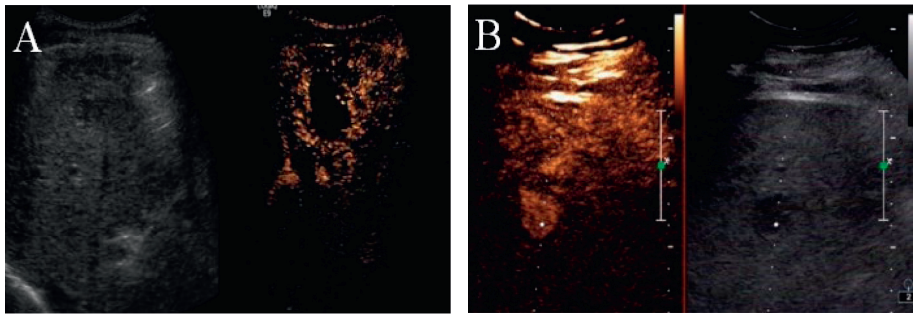

Figure 4: CEUS images of lesions located in the lower common bile duct. (a, b) The images of benign and malignant lesions, respectively.

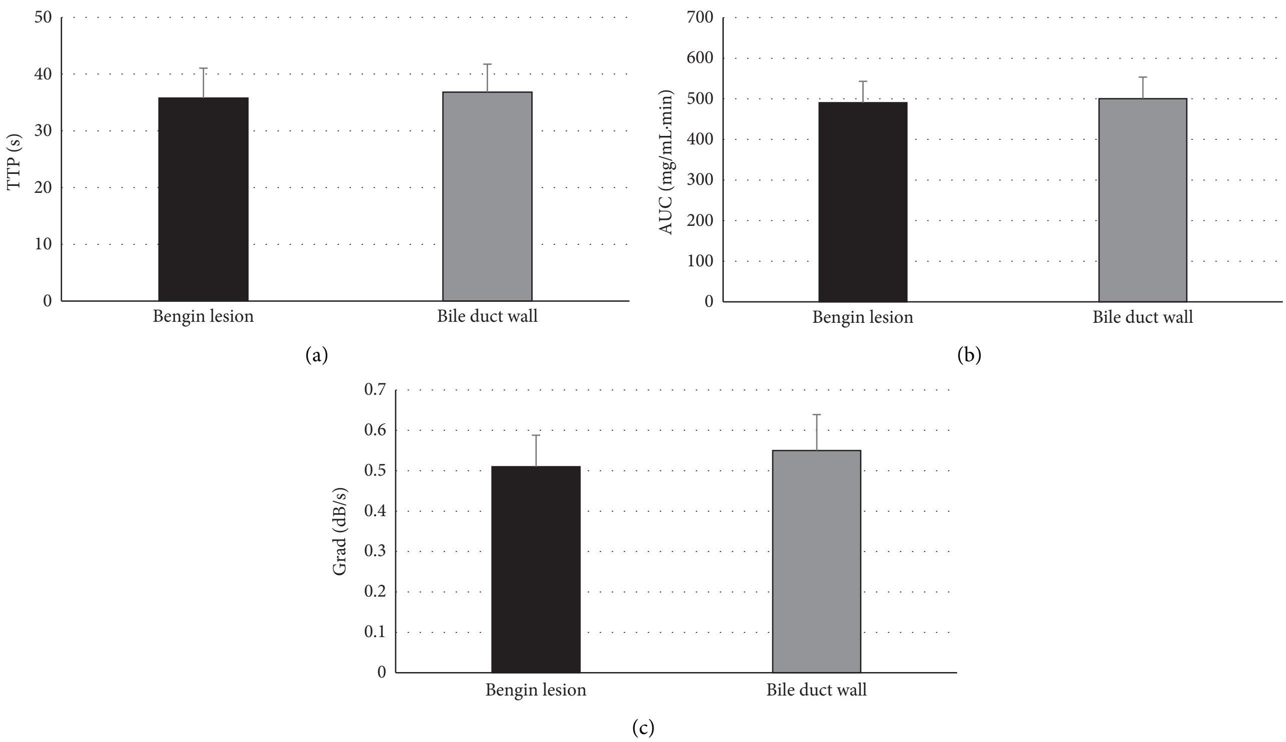

Figure 5: Comparison of CEUS indicators of lesions in the benign group and surrounding bile duct walls. (a–c) The comparisons of TTP, AUC, and Grad, respectively.

indicating that CEUS based on DEFLATE could increase the internal storage space of ultrasonic equipment to improve the detection efficiency. In this study, CEUS was applied to diagnose the lesions in the lower segment of the common bile duct. It was found that there were 25 patients with isoenhancement and 7 patients with high enhancement at the arterial phase in the benign group; and there were 8 patients with isoenhancement, 46 patients with high enhancement, and 2 patients with low enhancement at the arterial phase in the malignant group. This revealed that CEUS could effectively diagnose the benign and malignant lower common bile duct lesions, which is an effective imaging method for qualitative diagnosis of the lesions. The results showed that the differences in TTP, AUC, and Grad of lesions in the malignant group and common bile duct walls were statistically obvious ($P < 0.05$), while there were no statistically considerable differences in TTP, AUC, and Grad of lesions in the benign and malignant group ($P > 0.05$). AUC reflects the blood flow and the number of blood vessels at the lesion site. The AUC of lesions in the malignant group were higher than those of the benign group and surrounding normal bile duct walls because the microvessels inside the bile duct carcinoma were rich and densely distributed, and the bile duct carcinoma was a lesion rich in blood supply and had relatively more blood flow. The blood supply in the diseased area was more abundant than that in the normal bile duct wall, and the intervascular accesses were more complex so that the peak time was relatively short. However, when Grad of the malignant group was high, the malignant tissues grew rapidly and the blood vessel wall was easy to be damaged, to easily result in an arteriovenous short circuit [14].

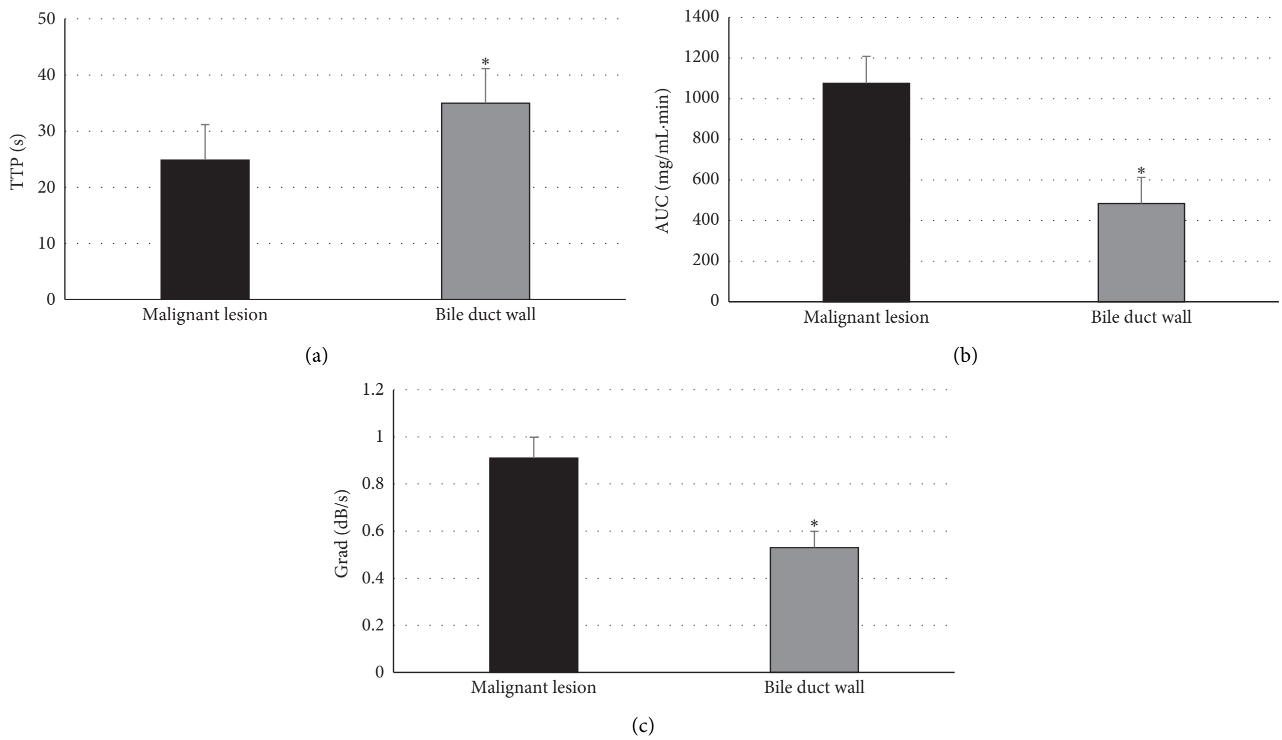

Figure 6: Comparison of CEUS indicators between malignant lesions and surrounding bile duct wall. (a–c) The comparisons of TTP, AUC, and Grad, respectively; $^*P < 0.05$ in contrast to malignant lesions.

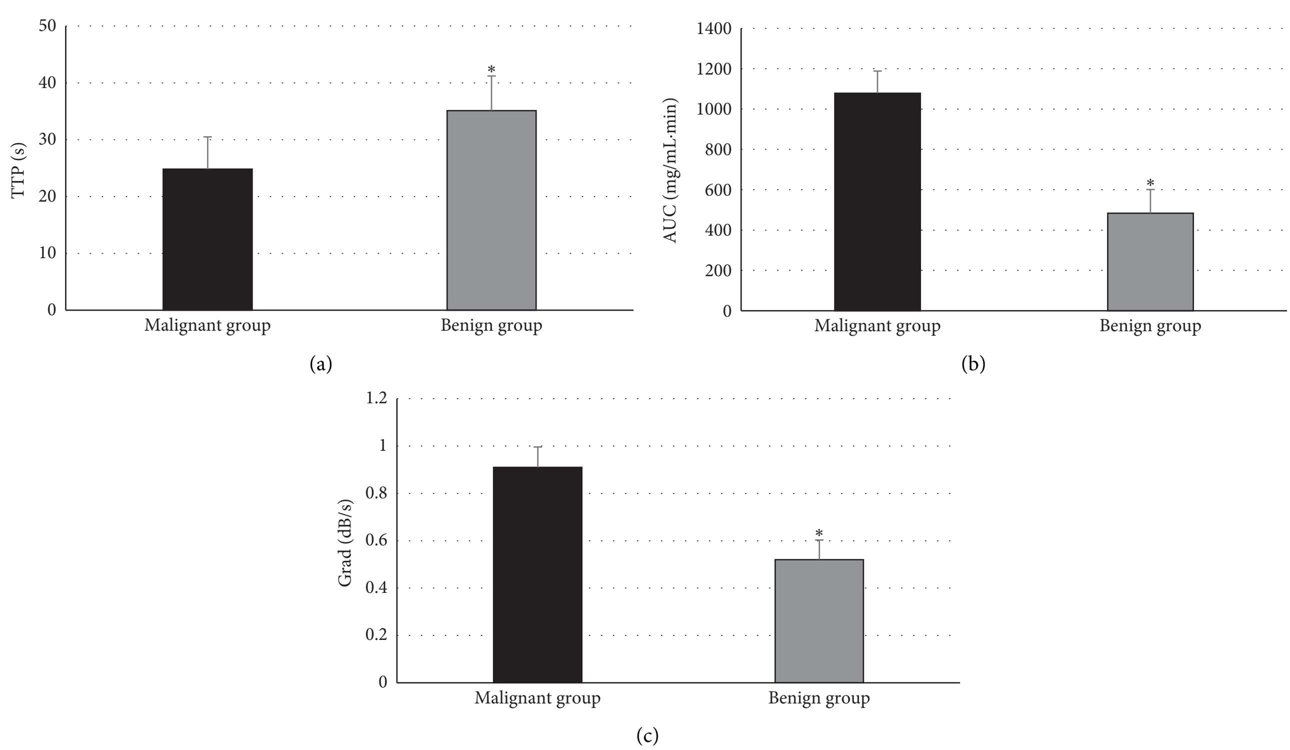

Figure 7: Comparison of CEUS indicators of patients in the benign and malignant group. (a–c) The comparisons of TTP, AUC, and Grad, respectively; $^*P < 0.05$ in contrast to the malignant group.

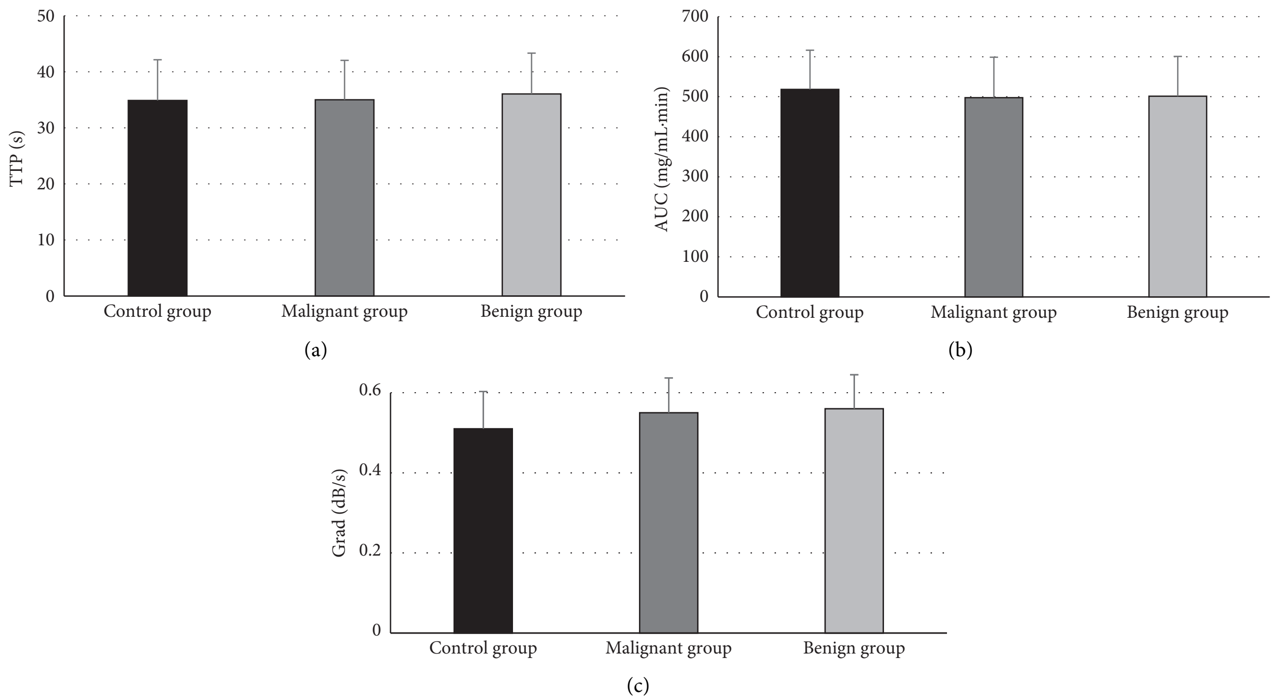

Figure 8: The comparison of CEUS indicators of surrounding bile duct walls in patients from the three groups. (a–c) The comparisons of TTP, AUC, and Grad, respectively.

Table 1: Diagnosis results of CEUS + US.

	Sensitivity (%)	Specificity (%)	Accuracy (%)	Positive predictive value (%)	Negative predictive value (%)
CEUS + US	92.83	87.14	89.54	91.23	86.43

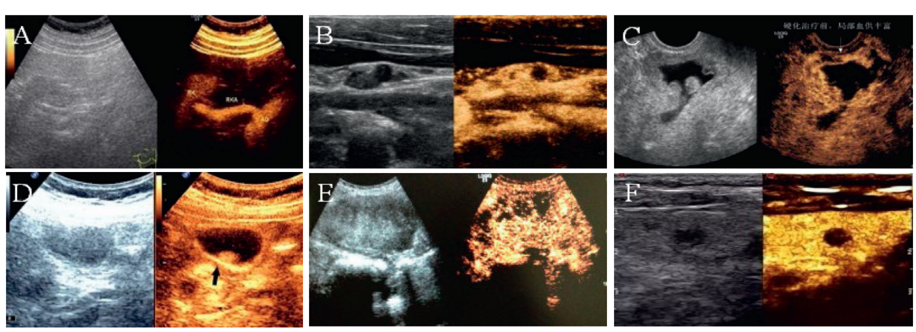

Figure 9: The CEUS images of superficial lymphoid lesions. (a, b) Images of a patient with reactive hyperplasia; (c, d) images of a patient with metastatic lymph nodes; (e) the image of a patient with lymphoma; (f) the image of a patient with tuberculous lymphadenitis.

Liu et al. [15] found that the sensitivity, accuracy, and positive/negative predictive values of conventional US in differentiating benign and malignant lymph nodes were 64.1%, 65.2%, 47.2%, and 66.7%, respectively, while the corresponding values of CEUS were 93.6%, 75.7%, 73.7%, and 83.9%, respectively. In addition, the sensitivity, specificity, accuracy, and positive/negative predictive values of CEUS + US in the diagnosis of benign and malignant lymph nodes were 92.83%, 87.14%, 89.54%, 91.23%, and 86.43%, respectively, which were in line with the results of Liu et al. [15]. The results of the study showed that there were statistical meanings in the comparison of I_{max} of patients from groups A, B, and C ($P < 0.05$). The TTP of patients in group B was extremely

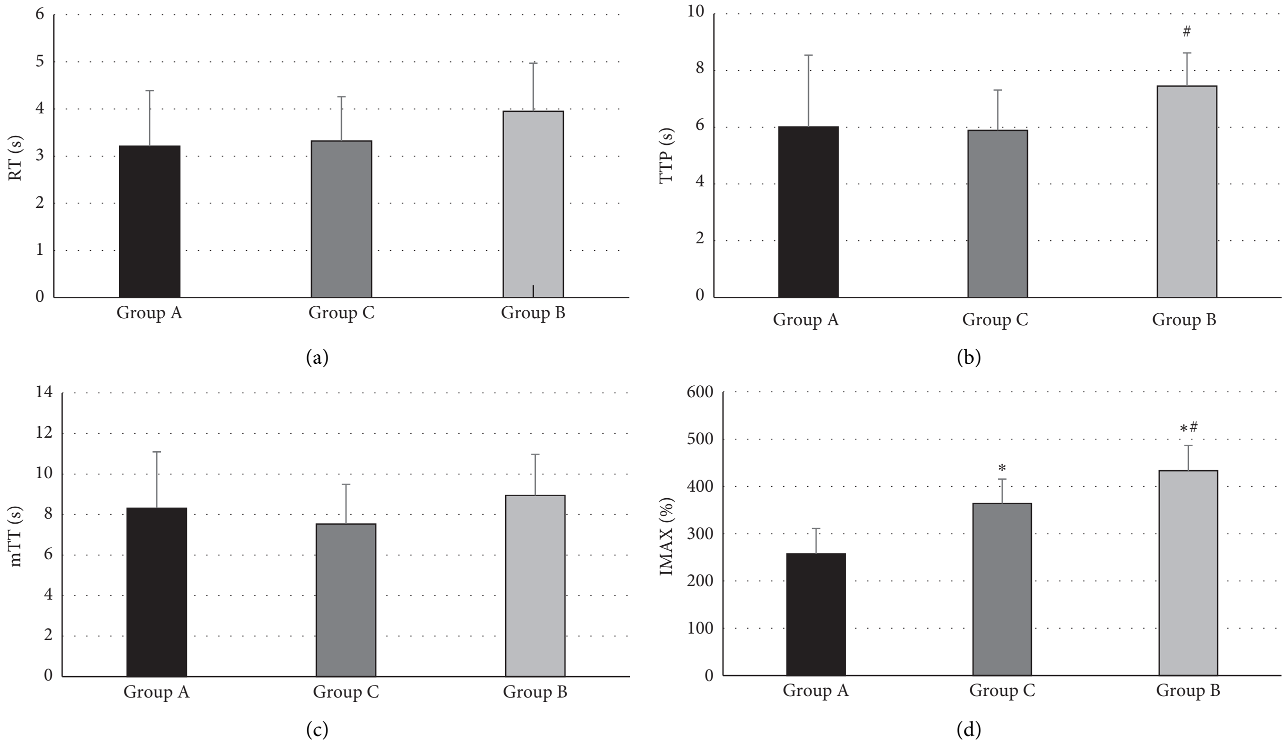

Figure 10: Comparison of CEUS indexes (a) RT, (b) TTP, (c) mTT, and (d) Imax of the patients in group A, B, and C. * and # stand for $P < 0.05$ in contrast to groups B and C, respectively.

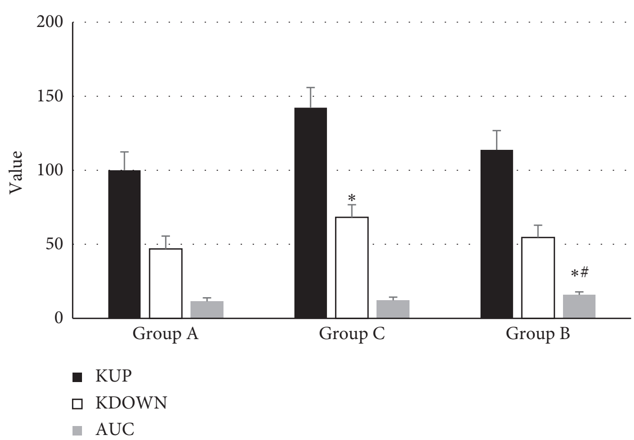

Figure 11: Comparison of K_{UP}, K_{DOWN}, and AUC of the patients in the three groups (* and # stand for $P < 0.05$ in contrast to groups A and C) respectively).

higher than that of group C ($P < 0.05$), K_{UP} and K_{DOWN} of patients in group C were obviously higher than those of group A ($P < 0.05$), and AUC of group B increased hugely in contrast to groups A and C ($P < 0.05$). Besides, RT and PI of patients in group A were markedly higher than the values of group B ($P < 0.05$). Therefore, it indicated that CEUS could effectively classify and diagnose superficial lymphoid lesions, which was consistent with the findings of Nie et al. [16].

5. Conclusion

Patients with the lower common bile duct lesions and superficial lymphoid lesions were taken as subjects investigated. CEUS based on DEFLATE was applied to analyze the CEUS characteristics and diagnostic efficiency for different lesion types. The results indicated that the DEFLATE-based CEUS proposed in this study could classify and diagnose the lower common bile duct lesions and superficial lymph nodes, which had reliable clinical application value. However, there were still some shortcomings in the study. For example, the number of subjects investigated was limited and distributed unevenly; many factors were affecting the morphology and indexes of TIC; and it was necessary to determine whether TIC could be considered as a standard for differentiating benign and malignant lymph nodes by further study. In subsequent studies, the number of samples could be increased and other TIC influence indicators should be supplemented for further research and analysis. In conclusion, the results of the study provided a critical basis for the imaging diagnosis of abdominal and superficial organ lesions.

Data Availability

The data used to support the findings of this study are available from the corresponding author upon request.

Conflicts of Interest

The authors declare that there are no conflicts of interest.

References

[1] T. H. Lee, J. H. Moon, and S. H. Park, "Biliary stenting for hilar malignant biliary obstruction," *Digestive Endoscopy*, vol. 32, no. 2, pp. 275–286, 2020.
[2] I. Durot, S. R. Wilson, and J. K. Willmann, "Contrast-enhanced ultrasound of malignant liver lesions," *Abdominal Radiology*, vol. 43, no. 4, pp. 819–847, 2018.
[3] W. K. Chong, V. Papadopoulou, and P. A. Dayton, "Imaging with ultrasound contrast agents: current status and future," *Abdominal Radiology*, vol. 43, no. 4, pp. 762–772, 2018.
[4] B. Kazmierski, C. Deurdulian, H. Tchelepi, and E. G. Grant, "Applications of contrast-enhanced ultrasound in the kidney," *Abdominal Radiology*, vol. 43, no. 4, pp. 880–898, 2018.
[5] Z. M. Lin, Q. Wen, C. X. Yan et al., "Combination of contrast-enhanced ultrasound and strain elastography to assess cytologically non-diagnostic thyroid nodules," *Oncology letters*, vol. 18, no. 6, pp. 6845–6851, 2019.
[6] V. Lehotska, K. Rauova, and L. Vanovcanova, "Pitfalls of contrast enhanced ultrasound (CEUS) in determination of breast tumor biological dignity," *Neoplasma*, vol. 65, no. 1, pp. 124–131, 2018.
[7] C. F. Dietrich, C. Tana, C. Caraiani, and Y. Dong, "Contrast enhanced ultrasound (CEUS) imaging of solid benign focal liver lesions," *Expert Review of Gastroenterology & Hepatology*, vol. 12, no. 5, pp. 479–489, 2018.
[8] H. P. Weskott, "Kontrastverstärkte slymphknotendiagnostik," *Radiologe, Der*, vol. 58, no. 6, pp. 563–571, 2018.
[9] P. Källback, A. Nilsson, M. Shariatgorji, and P. E. Andrén, "A space efficient direct access data compression approach for mass spectrometry imaging," *Analytical Chemistry*, vol. 90, no. 6, pp. 3676–3682, 2018.
[10] M. Brehm and M. Thomas, "An efficient lossless compression algorithm for trajectories of atom positions and volumetric data," *Journal of Chemical Information and Modeling*, vol. 58, no. 10, pp. 2092–2107, 2018.
[11] D. Y. Fu and J. Meiler, "RosettaLigandEnsemble: a small-molecule ensemble-driven docking approach," *ACS Omega*, vol. 3, no. 4, pp. 3655–3664, 2018.
[12] S. Alyami and C.-H. Huang, "Nongreedy unbalanced Huffman tree compressor for single and multifasta files," *Journal of Computational Biology*, vol. 27, no. 6, pp. 868–876, 2020.
[13] A. E. Bras and V. H. J. Velden, "Lossless compression of cytometric data," *Cytometry, Part A*, vol. 95, no. 10, pp. 1108–1112, 2019.
[14] E. S. Yoo, B. M. Yoo, J. H. Kim et al., "Evaluation of risk factors for recurrent primary common bile duct stone in patients with cholecystectomy," *Scandinavian Journal of Gastroenterology*, vol. 53, no. 4, pp. 466–470, 2018.
[15] N. X. Liu, L. N. Tang, Y. Q. Wang, and W. Q. Huang, "Evaluation of contrast-enhanced ultrasound in the differential diagnosis of benign and malignant lateral cervical lymph nodes," *Zhonghua Yixue Zazhi*, vol. 100, no. 29, pp. 2258–2262, 2020.
[16] J. Nie, W. Ling, Q. Yang, H. Jin, X. Ou, and X. Ma, "The value of CEUS in distinguishing cancerous lymph nodes from the primary lymphoma of the head and neck," *Frontiers in Oncology*, vol. 10, p. 473, 2020.

Hindawi
Journal of Healthcare Engineering
Volume 2021, Article ID 7758206, 13 pages
https://doi.org/10.1155/2021/7758206

Research Article

Intelligent Algorithm-Based Analysis on Ultrasound Image Characteristics of Patients with Lower Extremity Arteriosclerosis Occlusion and Its Correlation with Diabetic Mellitus Foot

YunShuang Wu,[1] **Yan Shen**,[2] **and Hailing Sun**[3]

[1]*Department of Ultrasound, Nanjing Integrated Traditional Chinese and Western Medicine Hospital, Affiliated with Nanjing University of Chinese Medicine, Nanjing 210014, Jiangsu, China*
[2]*Department of Ultrasound, Lianshui County People's Hospital, Lianshui, Huai'an 223400, Jiangsu, China*
[3]*Department of Ultrasound, Hongze District People's Hospital, Huai'an 223100, Jiangsu, China*

Correspondence should be addressed to Hailing Sun; fsyy00102@njucm.edu.cn

Received 28 June 2021; Revised 5 September 2021; Accepted 9 September 2021; Published 26 September 2021

Academic Editor: Enas Abdulhay

Objective. The study focused on the correlation between lower extremity arteriosclerosis and diabetic mellitus (DM) foot, and it was explored by virtue of ultrasound images processed by an intelligent algorithm. *Methods*. A total of 60 DM foot patients admitted to our hospital in the past three years were selected and divided into two groups according to their condition. Patients with DM foot alone were in group B (30 cases), and patients with DM foot combined with lower extremity arteriosclerosis occlusion were in group C (30 cases). 30 healthy people were in group A as a control. Color Doppler ultrasound was used to examine the arteries of the lower extremities of all subjects. It the intramedia thickness (IMT) from the femoral artery to the dorsal foot artery was recorded, whether there was plaque in the artery or knowing the size of the plaque, its echo, and distribution, and whether the artery had stenosis. Next, the stenosis percentage was calculated. Additionally, the general information of patients was analyzed. At the same time, an intelligent algorithm was used to process ultrasound images, and its effects on image quality were evaluated. *Results*. Doppler ultrasound images processed by Artificial Bee Colony (ABC) had less noise and better quality, and key information about the lesion was clearly displayed. There was no statistical difference between the general data of the three groups of patients; group B and group C had higher IMT value, plaque incidence, arterial stenosis incidence, and degree of stenosis versus group A, and there were statistically significant differences between groups B and C. In particular, the incidence of femoral artery stenosis and the degree of stenosis were significantly higher in group C than in group B. The rate of stenosis above grade I in group C was as high as 71%, while that in group B was only 19%; in Group C, the incidence of stenosis above grade II was 30%, and that in group B was 13.1%. Compared with group A, group B and group C had decreased peak arterial blood velocity (PSV), resistance index (RI), and pulse index (PI), and there were statistically significant differences between groups B and C. *Conclusion*. DM foot is a risk factor for arteriosclerosis occlusion; color Doppler ultrasound demonstrates good diagnostic effects on arteriosclerosis occlusion; the algorithm proposed in this study can improve the quality of Doppler ultrasound images and has a high application value.

1. Introduction

In recent years, with the continuous improvement of people's living standards and changes in dietary structure, the incidence of diabetes mellitus (DM) foot has been increasing year by year [1]. It is the third most common disease after tumors and cardiovascular diseases. DM foot is a common complication of DM patients. Statistics show that 15% of DM patients worldwide have foot ulcers and gangrene [2]. 50% of patients with amputation each year are DM patients, and more than 85% of these patients are amputated because of worsening foot ulcers leading to deep infection or gangrene. Domestic clinical data show that DM foot patients account for 2% of outpatients and 8% to 12% of inpatients. The per capita treatment cost for DM foot is more than 10,000 yuan. Worldwide, the incidence of DM foot is high, and the prognosis is poor [3].

As for why DM patients develop DM foot, it may be related to the influence of DM on the cardiac and cerebral vessels. To some extent, DM can be regarded as a cardiovascular and cerebrovascular disease and affects almost every blood vessel. The abnormal metabolism caused by DM can lead to changes in the structure and functions of arteries. These changes occur even before DM is diagnosed [4]. Peripheral arterial disease (PAD) is common in DM patients. It is a lower extremity occlusive disease, and its clinical symptoms are not obvious. PAD is an important indicator of thrombotic diseases of arteriosclerosis [5]. Statistics reveal that more than 40% of PAD patients suffer from DM, and DM is the strongest threat factor for PAD. Unlike PAD caused by other factors, DM is closely related to femoral-popliteal PAD and tibial artery PAD (below the knee). The DM foot arises from lower limb ischemia caused by arteriosclerosis occlusion [6]. Above, there is a huge correlation between DM foot and lower extremity arteriosclerosis occlusion. There are many commonalities but are different. Research has found that patients with both PAD and DM foot have a more complicated condition than patients with one of them alone, and the probability of cardiovascular diseases is greatly increased [7]. At present, the relationship between the two remains unclear. In the study, the correlation between the two was explored, in order to provide reference and basis for clinical research.

At present, the methods to diagnose lower extremity arteriosclerosis occlusion mainly include digital subtraction angiography (DSA), magnetic resonance angiography (MRA), CT angiography (CTA), and Doppler ultrasound. Among them, DSA is the recognized gold standard for peripheral vascular examination, but it is often not easily accepted by patients because it is invasive and expensive. As ultrasound technology marches forward continuously, it has been widely used in the detection of vascular diseases, especially in the research of atherosclerosis, because of its advantages, such as noninvasive, fast, efficient, safe, and accurate [8]. Statistics show that the accuracy of ultrasound examination for intraplaque hemorrhage is 90% and the sensitivity is 96%. B-mode ultrasound can display the anatomical images of the artery at longitudinal axis and at the transverse axis, providing rich information, such as artery thickness, plaque shape, size, range, and lumen stenosis and occlusion. Color blood flow imaging can reflect the blood filling and distribution state, which is of great significance for the evaluation of hemodynamic changes. In the early stage of atherosclerosis, it mainly manifests as expansion of the arterial wall or the thickening of MIT, which can be observed by ultrasound scan [9]. Thus, ultrasound has great advantages in the diagnosis of vascular diseases.

Nevertheless, its imaging effects are poor thanks to the reflection and random scattering. As a result, it is difficult to recognize the edges and details of the organs. Recently, Internet technology has developed rapidly, and some medical image processing technologies have also been developed, such as the arterial detection and tracking algorithm developed on the basis of ultrasound imaging, various ultrasonic 3D reconstruction algorithms, and computer-aided diagnostic systems. At present, the most widely used feature extraction and classification method in the field of medical image processing is the support vector machine. However, a large number of studies have shown that support vector machines are susceptible to extreme values in data classification and training. Therefore, in this article, the Artificial Bee Colony (ABC) was used to perform noise reduction and feature extraction on the ultrasound images of diabetes and arteriosclerosis occlusion [10], aiming to provide a scientific basis for the diagnosis and treatment of related diseases.

2. Materials and Methods

2.1. Research Subjects. 60 patients with DM foot and DM foot combined with lower extremity arteriosclerosis occlusion who were hospitalized in the hospital from March 2019 to June 2019 were selected as the research subjects. 30 healthy subjects were selected into group A as a control. The 30 subjects in group B were patients with DM foot alone. The diagnostic criteria of DM foot were based on the standards drawn up by the first DM foot academic conference of the Chinese Medical Association Diabetes Mellitus Society. The 30 subjects in group C were patients with DM foot and lower extremity arteriosclerosis occlusion. The diagnostic criteria for lower extremity arteriosclerosis occlusion were as follows. (1) Those with intermittent claudication; resting pain; soreness, swelling, numbness, and numbness (patients with one or more of them was included); dystrophic changes in skin, hair, muscles, and nails; and ulcers or gangrene were included. (2) The affected swelled and the pulsation of the middle artery was weakened or disappeared. (3) Those with sclerosis changes on fundus examination; electrocardiogram showing coronary artery ischemia, left ventricular hypertrophy, or old myocardial infarction; and Doppler or angiography showing limb arteriosclerosis were also included. The subjects were 62×6.5 years old on average, including 44 males and 46 females. All subjects need to be free of coronary heart disease, hyperlipidemia, and other cardiovascular and cerebrovascular diseases, with no long-term smoking history. The study met the requirements of medical ethics and the patients had signed an inform consent form.

2.2. Examination Methods

2.2.1. Inspection Instrument. Philips iu22 color Doppler ultrasonic diagnostic instrument, with a linear array probe, the probe frequency is 2–9 MHz. During the inspection process, conditions, such as emission energy, total gain, contrast, time gain compensation, and lateral gain compensation, need to be kept basically unchanged.

2.2.2. Inspection Content. The patient stayed in the supine and prone positions, and two-dimensional ultrasound scan was performed on the femoral artery, popliteal artery, anterior tibial artery, posterior tibial artery, dorsal foot artery lumen, and inner membrane of both lower limbs. The lumen inner diameter and intramedia thickness (IMT) were measured. It was observed that there were plaques on the tube wall, the position of plaques, and that there was stenosis in the lumen. The stenosis percentage was then calculated. Color Doppler was used to observe the blood vessel filling, and spectrum Doppler was used to detect blood flow spectrum. After a clear spectrum appeared, the blood flow parameters PSV, RI, and PI were measured. During the inspection, it should be noted not to compress the artery too much, and the angle between the sound beam and the blood flow direction should be less than 60°; each index is measured 3 times, and the average value is taken.

2.3. Image Processing. A total of 220 ultrasound images are collected as research data. Then, the NL algorithm is used to reduce the noise of the image. The original noise image is $Y \in R^{M\times N}$, and the image $\mathrm{NL}(Y)$ after noise reduction was

$$\mathrm{NL}(Y(p)) = \sum_{q=1}^{M\times N} w(p,q) = 1, \tag{1}$$

where p are the pixels to be denoised and q are the other pixels. $w(p,q)$ is the weight, $0 \le w(p,q) \le 1$, and $\sum_{q=1}^{M\times N} w(p,q) = 1$. The calculation of $w(p,q)$ is as follows:

$$w(p,q) = \frac{1}{Z(p)} \exp\left(-\frac{d(p,q)}{h^2}\right). \tag{2}$$

Then, the weighted Gaussian distance is used to judge the similarity:

$$d(p,q) = G_p \left\| g(N_p) - g(N_q) \right\|^2, \tag{3}$$

where G_p is the Gaussian weighting function and $Z(p)$ is the normalization parameter:

$$Z(p) = \sum_{q=1}^{M\times N} \exp\left(-\frac{d(p,q)}{h^2}\right), \tag{4}$$

where h are the attenuation control parameters. This algorithm has good noise reduction effects but long calculation time. In order to reduce the amount of calculation and shorten the calculation time, the search range is controlled in the large search box of $(2\times R_{\text{search}}+1)\times(2\times R_{\text{search}}+1)$.

2.3.1. Feature Extraction. The ultrasonic image features are divided into basic texture features and gray-level cooccurrence matrix features. The gray mean value of the k subblock is defined as

$$\overline{y}_k = \frac{1}{L2} \sum_{i=1}^{L} \sum_{j=1}^{L} \left[y_k(i,j) - \overline{y}_k \right]^2. \tag{5}$$

The gray-level variance $\sigma^2(y_k)$ of the k subblock is defined as follows:

$$\sigma^2(y_k) = \frac{1}{L2} \sum_{i=1}^{L} \sum_{j=1}^{L} \left[y_k(i,j) - \overline{y}_k \right]^2. \tag{6}$$

The probability that the pixels (i', j') with distance d, angle θ, and gray value g_2 appear at the same time is as follows:

$$P_{\theta,d}(g_1, g_2) = \#\{(i,j), (i',j') \in M\times N \mid f(i,j) = g_1, f(i',j') = g_2\}, \tag{7}$$

where $\#\{\cdot\}$ represents the number of elements in the set. For the sake of simplicity, θ and d are ignored, and the matrix is normalized as follows:

$$\frac{P_{\theta,d}(g_1, g_2)}{R} \longrightarrow P(g_1, g_2), \tag{8}$$

where R is the normalization constant and its value is the total number of point pairs in the gray-level cooccurrence matrix. CON is the contrast, and it can reflect the clarity and texture of the image. A greater grayscale difference of the pixel pair value leads to a greater value of CON:

$$\mathrm{CON} = \sum_{g_1=0}^{N_g-1} \sum_{g_2=0}^{N_g-1} \left| g_1 - g_2 \right|^2 p^2(g_1 - g_2). \tag{9}$$

Entropy ENT can be a measure of the complexity of the image texture, and it is calculated as follows:

$$\mathrm{ENT} = -\sum_{g_1=0}^{N_g-1} \sum_{g_2=0}^{N_g-1} P(g_1, g_2) \log\left[P(g_1, g_2)\right]. \tag{10}$$

The linear dependence of the image gray level depends on COR:

$$\mathrm{COR} = \frac{\sum_{g_1=0}^{N_g-1} \sum_{g_2=0}^{N_g-1} g_1 g_2 P(g_1, g_2) - \mu_{g_1}\mu_{g_2}}{\sigma_{g_1}\sigma_{g_2}}. \tag{11}$$

Energy ENG can reflect the uniformity of the image gray distribution and the thickness of the texture:

$$\mathrm{ENG} = -\sum_{g_1=0}^{N_g-1} \sum_{g_2=0}^{N_g-1} p^2(g_1, g_2). \tag{12}$$

2.4. Observation Indicators. The measurement of intramedia thickness (IMT) takes the average value of the left and right sides, and the thickest part of the arterial wall is measured in the diastolic phase of each segment of the lower limbs. It should be noted to be away from the plaque position during the measurement. IMT $\le$ 0.9 mm is the normal value, and IMT > 0.9 mm is the thickened IMT. Plaque is defined as: localized thickening of blood vessel wall greater than 1.2 mm or diffuse thickening of blood vessel greater than 1.2 mm. The calculation of vascular stenosis rate depends on the percentage reduction of inner diameter: vascular stenosis rate = $((d_2 - d_1)/d_2) \times 100\%$ (d_1 is the inner diameter of the lumen at the stenosis and d_2 is the original inner diameter of the lumen). The grades of stenosis were as follows: grade 0, no stenosis; grade I, stenosis rate 1%~19%; grade II, stenosis 20%~49%; grade III, stenosis 50%~99%; grade IV, occlusion, no blood flow information. If there are multiple plaques or stenosis in the same segment of blood vessel, the most severe part of the stenosis shall prevail.

2.5. Statistics. The data was processed by SPSS 17.0 software. The measurement data were expressed as ($\overline{x} \pm s$). The comparison of data between groups adopted analysis of variance, and the x^2 test was used to test the count data. $P < 0.05$ was the threshold for significance.

3. Results

3.1. The Basic Information of Subjects. The basic information of the subjects was shown in Table 1. The average ages of A, B, and C groups were 65.1 ± 6.8, 66.2 ± 5.4, and 64.2 ± 5.9, respectively. The number of male subjects in the three groups was 16, 18, and 17, respectively, and the number of female subjects was 14, 12, and 13, respectively; the proportions of smokers in each group were 16%, 15.1%, and 15.3%. It was noted that there was no significant difference between the general data of the three groups of subjects and it was comparable.

3.2. Ultrasound Images and Processing Results. The original ultrasound image and the processed image were shown in Figure 1. From column A in Figure 1, it was noted that although Doppler color ultrasound can reflect the arterial thickness, plaque shape, size, range, luminal stenosis and occlusion, blood flow filling, and other information in a comprehensive and detailed manner, the figure had much noise, with poor clarity and quality. It failed to show the edge and detailed information of diseased parts and tissue. As for column B in Figure 1, the clarity of the image was improved a lot, and the noise has also been reduced. At the same time, the key information of the disease was extracted, and the redundant information was removed that had nothing to do with the disease, to highlight the focus of the disease.

3.3. The Intramedia Thickness and Hemodynamic Test Results of the Lower Extremity Arteries of Each Group. The IMT measurement results of both lower limbs in the three groups were shown in Figure 2. Compared with group A, subjects in groups B and C had thicker IMT in the lower limb femoral artery, popliteal artery, anterior tibial artery, posterior tibial artery, and dorsal foot artery, and the difference was statistically significant, $P < 0.05$. The thickening of IMT in group C was more obvious versus group B, and the difference was statistically significant, $P < 0.05$.

The hemodynamic results of each group were shown in Figure 3. The test indicators included peak systolic velocity (PSV), resistance index (RI), and pulse index (PI), and the detection was located in femoral artery, popliteal artery, anterior tibial artery, posterior tibial artery, and dorsal foot artery. Compared with group A, PSV, RI, and PI of groups B and C decreased, and the difference was statistically significant, $P < 0.05$, and the decrease in group B was more obvious versus group C, and the difference was statistically significant, $P < 0.05$.

Table 1: The basic information of subjects.

Item		A (30 cases)	B (30 cases)	C (30 cases)
Case		30	30	30
Age (year)		65.1 ± 6.8	66.2 ± 5.4	64.2 ± 5.9
Gender	Male	16	18	17
	Female	14	12	13
Proportion of smokers (%)		16	15.1	15.3
TC (mol/L)		4.66 ± 1.08	4.55 ± 1.13	4.61 ± 1.14
TG (mol/L)		2.06 ± 1.16	2.08 ± 1.12	4.07 ± 1.19

3.4. Occurrence and Distribution of Atherosclerotic Plaques in the Lower Extremities of Each Group. Two-dimensional ultrasound results showed that the intima surface of the lower extremity arteries in groups B and C were not smooth, and there were patches or dots with localized or diffuse distribution and uneven echo. The plaques at the femoral artery were mostly single and large in volume. The plaques were often found at the bifurcation. The plaques of the popliteal artery, anterior tibial, posterior tibial, and dorsal foot artery were mostly diffusely distributed dots echoes and small in volume. Figure 4 showed the plaque incidence in each group, where (a) was the total number of arteries, (b) was the number of plaque arteries in each arterial segment, and (c) was the probability of plaque in each arterial segment. Compared with A, the incidence of plaque in the lower limb femoral artery, popliteal artery, anterior tibial artery, posterior tibial artery, and dorsal foot artery in the groups B and C was higher, $P < 0.05$, and the difference was statistically significant. The incidence of arterial plaque in each segment of the C group was higher than that of the B group, and the difference was statistically significant, $P < 0.05$.

3.5. Occurrence of Arteriosclerosis and Stenosis of the Lower Extremities. Two-dimensional ultrasound results showed that the arterial intima of the lower extremities of the two groups B and C showed varying degrees of thickening and plaques of different sizes and irregular shapes protruding into the lumen, resulting in varying degrees of stenosis of the vascular lumen. Figures 5–9 showed the occurrence and distribution of stenosis in each group. Compared with group A, the lower extremity arterial stenosis rate of groups B and C was higher, and the difference was statistically significant, $P < 0.05$. The incidence of stenosis in of group C was higher than that of group B, and the difference was statistically significant, $P < 0.05$. In particular, the incidence of femoral artery stenosis and the degree of stenosis was higher in group C than in group B. The stenosis rate of grade I and above in group C was as high as 71%, while that in group B was only 19%; in group C, the stenosis rate of grade II and above was 30%, and that in group B was 13.1%.

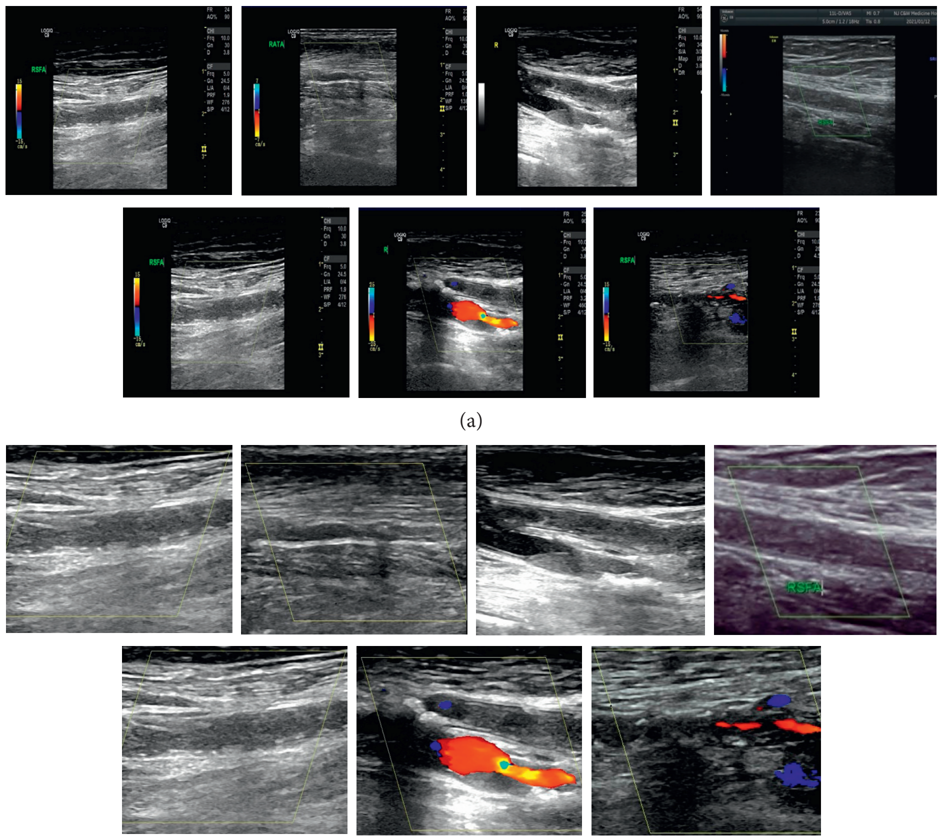

(a)

(b)

Figure 1: Comparison of the original ultrasound image and the processed image. *Note*. (a) The original image and (b) the processed image.

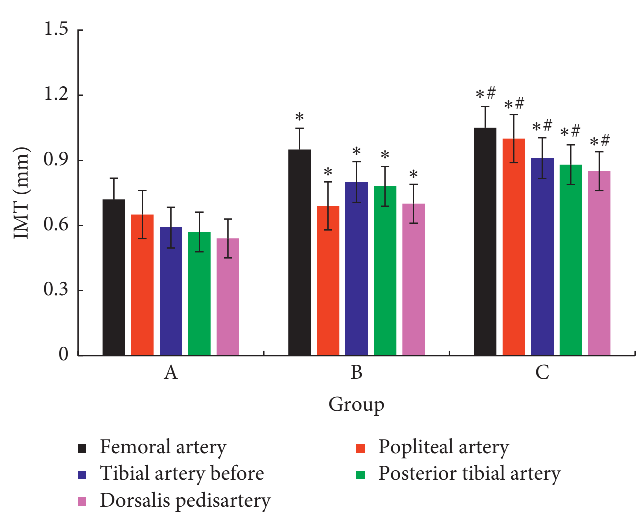

Figure 2: Comparison of intramedia thickness results of each group. *Note*. Compared with group A, $^{*}P < 0.05$; compared with group B, $^{\#}P < 0.05$.

4. Discussion

In China, diabetes is a common disease that threatens the lives and health of people. With the development of economy and the gradual westernization of lifestyle, the incidence of diabetes continues to rise [11]. DM foot is one of the most common complications of diabetes [12]. Studies have shown that 15 out of every 100 diabetic patients will suffer from DM foot. Clinical data show that diabetes is the culprit of 50% of amputation patients every year. In general,

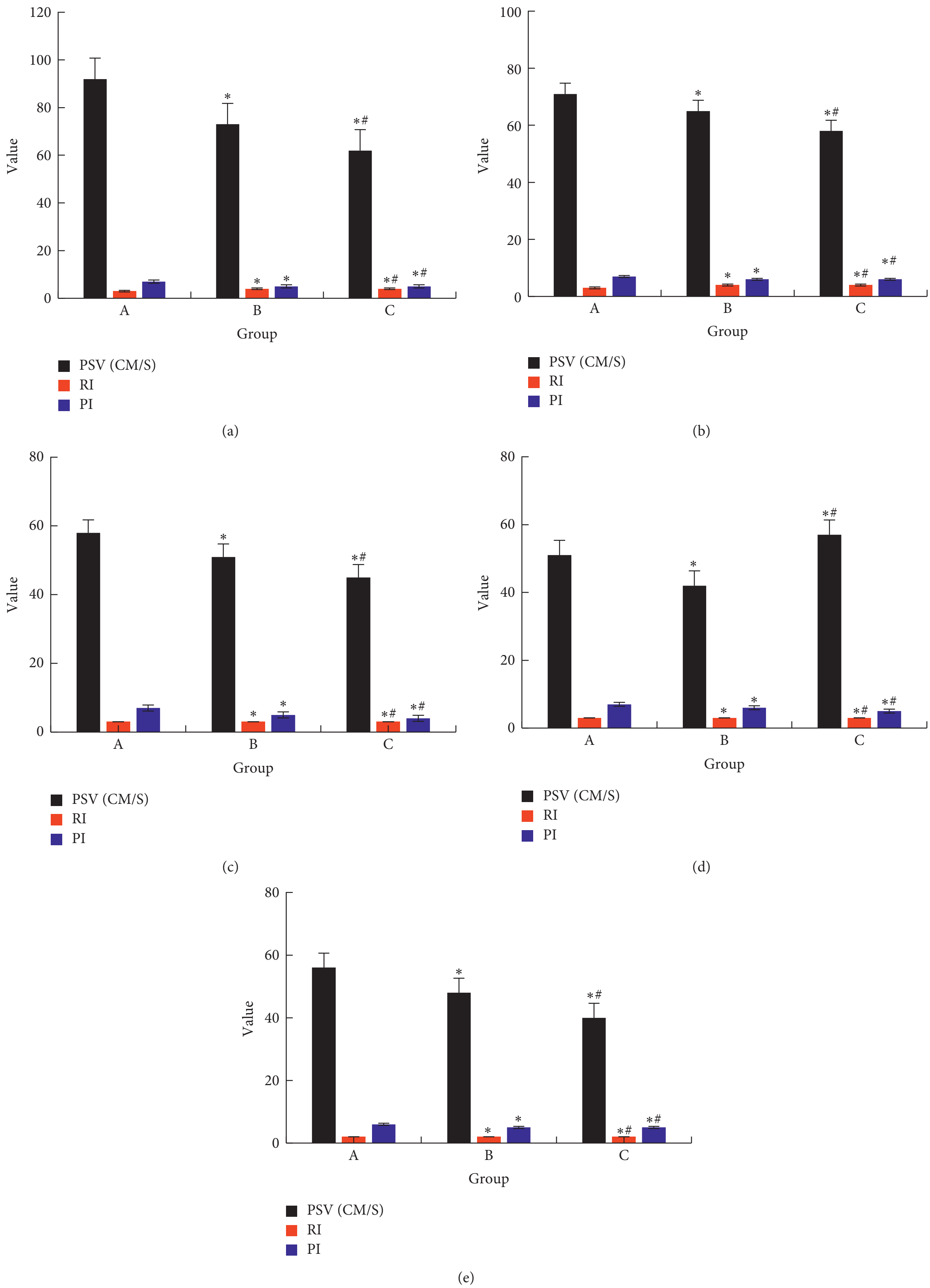

Figure 3: Hemodynamic examination results of each group. *Note*. Compared with group A, $^{*}P < 0.05$; compared with group B, $^{\#}P < 0.05$. (a) Femoral artery. (b) Popliteal artery. (c) Tibial artery before. (d) Posterior tibial artery. (e) Dorsalis pedis artery.

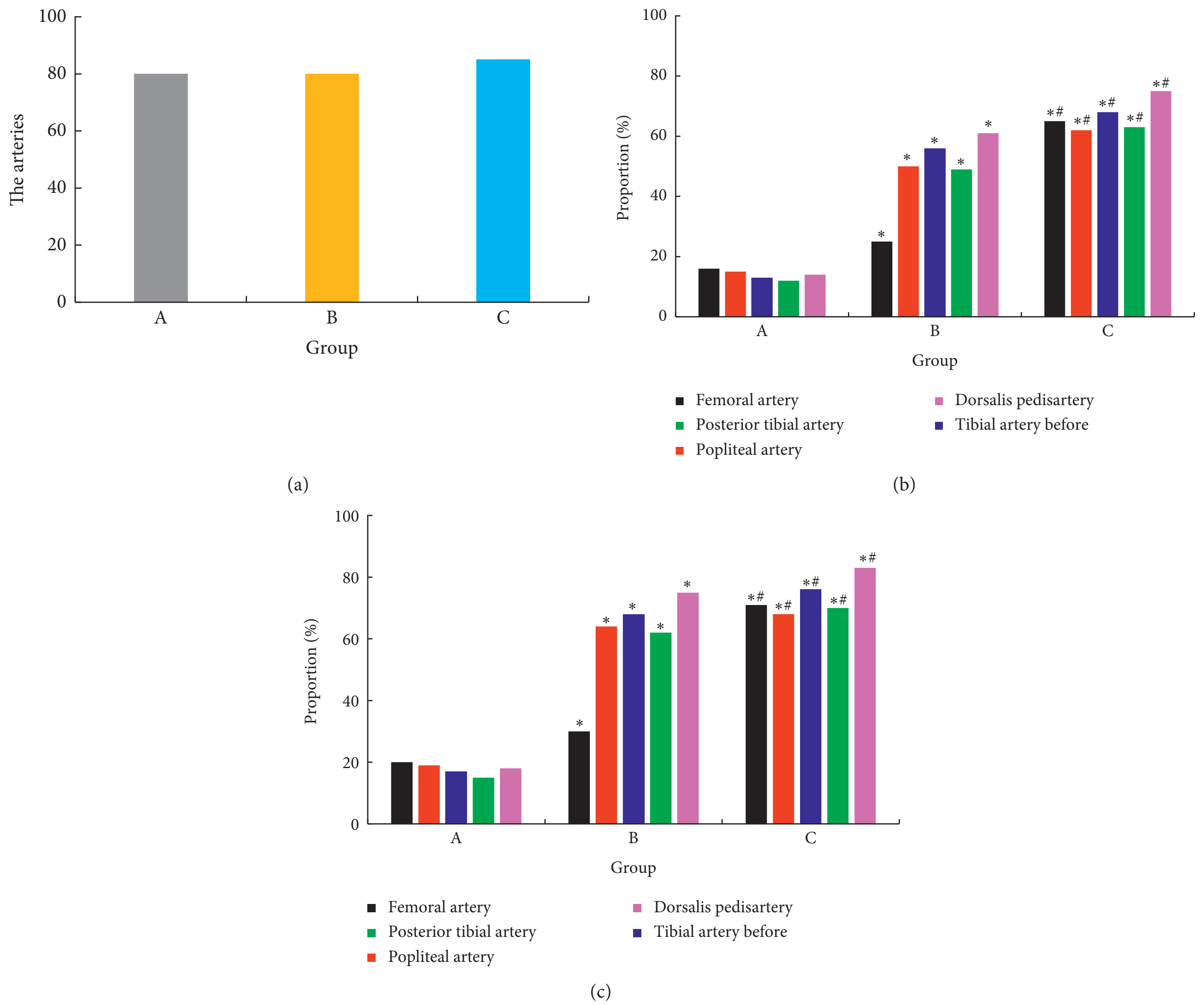

FIGURE 4: The occurrence and distribution of atherosclerotic plaques in the lower extremities of each group. *Note*. Compared with group A, $^{*}P < 0.05$; compared with group B, $^{\#}P < 0.05$.

DM foot can be divided into two types. One is DM foot combined with lower extremity arteriosclerosis occlusion, with the lower extremity arteriosclerosis being the main pathological change. It manifests as the coldness of the lower extremities, numbness, poor skin nutrition, and weakened or disappeared artery pulsation in distant end of lower extremities, that is, ischemic diabetes [13]. The other is DM foot with no obvious arteriosclerosis of the lower extremities, that is, nonischemic diabetes. Such patients have no obvious symptoms of lower limb ischemia, and the pulsation of dorsal foot artery and posterior tibial artery is also good. Clinical statistics show that the proportion of DM foot combined with lower extremity arteriosclerosis occlusion is different among countries, regions, and races [14]. The reason may be that we have different definitions of the two diseases, which has caused ambiguity. The international definitions of DM foot and fine arteriosclerosis occlusion are as follows. DM foot refers to the foot ischemia, infection, or neuropathy in diabetic patients; lower extremity arteriosclerosis occlusion is a systemic arterial disease, and it manifests as the appearance of atherosclerotic plaque, degeneration or calcification of the middle layer of the tissue, and the formation of secondary thrombosis in the lumen, which will eventually narrow or even completely occlude the lumen. In severe cases, ischemia in lower extremities may cause acronecrosis [15]. As per the definition, both DM foot and lower extremity arterial occlusion are related to ischemia. When a diabetic person has lower extremity arterial bleeding, whether it should be diagnosed as

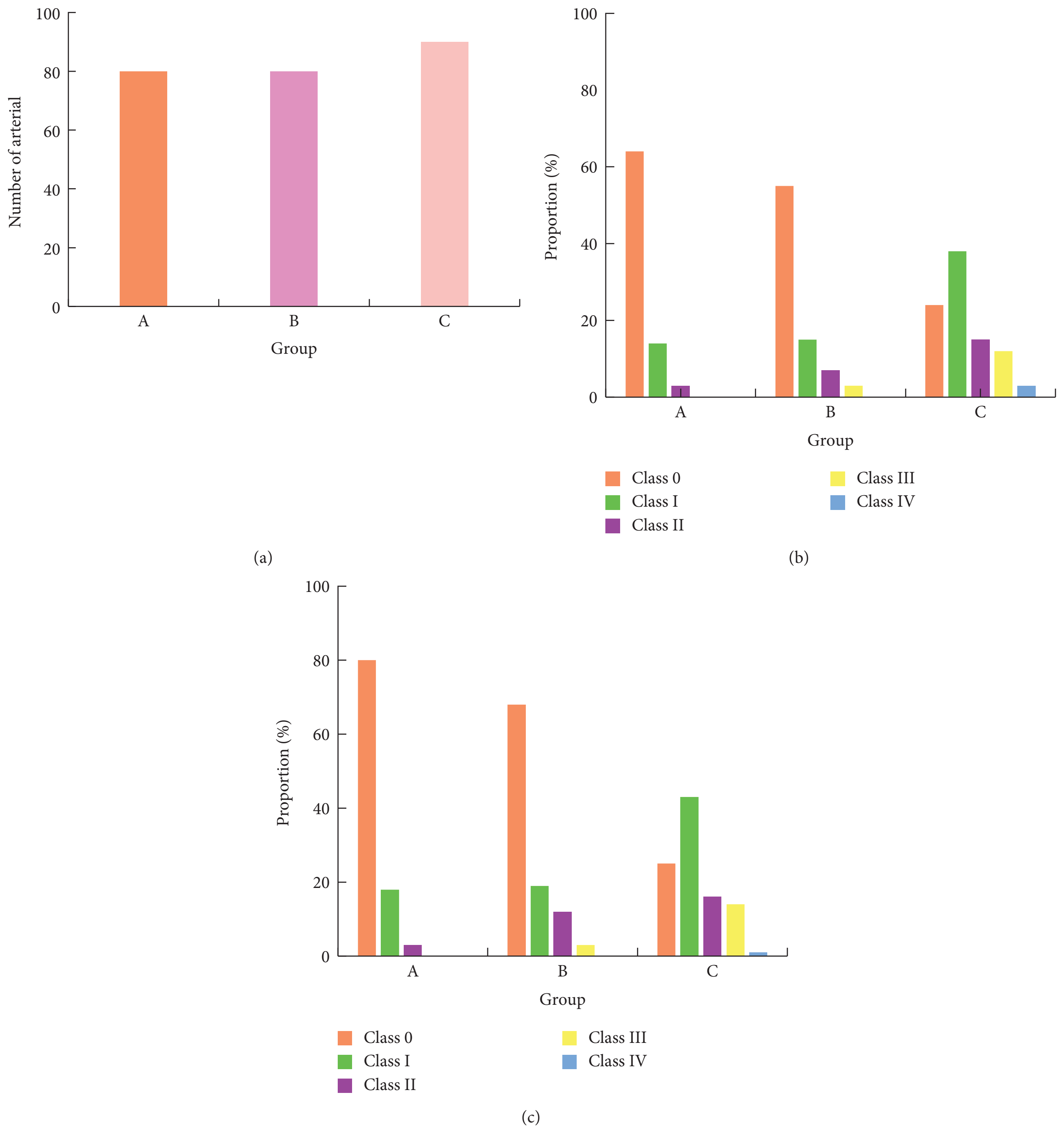

FIGURE 5: The occurrence of femoral artery stenosis in each group. (a) Total number of arteries in each group. (b) The number of arteries with stenosis in each group. (c) The occurrence probability of arterial stenosis in each group.

diabetic foot or lower extremity arteriosclerosis occlusion is a common problem that currently plagues clinicians [16]. If diagnosed as DM foot, it will enlarge the influence of DM foot and reduce the detection rate of arteriosclerosis occlusion; if diagnosed as lower extremity arteriosclerosis occlusion, it will reduce the detection rate of DM foot combined with lower extremity arteriosclerosis occlusion [17]. For the relationship between the two, scholars have used mathematical sets to express it; that is, those with DM foot alone and those with lower extremity arteriosclerosis occlusion alone are in mutually independent subsets, and those in the intersection have DM foot combined with arteriosclerosis occlusion. Hence, it is important to explore the difference and connection between the two [18].

Currently, except for the diagnosis method based on the clinical systems, the main methods to diagnose DM foot and

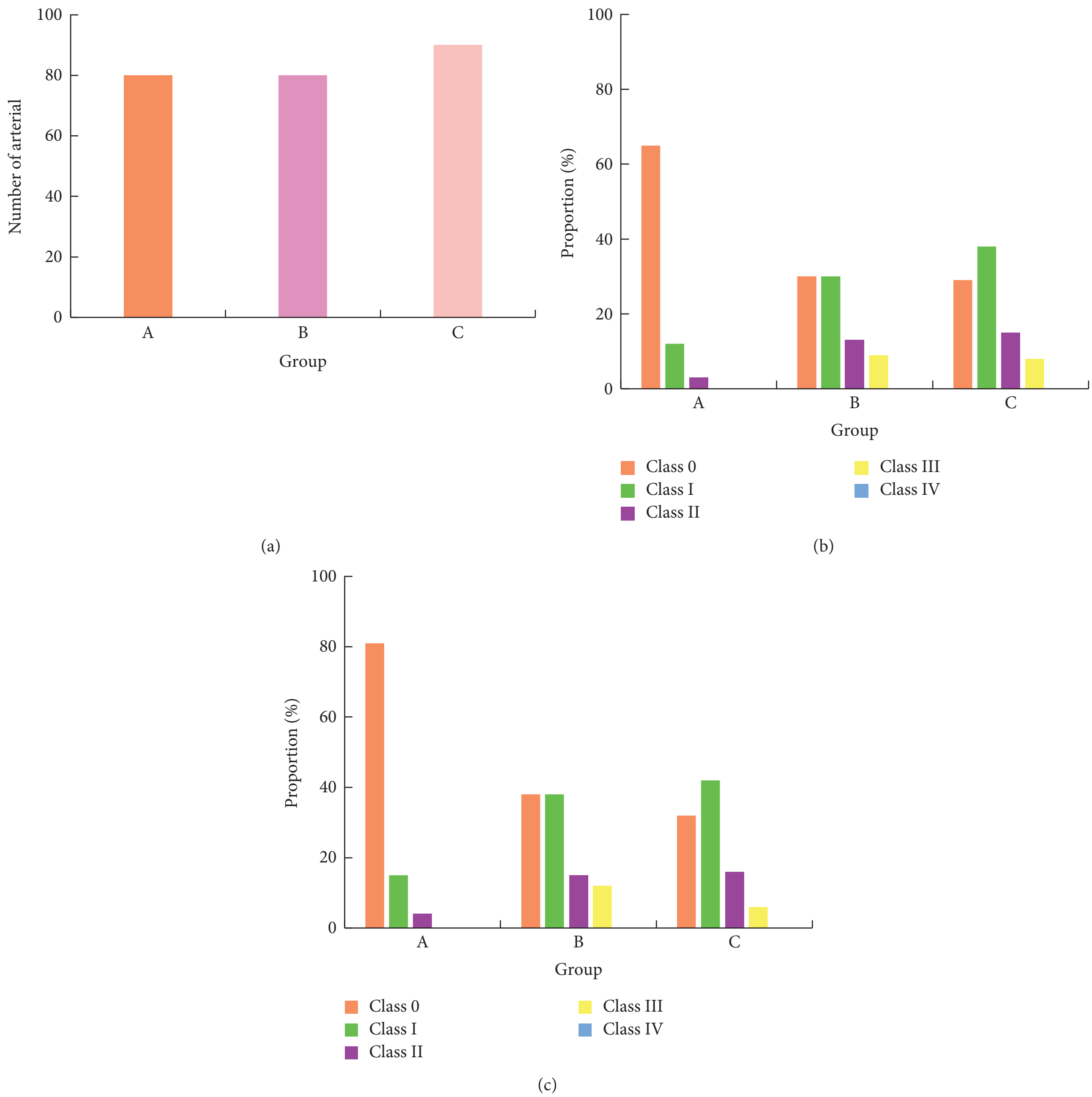

Figure 6: The occurrence of popliteal artery stenosis in each group. (a) Total number of arteries in each group. (b) The number of arteries with stenosis in each group. (c) The occurrence probability of arterial stenosis in each group.

lower extremity arteriosclerosis occlusion include DSA, MRA, CTA, and Doppler ultrasound. Among them, DSA is the gold standard for peripheral blood vessel examination, but it is invasive and expensive and thus poorly accepted by patients. Ultrasound examination has been widely used in clinical vascular examinations, especially the diagnosis of atherosclerosis, because of its fast speed, noninvasiveness, accuracy, and simple operation. It can detect early atherosclerosis and the location of small nonstenotic atherosclerotic plaques. Despite many advantages, the ultrasound examination is affected by reflection and random scattering, the image has large noise, and the edge of the lesion is often blurred. To further improve the quality of ultrasound images to more accurately grasp the patient's disease information, researchers have applied various image processing techniques to ultrasound image processing, such

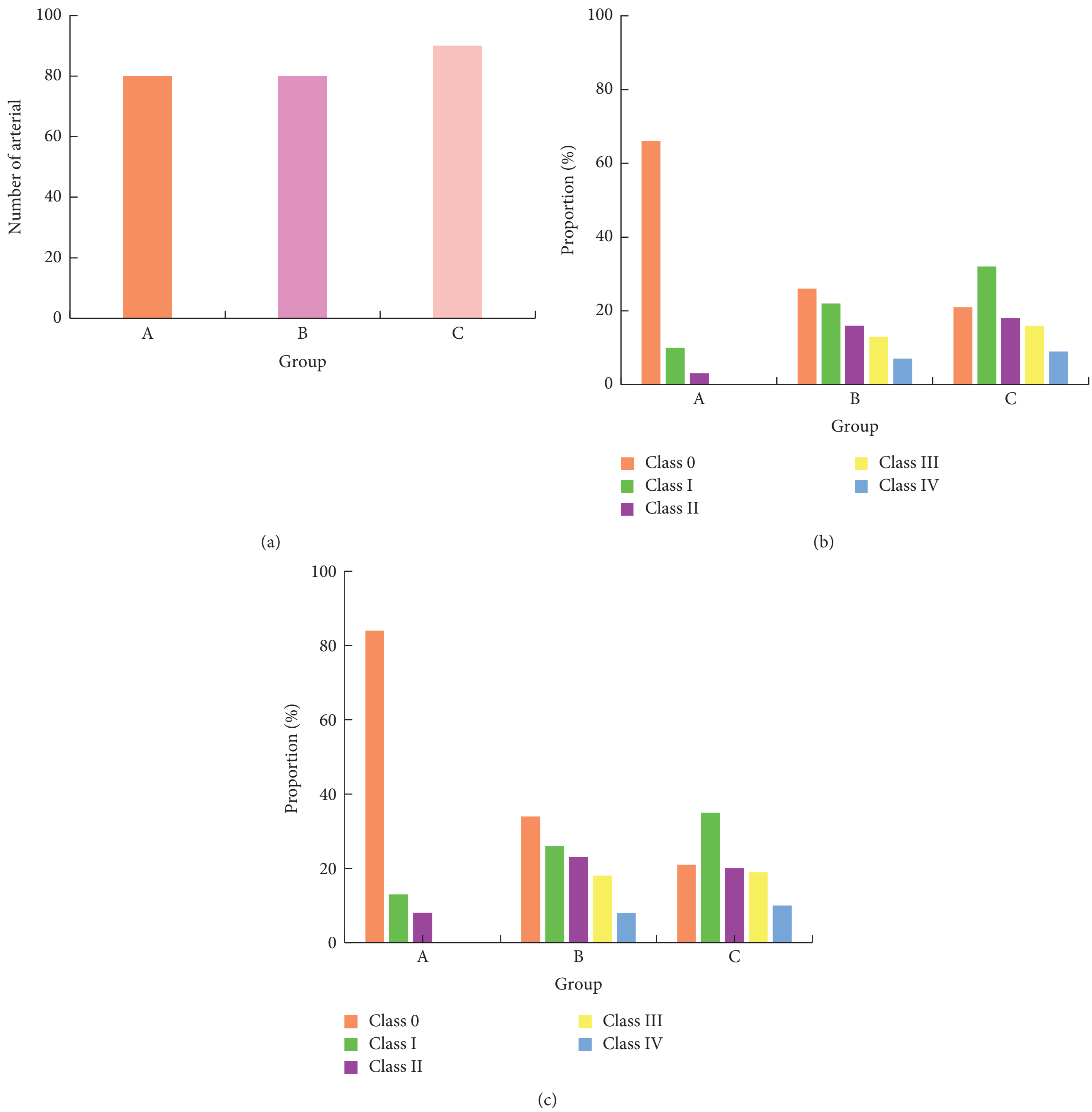

Figure 7: The occurrence of anterior tibial artery stenosis in each group. (a) Total number of arteries in each group. (b) The number of arteries with stenosis in each group. (c) The occurrence probability of arterial stenosis in each group.

as the arterial detection and tracking algorithm developed on the basis of ultrasound images [19]. In this study, the ABC algorithm was used to process the Doppler ultrasound images of all subjects. The study found that compared with the original image, the processed image was clearer, and the lesion features were more prominent. Then, the relationship

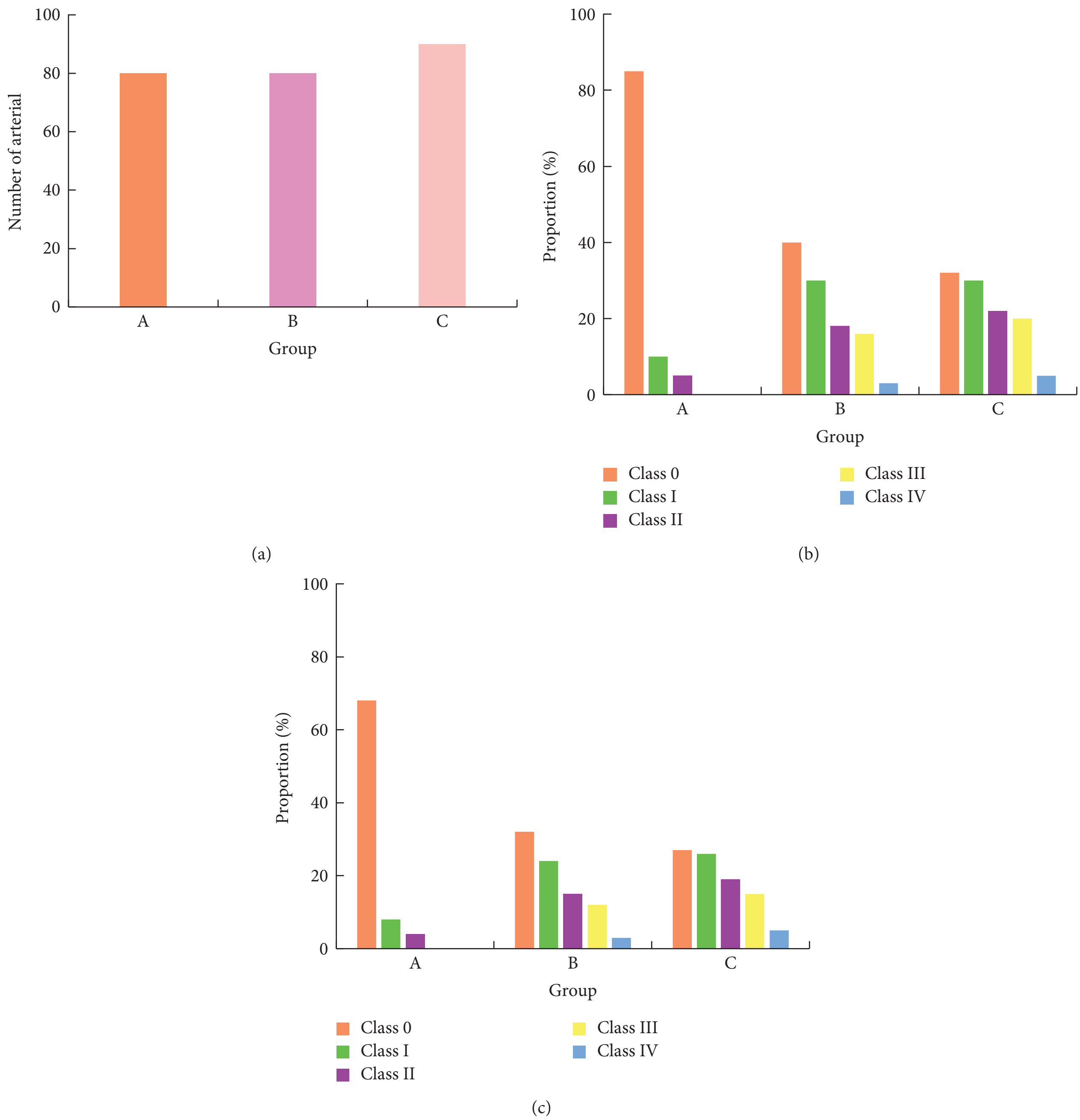

Figure 8: Occurrence of posterior tibial artery stenosis in each group. (a) Total number of arteries in each group. (b) The number of arteries with stenosis in each group. (c) The occurrence probability of arterial stenosis in each group.

between DM foot and lower extremity arteriosclerosis occlusion was analyzed on the basis. The study found that patients with DM foot combined with lower extremity arteriosclerosis occlusion had a higher incidence of lower extremity plaque and severe vascular stenosis compared with patients with DM foot alone. This suggested that DM foot is a risk factor for lower extremity arteriosclerosis occlusion.

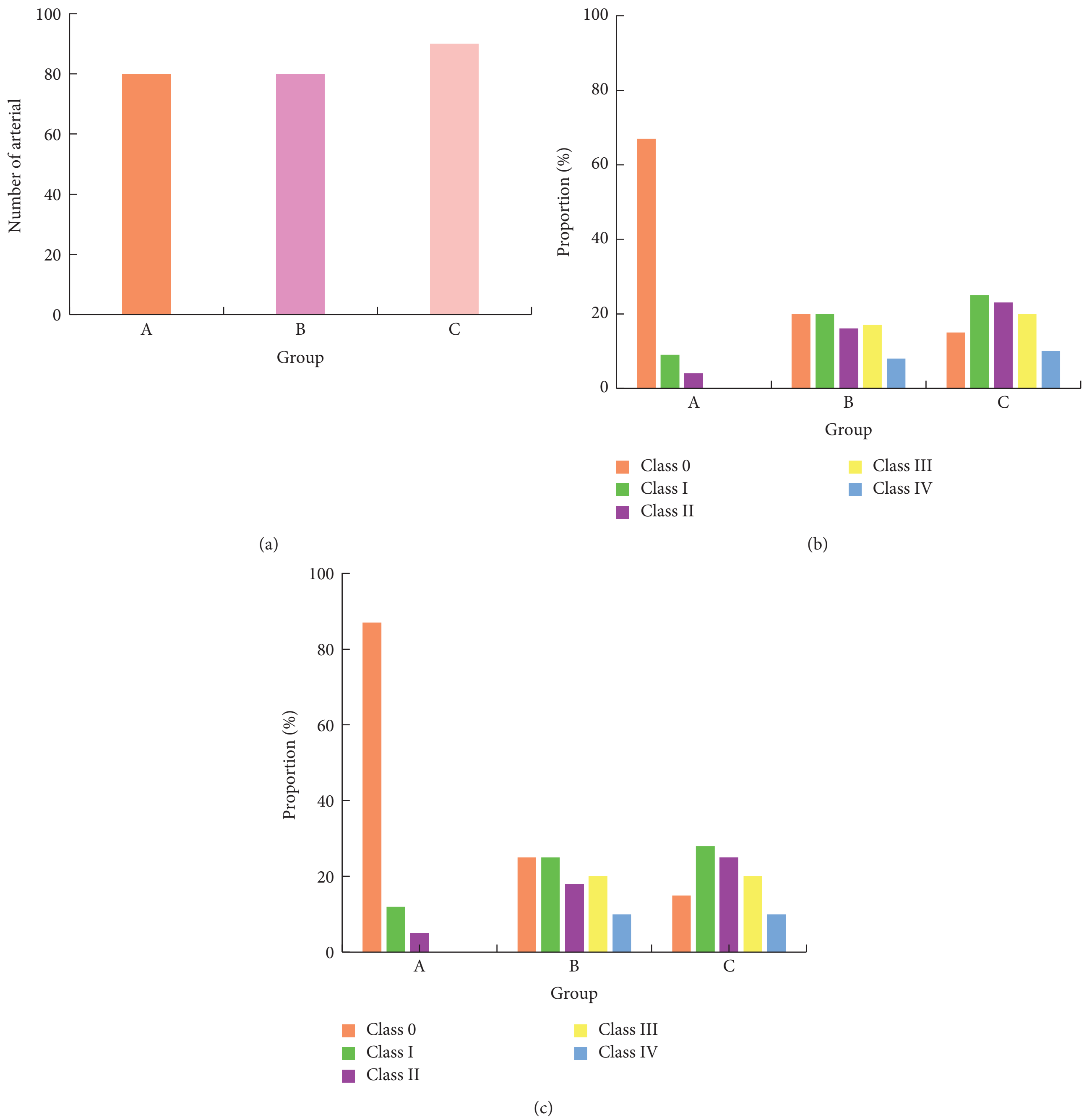

Figure 9: Occurrence of dorsal artery stenosis in each group. (a) Total number of arteries in each group. (b) The number of arteries with stenosis in each group. (c) The occurrence probability of arterial stenosis in each group.

5. Conclusion

In this study, patients with DM foot combined with PDA were selected, and they were analyzed for lower extremity arterial stenosis and plaque occurrence, as well as MIT thickness. Then, the correlation between DM foot and lower extremity arteriosclerosis occlusion was explored. It was found that DM foot was one of the risk factors for lower extremity arteriosclerosis occlusion, which negatively affect the prognosis of extremity arteriosclerosis occlusion. Meanwhile, an intelligent algorithm was used to process Doppler ultrasound images. It was found that the algorithm can highlight lesion information and improve image quality, with high application value and prospects. However, some limitations in the study should be noted. The sample size is small, which will reduce the power of the study. In the follow-up, an expanded sample size is necessary to strengthen the findings of the study.

Data Availability

The data used to support the findings of this study are available from the corresponding author upon request.

Conflicts of Interest

The authors declare no conflicts of interest.

References

[1] Y. Güneş, I. Sincer, and E. Erdal, "Catheter-directed intra-arterial thrombolysis for lower extremity arterial occlusions," *The Anatolian Journal of Cardiology*, vol. 22, no. 2, pp. 54–59, 2019.

[2] C. Martínez-Rico, X. Martí-Mestre, X. Jiménez-Guiu, E. Espinar-Garcia, D. Cervellera-Pérez, and R. Vila-Coll, "Ultrasound surveillance in endovascular revascularization of lower limbs," *Annals of Vascular Surgery*, vol. 56, pp. 274–279, 2019.

[3] P. Sapienza, A. Mingoli, V. Borrelli et al., "Inflammatory biomarkers, vascular procedures of lower limbs, and wound healing," *International Wound Journal*, vol. 16, no. 3, pp. 716–723, 2019.

[4] N. Narula, A. J. Dannenberg, J. W. Olin et al., "Pathology of peripheral artery disease in patients with critical limb ischemia," *Journal of the American College of Cardiology*, vol. 72, no. 18, pp. 2152–2163, 2018.

[5] T. Kassegne, N. Della Schiava, S. Henni, P. Feugier, J. Picquet, and M. Ammi, "What is the secondary patency of thrombosed bypasses of the lower limbs cleared by fibrinolysis in situ?" *Annals of Vascular Surgery*, vol. 61, pp. 48–54, 2019.

[6] V. C. Ganta, M. Choi, C. R. Farber, and B. H. Annex, "Antiangiogenic VEGF 165 b regulates macrophage polarization via S100A8/S100A9 in peripheral artery disease," *Circulation*, vol. 139, no. 2, pp. 226–242, 2019.

[7] P. Gogalniceanu, R. T. Lancaster, and V. I. Patel, "Clinical assessment of peripheral arterial disease of the lower limbs," *New England Journal of Medicine*, vol. 378, no. 18, p. e24, 2018.

[8] G. Adams, N. Shammas, S. Mangalmurti et al., "Intravascular lithotripsy for treatment of calcified lower extremity arterial stenosis: initial analysis of the disrupt PAD III study," *Journal of Endovascular Therapy*, vol. 27, no. 3, pp. 473–480, 2020.

[9] J. L. Heuslein, C. M. Gorick, and R. J. Price, "Epigenetic regulators of the revascularization response to chronic arterial occlusion," *Cardiovascular Research*, vol. 115, no. 4, pp. 701–712, 2019.

[10] Z. Lv, X. Li, and W. Li, "Virtual reality geographical interactive scene semantics research for immersive geography learning," *Neurocomputing*, vol. 254, pp. 71–78, 2017.

[11] J. A. Barnes, M. A. Eid, M. A. Creager, and P. P. Goodney, "Epidemiology and risk of amputation in patients with diabetes mellitus and peripheral artery disease," *Arteriosclerosis, Thrombosis, and Vascular Biology*, vol. 40, no. 8, pp. 1808–1817, 2020.

[12] Y. Shimada, N. Kino, D. Tonomura et al., "Efficacy of cutting balloon angioplasty for chronic total occlusion of femoropopliteal arteries," *Annals of Vascular Surgery*, vol. 58, pp. 91–100, 2019.

[13] B. Wang, W. Liu, Y. Huo et al., "Application of femoral-femoral artery bypass grafting combined with transverse tibial bone transporting for lower extremity arteriosclerosis obliterans or combined with diabetic foot," *Zhongguo Xiu Fu Chong Jian Wai Ke Za Zhi*, vol. 32, no. 12, pp. 1576–1580, 2018.

[14] D. V. Kosaev, "Early outcomes of therapy and indirect revascularization surgery in patients with critical ischemia of lower extremities," *Khirurgiya. Zhurnal im. N.I. Pirogova*, vol. 14, no. 8, pp. 55–60, 2020.

[15] S. H. Lai, J. Fenlon, B. B. Roush et al., "Analysis of the retrograde tibial artery approach in lower extremity revascularization in an office endovascular center," *Journal of Vascular Surgery*, vol. 70, no. 1, pp. 157–165, 2019.

[16] K. A. Chan and A. Junia, "Lower extremity peripheral artery disease: a basic approach," *British Journal of Hospital Medicine*, vol. 81, no. 3, pp. 1–9, 2020.

[17] R. J. Brouwer, R. C. Lalieu, R. Hoencamp, R. A. van Hulst, and D. T. Ubbink, "A systematic review and meta-analysis of hyperbaric oxygen therapy for diabetic foot ulcers with arterial insufficiency," *Journal of Vascular Surgery*, vol. 71, no. 2, pp. 682–692, 2020.

[18] A. Argenteri, G. de Donato, F. Setacci et al., "History of the diagnosis and treatment of critical limb ischemia and diabetic foot," *Seminars in Vascular Surgery*, vol. 31, no. 2-4, pp. 25–42, 2018.

[19] J. Hemingway, D. Emanuels, S. Aarabi et al., "Safety of transfer, type of procedure, and factors predictive of limb salvage in a modern series of acute limb ischemia," *Journal of Vascular Surgery*, vol. 69, no. 4, pp. 1174–1179, 2019.

Hindawi
Journal of Healthcare Engineering
Volume 2021, Article ID 9313201, 8 pages
https://doi.org/10.1155/2021/9313201

Review Article

Efficacy and Safety of Stem Cell Combination Therapy for Osteonecrosis of the Femoral Head: A Systematic Review and Meta-Analysis

Junqiao Li, Peng Su, Jian Li, Gang Chen, and Yan Xiong

Department of Orthopaedic Surgery, Orthopedic Research Institute, West China Hospital, Sichuan University, 37 Guoxue Lane, Wuhou District, Chengdu, China

Correspondence should be addressed to Yan Xiong; luyibingli@163.com

Received 14 July 2021; Revised 18 August 2021; Accepted 20 August 2021; Published 25 September 2021

Academic Editor: Enas Abdulhay

Background. The treatment results of core decompression (CD) and biomechanical support are not always satisfactory in osteonecrosis of the femoral head (ONFH). Stem cell therapy has been incorporated into traditional treatment in order to promote bone regeneration. The efficacy and safety of stem cell therapy combined with CD or biomechanical support on advanced and long-term patients with ONFH were unknown. The aim of this study was to assess whether stem cell combination therapy is superior to single CD or porous tantalum rod implantation treatment in ONFH. *Methods*. A systematic search of the literature was performed to evaluate all included randomized controlled trials (RCTs) on stem cell combination therapy for patients with ONFH in PubMed, Cochrane Library, Web of Science, and Embase sites. We assessed the quality and risk of bias for the included studies. And the outcomes of Harris hip score (HHS), visual analogue scale (VAS), and adverse events were statistically analyzed. *Results*. We included 10 randomized controlled trials, containing a total of 498 patients with 719 hips. Stem cell therapy combined with CD versus CD alone for HHS of ONFH was different (MD = 8.87, 95% CI = [5.53, 12.22], $P < 0.00001$). The combination of stem cell therapy and CD can effectively improve HHS. Similarly, the VAS of the stem cell combination therapy group also differed compared with the control group (MD = −14.07, 95% CI = [−18.32, −9.82], $P < 0.00001$). The result showed that stem cell combination therapy can relieve the pain of patients with ONFH. There was no significant difference in adverse response outcome events between the combination therapy group and the control group (RR = 1.57, 95% CI = [0.62, 3.97], $P = 0.34$). *Conclusions*. Stem cell therapy combined with core decompression is an effective and feasible method with few complications in the clinical treatment of early-stage ONFH. Even in the combination of porous tantalum rod implantation and peripheral blood stem cells, stem cell combination therapy is superior to single biomechanical support treatment. But high-quality, large-sample, multicenter, and long-term follow-up RCTs are still needed to corroborate the efficacy and safety of stem cell combination therapy in ONFH treatment.

1. Introduction

Osteonecrosis of the femoral head (ONFH) is a prevalent disease in relatively young patients, usually caused by hip trauma, alcoholism and long-term administration of steroid, which may lead to significant hip pain, articular surface collapse, and eventual osteoarthritis [1]. In clinical treatment, various methods are employed to avert or impede the progression of ONFH. The most common form of therapy is core decompression (CD) that has been universally administered for more than 30 years [2]. However, the treatment results of CD are not always satisfactory. This method of reconstructing necrotic areas may result in not only inadequate creeping substitution and but also bone remodeling [3]. Therefore, in order to promote bone regeneration, stem cell therapy has been incorporated into traditional CD treatment. When compared with treating ONFH with CD alone, the combined application of stem cell therapy and CD, in early treatment, has superior analgesic and clinical effects, and can more effectively delay the progress of femoral head collapse [4]. However, the efficacy and safety of these methods have been controversial and have yet to be proven in patients with advanced and long-term ONFH [5, 6].

To investigate the efficacy and safety of stem cell therapy combined with CD or porous tantalum rod implantation in ONFH patients, especially those with advanced stage and long-term follow-up [7], our research systematically retrieved the latest randomized controlled trials on stem cell combination therapy for ONFH according to the PRISMA guidelines [8]. Furthermore, the positive role and improvement of the new technologies in treatment were discussed, with a view of providing clinicians with scientific evidence for the treatment of ONFH patients.

2. Materials and Methods

2.1. Search Strategy. Two researchers independently searched databases from Cochrane Library, Web of Science, PubMed, and Embase. We integrated published randomized controlled studies of cell therapy for femur head necrosis in any language. The search period was from the date of the database establishment to January 2020. A manual supplementary search was performed before submission. The search terms were adjusted according to each database.

Taking PubMed database as an example, the search terms were as follows: ((Femur* Head Necros* [Title/Abstract]) OR (Necros* of Femur* Head [Title/Abstract]) OR ("Femur Head Necrosis" [Mesh])) AND (("Cell-and Tissue-Based Therapy" [Mesh]) OR (Cell-[Title/Abstract] AND Tissue-Based Therapy [Title/Abstract]) OR (cell therapy [Title/Abstract]) OR (Cell [Title/Abstract] AND Tissue Based Therapy [Title/Abstract]) OR (Cell Transplantation [Title/Abstract])) AND ((randomized controlled trial [Publication Type]) OR (controlled clinical trial [Publication Type]) OR (randomized [Title/Abstract]) OR (placebo [Title/Abstract]) OR (randomly [Title/Abstract]) OR (trial [Title]) OR ("Clinical Trials as Topic" [Mesh: noexp])).

2.2. Criteria for Inclusion and Exclusion. In our qualitative and quantitative analysis, only the studies that satisfied the following PICOS criteria were considered: (1) population: patients with stages I to IV of ONFH diagnosed by the Association Research Circulation Osseous classification (ARCO) [9] diagnostic criteria; (2) intervention: cell therapy combined with core decompression or porous tantalum rod implantation; (3) comparator: single core decompression or porous tantalum rod implantation therapy; (4) outcome: HHS, VAS, and adverse events; and (5) study design: randomized controlled trial (RCT).

We excluded studies with the following criteria: (1) republished studies with similar or identical content; (2) dissertation, conference, and review articles; (3) research in animal and basic experimental literature; (4) non-English published research; and (5) nonrandomized controlled trial or other irrelevant studies.

Two researchers followed the criteria for inclusion and exclusion separately. In case of disagreement, a third researcher intervened to resolve it.

2.3. Data Extraction. Two reviewers performed data extraction independently. In case of disputes, differences can be resolved through discussion or third parties until consensus was reached. The extracted information contained baseline information and feature information. The baseline information included: title, study ID, publication country, diagnostic criteria and stages, participants, age, sex ratio, intervention/control group, stem cell source, stem cell counts, the number of hips, and follow-up periods. The feature information included outcome indicators (HHS, VAS), adverse events, effect size, and 95% confidence interval.

2.4. Quality Assessment. The included studies were independently evaluated by two researchers in accordance with the Cochrane Handbook for Systematic Reviews of Interventions [10]. Cochrane Collaboration Risk of Bias Tool primarily includes selection (taking into account both allocation hiding and random sequence generation), execution (blinding of both subjects and researchers), measurement (research outcomes blind evaluation), and follow-up (outcome data completeness). A total of seven items in six aspects including gender, reporting, and further potential sources of bias were used to assess the bias risk. For each item, a categorization was specified, counting "low-risk bias," "high-risk bias," and "unclear," with this decision being made in accordance with the bias risk assessment criteria.

2.5. Statistical Analysis. Continuous variable values were expressed in mean difference (MD), and a 95% confidence interval (CI) was calculated for both. Regarding dichotomous variables, we used the risk ratio (RR) and 95% CI to describe. When $I^2 > 50\%$, heterogeneity was present within the data; hence, a random-effect model was used. When $I^2 < 50\%$, there was no heterogeneity present; hence, a fixed effects model was used. The findings of the meta-analysis were shown by the forest plot. We utilized RevMan 5.3 software for statistical analysis. $P < 0.05$ was used to evaluate statistical significance. If the number of the included studies was greater than ten, we would use a funnel plot to detect publication bias.

3. Results

3.1. Search Results. After searching various databases and a manual search method, we retrieved a total of 123 articles. Mechanical check and manual deduplication were performed by EndNote X9, 47 duplicate articles were deleted, 59 articles were excluded from our analysis after abstract screening, and 7 articles were omitted following a full-text screening, resulting in 10 randomized controlled trials being included in our qualitative and quantitative analysis [5, 6, 11–18]. The flowchart is shown in Figure 1.

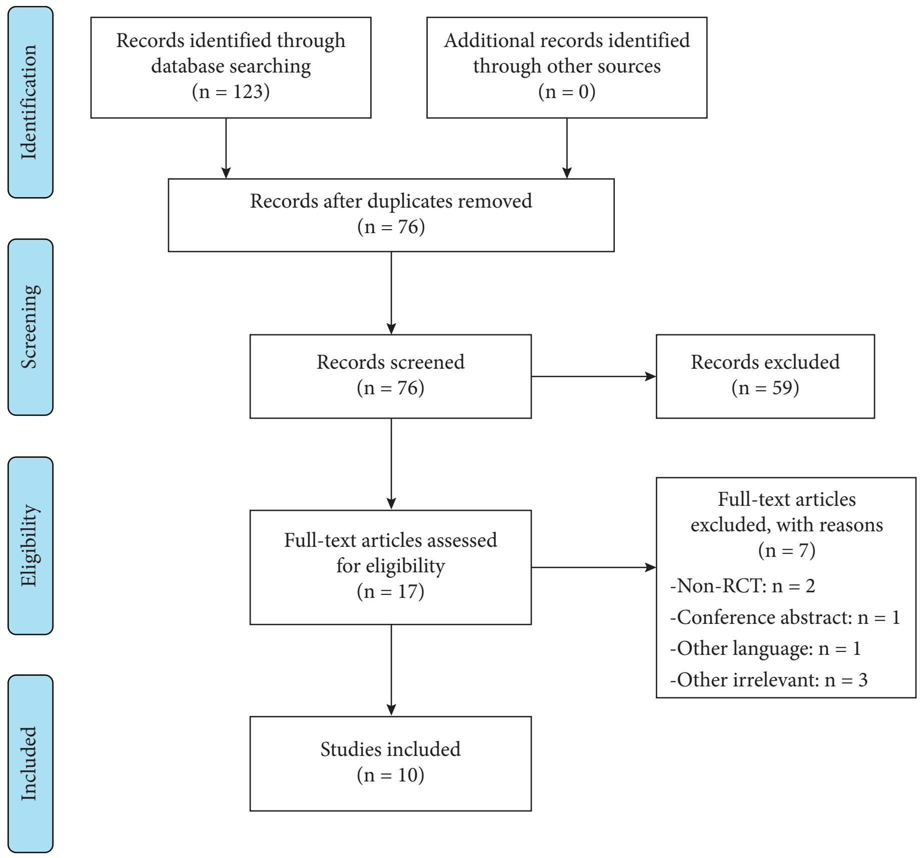

Figure 1: Flowchart of literature searching and screening process.

3.2. Study Characteristics. The publication dates of the included RCTs ranged from 2011 to 2018 and belonged to two regions in India [14, 15], one in Iran [16], one in Germany [13], three in China [11, 12, 17], two in Belgium [5, 18], and one in France [6]. All the studies used the ARCO stage as the diagnostic criteria. And the disease stage of the included patients with ONFH was mainly seen in the early phase. A total of 498 participants with 719 hips were included in this study. The longest average follow-up time was up to 25 years. See Table 1 for details.

3.3. Quality Assessment. According to the bias risk assessment method recommended by Cochrane Assistance Network, of the 10 studies included, 6 studies [5, 12, 13, 16–18] described the specific random grouping methods, 2 studies [11, 15] mentioned random grouping but did not detail the specific method, and the remaining 2 studies [6, 14] had a high risk of bias; 4 studies [6, 11, 14, 17] showed the unclear risk of bias for the allocation concealment assessment. As for the blinding of participants and personnel, 4 studies [6, 11, 13, 14] did not report whether double-blind information was used, and one study [17] had a high risk of bias; 4 studies [6, 11, 13, 14] showed the unclear risk of bias for the blinding of outcome assessment. Regarding the incomplete outcome data, one study [13] had an unclear risk of bias, and one study [17] showed a high risk of bias. All studies clearly described the selective reporting and had no other risk bias (Figures 2 and 3).

3.4. Meta-Analysis Results of HHS. Harris hip score was recorded in six studies [6, 12–15, 17] involving 572 hips. Stem cell therapy combined with core decompression treatment had higher heterogeneity ($\text{Chi}^2 = 34.21$, $I^2 = 85\%$, $P < 0.0001$) than core decompression alone, and a random effect model was used. The combination treatment group can effectively improve the Harris hip score (MD = 8.87, 95% CI = [5.53, 12.22]), and the difference was statistically significant ($P < 0.00001$). The forest plot is shown in Figure 4.

3.5. Meta-Analysis Results of VAS. Five studies [5, 6, 11, 16, 18] including a total of 397 hips reported visual analogue scales. It was evident that stem cell combination therapy yielded a higher heterogeneity than solely administering core decompression or porous tantalum rod implantation ($\text{Chi}^2 = 54.20$, $I^2 = 93\%$, $P < 0.00001$), and a random effect model was used. Stem cell combination therapy group can effectively relieve the patients' pain (MD = −14.07, 95% CI = [−18.32, −9.82]), with the difference observed between the two groups being statistically significant ($P < 0.00001$). See the forest plot in Figure 5.

3.6. Meta-Analysis Results of Adverse Events. The perioperative adverse events were reported in five studies [5, 12, 13, 17, 18]. Of these studies, three studies [5, 12, 18] reported the adverse response outcome events, including the postoperative pain at the great trochanter and iliac crest,

Table 1: Baseline characteristics of included RCTs.

Study	Year	Country	Study type	Diagnostic criteria	Disease stage	Patient	Age (years)	Sex ratio (M/F)	Intervention/control	Stem cell source	Stem cell counts	Hips	Follow-up (years)
Gangji [18]	2011	Belgium	RCT	ARCO	I/II	19	42.2 ± 2.6	NA	CD + cell therapy	BMMSCs	$92.6 \pm 22.4 \times 10^7$	13	5
Sen [15]	2012	India	RCT	ARCO	I/II	40	NA	NA	CD + cell therapy	BMMSCs	5.0×10^8	26	2
Zhao [17]	2012	China	RCT	ARCO	I/II	100	32.7 ± 10.5	27 : 23	CD + cell therapy	BMMSCs	2.0×10^6	53	5
Rastogi [14]	2013	India	RCT	ARCO	I/II/III	40	34.67 ± 7.02	5 : 2	CD + cell therapy	BMMSCs	1.1×10^8	30	2
Ma [11]	2014	China	RCT	ARCO	I/II/III	39	35.60 ± 8.05	15 : 6	CD + autologous bone graft with BBC	BMMSCs	3.0×10^9	25	2
Mao [12]	2015	China	RCT	ARCO	I/II/III	55	34.60 ± 11.50	17 : 13	Biomechanical support + cell therapy	PBSCs	$2.47 \pm 0.5 \times 10^9$	48	3
Tabatabaee [16]	2015	Iran	RCT	ARCO	I/II/III	18	31.0 ± 11.4	9 : 5	CD + cell therapy	BMMSCs	$5.0 \pm 2.0 \times 10^8$	14	2
Pepke [13]	2016	Germany	RCT	ARCO	II	24	44.3 ± 3.4	10 : 1	CD + cell therapy	BMMSCs	NA	11	2
Hauzeur [5]	2018	Belgium	RCT	ARCO	III	38	48.0 ± 2.8	14 : 5	CD + cell therapy	BMMSCs	$19.45 \pm 3.51 \times 10^9$	23	2
Hernigou [6]	2018	France	RCT	ARCO	I/II	125	18–54	78 : 47	CD + cell therapy	BMMSCs	$9.0 \pm 2.5 \times 10^4$	125	25

NA = not available; CD = core decompression; BBC = bone marrow buffy coat; BMMSCs = bone marrow mesenchymal stem cells; PBSCs = peripheral blood stem cells.

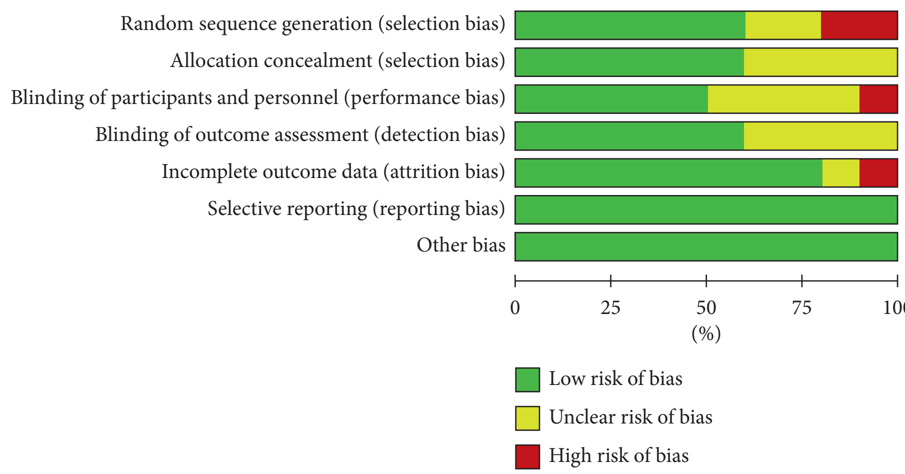

Figure 2: Bias graph risk.

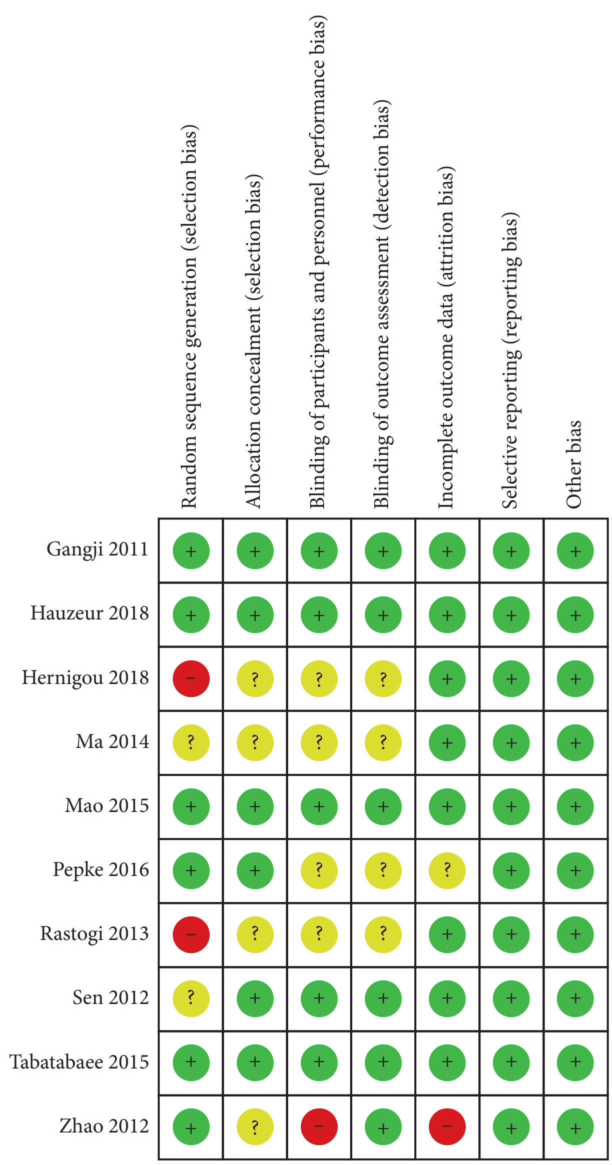

Figure 3: Bias summary risk.

hematoma, fever, nausea, infection, and porous tantalum rod displaced. Two studies [13, 17] reported that no adverse events were observed in both groups during the study period. The analysis showed that there was no significant difference in adverse events between the stem cell combination therapy group and the control group ($RR = 1.57$, 95% $CI = [0.62, 3.97]$, $P = 0.34$). The forest plot is shown in Figure 6.

3.7. Publication Bias. As no more than ten published studies were included, it was not possible to assess publication bias for the time being.

4. Discussion

4.1. Main Findings. Our findings demonstrate that in early-stage ONFH, stem cell therapy combined with core decompression is far more effective than core decompression alone. And the combination therapy has good safety with few complications. Moreover, even in the combination of porous tantalum rod implantation and peripheral blood stem cells, stem cell combination therapy is superior to single biomechanical support treatment.

4.2. Effectiveness of Stem Cell Combination Therapy. Stem cell combination therapy can relieve the symptoms of hip pain, improve patients' HHS, halt disease progression, and result in a reduction in the incidence of total hip replacement for the early-stage ONHF patients. This was confirmed in three independent systematic reviews conducted by Papakostidis et al. [19], Piuzzi et al. [20], and Wang et al. [4], respectively. However, in advanced patients, the evolution of necrosis was not significantly improved by stem cell therapy after core decompression [5]. Furthermore, the results of a network meta-analysis study by Yoon et al. [21] questioned the natural course of ONFH by CD treatment. The findings of this study suggested that the small lesions will not collapse, even without treatment being administered. This conclusion

Study or Subgroup	Combination therapy Mean	SD	Total	Control Mean	SD	Total	Weight (%)	Mean Difference IV, Random, 95% CI	Year
Sen 2012	16.23	11.7	26	22.67	16.2	25	10.8	−6.44 [−14.22, 1.34]	2012
Zhao 2012	30.1	3.1	53	19.9	4.7	44	24.4	10.20 [8.58, 11.82]	2012
Rastogi 2013	31.9	15.3	30	19.7	15.3	30	10.8	12.20 [4.46, 19.94]	2013
Mao 2015	25.4	9.9	48	13.91	21.4	41	11.9	11.49 [4.37, 18.61]	2015
Pepke 2016	21.2	6.5	11	14.6	5.4	14	16.9	6.60 [1.83, 11.37]	2016
Hernigou 2018	18	3.8	125	5	4.8	125	25.2	13.00 [11.93, 14.07]	2018
Total (95% CI)			293			279	100.0	8.87 [5.53, 12.22]	

Heterogeneity: $Tau^2 = 11.25$; $Chi^2 = 34.21$, df = 5 ($P < 0.00001$); $I^2 = 85\%$

Test for overall effect: Z = 5.20 ($P < 0.00001$)

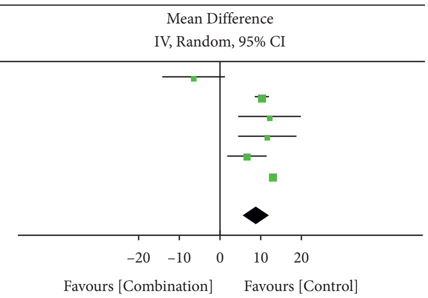

Figure 4: Forest plot of HHS.

Study or Subgroup	Combination therapy Mean	SD	Total	Control Mean	SD	Total	Weight (%)	Mean Difference IV, Random, 95% CI	Year
Gangji 2011	−12.2	7.5	13	5.3	8.2	11	15.2	−17.50 [−23.83, −11.17]	2011
Ma 2015	−18.66	3.96	25	1.25	3.09	24	21.9	−19.91 [−21.89, −17.93]	2015
Tabatabaee 2015	−19.9	4.2	14	−6.5	4.4	14	20.4	−13.40 [−16.59, −10.21]	2015
Hernigou 2018	−28.5	4.6	125	−14.2	5.7	125	22.6	−14.30 [−15.58, −13.02]	2018
Hauzeur 2018	−7.7	5.9	23	−2.3	6.4	23	19.8	−5.40 [−8.96, −1.84]	2018
Total (95% CI)			200			197	100.0	−14.07 [−18.32, −9.82]	

Heterogeneity: $Tau^2 = 20.40$; $Chi^2 = 54.20$, df = 4 ($P < 0.00001$); $I^2 = 93\%$

Test for overall effect: Z = 6.49 ($P < 0.00001$)

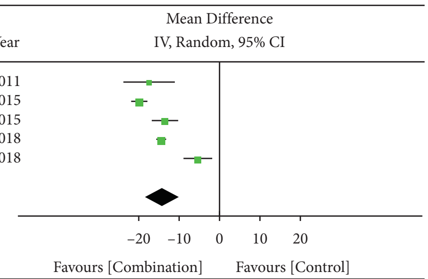

Figure 5: Forest plot of VAS.

Study or Subgroup	Combination therapy Events	Total	Control Events	Total	Weight (%)	Risk Ratio M-H, fixed, 95% CI	Year
Gangji 2011	3	13	1	11	17.6	2.54 [0.31, 21.06]	2011
Zhao 2012	0	53	0	44		Not estimable	2012
Mao 2015	1	48	1	41	17.5	0.85 [0.06, 13.23]	2015
Pepke 2016	0	11	0	14		Not estimable	2016
Hauzeur 2018	6	23	4	23	64.9	1.50 [0.49, 4.62]	2018
Total (95% CI)		148		133	100.0	1.57 [0.62, 3.97]	
Total events	10		6				

Heterogeneity: $Chi^2 = 0.39$, df = 2 ($P = 0.82$); $I^2 = 0\%$

Test for overall effect: Z = 0.95 ($P = 0.34$)

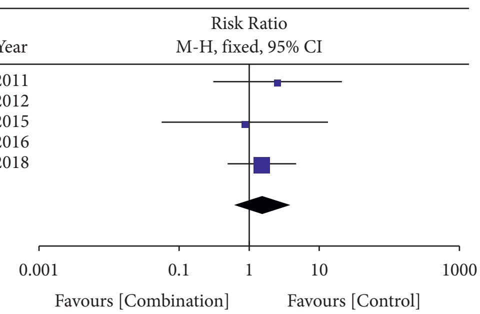

Figure 6: Forest plot of adverse events.

took into account that the extent of the decaying component was the primary factor of the necrotic femoral head fracture's collapse. However, even though the progression of osteonecrosis may result from numerous factors [6], an average follow-up time of 25-year prospective randomized study by Hernigou et al. [6] established that bone marrow cell implantation of necrotic lesions may potentially offer an effective treatment for early femoral head necrosis and impede the evolution of ailment, lessen the incidence of femoral head collapse, and elude the arthroplasty even at long-term follow-up.

4.3. Safety of Stem Cell Combination Therapy. The probability of adverse complications was extremely low, especially in the aspects of infection, excessive new bone formation, tumor induction, and local complications on the surviving side [13]. Stem cell therapy was safe for the treatment of ONFH. Even after 3–10 years of follow-up, there were no complications related to malignant tumors, bone overgrowth, core tract fractures, perforation of femoral head, deep vein thrombosis, infection, and so forth [7]. Ma et al. [11] conducted a prospective, double-blinded, randomized, controlled investigation. In order to reduce the failure rate, they improved the technology and used autologous bone grafts obtained by ring drilling with bone marrow buffy coat. Hernigou et al. [6] corroborated these findings and noted that computer navigation had the potential to be safely implemented in a basic procedure for the injection of stem cells. They all improved the overall safety of stem cell therapy and reduced the probability of complications. Additionally, Ciapetti et al. [22] demonstrated that, compared with bone marrow mesenchymal stem cells under normal conditions, the proliferation and colonization capacity of these stem cells were significantly enhanced in a hypoxic environment.

4.4. Strengths and Limitations. This systematic review was ultimately included in ten studies. All the studies were RCTs of stem cell combination therapy for ONFH, which would provide us with strong evidence for the efficacy and safety of this method in ONFH treatment. Owing to the small number of included studies, we could not make funnel charts to determine publication bias. The heterogeneity in the outcome indicators was large, which may result from certain differences in the included studies in aspects of stem cell concentration, treatment time, and the quality of the literature, leading to greater heterogeneity in each clinical study, and some outcome indicators were not stable.

The findings of this meta-analysis still had certain limitations: (1) the overall quality of the scope of included literature was not high, the sample size was small, and the short follow-up time in some studies may also lead to potential bias; (2) as no more than ten studies were included, publication bias cannot be assessed; (3) publication in English may result in language or regional bias; and (4) there was some heterogeneity in outcome indicators. High-quality, large-sample, multicenter, and long-term follow-up randomized controlled trials are still warranted to corroborate the differences in the efficacy and safety of stem cell combination therapy in ONFH.

5. Conclusion

Stem cell therapy combined with core decompression is an effective and feasible method with few complications in the clinical treatment of early-stage ONFH. Even in the combination of porous tantalum rod implantation and peripheral blood stem cells, stem cell combination therapy is superior to single biomechanical support treatment. But high-quality, large-sample, multicenter, and long-term follow-up RCTs are still needed to corroborate the efficacy and safety of stem cell combination therapy in ONFH treatment.

Data Availability

All data included in this study are available upon request by contact with the corresponding author.

Conflicts of Interest

All authors declare no conflicts of interest with this work.

Authors' Contributions

All authors read the manuscript and agreed to publish it.

References

[1] E. Larson, L. C. Jones, S. B. Goodman, K.-H. Koo, and Q. Cui, "Early-stage osteonecrosis of the femoral head: where are we and where are we going in year 2018?" *International Orthopaedics*, vol. 42, no. 7, pp. 1723–1728, 2018.

[2] I. Learmonth, S. Maloon, and G. Dall, "Core decompression for early atraumatic osteonecrosis of the femoral head," *Journal of Bone & Joint Surgery, British Volume*, vol. 72-B, no. 3, pp. 387–390, 1990.

[3] K. Koo, R. Kim, G. Ko, H. Song, S. Jeong, and S. Cho, "Preventing collapse in early osteonecrosis of the femoral head. a randomised clinical trial of core decompression," *Journal of Bone & Joint Surgery, British Volume*, vol. 77-B, no. 6, pp. 870–874, 1995.

[4] Z. Wang, Q.-M. Sun, F.-Q. Zhang, Q.-L. Zhang, L.-G. Wang, and W.-J. Wang, "Core decompression combined with autologous bone marrow stem cells versus core decompression alone for patients with osteonecrosis of the femoral head: a meta-analysis," *International Journal of Surgery*, vol. 69, pp. 23–31, 2019.

[5] J.-P. Hauzeur, V. De Maertelaer, E. Baudoux, M. Malaise, Y. Beguin, and V. Gangji, "Inefficacy of autologous bone marrow concentrate in stage three osteonecrosis: a randomized controlled double-blind trial," *International Orthopaedics*, vol. 42, no. 7, pp. 1429–1435, 2018.

[6] P. Hernigou, A. Dubory, Y. Homma et al., "Cell therapy versus simultaneous contralateral decompression in symptomatic corticosteroid osteonecrosis: a thirty year follow-up prospective randomized study of one hundred and twenty five adult patients," *International Orthopaedics*, vol. 42, no. 7, pp. 1639–1649, 2018.

[7] J. S. Kang, Y. J. Suh, K. H. Moon et al., "Clinical efficiency of bone marrow mesenchymal stem cell implantation for osteonecrosis of the femoral head: a matched pair control study with simple core decompression," *Stem Cell Research & Therapy*, vol. 9, no. 1, 2018.

[8] D. Moher, A. Liberati, J. Tetzlaff, D. G. Altman, and P. Group, "Preferred reporting items for systematic reviews and meta-analyses: the PRISMA statement," *Annals of Internal Medicine*, vol. 151, no. 4, pp. 264–269, 2009.

[9] J. W. M. Gardeniers, "ARCO (association research circulation osseous) committee on terminology and classification," *ARC News*, vol. 5, pp. 79–82, 1993.

[10] J. J. Deeks, J. Higgins, D. G. Altman, and S. Green, *Cochrane Handbook for Systematic Reviews of Interventions Version 5.1.0 (Updated March 2011)*, The Cochrane Collaboration, London, UK, 2011, http://www.cochrane-handbook.org.

[11] Y. Ma, T. Wang, J. Liao et al., "Efficacy of autologous bone marrow buffy coat grafting combined with core decompression in patients with avascular necrosis of femoral head: a prospective, double-blinded, randomized, controlled study," *Stem Cell Research & Therapy*, vol. 5, no. 5, p. 115, 2014.

[12] Q. Mao, W. Wang, T. Xu et al., "Combination treatment of biomechanical support and targeted intra-arterial infusion of peripheral blood stem cells mobilized by granulocyte-colony stimulating factor for the osteonecrosis of the femoral head: a randomized controlled clinical trial," *Journal of Bone and Mineral Research*, vol. 30, no. 4, pp. 647–656, 2015.

[13] W. Pepke, P. Kasten, N. A. Beckmann, P. Janicki, and M. Egermann, "Core decompression and autologous bone marrow concentrate for treatment of femoral head osteonecrosis: a randomized prospective study," *Orthopedic Reviews*, vol. 8, pp. 6162–6169, 2016.

[14] S. Rastogi, S. R. Sankineani, H. L. Nag et al., "Intralesional autologous mesenchymal stem cells in management of osteonecrosis of femur: a preliminary study," *Musculoskeletal surgery*, vol. 97, no. 3, pp. 223–228, 2013.

[15] R. K. Sen, S. K. Tripathy, S. Aggarwal, N. Marwaha, R. R. Sharma, and N. Khandelwal, "Early results of core decompression and autologous bone marrow mononuclear cells instillation in femoral head osteonecrosis," *The Journal of Arthroplasty*, vol. 27, no. 5, pp. 679–686, 2012.

[16] R. M. Tabatabaee, S. Saberi, J. Parvizi, S. M. J. Mortazavi, and M. Farzan, "Combining concentrated autologous bone marrow stem cells injection with core decompression improves outcome for patients with early-stage osteonecrosis of the femoral head: a comparative study," *The Journal of Arthroplasty*, vol. 30, no. 9, pp. 11–15, 2015.

[17] D. Zhao, D. Cui, B. Wang et al., “Treatment of early stage osteonecrosis of the femoral head with autologous implantation of bone marrow-derived and cultured mesenchymal stem cells,” *Bone*, vol. 50, no. 1, pp. 325–330, 2012.

[18] V. Gangji, V. De Maertelaer, and J.-P. Hauzeur, “Autologous bone marrow cell implantation in the treatment of non-traumatic osteonecrosis of the femoral head: five year follow-up of a prospective controlled study,” *Bone*, vol. 49, no. 5, pp. 1005–1009, 2011.

[19] C. Papakostidis, T. H. Tosounidis, E. Jones, and P. V. Giannoudis, “The role of “cell therapy” in osteonecrosis of the femoral head,” *Acta Orthopaedica*, vol. 87, no. 1, pp. 72–78, 2016.

[20] N. S. Piuzzi, J. Chahla, J. B. Schrock et al., “Evidence for the use of cell-based therapy for the treatment of osteonecrosis of the femoral head: a systematic review of the literature,” *The Journal of Arthroplasty*, vol. 32, no. 5, pp. 1698–1708, 2017.

[21] B.-H. Yoon, Y.-K. Lee, K.-C. Kim, Y.-C. Ha, and K.-H. Koo, “No differences in the efficacy among various core decompression modalities and non-operative treatment: a network meta-analysis,” *International Orthopaedics*, vol. 42, no. 12, pp. 2737–2743, 2018.

[22] G. Ciapetti, D. Granchi, C. Fotia et al., “Effects of hypoxia on osteogenic differentiation of mesenchymal stromal cells used as a cell therapy for avascular necrosis of the femoral head,” *Cytotherapy*, vol. 18, no. 9, pp. 1087–1099, 2016.

Hindawi
Journal of Healthcare Engineering
Volume 2021, Article ID 3284186, 8 pages
https://doi.org/10.1155/2021/3284186

Research Article

Analysis of the Significance of Immune Cell Infiltration and Prognosis of Non-Small-Cell Lung Cancer by Bioinformatics

Heng Sun,[1] Bowen Sui,[2] Yu Li,[1] Jun Yan,[1] Mingming Cao,[3] Lijia Zhang,[4] and Songjiang Liu[1]

[1]*The First Affiliated Hospital of Heilongjiang University of Chinese Medicine Department of Oncology, Harbin, China*
[2]*The First Affiliated Hospital of Heilongjiang University of Chinese Medicine Department of Oncology Respiratory, Harbin, China*
[3]*Heilongjiang University of Chinese Medicine, Harbin, China*
[4]*The First Affiliated Hospital of Heilongjiang University of Chinese Medicine Department of Oncology Ethics Office, Harbin, China*

Correspondence should be addressed to Songjiang Liu; liusongjiang@hljucm.net

Received 12 July 2021; Revised 24 August 2021; Accepted 25 August 2021; Published 22 September 2021

Academic Editor: Enas Abdulhay

Objective. To perform gene set enrichment analysis (GSEA) and analysis of immune cell infiltration on non-small-cell lung cancer (NSCLC) expression profiling microarray data based on bioinformatics, construct TICS scoring model to distinguish prognosis time, screen key genes and cancer-related pathways for NSCLC treatment, explore differential genes in NSCLC patients, predict potential therapeutic targets for NSCLC, and provide new directions for the treatment of NSCLC. *Methods*. Transcriptome data of 81 NSCLC patients and the GEO database were used to download matching clinical data (access number: GSE120622). Form the expression of non-small cell lung cancer (NSCLC). TICS values were calculated and grouped according to TICS values, and we used mRNA expression profile data to perform GSEA in non-small-cell lung cancer patients. Biological process (GO) analysis and DAVID and KOBAS were used to undertake pathway enrichment (KEGG) analysis of differential genes. Use protein interaction (PPI) to analyze the database STRING, and construct a PPI network model of target interaction. *Results*. We obtained 6 significantly related immune cells including activated B cells through the above analysis (Figure 1(b), $p < 0.001$). Based on the TICS values of significantly correlated immune cells, 41 high-risk and 40 low-risk samples were obtained. TICS values and immune score values were subjected to Pearson correlation coefficient calculation, and TICS and IMS values were found to be significantly correlated (Cor = 0.7952). Based on non-small-cell lung cancer mRNA expression profile data, a substantial change in mRNA was found between both the high TICS group as well as the low TICS group (FDR 0.01, FC > 2). The researchers discovered 730 mRNAs that were considerably upregulated in the high TICS group and 121 mRNAs that were considerably downregulated in the low TICS group. High confidence edges (combined score >0.7) were selected using STRING data; then, 191 mRNAs were matched to the reciprocal edges; finally, an undirected network including 164 points and 777 edges was constructed. Important members of cellular chemokine-mediated signaling pathways, such as CCL19, affect patient survival time. *Conclusion*. (1) The longevity of patients with non-small-cell lung cancer was substantially connected with the presence of immature B cells, activated B cells, MDSC, effector memory CD4 T cells, eosinophils, and regulatory T cells. (2) Immune-related genes such as CX3CR1, CXCR4, CXCR5, and CCR7, which are associated with the survival of NSCLC, affect the prognosis of NSCLC patients by regulating the immune process.

1. Introduction

The occurrence of tumors is not only related to the biological characteristics of the tumor cells themselves. And the interaction between cancer cells and tumor immune microenvironment and immune system also plays a very significance role. One of the problems that should be investigated is whether immune cell infiltration in tumor tissues is connected to tumor treatment and prognosis.

Lung carcinoma is a major cancer that has a high risk of morbidity and mortality, and data show that one person dies from lung cancer every 30 s worldwide [1] Lung tumor is

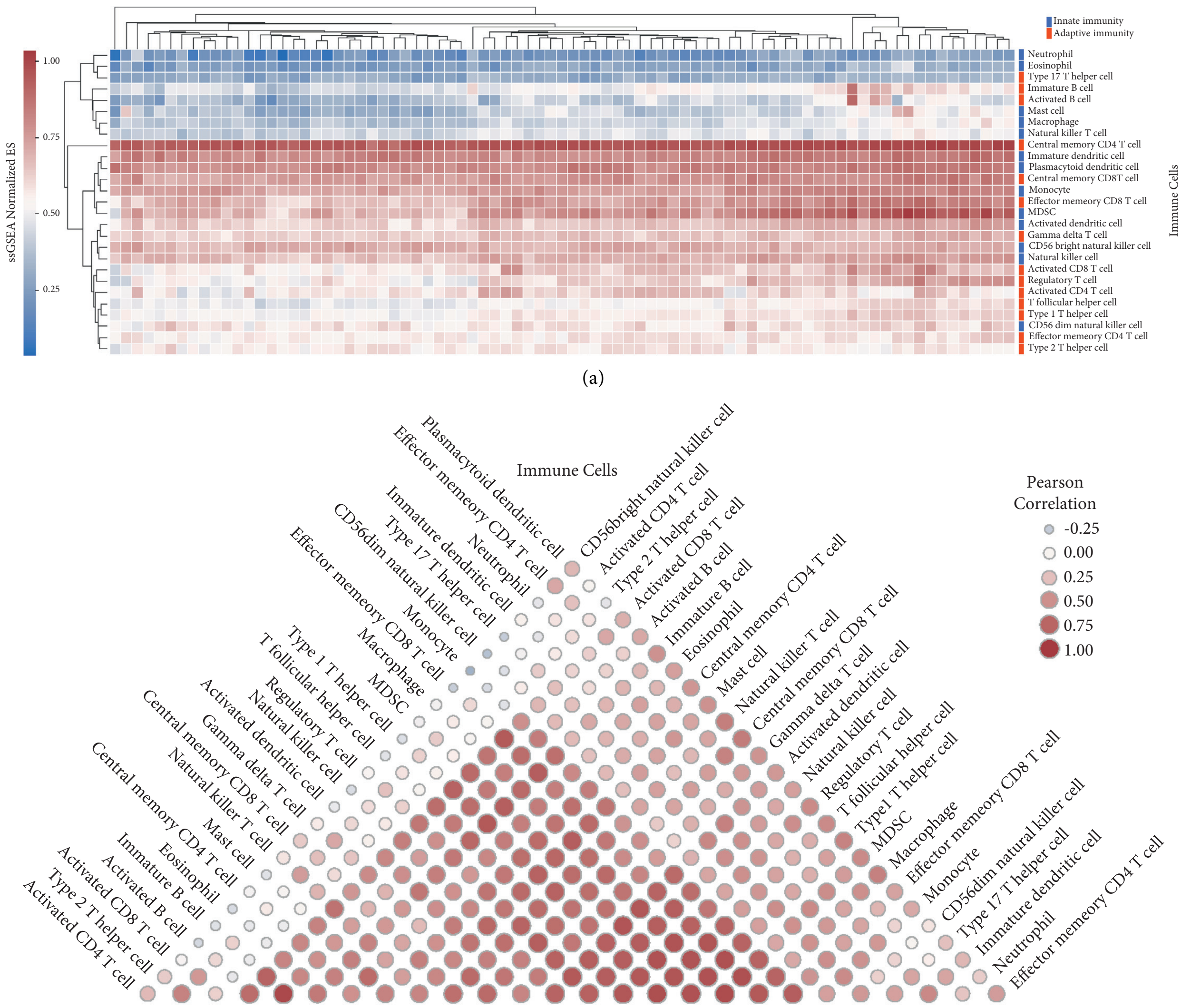

Figure 1: (a) Heat map of immune cell infiltration with the ssGSEA algorithm. (b) Construction of immune cell map based on the Pearson correlation.

divided into 2 types: small-cell lung cancer (SCLC) and non-small-cell lung cancer (NSCLC). Small-cell lung cancer (SCLC) accounts for around 85% of all lung cancer cases [2]. Because of the insidious onset, diversity of clinical manifestations, and lack of specificity of primary lung cancer patients, most patients are already in the middle and late stages of the disease when they are diagnosed with lung cancer, so whether lung cancer patients can be screened, diagnosed, and treated early becomes a key factor in prognosis.

The tumor microenvironment (TME) is a bidirectional, dynamic, and intricate network system composed of various cells (T cells, B lymphocytes, macrophages, NK cells, etc.) and extracellular components (cytokines, chemokines, and receptors, etc.), and each element of this network is capable of promoting malignant transformation and influencing both the onset, progression, and metastasis of lung cancer, development and metastasis, and the response to drug therapy [3] T-cell surface programmed cell death protein 1 (PD-1) in TME has been demonstrated to bind to programmed cell death ligand-1 (PD-L1) on the surface of cancer cells in recent years, causing T-cell dysfunction or depletion, resulting in immune tolerance and tumor cell response. Immune tolerance occurs, leading to immune escape of tumor cells [4], and in the process of killing tumor cells, the most central role in TME is played by CD8+ T cells [5], the quality and quantity of which are critical for immunotherapeutic efficacy [6]. Studies of PD-1 inhibitors for melanoma [7] have found that the number of CD8+ T cells correlates with efficacy. Tumor-infiltrating B cells are an important part of the immune system's microenvironment. In NSCLC patients, CD4+ T lymphocytes can be seen in tumor cells infiltrated by B cells and tumor cells with tertiary lymphoid structure. And high density of follicular B cells is associated with a better prognosis in NSCLC patients [8]. Bruno et al. [9] found that tumor-infiltrating B cells can present endogenous tumor antigens to CD4+ TIL and alter them in vitro. It has also been reported that bone marrow-derived suppressor cells (MDSCs) are able to produce factors like TGF-p and IL-10, which promotes the development of initial CD4+ T cells into Treg cells, resulting in the increase of Treg cells, thereby suppressing body immune response [10]. In addition, MDSC can block the secretion of natural killer cells (NK). IFN-NK cells in secreted substances refer to innate immune cells that can kill cancer cells and virus-infected cells. And IFN-NK cells can regulate the functions of other immune cells and promote tissue growth.

Chemokines are a group of small molecules (mostly 8–10 kD in molecular weight) that are capable of chemotactic cell movement. Chemokines can be classified into four groups according to the number and location of N-terminal cysteine residues: C, CC, CXC, and CX3C. For example, CCL2 chemokine has the ability to chemoattract monocytes, macrophages, and T lymphocytes [14]. It has been shown that anti-CCL2 antibodies blocking the effects of CCL2 such as reducing MDSC, increasing CD4+ and CD8+ T cell infiltration, and promoting IFNy secretion can enhance the tumor immune effect of PD-1 in treating lung cancer in mice [15]. CX3CL1 (FKN, fractalkine) is the only member of the CX3C type chemokine family, which possesses chemotactic functions common to chemokines and mediates the wandering and activation of leukocytes, especially lymphocytes and phagocytes. Li et al. [16] used gene silencing technology to confirm the stable high expression of CX3CL1 in the hepatocellular carcinoma cell line HepG2, which inhibited tumor angiogenesis. In breast cancer studies, CX3CL1 was found to have a possible role in tumor metastasis [17,18], and high CX3CL1 expression correlates with good prognosis in breast cancer [19] and can also be used as one of the indications for immunomodulatory therapy.

In summary, only a few reports have investigated the clinic pathological significance of immune cells in recent years, and the overall expression level and prognostic value of immune cell infiltration, especially in NSCLC patients, require further investigation. Therefore, in this study, we collected data from public databases and constructed statistical scoring models to analyze multiple datasets independently and pooled the analysis results in order to elucidate the prognosis-related molecular mechanisms of NSCLC, which not only helps to further understand the pathogenesis of NSCLC but also provides new ideas and targets for the early diagnosis and treatment of NSCLC.

2. Materials and Methods

2.1. Preprocessing of Data. The transcriptome and clinical data of NSCLC patients were obtained from the GEO database, using the study cohort GSE1206222 ($n = 81$). The enrolled patients' relevant somatic mutation data were also acquired from the aforesaid database. The original file was used to apply the robust multiarray average (RMA) technique on all of the expression data. Besides, "DeEseq2" and "affy" R packages were used to adjust the background, and log2 conversion was performed for the results of this analysis.

2.2. Immune Score, TICS Score, and Pearson Immune Cell Correlation Coefficient Calculation and Immune Cell Infiltration

(1) The relative abundance of 28 immune cells of tumor infiltrating in 81 patients with non-small-cell lung cancer was quantified using single-sample gene set enrichment analysis (ssGSEA). The prognosis of 28 immune cells was assessed using Cox risk regression analysis. The TICS value was calculated in terms of the risk value of immune cells and ssGSEA's NES value, and the Z-score was also calculated.

(2) We conducted principal component analysis on 81 patients' transcripts. In order to obtain genes related to high infiltration, *T*-test and FDR correction were performed. Then, we acquired upregulated and downregulated genes related to high infiltration and clustered upregulated genes and sample, comparing TICS value and immune score value and calculating Pearson correlation coefficient.

2.3. Enrichment Analysis on Function and Path.

(1) We explored the biological process of these different genes by GO and KEGG functional annotations. In addition, we used the "cluster analysis software" *R* package to implement the characteristic genes based on alternative TICS. Meanwhile, the overall relationship between GO terms and immune cells was acquired by the usage of GSEA.

(2) In order to find the relationship between GO terms, the signal pathways related to immune infiltration and the related genes involved were firstly used to construct network by STRING database. Secondly, we mined network modules and analyzed the correlation between genes and the biological processes involved.

(3) We examined and projected the survival of patients with non-small-cell lung cancer and drew a survival curve based on immune factor analyses.

3. Result 1: Construction of Immune Microenvironment Map of NSCLC

One of the most important treatments for non-small-cell lung cancer is immunotherapy (NSCLC). The heterogeneity of immune microenvironment of patients' tissues potentially affects the therapeutic effect. Therefore, the composition of immune cells in tumor tissue must be understood. First, we downloaded the transcriptome data and matched clinical data of 81 patients with NSCLC from GEO database (access number: gse120622). Based on ssGSEA algorithm, we used mRNA expression data of each patient to construct immune cell infiltration maps of NSCLC including 27 types of adaptive and innate immune cells. Central memory CD8 T cell, central memory CD4 T cell, and plasmacytoid dendritic cells are common immune cells in NSCLC tissues, which all exist in 81 patients. In addition, there are some individual specific immune cells, such as immature B cell (Figure 1(a)). We discovered that most immune cells had a high link with activated CD8 T cells, activated B cells, immature B cells, monocytes, effector memory CD8 T cells, and other cells. However, there is no evident link between some immune cells and others, such as the brilliant natural killer cell, activated CD4 T cell, and plasmacytoid dendritic cell (Figure 1(b)). This potentially indicates that there are complex interaction patterns among immune microenvironment of NSCLC patients.

4. Result 2: Construction of TICS Scoring Model Based on Immune Microenvironment of NSCLC Patients

Then, we used Cox regression to analyze and explore the relationship between 27 kinds of infiltrating immune cells and survival time on the basis of the survival data of patients. Meanwhile, we obtained the risk ratio and coefficient of 27 immune cells. The results showed that individual specific immune cells were significantly associated with the survival of NSCLC patients (Figure 2(a)). There was a high correlation between MDSC cells and other five kinds of immune cells (Figure 2(b)). We calculated a TICS score for each patient based on the quantity of these six tumor-infiltrating immune cells (see procedure) and then divided patients into high and low TICS groups based on the median TICS score. In the high TICS group, we discovered that immature B cells, activated B cells, MDSC effector memory CD4 T cells, eosinophils, and regulatory T cells had higher ssGSEA scores ($P < 0.01$) (Figure 2(c)). Various studies have found that the overall survival of many solid tumors, including NSCLC, is positively linked with tumor-infiltrating B cells [8, 20–26]. In addition, tumor-infiltrating B cells and tumor-infiltrating CD4 + T cells created three-level structures of lymphoid that was positively correlated with the survival rate of NSCLC [8, 26]. Furthermore, we analyzed the prognosis of NSCLC patients in accordance with the clinical survival data. We found a substantial difference in prognosis between the two groups, with the high TICS group having a much better prognosis than the low TICS group. This shows that the TICS score constructed can be a reference for clinical prognosis (Figure 2(d)).

5. Result 3: Related Genes of TICS Participate in Important Immune Pathways in NSCLC

Further study on the biological progress related to TICS will help to analyze the molecular mechanism affecting the prognosis of NSCLC. Firstly, we used mRNA expression data based on TICS group to conduct GSEA in patients with NSCLC. The results showed that the up-regulated genes affecting the prognosis of nonsmall cell lung cancer in the high TICS group were significantly related to the signal pathways of T cells and B cells (Figure 3(a)). This indicates that immune regulation is an important biological process affecting the prognosis of NSCLC, and the upregulated genes in the high TICS group are important molecules involved in its immune regulation. Next, we identified significantly different mRNA (FDR <0.01, FC > 2) between high TICS and low TICS groups based on the mRNA expression data of NSCLC.

Finally, 730 significantly upregulated mRNAs in the high TICS group and 121 significantly downregulated mRNAs in the low TICS group were obtained (Figure 3(b)). In accordance with our results, the upregulated mRNA is more likely to be associated with immune function such as CX3CR1, which mediates the migration and adhesion of leukocytes; CCL21 has no chemotactic effect on B cells, macrophages, or neutrophils. In order to further analyze the function of differential mRNA, we used DAVID tool to enrich it. Gene Ontology (GO) results showed that the upregulated mRNA was enriched in the top 10 biological functions. It mainly includes some function related to immune response. Similarly, the upregulated mRNA was enriched in the top ten pathways of Kyoto Encyclopedia of Genes and Genomes (KEGG). It mainly includes cell adhesion molecules and immune and other related signaling pathways. These results fully show that genes related to immune function can affect the prognosis of NSCLC. In addition, we also explored whether the top 10 biological functions (GO) are related. The result shows that these biological functions are closely related and can share the same gene set, indicating that these biological functions have some similarities.

6. Result 4: Immune-Related Genes Are the Key to Distinguish TICS

Next, we explored the interactions among the top 10 biologically functional related mRNAs. Firstly, we select high reliability edge (combined score >0.7) from STRING data. Then, 191 mRNAs were matched to the interaction edge. Finally, an undirected network with 164 points and 777 edges is constructed (Figure. 4(a)). Then, we used MCODE plug-in to obtain subnetworks and selected the subnetwork with high reliability for biological function annotation (Figures 4(b)–44(e)). We found that there was a close interaction among mRNA related to signaling pathway mediated by chemokine. At the same time, we explored whether the four subnetworks can effectively distinguish high TICS from low TICS. We find that the four small networks can distinguish high TICS from low TICS by drawing the ROC curve and calculating the area under the curve, indicating that they are potential markers to distinguish TICS (Figure 4(f)). Among them, CCL19 which is as an important member of chemokine-mediated signaling pathway has demonstrated that its expression level in tumor FSC is related to the degree of immune cell infiltration of CD8 + T cells and tumor accumulation (29391257). In conclusion, the level of CCL19 expression is related to tumor size. The lower the expression level, the larger the tumor. Besides, CX3CR1 is also a marker of T cell differentiation (33658501). These chemokines are also significantly associated with the survival of patients with NSCLC. It is reported that the expression levels of CX3CR1, CXCR4, CXCR5, and CCR7 in tumor tissues are

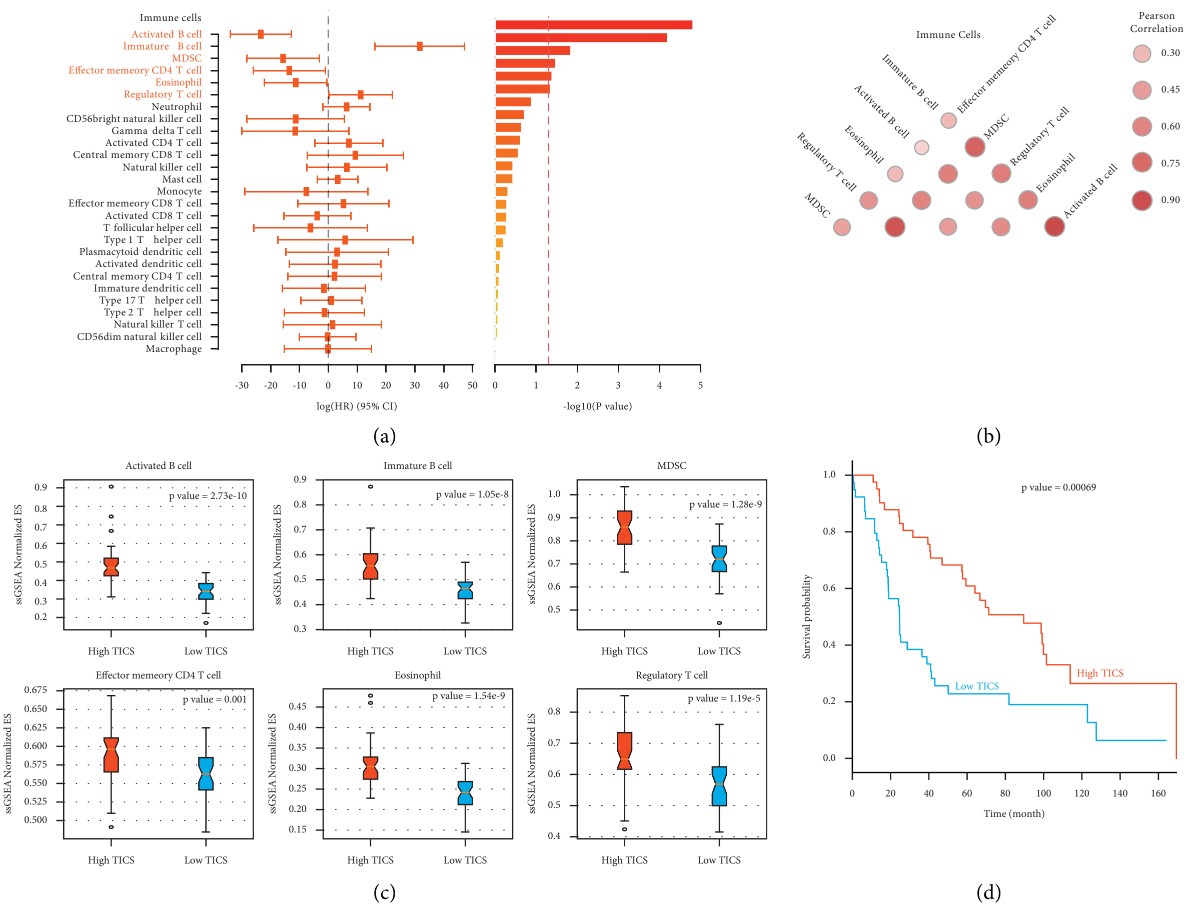

Figure 2:

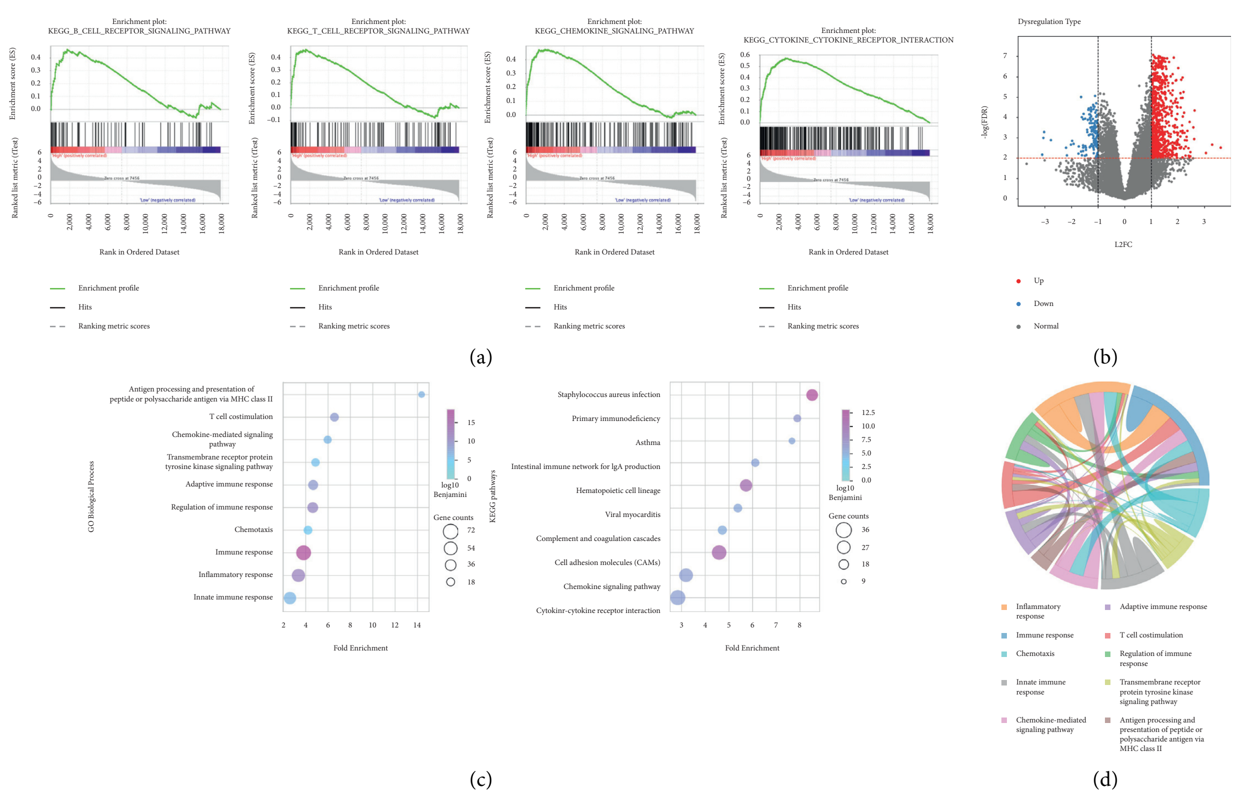

Figure 3:

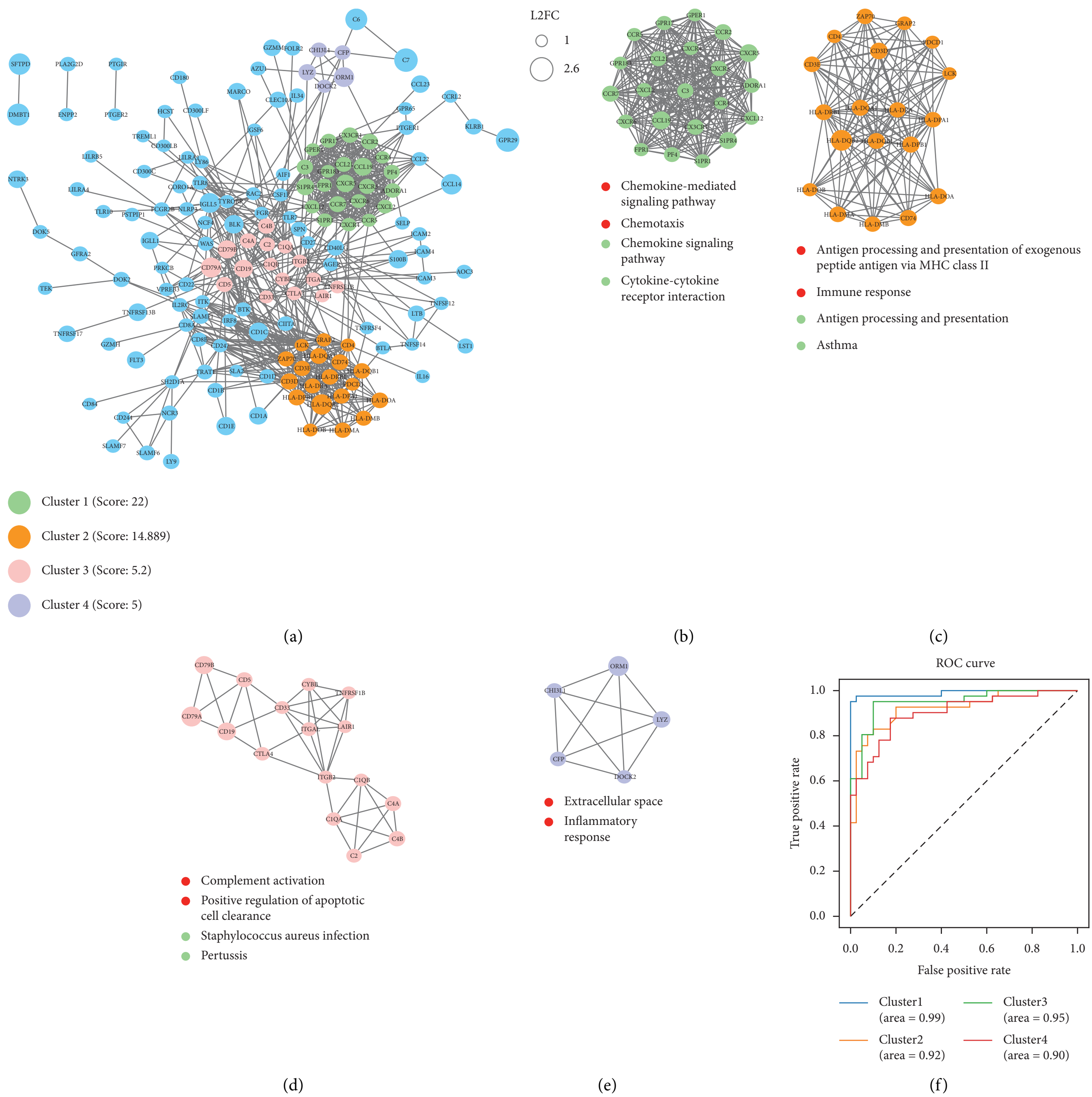

FIGURE 4:

significantly increased, which is able to affect the survival time of patients. The 5-year DFS and 5-year OS of patients with positive CCR7 expression are significantly higher (32896997).

7. Discussion

Tumor cells, fibroblasts, immune cells, different signal chemicals, and extracellular matrix make up the majority of the tumor microenvironment. Tumor microenvironment significantly affects diagnosis, survival, and clinical treatment sensitivity of tumor. Relevant studies have shown that immune cells of adaptive immune and innate immune system can penetrate into tumor tissue, forming tumor immune microenvironment and affecting tumor progression. Patients' survival following chemotherapy is influenced by the quantity of immune cells in the tumor. In this work, we used non-small-cell lung cancer mRNA expression data to create a microenvironment map of the internal immune system of tumor tissue. Combined with the analysis on immune cells combined with survival data of patients, it was found that there was a significant correlation between the survival of NSCLC patients and immature B cell, activated B cell, MDSC, effector memory CD4 T cell, eosinophil, and regulatory T cell. Next, we constructed the TICS scoring model and graded specific TICS score for patients in terms of prognosis-related immune cell content and its relationship with survival. TICS score can discriminate between patients with non-small-cell lung cancer who have a favourable prognosis and those who have a bad prognosis in terms of survival time.

Furthermore, we identified TICS-related genes by using prognostic markers and mRNA expression profiles. We found that many chemokines were significantly upregulated in the high TICS group. For example, there are CX3CR1, CXCR4, CXCR5, and CCR7 which are commonly associated with the survival of NSCLC. Also, high expression of CX3CR1 and CCL19 can affect the immune differentiation of T cells, such as CD8 + T cells. Previous studies have shown that C3 level in biopsy tissues of NSCLC is certainly correlated (24819254) with infiltrating CD4 + and CD8 + T lymphocytes. Moreover, the result of functional enrichment showed that TICS-related genes were involved in a variety of immune-related biological progresses and signaling pathways, which indicates that immune-related genes affect the prognosis of NSCLC patients by regulating the immune process.

We established PPIs among immune genes and high-confidence PPI network by using the top ten genes in biological function. PPI network results show that there is a close interaction between these genes, which indicates that immune genes may have complex coordination and interaction by which they can regulate the body's immune response. Furthermore, we explored four important subnetworks in PPI network. By drawing the ROC curve and calculating the area under the curve, we found that these four subnetworks are important molecular markers to distinguish patients from TICS. In conclusion, our study depicts a comprehensive immune map of NSCLC and constructs a TICS scoring model on the basis of the content of immune cells that can effectively distinguish the prognosis time of patients. Differential gene and enrichment analysis explains the prognosis-related molecular mechanism of NSCLC. PPI network and subnetwork mining effectively identified potential markers to distinguish TICS classification. We hope that the prognosis-related immune markers identified in our study will provide guidance for clinical diagnosis, medication, and prognosis prediction of patients.

Data Availability

The data that support the findings of this study are available from the corresponding author upon reasonable request.

Conflicts of Interest

The authors declare that they have no conflicts of interest.

Authors' Contributions

Heng Sun and Bowen Sui contributed equally to this study.

Acknowledgments

This study was supported through Heilongjiang Province Applied Technology Research and Development Plan Project, project number: GA19C109, project name: Study on the Toxic and Side Effects of Digestive Tract after Radiotherapy and Chemotherapy for Spleen Deficiency Lung Cancer Based on the Academic Thought of Professor Fujin Duan, a Master of Traditional Chinese Medicine, and supporting unit: the Heilongjiang University of Traditional Chinese Medicine and was supported by the Central Government Supports the Reform and Development of Local Colleges and Universities in Heilongjiang Province Undergraduate Colleges (High-Level Talent Project) (2020), project number: 2020GSP07, and project name: Exploration of "One Body, Two Wings" Operation Mode of Provincial TCM Cancer Diagnosis and Treatment Center.

References

[1] Z. Zhao, H. Bai, J. Duan, and J. Wang, "Recommendations of individualized medical treatment and common adverse events management for lung cancer patients during the outbreak of COVID-19 epidemic," *Thorac Cancer*, vol. 11, no. 6, pp. 1752–1757, 2020.

[2] P. L. Mitchell and T. John, "Lung cancer in 2016: immunotherapy comes of age," *Lancet Respir Med*, vol. 4, no. 12, pp. 947–949, 2016.

[3] T. Wu and Y. Dai, "Tumor microenvironment and therapeutic response," *Cancer Letters*, vol. 387, pp. 61–68, 2017.

[4] K. M. Zak, P. Grudnik, K. Magiera, A. Dömling, G. Dubin, and T. A. Holak, "Structural biology of the immune checkpoint receptor PD-1 and its ligands PD-L1/PD-L2," *Structure*, vol. 25, no. 8, pp. 1163–1174, 2017.

[5] P. S. Hegde, V. Karanikas, and S Evers, "The where, the when, and the how of immune monioring for cancer immunotherapes in the era of checkpoint inhibition," *Clinical Cancer Research*, vol. 22, no. 8, pp. 1865–1874, 2016.

[6] P. Sharma, L. S. Hu, J. A. Wargo, and A. Ribas, "Primary,adaptive, and acquired resistance to cancer immunotherapy," *Cell*, vol. 168, no. 4, pp. 707–723, 2017.

[7] P. C. Tumeh, C. L. Harview, and J. H. Yearley, "PD-1 blockade induces responses by inhibing adaptive immune resistance," *Nature*, vol. 515, no. 7528, pp. 568–571, 2014.

[8] C. Germain, S. Gnjatic, and F. Tamzalit, "Presence of B cells in tertiary lymphoid structures is associated with a protective immunity in patients with lung cancer," *American Journal of Respiratory and Critical Care Medicine*, vol. 189, no. 7, pp. 832–844, 2014.

[9] T. C. Bruno, P. J. Ebner, and B. L. Moore, "Antigen-presenting intratumoral B cells affect CD4+TIL phenotypes in NonSmall cell lung cancer patients," *Cancer Immunol Res*, vol. 5, no. 10, pp. 898–907, 2017.

[10] B. Huang, P. Y. Pan, and Q. Li, "Gr-1+CD115+ immature myeloid suppressor cells mediate the development of tumor-induced T regulatory cells and T-cell anergy in tumor-bearing host," *Cancer Research*, vol. 66, no. 2, pp. 1123–1131, 2006.

[11] E. Vivier, E. Tomasello, M. Baratin, T. Walzer, and S. Ugolini, "Functions of natural killer cells," *Nature Immunology*, vol. 9, no. 5, pp. 503–510, 2008.

[12] K. J. Malmberg, M. Carlsten, A. Bj rklund, E. Sohlberg, Y. T. Bryceson, and H.-G. Ljunggren, "Natural killer

cellmediated immunosurveillance of human cancer," *Seminars in Immunology*, vol. 31, pp. 20–29, 2017.

[13] L. Chiossone, P. Y. Dumas, M. Vienne, and E. Vivier, "Natural killer cells and other innate lymphoid cells in cancer," *Nature Reviews Immunology*, vol. 18, no. 11, pp. 671–688, 2018.

[14] T. Yoshimura, "The production of monocyte chemoattractant protein-1(MCP-1)/CCL2 in tumor microenvironments," *Cvtokine*, vol. 98, pp. 71–78, 2017.

[15] Y. Wang, X. Zhang, L. Yang, J. Xue, and G. Hu, "Blockade of CCL2 enhances effect of anti-PD1 in lung cancer," *J Bone Oncol*, vol. 11, pp. 27–32, 2018.

[16] F. Li, Z. Wang, Y. Liu, and J. Li, "Down-regulation of fractalkine inhibits the in vitro and in vivo angiogenesis of the hepatocellular carcinoma HepG2 cells," *Oncology Reports*, vol. 24, no. 3, pp. 669–675, 2010.

[17] F. Andre, N. Cabioglu, and H. Assi, "Expression of chemokine receptors predicts the site of metastatic relapse in patients with axillary node positive primary breast cancer," *Annals of Oncology*, vol. 17, no. 6, pp. 945–951, 2006.

[18] W. L. Jamieson-Gladney, Y. Zhang, A. M. Fong, O. Meucci, and A. Fatatis, "The chemokine receptor CX(3)CR1 is directly involved in the arrest of breast cancer cells to the skeleton," *Breast Cancer Research: BCR*, vol. 13, no. 5, p. R91, 2011.

[19] M. H. Park, J. S. Lee, and J. H. Yoon, "High expression of CX3CL1 by tumor cells correlates with a good prognosis and increased tumor-infiltrating CDB+ T cells, natural killer cells, and dendritic cells in breast carcinoma," *Journal of Surgical Oncology*, vol. 106, no. 4, pp. 386–392, 2012.

[20] K. I. Al-Shibli, T. Donnem, S. Al-Saad, M. Persson, R. M. Bremnes, and L. T. Busund, "Prognostic effect of epithelial and stromal lymphocyte infiltration in non-small cell lung cancer," *Clinical Cancer Research*, vol. 14, no. 16, pp. 5220–5227, 2008.

[21] K. Milne, M. Köbel, and S. E. Kalloger, "Systematic analysis of immune infiltrates in high-grade serous ovarian cancer reveals CD20, FoxP3 and TIA-1 as positive prognostic factors," *PLoS One*, vol. 4, no. 7, p. e6412, 2009.

[22] B. S. Nedergaard, M. Ladekarl, J. R. Nyengaard, and K. Nielsen, "A comparative study of the cellular immune response in patients with stage IB cervical squamous cell carcinoma. Low numbers of several immune cell subtypes are strongly associated with relapse of disease within 5 years," *Gynecologic Oncology*, vol. 108, pp. 106–111, 2008.

[23] J. R. Woo, M. A. Liss, and M. T. Muldong, "Tumor infiltrating B-cells are increased in prostate cancer tissue," *Journal of Translational Medicine*, vol. 12, no. 1, p. 30, 2014.

[24] J. Y. Shi, Q. Gao, and Z. C. Wang, "Margin-infiltrating CD20(+) B cells display an atypical memory phenotype and correlate with favorable prognosis in hepatocellular carcinoma," *Clinical Cancer Research*, vol. 19, no. 21, pp. 5994–6005, 2013.

[25] A. Shimabukuro-Vornhagen, H. A. Schlößer, and L. Gryschok, "Characterization of tumor-associated B-cell subsets in patients with colorectal cancer," *Oncotarget*, vol. 5, no. 13, pp. 4651–4664, 2014.

[26] M. C. Dieu-Nosjean, M. Antoine, and C. Danel, "Long-term survival for patients with non-small-cell lung cancer with intratumoral lymphoid structures," *Journal of Clinical Oncology*, vol. 26, no. 27, pp. 4410–4417, 2008.

Hindawi
Journal of Healthcare Engineering
Volume 2021, Article ID 4603475, 7 pages
https://doi.org/10.1155/2021/4603475

Research Article

Deep Learning-Based Image Segmentation of Cone-Beam Computed Tomography Images for Oral Lesion Detection

Xueling Wang[1], **Xianmin Meng**[1], **and Shu Yan**[2]

[1]*Department of Stomatology, Aerospace Center Hospital, Beijing 100049, China*
[2]*Department of Stomatology, PLA Strategic Support Force Characteristic Medical Center, Beijing 100101, China*

Correspondence should be addressed to Shu Yan; 201410710203@stu.shmtu.edu.cn

Received 27 June 2021; Accepted 8 September 2021; Published 21 September 2021

Academic Editor: Enas Abdulhay

This paper aimed to study the adoption of deep learning (DL) algorithm of oral lesions for segmentation of cone-beam computed tomography (CBCT) images. 90 patients with oral lesions were taken as research subjects, and they were grouped into blank, control, and experimental groups, whose images were treated by the manual segmentation method, threshold segmentation algorithm, and full convolutional neural network (FCNN) DL algorithm, respectively. Then, effects of different methods on oral lesion CBCT image recognition and segmentation were analyzed. The results showed that there was no substantial difference in the number of patients with different types of oral lesions among three groups ($P > 0.05$). The accuracy of lesion segmentation in the experimental group was as high as 98.3%, while those of the blank group and control group were 78.4% and 62.1%, respectively. The accuracy of segmentation of CBCT images in the blank group and control group was considerably inferior to the experimental group ($P < 0.05$). The segmentation effect on the lesion and the lesion model in the experimental group and control group was evidently superior to the blank group ($P < 0.05$). In short, the image segmentation accuracy of the FCNN DL method was better than the traditional manual segmentation and threshold segmentation algorithms. Applying the DL segmentation algorithm to CBCT images of oral lesions can accurately identify and segment the lesions.

1. Introduction

In recent years, with the development of computer technology and its popularity in various fields, medical institutions and other fields have been combined with computer technology, and computer-aided means are widely utilized. At present, computed tomography and magnetic resonance imaging (MRI) are widely adopted in the medical field [1]. CT is a type of X-ray computed tomography, in which different tissues absorb different amounts of X-rays. This technology can be applied to display the internal structure of the human body in the form of three-dimensional imaging, thus providing convenience and basis for clinical diagnosis and treatment of diseases and related research [2]. As a feedforward neural network, the CNN can effectively reduce the complexity of the feedback neural network, which can be utilized to identify some two-dimensional images with distorted and nondeformed forms such as displacement and scaling. The extensive application of DL in medical image classification, such as CNN, can provide convenience for researchers based on traditional research methods [3, 4]. CBCT is a cone-beam projection computer recombination tomography influence device. The X-ray generator surrounds the projection body with a low amount of radiation to make a circular digital projection [5, 6]. The projection data are two-dimensional, and a three-dimensional image will be obtained after reconstruction. Image segmentation is the main step and operation from image processing to image analysis. At present, the most commonly utilized segmentation methods are threshold-based, region-based, edge-based, and specific theory-based techniques [7, 8]. In addition, the artificial neural network recognition technology has begun to attract attention and is widely applied in image segmentation. The neural network has a large number of connections and is easy to introduce spatial information, which can better solve the problems such as uneven distribution and noise in image recognition [9].

Oral lesions include apical periodontitis, alveolar abscess, pericoronitis, periodontitis, and jaw osteomyelitis. When the oral lesion is stimulated by the external environment, the pathogenic microorganisms and related products in the lesion will diffuse outward. Then, damage to other systems or tissues and organs is caused, such as rheumatoid arthritis, chronic glomerulonephritis, erythema multiforme, and purulent nephropathy, which will aggravate the condition. However, the application of DL segmentation algorithm to oral lesion CBCT images is relatively lacking, and it is imperative to conduct in-depth research to study its clinical application [10, 11].

In this work, patients with oral lesions treated in the hospital were selected and divided into three groups and then the manual segmentation method, threshold segmentation algorithm, and FCNN DL algorithm were adopted for comparative research. They were applied to oral lesion CBCT image recognition and segmentation, so as to analyze and discuss the influence of FCNN DL algorithm on oral lesion and its effect on CBCT image analysis.

2. Materials and Methods

2.1. Selection and Grouping of Research Subjects. 90 patients who underwent oral lesion treatment in the hospital from September 2018 to September 2020 were selected as the research subjects, including 48 male patients and 42 female patients. Patients who voluntarily withdrew and transferred to the hospital were excluded. The included patients were randomly classified as three groups, blank group (manual segmentation method), control group (threshold segmentation algorithm), and experimental group (FCNN DL segmentation algorithm), with 30 cases in each group.

Inclusion criteria were as follows: (i) patients aged between 40 and 60; (ii) patients with clear consciousness and who could cooperate with treatment and sample collection; (iii) patients diagnosed with oral lesions; (iv) patients with complete clinical data and information; (v) patients without a history of mental illness and emotional stability.

Exclusion criteria were as follows: (i) patients who withdrew and transferred for treatment due to personal reasons; (ii) patients with other serious diseases or infectious diseases; (iii) patients with severe oral lesions or patients who had undergone treatment for similar diseases; (iv) patients with diseases of other systems or organs; (v) patients who had not received cooperative treatment due to personal or other reasons.

2.2. CBCT Data Set and Indicators. CBCT data of selected experimental sample patients were collected, and 90 patients with oral lesion CBCT data containing the final pathological test report were screened and selected. The CBCT data set contained CBCT cross-sectional images of patients with various oral lesions such as jaw osteomyelitis, periapical periodontitis, periodontal abscess, and pericoronitis. The image contained the overall three-dimensional structure of each patient's oral cavity, and the entire data set contained multiple CBCT images. The images were marked according to the type of the corresponding patient's lesion, and the above image marking was based on the medical gold standard of pathology test report and was jointly marked by multiple professional medical staff. After the labeling was completed, the corresponding preprocessing of the image was carried out. The CBCT images with value less than 0 were screened and set to 0, and the CBCT images with value greater than 3000 were screened and set to 3000. Then, the resulting image was divided by 3000 and multiplied by 255 to convert it into unit 8 digital format, and the preprocessed image was saved in the JPG image format. Finally, the accuracy and sensitivity of its classification were taken as evaluation indicators. The function of the denoising method in the two-dimensional image is defined as equation (1), and the function of the denoising method in the CBCT data CNN is defined as equation (2) in the three-dimensional space.

$$A(x, y) = \frac{1}{2\pi\theta^2} a^{\left(x^2+y^2/2\theta^2\right)}, \tag{1}$$

$$A(x, y, z) = \frac{1}{2\sqrt{2}\pi^{1.5}\theta^3} a^{\left(x^2+y^2+z^2/2\theta^2\right)}. \tag{2}$$

A represents the weight of each pixel; θ is the Gaussian distribution standard deviation parameter; the value of θ is 1.5; x is the abscissa value of the current pixel relative to the center pixel; and y is the abscissa value of the current pixel relative to the center pixel.

2.3. Three Different Segmentation Algorithms for CBCT Image Segmentation. Manual segmentation: manual image segmentation should be performed by doctors with rich clinical experience and over 10 years of experience in the evaluation of oral diseases. The doctor evaluated and analyzed oral lesions and utilized mimics14.11 software to sketch out the edge of lesions on the oral CBCT image by hand.

Threshold segmentation algorithm: the segmentation method referred to CBCT image segmentation by setting appropriate tissue threshold in advance. The threshold was set on the mimics14.11 software, and the threshold of the 3D oral image model was set. The HU value region was preliminarily selected and the tissues under this region were monitored in real time. The selected area was slightly adjusted by medical professionals with extensive clinical experience until the threshold was set to the segmentation edge.

FCNN DL segmentation algorithm: the CNN can identify the image through sliding window, selective search, and other methods. This algorithm can identify and judge whether the window is the target object. Its recognition is defined as the regression problem of the occurrence probability of each target in image segmentation. This method adopts FCNN DL based on CBCT image segmentation to perform image segmentation on oral lesion evaluation and utilizes average crossover ratio as the final indicator.

$$R = \frac{|M \cap N|}{|M \cup N|}. \tag{3}$$

R represents the average cross-union ratio, $M = \{(i, j)\}$ represents the point set that satisfies $Y_{i,j} = 1$ in the image, and $N = \{(i, j)\}$ represents the point set that satisfies $Y_{i,j} > 0.5$ in the image. The learning algorithm flow is shown in Figure 1.

2.4. Evaluation Indicators. The oral lesions of blank, control, and experimental groups were segmented according to the corresponding algorithm. The traditional manual segmentation, threshold segmentation algorithm, and FCNN DL algorithm were compared regarding the oral lesion CBCT image recognition and segmentation performance. Moreover, the running time, segmentation volume and surface area, image segmentation accuracy, and effect on lesions and lesion model segmentation of three methods were analyzed. The performances of the three algorithms were compared through the above indicators, and their recognition rate and accuracy of oral lesion image segmentation were studied.

2.5. Statistical Analysis. The data were processed via the SPSS19.0 version software. Measurement data were expressed as mean ± standard deviation, and count data were expressed as percentage. The t test was adopted to compare the segmentation volume and surface area, as well as running time of manual segmentation, threshold segmentation, and FCNN algorithm. Analysis of variance was utilized to compare the segmentation effect of lesions and lesion models. The difference was statistically significant at $P < 0.05$.

3. Results

3.1. Location and Type of Oral Lesions in Patients of the Three Groups. The 90 patients selected for the treatment of oral lesions were diagnosed in the experiment, and the location of the lesion was judged, as shown in Figure 2. The oral lesions of the three groups of patients were mainly periodontal, pulpal, periapical, and other chronic oral inflammations. The incidence of periodontal lesions was the highest, reaching 38%, followed by dental pulp and periapical infectious lesions, which was 29% and 17%, respectively.

The types of lesions were periodontal abscess, apical periodontitis, and jaw osteomyelitis. The types of oral lesions that occurred in the three groups of patients and the number of patients with each type of lesion are statistically shown in Figure 3. Three oral lesions of periodontal abscess, periapical periodontitis, and jaw osteomyelitis occurred in each group of patients, and there was no evident difference in the number of patients with different types of oral lesions in the three groups ($P > 0.05$).

3.2. Local Oral Lesion. Figure 4 is a partial view of the lesion in a patient with periodontal abscess. The gums at the lesion site were red and swollen, with protruding abscess formation accompanied by abscess flow and submaxillary lymph node enlargement.

Figure 5 is a partial view of the lesion in a patient with apical periodontitis. There were obvious inflammatory changes in the surrounding tissues and swelling of the surrounding tissues, apical cysts, discoloration of teeth, and hyperplasia of granulation tissue at the mouth of the apical mucosal fistula.

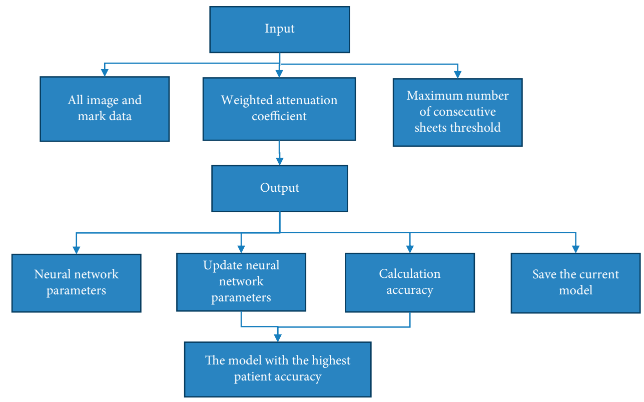

Figure 1: Schematic diagram of the DL segmentation algorithm flow.

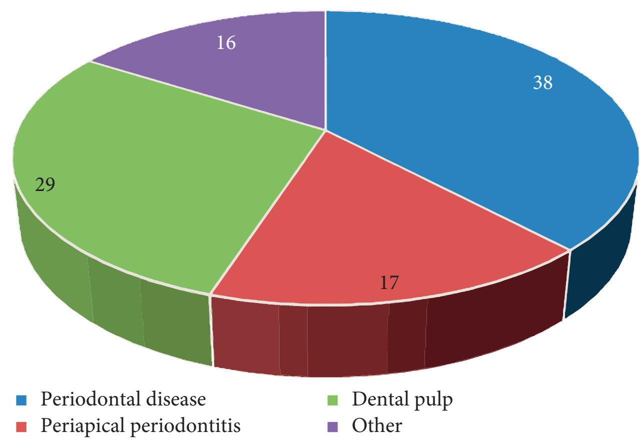

Figure 2: Location of the patients' oral lesions.

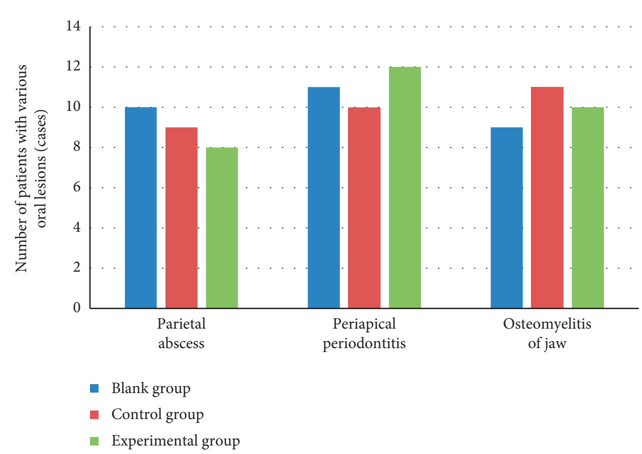

Figure 3: Types of oral lesions and number of patients.

3.3. Local Oral Lesion by Different Algorithms. Figure 6 shows the CBCT image of a patient with periapical periodontitis obtained by the traditional segmentation algorithm. The

Figure 4: Periodontal abscess.

Figure 5: Periapical inflammation.

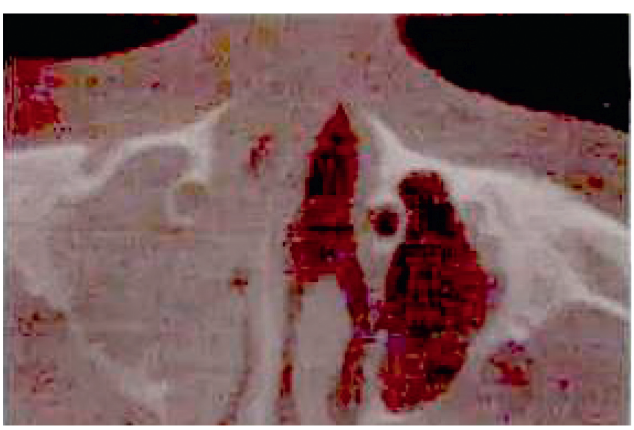

Figure 6: Traditional segmentation of the CBCT image of apical periodontitis.

lesion site showed continuous and complete low signal; obvious edema, abscess, and inflammatory reaction were observed at the lesion site; and the lesion edge segmentation was incomplete.

Figure 7 is a CBCT image of a patient with apical periodontitis obtained by the tissue threshold segmentation algorithm. The lesion site showed uneven high signal, and the surrounding tissue showed a flat oval low-signal shadow. There were obvious inflammatory changes in the lesion site,

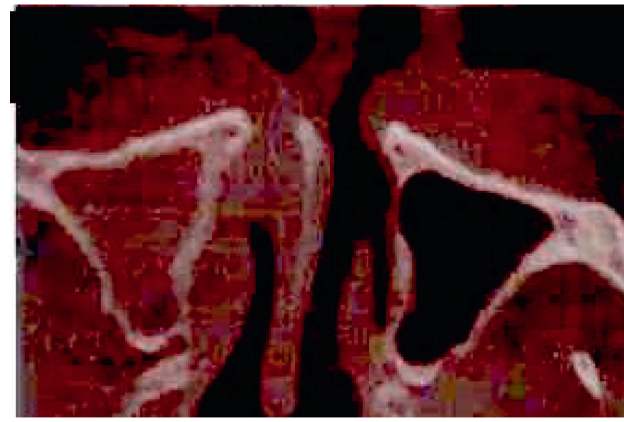

Figure 7: CBCT image of apical periodontitis by the threshold segmentation algorithm.

and the lesion edge segmentation was relatively complete and clear.

Figure 8 is a CBCT image of a patient with periodontal abscess by FCNN DL segmentation. Obvious abscesses appeared around the lesions and manifested as relatively loose mid-to-low-signal shadows, the edges of the lesions were completely segmented, and the lesion location was accurately identified.

3.4. Contrast of Segmentation Time and Accuracy of Three Segmentation Algorithms. Figure 9 shows the accuracy comparison results of the traditional segmentation algorithm, the tissue threshold segmentation algorithm, and the FCNN DL segmentation algorithm for oral lesion CBCT image segmentation. The segmentation accuracy of lesions in the experimental group was relatively higher and reached 98.3%, while those of the blank and control group were 78.4% and 62.1%, respectively. In contrast to the blank group, the accuracy of segmentation of CBCT images in the control and experimental group was notably higher ($P < 0.05$) and the accuracy of segmentation in the experimental group was considerably higher than in the control group ($P < 0.05$).

Figure 10 shows the comparison results of three segmentation algorithms for oral lesion CBCT image segmentation. The segmentation time of the FCNN DL segmentation algorithm was 10.2 ± 1.4 min, and that of threshold segmentation algorithm was 16.3 ± 1.6 min. The segmentation time of CBCT images in control and experimental groups was evidently shorter than in the blank group ($P < 0.05$), and the segmentation time in the experimental group was shorter than in control group ($P < 0.05$).

3.5. Contrast of Lesion Volume and Surface Area Obtained by Three Segmentation Algorithms. Figure 11 shows the comparison results of the volume and surface area of the oral lesion CBCT image segmentation by three segmentation algorithms. No evident difference was seen between the blank and experimental group in terms of split surface area and volume ($P > 0.05$). The volume and surface area in the

Figure 8: CBCT image of the lesion by DL segmentation.

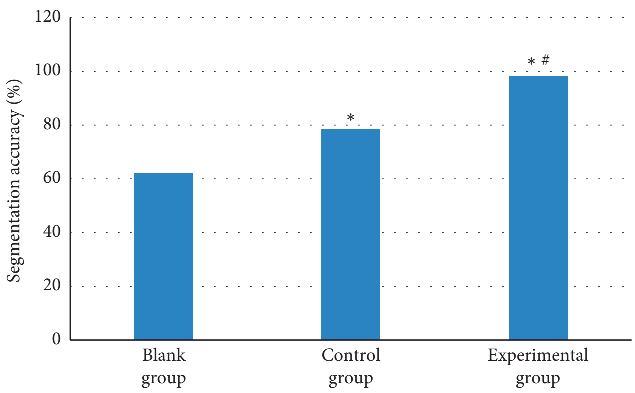

Figure 9: Contrast of accuracy of three segmentation algorithms. Note: the symbols * and # indicate that the difference was substantial, versus the blank group and control group, respectively ($P < 0.05$).

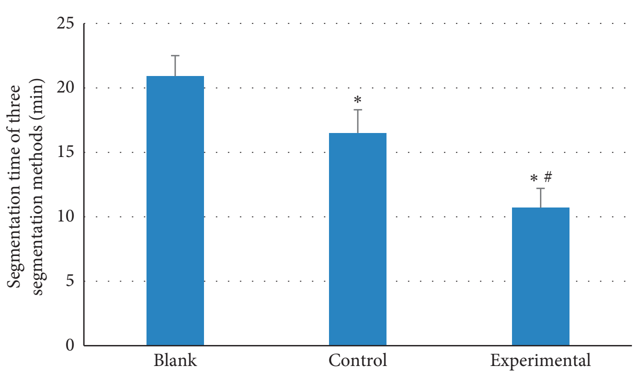

Figure 10: Contrast of running time of three segmentation algorithms. Note: the symbols * and # indicate that the difference was substantial, versus the blank group and control group, respectively ($P < 0.05$).

control group were considerably smaller than in the blank group ($P < 0.05$), and the split volume and surface area in the experimental group were remarkably larger than in the control group ($P < 0.05$).

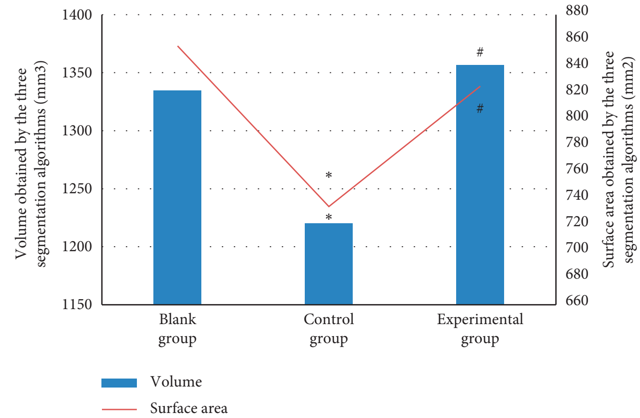

Figure 11: Contrast of the surface area and volume of the three segmentation algorithms. Note: the symbols * and # indicate that the difference was substantial, versus the blank group and control group, respectively ($P < 0.05$).

3.6. Segmentation Effect Comparison. Figure 12 shows the comparison results of the segmentation effects of the three segmentation algorithms on oral lesions and oral lesion models. The threshold segmentation algorithm and the FCNN DL algorithm had favorable segmentation effects on the lesion and the lesion model. The segmentation effect on the lesion and the lesion model in the experimental and control group was obviously superior to that in the blank group ($P < 0.05$). There was no substantial difference in the segmentation effect on lesions and lesion models between the control and experimental group ($P > 0.05$).

4. Discussion

With the application and popularization of CBCT and other three-dimensional medical imaging technologies in medical testing and treatment, as well as the improvement of human lifestyle, oral health has gradually attracted attention [12]. Stomatologists have begun to try to apply CBCT to the detection and treatment of oral lesions. Since the visualization of CBCT images and data provides important reference value for medical personnel to detect through image segmentation and analysis, the occurrence and development of diseases can be monitored intuitively [13, 14]. Early medical image research and learning algorithms often have large limitations and are not suitable for the diagnosis and treatment of all diseases. In addition, most of the research is on the human brain, chest, and abdominal organs. Therefore, it is necessary to conduct in-depth research on image analysis and algorithms and apply them to oral diseases [15, 16]. According to statistics, the rate of oral diseases in China is only 9~10%, which also has a great impact on oral health. Oral diseases, however, can cause serious bacterial or viral diseases if they fail to receive prompt diagnosis and treatment. Systemic diseases will even appear, such as chronic pharyngitis, rheumatoid arthritis, coronary heart disease, and chronic nephritis [17, 18]. In addition, relevant studies have found that oral therapy, such as periodontitis, has a bidirectional relationship with diabetes mellitus, in that

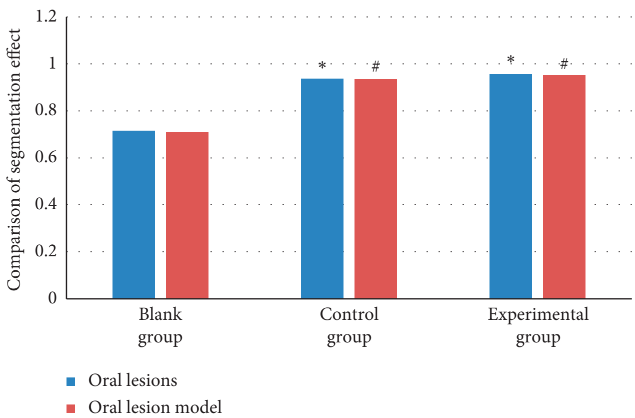

Figure 12: Comparison of the segmentation effects of three segmentation algorithms. Note: the symbols * and # indicate that the difference was substantial, versus the blank group and control group, respectively ($P < 0.05$).

severe periodontitis can aggravate diabetes mellitus and that patients' glycemic control ability is obviously worse than that of normal people. On the contrary, diabetes can also cause periodontitis and the bacteremia of periodontitis is likely to induce myocardial infarction and coronary heart disease [19]. Therefore, it is necessary to pay close attention to oral evaluation.

In this work, patients with oral lesions were selected and classified into three groups and then the manual segmentation method, threshold segmentation algorithm, and FCNN DL algorithm were adopted for comparative study. They were applied to oral lesion CBCT image recognition and segmentation, to analyze and discuss the influence of FCNN DL algorithm on oral lesions and its effect on CT images. The results showed that the experimental group was remarkably better than the blank and control group in terms of running time and accuracy of lesion segmentation. The experimental group and control group were remarkably better than the blank group in terms of the segmentation effect of lesions and lesion models ($P < 0.05$). The results were consistent with the research results of Sharma et al. [20], showing that the image segmentation accuracy of the FCNN DL method was better than the traditional manual segmentation and threshold segmentation algorithms, for it reduced the running time. Applying the DL segmentation algorithm to oral lesion CBCT images can accurately identify and segment the lesions, providing convenience for treatment, which can be applied to clinical diagnosis and treatment.

5. Conclusion

Based on the oral lesion CBCT images, the analysis and research on the FCNN DL segmentation algorithm were carried out. 90 patients were selected, and then, the DL algorithm was applied to their oral lesion CBCT images. The manual segmentation method, threshold segmentation algorithm, and FCNN DL algorithm were adopted to process images of patients in different groups for comparative study. It was found that the image segmentation effect accuracy of the FCNN DL was better than that of the traditional manual segmentation and threshold segmentation algorithms and the running time was notably reduced. The adoption of DL segmentation algorithm in oral lesion CBCT image segmentation can accurately identify and segment the lesions, which could provide convenience for treatment, and it was suitable to be applied in clinical diagnosis and treatment. However, the sample size selected in this study is small, which may have a certain impact on the experimental results, and the representativeness is low. Therefore, the sample size will be increased in subsequent experiments, and the influence of FCNN DL algorithm on oral lesion and CT image analysis will be further analyzed and discussed. In conclusion, this research provides data support and theoretical basis for the clinical diagnosis and treatment of oral lesions, as well as the adoption effect of FCNN DL segmentation algorithms on oral CBCT images.

Data Availability

The data used to support the findings of this study are available from the corresponding author upon request.

Conflicts of Interest

The authors declare no conflicts of interest.

Authors' Contributions

Xueling Wang and Xianmin Meng contributed equally to this work.

Acknowledgments

This work was supported by the Beijing Municipal Science and Technology Commission Capital Clinical Characteristic Applied Research (project number: Z171100001017177).

References

[1] W. Zhao, J. Yang, Y. Sun et al., "3D deep learning from CT scans predicts tumor invasiveness of subcentimeter pulmonary adenocarcinomas," *Cancer Research*, vol. 78, no. 24, pp. 6881–6889, 2018.

[2] B. Sahiner, A. Pezeshk, L. M. Hadjiiski et al., "Deep learning in medical imaging and radiation therapy," *Medical Physics*, vol. 46, no. 1, pp. e1–e36, 2019.

[3] R. Feng, M. Badgeley, J. Mocco, and E. K. Oermann, "Deep learning guided stroke management: a review of clinical applications," *Journal of Neurointerventional Surgery*, vol. 10, no. 4, pp. 358–362, 2018.

[4] A. Hosny, C. Parmar, T. P. Coroller et al., "Deep learning for lung cancer prognostication: a retrospective multi-cohort radiomics study," *PLoS Medicine*, vol. 15, no. 11, Article ID e1002711, 2018.

[5] F. Liu, H. Jang, R. Kijowski, T. Bradshaw, and A. B. McMillan, "Deep learning MR imaging-based attenuation correction for PET/MR imaging," *Radiology*, vol. 286, no. 2, pp. 676–684, 2018.

[6] J. Wallner, M. Schwaiger, K. Hochegger, C. Gsaxner, W. Zemann, and J. Egger, "A review on multiplatform

evaluations of semi-automatic open-source based image segmentation for cranio-maxillofacial surgery," *Computer Methods and Programs in Biomedicine*, vol. 182, Article ID 105102, 2019.

[7] B. Ibragimov and L. Xing, "Segmentation of organs-at-risks in head and neck CT images using convolutional neural networks," *Medical Physics*, vol. 44, no. 2, pp. 547–557, 2017.

[8] J. Schreier, A. Genghi, H. Laaksonen, T. Morgas, and B. Haas, "Clinical evaluation of a full-image deep segmentation algorithm for the male pelvis on cone-beam CT and CT," *Radiotherapy & Oncology*, vol. 145, pp. 1–6, 2020.

[9] F. Tang, S. Liang, T. Zhong et al., "Postoperative glioma segmentation in CT image using deep feature fusion model guided by multi-sequence MRIs," *European Radiology*, vol. 30, no. 2, pp. 823–832, 2020.

[10] J. Robertson, J. Urban, J. Stitzel, and B. E. Treeby, "The effects of image homogenisation on simulated transcranial ultrasound propagation," *Physics in Medicine and Biology*, vol. 63, no. 14, Article ID 145014, 2018.

[11] W. Li, S. Liao, Q. Feng, W. Chen, and D. Shen, "Learning image context for segmentation of the prostate in CT-guided radiotherapy," *Physics in Medicine and Biology*, vol. 57, no. 5, pp. 1283–1308, 2012.

[12] J. Minnema, M. van Eijnatten, W. Kouw, F. Diblen, A. Mendrik, and J. Wolff, "CT image segmentation of bone for medical additive manufacturing using a convolutional neural network," *Computers in Biology and Medicine*, vol. 103, pp. 130–139, 2018.

[13] A. P. Reeves, Y. Xie, and S. Liu, "Large-scale image region documentation for fully automated image biomarker algorithm development and evaluation," *Journal of Medical Imaging*, vol. 4, no. 2, Article ID 024505, 2017.

[14] E. Jafargholi Rangraz, W. Coudyzer, G. Maleux, K. Baete, C. M. Deroose, and J. Nuyts, "Multi-modal image analysis for semi-automatic segmentation of the total liver and liver arterial perfusion territories for radioembolization," *EJNMMI Research*, vol. 9, no. 1, p. 19, 2019.

[15] H. Kato, M. Kawaguchi, T. Ando, M. Aoki, B. Kuze, and M. Matsuo, "CT and MR imaging findings of non-neoplastic cystic lesions of the parotid gland," *Japanese Journal of Radiology*, vol. 37, no. 9, pp. 627–635, 2019.

[16] M. Oda, P. V. Staziaki, M. M. Qureshi et al., "Using CT texture analysis to differentiate cystic and cystic-appearing odontogenic lesions," *European Journal of Radiology*, vol. 120, Article ID 108654, 2019.

[17] S. Reddy, R. Prashanth, B. Yashodha Devi, N. Chugh, A. Kaur, and N. Thomas, "Prevalence of oral mucosal lesions among chewing tobacco users: a cross-sectional study," *Indian Journal of Dental Research*, vol. 26, no. 5, pp. 537–541, 2015.

[18] P. J. Pickhardt, V. P. Lam, J. M. Weiss, G. D. Kennedy, and D. H. Kim, "Carpet lesions detected at CT colonography: clinical, imaging, and pathologic features," *Radiology*, vol. 270, no. 2, pp. 435–443, 2014.

[19] C. Kruse, R. Spin-Neto, J. Reibel, A. Wenzel, and L.-L. Kirkevang, "Diagnostic validity of periapical radiography and CBCT for assessing periapical lesions that persist after endodontic surgery," *Dentomaxillofacial Radiology*, vol. 46, no. 7, Article ID 20170210, 2017.

[20] U. Sharma, P. Singhal, K. Bandil et al., "Genetic variations of TLRs and their association with HPV/EBV, co-infection along with nicotine exposure in the development of premalignant/malignant lesions of the oral cavity in Indian population," *Cancer Epidemiology*, vol. 61, pp. 38–49, 2019.

Hindawi
Journal of Healthcare Engineering
Volume 2021, Article ID 6128260, 7 pages
https://doi.org/10.1155/2021/6128260

Research Article

Wavelet Transform Artificial Intelligence Algorithm-Based Data Mining Technology for Norovirus Monitoring and Early Warning

Xucheng Fan,[1] **Na Xue**,[1] **Zhiguo Han**,[1] **Chao Wang**,[2] **Heer Ma**,[1] **and Yaoqin Lu**[1]

[1]*Department of Infectious Disease Control, Urumqi Center for Disease Control and Prevention, Urumqi 830026, Xinjiang, China*
[2]*Department of Microbiology, Urumqi Center for Disease Control and Prevention, Urumqi 830026, Xinjiang, China*

Correspondence should be addressed to Yaoqin Lu; 201823252501013@zcmu.edu.cn

Received 29 June 2021; Accepted 4 September 2021; Published 17 September 2021

Academic Editor: Enas Abdulhay

Norovirus monitoring and early warning can be used for diagnosis without etiological testing, and the treatment of this disease does not require the antibiotics. It often occurs in preschool children and affects their growth and development, so the coping measures for this disease are more prevention than treatment. In this study, the clinical data of 2133 children with diarrhea were collected. Based on the artificial intelligence (AI) algorithm of wavelet transform, a related model for data mining and processing of children's intestinal ultrasound images and stool specimens was constructed. Then, the norovirus infection trend was warned based on the wavelet analysis algorithm model. The results showed that the intestinal ultrasound image processed by the wavelet transform algorithm was clearer. The positive detection rate of norovirus in children with clinical diarrhea was as high as 59%, and the children had different degrees of body damage, of which the probability of compensatory metabolic acidosis was the highest. The epidemiological analysis found that children with norovirus infection were mainly concentrated in the age group under 2 years old and over 5 years old and showed a peak of infection in December. In summary, the intelligent algorithm based on wavelet transform can realize the noise reduction of intestinal ultrasound, and it should protect children with susceptible age and susceptible seasons to reduce the clinical infection rate of norovirus.

1. Introduction

Norovirus, also known as Norwalk virus, is highly similar to common viruses except for antigenicity [1]. The diarrhea caused by the virus is extremely prevalent, and infection can occur throughout the year. The main population of the disease includes adults and school-age children, with a high incidence in cold seasons [2]. In Western developed countries, more than 80% of all nonbacterial diarrhea outbreaks are infected by the virus every year. Besides, there are similar results in many developing countries [3]. Among children patients with diarrhea under 6 years old in China, the detection rate of norovirus is about 17%, and it has been found that the infection of this virus is also extremely common in the population of China through blood routine investigation [4]. The virus has distinct characteristics such as rapid mutation, strong resistance, and diverse transmission routes. Patients may have clinical manifestations such as diarrhea, vomiting, and fever after illness [5]. According to relevant investigations and studies, norovirus outbreaks have been dominated by other infectious diarrheal diseases in China since 2010. Especially, since the winter of 2014, norovirus outbreaks have increased significantly, higher markedly than previous years, so monitoring and early warning of this virus has become particularly important [6].

Clinical examinations for diarrhea caused by the virus usually use X-ray, endoscopy, B-mode ultrasound, and other examinations, among which B-mode ultrasound has become one of the main examination methods due to its noninvasive and nonradioactive advantages [7]. A large amount of information of the children patients have been recorded by B-mode ultrasound, such as abdominal changes after infection. It is necessary to carry out data mining and summarize the main data information so as to analyze the massive and complex data [8]. However, information deviation is caused due to the influence of noise during B-mode ultrasound examination, so the artificial intelligence algorithm is needed to deal with it [9]. Wavelet transform is a new type of the transform analysis method, which is evolved from the idea of localization of short-time Fourier transform. It overcomes the disadvantage that the window size does not change with frequency and provides a "time-frequency" window, which is an ideal tool to realize signal time-frequency analysis and processing at present [10]. Using the wavelet transform, noise and useful signal can be decomposed to different scales, and wavelet coefficients can be converted, so that useful signal can be distinguished from noise [11]. At present, the application in the science and technology information industry has made remarkable achievements, and it has become a critical part of contemporary scientific and technological work [12]. What is more, its application research in epidemic diseases is relatively small. In order to evaluate the feasibility and effectiveness of data mining technology based on the wavelet transform artificial intelligence algorithm for norovirus monitoring and early warning, wavelet transform artificial intelligence algorithm-based data mining technology was adopted in this study, so as to discuss the diarrhea caused by norovirus infection. Therefore, its feasibility in the monitoring and early warning of virus infection could be obtained, thereby providing reference significance for the application of other diseases.

2. Materials and Methods

2.1. General Data. 2,133 children patients with diarrhea admitted to hospital from April 2016 to June 2020 were selected as the research objects in this study. Among them, 1,154 were boys and 979 were girls, aged 30 days–6 years old after birth, with an average age of 2.13 ± 0.22 years old. The inclusion criteria were as follows: children patients defecated more than 3 times a day and had abnormal changes in fecal characteristics; children patients were younger than 6 years old and did not suffer from other diseases such as pus and blood in the stool and pneumonia; children patients had congenital digestive system diseases; and the family members of the children patients were aware of this study and signed the informed consent forms. The exclusion criteria were as follows: children patients were combined with other basic diseases that affected digestive function; the parents of the children patients did not cooperate with the researcher; the children patients had poor compliance; and the children patients were infected with other epidemic diseases during the research period. Most importantly, the medical ethics committee of hospital reviewed and approved this study.

2.2. Methods

2.2.1. Specimen Collection. 5 mL of the stool specimen of each included child patient was taken and put into a sterile and dried container. Then, it was placed in phosphate buffer, which was mixed into a 15% stool suspension. Afterwards, the suspension was divided into two evenly. One part was used to detect rotavirus, and the remaining one part was stored in a water tank at a temperature of −80°C to extract deoxyribonucleic acid (DNA) and ribonucleic acid (RNA) from the child patient.

2.2.2. Virus Detection. The norovirus detection kit (produced by Shanghai Fusheng Industrial Co., Ltd.) was adopted in this study, and the detection was carried out based on the operating instructions of the immunochromatography kit. The supernatant was extracted from the stool suspension, which was mixed with the enzyme marker evenly. Next, the mixture was added to the specimen well, which was placed at room temperature and then added with enzyme marker for incubation at room temperature. Finally, the incomplete binding peroxidase was rinsed with lotion, and the results in the kit were observed.

The rotavirus antigen kit (produced by Shanghai Kemin Biotechnology Co., Ltd.) was applied in this study, and the operating instructions of the enzyme-linked immunosorbent assay kit were refereed for detection. The specimens and standard specimens were added in the coated micropores with prereported captured antibodies and washed thoroughly after incubation. Then, the substrate tetramethylbenzidine (TMB) was used for color development. The absorbance value was calculated at 420 nm by using the enzyme-plate method.

2.3. Ultrasonic Testing. The Siemens 18L6HD and other color Doppler ultrasound diagnostic equipment was adopted in this study, with the high-frequency probe (7.0–12.0 MHz). Before the examination, the children patients should fast for 3-4 hours, the infants who used milk should fast for more than 4 hours, and the infants and children patients after supplementary food should be fasted for more than 6 hours. During the examination, each child patient was placed in a supine position. The examiner would probe coated with a small amount of the coupling agent and then put on the latex sleeve; in the case of children relaxed, the probe would slowly contact the skin of children, began ultrasound scanning, and carefully observe the stomach and intestinal wall layer changes of children patients.

2.4. Analysis of Wavelet Transform Algorithm. The wavelet analysis algorithm belonging to a kind of window size is fixed but the shape can be changed, which is called the "mathematical microscope." Moreover, it can play its high time resolution and low frequency resolution in the high-frequency part, which shows that the wavelet transform has the self-adaptability to the signal. The wavelet change algorithm was adopted in the denoising of the intestinal ultrasound images of children in this study, so as to provide data for the follow-up exploration of the body damage of children.

In the wavelet transform algorithm, the following can be obtained if $P(t)$ represents a square cocoa integrable function.

$$P(t) \in R^2(e). \tag{1}$$

In equation (1), e stands for a constant, R means the upper limit of space, and its Fourier transform $P(w)$ satisfies the following equation.

$$C_P = \int_{-\infty}^{+\infty} \frac{|P(w)|^2}{w} lw < \infty. \quad (2)$$

Then, the frequency domain of wavelet transform can be expressed as follows.

$$wt_i(a,s) = \frac{\sqrt{a}}{2\Pi} \int_{-\infty}^{+\infty} i(w)^P (awe)^{ws} w. \quad (3)$$

In equation (3), a represents different transformation scales, the signal to be analyzed is represented by i, and s indicates the displacement of the fundamental wavelet function.

Continuous wavelet transform is to expand and shift the mother wavelet $P(t)$ to obtain the function $P_{a,s}(t)$, which is expressed in the following equation.

$$P_{a,s}(t) = \frac{1}{\sqrt{a}} P\left(\frac{t-s}{a}\right). \quad (4)$$

In (4), $P_{a,s}(t)$ is the wavelet basis function that depends on the parameters. The expansion and contraction in the time domain and the time translation can be expressed in Figures 1 and 2.

Discrete wavelet transform usually adopts binary discrete form, as shown in the following equation.

$$a = 2^x. \quad (5)$$

Thus, (6) can be attained.

$$P_{x,s}(t) = 2^{x^2} P(2^x t - s). \quad (6)$$

The basic principle of wavelet transform noise reduction is presented in the following equation.

$$Y(o) = G(o) + e(o), \quad o = 1, 2, \ldots, n-1. \quad (7)$$

Among them, $Y(o)$ represents the signal with noise, $G(o)$ stands for the actual signal, and $e(o)$ expresses the magnitude of the noise.

Wavelet transform can decompose signal and noise and separate useful and useless signals. The specific performance is that useful signals have larger decomposition coefficients in some components, while the decomposition coefficients of noise are smaller. In addition, some components have the opposite performance. The decomposition coefficient of noise is large, while the decomposition coefficient of useful signal is small. Finally, the final result can be obtained by coefficient reconstruction after transformation (Figure 3).

The signal-to-noise ratio (SNR), root mean square error (MSE), and carrier-to-noise ratio (CNR) were adopted to evaluate the denoising effect of the algorithm. The calculation equations of SNR, MSE, and CNR are as follows:

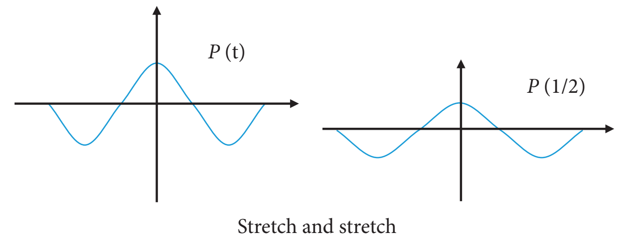

Figure 1: The stretching transformation of wavelet in time domain.

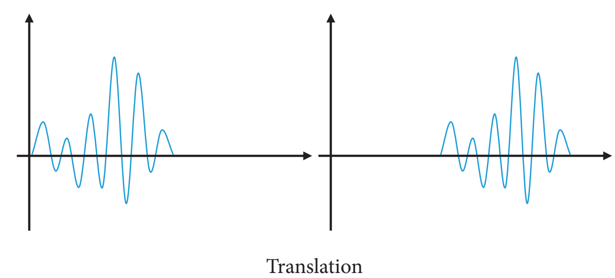

Figure 2: Time shift of wavelet.

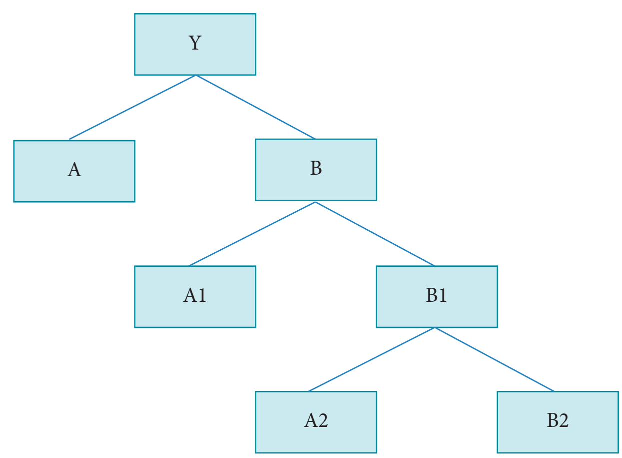

Figure 3: Three-layer decomposition of wavelet transform. A and B stand for weight.

$$\mathrm{SNR} = \frac{S}{N0B},$$
$$\mathrm{MSE}(y, \hat{y}) = \frac{1}{n} \sum_{i=1}^{n} (y_i - \hat{y})^2. \quad (8)$$
$$\mathrm{CNR} = \frac{S}{N0}.$$

In the above equations, S represents the signal power, $N0B$ represents the noise power, and $N0$ represents the noise power spectral density. The higher the SNR, the more prominent the signal and the better the quality of the original signal or transmission information signal. The smaller the MSE value, the better the accuracy of the processed image.

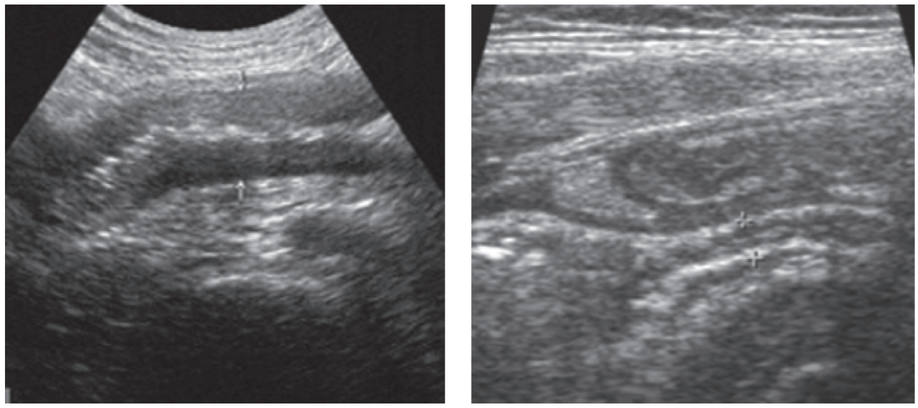

(a) (b)

Figure 4: Intestinal ultrasound images of a child patient. (a) The image of a child, female, 10 years old, suffered from abdominal pain and diarrhea for 2 weeks. (b) The image of a child, male, 9 years old, suffered from a tight abdomen, obvious diarrhea, and abdominal pain.

3. Results

3.1. Processing Performance and Results of Wavelet Transform Algorithm. The ultrasound examination results of a child patient with confirmed norovirus infection were selected randomly from the included research objects. Figure 4 shows that there was inhomogeneous echo in the center of the intestine of this child patient, hypoecho in the outer circle, and thickening of the mesentery at the margin of part of the intestinal wall with enlarged lymph nodes. Figure 5 shows the results of the noise reduction effect evaluation. Compared with the Contourlet threshold and Donoho threshold, the wavelet transform algorithm used in this study showed a higher SNR value after ultrasonic image denoising and a smaller MSE value. As illustrated in Figure 6, with the increase of the ultrasonic imaging parameter b value, the CNR value after wavelet transform denoising was always lower than the SNR value.

3.2. Detection Rate of Positive Virus. Figure 7 shows that the positive detection rate of norovirus was higher greatly than the positive detection rate of rotavirus, and the difference was statistically substantial ($P < 0.05$).

3.3. Laboratory Test Results of Children Patients with Positive Infections. Figure 8 shows that children patients with positive infections had different degrees of body damage. Among them, there were 132 cases of decompensated metabolic acidosis, 144 cases of compensatory metabolic acidosis, 32 cases of hypokalemia, 25 cases of hyponatremia, and 39 cases of liver damage.

3.4. Age Distribution Results of Children Patients Infected with the Virus and Seasonal Distribution of Virus Infection in Children Patients. Table 1 suggests that the age of children patients infected with the virus was concentrated in children under 2-3 years old and above 5 years old. In addition, the children patients were susceptible to the virus in winter, with the majority in December (Table 2).

4. Discussion

Norovirus belongs to a subfamily of Norovirus, namely, the prototype representative strain of human Caliciviridae [13]. Norovirus infections were first detected in China in the early 1990s. Besides, there were outbreaks all over the country since then. In recent years, the infection caused by this virus still shows an increasing trend [14]. The incubation period of the disease is within 1-2 days, which is relatively short [15]. There are two studies comparing the symptoms of diarrhea and vomiting in cases of different age groups [16]. The course of norovirus infection is relatively short, and the duration of clinical symptoms such as diarrhea and fever is only about 3 days. In addition, the patients show poor immunity, and the recovery time after infection is longer [17, 18]. Although the consequences caused by norovirus infection are not very serious, it still cannot be ignored. There are still cases of death caused by infection in clinical practice, and there is also the probability that healthy people will develop into severe cases after being infected with norovirus. Therefore, monitoring and early warning of norovirus has become an essential link.

Wavelet denoising is to eliminate noise through short waves, which is consistent with the basic principle of Gaussian denoising [19]. In recent years, the wave theory has developed rapidly, and it has been widely used in practice due to its good time-frequency characteristics. In new fields, the wave theory has also attracted the attention of many scholars because of its good application effects [20]. In mathematics, denoising is essentially a function approximation problem, that is, how to find the best approximation to the original signal in the function room, and the wave-generating function is expanded and shifted according to the proposed criteria, in order to complete the distinction between the original signal and the noise signal. In other words, the best mapping is found from the actual signal space to the wave function space. From the point of view of

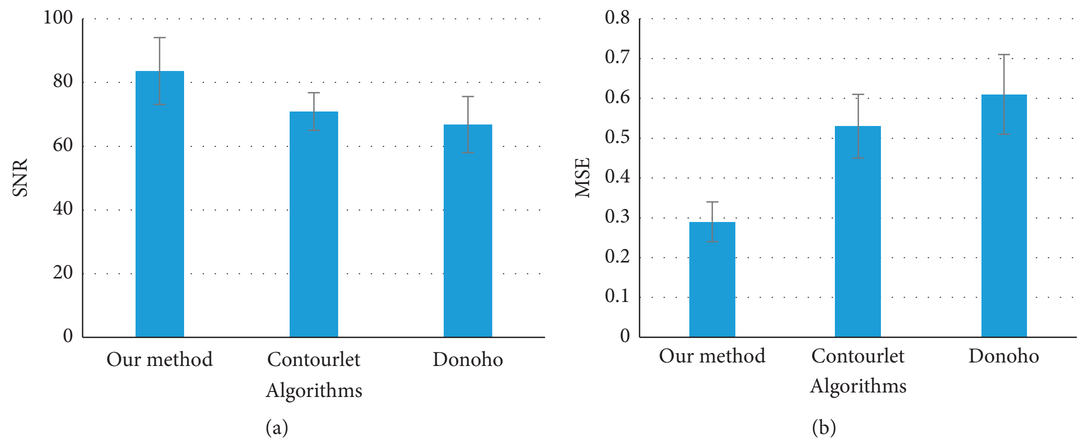

Figure 5: Evaluation of the noise reduction effect. (a) The comparison on SNR. (b) The comparison on MSE.

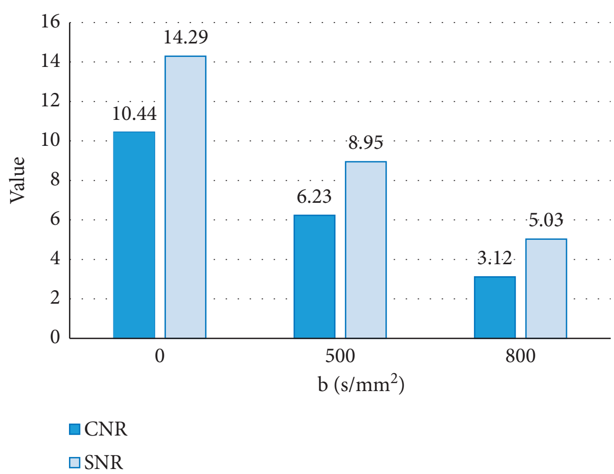

Figure 6: Comparison on SNR of images under different b values.

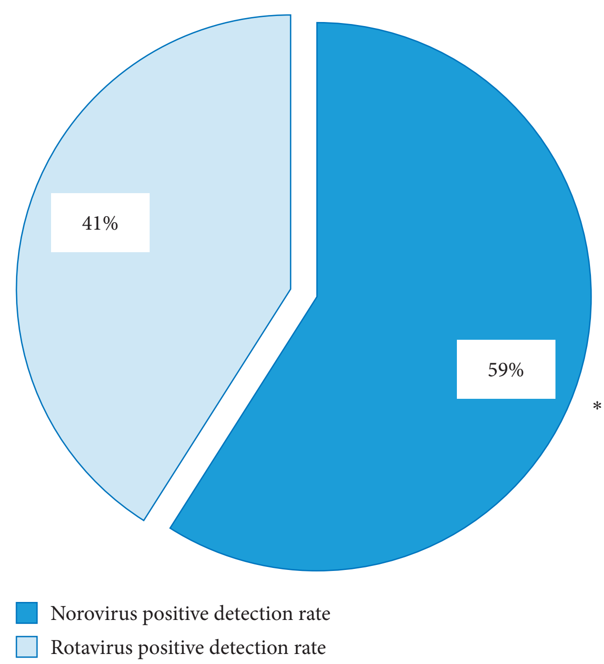

Figure 7: Detection rate of positive virus. *The difference among the groups was statistical obvious ($P < 0.05$).

signal science, denoising is a problem of signal filtering. Although denoising can be regarded as low-pass filtering to a large extent, it is better than the traditional low-pass filtering in retaining signal features completely after processing [21]. Thus, it is found that wavelet denoising is actually a combination of feature extraction and low-pass filtering. Through collecting a large number of cases, all the research objects underwent the ultrasound examinations in this study, and the results were processed by the wavelet transform algorithm, so the following conclusions were drawn. The positive detection rate of norovirus was higher than that of rotavirus. The age of children patients infected with norovirus was concentrated in children under 2-3 years old and above 5 years old, and the children were susceptible to norovirus in winter and most of them were in December. From this, the susceptible population and susceptible season of norovirus could be known.

Data mining technology is to obtain valuable knowledge and rules that users may be interested in from a large amount of data in the storage space, so as to tap out the potential of users [22]. These rules can provide useful information for business decisions and financial forecasts. In 1990, with the wide application of the network system and the rapid development of network technology, database technology has stepped into a new stage of management of graphs and images from the management of some simple data in the past, and the amount of data is also increasing [23]. According to the analysis, data mining is mainly carried out from the four aspects of classification, estimation, prediction, and clustering. Therefore, it is necessary to make sufficient preparations for the purpose of the operation and data collection before the operation. In this study, the ultrasound examination results and virus detection results of a large number of children patients were collected and analyzed, so as to construct the correlation model of related

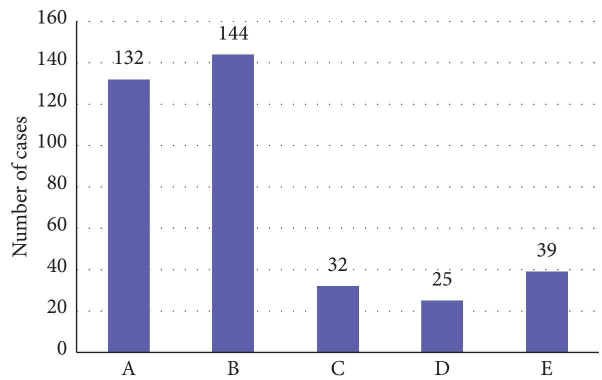

Figure 8: Laboratory test results of children patients with positive infections. (a) Decompensated metabolic acidosis. (b) Compensatory metabolic acidosis. (c) Hypokalemia. (d) Hyponatremia. (e) Liver damage.

Table 1: Age distribution results of children patients infected with the virus (cases).

Age distribution (years old)	Positive norovirus	Positive rotavirus
<1	211	214
1-2	204	131
2-3	122	83
3-4	79	60
4-5	65	54
>5	162	47

Table 2: Month distribution of virus infection in children patients (cases).

Month	Positive norovirus	Positive rotavirus
1	11	87
2	10	97
3	12	99
4	10	13
5	6	14
6	8	7
7	10	12
8	17	13
9	75	17
10	132	21
11	241	96
12	311	113

feature transformation. What is more, the data acquisition was mainly to prepare for the subsequent data mining. When data mining is performed, it is necessary to select data from the dataset and select the data needed to build the model from the original dataset. In this study, the data mining results found that the early ultrasound examinations of children patients in the susceptible age group showed slight intestinal edema or effusion and slight changes in gastrointestinal function, which affected the diet and rest of children. Some children patients might have clinical manifestations of vomiting, which was basically in line with the observation results of clinicians.

5. Conclusion

In this study, the main focus was the application of monitoring and early warning detection technology of norovirus, namely, data mining technology. Therefore, a large number of children patients with diarrhea symptoms were selected, and the ultrasonic examination results were collected. Meanwhile, the wavelet transform algorithm was applied to denoise processing of ultrasonic images to facilitate the normalization and collation of data. The research results showed that the ultrasound images processed by the wavelet transform algorithm had higher quality, which was convenient for doctors to diagnose the diseases of children in combination with the image data. Based on the results of data mining technology analysis of children infected with norovirus, it was found that in clinical practice, children with diarrhea were more likely to be infected with norovirus than rotavirus, and children younger than 2 years old or older than 5 years old are more susceptible to norovirus in December. In summary, data mining technology based on the wavelet transform artificial intelligence algorithm had a relatively accurate warning effect and could also predict the future trend of disease data, so it could be promoted and applied clinically. The disadvantage of this study is that the presentation of case data is less, which makes the research results lack of intuitive data support. Therefore, further research and analysis are needed to provide more effective clinical reference value.

Data Availability

The data used to support the findings of this study are available from the corresponding author upon request.

Conflicts of Interest

The authors declare that they have no conflicts of interest.

References

[1] N. Alam, E. L. Hobbelink, A. J. van Tienhoven, P. M. van de Ven, E. P. Jansma, and P. W. B. Nanayakkara, "The impact of the use of the early warning score (EWS) on patient outcomes: a systematic review," *Resuscitation*, vol. 85, no. 5, pp. 587–594, 2014.

[2] R. Trubey, C. Huang, F. V. Lugg-Widger et al., "Validity and effectiveness of paediatric early warning systems and track and trigger tools for identifying and reducing clinical deterioration in hospitalised children: a systematic review," *BMJ Open*, vol. 9, no. 5, Article ID e022105, 2019.

[3] T. Lam, M. Nagappa, J. Wong, M. Singh, D. Wong, and F. Chung, "Continuous pulse oximetry and capnography monitoring for postoperative respiratory depression and adverse events," *Anesthesia & Analgesia*, vol. 125, no. 6, pp. 2019–2029, 2017.

[4] M. Cardona-Morrell, M. Prgomet, R. Lake et al., "Vital signs monitoring and nurse-patient interaction: a qualitative observational study of hospital practice," *International Journal of Nursing Studies*, vol. 56, pp. 9–16, 2016.

[5] F. Haegdorens, K. G. Monsieurs, K. De Meester, and P. Van Bogaert, "An intervention including the national early

warning score improves patient monitoring practice and reduces mortality: a cluster randomized controlled trial," *Journal of Advanced Nursing*, vol. 75, no. 9, pp. 1996–2005, 2019.

[6] J. Keep, A. Messmer, R. Sladden et al., "National early warning score at Emergency Department triage may allow earlier identification of patients with severe sepsis and septic shock: a retrospective observational study," *Emergency Medicine Journal*, vol. 33, no. 1, pp. 37–41, 2016.

[7] S. Manetti, M. Vainieri, E. Guidotti et al., "Research protocol for the validation of a new portable technology for real-time continuous monitoring of Early Warning Score (EWS) in hospital practice and for an early-stage multistakeholder assessment," *BMJ Open*, vol. 10, no. 12, Article ID e040738, 2020.

[8] M. Hu, Y. Zhong, S. Xie, H. Lv, and Z. Lv, "Fuzzy system based medical image processing for brain disease prediction," *Frontiers in Neuroscience*, vol. 15, Article ID 714318, 2021.

[9] H. Zhou, H. Huang, X. Xie et al., "Development of early warning and rapid response system for patients with novel coronavirus pneumonia (COVID-19)," *Medicine (Baltimore)*, vol. 99, no. 34, Article ID e21874, 2020.

[10] M. E. H. Chowdhury, K. Alzoubi, A. Khandakar et al., "Wearable real-time heart attack detection and warning system to reduce road accidents," *Sensors*, vol. 19, no. 12, p. 2780, 2019.

[11] U. Kyriacos, D. Burger, and S. Jordan, "Testing effectiveness of the revised Cape Town modified early warning and SBAR systems: a pilot pragmatic parallel group randomised controlled trial," *Trials*, vol. 20, no. 1, p. 809, 2019.

[12] N. Jacob, Y. Moriarty, A. Lloyd et al., "Optimising paediatric afferent component early warning systems: a hermeneutic systematic literature review and model development," *BMJ Open*, vol. 9, no. 11, Article ID e028796, 2019.

[13] Ravikirti, "Early warning scoring system for early recognition of and timely intervention in deteriorating patients in the hospital," *Journal of the Association of Physicians of India*, vol. 64, no. 5, pp. 59–61, 2016.

[14] M. H. Van Velthoven, F. Adjei, D. Vavoulis, G. Wells, D. Brindley, and A. Kardos, "ChroniSense National Early Warning Score Study (CHESS): a wearable wrist device to measure vital signs in hospitalised patients-protocol and study design," *BMJ Open*, vol. 9, no. 9, Article ID e028219, 2019.

[15] C. Moldaenke, Y. Fang, F. Yang, and A. Dahlhaus, "Early warning method for cyanobacteria toxin, taste and odor problems by the evaluation of fluorescence signals," *The Science of the Total Environment*, vol. 667, pp. 681–690, 2019.

[16] K. Ioannidis, J. Serfontein, J. Deakin et al., "Early warning systems in inpatient anorexia nervosa: a validation of the MARSIPAN -based modified early warning system," *European Eating Disorders Review*, vol. 28, no. 5, pp. 551–558, 2020.

[17] J. Moore, D. Thomson, I. Pimentil, B. Fekad, and W. Graham, "Introduction of a modified obstetric early warning system (MOEWS) at an Ethiopian referral hospital: a feasibility assessment," *BMJ Open Quality*, vol. 8, no. 1, Article ID e000503, 2019.

[18] F. Wuytack, P. Meskell, A. Conway et al., "The effectiveness of physiologically based early warning or track and trigger systems after triage in adult patients presenting to emergency departments: a systematic review," *BMC Emergency Medicine*, vol. 17, no. 1, p. 38, 2017.

[19] K. Mao, K. Zhang, W. Du, W. Ali, X. Feng, and H. Zhang, "The potential of wastewater-based epidemiology as surveillance and early warning of infectious disease outbreaks," *Current Opinion in Environmental Science & Health*, vol. 17, pp. 1–7, 2020.

[20] S. S. Vyas and B. K. Bhattacharya, "Agricultural drought early warning from geostationary meteorological satellites: concept and demonstration over semi-arid tract in India," *Environmental Monitoring and Assessment*, vol. 192, no. 5, p. 311, 2020.

[21] C. Ye, O. Wang, M. Liu et al., "A real-time early warning system for monitoring inpatient mortality risk: prospective study using electronic medical record data," *Journal of Medical Internet Research*, vol. 21, no. 7, Article ID e13719, 2019.

[22] S. Guo, R. Chen, H. Li, T. Zhang, and Y. Liu, "Identify severity bug report with distribution imbalance by CR-SMOTE and ELM," *International Journal of Software Engineering and Knowledge Engineering*, vol. 29, no. 2, pp. 139–175, 2019.

[23] M. E. Ward, A. Wakai, R. McDowell et al., "Developing outcome, process and balancing measures for an emergency department longitudinal patient monitoring system using a modified Delphi," *BMC Emergency Medicine*, vol. 19, no. 1, p. 7, 2019.

Hindawi
Journal of Healthcare Engineering
Volume 2021, Article ID 6318936, 9 pages
https://doi.org/10.1155/2021/6318936

Research Article

Ultrasound Image Features under Deep Learning in Breast Conservation Surgery for Breast Cancer

Hongxu Zhang[1], **Haiwang Liu**[2], **Lihui Ma**[1], **Jianping Liu**[1], and **Dawei Hu**[1]

[1]*Department of Breast Surgery, Affiliated Hospital of Chengde Medical University, Chengde 067000, Hebei, China*
[2]*Department of Pathology, Affiliated Hospital of Chengde Medical university, Chengde 067000, Hebei, China*

Correspondence should be addressed to Dawei Hu; 3115501012@m.fafu.edu.cn

Received 29 June 2021; Revised 28 August 2021; Accepted 31 August 2021; Published 17 September 2021

Academic Editor: Enas Abdulhay

This study was to analyze the effect of the combined application of deep learning technology and ultrasound imaging on the effect of breast-conserving surgery for breast cancer. A deep label distribution learning (LDL) model was designed, and the semi-automatic segmentation algorithm based on the region growing and active contour technology (RA) and the segmentation model based on optimized nearest neighbors (ON) were introduced for comparison. The designed algorithm was applied to the breast-conserving surgery of breast cancer patients. According to the difference in intraoperative guidance methods, 102 female patients with early breast cancer were divided into three groups: 34 cases in W1 group (ultrasound guidance based on deep learning segmentation model), 34 cases in W2 group (ultrasound guidance), and 34 cases in W3 group (palpation guidance). The results revealed that the tumor area segmented by the LDL algorithm constructed in this study was closer to the real tumor area; the segmentation accuracy (AC), Jaccard, and true-positive (TP) values of the LDL algorithm were obviously greater than those of the RA and ON algorithms, while the false-positive (FP) value was significantly lower in contrast to the RA and ON algorithms, showing statistically observable differences ($P < 0.05$); the actual resection volume of the patients in the W1 group was the closest to the ideal resection volume, which was much smaller in contrast to that of the patients in the W2 and W3 groups, showing statistical differences ($P < 0.05$); the positive margins of the patients in the W1 group were statistically lower than those in the W2 and W3 groups ($P < 0.05$). In addition, 1 patient in the W1 group was not satisfied with the cosmetic effect, 3 patients in the W2 group were not satisfied with the cosmetic effect, and 9 patients in the W3 group were not satisfied with the cosmetic effect. Finally, it was found that the ultrasound image based on the deep LDL model effectively improved the AC of tumor resection and negative margins, reduced the probability of normal tissue being removed, and improved the postoperative cosmetic effect of breast.

1. Introduction

Breast cancer is a malignant tumor that occurs on the ductal epithelium and terminal ductal epithelium of the breast. It can manifest as breast lumps, nipple discharge, nipple retraction, skin adhesions, skin edema, and breast pain [1]. The invasive breast cancer is still major diseases threatening the lives and health of women [2]. In the past, the breast cancer was treated by removing the breasts for the classic surgical treatment, the expanded radical mastectomy, and modified radical mastectomy, which would leave women's chest long and ugly scar after the surgery [3]. In addition, large-scale mastectomy and axillary lymph node dissection will inevitably bring more surgical complications, such as the formation of postoperative scar tissue, which limits the range of movement of the upper limbs; the lymphatic circulation of the upper limbs is blocked, which leads to swelling of the upper limbs [4]. Therefore, modern clinical treatment recommends breast cancer conserving surgery. Compared with radical mastectomy, breast-conserving surgery has the characteristics of less trauma and less pain. While preserving the integrity of the breast shape, it also takes into account postoperative functional recovery, so the curative effect can be comparable to radical mastectomy by combining with postoperative comprehensive treatment [5, 6]. Although the current surgery is still generally based on modified radical mastectomy, breast-conserving surgery will gradually replace modified radical mastectomy as the main surgical procedure with the development of early diagnosis technology.

At present, the auxiliary methods suitable for breast-conserving surgery for breast cancer include intraoperative ultrasound guidance and palpation guidance. Although palpation guidance is a clinical standard surgical procedure, its performance in assessing the extent of resection of the disease is low, and excessive resection scope and positive margins may occur, which will not only affect the surgical effect but also lead to low cosmetic effect and unsuccessful surgery [7]. Ultrasound, as an imaging method widely used in clinical purposes, has developed from the initial diagnosis of breast cancer to aid surgical treatment. It can play an important role in breast cancer conserving surgery, and clinical ultrasound-guided breast-conserving surgery is necessary [8]. Deep learning, as a new field in machine learning research, allows computers to simulate the mechanism of the human brain to solve problems and enables the computers to improve their ability to solve problems on their own without human supervision [9, 10]. Clinical application of deep learning technology to ultrasound image segmentation is also a major trend. For example, the shape, color, and texture of the lesion can be classified through accurately segmenting the lesion, so that the machine can complete the doctor's diagnosis process or visualizing the images in three dimensions can effectively improve the diagnostic performance of doctors [11]. A multilabel classification task refers to a piece of data that may have one or more labels. For example, a patient's physical examination report may be labeled with multiple labels, such as high blood pressure and high blood sugar. Multilabel learning algorithms can be divided into problem conversion methods and algorithm adaptation methods. The problem conversion method is to convert the multilabel classification into other mature scenarios, so that the data can adapt to the algorithm, and the algorithm adaptation method is to adapt popular learning techniques to deal with multilabel data and let the algorithm adapt to the data. Therefore, it is necessary to combine the deep learning and ultrasound.

In short, the combined application of deep learning technology and imaging technology can be well developed in the field of medical diagnosis and treatment. In this study, a deep LDL model was designed and applied to breast cancer patients during breast-conserving surgery. The combined application of deep learning technology and ultrasound imaging on the effect of breast-conserving surgery for breast cancer was comprehensively evaluated by analyzing the amount of tumor resection, margins, and postoperative cosmetic effects in breast cancer patients.

2. Materials and Methods

2.1. Research Objects. One hundred and two female patients with early breast cancer (the clinical TNM staging is stage I and II) admitted in the hospital from February 10, 2018, to February 10, 2021, were selected as the research subjects. The patients with multicenter lesions, preoperative neoadjuvants, breast cancer surgery history, nontactile breast cancer, and invasive breast cancer were excluded. According to the different guidance methods used in the surgery, the research objects were rolled into three groups: 34 cases in W1 group (ultrasound guidance based on deep learning segmentation model), 34 cases in W2 group (ultrasound guidance), and 34 cases in W3 group (palpation guidance). This study had been approved by the Medical Ethics Committee of hospital, and the patients and their families had known the situation of the study and signed the informed consent forms.

2.2. Guidance Methods. Ultrasound guidance was performed as follows: Before the surgery, SonoScape was used to open the M11 ultrasound color Doppler diagnostic instrument to mark the tumor boundary on the patient's skin surface, and set 1 cm around the tumor as the ideal resection margin. After anesthesia, an appropriate incision was made, and an ultrasound probe was adopted to guide the surgical resection in real time. During the process, it had to pay attention to the gentle operation to avoid tumor compression. Ultrasonic testing was performed on the isolated specimens after surgery to ensure that the tumor was cleanly removed.

Palpation guidance was performed as follows. The SonoScape was adopted to open the M11 ultrasound color Doppler diagnostic instrument to mark the tumor boundary on the skin surface of the patient before the surgery, and set 1 cm around the tumor as the ideal resection margin. After anesthesia, a suitable incision was cut on the skin, and the palpation guidance was realized by figures. The tumor was marked and then completely removed based on past experience.

2.3. Pathological Examination and Data Collection. The pathological examination was performed on the tumor tissue resected by the two guiding methods; the circumferences (length, width, and height) of the tumor and the resected tissue were measured and the distance between each resection edge and the tumor edge was measured (obtain the longest/shortest resection edge). The resection edge was observed to check if the tumor cells were visible. Under a microscope, if there was no ink staining on the tumor tissue, it can be judged as a negative margin.

The tumor volume (V1), ideal resection tissue volume (V2), and actual resection tissue volume (V3) were calculated with following equations:

$$V1 = \frac{4}{3}\pi\bullet\frac{\alpha}{2}\bullet\frac{\beta}{2}\bullet\frac{\lambda}{2}, \tag{1}$$

$$V2 = \frac{4}{3}\pi\bullet\left(\frac{\alpha}{2}+1\right)\bullet\left(\frac{\beta}{2}+1\right)\bullet\left(\frac{\lambda}{2}+1\right), \tag{2}$$

$$V3 = \frac{4}{3}\pi\bullet\frac{\alpha *}{2}\bullet\frac{\beta *}{2}\bullet\frac{\lambda *}{2}. \tag{3}$$

In (1)–(3), α, β, and λ referred to the length, width, and height of the tumor, respectively, and α^*, β^*, and λ^* represented the length, width, and height of the actual resection tissue, respectively.

The age, weight, height, and tumor location of the patients were collected before the surgery. Long-term follow-up was carried out after the surgery. The breast shape, incision healing, and nipple, and areola positions of the patients were observed 2 and 5 months after the surgery.

2.4. Deep LDL Model. LDL can label an instance very naturally and assign a performance value to each label of the instance as much as possible. Compared with the traditional single-label learning, it showed more degrees of freedom to obtain more effective information [12]. Therefore, an encoder-decoder architecture deep network was designed based on LDL (Figure 1), which was composed of input layer, convolution module, pooling layer, subsequent branches of the convolution module, and softmax layer.

The network can perform Softmax operation [13] to obtain the label distribution map required. When the classification probability and cross entropy loss were calculated, the equations could be written as follows:

$$P_i = \frac{a^i}{\sum_i a^i}, \tag{4}$$

$$\text{Loss} = -\sum_m y_m \log P_m. \tag{5}$$

In (4) and (5), P was the classification probability, a_i was the element contained in the input data, and $y = \{y_0, y_1, y_2, \ldots, y_n\} \in \{0, 1\}$ represented the category. There were two categories in this study: tumor and background. When it was the tumor category, $\text{Loss}(P, y) = -\log P_1$ could be met; when it was the background category, $\text{Loss}(P, y) = -\log P_0$ was satisfied. From this, the fuzzy label distribution map can be initially obtained.

A label distribution fitting term [14] was proposed in this study to further integrate the obtained fuzzy label distribution map into the LDL model; then, the new energy function could be expressed as follows:

$$H = \varepsilon + \phi + D. \tag{6}$$

In equation (6), ε represented the gray-scale fitting term; ϕ and D represented the label fitting term and the regularization term, respectively. The following equation could be obtained by introducing the bias field hypothesis theory:

$$\varepsilon = \int_\Phi (M(x,y) - C(x,y)N(x,y))^2 \mathrm{d}x\mathrm{d}y. \tag{7}$$

In the above equation, M represented the image to be observed, N represented the real image, C was the bias field, and Φ referred to the interval. Then, the concept of local clustering properties was introduced. It was assumed that there was a circle with r as radius and s as center, the paranoid field value of any point s^* in this circle was similar to the center s. In addition, the values of the real image on multiple intervals [$\Phi 1$, $\Phi 2$, ... Φn] were [$v1$, $v2$,... v_n], respectively; then, equation (7) could be evolved as follows:

$$\varepsilon = \int \left(\sum_{i=1}^{n} \int L(s - s*)(M(s*) - C(s)v_i)^2 \right) \mathrm{d}s. \tag{8}$$

A label distribution fitting item was also added, which was different from the traditional model:

$$\phi = \sum_{i=1}^{n} \int_\Phi (S(s*) - v_i)^2 \mathrm{d}s. \tag{9}$$

In equation (9), $S(s^*)$ was the pixel value obtained from the label learning map and represented the tumor probability value in this study. Adding the abovementioned label distribution fitting item can solve the different qualitative gray levels. Therefore, the final energy function can be expressed as:

$$\begin{aligned} H = {} & \int \left(\sum_{i=1}^{n} \int L(s - s*)(M(s*) - C(s)v_i)^2 \right) \mathrm{d}s \\ & + \sum_{i=1}^{n} \int_\Phi (S(s*) - v_i)^2 \mathrm{d}s + |D|. \end{aligned} \tag{10}$$

2.5. Evaluation Indicators of Segmentation Performance. The semiautomatic segmentation algorithm based on the region growing and active contour technology (RA) and the segmentation model based on optimized nearest neighbors (ON) were introduced for comparison to further analyze the performance of the designed model. The accuracy (AC), true positive (TP), false positive (FP), and Jaccard were selected as the evaluation indicators, which could be expressed as follows:

$$\begin{aligned} \text{AC} &= \frac{|T_1 \cap T_2| \cup |C_1 \cap C_2|}{T_1 \cap C_1}, \\ \text{TP} &= \frac{|T_1 \cap T_2|}{T_1}, \\ \text{FP} &= \frac{|T_1 \cap T_2 - T_1|}{|T_1|}, \\ \text{Jaccard} &= \frac{|T_1 \cap T_2|}{|T_1 \cup T_2|}. \end{aligned} \tag{11}$$

In the above equations, T_1 referred the tumor area obtained by manual segmentation, and T_2 represented the tumor area obtained by the model segmentation.

2.6. Statistical Analysis. The data of this study was analyzed by SPSS19.0 version statistical software; the measurement data were expressed by the mean ± standard deviation ($\bar{x} \pm s$), and the count data were expressed in the form of percentage (%). One-way analysis of variance was used for pairwise comparison. The difference was statistically significant at $P < 0.05$.

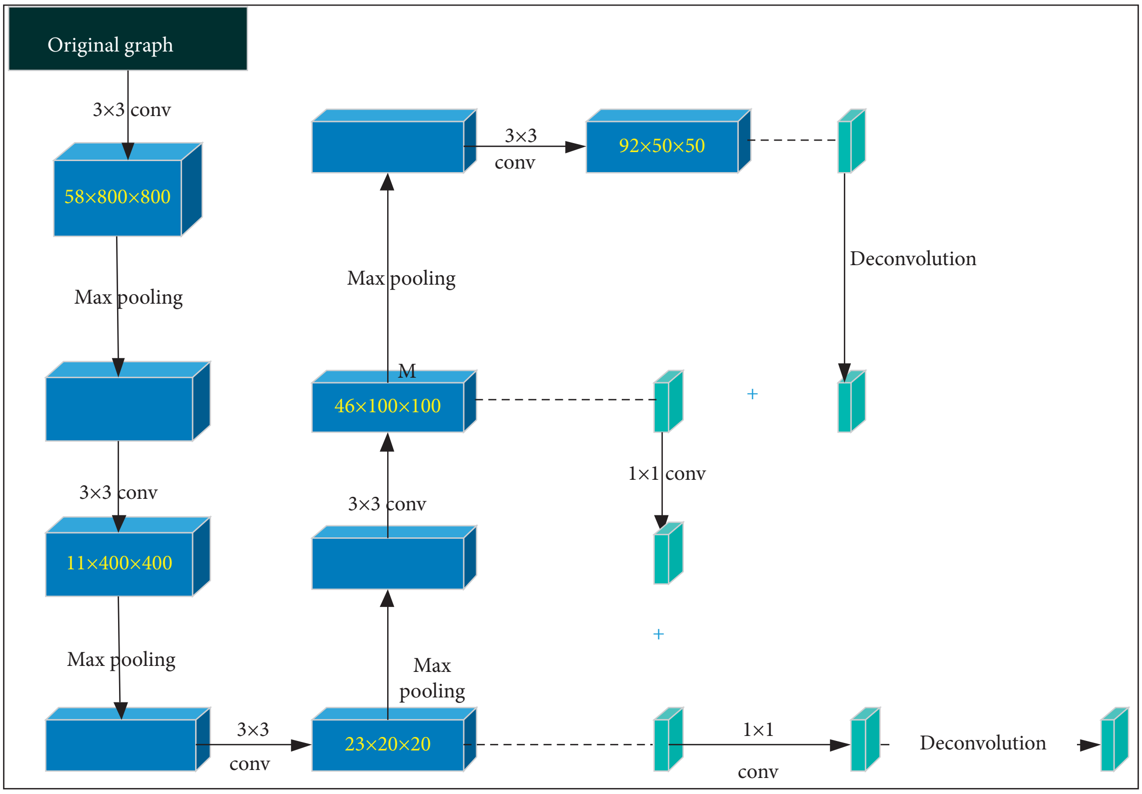

Figure 1: The architecture of LDL.

3. Results

3.1. Image Segmentation Performance of Deep LDL Model. Figure 2 shows the image segmentation effects of the three algorithms on some samples. It revealed that the tumor area segmented by the LDL algorithm constructed was closer to the real tumor area. Although the RA algorithm and the ON algorithm could also identify the tumor area better, the area selection range was too large, so that it was easy to include the background area, showing poor segmentation effect.

The quantitative indicators were compared to further clarify the segmentation performances of the three algorithms. As shown in Figures 3 and 4, the AC, Jaccard, and TP values of the LDL algorithm were greatly larger than those of the RA and ON algorithms, showing statistically obvious differences ($P < 0.05$); the FP value of the LDL algorithm was much smaller in contrast to that of the RA and ON algorithms, showing statistically great difference ($P < 0.05$).

3.2. Comparison on Basic Information of the Patients. As illustrated in Figures 5 and 6, the pairwise comparisons of age, body mass index (BMI), and tumor stage ratio of patients in W1, W2, and W3 groups were not statistically observable ($P > 0.05$).

Figure 7 shows an ultrasound image of a 46-year-old female patient with breast cancer. Ultrasound showed that the breast tissues on both sides were slightly thickened, the lobule structure was slightly thick and disordered, and the internal distribution was uneven. There were two hypoechoic masses of different sizes in the upper outer quadrant, with irregular shapes, and there was no echo in the capsule. The internal echo was uneven, and several sand particles showed strong echoes with weak sound shadows. In addition, the color Doppler ultrasound showed that there was no blood flow signal, right axillary lymph node was not reached, and multiple hypoechoic nodules were visible in the axillary.

3.3. Comparison on Resection Volume of Tumor. As given in Figure 8, the tumor volume and ideal resection volume of patients in the W1, W2, and W3 groups were relatively close, and the difference was not statistically significant ($P > 0.05$); the actual resection volume in the W1 group was the closest to the ideal resection volume and was greatly smaller than that in the W2 and W3 groups ($P < 0.05$).

Figure 9 shows the images of ultrasound reexamination in some patients after surgery. As shown in Figure 9(a), the ultrasound reexamination found that the right breast cancer of the patient was treated for one year after radiotherapy; the sonographic features were obvious, and the multiple hypoechoic nodules showed target ring signs, which were multiple liver metastases. Figure 9(b) reveals that the patient's left side breast cancer had an obstruction of lymphatic drainage, that is, lymphatic fluid accumulated in the axilla and formed a lymphatic cyst.

3.4. Comparison of Patient Margin Performance. As revealed in Figure 10, the positive margins and negative margins of the patients in the W1 group were 7.43% and 92.57%, respectively; the positive and negative margins of the patients

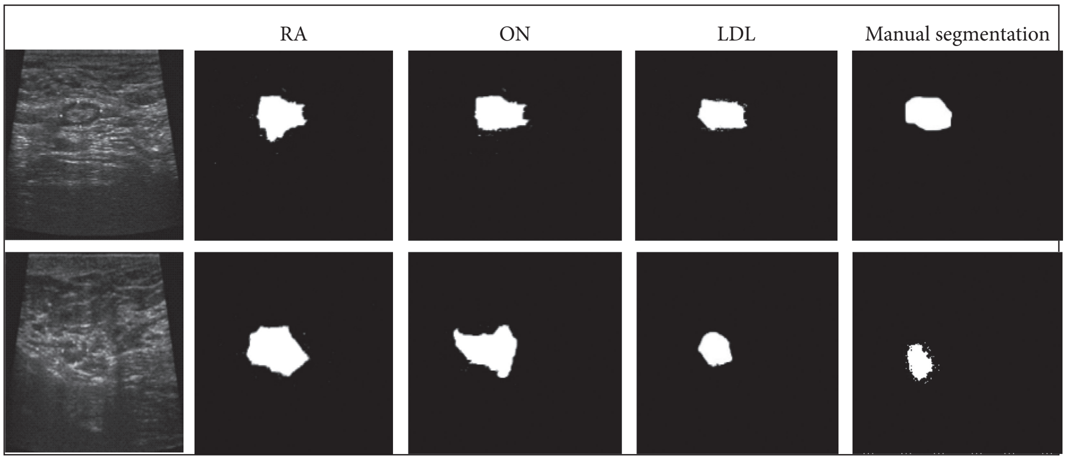

FIGURE 2: Comparison on image segmentation effects of different algorithms. (a, b) Original images.

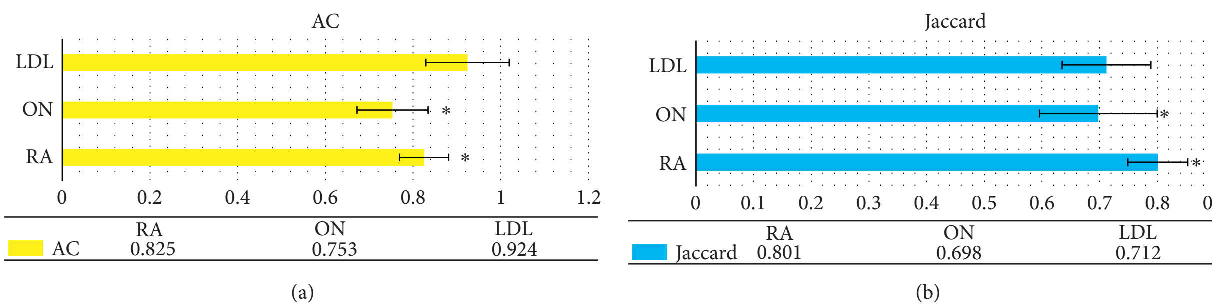

FIGURE 3: Comparison on AC and Jaccard of various algorithms. (a) The AC indicator and (b) the Jaccard indicator. * indicates that the difference was statistically obvious in contrast to the LDL algorithm ($P < 0.05$).

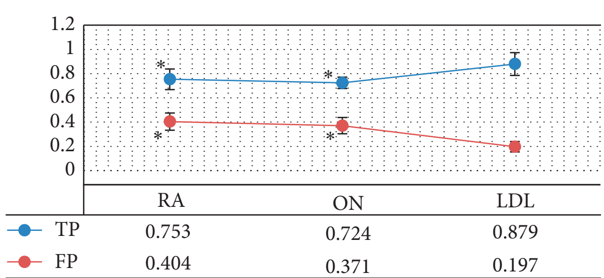

FIGURE 4: Comparison on TP and FP of various algorithms. * suggests that the difference was statistically obvious in contrast to the LDL algorithm ($P < 0.05$).

in the W2 group were 15.31% and 84.69%, respectively, and the positive and negative margins of the patients in the W3 group were 26.07% and 73.93%, respectively. It was clear that the positive margins of the patients in the W1 group were dramatically less than those in the W2 and W3 groups, and the differences were statistically observable ($P < 0.05$).

Figure 11reveals that the longest margin (1.35 cm) of the patients in the W1 group was smaller in contrast to that of the patients in the W2 and W3 groups, while the shortest margin (0.67 cm) was greater. Based on the difference between the longest resection margin and the ideal resection margin and the difference between the shortest resection margin and the ideal resection margin, it can be concluded that the longest and shortest resection margins of the patients in group W1 were closer to the ideal resection margin, and the variation among individuals was smaller.

3.5. Analysis on Postoperative Cosmetic Effect of Patients. The postoperative cosmetic effects of the three groups of patients were compared, and the results are shown in Figure 12. There was 1 patient in the W1 group who was not satisfied with the cosmetic effect because there was an obvious shift in the position of the nipple. In the W2 group, 3 patients were not satisfied with the cosmetic effect: 1 case suffered from a significant deviation in the position of the nipple, and 2 suffered from larger breast scar areas. In the W3 group, 9 patients were not satisfied with the cosmetic effect, including 3 patients with obvious deviation of the nipple position, 2 patients with large breast scar areas, 3 patients with visible breast deformation, and 1 patient with postoperative infection. As a result, patients in the W1 group were more satisfied with the cosmetic effect than those in the W2 and W3 groups, and the differences were statistically notable ($P < 0.05$).

4. Discussion

With the development of medical technology, the clinical treatment of breast cancer is constantly updated and progressed. Great changes have been realized from the initial

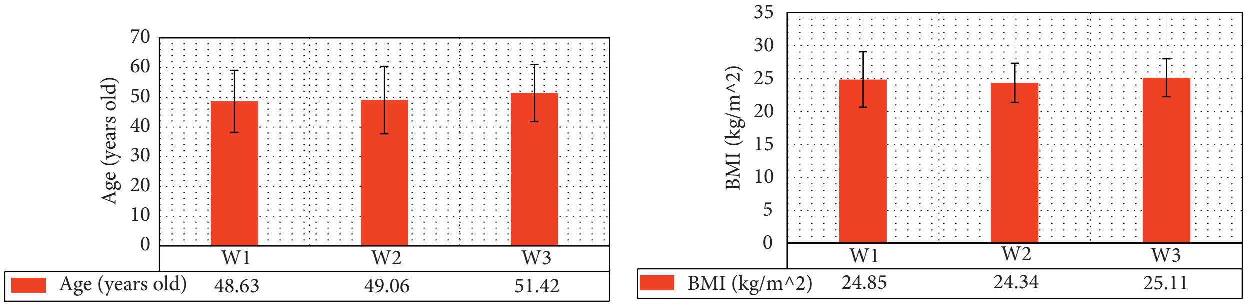

(a) (b)

Figure 5: Comparison on age and BMI of patients in three groups. (a, b) The statistical results of age and BMI, respectively.

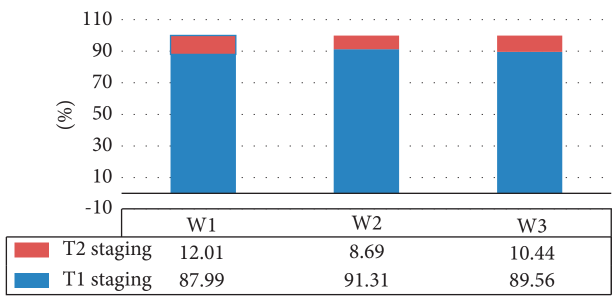

Figure 6: Comparison on tumor staging proportions of patients in three groups.

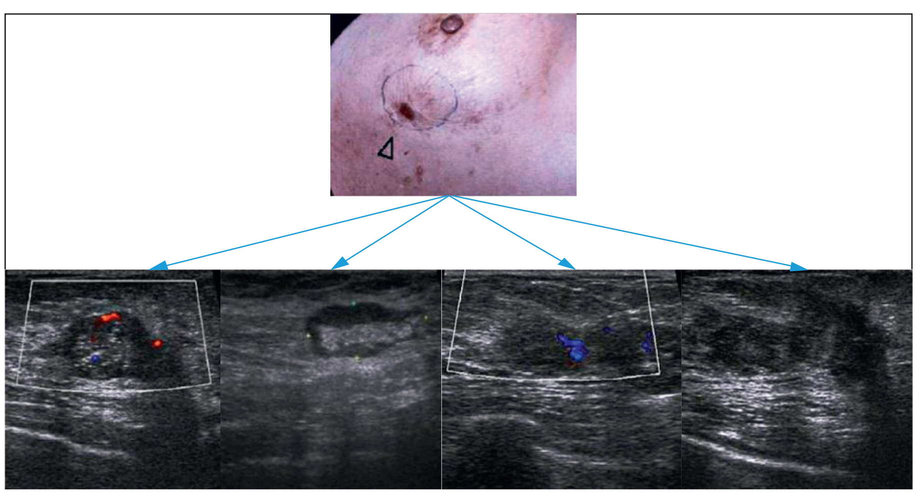

Figure 7: The ultrasound images of a 46-year-old female patient with breast cancer. The patient went to hospital for examination due to a lump in the left breast with obvious pain.

huge traumatic treatment to today's minimally invasive treatment. The breast-conserving surgery has become the best treatment way for early breast cancer in current years. On the other hand, the application of imaging methods in the surgical process is the current trend. As a diagnostic tool for early breast cancer, ultrasound has also been used in breast cancer, which shows very important value [15]. Therefore, a deep LDL model was designed for breast cancer patients during the breast-conserving surgery in this study. The semiautomatic segmentation algorithm based on the region growing and active contour technology (RA) and the segmentation model based on optimized nearest neighbors (ON) were introduced for comparison to further analyze the performance of the designed model. The results revealed that the tumor area segmented by the LDL algorithm was closer to the real tumor area; although the RA algorithm and the ON algorithm could also identify the tumor area better, the area selection range was too large, so that it was easy to include the background area, showing poor segmentation effect. The quantitative results suggested that the AC, Jaccard, and TP values of the LDL algorithm were greatly larger than those of the RA and ON algorithms, and the FP value of the LDL algorithm was much smaller in contrast to that of the RA and ON algorithms, showing statistically differences

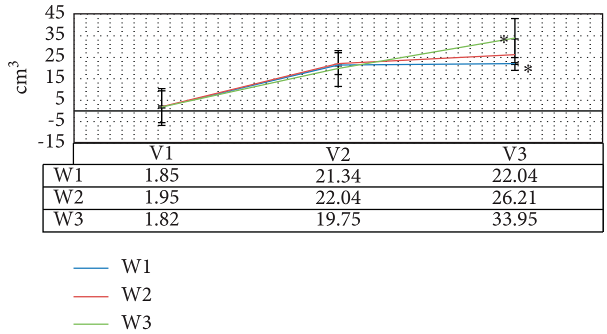

Figure 8: Comparison on resection volume of tumor. * indicates that the statistically visible difference could be found in contrast to the W1 group ($P < 0.05$).

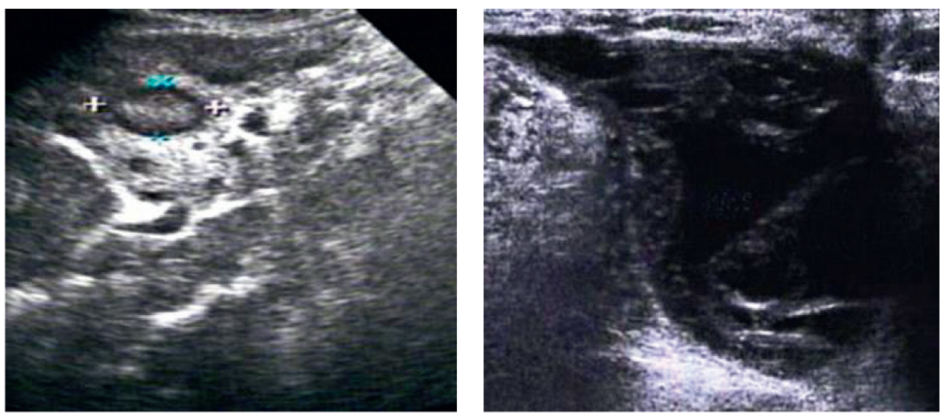

(a) (b)

Figure 9: Images of ultrasound reexamination of some patients after surgery. (a) Reexamination result of a 56-year-old female patient. (b) Reexamination result of a 43-year-old female patient.

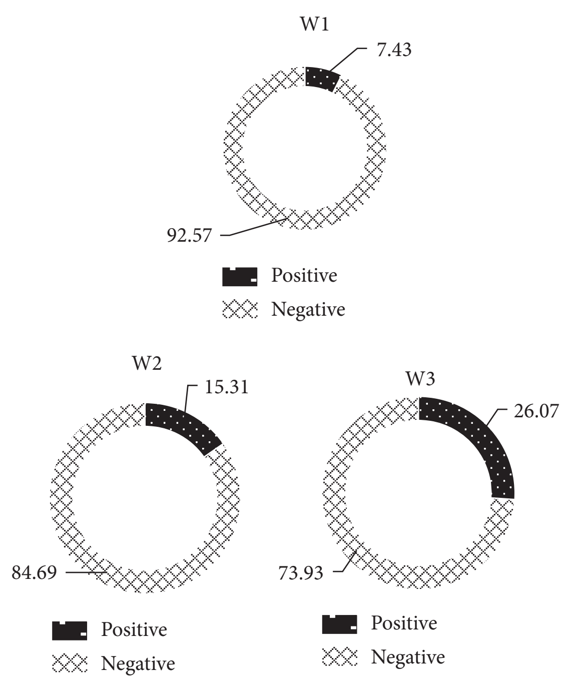

Figure 10: Comparison on positive margins of patients in three groups.

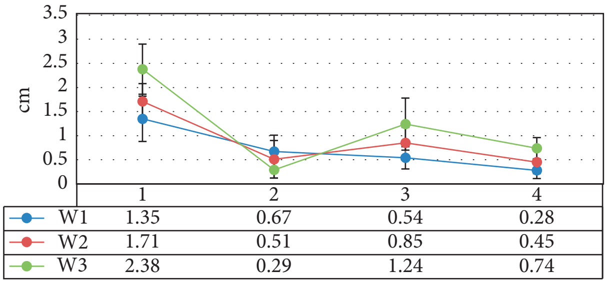

Figure 11: The longest and shortest margins of the three groups of patients.1 means the longest margin, 2 refers to the shortest margin, 3 marks the difference between the longest margin and the ideal margin, and 4 represents the difference between the shortest margin and the ideal margin value.

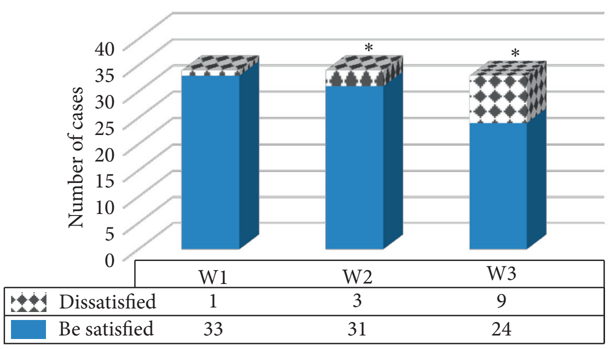

Figure 12: Comparison on postoperative cosmetic effects of patients in different groups. * indicates that the statistically visible difference could be found in contrast to the W1 group ($P < 0.05$).

($P < 0.05$). Such results were similar to the findings of Wang et al. [16], indicating that the LDL algorithm constructed in this study showed a good effect on tumor segmentation, improving the accuracy of tumor segmentation, so it was suitable for clinical promotion.

According to the difference in intraoperative guidance methods, 102 female patients with early breast cancer were divided into three groups: 34 cases in W1 group (ultrasound guidance based on deep learning segmentation model), 34 cases in W2 group (ultrasound guidance), and 34 cases in W3 group (palpation guidance). The results suggested that the actual resection volume of the patients in the W1 group was the closest to the ideal resection volume, which was much smaller in contrast to that of the patients in the W2 and W3 groups, showing statistical differences ($P < 0.05$). The amount of breast tissue removed will affect the appearance of the patient's breast after surgery. Excessive removal may cause the breast to collapse and deform, so it is necessary to reduce the amount of breast tissue resection under the premise of negative margins during the surgery to improve the success rate of breast preservation [17]. It was concluded that the ultrasound images based on the deep LDL model could effectively improve the AC of tumor resection and reduce the probability of normal tissue being resected. The positive margins of the patients in the W1 group were statistically lower than those in the W2 and W3 groups ($P < 0.05$), which was different with the research results of Guo et al. [18]. Resection margins are closely related to the postoperative recurrence of patients. Obtaining satisfactory negative margins is a topic of clinical concern. It was found in this study that ultrasound images based on the deep LDL model could effectively reduce the positive rate of resection margins in patients.

There are many side effects after breast cancer surgery, and the breast cosmetic effect has a great impact on the patient's physical and mental health. Previous studies have shown that breast asymmetry will make women's quality of life worse [19]. A follow-up survey was performed for the three groups of patients 6 months after the surgery. There was 1 patient in the W1 group who was not satisfied with the cosmetic effect because there was an obvious shift in the position of the nipple. In the W2 group, 3 patients were not satisfied with the cosmetic effect: 1 case suffered from a significant deviation in the position of the nipple, and 2 suffered from larger breast scar areas. In the W3 group, 9 patients were not satisfied with the cosmetic effect, including 3 patients with obvious deviation of the nipple position, 2 patients with large breast scar areas, 3 patients with visible breast deformation, and 1 patient with postoperative infection. Such results revealed that the ultrasound image based on the deep LDL model exerted reliable positive impacts on the cosmetic effect of the patient's breast after surgery, which was different from the results obtained by An et al. [20]. The possible reason may be that the resection amount of breast tissue during surgery could affect the postoperative cosmetic effect, resulting in significant differences in the cosmetic effect of the three groups.

5. Conclusion

A deep LDL model was designed, and the semiautomatic segmentation algorithm RA and the segmentation model ON were introduced for comparison. The designed algorithm was applied to the breast-conserving surgery of breast cancer patients. According to the difference of intraoperative guidance methods, 102 female patients with early breast cancer were divided into three groups: 34 cases in W1 group (ultrasound guidance based on deep learning segmentation model), 34 cases in W2 group (ultrasound guidance), and 34 cases in W3 group (palpation guidance). It was found that ultrasound images based on the deep LDL model effectively improved the tumor resection AC and negative margins, reduced the probability of normal tissue being removed, and enhanced the postoperative breast cosmetic effect. However, the constructed deep LDL model cannot be applied to all situations due to the complicated tumor edge characteristics, and the number of patients was small, so further empirical research was necessary in the follow-up. In summary, the image segmentation model proposed in this study showed a good application value for the implementation of clinical breast-conserving surgery for breast cancer.

Data Availability

The data used to support the findings of this study are available from the corresponding author upon request.

Conflicts of Interest

The authors declare no conflicts of interest.

Acknowledgments

This work was supported by Science and Technology Support Plan of Chengde City (201801A032).

References

[1] R. Guo, G. Lu, B. Qin, and B. Fei, "Ultrasound imaging technologies for breast cancer detection and management: a review," *Ultrasound in Medicine and Biology*, vol. 44, no. 1, pp. 37–70, Jan 2018.

[2] R. C. Ward, A. P. Lourenco, and M. B. Mainiero, "Ultrasound-guided breast cancer cryoablation," *American Journal of Roentgenology*, vol. 213, no. 3, pp. 716–722, Sep 2019.

[3] J. Geisel, M. Raghu, and R. Hooley, "The role of ultrasound in breast cancer screening: the case for and against ultrasound," *Seminars in Ultrasound, CT and MRI*, vol. 39, no. 1, pp. 25–34, Feb 2018.

[4] Q. Guo, Z. Dong, L. Zhang et al., "Ultrasound features of breast cancer for predicting axillary lymph node metastasis," *Journal of Ultrasound in Medicine*, vol. 37, no. 6, pp. 1354–1353, Jun 2018.

[5] A. Vourtsis, "Three-dimensional automated breast ultrasound: technical aspects and first results," *Diagnostic and Interventional Imaging*, vol. 100, no. 10, pp. 579–592, Oct 2019.

[6] N. Colakovic, D. Zdravkovic, Z. Skuric, D. Mrda, J. Gacic, and N. Ivanovic, "Intraoperative ultrasound in breast cancer surgery-from localization of non-palpable tumors to objectively measurable excision," *World Journal of Surgical Oncology*, vol. 16, no. 1, p. 184, Sep 11 2018.

[7] H.-P. Chan, R. K. Samala, and L. M. Hadjiiski, "CAD and AI for breast cancer-recent development and challenges," *British Journal of Radiology*, vol. 93, no. 1108, Article ID 20190580, Apr 2020.

[8] M. A. Leblond, N. Duchesne, L. Provencher, J. C. Hogue, and S. Pinault, "Is contralateral breast ultrasound worthwhile in preoperative staging of breast cancer?" *Journal of Clinical Ultrasound*, vol. 47, no. 4, pp. 195–200, May 2019.

[9] B. R. Kwon, J. M. Chang, S. Y. Kim et al., "Automated breast ultrasound system for breast cancer evaluation: diagnostic performance of the two-view scan technique in women with small breasts," *Korean Journal of Radiology*, vol. 21, no. 1, pp. 25–32, Jan 2020.

[10] B. T. Lawson, S. Vinnicombe, P. Whelehan, E. J. Macaskill, Y. T. Sim, and A. Evans, "Associations between the ultrasound features of invasive breast cancer and breast cancer specific survival," *Clinical Radiology*, vol. 75, no. 11, p. 879, Nov 2020.

[11] L. Ruby, S. J. Sanabria, K. Martini et al., "Breast cancer assessment with pulse-echo speed of sound ultrasound from intrinsic tissue reflections," *Investigative Radiology*, vol. 54, no. 7, pp. 419–427, Jul 2019.

[12] M. H. Yap, G. Pons, J. Marti et al., "Automated breast ultrasound lesions detection using convolutional neural networks," *IEEE Journal of Biomedical and Health Informatics*, vol. 22, no. 4, pp. 1218–1226, Jul 2018.

[13] Health Quality Ontario, "Ultrasound as an adjunct to mammography for breast cancer screening: a health technology assessment," *Ont Health Technol Assess Ser*, vol. 16, no. 15, pp. 1–71, Jul 1 2016.

[14] J. Hoffmann, M. Marx, A. Hengstmann et al., "Ultrasound-assisted tumor surgery in breast cancer - a prospective, randomized, single-center study (mac 001)," *Ultraschall in der Medizin - European Journal of Ultrasound*, vol. 40, pp. 326–332, Jun 2019.

[15] A. Nielsen Moody, J. Bull, A.-M. Culpan et al., "Preoperative sentinel lymph node identification, biopsy and localisation using contrast enhanced ultrasound (CEUS) in patients with breast cancer: a systematic review and meta-analysis," *Clinical Radiology*, vol. 72, no. 11, pp. 959–971, Nov 2017.

[16] Y. Wang, N. Wang, M. Xu et al., "Deeply-supervised networks with threshold loss for cancer detection in automated breast ultrasound," *IEEE Transactions on Medical Imaging*, vol. 39, no. 4, pp. 866–876, Apr 2020.

[17] Y. Lu, J. Li, X. Zhao, J. Li, J. Feng, and E. Fan, "Breast cancer research and treatment reconstruction of unilateral breast structure using three-dimensional ultrasound imaging to assess breast neoplasm," *Breast Cancer Research and Treatment*, vol. 176, no. 1, pp. 87–94, Jul 2019.

[18] Q. Guo, L. Zhang, Z. Di et al., "Assessing risk category of breast cancer by ultrasound imaging characteristics," *Ultrasound in Medicine and Biology*, vol. 44, no. 4, pp. 815–824, Apr 2018.

[19] J. M. Lee, S. C. Partridge, G. J. Liao et al., "Double reading of automated breast ultrasound with digital mammography or digital breast tomosynthesis for breast cancer screening," *Clinical Imaging*, vol. 55, pp. 119–125, May-Jun 2019.

[20] P. An, S. Zhong, R. Zhang, X. Hou, R. Xi, and Y. Wang, "A cross-sectional observational study to compare the role of ultrasound with mammography in women identified at high risk for breast cancer in a population in China," *Medical Science Monitor*, vol. 26, Jun 24 2020.

Hindawi
Journal of Healthcare Engineering
Volume 2021, Article ID 2254594, 8 pages
https://doi.org/10.1155/2021/2254594

Research Article

Deep Learning-Based Image Feature with Arthroscopy-Aided Early Diagnosis and Treatment of Meniscus Injury of Knee Joint

Zijian Li, Shiyou Ren, Xintao Zhang, Lu Bai, Changqing Jiang, Jiangyi Wu, and Wentao Zhang

Department of Sports Medicine and Rehabilitation, Peking University Shenzhen Hospital, Shenzhen 518036, China

Correspondence should be addressed to Wentao Zhang; 19zjli@stu.edu.cn

Received 29 June 2021; Revised 27 August 2021; Accepted 30 August 2021; Published 17 September 2021

Academic Editor: Enas Abdulhay

The aim of this study is to explore the clinical effect of deep learning-based MRI-assisted arthroscopy in the early treatment of knee meniscus sports injury. Based on convolutional neural network algorithm, Adam algorithm was introduced to optimize it, and the magnetic resonance imaging (MRI) image super-resolution reconstruction model (SRCNN) was established. Peak signal-to-noise ratio (PSNR) and structural similarity (SSIM) were compared between SRCNN and other algorithms. Sixty patients with meniscus injury of knee joint were studied. Arthroscopic surgery was performed according to the patients' actual type of injury, and knee scores were evaluated for all patients. Then, postoperative scores and MRI results were analyzed. The results showed that the PSNR and SSIM values of the SRCNN algorithm were (42.19 ± 4.37) dB and 0.9951, respectively, which were significantly higher than those of other algorithms ($P < 0.05$). Among patients with meniscus injury, 17 cases (28.33%) were treated with meniscus suture, 39 cases (65.00%) underwent secondary resection, 3 cases (5.00%) underwent partial resection, and 1 case (1.67%) underwent full resection. After meniscus suture, secondary resection, partial resection, and total resection, the knee function scores of patients after treatment were (83.17 ± 8.63), (80.06 ± 7.96), (84.34 ± 7.74), and (85.52 ± 5.97), respectively. There was no great difference in knee function scores after different methods of treatment ($P > 0.05$), and there were considerable differences compared with those before treatment ($P < 0.01$). Compared with the results of arthroscopy, there was no significant difference in the grading of meniscus injury by MRI ($P > 0.05$). To sum up, the SRCNN algorithm based on the deep convolutional network algorithm improved the MRI image quality and the diagnosis of knee meniscus injuries. Arthroscopic knee surgery had good results and had great clinical application and promotion value.

1. Introduction

The knee joint is the largest, most complex, and weight-bearing main joint in the human body. Patients with tibial plateau fractures are often accompanied by meniscal injuries, and the incidence is about 50% [1]. Meniscus injuries are difficult to repair themselves, which is a difficult and urgent problem in orthopedic treatment. Meniscus injuries are often diagnosed by arthroscopy, knee ultrasound, CT, and magnetic resonance imaging (MRI). Arthroscopy is the gold standard for meniscus diagnosis, but it is invasive and increases the probability of infection in patients [2]. The diagnostic accuracy of B-ultrasound for knee joint meniscus injury is not high [3]. CT cannot correctly grade the diagnosis. MRI has the characteristics of noninvasiveness, nonradiation, high soft tissue resolution, and high specificity. Moreover, MRI has high sensitivity and specificity to the injured area, so MRI has become an important method for knee joint injury following arthroscopy [4]. However, affected by the resolution of MRI images, the false positives and false negatives of meniscus injury diagnosis are relatively high.

MRI images are susceptible to noise pollution, resulting in distortion of MR images [5]. At present, MRI images are often processed by filtering-based denoising methods, but the image information is lost seriously in the denoising process, and additional noise may be introduced [6]. Convolutional neural networks have achieved very good results in natural image processing. At present, some scholars have applied them in the field of medical images. High-resolution MRI images can be obtained after being processed by super-resolution reconstruction algorithm [7]. Kobayashi et al. [8] pointed out that the image resolution processed by the three-layer convolutional neural network (CNN) (super-resolution CNN, SRCNN) was significantly improved. However, there are still obvious misdiagnosis and missed diagnosis in the diagnosis of clinical diseases, which need to be further improved.

In summary, the resolution of MRI images requires to be further improved. SRCNN based on deep CNN algorithm should be further optimized to increase its image quality. Therefore, SRCNN was optimized based on the deep CNN algorithm in this research. Patients with knee meniscus injury were taken as the research object to explore the diagnostic value of MRI images of deep CNN algorithm for meniscus injury. Moreover, the clinical effect of arthroscopic surgery based on MRI images in knee meniscus injuries was evaluated to provide guidance for the treatment of knee meniscus injuries.

2. Materials and Methods

2.1. Research Objects and Grouping. Sixty patients with knee meniscus injury who were admitted to the Orthopedics Department of our hospital from August 2019 to December 2020 were selected as the research objects. The age range was 18–70 years old, and the average age was (48.54 ± 5.46) years old. Among them, 41 were males and 19 were females. The meniscus injury time was seven days to five years, and the average injury time was (2.24 ± 1.04) years. There were 37 cases on the left and 23 cases on the right knee. All patients had no history of knee surgery and received knee MRI and knee arthroscopy during examination and treatment. Inclusion criteria were as follows: (i) age> 18 years; (ii) MRI examination showing meniscus injury, which was confirmed by knee arthroscopy; (iii) those who were hospitalized in time and can receive surgery; and (vi) those with no contraindications to surgery. Exclusion criteria were as follows: (i) patients with other fractures or severe system diseases; (ii) patients with meniscus congenital diseases or developmental abnormalities; (iii) patients combined with knee joint infection, tuberculosis, and so on; and (iv) meniscus injury caused by severe bone and joint disease. The experimental procedure had been approved by the hospital ethics committee, and all subjects included in the study had signed the informed consent form.

2.2. MRI Image Super-Resolution Algorithm Based on Deep CNN Algorithm. The convolutional layer of the deep CNN (DCNN) is mainly responsible for extracting features from the input data [9], and the extracted feature map X_l output by the first layer is expressed as follows:

$$X_l = X_{l-1} \odot A_l + b_l, \tag{1}$$

where X_{l-1} is the output of the l-th layer, $\odot$ is the convolution operation, A_l is the convolution layer parameter, and b_l is the bias. The activation function in DCNN can improve the expressive power of the entire network by introducing nonlinear operations [10]. The ReLU function can avoid the disappearance of the gradient when the input is saturated [11]. The ReLU function is expressed as follows:

$$g(x) = \begin{cases} x, & (x \geq 0), \\ 0, & (x < 0). \end{cases} \tag{2}$$

The training goal of DCNN is minimizing the loss function of the network [12]. The commonly used loss functions include mean square error loss function, cross-entropy loss function, and log-likelihood loss function. The mean square error loss function is expressed as follows:

$$B = \frac{\sum_{i=1}^{m} (y_i - \hat{y}_i)^2}{m}. \tag{3}$$

The cross-entropy loss function is expressed as follows:

$$B = \frac{1}{m} \sum_{i=1}^{m} y_i \log[h_0(x_i)] + (1 - y_i)\log[1 - h_0(x_i)]. \tag{4}$$

The log-likelihood loss function is expressed as follows:

$$B = -\sum_{i=1}^{m} y_i \ln h_0(x_i), \tag{5}$$

where m is the number of input samples, $\hat{y}_i$ is the corresponding model output of x_i, y_i is the corresponding target output, and $h_0(x_i)$ is the corresponding model probability output of x_i.

The DCNN-based super-resolution reconstruction algorithm (SRCNN) mainly includes image feature extraction, nonlinear mapping, and image reconstruction when processing low-resolution images. After the low-resolution images go through image data preprocessing, DCNN feature extraction, and nonlinear mapping and image reconstruction modules in the SRCNN module, a high-resolution MRI image is obtained. SRCNN processing flow for low-resolution images is shown in Figure 1.

Before low-resolution MRI image processing, it is necessary to perform preprocessing such as normalization, low-resolution image generation, image feature extraction, and data enhancement. The data types of MRI images are mostly 32-bit floating-point numbers. The calculation method for normalizing MRI images is as follows:

$$C_i' = \frac{C_i}{\max(C_i)}, \tag{6}$$

where C_i is the matrix of the original i-th MRI image and $C\prime$ is the normalized MRI image of the i-th image.

The neural network training process is divided into forward propagation process and backpropagation process. The forward propagation process uses the network input and existing parameters to calculate the network output. The backpropagation process first calculates the loss based on the network output and then transmits the loss back to each node in the network, thereby updating the weight value of each node [13]. For the simplest gradient descent algorithm, the weight update process is expressed as follows:

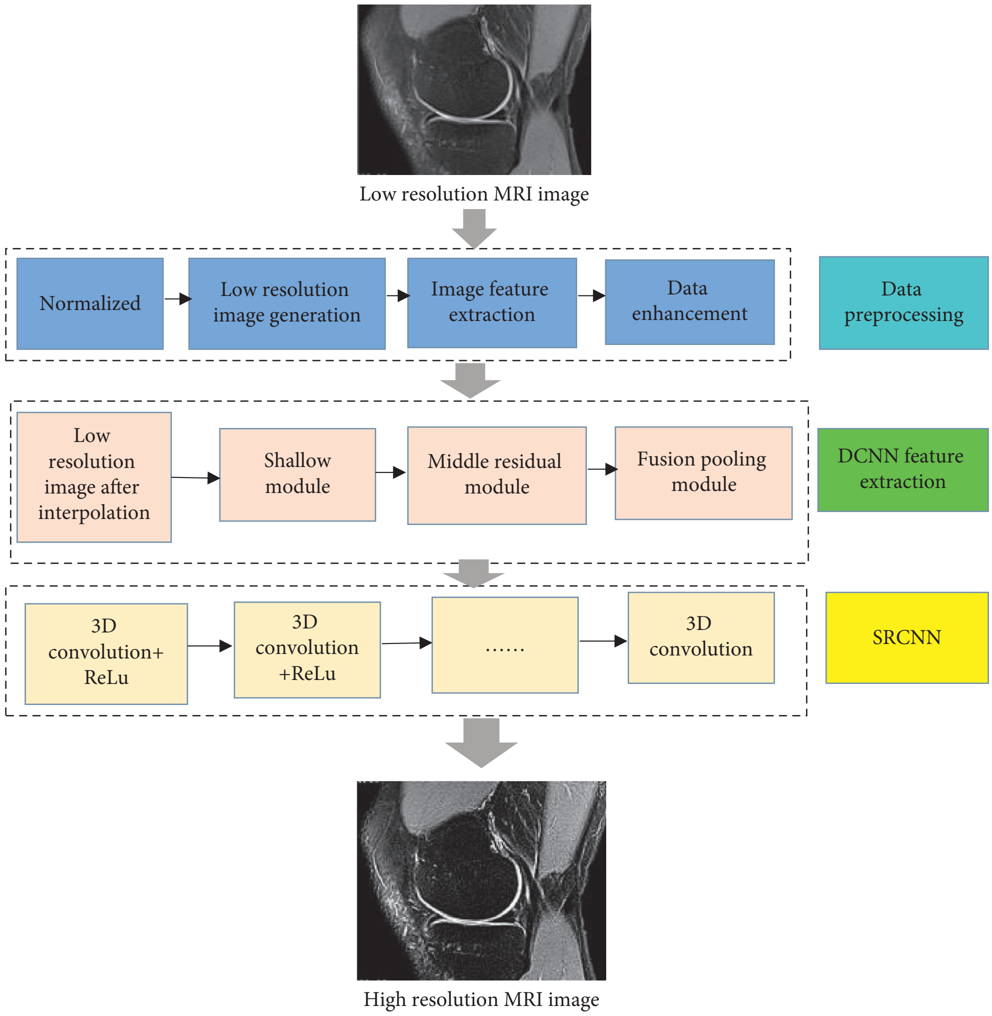

Figure 1: SRCNN processing flow for low-resolution image.

$$\begin{cases} \omega_{i+1} = \omega_i - \alpha \mathrm{d}\omega, \\ e_{i+1} = e_i - \alpha \mathrm{d}e, \end{cases} \tag{7}$$

where ω_i is the current weight, $\mathrm{d}\omega$ is the gradient of the loss function to ω, ω_{i+1} is the updated weight, e_i is the current bias term weight, $\mathrm{d}e$ is the gradient of the loss function to e, e_{i+1} is the updated bias term weight, and α is learning rate.

The momentum gradient descent algorithm is a common algorithm for parameter update in the network, and its update parameters are expressed as follows:

$$\begin{cases} D_{\mathrm{d}\omega} = \beta D_{\mathrm{d}\omega} + (1-\beta)\mathrm{d}\omega, \\ D_{\mathrm{d}e} = \beta D_{\mathrm{d}e} + (1-\beta)\mathrm{d}e, \\ \omega_{i+1} = \omega_i - \alpha D_{\mathrm{d}\omega}, \\ e_{i+1} = e_i - \alpha D_{\mathrm{d}e}, \end{cases} \tag{8}$$

where $\mathrm{d}\omega$ and $\mathrm{d}e$ represent the current gradients, $D_{\mathrm{d}\omega}$ and $D_{\mathrm{d}e}$ represent momentums, and β is a self-set hyperparameter.

The RMSProp algorithm has the advantages of fast convergence speed and small oscillation amplitude [14], and its parameter update process is expressed as shown in equation (9), where θ is a very small constant.

$$\begin{cases} E_{\mathrm{d}\omega} = \beta E_{\mathrm{d}\omega} + (1-\beta)(\mathrm{d}\omega)^2, \\ E_{\mathrm{d}e} = \beta E_{\mathrm{d}e} + (1-\beta)(\mathrm{d}e)^2, \\ \omega_{i+1} = \omega_i - \alpha \dfrac{\mathrm{d}\omega}{\sqrt{E_{\mathrm{d}\omega}} + \theta}, \\ e_{i+1} = e_i - \alpha \dfrac{\mathrm{d}e}{\sqrt{E_{\mathrm{d}e}} + \theta}. \end{cases} \tag{9}$$

Adaptive moment estimation (Adam) optimization algorithm combines the momentum gradient descent algorithm and the RMSProp algorithm, which can reduce the oscillation amplitude and accelerate the convergence speed of the network [15]. The Adam optimization algorithm was used to update the parameters. The parameter update process during the initial training of the Adam optimization algorithm is expressed as follows:

$$\begin{cases} D_{d\omega} = \beta_1 D_{d\omega} + (1-\beta_1)d\omega, \\ D_{de} = \beta_1 D_{de} + (1-\beta_1)de, \\ E_{d\omega} = \beta_2 E_{d\omega} + (1-\beta_2)(d\omega)^2, \\ E_{de} = \beta_2 E_{de} + (1-\beta_2)(de)^2. \end{cases} \tag{10}$$

At the t-th iteration, the cumulative amount of the modified gradient is expressed as follows:

$$\begin{cases} D^n_{d\omega} = \dfrac{D_{d\omega}}{\left(1-\beta_1{}^t\right)}, \\ D^n_{de} = \dfrac{D_{de}}{\left(1-\beta_1{}^t\right)}, \\ E^n_{d\omega} = \dfrac{E_{d\omega}}{\left(1-\beta_2{}^t\right)}, \\ E^n_{de} = \dfrac{E_{de}}{\left(1-\beta_2{}^t\right)}. \end{cases} \tag{11}$$

The parameters are updated according to the momentum and RMSProp algorithm, which are expressed as follows:

$$\begin{cases} \omega_{i+1} = \omega_i - \alpha \dfrac{D^n_{d\omega}}{\sqrt{E^n_{d\omega}} + \theta}, \\ e_{i+1} = e_i - \alpha \dfrac{D^n_{de}}{\sqrt{E^n_{de}} + \theta}. \end{cases} \tag{12}$$

In equations (9)-(12), β_1 and β_2 are 0.9 and 0.999, respectively, θ is 10^{-8}, y_i is the corresponding target output, and $h_0(x_i)$ is the corresponding model probability output of x_i.

2.3. Analysis of Reconstruction Performance of MRI Image Super-Resolution Algorithm Based on Deep CNN Algorithm. To avoid the impact of loss function, SRCNN still uses the same loss function as DCNN. The quality of the reconstructed image is evaluated regarding peak signal-to-noise ratio (PSNR) and structural similar image metric (SSIM). PSNR is commonly used to evaluate the differences between the image to be estimated and the ideal image, and its calculation equation is as follows:

$$\mathrm{PSNR}(f,g) = 10\log_{10}\left(\frac{L^2}{\mathrm{MSE}(f,g)}\right), \tag{13}$$

where L is the peak signal, f is the ideal image, g is the image to be estimated, $\mathrm{MSE}(f,g)$ is the mean square error of the image, $\mathrm{MSE}(f,g) = 1/\mathrm{MN}\sum_{i=1}^{M}\sum_{j=1}^{N}(f(i,j) - g(i,j))^2$, and $M \times N$ is the size of the image to be estimated.

The structural similarity (SSIM) evaluation result is similar to the human senses, which is calculated as follows:

$$\mathrm{SSIM}(f,g) = (L(f,g))^{\alpha} \cdot (C(f,g))^{\beta} \bullet (S(f,g))^{\gamma}, \tag{14}$$

where μ_f, μ_g, σ_f, and σ_g are the mean values and standard deviations of the ideal image f and the image g to be evaluated, respectively, σ_{fg} is the covariance of f and g, $c_1 = (k_1\ R)^2$, $c_2 = (k_2 R)^2$, R is the range of image pixel values, k_1 and k_2 are 0.01 and 0.03, respectively, $c_3 = c_2/2$, $\alpha = \beta = \gamma = 1$, and $L(f,g)$, $C(f,g)$, and $S(f,g)$ represent image brightness, structure, and contrast, respectively.

2.4. Knee MRI Examination and Diagnostic Criteria. 1.5 T superconducting MRI (Siemens, Germany) was used to examine the patient that was in the supine position, the knee joint was naturally externally rotated 25° during the examination, and the knee joint was fixed during the scan. The scanning layer thickness was 3 mm, the layer spacing was 0.2~0.4 mm, the matrix was 256×256, and the joint space was used as the scanning center. All patients underwent coronal and sagittal scans. The repetition time (TR) of T2WI was 800–1000 ms, and the echo time (TE) was 26 ms. The spin echo sequence T1WI had TR of 450–500 ms and TE of 14 ms. MRI diagnostic criteria were as follows: all patients' MRI scan images were individually read by three radiologists with senior titles, who provided reports to evaluate the lateral meniscus injury and its damage morphology.

2.5. Surgical Methods and Observation Indicators. Schatzker classification standard in the study of Kumar et al. [16] was referred, and the types of platform fractures of MRI images of all patients in the study were classified into six types. Different types of platform fractures received different surgical treatments.

The grading standard of meniscus injury was as follows. Grade 1: there is a patchy signal, showing mild degeneration. Grade 2: there is a linear signal, showing serious degeneration. Grade 3: there is a linear signal, showing a meniscus tear [17]. All patients were scored according to Lysholm knee joint function score before and after surgery, and the changes of knee joint function scores before and after treatment were compared to analyze the effect of surgical treatment.

2.6. Statistical Methods. The test data were processed using SPSS 19.0. The results of intraoperative exploration or arthroscopy were used as the standard to analyze the accuracy of MRI diagnosis. Enumeration data were expressed as a percentage (%), tested by the χ^2 test. $P < 0.05$ indicated that the difference was statistically considerable.

3. Results

3.1. The Influence of Loss Function and Number of Convolution Kernels on Reconstruction Performance. The comparison of training curves of the three loss functions is shown in Figure 2. PSNRs of the three loss functions all increased first and then became stable with the increase of the number of iterations. The PSNR of the mean square error loss function

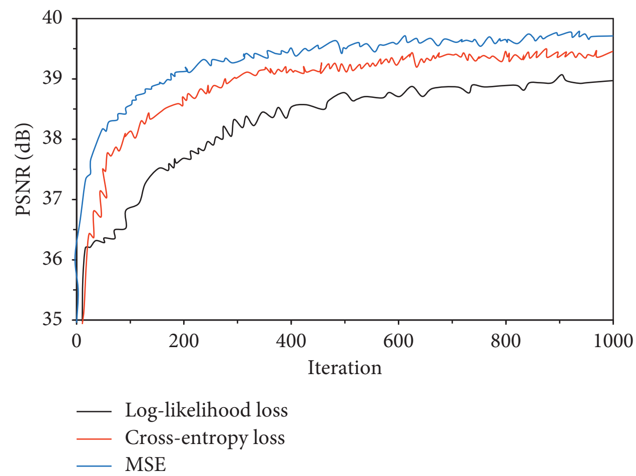

Figure 2: Comparison of training curves with the same loss function.

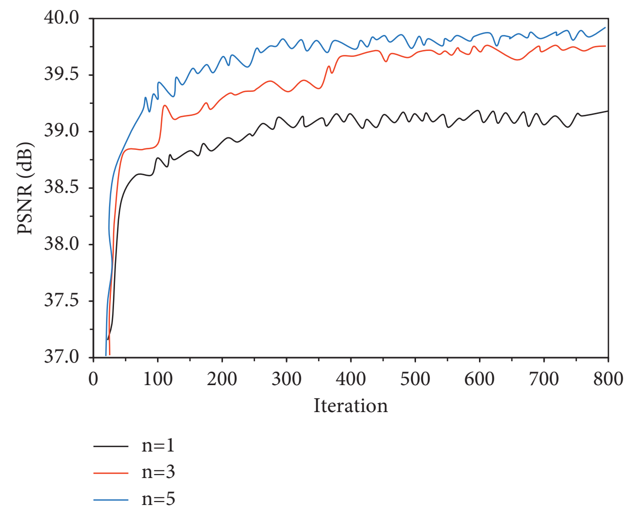

Figure 3: The influence of the number of convolution kernels on reconstruction performance.

was relatively higher under the same number of iterations, and the convergence was relatively faster during the training.

PSNRs of MRI reconstructed images under different numbers of convolution kernels are compared in Figure 3. With the increase of the number of iterations, the PSNR of the MRI reconstructed image under different convolutions and numbers showed a state of increasing first and then being stable in a certain region. As the number of convolution kernels increased, the PSNR of the MRI reconstructed image increased significantly. The number of convolution kernels was increased from 1 to 3, and the PSNR of the MRI reconstructed image was increased by 0.68 dB. The number of convolution kernels was increased from 3 to 5, and the PSNR of the MRI reconstructed image was increased by 0.16 dB.

3.2. Quality Analysis of Reconstructed MRI Image. PSNR value of the SRCNN algorithm was compared with the average PSNR value of DCNN, cubic spline interpolation, and deeply recursive convolutional network (DRCN) based on the residual learning algorithm (Figure 4). The PSNR of the SRCNN algorithm was (42.19 ± 4.37) dB, which was greatly higher than that of other algorithms, and the difference was remarkable ($P < 0.05$).

The average SSIMs of different algorithms were compared (Figure 5). The average SSIM of DCNN, cubic spline interpolation, DRCN, and SRCNN algorithms was 0.9447, 0.9316, 0.9764, and 0.9951, respectively. The SSIM of SRCNN algorithm was notably higher than that of other algorithms, and the difference was substantial ($P < 0.05$).

3.3. MRI Diagnosis Results of Meniscus Injury. The MRI results of patients with meniscus injury before and after treatment were analyzed (Figure 6). The normal meniscus MRI image showed uniform low signal and regular shape (Figure 6(a)). The MRI signal of meniscus injury patients showed focal ellipse or round high signal, which did not touch the articular surface of the meniscus (Figure 6(b)). The

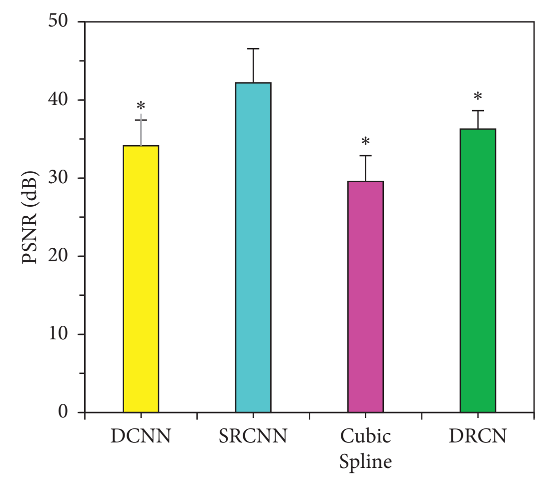

Figure 4: Comparison of PSNR of reconstructed MRI images with different algorithms.

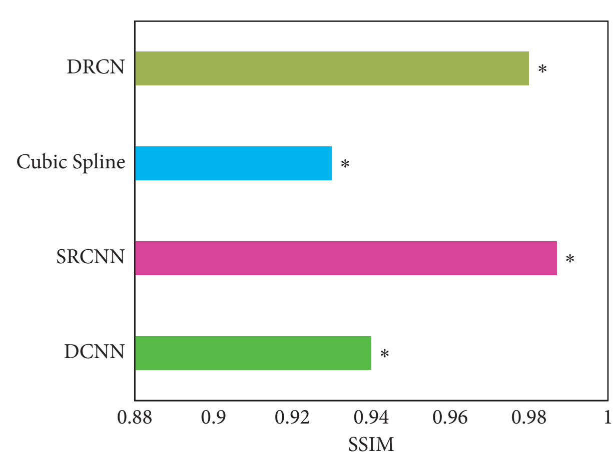

Figure 5: Comparison of SSIM of reconstructed MRI images with different algorithms.

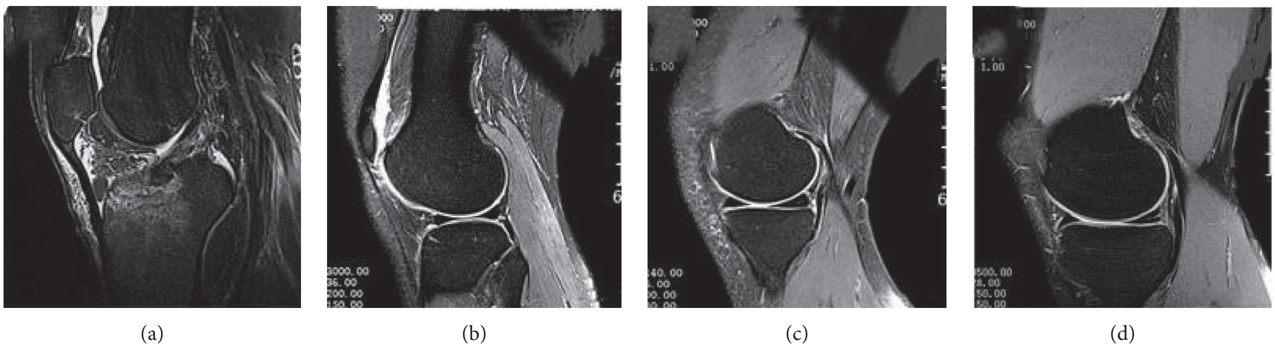

Figure 6: MRI image of meniscus. (a) MRI image of normal meniscus. (b) MRI image of grade I injury in the posterior horn of the medial meniscus (female, 24 years old). (c) MRI image of grade II injury of the posterior horn of the medial meniscus (female, 62 years old). (d) MRI image of grade III injury of the posterior horn of medial meniscus (male, 36 years old).

horizontal linear hyperintensity shadow extended to the edge of the joint capsule of the meniscus but did not exceed the articular surface of the meniscus (Figure 6(c)). In addition, there was an irregular high signal shadow in the meniscus (Figure 6(d)).

3.4. MRI Diagnosis Result of Meniscus Injury Degree. The results of arthroscopy or intraoperative exploration were used as the gold standard to evaluate the accuracy of MRI in the diagnosis of meniscus injury (Figure 7). There were 19 cases (31.67%), 34 cases (56.67%), and 7 cases (11.67%) of meniscus injury diagnosed by arthroscopy as grades I, II, and III, respectively. There were 20 cases (33.33%), 27 cases (45.99%), and 13 cases (21.67%) of meniscus injuries diagnosed by MRI as grades I, II, and III, respectively. There was no obvious difference in the grading of meniscus injury between results of MRI and arthroscopy ($P > 0.05$).

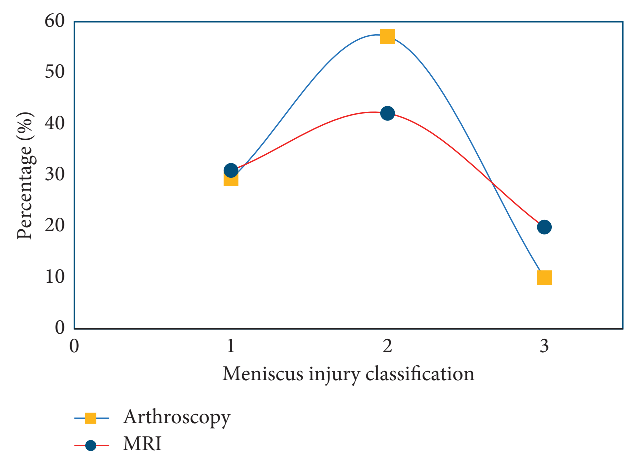

Figure 7: Analysis of the accuracy of MRI in the diagnosis of meniscus injury.

3.5. Statistics of Treatment Methods of MRI-Diagnosed Meniscus Injury. According to the degree and type of meniscus injury, different treatment methods were implemented for the 60 patients included in the study, and the proportion of patients in different methods was calculated (Figure 8). Seventeen cases (28.33%) were treated with meniscus suture, 39 cases (65.00%) underwent secondary resection, 3 cases (5.00%) underwent partial resection, and 1 case (1.67%) underwent total resection.

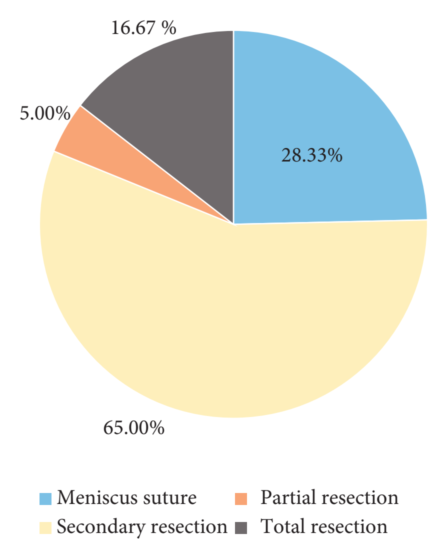

Figure 8: Statistics of treatment methods of MRI-diagnosed meniscus injury.

3.6. Knee Function Scores of Patients Treated with Different Methods before and after Treatment. The knee function scores of patients with different treatment methods were compared before and after treatment (Figure 9). There was no statistical difference in the knee function scores of all patients before treatment ($P > 0.05$). After meniscus suture, secondary resection, partial resection, and total resection were used to treat meniscus injury patients, and the knee function scores were (83.17 ± 8.63), (80.06 ± 7.96), (84.34 ± 7.74), and (85.52 ± 5.97), respectively. In addition, there was no great difference in the knee function scores among patients treated by different treatment methods after treatment ($P > 0.05$). The knee function scores of each group after treatment were significantly different from those before treatment ($P < 0.01$).

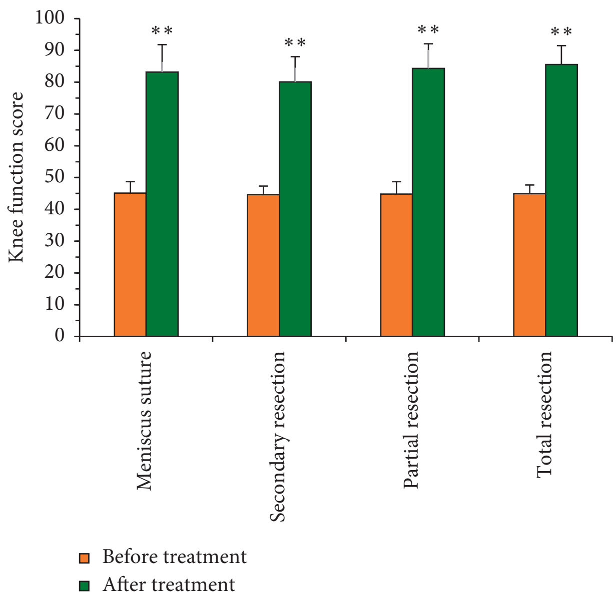

Figure 9: Comparison of knee joint function scores of patients with different treatment methods before and after treatment (** indicated a significant difference versus that before treatment, $P < 0.01$).

4. Discussion

The entire training process of SRCNN based on the deep CNN algorithm was calculating this round of loss according to the loss function after all levels and processing are passed through the input previous to the propagation. In this research, appropriate optimization methods such as stochastic gradient descent was adopted to update the parameters of each layer in the direction of reducing the loss. Therefore, the loss function was the instructor of the entire network learning, which had a great influence on the quality of the final learning result [18]. Then, the training curves of the three commonly used loss functions were compared. It was found that the PSNR of the mean square error loss function was high, and the convergence was fast during the training. The mean square error loss function belongs to the pixel-by-pixel loss function, which can well converge to the local minimum [19]. Therefore, the mean square error loss function was selected as the loss function. The depth of CNN has a great impact on network performance, and the depth of SRCNN is mainly determined by the number of convolution kernels in the network [20]. PSNRs of MRI reconstructed images under different numbers of convolution kernels were compared. It was found that as the number of convolution kernels increased, the PSNR of the MRI reconstructed image increased significantly. The number of convolution kernels was increased from 1 to 3, and the PSNR of the MRI reconstructed image was increased by 0.68 dB. The number of convolution kernels was increased from 3 to 5, and the PSNR of the MRI reconstructed image was increased by 0.16 dB. These results indicated that the PSNR increased with the increase in the number of S3D-RDBs, suggesting that the quality of the MRI images reconstructed by the SRCNN network was getting better and better. It was because the more the number of convolution kernels in the SRCNN network, the deeper the network depth, which can capture more feature maps of different levels to highlight more detailed information [21]. As the number of convolution kernels increased, the increase in PSNR became small. It may be because as the network deepened, information loss still occurred when information was transmitted in the network, which made the backpropagation of the gradient in the network more difficult [22].

Meniscus injury has a significant correlation with the stability of the knee joint, postoperative inflammation, and other complications [23]. Iqbal et al. [24] found that MRI diagnosis of articular surface collapse was consistent with the arthroscopic diagnosis. In this research, the results showed that the different degrees of MRI meniscus injury were not statistically significant with the results of arthroscopy ($P > 0.05$). It showed that there were still a small number of false positives and false negatives in MRI diagnosis. It may be related to the uneven confounding signal of connective tissues such as synovium and muscle health, which led to artifacts of meniscus damage during MRI scan. However, there was no considerable difference between MRI diagnosis results and arthroscopic diagnosis results, indicating that MRI had a certain potential value in the diagnosis of meniscus injury. Lu et al. [25] pointed out that arthroscopy had the characteristics of less surgical trauma and fast recovery speed and is used in the clinical treatment of meniscus injuries. Based on the imaging characteristics, different methods were used to treat patients with different degrees of meniscus injury. The results showed that there was no great difference in knee function scores among patients treated by different treatment methods after treatment ($P > 0.05$). The knee function scores of each group after treatment were significantly different from those before treatment ($P < 0.01$), which suggested that the effect of arthroscopic surgery on knee meniscus injury was significant.

5. Conclusion

Based on the deep CNN algorithm, the Adam optimization algorithm was introduced to optimize it, which was then applied to the knee joint meniscus injury diagnosis. The clinical effect of arthroscopic surgery in knee meniscus injury based on MRI images was evaluated. The results revealed that SRCNN based on deep CNN algorithm significantly improved the quality of knee MRI images. However, there are still some shortcomings in this research, which does not perform a statistical analysis on the parameters and calculation cost of the algorithm in MRI image processing. In the future work, we will further analyze it to clarify the value and significance of SRCNN based on deep CNN algorithm in the diagnosis of knee meniscus injury. In summary, the SRCNN algorithm based on the deep convolutional network algorithm improved the MRI image quality and the diagnosis of knee meniscus injuries. Moreover, arthroscopic knee surgery had good results and had great clinical application and promotion value.

Data Availability

The data used to support the findings of this study are available from the corresponding author upon request.

Conflicts of Interest

The authors declare that they have no conflicts of interest.

References

[1] J.-W. Cho, J. Kim, W.-T. Cho et al., "Approaches and fixation of the posterolateral fracture fragment in tibial plateau fractures: a review with an emphasis on rim plating via modified anterolateral approach," *International Orthopaedics*, vol. 41, no. 9, pp. 1887–1897, 2017.

[2] K. Asai, J. Nakase, T. Oshima, K. Shimozaki, K. Toyooka, and H. Tsuchiya, "Lateral meniscus posterior root tear in anterior cruciate ligament injury can be detected using MRI-specific signs in combination but not individually," *Knee Surgery, Sports Traumatology, Arthroscopy*, vol. 28, no. 10, pp. 3094–3100, 2020.

[3] B. D. Beynnon, N. Fiorentino, M. Gardner-Morse et al., "Combined injury to the ACL and lateral meniscus alters the geometry of articular cartilage and meniscus soon after initial trauma," *Journal of Orthopaedic Research*, vol. 38, no. 4, pp. 759–767, 2020.

[4] Y. Okazaki, T. Furumatsu, T. Yamaguchi et al., "Medial meniscus posterior root tear causes swelling of the medial meniscus and expansion of the extruded meniscus: a comparative analysis between 2D and 3D MRI," *Knee Surgery, Sports Traumatology, Arthroscopy*, vol. 28, no. 11, pp. 3405–3415, 2020.

[5] R. E. Gabr, G. B. Zunta-Soares, J. C. Soares, and P. A. Narayana, "MRI acoustic noise-modulated computer animations for patient distraction and entertainment with application in pediatric psychiatric patients," *Magnetic Resonance Imaging*, vol. 61, pp. 16–19, 2019.

[6] S. U. Khan, N. Ullah, I. Ahmed, I. Ahmad, and M. I. Mahsud, "MRI imaging, comparison of MRI with other modalities, noise in MRI images and machine learning techniques for noise removal: a review," *Current Medical Imaging Formerly Current Medical Imaging Reviews*, vol. 15, no. 3, pp. 243–254, 2019.

[7] J. Chun, H. Zhang, H. M. Gach et al., "MRI super-resolution reconstruction for MRI-guided adaptive radiotherapy using cascaded deep learning: in the presence of limited training data and unknown translation model," *Medical Physics*, vol. 46, no. 9, pp. 4148–4164, 2019.

[8] H. Kobayashi, R. Nakayama, A. Hizukuri, M. Ishida, K. Kitagawa, and H. Sakuma, "Improving image resolution of whole-heart coronary MRA using convolutional neural network," *Journal of Digital Imaging*, vol. 33, no. 2, pp. 497–503, 2020.

[9] S. Ramanarayanan, B. Murugesan, A. Kalyanasundaram et al., "MRI super-resolution using laplacian pyramid convolutional neural networks with isotropic undecimated wavelet loss," in *Proceedings of the 2020 42nd Annual International Conference of the IEEE Engineering in Medicine & Biology Society (EMBC)*, pp. 1584–1587, Montreal, Canada, August 2020.

[10] C. A. Hamm, C. J. Wang, L. J. Savic et al., "Deep learning for liver tumor diagnosis part I: development of a convolutional neural network classifier for multi-phasic MRI," *European Radiology*, vol. 29, no. 7, pp. 3338–3347, 2019.

[11] Y. Chen, S. Hu, H. Mao, W. Deng, and X. Gao, "Application of the best evacuation model of deep learning in the design of public structures," *Image and Vision Computing*, vol. 102, Article ID 103975, 2020.

[12] L. Sun, Z. Fan, X. Ding, Y. Huang, and J. Paisley, "Region-of-interest undersampled MRI reconstruction: a deep convolutional neural network approach," *Magnetic Resonance Imaging*, vol. 63, pp. 185–192, 2019.

[13] C. Guo, J. Lu, Z. Tian, W. Guo, and A. Darvishan, "Optimization of critical parameters of PEM fuel cell using TLBO-DE based on Elman neural network," *Energy Conversion and Management*, vol. 183, pp. 49–158, 2019.

[14] X. Han, "MR-based synthetic CT generation using a deep convolutional neural network method," *Medical Physics*, vol. 44, no. 4, pp. 1408–1419, 2017.

[15] C. J. Wang, C. A. Hamm, L. J. Savic et al., "Deep learning for liver tumor diagnosis part II: convolutional neural network interpretation using radiologic imaging features," *European Radiology*, vol. 29, no. 7, pp. 3348–3357, 2019.

[16] A. Kumar, A. Jain, S. Mittal, and N. Aga, "Letter to the e"rs," *Injury*, vol. 50, no. 3, pp. 820-821, 2019, Injury.

[17] X. Ouyang, B. Wei, S. D. Hong et al., "Arthroscopic characteristics of normal and discoid meniscus injury, and efficiency of recovery in each type of meniscus injury," *Cell Biochemistry and Biophysics*, vol. 72, no. 2, pp. 433–437, 2015.

[18] D. Rengasamy, M. Jafari, B. Rothwell, X. Chen, and G. P. Figueredo, "Deep learning with dynamically weighted loss function for sensor-based prognostics and health management," *Sensors*, vol. 20, no. 3, p. 723, 2020.

[19] J. W. Sanders, G. D. Lewis, H. D. Thames et al., "Machine segmentation of pelvic anatomy in MRI-assisted radiosurgery (MARS) for prostate cancer brachytherapy," *International Journal of Radiation Oncology, Biology, Physics*, vol. 108, no. 5, pp. 1292–1303, 2020.

[20] N. M. H. Elsaid and Y.-C. Wu, "Super-resolution diffusion tensor imaging using SRCNN: a feasibility study," in *Proceedings of the 2019 41st Annual International Conference of the IEEE Engineering in Medicine and Biology Society (EMBC)*, pp. 2830–2834, Berlin, Germany, October 2019.

[21] D. Qiu, S. Zhang, Y. Liu, J. Zhu, and L. Zheng, "Super-resolution reconstruction of knee magnetic resonance imaging based on deep learning," *Computer Methods and Programs in Biomedicine*, vol. 187, Article ID 105059, 2020.

[22] S. Celin and K. Vasanth, "ECG signal classification using various machine learning techniques," *Journal of Medical Systems*, vol. 42, no. 12, p. 241, 2018.

[23] Z. Lin, W. Huang, L. Ma et al., "Kinematic features in patients with lateral discoid meniscus injury during walking," *Scientific Reports*, vol. 8, no. 1, p. 5053, 2018.

[24] A. Iqbal, E. McLoughlin, R. Botchu, and S. L. James, "The ring-shaped meniscus: a case series demonstrating the variation of imaging appearances on MRI," *Skeletal Radiology*, vol. 49, no. 2, pp. 281–289, 2020.

[25] J. Lu, Y. Chen, M. Hu, and C. Sun, "Clinical efficacy of arthroscopy in the treatment of discoid meniscus injury and related risk factors for postoperative pain," *Annals of Palliative Medicine*, vol. 9, no. 6, pp. 4002–4009, 2020.

Hindawi
Journal of Healthcare Engineering
Volume 2021, Article ID 8251702, 4 pages
https://doi.org/10.1155/2021/8251702

Research Article

The Application of the Big Data Medical Imaging System in Improving the Medical and Health Examination

Xiaojuan Zhou [1] and Wenjun Ouyang [2]

[1] *Henan Vocational College of Economics and Trade, Zhengzhou 450018, Henan, China*
[2] *School of Economics and Management, China University of Geosciences (Wuhan), Wuhan 430000, China*

Correspondence should be addressed to Wenjun Ouyang; zhumihua@cug.edu.cn

Received 19 July 2021; Accepted 8 September 2021; Published 17 September 2021

Academic Editor: Enas Abdulhay

To explore the application effect of the big data medical imaging tertiary diagnostic system in improving the medical and health examination, cases in township health centers were collected by the medical imaging tertiary diagnosis system. Clinical cases examined by the tertiary diagnostic system of big data medical imaging will be set as the observation group. Clinical cases not involved in the tertiary diagnostic system of big data medical imaging were set as the control group. The qualified rate, film positive rate, and film diagnosis accuracy between the two groups are compared, and X-ray perspective, X-ray examination, and CT multiple medical imaging examinations are used in two groups. The experimental results showed that the pass rate was 86.57%, positive rate was 72.32%, and diagnosis rate was 80.17%. Pass rate, positive rate, and diagnostic accuracy were higher than the control group ($P < 0.05$). X-line film is the most cost effective. CT examination has a high diagnostic sensitivity and can achieve a clear diagnosis of the benign and malignant diseases. The three-level diagnosis system of medical imaging has significantly improved and improved the technical level in the medical and health examination, which has good practical value.

1. Introduction

China's medical resources are relatively lacking and highly unbalanced in distribution. With the accelerating aging process in China, the contradiction between high-quality medical resources and the people's ever-improving demand for health services is becoming more and more serious [1]. Regional sharing of medical image information is the key to solve this problem. At present, with the implementation of China's "Internet +" development strategy and the active promotion of medical reform on hierarchical diagnosis and treatment and medical consociation construction, many places in China are trying to conduct regional PACS [2]. Medical imaging software, diagnostic medical imaging software, is suitable for almost all types of images. It can diagnose computer X-ray, digital photography, active imaging radiography, angiography, ultrasound, nuclear medicine, endoscopy, and ophthalmic diseases [3]. It can help doctors view 3D images and combine them with other images to get more information about the diagnosis. Godinho et al. found in their 2012 investigation that, in processing CT scan images of stroke patients, radiologists using the ResolutionMD mobile terminal can improve the speed by 24% compared with the PACS workstation, saving one patient every 11 minutes on average [4]. Kong and Chen estimated that the gap of talents in relevant majors in China in the next five years would be as high as 1.3 million; especially, big data talents with solid theoretical foundation and business practice experience across biomedical science and information science are in great shortage [5]. Zhou et al. believed that the future development of teleradiology would be more important [6]. On the basis of the present research, this paper expounds the characteristics of several radiological examinations commonly used in health examination in order to make reasonable application of this kind of examination. Specific x-ray fluoroscopy, health examination, X-ray, and multiple medical imaging tests are involved in the physical examination program. Through discussion and comparison, it is concluded that the X-ray film is the first choice and the most cost-effective method for screening chest diseases in the routine physical examination of most people at present. Ultrasound shows a high diagnostic sensitivity and can make a clear diagnosis of benign and malignant diseases [7, 8].

2. Materials and Methods

2.1. Clinical Data. The patients received imaging health examination in the mobile health center and were set as the control group. There were 2316 cases in the observation group, including 1169 males and 1147 females, aged from 2 to 83 years, with an average age of 55 ± 16.9 years. In the control group, there were 1,982 cases, including 1006 males and 976 females, ranging in age from 1 to 81 years, with an average age of 52 ± 18.3 years. There was no significant difference in age and gender between the two groups ($P \geq 0.05$).

2.2. Research Methods. Doctors will upload the image data to the medical image level-3 diagnosis platform, so county hospital diagnostic center doctors can receive mobile phone SMS alerts and receive township hospital patients examination data. Doctors in the diagnostic center of county hospital can read diagnosis online, review, and issue diagnosis report and reply with electronic signature. Township health work site timely obtains and prints diagnostic reports to patients. For difficult cases, township doctors can upload the examination data to the central hospital for imaging consultation and generally complete the diagnosis or consultation within 1 hour [9].

2.3. Statistical Analysis. Data analysis was performed using SPSS 13.0. The measurement data are represented by mean ± standard difference ($x \pm s$), compared using the t-test and χ^2 test, and $P < 0.05$ is of statistical significance.

3. Results and Discussion

Among 2316 cases in the observation group, 2005 cases were qualified and 311 cases were unqualified, with a pass rate of 86.57%. In the control group of 1982 cases, 1391 cases were qualified and 591 cases were unqualified, with a qualified rate of 70.18%. The difference was statistically significant ($P < 0.05$), as shown in Table 1.

The main factors for unqualified cases are unphotographed positive position (32.13%), uploaded image quality defects (exposure, artifacts, and poor image quality) (28.58%), unmarked image left and right parts (25.12%), and failure to provide a complete medical history (14.17%).

In the observation group, 1675 cases were positive and 641 cases were negative, and the positive rate was 72.32%, while in the control group, 1167 cases were positive and 815 cases were negative, and the positive rate was 58.88%, among the 2316 cases. The difference was statistically significant ($P < 0.05$), as shown in Table 2.

Table 1: Comparison of imaging quality between the observation group and the control group.

Group	Qualified	Unqualified	Percentage of pass
Observation group ($n = 2316$)	2005	311	86.57
Control group ($n = 1983$)	1391	591	70.18

Table 2: Comparison of the positive rate of radiography between the observation group and the control group.

Group	Positive	Negative	Positive rate
Observation group ($n = 2316$)	1675	641	72.32
Control group ($n = 1982$)	1167	815	58.88

The use of the medical imaging system for sentinel lymph nodes in the treatment of breast cancer is characterized by the ability to detect sentinel lymph node metastasis through some diagnostic methods. At present, the main methods for the clinical diagnosis of sentinel lymph node micrometastasis include continuous section, immunohistochemistry, and biopsy. However, in the actual operation process of the former two methods, all lymph nodes of patients need to be tested, which is a heavy workload and has great limitations in practical use; it is difficult to achieve the purpose of detection, so sentinel lymph node biopsy for breast cancer has become a widely used means in clinics. However, with the continuous development of medical technology, some scholars have proposed that colour ultrasound has a good effect on the diagnosis of sentinel lymph node micrometastasis [10].

Sixty cases of breast cancer patients admitted to a hospital from December 2014 to December 2015 were randomly selected as the research objects. All the selected patients were female, aged from 21 to 68 years, with an average age of 50.6 ± 5.7 years. Sites: 33 on the right side and 27 on the left side; there were 22 cases of invasive ductal carcinoma, 7 cases of mucinous adenocarcinoma, 8 cases of invasive lobular carcinoma, 10 cases of papillary adenocarcinoma, and 13 cases of medullary carcinoma. According to TNM stage T1-2N0M0, 25 cases were of the T1 stage (tumor diameter: <2 cm), 35 cases were of the T2 stage (tumor diameter: 2–5 cm), as shown in Table 3.

According to the material of the X-ray bulb tube anode, there are tungsten target and rhodium target. At present, molybdenum target is more commonly used for X-ray photography, which is of great value for the examination of breast cancer, the classic textbook description of the X-ray signs of breast cancer typically involves lesions that have formed masses or prominent nodules, with the improvement of people's health awareness and the popularization of medical knowledge, and the typical breast cancer is rarely found in the health examination; however, mammography is more difficult to diagnose early breast cancer with no history, no symptoms, no signs, and lesions of less than a certain volume than breast cancer with a history, symptoms, signs, and lesions of a certain volume; it depends even more

Table 3: Colour ultrasound results of breast cancer patients.

Position and type	This is an infiltrating ductal carcinoma	Mucous adenocarcinoma	This is an invasive lobular carcinoma	Papillary adenocarcinoma	Medullary carcinoma
On the right side	10	3	4	3	5
On the left side	12	4	4	7	8

Table 4: CT examination data of thyroid cancer patients.

	The number of people	Age	You have thyroid nodules	Thyroid cancer	Papillary carcinoma of the thyroid	Medullary thyroid carcinoma
Man	50	40–50	16	3	2	0
Woman	95	19–75	45	6	5	1

Table 5: Comparison of diagnostic rates between observation and control imaging subjects.

Group	Clarify a diagnosis	No clear diagnosis	Positive rate (%)
Observation group ($n = 2316$)	2213	103	95.55
Control group ($n = 1982$)	1589	384	80.17

on the personal experience of the diagnostician and the thinking environment at the time of reading the film, especially in women of reproductive age whose breast tissue has not degenerated; the value of mammography may be higher for those who have already been examined or self-examined by a doctor, especially for those who have been found to have suspicious nodules by ultrasound. Molybdenum target mammography of the breast generally takes a total of four films for the comparison between the upper and lower positions of both sides of the breast and the internal and external oblique positions, and the total amount of X-ray radiation cannot be ignored. Therefore, the indications for mammography should be mastered from the aspects of family history, age, medical history of the present illness, marriage, and child history to prevent the abuse from causing harm to women [11]. Some foreign anthologies suggest annual mammography and MRI examination for high-risk groups, and Liu Peifang also advocates MRI participation in the census of high-risk groups in China. Regular screening for breast cancer is necessary for high-risk groups. If mammography has the most comprehensive advantages compared with MRJ and ultrasound, another method of screening for breast cancer, it is worthwhile to make mammography the preferred method for early breast cancer screening in high-risk groups.

Due to the popularity of CT, in routine physical examination, further CT examination of lesions of solid organs in the digestive system, urogenital system, and other systems found by ultrasound examination and lung lesions found by the chest X-ray film can be used to differentiate benign from malignant lesions or evaluate their functions: patients with special indications of biochemical examination results can be screened for diseases of related organs: for patients with frequent dizziness and headache, in order to exclude cerebrovascular lesions, head CT can be included in the physical examination items if conditions permit; as a routine test, because of the high dose of X-ray radiation, how to use this new technique to maximize the diagnostic effect and accord with the principle of X-ray examination optimization is a subject worth studying. So, people tend to use low-dose spiral CT scans to screen for early lung cancer, and because of the low dose X-ray scans in low dose spiral CT scans, the thin-layer reconstruction technique is used instead of the thin-layer scan so that the dose of iatrogenic X-ray radiation of the subject is greatly reduced, and because the low-dose spiral CT scan requires less X-ray dose, the thermal effect of the CT tube is reduced, the loss of the CT tube is correspondingly reduced, the life of the tube is prolonged, and it is possible to reduce the charge reasonably. In addition, CD is used instead of film, which further saves the cost and makes it possible to charge the same fee for the low-dose spiral CT scan and chest CR and DR examination, which is easy to be accepted by people. For patients with cardiac symptoms, CT coronary imaging is undoubtedly necessary, but this examination can increase the amount of X-ray radiation in the subject, and the screening for coronary artery disease in the routine physical examination is still under study and questionable; some occupations have special physical requirements for practitioners. After a certain age, CT coronary imaging can be performed to screen for coronary artery lesions. In any case, you should respect the advice of your doctor as to whether or not to have a CT scan on a healthy subject, and you should never ask for a CT scan unless recommended by your doctor.

A total of 150 patients (55 males and 95 females) underwent thyroid nodule examination. The average age was 45.39 ± 5.96 years from 19 to 75 years. For all physical examination personnel, colour Doppler ultrasound was selected to carry out thyroid nodule disease diagnosis. The frequency of the ultrasonic probe was adjusted from 7.5 to 12 MHz such as Table 4.

Patients with hyperplasia of thyroid tissue are more likely to present with thyroid nodules. If the nature of the thyroid nodule is different, different clinical intervention measures should be selected [12]. For patients with benign thyroid nodule, conservative treatment and follow-up observation were mainly selected clinically. For physical examination personnel in the implementation of the thyroid nodule diagnosis process, the method of ultrasound examination is chosen, showing a high diagnostic sensitivity, and can be a clear diagnosis of benign and malignant diseases so as to ensure the smooth implementation of clinical effective thyroid nodule treatment methods.

As shown in Table 5, in the observation group of 2316 cases, 2213 cases were clearly diagnosed, 103 cases were undiagnosed, and the diagnosis rate was 95.55%. In the control group, 1589 cases were definitely diagnosed, 384 cases were undiagnosed, and the diagnosis rate was 80.17%. The difference was statistically significant ($P < 0.05$).

4. Conclusions

This paper discusses the application of several radiological images in normal physical examination. X-ray fluoroscopy; X-ray photography; color Doppler imaging; X-ray radiography has developed from screen radiography to computer radiography (CR) and the latest digital X-ray radiography (DR). Through the comparison of the positive rate of radiography in the observation group of 2316 cases, 1675 cases were positive and 641 cases were negative, and the positive rate was 72.32%, while in the control group of 1982 cases, 1167 cases were positive and 815 cases were negative, and the positive rate was 58.88%. Thus, this demonstrates that X-rays are the preferred and most cost-effective method of screening for chest disease during routine physical examinations. The choice of the ultrasound examination method shows a high diagnostic sensitivity, and the benign and malignant disease can be clearly diagnosed so as to ensure the successful implementation of the clinical effective treatment of thyroid nodules. The development of information technology has indeed provided us with great convenience and also promoted the development of medical imaging, teaching, and scientific research. It is combined with biotechnology, genetic engineering, and medical engineering. Hospitals at all levels should improve the understanding of digital large imaging, update their ideas, actively promote its application in hospitals, and strengthen personnel training. The rapid development of video technology has promoted the explosive coverage of video visual culture in today's society. When video visual culture enters the field of education, it will have a huge impact on the educational mode.

Data Availability

The data used to support the findings of this study are available from the corresponding author upon request.

Conflicts of Interest

The authors declare no conflicts of interest.

References

[1] C. Tchito Tchapga, T. A. Mih, A. Tchagna Kouanou et al., "Biomedical image classification in a big data architecture using machine learning algorithms," *Journal of Healthcare Engineering*, vol. 2021, no. 2, 11 pages, Article ID 9998819, 2021.

[2] E. N. Huseyn, "Application of deep learning in medical imaging," *Nature and Science*, vol. 3, no. 4, pp. 7–13, 2020.

[3] A. Chandy, "A review on iot based medical imaging technology for healthcare applications," *Journal of Innovative Image Processing*, vol. 1, no. 1, pp. 51–60, 2019.

[4] T. M. Godinho, C. Costa, and J. L. Oliveira, "Intelligent generator of big data medical imaging repositories," *IET Software*, vol. 11, no. 3, pp. 100–104, 2017.

[5] H. Kong and J. Chen, "Medical monitoring and management system of mobile thyroid surgery based on internet of things and cloud computing," *Wireless Communications and Mobile Computing*, vol. 2021, no. 2, 10 pages, Article ID 7065910, 2021.

[6] C. Zhou, J. Hu, and N. Chen, "Remote care assistance in emergency department based on smart medical," *Journal of Healthcare Engineering*, vol. 2021, no. 10, 10 pages, Article ID 971960, 2021.

[7] X. Lv and M. Li, "Application and research of the intelligent management system based on internet of things technology in the era of big data," *Mobile Information Systems*, vol. 2021, no. 16, 6 pages, Article ID 6515792, 2021.

[8] Y. Yuan, W. Chen, L. Yan, B. Huang, and J. Li, "A similarity-based disease diagnosis system for medical big data," *Journal of Medical Imaging and Health Informatics*, vol. 7, no. 2, pp. 364–370, 2017.

[9] S. Ranjbar, K. W. Singleton, P. R. Jackson, C. R. Rickertsen, and L. S. Hu, "A deep convolutional neural network for annotation of magnetic resonance imaging sequence type," *Journal of Digital Imaging*, vol. 33, no. 112, pp. 1–8, 2019.

[10] K. Kaur and R. Rani, "Multi-model persistent solution for healthcare big data," *Journal of Medical Imaging and Health Informatics*, vol. 6, no. 4, pp. 937–947, 2016.

[11] Y. Li and S. Wang, "Research progress in application of artificial intelligence in diagnosis of upper digestive tract diseases," *Chinese Journal of Gastroenterology*, vol. 25, no. 5, pp. 298–300, 2020.

[12] Y. Liu, "Research on the application of infrared imaging system in the cervical syndrome treatment," *Revista de la Facultad de Ingenieria*, vol. 32, no. 6, pp. 191–199, 2017.

Hindawi
Journal of Healthcare Engineering
Volume 2021, Article ID 5436793, 11 pages
https://doi.org/10.1155/2021/5436793

Research Article

Deep Learning-Based CT Imaging in Diagnosing Myeloma and Its Prognosis Evaluation

Jinzhou Wang,[1] **Xiangjun Shi**,[2] **Xingchen Yao**,[1] **Jie Ren**,[1] **and Xinru Du**[1]

[1]*Department of Orthopedics, Beijing Chaoyang Hospital, Capital Medical University, Chaoyang District, 100032 Beijing, China*
[2]*Department of Hematology, Beijing Chaoyang Hospital, Capital Medical University, Chaoyang District, 100032 Beijing, China*

Correspondence should be addressed to Xinru Du; 122019000601@ccmu.edu.cn

Received 13 June 2021; Revised 20 August 2021; Accepted 23 August 2021; Published 13 September 2021

Academic Editor: Enas Abdulhay

Imaging examination plays an important role in the early diagnosis of myeloma. The study focused on the segmentation effects of deep learning-based models on CT images for myeloma, and the influence of different chemotherapy treatments on the prognosis of patients. Specifically, 186 patients with suspected myeloma were the research subjects. The U-Net model was adjusted to segment the CT images, and then, the Faster region convolutional neural network (RCNN) model was used to label the lesions. Patients were divided into bortezomib group (group 1, $n = 128$) and non-bortezomib group (group 2, $n = 58$). The biochemical indexes, blood routine indexes, and skeletal muscle of the two groups were compared before and after chemotherapy. The results showed that the improved U-Net model demonstrated good segmentation results, the Faster RCNN model can realize the labeling of the lesion area in the CT image, and the classification accuracy rate was as high as 99%. Compared with group 1, group 2 showed enlarged psoas major and erector spinae muscle after treatment and decreased bone marrow plasma cells content, blood M protein, urine 24 h light chain, pBNP, *ß*-2 microglobulin (β2MG), ALP, and white blood cell (WBC) levels ($P < 0.05$). In conclusion, deep learning is suggested in the segmentation and classification of CT images for myeloma, which can lift the detection accuracy. Two different chemotherapy regimens both improve the prognosis of patients, but the effects of non-bortezomib chemotherapy are better.

1. Introduction

Myeloma leads to increased levels of monoclonal immunoglobulin, which is attributed to malignant proliferation and abnormal accumulation of clonal plasma cells [1]. Studies have shown that the incidence of multiple myeloma has significantly exceeded that of acute leukemia and ranks second among hematological malignancies [2]. With the progress in research on treatment methods and the clinical promotion of hematopoietic stem cell transplantation technology, the complete remission rate of multiple myeloma has reached approximately 75% [3]. It has been confirmed that the median survival time of patients with multiple myeloma has been extended to 5 to 8 years [4]. Thanks to the unclear cause, the insidious onset, and low progress of myeloma, it is easy to cause the missed diagnosis and misdiagnosis [5]. In the treatment of myeloma, the chemotherapy regimen containing high-dose dexamethasone was generally selected in the past. This regimen has a rapid onset for newly discovered myeloma patients, with a median onset time of 1–1.5 months, which can quickly relieve patient symptoms. In recent years, with the emergence of new drugs such as immunomodulators and protease inhibitors, treatment programs have been further optimized. Nowadays, it is common to choose a combination of new drugs and traditional chemotherapy drugs for combined chemotherapy in clinical practice. This new combination chemotherapy regimen can significantly improve the remission rate of myeloma patients and the survival rate.

The clinical diagnosis method of myeloma is different from other general tumors. It requires obvious clinical symptoms of peripheral organ damage, such as renal function damage and osteolytic bone damage [6]. Recently, imaging techniques have been widely used in the diagnosis, differentiation, staging, and evaluation of therapeutic effects of multiple myeloma. Multiple myeloma is a blood system disease, involving multiple systems/organs. Systemic bone disease and extramedullary lesions have implications for the identification, diagnosis, and staging of the disease [7]. X-ray is always used in the imaging diagnosis of multiple myeloma, but it is positive only when more than 30% of the trabecular bone is destroyed and so it is easy to cause missed diagnosis [8]. CT imaging is characterized by cross-sectional scan, high-density resolution, and reconstruction. It is superior to X-ray scan in the diagnosis of multiple myeloma [9].

However, CT imaging cannot be used to stage the disease when there is no change in bone marrow infiltration and cortical bone. One of the most classic methods of deep learning is convolutional neural networks. Among them, Faster RCNN and U-Net are both earlier algorithms that use full convolutional networks for image segmentation. Deep learning used in the segmentation of medical images can greatly improve the segmentation effects [10]. The fully convolutional network (FCN) optimizes the fully connected layer in the traditional convolutional neural network into a convolutional layer, which reduces the complexity of the calculation and lifts the segmentation efficiency [11]. Compared with the FCN model, the U-Net model has higher segmentation accuracy and is not limited by the input sample size [12]. Using deep learning to process medical images can assist doctors in detecting lesions. It not only reduces the workload of doctors but also overcomes problems, such as poor diagnosis due to subjective differences.

In this study, a deep learning-based model was used to process CT images of patients with myeloma and then the effects of different chemotherapy treatments on the prognosis of patients were compared, aimed to provide reference for improving the clinical diagnosis, treatment, and staging effects of myeloma.

2. Methods

2.1. Research Subjects. A total of 186 suspected myeloma patients were selected, among whom 123 were initially diagnosed as myeloma by Durie–Salmon (DS) and International Staging System (ISS) methods. They all underwent surgery, pathological examination, and bone marrow aspiration biopsy and were diagnosed with myeloma. There were 93 males and 93 females, and the age ranged from 35 to 82 years, with an average age of 58.54 ± 10.15 years. The average interval between bone marrow biopsy and imaging examination was about 20 days.

The subjects were selected as per the following inclusion criteria: (i) those who met the diagnostic criteria for myeloma; (ii) those who had not received any radiotherapy, chemotherapy, or other therapies before treatment; (iii) those who had no other malignant tumors; and (iv) those agreeing with and accepting the study.

Exclusion criteria were as follows: (i) those with incomplete imaging data and (ii) those who cannot cooperate to complete the imaging examination. All patients have signed an informed consent form. All studies in this article have been approved by the Medical Ethics Committee.

2.2. CT Examination. The whole-body low-dose CT examination was performed using the Philips Brilliance ICT instrument. Under 120 kV and 50 mAs, the slice thickness was 2 mm, the slice spacing was 1 mm, the reconstruction slice thickness was 3 mm, the screw pitch was 0.811, and the collimation was 128×0.873 mm. During CT examination, the patient was in a supine position with arms crossed and placed on the lower abdomen. The scan was from the top of the skull to the proximal end of the tibia. After the scan, the collected images need to be transmitted to the image-processing workstation. The standardized bone algorithm was used to perform sagittal and coronal reconstruction.

2.3. CT Image Segmentation Based on U-Net. The U-Net model is used to segment skeletal CT images, and it is a typical "end-to-end" U-shaped network structure. To improve the segmentation effects, the original U-Net model was optimized, and the structure of the adjusted model is shown in Figure 1.

A loss function based on the Dice coefficient is used to balance the ratio of pixels in the bone area to the background area. The Dice coefficient is to measure the similarity between functions [13], and the Dice coefficient and its loss function are calculated as follows:

$$\begin{aligned} \text{Dice} &= \frac{2 \cdot \text{TP}}{2 \cdot \text{TP} + \text{FP} + \text{FN}}, \\ \text{loss} &= 1 - \frac{2 \cdot \text{TP}}{2 \cdot \text{TP} + \text{FP} + \text{FN}}, \end{aligned} \tag{1}$$

TP is the number of positive samples predicted as positive samples, FP is the number of positive samples predicted as negative samples, and FN is the number of positive samples predicted as negative samples.

Intersection over union metric (IOU) is used to evaluate the segmentation effects. IOU calculates the intersection ratio, which is often used in the field of image segmentation [14]. The calculation of IOU is as follows:

$$\text{IOU} = \frac{\text{TP}}{\text{TP} + \text{FP} + \text{FN}}. \tag{2}$$

2.4. Myeloma Detection Based on Faster RCNN. In order to realize the intelligent detection of myeloma using CT images, the Faster RCNN model is used to detect the lesion area. The Faster RCNN model mainly consists of two parts, namely, the region proposal network (RPN) and the region convolutional neural network (RCNN) [15]. The specific image processing steps using this model are as follows: First, the network classification model is used to extract the feature map, and then, the RPN is used to generate the region of interest (RoI), followed by the pooling operation. Finally, RCNN is used to classify the feature map and assign

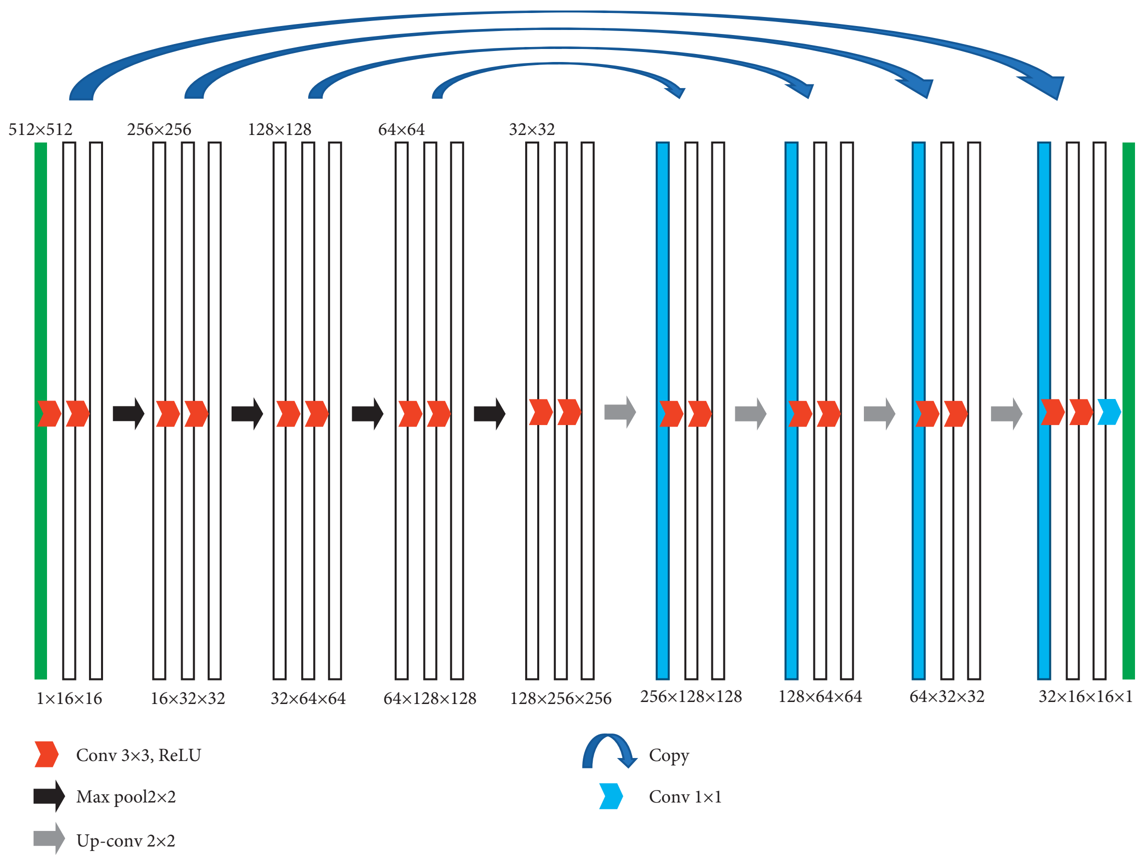

Figure 1: Basic framework and parameter settings of the U-Net model.

the probability value to the target category. The basic structure and parameters of Faster RCNN are shown in Figure 2.

The VGG basic model is used to extract the feature map. The basic structure of the VGG model is shown in Figure 3. The convolutional kernel sizes in the VGG model are 1×1 and 3×3. The activation function is a softmax function, and the reshape operation is performed before and after treatment to improve the classification effects.

The sample is input into the model for training, and the loss function of the model needs to include the RPN and detector, but the loss function is composed of classification loss and regression loss function, expressed as follows:

$$L(\{p_i\}, \{t_i\}) = \frac{1}{N_c} \sum L_c(p_i, p_i^*) + \alpha \frac{1}{N_r} \sum p_i^* L_r(t_i, t_i^*), \tag{3}$$

where p_i is the probability of the target area in the prediction box and p_i^* is the multiclass labels in softmax regression.

The mathematical expressions of classification loss L_c and regression loss L_r are as follows:

$$\begin{aligned} L_c(p_i, p_i^*) &= -\log(p_i^* p_i + (1 - p_i^*)(1 - p_i)), \\ L_r(t_i, t_i^*) &= R(t_i, t_i^*), \end{aligned} \tag{4}$$

where R is the smooth $L1$ function, t_i is the offset of the prediction frame during the RPN training process, and t_i^* has the same dimension as t_i. With the iteration of the loss function, the parameters of the softmax classifier are further optimized and clarified, which can distinguish different training samples.

2.5. Remission Induction Treatment Plan. With patients' economic levels and clinical differences taken into account, there were mainly two treatment plans: group 1 underwent bortezomib treatment, and group 2 underwent non-bortezomib treatment. There were 128 patients in group 1, and 58 patients in group 2.

2.6. Evaluation and Follow-Up. All patients were tested for laboratory indicators before treatment and after induction treatment, including blood routine, serum/urine protein electrophoresis, biochemical items (albumin, globulin, and blood creatinine), urine routine, and bone marrow examination, to explore clinical efficacy. All patients were followed up from the first visit, and the follow-up time was approximately 40 months. The overall survival time in this study was from the time of diagnosis to the end of the last follow-up. When patients were transferred halfway or gave up treatment, they were not included in the study of overall survival.

2.7. Statistical Processing. SPSS19.0 was used to process the data. Measurement data conforming to normal distribution were expressed as mean ± standard deviation, and

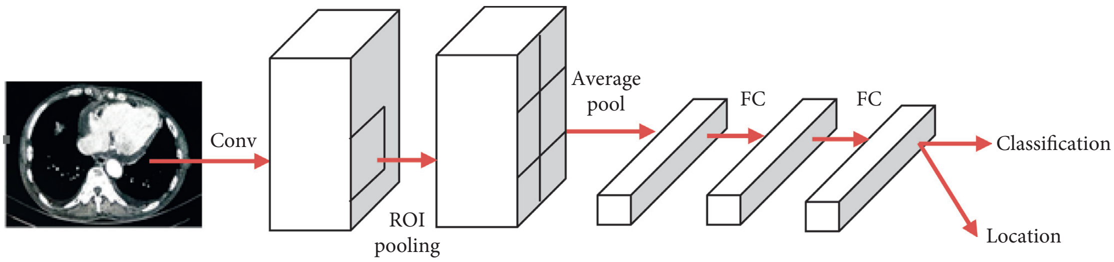

Figure 2: Basic structure of Faster RCNN.

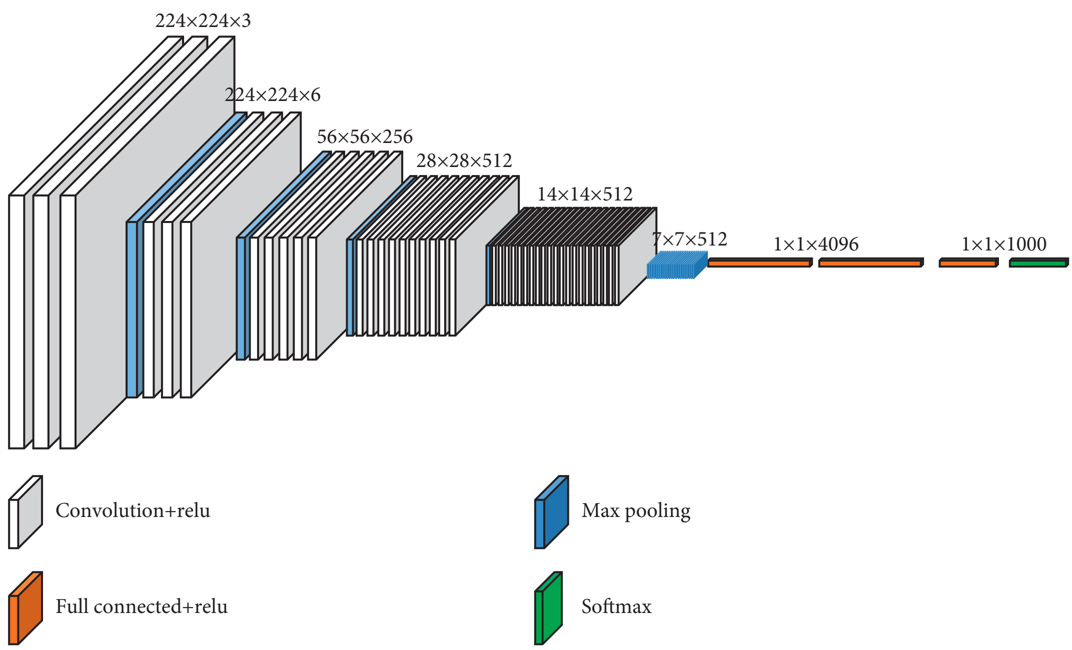

Figure 3: Basic structure of the VGG model.

comparisons between groups adopted the independent sample t test; measurement data that did not conform to normal distribution were represented by the median value, and the nonparametric rank sum test was used to analyze the difference between groups. The count data were expressed by percentage n, and the χ^2 test was for comparison between groups. $P < 0.05$ was the threshold for significance.

3. Results

3.1. Segmentation Performance of the U-Net Model. U-Net and the improved U-Net′ network were trained for 50 rounds, and the loss curve and IOU curve of the two models on the training set and the test set were compared before and after chemotherapy. It is noted in Figure 4 that the loss curve of the U-Net′ model on the training set and the test set converged more quickly, while the area under the IOU curve was larger.

The loss value and IOU value were compared between the U-Net and U-Net′ model when the maximum training times are reached, and the results are shown in Figure 5. It was noted that the loss values of the U-Net′ model on the training set and the test set were larger, than the IOU value.

Subjectively, the segmentation effects of the U-Net and U-Net′ model on CT images were compared for multiple myeloma, and the results are shown in Figure 6. The segmentation effects of the lesion area on the T1 and T2 images were compared. It was noted that the U-Net model had poor effects when segmenting small lesions in the CT image and the improved U-Net′ model can realize the segmentation of small lesions. The red area in the figure is the segmentation of the lesions of myeloma patients under the U-Net model algorithm.

3.2. Detection and Verification of the Faster RCNN Model. The Faster RCNN model was trained, and the training results are shown in Figure 7. It was noted that when training iterations were below 10 times, the classification accuracy and loss value of the model gradually stabilized. The classification accuracy of the Faster RCNN model was approximately 0.966, and the loss value was approximately 0.092.

The trained Faster RCNN model was then used to detect multiple myeloma, and the results are shown in Figure 8. It was noted that the classification results displayed the

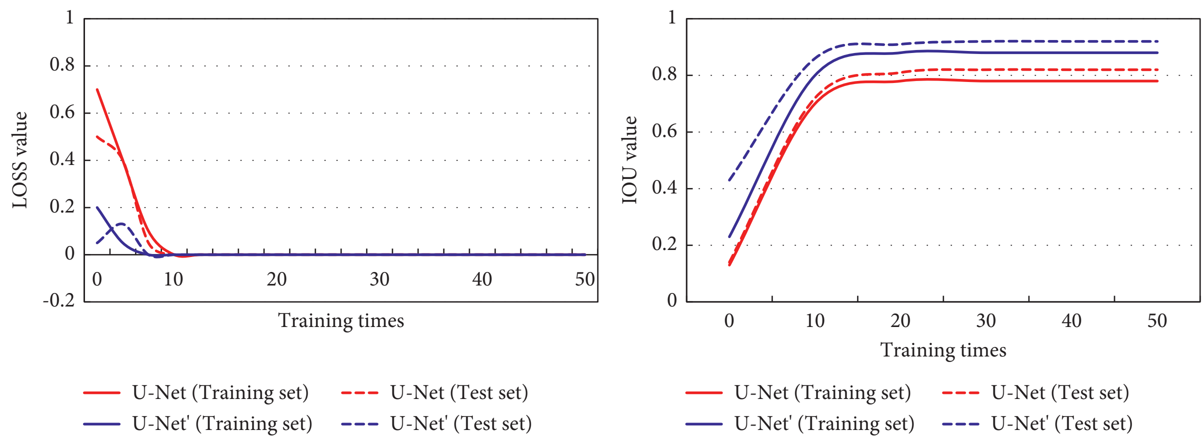

FIGURE 4: Loss and IOU curves on the training set and test set.

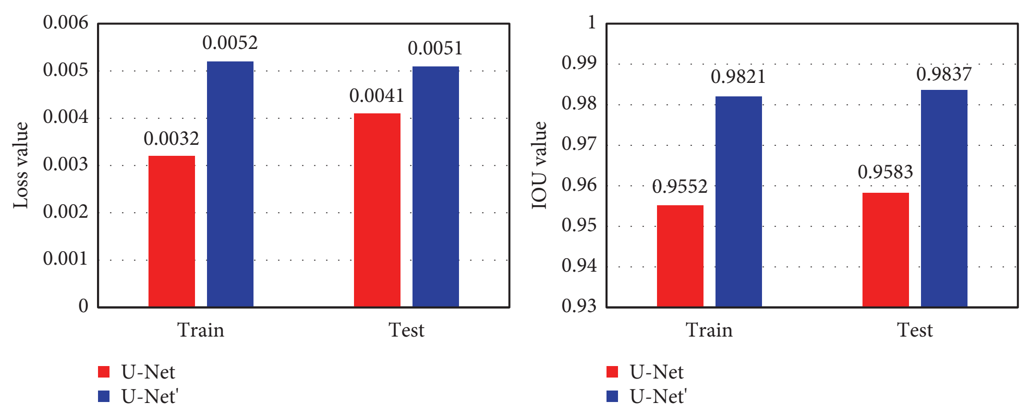

FIGURE 5: Loss and IOU values on the training set and test set.

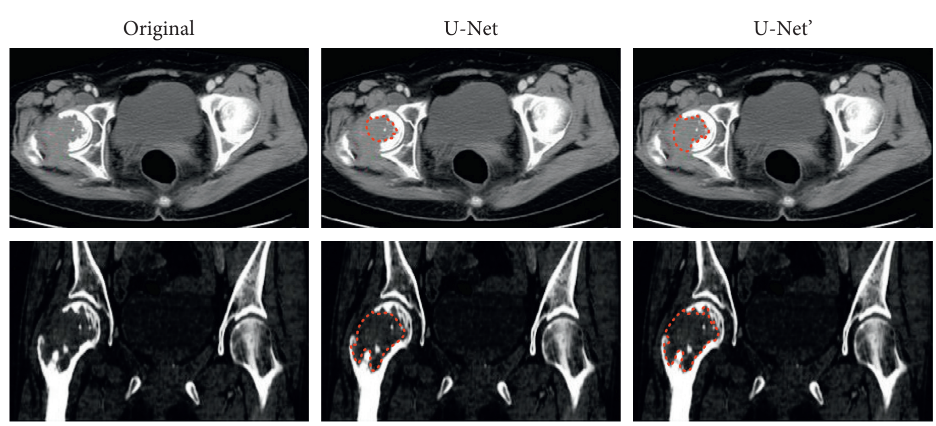

FIGURE 6: Segmentation of CT images for multiple myeloma.

prediction frame, the corresponding category, and the probability value of the target area. The red area in the figure is the part of the myeloma patient's lesion that was separated under the Faster RCNN model algorithm.

3.3. Basic Information of Patients. The baseline data of patients in group 1 and group 2 were compared, and the results are shown in Table 1. It was noted that there was no statistically significant difference between the two groups of patients in age, height, weight, gender, DS staging, and ISS staging ($P > 0.05$). Hence, the baseline data of the two groups were comparable.

3.4. CT Imaging for Waist Muscle of the Patient before and after Chemotherapy. The fat in psoas major, quadratus lumborum, erector spinae, and erector spinae was compared before

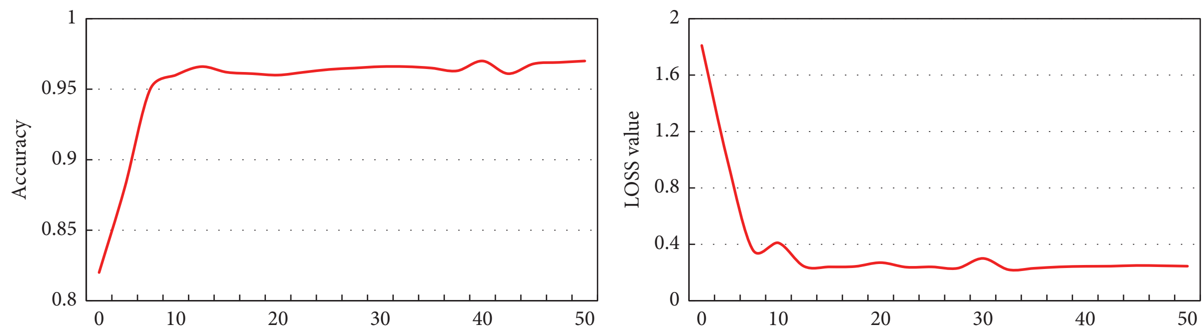

FIGURE 7: Classification accuracy and loss curve of the Faster RCNN model.

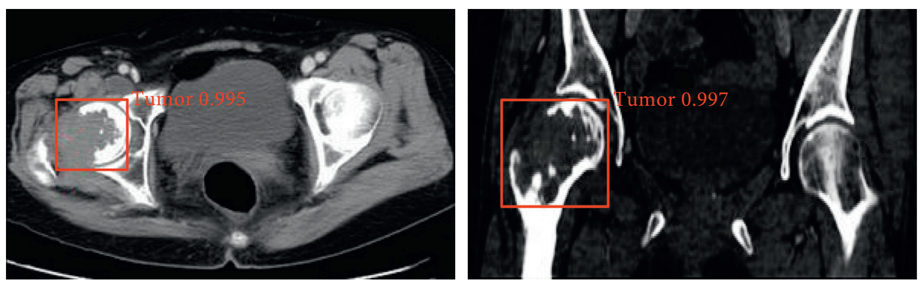

FIGURE 8: The detection results of the Faster RCNN model for multiple myeloma.

TABLE 1: Comparison of baseline data between the two groups.

Project		Group 1 ($n = 128$)	Group 2 ($n = 58$)	Statistics	P
Age (year)		58.93 ± 9.65	57.69 ± 11.12	$t = 0.771$	0.441
Height (m)		1.66 ± 0.08	1.65 ± 0.10	$t = 0.453$	0.652
Weight (kg)		67.52 ± 10.51	66.85 ± 11.86	$t = 0.317$	0.752
Gender (n/%)	Male	69/53.91	24/41.38	$\chi^2 = 0.839$	0.334
	Female	59/46.09	34/58.62		
DS staging (n/%)	I	3/2.34	4/6.90	$\chi^2 = 0.873$	0.467
	II	9/7.03	4/6.90		
	III	2/1.56	1/1.72		
	IV	9372.66	39/67.24		
	V	20/15.63	9/15.52		
ISS staging (n/%)	I	17/13.28	10/17.24	$\chi^2 = 0.797$	0.562
	II	54/42.19	22/37.93		
	III	52/40.63	22/37.93		
	IV	0/0.00	0/0.00		
	V	1/0.78	0/0.00		

and after chemotherapy, and the results are shown in Figure 9. It was noted that in group 2, the quadratus lumborum muscle was significantly reduced and the erector spinae muscle was significantly enlarged after treatment ($P < 0.05$) compared to before treatment; the psoas major and erector spinae muscle were significantly enlarged after treatment in group 2 compared to group 1, and the erector spinae muscle fat was significantly reduced ($P < 0.05$).

3.5. Biochemical Indicators before and after Chemotherapy. The ratio of bone marrow plasma cells, monoclonal immunoglobulin (M protein), urine 24 h light chain, pBNP, and β-2 microglobulin (β2MG) levels were compared before and after chemotherapy, and the results are shown in Figure 10. It was noted that compared to before treatment, the levels of urine 24 h light chain, pBNP, and β2MG in group 2 were significantly reduced ($P < 0.05$) while the level of β2MG in group 1 was also significantly reduced ($P < 0.05$). Compared with group 1, the ratio of bone marrow plasma cells, blood M protein, urine 24 h light chain, pBNP, and β2MG levels were significantly reduced after treatment in group 2 ($P < 0.05$).

3.6. Blood Routine Indexes before and after Chemotherapy. The blood routine indexes of ALP, LDH, Cr, Alb, Ca, WBC, Hb, and Plt were compared before and after chemotherapy, and the results are shown in Figure 11. It was noted that compared with before treatment, the Cr levels of group 1

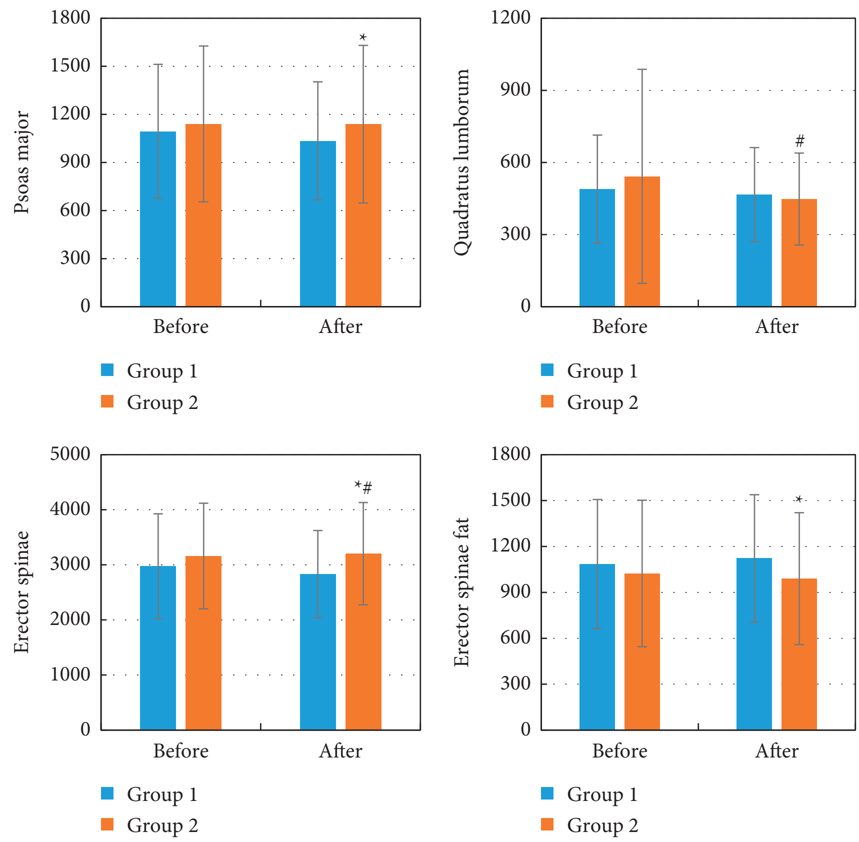

Figure 9: CT results of the patient's psoas major before and after chemotherapy. The four pictures show (a) psoas major, (b) quadratus lumborum, (c) erector spinae, and (d) erector spinae fat. Compared to before treatment, $^{\#}P<0.05$; compared to group 1, $^{*}P<0.05$.

and group 2 were significantly reduced ($P<0.05$). Compared with group 1, ALP before and after treatment in group 2 was significantly lower ($P<0.05$), the LDH level before and after treatment was significantly higher ($P<0.05$), and the WBC level after treatment was significantly lower ($P<0.05$).

4. Discussion

Threshold segmentation is the most common image segmentation method. The pixel values in the target area and background are similar, but the pixel values of different target areas are different. The algorithm segments the target area according to the peak value displayed in the histogram [16]. Traditional segmentation algorithms are affected by image noise and other factors, and thus, they tend to have poor segmentation results. The U-Net model has been proved to have excellent segmentation results [17], so it was used in the study. Its parameters were adjusted based on the original one, and then, the adjusted one was used to segment the lesion area in CT images. It was found that compared to the original one, the improved U-Net model demonstrated better convergence effects and the area under the IOU curve was larger. It suggested that the adjusted U-Net model had better segmentation effects on the CT image of multiple myeloma. Image processing is an integral part in the detection of lesion area [18]. The deep learning-based model needs to classify the target areas after the recognition and positioning [19]. Therefore, the Faster RCNN framework was used to detect the lesion area on CT images for myeloma and to locate the target area in the CT image and label the category. The results showed that the Faster RCNN model can realize the positioning and category labeling of the lesion area, which lifted the diagnosis efficiency.

Plasma cells are transformed into protoplasmic cells by B lymphocytes after antigen stimulation, and protoplasmic cells evolve into mature plasma cells through processes such as differentiation and reproduction [20]. M protein is an abnormal immunoglobulin produced by the monoclonal malignant proliferation of plasma cells or B lymphocytes [21]. Studies have confirmed that the proportion of plasma cells and the level of M protein in patients with multiple myeloma are significantly increased [22]. The results of this study found that the proportion of bone marrow plasma cells and the level of M protein in patients undergoing chemotherapy were significantly reduced and the decrease in the non-bortezomib group was more obvious. The molecular structure of immunoglobulin can be divided into two types: heavy chain and light chain, of which the light chain is divided into κ type and λ type [23]. The multiple myeloma arises from excessive proliferation of abnormal plasma cells in the bone marrow, which in turn causes an increased level of M protein, lifting

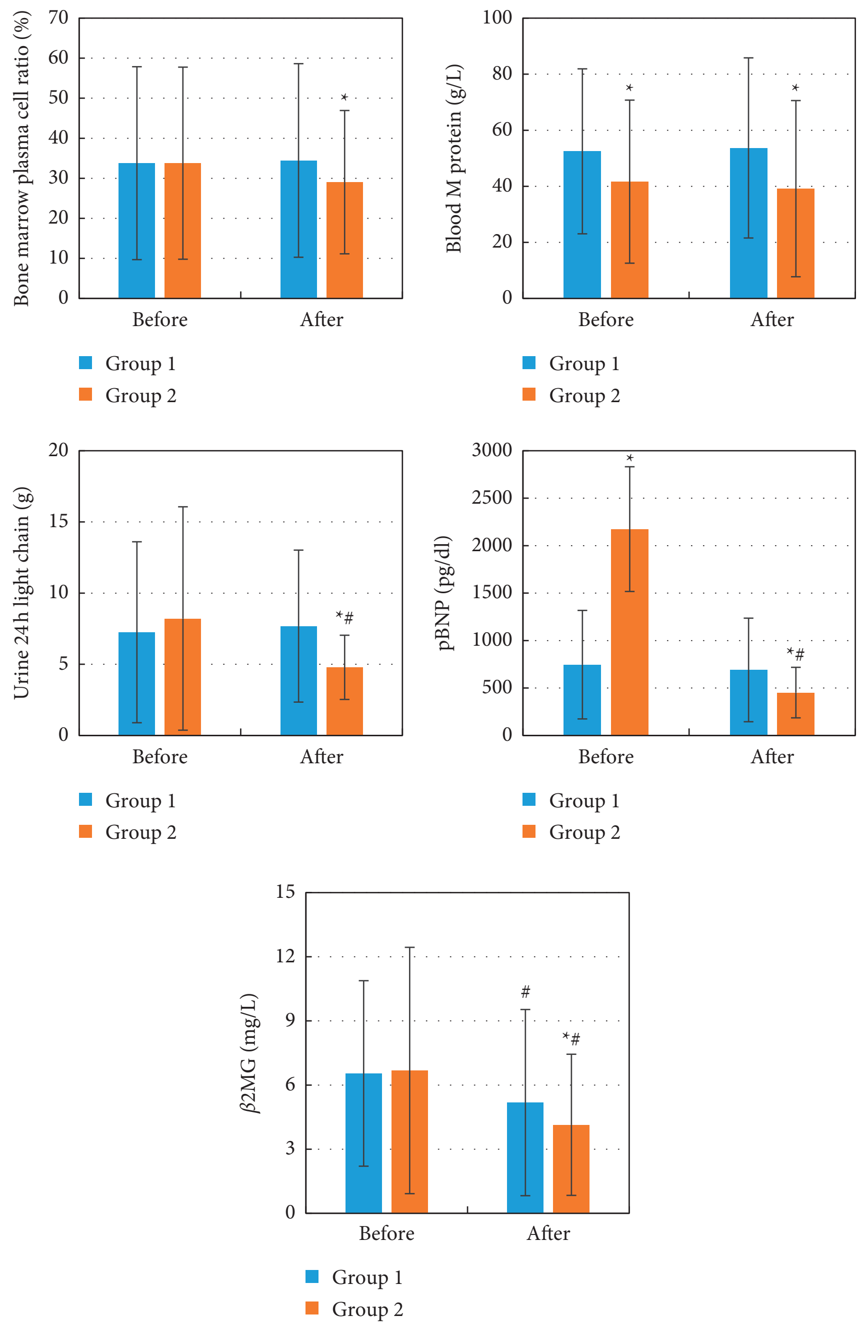

Figure 10: Biochemical indicators of the patient before and after chemotherapy. The five pictures show (a) bone marrow plasma cell ratio, (b) blood M protein, (c) urine 24 h light chain, (d) pBNP, and (e) β2MG. Compared to before treatment, $^{\#}P < 0.05$; compared to group 1, $^{*}P < 0.05$.

the level of urinary light chains, so the level of light-chain type of urine protein is an indicator for the diagnosis of multiple myeloma [24, 25]. β2MG is a small molecular protein synthesized by lymphocytes, which can be used to assess kidney function and can also be used for auxiliary diagnosis of malignant tumors [26, 27]. It was found in the study that, after non-bortezomib treatment, the patients' urine 24 h light chain and β2MG levels were significantly reduced, indicating that the treatment can effectively improve the prognosis of patients.

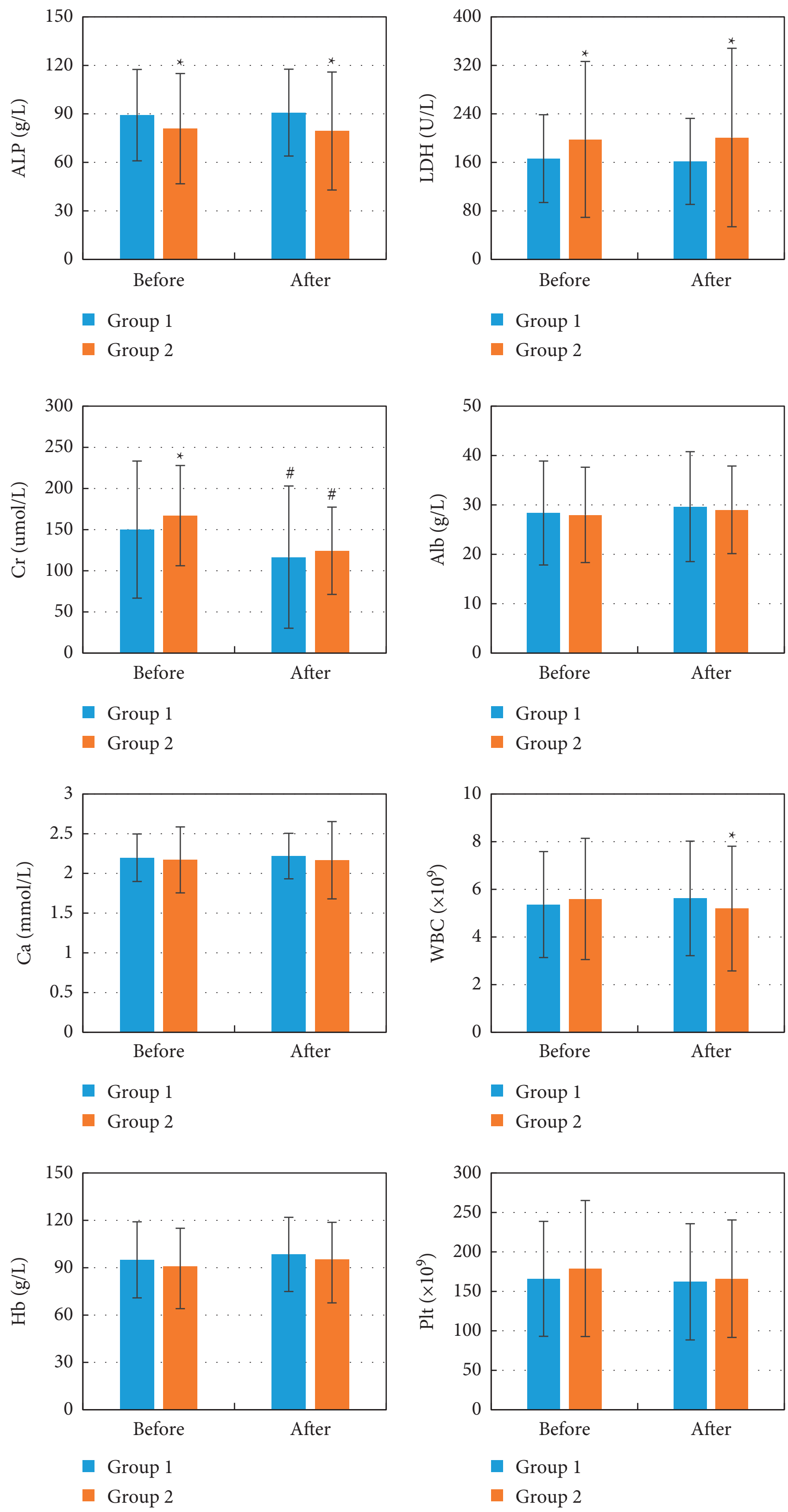

FIGURE 11: Routine blood indicators of patients before and after chemotherapy. The eight pictures were ALP, LDH, Cr, Alb, Ca, WBC, Hb, and Plt. Compared to before treatment, $^{\#}P < 0.05$; compared to group 1, $^{*}P < 0.05$.

5. Conclusion

The purpose of this article is to use deep learning technology to segment and classify myeloma CT images and to further improve the clinical diagnosis and treatment of myeloma patients. The results showed that U-Net and Faster RCNN models can realize lesion area segmentation and labeling. The effects of different chemotherapy treatments on the prognosis of patients were compared. It was found that non-bortezomib treatment can significantly reduce the proportion of bone marrow plasma cells, M protein, urine 24 h light chain, β2MG, and WBC levels, indicating that the treatment plan can improve the patient's chemotherapy effects. However, some limitations in the study should be noted. The deep learning is only used to segment and classify the lesion area in the CT image and not applied to the CT image after chemotherapy. However, the research content of this article still has certain limitations. The article does not analyze the correlation between different prognostic indicators and the overall survival of patients. And, this article only studies a single imaging diagnostic method, so more imaging diagnostic methods will be studied in depth in the future. Therefore, more clinical indicators will be involved in the follow-up, to strengthen the findings of the study. In summary, the results of this study can effectively improve the diagnostic accuracy of patients with myeloma, provide certain guidance for subsequent clinical treatment, and significantly improve the prognosis of patients. It provides a certain theoretical basis for the subsequent research on imaging examination methods.

Data Availability

The data used to support the findings of this study are available from the corresponding author upon request.

Conflicts of Interest

The authors declare no conflicts of interest.

Acknowledgments

This work was supported by the Beijing Natural Science Foundation (7192071).

References

[1] K. Brigle and B. Rogers, "Pathobiology and diagnosis of multiple myeloma," *Seminars in Oncology Nursing*, vol. 33, no. 3, pp. 225–236, 2017.

[2] D. Kazandjian, "Multiple myeloma epidemiology and survival: a unique malignancy," *Seminars in Oncology*, vol. 43, no. 6, pp. 676–681, 2016.

[3] G. Riccomi, G. Fornaciari, and V. Giuffra, "Multiple myeloma in paleopathology: a critical review," *International Journal of Paleopathology*, vol. 24, pp. 201–212, 2019.

[4] M. Kehrer, S. Koob, A. Strauss, D. Wirtz, and J. Schmolders, "Multiples myelom—aktuelle standards in diagnostik und therapie," *Zeitschrift für Orthopädie und Unfallchirurgie*, vol. 155, no. 5, pp. 575–586, 2017.

[5] A. Mehta, "Multiple myeloma," *Hematology*, vol. 20, no. 1, pp. 58-59, 2015.

[6] S. K. Kumar, N. S. Callander, M. Alsina et al., "NCCN guidelines insights: multiple myeloma, version 3.2018," *Journal of the National Comprehensive Cancer Network*, vol. 16, no. 1, pp. 11–20, 2018.

[7] C. Gerecke, S. Fuhrmann, S. Strifler, M. Schmidt-Hieber, H. Einsele, and S. Knop, "The diagnosis and treatment of multiple myeloma," *Deutsches Aerzteblatt Online*, vol. 113, no. 27-28, pp. 470–476, 2016.

[8] A. Kosmala, T. Bley, and B. Petritsch, "Imaging of multiple myeloma," *RöFo—Fortschritte auf dem Gebiet der Röntgenstrahlen und der bildgebenden Verfahren*, vol. 191, no. 9, pp. 805–816, 2019.

[9] M. Cavo, E. Terpos, C. Nanni et al., "Role of 18F-FDG PET/CT in the diagnosis and management of multiple myeloma and other plasma cell disorders: a consensus statement by the international myeloma working group," *The Lancet Oncology*, vol. 18, no. 4, pp. e206–e217, 2017.

[10] E. Moen, D. Bannon, T. Kudo, W. Graf, M. Covert, and D. Van Valen, "Deep learning for cellular image analysis," *Nature Methods*, vol. 16, no. 12, pp. 1233–1246, 2019.

[11] Y. Zheng, B. Zhen, A. Chen, F. Qi, X. Hao, and B. Qiu, "A hybrid convolutional neural network for super-resolution reconstruction of MR images," *Medical Physics*, vol. 47, no. 7, pp. 3013–3022, 2020.

[12] X. Dong, Y. Lei, T. Wang et al., "Automatic multiorgan segmentation in thorax CTimages using U-net-GAN," *Medical Physics*, vol. 46, no. 5, pp. 2157–2168, 2019.

[13] A. Machireddy, N. Meermeier, F. Coakley, and X. Song, "Malignancy detection in prostate multi-parametric MR images using U-net with attention," in *Proceedings of the 2020 42nd Annual International Conference of the IEEE Engineering in Medicine & Biology Society (EMBC)*, Montreal, Canada, July 2020.

[14] D. Abdelhafiz, J. Bi, R. Ammar, C. Yang, and S. Nabavi, "Convolutional neural network for automated mass segmentation in mammography," *BMC Bioinformatics*, vol. 21, no. S1, p. 192, 2020.

[15] S. Ma, Y. Huang, X. Che, and R. Gu, "Faster RCNN-based detection of cervical spinal cord injury and disc degeneration," *Journal of Applied Clinical Medical Physics*, vol. 21, no. 9, pp. 235–243, 2020.

[16] M. Tamal, "Intensity threshold based solid tumour segmentation method for positron emission tomography (PET) images: a review," *Heliyon*, vol. 6, no. 10, Article ID e05267, 2020.

[17] Z. Zhang, C. Wu, S. Coleman, and D. Kerr, "Dense-inception U-net for medical image segmentation," *Computer Methods and Programs in Biomedicine*, vol. 192, Article ID 105395, 2020.

[18] J. Mosebach, H. Thierjung, H.-P. Schlemmer, and S. Delorme, "Multiple myeloma guidelines and their recent updates: implications for imaging," *RöFo—Fortschritte auf dem Gebiet der Röntgenstrahlen und der bildgebenden Verfahren*, vol. 191, no. 11, pp. 998–1009, 2019.

[19] P. Schelb, S. Kohl, J. P. Radtke et al., "Classification of cancer at prostate MRI: deep learning versus clinical PI-rads assessment," *Radiology*, vol. 293, no. 3, pp. 607–617, 2019.

[20] D. Suan, C. Sundling, and R. Brink, "Plasma cell and memory b cell differentiation from the germinal center," *Current Opinion in Immunology*, vol. 45, pp. 97–102, 2017.

[21] S. C. Ragbourne, N. Maghsoodi, M. Streetly, and M. A. Crook, "The association between metabolic syndrome and multiple

myeloma," *Acta Haematologica*, vol. 144, no. 1, pp. 24–33, 2021.
[22] M.-V. Mateos and O. Landgren, "MGUS and smoldering multiple myeloma: diagnosis and epidemiology," *Plasma Cell Dyscrasias*, vol. 169, pp. 3–12, 2016.
[23] I. J. Sathick, M. E. Drosou, and N. Leung, "Myeloma light chain cast nephropathy, a review," *Journal of Nephrology*, vol. 32, no. 2, pp. 189–198, 2019.
[24] M. Andrei and J. C. Wang, "Cutaneous light chain amyloidosis with multiple myeloma: a concise review," *Hematology/Oncology and Stem Cell Therapy*, vol. 12, no. 2, pp. 71–81, 2019.
[25] H. Y. Ting, P. Sthaneshwar, P. C. Bee, H. Shanmugam, and M. Lim, "Heavy/light chain assay in the monitoring of multiple myeloma," *Pathology*, vol. 51, no. 5, pp. 507–511, 2019.
[26] T. Kuragano, A. Kida, M. Yahiro, and T. Nakanishi, "Clinical benefit of an adsorptive technique for elderly long-term hemodialysis patients," *CKD-Associated Complications: Progress in the Last Half Century*, vol. 198, pp. 94–102, 2019.
[27] N. Wang, N. Tesfaluul, J. Li, X. Gao, S. Liu, and B. Yue, "Enrichment of circulating myeloma cells by immunomagnetic beads combined with flow cytometry for monitoring minimal residual disease and relapse in patients with multiple myeloma," *Annals of Hematology*, vol. 98, no. 12, pp. 2769–2780, 2019.

Hindawi
Journal of Healthcare Engineering
Volume 2021, Article ID 1640870, 8 pages
https://doi.org/10.1155/2021/1640870

Research Article

Diagnosis of Arrhythmia for Patients with Occult Coronary Heart Disease Guided by Intracavitary Electrocardiogram under Data Mining Algorithm

Gang Wang,[1] **Li Luo**,[2] **and Xia Zhao**[3]

[1]*Department of Geriatrics, Lianshui County People's Hospital, Lianshui 223400, China*
[2]*Department of Cardiology, The Affiliated Huai'an Hospital of Xuzhou Medical University and The Second People's Hospital of Huai'an, Huai'an 223002, China*
[3]*Department of Cardiology, The Second Affiliated Hospital of Jiaxing University, Jiaxing, Zhejiang 314000, China*

Correspondence should be addressed to Xia Zhao; 29101@njnu.edu.cn

Received 29 June 2021; Revised 28 August 2021; Accepted 31 August 2021; Published 13 September 2021

Academic Editor: Enas Abdulhay

The objective of this study was to explore the application value of intracavitary electrocardiogram- (IEGM-) guided diagnosis of occult heart disease and conventional electrocardiogram (EGM) in the diagnosis of occult coronary heart disease (CHD) based on the classification and regression tree (CART) mining algorithm, hoping to provide a more effective basis for clinical diagnosis of the occult CHD. In this study, 100 patients with occult CHD admitted to our hospital from February 2016 to December 2020 were selected as the research objects. Based on the random number table method, 100 patients were randomly rolled into two groups, each with 50 cases. The patients diagnosed with conventional ECG were set as the control group, and patients in the experimental group were diagnosed with IEGM under the data mining algorithms. The diagnostic effects of the two groups were compared. The results showed that the processing effect of the CART algorithm (94%) was much better than that of the multiple linear regression algorithm (78%) and the random forest algorithm (69%) ($P < 0.05$), the agreement between the results of the experimental group and the results of coronary angiography (80%) and Kappa (0.7) was higher than those of the control group (55%, 0.45), and the difference was statistically significant ($P < 0.05$). In addition, the sensitivity (93%) and accuracy (80%) of the experimental group were obviously higher than those of the control group (62% and 55%), and the differences were remarkably significant ($P < 0.05$). In conclusion, the consistency ratio of the IEGM examination was higher, showing high accuracy; the intracavitary examination was invasive, so IEGM was not recommended when the diagnosis result of the examination may cause more harm than good.

1. Introduction

The economic, cultural, and technological development of today's society is quite rapid, including the medical technology. With the development of society, it is not only people's living standards that have been improved, but the incidence of various diseases has also increased, which has had a great impact on people's lives and health, including the hidden coronary heart disease (occult CHD) [1, 2]. The pathogenesis of coronary heart disease (CHD) is mainly due to coronary artery stenosis that causes the circulatory system to not provide enough blood to the body, which indirectly leads to myocardial dysfunction. CHD can be said to be a common disease with a high clinical incidence, and its occurrence trend is also increasing year by year with time [3, 4]. The occult CHD, also known as painless myocardial ischemia, is a special type of CHD [5]. Most people with occult CHD are middle-aged or older. Simply speaking, it means that there is no obvious clinical manifestation. However, myocardial ischemia and coronary atherosclerosis can be found under the relevant examinations of electrocardiogram (EGM), dynamic EGM, and cardiac color Doppler ultrasound [6, 7].

Since the diagnosis of occult CHD is relatively difficult, the clinically frequently used diagnostic method is EGM, including dynamic EGM and stress test EGM. However, the operations of these two examination methods are more complicated and difficult to use, which makes it difficult for their clinical applications to be popularized. Although selective coronary angiography can improve the clinical detection rate, it is an invasive operation. To a certain extent, the patient's tolerance must be taken into account, so it will lead to high clinical misdiagnosis and missed diagnosis [8, 9]. As a mapping technique that places electrode catheters in different parts of the heart to record cardiac indicators, intracavitary electrocardiogram (IEGM) uses the guide wire in the catheter as the electrode and monitors the changes in the EGM P wave that occur during catheter placement to determine the tip of the catheter location [10]. The IEGM is a new cutting-edge positioning method for peripherally inserted central venous catheters (PICC), which can effectively dilute high-concentration and irritating drugs, protecting the blood vessels and relieving patients' pain [11]. But there are still limitations in the application of this technology. It is difficult to distinguish between atrial and ventricular waves by observing the results of IEGM alone, and the extracavitary electrocardiogram has to be required during the analysis process.

With the widespread application of intelligent algorithms in the medical field, people also try to combine intelligent algorithms with intracavitary electrocardiogram inspection methods to obtain a good diagnosis of occult coronary heart disease. However, there are relatively few researches on this type. Data mining algorithm is a set of heuristics and calculations to create a data mining model based on data. The provided data were analyzed firstly using the algorithm, and a specific type of pattern and trend would be found to create the model [12]. This study was intended to explore the application value of IEGM based on data mining algorithms and conventional EGM in diagnosis of occult CHD, hoping to provide a more effective basis for its clinical diagnosis.

2. Methods

2.1. Research Objects. 100 patients with occult CHD admitted to the hospital from February 2016 to December 2020 were selected as the research objects. There were 52 males and 48 females, aged 45–72 years (with an average age of 56.1 ± 3.8 years). Based on the random number table method, 100 patients were randomly rolled into two groups, each with 50 cases. The patients diagnosed with conventional ECG were set as the control group, and patients in the experimental group were diagnosed with IEGM under the classification and regression tree (CART) data mining algorithm. The diagnostic effects of the two groups were compared. The general clinical data of the two groups of patients (Table 1) revealed that the comparison was not statistically significant ($P > 0.05$) but comparable, suggesting the feasibility of this experiment. This study had been reviewed by the Ethics Committee of our hospital.

The inclusion criteria were given as follows: patients over 18 years, patients who suffered with coronary atherosclerosis and myocardial ischemia without pain, patients with at least one coronary artery stenosis $\geq 50\%$ diagnosed by selective coronary angiography, and patients who were informed about the study and signed the informed consent forms.

The exclusion criteria were defined as follows: patients with malignant tumor disease; patients with severe immunization and infectious diseases; patients with cognitive impairment and unable to complete the study; patients with pacemakers and 24 h dynamic EGM; patients who had been diagnosed with atrial fibrillation, supraventricular tachycardia, pulmonary heart disease, and other heart diseases that affected the shape of the P wave; patients who were prone to muscle tremor, such as hyperthyroidism; and patients whose basic EGMs were difficult to clearly identify.

2.2. Research Methods. The conventional EGM was performed as for patients in the control group. The posture of the patient was guided by professional person so that they were relaxed enough. The specific operation process is shown in Figure 1.

The IEGM was performed for patients in the experimental group, and the involved materials and instruments included catheter material (1.9 F PICC catheter with guide wire), EGM monitor (PHILPS MP20), IEGM wire, EGM electrode clips, and conversion adapter.

The specific operation process is shown in Figure 2: the catheter placement was performed by the static therapy specialist nurses in accordance with the PICC catheter placement in the hospital and the standardized operating procedures for IEGM positioning.

2.3. Analysis Model of Data Mining Algorithm. In this study, the classification and regression tree (CART) mining algorithm in the data mining algorithm was adopted to build the analysis model. The CART is commonly used to process continuous data, and heuristic methods are used to minimize the quadratic variance of each node, thus completing the division of the input space [13].

The n^{th} variable x^n and its value m were selected as the segmentation variable and segmentation point, respectively, and two regions Q_1 and Q_2 were defined as shown in the following equations:

$$Q_1(n,m) = \{x \mid x^n \leq m\}, \tag{1}$$

$$Q_2(n,m) = \{x \mid x^n > m\}. \tag{2}$$

Then, the best segmentation variable n and segmentation point m were found out, and the specific solution process is shown as follows:

$$\min_{n,m}\left[\min_{z_1}\sum_{x_1\in Q_1(n,m)}(y_i - z_1)^2 + \min_{z_2}\sum_{x_1\in Q_2(n,m)}(y_i - z_2)^2\right], \tag{3}$$

$$Z_1 = \mathrm{ave}(y_i \mid x_i \in Q_1(n,m)), \tag{4}$$

$$Z_2 = \mathrm{ave}(y_i \mid x_i \in Q_2(n,m)). \tag{5}$$

In the above equation, x_i, y_i, and Z_1 referred to independent variable, dependent variable, and optimal solution,

Table 1: The general clinical data of the two groups of patients.

Group	Gender		Age range (years)	Average age (years)
	Males ($n = 52$)	Females ($n = 48$)		
Experimental group (50 cases)	27	23	45–70	56.4 ± 3.1
Control group (50 cases)	25	25	45–71	55.8 ± 3.8
χ^2	3.182	2.198	2.391	2.981
P	0.121	0.081	0.096	0.101

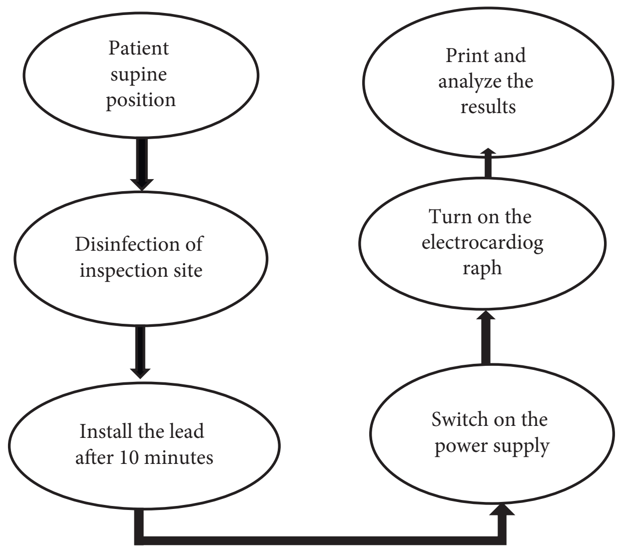

Figure 1: The specific operation process of conventional EGM.

respectively. In this study, the CART mining algorithm was adopted to process a large amount of particle information in the IC-EGM detection to increase the accuracy of the inspection results.

2.4. Observation Indicators. Two experienced and highly qualified physicians were invited to judge all examination results. The result of coronary angiography was undertaken as the gold standard to compare the consistency of the results. The sensitivity, specificity, accuracy, positive predictive value, and negative predictive value were calculated based on the test results. The calculation standard of curative effect was shown in Table 2.

2.5. Statistical Methods. The SPSS22.0 was adopted for data entry, sorting, and statistical analysis. The enumeration data were compared using χ^2 test; and the measurement data were compared using t-test. The multiple sample means were compared with the analysis of variance. The LSD method was used when the variance was uniform, and the Dunnett T3 method was used when the variance was uneven. $P < 0.05$ indicated that the difference was statistically significant. Kappa test was performed on the consistency ratio between the examination result and the coronary angiography results in two groups. When Kappa > 0.75, the consistency rate between the two results was high; when $0.4 \leq$ Kappa < 0.75, the consistency rate was normal; and when Kappa < 0.4, the consistency rate was low.

3. Results

3.1. Comparison on IC-EGM Processing Effect. In the research process, the effect of multiple linear regression algorithm, random forest algorithm, and CART algorithm were compared on IC-EGM processing. The final diagnosis result was undertaken as the gold standard to compare the accuracy of the diagnosis result. The results showed that the accuracy of the IC-EGM detection results processed by the multiple linear regression algorithm was 78%, and that was 69% for the random forest algorithm and 94% for CART algorithm. The comparison revealed that the processing effect of the CART algorithm was much better than the multiple linear regression algorithm and the random forest algorithm ($P < 0.05$), as shown in Figure 3.

3.2. Comparison of EGM Results of Healthy Person and Patients with CHD. Figure 4(a) shows the standard EGM results of normal people, and Figure 4(b) shows the EGM manifestations of patients with CHD. Comparison of the two EGM results revealed that the trend of P wave in the EGM of patients with CHD weakened and decreased, with basically disappeared Q wave and lower position of ST segment compared with the results of normal people, showing an oblique ST segment decline, inverted T wave, and basically normal QRS band.

3.3. Comparison on the Diagnosis Results of the ECG of the Two Groups of Patients. Figure 5 shows the test results under a conventional EGM. It disclosed that there were 31 patients

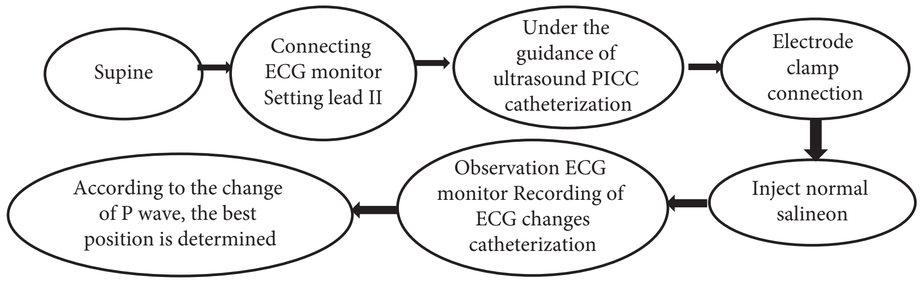

Figure 2: The specific operation process of IEGM.

Table 2: The calculation standard of curative effect.

Indicators	Calculation methods
Sensitivity	Number of true-positive cases/(number of true-positive cases + number of false-negative cases) × 100%
Specificity	Number of true-negative cases/(number of true-negative cases + number of false-positive cases) × 100%
Accuracy	EGM result/coronary angiography result × 100%

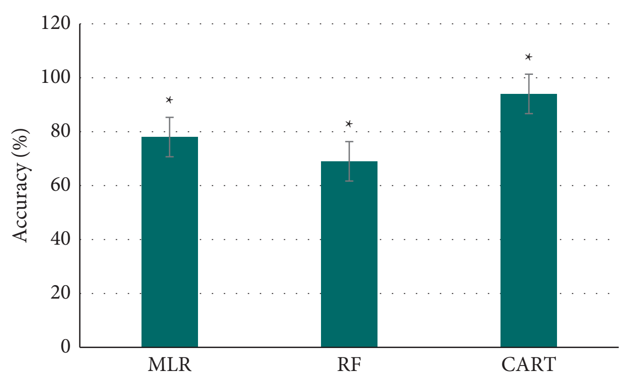

Figure 3: Comparison on diagnosis accuracy of different algorithms. *Note.* $^*P < 0.05$.

with positive test results and 19 with negative results in the control group. The comparison between the positive rate and the negative rate in this group of patients suggested that the positive rate was higher than the negative rate, and the difference was statistically significant ($P < 0.05$). Figure 6 shows the test results under IEGM. It revealed that there were 46 patients with positive test results and 4 patients with negative results in the experimental group. The comparison showed that the positive rate was higher than the negative rate, and the difference was statistically obvious ($P < 0.05$).

3.4. Comparison on the Consistency between Examination Results and the Coronary Angiography Results between Two Groups. Table 3 shows the statistics of the results in the control group. It disclosed that in the control group, there were 28 cases with the consistent results between the conventional EGM and the coronary angiography, including 21 positive cases and 7 negative cases. Therefore, the consistency ratio was 55%. Table 4 shows the statistics of the results in the experimental group. It was clear that in the experimental group, there were 42 cases with the consistent results between the IEGM examination and the coronary angiography, including 39 positive cases and 3 negative cases, so the consistency ratio was 80%. The consistency ratios between the examination results and the coronary angiography results and the Kappa test results were compared, and the results are illustrated in Figure 7. The results in the experimental group were higher than those of the control group, showing statistically great difference ($P < 0.05$), indicating the IEGM examination showed higher consistency, so the accuracy was higher.

3.5. Comparison on Diagnostic Effect of Two Different Examinations. The diagnostic effect between the experimental group and the control group after examination was compared, as illustrated in Figure 8. The diagnostic sensitivity and accuracy in the experimental group were 93% and 80%, respectively, while those in the control group were 62% and 55%, respectively. Thus, the diagnostic sensitivity and accuracy in the experimental group were much higher in contrast to those in the control group, and the difference was statistically great ($P < 0.05$). The specificity in control group was slightly higher in contrast to the experimental group, showing not statistically obvious difference ($P > 0.05$).

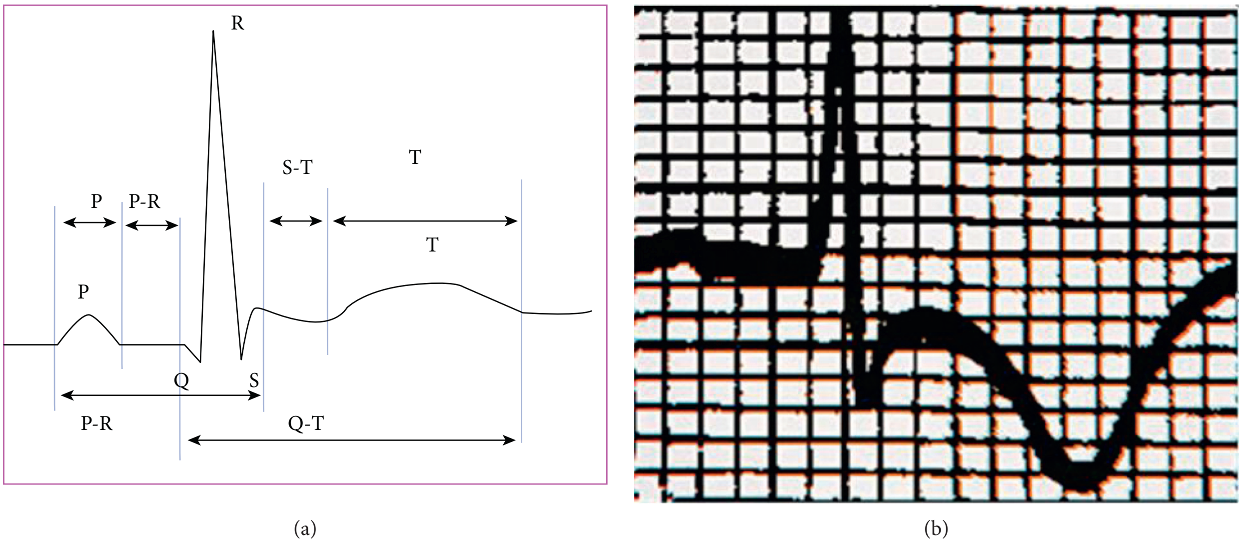

Figure 4: Comparison of EGM results of healthy person and patients with CHD. (a) The standard EGM results of normal people and (b) the EGM manifestations of patients with CHD.

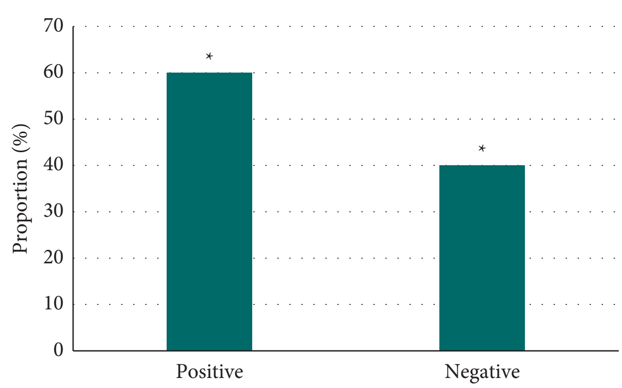

Figure 5: EGM results of patients in the control group. *Note*. $^{*}P < 0.05$.

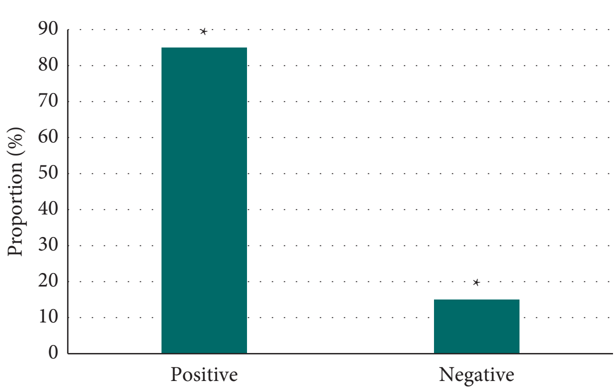

Figure 6: IEGM results of patients in the experimental group. *Note*. $^{*}P < 0.05$.

4. Discussion

As the quality of life of people in today's society has been greatly improved, the food, clothing, housing, and transportation have been greatly improved, especially in terms of diet [14]. As the pace of people's lives continues to accelerate, the dietary structure, types of diet, and dietary styles have become diversified. In addition, the diseases have become diversified, and the incidence of various diseases has increased year by year [15]. At present, the incidence of CHD is showing a slow upward trend. CHD is mainly due to the vascular blockage or stenosis caused by coronary atherosclerosis in patients. The blood circulation in the patient's blood vessels is blocked, so that the normal function is affected, and then convulsions occur, which eventually leads to myocardial hypoxia and ischemia [16]. If the patient cannot be treated in time after the onset of the CHD, it will lead to sudden death and endanger the patient's life. According to clinical studies, the types of CHD are relatively diverse, mainly manifested as angina pectoris, myocardial infarction, and occult [17, 18]. The occult CHD has a particularly high clinical incidence, and it is mainly in the elderly. As a CHD lacking relevant clinical symptoms, occult CHD is also a cardiovascular event with higher risk factors, and it is affected by no obvious clinical symptoms,

Table 3: The statistics of the results in the control group.

Control group	Coronary angiography		Total
	Positive	Negative	
Positive	21	10	31
Negative	12	7	19
Number of consistent results	21	7	28

Table 4: The statistics of the results in the experimental group.

Experimental group	Coronary angiography		Total
	Positive	Negative	
Positive	39	7	46
Negative	1	3	4
Number of consistent results	39	3	42

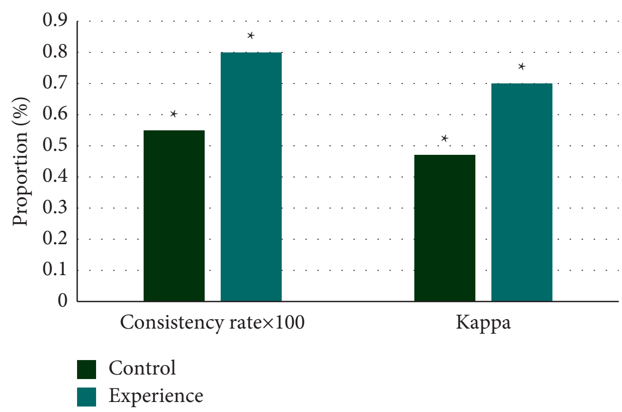

Figure 7: Comparisons on consistency ratio and Kappa results. *Note*. $^*P < 0.05$.

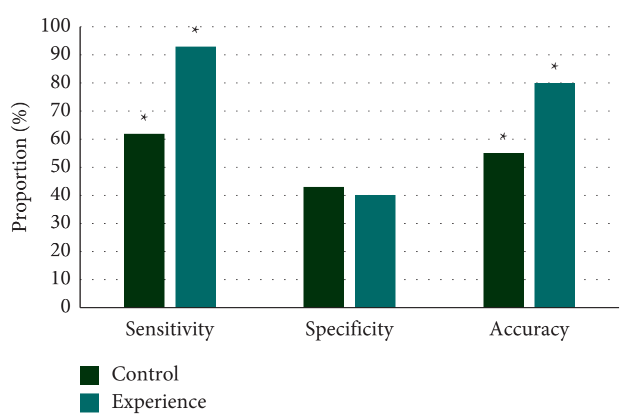

Figure 8: Comparison on diagnostic effect of two different examinations. *Note*. $^*P < 0.05$.

so the missed diagnosis rate is high, which brings great hidden dangers to the life safety of patients [7, 19].

In order to effectively improve the diagnostic accuracy of patients with occult CHD, the current clinical diagnosis is mainly based on EGM, which greatly improves the clinical diagnosis effect of patients. However, there are still some shortcomings in conventional EGM diagnosis. Therefore, the conventional EGM was adopted to diagnose 50 patients with suspected occult CHD in the control group, and the IEGM based on data mining algorithms was adopted to diagnose and analyze the other 50 patients in the experimental group in this study. In addition, the consistency between the examination results of the coronary angiography results was calculated and compared between two groups. According to the diagnosis results, the diagnostic sensitivity and accuracy in the experimental group were higher than those in the control group, and the specificity was basically similar, indicating that the IEGM showed higher diagnostic accuracy in occult CHD patients clinically. The application of IEGM not only is applicable in the diagnosis of heart disease, but also can assist the positioning of the PICC catheter to reduce the occurrence of neonatal complications. Many experts have discussed the impacts of IEGM-assisted positioning technology on the complications of PICC in neonates. Research results have shown that in the process of neonatal PICC catheterization, the use of IEGM-assisted positioning can reduce catheter-related complications [20, 21]. There are also research experts selected by typical EGMs of different parts of the heart cavity and their evolutionary characteristics as the guidance to replace the X-ray fluoroscopy for bedside temporary endocardial pacing of 22 cases; the success rate was 100%, the average operation time was 18 minutes, the average pacing from intubation to the right ventricle was 48 seconds, and the average pacing threshold was 0.72 V; there were no other complications except for electrode dislocation. Compared with 30 cases of temporary pacing under traditional fluoroscopy, there was no significant difference in various indicators. The results showed that cardiac IEGM-guided bedside pacing was a first-aid measure that was reliable, easy to operate, safe, practical, and easy to popularize [22]. The retrospective analysis in this study suggested that the high-frequency wavelet part had to be filtered in the conventional EGM examination to keep the waveform smooth and clear. As a result, the high-frequency signal cannot be fully displayed in the conventional EGM examination result, which in turn caused some high-frequency signals to be lost in the EGM result. Therefore, conventional EGM examination is only suitable for patients with a wide range of myocardial ischemic necrosis, and occult CHD patients with mild myocardial ischemia cannot show typical EGM signs of CHD [23].

Lupi et al. (2016) [24] found that IEGM is more sensitive than the extracavitary electrocardiogram in reflecting the myocardial ischemia during percutaneous transluminal coronary angioplasty (PT-CA). Drago et al. (2018) [25] suggested that the change of IEGM into the ST segment can reflect the viability of the residual myocardium to a certain extent. Moreover, some people have studied and proposed that IEGM can detect the viable myocardium at the infarcted area of patients with acute myocardial infarction and predict the postoperative efficacy of coronary intervention. Therefore, the clinical application value of IEGM is very high [26].

5. Conclusion

Based on the above research results, it could be concluded that the sensitivity and accuracy of IEGM results based on data mining algorithm analysis were higher than those of conventional EGM, and it showed very high application value in diagnosis of related diseases and in the guidance for treatment of related diseases, reflecting the good development prospects of IEGM in the clinical field. However, the intracavitary examination was invasive, so it was not recommended when the diagnosis result of the examination may cause more harm than good.

Data Availability

The data used to support the findings of this study are available from the corresponding author upon request.

Conflicts of Interest

The authors declare no conflicts of interest.

Authors' Contributions

Gang Wang and Li Luo contributed equally to this work.

References

[1] Y. Tian, P. Deng, B. Li et al., "Treatment models of cardiac rehabilitation in patients with coronary heart disease and related factors affecting patient compliance," *Reviews in Cardiovascular Medicine*, vol. 20, no. 1, pp. 27–33, 2019.

[2] T. L. Braber, A. Mosterd, N. H. Prakken et al., "Occult coronary artery disease in middle-aged sportsmen with a low cardiovascular risk score: the measuring athlete's risk of cardiovascular events (MARC) study," *European Journal of Preventive Cardiology*, vol. 23, no. 15, pp. 1677–1684, 2016.

[3] B. Cybulska and L. Kłosiewicz-Latoszek, "Landmark studies in coronary heart disease epidemiology. the framingham heart study after 70 years and the seven Countries study after 60 years," *Kardiologia Polska*, vol. 77, no. 2, pp. 173–180, 2019.

[4] F. Lin, G. Zhao, Z. Chen et al., "circRNA-miRNA association for coronary heart disease," *Molecular Medicine Reports*, vol. 19, no. 4, pp. 2527–2536, 2019.

[5] S. Chandra, S. Saraf, G. Chaudhary et al., "Prevalence and trends of occult coronary artery disease in patients with dilated cardiomyopathy," *American journal of cardiovascular disease*, vol. 10, no. 5, pp. 557–563, 2020.

[6] O. M. Kobo, E. Vainer Evgrafov, Y. Cohen et al., "Non-ST-elevation myocardial infarction with non-significant coronary artery disease as a symptom of occult or new malignancy," *The Israel Medical Association Journal : The Israel Medical Association Journal*, vol. 21, no. 6, pp. 381–385, 2019.

[7] P. Caap, J. C. H. Jensen, and M. Schmidt, "A 66-year-old woman with intermittent chest pain and dyspnea who underwent continued st-segment monitoring to identify occult st-segment elevation that expedited coronary angiography and revascularization," *American Journal of Case Reports*, vol. 22, Article ID e929736, 2021.

[8] G. Teressa, V. Bhasin, P. Noack, and M. Poon, "Comparing the modified history, electrocardiogram, age, risk factors, and troponin score and coronary artery disease consortium model for predicting obstructive coronary artery disease and cardiovascular events in patients with acute chest pain," *Critical Pathways in Cardiology: Journal of Evidence-Based Medicine*, vol. 18, no. 3, pp. 125–129, 2019.

[9] T. W. Johnson, L. Räber, C. di Mario et al., "Clinical use of intracoronary imaging. Part 2: acute coronary syndromes, ambiguous coronary angiography findings, and guiding interventional decision-making: an expert consensus document of the european association of percutaneous cardiovascular interventions," *European Heart Journal*, vol. 40, no. 31, pp. 2566–2584, 2019.

[10] T. Yu, L. Wu, L. Yuan et al., "The diagnostic value of intracavitary electrocardiogram for verifying tip position of peripherally inserted central catheters in cancer patients: a retrospective multicenter study," *The Journal of Vascular Access*, vol. 20, no. 6, pp. 636–645, 2019.

[11] A.-q. Xiao, J. Sun, L.-h. Zhu et al., "Effectiveness of intracavitary electrocardiogram-guided peripherally inserted central catheter tip placement in premature infants: a multicentre pre-post intervention study," *European Journal of Pediatrics*, vol. 179, no. 3, pp. 439–446, 2020.

[12] H. M. van Loo, T. B. Bigdeli, Y. Milaneschi, S. H. Aggen, and K. S. Kendler, "Data mining algorithm predicts a range of adverse outcomes in major depression," *Journal of Affective Disorders*, vol. 276, pp. 945–953, 2020.

[13] P. Tavallali, M. Razavi, and S. Brady, "A non-linear data mining parameter selection algorithm for continuous variables," *PloS One*, vol. 12, no. 11, Article ID e0187676, 2017.

[14] J. L. Bühler and J. Nikitin, "Sociohistorical context and adult social development: new directions for 21st century research," *American Psychologist*, vol. 75, no. 4, pp. 457–469, 2020.

[15] J. Jiang, L. Luo, P. Xu, and P. Wang, "How does social development influence life expectancy? a geographically weighted regression analysis in China," *Public Health*, vol. 163, pp. 95–104, 2018.

[16] K. G. Aragam and P. Natarajan, "Polygenic scores to assess atherosclerotic cardiovascular disease risk," *Circulation Research*, vol. 126, no. 9, pp. 1159–1177, 2020.

[17] C. Chen, J. Wei, A. AlBadri, P. Zarrini, and C. N. Bairey Merz, "Coronary microvascular dysfunction - epidemiology, pathogenesis, prognosis, diagnosis, risk factors and therapy," *Circulation Journal*, vol. 81, no. 1, pp. 3–11, 2017.

[18] G. Wang, Y. Li, Y. Peng, J. Tang, and H. Li, "Association of polymorphisms in MALAT1 with risk of coronary atherosclerotic heart disease in a Chinese population," *Lipids in Health and Disease*, vol. 17, no. 1, p. 75, 2018.

[19] J. J. Sico, F. Baye, L. J. Myers et al., "Receipt of cardiac screening does not influence 1-year post-cerebrovascular event mortality," *Neurology: Clinical Practice*, vol. 8, no. 3, pp. 192–200, 2018.

[20] Z. Lianjuan, X. Hongzhen, L. Jianfeng, X. Meifang, and Y. Jun, "Effectiveness of intracavitary electrocardiogram guidance in peripherally inserted central catheter tip placement in neonates," *Journal of Perinatal and Neonatal Nursing*, vol. 31, no. 4, p. E2, 2017.

[21] L. Yang, X. Bing, L. Song, C. Na, D. Minghong, and L. Annuo, "Intracavitary electrocardiogram guidance for placement of peripherally inserted central catheters in premature infants," *Medicine*, vol. 98, no. 50, p. e18368, Article ID e18368, 2019.

[22] P. Blanco, "Temporary transvenous pacing guided by the combined use of ultrasound and intracavitary electrocardiography: a feasible and safe technique," *The Ultrasound Journal*, vol. 11, no. 1, p. 8, 2019.

[23] N. A. Chatterjee, J. T. Tikkanen, G. K. Panicker et al., "Simple electrocardiographic measures improve sudden arrhythmic death prediction in coronary disease," *European Heart Journal*, vol. 41, no. 21, pp. 1988–1999, 2020.

[24] A. Lupi, A. Schaffer, A. Rognoni et al., "Intracoronary bivalirudin bolus in st-elevation myocardial infarction patients treated with primary angioplasty: theoretical bases, clinical experience, and future applications," *American Journal of Cardiovascular Drugs*, vol. 16, no. 6, pp. 391–397, 2016.

[25] F. Drago, I. Battipaglia, and C. Di Mambro, "Neonatal and pediatric arrhythmias," *Cardiac Electrophysiology Clinics*, vol. 10, no. 2, pp. 397–412, 2018.

[26] M. Nakayama, T. Uchiyama, N. Tanaka et al., "Diagnostic Performance and pressure stability of a novel myocardial ischemic diagnostic index - the intracoronary-electrocardiogram-triggered distal pressure/aortic pressure ratio," *Circulation Reports*, vol. 2, no. 11, pp. 665–673, 2020.

Hindawi
Journal of Healthcare Engineering
Volume 2021, Article ID 8960465, 9 pages
https://doi.org/10.1155/2021/8960465

Research Article

Wavelet Transform Image Enhancement Algorithm-Based Evaluation of Lung Recruitment Effect and Nursing of Acute Respiratory Distress Syndrome by Ultrasound Image

Wangyan Jin, Ling Dai, Liuyan Ge, Xuhua Huang, Guanhua Xu, Chunhong Qu, and Jianfei Sun

Department of Critical Medicine, The First People's Hospital of Xiaoshan District, Hangzhou 311201, Zhejiang, China

Correspondence should be addressed to Jianfei Sun; jianfeisun_5429@yeah.net

Received 4 June 2021; Accepted 31 August 2021; Published 11 September 2021

Academic Editor: Enas Abdulhay

This study aimed to analyze the application of ultrasound images of lung recruitment (LR) nursing treatment guided by positive-end expiratory pressure (PEEP) in patients with acute respiratory distress syndrome (ARDS). An ultrasound image enhancement algorithm (UIEA) wavelet transform (WT) was constructed, and the soft threshold (ST) and adjacent region average (ARA) were introduced for simulation comparison. In addition, the signal-to-noise ratio (SNR), peak signal-to-noise ratio (PSNR), and running time were undertaken as the evaluation indexes. The WT algorithm was applied to the ultrasound images of 85 ARDS patients before and after PEEP recruitment. The mean artery pressure (MAP), heart rate (HR), and central venous pressure (CVP), peak inspiratory pressure (Ppeak), mean inspiratory pressure (Pmean), dynamic lung compliance (DLC), PCO_2, and PaO_2/FiO_2 of the patients were recorded before and after the LR. The results showed that the signal-to-noise ratio (SNR) (19.67 ± 3.15 dB) and PSNR (23.08 ± 2.08 dB) of the images enhanced by the WT algorithm were much higher than those of ST (13.88 ± 2.74 dB and 14.62 ± 1.76 dB, respectively) and ARA (14.96 ± 3.06 dB and 15.11 ± 1.94 dB, respectively), while the running time was in adverse ($P < 0.05$); the HR and CVP of patients after LR nursing treatment were increased greatly, while the MAP was in the opposite case ($P < 0.05$); after LR nursing treatment, Ppeak, Pmean, DLC, PCO_2, and PaO_2/FiO_2 of the patient were significantly greater than those before the LR, and the difference was statistically significant ($P < 0.05$). In short, the WT algorithm not only enhanced the quality of ultrasound images but also shortened the running time and improved the processing efficiency. PEEP LR nursing treatment could effectively improve the vascular patency, cardiac ejection capacity, and DLC in patients with ARDS, thereby increasing the airway pressure and maintaining the unobstructed expiration.

1. Introduction

ARDS refers to the diffuse damage caused by lung capillary endothelial cells and alveolar epithelial cells in the process of noncardiac diseases such as severe infection, shock, high-risk surgery, trauma, and burns. Pulmonary interstitial and alveolar edema, can lead to acute hypoxic respiratory insufficiency or failure [1]. Onset of ARDS is so rapid that it can occur within 24–48 hours, and the ARDS is mainly characterized by reduced lung volume, reduced lung compliance, severe ventilation, or blood flow imbalance [2, 3]. It is necessary to apply the sensitive antibiotics to the bacteria to prevent the inflammatory reaction from further damage to the lungs. It is more urgent to correct the severe hypoxia of the patient in time to win precious time for the treatment of underlying diseases [4]. Currently, PEEP nursing scheme is mainly adopted to treat patients with ARDS, mainly by expanding the trachea and closing the alveoli, reducing the static blood shunt in the lungs, and improving the ventilation/blood flow ratio and diffusion function, thereby improving the respiratory function of patient [5]. Therefore, PEEP nursing scheme was used in this study to treat the ARDS patients.

With the development of imaging technology, ultrasound imaging is gradually utilized in the diagnosis of ARDS.

Compared with the gold standard chest computed tomography (CT) with high cost, large radiation, and complicated operation, thoracic lung ultrasound can clearly show diseases such as pulmonary interstitial syndrome, pulmonary consolidation, pneumonia, pleural exudation, and pneumothorax [6]. It is safer, noninvasive, cost-effective, low-cost, and dynamic observation. Tang et al. (2017) [7] discussed the clinical value of ultrasound monitoring in assessing LR and PEEP and found that lung ultrasound could be used to detect the LR endpoints and optimal PEEP, improving the DLC and oxygenation effectively. Therefore, ultrasound images were intended to be applied to evaluate the therapeutic effect of PEEP on ARDS patients in this study [8]. WT refers to the use of finite-length or fast-decaying oscillating waveforms to represent signals. It is an effective time, space, and scale analysis method and has been widely applied in many research fields of signal and image processing technology. WT is able for resolution analysis and time-frequency localization capabilities, can effectively distinguish the useful signals from noise, and has a good effect on image denoising and edge feature retention [9, 10]. Therefore, the WT algorithm was introduced in this study to process the ultrasound images of lung.

In summary, an UIEA WT was constructed based on the conventional WT, and the ST and ARA were employed for comparison and applied to the ultrasound images of 85 patients with ARDS before and after PEEP LR nursing treatment. The hemodynamic indexes (MAP, HR, and CVP), lung mechanical indexes (Ppeak, Pmean, and DLC), and blood-gas parameters (PCO_2 and PaO_2/FiO_2) of the patients were comprehensively compared and analyzed to evaluate the application of ultrasound image in PEEP-guided LR treatment in ARDS patients.

2. Materials and Methods

2.1. Selection of Research Samples. 85 patients with ARDS who were admitted to the hospital for PEEP LR treatment from February 11, 2019, to February 10, 2020, were selected as the research objects. The study had been approved by the Medical Ethics Committee of Hospital, and the patients and their families had understood the study and signed the informed consents and the inspection failure consents.

Inclusion criteria were given as follows: patients with acute onset; patients with oxygenation index less than 200 mmHg; patients older than 18 years old; patients with clear consciousness and ability of cooperating with the examination; and patients whose X-ray chest radiograph showed patchy shadows in the lungs.

Exclusion criteria were determined as follows: patients with pulmonary incarceration pressure greater than 20 mmHg; patients with psychiatric diseases; patients with hemodynamic insufficiency during treatment; patients with oxygenation index less than 100 mmHg; patients with intracranial hypertension; patients with pneumothorax; and patients with incomplete clinical information.

2.2. Treatment Methods. The patient was placed in a supine position, and the lung recruitment therapy was realized with the method of increasing PEEP. Firstly, the medical ventilator produced by Philips Respironics was set to the pressure mode, the PEEP was filled with 15 cmH_2O and PC20 cmH_2O, the inhaled oxygen concentration was adjusted to 1.0, and the oxygen saturation was set to about 92% for 20 minutes. The PEEP was increased at an interval of 5 cmH_2O, and the personal computer (PC) was fixed. After each increase of PEEP, it was ventilated for 1 minute, and then the PEEP was adjusted to 15 cmH_2O for 20 minutes. The LR was considered sufficient when the ultrasound score was no longer increased. Finally, the PEEP was adjusted back to 20 cmH_2O until the tidal volume reached 6.5 mL/kg.

2.3. Lung Ultrasound Scan Method. An intelligent ultrasound system (Philips IU22) was adopted to scan the lungs of patients with a probe frequency of 2–5 MHz. The lung was divided into 12 areas, including 4 areas (up, down, left, and right) in the chest based on the sternal angle plane and the human body's midaxis plane, and each area was divided into 3 subareas (front, middle, and back area) based on the front and back axillary lines area. During the scan, the patient was placed in a supine position, and the scan was started from the second intercostal space from top to bottom and front to back as well as along the intercostal space. The probe was rotated 90° so that the probe was perpendicular to the chest wall, and then one side of the patient's body was elevated to scan the lung field in the back. The characteristics of the patient's effusion and consolidation stroma were observed and recorded, and the images were sent to the workstation for processing. The hemodynamic indexes (MAP, HR, and CVP), lung mechanical indexes (Ppeak, Pmean, and DLC), and blood-gas parameters (PCO_2 and PaO_2/FiO_2) of the patients were measured and recorded.

2.4. Ultrasound Image Enhancement Algorithm Based on Wavelet Transform. In ultrasound imaging, the single-frequency ultrasound emitted by the ultrasound probe would scatter when it touched the surface of tissue, resulting in a series of coherent waves and causing a lot of noise. Thus, how to deal with such speckle noise was a very important research hotspot. It was assumed that the observed image was $u(x, y)$ and the actual image was $p(x, y)$, then the following equation could be obtained:

$$u(x, y) = p(x, y) + \xi(x, y) \bullet p(x, y). \tag{1}$$

In the above equation, $\xi(x, y)$ represented the noise. The traditional denoising methods cannot meet the two requirements of filtering noise and optimizing image edge features, and the image details were fuzzed when the noise was removed. On the contrary, WT could solve the above problems based on its decorrelation and multiresolution characteristics. Therefore, the concept of WT was introduced in this study to denoise the ultrasound images. The basic process was defined as follows: after the original ultrasound image was inputted, an appropriate wavelet function was selected to decompose the image in multiple layers to obtain the corresponding wavelet coefficients. Then, appropriate threshold processing was performed on each decomposed layer, the obtained wavelet decomposition coefficients and threshold processing coefficients were combined to calculate the wavelet reconstruction of the image, so as to obtain the denoising processed image.

In the wavelet algorithm, the selection of an appropriate threshold was very critical. If the threshold was too large, the wavelet coefficient would become zero, and the image became too blurry. If the threshold was too small, the image would retain too much noise. Therefore, the BayesShrink threshold [11] was adopted for processing, which carried different subequations in images of different scales and directions and could be adjusted adaptively with subbands. The equation could be expressed as follows:

$$T_B = \frac{\theta^2}{\theta_x}. \tag{2}$$

In the above equation, T_B referred to the BayesShrink threshold, θ^2 referred to the noise standard deviation, and θ_x represented the Gaussian standard deviation. The threshold function was to reconstruct the continuity and accuracy of the signal and had a great influence on the image denoising effect. The hard threshold (HT) method was combined with the ST method in this study to obtain a semisoft threshold function. Firstly, the HT function could be expressed as

$$m = \begin{cases} n, & |n > \kappa,| \\ 0, & \text{others.} \end{cases} \tag{3}$$

In the above equation, m represented the point on the abscissa of the image pixel, n represented the point on the ordinate of the image pixel, and κ referred to the set threshold point. The ST was to replace the coefficients less than the set threshold with 0, and its equation could be written as follows:

$$m = \begin{cases} \operatorname{sigm}(n)(|n| - \kappa), & |n| > \kappa, \\ 0, & \text{others.} \end{cases} \tag{4}$$

In (4), $\operatorname{sigm}(n)$ represents the symbolic function, and $\operatorname{sigm}(n) = \begin{cases} 1 & n > 0 \\ -1 & n < 0 \end{cases}$. A compromise solution could be obtained based on the HT and ST, which could be expressed as follows:

$$\begin{aligned} m &= n, \\ |n| &> \kappa_2, \end{aligned} \tag{5}$$

$$m = \operatorname{sigm}(n) \frac{\kappa_2 (|n| - \kappa_1)}{\kappa_2 - \kappa_1}, \quad \kappa_2 < |n| < \kappa_1, \tag{6}$$

$$\begin{aligned} m &= 0, \\ |n| &< \kappa_1. \end{aligned} \tag{7}$$

In the above equations, κ_2 represented the higher threshold, κ_1 referred to the lower threshold, and $\kappa_2 = 2\kappa_1$. The wavelet function used in WT was diverse. Thus, the wavelet function was selected based on the principles of orthogonality, support length, symmetry, and regularity in this study, and the decomposition filter and reconstruction filter of the biorthogonal WT were selected for processing. The boundary extension was required due to the length of actual signal. The symmetric extension was adopted to process signals of limited length to avoid the inconsistency of the signal caused by the period extension. Therefore, the above process was to build the UIEA WT based on WT.

2.5. Evaluation Indexes of Image Enhancement Performance. The ST [12] and the ARA [13] were introduced to compare with the WT algorithm constructed in this study, taking SNR, PSNR, and running time as evaluation indexes.

SNR was a common evaluation index to measure the amount of image signal noise (decibel, Db) and could be expressed as follows:

$$\mathrm{SNR} = 10 \times \log 10\left(\frac{P_1}{P_2}\right), \tag{8}$$

$$P_1 = \frac{1}{K \times H} \sum_{n}^{K \times H} S^*(m,n)^2, \tag{9}$$

$$P_2 = \frac{1}{K \times H} \sum_{n}^{K \times H} \left(S(m,n) - S^*(m,n)\right)^2. \tag{10}$$

In equations (8)–(10), P_1 represented the power of the signal, P_2 referred to the noise power, $S(m,n)$ indicated the initial signal, $S^*(m,n)$ represented the signal after wavelet processing, K referred to the dimension of the image row, and H represented the dimension of the image column.

PSNR was to evaluate the fidelity of the image, with the unit of decibel (dB). It could be calculated with the following equation:

$$\mathrm{PSNR} = 10 \times \log_{10}\left(\frac{N^2}{\mathrm{MSE}}\right), \tag{11}$$

$$\mathrm{MSE} = \frac{\sum_n^{K \times H} (O^n - F^n)^2}{K \times H}, \tag{12}$$

where N represented the maximum gray value of the image, O^n referred to the n^{th} pixel value of the original image, and F^n indicated the n^{th} pixel value of the processed image.

2.6. Statistical Methods. The data processing in this study was analyzed by SPSS19.0 version statistical software, the measurement data was expressed as mean ± standard deviation ($\bar{x} \pm s$), and the count data was indicated with percentage. The pairwise comparison of SNR, PSNR, and running time of WT, ARA, and ST algorithms was realized with the single-factor analysis of variance. The hemodynamic indexes (MAP, HR, and CVP), lung mechanical indexes (Ppeak, Pmean, and DLC), and blood-gas parameters (PCO_2 and PaO_2/FiO_2) before and after LR nursing treatment were compared by the independent t-test. The difference was statistically significant at $P < 0.05$.

3. Results

3.1. Comparison of Three Algorithms for Denoising Performance of Lung Ultrasound Images. Figure 1 shows the comparison of the denoising performance of three algorithms on lung ultrasound images. It revealed that the SNR and PSNR of the ST algorithm for lung ultrasound image reconstruction were 13.88 ± 2.74 dB and 14.62 ± 1.76 dB, respectively; the SNR and PSNR of the ARA algorithm for lung ultrasound image reconstruction were 14.96 ± 3.06 dB and 15.11 ± 1.94 dB, respectively; the SNR and PSNR of WT algorithm for the lung ultrasound image reconstruction were 19.67 ± 3.15 dB and 23.08 ± 2.08 dB, respectively. Thus, the SNR and PSNR of WT algorithm for lung ultrasound image reconstruction were higher observably than those of the ARA and ST algorithm ($P < 0.05$).

Figure 2 illustrates the comparison in the running time of three algorithms for lung ultrasound image denoising. It disclosed that the running time of ST, ARA, and WT algorithm for lung ultrasound image reconstruction was 15.17 ± 1.05 s, 14.84 ± 0.77 s, and 23.08 ± 2.56 s, respectively. In addition, the running time of WT algorithm was much shorter than that of ARA algorithm and ST algorithm, and the difference was statistically significant ($P < 0.05$).

3.2. Reconstruction Results of Lung Ultrasound Images with Three Algorithms. The results of lung ultrasound image reconstruction of the three algorithms were compared and analyzed, and the results were given in Figure 3. Figure 3(a) is an original ultrasound image of a patient, which included a lot of artifacts and noises, and the clarity was so poor that the needs of imaging diagnosis could not be satisfied. The clarity of Figure 3(d) was higher obviously than that of Figures 3(b) and 3(c), and it could display the lung lesions perfectly.

3.3. Comparison of Hemodynamic Parameters before and after Lung Recruitment Nursing Treatment. Figure 4 illustrates the comparison of HR and MAP before and after LR nursing treatment. The HR and MAP before LR was 95.71 ± 5.11 beats/min and 101.42 ± 10.33 mmHg, respectively, while the HR and MAP after LR was 118.62 ± 8.37 beats/min and 79.41 ± 7.26 mmHg, respectively. In addition, the HR of patients after LR was faster extremely than that before LR ($P < 0.05$); and the MAP of patients after LR was greatly decreased in contrast to that before ($P < 0.05$).

Figure 5 reveals the comparison of CVP before and after LR. The CVP before and after LR was 7.33 ± 2.01 mmHg and 12.15 ± 1.85 mmHg, respectively. Besides, the CVP of patients after LR was increased greatly than that before LR ($P < 0.05$).

3.4. Comparison of Blood-Gas Parameters before and after Lung Recruitment Nursing Treatment. Figure 6 shows the comparison of blood-gas parameters (PCO_2 and PaO_2/FiO_2) before and after LR nursing treatment. As it indicated, the PCO_2 and PaO_2/FiO_2 before LR were 42.74 ± 10.64 mmHg and 175.37 ± 12.41 mmHg, respectively; and the PCO_2 and PaO_2/FiO_2 after LR were 56.38 ± 9.78 mmHg and 385.15 ± 15.93 mmHg, of which, the blood-gas parameters (PCO_2 and PaO_2/FiO_2) after LR were observably increased than those before LR ($P < 0.05$).

3.5. Comparison of Respiratory Mechanical Parameters before and after Lung Recruitment Nursing Treatment. The respiratory mechanical parameter Cdyn before and after LR nursing treatment was analyzed and compared, as shown in Figure 7. The Cdyn before LR was 22.54 ± 1.51 mL/cH_2O, and the Cdyn after LR was 42.74 ± 2.65 mL/cH_2O. Among them, the Cdyn of patients after LR was significantly greater than before LR, and the difference was statistically significant ($P < 0.05$).

As shown in Figure 8, the comparison of the respiratory mechanical parameter Pmean and Ppeak before and after LR revealed that the Pmean and Ppeak before LR were 15.76 ± 3.03 mL/cH_2O and 27.17 ± 1.34 mL/cH_2O, respectively; and the Pmean and Ppeak after LR were 30.57 ± 4.02 mL/cH_2O and 46.11 ± 3.42 mL/cH_2O, respectively. Thus, the Pmean and Ppeak of patients after LR were higher obviously than those before LR ($P < 0.05$).

4. Discussion

As a common critical symptom, ARDS has a fatality rate of 30–40%, which is extremely threatening to the life safety of patients. Its typical physiological changes include reduced lung volume, reduced compliance, and imbalanced ventilation/blood flow ratio. Thus, how to realize the protective ventilation of lung is essential to improve the respiratory function of the patient [14]. Therefore, an UIEA WT was constructed based on WT, and the ST and ARA were introduced for comparison and analysis. The results showed that the SNR and PSNR of the WT algorithm for lung ultrasound image reconstruction were much higher than those of the ARA algorithm and the ST algorithm ($P < 0.05$), which was similar to the research results of Bein et al. (2016) [15]. Thus, it indicated that the WT algorithm constructed in this study had better performance in denoising ultrasound images and reducing the influence of artifacts and noises. The running time of the ST algorithm for lung ultrasound image reconstruction was obviously longer than that of the ARA algorithm and the WT algorithm ($P < 0.05$), which indicated that the WT algorithm based on WT was very rapid for ultrasound images. Therefore, the WT algorithm not only enhanced the quality of ultrasound images but also shortened the running time and improved the processing efficiency [16].

The WT algorithm was applied to the diagnosis of ultrasound images of 85 patients with ARDS. The results disclosed that the HR and CVP of patients after LR were increased greatly than those before LR ($P < 0.05$), which was similar to the results of Sahetya and Brower (2017) [17], indicating that the PEEP LR nursing treatment could effectively improve the patency of vascular circulation in patients with ARDS and reduce the degree of blood viscosity. The MAP of patients after LR was observably smaller than

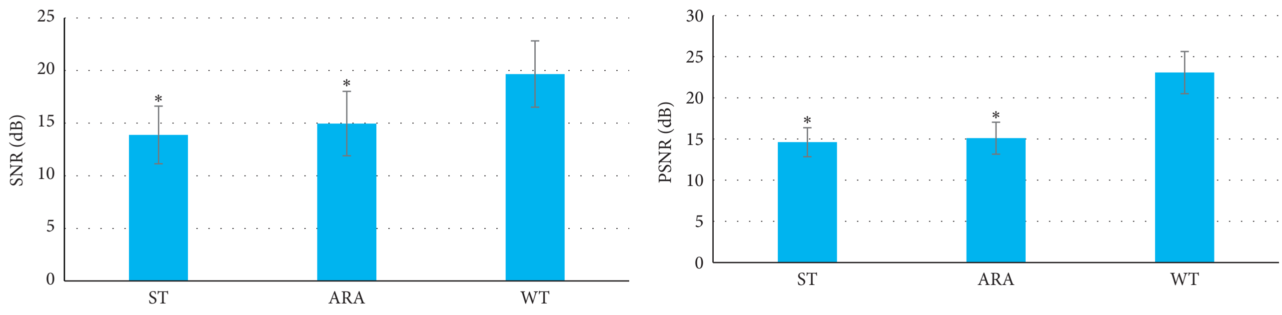

Figure 1: The comparison of the denoising performance of three algorithms on lung ultrasound images. (a) The SNR and (b) PSNR of the three algorithms for lung ultrasound image reconstruction, respectively. * indicates $P < 0.05$ in contrast to the WT algorithm.

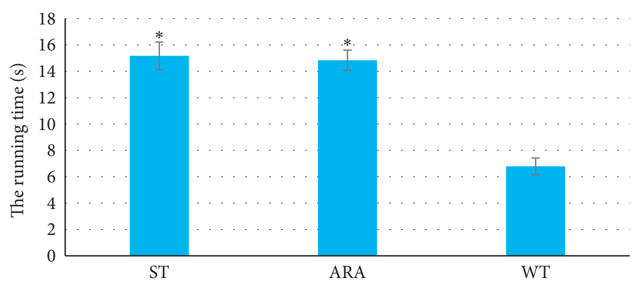

Figure 2: The comparison in the running time of three algorithms for lung ultrasound image denoising. * indicates $P < 0.05$ in contrast to the WT algorithm.

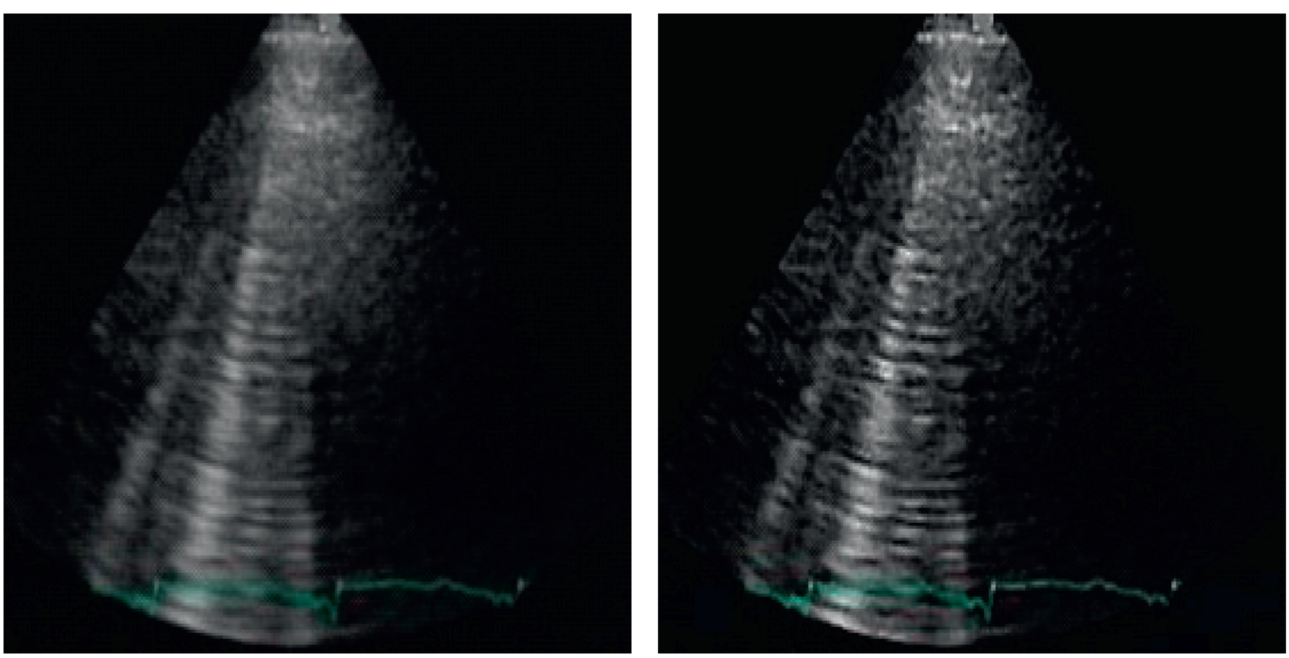

(a) (b)

Figure 3: Continued.

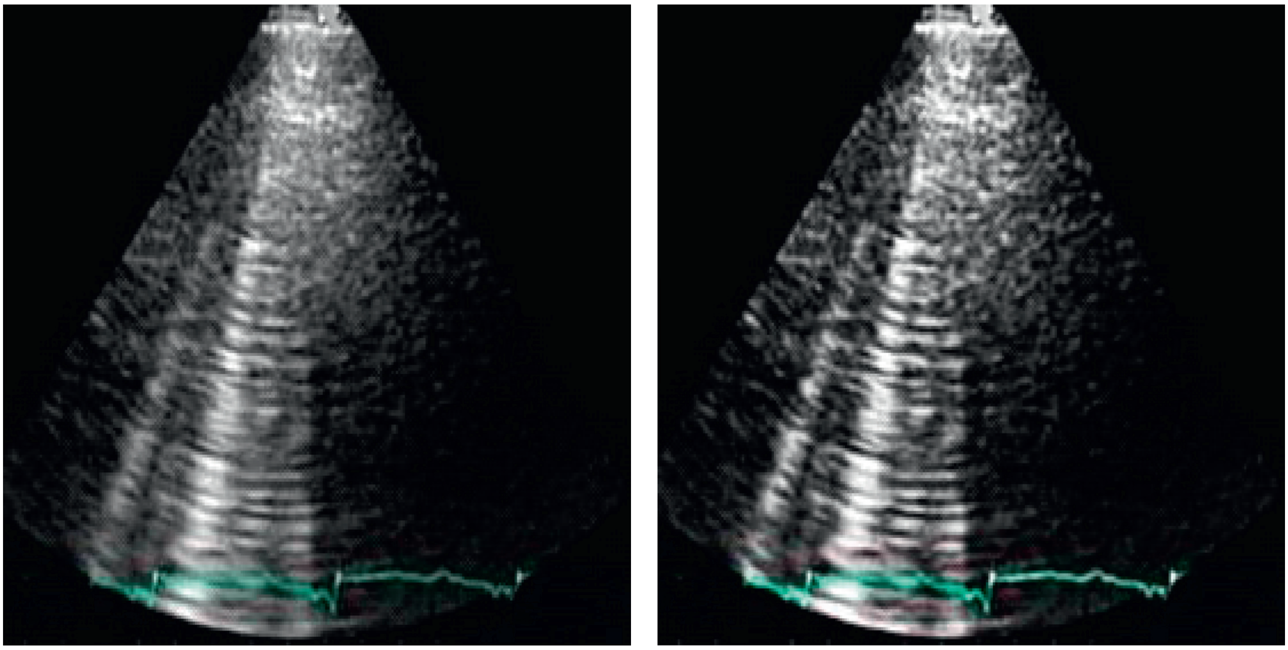

(c) (d)

Figure 3: The results of lung ultrasound image reconstruction of the three algorithms. (a) An original ultrasound image of a patient; (b–d) the reconstructed images with ST, ARA, and WT algorithms, respectively.

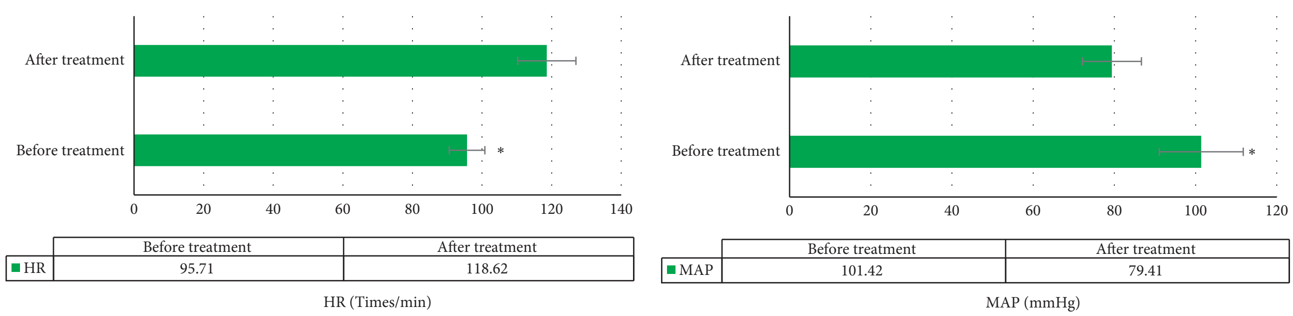

(a) (b)

Figure 4: The comparison of (a) HR and (b) MAP before and after lung recruitment. * suggests $P < 0.05$ in contrast to the values before lung recruitment.

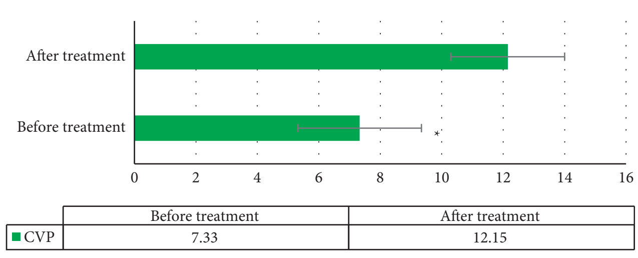

Figure 5: The comparison of CVP before and after lung recruitment. *suggests $P < 0.05$ in contrast to the values before lung recruitment.

that before LR ($P < 0.05$). CVP is the pressure where the upper and inferior vena cava enter the right atrium. It can be measured through the upper and inferior vena cava or the right atrium tube and can reflect the ejection ability of the heart. The results of this article showed that the treatment after LR effectively improved the cardiac ejection ability of

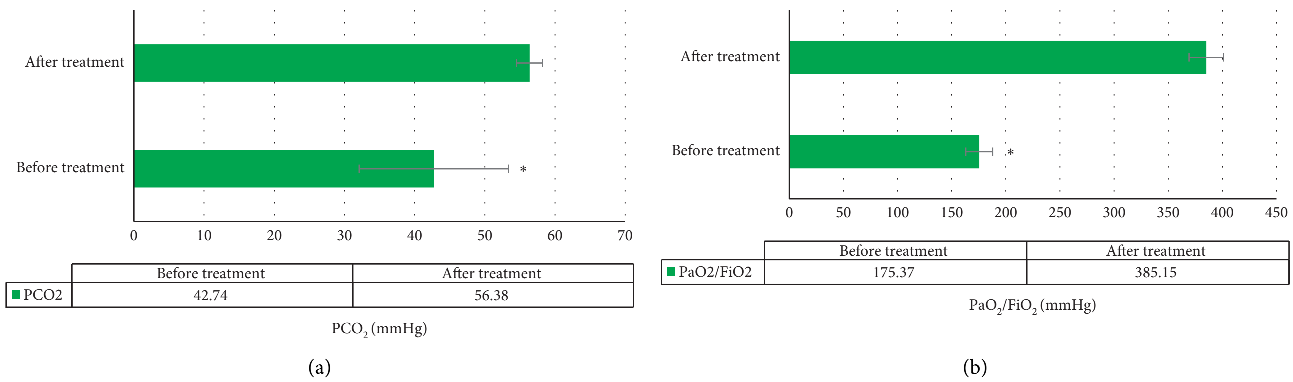

FIGURE 6: The comparison of blood-gas parameters ((a) PCO_2 and (b) PaO_2/FiO_2) before and after lung recruitment. *indicates $P < 0.05$ in contrast to the values before lung recruitment.

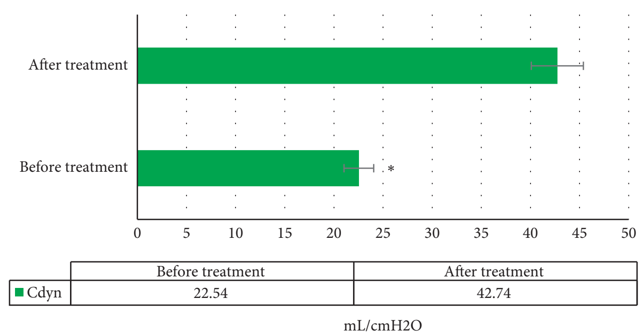

FIGURE 7: The respiratory mechanical parameter Cdyn before and after lung recruitment. *indicates $P < 0.05$ in contrast to the values before lung recruitment.

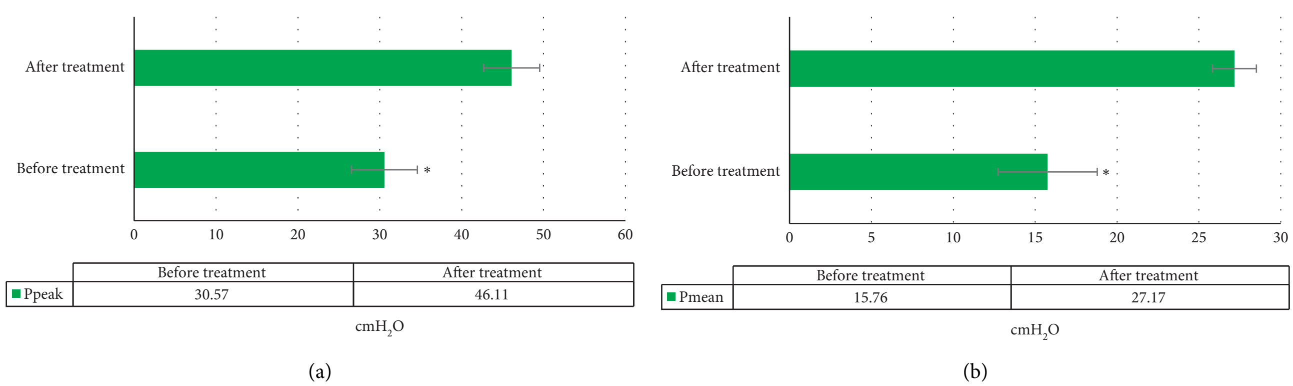

FIGURE 8: The comparison of the respiratory mechanical parameters (a) Ppeakand (b) Pmean before and after lung recruitment. *means $P < 0.05$ in contrast to the values before lung recruitment.

the patient, which was beneficial for the patient to eject the returned blood into the artery in time. The blood-gas parameters PCO_2 and PaO_2/FiO_2 of patients after LR were increased obviously in contrast to those before LR ($P < 0.05$), which indicated that the alveoli of patients after LR treatment could maintain more open state and increase oxygenation level. The Cdyn of patients after LR was higher hugely than that before LR ($P < 0.05$), which was different with the results of Karlsson et al. (2018) [18]. The reason of which may be that DLC differed in the compliance expressed by the respiratory muscles during lung breathing. The better the compliance, the smoother the breathing, and vice versa. The results of this study indicated that LR nursing treatment could effectively improve the DLC of the patient's respiratory system [19]. The Pmean and Ppeak of patients after LR were higher significantly than before LR ($P < 0.05$), which was not similar to the results of Sigmundsson et al. (2020) [20]. Ppeak is the maximum pressure during lung ventilation, while Pmean is the mean pressure experienced by the lungs during the respiratory cycle. The results of this study suggested that LR nursing treatment could increase the pressure in the airway to prevent airway trapping and maintain a clear breath.

5. Conclusion

An UIEA WT was constructed based on the WT, the ST and ARA were introduced for comparison, and then the WT algorithm was applied to the ultrasound images of 85 ARDS patients before and after PEEP LR nursing treatment. It was found that the WT algorithm not only enhanced the quality of ultrasound images but also shortened the running time and improved the processing efficiency. PEEP LR nursing treatment could effectively improve the vascular patency, cardiac ejection capacity, and DLC in patients with ARDS, so as to increase the airway pressure and maintain the unobstructed expiration. However, there were still some shortcomings for this study. The sample size of the selected patients was relatively small and the source was single, which may have some impact on the experimental results. In the future, we will consider increasing the sample size of patients to further explore the diagnostic value of the WT algorithm for the prognosis of ARDS patients. In conclusion, the results of this study provided a theoretical basis for the clinical application of PEEP LR nursing scheme in the treatment of ARDS patients.

Data Availability

The data used to support the findings of this study are available from the corresponding author upon request.

Conflicts of Interest

The authors declare no conflicts of interest.

References

[1] F. Lovisari, G. H. Fodor, and F. Peták, "Effect of PEEP and I:E ratio on cerebral oxygenation in ARDS: an experimental study in anesthetized rabbit," *BMC Anesthesiology*, vol. 19, no. 1, p. 110, 2019.

[2] H. Zhao, X. Wang, D. Liu, H. Zhang, H. He, and Y. Long, "Effects of critical ultrasonic management of Peking Union Medical College Hospital on the etiological diagnosis of patients with acute respiratory failure," *Zhonghua Yixue Zazhi*, vol. 95, no. 47, pp. 3843–3847, 2015.

[3] Z. Jia, X. Liu, and Z. Liu, "Evaluation value of oxygenation index of mechanical ventilation on the prognosis of patients with ARDS: a retrospective analysis with 228 patients," *Zhonghua Wei Zhong Bing Ji Jiu Yi Xue*, vol. 29, no. 1, pp. 45–50, 2017.

[4] J. R. Beitler, T. Sarge, V. M. Banner-Goodspeed et al., "Effect of titrating positive end-expiratory pressure (PEEP) with an esophageal pressure-guided strategy vs an empirical high PEEP-fio2 strategy on death and days free from mechanical ventilation among patients with acute respiratory distress syndrome," *Journal of the American Medical Association*, vol. 321, no. 9, pp. 846–857, 2019.

[5] P. van der Zee and D. Gommers, "Recruitment maneuvers and higher PEEP, the so-called open lung concept, in patients with ARDS," *Critical Care*, vol. 23, no. 1, p. 73, 2019.

[6] S. K. Sahetya, D. N. Hager, R. S. Stephens, D. M. Needham, and R. G. Brower, "PEEP titration to minimize driving pressure in subjects with ARDS: a prospective physiological study," *Respiratory Care*, vol. 65, no. 5, pp. 583–589, 2020.

[7] K.-Q. Tang, S.-L. Yang, B. Zhang et al., "Ultrasonic monitoring in the assessment of pulmonary recruitment and the best positive end-expiratory pressure," *Medicine*, vol. 96, no. 39, Article ID e8168, 2017.

[8] E. Fan, D. Brodie, and A. S. Slutsky, "Acute respiratory distress syndrome," *Journal of the American Medical Association*, vol. 319, no. 7, pp. 698–710, 2018.

[9] D. L. Grieco, L. S. Menga, D. Eleuteri, and M. Antonelli, "Patient self-inflicted lung injury: implications for acute hypoxemic respiratory failure and ARDS patients on non-invasive support," *Minerva Anestesiologica*, vol. 85, no. 9, pp. 1014–1023, 2019.

[10] A. J. Walkey, L. Del Sorbo, C. L. Hodgson et al., "Higher PEEP versus lower PEEP strategies for patients with acute respiratory distress syndrome. A systematic review and meta-analysis," *Annals of the American Thoracic Society*, vol. 14, no. Supplement_4, pp. S297–S303, 2017.

[11] M. Bergez, N. Fritsch, D. Tran-Van et al., "PEEP titration in moderate to severe ARDS: plateau versus transpulmonary pressure," *Annals of Intensive Care*, vol. 9, no. 1, p. 81, 2019.

[12] E. Fan, L. Del Sorbo, E. C. Goligher et al., "An official American thoracic society/European society of intensive care medicine/society of critical care medicine clinical practice guideline: mechanical ventilation in adult patients with acute respiratory distress syndrome," *American Journal of Respiratory and Critical Care Medicine*, vol. 195, no. 9, pp. 1253–1263, 2017.

[13] S. K. Sahetya, E. C. Goligher, and R. G. Brower, "Fifty years of research in ARDS.Setting positive end-expiratory pressure in acute respiratory distress syndrome," *American Journal of Respiratory and Critical Care Medicine*, vol. 195, no. 11, pp. 1429–1438, 2017.

[14] J. C. Keenan, G. A. Cortes-Puentes, L. Zhang, A. B. Adams, D. J. Dries, and J. J. Marini, "PEEP titration: the effect of prone position and abdominal pressure in an ARDS model," *Intensive Care Medicine Experimental*, vol. 6, no. 1, p. 3, 2018.

[15] T. Bein, S. Grasso, O. Moerer et al., "The standard of care of patients with ARDS: ventilatory settings and rescue therapies for refractory hypoxemia," *Intensive Care Medicine*, vol. 42, no. 5, pp. 699–711, 2016.

[16] C. Guérin, L. Papazian, L. Papazian et al., "Effect of driving pressure on mortality in ARDS patients during lung protective mechanical ventilation in two randomized controlled trials," *Critical Care*, vol. 20, no. 1, p. 384, 2016.

[17] S. K. Sahetya and R. G. Brower, "Lung recruitment and titrated PEEP in moderate to severe ARDS," *Journal of the American Medical Association*, vol. 318, no. 14, pp. 1327–1329, 2017.

[18] J. Karlsson, P. Winberg, B. Scarr et al., "Validation of capnodynamic determination of cardiac output by measuring effective pulmonary blood flow: a study in anaesthetised children and piglets," *British Journal of Anaesthesia*, vol. 121, no. 3, pp. 550–558, 2018.

[19] R. G. Khemani, K. Parvathaneni, N. Yehya, A. K. Bhalla, N. J. Thomas, and C. J. L. Newth, "Positive end-expiratory

pressure lower than the ARDS network protocol is associated with higher pediatric acute respiratory distress syndrome mortality," *American Journal of Respiratory and Critical Care Medicine*, vol. 198, no. 1, pp. 77–89, 2018.

[20] T. S. Sigmundsson, T. Öhman, M. Hallbäck et al., "Performance of a capnodynamic method estimating cardiac output during respiratory failure–before and after lung recruitment," *Journal of Clinical Monitoring and Computing*, vol. 34, no. 6, pp. 1199–1207, 2020.

Hindawi
Journal of Healthcare Engineering
Volume 2021, Article ID 7161901, 6 pages
https://doi.org/10.1155/2021/7161901

Research Article

Postoperative Effects of Dexmedetomidine on Serum Inflammatory Factors and Cognitive Malfunctioning in Patients with General Anesthesia

Zitan Zhang,[1] Wei Li,[2] and Huiqun Jia[1]

[1]*Department of Anesthesiology, The Fourth Hospital of Hebei Medical University, 12 Jiankang Road Shijiazhuang, Hebei 050011, China*
[2]*Department of Anesthesiology, The Second Hospital of Hebei Medical University, 215 Heping West Road Shijiazhuang, Hebei 050000, China*

Correspondence should be addressed to Huiqun Jia; jiahuiqun1986@outlook.com

Received 4 July 2021; Revised 18 August 2021; Accepted 20 August 2021; Published 8 September 2021

Academic Editor: Enas Abdulhay

Objective. To investigate the effects of dexmedetomidine intervention on serum inflammatory factor concentration and postoperative cognitive malfunction in elderly patients with general anesthesia. *Methodology*. 174 patients with general anesthesia were selected, who were categorized into a control group (HC) and a dexmedetomidine group (HS) using the random number table method, with 87 patients in individual groups. The dexmedetomidine group was pumped intravenously with dexmedetomidine at a loading dose of 1 μg/kg before induction of anesthesia for 15 min, followed by continuous intravenous pumping at a rate of 0.4 μg/kg/h, and the dosing was stopped at 30 min before concluding the surgery. The control group was administered the identical dose of saline in the same manner. Interleukin 6 (IL-6) and tumor necrosis factor α (TNF-α) levels and MMES scores were tested at 1 h before and 24 h after anesthesia. *Results*. Comparing to HC group, patients in the HS group had lower TNF-α and IL-6 levels at both scheduled points ($P < 0.05$). *Conclusion*. Dexmedetomidine reduced the expression of inflammatory factors in elderly patients with general anesthesia and effectively reduced the incidence of postoperative cognitive dysfunction after general anesthesia surgery.

1. Introduction

Postoperative cognitive dysfunction (POCD) has a high incidence in elderly patients undergoing general anesthesia, and there is still no clear pathogenesis. It is generally believed that POCD refers to a group of complications of the patient's central nervous system (CNS) after anesthesia surgery. Its formation mechanism is complex, which may be related to age, surgery type, and anesthetic type [1]. It is more common in elderly patients, manifesting as impairment in patients' memory, attention, learning ability, abstract thinking, and orientation. Most are accompanied by a decrease in the ability to adapt to society, to interact with others, and to perform daily activities. It often lasts for several days, with a few lasting for several weeks. POCD has become a common and frequent disease in the elderly after surgery. With the development of economy and society, Chinese society is rapidly entering the aging society. Therefore, strengthening the research on POCD is in line with the trend of social development and has significant socioeconomic significance.

The neuroinflammatory mechanism is one of the most important theories in the current mechanistic studies. Neuroinflammation is mostly caused by systemic inflammation, and the body causes central nervous system inflammation through different pathways and mechanisms, leading to constructional and functional alterations in the central nerve cells, resulting in POCD. The main view is that POCD is a neurological disorder induced by surgical and anesthesia-induced changes in the structure of central nerve cells in elderly patients based on degenerative changes in the brain and preexisting diseases in other organs and systems of the body. Since POCD is a kind of central nerve injury, clinical anesthesia needs to find a drug that can protect the central nerve and suppress the inflammatory response. Dexmedetomidine (DEX) is one of the most recently studied anesthetic adjuncts that can protect organ function by decreasing the release of sympathetic ganglion fiber neurotransmitters, thereby reducing the production of related inflammatory factors, and by inhibiting oxidative stress and reducing reperfusion injury. This study was conducted to try to understand the relationship between inflammatory factors, dexmedetomidine, and postoperative cognitive dysfunction by preoperative- and postoperative-related inflammatory factors in patients undergoing general anesthesia.

2. Materials and Methods

A total of 174 elderly patients scheduled for surgery with ASA grade I–III from January 2018 to June 2019 were selected. Among them, there were 75 patients with lumbar disc herniation, 36 prostatectomy patients, 31 cholecystectomy patients, and 6 patients with radical rectal cancer. These patients were randomized into two categories: the "dexmedetomidine group" and the "saline control group." Eighty-seven patients were included in the dexmedetomidine group, 56/32 males/females of 61–89 years of age with mean age of 70.6 ± 4.2 years; body weight was 45–95 Kg with mean weight of 65.8 ± 5.8 kg. Education outlined was illiterate 11, primary 21, secondary 35, and above secondary 20, respectively. A total of 31 cases were classified as ASA grade I, 47 cases as ASA grade II, and 9 cases as ASA grade III. The control group included 87 patients, 58 males and 19 females from 61 to 92 years of age with 71.4 ± 4.9 mean age and body weight 47–94 kilograms with 66.2 ± 5.5 mean weight. Education outlined was illiterate 8, primary 16, secondary 23, and above secondary 14, respectively. A total of 22 cases were classified as ASA grade I, ASA grade II had 32 cases, and ASA grade III had 7 cases. Reportedly, the two groups had no statistically significant difference in general information such as age and gender ($P > 0.05$), and they were comparable (Table 1).

2.1. Inclusion and Exclusion Criteria. Inclusion criteria: patients with 18–79 years of age; ASA grade I–III; operation time within 24 hours; preoperative approval by the ethical board committee and voluntary signing of the study consent form. Exclusion criteria: those with a history of dementia and psychosis; those with severe cerebrovascular disease; those with a history of multiple surgeries; those with a history of severe perioperative infections in various systems; those with perioperative massive hemorrhage and severe acid-base imbalance and electrolyte imbalance; those with diabetes mellitus; and those with perioperative hormone.

2.2. Experimental Protocol. All patients were fasted for 8 h and dehydrated for 2 h before surgery, and no drugs were administered before surgery. After entering the operating room, peripheral veins were routinely opened and patients' heart rate, blood pressure, oxygen saturation, and EEG dual-frequency index were monitored, and internal jugular venipuncture and radial artery puncture were conducted after anesthesia induction to monitor patients' central venous pressure and invasive arterial pressure. Anesthesia method: sufentanil 0.4 μg/kg, propofol 1 mg/kg, midazolam 0.05 mg/kg, and cis-atracurium 0.3 mg/kg were injected intravenously for anesthesia induction and wind pipe (tracheal tube) was inserted after 5 min. The anesthesia machine was connected for mechanical ventilation after determining the correct position of the tracheal tube, with VT 8–10 mL/kg, RR 12–16 times/min, and IE 1 : 2. $PETCO_2$ was maintained at 35–40 mmHg and FiO_2 at 60%. Anesthesia was maintained by inhalation of sevoflurane at concentrations of 1% to 2% and intravenous infusion of ~6 mg/kg/h of propofol , 0.1~0.5 μg/kg/min remifentanil, and 0.1~0.2 mg/kg/h cis-atracurium. The intraoperative inhaled concentration of sevoflurane was regulated according to the hemodynamic and BIS values, maintaining a BIS value of 40 to 60. Narcotic analgesics and vasoactive drugs were used so that the intraoperative BP and HR fluctuations did not exceed 20% of the basic value, and the mean value of arterial pressure must not be below 60 mmHg. If the fluctuation of BP and HR was greater than 20% of the preoperative base value, a comprehensive analysis and judgment would be made by using the depth of anesthesia monitor, and the specific intervention was to add 5 μg of sufentanil and 0.3 mg of atropine or 2 μg of norepinephrine each time and dexmedetomidine loading dose 1 μg/kg was administered intravenously for 10 min, which were all monitored until medications took effect and vital signs returned to stability. When the adverse reaction of dextrometomidine happened, such as hypotension, hypertension, nausea, bradycardia, and dry mouth, the infusion was immediately discontinued. Over the next 24 hours, patients receiving the drug were closely monitored. After surgery and anesthesia, the patient was transferred to the postanesthesia recovery unit for resuscitation. All procedures were performed by the same group of physicians.

2.3. Examination Indicators and Methods. A total of 4 mL of elbow venous blood was collected before surgery (T1) and 24 h after surgery (T2), respectively, and centrifugation was performed to separate the serum. Enzyme-linked immunosorbent assay was used to detect the concentration of serum TNF-α and IL-6, in strict accordance with the instructions for use of the kit.

2.4. The POCD and Inflammatory Mediators Link Was Assessed by Quartiles. The values of TNF-α and IL-6 were arranged from smallest to largest and the three quartiles (Q1, Q2, and Q3) were $Ql = (87 + 1)/4 = 22$, $Q2 = 2^*(87 + 1)/4 = 44$, and $Q3 = 3^*(87 + 1)/4 = 66$. These four individuals divided 87 patients into four segments (q1, q2, q3, and q4). A comparison was performed with the POCD number within this quartet intersegments and then the correlation between POCD and these two inflammatory mediators was evaluated using Pearson's correlation analysis.

2.5. Statistical Analysis. The extracted data were statistically analyzed by using statistical software SPSS 17.0 (SPSS Inc., Chicago, II). For numerical variables, *t*-tests were performed both with paired and independent samples. If the data values conformed to normality and chi-squaredness, otherwise, signed rank sum test and Kruskal–Wallis test were used. The chi-square test was used for categorical variables. Correlation analysis was expressed as Pearson correlation coefficient. The test level was $P = 0.05$.

3. Results

The incidence of POCD was calculated in both experimental and control groups as 9.20% and 21.31%, respectively. There was a statistically significant difference between both experimental and control groups ($P = 0.038$). The levels of IL-6 and TNF-α in both groups were significantly higher than before surgery (Table 2). The increase was significantly suppressed in the dexmedetomidine group comparing to the control group ($P < 0.05$). POCD occurrence was also analyzed and statistically significant difference was also reported between the odds, when the levels of inflammatory mediators were different in the quartile grouping ($P < 0.05$). The relationship between two inflammatory mediators and POCD was calculated by Pearson's correlation analysis, and the correlation coefficients were $R = 0.689$ for IL-6 and $P = 0.043$ for POCD and $R = 0.711$ and $P = 0.038$ for TNF-α and POCD (Table 3).

Table 4 shows that with the increase of TNF-α values, the number of POCD also increases significantly ($P < 0.05$).

The data from Tables 4 and 5 were analyzed by Pearson's correlation analysis, which showed that the serum value of IL-6 concentration was significantly correlated with the number of POCD, i.e., $r = 0.689$ and $P = 0.043$. Likewise, serum concentration of TNF-α was also significantly and positively linked with POCD, i.e., $r = 0.711$ and $P = 0.038$. $P < 0.05$, suggesting that the elevated concentrations of proinflammatory factors were correlated with POCD (Tables 4 and 5).

4. Discussion

Studies have shown that the POCD incidence in elderly individuals encountering noncardiac surgical procedure is up to 25.8% and 9.9% at 1 week and 3 months postoperatively [2]. POCD is a degenerative change in neurological function induced or aggravated by a combination of surgical, anesthetic, and preexisting diseases based on the degeneration of the central nervous system. Monk and Price [3] have confirmed that the occurrence of POCD not only prolongs hospitalization time and increases patients' hospital costs but also leads to neurological impairment.

Numerous factors influence POCD in clinical practice, such as patient age, gender, education level, type of surgery, anesthesia method, and medications [4]. In this trial, a randomized approach was used in the design regarding the abovementioned factors, and there were no statistically significant differences in age, education level, duration of surgical anesthesia, and intraoperative medication between the two groups in this study. Besides, BIS was used to maintain the same depth of anesthesia during the operation, so as to ensure the homogeneity of the study population.

In the mechanisms of POCD, the theory of inflammatory response of central nervous system has gradually become a research hotspot, and validation plays an important role in this process [5], where tissue damage due to surgery can activate the peripheral intrinsic immune system and cause inflammatory cell infiltration, which in turn releases inflammatory mediators (TNF-α, IL-6, IL-1, etc.) [6]. Inflammatory reactions of the central nerve system can be caused by peripheral inflammatory factors entering the central nervous system. Peripheral inflammatory factors can enter the central nervous system through the blood-brain barrier or synthesize and release inflammatory factors by activating neuroendocrine cells in the blood-brain barrier, causing central inflammation. Inflammatory factors entering the CNS interfere with neuronal activity, thereby disrupting intersynaptic connections and signaling [7]. It has been shown that the degree of increased expression of proinflammatory factors and its presence in the central nervous system and body circulation of surgical patients may correlate with the degree of cognitive decline [8,9]. Interleukin 6 plays an important role in body's defense mechanism, immune system, and generating inflammatory responses in vivo. It also affects the growth and differentiation of central nerve cells in the CNS, which also influence cerebral functionality, specifically learning, investigation, and recollection of memory. IL-6 is secreted by intracranial microglia, neuronal cells, and astrocytes and has been implicated in brain injury. Normal concentrations of IL-6 levels are important for neuronal cell protection and repair; however, if the concentrations are too high, they instead exacerbate neuronal and microglial cell damage [10]. These processes may include synaptic plasticity or neuronal cell growth regulation [11].

TNF-α is secreted by macrophages and has a wide range of biological activities with extremely important roles in immune body regulation, regulation of inflammatory responses, neuroendocrine regulation, and other systems. TNF-α is involved in many aspects of daily activities of life such as sleeping, eating, bathing, and other autonomous processes. Recent studies have found that it is involved in the processes of learning and memory and plays a vital role in the pathology of POCD. The mechanism may be related to the processes that affect synaptic shaping and inhibit the growth and differentiation of nerve cells [12]. After surgery, TNF-α is the first cytokine to be released, and it is the initiating and amplifying factor of the inflammatory cascade response. Animal studies have shown that peripheral TNF-α can cause neuronal inflammation and lead to cognitive decline by inducing the release of IL-1 in the brain [13]. The hippocampus-dependent cognitive decline induced by chronic neuronal inflammation can be significantly reversed when using TNF-α synthesis inhibitors, suggesting that TNF-α is an important mediator of neuronal dysfunction and cognitive impairment triggered by chronic neuroinflammation.

In our study, patients were divided into 4 segments based on the serum concentration of defined parameters IL-6 and TNF-α. Based on the result output, the number of POCD was significantly different in these four segments. With the increase of the concentration of these two inflammatory

Table 1: Comparison of general data and intraoperative conditions of each indicator between two groups of patients ($\bar{\chi} \pm s$).

Groups	No. of cases	Age	Gender (M/F)	Weight (kg)	ASA grade (cases, II/III)	Education (years)	Operative time (min)	Bleeding volume (ml)	Sufentanil dosage (μg)	Remifentanil dosage (mg)	Isoproterenol dosage (mg)
HC	87	71.4 ± 4.9	56/31	67 ± 8	71/16	10 ± 4	168 ± 53	406 ± 142	30.3 ± 3.8	2.38 ± 0.61	1485 ± 238
HS	87	70.6 ± 4.2	58/29	69 ± 8	76/11	11 ± 4	170 ± 48	428 ± 166	31.6 ± 4.2	2.51 ± 0.65	1533 ± 264

Table 2: TNF-α and IL-6 changes of serum concentrations of both groups ($n = 30$).

Indicators	Groups	Preoperative (T0)	Postoperative (T1h)
TNF-α (ng/L) HS	HC	46.20 ± 9.42	75.74 ± 10.39*
	HS	45.28 ± 8.99*	64.82 ± 9.71***
IL-6 (ng/L)	HC	51.02 ± 10.19	86.48 ± 13.51*
	HS	49.44 ± 9.25#	69.04 ± 12.14***

*$P < 0.05$ indicates comparing postoperative with preoperative, **$P < 0.05$ indicates comparing both experimental and control group, and# indicates $P > 0.05$ when comparing both experimental and control group.

Table 3: Comparing Mini-Mental State Examination (MMSE) scores and incidence of postoperative POCD between two groups of patients at different time points (scores, $\bar{\chi} \pm s$).

Groups	No. of cases	MMSE score		Incidence of POCD (cases (%))
		Preoperative (T10)	Postoperative T1 (1d)	
HC	87	25.8 ± 0.8	25.6 ± 1.1*	8(9.2)
HS	87	26.1 ± 0.7	22.2 ± 1.9***	13 (21.3)*
P values		0.86	0.04	0.038

*$P < 0.05$ indicates comparing postoperative and preoperative and **$P < 0.05$ indicates comparing both experimental and control group.

Table 4: The cases of POCD in the data segment of the two proinflammatory factor quartiles.

Grade	No. of cases	IL-6 (ng/ml)	Incidence of POCD (cases (%))
Q1	22	57.96 (±10.06)	0 (0.00)
Q2	22	65.27 (±10.62)	1 (4.55)
Q3	22	70.34 (±11.82)	2 (9.09)
Q4	21	83.24 (±14.82)	5 (22.73)

Table 5: With the increase in the level of IL-6 concentration, the number of POCD increases significantly ($P < 0.05$).

Grade	No. of cases	TNF-α (ng/ml)	Incidence of POCD (cases (%))
Q1	22	55.28 (±11.27)	0 (0.00)
Q2	22	61.94 (±10.72)	1 (4.55)
Q3	22	66.18 (±11.71)	2 (9.09)
Q4	21	76.41 (±14.20)	5 (22.73)

factors, the frequency of POCD increased significantly. Analysis of Pearson correlation indicated the positive correlation of IL-6 concentration with POCD, i.e., $r = 0.689$ and $P = 0.043$. Likewise, plasma TNF-α concentration was also significantly correlated with POCD, i.e., $r = 0.711$ and $P = 0.038$. Both IL-6 and TNF-α play important roles in neurocognitive function, and their increased concentrations are predictive of decreased cognitive function; similarly, it is seen that the concentrations of both proinflammatory factors increase when POCD occurs. Concluding all, IL-6 and TNF-α concentrations were significantly correlated with the POCD values. The results of this trial further proved the validity of this theory.

Dexmedetomidine is the most discriminating and selective alpha-2 adrenergic receptor agonist. The most common uses of this receptor are sedation, narcotic analgesia, and anxiolysis. In this trial, the incidence of POCD was reduced from 21.31% to 9.2% both in the control and experimental group, respectively. The anti-inflammatory effect of dexmedetomidine has been found in recent years and may have a good protective effect on humans. There may be three ways for it to exert its anti-inflammatory effect [14,15]: (1) it activates the central a-Z receptor, inhibits the activity of sympathetic nerves, activates the anti-inflammatory pathway of cholinergic nerves, and reduces the level of proinflammatory factors. (2) It inhibits macrophages and reduces the secretion of tissue necrotizing factor α. (3) It reduces the concentration of IL-6 and TNF-α by gene regulation of kappa-B. This trial is concluded; dexmedetomidine reportedly reduced the increased concentration levels of IL-6 and TNF-α in the experimental group, which proved its anti-inflammatory effect. At the same time, dexmedetomidine has a protective effect on brain tissue. Some studies [16] have shown that dexmedetomidine can improve the oxygen metabolism in areas of cerebral hypoxia-reperfusion damage in rats and reduce the area of necrotic foci. A number of studies [17] at home and abroad showed that the postoperative MMSE score of the observational group is markedly lower than the dexmedetomidine intervention group, and the TNF-α and IL-6 levels and the incidence of postoperative POCD are markedly lower than those reported in the control group. The above results suggest that dexmedetomidine used for surgery in elderly patients can significantly improve patients' MMSE scores and minimize the incidence of early postsurgical cognitive dysfunction. The diagnosis of POCD still relies mainly on neuropsychological tests. The MMSE score is a simple, easy, and most influential screening tool for determining cognitive function. Therefore, in this study, the score was used, while the test was administered by the same specialized anesthesiologist at a fixed time, and the test details were explained to the patient before the test to minimize the possible influencing factors related to the test.

The incidence of postoperative POCD in the control group was 26.7% in this study, and the MMSE score increased and the incidence of POCD decreased after dexmedetomidine pretreatment, suggesting that dexmedetomidine pretreatment helps to prevent the occurrence of postoperative POCD in elderly patients with general anesthesia. The mechanism may be related to the ability of dexmedetomidine pretreatment to reduce the occurrence of inflammatory immunity and decrease the damage to the central nervous system of the organism.

5. Conclusion

(1) Dexmedetomidine reduces the incidence of postoperative POCD in elderly patients.

(2) Dexmedetomidine significantly reduces the increase in the postsurgical interleukin 6 and tissue necrotizing factor α.

(3) The increase of interleukin 6 and tissue necrotizing factor α after surgery is significantly correlated with the increase of POCD.

Data Availability

The data used to support the findings of this study are available from the corresponding author upon request.

Conflicts of Interest

The authors declare that they have no conflicts of interest.

References

[1] I. K. Koleli, E. Ozdogan, B. Sariibrahim, L. B Ozturk, and A Karateke, "Prognostic factors affecting lymph node involvement in cervical cancer," *European Journal of Gynaecological Oncology*, vol. 35, no. 4, pp. 425–428, 2014.

[2] J. Moller, P. Cluitmans, L. Rasmussen et al., "Long-term postoperative cognitive dysfunction in the elderly: ISPOCD1 study," *The Lancet*, vol. 351, no. 9106, pp. 857–861, 1998.

[3] T. G. Monk and C. C. Price, "Postoperative cognitive disorders," *Current Opinion in Critical Care*, vol. 17, no. 4, pp. 376–381, 2011.

[4] S. S. Arora, J. L. Gooch, and P. S. García, "Postoperative cognitive dysfunction, Alzheimer's disease, and anesthesia," *International Journal of Neuroscience*, vol. 124, no. 4, pp. 236–242, 2014.

[5] H. Ri1ia, T. Kotulak, A. Brezina et al., "Comparison of the sevoflurane-sufentanil anesthesia observational study," *Physiol Res on effects of ketamine-mex cardiac biomarkers after cardiac surgery:an*, vol. 61, pp. 63–72, 2012.

[6] H. A. Rosczyk, N. L. Sparkman, and R. W. Johnson, "Neuroinflammation and cognitive function in aged mice following minor surgery," *Experimental Gerontology*, vol. 43, no. 9, pp. 840–846, 2008.

[7] Y. Liu and Y. Yin, "Emerging roles of immune cells in postoperative cognitive dysfunction," *Mediators of Inflammation*, vol. 2018, Article ID 6215350, , 2018.

[8] Y. Beloosesky, D. Hendel, A. Weiss et al., "Cytokines and C-reactive protein production in hip-fracture-operated elderly patients," *The Journals of Gerontology Series A: Biological Sciences and Medical Sciences*, vol. 62, no. 4, pp. 420–426, 2007.

[9] A. Buvanendran, J. S. Kroin, R. A. Berger et al., "Upregulation of p interleukins in the central nervous system and peripheral tissue during and after surgery in humans," *Anesthesiology*, vol. 104, no. 3, pp. 403–410, 2006.

[10] W. X. Tan, N. Hai, and M. Z. Mo, "The relationship between the serum levels of NSE, S-100 beta-protein and IL-6 and postoperative cognitivedysfunction in aged patients with general anesthesia," *Guangdong Medicine*, vol. 34, pp. 3178-3179, 2013.

[11] J. A. Hudetz, S. D. Gandhi, Z. Iqbal, K. M. Patterson, and P. S. Pagel, "Elevated postoperative inflammatory biomarkers are associated with short- and medium-term cognitive dysfunction after coronary artery surgery," *Journal of Anesthesia*, vol. 25, no. 1, pp. 1–9, 2011.

[12] D. Stellwagen and R. C. Malenka, "Synaptic scaling mediated by glial TNF-α," *Nature*, vol. 440, no. 7087, pp. 1054–1059, 2006.

[13] N. Terrando, C. Monaco, and D. Ma, "Tumor necrosis factor-alphatriggers a cytokine cascade yielding postoperative cognitive decline," *Proceedings of the National Academy of Sciences*, vol. 107, no. 47, pp. 20518–20522, 2010.

[14] J. J. Ke, Z. Z. Zhang, and X. B. Feng, "The effect of various dose of dexmedetomidine on the prevention of postoperative cognitive dysfunction in aged patients with intraperitoneal hyperthermic perfusion chemotherapy," *Chinese Journal of Anesthesiology*, vol. 33, pp. 1192–1194, 2013.

[15] J. Gu, J. Chen, and P. Xia, "Dexmedetomidine attenuates temote lung injury by renal ischemia-reperfusion in mice," *Acta Anaesthesiologica Scandinavica*, vol. 55, pp. 1272–1278, 2011.

[16] O. Z. Chi, J. Grayson, S. Barsoum, L. Xia, A. Dinani, and R. W. Harvey, "Effect of dexmedetomidine on microregional

O2 balance during reperfusion after focal cerebral ischemia," *J Strole CerebrovascDis*, vol. 24, no. 1, pp. 163–170, 2015.

[17] P. G. Rose, J. Java, C. W. Whitney et al., "Nomograms predicting progression-free survival overall survival and pelvic recurrence in locally advanced cervical cancer developed from an analysis of identifiable prognostic factorsin patients from NRG oncology/gynecologic oncology group randomized trials of chemoradiotherapy," *Journal of Clinical Oncology*, vol. 33, no. 19, pp. 2136–2142, 2015.

Hindawi
Journal of Healthcare Engineering
Volume 2021, Article ID 1846886, 7 pages
https://doi.org/10.1155/2021/1846886

Research Article

Thoracic Paravertebral Nerve Block with Ropivacaine and Adjuvant Dexmedetomidine Produced Longer Analgesia in Patients Undergoing Video-Assisted Thoracoscopic Lobectomy: A Randomized Trial

Jun Zha[1], **Shiliang Ji**[2], **Chen Wang**[1], **Zhe Yang**[1], **Shigang Qiao**[1,3] **and Jianzhong An**[3]

[1]*Department of Anesthesiology and Perioperative Medicine, The Affiliated Suzhou Science & Technology Town Hospital of Nanjing Medical University, No. 1 Lijiang Road, Suzhou 215153, China*
[2]*Department of Pharmacy, The Affiliated Suzhou Science & Technology Town Hospital of Nanjing Medical University, No. 1 Lijiang Road, Suzhou 215153, China*
[3]*Institute of Clinical Medicine Research, The Affiliated Suzhou Science & Technology Town Hospital of Nanjing Medical University, No. 1 Lijiang Road, Suzhou 215153, China*

Correspondence should be addressed to Shigang Qiao; qiaoshigang@163.com and Jianzhong An; szkjcyy_ajz@126.com

Received 23 July 2021; Revised 11 August 2021; Accepted 21 August 2021; Published 8 September 2021

Academic Editor: Enas Abdulhay

Purpose. This study evaluated the postoperative analgesic effect of ultrasound-guided single-point thoracic paravertebral nerve block (TPVB) combined with dexmedetomidine (DEX) in patients undergoing video-assisted thoracoscopic lobectomy. *Methods*. Sixty adult patients of the American Society of Anesthesiologists (ASA) I–III were randomly assigned into three groups ($n = 20$ each). G group: patients received routine general anesthesia; PR group: patients received 0.5% ropivacaine; and PRD group: patients received 0.5% ropivacaine with 1 μg/kg DEX. TPVB was performed in the T5 space before surgery, and then, general anesthesia induction and video-assisted thoracoscopic lobectomy were performed. Analgesics were administered through the patient-controlled analgesia (PCA) device intravenously. The background infusion of each PCA device was set to administer 0.02 μg/kg/h sufentanil, with a lockout time of 15 min, and a total allowable volume is 100 ml. *Results*. Compared to PR and G groups, the total sufentanil consumption after operation, the times of analgesic pump pressing, the pain score, and the incidence of postoperative nausea or vomiting in the PRD group were significantly reduced ($p < 0.05$). Also, the duration of first time of usage of the patient-controlled analgesia (PCA) was longer. The heart rate (HR) and mean arterial pressure (MAP) during operation were lower in the PRD group as compared with the other two groups in most of the time. However, hypotension and arrhythmia occurred in three groups with no statistically significant difference. *Conclusions*. A small volume of TPVB with ropivacaine and DEX by single injection produced longer analgesia in patients undergoing video-assisted thoracoscopic lobectomy, reduced postoperative opioids consumption, and the incidence of side effects.

1. Introduction

Video-assisted thoracoscopic surgery (VATS) is mainly used for the treatment of the lung, mediastinum, and pleural lesions. The main advantage is to avoid the injury of thoracotomy. Compared with thoracotomy, the operation time is shorter, the postoperative morbidity is lower, and the time for returning to normal activities is earlier [1]. However, effective analgesia is still needed to reduce postoperative pain and postoperative nausea and vomiting.

Thoracic paravertebral block (TPVB) as part of a multimodal analgesia strategy after thoracotomy [2] and breast surgery [3] has a broad evidence base and along with ultrasound-guided techniques. It has become increasingly popular. Recent randomized controlled trials and reviews have shown that paravertebral block (PVB) causes prolonged directional analgesia and reduces the risk of postoperative nausea, vomiting, and complications [4, 5]. However, a large body of literature has shown that the duration of analgesia is controversial, and PVB is only beneficial immediately after surgery [6, 7]. There are few studies on the effectiveness and tolerability of adjuvant analgesics in paraspinal analgesia. The addition of magnesium, clonidine, ketamine, dexamethasone, opioids, and other analgesics and local anesthetics can enhance and prolong the analgesic effect provided by PVB [8, 9].

Dexmedetomidine (DEX) is a novel alpha-2 adrenergic receptor agonist with dose-dependent sedative, anxiolytic, and analgesic effects and has an advantage of minimum respiratory depression compared with alternative drugs [10]. It is well known that α_{-2} receptor agonists, due to their own sympathetic properties, provide stable hemodynamics during surgery and reduce the amount of narcotic analgesics. When DEX is used as an anesthetic for epidural anesthesia [11], subarachnoid block [12, 13], PVB [14, 15], and brachial plexus block analgesia [16], the time is significantly extended. However, there are few studies evaluating the efficacy of DEX as an adjuvant in the treatment of analgesia after thoracoscopic surgery, only in partial breast surgery [15].

Therefore, this study was designed to evaluate whether TPVB combined with ropivacaine and DEX could improve the analgesic effect of patients undergoing VATS, thereby reducing postoperative opioid drugs consumption.

2. Methods

This study was approved by the Affiliated Suzhou Science and Technology Town Hospital of Nanjing Medical University' Ethics Committee, and written informed consent was obtained from all patients. The trial is registered at the Chinese Clinical Trial Registry, number ChiCTR-IOR-17013034. After obtaining approval and written informed consent from the institutional ethics committee, the study enrolled 60 ASA I–III patients (18–65 years old, either gender, weighing 50–85 kg) who were scheduled to undergo elective thoracoscopic lobectomy. Patients undergoing elective general anesthesia and video-assisted thoracoscopic unilateral lobectomy had no history of cardiopulmonary disease, no sinus bradycardia, no functional lesions of the sinoatrial node, no serious arrhythmia, and no thoracic deformity. Surgery time was more than 2 hours. Exclusion criteria: minimental state examination scores below 23 points; the history of dementia, psychosis, or other central nervous system disease or drug dependence and poor compliance; and those who did not complete video-assisted thoracoscopic lobectomy under general anesthesia or have to convert to thoracotomy.

All patients did not use preoperative medication, and in the preoperative preparation room, the patients were explained in detail the numerical rating scale (NRS) scoring rules (scores from 0 to 10: 0 = no pain, 10 = most severe pain). Patients were randomized into three groups of 20 individuals each using a computer-generated random number table (random number table method) with sealed envelope technology for assignment concealment (distribution hidden). In the operating room, ultrasound-guided right internal jugular vein catheterization for infusion and left radial artery catheterization for monitoring the changes of pressure have been performed. Conventional general anesthesia induction included sufentanil 5 ug/kg + etomidate 2 mg/kg + cisatracurium 2 mg/kg intravenous slow bolus injection; anesthesia maintenance: propofol 2.5 ug/ml, sevoflurane 0.8 MAC, remifentanil 3 ng/ml, bispectral index monitoring, and the depth of anesthesia is maintained between 40 and 60. Patients were classified into three groups as follows: G group: patients received routine general anesthesia; PR group: patients received 0.5% ropivacaine for TPVB; PRD group: patients received 0.5% ropivacaine with 1 μg/kg DEX for TPVB. Paravertebral blockade was performed under ultrasound guidance. A linear ultrasound transducer (HITACHI Arietta 60) was placed intercostally to identify the thoracic paravertebral space (TPVS), and a 20-gauge needle was inserted into the plane of the transducer. When the needle tip reached TPVS, 10 mL 0.5% ropivacaine with 1 μg/kg DEX in T5 paravertebral space was injected.

The gender, age, ASA grade, height, weight, body mass index (BMI), heart rate (HR), mean artery pressure (MAP) baseline, duration of surgery (h), anesthesia (h), the time to first analgesic request since paravertebral injection (TFR1), first use of patient-controlled analgesia (PCA1) intravenously, total sufentanil dosage, and the pressing times of analgesic pumps were all recorded in three groups. The intraoperative MAP and HR were measured after starting TPVB bolus injection. Hypotension defined as a 30% decrease or less than 80 mmHg in systolic blood pressure from baseline was treated with ephedrine 5 mg intravenously and further boluses as required. Bradycardia defined as heart rate <55 beats per minute was treated with 0.6 mg intravenously. Analgesics were administered through the PCA device (ZZB-150, Apon, Nantong, China). The background infusion of each PCA device was set to administer 0.02 μg/kg/h sufentanil, with a lockout time of 15 min, and a total allowable volume is 100 ml. The anesthetist conducted postoperative monitoring, pain assessment, and management was blinded to the patient groups. The flowchart of the study protocol is shown in Figure 1.

Ramsay sedation scores of patients were recorded at 30 minutes, 1 hour, 2 hours, 4 hour, 6 hours, 8 hours, 12 hours, and 24 hours after anesthetic recovery in three groups (score 1: patient anxiety, agitated or restlessness, or both; score 2: patient cooperation, orientation, and calm; score 3: patient only responds to orders; score 4: patient with light outer membrane percussion, or a loud auditory stimuli showed a rapid response; score 5: the patient showed a slow response to light eyebrows or loud auditory stimuli; score 6: the patient did not respond; score 2–4 is an ideal sedation level). The intraoperative MAP and HR were recorded at 10

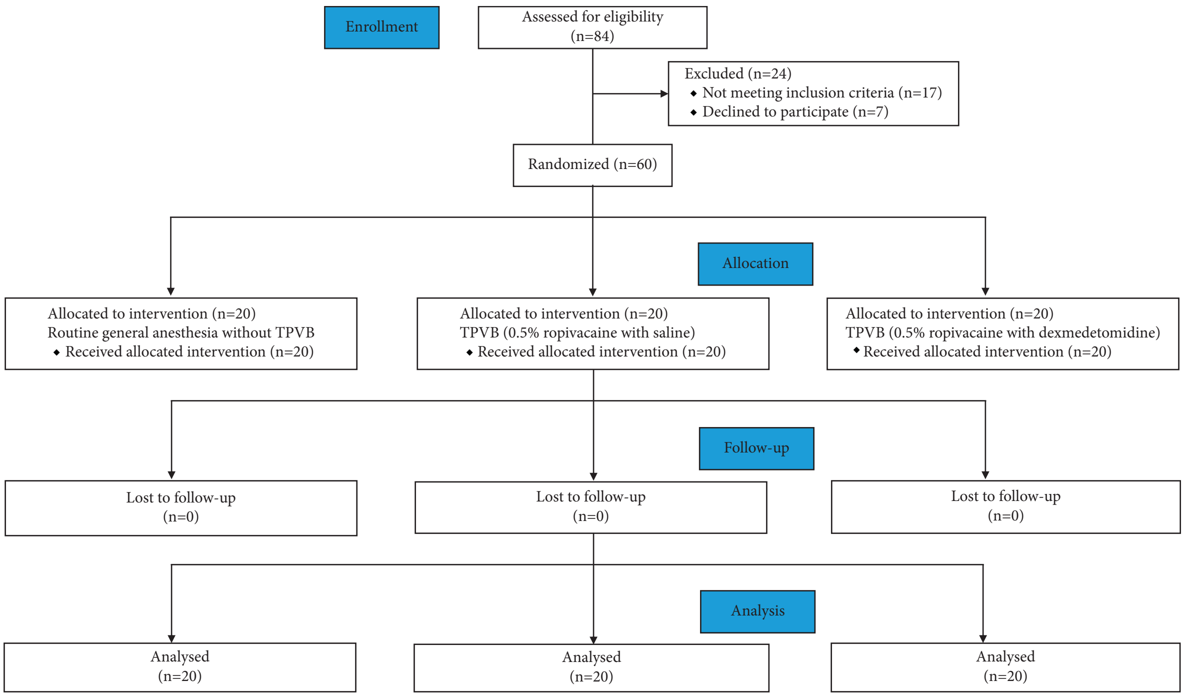

Figure 1: CONSORT flow diagram of the study.

minutes, 20 min, 30 min, 40 min, 50 min, 60 min, 70 min, 80 min, 90 min, and 100 min after starting TPVB bolus injection. Postoperative pain ratings (NRS) during rest and movement were recorded every two hours within 24 hours (NRS: NRS uses 0–10 to represent different degrees of pain. Score 0: no pain; score 1–3: mild pain; score 4–6: moderate pain; score 7–10: severe pain).

All values are mean ± SEM. Two-way ANOVA for repeated measures was used when appropriate (SPSS 20.0 for Windows, SPSS Inc.). The Student–Newman–Keuls multiple comparison post hoc test was used to differentiate within the groups. A probability value less than 0.05 was considered to indicate a significant difference between the groups, while a value greater than 0.05 was considered to indicate no significant difference between the groups.

3. Results

There were no significant differences among the G group, PR group, and PRD group in demographic data such as age, weight, height, BMI, and baseline hemodynamic parameters durations of surgery and anesthesia ($p > 0.05$) (Table 1). All patients underwent the surgery successfully without local anesthetic toxicity or diclofenac sodium contraindications.

Postoperative sufentanil (over 24 hours) consumptions were reduced significantly in the PRD group compared to other two groups ($p < 0.05$; Table 2). Moreover, all the abovementioned parameters did not reach significant difference between the G group and PR group as given in Table 2 ($p > 0.05$). There was no significant difference of postoperative Ramsay sedation scores among all groups before 12 h; however, the score values in the G group were significantly lower than that in the PR or PRD group ($p < 0.05$; Table 3).

The NRS pain scores of ipsilateral arm were, respectively, indicated in Figure 2 and 3 in rest or movement status. There was no significant difference in pain score among three groups in rest or movement status within 1 hour after surgery; 2 hours after surgery, the pain scores of the PRD group were lower than other two groups. In the PRD group, TFR1 and PCA1 were significantly longer than those in the PR group ($p < 0.05$) and G group ($p < 0.05$) (Table 2). There were significant differences of TFR1 and PCA1 between the PR group and G group ($p < 0.05$).

Hemodynamic parameters were monitored during surgery. HR and MAP trends are shown in Figures 4 and 5, respectively. There were no differences of hypotension and bradycardia among groups and the requirement of vasopressors for maintenance of stable hemodynamic parameters during the induction period did not show significant differences among groups (data not shown). The intraoperative HR and MAP in the PRD group were lower compared to other two groups. After 10 minutes, the intraoperative HR of all three groups decreased, but it was more obvious in the PR group and G group than that in the PRD group ($p < 0.05$). In the PR group and G group, the intraoperative HR tended to stabilize and increased slowly until 40 minutes, but the HR of the PRD group was lower than other G groups at 80 and 100 minutes. In the PR group and G group, the intraoperative MAP decreased significantly around 20 minutes, while MAP of the PRD group decreased to (77.1 ± 1.7) mmHg around 40 minutes, and it gradually returned to the baseline level around 100 minutes ($p < 0.05$). However, there was no significant difference in the consumption of sufentanil dose or the

Table 1: Characteristics of the patients and surgery.

Items	G group ($n = 20$)	PR group ($n = 20$)	PRD group ($n = 20$)	P value
Age (years)	45.7 ± 1.3	47.1 ± 1.7	48.1 ± 1.5	0.962
Height (cm)	165.4 ± 1.4	165.9 ± 1.2	164.6 ± 1.4	0.594
Weight (kg)	68.0 ± 2.1	67.3 ± 2.3	72.4 ± 2.1	0.719
BMI (kg/m^2)	23.2 ± 0.5	23.4 ± 0.6	24.1 ± 0.6	0.574
Baseline HR (beats/min)	83.0 ± 1.6	82.3 ± 2.9	84.8 ± 2.3	0.922
Baseline MAP (mmHg)	96.7 ± 1.8	97.1 ± 1.5	95.5 ± 1.9	0.460
Surgery time (h)	2.2 ± 0.1	2.2 ± 0.1	2.2 ± 0.1	0.614
Anesthesia time (h)	2.5 ± 0.1	2.8 ± 0.1	2.9 ± 0.1	0.067

Values are mean ± SEM. G: general anesthesia; PR, paravertebral ropivacaine; PRD, paravertebral ropivacaine and dexmedetomidine; BMI, body mass index; HR, heart rate; MAP, mean arterial pressure.

Table 2: Analgesic efficacy and postoperative adverse effects.

Items	G group ($n = 20$)	PR group ($n = 20$)	PRD group ($n = 20$)	P value
TFR1 (h)	2.6 ± 1.5	5.6 ± 2.0	24.1 ± 2.9	<0.05$^{*\#\$}$
Numbers of pressing analgesic pump	5.3 ± 0.2	3.2 ± 0.1	1.6 ± 0.2	<0.05$^{*\#\$}$
Total sufentanil dosage (μg)	142.2 ± 7.3	105.1 ± 5.7	78.2 ± 6.2	<0.05$^{*\#\$}$
Nausea	5(25%)	3(15%)	0	<0.05$^{*\#\$}$
Vomiting	2(10%)	1(5%)	0	<0.05$^{*\#\$}$

Values are mean ± SEM or n (%). TFR1, time from paravertebral injection to first analgesic request. $P < 0.05$, *G group vs. PR group; $^\#$G group vs. PRD group; $^\$$PR group vs. PRD group.

Table 3: Postoperative Ramsay sedation scores at different intervals.

Time points	G group ($n = 20$)	PR group ($n = 20$)	PRD group ($n = 20$)	P value
30 min	2.5 (2.0–5.0)	2.5 (2.0–5.0)	2.0 (2.0–5.0)	0.409
1 h	2.0 (2.0–4.0)	2.0 (2.0–4.0)	2.0 (2.0–4.0)	0.995
2 h	2.0 (2.0–4.0)	2.0 (2.0–4.0)	2.0 (2.0–4.0)	1.000
4 h	2.0 (2.0-3.0)	2.0 (2.0-3.0)	2.0 (2.0-3.0)	0.415
8 h	2.0 (2.0-3.0)	2.0 (2.0-3.0)	2.0 (2.0-3.0)	0.216
12 h	2.0 (2.0-3.0)	2.0 (2.0-3.0)	2.0 (2.0-3.0)	0.331
24 h	1.0 (0.0–2.0)	2.0 (1.0–3.0)	2.0 (0.0–3.0)	<0.05$^{*\#}$

Values as median (interquartile range). *G group versus PR group; $^\#$G group versus PRD group.

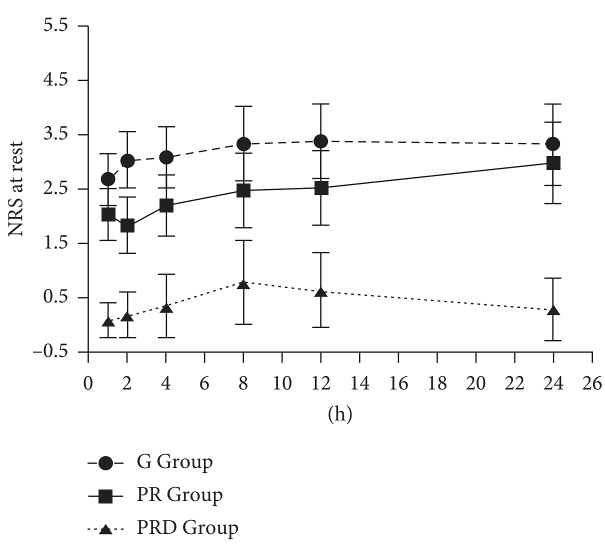

Figure 2: Postoperative NRS.R. Values in all groups. Values in the PRD group compared to the G group and the PR group at all time points. There was no difference between the G group and PR group ($p > 0.05$).

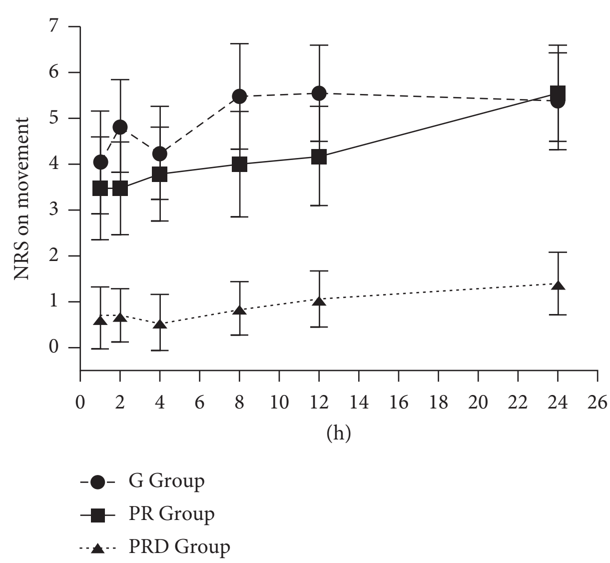

Figure 3: Postoperative NRS.M. Values in all groups. Values in the PRD group compared to the G group and the PR group at all time points ($p < 0.05$). There was no difference between the G group and PR group.

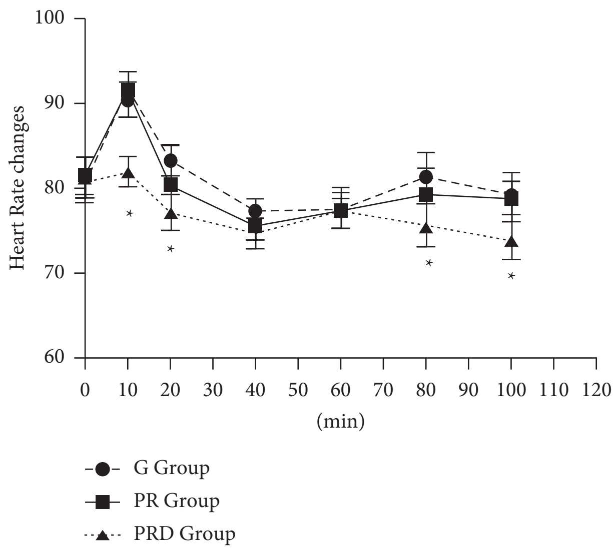

Figure 4: Intraoperative heart rate values in all groups. The PRD group compared to the G group and PR group except at 40 minutes and 60 minutes ($^* p < 0.05$).

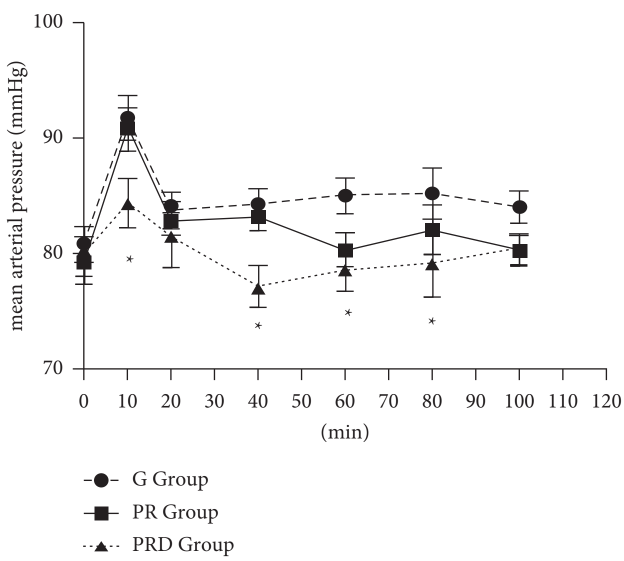

Figure 5: Intraoperative MAP values in all groups. The PRD group compared to the G group and PR group except at 20 min and 100 min ($^* p < 0.05$). There were significant differences between the G group and PR group at 60, 80, and then 100 min; the G group and PRD group at all time points except 20 min; and the PR group and PRD group at 20 and 100 min ($p < 0.05$).

incidence of hypotension and the occurrence of bradycardia during the surgery.

4. Discussion

TPVB has been used wildly to reduce postoperative opioid consumption and provide effective pain control. The injection site and volume are quite different in different studies, and there are single and multiple injections with volumes of 5, 7, 10, 15, 20, or 0.3 ml/kg [17]. A cadaver study observed distribution of 20 ml injected dye over three to four TPVS (range, 1–10) with 40% incidence of epidural spread [2]. Therefore, the analgesic effect produced by the volume of 15 or 20 ml may also include the effect of the epidural spread. In this study, we applied a volume of 10 ml of DEX combined with ropivacaine TPVB for patients with thoracoscopic lobectomy had a better analgesic effect than patients with only TPVB or no TPVB and may reduce the incidence of epidural spread.

DEX acts as a potential adjuvant for both axons and peripheral nerve blocks [16, 18], and studies have confirmed that epidural injection of DEX enhanced local anesthetics on nerves, reduced the need for intraoperative anesthesia, and provided a better analgesic effect after thoracotomy [19]. The analgesic effect is concentrated by inhibiting the release of substance P in the nociceptive pathway of dorsal root neurons and activating the alpha-2 receptor in the blue spot. This alpha-2 agonist mediates peripheral analgesia by reducing the release of norepinephrine and the independent inhibition of neurofibrillary action potential by the alpha-2 receptor. None of the various animal studies showed any adverse neurological effects of DEX [20, 21] and neuroprotective effects of dexmedetomidine, induced by intrathecal administration is similar to methylprednisolone [21]. DEX has also been used in human studies as an adjuvant for local anesthetics [14, 15]. Mahendru et al. compared the effects of intrathecal DEX and fentanil as bupivacaine adjuvants; the results showed that intrathecal DEX prolonged exercise and sensory block, more hemodynamic stability, and reduced need for analgesics within 24 hours compared with fentanil [22]. In other studies, DEX improved blocker efficiencies have been shown, with no reported neurological side effects. Further study of the neuronal effects of DEX was encouraged by the researchers [15, 16]. In the current study, the consumption of sufentanil in the two paravertebral nerve block patients was significantly lower than that in the control group, indicating that paravertebral nerve block can prolong the analgesic time. None of the patients in the PRD group required an additional dose of sufentanil, while only one patient in the PR group required an additional dose of sufentanil. Compared with the PR group and the G group, the first analgesia request time was much longer in the PRD group, and the postoperative PRD group had a longer PCA1 time, but the total number of PCA (or sufentanil consumption) and pain score are lower. This indicates that ropivacaine supplemented with DEX prolongs the time of analgesia after PVB. In addition, patients receiving DEX had less opioid-related complications such as nausea and vomiting. On the other hand, all of these parameters were comparable in the PR group and G group, indicating that there was no significant TPVB analgesic effect of ropivacaine alone compared with patients who did not receive TPVB. The use of local anesthetic TPVB alone improved intraoperative analgesia and reduced the need for sufentanil, but did not provide adequate postoperative analgesia. A recent RCT meta-analysis study evaluated the analgesic effects of multilevel TPVB in combination with ropivacaine or bupivacaine in postoperative breast cancer [23], and the results showed the overall analgesic consumption was lower in the intraoperative and postoperative ropivacaine groups or bupivacaine group, and the number of patients with NRS >3 after PACU was significantly reduced in the TPVB group. The local anesthetic infiltration group immediately reduced postoperative pain, especially in the 2 hours after surgery, but there was no significant difference of analgesia between 12 hours and 24 hours after surgery.

In this study, the requirement of vasopressors for maintenance of stable hemodynamic parameters did not reveal any significant difference during the induction period among groups. However, the HR and MAP in the PRD group were lower than those in the other two groups during surgery. It has been reported that the stable hemodynamics may possibly be explained on the basis of lower volume of local anesthetics used and a suitable selection of the dose of adjuvant [11]. The sedative effects found in the study may be related to the use of DEX [24]. A higher sedation score in the PR and PRD groups than the G group may due to better analgesia effects in PR and PRD groups.

More recently, Hong et al. reported that DEX as an adjunct in TPVB provided effective pain relief and significantly reduced opioid requirement in VATS [25]. Our results are consistent with the Hong et al.' study. However, there are two differences between our study and Hong et al. study'. (1) In our study, only on injection at T5 space before surgery, while there are two injections at the T3-T4 and T4-T5 levels after surgery in Hong et al.' study. It has been reported that TPVB performed prior to general anesthesia for laparoscopic cholecystectomy can provide early discharge and better postoperative pain management [6]. (2) The injection volume of the ropivacaine and DEX is different. The injection volume of ropivacaine and DEX mixture in our study is 10 ml at the single site, while the total volume of the two site injections was 30 ml in Hong et al.' study. Our results demonstrated that a small injection volume (10 ml 0.5% ropivacaine with 1 μg/kg DEX) at site of T5 space before surgery also achieved effective postoperative analgesia. It may have beneficial clinical effects for reducing the side effects of drugs, puncture injury, and discomfort to patients and enhancing recovery after surgery.

There are certain limitations to our study. First, it was a retrospective study with a small sample size and the findings therefore have to be confirmed with a larger randomized controlled trial. Second, the small sample size and recruitment of relatively healthy patients (ASA I and II) limited the possibility of drawing a definitive conclusion. Greater numbers of patients and patients with multiple comorbidities (i.e., ASA III or IV) need to be included in future studies to verify these findings. Third, since a single dose of TPVB can provide sufficient pain relief, inserting a catheter into the paravertebral space for continuous infusion of local anesthetics may provide protracted postsurgery analgesia. Furthermore, different doses and drugs used in TPVB may cause bias of the results. More studies have to be conducted to clarify this question.

5. Conclusions

In summary, a small volume of TPVB with 1 μg/kg DEX combined with 0.5% ropivacaine by single injection at T5 space before surgery for patients undergoing thoracoscopic lobectomy prolonged the overall analgesia time after surgery and reduced the dose and side effects of opioids.

Data Availability

The data used to support the findings of this study are available from the corresponding author upon request.

Disclosure

The funding body had no role in the design of this study, analyses, interpretation of the data, or writing the manuscript.

Conflicts of Interest

The authors declare that they have no conflicts of interest.

Authors' Contributions

Jun Zha and Shiliang Ji contributed equally to this work.

Acknowledgments

This work was supported by grants QNRC2016219 from Jiangsu Key Talent Youth Awards in Medicine, GSWS2019092 from Gusu Health Youth Talent Awards, and 2016Z002 (to Dr. Qiao) and SGXWS2020 (to Dr. Ji) from the Third Batch of Suzhou High-Tech District Health Talents Project. The funding body contributed with research equipment.

References

[1] S. Kaseda, T. Aoki, N. Hangai, and K. Shimizu, "Better pulmonary function and prognosis with video-assisted thoracic surgery than with thoracotomy," *The Annals of Thoracic Surgery*, vol. 70, no. 5, pp. 1644–1646, 2000.

[2] A. C. Krediet, N. Moayeri, G. J. V. Geffen et al., "Different approaches to ultrasound-guided thoracic paravertebral block," *Anesthesiology*, vol. 123, no. 2, pp. 459–474, 2015.

[3] A. Schnabel, S. U. Reichl, P. Kranke, E. M. Z. Pogatzki, and P. K. Zahn, "Efficacy and safety of paravertebral blocks in breast surgery: a meta-analysis of randomized controlled trials," *British Journal of Anaesthesia*, vol. 105, no. 6, pp. 842–852, 2010.

[4] Y. Tahiri, D. Q. H. Tran, J. Bouteaud et al., "General anaesthesia versus thoracic paravertebral block for breast surgery: a meta-analysis," *Journal of Plastic, Reconstructive & Aesthetic Surgery*, vol. 64, no. 10, pp. 1261–1269, 2011.

[5] J. F. Moller, L. Nikolajsen, S. A. Rodt, H. Ronning, and P. S. Carlsson, "Thoracic paravertebral block for breast cancer surgery: a randomized double-blind study," *Anesthesia and Analgesia*, vol. 105, no. 6, pp. 1848–1851, 2007.

[6] Z. M. Naja, M. E. Rajab, F. Ziade, M. A. Tannir, and T. Itani, "Preoperative vs. postoperative bilateral paravertebral blocks for laparoscopic cholecystectomy: a prospective randomized clinical trial," *Pain Practice*, vol. 11, no. 6, pp. 509–515, 2011.

[7] J. C. Boughey, F. Goravanchi, R. N. Parris, S. S. Kee, A. M. Kowalski, and J. C. Frenzel, "Prospective randomized trial of paravertebral block for patients undergoing breast

cancer surgery," *The American Journal of Surgery*, vol. 198, no. 5, pp. 720–725, 2009.

[8] S. S. Liu and F. V. Salinas, "Continuous plexus and peripheral nerve blocks for postoperative analgesia," *Anesthesia and Analgesia*, vol. 96, no. 1, pp. 263–272, 2003.

[9] M. E. Mourad and A. Amer, "Effects of adding dexamethasone or ketamine to bupivacaine for ultrasound-guided thoracic paravertebral block in patients undergoing modified radical mastectomy: a prospective randomized controlled study," *Indian Journal of Anaesthesia*, vol. 62, no. 4, pp. 285–291, 2018.

[10] L. Wang, Y. Zhou, T. Zhang, L. Huang, and W. Peng, "Comparison in sedative effects between dexmedetomidine and midazolam in dental implantation: a randomized clinical trial," *BioMed Research International*, vol. 2020, Article ID 6130162, 7 pages, 2020.

[11] S. J. S. Bajwa, A. Singh, V. Arora, J. Kaur, and S. Parmar, "Comparative evaluation of dexmedetomidine and fentanyl for epidural analgesia in lower limb orthopedic surgeries," *Saudi Journal of Anaesthesia*, vol. 5, no. 4, pp. 365–370, 2011.

[12] R. Gupta, J. Bogra, R. Verma, M. Kohli, J. K. Kushwaha, and S. Kumar, "Dexmedetomidine as an intrathecal adjuvant for postoperative analgesia," *Indian Journal of Anaesthesia*, vol. 55, pp. 347–351, 2011.

[13] R. Gupta, R. Verma, J. Bogra, M. Kohli, R. Raman, and J. K. Kushwaha, "A comparative study of intrathecal dexmedetomidine and fentanyl as adjuvants to Bupivacaine," *Journal of Anaesthesiology, Clinical Pharmacology*, vol. 27, pp. 339–343, 2011.

[14] S. A. Mohamed, K. M. Fares, A. A. Mohamed, and N. H. Alieldin, "Dexmedetomidine as an adjunctive analgesic with bupivacaine in paravertebral analgesia for breast cancer surgery," *Pain Physician*, vol. 17, no. 5, pp. E589–E598, 2014.

[15] M. Mohta, B. Kalra, A. K. Sethi, and N. Kaur, "Efficacy of dexmedetomidine as an adjuvant in paravertebral block in breast cancer surgery," *Journal of Anesthesia*, vol. 30, no. 2, pp. 252–260, 2016.

[16] G. Fritsch, T. Danninger, K. Allerberger, A. Tsodikov, T. K. Felder, and M. Kapeller, "Dexmedetomidine added to ropivacaine extends the duration of interscalene brachial plexus blocks for elective shoulder surgery when compared with ropivacaine alone," *Regional Anesthesia and Pain Medicine*, vol. 39, no. 1, pp. 37–47, 2014.

[17] K. E. Boghdadly, C. Madjdpour, and K. J. Chin, "Thoracic paravertebral blocks in abdominal surgery - a systematic review of randomized controlled trials," *British Journal of Anaesthesia*, vol. 117, no. 3, pp. 297–308, 2016.

[18] F. W. Abdallah and R. Brull, "Facilitatory effects of perineural dexmedetomidine on neuraxial and peripheral nerve block: a systematic review and meta-analysis," *British Journal of Anaesthesia*, vol. 110, no. 6, pp. 915–925, 2013.

[19] X. Zeng, J. Jiang, L. Yang, and W. Ding, "Epidural dexmedetomidine reduces the requirement of propofol during total intravenous anaesthesia and improves analgesia after surgery in patients undergoing open thoracic surgery," *Scientific Reports*, vol. 7, no. 1, p. 3992, 2017.

[20] E. Koksal, D. Karakaya, B. Can et al., "Intracerebroventricular application of dexmedetomidine produces antinociception and does not cause neurotoxicity in rats," *Balkan Medical Journal*, vol. 30, no. 4, pp. 355–361, 2013.

[21] F. Celik, C. Göçmez, K. Kamaşak, A. Tufek, A. Guzel, and O. Tokgoz, "The comparison of neuroprotective effects of intrathecal dexmedetomidine and metilprednisolone in spinal cord injury," *International Journal of Surgery*, vol. 11, no. 5, pp. 414–418, 2013.

[22] V. Mahendru, A. Tewari, S. Katyal, A. Grewal, M. Singh, and R. Katyal, "A comparison of intrathecal dexmedetomidine, clonidine, and fentanyl as adjuvants to hyperbaric bupivacaine for lower limb surgery: a double blind controlled study," *Journal of Anaesthesiology Clinical Pharmacology*, vol. 29, no. 4, pp. 496–502, 2013.

[23] K. W. Tam, S. Y. Chen, T. W. Huang, C. C. Lin, C. M. Su, and C. L. Li, "Effect of wound infiltration with ropivacaine or bupivacaine analgesia in breast cancer surgery: a meta-analysis of randomized controlled trials," *International Journal of Surgery*, vol. 22, pp. 79–85, 2015.

[24] Y. Lin, B. He, J. Chen, and Z. Wang, "Can dexmedetomidine be a safe and efficacious sedative agent in post-cardiac surgery patients? a meta-analysis," *Critical Care*, vol. 16, no. 5, p. R169, 2012.

[25] B. Hong, C. Lim, H. Kang, H. Eom, Y. Kim, and H. J. Cho, "Thoracic paravertebral block with adjuvant dexmedetomidine in video-assisted thoracoscopic surgery: a randomized, double-blind study," *Journal of Clinical Medicine*, vol. 8, 2019.

Hindawi
Journal of Healthcare Engineering
Volume 2021, Article ID 6343677, 7 pages
https://doi.org/10.1155/2021/6343677

Research Article

Cardioprotective Action of Glycyrrhizin on Diabetic Rats with Myocardial Remodeling

Fuxu Chen [1] **and Jie Song** [2]

[1]*Department of Cardiology, The Fourth Affiliated Hospital, Zhejiang University School of Medicine, N1 Shangcheng Road, Yiwu, Zhejiang, China*
[2]*Electroencephalogram Room, The Fourth Affiliated Hospital, Zhejiang University School of Medicine, N1 Shangcheng Road, Yiwu, Zhejiang, China*

Correspondence should be addressed to Fuxu Chen; 8013012@zju.edu.cn

Received 17 July 2021; Revised 15 August 2021; Accepted 16 August 2021; Published 1 September 2021

Academic Editor: Enas Abdulhay

Introduction. Cardiovascular disorders are one of the prominent causes of risks of mortality which accounts for high rate of the deaths at a global level. The risk of deadly myocardial infraction grows because of diabetes which even causes the development of heart failure. *Objective*. The objective of this study was to understand and study the effect of glycyrrhizin on diabetes suffering rats with myocardial remodeling. *Materials and Methods*. Streptozotocin was used for induction of diabetes, and 8–12 weeks later, the assessment of inflammation, fibrosis, and cardiac damage was evaluated. Histopathological analysis and immunohistochemistry was performed to analyze the effect in various groups. Western blotting was performed to understand the proteins expressed in diabetes, and also, their expression was noted in treatment groups. *Results*. There was a significant rise in TNF-α, dense fibrosis, and collagen deposits in the STZ diabetes group. The effects of hyperglycemia were significantly improved in the glycyrrhizin-treated group. DAPI, BrDu, and caspase staining was also performed to understand apoptosis in tissues where the diabetic groups reported significant apoptosis, while the effects were significantly lower in the treated group. *Conclusion*. All the observations indicate that glycyrrhizin has cardioprotective action in diabetic rats with myocardial remodeling and is due to the inhibition of the NF-κB signaling pathway in the myocardial layer.

1. Introduction

Approximately 30% of all deaths worldwide occur due to the cardiovascular disorders [1]. Acute myocardial infraction (AMI) is considered among those with the high mortality rate, and the infarct size is a chief determinant of prognosis in the patients. Restoration of the coronary blood circulation by the percutaneous coronary interventions (PCI) is considered to be the only clinically accepted and approved procedure to bound the infarct size [2]. The circulation of the high level of glucose might guide to the modified cardiomyocyte signaling which results in oxidative stress, fibrosis, and finally to the death of the myocyte cell [3].

The cardiac cells might face early transitions due to hyperglycemic conditions which may cause the discharge of important inflammatory mediators such as cytokines and chemokines [4]. The myocardial revascularization involvement is regularly demonstrating throughout the period of medication of patients with the persistent coronary artery disease (CAD). Advancement of angina and exercise potential in the patients with bounded symptoms is the most important observed advantages with these mediations [5].

The acute myocardial infarction heads to the ischemic necrosis of the myocardium which is considered to be harmful to the health of the mass population [6]. The timely widening of the coronary arteries in the patients suffering from the myocardial infraction diminishes the region of myocardial infraction, and there is an outstanding reduction in the mortality rate [7]. There is multiple known as well as unknown components that might affect the myocardial impairments followed by interferences.

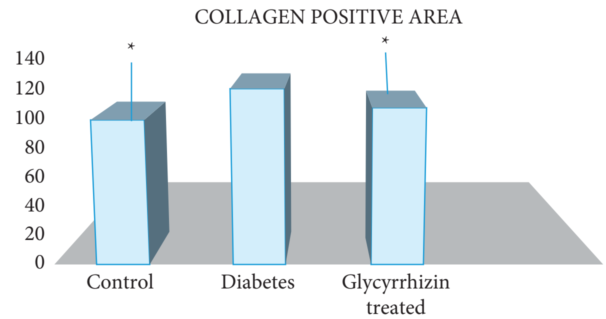

Figure 1: Percentage of collagen positive area in all groups.

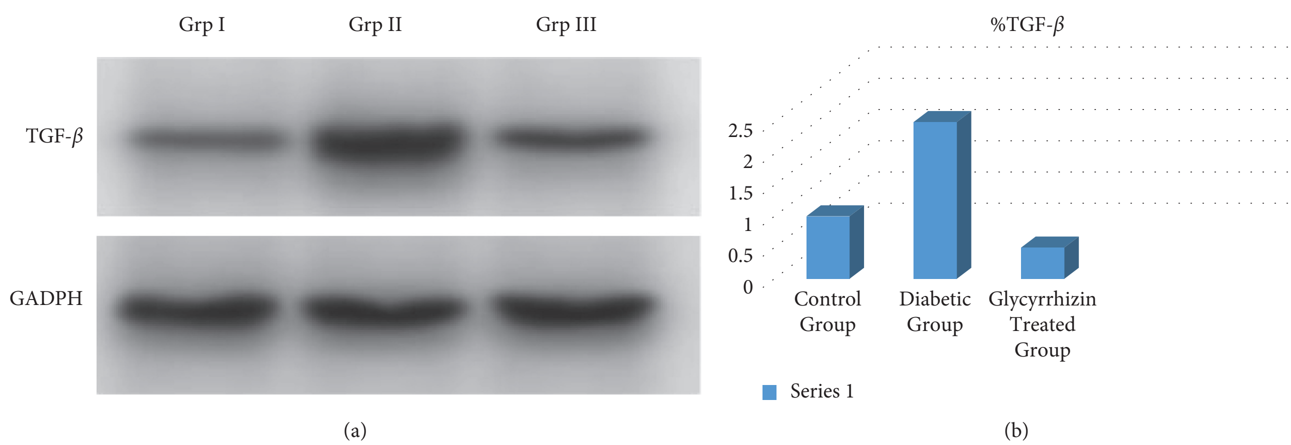

Figure 2: TGF-β expressions recorded by (a) Western blotting and (b) quantification in control, diabetic, and treated groups.

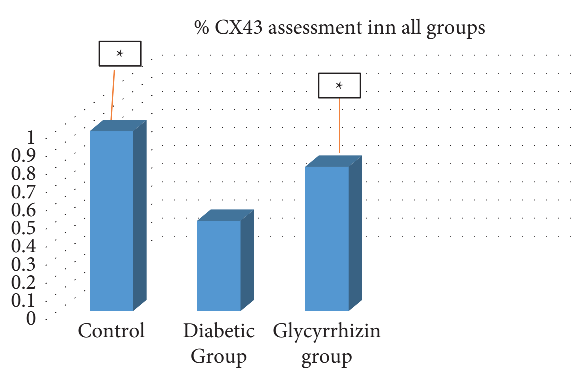

Figure 3: Glycyrrhizin alters CXCR4 expressions in myocardial tissues in STZ-diabetic rats.

However, this is still considered debatable as the diabetes mellitus might alter the myocardial responsibilities and possibly make the myocardium more prone to ischemic impairment [8, 9]. The cardiac muscles might even die, and the region of the myocardial necrosis leads to affect the prognosis of the patient suffering from myocardial infraction. In clinical practices, the myocardial damages lead to the disorder of the electric roles within the myocardial and cardiac deficiency along with arrhythmia. One of the crucial elements of root extraction from the liquorice is the acid, i.e., glycyrrhizin which is soluble in water. It consists of the glucuronic acid as well as the glycyrrhetinic acid [10].

The research study conducted by [11] demonstrates that the glycyrrhizin is a successful element in the liquorice that comprises of antiallergic, antioxidant, immunomodulatory, anticancer, antiulcer, and antiviral properties. The risk of lethal myocardial infarction and evolution of heart failure is intensified because of diabetes [12, 13]. The fundamental

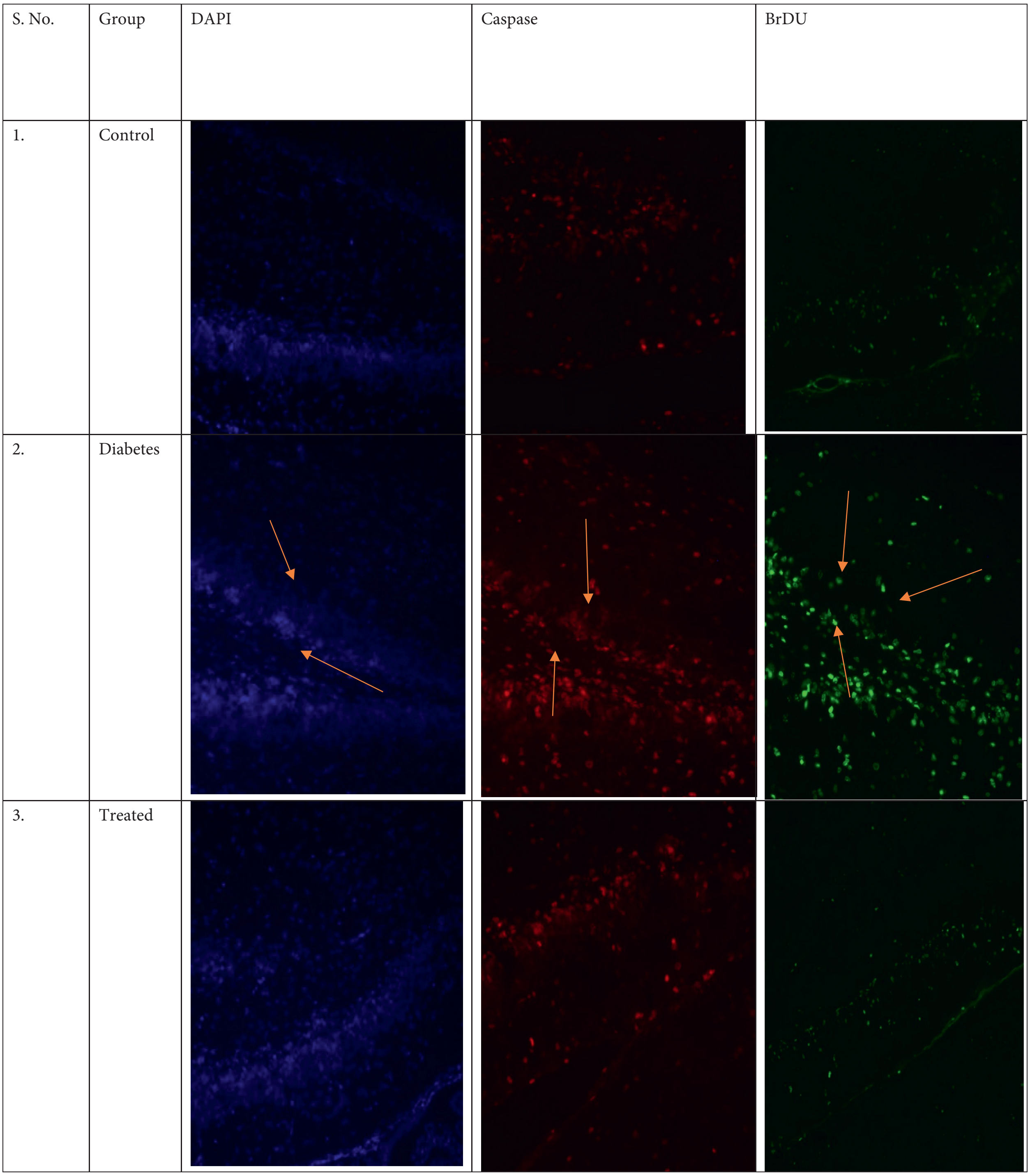

Figure 4: Immunofluorescent staining of tissues from all groups with DAPI, caspase, and BrDU for analysis of apoptosis.

diabetic cardiomyopathy which is aggravated by other components such as the hypertension as well as ischemic heart disorders justifies the defective prognosis after the myocardial infarction.

The reactive oxygen species (ROS) as well as the reactive nitrogen species (RNS) is built as an outcome of hyperglycemia. This in turn persuades the p53 and the cytochrome-c moderated caspase-3-dependent apoptosis [14, 15]. Correspondingly, termination of myocardial cells in diabetes is averted by the utilization of the antioxidants and the caspase inhibitors which shows a spontaneous task for the apoptosis in the pathogenesis of diabetes-instigated cardiomyocyte loss.

2. Materials and Methods

Male Wistar rats weighing around 200–250 gm were obtained from the animal house. The rats were kept at a

Figure 5: Isolated heart from the experimental rats. (a) Freshly isolated heart for fixing. (b) Fixed organ in 10% formalin solution.

constant temperature of 25°C ± 2°C in cages. Food pellet and water were provided freely ad libitum, and 12 h light/12 h dark cycle was maintained. All experiments were duly approved by the ethical committee, and protocols were followed in accordance to National Institutes of Health Guidelines.

2.1. Induction of Diabetes. Type 2 diabetes was induced using streptozotocin 45 mg/kg via i.p., route. After 4 days of dose administration, the blood glucose levels were tested to ensure the induction diabetes in rats. Evaluation of inflammation and cardiac damage was done 8–12 weeks postinduction of diabetes. Animals were housed in the animal facility. Diabetic rats were administered Formulab Diet 5008 Purina ad libitum throughout the experiment. Accucheck glucometer (UK) was used for measuring the blood glucose levels via the tail region once in seven days.

2.2. Western Blotting. Rats tissues from the heart were harvested from all 3 groups and then processed for Western blotting. The primary antibodies used were CX43, GAPDH, CXCR4, RAGE, and TGF-β (Cell Signaling, Danvers, MA, USA) ET-1, NaV1.5, phospho-p38, Nrf2 (Thermo Fischer Scientific), and secondary antibodies used were anti-mouse IgG or anti-rabbit IgG (1 : 5000; Sigma Aldrich) and were used as control where the data's were compared with β-actin levels using the analytical software for processing images and determining the intensity and percentage of control.

2.3. Morphometric Analysis. At the end of experimentation, the rats were sacrificed, and tissues from the heart were fixed in 10% formalin solution. The tissues were embedded in paraffin, and 4 mm thick sections were cut. Myocyte obtained from sections were stained with hematoxylin and eosin, and captured images were analyzed.

Collagen fibers were stained and were quantified so as to measure the fibrosis. The collagen positive area was measured for all groups. Myocardial tissues were frozen and stained in oil-red and then washed and counterstained with hematoxylin. Images were captured using a microscope (Leica microsystems).

2.4. Immunofluorescence Staining. The paraffin sections were cut from control and treatment groups which underwent immunohistochemistry tests by using antigen retrieval methods. Tissue sections were incubated with primary antibodies for interleukin 6 (IL-6) (Genescript), interleukin 6 (IL-6) (Thermo Fischer), rabbit polyclonal collagens I and III (Thermo Fischer), and tumor necrosis factor TNF-α (Sino Biological) overnight, and then, they were stained with secondary antibodies at 370°C for thirty minutes. The stained sections were developed using diaminobenzidine and hematoxylin was used for counterstaining. All sections were viewed and captured using the ZEISS LSM 780 laser scanning microscope (Zeiss).

Sections were also stained with DAPI after three washings and then mounted on Fluoromount-G (Southern Biotech). Sections from cardiac tissue which were stained with troponin-I initially were analyzed for troponin intensity

S. No.	Tissue Micrograph	Description
1.	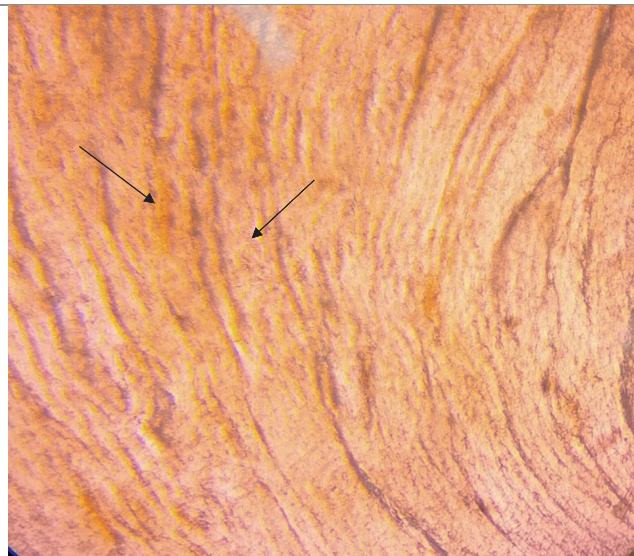	Arrows indicate clear zone from any collagen deposit or fibrosis
2.	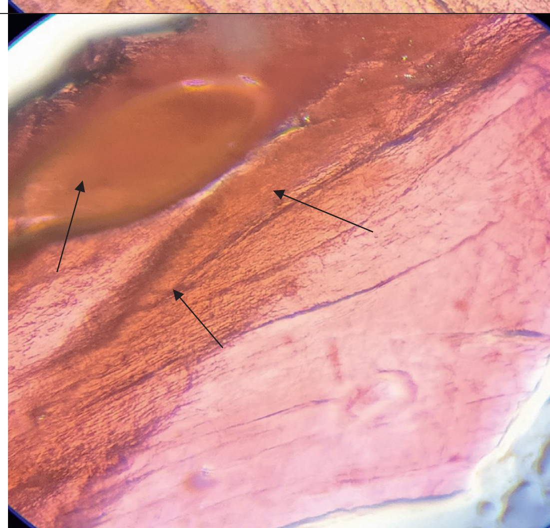	Arrows indicate deposition of collagen and fibrosis tissues
3.	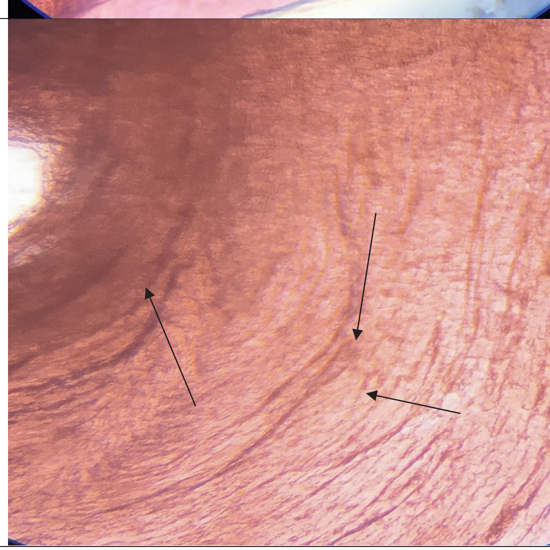	Arrows indicate clear zone from any collagen deposit or fibrosis

Figure 6: Histological analysis of tissues in all groups with collagen and fibrosis assessment.

changes and compared with control, diabetic only, and diabetic rats with treatment for identification of the effects of glycyrrhizin on troponin-I in ventricular cardiac muscle.

Myocardial apoptosis: the effect of glycyrrhizin on apoptosis in cardiomyocytes in the diabetic rats was evaluated using DAPI, caspase, and BrDU staining.

2.5. Statistical Analysis. The results were expressed in mean ± SD. We used one-way ANOVA was used for checking the significant differences followed by the post hoc multiple comparison Tukey's test where $p < 0.05$ was considered as significant.

3. Results

The tissues collected from the ventricular heart in case of diabetic rats have shown a significant rise in collagen deposition which was improved in the glycyrrhizin treatment group (Figure 1). The collagen positive area was measured by positive trichrome staining. Means ± SE; $p < 0.001$; $n = 6$.

The expressions of TGF-β were increased in cardiomyocytes cells and cardiac tissues of the diabetic group which was improved with CXCR4 antagonist in case of the glycyrrhizin-treated group. TGF-β: fibrosis marker was evaluated in STZ-diabetic rats where a significant increase was shown on comparison to the control group. Treatment of four weeks in the glycyrrhizin-treated group caused a significant decrease in the TGFβ expression in tissues of group II (treatment group) animals (Figures 2(a) and 2(b)).

Glycyrrhizin has shown increased levels in connexin43 (gap junction protein) in the cardiac tissues (Figure 3).

The stained cells in the diabetic group were higher on comparison to the normal control group, hence showing confirmed apoptosis in the myocardial region of the diabetic rats. Glycyrrhizin has shown a significant decrease in the apoptosis in myocardial cells, hence confirming the cardioprotective action of glycyrrhizin (Figure 4).

4. Discussion

Glycyrrhizin is a crucial water-soluble acid which is prominently used in Asian countries, in root extraction from liquorice. One of the major complicated disorders of chronic diabetes is myocardial fibrosis where many studies demonstrate high cardiac impairment postischemic results. Multiple clinical studies show the scenario of acute coronary syndromes which have direct impact over the high susceptibility of patients suffering from diabetes to a higher risk of heart failures.

The heart was isolated from rats and then fixed with formalin for further studies (Figures 5(a) and 5(b)). Deposition of collagen in cardiac fibrosis in the STZ diabetic rats, control group, and glycyrrhizin-treated groups was analyzed histopathologically, where it was found that collagen deposits were significantly higher in the diabetic groups as compared to the treated and control groups (Figure 6). Stained tissues were observed for fibrosis and collagen deposits.

The hyperglycemia condition mediates fibrosis in cardiac tissues which was analyzed by TGF-β (transforming growth factor beta), thus showing a significant increase in its expressions in the STZ rat cardiac tissues, while the expressions of TGF-β were significantly reduced in glycyrrhizin groups in treatment duration of four weeks. AC16 cardiomyocyte cells were also treated overnight with 25 mM of glucose and hyperglycemia cells were treated with AMD3100 (CXCR4 antagonist) to estimate the connection between TGF-β and CXCR4 pathways. Increase in TGFβ expression was in hyperglycemic cardiomyocytes, while the treated group receiving AMD3100 had noted a decreased expression of TGF-β (Figure 2), hence showing the anti-inflammatory action of glycyrrhizin.

The regulation of cell adhesion for diabetic groups was performed by assessing the connexin43. Western blotting tests were performed for showing the reduced CX43 expression in heart tissues of diabetic rats on comparison to the control group. A restoration of the CX43 expression was shown in the treatment group. Western blot analysis was performed for tissue of STZ rats to understand the mechanisms involved in inflammatory responses during hyperglycemia and in cardiac fibrosis. A significant increase in expression of CXCR4 was found in diabetic groups versus the treated group, hence showing role of glycyrrhizin in CXCR4 expression, thus confirming the anti-inflammatory action of glycyrrhizin. Reduced CXCR4 expression showed the anti-inflammatory effect in diabetic rats with cardiac atrophy.

TGFβ is a prime factor involved in contributing towards cardiac fibrosis. Hence, in this study, we concluded that STZ-induced hyperglycemia has shown activated cardiac fibroblasts and deposition of matrix proteins extracellularly. As the elevated factor TGF-β is responsible for fibrogenesis, the fibroblast production is seen to be prominent in diabetic rats but were ameliorated in the treatment group. Hence, we can say that there is an association of chemokines with cardiac fibrosis. Expressions of TGF-β in the myocardium were increased leading to fibrosis. Collagen fibers were also found significantly higher in the diabetic groups, whereas they were reduced in the glycyrrhizin group. Apoptosis was also noted in diabetic groups and was significantly reduced in the treated groups.

5. Conclusion

Hyperglycemia can lead to increased inflammation and oxidative stress which leads to cardiac remodeling and hence causes hypertrophy in the myocardium. The STZ rats showed an increased level of inflammation which may lead to cardiac injury and damage. The research concludes with findings about the anti-inflammatory and preventive cardiac damage properties of glycyrrhizin.

Abbreviations

STZ: Streptozotocin
TGF-β: Transforming growth factor-beta
CXCR4: Chemokine receptor type 4

DAPI: 4′,6-Diamidino-2-phenylindole
BrDU: Bromodeoxyuridine.

Data Availability

The data used to support the results of the study are available from the first author or corresponding author upon request.

Conflicts of Interest

The authors declare that they have no conflicts of interest.

Acknowledgments

This research was funded by the project of Zhejiang Provincial Education Department: the role of endoplasmic reticulum stress in the pathogenesis of diabetic cardiomyopathy (No. Y201942034).

References

[1] L. J. Williams, B. G. Nye, and A. R. Wende, "Diabetes-related cardiac dysfunction," *Endocrinology and Metabolism*, vol. 32, no. 2, p. 171, 2017.

[2] T. Miki, T. Itoh, D. Sunaga, and T. Miura, "Effects of diabetes on myocardial infarct size and cardioprotection by preconditioning and postconditioning," *Cardiovascular Diabetology*, vol. 11, no. 1, p. 67, 2012.

[3] A. Tao, J. Song, T. Lan et al., "Cardiomyocyte-fibroblast interaction contributes to diabetic cardiomyopathy in mice: role of HMGB1/TLR4/IL-33 axis," *Biochimica et Biophysica Acta-Molecular Basis of Disease*, vol. 1852, no. 10, pp. 2075–2085, 2015.

[4] I. Russo and N. G. Frangogiannis, "Diabetes-associated cardiac fibrosis: cellular effectors, molecular mechanisms and therapeutic opportunities," *Journal of Molecular and Cellular Cardiology*, vol. 90, pp. 84–93, 2016.

[5] G. R. Dagenais, J. Lu, D. P. Faxon et al., "Effects of optimal medical treatment with or without coronary revascularization on angina and subsequent revascularizations in patients with type 2 diabetes mellitus and stable ischemic heart disease," *Circulation*, vol. 123, no. 14, pp. 1492–1500, 2011.

[6] Z. Sun, J. Zeng, and H. Huang, "Intracoronary injection of tirofiban prevents microcirculation dysfunction during delayed percutaneous coronary intervention in patients with acute myocardial infarction," *International Journal of Cardiology*, vol. 208, pp. 137–140, 2016.

[7] S. Ota, T. Tanimoto, K. Hirata et al., "Assessment of circumferential endocardial extent of myocardial edema and infarction in patients with reperfused acute myocardial infarction," *International Heart Journal*, vol. 55, no. 3, pp. 234–238, 2014.

[8] A. Barsotti, A. Giannoni, P. Di Napoli, and M. Emdin, "Energy metabolism in the normal and in the diabetic heart," *Current Pharmaceutical Design*, vol. 15, no. 8, pp. 836–840, 2009.

[9] I. D. Moussa, L. W. Klein, B. Shah et al., "Consideration of a new definition of clinically relevant myocardial infarction after coronary revascularization," *Journal of the American College of Cardiology*, vol. 62, no. 17, pp. 1563–1570, 2013.

[10] R. Jose, G. R. Sajitha, and K. T. Augusti, "A review on the role of nutraceuticals as simple as Se2+ to complex organic molecules such as glycyrrhizin that prevent as well as cure diseases," *Indian Journal of Clinical Biochemistry*, vol. 29, no. 2, pp. 119–132, 2013.

[11] S. Rahman and S. Sultana, "Glycyrrhizin exhibits potential chemopreventive activity on 12-O-tetradecanoyl phorbol-13-acetate-induced cutaneous oxidative stress and tumor promotion in swiss albino mice," *Journal of Enzyme Inhibition and Medicinal Chemistry*, vol. 22, no. 3, pp. 363–369, 2007.

[12] S. M. Donahoe, G. C. Stewart, C. H. McCabe et al., "Diabetes and mortality following acute coronary syndromes," *Journal of the American Medical Association*, vol. 298, no. 7, p. 765, 2007.

[13] R. Huxley, F. Barzi, and M. Woodward, "Excess risk of fatal coronary heart disease associated with diabetes in men and women: meta-analysis of 37 prospective cohort studies," *BMJ*, vol. 332, no. 7533, pp. 73–78, 2005.

[14] R. Marfella, M. Siniscalchi, K. Esposito et al., "Effects of stress hyperglycemia on acute myocardial infarction: role of inflammatory immune process in functional cardiac outcome," *Diabetes Care*, vol. 26, no. 11, pp. 3129–3135, 2003.

[15] D. M. Yellon and J. M. Downey, "Preconditioning the myocardium: from cellular physiology to clinical cardiology," *Physiological Reviews*, vol. 83, no. 4, pp. 1113–1151, 2003.

Hindawi
Journal of Healthcare Engineering
Volume 2021, Article ID 3293457, 9 pages
https://doi.org/10.1155/2021/3293457

Research Article

Artificial Intelligence Algorithm with ICD Coding Technology Guided by the Embedded Electronic Medical Record System in Medical Record Information Management

Cheng Wang,[1] **Chenlong Yao**,[2] **Pengfei Chen**,[3] **Jiamin Shi**,[1] **Zhe Gu**,[1] **and Zheying Zhou**[1]

[1]*Medical History Room, Shanghai First Maternity and Infant Hospital, Shanghai 200000, China*
[2]*Department of Information, Children's Hospital Affiliated to Jiaotong University, Shanghai 200000, China*
[3]*Unionnet Co. Ltd., Shanghai 200000, China*

Correspondence should be addressed to Cheng Wang; 1751010011@xzyz.edu.cn

Received 29 June 2021; Revised 4 August 2021; Accepted 16 August 2021; Published 30 August 2021

Academic Editor: Enas Abdulhay

The study aims to explore the application of international classification of diseases (ICD) coding technology and embedded electronic medical record (EMR) system. The study established an EMR information knowledge system and collected the data of patient medical records and disease diagnostic codes on the front pages of 8 clinical departments of endocrinology, oncology, obstetrics and gynecology, ophthalmology, orthopedics, neurosurgery, and cardiovascular medicine for statistical analysis. Natural language processing-bidirectional recurrent neural network (NLP-BIRNN) algorithm was used to optimize medical records. The results showed that the coder was not clear about the basic rules of main diagnosis selection and the classification of disease coding and did not code according to the main diagnosis principles. The disease was not coded according to different conditions or specific classification, the code of postoperative complications was inaccurate, the disease diagnosis was incomplete, and the code selection was too general. The solutions adopted were as follows: communication and knowledge training should be strengthened for coders and medical personnel. BIRNN was compared with the convolutional neural network (CNN) and recurrent neural network (RNN) in accuracy, symptom accuracy, and symptom recall, and it suggested that the proposed BIRNN has higher value. Pathological language reading under artificial intelligence algorithm provides some convenience for disease diagnosis and treatment.

1. Introduction

With the improvement of living standards, people's attention to their health is also increasing. At the same time, they are concerned about the medical conditions and facilities of the hospital. The hospital will conduct statistical analysis and comparison of the annual medical data to form an indicator of medical quality management [1]. Most of the data in the medical industry come from electronic medical records (EMRs). EMR is also called computerized medical record system or computer-based patient record (CPR). It is a digital medical record saved, managed, transmitted, and reproduced by electronic devices (computers, health cards, etc.) to replace handwritten paper medical records. Its content includes all the information of paper medical records. The National Institute of Medicine defines EMR as an electronic patient record based on a specific system, which provides users with the ability to access complete and accurate data, warnings, prompts, and clinical decision support systems.

Through the extraction and statistical analysis of these data, relevant indicators are formed to provide convenience for medical personnel, which help them better understand the relevant medical conditions and improve the quality of medical care [2]. With the rise and wide application of computer network technology, its application in the medical industry is becoming more common. Most medical institutions use a unified medical record front page, which provides great convenience for the information statistics of the medical industry [3]. The medical record records the detailed condition of the patient, from the initial diagnosis to the final treatment result, which provides a detailed basis for the follow-up [4, 5]. The detailed record of the patient's condition in the medical record provides important support for medical staff to understand the patient's condition. Both the past medical history and the current diagnosis and treatment of diseases can be consulted [6]. With the development of electronic information on the Internet, case records have also changed from the original paper version to an electronic version, completing the digital management mode of medical records [7, 8]. Electronic cases have greatly improved the efficiency of using medical records. The use of EMRs provides convenience for medical staff and management staff.

ICD coding technology is a relatively complete and mature disease-coding method. Almost every hospital unit uses its rules to code diseases on the front page of medical records [9]. The combination of English and numbers is used for coding to avoid coding inconsistencies [10]. It promotes exchanges between people from different countries and regions. With the continuous improvement of disease classification by scholars, more and more disease types are covered [11]. The coding method is characterized by scientificity, integrity, applicability, and operability. Therefore, it is widely used in the field of medicine [12]. In clinical medicine, the use of LCD can bring great convenience, unify the code for global diseases, facilitate researchers' research, and contribute to the development of medicine.

In this experiment, the statistical analysis of the first page of medical records is conducted through the sample survey. The causes of errors in the disease classification on the first page of the medical record are analyzed and summarized. Meanwhile, the embedded medical record information knowledge system is established, and the NLP-BIRNN algorithm is used to optimize the medical record text. Also, the detailed improvement measures are proposed to provide a basis for the investigation of disease classification.

2. Materials and Methods

2.1. Experimental Materials. The data were randomly selected from the EMR database of our hospital, and the patient medical records and disease diagnostic code data on the front pages of 8 clinical departments of endocrinology, oncology, obstetrics and gynecology, ophthalmology, orthopedics, neurosurgery, and cardiovascular medicine were collected.

2.2. Case Statistics. The medical record information is randomly extracted from the EMR management system for analysis. Statistics on the diagnosis selection and the number of disease-coding errors are conducted. The statistical analysis of the data of clinicians and medical coders before and after training is performed. Through research, self-examination, training, and feedback, the disease-coding knowledge topics of the above eight clinical departments are explored. The coder calls up the medical record data of a certain department. According to ICD-10's undergraduate disease-coding rules, such as clinical knowledge and main diagnosis selection principles of the disease's physiological mechanism, development process, clinical manifestations, and treatment methods, the disease-coding process is conducted. During the coding process, the coder must carefully read the case, especially the admission records (judgment of the main diagnosis selection), surgical records (surgical name, postoperative method, surgical grade, surgical incision, and anesthesia method), course records (development of the disease, such as whether the disease is aggravated, whether it is improved, and whether it is treated), and discharge records (diagnosis and treatment process, whether the diagnosis at admission and discharge are consistent). Pathology, imaging, ultrasound, and laboratory reports should also be paid attention to.

2.3. Self-Examination and Training. According to the results, the coder reexamines the previous medical records, mainly checking the diagnosis selection and disease coding. Statistics on the data of diagnosis selection errors and disease-coding errors are conducted. Then, ICD-10 training will be given to the relevant doctors and coders of the above eight clinical departments on the problems examined this time.

2.4. Feedback. The coder compares and analyzes the data of main diagnosis selection errors and disease-coding errors before and after the training. The results are then shared to the relevant personnel with feedback, to explore rectification measures and improve the coding level.

2.5. Establishment of Embedded EMR Information Knowledge System. The system establishes conditions. First, conditions are written based on the writing standard of medical records stipulated by the national health department. The data content expressed in the medical record should be a common medical term without ambiguity. Second, the knowledge system must contain descriptive and conclusive knowledge about medical records. Descriptive knowledge refers to the detailed description of the disease. For example, the types of cold are wind chill and wind heat and their common symptoms are headache and cough, which is descriptive knowledge. On the contrary, it is conclusive knowledge to judge the type of cold according to the description of the disease. The knowledge system needs to combine the structured input interface of medical records and provide a selective input prompt based on the user input. Third, the medical record information is stored as an XML document, which has hierarchical structure. The knowledge base is also represented by the hierarchical XML document to achieve efficient synchronization of medical record input interface, which corresponds to the medical record information document. For some simple information input without prompt, the node can be set to null value. For items with multiple choices, multiple child nodes can be set when prompted, read into memory, and displayed in the medical record interface for users to choose. Fourth, the semantics should be concise and include the hints about limiting the use of characters.

The information base of the embedded medical record knowledge system contains knowledge, as shown in Table 1:

There are seven pages in the embedded EMR input system, and seven XML documents of medical record knowledge base are established accordingly. When doctors create a new medical record page, the system will automatically call the knowledge base XML document according to the current page. When doctors input specific document node information, they can input medical record information according to prompt operation to improve the recording speed and reduce expression errors.

2.6. Steps of NLP-BIRNN Algorithm. First, the data preprocessing of EMR is carried out, including data processing, cleaning, and screening.

Second, NLP based on medical tagging (medical record tagging, character extraction, word vector transformation, deep neural network, automatic tagging, and feature vector splicing) and NLP without medical tagging (no medical record, part of speech tagging, keyword selection, word vector transformation, and feature vector splicing) are performed.

Third, calculation is done. The symptom feature vectors involved in NLP solutions are normalized, and the values at each position of vector data are limited to [0, 1]. The ICD is coded by one hot representation to become the tag of deep learning training. The normalized feature vector and label are imported into the deep learning model for training, the auxiliary diagnosis model is obtained, and the test set is used to complete the test of the model results.

2.7. Data Analysis. The SPSS24.0 software was adopted for data statistics and analysis. The difference between the two groups of data was analyzed by the t-test. The count data were compared by the Chi-square test. $P < 0.05$ indicated significant difference, and $P < 0.01$ indicated highly significant difference.

3. Results

3.1. CT and Ultrasound Images of Some Diseases. At present, the diagnosis basis of 2019 novel coronavirus (2019-nCoV) is mainly nucleic acid testing and medical imaging detection. The combination of the two is more conducive to diagnosis. It is found from the announcement of officially confirmed cases that some patients showed a positive result after more than 2 nucleic acid tests and even showed a positive result after the fifth nucleic acid test. Therefore, while performing nucleic acid testing, lung CT imaging examination is carried out. Patients with lung CT presenting with signs of acute inflammation should be admitted as soon as possible in accordance with the principle of "suspected disease is always present." The CT and ultrasound results of some diseases are shown in Figure 1. Figure 1(a) is a chest CT image of coronavirus disease 2019 (COVID-19). Figure 1(b) is a segmented image of the pneumonia-infected area. Figure 1(c) is a CT of the abdomen. The accuracy of diagnosing the mild fatty liver using CT is 88.75%. Figure 1(d) is an ultrasound image of the abdomen. The accuracy of diagnosing the mild fatty liver using ultrasound is 73.75%. It shows that CT diagnosis is more accurate than ultrasound diagnosis.

3.2. Results of Main Diagnosis Selection Errors and Disease-Coding Errors of the Obstetrics and Gynecology Department. Results of main diagnosis selection errors and disease-coding errors of the obstetrics and gynecology department are shown in Figure 2. Figure 2(a) is the results of the main diagnosis selection errors. There are 280 errors in the discharge case statistics before the training and 80 errors after the training. The statistics on the four types of main diagnosis selection errors are conducted, including that C-section is the main diagnosis, singleton live birth diagnosis is the first, tumor morphological coding is the main diagnosis, and major treatable diseases are not major diagnosed. It is found that the difference in each index between groups before and after training is significant ($P < 0.05$). Figure 2(b) is the results of disease-coding errors. There are 240 errors in the discharge case statistics before the training and 60 errors after the training. The statistics on the four types of disease-coding errors of pregnancy hypertension, premature rupture of membranes, tumors, and mass, and vomitus gravidarum are conducted. It is found that the difference in each index between groups before and after training is significant ($P < 0.05$).

3.3. Results of Main Diagnosis Selection Errors and Disease-Coding Errors of the Endocrinology Department. Results of the main diagnosis selection errors and disease-coding errors of the endocrinology department are shown in Figure 3. Figure 3(a) is the results of the main diagnosis selection errors. There are 180 errors in the discharge case statistics before the training and 50 errors after the training. The statistics on the three types of main diagnosis selection errors are conducted, including that the treatment of the disease is not a major diagnosis, multiple complications are not primarily diagnosed, and no major diagnosis is made for a single complication. It is found that the difference in each index between groups before and after training is significant ($P < 0.05$). Figure 3(b) is the results of disease-coding errors. There are 160 errors in the discharge case statistics before the training and 30 errors after the training. The statistics on the five types of disease-coding errors are conducted, including the merge coding error, no additional coding used, neonatal diabetes mellitus, gestational diabetes mellitus, and screening for diabetes. It is found that the difference in each index between groups before and after training is significant ($P < 0.05$).

3.4. Results of Main Diagnosis Selection Errors and Disease-Coding Errors of the Orthopedics Department. Results of the main diagnosis selection errors and disease-coding errors of the orthopedics department are shown in Figure 4.

Table 1: Content of database construction of the embedded medical record knowledge system.

Descriptive knowledge of disease	Terms of disease characteristics and selection of entry
Conclusive knowledge of disease	Keywords given for pathological conclusion are given
Normative data content	Age
XML document input information	Restrictions on character entry

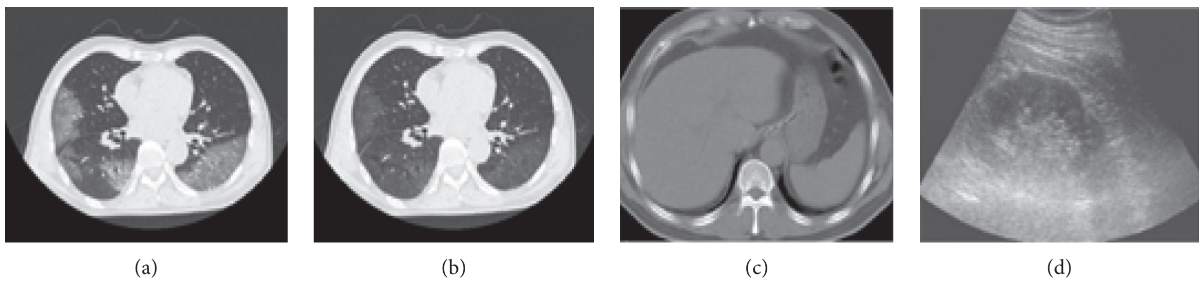

Figure 1: CT and ultrasound images. (a) The chest CT image of COVID-19 cases. (b) The segmented image of the pneumonia-infected area. (c) CT of the abdomen. (d) Ultrasound of the abdomen.

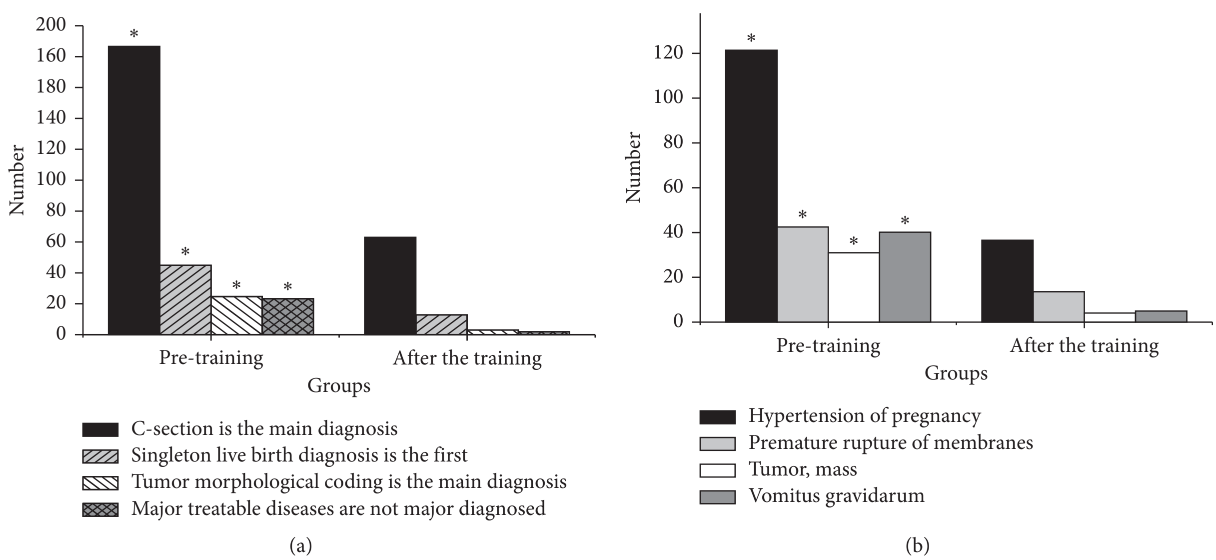

Figure 2: (a) Main diagnosis selection errors and (b) disease-coding errors of the obstetrics and gynecology department ($^*P < 0.05$).

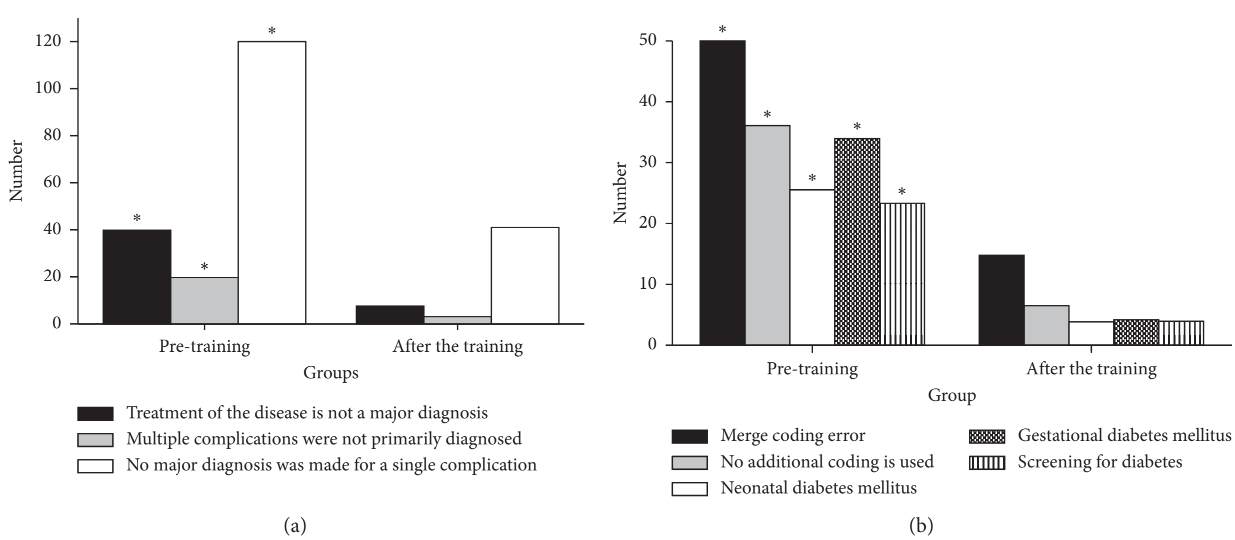

Figure 3: (a) Main diagnosis selection errors and (b) disease-coding errors of the endocrinology department ($^*P < 0.05$).

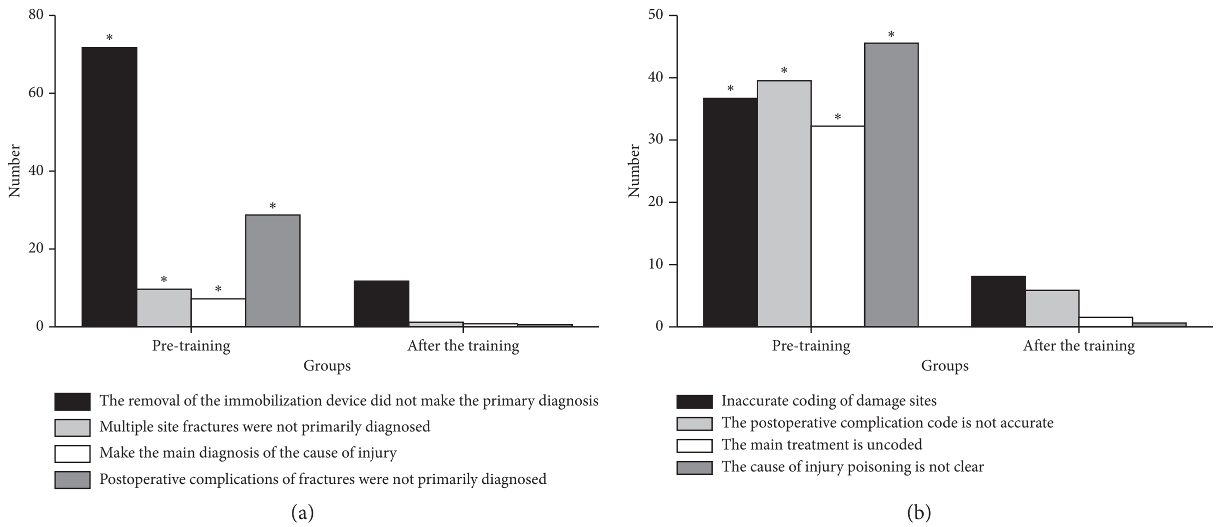

Figure 4: (a) Main diagnosis selection errors and (b) disease-coding errors of orthopedics department ($^{*}P < 0.05$).

Figure 4(a) is the results of the main diagnosis selection errors. There are 120 errors in the discharge case statistics before the training and 30 errors after the training. The statistics on the four types of main diagnosis selection errors are conducted, including that the removal of the immobilization device does not make the primary diagnosis, multiple site fractures are not primarily diagnosed, the main diagnosis is made for the cause of injury, and postoperative complications of fractures are not primarily diagnosed. It is found that the difference in each index between groups before and after training is significant ($P < 0.05$). Figure 4(b) is the results of disease-coding errors. There are 160 errors in the discharge case statistics before the training and 25 errors after the training. The statistics on the four types of disease-coding errors are conducted, including that the coding of damage sites is inaccurate, the postoperative complication coding is not accurate, the main treatment is uncoded, and the cause of injury poisoning is not clear. It is found that the difference in each index between groups before and after training is significant ($P < 0.05$).

3.5. Results of Main Diagnosis Selection Errors of the Oncology and Neurosurgery Department. Results of the main diagnosis selection errors of the oncology and neurosurgery department are shown in Figure 5. Figure 5(a) is the results of the main diagnosis selection errors of oncology. There are 260 errors in the discharge case statistics before the training and 60 errors after the training. The statistics on the four types of main diagnosis selection errors are conducted, including that the primary diagnosis of the tumor is not made in Z code, using Z code to make the primary diagnosis is inaccurate, major diagnosis is not made for the major treatment of disease, and tumor morphology code is the main diagnosis. It is found that the difference in each index between groups before and after training is significant ($P < 0.05$). Figure 5(b) is the results of the main diagnosis selection errors of the neurosurgery department. There are 180 errors in the discharge case statistics before the training and 50 errors after the training. The statistics on the five types of main diagnosis selection errors are conducted, including that the main diagnosis is head trauma, tumor morphological code is not written, the rehabilitation Z code is not used, coding of disease sites is inaccurate, and the cause of injury poisoning is not written. It is found that the difference in each index between groups before and after training is significant ($P < 0.05$).

3.6. Results of Disease-Coding Errors of Cardiovascular Medicine, Burns Surgery, and Ophthalmology Departments. Results of disease-coding errors of cardiovascular medicine, burns surgery, and ophthalmology departments are shown in Figure 6. Figure 6(a) is the results of the coding errors of the cardiovascular medicine department. There are 420 errors in the discharge case statistics before the training and 180 errors after the training. The statistics on the five types of disease-coding errors are conducted, including arrhythmia, myocardial infarction (MI), coronary heart disease (CHD), sudden coronary death (SCD), and myocardial ischemia. It is found that the difference in each index between groups before and after training is significant ($P < 0.05$). Figure 6(b) is the result of disease-coding errors of the burns surgery department. There are 170 errors in the discharge case statistics before the training and 35 errors after the training. The statistics on the seven types of disease-coding errors are conducted, including that multiple burns are the main diagnosis, the burn degree and area not written, the burn site is not filled in accurately, scald/burn is not written clearly, coding of chilblain and frostbite is confusing, burn complications are coded, and the cause of injury poisoning is not coded. It is found that the difference in each index between groups before and after training is significant ($P < 0.05$). Figure 6(c) is the results of disease-coding errors of the ophthalmology department. There are 160 errors in the discharge case statistics before the training and 30 errors after the training. The statistics on the five types of disease-coding errors are conducted, including that the diagnosis of

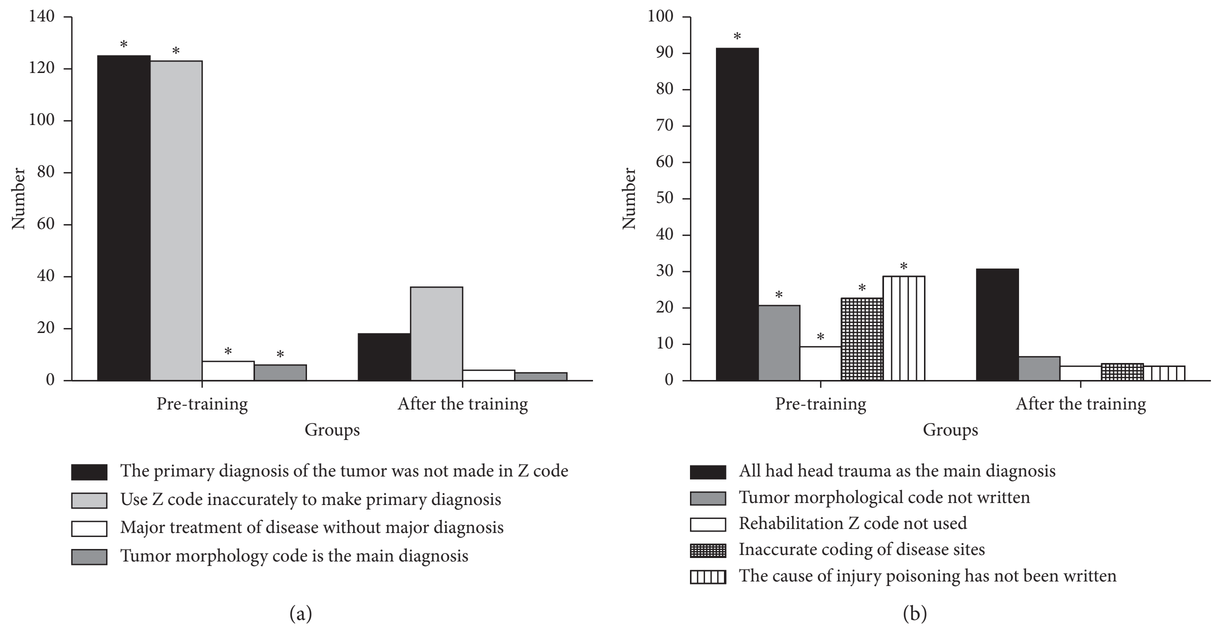

Figure 5: Main diagnosis selection errors of (a) oncology and (b) neurosurgery ($^{*}P < 0.05$).

the disease is filled incompletely, the disease diagnosis name localization is not accurate, coding choices are too general, the diagnosis name is not detailed, and the disease is not coded according to coding principles. It is found that the difference in each index between groups before and after training is significant ($P < 0.05$).

3.7. Automatic Annotation Results of the Medical Record Language. The results of automatic annotation of the medical record language under different artificial intelligence algorithms are statistically analyzed (Figure 7).

Figure 7 indicates that the accuracy rate, symptom precision, and symptom recall of BIRNN are higher than those of CNN and RNN, which indicates that BIRNN has better automatic annotation effect of pathological language.

4. Discussion

In medicine, disease classification reflects the medical level of a hospital to a certain extent. Disease classification refers to the scientific classification of various diseases through coding to provide a basis for clinical diagnosis and treatment. Hospital requirements for accurate classification of diseases have also increased the requirements for disease coders [13, 14]. EMR is defined in *The Basic Framework and Data Standard Electronic Medical Record of Electronic Medical Record* issued by the Ministry of Health as follows: an electronic medical record is a digital medical service record of clinical diagnosis and treatment, guidance, and intervention of outpatients and inpatients (or health care objects) by medical institutions. Studies have shown that coders need to collect, classify, organize, analyze, and use medical record information through the criteria for disease classification. It requires coders to fully understand the clinical knowledge of various diseases [15–17]. This experiment analyzes the reasons for the main diagnosis selection error. The coders are not familiar with the basic rules of the main diagnosis selection, which leads to the misunderstanding of the main diagnosis as an outpatient diagnosis. The classification of disease codes is unclear, and it is believed that the same names have the same codes. The result is the same as that of Nhut Pham et al. [18]. It is difficult to make accurate main diagnosis selection for situations with multiple diseases at the same time. Complications are not the main diagnosis. The morphological coding is mistaken as the main diagnosis. Some studies have found that some coders do not code according to specific medical purposes [19]. The classification of the treatment period and the recovery period is unclear. The disease is not coded according to the main diagnosis principles. It is wrong to regard some damage causes as the main diagnosis. Other investigations have found that when multiple fractures occur, some coders will mistake a certain fracture as the main diagnosis, causing errors [20]. When there is a complication, the previous disease is mistaken as the main diagnosis. The most serious injury is not taken as the main diagnosis. Rehabilitation treatment is not taken as the main diagnosis. The coding of many kinds of diseases is not detailed and accurate.

The experiment analyzes the causes of disease-coding errors. There is no merge coding for diseases that should be merged. Studies have found that coding undiagnosed diseases according to diagnosed diseases is also one of the reasons for coding errors [21]. When accompanied by complications, accurate coding is not performed. Patients of different ages are not coded differently. Drug-induced diseases are not coded correctly. The diseases are not coded according to different conditions. This is consistent with the results of Mahajan et al. [22]. The diseases are not coded according to different sites and different onset times. The

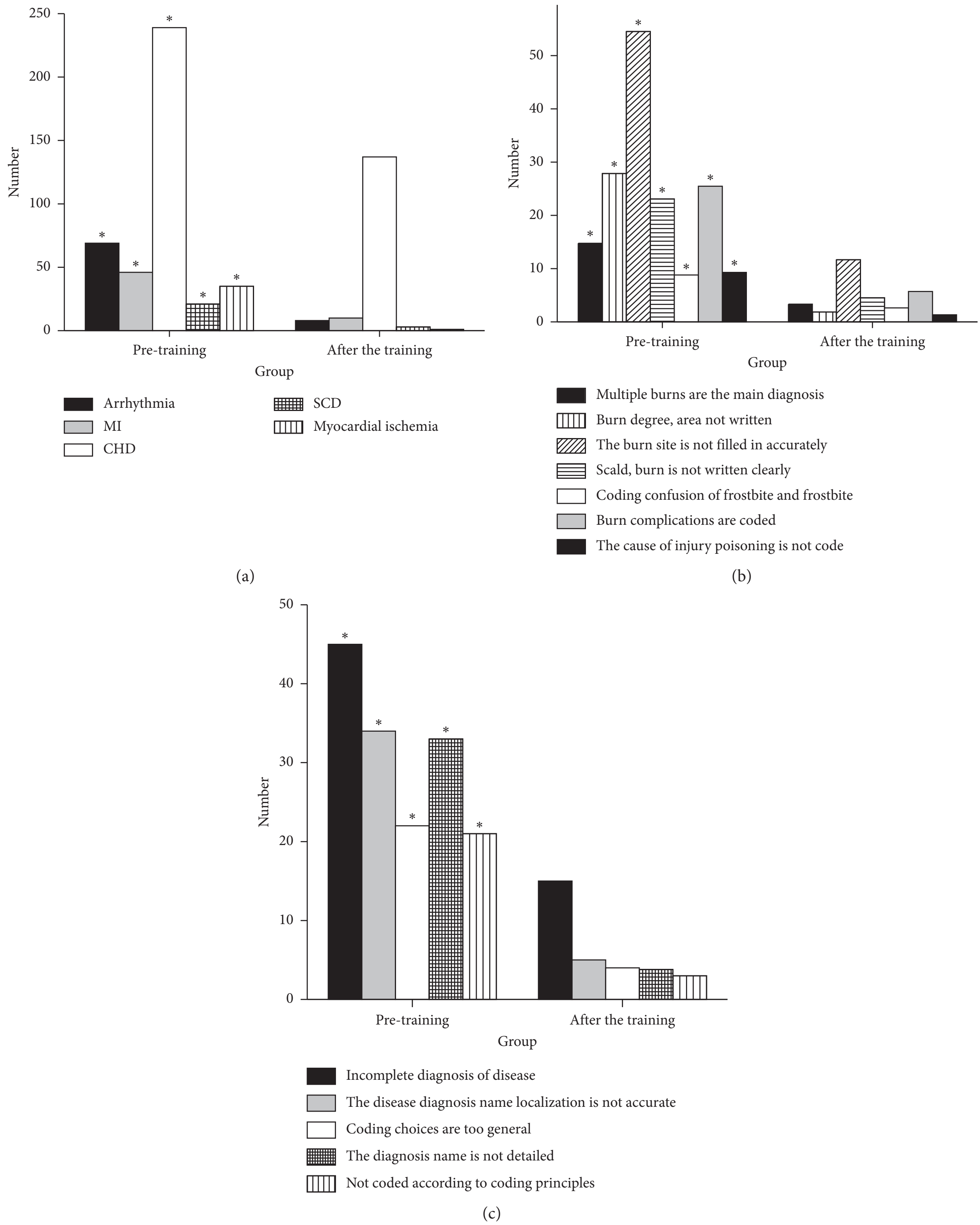

Figure 6: Disease-coding errors of (a) cardiovascular medicine, (b) burns surgery, and (c) ophthalmology departments ($^*P < 0.05$).

diseases are not coded according to the specific classification and according to cause. When coding, it is not carried out in the order of first determining the site and then looking at the severity of the disease. Postoperative complication codes are inaccurate. The coding is not performed according to diagnostic purposes. The filling of the disease diagnosis is incomplete. The name of the disease diagnosis site is inaccurate. Coding selection is too general. The solutions to these problems are as follows. The relevant knowledge training is provided for coders and clinicians. The doctors are regulated to fill in medical record templates. The communication is enhanced between coders and medical

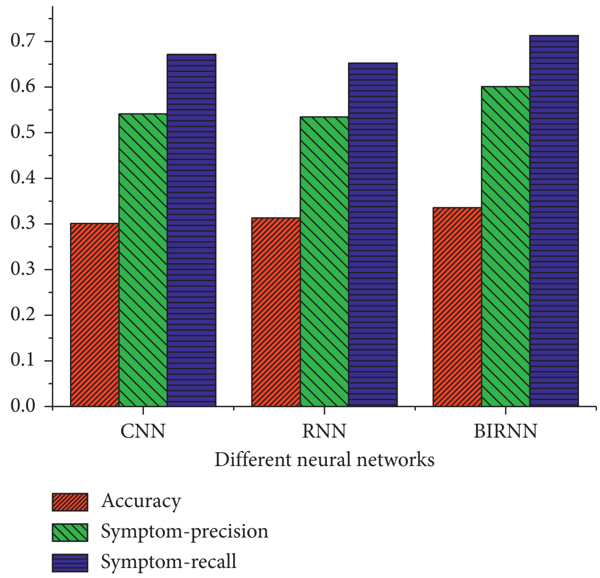

Figure 7: Performance comparison of different artificial intelligence algorithms.

staff. The new coding requirements should be mastered at any time. Tanno et al. [23] reviewed the history of changes in the classification and coding of allergic reactions and found that better ICD codes could reduce the mortality of allergic diseases.

This experiment shows that the main reason for the main diagnosis selection errors and coding errors for coders is that they do not fully understand the various diseases and their classification. Therefore, relevant training in this area should be strengthened.

5. Conclusion

The study analyzes the reasons for the wrong selection of main diagnosis before and after training in obstetrics and gynecology, endocrinology, oncology, orthopedics, and neurosurgery, as well as the wrong disease coding in these departments. It is found that the statistical errors of various diseases before and after training are significantly different between the groups. It shows that the coding personnel do not have a thorough understanding of various diseases and their specific classification, and the medical staff cannot clearly fill in the medical records of diseases. Therefore, the relevant training of coders and medical personnel should be strengthened. However, there are also some shortcomings, such as the small number of samples. Later, the scope of sample collection can be expanded to provide some support for the main diagnosis selection and disease-coding research.

Data Availability

The data used to support the findings of this study are available from the corresponding author upon request.

Conflicts of Interest

The authors declare no conflicts of interest.

References

[1] M. A. Alkureishi, W. W. Lee, M. Lyons et al., "Impact of electronic medical record use on the patient-doctor relationship and communication: a systematic review," *Journal of General Internal Medicine*, vol. 31, no. 5, pp. 548–560, 2016.

[2] A. Goyal, T. J. Gluckman, and J. E. Tcheng, "What's in a name?" *Circulation*, vol. 136, no. 13, pp. 1180–1182, 2017.

[3] Y. Halpern, S. Horng, Y. Choi, and D. Sontag, "Electronic medical record phenotyping using the anchor and learn framework," *Journal of the American Medical Informatics Association*, vol. 23, no. 4, pp. 731–740, 2016.

[4] Y. Chen, H. Lu, and L. Li, "Automatic ICD-10 coding algorithm using an improved longest common subsequence based on semantic similarity," *PLoS One*, vol. 12, no. 3, Article ID e0173410, 2017.

[5] Z. Jia, W. Qin, H. Duan, X. Lv, and H. Li, "A hybrid method for ICD-10 auto-coding of Chinese diagnoses," *Studies in Health Technology and Informatics*, vol. 245, no. 4, pp. 427–431, 2017.

[6] A. Segolene, B. Bellet, and A. Rath, "Rare diseases in ICD11: making rare diseases visible in health information systems through appropriate coding," *Orphanet Journal of Rare Diseases*, vol. 10, no. 1, pp. 1–14, 2015.

[7] G. Tyler and C. Christopher, "ICD-10:A primer for the orthopedic foot and ankle surgeon," *Foot & Ankle International*, vol. 36, no. 9, pp. 1110–1116, 2015.

[8] S. Tim, "Library management for the digital age: a new paradigm," *Technical Services Quarterly*, vol. 33, no. 12, pp. 322–324, 2015.

[9] H. Lu, R. Setiono, and H. Liu, "Effective data mining using neural networks," *IEEE Transactions on Knowledge and Data Engineering*, vol. 8, no. 6, pp. 957–961, 2016.

[10] K. M. Heiden-Rootes, J. Salas, S. Gebauer et al., "Sexual dysfunction in primary care: an exploratory descriptive analysis of medical record diagnoses," *The Journal of Sexual Medicine*, vol. 14, no. 11, pp. 1318–1326, 2017.

[11] T. H. Neville, D. M. Tarn, M. Yamamoto, B. J. Garber, and N. Wenger, "Understanding factors contributing to inappropriate critical care: a mixed-methods analysis of medical record documentation," *Journal of Palliative Medicine*, vol. 17, Article ID 0023, 2017.

[12] M. H. Amir, A. W. Bayu, Tommy, A. Marwan, and R. Siregar, "Performance analysis of AES-Blowfish hybrid algorithm for security of patient medical record data," *Journal of Physics: Conference Series*, vol. 1007, no. 2, Article ID 012018, 2018.

[13] Y. Chen, N. M. Lorenzi, W. S. Sandberg, K. Wolgast, and B. A. Malin, "Identifying collaborative care teams through electronic medical record utilization patterns," *Journal of the American Medical Informatics Association*, vol. 24, no. e1, pp. e111–e120, 2016.

[14] P. Li, C. Xie, T. Pollard et al., "Promoting secondary analysis of electronic medical records in China: summary of the PLAGH-MIT critical data conference and health datathon," *JMIR Medical Informatics*, vol. 5, no. 4, p. e43, 2017.

[15] M. B. Mayhew, B. K. Petersen, A. P. Sales, J. D. Greene, V. X. Liu, and T. S. Wasson, "Flexible, cluster-based analysis of the electronic medical record of sepsis with composite mixture models," *Journal of Biomedical Informatics*, vol. 78, 2017.

[16] R. K. Hernandez, S. W. Wade, A. Reich, M. Pirolli, A. Liede, and G. H. Lyman, "Incidence of bone metastases in patients with solid tumors: analysis of oncology electronic medical records in the United States," *BMC Cancer*, vol. 18, no. 1, p. 44, 2018.

[17] X. Ma, X. Zhai, J. Liu et al., “Study on the biological basis of hypertension and syndrome with liver-fire hyperactivity based on data mining technology,” *Pro Quest*, vol. 4, no. 4, pp. 176–180, 2018.
[18] N. M. Nhut Pham, V. S. Le, and H. H. C. Nguyen, “Energy efficient resource allocation for virtual services based on heterogeneous shared hosting platforms in cloud computing,” *Cybernetics and Information Technologies*, vol. 17, no. 3, pp. 47–58, 2017.
[19] J. Zhang, “UtEnables collaborative decision making between healthcare providers and patients,” *Diabetes Technology amp; Therapeutics*, vol. 18, no. 2, pp. 59–67, 2016.
[20] T. Song, “Ronowimanufacturing process based on a decision tree algorithm,” *European Journal of Pharmaceutical Sciences*, vol. 73, pp. 44–48, 2015.
[21] C. Boettiger, “An introduction to Docker for reproducible research,” *ACM SIGOPS–Operating Systems Review*, vol. 49, no. 1, pp. 71–79, 2015.
[22] D. Mahajan, C. Blakeney, and Z. Zong, “Improving the energy efficiency of relational and NoSQL databases via query optimizations,” *Sustainable Computing: Informatics and Systems*, vol. 22, no. 1, pp. 120–133, 2019.
[23] L. K. Tanno, R. Chalmers, A. L. Bierrenbach et al., “Changing the history of anaphylaxis mortality statistics through the world health organization’s international classification of diseases-11,” *The Journal of Allergy and Clinical Immunology*, vol. 144, no. 3, pp. 627–633, 2019.

Hindawi
Journal of Healthcare Engineering
Volume 2021, Article ID 1148309, 8 pages
https://doi.org/10.1155/2021/1148309

Research Article

Deep Learning for Intelligent Recognition and Prediction of Endometrial Cancer

Yan Zhang,[1] **Cuilan Gong**,[2] **Ling Zheng**,[1] **Xiaoyan Li**,[1] **and Xiaomei Yang**[2]

[1]*Department of Obstetrics, Huangdao District Hospital of Traditional Chinese Medicine, Qingdao 266500, China*
[2]*Department of Gynaecology, Huangdao District Chinese Medicine Hospital, Qingdao 266500, China*

Correspondence should be addressed to Xiaomei Yang; 1410601307@stu.cque.edu.cn

Received 27 June 2021; Accepted 29 July 2021; Published 26 August 2021

Academic Editor: Enas Abdulhay

The aim of the study was to investigate the intelligent recognition of radiomics based on the convolutional neural network (CNN) in predicting endometrial cancer (EC). In this study, 158 patients with EC in hospital were selected as the research objects and divided into a training group and a test group. All the patients underwent magnetic resonance imaging (MRI) before surgery. Based on the CNN, the imaging model of EC prediction was constructed according to the characteristics. Besides, the comprehensive prediction model was established through the clinical information and imaging parameters. The results showed that the area under the working characteristic curve (AUC) of the radiomics model and comprehensive prediction model was 0.897 and 0.913 in the training group, respectively. In addition, the AUC of the radiomics model was 0.889 in the test group and that of the comprehensive prediction model was 0.897. The comprehensive prediction model was established through specific imaging parameters and clinical pathological information, and its prediction performance was good, indicating that radiomics parameters could be applied as noninvasive markers to predict EC.

1. Introduction

EC is a group of epithelial malignant tumors that occur in the endometrium, the most frequent is adenocarcinoma originating from the endometrial glands [1]. What is more, EC often emerges in postmenopausal and perimenopausal women. It is one of the most common tumors of the female reproductive system, with nearly 200,000 new cases every year [2]. Among the gynecological malignant tumors that cause death, it ranks third after ovarian cancer and cervical cancer. With the rapid development of social economy, the incidence of EC is gradually increasing in China, and it is the second place among malignant tumors [3]. At present, the cause of EC is still unclear. Some scholars have pointed out that its risk factors are related to fertility, hormones, metabolism, and physiological behavior [4]. Endometrial hyperplasia is the pathological change of the endometrium before canceration and has the potential to deteriorate. The morphology of atypical endometrial hyperplasia is similar to that of EC, and it is difficult to distinguish in clinical diagnosis [5]. Based on the danger of endometrial hyperplasia and the difficulty of clinical diagnosis, it is necessary to find a method that can intelligently identify normal endometrial, endometrial hyperplasia, and endometrial cancerous tissues.

The artificial neural network (ANN) is an artificial intelligence method that attempts to simulate the function of the human brain [6]. The convolutional neural network (CNN) is an artificial intelligence method that attempts to simulate the function of the human brain [6]. Based on the combination of biology and neurology, deep learning technology is a kind of the deep network model with hierarchical structure constructed by simulating the hierarchical working mode of the human brain visual system, which is inspired by the field of the human brain visual nerve [7]. What is more, the CNN is a derived ANN with the characteristics of hierarchical structure, extracting features, perceiving local areas, and classification due to a perfect combination of the ANN and deep learning technology [8]. The task requirement of modern image recognition is that the classification system can adapt to different kinds of recognition requirements, and the CNN has become a hot topic in the field of the ANN because of its high-efficiency recognition advantages. MRI is a medical imaging technique applied in radiology, which employs the combined action of a strong magnetic field, magnetic field gradients, and silent electric waves to form images of human organs to analyze the physiological processes or anatomy of the body image [9]. The radiomics is the most widely applied in the oncology, which includes tumor classification, shunt staging, and prognosis prediction. Ge et al. [10] combined the parameters of CT radiomics with clinicopathological characteristics for investigation, established a preoperative prediction model for EC, and verified the application value of this model in clinical diagnosis.

In this study, radiomics based on CNN modeling was adopted to intelligently identify the normal, hyperplastic, and cancerous tissues of the endometrium, providing a new method for clinical prediction of the emerging and development of EC.

2. Materials and Methods

2.1. Research Objects. In this study, 158 patients with EC, who underwent staged surgery in hospital from October 17, 2018, to May 21, 2020, were selected as the research objects and divided into the training group and the test group (79 cases in each group), with an average age of 56.9 ± 17.5 years. The medical ethics committee of hospital had approved this experiment, and each patient and his or her family members had understood the situation of this experiment and signed the informed consent form.

The criteria for inclusion were defined to include patients who were diagnosed with EC after surgery, had no contraindications to MRI scanning, were younger than 70 years old, and had clear consciousness for normal examination.

The criteria for exclusion were defined to include patients who suffered from mental disorders, had other malignant tumors such as cervical cancer, had incomplete clinical data, withdrew from this experiment due to their own reasons, and had poor MRI image quality for difficult recognition of the lesion.

2.2. Research Methods for Intelligent Recognition of Endometrial Cancer. Each patient underwent sagittal T1- and T2-weighted images of pelvic enhanced MRI before surgery. The CNN model was constructed, the imaging model for EC prediction was screened out based on features, and the comprehensive prediction model for EC was established based on clinical pathological information and imaging parameters. The patient's region of interest (ROI) was drawn, and the AUC, sensitivity, specificity, and accuracy were applied to evaluate the diagnostic effect of the constructed model, and its effect was verified in patients of the test group.

2.3. Dynamic Enhancement Magnetic Resonance Scanning. In this study, the MR Prisma 3.0 magnetic resonance instrument produced by Siemens, Germany, was employed to examine the patients. Before the scanning, the examination procedure should be described in detail to the patients. They should be in the supine position and maintain steady breathing. After MRI scanning, a high-pressure syringe was adopted to inject a 0.2 mmol/L contrast enhancer gadolinium-diethylenetriamine pentaacetic acid (Gd-DTPA) through the back of the hand vein at an injection rate of 2.5 mL/s. Then, the same amount of normal saline was injected. The scanning parameters were as follows. The matrix was 251×251, the layer thickness was 3.5 mm, the field of view was 25×25 cm, the flip angle was 15°, and the layer spacing was 6.1 mm. The obtained dynamic enhanced magnetic resonance images were sent to the workstation, and the images were processed by Functool II software.

2.4. Steps of the Back-Propagation Algorithm. Under the principle of gradient descent, the back-propagation (BP) algorithm searched for the minimum value on the error surface. The iterative process of each BP was divided into two steps. The first step was that an output result was generated during propagation before inputting the data. The second step was that the corresponding weights in the network were adjusted by back propagation to compute errors. The feedforward process and BP process were alternated, and the error was less than the set value or the time of iterations that reaches a set value unless the output result of the network reached a preset condition. For the multicategory classification problem with B categories and M training examples, the error function is

$$F^M = \frac{1}{2}\sum_{m=1}^{M}\sum_{k=1}^{B}\left(p_k^m - q_k^m\right)^2. \tag{1}$$

In equation (1), p_k^m represents the target value corresponding to the k^{th} dimension in the m^{th} sample, and q_k^m stood for the network output value corresponding to k^{th} dimension in the m^{th} input. The error of the whole dataset was the sum of all single data errors. The BP of a single sample could be expressed as the following equation.

$$F^m = \frac{1}{2}\sum_{k=1}^{B}\left(p_k^m - q_k^m\right)^2 = \frac{1}{2}\left\| p^m - q^m \right\|_2^2. \tag{2}$$

In equation (2), p_k^m expresses the target value corresponding to the k^{th} dimension in the m^{th} sample, and q_k^m stood for the network output value corresponding to k^{th} dimension in the m^{th} input. For a normal full connection layer, the partial derivative of F relative to corresponding network weight could be calculated by the following form of the back-propagation rule. The output equation of the input layer is as follows.

$$x^r = g\left(v^r\right), \text{there into } v^r = W^r x^{r-1} + c^r. \tag{3}$$

In equation (3), r represents the current layer, the output layer was defined as the R layer, and the input layer was specified as the 1st layer.

The basic idea of the gradient learning algorithm was to find the error, calculate the partial derivative of parameters in the CNN, and identify the "error" in the BP network as the error signal of each unit pair's deviation. Besides, the equation could be as follows.

$$\frac{\partial F}{\partial c} = \frac{\partial F}{\partial v}\frac{\partial v}{\partial c} = \delta. \tag{4}$$

In equation (4), $(\partial F/\partial c)$ represents the partial derivative of the error with respect to the network parameter, and $(\partial v/\partial c)$ was equal to 1. Therefore, the error signal was equal to the error relative to all the input partial derivatives of a unit. For R layer of the input layer, the partial derivative equation is obtained as follows.

$$\delta^R = g'\left(v^R\right) \circ \left(q^m - p^m\right). \tag{5}$$

In equation (5), R represents the input layer, and "$\circ$" expresses the point-by-point product. The partial derivative δ^R was back-propagated from the upper layer through the network, and its equation could be shown as follows.

$$\delta^r = \left(w^{r+1}\right)^T \delta^{r+1} \circ g'\left(v^r\right). \tag{6}$$

In equation (6), δ^r represents the partial derivative, and "$\circ$" expresses the point-by-point product. Finally, the rule of the weight of a certain neuron for updating was that the neuron was input and multiplied by its triangular array. It was represented by a vector, which was the outer product of the input vector and the error signal vector, as shown in the following equations.

$$\frac{\partial F}{\partial W^r} = x^{r-1}\left(\partial^r\right)^T, \tag{7}$$

$$\Delta W^r = -\xi \frac{\partial F}{\partial W^r}. \tag{8}$$

Corresponding to the deviation c of equation (4), each weight W_{ij} usually had a corresponding ξ_{ij} in practical applications.

2.5. Structure of the Convolutional Neural Network Model. The network structure of LeNet-5 was adopted in this study, and the input data were a matrix formed by 32×32 pixels. The first feature image layer included 6 feature maps, and a 5×5 window was applied to convolve the input image, so as to obtain a 28×28 feature map. Then, it entered the first downsampling layer, and the first feature image layer was for downsampling operations to obtain 6 feature maps with a size of 14×14. The C3 layer was a convolutional layer, and the size of its convolution kernel was 5×5, which was the same as that of the C1 layer. It entered the S4 layer to continue the downsampling operation. The S4 layer was for convolutional operation by the C5 layer, and a fully connected method was adopted to perform convolution operations on the convolution kernel of each C5 layer on the basis of the S4 feature map. The C5 layer included 120 feature maps with a size of 1×1, and finally, the process of feature extraction was ended. Then, the result of 1×10 result was eventually output through a fully connected network on the basis of the C5 layer. In the vector whose output was 1×10, the classification result output by the network was the position corresponding to the largest component (Figure 1).

2.6. Data Preprocessing and the Convolutional Neural Network Model. In order to accelerate the convergence speed of the training algorithm, data preprocessing techniques were often adopted, including noise removal, dimensionality reduction of input data, and deletion of irrelevant data. Balanced data were very crucial in classification, and it was often considered that the data in the training set should be approximately evenly distributed relative to the label category. In order to balance the dataset, some redundant classification data should be appropriately removed, and some classification data with rare examples should be supplemented as much as possible.

CNN applied the structure that was the same as that of LeNet-5, but the following modifications had to be made. First, the tanh function should be employed to the output values of all layers in the network in LeNet-5, including the output layer results in the interval [0, 1], and the activation function applied in the CNN was the sigmoid function. Second, the radial basis function network structure was adopted in LeNet-5, and the CNN output layer was connected with the C5 layer to omit the F6 layer, so as to employ the fully connected method. Third, LeNet-5 applied a special learning rate sequence, and the learning rate during CNN training was fixed at 0.002. Fourth, the input data size of LeNet-5 was 28×28, while the CNN adopted the border filling method to expand the size to 32×32.

2.7. Technical Process of Radiomics. There was the technical process of radiomics, including 4 steps. The first step was to acquire images. Up to now, the images applied in radiomics research included MRI, computed tomography (CT), positron emission tomography (PET), and ultrasound. The second step was the image segmentation. The ROI or focus was sketched to prepare for the next feature extraction. The frequently applied segmentation methods included automatic, manual, and semiautomatic segmentation. The third step was to extract the image features. The extraction of image features was one of the critical steps of radiomics, which was to extract image features from the segmented ROI with high throughput to achieve the transition from image to quantitative data. At present, image extraction features contained morphological features and nonmorphological features. Morphological features described the shape, size, and location of lesions through traditional imaging methods. In addition, nonmorphological features included first-order, second-order, and high-order features. First-order features described the statistical distribution of each voxel, such as statistical features (mean, median, and skewness) generated through histograms; second-order features were texture features that described the relationship between voxels and reflect tumor abnormalities; and high-order features included wavelet features and fractal analysis. The fourth step was to analyze data and build models. The extracted image features were combined with statistics, pathological features, clinical data, and other information to construct an imaging prediction model that was suitable for clinical application. The specific radiomics flowchart is shown in Figure 2.

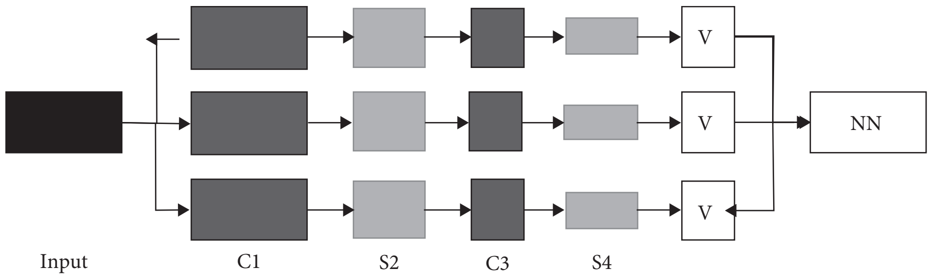

Figure 1: The structure of the CNN model.

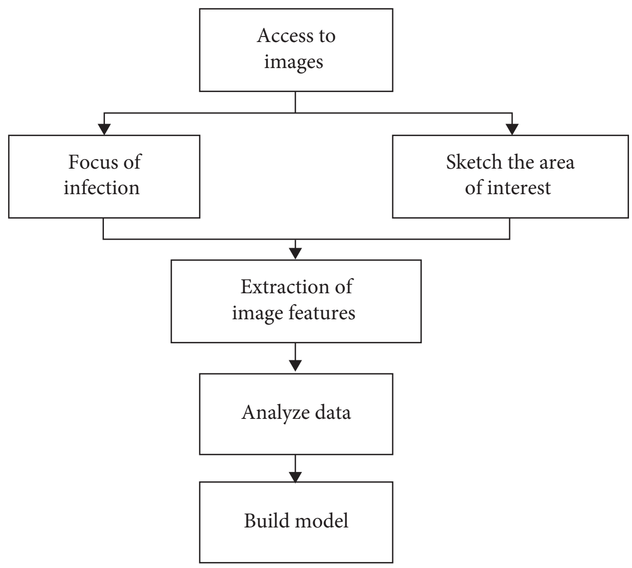

Figure 2: Technical process of radiomics.

2.8. Statistical Methods. The data processing of this study was analyzed by SPSS19.0 version statistical software. The measurement data conforming to the normal distribution were expressed by the mean ± standard deviation ($\overline{x} \pm s$), and the nonconforming measurement data were represented by frequency (%). The accuracy, sensitivity, and specificity were collected in the prediction of the radiomics model and the comprehensive prediction model. $P < 0.05$ revealed that the difference was statistically obvious.

3. Results

3.1. Feature Distribution of all Patients. The patients were grouped into the training group and the test group, so as to investigate the feature distribution of patients in the two groups. There was no statistical difference in the feature distribution among patients in the two groups. Figure 3 shows the comparison results of high-risk and low-risk data of preoperative biopsy pathology among patients in both groups. Moreover, there were comparisons on the normal and rising levels of CA125 in serums among patients in the two groups (Figure 4).

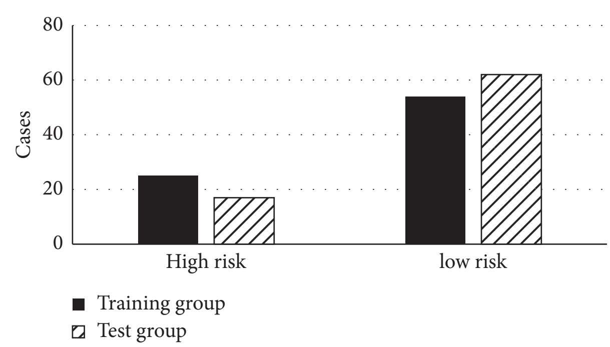

Figure 3: Pathological comparison of preoperative biopsy among patients in the test and training groups.

3.2. Imaging Features of Endometrial Cancer. The MRI imaging manifestations of each stage of EC were best shown on sagittal T2WI, which could clearly reflect the anatomical structure of the uterus. The typical manifestations were as follows. The endometrium was widened, the endometrial cavity was expanded, there were medium or low signal areas mixed with nodules in the high signal endometrial cavity, and larger masses presented different signal intensities due to necrosis, bleeding, and other reasons.

Endometrial hyperplasia was manifested as diffuse lesions in the uterine cavity, the endometrial was uniform and extensively thickened, diffusion weighted imaging (DWI) showed slightly high signal, and the endometrial thickening was limited and asymmetric (Figure 5). Endometrial polyps

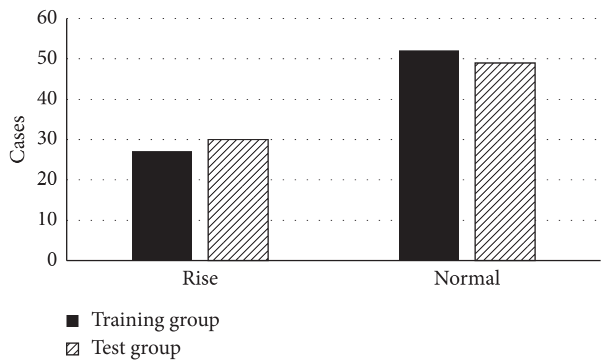

Figure 4: Comparison of CA125 levels in serums from patients.

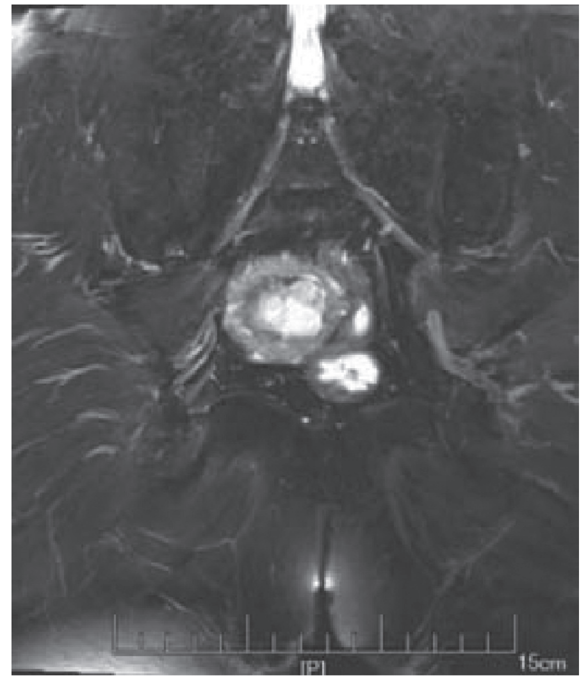

Figure 5: The image of endometrial tissue hyperplasia.

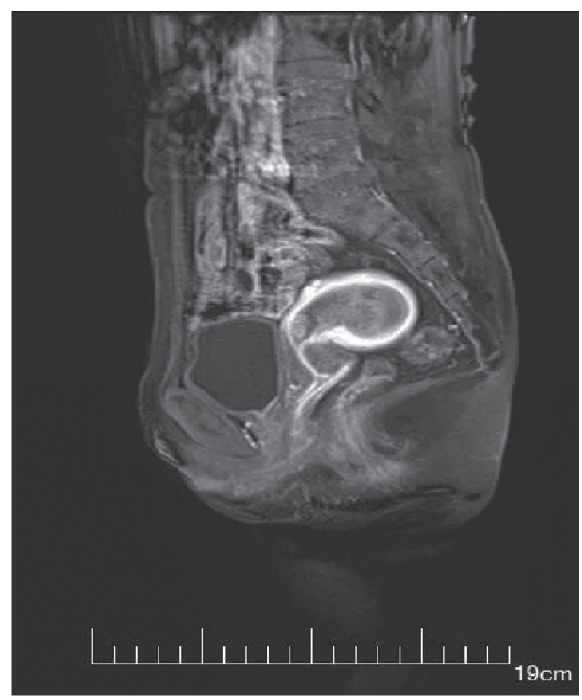

Figure 6: The image of endometrial polyps.

appeared as nodules or masses in the uterine cavity, showing a woven mesh-like uneven high signal on T2WI, and DWI indicated a slightly high signal (Figure 6). The T2WI of submucosal fibroids was like circular low signal, or nodules or tumors were dominated by low signal, and the surrounding boundary was light. If uterine bleeding was caused in the early stage, the surrounding boundary of the tumor would be unclear (Figure 7).

3.3. Experimental Results of the Convolutional Neural Network in Dataset. The network structure of the CNN was similar to that of LeNet-5. The main difference was that the CNN did not adopt some of the previous parameters in LeNet-5 and applied a fully connected network in the final classifier part. The misclassification rate curve of the CNN in the training process is shown in Figure 8. The abscissa stood for the times of iterations, and the ordinate represented the misclassification rate. The test misclassification rate after the CNN convergence was higher than that of LeNet-5, and the CNN test misclassification rate and training misclassification rate were higher than those of LeNet-5 during the entire training process.

3.4. Predictive Efficacy of the Radiomics Model. The prediction efficacy of the radiomics model of patients in the two groups was compared, including the accuracy, sensitivity, and specificity of patients from the two groups in predicting EC before surgery. It was found that the accuracy and specificity of patients in the two groups were not large, and the difference was not statistically obvious ($p > 0.05$). In addition, the sensitivity of patients in the training group was sharply lower than that of the test group, and there was a statistically great difference ($p < 0.05$) (Figure 9).

3.5. Predictive Efficacy of the Comprehensive Predictive Model. There were comparisons on the prediction efficacy of the comprehensive prediction model of patients in both groups, including the accuracy, sensitivity, and specificity of patients in the test group and training group in predicting EC before surgery. As shown in Figure 10, the accuracy and specificity of patients in the two groups were not marked, with no statistically huge difference ($p > 0.05$), while the sensitivity of patients in the training group was dramatically higher than that of the test group, and the difference was statistically substantial ($p < 0.05$).

3.6. Comparison on the Area under the Working Characteristic Curve of the Radiomics Model and Comprehensive Prediction Model. The AUC of the radiomics model was 0.897 in the

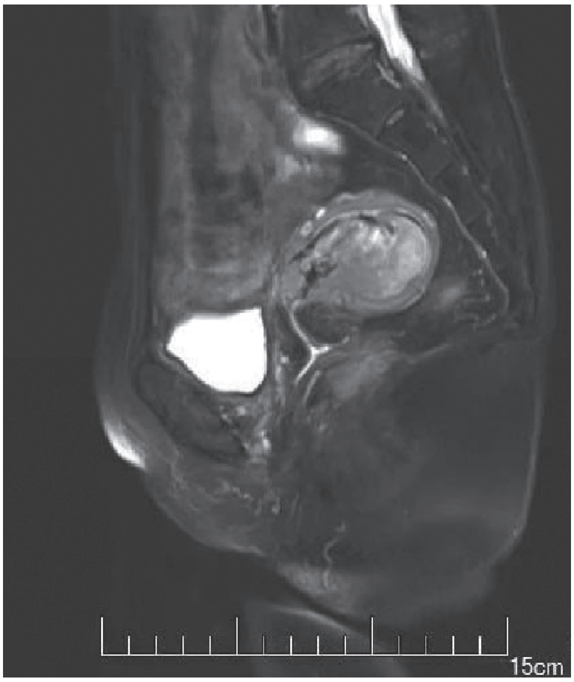

Figure 7: The image of endometrial tissue submucosal fibroids.

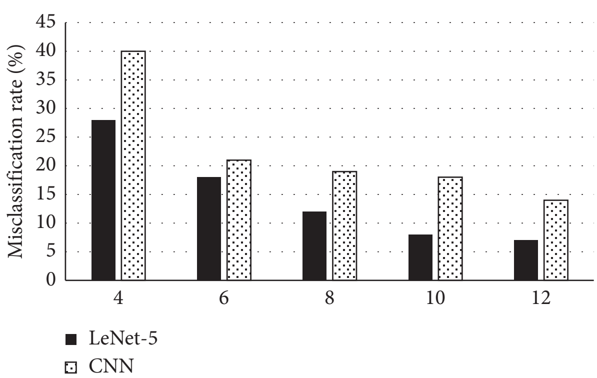

Figure 8: Comparison of the CNN and LeNet-5 misclassification rate trend.

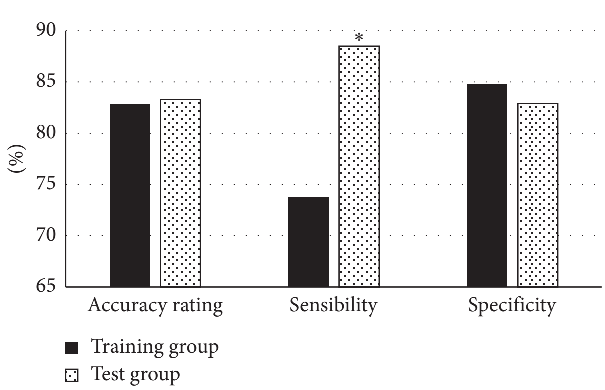

Figure 9: Comparison on prediction efficiency of the radiomics model. (Note: *The difference was statistically substantial in contrast to the sensitivity of the training group ($p < 0.05$).).

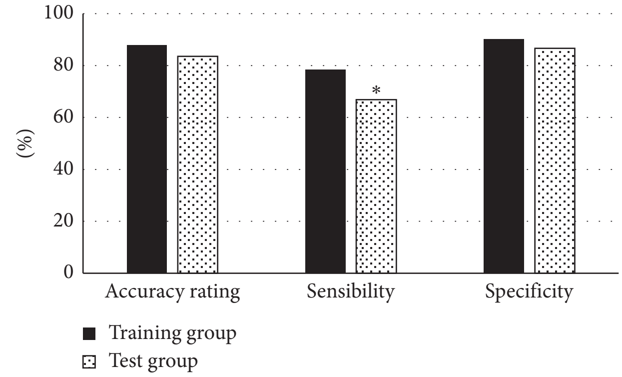

Figure 10: Comparison on prediction efficiency of the comprehensive prediction model. (Note: *A statistically great difference in contrast to the sensitivity of the training group ($p < 0.05$).).

training group and that of the comprehensive prediction model was 0.913 in the training group. It indicated that the two models constructed in this study had good prediction performance, and the effect of the comprehensive prediction model was better than that of the radiomic model. The AUC of the radiomics model and comprehensive prediction model in the test group was 0.889 and 0.897 in turn, which was similar to the above results. Therefore, it revealed that both models had great predictive performance, which again verified that the effect of the comprehensive prediction model was superior to the radiomics model (Figures 11 and 12).

4. Discussion

The etiology of EC has not been clear up to now. Metin et al. [11] employed the radiomics to establish a preoperative predictive model of EC. The radiomics preoperative prediction research also had been reported in the early cervical cancer [12] and bladder cancer [13]; the radiomics models of these research were the images based on different sequences of CT or MRI. Moreover, some other clinical pathological information was integrated. They could achieve the ideal prediction, which was consistent with the results of this study. The comprehensive prediction model was constructed in this study by combining specific imaging parameters with clinical pathological information. The results showed that the prediction performance was great and confirmed in the test group, indicating that the imaging parameters could be used as noninvasive markers for the prediction of EC.

In the research of EC, Takagi et al. [14] evaluated EC through the prediction model based on PET. It was found that PET was not suitable for routine examination of EC. Xuet al. [15] analyzed the single texture features of EC based on the MRI model, without complete radiomics analysis and independent risk factor validation. In this study, EC was for the complete MRI radiomics analysis under the CNN-based BP algorithm. From the results, the established model could achieve good specificity and sensitivity, which was superior to the above two models.

In this study, the diagnostic efficacy of the comprehensive predictive model in the training group and the test

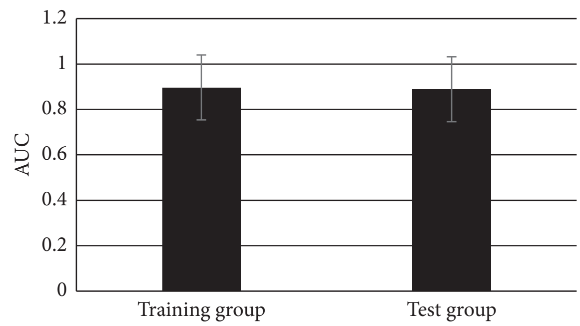

Figure 11: The AUC of the radiomics prediction model in the two groups.

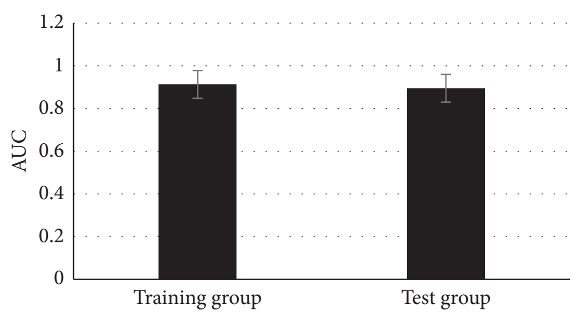

Figure 12: The AUC of the comprehensive prediction model in the two groups.

group was higher than that of the radiomics model, indicating that the diagnosis of disease required the comprehensive evaluation of clinical pathological features, pathological information, and various data of the radiomics. On the basis of the development of the CNN and the famous LeNet-5, a simple neural network model was constructed and applied to the identification of EC. The experimental results revealed that the simplified structure of the CNN could also achieve a better classification identification rate.

5. Conclusion

The enhanced MRI imaging analysis was for preoperative pelvic cavity in patients with EC based on radiomics of the CNN, the CNN model of preoperative EC was constructed, and the imaging specific parameters were combined with the clinical pathological information to establish the comprehensive prediction model. The results indicated that the prediction performance of the above models was good and verified in the test group, suggesting that the model constructed in this study could be applied in clinical practice. The limitations of this study were that all subjects came from the same hospital, MRI images were all from the same instrument, and the number of samples was also limited. Furthermore, the production of cancer markers was not taken into account during the research, so further investigation was needed. To sum up, the CNN model constructed in this study could be adopted to the clinical prediction and diagnosis of EC by radiomics analysis.

Data Availability

The data used to support the findings of this study are available from the corresponding author upon request.

Conflicts of Interest

The authors declare that they have no conflicts of interest.

References

[1] E. A. Goebel, A. Vidal, X. Matias-Guiu, and C. Blake Gilks, "The evolution of endometrial carcinoma classification through application of immunohistochemistry and molecular diagnostics: past, present and future," *Virchows Archiv*, vol. 472, no. 6, pp. 885–896, 2018.

[2] R. A. Soslow, C. Tornos, K. J. Park et al., "Endometrial carcinoma diagnosis," *International Journal of Gynecological Pathology*, vol. 38, no. 1, pp. S64–S74, 2019.

[3] J. Ventriglia, I. Paciolla, C. Pisano et al., "Immunotherapy in ovarian, endometrial and cervical cancer: state of the art and future perspectives," *Cancer Treatment Reviews*, vol. 59, pp. 109–116, 2017.

[4] B. G. Wortman, C. L. Creutzberg, C. L. Creutzberg et al., "Ten-year results of the PORTEC-2 trial for high-intermediate risk endometrial carcinoma: improving patient selection for adjuvant therapy," *British Journal of Cancer*, vol. 119, no. 9, pp. 1067–1074, 2018.

[5] V. Charalampakis, A. A. Tahrani, A. Helmy, J. K. Gupta, and R. Singhal, "Polycystic ovary syndrome and endometrial hyperplasia: an overview of the role of bariatric surgery in female fertility," *European Journal of Obstetrics & Gynecology and Reproductive Biology*, vol. 207, pp. 220–226, 2016.

[6] J. Gao, Q. Jiang, Q. Jiang, B. Zhou, and D. Chen, "Convolutional neural networks for computer-aided detection or diagnosis in medical image analysis: an overview," *Mathematical Biosciences and Engineering*, vol. 16, no. 6, pp. 6536–6561, 2019.

[7] Y. Q. Xu and R. F. Zhao, "A prediction model of endometrial cancer lesion metastasis under region of interest target detection algorithm," *Scientific Programming*, vol. 2021, Article ID 9928842, 7 pages, 2021.

[8] Y. Horie, T. Yoshio, K. Aoyama et al., "Diagnostic outcomes of esophageal cancer by artificial intelligence using convolutional neural networks," *Gastrointestinal Endoscopy*, vol. 89, no. 1, pp. 25–32, 2019.

[9] W. J. Shi, X. Y. Kong, W. Tian, Y. Yan, and Y. Chen, "Segmentation algorithm for intracranial magnetic resonance images for cerebral stroke identification and nursing evaluation," *Scientific Programming*, vol. 2021, Article ID 9996977, 8 pages, 2021.

[10] G. Ge, J. Zhang, M. Winkler, C. Lumby, W. Cong, and G. Wang, "Clinical validation of CT image reconstruction with interior tomography," *Journal of X-Ray Science and Technology*, vol. 26, no. 2, pp. 303–309, 2018.

[11] M. R. Metin, H. Aydın, Ö. Ünal et al., "Differentiation between endometrial carcinoma and atypical endometrial hyperplasia with transvaginal sonographic elastography," *Diagnostic and Interventional Imaging*, vol. 97, no. 4, pp. 425–431, 2016.

[12] W. William, A. Ware, A. H. Basaza-Ejiri, and J. Obungoloch, "A review of image analysis and machine learning techniques for automated cervical cancer screening from pap-smear images," *Computer Methods and Programs in Biomedicine*, vol. 164, pp. 15–22, 2018.

[13] A. J. Leffler, E. T. Hostnik, E. E. Warry et al., "Canine urinary bladder transitional cell carcinoma tumor volume is dependent on imaging modality and measurement technique," *Veterinary Radiology & Ultrasound*, vol. 59, no. 6, pp. 767–776, 2018.

[14] H. Takagi, T. Sasagawa, T. Shibata, H. Minato, and T. Takahashi, "Association between 18F-fluorodeoxyglucose-PET/CT and histological grade of uterine endometrial carcinoma," *Taiwanese Journal of Obstetrics & Gynecology*, vol. 57, no. 2, pp. 283–288, 2018.

[15] X. Xu, N. Li, Y. Chen, H. Ouyang, X. Zhao, and J. Zhou, "Diagnostic efficacy of MRI for pre-operative assessment of ovarian malignancy in endometrial carcinoma: a decision tree analysis," *Magnetic Resonance Imaging*, vol. 57, pp. 285–292, 2019.

Hindawi
Journal of Healthcare Engineering
Volume 2021, Article ID 9059411, 6 pages
https://doi.org/10.1155/2021/9059411

Research Article

Deep Learning-Based Image Automatic Assessment and Nursing of Upper Limb Motor Function in Stroke Patients

Xue Chen,[1] **Yuanyuan Shi**,[2] **Yanjun Wang**,[2] **and Yuanjuan Cheng**[2]

[1]*Department of Orthopedics, The Second Hospital of Jilin University, Changchun 130041, China*
[2]*Department of Nursing, The Second Hospital of Jilin University, Changchun 130041, China*

Correspondence should be addressed to Yuanjuan Cheng; 2001010211@st.btbu.edu.cn

Received 24 June 2021; Accepted 13 August 2021; Published 24 August 2021

Academic Editor: Enas Abdulhay

This paper mainly introduces the relevant contents of automatic assessment of upper limb mobility after stroke, including the relevant knowledge of clinical assessment of upper limb mobility, Kinect sensor to realize spatial location tracking of upper limb bone points, and GCRNN model construction process. Through the detailed analysis of all FMA evaluation items, a unique experimental data acquisition environment and evaluation tasks were set up, and the results of FMA prediction using bone point data of each evaluation task were obtained. Through different number and combination of tasks, the best coefficient of determination was achieved when task 1, task 2, and task 5 were simultaneously used as input for FMA prediction. At the same time, in order to verify the superior performance of the proposed method, a comparative experiment was set with LSTM, CNN, and other deep learning algorithms widely used. *Conclusion*. GCRNN was able to extract the motion features of the upper limb during the process of movement from the two dimensions of space and time and finally reached the best prediction performance with a coefficient of determination of 0.89.

1. Introduction

Cerebral apoplexy (CA), also known as cerebral stroke or cerebral vascular accident (CVA), is a kind of acute cerebrovascular disease and is due to the sudden rupture of blood vessels in the brain or due to blood circulation obstruction caused by blood vessel damage caused by a group of diseases. Stroke is one of the three major diseases leading to human death. It has the characteristics of high morbidity, high mortality, high disability, and high recurrence rate. China is a region with a high incidence of stroke. According to the data of "2018 China Health Statistics Summary," in 2017, the proportion of cerebrovascular diseases in the deaths of Chinese residents was 23.18% in the rural population and 20.52% in the urban population, which means that at least one person in every five deaths died from stroke. According to the 2018 Report on Stroke Prevention and Treatment in China, the number of stroke patients in residents over 40 years old has reached 12.42 million, and since 2002, the incidence of the first stroke in residents between 40 and 74 years old has increased by 8.3% on average every year, and the number of deaths caused by stroke has reached 1.96 million every year. Stroke has overtaken diseases such as ischemic heart disease, traffic accidents, chronic pulmonary obstruction, and lung cancer to become the leading cause of death. With the development of modern medicine, the level of treatment in the acute stage of the disease has been improved, and the number of death cases caused by stroke has gradually decreased, but the residual dysfunction has also led to a gradual increase in the rate of disability, which greatly affects the healthy life of patients and their families.

Stroke can be divided into hemorrhagic and ischemic diseases pathologically. Different clinical manifestations may occur due to different sites and properties of the lesions. 55%~75% of surviving stroke patients will remain with limb dysfunction, and 85% of patients will have lateral limb motor dysfunction after onset. In patients with hemiplegia, the incidence of motor function injury of the half limb, especially the hand function and upper limb motor dysfunction, is higher than that of the lower limb, and its rehabilitation difficulty is higher than that of the lower limb. These functional disorders seriously affect the ability of patients to live independently and reduce the quality of life of patients. Clinical observation shows that rehabilitation treatment is the most effective way to reduce the disability rate of stroke patients. Effective rehabilitation training plays an important role in improving the motor ability, sensory ability, and behavioral ability of stroke patients. Rehabilitation training can improve the daily living ability of patients, improve the ability to recover from brain lesions, reduce the degree of disability, restore the ability of independent living, better return to family and society, reduce potential nursing costs, and save social resources.

Stroke rehabilitation is a circular process, mainly including the following links: (1) rehabilitation assessment, identification, and determination of patients' needs; (2) rehabilitation goal setting, to develop practical and achievable rehabilitation goals and health training plans for patients; (3) rehabilitation treatment to achieve rehabilitation goals; and (4) evaluation of rehabilitation again to evaluate the therapeutic effect of the rehabilitation process.

In this paper, sensor technology and artificial intelligence were integrated to carry out the research on automatic assessment of stroke upper limb motor function based on deep learning. A motion measurement system was designed from the upper limb motor ability, and three different deep learning methods were proposed to extract features based on sensor data to achieve clinical scale stages and score prediction.

Upper limb hemiplegia is one of the most serious disabling consequences of stroke [1]. There are many studies on the influence of upper limb motor function of patients. Mullick et al. discussed the influence of motion observation training based on the mirror neuron system on upper limb motor function of stroke patients [2]. Gunduz et al. aimed to investigate the influence of hand robot assisted training based on motion imagery on upper limb function of stroke patients [3]. Brewer et al. investigated the effect of high frequency repetitive transcranial magnetic stimulation (HF-rTMS) on upper limb motor function in the early stage of stroke [4]. Strippoli et al. discussed the effect of restrictive exercise therapy (CIMT) on the rehabilitation of upper limb motor function in stroke patients [5]. Simpkins et al. investigated the effect of upper limb isokinetic muscle strength training on motor function of stroke patients [6]. Liou et al. discussed the influence of mirror therapy on upper limb function and daily living ability of stroke patients with hemiplegia [7].

In order to objectively quantify the upper limb motor injuries of stroke patients with hemiplegia, Fu et al. proposed an assessment method based on motion coordination quantization and multimodal fusion. Principal component analysis (PCA) and K-weighted angular similarity (K-WAS) algorithm were used to quantify the synergistic effect and muscle synergistic effect so as to further analyze the synergistic activation characteristics leading to visible sports injuries [8].

Quantitative assessment of motor function is important for post-stroke patients because it can be used to personalize treatment strategies. Pan et al. studied the assessment method of upper limb motor function in stroke patients. During voluntary upward extension, inertial sensor data and surface electromyography (sEMG) signals were collected from the upper limb. Five features include the maximum shoulder joint angle, peak and average velocity, trunk balance calculated from inertial sensor data, and muscle cooperative similarity extracted from surface EMG data by the nonnegative matrix factorization algorithm [9]. Sang-Mi et al. used BCT to quantitatively detect the motor imaging ability of stroke patients and clarified the relationship between the motor imaging ability of the upper limb of hemiplegia, motor function, and the use level of paralyzed limbs [10].

Fusion in sensor technology and artificial intelligence in this paper, based on in-depth study of the upper limb movement function stroke automatic evaluation of research, probes into the upper limb after stroke activity ability to automatically assess the related content, including the clinical ability of upper limb activity in clinical evaluation of relevant knowledge, called sensors for upper limb bones point spatial location tracking, and GCRNN model building process.

2. Materials and Methods

In order to evaluate the performance of the proposed deep learning method for predicting the FMA score of upper limb motor function, Kinect V2 was selected in this paper to measure the upper limb motor function of stroke patients. Group-constrained convolutional recurrent neural network (GCRNN) is used to achieve this task. We first designed a unique experimental environment and called volunteers to complete the required data collection of upper limb skeletal map. By analyzing the correlation between the predicted value of the model and the actual evaluation score of clinicians, we verified the performance of the model in each evaluation task and the overall performance.

In order to avoid the interference of background and other external factors, improve the quality of data, and ensure the consistency, we first set up a unique experimental environment for the collection experiment of bone point position sequence required by model training. The Kinect V2 is mounted 1.5 meters away from a chair with a small armrest. The subject will sit in this chair and complete the rating task. The Kinect V2 connects to a PC via a USB cable to transfer data and instructions. When subjects performed the upper limb assessment task, Kinect collected the three-dimensional spatial location information of the upper limb bone points in the process at a frequency of 30 Hz and transmitted and stored it to the PC in real time. Before the FMA test, we adjusted the Kinect V2's installation angle so that it could track the entire upper limb of the subject.

A total of 15 healthy volunteers were recruited in this experiment, including 9 males and 6 females, with an average age of 22.6 ($\pm$1.4) years old. Each volunteer was a stroke patient whose FMA score of upper limb motor function was randomly simulated between 30 and 100 points and who could keep sitting position. The basic information of the subjects is shown in Table 1.

Table 1: Subject information table.

Attribute	Value
Male	9
Female	6
Age range	21–24
FMA score range	30–100

Subjects sit on chairs in the experimental environment by themselves and coordinate with the experimenter to adjust the posture angle for better data collection. Then, subjects need to repeat the following upper limb assessment movements successively under the guidance:

2.1. Shoulder Buckling. Subject will sit in a chair and raise the upper limb of the hemiplegia side as far forward as possible, hold for 5 seconds, and finally return to the starting position.

2.2. Shoulder Abduction. Subjects sit in a chair and extend their upper limb on the hemiplegic side as far as possible, then hold it for 5 seconds, and finally return to the starting position.

2.3. The Forearm before and after the Rotation. Subject is sitting in a chair with shoulder 0° and elbow 90° flexed and forearm pronated forward and backward.

2.4. Finger Pinch. When the shoulder of the affected side is 0° and the elbow is 90° flexed, try to touch the little finger with the thumb and then move back to the initial position.

2.5. Move the Cylinder Object. Use the affected hand to pick up a cylinder on one side of the table and then move it to the other side of the table and lower it.

Each rating action was provided with an instructive video, and the subjects were asked to try their best to complete the rating action (simulation) while watching the video. At the same time, two raters were responsible for rating according to the FMA requirements and experience according to the completion of the action. Then, the average of the FMA scores obtained by the two raters was calculated. The actual FMA score of the subject was used for model training. Before the experiment, each subject will watch the instruction video of learning movements and practice the familiar movements for 3–5 times before starting the experiment. During the experiment, the subjects need to complete all the 5 movements continuously with a short rest interval of 2-3 seconds to facilitate the later data separation. The subjects can repeat 3–5 times according to their own physical conditions. Cameras were also used to record the whole experiment process, measure the time required for each experiment process, and analyze the movements of the subjects.

3. Results and Discussion

We verify the performance of the method proposed in this paper, namely, the comparison algorithm, by using five-fold cross validation of the data set. Each method iterates 100 times in the near row of the training set, and the iteration parameter with the best performance on the validation set is taken as the final result. The model outputs were predictive FMA scores of upper limb motor function. Performance was evaluated by correlation analysis with clinician scores, and coefficient of determination (R^2), root mean square error (RMSE), and adjustment-R^2 were used as model performance indicators.

First, we analyzed the correlation analysis results of the proposed algorithm for the 5 scoring tasks separately, as well as the correlation analysis results of FMA prediction using the data of the 5 tasks, as shown in Figure 1, and it can be found that task 1, task 2, and task 5 have a high correlation with FMA, and the determination coefficients of 0.88, 0.85, and 0.87 can be reached when using these rating tasks alone. Because task 3 and task 4 only have local hand movements, the correlation with the overall FMA rating item is weaker. Therefore, the consistency with the clinician's FMA assessment was only 0.78 and 0.72. When we input all the bone point data of the five assessment tasks into the model for FMA prediction, as shown in Figure 1(f), although the determination coefficient obtained is improved compared with that when using single task data as input, the improvement effect is not obvious. The coefficient of determination is 0.86, which is lower than that of Task 1 (Figure 1(b)) and Task 5 (Figure 1(e)).

In order to achieve automatic upper body activity assessment using as few assessment tasks as possible, we conducted prediction performance under different number and combination of tasks in order to find the most appropriate number and combination of assessment tasks. According to the experimental results shown in Figure 1, we conducted a comparative verification experiment in accordance with some combinations that might be better. The results are shown in Table 2.

As can be seen from the table, when the task combination is Task 1-2-3-5, the maximum coefficient of determination can be reached to 0.89; when the number of tasks is 2, the overall coefficient of determination is relatively low because there are too few FMA assessment items covered and the upper limb movement features can be provided. When the number of assessed tasks was 3, compared with the number of assessed tasks was 2, there was a significant improvement, but different combination of tasks also had an impact on the experimental results. Because task 4 and task 5 were both hand functional assessments, the combination of task 4 and task 5 provided overlapping motor function characteristics. In addition, it can be seen from Table 2 that the task combination of Task 1, 2, and 5 can provide more motor characteristics from multiple dimensions such as shoulder abduction, forward bending, and grasping ability, covering more FMA assessment items.

In order to verify the performance of the proposed deep learning framework, we used the optimal combined task data of Task 1, 2, 3, and 5 mentioned above to conduct comparative

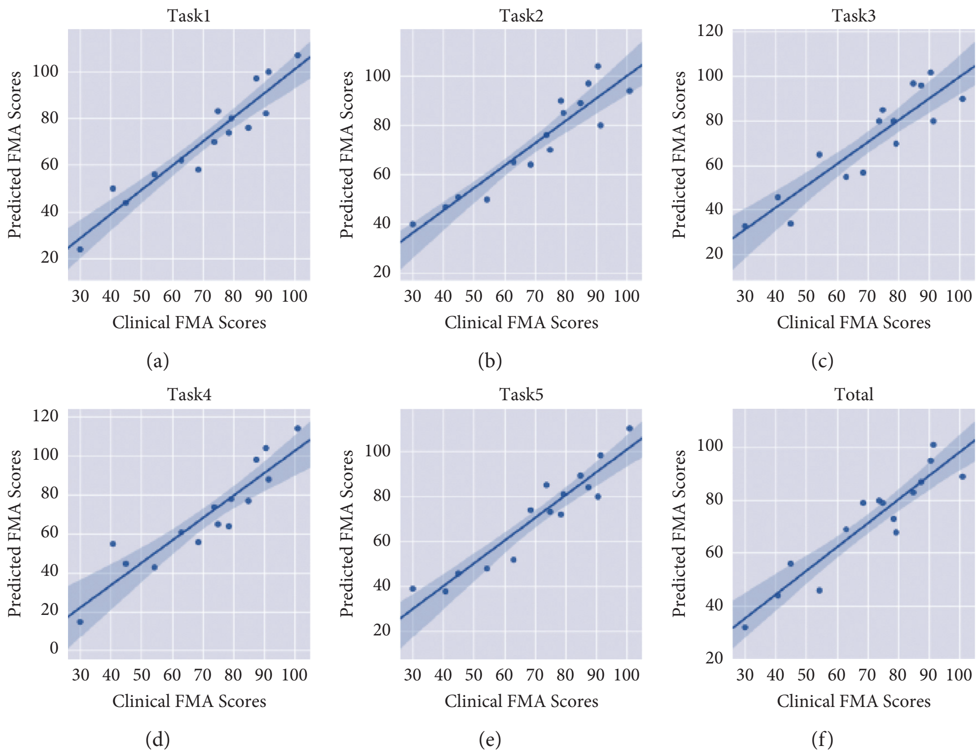

Figure 1: Individual assessment task data predicts FMA results.

Table 2: Comparison of evaluation task combinations.

Number of tasks	Task combination	RMSE	R^2	Adjust-R^2
2	Task 1-2	7.29	0.86	1.19
	Task 2-5	7.30	0.86	1.21
3	Task 1-2-5	7.25	0.88	1.23
	Task 2-4-5	7.90	0.84	1.25
	Task 2-3-5	7.26	0.87	1.19
4	Task 2-3-4-5	7.81	0.85	1.24
	Task 1-2-3-5	6.57	0.89	1.17
	Task 1-2-4-5	7.40	0.86	1.22
5	Task 1-2-3-4-5	7.37	0.86	1.21

experiments with the GCRNN algorithm in this paper, LSTM and CNN algorithm. Regression analysis was performed on clinician evaluation scores and model-predicted FMA scores of 15 subjects, and determination coefficients were calculated, and correlation analysis graphs were drawn, as shown in Figures 2–4. The GRCNN model fully extracts the spatial location sequence data features of bone points from the two dimensions of data sequences between data sequences and the context of a single data sequence through convolution and cyclic neural network modules and finally predicts the optimal performance when the coefficient of determination of FMA fraction reaches 0.89 (Figure 2). In the manifestation of upper limb motor dysfunction, the relationship between bone nodes in the human body can reflect the cooperative movement mode often manifested in clinical practice and so on. Compared with LSTM, CNN pays more attention to the feature extraction of the relationship between data, and in the upper limb motor ability assessment task in this paper, it also obtains a coefficient of determination of 0.87 (Figure 3). The LSTM model pays more attention to the before and after dependence of the sequence. Stroke-related patients have a small range of upper limb motion, weak features of the before and after changes in the sequence data, and relatively weak performance in automatic assessment tasks. The coefficient of determination in the data set in this paper is 0.85 (Figure 4).

IMU, glove sensor, and motion capture system often used in existing studies need quite a long time to complete the wearing and marking, and it is already difficult to fix the sensor or marker on the body of stroke patients, and it is easy to cause discomfort to patients and affect normal activities. The automatic evaluation system proposed in this paper uses the Kinect V2 depth sensor based on vision to collect motion data. It does not require the time-consuming process of sensor wearing. It only takes about 5 minutes to set up the initial (perspective setting) and has a generally acceptable low cost. The rich

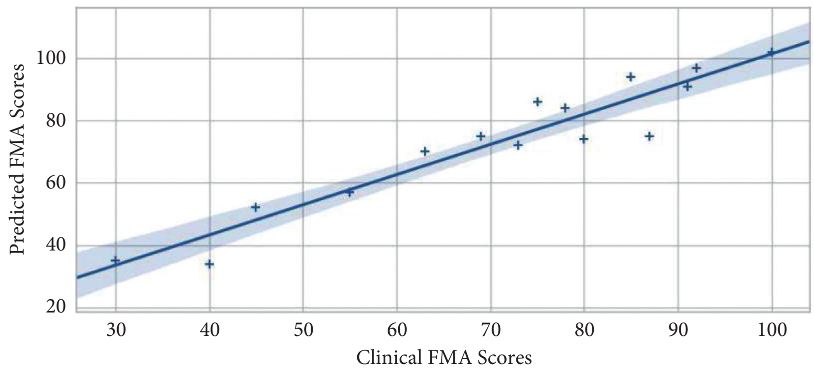

Figure 2: GCRNN performed FMA prediction performance.

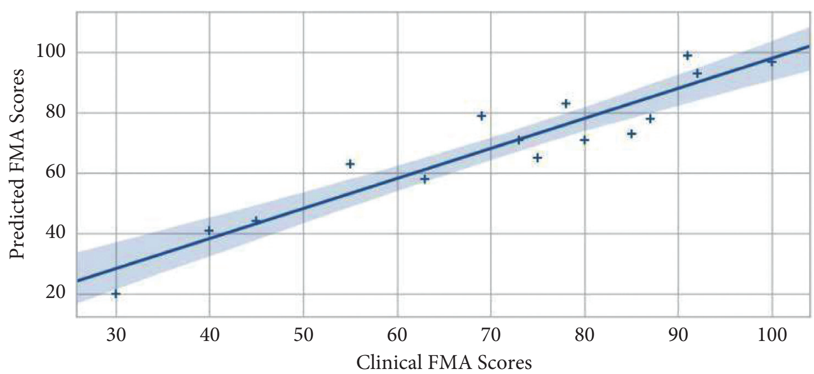

Figure 3: FMA prediction performance by CNN.

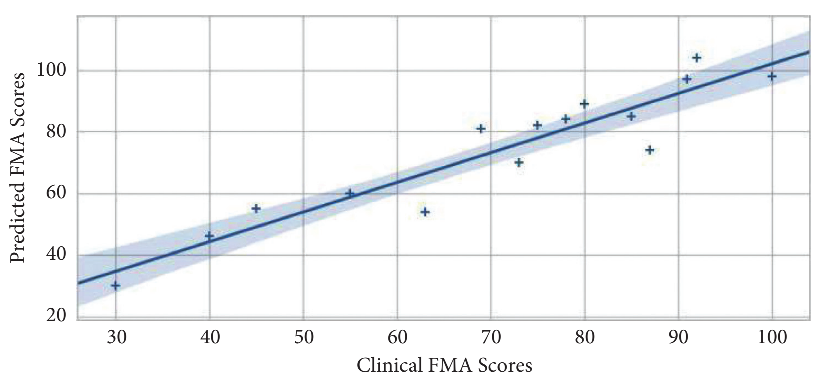

Figure 4: LSTM performed FMA to predict performance.

SDK provided by Kinect can obtain various motion tracking data, such as RGB image, depth image, and spatial position of bone points. In this paper, the spatial position data of human upper limb bone points were only used to complete the task of upper limb mobility assessment. In the future work, we can also consider the use of depth image, RGB, and combined data for automatic evaluation research. In addition, we also found that there are some insurmountable errors in acquiring it through noncontact motor consciousness in our experiment. When subjects wear loose clothes, there is a deviation in the recognition and tracking of shoulders and elbows. When human beings are active, it will bring great interference to the data. Such data patterns can be confused with data disturbances caused by limb spasms. Second, the Kinect V2 only has two bone points on the hand, the thumb, and the fingertip, which poses a huge challenge to complete the measurement of hand extension/flexion motion in FMA. In addition, when a single Kinect performs task 5: upper limb activity tracking of moving pencil and limb occlusion is easy to occur, which will cause the data loss of occluded bone points, thus affecting the accuracy. Of course, this problem of being easily obscured can be solved in the future by setting up multiple Kinect devices to track human activities from different angles.

4. Conclusions

The focus of this paper is to propose a deep learning framework for data analysis, to achieve the use of as few assessment tasks as possible to complete the complex clinical FMA assessment tasks, and to achieve a high degree of consistency with the clinician assessment. Through a detailed analysis of all FMA evaluation items, we set up a unique experimental data collection environment and evaluation tasks. The results of FMA prediction using bone point data of each evaluation task are shown in Figure 1. Through different number and combination of tasks, it can be seen in Table 2. The best coefficient of determination was achieved when task 1, task 2, and task 5 were simultaneously used as inputs for the FMA prediction. At the same time, in order to verify the superior performance of the proposed method, a comparative experiment was set with LSTM, CNN, and other deep learning algorithms widely used. GCRNN was able to extract the motion features of the upper limb during the process of movement from the two dimensions of space and time and finally reached the best prediction performance with a coefficient of determination of 0.89.

Data Availability

The data used to support the findings of this study are available from the corresponding author upon request.

Conflicts of Interest

The authors declare that there are no conflicts of interest.

References

[1] L. Piron, A. Turolla, M Agostini et al., "Assessment and treatment of the upper limb by means of virtual reality in post-stroke patients," *Studies in Health Technology and Informatics*, vol. 145, pp. 55–62, 2009.

[2] A. A. Mullick, S. K. Subramanian, and M. F. Levin, "Emerging evidence of the association between cognitive deficits and arm motor recovery after stroke: a meta-analysis," *Restorative Neurology and Neuroscience*, vol. 33, no. 3, pp. 389–403, 2015.

[3] H. Gunduz, "Deep learning-based Parkinson's disease classification using vocal feature sets," *IEEE Access*, vol. 7, no. 99, pp. 115540–115551, 2019.

[4] L. Brewer, F. Horgan, A. Hickey, and D. Williams, "Stroke rehabilitation: recent advances and future therapies," *QJM*, vol. 106, no. 1, pp. 11–25, 2013.

[5] Clinical Evaluation of the Dose of Erythropoietins Study Group (C.E. Dose) and G. Strippoli, "Effects of the dose of erythropoiesis stimulating agents on cardiovascular events, quality of life, and health-related costs in hemodialysis patients: the clinical evaluation of the dose of erythropoietins (C.E. DOSE) trial protocol," *Trials*, vol. 11, no. 1, p. 70, 2010.

[6] S. D. Simpkins, P. E. Davis-Kean, and J. S. Eccles, "Parents' socializing behavior and children's participation in math, science, and computer out-of-school activities," *Applied Developmental Science*, vol. 9, no. 1, pp. 14–30, 2005.

[7] J.-C. Liou, Y.-T. Chang, "Investigated of the reproducibility of upper-limb motor function in stroke patients," *Journal of Nanoelectronics and Optoelectronics*, vol. 12, no. 8, pp. 862–867, 2017.

[8] Q. Fu, W. Chen, and J. Yu, "The effects of motor imagery therapy on the upper limb motor function in hemiplegic stroke patients," *Chinese Journal of Rehabilitation Medicine*, vol. 25, no. 1, pp. 53–55, 2010.

[9] F. Molteni, M. Caimmi, S. Carda et al., "Kinematic upper limb analysis in stroke patients undergoing constraint-induced movement therapy: 3-month follow-up," *Gait & Posture*, vol. 24, no. supp-S2, pp. S42–S43, 2006.

[10] J. Sang-Mi, J. Byeong-Rok, and Y. Seung-Hoon, "A study of correlation among balance, upper limb function and activities of daliy living in stroke patients," *Journal of the Korea Entertainment Industry Association*, vol. 7, no. 3, pp. 223–228, 2013.

Hindawi
Journal of Healthcare Engineering
Volume 2021, Article ID 3051578, 7 pages
https://doi.org/10.1155/2021/3051578

Research Article

Application Value of Magnetic Resonance Arthrography of the Shoulder in Nursing and Diagnosis of Patients with Shoulder Joint Injury

Si Chen,[1] **Yuanyuan Shi**,[2] **Pan Xue**,[3] **and Xue Chen**[3]

[1]*Geriatric Medicine, The Second Hospital of Jilin University, Changchun 130041, China*
[2]*Department of Nursing, The Second Hospital of Jilin University, Changchun 130041, China*
[3]*Department of Orthopedics, The Second Hospital of Jilin University, Changchun 130041, China*

Correspondence should be addressed to Xue Chen; 2005010227@st.btbu.edu.cn

Received 24 June 2021; Accepted 6 August 2021; Published 24 August 2021

Academic Editor: Enas Abdulhay

Supraspinatus tendon injury is a common clinical shoulder joint disease and is one of the most common causes of shoulder pain and dysfunction. Supraspinatus tendon injury will lead to articular cartilage injury and degeneration, then cause joint disease, seriously affect the quality of life of patients, and bring a huge burden to the family and society. This paper mainly studies and evaluates the application value of special signs of shoulder joint and indirect MR imaging in the diagnosis of supraspinatus tendon injury. Through a series of special examinations for the diagnosis of supraspinatus tendon injury in 90 patients, including zero degree abduction resistance test, arm drop test, Jobe test, Neer sign, and Hawkins sign, all patients in the study underwent indirect magnetic resonance imaging of the shoulder joint. Finally, arthroscopic examination results were used as the "gold standard" to evaluate and analyze the diagnosis. The results showed that among the special signs, the specificity of the falling-arm test was the highest (72.2%) in the diagnosis of full-thickness supraspinatus tendon injury. Hawkins sign had the highest sensitivity (84.0%). In the diagnosis of partial supraspinatus tendon injury, the specificity of the Jobe test was the highest, which was 66.6%. The Neer sign had the highest sensitivity of 50.0%. In the diagnosis of full-thickness supraspinatus tendon injury, there was no significant difference in sensitivity between indirect MRI and Hawkins sign, but the diagnostic specificity of indirect MRI was higher than that of special sign examination. In the diagnosis of partial supraspinatus tendon injury, the sensitivity and specificity of indirect MR imaging are higher than those of special sign examination.

1. Introduction

Rotator cuff injury has attracted much attention since Smith first put forward the concept of rotator cuff injury in 1834. These concerns are not only due to the research interest of scholars, but also due to the needs of a large number of patients. The study found that the incidence of partial or full-thickness rotator cuff injury increased significantly after age 50, exceeding 50 percent in people over 70 and more than 80 percent in people over 80. What deserves more attention is the progression of the disease after the injury of the rotator cuff. Yamanaka et al. observed 40 patients with partial rotator cuff injury without surgical treatment. After more than one year of follow-up, changes of rotator cuff injury is examined with shoulder arthrography. The results showed that only 4 patients had obvious healing of injured rotator cuff. The extent of injury was reduced in four patients. At the same time, 21 patients had an expanded rotator cuff lesion, and 11 patients shifted from a partial rotator cuff lesion to a full-thickness lesion.

Among the tendons that make up the rotator cuff, the supraspinatus tendon is located at the top of the rotator cuff. Compared with other tendons, the supraspinatus tendon is most vulnerable to the extrusion of the acromial peak and the coracoacromial arch and is the tendon with the highest incidence of degeneration and injury. Because of the high incidence of rotator cuff injury and the exacerbation of the course of disease, it is of great significance to improve the understanding of rotator cuff injury, especially supraspinatus tendon injury. The previous concept of "periarthritis of the shoulder" is obviously too broad and general, and the early diagnosis of supraspinatus tendon injury is essential to prevent further progression of the disease. However, the clinical symptoms of supraspinatus tendon injury are diverse, and there is a lack of special clinical symptoms for diagnosis. Routine physical examination often fails to provide sufficient diagnostic reference information. Therefore, various specific examinations for special signs have emerged as the times require. At the same time, a variety of imaging examinations also provide useful diagnostic information from different perspectives, and how to choose efficient and reliable diagnostic techniques to help the clinical screening and diagnosis of supraspinatus tendon injury has become one of the hot spots of attention and research.

Physical examination was performed to assess supraspinatus tendon injury by an impingement test that elicits pain and by examining the strength of the supraspinatus muscle, and the diagnosis of supraspinatus tendon injury by indirect magnetic resonance arthrography was performed.

Imaging examination is an essential and important means for the diagnosis of supraspinatus tendon injury, and it is also helpful to determine the degree and type of supraspinatus tendon injury and whether there are other accompanying shoulder diseases. There is no doubt that imaging examination plays an important role in the diagnosis, treatment, and prognosis evaluation of supraspinatus tendon injury. Imaging examinations for supraspinatus tendon injuries mainly include the following types: X-ray examination (X-ray examination cannot directly observe the rotator cuff and other soft tissues, mainly through some indirect signs to determine whether there is rotator cuff injury), CT examination (CT examination can clearly show the shoulder joint fault structure and three-dimensional reconstruction), ultrasound, which uses a range of physical properties of ultrasound to identify and image soft tissue, and MRI, which is a great advance in the imaging diagnosis of rotator cuff. The basic element of the imaging principle of MRI is the hydrogen nuclei contained in the tissues of the body. Currently, the diagnosis of the supraspinatus tendon injury mainly includes plain MRI, direct MRI arthrography, and indirect MRI arthrography.

The research of MR arthrography in the examination of shoulder joint injury is developing continuously. MR arthrography (MRA) is often used to evaluate intra-articular disorders of the shoulder. Liao et al. discussed the diagnostic value of MR arthrography for rotator cuff injury [1]. Zhang et al. discussed the diagnostic value of conventional MRI and MR arthrography in flapping injury of shoulder joint [2]. Xiao et al. discussed the diagnostic value of magnetic resonance arthrography of the shoulder for partial rotator cuff tear [3]. Nassef et al. proved that MR arthrography is the preferred imaging examination method for patients with shoulder instability [4]. Alaia et al. discussed the standard MR imaging and arthrography protocols routinely used in clinical practice, as well as more innovative sequence and reconstruction techniques facilitated by the increase of high field intensity magnets and multichannel phased array surface coils and the combination of artificial intelligence [5].

Studies are also under way to combine MRI arthrography with other procedures. Pan et al. summarized the diagnosis and measurement methods of bone defect in anterior shoulder instability (scapular glenoid defect and Hill–Sachs lesion): X-ray, CT, MRI, arthroscopy, and arthrography are common methods for the diagnosis of humeral head anterior glenoid defect and Hill–Sachs lesion [6]. Foti et al. compared the diagnostic accuracy of dual-energy CT arthrography (DE-CTA) and magnetic resonance arthrography (MRA) in describing labial lacerations [7]. Fu et al.'s objective was to explore the application of CT combined with MRI in the diagnosis of shoulder injury and to provide reference for clinical application [8]. Bucha et al. studied the value of shoulder magnetic resonance in the diagnosis of shoulder instability and compared it with arthroscopy [9].

This paper mainly studies and evaluates the application value of special signs of shoulder joint and indirect MR imaging in the diagnosis of supraspinatus tendon injury.

2. Research Methods

2.1. Research Object. A total of 90 cases were enrolled, including 46 males and 44 females, aged 42 to 75, with an average age of 58.6 years (48 cases of right shoulder and 42 cases of left shoulder and duration ranging from 4 to 24 months, with an average of 8.5 months). Eighteen patients had a history of shoulder trauma, and 12 patients complained of shoulder strain. The other cases had no obvious cause of disease. There were 10 cases of coronary heart disease, 12 cases of diabetes, and 19 cases of hypertension in this group. There were 52 cases of dominant limb and 38 cases of nondominant limb. Visual analog scale of pain (VAS score), shoulder function score (UCLA score, Constant score, and ASE score), and range of motion of shoulder were measured preoperatively in all patients.

2.2. Examination of Special Physical Signs. The examination of special physical signs was performed and recorded by an attending physician with more than 5 years of experience in sports medicine and a doctoral candidate in sports medicine. All the patients were examined on both sides of the shoulder. The order of examination was first the physical examination of the walking side of the shoulder and then the physical examination of the affected side of the shoulder. The contents of special physical examination are mainly for the muscle strength examination of the supraspinatus muscle and the impact test to induce shoulder pain. In order to avoid the interference of pain on the muscle strength examination results as far as possible, the impact test is arranged after the muscle strength examination.

2.3. Indirect Magnetic Resonance Angiography. Instruments and materials used: the MRI scanner used for scanning was the Philips Ingenia 3.0 T MRI scanner (Netherlands). The contrast agent used for indirect imaging was gadolinium spray acid meglumine gadolinate (trade name: Magenweisen (Germany); chemical name: dihydro-[N, N-bis [2-{bis (carboxymethyl) amino} ethyl] glycoyl (5-)] gadolinic acid (2-) combined with 1-deoxy-1-(methylamino)-D-glucosol (1 : 2); molecular weight: 938.00). Accessories: meglumine and water for injection.

2.4. Shoulder Arthroscopy. Arthroscopic personnel and equipment: all arthroscopes are performed by a team of a chief physician in sports medicine and an attending physician. Arthroscopic instruments and lenses: Smith & Nephew arthroscopic system equipment was used.

2.5. Statistical Methods. The diagnosis results under shoulder arthroscopy are regarded as the "gold standard" of the final diagnostic standard of all cases. Special signs of shoulder and indirect magnetic resonance angiography were used as screening diagnostic methods to be evaluated, and the results of shoulder arthroscopy were compared with the "gold standard" diagnostic results and statistically analyzed. SPSS19.0 statistical software package was used for data analysis, and X2 test was used for data statistical analysis. If $P < 0.05$, the difference was considered to be statistically significant.

3. Results

3.1. Examination of Special Physical Signs. Procedures for checking special physical signs are as follows:

> Abduction resistance test at zero position: the patient's two upper limbs are placed at the side of the body, and the examinator stands behind the patient's body against the patient's upper limb abduction movement. If the patient feels obvious pain or cannot resist resistance and cannot abduct the upper limbs, the test is positive.
>
> The dropping arm test: the examiner abducted the patient's shoulder joint to more than 90 degrees and let the patient keep it by himself. The test is positive if the patient is unable to maintain the abduction position until the upper limb falls.
>
> Jobe test (empty can test): The patient's shoulder joint abducted 80 to 90 degrees in coronal position and retracted 30 degrees in horizontal position. With the forearm pronated and the thumb pointed to the ground, the examiner applied downward pressure on the patient's wrist. Patients who are unable to resist resistance and experience significant pain and weakness are considered to be positive for the Jobe test.
>
> Neer sign: the examiner stands behind the patient, stabilizes the scapula on the examining side with one hand, and maintains the shoulder joint in internal rotation with the other hand, so that the fingertip of the thumb of the upper limb is downward, and then the shoulder joint on the examining side is flexed forward and lifted over the top. If pain is induced, Neer sign is positive.
>
> Hawkins sign: the examiner flexes the patient's elbow 90 degrees, with the shoulder adducted forward 90 degrees and the forearm in horizontal position. The examiner forces the affected forearm downward to produce internal rotation of the shoulder. If significant pain is induced, Hawkins sign is positive.

The examination results of special physical signs are as follows.

As can be seen from Table 1, in patients with full-thickness supraspinatus tendon injury, the sensitivity and specificity of the zero degree abduction resistance test were 48.0% and 65.0%, respectively. The sensitivity and specificity of falling arm test were 51.9% and 72.2%, respectively. The sensitivity and specificity of the Jobe test were 45.8% and 66.7%. The sensitivity and specificity of Neer sign were 54.2% and 61.9%. The sensitivity and specificity of Hawkins sign were 84.0% and 60.0%, respectively. The sensitivity and specificity of the zero degree abduction resistance test were 46.2% and 57.9% in patients with partial supraspinatus tendon injury. The sensitivity and specificity of falling arm test were 39.2% and 64.7%. The sensitivity and specificity of Jobe test were 40.7% and 66.6%. The sensitivity and specificity of Neer sign were 50.0% and 52.6%, respectively. The sensitivity and specificity of Hawkins sign were 45.8% and 57.1%, respectively.

Among the examinations of special signs, the falling arm test has the highest specificity and the highest sensitivity in the diagnosis of the full-thickness supraspinatus tendon injury. In the diagnosis of partial supraspinatus tendon injury, the Jobe test has the highest specificity and the highest sensitivity of Neer sign. The diagnostic accuracy of the full layer injury of supraspinatus tendon was higher than that of partial injury by special sign examination.

3.2. Indirect MRI Examination. Prior to MRI, the patient received a rapid injection of gadolinium spray diglumethamine at a dose of 0.1 mmol/kg from a peripheral vein in front of the elbow. Immediately after the injection of contrast agent, the patient was instructed to examine the lateral shoulder joint for about 15 minutes and then underwent magnetic resonance scanning. Figures 1–4 show typical cases of joint injury. During the scanning, the patient was placed in supine position, and the range value of the scanning field of view (FOV) was $160 * 160 * 71$ mm. The scanning thickness was 3 mm, and the scanning gap was 1 mm. The precise frequency reversal recovery (SPAIR) PDW fat suppression sequence (TR 2800 ms, TE 30 ms) and matrix (Matrix) $320 * 228 * 18$ mm were used to scan the oblique coronal plane. SPAIR T1W fat suppression sequence (TR635 ms, TE 15 ms), matrix $292 * 242 * 18$ mm was used to scan the oblique coronal plane as well. Fast spin echo (FSE) T1WI (TR561 ms, TE15 ms) with a matrix of $320 * 263 * 18$ mm was used for oblique sagittal scanning. For cross-sectional scanning, the SPAIR fat-inhibited PDW sequence (TR 2800 ms, TE30 ms) with a matrix of $268 * 181 * 18$ mm was used. The MRI scan was perpendicular to the humeral shaft, extending from above the acromioclavicular joint to below the pelvis of the scapula

Table 1: Results of special physical signs.

Test	Abduction resistance test		The left arm test		Jobe test		Neer		Hawkins	
Parts	Full-thickness injury	Part of the damage	Full-thickness injury	Part of the damage	Full-thickness injury	Part of the damage	Full-thickness injury	Part of the damage	Full-thickness injury	Part of the damage
True positive	12	12	14	11	11	11	13	13	21	11
A false positive	7	8	5	6	7	6	8	9	8	9
True negative	13	11	13	11	14	12	13	10	12	12
False negative	13	14	13	17	13	16	11	13	4	13
Sensitivity (%)	48	46.2	51.9	39.2	45.8	40.7	54.2	50.0	84.0	45.8
Specificity (%)	65	57.9	72.2	64.7	66.7	66.6	61.9	52.6	60.0	57.1
Positive predictive value (%)	63.2	60.0	73.7	64.7	61.1	64.7	61.9	59.1	72.4	55.0
Negative predictive value (%)	50.0	44.0	50.0	39.3	51.9	42.9	54.2	43.5	75.0	48.0
Accuracy (%)	13.0	4.1	24.1	3.9	12.5	7.3	16.1	2.6	44.0	2.9

Figure 1: Injury of the articular portion of supraspinatus tendon 1.

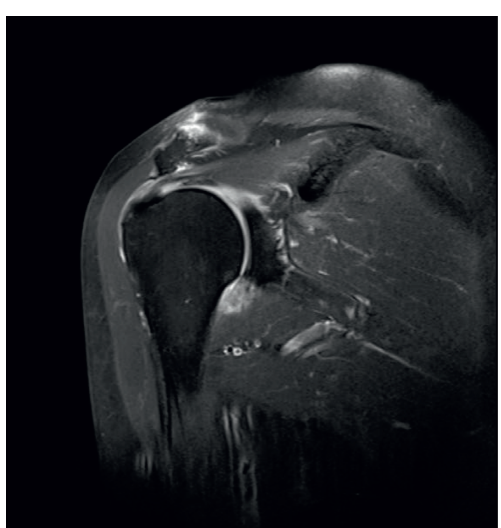

Figure 2: Injury of the articular part of supraspinatus tendon 2.

Figure 3: Injury of the articular part of supraspinatus tendon 3.

Figure 4: Injury of the articular part of supraspinatus tendon 4.

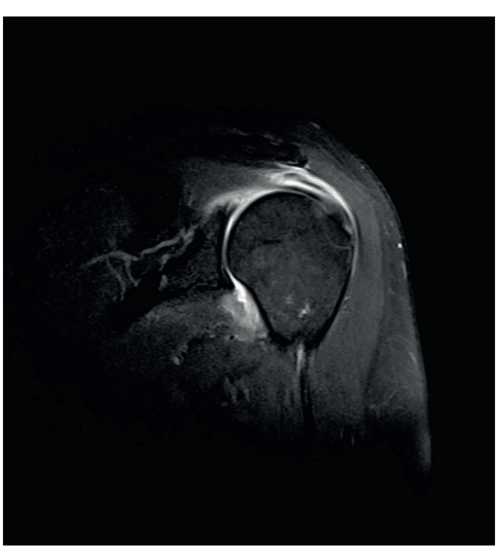

Figure 5: Injury of the supraspinatus tendon in tendon 1.

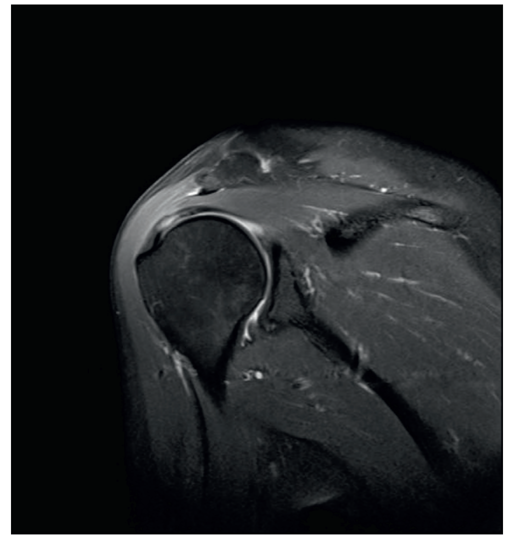

Figure 6: Injury of supraspinatus tendon in tendon 2.

Figure 7: Injury of the supraspinatus tendon in tendon 3.

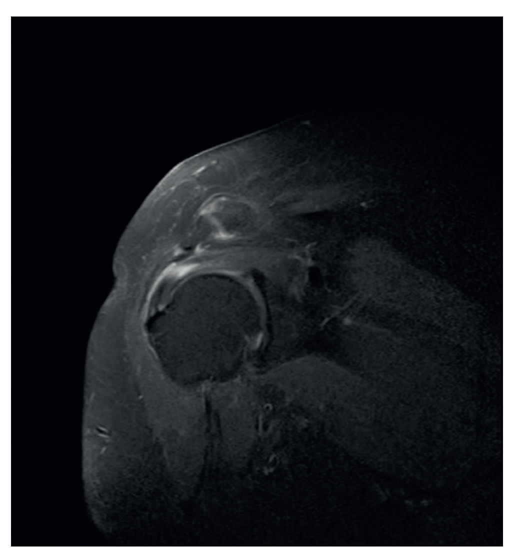

Figure 8: Injury of supraspinatus tendon in tendon 4.

Table 2: Results of indirect magnetic resonance angiography.

Parameter	Indirect magnetic resonance angiography	
Parts	Full-thickness injury	Part of the damage
True positive	29	29
A false positive	1	1
True negative	14	12
False negative	1	3
Sensitivity (%)	96.7	90.6
Specificity (%)	93.3	92.3
Positive predictive value (%)	96.7	93.5
Negative predictive value (%)	93.3	85.7
Accuracy (%)	90.0	82.9

joint. The oblique coronal scanning direction was parallel to the long axis of the supraspinatus muscle, extending from the front of the tip of the coracoid process to the rear of the scapulae. The oblique sagittal scanning direction was perpendicular to the long axis of the supraspinatus muscle and ranged from the lateral humeral head to the medial supraspinatus fossa of the shoulder joint. Figures 5–8 show a typical MRI of partial injury to the upper tendon. Table 2 shows the results of indirect magnetic resonance angiography.

As can be seen from Table 2, the sensitivity and specificity of indirect MR imaging in the diagnosis of full-thickness injury of supraspinatus tendon were 96.7% and 93.3%, and the sensitivity and specificity of partial injury of supraspinatus tendon were 90.6% and 92.3%.

The accuracy of indirect MR imaging in the diagnosis of the full thickness injury of supraspinatus tendon was higher than that of the partial injury of supraspinatus tendon.

3.3. Comparison of the Results of Special Sign Examination and Indirect Magnetic Resonance Angiography. For the full-thickness injury and partial injury of supraspinatus tendon, the sensitivity and specificity of the examination with the highest sensitivity and specificity were compared with those of the indirect MRI examination (see Tables 3 and 4 for details).

In the diagnosis of full-thickness supraspinatus tendon injury, there was no significant difference between the sensitivity of MR indirect imaging and Hawkins sign, the most sensitive of the special signs ($P > 0.05$).

In the diagnosis of partial supraspinatus tendon injury, there was a significant difference between the sensitivity of MR indirect imaging and Neer sign, the most sensitive of the special signs ($P < 0.05$).

In the diagnosis of full-thickness supraspinatus tendon injury, there was a significant difference between the highest specificity of the arm test and indirect MR imaging ($P < 0.05$).

Table 3: Comparison of sensitivity between indirect MRI and specific signs.

Parameter	Indirect magnetic resonance angiography	
Special signs	Full-thickness injury	Part of the damage
Pairing X^2	1.273	19.361
P value	0.214	0.000

Table 4: Comparison of specificity between indirect MRI and specific signs.

Parameter	Indirect magnetic resonance angiography	
Special signs	Full-thickness injury	Part of the damage
Pairing X^2	6.142	10.313
P value	0.033	0.023

In the diagnosis of partial supraspinatus tendon injury, there was a significant difference between the specificity of Jobes test and indirect magnetic resonance imaging ($P < 0.05$).

4. Conclusions

(1) Among the examinations of special physical signs, the falling arm test has the highest specificity and the highest sensitivity for the diagnosis of full-thickness supraspinatus tendon injury. In the diagnosis of partial supraspinatus tendon injury, the Jobe test has the highest specificity and the Neer sign has the highest sensitivity.

(2) In the diagnosis of full-thickness supraspinatus tendon injury, there was no significant difference in sensitivity between indirect MR imaging and Hawkins sign, but the specificity of indirect MR imaging was higher than that of special signs.

(3) In the diagnosis of partial supraspinatus tendon injury, the sensitivity and specificity of indirect MR imaging are higher than those of special sign examination.

The examination of special signs is simple and quick, which is helpful to the diagnosis of supraspinatus tendon injury and should be used as the basic diagnostic method. Indirect MR imaging is an important auxiliary diagnostic method with high sensitivity and specificity, which can be examined by multiplane images.

Data Availability

The data used to support the findings of this study are available from the corresponding author upon request.

Conflicts of Interest

The authors declare that they have no conflicts of interest.

References

[1] R. Liao, Y. Zhang, Q. U. Zhongwei, G. Zou, and L. Zhou, "The value analysis of 3.0t MR shoulder arthrography in diagnosis of rotator cuff injury," *Journal of Medical Imaging*, vol. 29, no. 1, 2019.

[2] Z. G. Zhang, R. M. Peng, L. Yu-Dan, H. E. Chuan, F. K. Wang, and Y. M. Jiang, "Correlation between MRI and MR arthrography in the diagnosis of SCAP injury that compared with arthroscopy," *Journal of Kunming Medical University*, vol. 40, no. 5, 2019.

[3] L. Xiao, X. Fan, and L. Guiping, "Diagnostic value of MRI and MR arthrography in rotator cuff tears," *Hebei Medicine*, vol. 25, no. 1, 2019.

[4] M. A. Nassef, S. Abdulrahim, and D. Eldesouki, "Role of MRI arthrography compared to conventional MRI in assessment of shoulder joint disorders," *QJM: Monthly Journal of the Association of Physicians*, vol. 113, no. 1, 2020.

[5] E. F. Alaia and N. Subhas, "Shoulder MR imaging and MR arthrography techniques," *Magnetic Resonance Imaging Clinics of North America*, vol. 28, no. 2, 2020.

[6] Z. Pan, F. Huang, L. I. Jian, X. Tang, and D. O. Orthopaedics, "Current concepts of diagnostic techniques and measurement methods for bone defect in patient with anterior shoulder instability," *Chinese Journal of Reparative and Reconstructive Surgery*, vol. 33, no. 6, 2019.

[7] G. Foti, W. Mantovani, M. Catania, P. Avanzi, and S. Caia, "Evaluation of glenoid labral tears: comparison between dual-energy CT arthrography and MR arthrography of the shoulder," *La Radiologia Medica*, vol. 125, no. 1, pp. 39–47, 2020.

[8] W. Fu and D. O. Radiology, "Application of combined diagnosis of CT and MRI in shoulder joint injury," *Contemporary Medicine*, 2019.

[9] A. Bucha, S. Dashottar, and A. Shukla, "Shoulder MRI in diagnostic evaluation of shoulder joint instability: a comparison with shoulder arthroscopy," *International Journal of Radiology and Diagnostic Imaging*, vol. 2, no. 2, 2019.

Hindawi
Journal of Healthcare Engineering
Volume 2021, Article ID 7865155, 4 pages
https://doi.org/10.1155/2021/7865155

Research Article

The Value of CT Three-Dimensional Reconstruction in Nursing and Diagnosis of Senile Hip Fracture

Yuanyuan Shi[1] **Si Chen**[2] **Xue Chen**[3] **and Pan Xue**[3]

[1]*Department of Nursing, The Second Hospital of Jilin University, Changchun 130041, China*
[2]*Geriatric Medicine, The Second Hospital of Jilin University, Changchun 130041, China*
[3]*Department of Orthopedics, The Second Hospital of Jilin University, Changchun 130041, China*

Correspondence should be addressed to Pan Xue; 2001010212@st.btbu.edu.cn

Received 24 June 2021; Accepted 12 August 2021; Published 20 August 2021

Academic Editor: Enas Abdulhay

Aim. To study the diagnostic effect of hip fracture in the elderly. In this paper, a total of 100 elderly patients with hip fracture from January 2020 to May 2021 were selected for X-ray and CT examination after admission. The operation was taken as the final criteria for determining hip fracture type, and the diagnosis of hip fracture by CT three-dimensional reconstruction was analyzed and studied. The results showed that the diagnostic rate of CT 3D reconstruction for various types of hip fracture in the elderly was higher than that of CT plain scan and X-ray ($P < 0.05$). For the diagnosis of intra-articular small bone fragments, the rate of missed diagnosis was 2% (2/100) with CT 3D reconstruction, 10% (10/100) with conventional CT scan, and 20% (20/100) with X-ray. The rate of misdiagnosis was 5.0% (5/100) with CT 3D reconstruction. Routine CT scan was 15% (15/100), X-ray was 30% (30/100), and CT 3D reconstruction was significantly lower than other examinations ($P < 0.05$). *Conclusion.* CT 3D reconstruction has high accuracy in the diagnosis of various types of hip fractures in the elderly.

1. Introduction

Artificial hip arthroplasty has developed for nearly half a century since its development. At present, this technology has become a method for the treatment of hip diseases such as femoral neck fracture, hip osteoarthritis, femoral head necrosis, rheumatoid hip arthritis, ankylosing spondylitis complicated with hip ankylosis, congenital acetabular dysplasia, and hip tumor, It is an effective means to relieve hip pain, restore joint activity, and improve joint stability. It is an effective means to restore joint motion and improve joint stability. Artificial hip replacement includes total hip arthroplasty (THA), total hip replacement (THR), and artificial femoral-head replacement (AFR) [1]. According to statistics, more than 1 million cases of artificial hip arthroplasty have been carried out globally every year, and the number of THA is increasing year by year. By 2015, 0.83% of the total population of the United States has received artificial hip arthroplasty, and the number of artificial hip arthroplasty in China is as high as 200,000 cases every year. At present, the length of hospital stay of patients with hip arthroplasty in China is 13.07 ± 3.49 days, which is generally longer than that of patients in Western countries or regions (5.3 ± 1.6 days). On the one hand, it may be due to the delayed start of functional exercise and getting out of bed. Hip replacement patients, on the other hand, have early postoperative complications such as lower extremity deep vein thrombosis (DVT), infection, postoperative nausea and vomiting (PONV), and prosthesis peripheral fracture. Prolongation of hospitalization time brings an increase in hospitalization costs, increasing the economic burden of medical treatment [2].

Musculoskeletal diseases, including osteoarthritis of the hip and knee, are the second leading cause of disability in almost every country and region in the world, according to a 2010 study on the global burden of disease in the Lancet. The incidence of hip and knee osteoarthritis is increasing year by year worldwide, especially in the elderly population [3].

March et al. have shown that hip diseases, mainly osteoarthritis of the hip, affect nearly 15% of the global population and are a major cause of pain and disability in the elderly. Although there are many treatments available for hip osteoarthritis, joint replacement remains the primary treatment of choice. With the acceleration of population aging process and the development of transportation and construction industry, the incidence of femoral neck fracture increases year by year [4]. Based on data on the incidence of hip fractures, changes in the age composition of the population, and long-term changes in the risk of hip fractures, there are estimates that by 2025, the number of hip fractures will reach 2.6 million (37% in Asia), and by 2050, it will reach 4.5 million (45% in Asia). After China enters the aging society, the incidence of senile fracture increases by 30% every 10 years, and the number of hip fracture also increases at a rate of four times. Hip fractures account for 50% of all fractures caused by osteoporosis in the elderly. Femoral neck fracture is the most common and serious hip fracture. Through retrospective study and comparative analysis, Lee et al. investigated the pelvis of 136 normal adults in order to provide anatomic and morphological data of the coccyx with three-dimensional images for the diagnosis of idiopathic coccygeal pain. Computed tomography used software to reconstruct a three-dimensional model of the pelvis from X-ray images of all the specimens. Unilateral or bilateral fusion of the sacral and coccygeal angles is not uncommon. As far as the transverse processes of sacrum and coccyx are concerned, the separation type is more than the fusion type. The incidence and angle of coccyx deviation vary greatly from individual to individual. A three-dimensional model of the gross anatomy of the coccyx will help to understand the mechanisms underlying the development of idiopathic coccygeal pain [5]. Morgagni hernias can be diagnosed in different ways, but they are not always 100% accurate. A three-dimensional reconstruction of the model may help to better understand important anatomical structures. Zhang et al. performed laparoscopic repair based on a three-dimensional reconstruction model. This case demonstrates that the three-dimensional reconstruction model is a useful tool for the diagnosis and preoperative evaluation of MH patients, especially when the diagnosis is confused in clinical practice [6]. In recent years, with the aging of China's social population, the improvement of people's requirements for the quality of life, the continuous improvement of the medical insurance system, and the rapid development of medicine, the demand for hip replacement in China has increased significantly. It has been more than ten years since ERAS was introduced into China. Through continuous exploration and practice by scholars, remarkable achievements have been made [7]. 2015 was the year of rapid development of ERAS, and the first ERAS collaboration group was established in China. The first ERAS national conference was held in Nanjing in July; the consensus of Chinese experts on the application of accelerated rehabilitation surgery in colorectal surgery (2015 Edition) was released, which includes 19 perioperative measures, mainly including shorten the preoperative ban drink, multimodal analgesia, early postoperative fasting time bed, early to eat drink, restrictive transfusion and minimally invasive surgical operation, the consensus for our country the first ERAS expert consensus. Since then, Chinese scholars have successively published the consensus of ERAS experts in many surgical fields. Including the GanDanYi surgery accelerate rehabilitation expert consensus (2015 edition), the biliary tract surgery accelerate rehabilitation surgery expert consensus (2016 edition), the stomach gastric resection surgery accelerate rehabilitation surgery expert consensus (2016 edition), the laparoscopic hepatectomy accelerate rehabilitation surgery expert consensus (2017 edition)," "China accelerated rehabilitation surgery perioperative tube Consensus of Science Experts (2016 Edition), etc. A systematic evaluation of the application status of ERAS in China shows that ERAS can effectively shorten the length of stay, reduce hospitalization costs, reduce postoperative complications, improve patient satisfaction, improve prognosis and improve the quality of medical care in the surgical fields of gastrointestinal surgery, hepatobiliary surgery, cardiothoracic surgery, urology and obstetrics and gynecology. However, there are still few reports on the application of this advanced surgical concept and technology in the field of orthopedics, especially in hip arthroplasty, and there is still a large research space at present [8].

The innovation point of this paper is that CT 3D reconstruction can not only clearly show the situation of joint fracture, but also select the best Angle of observation of fracture through rotation Angle. In addition, 3D reconstruction can effectively observe the situation of bone fragments, which is conducive to the judgment of hip fracture type and the formulation of surgical plan. The results of this study fully prove that CT examination has a high sensitivity to fracture.CT 3D reconstruction has a high accuracy in the diagnosis of various types of hip fractures in the elderly.

2. Materials and Methods

2.1. General Information. There were 100 cases in this study, including 53 males and 47 females. The average age was (75.06 ± 2.33) years from 61 to 82 years old. The time from hip injury to admission to hospital ranged from 5 to 52 hours (19.49 ± 6.32) hours on average. Causes of injury: traffic accident injury 45 cases, falling injury 30 cases, fall and fall injury 25 cases. Inclusion criteria: ① All the elderly patients were over 60 years old; ② The symptoms of hip fracture were obvious on admission; ③ All patients had a history of hip trauma before admission; ④ All patients were finally treated by surgery, and the type of hip joint injury was determined by surgery. ⑤ All the patients and their family members agreed to participate in this study, and signed the surgical consent and informed consent. Exclusion criteria: ① Involuntary participation in the study; ② Old or pathological hip fracture; ③ Mental disorders can not take the initiative to participate in surgical treatment.

Table 1: The diagnosis of various types of senile hip fractures by different examination methods.

The fracture types	CT 3D reconstruction	Routine CT	X-ray
Femoral neck fracture	100.0% (58/58)	94.83% (55/58)	86.21% (50/58)
Intertrochanteric fracture of femur	100.0% (29/29)	93.10% (27/29)	75.86% (22/29)
Acetabulum fracture	96.67% (29/30)	86.67% (26/30)	56.67% (17/30)

Note. ① Femoral neck fracture: Comparison of 3D reconstruction and conventional CT, $\chi 2 = 4.1039$, $P < 0.05$; Three-dimensional reconstruction compared to X-ray, $\chi 2 = 7.6631$, $P < 0.05$; Conventional CT versus X-ray, $\chi 2 = 6.0583$, $P < 0.05$; ② Intertrochanteric fracture of femur: comparison of three-dimensional reconstruction and conventional CT, $\chi 2 = 5.2043$, $P < 0.05$; Three-dimensional reconstruction compared to X-ray, $\chi 2 = 11.0926$, $P < 0.05$; Conventional CT versus X-ray, $\chi 2 = 9.2235$, $P < 0.05$; ③ Acetabular fractures: Comparison of 3D reconstruction and conventional CT, $\chi 2 = 8.4921$, $P < 0.05$; Three-dimensional reconstruction compared to X-ray, $\chi 2 = 16.3928$, $P < 0.05$; Conventional CT versus X-ray, $\chi 2 = 12.1149$, $P < 0.05$.

2.2. Examination and Treatment Methods

① X-ray examination: the machine model is Siemens YSIO, and the hip joint and pelvis are scanned in the positive position.

② CT examination: CT models were Siemens SOMATOMdefinionAS and GebrightSpeed, scanning from both iliac wings to ischial nodular, voltage: 120 kV, current: 90 mA, matrix: 512×512, layer thickness: 2.5 mm, field: 400×400 mm.

③ CT three dimensional reconstruction: 1~1.25 mm, with a thick layer of layer spacing of 1 mm, relevant data import post-processing software, multiplanar reconstruction (MPR), bone reconstruction algorithm was used to rebuild, according to the direction of horizontal, vertical axis coordinates of human body adjust, select effective fracture plane imaging, further analyze the fracture type, form, and so on and so forth. Surgical treatment: ① Joint replacement for femoral neck fracture; ② Femoral trochanteric fracture should be treated with proximal femoral anti-rotation intramedullary nail; ③ Acetabular fractures were treated with open reduction plate fixation.

2.3. To Observe. Using surgery as the final criteria to determine the type of hip fracture, we compared the diagnosis of various types of hip fracture with X-ray, conventional CT scan and CT three-dimensional reconstruction. Two attending radiologists read the radiographs respectively. When the results were inconsistent, the same conclusion could be reached after joint discussion.

2.4. Statistical Method. SPSS18.0 data statistical software was used to establish a database and statistical analysis was conducted. Measurement data was expressed as $(x \pm s)$, enumulation data as rate (%), $\chi 2$ test was used for comparison, $P < 0.05$, which was statistically significant.

The materials and methods section should contain sufficient detail so that all procedures can be repeated. It may be divided into headed subsections if several methods are described.

3. Results and Discussion

3.1. The Diagnosis of Various Types of Senile Hip Fractures by Different Examination Methods. The diagnosis of various types of senile hip fracture by different examination methods: in 80 cases of senile hip fracture patients, conventional CT scan and CT three-dimensional reconstruction were completely detected (100.0%), and the detection rate of X-ray examination was 81.25% (81.25/100), the difference was statistically significant($\chi 2 = 5.2396$, $P > 0.05$); In this study, 117 hip fractures were found, including 58 femoral neck fractures, 29 intertrochanteric fractures, and 30 acetabulum fractures. In the acetabular fractures, 5 anterior wall, 8 posterior wall, 6 anterior column, 7 posterior column and 4 acetabular floor were involved. The detection rate of CT three-dimensional reconstruction for femoral neck fracture, intertrochanteric fracture and acetabular fracture was higher than that of conventional CT scan and X ray ($P < 0.05$). See Table 1.

Table 2: Diagnosis of intraarticular small bone fragments by different examination methods.

The fracture types	The missed diagnosis (%)	The misdiagnosis rate (%)
CT 3D reconstruction	2.5	5.0
Routine CT	8.75	12.50
X-ray	18.75	27.50

Note. In terms of missed diagnosis rate, the comparison between CT 3D reconstruction and conventional CT, $\chi 2 = 3.3649$, $P < 0.05$; Comparison of CT 3D reconstruction and X-ray, $\chi 2 = 8.0237$, $P < 0.05$; Routine CT scans compared to x-rays, $\chi 2 = 5.1282$, $P < 0.05$; In terms of misdiagnosis rate, the comparison between CT 3D reconstruction and conventional CT, $\chi 2 = 3.4035$, $P < 0.05$; Comparison of CT 3D reconstruction and X-ray, $\chi 2 = 11.2391$, $P < 0.05$; Routine CT scans compared to x-rays, $\chi 2 = 8.0907$, $P < 0.05$.

3.2. Diagnosis of Intra-Articular Small Bone Fragments by Different Examination Methods. Different examination methods for the diagnosis of intraarticular small bone fragments: For the diagnosis of intraarticular small bone fragments, the rate of missed diagnosis was 2% (2/100) with CT 3D reconstruction, 10% (10/100) with conventional CT scan and 20% (20/100) with X-ray. The rate of misdiagnosis was 5.0% (5/100) with CT 3D reconstruction. Routine CT scan was 15% (15/100), X-ray was 30% (30/100), CT 3D reconstruction was significantly lower than other examinations ($P < 0.05$). See Table 2.

4. Conclusions

The acetabulum, femoral head and other tissues together constitute the hip joint, which can cause hip injury when it is subjected to the external force of several times the weight of human body. Since osteoporosis is common in older people, mild violence can lead to hip fractures. Because of the decline in the metabolism of the elderly patients themselves, the recovery time is prolonged after the trauma, and in severe cases, other serious concurrent diseases will be caused. For the elderly patients with hip fracture, timely diagnosis and treatment is very important. CT examination has the characteristics of short time and quick scan, and can collect volumetric data at the same time, the thickness of the layer is extremely thin. CT post - processing technology can obtain three - dimensional images. In addition, the examination results of various types of hip fractures in this study showed that CT three-dimensional reconstruction had the highest diagnostic rate for femoral neck, intertrochanteric and acetabular fractures. Because hip fracture is often accompanied by bone fragments displaced, some of the bone fragments are easy to embed in the joint, and it is not easy to be observed in the examination process. In severe cases, it can lead to necrosis of the femoral head or arthritis, which can affect the prognosis of elderly patients to a certain extent. The results of this study effectively proved the advantage of 3D reconstruction in the diagnosis of small intraarticular bone fragments. Multi-plane reconstruction can clearly display the femoral head and acetabulum, and observe the joint fracture from multiple angles. Higher tissue resolution can improve the recognition of small fragments of bone, and further improve the diagnosis rate of hip fracture. In conclusion, CT 3D reconstruction has a high accuracy in the diagnosis of various types of hip fractures in the elderly.

Data Availability

The data used to support the findings of this study are available from the corresponding author upon request.

Conflicts of Interest

The authors declare no conflicts of interest.

Acknowledgments

This study was not funded.

References

[1] S. Kolta, A. L. Bras, D. Mitton et al., "Three-dimensional X-ray absorptiometry (3D-XA): a method for reconstruction of human bones using a dual X-ray absorptiometry device," *Osteoporosis International*, vol. 16, no. 8, pp. 969–976, 2015.

[2] J. Watt, L. Cox, and R. G. Crilly, "Distribution of vertebral fractures varies among patients according to hip fracture type," *Osteoporosis International*, vol. 26, no. 3, pp. 885–890, 2015.

[3] O. Cvijanovi, S. Z. Cvek, G. Gulan et al., "The effect of age, anthropometric parameters, vertebral bone densitometry and ash density on iliac crest bone volume and microstructure," *Periodicum Biologorum*, vol. 117, no. 1, pp. 53–57, 2015.

[4] Y. Chen, H. Zhou, Y. Hu et al., "[Risk factors of pulmonary embolism in senile and non-senile inpatients and the predictive value of Caprini risk assessment model in these two populations]," *Zhonghua Yi Xue Za Zhi*, vol. 97, no. 10, pp. 755–760, 2017.

[5] J.-Y. Lee, Y.-C. Gil, K.-J. Shin et al., "An anatomical and morphometric study of the coccyx using three-dimensional reconstruction," *The Anatomical Record*, vol. 299, no. 3, pp. 307–312, 2016.

[6] Z. Zhang, Y. Fu, and B. Hu, "Three-dimensional reconstruction model in the diagnosis of Morgagni's hernia," *BMJ Case Reports*, vol. 14, no. 2, Article ID e239911, 2021.

[7] H. Ulutürk, E. Yücel, B. Okur et al., "Surgical management of a bilateral bifid condyle: diagnosis, three-dimensional reconstruction, and treatment - a report of a case and review of the literature," *Nigerian Journal of Clinical Practice*, vol. 21, no. 2, pp. 251–255, 2018.

[8] E. Fanning, T. Donnelly, J. G. Lunney, D. B. Murray, and T. Persoons, "Application of gaseous laser-induced fluorescence in low-temperature convective heat transfer research," *Experiments in Fluids*, vol. 61, no. 5, pp. 1–20, 2020.

Hindawi
Journal of Healthcare Engineering
Volume 2021, Article ID 5666136, 6 pages
https://doi.org/10.1155/2021/5666136

Research Article

The Role of Digital X-Ray in Curative Effect and Nursing Evaluation of Cervical Spondylotic Radiculopathy

Xue Chen[1] **Pan Xue**[1] **Yuanyuan Shi**[2] **and Si Chen**[3]

[1]*Department of Orthopedics, The Second Hospital of Jilin University, Changchun 130041, China*
[2]*Department of Nursing, The Second Hospital of Jilin University, Changchun 130041, China*
[3]*Geriatric Medicine, The Second Hospital of Jilin University, Changchun 130041, China*

Correspondence should be addressed to Si Chen; 2005010224@st.btbu.edu.cn

Received 24 June 2021; Accepted 7 August 2021; Published 17 August 2021

Academic Editor: Enas Abdulhay

The present study attempted to analyze the features of atlanto-occipital radiograph in patients with cervical spondylotic radiculopathy or vertebral artery type. In order to reduce the interference of human factors and the measurement error as much as possible, this experiment adopts the blind design and analyzes the digital format X-ray films by using the computer software ImageJ. Because the tangent line between the outer plates of the anterior and posterior margin of the foramen magnum was not accurately located on the X-ray film, the angle formed by the line between the saddle dorsal slope and the center point of the anterior and posterior nodule with a clear display was selected as the measurement method of the angle between the atlanto-occipital joints. The results showed that the lateral cervical curvature of the VCS group was 0.43 ± 0.51, and the lateral cervical curvature of the CSR group was 0.46 ± 0.49, both of which were significantly lower than the normal value (1.2 ± 0.5 cm). Patients in both groups had the characteristic of cervical curvature straightening. The changes of cervical curvature in overflexion and overextension positions can indirectly reflect the state of cervical motion. The anterior flexion neck curve of the VCS group was less than that of the CSR group ($P < 0.05$). Compared with the CSR group, VCS showed limited cervical anterior flexion movement. In this study, X-ray films of both CSR and VCS showed occipitocervical flexion and extension disorders, cervical curvature straightening, and lower cervical instability. In VCS, occipitocervical flexion and extension disorders were mainly manifested in atlantoaxial flexion disorders, while in CSR, atlanto-occipitocervical flexion and extension disorders were mainly manifested in atlantoaxial flexion disorders.

1. Introduction

Cervical spondylosis is a common disease in orthopedic department. The prevalence rate of cervical spondylosis in China is about 3.8%~17.5%, and it shows a rapid increase and younger trend. Cervical spondylotic radiculopathy accounted for more than 60% of all types of cervical spondylopathy. The rotation and lifting technique is an important TCM method to treat cervical spondylotic radiculopathy. The method has been approved by the National Tenth Five-Year Project, the National Eleventh Five-Year Support Plan, and the National Natural Science Foundation of China, has proved its effectiveness and safety, and has been approved by the State Administration of Traditional Chinese Medicine to promote and apply nationwide. However, the basic research on the mechanism of action of this technique has been lagging behind and cannot meet the clinical needs.

In the preliminary clinical study, it was found that the X-ray manifestations of cervical spondylotic radiculopathy may be different from those of other types of cervical spondylopathy. Reviewing the previous literature, it is found that the summary analysis on the imaging manifestations of cervical spondylopathy of nerve radiculopathy is more common, but the comparative studies on the imaging manifestations of cervical spondylopathy of nerve radiculopathy and other types of cervical spondylopathy are rarely carried out.

Cervical spondylosis is caused by a series of clinical manifestations caused by cervical intervertebral disc degeneration, intervertebral instability, osteophyte or disc rupture at the vertebral edge, pulposus prolapse, and other compression of nerve roots, spinal cord, or vertebral artery. Cervical spondylotic radiculopathy (CSR) and vertebral artery spondylopathy (VCS) are the most common types of cervical spondylopathy. Clinically, both of them have their own unique clinical manifestations. However, there is no consensus on whether there is the same difference in imaging between the two. With the development of science and technology, imaging diagnostic technology has been improved and developed, and CT and MRI examination has been basically the universal application. However, because it is cheap and easy to perform, X-ray examination is still the most commonly used examination method for cervical spondylosis. Reviewing the previous literature, the summary and analysis of X-ray films of cervical spondylosis are more common, but the comparative analysis of X-ray findings of cervical spondylosis of nerve root type and cervical spondylosis of vertebral artery type is rarely carried out. The analysis of the imaging findings of CSR and VCS is helpful to understand the pathogenesis of both and can improve the level of clinical diagnosis, which has important clinical value. Therefore, this experiment was designed to compare and analyze the X-ray characteristics of CSR and VCS.

Cervical spondylosis is caused by a series of clinical manifestations caused by cervical intervertebral disc degeneration, intervertebral instability, osteophyte or disc rupture at the vertebral edge, pulposus prolapse, and other compression of nerve roots, spinal cord, or vertebral artery. There are many research studies on the treatment of cervical spondylosis. The objective of this study was to investigate the curative effect of shock wave combined with acupuncture in the treatment of senile cervical spondylotic radiculopathy [1]. Zhou et al. studied the clinical efficacy of Baimai plaster massage combined with cervical pain granules in the treatment of cervical spondylotic radiculopathy [2]. Cui et al. discussed the efficacy of low-weight continuous traction in treating nocturnal pain of cervical spondylosis [3]. Juan et al. discussed the clinical efficacy of joint loosening combined with nerve loosening in the treatment of cervical spondylotic radiculopathy [4]. Sheng et al. discussed the clinical efficacy of acupuncture combined with cervical pain granules in treating cervical spondylotic radiculopathy [5]. Zhang et al. studied the clinical efficacy of warm acupuncture under the guidance of high-frequency ultrasound in the treatment of cervical spondylotic radiculopathy [6]. Jiang et al. discussed the application effect of TCM nursing clinical pathway in patients with cervical spondylotic radiculopathy [7]. Chen et al. analyzed the clinical efficacy of acupuncture, traction, and cervical vertebra in the treatment of cervical spondylotic radiculopathy [8]. Yang et al. analyzed the efficacy of Xifeng dredging collaterals combined with Shujing tongdu point in the treatment of vertebral artery type cervical spondylosis [9].

X-ray examination is the cheapest, is simple and easy to perform, and is often used in routine detection and diagnosis of cervical spondylosis [10]; it is a routine examination method for cervical spondylosis and has important clinical significance for the diagnosis of cervical spondylosis. It is generally believed that radiculotype cervical spondylopathy is mainly related to lower cervical spondylopathy and osteophyte hyperplasia, while vertebral artery type cervical spondylopathy is mainly manifested as atlantoaxial joint unalignment or cervical instability. In the previous literature, experimental designs were designed to summarize the X-ray manifestations of cervical spondylotic radiculopathy or vertebral artery spondylopathy without comparative analysis of the X-ray manifestations of the two. The difference in radiographic appearance between the two is inconclusive. There have been few studies on the findings of atlanto-occipital radiograph in patients with cervical spondylotic radiculopathy or vertebral artery type. Therefore, on this basis, this paper studied the curative effect of digital X-ray in cervical spondylotic radiculopathy. Cervical spondylotic radiculopathy is mainly manifested in atlanto-occipital joint extension disorder, while vertebral artery type cervical spondylopathy is mainly manifested in atlantoaxial joint flexion disorder, and this difference is closely related to its pathological mechanism.

2. Research Methods

2.1. Experiment Design: Single-Blind Control

2.1.1. Sample Size

Observation group: 60 cases of cervical spondylotic radiculopathy.

Control group: 60 cases of vertebral artery type of cervical spondylosis.

2.2. Implementation Method. 120 cases of X-ray films were randomly sorted, and then four clinicians trained in measurement were assigned to measure the numbered X-ray films without knowing the type of cervical spondylosis and input corresponding data. After data entry is completed, the analyst will break the blind and complete data statistical analysis.

2.3. Content and Method of Line Slice Measurement. The computer software ImageJ was used for imaging measurement. During measurement, X-ray film in DICOM format was imported into the program to open, and the drawing tool and measurement tool of ImageJ were used for measurement. Specific measurement contents and methods are as follows:

(1) Cervical curvature: the distance between the posterior edge of the cervical curvature vertex vertebra and the tip edge of the axial odontoid process and the posterior lower edge of the seventh cervical vertebra was measured (curve convex is positive, and curve backward tensioning is negative).

(2) Interangle: the angle formed along the saddle dorsal slope and the central point of the anteroposterior atlas nodules (positive angles are those located behind the cervical vertebra and negative angles are those located in front of the cervical vertebra) (see Figure 1).

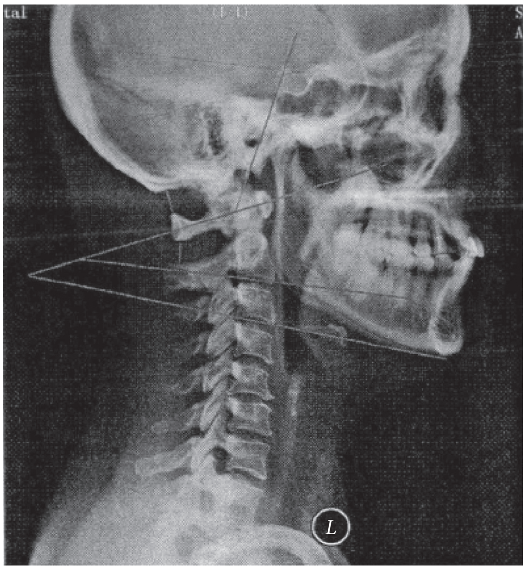

Figure 1: Measurement method of upper cervical intervertebral angle and posterior space.

(3) C1/C2 angle: the angle between the line between the central point of the anterior and posterior atlas nodules and the tangent line of the lower margin of the C2 vertebral body (positive angle is located behind the cervical vertebra body, and negative angle is located in front of the cervical vertebra body).

(4) C2/C3 angle: the degree formed by the tangent of the articular plane of the lower edge of the C2 vertebral body and the tangent of the lower edge of the C3 vertebral body (positive angle is located behind the cervical vertebra body, and negative angle is located in front of the cervical vertebra body).

(5) Posterior spacing of C0/C1: the shortest distance between the occipital bone and the posterior atlas tubercle.

(6) Posterior spacing of C1/C2: the shortest distance between the posterior atlas tubercle and the axial spinous process.

(7) Lower cervical instability segment: on the cervical functional radiograph, angle $>11^{\circ}$ was formed between the vertebrae at the point where the extension line intersected the lower edge of the sliding vertebrae and the sum of the distance from the lower edge of the sliding vertebrae to the sum of the distance from the same vertebrae to the posterior edge of the same vertebrae ≥ 2 mm.

(8) Interarticular angle flexion range: the difference between the interarticular angle on the anterior flexion film and the interarticular angle on the lateral film.

(9) Extension range of motion of inter-articular angle: the difference between the inter-articular angle of the post extension film and the inter-articular angle of the lateral film.

3. Result Analysis and Discussion

3.1. X-Ray Analysis

3.1.1. Cervical Curvature. Comparison of cervical curvature between the two groups is shown in Table 1.

3.1.2. Angle between C0 and C1. Comparison of angle between C0 and C1 between the two groups is given in Table 2.

3.1.3. Angle between C1 and C2. Comparison of C1 and C2 angles between the two groups is given in Table 3.

3.1.4. Angle between C2 and C3. Comparison of C2 and C3 angles between the two groups is given in Table 4.

3.1.5. C0/C1 Rear Spacing. Comparison of posterior spacing of C0/C1 between the two groups is given in Table 5.

3.1.6. Back Spacing of C1/C2. Comparison of posterior spacing of C1/C2 between the two groups is given in Table 6.

3.1.7. Correlation Analysis of Angular Flexion Change between C1 and C2 and Posterior Space Flexion Change. Correlation between anterior flexion of C1/C2 angle and posterior distance is given in Table 7.

3.1.8. Lower Cervical Instability. Comparison of the proportion of lower cervical instability between the two groups is given in Table 8, and comparison of the distribution of lower cervical instability segments between the two groups is given in Table 9.

4. Discussion

The experimental results, as known from Table 1, show that the lateral cervical curvature of the VCS group was 0.43 ± 0.51 and the lateral cervical curvature of the CSR group was 0.46 ± 0.49, both of which were significantly lower than the normal value (1.2 ± 0.5 cm), as shown in Figure 2, suggesting that patients in both groups had the characteristics of cervical curvature straightening. When the cervical spine flexes forward, the cervical spine flexes and moves forward, causing the reduction of cervical curvature. The opposite is true for stretching. Therefore, the changes of cervical curvature in the overflexion and overextension positions can indirectly reflect the state of cervical motion. The anterior flexion neck curvature of the VCS group was less than that of the CSR group ($P < 0.05$), as shown in Figure 3, suggesting that the VCS had limited cervical anterior flexion movement compared with the CSR group.

The occipital neck has a large range of flexion, extension, and rotation. The flexion and extension of the neck is mainly completed by the atlanto-occipital joint, which accounts for half of the whole range of neck motion. The left and right rotations of the head and neck are mainly completed by the

Table 1: Comparison of cervical curvature between the two groups (unit: cm).

The neck piece	Group	Mean ± SD (cm)	t	P
Side a	VCS CSR	0.43 ± 0.51 0.46 ± 0.49	−0.313	0.755
Top down	VCS CSR	−0.62 ± 0.41 −0.77 ± 0.37	2.088	0.039*
After sticking a	VCS CSR	1.24 ± 0.55 1.20 ± 0.51	0.403	0.688
Flexion or value	VCS CSR	1.83 ± 0.70 1.97 ± 0.60	−1.138	0.257

*The curvature of the anterior flexion cervical spine in the VCS group was lower than that in the CSR group, with statistically significant difference ($P < 0.05$).

Table 2: Comparison of angle between C0 and C1 between the two groups (unit: angle).

	Group	Mean ± SD (cm)	t	P
Side a	VCS CSR	57.50 ± 8.49 58.13 ± 10.35	−0.340	0.735
Top down	VCS CSR	53.86 ± 9.84 53.80 ± 9.42	0.032	0.974
After sticking a	VCS CSR	66.70 ± 9.59 63.73 ± 11.49	1.435	0.154
Before the degree	VCS CSR	2.96 ± 5.23 4.12 ± 5.49	−1.038	0.302
After elongation	VCS CSR	8.81 ± 5.93 5.64 ± 5.10	2.927	0.004*
Flexion extension range	VCS CSR	12.28 ± 6.10 9.78 ± 7.17	1.780	0.078

*The extension range of motion between C0 and C1 angles in the VCS group was significantly larger than that in the CSR group. The difference was statistically significant ($P < 0.01$).

Table 3: Comparison of C1 and C2 angles between the two groups (unit: angle).

	Group	Mean ± SD (cm)	t	P
Side a	VCS CSR	27.11 ± 4.76 29.40 ± 5.74	−2.325	0.022*
Top down	VCS CSR	20.98 ± 6.31 22.04 ± 5.43	−0.979	0.330
After sticking a	VCS CSR	31.72 ± 5.66 32.74 ± 5.43	−0.990	0.324
Before the degree	VCS CSR	5.94 ± 3.45 7.35 ± 3.89	−2.045	0.043#
After elongation	VCS CSR	4.62 ± 4.21 3.34 ± 3.22	1.840	0.068
Flexion extension range	VCS CSR	10.74 ± 4.79 10.69 ± 4.53	−0.056	0.956

*Lateral C1/C2 angle in the VCS group was lower than that in the CSR group, with statistically significant difference ($P < 0.05$). #The flexion range of C1/C2 angle in the VCS group was smaller than that in the CSR group ($P < 0.05$).

atlantoaxial joint, and its motion range can also account for about half of the entire rotation of the neck. The normal range of flexion and extension of atlanto-occipital joint and

Table 4: Comparison of C2 and C3 angles between the two groups (unit: angle).

	Group	Mean ± SD (cm)	t	P
Side a	VCS CSR	1.75 ± 4.27 2.47 ± 3.23	−0.743	0.457
Top down	VCS CSR	−2.55 ± 4.40 −1.65 ± 4.06	−1.146	0.254
After sticking a	VCS CSR	4.75 ± 4.94 4.15 ± 3.42	0.762	0.448
Before the degree	VCS CSR	4.54 ± 3.72 4.12 ± 3.49	0.619	0.537
After elongation	VCS CSR	2.72 ± 3.63 1.68 ± 2.51	1.800	0.075
Flexion extension range	VCS CSR	7.30 ± 4.36 5.80 ± 3.65	2.011	0.047

There was no statistically significant difference in the angle between the two groups.

Table 5: Comparison of posterior spacing of C0/C1 between the two groups (unit: cm).

	Group	Mean ± SD (cm)	T or Z	P
Side a	VCS CSR	0.57 ± 0.30 0.57 ± 0.28	−0.065	0.948
Before the degree	VCS CSR	0.64 ± 0.30 0.68 ± 0.28	−0.849	0.398
After elongation	VCS CSR	0.20 ± 0.23 0.20 ± 0.22	0.165	0.869
Forward bending change value	VCS CSR	0.06 ± 0.23 0.11 ± 0.24	−1.229	0.222
Change in extension	VCS CSR	0.38 ± 0.25 0.28 ± 0.25	0.007	0.994
Flexion or value	VCS CSR	0.44 ± 0.28 0.49 ± 0.31	−0.975	0.311

There was no statistically significant difference in the posterior space between the two groups.

Table 6: Comparison of posterior spacing of C1/C2 between the two groups (unit: cm).

	Group	Mean ± SD (cm)	T or Z	P
Side a	VCS CSR	0.48 ± 0.23 0.46 ± 0.21	0.474	0.637
Before the degree	VCS CSR	0.74 ± 0.28 0.80 ± 0.28	−1.051	0.296
After elongation	VCS CSR	0.31 ± 0.15 0.33 ± 0.15	−0.673	0.503
Forward bending change value	VCS CSR	0.26 ± 0.16 0.33 ± 0.20	−2.157	0.033*
Change in extension	VCS CSR	0.17 ± 0.18 0.14 ± 0.11	1.192	0.236
Flexion or value	VCS CSR	0.43 ± 0.22 0.47 ± 0.21	−0.896	0.372

*The flexion change of C1/C2 posterior space in the VCS group was less than that in the CSR group, with statistically significant difference ($P < 0.05$).

Table 7: Correlation between anterior flexion of C1/C2 angle and posterior distance.

Indicators	Forward flexion variation of the posterior spacing of C1/C2
Forward flexion between C1 and C2 angles	0.622**

** $P < 0.001$ indicates a significant correlation between the two.

Table 8: Comparison of the proportion of lower cervical instability between the two groups.

	Instability	No instability	X2	P
VCS	35	25	0.539	0.463
CSR	31	29		

There was no statistically significant difference in the proportion of lower cervical instability between the two groups.

Table 9: Comparison of the distribution of lower cervical instability segments between the two groups.

The section of instability	VCS	CSR	X2	P
C3	9	9		
C4	17	15		
C5	8	6	0.133	0.936
C6	1	1		
C7	0	0		

There was no statistically significant difference in the distribution of lower cervical instability between the two groups.

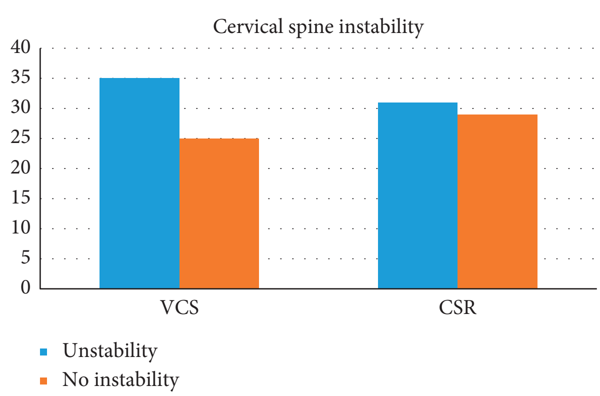

Figure 2: Comparison of cervical instability between the two groups.

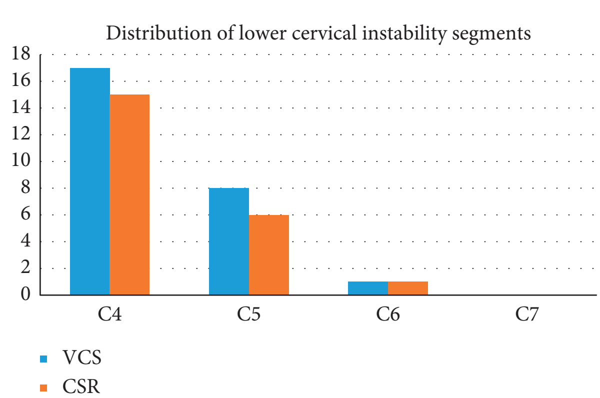

Figure 3: Comparison of cervical instability segment distribution between the two groups.

atlantoaxial joint was ±13° and ±10°, respectively. In this experiment, from Tables 2–6, the range of flexion and extension of atlanto-occipital joint in both groups was significantly less than the normal range, suggesting that both groups had atlanto-occipital flexion and extension disorders. Among them, the atlanto occipital joint extension dysfunction of CSR is more serious than that of VCs ($P < 0.01$). The range of flexion and extension of the atlantoaxial joint in both groups was significantly less than the normal range, indicating the presence of atlantoaxial flexion and extension dysfunction in both groups. Among them, the atlantoaxial flexion dysfunction of VCS was more significant than that of CSR ($P < 0.05$).

Radical cervical spondylopathy (CSR) is caused by disc degeneration, herniation, segmental instability, hyperosteogenesis, or osteophyte formation that irritates and compacts the cervical nerve roots in the spinal canal or in the foraminal area. During cervical anterior flexion, the ligamentum flavum and the posterior longitudinal ligament were elongated, and the sagittal diameter of the cervical canal and the area of the intervertebral foramen were increased accordingly, which could relieve the mechanical compression of nerve roots. However, cervical posterior extension activity can cause contraction of posterior cervical muscle group and reduction of intervertebral foraminal area and further aggravate neck, shoulder, and arm pain by irritating the pathological segmental nerve roots. Therefore, in patients with CSR, posterior extension activity disorders in upper neck are particularly obvious, while anterior flexion activity disorders are less severe than VCS. The two major curves of the vertebral artery are located in the occipital atlantoaxial complex. According to the mechanical compression theory, excessive cervical spine movement can cause the spatial changes of the cervical structure, especially the spatial changes of the occipito-atlantoaxial complex, resulting in the insufficiency of blood supply to the vertebral artery and inducing dizziness. Therefore, upper cervical flexion and extension dysfunction in VCS patients is a state of self-preservation. Furthermore, the vertebral artery was bent almost at right angles above the upper mouth of the transverse foramen of the atlas and was fixed in the groove of the vertebral artery of the atlas by the posterior membrane of the atlas. During cervical anterior flexion, the posterior atlanto-occipital membrane is stretched and local tension is increased, thereby compacting the vertebral artery across the atlanto-vertebral artery sulcus, resulting in insufficient blood supply. Thus, atlanto-occipital flexion dysfunction was more pronounced in VCS patients than in CSR.

In the course of flexion and extension of occipito-atlantoaxial joint, the posterior distance of occipito-atlantoaxial joint and occipito occipital joint changed accordingly. Therefore, this experiment is an attempt to analyze and study this index. The experimental results are given in Table 7, and there was no significant difference between the two groups in the statistical analysis of the posterior space between the occipito-atlanto joints at all states, and no statistical results consistent with the occipito-atlanto angle were obtained. The consideration is related to the difficulty in determining the occipital condylar boundary. In the VCS group, the change value of flexion activity in the posterior space of the atlantoaxial joint was smaller than that in the CSR group ($P < 0.05$), suggesting that the flexion activity of the atlantoaxial joint was limited in the VCS patients, which was consistent with the statistical results of the atlantoaxial angle. There was a positive correlation between the atlantoaxial angle and the change of flexion activity in the distance behind the atlantoaxial joint ($R = 0.622$) ($P < 0.001$). Comparatively speaking, the posterior distance of atlantoaxial joint is easier to measure than the angle between atlantoaxial joints, so the former is recommended in clinical practice.

Lower cervical instability is one of the imaging diagnostic criteria for vertebral artery type of cervical spondylosis, but it is also common in other types of cervical spondylosis. The results of this experiment are given in Tables 8 and 9, and the incidence of lower cervical instability was 58.3% in the VCS group and 51.7% in the CSR group, and there was no statistical difference between the two groups. The distribution of lower cervical instability segments in both the CSR group and the VCS group was concentrated in C3, C4, and C5, which was consistent with previous literature. There was also no statistical difference in the distribution of lower cervical instability between the two groups. These results suggest that lower cervical instability is only a manifestation of cervical degeneration and is not the characteristic X-ray finding of vertebral artery or radiculotype cervical spondylosis.

In this study, X-ray films of both CSR and VCS showed occipitocervical flexion and extension disorders, cervical curvature straightening, and lower cervical instability. However, there were some differences in the X-ray findings between the two, among which the occipitocervical flexion and extension disorders in VCS were mainly manifested in atlantoaxial flexion disorders, while the CSR was mainly manifested in atlanto-occipitocervical flexion and extension disorders, and the differences were closely related to their respective pathological mechanisms. In this study, the open position and double oblique profile of CSR and VCS have not been compared and analyzed, and further study is needed.

5. Conclusions

Occipital and cervical flexion and extension disorders, cervical curvature straightening, and lower cervical instability are common X-ray manifestations of radiculotype cervical spondylopathy and vertebral artery type cervical spondylopathy.

Cervical spondylotic radiculopathy is mainly manifested in atlanto-occipital joint extension disorder, while vertebral artery type cervical spondylopathy is mainly manifested in atlantoaxial joint flexion disorder, and this difference is closely related to its pathological mechanism.

Data Availability

The data used to support the findings of this study are available from the corresponding author upon request.

Conflicts of Interest

The authors declare that they have no conflicts of interest.

References

[1] H. R. Khedmatgozar and M. Alipour-Hafezi, "The role of digital identifier systems in the theory of digital objects," *International Journal of Information Management*, vol. 37, no. 3, pp. 162–165, 2017.

[2] S. A. Rodrigues, A. G. C. Presotto, V. A. R. Barão, R. L. X. Consani, M. A. A. Nóbilo, and M. F. Mesquita, "The role of welding techniques in the biomechanical behavior of implant-supported prostheses," *Materials Science and Engineering: C*, vol. 78, pp. 435–442, 2017.

[3] T. W. Kim, W. Yun, and A. R. Kovscek, "Application of digital volume correlation to x-ray computed tomography images of shale," *Energy & Fuels*, vol. 34, no. 11, pp. 13636–13649, 2020.

[4] M. L. Wilczek, L. Bhatta, B. M. Brumpton et al., "Screening for women with increased risk of fragility fractures in a general female population using digital x-ray radiogrammetry (DXR)," *Maturitas*, vol. 144, pp. 60–67, Article ID 10169, 2020.

[5] S. A. Kruchinin, "A method for the routine testing of digital x-ray units," *Biomedical Engineering*, vol. 53, no. 5, pp. 341–344, 2020.

[6] R. Sheikh, Q. Haq, and U. Abdullah, "Diagnostic role of ultrasonography and x-ray combined versus intravenous urography in evaluation of renal colic," *The Professional Medical Journal*, vol. 28, no. 5, pp. 725–730, 2021.

[7] A. Jh, F. Chen, G. Qiu et al., "Jingshu Keli for treating cervical spondylotic radiculopathy: the first multicenter, randomized, controlled clinical trial," *Journal of Orthopaedic Translation*, vol. 27, pp. 44–56, 2021.

[8] M. Pietragalla, C. Nardi, L. Bonasera et al., "The role of diffusion-weighted and dynamic contrast enhancement perfusion-weighted imaging in the evaluation of salivary glands neoplasms," *La radiologia medica*, vol. 125, no. 9, pp. 851–863, 2020.

[9] D. T. Goldman, H. Sharma, M. Finkelstein et al., "The role of telemedicine in the maintenance of IR outpatient evaluation and management volume during the COVID-19 global pandemic," *Journal of Vascular and Interventional Radiology*, vol. 32, no. 3, pp. 479–481, 2021.

[10] A. J. Schneider and M. J. Gonsalves, "The role and relationship of science and ethics in the evaluation of fairness in sport," *Sport in Society*, vol. 22, no. 2, pp. 1–17, 2018.

Hindawi
Journal of Healthcare Engineering
Volume 2021, Article ID 7569908, 8 pages
https://doi.org/10.1155/2021/7569908

Research Article

Cardiac Ultrasound under Speckle Tracking Technology Based Analysis of Efficacy of Respiratory Rehabilitation on Chronic Obstructive Pulmonary Disease

Chuangen Ren [1] and Wantian Liu [2]

[1] Department of Ultrasound, The First Affiliated Hospital of Wenzhou Medical University, Wenzhou 325000, Zhejiang, China
[2] Department of Ultrasound Medicine, Wenzhou Traditional Chinese Medicine Affiliated to Zhejiang Chinese Medicine University, Wenzhou 325000, Zhejiang, China

Correspondence should be addressed to Wantian Liu; 201701350223@lzpcc.edu.cn

Received 26 May 2021; Revised 6 July 2021; Accepted 3 August 2021; Published 12 August 2021

Academic Editor: Enas Abdulhay

The study shined spotlight on the effect of respiratory rehabilitation training on chronic obstructive pulmonary disease (COPD), which was evaluated using speckle ultrasound algorithm-based cardiac ultrasound. Then, 90 patients with stable COPD, who were admitted to the hospital from January 2018 to December 2019, were randomly rolled into three groups, namely, the fast inhalation and slow exhalation (A) group, abdominal breathing (B) group, and control (C) group. For group A, on the basis of the conventional treatment, the method of rapid inhalation and slow exhalation was adopted. The group B ($n = 30$) adopted the abdominal breathing method besides the conventional treatment. In addition, the group C ($n = 30$) received only conventional treatment. Finally, the efficacy and parameters of the three treatment methods were compared. The echocardiographic parameters and echocardiographic images were calculated and processed by the speckle tracking method. Three kinds of operators were used to track the myocardial spots successfully, and the corresponding points in the image were obtained and calculated. It was found that there was no significant difference in the degree of dyspnea, exercise endurance, lung function, respiratory muscle function, and quality of life (QOL) before treatment ($P > 0.05$). After treatment, in contrast with group C, the previously mentioned indicators in groups A and B were obviously better ($P < 0.05$). Further, both the echocardiographic images and echocardiographic parameters of groups A and B were obviously improved, and there was no obvious difference between groups A and B. Hence, some degree of respiratory rehabilitation was very effective in the diagnosis of patients with chronic pulmonary obstruction. In conclusion, the speckle tracking algorithm-based cardiac ultrasound improves the image quality. At the same time, respiratory rehabilitation training is effective on COPD and worthy of clinical promotion.

1. Introduction

The common symptoms of COPD are characterized by irreversible airflow limitation and difficulty in breathing, and patients often have more severe dyspnea at the onset. At the same time, as the disease progresses, the patient's airflow limitation aggravates, and this symptom is largely related to the inhalation of harmful gases and particles [1, 2]. As a modern disease, COPD has high fatality and disability rates.

With the development of modern medicine, ultrasound diagnosis is adopted in the detection of heart function in patients with COPD. At this stage, some speckles often appear in cardiac ultrasound images. For these speckles, there are two common points at this stage. One point is that it is a kind of noise that influences the image quality. The other point claims that it is a structural signal, which mainly reflects the information between the organ tissue and the imaging medium [3, 4]. Although the two viewpoints are quite different, their purpose is consistent, that is, for better diagnosis, research, and treatment of lesions. At the same time, due to the complexity of COPD itself, it often has complex effects on body functions, which not only acts on the respiratory system, but also has an impact on the structure of skeletal muscle as a result of inflammation in the body caused by COPD. Then, it causes dysfunctions in the respiratory muscles and further aggravates the patient's condition [5, 6]. The symptoms of weakened respiratory muscle function include decreased muscle function and decreased muscle endurance, which are often accompanied by dyspnea, increased carbon dioxide content in the blood, and decreased exercise capacity.

Further research on related phenomena shows that the increase in number of patients with reduced respiratory muscle function will greatly aggravate the consumption of medical resources, and the decline in respiratory muscle function also directly affects the survival rate of COPD patients [7, 8]. Therefore, it is necessary for COPD patients to exercise to improve their respiratory muscle function, and the way to realize it is to perform breathing training.

Therefore, the therapeutic effect of respiratory rehabilitation training on COPD patients was further studied utilizing speckle tracking algorithm-based ultrasound images.

2. Methods and Materials

2.1. Feature Point Operator Construction and Matching Pursuit. The speckles in cardiac ultrasound generally reflect the movement information of the epicardium and myocardium. At the same time, the speckles move with the movement of the myocardium. On this basis, the speckle information closely related to the movement of the myocardium is needed. In the study, the Forstner operator, SUSAN operator, and Harris operator were selected as the research subjects.

The Forstner operator is a well-known positioning operator in photogrammetry. It has the characteristics of fast speed and high accuracy. This operator takes the distance from the origin to the edge line of the inner edge of the window as the observed value, takes the gradient modulus square as the weight, and estimates the coordinates of the intersection point by the least square method. First, points with greater gray-scale differences from the surroundings were selected as feature points. The absolute values of the gray-scale differences in the four directions (up, down, left, and right) of the pixel point were calculated as follows:

$$\begin{cases} \mathrm{d}f_1 = \left|f_{a,b} - f_{a+1,b}\right|, \\ \mathrm{d}f_2 = \left|f_{a,b} - f_{a,b+1}\right|, \\ \mathrm{d}f_3 = \left|f_{a,b} - f_{a-1,b}\right|, \\ \mathrm{d}f_4 = \left|f_{a,b} - f_{a,b-1}\right|, \end{cases} \tag{1}$$

where $f_{a,b}$ is the gray value of (a, b), and $f_{a+1,b}, f_{a,b+1}, f_{a,b+1}$, and $f_{a,b-1}$ are the gray values of the four neighboring points of up, down, left, and right (a, b). Then, the mean value of these four absolute differences is calculated as $M = \text{mean}\{\mathrm{d}f_1, \mathrm{d}f_2, \mathrm{d}f_3, \mathrm{d}f_4\}$. For a given threshold Y, if $M > Y$, then (a, b) is the primary selected point.

In the 3×3 window with the primary selection point (a, b) as the center, the covariance matrix T and the interest value I are calculated according to the simplified Forstner operator, and the equations for T and I are as follows:

$$T = \begin{pmatrix} \sum g_x^2 \sum g_x g_y \\ \sum g_x g_y \sum g_y^2 \end{pmatrix}, \qquad I = \frac{4\mathrm{DeT}(T)}{(\mathrm{trT})^2}, \tag{2}$$

whereg_x and g_y are the Roberts gradients, $\mathrm{Det}(T)$ is the determinant of matrix T, trT is the trace of matrix T (the sum of diagonal elements), and$\mathrm{trT} = \sum g_x^2 + \sum g_y^2$. g_{x1}. The g_{x1} and $g_{y1}g_{y2}$ are as calculated as follows:

$$\begin{cases} g_{x1} = f(a,b) - f(a-1,b+1), \\ g_{x2} = f(a+1,b-1) - f(a,b), \\ g_{y1} = f(a,b) - f(a+1,b+1), \\ g_{y2} = f(a-1,b-1) - f(a,b). \end{cases} \tag{3}$$

The SUSAN operator adopts the USAN corner detection, that is, the pixel to be detected in the center of the circular window template, is called core point. The SUSAN template slides over the image, and the gray value of the image pixel in the template is compared with the gray value of the core point at each position:

$$C(x, x_0) = \begin{cases} 1, & \left|Z(x) - Z(x_0)\right| \le t, \\ 0, & \left|Z(x) - Z(x_0)\right| \ge t, \end{cases} \tag{4}$$

where x_0 is the position of the core point of the image, x is the position of other points in the template, Z_0 is the gray value function, t is the threshold to restore to the difference value, and $c(x, x_0)$ is the comparison result. The brightness difference between points in the template and the core point is calculated, and the sum is as follows:

$$n(x_0) = \sum c(x, x_0). \tag{5}$$

Then, n is compared with a given threshold, and SUSAN sets g as half of the size of $n_{\max}$. Finally, the local maximum value of the corner response is obtained, and the corresponding pixel is marked as a corner point.

Inspired by the autocorrelation function in the signal processing, Harris operator gives the matrix N related to the autocorrelation function. The eigenvalue of the N matrix is the first-order curvature of the autocorrelation. If the two curvature values are both high, the point is considered to be a feature point, and the expression of the Harris operator is as follows:

$$M = G(\tilde{s}) \otimes \begin{bmatrix} g_u & g_u g_v \\ g_u g_v & g_v \end{bmatrix}, \tag{6}$$

where $q = \mathrm{Det}(T) - k\mathrm{Trac}^2(T)$, $k = 0.04$, g_u is the gradient in the direction of x, g_v is the gradient in the direction of y, $G(\tilde{s})$ is the Gaussian template, $\otimes$ is the convolution operation, q is the interest value of each point, DeT is the determinant of the matrix, Trac is the trace of the matrix, and k is the threshold.

2.2. Research Subjects and Groups. Ninety COPD patients admitted to our hospital from January 2018 to December 2019 were selected. All patients admitted met the following criteria: (i) patients had clinically confirmed COPD; (ii) they were older than 50 years and younger than 75 years; (iii) they had normal liver and kidney functions. Patients with the following conditions were excluded: (i) those who had type I or II respiratory failure; (ii) those who had pleural disease or thoracic deformity, bone and joint disease, and neuromuscular junction disease; (iii) those who had received other treatments including traditional Chinese medicine; (iv) those who refused to receive rehabilitation training and had poor compliance. All patients participating in the experiment signed informed consent forms, and this study got permission from the hospital ethics committee.

Ninety patients were randomly divided into three groups, each with 30 cases, namely, the fast inhalation and slow exhalation (A) group, abdominal breathing (B) group, and control (C) group. For group A, on the basis of the conventional treatment, the method of rapid inhalation and slow exhalation was adopted. The group B ($n = 30$) adopted the abdominal breathing method besides the conventional treatment. In addition, the group C ($n = 30$) received only conventional treatment.

2.3. Respiratory Rehabilitation Training Methods. The three groups were all treated with conventional medical treatment, which lasted for eight weeks. On this basis, the group A accepted fast inhalation and slow-exhalation training, and the group B accepted abdominal breathing training. Fast inhalation and slow exhalation training method: the patient was asked breathe quickly through the nose, breathe as much as possible until the lungs were saturated, and the saturated state should be maintained for a short time. Then, the patient breathed out slowly. The exhalation process was also completed through the nose, and the whole breathing was about five seconds, and the time ratio of inhalation and exhalation was 1 : 3 or 1 : 4. Abdominal breathing training method was as the patient's left hand was placed on the chest and the right hand on the upper abdomen. The patient should keep the abdomen swelling when inhaling and make the abdomen actively collapse when exhaling and place the right hand on the back when exhaling, to give a certain pressure in the direction so that the diaphragm can effectively recover, while the left hand remains motionless during the entire breathing process.

2.4. Related Testing Indicators. The basic examinations for all selected patients included lung ventilation function, respiratory muscle function, exercise endurance test, QOL score, and dyspnea score. Among them, the QOL score was measured using SGRQ, the score was within 0–100 points, and the score was negatively correlated with the patient's health status.

The functional dyspnea score was based on the British medical research council (MRC) dyspnea scale. Level 0 means dyspnea during hard exercise; level 1 means shortness of breath when people walk on flat ground or on small slopes; level 2 is shortness of breath when people walk on flat ground; therefore, they are slower than others of the same age and need to stop and rest; level 3 means walking on flat ground for about 100 meters or a few minutes and needs to stop and breathe; level 4 means being unable to leave home due to severe breathing difficulties or having difficulties putting on or taking off clothes.

2.5. Statistical Analysis. The SPSS 22.0 was adopted for statistical analysis, and the mean ± standard deviation was adopted to express the counting results. The comparison between the two groups was realized by t-test, and $P < 0.05$ was statistically significant.

3. Results

3.1. Feature Point Extraction and Matching of Speckle Tracking Algorithm. The extraction results of the feature points of the echocardiogram by the Forstner operator, SUSAN operator, and Harris operator were compared, and the results are shown in Figure 1. Figure 1(a) is the first image of the short-axis motion of the left ventricle during diastole in echocardiography, Figure 1(b) is the image processed by the Forstner operator, Figure 1(c) is the image processed by the SUSAN operator, and Figure 1(d) is the image processed by the Harris operator. It was evident that the SUSAN operator and Harris operator were obviously better than the Forstner operator in extracting features at the corners of the contour. At the same time, the running time of the Forstner operator algorithm was 2.054 s, that of the SUSAN operator algorithm was 2.291 s, and that of the Harris operator was 3.249 s ($P < 0.05$).

3.2. General Information. This study included 90 patients in the experiment, including 30 in groups A, B, and C, respectively. Among them, there were 17 males and 13 females in group A. They were 65.17 ± 5.78 years old in average, and the average course of disease was 8.17 ± 1.24 years; in group B, there were 14 males and 16 females, and they were 66.45 ± 7.22 years old in average, with an average course of 8.73 ± 1.34 years; group C included 20 males and 10 females, and they were 66.14 ± 6.17 years old in average, and the average course of disease was 8.01 ± 1.13 years. During the experiment, there were no patients who were omitted to follow-up, and the loss-to-follow-up rate was 0%. Then, the previously mentioned information was compared ($P < 0.05$) (Figure 2).

3.3. The Difficulty to Learn Respiratory Rehabilitation Training. Groups A and B undergoing breathing rehabilitation training were evaluated for the difficulty of learning. The lower the score, the easier it was to master, and vice versa. The results are shown in Figure 3. The score of group A was 2.14 ± 0.57, and that of group B was 2.58 ± 0.95 ($P > 0.05$).

3.4. Changes in Exercise Endurance and Dyspnea. Figure 4 shows the changes in exercise endurance and dyspnea before and after breathing rehabilitation training,

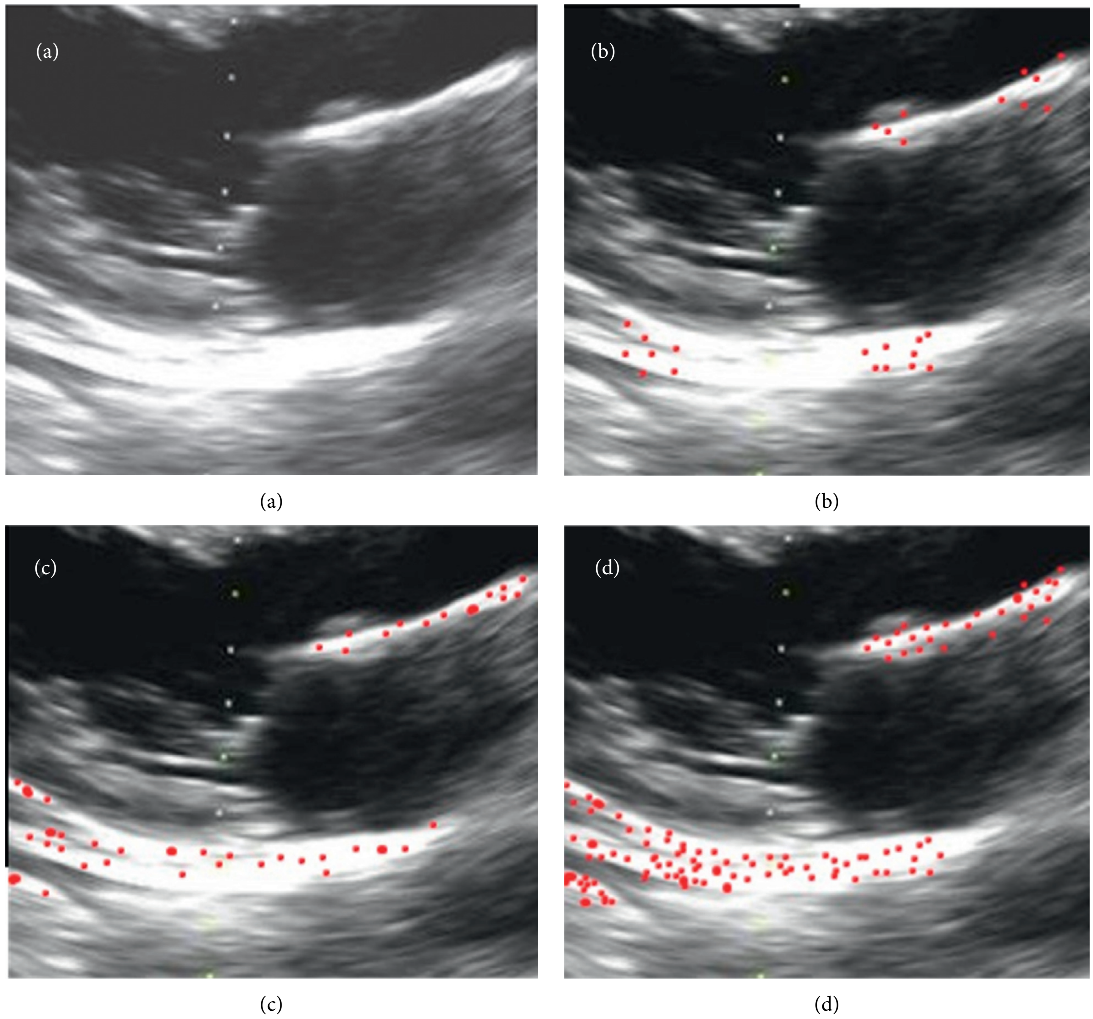

Figure 1: Feature point extraction effect.

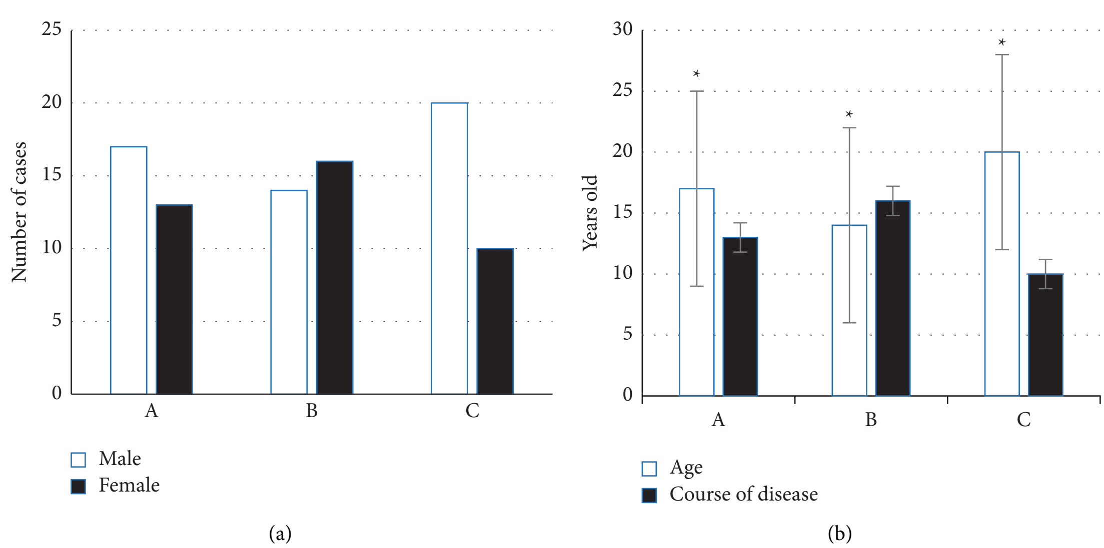

Figure 2: Comparison of general patient data. (a) Gender; (b) age and course of disease (* means that the difference was statistically significant $P < 0.05$).

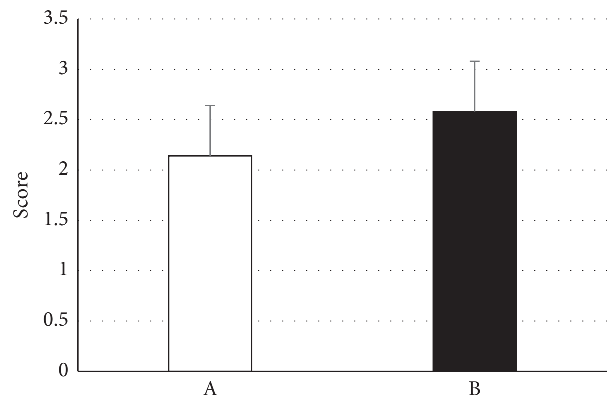

Figure 3: Learning difficulty of different breathing rehabilitation training.

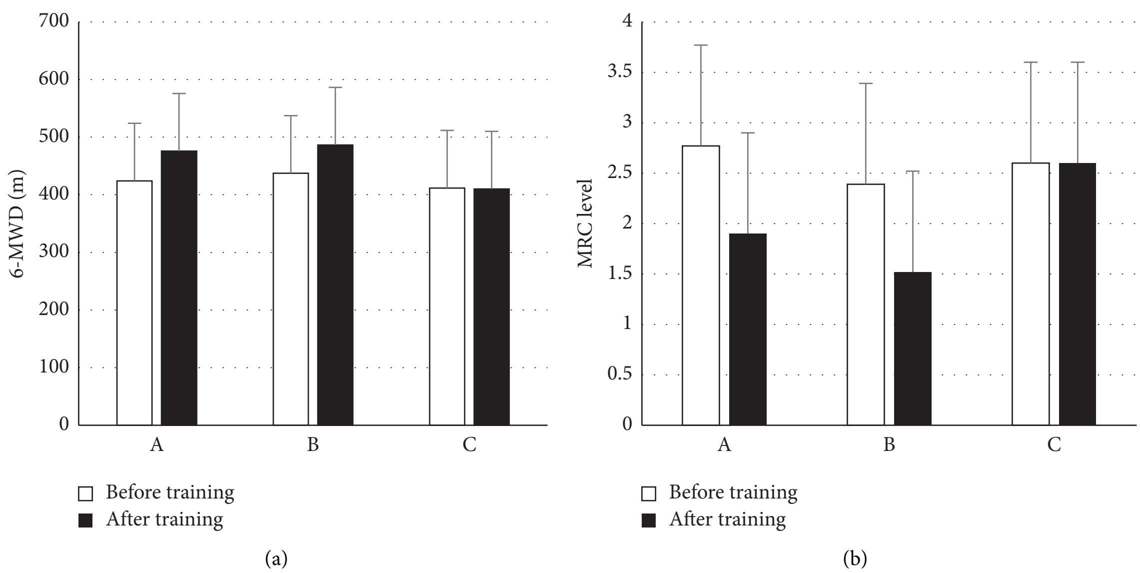

Figure 4: Changes in exercise endurance and dyspnea. (a) Exercise endurance; (b) difficulty breathing.

and there was no obvious difference in exercise endurance and dyspnea before the three groups of patients ($P > 0.05$). After training, in contrast with C, patients in groups A and B had a significant increase in exercise endurance and a significant improvement in dyspnea ($P < 0.05$), and the difference between groups A and B was not obvious ($P > 0.05$).

3.5. Changes in Lung Function. The changes in lung function before and after respiratory rehabilitation training are shown in Figure 5. There was no obvious difference between the deep inspiratory volume (IC) and peak inspiratory flow rate (PIF) of patients in groups A, B, and C before training ($P > 0.05$). After training, in contrast with group C, the IC and PIF of groups A and B were obviously increased ($P < 0.05$), and there was no obvious difference between groups A and B ($P > 0.05$).

3.6. Changes in Cardiac Function. This part of the detection was carried out using the spot tracking algorithm, and the changes in the heart function before and after the respiratory rehabilitation training are shown in Figure 6. Before training, the difference between left ventricular EDVI and left ventricular ESVI was not obvious ($P > 0.05$) in groups A, B, and C. After training, in contrast with group C, the EDVI and ESVI of groups A and B were obviously reduced ($P < 0.05$), and the difference between the groups A and B was not obvious ($P > 0.05$).

3.7. Changes in Respiratory Muscle Function. The changes in respiratory muscle function before and after respiratory rehabilitation training are shown in Figure 7. There was no obvious difference between pretraining MIP and MEP in groups A, B, and C ($P > 0.05$). After training, in contrast with group C, the MIP and MEP of groups A and B were obviously increased ($P < 0.05$), and there was no obvious difference between groups A and B ($P > 0.05$).H_2O

3.8. Changes in the QOL. The changes in the QOL before and after respiratory rehabilitation training are indicated in Figure 8. The overall QOL in groups A, B, and C before

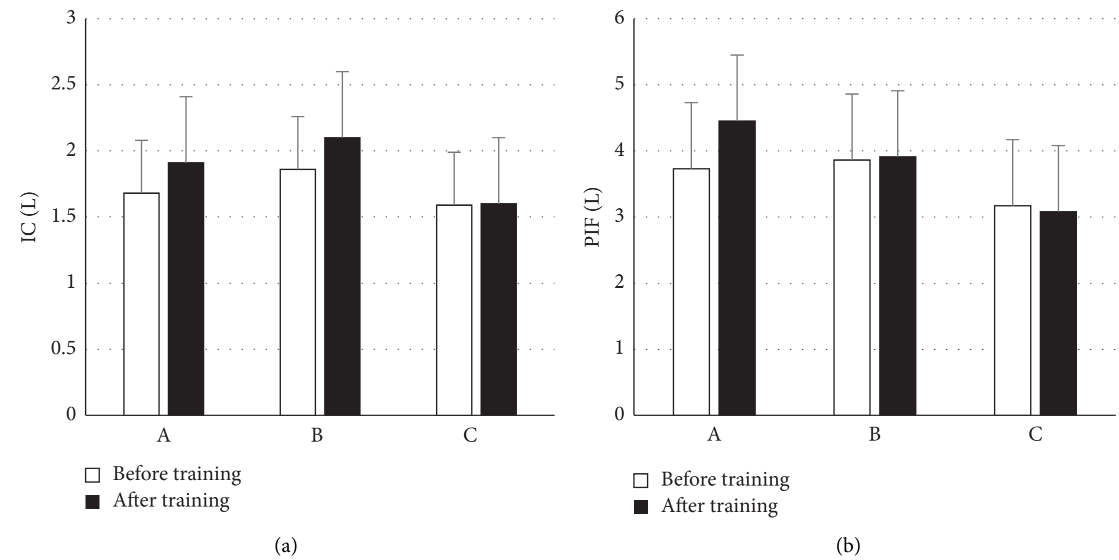

Figure 5: Changes in lung function. (a) Inspiratory volume (IC); (b) peak inspiratory flow (PIF) rate.

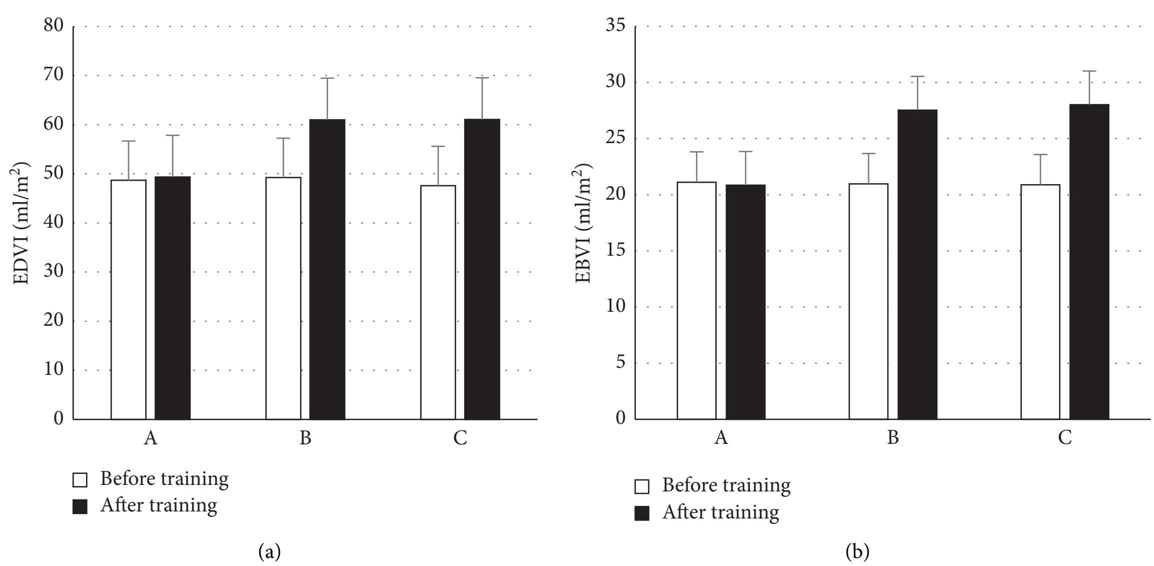

Figure 6: Changes in cardiac function. (a) EDVI; (b) ESVI.

training was low ($P > 0.05$). After training, in contrast with group C, the QOL of groups A and B had a significant increase ($P < 0.05$), and there was no obvious difference between groups A and B ($P > 0.05$).

4. Discussion

At this stage, the main treatment methods for patients in the stable phase of COPD are drug therapy and nondrug therapy, and respiratory rehabilitation therapy is not the mainstream treatment method [9]. COPD patients often have problems not only with lung function, but also with heart function. In the study, speckle tracking algorithm was adopted to analyze cardiac ultrasound. It was found that the point of motion between adjacent frames was small, and it was limited to calculate the elastic strain parameter rotation angle of the local area according to this. However, it was sensible to calculate the movement displacement length by combining the movement displacement vector of each point in the movement process. Movement restriction is one of the main symptoms that can be observed in patients with COPD. Due to functional impairment of the respiratory muscles, the patient often suffers a significant increase in load at the same time, which in turn causes that the patient's ventilation volume is unable to meet the increased demand for ventilation during exercise [10]. Berry et al. showed that systematic breathing training can obviously improve the patient's exercise endurance. In this study, the 6-MWD of groups A and B were obviously increased compared with before training, indicating that the two training methods can also improve the exercise endurance of patients with COPD [11]. It was confirmed in the study that both breathing

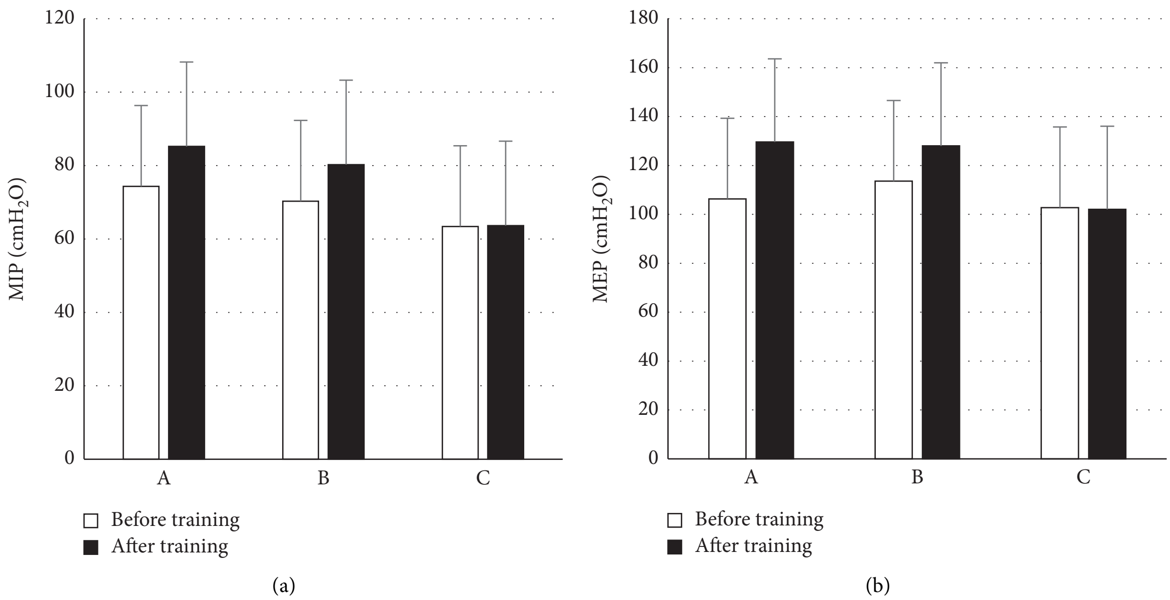

Figure 7: Changes in respiratory muscle function. (a) MIP; (b) MEP.

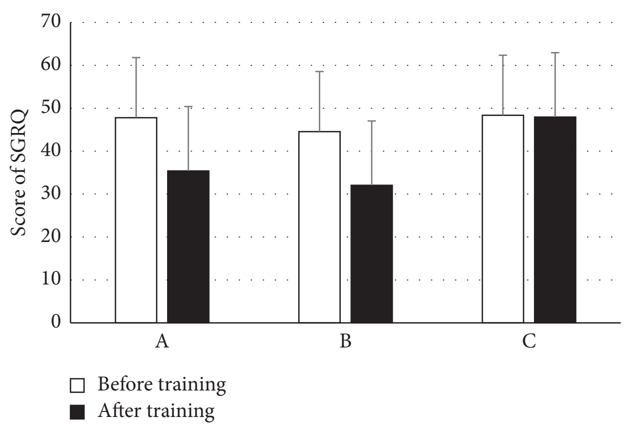

Figure 8: Changes in QOL.

training methods can increase the patient's IC value, suggesting that the increase in IC may be an important reason for the improvement of patients' exercise endurance. In addition, exercise endurance is not only related to the patient's ventilation ability, but also related to the function of the limbs and respiratory muscles. Langer et al. found that MIP was an important factor affecting exercise endurance in patients with severe COPD, indicating that respiratory muscle function was related to exercise endurance. In this study, the respiratory muscle strength of the two groups of patients was obviously improved compared with before training [12].

Due to the particularity of the disease itself, COPD often manifests as a complex respiratory system disease, accompanied by chronic disease of multiple organs throughout the body, which affects a variety of extrapulmonary tissues including skeletal muscle [13]. Due to the appearance of inflammation, the system has an impact on the structure of organs including skeletal muscles, which further leads to the dysfunction of the body including respiratory muscles [14]. Respiratory muscle dysfunction is often caused by a combination of many factors and, to a large extent, is closely related to the clinical manifestations of COPD patients and the severity of the disease [15]. Breathing training can improve the breathing of patients. The study of Kerti et al. showed that, after breathing muscle training in COPD patients, MIP increased obviously before training [16]. In this study, the MIP and MEP of patients in groups A and B were obviously increased than before training, suggesting that both training methods can improve the respiratory muscle function of COPD patients.

5. Conclusion

In this research, the three operators of the speckle tracking algorithm were studied and verified accordingly. Then, the therapeutic effect of respiratory rehabilitation training on COPD patients was further explored, and it was found that, in contrast with the control group, the degree of dyspnea, exercise endurance, lung function, respiratory muscle function, and life quality were obviously improved ($P < 0.05$). In the study, MIP and MEP in group A and group B were significantly higher than those before training, indicating that both the two training methods can improve the respiratory muscle function of COPD patients. However, the research on the algorithm in this study is limited to cardiac ultrasound images. Whether the speckle tracking algorithm is useful for other ultrasound images and needs to be further explored. At the same time, the experimental research samples are small and the types of patients are not subdivided, which should be improved in the future.

Data Availability

The data used to support the findings of this study are available from the corresponding author upon request.

Conflicts of Interest

The authors declare no conflicts of interest.

Acknowledgments

This work was supported by Wenzhou science and Technology Bureau (Y20190671).

References

[1] U. W. Iepsen, K. J. Jørgensen, T. Ringbaek, H. Hansen, C. Skrubbeltrang, and P. Lange, "A systematic review of resistance training versus endurance training in COPD," *Journal of Cardiopulmonary Rehabilitation and Prevention*, vol. 35, no. 3, pp. 163–172, 2015.

[2] A. Marques, C. Jácome, J. Cruz, R. Gabriel, and D. Figueiredo, "Effects of a pulmonary rehabilitation program with balance training on patients with COPD," *Journal of Cardiopulmonary Rehabilitation and Prevention*, vol. 35, no. 2, pp. 154–158, 2015.

[3] U. W. Iepsen, K. J. Jørgensen, T. Ringbæk, H. Hansen, C. Skrubbeltrang, and P. Lange, "A combination of resistance and endurance training increases leg muscle strength in COPD," *Chronic Respiratory Disease*, vol. 12, no. 2, pp. 132–145, 2015.

[4] J. A. Neder, M. Marillier, A.-C. Bernard, M. D. James, K. M. Milne, and D. E. O'Donnell, "The integrative physiology of exercise training in patients with COPD," *COPD: Journal of Chronic Obstructive Pulmonary Disease*, vol. 16, no. 2, pp. 182–195, 2019.

[5] Y. Zeng, F. Jiang, Y. Chen, P. Chen, and S. Cai, "Exercise assessments and trainings of pulmonary rehabilitation in COPD: a literature review," *International Journal of Chronic Obstructive Pulmonary Disease*, vol. 13, pp. 2013–2023, 2018.

[6] W.-H. Liao, J.-W. Chen, X. Chen et al., "Impact of resistance training in subjects with COPD: a systematic review and meta-analysis," *Respiratory Care*, vol. 60, no. 8, pp. 1130–1145, 2015.

[7] K. Schultz, D. Jelusic, M. Wittmann et al., "Inspiratory muscle training does not improve clinical outcomes in 3-week COPD rehabilitation: results from a randomised controlled trial," *European Respiratory Journal*, vol. 51, no. 1, Article ID 1702000, 2018.

[8] H. Hansen, T. Bieler, N. Beyer, N. Godtfredsen, T. Kallemose, and A. Frølich, "COPD online-rehabilitation versus conventional COPD rehabilitation-rationale and design for a multicenter randomized controlled trial study protocol (CORe trial)," *BMC Pulmonary Medicine*, vol. 17, no. 1, p. 140, 2017.

[9] V. C. Huynh, D. P. Fuhr, B. W. Byers, A.-M. Selzler, L. E. Moore, and M. K. Stickland, "Influence of disease severity and exercise limitation on exercise training intensity and load and health benefits from pulmonary rehabilitation in patients with COPD," *Journal of Cardiopulmonary Rehabilitation and Prevention*, vol. 38, no. 5, pp. 320–326, 2018.

[10] R. Gloeckl, T. Schneeberger, I. Jarosch, and K. Kenn, "Pulmonary rehabilitation and exercise training in chronic obstructive pulmonary disease," *Deutsches Aerzteblatt Online*, vol. 115, no. 8, pp. 117–123, 2018.

[11] M. J. Berry, K. L. Shields, and N. E. Adair, "Comparison of effects of endurance and strength training programs in patients with COPD," *COPD: Journal of Chronic Obstructive Pulmonary Disease*, vol. 15, no. 2, pp. 192–199, 2018.

[12] D. Langer, N. Charususin, C. Jácome et al., "Efficacy of a novel method for inspiratory muscle training in people with chronic obstructive pulmonary disease," *Physical Therapy*, vol. 95, no. 9, pp. 1264–1273, 2015.

[13] J. M. Felcar, V. S. Probst, D. R. De Carvalho et al., "Effects of exercise training in water and on land in patients with COPD: a randomised clinical trial," *Physiotherapy*, vol. 104, no. 4, pp. 408–416, 2018.

[14] M. Vitacca, I. Pietta, I. Pietta, M. Lazzeri, and M. Paneroni, "Effect of high-flow nasal therapy during exercise training in COPD patients with chronic respiratory failure: study protocol for a randomised controlled trial," *Trials*, vol. 20, no. 1, p. 336, 2019.

[15] W. Wu, X. Zhang, L. Lin et al., "Transdiaphragmatic pressure and neural respiratory drive measured during inspiratory muscle training in stable patients with chronic obstructive pulmonary disease," *International Journal of Chronic Obstructive Pulmonary Disease*, vol. 12, pp. 773–781, 2017.

[16] M. Kerti, Z. Balogh, K. Kelemen, and J. Varga, "The relationship between exercise capacity and different functional markers in pulmonary rehabilitation for COPD," *International Journal of Chronic Obstructive Pulmonary Disease*, vol. 13, pp. 717–724, 2018.

Hindawi
Journal of Healthcare Engineering
Volume 2021, Article ID 2178281, 13 pages
https://doi.org/10.1155/2021/2178281

Research Article

Research Progress of Ferroptosis: A Bibliometrics and Visual Analysis Study

Jian Xiong,[1] **Wenchuan Qi**,[1] **Jiacheng Liu**,[2] **Zhenqing Zhang**,[2] **Ziwen Wang**,[1] **Jinku Bao**,[3] **Chuanfang Wu**,[3] **and Fanrong Liang**[1]

[1]*Chengdu University of Traditional Chinese Medicine, Chengdu 610075, China*
[2]*Guangxi University of Traditional Chinese Medicine, Nanning 530001, China*
[3]*Key Laboratory of Bio-Resource and Eco-Environment of Ministry of Education, College of Life Sciences, Sichuan University, Chengdu 610041, China*

Correspondence should be addressed to Fanrong Liang; 19821001@cdutcm.edu.cn

Received 28 May 2021; Revised 13 July 2021; Accepted 29 July 2021; Published 10 August 2021

Academic Editor: Enas Abdulhay

Background. Ferroptosis is a type of cell death with major topic of debate under current research and plays an important role in disease regulation. *Objective*. In this study, the literature management software Bibexcel and knowledge graph tool VOSviewer were used to summarize and analyze the international research trends and hotspots about ferroptosis in recent years, which highlight the disease mechanism, diagnosis, and treatment related to ferroptosis. *Material/Methods*. The core collection database of Web of Science was used for retrieving ferroptosis research literature. The information such as the amount of text, the country, the period, the institution, the fund, and the keywords was extracted by the bibliometric tool Bibexcel. The cooccurrence and clustering function of VOSviewer were used to analyze the high-frequency keywords and the cooperative network of the author, institution, and country. *Results*. The research of ferroptosis started late and was formally proposed in 2012. It has developed rapidly and presented an "exponential" growth trend. China, the United States, Germany, Japan, and France are the main national forces of ferroptosis research development. The United States and China have a relatively high degree of support and attention to ferroptosis. Exploring oxidative stress, inducers/inhibitors, synergistic antitumor effect, relationships with other cell death types, GSH/GPX4 and iron metabolism imbalance related mechanisms of ferroptosis, and ferroptosis in the nervous system disease, ischemia-reperfusion injury, tumor, inflammation, and age-related diseases are the hot research directions. *Conclusion*. Ferroptosis has been a research hotspot in the field of biomedicine in recent years and has attracted the attention of scholars all over the world. The occurrence mechanism of ferroptosis and its application in neurological diseases, ischemia and reperfusion injury, tumors, inflammation, and aging are the hot directions of current research. In the future, ferroptosis can be appropriately considered for strengthening new approaches, new diseases, new inductors, new inhibitors, clinical transformation, and traditional medicine research.

1. Introduction

Ferroptosis is an iron ion-related metabolic abnormality with the main feature of lipid peroxidation programmed cell death which has caused extensive attention in recent years. Its gene expression, reaction molecules, biochemical characteristics, and influence morphology are different from other known cell death types: apoptosis, autophagy, necrosis, and pyroptosis. The related mechanisms of ferroptosis such as iron metabolism imbalance, oxidative stress, abnormal glutamate metabolism, and lipid metabolism are involved in the occurrence and development of many diseases and have common mechanisms with the pathological changes of many diseases. These original and important discoveries provide new potential targets for the prevention and control of ferroptosis related diseases. Current evidence shows that ferroptosis plays an important role in ischemia-reperfusion injury, tumor disease, renal failure, circulatory system disease, and nervous system disease [1]. Therefore, it is of positive significance to summarize the existing research results of ferroptosis, discuss the research trends and frontier hotspots of ferroptosis, and reveal the new detailed molecular targets and mechanisms of ferroptosis in depth.

At present, many research summaries and analyses are often confined to literature reading combined with personal experience, lacking a general overview and overall grasp. In this study, literature management software Bibexcel and knowledge map tool VOSviewer were used to conduct bibliometric and visual analysis of ferroptosis. Through the analysis of literature keywords, authors, countries, institutions, funds, and cocitations in the field of ferroptosis research, it explores its research background, research status, research hotspots, and dynamic trends. It hopes to provide references and suggestions for the research on the pathogenesis and clinical application of ferroptosis in the future.

2. Materials and Statistical Analysis

2.1. The Data Source. The literature in this study is mainly from the Web of Science core collection database, Science Citation Index Expanded. The timeline is limited to 2020 from the beginning of the construction of the database. The types of literatures were restricted to ARTICLE and REVIEW, and two researchers independently searched and screened the literatures with TS = (“Ferroptosis” OR “Iron Death”), regardless of language. The search date was December 17, 2020. A total of 1,363 effective literatures were obtained.

2.2. Statistics and Analysis. After selecting the valid documents related to the research, they were downloaded and saved in plain text format. Bibexcel was used to extract the number of papers, year, journal, country, fund, and keywords from the effective bibliography, and the software was used to calculate the H-index of the corresponding author. The H-index indicates that the author’s H paper has been cited at least H times at most. The H-index can accurately evaluate and reflect the academic achievement and level of researchers, so as to discuss and compare the contributions of researchers to the field [2]. The research results show that the higher the H-index value, the higher its quantity, quality, and academic influence. Frequency statistics and keyword analysis of VOSviewer 1.6.15 and Pajek5.13 were used to perform biclustering analysis of high-frequency keywords, and VOSviewer software network analysis and density analysis modules for visual map analysis were used so as to objectively reflect research hotspots. The author’s collaboration network, institutional collaboration network, and country-regional collaboration network visualized collaborative analysis were all realized through VOSviewer [3, 4], which provides guidance and reference for scholars to understand the current situation of cooperation in the research field and carry out extensive scientific research cooperation. Data entry, analysis, and verification were independently completed by two researchers. The rest of the chart-making and analysis were done in Excel 2013.

3. Results

3.1. Basic Features of the Literature

3.1.1. Distribution of Publication Output. From 2012 to 2020, A total of 1363 articles related to the ferroptosis field can be collected. The number of publications in the field of ferroptosis is increasing, overall showing the “exponential” rapid growth. It shows that ferroptosis research is in its development process of “growing period” with a great potential to grow. The earliest research was carried out in 2012. After 2018, the number of published articles was more than 100, and the number of published articles was the highest in 2020. This indicates that the research of ferroptosis has been the focus of scholars’ attention in recent years and is a hot research direction of future medical research (Figure 1).

3.1.2. Distribution of Country. Through Bibexcel software, a scientific metrological analysis is made of the national characteristics of ferroptosis research. The results show that more than 100 papers were published in four countries, accounting for 96.99% of the total number of papers published. The top 5 countries are China, the United States, Germany, Japan, and France (Table 1), indicating that these 5 countries are the core strength of international ferroptosis research field. In addition, the number distribution map of the world presents that Eastern Asia, North America, Europe, and Oceania are the core region for ferroptosis research, which is basically in line with the world’s regional economic, social, and cultural level of spatial distribution pattern. China located in the Eastern Asia region is the rapid development country of ferroptosis research, but the average cited frequency and H-index are on the low side (Figure 2).

3.1.3. Distribution of Academic Journals. The journals of ferroptosis were analyzed, the number of journals was counted, as well as citations and influencing factors, and the number of articles published by the top 10 journals accounted for 18.78% of the total number of articles published. Among them, more than 30 papers have been published in “Cell Death and Disease,” “Biochemical and Biophysical Research Communications,” and “Free Radical Biology and Medicine.” Combining the influencing factors and citations of major journals, it can be found that “Cell Death & Disease,” “Free Radical Biology and Medicine,” “Redox Biology,” “Cell Death and Differentiation,” and “Oxidative Medicine and Cellular Longevity” are also high-impact journals with an impact factor over 5 (Table 2). To a certain extent, such journals can be regarded as the main position and representative of ferroptosis. Well-known journals about cytology, biomolecular science, comprehensive medicine, and oncology have shown greater interest and tendency in the research of ferroptosis, reflecting the comprehensiveness and intersectionality of the research.

3.1.4. Distribution of Funding Institutions. The funded projects of the thesis results often reflect the attention rate of the country and institutions to the research field and also

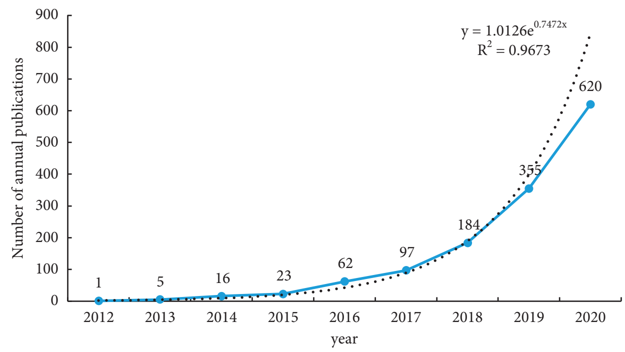

Figure 1: Number of annual publications.

Table 1: Country distribution (top 10).

Rank	Country (region)	Freq.	Total citation frequency	The average cited frequency	H-index
1	China	620	10828	17.46	73
2	USA	434	22377	51.56	48
3	Germany	161	9366	58.17	45
4	Japan	107	4264	39.85	25
5	France	62	2982	48.10	25
6	Australia	51	3010	59.02	22
7	UK	50	3752	75.04	20
8	Canada	46	2092	45.48	18
9	Italy	44	1539	34.98	17
10	Russia	35	1640	46.86	15

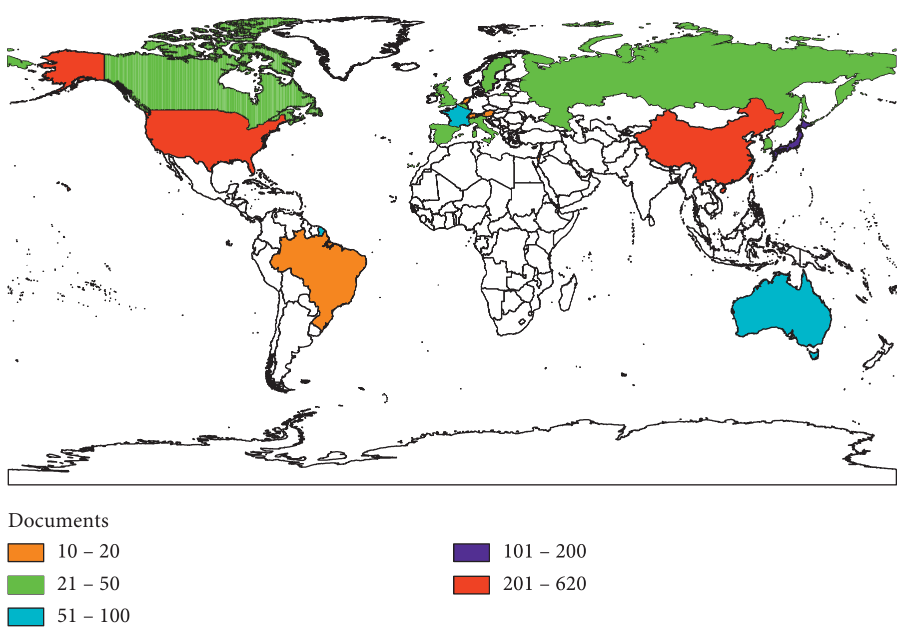

Figure 2: Distribution of countries with more than 10 publications.

Table 2: The characteristics of main academic journals publications about ferroptosis (top 10).

Rank	Journals	Publications	Total citation frequency	The average cited frequency	Impact factor
1	Cell Death and Disease	45	588	13.07	6.486
2	Biochemical and Biophysical Research Communications	36	904	25.11	2.75
3	Free Radical Biology and Medicine	31	1112	35.87	6.457

Table 2: Continued.

Rank	Journals	Publications	Total citation frequency	The average cited frequency	Impact factor
4	Redox Biology	27	740	27.41	9.789
5	International Journal of Molecular Sciences	25	200	8.00	4.653
6	Cell Death and Differentiation	22	1999	90.86	9.597
7	Oxidative Medicine and Cellular Longevity	20	193	9.65	5.608
8	Scientific Reports	18	237	13.17	4.576
9	Frontiers in Neuroscience	16	261	16.31	2.649
10	Cancers	16	56	3.50	6.433

represent the development trend of the corresponding research, the existing research resources, and the research level of related fields [5]. In these 1363 articles, a total of 5095 funds were found (Table 3). Five of the top 10 publications funded by projects in the United States are leading. They are National Institutes of Health (NIH), USA, United States Department of Health Human Services, NIH National Cancer Institute (NCI), NIH National Institute of General Medical Sciences (NIGMS), and NIH National Institute of Neurological Disorders Stroke (NINDS). In addition, the number of published papers funded by the National Natural Science Foundation of China is 427, ranking first (Figure 3). Although in essence academic output level and academic output quantity are not necessarily related to funding projects, it can be found that the support and attention from the United States and China to the field of ferroptosis research are still relatively leading.

3.1.5. H-Index of Main Authors. Before the development and application of the Hirsch index, various indicators for evaluating the personal influence of researchers had their own advantages. Compared with other indicators, the H-index can organically combine the researcher's output and influence through algorithm technology, thus comprehensively considering the "quality" and "quantity" of academic achievements [6]. Table 4 lists the H-index value and the total number of citations of the top 15 authors whose H-index was more than 10. Judging from the essential significance of Hirsch index, 7 of the authors with an H-index more than 10 are from the United States, accounting for 46.7%, mainly from Columbia University and the University of Pittsburgh. This shows that these universities and research institutions have scientific research resources in the field of ferroptosis with the leading level in the world. At the same time, three Chinese authors, Tang Deli, Wang Hao, and Wang Xu, whose H-index exceeds 10, show that they play an indispensable role in the field of ferroptosis and have a certain influence.

3.2. Visual Analysis

3.2.1. Analysis of the Author Partnership Network. A visual analysis of the collaborative network of authors who published more than 7 papers is shown in Figure 4. The size of the dots indicates the academic influence and cooperation degree of authors; the width of the line between the dots indicates the strength of the cooperative relationship between corresponding authors; and the color indicates the subcluster network to which the authors belong. Author's network of cooperative relations of ferroptosis presents the characteristics of "overall dispersion and multicenter and regional concentration." "Tang DL"-"Kang R," "Stockwell BR," "Conrad M," and "Angeli JPF" formed a larger net cooperation subgroup and branch outward radiation. Exploring the author collaboration network relationship can fully show the research achievements communication situation in the field.

3.2.2. Analysis of Cooperation Network Relationship about Institutions. The analysis of the cooperative network of institutions that have published more than 10 papers is shown in Figure 5. The size of the dots indicates the academic influence and cooperation degree of the institutions; the width of the lines between the dots indicates the strength of the cooperative relationship between the corresponding institutions; and the color represents the subcluster network to which the institutions belong. There were roughly 6 major cooperative subclusters. In cluster 4, the number and the quantitative index of "Univ Pittsburgh" ranked first. According to the literature, the University of Pittsburgh has cooperated with 11 organizations such as "Guangzhoumeduniv" and "Centsuniv." The University of Pittsburgh researchers have succeeded in deciphering the ferroptosis trigger signals language in cell, in 2020. "Univ Pittsburgh" associated with "Jinan University" found iPLA2β is an important regulatory protein for ferroptosis. The accumulation of lipid peroxides caused by loss of activity is closely related to the occurrence of Parkinson's disease. Inhibition of ferroptosis is expected to be a new strategy for the treatment of Parkinson's disease [7]. In cluster 1, "Chinese Acad Sci"-"Zhejiang Univ"-"Shanghai Jiao Tong Univ" as representatives of Chinese university and research institutions accounted for 27.1% of the total. Professor H. D. Wang from Zhejiang University and others from Zhengzhou University have discovered a drug for rheumatoid arthritis known as Auranofin; it can significantly activate Hepcidin and effectively reduce the iron overload burden. Furthermore, the researchers found that the molecular mechanism for this phenomenon is to reduce iron overload by activating the NF-κB/IL-6/JAK-STAT signaling pathway [8]. In 2020, together with the Chinese Academy of Medical Sciences and others, Professor H. D. Wang clarified the effect and molecular regulation mechanism of ferritin inhibiting the

Table 3: Funds distribution (top 10).

Rank	Fund subvented organizations	Number of literatures (articles)
1	National Natural Science Foundation of China (NSFC)	427
2	National Institutes of Health (NIH), USA	307
3	United States Department of Health Human Services	307
4	NIH National Cancer Institute (NCI)	160
5	NIH National Institute of General Medical Sciences (NIGMS)	93
6	German Research Foundation (DFG)	74
7	Ministry of Education, Culture, Sports, Science and Technology (MEXT), Japan	70
8	Japan Society for the Promotion of Science	61
9	Grants-in-Aid for Scientific Research (KAKENHI)	46
10	NIH National Institute of Neurological Disorders Stroke (NINDS)	40

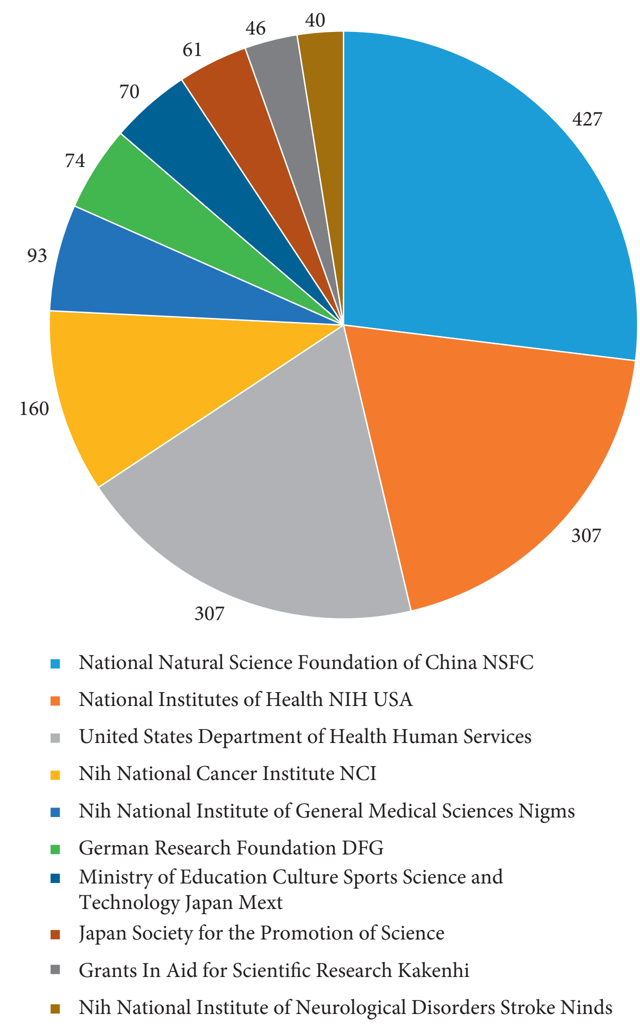

Figure 3: Top 10 fund organizations and number of publications.

Table 4: H-index of main authors (H-index more than 10).

Rank	Author	Country	Publications	Total citation frequency	The average cited frequency	H-index
1	Stockwell	USA	47	10054	213.91	33
2	Conrad	Germany	36	5059	140.53	26
3	Linkermann	Germany	28	4157	148.46	21
4	Tang	China	39	3525	90.38	20

Table 4: Continued.

Rank	Author	Country	Publications	Total citation frequency	The average cited frequency	H-index
5	Kang	USA	38	2418	63.63	20
6	Dixon	USA	25	5945	237.80	19
7	Angeli	Germany	21	3164	150.67	16
8	Kagan	USA	25	2628	105.12	14
9	Kroemer	France	14	1749	124.93	13
10	Bayir	USA	22	1913	86.95	12
11	Tyurina	USA	20	1770	88.50	12
12	Wang	China	21	623	29.67	11
13	Wang	China	18	370	20.56	11
14	Vandenabeele	Belgium	13	2790	214.62	11
15	Gu	USA	13	1154	88.77	11

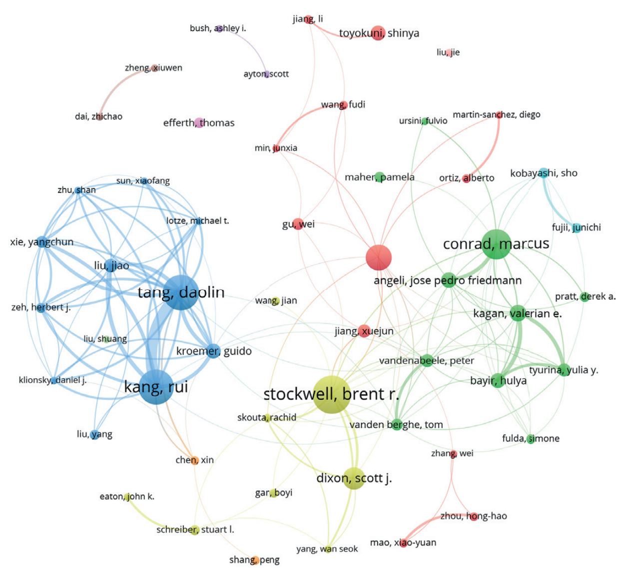

Figure 4: Cooperative network of individual authors.

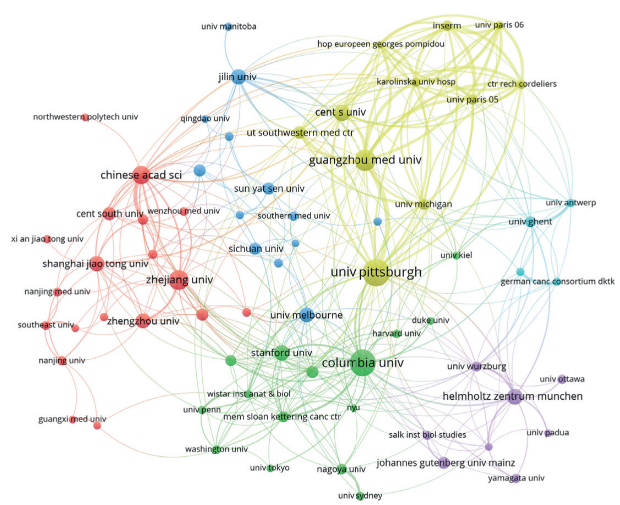

Figure 5: Institutional cooperation network.

occurrence of cardiomyopathy by regulating ferroptosis. It was first revealed in vivo that membrane protein SLC7A11 can effectively reverse cardiomyopathy caused by ferritin deficiency by blocking ferroptosis in cardiomyocytes, which is expected to become a new target for the prevention and treatment of heart diseases [9]. University of Science and Technology of China (USTC) and others jointly found that monodispersed amorphous Fe carbonate containing nanodrug assembly (calcium carbonate based Fe2+ -adriamycin complex, ACC@DOX.Fe2+ -CASI-PAMAM-FA/MPEG) can synergically induce ferroptosis and apoptosis of tumor cells [10]. In cluster 2, “Columbia Univ”-“Stanford Univ”-“Harvard Med Sch” asrepresentatives of university and research institutions accounted for 21.4% of the total. In 2017, Columbia University in the United States, as the origin and core institution of ferroptosis research, invited researchers from 27 institutions around the world to publish a programmatic guide on ferroptosis research, systematically expounding the mechanism of ferroptosis and its relationship with human diseases [11]. In cluster 3, “Jilin Univ”-“Univ Melbourne”-“Shandong Univ” as representatives of universities and research institutions in China and Australia accounted for 18.5% of the total. Sun et al. from Jilin University published their important research results, discussing how to regulate ferroptosis and lipid metabolism abnormality through overexpression and knockdown of perilipin2, a potential predictive biomarker in gastric cancer [12]. In cluster 5, “Helmholtz Zentrum Munchen”-“Johannes Gutenberg Univ Mainz”-“Univ Wurzburg” as representatives of German research institution groups accounted for 11.4% of the total. “Targeting Ferroptosis: New Hope for As-Yet-Incurable Diseases” was published in Trends in Molecular Medicine by Marcus Conrad, Svenja M.Lorenz, and Bettina Proneth form the German Institute for Metabolism and Cell Death in October 2020. This paper argues that because ferroptosis pathway provides a variety of drug-addable nodes, it is expected that the preclinical and clinical development of ferroptosis modulators will bring about unprecedented opportunities for treating uncured diseases [13]. In cluster 6, German research group with the core of “Univ Ghent” accounted for 5.7% of the total.

3.2.3. Analysis of the Network of Country Cooperation. An analysis of the country cooperation relationship with 5 or more papers published is shown in Figures 6 and 7. The size of the dot indicates the academic influence and degree of cooperation of a country; the width of the line between the dots indicates the strength of the cooperation relationship between the corresponding countries; the color indicates the

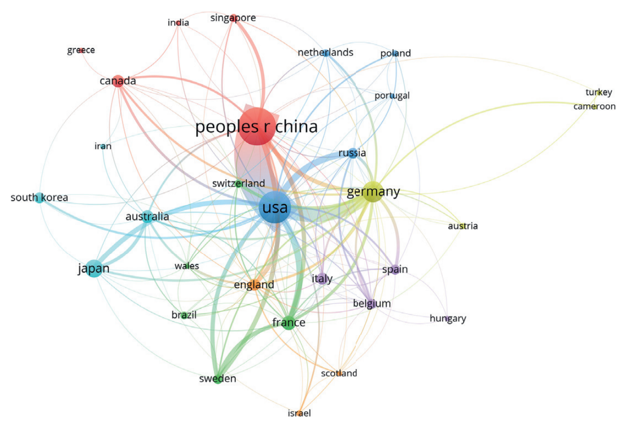

Figure 6: National cooperation network.

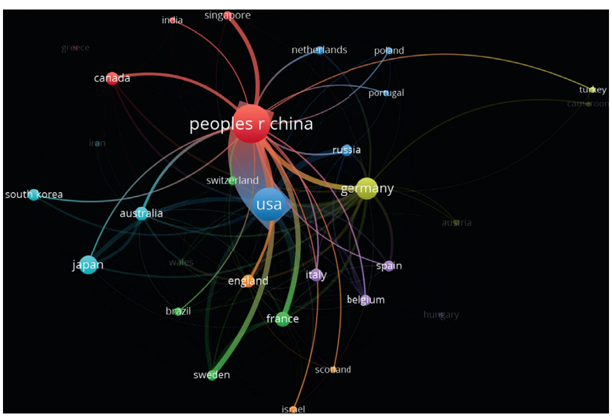

Figure 7: Chinese network of cooperation with other countries.

subcluster network to which they belong. The results of the study show that the United States, China, and Germany have close cooperative relations, and the overall performance of international cooperation is good. It can be seen from the network map of China's scientific research cooperation that China maintains scientific research cooperation with many countries such as the United States, Germany, France, Sweden, Japan, Australia, and Russia. Strengthening international cooperation is an important factor in promoting the output, dissemination, and commercialization of high-quality research results. While integrating into the internationalization process of frequencies and strengthening cooperation between countries, China should also focus on its own independent innovation and improvement of original results in order to enhance its influence and voice in this field.

3.2.4. Cooccurrence and Cluster Analysis of Keywords. Summarizing the themes of keywords and analyzing keywords can help understand the research hotspots and trends in this field. In this study, VOSviewer software was used to extract the cooccurrence frequencies of more than 8. Cluster analysis with 64 keywords was performed. The 53 keywords were divided into 6 categories, combined with the meaning and logical analysis of the research subject words between the words, as shown in Figure 8: (1) oxidative stress response of ferroptosis and its application in stroke, Alzheimer's disease, and breast cancer (red): iron drop, active oxygen, iron overload, antioxidants, iron, mitochondria, stroke, Alzheimer's disease, oxidative stress, induced labor, nrf2, and breast cancer; (2) the inducer/inhibitor of ferroptosis response and its role in cerebral hemorrhage and diseases of aging (yellow): erastin, ferrostatin-1, cerebral hemorrhage, Fenton reaction, and aging; (3) ferroptosis mechanism involved in antitumor research (sky blue): sorafenib and pancreatic cancer; (4) relationship between ferroptosis and other cell death types, where ferroptosis is involved in inflammation and ischemia-reperfusion (dark blue): autophagy, cell death, pyroptosis, necroptosis, and apoptosis; (5) ferroptosis glutathione and peroxidase-4 systems and antimelanoma and glioma studies (purple): melanoma, glutathione, glioma, and GPX4; (6) correlation between iron metabolism imbalance and tumor microenvironment and antitumor genes (green): cancer stem cell, iron metabolism, tumor microenvironment, and p53.

The density view of the VOSviewer software was used to perform cooccurrence analysis on keywords (Figure 9). The frequency of keyword occurrences is related to the image density. The higher the frequency, the darker the color and the higher the density. At the same time, with larger gray value of the color, it also represents the bias of the research hotspot in this field. The keywords in the middle area of the figure are divided into five parts according to their location distribution, similar to the result of keyword clustering analysis. The first part is in the center of the view. Keywords were the following: iron drop disease, reactive oxygen species, iron overload, cancer, p53, and metabolism; the darkest part indicates that it is an international research hotspot in this field. Among them, ferroptosis has a large hotspot distribution area and is a high-frequency keyword. The oxidative stress response, iron metabolism, tumor, and tumor suppressor genes of ferroptosis occupy the core research position. The second part is located at the bottom left of the first part. The keywords were iron, Alzheimer's disease, oxidative stress, mitochondria, and stroke, focusing on the application of ferroptosis in stroke, Alzheimer's disease, and other neurological diseases. The third part is mainly located at the bottom right of the first part. Taking necrosis, scorch, apoptosis, and autophagy as keywords, this part focuses on the relationship between ferroptosis and other types of cell death. The fourth part is mainly located at the upper right of the first part. The keywords were glutathione, glioma, and GPX4, mainly related to glutathione and its peroxidase 4. The fifth part is mainly located on the upper part of the first part. Keywords were iron metabolism and tumor microenvironment, focusing on the research about abnormal iron metabolism, tumor microenvironment, and tumor stem cells.

4. Discussions

4.1. International Ferroptosis Research Development Trend. In this study, bibliometrics and visual analysis were used to make a macroscopic description and retrospective analysis

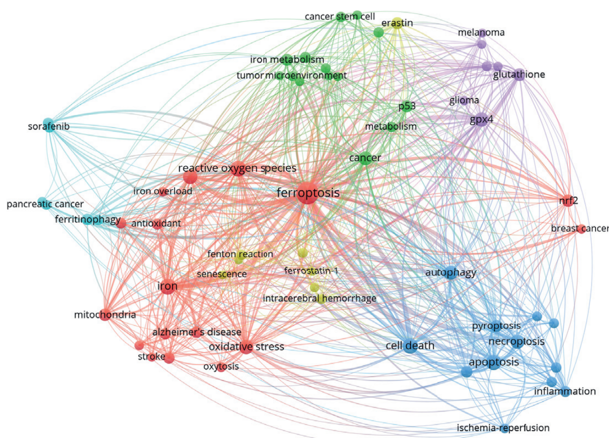

Figure 8: Keyword clustering visualization.

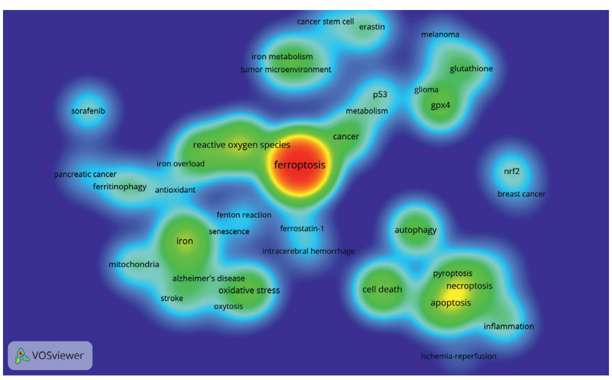

Figure 9: Density map of keywords.

of the research literature on ferroptosis, presenting research trends, hotspots, topics, major researchers, major research institutions, important research journals, and funding in this field. In recent years, a large number of literatures about ferroptosis have been published, showing an "exponential" rapid growth trend, which is the focus of international medical research and a hot research direction. By combining the historical axle of landmark research achievements on ferroptosis (Figure 10) and the number of published articles (Figure 1), the research on ferroptosis started late, officially in 2012. Dixons et al. [14] formally proposed the concept and characteristics of ferroptosis. In 2014, Yang et al. [1] found that GPX4 can regulate the death of eosinophilic cancer cells through the ferroptosis pathway. In 2016, ferroptosis inducers inhibited GPX4 by covalently targeting the active site selenocysteine, leading to accumulation of PUFA hydroperoxides [15]. In 2017, Doll et al. [16] found that ACSL4 inhibition is an important mechanism to improve the occurrence of ferroptosis. In 2018, Ingold et al. [17] found that GPX4 was selenium-dependent in preventing ferroptosis caused by hydrogen peroxide. In 2019, FSP1 is a key component of a nonmitochondrial coantioxidant system that acts in parallel with the GPX4 pathway based on glutathione [18]. In 2020, Zou et al. [19] revealed the role of peroxisomal-ether-phospholipid axis in the development of susceptibility and avoidance of ferroptosis and emphasized that PUFA-EPL is a unique functional lipid class, which is dynamically regulated in the process of cell state transition and provides multiple regulatory nodes for therapeutic intervention of disease. Zhou and Jinku [20] established a database of manually collected and managed ferroptosis-related markers and regulators and ferroptosis-related diseases.

4.2. Ferroptosis Research of High-Influence Scholar-Institution-Country and Cooperative Relationship. Stockwell BR (Columbia University), Conrad M (Helmholtz Zentrum Munchen), Linkermann A (Dresden University of Technology), Tang DL (Guangzhou Medical University), and Kang R (University of Pittsburgh) are influential in the field of ferroptosis. The cooperation between authors has increased, including interorganizational cooperation and international cooperation. Author-institution-country has a certain correlation in the number of papers published. China, the United States, Germany, Japan, and France are the countries with the biggest numbers of publications. There are many highly productive scholars in China, the United States, and Germany, and the team of them cooperates closely with the international community. A large-scale research team has initially formed, and each research direction has its own characteristics. However, it is also necessary to strengthen interagency and interregional cooperation and carry out high-quality academic exchanges and cooperation.

4.3. Ferroptosis Research Fund Support and Main Journal Position. The scientific research results of funded projects often reflect the attention rate of the country and institutions. The number of papers in the journals about the research field can reflect the interests of the journals and provide a reference to the paper publication and hot follow-up research information. The National Natural Science Foundation of China, National Institutes of Health (NIH), U.S. Department of Public Services, National Institutes of Health National Cancer Institute (NCI), and National Institutes of Health National Institute of General Medical Sciences (NIGMS) are the main fund project institutes in supporting ferroptosis research with a positive significance. The journals with the highest output are "Cell Death and Disease," "Biochemical and Biophysical Research Communications," "Free Radical Biology and Medicine," "Redox Biology," and "International Journal of Molecular Science." To a certain extent, this reflects the status of major journals in the study of ferroptosis. However, due to the limitations of space and review requirements, the publication of research results from top international journals cannot be ignored. Secondly, the study of ferroptosis is a multidisciplinary research topic, which can be further explored from the perspective of diseases in various disciplines.

4.4. Analysis of Ferroptosis Research Hotspot Trend. The visualization analysis of keyword clustering found that 53 keywords were clustered into 6 topic directions. Oxidative

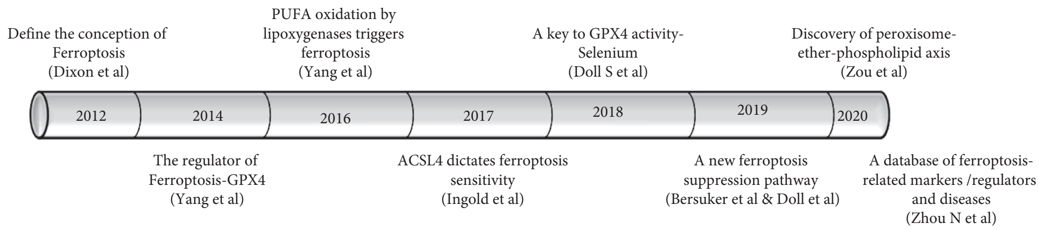

Figure 10: Historical axis of landmark achievements in ferroptosis research development.

stress, inducers/inhibitors, synergistic antitumor effect, relationships with other cell death types, glutathione peroxidase, GPX4, and iron metabolism imbalance related mechanisms of ferroptosis were discussed. The application of ferroptosis in nervous system diseases, ischemia-reperfusion injury, tumor, inflammation, and aging related diseases is a hot research direction (Figure 8; Table 5).

4.4.1. Oxidative Stress Response of Ferroptosis and Its Application in Stroke, Alzheimer's Disease, and Breast Cancer. Cluster 1 (red) of keywords focuses on ferroptosis oxidative stress and its application in stroke, Alzheimer's disease, and breast cancer. Oxidative stress is a reaction process in which reactive oxygen species generated during the aerobic metabolism of the body accumulate excessively in cells, leading to cell damage and death. Its essence is the imbalance between the body's [21] antioxidant defense and the production of reactive oxygen species. The mechanism of ferroptosis is due to the damage of the glutathione- (GSH-) dependent lipid peroxide repair system, which leads to the accumulation of reactive oxygen species in lipids [11, 14]. Mitochondrial electron transport chain complex I inhibitor DPI can inhibit oxidative stress response [22], and mitochondrial complex III inhibitor antimycin A can inhibit erastin-induced ferroptosis [14, 23], indicating that both ferroptosis and oxidative stress pathways rely on mechanisms for GSH reduction and related antioxidant system damage. A large number of studies have shown that ferroptosis is an important potential target for stroke prevention and treatment. Inhibition of ferroptosis response can reduce stroke injury [24–28], and its mechanism is related to excitement related to iron overload [28], ACSL4 protein [29], 12/15-LOX expression [30], XCT expression [31], and increased sexual toxicity. Abnormal iron metabolism plays an important role in the occurrence and development of Alzheimer's disease. Patients with Alzheimer's disease have obvious iron deposits in the cerebral cortex and hippocampus, which corresponds to the distribution of Aβ plaques [32, 33]. Elevated iron content in the brain can aggravate the disease, and Aβ accumulation [33] and iron chelating agents can reduce the level of iron in the brain and relieve symptoms [34]. Cys deletion in triple-negative breast cancer (TNBC) cells can induce ferroptosis, and DFO and Tistatin-1 can block the corresponding cell death [35]. Ferroptosis may also mediate the synergistic anti-breast-cancer effect of cyclamine and lapatinib [36].

4.4.2. The Inducer/Inhibitor of Ferroptosis Response and Its Role in Cerebral Hemorrhage and Diseases of Aging. Cluster 2 of keywords (yellow) mainly focuses on the inducer/inhibitor of ferroptosis response and its role in cerebral hemorrhage and diseases of aging. Erastin is a classic inducer of ferroptosis reaction, which can inhibit System XC- activity and affect glutathione (GSH) synthesis, combined with VDAC2/3 inducing mitochondrial dysfunction [14, 22, 37]. Ferrostatin1 classical inhibitor of ferroptosis reaction eliminates lipid reactive oxygen species (ROS), inhibits lipid peroxidation, regulates the expression of oxidization-related proteins, and reduces unstable iron in cells [14, 38–43]. Intracerebral hemorrhage injury also has the phenomenon of neuronal ferroptosis [44]. Intracerebral hemorrhage injury can be alleviated by the administration of ferroptosis inhibitors, the mechanism of which is mainly related to iron overload [45], decreased expression of glutathione peroxidase 4 [46], and increased activity of arachidonic acid-dependent lipoxygenase-5 (ALOX5) [47]. Aging can cause excessive accumulation of iron ions in cells, damage DNA, and inhibit the ability to repair DNA damage, while incomplete DNA loss accelerates cellular neurodegeneration and aging of the body [48, 49]. The mechanism may be that iron ions take up the binding site of p53 protein, thus weakening p53 to repair DNA damage [49].

4.4.3. Ferroptosis Mechanism Involved in Antitumor Research. Cluster 3 of keywords (sky blue) mainly focuses on ferroptosis mechanism involved in antitumor research. Sorafenib is a clinical multitargeted antitumor drug and also an important inducer of ferroptosis. Deferriamine can block the oxidative stress response induced by sorafenib in HCC HUH7 cells, suggesting that the antitumor targeting effect of sorafenib may be mediated through the ferroptosis pathway [50]. Sorafenib can induce the expression of metallothionein-1G (MT-1G) gene in liver cancer cells, thereby inhibiting ferroptosis and promoting drug resistance [51, 52]. Studies have shown that inhibition of p62-KEAP1-Nrf2 antioxidant signaling pathway can significantly enhance the anti-HCC activity of erastin and sorafenib, indicating that the induction of ferroptosis can promote the anti-HCC targeted sensitization of erastin and sorafenib [53]. Sorafenib and low-dose PDT have a synergistic effect in inhibiting tumor progression, and the mechanism may be to reshape tumor immune microenvironment by inducing T cell-dependent local and systemic antitumor immune response [54].

Table 5: Keywords clustering table.

Clustering number	Color	Key keywords
Cluster 1	Red	Ferroptosis, reactive oxygen species, iron overload, antioxidant, iron, mitochondria, stroke, Alzheimer's disease, oxidative stress, oxytosis, nrf2, breast cancer
Cluster 2	Yellow	Erastin, ferrostatin-1, intracerebral hemorrhage, Fenton reaction, senescence
Cluster 3	Sky blue	Sorafenib, pancreatic cancer, ferritinophagy
Cluster 4	Dark blue	Autophagy, cell death, pyroptosis, necroptosis, apoptosis, inflammation, ischemia-reperfusion
Cluster 5	Purple	Melanoma, glutathione, glioma, GPX4
Cluster 6	Green	Cancer stem cell, iron metabolism, tumor microenvironment, p53, metabolism, cancer

4.4.4. Relationship between Ferroptosis and Other Cell Death Types: Ferroptosis Is Involved in Inflammation and Ischemia Reperfusion. Cluster 4 of keywords (dark blue) mainly focuses on the relationship between ferroptosis and other cell death types. Ferroptosis is involved in inflammation and ischemia-reperfusion. The morphology of ferroptosis is different from those of apoptosis, necrosis, and autophagy. Ferroptosis is mainly manifested as mitochondrial atrophy, cristae disappearance, increased membrane density, and outer membrane rupture [14]. In the past, inhibitors widely used for apoptosis, necrosis, or autophagy could not prevent ferroptosis. However, there is a certain correlation between ferroptosis and other types of cell death. Under certain conditions, cell apoptosis can be transformed into ferroptosis, which also can promote the sensitivity of cells to apoptosis. The tumor suppressor gene p53 can not only fight tumors through cell cycle arrest and apoptosis but also induce ferroptosis reactions in tumor cells under certain conditions. Studies have shown that autophagy activation can degrade ferritin, leading to ferroptosis in tumor cells [55]. Ferroptosis may be the process of autophagy death, which is induced by autophagy [56]. Ferroptosis and programmed necrosis are complementary forms of cell death. When the programmed necrosis pathway is weakened, ferroptosis pathway becomes more sensitive [57]. Ferroptosis is often related to the inflammatory immune process, and the two are closely related. In acute kidney injury (AKI) model and tamoxifen-induced systemic GPX4 deletion knockout mice, it is shown that inflammation is associated with ferroptosis of the kidney [58]. The significant activation of macrophages is observed through the development of ferroptosis tissues involved in the inflammatory response [59]. The occurrence of pancreatic cancer is related to iron metabolism and lipid peroxidation. The possible mechanism of antitumor action of Ruscogenin is to regulate transferrin to increase intracellular Fe ion concentration, inducing ferroptosis [60]. The activation of the Atg5/Atg7-NCoA4 axis in pancreas cancer PANC-1 cells can degrade ferritin, inhibit the expression of the heavy chain of ferroprotein, and induce ferroptosis [61]. In the study of pancreatic cancer PANC-1 cells, the antioncogene p53 may exert a tumor suppressor effect through the ferroptosis mediated by the SAT1-ALOX15 axis [62].

4.4.5. Ferroptosis Glutathione and Peroxidase 4 Systems, Antimelanoma, and Glioma Studies. Cluster 5 of keywords (purple) mainly focuses on ferroptosis glutathione and peroxidase 4 system and antimelanoma and glioma research. Cystine/glutamate antiporter system XC- is exchanged between intracellular cystine and glutamate in a 1 : 1 ratio, and extracellular glutamate accumulation is an important regulator of ferroptosis [56]. Glutathione (GSH) is the main substrate of glutathione peroxidase 4 (GPX4), a key regulator of death [63]. Inhibition of GPX4 can induce a large number of lipid peroxides to aggregate in cells and form a marker reaction of ferroptosis [64]. Melanoma is a kind of skin tumor with high malignant degree, and miR-137 can mediate the glutamine transporter SLC1A5 to regulate the occurrence of ferroptosis in melanoma cells [65]. Erastin, a classic inducer of ferroptosis, can significantly enhance the killing ability of vemurafenib against M229R and M238R melanoma cells [66]. Activation of ferroptosis in glioblastoma stem cells increases the sensitivity of tumor cells to temozolomide, opening a new pathway for glioblastoma therapy [67–69].

4.4.6. Correlation between Iron Metabolism Imbalance and Tumor Microenvironment and Antitumor Genes. Cluster 6 of keywords (green) mainly focuses on the correlation between iron metabolism imbalance and tumor microenvironment and antitumor genes. Iron is an important factor in the accumulation of lipid peroxides in ferroptosis. Iron metabolism imbalance and ferritin autophagy are important regulatory targets for ferroptosis. Iron responsive element binding protein 2 (IREB2) can mediate transferrin and transferrin receptor iron import cells to induce ferroptosis, and silencing the IREB2 gene can inhibit ferroptosis [56]. This process is affected by IREB2 [14]. Autophagy can also affect the iron metabolism pathway and regulate the ferroptosis response [70, 71]. p53 is an important tumor suppressor molecule, which can induce the occurrence of ferroptosis and mediate its antitumor effect through the sensitivity of cells to ferroptosis. p53 can inhibit the SLC7A11-induced ferroptosis response through a transcription-dependent pathway and play a role in suppressing tumors [72, 73]. It is found that p53 can delay ferroptosis, and erastin does not significantly stimulate the ferroptosis of p53 in colorectal cancer (CRC). Inhibition or knockout of p53 can restore the ferroptosis response caused by erastin [74], indicating that p53 plays a complicated role in the death mechanism of ferroptosis cells, and further research is needed.

5. Conclusion

This article studies the English literature of ferroptosis published in the Web of Science core collection database. The earliest article to clarify the concept of ferroptosis was published in 2012, and the number of articles presents an exponential growth trend, indicating that ferroptosis research started late and has been a hot research spot in the field of biomedical science in recent years. It has attracted wide attention from scholars all over the world. The occurrence mechanism of ferroptosis is the hot directions of current research. In terms of disease carrier selection, stroke, Alzheimer's disease, cerebral hemorrhage, ischemia and reperfusion, inflammation, aging, breast cancer, liver cancer, melanoma, and glioma are the key subjects of the current ferroptosis mechanism-related disease research. Secondly, is there a new way in the study of the action mechanism of ferroptosis? Can new inductors and inhibitors of ferroptosis be screened? What are the complete mechanism and pathway for ferroptosis involved in anti-inflammatory and antitumor activation of the immune system? Can the research results of antitumor mechanism based on ferroptosis be better applied and transformed into clinical front-line? Discuss the relationship between traditional medicine and ferroptosis. These issues still need extensive and thorough research.

Data Availability

The data used to support the findings of this study are available from the corresponding author upon request.

Additional Points

The limitation of visual analysis mainly lies in that some high-quality but low-impact factor literatures cannot analyze it, so as to provide more comprehensive suggestions for related research fields.

Conflicts of Interest

The authors declare that there are no conflicts of interest.

Authors' Contributions

Jian Xiong and Wenchuan Qi made similar contributions to this study and are co-lead authors. Jian Xiong and Wenchuan Qi were responsible for the conception and design of the research and drafted the article. Jiacheng Liu, Ziwen Wang, and Zhenqing Zhang were responsible for literature retrieval and acquisition and contributed to the analysis and interpretation of the data. Jinku Bao, Chuanfang Wu, and Fanrong Liang reviewed and critically revised the content of the study and finally approved the version to be published.

Acknowledgments

The authors thank all the authors of the original studies included in this analysis. This paper was supported by the National Natural Science Foundation of China (nos. 81590951 and 82074556), China Postdoctoral Science Foundation (no. 260350), Support Fund for National "Ten Thousand Talents Plan" Famous Teachers (no. 6 [2018] of Group Office), National Administration of Traditional Chinese Medicine "Hundreds of Millions" Talent Project for TCM Inheritance and Innovation (Qhuang Project) Qhuang Scholar Support Fund (National Letter of Education of TCM Scholars [2018] no. 288), and Special Project of "Central Government Guides Local Science and Technology Development" in Sichuan Provincial Department of Science and Technology (2020ZYD046).

References

[1] W. S. Yang, R. SriRamaratnam, and M. E Welsch, "Regulation of ferroptotic cancer cell death by GPX4," *Cell*, vol. 156, no. 1-2, pp. 317–331, 2014.

[2] E. Roldan-Valadez, S. Y. Salazar-Ruiz, R. Ibarra-Contreras, and C. Rios, "Current concepts on bibliometrics: a brief review about impact factor, Eigenfactor score, CiteScore, SCImago Journal Rank, Source-Normalised Impact per Paper, H-index, and alternative metrics," *Irish Journal of Medical Science*, vol. 188, no. 3, pp. 939–951, 2019.

[3] M. Li, X. Zhuang, W. Liu, and P. Zhang, "More stable ties or better structure? An examination of the impact of Co-author network on team knowledge creation," *Frontiers in Psychology*, vol. 8, p. 1484, 2017.

[4] C. A. Hamilton, R. Vacca, and J.-M. R. Stacciarini, "The emergence of team science: understanding the state of adoption research through social network analysis," *Adoption and Fostering*, vol. 41, no. 4, pp. 369–390, 2017.

[5] Y. Huang, Y. Zhang, J. Youtie, A. L. Porter, and X. Wang, "How does national scientific funding support emerging interdisciplinary research: a comparison study of big data research in the US and China," *PloS One*, vol. 11, no. 5, Article ID e0154509, 2016.

[6] B. Sharma, S. Boet, T. Grantcharov, E. Shin, N. J. Barrowman, and M. D. Bould, "The h-index outperforms other bibliometrics in the assessment of research performance in general surgery: a province-wide study," *Surgery*, vol. 153, no. 4, pp. 493–501, 2013.

[7] W.-Y. Sun, V. A. Tyurin, K. Mikulska-Ruminska et al., "Phospholipase iPLA2β averts ferroptosis by eliminating a redox lipid death signal," *Nature Chemical Biology*, vol. 17, no. 4, pp. 465–476, 2021.

[8] L. Yang, H. Wang, X. Yang et al., "Auranofin mitigates systemic iron overload and induces ferroptosis via distinct mechanisms," *Signal Transduction and Targeted Therapy*, vol. 5, no. 1, p. 138, 2020.

[9] X. Fang, Z. Cai, H. Wang et al., "Loss of cardiac ferritin H facilitates cardiomyopathy via slc7a11-mediated ferroptosis," *Circulation Research*, vol. 127, no. 4, pp. 486–501, 2020.

[10] C.-C. Xue, M.-H. Li, Y. Zhao et al., "Tumor microenvironment-activatable Fe-doxorubicin preloaded amorphous CaCO3 nanoformulation triggers ferroptosis in target tumor cells," *Science Advances*, vol. 6, no. 18, Article ID eaax1346, 2020.

[11] B. R. Stockwell, J. P. Friedmann Angeli, H. Bayir et al., "Ferroptosis: a regulated cell death nexus linking metabolism, redox Biology, and disease," *Cell*, vol. 171, no. 2, pp. 273–285, 2017.

[12] X. Sun, S. Yang, X. Feng et al., "The modification of ferroptosis and abnormal lipometabolism through overexpression and

knockdown of potential prognostic biomarker perilipin2 in gastric carcinoma," *Gastric Cancer*, vol. 23, no. 2, pp. 241–259, 2020.

[13] M. Conrad, S. M. Lorenz, and B. Proneth, "Targeting ferroptosis: new hope for as-yet-incurable diseases," *Trends in Molecular Medicine*, vol. 27, no. 2, pp. 113–122, 2021.

[14] S. J. Dixon, K. M. Lemberg, M. R. Lamprecht et al., "Ferroptosis: an iron-dependent form of nonapoptotic cell death," *Cell*, vol. 149, no. 5, pp. 1060–1072, 2012.

[15] W. S. Yang, K. J. Kim, M. M. Gaschler, M. Patel, M. S. Shchepinov, and B. R. Stockwell, "Peroxidation of polyunsaturated fatty acids by lipoxygenases drives ferroptosis," *Proceedings of the National Academy of Sciences*, vol. 113, no. 34, pp. E4966–E4975, 2016.

[16] S. Doll, B. Proneth, Y. Y. Tyurina et al., "ACSL4 dictates ferroptosis sensitivity by shaping cellular lipid composition," *Nature Chemical Biology*, vol. 13, no. 1, pp. 91–98, 2017.

[17] I. Ingold, C. Berndt, S. Schmitt et al., "Selenium utilization by GPX4 is required to prevent hydroperoxide-induced ferroptosis," *Cell*, vol. 172, no. 3, pp. 409–422, 2018, e21.

[18] K. Bersuker, J. M. Hendricks, Z. Li et al., "The CoQ oxidoreductase FSP1 acts parallel to GPX4 to inhibit ferroptosis," *Nature*, vol. 575, no. 7784, pp. 688–692, 2019.

[19] Y. Zou, W. S. Henry, E. L. Ricq et al., "Plasticity of ether lipids promotes ferroptosis susceptibility and evasion," *Nature*, vol. 585, no. 7826, pp. 603–608, 2020.

[20] N. Zhou and B. Jinku, "FerrDb: a manually curated resource for regulators and markers of ferroptosis and ferroptosis-disease associations," *Database*, vol. 2020, 2020.

[21] N. Sinha and P. Dabla, "Oxidative stress and antioxidants in hypertension-a current review," *Current Hypertension Reviews*, vol. 11, no. 2, pp. 132–142, 2015.

[22] S. Tan, Y. Sagara, Y. Liu, P. Maher, and D. Schubert, "The regulation of reactive oxygen species production during programmed cell death," *Journal of Cell Biology*, vol. 141, no. 6, pp. 1423–1432, 1998.

[23] N. Yagoda, M. von Rechenberg, and E Zaganjor, "RAS-RAF-MEK-dependent oxidative cell death involving voltage-dependent anion channels," *Nature*, vol. 447, no. 7146, pp. 864–868, 2007.

[24] M. Zille, S. S. Karuppagounder, Y. Chen et al., "Neuronal death after hemorrhagic stroke in vitro and in vivo shares features of ferroptosis and necroptosis," *Stroke*, vol. 48, no. 4, pp. 1033–1043, 2017.

[25] N. DeGregorio-Rocasolano, O. Martí-Sistac, and T. Gasull, "Deciphering the iron side of stroke: neurodegeneration at the crossroads between iron dyshomeostasis, excitotoxicity, and ferroptosis," *Frontiers in Neuroscience*, vol. 13, p. 85, 2019.

[26] L. Li, Y. Hao, and Y Zhao, "Ferroptosis is associated with oxygen-glucose deprivation/reoxygenation-induced Sertoli cell death," *International Journal of Molecular Medicine*, vol. 41, no. 5, pp. 3051–3062, 2018.

[27] Q. Li, X. Han, and X Lan, "Inhibition of neuronal ferroptosis protects hemorrhagic brain," *JCI Insight*, vol. 2, no. 7, Article ID e90777, 2017.

[28] Q.-z. Tuo, P. Lei, K. A. Jackman et al., "Tau-mediated iron export prevents ferroptotic damage after ischemic stroke," *Molecular Psychiatry*, vol. 22, no. 11, pp. 1520–1530, 2017.

[29] C. Gubern, S. Camós, I. Ballesteros et al., "miRNA expression is modulated over time after focal ischaemia: up-regulation of miR-347 promotes neuronal apoptosis," *FEBS Journal*, vol. 280, no. 23, pp. 6233–6246, 2013.

[30] K. Yigitkanli, Y. Zheng, A. Pekcec, E. H. Lo, and K. van Leyen, "Increased 12/15-lipoxygenase leads to widespread brain injury following global cerebral ischemia," *Translational Stroke Research*, vol. 8, no. 2, pp. 194–202, 2017.

[31] J. H. Cheah, S. F. Kim, L. D. Hester et al., "NMDA receptor-nitric oxide transmission mediates neuronal iron homeostasis via the GTPase Dexras1," *Neuron*, vol. 51, no. 4, pp. 431–440, 2006.

[32] D. J. R. Lane, S. Ayton, and A. I. Bush, "Iron and Alzheimer's disease: an update on emerging mechanisms," *Journal of Alzheimer's Disease*, vol. 64, no. s1, pp. S379–S395, 2018.

[33] M. D. Meadowcroft, J. R. Connor, M. B. Smith, and Q. X. Yang, "MRI and histological analysis of beta-amyloid plaques in both human Alzheimer's disease and APP/PS1 transgenic mice," *Journal of Magnetic Resonance Imaging*, vol. 29, no. 5, pp. 997–1007, 2009.

[34] S. Ayton, P. Lei, and A. I. Bush, "Biometals and their therapeutic implications in Alzheimer's disease," *Neurotherapeutics*, vol. 12, no. 1, pp. 109–120, 2015.

[35] M.-S. Chen, S.-F. Wang, C.-Y. Hsu et al., "CHAC1 degradation of glutathione enhances cystine-starvation-induced necroptosis and ferroptosis in human triple negative breast cancer cells via the GCN2-eIF2α-ATF4 pathway," *Oncotarget*, vol. 8, no. 70, pp. 114588–114602, 2017.

[36] S. Ma, E. S. Henson, Y. Chen, and S. B. Gibson, "Ferroptosis is induced following siramesine and lapatinib treatment of breast cancer cells," *Cell Death & Disease*, vol. 7, no. 7, e2307 pages, 2016.

[37] S. J. Dixon, D. N. Patel, and M Welsch, "Pharmacological inhibition of cystine-glutamate exchange induces endoplasmic reticulum stress and ferroptosis," *Elife*, vol. 3, Article ID e02523, 2014.

[38] J. Chu, C. X. Liu, R. Song, and Q. L. Li, "Ferrostatin-1 protects HT-22 cells from oxidative toxicity," *Neural regeneration research*, vol. 15, no. 3, pp. 528–536, 2020.

[39] P. Liu, Y. Feng, H. Li et al., "Ferrostatin-1 alleviates lipopolysaccharide-induced acute lung injury via inhibiting ferroptosis," *Cellular and Molecular Biology Letters*, vol. 25, no. 1, p. 10, 2020.

[40] R. Skouta, S. J. Dixon, J. Wang et al., "Ferrostatins inhibit oxidative lipid damage and cell death in diverse disease models," *Journal of the American Chemical Society*, vol. 136, no. 12, pp. 4551–4556, 2014.

[41] A. Linkermann, R. Skouta, N. Himmerkus et al., "Synchronized renal tubular cell death involves ferroptosis," *Proceedings of the National Academy of Sciences*, vol. 111, no. 47, pp. 16836–16841, 2014.

[42] G. Miotto, M. Rossetto, M. L. Di Paolo et al., "Insight into the mechanism of ferroptosis inhibition by ferrostatin-1," *Redox Biology*, vol. 28, Article ID 101328, 2020.

[43] O. Zilka, R. Shah, B. Li et al., "On the mechanism of cytoprotection by ferrostatin-1 and liproxstatin-1 and the role of lipid peroxidation in ferroptotic cell death," *ACS Central Science*, vol. 3, no. 3, pp. 232–243, 2017.

[44] Y. N. Jin and G. V. W. Johnson, "The interrelationship between mitochondrial dysfunction and transcriptional dysregulation in Huntington disease," *Journal of Bioenergetics and Biomembranes*, vol. 42, no. 3, pp. 199–205, 2010.

[45] J. Wan, H. Ren, and J. Wang, "Iron toxicity, lipid peroxidation and ferroptosis after intracerebral haemorrhage," *Stroke and Vascular Neurology*, vol. 4, no. 2, pp. 93–95, 2019.

[46] Z. Zhang, Y. Wu, S. Yuan et al., "Glutathione peroxidase 4 participates in secondary brain injury through mediating ferroptosis in a rat model of intracerebral hemorrhage," *Brain Research*, vol. 1701, pp. 112–125, 2018.

[47] S. S. Karuppagounder, L. Alin, Y. Chen et al., “N-acetylcysteine targets 5 lipoxygenase-derived, toxic lipids and can synergize with prostaglandin E2to inhibit ferroptosis and improve outcomes following hemorrhagic stroke in mice,” *Annals of Neurology*, vol. 84, no. 6, pp. 854–872, 2018.

[48] J.-H. Park, J. Zhuang, J. Li, and P. M. Hwang, “p53 as guardian of the mitochondrial genome,” *FEBS Letters*, vol. 590, no. 7, pp. 924–934, 2016.

[49] J. Shen, X. Sheng, Z. Chang et al., “Iron metabolism regulates p53 signaling through direct heme-p53 interaction and modulation of p53 localization, stability, and function,” *Cell Reports*, vol. 7, no. 1, pp. 180–193, 2014.

[50] C. Louandre, Z. Ezzoukhry, C. Godin et al., “Iron-dependent cell death of hepatocellular carcinoma cells exposed to sorafenib,” *International Journal of Cancer*, vol. 133, no. 7, pp. 1732–1742, 2013.

[51] A. Houessinon, C. François, C. Sauzay et al., “Metallothionein-1 as a biomarker of altered redox metabolism in hepatocellular carcinoma cells exposed to sorafenib,” *Molecular Cancer*, vol. 15, no. 1, p. 38, 2016.

[52] X. Sun, X. Niu, R. Chen et al., “Metallothionein-1G facilitates sorafenib resistance through inhibition of ferroptosis,” *Hepatology*, vol. 64, no. 2, pp. 488–500, 2016.

[53] X. Sun, Z. Ou, R. Chen et al., “Activation of the p62-Keap1-NRF2 pathway protects against ferroptosis in hepatocellular carcinoma cells,” *Hepatology*, vol. 63, no. 1, pp. 173–184, 2016.

[54] X. Sun, Z. Cao, K. Mao et al., “Photodynamic therapy produces enhanced efficacy of antitumor immunotherapy by simultaneously inducing intratumoral release of sorafenib,” *Biomaterials*, vol. 240, Article ID 119845, 2020.

[55] S. Ma, R. F. Dielschneider, E. S. Henson et al., “Ferroptosis and autophagy induced cell death occur independently after siramesine and lapatinib treatment in breast cancer cells,” *PloS One*, vol. 12, no. 8, Article ID e0182921, 2017.

[56] M. Gao, P. Monian, Q. Pan, W. Zhang, J. Xiang, and X. Jiang, “Ferroptosis is an autophagic cell death process,” *Cell Research*, vol. 26, no. 9, pp. 1021–1032, 2016.

[57] T. Müller, C. Dewitz, J. Schmitz et al., “Necroptosis and ferroptosis are alternative cell death pathways that operate in acute kidney failure,” *Cellular and Molecular Life Sciences*, vol. 74, no. 19, pp. 3631–3645, 2017.

[58] A. von Mässenhausen, W. Tonnus, and A. Linkermann, “Cell death pathways drive necroinflammation during acute kidney injury,” *Nephron*, vol. 140, no. 2, pp. 144–147, 2018.

[59] R. Shah, M. S. Shchepinov, and D. A. Pratt, “Resolving the role of lipoxygenases in the initiation and execution of ferroptosis,” *ACS Central Science*, vol. 4, no. 3, pp. 387–396, 2018.

[60] Z. Song, X. Xiang, and J Li, “Ruscogenin induces ferroptosis in pancreatic cancer cells,” *Oncology Reports*, vol. 43, no. 2, pp. 516–524, 2020.

[61] B. Zhou, J. Liu, R. Kang, D. J. Klionsky, G. Kroemer, and D. Tang, “Ferroptosis is a type of autophagy-dependent cell death,” *Seminars in Cancer Biology*, vol. 66, pp. 89–100, 2020.

[62] R. Shintoku, Y. Takigawa, K. Yamada et al., “Lipoxygenase-mediated generation of lipid peroxides enhances ferroptosis induced by erastin and RSL3,” *Cancer Science*, vol. 108, no. 11, pp. 2187–2194, 2017.

[63] J. P. Friedmann Angeli, M. Schneider, B. Proneth et al., “Inactivation of the ferroptosis regulator Gpx4 triggers acute renal failure in mice,” *Nature Cell Biology*, vol. 16, no. 12, pp. 1180–1191, 2014.

[64] J. H. Woo, Y. Shimoni, W. S. Yang et al., “Elucidating compound mechanism of action by network perturbation analysis,” *Cell*, vol. 162, no. 2, pp. 441–451, 2015.

[65] M. Luo, L. Wu, K. Zhang et al., “miR-137 regulates ferroptosis by targeting glutamine transporter SLC1A5 in melanoma,” *Cell Death & Differentiation*, vol. 25, no. 8, pp. 1457–1472, 2018.

[66] J. Tsoi, L. Robert, K. Paraiso et al., “Multi-stage differentiation defines melanoma subtypes with differential vulnerability to drug-induced iron-dependent oxidative stress,” *Cancer Cell*, vol. 33, no. 5, pp. 890–904, 2018.

[67] M. Buccarelli, M. Marconi, S. Pacioni et al., “Inhibition of autophagy increases susceptibility of glioblastoma stem cells to temozolomide by igniting ferroptosis,” *Cell Death & Disease*, vol. 9, no. 8, p. 841, 2018.

[68] T. Sehm, M. Rauh, K. Wiendieck, M. Buchfelder, I. Y. Eyüpoglu, and N. E. Savaskan, “Temozolomide toxicity operates in a xCT/SLC7a11 dependent manner and is fostered by ferroptosis,” *Oncotarget*, vol. 7, no. 46, pp. 74630–74647, 2016.

[69] Z. Hu, Y. Mi, H. Qian et al., “A potential mechanism of temozolomide resistance in glioma-ferroptosis,” *Frontiers in Oncology*, vol. 10, p. 897, 2020.

[70] M. Gao, P. Monian, N. Quadri, R. Ramasamy, and X. Jiang, “Glutaminolysis and transferrin regulate ferroptosis,” *Molecular Cell*, vol. 59, no. 2, pp. 298–308, 2015.

[71] W. Hou, Y. Xie, X. Song et al., “Autophagy promotes ferroptosis by degradation of ferritin,” *Autophagy*, vol. 12, no. 8, pp. 1425–1428, 2016.

[72] L. Jiang, N. Kon, T. Li et al., “Ferroptosis as a p53-mediated activity during tumour suppression,” *Nature*, vol. 520, no. 7545, pp. 57–62, 2015.

[73] S.-J. Wang, D. Li, Y. Ou et al., “Acetylation is crucial for p53-mediated ferroptosis and tumor suppression,” *Cell Reports*, vol. 17, no. 2, pp. 366–373, 2016.

[74] Y. Xie, S. Zhu, X. Song et al., “The tumor suppressor p53 limits ferroptosis by blocking DPP4 activity,” *Cell Reports*, vol. 20, no. 7, pp. 1692–1704, 2017.

[75] Y. Mou, J. Wang, J. Wu et al., “Ferroptosis, a new form of cell death: opportunities and challenges in cancer,” *Journal of Hematology & Oncology*, vol. 12, no. 1, p. 34, 2019.

Hindawi
Journal of Healthcare Engineering
Volume 2021, Article ID 9596518, 5 pages
https://doi.org/10.1155/2021/9596518

Research Article

The Value of CT 3D Reconstruction in the Classification and Nursing Effect Evaluation of Ankle Fracture

Pan Xue,[1] **Xue Chen**,[1] **Si Chen**,[2] **and Yuanyuan Shi**[3]

[1]*Department of Orthopedics, The Second Hospital of Jilin University, Changchun 130041, China*
[2]*Geriatric Medicine, The Second Hospital of Jilin University, Changchun 130041, China*
[3]*Department of Nursing, The Second Hospital of Jilin University, Changchun 130041, China*

Correspondence should be addressed to Yuanyuan Shi; 2001010122@st.btbu.edu.cn

Received 24 June 2021; Accepted 2 August 2021; Published 10 August 2021

Academic Editor: Enas Abdulhay

Aim. To study the application value of ankle fracture classification and diagnosis. In this paper, the clinical data of 100 cases of ankle fracture patients admitted from May 2020 to May 2021 were analyzed by CT 3D reconstruction. All patients received surgical treatment and underwent spiral CT 3D reconstruction and X-ray examination before surgery. The results showed that 20 cases (20.00%) of the 100 cases were PER, 24 cases (24%) of the 100 cases were PAB, 31 cases (31%) of the 100 cases were SER, and 25 cases (25%) of the 100 cases were SAB, respectively. *Conclusion*. The diagnostic accuracy of CT 3D reconstruction for different types of ankle fracture is higher than that of X-ray, and the differences are statistically significant ($P < 0.05$). CT 3D reconstruction is applied in the early diagnosis of ankle fracture, which can accurately detect the classification of patients. It has important clinical application value and can be used as the first choice for the early classification diagnosis of ankle fracture.

1. Introduction

Manic joint fracture is the most common intra-articular fracture, accounting for about 3.9% of systemic fractures, which is most likely to occur in young adults. Due to the different mechanism of injury, the manifestation of ankle fracture is different. With the in-depth understanding of the anatomy, function, biomechanical properties of the disc joint, and injury mechanism, the classification methods pay more attention to comprehensive factors, such as the location of foot injury, the magnitude and direction of external force, the relationship between inlay and fracture, and the process and degree of fracture [1]. The area of ankle joint is smaller than that of hip joint and knee joint, but the pressure is the largest among the three. In addition, the ankle joint is close to the ground, and the load-bearing stress acting on it cannot be buffered. Therefore, the treatment of ankle fracture is higher than that of other parts. The importance of anatomical reduction of ankle joint has become a consensus. Uneven articular surfaces or poor reduction of the ankle after a manic joint fracture can lead to limited joint movement, pain, and traumatic arthritis. How to choose the most appropriate treatment is closely related to the classification and diagnosis of fracture. Currently, there are three commonly accepted and commonly used classifications in clinical practice: mechanical classification, surgical classification, and Ashurst–Bromer classification. The above classification methods have their own advantages, but for disc fracture, there are many factors that affect the prognosis, and there is no effective and comprehensive classification method to judge the prognosis at present. In addition, the classification diagnosis mentioned above is usually based on radiography, but due to the special anatomical structure of foot manic part, conventional ankle radiographs are difficult to comprehensively and clearly show the X-ray and bone fragments, which makes the classification diagnosis of ankle more difficult [2]. In recent years, with the continuous progress and improvement of spiral CT three-dimensional reconstruction technology, fracture positioning is more accurate and intuitive and can better display the spatial morphology of ankle fracture, which provides convenience for classification and diagnosis.

Injures of the primary triangle of the ankle joint can be divided into acute and chronic injuries. The acute injury is usually manifested by tenderness and hematoma of the angular band at the medial malleolus, while the chronic injury is manifested by dull pain of the medial sulcus of the ankle joint, which is typically caused by palpation of the anterior medial malleolus. There is obvious tenderness before and below the tip of the medial malleolus, subcutaneous spots can be seen, and there is a sense of depression or emptiness when pressing the inner side of the heel joint. Due to acute injury, patients have obvious clinical symptoms, so they can usually attract the attention of patients and take corresponding measures to prevent the aggravation of ligament damage. However, chronic injury is not easy to attract the attention of patients because the symptoms occur from time to time. As a result, the triangular ligament cannot rest, but it is more likely to lead to the instability of the medial disc joint, which is mainly manifested as "hitting the soft leg" when walking on uneven ground, downhill, or down stairs [3]. Qi Xiaoyang et al. pointed out that the smoothness and displacement of the ankle joint surface are closely related to the elasticity of the joint ligament and the articular surface stress. If the articular surface shifts outward by 1 mm, the contact area of the tibial talar joint will be reduced by about 40%. If the displacement or shortening of the articular surface is more than 2 mm or external rotation is more than 5°, the stress of the ankle will be abnormally distributed, which is very easy to lead to many complications such as traumatic arthritis. Therefore, in case of ankle fracture, patients should be classified and diagnosed in time in the early stage, so that clinicians can design a reasonable surgical treatment plan to ensure the postoperative rehabilitation of patients and achieve the purpose of effective anatomical reduction and internal fixation [4]. In the past, the diagnosis of ankle fractures mostly relied on conventional CT plane scan and X-ray film. However, the use of X-ray film is easy to appear like the overlapping image of ankle fractures and unable to clearly show the small broken end displacement, fracture line, articular surface, and other conditions, resulting in a high rate of missed diagnosis and misdiagnosis. Two-dimensional CT has a higher resolution than X-ray film without overlapping images, but due to the poor stereoscopic sense of the sectional plane images, it is unable to comprehensively and accurately evaluate the overall situation of ankle fracture, and its application also has certain limitations [5].

Hinb et al. proposed the "foot free suspension test" to check whether the triangle facing belt is damaged. The specific methods are as follows: the examinee holds the subject's heel on the affected side with one hand and the ipsilateral cavity bone with the other hand and imposes a valgus force and valgus force on the heel, respectively. The degree of valgus is checked and then compared with the contralateral side, so as to infer the damage of the triangular zone. In addition, the drawer test commonly used in orthopedics to check the degree of relaxation of Bremsstrahlung can also be used to infer the condition of sonic injury of the primary triangular band. The principle of treatment of manic joint fracture is to completely remove the intra-articular bone fragments and achieve anatomic reduction at the ankle point. However, it has been reported abroad that it is very difficult to completely rely on surgical anatomical reduction for the treatment of ankle fractures, and it is almost impossible to achieve anatomical reduction by surgical treatment, not because of the limited surgical techniques, but because of the failure to correctly evaluate the degree of fracture injury of patients before surgery [6]. So, an accurate assessment of preoperative plan formulation, treatment effect of surgery, has important meaning, and 3D reconstruction technology in this advantage is particularly prominent in the presence of displaced fractures, more blocks, more severe compression or comminuted fracture, intra-articular fractures cases, which ordinary methods do not have. Through clinical practice, many scholars at home and abroad put forward that 3D reconstruction can not only display the trend of fracture line, the damage of joint surface, joint cavity and joint capsule, the position of fracture fragments, dislocation, and subluxation comprehensively, intuitively, three-dimensional, and accurately but also can accurately display the subtle anatomical structure of ankle joint and clearly show the bleeding of soft tissue around manic joint. It is not only conducive to judge the fracture classification and provide more effective and valuable information but also has far more advantages than the traditional examination methods. Clinical practice also shows that preoperative preparation can be fully completed through three-dimensional reconstruction examination and further evaluation of the risk of surgery, so as to achieve anatomical reduction of fracture as far as possible and maximize the recovery of patients' manic joint function [7].

The innovation of this paper: spiral CT reconstruction is targeted at different fracture sites of patients and can comprehensively display the specific situation of ankle fracture, which can not only eliminate image overlap but also improve the accuracy of classification diagnosis of ankle fracture and provide reliable diagnostic basis for patients' future treatment.

2. Materials and Methods

2.1. General Information. Retrospective analysis was performed on the imaging and clinical data of 100 patients with ankle joint fracture admitted to the hospital of the author from May 2020 to May 2021. This study was approved by the medical ethics committee of the hospital of the author. Among the 100 patients, 59 were male and 41 were female. The average age was (44.79 ± 10.51) years from 21 to 67 years old.

2.2. Inclusion Criteria. Inclusion criteria: (1) all patients had new ankle fractures; (2) no pathological fracture was found; (3) daily life before fracture can be self-care; (4) have good language skills; (5) all patients received surgical treatment; (6) complete clinical data. Exclusion criteria: (1) patients with severe consciousness impairment, cognitive impairment, and mental disorder; (2) patients with systemic blood diseases; (3) patients with combined diseases that have influence on imaging examination.

3. Methods

All patients underwent X-ray examination and spiral CT three-dimensional reconstruction.

(1) Data collection preoperative imaging examination data, physical sign examination data, trauma history, and intraoperative conditions of the patients were collected, and relevant imaging images were analyzed using Digimizer measurement software. Anteroposterior radiographs of the ankle included TFCS, TFO, coin sign, and Shenton line. Ankle acupoint films: tibial talus angle, talus leg and foot, talus tibial space (TCS), and talus medial malleolus space (MCS). CT reconstruction: medial malleolus space of talus (MCS) and inferior tibiofibular space (RFCS). Intraoperative: cotton test, abductor and pronator stress test, lateral forward stress radiograph, anterior drawer test, varus stress radiograph, and ankle radiograph under varus stress. Combined with the imaging signs, trauma history, and physical index examination results of the patients, the diagnosis was made. According to CT reconstruction, X-ray, and intraoperative conditions of each patient and Lauge-Hansen classification, the application value of X-ray and spiral CT three-dimensional reconstruction was analyzed and compared with intraoperative diagnosis as the gold standard.

(2) Examination method X-ray film: Philips DR camera was used to perform anteroposterior and lateral X-ray photography for the affected side of the ankle. The CT examination instrument was Toshiba Aquilion 16-Slice Spiral CT Scanner. During the scanning, the patient was placed in supine position. The scanning range was distal to proximal, and the axial scanning range was from 1/3 of the lower tibia to the foot, including the range of 2 cm above and below the fracture line. Parameters: current, 200~250 mA; voltage, 135 kV; layer thickness, 5 mm; reconstruction spacing, 1 mm; pitch, 1, the standard algorithm for reconstruction calculation. After the scanning, the obtained two-dimensional volume image was transferred to the workstation, and the computer was used to perform three-dimensional image reconstruction, including sagittal and coronal multiplane reconstruction (MPR), maximum density projection (MIP), and surface occlusion imaging (SSD). The free cross-section multiplane recombination mode was used to observe the fracture fragments and details, the surface reconstruction method was used to reconstruct the three-dimensional image of the bone structure around the ankle joint, and the three-dimensional shape of the ankle joint was carefully observed by the maximum density projection.

3.1. Observation Indexes and Evaluation Criteria. To compare the diagnosis of different types of ankle fractures by two examination methods. Ankle fractures are classified according to the Lauge–Hansen classification, including pronation-external rotation type (PER), pronation-abduction (PAB), supination external rotation (SER), and supination-adduction (SAB). According to the degree of injury of the patient, the classification of ankle fracture types can be as follows: PER, I~IV degree; PAB, I~III degree; SER, I~IV degree; SAB, I~II degree.

3.2. Statistical Treatment. SPSS 20.0 statistical software was used to process the data. Enumeration data were represented as rate (%), word 2 test was used, measurement data were represented as (X- $\pm S$), and $P < 0.05$ indicated statistically significant difference [8].

4. Results and Discussion

4.1. Intraoperative Typing Results. Among the 100 patients, 24 patients were PAB, accounting for 24%, including 12 patients with I degree, 8 patients with critical degree, and 4 patients with radiance. 20 cases belonged to PER, accounting for 20.00%, including 9 cases of I degree, 6 cases of power degree, 3 cases of bulkiness, and 2 cases of compliance; 31 cases (31%) belonged to SAB type, of which 21 cases were I degree and 10 cases were normal degree. 25 cases (25%) were SER, including 13 cases with I degree, 7 cases with power degree, 3 cases with universality degree, and 2 cases with adequacy degree. The diagnostic value of X-ray and spiral CT 3D reconstruction for PAB ankle fracture was found by intraoperative typing results as the gold standard; the specificity, sensitivity, and accuracy of spiral CT 3D reconstruction in the diagnosis of PAB ankle fracture were 100% (91/91), 100% (29/29), and 100% (100/100), respectively, and the X-ray values were 95.6% (87/91), 75.86% (22/29), and 90.83% (109/100), respectively; the specificity, sensitivity, and accuracy of 3D reconstruction of spiral CT were all higher than that of X-ray, and the differences were statistically significant (word 2 = 2.301, 5.849, 11.528; $P < 0.05$), as shown in Table 1.

4.2. The Value of X-Ray and Spiral CT 3D Reconstruction in the Diagnosis of PER Ankle Fracture. Using intraoperative typing results as the gold standard, the specificity, sensitivity, and accuracy of spiral CT 3D reconstruction for PER ankle fracture were 100%(96/96), 95.83%(23/24), and 99.17%(119/100), respectively. X-ray values were 93.75% (90/96), 91.67% (22/24), and 93.33% (112/100), respectively; the difference was not statistically significant (word 2 = 0.000; P = 0.551), and the diagnostic specificity and accuracy of spiral CT 3D reconstruction were both higher than that of X-ray, and the difference was statistically significant (word 2 = 4.301, 4.156; $P < 0.05$), as shown in Table 2.

4.3. The Value of X-Ray and Spiral CT 3D Reconstruction in the Diagnosis of SAB Ankle Fracture. Using intraoperative typing results as the gold standard, the specificity, sensitivity, and accuracy of spiral CT 3D reconstruction in the diagnosis of SAB articular fractures were 100% (87/87), 100% (33/33),

Table 1: Comparison of the value of X-ray and spiral CT 3D reconstruction in the diagnosis of PAB type of ankle fracture.

X-ray	Intraoperative		A combined	CT	Intraoperative		A combined
	+	−			+	−	
+	20	3	23	+	25	0	25
−	7	70	77	−	0	75	75
A combined	27	73	100	A combined	25	75	100

Table 2: Comparison of diagnostic value of 2X scan and spiral CT 3D reconstruction in PER ankle fracture.

X-ray	Intraoperative		A combined	CT	Intraoperative		A combined
	+	−			+	−	
+	18	3	21	+	19	0	19
−	1	78	79	−	1	80	81
A combined	19	81	100	A combined	20	80	100

Table 3: Comparison of X-ray and spiral CT 3D reconstruction in the diagnosis of SAB ankle fracture.

X-ray	Intraoperative		A combined	CT	Intraoperative		A combined
	+	−			+	−	
+	22	5	27	+	31	0	31
−	1	72	73	−	0	69	69
A combined	23	77	100	A combined	31	69	100

Table 4: Comparison of the diagnostic value of X-ray and spiral CT 3D reconstruction in SER ankle fracture.

X-ray	Intraoperative		A combined	CT	Intraoperative		A combined
	+	−			+	−	
+	16	4	20	+	17	7	24
−	5	75	80	−	1	75	76
A combined	21	79	100	A combined	18	82	100

and 100% (100/100), respectively; X-ray examination was 93.75% (80/87), 91.67% (30/33), and 93.33% (110/100), respectively; there was no significant difference in sensitivity between the two methods (word $2 = 1.397$; $P = 0.076$). The sensitivity and accuracy of 3D reconstruction of spiral CT were both higher than that of X-ray, and the differences were statistically significant (word $2 = 5.358$, 10.435; $P < 0.05$), as shown in Table 3.

4.4. Diagnostic Value of X-Ray and Spiral CT 3D Reconstruction in SER Ankle Fracture. Using intraoperative classification as the gold standard, the diagnostic specificity, sensitivity, and accuracy of spiral CT 3D reconstruction for SER ankle fracture were 96.51% (83/86), 97.06% (33/34), and 96.67% (116/100), respectively; X-ray results were 95.35% (82/86), 76.47% (26/34), and 90.00% (108/100), respectively. There was no significant difference in the specificity of the two methods (word $2 = 0.000$; $P = 0.670$). The sensitivity and accuracy of spiral CT 3D reconstruction diagnosis were higher than that of X-ray. The difference was statistically significant (word $2 = 4.610$, 4.286; $P < 0.05$), as shown in Table 4.

5. Conclusions

The treatment of ankle fracture is mainly to achieve the best anatomical reduction and fixation, so as to realize the effective recovery of the patient's ankle function. Therefore, strengthening the clinical diagnosis of patients with ankle fracture is of great significance to improve the treatment effect of patients in the future. Ankle fracture is prone to misdiagnosis or missed diagnosis due to its complex anatomical structure, many types of fracture and easy displacement of bone block, which increases the clinical diagnosis difficulty of X-ray and CT scan examination, leading to misdiagnosis or missed diagnosis of ankle fracture. In conclusion, the application of spiral CT reconstruction in the diagnosis of ankle fracture can visually and comprehensively display the fracture site, provide a reliable basis for doctors' clinical diagnosis and treatment, and promote the gradual improvement of patients' clinical treatment effect.

This study retrospectively analyzed the clinical data of patients with ankle fracture admitted to our hospital in the past two years and found that all patients received surgical treatment, preoperative X-ray examination, and spiral CT three-dimensional reconstruction. The intraoperative typing results showed that, of the 100 patients, 20 (20.00%) were found to have pronation and extrapolation (PER), 24 (24%) to have pronation and extrapolation (SER), and 25 (25%) to have pronation and adduction (SAB), respectively. Using the intraoperative classification results as the gold standard, the diagnostic accuracy of spiral CT 3D reconstruction for different types of ankle fracture was higher than that of X-ray, suggesting that the application of spiral CT 3D reconstruction in the early diagnosis of different types of ankle fracture has more clinical application value than that of X-ray. In conclusion, the application of spiral CT three-dimensional reconstruction in the early diagnosis of ankle fracture can accurately detect the classification of patients, which has important clinical application value and can be used as the first choice for the early classification diagnosis of ankle fracture.

Data Availability

The data used to support the findings of this study are available from the corresponding author upon request.

Conflicts of Interest

The authors declare no conflicts of interest.

References

[1] X. F. Gong, Y. W. Lyu, J. H. Wang, Y. Wang, Y. Wu, and M. Y. Wang, “A correlation analysis of the ankle CT and ankle fracture classification,” *Beijing da xue xue bao. Yi xue ban = Journal of Peking University Health Sciences*, vol. 49, no. 2, pp. 281–285, 2017.

[2] R. Patil and S. Tamane, “A comparative analysis on the evaluation of classification algorithms in the prediction of diabetes,” *International Journal of Electrical and Computer Engineering*, vol. 8, no. 5, pp. 3966–3975, 2018.

[3] C. Anuradha and T. Velmurugan, “A comparative analysis on the evaluation of classification algorithms in the prediction of students performance,” *Indian Journal of Science & Technology*, vol. 8, no. 15, pp. 974–6846, 2015.

[4] J. Su, J. Li, J. Zhang, Z. Nan, and Z. Liu, “Classification and evaluation of relative permeability based on the analysis of petrophysical facies: a case study on Chang 8 reservoir in Zhenjing region,Ordos Basin,” *Journal of Shenzhen University Science and Engineering*, vol. 32, no. 5, pp. 480–487, 2015.

[5] W. Kristina and S. Darko, M. Sue and T. Regina, Evaluation of the effect of laboratory methods on semen analysis and breeding soundness examination (BSE) classification in stallions,” *Theriogenology*, vol. 142, no. 2, pp. 67–76, 2019.

[6] M. Bellomi, F. De Piano, E. Ancona et al., “Evaluation of inter-observer variability according to RECIST 1.1 and its influence on response classification in CT measurement of liver metastases,” *European Journal of Radiology*, vol. 95, no. 3, pp. 96–101, 2017.

[7] J. Bartoníček, S. Rammelt, K. Kostlivý, V. Vaněček, D. Klika, and I. Trešl, “Anatomy and classification of the posterior tibial fragment in ankle fractures,” *Archives of Orthopaedic and Trauma Surgery*, vol. 135, no. 4, pp. 505–516, 2015.

[8] H. Tao, H. Li, Y. Hua, Z. Chen, X. Feng, and S. Chen, “Quantitative magnetic resonance imaging (MRI) evaluation of cartilage repair after microfracture treatment for full-thickness cartilage defect models in rabbit knee joints: correlations with histological findings,” *Skeletal Radiology*, vol. 44, no. 3, pp. 393–402, 2015.

Hindawi
Journal of Healthcare Engineering
Volume 2021, Article ID 2302379, 6 pages
https://doi.org/10.1155/2021/2302379

Research Article

Cognitive Dysfunction of Pregnant Women with Gestational Diabetes Mellitus in Perinatal Period

Siriguleng Sana,[1] **Xijin Deng**,[2] **Lei Guo**,[1] **Xunhong Wang**,[3] **and Enyou Li**[1]

[1]*Department of Anesthesiology, The First Affiliated Hospital of Harbin Medical University, Harbin 150001, Heilongjiang Province, China*
[2]*Department of Anesthesiology, The Second Affiliated Hospital of Harbin Medical University, Harbin 150001, Heilongjiang Province, China*
[3]*Department of Obstetrics, The First Affiliated Hospital of Harbin Medical University, Harbin 150001, Heilongjiang Province, China*

Correspondence should be addressed to Enyou Li; lienyou_1111@163.com

Received 29 May 2021; Revised 10 July 2021; Accepted 27 July 2021; Published 10 August 2021

Academic Editor: Enas Abdulhay

Purpose. To explore whether pregnant women with gestational diabetes mellitus (GDM) had cognitive impairment and assess cognitive function in normal pregnant women. *Methods*. A total of 75 consecutive women diagnosed with GDM (GDM group), 70 normal pregnant women (NP group) without diabetes and matched for age, and 51 female volunteers (CG group) with the similar age level, normal blood glucose, and nonpregnancy were included in the study. For the assessment of cognitive functions, Montreal Cognitive Assessment (MoCA) was performed. Venous blood samples were collected to measure blood glucose, glycated hemoglobin (HbA1c), methylglyoxal (MGO), beta amyloid (Aβ), and tau protein. *Results*. The score of MoCA of GDM was lowest, and the score of the NP group was lower than volunteers ($P < 0.05$). The incidence of cognitive dysfunction increased significantly in the GDM group with statistical significance ($P < 0.05$). The levels of tau and MGO in the GDM group were significantly less than those in the NP and CG groups, and Aβ in the GDM group was significantly more than that in the NP and CG groups ($P < 0.05$), but the differences between NP and CG groups were not statistically significant ($P < 0.05$). *Conclusion*. The pregnant women with GDM showed a significant decline in cognitive function, and the normal pregnant women also showed a decline in cognitive function which is very light.

1. Introduction

Gestational diabetes mellitus (GDM) occurs in pregnant women who were not diagnosed with diabetes before pregnancy but have abnormal result of OGTT or/and high blood glucose levels during pregnancy, usually around the 24th week, by the American Diabetes Association [1]. According to the most recent International Diabetes Federation (IDF) estimates (2019), GDM affects approximately 13.2% of pregnancies worldwide, representing approximately 17 million births annually. The risk factors of GDM include older age, overweight and obesity, previous GDM, a family history of diabetes, and a history of stillbirth or giving birth to an infant with a congenital abnormality. GDM usually exists as a transient disorder during pregnancy and resolves once the pregnancy ends. However, it can have long-lasting health consequences, including increased risk for type 2 diabetes (T2DM) and cardiovascular disease (CVD) in the mother, and future obesity, and/or GDM in the child [2].

The pathogenesis of GDM is still not clear, although there are many risk factors, similar to type 2 diabetes (T2DM). Cognitive dysfunction in cases with long standing T2DM has been widely reported [3]. And, decline of verbal memory, associate learning, and verbal recall in normal pregnant women have been reported [4–6]. However, few studies have identified cognitive dysfunction in GDM patients [7]. Therefore, this study observed the cognitive function of pregnant women, especially who are suffering from GDM and tried to improve the evidence from the serological point of view.

2. Materials and Methods

2.1. Subjects and Protocol. Patients aged 18–35 years with American Society of Anaesthesiologists (ASA) physical status I-II were admitted to the study. A total of 101 consecutive women with GDM who were diagnosed, followed, and treated at the First Affiliated Hospital of Harbin Medical University included in the study. 76 pregnant women without diabetes and matched for age constituted the normal pregnancy group (NP). And, we recruited 51 female volunteers with the similar age level, normal blood glucose, and are not pregnant formed the control group (CG). All the patients and volunteers read and signed the informed consent forms before enrolling in the study. The study protocol was approved by the Ethics Committee of First Affiliated Hospital of Harbin Medical University, which was registered with the Chinese Clinical Trial Register (registration number: ChiCTR2000038703).

GDM was diagnosed with at least one abnormal result during OGTT: plasma glucose during fasting ≥92 mg/dL (5.1 mmol/L) or at 1 h ≥180 mg/dL (10.0 mmol/L) or at 2 h ≥153 mg/dL (8.5 mmol/L). Cases with fasting plasma glucose ≥126 mg/dL (7.0 mmol/L), HbA1c ≥6.5%, or a random plasma glucose ≥200 mg/dL (11.1 mmol/L) were diagnosed with overt diabetes and excluded. Cases with pregestational T1 or T2DM were not included in the study. Cases with unnatural pregnancy or gestational period <37 weeks or >41 weeks were excluded. Subjects on medications affecting cognitive functions including corticosteroids, antidepressants, or antiepileptics were also not included. Additionally, subjects suffering from any chronic metabolic, endocrine, inflammatory diseases, cancer, subjects who had drug or alcohol dependency, history of major brain abnormalities (e.g., tumors and hydrocephaly), epilepsy, and Parkinson's disease were excluded. The Hamilton Depression Rating Scale (HAMD) was used to assess the psychological status of pregnant women and those with a score of more than 7 might have depression and were excluded [8].

On the survey date, all enrolled patients underwent routine medical history inquiries, physical examinations, and laboratory measurements. Clinical research coordinators used a standard questionnaire to collect information on demographic characteristics and a medical history. There were no racial/ethnic, educational, or socioeconomic differences between the groups (Table 1). All pregnant women were instructed to maintain their usual physical activity and diet for at least 3 days before the survey. After an overnight fasting of ≥10 h, venous blood samples were collected to measure blood lipids, glycated hemoglobin (HbA1c), methylglyoxal (MGO), beta amyloid (Aβ), and tau protein activity. Blood samples were stored at −80°C, and all parameters were measured within 6 months of sample collection.

2.2. Assessment of Cognitive Function. For the assessment of cognitive functions, Montreal Cognitive Assessment (MoCA), which is a brief cognitive screen across a variety of clinical settings and widely used, was performed [9]. The assessment was conducted in a quiet room without distractions by a physical therapist trained in the administration of the MoCA questionnaire. The total score of the respondents with less than 12 years of education can be increased by one point on the premise that the total score does not exceed 30 points.

2.3. Statistical Analysis. The data were statistically analyzed with the SPSS 19.0 package program. All measures were tested for normality and homogeneity of variance. Normally distributed data are expressed as means ± SD. Continuous variables with normal distribution were compared by using the Student's *t*-test and those with nonnormal distributions were compared by using the Mann–Whitney *U*-test, and the multiple comparison between groups was performed by the LSD method. The count data were described by percentage, and the comparison between groups was performed by χ^2-test, which were two-sided tests. $P < 0.05$ was considered statistically significant.

3. Results

The study plan included 177 pregnant women and 51 volunteers, and a total of 145 pregnant women and 51 volunteers were eventually enrolled, including 75 pregnant women with GDM in the GDM group, 70 normal pregnant women in the NP group, and 51 volunteers in the CG group (Figure 1).

Compared with the CG group, the score of visuospatial/executive, attention, delayed recall, and total was significantly lower in the GDM and NP group, and the language score was lower in the GDM group ($P < 0.05$). Compared with the NP group, the score of visuospatial/executive, language, delayed recall, and total was significantly lower in the GDM group ($P < 0.05$) (Table 2).

The levels of tau and MGO in the GDM group was significantly less than these in the NP and CG groups ($P < 0.05$), but the differences between NP and CG groups were not statistically significant ($P < 0.05$). The level of Aβ in the GDM group was significantly more than that in the NP and CG groups ($P < 0.05$), and the differences between NP and CG groups were not statistically significant ($P < 0.05$), though the level of tau in NP was more than that in the CG group (Figure 2).

4. Discussion

The viewpoint that pregnant women suffer from deficits in memory is widespread, while the related documents are limited, especially in humans [10]. In this study, we found pregnant women did have a decrease in cognitive function scores. And, the incidence of cognitive dysfunction in pregnant women with GDM is much higher than that in normal pregnant women. Among all the tests of MoCA score, the most significant change was delayed recall.

Table 1: Demographic characteristics.

	GDM	NP	CG	F	*P*
Sample	73	70	51		
Age	29.70 ± 3.06	29.56 ± 3.39	29.52 ± 3.33	0.06	0.95
Height (cm)	164.75 ± 4.58	164.61 ± 5.08	164.28 ± 5.03	0.14	0.87
Weight (kg)	77.86 ± 10.46	74.25 ± 8.97	58.65 ± 7.49	68.32	<0.001
Glucose	4.95 ± 1.29	3.99 ± 0.76	4.69 ± 0.55	18.90	<0.001
Hba1c (%)	5.83 ± 0.63	4.74 ± 0.93		8.24	<0.001
Education (%)				0.02	0.99
Primary school	4 (5.5)	3 (4.3)	1 (2.0)		
High school	19 (26.0)	18 (25.7)	14 (27.5)		
University	50 (68.5)	49 (70.0)	36 (70.6)		

Data are expressed as means ± SD or number.

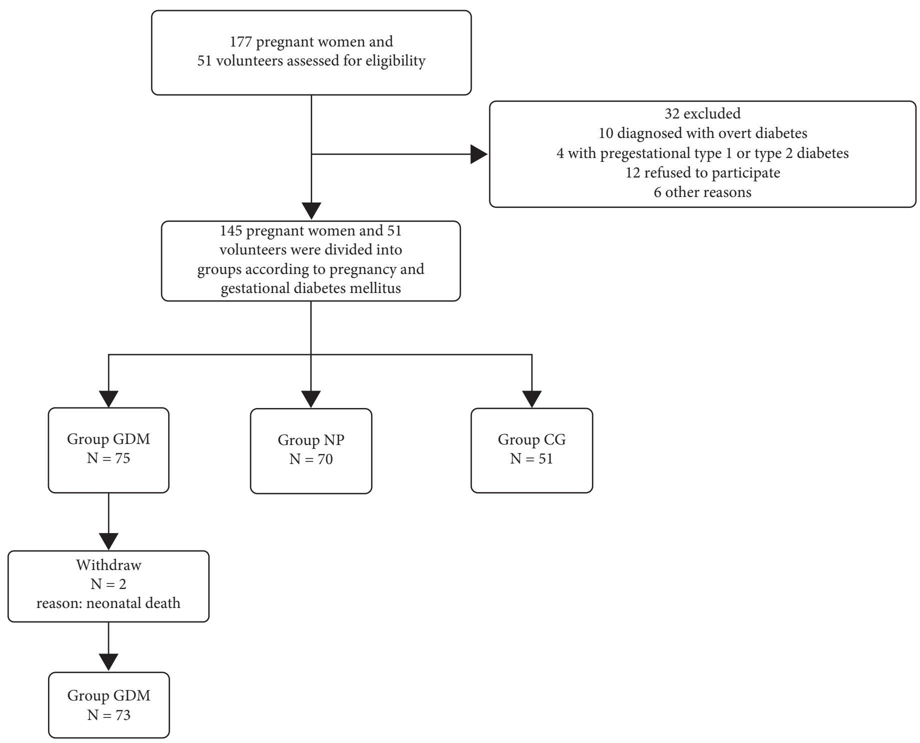

Figure 1: Patient recruitment flowchart.

Table 2: MoCA test score.

	GDM	NP	CG	*P* (GDM vs. NP)	*P* (GDM vs. CG)	*P* (NP vs. CG)
Sample	73	70	51			
Visuospatial/executive	4.42 ± 0.84	4.55 ± 0.63	4.94 ± 0.35	0.24	<0.001	0.002
Naming	3.00 ± 0.00	3.00 ± 0.00	3.00 ± 0.00	—	—	—
Attention	5.52 ± 0.84	5.57 ± 0.70	5.82 ± 0.27	0.66	0.02	0.04
Language	2.64 ± 0.52	2.82 ± 0.41	2.95 ± 0.21	0.01	<0.001	0.09
Abstraction	1.97 ± 0.15	1.97 ± 0.14	2.00 ± 0.00	—	—	—
Orientation	6.00 ± 0.00	5.99 ± 0.10	6.00 ± 0.00	—	—	—
Delayed recall	2.81 ± 1.15	3.62 ± 1.21	4.18 ± 0.91	<0.001	<0.001	0.01
Total	26.98 ± 1.79	28.01 ± 1.85	29.00 ± 1.18	<0.001	<0.001	<0.001

Data are expressed as means ± SD or number.

In fact, the effect of childbirth on women's cognitive ability is an obscure issue, because it may affect the job opportunities of working women of childbearing age. So, we discuss the impact of pregnancy on women's cognitive function with caution. Actually, the average score of normal pregnant women is indeed lower than that of volunteer women with the similar age, from the MoCA score point of view. But the degree of this cognitive function decline is

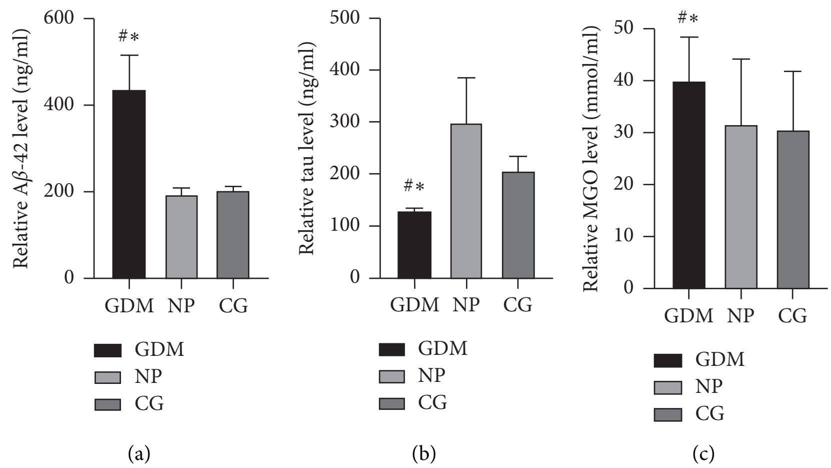

Figure 2: Concentration of (a) Aβ-42, (b) tau, and (c) MGO of each group; compared with NP group, $^{\#}P < 0.05$; compared with CG group, $^{*}P < 0.05$.

lighter comparing with the pregnant women with GDM. In the late stages of pregnancy, most pregnant women will be out of the working environment, and the brain belongs to excessive relaxation state in terms of cognition that may be one of the reasons of the mild cognitive decline in pregnant women [11, 12]. Mild stress, anxiety, and depression about childbirth during pregnancy may also affect the cognitive function of pregnant women to a certain extent [13, 14]. However, most of these bad emotions during pregnancy would disappear with childbirth. On the other hand, the levels of Aβ and tau were much closer to normal women. Therefore, we think the decline of cognitive of pregnant women was minimal and less influential.

However, cognitive decline in women with GDM is less optimistic. At first, the average score of MoCA was the lowest, and the difference was statistically significant. And, the levels of tau were lowest, while those of Aβ were highest. The changes of these plasma markers should be paid much more attention, though the pregnant women with GDM may need to face more serious emotions problems that may affect cognitive function.

Aβ and tau are a group of plasma markers related to cognitive function. The primary pathological changes in Alzheimer's disease (AD) are intracellular neurofibrillary tangles induced by tau phosphorylation and intercellular senile plaque accumulation induced by oligomerization of Aβ protein [15]. The toxic effects of Aβ can lead to dysfunction in neurotrophic factor expression. Compared with cognitive impairment, we are more worried about the changes of serum markers, suggesting that the effect of this cognitive impairment is long-term and even can cause AD.

MGO is advanced glycation endproducts (AGEs), a highly reactive α-dicarbonyl that is mainly generated as a byproduct of glycolysis and auto-oxidation of glucose which can initiate potentially deleterious changes, leading to protein dysfunction, have raised concern in relation to healthy living [16, 17]. MGO has been implicated in the pathogenesis of T2DM, vascular complications of diabetes, and several other age-related chronic inflammatory diseases such as cardiovascular disease, cancer, and disorders of the central nervous system [18].

Increased levels of AGEs were reported in brains of AD patients and were also found to be associated with the amyloid plaques and the neurofibrillary tangles (NFTs) [19, 20]. Many studies have reported the capacity of MGO intermediates to induce cellular damage and contribute to the pathogenesis of many neurodegenerative diseases [21]. For instance, increased intracellular reactive oxygen species production, tau hyperphosphorylation, and mitochondrial dysfunction were observed in neuronal cells following MGO treatment [22]. The intracerebroventricular (ICV) administration of MGO induced tau hyperphosphorylation and caused hippocampal damage and memory impairment in mice [23]. So, we believe that the increasing MGO of GDM pregnant women is the reason of mild cognition decline.

In this experiment, the results of MOCA score and serum indicators of perinatal GDM pregnant women are consistent. The mechanism of memory loss in pregnant women with perinatal GDM may be complex. In recent years, more and more attention has been paid to the relationship between diabetes and cognitive impairment. Compared with the general population, cognitive dysfunction in patients with type 2 diabetes is 1.5–2 times higher [24, 25]. Many studies support this view, and diabetic patients have a greater risk of cognitive impairment [26, 27]. The mechanism may be related to protein aggregation, insulin damage, oxidative stress, inflammatory reaction, and the generation of diabetes end products. This study is also in line with this view.

GDM is considered to be a prediabetic state, and the pathology of them is significantly correlated. In recent years, studies have shown that abnormal lipid metabolism can be widely involved in the pathophysiological process of a series of metabolic diseases such as obesity and type 2 diabetes by mediating oxidative stress and other signal transduction pathways. There are many studies on oxidative stress and inflammatory reaction in GDM pregnant women. Monitoring the serum C-reactive protein (CRP) level in early pregnancy is of great significance for predicting GDM [28].

Moreover, the study indicates that interleukin-6 (IL-6) and 8-isoprostaglandin F2 α (8-iso-pgf2 α) are significantly increased in GDM. These mechanisms may be involved in the cognitive dysfunction of GDM pregnant women, and the specific mechanism needs to be further studied.

5. Conclusion

The pregnant women with GDM have a significant decline in cognitive function, and the normal pregnant women have also a decline in cognitive function which very light.

Data Availability

The datasets generated during and/or analyzed during the current study are not publicly available but are available from the corresponding author on reasonable request.

Ethical Approval

The study protocol was approved by the Ethics Committee of the First Affiliated Hospital of Harbin Medical University, which was registered with the Chinese Clinical Trial Register (registration number: ChiCTR2000038703).

Consent

All the patients and volunteers read and signed the informed consent forms before enrolling in the study.

Conflicts of Interest

The authors declare no potential conflicts of interest with respect to the research, authorship, and/or publication of this article.

Authors' Contributions

Enyou Li designed the study. Si ri gu leng Sa na designed the study, collected data, and wrote and revised the manuscript. Xijin Deng interpreted and analyzed the data. Xunhong Wang interpreted and analyzed the data. Lei Guo collected data.

Acknowledgments

The authors greatly appreciate the support from the Department of Obstetrics of the First Affiliated Hospital of Harbin Medical University.

References

[1] American Diabetes Association, "Classification and diagnosis of diabetes," *Diabetes Care*, vol. 39, no. 1, pp. 13–22, 2016.
[2] J. Plows, J. Stanley, P. Baker, C. Reynolds, and M. Vickers, "The pathophysiology of gestational diabetes mellitus," *International Journal of Molecular Sciences*, vol. 19, no. 11, Article ID 3342, 2018.
[3] H. Umegaki, T. Hayashi, H. Nomura et al., "Cognitive dysfunction: an emerging concept of a new diabetic complication in the elderly," *Geriatrics and Gerontology International*, vol. 13, no. 1, pp. 28–34, 2013.
[4] L. M. Glynn, "Giving birth to a new brain: hormone exposures of pregnancy influence human memory," *Psychoneuroendocrinology*, vol. 35, no. 8, pp. 1148–1155, 2010.
[5] C. Janes, P. Casey, C. Huntsdale, and G. Angus, "Memory in pregnancy. I: subjective experiences and objective assessment of implicit, explicit and working memory in primigravid and primiparous women," *Journal of Psychosomatic Obstetrics and Gynaecology*, vol. 20, no. 2, pp. 80–87, 1999.
[6] P. Casey, C. Huntsdale, G. Angus, and C. Janes, "Memory in pregnancy. II: implicit, incidental, explicit, semantic, short-term, working and prospective memory in primigravid, multigravid and postpartum women," *Journal of Psychosomatic Obstetrics and Gynaecology*, vol. 20, no. 3, pp. 158–164, 1999.
[7] F. E. Keskin, M. Ozyazar, A. S. Pala et al., "Evaluation of cognitive functions in gestational diabetes mellitus," *Experimental and Clinical Endocrinology & Diabetes*, vol. 123, no. 4, pp. 246–251, 2015.
[8] M. Zimmerman, J. H. Martinez, D. Young, I. Chelminski, and K. Dalrymple, "Severity classification on the Hamilton depression rating scale," *Journal of Affective Disorders*, vol. 150, no. 2, pp. 384–388, 2013.
[9] C. O'Driscoll and M. Shaikh, "Cross-cultural applicability of the montreal cognitive assessment (MoCA): a systematic review," *Journal of Alzheimer's Disease*, vol. 58, no. 3, pp. 789–801, 2017.
[10] E. Brown and J. Schaffir, "Pregnancy brain: a review of cognitive changes in pregnancy and postpartum," *Obstetrical & gynecological survey*, vol. 74, no. 3, pp. 178–185, 2019.
[11] A. Al-Thaqib, F. Al-Sultan, A. Al-Zahrani et al., "Brain training games enhance cognitive function in healthy subjects," *Medical science monitor basic research*, vol. 24, pp. 63–69, 2018.
[12] R. Nouchi, Y. Taki, H. Takeuchi et al., "Brain training game boosts executive functions, working memory and processing speed in the young adults: a randomized controlled trial," *PloS One*, vol. 8, no. 2, Article ID e55518, 2013.
[13] N. B. Gawali, V. D. Bulani, M. S. Gursahani, P. S. Deshpande, P. S. Kothavade, and A. R. Juvekar, "Agmatine attenuates chronic unpredictable mild stress-induced anxiety, depression-like behaviours and cognitive impairment by modulating nitrergic signalling pathway," *Brain Research*, vol. 1663, pp. 66–77, 2017.
[14] V. Glover, "Maternal depression, anxiety and stress during pregnancy and child outcome; what needs to be done," *Best Practice & Research Clinical Obstetrics&gynaecology*, vol. 28, no. 1, pp. 25–35, 2014.
[15] Q. Chen, H. Ma, X. Guo, J. Liu, T. Gui, and Z. Gai, "Farnesoid X receptor (FXR) aggravates amyloid-β-triggered apoptosis by modulating the cAMP-response element-binding protein (CREB)/brain-derived neurotrophic factor (BDNF) pathway in vitro," *Medical Science Monitor : International Medical Journal of Experimental and Clinical Research*, vol. 25, pp. 9335–9345, 2019.
[16] D. E. Maessen, C. D. Stehouwer, and C. G. Schalkwijk, "The role of methylglyoxal and the glyoxalase system in diabetes and other age-related diseases," *Clinical science (London, England : 1979)*, vol. 128, no. 12, pp. 839–861, 2015.
[17] Y. Wang, L. M. Hall, M. Kujawa et al., "Methylglyoxal triggers human aortic endothelial cell dysfunction via modulation of the K (ATP)/MAPK pathway," *American Journal of Physiology Cell Physiology*, vol. 317, no. 1, pp. C68–c81, 2019.

[18] C. G. Schalkwijk and C. D. A. Stehouwer, "Methylglyoxal, a highly reactive dicarbonyl compound, in diabetes, its vascular complications, and other age-related diseases," *Physiological Reviews*, vol. 100, no. 1, pp. 407–461, 2020.

[19] M. Haddad, M. Perrotte, M. R. B. Khedher et al., "Methylglyoxal and glyoxal as potential peripheral markers for mci diagnosis and their effects on the expression of neurotrophic, inflammatory and neurodegenerative factors in neurons and in neuronal derived-extracellular vesicles," *International Journal of Molecular Sciences*, vol. 20, no. 19, 2019.

[20] H. J. Lüth, V. Ogunlade, B. Kuhla et al., "Age- and stage-dependent accumulation of advanced glycation end products in intracellular deposits in normal and Alzheimer's disease brains," *Cerebral Cortex (New York, NY : 1991)*, vol. 15, no. 2, pp. 211–220, 2005.

[21] X. H. Li, J. Z. Xie, X. Jiang et al., "Methylglyoxal induces tau hyperphosphorylation via promoting AGEs formation," *NeuroMolecular Medicine*, vol. 14, no. 4, pp. 338–348, 2012.

[22] M. Tajes, A. Eraso-Pichot, F. Rubio-Moscardó et al., "Methylglyoxal reduces mitochondrial potential and activates bax and caspase-3 in neurons: implications for Alzheimer's disease," *Neuroscience Letters*, vol. 580, pp. 78–82, 2014.

[23] Y. J. Chen, X. B. Huang, Z. X. Li, L. L. Yin, W. Q. Chen, and L. Li, "Tenuigenin protects cultured hippocampal neurons against methylglyoxal-induced neurotoxicity," *European Journal of Pharmacology*, vol. 645, no. 1-3, pp. 1–8, 2010.

[24] J. A. Luchsinger, C. Reitz, B. Patel, M. X. Tang, J. J. Manly, and R. Mayeux, "Relation of diabetes to mild cognitive impairment," *Archives of Neurology*, vol. 64, no. 4, pp. 570–575, 2007.

[25] Y. D. Reijmer, E. van den Berg, C. Ruis, L. J. Kappelle, and G. J. Biessels, "Cognitive dysfunction in patients with type 2 diabetes," *Diabetes/metabolism research and reviews*, vol. 26, no. 7, pp. 507–519, 2010.

[26] I. Feinkohl, G. Winterer, and T. Pischon, "Diabetes is associated with risk of postoperative cognitive dysfunction: a meta-analysis," *Diabetes/metabolism research and reviews*, vol. 33, no. 5, 2017.

[27] X. Zhang, H. Dong, S. Zhang, S. Lu, J. Sun, and Y. Qian, "Enhancement of LPS-induced microglial inflammation response via TLR4 under high glucose conditions," *Cellular Physiology and Biochemistry: International Journal of Experimental Cellular Physiology, Biochemistry, and Pharmacology*, vol. 35, no. 4, pp. 1571–1581, 2015.

[28] N. Fatema, F. Deeba, S. Akter et al., "CRP (C-reactive protein) in early pregnancy predictor for development of GDM," *Mymensingh Medical Journal : MMJ*, vol. 25, no. 2, pp. 271–276, 2016.

Hindawi
Journal of Healthcare Engineering
Volume 2021, Article ID 7098924, 9 pages
https://doi.org/10.1155/2021/7098924

Research Article

Computed Tomography Image Segmentation Algorithm to Detect the Curative Effect of Radial Shock Wave Therapy for Knee Osteoarthritis

Jinghai Tian,[1] **Guoyong Chen**,[2] **Fuhong Peng**,[3] **and Guotang Lan**[1]

[1]*Department of Orthopedics, People's Hospital of Dongxihu District, Wuhan 430030, Hubei, China*
[2]*Department of Orthopedics, Wuhan Asia Heart General Hospital, Wuhan 430000, Hubei, China*
[3]*Department of Orthopedics, Tongji Hospital, Tongji Medical College, Huazhong University of Science and Technology, Wuhan 430000, Hubei, China*

Correspondence should be addressed to Guotang Lan; 2006010118@st.btbu.edu.cn

Received 2 June 2021; Accepted 28 July 2021; Published 6 August 2021

Academic Editor: Enas Abdulhay

The aim of this study was to investigate the values of computed tomography (CT) imaging technology based on image segmentation algorithm (ISA). It was applied in the radial shock wave therapy (RSWT) to treat knee osteoarthritis (KOA), so its curative effect and rehabilitation effect on nerve function were mainly analyzed in this study. 84 patients with KOA were selected and grouped into an ultrasonic treatment group (group A) and a RSW group (group B). All the patients received the ISA-based CT examination and high-quality nursing intervention. There were comparisons on the effects of pain improvement, knee joint function, and nerve function rehabilitation of patients in groups A and B. Results showed that visual analogue scale (VAS) scores before and after treatment were markedly different among all patients, and the pain degree of patients in group B was lower than the degree of group A ($P < 0.05$). The knee joint function of group B after treatment was greatly better than group A ($P < 0.05$). Scandinavian stroke scale (SSS) scores of nerve function rehabilitation after nursing in patients from group B were sharply lower than the scores of group A ($P < 0.05$). Results indicated that ISA-based CT images could be applied in analysis of curative effect on KOA, and there was more obvious effect of RSWT in the treatment of KOA.

1. Introduction

KOA is a relatively common type of chronic osteoarthritis, which accounts for about 6% of all osteoarthritis [1]. The incidence of KOA is related to age; namely, the higher the age, the higher the incidence of KOA [2]. Studies have shown that the incidence of KOA in people who have been in semisquat or kneeling positions for a long time, such as underground coal miners and construction workers, is higher than that in the normal population [3]. KOA is usually caused by degeneration of the knee joint, overwork, trauma, and other factors, but the specific pathogenesis is not clear. Besides, RSWT is a common treatment for bone diseases [4]. It is mainly employed to collect a variety of acoustic energy single fluctuations into the focus area of targeted tissues by inducing energy convergence and to achieve a variety of therapeutic stimuli of different degrees by applying angle and pressure adjustment. RSWT is very effective in relieving pain and treating bone diseases such as supracondylar, calcified tendonitis, and plantar fasciitis [5, 6]. In addition, RSWT is a noninvasive treatment with minimal trauma and relatively few complications for patients, which does not require hospitalization. As a result, the economic pressure on patients is greatly reduced, so it is widely applied in clinical treatment. Therefore, as a treatment method with little trauma and side effects, RSWT has a very critical clinical significance in the treatment of KOA.

CT imaging is an effective method for the clinical diagnosis of KOA [7]. CT imaging can clearly observe the osteoarthritis lesions of knee joint, thus providing a strong help for the diagnosis and follow-up treatment of doctors [8]. In recent years, the resolution of medical image is constantly improved with the rapid development of modern medical image technology, while the traditional segmentation technology is difficult to obtain satisfactory segmentation results. Image segmentation is a critical step for image analysis and three-dimensional reconstruction in medical imaging, and the realization of accurate segmentation helps doctors understand the actual condition of patients and make reasonable treatment plans [9, 10]. Image segmentation technology based on graph theory is a hot research topic in the image segmentation in recent years [11]. It not only emphasizes global constraints, but also pays special attention to local information processing, so the segmentation results are better than those of traditional segmentation methods. The regions or pixels in the original image based on ISA are interpreted as nodes in the graph, transforming medical image segmentation into the graph-based energy minimization and dealing with the application of maximum flow/minimum segmentation algorithm [12]. Thus, ISA was used for image segmentation processing of CT imaging techniques and applied in the analysis of curative effect of RSWT for KOA. Through the analysis of pain symptoms before and after treatment, the knee joint function, and nerve function recovery, there was a theoretical basis for the clinical diagnosis and treatment of KOA.

2. Materials and Methods

2.1. Subjects Investigated and Grouping. 84 patients with KOA were selected as the subjects investigated, who were admitted to hospital from October 2018 to May 2020, including 46 males and 38 females. All patients were rolled into the ultrasound treatment group (group A) and RSW group (group B) based on different treatment methods, with 42 cases in each group. The ethics committee of the hospital had approved this experiment, and all the subjects included in this experiment had known and agreed.

The criteria for inclusion were defined to include patients who were diagnosed with KOA, were older than 42 years and younger than 70 years, had been informed and agreed, and had complete clinical data.

The criteria for exclusion were defined to include patients who suffered from severe heart, brain, and hematopoietic diseases, mental illness, knee joint infection, tumor, or rheumatic immune system diseases, were in the pregnant and lactating period, and had contraindications for ultrasound or RSWT.

2.2. Therapeutic Methods. The patients of group A were given ultrasonic treatment. Coupling agent was applied to the head of the ultrasonic arthritis treatment instrument, so as to treat the pain points around the knee joints. The intensity was set at 1.0–1.2 W/cm during the treatment, and the ultrasonic arthritis treatment instrument was first moved around pain points at a constant speed of 5 minutes with a speed of 5 mm/s. Then, the fixed treatment was for the pain points of the knee joints for 10 minutes. The treatment was once a day, five times a week for a four-week course.

The patients of group B were treated with RSWT apparatus. The impact points of knee pain points and calcification were selected according to the imaging data of patients. 7 treatment points were selected for each treatment, and each point was impacted 600–800 times. The output pressure was set as 2.5–3.5 bar, and the frequency was within the range of 10–15 Hz. The interval of each treatment was 5 days, and 5 consecutive treatments were regarded as a course of treatment. Besides, adverse reactions were observed and recorded during the treatment.

2.3. Computed Tomography Examination. All patients were examined by CT imaging and the instrument was Philips 128-slice spiral CT. The specific examination method was as follows. The patient was placed in the supine position and the flat foot was first entered. Then, the local position of the knee joint was scanned, the layer thickness was set at 0.6 mm, the layer spacing was set at 2 mm, and the pitch parameter was 1.0. The data were uploaded to the workstation for coronal and sagittal reconstruction after the scanning.

2.4. Computed Tomography Imaging Technology Based on Image Segmentation Algorithm. Graph Cuts algorithm fused all the information of the global and local images and fully reflected the correlation of image pixels, so it has marked advantages in the image segmentation. Graph Cuts algorithm input source image and corresponding label. Suppose that there was $l \in \{0, 1\}$ marked by any pixel point q of the image, and 0 represented the background and 1 stood for the foreground. In order to obtain the best binary segmentation result, the expression of the quantity function was defined as follows:

$$E(L) = \lambda * \sum_{p\in N} R_p(l_p) + \sum_{\{p,q\}\in N} A_{\{p,q\}} \cdot \delta(l_p, l_q). \tag{1}$$

There were two equations below to supplement and explain (1):

$$\begin{cases} R_p(\text{“}obj\text{”}) = -lnP_r(I_p|O), \\ R_p(\text{“bkg”}) = -lnP_r(I_p|B), \end{cases} \tag{2}$$

$$\delta l_p, l_q = \begin{cases} 1, & l_p \neq l_q, \\ 0, & l_p = l_q. \end{cases} \tag{3}$$

In equations (2) and (3), λ expressed the weighted factor; N stood for the collection of pixel points; p and q represented any pixel points in N; I meant the gray value; and A stood for the discontinuous penalty.

In order to solve the deficiencies of traditional Graph Cuts algorithm that required manual setting of foreground and background markers, automatic generation of threshold markers was for improvement in this study, so as to be more suitable for bone tissue CT image segmentation. Firstly, there was format conversion, and the DICOM file of medical image was converted into bitmap for the convenience of subsequent processing. Then, the regional and boundary items were established. The weight of n-links edge was very critical for the image segmentation quality, so it was necessary to consider not only the pixel position relationship between the two endpoints, but also the pixel difference value. The weight calculation method based on gray scale and distance was expressed as follows:

$$A_{\{p,q\}} = \exp\left(-\frac{\left(I_p - I_q\right)^2}{2\sigma^2}\right) \cdot \frac{1}{\mathrm{dist}\,(p,q)}, \tag{4}$$

where $\mathrm{dist}\,(p,q)$ stood for distance from the pixel q to the pixel p.

The model shown in equation (2) was still used for the setting of regional item. After threshold segmentation was processed, there were three types of images (Label-Back-Ground, Label-Object, and pixel points to be segmented). The network diagram was established, and the regional and boundary items corresponded to t-links and n-links, respectively. The maximum flow/minimum segmentation algorithm was adopted to seek the solution, so as to obtain the initial segmentation results. At this time, most foreground and background points could be identified, and the marking errors caused by small differences between foreground and background in some regions could be corrected manually.

In order to deal with threshold selection difficulty and noise sensitivity in the above algorithm, the morphological marker automatic generation method was adopted to optimize the algorithm. Open operation and closed operation were two crucial operations in morphology. Open operation could reduce image noise to make contour boundary smoother. The horizontal direction was of $1 * 3$ structural elements, morphological opening was applied to get the initial mark image, and the mark point image with the original image was input to the Graph Cut algorithm. The maximum flow/minimum segmentation algorithm was adopted to improve the initial segmentation, there was judgment for initial segmentation image quality, and there was manual modification by combining with man-machine interaction for continuous iteration until there was no segmentation error. The specific process is shown in Figure 1.

2.5. Evaluation of Therapeutic Effects. VAS was employed to assess the pain degree of knee joint. The pain degrees of patients were graded by themselves based on their own pain conditions, and the score ranged from 0 to 10. In addition, the pain degree increased gradually from 0 to 10 (0 meant no pain and 10 stood for the most severe pain).

The Roles and Maudsley (RM) scale was applied to assess the physical activity of patient. It included 4 grades, namely, excellent, good, general, and poor, corresponding to 1, 2, 3, and 4 points, respectively. There was 1 point if the patient had no pain during exercise and in normal life. The patient sometimes felt pain during exercise and in normal life, so there were 2 points. If the patient felt pain after a little activity, it was 3 points. If the patient was unable to do normal activities, the score was 4 points.

The Western Ontario and McMaster Universities osteoarthritis index (WOMAC) and Lequesne index scales were adopted to assess the body function of patient. The WOMAC score scale included pain, joint function, and stiffness. There were 5 ratings including difficult, mild, medium, very, and extreme that corresponded to 0, 1, 2, 3, 4, and 5 points in sequence. The Lequesne index scale involved tenderness, swelling, morning stiffness, walking ability, knee joint exercise pain, and rest pain, with 0, 1, 2, and 3 points for each aspect.

2.6. Quality Nursing Intervention. All patients were treated with high-quality nursing intervention after surgery, and the nursing effect was evaluated by SSS. First, the head nurse was selected as the group leader to set up a nursing team and reasonably arrange the nursing work and specific division of labor of the staff within the group, so as to ensure that the nursing staff were on duty 24 hours a day and give comprehensive and meticulous care to each patient.

The drug therapy included was as follows: 2 mL of sodium hyaluronate was injected into the articular cavity of the patient 1–2 times a week for a total of 6 weeks. If the patient suffered from severe pain, external application could be made with dressings of activating blood circulation and dissipating blood stasis. If the patient was well tolerated and in good condition, the traditional Chinese medicine with activating blood circulation to dissipate blood stasis could be adopted as adjuvant therapy.

The rehabilitation exercise was as follows. According to the condition of patient, the nursing staff should guide and help the patient to do some rehabilitation exercises, such as limb stretching and limb twisting. In addition, there was also appropriate massage, foot bath, and physical therapy to improve the symptoms of pain and swelling and promote the recovery of patients.

2.7. Statistical Analysis. SPSS20.0 statistical software was used for analysis, the measurement data were expressed as mean ± standard deviation ($\overline{x} \pm s$), and there was the pairwise comparison analyzed by one-way variance (ANOVA) and tested by least significant difference (LSD). Besides, χ^2 test was used for pairwise comparison and analysis of count data. If $P < 0.05$, there was a statistically substantial difference.

3. Results

3.1. Computed Tomography Imaging Segmentation Results Based on Image Segmentation Algorithm. Dice similarity coefficient was employed to evaluate the segmentation results of different algorithms, and the definition of Dice similarity coefficient was expressed as follows:

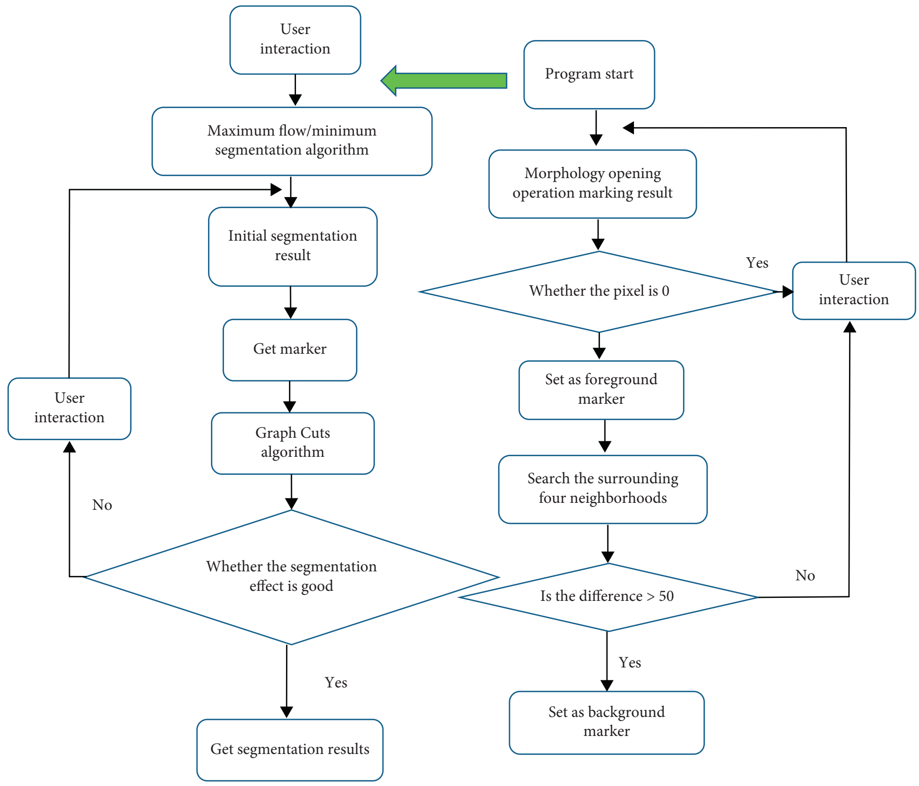

Figure 1: Flowchart of morphological marker graph cut algorithm.

$$\mathrm{Dice}\,(M, N) = \frac{2|M \cap N|}{|M| + |N|}. \quad (5)$$

In equation (5), M and N stood for the image pixel set obtained by the gold standard and the segmentation algorithm, respectively.

Figures 2 and 3 indicated the segmentation results of different algorithms. The Dice similarity coefficients of the traditional Graph Cuts algorithm, threshold + Graph Cuts algorithm, and morphology + Graph Cuts algorithm were 0.528, 0.854, and 0.926, respectively, and the running time was 0.112 seconds, 0.045 seconds, and 0.069 seconds in sequence. Dice similarity coefficient ranged within 0-1, and the larger the value was, the smaller the gap between algorithm segmentation and standard segmentation was. According to the above results, the segmentation quality and algorithm efficiency of morphology + Graph Cuts algorithm were more excellent.

CT images of patients with KOA were segmented by different segmentation algorithms, as shown in Figure 4. The number of seed points required by the traditional Graph Cuts algorithm was large but its segmentation effect was poor. Threshold + Graph Cuts algorithm segmentation was more accurate, but there were holes and isolated points. Compared with the traditional Graph Cuts algorithm and threshold + Graph Cuts algorithm, the morphology + Graph Cuts algorithm had the best segmentation effect on CT images.

3.2. Clinical Data of Patients with KOA from Both Groups. Table 1 showed the comparison results of clinical data of patients with KOA from groups A and B. In group A, there were 22 male and 20 female patients with KOA, with an average age of 53.14 ± 10.39 years, an average height of 165.23 ± 8.98 cm, an average weight of 67.87 ± 4.36 kg, and the body mass index (BMI) of $24.36 \pm 1.54\,\text{kg/m}^2$. Furthermore, there were 20 male and 18 female patients with KOA in group B, with an average age of 54.03 ± 9.76 years, an average height of 167.24 ± 8.02 cm, an average weight of 68.36 ± 5.02 kg, and the BMI of $23.98 \pm 1.25\,\text{kg/m}^2$. There were no statistically obvious differences in gender, age, height, weight, and BMI of patients with KOA from groups A and B ($P > 0.05$).

3.3. Comparison of Knee Joint Pain Improvement among Patients in the Two Groups. Figure 5 revealed the comparison of VAS scores of KOA patients from both groups before and after treatment. VAS scores of patients in group A were 5.95 ± 1.09 points, 4.78 ± 0.52 points, 2.76 ± 0.55 points, and 1.92 ± 0.67 points before treatment, after treatment, 1 month after treatment, and 3 months after treatment, respectively. Moreover, VAS scores of patients from group B were 6.09 ± 1.15 points, 5.15 ± 0.80 points, 2.72 ± 0.78 points, and 1.56 ± 0.54 points before treatment, after treatment, 1 month after treatment, and 3 months after treatment in turn. VAS scores after treatment of patients in both groups A and B decreased in contrast to those before treatment, and the difference was statistically substantial ($P < 0.05$). VAS scores after treatment and 3 months after treatment of patients in group B reduced sharply in contrast to the scores of group A ($P < 0.05$).

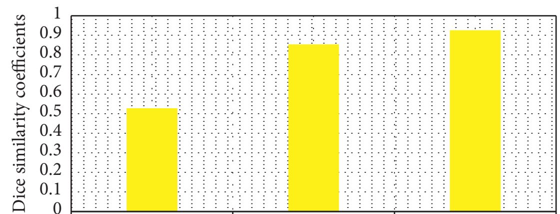

	Graph Cuts	Threshold + Graph Cuts	Morphology + Graph Cuts
Dice similarity coefficients	0.528	0.854	0.926

Figure 2: Comparison of Dice similarity coefficient among different algorithms.

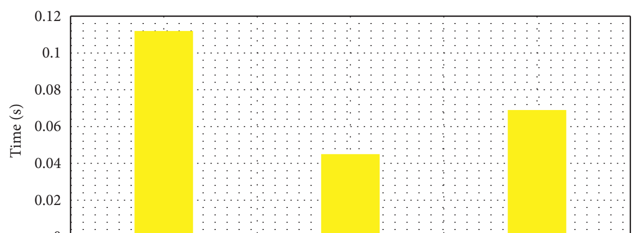

	Graph Cuts	Threshold + Graph Cuts	Morphology + Graph Cuts
Time	0.112	0.045	0.069

Figure 3: Comparison of running time among different algorithms.

3.4. Comparison on Knee Joint Function Improvement of Patients with KOA from the Two Groups. There were the comparison results of RM scores of patients in groups A and B before and after treatment (Figure 6). The RM scores of patients in group A were 3.26 ± 0.77 points, 2.45 ± 0.59 points, 1.71 ± 0.62 points, and 1.24 ± 0.47 points before treatment, after treatment, 1 month after treatment, and 3 months after treatment in sequence. In addition, RM scores of patients in group B before treatment, after treatment, 1 month after treatment, and 3 months after treatment were 3.25 ± 0.72 points, 3.25 ± 0.72 points, 1.42 ± 0.48 points, and 1.11 ± 0.32 points, respectively. RM scores of patients in groups A and B decreased after treatment compared with those before treatment, and there was a statistically remarkable difference ($P < 0.05$). RM scores of KOA patients from group B were steeply lower than the scores of group A after treatment and 1 month after treatment ($P < 0.05$).

The WOMAC scores of patients with KOA in groups A and B were compared before and after treatment as shown in Figure 7. WOMAC scores of patients in group A before treatment, after treatment, 1 month after treatment, and 3 months after treatment were 56.94 ± 10.87 points, 49.20 ± 10.23 points, 38.87 ± 8.35 points, and 32.54 ± 7.12 points, respectively. Besides, WOMAC scores of patients in group B were 57.45 ± 10.23 points, 49.02 ± 11.25 points, 31.64 ± 9.15 points, and 24.27 ± 7.27 points, respectively, before treatment, after treatment, 1 month after treatment, and 3 months after treatment. WOMAC scores of all patients from groups A and B after treatment reduced dramatically in contrast to those before treatment ($P < 0.05$). In addition, WOMAC scores of patients with KOA from group B were sharply lower than scores of group A 1 month and 3 months after treatment ($P < 0.05$).

Figure 8 expresses the comparison results of Lequesne index scores of patients from groups A and B before and after treatment. The Lequesne scores of patients in group A before treatment, after treatment, 1 month after treatment, and 3 months after treatment were 15.06 ± 4.52 points, 14.55 ± 3.85 points, 10.77 ± 3.91 points, and 8.46 ± 2.17 points in turn. What is more, Lequesne scores of patients in group B before treatment, after treatment, 1 month after treatment, and 3 months after treatment were 15.08 ± 4.22 points, 13.74 ± 3.13 points, 9.56 ± 3.42 points, and 6.05 ± 2.07 points, respectively. Lequesne scores of patients in groups A and B dropped after treatment by comparing with those before treatment, and the difference was statistically marked ($P < 0.05$). The Lequesne score of patients in group B 3 months after treatment was markedly lower than the score of group A ($P < 0.05$).

3.5. Comparison on Adverse Reactions of KOA Patients in Groups A and B. During the treatment, 3 cases of group A and 1 case of group B showed mild redness and swelling, which disappeared after local cold application for 24 hours. Furthermore, 1 patient in group B was unbearable for the pain, so the treatment was stopped immediately, and the pain was gradually eased after the patient rested for 1 hour. The comparison results of the adverse reaction rate of KOA patients in the two groups are shown in Figure 9. Besides, the adverse reaction rates of patients in groups A and B were

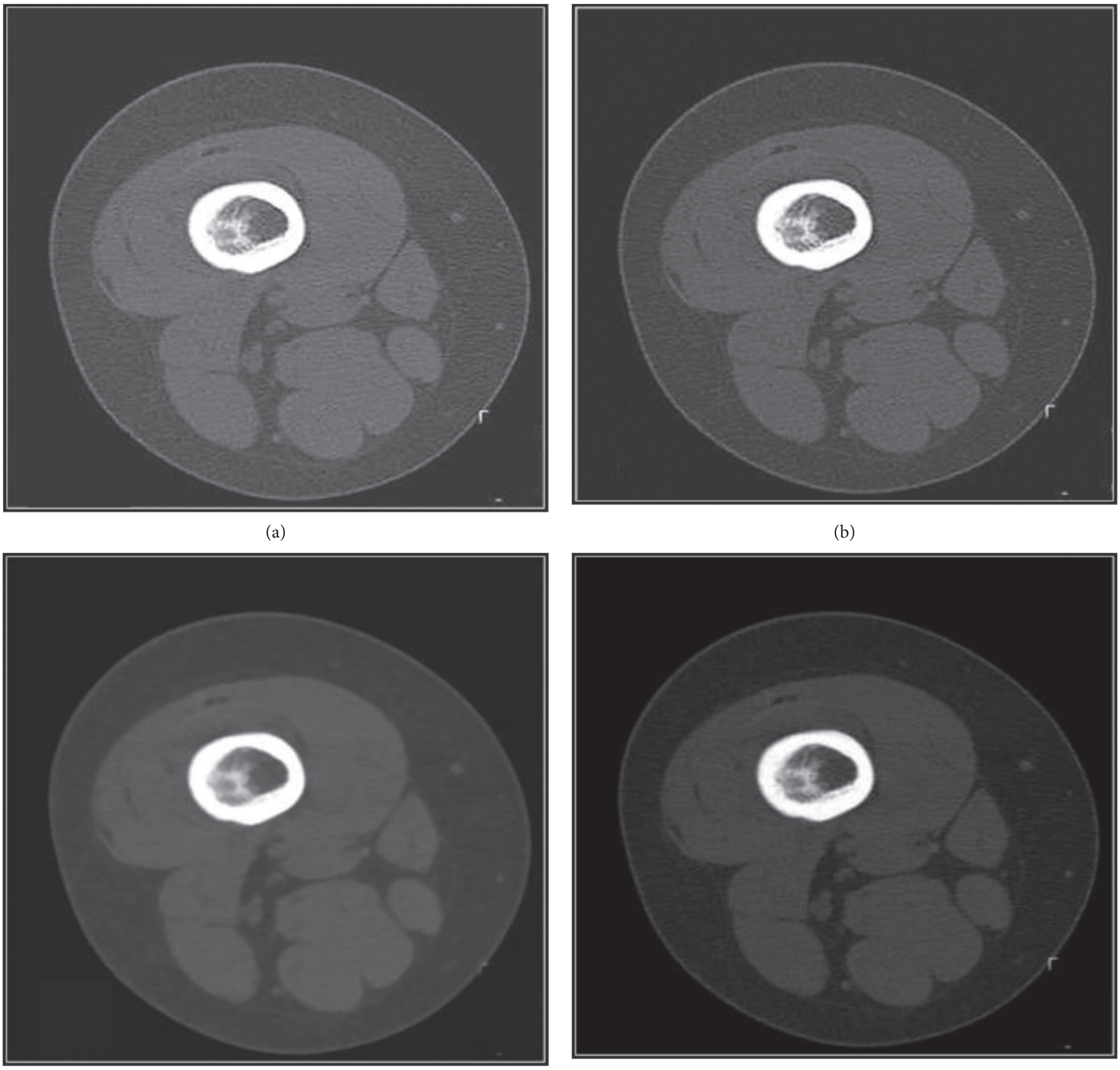

(a) (b) (c) (d)

Figure 4: CT image segmentation results of different segmentation algorithms: (a) The source image, (b) The image of Graph Cuts algorithm, (c) The image of threshold + Graph Cuts algorithm, and (d) The image of morphology + Graph Cuts algorithm.

Table 1: Comparison on clinical data of all patients in both groups.

	Group A ($n = 42$)	Group B ($n = 42$)	P
Gender (male/female)	22/20	24/18	0.123
Age (years old)	53.14 ± 10.39	54.03 ± 9.76	0.113
Height (cm)	165.23 ± 8.98	167.24 ± 8.02	0.097
Weight (kg)	67.87 ± 4.36	68.36 ± 5.02	0.068
BMI (kg/m^2)	24.36 ± 1.54	23.98 ± 1.25	0.612

7.1% and 4.8% in turn. There were no statistically great differences in the adverse reaction rates of KOA patients from the two groups ($P > 0.05$).

3.6. Comparison on Nerve Function Rehabilitation of KOA Patients in the Two Groups. The comparison results of SSS scores of patients in groups A and B before and after nursing

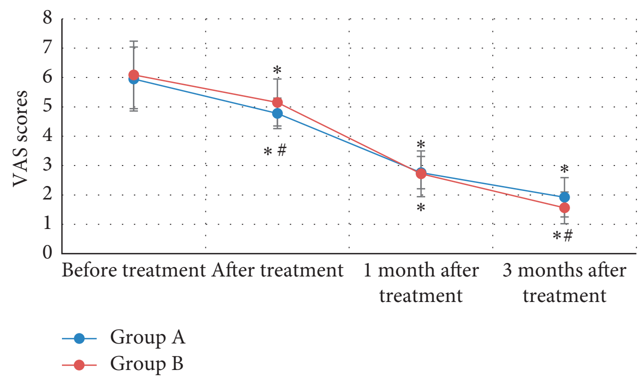

Figure 5: Comparison on VAS scores of patients with KOA from both groups before and after treatment. *Note*. * indicated $P < 0.05$ compared with before treatment; and # meant $P < 0.05$ in contrast to group A.

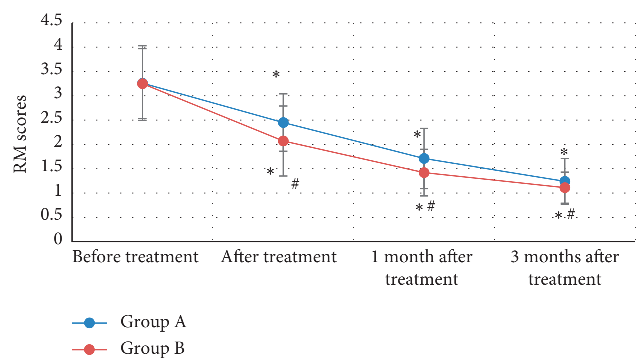

Figure 6: Comparison on RM scores of KOA patients from groups A and B before and after treatment. *Note*. * indicated $P < 0.05$ compared to before treatment; and # showed $P < 0.05$ in contrast to group A.

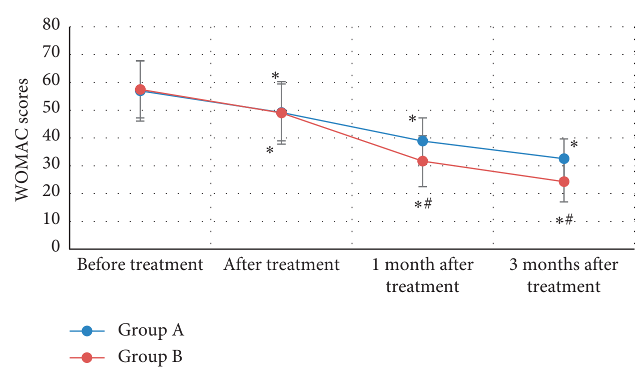

Figure 7: Comparison on WOMAC scores of KOA patients from groups A and B before and after treatment. *Note*. * showed that there was a statistically obvious difference compared to before treatment ($P < 0.05$); and # indicated that there were statistically considerable differences in contrast to group A ($P < 0.05$).

are shown in Figure 10. In group A, SSS score of patients before nursing was 34.69 ± 3.13 points and that after nursing was 28.15 ± 1.98 points. Before and after nursing, SSS scores of patients with KOA from group B were 34.72 ± 3.09 points and 16.35 ± 2.12 points, respectively. Thus, SSS scores of patients in groups A and B were compared before nursing, suggesting that the difference was not statistically remarkable ($P > 0.05$), while the SSS scores of patients from group B after nursing were dramatically lower than the scores of group A ($P < 0.05$).

4. Discussion

ISA was applied to improve and optimize the segmentation effect of medical images, and the results showed that the morphology + Graph Cuts algorithm had the best segmentation effect on CT images in contrast to the threshold + Graph Cuts algorithm and traditional Graph Cuts algorithm. This was consistent with the research results of Wu et al. [13], indicating that the CT segmentation method based on ISA could promote the segmentation accuracy of

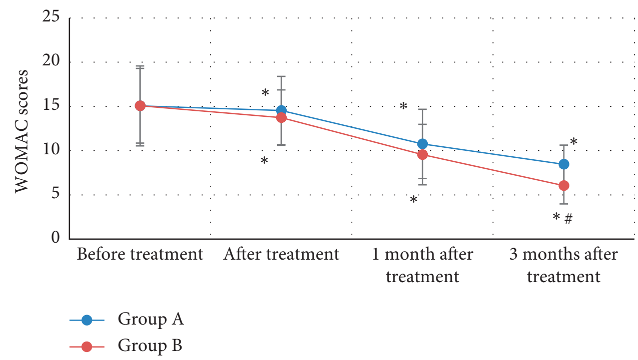

FIGURE 8: Comparison on Lequesne scores of KOA patients from groups A and B before and after treatment. *Note*. * showed that there was a statistically substantial difference compared with before treatment ($P < 0.05$); and # indicated that there were statistically marked differences in contrast to group A ($P < 0.05$).

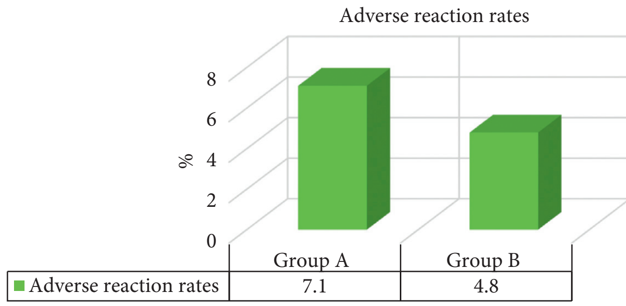

FIGURE 9: Comparison on adverse reaction rates of KOA patients in groups A and B.

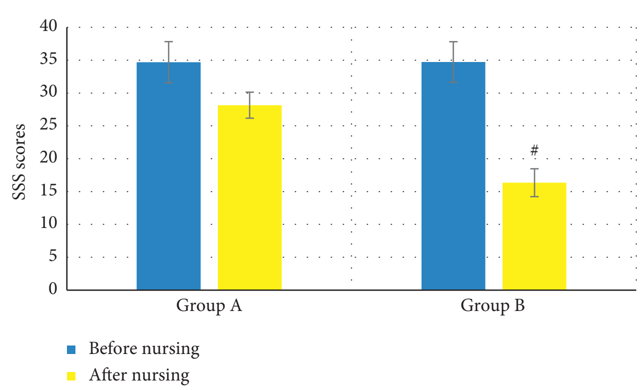

FIGURE 10: Comparison on SSS scores of KOA patients in the two groups. *Note*. # indicated that the difference was statistically obvious in contrast to group A ($P < 0.05$).

medical CT images. KOA is the leading cause of chronic bone and muscle pain. In recent years, RSWT has been employed to treat patients with KOA. In this study, there was a comparison on the curative effect of ultrasound treatment and RSWT for KOA. It was found that VAS scores before and after treatment were extremely different among KOA patients in the two groups, and the pain degree of patients in group B decreased hugely by comparing with the degree of group A ($P < 0.05$). This suggested that both ultrasound therapy and RSWT could help patients with pain symptoms, and RSWT was more effective. This was in accordance with the research results of Lee et al. [14] and Kang et al. [15]. The knee joint function rehabilitation of KOA patients was evaluated by RM, WOMAC, and Lequesne index scores in this study, and it was found that there were statistically marked differences in the RM, WOMAC, and Lequesne index scores of patients in groups A and B before and after treatment ($P < 0.05$). With the extension of treatment time, RM, WOMAC, and Lequesne index scores decreased gradually ($P < 0.05$). Therefore, the knee joint function of patients in group B was obviously better than that of group A ($P < 0.05$). There was no statistically great difference in the adverse reaction rates of patients in the two groups ($P > 0.05$). Lizis et al. [16] pointed out that the WOMAC and

ROM scores of KOA patients treated with RSWT were superior to those of KOA patients treated with kinesitherapy (KIN) by comparing the influences of RSWT and KIN for KOA patients. The research findings of Zhong et al. [17] reflected that VAS, WOMAC, and Lequesne index scores of KOA patients with RSWT were extremely better than those of KOA patients with placebo at the 5th and 12th week ($P < 0.05$). Moreover, all the patients showed improvement in pain and disability scores during 12 weeks of follow-up ($P < 0.05$), the adverse reaction rates of them were similar, and there were no serious side effects. This was consistent with the research results of this study. In this study, high-quality nursing was used for intervention treatment, and it was found that the SSS scores of nerve function rehabilitation after nursing in patients of group B were steeply lower than the scores of group A ($P < 0.05$). To some extent, it revealed that RSWT could promote tissue repair, thus contributing to nerve function rehabilitation. Based on the above results, RSWT had a better effect on alleviating pain and improving knee joint function in KOA patients.

5. Conclusion

The ISA-based CT imaging technology was for analysis of curative effects on KOA. It was found that RSWT had a more marked clinical effect, which could effectively relieve patients' pain and promote the knee joint and nerve function rehabilitation, and it was better than that of ultrasonic treatment through the analysis of the pain symptoms and knee joint and nerve function rehabilitation in patients with KOA before and after treatment. However, there were still some deficiencies in this study; for example, the sample size was limited, there was evaluation of only 3 months, and there was a lack of long-term efficacy evaluation. In the future, the number of samples and observation time should be increased to assess the long-term efficacy, so as to further analyze the therapeutic effects of KOA. In summary, the results of this study could provide reference for the imaging diagnosis and treatment of KOA.

Data Availability

The data used to support the findings of this study are available from the corresponding author upon request.

Conflicts of Interest

The authors declare no conflicts of interest.

Authors' Contributions

Jinghai Tian and Guoyong Chen contributed equally to this work.

References

[1] E. C. Rodriguez-Merchan and H. De La Corte-Rodriguez, "The role of orthoses in knee osteoarthritis," *Hospital Practice (1995)*, vol. 47, no. 1, pp. 1–5, 2019.

[2] S. Hussain, D. Neilly, S. Baliga, S. Patil, and R. Meek, "Knee osteoarthritis: a review of management options," *Scottish Medical Journal*, vol. 61, no. 1, pp. 7–16, 2016.

[3] K. A. Timmins, R. D. Leech, M. E. Batt, and K. L. Edwards, "Running and knee osteoarthritis: a systematic review and meta-analysis," *The American Journal of Sports Medicine*, vol. 45, no. 6, pp. 1447–1457, 2017.

[4] B. Yalvaç, N. Mesci, D. Geler Külcü, and O. Volkan Yurdakul, "Comparison of ultrasound and extracorporeal shock wave therapy in lateral epicondylosis," *Acta Orthopaedica et Traumatologica Turcica*, vol. 52, no. 5, pp. 357–362, 2018.

[5] B. Cooper and P. Bachoo, "Extracorporeal shock wave therapy for the healing and management of venous leg ulcers," *Cochrane Database of Systematic Reviews*, vol. 6, no. 6, Article ID CD011842, 2018.

[6] D. Stasinopoulos, "Can extracorporeal shock-wave therapy be used for the management of lateral elbow tendinopathy?" *World Journal of Methodology*, vol. 8, no. 3, pp. 37–39, 2018.

[7] D. Zarringam, D. B. F. Saris, and J. E. J. Bekkers, "The value of SPECT/CT for knee osteoarthritis: a systematic review," *Cartilage*, vol. 19, 2019.

[8] R. De Laroche, E. Simon, N. Suignard et al., "Clinical interest of quantitative bone SPECT-CT in the preoperative assessment of knee osteoarthritis," *Medicine*, vol. 97, no. 35, Article ID e11943, 2018.

[9] F. P. An and Z. W. Liu, "Medical image segmentation algorithm based on feedback mechanism CNN," *Contrast Media and Molecular Imaging*, vol. 2019, Article ID 6134942, 13 pages, 2019.

[10] G. Wang, M. A. Zuluaga, W. Li et al., "DeepIGeoS: a deep interactive geodesic framework for medical image segmentation," *IEEE Transactions on Pattern Analysis and Machine Intelligence*, vol. 41, no. 7, pp. 1559–1572, 2019.

[11] S. Janardhanaprabhu and V. Malathi, "Brain tumor detection using depth-first search tree segmentation," *Journal of Medical Systems*, vol. 43, no. 8, p. 254, 2019.

[12] X. Chen and L. Pan, "A survey of graph cuts/graph search based medical image segmentation," *IEEE Reviews in Biomedical Engineering*, vol. 11, pp. 112–124, 2018.

[13] W. Wu, Z. Zhou, S. Wu, and Y Zhang, "Automatic liver segmentation on volumetric CT images using supervoxel-based graph cuts," *Computational and mathematical methods in medicine*, vol. 2016, Article ID 9093721, 14 pages, 2016.

[14] J.-H. Lee, S. Lee, S. Choi, Y.-H. Choi, and K. Lee, "The effects of extracorporeal shock wave therapy on the pain and function of patients with degenerative knee arthritis," *Journal of Physical Therapy Science*, vol. 29, no. 3, pp. 536–538, 2017.

[15] S. Kang, F. Gao, J. Han et al., "Extracorporeal shock wave treatment can normalize painful bone marrow edema in knee osteoarthritis," *Medicine*, vol. 97, no. 5, Article ID e9796, 2018.

[16] P. Lizis, W. Kobza, and G. Manko, "Extracorporeal shockwave therapy vs. kinesiotherapy for osteoarthritis of the knee: a pilot randomized controlled trial," *Journal of Back and Musculoskeletal Rehabilitation*, vol. 30, no. 5, pp. 1121–1128, 2017.

[17] Z. Zhong, B. Liu, G. Liu et al., "A randomized controlled trial on the effects of low-dose extracorporeal shockwave therapy in patients with knee osteoarthritis," *Archives of Physical Medicine and Rehabilitation*, vol. 100, no. 9, pp. 1695–1702, 2019.

Hindawi
Journal of Healthcare Engineering
Volume 2021, Article ID 3819900, 7 pages
https://doi.org/10.1155/2021/3819900

Research Article

Block Matching Pyramid Algorithm-Based Analysis on Efficacy of Shexiang Baoxin Pills Guided by Echocardiogram (ECG) on Patients with Angina Pectoris in Coronary Heart Disease

Junqing Gao, Xu Wang, Lingyan Li, Hong Zhang, Ruiqing He, Bingyu Han, and Zongjun Liu

Department of Cardiology, Putuo Hospital, Shanghai University of Traditional Chinese Medicine, Putuo District, Shanghai 200062, China

Correspondence should be addressed to Zongjun Liu; xrys@nefu.edu.cn

Received 5 June 2021; Revised 5 July 2021; Accepted 22 July 2021; Published 6 August 2021

Academic Editor: Enas Abdulhay

This paper was aimed to explore the application of the block matching pyramid (BMP) algorithm in echocardiographic spot tracking in patients with coronary heart disease (CHD) and angina pectoris, as well as the effect of Shexiang Baoxin pills (a kind of drug containing musk, which is good for cardiac diseases) on blood lipids, cardiac function, and curative effect. 206 patients with CHD angina pectoris in the hospital from July 2018 to May 2020 were selected as the research subjects and were enrolled into the control (Ctrl) group (conventional treatment, $n = 103$) and the observation group (the Shexiang Baoxin pill was given on the basis of conventional treatment, $n = 103$) in random. Then, the patients' echocardiograms were obtained, and the BMP algorithm was used to track the echocardiograms. At 12 months after treatment, the total cholesterol (TC), triglycerides (TG), low-density lipoprotein cholesterol (LDL-C), and high-density lipoprotein cholesterol (HDL-C) were compared. Besides, the differences between left ventricular end-systolic volume (LVESV), left ventricular end-systolic diameter (LVESD), left ventricular end-diastolic volume (LVEDV), left ventricular end-diastolic dimension (LVEDD), cardiac index (CI), cardiac output (CO), and LVEF were observed. Finally, the efficacy of angina pectoris and electrocardiogram was calculated. It was found that the BMP algorithm can track the echocardiograms and display the movement and displacement of the patients' left ventricle. After treatment, in contrast with the Ctrl, the levels of TC, TG, and LDL-C in the observation group were obviously lower ($P < 0.05$); the LVESV, LVEDV, and LVEF were obviously lower ($P < 0.05$), the LVESD, LVEDD, CO, and CI were obviously higher ($P < 0.05$), the total score of angina after treatment was obviously lower ($P < 0.05$), and the total effective rates of angina pectoris and echocardiogram were obviously higher ($P < 0.05$). In conclusion, echocardiographic spot tracking can realize the diagnosis of patients with CHD angina pectoris, and Shexiang Baoxin pill can regulate the blood lipid level and improve the echocardiographic indicators and the clinical efficacy is obvious.

1. Introduction

In recent years, the incidence and mortality of CHD in China have shown an upward trend year by year, which has seriously threatened people's lives and health. At present, the methods commonly used in clinical treatment of CHD are percutaneous coronary intervention or coronary artery bypass surgery. Surgical treatment can realize the recanalization of the occluded blood vessels, improve the symptoms, and reduce cardiovascular events such as myocardial infarction [1, 2]. The occurrence of CHD angina is correlated with the increase of blood lipid levels and vascular endothelial injury [3]. Therefore, the clinical treatment of CHD not only needs to relieve the symptoms of patients with angina but also needs to control blood lipids and other risk factors for cardiovascular diseases. Traditional Chinese medicine (TCM) has a long history of treating CHD angina pectoris, and studies have confirmed that TCM is better than Western medicine in treating CHD angina. Shexiang Baoxin pill is a TCM preparation, which is developed for clinical treatment of cardiovascular diseases such as CHD [4]. Studies have proved that Shexiang Baoxin pills can improve patients' ECG performance and reduce the incidence of cardiovascular events [5].

Cardiac ultrasound imaging technology is also often used in clinical disease diagnosis and treatment effect evaluation, and the new type of echocardiogram technology can be used for the evaluation of myocardial strain. In addition, it can also measure myocardial deformation [6]. The traditional echocardiographic parameters based on volume measurement are not very sensitive to the early changes of myocardial function, but the spot tracking detection of echocardiogram can realize the assessment of ventricular function in patients with early myocardial diseases [7, 8]. Moinfar et al. used 2-d speckle to track echocardiography. It was found that the left atrial fluid storage and catheter capacity decreased in patients with type 2 diabetes complicated with urinary protein coronary disease [9]. However, there are relatively few studies on echocardiogram in patients with CHD angina.

Therefore, in this study, CHD angina pectoris patients were taken as the research subjects. Then, the patients' echocardiograms were obtained, and the changes of the ventricular function were explored through spot tracking. Subsequently, Shexiang Baoxin pills were given to compare the differences in the blood lipid levels, echocardiographic parameters, and treatment efficiency of different methods. The results provided a reference for improving the clinical treatment of patients with CHD angina.

2. Methods and Materials

2.1. Research Subjects. 206 patients with CHD angina in the hospital from July 2018 to May 2020 were taken as the research subjects. The diagnosis of CHD angina meets the requirements stipulated by WHO. Inclusion criteria: patients must be over 20 years old; patients who clinically demonstrated myocardial ischemia and hypoxia for more than 30 days; and patients who have had acute myocardial infarction for more than 6 months, who have undergone percutaneous coronary intervention or coronary artery bypass surgery, or whose imaging revealed that at least one main branch had a stenosis of more than 50%. At least one of the above events occurred. Exclusion criteria: patients with myocardial infarction or revascularization therapy in the past 6 months; patients with severe respiratory disease; patients with severe other organ dysfunction; patients with serious diseases such as malignant tumors; pregnant women; and patients with severe mental illness. 206 patients with CHD angina were enrolled into the observation group and Ctrl, with 103 in each. Patients in the Ctrl were given conventional treatments, and patients in the other group were given 2 capsules/time and 3 times/d Shexiang Baoxin pills based on the above treatment. This trial had got permission from the ethics committee of the hospital, and the subjects or their families had signed informed consents.

2.2. Collection of Echocardiograms. The color Doppler ultrasound diagnostic apparatus was adopted to collect the patients' echocardiograms, and the frequency of the S4 probe was set to 2~4 MHz. During the examination, the probe was needed to be placed between the 3rd and 4th ribs on the left side of sternum to obtain the 4 chambers of the heart. Then, the dimensions of the heart chamber, the thickness of the ventricular wall, the thickness of the left atrium, and contraction and relaxation ability of the left ventricle were observed.

2.3. Echocardiogram Spot Tracking Based on Block Matching Algorithm. BMP combines image pyramid and block matching algorithm, which can measure the similarity of image spot position. At the same time, through the sampling of image blocks, there is only a small amount of calculation [10]. The process of BMP algorithm is shown in Figure 1. After the spots to be tracked in the echocardiogram were calibrated, block matching and pyramid models were needed to be built. Then, the SAD value at the current time was calculated, and the similarity of all pixels in the view field was calculated. The comparison ends until all pixels were compared.

In Figure 1, when the BMP algorithm was adopted, the calculation equation of the sum of absolute differences (SAD) value was as follows:

$$\mathrm{SAD}_m(x, y) = \sum_{i=1}^{2^m} \sum_{j=1}^{2^m} \left| x^m(i, j) - y^m(i, j) \right|, \tag{1}$$

in which $x^m(i, j)$ represents the value of the pixel at point (i, j) in the mth layer of the pyramid.

After the above equation was unfolded and Minkowski's inequality was used, the following equation was obtained:

$$\begin{aligned} \mathrm{SAD}_m(i, j) &\geq \mathrm{SAD}_{m-1}(i, j) \geq \mathrm{SAD}_{m-2}(i, j) \\ &\geq \cdots \geq \mathrm{SAD}(i, j). \end{aligned} \tag{2}$$

2.4. Observation Indicators. Blood biochemical indicators and renal function were tested before treatment and 3 months and 12 months after treatment. The patient was in the left decubitus position, and LVESV, LVESD, LVEDV, and LVEDD were collected before and 12 months after treatment. After the collection, the patients' CI, CO, and LVEF were calculated.

2.5. Efficacy Criteria. Criteria for determining the effect of angina pectoris: obviously effective (decrease in total angina pectoris points by at least 60%), effective (decrease in total angina pectoris points by at least 30%), ineffective (decrease in total angina pectoris points by less than 30%), and worsening of disease (no decrease in total angina pectoris points).

Criteria for determining the effect of echocardiogram treatment: obviously effective (the echocardiograms returned to the normal range), effective (ST segment was reduced, and after treatment, it rose above 0.05 mV, but did not reach the normal level, or the *T* wave changed from a flat state to an upright state), ineffective (the ECG had no significant changes compared to before treatment), and

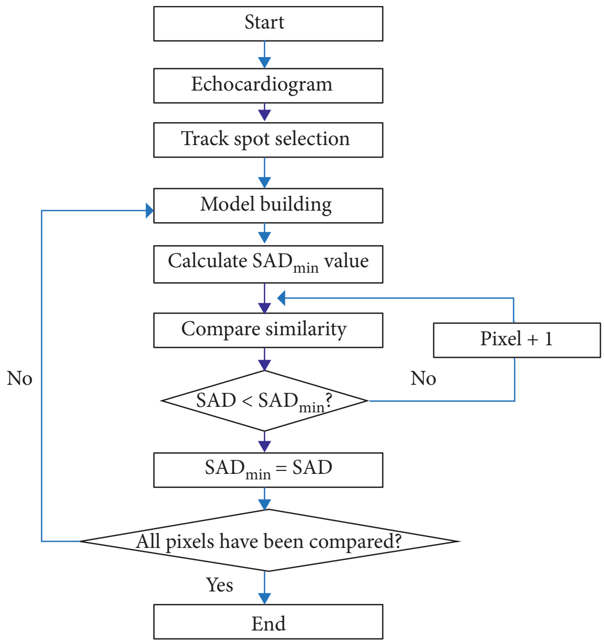

Figure 1: The spots marking process of echocardiograms based on BMP algorithm.

worsening of disease (the ST segment was reduced by more than 0.05 mV after treatment; the *T* wave state was completely changed, and ectopic heart rate occurred).

2.6. Statistics and Analysis. The data were processed by SPSS 20.0. Mean ± standard deviation ($\overline{x} \pm s$) was how measurement data were expressed, and comparison between groups was realized through independent sample t-test. Count data were expressed as frequency or percentage, and the χ^2 test was used to compare differences between groups. When $P < 0.05$, the difference was considered to be statistically significant.

3. Results

3.1. General Information Comparison. Before treatment, the differences were compared in baseline data, biochemical indicators, and cardiac function indicators. From Table 1, it was evident that there was no obvious difference in baseline data, biochemical indexes, and cardiac function indexes ($P > 0.05$).

3.2. Evaluation of Echocardiographic Speckle Tracking Algorithm. First, the difference between the accuracy and time was compared when the global search method or the logarithmic search method was adopted to analyze the pixel points in the motion vector search window in the BMP algorithm (Figure 2). It was evident from Figure 2(a) that the change of the size of search window had a small effect on the search accuracy of the global search algorithm. As the size of search window increased, the accuracy of the logarithmic search method gradually decreased. However, the accuracy rate of the two algorithms was always higher than 90%. It was evident from Figure 2(b) that as the size of search window increased, the running time of the two algorithms gradually increased, but that of the logarithmic search method was always lower than that of the global search method.

The heartbeat sequence was selected; each sequence contained 250 frames of heartbeat images and multiple heart motion cycles. It was evident from Figure 3(a) that the red smooth closed contour was the segmentation line of the ventricle and atrium, and the yellow dots around were the marked spots. By tracking these spots, the direction of heart movement was finally obtained (Figure 3(b)). It was evident that the maximum displacement of the heart was about 15 pixels, which was about 13.8 mm.

3.3. The Effect of Shexiang Baoxin Pill on Biochemical Indexes. The changes were compared in the levels of biochemical indexes 3 months and 12 months after treatment (Figure 4). It was evident that the levels of biochemical indexes of all patients decreased 12 months after treatment in contrast with those 3 months after treatment. In contrast with Ctrl, at 3 months after treatment, the levels of TC and LDL-C in the observation group were obviously lower ($P < 0.05$); at 12 months after treatment, the levels of TC, TG, and LDL-C were obviously lower ($P < 0.05$). Although the difference in TG levels 3 months after treatment and HDL-C levels 3 months and 12 months after treatment was not obvious ($P > 0.05$), it was observed that those in the observation group were still lower than Ctrl.

3.4. The Effect of Shexiang Baoxin Pill on Cardiac Function. The differences were compared in LVESV, LVEDV, LVESD, and LVEDD 12 months after treatment (Figure 5). It was evident that in contrast with Ctrl, the levels of LVESV and LVEDV of the observation group after treatment were obviously lower ($P < 0.05$); the LVESD and LVEDD were obviously higher after treatment ($P < 0.05$) .

The differences were compared in LVEF, CO, and CI 12 months after treatment (Figure 6). In contrast with Ctrl, in Figure 6(a), the LVEF of the observation group after treatment was obviously lower ($P < 0.05$); in Figure 6(b), the CO was obviously higher after treatment ($P < 0.05$); in Figure 6(c), the CI after treatment was obviously higher ($P < 0.05$).

3.5. Therapeutic Effect Analysis of Shexiang Baoxin Pills. The difference was compared between the total scores of patients with angina before treatment (0 month) and 12 months after treatment (Figure 7). There was no obvious difference in the total score of angina before treatment ($P > 0.05$). After treatment, that in the observation group was obviously lower than Ctrl ($P < 0.05$).

After 12 months of treatment, the difference was compared in the efficacy of angina pectoris and echocardiogram (Table 2). There was no case with aggravated angina pectoris and echocardiogram efficacy in both groups, while the total effective rate of angina pectoris efficacy and echocardiogram efficacy in the observation group was obviously higher than Ctrl ($P < 0.05$).

Table 1: Comparison of general information.

Baseline data	Ctrl ($n = 103$)	Observation group ($n = 103$)	t/χ^2	P value
Male (case/%)	66 (64.1)	63 (61.2)	1.232	0.153
Age (year)	62.33 ± 8.47	63.28 ± 9.77	0.785	0.229
Course of disease (year)	2.62 ± 1.35	2.53 ± 1.72	0.633	0.314
BMI (kg/m^2)	22.17 ± 5.43	21.80 ± 4.62	0.791	0.221
TC (mmol/L)	6.52 ± 0.82	6.54 ± 0.67	0.626	0.335
TG (mmol/L)	2.24 ± 0.53	2.35 ± 0.74	0.729	0.304
LDL-C (mmol/L)	4.11 ± 0.58	4.09 ± 0.52	1.223	0.170
HDL-C (mmol/L)	1.35 ± 0.42	1.33 ± 0.21	1.121	0.197
LVESV (mL)	58.92 ± 6.57	58.17 ± 5.93	0.789	0.237
LVESD (mm)	45.83 ± 3.62	44.23 ± 4.11	0.826	0.219
LVEDV (mL)	111.93 ± 10.37	112.76 ± 10.83	0.627	0.335
LVEDD (mm)	66.85 ± 7.68	67.42 ± 8.08	1.109	0.203
CO (L/min)	6.10 ± 1.30	6.00 ± 0.70	1.203	0.188
CI (L/min·m^2)	4.00 ± 0.20	4.30 ± 0.30	0.668	0.326
LVEF (%)	40.33 ± 4.35	41.63 ± 4.78	0.718	0.315

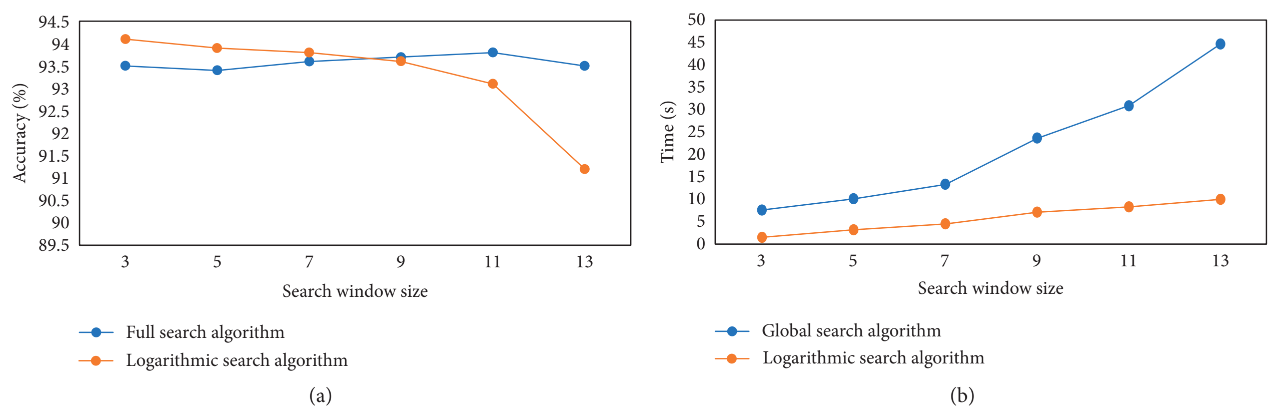

Figure 2: Performance comparison of global search method and logarithmic search method. (a) The accuracy rate; (b) the running time.

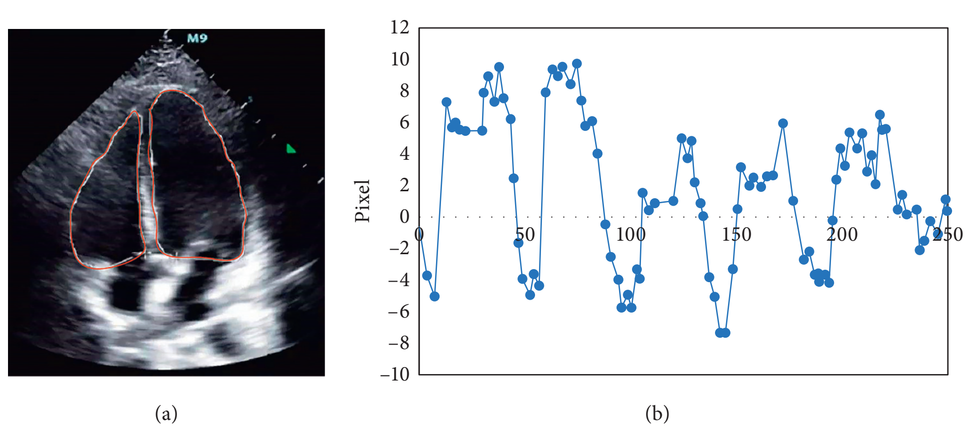

Figure 3: Results of echocardiographic spot tracking. (a) The calibration of echocardiographic spots; (b) the displacement of echocardiographic spots.

4. Discussion

The occurrence and development of CHD angina are closely related to the ischemia and hypoxia of myocardial cells [11]. At present, many studies have proved that hyperlipidemia is an important factor, leading to a variety of cardiovascular and cerebrovascular diseases [12]. Therefore, in the study, the effect of Shexiang Baoxin pills on the levels of TC, TG, LDL-C, and HDL-C in patients with CHD angina pectoris was explored. It was revealed that at 3 months and 12 months after treatment, the levels of the abovementioned indexes were obviously lower than Ctrl. It was basically in

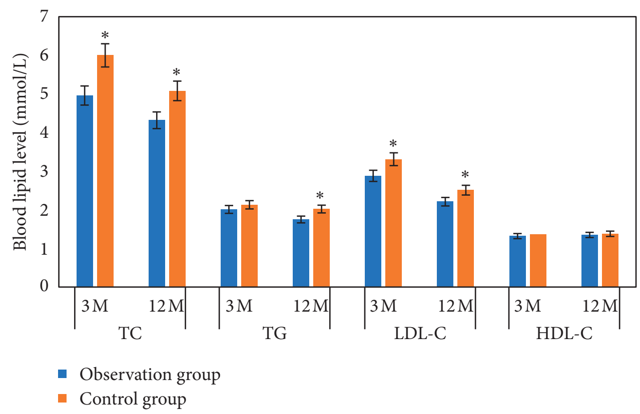

Figure 4: Comparison of blood lipid indexes after treatment. * indicates that the difference between groups was obvious, $P < 0.05$ (with the same meaning in Figures 5–7).

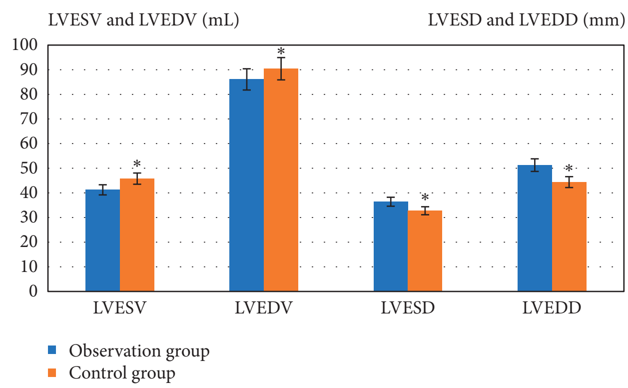

Figure 5: Comparison of differences in cardiac function indexes after treatment.

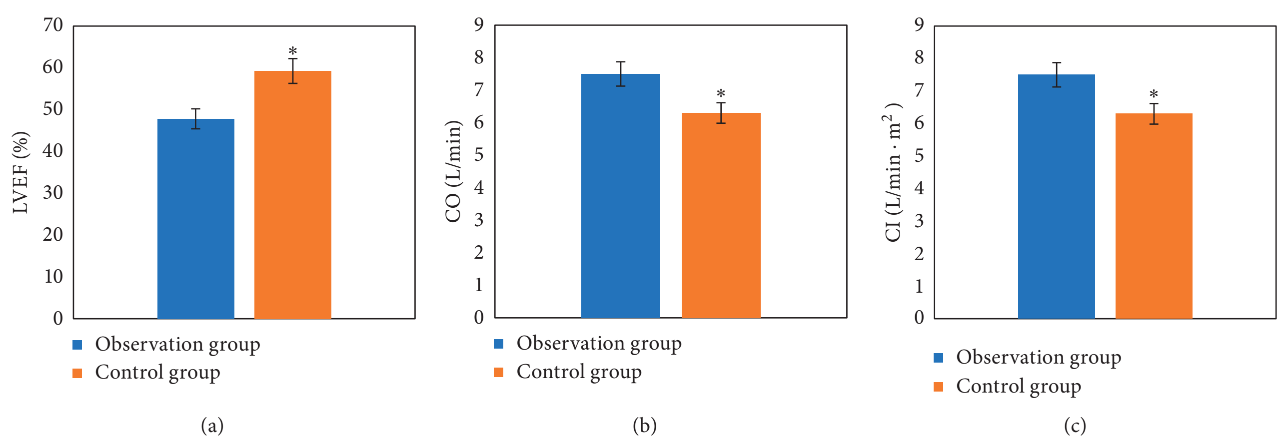

Figure 6: Comparisons of differences in (a) LVEF, (b) CO, and (c) CI after treatment.

line with the research results of Tian et al. [13], suggesting that Shexiang Baoxin pills can reduce the blood lipid levels in patients with CHD angina pectoris, thereby slowing down the process of coronary atherosclerosis.

Cardiac imaging technology has been widely used in disease prevention, diagnosis, and treatment. Among them, echocardiogram imaging technology has small side effects and is economical. Therefore, it is one of the imaging technologies commonly used in the diagnosis of heart diseases [14, 15]. The echocardiogram spot tracking can realize the assessment of cardiac strain in severe cardiac patients [16]. Therefore, the image pyramid and block matching method were combined to track the echocardiogram of CHD angina pectoris patients in the study. Clinically, the computational complexity of the block matching algorithm makes it difficult to meet the needs of timeliness.

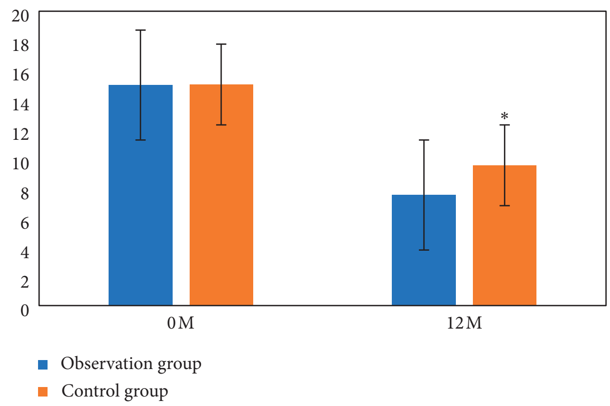

Figure 7: Comparison of total scores of angina pectoris.

Table 2: Comparison of efficacy between angina pectoris and echocardiogram.

Grade	Angina pectoris efficacy				Echocardiogram efficacy			
	Ctrl ($n = 103$)	Observation group ($n = 103$)	χ^2	P value	Ctrl ($n = 103$)	Observation group ($n = 103$)	χ^2	P value
Obviously effective	41 (39.8)	45 (43.7)	—	—	34 (33.0)	41 (39.8)	—	—
Effective	52 (50.5)	54 (52.4)	—	—	52 (50.5)	55 (53.4)	—	—
Ineffective	10 (9.7)	4 (3.9)	—	—	17 (16.5)	7 (6.8)	—	—
Aggravated	0 (0.0)	0 (0.0)	—	—	0 (0.0)	0 (0.0)	—	—
Effective rate (%)	90.3	96.1	8.325	0.027	83.5	93.2	11.231	0.004

Therefore, first, the impact of global search [17] and logarithmic search [18] on the efficiency of the algorithm was analyzed. It was found the tracking accuracy of the two search methods was both higher than 93%. Although the logarithmic search method reduces the tracking accuracy due to the increase of the search window, the tracking time is always lower than that of the global search method. Therefore, the parameters can be adjusted in clinical application to improve tracking effect. When the echocardiograms of patients with CHD angina pectoris were tracked subsequently, it was found that the displacement of the patients' left ventricle could be clearly tracked through the calibrated spots. What's more, the patients' heart motion trajectory showed a certain periodicity, which was in line with the clinical cardiac motion state. However, after tracking, it was found that the maximum displacement of the heart was 15 pixels, about 13.8 mm. Besides, the heart beat was too strong, indicating that the heart function was abnormal. It was in line with the actual situation of CHD angina patients [19].

Subsequently, the effect of Shexiang Baoxin pill on the heart function was studied. It was found that the patients in observation group had obviously lower LVESV, LVEDV, and LVEF than the Ctrl ($P < 0.05$), and LVESD, LVEDD, CO, and CI were obviously higher ($P < 0.05$). LVESV, LVEDV, LVEF, LVESD, LVEDD, CO, and CI indicators are important indicators used to evaluate the volume, shape, function, and structure of the heart [20]. It was found that Shexiang Baoxin pills could reduce the left ventricular volume, increase the left ventricular inner diameter, and improve the heart function by increasing cardiac output and enhancing cardiac systolic function. It was in line with the research results of Tian et al. and Zhang et al. [13, 21]. Finally, the difference between the total effective rates of and echocardiogram in two groups was evaluated. It was found that the total effective rates of angina pectoris and echocardiogram in observation were 96.1% and 93.2%, respectively, both of which were obviously higher than Ctrl ($P < 0.05$). It was in line with the results of Chen et al. [22], indicating that the clinical treatment of Shexiang Baoxin pills can obviously improve the symptoms of angina pectoris and enhance the cardiac function of patients, which was consistent with the results of the previous echocardiographic evaluation.

5. Conclusion

In the study, the application of the BMP algorithm in echocardiographic spot tracking of patients with CHD angina pectoris, as well as the effect of Shexiang Baoxin pills on blood lipid levels, cardiac function, and treatment efficiency, was explored. It was found that echocardiographic speckle tracking can detect the abnormal displacement of the left ventricle, and giving Shexiang Baoxin pills on the basis of conventional treatment can improve the patients' echocardiographic indicators and increase the total effective rate of treatment. However, only the BMP algorithm is used to realize the echocardiographic speckle tracking. The follow-up studies need to compare and analyze the differences in the results of echocardiographic speckle tracking before and after treatment. In short, the results can provide a theoretical basis for improving the clinical treatment of patients with CHD angina and the quality of life of patients.

Data Availability

The data used to support the findings of this study are available from the corresponding author upon request.

Conflicts of Interest

The authors declare no conflicts of interest.

Authors' Contributions

Junqing Gao and Xu Wang contributed equally to this work.

Acknowledgments

This work was supported by The Shanghai Key Medical Specialties Construction Project (ZK2019A11); Shanghai Health and Family Planning Commission Medical Clinical Special Project (201840247); Young Elite Scientists Sponsorship Program by CAST (QNRC2-B03); Clinical Advantage Discipline of Health System of Putuo District in Shanghai (2019ysxk01); and Shanghai Traditional Chinese Medicine Inheritance and Technological Innovation Project (ZYCC2019026).

References

[1] W. Jian, L. Li, X. M. Wei, C. Q. Wu, and C. Gui, "Prognostic value of angiopoietin-2 for patients with coronary heart disease after elective PCI," *Medicine (Baltimore)*, vol. 98, no. 5, Article ID e14216, 2019.

[2] L. R. K. Al, A. N. Nowbar, and D. P. Francis, "Percutaneous coronary intervention for stable coronary artery disease," *Heart*, vol. 105, no. 1, pp. 11–19, 2019.

[3] Y. Zhao, X. Yu, and X. Cao, "Cluster analysis for syndromes of real-world coronary heart disease with angina pectoris," *Frontiers of Medicine*, vol. 12, no. 5, pp. 566–571, 2018.

[4] K. J. Zhang, J. Z. Zhu, X. Y. Bao, Q. Zheng, G. Q. Zheng, and Y. Wang, "Shexiang Baoxin pills for coronary heart disease in animal models: preclinical evidence and promoting angiogenesis mechanism," *Frontiers in Pharmacology*, vol. 8, 2017.

[5] F. Huang, Y. Liu, and X. Yang, "Shexiang Baoxin pills promotes angiogenesis in myocardial infarction rats via upregulation of 20-HETE-mediated endothelial progenitor cells mobilization," *Atherosclerosis*, vol. 263, pp. 184–191, 2017.

[6] P. Premkumar, "Utility of echocardiogram in the evaluation of heart murmurs," *Medical Clinics of North America*, vol. 100, no. 5, pp. 991–1001, 2016.

[7] P. Collier, D. Phelan, and A. Klein, "A test in context: myocardial strain measured by speckle-tracking echocardiography," *Journal of the American College of Cardiology*, vol. 69, no. 8, pp. 1043–1056, 2017.

[8] M. Bonizzoli, S. Cipani, and C. Lazzeri, "Speckle tracking echocardiography and right ventricle dysfunction in acute respiratory distress syndrome: a pilot study," *Echocardiography*, vol. 35, no. 12, pp. 1982–1987, 2018.

[9] A. Moinfar, A. Hosseinsabet, and A. M. Sotudeh, "Association between atrial function assessed by 2D-speckle tracking echocardiography and albuminuria in patients with type 2 diabetes and coronary artery disease," *Journal of Clinical Ultrasound*, vol. 44, no. 9, pp. 561–570, 2016.

[10] F. Massanes, M. Cadennes, and J. G. Brankov, "Compute-unified device architecture implementation of a block-matching algorithm for multiple graphical processing unit cards," *Journal of Electronic Imaging*, vol. 20, no. 3, Article ID 33004, 2011.

[11] K. Deckers, S. H. J. Schievink, and M. M. F. Rodriquez, "Coronary heart disease and risk for cognitive impairment or dementia: systematic review and meta-analysis," *PLoS One*, vol. 12, no. 9, Article ID e0184244, 2017.

[12] X. F. Hu, T.-A. Kenny, and H. M. Chan, "Inuit country food diet pattern is associated with lower risk of coronary heart disease," *Journal of the Academy of Nutrition and Dietetics*, vol. 118, no. 7, pp. 1237–1248, 2018.

[13] P.-p. Tian, J. Li, J. Gao, and Y. Li, "Efficacy and safety of the Shexiang Baoxin Pill for the treatment of coronary artery disease not amenable to revascularisation: study protocol for a randomised, placebo-controlled, double-blinded trial," *BMJ Open*, vol. 8, no. 2, Article ID e018052, 2018.

[14] B. W. McCrindle and B. Cifra, "The role of echocardiography in Kawasaki disease," *International Journal of Rheumatic Diseases*, vol. 21, no. 1, pp. 50–55, 2018.

[15] S. Gurunathan and R. Senior, "Stress echocardiography in stable coronary artery disease," *Current Cardiology Reports*, vol. 19, no. 12, 2017.

[16] F. Pathan, N. D'Elia, M. T. Nolan, T. H. Marwick, and K. Negishi, "Normal ranges of left atrial strain by speckle-tracking echocardiography: a systematic review and meta-analysis," *Journal of the American Society of Echocardiography*, vol. 30, no. 1, pp. 59–70, 2017.

[17] L. Meenachi and S. Ramakrishnan, "Random global and local optimal search algorithm based subset generation for diagnosis of cancer," *Current Medical Imaging Formerly Current Medical Imaging Reviews*, vol. 16, no. 3, pp. 249–261, 2020.

[18] P. Joos, J. Poree, and H. Liebgott, "High-frame-rate speckle-tracking echocardiography," *IEEE Transactions on Ultrasonics, Ferroelectrics, and Frequency Control*, vol. 65, no. 5, pp. 720–728, 2018.

[19] M. Dogdus, E. Simsek, and C. S. Cinar, "3D-speckle tracking echocardiography for assessment of coronary artery disease severity in stable angina pectoris," *Echocardiography*, vol. 36, no. 2, pp. 320–327, 2019.

[20] Á. Árnadóttir, K. R. Vestergaard, G. Sölétormos, R. Steffensen, J. P. Goetze, and K. Iversen, "Prediction of coronary heart disease or heart failure using high-sensitivity cardiac troponin T: a pilot study," *European Journal of Clinical Investigation*, vol. 48, no. 10, Article ID e13009, 2018.

[21] J. Zhang, Q. Cui, and Y. Zhao, "Mechanism of angiogenesis promotion with Shexiang Baoxin Pills by regulating function and signaling pathway of endothelial cells through macrophages," *Atherosclerosis*, vol. 292, pp. 99–111, 2020.

[22] H. Chen, Q. Dong, and X. Zheng, "Efficacy of Shexiang Baoxin Pills for the treatment of unstable angina pectoris," *Medicine (Baltimore)*, vol. 98, no. 37, Article ID e17119, 2019.

Hindawi
Journal of Healthcare Engineering
Volume 2021, Article ID 5000102, 8 pages
https://doi.org/10.1155/2021/5000102

Research Article

Study on Model Iterative Reconstruction Algorithm vs. Filter Back Projection Algorithm for Diagnosis of Acute Cerebral Infarction Using CT Images

Songlin Tang,[1] **Yan Liu**,[2] **Zhifu Wang**,[1] **Yajie Liu**,[1] **and Huafei Liu**[1]

[1]*Department of Neurology, The First Affiliated Hospital of Shaoyang College, Shaoyang 422039, Hunan, China*
[2]*Department of Imaging, Shaoyang Central Hospital, Shaoyang 422100, Hunan, China*

Correspondence should be addressed to Songlin Tang; 201430120311@stu.scau.edu.cn

Received 26 May 2021; Accepted 22 July 2021; Published 5 August 2021

Academic Editor: Enas Abdulhay

The aim was to explore the application value of computed tomography (CT) perfusion (CTP) imaging based on the iterative model reconstruction (IMR) in the diagnosis of acute cerebral infarction (ACI). 80 patients with ACI, admitted to hospital, were selected as the research objects and divided randomly into a routine treatment group (group A) and a low-dose group (group B) (each group with 40 patients). Patients in group A were scanned at 80 kV–150 mAs, and the traditional filtered back projection (FBP) algorithm was employed to reconstruct the images; besides, 80 kV–30 mAs was adopted to scan the patients in group B, and the images were reconstructed by IMR1, IMR2, IMR3, iDose4 (a kind of hybrid iterative reconstruction technology), and FBP, respectively. The application values of different algorithms were evaluated by CTP based on the collected CTP images of patients and detecting indicators. The results showed that the gray and white matter CT value, SD value, SNR, CNR, and subjective image scores of patients in group B were basically consistent with those of group A ($p > 0.05$) after the IMR1 reconstruction, and the CT and SD of gray and white matter in patients from group B reduced steeply ($p < 0.05$), while SNR and CNR increased dramatically after IMR2 and IMR3 reconstruction in contrast to group A ($p < 0.05$). Furthermore, the cerebral blood volume (CBV), cerebral blood flow (CBF), mean transit time (MTT) of contrast agent, and time to peak (TTP) of contrast agent in patients from group B after iDose4 and IMR reconstruction were basically the same as those of group A ($p > 0.05$). Therefore, IMR combined with low-dose CTP could obtain high-quality CTP images of the brain with stable perfusion indicators and low radiation dose, which could be clinically applied in the diagnosis of ACI.

1. Introduction

ACI is a common disease and also known as acute ischemic stroke. Its main feature is that blood clots emerges in the brain blood vessels or various reasons lead to insufficient blood supply to the brain, which causes brain tissue ischemia and hypoxia to result in the irreversible apoptosis which is the main cause of death and disability in the old people [1, 2]. It is of great importance to determine the time window of reperfusion therapy for patients with ACI. Moreover, CTP can determine the core of lesion and ischemic area of patients with ACI to make clinical diagnosis and determine the treatment plan in a relatively short time, so as to avoid the constraints of time window, reduce the mortality and disability rate of patients, and monitor patient's prognosis [3].

Although CTP is irreplaceably featured with the diagnosis of patients with ACI, excessive radiation dose is its biggest shortcoming in the diagnosis. CTP requires continuous and repeated scanning of the target area of the brain, resulting in a huge increase in the X-ray radiation dose received by a patient by comparing with conventional CT. Therefore, reducing radiation dose is an urgent clinical topic in the process of CTP application [4, 5]. The main factors that affect CTP radiation dose are voltage, current, collection time, and frequency. Reducing the scanning time and increasing the scanning interval can reduce the radiation, but its effect is extremely limited. An effective method is to reduce the voltage and current, but it is necessary to pay attention to maintaining the quality stability of the perfusion images. Algorithm reconstruction plays an irreplaceable role in maintaining the quality of perfusion images [6].

FBP has been called the gold standard of CT image reconstruction, and it plays a vital role in CT image reconstruction. The amount of projection data reconstructed by FBP has a positive correlation with the resolution of image space and a negative correlation with the image noise, which affects the radiation dose reduction of CT scanning [7, 8]. In order to ensure the image quality of low-dose radiation CT scanning, scholars have focused on the iterative reconstruction technology of CT images, including the iterative reconstruction in image space (IRIS), adaptive statistical iterative reconstruction technology (AsiR), iDose (a kind of hybrid iterative reconstruction technology), and adaptive iterative dose reduction (AIDR) algorithm [9, 10]. Philips' iDose is taken as an example, which applies a dual-model iterative reconstruction algorithm. First, a data model is reconstructed by FBP, and then, it is identified and denoised through a mathematical model and matrix algebra [11]. However, iDose iterative reconstruction algorithm based on FBP is still a partial iterative algorithm. It still does not considers factors such as system hardware problems and X-ray photonic characteristics, which will affect the image quality, thereby limiting the further reduction of scanning radiation dose. After the iDose, Philips' researchers have further developed IMR (a fully iterative reconstruction technology that does not contain FBP components). The mechanism of IMR is to continuously optimize an image and data statistical model and a system model in the image and data space, so as to achieve the objective of denoising. Compared with iDose, IMR can not only reduce noise but also improve the resolution of the image [6, 12, 13].

In summary, the combination of IMR and low-dose CT can achieve the optimization of CTP radiation dose and image quality. This study would explore the application value of IMR-based CTP in the diagnosis of ACI, aiming to provide reliable basic data for clinical applications.

2. Materials and Methods

2.1. Establishment of Research Objects. 80 patients with ACI, who were admitted in hospital, were selected as the research objects. The criteria for inclusion were defined to include patients suffered from ACI, were 18–80 years old, and had signed the informed consents. The criteria for exclusion were defined to contain patients suffered from severe cardiovascular and cerebrovascular diseases, were allergic to the iodine contrast agent, were pregnant or in the lactation period, and had received the arterial stent implantation in the brain. This study had been approved by the ethics committee of hospital. The research objects in the experiment were grouped randomly into group A and B. The tube current in patients of group A was 150 mAs detected by CT, and the tube current of patients in group B was 30 mAs. The FBP image reconstruction was adopted for patients in group A, and FBP, iDose4, IMR1, IMR2, and IMR3 were employed to reconstruct the images of the patients in group B.

2.2. Computed Tomography Scanning and Methods. Brilliance iCT Elite CT machine was used for CT scanning. The tube current of patients in group A was 150 mAs, tube current of patients in group B was 30 mAs, tube voltage of patients in both groups was 80 kV, rotation time was 0.33 s, and both of layer thickness and spacing were 5 mm. A double-tube high pressure syringe was applied to inject the contrast agent. After the contrast agent was injected for 4 seconds, it was time to scan. The scan time was 2 seconds, and scanning was repeated 25 times, so the total scan time was 50 seconds. The image reconstruction indicators of FBP and iDose were all standard, and those of IMR1, IMR2, and IMR3 were all normal.

2.3. Image Postprocessing. The original image of CTP was transmitted to the workstation (Extend Brilliance Workspace, Philips Healthcare), and the Brain Perfusion software was employed to form a pseudocolor perfusion image of CBF, CBV, MTT, and TTP.

2.4. Analysis on the Quality of Images and Objective Evaluation. First, the CT value of white and gray matter on the instantaneous maximum density projection image was measured, and SD of the CT value was regarded as the image noise to calculate the SNR and CNR. The calculation equations were shown as follows. SNR = CT/SD and CNR = (gray matter CT value − white matter of CT value)/(white matter of SD^2 + gray matter of SD^2). Second, the values of CBF, CBV, MTT, and TTP were recorded on each pseudocolor image.

2.5. Subjective Evaluation of Image Quality Analysis. The 3-level scoring method was for the subjective evaluation standard, with 2 points for good quality, 1 point for average quality, and 0 points for bad quality. The subjective evaluation criteria included the difference of gray and white matter perfusion value on the perfusion pseudocolor image, difference between the focal ischemia and normal tissue, homogeneity of image, contrast of infarction, contour, degrees of concentration and dispersion, and presence or absence of artifacts. The highest score was 8; a score greater than 6 indicated an image with high quality, a score of 3–6 meant a medium-quality image, and a score less than 3 indicated an image of poor quality.

2.6. Statistical Analysis. SPSS22.0 was used for statistical analysis of the data. The subjective scores of images from patients in each group were compared by the rank sum test, the variance was employed to analyze the perfusion indicators, CT value, SD value, SNR, and CNR of gray and white matter, and the independent sample t-test was applied to the pairwise comparison between groups. $P < 0.05$ meant that there was statistically significant difference.

3. Results

3.1. Objective Indicators. As given in Table 1, there were the statistically substantial overall differences in the CT value, SD value, SNR, and CNR of gray and white matter among patients from the two groups through the 6 reconstruction methods ($p < 0.05$) after the variance analysis. Figure 1 shows the CT images processed by different reconstruction methods, including the images of group A reconstructed by FBP, and the images of group B reconstructed by FBP, iDose4, IMR1, IMR2, and IMR3, respectively. It was found that the images with high current were relatively clear (A-FBP), while the CT images obtained by different reconstruction algorithms in group B were slightly different in quality. The reconstructed images of FBP, IMR1, IMR2, and IMR3 were relatively clear, but the reconstructed images of iDose4 were quite fuzzy, which was not good for observation.

3.2. Computed Tomography Values of Gray and White Matter in the Brain. Table 1 and Figure 2 show that the CT values of gray and white matter reconstructed by FBP in patients from group A were 56.23 ± 2.45 Hu and 36.23 ± 2.12 Hu, respectively. In contrast to group A, the obtained CT values of gray and white matter reconstructed by FBP and iDose4 increased dramatically in patients of group B ($p < 0.05$); there were no obvious differences in CT values of gray and white matter reconstructed by IMR1 in patients from group B ($p > 0.05$); the CT value of gray matter reconstructed by IMR2 reduced sharply ($p < 0.05$), but the value of CT in white matter was not considerably different ($p > 0.05$); and the values of CT in gray and white matter reconstructed by IMR3 reduced hugely both ($p < 0.05$).

3.3. Standard Deviation Values of Gray and White Matter in the Brain. Table 1 and Figure 3 reveal that the values of SD in gray and white matter reconstructed by FBP were 7.82 ± 1.43 Hu and 5.21 ± 0.98 Hu in patients from group A, respectively. By comparing with group A, the SD values of gray and white matter obtained from FBP and iDose4 image reconstruction increased markedly in patients from group B ($p < 0.05$); the values of SD in gray and white matter reconstructed by IMR1 were not significantly different ($p > 0.05$); and the SD values of gray and white matter reconstructed by IMR2 and IMR3 reduced extremely ($p < 0.05$).

3.4. The Values of Signal-to-Noise Ratio in Gray and White Matter from the Brain. Table 1 and Figure 4 indicate that the values of SNR in gray and white matter reconstructed by FBP in patients from group A were 9.41 ± 1.53 and 10.06 ± 1.32, respectively. Besides, the SNR values of gray and white matter reconstructed by FBP and iDose4 decreased enormously in patients from group B compared with those of group A ($p < 0.05$); the SNR of gray matter did not change significantly under the reconstruction of IMR1 ($p > 0.05$), but the white matter SNR value rose dramatically ($p < 0.05$); and the SNR values of gray and white matter reconstructed by IMR2 and IMR3 grew hugely in patients from group B.

3.5. The Values of Contrast-to-Noise Ratio in Gray and White Matter from the Brain. Table 1 and Figure 5 show that the CNR of gray matter in patients from group A was 0.40 ± 0.09 after the reconstruction. The CNR of gray matter reconstructed by FBP and iDose4 dropped extremely in patients from group B ($p < 0.05$) compared with that of group A; there was no great difference in the CNR of patients from group B after IMR1 reconstruction ($p > 0.05$); besides, CNR of gray matter increased dramatically in patients from group B after the reconstruction of IMR2 and IMR3 ($p < 0.05$).

3.6. Comparison of Subjective Indicators. The subjective score of FBP and iDose4 image reconstruction was 0 in patients of group B, which could not meet the standard of clinical diagnosis. The subjective scores of FBP reconstruction in patients of group A and IMRE1, IMR2, and IMR3 reconstruction in patients of group B were 7.45 ± 0.34, 7.84 ± 0.84, 7.29 ± 0.62, and 7.34 ± 0.67, respectively. There were no huge differences in the subjective scores of image quality among patients from the two groups after multiple rank sum tests ($\chi^2 = 0.78$ and $p = 0.92$).

3.7. Comparison on the Values of Perfusion Indicators. Table 2 presents that there were statistically obvious differences in CBV of white matter and CBF and MTT of gray matter among patients in the two groups under the six reconstruction methods ($p < 0.05$) based on the analysis of variance. In addition, the overall differences of white matter CBV and gray matter TPP were statistically marked among patients in the two groups under the six reconstruction methods ($p < 0.05$).

3.8. The Values of Cerebral Blood Volume in the Gray and White Matter. As given in Table 2 and Figure 6, CBV of gray and white matter reconstructed by FBP was 5.08 ± 0.42 mL/100 g and 3.12 ± 0.23 mL/100 g in patients of group A, respectively. In contrast to group A, CBV of gray and white matter reconstructed by iDose4, IMR1, IMR2, and IMR3 had no obvious difference ($p > 0.05$) and CBV of white matter showed no obvious difference in patients from group B ($P > 0.05$), while those reconstructed by FBP reduced steeply ($p < 0.05$).

3.9. The Values of Cerebral Blood Flow in the Gray and White Matter. As given in Table 2 and Figure 7, the CBF of gray and white matter reconstructed by FBP in patients from group A was 54.23 ± 4.97 mL/100 g/min and 23.32 ± 2.16 mL/100 g/min, respectively. In contrast to group A, there was no considerable difference in CBF of gray and white matter in patients from group B under the reconstruction of iDose4, IMR1, IMR2, and IMR3 ($P > 0.05$), while the CBF of gray and white matter reconstructed by FBP increased substantially ($p < 0.05$).

Table 1: Comparison results of objective values of image quality among patients from the two groups.

Group	Reconstruction methods		CT (Hu)	SD (Hu)	SNR	CNR
Group A	FBP	Gray matter	56.23 ± 2.45	7.82 ± 1.43	9.41 ± 1.53	0.40 ± 0.09
		White matter	36.23 ± 2.12	5.21 ± 0.98	10.06 ± 1.32	
Group B	FBP	Gray matter	78.69 ± 3.12	12.43 ± 1.54	7.83 ± 0.93	0.21 ± 0.03
		White matter	57.12 ± 2.56	9.26 ± 0.98	7.82 ± 0.72	
	iDose4	Gray matter	65.98 ± 3.12	10.79 ± 1.87	8.21 ± 1.10	0.24 ± 0.02
		White matter	48.34 ± 2.17	8.15 ± 0.85	7.73 ± 0.91	
	IMR1	Gray matter	55.43 ± 3.45	7.24 ± 1.27	10.52 ± 2.13	0.42 ± 0.06
		White matter	38.63 ± 1.91	4.83 ± 0.62	10.98 ± 1.17	
	IMR2	Gray matter	53.24 ± 3.19	6.39 ± 1.28	11.23 ± 2.15	0.57 ± 0.11
		White matter	37.03 ± 4.23	4.97 ± 0.92	11.83 ± 1.86	
	IMR3	Gray matter	52.34 ± 3.92	6.82 ± 1.97	11.65 ± 2.31	0.68 ± 0.21
		White matter	34.61 ± 1.97	3.94 ± 0.82	12.82 ± 1.91	
Z		Gray matter	234.96	70.98	36.87	65.14
		White matter	267.25	235.87	75.61	
p		Gray matter	<0.001	<0.001	<0.001	<0.001
		White matter	<0.001	<0.001	<0.001	

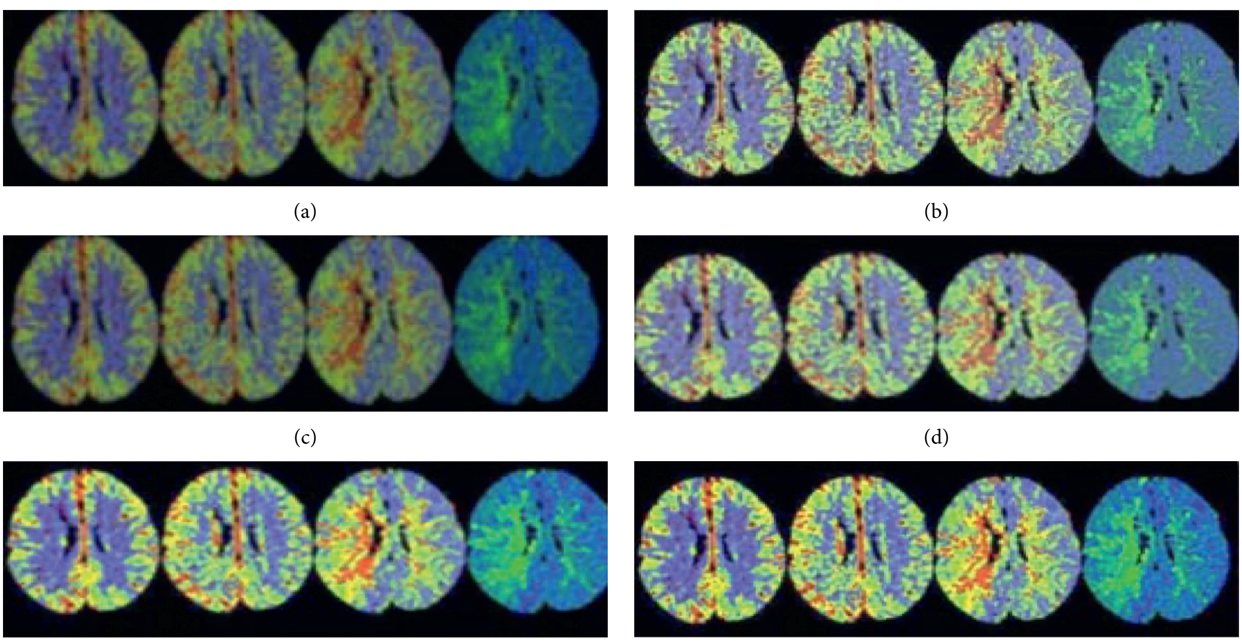

Figure 1: The processing results of CT image under different reconstruction methods. (a) A-FBP. (b) B-FBP. (c) B-iDose4. (d) B-IMR1. (e) B-IMR2. (f) B-IMR3.

3.10. The Values of Mean Transit Time in the Gray and White Matter. As given in Table 2 and Figure 8, the values of MTT in gray and white matter reconstructed by FBP in patients from group A were 5.65 ± 0.76 seconds and 7.38 ± 1.12 seconds, respectively. In contrast to group A, the MTT values of gray and white matter reconstructed by FBP and iDose4 rose remarkably in patients from group B ($p < 0.05$), while there were no marked differences in the values of MTT reconstructed by IMR1, IMR2, and IMR3 ($p > 0.05$).

3.11. Computed Tomography Perfusion Image Example. Figure 9 shows the CT images of ACI. To be specific, Figure 9(a) is the CT image and Figure 9(b) is the CTP image. It was found that CTP could present richer intracranial information by comparing with CT, which was beneficial to diagnose accurately the patient's lesions.

4. Discussion

The normal physiological activity of brain tissues depends on certain blood oxygen supply, and the compensatory contraction of capillary smooth muscle and small artery can alleviate the limited fluctuation of cerebral blood perfusion pressure, so as to maintain basically stable cerebral blood flow [14]. When the reduction in perfusion pressure is less than the circulating reserve capacity of the brain, CBF

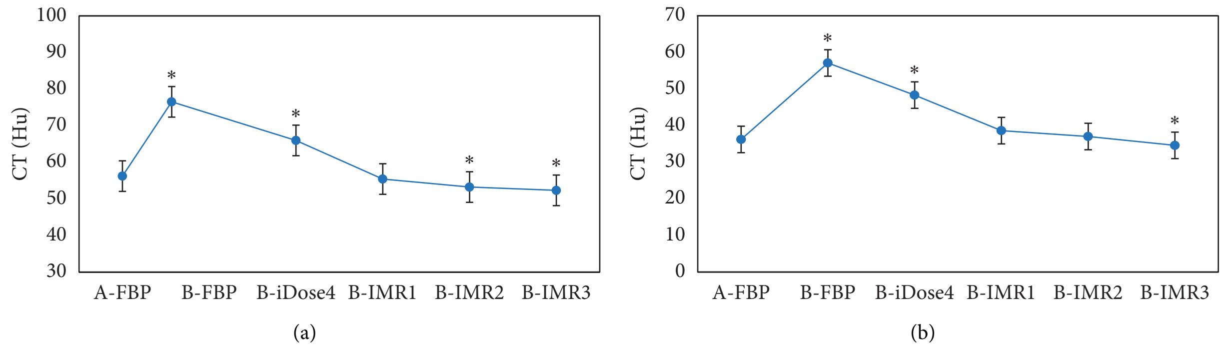

Figure 2: Statistical results of CT values of gray and white matter in the brain among patients from groups A and B by different reconstruction methods. A and B are the statistical results of gray and white matter in patients from both groups under various reconstruction methods, respectively. *CT value of patients from group B was dramatically different compared with group A ($p < 0.05$).

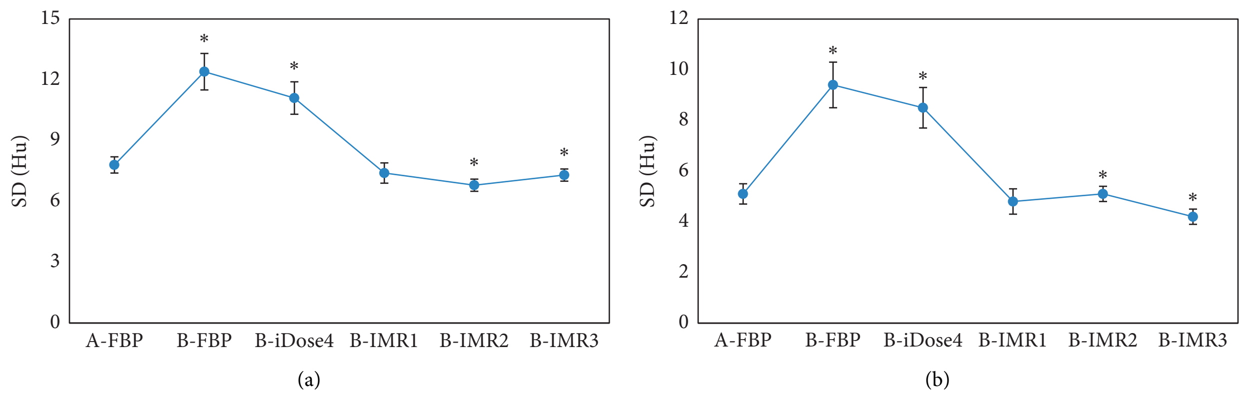

Figure 3: Statistical results of SD values of gray and white matter in the brain among patients from groups A and B by different reconstruction methods. A and B are the statistical results of gray and white matter in patients from the two groups under various reconstruction methods, respectively. *The SD value of patients from group B was different greatly in contrast to group A ($p < 0.05$).

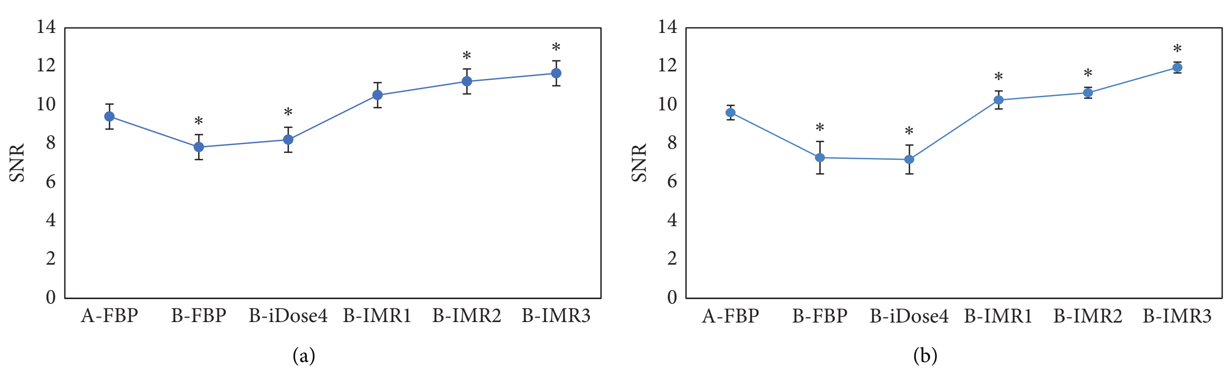

Figure 4: Statistical results of SNR values of gray and white matter in the brain among patients from groups A and B by different reconstruction methods. A is the statistical result of gray matter in patients from the two groups under various reconstruction methods; B is the statistical result of white matter in patients from the two groups under different reconstruction methods. *The SNR value of patients from group B was different obviously compared to group A ($p < 0.05$).

expresses to be normal or a slight decrease, and CBV often increases at this moment due to arteriolar and capillary dilatation. When the decrease of CBF is greater than that of cerebral circulation reserve force, neurons absorb excess glucose and increase oxygen content to maintain normal cell physiological metabolism. At this time, CBF falls below the threshold of electrical failure, so CBF reduces significantly and CBV is normal or decreases. With the continuous decline of CBF, the metabolism level in the brain changes dramatically, the balance of various substances is disrupted, and there is irreversible apoptosis in neurons, namely, ACI [15], with CBF and CBV both dropping obviously.

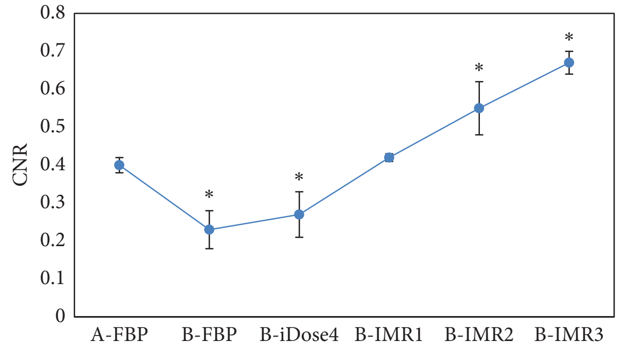

Figure 5: Statistical results of CNR of gray matter in the brain among patients from both groups by various reconstruction methods. *The CNR value of group B was different hugely from that of group A ($p < 0.05$).

Table 2: Comparison results of perfusion indicators in gray and white matter among patients in the two groups.

Group	Reconstruction methods		CBV (mL/100 g)	CBF (mL/100 g/min)	MTT (s)	TTP (s)
A	FBP	Gray matter	5.08 ± 0.42	54.23 ± 4.97	5.65 ± 0.76	18.65 ± 2.87
		White matter	3.12 ± 0.23	23.32 ± 2.16	7.38 ± 1.12	19.86 ± 2.97
B	FBP	Gray matter	4.76 ± 0.45	61.65 ± 8.32	8.23 ± 1.98	18.74 ± 2.31
		White matter	3.16 ± 0.72	31.54 ± 3.21	11.76 ± 2.12	19.23 ± 2.76
	iDose4	Gray matter	4.98 ± 0.47	53.09 ± 3.97	6.54 ± 1.19	18.54 ± 2.13
		White matter	3.17 ± 0.64	25.76 ± 2.96	10.09 ± 2.01	19.76 ± 3.21
	IMR1	Gray matter	5.32 ± 0.71	51.85 ± 3.21	6.21 ± 0.87	18.65 ± 2.45
		White matter	3.16 ± 0.42	23.76 ± 2.93	7.86 ± 1.32	19.93 ± 2.87
	IMR2	Gray matter	5.54 ± 0.89	51.23 ± 3.63	6.26 ± 0.76	18.65 ± 2.52
		White matter	3.21 ± 0.41	23.67 ± 2.87	7.63 ± 1.06	19.78 ± 2.76
	IMR3	Gray matter	5.39 ± 0.75	52.98 ± 5.87	6.24 ± 0.52	18.76 ± 2.61
		White matter	3.23 ± 0.51	22.54 ± 2.12	7.80 ± 1.13	19.72 ± 2.84
Z		Gray matter	5.42	4.87	18.65	0.008
		White matter	0.8	12.43	39.76	0.5
p		Gray matter	<0.001	0.001	<0.001	1.8
		White matter	0.72	<0.001	<0.001	0.93

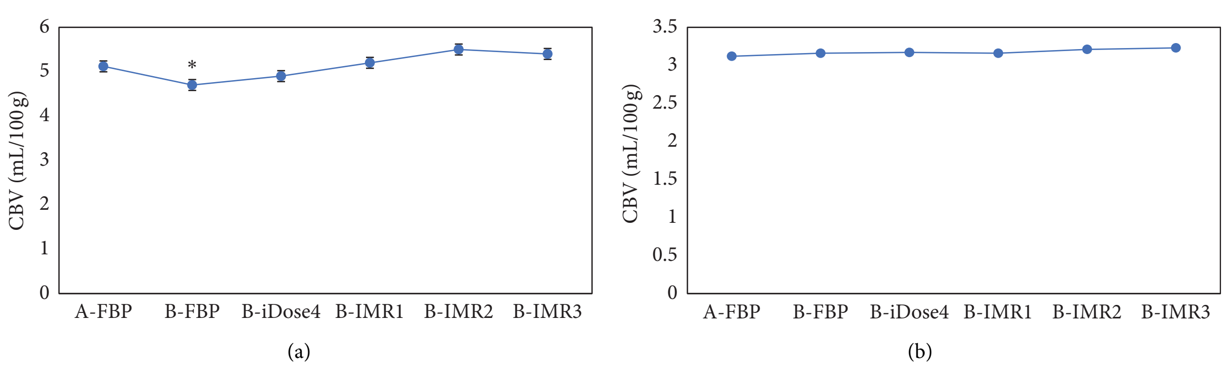

Figure 6: Statistical results of CBV of gray and white matter in the brain among patients from groups A and B under the six reconstruction methods. A is the statistical result of gray matter in patients from the two groups under various reconstruction methods; B is the statistical result of white matter in patients from the two groups under different reconstruction methods. *The CBV value of patients from group B was different considerably by comparing with group A ($p < 0.05$).

CTP requires continuous repeated scanning of the target area, so the radiation dose of a patient is higher enormously than that of CT scanning. Therefore, how to reduce the radiation dose of CTP has been attracting the attention of scholars. The traditional methods for radiation reduction include reducing tube voltage, tube current, and acquisition

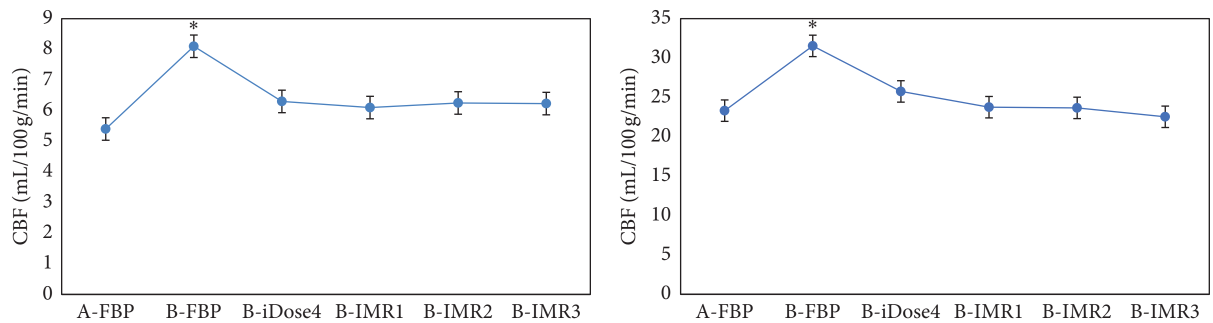

(a) (b)

Figure 7: Statistical results of CBF of gray and white matter among patients from the two groups under different reconstruction methods. A is the statistical result of gray matter in patients from the two groups under the six reconstruction methods; B is the statistical result of white matter in patients from the two groups under different reconstruction methods. *The CBF value of patients from group B had a significant difference compared with group A ($p < 0.05$).

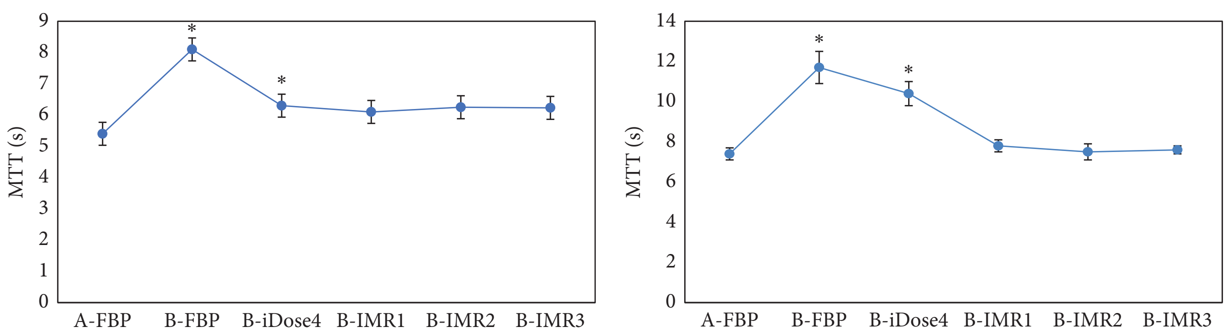

(a) (b)

Figure 8: Statistical results of MTT of gray and white matter among patients from both groups under the six reconstruction methods. A and B are the statistical results of gray and white matter in patients from the two groups under the six reconstruction methods, respectively. *The MTT value of patients from group B had an obvious difference compared with group A ($p < 0.05$).

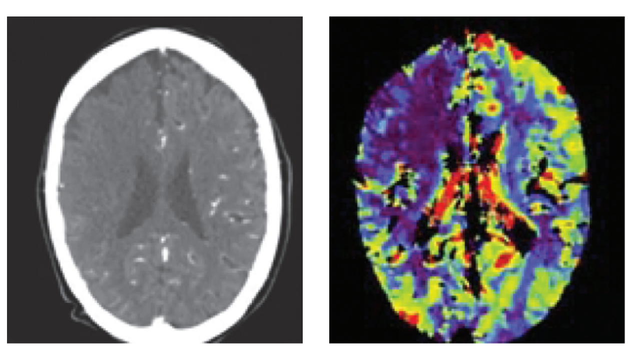

(a) (b)

Figure 9: The (a) CT and (b) CTP images of ACI.

time and frequency, but these measures are easy to increase image noise. With the application of IMR, the image quality can be guaranteed within the maximum range, thus making the traditional methods well applied [16]. In this study, patients with the CTP scanning mode of 80 kV–150 mAs routine dose combined with FBP image reconstruction were regarded as group A to evaluate the changing patterns of each indicator of gray and white matter in patients from group B under different image reconstruction methods. The results indicated that FBP was for reconstruction in the mode of low dose, and the average CT values of gray and white matter in patients from group B were 40% and 55% higher than that of group A, respectively. Moreover, the average CT values of gray and white matter in patients from group B increased by 20% and 28% after the iDose4 reconstruction, respectively. Therefore, the above data could determine that FBP and iDose4 reconstruction were not suitable for the image reconstruction of the low-dose scanning mode. On the contrary, there was no obvious change in the CT value of gray and white matter in the brain with the application of IMR, the CT value of gray and white matter reconstructed by IMR1 in patients of group B had no great difference from those of group A, the CT value reconstructed by IMR2 in patients of group B was at the middle level, and the CT value reconstructed by IMR3 in patients of group B was less than that of group A. This was related to the superior noise reduction function of IMR, making the CT value of gray and white matter return to normal or even lower than the normal value. Previous studies have shown that IMR has an excellent image noise reduction capability and can also improve image resolution [17]. In addition, studies have indicated that the average image noise and CNR under IMR reconstruction are superior markedly to hybrid iterative reconstruction and FBP technology, and IMR improves remarkably the image quality under low-tube voltage that especially helps to promote the display effect of distal vessels [18]. This is consistent with the results of this study.

5. Conclusion

The advantages of the IMR full-model iterative reconstruction algorithm in CTP image reconstruction were verified by comparing with low and conventional dose CTP. The results showed that IMR could ensure the quality of CT images under lower dose of radiation and complete the diagnosis of patients with ACI compared with FBP and iDose4, which could be promoted clinically. Therefore, a new direction was provided by this study for the diagnosis of patients with ACI, and the safety of patients was greatly enhanced during examination. The shortcoming of this study was that it had not been compared with other imaging methods, leading to a relatively single standard for judgment.

Data Availability

The data used to support the findings of this study are available from the corresponding author upon request.

Conflicts of Interest

The authors declare that they have no conflicts of interest.

References

[1] J. Lyu, Y. Xie, Z. Wang, and L. Wang, "Salvianolic acids for injection combined with conventional treatment for patients with acute cerebral infarction: a systematic review and meta-analysis of randomized controlled trials," *Medical Science Monitor*, vol. 25, pp. 7914–7927, 2019.

[2] K. Malhotra, J. J. Chang, A. Khunger et al., "Minocycline for acute stroke treatment: a systematic review and meta-analysis of randomized clinical trials," *Journal of Neurology*, vol. 265, no. 8, pp. 1871–1879, 2018.

[3] M. Grigoryan, D. C. Haussen, A. E. Hassan et al., "Endovascular treatment of acute ischemic stroke due to tandem occlusions: large multicenter series and systematic review," *Cerebrovascular Diseases*, vol. 41, no. 5-6, pp. 306–312, 2016.

[4] C. O. Santos, L. Caeiro, J. M. Ferro, and M. L. Figueira, "Mania and stroke: a systematic review," *Cerebrovascular Diseases*, vol. 32, no. 1, pp. 11–21, 2011.

[5] A. Mattioni, S. Cenciarelli, P. Eusebi et al., "Transcranial Doppler sonography for detecting stenosis or occlusion of intracranial arteries in people with acute ischaemic stroke," *Cochrane Database of Systematic Reviews*, vol. 2, no. 2, Article ID CD010722, 2020.

[6] J. Shen, X. Li, Y. Li, and B. Wu, "Comparative accuracy of CT perfusion in diagnosing acute ischemic stroke: a systematic review of 27 trials," *PLoS One*, vol. 12, no. 5, Article ID e0176622, 2017.

[7] C. H. Suh, S. C. Jung, S. J. Cho et al., "Perfusion CT for prediction of hemorrhagic transformation in acute ischemic stroke: a systematic review and meta-analysis," *European Radiology*, vol. 29, no. 8, pp. 4077–4087, 2019.

[8] K. R. Burton, D. Dhanoa, R. I. Aviv, A. R. Moody, M. K. Kapral, and A. Laupacis, "Perfusion CT for selecting patients with acute ischemic stroke for intravenous thrombolytic therapy," *Radiology*, vol. 274, no. 1, pp. 103–114, 2015.

[9] C. A. Potter, A. S. Vagal, M. Goyal, D. B. Nunez, T. M. Leslie-Mazwi, and M. H. Lev, "CT for treatment selection in acute ischemic stroke: a code stroke primer," *RadioGraphics*, vol. 39, no. 6, pp. 1717–1738, 2019.

[10] L. Bouchez, R. Sztajzel, M. I. Vargas et al., "CT imaging selection in acute stroke," *European Journal of Radiology*, vol. 96, pp. 153–161, 2017.

[11] A. Vagal, M. Wintermark, K. Nael et al., "Automated CT perfusion imaging for acute ischemic stroke: pearls and pitfalls for real-world use," *Neurology*, vol. 93, no. 20, pp. 888–898, 2019.

[12] A. Kalnins, L. J. Mickelsen, D. Marsh et al., "Decreasing stroke code to CT time in patients presenting with stroke symptoms," *RadioGraphics*, vol. 37, no. 5, pp. 1559–1568, 2017.

[13] O. Bill, N. M. Inácio, D. Lambrou et al., "Focal hypoperfusion in acute ischemic stroke perfusion CT: clinical and radiologic predictors and accuracy for infarct prediction," *American Journal Neuroradiology*, vol. 40, no. 3, pp. 483–489, 2019.

[14] J. R. Leonard, M. Henry, M. Rahouma et al., "Systematic preoperative CT scan is associated with reduced risk of stroke in minimally invasive mitral valve surgery: a meta-analysis," *International Journal of Cardiology*, vol. 278, pp. 300–306, 2019.

[15] P. Caruso, M. Naccarato, G. Furlanis et al., "Wake-up stroke and CT perfusion: effectiveness and safety of reperfusion therapy," *Neurological Sciences*, vol. 39, no. 10, pp. 1705–1712, 2018.

[16] A. T. Wilson, S. Dey, J. W. Evans, M. Najm, W. Qiu, and B. K. Menon, "Minds treating brains: understanding the interpretation of non-contrast CT aspects in acute ischemic stroke," *Expert Review of Cardiovascular Therapy*, vol. 16, no. 2, pp. 143–153, 2018.

[17] A. M. Ajlan, R. R. Bagdadi, M. N. Alama, and O. Ayoub, "Impact of implementing cardiac CT in evaluating patients suspected of cardioembolic stroke," *Journal of Computer Assisted Tomography*, vol. 40, no. 3, pp. 380–386, 2016.

[18] S. Oda, G. Weissman, M. Vembar, and W. G. Weigold, "Iterative model reconstruction: improved image quality of low-tube-voltage prospective ECG-gated coronary CT angiography images at 256-slice CT," *European Journal of Radiology*, vol. 83, no. 8, pp. 1408–1415, 2014.

Hindawi
Journal of Healthcare Engineering
Volume 2021, Article ID 3706265, 10 pages
https://doi.org/10.1155/2021/3706265

Research Article

Deep Learning-Based Computed Tomography Image Features in the Detection and Diagnosis of Perianal Abscess Tissue

Song Han, Jun Yang, and Jihua Xu

Department of Anorectal Surgery, Qilu Hospital (Qingdao), Cheeloo College of Medicine, Shandong University, 758 Hefei Road, Qingdao 266035, Shandong, China

Correspondence should be addressed to Jun Yang; 2004020125@st.btbu.edu.cn

Received 24 May 2021; Revised 24 June 2021; Accepted 28 July 2021; Published 4 August 2021

Academic Editor: Enas Abdulhay

The performance characteristics of deep learning fully convolutional neural network (DLFCNN) algorithm-based computed tomography (CT) images were investigated in the detection and diagnosis of perianal abscess tissue. 60 patients who were medically diagnosed as perianal abscesses in the hospital were selected as the experimental group, and 60 healthy volunteers were selected as the control group. In this study, the DLFCNN algorithm based on deep learning was compared with the CNN algorithm and applied to the segmentation training of CT images of patients with perianal abscesses. Then, the segmentation metrics Jaccard, Dice coefficient, precision rate, and recall rate were compared by extracting the region of interest. The results showed that Jaccard (0.7326) calculated by the CNN algorithm was sharply lower than that of the DLFCNN algorithm (0.8525), and the Dice coefficient (0.7264) was also steeply lower than that of the DLFCNN algorithm (0.8434) ($P < 0.05$). The thickness range of the epidermis and dermis in patients from the experimental group was 4.1–4.9 mm, which was markedly greater than the range of the control group (1.8–3.6 mm) ($P < 0.05$). Besides, the CT value of the subcutaneous fascia in the experimental group (-95.45 ± 8.26) hugely reduced compared with the control group (-76.34 ± 7.69) ($P < 0.05$). The accuracy rate of the patients with perianal abscesses was 96.67% by multislice spiral CT (MSCT). Therefore, the DLFCNN algorithm in this study had good stability and good segmentation effect. The skin at the focal site of anal abscess was obviously thickened, and it was simple and accurate to use CT images in the diagnosis of patients with perianal abscesses, which could effectively locate the lesion and clarify the relationship between the lesion and the surrounding structure.

1. Introduction

Perianal region refers to the area extending 5-6 cm from the junction between the anal squamous mucosa and the skin [1]. Perianal abscess is an abscess caused by acute and chronic infections of the perianal space [2], which is manifested as redness, pain, swelling, and agglomeration of the skin around the anus, accompanied by systemic symptoms of varying degrees [3]. Perianal abscess is a common and frequently occurring disease in surgery, which has a high incidence and seriously affects the normal life and work of patients. In the past, the comprehensive diagnosis of perianal abscess was mainly made by digital surgical rectal examination, clinical symptoms, clinical vital signs, etc., which could not directly determine the location and range of the lesion and resulted in high blindness in diagnosis and treatment [4]. Therefore, the surgical treatment of perianal abscess has to be accurately positioned and diagnosed preoperatively to improve the safety of the surgery.

In recent years, with the continuous development of electronic imaging technology, multislice spiral computed tomography (MSCT) has gradually been applied in the clinical treatment of perianal abscess [5]. CT scanning has the characteristics of fast scanning speed, powerful image postprocessing function, and clear image [6]. Furthermore, CT scanning is used for the examination of the human abdomen and pelvis, without special bowel preparation such as enema or inflation [7]. Therefore, the application of CT scanning to examine the tissue structure of human perianal abscesses will help improve the clinical diagnosis of anal diseases.

Segmentation algorithms based on deep learning can deeply learn the mapping relationship between images and are widely used in computer vision and sound effects. They can methodically sort out a large amount of data, extract image features, and efficiently deal with complex problems, which have become the mainstream application of segmentation algorithms at present [8, 9]. Mastragostino et al. [10] used the deep learning-based convolutional neural network to evaluate CT images of liver tissue with high segmentation accuracy. In this study, a deep learning fully convolutional neural network (DLFCNN) algorithm was proposed to replace the full connection layer in the later stage of the CNN with the convolutional layer so that the number of neurons in the input layer was not restricted. The input of the convolutional layer could accept images of different sizes; the window for each value in the output to be mapped to the receptive field in the input image was fixed, which greatly improved the speed.

In this study, DLFCNN algorithm was proposed and compared with the CNN algorithm, which was applied in the CT imaging diagnosis of 60 patients with perianal abscesses. The objective of this study was to investigate the ability of CT images to distinguish the structure of perianal abscess tissue and to summarize the specific signs of perianal abscess tissue, so as to lay a foundation for the CT diagnosis of anorectal diseases.

2. Materials and Methods

2.1. General Data. In this study, 60 patients with medical diagnosis of perianal abscess in the Department of Anorectal Surgery of our hospital from October 2018 to December 2019 were selected as the experimental group, including 68 males and 52 females, with an average age of 54.23 ± 11.46 years. Another 60 healthy volunteers were selected as the control group, and the experimental group was diagnosed by MSCT scanning. The study was approved by the Medical Ethics Committee of the hospital, and the research objects and their family members learnt about the study and signed informed consent forms.

The criteria for inclusion were defined to include research objects who were diagnosed with perianal abscesses and had anal mass with pain, had complete clinical data and imaging data, and had suffered from the disease for more than 4 weeks.

The criteria for exclusion were defined to include research objects who were combined with cardiovascular disease, mental illness, speech impairment, and hearing impairment, did not undergo anorectal surgery in the past 6 months, and had unclear CT images.

2.2. Deep Learning Fully Convolutional Neural Network (DLFCNN) Algorithm. Neuron is the basic functional unit of the whole neural network structure (Figure 1). A large number of neurons together form a neural network structure. The essence of the internal convolution operation of the DLFCNN algorithm model is the integral operation, and the calculation equation is as follows:

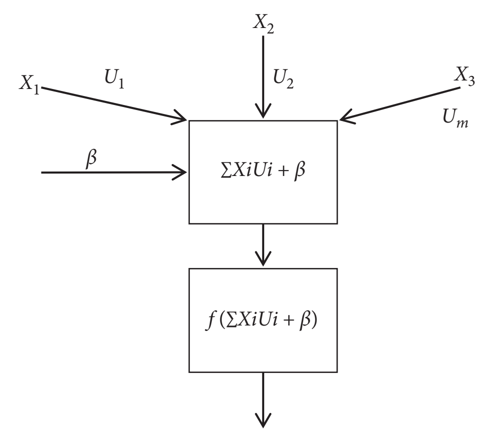

Figure 1: The basic structure of a neuron.

$$(g \cdot h)(s) \triangleq \int_{-\infty}^{\infty} g(\gamma)h(s-\gamma)\mathrm{d}\gamma. \quad (1)$$

In equation (1), function g and function h represent continuous functions, and both of them are integrable functions in the range of real numbers. Assume that the two-dimensional vector P and the convolution kernel Q are the input, and the output L is a two-dimensional tensor, which can be expressed in the following:

$$L(i,j) = (P \cdot Q)(i,j) = \sum_a \sum_b P(a+i, b+i) \cdot Q(a,b). \quad (2)$$

In equation (2), P is a 6×6 two-dimensional vector, Q is a 4×4 convolution kernel, and the output L is a two-dimensional tensor with 4×4. According to the equation, the size of the input image $(i \times i)$ directly affects the size of the output image $(L \times L)$, and it will also be affected by the size of the convolution kernel $(q \times q)$ during the operation. In order to better segment the edge of the image, a supplementary parameter o is often added. The specific equation is as follows:

$$L = \left[\frac{i-q+2o}{t}\right] + 1. \quad (3)$$

In equation (3), i stands for the size of the input image, q represents the size of the convolution kernel, and L means the size of the output image. Model networks often have multilayer superimposed hollow convolution, and the use of a zigzag structure can avoid the superposition of information and maintain the continuity of information. The zigzag structure uses time intervals of different lengths to integrate information from different distances and nearby locations. Thus, the following equation can be obtained:

$$N_i = \max\left[N_{i+1} - 2\lambda_i, N_{i+1} - 2\left(N_{i+1} - \lambda_i\right), \lambda_i\right]. \quad (4)$$

In equation (4), λ_i represents the hole interval of the ith layer, and N_i indicates the hole interval of the last layer, which is also the maximum value of the hole interval. In this study, the void interval was set to (2, 4, 5). The essence of the operation of the convolutional layer is to perform weighted summation. The function used in this study was the sigmoid function for classifying and outputting, and the ReLU function was adopted for extracting image features. Among them, the calculation and derivative equations of the sigmoid function are shown in the following:

$$\mathrm{Sig} = \frac{1}{1+e^{-c}} = \frac{1}{1+e^{-(vx+b)}}, \tag{5}$$

$$\mathrm{Sig}'(c) = \frac{e^{-c}}{\left(1+e^{-c}\right)^2}. \tag{6}$$

The function values in equations (5) and (6) are both in (0, 1), and the sigmoid function is a differentiable function. The ReLU function can reduce the problem of the disappearance of the gradient, and its mathematical operation and derivative equations are as follows:

$$\mathrm{ReLU}(c) = \max(0, c), \tag{7}$$

$$\mathrm{ReLU}'(c) = \begin{cases} 0, & c<0, \\ 1, & c>0. \end{cases} \tag{8}$$

In equations (7) and (8), the derivative of the ReLU function is negative, and the gradient is in a saturated state when $c<0$. When $c>0$, the derivative of the ReLU function is 1, and no gradient disappears. Compared with the sigmoid function, the ReLU function has a faster calculation speed and convergence speed. For the input P, the gap between $g(P)$ obtained by the model output and the actual value K usually requires a loss function to express the degree of deviation, which is recorded as $R(K, g(P))$ that is presented in the following equation:

$$R = \frac{1}{2m}\sum (K - g(P))^2. \tag{9}$$

2.3. Extraction of the Region of Interest from the CT Image of the Perianal Abscess Tissue. The main purpose of segmenting the CT image of the perianal abscess tissue was to classify the lesion. There was some irrelevant noise information in the CT image. If there was an error in the segmentation process, the classification result would be inaccurate, resulting in the perianal abscess. The iterative threshold method was adopted in this study to effectively solve the problems of inconspicuous contrast of light and dark in CT images, the dark overall image, and the too small difference between pixels. A clear CT image of perianal abscess could be obtained after a series of operations, such as expansion, corrosion, cavity filling, open operation, close operation, and mask operation. Figure 2 shows the extraction process of the region of interest in the image of perianal abscess tissue through the iterative threshold method. After the extraction of the region of interest, the image of perianal abscess tissue could reduce the amount of data and the interference of noise, complete the outline of the lesion, and realize the preprocessing of the image.

2.4. Examination Method. The diagnosis was made by using Somatom Definition AS+ 64-slice, 128-slice 4-dimensional spiral CT (Siemens, Germany). Before the examination, routine bowel preparations were performed. After the bladder was properly filled, the scanning was started. Each patient held his head with his hands, his lower limbs were in an external stand, and he was in a supine position in the center of the examination bed. The central sagittal position of his body was perpendicular to the plane of the bed, and his head was advanced. During the examination, the patient should keep a calm state of mind, not move his body, and hold his breath as required.

Scanning parameters were as follows: the flat sweep tube voltage was 120 kV and tube current was 175 mA; layer thickness was 2.5 mm and layer spacing was 5.0 mm; enhanced tube voltage and tube current were also 120 kV and 175 mA in turn; scanning rotation speed was 0.8 s/r, pitch was 1.0, field of view (FOV) was 250 mm × 250 mm, and the matrix was 512 × 512; the reconstruction layer thickness was 1.5 mm, and the layer spacing was 1.5 mm. 0.9% sodium chloride (NaCl) injection and 20 mL of iohexol injection were used as contrast agents. After probe exploration, the catheter was inserted, and the contrast agent was injected. After completion, image processing was carried out. On the AmbiVU 4.2.3 workstation, the image of the third sacral vertebra-anus area was reconstructed with a thickness of 1.5 mm, and the multiplanar reconstruction and maximum intensity projection reconstruction technology were employed to observe and save the relevant data. Two experienced doctors reviewed the CT images separately and reached a conclusion after discussion when their opinions were inconsistent.

2.5. Simulation Experiment Design of Deep Learning Fully Convolutional Neural Network Algorithm. In order to verify the effectiveness of the CT image segmentation method of perianal abscess tissue based on DLFCNN, a comparative experimental platform was designed in this study. The CT images of 60 patients with perianal abscesses were processed in batch by DLFCNN based on deep learning. Colloidal operation was performed in the convolutional layer of the convolutional network. Finally, the segmentation results were output in the output layer of the full connection layer. Table 1 shows the number of feature graphs and the size of the convolution kernel in each convolutional layer of DLFCNN. Moreover, C1 represented the convolutional layer, which mainly performed the convolution operation of the filter and then output the activation function. S2 stood for the sampling layer, and the input data of the previous layer were processed by dimensionality reduction. C3 and S4 both expressed the network layers, C3 was similar to C1, and S4 was similar to S2, which indicated the second downsampling layer. C5 meant the convolutional layer, which had 28 feature maps; the size of the feature map was changed after processing. S6 represented the downsampling layer, and the principles of C7 and S8 were the same as before. In addition, F9 stood for the full connection layer, which contained multiple neural units, and each neural unit was fully connected to the previous layer.

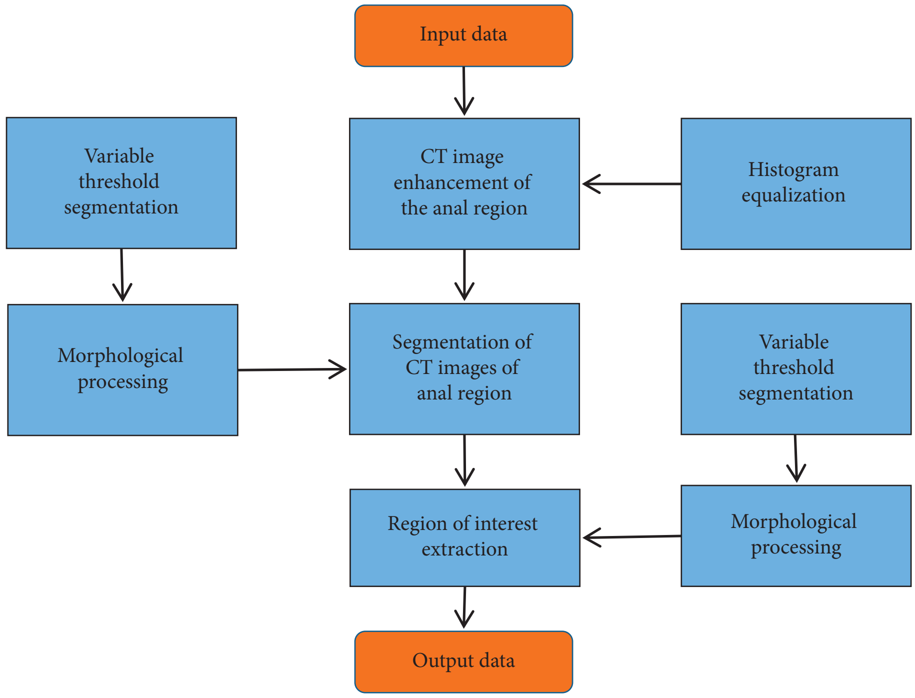

Figure 2: The extraction process of the region of interest in the image of perianal abscess tissue by the iterative threshold method.

2.6. Design of Evaluation Indicators for Deep Learning Fully Convolutional Neural Network Algorithm. In this study, it was necessary to select the appropriate image segmentation indicators in order to evaluate the extraction effect of the perianal abscess tissue segmentation process in the segmentation method. Commonly used segmentation metrics included Jaccard, Dice coefficient, precision rate, and recall rate. Jaccard was mainly employed to evaluate the effect of image segmentation, which could be calculated as follows:

$$\text{Jaccard} = \frac{C \cap D}{C \cup D}. \tag{10}$$

In equation (10), C stood for the label of the anal abscess tissue delineated in the image segmentation, representing the gold standard; D meant the segmentation result. If $\text{Jaccard} = 1$, the segmentation result completely overlapped with the gold standard. The Dice coefficient could be adopted to evaluate the similarity of two sets, and its equation is expressed as follows:

$$\text{Dice} = \frac{2|C \cap D|}{|C| + |D|}. \tag{11}$$

In equation (11), $\text{Dice} = 1$ indicated that the segmentation result was very ideal. Besides, the calculation of accuracy was as follows:

$$\text{Accuracy rate} = \frac{\text{TP}}{\text{TP} + \text{FP}}. \tag{12}$$

In equation (12), TP stood for that the detected perianal abscess tissue showed a true positive, and FP meant that the detected perianal abscess tissue showed a false positive. Furthermore, the equation for calculating the recall rate was as follows:

$$\text{RR} = \frac{\text{TP}}{\text{TP} + \text{FN}}. \tag{13}$$

In equation (13), TP suggested that the detected perianal abscess tissue presented a true positive, and FN indicated that the detected perianal abscess tissue presented a false negative.

2.7. Statistical Methods. SPSS 22.0 statistical software was used for analysis. The data which met the normal distribution were represented by the mean ± standard deviation ($\overline{x} + s$), and the data of the nonnormal distribution were expressed as the frequency and percentage. Furthermore, the t-test or χ^2 test was used for comparison between the control group and the experimental group. In addition, $P < 0.05$ indicated that the difference was statistically substantial.

3. Results

3.1. Comparison on CT Image Segmentation Effects of the Two Algorithms. Figure 3 shows the comparison of the CT image segmentation effect between the CNN and FCNN. In this study, the DLFCNN algorithm was proposed based on deep learning and compared with the CNN algorithm, which were applied in the CT image evaluation of 60 patients with perianal abscesses. According to the general structure, the segmentation effect of the CNN was not particularly prominent, while the segmentation of the DLFCNN was relatively accurate.

3.2. Analysis on the Simulation Effects of the Two Algorithms. The simulation effects of the two algorithms were compared, and the results are shown in Figure 4. The maximum entropy

Table 1: The number of feature maps of the DLFCNN and the size of the convolution kernel.

Convolutional layer	The number of feature maps	The size of the convolution kernel
C1	14	2×2
S2	14	5×5
C3	14	5×5
S4	14	2×2
C5	28	5×5
S6	28	2×2
C7	28	5×5
S8	28	2×2
F9	52	5×5

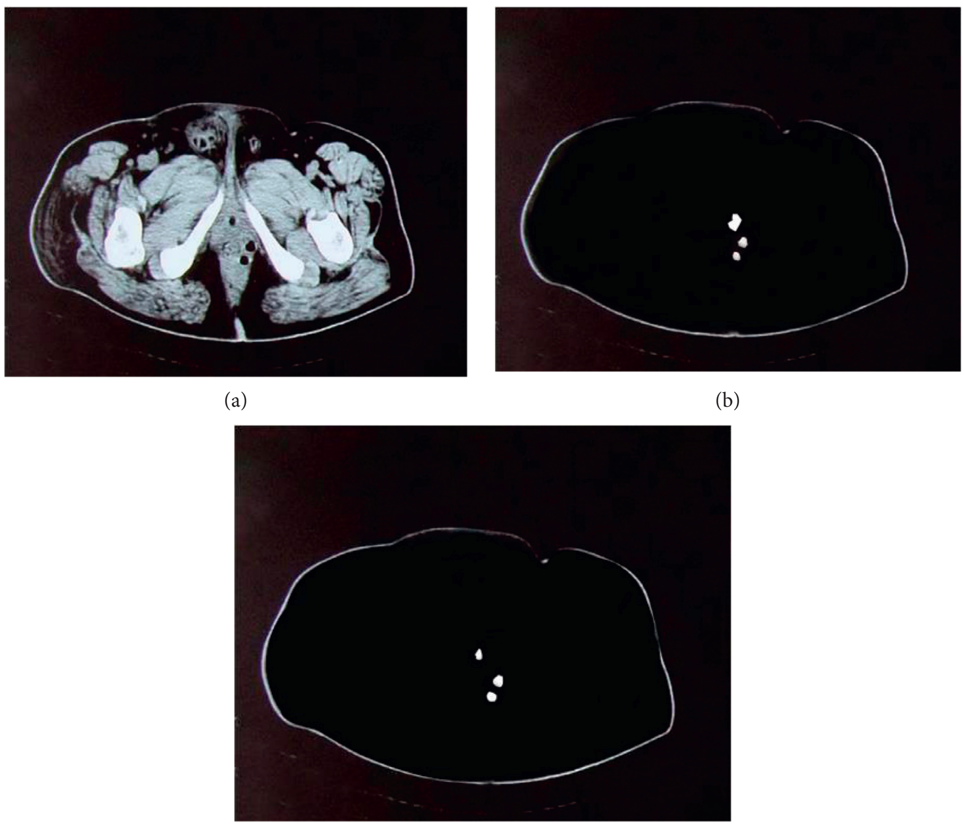

(a) (b) (c)

Figure 3: Comparison on the segmentation effect of the two algorithms. (a) Input CT image of perianal abscess tissue. (b) Segmentation effect of CNN algorithm. (c) Segmentation effect of DLFCNN algorithm.

method of the DLFCNN algorithm in this study began to converge around 25 iterations. The final loss value of the CNN was around 0.09. The image segmentation algorithm of the algorithm explored in this study had a faster convergence rate than the CNN in the training process, and the lowest final loss value was between 0.03 and 0.04.

Jaccard (0.7326) calculated by the CNN algorithm was sharply lower than that of the DLFCNN algorithm (0.8525) ($P < 0.05$), and the Dice coefficient (0.7264) hugely dropped in contrast to that of the DLFCNN algorithm (0.8434) ($P < 0.05$). The precision rate and recall rate of the CNN were also lower than the rates of the FCNN, but there was no significant difference. It revealed that the CNN was prone to oversegmentation and missing-segmentation. If the gold standard was taken as a reference, it indicated that the segmentation results differed greatly between the gold standards. However, the segmentation indicators of the DLFCNN in this study were improved to varying degrees, and the segmentation effect was better than that of the CNN.

3.3. Comparison on the General Data of Research Objects from the Two Groups. There was a comparison on the general data of research objects from the two groups, as shown in Figure 5. There were 36 males (60%) and 24 females (40%) in the experimental group, while there were 32 males (53.33%) and 28 females (46.67%) in the control group. Thus, the gender ratio of the two groups had no obvious difference ($P > 0.05$).

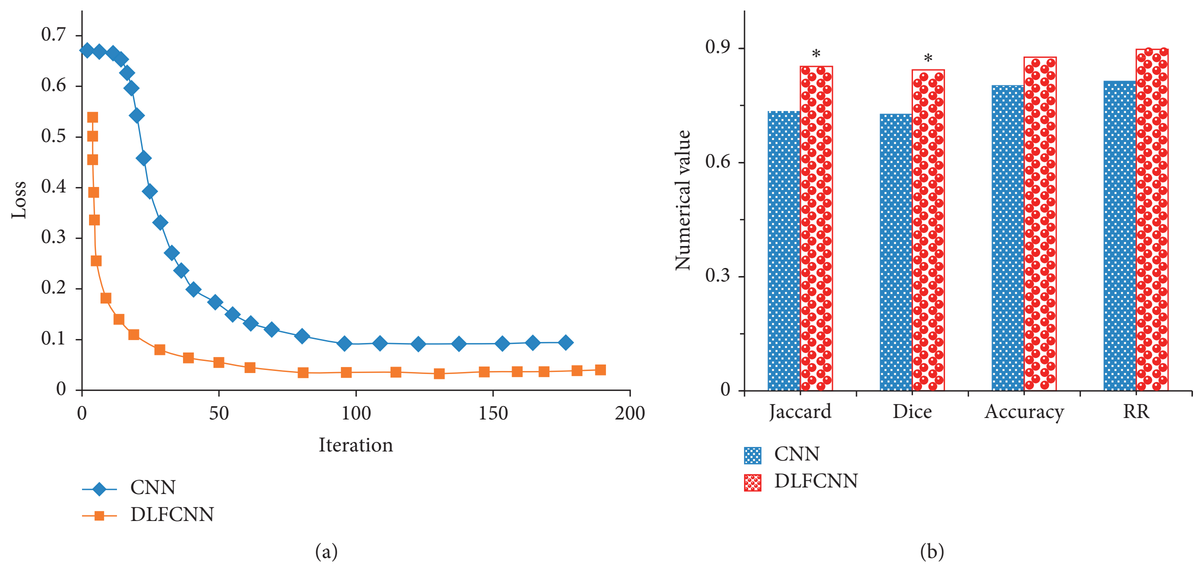

FIGURE 4: Comparison on simulation effects of the two algorithms. (a) Loss training curve diagram of the two algorithms. (b) Comparison of the segmentation indicators of the two algorithms; *meant $P < 0.05$ compared with the CNN.

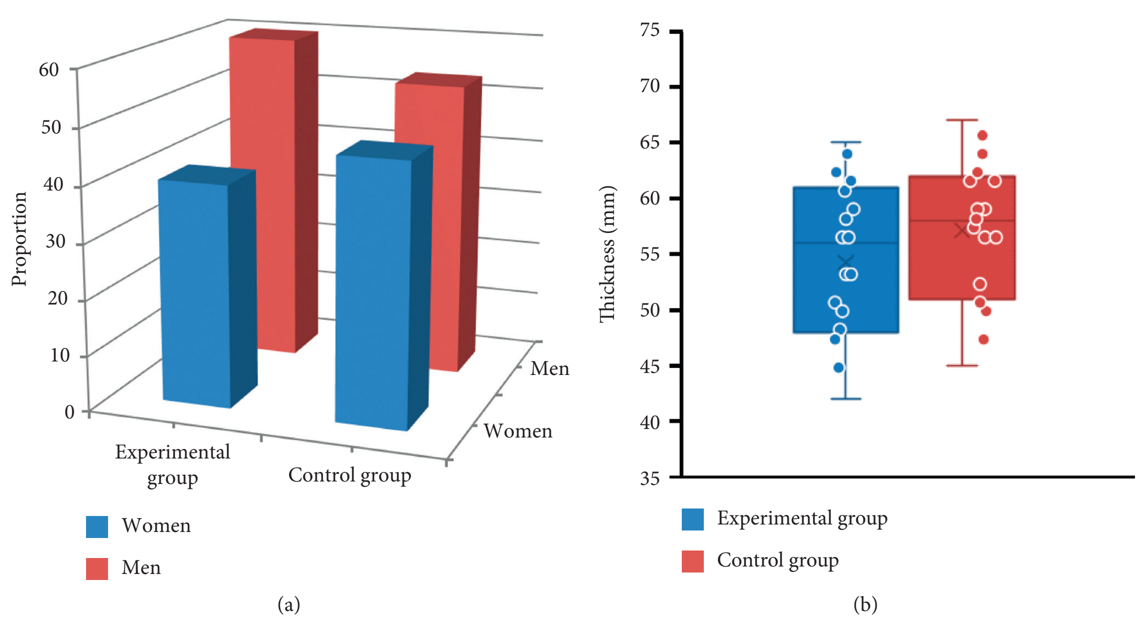

FIGURE 5: Comparison on the general data of research objects from the two groups. (a) The proportion of gender between the experimental group and the control group. (b) The age distribution of the experimental group and the control group.

The age range of the experimental group was 42–65 years, and the age range of the control group was 45–67 years. There was no marked difference in age between the experimental group and the control group ($P > 0.05$).

3.4. CT Imaging Features of Patients with Perianal Abscesses. Figures 6 and 7 display the axial and coronal CT images of two cases with perianal abscesses, respectively. The CT image of the soft tissue around the anal canal showed U-shaped thickening, uneven density, low-density shadows in the center, blurred edges of the lesion, and obvious enhancement of the central lesion on the enhanced scan. The central low-density shadow showed no obvious enhancement. The short strips were clearly intensified and connected with the posterior edge of the anal canal.

3.5. The Thickness of the Epidermis and Dermis in the Research Objects from the Experimental Group and the Control Group. According to the statistical results, it was found that the thickness of the epidermis and dermis of men was 2.8–3.6 mm, and the thickness of the epidermis and dermis of women was 1.8–2.6 mm. The thickness of the epidermis and dermis of men was obviously greater than the thickness of women, and the difference was statistically significant

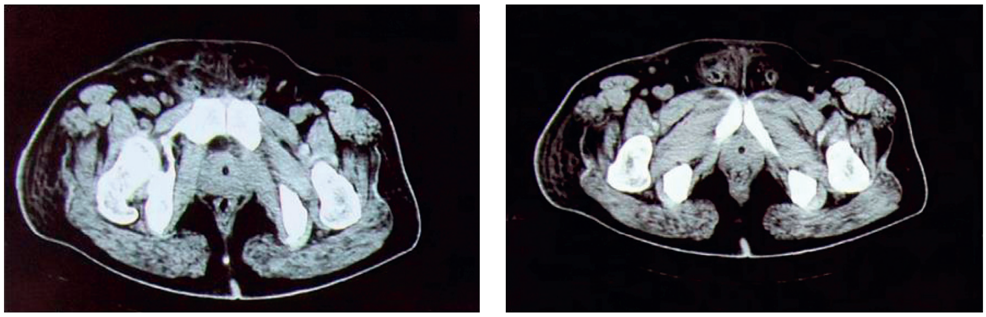

(a) (b)

Figure 6: CT image with a perianal horseshoe abscess (asterisk) (case 1, a male patient, aged 53 years). (a) Axial CT image. (b) Coronal CT image.

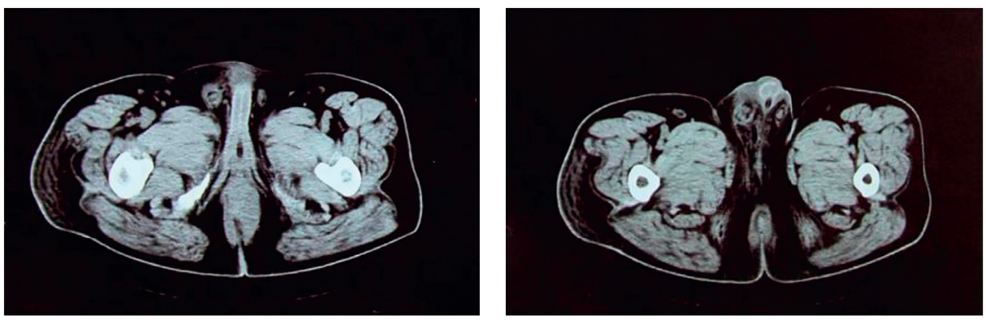

(a) (b)

Figure 7: CT image with the spread of abscess upward to the left levator ani muscle, forming an abscess (case 2, a male patient, aged 56 years). (a) Axial CT image. (b) Coronal CT image.

($P < 0.05$) (Figure 8); the thickness of the epidermis and dermis of the experimental group was 4.1–4.9 mm, and the thickness of the control group was 1.8–3.6 mm, so the thickness of the experimental group markedly increased compared with that of the control group ($P < 0.05$) (Figure 9).

3.6. Comparison on the CT Observation of the Superficial Fascia and Subcutaneous Fascia between the Experimental Group and the Control Group. The comparison results of the CT observation of the superficial fascia and subcutaneous fascia between the experimental group and the control group are presented in Figure 10. The display rate of the superficial fascia in the experimental group was 46.35%, and the display rate of the control group was 37.56%, so there was no marked difference between the two ($P > 0.05$). Furthermore, the CT value (-95.45 ± 8.26) of the subcutaneous fascia in patients from the experimental group was substantially greater than the value of the control group (-76.34 ± 7.69), with a statistical difference ($P < 0.05$).

3.7. The Detection Rate of CT Images in Patients with Perianal Abscesses. Figure 11 shows the accuracy and misdiagnosis rate of lesions in patients with perianal abscesses. 60 cases of perianal abscesses were examined by MSCT, 58 cases were in line with pathological examination, and 2 cases were misdiagnosed. After postoperative pathological examination, 58 patients had accurate location of the lesions, with an accuracy rate of 96.67%, including 21 cases of upper levator ani muscle abscess and 37 cases of lower levator ani muscle abscess.

4. Discussion

In this study, the deep learning fully convolutional neural network algorithm was compared with the CNN algorithm, which were applied to the segmentation training of CT images of patients with perianal abscesses to solve the problem that the segmentation effect was not ideal due to incomplete feature extraction of the CNN segmentation. By extracting the region of interest, the commonly applied segmentation metrics of medical images were compared, including Jaccard, Dice coefficient, accuracy, and recall rate [11]. The results disclosed that the maximum entropy method of the DLFCNN algorithm in this study started to converge when the times of iteration were around 25, and the final loss value of the CNN was around 0.09. The lowest loss value of the image segmentation algorithm in this study was between 0.03 and 0.04 in the final training, suggesting that the convergence speed of the DLFCNN was fast. Jaccard (0.7326) calculated by the CNN algorithm sharply reduced compared with the DLFCNN algorithm (0.8525); the Dice coefficient (0.7264) was obviously lower than the Dice coefficient (0.8434) of the DLFCNN algorithm ($P < 0.05$) [12].

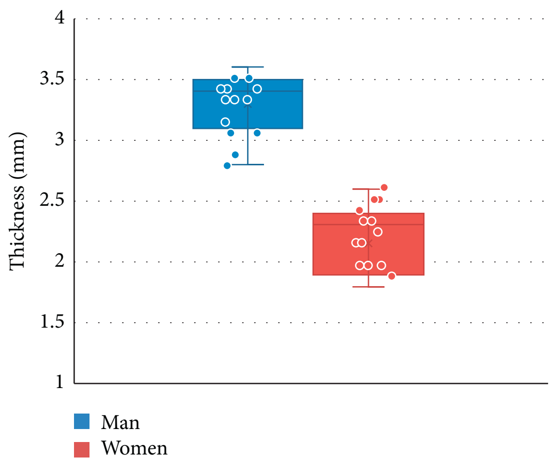

Figure 8: Comparison on dermal and epidermal thickness between men and women in the control group. *indicated $P < 0.05$ compared with men.

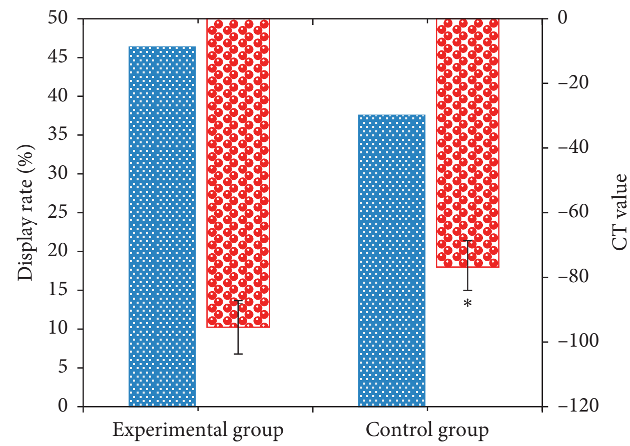

Figure 10: Comparison on the CT observation of the superficial fascia and subcutaneous fascia between the experimental group and the control group. *indicated $P < 0.05$ in contrast to the experimental group.

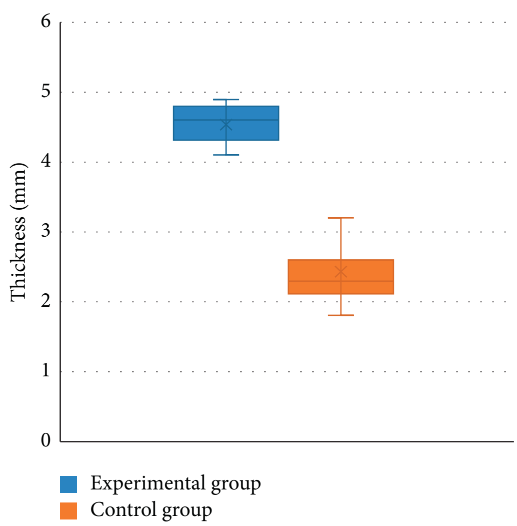

Figure 9: Comparison on epidermal and dermal thickness between the experimental group and the control group. *meant $P < 0.05$ compared with the experimental group.

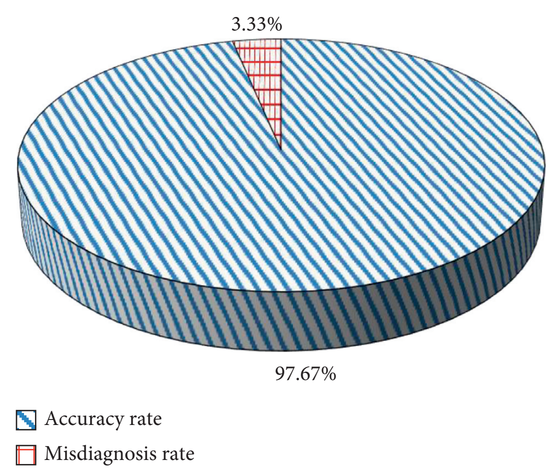

Figure 11: The accuracy and misdiagnosis rate of lesions in patients with perianal abscesses.

It showed that the CNN was prone to oversegmentation and missing-segmentation. If the gold standard was used as a reference, it indicated that the segmentation results were quite different among the gold standards [13]. DLFCNN in this study was improved to varying degrees in terms of segmentation indicators, with good stability and good segmentation effects [14].

Perianal abscess is a common and frequently occurring disease after clinical surgery, which is generally caused by primary infection. Some perianal abscesses are caused by trauma, inflammatory lesions, and drug injection [15]. Under normal circumstances, clinical diagnosis focuses on the number of lesions and the location of the relationship between the lesion location and the levator ani muscle. Besides, the use of CT imaging diagnosis before surgery has a very positive significance in preventing postoperative recurrence. MSCT images continue to expand the diagnostic methods of perianal abscess tissue imaging. It has the characteristics of fast inspection, thin layers, and high resolution and is widely used in the diagnosis of anal diseases [16]. When perianal abscess is detected with MSCT, it is usually not affected by the weak peristalsis of the anorectum, with few motion artifacts, and the lesion can be clearly shown in the image. Perianal abscesses are affected by the pus, the boundaries are not clear, and the density of the abscess is not uniform over time. In this study, the CT value of the subcutaneous fascia of the experimental group was -95.45 ± 8.26, which was significantly lower than the value of the control group (-76.34 ± 7.69) ($P < 0.05$). It might be that patients with early perianal abscess had more inflammatory exudate, and the CT scan had a uniform density and a low CT value [17]. In the middle and late stages of the formation of pus in the perianal abscess tissue, the absorption or discharge of pus will occur, forming an abscess cavity, which is manifested as a thick wall and abscess cavity [18]. With enhanced CT scanning, it can be observed that the thick wall of the abscess is obviously strengthened, in a ring shape, and the abscess cavity is not strengthened, showing a lower density. After the CT image is segmented by the DLFCNN algorithm, the relationship between the perianal abscess and the anorectum can be better displayed, and the number and location of the abscess can be accurately located, providing a reliable basis for the treatment of clinicians [19]. 60 patients with perianal abscesses were examined by MSCT. 58 patients had accurate location of the lesion with an accuracy rate of 96.67%, which confirmed that the MSCT scan could clearly show the morphology and structure of the lesion, thereby providing intuitive clinical diagnosis. This was consistent with the research findings of Zhao et al. [20].

CT image measurement of skin thickness is mainly used in the application research of breast skin, but there are few reports on the research of skin thickness measurement in the anal area. The statistical results of this study found that the thickness of the epidermis and dermis of men was in the range of 2.8–3.6 mm, and the thickness of the epidermis and dermis of women was 1.8–2.6 mm. The thickness of the epidermis and dermis of men was markedly greater than that of women, and there was a statistically great difference ($P < 0.05$). Moreover, the thickness of the epidermis and dermis of the experimental group was 4.1–4.9 mm, and the thickness of the control group was 1.8–3.6 mm. The thickness of the epidermis and dermis of the experimental group was greatly larger than that of the control group ($P < 0.05$), meaning that the skin at the lesion site was significantly thickened when a lesion occurred in the anal area, which could clearly distinguish between perianal abscess and other anal diseases.

5. Conclusion

In this study, DLFCNN was compared with the CNN and applied to the CT images of 60 patients with perianal abscesses. The DLFCNN algorithm had good stability and segmentation effect, and the skin at the focal area of anal abscess was obviously thickened. The CT image was simple and accurate in the diagnosis of patients with perianal abscess, which could be applied to effectively locate the lesion and clarify the relationship between the lesion and the surrounding structure. The shortcomings of this study are that the sample size is small, and the DLFCNN training images are few. Subsequently, the sample size should be expanded to further improve the accuracy of image segmentation. In this study, MSCT was adopted to detect the perianal abscess tissue, which could improve the reference basis for the clinical development of the scientific surgical treatment plan, effectively reduce the incidence of lesion omission, and prevent the recurrence of the patient's disease.

Data Availability

No data were used to support this study.

Conflicts of Interest

The authors declare no conflicts of interest.

References

[1] Y. Hiraoka, S. Shinozaki, and T Yano, "Recurrent intestinal inflammation with a perianal abscess is not always Crohn's disease: a patient with a complex Meckel's diverticulum diagnosed by double-balloon endoscopy," *Clinical Journal of Gastroenterology*, vol. 13, no. 1, pp. 26–30, 2020.

[2] F. P. Azmi, N. A. A. Rahman, L. Mazlan, N. Basiron, and F. H. Imran, "A case of large perianal mucinous adenocarcinoma arising from recurrent abscess and complex fistulae," *Case Reports in Surgery*, vol. 2020, Article ID 1798543, 4 pages, 2020.

[3] E. Solis, Y. Liang, G. Ctercteko, and J. W. T. Toh, "Dangers of delayed diagnosis of perianal abscess and undrained perianal sepsis in Fournier's gangrene: a case series," *BMJ Case Reports*, vol. 13, no. 10, Article ID e236503, 2020.

[4] Y. H. Liu, Z. B. Lv, J. B. Liu, and Q. F. Sheng, "Perianorectal abscesses and fistula due to ingested jujube pit in infant: two case reports," *World J Clin Cases*, vol. 8, no. 20, pp. 4930–4937, 2020.

[5] K. Bałaż, A. Trypens, D. Polnik, K. Pankowska-Woźniak, and P. Kaliciński, "Perianal abscess and fistula-in-ano in children - evaluation of treatment efficacy. Is it possible to avoid recurrence?" *Polski Przeglad Chirurgiczny*, vol. 92, no. 2, pp. 29–33, 2020.

[6] L. Ghahramani, M. R. Minaie, and P Arasteh, "Antibiotic therapy for prevention of fistula in-ano after incision and drainage of simple perianal abscess: a randomized single blind clinical trial," *Surgery*, vol. 162, no. 5, pp. 1017–1025, 2017.

[7] J. P. Wang, C. Cai, and J. L. Du, "Role of interleukin-17 in the pathogenesis of perianal abscess and anal fistula: a clinical study on 50 patients with perianal abscess," *ANZ Journal of Surgery*, vol. 89, no. 3, pp. 244–247, 2019.

[8] W. Ding, Y. R. Sun, and Z. J. Wu, "Treatment of perianal abscess and fistula in infants and young children: from basic etiology to clinical features," *The American Surgeon*, vol. 28, Article ID 3134820954829, 2020.

[9] H. Chang, M. C. Kuo, and T. C. Tang, "Clinical features and recurrence pattern of perianal abscess in patients with acute myeloid leukemia," *Acta Haematologica*, vol. 138, no. 1, pp. 10–13, 2017.

[10] P. Mastragostino, A. D. Lee, and P. J. Battaglia, "Perianal abscess mimicking levator ani syndrome: a case report and approach to the differential diagnosis of anorectal pain," *Journal of the Canadian Chiropractic Association*, vol. 61, no. 2, pp. 145–152, 2017.

[11] J. D. Dormer, M. Halicek, L. Ma, C. M. Reilly, E. Schreibmann, and B. Fei, "Convolutional neural networks for the detection of diseased hearts using ct images and left atrium patches," *Proceedings of SPIE-The International Society for Optical Engineering*, vol. 10575, Article ID 1057530, 2018.

[12] T. Zhao, G. M. McNitt, and D. Ruan, "A convolutional neural network for ultra-low-dose CT denoising and emphysema screening," *Medical Physics*, vol. 46, no. 9, pp. 3941–3950, 2019.

[13] G. Chlebus, A. Schenk, J. H. Moltz, B. V. Ginneken, H. K. Hahn, and H. Meine, "Automatic liver tumor segmentation in CT with fully convolutional neural networks and object-based postprocessing," *Scientific Reports*, vol. 8, no. 1, Article ID 15497, 2018.

[14] K. A. J. Eppenhof and J. P. W. Pluim, "Error estimation of deformable image registration of pulmonary CT scans using convolutional neural networks," *Journal of Medical Imaging*, vol. 5, no. 2, Article ID 024003, 2018.

[15] D. Zhang, J. H. Noble, and B. M. Dawant, "Automatic detection of the inner ears in head CT images using deep convolutional neural networks," *Proceedings of SPIE-The International Society for Optical Engineering*, vol. 10574, Article ID 1057427, 2018.
[16] S. Chen, X. Zhong, and S Hu, "Automatic multi-organ segmentation in dual-energy CT (DECT) with dedicated 3D fully convolutional DECT networks," *Medical Physics*, vol. 47, no. 2, pp. 552–562, 2020.
[17] H. C. Shin, H. R. Roth, and M Gao, "Deep convolutional neural networks for computer-aided detection: CNN architectures, dataset characteristics and transfer learning," *IEEE Transactions on Medical Imaging*, vol. 35, no. 5, pp. 1285–1298, 2016.
[18] L. Sibille, R. Seifert, and N Avramovic, "18F-FDG PET/CT Uptake classification in lymphoma and lung cancer by using deep convolutional neural networks," *Radiology*, vol. 294, no. 2, pp. 445–452, 2020.
[19] K. Men, J. Dai, and Y. Li, "Automatic segmentation of the clinical target volume and organs at risk in the planning CT for rectal cancer using deep dilated convolutional neural networks," *Medical Physics*, vol. 44, no. 12, pp. 6377–6389, 2017.
[20] Z. Zhao, C. Ye, Y. Hu, C. Li, and X. Li, "Cascade and fusion of multitask convolutional neural networks for detection of thyroid nodules in contrast-enhanced CT," *Computational Intelligence and Neuroscience*, vol. 2019, Article ID 7401235, 13 pages, 2019.

Hindawi
Journal of Healthcare Engineering
Volume 2021, Article ID 4959727, 10 pages
https://doi.org/10.1155/2021/4959727

Research Article

Feature Point Extraction and Motion Tracking of Cardiac Color Ultrasound under Improved Lucas–Kanade Algorithm

Xiaoli Zhang[1] **Punan Li**[1] **and Yibing Li**[2]

[1]*Department of Ultrasound Medicine, Jincheng People's Hospital, Jincheng, Shanxi 048000, China*
[2]*Department of Ultrasound Medicine, Zhengzhou Maternity Hospital Affiliated to Henan University, Zhengzhou, Henan 450000, China*

Correspondence should be addressed to Yibing Li; huidong.li@cumt.edu.cn

Received 13 June 2021; Revised 13 July 2021; Accepted 26 July 2021; Published 4 August 2021

Academic Editor: Enas Abdulhay

The purpose of this research is to study the application effect of Lucas–Kanade algorithm in right ventricular color Doppler ultrasound feature point extraction and motion tracking under the condition of scale invariant feature transform (SIFT). This study took the right ventricle as an example to analyze the extraction effect and calculation rate of SIFT algorithm and improved Lucas–Kanade algorithm. It was found that the calculation time before and after noise removal by the SIFT algorithm was 0.49 s and 0.46 s, respectively, and the number of extracted feature points was 703 and 698, respectively. The number of feature points extracted by the SIFT algorithm and the calculation time were significantly better than those of other algorithms ($P < 0.01$). The mean logarithm of the matching points of the SIFT algorithm for order matching and reverse order matching was 20.54 and 20.46, respectively. The calculation time and the number of feature points for the SIFT speckle tracking method were 1198.85 s and 81, respectively, and those of the optical flow method were 3274.19 s and 80, respectively. The calculation time of the SIFT speckle tracking method was significantly lower than that of the optical flow method ($P < 0.05$), and there was no statistical difference in the number of feature points between the SIFT speckle tracking method and the optical flow method ($P > 0.05$). In conclusion, the improved Lucas–Kanade algorithm based on SIFT significantly improves the accuracy of feature extraction and motion tracking of color Doppler ultrasound, which shows the value of the algorithm in the clinical application of color Doppler ultrasound.

1. Introduction

Commonly used imaging techniques for evaluating cardiac tissue function include Doppler tissue imaging, magnetic resonance imaging (MRI), computerized tomography (CT), and ultrasound. Ultrasound imaging is widely used in the evaluation of cardiac tissue function due to its advantages of fast imaging speed, high safety, and low price [1]. At present, the evaluation of cardiac function by clinical diagnostic technology is mainly the evaluation of left ventricular function, and the research of right ventricle is still relatively vacant in the medical field. The change of right ventricular function is of great significance for the evaluation, diagnosis, and prognosis of pulmonary hypertension and a variety of heart diseases [2]. Cardiac color Doppler ultrasound is the main examination method in the clinical diagnosis of CHF, and it is also the only imaging method that can display the internal structure of the heart and internal circulation of organs. This method is simple to operate, has no wound, and can carry out repeated operation. When examining patients with CHF, it can display the cardiac image structure comprehensively and intuitively, Therefore, cardiac color Doppler ultrasound can accurately and comprehensively evaluate the function of right ventricle and myocardium, which plays an important role in the diagnosis and treatment of heart disease [3]. Due to the randomness of ultrasound scattering signals in biological tissues, a large amount of irregular speckle noise will be distributed in the generated image, which will make the image blurred, and the artifacts of different organs will also affect the ultrasound imaging [4]. The acoustic field characteristics of the ultrasound beam make the lateral resolution of ultrasound imaging low. Ordinary ultrasound images usually cannot clearly reflect the tissue morphology and differences between tissues [5]. The complexity of the geometry leads to the lack of accurate measurement of right ventricular function by ultrasound inspection methods [6].

The optical flow method can process continuous image sequences and has real-time characteristics in digital image data. Lucas–Kanade algorithm is an optical flow estimation algorithm based on two-frame difference. Lucas–Kanade point matching algorithm has a wide range of applications in realizing single and multiple target tracking because of its fast calculation speed and simple application [6]. However, the tracking effect of Lucas–Kanade algorithm in practice is not good [7]. Some researchers proposed that the idea of image pyramids can be introduced into the Lucas–Kanade algorithm, which can significantly increase its tracking effect [8]. There were studies applying the Lucas–Kanade algorithm to the motion tracking of cardiac color Doppler ultrasound. However, the effect of feature point extraction and tracking is still poor when the motion between frames of the sequence image is large, because the Lucas–Kanade algorithm uses linear estimation [6], and further optimization is needed.

In summary, although Lucas–Kanade algorithm has significant advantages in target tracking, it still needs further improvement in cardiac color Doppler ultrasound feature point extraction and motion tracking. Therefore, the idea of pyramid was proposed based on the Lucas–Kanade algorithm and the SIFT algorithm to improve the accuracy and computing speed of the Lucas–Kanade algorithm, which was applied to the right ventricular color Doppler ultrasound feature point extraction and motion tracking. It was hoped that this research can provide a reference basis for the evaluation, diagnosis, and prognosis of pulmonary hypertension and a variety of heart diseases.

2. Materials and Methods

2.1. Lucas–Kanade Algorithm Improvement. Differentiation method [9] and region-based matching method [10] are the most commonly used algorithms for optical flow algorithms, and Lucas–Kanade algorithm is an algorithm based on the local constraints of optical flow. For the small plane S with the center line A, the gray values of the pixels in the regional coordinates of any two images in the image sequence are $F(x)$ and $G(x)$, respectively. Then, the smallest difference between the two images is expressed as shown in equation (1), where b is the vector for calculating the matching.

$$D = \sum_{x \in S} |F(x+b) - G(x)|. \tag{1}$$

If $b \longrightarrow 0$, then there the following equations:

$$\begin{aligned} F(x) &\approx \frac{F(x+b) - F(x)}{b} = \frac{G(x) - F(x)}{F(x)}, \\ b &\approx \frac{G(x) - F(x)}{F(x)}. \end{aligned} \tag{2}$$

The weight of b obtained at the x field is expressed as follows:

$$w(x) = \frac{1}{|G(x) - F(x)|}. \tag{3}$$

The iterative equation of the matched vector b is expressed as equation (4), where k is the number of iterations.

$$b_{k+1} = b_k + \frac{\sum_x \left(\left(w(x)\left[G(x) - F\left(x + b_k\right)\right]\right) / \left(F\left(x + b_k\right)\right)\right)}{\sum_x w(x)}. \tag{4}$$

For the accuracy and speed of the Lucas–Kanade algorithm, the pyramid idea was introduced into the Lucas–Kanade algorithm to iterate the Lucas–Kanade algorithm by levels and reduce the calculation amount of Lucas–Kanade algorithm caused by excessive image pixel motion [11]. For the point (x, y) on the ultrasound image, the iterative equation of the improved Lucas–Kanade algorithm based on the pyramid idea is expressed as follows:

$$\begin{aligned} C^l = \frac{1}{4}(2x, 2y) &+ \frac{1}{8}\left[C^{l-1}(2x-1, 2y) + C^{l-1}(2x+1, 2y)\right. \\ &\left. + C^{l-1}(2x, 2y-1) + C^{l-1}(2x, 2y+1)\right] \\ &+ 16\left[C^{l-1}(2x-1, 2y-1) + C^{l-1}(2x-1, 2y+1)\right. \\ &\left. + C^{l-1}(2x+1, 2y-1) + C^{l-1}(2x+1, 2y+1)\right]. \end{aligned} \tag{5}$$

In equation (6), C^{l-1} is the gray value of the point (x, y) at time l.

As the number of pyramid layers progresses downwards, the resolution of the image gradually decreases. The optical flow field motion result obtained in the image of the previous resolution will be used as the initial value for the calculation of the next resolution. Calculating the Lucas–Kanade algorithm in a hierarchical manner can greatly reduce the massive data calculations generated when a large amount of optical flow moves and shortens the calculation time. The iterations were repeated until the final optical flow result was calculated. The schematic diagram of the improved operation of the Lucas–Kanade algorithm pyramid is shown in Figure 1.

2.2. Ultrasonic Image Preprocessing. The ultrasound imaging system will cause the image to be damaged to a certain extent during image acquisition, transmission, and preservation. Therefore, it is necessary to perform operations such as line filtering noise on the cardiac color Doppler ultrasound image to reduce the impact on the image before the data analysis on cardiac color Doppler ultrasound. Commonly used medical image noise reduction methods include mean filter, adaptive Wiener filter, and median filter [12]. The linear-mean filtering method filters out isolated noise points by means of averaging neighborhoods and has a good removal effect on salt and pepper noise, Gaussian noise, and impulse noise [13]. For the image pixel point (x, y) to be filtered, the corresponding R of the linear-mean filtering is expressed as follows:

$$\begin{aligned} R = w(-1,-1)f(x-1, y-1) &+ w(-1,0)f(x-1, y) \\ &+ w(0,0)f(x, y) + \cdots + w(1,0)f(x+1, y) \\ &+ w(1,1)f(x+1, y+1). \end{aligned} \tag{6}$$

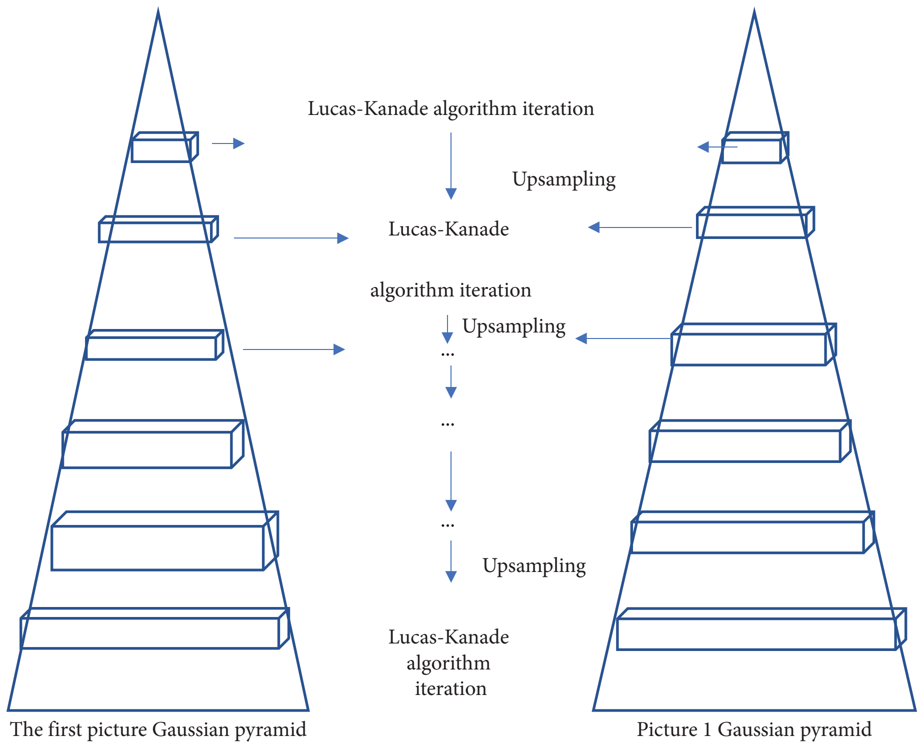

FIGURE 1: Schematic diagram of pyramid improvement of Lucas–Kanade algorithm.

On the image g with a mask size of $M \times N$, the filter mask of linear-mean filtering is $m \times n$, and the corresponding pixel is expressed as follows:

$$f(x, y) = \frac{1}{D} \sum_{(x,y)\in N} g(x, y). \tag{7}$$

D represents the sum of pixels in the mask including the current pixel, and $g(x, y)$ is the pixel value in the x-th row and y-column.

2.3. Feature Points Extraction of Cardiac Ultrasound Images. Ultrasound image speckle is a feature often used in medical ultrasound image processing. The feature speckles of cardiac ultrasound images usually reflect changes in the heart cavity, myocardium, and valves during movement. Forstner algorithm, SUNSAN algorithm, SIFT algorithm, and Harris algorithm are commonly used point feature extraction methods in the field of image registration. Among them, the SIFT algorithm has the characteristics of strong matching ability, stable extraction of features, and high matching accuracy. It can also match features between two images with large differences [14]. Gaussian normal distribution function $G(x, y, \sigma)$ of the SIFT algorithm in a two-dimensional plane image is expressed as follows:

$$G(x, y, \sigma) = \frac{1^{e-(x2+y2)/2\sigma^2}}{2\pi\sigma^2}. \tag{8}$$

Its scale space is expressed as follows:

$$L(x, y, \sigma) = G(x, y, \sigma) * I(x, y). \tag{9}$$

In equations (8) and (9), (x, y) is the position of a certain pixel of the target image, $L(x, y, \sigma)$ is the scale space of the target image, and σ is the scale coordinate. σ is related to the smoothness of the image. The smaller the σ, the lower the smoothness. The calculation of Gaussian difference scale space is as follows:

$$\begin{aligned} D(x, y, \sigma) &= [G(x, y, k\sigma) - G(x, y, \sigma)] * I(x, y) \\ &= L(x, y, k\sigma) - L(x, y, \sigma). \end{aligned} \tag{10}$$

A fitted quadratic function was used to increase the accuracy of the position detection of the feature point. For the key points and boundary points with insignificant features in the extraction process, the spatial scale function was used to eliminate the algorithm to enhance the robustness and accuracy of the algorithm. The spatial scale function is expressed as follows:

$$D(x, y, \sigma) = D(x, y, \sigma) + \left(\frac{\partial D^t}{\partial x} + \frac{1}{2} x^t \frac{\partial^2 D}{\partial x^2} x \right). \tag{11}$$

Derivation of the above function is the calculation method of accurate position.

$$\hat{x} = -\frac{\partial^2 D^{-1^t}}{\partial x^2} \frac{\partial D}{\partial x}. \tag{12}$$

The key points with insignificant features are eliminated, and the following equation is obtained.

$$D(\hat{x}) = D(x, y, \sigma) + \frac{1}{2} x \frac{\partial D^t}{\partial x}, \tag{13}$$

$\hat{x}$ is the transpose of the matrix (x, y, σ). If $D(\hat{x}) \geq 0.03$, the feature point is retained; otherwise, it is discarded.

SIFT algorithm makes use of the gradient direction distribution characteristics of neighborhood pixels of key points to specify direction parameters for each key point, so that the operator has rotation invariance [15].

$$m(x, y) = \sqrt{[L(x+1, y) - L(x-1, y)]^2 + [L(x, y+1) - L(x, y-1)]^2}, \tag{14}$$

$$\vartheta(x, y) = \alpha \tan 2\left[\frac{L(x+1, y) - L(x-1, y)}{L(x, y+1) - L(x, y-1)}\right]. \tag{15}$$

In equations (15) and (16), $m(x, y)$ is the calculation equation for gradient modulus at position (x, y), and $\delta(x, y)$ is the calculation equation for Angle at position (x, y). L is the scale space.

The required calculation method of the circular image area in the process of generating the features of key points is as follows:

$$R = \frac{3\sqrt{2}\sigma(d+1) + 1}{2}. \tag{16}$$

The coordinate of rotation Angle obtained after movement is expressed as follows:

$$\begin{bmatrix} \hat{x} \\ \hat{y} \end{bmatrix} = \begin{bmatrix} \cos\alpha - \sin\alpha \\ \cos\alpha + \sin\alpha \end{bmatrix} \times \begin{bmatrix} x \\ y \end{bmatrix}, \tag{17}$$

In equations (16) and (17), σ is the intragroup scale of the group, where the feature points are located, and α is the rotation Angle.

The calculation method of specification description subvector element is as follows:

$$l_j = \frac{w_j}{\sqrt{\sum_{i=1}^{128} w_i}}, \tag{18}$$

w_i and w_j are eigenvectors of i and j dimensions, and l_i is normalized vector.

The extraction steps of feature points in cardiac ultrasound images based on SIFT algorithm mainly included five parts: generation of scale space, detection of extreme points in scale space, accurate positioning of extreme points, direction parameters of key points, and generation of feature vectors of key points. The specific SIFT algorithm feature point extraction flow chart is shown in Figure 2.

2.4. Feature Point Matching and Tracking Based on Improved Lucas–Kanade Algorithm. Euclidean distance is often used to verify whether the feature points of two images match [16]. It is assumed that the two images to be matched are A and B, and SIFT is used to extract feature points for the two images. If $f_a = \{a_1, a_2, \ldots, a_m\}$ and $f_b = \{b_1, b_2, \ldots, b_m\}$ are the feature point sets of A and B, respectively, and m and n are the number of feature points of A and B, respectively, then the Euclidean distance of k-dimensional space is expressed as follows:

$$s(f_a, f_b) = \mathrm{sqrt}\left[\sum_{i=1}^{k} (a_i - b_i)^2\right]. \tag{19}$$

For a certain point, the Euclidean distance in f_a and f_b was calculated to find the minimum distance and the second smallest distance $\widetilde{d}_{\min}$, $r = d_{\min}/\widetilde{d}_{\min}$. Whether the feature points are matched is evaluated according to the following equation, where evaluation is the threshold set by the experiment, which was set as 0.44 in this research.

$$\begin{cases} r < \eta, & \text{success}, \\ r \geq \eta, & \text{failure}. \end{cases} \tag{20}$$

K-D tree index tree and Best Bin First (BBF) algorithm are commonly used in feature point matching process. BBF algorithm reduces the node backtracking of K-D tree nearest neighbor search algorithm, improves the search efficiency, and is suitable for high-dimensional data search. For two images to be matched, feature points extraction and feature vector set analysis were carried out by SIFT, and the corresponding point set of SIFT feature matching was finally obtained. The flowchart of feature point matching based on the improved Lucas–Kanade algorithm is shown in Figure 3.

2.5. Statistical Methods. The experimental data was processed using SPSS 19.0, the count data was tested by χ^2 test, and $P < 0.05$ indicated that the difference was statistically considerable.

3. Results and Discussion

3.1. Image Motion Feature Point Detection Based on Improved Lucas–Kanade Algorithm. The image sequence of frames 1 to 2 of the right ventricular movement cycle was selected for comparative analysis, and the vector image of gray-scale movement from frame 1 to frame 2 was obtained. The results are shown in Figure 4. It can be concluded from Figure 4(c) that the improved Lucas–Kanade algorithm has better real-time performance in feature point tracking. The gradient direction histogram of Lucas–Kanade algorithm represented the gradient direction and the total number of gradients. Gradient direction histogram was used to obtain the direction synthesis vector of an image pixel in a certain area. The reference direction was calculated through the small area, where the key points were obtained, so that the algorithm had spatial rotation invariance [17].

3.2. Special Point Trajectory Based on Improved Lucas–Kanade Algorithm. The improved Lucas–Kanade algorithm was used to compare the movement tracks of right

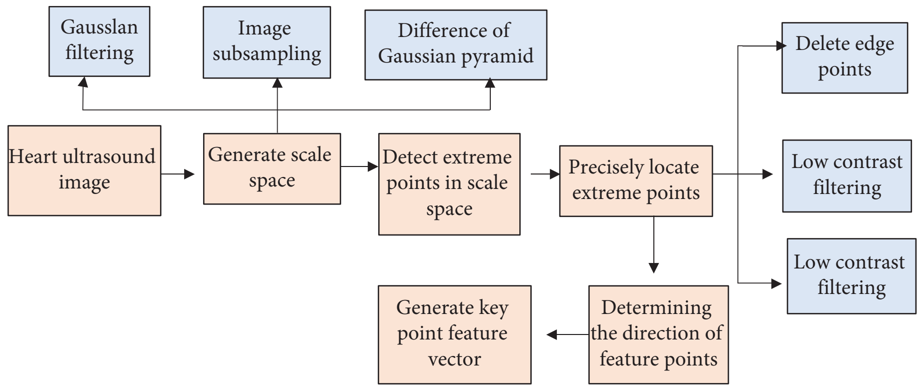

FIGURE 2: Specific flow chart of feature point extraction of SIFT algorithm.

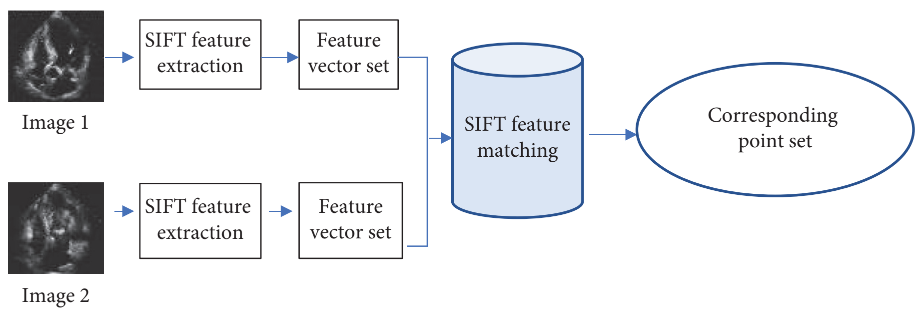

FIGURE 3: Flow chart of feature point matching based on improved Lucas-Kanade algorithm.

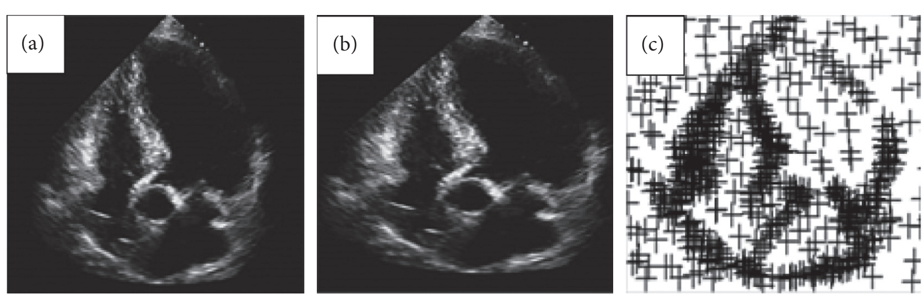

FIGURE 4: Image sequence of frames 1-2 of right ventricular movement cycle. (a) Image of frame 1; (b) Image of frame 2; (c) vector diagram of gray-scale motion.

ventricular myocardium, right atrioventricular septal tricuspid valve ring, and left atrioventricular septal tricuspid valve ring (Figure 5). The motion trajectory of feature points based on the improved Lucas–Kanade algorithm had significant differences for different parts. The variation range of the right ventricular myocardium in the X direction was 372~405, and the variation range of the right atrioventricular septal tricuspid valve in the X direction was 385~450. The left ring of the atrioventricular septal tricuspid valve varied from 415 to 450 in the X direction. Heart movement is a very complex nonlinear movement, which includes rotation, torsion, and circular movement, in addition to contraction and diastole, and the motion parameters of each point and region are often different [18].

3.3. Analysis of Feature Point Extraction Results Based on Improved Lucas–Kanade Algorithm. The improved Lucas–Kanade algorithm was used to extract ultrasonic images with feature points, and the number of feature points under different image frame sequences was statistically analyzed (Figure 6). The number of feature points extracted under different image frame order had great difference. When the image frame order was 1, the maximum number of feature points extracted was 75.

The calculation time and the number of feature points of different algorithms before and after noise removal were compared (Figure 7). The calculation time of SIFT algorithm before noise removal was 0.49 s, and the calculation time of Forstner, SUNSAN, and Harris was 1.71 s, 3.04 s, and 2.25 s,

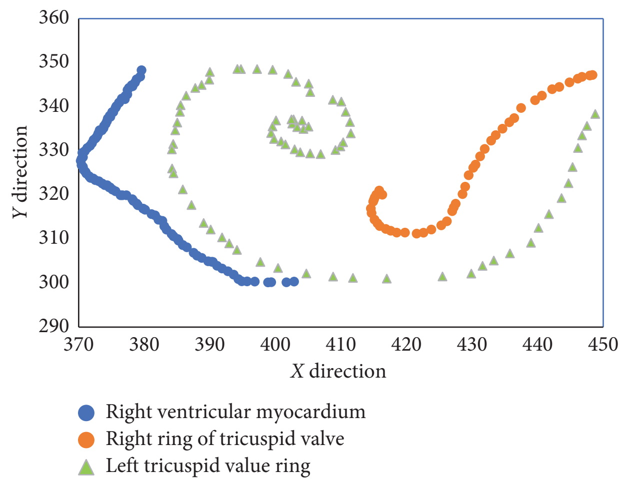

FIGURE 5: Motion trajectories of special points in optical flow method.

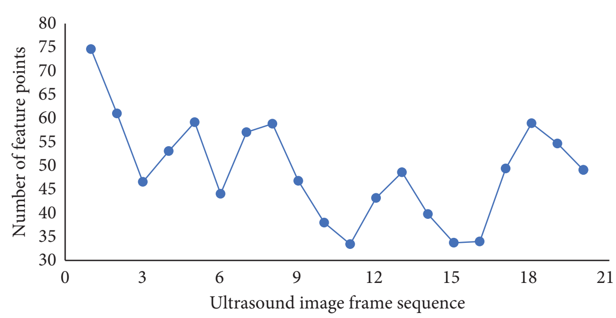

FIGURE 6: Statistics of the number of special points extracted by the SIFT algorithm.

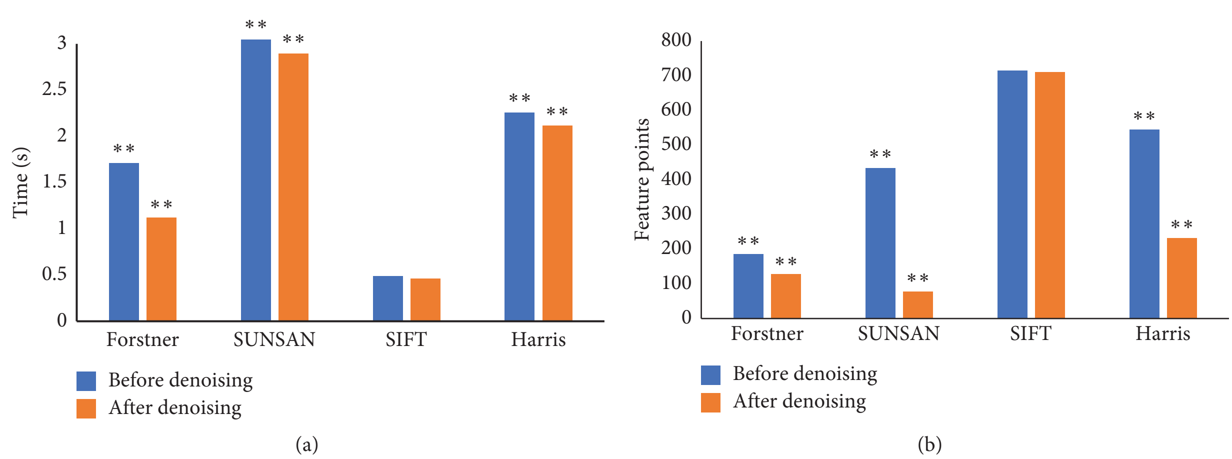

FIGURE 7: Comparison of calculation time and number of feature points before and after noise removal by different algorithms. (a) Comparison of calculation time before and after noise removal by different algorithms; (b) comparison of the number of feature points before and after noise removal by different algorithms. *indicates a remarkable difference compared with SIFT, $P < 0.01$.

respectively. The calculation time of SIFT algorithm after noise removal was 0.46 s, and the calculation time of Forstner, SUNSAN, and Harris was 1.12 s, 2.89 s, and 2.11 s, respectively. The calculation time of the SIFT algorithm before and after the noise was removed was obviously shorter than that of other algorithms. The calculation time of all algorithms after noise removal was significantly shorter than that before noise removal. The number of feature points extracted by the SIFT algorithm before noise removal was 703, and the number of feature points extracted by the Forstner, SUNSAN, and Harris algorithms was 182, 426, and 535, respectively. The number of feature points extracted by the SIFT algorithm after noise removal was 698, and the number of feature points extracted by the Forstner, SUNSAN, and Harris algorithms was 126, 76, and 228, respectively. The number of feature points extracted by SIFT algorithm before and after noise removal was more than that of other algorithms, and the number of feature points extracted by all algorithms after noise removal was significantly less than that before noise removal. It showed that, among the four feature point extraction algorithms, the SIFT algorithm extracted the largest number of speckles and took the least time. The number of feature points extracted by the SIFT algorithm and the calculation time were significantly better than those of other algorithms ($P < 0.01$).

The different algorithms before and after noise removal were compared on the first frame of the heart motion image to extract the feature point images (Figure 8). Different algorithms had large differences in the number of feature points extracted from the diastolic motion image of the short-axis motion of the left ventricle with a size of 172×172. The speckles extracted by the Forstner operator were more uniformly dispersed, but the number of extracted feature points was small. Although SUNSAN and Harris algorithms extracted more features than Forstner operators, their calculation time was longer. The number of feature extraction points of SIFT algorithm was obviously more than that of other algorithms. Forstner operator was the best method for feature points compared with the other three methods.

3.4. Analysis of Feature Point Matching Results Based on Improved Lucas–Kanade Algorithm. To test the accuracy of the SIFT algorithm, the ultrasound images of the first and second frames of the same heart were matched, and the results were shown in Figure 9. By observing the distribution of red spots in the image, it can be concluded that sift algorithm has good stability and accuracy.

To further objectively analyze the accuracy of the feature point matching of the SIFT algorithm, the order matching method and the reverse order matching method were used to extract the matching point logarithms under different frame sequences (Figure 10(a)). The logarithm of the matching points extracted by the sequential matching method and the reverse matching method was not much different. The mean logarithm of the matching points of the sequential matching method and the reverse matching method was 20.54 and 20.46, respectively, which indicated that, for the same two sets of images, the matching algorithm can be used as a template for each other, which had little effect. The matching results of different ultrasonic image feature extraction points were compared (Figure 10(b)). When the image frame order was 5–11, the feature extraction point matching effect was ideal.

3.5. Analysis of Feature Point Tracking Results Based on Improved Lucas–Kanade Algorithm. Based on the characteristics of two-dimensional speckle tracking in ultrasonic image, the tolerance method was selected to track the image sequence. The selected feature points were modified within 1~20 pixels, and a point (130,165) on the myocardial interval between the left and right ventricles was selected for tracking under different tolerance conditions. The tracking results of the first 30 frames of the ultrasonic image sequence were shown in Table 1 and Figure 11. Feature points were extracted in both the 6th and 7th frames. The reason may be that the sequences of matching points between two adjacent frames are not identical, leading to the occurrence of missing matching [19].

3.6. Comparison of Tracking Results of Feature Points by Different Algorithms. The shrinkage of feature points per frame of SIFT speckle tracking method and optical flow method was compared (Figure 12). The highest point and curvature of SIFT speckle tracking method were close to the original curve, while the highest point and curvature of optical flow method were different from the original curve. The differences between the two methods were analyzed. The possible reason was that the intraregion matching of SIFT speckle tracking method improved the accuracy of matching, while optical flow tracking in the neighborhood of key points was less affected by noise and had good stability, but its accuracy was low [20].

The calculation time and number of tracking speckles of SIFT speckle tracking method and optical flow method were compared (Figure 13). The calculation time and number of tracking speckles of SIFT speckle tracking method were 1198.85 s and 81, respectively, and the calculation time and number of tracking speckles of optical flow method were 3274.19 s and 80, respectively. The calculation time of SIFT speckle tracking method was significantly lower than that of optical flow method, and the difference between them was great ($P < 0.05$). There was no remarkable difference in the number of tracking speckles between SIFT and optical flow method ($P > 0.05$).

The above results show that Lucas–Kanade algorithm improved by pyramid idea, SIFT algorithm, and denoising algorithm is superior to other algorithms in terms of calculation time, number of feature points identified, and number of tracking spots. Yang et al. [21] used the improved ROAM algorithm based on pyramid idea to preprocess large amount of terrain and texture data in layers and blocks and obtained the conclusion combined with the algorithm, the 3D terrain of Huairou Reservoir in Beijing was rendered, and the real-time network roaming was carried out. Liu et al. [22] also studied the defect image registration based on SIFT algorithm and found that the algorithm can effectively register the defect image and lay a good foundation for the subsequent defect information extraction. The above research results show that the application effect of pyramid idea and sift algorithm is basically consistent with this research. However, Lv et al. [23] used the pyramid Lucas–Kanade combined with U-net technology to study its matching performance on renal free breathing multi-b-value diffusion MRI and obtained the segmentation based on U-net and pyramid Lucas–Kanade registration method, so as to improve the alignment of multi-b-value diffusion weighted MRI and reduce the interference in free breathing.

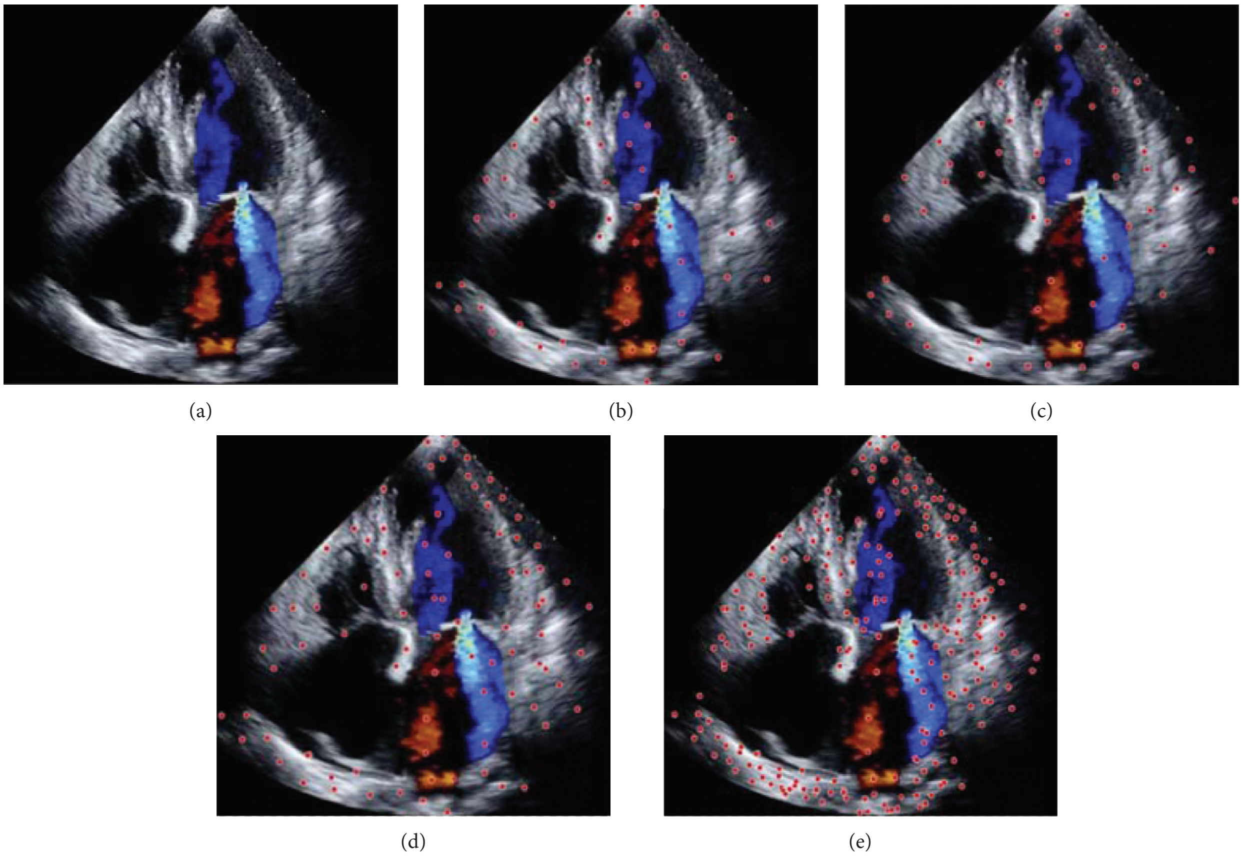

Figure 8: Analysis of feature point extraction results of different algorithms. (a) Original image; (b) feature point extraction effect of Forstner algorithm; (c) feature point extraction effect of SUNSAN algorithm; (d) feature point extraction effect of Harris algorithm; (e) feature point extraction effect of SIFT algorithm.

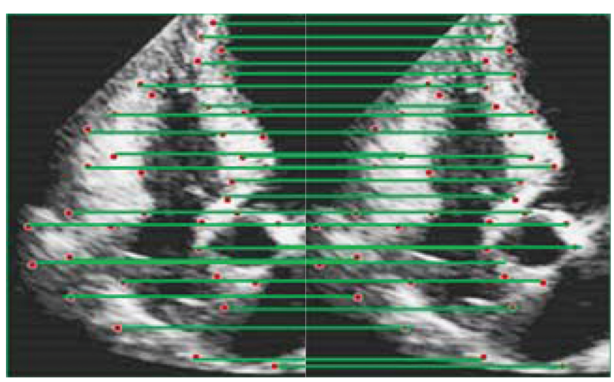

Figure 9: Matching results of cardiac ultrasound images in frames 1-2.

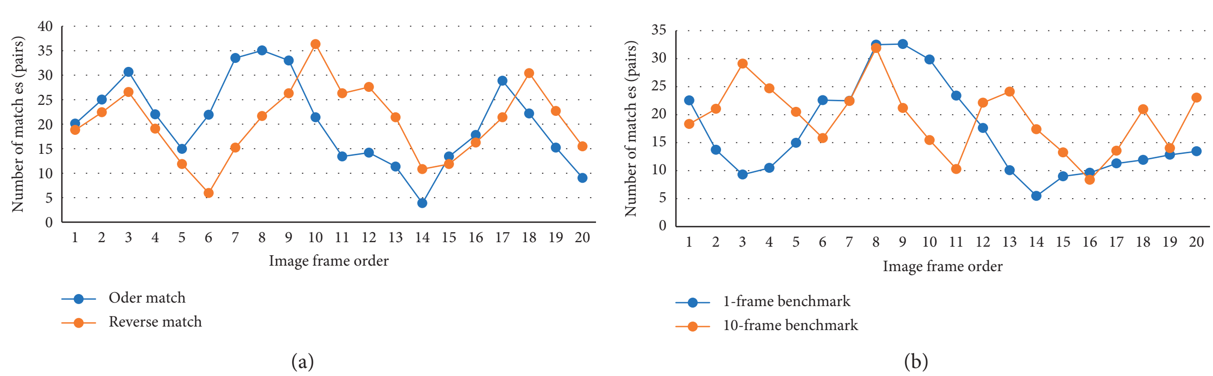

Figure 10: Feature point matching results based on the improved Lucas–Kanade algorithm. (a) Comparison of the results of sequential matching and reverse matching; (b) comparison of matching results of different templates.

Table 1: Image tracking table for frames 1 to 30.

Point	Abscissa	Ordinate	Point	Abscissa	Ordinate	Point	Abscissa	Ordinate
1	129.17	158.17	11	129.17	108.19	21	124.11	39.17
2	130	141.92	12	131.52	98.49	22	112.98	33.25
3	128	115.54	13	122.68	99.12	23	121.00	33.16
4	110.92	112.68	14	118.45	80.16	24	115.19	39.45
5	121.41	111.54	15	125.14	88.12	25	112.58	38.12
6	0	0	16	112.52	78.16	26	114.16	110.17
7	0	0	17	133.41	75.54	27	124.51	39.54
8	117.41	104.19	18	128.26	67.77	28	112.51	38.77
9	129.16	112.44	19	124.71	41.25	29	114.79	35.75
10	119.28	110.62	20	122.64	51.22	30	120.18	38.16

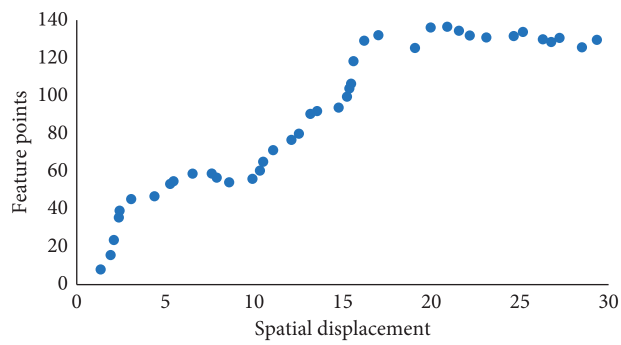

Figure 11: Spatial displacement of feature point matching based on the improved Lucas–Kanade algorithm.

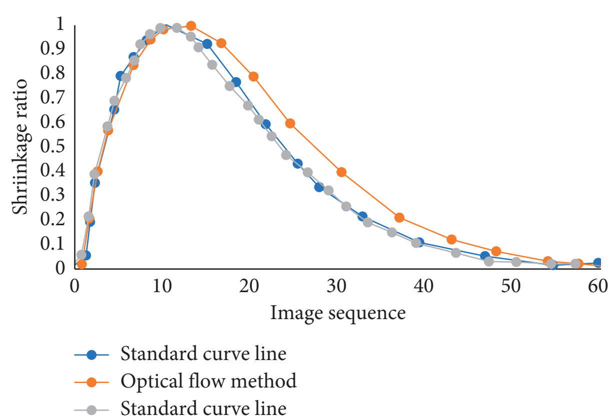

Figure 12: Comparison of shrinkage per frame under different algorithms.

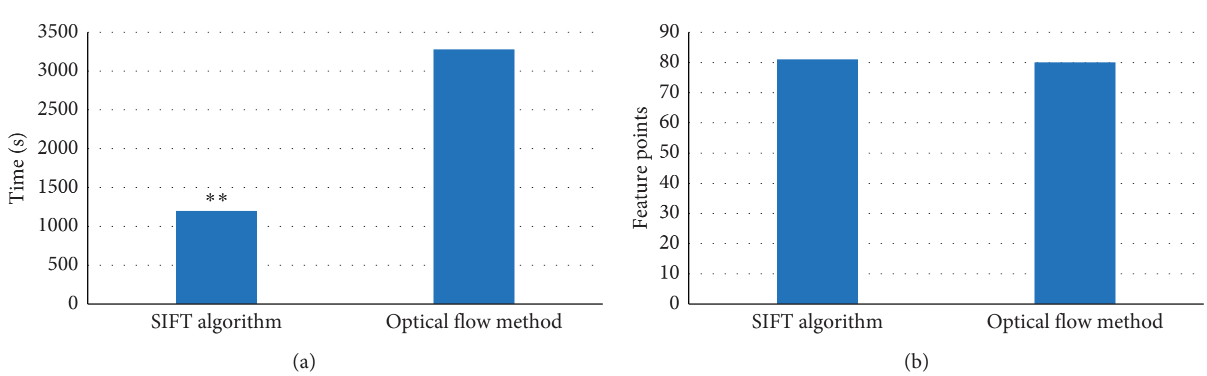

Figure 13: Comparison of the number of tracking speckles and calculation time of different algorithms. (a) Comparison of calculation time of different algorithms; (b) comparison of the number of tracking speckles of different algorithms. * indicates remarkable difference versus SIFT, $P < 0.05$.

4. Conclusion

The application value of the improved Lucas–Kanade algorithm based on SIFT in the extraction of feature points and motion tracking of heart color ultrasound was discussed. Pyramid idea, SIFT algorithm, and noise reduction algorithm were introduced to improve the Lucas–Kanade algorithm. The results showed that the improved Lucas–Kanade algorithm was better than other algorithms in the computation time, the number of recognized feature points, and the number of tracking speckles. However, there are still some shortcomings in this study. There are mismatching problems in multiple similar regions in the process of speckle tracking. In the future work, the coherence of the feature points of the image sequence will be enhanced according to the image features of the heart color ultrasound, so as to reduce the mismatching phenomenon and further improve the accuracy of the matching of the feature points. In conclusion, the improved Lucas–Kanade algorithm based on SIFT proposed significantly improves the accuracy of feature point extraction and motion tracking of cardiac color ultrasound. It shows that the algorithm has a good prospect in the clinical application of cardiac color Doppler ultrasound.

Data Availability

The data used to support the findings of this study are available from the corresponding author upon request.

Conflicts of Interest

The authors declare no conflicts of interest.

Authors' Contributions

Xiaoli Zhang and Punan Li equally contributed to this work.

References

[1] J. J. Bax and V. Delgado, "Advanced imaging in valvular heart disease," *Nature Reviews Cardiology*, vol. 14, no. 4, pp. 209–223, 2017.

[2] A. Mondal, J. Lackey, M. Saeed et al., "An imaging protocol to discriminate specialized conduction tissue during congenital heart surgery," *Seminars in Thoracic and Cardiovascular Surgery*, vol. 31, no. 3, pp. 537–546, 2019.

[3] M. A. Chamsi-Pasha, P. P. Sengupta, W. A. Zoghbi, C. State, and F. Perspectives, "Handheld echocardiography," *Circulation*, vol. 136, no. 22, pp. 2178–2188, 2017.

[4] C. C. Schwarzwald, "Equine echocardiography," *Veterinary Clinics of North America: Equine Practice*, vol. 35, no. 1, pp. 43–64, 2019.

[5] J. Shiber, E. Fontane, and M. Newberry, "Transesophageal echocardiography use during cardiopulmonary resuscitation," *Annals of Emergency Medicine*, vol. 74, no. 6, p. 823, 2019.

[6] K. Karamanidis, A. Travlou, P. Krauss, and U. Jaekel, "Use of a Lucas-Kanade-based template tracking algorithm to examine in vivo tendon excursion during voluntary contraction using ultrasonography," *Ultrasound in Medicine and Biology*, vol. 42, no. 7, pp. 1689–1700, 2016.

[7] J. Guo, C. a. Zhu, S. Lu, D. Zhang, and C. Zhang, "Vision-based measurement for rotational speed by improving Lucas-Kanade template tracking algorithm," *Applied Optics*, vol. 55, no. 25, pp. 7186–7194, 2016.

[8] E. Antonakos, J. Alabort-i-Medina, G. Tzimiropoulos, and S. P. Zafeiriou, "Feature-based Lucas-Kanade and AAM," *IEEE Transactions on Image Processing*, vol. 24, no. 9, pp. 2617–2632, 2015.

[9] H.-Q. Yang, X. Chen, L. Zhang, J. Zhang, X. Wei, and C. Tang, "Conditions of hydraulic heterogeneity under which Bayesian estimation is more reliable," *Water*, vol. 12, no. 1, p. 160, 2020.

[10] C. Guo, J. Lu, Z. Tian, W. Guo, and A. Darvishan, "Optimization of critical parameters of PEM fuel cell using TLBO-DE based on Elman neural network," *Energy Conversion and Management*, vol. 183, pp. 49–158, 2019.

[11] Y. Niu, Z. Xu, and X. Che, "Dynamically removing false features in pyramidal Lucas-Kanade registration," *IEEE Transactions on Image Processing*, vol. 23, no. 8, pp. 3535–3544, 2014.

[12] Y. Chen, S. Hu, H. Mao, W. Deng, and X. Gao, "Application of the best evacuation model of deep learning in the design of public structures," *Image and Vision Computing*, vol. 102, Article ID 103975, 2020.

[13] Y. Xu, C. Xu, X. Kuang et al., "3D-SIFT-Flow for atlas-based CT liver image segmentation," *Medical Physics*, vol. 43, no. 5, pp. 2229–2241, 2016.

[14] R. Vaser, S. Adusumalli, S. N. Leng, M. Sikic, and P. C. Ng, "SIFT missense predictions for genomes," *Nature Protocols*, vol. 11, no. 1, pp. 1–9, 2016.

[15] I. N. Daliakopoulos and I. K. Tsanis, "A SIFT-based DEM extraction approach using GEOEYE-1 satellite stereo pairs," *Sensors*, vol. 19, no. 5, p. 1123, 2019.

[16] X. Gao, J. Cai, Y. Long, and Z. A. Song, "Study on traffic organization for primary roads with super small spacing," *Advances in Transportation Studies*, vol. 10, no. 2, pp. 3–12, 2017.

[17] K. Říha, M. Zukal, and F. Hlawatsch, "Analysis of carotid artery transverse sections in long ultrasound video sequences," *Ultrasound in Medicine & Biology*, vol. 44, no. 1, pp. 153–167, 2018.

[18] S. Chai, P. Tan, and K. Tong, "A review of the safety and clinical utility of contrast echocardiography," *Singapore Medical Journal*, vol. 61, no. 4, pp. 181–183, 2020.

[19] H. Miura, S. Ozawa, T. Matsuura, K. Yamada, and Y. Nagata, "Proposed patient motion monitoring system using feature point tracking with a web camera," *Australasian Physical & Engineering Sciences in Medicine*, vol. 40, no. 4, pp. 939–942, 2017.

[20] Z. M. Qian and Y. Q. Chen, "Feature point based 3D tracking of multiple fish from multi-view images," *PLoS One*, vol. 12, Article ID e0180254, 2017.

[21] H. Yang, E. Willert, and S. Ramani, "ROAM algorithm based on Pyramid," *Journal of General Internal Medicine*, vol. 34, no. 8, pp. 1631–1636, 2019.

[22] P. Liu, S. Henikoff, and P. C. Ng, "Defect image registration based on SIFT algorithm," *Nature Protocols*, vol. 4, no. 7, pp. 1073–1081, 2009.

[23] J. Lv, W. Huang, J. Zhang, and X. Wang, "Performance of U-net based pyramidal Lucas-Kanade registration on free-breathing multi-b-value diffusion MRI of the kidney," *British Journal of Radiology*, vol. 91, no. 1086, Article ID 20170813, 2018.

Hindawi
Journal of Healthcare Engineering
Volume 2021, Article ID 8563181, 11 pages
https://doi.org/10.1155/2021/8563181

Research Article

Computerized Tomography Image Feature under Convolutional Neural Network Algorithm Evaluated for Therapeutic Effect of Clarithromycin Combined with Salmeterol/Fluticasone on Chronic Obstructive Pulmonary Disease

Guoping Luo, Anqi Lin, Zhaoqiang Yang, Yujian Chen, and Cuiying Mo [2]

[1] *Department of Respiration, Shunde Hospital of Guangzhou University of Traditional Chinese Medicine, Shunde District, Foshan City 528300, Guangdong Province, China*
[2] *Psychosomatic Medicine, Wuzhongpei Memorial Hospital, Shunde District, Foshan City 528300, Guangdong Province, China*

Correspondence should be addressed to Cuiying Mo; 201823252501009@zcmu.edu.cn

Received 13 June 2021; Revised 13 July 2021; Accepted 22 July 2021; Published 2 August 2021

Academic Editor: Enas Abdulhay

This study was to explore the use of convolutional neural network (CNN) for the classification and recognition of computerized tomography (CT) images of chronic obstructive pulmonary disease (COPD) and the therapeutic effect of clarithromycin combined with salmeterol/fluticasone. First, the clinical data of COPD patients treated in hospital from September 2018 to December 2020 were collected, and CT and X-ray images were also collected. CT-CNN and X ray-CNN single modal models were constructed based on the LeNet-5 model. The randomized fusion algorithm was introduced to construct a fused CNN model for the diagnosis of COPD patients, and the recognition effect of the model was verified. Subsequently, the three-dimensional reconstruction of the patient's bronchus was performed using the classified CT images, and the changes of CT quantitative parameters in COPD patients were compared and analyzed. Finally, COPD patients were treated with salmeterol/fluticasone (COPD-C) and combined with clarithromycin (COPD-T). In addition, the differences between patients' lung function indexes, blood gas indexes, St. George respiratory questionnaire (SGRQ) scores, and the number of acute exacerbations (AECOPD) before and after treatment were evaluated. The results showed that the randomized fusion model under different iteration times and batch sizes always had the highest recognition rate, sensitivity, and specificity compared to the two single modal CNN models, but it also had longer training time. After CT images were used to quantitatively evaluate the changes of the patient's bronchus, it was found that the area of the upper and lower lung lobes of the affected side of COPD patients and the ratio of the area of the tube wall to the bronchus were significantly changed. The lung function, blood gas index, and SGRQ score of COPD-T patients were significantly improved compared with the COPD-C group ($P < 0.05$), but there was no considerable difference in AECOPD ($P > 0.05$). In summary, the randomized fusion-based CNN model can improve the recognition rate of COPD, and salmeterol/fluticasone combined with clarithromycin therapy can significantly improve the clinical treatment effect of COPD patients.

1. Introduction

Chronic obstructive pulmonary disease (COPD) is a disease with a high prevalence and fatality rate in the world. The quality of life of patients with advanced COPD will be significantly reduced, and long-term oxygen therapy and drug treatment are required, which brings a huge burden to the patient's family [1]. The main pathological changes of COPD are lung parenchymal damage and airway damage, among which the main manifestation of lung parenchymal damage is emphysema, and airway damage is classified into central trachea or small trachea injury [2]. The main clinical methods used to detect COPD small airway damage are computerized tomography (CT) and pulmonary function test (PFT) examinations. PFT examination focuses on spirometry, single breathing method, repeated breathing method, and pulse oscillation method, which is the gold standard for clinical diagnosis and grading of COPD [3, 4].

With the improvement of the computing level, deep learning has harvested excellent results in many fields such as speech recognition, and medical image classification based on deep learning has gradually replaced manual operation [5, 6]. The deep learning method mostly used in the field of medical imaging is convolutional neural network (CNN). The model contains special structures such as convolutional layer and pooling layer, which significantly improve the classification and recognition accuracy of the model [7].

At present, anti-inflammatory therapy is of great significance in the treatment of COPD disease. The drugs used in anti-inflammatory treatment are mainly glucocorticoids. Most studies recommend the use of salmeterol/fluticasone inhalation [8]. However, the drug used in the treatment of COPD can increase the risk of pneumonia, and it is difficult for most patients to accept it. In recent years, studies found that macrolide antibiotics have certain antibacterial effects, as well as anti-inflammatory and immunomodulatory effects, which have good results in the treatment of chronic inflammatory reactive lung diseases [9]. Studies have shown that oral clarithromycin combined with inhaled salmeterol in the treatment of chronic pulmonary obstruction has a good effect and high safety.

A model for image classification and recognition of COPD patients was proposed based on the CNN model, and the morphological changes of the small trachea of COPD patients were quantitatively analyzed based on the CT images after classification. Moreover, the therapeutic effects of inhaled corticosteroids on COPD patients were compared and analyzed, aiming to provide a reference for improving the clinical diagnosis rate of COPD and improving the treatment effect of patients.

2. Materials and Methods

2.1. Research Subjects. The clinical data of 58 patients with COPD who were treated in hospital from September 2018 to December 2020 were collected. COPD patients met the diagnostic criteria of the *Guidelines for the Diagnosis of Chronic Obstructive Pulmonary Disease Pulmonary Diseases* (2013 revision). Among them, 35 were males and 23 were females, aged 44 to 63 years old. The 50 healthy people who had undergone physical examinations in the hospital served as controls. Among them, 32 were males and 18 were females, aged 42–61 years old. Exclusion criteria: (i) those with bronchiectasis, pulmonary bullae, pulmonary fibrosis, and pulmonary space-occupying diseases that affect lung function; (ii) those with organic heart disease; (iii) those underwent chest surgery in history; and (iv) those who suffered from other diseases that restrict respiratory movement. The experimental procedure of this study had been approved by the Medical Ethics Committee of the Hospital, and all subjects had signed written informed consent.

2.2. Lung Function and Blood Gas Index Measurement. All subjects were required to complete pulmonary function measurements within seven days before and after the CT scan. Measurement function parameters included forced expiration in the first second (FEV1), forced expiratory volume percentage (FEV%), and forced expiratory volume in the first second/forced vital capacity (FEV1/FVC%). In addition, the PaO_2 and $PaCO_2$ blood gas indexes in the arterial blood of the patient were measured. All patients needed to undergo pulmonary function tests and be able to meet the criteria for diagnosing COPD.

2.3. CT Scan Process. The patient's chest image was scanned using 64-slice MSCT, and the patient underwent breathing training before the scan. During the examination, the patient was placed in the supine position for CT scan, and the whole lung was examined when the patient took a deep breath and reached the optimal inflatable state after holding his breath. Scanning parameters were set as follows: 0.875 pitch, 38×38 cm field of view, 512×512 matrix, 1500 window width, −650U window level, 0.5 cm layer thickness, and 0.5 cm layer spacing. CT image reconstruction was performed using the standard CT reconstruction algorithm, and the layer thickness was set as 0.625 mm and the layer spacing was set as 0.625 mm. The reconstructed CT images were uploaded to the workstation, and Thoracic VCAR Airway Analysis software was used to measure the airway. The lumen diameter, area ratio of trachea to bronchial wall, wall thickness, and diameter ratio of the air duct (trachea, main bronchus, apical segment of upper lobe/posterior segment/anterior segment, etc.) were measured.

2.4. COPD Image Classification and Recognition Based on CNN. Firstly, a single mode CNN model was constructed to extract the feature vectors of the CNN full connection layer, and a randomized function was constructed. The data of the full connection layer of different modes were randomly fused, and the fused feature recognition was used for the classification of COPD images, so as to improve the image classification effect.

2.4.1. Multimodal Feature Fusion Based on Stochastic Fusion. The methods of multimodal feature fusion recognition designed in this study were (i) the processing of CT images and chest X-ray images; (ii) multimodal lung image features extracted using LeNet-5 network; (iii) stochastic function used for the fusion of parallel multimodal features and the reconstruction of target features in the same dimension; and (iv) the full connection layer and the classification layer added to carry out the regression training of the network, so as to get the results after classification.

The basic structure of the LeNet-5 network model [10] is shown in Figure 1, and the algorithm flow of using randomized fusion algorithm combined with multimodal CNN lung image recognition is shown in Figure 2.

The LeNet-5 model was employed to extract the features of the image, and then the model's own parameter transfer learning ability was adopted to adjust the parameters of the model. The size of the training data needed to be randomly selected when the model was trained, and the data were

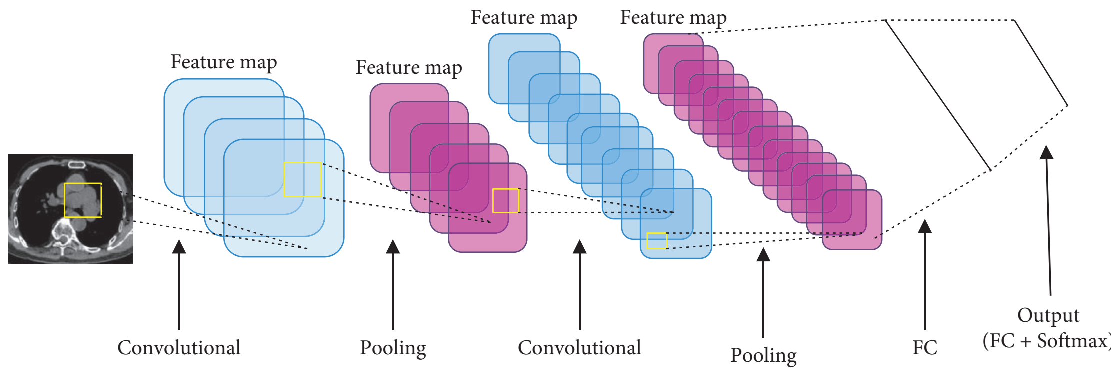

FIGURE 1: The basic structure of the LeNet-5 model. FC is the fully connected layer; Softmax is the activation function.

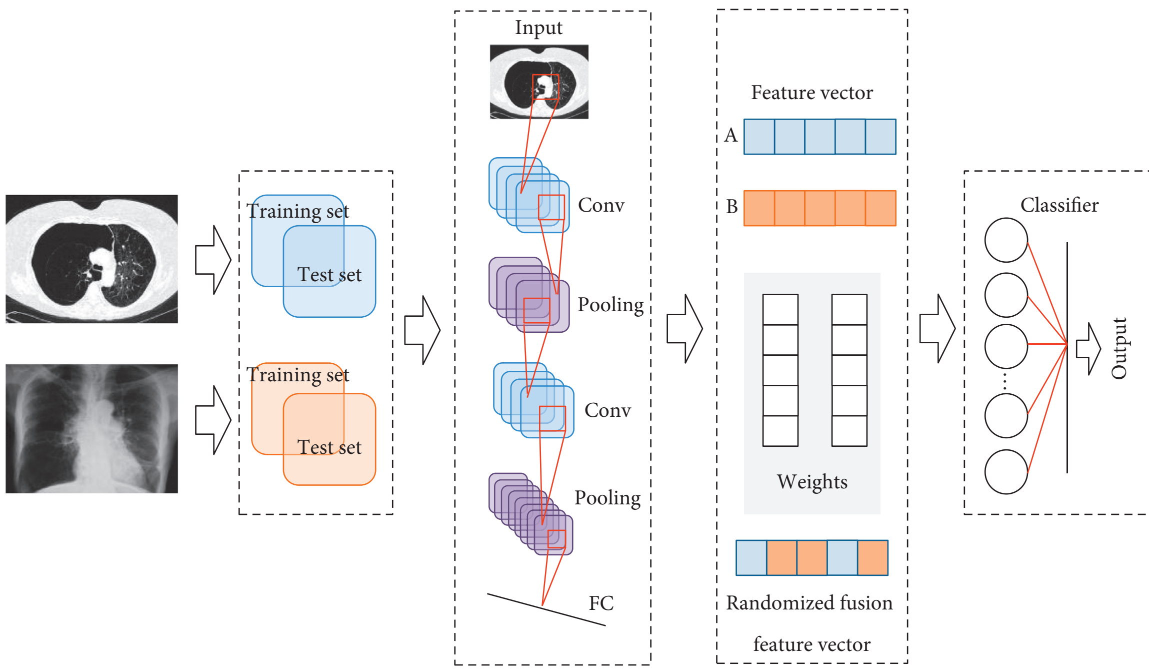

FIGURE 2: Multimodal CNN lung image recognition process based on randomized fusion algorithm.

sequentially input into the model for training according to the set batches. At the same time, the weight value and bias of the model needed to be adjusted. It is required to input all the data in the test set into the network when the model was tested. The network parameters were set to the optimal number of adoption during training, and the classifier was used to recognize COPD. The network structure constructed in this study is shown in Figure 3.

From Figure 3, there were two CNN network models designed, namely, CT-CNN and X ray-CNN, and the specific parameter settings of the network are shown in Table 1. There were certain differences in the parameters between different network layers. The input data of the input layer needed to be randomly selected from the training set according to the size of the batch and form a vector with a certain dimension. The convolutional layer needed to initialize the convolution kernel size, weight value, and bias. Then, the convolution kernel and the input data were convolved to enhance the feature matrix in the image and remove noise. The activation function used was the Sigmoid function [11], and the pooling operation was an average pooling operation. Rand random function [12] was used to randomize the feature vector, weight, and bias in the last layer of the fully connected layer.

2.5. Treatment Methods. 58 COPD patients were randomly divided into two groups—the control group (COPD-C) and the treatment group (COPD-T)—with 28 and 30 patients, respectively. Patients in the COPD-C group inhaled 50/250 μg of salmeterol/fluticasone twice a day. Patients in the COPD-T group were given oral clarithromycin sustained-release tablets for combination therapy based on the inhalation of salmeterol/fluticasone. In addition, 0.5 g clarithromycin sustained-release tablets should be taken orally once a day, and 50/250 μg salmeterol/fluticasone should be inhaled twice a day. All patients took 10 days as a course of treatment and cannot take β-agonist and hormone

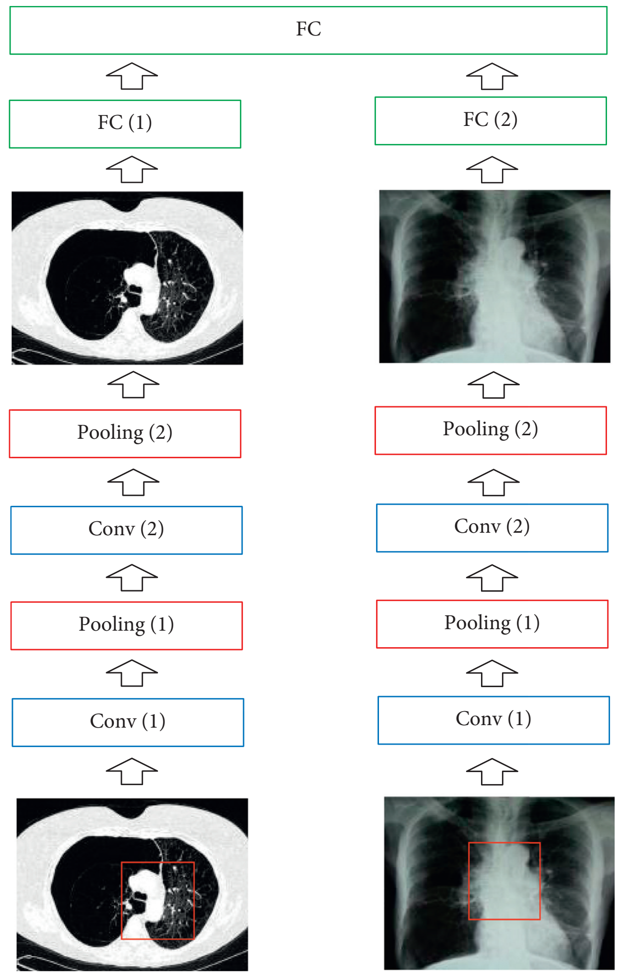

Figure 3: The basic structure of the CNN model.

Table 1: Structure and parameter setting of the CNN model.

Framework	Input	Convolution		Pooling		Structure				
		Convolution kernel	Step size	Size	Step size	Convolutional layer	Sigmoid	Average pooling	Fc	Rand
Input layer	28 × 28	—	—	—	—	—	—	—	—	—
Conv (1)	24 × 24 × 6	3 × 3	1	2 × 2	2	+	+	+	—	—
Conv (2)	8 × 8 × 12	3 × 3	1	2 × 2	2	+	+	+	—	—
Fc (1)	4 × 4 × 12	1 × 1	—	—	—	—	+	—	+	—
Fc (2)	192 × 3	1 × 1	—	—	—	—	+	—	+	+

Note. + means yes; —means no.

inhalation therapy within 15 days before receiving the treatment. After treatment, a 3-month follow-up was conducted to record the patient's drug use, changes in the condition, the number of acute exacerbations, and adverse reactions.

2.6. Evaluation Indexes. The number of acute exacerbations of COPD (AECOPD) in the patient was recorded. St. George Respiratory Questionnaire (SGRQ) score sheet was used to evaluate the patient. The lower the score is, the better the patient's function is, and it was meaningful to reduce the total score of SGRQ by more than 4 points in clinical practice. After treatment, the lung function indexes were evaluated, as shown in Section 2.2. Moreover, the probability of adverse reactions in patients after treatment was recorded.

The recognition rate, sensitivity, and specificity were calculated to evaluate the construction model. The calculation equations for different indexes were as follows:

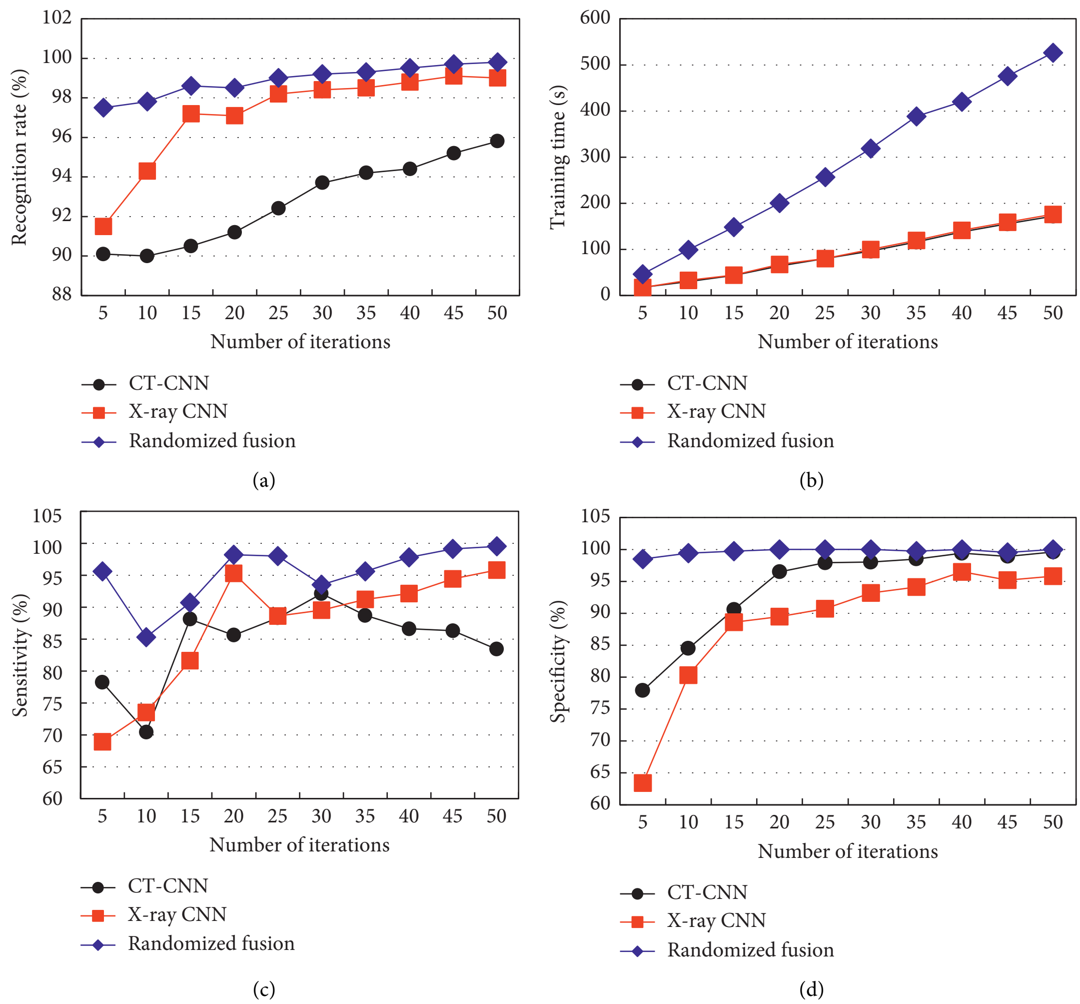

FIGURE 4: Changes in the recognition efficiency of single-modal CNN and randomized fusion models under different iteration times. (a) The recognition rate. (b) The training time. (c) The recognition sensitivity. (d) The recognition specificity.

$$\text{recognition} = \frac{TP + TN}{TP + TN + FP + FN},$$
$$\text{sensitivity} = \frac{TP}{TP + FN}, \tag{1}$$
$$\text{specificity} = \frac{TN}{TN + FP}.$$

TP is true positive, FP is false positive, TN is true negative, and FN is false negative.

2.7. Statistical Methods. Subsequently, SPSS 19.0 was used for statistical analysis. Measurement data were expressed as mean ± standard deviation, and independent sample *t*-test was used for difference comparison. Count data were expressed by frequency (percentage), and the difference was compared using chi-square test or Fisher's test. $P < 0.05$ means that the difference was statistically significant.

3. Results

3.1. Model Training for CT Image Classification. The parameter transfer method was adopted to train the constructed CNN model. Comparison and analysis of the differences among model recognition rate, training time, sensitivity, and specificity under different iteration times are shown in Figure 4. From Figure 4(a), as the number of iterations increased, the recognition rates of CT-CNN, X ray-CNN, and randomized fusion showed a gradual increase trend. However, the recognition rate of the randomized fusion model was always higher than that of other models. The recognition rates of CT-CNN, X ray-CNN, and randomized fusion under the maximum number of iterations were 95.8%, 99.0%, and 99.8%, respectively. From Figure 4(b), as the number of iterations increased, the training times of different models showed a gradual increase trend. Among them, the training time of the randomized fusion model was always the longest, and there was no significant difference between the training time of the CT-CNN and X ray-CNN models. From Figure 4(c), the recognition sensitivity of different models showed different changes as the number of iterations increased. The sensitivities of CT-CNN, X ray-CNN, and randomized fusion at the maximum number of iterations were 83.4%, 95.8%, and 99.5%, respectively. From Figure 4(d), as the number of iterations increased, the recognition specificity of different models gradually increased. CT-CNN, X ray-CNN, and the recognition specificity of the randomized fusion model was 99.6%, 95.8%, and 100.0%, respectively.

The differences of model recognition rate, training time, sensitivity, and specificity under different batch sizes are shown in Figure 5. From Figures 5(a) and 5(b), as the training batch increased, the recognition rate and training time of CT-CNN, X ray-CNN, and randomized fusion models showed a gradual decline. When the maximum training batch was reached, the recognition rates were 97.4%, 96.0%, and 98.6%, and the training time was 67.2 s, 63.4%, and 193.6 s, respectively. Among them, the randomized fusion model had the highest recognition rate and the longest training time. From Figure 5(c), with the increase of training batches, the recognition sensitivity of different models first increased and then decreased. When the training batch reached 100, the sensitivity was the lowest, but the randomized fusion model had the highest sensitivity compared with the CT-CNN and X ray-CNN models. From Figure 5(d), the recognition specificity of each model changed with the training batch, and the recognition specificity of the randomized fusion model was always the highest.

3.2. Quantitative Analysis of CT Bronchus in Patients with COPD. The differences between the baseline data of the healthy control group and COPD patients are shown in Table 2. There was no significant difference in average age, sex ratio, and BMI indexes between the control group and COPD group ($P > 0.05$

The difference between the LA and WA% of the bronchi of the upper and lower lobe of the affected lung in the control group and the COPD group was evaluated (Figure 6). CT images classified by CNN were used to reconstruct the patient's bronchi in three dimensions. From Figure 6(a), the lung bronchus of the COPD group showed obvious obstruction. From Figures 6(b) and 6(c), the upper lobe of the affected side of the COPD group had significantly increased LA in the upper lobe of the lung and significantly reduced LA in the 5 and 6 levels compared with the control group ($P < 0.05$), and WA% in the 5 and 6 levels greatly increased ($P < 0.05$). From Figures 6(d) and 6(e), the LA of the lower lobe of the affected lung in the COPD group was significantly reduced in grade 6, 7, and 8, while the WA% was significantly increased compared with the control group ($P < 0.05$).

3.3. Analysis of the Treatment Effect of Patients with COPD

3.3.1. Changes in Lung Function and Blood Gas Indexes in Patients with COPD. The changes in lung function and blood gas indexes of patients before and after treatment are compared in Figure 7. There was no significant difference in the FEV1, FVC, FEV1/FVC, PaO_2, and $PaCO_2$ between patients in COPD-C group and COPD-T group before treatment ($P > 0.05$). After treatment, compared with patients in the COPD-C group, FEV1, FVC, FEV1/FVC, and PaO_2 in COPD-T patients increased significantly, and $PaCO_2$ decreased significantly ($P < 0.05$).

3.3.2. Comparison of Differences in Other Indexes of COPD Patients after Treatment. The difference of the SGRQ scores before and after treatment and the number of AECOPD during treatment between the two groups of patients is compared in Figure 8. From Figure 8(a), there was no considerable difference in SGRQ scores between the two groups before treatment ($P > 0.05$). Compared with the COPD-C group, the SGRQ score of the COPD-T group was significantly reduced after treatment ($P < 0.05$). From Figure 8(b), there was no great difference in the number of AECOPDs between the two groups of patients during treatment ($P > 0.05$).

4. Discussion

The CNN model is a feed forward neural network, and it is a multilayer perceptron model constructed to recognize two-dimensional and above images [13,14]. The current CNN model includes LeNet and AlexNet models, among which the LeNet-5 model is relatively mature, and the network structure is simpler [15,16]. To improve the clinical diagnosis rate of COPD, two single-modal CNN models were constructed using patient CT images and X-ray images. Then, the randomized fusion algorithm was adopted to fuse the CT-CNN and X ray-CNN models to obtain a randomized fusion model. The model recognition effect was evaluated, and the test results showed that the recognition rate, sensitivity, and specificity of the randomized fusion model increased greatly. It showed that the use of single-modal CNN model fusion for feature extraction of patient images can improve the effect of patient feature extraction and classification and recognition.

COPD is a common and frequent disease in respiratory system diseases. Clarithromycin combined with salmeterol and fluticasone has a significant effect in the treatment of chronic pulmonary obstruction. Patients with stable chronic obstructive pulmonary disease have a relatively stable condition. However, if patients with acute-onset chronic obstructive pulmonary disease cannot be further treated, their condition will become worse and cause respiratory failure, hypoxemia, and other serious complications [17,18]. The results of Renkema et al. [19] showed that the airway hyper-responsiveness of nonallergic patients with chronic obstructive malignant disease increased over time. In this research, the patient's affected lung lobe bronchus was scanned for quantitative evaluation. The results showed that COPD patients had significant changes in LA and WA% of grades 5~6 bronchus in the upper lobes of the lung and had LA and WA% of grades 6~8 in the lower lobes of the lung compared with healthy people. Studies revealed that, with

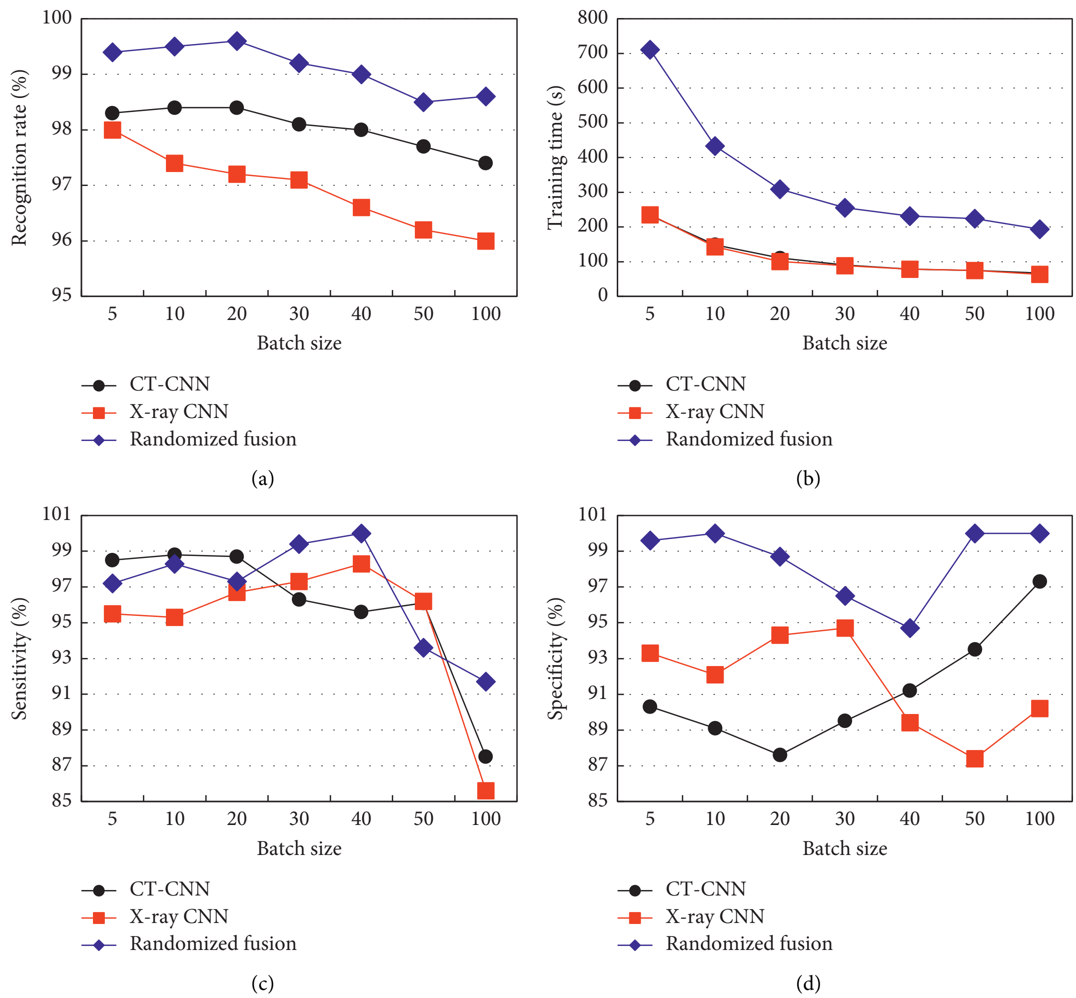

Figure 5: Changes in the recognition efficiency of single-modal CNN and randomized fusion models under different batches. (a) The recognition rate. (b) The training time. (c) The recognition sensitivity. (d) The recognition specificity.

Table 2: Comparison of baseline data of patients.

Item	Control group ($n = 50$)	COPD group ($n = 58$)	Statistics	P
Age (years old)	56.7 ± 5.7	58.3 ± 6.2	$t = 0.133$	0.883
Male (cases/%)	32/64.0	35/60.3	$\chi^2 = 1.204$	0.559
BMI (kg/m^2)	21.4 ± 1.6	21.6 ± 1.4	$t = -2.125$	0.936

BMI: body mass index.

the aggravation of COPD disease, LA gradually decreases, while WA% gradually increases.

Due to the relatively poor diffusion function of small airways, the inflammatory response of COPD is determined by the activation of respiratory epithelial cells and macrophages. Therefore, the bronchial tube wall is thickened, and the lumen is narrowed in patients with COPD. Combined with the results obtained in this study, it was suggested that LA and WA% can be used to quantitatively assess the morphological changes of the bronchus in patients with COPD and can also be used for the diagnosis of COPD.

Salmeterol is a long-acting $\beta 2$ receptor agonist, which is used for the relaxation of airway smooth muscle and can also inhibit the release of inflammatory mediators [20]. Fluticasone is an inhaled glucocorticoid, which acts on glucocorticoid receptors and increases the sensitivity of $\beta 2$ receptors, thereby delaying airway remodeling. The results of Jin [21] and other studies showed that patients with chronic obstructive disease had higher serum levels, and the impairment of lung function was related to symptoms such as serum levels and dyspnea. In addition to antibacterial properties, clarithromycin also has anti-inflammatory and immunomodulatory effects. Salmeterol/fluticasone and clarithromycin were combined for the treatment of COPD in this research. The results showed that salmeterol/fluticasone and combined clarithromycin treatment can significantly reduce the SGRQ score of COPD patients. It was proved that salmeterol/fluticasone combined with

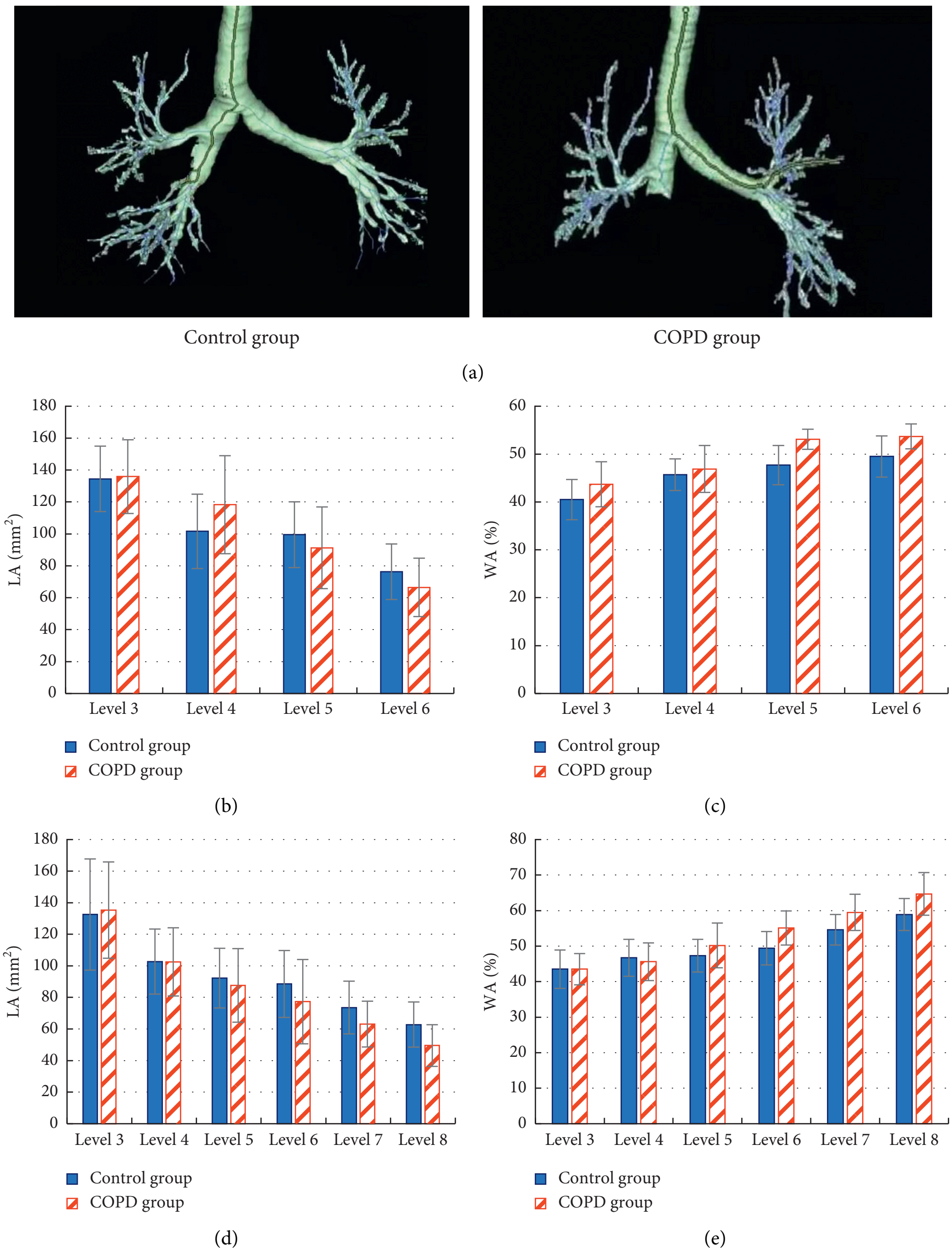

Figure 6: Comparison of quantitative parameters of bronchus between normal and COPD patients based on CT reconstruction. (a) The three-dimensional reconstruction of the bronchial CT image. (b) The LA detection of the upper lobe of the affected side of the lung. (c) The WA% detection of the upper lobe of the affected side of the lung. (d) The LA detection of the lower lobe of the affected side of the lung. (e) The WA% detection of the lower lobe of the affected side of the lung. $^*P < 0.05$.

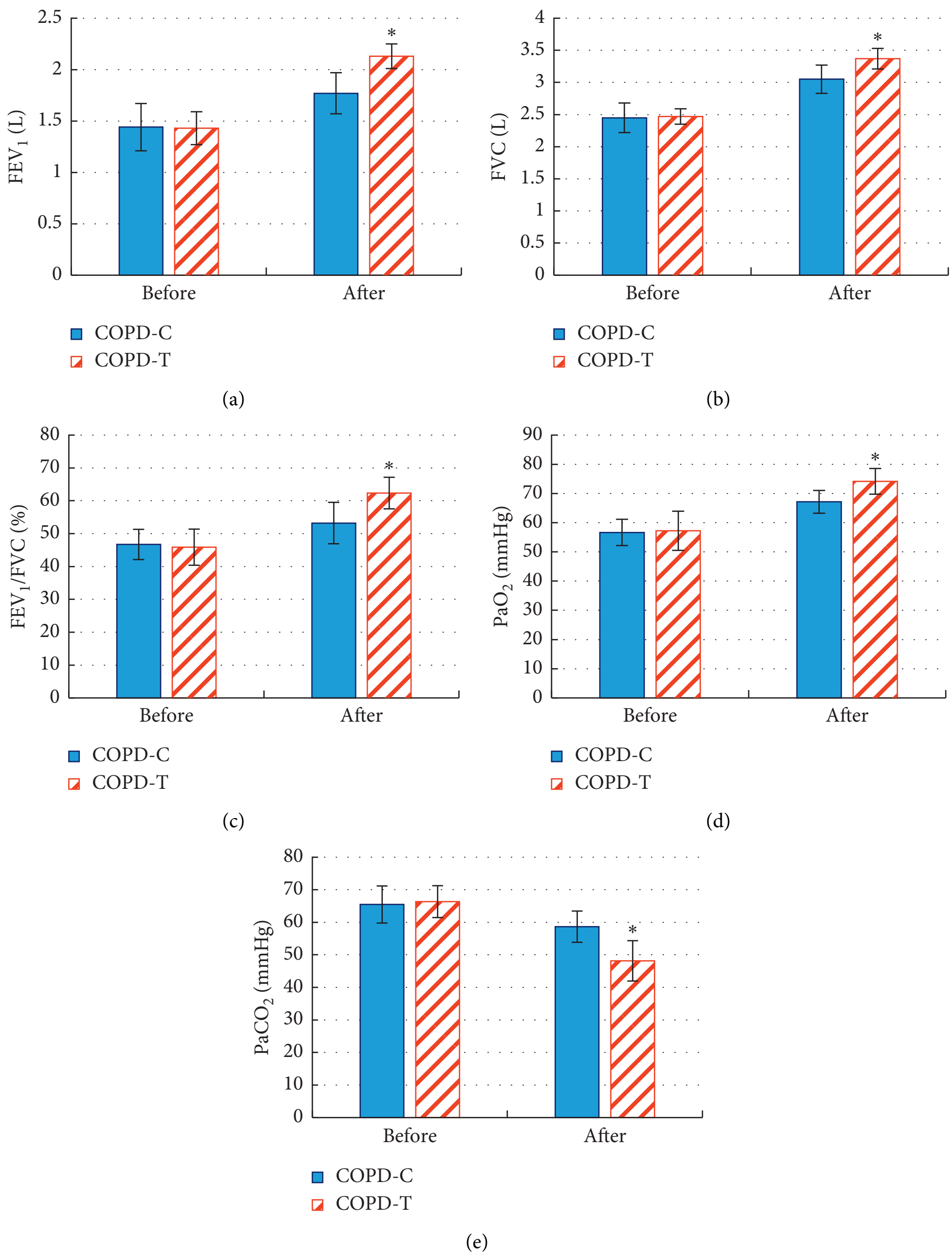

Figure 7: Comparison of lung function and blood gas indexes between two groups of COPD patients before and after treatment. (a) FEV1. (b) FVC. (c) FEV1/FVC. (d) PaO_2. (e) $PaCO_2$. $^*P < 0.05$.

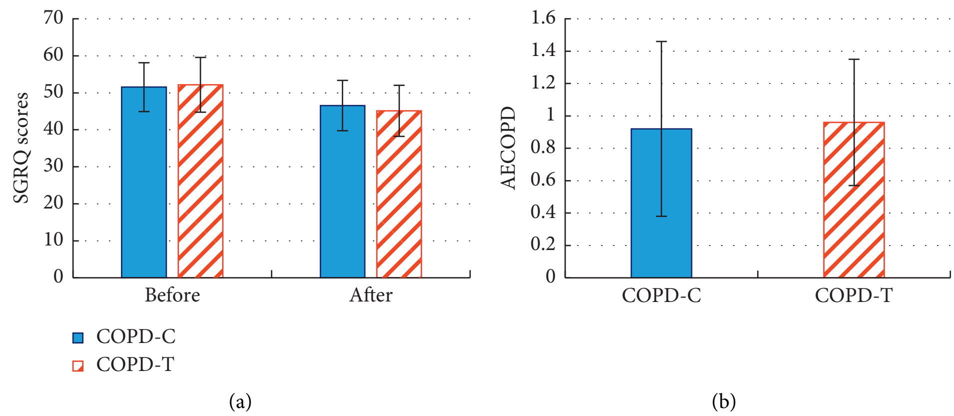

Figure 8: Comparison of SGRQ scores and AECOPD times between two groups of COPD patients before and after treatment. (a) The comparison of SGRQ scores before and after treatment. (b) The comparison of AECOPD times during treatment. $^{*}P < 0.05$.

clarithromycin treatment can significantly improve the lung function of COPD patients.

5. Conclusion

The randomization and fusion of the single-modal CNN model can improve the recognition effect of COPD, and CT quantitative indexes can be used for the diagnosis of COPD. Moreover, combined treatment of salmeterol/fluticasone and clarithromycin can significantly improve the lung function of COPD patients and enhance the clinical treatment effect. However, this study only analyzed the CT image and X-ray image of COPD patients based on the constructed CNN model. Follow-up work should combine it with clinical biology and other indexes to comprehensively compare the differences between the diagnosis rates of COPD. In short, this study can provide a reference for improving the clinical diagnosis and treatment of COPD.

Data Availability

The data used to support the findings of this study are included within the article.

Conflicts of Interest

The authors declare that they have no conflicts of interest.

References

[1] K. F. Rabe and H. Watz, "Chronic obstructive pulmonary disease," *The Lancet*, vol. 389, no. 10082, pp. 1931–1940, 2017.

[2] W. W. Labaki and S. R. Rosenberg, "Chronic obstructive pulmonary disease," *Annals of Internal Medicine*, vol. 173, no. 3, pp. ITC17–ITC32, 2020.

[3] H. J. Koo, S. M. Lee, J. B. Seo et al., "Prediction of pulmonary function in patients with chronic obstructive pulmonary disease: correlation with quantitative CT parameters," *Korean Journal of Radiology*, vol. 20, no. 4, pp. 683–692, 2019.

[4] D. A. Lynch, J. H. M. Austin, J. C. Hogg et al., "CT-definable subtypes of chronic obstructive pulmonary disease: a statement of the fleischner society," *Radiology*, vol. 277, no. 1, pp. 192–205, 2015.

[5] O. F. Ahmad, A. S. Soares, E. Mazomenos et al., "Artificial intelligence and computer-aided diagnosis in colonoscopy: current evidence and future directions," *The Lancet Gastroenterology & Hepatology*, vol. 4, no. 1, pp. 71–80, 2019.

[6] C. Guo, J. Lu, Z. Tian, W. Guo, and A. Darvishan, "Optimization of critical parameters of pem fuel cell using tlbo-de based on elman neural network," *Energy Conversion and Management*, vol. 183, pp. 149–158, 2019.

[7] S. Guo, R. Chen, H. Li, T. Zhang, and Y. Liu, "Identify severity bug report with distribution imbalance by cr-smote and elm," *International Journal of Software Engineering and Knowledge Engineering*, vol. 29, no. 2, pp. 139–175, 2019.

[8] J. A. Wedzicha, D. Banerji, K. R. Chapman et al., "Indacaterol-glycopyrronium versus salmeterol-fluticasone for COPD," *New England Journal of Medicine*, vol. 374, no. 23, pp. 2222–2234, 2016.

[9] A. W. Huckle, L. C. Fairclough, and I. Todd, "Prophylactic antibiotic use in COPD and the potential anti-inflammatory activities of antibiotics," *Respiratory Care*, vol. 63, no. 5, pp. 609–619, 2018.

[10] G. Wei, G. Li, J. Zhao, and A. He, "Development of a LeNet-5 gas identification CNN Structure for electronic noses," *Sensors*, vol. 19, no. 1, 217 pages, 2019.

[11] K. Kim and J. Jeong, "Real-time monitoring for hydraulic states based on convolutional bidirectional LSTM with attention mechanism," *Sensors*, vol. 20, no. 24, 7099 pages, 2020.

[12] S. Fan, Y. Bian, E. Wang et al., "An automatic estimation of arterial input function based on multi-stream 3D CNN," *Frontiers in Neuroinformatics*, vol. 1349 pages, 2019.

[13] K. He, G. Gkioxari, P. Dollar, and R. Girshick, "Mask R-CNN," *IEEE Transactions on Pattern Analysis and Machine Intelligence*, vol. 42, no. 2, pp. 386–397, 2020.

[14] M. Sadrawi, Y.-T. Lin, C.-H. Lin et al., "Genetic deep convolutional autoencoder applied for generative continuous arterial blood pressure via photoplethysmography," *Sensors*, vol. 20, no. 14, 3829 pages, 2020.

[15] D. Močnik, B. Ibragimov, L. Xing et al., "Segmentation of parotid glands from registered CT and MR images," *Physica Medica*, vol. 52, pp. 33–41, 2018.

[16] Z. Tang, Y. Xu, L. Jin et al., "Deep learning of imaging phenotype and genotype for predicting overall survival time of glioblastoma patients," *IEEE Transactions on Medical Imaging*, vol. 39, no. 6, pp. 2100–2109, 2020.

[17] J. Park, B. D. Hobbs, J. D. Crapo et al., "Subtyping COPD by using visual and quantitative CT imaging features," *Chest*, vol. 157, no. 1, pp. 47–60, 2020.

[18] A. Verma, I. Kumar, A. Jain, and S. Agarwal, "Performance of quantitative CT parameters in assessment of disease severity in COPD: a prospective study," *Indian Journal of Radiology and Imaging*, vol. 28, no. 1, pp. 99–106, 2018.

[19] T. E. Renkema, H. A. Kerstjens, J. P. Schouten, J. M. Vonk, G. H. Koëter, and D. S. Postma, "The importance of serum IgE for level and longitudinal change in airways hyper-responsiveness in COPD," *Clinical and Experimental Allergy*, vol. 28, no. 10, pp. 1210–1218, 1998.

[20] M. Kirjavainen, L. Mattila, M. Vahteristo, J. Korhonen, and S. Lähelmä, "Pharmacokinetics of salmeterol and fluticasone propionate delivered in combination via easyhaler and diskus dry powder inhalers in healthy subjects," *Journal of Aerosol Medicine and Pulmonary Drug Delivery*, vol. 31, no. 5, pp. 290–297, 2018.

[21] J. Jin, X. Liu, and Y. Sun, "The prevalence of increased serum IgE and aspergillus sensitization in patients with COPD and their association with symptoms and lung function," *Respiratory Research*, vol. 15, no. 1, 130 pages, 2014.

Hindawi
Journal of Healthcare Engineering
Volume 2021, Article ID 2584291, 8 pages
https://doi.org/10.1155/2021/2584291

Research Article

Back Propagation Neural Network-Based Ultrasound Image for Diagnosis of Cartilage Lesions in Knee Osteoarthritis

Xiaoming Zhao[1] **Wei Gong**[1] **Xing Li**[1] **Weibing Yang**[2] **Dengfeng Yang**[2] **and Zhiguo Liu**[2]

[1]*Department of Orthopaedics, Baoji Central Hospital of Shaanxi Province, Baoji 721008, Shaanxi, China*
[2]*Department of Bone and Joint Trauma, Hanzhong City Center Hospital, Hanzhong 713000, Shaanxi, China*

Correspondence should be addressed to Zhiguo Liu; hellomaria@zjnu.edu.cn

Received 13 June 2021; Revised 12 July 2021; Accepted 22 July 2021; Published 31 July 2021

Academic Editor: Enas Abdulhay

Objective. To explore the application value of ultrasound image based on back propagation (BP) neural network algorithm in knee osteoarthritis (KOA) and evaluate the application effect and value of ultrasound image technology based on the BP neural network in the diagnosis of knee osteoarthritis cartilage lesions, 98 patients who were admitted to our hospital were diagnosed with KOA and had undergone arthroscopic soft tissue examinations were randomly selected. According to whether image processing was performed, the ultrasound images of all patients were divided into two groups. The control group was image before processing, and the experimental group was image after processing optimization. The consistency of the inspection results of the ultrasound images before and after the processing with the arthroscopy results was compared. The results showed that the staging accuracy of the control group was 68.3% and that of the experimental group was 76.9%. The accuracy of staging cartilage degeneration of the experimental group was higher than that of the control group, and the difference was not remarkable ($P > 0.05$). The kappa coefficient of the experimental group was 0.61, and that of the control group was 0.40. The kappa coefficient of the experimental group was higher than that of the control group, and the difference was significant ($P < 0.05$). *Conclusion*. The inspection effect of the ultrasound image processed by the BP neural network was superior to that of the conventional ultrasound image. It reflected the good adoption prospect of neural networks in image processing.

1. Introduction

Knee osteoarthritis (KOA) is a common joint degenerative disease in clinical orthopedic diseases, also known as osteoarthritis, degenerative arthritis, etc. [1]. Most of the people with high incidence of KOA are the elderly. Therefore, with the aging of China's population, the disease also gradually presents an upward trend [2]. The general clinical manifestations of KOA are knee pain and limitation of movement, but it often causes joint soft tissue lesions such as cartilage, subchondral bone, synovial capsule of the joint, and knee osteoarticular ligament in severe cases. Then, along with the development of pathological changes, cartilage tissue damage, bone spurs, and even joint deformation can lead to bone and joint failure [3–5], which will bring great inconvenience to the life of patients. At present, the main treatment for knee cartilage lesions is conservative treatment, which is targeted at the early stage of knee cartilage lesions. Arthroscopic therapy may be appropriate for patients with stage II lesions according to the condition of the disease. Surgical treatment is recommended for patients with stage III to moderate lesion stage [6–8]. Accurate diagnosis is essential in order to adopt reasonable and appropriate treatment methods and ensure the treatment effect. At present, the diagnosis of KOA joint disease is mainly based on the results of imaging techniques, including X-ray, CT, MRI, and ultrasound. However, X-ray and CT have great limitations in the display of soft tissue around the joint, which cannot be well displayed. Although MRI can display the soft tissue lesions around the joint, there are still many inconveniences [4, 9, 10]. Therefore, ultrasonic testing has been favored by more people due to its high-resolution display characteristics, noninvasiveness, safety and simple operation mode, and easy-to-accept test price [11]. With the continuous adoption of this technique in clinical practice, its accuracy in the examination of KOA disease and peripheral soft tissue lesions caused by this disease has become a hot spot in clinical research.

At present, ultrasound imaging technology is mainly used for the detection of Doppler ultrasound imaging, by showing the patient's disease location to the doctor in the form of black-and-white image to diagnose the disease. With the rapid development of artificial intelligence (AI) technology, its algorithm has been widely used in medical image processing. The principle of this technology is extracting the feature map of the original image and comparing it with the expert's to make a detection diagnosis [12]. AI algorithms include a kind of neural network calculation that has been used in various industries. Among them, the back propagation (BP) feed forward neural network is a kind of AI learning algorithm, which is widely used at this stage. It can well process images and has good adoption value in forecasting [13]. The principle of the BP neural network is as follows. Firstly, the corresponding network connection weight is obtained through the given training samples. Secondly, the input samples to be processed are taken to obtain the corresponding output samples. When the process is completed, the weight will not be changed. To put it simply, the training process of neural network algorithm for image processing is actually a process of obtaining network weights, and the methods to obtain them are mainly the back propagation of error and the speediest gradient method [14].

In this study, it used the BP neural network algorithm to optimize the ultrasound image of KOA cartilage lesions for the diagnosis of the disease and compare with the results of conventional ultrasound image examination, so as to evaluate the application effect and value of ultrasound image technology based on the BP neural network in the diagnosis of knee osteoarthritis cartilage lesions. It aimed to study more effective and feasible detection techniques for clinical diagnosis and treatment of KOA patients.

2. Methods

2.1. Research Objects. A total of 98 patients with KOA who were admitted to our hospital from October 2018 to March 2020 and had undergone arthroscopic soft tissue examination by arthroscopy were randomly selected in this study. Among them, 42 male patients and 56 female patients ranged in age from 50 to 78 years old, with an average age of (64.3 ± 7.9) years old. All patients had completed ultrasound diagnosis at admission, with complete arthroscopic results and general clinical data. The ultrasound images of all patients were processed and optimized by the BP neural network algorithm, and the consistency between the ultrasound images and arthroscopy results before and after treatment was compared. Ultrasound images of all patients were divided into two groups according to whether image processing was performed. The group before processing was set as the control group, and the group after optimized processing was set as the experimental group. This study had been approved by the medical ethics committee of our hospital. The patients and their families were informed of the study and signed the informed consent.

Inclusion criteria: (a) according to the diagnostic criteria for KOA prescribed by the American Rheumatology Association (ACR) in 2001 [15], as shown in Figure 1, patients with knee pain were diagnosed as KOA if they had five of the following nine items. (b) All patients were over 50 years old (inclusive). (c) None of the patients had undergone surgical treatment for KOA.

Exclusion criteria: (a) patients complicated with severe cardiovascular and cerebrovascular diseases and severe dysfunction of the liver, kidney, and hematopoietic system. (b) Patients with KOA lesions due to other causes and cartilage lesions around joints.

2.2. Experimental Methods

2.2.1. Inspection Method. First, high-frequency ultrasound examination was performed on all patients. All patients were scanned using the same machine and equipment, and all the examination process were carried out by the same experienced, skilled, and accurate imaging doctor. The linear array probe was used for the ultrasonic equipment, and the probe frequency was set at 10 MHz. Figure 2 showed the specific operation. Then, arthroscopy was performed on the patients who needed it. The procedure must be performed by two experienced orthopedic surgeons, and all patients were treated with a unified arthroscopic device to avoid greater individual differences. The degeneration of knee cartilage was staged according to the staging criteria in Table 1. The process of reviewing the ultrasound images was carried out by two highly qualified imaging doctors. The state of the cartilage surface around the joint, the echo state of the ultrasonic image inside the cartilage, and the morphological changes of part of the cartilage were mainly evaluated, and the thickness of the cartilage was measured. According to Table 2, lesions were staged. When the result is different, the final result should be agreed through discussion and consultation.

2.2.2. Ultrasonic Image Based on the BP Neural Network Algorithm. BP neural network algorithm was adopted to denoise and optimize the image under the ultrasonic image technology. The algorithm process is as follows.

First of all, the speckle noise in the ultrasonic image was studied. According to the study, if the particles scattered in the human tissues are sufficient and evenly distributed, the distribution of speckle noise in ultrasonic images conforms to Rayleigh distribution and is expressed by the multiplicative model in the following equation:

$$Q = we. \tag{1}$$

Q in equation (1) represents the undenoised image disturbed by noise e, and w is the original undisturbed image. If the noise distribution conforms to Rayleigh distribution, the following equation is obtained:

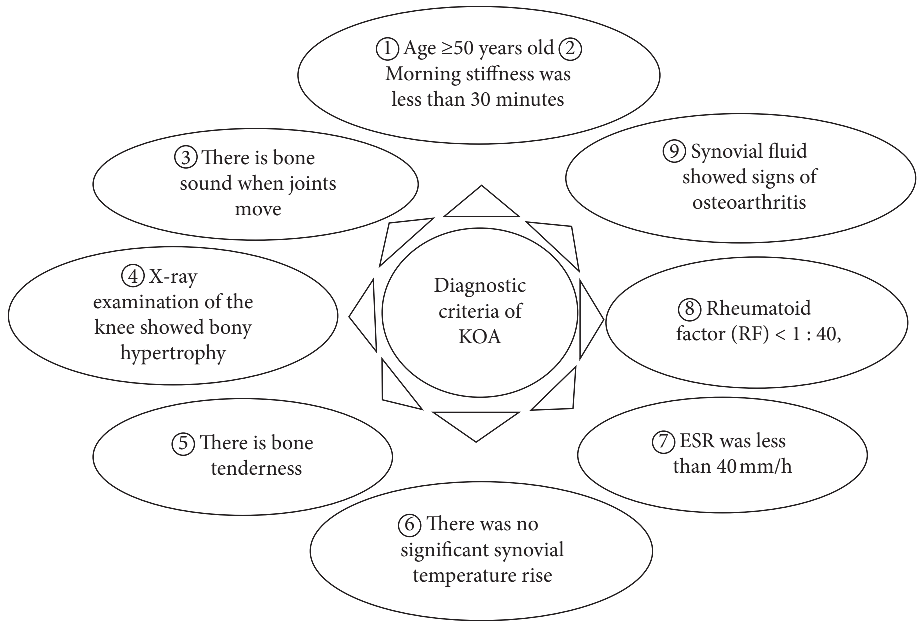

Figure 1: KOA diagnostic criteria customized by the American Association of Rheumatology (ACR) in 2001.

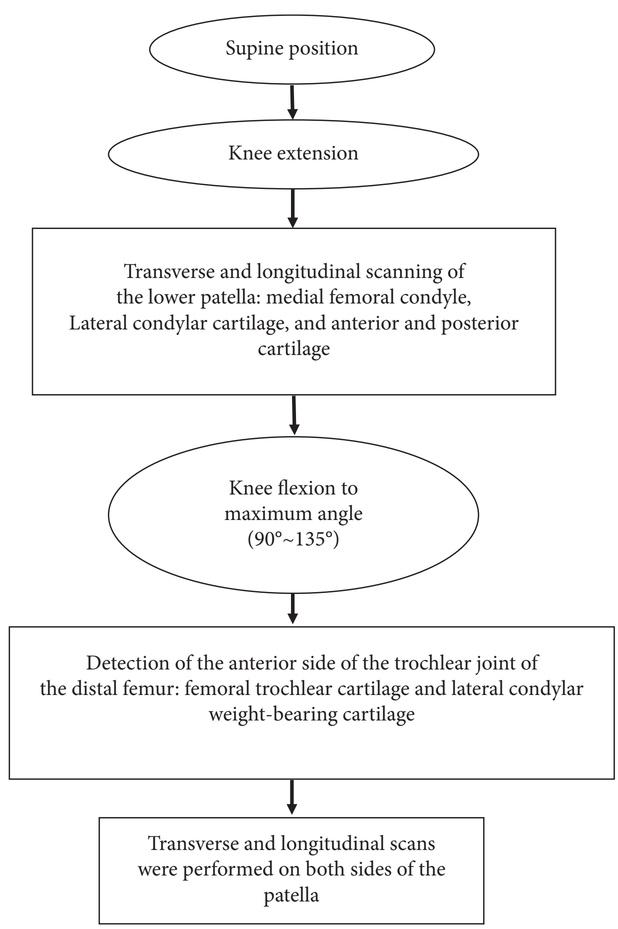

Figure 2: Process of high-frequency ultrasound examination.

Table 1: Staging criteria of knee cartilage degeneration under arthroscopy.

Stage	The state of cartilage lesions
Stage I	The cartilage tissue loses its luster and becomes hard in texture
Stage II	The surface of the cartilage is not smooth, with blisters or velvet-like changes, and the invasion range of the damage is less than 1/2 of the depth of the cartilage.
Stage III	The cartilage lesions are severe, with local thinning or even fibrosis, and the invasion range of the injury is more than 1/2 of the cartilage depth.
Stage IV	The cartilage has ulcerated lesions, complete defects, and exposed subchondral bone tissue.

Table 2: Staging criteria of knee cartilage degeneration under ultrasound detection.

Stage	Cartilage status under ultrasound
No lesion	The surface shows high echo and the lines are smooth, clear, and continuous. The boundary between cartilage and its inferior bone is normal, and the lower vocal cords are evenly distributed and of normal thickness.
Stage I	The change degree is small or the surface is rough, the thickness is close to normal, the degenerated deep layer shows high echo, the sound line is continuous, the smooth slightly less, and the internal echo distribution is basically uniform
Stage II	The surface shows hyperecho and coarse sound line with localized uplift. The deep sound line of the lesion site shows continuous hyperecho with increased echo and uneven distribution.
Stage III	Thin, with obvious defect, but no invasion of subchondral tissue, uneven distribution of low vocal cords, cartilage interruption defect, degenerative deep high echo, irregular voice line increase, showing extremely coarse, local defect
Stage IV	The subchondral bone is exposed, the deep high echo line is discontinuous, the central low echo cord is thinned, the cartilage defect area is enlarged, and the subchondral bone is invaded, obviously thinned, and the whole layer is thinned.

$$R = f\left[\sum tQ\right]. \quad (2)$$

In equation (2), f is a nonlinear function, which is relatively complex; t is the nonlinear coefficient; and R is the result of nonlinear transformation after the weighted sum of gray values of all pixels in the noisy image Q.

The processing of the BP neural network is the forward signal transmission of the original image-reverse transmission error-continuous training and correction-inspection effect. The BP network includes input layer, hidden layer, and input layer. During training, the output relationship of the BP neural network is represented by equation (3), where W_i, X_i, O_i, and y represent the weight, input value, bias, and output value of the ith neuron in the hidden layer, respectively.

$$y = \sum_{i=0}^{T-1} w_i x_i + o_i. \quad (3)$$

The error function calculation method in the back propagation process is shown in the following equation, where a_j is the output result of node j.

$$P(w,o) = \frac{1}{2}\sum_{j=0}^{s-1}\left(a_j - d_j\right)^2. \quad (4)$$

The optimization algorithm of the BP neural network often uses the gradient descent method, as shown in equation (5), where β_{i+1} is the weight after optimization, β_i is the weight before optimization, α is the learning probability, and $\chi J(\beta)/\chi\beta_i$ is the gradient in the weight direction.

$$\beta_{i+1} = \beta_i - \alpha\frac{\chi J(\beta)}{\chi\beta_i}. \quad (5)$$

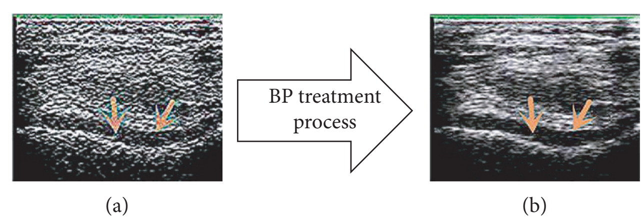

Figure 3: Comparison of ultrasound images (a) before and (b) after BP neural network algorithm processing. The red arrow refers to the articular cavity.

At this time, the BP neural network obtains the relational expression of the function, and the training is completed. The denoising effect is evaluated regarding peak signal-to-noise ratio, which is expressed by the following equation:

$$F = 101g\left[\frac{\max(h)^2}{\text{MSE}}\right]. \quad (6)$$

In equation (6), h is the ultrasonic image after denoising and MSE is mean square error, which is calculated in equation (7), where h_0 is the original unprocessed ultrasound image and M is the ultrasound image number:

$$\text{MSE} = \frac{\sqrt{\sum_{i=1}^{M}(h - h_0)^2}}{M}. \quad (7)$$

The before and after comparison of the optimized ultrasound image processed by the BP neural network algorithm is shown in Figure 3.

2.3. Statistical Methods. SPSS 22.0 was employed for data entry, sorting, and statistical analysis. The comparison of count data was performed by χ^2 test, while the comparison of measurement data was performed by t-test. Multiple sample means were compared using analysis of variance. The LSD method was used when the variance was uniform, and the Dunnett T3 method was used when the variance was uneven. $P < 0.05$ was statistically different. The kappa test was performed on the consistency between the staging results shown in the two groups of ultrasound images and those seen under arthroscopy. When kappa > 0.75, the consistency between the two was strong. When $0.4 \leq$ kappa < 0.75, the consistency between the two was general. When kappa < 0.4, the consistency between the two was poor.

3. Results

3.1. Staging Results of Cartilage Lesions under Arthroscopy. 98 patients were examined for cartilage lesions on a total of 490 articular surfaces under arthroscopic surgery. Among them, the cartilage of 206 articular surfaces was normal and uninvolved and caused disease. The cartilage of the remaining 284 articular surfaces had different degrees of disease, with a total of 320. Among them, 56 were in stage I, 85 were in stage II, 94 were in stage III, and 85 were in stage IV. The staging results of different detection parts are summarized in Table 3. Figure 4 shows the performance of different stages under arthroscopy. It was obvious that the pathological differences of the cartilage around the joints in each stage can be observed.

3.2. The Staging Results of Cartilage Lesions under Ultrasound Imaging in the Control Group. Among cartilage lesions on 490 articular surfaces of 98 patients in the staging results of the ultrasound image of the control group, the echo distribution of the ultrasound image of cartilage with 242 articular surfaces was a normal high-low-high distribution. The cartilage of the remaining 248 articular surfaces all had different degrees of lesions, with a total of 284 lesions. Among them, 38 were in stage I, 99 were in stage II, 83 were in stage III, and 64 were in stage IV. The staging results of different detection sites are summarized in Table 4. Figure 5 shows the ultrasound imaging manifestations of different stages of the control group. There were certain differences in the pathological changes of the cartilage around the joints in each stage.

3.3. The Results of Staging of Cartilage Lesions under Ultrasound Imaging in the Experimental Group. Among cartilage lesions on 490 joint surfaces of 98 patients in the staging results of the ultrasound image of the experimental group, the echo distribution of the ultrasound image of cartilage with 231 articular surfaces was normal. The cartilage of the remaining 269 articular surfaces had different degrees of lesions, with a total of 307 lesions. Among them, 44 were in stage I, 87 were in stage II, 87 were in stage III, and 89 were in stage IV. The staging results of different detection sites are summarized in Table 5. Figure 6 shows the ultrasound image manifestations of different stages in the experimental group. There were certain differences in the lesions of the cartilage around the joints in each stage.

3.4. Comparison of Consistency between the Staging Results of the Two Groups of Ultrasound Images and the Results under Arthroscopy. The examination results of the two sets of ultrasound images of the cartilage lesions around the KOA of all patients were compared with the results observed under arthroscopy. There were 335 cartilage degenerations that were accurately detected by the ultrasound image of the control group, and the staging accuracy of the inspection results was 68.3%. In the experimental group, 377 cartilage degenerations were detected, and the staging accuracy of the inspection results was 76.9%. The accuracy of staging of cartilage degeneration in the experimental group was higher than that in the control group, but the difference was not remarkable ($P > 0.05$). Moreover, the kappa coefficient of the ultrasound image staging and arthroscopic staging results of the experimental group was 0.61, while the kappa coefficient of the control group and arthroscopic staging was 0.40. The kappa coefficient of the two groups indicated that they were generally consistent with the arthroscopic staging results, but the kappa coefficient of the experimental group was higher than that of the control group, with considerable difference ($P < 0.05$), as presented in Figure 7.

4. Discussion

The progression of KOA disease is very likely to cause degenerative lesions of the cartilage around the knee joint. Patients will feel the pain of the knee joint, flexion, and extension, which even bring difficulties in walking, seriously affecting the patient's daily life. Therefore, timely and effective diagnosis is necessary for the control of cartilage involvement in patients with KOA. In order for the treatment to be effective, symptomatic treatment is necessary. The accuracy of examination of the degree of knee cartilage degeneration has an effective guiding significance for doctors to make a reasonable clinical treatment plan. There are a variety of detection methods for KOA disease, including MRI, X-ray, CT, and ultrasound, but all of them have certain adoption limitations. Ultrasound diagnosis has been welcomed by its effect on the adoption of research analysis which has been analyzed by a lot of researchers and clinicians for its excellent characteristics such as no radiation, low cost, short examination time, and simple operation, especially for the diagnosis of osteoarthritis. Researchers studied the effectiveness of ultrasound in the detection of cartilage lesions in the knee. It was found that when the knee joint was in complete flexion, ultrasound examination could clearly show the tissue structure of the cartilage around the joint, including the trochlea, femur, and medial and lateral condyle. Other researchers proposed that when the knee flexion angle was maximized, the articular surface of the patella pulley was fully exposed. The blocked range of the medial and lateral condyles of the femur can also be reduced, so that it can observe the cartilage lesions on the articular surface of the femur more completely [16]. In this study, the knee flexion of the two aspects was observed, and the results were basically the same, except that the femoral articular surface could not be fully exposed due to various obstructions. In addition, it was found through studies that

Table 3: Staging results of different articular surface cartilage lesions under arthroscopic examination (place).

Staging		Inspection area				
		Stage I	Stage II	Stage III	Stage IV	Total
Central groove of pulley	The central sulcus	10	18	11	7	164
	The inside of the slope	12	18	16	17	
	The outside of the slope	9	17	18	11	
The femoral	The medial condyle	12	21	25	27	155
	The lateral condyle	12	11	24	23	

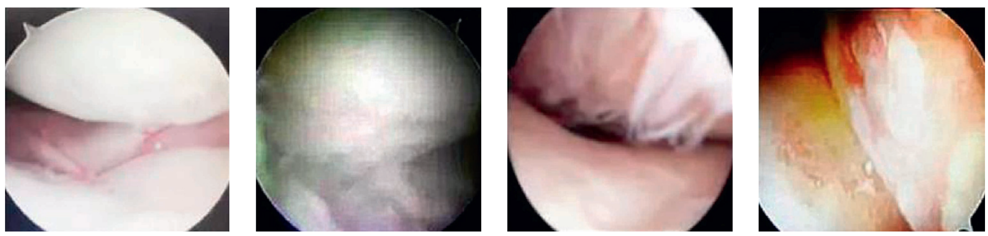

(a) (b) (c) (d)

Figure 4: The manifestations of different stages under arthroscopy. (a) Stage I. (b) Stage II. (c) Stage III. (d) Stage IV.

Table 4: Results of different articular surface cartilage lesion stages in the control group (place).

Staging		Inspection area				
		Stage I	Stage II	Stage III	Stage IV	Total
Central groove of pulley	The central sulcus	7	11	10	11	164
	The inside of the slope	6	20	17	26	
	The outside of the slope	5	17	20	14	
The femoral	The medial condyle	15	22	25	5	120
	The lateral condyle	7	29	11	8	

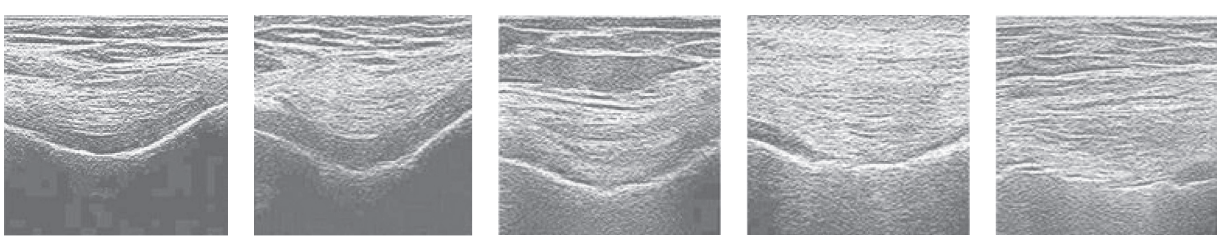

(a) (b) (c) (d) (e)

Figure 5: The ultrasound imaging manifestations of different stages in the control group. (a) Normal. (b) Stage I. (c) Stage II. (d) Stage III. (e) Stage IV.

ultrasound imaging can show significant differences in the degree of cartilage degeneration, which can be regarded as an important examination and evaluation method for staging of knee cartilage lesions [17].

With the development of AI, deep neural network algorithm has been applied more and more widely in various fields [18, 19]. Some researchers have studied and analyzed the application of BP neural network in medical ultrasound image denoising. The results showed that the BP neural network has a good denoising effect on the ultrasonic image and can also preserve the edge features of the ultrasonic image well [20]. Other researchers studied the feed forward neural network ultrasonic diagnosis method based on BP algorithm and proposed the results of continuous clinical testing. BP neural network ultrasonic diagnosis software can not only improve the efficiency of ultrasonic diagnosis and reduce the time of medical treatment but also use expert knowledge base to share expert knowledge, so as to improve the accuracy of disease diagnosis [21]. The BP neural network algorithm in AI algorithm was used to process the ultrasonic image of knee cartilage to study the stage of cartilage lesions, and a good effect was obtained. The adoption of BP neural network algorithm is very wide, not only in the medical field. For example, some research experts have done a study on using the denoising characteristics of the BP neural network to deal with the noise in seismic data.

Table 5: Results of different articular surface cartilage lesion stages in the experimental group (place).

Staging		Inspection area				
		Stage I	Stage II	Stage III	Stage IV	Total
Central groove of pulley	The central sulcus	8	16	11	9	169
	The inside of the slope	7	20	18	25	
	The outside of the slope	7	15	20	13	
The femoral	The medial condyle	13	20	20	22	138
	The lateral condyle	9	16	18	20	

(a) (b) (c) (d) (e)

Figure 6: The ultrasound imaging manifestations of different stages in the experimental group. (a) Normal. (b) Stage I. (c) Stage II. (d) Stage III. (e) Stage IV.

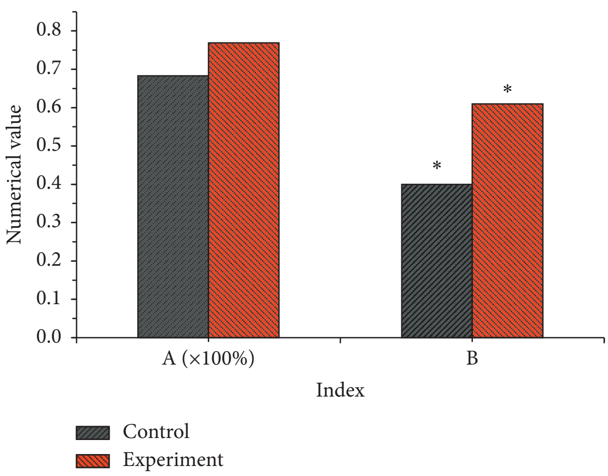

Figure 7: Comparison of the staging results of the two groups of ultrasound images with the results under arthroscopy. A: staging accuracy. B: kappa coefficient. *: the kappa value of the two groups was statistically significant ($P < 0.05$).

The experimental results showed that if BP neural network was used to denoise the seismic data, the peak signal-to-noise ratio was greatly improved, and the details of the effective information were well protected, which was in line with the expected results [22]. For the evacuation of public places, the simulation of subway station building based on the deep neural network model is used to conduct evacuation training.

5. Conclusion

In this study, it observed the cartilage degeneration stage of KOA under arthroscopy as the standard, observed the consistency between the ultrasound images of KOA cartilage lesions processed by the BP neural network algorithm and the conventional ultrasound images and the results under arthroscopy, and compared the results of the two groups. The results showed that the inspection effect of the ultrasonic image processed by the BP neural network was better than that of the conventional ultrasonic image. However, due to the small amount of data in this study, there was a lack of strong representativeness, but it also reflected the good application prospect of neural network technology in image processing. In the future, more ultrasound images will be optimized to improve the recognition accuracy of the neural network and bring more convenience for clinical ultrasound image diagnosis.

Data Availability

The data used to support the findings of this study are available from the corresponding author upon request.

Conflicts of Interest

The authors declare no conflicts of interest.

References

[1] T. Georgiev and A. K. Angelov, "Modifiable risk factors in knee osteoarthritis: treatment implications," *Rheumatology International*, vol. 39, no. 7, pp. 1145–1157, 2019.

[2] M. Vitaloni, A. Botto-van Bemden, R. M. Sciortino Contreras et al., "Global management of patients with knee osteoarthritis begins with quality of life assessment: a systematic review," *BMC Musculoskeletal Disorders*, vol. 20, no. 1, p. 493, 2019.

[3] E. Kon, M. Ronga, G. Filardo et al., "Bone marrow lesions and subchondral bone pathology of the knee," *Knee Surgery, Sports Traumatology, Arthroscopy*, vol. 24, no. 6, pp. 1797–1814, 2016.

[4] T. Gorbachova, Y. Melenevsky, M. Cohen, and B. W. Cerniglia, "Osteochondral lesions of the knee: differentiating the most common entities at MRI," *RadioGraphics*, vol. 38, no. 5, pp. 1478–1495, 2018.

[5] K. Aso, S. M. Shahtaheri, R. Hill, D. Wilson, D. F. McWilliams, and D. A. Walsh, "Associations of symptomatic knee osteoarthritis with histopathologic features in subchondral bone," *Arthritis & Rheumatology*, vol. 71, no. 6, pp. 916–924, 2019.
[6] L. Andriolo, C. Candrian, T. Papio, A. Cavicchioli, F. Perdisa, and G. Filardo, "Osteochondritis dissecans of the knee - conservative treatment strategies: a systematic review," *Cartilage*, vol. 10, no. 3, pp. 267–277, 2019.
[7] G. C. Gracitelli, V. Y. Moraes, C. E. Franciozi, M. V. Luzo, and J. C. Belloti, "Surgical interventions (microfracture, drilling, mosaicplasty and allograft transplantation) for treating isolated cartilage defects of the knee in adults," *Cochrane Database of Systematic Reviews*, vol. 9, no. 9, Article ID CD010675, 2016.
[8] T. Totlis, T. Marín Fermín, G. Kalifis, I. Terzidis, N. Maffulli, and E. Papakostas, "Arthroscopic debridement for focal articular cartilage lesions of the knee: a systematic review," *The Surgeon*, vol. 85, pp. 129–141, 2021.
[9] C. Rehnitz, M.-A. Weber, and F. Wuennemann, "Imaging of the knee following repair of focal articular cartilage lesions," *Seminars in Musculoskeletal Radiology*, vol. 22, no. 4, pp. 377–385, 2018.
[10] B. Klaan, F. Wuennemann, L. Kintzelé, A. S. Gersing, and M.-A. Weber, "MR- und CT-Arthrographie zur Knorpeldiagnostik," *Der Radiologe*, vol. 59, no. 8, pp. 710–721, 2019.
[11] L. Aghaghazvini, M. N. Tahmasebi, R. Gerami et al., "Sonography: a sensitive and specific method for detecting trochlear cartilage pathologies," *Journal of Ultrasound*, vol. 23, no. 3, pp. 259–263, 2020.
[12] C. Tack, "Artificial intelligence and machine learning | applications in musculoskeletal physiotherapy," *Musculoskeletal Science and Practice*, vol. 39, pp. 164–169, 2019.
[13] V. Geetha, K. S. Aprameya, and D. M. Hinduja, "Dental caries diagnosis in digital radiographs using back-propagation neural network," *Health Information Science and Systems*, vol. 8, no. 1, p. 8, 2020.
[14] N. Frolov, V. Maksimenko, A. Lüttjohann, A. Koronovskii, and A. Hramov, "Feed-forward artificial neural network provides data-driven inference of functional connectivity," *Chaos: An Interdisciplinary Journal of Nonlinear Science*, vol. 29, no. 9, Article ID 091101, 2019.
[15] M. Boylan, "Should ultrasound be used routinely in the diagnosis of rheumatoid arthritis?" *Irish Journal of Medical Science*, vol. 189, no. 2, pp. 735–748, 2020.
[16] E. A. Haavardsholm, A.-B. Aga, I. C. Olsen et al., "Ultrasound in management of rheumatoid arthritis: ARCTIC randomised controlled strategy trial," *BMJ*, vol. 354, p. i4205, Article ID i4205, 2016.
[17] X. Li, Y. Sun, Z. Zhou et al., "Mitigation of articular cartilage degeneration and subchondral bone sclerosis in osteoarthritis progression using low-intensity ultrasound stimulation," *Ultrasound in Medicine and Biology*, vol. 45, no. 1, pp. 148–159, 2019.
[18] C. Guo, J. Lu, Z. Tian, W. Guo, and A. Darvishan, "Optimization of critical parameters of PEM fuel cell using TLBO-DE based on Elman neural network," *Energy Conversion and Management*, vol. 183, pp. 149–158, 2019.
[19] S. Guo, R. Chen, H. Li, T. Zhang, and Y. Liu, "Identify severity bug report with distribution imbalance by CR-SMOTE and ELM," *International Journal of Software Engineering and Knowledge Engineering*, vol. 29, no. 2, pp. 139–175, 2019.
[20] W. Dong, P. Wang, W. Yin, G. Shi, F. Wu, and X. Lu, "Denoising prior driven deep neural network for image restoration," *IEEE Transactions on Pattern Analysis and Machine Intelligence*, vol. 41, no. 10, pp. 2305–2318, 2019.
[21] Y. Shi, Y. Li, M. Cai, and X. D. Zhang, "A lung sound category recognition method based on wavelet decomposition and BP neural network," *International Journal of Biological Sciences*, vol. 15, no. 1, pp. 195–207, 2019.
[22] S. Liu, Z. Hou, and C. Yin, "Data-driven modeling for UGI gasification processes via an enhanced genetic BP neural network with link switches," *IEEE Transactions on Neural Networks and Learning Systems*, vol. 27, no. 12, pp. 2718–2729, 2016.

Hindawi
Journal of Healthcare Engineering
Volume 2021, Article ID 2603842, 8 pages
https://doi.org/10.1155/2021/2603842

Research Article

Deep-Learning-Based Color Doppler Ultrasound Image Feature in the Diagnosis of Elderly Patients with Chronic Heart Failure Complicated with Sarcopenia

Peng Bian,[1] **Xiyu Zhang**,[1] **Ruihong Liu**,[1] **Huijie Li**,[1] **Qingqing Zhang**,[1] **and Baoling Dai**[2]

[1]*Department of Statistics and Medical Record Management, Provincial Hospital Affiliated to Shandong First Medical University, Jinan 250021, Shandong, China*
[2]*Medical Office, Liaocheng Hospital of Traditional Chinese Medicine of Shandong Province, Liaocheng 252000, Shandong, China*

Correspondence should be addressed to Baoling Dai; 20100246004@lfnu.edu.cn

Received 12 June 2021; Revised 12 July 2021; Accepted 22 July 2021; Published 30 July 2021

Academic Editor: Enas Abdulhay

The neural network algorithm of deep learning was applied to optimize and improve color Doppler ultrasound images, which was used for the research on elderly patients with chronic heart failure (CHF) complicated with sarcopenia, so as to analyze the effect of the deep-learning-based color Doppler ultrasound image on the diagnosis of CHF. 259 patients were selected randomly in this study, who were admitted to hospital from October 2017 to March 2020 and were diagnosed with sarcopenia. Then, all of them underwent cardiac ultrasound examination and were divided into two groups according to whether deep learning technology was used for image processing or not. A group of routine unprocessed images was set as the control group, and the images processed by deep learning were set as the experimental group. The results of color Doppler images before and after processing were analyzed and compared; that is, the processed images of the experimental group were clearer and had higher resolution than the unprocessed images of the control group, with the peak signal-to-noise ratio (PSNR) = 20 and structural similarity index measure (SSIM) = 0.09; the similarity between the final diagnosis results and the examination results of the experimental group (93.5%) was higher than that of the control group (87.0%), and the comparison was statistically significant ($P < 0.05$); among all the patients diagnosed with sarcopenia, 88.9% were also eventually diagnosed with CHF and only a small part of them were diagnosed with other diseases, with statistical significance ($P < 0.05$). In conclusion, deep learning technology had certain application value in processing color Doppler ultrasound images. Although there was no obvious difference between the color Doppler ultrasound images before and after processing, they could all make a better diagnosis. Moreover, the research results showed the correlation between CHF and sarcopenia.

1. Introduction

Cardiovascular and cerebrovascular diseases are high-morbidity diseases in the elderly population. With the aging of the population in China, the occurrence and mortality of cardiovascular and cerebrovascular diseases are gradually increasing, especially in the aspect of heart. Chronic heart failure (CHF) will appear in the late stage of heart disease development [1]. According to the statistics, the probability of suffering from CHF is between 1.3% and 1.8% in our population at the present stage and 30% to 50% of the CHF patients eventually die [2]. Sarcopenia, also known as age-related sarcopenia, is a complication of developing CHF, which mainly refers to an age-related degenerative syndrome in which the content of human skeletal muscle gradually decreases with the increase of age, as well as the strength and function of muscle gradually deteriorates [3]. The incidence of sarcopenia varies by region and race, but it is a general trend that increases with age, so it can also be called a progressive geriatric syndrome [4]. Studies have shown that grip strength, muscle strength of quadriceps femoris, 6-minute walking distance, reduced left ventricular ejection fraction, and high oxygen consumption will appear due to low exercise peak when CHF patients are complicated with sarcopenia [5]. Moreover, it is proposed that this complication will not only reduce the quality of life of the patients but also increase the probability of death of the patients through the analysis of patients with CHF complicated with sarcopenia [3].

Cardiac color Doppler ultrasound is a major examination method in diagnosing CHF disease, which is now the only imaging method that can display circulation situation in the internal structure of the heart and organs, and the method has simple operation, causes no wound, and can be repeated [6]. When patients with CHF are examined, the cardiac image structure is comprehensively and intuitively displayed, thereby providing a more favorable and reliable basis for doctors' diagnosis [7].

Deep learning is a kind of artificial intelligence technology that has developed very rapidly in recent years. The neural network system of deep learning has made great progress in image classification and examination. Furthermore, this technology is also widely applied in the medical field. Intelligent medical care, which is a combination of deep learning artificial intelligence and the medical industry, has become a research hotspot [8]. It also solves two major problems for the medical industry: the first one is the imbalance between the amount of imaging data and the amount of clinical imaging data, and the second one is the imbalance between the level of imaging doctors and the allocation of resources [9]. Deep learning methods have been fully and reasonably utilized in image processing and analysis in the medical field. In particular, the deep convolutional network model can more effectively learn image features from a large number of samples, avoid the complex feature extraction process in traditional image classification algorithms, and realize end-to-end classification and detection [10].

In this study, deep learning convolutional neural network technology was combined with color Doppler ultrasound images, which was used for the diagnosis of CHF to analyze the correlation between CHF and sarcopenia.

2. Methods

2.1. Research Objects. A total of 259 patients were randomly selected in this study, who were diagnosed as sarcopenia and admitted to hospital from October 2017 to March 2021, including 119 males and 140 females. They were 60 to 76 years old, with an average age of 69.5 ± 3.5 years. All patients underwent cardiac ultrasound examinations, who were rolled into two groups according to whether deep learning technology was used for image processing or not. A group of routine unprocessed images was set as the control group, and the images processed by deep learning were set as the experimental group. This study was approved by the Medical Ethics Committee, and all the patients participating in the study signed the informed consent forms.

The criteria for inclusion were defined to include patients who were over 50 years of age, were diagnosed as sarcopenia based on the diagnostic criteria proposed by the Asian Working Group for Sarcopenia (AWGS) [11] (Table 1), and were able to undergo a complete color ultrasound examination, whose color ultrasound images were well preserved.

The criteria for exclusion were defined to include patients who had skeletal disease or motor obstruction disease, had previous history of fracture, suffered from diabetes, thyroid, and parathyroid gland and other endocrine system diseases, had diseases of the digestive system and renal insufficiency that affected skeletal muscle metabolism, suffered from malignant tumors and connective tissue diseases, and took calcium, hormone drugs, and antitumor drugs within 1 year, with female ovarian lesions.

2.2. Research Methods

2.2.1. Diagnostic Methods of Chronic Heart Failure. For the diagnosis of CHF, the method of combining the clinical manifestations with the results of other auxiliary examinations was adopted to make the combined diagnosis, as shown in Figure 1.

2.2.2. Convolution Neural Network Algorithm Model. In this study, a convolutional neural network algorithm-based color Doppler ultrasound image model would be established according to the pixel resolution and the performance of stable deep neural network. Then, it would be trained and applied in this study.

The convolution layer was set as the layer q, so the feature graph of the input color ultrasound image at the layer $q-1$ could be expressed as follows:

$$W(q,p) = \sum_{e=1}^{E} Y^{(q,p,e)} \otimes Z^{(q-1,e)} + l^{(q,p)}. \tag{1}$$

In addition, $W^{(q,p,e)}$ represented the convolution kernel, $l^{(q,p)}$ stood for the bias, and e meant the number of feature graphs.

In this study, the commonly used and high-rate ReLu was used as the activation function, which is shown in equation (2), and the corresponding derivative function expression is presented in equation (3). However, due to the excessive data gradient passing through the ReLu neuron, once the data were updated, the neuron would not be able to activate any data again, so it was improved into equation (3). It was a self-gated activation function, which could be called swish.

$$f(x) = \max(0,x), \tag{2}$$

$$f'(x) = \begin{cases} x, & x > 0, \\ 0, & x \leq 0, \end{cases} \tag{3}$$

$$F_1(x) = \left(R_1 * X + L_1\right) \times \frac{Y}{Y + u^{-\alpha\left(R_1 * X + L_1\right)}}. \tag{4}$$

In equation (4), R_1 stands for the convolution kernel, $i \times f_1 \times f_1$ expresses the size, i indicates the number of channels of the input graph, L_1 represents the offset vector,

Table 1: Diagnostic criteria for AWGS sarcopenia.

	Evaluation content	Gender	Criteria
One	The mass of skeletal muscle measured by the dual energy X-ray absorption method; calculation of the ratio of the mass to the height square	Male	<7.0 kg/m^2
		Female	<5.4 kg/m^2
Two	Grip strength	Male	<26 kg
		Female	<18 kg
	Walking speed	6-minute walking speed	<0.8 m/s

Note. Patients who met any of these criteria could be diagnosed with sarcopenia.

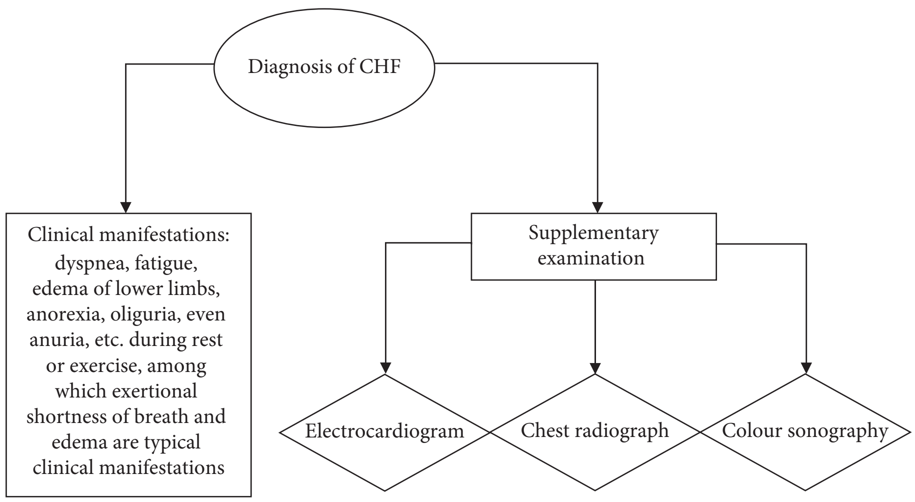

Figure 1: Diagnostic criteria for CHF.

$*$ means the convolution operation, and α stands for the parameter that could be trained.

In this model, the first layer was mainly for the operation of extracting the feature map of the original color ultrasound image, and the second layer to the $q-2$ layer was the nonlinear mapping process of the extracted feature map, which could be expressed by the following equation:

$$F_2(x) = (R_2 * X + L_2) \times \frac{Y}{Y + u^{-\alpha(R_2 * X + L_2)}}. \quad (5)$$

The reconstruction process of the image could be expressed as equation (6), where R_3 represents the mean filter and L_3 expresses the offset of dimension i.

$$F_3(x) = R_3 * F_2(X) + L_3. \quad (6)$$

The convolutional neural network algorithm needed to be reconstructed according to the error, and the parameter error in the propagation process was constantly corrected. If the current propagation was q, the output parameter of the layer was x^q, and the weight and bias could be expressed by R^q and L^q in turn, as shown in the following equations:

$$x^q = f(p^q), \quad (7)$$

$$(p^q) = R^q x^{q-1} + l^q. \quad (8)$$

The expression of loss function was as shown in the following equation:

$$\mathrm{Loss}(s, s') = \frac{1}{n}\sum_{j=1}^{n}\left(s_j, s_j'\right)^2. \quad (9)$$

The method of reducing the gradient was adopted to minimize the sum of squares of errors, and the specific algorithm is shown in the following equations:

$$R_j = R_j - \beta\frac{\chi}{\chi R_j} M(R, l), \quad (10)$$

$$R_j = R_{jk} - \beta\frac{1}{z}\sum_{j=1}^{z}\left[V_{r,l}\left(x^j\right) - s^j\right]x^j. \quad (11)$$

Among them, β represents the weight, χ represents the volume number, and s refers to the loss data.

For the semisupervised learning algorithm aiming at the inherent noise and uncertainty in ultrasonic images, its calculation method was displayed as follows, but the derivation process was omitted:

$$L_{\mathrm{label}} = -B[\ln g(y \mid x)] = -ly + \mathrm{LSE}(l), \quad (12)$$

$$\begin{aligned} L_{\mathrm{unlabel}} &= -E[\ln(1 - g(H+1) \mid x)] \\ &= -\mathrm{LSE}(l) + \mathrm{sofplus}(\mathrm{LSE}(l)), \end{aligned} \quad (13)$$

$$L_{\text{fake}} = -E[\ln g(H+1 \mid x)] = \text{softplus}(\text{LSE}(l)), \tag{14}$$

$$L_D = L_{\text{label}} + \frac{v(L_{\text{unlabel}} + L_{\text{fake}})}{2}. \tag{15}$$

In equations (12)–(15), H stands for the classifier and $H+1$ means the output graph of the discriminator. The whole system included real data with labels, noise data without labels, and generated data, and the corresponding probabilities were L_{label}, L_{unlabel}, and L_{fake}, respectively.

Figure 2 shows the comparison of the cardiac color ultrasound images before and after processing and optimization by this algorithm.

2.2.3. Evaluation Criteria for the Algorithm Effect. In order to evaluate the effect achieved by the abovementioned algorithm model, the peak signal-to-noise ratio (PSNR) and structural similarity index measure (SSIM) were applied in this study. Besides, the smaller the value of PSNR, the smaller the degree of image distortion. However, the closer the SSIM value was to 1, the more similar the processed image would be to the original. The specific algorithm of PSNR is shown in equations (16) and (17), where K expresses the image height, H means the image width, and n stands for the bit value of each pixel.

$$\text{MSE} = \frac{1}{K \times L} \sum_{i=1}^{K} \sum_{j=1}^{H} (X(i,j) - Y(i,j))^2, \tag{16}$$

$$P = 10 \log_{10}\left(\frac{(2^n - 1)^2}{\text{MSE}}\right). \tag{17}$$

SSIM could be calculated as in equation (18), where α_x indicates the average value of x, α_y means the average value of y, β_x^2 represents the variance of x, β_y^2 stands for the variance of y, and β_{xy} expresses the covariance of x and y.

$$\text{SSIM}(x,y) = \frac{(2\alpha_x\alpha_y + e_1)(2\beta_{xy} + e_2)}{(\alpha_x^2 + \alpha_y^2 + e_1)(\beta_x^2 + \beta_y^2 + e_2)}. \tag{18}$$

2.3. Observation Indicators. The left atrial diameter (LAD), left ventricular ejection fraction (LVEF), and left ventricular end-diastolic diameter (LVDD) of the two groups were observed and recorded by using a color Doppler ultrasound, so as to evaluate and compare the positive rates of LAD, LVEF, and LCDD in the two groups. Positive criteria for diagnosis of CHF by using the cardiac ultrasound [12]: ① LAD > 30 mm was positive; ② LVDD > 55 mm in male and >50 mm in female were positive; and ③ LVEF < 50% was positive.

The detection results of the two groups were compared, the number of sarcopenia patients diagnosed with CHF was contrasted, and the clinical manifestations and other auxiliary examinations were combined to confirm the diagnosis, so as to analyze the accuracy of the cardiac ultrasound examination.

2.4. Statistical Methods. SPSS 23.0 statistical software was used for data processing, in which measurement data were expressed as ($x \pm s$), and the two independent samples t-test was used for comparison between groups. Count data were represented by [n (%)], and the χ^2 test was used for comparison between groups. In addition, $P < 0.05$ indicated that the difference was statistically substantial.

3. Results

3.1. Comparison on Cardiac Color Ultrasound Images of Patients with Chronic Heart Failure and Other Heart Diseases from Two Groups. The cardiac color ultrasound images of patients from the two groups were observed, clearly showing that the processed images of the experimental group were clearer than the untreated images of the control group, which also had higher resolution. Therefore, it indicated that the deep learning convolutional neural network algorithm had a certain effect on optimization for color ultrasound images, and the specific comparison is shown in Figures 3 and 4. In addition, PSNR and SSIM were adopted to evaluate the effect of processing, achieving good results (PSNR = 20 and SSIM = 0.09).

3.2. Comparison of LVEF, LCDD, and LAD Results between the Two Groups. By statistical analysis of the diagnostic results of LVEF, LCDD, and LAD in the two groups of cardiac color ultrasound of all patients (Table 2), it was found that the indicators of LVEF, LCDD, and LAD of the control group were lower than the indicators of the experimental group, and the comparison was statistically significant ($P < 0.05$), as shown in Figure 5.

3.3. Statistical Comparison on the Positive Rates of LVEF, LCDD, and LAD Results from Cardiac Color Ultrasound Diagnosis between the Two Groups. There was statistical analysis on the positive rates of diagnostic results of LVEF, LCDD, and LAD in the two groups of heart color ultrasound of all patients (Table 3). Figure 6 reveals that the positive rates of LVEF, LCDD, and LAD of the experimental group were higher than the rates of the control group, and the comparison was statistically significant ($P < 0.05$).

3.4. Comparison on the Results of CHF Patients Diagnosed in the Two Groups and the Final Confirmed Results. Table 4 shows the comparison of the number of patients diagnosed with CHF by using the cardiac color ultrasound and the final diagnosis combined with other clinical examinations. The study results suggested that the similarity between the final diagnosis results and the examination results of the experimental group was 93.5%, while the similarity between the results and the control group was 87.0%. Thus, the similarity between the experimental group and the control group was higher, and the comparison was statistically significant ($P < 0.05$). Among all the patients diagnosed with sarcopenia in this study, 88.9% were also finally diagnosed with CHF, and only a small part suffered from other diseases,

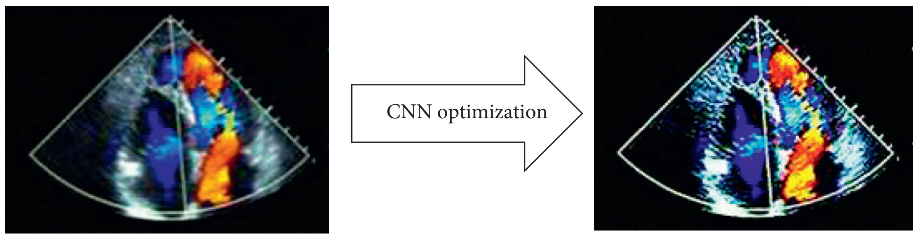

Before treatment After treatment

Figure 2: Comparison on cardiac color ultrasound images before and after optimization by convolutional neural network algorithm.

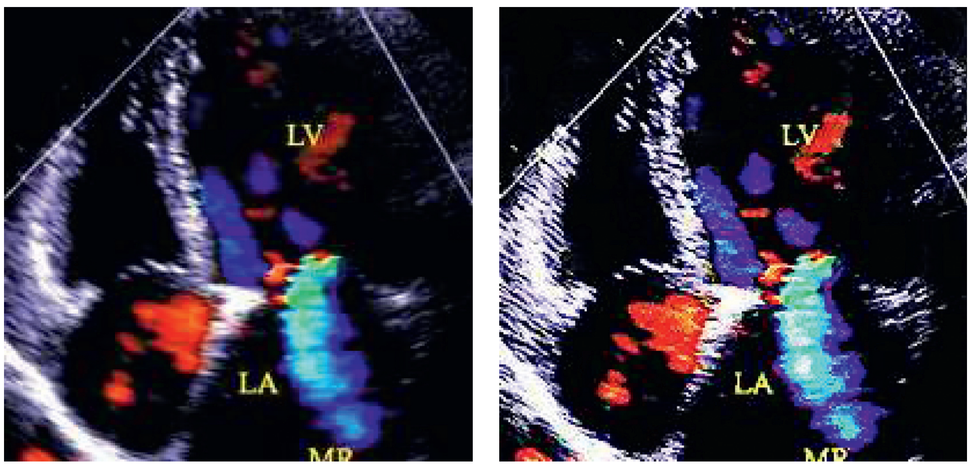

(a) (b)

Figure 3: Comparison on cardiac color ultrasound images of CHF patients between the two groups. (a) Control group; (b) experimental group.

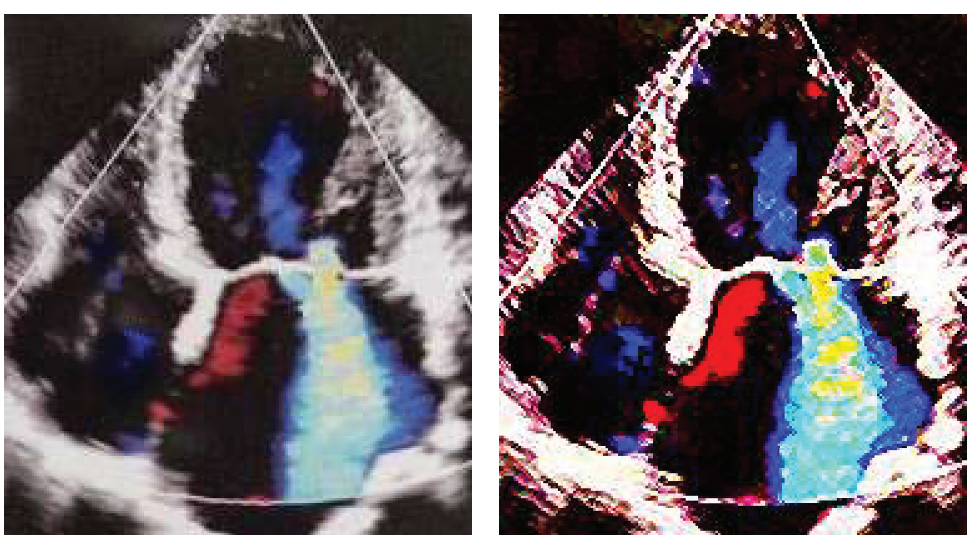

(a) (b)

Figure 4: Comparison on cardiac color ultrasound images between the two groups of patients with other heart diseases. (a) Control group; (b) experimental group.

Table 2: Statistical results of LVEF, LCDD, and LAD diagnosed by using a cardiac ultrasound in the two groups.

Indicators	Group	
	Control group	Experimental group
LVEF (%)	54.05 ± 4.79	60.09 ± 4.34
LCDD (mm)	51.35 ± 3.97	56.05 ± 3.09
LAD (mm)	33.45 ± 4.01	40.05 ± 4.12

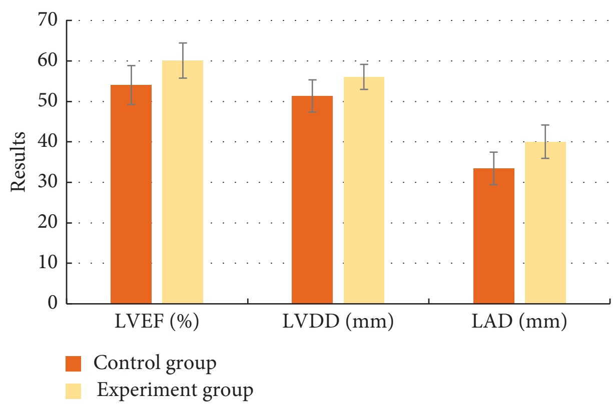

Figure 5: Comparison on the results of LVEF, LCDD, and LAD diagnosed by using a cardiac color ultrasound between the two groups.

Table 3: Statistical results of positive rates of cardiac ultrasound in LVEF, LCDD, and LAD in the two groups.

Indicators	Positive rate (n %)	
	Control group	Experimental group
LVEF (%)	56	65
LCDD (mm)	59	69
LAD (mm)	57	66

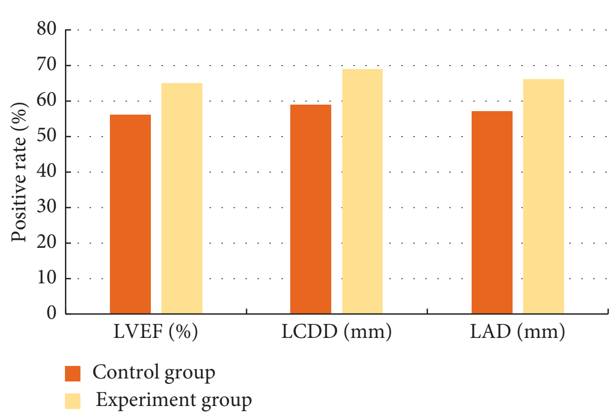

Figure 6: Comparison on positive rates of LVEF, LCDD, and LAD diagnosed by using a color Doppler ultrasound between the two groups.

which showed statistical significance ($P < 0.05$). In contrast, 77.2% of the patients from the control group and 83% from the experimental group had the combination of the two diseases. There was statistical significance in comparing the probability of patients with CHF among the three groups ($P < 0.05$), as shown in Figure 7.

4. Discussion

In today's medical field, the application of medical imaging technology in the screening, diagnosis and treatment, and evaluation of clinical diseases has become more and more extensive, and it is a very critical examination method [13]. Since the diagnosis and evaluation of image maps in the past was mainly carried out by excellent doctors and they had the uneven experience level, the results of the review were very different, and it was also highly subjective [14]. Therefore, as the deep learning artificial intelligence technology research has achieved excellent results, the technology has been extensively used in all aspects of the medical field, especially in the improvement and promotion of medical imaging technology, and has achieved good research results, showing good results in clinical examination and diagnosis [15]. At this stage, the medical imaging technology system and medical image processing and analysis are the most typical application scenarios of medical technology based on deep learning methods, and significant results have been achieved.

In this study, the neural network algorithm of deep learning was adopted to optimize and improve the color Doppler ultrasound images, which was applied in the diagnosis of CHF complicated with sarcopenia. The comparison of images before and after processing showed that the algorithm model had certain effect on image improvement, not only for color Doppler ultrasound image processing but also for other commonly used imaging techniques such as CT and MRI. Voets et al. [16] reported on the diagnosis of diabetic retinopathy in the *Journal of the American Medical Association*. It was proved that the end-to-end deep learning model could be directly applied to medical image processing, and the diagnostic results obtained were very similar with experts, which were even better than the diagnosis made by experts. Varghese et al. [17] combined imaging with machine learning (ML) to cross examine the accuracy of multiple ML algorithms for the detection of clinically significant PCa (csPCa). The results showed that the second kernel-based support vector machine (SVM) had the best accuracy, up to 92%. Zhang et al. [18] applied MSCTA three-dimensional reconstruction technology in the treatment of colorectal cancer. By comparing the consistency of the MSCTA three-dimensional reconstruction with the actual surgical plan, they found that the kappa consistency test between the two was $k = 0.769$,

Table 4: Comparison on the results of CHF patients diagnosed from the two groups and the final diagnosis results.

Symptom	Group		
	Control group	Experimental group	The final diagnosis results
CHF	200	215	230
Other diseases	59	44	29
CHF proportion	77.4%	83.1%	88.9%

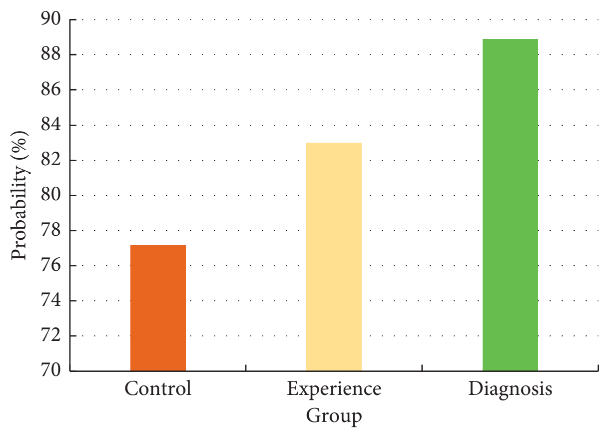

Figure 7: Comparison on the probability of patients with CHF in the three groups.

which proved MSCTA three-dimensional reconstruction had a good effect in guiding the treatment of colorectal cancer under laparoscopy.

In this study, CHF patients complicated with sarcopenia accounted for a large part of the total number of patients, which fully reflected that there was a certain connection between the two. Besides, the correlation between CHF and sarcopenia was extensively investigated. Some experts conducted a statistical study on 200 CHF patients with an average age of 70.8 ± 8.3 years, and the results showed that the incidence of CHF with sarcopenia was 19.5% [19]. A large number of studies have shown that 68% of patients with CHF are complicated with muscle fiber atrophy, the body mass of elderly patients with CHF is decreased, and the decreased exercise tolerance may be related to skeletal muscle fiber and skeletal muscle mass loss [20]. By exploring and analyzing CHF patients complicated with sarcopenia, foreign research experts have found recently that there is a certain correlation between skeletal muscle decline and pathological changes such as coronary atherosclerosis in elderly people and have proposed that sarcopenia may also have a reliable influence on the disease development of CHF [21]. Those mentioned above were similar to the results of this study, and there was a close correlation between CHF and the occurrence of sarcopenia.

5. Conclusions

In this study, the deep learning neural network algorithm is used to optimize and improve the color Doppler ultrasound image for the diagnosis of CHF complicated with myopenia. It is found that the processed image of the experimental group is clearer and has higher resolution than the unprocessed image of the control group. The final diagnosis result is more similar to the experimental group, which also indicates the correlation between CHF and myopenia. However, due to the limitation of the research scope, this study lacks a certain representativeness. However, the overall results show that the application of deep learning artificial intelligence in the field of imaging is still very promising.

Data Availability

The data used to support the findings of this study are available from the corresponding author upon request.

Conflicts of Interest

The authors declare no conflicts of interest.

Acknowledgments

This work was supported by the National Key Research and Development Plan of China (2020YFC2005600).

References

[1] T. M. Hoffman, "Chronic heart failure," *Pediatric Critical Care Medicine*, vol. 17, no. 8, pp. S119–23, 2016.

[2] A. Skrzypek, M. Mostowik, M. Szeliga, M. Wilczyńska-Golonka, D. Dębicka-Dąbrowska, and J. Nessler, "Chronic heart failure in the elderly: still a current medical problem," *Folia Medica Cracoviensia*, vol. 58, no. 4, pp. 47–56, 2018.

[3] J. Yin, X. Lu, Z. Qian, W. Xu, and X. Zhou, "New insights into the pathogenesis and treatment of sarcopenia in chronic heart failure," *Theranostics*, vol. 9, no. 14, pp. 4019–4029, 2019.

[4] A. Tournadre, G. Vial, F. Capel, M. Soubrier, and Y. Boirie, "Sarcopenia," *Joint Bone Spine*, vol. 86, no. 3, pp. 309–314, 2019.

[5] A. J. Cruz-Jentoft, G. Bahat, J. Bauer et al., "Sarcopenia: revised European consensus on definition and diagnosis," *Age Ageing*, vol. 48, no. 1, pp. 16–31, 2019.

[6] J. P. Sousa and M. Santos, "Symptom management and hospital readmission in heart failure patients: a qualitative study from Portugal," *Critical Care Nursing Quarterly*, vol. 42, no. 1, pp. 81–88, 2019.

[7] T. Vezzosi and K. E. Schober, "Doppler-derived echocardiographic evidence of pulmonary hypertension in cats with left-sided congestive heart failure," *Journal of Veterinary Cardiology*, vol. 23, pp. 58–68, 2019.

[8] B. Sahiner, A. Pezeshk, L. M. Hadjiiski et al., "Deep learning in medical imaging and radiation therapy," *Medical Physics*, vol. 46, no. 1, pp. e1–e36, 2019.

[9] A. Choudhary, L. Tong, Y. Zhu, and M. D. Wang, "Advancing medical imaging informatics by deep learning-based domain

adaptation," *Yearbook of Medical Informatics*, vol. 29, no. 1, pp. 129–138, 2020.

[10] H. P. Chan, R. K. Samala, L. M. Hadjiiski, and C. Zhou, "Deep learning in medical image analysis," *Advances in Experimental Medicine and Biology*, vol. 1213, pp. 3–21, 2020.

[11] L. K. Chen, L. K. Liu, J. Woo et al., "Sarcopenia in Asia: consensus report of the Asian working group for sarcopenia," *Journal of the American Medical Directors Association*, vol. 15, no. 2, pp. 95–101, 2018.

[12] J. D. Gazewood and P. L. Turner, "Heart failure with preserved ejection fraction: diagnosis and management," *American Family Physician*, vol. 96, no. 9, pp. 582–588, 2017.

[13] M. Biswas, V. Kuppili, L. Saba et al., "State-of-the-art review on deep learning in medical imaging," *Frontiers in Bioscience*, vol. 24, pp. 392–426, 2019.

[14] P. B. Zanzonico, "Benefits and risks in medical imaging," *Health Physics*, vol. 116, no. 2, pp. 135–137, 2019.

[15] J. C. Gore, "Artificial intelligence in medical imaging," *Magnetic Resonance and Imaging*, vol. 68, pp. A1–A4, 2020.

[16] M. Voets, K. Møllersen, and L. A. Bongo, "Reproduction study using public data of: development and validation of a deep learning algorithm for detection of diabetic retinopathy in retinal fundus photographs," *PLoS One*, vol. 14, no. 6, Article ID e0217541, 2019.

[17] B. Varghese, F. Chen, D. Hwang et al., "Objective risk stratification of prostate cancer using machine learning and radiomics applied to multiparametric magnetic resonance images," *Scientific Reports*, vol. 9, no. 1, p. 1570, 2019.

[18] J. L. Zhang, X. C. Guo, J. Liu et al., "Preoperative evaluation using multi-slice spiral CT angiography of right-side colon vascular in laparoscopic radical operation for right colon cancer," *Chinese Journal of Surgery*, vol. 57, no. 12, pp. 927–933, 2019, in Chinese.

[19] S. Fülster, M. Tacke, A. Sandek et al., "Muscle wasting in patients with chronic heart failure: results from the studies investigating co-morbidities aggravating heart failure (SICA-HF)," *European Heart Journal*, vol. 34, no. 7, pp. 512–519, 2013.

[20] D. W. Kitzman, B. Nicklas, W. E. Kraus et al., "Skeletal muscle abnormalities and exercise intolerance in older patients with heart failure and preserved ejection fraction," *American Journal of Physiology-Heart and Circulatory Physiology*, vol. 306, no. 9, Article ID H1364, 2014.

[21] S. Uchida, K. Kamiya, N. Hamazaki et al., "Association between sarcopenia and atherosclerosis in elderly patients with ischemic heart disease," *Heart Vessels*, vol. 35, no. 6, pp. 769–775, 2020.

Hindawi
Journal of Healthcare Engineering
Volume 2021, Article ID 9687591, 7 pages
https://doi.org/10.1155/2021/9687591

Research Article

Deep Learning-Based Denoised MRI Images for Correlation Analysis between Lumbar Facet Joint and Lumbar Disc Herniation in Spine Surgery

Feng Gao [1,2] and Mingcan Wu [3]

[1]*Department of Spine Surgery, Tongji Hospital, Tongji University School of Medicine, Shanghai 200065, China*
[2]*Spine Surgery, Yuyao People's Hospital of Zhejiang Province, Yuyao 315400, Zhejiang, China*
[3]*Department of Radiology, Yuyao People's Hospital of Zhejiang Province, Yuyao 315400, Zhejiang, China*

Correspondence should be addressed to Mingcan Wu; 202003000189@hceb.edu.cn

Received 26 May 2021; Revised 13 July 2021; Accepted 23 July 2021; Published 30 July 2021

Academic Editor: Enas Abdulhay

This work aimed to explore the relationship between spine surgery lumbar facet joint (LFJ) and lumbar disc herniation (LDH) via compressed sensing algorithm-based MRI images to analyze the clinical symptoms of patients with residual neurological symptoms after LDH. Under weighted BM3D denoising, Epigraph method was introduced to establish the novel CSMRI reconstruction algorithm (BEMRI). 127 patients with LDH were taken as the research objects. The BEMRI algorithm was compared with others regarding peak signal-to-noise ratio (PSNR) and structural similarity index (SSIM). Patients' bilateral LFJ angles were compared. The relationships between LFJ angles, lumbar disc degeneration, and LFJ degeneration were analyzed. It turned out that the PSNR and SSIM of BEMRI algorithm were evidently superior to those of other algorithms. The proportion of patients with grade IV degeneration was at most 31.76%. Lumbar disc grading was positively correlated with change grading of LFJ degeneration ($P < 0.001$). LFJ asymmetry was positively correlated with LFJ degeneration grade and LDH ($P < 0.001$). Incidence of residual neurological symptoms in patients aged 61–70 years was as high as 63.77%. The proportion of patients with severe urinary excretion disorders was 71.96%. Therefore, the BEMRI algorithm improved the quality of MRI images. Degeneration of LDH was positively correlated with degeneration of LFJ. Asymmetry of LFJ was notably positively correlated with the degeneration of LFJ and LDH. Patients aged 61–70 years had a high incidence of residual neurological symptoms after surgery, most of which were manifested as urinary excretion disorders.

1. Introduction

LDH is a common chronic spinal degenerative disease [1]. In recent years, the incidence of LDH has shown a significant upward trend, and a large number of studies have shown that LFJs are related to the occurrence of LDH [2]. In addition, studies have shown that the angle and asymmetry of LFJs are related to the occurrence of LDH [3]. Magnetic resonance imaging (MRI) technology is utilized in the diagnosis of LDH due to its noninvasiveness and multiple imaging angles. However, in the current research, there are generally cases where the results of imaging examinations do not match the patient's signs and symptoms. Moreover, due to the limited quality of MRI images, there are certain controversies about the occurrence of LFJ and LDH. Clinically, there are also cases where the images and physical signs do not match [4]. The quality of reconstructed images in traditional MRI algorithms is low. Some researchers applied compressed sensing (CS) theory to the reconstruction of MRI images and established the CSMRI algorithm, which can not only obtain the precise sparsity prior of the image but also capture the rich structural information of the image, and thus it is widely adopted in the field of MR image reconstruction. However, the CSMRI algorithm still cannot manage both image quality and calculation speed, and there is still room for further improvement in the quality of MR image reconstruction at low sampling rates [5].

At present, surgical methods are often adopted to treat LDH in clinic. Although surgical methods can significantly relieve the clinical symptoms of LDH patients, some patients still have residual neurological symptoms after surgery. The incidence of residual neurological symptoms after LDH is 5%–40%, with an average of 15%. The main manifestations are swelling, numbness, limp, and weakness of the lower limbs. Studies pointed out that the proportion of patients with lower extremity numbness after LDH operation was up to 21%–67%, and studies reported that patients with hip pain after LDH operation accounted for 63.1% [1]. At present, there are few studies on residual neurological symptoms in patients with LDH. Moreover, the proportion of symptoms after LDH is quite different, and further research on its symptoms is needed to provide a reference for the prognosis of LDH.

The deep ResNet method was introduced based on the deep learning algorithm to remove the Rician noise in MRI images and was applied to the diagnosis of LDH patients. From June 2018 to March 2020, 127 patients who underwent MRI diagnosis and were confirmed as LDH with residual neurological symptoms in our hospital's spine surgery were taken as the research objects. The relationship between LFJ, LDH, and residual neurological symptoms after surgery was explored to find out the cause of LDH and the residual neurological symptoms after surgery and provide a reference for the diagnosis and prognosis of LDH.

2. Materials and Methods

2.1. Research Objects. From June 2018 to March 2020, 127 patients who underwent MRI diagnosis and were confirmed as LDH with residual neurological symptoms in our hospital's spine surgery were taken as the research objects. 381 lumbar intervertebral discs and 381 pairs of LFJs and LFJs were measured.

The inclusion criteria in this study were defined as follows: patients diagnosed as LDH; patients without a history of lumbar spine surgery; patients who suffered from recurrent or persistent low back pain, sciatica, or its branch nerve compression symptoms 3 months after LDH surgery; and patients without prominent or nerve root compression or damage of original surgery segment after the surgery. The exclusion criteria could be determined as follows: patients whose MRI diagnosis images could not be found in the information query system of the hospital; patients with ankylosing spondylitis; patients with spinal tumors or lumbar tuberculosis; patients with failed LDH surgery; and patients accompanied by serious cardiovascular, cerebrovascular, liver and kidney, hematopoietic system or other serious diseases of other organs. The experimental process had been approved by the Ethics Committee of the hospital, and all subjects included in the study had signed the informed consent forms.

2.2. Denoising Algorithms for MRI Images Based on the Deep Learning. The traditional image denoising algorithms cannot completely remove the Rician noise in MRI images with relatively fuzzy image edge contours, and the deep learning mainly focuses on removing the Gaussian white noise. Therefore, the deep ResNet method was proposed based on the deep learning to remove the Rician noise in MRI images.

Gradient reduction could be found during the training of convolutional neural network (CNN) model, while the ResNet idea could solve this problem well. It was assumed that the input neural network of the ResNet was x and the function mapping was $H(x)$; then the expression of the residual mapping $F(x)$ was as follows:

$$F(x) = H(x) - x. \tag{1}$$

The expression equation of the hidden layer could be written as follows:

$$H(x) = F(x) + x. \tag{2}$$

It was expected to obtain the mapping $H(x)$ by training the deep network, while the residual learning could fit the residual mapping $F(x)$, and the residual learning equation was more suitable for solving the image denoising. The structure of ResNet is shown in Figure 1.

In the ResNet, the batch normalization (BN) method was used for intermediate preprocessing, so that the input of the previous layer was processed by BN before entering the next layer, which can avoid gradient explosion and improve the training speed. When the model was designed, BN was introduced after each convolutional layer. If one layer of the network was a d-dimensional input $x = \{x_1, x_2, \ldots, x_d\}$, it could be normalized as in the following equation:

$$x_k = \frac{x_k - E(x_k)}{\sqrt{\mathrm{Var}(x_k)}}, \tag{3}$$

where $E(x_k)$ refers to the expectation and $\mathrm{Var}(x_k)$ represents the variance.

Parameters γ_k and β_K were introduced to avoid influences on network learning features of this layer:

$$y_k = \gamma_k x_k + \beta_k. \tag{4}$$

If BN was not introduced, the activation function layer y could be expressed as follows:

$$y = s(\omega x + b), \tag{5}$$

where w refers to the weight; b and s represent the bias and activation function, respectively.

If the BN was introduced, the forward conduction could be written as in the following equation:

$$y = s(BN(\omega x + b)). \tag{6}$$

The above equation could be normalized as follows:

$$y = s(BN(\omega x)). \tag{7}$$

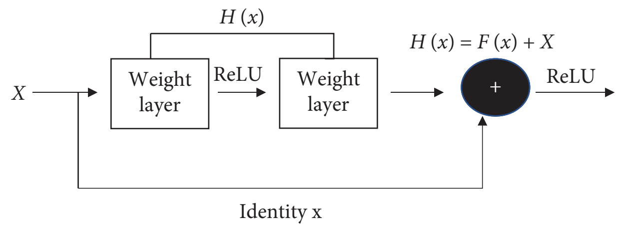

Figure 1: The structure of residual network.

The gradient descent algorithm was the commonly used optimization algorithm in the neural network training process so as to obtain the minimum parameters of the loss function. The single-step weight and bias update expressions were as follows:

$$\omega_k \longrightarrow \omega_k' = \omega_k - \left(\partial\frac{\delta C}{\delta \omega_k}\right),$$
$$b_l \longrightarrow b_l' = b_l - \left(\partial\frac{\delta C}{\delta b_l}\right). \tag{8}$$

The gradient descent algorithm was slow when the amount of data was large, so a stochastic gradient descent (SGD) algorithm was proposed. However, it adopted individuals to represent the overall change and cannot obtain the global optimal solution in each iteration. Therefore, the Adam algorithm was proposed in this study. The SGD algorithm updated all weights so that the learning rate remained stable during the network training. The Adam algorithm iteratively updated the weights of the neural network, which can solve the high-intensity noise or sparse gradient well.

As regards the Adam algorithm, the noise objective function was set to $f(\theta)$; the exponential moving average and square gradient were updated; and the deviation correction term was initialized.

$$v_t = (1-\beta_2)\sum_{i=1}^{t}\beta_2^{t-i}\cdot g_i^2, \tag{9}$$

where t represents the time step; β_2 refers to the exponential decay rate; and g represents the gradient.

After deviation correction, the expected value could be written as in the following equation:

$$\begin{aligned} E[v_t] &= E\left[(1-\beta_2)\sum_{i=1}^{t}\beta_2^{i-1}\cdot g_i^2\right],\\ &= E\left[g_t^2\right]\cdot(1-\beta_2)\sum_{i=1}^{t}\beta_2^{i-1} + \varsigma\\ &= E\left[g_t^2\right]\cdot(1-\beta_2) + \varsigma. \end{aligned} \tag{10}$$

If the second moment $E[g_t^2]$ was static, the ς value was 0.

The structure of the deep ResNet denoising model proposed in this study is shown in Figure 2. There were 15 network layers in total, 13 of which were hidden layers. Both the training image and the test image were grayscale ones. The size of the input layer was $3\times3\times1\times64$, including the activation function and the convolutional layer. The size of the hidden layer was $3\times3\times64\times64$, including activation function, BN, convolution, and pooling operations. The output layer size was $3\times3\times64\times1$, and the convolutional layer was reconstructed to output the image.

2.3. Degeneration Classification and Measurement Methods of LFJs and Lumbar Disc. The classification of LFJs could refer to the classification standards (0–3 levels) of LFJs degradation image defined by Song et al. [6]. L3/4, L4/5, and L5/S1 of the patients were scanned with MRI, and the scan line was parallel to the intervertebral space and passed through the corresponding LFJs. If the angle difference between two sides of LFJs of the same segment was greater than 7°, it was deemed that LFJs were asymmetric.

The grades of lumbar disc degeneration were divided into grades I–V [7]. The height of the first-level lumbar disc of the MRI image was to determine the degeneration grade. The vertical height of the center of the lumbar disc was calculated according to the two reference lines. According to the results of Brayda-Bruno et al. (2018) [8], the normal values of the height of each lumbar disc were 1.073 cm–1.247 cm for L3/4, 1.18 cm–1.272 cm for L4/5, and 0.939 cm–1.121 cm for L5/S1. It was determined as the slight decrease if the height was higher than 80% of the normal height. If the height was lower than 80% and higher than 60% of the normal height, it was deemed as a moderate decrease; and it was determined as gap collapse if the height was lower than 60% of the normal height.

2.4. Observation Indicators. The asymmetry of LFJs, LFJs degeneration grade, and lumbar disc degeneration were measured based on the MRI images of all patients. The basic clinical data, postoperative clinical manifestations, influencing factors, and nerve entrapment points were recorded for all patients.

2.5. Statistical Analysis. The experimental data was processed using SPSS 19.0 statistical software, the mean $\pm$ standard deviation ($\overline{x}\pm s$) was adopted to show the measurement data, and the t-test was employed for normal distribution. Spearman's rank correlation analysis was to analyze the lumbar disc degeneration grades, LFJs asymmetry, LFJs degeneration grades, LDH, and age, which did not obey the normal distribution ($\alpha = 0.005$). The count data of patients with postoperative residual neurological symptoms of different ages and different genders were expressed in percentage (%), tested by the χ^2 test. $P < 0.05$ indicated that the difference was considerable.

3. Results

3.1. Analysis of Denoising Performance of Different Algorithms. The proposed deep learning denoising algorithm was compared with the weighted stable matching (WSM) algorithm and denoising CNN (DnCNN) algorithm in terms of PSNR value (Figure 3(a)). The PSNR value of the

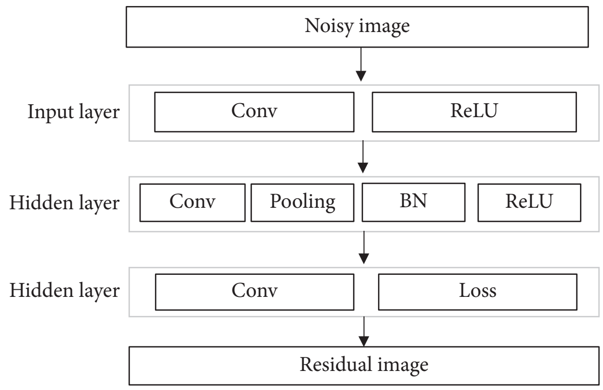

FIGURE 2: The structure of the deep ResNet denoising model.

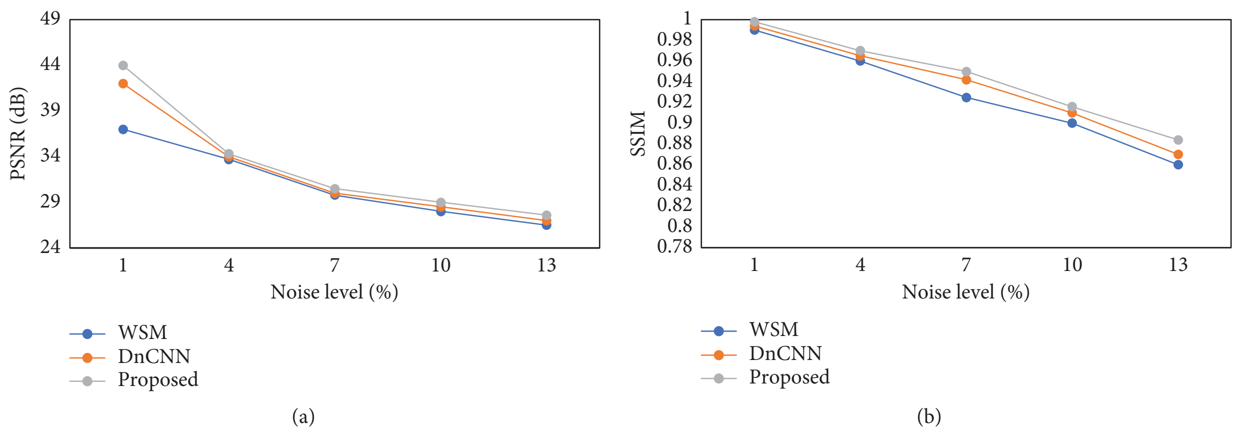

FIGURE 3: Comparison of PSNR and SSIM values under different algorithms. *Note.* (a) illustrates the comparison results of PSNR, and (b) discloses the comparison results of SSIM.

image after denoising by the proposed algorithm was higher than those of the WSM algorithm and DnCNN algorithm under different noise intensities. Further analysis of the SSIM values of various algorithms (Figure 3(b)) revealed that the SSIM value of the image after denoising by the proposed algorithm was still higher than those of other algorithms. Based on the above results, it was obtained that the proposed algorithm had obvious advantages in denoising of the medical MRI images.

3.2. MRI Examination of Patients with Lumbar Disc Herniation. The MRI image of the LDH patient was compared with the MRI image of the normal human body, and the results are shown in Figure 4. The MRI image of the patient showed an obvious disc herniation and compression of the nerve root and the right dural sac.

3.3. The Correlation between the Grades of Lumbar Disc Degeneration and Lumbar Facet Joint. The proportion of patients in different lumbar disc degeneration grades was analyzed and compared, as shown in Figure 5. The proportion of patients with degeneration grade 4 was up to 31.76%. Further, there was an obviously positive correlation between the lumbar disc degeneration grade and the LFJ degeneration grade ($r = 0.753$, and $P < 0.001$).

3.4. Correlation between Lumbar Facet Joint Degeneration and Lumbar Disc Herniation. The correlation between LFJ degeneration grade and LDH was analyzed, and the results are shown in Table 1. They were extremely and negatively correlated ($r = -0.306$, and $P < 0.001$).

3.5. Correlation between Lumbar Facet Joint Asymmetry and Lumbar Disc Herniation. As shown in Table 2, LFJ asymmetry was extremely and positively correlated with the LDH ($r = 0.543$, and $P < 0.001$).

3.6. Distribution of Patients with Postoperative Residual Neurological Symptoms. A total of 81 patients with LDH had postoperative residual neurological symptoms, accounting for 63.77%. As age increased, the number of patients with postoperative residual neurological symptoms tended to increase and then decrease. Moreover, the patients aged 61–70 years accounted for the highest proportion (Figure 6). There were 18 male patients (22.22%) and 15 female patients (18.52%) with residual neurological symptoms in the age

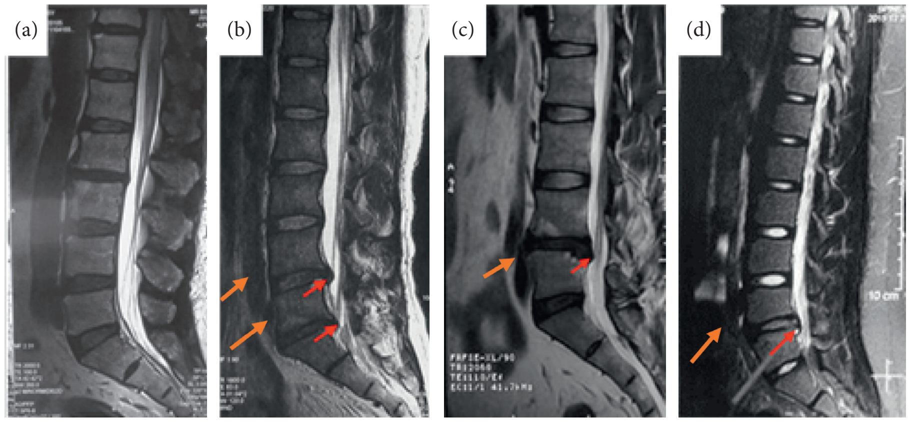

FIGURE 4: MRI of patients with LDH. (a) shows an MRI image of lumbar disc of a normal human body; (b) shows an MRI image of a male patient aged 42 years with L4/5 disc herniation; (c) shows an MRI image of L3/4 disc herniation for a female patient aged 39 years; and (d) shows an MRI image of L5/S1 right disc herniation for a male patient aged 64 years.

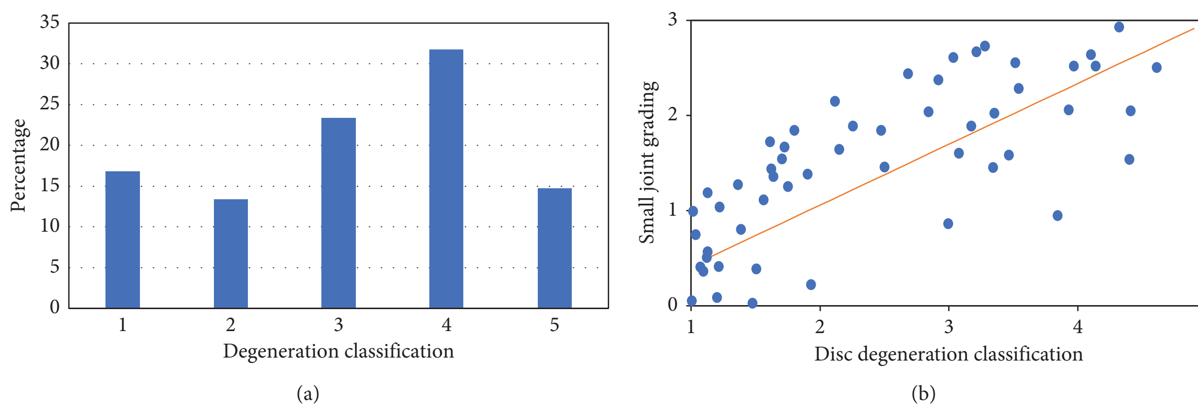

FIGURE 5: Distribution of lumbar disc degeneration grade and its correlation with LFJ degeneration grade. (a) illustrates the analysis of the proportion of patients in different grades of lumbar intervertebral disc degeneration; and (b) illustrates the correlation between the grades of lumbar intervertebral disc degeneration and LFJ degeneration.

TABLE 1: Correlation between LFJ degeneration and LDH.

LFJ degeneration grade	LDH		
	LDH (52 cases)	Lumbar disc bulging (69 cases)	No obvious herniation or bulging (6 cases)
Grade 0	14 (26.92%)	20 (38.46%)	2 (3.85%)
Grade 1	21 (40.38%)	31 (59.62%)	4 (7.69%)
Grade 2	10 (19.23%)	11 (21.15%)	0 (0)
Grade 3	7 (13.46%)	7 (13.46%)	0 (0)

TABLE 2: Correlation between LFJ asymmetry and LDH.

LFJs asymmetry	LDH		
	LDH (52 cases)	Lumbar disc bulging (69 cases)	No obvious herniation or bulging (6 cases)
L3/4	25 (48.08%)	23 (44.23%)	2 (3.85%)
L4/5	9 (17.31%)	15 (28.85%)	3 (5.77%)
L5/S1	18 (34.62%)	31 (59.62%)	1 (1.92%)

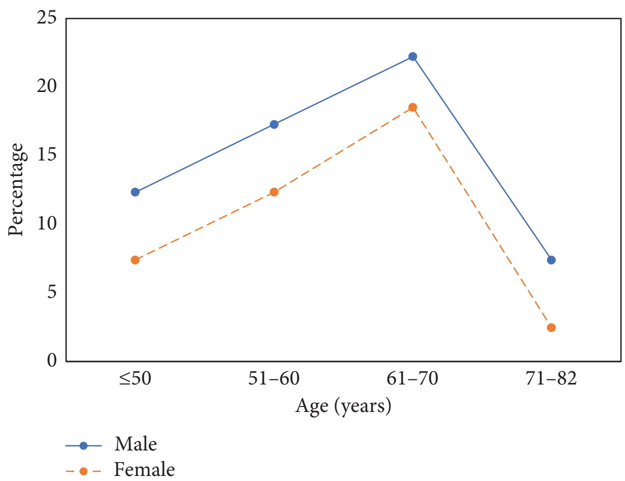

Figure 6: Analysis of the age and gender distribution of patients with postoperative residual neurological symptoms.

group of 61–70 years. In the entire age distribution, the proportion of males was higher than that of women, but the differences were not considerable ($P > 0.05$).

3.7. Symptoms of Postoperative Residual Neurological Symptoms. In this study, PRNSs of LDH were mainly manifested in waist pain, lower extremity radiating pain, buttock pain, waist movement limitation, lower extremity pain, lower extremity paresthesia, lower extremity weakness, severe urinary excretion disorder, and intermittent claudication (Figure 7). Most of patients suffered from serious urinary excretion disorders, reaching 71.96%.

4. Discussion

In this study, PSNR and SSIM values of the deep learning denoising algorithm were higher than those of other algorithms, showing that the quality of image treated with the deep learning denoising algorithm was higher [9, 10]. The proportion of patients with grade 4 degeneration was as high as 31.76%, and there was a dramatically positive correlation between the degeneration grade of lumbar disc and the degeneration grade of LFJ and age ($r = 0.753$, and $P < 0.001$). Ezemagu et al. [11] believed that herniation was caused when the pressure of the lumbar disc exceeded the load pressure. LFJs could protect the lumbar disc from damage due to excessive spine activity, so LFJ was positively correlated with herniation [12], which was similar to the results of this study. Cao et al. (2020) [13] found that the degeneration of LFJ could cause differences in the direction of the force on the lumbar disc nucleus pulposus, which could lead to different positions of LDH. There was a significantly positive correlation between LFJ degeneration grade and patient age ($r = 0.694$, and $P < 0.001$). There was a considerably negative correlation between LFJ degeneration and LDH ($r = -0.306$, and $P < 0.001$), and there was a significantly positive correlation between the asymmetry of LFJs and LDH ($r = 0.543$, and $P < 0.001$). The asymmetry of LFJs could cause the LFJs on one side to bear greater pressure, aggravate the degeneration and damage of the

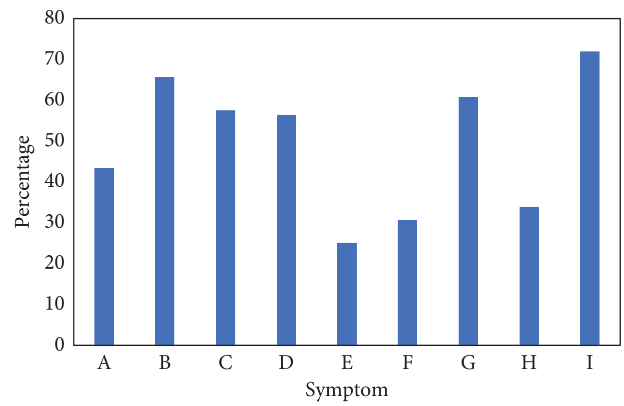

Figure 7: Symptoms of postoperative residual neurological symptoms. Note: A, B, C, D, E, F, G, H, and I in the horizontal coordinate refer to waist pain, hip pain, lower extremity radiating pain, lower extremity pain, waist movement limitation, lower extremity weakness, lower extremity paresthesia, intermittent claudication, and severe urinary excretion disorder, respectively.

lumbar disc, and result in the occurrence of LDH [14]. LDH patients with PRNSs accounted for 63.77%, and patients aged 61–70 years accounted for the highest proportion, which was consistent with the results of Wu et al. (2020) [15]. The proportion of patients with severe urinary excretion disorders accounted for more than 71.96%, which might be because most of patients were 61–70 years old and some older patients suffered from different degrees of prostate disease.

5. Conclusion

The deep ResNet method was introduced based on the deep learning algorithm to construct a deep learning denoising algorithm for MRI image. The constructed denoising algorithm was applied to the diagnosis of LDH patients. The correlations among LFJ angle, lumbar disc degeneration, and LFJ degeneration were analyzed. However, there were still some shortcomings in this study. The age span of the observation objects was large, and the different age groups were not classified and analyzed with the grading of intervertebral disc degeneration and the degree of degeneration of LFJs. It will supplement related data in the future research. In summary, the deep learning denoising algorithm can improve the quality of MRI image. The degeneration of the lumbar disc was extremely and positively correlated with the degeneration of LFJ; the asymmetry of LFJs was significantly and positively correlated with LFJ degeneration grade and LDH; and PRNSs were mainly concentrated in the people aged 61–70 years. This work provides a reference basis for the diagnosis, treatment, and prognosis of LDH [16–18].

Data Availability

The data used to support the findings of this study are available from the corresponding author upon request.

Conflicts of Interest

The authors declare no conflicts of interest.

References

[1] A. Rogerson, J. Aidlen, and L. G. Jenis, "Persistent radiculopathy after surgical treatment for lumbar disc herniation: causes and treatment options," *International Orthopaedics*, vol. 43, no. 4, pp. 969–973, 2019.

[2] A. Demirel, M. Yorubulut, and N. Ergun, "Regression of lumbar disc herniation by physiotherapy. Does non-surgical spinal decompression therapy make a difference? Double-blind randomized controlled trial," *Journal of Back Musculoskelet Rehabilitation*, vol. 30, no. 5, pp. 1015–1022, 2017.

[3] M. A. Alvi, P. Kerezoudis, W. Wahood, A. Goyal, and M. Bydon, "Operative approaches for lumbar disc herniation: a systematic review and multiple treatment Meta-analysis of conventional and minimally invasive surgeries," *World Neurosurgery*, vol. 114, pp. 391–407, 2018.

[4] N. Karimi, P. Akbarov, and L. Rahnama, "Effects of segmental traction therapy on lumbar disc herniation in patients with acute low back pain measured by magnetic resonance imaging: a single arm clinical trial," *Journal of Back Musculoskelet Rehabilitation*, vol. 30, no. 2, pp. 247–253, 2017.

[5] K. Zhang, W. Zuo, Y. Chen, D. Meng, and L. Zhang, "Beyond a Gaussian denoiser: residual learning of deep CNN for image denoising," *IEEE Transactions on Image Processing*, vol. 26, no. 7, pp. 3142–3155, 2017.

[6] Q. Song, X. Liu, D. J. Chen et al., "Evaluation of MRI and CT parameters to analyze the correlation between disc and facet joint degeneration in the lumbar three-joint complex," *Medicine (Baltimore)*, vol. 98, no. 40, Article ID e17336, 2019.

[7] Z. Feng, Y. Liu, G. Yang, M. C. Battié, and Y. Wang, "Lumbar vertebral endplate defects on magnetic resonance images: classification, distribution patterns, and associations with Modic changes and disc degeneration," *Spine (Phila Pa 1976)*, vol. 43, no. 13, pp. 919–927, 2018.

[8] M. Brayda-Bruno, D. Albano, G. Cannella, F. Galbusera, and A. Zerbi, "Endplate lesions in the lumbar spine: a novel MRI-based classification scheme and epidemiology in low back pain patients," *European Spine Journal*, vol. 27, no. 11, pp. 2854–2861, 2018.

[9] C. Tian, L. Fei, W. Zheng, Y. Xu, W. Zuo, and C. W. Lin, "Deep learning on image denoising: an overview," *Neural Networks*, vol. 131, pp. 251–275, 2020.

[10] D. Jiang, W. Dou, L. Vosters, X. Xu, Y. Sun, and T. Tan, "Denoising of 3D magnetic resonance images with multi-channel residual learning of convolutional neural network," *Japanese Journal of Radiology*, vol. 36, no. 9, pp. 566–574, 2018.

[11] U. K. Ezemagu, C. P. Anibeze, and C. F. Akpuaka, "Considering the inferior surface area of lower lumbar vertebrae: determining weight transmission pattern at the lumbosacral junction," *Anatomical Science International*, vol. 93, no. 2, pp. 277–283, 2018.

[12] J. Sutovsky, M. Benco, M. Sutovska et al., "Cytokine and chemokine profile changes in patients with lower segment lumbar degenerative spondylolisthesis," *International Journal of Surgery*, vol. 43, pp. 163–170, 2017.

[13] L. Cao, Y. Liu, W. Mei, J. Xu, and S. Zhan, "Biomechanical changes of degenerated adjacent segment and intact lumbar spine after lumbosacral topping-off surgery: a three-dimensional finite element analysis," *BMC Musculoskelet Disorders*, vol. 21, no. 1, p. 104, 2020.

[14] H. Sadeghian and R. Motiei-Langroudi, "Sonography guided lumbar nerve and facet blocks: the first report of clinical outcome from Iran," *Radiography (London)*, vol. 24, no. 1, pp. 52–56, 2018.

[15] X. B. Wu, Z. H. Li, Y. F. Yang, and X. Gu, "Two-level percutaneous endoscopic lumbar discectomy for highly migrated upper lumbar disc herniation: a case report," *World Journal of Clinical Cases*, vol. 8, no. 1, pp. 168–174, 2020.

[16] S. Elahi, M. Kaleem, and H. Omer, "Compressively sampled MR image reconstruction using generalized thresholding iterative algorithm," *Journal of Magnetic Resonance*, vol. 286, pp. 91–98, 2018.

[17] Y. Liu, Z. Zhan, J.-F. Cai, Di Guo, Z. Chen, and X. Qu, "Projected iterative soft-thresholding algorithm for tight frames in compressed sensing magnetic resonance imaging," *IEEE Transactions on Medical Imaging*, vol. 35, no. 9, pp. 2130–2140, 2016.

[18] E. Ahishakiye, M. B. Van Gijzen, J. Tumwiine, and J. Obungoloch, "Adaptive-size dictionary learning using information theoretic criteria for image reconstruction from undersampled k-space data in low field magnetic resonance imaging," *BMC Medical Imaging*, vol. 20, no. 1, p. 72, 2020.

Hindawi
Journal of Healthcare Engineering
Volume 2021, Article ID 1730158, 8 pages
https://doi.org/10.1155/2021/1730158

Research Article

Deep Learning-Based CT Image Characteristics and Postoperative Anal Function Restoration for Patients with Complex Anal Fistula

Lingling Han, Yue Chen, Weidong Cheng, He Bai, Jian Wang, and Miaozhi Yu

Department of Anorectal, Xinhua Hospital, Affiliated Hospital of Dalian University, Dalian 116021, China

Correspondence should be addressed to Lingling Han; 20151519@huanghuai.edu.cn

Received 24 May 2021; Revised 24 June 2021; Accepted 7 July 2021; Published 28 July 2021

Academic Editor: Enas Abdulhay

Objective. This study aimed to optimize the CT images of anal fistula patients using a convolutional neural network (CNN) algorithm to investigate the anal function recovery. *Methods*. 57 patients with complex anal fistulas admitted to our hospital from January 2020 to February 2021 were selected as research subjects. Of them, CT images of 34 cases were processed using the deep learning neural network, defined as the experimental group, and the remaining unprocessed 23 cases were in the control group. Whether to process CT images depended on the patient's own wish. The imaging results were compared with the results observed during the surgery. *Results*. It was found that, in the experimental group, the images were clearer, with DSC = 0.89, precision = 0.98, and recall = 0.87, indicating that the processing effects were good; that the CT imaging results in the experimental group were more consistent with those observed during the surgery, and the difference was notable ($P < 0.05$). Furthermore, the experimental group had lower RP (mmHg), AMCP (mmHg) scores, and postoperative recurrence rate, with notable differences noted ($P < 0.05$). *Conclusion*. CT images processed by deep learning are clearer, leading to higher accuracy of preoperative diagnosis, which is suggested in clinics.

1. Introduction

Anal fistula, also known as "anal leakage," is a chronic inflammatory disease that starts with the anal gland and then invades the anal canal and other normal skin tissues around the anus [1], so it is also defined as inflammatory rectum disease (RD) [2]. The anal fistula is composed of the internal opening, the fistula, and the external opening [3]. Complex anal fistula refers to the one with 2 or more internal or external openings and fistulas [4], which will bring great inconvenience to the patient's life. Its incidence is reported to be approximately 0.01%, and the young are predominantly affected [5]. There are two main treatment methods for anal fistula: one is conservative treatment based on traditional Chinese medicine, and the other is surgical treatment [6]. Nevertheless, for complex anal fistula, it is reported that the recurrence rate is as high as 30% to 50% or even 10% patients cannot be radically cured after another operation [7]. There are many factors that affect surgical treatment. The main factor is whether the positioning of the internal mouth is accurate before surgery [8, 9], and the symptomatic degree of the surgical plan will affect the probability of recurrence and the degree of anal function retention [10, 11]. The complex anal fistula is mainly treated by the surgery, with traditional Chinese medicine used for adjuvant treatment. Therefore, imaging examination is of great significance for the treatment of the complex anal fistula [12, 13].

The commonly used imaging examination methods include CT, MRI, and B-ultrasound. However, in the examination of complex anal fistulas, CT has low resolution for soft tissues, such as pelvic tissue and anal sphincter, so the accuracy rate is only 24%~60% [14]. With the rapid development of the technology, deep learning artificial intelligence technology is widely used in the field of imaging and the neural network system has made great progress in processing medical images, which has become a research hotspot [15]. Deep learning has solved two major problems in the medical field: one is the imbalance between the number of imaging doctors and clinical imaging data; the other is the imbalance in the level of imaging doctors and the allocation of resources [16]. Deep convolutional network models can learn image features from a large number of samples, achieving end-to-end classification and detection [17].

In this study, deep learning was used to process CT images of patients with complex anal fistula, which was expected to provide guidance for the clinical diagnosis and treatment of the disease.

2. Methods

2.1. Research Subjects. 57 patients admitted to our hospital from January 2019 to February 2020 who had been diagnosed with complex anal fistula were selected as research subjects, including 35 males and 22 females, aged 18~70, with an average age of (39.2 ± 2.1) years. All patients had the CT examination, and the CT images of 34 cases were processed using the convolutional neural network, defined as the experimental group, while the remaining unprocessed 23 cases were in the control group. Whether to process CT images depended on the patient's own wish. Clinically, all patients suffered from repeated swelling and pain around the anus, accompanied by pus discharge. The duration of the disease was 3 to 12 months, and the average duration of the disease was 7 months. Physical examination revealed purulent secretions around the anus and external opening on the skin surface. This study has been approved by the ethics committee, and the patients and their families have signed the informed consent forms. Intrarectal ultrasound, MRI, and CT examinations were conducted [18].

Patients were selected as per these inclusion criteria: (1) patients diagnosed with complex anal fistulas based on digital rectal examination, (2) the disease course lasted more than 3 months, (3) the length of the fistula was more than 3 cm (including 3 cm), (4) patients who had not undergone anal fistula surgery before, and (5) those aged between 18 and 75.

Exclusion criteria were as follows: (1) patients with the complex anal fistula caused by trauma, foreign body, infection, etc.; (2) patients accompanied by severe heart, lung, liver, and kidney dysfunction; (3) patients with cervical cancer, vaginal rectal fistula, rectal tumor, etc.; (4) patients in pregnancy and lactation; (5) patients with mental disorders; (6) patients with a history of pelvic and rectal radiotherapy; (7) patients with hematopoietic, endocrine, and immune system diseases.

2.2. Research Methods

2.2.1. CT Examination. The anti-infection treatment was performed on all patients 1 to 2 weeks before the CT scan, to improve the symptoms of the patients to meet the examination standards. 2 hours before the scan, intestine cleaning was needed. The specific process is shown in Figure 1. All patients shared an instrument and the same skilled and experienced imaging doctor who was responsible for the CT examination and image reconstruction. After image reconstruction, 2 experienced radiologists and anorectal doctors read the films together and recorded the various conditions of the fistula. Surgical plans were formulated based on the results of the CT examination and other auxiliary examinations.

2.2.2. CT Image Optimization Model Based on Convolutional Neural Network Algorithm. In this research, the convolutional neural network was used to optimize CT images. The convolutional neural network consists of the convolutional layer, the pooling layer, the fully connected layer, and the deconvolutional layer [19].

First, it is needed to collect the feature map of the CT image, provided that the convolutional layer has q layers, and then the feature map of the CT image input at the q-1 layer can be expressed by equation (1). Then, the feature map of the CT image input at the $q-1$ layer can be expressed by the following equation:

$$W(q,p) = \sum_{b=1}^{B} Y^{(q,p,b)} \otimes Z^{(q-1,b)} + l^{(q,p)}, \tag{1}$$

where $Y^{(q,p,b)}$ is the convolutional kernel, b is the number of feature maps, and $Y^{(q,p,b)}$ is the bias.

The activation function is a sigmoid transfer function, with a domain of $(-\infty, +\infty)$ and a value domain of (0, 1). It is continuously derivable in the domain, and its reciprocal $f(x)$ is easy to calculate. The specific equation is as follows:

$$\begin{aligned} Y &= f(x) = \frac{1}{1+e^{-x}}, \\ f'(x) &= f(x)(1-f(x)). \end{aligned} \tag{2}$$

Assume T is the CT image and U represents all pixels in T. The segmentation part of T is represented by O. Then, the probability that U_n outputs O_i in the i-th path can be expressed as follows:

$$T(u_n = O_i) = \frac{1}{A}\exp(\alpha(O_i)), \tag{3}$$

where $\alpha(O_i)$ is the value of Oi and A is a regularization term. Then, the S_n predicted by U_n can be expressed as follows:

$$Sn = argmax[T(u_n = O_i)]. \tag{4}$$

The corresponding loss function is as follows:

$$L = -\frac{1}{c\ d}\sum_n \sum_j y_{nj} \ln[T(u_n = O_i)]. \tag{5}$$

To minimize the loss function, the stochastic gradient descent [20] is used to solve equation (5).

If the function to be fitted is expressed as follows:

$$g(\delta) = \sum_{j=0}^{l} \delta_j x_j, \tag{6}$$

then the square loss function is

$$B(\delta) = \frac{1}{2m}\sum_{i=1}^{1}\left(y^i - g_\delta\left(x^i\right)\right)^2. \tag{7}$$

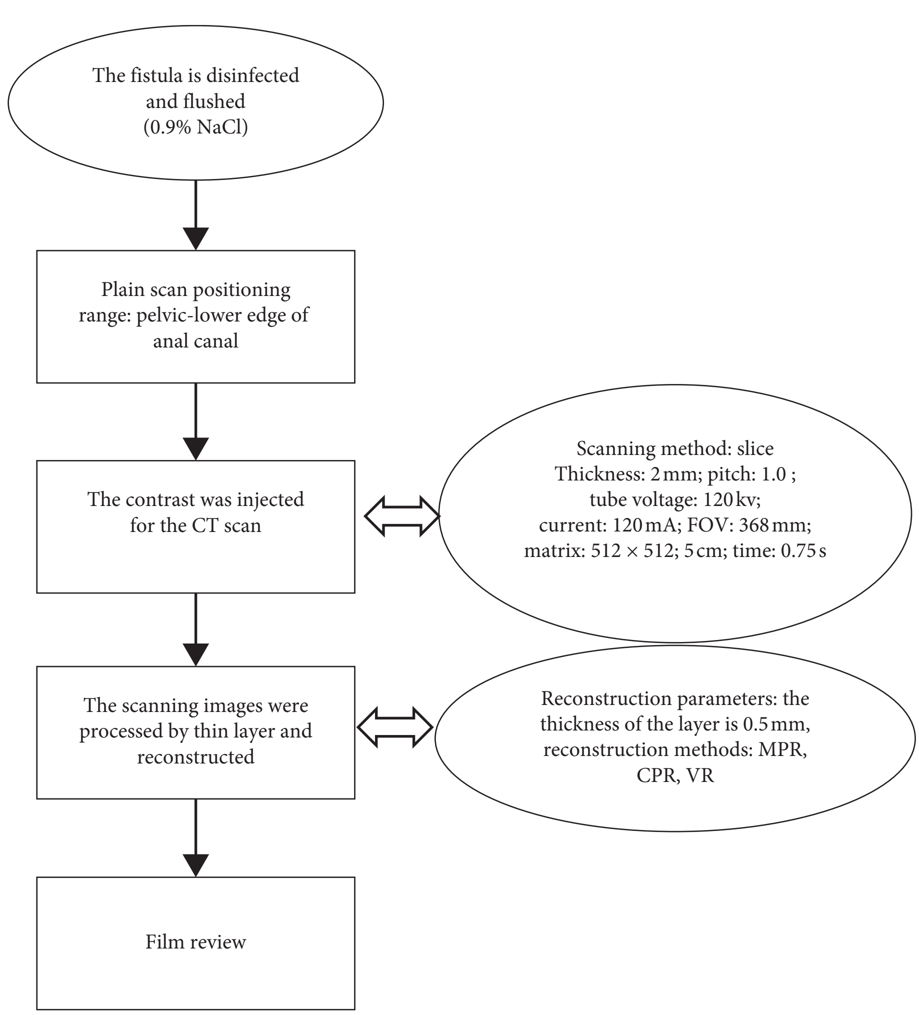

Figure 1: The specific process of CT examination.

The stochastic gradient descent method is used to update δ_j according to the sample:

$$\delta_j' = \delta_j + \left(y^i - g_\delta\left(x^i\right)\right)x^i. \tag{8}$$

The network parameters are obtained by solving equation (9), so as to obtain the network model as follows:

$$NLL(\delta, M) = -\sum_{i=0}^{|M|} logK\left(Y = y^{(i)}|x^{(i)}, \delta\right). \tag{9}$$

The processed pelvic CT image through the CNN algorithm is shown in Figure 2.

2.3. Evaluation of the Processed CT Image

2.3.1. Dice Similarity Coefficient. Dice similarity coefficient (DSC) is used to measure the similarity of two sets. The data pile can be regarded as a set, and the Dice distance is used to measure the similarity of strings.

The DSC is expressed as follows:

$$\mathrm{DSC} = \frac{2\times|G\cap J|}{|G| + |J|}\times 100\%, \tag{10}$$

where G is the algorithm segmentation result and J is the gold standard. If the DSC is closer to 1, the segmentation result is more accurate. If the DSC value is infinitely close to 0, it indicates that the segmentation result basically does not overlap with the gold standard and the segmentation fails.

2.3.2. Precision. Precision refers to the proportion of the number of correctly classified positive samples to the total number of classified positive samples. A closer precision value to 1 indicates a lower error rate. The precision is expressed as follows:

$$Pre = \frac{TP}{TP + FP}\times 100\%, \tag{11}$$

where TP stands for true positive, which is consistent with the gold standard; on the contrary, FP stands for false positive, which is inconsistent with the gold standard.

2.3.3. Recall Rate. Recall represents the ratio of the number of correctly classified positive samples to the total number of positive samples. A closer recall value to 1 indicates an error

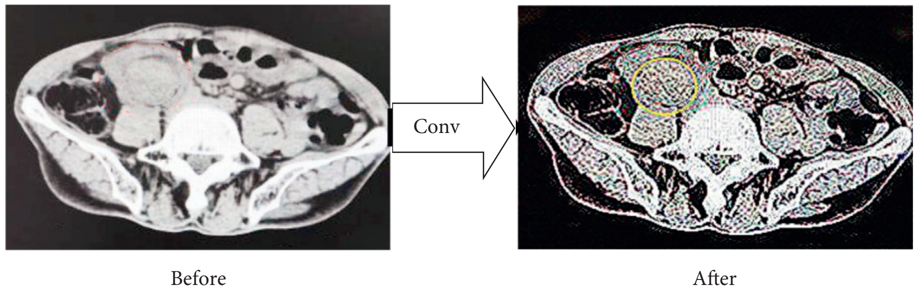

Figure 2: The processed pelvic CT image.

rate that the positive samples are incorrectly classified as negative samples. Recall is expressed as follows:

$$RE = \frac{TP}{TP + FN} \times 100\%, \quad (12)$$

where TP stands for true positive, FN stands for false negative, and the classification is also inconsistent with the gold standard.

Finally, it is concluded that DSC = 0.89, precision = 0.98, and recall = 0.87, which proves the feasibility of the model established in Section 2.3 and the effectiveness of image processing.

2.4. Observation Indicators

(1) The number and position of the internal and external openings of the fistula, whether the rectum, anal sphincter, and levator ani, are associated with the fistula, the area and length of the fistula, the diameter of the fistula, the fistula trend, whether there are complicated branches, and whether there is abscess formation.

(2) The recovery of anal function of the two groups of patients after surgical treatment was observed based on the CT images before and after the treatment. The Wexner anal incontinence score (Table 1) and anorectal manometry were used to evaluate its function. The parameters of anorectal manometry were anal rest pressure (ARP) and anal maximal construction pressure (AMCP).

2.5. Statistics. SPSS 22.0 was used to process data. Count data were expressed by percentage (%), the $Y2$ test was performed, and the rank sum test was performed for grade count data. The measurement data were expressed by the mean ± standard deviation, and the t-test was performed. $P < 0.05$ was the threshold for significance.

3. Results

3.1. Basic Information of Patients. As shown in Table 2, there was no notable difference in age, gender, and disease course of patients in the control group and the experimental group ($P > 0.05$), suggesting the feasibility of this study.

3.2. Examination Results and the Results after Surgical Treatment. After analyses, there was no difference in the external opening, while parameters such as the internal openings, the trend of the fistula, whether there was branch, whether the fistula was associated with the perianal muscle, and fistula diameter ≥ 2 mm were different from the results observed during the surgical treatment in both the experimental group and the control group, and notable differences were noted between the CT examination results and the postoperative results in both groups ($P < 0.05$), suggesting that the accuracy of CT examination was insufficient (Table 3). Figure 3 shows the CT images of the two groups of patients. Obviously, the optimized CT images were clearer.

3.3. Consistency between Examination Results and Postoperative Results. Table 4 shows the consistency between the examination results and the postoperative results. It was observed that in the experimental group, the consistency of the CT examination results and the postoperative results were higher than in the control group ($P < 0.05$) (Figure 4).

3.4. Postoperative Anal Function Recovery and Postoperative Recurrence Rate. Table 5 shows the statistics of Wexner anal incontinence score and anorectal manometry scores. It was found that the postoperative Wexner anal incontinence score of the experimental group was lower than that of the control group, showing notable differences. Additionally, the experimental group had lower RP (mmHg), AMCP (mmHg) scores, and the postoperative recurrence rate, and the difference was notable ($P < 0.05$). Figure 5 shows the CT images and the postoperative recovery of the two groups of patients, suggesting that both had good curative effects.

4. Discussion

Recently, CT imaging has been widely used in the examination of anal fistula diseases and it has certain advantages compared with other imaging techniques. Researchers have conducted a comparative study on the ordinary X-ray and CT imaging. The study found that the diagnosis of anal fistula with CT imaging is almost the same as the results of the surgery, with 96.7% of patients radically cured at one time, while the one-time cure rate of X-ray angiography is 70% [21]. The trend of fistulas is diverse and extremely irregular. Conventional two-dimensional CT images cannot

Table 1: Wexner anal incontinence score sheet.

Grade	Characteristics
Grade A	The anus function is normal, and the solid, liquid, and gas are well controlled
Grade B	The solid and liquid is well controlled but the gas is out of control
Grade C	Good control of solids, but there is a little liquid, infiltrating clothing
Grade D	Unable to control the liquid, it will often stain the clothes
Grade E	Both solids and liquids are out of control

Note. Grades A, B, and C indicate good anal function, while grades D and E indicate poor anal function.

Table 2: The basic information of patients.

Group	Gender		Age (year)	Disease course (month)
	Male ($n = 35$)	Female ($n = 22$)		
Control group ($n = 23$)	17	10	36.8 ± 4.1	8.3 ± 3.7
Experimental group ($n = 34$)	18	12	38.2 ± 5.0	7.6 ± 4.2

Table 3: Comparison of examination results and postoperative results.

		Anal fistula situation			
		Experimental group and postoperative results		Control group and postoperative results	
Grouping ($n = 34$)		Experimental group	Postoperative results	Control group	Postoperative results
2/2 or more internal openings		23	27	14	20
2/2 or more external openings		24	24	21	21
Fistula trend	"Y" sinus	12	14	7	10
	"U" sinus	11	15	5	8
	Other irregular sinuses	11	5	11	5
Whether there are branches beside the fistula		2	7	0	7
Whether it is associated with perianal muscles		14	17	12	19
Diameter of fistula ≥ 2 mm		24	29	13	21

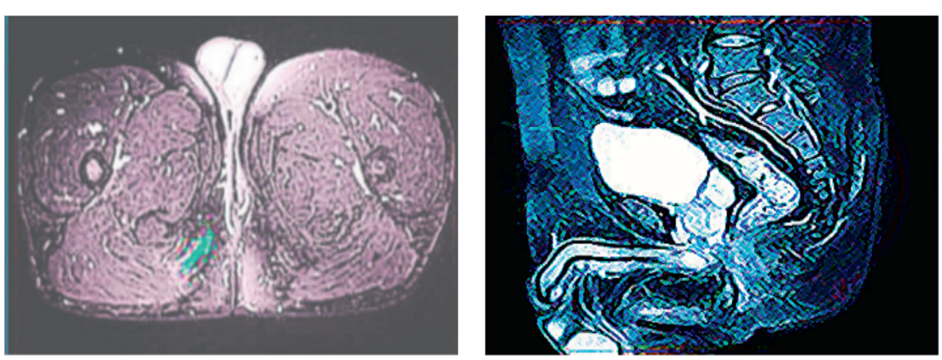

(a) (b)

Figure 3: Comparison of CT images of the two groups of patients. (a) Control group. (b) Experimental group.

Table 4: Consistency between the examination results and the postoperative results (n%).

Grouping		Anal fistula situation			
		Experimental group ($n = 34$)		Control group ($n = 23$)	
2/2 or more internal openings		85.1		70.0	
Fistula trend	"Y" sinus	85.7	79.5	70.0	66.3
	"U" sinus	73.3		62.5	

Table 4: Continued.

Grouping	Anal fistula situation	
	Experimental group ($n = 34$)	Control group ($n = 23$)
Whether there are branches beside the fistula	28.6	0
Whether it is associated with perianal muscles	82.4	61.2
Diameter of fistula ≥ 3 mm	82.8	62.0

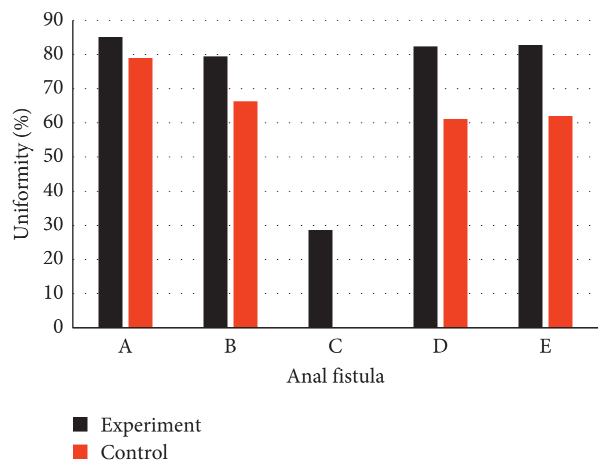

Figure 4: Comparison of the consistency with the results observed during the surgery. (a) 2/2 or more internal openings; (b) Fistula trend; (c) Whether there are branches beside the fistula; (d) Whether it is associated with perianal muscles; (e) Diameter of fistula ≥ 3 mm.

Table 5: Postoperative anal function recovery and recurrence rate.

Grouping	Wexner anal incontinence score		Anorectal manometry		Recurrence rate (n%)
	Preoperative	Postoperative	ARP (mmHg)	AMCP (mmHg)	
Experimental group	0.10 ± 0.24	1.06 ± 1.34	43.43 ± 9.41	122.71 ± 12.56	20
Control group	0.14 ± 0.29	0.34 ± 0.61	47.98 ± 10.21	137.63 ± 16.99	54

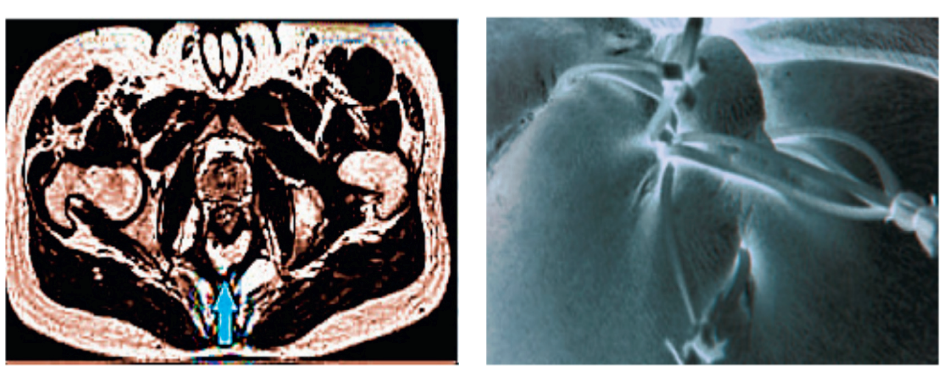

(a) (b)

Figure 5: Continued.

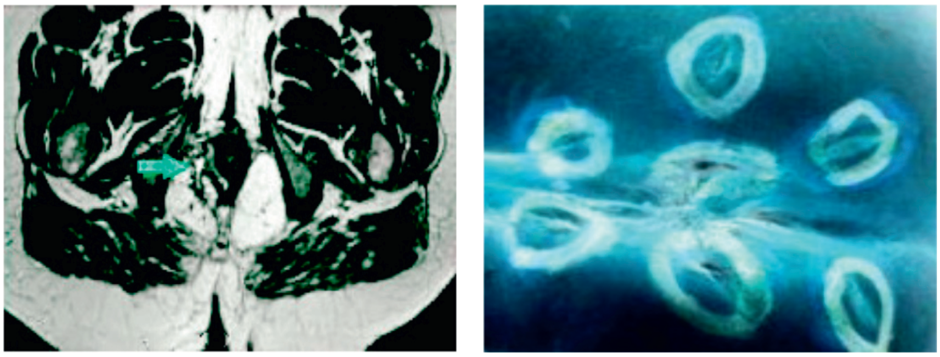

Figure 5: CT images and postoperative results. (a) CT image of the experimental group; (b) postoperative performance of the experimental group; (c) CT image of the control group; (d) postoperative performance of the control group.

fully display its distribution, and it is impossible to make accurate judgment. Hence, it is urgent to optimize the technology. There is abundant research combining CT imaging technology with three-dimensional reconstruction and applying them to the examination of anal fistulas. The results found that the accuracy, sensitivity, and specificity of the diagnosis of the internal opening of anal fistula have reached more than 90%, suggesting good effects [15]. The artificial intelligence in deep learning has made good progress in the field of medicine, especially in the field of medical imaging. Higaki et al. [22] applied fully convolutional neural networks and dense 3D conditional random field (CRF) technology to CT images for liver segmentation studies, to understand liver lesions. Tao et al. [23] applied FCN technology to the automatic analysis of cardiac magnetic resonance (CMR). In this study, the deep neural network was used to process the CT images of patients with anal fistulas. It was found that the deep learning-based CT imaging demonstrated good examination, diagnosis, and treatment results. Studies have also shown that higher accuracy of the preoperative diagnosis leads to better surgical effects, a greater possibility of recovery of anal function, and a lower probability of recurrence. Some experts have statistically studied 17 patients with complex anal fistula who underwent MSCT angiography diagnosis before the surgery. Some experts have statistically studied 17 patients with complex anal fistula who underwent multislice CT (MSCT) angiography diagnosis before the surgery. It was found that the consistency between the preoperative diagnosis and the surgical findings was close to 100%, and in the 1-year follow-up survey, there was no recurrence and the anal function recovered well [24]. In conclusion, deep learning-based CT imaging is worthy of promotion for the preoperative diagnosis of patients with anal fistula.

5. Conclusion

In this study, the deep learning neural network was used to process the CT images of patients with anal fistula and the preoperative imaging results were compared with the results observed during the surgery. It was found that in the experimental group, the CT imaging results were more consistent with those observed during the surgery ($P < 0.05$) and the images were clearer. Furthermore, the anal function recovery in the experimental was better.

To sum up, CT images processed by deep learning are clearer, leading to higher accuracy of preoperative diagnosis, better surgical effects, a higher possibility of recovery, and a lower recurrence rate, which is suggested in clinics.

Data Availability

No data were used to support this study.

Conflicts of Interest

The authors declare that they have no conflicts of interest.

References

[1] A. Amato, C. Bottini, P. De Nardi et al., “Evaluation and management of perianal abscess and anal fistula: SICCR position statement,” *Techniques in Coloproctology*, vol. 24, no. 2, pp. 127–143, 2020.

[2] S. Balci, M. R. Onur, M. R. Onur et al., “MRI evaluation of anal and perianal diseases,” *Diagnostic and interventional radiology*, vol. 25, no. 1, pp. 21–27, 2019 Jan.

[3] B. K. Jain, “Pre-surgery assessment of anal fistula,” *Techniques in Coloproctology*, vol. 24, no. 7, pp. 775-776, 2020 Jul.

[4] B. Schulze and Y.-H. Ho, “Management of complex anorectal fistulas with seton drainage plus partial fistulotomy and subsequent ligation of intersphincteric fistula tract (LIFT),” *Techniques in Coloproctology*, vol. 19, no. 2, pp. 89–95, 2015 Feb.

[5] M. Ferrer-Márquez, N. Espínola-Cortés, Á. Reina-Duarte, J. Granero-Molina, C. Fernández-Sola, and J. M. Hernández-Padilla, “Analysis and description of disease-specific quality of life in patients with anal fistula,” *Cirugía Española*, vol. 96, no. 4, pp. 213–220, 2018 Apr.

[6] S. Schlichtemeier and S. Tou, “Treatment for complex anal fistula, are we any wiser?” *Colorectal Disease*, vol. 20, no. 12, pp. 1067-1068, 2018 Dec.

[7] F. Cadeddu, F. Salis, G. Lisi, F. Cao, I. Ciangola, and G. Milito, “Complex anal fistula remains a challenge for colorectal surgeon,” *International Journal of Colorectal Disease*, vol. 30, no. 5, pp. 595–603, 2015.

[8] C. M. Rosenbaum, M. W. Vetterlein, and M. Fisch, "Fistelchirurgie," *Urologe A, Der*, vol. 59, no. 4, pp. 489–498, 2020 Apr.

[9] P. Garg, S. S. Sodhi, and N. Garg, "Management of complex cryptoglandular anal fistula: challenges and solutions," *Clinical and Experimental Gastroenterology*, vol. 13, pp. 555–567, 2020 Nov.

[10] S. M. Murad-Regadas, F. S. P. Regadas Filho, E. d. C. Holanda, L. B. Veras, A. d. S. Vilarinho, and M. S. Lopes, "Can three-dimensional anorectal ultrasonography be included as a diagnostic tool for the assessment OF anal fistula before and after surgical treatment?" *Arquivos de Gastroenterologia*, vol. 55, no. 1, pp. 18–24, 2018 Nov.

[11] A. Brillantino, F. Iacobellis, A. Reginelli et al., "Preoperative assessment of simple and complex anorectal fistulas: tridimensional endoanal ultrasound? Magnetic resonance? Both?" *La radiologia medica*, vol. 124, no. 5, pp. 339–349, 2019 May.

[12] A. Konan, M. R. Onur, M. R. Onur, and M. N. Ozmen, "The contribution of preoperative MRI to the surgical management of anal fistulas," *Diagnostic and interventional radiology*, vol. 24, no. 6, pp. 321–327, 2018 Nov.

[13] W. Wanitsuwan, K. Junmitsakul, S. Jearanai, and V. Lohsiriwat, "Video-assisted ligation of intersphincteric fistula tract for complex anal fistula: technique and preliminary outcomes," *Diseases of the Colon & Rectum*, vol. 63, no. 11, pp. 1534–1540, 2020 Nov.

[14] Z. Zhou, "[Pay attention to the imaging diagnosis of complex anal fistula]," *Zhonghua Wei Chang Wai Ke Za Zhi*, vol. 18, no. 12, pp. 1193–1196, 2015 Dec.

[15] S. Bhatt, B. K. Jain, and V. K. Singh, "Multi detector computed tomography fistulography in patients of fistula-in-ano: an imaging collage," *Polish Journal of Radiology*, vol. 82, pp. 516–523, 2017 Sep.

[16] G. Zaharchuk, E. Gong, M. Wintermark, D. Rubin, and C. P. Langlotz, "Deep learning in neuroradiology," *American Journal of Neuroradiology*, vol. 39, no. 10, pp. 1776–1784, 2018 Oct.

[17] P. Lakhani, D. L. Gray, C. R. Pett, P. Nagy, and G. Shih, "Hello world deep learning in medical imaging," *Journal of Digital Imaging*, vol. 31, no. 3, pp. 283–289, 2018 Jun.

[18] H.-P. Chan, R. K. Samala, L. M. Hadjiiski, and C. Zhou, "Deep learning in medical image analysis," *Advances in Experimental Medicine & Biology*, vol. 1213, pp. 3–21, 2020.

[19] M. Jimenez and N. Mandava, *Anorectal Fistula*, StatPearls Publishing, Treasure Island, FL, USA, 2021 Jan.

[20] N. Kriegeskorte and T. Golan, "Neural network models and deep learning," *Current Biology*, vol. 29, no. 7, pp. R231–R236, 2019 Apr.

[21] S. Thipphavong, A. F. Costa, H. A. Ali, D. C. Wang, M. S. Brar, and K. S. Jhaveri, "Structured reporting of MRI for perianal fistula," *Abdominal Radiology*, vol. 44, no. 4, pp. 1295–1305, 2019 Apr.

[22] T. Higaki, Y. Nakamura, F. Tatsugami, T. Nakaura, and K. Awai, "Improvement of image quality at CT and MRI using deep learning," *Japanese Journal of Radiology*, vol. 37, no. 1, pp. 73–80, 2019 Jan.

[23] Q. Tao, B. P. F. Lelieveldt, and R. J. van der Geest, "Deep learning for quantitative cardiac MRI," *American Journal of Roentgenology*, vol. 214, no. 3, pp. 529–535, 2020 Mar.

[24] A. Taccone, G. Martucciello, and P Dodero, "Preoperative evaluation of anal fistula by multi-slice spiral CT combined with fistulography," *Colorectal diseases of integrated traditional Chinese and Western medicine*, vol. 1, no. 3, pp. 154–156, 2007.

Hindawi
Journal of Healthcare Engineering
Volume 2021, Article ID 6095676, 7 pages
https://doi.org/10.1155/2021/6095676

Research Article

Edge-Preserving Median Filter and Weighted Coding with Sparse Nonlocal Regularization for Low-Dose CT Image Denoising Algorithm

Quan Yuan,[1] **Zhenyun Peng**,[1] **Zhencheng Chen**,[1] **Yanke Guo**,[1] **Bin Yang**,[2] **and Xiangyan Zeng**[3]

[1]*School of Electronic Engineering and Automation, Guilin University of Electronic Technology, Guilin 541004, Guangxi, China*
[2]*Xi'an Tapo Primary School, Chang'an District, Xi'an 710119, Shaanxi, China*
[3]*School of Mathematics and Computing Science, Guilin University of Electronic Technology, Guilin 541004, Guangxi, China*

Correspondence should be addressed to Zhencheng Chen; 1808008004@mails.guet.edu.cn

Received 26 May 2021; Accepted 16 July 2021; Published 27 July 2021

Academic Editor: Enas Abdulhay

The impulse noise in CT image was removed based on edge-preserving median filter algorithm. The sparse nonlocal regularization algorithm weighted coding was used to remove the impulse noise and Gaussian noise in the mixed noise, and the peak signal-to-noise ratio (PSNR) and structural similarity index (SSIM) were calculated to evaluate the quality of the denoised CT image. It was found that in nine different proportions of Gaussian noise and salt-and-pepper noise in Shepp-Logan image and CT image processing, the PSNR and SSIM values of the proposed denoising algorithm based on edge-preserving median filter (EP median filter) and weighted encoding with sparse nonlocal regularization (WESNR) were significantly higher than those of using EP median filter and WESNR alone. It was shown that the weighted coding algorithm based on edge-preserving median filtering and sparse nonlocal regularization had potential application value in low-dose CT image denoising.

1. Introduction

CT images are susceptible to the interference of quantum noise and electronic noise of detectors and other noises during the acquisition process, which causes the quality of reconstructed images to decrease, which in turn affects the diagnosis of diseases by doctors [1]. Under normal circumstances, the scan dose is proportional to the sharpness of the CT image. However, CT radiation dose is accumulated throughout the life, and multiple CT scans will increase the risk of cancer [2, 3]. Low-dose CT scan can reduce the radiation dose of patients, reduce equipment damage, reduce costs, and is conducive to the general investigation and cure of certain diseases [4]. However, the reduction of low-dose CT tube current leads to rapid degradation of projection data. After traditional algorithms are reconstructed, there are still obvious noises and artifacts in the CT reconstructed image, which seriously affects the credibility of the doctor's diagnosis. Low-dose CT scan technology is unable to give full play to its accurate diagnostic efficacy in clinical practice [5]. There may be some isolated impulse noise points in some areas of low-dose CT images. After these isolated impulse noise points are filtered, the CT image data is distributed in the form of Gaussian noise [6]. Due to the complexity of the distribution of noise and artifacts in low-dose CT images, it is difficult to establish a suitable and accurate prior model of noise in the image domain reconstruction method. The image preprocessing is complex, and the calculation is large, which affects the real-time clinical application of CT. The postprocessing method is a method that is directly applied to the reconstructed low-dose CT image to improve its image quality [7]. The method is simple and easy to implement and has good compatibility with existing CT equipment.

According to the sparse representation theory, the differences in the learning dictionary caused by individual differences and differences in tissues and organs in CT images are very small [8]. Chen et al. [5] improved the reconstruction quality of low-dose CT images with a sparse image reconstruction method. Cui et al. [9] proposed a learning method based on morphological component analysis, which can automatically generate an adaptive discriminant dictionary and effectively suppress the artifacts of low-dose CT images under the framework of sparse representation. Jiang et al. [10] proposed a denoising algorithm based on weighted coding and sparse nonlocal regularization (WESNR), which simultaneously removes impulse noise and Gaussian noise through soft impulse pixel detection. The principal component analysis (PCA) dictionary was used to encode image blocks, and the coding residuals were weighted to suppress the heavy tail of the distribution. The image sparse prior and nonlocal self-similarity prior were merged into a single nonlocal sparse regularization term, which enhances the stability of weighted coding. However, when this method was applied to low-dose CT image denoising, details were lost, and edges were destroyed. A variety of edge preservation filters can solve the problem of incorrect removal of edges and lines in the image denoising process. The feature of edge-preserving filtering is that it can extract the spatial constraint factors of the edge information in the reference image to process the original image, thereby smoothing and edge-preserving it. Among them, edge-preserving median filter (EP median filter) has a good performance in terms of operation speed and edge protection [11]. However, the edge-preserving filtering algorithm is not effective for mixed noise and noise with low signal-to-noise ratio.

In this exploration, a denoising algorithm based on EP median filter and WESNR is proposed, which can remove the mixed noise of low-dose CT image and preserve the edge information of the image.

2. Algorithm Based on WESNR and EP Median Filter

2.1. Mixed Noise Model. For image x with size $m \times n$, $x_{i,j}$ is the gray value at (i, j), and y is set as the observed image of image x. For adding Gaussian noise, the pixels $y_{i,j}$ in y are defined as $y_{i,j} = x_{i,j} + v_{i,j}$, where $v_{i,j}$ is the independent and identically distributed noise; for the salt-and-pepper noise, $[d_{\min}, d_{\max}]$ represents the dynamic range of y pixels in the observation image, and the probability of salt-and-pepper noise is s, $0 \le s \le 1$. Then, the probability of $y_{i,j} = d_{\min}$ is $s/2$, and the probability of $y_{i,j} = d_{\max}$ is $s/2$. Therefore, the observation image mixed with Gaussian noise and salt-and-pepper noise can be described as follows:

$$y_{i,j} = \begin{cases} d_{\min}, & \text{the probability is } \dfrac{s}{2}, \\ d_{\max}, & \text{the probability is } \dfrac{s}{2}, \\ x_{i,j} + v_{i,j}, & \text{the probability is } 1 - s. \end{cases} \tag{1}$$

2.2. EP Median Filter Algorithm. The pixel at $(i, j)(3 \le i \le m-2, 3 \le j \le n-2)$ in image y has the neighborhood of 5×5 in Figure 1. If (i, j) is a point in a flat area, most of the gray values of 24 pixels in its neighborhood should be close to it. Even if there are few noise points, it can be set to less than one-fourth; that is, the number $t_{i,j}$ of absolute values of gray value difference greater than a certain threshold T is less than or equal to 6; if (i, j) is an edge point, about half of the gray values of the 24 pixels in its neighborhood should be close to it, and the other half should have a large difference with it; that is, the number $t_{i,j}$ of gray values whose absolute value is greater than a certain threshold T should be about 12; if (i, j) is a noise point, most of the gray values of the 24 pixels in its neighborhood should not be close to it. It can be set as no less than three-fourths; that is, the number $t_{i,j}$ of absolute values of gray value difference greater than a certain threshold value T is greater than or equal to 18.

The standard deviation of image y is taken as the threshold T; that is,

$$T = \sqrt{\frac{\sum_{i=1}^{m} \sum_{j=1}^{n} \left(y_{i,j} - \overline{y}\right)^2}{m \cdot n}}, \tag{2}$$

where $\overline{y}$ is the mean value of all gray values of image y; that is,

$$\overline{y} = \sqrt{\frac{\sum_{i=1}^{m} \sum_{j=1}^{n} \left(y_{i,j}\right)}{m \cdot n}}, \tag{3}$$

Based on the above assumption, $(i, j)(3 \le i \le m-2, 3 \le j \le n-2)$ can be divided into points in flat area, edge points, and noises.

① $t_{i,j} \le 6$, (i, j) is the point of the flat area.

② $6 < t_{i,j} < 18$, (i, j) is the edge point.

③ $t_{i,j} \ge 18$, (i, j) is the noise.

When (i, j) is noise, the gray value at (i, j) of the original image is replaced by the mean value of $y_{i,j}$, $y_{i,j-1}$, $y_{i-1,j}$, $y_{i+1,j}$, $y_{i,j+1}$, $y_{i-1,j-2}$, $y_{i+1,j-2}$, $y_{i-2,j-1}$, $y_{i+2,j-1}$, $y_{i-2,j+1}$, $y_{i+2,j+1}$, $y_{i-1,j+2}$, and $y_{i+1,j+2}$. The pixels participating in the assignment and their gray values are the shadow parts in Algorithm 1, and the mean value is $a_{i,j}$; that is,

$y_{i-2,j-2}$	$y_{i-2,j-1}$	$y_{i-2,j}$	$y_{i-2,j+1}$	$y_{i-2,j+2}$
$y_{i-1,j-2}$	$y_{i-1,j-1}$	$y_{i-1,j}$	$y_{i-1,j+1}$	$y_{i-1,j+2}$
$y_{i,j-2}$	$y_{i,j-1}$	$y_{i,j}$	$y_{i,j+1}$	$y_{i,j+2}$
$y_{i+1,j-2}$	$y_{i+1,j-1}$	$y_{i+1,j}$	$y_{i+1,j+1}$	$y_{i+1,j+2}$
$y_{i+2,j-2}$	$y_{i+2,j-1}$	$y_{i+2,j}$	$y_{i+2,j+1}$	$y_{i+2,j+2}$

$y_{i-2,j-2}$	$y_{i-2,j-1}$	$y_{i-2,j}$	$y_{i-2,j+1}$	$y_{i-2,j+2}$
$y_{i-1,j-2}$	$y_{i-1,j-1}$	$y_{i-1,j}$	$y_{i-1,j+1}$	$y_{i-1,j+2}$
$y_{i,j-2}$	$y_{i,j-1}$	$y_{i,j}$	$y_{i,j+1}$	$y_{i,j+2}$
$y_{i+1,j-2}$	$y_{i+1,j-1}$	$y_{i+1,j}$	$y_{i+1,j+1}$	$y_{i+1,j+2}$
$y_{i+2,j-2}$	$y_{i+2,j-1}$	$y_{i+2,j}$	$y_{i+2,j+1}$	$y_{i+2,j+2}$

Figure 1: Gray value of (i, j) and its neighborhood Algorithm 1 Pixels participating in $a'_{i,j}$ assignment and their gray values.

Input: noisy image y.
For $(i, j)\,(1 \le i \le m, 1 \le j \le n)$:
① When $i \le 2$, or $i \ge m-1$, or $j \le 2$, or $j \ge n-1$, make: $y'_{i,j} = y_{i,j}$.
② When $3 < i < m-2$, $3 < j < n-2$, and $t_{i,j} < 18$, make: $y'_{i,j} = y_{i,j}$.
③ When $3 < i < m-2$, $3 < j < n-2$, and $t_{i,j} \ge 18$, make: $y'_{i,j} = a_{i,j}$.
Image y' is obtained.
Initialization: $e^{(0)} = y' - x^{(0)}$, $W_{ii} = \exp(-ae_i^2)$, $\mu = 0$, $k = 1$, $y''^{(0)} = y'$.
When $k \le K$, the following cycle is performed:
(1) $\hat{\alpha}^{(k)} = (\Phi^T W \Phi + V^{(k)})^{-1} (\Phi^T W y' - \Phi^T W \Phi \mu) + \mu$ is calculated;
(2) $y''^{(k)} = \Phi \alpha^{(k)}$ is calculated and the nonlocal coding vector μ is updated;
(3) $e^{(k)} = y' - y''^{(k)}$ is calculated;
(4) $W_{ii} = \exp(-ae_i{}^2)$ is used to calculate weight W;
(5) $k \le k+1$
$y'' = \Phi \alpha^{(K)}$
Output: denoised image y''.

Algorithm 1: Flow chart of the algorithm proposed.

$$a_{i,j} = \frac{\left(y_{i,j} + y_{i,j-1} + y_{i-1,j} + y_{i+1,j} + y_{i,j+1} + y_{i-1,j-2} + y_{i+1,j-2} + y_{i-2,j-1} + y_{i+2,j-1} + y_{i-2,j+1} + y_{i+2,j+1} + y_{i-1,j+2} + y_{i+1,j+2}\right)}{13}. \tag{4}$$

The gray values of all the pixels in $(i, j)\,(i \le 2$, or $i \ge m-2$, or $j \le 2$, or $j \ge n-2)$ are not modified, the gray values of the points in the flat area and the edge points in $(i, j)\,(3 \le i \le m-2, 3 \le j \le n-2)$ are not modified, and the noise in $(i, j)\,(3 \le i \le m-2, 3 \le j \le n-2)$ is replaced by the value of $a_{i,j}$, so that the gray values of the pixels in the (i, j) position of the denoised image are $y'_{i,j}$. There is

$$y'_{i,j} = \begin{cases} y_{i,j}, & i \le 2, \text{ or } i \ge m-1, \text{ or } j \le 2 \text{ or } j \ge n-1, \\ y_{i,j}, & 3 < i < m-2,\ 3 < j < n-2 \text{ and } t_{i,j} < 18, \\ a_{i,j}, & 3 < i < m-2,\ 3 < j < n-2 \text{ and } t_{i,j} \ge 18. \end{cases} \tag{5}$$

If y' is the image with size $m \times n$ and the gray value at (i, j) is $y'_{i,j}$, y' is the denoised image of observation image y by EP median filter algorithm.

2.3. WESNR Algorithm. For image x, $x_i = R_i x \in R^{n'}$ represent the image block of size $\sqrt{n'} \times \sqrt{n'}$, where R_i is the matrix vector. Based on the sparse representation theory, the image block is sparse-coded through the overcomplete dictionary $\Phi = [\phi_1; \phi_2; \ldots; \phi_n] \in R^{n' \times m'}$, so that $x_i = \Phi\alpha_i$, where α_i is the sparse coding vector of nonzero matrix. The results are as follows:

$$x = \Phi\alpha, \quad (6)$$

where α is the set of all sparse coding vectors α_i.

The traditional sparse representation denoising algorithm can be expressed as

$$\widehat{\alpha} = \arg\min_{\alpha} \|y - \Phi\alpha\|_2^2 + \lambda R(\alpha), \quad (7)$$

where $R(\alpha)$ is a regularization term corresponding to α and λ is a regularization parameter.

To make the distribution of data fitting residuals more regular, data residuals are weighted [12]. A new loss function is used, and the following mixed noise removal model is obtained:

$$\widehat{\alpha} = \arg\min_{\alpha} \left\|W^{(1/2)}(y - \Phi\alpha)\right\|_2^2 + \lambda R(\alpha), \quad (8)$$

where W is a diagonal weight matrix with diagonal elements.

Image block x_i and its nonlocal prediction are encoded by a given dictionary ϕ_i; that is, $x_i = \phi_i\alpha_i$ and $\widehat{x}_i = \phi_i\mu_i$, and then the encoding coefficients x_i and μ_i are similar. Therefore, $\sum_i \|\alpha_i - \mu_i\|_{l_p}$ is used as the regularization term and applied to the above equation. There is

$$\widehat{\alpha} = \arg\min_{\alpha} \left\|W^{(1/2)}(y - \Phi\alpha)\right\|_2^2 + \lambda \sum_i \left\|\alpha_i - \mu_i\right\|_{l_p}, \quad (9)$$

where l_p ($p = 1$ or $p = 2$) is the l_p norm. l_1 is chosen as the norm. The model is as follows:

$$\widehat{\alpha} = \arg\min_{\alpha} \left\|W^{(1/2)}(y - \Phi\alpha)\right\|_2^2 + \lambda \sum_i \left\|\alpha_i - \mu_i\right\|_1, \quad (10)$$

where W is a diagonal weighted matrix whose element W_{ii} will be determined automatically. The coding residual e_i can be used to determine the weight W_{ii}, and the strength of W_{ii} is inversely proportional to that of e_i. $W_{ii} \in [0, 1]$ is set. W_{ii} is determined as

$$W_{ii} = \exp\left(-ae_i^2\right). \quad (11)$$

Iterative reweighting is used to solve the problem. V is set to a diagonal matrix and initialized as an identity matrix. In $k+1$ times of iteration, each element of V is updated as follows:

$$V_{ii}^{(k+1)} = \frac{\lambda}{\left(\left(\alpha_i^{(k)} - \mu_i\right)^2 + \varepsilon^2\right)^{(1/2)}}, \quad (12)$$

where ε is a scalar and α_i^k is the i-th element of the coding vector α in the k-th iteration. The sparse coding α is updated by the following function:

$$\widehat{\alpha}^{(k+1)} = \left(\Phi^T W \Phi + V^{(k+1)}\right)^{-1}\left(\Phi^T W y - \Phi^T W \Phi\mu\right) + \mu. \quad (13)$$

A set of local PCA dictionaries are learned from natural images, and the model can be solved by iteratively updating W and α. The update of W depends on the coding residual e, and the adaptive median filter is selected for y to get an initial image $x^{(0)}$. Then, e is initialized to

$$e^{(0)} = y - x^{(0)}. \quad (14)$$

The above optimization is repeated for the subproblem until the iteration stop condition is satisfied. When there is no significant change in the solution of continuous iteration or the corresponding objective function value, that is, when the difference norm between two continuous iterative solutions is less than the given positive norm, the algorithm stops, or when the running time exceeds the upper limit, the iterative process stops. In this exploration, $t = \|\Phi\alpha^{(k+1)} - \Phi\alpha^{(k)}\|_2 / \|\Phi\alpha^{(k)}\|_2 < \tau$ is regarded as the termination condition. The obtained image is the denoised image of the observed image y by the WESNR algorithm.

2.4. Denoising Algorithm Based on EP Median Filter and WESNR. The general denoising algorithm will inevitably lose the details of the image. In particular, for the image with more lines, it will cause the blurring of the visual effect. In order to avoid the situation that the lines and edges of objects in the image are eliminated by mistake in the process of denoising, EP median filter algorithm distinguishes lines or edges from noise in advance, which has good performance in image details and edge preservation. However, EP median filter algorithm is only suitable for the removal of impulse noise in the image, and it does not perform well in the removal of other noises or mixed noises. When low-dose CT images with complex noise are processed, the phenomenon of incomplete noise removal will appear.

WESNR algorithm encodes each noise contaminated block, which can remove the mixed noise of impulse noise and Gaussian noise at the same time. However, for low-dose CT image denoising, when WESNR algorithm is used directly, there will be loss of details and edge damage.

In order to achieve the purpose of removing mixed noise in the process of low-dose CT image denoising without destroying the details and edges, EP median filter algorithm is combined with WESNR algorithm. First, the points in the center region of the noisy image y are classified into points in flat areas, edge points, and noise points. The points in the flat area, the edge points, and the points outside the central area are not replaced. The noise in the central region is replaced by the mean value of the gray value of 13 pixels around it to get image y' after the first step. Then, y' is input into WESNR algorithm as noisy image, and local PCA dictionary is selected to iterate the target problem, subproblem, and parameters. When the preset termination condition is satisfied, image y'' is the result of the denoising algorithm based on EP median filter and WESNR. Algorithm 1 shows the flow of the algorithm.

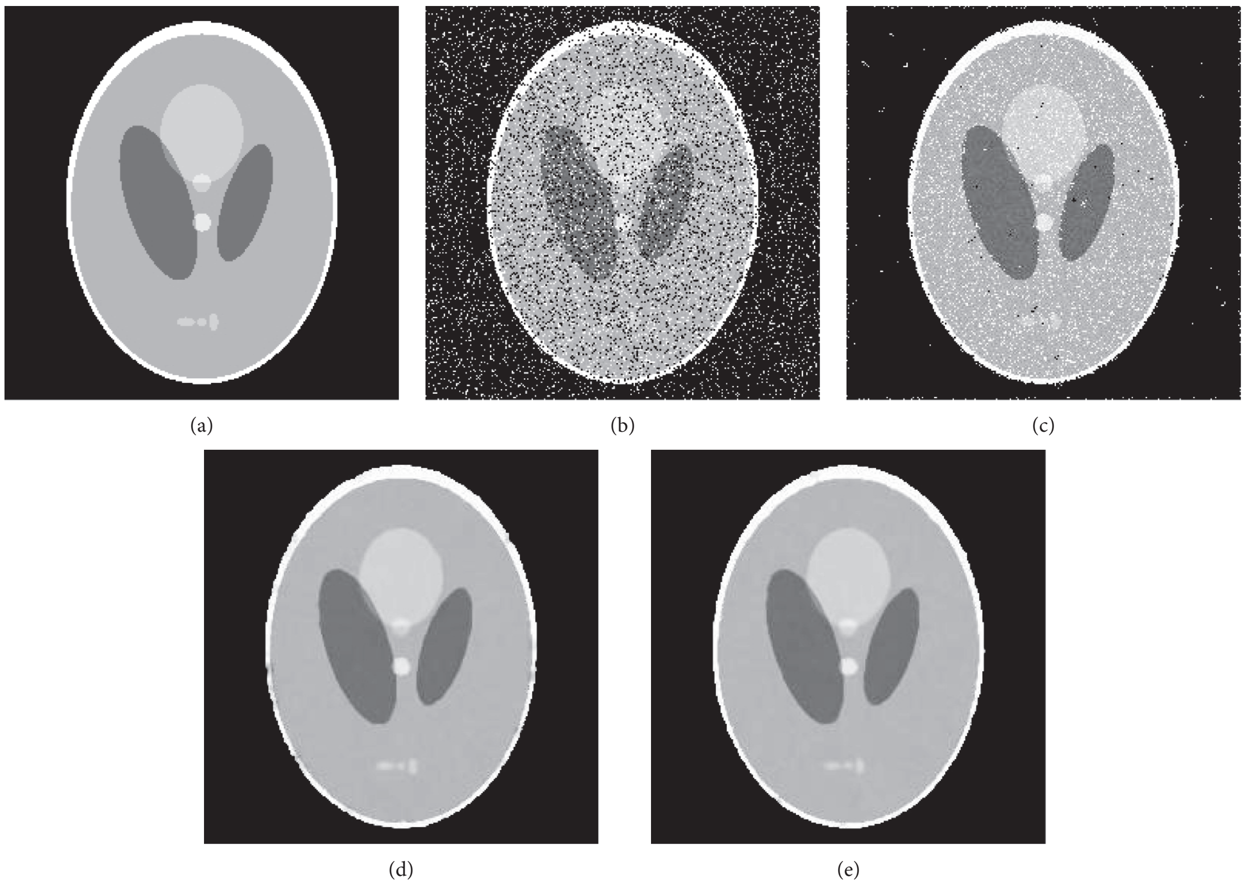

Figure 2: Denoising effect of different methods on Shepp-Logan image. (a) The original Shepp-Logan image. (b) The Shepp-Logan image after adding mixed noise $\sigma = 5$, $\rho = 20\%$. (c) Denoising effect of EP median filter algorithm. (d) Denoising effect of WESNR algorithm. (e) Denoising effect of the algorithm proposed in this exploration.

The steps of denoising algorithm based on EP median filter and WESNR are as follows.

3. Experiment

In addition to the visual effect comparison, the following numerical criteria are given: peak signal-to-noise ratio (PSNR) and structural similarity (SSIM). PSNR is the most commonly used objective index to evaluate image quality, which is an objective description of the degradation degree of an image. The higher the value of PSNR is, the closer it is to the original image. SSIM is mainly used to measure the similarity between the original image and the restored image. The higher the SSIM, the higher the image quality [13].

3.1. Shepp-Logan Head Model Experiment. The Shepp-Logan head model of $256 * 256$ is selected as the experimental object. This model was proposed by Shepp and Logan in 1974 [14]. The image is composed of 10 ellipses with different positions, sizes, directions, and densities. Different gray value of ellipse can simulate attenuation coefficient of different tissues, and Shepp-Logan head model can simulate human head sectional image well. In Shepp-Logan image, the mixed noise with different proportions of Gaussian noise and salt-and-pepper noise are added, respectively. EP median filter algorithm, WESNR algorithm, and the algorithm proposed in this exploration are used to denoise the image. The reconstruction effect and numerical comparison of various algorithms under nine kinds of noise are listed, as shown in Figure 2 and Table 1. The bold fonts in the table indicate the advantages of the algorithm.

The experimental results show that, for nine kinds of Shepp-Logan images with different proportions of Gaussian noise and salt-and-pepper noise, the reconstruction effect and numerical comparison of the proposed denoising algorithm based on EP median filter and WESNR are better than those of EP median filter algorithm and WESNR algorithm alone. Moreover, the proposed algorithm has the advantages of good edge preservation and good effect of removing mixed noise.

3.2. Low-Dose Brain CT Simulation Image. A brain CT image with $512 * 512$ pixels is selected as the experimental object. Different proportions of Gaussian noise and salt-and-pepper noise are added to simulate the image output effect of low-dose CT. The reconstruction effect and numerical comparison of various algorithms under nine kinds of noise are

Table 1: Comparison of PSNR and SSIM of denoised Shepp-Logan image.

σ	ρ (%)	EP median filter		WESNR		The algorithm proposed in this exploration	
		PSNR	SSIM	PSNR	SSIM	PSNR	SSIM
5	10	23.25	0.5233	32.76	0.8589	33.31	0.8841
	20	19.85	0.4511	28.68	0.8341	30.01	0.9026
	30	16.78	0.3399	27.14	0.8153	27.59	0.9028
10	10	22.60	0.3337	31.22	0.6922	31.94	0.7393
	20	19.62	0.2963	29.29	0.6829	30.20	0.7766
	30	16.24	0.2192	26.43	0.6534	26.73	0.7819
20	10	20.77	0.1943	28.16	0.4816	28.96	0.5349
	20	18.28	0.1681	26.83	0.4482	27.85	0.5418
	30	15.85	0.1382	25.99	0.4413	27.38	0.5813

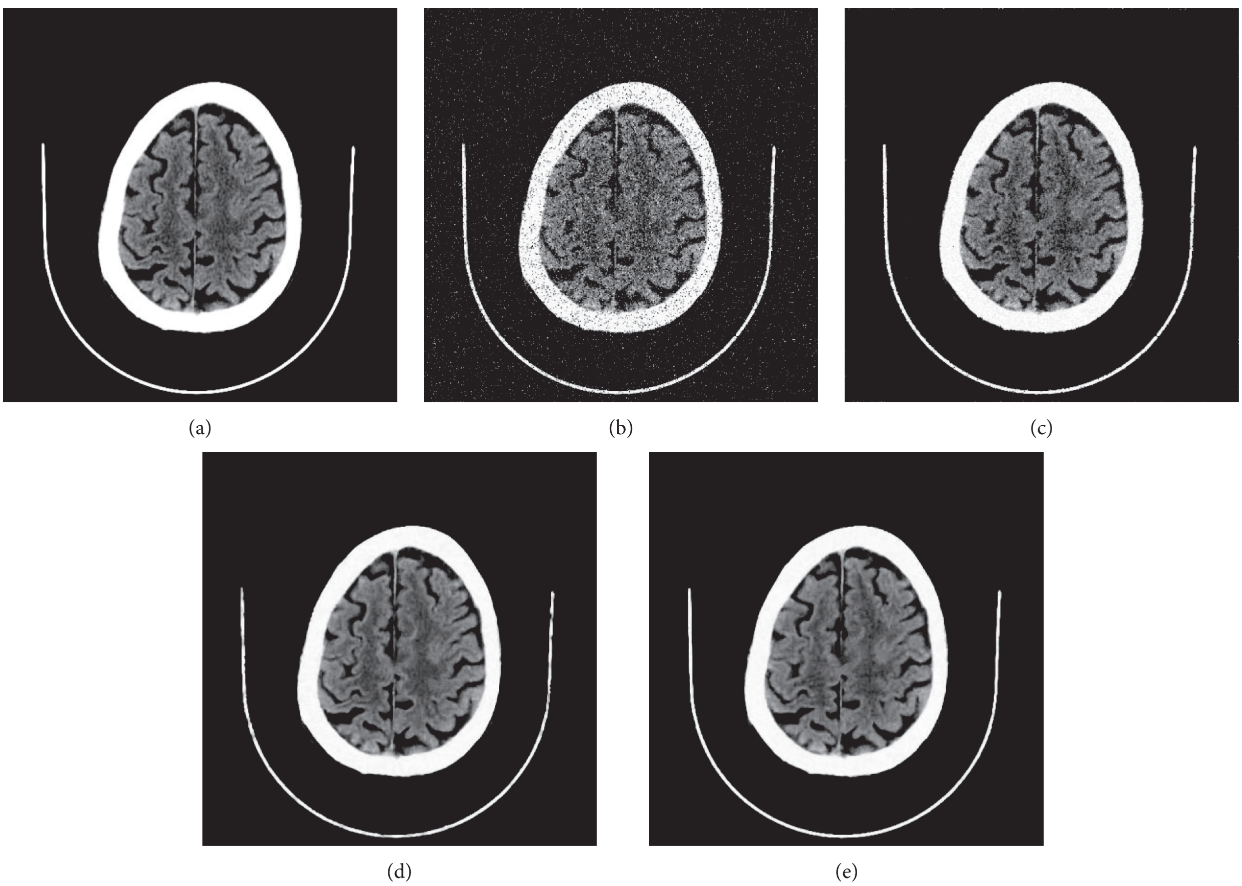

Figure 3: Denoising effect of different methods on brain CT image. (a) The original image of brain CT. (b) Simulated low-dose brain CT images with mixed noise of $\sigma = 5$, $\rho = 20\%$. (c) Denoising effect of EP median filter algorithm. (d) Denoising effect of WESNR algorithm. (e) Denoising effect of the algorithm proposed in this exploration.

listed, as shown in Figure 3 and Table 2. The bold fonts in the table indicate the advantages of the algorithm.

The experimental results show that, for nine kinds of simulated low-dose brain CT images with different proportions of Gaussian noise and salt-and-pepper noise, the proposed denoising algorithm based on EP median filter and WESNR outperforms EP median filter algorithm and WESNR algorithm alone in terms of reconstruction effect and numerical comparison. Moreover, the proposed algorithm has the advantages of good details and edge preservation and good effect of removing mixed noise.

Table 2: Numerical comparison of PSNR and SSIM after denoising of simulated low-dose brain CT images.

σ	ρ (%)	EP median filter		WESNR		The algorithm proposed in this exploration	
		PSNR	SSIM	PSNR	SSIM	PSNR	SSIM
10	10	25.40	0.4115	33.87	0.5428	34.20	0.6123
	20	21.41	0.3813	31.95	0.5304	32.26	0.6757
	30	17.11	0.2933	28.68	0.5302	29.41	0.7335
20	10	22.49	0.2165	28.38	0.3950	30.00	0.4107
	20	20.11	0.1970	27.84	0.3526	29.17	0.4710
	30	16.43	0.1539	26.75	0.3376	27.79	0.5054
30	10	20.05	0.1498	25.67	0.2773	26.92	0.3162
	20	18.48	0.1337	25.14	0.2702	26.83	0.3604
	30	15.52	0.1089	24.29	0.2632	25.94	0.4110

4. Conclusion

In this exploration, a new low-dose CT image denoising algorithm is proposed. According to the characteristics of low-dose CT image and noise, this algorithm is to combine EP median filter with WESNR. The experimental results show that the algorithm proposed in this exploration has a good ability to suppress the mixed noise in low-dose CT images, and the edge information is well preserved. However, this study still has some shortcomings. The proposed method is not compared with other related low-dose CT image noise reduction algorithms, and its effect on low-dose CT image noise reduction needs further study. In the future work, we will continue to compare it with related algorithms to clarify the value of this algorithm in low-dose CT images for noise reduction. In short, the algorithm of this research has a significant effect on denoising mixed noise in low-dose CT images.

Data Availability

The data used to support the findings of this study are available from the corresponding author upon request.

Conflicts of Interest

The authors declare that there are no conflicts of interest.

Acknowledgments

This work was supported by the National Natural Science Foundation of China (11961012 and 71801060), Provincial Natural Science Foundation of Guangxi (2018GXNSFBA281192, 2017GXNSFAA198248, and 2017GXNSFBA198182), and National Major Scientific Research Instruments Development Program (61627807).

References

[1] J. Hsieh, *Computed Tomography Principles, Design, Artifacts, and Recent Advances*, SPIE Press, Bellingham, WA, USA, 2nd edition, 2009.

[2] D. Hart and B. F. Wall, "UK population dose from medical X-ray examinations," *European Journal of Radiology*, vol. 50, no. 3, pp. 285–291, 2004.

[3] T. L. Slovis, "Children, computed tomography radiation dose, and the as low as reasonably achievable (ALARA) concept," *Pediatrics*, vol. 112, no. 4, pp. 971-972, 2003.

[4] D. J. Brenner, "Radiation risks potentially associated with low-dose CT screening of adult smokers for lung cancer," *Radiology*, vol. 231, no. 2, pp. 440–445, 2004.

[5] Y. Chen, L. Shi, Q. Feng et al., "Artifact suppressed dictionary learning for low-dose CT image processing," *IEEE Transactions on Medical Imaging*, vol. 33, no. 12, pp. 2271–2292, 2014.

[6] Y. Zhang, J. Zhang, and H. Lu, "Statistical s smoothing for low-dose CT with segmentation-based adaptive filtering," *IEEE Transactions on Nuclear Science*, vol. 57, no. 5, pp. 2587–2598, 2010.

[7] Y. Chen, J. Liu, Y. Hu et al., "Discriminative feature representation: an effective postprocessing solution to low dose CT imaging," *Physics in Medicine and Biology*, vol. 62, no. 6, pp. 2103–2131, 2017.

[8] Y. Chen, X. Yin, L. Shi et al., "Improving abdomen tumor low-dose CT images using a fast dictionary learning based processing," *Physics in Medicine and Biology*, vol. 58, no. 16, pp. 5803–5820, 2013.

[9] X.-Y. Cui, Z.-G. Gui, Q. Zhang, H. Shangguan, and A.-H. Wang, "Learning-based artifact removal via image decomposition for low-dose CT image processing," *IEEE Transactions on Nuclear Science*, vol. 63, no. 3, pp. 1860–1873, 2016.

[10] J. Jiang, L. Zhang, and J. Yang, "Mixed noise removal by weighted encoding with sparse nonlocal regularization," *IEEE Transactions on Image Processing*, vol. 23, no. 6, pp. 2651–2662, 2014.

[11] M. Sun, *Fundamentals of Digital Image Processing and Analysis: MATLAB and VC++ Implementation*, Publishing House of Electronics Industry, Beijing, China, 2013.

[12] Y. Chen, S. Hu, H. Mao, W. Deng, and X. Gao, "Application of the best evacuation model of deep learning in the design of public structures," *Image and Vision Computing*, vol. 102, Article ID 103975, 2020.

[13] C. Guo, J. Lu, Z. Tian, W. Guo, and A. Darvishan, "Optimization of critical parameters of PEM fuel cell using TLBO-DE based on Elman neural network," *Energy Conversion and Management*, vol. 183, pp. 49–158, 2019.

[14] L. A. Shepp and B. F. Logan, "The fourier reconstruction of a head section," *IEEE Transactions on Nuclear Science*, vol. 21, no. 3, pp. 21–43, 1974.

Hindawi
Journal of Healthcare Engineering
Volume 2021, Article ID 4650794, 9 pages
https://doi.org/10.1155/2021/4650794

Research Article

miR-130-3p Promotes MTX-Induced Immune Killing of Hepatocellular Carcinoma Cells by Targeting EPHB4

Liangtian Shao [1] **Qing Ye,** [2] **and Moyang Jia** [1]

[1] *The Second Affiliated Hospital of Shandong First Medical University, Tai'an 271000, Shandong, China*
[2] *Taian Maternal and Child Health Hospital, Tai'an 271000, Shandong, China*

Correspondence should be addressed to Liangtian Shao; shaoliangtian2020@163.com

Received 13 April 2021; Revised 25 May 2021; Accepted 12 July 2021; Published 23 July 2021

Academic Editor: Enas Abdulhay

The vast majority of primary hepatocellular cancer is hepatocellular carcinomas (HCCs). Currently, HCC is one of the more common cancers in humans, and it has a high mortality and disability rate. Mitoxantrone (MTX) is an antitumor drug that can block type II topoisomerase. It has been reported that immunogenic cell death evoked by MTX can induce the discharge of damage associated with molecular patterns (DAMPs) and subsequently influence immune cell infiltration in the tumor microenvironment. High mobilities aggregation box 1 (HMGB1) is the prototypical extracellular DAMP. Many cellular processes have been reported to involve EPHB4 receptor tyrosine kinases, but the relation of DAMP and EPHB4 is uncertain. In this research, we assessed the impact of miR-130-3p by Edu incorporation test on cell proliferation, and we have proven its impact on HCC cell migration through Transwell and wound healing tests. Flow cytometry was applied to study its influence on apoptosis. Luciferase report test was integrated in detecting the miR-130-3p target gene. The influence of miR-130-3p on the manifestation of classical DAMPs was studied, such as HMGB1, ATP, and Calreticulin. A coculture experiment was carried out to further confirm its effects on immune cell infiltration. The result displayed that miR-130-3p overexpression considerably facilitates apoptosis and suppresses the migration or proliferation of HCC cells. EPHB4 was confirmed as the target gene of miR-130-3p. Overexpression of this target gene promotes emission of Calreticulin, ATP, and HMGB1 and subsequently promotes DCs maturation and proliferation of CD4+ T cells. In summary, our results demonstrated that miR-130-3p inhibits HCC cell proliferation and migration by targeting EPHB4 and promotes drug-induced immunogenic cell death.

1. Introduction

Primary liver cancer is predominantly hepatocellular carcinoma [1–3], which is currently the leading cause of cancer worldwide. Traditional therapeutic strategies for HCC include surgery, radiotherapy, and chemotherapy [4, 5]. However, the effect of this treatment is not satisfactory.

Mitoxantrone, also known as MTX, is an Adriamycin analogue that was developed in the 1980s to specifically inhibit type II topoisomerase based on its antitumor properties [6]. It is often employed for the management of various cancer types, including acute leukemia, breast cancer, myeloma, and lymphomas [7].

Most importantly, MTX can induce immunogenic cell death and promote immune cell infiltration. Immunogenic cell death is known to induce adaptive immunity against dead cell antigens, especially when they are released from cancer cells [8–10].

DAMPs are signals that can be released or exposed when dying, stressed, or injured cells are present. These molecules often play the role of danger signals or adjuvants, thus helping the immune system [11]. HMGB1 is a highly conserved nuclear protein that senses and coordinates the stress response of cells. It plays an especially important part not only as it was intracellularly a defender of DNA chaperones, apoptosis, and autophagy, but also outside the cell as the prototypic DAMP. Classical DAMPs include ATP and HMGB1, and the DAMPs advance the development of dendritic cells and further activate the immune system [12].

EPHB4, a part of the biggest group of receptor tyrosine kinases-protein tyrosine kinases is ordinarily communicated on neurons and endothelial cells, where it plays a vital part in the vascular era and organizes gathering.

EPHB4 is a constituent of the biggest family of receptor tyrosine kinases. It is often manifested as a protein tyrosine kinase on endothelial and neuronal cells and has a significant role in multiple cellular processes including cell growth, survival, and angiogenesis. Its receptor could be a tyrosine kinase, which is included in numerous cellular forms such as angiogenesis, cell development, and survival.

A few reports propose that EPHB4 is overexpressed in different cancers, counting breast, prostate, and colon [13, 14]. MicroRNAs are evolutionarily conserved small RNAs that do not code and which are useful in almost all bioprocesses by targeting mRNAs [15, 16]. A new study suggests that miRNA dysregulation is included in tumor movement [17]. Nevertheless, the potential part played by miR-130-3p in HCC cells still remains unknown. MiR-130 was first found in regulating respiratory syndrome virus replication and porcine reproduction. A previous study demonstrated that the downregulation of miR-130 contributed to the activation of lung fibroblasts by targeting IGF-1. A previous study demonstrated that miR-130 was served as a tumor promotive miRNA in most human cancer.

In this study, our research was aimed at exploring the embedded mechanism on molecules of miR-130-3p-EPHB4 in terms of transfer of MTX-induced immunogenicity in hepatocellular carcinoma cells, as well as providing any potential effective targets of therapy for PC treatment.

2. Materials and Methods

2.1. Patients and Tumor Samples. Our experimental samples were all provided by the Department of the Second Affiliated Hospital of Shandong First Medical University. We obtained approval letters from the University's ethics committee. Our conducted study was also aligned with Helsinki Declaration in terms of the guidelines and principles. We examined the samples (patients) by PCR and explored the pattern of expression in EPHB4 in liver cancer tissues and regular controls with the help of TANRIC software platform.

2.2. Cell Lines and Antibodies for Immunoblotting. The HepG2 cells employed in the experiment were acquired from ATCC Cell Bank (Manassas, VA, USA). Under suitable conditions of 5% CO_2 and 37°C, these cell cultures are cultured in Dulbecco's modified Eagle medium (DMEM). The first antibody (CST, Trask Lane Danvers, MA) was a rabbit polyclonal antibody at a dilution of 1 : 1000. The first antibodies are Cleaved Caspase-3, AIFM1, Pro-Caspase-3, and Bcl-2. The secondary antibody is the anti-rabbit polyclonal antibody GADPH (CST, Trask Lane Danvers, MA) at a dilution of 1 : 2000.

2.3. In Vitro Cell Multiplication Measure. 96-well plates with a density of 5,000 cells/well in the total medium were used to inoculate the cells. After 24 hours of cell culture, the cells became precipitated with 4% formaldehyde and recolored with 0.5% crystal violet. Finally, the crystal violet was dissolved in 10% acetic acid and cells were tested for transfection at $\lambda = 580$ nm using an ELx800 spectrophotometer after 24 and 48 h, respectively.

2.4. Plasmid Development and Transfection. We transfected inhibitors and mimics of miR-130-3p using Lipofectamine 3000, which was sourced from Life Technologies. The concentration of the solution was set at 20 nM according to the instructions from the manufacturer. Based on the expression of green fluorescent protein (GFP), we harvested and cultured cells after sorting lentivirus-infected cells with MoFlo XDP (Beckman, USA) for subsequent functional studies. In addition, to explore whether miR-130-3p could regulate EPHB4 manifestation by directly binding to the established 3′ UTR sequence, we established luciferase reporter plasmids that had binding sites or wild-type for EPHB4. To induce the overexpression of circ-EPHB4, we cloned the coding sequence into the pEX-3 vector (Shanghai Gene Pharma Co., Ltd.), respectively. We transfected the above vectors with Lipofectamine® 3000 (Invitrogen, Thermo Fisher Scientific, USA) based on the instructions of the manufacturer. Following a 48 hour transfection, the efficiency of each group of cells was identified using qRT-PCR.

2.5. Public Clinical Datasets. We obtained immune infiltration information associated with EPHB4 expression from the TIMER2.0 online dataset.

2.6. Wound Healing Test. After the cells have grown all over the cell vial, a fine needle is scraped in one direction over the cell monolayer. Wounded cell monolayers were washed with phosphate-buffered saline to remove cellular debris. We analyzed the wound healing and migration of cells in the remaining slits at different time points by using an inverted microscope.

2.7. Western Blotting Analysis. Based on the instructions of the manufacturer, we extracted the total protein from each group. The selected protein assay kit was then employed in determining the concentration of total cellular proteins. Samples of denatured protein were denatured at 100°C for 10 min and then analyzed on 10% SDS-PAGE gels and moved to PVDF membranes (Millipore, MA, USA) through electroblotting. The membrane was closed with 5% skim milk for 1 h at room temperature before incubating them overnight using primary antibody at 4°C. Then, a secondary antibody was used in incubating the membrane after its washing (Proteintech) for 2 hours at room temperature. Finally, the immunoblots were visualized and analyzed with an ECL chemiluminescence detection system (Thermo Scientific), and the relative integrated density values (IDVs) were determined using GAPDH as an internal control. The assessments were performed in three samples. The main antibodies included the following: IKKβ (1 : 1000; Cell Signaling Technology, USA); GAPDH (1 : 6000, Sigma, St. Louis, MO, USA).

2.8. ATP Detection. Intracellular and extracellular ATP concentrations were measured by utilizing the fluorescein-based ENLITEN ATP test (Promega, Madison, WI, USA).

2.9. Stream Cytometry Examination. The processing of cells was achieved through trypsin before being washed using PBS. Apoptosis tests were performed utilizing Annexin V-FITC Apoptosis Detection Kit (Beyotime). According to the instructions provided by the manufacturer, anaplastic cells were dual-stained with PI and Annexin V-FITC utilizing the Annexin V/FITC kit (Thermo Logical, Shanghai, China). Analysis was performed on a BDTM LSRII stream cytometer (BD Biosciences).

2.10. Luciferase Columnist Test. Firefly correspondent quality expression vectors driven by SV40 enhancers were acquired from Gene Copeia. 3′-UTR arrangements of wild-type or mutant EPHB4 were included downstream of the luciferase quality, where no oligonucleotides were included within the control vector. Renilla luciferase was utilized as a marker to screen transfection productivity. The luciferase movement was measured with a discuss photo-switch reagent.

2.11. Statistical Analysis. All collected data are expressed as mean ± SEM. A single evaluation of variance via ANOVA used to be carried out using SPSS 21.0 (SPSS Inc., Chicago, Illinois, USA) for assessment between groups. We also performed pairwise comparisons between groups using the Student-Newman-Coors (SNK) test. The statistical results with P values of below 0.05 were identified as significant, with significant differences.

3. Results

3.1. miR-130-3p Suppresses Restraint of Movement and Overgrowth of HCC Cells. The miR-130-3p expression in the clinical sample was confirmed by PCR. As shown in Figure 1(a), HCC tumor tissue expresses lower miR-130-3p than paracancer normal tissue, implying that miR-130-3p may serve as a tumor-suppression effect. To affirm the function of miR-130-3p of HCC cells, EdU incorporation assay was confirmed. As shown in Figure 1(b), after the transfection of miR-130-3p mimic, the percentage of EdU positive cells decreased, showing that miR-130-3p suppressed HCC proliferation. To explore the impacts of miR-130-3p on HCC cell migration, a Transwell assay was performed. As shown in Figure 1(c), after the transfection of miR-130-3p mimic, migrated cancer cells decreased significantly. The result showed that miR-130-3p suppresses the migration of HCC cells. To further confirm this conclusion, a wound healing assay was performed. As shown in Figure 1(d), the result confirmed our previous conclusion that miR-130-3p overexpression impaired HCC cells migration. We further confirmed the impacts of miR-130-3p on the overgrowth of cells. As shown in Figure 1(e), the CCK8 assay indicated that after transfection of mimic, the proliferation of tumor cells was suppressed. To confirm if miR-130-3p overexpression promotes MTX-induced apoptosis, flow cytometry was used. As shown in Figure 1(f), 12 treatments of MTX increased the apoptosis rate of HCC cells. After miR-130-3p overexpression, the apoptosis rate was further enhanced. Western blot was conducted to investigate the underlying mechanism. As shown in Figure 1(g), Bcl-2 was suppressed by MTX, Bax, and cleaved caspase-3 expression was enhanced by MTX treatment. After the transfection of miR-130-3p mimic, the expression of cleaved caspase3 was further enhanced. Those results indicated that the overexpression of miR-130-3p promotes MTX-induced apoptosis.

Our result affirmed that miR-130-3p suppresses the migration and proliferation of HCC cells, and the overexpression of miR-130-3p promotes MTX-induced apoptosis.

3.2. miR-130-3p Targeting EPHB4 and Promotes Apoptosis of HCC Cells. To confirm target gene of miR-130-3p, TargetScan dataset was used. Given the dataset, EPHB4 may act as the target protein of miR-130-3p. As shown in Figure 2(a), the *d* showed that EPHB4 expresses higher in tumor tissue relative to normal tissue, indicating that EPHB4 may function as a tumor-promote gene. As shown in Figure 1(c), the online dataset showed that the expression of EPHB4 is negatively associated with the expression of miR-130a-3p in HCC. After the overexpression of miR-130-3p, as shown in Figure 2(d), EPHB4 expression was limited, indicating that miR-130-3p expression may regulate EPHB4 expression. To further confirm that EPHB4 is a direct target gene for miR-130-3p, a luciferase report measure was undertaken. Wild-type EPHB4 3′-UTR and mutant EPHB4 3′-UTR with nucleotide substitution within the putative binding site were built, and after that, subcloned into luciferase columnist vectors. As displayed in Figure 2(b), the transfection of miR-130-3p significantly suppresses luciferase activity, and insignificant differences were observed in luciferase with mutating UTR.

We are curious about whether the effects of miR-130-3p are through the regulation of EPHB4. To answer this question, the development of the EPHB4 overexpression vector and the effects of EPHB4 overexpression were evaluated by western blot. As shown in Figure 2(e), the result indicated that EPHB4 was successfully overexpressed. The mechanism of miR-130-3p-induced effects was further studied. As shown in Figure 2(f), as previously mentioned, the integration of MTX enhances the manifestation of Bax and cleaved caspase-3, and the transfection of miR-130-3p mimic further promotes these effects. But after transfection of the EPHB4 overexpression vector, miR-130-3p induced apoptosis was partly inhibited. The effect was also affirmed

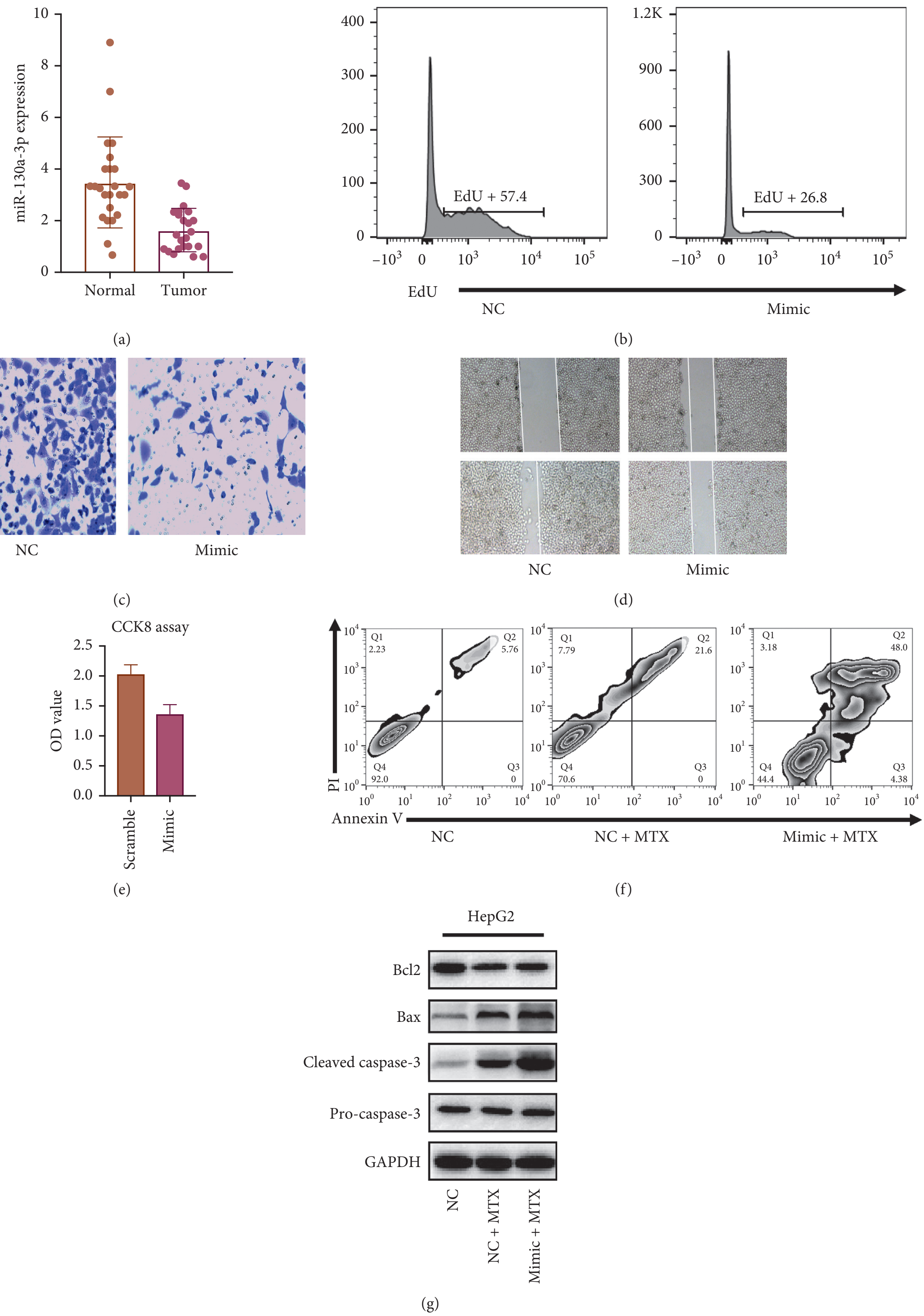

FIGURE 1: miR-130-3p suppresses migration and proliferation of HCC cells. (a) CR evaluation of miR-130a-3p expression in HCC tumor tissues and regular tissues adjoining to cancer. (b) EdU binding assay after transfection of HCC cells with NC and mimic. (c) Transwell assay after transfection of HCC cells with NC and mimic. (d) Wound healing test of HCC cells after transfection of HCC cells with NC and mimic. (e) CCK8 assay after therapy of HCC cells with MTX for 24 hours. (f) AnnexinV analysis of apoptosis rate. (g) Western blot evaluation of molecules linked to the apoptotic pathway.

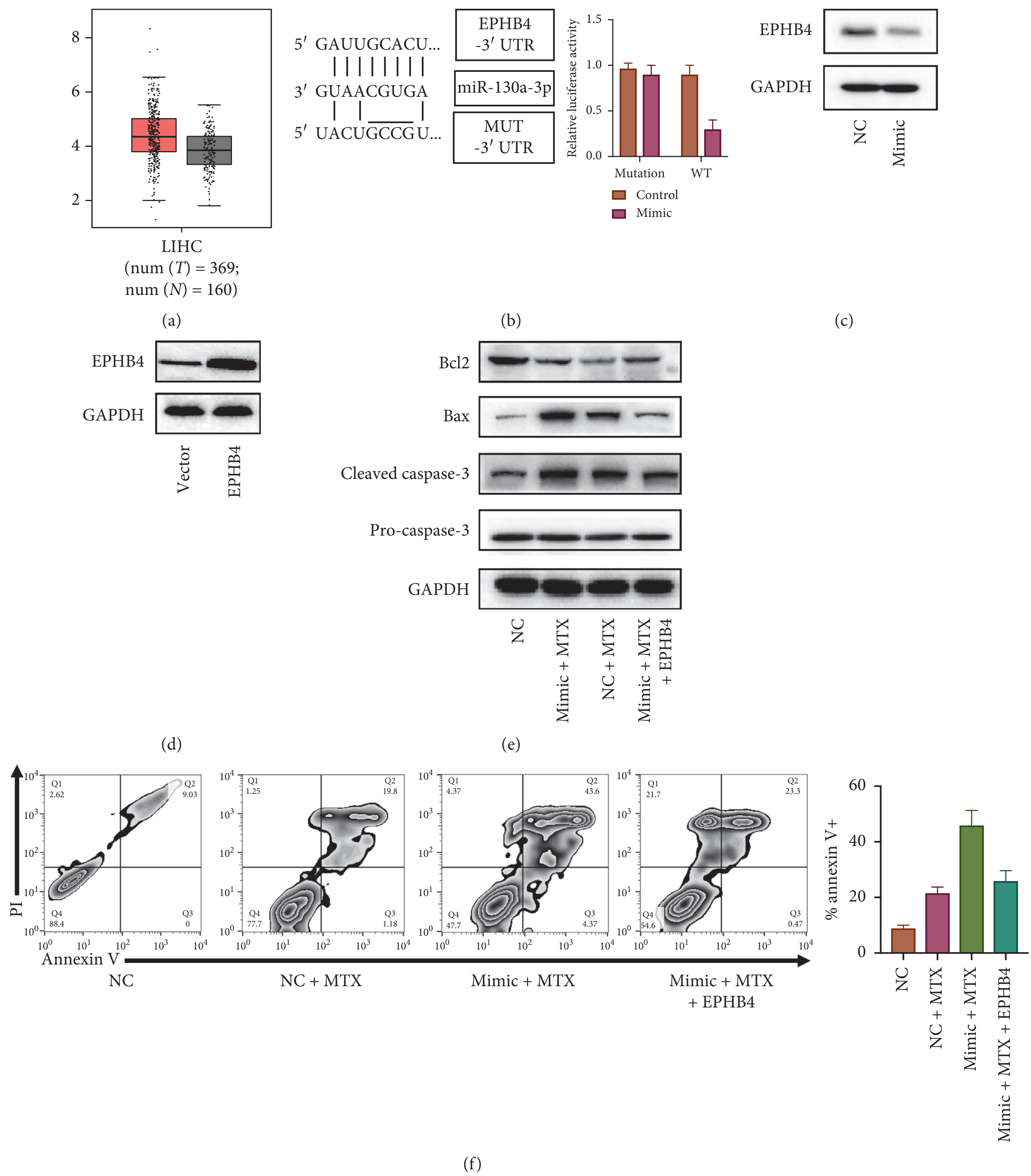

Figure 2: miR-130-3p targets EPHB4 and promotes apoptosis of HCC cells. (a) EPHB4 expression in HCC cancer tissue and normal tissue. (b) Luciferase assay was used to evaluated the relationship between miR-130-3p and mRNA of EPHB4. (c) Correlation between miR-130a-3p expression and EPHB4 expression. (d) Immunoblot evaluation of EPHB4 expression after transfection with mock or NC. (e) Immunoblot evaluation of EPHB4 expression after overexpression vector. (f) Western blot analysis of apoptosis-associated molecular. (g) AnnexinV analysis of apoptosis rate.

by flow cytometry, as depicted in Figure 2(f); overexpression of EPHB4 reversed miR-130-3p induced apoptosis. These results indicated that miR-130-3p promotes the apoptosis of HCC cells through the downregulation of EPHB4.

Taken together, our result indicated that miR-130-3p targets EPHB4 and promotes the apoptosis of HCC cells.

3.3. miR-130-3p Overexpression Promotes Emission of DAMPs upon MTX Treatment. Based on the prediction of the TIMER dataset, EPHB4 expression is associated with the alternation of immune cell infiltration, including macrophages, as shown in Figure 3(a). We next study the effects of miR-130-3p on immune cells. Immunogenic cell death is a

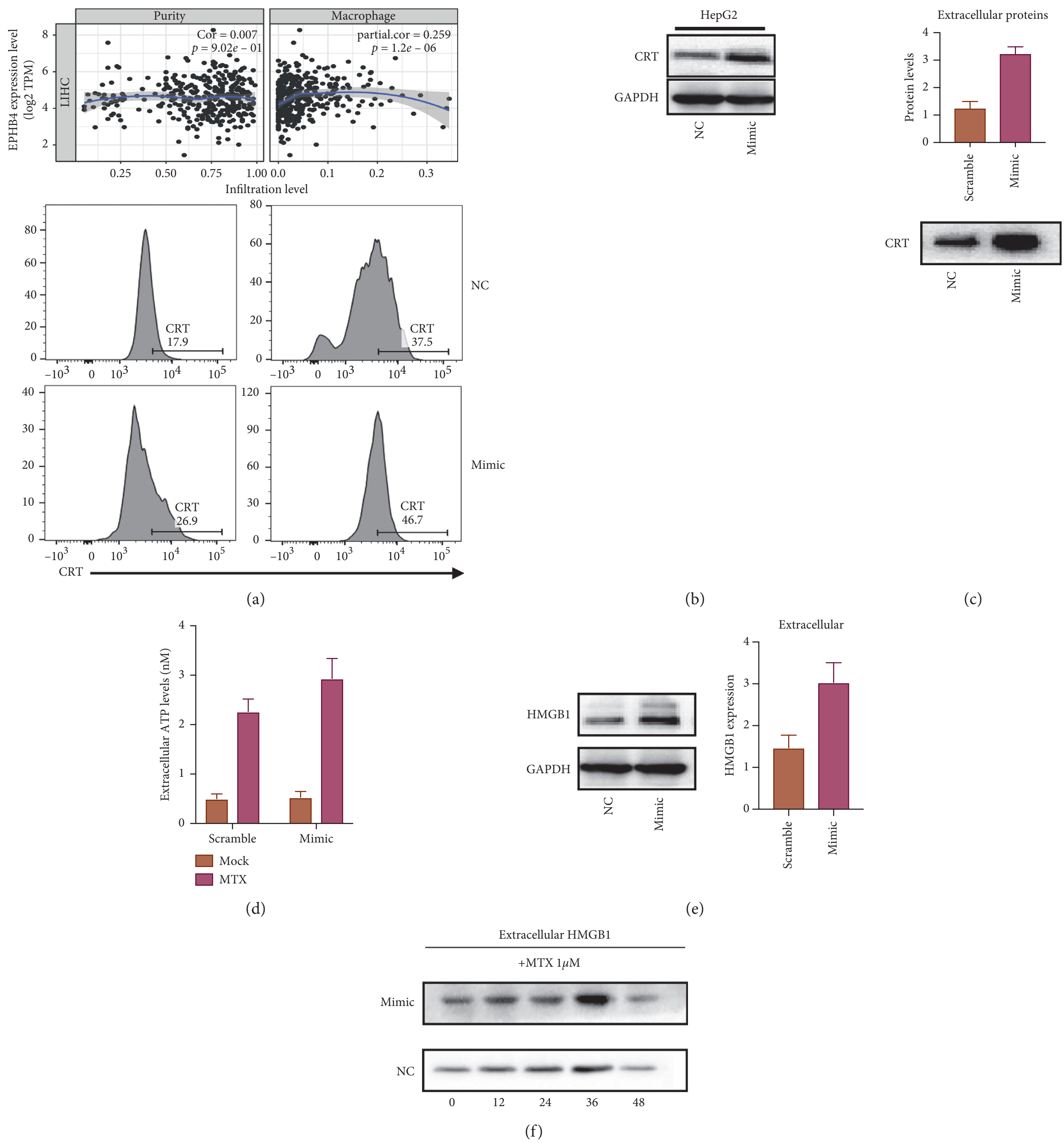

Figure 3: miR-130-3p overexpression promotes emission of DAMPs upon MTX treatment. The best segment shows the affiliation of safe cell invasion with EPHB4 expression. (b) Western smudge investigation of calreticulin after overexpression of miR-130-3p. (c) Immunodetection of CRT within the medium and extracellular calmodulin communicated by entirety cell lysis. (d) The energy of initiated ATP discharge. (e) Immunodetection of extracellular HMGB1 and HMGB1 in medium. (f) Time course of HMGB1 discharge after MTX treatment. Blunder bars imply ± s.d.

cell death that does stimulate an immune response by the emission of DAMPs. Classical DAMPs include ATP, high mobility group protein B, and calreticulin, and miR-130-3p may influence the emission of DAMPs and subsequently affect immune cells. As shown in Figure 3(a), the calreticulin expression in the cell surface was detected by flow cytometry. Our results showed that MTX treatment greatly increased the expression of calmodulin on the cell surface. After the overexpression of miR-130-3p, it was further increased. Interestingly, the basement expression of calreticulin was moreover expanded after the transfection of the miR-130-3p mirror. As shown in Figure 3(b), calreticulin expression in HCC cells was evaluated by western blot. After the transfection of mimic, the calreticulin expression in HCC cells was increased. We then tested the amount of calreticulin that was released by HCC cells after MTX treatment. As shown in Figure 3(c), secreted calreticulin that was induced by MTX treatment was increased as miR-130-3p was overexpressed in HCC cells.

As illustrated in Figure 3(d), the kinetics of ATP release in cell culture medium showed that cells overexpressing miR-130-3p had a stronger response to MTX's along with an increase in the amount of ATP secreted. HMGB1 expression was also evaluated. As shown in Figure 3(e), after miR-130-3p overexpression, the total expression of HMGB1 and its secretion were increased. As shown in Figure 3(f), the temporal profile of the HMGB1 release indicated that the HMGB1 release was slightly amplified by MTX treatment. miR-130-3p overexpression generally amplified extracellular HMGB1.

In conclusion, our results confirm that overexpression of miR-130-3p promotes the release of DAMPs when MTX is treated.

3.4. miR-130-3p Overexpression Promotes T-Cell Proliferation and DC Maturation. It has been reported that the DAMPs advance the further active immune system and the maturation of dendritic cells. In order to confirm whether miR-130-3p overexpression induced DAMPs influence activation of immune cells, HCC cells were transfected with miR-130-3p mimic. NC served as control and was treated with MTX for 12 h and cocultured with human youthful DCs for 24 hours.

As shown in Figure 4(a), after DC was cocultured with HCC cells and miR-130-3p overexpression, the maturation marker of DCs such as CD80 and CD83 was increased compared with the coculture and HCC cells without miR-130-3p overexpression.

Phagocytosis of dying tumor cells and mature DCs play an active immune role, so we stimulated the proliferation of T-cell receptors (CD3/CD28) using a medium with DCs cocultured with tumor cells under such conditions. As shown in Figure 4(b), the conditioned medium derived from coculture of DCs and HCC cells with miR-130-3p overexpression significantly promotes the proliferation of CD4+ T cells. The released IFN from CD4+ T cells was evaluated by ELISA. As shown in Figure 4(c), the conditioned medium derived from the coculture of DCs and HCC cells with miR-130-3p overexpression promotes the IFN production from CD4+ T cells.

Our result indicated that miR-130-3p overexpression promotes DC maturation and T-cell proliferation.

4. Discussion

Liver cancer is one of the common cancers in humans. It has the characteristics of a high fatality rate and high disability rate. Despite the continuous development of surgical technology, it is still a medical problem [18]. Chemotherapy is the traditional remedy approach for hepatocellular carcinoma, and MTX is one of the most secure and most famous anticancer marketers at therapeutically utilized doses and has anticancer outcomes on a range of hepatocellular carcinoma cellphone lines, inclusive of HepG2, MHCC97, Huh7, and Morris 5123 cells.

For the patient with advanced HCC, MTX did now not exhibit a favorable tumor response or normal survival. However, the combination of MTX with other chemotherapy strategies is under investigation [19, 20].

EphB4 has been detailed in that EphB4 includes a potential oncogenic part and is a critical controller of essential physiological and pathophysiological forms, such as tissue designing, amid advancement, angiogenesis, and tumor movement. It has been reported that EPHB4 overexpression is related to destitute forecast in patients with ovarian cancer. The overexpression of EPHB4 in colorectal cancer cells promotes its proliferation and migration, invasion, and angiogenesis [21, 22]. EphB4 expression was too essentially higher in delicate tissue sarcomas, and mRNA and protein expression were altogether expanded in synovial sarcomas, while the regulation mechanism of EPHB4 still remains unknown [23]. In this experiment, the Edu incorporation assay method was conducted to detect the effects of miR-130-3p on cell proliferation. At the same time, we also detected the effect of HCC cell migration by the Transwell method and other experiments. Flow cytometry was performed to study its influence on apoptosis. Luciferase report assay was carried out to confirm the target gene of miR-130-3p. The influence of miR-130-3p on the expression of classical DAMPs such as Calreticulin, ATP, and HMGB1 was studied. A coculture experiment was used to further confirm its effects on immune cells infiltration.

In this study, we confirmed that EPHB4 is a target gene of miR-130-3p. After miR-130-3p was overexpressed, the migration and proliferation of HCC cells were significantly inhibited. miR-130-3p overexpression also promotes MTX-induced cancer cell apoptosis. After EPHB4 was reexpressed, miR-130-3p induced proapoptosis effect was partly inhibited, indicating that miR-130-3p promotes MTX-induced apoptosis through the downregulation of EPHB4.

It has been reported that MTX treatment can induce Immunogenic Cell Death (ICD) melanoma, osteosarcoma, and mouse colon cancer cells, acting through an eIF2α phosphorylation-dependent mechanism [24, 25]. Immunogenic cell death is the effect. Dying cancer cell triggers robust immunological memory and immune response [26]. It has been reported that ICD is actuated by harm related atomic designs (DAMPs) and the outflow of numerous DAMPs. Cell surface presentation to CALR, extracellular discharge of ATP, and the atomic protein HMGB1 are considered to be all-inclusive donors to nearly all ICD sorts. Subsequently, these DAMPs are commonly utilized as markers for in vitro evaluation of ICD inducers.

In this basic study of liver cancer, we confirmed that after miR-130-3p increased, and the expression of calmodulin on the cell surface also increased significantly. After the

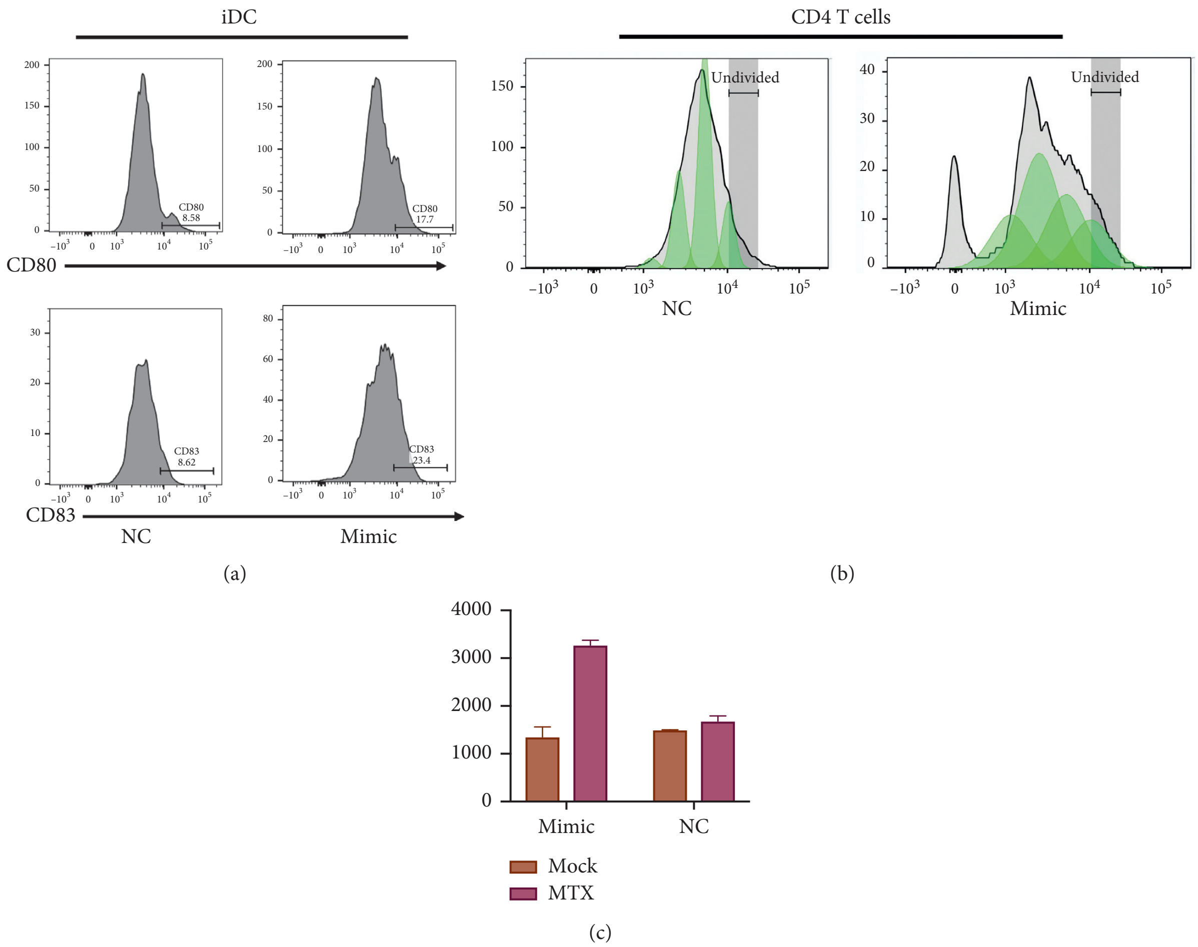

Figure 4: miR-130-3p overexpression promotes DC maturation and T-cell proliferation. (a) Investigation of expression of CD86 and CD80 by flow cytometry following DC coculture with cancer cells. (b) Analysis of CD4 T-cell proliferation by CFSE following treatment with CM acquired from tumour cells cultured with DC. (c) IFN expression in conditioned medium of CD4+ T cells by ELISA.

transfection of mimic, the total calreticulin expression in HCC cells was increased. We then tested the amount of calreticulin that is released by HCC cells after MTX treatment. Secreted calreticulin that was induced by MTX treatment was increased because miR-130-3p was overexpressed in HCC cells. After miR-130-3p overexpression, the total expression of HMGB1 and its secretion were all increased. The increased emission of DAMPs increased DCs maturation and subsequently promoted CD4+ T-cell proliferation. Increased IFN secretion was also observed when CD4+ T cells were treated by condition medium derived from the coculture of DCs and HCC cells with miR-130-3p overexpression.

In summary, our results confirm that miR-130-3p inhibits the proliferation and migration of HCC cells by targeting EPHB4 and induces immune death of hepatocellular carcinoma cells by promoting drug.

Nonetheless, there are several limitations to the present study. The study did not investigate the association between other MircroRNAs and primary hepatocellular cancer and any other potential interactions between genes. Therefore, future studies will focus on the interactions between microRNAs.

Data Availability

The data of this article are included in pictures and illustrations. The datasets used and analyzed during the current study are available from the corresponding author upon reasonable request.

Ethical Approval

The protocol of this experiment was considered and affirmed by the Ethics Committee of the Second Affiliated Hospital of Shandong First Medical University. The review and approval were based on the acquisition of written informed consent from each participant.

Consent

Written informed consent was obtained from each participant.

Conflicts of Interest

The authors declare that they have no conflicts of interest.

Authors' Contributions

Liangtian Shao drafted the paper and cooperated with Qing Ye to conduct the experiment. Liangtian Shao collected the data, with Moyang Jia to interpret the data. Liangtian Shao designed this work.

References

[1] M. F. Chedid, C. R. P. Kruel, M. A. Pinto et al., "Hepatocellular carcinoma: diagnosis and operative management," *ABCD. Arquivos Brasileiros de Cirurgia Digestiva (São Paulo)*, vol. 30, no. 4, pp. 272–278, 2017.

[2] M. Kanematsu, R. C. Semelka, S. Osada, and N. Amaoka, "Magnetic resonance imaging and expression of vascular endothelial growth factor in hepatocellular nodules in cirrhosis and hepatocellular carcinomas," *Topics in Magnetic Resonance Imaging : TMRI*, vol. 16, pp. 67–75, 2005.

[3] H. Sun and T. Song, "Hepatocellular carcinoma: advances in diagnostic imaging," *Drug Discoveries & Therapeutics*, vol. 9, no. 5, pp. 310–318, 2015.

[4] S. S. Shah, T.-T. Wu, M. S. Torbenson, and V. S. Chandan, "Aberrant CDX2 expression in hepatocellular carcinomas: an important diagnostic pitfall," *Human Pathology*, vol. 64, pp. 13–18, 2017.

[5] H. Rhee, J. H. Nahm, H. Kim et al., "Poor outcome of hepatocellular carcinoma with stemness marker under hypoxia: resistance to transarterial chemoembolization," *Modern Pathology*, vol. 29, no. 9, pp. 1038–1049, 2016.

[6] B. Xie, X. He, G. Guo et al., "High-throughput screening identified mitoxantrone to induce death of hepatocellular carcinoma cells with autophagy involvement," *Biochemical and Biophysical Research Communications*, vol. 521, no. 1, pp. 232–237, 2020.

[7] M. Ikeda, T. Okusaka, Y. Sato et al., "A Phase I/II trial of continuous hepatic intra-arterial infusion of 5-fluorouracil, mitoxantrone and cisplatin for advanced hepatocellular carcinoma," *Japanese Journal of Clinical Oncology*, vol. 47, no. 6, pp. 512–519, 2017.

[8] G. Kroemer, L. Galluzzi, O. Kepp, and L. Zitvogel, "Immunogenic cell death in cancer therapy," *Annual Review of Immunology*, vol. 31, no. 1, pp. 51–72, 2013.

[9] J. Zhou, G. Wang, Y. Chen, H. Wang, Y. Hua, and Z. Cai, "Immunogenic cell death in cancer therapy: present and emerging inducers," *Journal of Cellular and Molecular Medicine*, vol. 23, no. 8, pp. 4854–4865, 2019.

[10] X. Li, "The inducers of immunogenic cell death for tumor immunotherapy," *Tumori Journal*, vol. 104, no. 1, pp. 1–8, 2018.

[11] D. V. Krysko, A. D. Garg, A. Kaczmarek, O. Krysko, P. Agostinis, and P. Vandenabeele, "Immunogenic cell death and DAMPs in cancer therapy," *Nature Reviews Cancer*, vol. 12, no. 12, pp. 860–875, 2012.

[12] Y.-J. Wang, R. Fletcher, J. Yu, and L. Zhang, "Immunogenic effects of chemotherapy-induced tumor cell death," *Genes & Diseases*, vol. 5, no. 3, pp. 194–203, 2018.

[13] Y. Chen, H. Zhang, and Y. Zhang, "Targeting receptor tyrosine kinase EphB4 in cancer therapy," *Seminars in Cancer Biology*, vol. 56, pp. 37–46, 2019.

[14] E. Kadife, T. M. B. Ware, R. B. Luwor, S. T. F. Chan, K. Nurgali, and P. V. Senior, "Effects of EphB4 receptor expression on colorectal cancer cells, tumor growth, vascularization and composition," *Acta Oncologica*, vol. 57, no. 8, pp. 1043–1056, 2018.

[15] R. Rupaimoole and F. J. Slack, "MicroRNA therapeutics: towards a new era for the management of cancer and other diseases," *Nature Reviews Drug Discovery*, vol. 16, no. 3, pp. 203–222, 2017.

[16] Y. S. Lee and A. Dutta, "Micrornas in cancer," *Annual Review of Pathology: Mechanisms of Disease*, vol. 4, no. 1, pp. 199–227, 2009.

[17] G. Di Leva, M. Garofalo, and C. M. Croce, "Micrornas in cancer," *Annual Review of Pathology: Mechanisms of Disease*, vol. 9, no. 1, pp. 287–314, 2014.

[18] A. S. Befeler and A. M. di Bisceglie, "Hepatocellular carcinoma: diagnosis and treatment," *Gastroenterology*, vol. 122, no. 6, pp. 1609–1619, 2002.

[19] X.-l. Cheng, T.-y. Zhou, B. Li et al., "Methotrexate and 5-aminoimidazole-4-carboxamide riboside exert synergistic anticancer action against human breast cancer and hepatocellular carcinoma," *Acta Pharmacologica Sinica*, vol. 34, no. 7, pp. 951–959, 2013.

[20] G.-T. Yiang, P.-L. Chou, Y.-T. Hung et al., "Vitamin C enhances anticancer activity in methotrexate-treated Hep3B hepatocellular carcinoma cells," *Oncology Reports*, vol. 32, no. 3, pp. 1057–1063, 2014.

[21] J. Lv, Q. Xia, J. Wang, Q. Shen, J. Zhang, and X. Zhou, "EphB4 promotes the proliferation, invasion, and angiogenesis of human colorectal cancer," *Experimental and Molecular Pathology*, vol. 100, no. 3, pp. 402–408, 2016.

[22] S. Bhatia, A. Oweida, S. Lennon et al., "Inhibition of EphB4-ephrin-B2 signaling reprograms the tumor immune microenvironment in head and neck cancers," *Cancer Research*, vol. 79, no. 10, pp. 2722–2735, 2019.

[23] I. Mertens-Walker, J. E. Lisle, W. A. Nyberg et al., "EphB4 localises to the nucleus of prostate cancer cells," *Experimental Cell Research*, vol. 333, no. 1, pp. 105–115, 2015.

[24] A. D. Garg, S More, N Rufo et al., "Trial watch: immunogenic cell death induction by anticancer chemotherapeutics," *OncoImmunology*, vol. 6, Article ID e1386829, 2017.

[25] A. Serrano-del Valle, A. Anel, J. Naval, and I. Marzo, "Immunogenic cell death and immunotherapy of multiple myeloma," *Frontiers in Cell and Developmental Biology*, vol. 7, p. 50, 2019.

[26] Q. Wang, X. Ju, J. Wang, Y. Fan, M. Ren, and H. Zhang, "Immunogenic cell death in anticancer chemotherapy and its impact on clinical studies," *Cancer Letters*, vol. 438, pp. 17–23, 2018.

Hindawi
Journal of Healthcare Engineering
Volume 2021, Article ID 4543702, 8 pages
https://doi.org/10.1155/2021/4543702

Research Article

Computed Tomography Angiography under Deep Learning in the Treatment of Atherosclerosis with Rapamycin

Fuguang Ji[1], **Shuai Zhou**[2], **and Zhangshuan Bi**[1]

[1] *Intensive Care Unit, People's Hospital of Zhongmou, Zhengzhou 451450, Henan, China*
[2] *Department of Cardiology, The First Affiliated Hospital of Zhengzhou University, Zhengzhou 450052, Henan, China*

Correspondence should be addressed to Shuai Zhou; 0112031@yzpc.edu.cn

Received 24 May 2021; Revised 30 June 2021; Accepted 15 July 2021; Published 22 July 2021

Academic Editor: Enas Abdulhay

The clinical characteristics and vascular computed tomography (CT) imaging characteristics of patients were explored so as to assist clinicians in diagnosing patients with atherosclerosis. 316 patients with atherosclerosis who were hospitalized for emergency treatment were treated with rapamycin (RAPA) in the hospital. A group of manually delineated left ventricular myocardia (LVM) on the patient's coronary computed tomography angiography (CCTA) were selected as the region of interest for imaging features extracted. The CCTA images of 80% of patients were randomly selected for training, and those of 20% of patients were used for verification. The correlation matrix method was used to remove redundant image omics features under different correlation thresholds. In the validation set, CCTA diagnostic parameters were about 40 times higher than the manually segmented data. The average dice similarity coefficient was 91.6%. The proposed method also produced a very small centroid distance (mean 1.058 mm, standard deviation 1.245 mm) and volume difference (mean 1.640), with a segmentation time of about 1.45 ± 0.51 s, compared to about 744.8 ± 117.49 s for physician manual segmentation. Therefore, the deep learning model effectively segmented the atherosclerotic lesion area, measured and assisted the diagnosis of future atherosclerosis clinical cases, improved medical efficiency, and accurately identified the patient's lesion area. It had great application potential in helping diagnosis and curative effect analysis of atherosclerosis.

1. Introduction

The coronary atherosclerotic heart disease (CAHD) is a common cardiovascular disease endangering human physical and mental health in China. It is the most common type of organ disease caused by atherosclerosis, and the acute myocardial infarction (AMI) is the most serious type of coronary heart disease [1, 2]. In recent years, with the continuous development of China's economy and the continuous rise of the people's happiness index, the incidence of atherosclerosis in China has also increased year by year, with 45–55 deaths per 100,000 people from atherosclerosis. Besides, people who get sick are getting younger and younger, making the occurrence and prognosis of AMI a central issue in current research [3].

Rapamycin (RAPA) is the first known mammalian target of rapamycin (mTOR) pathway inhibitor, and the molecular formula is $C_{51}H_{79}NO_{13}$. As a traditional macrolide antibiotic, RAPA was first isolated from the fungus *Streptomyces hygroscopicus* and used as an antifungal drug in the 1970s. It was certified by the U.S. Food and Drug Administration in 1999 to resist acute immune rejection of organ transplant patients [1]. In recent years, the antitumor activity and antiaging function of RAPA and its analogues have been gradually discovered; they also have certain effects on diabetes and cardiovascular diseases (CVD) and so forth and have been gradually applied in relevant clinical treatment [4].

The imaging examination plays an important role in assessing whether patients with coronary heart disease are accompanied by myocardial ischemia [5]. However, ultrasound examination has strong subjective dependence, which is related to the experience of the operator. Its current application value in diagnosing myocardial ischemia is limited. Coronary computed tomography angiography (CCTA) can clearly show the structure of the heart and the condition of the coronary arteries [6]. Clinicians can assess the degree of stenosis of the coronary arteries and the characteristics of stenosis plaques, and then they can stratify patients for risk. However, the radiology department or clinician cannot directly identify whether the patient is accompanied by myocardial ischemia on the resting CCTA. CCTA combined with stress perfusion examination can visually display whether the myocardium has perfusion defects and can identify myocardial ischemia. However, compared with resting state CCTA, stress perfusion examination will increase the radiation dose, and the use of stress drugs will increase the risk of patient examination, and some patients cannot tolerate it [7]. Therefore, if advanced image analysis methods, such as artificial intelligence (AI) technologies, can be used to identify myocardial ischemia on the CCTA in the conventional resting state, the various follow-up invasive examinations can be reduced, which has important clinical significance.

AI is a branch of the field of computer science, which aims to imitate human thinking process, learning ability, and knowledge storage as much as possible [8]. Some research limitations based on traditional methods have gradually become prominent with the advent of the "big data" era. With the development of computer hardware and software, the application research of AI in the medical field has become a hot topic [9]. At present, the research results of AI in the medical field continue to emerge, and it has applications in disease screening, diagnosis, choice of treatment methods, and patient prognosis judgments. At present, many studies showed that some diagnostic or predictive models based on AI methods were better than those based on traditional methods. For example, Esteva et al. [10, 11] established a machine learning-based model to predict the 5-year all-cause mortality of patients with suspected coronary heart disease. This model evaluated 25 clinical features and 44 CCTA-based features. This model based on machine learning had better predictive performance than the Framingham risk assessment model established by traditional statistical methods. However, the above-mentioned work required the clinician to manually outline the contour of the myocardium on the corresponding image, which was undoubtedly a heavy and laborious work [12]. At present, studies showed that some deep learning-based methods can quickly, efficiently, and automatically outline the structure of interest, which not only greatly reduced the workload of clinicians, but also avoided subjective differences between different doctors to a certain extent [13].

Therefore, the research aimed to study the use of imaging omics methods combined with machine learning methods to analyze LVM characteristics. As a reference, the fractional flow reserve (FFR) of invasive coronary artery was compared with the hemodynamically significant stenosis judged by CCTA and invasive coronary angiography (ICA) to evaluate the effectiveness of different methods in diagnosing atherosclerosis. In addition, through the deep learning method and with the contour of the left ventricle myocardium manually drawn by the clinician as a reference, a deep learning model that can accurately and automatically outline the left ventricle was constructed to reduce the workload of the clinician.

2. Methods

2.1. Research Object. 316 patients with CAHD who underwent emergency treatment for the first time within 12 hours of onset of hospitalization were selected in the research from May 2017 to March 2021. There were 221 males and 95 females, aged 60.66 ± 12.19 years. The CAHD patients met the 2014 American College of Cardiology/American Heart Association (ACC/AHA) AMI diagnostic criteria.

Inclusion criteria were as follows: a) patients who met the diagnostic criteria of AMI and received emergency treatment within twelve hours; b) patients with complete case data and complete follow-up on time.

Exclusion criteria were as follows: (a) patients with a history of myocardial infarction or coronary revascularization; (b) patients with previous arrhythmia such as persistent atrial fibrillation; (c) patients with hematological diseases, malignant tumors, autoimmune diseases, infections, or inflammatory diseases; (d) patients with severe heart, liver, and kidney dysfunction; (e) patients with recent major trauma and major surgery; (f) patients with incomplete clinical data.

A total of 316 patients with coronary atherosclerosis met the above inclusion criteria and exclusion criteria in the research. The research had been approved by the medical ethics committee of hospital, and the family members of the patients included in the research had signed an informed consent form.

2.2. Data Acquisition and Image Analysis

2.2.1. CCTA Data Collection. The CCTA data was collected for all patients using 64 rows, and CCTA images were collected by scanning machines from four different CT manufacturers (Siemens, Somatom Flash, Definition Flash, Somatom Definition FlashAS+, Force; GE Discovery CT 750 HD, Light Speed VCT; Toshiba, Aquilion One Vision; Philips BrillianceiCT 256). The patients took nitroglycerin sublingually to dilate the coronary arteries five minutes before the CCTA examination. For patients with a fast heart rate, they can consider taking oral p-blockers (25–75 mg) before the examination according to the doctor's recommendation. The CT scan range was determined according to location phase, which was from tracheal protrusion to lower edge of the heart. All patients received adaptive sequence acquisition triggered by prospective electrocardiogram.

2.2.2. Image Analysis. The CCTA images of all patients were locally anonymized to remove sensitive information, then transmitted to the core laboratory, and imported into the Siemens postprocessing workstation for further analysis. The CCTA image quality was assessed by two experienced imaging doctors (with 3 years and 18 years of CCTA-related work experience, respectively). A 4-point method was used for evaluation: 1 = undiagnosable; 2 = acceptable; 3 = good; 4 = excellent. When there was a difference, the two radiologists reached a consensus through consultation. The cases with an image quality score of one were excluded.

2.3. Experiment Environment

2.3.1. Construction of the Deep Learning Segmentation Model. Before the deep learning model was constructed, the contours of the left ventricular myocardium (LVM) of 100 patients were manually sketched as a reference for the deep learning method to learn from CCTA images. The deep learning model was composed of U-Net and deep attention, which mainly included two parts: training phase and segmentation phase. The flow chart of the research is shown in Figure 1. Before the training was started, the 3D-patches on the CCTA images and the corresponding hand-drawn myocardial contours were collected. A voxel window with a window size of $512 \times 512 \times 32$ was used to slide on the Z axis of the image to extract 3D-patches. The data augmentation methods were used, such as flipping, rotating, and scaling, to increase the heterogeneity of the training set. Figure 2 shows that the deep learning network was composed by an encoding path and a decoding path. The long-hop connection bypassed the feature extracted from the encoding path and was mapped to the decoding path.

2.3.2. Deep Learning Model. After training, first the 3D-patches of the CCTA image were input into the trained model to obtain the probability map that each pixel on the CCTA image was the myocardial tissue, so as to obtain the myocardial segmentation result of the new patient. Then, these probability maps were merged into the entire image, and the final segmentation result of the LVM contour was obtained by gathering the myocardial probability maps and merging them on average. The fivefold cross-validation was used to verify the segmentation performance of the deep learning model. That is, the data of the above-mentioned patients were randomly classified into five equal parts, and four groups were selected for training, and the remaining group was used for verification. The dice similarity coefficient (DSC), mean surface distance (MSD), residual mean square distance (RMSD), center mass distance (CMD), and volume of difference (VOD) were used to evaluate the difference between LVM contour drawn by the model and that drawn manually by the doctor. The image segmentation accuracy was evaluated visually, and the segmentation time was recorded.

2.3.3. Statistical Analysis. The data conforming to the normal distribution was represented by the mean ± standard deviation in the research, and the data not conforming to the normal distribution was represented by the median or percentage. The categorical variables were expressed in frequency and percentage. The commercial software (Med Calc; version 18.2.1) and SPSS 22.0 version were used for statistical analysis of data. The Kolmogorov–Smirnov test was used to determine whether the data fit a normal distribution. The t-test was used to compare the difference between LVM time by the automatic segmentation model and that drawn manually by the doctor. The bilateral $P < 0.05$ was considered statistically significant in the research.

2.4. Therapeutic Reagents and Methods

2.4.1. Preparation of Therapeutic Reagent RAPA Nanoparticles (RAPA NP). 10 mg of RAPA and 20 mg of indomethacin (IND) were accurately weighed and added into 1 mL dimethyl sulfoxide (DMSO), which were fully suspended and dissolved with ultrasound. Then, 1 mL of DMSO suspension solution of 10 mg/mL PEI was added. After full and uniform mixing, the mixed solution was transferred into a dialysis bag (molecular weight was 3500 Da). The suspension of RAPA nanoparticles (PEI/IND/RAP) was obtained after dialyzed with ultrapure water for 24 hours. The suspensions containing different masses of small molecule shuttle-based drugs ursodeoxycholic acid (UDCA) were prepared in the same way.

2.4.2. Treatment Method. 300 mg aspirin and 180 mg ticagrelor/300 mg clopidogrel were given before treatment. RAPA was injected intravenously during treatment. Coronary angiography was performed via femoral artery or radial artery using standard techniques to assess coronary artery disease. Other treatments included angiotensin converting enzyme inhibitors (ACED) receptor blockers, diuretics, and nitrates, which can be used depending on the patient's own specific conditions.

2.5. Observation Index. The 0, 12, and 24 weeks were selected as the evaluation time points. The intima-media thickness (IMT) and plaque thickness (course integral) were detected at each evaluation point, and the patients in the treatment group were followed up to test the carotid artery intima-media thickness after three months to monitor the degree of treatment.

2.6. Statistical Method. The appropriate statistical analysis method was selected according to the nature of clinical trial data (measurement, classification, and grade data). The chi-square test or exact probability test was used for classification data, normality test and homogeneity test of variance were used for measurement data first, t-test was used for comparison of sample means for those who met the requirements, and paired t-test was used for the comparison of sample mean before and after treatment. The paired signed rank sum test was used to compare the samples that did not meet the conditions. The Wilcoxon rank sum test (correction) for sample comparisons or the Kruskal–Wallis test for multigroup comparisons were used for grade data. The repeated measure analysis of variance was used for quantitative primary outcome indexes at multiple observation time points. A two-sided test was used, with the baseline comparison test level $P = 0.05$, the efficacy group comparison test level $P = 0.05$, and the pairwise comparison between groups $P = 0.01670$.

3. Results

3.1. Visual Assessment of the Results of the Deep Learning Model and the Doctor's Manual Segmentation. In the axial CCTA image, the comparison of the contour results of visual assessment method and the left ventricular muscle manually segmented by the doctor is shown in Figure 3. On the CCTA image, the contrast between the LVM and the surrounding tissues was not very different, while the segmentation effect of the proposed deep learning-based segmentation method was basically consistent with the contour of the myocardium manually segmented by the doctor.

3.2. Objective Parameters Evaluating the Results of the Deep Learning Model and Manual Segmentation by Doctors. In the data set of all patients, the LVM contour segmented by the proposed method was consistent with the myocardial contour drawn by doctors. The average DSC = 91.6%, and the standard deviation was 4.1%. The proposed method also produced very small CMD (average of 1.058 mm, standard deviation of 1.245 mm) and VOD (average of 1.640, standard deviation of 1.777), and the specific results are shown in Figure 4. The distance of HI was less than 10 mm, which meant that the pixels of the myocardium segmented by this method were very close to the pixels of the manually segmented myocardium, and LVM can be well positioned by this method.

In addition, the MSD and RMSD were both less than 2 mm, which indicated that the accuracy of the segmentation method was high. The differences of DSC and VOD between this method and manual segmentation of myocardium were evaluated at different levels of myocardium, and the results are shown in Figure 5.

3.3. The Time Required for Automatic Segmentation of Deep Learning Models and Manual Segmentation of LVM by Physicians. The time required for LVM by the automatic segmentation model and that of manual segmentation by the doctor were compared in the research. Through a randomized analysis of the time required for myocardial segmentation in 20 patients, it was found that LVM segmentation based on deep learning method required significantly short time. The deep learning method only needed an average of about 1.45 ± 0.51 seconds to complete segmentation, while the doctor's manual segmentation needed about 744.8 ± 117.49 seconds to complete segmentation ($P < 0.001$). The results showed that the efficiency and quality of automatic segmentation were much higher than those of manual segmentation by doctors.

3.4. Data Results after RAPA Treatment

3.4.1. IMT Results. A paired t-test was performed in the control group and the treatment group to test the data before and after treatment. Wilcoxon signed rank test was used for the measurement data that did not meet the conditions before and after treatment. The Shapiro-Wilk normality test is shown in Figure 6. After inspection, the difference of the left carotid artery before and after IMT treatment in the treatment group showed that $P = 0.043$, and the difference of the right carotid artery before and after IMT treatment showed that $P = 0.025$. There were statistical differences before and after treatment, which proved that the use of a deep learning-based imaging system had a certain therapeutic effect in improving the thickness of carotid artery intima-media in patients with carotid atherosclerotic plaque.

3.4.2. Carotid Artery Intima-Media Thickness Results. Before treatment, at the end of treatment, and during follow-up, the thickness of carotid medial artery was statistically analyzed and compared between groups, as shown in Figure 7. The IMT of left carotid artery was significantly different between the three groups at the end of treatment and 3 months of follow-up ($P = 0.025$). At the end of treatment, there was a difference between the control group and the treatment group ($P = 0.011$), while there was no statistical difference between the control group and the treatment group ($P = 0.618$). After three months of follow-up, there was a difference between the control group and the treatment group ($P = 0.019$), while there was no statistical difference between the control group and the treatment group ($P = 0.865$). It was concluded that, in terms of the improvement of carotid artery thickness, the group using deep learning-based CT imaging characteristics analysis was superior to the control group with respect to the left carotid artery.

4. Discussion

How to accurately monitor the occurrence of adverse cardiac events in patients with atherosclerosis is always the core of cardiovascular disease research. The process of diagnosis and treatment of cardiovascular patients generates a large amount of data, including the patient's symptoms, laboratory test results, medical imaging data, and drug prescriptions. In general, clinicians judge the prognosis of patients based on their own models, their own experience, and the current condition of the patient. However, most prediction models were based on regression models and only used limited variables, which may not meet the requirements of accurate prediction [14]. The routine diagnosis and treatment of patients with CVD generated a large amount of data. At the same time, the amount of cardiovascular imaging data was also increasing. Clinically, doctors were unlikely to be familiar with various electronic medical record information including genetic data and cardiovascular imaging data and made full use of this information in clinical practice. This may lead to misdiagnosis due to insufficient information utilization. A recent study pointed out that about 40,000–80,000 people die every year because of diagnostic errors [15]. The autopsy studies found that diagnosis based on imaging data had an error rate of up to 20%. However, a fivefold cross-validation method was used to verify the

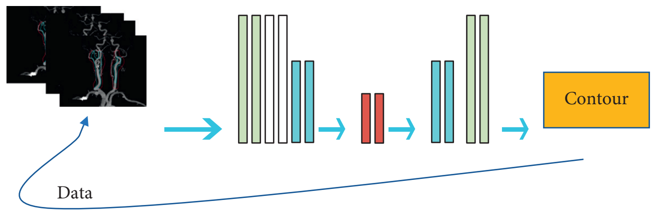

Figure 1: Data analysis model.

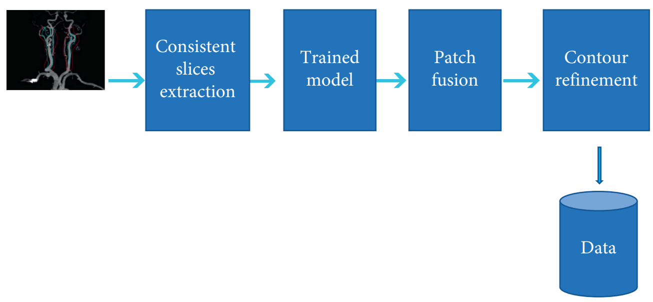

Figure 2: Data gain model.

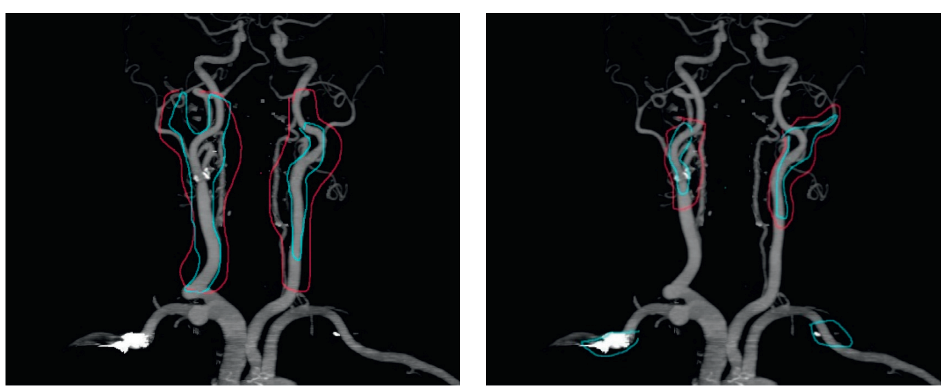

(a) (b)

Figure 3: Manual segmentation (a) and deep learning segmentation (b).

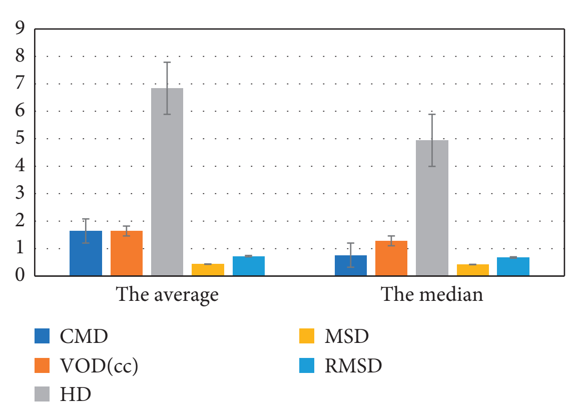

Figure 4: The results of objective parameter evaluation of automatic and manual myocardial segmentation.

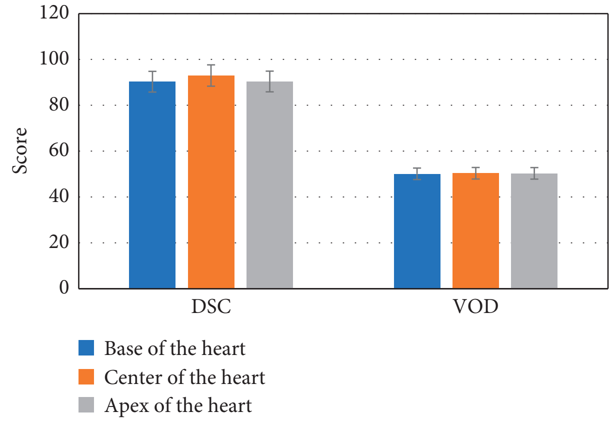

Figure 5: Evaluation of the parameter results of automatic and manual myocardial segmentation at different myocardial levels.

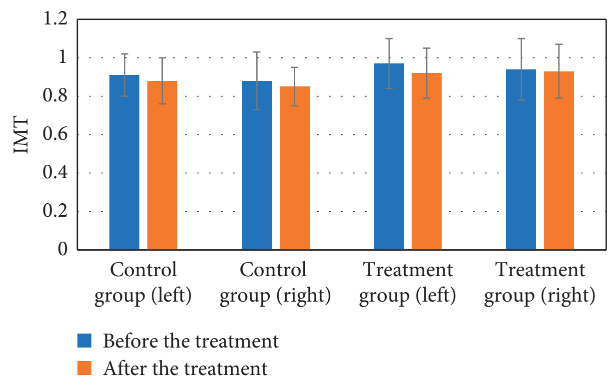

Figure 6: Comparison before and after IMT treatment.

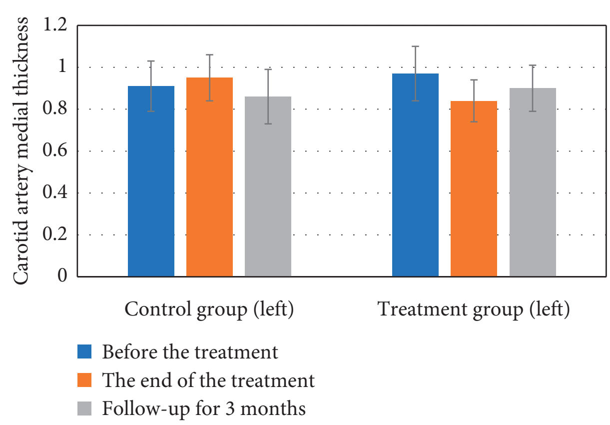

Figure 7: The thickness of the left carotid artery intima-media at different time points in the two groups.

segmentation effect of the LVM based on the proposed deep learning model. The subjective and objective methods were used to evaluate the contour difference between the proposed method of automatic segmentation of the LVM contour and the manual segmentation drawn by the doctor. It was verified that the proposed method could accurately segment the LVM tissue from CCTA images by analyzing six objective parameters, including DSC, HD, MSD, RMSD, C1VID, and VOD, and the proposed method significantly shortened the time needed to segment LVM from CCTA images. It reduced the time that would normally take about 12 minutes on average to about a second, which greatly reduced the workload of the doctor [16].

In the past, some scholars had achieved good results by establishing a deep learning-based method to automatically segment cardiac tissue of cardiac MRI images [17]. However, the contrast of myocardial tissue on CCTA images was not obvious compared with cardiac MR images, so there were few studies on the automatic segmentation of LVM on CCTA images. For the first time in the research, a neural learning network was used to integrate a deep-attention network to detect and segment LVM on CCTA images. After the model was trained, automatic LVM recognition and segmentation were performed on newly inputted CCTA images of patients. At present, some scholars have proposed to use different AI-based methods to segment the LVM on CCTA images. The imaging omics method used in this study can extract many quantitative and qualitative features from the region of interest on the image with high throughput. These imaging omics features can reflect the internal features of the organizational structure. Combined with machine learning methods, a lot of information was provided for the diagnosis of myocardial ischemia, which overcame the limitation of clinicians to analyze CCTA solely based on the naked eye. For example, Smyth et al. [18] used a multiscale convolutional neural network (CNN) to segment the LVM. The segmentation performance of CNN network on CCTA images of 20 patients was analyzed, and the average DSC was 0.910. Gertsen et al. [19] used a fully convolutional network to analyze the virtual single-energy CCTA data, and the best DSC value was 90.1 through CCTA image verification in 40 patients. The 3D fully convolutional neural network was used for CT brain tissue image segmentation, which can improve the accuracy of image analysis of atherosclerotic hard blood vessel function, and significantly improved the clearance rate of vascular plaque deposition and the recovery of carotid artery intima-media thickness after treatment. In this retrospective study, the feasibility of using imaging omics combined with machine learning method to analyze the characteristics of left ventricular myocardium on CCTA images to predict whether patients with coronary heart disease had myocardial ischemia was established and verified. Compared with the method that clinicians identify lesions based on CT images and determine myocardial ischemia based on the degree of coronary artery stenosis, the proposed method of image omics combined with machine learning had a better performance in predicting myocardial ischemia. The ability of the model to predict myocardial ischemia was relatively stable, and the accuracy was still high in the validation group. In addition, CCTA images generated by a number of hospitals and a variety of CT devices across the country were collected, and the model was randomly trained and verified, which reflected the universality and generalization of the model. To our knowledge, this was the first time that left ventricular myocardial features were analyzed using image omics to investigate whether patients with coronary heart disease had myocardial ischemia. Unlike the traditional clinical use of the degree of coronary artery stenosis as a standard to determine whether patients with CHD had myocardial ischemia, the characteristics of myocardium supplied by coronary arteries were analyzed to assess whether patients with CHD had myocardial ischemia, which also provided a new idea for future research.

5. Conclusion

The research showed that the CT angiography images were used during the treatment of atherosclerosis with rapamycin. Compared with the LVM contour manually drawn by the doctor on the CCTA image, the method proposed in the research had little difference with the LVM contour manually drawn by the doctor regardless of whether subjective or objective evaluation methods were used. The method significantly reduced the time required to segment LVM compared with traditional manual segmentation. However, there are still some shortcomings in this study. First, although patients with atherosclerosis were included in this study, CCTA images of only 100 patients were randomly and continuously selected for model training and validation. The results need to be further validated for the segmentation of myocardium on CCTA images collected by hospitals and CT scanning equipment in the future. Due to the different expertise and experience of imaging doctors, each doctor will have different contour labeling of the left ventricular myocardium, and such difference cannot be corrected by this deep learning algorithm. Second, there are only patients with suspected or confirmed coronary heart disease involved. The results of the myocardial segmentation model in patients with other diseases and at different stages of the disease need further study. Finally, the model is currently in the initial stage of establishment, and the extent to which it can reduce the workload of doctors in clinical practice is still unknown. Future research needs to be improved.

Data Availability

No data were used to support this study.

Conflicts of Interest

The authors declare that they have no conflicts of interest.

References

[1] W. L. Bi, A. Hosny, M. B. Schabath et al., "Artificial intelligence in cancer imaging: clinical challenges and applications," *CA: A Cancer Journal for Clinicians*, vol. 69, no. 2, pp. 127–157, 2019.

[2] F. D. Verbraak, M. D. Abramoff, G. C. F. Bausch et al., "Diagnostic accuracy of a device for the automated detection of diabetic retinopathy in a primary care setting," *Diabetes Care*, vol. 42, no. 4, pp. 651–656, 2019.

[3] M. M. Braun, W. A. Stevens, and C. H. Barstow, "Stable coronary artery disease: treatment," *American Family Physician*, vol. 97, no. 6, pp. 376–384, 2018.

[4] B. Koçak, E. Ş. Durmaz, E. S. Durmaz, E. Ates, and O. Kilickesmez, "Radiomics with artificial intelligence: a practical guide for beginners," *Diagnostic and interventional radiology*, vol. 25, no. 6, pp. 485–495, 2019.

[5] K. Chang, A. L. Beers, and H. X. Bai, "Automatic assessment of glioma burden: a deep learning algorithm for fully automated volumetric and bidimensional measurement," *Neuro-Oncology*, vol. 21, no. 11, pp. 1412–1422, 2019.

[6] S. A. Taghanaki, K. Abhishek, J. P. Cohen, C. A. Julian, and H. Ghassan, "Deep semantic segmentation of natural and medical images: a review," *Artificial Intelligence Review*, vol. 54, 2020.

[7] G. Wang, W. Li, S. Ourselin et al., "Automatic brain tumor segmentation using cascaded anisotropic convolutional neural networks," in *Proceedings of the International MICCAI*

Brainlesion Workshop, Springer, Quebec City, Canada, September 2017.
[8] Y. Yuan, M. Chao, and Y.-C. Lo, "Automatic skin lesion segmentation using deep fully convolutional networks with jaccard distance," *IEEE Transactions on Medical Imaging*, vol. 36, no. 9, pp. 1876–1886, 2017.
[9] J. J. Titano, M. Badgeley, and J. Schefflein, "Automated deep-neural-network surveillance of cranial images for acute neurologic events," *Nature Medicine*, vol. 24, no. 9, pp. 1337–1341, 2018.
[10] H. Liang, B. Y. Tsui, and H. Ni, "Evaluation and accurate diagnoses of pediatric diseases using artificial intelligence," *Nature Medicine*, vol. 25, no. 3, pp. 433–438, 2019.
[11] A. Esteva, B. Kuprel, and R. A. Novoa, "Dermatologist-level classification of skin cancer with deep neural networks," *Nature*, vol. 542, no. 7639, pp. 115–118, 2017.
[12] G. A. Bello, T. J. W. Dawes, and J. Duan, "Deep-learning cardiac motion analysis for human survival prediction," *Nature Machine Intelligence*, vol. 1, no. 2, pp. 95–104, 2019.
[13] M. J. Willemink and P. B. Noël, "The evolution of image reconstruction for CT-from filtered back projection to artificial intelligence," *European Radiology*, vol. 29, no. 5, pp. 2185–2195, 2019.
[14] F. J. Neumann, U. M. Sousa, and A Ahlsson, "ESC/EACTS Guidelines on myocardial revascularization," *European Heart Journal*, vol. 40, no. 2, pp. 87–165, 2019.
[15] M. J. Blaha, M. Cainzos-Achirica, P. Greenland et al., "Role of coronary artery calcium score of zero and other negative risk markers for cardiovascular disease," *Circulation*, vol. 133, no. 9, pp. 849–858, 2016.
[16] T. Braun, S. Spiliopoulos, and C. Veltman, "Detection of myocardial ischemia due to clinically asymptomatic coronary artery stenosis at rest using supervised artificial intelligence-enabled vectorcardiography - a five-fold cross validation of accuracy," *Journal of Electrocardiology*, vol. 59, pp. 100–105, 2020.
[17] S. Liu, H. Shi, and C. Ji, "Preoperative CT texture analysis of gastric cancer: correlations with postoperative TNM staging," *Clinical Radiology*, vol. 73, no. 8, pp. 756.e1–756.e9, 2018.
[18] E. C. Smyth, M. Nilsson, H. I. Grabsch, N. C. V. Grieken, and F. Lordick, "Gastric cancer," *The Lancet*, vol. 396, no. 10251, pp. 635–648, 2020.
[19] E. C. Gertsen, C. D. Jongh, and H. J. F. Brenkman, "The additive value of restaging-CT during neoadjuvant chemotherapy for gastric cancer," *European Journal of Surgical Oncology*, vol. 46, no. 7, pp. 1247–1253, 2020.

Hindawi
Journal of Healthcare Engineering
Volume 2021, Article ID 5063021, 7 pages
https://doi.org/10.1155/2021/5063021

Research Article

Fast Independent Component Analysis Algorithm-Based Diagnosis of L5 Nerve Root Compression and Changes of Brain Functional Areas Using 3D Functional Magnetic Resonance Imaging

Bofeng Zhao[1] **Fuxia Yang**[2] **Lan Guan**[1] **Xinbei Li**[1] **Yuanming Hu**[1] **Chunlei Zhang**[3] **Yang Liu**[1] **Xiutao Li**[1] **Wucheng Wen**[1] **and Hanqing Lyu**[1]

[1]*Department of Radiology, Shenzhen Traditional Chinese Medicine Hospital, The Fourth Clinical Medical College of Guangzhou University of Chinese Medicine, Shenzhen 518033, Guangdong, China*
[2]*Department of Acupuncture and Moxibustion, Shenzhen Traditional Chinese Medicine Hospital, The Fourth Clinical Medical College of Guangzhou University of Chinese Medicine, Shenzhen 518033, Guangdong, China*
[3]*Department of Clinical Laboratory, Shenzhen Traditional Chinese Medicine Hospital, The Fourth Clinical Medical College of Guangzhou University of Chinese Medicine, Shenzhen 518033, Guangdong, China*

Correspondence should be addressed to Hanqing Lyu; 151009020109@st.sdju.edu.cn

Received 4 June 2021; Accepted 14 July 2021; Published 22 July 2021

Academic Editor: Enas Abdulhay

In this paper, the application of 3-dimensional (3D) functional magnetic resonance imaging (FMRI) in the diagnosis of the 5th lumbar (L5) nerve root compression and brain functional areas in patients with lumbar disc herniation (LDH) was analyzed. The traditional fast independent component analysis (Fast ICA) algorithm was optimized based on the modified whitening matrix to establish a new type of Modified-Fast ICA (M-Fast ICA) algorithm that was compared with the introduced traditional Fast ICA and ICA. M-Fast ICA was applied to the 3D FMRI diffusion tensor imaging (DTI) evaluation of 65 patients with L5 nerve root pain due to LDH (group A) and 50 healthy volunteers (group B). The values of fractional anisotropy (FA) and apparent diffusion coefficient (ADC) in the lumbar nerve roots (L3, L4, L5, and the 1st sacral vertebra (S1)) were recorded among subjects from the two groups. Besides, the score of edema degree in the lumbar nerve roots (L5 and S1) and activity of brain functional areas were also recorded among all subjects of the two groups. The results showed that the mean square error of M-Fast ICA was smaller than that of traditional Fast ICA and ICA, while its signal-to-noise ratio (SNR) was greater than that of Fast ICA and ICA ($P < 0.05$). The FA of L5 and S1 nerve roots in patients of group A was sharply lower than the values of group B, while the ADC of patients in group A was greater than that of the control group ($P < 0.05$). Besides, the score of edema in L5 and S1 nerve roots of patients in group A increased in contrast to group B ($P < 0.05$). The brain areas were activated after surgery including bilateral temporal lobe, left thalamus, splenium of corpus callosum, and right internal capsule. In conclusion, the 3D image denoising performance of M-Fast ICA optimized and constructed in this study was superior to that of the traditional Fast ICA and ICA. The FA of patients with L5 nerve root pain due to LDH decreased steeply, while the ADC increased dramatically. L5 nerve root pain caused by LDH resulted in changes in brain functional areas of the patients to inhibit the resting state default network activity, and the corresponding brain functional areas could be activated through treatment.

1. Introduction

LDH is a common and frequent-occurring disease in spine surgery, and low back pain and lumbocrural pain are the most common causes. Its clinical manifestations include low back pain, sciatica, and lower extremity radiation pain and weakness, and patients with severe symptoms suffer from incontinence of defecation and urination and abnormal sensation in the saddle area [1, 2]. Moreover, the main pathogenic factors of this disease include degenerative changes, annulus fibrosus disruption, or nerve root and cauda equina nerve stimulated and compressed by disc herniation in various parts of lumbar intervertebral disc (nucleus pulposus, annulus fibrosus, and cartilage plate) [3]. In addition, the incidence of L4-L5 and L5-S1 is the highest of patients with LDH, accounting for about 95% of the whole symptoms, while the incidence of multiple intervertebral disc herniation only occupies about 15%. LDH tends to emerge in young adults aged 20–40 years old (more males suffer from this disease than females), and it is often common in information technology (IT) practitioners, teachers, civil servants, drivers, and other long-term office workers [4, 5]. Excessive bending down should be avoided in life, and the back muscle should be exercised in order to improve lumbar muscle strength. Generally speaking, LDH cannot be completely cured, and most patients need mild conservative treatment to alleviate the disease. Therefore, it is very important to discuss the compression conditions of each lumbar vertebra in patients with LDH [6].

With the rapid development of imaging, MRI has been gradually applied in the diagnosis of LDH. By comparing with multiple indicators, it can clearly show the height, outline, annular tear, and high signal area of the intervertebral disc, with advantages of multidimensional imaging, high resolution, and high sensitivity. However, conventional MRI has a false positive rate and false negative rate in the diagnosis of elderly patients with lumbar nerve root pain, so it is necessary to adopt more excellent diagnostic tools [7,8]. Theoretically speaking, FMRI is designed to reflect the functional states of tissues and organs, and DTI, as an extension technique of conventional MRI, can visually display highly anisotropic nerve fibers [9]. On this basis, 3D MRI can process the cross-sectional images of any part or direction of one scan through electronic computers to form a 3D image, which can be further applied to diagnose the patient. ICA has been a new signal processing technology since the 1990s and mainly refers to the way to separate the source signals from the linear mixed signals of multiple source signals, which is featured with rapid convergence. However, it is easy to be interfered with by the SNR of data when processing FMRI data, which affects the results of analysis [10, 11]. Therefore, this study intended to optimize Fast ICA to explore its value in the MRI diagnosis of LDH.

To sum up, ICA is a traditional method for FMRI denoising, but it has some defects. On this basis, the traditional Fast ICA was optimized through the modified whitening matrix to construct the M-Fast ICA, so as to apply to the DTI evaluation of 65 patients with L5 nerve root pain due to LDH (group A) and 50 healthy volunteers (group B). Besides, the traditional Fast ICA and ICA were compared with M-Fast ICA. The FA and ADC of L3, L4, L5, and S1 lumbar nerve roots and brain activation areas after surgery in patients from the two groups were compared to comprehensively evaluate the application of FMRI in the diagnosis of L5 nerve root compression and brain functional areas in patients with LDH.

2. Materials and Methods

2.1. Sample Selection. In this study, 65 patients with L5 nerve root pain due to LDH were selected as group A, who were admitted to the hospital from January 1, 2019, to July 15, 2020; and 50 healthy volunteers were selected as group B, who underwent physical examination during the same period. During the surgery, the edema degree of the diseased nerve roots was evaluated based on the color of nerve roots (1 point for yellow-white, 2 points for pink, and 2 points for purplish red) and the thickness (0 points for no obvious thickening and 1 point for thickening). In addition, the higher the score, the greater the edema. This study had been approved by the Medical Ethics Committee of the hospital. Moreover, the subjects and their family members had known about this study and signed informed consent and failed examination consent.

The criteria for inclusion were defined to include the subjects who were older than 18 years old, were right-handed, had clear consciousness, could cooperate with the examination, were diagnosed with LDH accompanied by root pain, and suffered from LDH of the unilateral lower extremity.

The criteria for exclusion were defined to include the subjects who were pregnant, suffered from cardiovascular diseases, had taken relevant drugs, had mental diseases, and interrupted the examination.

2.2. Magnetic Resonance Imaging Scanning. MR Prisma 3.0 magnetic resonance machine produced by Siemens, Germany, was adopted to scan all subjects. Subjects were placed in the supine position with quiet breathing. Standard Siemens spinal coils were placed in the subject's scanning sequence and scanned based on the location of LDH. Conventional MRI scan parameters were shown as follows: the repeat time was 4,500 ms, echo time was 115 ms, field of view was 250×250 mm, matrix was 251×325, the thickness of a layer was 3.5 mm, and the number of layers was 10. The scan parameters of DTI included repeat time of 7,500 ms, echo time of 82 ms, view field of 310×150 mm, matrix of 108×308, thickness of 3.5 mm, layer number of 40, and scanning time of 20 minutes. The obtained image sent to the workstation was completed after the scanning, and the Neuro Space was employed to select the region of interest (near the lumbar intervertebral foramen) to measure the FA and ADC. What is more, the activation rate of each brain area was recorded (it indicated that the low-frequency fluctuation amplitude was active brain area with statistical significance when the voxel value in the magnetic resonance image was equaled to or more than 2.262).

2.3. Magnetic Resonance Imaging Denoising Algorithm Based on Fast Independent Component Analysis Algorithm. Fast ICA was a fixed point recursive algorithm proposed by Hyvarinen et al. from the University of Helsinki, Finland. With its fast convergence speed and good separation effect, Fast ICA was widely applied in signal processing and could well estimate the mutually statistically independent original signals mixed by unknown factors from the observed signals.

This algorithm firstly centralized the observed signals so that the mean vectors of the observed signals were all 0, and then, the centralized observed signals were whitened. It could be expressed as follows:

$$F = W_N (S - \overline{S}), \tag{1}$$

where S stood for an observed signal, $\overline{S}$ expressed the mean vector of an observed signal, W_N represented a whitening matrix, and f stood for a whitened signal. Then, the matrix N was initially separated so that $\|N\| = 1$. The matrix should be updated, and the iterative processing was for the separated matrix by Newton iteration method to obtain N_1 that was orthogonalized. Thus, the matrix N was shown as the following equation:

$$N = \left(N_1 N_1^T\right)^{-(1/2)} N_1, \tag{2}$$

where T represented the orthogonalization factor. Finally, the convergence of the separated matrix N was judged. If the convergence state was reached, the optimal estimation value of the source signal at this time could be calculated as follows:

$$\overrightarrow{U} = NS, \tag{3}$$

where U stood for a source signal. If the separation matrix N did not converge, the return iteration continued until it converged. Considering that the traditional Fast ICA did not exclude the interference of image noise to the signal during whitening, the whitening processing was optimized and the whitening matrix was formed by the combination of eigenvalues of the noise subspace and the eigenvalues of the signal subspace. Firstly, the autocorrelation matrix of the observed matrix was obtained through the following equation:

$$R_{ss} = G\left[SS^T\right], \tag{4}$$

where R_{ss}, T, and $G[\cdot]$ expressed the autocorrelation matrix, the orthogonalization factor, and the autocorrelation function, respectively. Then, the eigenvalues were discomposed, as shown in the following:

$$R_{ss} = V_s \exists V_S^H, \tag{5}$$

where $\exists$, V, and H represented the eigenvalue corresponding to signal subspace, the eigenvalue vector corresponding to signal subspace, and the signal factor of the matrix, respectively. Besides, $\exists = \mathrm{diag}(\lambda_1, \lambda_2, \ldots, \lambda_n)$ and $V_S^H = [V_i / V_{n-i}]^H$. Thus, the whitening matrix was formed by the eigenvalues and eigenvalue vectors, which was expressed in the following equation:

$$N = \exists_i^{-(1/2)} V_i^H. \tag{6}$$

Then, the main eigenvalue was modified to obtain the following:

$$\exists_i = \exists_i - \overline{\Delta}^2 \sigma_i, \tag{7}$$

where $\exists_i$ stood for the main eigenvalue after modification, $\overline{\Delta}^2$ expressed the weight matrix corresponding to the average eigenvalue of noise, and σ_i represented the weight matrix corresponding to the eigenvalues of the signal subspace. What is more, $\overline{\Delta}^2 = \sum_{i+1}^{n} (\lambda_{i+1} / (n - i))$ and $\sigma_i = \mathrm{diag}(\sigma_1, \sigma_2, \ldots, \sigma_n)$. The new whitening matrix could be calculated as follows:

$$N = \exists_i^{-(1/2)} V. \tag{8}$$

The above was the M-Fast ICA optimized on the basis of the modified whitening matrix, which fully considered the impact of noise and helped to separate the signal with low signal noise.

2.4. Evaluation Indicators of Image Enhancement Performance. The traditional Fast ICA [12] and ICA [13] were introduced to compare with M-Fast ICA constructed in this study. The root mean square error (RMSE) and SNR were regarded as evaluation indicators.

RMSE referred to the square root of the variance between the original signal and the denoised signal, which can be expressed as follows:

$$\mathrm{RMSE} = \left\{ \frac{[f(n) - f(n)^*]^2}{n} \right\}^{1/2}, \tag{9}$$

where $f(n)$ and $f(n)^*$ stood for the original signal and the denoised signal, respectively.

SNR was a traditional method for detecting noise measurement in signals, which can be calculated as the following:

$$\mathrm{SNR} = 10 \log 10 \left(\frac{P_s}{P_z} \right), \tag{10}$$

where P_s and P represented the power of the original signal and the power of noise, respectively. In addition, $P_s = \{[\sum f^2(n)]/n\}$ and $P_z = \mathrm{RMSE}^2$.

2.5. Statistical Methods. SPSS19.0 version statistical software was adopted to analyze the data processing in the study, measurement data were expressed as mean ± standard deviation, and enumeration data was represented by percentage (%). The SNR and RMSE of Fast ICA, ICA, and M-Fast ICA were pairwise compared through the one-way variance analysis. The independent t-test was applied to compare the FA and ADC of the lumbar nerve roots (L3, L4, L5, and S1) with the edema degree score of the lumbar nerve roots (L5 and S1) of the subjects in the two groups. $P < 0.05$ meant the difference was statistically significant.

3. Results

3.1. Comparison of Basic Information of the Subjects in the Two Groups. Figure 1 shows the comparison of basic information of the subjects in the two groups. It indicates that the age of the subjects in group A was 50.17 ± 8.83 years old, the height was 160.21 ± 12.33 cm, the weight was 58.28 ± 7.82 kg, the male proportion was 56.08%, and the female proportion was 43.92%. Besides, the age, height, weight, male

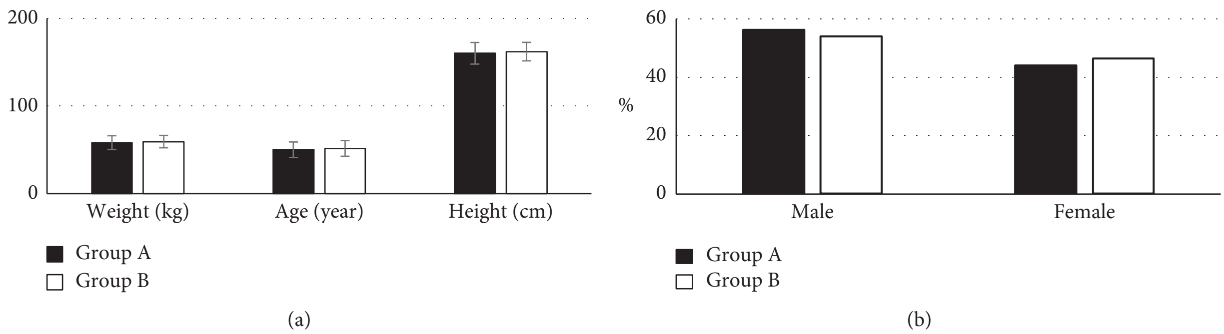

Figure 1: Comparison of basic information of the subjects in both groups. (a) Comparison of the age, height, and weight of the subjects in groups A and B; (b) comparison of the male and female proportion of the subjects in the two groups.

proportion, and female proportion of the subjects in group B were 51.62 ± 8.91 years old, 162.13 ± 10.56 cm, 59.41 ± 7.07 kg, 53.81%, and 46.19%, respectively. There were no great differences in the age, height, weight, male proportion, and female proportion of the subjects from groups A and B ($P > 0.05$).

3.2. Comparison of the Root Mean Square Error and Signal-to-Noise Ratio of the Three Algorithms. Figure 2 indicates the comparison of RMSE and SNR of the three algorithms. It reveals that the values of RMSE in the ICA, Fast ICA, and M-Fast ICA were 6.38 ± 0.52, 6.25 ± 0.72, and 4.91 ± 0.38, respectively; and the values of SNR in the ICA, Fast ICA, and M-Fast ICA were 71.42 ± 5.49 dB, 72.37 ± 5.18 dB, and 86.36 ± 6.77 dB, respectively. Therefore, the RMSE of M-Fast ICA was obviously higher than the values of ICA and Fast ICA, showing a statistical substantial difference ($P < 0.05$). However, the SNR of M-Fast ICA increased dramatically in contrast to ICA and Fast ICA, with a statistical great difference ($P < 0.05$).

Figure 3 expresses the MRI image reconstruction results of the lumbar spine by the three algorithms. Figure 3 shows the original ultrasound image of one patient, with a blurred lumbar spine and a lot of noise. The image resolution of M-Fast ICA was higher markedly than that of ICA and Fast ICA after denoising, and the noise reduction was obvious, so M-Fast ICA could fully meet the requirements of clinical imaging diagnosis.

3.3. Comparison of the Fractional Anisotropy of the 3rd, 4th, and 5th Lumbar and the 1st Sacral Vertebra Nerve Roots in the Subjects from Both Groups. Figure 4 shows the comparison of FA of L3 and L4 lumbar nerve roots among the subjects in the two groups. It was known that the FA of L3 and L4 lumbar nerve roots were 314.24 ± 17.71 and 308.41 ± 17.55 in patients from group A, respectively. Besides, the FA of L3 lumbar nerve root was 319.41 ± 30.31 and the FA of L4 lumbar nerve root was 315.76 ± 27.45 in the subjects from group B. The values of FA in L3 and L4 lumbar nerve roots of patients from group A were not statistically considerable in contrast to group B ($P > 0.05$).

Figure 5 indicates the comparison of FA in the L5 and S1 lumbar nerve roots among the subjects from the two groups. The FA of L5 lumbar nerve root was 250.58 ± 16.62 and its S1 lumbar nerve root was 239.64 ± 18.85 in patients of group A; and the values of FA in L5 and S1 lumbar nerve roots were 331.71 ± 18.93 and 316.46 ± 28.82, respectively. Among them, the values of FA in the L5 and S1 lumbar nerve roots were lower sharply in patients of group A than those of group B, and the difference was statistically remarkable ($P < 0.05$).

3.4. Comparison of the Apparent Diffusion Coefficient of the 3rd, 4th, and 5th Lumbar and the 1st Sacral Vertebra Nerve Roots in the Subjects from Both Groups. In Figure 6, there are comparisons of the ADC of L3, L4, L5, and S1 lumbar nerve roots among the subjects in the two groups. It was observed that the values of ADC in the L3, L4, L5, and S1 lumbar nerve roots were $0.64 \pm 0.025 \times 10^3$ s/mm^2, $0.52 \pm 0.016 \times 10^3$ s/mm^2, $0.86 \pm 0.024 \times 10^3$ s/mm^2, and $0.79 \pm 0.033 \times 10^3$ s/mm^2 in the patients from group A, respectively. What is more, the values of ADC in the S1, L3, L4, and L5 lumbar nerve roots were $0.58 \pm 0.011 \times 10^3$ s/mm^2, $0.71 \pm 0.018 \times 10^3$ s/mm^2, $0.54 \pm 0.021 \times 10^3$ s/mm^2, and $0.51 \pm 0.016 \times 10^3$ s/mm^2 in the subjects from group B, respectively. The ADC of the L3 and L4 lumbar nerve roots in the subjects from group A was not statistically substantial compared with that of group B ($P > 0.05$). However, ADC of the L5 and S1 lumbar nerve roots in the subjects from group A increased enormously in contrast to group B, and there was a statistically obvious difference ($P < 0.05$).

3.5. The Edema Scoring of the 3rd, 4th, and 5th Lumbar and the 1st Sacral Vertebra Nerve Roots in the Subjects from the Two Groups. There was a comparison of edema scoring of the L5 and S1 lumbar nerve roots among the subjects in the two groups, as shown in Figure 7. It revealed that the edema scores of the L5 and S1 lumbar nerve roots were 5.62 ± 1.43 and 4.07 ± 1.13 in the patients of group A, respectively. The edema scores of the L5 and S1 lumbar nerve roots were 1.62 ± 0.33 and 1.25 ± 0.24 in the patients of group B, respectively. Among them, the edema scores of the L5 and S1 lumbar nerve roots were higher hugely in the subjects of group A than those of group B, indicating a statistically great difference ($P < 0.05$).

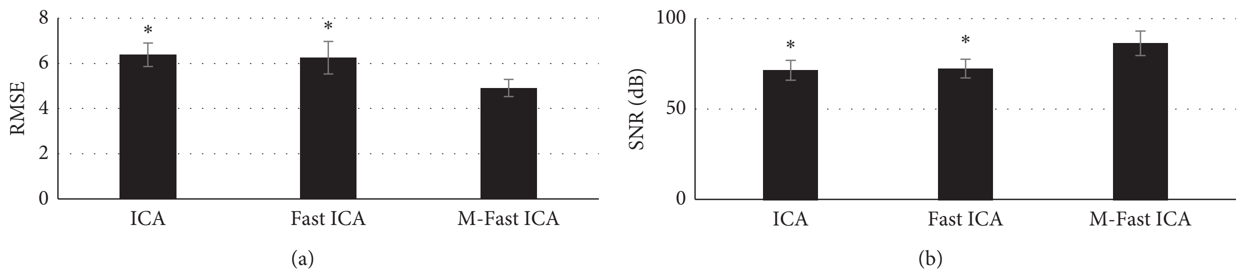

Figure 2: (a, b) Comparison of RMSE and SNR of the three algorithms. *There was a statistical difference in contrast to M-Fast ICA ($P < 0.05$).

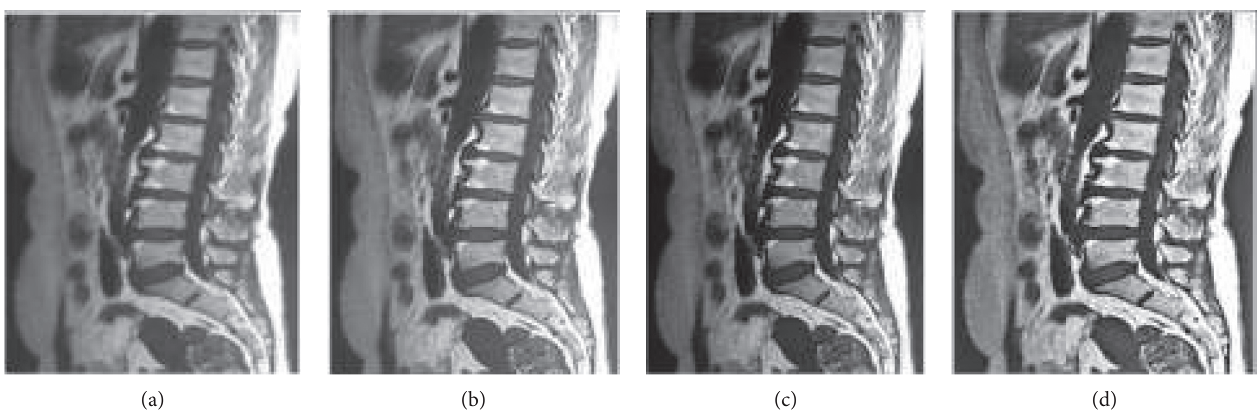

Figure 3: MRI image reconstruction results of lumbar nerves by the three algorithms. (a) Original MRI image of a male patient; (b) image denoised by ICA; (c) image denoised by Fast ICA; and (d) image denoised by M-Fast ICA.

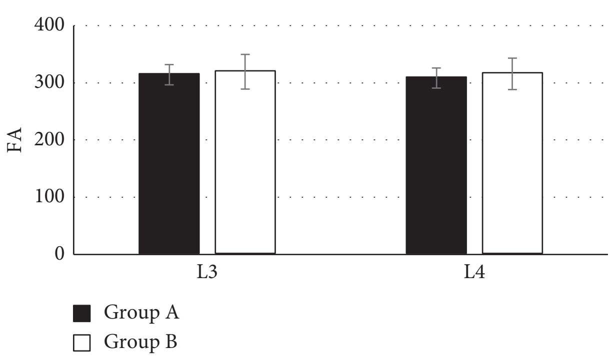

Figure 4: Comparison of FA of L3 and L4 lumbar nerve roots among the subjects in both groups.

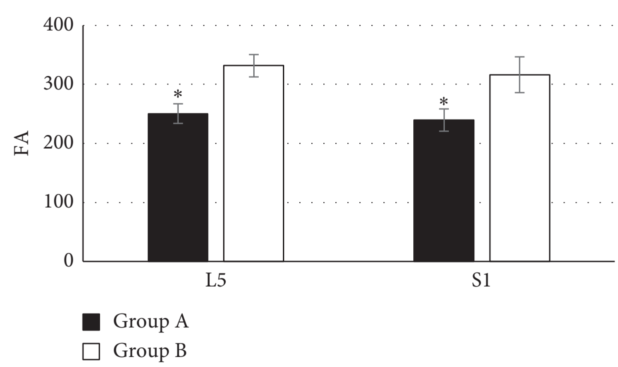

Figure 5: Comparison of FA of L5 and S1 lumbar nerve roots among the subjects in both groups. *There was a statistical difference in contrast to group B ($P < 0.05$).

3.6. Brain Areas with Higher Activation Rates in the Patients of Group A after Surgery. Figure 8 shows the brain regions after surgery with a higher rate of activation in all patients of group A. It indicates that the activation rates of the left temporal lobe, right temporal lobe, left thalamus, splenium of corpus callosum, and right internal capsule were 100%, 100%, 100%, 68.31%, and 87.43%, respectively.

4. Discussion

LDH is a very common medical lesion, with about 80% of people experiencing low back pain in their lifetime. Herniated lumbar disc can lead to lumbar nerve root compression, so as to let patients suffer from sciatica, and the area with the highest incidence is the gap between the L4 and L5 lumbar roots [14]. The 3D FMRI is a typical method for the clinical diagnosis of LDH. Due to various objective factors that cause the original FMRI image quality, the traditional Fast ICA was optimized based on the modified whitening matrix to establish the M-Fast ICA, and the traditional Fast ICA and ICA were introduced for simulation denoising comparison with M-Fast ICA. The results showed that the RMSE of M-Fast ICA was greater markedly than that of ICA and Fast ICA, indicating that the difference was statistically obvious ($P < 0.05$), while the SNR of M-Fast ICA

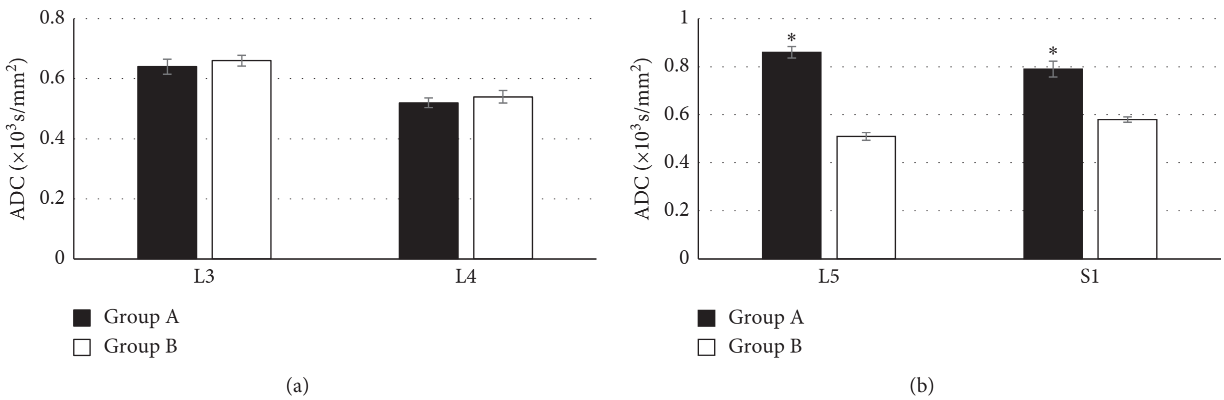

Figure 6: Comparison on ADC of the L3, L4, L5, and S1 lumbar nerve roots among the subjects in the two groups. *The difference was statistically significant in contrast to group B ($P < 0.05$).

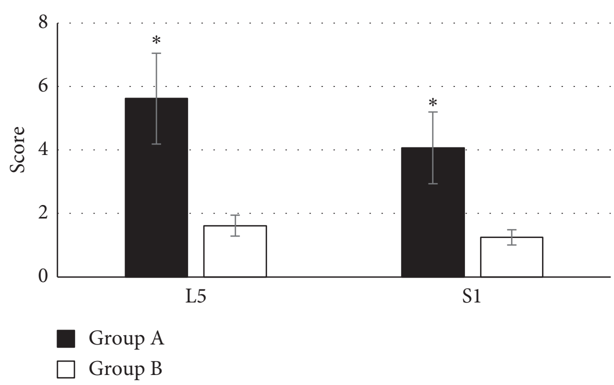

Figure 7: Comparison of the edema scores of the L5 and S1 lumbar nerve roots among the subjects in both groups. *The difference was statistically obvious in contrast to group B ($P < 0.05$).

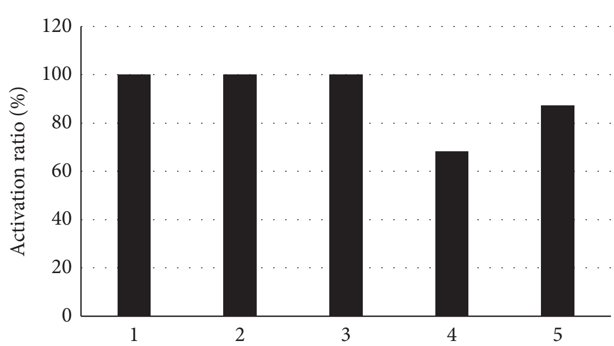

Figure 8: Brain regions with a higher activation rate in the patients of group A after surgery. 1, 2, 3, 4, and 5 stand for the activation rates of the left temporal lobe, right temporal lobe, left thalamus, splenium of corpus callosum, and right internal capsule in sequence.

was smaller extremely than that of ICA and Fast ICA, suggesting that there was a statistically huge difference ($P < 0.05$). It was similar to the research results of Ariyasu et al. [15], showing that the denoising effect of M-Fast ICA constructed in this study with good generalization was far better than that of Fast ICA and ICA for FMRI images. Under the reconstruction results of lumbar neurological MRI images by the three algorithms, the image definition after denoising by M-Fast ICA was higher dramatically than that of ICA and Fast ICA, and the noise reduced sharply. In addition, it was consistent with the above quantitative data results and also demonstrated the superiority of M-Fast ICA [16].

M-Fast ICA was applied to evaluate the DTI of 65 patients with L5 nerve root pain caused by LDH (group A) and 50 healthy volunteers (group B). The results suggested that the FA of L3 and L4 lumbar nerve roots in the subjects of group A were not statistically extreme compared with that of group B ($P > 0.05$), which was similar to the research results of Wang et al. [17], indicating that patients with L5 nerve root pain caused by LDH had no lesion changes in L3 and L4 lumbar nerve roots, which were not different from healthy volunteers. The FA of L5 and S1 lumbar nerve roots was lower steeply in the subjects of group A than that of group B, and the difference has statistical significance ($P < 0.05$), which was different from the results of Wu et al. [18]. It might be associated with histopathological changes in nerve roots generated from the nerve root compressed by herniated disc, and DTI images presented the disorder and narrow of nerve fibers and the decline of FA. The ADC of L3 and L4 lumbar nerve roots in the subjects from group A was not statistically substantial compared to that of group B ($P > 0.05$), but its ADC of L5 and S1 lumbar nerve roots was higher greatly than that of group B ($P < 0.05$). Chronic compression of the same lumbar nerve roots would lead to changes of edema and hyperemia in the nerves, and their continuous development would even reduce blood flow to the blood vessels, resulting in nerve root ischemia; thus, the ADC increased. The edema score of L5 and S1 lumbar nerve roots in the patients from group A was obviously higher than that of group B, and the difference was statistically remarkable ($P < 0.05$), indicating that there were pathological tissue changes and the increasing edema degree of the nerve roots in patients with LDH [19]. The activation rates of the right temporal lobe, left temporal lobe, left thalamus, right internal capsule, and splenium of corpus callosum were 100%, 100%, 100%, 87.43%, and 68.31%, respectively, in the patients of group A. Therefore, it revealed that the L5 nerve root pain result caused by LDH led to the changes in the brain functional area to restrain the resting state of the default network activity, which could be activating the corresponding brain regions through treatment.

5. Conclusion

This study optimized the traditional Fast ICA based on the modified whitening matrix to construct the M-Fast ICA that was compared with the introduced traditional Fast ICA and ICA. Moreover, M-Fast ICA was adopted to the 3D DTI evaluation of 65 patients with L5 nerve root pain caused by LDH and 50 healthy volunteers. It was found that the image denoising performance of M-Fast ICA constructed in this study was better than the traditional Fast ICA and ICA. The FA of patients with L5 nerve root pain caused by LDH dropped sharply but its ADC rose obviously. Changes in the functional areas of the patient's brain were affected by L5 nerve root pain caused by LDH to inhibit the resting state default network activity, and the corresponding brain functional areas could be activated by the treatment. However, the number of lumbar disc herniation patients with L5 nerve root pain was relatively small in this study and from a single source, which was less supportive of the results. Therefore, the sample size of patients should be increased in the future to further explore the application value of Fast ICA. In summary, the results of this study provided a theoretical basis for the clinical diagnosis of nerve roots in patients with lumbar disc herniation.

Data Availability

No data were used to support this study.

Conflicts of Interest

The authors declare that they have no conflicts of interest.

References

[1] M. Zhong, J. T. Liu, H. Jiang et al., "Incidence of spontaneous resorption of lumbar disc herniation: a meta-analysis," *Pain Physician*, vol. 20, no. 1, pp. E45–E52, 2017.

[2] N. Karimi, P. Akbarov, and L. Rahnama, "Effects of segmental traction therapy on lumbar disc herniation in patients with acute low back pain measured by magnetic resonance imaging: a single arm clinical trial," *Journal of Back and Musculoskeletal Rehabilitation*, vol. 30, no. 2, pp. 247–253, 2017.

[3] M. Karademir, O. Eser, and E. Karavelioglu, "Adolescent lumbar disc herniation: impact, diagnosis, and treatment," *Journal of Back and Musculoskeletal Rehabilitation*, vol. 30, no. 2, pp. 347–352, 2017.

[4] E. Shokri, F. Kamali, E. Sinaei, and F. Ghafarinejad, "Spinal manipulation in the treatment of patients with MRI-confirmed lumbar disc herniation and sacroiliac joint hypomobility: a quasi-experimental study," *Chiropractic & Manual Therapies*, vol. 26, no. 1, p. 16, 2018.

[5] J.-H. Kim, R. M. Van Rijn, and M. W. Van Tulder, "Diagnostic accuracy of diagnostic imaging for lumbar disc herniation in adults with low back pain or sciatica is unknown; a systematic review," *Chiropractic & Manual Therapies*, vol. 26, no. 1, p. 37, 2018.

[6] İ Coşkun Benlidayı, S. Başaran, and G. Seydaoğlu, "Lumbosacral morphology in lumbar disc herniation: a "chicken and egg" issue," *Acta Orthopaedica et Traumatologica Turcica*, vol. 50, no. 3, pp. 346–350, 2016.

[7] S. Jafari, T. Dehesh, and F. Iranmanesh, "Classifying patients with lumbar disc herniation and exploring the most effective risk factors for this disease," *Journal of Pain Research*, vol. 12, pp. 1179–1187, 2019.

[8] S. Huang, K. Wakaizumi, and B. Wu, "Whole-brain functional network disruption in chronic pain with disk herniation," *Pain*, vol. 160, no. 12, pp. 2829–2840, 2019.

[9] W. Li, Y.-C. Liu, and C.-F. Zheng, "Diagnosis of compressed nerve root in lumbar disc herniation patients by surface electromyography," *Orthopaedic Surgery*, vol. 10, no. 1, pp. 47–55, 2018.

[10] O. Komolafe, S. P. Pereira, B. R. Davidson, and K. S. Gurusamy, "Serum C-reactive protein, procalcitonin, and lactate dehydrogenase for the diagnosis of pancreatic necrosis," *Cochrane Database of Systematic Reviews*, vol. 4, no. 4, Article ID CD012645, 2017.

[11] P. Fritzell, C. Welinder-Olsson, and B. Jönsson, "Bacteria: back pain, leg pain and Modic sign—a surgical multicentre comparative study," *European Spine Journal*, vol. 28, no. 12, pp. 2981–2989, 2019.

[12] L. Zhao, M. Dong, M. Ren, C. Li, H. Zheng, and H. Gao, "Metabolomic analysis identifies lactate as an important pathogenic factor in diabetes-associated cognitive decline rats," *Molecular & Cellular Proteomics*, vol. 17, no. 12, pp. 2335–2346, 2018.

[13] D. H. Lee, P. Lee, and S. W. Seo, "Neural substrates of cognitive reserve in Alzheimer's disease spectrum and normal aging," *NeuroImage*, vol. 186, pp. 690–702, 2019.

[14] C. He, S. Jiang, and H. Yao, "Endoplasmic reticulum stress mediates inflammatory response triggered by ultra-small superparamagnetic iron oxide nanoparticles in hepatocytes," *Nanotoxicology*, vol. 12, no. 10, pp. 1198–1214, 2018.

[15] H. Ariyasu, H. Inaba, and T. Ota, "Thyrotoxicosis and adrenocortical hormone deficiency during immune-checkpoint inhibitor treatment for malignant melanoma," *In Vivo*, vol. 32, no. 2, pp. 345–351, 2018.

[16] W. Hu, S. Kan, and G. Liu, "The expression of P16 and S100 associated with elastin degradation and fibrosis of the Ligamentum Flavum hypertrophy," *BMC Musculoskeletal Disorders*, vol. 20, no. 1, p. 458, 2019.

[17] Q. Wang, H. Zhang, and J. Zhang, "The relationship of the shear wave elastography findings of patients with unilateral lumbar disc herniation and clinical characteristics," *BMC Musculoskeletal Disorders*, vol. 20, no. 1, p. 438, 2019.

[18] W. Wu, Y. Chen, and L. Yu, "Coronal and sagittal spinal alignment in lumbar disc herniation with scoliosis and trunk shift," *Journal of Orthopaedic Surgery and Research*, vol. 14, no. 1, p. 264, 2019.

[19] M. Annen, C. Peterson, and S. Leemann, "Comparison of outcomes in MRI confirmed lumbar disc herniation patients with and without modic changes treated with high velocity, low amplitude spinal manipulation," *Journal of Manipulative and Physiological Therapeutics*, vol. 39, no. 3, pp. 200–209, 2016.

Hindawi
Journal of Healthcare Engineering
Volume 2023, Article ID 9836380, 1 page
https://doi.org/10.1155/2023/9836380

Retraction

Retracted: ANOVA-Based Analysis of Early Blood Transfusions on Hemodynamics with Severely Injured Trauma Using Bedside Ultrasound Imaging

Journal of Healthcare Engineering

Received 8 August 2023; Accepted 8 August 2023; Published 9 August 2023

This article has been retracted by Hindawi following an investigation undertaken by the publisher [1]. This investigation has uncovered evidence of one or more of the following indicators of systematic manipulation of the publication process:

(1) Discrepancies in scope
(2) Discrepancies in the description of the research reported
(3) Discrepancies between the availability of data and the research described
(4) Inappropriate citations
(5) Incoherent, meaningless and/or irrelevant content included in the article
(6) Peer-review manipulation

The presence of these indicators undermines our confidence in the integrity of the article's content and we cannot, therefore, vouch for its reliability. Please note that this notice is intended solely to alert readers that the content of this article is unreliable. We have not investigated whether authors were aware of or involved in the systematic manipulation of the publication process.

In addition, our investigation has also shown that one or more of the following human-subject reporting requirements has not been met in this article: ethical approval by an Institutional Review Board (IRB) committee or equivalent, patient/participant consent to participate, and/or agreement to publish patient/participant details (where relevant).

Wiley and Hindawi regrets that the usual quality checks did not identify these issues before publication and have since put additional measures in place to safeguard research integrity.

We wish to credit our own Research Integrity and Research Publishing teams and anonymous and named external researchers and research integrity experts for contributing to this investigation.

The corresponding author, as the representative of all authors, has been given the opportunity to register their agreement or disagreement to this retraction. We have kept a record of any response received.

References

[1] L. Song, J. Zhang, and J. Liu, "ANOVA-Based Analysis of Early Blood Transfusions on Hemodynamics with Severely Injured Trauma Using Bedside Ultrasound Imaging," *Journal of Healthcare Engineering*, vol. 2021, Article ID 5263454, 6 pages, 2021.

Hindawi
Journal of Healthcare Engineering
Volume 2021, Article ID 5263454, 6 pages
https://doi.org/10.1155/2021/5263454

Research Article

ANOVA-Based Analysis of Early Blood Transfusions on Hemodynamics with Severely Injured Trauma Using Bedside Ultrasound Imaging

Lei Song, Jianguo Zhang, and Junliang Liu

Department of Intensive Care Unit, The Affiliated Qingdao Hospital of Shandong First Medical University, Qingdao 266109, Shandong, China

Correspondence should be addressed to Junliang Liu; 2201800164@neepu.edu.cn

Received 2 June 2021; Accepted 14 July 2021; Published 22 July 2021

Academic Editor: Enas Abdulhay

The focus of the study was to quantitatively analyze the influence of early massive blood transfusions (MBTs) on the hemodynamics and prognostic living quality of patients with severely injured trauma. 114 patients with severely injured trauma were enrolled into MBT group (67 cases) and nonmassive blood transfusions (NBT) group (47 cases) according to whether they accepted MBTs within 24 hours after the admission. All patients had bedside ultrasound technology scanning. Furthermore, the indexes were calculated for inferior vena cava (IVC), peripheral arteries, and heart. The prognostic deaths were recorded. It was found that, in the MBT group, the mortality was lower (7.55% vs. 24.23%) ($P < 0.05$), and these indexes were higher for the IVC expansion (IVCE), the respiration variation index (RVI) of IVC (ΔIVC_2), the peak flow velocity RVI of brachial artery ($\Delta Vpeak_{BA}$), femoral artery ($\Delta Vpeak_{FA}$), left ventricular outflow tract ($\Delta Vpeak_{L}$), and aorta ($\Delta Vpeak_{AO}$), as well as peak flow velocity time integral RVI of aorta (ΔVTI_{AO}) ($P < 0.05$). In conclusion, early MBTs can elevate survival rate and prognostic living quality and alleviate the atrophy degree of IVC, peripheral artery, and blood vessel of patients with severely injured trauma. Furthermore, bedside ultrasound scanning demonstrated superb capabilities in quantitatively displaying hemodynamics and outcomes of MBTs of patients with severely injured trauma.

1. Introduction

Trauma refers to the destruction of tissues or organs caused by mechanical factors. Due to the differences in injured parts, injured tissues, and skin integrity, the severity of trauma is also different [1, 2]. Among them, severely injured trauma may cause systemic reactions, with local manifestations such as pain, swelling, tenderness in the injured area, and even fatal symptoms such as hemorrhage, shock, suffocation, and disturbance of consciousness [3]. Relevant studies have reported that trauma has become the leading cause of death for people under the age of 40, even exceeding the total number of deaths from AIDS, tuberculosis, and malaria [4]. Furthermore, the people who die from trauma every year are mostly teenagers, which greatly affect social stability and economic development. Traumatic bleeding has always been the main cause of death in trauma patients. Clinical observations have revealed that, in addition to bleeding caused by liver and spleen lacerations and fractures, the abnormal coagulation function of patients is also a very key factor for continuous bleeding [5, 6]. At present, the clinical treatment methods of bleeding in patients with severely injured trauma mainly contain permissive hypotension, hemostasis, and resuscitation. Patients with heavy bleeding need timely blood transfusion therapy to correct coagulation disorders and improve the prognosis of trauma patients. Therefore, the primary objective of the study was to explore the influence of massive transfusions on patients with severely injured trauma.

With the advancement of imaging, there are various imaging examination methods used in clinical practice. However, being time-consuming, the routine imaging scan is not suitable for the diagnosis of trauma and bleeding patients, such as ultrasound, conventional CT, X-ray, and angiography [7]. Plain X-ray is the earliest imaging method used. It features simple operation and low price, but the display of soft tissue is poor, and it is prone to misdiagnosis and missed diagnosis [8, 9]. Angiography can be used to observe the blood flow in the arteries or veins of the head, arms, legs, chest, back, or abdomen, but it is easily affected by body movements. Although conventional CT is easy to operate, it cannot show minor damage [10]. As a result, bedside ultrasound has been a hotspot in clinical research in recent years. It is usually used in emergency and life-threatening conditions to speed up diagnosis and treatment [11]. Because bedside real-time ultrasound performs a single or local examination for a specific clinical phenotype, it greatly shortens the examination time and can quickly provide crucial information, such as the patient's systolic, diastolic function, volume load, heart structure, and hemodynamics. Balík [12] adopted transcranial Doppler ultrasound to monitor the cerebral blood flow of severely injured trauma patients. The results showed that ultrasound images can accurately diagnose the hemodynamics and position the blood vessels before intubation to avoid potential complications and unnecessary platelet transfusion. Gomora-García et al. [13] used ultrasound to guide the treatment of patients with painful shoulder trauma syndrome. The results found that ultrasound-guided treatment demonstrated better effects in contrast with conventional treatment and was safer. Therefore, the further aim was to apply bedside ultrasound to analyze the diagnostic results of severely injured trauma.

In summary, bedside ultrasound demonstrated superb capabilities in clinical diagnosis and treatment of severely injured trauma patients. Based on this, 114 patients with severely injured trauma were enrolled into MBT group (67 cases) and NBT group (47 cases) according to whether they accepted MBTs within 24 hours after the admission. All patients had bedside ultrasound technology scanning. Furthermore, the indexes were calculated for IVC, peripheral arteries, and heart, to quantitatively analyze the influence of early MBTs on the hemodynamics and prognostic living quality of patients with severely injured trauma.

2. Materials and Methods

2.1. Selection of Samples. 114 patients with severely injured trauma, who were admitted to the hospital between November 25, 2017, and February 10, 2020, were selected for analysis, with an average age between 20 and 67. All of them had bedside ultrasound scanning. The study has been approved by the Medical Ethics Committee of the hospital. The patient and his/her family members have been informed of the study and signed the consent letters.

Inclusion criteria: (i) patients older than 18 years; (ii) patients who underwent bedside ultrasound within 12 hours after trauma; (iii) patients with an abbreviated injury scale (AIS) score greater than 3; (iv) patients who can cooperate with the doctors.

Exclusion criteria: (i) patients with unstable hemodynamics; (ii) patients with congenital heart disease; (iii) patients with severe kidney disease; (iv) patients with aortic and great vessel split; (v) patients with incomplete clinical data; and (vi) patients with head trauma.

2.2. Grouping of Subjects. 114 patients with severely injured trauma were enrolled into MBT group (67 cases) and NBT group (47 cases) according to whether they accepted MBTs within 24 hours after the admission. The standard of massive blood transfusions no less than 20 U red blood cells were injected within 24 hours after admission.

2.3. Bedside Ultrasound Scanning. Patients accepted bedside ultrasound scanning before and after treatment by Sono ultrasonic machine (USA). A 2.5 MHz heart probe was used. The patient was in a supine position. The long axis of the left heart next to the sternum was selected, that is, the long axis of the left ventricle. The heart probe was placed between 3 and 4 intercostals of the left edge of the sternum. The detection direction was parallel to the right sternoclavicular joint to center the transverse section of the thoracic aorta. The probe was slightly upward on the basis of the four-chamber heart at the apex of the heart, and the scanning plane passed through the aortic root to obtain the transverse section of the aortic root, the longitudinal section of the left ventricle, the longitudinal section of the right atrium, the longitudinal section of the right ventricle, and the longitudinal section of the right atrium, namely, the image of the five-chamber heart at the apex. IVCE, ΔIVC_2, $\Delta Vpeak_{BA}$, $\Delta Vpeak_{FA}$, $\Delta Vpeak_L$, $\Delta Vpeak_{AO}$, and ΔVTI_{AO} were recorded. IVCE refers to the difference between the maximum diameter (IVC_{max}) and the minimum diameter (IVC_{min}) of IVC at 2 cm of the opening of right atrium which was then divided by IVC_{min}. The equation is as follows:

$$IVCE = \frac{IVC_{max} - IVC_{min}}{IVC_{min}} \times 100\%. \quad (1)$$

2.4. Statistics. The data were processed by SPSS19.0. The mean ± standard deviation ($\overline{x} \pm s$) illustrated how to calculate the measurement data. Count data were expressed as a percentage (%). Age, BMI, length of hospital stays, male-female ratio, and mortality were compared using independent t-test. The analysis of variance was applied to compare indexes for IVC, peripheral arteries, and heart. $P < 0.05$ indicated statistically significant differences.

3. Results

3.1. Comparison of Basic Data. Figures 1 and 2 show the comparison of basic data of patients. In the MBT group, the patients were 43.51 ± 9.73 years old, their BMIs were $24.76 \pm 4.79\ m^2/kg$, the ratio of males was 68.56%, and the length of hospital stay was 33.51 ± 7.53 days. In the NBT group, the patients were 41.73 ± 11.24 years old, their BMIs were $26.11 \pm 5.22\ m^2/kg$, the proportion of males was 64.37%, and the length of hospital stay was 31.75 ± 8.22 days. There was no notable difference in age, BMI, the ratio of males, and the length of hospital stays ($P > 0.05$).

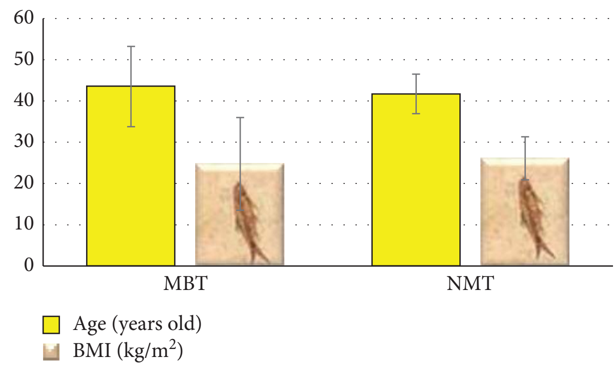

Figure 1: Comparison of the age and the BMI.

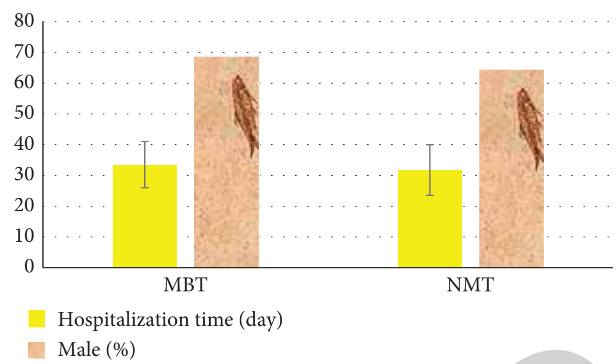

Figure 2: Comparison of the hospitalization time and the male ratio.

Figure 3 shows traumatic kidney injury in a male patient (aged 34 years old) caused by a car accident. It was evident that the lower part of the right kidney was morphologically abnormal, there was a heterogeneous echogenic mass, and an acoustic image of a clot can be seen in the bladder. Figure 4 shows traumatic renal parenchymal laceration caused by a car accident in a female (aged 26 years old). The renal parenchymal laceration with hematoma was visible, the renal capsule was intact, and a hypoechoic mass was seen in the middle parenchyma with a clear boundary.

3.2. Comparison of Mortality. Figure 5 shows the comparison of mortality of the two groups. It was evident that, in the MBT group, the mortality was lower (7.55% vs. 24.23%) ($P < 0.05$).

3.3. Comparison of IVCE and IVC_2. Figure 6 shows the comparison of IVCE and IVC_2. It was evident that, in the MBT group, IVCE (21.54 ± 4.11 vs. 13.52 ± 3.27) and IVC_2 (13.52 ± 3.27 vs. 13.17 ± 2.86) were obviously higher ($P < 0.05$).

3.4. Comparison of $\Delta Vpeak_L$. Figure 7 shows the comparison of $\Delta Vpeak_L$. It was evident that, in the MBT group, $\Delta Vpeak_L$ was obviously higher (19.56 ± 2.76 vs. 14.11 ± 1.85) ($P < 0.05$).

Figure 3: The ultrasound image of a male (aged 34) with traumatic renal laceration caused by a car accident.

Figure 4: The ultrasound image of a female (aged 26) with traumatic renal parenchymal laceration caused by a car accident.

3.5. Comparison of $\Delta Vpeak_{AO}$ and ΔVTI_{AO}. Figure 8 presented the comparison of $\Delta Vpeak_{AO}$ and ΔVTI_{AO}. It was evident that, in the MBT group, $\Delta Vpeak_{AO}$ (15.77 ± 1.48 vs. 12.75 ± 1.51) and ΔVTI_{AO} (18.88 ± 1.62 vs. 13.47 ± 1.36) were obviously higher ($P < 0.05$).

3.6. Comparison of $\Delta Vpeak_{BA}$ and $\Delta Vpeak_{FA}$. Figure 9 shows the comparison of $\Delta Vpeak_{BA}$ and $\Delta Vpeak_{FA}$. It was evident that, in the MBT group, $\Delta Vpeak_{BA}$ (21.55 ± 1.42 vs. 14.92 ± 1.36) and $\Delta Vpeak_{FA}$ (17.53 ± 1.38 vs. 13.66 ± 1.51) were obviously higher ($P < 0.05$).

4. Discussion

Patients with severely injured trauma should see a doctor in time to determine the degree of trauma as quickly as possible, so as to provide targeted clinical treatment. Although the domestic diagnostic technology has been greatly improved in recent years, the shock and mortality caused by severely injured trauma are still high, so it is very important to adopt effective diagnostic methods [14, 15]. In the study, bedside ultrasound scanning was applied to patients to analyze the influence of early MBTs on hemodynamics and

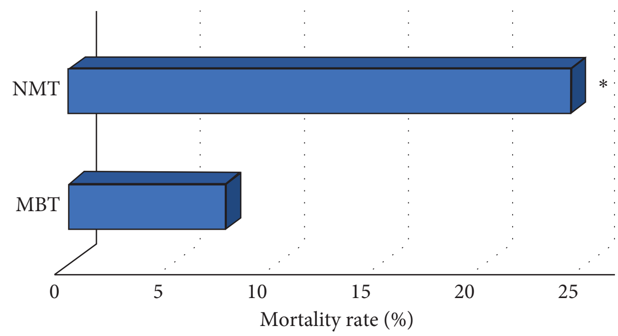

FIGURE 5: Comparison of mortality. *Note.* * indicates that there was a notable difference in contrast with the MBT group ($P < 0.05$).

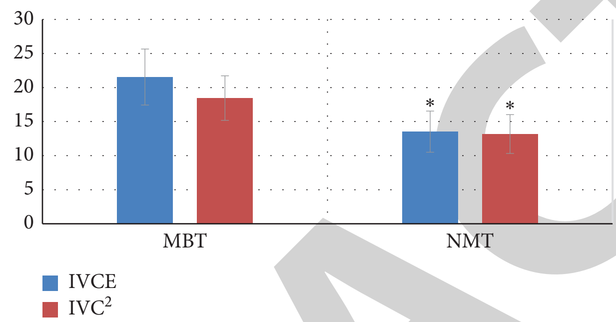

FIGURE 6: Comparison of IVCE and RVI. *Note.* * indicates that there was a notable difference in contrast with the MBT group ($P < 0.05$).

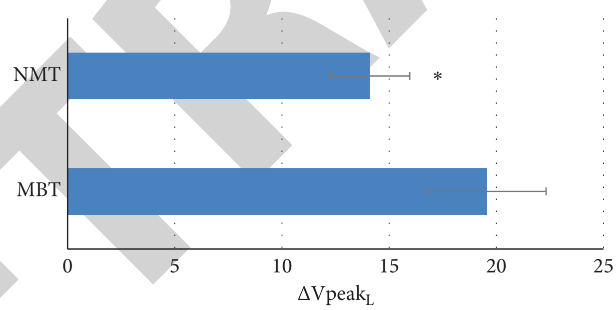

FIGURE 7: Comparison of $\Delta Vpeak_{L}$. *Note.* * indicated that there was a notable difference in contrast with MBT group ($P < 0.05$).

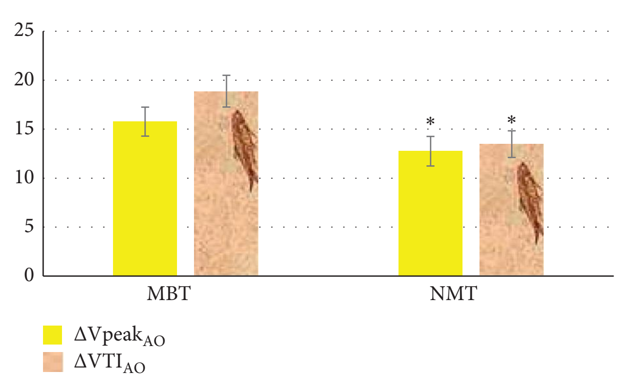

FIGURE 8: Comparison of $\Delta Vpeak_{AO}$ and ΔVTI_{AO}. *Note.* * indicates that there was a notable difference in contrast with the MBT group ($P < 0.05$).

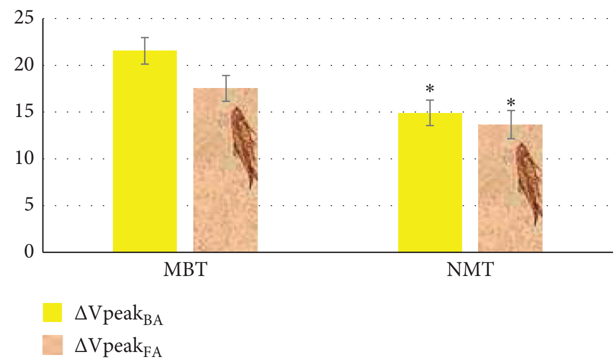

FIGURE 9: Comparison of $\Delta Vpeak_{BA}$ and $\Delta Vpeak_{FA}$. *Note.* * indicates that there was a notable difference in contrast with the MBT group ($P < 0.05$).

prognostic living quality of them. It was found that, in the MBT group, the mortality was lower (7.55% vs. 24.23%) ($P < 0.05$). This was in line with the research results of Nolte et al. [16]. Existing research believes that early MBTs for severely injured trauma can actively improve the coagulation disorder after acute trauma, thereby enhancing the prognosis of trauma patients. It suggested that early MBTs can elevate survival rate and prognostic quality of patients and reduce shock death. In the MBT group, IVCE (21.54 ± 4.11 vs. 13.52 ± 3.27) and IVC_2 (13.52 ± 3.27 vs. 13.17 ± 2.86) were obviously higher ($P < 0.05$). This was inconsistent with the research results of Cui and Wu [17]. IVC is the main blood vessel that returns blood to the abdominal organs and lower limbs. In the early stage of trauma, the internal diameter is reduced due to the reduction of blood flow back to the lower limbs and abdomen. However, early MBTs can effectively compensate for the ischemic state of patients with severely injured trauma and improve IVCE and IVC_2.

In the MBT group, $\Delta Vpeak_L$ was obviously higher (19.56 ± 2.76 vs. 14.11 ± 1.85) ($P < 0.05$). This was different from the research results of Endo et al. [18], which may be because of the different sample sources. It demonstrated that MBTs allow the patient to receive enough blood to restore normal blood flow. In the MBT group, $\Delta Vpeak_{AO}$ (15.77 ± 1.48 vs. 12.75 ± 1.51) and ΔVTI_{AO} (18.88 ± 1.62 vs. 13.47 ± 1.36) were obviously higher ($P < 0.05$). This illustrated that the early MBTs greatly affected the abdominal aortic vessels, which may be due to the fact that the abdominal aortic vessels mainly regulate blood flow through changes in tube diameter and distal resistance and will supplement the overall capacity of human body by reducing its own blood flow when there is trauma [19]. In the MBT group, $\Delta Vpeak_{BA}$ (21.55 ± 1.42 vs. 14.92 ± 1.36) and $\Delta Vpeak_{FA}$ (17.53 ± 1.38 vs. 13.66 ± 1.51) were obviously higher ($P < 0.05$). This was aligned with the research results of Roden-Foreman et al. [20]. Arteries transport blood rich in oxygen and various nutrients to various parts of the body, while severely injured trauma can cause abnormal operation of peripheral arteries. As a result, arterial lumen becomes narrow or even completely occluded. The early MBTs can effectively promote the recovery of the blood flow of the peripheral arteries, expand the peripheral arteries, and even make them return to normal.

5. Conclusion

In the study, 114 patients with severely injured trauma were enrolled into MBT group (67 cases) and NBT group (47 cases) according to whether they accepted MBTs within 24 hours after the admission. They all had bedside ultrasound scanning. The results revealed that early MBTs can elevate survival rate and prognostic living quality and alleviate the atrophy degree of IVC, peripheral artery, and blood vessel of patients with severely injured trauma. Furthermore, bedside ultrasound scanning demonstrated superb capabilities in quantitatively displaying hemodynamics and outcomes of MBTs of patients with severely injured trauma. However, some limitations should be noted in the study. The sample size is relatively small, which may reduce the power and increase the margin of error of the study. A study with an expanded sample size is necessary to strengthen the findings. In summary, the results obtained provide a theoretical basis for the application of bedside ultrasound scanning in diagnosis of patients with severely injured trauma.

Data Availability

No data were used to support this study.

Conflicts of Interest

The authors declare that they have no conflicts of interest.

References

[1] T. Wolny, E. Saulicz, P. Linek, M. Shacklock, and A. Myśliwiec, "Efficacy of manual therapy including neurodynamic techniques for the treatment of carpal tunnel syndrome: a randomized controlled trial," *Journal of Manipulative and Physiological Therapeutics*, vol. 40, no. 4, pp. 263–272, 2017.

Hindawi
Journal of Healthcare Engineering
Volume 2021, Article ID 8830260, 8 pages
https://doi.org/10.1155/2021/8830260

Research Article

Artificial Intelligence Algorithm-Based Ultrasound Image Segmentation Technology in the Diagnosis of Breast Cancer Axillary Lymph Node Metastasis

Lianhua Zhang, Zhiying Jia, Xiaoling Leng, and Fucheng Ma

Department of Ultrasound, Tumor Hospital Affiliated to Xinjiang Medical University, Urumqi 830011, Xinjiang, China

Correspondence should be addressed to Fucheng Ma; 20160622@ayit.edu.cn

Received 24 May 2021; Accepted 14 July 2021; Published 22 July 2021

Academic Editor: Enas Abdulhay

This paper aimed to investigate the application of ultrasound image segmentation technology based on the back propagation neural network (BPNN) artificial intelligence algorithm in the diagnosis of breast cancer axillary lymph node metastasis, thereby providing a theoretical basis for clinical diagnosis. In this study, 90 breast cancer patients with axillary lymph node metastasis were selected as the research objects and rolled randomly into an experimental group and a control group. Besides, all of them were examined by ultrasound. The BPNN algorithm for the ultrasound image segmentation diagnosis method was applied to the patiens from the experimental group, while the control group was given routine ultrasound diagnosis. Thus, the value of this algorithm in ultrasonic diagnosis was compared and explored. The results showed that when the number of hidden layer nodes based on the BPNN artificial intelligence algorithm was 2, 3, 4, 5, 6, 7, and 8, the corresponding segmentation accuracy was 97.3%, 96.5%, 94.8%, 94.8%, and 94.1% in turn. Among them, the segmentation accuracy was the highest when the number of hidden layer nodes was 2. The correlation of independent variable bubble plot analysis showed that the presence or absence of capsules, the presence of crab feet or burrs in breast cancer lesions was critical influencing factors for the occurrence of axillary lymph node metastasis, and the standardized importance was 99.7% and 70.8%, respectively. Besides, the area under the two-dimensional receiver operating characteristic (ROC) curve of the BPNN artificial intelligence algorithm model classification was always greater than the area under the curve of manual segmentation, and the segmentation accuracy was 90.31%, 94.88%, 95.48%, 95.44%, and 97.65% in sequence. In addition, the segmentation specificity of different running times was higher than that of manual segmentation. In conclusion, the BPNN artificial intelligence algorithm had high accuracy, sensitivity, and specificity for ultrasound image segmentation, with a better segmentation effect. Therefore, it had a better diagnostic effect for breast cancer axillary lymph node metastasis.

1. Introduction

Breast cancer refers to the appearance of malignant tumors in the breast; that is, the cancer cells originate from the lobules of the ductal epithelium of the breast, and the breast cells grow out of control and are formed. Breast cancer can be divided into carcinoma in situ and invasive carcinoma based on histopathology. According to immunohistochemistry, it can also be divided into luminal A, luminal B, and triple-negative breast cancer [1]. The incidence of breast cancer is very high, ranking at the top of malignant tumors. In developed countries such as Europe and America, the incidence of breast cancer ranks first in malignant tumors [2]. According to the data released by the National Cancer Center, there were nearly 300,000 new cases of breast cancer and more than 700,000 deaths in China in 2018, with the highest incidence among women aged 45–74 years [3]. In the growth process of breast cancer, regional lymph node metastasis is prone to occur as the tumor infiltrates into the surrounding mammary gland tissues. The most common manifestation of lymph node metastasis of breast cancer is local lymph node enlargement, hardening, fusion, agglomeration, and fixation [4]. Lymph nodes, as an important filtration structure of the human body, are responsible for phagocytosis of killer cells and removal of degenerating and broken cells [5]. After cancerous transformation, the cancer cells fall off and enter the lymph node reflux, which is intercepted by the lymph nodes, so that the cancer cells stay in the lymph nodes. Due to immune and other reasons, the cancer cells cannot be killed by the lymph nodes and survive for a long time to form lymph node metastasis [6]. Generally, lymph node metastasis in superficial sites is easy to find and diagnose, while some deep lymph nodes (internal mammary lymph nodes, mediastinal lymph nodes, etc.) are not easy to find. Therefore, computed tomography (CT) and ultrasound imaging are needed for auxiliary diagnosis to improve the accuracy of diagnosis [7, 8]. However, current ultrasound is not diagnostic for some small or unformed nodules.

The back propagation neural network (BPNN) is a multilayer feedforward network trained according to the error BP algorithm, which is one of the most widely applied neural networks at present [9]. The human brain is composed of multiple neurons, and there is a certain connection between these neurons, which becomes the basic element of the brain to process information [10]. An artificial neural network is a technology that can optimize the process of calculation and judgment by imitating the structure of the human brain, to achieve functions that cannot be realized by current computers [11]. At present, BPNN is extensively used in disease auxiliary diagnosis and survival analysis, and it can be employed to screen breast cancer, cervical cancer, and diabetes [12, 13]. Medical image classification is a key point of current medical diagnosis and pattern recognition. Through image recognition and classification, the identification of diseased tissues in medical images (such as ultrasound and CT) can be realized, and information such as the location of the disease and the size and quantity of the disease can be determined [14, 15]. Studies have found that combining the texture features of medical images with BPNN, using the feature information of pixels as training samples to train the neural network, and using the trained neural network to classify and recognize images can effectively and accurately classify a given medical image [16].

To improve the accuracy of the diagnosis of breast cancer and other diseases, and to determine whether breast cancer has metastasis to lymph nodes and other parts, the clinical diagnosis is usually combined with CT, magnetic resonance, and ultrasound imaging examinations. Therefore, the BPNN algorithm model was established in this study and applied to the segmentation of ultrasound diagnostic images of patients with breast cancer axillary lymph node metastasis, to explore the application of ultrasound image segmentation technology based on artificial intelligence algorithms in the diagnosis of breast cancer axillary lymph node metastasis.

2. Materials and Methods

2.1. Research Objects and Grouping. 90 breast cancer patients with axillary lymph node metastasis were selected in this study, who were treated in hospital from January 2017 to September 2020. The cases included in this study were subjected to pathological examination and ultrasound diagnostic examination before surgical treatment. In this study, all breast cancer patients were grouped randomly into two groups and underwent ultrasound examinations. After the examination, the ultrasound images of the experimental group were processed by artificial intelligent-based ultrasound image segmentation technology to diagnose breast cancer axillary lymph nodes, while the control group was directly diagnosed by routine ultrasound images. The study had been approved by the medical ethics committee of the hospital, and the patients and their family members understood the content and methods of this study and agreed to sign the corresponding informed consent.

The criteria for inclusion were defined to include patients who were diagnosed with axillary lymph node metastasis of breast cancer by previous pathological diagnosis and imaging examination, did not receive other drugs or antibiotics in the recent research, did not receive radiotherapy or chemotherapy, and were conscious and in good mental state.

The criteria for exclusion were defined to include patients who were combined with psychiatric diseases or other system diseases, suffered from tumor metastasis to other systems and tissues other than lymph nodes, had incomplete clinical data and medical history information, did not receive treatment due to personal or other factors, and had axillary lymph nodes more than 30 mm in depth.

2.2. Patient Ultrasound Examination. The E-ultrasound equipment (French acoustic department Aixplorer type) and SL15-4 probe were adopted in this study, and the frequency range was 4–15 MHz. Then, each patient underwent B-type grayscale, energy Doppler, and AP examinations in sequence, and the imaging parameters of each mode and the size of the sampling box remained unchanged during the study. The operation was carried out by medical staff with about 10 years of breast ultrasound examination experience, and two full-time doctors would double-blindly read the images and record the reading results. If there was a disagreement, a third experienced physician would interpret the results.

2.3. BPNN Artificial Intelligence Algorithm Image Segmentation. BPNN includes three layers of feedforward network, namely, input layer, hidden layer, and output layer, and its topological structure is shown in Figure 1. The neurons of each layer are only fully connected with the neurons of the adjacent layer but not connected with the neurons of the same layer, and there is no feedback connection between the neurons of each layer, forming a feedforward neural network system with a hierarchical structure.

In the BPNN as shown in the figure, the input layer and the output layer contain a nodes and b nodes, so the neural network can be regarded as a mapping from an a-dimensional vector to a b-dimensional vector. According to the nodes of the input layer and output layer, the number of nodes in the hidden layer of the network can be calculated as follows:

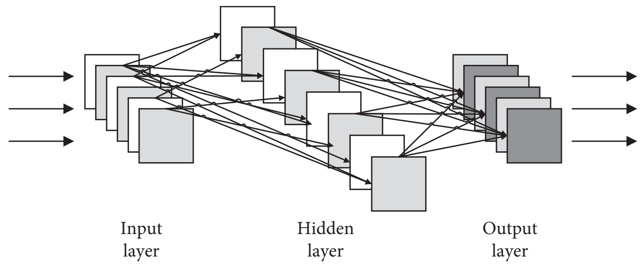

Figure 1: The structure of BPNN.

$$N = \sqrt{a+b} + C. \tag{1}$$

In (1), N stands for the number of nodes in the hidden layer, a means the number of nodes in the input layer, b represents the number of nodes in the output layer, and C expresses the adjustment constant. The relationship between the output and input of the artificial neural network can be expressed as follows:

$$\mathrm{net}_u = \sum_{v=1}^{b} Q_{uv} I_v - p, \tag{2}$$

$$O_u = A(\mathrm{net}_u). \tag{3}$$

In (2) and (3), I, Q, p, O, and A stand for the input signal from the neuron, the connection weight between neurons, the bias, the output of the neuron, and the activation function in turn, so the net is the net activation. Besides, v and u represent the number of neurons. Suppose there is an a-layer neural network and the sample m is added to the input layer, so the input sum of u neurons at layer n is S_u^n and the output is I_u^n. The weight coefficient from the v-th neuron in the $n-1$-th layer to the n-th neuron in the $n-1$-th layer is Q_{uv}, and the excitation function of each neuron is A:

$$A(m) = \frac{1}{1+\exp(-m)}. \tag{4}$$

In the above equation, m represents the number of samples. The relationship between each variable can be expressed as a mathematical relationship in

$$m_u^n = A(S_u^n), \tag{5}$$

$$S_u^n = \sum_v Q_{uv} m_v^{n-1}. \tag{6}$$

The BPNN algorithm is divided into two steps: forward propagation and back propagation. The forward propagation is carried out in the order of the input layer-hidden layer-output layer. What is more, the actual output is compared with the expected output. If there is a difference between the two, it enters BP. Then, the error signal will be transmitted back in reverse according to the forward propagation path, and the weight coefficient of each neuron in each hidden layer will be modified to minimize the error signal. The propagation process is shown in Figure 2.

The BP error function is defined as (7), and its gradient is determined as (8):

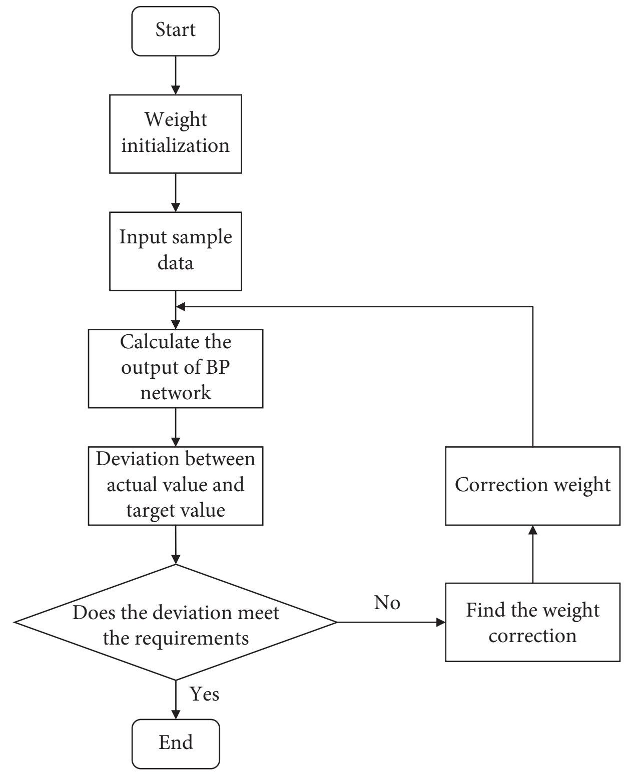

Figure 2: BPNN workflow chart.

$$r = \frac{1}{2}\sum_u \left(I_u^a - O_u\right)^2, \tag{7}$$

$$\frac{\partial r}{\partial Q_{uv}} = \frac{\partial r}{\partial S_u^n} \cdot \frac{\partial S_u^n}{\partial Q_{uv}}. \tag{8}$$

Among them, r represents the BP error, Q indicates the weight, and Ou means the output of the neuron u. If $d_u^n = \partial r/\partial S_u^n$, the following equation can be obtained:

$$\frac{\partial r}{\partial S_u^n} = \frac{\partial r}{\partial I_u^n} \cdot \frac{\partial I_u^n}{\partial S_u^n}. \tag{9}$$

In (9), I_u represents the input of neuron u, S_u^n stands for the total input of neuron u in the n-th layer, and $\partial I_u^n/\partial S_u^n = A'(S_u^n)$; $A'(S_u^n) = (1/1+\exp(-S_u^n))'$; $(1/1+\exp(-S_u^n))' = I_u^n(1-I_u^n)$. Besides, $\partial r/\partial I_u^n = \partial r/\partial I_u^a$ and $\partial r/\partial I_u^a = (I_u^a - O_u)$ when $n=a$, but $\partial r/\partial I_u^n = \sum_1 (\partial r/\partial S_1^{n+1}) \cdot (\partial S_1^{n+1}/\partial I_u^a)$ and $\sum_1 (\partial r/\partial S_1^{n+1}) \cdot (\partial S_1^{n+1}/\partial I_u^a) = \sum_1 Q_{Iu} \cdot d_1^{n+1}$ when $n < a$.

Therefore, the neural network weight modification equation is presented in

$$\Delta Q_{uv}(t+1) = \alpha \Delta Q_{uv}(t) - \theta \cdot d_1^n \cdot I_v^{n-1}. \tag{10}$$

If $I_u^n = e$, $d_1^n = I_u^n(1-I_u^n)\sum Q_{Iu} \cdot d_1^{n+1}$. In addition, Q, I, r, and a stand for the weight, the input, the propagation error, and the number of nodes in the input layer, respectively.

2.4. Evaluation Indicators. In this study, specificity (Spe), sensitivity (Sen), and accuracy (Acc) were employed to quantitatively evaluate the performance of the processing model. The calculation method of Spe was displayed in (11), which represented the proportion of correctly classified samples in all negative samples; the calculation method of Sen is shown in (12), which indicated the proportion of samples that were correctly classified in all positive samples; Acc could be calculated in (13), which represented the proportion of training positive samples in all predicted positive samples:

$$\mathrm{Spe} = \frac{\mathrm{TN}}{\mathrm{TN} + \mathrm{FP}}, \tag{11}$$

$$\mathrm{Sen} = \frac{\mathrm{TP}}{\mathrm{TP} + \mathrm{FN}}, \tag{12}$$

$$\mathrm{Acc} = \frac{\mathrm{TN} + \mathrm{TP}}{\mathrm{TN} + \mathrm{TP} + \mathrm{FP} + \mathrm{FN}}. \tag{13}$$

In the above equations, TN stood for the number of true negative samples, representing the number of actual negative samples classified as negative samples; FP was the number of false positive samples, expressing the number of actual negative samples classified as true samples; TP was the number of true samples, which represented the number of actual positive samples classified as true samples; FN meant the number of false negative samples, which expressed the number of actual positive samples classified into negative samples.

BPNN has three or more layers of the forward network, the number of layers mainly depends on the number of hidden layers, and any continuous function in a closed interval can be approached by a single hidden layer of BPNN. Therefore, a three-layer BPNN can complete the mapping from the n dimension to the m dimension. In a neural network, the determination of the number of hidden layer nodes is the most important link in the determination of the whole network structure. In this study, through a simple cross-validation method, the number of potential hidden layer nodes was tested from 2 to 8, to explore the influence of neural network structure of different hidden layer node number models on the segmentation accuracy of ultrasonic images.

2.5. Statistical Methods. The data processing in this study was analyzed by SPSS 19.0 version statistical software, the measurement data were expressed as the mean ± standard deviation (□$x \pm s$), and the count data were represented by the percentage (%). The analysis of variance was used for pairwise comparison. In addition, $P < 0.05$ indicated that the difference was statistically substantial.

3. Results

3.1. Ultrasound Images of Breast Cancer Axillary Lymph Node Metastasis. Figure 3 shows the ultrasonographic images of breast cancer patients with axillary lymph node metastasis. It was found that most lymph nodes of breast cancer patients were oval, and the ultrasonographic images included the outer hypoechoic cortex and the inner hyperechoic medulla. In Figures 3(d)–3(f), the structure of lymph node metastasis was destroyed, the skin and medulla structure were not clear, and the local cortex showed obvious uneven thickening, with localized protrusion and eccentricity thickening (the thickness of one end of the cortex was about twice that of the other end).

3.2. Diagnosis Accuracy Rate of Different Hidden Layer Nodes. The average accuracy of different hidden layer nodes was compared, and the results are presented in Figure 4. When the number of hidden layer nodes was 2, 3, 4, 5, 6, 7, and 8, the corresponding segmentation accuracy was 97.3%, 96.5%, 94.8%, 94.8%, and 94.1%, respectively. In other words, the segmentation accuracy was the highest (97.3%) when the number of nodes in the hidden layer is 2. With the increase of the number of nodes in the hidden layer, the segmentation accuracy of ultrasonic images decreased continuously.

3.3. Analysis of the Importance of Ultrasound Manifestations and Pathological Results of Independent Variables. Figure 5 indicates the pathological findings of axillary lymph node metastasis in patients with breast cancer. The ultrasound imaging data of the patients included in the study were analyzed, and the pathological examination results of breast cancer patients with axillary lymph node metastasis were classified, including morphological regularity, echo intensity, and presence or absence of sand-like microcalcification. Different imaging features were used as independent variables, patient age was used as a covariate, and the occurrence of axillary lymph node metastasis was used as a dependent variable to establish an analysis model. According to the correlation analysis of the independent variable bubble chart (Figure 5), the presence or absence of the capsule and the presence or absence of crab feet or burrs in breast cancer lesions were important influencing factors for the occurrence of axillary lymph node metastasis, and the standardization importance was 99.7% and 70.8%, respectively.

3.4. Sensitivity Curve of the Algorithm Model. To determine the classification sensitivity of the BPNN model in this study, a two-dimensional ROC was drawn, and the area under the ROC curves segmented by artificial segmentation and the BPNN artificial intelligence algorithm were compared. Thus, there was an investigation on the sensitivity of the BPNN artificial intelligence algorithm to segment ultrasound images, and the results are shown in Figure 6. The area under the ROC curve classified by the BPNN artificial intelligence algorithm model was always larger than the area under the artificial segmentation curve. In other words, the BPNN artificial intelligence algorithm model had a better classification effect and high sensitivity.

3.5. Analysis of the Accuracy of the Algorithm Model. Figure 7 shows the accuracy analysis results of ultrasound images of breast cancer axillary lymph node metastasis by

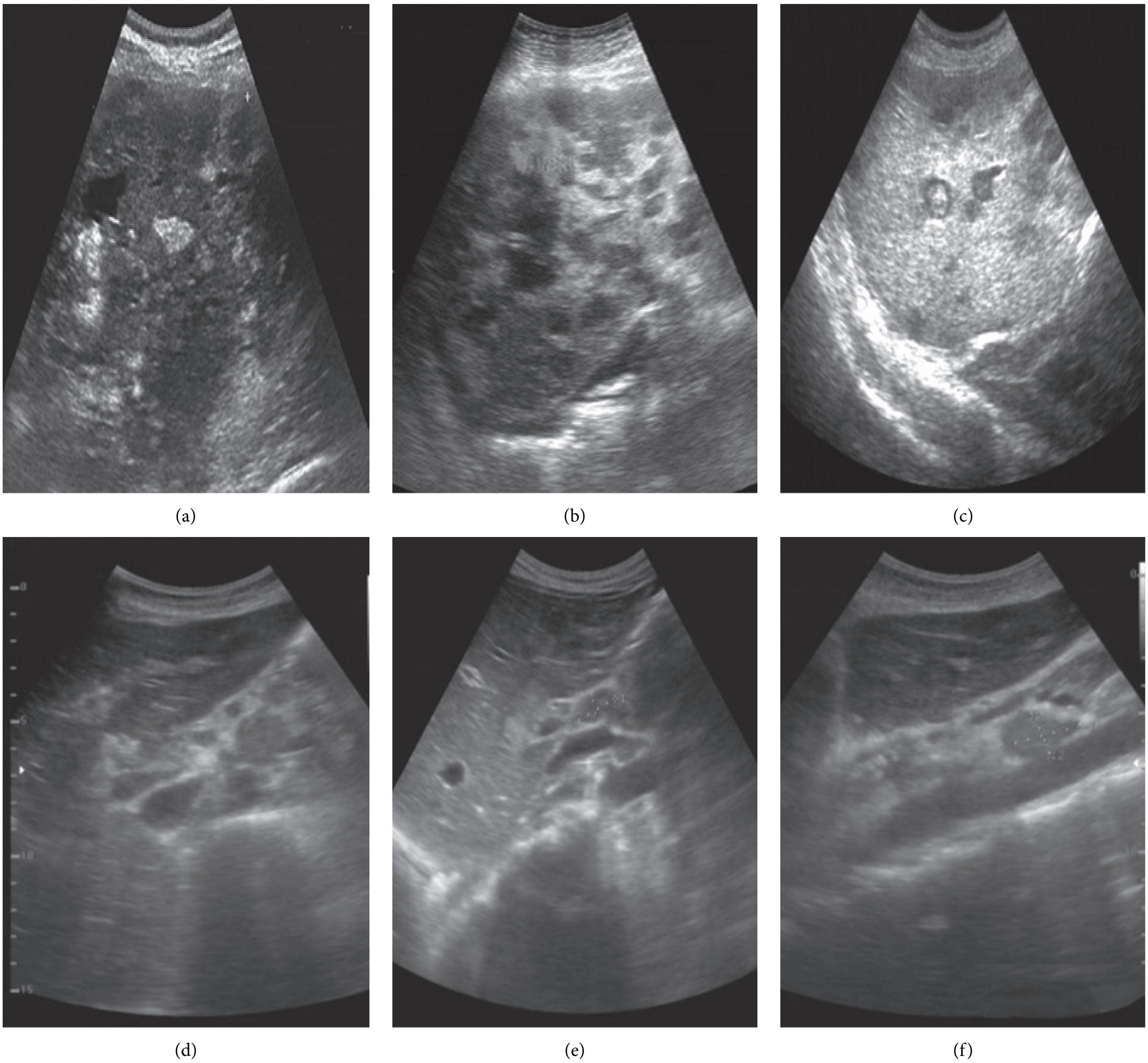

Figure 3: Ultrasound images of breast cancer axillary lymph node metastasis (note: (a–c) were left axillary lymph nodes; (d–f) were right axillary lymph nodes).

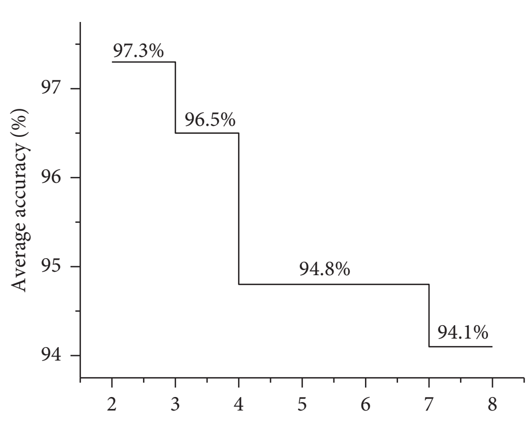

Figure 4: The average correct rate of different hidden layer nodes.

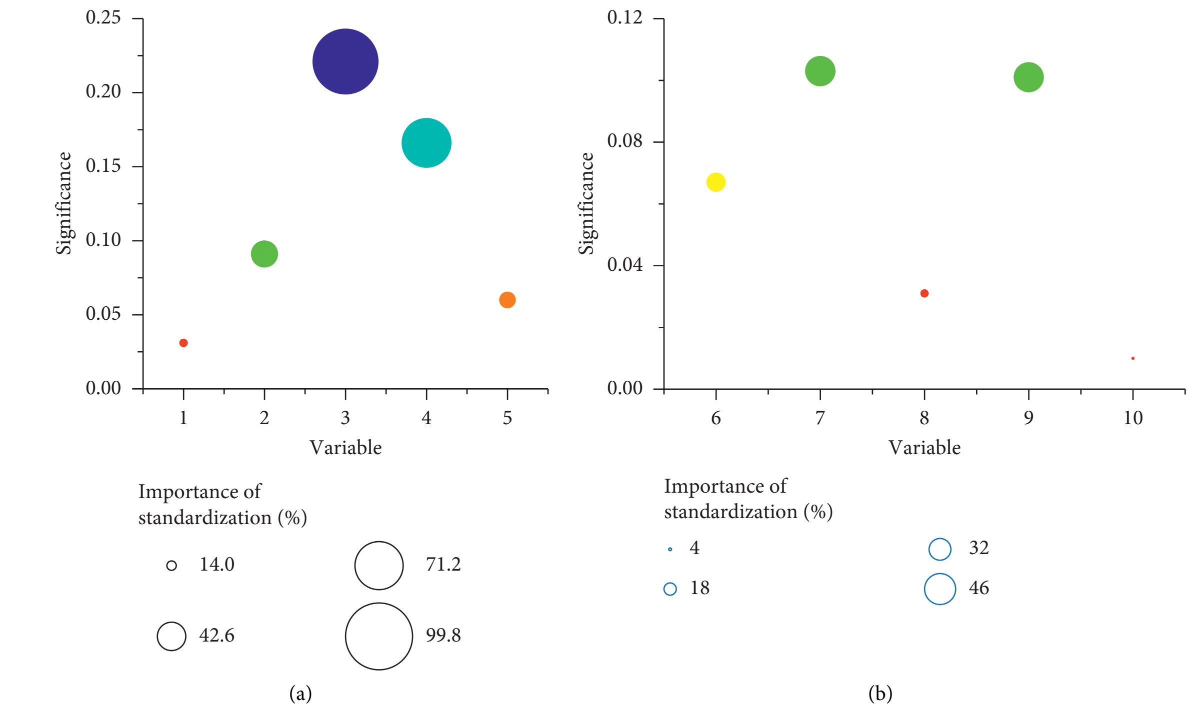

Figure 5: Comparison of the importance of the pathological results of independent variables (the independent variables 1–10 in the above figures represented the tumor shape, boundary, capsule, crab feet or burrs, internal echo, whether the echo was uniform, posterior echo, sand-like microcalcification, blood flow, and axillary lymph nodes).

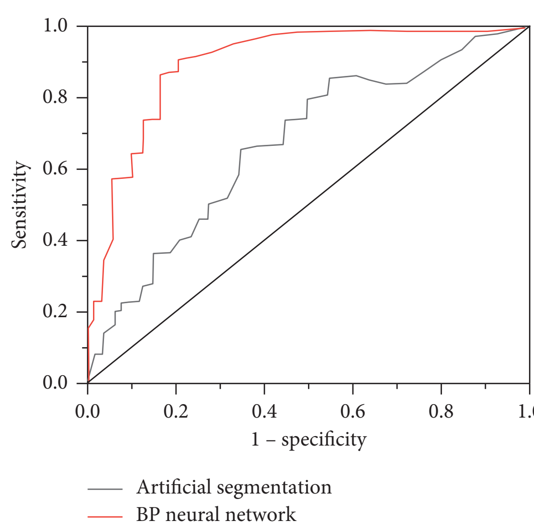

Figure 6: ROC curve of BPNN.

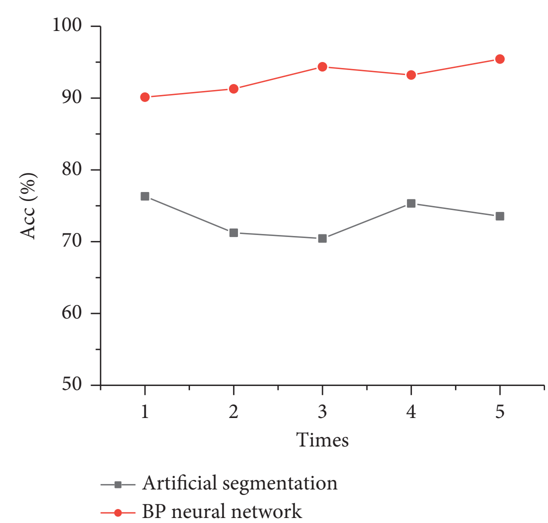

Figure 7: Algorithm segmentation accuracy analysis.

artificial segmentation and BPNN artificial intelligence algorithm. When the running times were 1, 2, 3, 4, and 5, the segmentation accuracy of the BPNN artificial intelligence algorithm model was 90.12%, 91.28%, 94.35%, 93.21%, and 95.43%, respectively. Furthermore, the accuracy was high.

3.6. Analysis of the Specificity of the Algorithm Model. The accuracy results of ultrasound images of breast cancer axillary lymph node metastasis by artificial segmentation and BPNN artificial intelligence algorithm were analyzed, as shown in Figure 8. When the number of running times was 1, 2, 3, 4, and 5, the segmentation accuracy of the BPNN artificial intelligence algorithm model was 90.31%, 94.88%, 95.48%, 95.44%, and 97.65% in turn. Therefore, the segmentation specificity of different running times was all higher than the manual segmentation method.

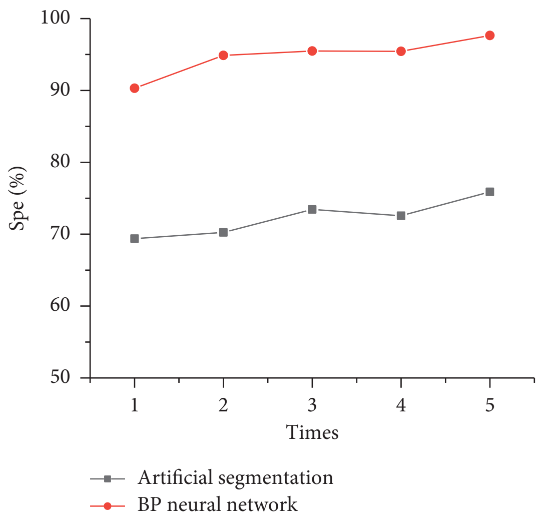

Figure 8: Algorithm segmentation specificity analysis.

4. Discussion

The lymphatic system is a crucial defensive system in the human body, which is distributed throughout the body, and the lymph nodes are an important part of the lymphatic system, mostly located in the armpits, groin, neck, etc. [17]. The presence or absence of breast cancer with axillary lymph node metastasis not only affects the choice of treatment options, but also has important implications for prognostic evaluation. Chien et al. [18] found that about 60% of breast cancer patients had regional lymph node metastasis (axillary, internal breast, and supraclavicular), and 40% of them had axillary lymph node metastasis, and most of them were sentinel lymph node metastasis. What is more, the 10-year survival rate of patients without axillary lymph node metastasis was higher than the rate of patients with axillary lymph node metastasis. Therefore, the noninvasive examination of axillary lymph node metastasis for early diagnosis has become a critical issue worthy of attention in clinical work. The scope of breast cancer surgery includes breast and axillary lymph nodes [19], and breast surgery includes enlarged tumor resection and total mastectomy. Sentinel lymph node biopsy and axillary lymph node dissection are available for axillary lymph nodes, and axillary lymph node status is required except for carcinoma in situ. The choice of surgical procedure should consider the clinical stage of the tumor and the patient's physical condition. In this study, patients with breast cancer axillary lymph node metastasis were selected as the research objects. The patients were diagnosed by ultrasound and the images were segmented by artificial segmentation and BPNN artificial intelligence algorithm, and the accuracy, specificity, and sensitivity of the two segmentation methods were compared, so as to investigate the application of ultrasonic image segmentation technology based on artificial intelligence algorithm in the diagnosis of breast cancer axillary lymph node metastasis. As a result, when the number of hidden layer nodes was 2, 3, 4, 5, 6, 7, and 8, the corresponding segmentation accuracy rates were 97.3%, 96.5%, 94.8%, 94.8%, and 94.1%, respectively. It showed that the segmentation accuracy rate was the highest when the number of hidden layer nodes was 2 in the algorithm model constructed by this research, so the optimal number of hidden layer nodes for this model was 2. According to the correlation analysis of the independent variable bubble chart, the presence or absence of the capsule and the presence or absence of crab feet or burrs in breast cancer lesions were important influencing factors for the occurrence of axillary lymph node metastasis, and the standardization importance was 99.7% and 70.8%, respectively. It indicated that tumor metastasis was affected greatly by the presence or absence of the capsule and the presence or absence of crab feet or burrs in the tumor lesion. The area under the ROC curve classified by the BPNN artificial intelligence algorithm model was always greater than the area under the artificial segmentation curve, namely, the BPNN artificial intelligence algorithm model had a better classification effect and high sensitivity; the algorithm's segmentation accuracy was 90.31%, 94.88%, 95.48%, 95.44%, and 97.65% in turn, suggesting that the segmentation specificity after different running times was higher than the manual segmentation method. This was similar to the research findings of Yang et al. [20], which disclosed that the BPNN artificial intelligence algorithm had high accuracy, sensitivity, and specificity for ultrasound image segmentation, and the segmentation effect was better. Moreover, it also had a better diagnostic effect for breast cancer axillary lymph node metastasis.

5. Conclusion

In this study, the BPNN artificial intelligence algorithm model was constructed and applied to the ultrasound images of breast cancer lymph node metastasis, and the images were segmented, so as to explore its application value in the diagnosis of breast cancer axillary lymph node metastasis. The results showed that the BPNN artificial intelligence algorithm had high accuracy, sensitivity, and specificity for ultrasound image segmentation, with better segmentation effect, which also had a better diagnostic effect for breast cancer axillary lymph node metastasis. However, the selected case samples in this study are small, which may have a certain impact on the experimental results. In addition, it lacks a comparison with other intelligent algorithm segmentation effects, and the representativeness is low. Therefore, the sample size will be increased in subsequent experiments, thereby further analyzing the application of ultrasound segmentation technology based on artificial intelligence algorithm in the diagnosis of breast cancer axillary lymph node metastasis. All in all, the results of this study can provide data support and theoretical basis for clinical diagnosis of breast cancer lymph node metastasis and other diseases.

Data Availability

No data were used to support this study.

Conflicts of Interest

The authors declare that they have no conflicts of interest.

Acknowledgments

This work was supported by National Natural Science Foundation of China Regional Fund Project (Grant number: 81660496).

References

[1] S. X. Sun, T. W. Moseley, H. M. Kuerer, and W. T. Yang, "Imaging-based approach to axillary lymph node staging and sentinel lymph node biopsy in patients with breast cancer," *American Journal of Roentgenology*, vol. 214, no. 2, pp. 249–258, 2020.

[2] S. Sasada, N. Masumoto, Y. Kimura et al., "Identification of axillary lymph node metastasis in patients with breast cancer using dual-phase FDG PET/CT," *American Journal of Roentgenology*, vol. 213, no. 5, pp. 1129–1135, 2019.

[3] T. N. Tan-Nai Wang, C. H. Chung-Hao Cheng, and H. W. Hung-Wen Chiu, "Predicting post-treatment survivability of patients with breast cancer using artificial neural network methods," in *Proceedings of the 2013 35th Annual International Conference of the IEEE Engineering in Medicine and Biology Society (EMBC)*, pp. 1290–1293, Osaka, Japan, July 2013.

[4] D. K. Lee, D. J. Sung, C.-S. Kim et al., "Three-dimensional convolutional neural network for prostate MRI segmentation and comparison of prostate volume measurements by use of artificial neural network and ellipsoid formula," *American Journal of Roentgenology*, vol. 214, no. 6, pp. 1229–1238, 2020.

[5] R. Kim, J. M. Chang, H.-B. Lee et al., "Predicting axillary response to neoadjuvant chemotherapy: breast MRI and US in patients with node-positive breast cancer," *Radiology*, vol. 293, no. 1, pp. 49–57, 2019.

[6] L. Dihge, J. Vallon-Christersson, C. Hegardt et al., "Prediction of lymph node metastasis in breast cancer by gene expression and clinicopathological models: development and validation within a population-based cohort," *Clinical Cancer Research*, vol. 25, no. 21, pp. 6368–6381, 2019.

[7] C. L. Quan, N. S. Huang, B. L Yang et al., "Incidental internal mammary lymph node biopsy in 113 cases of breast cancer undergoingfree abdominal flap breast reconstruction and its influencing factors," *Zhonghua Zhongliu Zazhi*, vol. 38, no. 10, pp. 769–773, 2016, Chinese.

[8] F. Fu, J. Wei, M. Zhang et al., "Rapid vessel segmentation and reconstruction of head and neck angiograms using 3D convolutional neural network," *Nature Communications*, vol. 11, no. 1, p. 4829, 2020.

[9] Y. Liang, X. Chen, Y. Tong et al., "Higher axillary lymph node metastasis burden in breast cancer patients with positive preoperative node biopsy: may not be appropriate to receive sentinel lymph node biopsy in the post-ACOSOG Z0011 trial era," *World Journal of Surgical Oncology*, vol. 17, no. 1, p. 37, 2019.

[10] X.-w. Qi, J.-z. Du, P. Tang et al., "Clinical significance of internal mammary lymph node metastasis for breast cancer: analysis of 337 breast cancer patients," *Surgical Oncology*, vol. 27, no. 2, pp. 185–191, 2018.

[11] Y. Chen, S. Hu, H. Mao, W. Deng, and X. Gao, "Application of the best evacuation model of deep learning in the design of public structures," *Image and Vision Computing*, vol. 102, Article ID 103975, 2020.

[12] A. Inaki, K. Nakajima, H. Wakabayashi, T. Mochizuki, and S. Kinuya, "Fully automated analysis for bone scintigraphy with artificial neural network: usefulness of bone scan index (BSI) in breast cancer," *Annals of Nuclear Medicine*, vol. 33, no. 10, pp. 755–765, 2019.

[13] A. López-Cortés, A. Cabrera-Andrade, J. M. Vázquez-Naya et al., "Prediction of breast cancer proteins involved in immunotherapy, metastasis, and RNA-binding using molecular descriptors and artificial neural networks," *Scientific Reports*, vol. 10, no. 1, p. 8515, 2020.

[14] G. V. Sherbet, W. L. Woo, and S. Dlay, "Application of artificial intelligence-based technology in cancer management: a commentary on the deployment of artificial neural networks," *Anticancer Research*, vol. 38, no. 12, pp. 6607–6613, 2018.

[15] K. Terata, S. Motoyama, S. Kamata et al., "Evaluation of the potential for lymph node metastasis using CRP 1846C>T genetic polymorphism in invasive breast cancer," *Tumor Biology*, vol. 35, no. 6, pp. 5931–5935, 2014.

[16] D. Farrokh, L. Ameri, F. Oliaee et al., "Can ultrasound be considered as a potential alternative for sentinel lymph node biopsy for axillary lymph node metastasis detection in breast cancer patients?" *Breast Journal*, vol. 25, no. 6, pp. 1300–1302, 2019.

[17] A. Lale, M. Yur, H. Özgül et al., "Predictors of non-sentinel lymph node metastasis in clinical early stage (Ct1-2N0) breast cancer patients with 1-2 metastatic sentinel lymph nodes," *Asian Journal of Surgery*, vol. 43, no. 4, pp. 538–549, 2020.

[18] C.-Y. Chien, S.-W. Hsu, T.-L. Lee, P.-S. Sung, and C.-C. Lin, "Using artificial neural network to discriminate Parkinson's disease from other parkinsonisms by focusing on putamen of dopamine transporter SPECT images," *Biomedicines*, vol. 9, no. 1, p. 12, 2020.

[19] M. Toğaçar, B. Ergen, and Z. Cömert, "Application of breast cancer diagnosis based on a combination of convolutional neural networks, ridge regression and linear discriminant analysis using invasive breast cancer images processed with autoencoders," *Medical Hypotheses*, vol. 135, Article ID 109503, 2020.

[20] Z. B. Yang, Z. Huang, S. L Wang et al., "A nomogram to predict non-sentinel lymph node metastasis for breast cancer patients with positive axillary sentinel lymph node," *Zhonghua Zhongliu Zazhi*, vol. 42, no. 8, pp. 653–659, 2020, Chinese.

Hindawi
Journal of Healthcare Engineering
Volume 2021, Article ID 4505227, 7 pages
https://doi.org/10.1155/2021/4505227

Research Article

Application of PET Imaging in the Brain Regions of the Emotional Control Loop in Patients with Generalized Anxiety Disorder

Jing Li[1] and Wenjun Ouyang[2]

[1]*Hubei Provincial Hospital of Traditional Chinese Medicine, Wuhan 430000, China*
[2]*School of Economics and Management, China University of Geosciences (Wuhan), Wuhan 430000, China*

Correspondence should be addressed to Wenjun Ouyang; zhumihua@cug.edu.cn

Received 3 June 2021; Revised 3 July 2021; Accepted 14 July 2021; Published 22 July 2021

Academic Editor: Enas Abdulhay

Objective. This study uses PET imaging to observe the uptake and metabolism of 18F-fluorodeoxyglucose (^{18}F-FDG) in the multibrain areas of the emotional control loop in patients with generalized anxiety disorder (GAD) and investigate the brain of GAD patient's functional abnormality mechanism. *Methods*. The thesis clinically collected 20 GAD patients and 20 healthy subjects. Dynamic PET-CT scans were used. At the same time, ^{18}F-FDG whole-brain uptake and metabolism data were collected. Image fusion and semiquantitative analysis were used to measure emotional control loops. The maximum standard uptake value (SUVmax) and dynamic uptake and metabolic changes of 11 time points in the brain area at 150 min were measured. *Results*. Compared with the healthy control group, the peak uptake of the bilateral prefrontal cortex and the average uptake rate before the peak in GAD patients were significantly reduced ($P < 0.05$), and the average metabolic rate after the peak was significantly increased ($P < 0.05$). The peak uptake of the left striatum and the left hippocampus, the average uptake rate before the peak, and the average metabolic rate after the peak were all significantly reduced ($P < 0.05$); There were no obvious changes in the three indexes of the right striatum and the right hippocampus. *Conclusion*. There are ^{18}F-FDG uptake and metabolic disorders in multiple brain areas of the affective control loop of GAD patients. The abnormal peak and rate of uptake may be related to the pathogenesis of GAD.

1. Introduction

Generalized Anxiety Disorder (GAD) is a common mental illness. Patients have emotional disorders such as anxiety, tension, and fear, which often seriously affect normal life. Research on the pathogenesis of GAD is currently mostly focused on the fields of neurotransmitter and brain structure and function, and there are few studies from the level of molecular imaging. 18F-Fluorodeoxyglucose (^{18}F-FDG) PET-CT imaging is a technology that has been gradually used in clinical work in recent years. It can reflect the degree of somatic cell activity from the side, especially in the research of central nervous disease. The level reflects the function of nerve cells. At present, it has been well used in many fields such as stroke, brain tumor, and Alzheimer's disease and can accurately determine the distribution, range, and degree of nerve cell activity [1, 2]. There are many abnormalities in GAD, such as atrophy of gray matter nuclei in the brain area of the affect-regulated brain area, functional link disorder of the brain area, and neurotransmitter imbalance. These abnormal changes affect and interact with each other, and the pathogenesis is very complicated. Based on whole-brain imaging, this study dynamically observed the ^{18}F-FDG uptake and metabolism characteristics of nerve cells in the brain area of the emotional control loop and provided an objective basis for abnormal information interaction feedback and regulatory disorders in each brain area to supplement and improve the pathogenesis of GAD.

2. Materials and Methods

2.1. Clinical Data. The thesis collected 20 GAD patients in the neurology clinic of our hospital. All patients included 9 males and 11 females, aged 21 to 58 years, with an average of 33.9 ± 3.4 years; the patient's years of education were 9–16 (14.5 ± 3.5) years; height was 150 ~ 179 (155 ± 12) cm; weight

47 ~ 82 (60 ± 11) kg; and all patients were right handed [3, 4]. Conditions for patients to enter the group: (1) they all met the GAD diagnostic criteria of the Chinese Classification and Diagnostic Criteria for Mental Disorders 3rd Edition (CCMD3) and Hamilton Anxiety Scale (HAMA) score ≥ 14 points; (2) head MRI excludes brain organic diseases or development abnormality; (3) clinical-scale evaluation excludes depression, schizophrenia, and other mental diseases; and (4) not recently (within 3 months) taking hormones, antianxiety, and other psychotropic drugs that affect glucose intake.

Taking the staff of the hospital and their families as sources, this study collected a total of 20 cases in the healthy control group. There were 9 males and 11 females in the healthy group, aged 23 to 60 years, with an average of 35.3 ± 3.7 years; the years of education in the group were 9–19 (15.4 ± 2.7) years; height was 155–180 (160 ± 10) cm; weight was 41–79 (56 ± 9) kg; and all were right handed. Inclusion criteria: (1) clinical-scale evaluation to exclude any mental illness; (2) head MRI to exclude brain organic diseases or developmental abnormalities; and (3) recently (within 3 months), no drugs that affect glucose uptake have been taken.

2.2. PET-CT Image Acquisition. Preparations before and during the scan: the subject started smoking and alcohol prohibition 1 day before the examination, avoiding the intake of drinks such as coffee, strong tea, and sugar water, sitting still for half an hour before the scan, closing the eyes during the scan, and trying to keep calm breathing. The study used a SIEMENS52 ring 128-layer high-resolution PET-CT scanner; the imaging agent ^{18}F-FDG was produced by Canada's EBCOTR19 medical cyclotron, with radiochemical purity >95%. The data collection method is as follows: after the subject's measured blood glucose reaches the target, they will be injected with ^{18}F-FDG intravenously, the total amount of injection = body weight (kg) × 0.1 mCi, and keep calm for 10 minutes. All of them first performed CT head scan for anatomical positioning and then used the dynamic list mode to collect PET data at 11 time points at an interval of 15 minutes [5]. The data are reconstructed by the iterative method after attenuation correction and processed in the syngo True DVE12A workstation to obtain multiplanar reconstruction images.

2.3. A Semiquantitative Analysis of the Region of Interest of ^{18}F-FDG Uptake in the Emotional Regulation Brain Area. Because the CT anatomy of the brain tissue is fuzzy and the accuracy is not good, the subjects in this study have been examined by the head MRI before being enrolled. Based on the 3D-T1WI sequence of the same subject, a multiresolution nonparametric density model was used (MRNDM), image fusion method, which transforms the RGB space of the source multimodal medical image registration into a generalized intensity-hue-saturation space (GIHS). Then, the MRI brain image of the patient is decomposed into low- and high-frequency components using nonsubsampled contour transformation (NSCT), and the fusion image is constructed by inverse operation of the NSCT operation of all composite coefficients. This method effectively overcomes the problem of model mismatch and can provide an accurate anatomical positioning basis for the outline of the region of interest [6]. The outline of the region of interest based on the ALL template and the anatomical landmark points of each brain area proposed by Ax macher, respectively, outlines the prefrontal cortex, striatum, hippocampus, and thalamus in the emotional control brain area. After the region of interest is delineated, the highest dynamic standard uptake value (SUVmax value, unit of Bq/cc) of ^{18}F-FDG in the region is measured, and the data are automatically generated by the PET workstation software. The data of each point of 11 time points measured in each brain area were measured 3 times and averaged. Since ^{18}F-FDG uptake and metabolism in the cerebellar region are recognized as relatively stable, the SUVmax value of the ipsilateral cerebellar structure of the same subject was standardized based on SUVmax (standardized) = SUVmax (brain area of interest)/SUVmax (same as the lateral cerebellum). The ^{18}F-FDG peak value (the highest value of SUVmax in all time points), the average uptake rate before the peak, and the average metabolic rate after the peak of the brain area of interest were recorded. Average uptake rate before peak = [SUVmax peak − SUVmax (time starting point)]/peak time and average metabolic rate after peak = [SUVmax peak − SUVmax (time end point)]/postpeak time were recorded. Finally, Graph Pad Prism software was used to draw the time dynamic curve.

2.4. Statistical Analysis. Using SPSS11.0 software for statistical analysis, the data obtained in the experiment accord with the normal distribution, and the measurement data are expressed as mean ± standard deviation. A two-sample t-test was used to compare the two groups, and $P < 0.05$ indicated that the difference was statistically significant [7].

Context Awareness (CA) is a visual saliency model based on the contrast method. It uses LAB color space features to calculate the distance between two pixel blocks and define dissimilarity and then calculate the contrast of the 64 nearest neighbors of the current block; finally, feature maps such as color and distance are merged, and context correction and enhancement are performed to obtain a saliency map. The context-aware model follows the four criteria of bottom-level features, global features, organizational rules, and high-level elements. Among them, the first three points are calculated by color mode difference, global feature universality, and the relative concentration of salient feature pixels to calculate the salient area [8]. Finally, this paper adds feature elements to postprocess the salient map. The specific steps and calculation formula are as follows.

We divide the target image into $n \times n$ blocks and calculate the Euclidean color distance and the Euclidean space distance of the two pixel blocks in the LAB space, denoted by $d_{\text{color}}(p_i, p_j)$ and $d_{\text{position}}(p_i, p_j)$, respectively. Among them, p_i and p_j represent pixel block i and pixel block j. The saliency of a pixel block is jointly determined by $d_{\text{color}}(p_i, p_j)$ and $d_{\text{position}}(p_i, p_j)$. The larger the color distance and the smaller the position distance, the greater the difference between the two pixel blocks. The pixel block dissimilarity calculation formula is

$$D\left(p_i, p_j\right) = \frac{d_{\text{color}}\left(p_i, p_j\right)}{1 + c \times d_{\text{position}}\left(p_i, p_j\right)}. \quad (1)$$

Here, c is a constant. Taking the saliency value of the pixel block pi as an example, the greater the difference between p_i and the surrounding pixel blocks, the higher the saliency. The reference set is $\{q_k\}_{k=1}^{K}$. $K = 64$ is the number of selected pixel blocks, calculated as

$$S_i^r = 1 - \exp\left\{-\frac{1}{K}\sum_{k=1}^{K} d\left(p_i^r, q_k^r\right)\right\}. \quad (2)$$

Equation (2) can be used improve the contrast between the salient area and the insignificant area by taking the average value. The calculation formula is

$$S_i^r = 1 - \exp\left\{-\frac{1}{K}\sum_{k=1}^{K} d\left(p_i^r, q_k^{rk}\right)\right\}. \quad (3)$$

The range of saliency value is $[0, 1]$; the larger the two pixel blocks, the higher the saliency and the smaller the less significant for pixels around salient points. The paper needs to add context for correction, by setting the saliency threshold and calculating the Euclidean distance weighted value between the salient point and the surrounding pixels to obtain the saliency value of the information [9]. After the thesis is revised, the saliency value of the salient area is enhanced. The context correction calculation method is shown as follows:

$$\widehat{S}_i = \overline{S}_i\left(1 - d_{\text{foci}}(i)\right), \quad \overline{S}_i = \frac{1}{M}\sum_{r\in R} S_i^r. \quad (4)$$

After the target image is processed as mentioned above, a two-dimensional saliency map with the same size as the original image is obtained, as shown in Figure 1.

Grab cut characterizes the probability distribution of color information by estimating the Gaussian Mixture Model (GMM) of the target area and the background area. On the RGB space color image, the pixel GMM Gaussian component is allocated, the parameters are optimized, and the segmentation prediction is iterated to converge to obtain the foreground area. Finally, the paper uses the smoothest boundary of the foreground area to improve the edge accuracy of the segmented image [10].

The Grab Cut algorithm requires user initialization to divide the target image into a background area and possible target areas. The pixels in the two areas are initialized to 0 and 1, respectively [11]. The pixel point set $a = (a_1, \ldots a_n, \ldots, a_N), a_n \in \{0, 1\}$ corresponds to the pixel point label set $K = (k_1, \ldots k_n, \ldots, k_N)$. Among them, N is the number of pixels; θ is the color probability distribution model of the target area and the background area; and K is the number of Gaussian distribution ($K = 5$). The problem is described as follows:

$$a = \arg\min_{a} E(a, \theta). \quad (5)$$

The Gibbs energy used by Grab Cut on the RGB space color image is

$$E\left(\underline{a}, k, \underline{\theta}, z\right) = U\left(\underline{a}, k, \underline{\theta}, z\right) + V\left(\underline{a}, z\right). \quad (6)$$

Here, E is the Gibbs energy, U is the data item, V is the smooth item, and z is the image gray value array, $z = (z_1, \ldots z_n, \ldots, z_N)$. The parameters of the Gaussian mixture model are

$$\underline{\theta} = \left\{\pi(a, z), u(a, k), \sum(a, k)\right\}. \quad (7)$$

Here, $a = 0, k = 1, \ldots, K$. The boundary energy term V is solved using the Euclidean distance formula in the RGB space:

$$V\left(\underline{a}, z\right) = y\sum_{(m,n)\in C}\left[a_n \neq a_m\right]\exp - \beta\left\|z_m - z_n\right\|^2. \quad (8)$$

Here, m and n represent two neighborhood pixels; the value of parameter β is inversely proportional to the contrast of the image, so that the boundary energy term V can be applied to high-contrast and low-contrast images; and the constant γ is obtained from image training. This paper uses this method to obtain a segmentation curve with smooth edges, as shown in Figure 2.

3. Results

3.1. The Distribution of Abnormal Uptake in the Emotional Control Loop. F-FDGPET-CT imaging showed that the whole-brain uptake distribution of the GAD group and healthy control group was clear. Compared with the healthy control group, the peak uptake of the bilateral prefrontal cortex and the average uptake rate before the peak in the GAD group were significantly reduced ($P < 0.05$), and the average metabolic rate after the peak was significantly increased ($P < 0.05$); the peak uptake in the lateral striatum and the left hippocampus, the average uptake rate before the peak, and the average metabolic rate after the peak were all significantly reduced ($P < 0.05$); the peak uptake in the left thalamus, the average uptake rate before the peak, and the peak average metabolic rate after the peak increased significantly ($P < 0.05$); and the peak uptake in the right thalamus and the average uptake rate before the peak increased significantly ($P < 0.05$), and there was no significant difference in the average metabolic rate after the peak [12]. There were no obvious changes in the three indexes of the right striatum and the right hippocampus. The specific data in the paper are shown in Tables 1–3.

3.2. Dynamic Characteristics of Abnormal Uptake in the Brain Area of the Emotional Control Loop. Compared with the healthy control group, during the ^{18}F-FDG imaging process, the GAD group showed slow advancement and faster delivery and decreased total amount on both sides of the prefrontal cortex; the left striatum showed slow advancement and slow exit and decreased total amount. There was

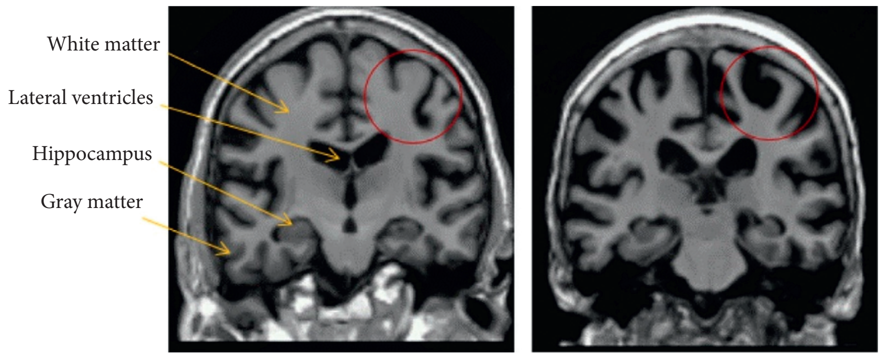

Figure 1: Two-dimensional saliency map of brain PET.

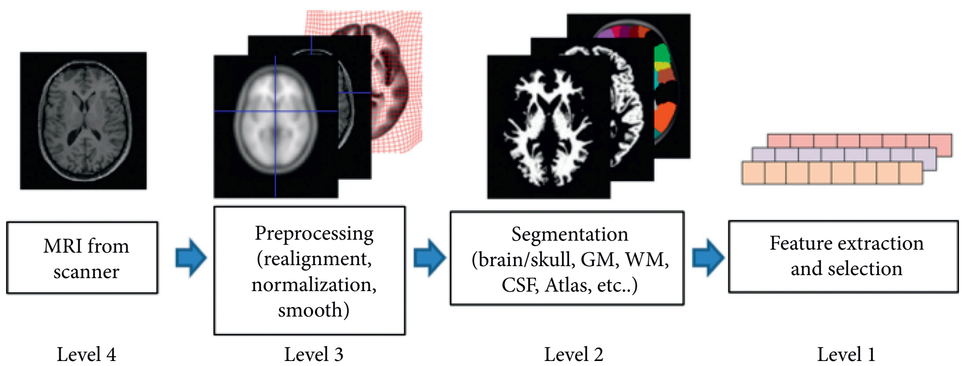

Figure 2: Segmentation curve with smooth edges.

Table 1: The difference of the peak uptake of the two groups of emotional control loops in multiple brain regions (Bq/cc).

Grouping	Left prefrontal cortex	Right prefrontal cortex	Left striatum	Right striatum	Left hippocampus	Right hippocampus	Left thalamus	Right thalamus
Healthy control group	2.41 ± 0.21	2.52 ± 0.24	1.95 ± 0.17	1.97 ± 0.22	1.65 ± 0.20	1.63 ± 0.19	1.71 ± 0.17	1.69 ± 0.15
GAD group	2.04 ± 0.20	2.06 ± 0.18	1.41 ± 0.19	1.97 ± 0.18	1.16 ± 0.15	1.63 ± 0.16	2.13 ± 0.24	2.08 ± 0.20
t value	5.71	6.86	9.47	0	8.77	0	6.39	6.98
P value	<0.05	<0.05	<0.05	>0.05	<0.05	>0.05	<0.05	<0.05

no significant difference in changes in the lateral striatum; the left hippocampus showed slow entry and slow exit, and the total amount decreased, and the right hippocampus showed no significant difference; the left thalamus showed fast forward and faster exit, and the total amount increased, the right thalamus showed fast in and out, and the total volume increases performance [13] (see Figures 3 and 4).

4. Discussion

GAD has a number of functional abnormalities in brain structures, and the dysfunction of the affect regulation loop is a key factor leading to the disease. Structural magnetic resonance studies have shown that the prefrontal cortex, striatum, hippocampus, and thalamus contained in this loop have varying degrees of morphological abnormalities. The main manifestations are the reduction of brain volume and the reduction of gray matter thickness; functional magnetic resonance is here on the basis of this, and it is further confirmed that there are abnormal functional linkages between multiple brain areas of the emotional control loop. For example, there is an increase in the activation of the thalamus and the hippocampus, the prefrontal cortex, and the decrease of the activation of the hippocampus and the prefrontal cortex while the brain structure is atrophy [14]. Conventional MRI technology can certainly observe and explore the mechanism of GAD imaging performance to a certain extent, but due to differences in data collection, correction, and normalization steps, there are still many differences and controversies in the final results, and MRI lacks dynamic brain function. Technical means of change observation.

Table 2: The difference in the average uptake rate of the two groups of emotional control loops before the peak of the multibrain area [Bq/(cc·min)].

Grouping	Left prefrontal cortex	Right prefrontal cortex	Left striatum	Right striatum	Left hippocampus	Right hippocampus	Left thalamus	Right thalamus
Healthy control group	0.34 ± 0.02	0.24 ± 0.02	0.14 ± 0.01	0.09 ± 0.01	0.12 ± 0.02	0.11 ± 0.02	0.21 ± 0.02	0.08 ± 0.01
GAD group	0.15 ± 0.01	0.15 ± 0.02	0.09 ± 0.01	0.09 ± 0.01	0.06 ± 0.01	0.11 ± 0.01	0.45 ± 0.03	0.14 ± 0.01
t value	38	14.23	15.81	0	12	0	29.77	18.97
P value	<0.05	<0.05	<0.05	>0.05	<0.05	>0.05	<0.05	<0.05

Table 3: Differences in the average metabolic rate of the two groups of emotional control loops after peaking in multiple brain regions [Bq/(cc·min)].

Grouping	Left prefrontal cortex	Right prefrontal cortex	Left striatum	Right striatum	Left hippocampus	Right hippocampus	Left thalamus	Right thalamus
Healthy control group	0.07 ± 0.01	0.05 ± 0.02	0.08 ± 0.01	0.12 ± 0.02	0.09 ± 0.01	0.11 ± 0.02	0.05 ± 0.01	0.10 ± 0.01
GAD group	0.10 ± 0.01	0.12 ± 0.02	0.03 ± 0.01	0.11 ± 0.02	0.05 ± 0.01	0.10 ± 0.01	0.08 ± 0.01	0.09 ± 0.02
t value	9.49	11.07	15.81	1.58	12.65	2.1	9.49	2.1
P value	<0.05	<0.05	<0.05	>0.05	<0.05	>0.05	<0.05	>0.05

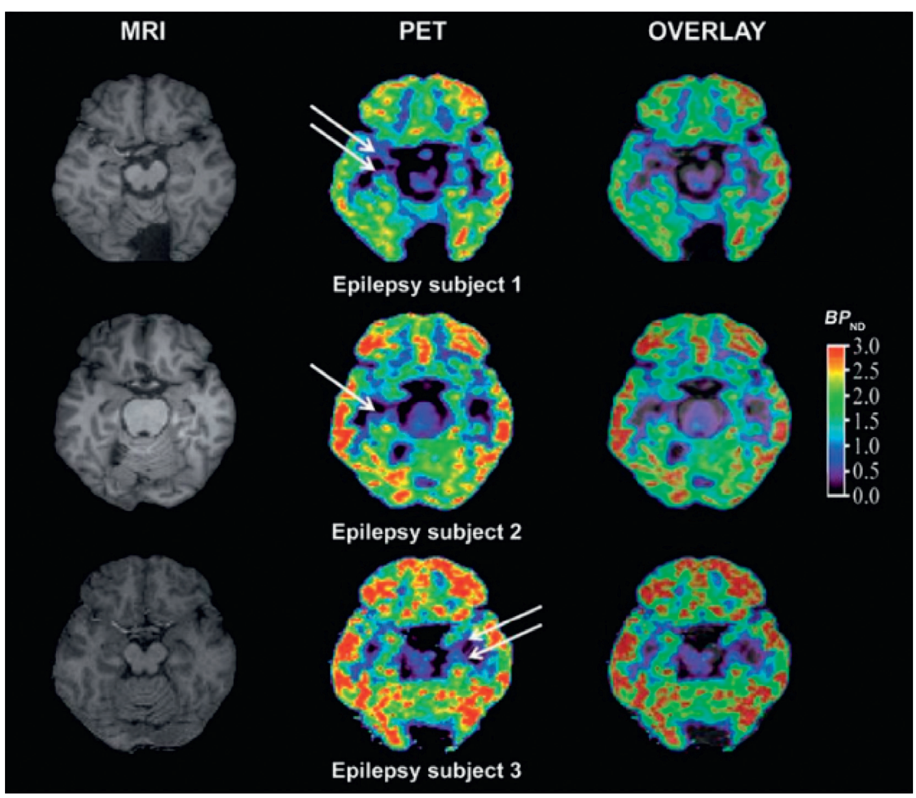

Figure 3: ^{18}F-FDG imaging of the bilateral prefrontal cortex showed slow advance and fast exit, and the total amount decreased.

F-FDGPET-CT, as a new technology for observing changes in brain nerve cell function in recent years, can clearly visualize the glucose uptake and metabolism process of nerve cells. This technology presents brain function changes in image data through the dynamic acquisition mode, which can compensate for MRI observation of the cell metabolism process that is difficult to achieve in brain function research, realizing the real molecular imaging level

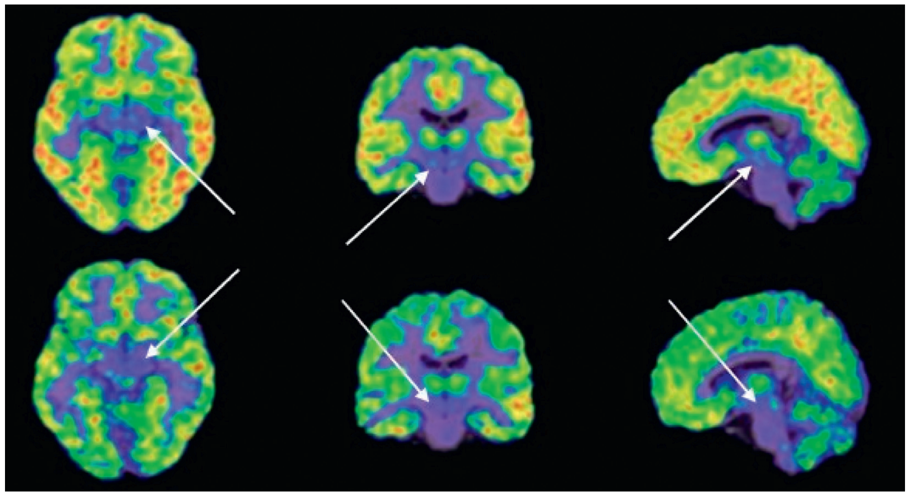

Figure 4: The left striatum of ^{18}F-FDG showed slow in and slow out, and the total amount decreased.

research. GAD patients have significant mental disorders such as anxiety, tension, and fear, and the nerve cells in the brain area of the emotional control loop have a significantly different demand for glucose energy from healthy people [15].

The results of this study showed that the peak uptake of the bilateral prefrontal cortex in GAD patients decreased and the average uptake rate before the peak decreased, which was consistent with the results of PET experiments in rat models of other scholars, but the time gradient results suggested that the brain area was average after the peak. The metabolic rate is significantly accelerated; the peak uptake of the hippocampus and striatum on the left side decreases, and the average postpeak metabolic rate slows down, similar to the results of the literature; our results also show that the peak uptake of the bilateral thalamus increases, reaching the prepeak The average uptake rate increases, and the average metabolic rate after the left thalamic peak increases [16]. Dynamic analysis of abnormal ^{18}F-FDG uptake in various brain regions shows that, in the emotional regulation loop of GAD patients, the thalamus structure, which is a rough information processing area, has a significant increase in the demand for glucose energy and the use of conversion rate is accelerated, as a fine information adjustment transmission The hippocampus and striatum in the central part of the hippocampus and striatum have a significant insufficient demand for glucose energy and a tendency to stagnate conversion. The prefrontal cortex, which has information executive functions, has insufficient demand for glucose energy but uses it to transform too quickly [17]. The possible mechanism for the occurrence of this misaligned energy demand and application inequality is that, with the continuous increase in external stress events, sensitive individuals absorb too many negative stimuli, resulting in a certain degree of regulatory transmission dysfunction.There are insufficient executive functions, unable to adapt and deal with too many adverse events, and there are also obstacles to the feedback implementation of benign regulation, which are prone to anxiety and fear-like behaviors and eventually lead to the occurrence of GAD. For the right emotional regulation loop, the study only shows abnormalities in the thalamus and prefrontal cortex, and the intermediate regulatory transmission center is not affected. In addition to the theory of the dominant hemisphere of the brain, the thesis needs to further study its mechanism.

5. Conclusions

To sum up, there are abnormalities in ^{18}F-FDG uptake and metabolism in multiple brain regions in the nutriregulation circuit of GAD patients. Abnormal uptake peaks and rates may be related to the onset of GAD. Dynamic observation of its changes can help reveal deeper the pathogenesis of GAD.

Data Availability

The data used to support the findings of this study are available from the corresponding author upon request.

Conflicts of Interest

The authors declare no conflicts of interest.

References

[1] J. D. Watson and F. H. C. Crick, "A structure for deoxyribose nucleic acid," *Nature*, vol. 171, no. 43, pp. 737-738, 1953.

[2] M. Nojoumi, P. Ghaeli, S. Salimi, A. Sharifi, and F. Raisi, "Effects of passion flower extract, as an add-on treatment to sertraline, on reaction time in patients with generalized anxiety disorder: a double-blind placebo-controlled study," *Iranian Journal of Psychiatry*, vol. 11, no. 3, pp. 191–197, 2016.

[3] B. P. Abbott, R. Abbott, and T. D. Abbott, "Observation of gravitational waves from a binary black hole merger," *Physical Review Letters*, vol. 116, no. 6, Article ID 061102, 2016.

[4] M. Latas, J. Samardi, S. Perovi, Z. Nei, and S. Milovanovi, "An observational study comparing the efficacy of duloxetine and pregabalin in patients with generalized anxiety disorder," *Engrami*, vol. 42, no. 1, pp. 20–31, 2020.

[5] N. T. T. Hmwe, P. Subramanian, L. P. Tan, and W. K. Chong, "The effects of acupressure on depression, anxiety and stress in patients with hemodialysis: a randomized controlled trial,"

International Journal of Nursing Studies, vol. 52, no. 2, pp. 509–518, 2015.

[6] L. Eduardo, B. Henning, F. Paes et al., "Effects of aerobic exercise on anxiety symptoms and cortical activity in patients with panic disorder: a pilot study," *Clinical Practice & Epidemiology in Mental Health Cp & Emh*, vol. 14, no. 1, pp. 11–25, 2018.

[7] N. Galldiks, K. J. Langen, N. L. Albert et al., "PET imaging in patients with brain metastasis--report of the RANO/PET group," *Neuro-Oncology*, vol. 21, no. 5, pp. 585–595, 2019.

[8] Z. Chen, S. D. Jamadar, S. Li et al., "From simultaneous to synergistic MR-PET brain imaging: a review of hybrid MR-PET imaging methodologies," *Human Brain Mapping*, vol. 39, no. 12, pp. 5126–5144, 2018.

[9] N. Quartuccio and M. C. Asselin, "The validation path of hypoxia PET imaging: focus on brain tumours," *Current Medicinal Chemistry*, vol. 25, no. 26, pp. 3074–3095, 2018.

[10] K. Gong, J. Yang, K. Kim, G. El Fakhri, Y. Seo, and Q. Li, "Attenuation correction for brain PET imaging using deep neural network based on Dixon and ZTE MR images," *Physics in Medicine and Biology*, vol. 63, no. 12, Article ID 125011, 2018.

[11] L. Michaud, B. J. Beattie, T. Akhurst et al., "18 F-Fluciclovine (18 F-FACBC) PET imaging of recurrent brain tumors," *European Journal of Nuclear Medicine and Molecular Imaging*, vol. 471, no. 6, pp. 1353–1367, 2020.

[12] K. Chiotis, P. Stenkrona, O. Almkvist, D. Ferreira, R. Arakawa, and H. Shimada, "Dual tracer tau PET imaging reveals different molecular targets for 11 C-THK5351 and 11 C-PBB3 in the Alzheimer brain," *European Journal of Nuclear Medicine and Molecular Imaging*, vol. 45, no. 9, pp. 1605–1617, 2018.

[13] S. Minoshima, A. E. Drzezga, H. Barthel et al., "SNMMI procedure standard/EANM practice guideline for amyloid PET imaging of the brain 1.0," *Journal of Nuclear Medicine*, vol. 57, no. 8, pp. 1316–1322, 2016.

[14] W. G. Lesniak, C. Chu, A. Jablonska et al., "A distinct advantage to intraarterial delivery of 89Zr-bevacizumab in PET imaging of mice with and without osmotic opening of the blood–brain barrier," *Journal of Nuclear Medicine*, vol. 60, no. 5, pp. 617–622, 2019.

[15] T. Sekine, N. Burgos, G. Warnock et al., "Multi-atlas–based attenuation correction for brain ^{18}F-FDG PET imaging using a time-of-flight PET/MR scanner: comparison with clinical single-atlas–and CT-based attenuation correction," *Journal of Nuclear Medicine*, vol. 57, no. 8, pp. 1258–1264, 2016.

[16] A. G. Horti, R. Naik, C. A. Foss et al., "PET imaging of microglia by targeting macrophage colony-stimulating factor 1 receptor (CSF1R)," *Proceedings of the National Academy of Sciences*, vol. 116, no. 5, pp. 1686–1691, 2019.

[17] M. A. Nettis, M. Veronese, N. Nikkheslat et al., "PET imaging shows no changes in TSPO brain density after IFN-α immune challenge in healthy human volunteers," *Translational Psychiatry*, vol. 10, no. 1, pp. 1–11, 2020.

Hindawi
Journal of Healthcare Engineering
Volume 2021, Article ID 5169803, 8 pages
https://doi.org/10.1155/2021/5169803

Research Article

Wavelet Transform-Based Ultrasound Image Enhancement Algorithm for Guided Gynecological Laparoscopy Imaging of Local Anesthetics in Perioperative Gynecological Laparoscopy

Bingbing Sheng, Qiaoqin Yan, Xianda Zhao, and Wujian Yang

Department of Anaesthesiology, The First People's Hospital of Wenling, Taizhou 317500, Zhejiang, China

Correspondence should be addressed to Wujian Yang; 102253011049@m.fafu.edu.cn

Received 2 June 2021; Revised 4 July 2021; Accepted 14 July 2021; Published 22 July 2021

Academic Editor: Enas Abdulhay

This paper aimed to study the application of local anesthetics combined with transversus abdominis plane (TAP) block in gynecological laparoscopy (GLS) surgery during perioperative period under the guidance of ultrasound image enhanced by the wavelet transform image enhancement (WTIE) algorithm. 56 patients who underwent GLS surgery in hospital were selected and classified as the infiltrating group and block group. The puncture needle was guided by ultrasound images under WTIE algorithm, and 0.375% ropivacaine was adopted to block TAP. The results showed that the dosage of propofol in the infiltrating group (313.23 ± 19.67 mg) was remarkably inferior to the infiltrating group (377.67 ± 21.56 mg) ($P < 0.05$). The hospitalization time of patients in the infiltrating group (2.14 ± 0.18 days) was obviously shorter than that of the infiltrating group (3.23 ± 0.27 days) ($P < 0.05$). 3 h, 6 h, and 12 h after the operation, the visual analogue scores (3.82 ± 1.58 points, 2.97 ± 1.53 points, and 1.38 ± 0.57 points) of the patients in the infiltration group were considerably higher than the infiltrating group (2.31 ± 1.46 points, 1.06 ± 1.28 points, and 0.95 ± 0.43 points) ($P < 0.05$). 3 h, 6 h, and 12 h after the operation, the number of patients in the infiltrating group who used tramadol for salvage analgesia (2 cases, 1 case, and 1 case) was notably less than that in the infiltration group (9 cases, 7 cases, and 3 cases) ($P < 0.05$). In short, local anesthetics combined with TAP block can reduce postoperative VAS score and postoperative nausea and vomiting (PONV) score, which also reduced the incidence of postoperative analgesia.

1. Introduction

Gynecological laparoscopy has been widely adopted in clinical treatment because of its advantages of small trauma, light pain, and quick recovery [1]. However, due to the different physiques of the patients, the pain is still unbearable. After GLS, patient-controlled intravenous analgesia is commonly adopted, and the analgesic effect is very significant. Due to general anesthesia, it causes more side effects, and it is prone to adverse symptoms such as respiratory depression, nausea, vomiting, and skin itching [2]. Transversus abdominis plane (TAP) block refers to injecting anesthetics into the neurofascial layer between the internal oblique muscle and the transversus abdominis muscle, to block the relevant nerve sensory conduction. Therefore, the pain of the skin, muscles, and peritoneum of the front abdomen is weakened, and a relatively ideal abdominal wall analgesic effect is achieved [3]. In recent years, the application of TAP block in postoperative analgesia has gradually increased. Ping-Chen et al. [4] found that different drug concentrations had a greater impact on laparoscopic surgery, so it was urgent to determine the optimal drug concentration.

With the rapid development of computer image processing technology, its application in medical imaging has been gradually extensive [5]. Ultrasound imaging medicine is one of the important tools for clinicopathological diagnosis, which can improve the efficiency of clinical diagnosis by locating and recognizing ultrasonic images and extracting graphic features. On the premise of feature extraction, image segmentation, image enhancement, and edge features of ultrasonic images, abnormal feature points are extracted from ultrasonic images to enhance the judgment ability of ultrasonic images [6]. Abraham et al. [7] proposed a small porter feature decomposition for the extraction of abnormal feature points in ultrasonic images and decomposed the edge contour features of ultrasonic images. Then, according to the decomposition results, the adaptive information fusion was enhanced to improve the detection of ultrasonic images. Sadek et al. [8] proposed an ultrasonic image localization of correlation characteristics and conducted batch processing of ultrasonic image edges. Based on the above reports, this work proposed an ultrasonic image localization technique based on WTIE algorithm. Firstly, edge feature fusion method was adopted for contour detection of ultrasonic images, color gradient decomposition was carried out in the region, and the ultrasonic image region was fused and filtered. Then, the wavelet transform method was combined to perform feature decomposition and scale template matching on the ultrasound image and process the color feature decomposition value of the ultrasound image, so that the region of the image was equalized. According to the color and texture features of ultrasonic images, the abnormal feature points of the image were located and monitored. Finally, the simulation experiment was utilized for analysis, and the conclusion was reached [9].

In this work, WTIE algorithm was applied to the ultrasound images of 56 patients undergoing GLS. The purpose was to explore the analgesic effect of different concentrations of ropivacaine combined with TAP block on the perioperative period of GLS and provide good clinical adoption reference in the analgesic aspect of GLS.

2. Materials and Methods

2.1. Selection of Research Subjects. 56 patients who were admitted to the hospital from October 17, 2018, to November 19, 2019, that underwent GLS were selected. The average age was 40.32 ± 1.24 years old. All patients were classified as grade I and grade II according to American Society of Anesthesiologists (ASA). The random number table method was utilized to divide the patients into the infiltrating group ($n = 28$) and block group ($n = 28$). The study had been approved by the Medical Ethics Committee of Hospital, and the patients and their families understood the situation of the study and signed the informed consent forms.

Inclusion criteria: (1) patients aged 20–60 years; (2) patients underwent surgery including hysterectomy, ectopic tubal pregnancy removal, and ovarian cyst removal; and (3) patients with clear consciousness and could receive normal examinations.

Exclusion criteria: (1) patients with mental illness; (2) patients with surgery time greater than 3 hours; (3) patients allergic to local anesthetics and drugs during surgery; (4) patients who withdrew from the experiment due to their own reasons; (5) patients with coagulopathy or peptic ulcer.

2.2. Observation Indicators. The clinical data of the patients were collected, and various examination indicators of the patient were detected, including blood routine, cardiac color Doppler ultrasound, lung ventilation function, blood biochemical results, infectious disease examinations, electrocardiogram, and chest radiograph. The presurgery inspections were performed in time, to fully understand the diagnosis process. Communications with the attending physician about surgery method and surgery time should be made in time. The patient's mental outlook was observed, to understand the patient's physical condition and take medication. ASA classification: before the anesthesia, the American Society of Anesthesiologists clearly categorized the risk of the upcoming surgery based on the patient's physical condition, which was divided into six levels. VAS score of pain: 0 meant no pain, less than 4 meant slight pain, 5 to 6 indicated moderate pain that can be tolerated, and a score of 7 to 10 indicated severe pain that was unbearable. PONV score: 0 meant no nausea and vomiting, 4 points or less meant slight nausea and vomiting, a score of 5 to 6 indicated moderate nausea and vomiting, and a score of 7 to 10 indicated severe nausea and vomiting. The patient needed to fast for 4 hours before the surgery.

General information of patients including average age, average height, and average weight of ASA classification was counted. The TAP blocking effect was measured after half an hour using the alcohol method to measure the patient's sensation, and the final data were recorded. The amount of anesthesia used was recorded, especially the amount of propofol used during surgery. The analgesic effect of the patients after surgery was recorded, and the VAS score of pain and PONV score were recorded 3 h, 6 h, and 12 h after the surgery. After the surgery, the number of patients using tramadol was recorded at 3 h, 6 h, and 12 h. Finally, the length of stay of all patients was recorded.

2.3. TAP Block Method. For TAP block guided by ultrasonic images, TAP localization should be performed first. Firstly, the ultrasonic probe (5.5~12 MHz) was placed under the xiphoid process to locate the rectus abdominis and the linea alba, and the probe was rotated to move along the costal margin. In the section position, it could be seen that the TAP was located between the rectus abdominis and the transverse abdominis. If TAP was not observed at the sectionals, it was because the transabdominal muscle terminated at the side of the rectus abdominis in some patients. If the probe was then moved along the costal margin to the position of the semilunar line at the lateral margin of the rectus abdominis, the three layers of the abdominal wall can be clearly identified, which were transverse abdominis, internal oblique, and external oblique from inside to outside, respectively. The probe was continuously moved to the midaxillary line, which was moved up and down between the costal margin and the iliac crest, so that the three bases can be clearly seen. The patient was told to lie on the opposite side, and the probe was moved to the direction of the posterior axillary line. It could be seen that the internal oblique muscle and the transverse abdominis were fused into a layer of fascia, which was called the pectoralis lumbar fascia, and was connected with the outer edge of the quadratus psoas. TAP was located between the transverse abdominis muscle and the internal oblique and was connected with the pectoralis lumbar fascia. A slightly mobile ultrasound probe scanned the ideal position, the area around the puncture site was disinfected with Jill iodine, and the ultrasound probe was wrapped in a sterile protective sleeve. The in-plane technique was adopted, and the nerve blocker was inserted from the medial side to the lateral side. When the puncture needle reached the TAP close to the quadratus psoas, if there was no blood loss during the withdrawal, 0.375% ropivacaine 20 mL would be injected, the ultrasonic image would be utilized to observe the diffusion of local anesthetics, and the step of the nerve blocking needle would be adjusted to continue the injection. 30 minutes after the TAP block, the block plane was detected by alcohol method. If the block scope covered T9~T12, the block effect was considered to be ideal; but if the block effect was not good, the patient would be withdrawn from the study.

Before surgery, patients in the block group were deflated in the abdominal cavity and sutured four holes. On each of the abdominal wall, a hole was made and injected with 5 mL of 0.375% ropivacaine, a total of 20 mL, for infiltration. The infiltrating group received local anesthetics combined with TAP block method for treatment.

2.4. Anesthesia Process and Surgical Method. After the TAP block was over, the patient was anesthetized. Both groups of patients were given intravenous anesthesia, and it was necessary to inject etomidate and sufentanil into the patient's veins. After the muscles were fully relaxed, the patient was put on a ventilator, and the working mode, tidal volume, respiratory rate, and respiratory ratio were determined. During surgery, it was necessary to continue to inject propofol for anesthesia and continue to add atracurium according to the actual surgery. The GLS surgery adopted the laparoscopic four-hole method. The specific positions of the four holes were the upper edge of the umbilical chakra, the right McBurney point, two fingers above the attachment between the left umbilical foramen and the left anterior superior spine of the ilium, and site with no blood vessels in the middle and lower abdomen. After surgery, the patients were transferred to the anesthesia recovery room for postoperative observation, and when they recovered consciousness, they were transferred to the general ward.

2.5. WTIE Algorithm. Wavelet transform is based on the frequency localization idea of Fourier transform. It is an analysis method in which the window size is fixed, but the shape, time window, and frequency window can be changed, and the local characteristics of the signal can be characterized in the time domain and frequency domain.

If the function $\phi(s)$ has finite energy, then, $\phi(s) \in M^2(T)$. The Fourier transform should be conducted on it, and $\phi(s)$ satisfies the following equation:

$$B_\phi = \int_T \frac{|\phi(\alpha)|^2}{|\alpha|} d\alpha < \infty. \tag{1}$$

In equation (1), B_ϕ represents the coefficient of the wavelet function, and then $\phi(s)$ is called the mother wavelet. After it is scaled and translated, the wavelet sequence $\phi_{a,b}(s)$ can be obtained, and equation is as follows:

$$\phi_{a,b}(s) = \frac{1}{\sqrt{|u|}}\phi\left(\frac{s-v}{u}\right) \quad u, v \in T;\ u \neq 0. \tag{2}$$

In equation (2), u represents the scaling factor, which corresponds to frequency information and v represents the translation factor, which corresponds to space-time information. For continuous wavelet transform of function $g(s) \in M^2(T)$, the calculation is shown as follows:

$$A_g(u, v) = \frac{1}{\sqrt{|u|}}\int_T g(s)\phi\left(\frac{t-v}{u}\right) ds. \tag{3}$$

In equation (3), $A_g(u, v)$ represents the wavelet coefficient. The wavelet function is reconstructed, and the equation is as follows:

$$g(s) = \frac{1}{B_\phi}\int_{-\infty}^{\infty}\int_{-\infty}^{\infty}\frac{1}{u^2}A_g(u, v)\phi\left(\frac{s-u}{v}\right) du dv. \tag{4}$$

In equation (4), $g(s)$ represents the wavelet transform function. Since the continuous wavelet transform function is mainly utilized in theoretical analysis, the continuous wavelet and transform should be discretized in the actual application process. Discretizing the scaling factor u and the translation factor v as $u = u_0^j$ and $v = ku_0^j v_0$, respectively, the time variable is unchanged, and the discrete wavelet function of the continuous wavelet function is as follows:

$$\phi_{j,k}(s) = u^{-j/2}\phi\left(\frac{s - ku_0^j v_0}{u_0^j}\right). \tag{5}$$

Therefore, the discretized wavelet coefficient is calculated as follows:

$$B_{i,j} = \int_{-\infty}^{\infty} g(s)\phi_{j,k}^{\circ}(s) ds. \tag{6}$$

The inverse wavelet transform for discretization is as follows:

$$g(s) = b\sum_{j=-\infty}^{\infty}\sum_{k=-\infty}^{\infty} b_{j,k}\phi_{j,k}(s). \tag{7}$$

In equation (7), b is a constant. It can be seen that the smaller the u_0 and v_0, the higher the signal reconstruction accuracy.

Infrared image is a two-dimensional discrete image $A(u, v)$, which can be regarded as a two-dimensional matrix and subjected to two-dimensional wavelet transformation. Then, it is decomposed into low-frequency components PP1, PQ1, QP1, and QQ1 at each resolution of each layer, and high-frequency components PP2, PQ2, QP2, and QQ2 in the three directions of horizontal, vertical, and diagonal. The schematic diagram of wavelet transform is shown in Figure 1, and the image reconstruction process is just the opposite.

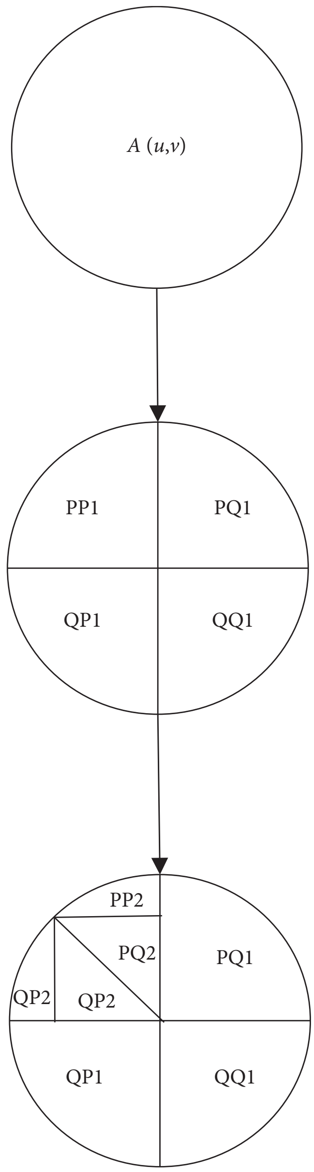

Figure 1: Schematic diagram of two-dimensional wavelet transform.

A threshold function is adopted to modify the positive wavelet coefficients. Commonly utilized threshold functions include hard threshold functions and soft threshold functions. It is assumed that A is a wavelet function, and A_S is threshold-treated wavelet coefficient, where S is the threshold. The hard threshold function means that when the absolute value of the wavelet coefficient is less than the threshold, it is equal to 0, and when it is greater than or equal to the threshold, it remains unchanged. The equation is as follows:

$$A_s = \begin{cases} A, & |A| \geq S \\ 0, & |A| < S \end{cases}. \tag{8}$$

The hard threshold function means that when the absolute value of the wavelet function is less than the threshold, it is equal to 0, and when it is greater than or equal to the threshold, the threshold is subtracted. The equation is as follows:

$$A_s = \begin{cases} \operatorname{sign}(A)(|A| - S) & |A| \geq S \\ 0 & |A| < S \end{cases}. \tag{9}$$

The key point of threshold denoising is the choice of threshold. If the choice of threshold is too large, it is possible to delete a lot of important information, and if the threshold is too small, it may affect the denoising effect. The VisuShrink threshold and the universal unified threshold is adopted. The calculation equation of the threshold S is as follows:

$$S = \sigma_m \sqrt{2 \ln M}. \tag{10}$$

In equation (10), σ_m represents the standard deviation of noise and M represents the length of the signal. Moreover, for the details of high-frequency components, the adoption of coefficient transformation can improve the contrast of the image and enhance the visual effect. The equation is as follows:

$$S_{\mathrm{OUT}} = H(S_A + f). \tag{11}$$

In equation (11), S_{OUT} represents the wavelet function after detail enhancement, S_A represents the wavelet function after threshold processing, H represents the gain factor, and f represents the offset.

2.6. Statistical Methods. Data processing adopted SPSS19.0 version statistical software analysis, measurement data conformed to normal distribution were recorded in the form of mean ± standard deviation ($\overline{x} \pm s$), and count data were recorded as percentage (%). The surgery time, length of stay, dosage, pain VAS score, and PONV scores of two groups were all analyzed by variance. The difference was considerable at $P < 0.05$.

3. Results

3.1. Statistics of General Information of Patients. There was no considerable difference in the average age, average weight, average height, and ASA classification results between the two groups ($P > 0.05$) (Figure 2). The GLS surgery received by the two groups of patients included ovarian cyst removal, hysteromyoma removal, and subtotal hysterectomy. Among them, of the majority of patients undergoing ovarian cyst removal, no notable difference was shown within or between groups ($P > 0.05$) (Figure 3).

3.2. Ultrasound Image of Gynecological Abdominal Cavity during Perioperative Period. There was a huge cystic mass in the peritoneal cavity of the ovarian cyst, with multiple compartments and compartments inside, large intra-atrial sound transmission difference, and dense spot echo. Other parts showed multiple vesicle-like aggregation. Ultrasonography showed a large amount of effusion in the abdominal cavity, with poor sound transmission, which was manifested as dense punctate echo. Original abdominal mass

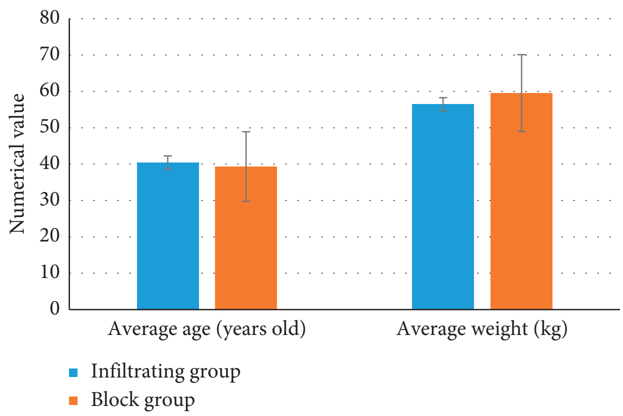

Figure 2: Contrast of general conditions of the two groups of patients.

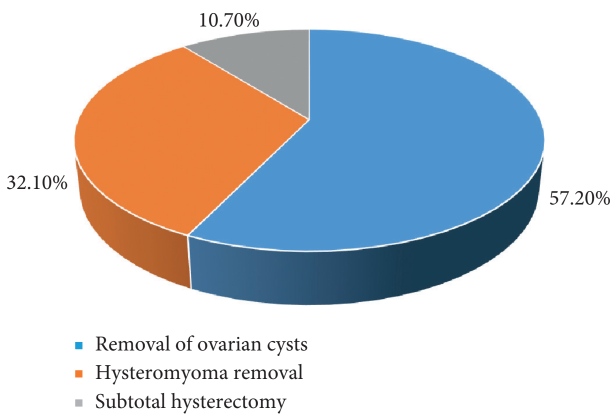

Figure 3: The proportion of ovarian cyst removal, hysteromyoma removal, and subtotal hysterectomy.

and whole volume manifestation were confined to the lower abdomen and pelvic cavity (Figure 4).

Uterine fibroids showed that the original lesion still had an echo mass with a diameter similar to that of the original lesion. This was the result of inflammatory response edema in local tissues after lesion coagulation. When ultrasound imaging was adopted for inspection, it can be seen that the original lesion still had echogenic light mass, and the diameter of the echogenic light group was generally significantly smaller than that of the original lesion, with irregular boundary and blood vessels piercing into it. This was the result of solidification of a fibroid or adenomyoma into scar tissue, which was a normal phenomenon (Figure 5).

3.3. Distribution of Blocking Planes. The anterior abdominal skin, muscles, and parietal peritoneum were innervated by T9~L1 anterior spinal nerves. After these spinal nerves left the intervertebral foramen, the anterior branch passed through the lateral abdominal wall muscles and run along the transverse abdominal muscle plane to innervate the anterior abdominal muscles and skin. The T9~T12 anterior branch entered the TAP layer from the inside of the anterior

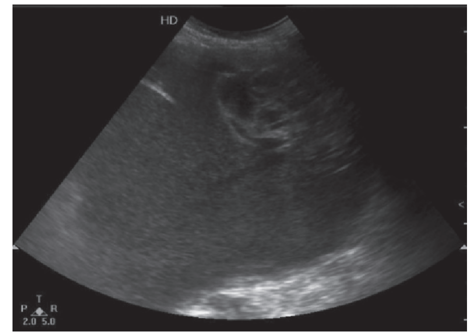

Figure 4: Ultrasound image of ovarian cyst of a female patient who underwent GLS (38 years old).

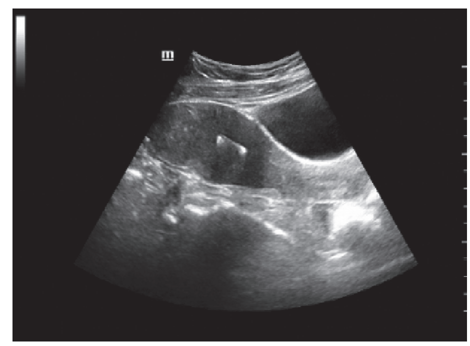

Figure 5: Ultrasound image of uterine fibroids of a female patient who underwent GLS (35 years old).

axillary line. Local anesthetics combined with TAP block were received by the two groups of patients, and no considerable difference in the block distribution was found after half an hour of surgery, as shown in Figure 6 ($P > 0.05$), and the block effect of the two groups was ideal.

3.4. Propofol Dosage during Surgery. The dosage of propofol in the block group (313.23 ± 19.67 mg) was substantially lower than that of the infiltration group (377.67 ± 21.56 mg) ($P < 0.05$) (Figure 7). In terms of surgery time, no evident differences between the two groups were found ($P > 0.05$) (Figure 8). The hospitalization time of patients in the block group (2.14 ± 0.18 days) was significantly shorter relative to the infiltrating group (3.23 ± 0.27 days) ($P < 0.05$) (Figure 9).

3.5. VAS Score and PONV Score for Postoperative Pain. 3 h, 6 h, and 12 h after the operation, the VAS scores (3.82 ± 1.58 points, 2.97 ± 1.53 points, and 1.38 ± 0.57 points) of the infiltrating group were greatly superior to the block group (2.31 ± 1.46 points, 1.06 ± 1.28 points, and 0.95 ± 0.43 points) ($P < 0.05$) (Figure 10); PONV score of the infiltrating group (1.84 ± 0.65, 1.53 ± 0.82, and 1.16 ± 0.36) was notably less than the block group (2.37 ± 0.46, 1.94 ± 0.52, and 1.57 ± 0.42) ($P < 0.05$) (Figure 11).

3.6. Tramadol Used for Postoperative Salvage Analgesia. 3 hours after the operation, 2 patients in the block group used tramadol for salvage analgesia. 6 hours after the operation, 1

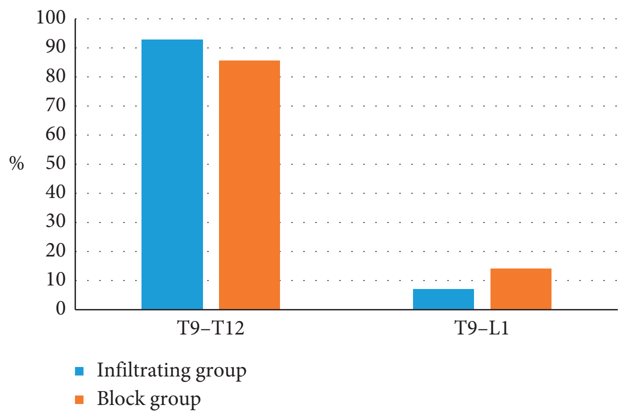

Figure 6: Contrast of block plane distribution.

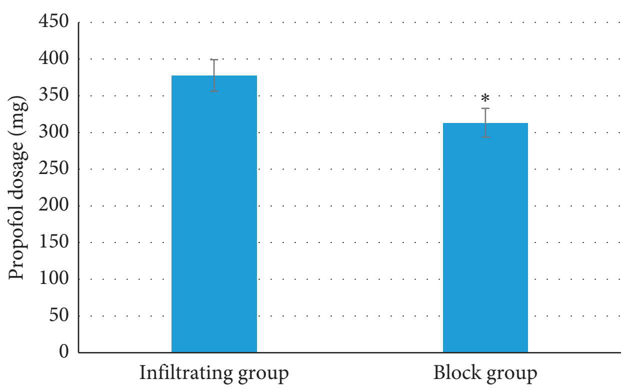

Figure 7: Contrast of propofol dosage during surgery between the two groups. Note: * meant $P < 0.05$ versus infiltrating group, the same for Figures 8 and 9.

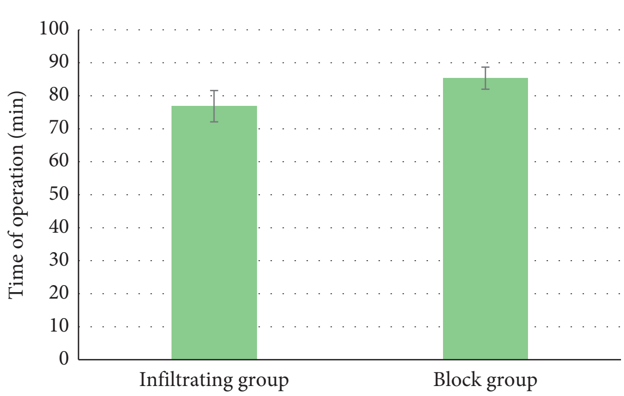

Figure 8: Contrast of surgery time between two groups of patients.

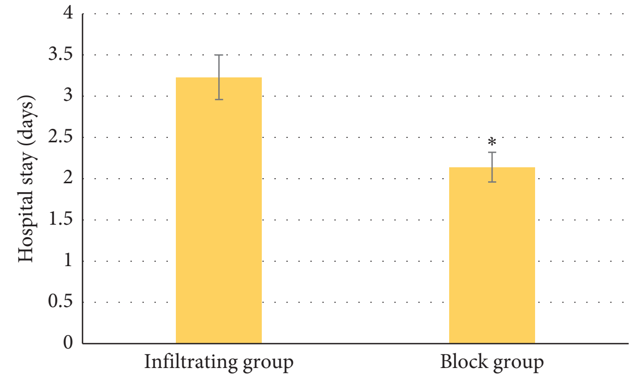

Figure 9: Contrast of length of stay between two groups of patients.

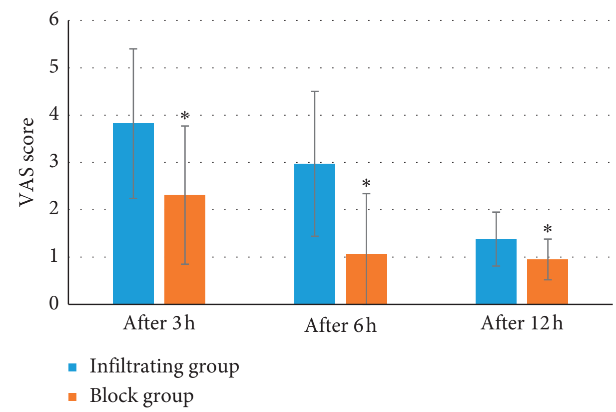

Figure 10: VAS score of postoperative pain of patients. Note: * meant $P < 0.05$ versus infiltrating group.

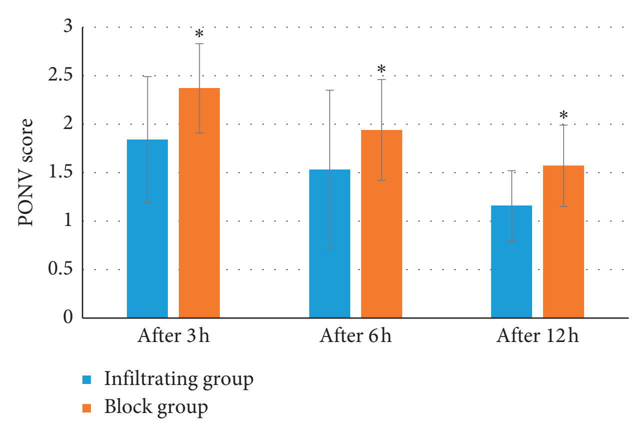

Figure 11: PONV score of postoperative pain of patients. Note: * meant $P < 0.05$ versus infiltrating group.

patient in the block group used tramadol. 12 hours after the operation, one patient in the block group was treated with tramadol. 3 hours after the operation, 9 patients in the infiltration group used tramadol. 6 hours after the operation, 7 patients in the infiltration group used tramadol. 12 hours after the operation, 3 patients in the infiltration group received tramadol. The difference between the two groups at each time point was obvious ($P < 0.05$) (Figure 12).

4. Discussion

Pain after laparoscopic gynecological surgery includes pain at the incision site of abdominal surgery, pain in internal organs around organs, pain caused by phrenic nerve stimulation, and pain caused by tissue inflammation caused by surgery. Blanco et al. [10] deemed that the utilization of

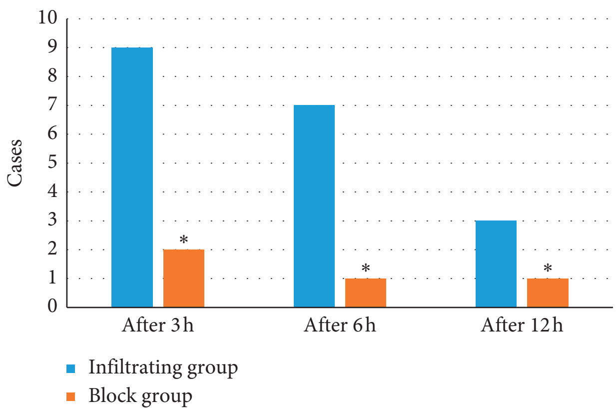

Figure 12: Contrast of the number of cases using tramadol in the two groups. Note: * meant $P < 0.05$ versus infiltrating group.

posterior approach for TAP block had a certain relief effect on peripheral visceral pain. Öksüz et al. [11] pointed out that the TAP block method can reduce the pain in the front of the abdomen, but it cannot reduce the pain in the internal organs. Studies have reported that intravenous injection of propofol before surgery can prevent the synthesis of cyclooxygenase and reduce the prostatic hormone content of the surgical site, thereby achieving the purpose of analgesia [12]. This work revealed that when patients received propofol combined with TAP block, in contrast to the infiltrating group, the dose of propofol used in the block group was greatly reduced during surgery, which can significantly reduce the pain VAS score after surgery, and the results were consistent with the above research results.

Previous studies have pointed out that local anesthetics combined with nerve block can reduce the dosage of opioid analgesics [13]. The results showed that the VAS scores and PONV scores of patients with TAP block decreased evidently at 3 h, 6 h, and 12 h after surgery, and the number of patients who used tramadol for analgesic remedy after surgery was reduced, which greatly improved patient satisfaction. The results were consistent with those of Zhang et al. [14].

TAP block adopted the water separation method to separate and diffuse local anesthetics and utilized local anesthetics to infiltrate the blocked nerves. The low concentration of local anesthetics will make the analgesic effect insignificant, while the high concentration will increase the drug concentration in plasma. Therefore, TAP block requires the adoption of appropriate drug concentration and dosage [14]. In this work, 20 mL of 0.375% ropivacaine was used to observe the block plane distribution between the two groups within 30 minutes after the TAP block, and the difference was not considerable ($P < 0.05$). Sun et al. [15] performed GLS on women after TAP block, and the concentrations of ropivacaine were 0.25%, 0.40%, and 0.45%, respectively, and the dosage was 40 mL. Plasma levels of ropivacaine in each group were measured after TAP block. The results showed that the maximum blood concentration changed with the injection. Adverse reactions to local anesthetics generally occurred within 10 minutes after completion of TAP block. The results of this work were different from those of the above studies, which may be related to the cases of the patients in this work, and it should further determine the concentration of ropivacaine in the blood.

5. Conclusion

Wavelet transform was adopted to enhance the ultrasound images, and it was revealed that the algorithm can enhance the image contrast, and the denoising effect was very strong. Ultrasound imaging technology was utilized to intuitively guide the direction of needle insertion during puncture, and it was proved that 0.375% ropivacaine can accurately enter the TAP, maximizing the analgesic effect. It also reduced the VAS score and PONV score of patients after surgery and reduced the incidence of postoperative analgesia. Moreover, the amounts of opioid analgesics during the GLS perioperative period and the occurrence of malignant reactions were also reduced. In contrast to the previous intravenous analgesia treatment, it greatly improved the comfort and satisfaction of patients after surgery. The limitation of this study is that only the clinical effects of the two groups of patients were compared, yet the concentration of ropivacaine in the blood was not further measured. In conclusion, local anesthetic combined with TAP block was used in this work, which provided a good reference for clinical GLS perioperative period.

Data Availability

No data were used to support this study.

Conflicts of Interest

The authors declare that they have no conflicts of interest.

References

[1] S. Uccella, V. A. Capozzi, M. Ricco' et al., "Sexual function following laparoscopic versus transvaginal closure of the vaginal vault after laparoscopic hysterectomy: secondary analysis of a randomized trial by the Italian society of gynecological endoscopy using a validated questionnaire," *Journal of Minimally Invasive Gynecology*, vol. 27, no. 1, pp. 186–194, 2020.

[2] T. Wedel, J. Ackermann, H. Hagedorn, L. Mettler, N. Maass, and I. Alkatout, "Educational training in laparoscopic gynecological surgery based on ethanol-glycerol-lysoformin-preserved body donors," *Annals of Anatomy*, vol. 221, pp. 157–164, 2019.

[3] N. Ma, J. K. Duncan, A. J. Scarfe, S. Schuhmann, and A. L. Cameron, "Clinical safety and effectiveness of transversus abdominis plane (TAP) block in post-operative analgesia: a systematic review and meta-analysis," *Journal of Anesthesia*, vol. 31, no. 3, pp. 432–452, 2017.

[4] C. Ping-Chen, Q.-S. Lin, and X.-Z. Lin, "Optimal concentration of the transversus abdominis plane block in enhanced recovery after surgery protocols for patients of advanced age undergoing laparoscopic rectal cancer surgery," *Journal of International Medical Research*, vol. 46, no. 11, pp. 4437–4446, 2018.

[5] C. J. Boushey, M. Spoden, F. M. Zhu, E. J. Delp, and D. A. Kerr, "New mobile methods for dietary assessment:

review of image-assisted and image-based dietary assessment methods," *Proceedings of the Nutrition Society*, vol. 76, no. 3, pp. 283–294, 2017.
[6] S. Jorge, K. Pereira, H. López-Fernández et al., "Ultrasonic-assisted extraction and digestion of proteins from solid biopsies followed by peptide sequential extraction hyphenated to MALDI-based profiling holds the promise of distinguishing renal oncocytoma from chromophobe renal cell carcinoma," *Talanta*, vol. 206, Article ID 120180, 2020.
[7] A. C. Abraham, L. K. Cheng, T. R. Angeli, S. Alighaleh, and N. Paskaranandavadivel, "Dynamic slow-wave interactions in the rabbit small intestine defined using high-resolution mapping," *Neuro-Gastroenterology and Motility*, vol. 31, no. 9, Article ID e13670, 2019.
[8] M. Sadek, C. Roger, S. Bastide et al., "The influence of arm positioning on ultrasonic visualization of the subclavian vein," *Anesthesia & Analgesia*, vol. 123, no. 1, pp. 129–132, 2016.
[9] M. Zhao, L. Du, L. Qi, Y. Li, Y. Li, and X. Li, "Numerical simulations and electrochemical experiments of the mass transfer of microvias electroforming under ultrasonic agitation," *Ultrasonics Sonochemistry*, vol. 48, pp. 424–431, 2018.
[10] R. Blanco, T. Ansari, W. Riad, and N. Shetty, "Quadratus lumborum block versus transversus abdominis plane block for postoperative pain after cesarean delivery," *Regional Anesthesia and Pain Medicine*, vol. 41, no. 6, pp. 757–762, 2016.
[11] G. Öksüz, B. Bilal, Y. Gürkan et al., "Quadratus lumborum block versus transversus abdominis plane block in children undergoing low abdominal surgery," *Regional Anesthesia and Pain Medicine*, vol. 42, no. 5, pp. 674–679, 2017.
[12] S. Sen, S. Arulkumar, E. M. Cornett et al., "New pain management options for the surgical patient on methadone and buprenorphine," *Current Pain and Headache Reports*, vol. 20, no. 3, p. 16, 2016.
[13] R. Aslan, A. Erbin, S. Celik, B. Ucpinar, R. Eryilmaz, and K. Taken, "Periprostatic nerve block alone versus combined with perineal pudendal nerve block or intrarectal local anesthesia during transrectal ultrasound-guided prostate biopsy: a prospective randomized controlled trial," *International Journal of Urology*, vol. 26, no. 8, pp. 833–838, 2019.
[14] X.-h. Zhang, Y.-j. Li, W.-q. He et al., "Combined ultrasound and nerve stimulator-guided deep nerve block may decrease the rate of local anesthetics systemic toxicity: a randomized clinical trial," *BMC Anesthesiology*, vol. 19, no. 1, p. 103, 2019.
[15] N. Sun, S. Wang, P. Ma, S. Liu, A. Shao, and L. Xiong, "Postoperative analgesia by a transversus abdominis plane block using different concentrations of ropivacaine for abdominal surgery," *The Clinical Journal of Pain*, vol. 33, no. 9, pp. 853–863, 2017.

Hindawi
Journal of Healthcare Engineering
Volume 2021, Article ID 5755671, 8 pages
https://doi.org/10.1155/2021/5755671

Research Article

Effect of Interventional Therapy on Iliac Venous Compression Syndrome Evaluated and Diagnosed by Artificial Intelligence Algorithm-Based Ultrasound Images

Ye Bai,[1] **Fei Bo**,[2] **Wencan Ma**,[3] **Hongwei Xu**,[3] **and Dawei Liu**[4]

[1]*Department of Interventional Operating, Chengde City Central Hospital, Chengde 067000, Hebei, China*
[2]*Department of Ultrasound Diagnosis, Chengde City Central Hospital, Chengde 067000, Hebei, China*
[3]*Department of Radiology, Chengde City Central Hospital, Chengde 067000, Hebei, China*
[4]*Department of Interventional Vascular Surgery, Chengde City Central Hospital, Chengde 067000, Hebei, China*

Correspondence should be addressed to Dawei Liu; cdszxyyjrxgwk@chengde.gov.cn

Received 20 May 2021; Revised 6 July 2021; Accepted 16 July 2021; Published 22 July 2021

Academic Editor: Enas Abdulhay

In order to explore the efficacy of using artificial intelligence (AI) algorithm-based ultrasound images to diagnose iliac vein compression syndrome (IVCS) and assist clinicians in the diagnosis of diseases, the characteristics of vein imaging in patients with IVCS were summarized. After ultrasound image acquisition, the image data were preprocessed to construct a deep learning model to realize the position detection of venous compression and the recognition of benign and malignant lesions. In addition, a dataset was built for model evaluation. The data came from patients with thrombotic chronic venous disease (CVD) and deep vein thrombosis (DVT) in hospital. The image feature group of IVCS extracted by cavity convolution was the artificial intelligence algorithm imaging group, and the ultrasound images were directly taken as the control group without processing. Digital subtraction angiography (DSA) was performed to check the patient's veins one week in advance. Then, the patients were rolled into the AI algorithm imaging group and control group, and the correlation between May–Thurner syndrome (MTS) and AI algorithm imaging was analyzed based on DSA and ultrasound results. Satisfaction of intestinal venous stenosis (or occlusion) or formation of collateral circulation was used as a diagnostic index for MTS. Ultrasound showed that the AI algorithm imaging group had a higher percentage of good treatment effects than that of the control group. The call-up rate of the DMRF-convolutional neural network (CNN), precision, and accuracy were all superior to those of the control group. In addition, the degree of venous swelling of patients in the artificial intelligence algorithm imaging group was weak, the degree of pain relief was high after treatment, and the difference between the artificial intelligence algorithm imaging group and control group was statistically considerable ($p < 0.005$). Through grouped experiments, it was found that the construction of the AI imaging model was effective for the detection and recognition of lower extremity vein lesions in ultrasound images. To sum up, the ultrasound image evaluation and analysis using AI algorithm during MTS treatment was accurate and efficient, which laid a good foundation for future research, diagnosis, and treatment.

1. Introduction

Iliac vein compression syndrome (IVCS) is called Cockett syndrome and May–Thurner syndrome. It is a disease of physiological changes such as changes in the venous pressure of the lower extremities and venous return disorders caused by continuous compression of the iliac veins, which is also a common disease in clinical vascular disease [1]. In the early 1957, May and Thurner first proposed the anatomical basis of IVCS through autopsy research. Since the position of the iliac vein is different from the usual anatomy, the left common iliac vein receives the pressure of the bone and the stimulation of the blood vessels from the right common iliac artery and the lumbar spine. Compression of the left common iliac vein is the most common clinical case [2–4]. In addition, other general factors such as abdominal aorta, bladder disease, local kidney, pelvic tumor, and other high branches would also put pressure on the iliac vein [5–7]. The most important methods for detecting IVCS include ultrasound, computed tomography (CT), magnetic resonance imaging (MRI), and positron emission tomography (PET) [8–11]. To save time and money, ultrasound has become the first choice for IVCS. However, the iliac vein compression point is combined with the surrounding mechanism in the ultrasound image of IVCS, which is difficult to distinguish with the naked eye. Due to the various experiences of doctors, needle biopsy, ablation, and other surgical treatment methods are used for various diagnostic results. Sometimes when surgery is not needed, it will bring unnecessary worry to the patient. Therefore, the correct detection and diagnosis of iliac vein disease is very important [12].

With the rapid expansion of AI's core technology, the in-depth learning model in the field of medical image diagnosis has been improved. A deep learning mode was established in the recognition of iliac vein compression points based on ultrasound images to realize the classification of the severity of various lesions and automatically identify the disease and effectively help doctors to diagnose and treat it. Due to different compression point sizes, shapes, and textures, the establishment of an accurate and effective recognition model is of specific research value and clinical application value. Since the application of AI in medical treatment, especially the development of deep learning in images, many deep learning methods have been applied to medical image processing. The convolutional neural network (CNN) is the most common network model in image extraction. All effective networks include networks that provide excellent results for daily graphics, including the residual neural network, dense convolutional neural network (DenseNet), Mobile Net, and the top-ranked ImageNet network [13]. However, vein ultrasound images have higher noise and higher volatility compared with ordinary images, and the imaging of the vein end is not obvious. The common network limits the extraction of edges and textures. In addition, the resolution of the traditional convolution kernel gradually decreases as the number of layers increases, which can reduce the acquisition of more detailed position information [14–16]. Hole convolution has a wider field of view under the same convolution kernel size compared with traditional convolution.

A dense multireceptive field convolutional neural network based on AI was proposed in this research. It can detect iliac vein compression lesions efficiently and accurately and can evaluate the effectiveness of contrast-enhanced ultrasound in the diagnosis of iliac vein compression by different methods. In addition, a model that can automatically identify compression points was constructed based on deep learning methods to reduce the workload of clinicians.

2. Methods

2.1. Research Objects. A total of 280 CVD and DVT inpatients (363 affected limbs) in the hospital from January 2017 to January 2021 were selected as the research objects. There were 194 patients with nonthrombotic CVD (265 limbs), including 126 males and 68 females, aged from 25 to 80 years, with an average age of 40.7 ± 11.24 years. There were 90 patients with DVT (98 limbs), including 45 males and 45 females, aged from 25 to 80 years, with an average age of 60.23 ± 12.15 years. The patient's general information, clinical symptoms, history of intravenous treatment, and thrombus cases were recorded.

Inclusion criteria: (i) clinical inpatients diagnosed with CVD or DVT after vascular surgery and (ii) ultrasound and DSA examination of the iliac vein were performed before surgery or surgical treatment, and no venous related treatment was performed.

Exclusion criteria: (i) other diseases may lead to varicose veins (such as Budd–Chiari syndrome), right heart failure, pelvic tumors, pregnancy, and other lower limb venous insufficiency; (ii) diseases affecting the amount of blood in large amounts of chest, ascites, and hypoproteinemia; and (iii) patients who were allergic to contrast media and cannot be tested with DSA.

Patients were randomly rolled into the AI algorithm imaging group and control group according to ultrasound diagnosis results.

In this study, a total of 284 patients with IVCS met the above inclusion criteria and exclusion criteria. This study had been approved by the medical ethics committee of the hospital, and the families of the patients included in the study had all signed informed consent.

2.2. Data Acquisition and Image Analysis

2.2.1. Ultrasonic Data Acquisition. The patient needed to fast for more than eight hours before the ultrasound examination of the iliac vein. The patient was in a supine position with his lower extremities slightly eversion. Two-dimensional ultrasonic imaging (2D-US), color Doppler flow imaging (CDFI), and color Doppler energy imaging (CDE) were performed to analyze the energy imaging, vascular enhancement technology (VET), and pulse wave (PW). The abnormal echo of the iliac vein cavity, stenosis, or dilation was observed, so did the formation of collateral blood circulation, the reflux and abnormal echo of the internal bowel veins, and the expansion of the venous cavity of the lower extremities.

2.2.2. Equipment. A 52000 type Doppler ultrasonic diagnostic device was used. The 4c1 convex array detection frequency was 14 mHz, and the 9l4 linear array detection frequency was 4×9 mHz. Philips FD2.0 digital subtraction angiography machine was employed.

2.3. Experimental Environment

2.3.1. Convolutional Layer Model Construction. CNN realizes image point extraction through convolutional layers. The convolutional layer requires fewer parameters compared with the fully connected layer (the number of weights does not change with the size of the image). In the convolutional layer, the image convolution operation shares the weight of the network. Therefore, the model does not require separate detectors for the same object, and the network translation is consistent with the input result. The convolution operation is between the first layer and the second layer, and the complete connection operation is between the third layer and the fourth layer. Figure 1 shows a schematic diagram of a convolutional layer and a fully connected layer. The dense multireceptive field CNN (DMRF-CNN) was utilized to extract features from ultrasound images of thyroid nodules. The method of multiporosity convolution and dense connection was used to extract the features of the nodules and transfer the features. "d-x-conv-y" represents the feature map obtained after this kind of hole convolution, x represents the size of the hole rate ($x \in \{2, 3, 4\}$), and y represents the number of convolutional layers. "conv" represents the feature map after the traditional convolution kernel convolution, that is, the convolution kernel with a hole rate of 1, which is equivalent to "d1conv-y." "Cx" represents different cross-layer connections, and different colors represent the feature maps obtained after convolution kernels with different void ratios. This model realizes the fusion of multiple receptive fields with the help of four convolution kernel fusion methods with different void ratios, which can not only achieve the goal but also reduce the parameters and prevent overfitting to a certain extent. In addition, for each dilated convolution module (Dilated Conv), the convolution module of the 0Darknet network was used. A 3×3 convolution kernel was utilized, and then, a batch normalization layer was employed to normalize the feature map to prevent the gradient from disappearing, and finally, the LeakyReLU activation function was used. In the DMRF-CNN, information between various layers is exchanged through dense cross-layer connections. The fusion of deep-level feature maps with shallow-level feature maps can make edge features well recognized.

2.3.2. R-CNN. Figure 2 shows the flowchart of the R-CNN (Region-CNN), which is classified into three stages: generating regions of interest, feature extraction based on convolutional neural networks, and classification and positioning.

Since the R-CNN uses a selective search method to generate about 2,000 regional feature points for each image, accurate data points can be selected and the search space can be reduced in target detection. Therefore, the AlexNet CNN is used to extract the features of the image. Because of the automatic AI of the network, it can learn data processing and gradually improves the accuracy.

2.3.3. Dataset and Evaluation Criteria. The dataset from the hospital physical examination center was utilized to conduct the experiment, and finally, 699 vein images were selected, among which each image contained at least one lesion point. Venous compression images of 34 men and 177 women were extracted. The sample underwent data expansion, and the process included color dithering, changing saturation, exposure, and color. In particular, the aspect ratio of the lesion point may interfere with the judgment of the disease, so the random angle change was not used in this experiment. After zooming in, 10,377 images were obtained. Figure 3 shows the detailed number of training sets and test sets.

2.3.4. Deep Learning Mode. In this experiment, the compression site of the vein was first obtained, and then, the vein ultrasonic image was edited out with the same size, i.e., 240×240. Different models were used to categorize data graphs. In the experiment, the probability gradient descent algorithm was used to upgrade the quality and efficiency. The learning efficiency at the beginning of the experiment was 0.01, the number of iterations was 600, and the final training time of the model was about 4 hours. In addition, the rate of Jitter was set to 0.3 during data amplification. The ultrasonic image was edited and randomly inverted at a rate of 0.3. The chroma and exposure was set to 2.5 and the hue to 0.1 to represent the random generation of the image in the range of 0.05–0.12 tones. A 3070 graphics card (13G memory), 8-core CPU, and 16G memory were used to implement the model and Kersa architecture for training as the experimental environment.

2.4. Treatment Methods

2.4.1. Treatment Measures. The patient's physical data and the lower extremity venous ultrasound results were recorded. A lateral thigh artery puncture was performed by the Seldinger method in the supine position, depending on the polymortem level, which was through the affected vein in advance of B ultrasound. The sheath of 6F was inserted. The degree, location, extent, and collateral circulation of iliac vein stenosis were determined by angiography. If the skeleton has severe narrowing in the vein or occlusion of the vein, adjuvant treatment can be done through the spinal canal at the occlusion site. Reconfirming of the angiogram in the inferior great vein was carried out, and severe stenosis or occlusion can be found in images with small openings in the lumen. To open the narrow part of the iliac vein, the loach guide wire was inserted. A V-18 guide wire was used to pass through the occlusion without opening. With the majority of the orbital catheter, the majority of the lesions were detected. After balloon dilation, the lesion segment of angiogram intestinal venous stenosis was less than 50%, the vascular elasticity recovery was reduced to 1/3, or the balloon dilation was performed after peripheral collateral circulation was greatly reduced.

2.4.2. Anticoagulation Therapy and Compression Therapy. To prevent puncture bleeding after intracavitary treatment, sterile gauze and elastic bandage should be used for pressure protection of puncture site and 12 h clinical observation. Anticoagulant therapy referred to a subcutaneous injection of low molecular weight heparin (LMWH) with oral administration of Beritol 10 mg twice daily for three months. For patients with high thrombosis risk factors, this may be extended to six months. Patients needed to wear stretch socks for six months after discharge.

2.4.3. Diagnostic Criteria and Cure Indicators. Ultrasonic diagnostic criteria were as follows. During CT venography of completely obstructed thrombosis, this segment of blood

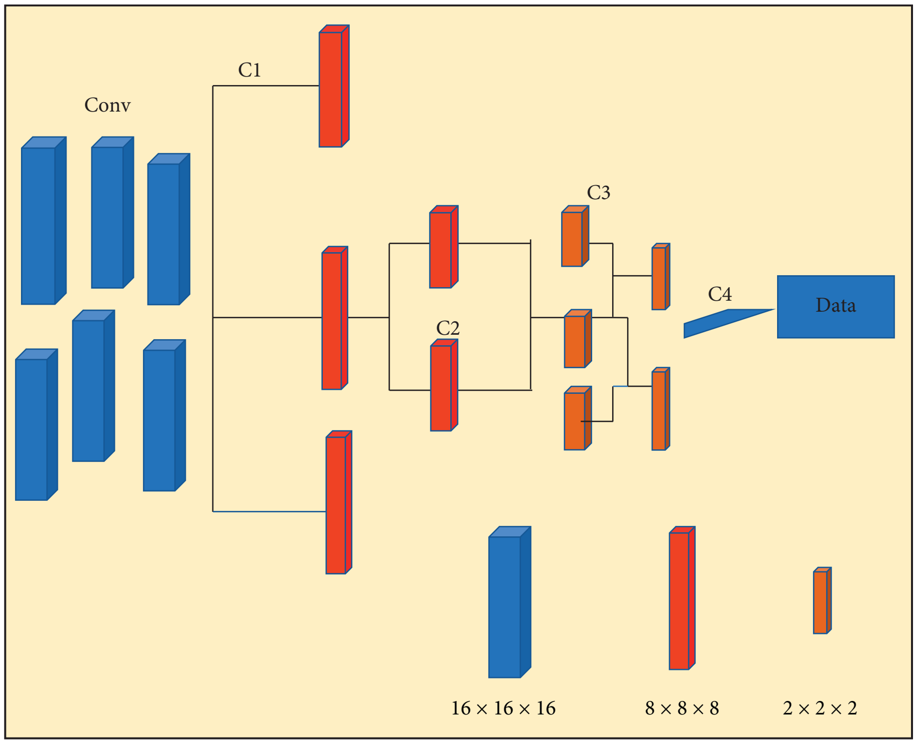

Figure 1: Schematic diagram of the convolutional layer and fully connected layer.

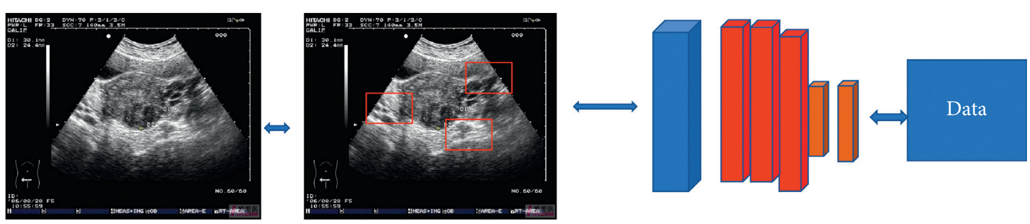

Figure 2: Flowcharts of the R-CNN.

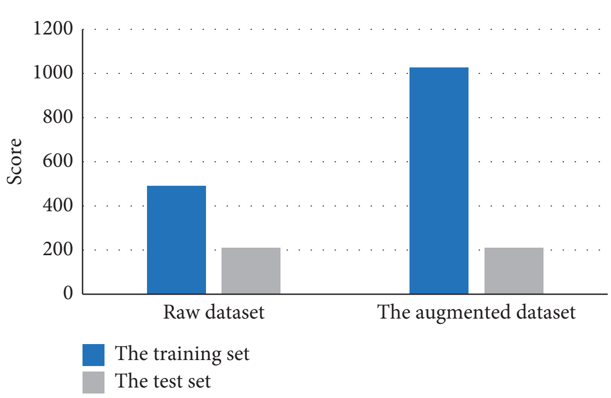

Figure 3: Detailed number of the training set and test set.

vessel did not develop at all or showed signs of sudden interruption of contrast medium at a certain level. For incomplete obstructed thrombosis, CT venography showed cylindrical or low-density contrast areas with different lengths in the venous lumen, and the edge of the venous lumen may have orbit disease caused by the contrast agent alignment. After mechanization and recanalization, CT venography showed that the venous lumen was irregular, narrow, and multibranched, partly dilated, or even twisted. Collateral circulation was established, and CT venography showed irregular collateral vein development around the obstructed vessel. Physical examination of the affected limb was implemented to assess relief of symptoms associated with venous hypertension in the lower extremity with a venous clinical severity score (VCSS). The VCSS scale includes ten clinical symptoms, such as, pain, varicose veins, venous edema, pigmentation, inflammation, sclerosis, number of ulcers, duration of ulcers, diameter of ulcers, and compression treatment. According to the classification of none, light, medium, and heavy, the corresponding score is 0, 1, 2, and 3. The patency rate of the stent was examined by color Doppler ultrasonography or venography to evaluate the patency of the venous outflow tract.

2.4.4. Follow-Up after Treatment. Hospitalization or telephone appointments were made at 3 months, 6 months, and 1 year. Patients were required to wear stretch socks and take anticoagulants. To assess the VCSS for reducing symptoms associated with venous hypertension of the lower extremities, physical examinations of the limbs were performed. The VCSS included ten clinical symptoms, such as varicose veins, edema of veins, pain, pigmentation, inflammation, sclerosis, number of ulcers, duration of ulcers, and diameter of ulcers. The patency rate of the stent was examined by color Doppler ultrasound or venography, and the smoothness of the venous outflow path was assessed.

2.5. Statistical Processing. SPSS 20.0 was employed for statistical analysis. The data were expressed as n, and the chi-square test was used for comparison in the same group. The measurement data were expressed as positive and negative standard deviations, and the normality test and the variance homogeneity test were performed before the analysis of the two sets of measurement data. The t-test was used for the comparison of the average between the normal groups, and the rank sum test was used to compare the mean between groups for normality. When $p < 0.005$, the difference was statistically significant.

3. Results

3.1. Evaluation of Hole Convolution. Figure 4 shows the difference comparison of the feature extraction effect of the hole convolution with four different kinds of hole ratios. When the hole ratio was two, the effect was ideal. In addition, the accuracy of vein compression image recognition can be improved to a certain extent by introducing the hole ratio. Figure 5 shows the segmentation and lesion identification of venous compression ultrasound images.

3.2. Comparison between Different Models. Figure 6 shows the segmentation comparison between different models. In the traditional feature extraction method, the recall rate was very high and the accuracy was very low. The deep learning methods improved accuracy compared with traditional feature extraction methods. However, the recall rate and accuracy of these methods had changed a lot, and the stability of model recognition was not good. The recall rate and accuracy of the DMRF-CNN were not significantly different. Therefore, the DMRF-CNN had good stability for identifying venous compression points and achieved good accuracy. Figure 7 shows the efficiency graph compared with other feature extraction methods.

3.3. Technical Success Rate. Sixty-six patients in the two groups successfully completed endovascular treatment for iliac vein stenosis or occlusion. After endovascular treatment, angiography confirmed different degrees of intestinal vein stenosis or occlusion, and the pelvic side blood circulation was significantly reduced. Twenty-three patients with venous flow received a second treatment in the observation group. Figure 8 shows that there was no statistical difference in the ratio of venous flow between the two groups.

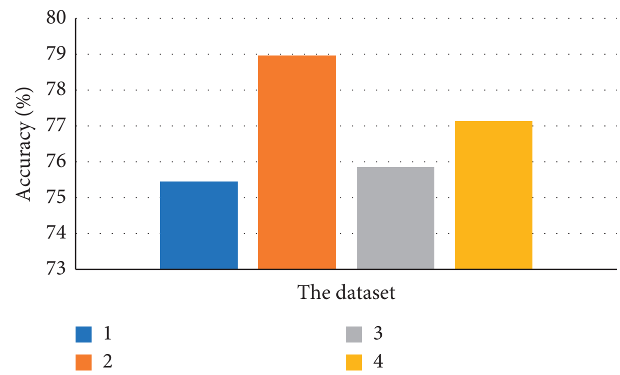

Figure 4: The influence of four kinds of hole convolutions on the feature extraction effect (1, 2, 3, and 4 represent four kinds of hole rate labels).

3.4. Relief of Intravenous Clinical Symptoms. The analgesic rate of 66 patients in the angiographic group was 88.42% and that in the control group was 86.3%. Most of the symptoms of limb swelling disappeared, and the patients' pain significantly reduced. The swelling rate of the angiographic group was 91.1%, and the swelling rate of the control group was 89.72%. Among patients with compound ulcers, the ulcer cure rate in the observation group was 83.20% in groups with different improvement and cure degrees. The average VCSS score at 3 months after treatment was 11.37 ± 3.12 points, that at 6 months after treatment was 7.98 ± 3.66, that at 12 months after treatment was 7.33 ± 2.12, that at 24 months after treatment was 15.15 ± 4.57, and that at 36 months after treatment was 14.33 ± 2.13. The average VCSS score of each follow-up point was 6.53 ± 2.33, which was lower than that before treatment, and there were statistical differences before and after treatment ($p < 0.005$). Therefore, the treatment method of the angiography group was effective. Figure 9 shows the comparison of pain relief rates between the two groups.

Comparison of VCSS scores before treatment, 3 months after treatment, and 6 months after treatment between the two groups showed that $p > 0.005$. There was no difference in the severity of intravenous clinical symptoms between the two groups before treatment. The curative effect was equivalent within 6 months. The average score of VCSS at 12 months after treatment, 24 months after treatment, and 36 months after treatment was compared, and there were statistical differences, $p < 0.005$. The average VCSS score of the angiographic group was significantly lower than that of the control group, indicating that the angiographic group had a more significant clinical effect than the control group in the midterm effect at 12, 24, and 36 months. Figure 10 shows the comparison of VCSS scores between the two groups at 3, 6, 12, 24, and 36 months after treatment.

The VCSS scores before treatment, 3 months after treatment, and 6 months after treatment were compared, and $p > 0.05$. The severity of intravenous clinical symptoms was compared between the two groups within 6 months, and there was no difference between the two groups. The average VCSS score at 12 months after treatment, 24 months after treatment, and 36 months after treatment was compared,

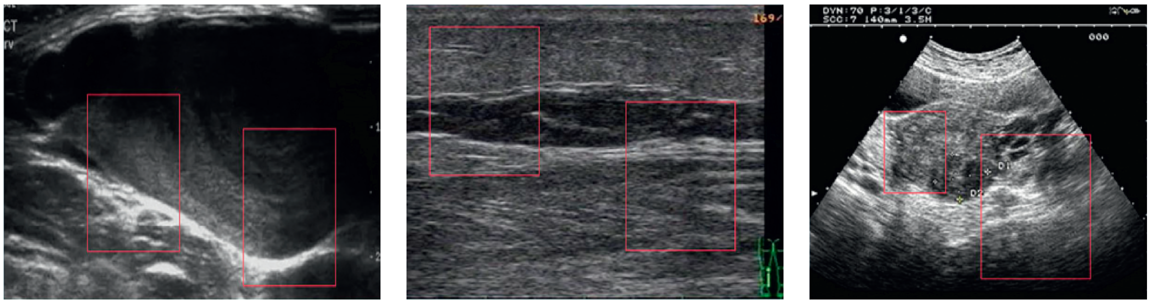

(a) (b) (c)

Figure 5: The effect of hole convolution on feature extraction (The red parts are the focus points extracted by the artificial intelligence algorithm, and the three images are from three randomly selected patients).

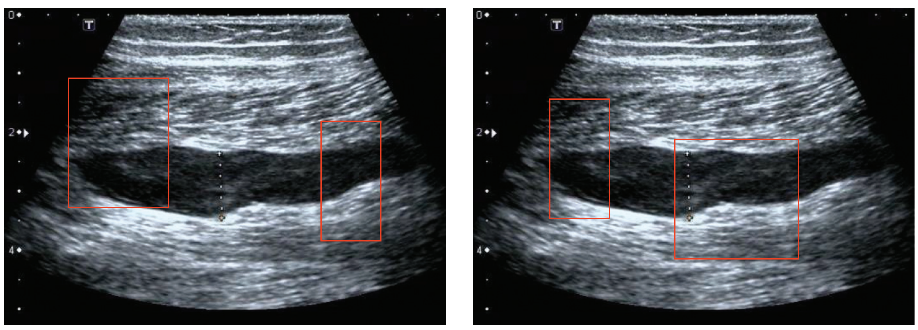

(a) (b)

Figure 6: Traditional extraction method (a) and DMRF-CNN extraction (b) (the red parts are the focus points extracted by the artificial intelligence algorithm).

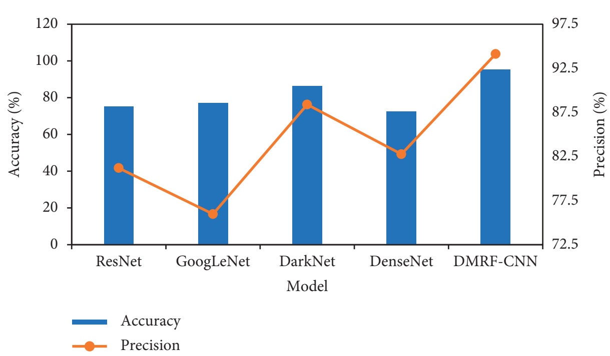

Figure 7: Accuracy and precision comparison with other model extraction methods.

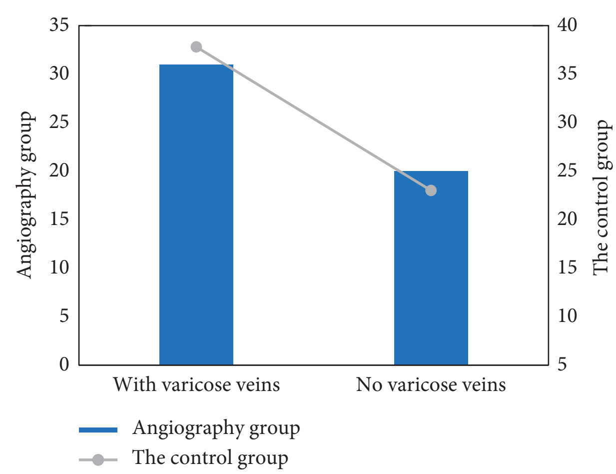

Figure 8: The proportion of varicose veins in the two groups.

and the results showed statistical differences, $p < 0.005$. The average VCSS score of the control group was significantly lower than that of the angiographic group. Significant effects were achieved within 12, 24, and 36 months. Figure 10 shows the comparison of the VCSS scores of the two groups at 3, 6, 12, 24, and 36 months after treatment.

4. Discussion

IVCS is caused by a series of clinical symptoms of pelvic or venous return disorders due to venous pressure and/or an unusual bonding structure. The main manifestations are lower extremity skin pigmentation, lower extremity vein collapse, and spermatic vein flow [17]. MTS was thought to be a rare disease in the past. With the development of imaging techniques and improved understanding of MTS, it has been applied to a variety of lesions; however, the extent of its use is now overrated. Compression of the right common iliac vein is rare and is related to anatomical differences between the bony veins of the two intestines. The high rate of MTS in young women may be related to the

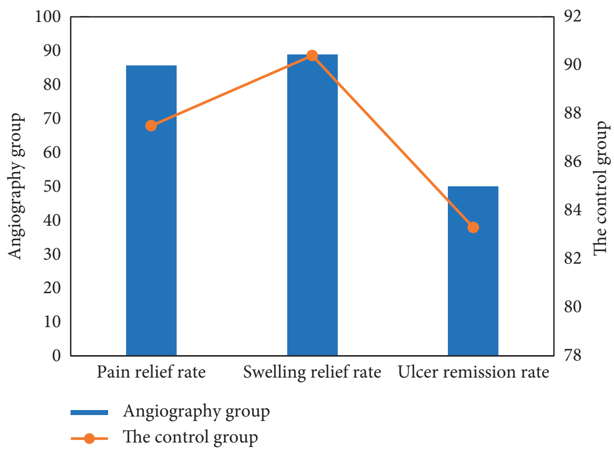

Figure 9: Comparison of pain relief rates between the two groups.

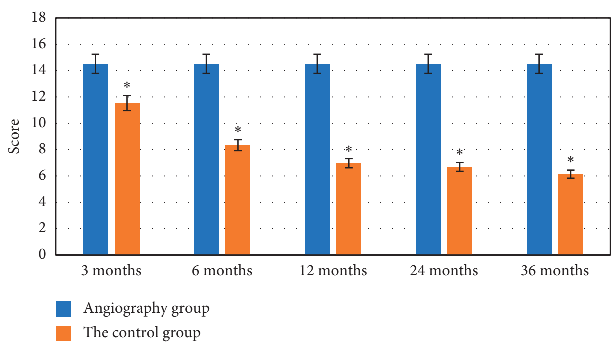

Figure 10: Comparison of VCSS scores between the two groups at 3, 6, 12, 24, and 3 months after treatment. *Significance of the difference.

obvious lumbar vertebra physiology of women and the long-term use of contraceptives in young women. The extent of enteric venous compression stenosis is not well defined. Collateral circulation may be observed by imaging [18].

With the improvement of people's living standard and the progress of medical technology, many people can get a physical examination at a very low cost. Intravenous compression examination is one of the most common items of physical examination. This has also led to an increase in the detection rate of venous compression syndrome. In addition, the same compression site can be identified with different results, depending on the clinician's clinical judgment. In addition, the gap between urban and rural medical level also makes it difficult for the county hospitals to distinguish compression lesions. Experience is likely to lead to overtreatment of patients [19]. It brings unnecessary pain and burden to patients. To solve this problem, an effective deep learning framework was proposed in this research to help doctors identify and judge the disease.

The general structure flowchart of this method was proposed and compared with other backbone networks based on YOLOV3. The dataset for comparison was from our hospital, and 699 ultrasound images of thyroid nodules were eventually collected. The graph features on the test set and detection time were used to evaluate the validity of the model. Then, YOLOV3-DMRF was verified to have the best detection performance. The graph features reached 91.77% in the dataset collected by myself, and the detection time was 4.2 seconds. In the open dataset, the mapping reached 94.72%, and the detection time was 2.3 seconds. To prove the feature extraction effect of the DMRF-CNN, the classification performance of the DMRF-CNN was compared with that of other AI networks. Finally, it was proved that the DMRF-CNN was superior to other CNNs in classification performance based on different evaluation criteria.

5. Conclusion

The contrast-enhanced ultrasound images were used in the treatment of venous compression syndrome. Compared with the lesion site manually delineated by the doctor on the angiography image, the method proposed in this study had little difference in both the therapeutic effect and the convenience of operation. This method significantly shortened the time needed for outlining compared with traditional manual segmentation. In the future, it needs to verify the performance of our model in more centers, CEUS models, and more disease types. In addition, to study various parameters of image formation based on this method, its clinical diagnosis and prognosis prediction need to be further studied.

Data Availability

The data used to support the findings of this study are available from the corresponding author upon request.

Conflicts of Interest

The authors declare that they have no conflicts of interest.

Authors' Contributions

Ye Bai and Fei Bo contributed equally to this work.

References

[1] M. Castellana, C. Castellana, and G. Treglia, "Performance of five ultrasound risk stratification systems in selecting thyroid nodules for FNA," *Journal of Clinical Endocrinology & Metabolism*, vol. 105, no. 5, pp. 1659–1669, 2020.

[2] Z. Hou, J. Zhao, and J. Sun, "Inner focus iterative reconstruction method with the interlaced phase stepping scanning for grating-based phase contrast tomography," in *Proceedings of 41st Annual International Conference of the IEEE Engineering in Medicine and Biology Society (EMBC)*, pp. 6251–6254, IEEE, Berlin, Germany, July 2019.

[3] Y. Wang, W. Liu, Y. Yu et al., "CT radiomics nomogram for the preoperative prediction of lymph node metastasis in gastric cancer," *European Radiology*, vol. 30, no. 2, pp. 976–986, 2020.

[4] S. Chang, M. Li, H. Yu et al., "Spectrum estimation-guided iterative reconstruction algorithm for dual energy CT," *IEEE Transactions on Medical Imaging*, vol. 39, no. 1, pp. 246–258, 2020.

[5] Y. Chen, S. Hu, H. Mao, W. Deng, and X. Gao, "Application of the best evacuation model of deep learning in the design of

public structures," *Image and Vision Computing*, vol. 102, Article ID 103975, 2020.
[6] J. Li, Y. Tan, D. Zhang et al., "Value and necessity of pelvic CT in gastric cancer staging: an observational study," *Scandinavian Journal of Gastroenterology*, vol. 53, no. 9, pp. 1097–1099, 2018.
[7] G. Sun, C. Cheng, X. Li, T. Wang, J. Yang, and D. Li, "Metabolic tumor burden on postsurgical PET/CT predicts survival of patients with gastric cancer," *Cancer Imaging*, vol. 19, no. 1, p. 18, 2019.
[8] C. W. Shen and J. T. Ho, "Technology-enhanced learning in higher education: a bibliometric analysis with latent semantic approach," *Computers in Human Behavior*, vol. 104, Article ID 106177, 2020.
[9] S. Schur, P. Martel, and J. Marcoux, "Optimal bone flap size for decompressive craniectomy for refractory increased intracranial pressure in traumatic brain injury: taking the patient's head size into account," *World Neurosurgery*, vol. 137, pp. e430–e436, 2020.
[10] S. Inokuchi, N. Fujita, H. Hasegawa et al., "[Frontal base penetrating brain injury by a gardening scissors:A case report]," *Noshinkeigeka*, vol. 46, no. 11, pp. 999–1005, 2018.
[11] A. Pezeshk, S. Hamidian, N. Petrick, and B. Sahiner, "3-D convolutional neural networks for automatic detection of pulmonary nodules in chest CT," *IEEE Journal of Biomedical and Health Informatics*, vol. 23, no. 5, pp. 2080–2090, 2019.
[12] P.-H. Tsai, Y.-C. Chen, S.-W. Chiang et al., "Changes in sensorimotor-related thalamic diffusion properties and cerebrospinal fluid hydrodynamics predict gait responses to tap test in idiopathic normal-pressure hydrocephalus," *European Radiology*, vol. 28, no. 11, pp. 4504–4513, 2018.
[13] S. L. Al-Khafaji, J. Zhou, A. Zia, and A. W.-C. Liew, "Spectral-spatial scale invariant feature transform for hyperspectral images," *IEEE Transactions on Image Processing*, vol. 27, no. 2, pp. 837–850, 2018.
[14] X. Shao, H. Zhang, Y. Wang et al., "Deep convolutional neural networks combine Raman spectral signature of serum for prostate cancer bone metastases screening," *Nanomedicine: Nanotechnology, Biology and Medicine*, vol. 29, Article ID 102245, 2020.
[15] Q. Guan, Y. Wang, B. Ping et al., "Deep convolutional neural network VGG-16 model for differential diagnosing of papillary thyroid carcinomas in cytological images: a pilot study," *Journal of Cancer*, vol. 10, no. 20, pp. 4876–4882, 2019.
[16] Q. R. Chen and S. P. Xie, *Lung Cancer Detection Method Based on Deep Learning*, Computer Technology and Development, 2018.
[17] H. Seo, M. B. Khuzani, V. Vasudevan et al., "Machine learning techniques for biomedical image segmentation: An overview of technical aspects and introduction to state-of-art applications," *Medical Physics*, vol. 47, no. 5, 2019.
[18] S. A. Taghanaki, K. Abhishek, J. P. Cohen et al., "Deep semantic segmentation of natural and medical images: a review," *Artificial Intelligence Review*, vol. 54, no. 1, pp. 137–178, 2020.
[19] G. Wang, W. Li, S. Ourselin, and T. Vercauteren, "Automatic brain tumor segmentation using cascaded anisotropic convolutional neural networks," in *Proceedings of the International MICCAI Brainlesion Workshop*, pp. 178–190, Springer, Cham, Granada, Spain, September 2017.

Hindawi
Journal of Healthcare Engineering
Volume 2021, Article ID 6472440, 9 pages
https://doi.org/10.1155/2021/6472440

Research Article

Value of Rehabilitation Training for Children with Cerebral Palsy Diagnosed and Analyzed by Computed Tomography Imaging Information Features under Deep Learning

Xi Zhang,[1] **Zhenfang Wang**,[1] **Jun Liu**,[2] **Lulin Bi**,[3] **Weilan Yan**,[1] **and Yueyue Yan**[1]

[1]*Department of Rehabilitation, Children's Hospital of Shanxi Province, Taiyuan 030025, Shanxi, China*
[2]*Outpatient Department of Infectious Diseases, Children's Hospital of Shanxi Province, Taiyuan 030025, Shanxi, China*
[3]*Imaging Department of CT Room, Children's Hospital of Shanxi Province, Taiyuan 030025, Shanxi, China*

Correspondence should be addressed to Zhenfang Wang; lyt@zjnu.edu.cn

Received 26 May 2021; Revised 30 June 2021; Accepted 12 July 2021; Published 21 July 2021

Academic Editor: Enas Abdulhay

To analyze the brain CT imaging data of children with cerebral palsy (CP), deep learning-based electronic computed tomography (CT) imaging information characteristics were used, thereby providing help for the rehabilitation analysis of children with CP and comorbid epilepsy. The brain CT imaging data of 73 children with CP were collected, who were outpatients or inpatients in our hospital. The images were randomly divided into two groups. One group was the artificial intelligence image group, and hybrid segmentation network (HSN) model was employed to analyze brain images to help the treatment. The other group was the control group, and original images were used to help diagnosis and treatment. The deep learning-based HSN was used to segment the CT image of the head of patients and was compared with other CNN methods. It was found that HSN had the highest Dice score (DSC) among all models. After treatment, six cases in the artificial intelligence image group returned to normal (20.7%), and the artificial intelligence image group was significantly higher than the control group ($X^2 = 335191$, $P < 0.001$). The cerebral hemodynamic changes were obviously different in the two groups of children before and after treatment. The VP of the cerebral artery in the child was (139.68 ± 15.66) cm/s after treatment, which was significantly faster than (131.84 ± 15.93) cm/s before treatment, $P < 0.05$. To sum up, the deep learning model can effectively segment the CP area, which can measure and assist the diagnosis of future clinical cases of children with CP. It can also improve medical efficiency and accurately identify the patient's focus area, which had great application potential in helping to identify the rehabilitation training results of children with CP.

1. Introduction

Cerebral palsy (CP) is one of the common causes of disability in children. It is the brain tissue damage caused by the immature brain (fetal period to within one year of life) due to congenital malformations or hypoxia, trauma, infection, and other factors after birth, which further causes a group of neurological syndromes in children with nonprogressive movement abnormalities and postural abnormalities as the main manifestations, accompanied by cognition, sensory, and communication disorders and other complications [1]. With the continuous development of perinatal medicine and neonatal life support technology and the improvement of rescue technology, more and more ultrapremature babies are able to survive. These premature babies are extremely immature and face severe challenge such as breathing, nutrition, metabolism, and infection. Their brain damage easily occurs, CP is caused, and the risk of disability is increased [2, 3]. Neuroimaging examination is an important auxiliary examination for central nervous system damage, which can provide objective basis for changes in tissue morphology for clinical diagnosis and treatment. The traditional cranial CT has been widely used in the cranial imaging examination of children with CP and has accumulated certain experience [4]. The other functional imaging examinations developed based on traditional techniques such as magnetic resonance imaging (MRI), ultrasound (US), positron emission tomography (PET), and other devices can assess the function of brain tissue through local blood flow changes, water molecular activity, and metabolic status. The lesions associated with the occurrence of CP were mapped in more detail to provide evidence of functional and metabolic abnormalities for some lesions with insignificant morphological changes. Up to now, medical imaging is an indispensable part of the clinic, and it plays an irreplaceable role in diagnosis and treatment. However, the workload of doctors is huge. Studies showed that, in some cases, general radiologists must make a diagnosis every three to four seconds in an 8-hour working day to meet the needs of the workload [5]. The accuracy of doctors' diagnosis results will be greatly affected by such a large work intensity, and misdiagnosis and missed diagnosis will be caused. However, there are also obvious problems in the current study. (I) The commonly used brain images have millimeter resolution. However, some diseases do not cause significant structural changes and require high resolution and small-scale brain imaging techniques. (II) The sample data only contains a certain kind of special diseases and health data. In actual diagnosis, the patient may suffer from ten related diseases. (III) The excessive number of extracted features consumes a large amount of storage space and at the same time greatly increases the computational complexity and leads to dimensional disaster. (IV) The classification accuracy should be further improved to meet the requirements of practical use. (V) The generalization performance of the classifier is poor, and the prediction effect of the new samples is obviously lower than that of the training samples.

With the development of artificial intelligence (AI), people began to try to use computer technology to assist doctors in diagnosis, which produced a computer-aided diagnosis (CAD) [6]. Taking the most widely used mammography CAD screening as an example, more than 74% of mammograms in the United States were performed with the aid of the CAD system by 2010 [7]. However, the advantages of CAD were questionable; several large trials concluded that there was little benefit from CAD. The accuracy of radiologists' diagnoses was reduced; thus high biopsy rates were caused. To eliminate the false alarms generated by these systems, the diagnostic process becomes more complex [8]. At present, diagnosis based on medical imaging mainly relies on radiologists' manual review of images and manual analysis of radiological images. This is a very time-consuming work, requiring radiologists to consult hundreds of sections and multiple lesions through three-dimensional CT scanning equipment [9]. For early detection, detecting lesions that are "too small to characterize" is particularly important, which requires time and effort on the part of the radiologist. In addition, the increasing huge amount of image data also brings great challenges for image reading. To effectively improve the efficiency of medical image reading, reduce the error rate of diagnosis, and provide effective auxiliary information for imaging physicians, the auxiliary diagnostic technology based on intelligent image analysis is becoming more and more important. In recent years, computer-aided diagnosis based on intelligent image analysis has gradually become a research hotspot in the medical field. Artificial intelligence algorithms have been used in the field of medical image data analysis and processing. By integrating these algorithms into clinical practice, effective and accurate diagnostic results are obtained. The traditional method of intelligent imaging diagnosis compares the automatically labeled or segmented area with the predefined benchmark template, but it still needs the imaging expert to give the final diagnosis result. In the application of disease diagnosis, abdominal CT imaging is the most important imaging means in the clinical diagnosis and follow-up of tumor diseases, which is widely used in the detection, segmentation, and diagnosis of lesions. Since different types of lesions correspond to different characteristics, how to separate the lesion area from the image is the key to the success of the high-precision diagnosis system [10]. To improve the accuracy of the automatic diagnosis system, the medical image assisted diagnosis system based on artificial intelligence mainly includes four aspects as follows: (I) image preprocessing, which improves the image quality and enhances the contrast of lesions; (II) detection and segmentation of the region of interest (ROI), which reduces the influence of interference background on the system; (III) feature extraction, selection, and classification, which improve the characterization ability of the target; (IV) the semantic segmentation of tumor, which can obtain the semantic features of lesions and improve the accuracy of recognition. The extraction of efficient features in the four key steps of the auxiliary diagnosis system is the core technology of the system. At present, the performance of medical image aided diagnosis system based on shallow learning completely depends on the characterization ability of features and the generalization performance of classification diagnosis model.

In short, the development of AI technology has provided new ideas to solve such medical problems. In particular, multidisciplinary knowledge such as radiology and computer science was integrated by imaging omics. High-throughput features can be mined from medical images and modeled and analyzed to provide clinical decision support for rehabilitation training for children with CP.

2. Methods

2.1. Research Object. Children with CP who were outpatient or hospitalized in our hospital from June 2017 to June 2020 were taken as research subjects. A total of 73 cases met the requirements; 44 were males and 29 were females. The age range was 1 to 14 years and the average age was 47.7 ± 37.2 months.

The classification was carried out according to the gross motor function classification system (GMFCS) [11]. There were 8 cases of GMFCS I (4 males, 4 females), 21 cases of GMFCS II (12 males, 9 females), 23 cases of GMFCS III (13 males, 10 females), 11 cases of GMFCS IV (8 males, 3 females), and 10 cases of GMFCS V (7 males, 3 females).

2.1.1. Inclusion Criteria. The abovementioned children met the diagnostic criteria for CP and must meet the following four necessary conditions: (a) nonprogressive aggravating dysfunction that persisted, which was caused by central nervous system damage; children with complications such as muscle damage and joint deformation as the course of CP was prolonged; (b) children with deviations in motor development and abnormal postures (motor development was included or not included); (c) the original reflex not disappearing or the erection reflex and balance response delayed or absent, which may be accompanied by a positive pathological reflex; (d) children with abnormal muscle tone and strength. In addition, there were two reference conditions whether it met the diagnosis of CP: (a) children with a history or risk factors that cause CP; (b) children with cranial imaging evidence.

2.1.2. Exclusion Criteria. The exclusion criteria included (a) the diagnosis of abnormal motor development in children that was consistent with general developmental retardation and developmental coordination disorder; (b) children with induced epileptic seizures caused by acute ketoacidosis, water and electrolyte disorders, acute brain injury, febrile convulsions, hypoglycemia, and drug poisoning, etc.; (c) children with metal implants or other contraindications for CT examination; (d) children with abnormal motor function caused by other genetic metabolic reasons; (e) children with motor dysfunction and epileptic seizures caused by tumors, peripheral neuropathy, and genetic metabolic diseases, etc.

A total of 73 children with CP met the above inclusion criteria and were included in the research. The research had been approved by the medical ethics committee of *X* hospital, and the informed consent form had been signed by the families of the children involved in the research.

2.2. Experimental Equipment. 74 contrast-enhanced CT samples constituted the dataset of the research. The Philips Brilliance 1281 CT scanner (Philips Healthcare, Amsterdam, Netherlands) was used. The tube voltage and current were 120 kV and 220 mA, respectively, the size of the collimator was 64×0.625 mm, and the Fov was 20×20 cm. The 512×512 size imaging matrix was used, the pixel size range was 0.58 to 0.98 mm, and the reconstruction interval was 5 mm. All scans were manually segmented by two radiologists using Itk snap software (version 3.4; http://www.itksnap.org), and the segmentation differences were resolved through discussion until a consensus was reached. The data set was randomly divided into three subsets, and 84, 20, and 30 samples were included for training, verification, and testing, respectively.

2.3. Experimental Environment

2.3.1. CNN Model. The proposed CNN model is shown in Figure 1, which was similar to 3D U-NET. The image features can be extracted layer by layer by the encoder, and the segmentation map can be generated by the decoder. The 3D U-Net was modified to be suitable for this task. In the original 3D U-Net, there were two $3 \times 3 \times 3$ convolutions included in each level, which was replaced by two modules. To reduce the size of the feature map, the step S3D convolution was used to replace the pooling operation. The goal of the decoder was generating high resolution feature maps. First, the feature graph was upsampled, and then the upsampled feature graph was cascaded with the feature graph from the corresponding level of the encoder. After cascading, the MSC module was used to adjust the number of feature graphs. The lightweight 3D CNN had fewer parameters and computational costs compared to the original 3D U-NET.

2.3.2. Deep Learning Mode. The Python deep learning framework was used to write code, which was trained on NVIDIA GeForce GTX 1080TIGPU. There were 100 training cycles and the training time was about 12 hours. The Adam optimizer was used with an initial learning rate of 0.001. The GDL loss function similar to the previous chapter was used to optimize network parameters. If the validation set loss was not decreased in the last 20 training cycles, the learning rate was reduced to 1/5 of the original. The rotation, scaling, deformation, mirroring, and other data were not used to enhance technology to focus on the impact of network structure. The LeakyReLU was used as the activation function. The negative part of the feature information can be retained by LeakyReLU to prevent falling into a local minimum compared with the standard ReLU. For 2D CNN, batch normalization was used to reduce internal covariant offset problems. For 3D CNN, a number of criteria were calculated using instance normalization as performance indicators to quantify the segmentation results, including DSC, sensitivity, and positive predictive value (PPV).

2.4. Comparative Test with 3DCNN Method. Compared with the 3D CNN method, each CT was first resampled to $256 \times 256 \times 64$ to maximize the utilization of 11 GB of GPU memory. In the decoder, each layer was composed of a trilinear upsampling layer with a factor of two, followed by two $3 \times 3 \times 3$ convolutions, and instance normalization and LeakyReLU were used to activate each layer. The jump connection was used to provide the decoder with spatial information from the encoder. Finally, the nearest neighbor sampling was used to upsample the segmentation result to the size of $512 \times 512 \times 64$.

2.5. Treatment Methods. The physical therapy (PT), occupational therapy (OT), and speech therapy (ST) were used as the main treatment methods. The selected method was Bobath's method to suppress the abnormal posture, abnormal posture reflex, and abnormal movement patterns of children with CP. The facilitating techniques were used to promote cervical erection, sitting erection, standing erection, and static and dynamic balance in children with CP. The German Voyt method was selected to perform reflex movement of the body to promote normal motor development and induce training with reflex turning over and reflex abdominal crawling. According to the child's condition, one-to-one rehabilitation training was carried out by

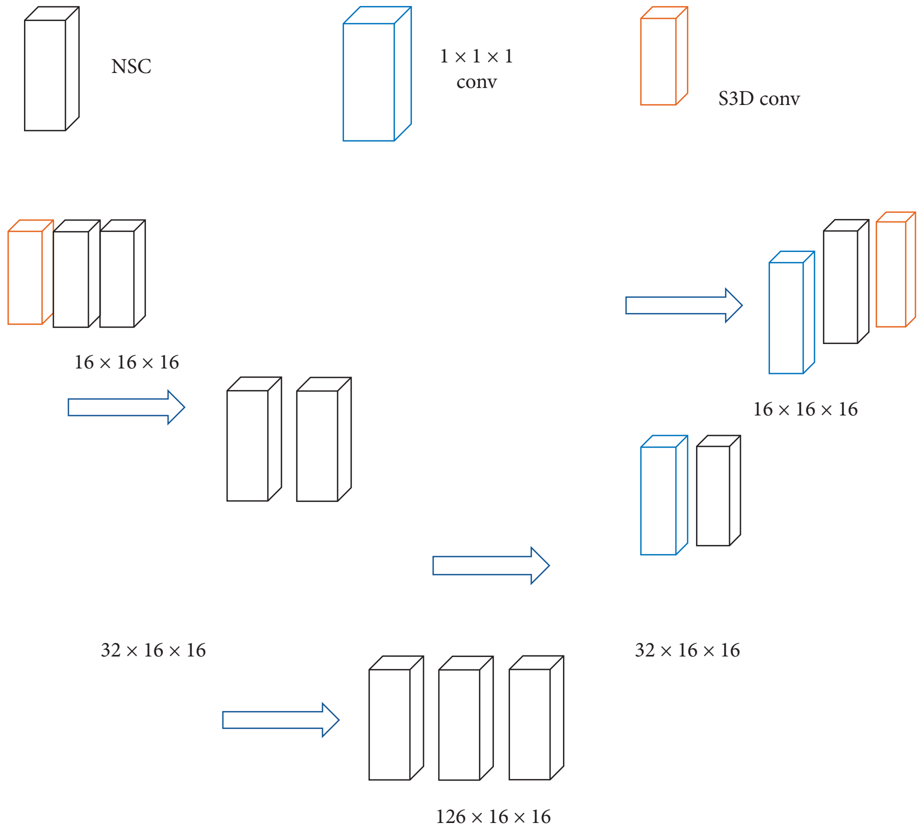

Figure 1: CNN model.

the rehabilitation therapist. The training was one to two hours a day, and 90 days was a course of treatment. The rehabilitation training for children with mild CP was one to two courses, and the rehabilitation training for children with severe CP was three to four courses.

2.6. Observation Indicators. Before and after treatment, the cerebral artery blood flow velocity (VP) and the vascular pulse index (PI) of the children in both groups were examined by Libong CBC-II transcranial doppler (TCD) cerebrovascular ultrasound to understand the recovery of cerebral blood circulation. The routine EEG and single photon emission cranial computed tomography (SPELT) were performed before and after treatment to assess cerebral perfusion and neuronal functional status. The CT scans of the head were performed after three to six months of treatment to observe the morphological and structural recovery of the brain. The development quotient (DQ) of the children was assessed using the Geisel method to assess the children's social adaptability, personal social ability, language ability, general motor, and fine motor recovery before and after treatment.

2.7. Statistical Analysis. SPSS 20.0 was used for statistical analysis of the data. Measurement data such as body weight and scores were expressed as mean ± standard deviation, and *t*-test was used to compare the data of normal distribution between the two groups. When three groups or more were compared, analysis of variance was carried out first, and then pairwise comparison was made. Enumeration data were expressed as percentage (%), and comparison between two groups was performed by χ^2 test or corrected χ^2 test. $P < 0.05$ was considered statistically significant.

3. Results

3.1. Comparative Test with 2DCNN Method. It was compared with 2D CNN method. The 2D models allowed larger images as input than 3D models (Figure 2). Therefore, full-resolution CT slices were used to collect detailed contextual information. The 2D CNN similar to 3D CNN was constructed, and the difference was that 3D convolution was replaced with 2D convolution. The 3D trilinear upsampling layer was replaced with 2D bilinear upsampling layer, and batch normalization was used in convolution.

3.2. Segmentation Results in Different Ways. Figures 3 and 4 show the segmentation results of 2D CNN and 3DCNN on the test set, respectively. The blue represented the gold standard for segmentation, and the red represented the result of automatic segmentation. These segmentation results indicated that 3D CNN can segment cancer regions more accurately than 2DCNN.

3.3. Comparative Experiment of Loss Correspondence Teaching. The choice of loss function was crucial to obtain accurate segmentation results when dealing with serious

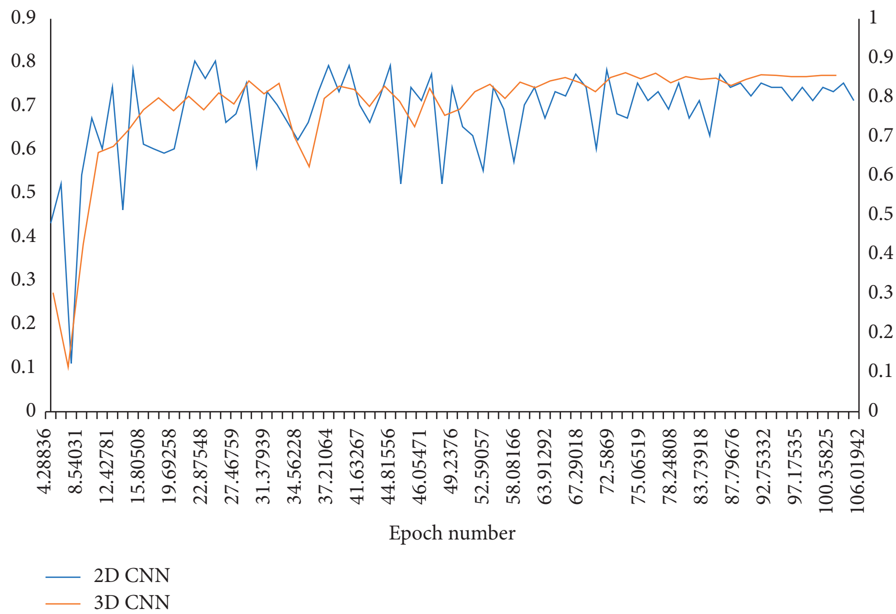

Figure 2: The average validation set DSC of 2D CNN and 3D CNN in 100 training cycles.

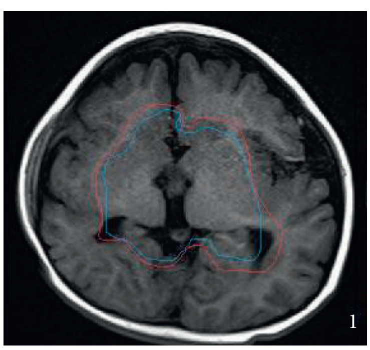

Figure 3: 2D CNN.

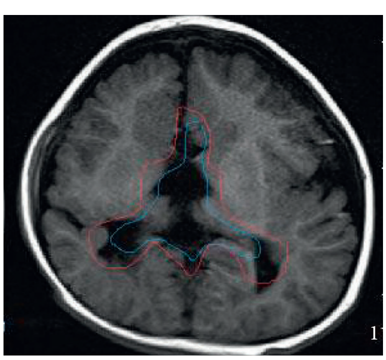

Figure 4: 3D CNN.

category imbalance. The GDL loss function was used to solve the class imbalance problem in CT images. Since many works proved that Dice loss can obtain more reliable results than cross-direction loss, there was a performance difference between Dice loss and GDL loss. Figures 5 and 6 show the average DSC on the validation set, and the loss of the model trained with GDL was smaller than the loss of the model trained with Dice. The DSC curve of the model's validation set was smoother when GDL was used for training, which indicated that GDL was more stable for CT image segmentation.

3.4. Quantitative Results of the Test Set. Figure 7 shows the quantitative results of the test set. The model with Dice loss training had lower DSC, lower PPV, and higher sensitivity compared with HSN, but all the deviations were large. The results showed that the problem of category imbalance can be effectively solved by GDL.

3.5. Spatial Convolution Contrast Experiment. The goal of 2D CNN was providing fine-grained semantic information about smaller and less salient objects for accurate segmentation. Therefore, the high spatial resolution must be retained in the output feature map. A simple reduction of the pooled or stepped convolution layer resulted in a reduction of the receptive field. Therefore, the cavity convolution was proposed to enlarge the receptive field and the resolution of the feature map was maintained. To study whether the hole convolution helped to learn fine-grained semantic information, it was compared with the standard 2D convolution version (HSN-N). The standard 2D convolution version (HSN-N) had the same architecture as HSN, but all 2D convolution layers did not use hole convolution. The convolution kernels with large void ratios may be too sparse to capture local features, which led to the "grid problem." To investigate the effect of large void rate on segmentation performance, another HSN model (2D HSN-L) with larger void rate was evaluated. The void rate of the original HSN was increased from three to five by this model. Figure 8 shows the qualitative segmentation results of different experiments on the test set. The blue represented the gold standard, and red represented the result of automatic

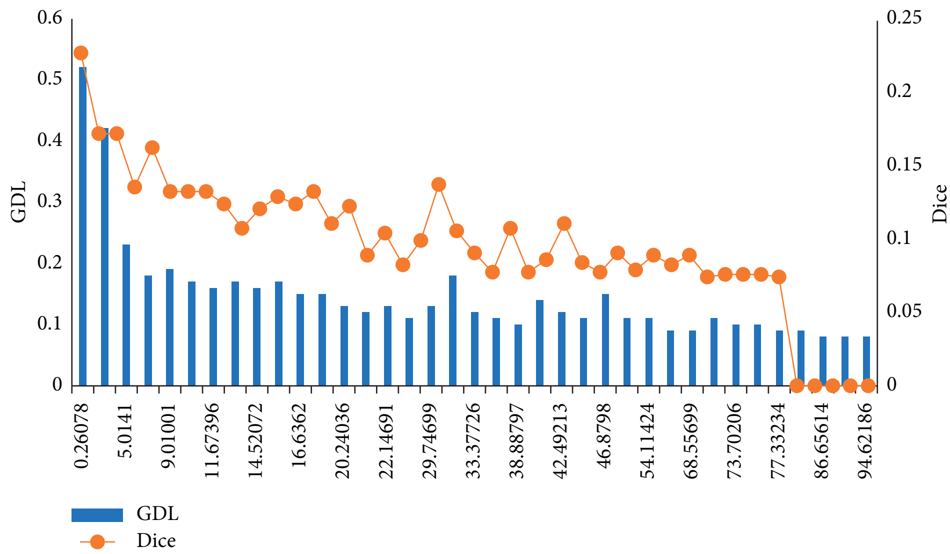

Figure 5: Training process of different loss function.

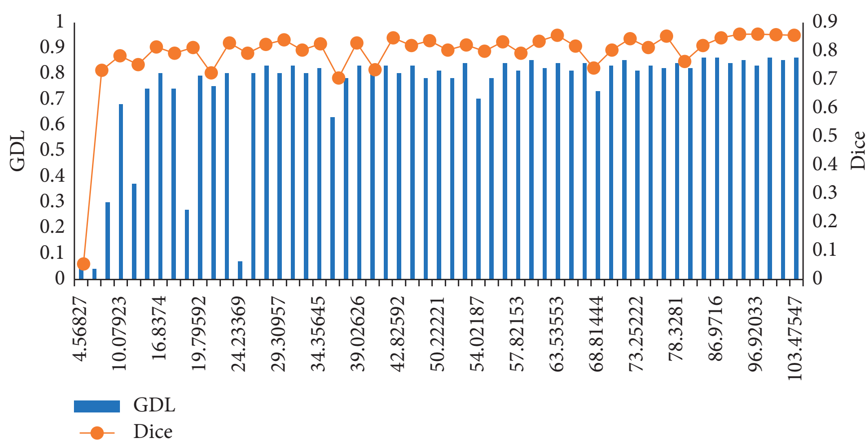

Figure 6: The average DSC of the verification set of different loss functions.

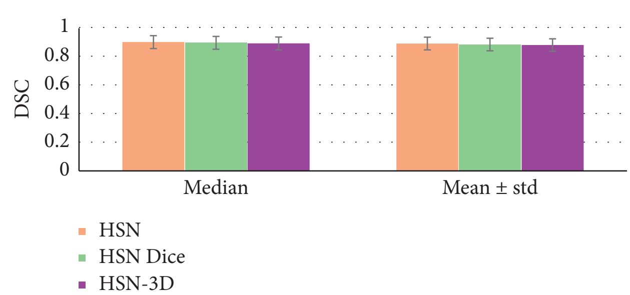

Figure 7: Quantitative results of the test set.

segmentation. These segmentation results showed that HSN performed well in segmenting lung cancer even in a small area. This was because the model can learn remote 3D context information and fine-grained 2D semantic information.

3.6. Results of Children's Rehabilitation Data. The SPECT examination showed hypoperfusion of cerebral blood flow and decreased functional activity of neurons in the treatment group before treatment, and 27 cases returned to normal after treatment (96.4%). There were 29 cases of

(a) (b) (c)

Figure 8: Qualitative segmentation results of different experiments on the test set (red was the artificial segmentation area, and blue was the model segmentation area). (a) HSN; (b) HSN-Dice; (c) HSN-S3D.

hypoperfusion of cerebral blood flow and decreased functional activity of neurons in the control group before treatment, and 6 cases returned to normal after treatment (20.7%). The return to normal rate of SPECT in the treatment group was significantly higher than that in the control group (XPINGFANG = 33 5191, $P < 0.001$). The cerebral hemodynamic changes of the two groups of children before and after treatment showed that VP of the cerebral artery in children was (139.68 ± 15.66) cm/s after treatment, which was significantly faster than that before treatment (131.84 ± 15.93) cm/s, $P < 0.05$. The cerebral artery PI of the children was 0.91 ± 0.19 after treatment, which was significantly lower than that of 1.18 ± 0.24 before treatment, $P < 0.05$. However, in the control group, the cerebral artery VP and PI of the children had no significant difference before and after treatment, $P > 0.5$. After treatment, there were significant differences in VP and PI between groups ($P < 0.05$). The changes in DQ of the two groups of children before and after treatment are shown in Figure 9. The difference of GM FM scale scores before and after treatment in the two groups of children is shown in Figure 10.

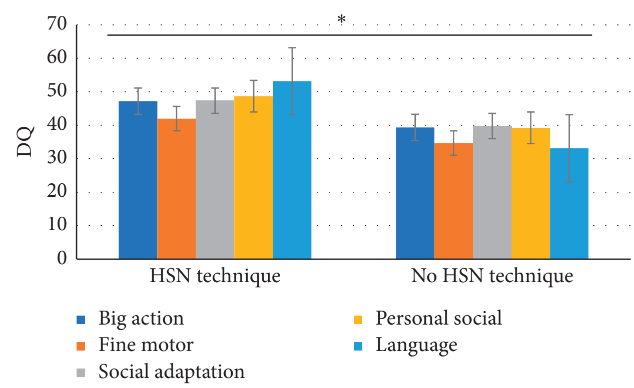

Figure 9: Changes in DQ of the two groups of children before and after treatment (*indicated significant difference.).

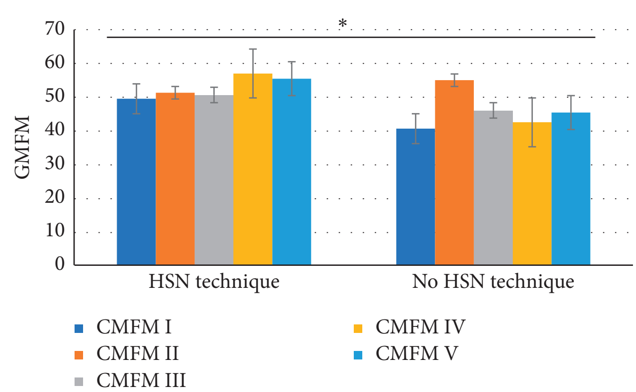

Figure 10: Difference of GM FM scale scores before and after treatment in the two groups of children (*indicated significant difference).

4. Discussion

A large amount of image data was generated in the process of diagnosis and treatment of CP lesions. These data were usually subjectively evaluated by doctors based on experience, and then the corresponding diagnosis and treatment plan were made. However, the features observed by doctors with only naked eyes from image data were very limited, and the potential of image data was often not fully utilized. For many years, the quantitative information that was not available to the human eye was extracted by many scholars with the help of complex mathematical and statistical algorithms, based on which the corresponding diagnosis and treatment plan were carried out, and even the progress of the disease was predicted. The image omics came into being with the development of AI technology. The machine learning algorithms were used to mine high-throughput features from medical images and perform modeling analysis [12]. More and more evidence showed that imaging omics can be used for the quantitative characterization of CP lesions for the diagnosis, treatment planning, and prognosis of the disease. Thus, an important research direction of AI technology in the field of medical applications was constituted [13–17].

In recent years, with the rise of deep learning technology and computer vision technology, it has become more and more urgent to develop automatic segmentation algorithms with high accuracy and high stability [9]. The problem of CT image segmentation was studied based on the brain MRI and lung CT images and the use of deep learning technology. In addition, for the grading of brain lesions, the impact of deep learning segmentation results and manual segmentation results on imaging omics research was compared in the research. For the prediction of chemotherapy outcomes in patients with CP, imaging omics models were also constructed and analyzed in combination with clinical features. The reproducibility of imaging omics research was still an unresolved problem, and the clinical application of imaging omics was greatly affected by this problem. Studies showed that more than 90% of research had not undergone rigorous external verification and lacked multicenter diversity data [18, 19]. A hybrid segmentation network based on deep learning (HSN) was used for CT brain image segmentation and the accuracy of image analysis of brain cell function in children with CP can be improved. The language function, motor function, cognitive function, language quotient, great motor development quotient, fine motor development quotient, personal social, and social adaptation development of the brain of children with CP in the HSN group were significantly improved after treatment compared to before treatment.

In this research, a hybrid segmentation network HSN based on deep learning was proposed for CT brain tissue image segmentation. CT images often have higher resolution than MRI images. How to segment CT images effectively is always a difficult problem. HSN can effectively solve this problem. HSN includes a lightweight 3D CNN and a refined 2D CNN. 3D CNN uses desampled images and spatio-temporal separable 3D convolution to reduce memory requirements and computational costs. 2D CNN can learn fine-grained semantic information while maintaining a high spatial resolution. A hybrid feature fusion module was proposed to effectively integrate 2D and 3D features. This network structure combines the advantages of 3D CNN learning long-range contextual information and 2D CNN learning semantic information. The results showed that this model can segment CP lesion area accurately on CT images. The development of deep learning and imaging omics has promoted the progress of medical imaging. Radiology using artificial intelligence can automate certain clinical tasks to some extent. In addition, it can reduce the heavy workload of doctors and improve the diagnostic efficiency, so as to optimize the allocation of social medical resources. However, there are still some shortcomings, which need to be further strengthened in the future. For example, traditional image omics feature extraction methods have certain limitations without adoption of deep learning in feature extraction. Deep learning methods, especially CNNs, can learn rich texture information from medical images in a hierarchical manner. Deep features have a more powerful feature representation than hand-designed features. In the future work, we will carry out related studies on feature extraction based on deep learning to further explore the potential of image data.

5. Conclusion

In this study, a hybrid segmentation network HSN based on deep learning was proposed for CT brain tissue image segmentation. After treatment, six patients in the artificial intelligence group returned to normal (20.7%), which was significantly higher than the control group ($X^2 = 335191$, $P < 0.001$). Cerebral hemodynamic changes were obvious in both groups before and after treatment. VP of the cerebral artery was (139.68 ± 15.66) cm/s after treatment, which was greatly faster than that before treatment (131.84 ± 15.93) cm/s, $P < 0.05$. In general, the deep learning model can effectively segment the CP area and assist in the clinical case measurement and diagnosis of future CP children. In addition, the deep learning model can improve medical efficiency and accurately identify patients' focal areas, which has great application potential in helping to identify the rehabilitation training results of children with CP.

Data Availability

No data were used to support this study.

Conflicts of Interest

The authors declare that they have no conflicts of interest.

References

[1] M. J. Maenner, S. J. Blumberg, M. D. Kogan, D. Christensen, M. Yeargin-Allsopp, and L. A. Schieve, "Prevalence of cerebral palsy and intellectual disability among children identified in two U.S. National Surveys, 2011-2013," *Annals of Epidemiology*, vol. 26, no. 3, pp. 222–226, 2016, Epub 2016 Jan 12. PMID: 26851824 PMC5144825.

[2] A. Hosny, C. Parmar, J. Quackenbush, L. H. Schwartz, and H. J. W. L. Aerts, "Artificial intelligence in radiology," *Nature Reviews Cancer*, vol. 18, no. 8, pp. 500–510, 2018, PMID: 29777175 PMC6268174.

[3] L. Oakden-Rayner, "The rebirth of CAD: how is modern AI different from the CAD we know?" *Radiology: Artificial Intelligence*, vol. 1, no. 3, Article ID e180089, 2019.

[4] W. L. Bi, A. Hosny, M. B. Schabath et al., "Artificial intelligence in cancer imaging: clinical challenges and applications," *CA: A Cancer Journal for Clinicians*, vol. 69, no. 2, 2019.

[5] B. Koçak, E. Ş Durmaz, E. S. Durmaz, E. Ates, and O. Kilickesmez, "Radiomics with artificial intelligence: a practical guide for beginners," *Diagnostic and interventional radiology*, vol. 25, no. 6, pp. 485–495, 2019, PMC6837295.

[6] K. Chang, A. L. Beers, H. X. Bai et al., "Automatic assessment of glioma burden: a deep learning algorithm for fully automated volumetric and bidimensional measurement," *Neuro-Oncology*, vol. 21, no. 11, pp. 1412–1422, 2019, PMC6827825.

[7] Z. Qian, Y. Li, Y. Wang et al., "Differentiation of glioblastoma from solitary brain metastases using radiomic machine-learning classifiers," *Cancer Letters*, vol. 451, pp. 128–135, 2019, Epub 2019 Mar 13. PMID: 30878526.

[8] Q. Hu, L. F. de F Souza, G. B. Holanda et al., "An effective approach for CT lung segmentation using mask region-based convolutional neural networks," *Artificial Intelligence in Medicine*, vol. 103, 2020 Epub 2020 Jan 8. PMID: 32143797, Article ID 101792.

[9] S. A. Taghanaki, K. Abhishek, J. P. Cohen, J. Cohen-Adad, and G. Hamarneh, "Deep semantic segmentation of natural and medical images: a review," *Artificial Intelligence Review*, vol. 54, no. 1, pp. 137–178, 2020.

[10] X. Zhu, D. Dong, Z. Chen et al., "Radiomic signature as a diagnostic factor for histologic subtype classification of non-small cell lung cancer," *European Radiology*, vol. 28, no. 7, pp. 2772–2778, 2018, Epub 2018 Feb 15. PMID: 29450713.

[11] R. Palisano, P. Rosenbaum, S. Walter, D. Russell, E. Wood, and B. Galuppi, "Development and reliability of a system to classify gross motor function in children with cerebral palsy," *Developmental Medicine and Child Neurology*, vol. 39, no. 4, pp. 214–223, 1997.

[12] S. Rizzo, F. Botta, S. Raimondi et al., "Radiomics: the facts and the challenges of image analysis," *European Radiology Experimental*, vol. 2, no. 1, p. 36, 2018 PMID: 30426318 PMC6234198.

[13] T. Kagawa, S. Yoshida, T. Shiraishi et al., "Basic principles of magnetic resonance imaging for beginner oral and maxillofacial radiologists," *Oral Radiology*, vol. 33, no. 2, pp. 92–100, 2017.

[14] P. Korfiatis, T. L. Kline, Z. Akkus et al., *Predictive Modeling, Machine Learning, and Statistical Issues*, CRC Press, Boca Raton, Florida, 2019.

[15] M. Shafiq-Ul-Hassan, G. G. Zhang, K. Latifi et al., "Intrinsic dependencies of CT radiomic features on voxel size and number of gray levels," *Medical Physics*, vol. 44, no. 3, pp. 1050–1062, 2017, PMID: 28112418 PMC5462462.

[16] C. A. Owens, C. B. Peterson, C. Tang et al., "Lung tumor segmentation methods: impact on the uncertainty of radiomics features for non-small cell lung cancer," *PLoS One*, vol. 13, no. 10, PMID: 30286184 PMC6171919, Article ID e0205003, 2018.

[17] H. Seo, M. Badiei Khuzani, V. Vasudevan et al., "Machine learning techniques for biomedical image segmentation: an overview of technical aspects and introduction to state-of-art applications," *Medical Physics*, vol. 47, no. 5, pp. e148–e167, 2020 Jun, PMID: 32418337 PMC7338207.

[18] G. Wang, W. Li, S. Ourselin, and T. Vercauteren, "Automatic brain tumor segmentation using cascaded anisotropic convolutional neural networks," *International MICCAI Brainlesion Workshop*, Springer, New York, NW, USA, 2017.

[19] Y. Yuan, M. Chao, and Y.-C. Lo, "Automatic skin lesion segmentation using deep fully convolutional networks with jaccard distance," *IEEE Transactions on Medical Imaging*, vol. 36, no. 9, pp. 1876–1886, 2017, Epub 2017 Apr 18. PMID: 28436853.

Hindawi
Journal of Healthcare Engineering
Volume 2021, Article ID 6761364, 8 pages
https://doi.org/10.1155/2021/6761364

Research Article

Artificial Intelligence Pulse Coupled Neural Network Algorithm in the Diagnosis and Treatment of Severe Sepsis Complicated with Acute Kidney Injury under Ultrasound Image

Fu Ying [1] **Shuhua Chen** [2] **Guojun Pan** [2] **and Zemin He** [1]

[1] *Department of Emergency Medicine, Changzhou Cancer Hospital, Changzhou 213000, Jiangsu, China*
[2] *Department of Intensive Care Unit, Changzhou Cancer Hospital, Changzhou 213000, Jiangsu, China*

Correspondence should be addressed to Zemin He; 1513402027@stu.suda.edu.cn

Received 20 May 2021; Revised 24 June 2021; Accepted 12 July 2021; Published 20 July 2021

Academic Editor: Enas Abdulhay

The objective of this study was to explore the diagnosis of severe sepsis complicated with acute kidney injury (AKI) by ultrasonic image information based on the artificial intelligence pulse coupled neural network (PCNN) algorithm. In this study, an algorithm of ultrasonic image information enhancement based on the artificial intelligence PCNN was constructed and compared with the histogram equalization algorithm and linear transformation algorithm. After that, it was applied to the ultrasonic image diagnosis of 20 cases of severe sepsis combined with AKI in hospital. The condition of each patient was diagnosed by ultrasound image performance, change of renal resistance index (RRI), ultrasound score, and receiver operator characteristic curve (ROC) analysis. It was found that the histogram distribution of this algorithm was relatively uniform, and the information of each gray level was obviously retained and enhanced, which had the best effect in this algorithm; there was a marked individual difference in the values of RRI. Overall, the values of RRI showed a slight upward trend after admission to the intensive care unit (ICU). The RRI was taken as the dependent variable, time as the fixed-effect model, and patients as the random effect; the parameter value of time was between 0.012 and 0.015, $p = 0.000 < 0.05$. Besides, there was no huge difference in the ultrasonic score among different time measurements ($t = 1.348$ and $p = 0.128 > 0.05$). The area under the ROC curve of the RRI for the diagnosis of AKI at the 2nd day, 4th day, and 6th day was 0.758, 0.841, and 0.856, respectively, which was all greater than 0.5 ($p < 0.05$). In conclusion, the proposed algorithm in this study could significantly enhance the amount of information in ultrasound images. In addition, the change of RRI values measured by ultrasound images based on the artificial intelligence PCNN was associated with AKI.

1. Introduction

Acute kidney injury (AKI) refers to a clinical syndrome caused by a rapid decline in renal function within a short period that led to various etiologies. It can occur in people without previous kidney disease or in patients with existing chronic kidney disease [1]. AKI is a common emergency and critical illness, and its prevalence in ordinary hospitalized patients is 3–5%. Moreover, the prevalence of AKI is as high as 30–50% in the intensive care unit (ICU) [2]. Although blood purification technology is constantly being updated, the mortality rate of patients with AKI has not been markedly reduced, which is an acute and critical disease in kidney disease [3]. The early course of AKI is reversible, but its treatment window is narrow. Once the injury period is entered, the incidence of death or uremia will exceed 30% [4]. Therefore, the early diagnosis of AKI, the improvement of the treatment effect of AKI, and the reduction of the mortality rate of AKI have a very critical scientific value and clinical significance.

In patients with AKI, Doppler ultrasound (DU) is often adopted to determine the renal resistance index (RRI) of the renal interlobular artery [5]. Bragato et al. [6] reported that RRI could assess the renal function of patients with AKI. Most importantly, RRI is correlated with renal vascular resistance, renal vascular compliance, renal blood flow, oxygen partial pressure, renal interstitial pressure, and other aspects, most of which are risk factors for AKI, so it can be used to effectively evaluate AKI [7]. In recent years, Kim et al. [8] have shown that DU can be used for the early diagnosis of kidney injury in patients with severe sepsis. DU can evaluate the ultrasound score of patients in a semiquantitative manner, and the operation is simple. However, there are few reports on the application of DU to evaluate the renal function of patients with severe sepsis and AKI [9].

The artificial intelligence pulse coupled neural network (PCNN) algorithm can construct neuron mapping into a phase-based model, which carries information not only the pulse frequency but also a sign of the transmission channel [10]. The artificial intelligence PCNN makes the way of selecting communication routes and the construction of computers simpler and more effective. Compared with other neural network models, the PCNN is more practical. The artificial intelligence PCNN uses a single-layer neural network model, which can be directly applied to image segmentation, pattern recognition, and image fusion without training [11]. Lotfinejad et al. [12] have adopted the artificial intelligence PCNN to image processing, finding that the PCNN had the advantages of constant signal strength, constant rotation, and constant scale under weak connection conditions.

In this study, the artificial intelligence PCNN algorithm was compared with the histogram equalization algorithm and linear transformation algorithm. Then, they were applied to the ultrasound images of 20 patients with severe sepsis combined with AKI, aiming to explore the ultrasound image characteristics of severe sepsis combined with AKI. Therefore, it could provide a reliable reference basis for early diagnosis and early treatment of clinical AKI patients.

2. Materials and Methods

2.1. Research Objects. In this study, 20 patients diagnosed with severe sepsis and AKI in the hospital from December 2018 to October 2019 were selected as the research objects. Besides, all of them underwent ultrasound examinations. There were 13 males and 7 females, with an average age of 48.69 ± 12.47 years. This study had been approved by the ethics committee of the hospital, and the research objects included in this study and their family members signed the informed consent forms.

The criteria for inclusion were defined to include patients who met the diagnostic criteria for severe sepsis, with tissue hypoperfusion and renal dysfunction caused by sepsis, can undergo the assisted breathing treatment through a ventilator, and were 18–75 years old.

The criteria for exclusion were defined to include patients who were younger than 18 years old, were in the recovery period of AKI, were accompanied with obstructive renal failure, intraabdominal hypertension, arrhythmia, and other diseases that would affect the value of RRI, suffered from chronic renal insufficiency, and were combined with heart, spleen, and cardiovascular and cerebrovascular diseases.

2.2. Construction of Ultrasound Images Based on Artificial Intelligence Pulse Coupled Neural Network Algorithm. Figure 1 shows the artificial intelligence PCNN algorithm model. When the PCNN processed the images, it was a single-layer two-dimensional network. The number of neurons was consistent with the number of pixels in the output image. The pixel intensity of the gray-scale image was the excitation condition of the neuron. The surrounding input neurons connected with each output neuron to form an image processing system based on the PCNN algorithm. In this study, a threshold $F_{i,j}$ was constructed to represent the Mach band effect. The Laplacian operator $L = \begin{bmatrix} -1 & -1 & -1 \\ -1 & 6 & -1 \\ -1 & -1 & -1 \end{bmatrix}$ was convolved with the gray-scale image of the input excitation, so that the size of the threshold $F_{i,j}$ was redefined as follows.

$$F_{i,j}(0) = \mathrm{BPG} - \mathrm{CPG}_{i,j}. \tag{1}$$

In equation (1), BPG represents the gray value of the brightest pixel of the original image input, and $\mathrm{CPG}_{i,j}$ represents the gray value of the neuron (i, j) point image after convolution processing. The network output of the PCNN was transformed into the gray-scale excitation value perceived by the network to obtain the final enhanced image. Besides, the equation was as follows.

$$\mathrm{EIG} = \mathrm{In}(\mathrm{BPG}) - \tau (S(i, j) - 1). \tag{2}$$

In equation (2), EIG represents the gray value of the enhanced image, BPG represents the brightest pixel gray value of the original image input, $S(i, j)$ represents the ignition timing of the neuron (i, j), and τ represents the attenuation constant.

The specific steps of the PCNN algorithm included the following.

Step 1: first, the parameters of the PCNN were set, and the number of cycles was set as M, so that all neurons were in the inhibited state. The gray value of the PCNN algorithm image was calculated to construct the matrix S of neuron ignition time and determine the threshold $F_{i,j}$. The specific algorithm flow steps were expressed in the following equations.

$$F_{i,j}[m] = S_{i,j}[m], \tag{3}$$

$$R_{i,j}[m] = W_L \sum VY[m], \tag{4}$$

$$U[m] = F_{i.j}[m]\left(1 + \alpha R_{i,j}[m]\right), \tag{5}$$

$$Y_{i,j}[m] = 1, \quad \text{if } U[m] > F_{i,j}[m] \text{ or otherwise}, \tag{6}$$

$$F_{i,j}[m] = \exp(-\tau) \times F(i, j) + W_E \times Y(i, j). \tag{7}$$

In the above equations, the PCNN parameters $\alpha = 0.2, \tau = 0.7, W_L = 1, W_F = 278$, $F_{i,j}$ represents the dynamic threshold, m represents the number of

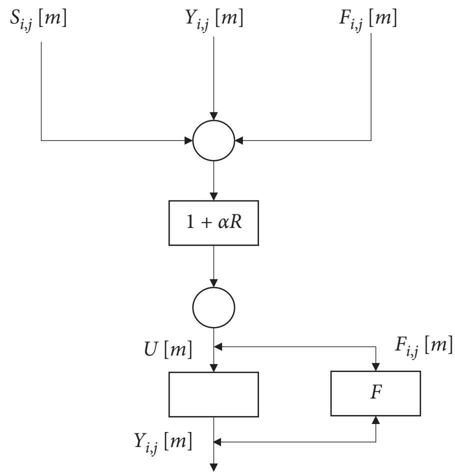

Figure 1: Artificial intelligence PCNN algorithm model.

iterations, $S(i, j)$ represents the ignition timing of the neuron (i, j), $R_{i,j}[m]$ represents the feedback input of the neuron (i, j)'s m^{th} iteration, $Y_{i,j}[m]$ represents the feedback output of the neuron (i, j)'s m^{th} iteration, α represents the strength constant of links between synapses, $U[m]$ represents the internal activity item, W_L represents the amplitude constant of $F_{i,j}[m]$, and W_F represents the threshold decay time coefficient.

Step 2: the neuron ignited at a certain moment and could output a pulse to record the ignition moment in S. The threshold of the neuron was taken as the maximum value to inhibit the occurrence of reignition. What is more, the equations are given as follows:

$$S_{i,j}[m] = m, \quad \text{if } E_{i,j}[m] = 1, \text{mark}_{i,j}[m] = 0, \tag{8}$$

$$\text{mark}_{i,j}[m] = \infty i, \quad \text{if } E_{i,j}[m] = 1, \text{ otherwise } 0, \tag{9}$$

$$E_{i,j}[m] = \infty, \quad \text{if } Y_{i,j}[m] = 1. \tag{10}$$

Step 3: if one of the neurons ignited, the final output value was 1, and the gray value of the image could be enhanced according to equation (2).

Step 4: all gray values were processed, so it would be ended; otherwise, return to Step 2.

2.3. Ultrasound Scoring Standards for Severe Sepsis Patients Combined with Kidney Injury. The diagnostic criteria of severe sepsis combined with AKI in this study referred to the diagnostic criteria of severe sepsis in the 2012 Scientific Steering Committee (SSC) guidelines [13]. The patients received the DU examinations, and their ultrasound images were saved in ultrasound equipment, which was scored (DU scoring) by 3 physicians who were specially trained in emergency and critical ultrasound. Using a 0–3 semi-quantitative scoring standard, the ultrasound scoring was as follows. 0 point indicated that no renal blood vessels could be detected, 1 point meant that a few blood vessels could be observed in the renal hilum, 2 points showed that interlobular blood vessels could be observed in the renal parenchyma, and 3 points presented that the renal arcuate artery level could be found in the kidney.

2.4. Renal Ultrasound Examination. Within 24 hours of entering ICU, each patient was given with renal ultrasound examination when the hemodynamics was stable. The patients were detected through ultrasound once a day for 7 consecutive days until they left the ICU. Besides, the ultrasound examinations were conducted by the physicians who were specially trained in emergency and critical ultrasound and were not involved in the treatment. The Vivid i portable Doppler ultrasound (produced by GE, USA) was employed to explore the kidneys on both sides of the patient, and a 5 Hz ultrasound probe was adopted to observe whether the kidneys had contusions or hematomas and whether there was damage to the bilateral renal arteries. Finally, RRI was measured, first on the right kidney and then on the left.

The measurement of RRI was as follows. First, the protruding probe was used for the detection of the patient's abdomen, and the long axial section of the kidney was intercepted from the posterolateral position of the two-dimensional ultrasound. Doppler was applied to identify the renal vessels to locate an interlobular artery. Then, the minimum Doppler sampling gate 3–6 mm and minimum pulse repetition frequency (PRF) where graphics did not overlap were set to obtain 4–6 consecutive similar spectra. Moreover, statistical measurements of the peak systolic velocity (SV) and the minimum diastolic velocity (DV) were made to calculate the RRI of each spectrum. In addition, the RRI for each spectrum could be calculated by the following equation.

$$\text{RRI} = \frac{(\text{SV} - \text{DV})}{\text{SV}}. \tag{11}$$

In equation (11), SV represents the peak flow velocity in the systolic period and DV represents the lowest diastolic flow rate. Furthermore, the average value of the RRI was taken after 4–6 measurements.

2.5. Statistical Methods. The test data processing was carried out using SPSS20.0 statistical software. The measurement data were expressed as the mean ± standard deviation ($\overline{x} \pm s$), and the t-test was used for the comparison of the average values between each group. The count data were represented by the percentage (%), and the χ^2 test was used. The RRI at different time points was used as the diagnostic evaluation test to draw the ROC and determine the optimal critical value of RRI for the diagnosis of AKI. What is more, the AUC of ROC was compared between each time point. In addition, $p < 0.05$ indicated that the difference was statistically substantial.

3. Results

3.1. Ultrasound Image Quality Evaluation Results Based on Artificial Intelligence Pulse Coupled Neural Network Algorithm. Figure 2 shows the ultrasound images of

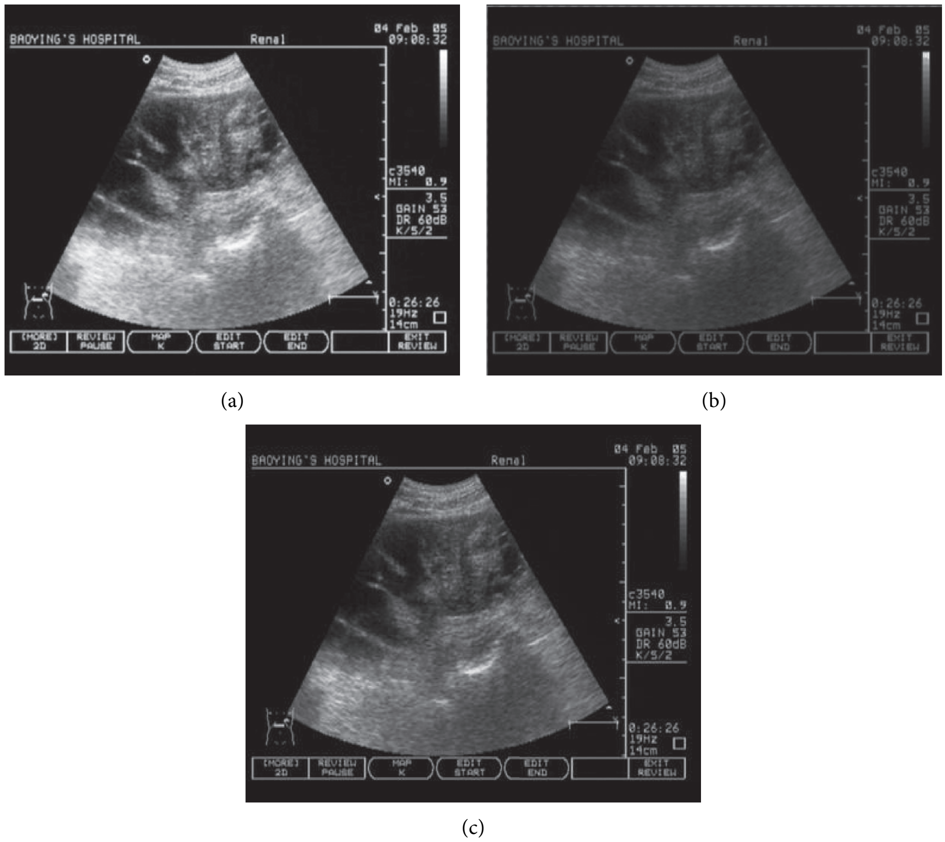

Figure 2: The ultrasound images of (a) histogram equalization, (b) linear transformation algorithm, and (c) artificial intelligence PCNN algorithm.

equalization, linear transformation algorithm, and artificial intelligence PCNN algorithm. The results showed that histogram equalization was a global image enhancement algorithm that could extend the gray scale of low-brightness ultrasound images, and eventually, over-enhancement occurred. The transformation function adopted by the linear transformation algorithm was relatively simple, and the final imaging effect was not ideal. The artificial intelligence PCNN algorithm proposed in this study not only considered the global information but also enhanced the local information. After enhancement, the gray value of the ultrasound image was evenly distributed near the gray value sensitive to the human eye, and the overall image effect was suitable for direct observation with naked eyes.

The histograms of AKI, histogram equalization, linear transformation algorithm, and artificial intelligence PCNN algorithm are shown in Figure 3. To verify the effectiveness of the artificial intelligence PCNN algorithm, it was compared with the equalization method and the linear transformation algorithm. It was found that the histogram of the equalization method was mainly concentrated in a large area and the distribution was relatively uniform, but there was the enhancement after the image was enhanced, and the overall image effect was not very good. The linear transformation algorithm was mainly concentrated in the darker area, the enhancement was not obvious, and the overall effect was not good. The histogram of the artificial intelligence PCNN algorithm was relatively evenly distributed, and each gray level was retained, with significantly enhanced ultrasound image information, which was convenient for the medical diagnosis of AKI. Therefore, it showed that the artificial intelligence PCNN algorithm was the best among the three algorithms in enhancing the information content of the ultrasonic images.

3.2. General Information of Patients with Severe Sepsis Combined with Acute Kidney Injury. Figure 4 shows the general data of patients with severe sepsis combined with AKI. In this study, there were a total of 20 severe sepsis patients with AKI, including 13 males (65%) and 7 females (35%), with an average age of 48.69 ± 12.47 years. The patient's injury severity score (ISS) was 32.5 ± 8.9 points, and the acute physiology and chronic health status score II (APACHE II score) was 16.2 ± 9.4 points. Among them, 7 cases (35%) were injured by road traffic accidents, followed by 4 cases (20%) injured by falling from a height, 3 cases (15%) injured by heavy objects, 2 cases (10%) injured by beatings, 3 cases (15%) with machine strangulation injuries, and 1 case (5%) with explosion injury. Finally, 3 cases died, 1 case died of hemorrhage at the trauma site, 1 case died of severe sepsis, and 1 case died of multiple organ failure after severe head injury.

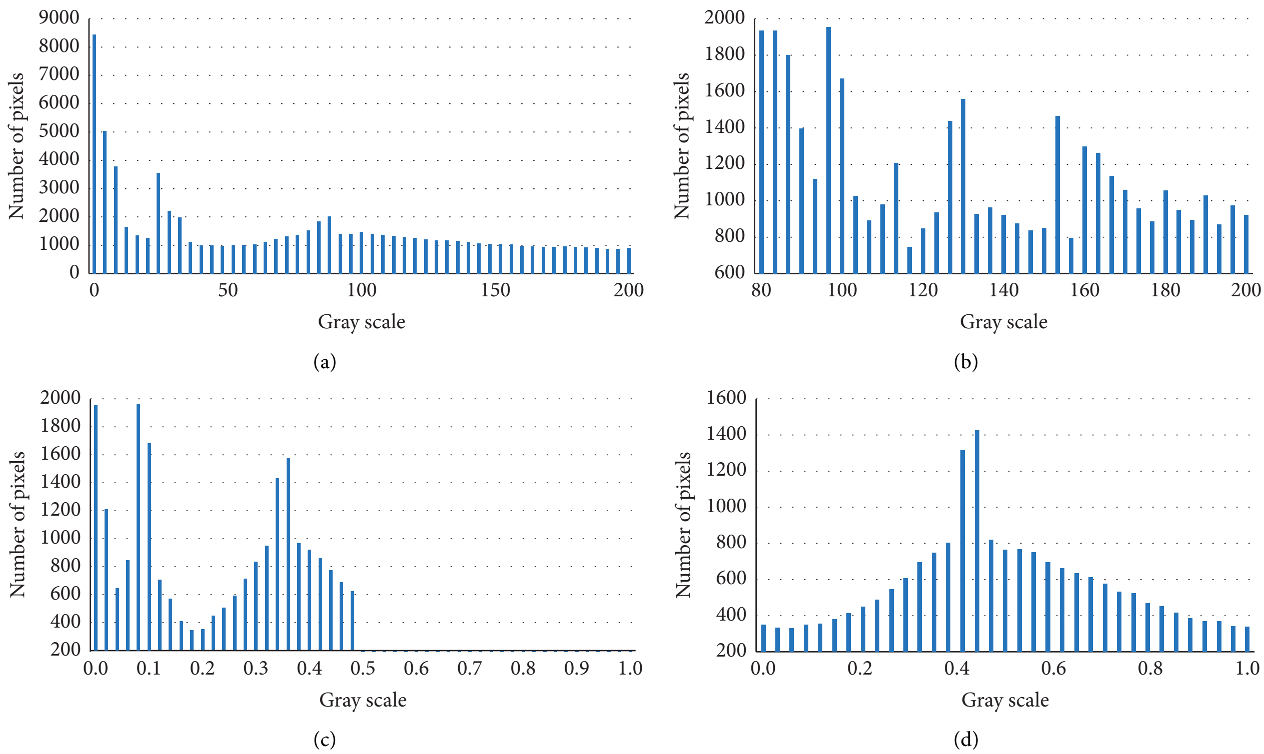

Figure 3: The histograms of (a) severe sepsis with AKI, (b) histogram equalization, (c) linear transformation method, and (d) artificial intelligence PCNN algorithm.

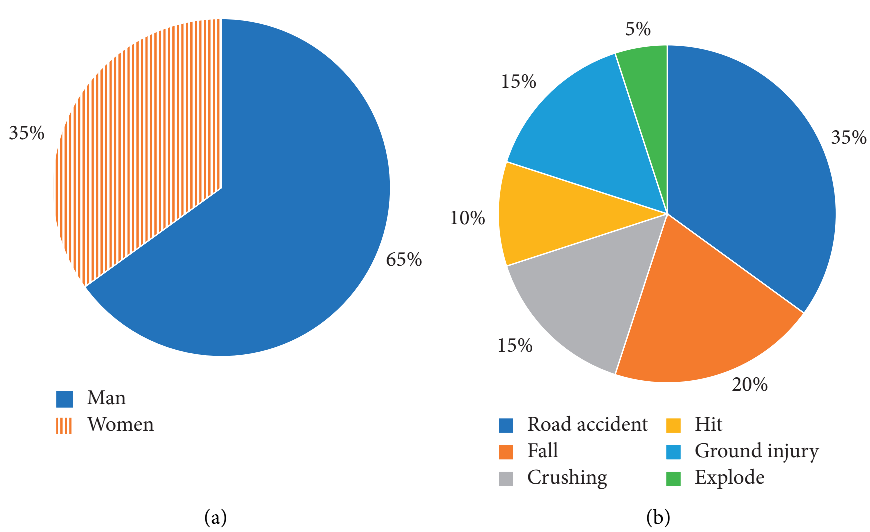

Figure 4: General data of patients with severe sepsis combined with AKI. (a) Ratio of male to female in severe sepsis patients with AKI. (b) Types of injury in severe sepsis patients with AKI.

3.3. Ultrasound Image Performance Characteristics Based on Artificial Intelligence Pulse Coupled Neural Network Algorithm. The ultrasound images based on the artificial intelligence PCNN algorithm are shown in Figure 5. Ultrasound is an important method for diagnosing AKI and judging the prognosis. Whether it was glomerular sclerosis, renal tubular atrophy, interstitial fibrosis, or inflammation, ultrasound imaging showed enhanced cortical echo. The cortex became thinner and the echo was enhanced; the renal cortex and the medulla echo were not demarcated; the focal cortex was thinned; the echo was enhanced, with the uniform structure, and the renal parenchyma and the renal sinus could not be distinguished by naked eyes; the cortical echo was enhanced, and the upper pole of the kidney was

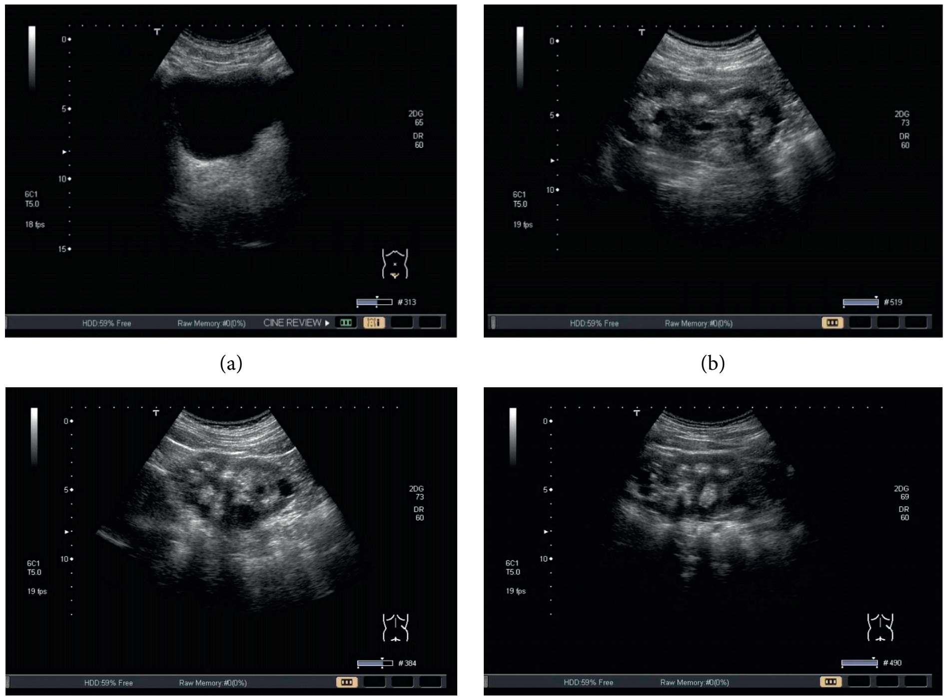

(a) (b) (c) (d)

Figure 5: Ultrasound images based on artificial intelligence PCNN algorithm. (a) Ultrasound image of renal cortex thinning and echo enhancement. (b) Ultrasound image of renal cortex and medulla echo being unclear. (c) Cortical echo enhancement and an ultrasound image of renal enlargement. (d) Ultrasound image of renal inferior pole laceration and subcapsular effusion.

unclear; the cortex echoes enhanced, and the kidneys enlarged; the lower pole of the kidney was lacerated, and the subcapsular fluid was accumulated.

3.4. Changes in Ultrasound Renal Resistance Index in Severe Sepsis Patients Combined with Acute Kidney Injury. Figure 6 includes the two graphs showing the changing trend of ultrasound RRI in patients with severe sepsis combined with AKI. According to the changing trend in the figure, there were obvious individual differences in RRI; on the whole, RRI indicated a slight upward trend after the patient entered ICU.

The analysis results of the linear mixed model of RRI and time are presented in Table 1. The RRI was used as the dependent variable, time was used as a fixed-effect model, and the patient was treated as a random effect. The parameter value of time was 0.012–0.015, $p < 0.001$, which verified that RRI would increase over time. Among them, 2 patients had AKI after entering ICU, 1 patient had a marked increase in RRI after AKI, and 1 patient showed a significant downward trend.

3.5. Ultrasound Scores of Severe Sepsis Patients Combined with Acute Kidney Injury. The ultrasound scores of patients with severe sepsis and AKI are shown in Figure 7. Over time, the ultrasound scores of patients with severe sepsis and AKI were mainly distributed in 2 points.

Table 2 reveals the analysis results of the linear mixed model of RRI and time. The ultrasound score was used as the dependent variable, time was a fixed-effect, patient time was used as a fixed-effect model, and the patient was taken as a random effect. The parameter value of time was 0.001–0.015, $p = 0.128 > 0.05$, indicating that there was no substantial difference in the ultrasound scores of patients with severe sepsis complicated with AKI ($t = 1.348$ and $p = 0.128 > 0.05$).

3.6. ROC Curve Analysis of Renal Resistance Index at Different Time Points in the Diagnosis of Severe Sepsis with Acute Kidney Injury. Figure 8 shows the ROC curves of the RRI for the diagnosis of AKI on the 2^{nd} day, 4^{th} day, and 6^{th} day after entering the ICU. Besides, the AUC values of ROC for RRI diagnosis of AKI at different time points were analyzed, and the analysis results are given in Table 3. The patient with AKI was defined as a positive index as 1, and the ROC of RRI on the 2^{nd} day, 4^{th} day, and 6^{th} day after entering ICU was drawn to the diagnosis of AKI. Furthermore, the values of AUC were 0.758, 0.841, and 0.856 in turn, which were all greater than 0.5 ($p < 0.05$).

4. Discussion

AKI is a complication of traumatic diseases, and the common risk factors for its occurrence include the severity of the trauma, the degree of bleeding, shock, traumatic inflammation, and severe sepsis [14]. In this study, 20 patients with severe sepsis combined with AKI were included, and there were no marked differences in gender, age, and ISS.

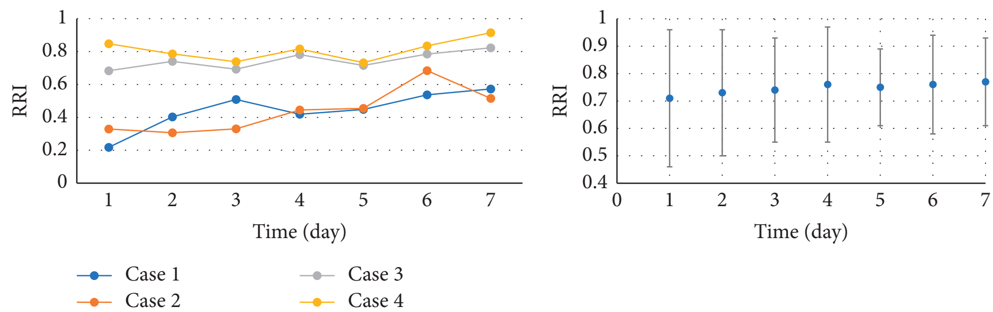

(a) (b)

FIGURE 6: Trend chart of ultrasound RRI changes in severe sepsis patients combined with AKI. (a) The changing trend of RRI of randomly selected cases. (b) The changing trend of average RRI of patients on ultrasound.

TABLE 1: Analysis of the linear mixed model of RRI and time effect.

Parameters	Standard error	95% CI	t	P
Time	0.002	0.012–0.015	12.348	<0.001
Intercept	0.007	0.638–0.758	64.854	<0.001

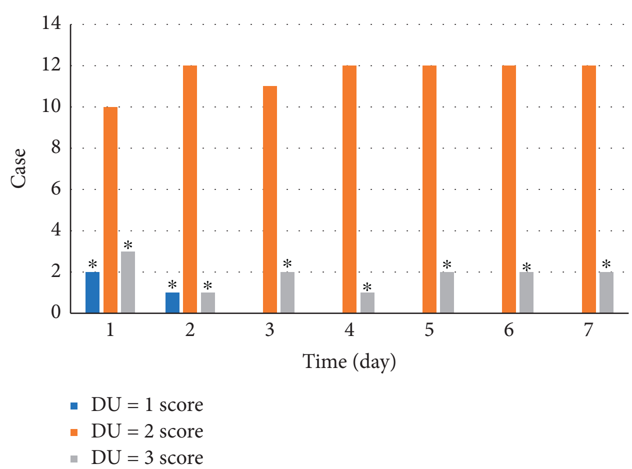

FIGURE 7: Ultrasound scores of severe sepsis patients combined with AKI. *Compared to DU = 2 points, $p < 0.05$.

TABLE 2: Linear mixed model analysis of ultrasound scores and time effect.

Parameters	Standard error	95% CI	t	P
Time	0.003	0.001–0.015	1.348	0.128
Intercept	1.225	1.126–2.154	13.238	<0.001

DU has the advantages of high reproducibility and noninvasiveness, which is extensively applied in the field of acute and critical illness and has shown a good diagnostic value in the assessment of renal trauma [15–17]. DU can quantitatively determine the resistance index of renal interlobular arteries. Xia et al. [18] confirmed that RRI could predict the occurrence of AKI in the state of severe sepsis. According to the changing trend of the RRI within 1–7 days

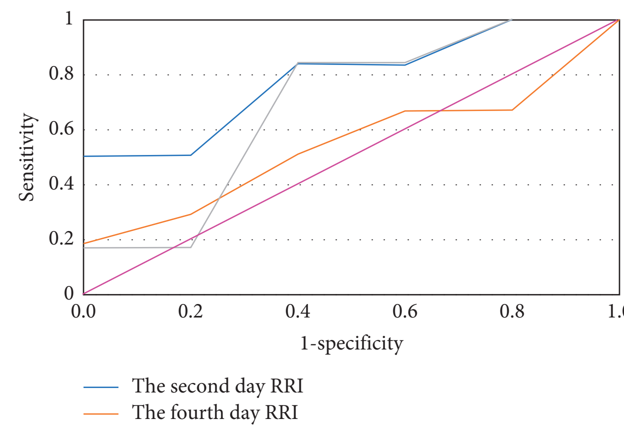

FIGURE 8: The ROC curves of the RRI on the 2^{nd} day, 4^{th} day, and 6^{th} day after entering the ICU for the diagnosis of AKI. The AUC values were 0.758, 0.841, and 0.856, respectively, which were all greater than 0.5 ($p < 0.05$).

TABLE 3: Analysis of the AUC of the ROC curves of RRI at different time points in the diagnosis of AKI.

Time	AUC	95% CI	Standard error	P value
The 2^{nd} day	0.758	0.526–0.974	0.148	1.241
The 4^{th} day	0.841	0.540–0.985	0.134	1.126
The 6^{th} day	0.8526	0.623–1.000	0.012	1.364

Note. The P value was compared with the value of AUC (0.5).

after entering the ICU, there were obvious individual differences in RRI [19]. On the whole, the RRI had a slight upward trend after entering the ICU. The RRI, time, and the patient were taken as the dependent variable, a fixed-effect model, and a random effect, respectively. The parameter value of time was 0.012–0.015, $p < 0.001$, verifying that RRI would rise over time.

The AUC of ROC for the diagnosis of AKI was drawn on the 2^{nd} day, 4^{th} day, and 6^{th} day of entering the ICU [20]. The patient with AKI was defined as a positive index as 1, and the ROC curves of RRI on the 2^{nd} day, 4^{th} day, and 6^{th} day after entering the ICU were drawn to the diagnosis of AKI. What is more, the values of AUC were 0.758, 0.841, and 0.856 in sequence, all greater than 0.5 ($p < 0.05$), suggesting that the AUC of ROC drawn in this study had high accuracy. Thus, RRI could be used as a predictive index of AKI.

5. Conclusion

The artificial intelligence PCNN algorithm in this study was compared with histogram equalization algorithm and linear transformation algorithm, which were adopted for the ultrasound images of 20 patients with severe sepsis and AKI. The results disclosed that the artificial intelligence PCNN algorithm proposed in this study not only considered the global information of ultrasound images but also enhanced the local information of ultrasound images. In addition, the changes in RRI measured by ultrasound images were related to AKI. The shortcomings of this study are that the time is limited, the number of samples collected is small, and the patient observation time is only about 1 week. It is impossible to observe the changes of RRI before and after kidney injury and during the recovery period of AKI. Further research is needed in the later period. All in all, the artificial intelligence PCNN algorithm has a significant effect on ultrasound image enhancement, thereby providing a reference theoretical basis for the diagnosis of severe sepsis with AKI.

Data Availability

No data were used to support this study.

Conflicts of Interest

The authors declare that they have no conflicts of interest.

References

[1] S. Peerapornratana, C. L. Manrique-Caballero, H. Gómez, and J. A. Kellum, "Acute kidney injury from sepsis: current concepts, epidemiology, pathophysiology, prevention and treatment," *Kidney International*, vol. 96, no. 5, pp. 1083–1099, 2019.

[2] E. V. Schrezenmeier, J. Barasch, K. Budde, T. Westhoff, and K. M. Schmidt-Ott, "Biomarkers in acute kidney injury - pathophysiological basis and clinical performance," *Acta Physiologica*, vol. 219, no. 3, pp. 556–574, 2017.

[3] D. G. Moledina and C. R. Parikh, "Phenotyping of acute kidney injury: beyond serum creatinine," *Seminars in Nephrology*, vol. 38, no. 1, pp. 3–11, 2018.

[4] S. Negi, D. Koreeda, S. Kobayashi et al., "Acute kidney injury: epidemiology, outcomes, complications, and therapeutic strategies," *Seminars in Dialysis*, vol. 31, no. 5, pp. 519–527, 2018.

[5] Y. Chen, S. Hu, H. Mao, W. Deng, and X. Gao, "Application of the best evacuation model of deep learning in the design of public structures," *Image and Vision Computing*, vol. 102, Article ID 103975, 2020.

[6] N. Bragato, N. C. Borges, and M. C. S. Fioravanti, "B-mode and Doppler ultrasound of chronic kidney disease in dogs and cats," *Veterinary Research Communications*, vol. 41, no. 4, pp. 307–315, 2017.

[7] C. G. Varela, L. A. M. Yeguas, I. C. Rodríguez, and M. D. D. Vila, "Penile doppler ultrasound for erectile dysfunction: technique and interpretation," *American Journal of Roentgenology*, vol. 214, no. 5, pp. 1112–1121, 2020.

[8] E. S. Kim, A. M. Sharma, R. Scissons et al., "Interpretation of peripheral arterial and venous Doppler waveforms: a consensus statement from the society for vascular medicine and society for vascular ultrasound," *Vascular Medicine*, vol. 25, no. 5, pp. 484–506, 2020.

[9] E. Quaia, J. M. Correas, M. Mehta, J. T. Murchison, A. G. Gennari, and E. J. R. Van Beek, "Gray scale ultrasound, color Doppler ultrasound, and contrast-enhanced ultrasound in renal parenchymal diseases," *Ultrasound Quarterly*, vol. 34, no. 4, pp. 250–267, 2018.

[10] E. Merino García, F. J. Borrego Utiel, M. Polaina Rusillo, and M. J. García Cortés, "Vascular renal resistance index is not related with prognosis in kidney transplantation," *Nefrologia*, vol. 41, no. 1, pp. 69–71, 2021.

[11] Z. Lv and W. Xiu, "Interaction of edge-cloud computing based on SDN and NFV for next generation IoT," *IEEE Internet of Things Journal*, vol. 7, no. 7, pp. 5706–5712, 2020.

[12] M. Lotfinejad, A. Rashedi, and S. Amirkhanlou, "The survey of relationship between resistance index of renal artery and albuminuria in diabetic patients referring to Shahid Sayyad Shirazi hospital, 2017 to 2018," *Iranian Journal of Kidney Diseases*, vol. 14, no. 5, pp. 358–364, 2020.

[13] M. Bejic, S. Déglise, J. P. Venetz et al., "Use of intraoperative duplex ultrasound and resistance index reduces complications in living renal donor transplantation," *Transplantation Proceedings*, vol. 50, no. 10, pp. 3192–3198, 2018.

[14] R. Cianci, A. Gigante, D. Bagordo et al., "Renal resistive index in IgA nephropathy and renal scleroderma vasculopathy," *Microvascular Research*, vol. 133, Article ID 104095, 2021.

[15] W. Beaubien-Souligny, G. Huard, J. Bouchard, Y. Lamarche, A. Denault, and M. Albert, "Doppler renal resistance index for the prediction of response to passive leg-raising following cardiac surgery," *Journal of Clinical Ultrasound*, vol. 46, no. 7, pp. 455–460, 2018.

[16] C. Huang, G. Tian, Y. Lan et al., "A new pulse coupled neural network (PCNN) for brain medical image fusion empowered by shuffled frog leaping algorithm," *Frontiers in Neuroscience*, vol. 13, p. 210, 2019.

[17] Q. Wu, B. Dang, C. Lu et al., "Spike encoding with optic sensory neurons enable a pulse coupled neural network for ultraviolet image segmentation," *Nano Letters*, vol. 20, no. 11, pp. 8015–8023, 2020.

[18] J. Xia, Y. Lu, and L. Tan, "Research of multimodal medical image fusion based on parameter-adaptive pulse-coupled neural network and convolutional sparse representation," *Comput Math Methods Med*, vol. 2020, Article ID 3290136, 13 pages, 2020.

[19] M. Zareie, H. Parsaei, S. Amiri, M. S. Awan, and M. Ghofrani, "Automatic segmentation of vertebrae in 3D CT images using adaptive fast 3D pulse coupled neural networks," *Australasian Physical & Engineering Sciences in Medicine*, vol. 41, no. 4, pp. 1009–1020, 2018.

[20] X. Jin, D. Zhou, Q. Jiang et al., "How to analyze the neurodynamic characteristics of pulse-coupled neural networks? A theoretical analysis and case study of intersecting cortical model," *IEEE Transactions on Cybernetics*, vol. 99, pp. 1–15, 2021.

Hindawi
Journal of Healthcare Engineering
Volume 2023, Article ID 9761493, 1 page
https://doi.org/10.1155/2023/9761493

Retraction

Retracted: The Effect of lncRNA SNHG3 Overexpression on Lung Adenocarcinoma by Regulating the Expression of miR-890

Journal of Healthcare Engineering

Received 8 August 2023; Accepted 8 August 2023; Published 9 August 2023

This article has been retracted by Hindawi following an investigation undertaken by the publisher [1]. This investigation has uncovered evidence of one or more of the following indicators of systematic manipulation of the publication process:

(1) Discrepancies in scope
(2) Discrepancies in the description of the research reported
(3) Discrepancies between the availability of data and the research described
(4) Inappropriate citations
(5) Incoherent, meaningless and/or irrelevant content included in the article
(6) Peer-review manipulation

The presence of these indicators undermines our confidence in the integrity of the article's content and we cannot, therefore, vouch for its reliability. Please note that this notice is intended solely to alert readers that the content of this article is unreliable. We have not investigated whether authors were aware of or involved in the systematic manipulation of the publication process.

Wiley and Hindawi regrets that the usual quality checks did not identify these issues before publication and have since put additional measures in place to safeguard research integrity.

We wish to credit our own Research Integrity and Research Publishing teams and anonymous and named external researchers and research integrity experts for contributing to this investigation.

The corresponding author, as the representative of all authors, has been given the opportunity to register their agreement or disagreement to this retraction. We have kept a record of any response received.

References

[1] B. Kang, C. Qiu, and Y. Zhang, "The Effect of lncRNA SNHG3 Overexpression on Lung Adenocarcinoma by Regulating the Expression of miR-890," *Journal of Healthcare Engineering*, vol. 2021, Article ID 1643788, 9 pages, 2021.

Hindawi
Journal of Healthcare Engineering
Volume 2021, Article ID 1643788, 9 pages
https://doi.org/10.1155/2021/1643788

Research Article

The Effect of lncRNA SNHG3 Overexpression on Lung Adenocarcinoma by Regulating the Expression of miR-890

Baojie Kang,[1] Caihong Qiu,[1] and Ying Zhang[2]

[1]*Department of Respiratory, Weifang Yidu Central Hospital, Weifang City, Shandong, China*
[2]*Department of ICU, Zibo Central Hospital, Zibo City, Shandong, China*

Correspondence should be addressed to Ying Zhang; ziboicuzhagying@163.com

Received 14 April 2021; Accepted 25 June 2021; Published 9 July 2021

Academic Editor: Enas Abdulhay

The lncRNA small nucleolar host gene 3 (SNHG3) was discovered to play an important role in the occurrence and development of lung adenocarcinoma (LUAD). However, the underlying molecular mechanism of SNHG3 in LUAD remains unclear. In the present study, SNHG3 expression levels in LUAD tissues and cell lines were analyzed using reverse transcription-quantitative PCR. The effects of SNHG3 on the proliferation, apoptosis, migration, and invasion of LUAD cells were determined using Cell Counting Kit-8, colony formation, flow cytometry, wound healing, and Transwell chamber assays, respectively. The specific underlying mechanism of SNHG3 in LUAD was investigated using bioinformatics analysis and a dual luciferase reporter assay. The results revealed that SNHG3 expression levels were downregulated in LUAD tissues and cell lines. Functionally, SNHG3 overexpression suppressed the proliferation, migration, and invasion of LUAD cells, while promoting apoptosis. Mechanistically, microRNA- (miR-) 890 was identified as a potential target of SNHG3, and its expression was negatively regulated by SNHG3. Notably, SNHG3 was found to promote LUAD progression by targeting miR-890. In conclusion, the findings of the present study revealed that lncRNA SNHG3 promoted the occurrence and progression of LUAD by regulating miR-890 expression.

1. Introduction

Lung cancer is a common type of cancer with high incidence and mortality rates worldwide [1]. Non-small-cell lung cancer (NSCLC) represents ~85% of all lung cancer types and has a mortality rate of ~50%. Lung adenocarcinoma (LUAD), a leading cause of cancer-related mortality, accounts for ~40% of NSCLCs and has a 5-year survival rate of only 15% [2]. At present, patients with LUAD are usually diagnosed at the terminal stage or following metastasis due to the lack of effective biomarkers and obvious early symptoms [3, 4]. For more than half a century, even with the significant progress and development made in molecular biology, oncology, and medicinal technology, the treatment of LUAD has been and remains ineffective [5]. In addition, although a large number of molecular biology studies have focused on investigating the mechanisms underlying LUAD, the exact molecular mechanism of LUAD remains unclear. Thus, further investigations to identify LUAD-associated pathogenic genes and the underlying molecular mechanisms of LUAD are required.

Long noncoding RNAs (lncRNAs), which are functional transcripts of >200 nucleotides in length, have been discovered to serve important roles in modulating the pathological and physiological progression of numerous cancer types [6–9]. Accumulating studies have reported that the abnormal expression of lncRNAs was associated with the progression of different malignant tumor types, including breast cancer [9], prostate cancer [10], liver cancer [11], and LUAD [12, 13]. Numerous lncRNAs, such as metastasis-associated lung adenocarcinoma transcript 1 [12], long intergenic non-protein-coding RNA 1512 [13], MIR31 host gene [14], FEZ family zinc finger 1 antisense RNA 1 [15], and urothelial cancer associated 1 [16], were found to be closely associated with LUAD occurrence and development. In addition, the lncRNA DiGeorge syndrome critical region gene 5 was reported to promote the progression of LUAD by downregulating microRNA- (miRNA/miR-) 22-3p expression [17]. The lncRNA small nucleolar host gene 3(SNHG3) is a long noncoding RNA. At present, its potential role and mechanism in lung adenocarcinoma have not been reported. SNHG3, also known as the host gene of U17 (U17HG), is located in band 6 in region 3 of the short arm of chromosome 1. The lncRNA small nucleolar host gene 3 (SNHG3) has been demonstrated to serve a role in multiple types of cancer. In fact, an increasing number of studies have revealed that the expression levels of SNHG3 were upregulated in numerous tumor types, and SNHG3 upregulation markedly promoted tumor cell proliferation, migration, and invasion, thereby indicating that SNHG3 may represent a novel oncogenic lncRNA [18]. For example, SNHG3 promoted the migration and invasion of osteosarcoma cells by regulating the miR-151a-3p/RAB22A, member RAS oncogene family axis [19]. In NSCLC, SNHG3 promoted the proliferation, migration, and invasion of NSCLC cells by activating the TGF-β and IL-6/JAK2/STAT3 signaling pathways [20]. These studies suggested that SNHG3 may serve a role as a novel oncogene in numerous cancer types. Nevertheless, the specific regulatory mechanism of SNHG3 in LUAD requires further study.

The current study hypothesized that SNHG3 may promote LUAD occurrence and development by targeting miR-890 expression. Thus, the expression levels of SNHG3 and miR-890 in LUAD tissues and cell lines were analyzed. The potential functions of SNHG3 and its association with miR-890 were also investigated *in vitro*. The results of the present study may provide a novel insight into potential targets for the treatment of LUAD.

2. Materials and Methods

2.1. Patient Studies. LUAD and adjacent normal tissues were obtained from 66 patients with LUAD (men and women account for 50%, respectively) who were diagnosed at Weifang Yidu Central Hospital (China). Included patients had neither received surgery nor chemotherapy prior to sample collection. The present study was approved by the Ethics Committee of Weifang Yidu Central Hospital, and all enrolled patients provided written informed consent. All tissues were stored at −80°C before use.

2.2. Cell Lines and Culture. The human normal lung epithelial cell line, 16HBE, and human LUAD cell lines (A549, H1299, and H1975) were obtained from the Cell Bank of Type Culture Collection of the Chinese Academy of Sciences. All cells were cultured in DMEM (Nanjing KeyGen Biotech Co., Ltd.) and maintained in a humidified atmosphere with 5% CO_2 at 37°C.

2.3. Cell Transfection. The pcDNA 3.1 and pcDNA3.1 SNHG3 plasmids, negative control (NC) inhibitor, miR-890 inhibitor, NC mimic, and miR-890 mimic were purchased from Invitrogen; Thermo Fisher Scientific, Inc. The synthetic oligonucleotides or plasmids were transfected into cells using Lipofectamine® 2000 (Invitrogen; Thermo Fisher Scientific, Inc.).

2.4. Cell Counting Kit-8 (CCK-8) Assay. The cells were gently seeded at a density of 1 × 106 cells/well into 96-well plates by the experimenter. Following 24, 48, 72, 96, or 120 h of culture, the CCK-8 reagent (Beyotime Institute of Biotechnology) was added to each well. The cell density was measured at a wavelength of 450 nm.

2.5. Colony Formation Assay. The transfected cells were seeded into a 6-well plate and cultured for 14 days; during this process, the medium was replaced every 2 days. Following the incubation, the formed colonies were fixed with 4% formaldehyde and stained with crystal violet (Sangon Biotech Co., Ltd.) for 3 min to visualize the colonies, which were defined as >50 cells. The colony formation rate was calculated using the following equation: colony formation rate (%) = (number of colonies/number of seeded cells) × 100.

2.6. Reverse Transcription-Quantitative PCR (RT-qPCR). Total RNA was extracted from LUAD cell lines and tissues using TRIzol® reagent (Invitrogen; Thermo Fisher Scientific, Inc.). Total RNA was reverse transcribed into cDNA using a PrimeScript RT reagent kit (Qiagen, Inc.). qPCR was subsequently performed using SYBR Green (Takara Bio, Inc.), with U6 as the control gene. The following primer pairs were used for the qPCR: SNHG3 forward, 5′-TTCAAGCGATTCTCGTGCC-3′ and reverse, 5′-AAGATTGTCAAACCCTCCCTGT-3′; miR-890 forward, 5′-CGGCTTCCTGTGCTAAGCGT-3′ and reverse, 5′- AACGCTTCACGAATTTGCGT-3′; and U6 forward, 5′-CTCGCTTTCGGCAGCACA-3′ and reverse, 5′-AACGCTTCACGAAATTTGCGT-3′.

2.7. Cell Apoptosis Assay. Following trypsinization and centrifugation, 1×10^6 cells were collected and incubated with 500 μl buffering agent containing Annexin V-FITC and PI in the dark for 30 min. The cell apoptotic rate was analyzed using flow cytometry (Beckman Coulter, Inc.).

2.8. Wound Healing Assay. The migratory ability of LUAD cells was analyzed using a wound healing assay. Briefly, 1×10^6 transfected cells were cultured for 24 h, and upon reaching confluence, a straight line was scratched into the cell monolayer to generate an artificial wound. The area of the scratch was visualized under a microscope at 0 and 48 h and analyzed using an image analysis and detection system.

2.9. Cell Invasion Assay. The invasive ability of LUAD cells was measured using Transwell plates (8.0 μm pores; Nanjing KeyGen Biotech Co., Ltd.). Briefly, 1×10^6 cells/well were seeded into the upper chamber of the Transwell plates. Following 48 h of incubation, the invasive cells were fixed and stained with crystal violet. Stained cells were visualized and semiquantified using a microscope (Nikon Corporation).

2.10. Dual Luciferase Reporter Assay. Wild-type (WT) or mutant (Mut) SNHG3 3′-untranslated region (UTR) fragments containing the miR-890 binding sites were synthesized and inserted into the pGL3-basic plasmid (Promega Corporation) to construct SNHG3-WT or SNHG3-Mut reporter vectors, respectively. LUAD cells were cotransfected with the aforementioned reporter vectors and miR-890 inhibitor or NC inhibitor. Following 48 h of transfection, the relative luciferase activity was measured using a Dual Luciferase Reporter assay system (Promega Corporation).

2.11. Statistical Analysis. Statistical analysis was performed using SPSS 19.0 software (IBM Corp.), and data are presented as the mean ± SD. Statistical differences between two or more groups were performed using Student's *t*-test or one-way ANOVA, respectively. Kaplan–Meier survival analysis was used to evaluate the association between the overall survival of patients with LUAD and SNHG3 expression levels. The Gene Expression Profiling Interactive Analysis (GEPIA) database was used to analyze the survival of patients with either low or high expression of SNHG3. $P < 0.05$ was considered to indicate a statistically significant difference.

3. Results

3.1. SNHG3 Expression Levels Are Downregulated in LUAD Tissues and Cell Lines. To determine the potential regulatory roles of SNHG3 in LUAD, RT-qPCR analysis was performed. The clinicopathological characteristics of patients are shown in Table 1. SNHG3 expression levels were downregulated in LUAD tissues compared with adjacent normal tissues (Figure 1(a)). The results of the Kaplan–Meier analysis revealed that patients with low SNHG3 expression levels had a shorter overall survival compared with those with high SNHG3 expression levels (Figure 1(b)). Similar to the patient studies, SNHG3 expression levels were also found to be markedly downregulated in LUAD cell lines (A549, H1299, and H1975) compared with 16HBE cells (Figure 1(c)). The expression levels of SNHG3 were downregulated to the greatest extent in A549 and H1299 cells; therefore, these two cell lines were selected for use in subsequent experiments. These results indicated that SNHG3 expression levels may be significantly downregulated in LUAD tissues and cells.

3.2. SNHG3 Overexpression Inhibits the Proliferation, Migration, and Invasion, and Promotes the Apoptosis, of LUAD Cells. To determine the function of SNHG3 in LUAD, pcDNA3.1 SNHG3 vectors were transfected into A549 and H1299 cells. Following transfection, SNHG3 expression levels were markedly upregulated (Figure 2(a)). The results of the CCK-8 and colony formation assays demonstrated that SNHG3 overexpression inhibited the proliferation of LUAD cells (Figures 2(b) and 2(c)). In addition, flow cytometric analysis found that SNHG3 overexpression induced the apoptosis of LUAD cells (Figure 2(d)). To investigate the effects of SNHG3 on the migration and invasion of A549 and H1299 cells, wound healing and Transwell invasion assays were performed. The results of the wound healing assay revealed that the migration was decreased following the overexpression of SNHG3 in LUAD cells (Figure 2(e)). Similarly, the results of the Transwell assay demonstrated that SNHG3 overexpression inhibited the invasive abilities of LUAD cells (Figure 2(f)). These findings suggested that SNHG3 overexpression may inhibit the proliferation, migration, and invasion and promote the apoptosis of LUAD cells.

3.3. SNHG3 Directly Binds to miR-890 and Downregulates miR-890 Expression. To identify specific miRNAs modulated by SNHG3 in LUAD, downstream genes of SNHG3 were searched for using bioinformatics analysis. Data from The Cancer Genome Atlas database identified a potential binding site between SNHG3 and miR-890 (Figure 3(a)). Furthermore, a dual luciferase reporter assay was performed, and the results found that the cotransfection with the miR-890 inhibitor increased the relative luciferase activity of the SNHG3-Wt reporter vector compared with the cotransfection with the NC inhibitor. However, no significant differences were observed in the relative luciferase activity of the SNHG3-Mut reporter vectors between cells cotransfected with the miR-890 inhibitor or NC inhibitor (Figure 3(b)). In addition, SNHG3 overexpression was found to downregulate miR-890 expression (Figure 3(c)). Thus, the expression levels of miR-890 in LUAD tissues and cell lines were further analyzed. RT-qPCR analysis revealed that the expression levels of miR-890 were upregulated in LUAD tissues and cell lines (Figures 3(d) and 3(e)). These results indicated that miR-890 may be a target of SNHG3 and be negatively regulated by SNHG3.

3.4. SNHG3 Exerts Its Effects in LUAD by Regulating miR-890 Expression. To determine whether miR-890 was involved in promoting the effects of SNHG3 in LUAD, a miR-890 mimic was transfected into A549 and H1299 cells following the overexpression of SNHG3. The transfection efficiencies of the miR-890 mimic transfection and cotransfection of the miR-890 mimic and SNHG3 overexpression plasmid are presented in Figure 4(a). The expression levels of miR-890 were upregulated following the overexpression of miR-890, while the expression levels of miR-890 were downregulated following the overexpression of SNHG3. The results of the CCK-8 and colony formation assays demonstrated that miR-890 overexpression increased the proliferation of LUAD cells, while the SNHG3-overexpression-induced inhibition of LUAD cell proliferation was impaired following miR-890 overexpression (Figures 4(b) and 4(c)). Flow cytometric analysis showed that miR-890 overexpression inhibited the apoptosis of LUAD cells. Conversely, the increased apoptotic rate following SNHG3 overexpression was weakened following miR-890 overexpression (Figure 4(d)). The results of the wound healing and Transwell chamber assays showed that the migratory and invasive abilities of LUAD cells were increased following the overexpression of miR-890, while the inhibitory effects of SNHG3 overexpression on migration and invasion were partially antagonized by miR-890

Table 1: The expression of SNHG3 and clinicopathological features in 66 lung adenocarcinoma. *P values are calculated with the chi-square test.

Clinicopathological features	Cases ($n = 66$)	SNHG3 expression 38 high (%)	SNHG3 expression 28 low (%)	P value*
Gender				
Male	34	20 (58.8)	14 (41.2)	0.833
Female	32	18 (56.3)	14 (43.8)	
Age (years)				
≤60	33	17 (51.5)	16 (48.5)	0.319
>60	33	21 (63.6)	12 (36.4)	
Tumor size (mm)				
≤5.0	39	24 (61.5)	15 (38.5)	0.434
>5.0	27	14 (51.9)	13 (48.1)	
TNM stage				
I-II	38	27 (71.1)	11 (28.9)	0.010*
III-IV	28	11 (39.3)	17 (60.7)	
Lymph node metastasis				
0–2	41	29 (70.7)	12 (29.3)	0.014*
>2	25	11 (40.7)	16 (59.3)	

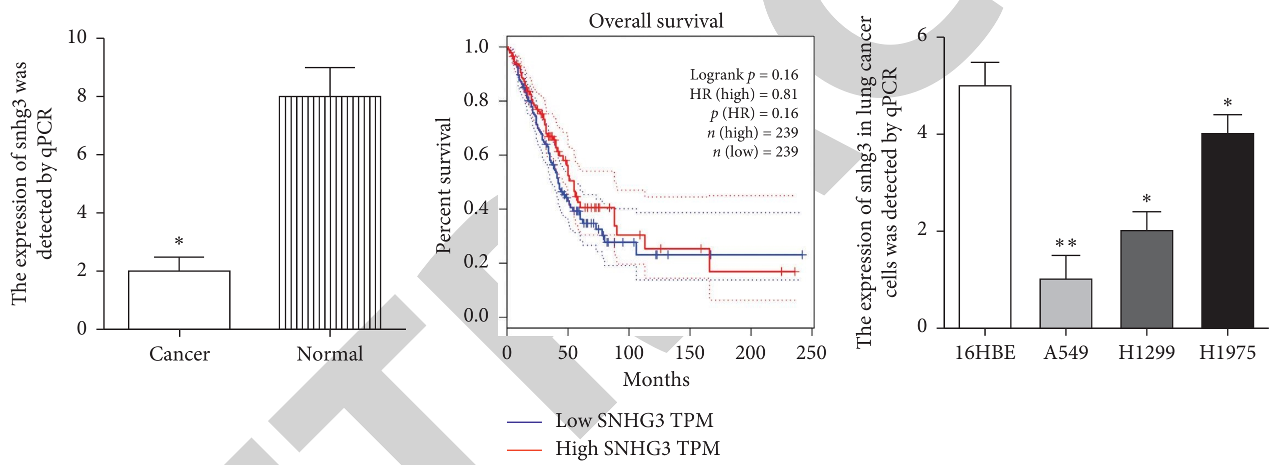

Figure 1: The SNHG3 expression is downregulated in LUAD tissues and cell lines. (a) Relative expression levels of lncRNA SNHG3 in LUAD tissues and normal tissues were detected by RT-qPCR. *$P < 0.05$ vs. the normal tissue. (b) The GEPIA database was used to evaluate the relationship between SNHG3 expression and the prognosis of LUAD patients with overall survival (OS). (c) Relative expression levels of lncRNA SNHG3 in different LUAD cell lines were detected by RT-qPCR. *$P < 0.05$, **$P < 0.01$ vs. the normal tissue the 16HBE cell line.

overexpression (Figures 4(e) and 4(f)). Therefore, miR-890 overexpression promoted the progression of LUAD. SNHG3 activated LUAD progression by regulating miR-890.

4. Discussion

LUAD is one of the most common types of malignancy worldwide, accounting for high mortality rates [1, 2]. Therefore, determining the specific underlying mechanisms of LUAD remains a priority for the development of effective treatments for patients with LUAD. Currently, numerous studies have reported roles for and determined the underlying mechanisms of lncRNAs in LUAD [12–17]. In particular, the lncRNA SNHG3 was discovered to serve as a competing endogenous RNA to regulate the progression of various cancer types [18–20]. For example, SNHG3 promoted hepatocellular tumorigenesis by regulating miR-326 expression [21], and SNHG3 modulated the miR-384/WEE1 G_2 checkpoint kinase axis to regulate laryngeal carcinoma cell proliferation and migration [22]. In addition, the lncRNA SNHG3 was reported to play a vital role in LUAD progression [23, 24]. However, to the best of our knowledge, the tumorigenic properties and underlying mechanism of action of SNHG3 in LUAD progression remain to the determined. The present study characterized the expression pattern and molecular mechanism of SNHG3 in LUAD. The expression levels of SNHG3 were found to be downregulated in both clinical samples from patients with LUAD and LUAD cell lines. Furthermore, SNHG3 overexpression inhibited the proliferation, migration, and invasion and promoted the apoptosis of LUAD cells, which indicated that SNHG3 may regulate the malignant behavior of LUAD cells by serving as an oncogene in LUAD. Mechanistically,

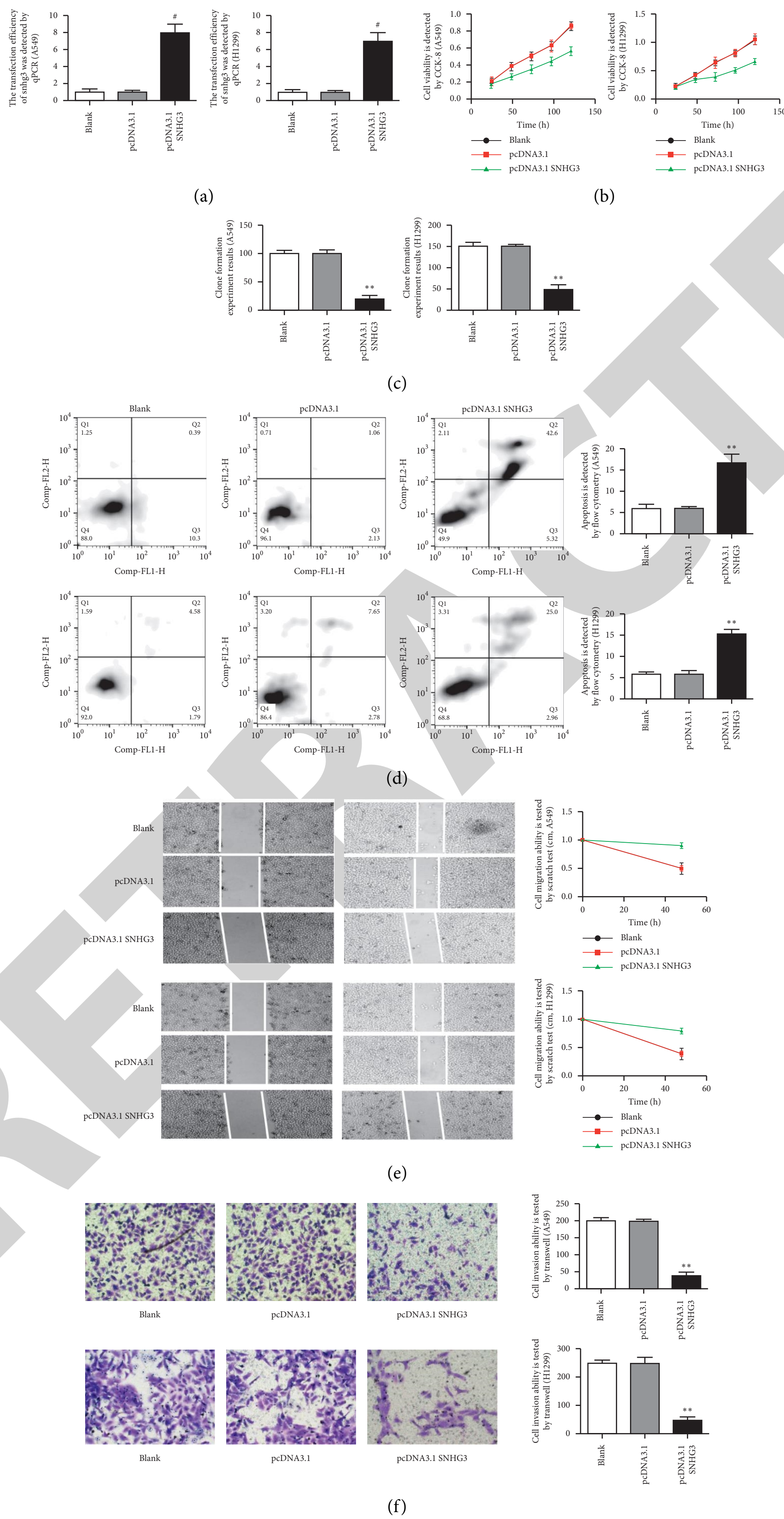

Figure 2: SNHG3 overexpression inhibits the progression of LUAD cells. (a) The transfection efficiency of pcDNA3.1 SNHG3 was verified by RT-qPCR assay. (b) Cell viability was detected by CCK-8 assay. (c) Cell proliferation was detected by clone formation assay. (d) Cell apoptosis was determined by flow cytometry assay. (e) Cell migration was detected by wound scratch assay. (f) Cell invasion was detected by transwell chamber assay. $^{\#}P < 0.05$, $^{**}P < 0.01$ vs. blank and pcDNA3.1.

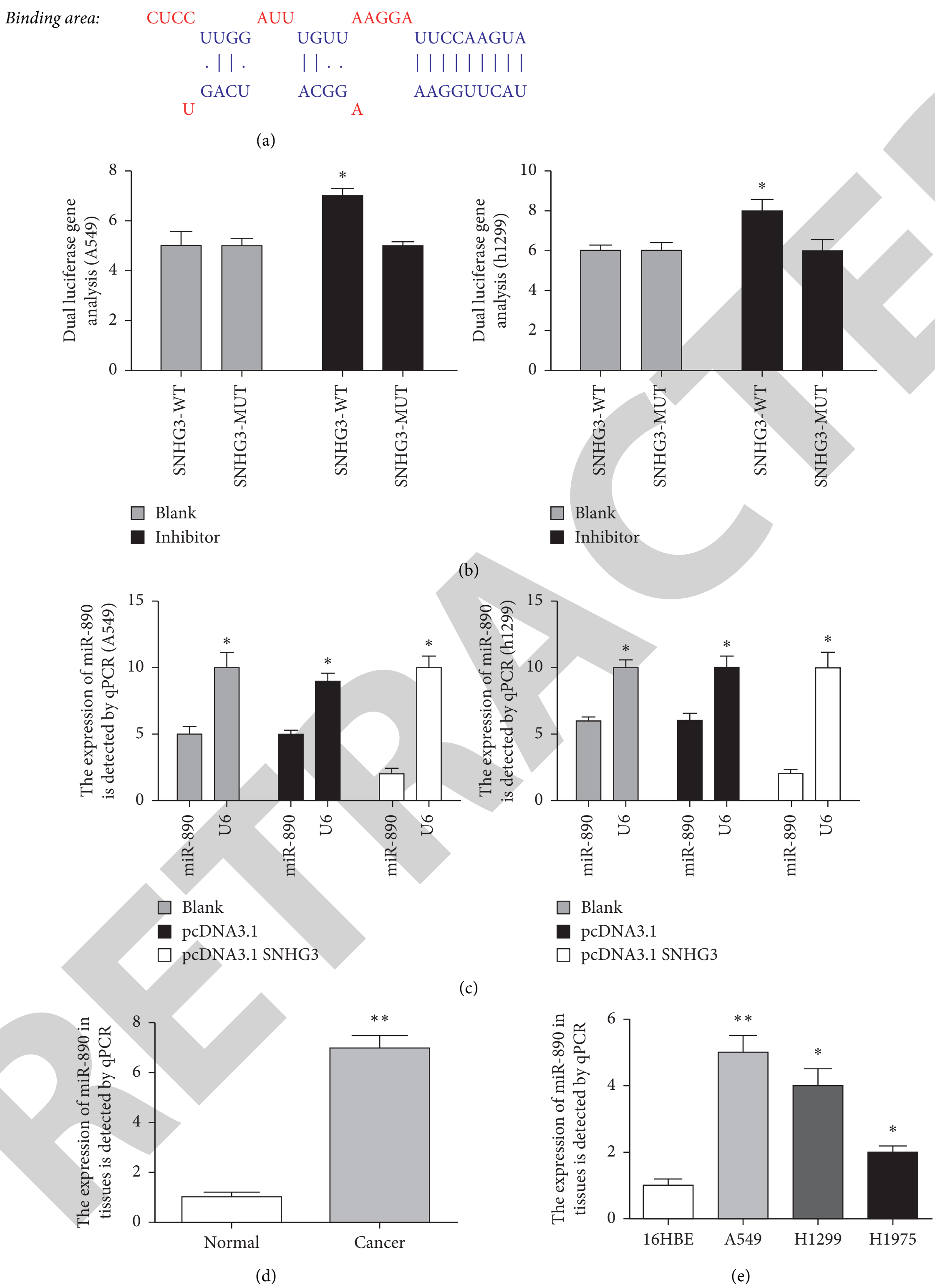

Figure 3: SNHG3 directly binds to miR-890 and downregulates the miR-890 expression. (a) The putative miR-890 binding sites for SNHG3. (b) Luciferase reporter assay was applied to assess the relationship between SNHG3 and miR-890. $^*P < 0.05$ vs. blank and NC-inhibitor. (c) Relative mRNA expression level of miR-890 was detected by RT-qPCR when cells were transfected with pcDNA3.1 SNHG3. $^*P < 0.05$ vs. blank and pcDNA3.1. (d) Relative expression levels of miR-890 in LUAD tissues and normal tissues were detected by RT-qPCR. $^{**}P < 0.01$ vs. the normal tissue. (e) Relative expression levels of lncRNA SNHG3 in different LUAD cell lines were detected by RT-qPCR. $^*P < 0.05$, $^{**}P < 0.01$ vs. the normal tissue the 16HBE cell line.

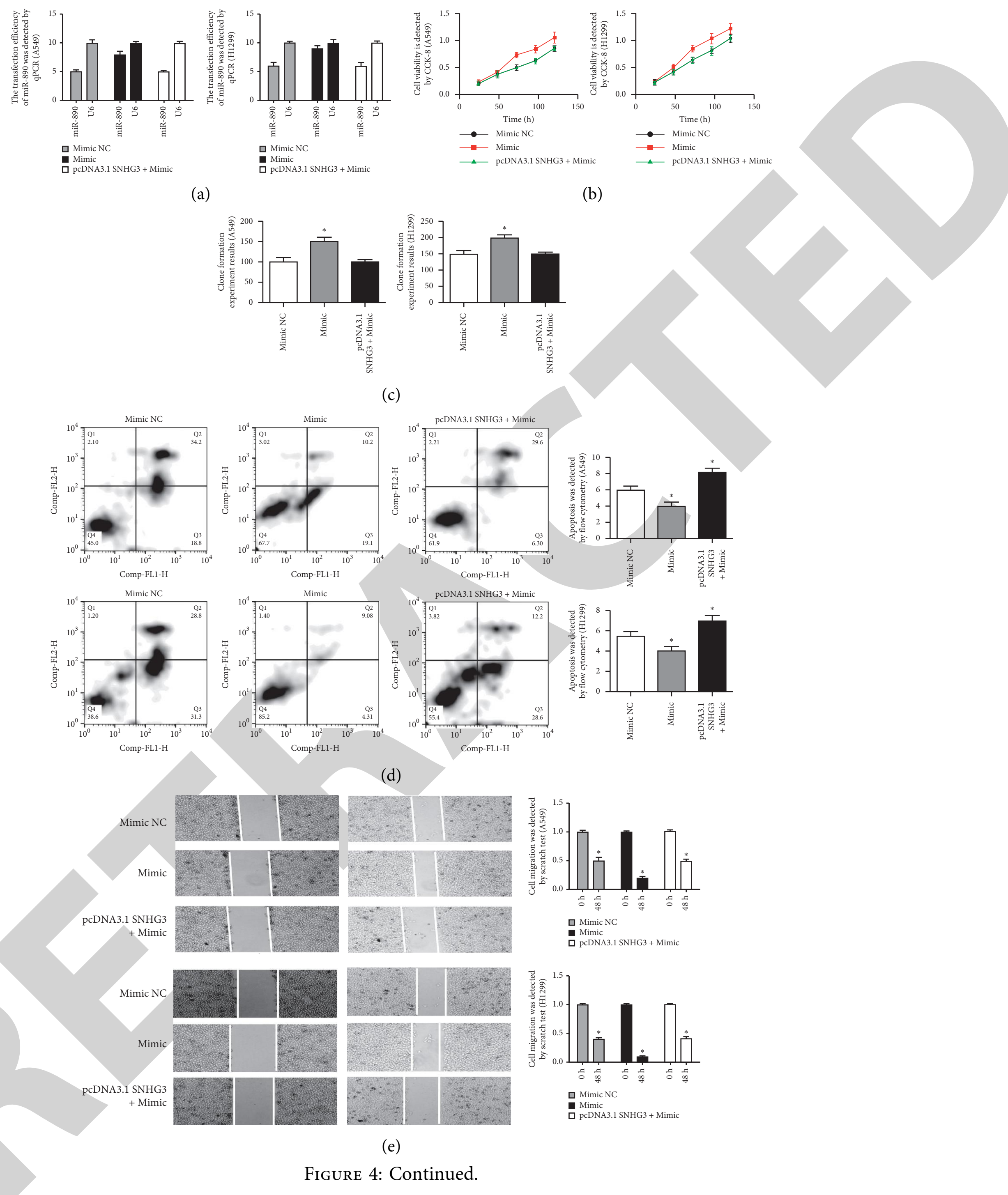

Figure 4: Continued.

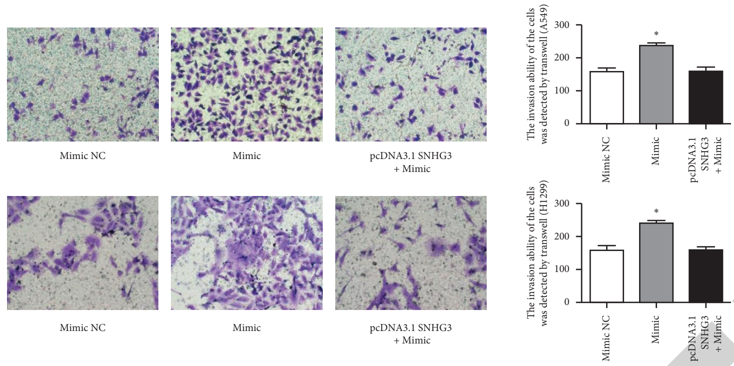

Figure 4: SNHG3 promotes the progression of LUAD by regulating miR-890. (a) The relative expression level of miR-890 in A549 and H1299 cells transfected with miR-890 mimic and pcDNA3.1 SNHG3+miR-216a-3p mimic was measured by RT-qPCR. (b) Cell viability was detected by CCK-8 assay. (c) Cell proliferation was detected by clone formation assay. (d) Cell apoptosis was determined by flow cytometry assay. (e) Cell migration was determined by wound healing assay. (f) Cell invasion was determined by transwell chamber assay. $^{*}P < 0.05$, $^{**}P < 0.01$ vs. blank and NC mimic.

SNHG3 promoted LUAD progression by regulating miR-890 expression.

An increasing number of studies have demonstrated that miRNAs exert both tumor suppressive and oncogenic roles in tumorigenesis, and the expression of lncRNAs can regulate the activities of miRNAs [25, 26]. Therefore, miRNAs have shown promise as potential clinical biomarkers and therapeutic targets for the treatment of patients with LUAD [27–29]. To date, numerous studies have revealed that miR-890 was associated with the progression of a large number of cancer types [30, 31]. For instance, miR-890 repressed the proliferation and invasion and induced apoptosis in breast cancer cells by regulating CD147 expression [32]. Nevertheless, to the best of our knowledge, the functional role of miR-890 in the evaluation of LUAD status remains unclear. Based on the results of a previous study, the present study further investigated the function of miR-890 in LUAD development. Using bioinformatics analysis and a dual luciferase reporter assay, SNHG3 was predicted to directly bind to miR-890. Moreover, miR-890 expression was negatively regulated by SNHG3, and miR-890 expression levels were found to be upregulated in both LUAD tissues and cell lines. In addition, miR-890 overexpression promoted the proliferation, migration, and invasion and inhibited the apoptosis of LUAD cells. Thus, miR-890 overexpression abrogated the effects of SNHG3 overexpression on LUAD cells. Thus, it is suggested that SNHG3 may promote the occurrence and progression of LUAD by regulating miR-890 expression.

Nonetheless, there are several limitations to the present study. First, although there are a large number of lncRNAs, the current study only determined the role of lncRNA SNHG3 and miR-890 in LUAD. Second, the study did not investigate the association between other lncRNAs and lung cancer and any other potential interactions between genes. Therefore, future studies will focus on the interactions between lncRNAs.

In conclusion, to the best of our knowledge, the current study was the first to report the function and regulatory mechanism of the lncRNA SNHG3 in LUAD. The findings suggested that SNHG3 may function as an oncogene in LUAD by modulating the expression levels of miR-890. Therefore, lncRNA SNHG3 and miR-890 may serve as novel biomarkers or potential targets for the treatment of LUAD.

Data Availability

The simulation experiment data used to support the findings of this study are available from the corresponding author upon request.

Disclosure

Baojie Kang and Caihong Qiu should be considered co-first authors.

Conflicts of Interest

The authors declare that they have no conflicts of interest.

Authors' Contributions

Baojie Kang and Caihong Qiu contributed equally to this work. Baojie Kang drafted the manuscript and cooperated with Caihong Qiu to conduct the experiment and with Yingzhang to collect the data.

References

[1] T. V. Denisenko, I. N. Budkevich, and B. Zhivotovsky, "Cell death-based treatment of lung adenocarcinoma," *Cell Death & Disease*, vol. 9, no. 2, p. 117, 2018.

[2] B. D. Hutchinson, G. S. Shroff, M. T. Truong, and J. P. Ko, "Spectrum of lung adenocarcinoma," *Seminars in Ultrasound, CT and MRI*, vol. 40, no. 3, pp. 255–264, 2019.

Hindawi
Journal of Healthcare Engineering
Volume 2021, Article ID 5678994, 9 pages
https://doi.org/10.1155/2021/5678994

Research Article

Optimized Fuzzy C-Means Algorithm-Based Coronal Magnetic Resonance Imaging Scanning in Tracheal Foreign Bodies of Children

Lan Jin and Ke Chang

Department of Pediatrics, Hospital of Chengdu University of Traditional Chinese Medicine, Chengdu 610072, Sichuan, China

Correspondence should be addressed to Ke Chang; jinlan168@stu.cdutcm.edu.cn

Received 15 April 2021; Revised 24 May 2021; Accepted 18 June 2021; Published 7 July 2021

Academic Editor: Enas Abdulhay

In order to provide theoretical support for clinical diagnosis, the diagnostic value of the optimized fuzzy C-means (FCM) algorithm combined with coronal magnetic resonance imaging (MRI) scan was investigated in the diagnosis of tracheal foreign bodies in children. The anisotropic filtering was applied to optimize the traditional FCM algorithm, so as to construct a new MRI image segmentation algorithm, namely, AFFCM algorithm. Then, the traditional FCM algorithm, the FCM algorithm based on the kernel function (KFCM), and the FCM algorithm based on the spatial neighborhood information (RFCM) were introduced for comparison with the AFFCM. 28 children diagnosed with foreign bodies in the trachea were selected for MRI diagnosis, and AFFCM was used for segmentation. The partition coefficient, segmentation entropy, and the correlation degree between classes after fuzzy division of the four algorithms were recorded, and the location and distribution of foreign bodies in the trachea and the types of foreign bodies were also collected. Besides, the MRI scanning and chest X-rays of the children with foreign bodies in the trachea should also be recorded in terms of the positive rate, diagnosis rate, and indirect signs. The class division coefficient and interclass correlation degree after fuzzy division of AFFCM were markedly greater than those of FCM, KFCM, and RFCM ($P < 0.05$), while the segmentation entropy of AFFCM was less sharp than the entropies of FCM, KFCM, and RFCM ($P < 0.05$). Among the 28 children, there were 5 cases with foreign bodies in the trachea (17.86%), 10 cases in the left bronchus (35.71%), and 13 cases in the right bronchus (46.43%). Among the foreign body types, there were 10 cases of melon seeds (35.71%), 6 cases of peanuts (21.43%), and 5 cases of beans (17.86%). The positive rate (89.29%) and diagnosis rate (96.43%) of MRI for bronchial foreign bodies increased obviously in contrast to the rates of X-ray chest radiographs (57.14% and 67.86%) ($P < 0.05$). Therefore, it was indicated that AFFCM showed higher partition coefficient value, lower segmentation entropy, larger similarity among classes, and better image segmentation effect. Furthermore, AFFCM-based coronal MRI scan had a higher positive rate and diagnosis rate for children's tracheal foreign bodies, and the main signs were emphysema and atelectasis.

1. Introduction

Tracheal foreign bodies in children refer to foreign bodies entering the airway, causing airway blockage. In mild cases, it can result in lung damage, and, in severe cases, suffocation death is more common in children below 5 years of age [1]. The most common manifestations of foreign bodies in the trachea of children are severe coughing, suffocation, nausea, excessive phlegm, and difficulty breathing [2]. If it is not treated in time, it will easily lead to suffocation, atelectasis, recurrent pneumonia, which will not heal for a long time, and even death in severe cases. Therefore, timely diagnosis of foreign bodies in the trachea of children is necessary. The clinical diagnosis methods for foreign bodies in the trachea of children mainly include X-ray, ordinary computed tomography (CT), and multislice spiral CT [3, 4]. When diagnosing atypical foreign bodies in the trachea of infants and young children, it is necessary to use X-rays for chest plain radiographs and fluoroscopy to determine the presence of foreign bodies through indirect signs. However, when the imaging manifestations such as pulmonary obstruction, pulmonary block shadows, and atelectasis occur, it is easy to be misdiagnosed as bronchial pneumonia, bronchial lung cancer, bronchial asthma, and other diseases, and the misdiagnosis rate is high [5]. Ordinary CT axial images increase the detection rate of foreign bodies, and the display clarity of indirect lung signs is better than X-ray, but it has the disadvantages of slow scanning speed, only presenting axial images, and easy to miss small foreign bodies. Multislice spiral CT is developed based on common CT technology, which greatly shortens the scanning time, and has higher resolution and image clarity, but it does not perform well in soft tissue display and needs further improvement. MRI examination is an auxiliary examination method that is extensively applied in clinical practice. It is different from X-ray film, CT, and other methods, which can accurately locate the lesion and make qualitative diagnosis of the lesion. It is mainly suitable for soft tissues, bones and joints, nervous system, and chest and abdomen [6, 7].

Due to the uncertainty of the gray scale and geometric shape of the digital image, it is quite difficult to use the digital image. Therefore, it is necessary to apply fuzzy theory and robust algorithm to process these digital images [8]. Among them, fuzzy C-means (FCM) is the most widely used objective function-based fuzzy clustering method in daily life applications. It occupies a key position in the field of image segmentation and can be used for gray image or color image segmentation [9]. FCM can obtain the minimum value of the objective function through an iterative optimization method, thereby updating the membership of the elements in the sample set and finally obtaining the optimal cluster center [10, 11]. However, FCM also has some inherent shortcomings. For example, FCM will become very sensitive and affect the accuracy of the segmentation results when some sample images with natural noise are encountered. Based on this, the introduction of anisotropic filtering was considered in this study to optimize the FCM algorithm and apply it to the sagittal MRI image processing of pediatric bronchial foreign bodies.

To sum up, the application of mathematical algorithms and magnetic resonance imaging (MRI) images in the field of medical diagnosis is the focus of the current research. On this basis, anisotropic filtering was employed to optimize the traditional fuzzy clustering method, and a new MRI image segmentation algorithm was constructed in this study. In addition, the traditional fuzzy clustering algorithm, the FCM algorithm based on the kernel function (KFCM), and the rough FCM (RFCM) were also introduced, which were compared with the fuzzy clustering algorithm. 28 pediatric patients diagnosed with foreign bodies in the trachea were selected for MRI diagnosis, and AFFCM was used for segmentation to comprehensively evaluate the diagnostic value of modified FCM combined with coronal MRI scanning in children with foreign bodies in the trachea.

2. Materials and Methods

2.1. Research Objects. 28 child patients, who were hospitalized with foreign bodies in the trachea in the hospital from October 2019 to November 2020, were selected as the research objects in this study. There were 17 males and 11 females, with the age ranging from 5 months to 10 years, and the history of foreign body inhalation ranged from 5 hours to 32 days. This study had been approved by the ethics committee of the hospital, and the family members of the child patients included in the study were known and signed the informed consent forms.

The inclusion criteria were defined to include child patients who were diagnosed with foreign bodies in the trachea, signed the informed consent forms, and had no contraindications to MRI scanning.

The exclusion criteria were defined to include child patients who had received relevant treatment, withdrew from the experiment halfway, and had other lung diseases.

2.2. Coronary MRI and X-Ray Scanning. The requirements of MRI scanning were as follows: A 3.0 T superconducting magnetic resonance MAGNETOM Skyra imaging system (produced by Siemens, Germany) was adopted in this study to scan the child patients. First, each child patient was placed in a supine position and underwent the cross-sectional and sagittal positioning scanning. Besides, a coronal scanning was performed with the child's trachea and bronchus bifurcation as the center to obtain the coronal T1-weighted imagining (T1WI) of the self-cyclotron wave sequence. The scanning parameters included repetition time (TR) of 400 ms, echo time (TE) of 15 ms, and layer thickness of 5 mm.

The requirements of chest X-ray were shown in the following. In this study, PHILIPS DR machine (produced by Royal Philips, Netherlands) was used for X-ray examination, and each child patient was placed in a supine position, inhaled, and taken X-ray after the chest was in the center.

2.3. FCM Based on Anisotropic Filtering Optimization. FCM can minimize the objective function through the iterative calculation of the membership matrix and clustering center, and then the data sample set is partitioned by defuzzing operation according to the membership matrix [4]. When FCM is applied to image segmentation, all pixels on the image to be segmented are the sample set of data, and its objective function can be expressed as follows:

$$G_\alpha(W, Z) = \sum_{i=1}^{n} \sum_{j=1}^{s} \left(w_{ji}\right)^\alpha l^2(x_i, z), \tag{1}$$

$$\sum_{j=1}^{s} \left(w_{ji}\right) = 1. \tag{2}$$

In equations (1) and (2), s represents the number of clusters, n stands for the number of pixels, W expresses the value of the membership function, $S = (w_{ji})_{s\times n}$, Z indicates the central value of all clusters, $Z = (z_1, z_2, \ldots z_n)$, x_i means the gray value of the image pixel, α represents the fuzzy weighted index, and $l^2(x_i, z)$ indicates the square of the error within the class. Then, the Lagrangian multiplier method is introduced to solve equations (1) and (2):

$$H = \sum_{j=1}^{s} \left(w_{ji}\right)^{\alpha} l_{ji}^{2} + \beta\left(1 - \sum_{j=1}^{s} w_{ji}\right). \tag{3}$$

In equation (3), H represents the Lagrangian multiplier solution, and α and β stand for the parameters. Then, the necessary conditions for the optimization of the Lagrangian equation should be the following:

$$\frac{\partial H}{\partial \beta} = 1 - \sum_{j=1}^{s} w_{ji} = 0, \tag{4}$$

$$\frac{\partial H}{\partial w_{ji}} = \alpha\left(w_{ji}\right)^{\alpha-1}\left(l_{ji}\right)^{2} - \beta = 0. \tag{5}$$

From equation (4), the following equation can be obtained:

$$w_{ji} = \left[\frac{\beta}{\alpha\left(l_{ji}\right)^{2}}\right]^{(1/\alpha-1)}. \tag{6}$$

Equation (5) is substituted into equation (2), so as to obtain the two following equations:

$$\sum_{j=1}^{s} w_{ji} = \left(\frac{\beta}{\alpha}\right)^{1/\alpha-1}\left\{\sum_{j=1}^{s}\left[\frac{1}{\left(l_{ji}\right)^{2}}^{1/\alpha-1}\right]\right\} = 1, \tag{7}$$

$$\left(\frac{\beta}{\alpha}\right)^{1/\alpha-1} = \frac{1}{\sum_{j=1}^{s}\left[1/\left(l_{ji}\right)^{2}\right]^{1/\alpha-1}}. \tag{8}$$

Equation (9) can be obtained by substituting equation (8) into equation (5).

$$w_{ji} = \frac{1}{\sum_{p=1}^{s}\left[l_{ji}/l_{jp}\right]^{2/\alpha-1}}. \tag{9}$$

Then, $G_{\alpha}(W, Z)$ is made to be the minimum membership function value, which can be shown in the following equation:

$$w_{ji} = \left[\frac{\beta}{\alpha\left(l_{ji}\right)^{2}}\right]^{1/\alpha-1}. \tag{10}$$

In the same way, $G_{\alpha}(W, Z)$ is made to be the smallest cluster center value, as shown in the following equation:

$$Z_i = \frac{\sum_{i=1}^{n}\left(w_{ji}\right)^{\alpha} x_i}{\sum_{i=1}^{n}\left(w_{ji}\right)^{\alpha}}. \tag{11}$$

Therefore, the cluster center and the best classification matrix can be determined by equations (10) and (11) according to the number of cluster categories of the data sample set and the specified sample fuzzy weight. What is more, the defuzzy algorithm [12] is applied to operate the membership matrix to complete the partition effect of samples. However, the standard FCM algorithm does not consider the association of the neighboring pixels of each element when performing image segmentation, which makes the algorithm very sensitive to images with noise. Therefore, the anisotropic filtering method was introduced in this study to denoise the image by anisotropic filtering, and its objective function can be updated as follows:

$$\begin{aligned} G^{*} &= \sum_{j=1}^{s}\sum_{t=0}^{T-1} f_{x}(t) w_{jt}^{\alpha}\left\|\Phi\left(x_t\right) - \Phi\left(z_j\right)\right\|^{2} \\ &\quad + \kappa \sum_{j=1}^{s}\sum_{t=0}^{T-1} f_{y}(t) w_{jt}^{\alpha}\left\|\Phi\left(y_t\right) - \Phi\left(z_j\right)\right\|^{2}. \end{aligned} \tag{12}$$

In equation (12), t stands for the gray level in the image, T represents the highest gray level in the image, $f(t)$ means the gray domain histogram statistical function of the image before and after processing, κ indicates the coefficient of fuzzy weight correction, y represents the gray value of the postprocessing image, and $\Phi(x)$ represents the kernel function. $\Phi(x)$ is set as the Gaussian kernel function ([K]), so the following equations can be gotten:

$$\left\|\Phi\left(x_i\right) - \Phi\left(z_j\right)\right\|^{2} = K(x, x) + K(y, y) - 2K(x, y), \tag{13}$$

$$K(x, y) = \exp\left(-\frac{\|x - y\|^{2}}{\theta^{2}}\right). \tag{14}$$

From equations (13) and (14), the following equation can be obtained:

$$\left\|\Phi\left(x_i\right) - \Phi\left(z_j\right)\right\|^{2} = 2\left(1 - K\left(x_i, z_j\right)\right). \tag{15}$$

Thus, the objective function can be updated as follows:

$$\begin{aligned} G^{*} &= \sum_{j=1}^{s}\sum_{t=0}^{T-1} f_{x}(t) w_{jt}^{\alpha}\left(1 - K\left(x_i, z_j\right)\right) \\ &\quad + \kappa \sum_{j=1}^{s}\sum_{t=0}^{T-1} f_{y}(t) w_{jt}^{\alpha}\left(1 - K\left(y_i, z_j\right)\right). \end{aligned} \tag{16}$$

The same can be solved to make $G*(W, Z)$ the minimum membership function value and cluster center value, which can be expressed in the two following equations:

$$w_{ji} = \frac{\left[f_x(t)\left(1 - K\left(x_i, z_j\right)\right) + \beta f_y(t)\left(1 - K\left(y_i, z_j\right)\right)\right]^{1/\alpha - 1}}{\sum_{j=1}^{s}\left[f_x(t)\left(1 - K\left(x_i, z_j\right)\right) + \beta f_y(t)\left(1 - K\left(y_i, z_j\right)\right)^{1/\alpha - 1}\right]}, \tag{17}$$

$$Z_i = \frac{\sum_{t=0}^{T-1}\left[f_x(t)w_{jt}^{\alpha}K\left(x_i, z_j\right)x_t + \beta f_y(t)w_{jt}^{\alpha}K\left(y_i, z_j\right)y_t\right]}{\sum_{j=1}^{s}\left[f_x(t)w_{jt}^{\alpha}K\left(x_i, z_j\right) + \beta f_y(t)w_{jt}^{\alpha}K\left(y_i, z_j\right)\right]}. \tag{18}$$

Therefore, an optimized FCM algorithm based on anisotropic filtering can be obtained, which is set as AFFCM. The calculation process is shown in Figure 1. First, the FCM algorithm's parameters are initialized, the image is preprocessed by anisotropic filtering, and the histogram function of the original image and the filtered image is obtained. Then, the membership matrix and clustering center are calculated and updated. If $t \le T$, the algorithm ends. Otherwise, the above steps are repeated. Finally, the image is deblurred to judge the categories of image elements.

2.4. Evaluation Criteria for Image Segmentation. The traditional FCM algorithm, KFCM [13], and RFCM [14] were introduced for comparison with AFFCM constructed in this study. Moreover, the results of image segmentation were evaluated by using three indicators of correlation degree between classes after fuzzy, partition coefficient, and segmentation entropy, which could be calculated as follows:

$$Q_{pc} = \frac{\sum_{i=1}^{s}\sum_{j=1}^{n} w_{ij}^{2}}{n}. \tag{19}$$

$$Q_{pe} = -\frac{\sum_{i=1}^{s}\sum_{j=1}^{n}\left(w_{ij}\log w_{ij}\right)}{n}. \tag{20}$$

$$Q_{da} = -\frac{\sum_{j=1}^{s}\sum_{j=1}^{n} w_{ij}\left\|x_j - z_i\right\|^2}{n\left(\min i \ne k\left\|z_k - z_i\right\|\right)}. \tag{21}$$

In equations (19), (20), and (21), Q_{pc} represented the partition coefficient, Q_{pe} stood for the segmentation entropy, Q_{da} meant the correlation degree between classes after fuzzy, and the other letters had the same meaning as above. When performing image segmentation, the larger the value Q_{pc}, the better the segmentation effect; the smaller the value Q_{pe}, the better the segmentation effect; the smaller the value Q_{da}, the better the segmentation effect.

2.5. Observation Indicators. Three indicators of AFFCM, FCM, KFCM, and RFCM needed to be recorded, which were the partition coefficient, segmentation entropy, and the correlation degree between classes after fuzzy. Then, the location and distribution of foreign bodies in the trachea and the types of foreign bodies should be collected. MRI scanning and chest X-ray were recorded for the diagnosis of tracheal foreign body (positive and negative), and the positive rate of diagnosis was calculated. In addition, the indirect signs of tracheal foreign bodies in the children were recorded by MRI scanning and chest X-ray.

2.6. Statistical Methods. SPSS 19.0 statistical software was used for test data processing, the measurement data were expressed as the mean ± standard deviation ($\overline{x} \pm s$), the count data were represented by percentage (%), and the AFFCM, FCM, KFCM, and RFCM were compared by one-way analysis of variance (ANOVA). Furthermore, MRI scanning and X-ray chest radiographs adopted t-test to compare the positive rate and the diagnosis rate of tracheal foreign bodies in children, and $P < 0.05$ indicated that the difference was statistically marked.

3. Results

3.1. Comparison on the Segmentation Performance of Different Algorithms. Figure 2 reveals that the partition coefficient and the correlation degree between classes after fuzziness of AFFCM increased greatly in contrast to those of FCM, KFCM, and RFCM, with a statistically marked difference ($P < 0.05$). The segmentation entropy of AFFCM (0.137) was smaller steeply than the entropies of FCM (0.447), KFCM (0.322), and RFCM (0.275), and there was a statistically obvious difference ($P < 0.05$). The partition coefficient and the correlation degree between classes after fuzziness of KFCM (0.347) and RFCM (0.406) were markedly greater than those of FCM (0.288) ($P < 0.05$), while the segmentation entropies of KFCM and RFCM were both hugely smaller than that of FCM ($P < 0.05$).

Figure 3 shows the comparison of MRI images processed by different algorithms. It was found that the original image map had poor clarity and more artifacts and noises, and the observation of image features was not clear enough, with poor quality. After the four algorithms, the sharpness of the image was improved to a certain extent, and the noise was correspondingly reduced. Among them, the sharpness of the image processed by AFFCM was the highest, with less noise and artifacts, and the quality was improved hugely.

3.2. X-Ray and MRI Imaging Evaluation of One Child Patient. Figure 4 shows the X-ray and MRI image evaluation of one case (male, 2 years old). X-ray film revealed that the transmittance of the left lung field decreased, the mediastinum moved to the left, the transmittance of the right lung field increased, the air content rose, and there were obvious manifestations of emphysema. Considering the valve function of the foreign body, the volume of air inhaled was more than the volume of air exhaled, resulting in the increased volume of air in the right lung and emphysema, so he was diagnosed as a right bronchial foreign body. The right lung emphysema could be observed from the MRI image, the

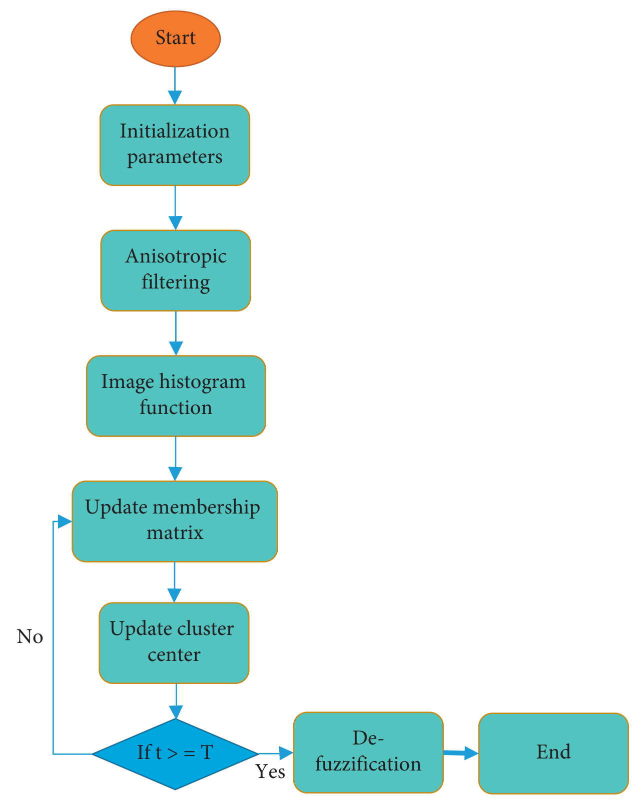

Figure 1: Algorithm's flow chart.

T1-weighted image was an iso-signal shadow, and the T2-weighted image was a high-intensity shadow. Thus, the diagnosis was a vegetative bronchial foreign body.

3.3. The Situation of Foreign Bodies in the Bronchus of 28 Child Patients. Figure 5 reveals that there were 5 cases of foreign bodies in the trachea (17.86%), 10 cases of foreign bodies in the left bronchus (35.71%), and 13 cases of foreign bodies in the right bronchus (46.43%) among the 28 child patients.

As for the types of foreign bodies, 10 cases were melon seeds (35.71%), 6 cases were peanuts (21.43%), 5 cases were beans (17.86%), 3 cases were pistachios (10.71%), 3 cases were plastic (10.71%), 1 case was fish bone (3.57%), most of which were plant-based foreign bodies, as shown in Figure 6.

3.4. Comparison on Positive Rate and Diagnosis Rate of MRI and X-Ray Diagnosis of Bronchial Foreign Bodies. Figure 7 discloses the comparison results of the positive rates of MRI and X-ray diagnosis of bronchial foreign bodies. It was found that MRI diagnosis of bronchial foreign bodies was positive in 25 cases and negative in 3 cases; chest X-ray diagnosis of bronchial foreign bodies was positive in 16 cases and negative in 12 cases. The positive rate of MRI diagnosis of bronchial foreign bodies (89.29%) rose substantially compared with X-ray chest radiograph (57.14%), and the difference was obvious ($P < 0.05$). Besides, the negative rate of MRI diagnosis of bronchial foreign bodies (10.71%) dropped sharply in contrast to the rate of X-ray chest radiograph (42.86%), showing a statistically huge difference ($P < 0.05$).

The diagnosis rates of MRI and X-ray diagnosis of tracheal foreign bodies were compared, and the results are presented in Figure 8. It shows that the diagnosis rate of tracheal foreign bodies diagnosed by MRI (96.43%) elevated obviously compared with chest X-ray (67.96%) ($P < 0.05$). However, the negative diagnosis rate of tracheal foreign bodies diagnosed by MRI (3.57%) reduced steeply in contrast to the rate of chest X-ray (32.14%) ($P < 0.05$).

3.5. MRI and X-Ray Diagnosis of Tracheal Foreign Body Signs. Figure 9 displays the signs of foreign bodies in trachea diagnosed by MRI and X-ray. It reveals that the X-ray diagnosis of bronchial foreign body signs included emphysema, atelectasis, limited obstruction, and mediastinal displacement. Among them, 21 child patients suffered from emphysema, 8 child patients had atelectasis, 1 child patient suffered from limited obstruction, and 2 child patients showed mediastinal displacement; thus emphysema > atelectasis > mediastinal displacement > limited obstruction. The bronchial foreign body signs diagnosed through MRI were emphysema, atelectasis, mediastinal swing, limited obstruction, mediastinal displacement, and pulmonary infection. Among them, there were 25 cases with emphysema, 22 cases with atelectasis, 17 cases with mediastinal swing, 10 cases with limited obstruction, 3 cases with mediastinal displacement, and 19 cases with pulmonary infection, so emphysema > atelectasis > pulmonary infection > mediastinal swing > limited obstruction > mediastinal displacement.

4. Discussion

Tracheal and bronchial foreign bodies refer to the symptoms of coughing, wheezing, and dyspnea caused by foreign bodies entering the respiratory tract through inhalation, ingestion, suffocation, and so forth. Kozaci et al. (2019) [15] found that when a foreign body entered the human airway, it would stimulate the airway mucosa and cause mucosal edema. If it stayed in the airway for too long, it would also lead to pneumonia and lung abscess. Therefore, it is necessary to choose an accurate way to diagnose and treat airway foreign bodies. MRI, as an imaging method extensively used in the field of medical diagnosis in recent years, has very prominent advantages, but it is rarely applied in the diagnosis of foreign bodies in the trachea. In this study, the traditional FCM algorithm was first optimized based on anisotropic filtering (AFFCM), which was compared with FCM, KFCM, and RFCM. The result indicated that the partition coefficient and the correlation degree between classes after fuzziness of AFFCM were hugely greater than those of FCM, KFCM, and RFCM, but the segmentation entropy of AFFCM was obviously smaller than those of FCM, KFCM, and RFCM ($P < 0.05$). This was similar to the research findings of Tamiru et al. (2012) [16], which showed that, compared with the traditional algorithm, the proposed algorithm AFFCM had higher segmentation coefficient value, lower segmentation entropy, higher similarity between classes, and better image segmentation effect [17].

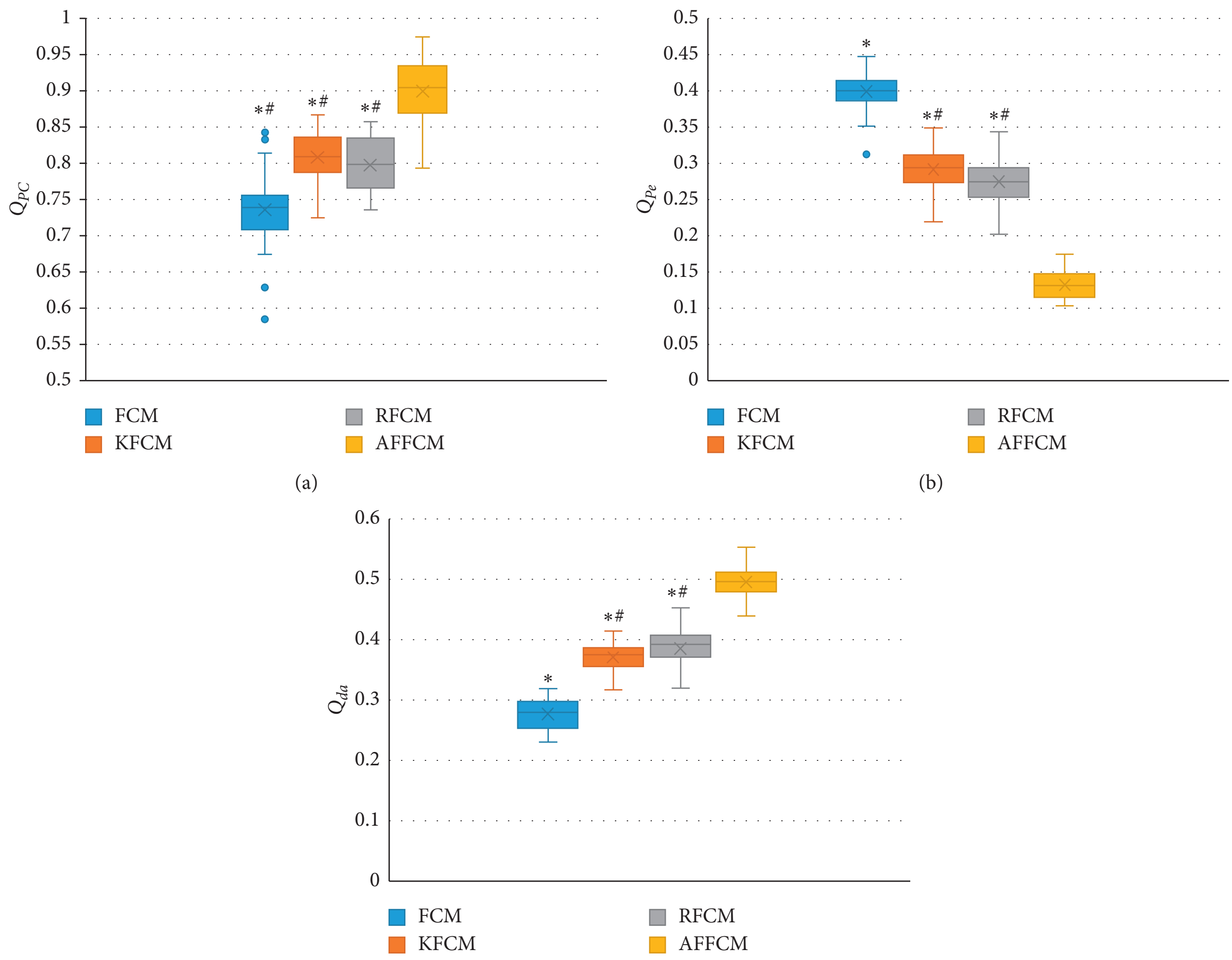

Figure 2: Comparison on partition coefficients, segmentation entropy, and the correlation degree between classes after fuzziness of different algorithms: (a) the partition coefficient; (b) the segmentation entropy; (c) the correlation degree between classes after fuzziness. $*$ indicates $P < 0.05$ compared with AFFCM; # indicates $P < 0.05$ compared with FCM.

(a) (b) (c)

Figure 3: Continued.

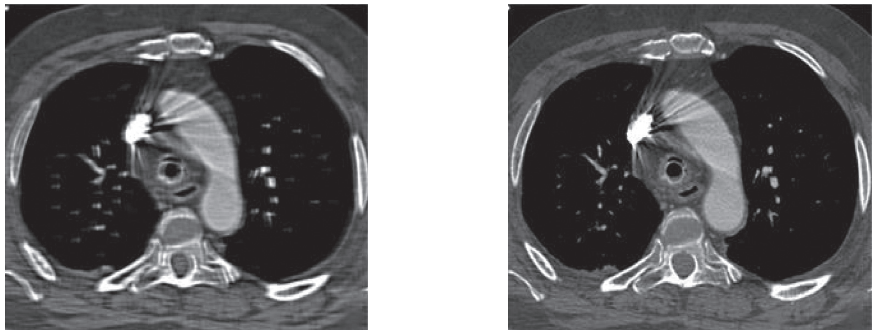

(d) (e)

Figure 3: Comparison on the segmentation performance of different algorithms: (a) the original image; (b) the image processed by FCM; (c) the image processed by KFCM; (d) the image processed by RFCM; and (e) the image processed by AFFCM constructed in this study.

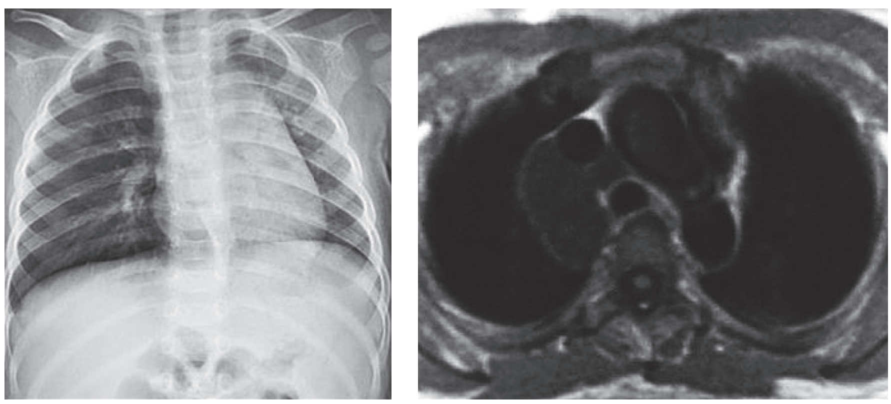

(a) (b)

Figure 4: X-ray and MRI image evaluation of a male case (2 years old): (a) a chest X-ray; (b) an MRI image.

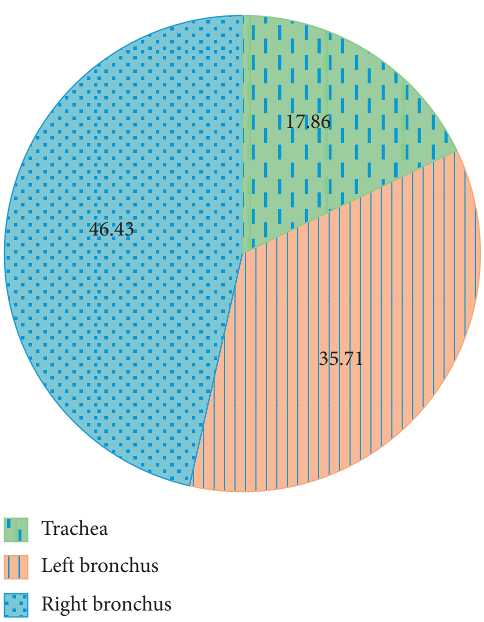

Figure 5: The distribution of foreign bodies in the bronchus of 28 child patients: 1: the foreign bodies in the trachea; 2: the foreign bodies in the left bronchus; 3: the foreign bodies in the right bronchus.

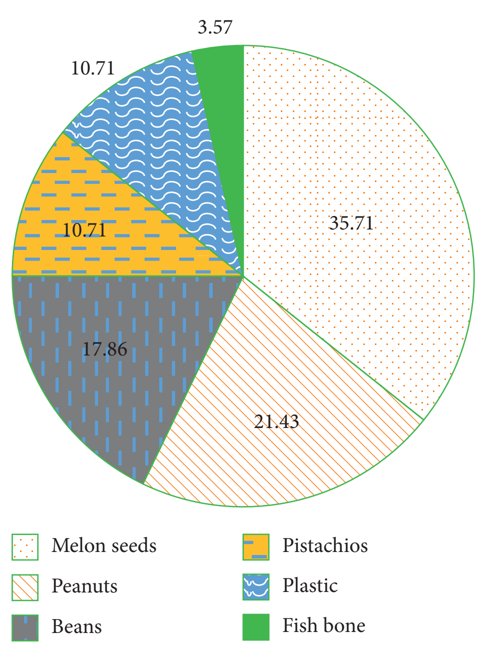

Figure 6: Types of bronchial foreign bodies in 28 child patients.

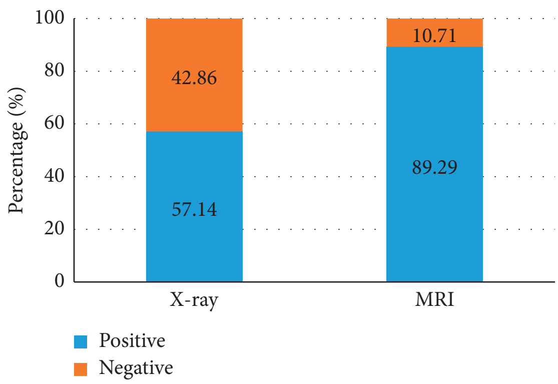

Figure 7: Comparison on positive rates of MRI and X-ray diagnosis of bronchial foreign bodies: $*$ indicates $P < 0.05$ by comparison with MRI.

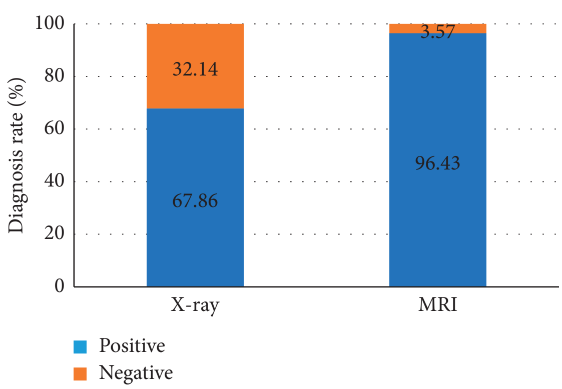

Figure 8: Comparison of the diagnosis rates of MRI and X-ray diagnosis of tracheal foreign bodies: $*$ indicates $P < 0.05$ compared to MRI.

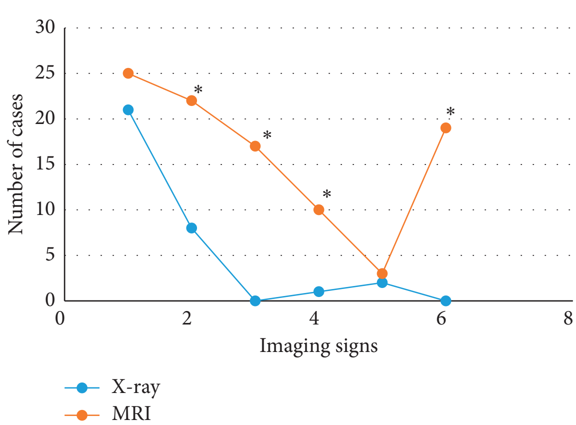

Figure 9: Comparison of the tracheal foreign body signs of MRI and X-ray diagnosis: $*$ indicates $P < 0.05$ compared with X-ray.

Based on the processed MRI images, AFFCM could overcome noise and improve image quality.

In this study, MRI and X-ray scanning based on AFFCM were performed on 28 children who were diagnosed with tracheal foreign bodies and admitted to the hospital from October 2019 to November 2020. It was found that there were 5 cases (17.86%) of tracheal foreign bodies, 10 cases (35.71%) of left bronchial foreign bodies, and 13 cases (46.43%) of right bronchial foreign bodies in the 28 children, which was consistent with previous studies, showing that the right bronchial foreign body was the most common site. Among the 28 cases of foreign bodies, 10 cases were melon seeds (35.71%), 6 cases were peanuts (21.43%), 5 cases were beans (17.86%), and other types were few, most of which were plant foreign bodies. This may be due to the fact that melon seeds are always available in every family. When children are frightened, crying, and naughty, and there are other predisposing factors, it is easy to accidentally choke into the airway [18]. The positive rate (89.29%) and diagnosis rate (96.43%) of bronchial foreign body diagnosed by MRI were substantially higher than the rates of chest X-ray (57.14% and 67.86%) ($P < 0.05$), which was similar to the research findings of Gao et al. (2015) [19], indicating that the diagnostic level of coronal MRI for airway foreign bodies was better than that of chest X-ray film. What is more, it could clearly show the size, shape, and type of foreign bodies as well as the complications caused to the lungs, and it was easier to identify the related diseases. The bronchial foreign body signs through MRI diagnosis were emphysema > atelectasis > lung infection > mediastinal swing > limited obstruction > mediastinal displacement, in which emphysema and atelectasis were the most common cases, suggesting that emphysema and atelectasis could be the main signs of bronchial foreign body in MRI diagnosis. In the X-ray diagnosis of bronchial foreign body signs, emphysema > atelectasis > mediastinal displacement > limited obstruction, where the number of emphysema cases was the largest, which indicated that emphysema could be used as the primary sign of X-ray diagnosis of bronchial foreign bodies.

5. Conclusion

In this study, the traditional FCM algorithm was optimized based on anisotropic filtering to obtain AFFCM, and it was compared with FCM, KFCM, and RFCM, which was also applied to 28 cases of pediatric tracheal foreign body MRI diagnosis. It was found that AFFCM had a relatively high partition coefficient value, a lower segmentation entropy, and a greater degree of similarity between classes, with better image segmentation effect. MRI based on AFFCM also had a higher positive rate and diagnosis rate for children with foreign bodies in the trachea, and the main signs were emphysema and atelectasis. However, the selection of children's samples is small in this study, and more detailed group discussions are not possible. Further consideration is given to the selection of more children to further explore the characteristics of tracheal foreign body in MRI images of child patients. All in all, the results of this study can provide a good theoretical basis for the clinical diagnosis of foreign bodies in the trachea of children.

Data Availability

No data were used to support this study.

Conflicts of Interest

The authors declare that they have no conflicts of interest.

Acknowledgments

This work was supported by Sichuan Administration of Traditional Chinese Medicine (2013BAI02B07), State Food and Drug Administration Bureau (H2014017), and Chengdu University of Traditional Chinese Medicine Foundation Project (301-568).

References

[1] O. Eyekpegha, U. Onakpoya, P. Obiajunwa, O. Famurewa, and A. Ogunrombi, "Missed distal tracheal foreign body in consecutive bronchoscopies in a 6-year-old boy," *Nigerian Journal of Surgery*, vol. 23, no. 1, PMCID, PMID: 28584516, pp. 67–70, 2017.

[2] V. Vieitez, M. Martín-Cuervo, V. López-Ramis, and L. J. Ezquerra, "Acute upper airway obstruction due to retropharyngeal hematoma in a dog with Anaplasma species: a case study," *BMC Veterinary Research*, vol. 11, no. 1, PMCID, PMID: 26452479, p. 257, 2015 .

[3] E. L. Riedesel, E. J. Richer, E. M. Sinclair et al., "Serial MRI findings after endoscopic removal of button battery from the esophagus," *American Journal of Roentgenology*, vol. 215, no. 5, pp. 1238–1246, 2020, Epub 2020 Sep 22. PMID: 32960667.

[4] L. Gonzalez, A. Candelario, Y. Otero, L. Torres-Luna, O. Cantres, and W. Rodriguez-Cintron, "Chronic non-asphyxiating bronchial foreign body removal," *Journal of Bronchology & Interventional Pulmonology*, vol. 26, no. 3, pp. e34–e37, 2019, PMID: 31233475.

[5] C. K. Hughes, C. L. Christensen, S. C. Maturo, P. R. O'Connor, and G. R. Dion, "Organic vs. Inorganic tracheobronchial airway foreign body aspiration: does type/duration matter?" *The Laryngoscope*, vol. 131, no. 3, pp. 490–495, 2021, Epub 2020 Aug 14. PMID: 32797684.

[6] W. W. Wang, H. J. Cheng, M. Li et al., "Analyses of diagnosis and treatment of foreign body aspiration in children with tracheobronchial variations]," *Zhonghua er bi yan hou tou jing wai ke za zhi*, vol. 54, no. 10, pp. 760–763, 2019, PMID: 31606989.

[7] B. Zhong, S.-L. Sun, J.-T. Du et al., "Risk factors for lower respiratory tract infection in children with tracheobronchial foreign body aspiration," *Medicine*, vol. 98, no. 10, PMCID, PMID: 30855455, , p. PMC6417600, 2019 , Article ID e14655.

[8] C. W. Fidkowski, H. Zheng, and P. G. Firth, "The anesthetic considerations of tracheobronchial foreign bodies in children: a literature review of 12,979 cases," *Anesthesia & Analgesia*, vol. 111, no. 4, pp. 1–25, 2010, Epub 2010 Aug 27. PMID: 20802055.

[9] K. Tachi, S. Yamashita, and M. Tanaka, "Tracheal foreign body removal under rigid bronchoscope in a child with fistula-like structure in the trachea after surgery of congenital esophageal atresia," *Masui*, vol. 65, no. 8, pp. 824–827, 2016, Japanese. PMID: 30351595.

[10] J. Shen, L. Huang, and C. Hao, "Value of multi-slice spiral computed tomography for diagnosis of tracheobronchial foreign body aspiration in children: 5-year retrospective study," *Pediatrics International*, vol. 62, no. 10, pp. 1184–1188, 2020.

[11] H. Gao, Z. X. Dou, L. Mu, X. Q. Li, F. Liu, and Y. Yang, "The application effect and safety analysis of dyclonine in children's removal of tracheal foreign body in trachea through bronchoscopy," *Lin Chung Er Bi Yan Hou Tou Jing Wai Ke Za Zhi*, vol. 30, no. 6, pp. 492–494, 2016, PMID: 29871048.

[12] R. Kapoor, T. Chandra, H. Mendpara, R. Gupta, and S. Garg, "Flexible bronchoscopic removal of foreign bodies from airway of children: single center experience over 12 years," *Indian Pediatrics*, vol. 56, no. 7, pp. 560–562, 2019, PMID: 31333209.

[13] S. Goyal, S. Jain, G. Rai et al., "Clinical variables responsible for early and late diagnosis of foreign body aspiration in pediatrics age group," *Journal of Cardiothoracic Surgery*, vol. 15, no. 1, p. 271, 2020 PMID: 32993750; PMCID: PMC7526158.

[14] A. B. Le Roux and D. Cahn, "What is your diagnosis?" *Journal of the American Veterinary Medical Association*, vol. 248, no. 8, pp. 879–881, 2016, PMID: 27031411.

[15] N. Kozaci, M. Avci, G. Ayhan, G. S. Ozgunlu, and F. Selvi, "The visualization of a foreign body in a Patient's subglottic region using point-of-care ultrasonography," *Pediatric Emergency Care*, vol. 35, no. 9, pp. 659-660, 2019, PMID: 31425476.

[16] T. Tamiru, P. E. Gray, and J. D. Pollock, "An alternative method of management of pediatric airway foreign bodies in the absence of rigid bronchoscopy," *International Journal of Pediatric Otorhinolaryngology*, vol. 77, no. 4, pp. 480–482, 2013, Epub 2013 Jan 5. PMID: 23294930.

[17] S. H. Woo, J. J. Park, M. Kwon, J. S. Ryu, and J. P. Kim, "Tracheobronchial foreign body removal in infants who had very small airways: a prospective clinical trial," *The Clinical Respiratory Journal*, vol. 12, no. 2, pp. 738–745, 2018, Epub 2016 Nov 23. PMID: 27860324.

[18] A. K. Jayaraj, P. K. Jayaraj, M. Murugesh, S. Aruchamy, A. Yousefzadeh, and N. T. Siddiqui, "Tracheal foreign body removal using flexible bronchoscope in a pediatric patient. A novel approach," *American Journal of Respiratory and Critical Care Medicine*, vol. 196, no. 8, pp. 1071-1072, 2017, PMID: 28862874.

[19] Z. Gao, X. Cai, and X. Zhou, "Application of endotracheal intubation in the rescue of children with severe trachea and bronchial foreign body]," *Lin Chung Er Bi Yan Hou Tou Jing Wai Ke Za Zhi*, vol. 29, no. 11, pp. 988–990, 2015, Chinese. PMID: 26536699.

Hindawi
Journal of Healthcare Engineering
Volume 2021, Article ID 4076175, 9 pages
https://doi.org/10.1155/2021/4076175

Research Article

Deep Learning-Based Magnetic Resonance Imaging Image Features for Diagnosis of Anterior Cruciate Ligament Injury

Zijian Li, Shiyou Ren, Ri Zhou, Xiaocheng Jiang, Tian You, Canfeng Li, and Wentao Zhang

Department of Sports Medicine and Rehabilitation, Peking University Shenzhen Hospital, Shenzhen 518036, China

Correspondence should be addressed to Wentao Zhang; 19zjli@stu.edu.cn

Received 15 April 2021; Revised 10 June 2021; Accepted 21 June 2021; Published 3 July 2021

Academic Editor: Enas Abdulhay

To study and explore the adoption value of magnetic resonance imaging (MRI) in the diagnosis of anterior cruciate ligament (ACL) injuries, a multimodal feature fusion model based on deep learning was proposed for MRI diagnosis. After the related performance of the proposed algorithm was evaluated, it was utilized in the diagnosis of knee joint injuries. Thirty patients with knee joint injuries who came to our hospital for treatment were selected, and all patients were diagnosed with MRI based on deep learning multimodal feature fusion model (MRI group) and arthroscopy (arthroscopy group). The results showed that deep learning-based MRI sagittal plane detection had a great advantage and a high accuracy of 96.28% in the prediction task of ACL tearing. The sensitivity, specificity, and accuracy of MRI in the diagnosis of ACL injury was 96.78%, 90.62%, and 92.17%, respectively, and there was no considerable difference in contrast to the results obtained through arthroscopy ($P > 0.05$). The positive rate of acute ACL patients with bone contusion and medial collateral ligament injury was substantially superior to that of chronic injury. Moreover, the incidence of chronic injury ACL injury with meniscus tear and cartilage injury was notably higher than that of acute injury, with remarkable differences ($P < 0.05$). In summary, MRI images based on deep learning improved the sensitivity, specificity, and accuracy of ACL injury diagnosis and can accurately determined the type of ACL injury. In addition, it can provide reference information for clinical treatment plan selection and surgery and can be applied and promoted in clinical diagnosis.

1. Introduction

The knee joint is a very important compound joint in the human body, which not only undertakes frequent and complex movements but also is the most important weight-bearing joint of the human body [1]. Therefore, knee injuries are inevitable in life. Most knee injuries are caused by high-intensity exercises, sports competitions, and falls from high altitudes. The most common knee injuries include anterior cruciate ligament (ACL) injury and meniscus injury, and the combination of the two injuries is also common. According to reports, the incidence of ACL injury with meniscus injury was more than 85%, which may cause joint swelling, pain, and movement inconvenience in patients, thus substantially affecting the life and work of patients [2, 3]. In the case of knee injury, timely and accurate assessment of ACL injury is helpful to select the best treatment plan and effectively evaluate the prognosis of patients. It is of great clinical significance for patients to recover the normal stability and normal motor function of knee joint and to avoid or reduce the secondary injury of other knee joint structures [4]. Clinically, complete tears and partial tears are often taken as the basis for judging ACL damage [5]. All in all, the early and correct diagnosis after ACL injury is of great significance for the choice of clinical treatment plan and prognosis [6, 7].

The commonly used methods for diagnosing ACL injury are roughly classified into three categories, clinical stability examinations, such as anterior drawer test and axis shift test, imaging examinations such as ultrasound diagnosis, CT diagnosis, and MRI diagnosis, and arthroscopy [8]. Ultrasound examination and CT examination require high operational experience of medical staff. Arthroscopic diagnosis is an effective standard for ACL injury, but the inspection method is limited to the case of trauma [9]. Therefore, clinical stability check is an important method for doctors to check ACL injury. Due to the good tissue resolution and high spatial resolution, MRI can not only objectively evaluate knee joint injuries but also evaluate knee joint injuries such as meniscus injuries and cartilage injuries [10].

Since MRI examinations show high clinical diagnosis accuracy of ACL tears and meniscus, knee MRI has become the first choice for the diagnosis of knee joint injuries in recent years. The deep learning approaches can automatically learn multilayer features, which are very suitable for the auxiliary diagnosis of medical images [11]. At present, deep learning approaches have surpassed traditional medical image analysis methods and have made great progress in the field of knee MRI. Mayo et al. [12] developed a fully automatic knee joint magnetic resonance cartilage damage detection system based on deep learning. The system consisted of two CNN networks. The first CNN network was utilized for the rapid segmentation of cartilage and bone, while the second CNN network evaluated the structural abnormalities of articular cartilage. The total accuracy of the experiment reached 98.37%. Therefore, the deep learning-based MRI cartilage injury detection system of the knee joint shows a high diagnostic accuracy, can quickly analyze images, significantly saves the diagnostic time, and improves the diagnostic efficiency. This diagnosis method is worthy of promotion and adoption.

In summary, the knee joint injury patients were taken as the research object in this research. MRI images of patients were optimized based on deep learning algorithms, which were then applied to the diagnosis of knee joint injury patients, and the adoption value of MRI image diagnosis in ACL injury was evaluated.

2. Materials and Methods

2.1. Research Objects and Grouping. Thirty patients with knee joint injuries diagnosed in our Hospital from May 2019 to March 2020 were selected as the research objects. All patients underwent MRI and the results were compared with those obtained by arthroscopy. There were 21 males and 9 females. The age range of the patients was 18–75 years, and the average age was (37.82 ± 5.18) years. The patients were rolled into two groups according to diagnosis methods. One group was MRI diagnose and the other group was arthroscopic diagnose, and they were compared within the groups. The experimental process had been approved by the ethics committee of the hospital, and all subjects included in the study had signed the informed consent forms.

Inclusion criteria: (i) clinical symptoms were joint pain, swelling, joint instability, etc.; (ii) physical examination methods (anterior drawer test, Lachman test, etc.) showed at least one positive sign; (iii) those who aged 18–75 years old.

Exclusion criteria: (i) patients with a previous history of knee joints, such as tuberculosis arthritis and rheumatoid arthritis; (ii) the patient's joints were found to have tumors or tumor-like lesions through examination; (iii) patients with a history of knee surgery; (iv) patients whose age was under 18.

2.2. MRI Examination. The patient's original image was sent to a postprocessing workstation. Three associate chief doctors with more than five years of experience in MRI diagnosis in the radiology department performed oblique coronal and cross-sectional multiplane recombination. The thickness was 0.4 mm, and there was no spacing between the layers. The three-dimensional reconstructed ACL and its surrounding structures were observed, and consensus was reached and recorded through consultation. At the same time, the MRI scan sequences (T2WI-SPAIR sagittal images, T2WI cross-sectional images, etc.) were observed and analyzed, and the corresponding diagnostic opinions were recorded. According to the characteristics, continuity, edge, shape, and signal of ACL damage, whether ACL was damaged and the extent of damage were judged. According to the comprehensive literature, MRI diagnostic criteria of ACL injury were established, and the MRI signs of ACL injury were classified into four categories [13] as follows. Grade 0: no abnormalities in initial profile, walk, and signal. Grade I: the ligament continuity was still good, the contour was still intact, the ligament was not thickened or slightly thickened and expanded, small patches or streaks of signal can be seen, and damage area was less than 50%. Grade II: ligamentous continuity was poor, but some continuous fibers were still visible; locally thickened or diffused ligaments were visible; incomplete or well-defined edges were at the site of ligament injury, or there were locally notched areas; abnormally high signal can be seen, with damage area greater than or equal to 50%. Grade III: there was intact rupture of the ligament, characterized by broken continuity of the ligament, displacement of the bent or broken end, clumpy ligament, increased signal, and unclear boundary.

After the patient's medical history and MRI results were provided, radiologists would observe and analyze the knee images of the patient to determine whether there was a tear in the ACL of the knee and the degree of the tear. If there was a difference of opinion, the three experts could reach a conclusion after consultation.

2.3. Arthroscopy Examination. Arthroscopy with a diameter of 4.0 mm and a wide angle of 30 degrees from Stryker and Smith & Nephew were utilized. The arthroscopy was performed by two joint surgeons. A detailed medical history was taken before surgery, and a physical examination was performed in combination with X-rays and MRI. The knee ACL was carefully examined during surgery. If there was a partial injury, a detailed examination with a probe was performed to avoid misdiagnosis. If a ligament injury was found arthroscopically, the physician could take further appropriate treatment and recorded the surgical plan and procedure. MRI findings and arthroscopic findings were studied and analyzed.

2.4. Deep Learning Model Construction Based on Multimodal Feature Fusion

2.4.1. Deep Feature Extraction. At present, convolutional neural networks are more and more widely used in the field of medical image diagnosis and have made good progress. The mechanism of convolutional neural network refers to automatically performing the feature extraction of the image through the convolution operation of the image, and such feature has advanced semantic information and is more robust [14]. Since the deep learning model can only achieve ideal results when trained on annotated images, transfer learning is adopted to directly use the second to fifth convolution blocks of the pretrained VGG16 [15]. The feature map of the last layer of each convolution block is extracted, which is $H(g)$, $g = 1, 2, 3, 4, 5$. After the up-sampling $K(g-1)$ of $H(g-1)$ was obtained, the result image after 2^*2 convolution processing is pixel fused, and then, 5^*5 convolution kernel is used again to correct the fused image, which can eliminate the aliasing effect used above and obtain a new feature map $H(g-1)$. The pyramid fusion equation is as follows:

$$\begin{aligned} K(g-1) &= y_{2\times 2}(H(g-1)), \\ H(g-1) &= y_{5\times 5}(H(g) + H(g-1)). \end{aligned} \tag{1}$$

After the last layer $H(2)$ is acquired, it passes through the batch normalization (BN) layer, the adaptive maximum pooling layer, and the fully connected layer in turn. The BN layer can speed up the convergence speed and classification effect of the model. $y^{(n)}$ is set as the nth dimension feature of $H(2)$, the BN layer is $H(2)$ introduced with the parameters $\partial^{(n)}$ and $D^{(n)}$, and the indifference estimation is conducted to output the nth dimension feature as follows:

$$y^{(n)} = \partial^{(n)}\overline{s}^{(n)} + D^{(n)}, \tag{2}$$

$$\begin{aligned} \overline{s_l} &= \frac{s_l - q}{\sqrt{w_x^2 + \vartheta}}, \\ q &= \frac{1}{e}\sum_{l=1}^{a} s_l, \end{aligned} \tag{3}$$

$$w_x^2 = \frac{1}{e}\sum_{l=1}^{a}(s_l - w_x). \tag{4}$$

In the above equation, equation (3) is the average value of batch size q, and equation (4) is the variance of batch size q.

When nonlinear factors are added to the ReLU layer, the expression ability of the increased model will be weakened. The activation function of ReLU is as follows:

$$f(m) = \max\{0, m\}. \tag{5}$$

The main difference between the adaptive maximum pooling layer and the standard Max Pooling is that the former will control the output size (Out) according to the input size (In), and stride and kernel size are as follows:

$$\begin{aligned} \text{stride} &= \text{floor}\left(\frac{\text{In}}{\text{Out}}\right), \\ \text{kernel size} &= \text{In} - (\text{Out} - 1) \times \text{stride}, \\ \text{Padding} &= 0. \end{aligned} \tag{6}$$

The fully connected layer can be regarded as the full-scale convolution of $s \times u$; s and u are the output size of the previous layer, and finally, 1026-dimensional features extracted by the convolutional neural network can be obtained:

$$h = (h_1, h_2, h_3, \ldots, h_{1026}). \tag{7}$$

2.4.2. Multimodal Feature Adaptive Fusion. Due to the different features of different modalities [16], a deep learning model of multimodal feature fusion is constructed to retain the correlation of multimodality. The model contains a hidden layer with a number of neurons less than the feature dimension and a Sigmoid layer. The entire network is trained by maximizing the energy proportion of the feature layer. The Sigmoid layer can map the feature interval after feature fusion to (0, 1), which is the prediction probability. The feature vector $m = (c, o)$, and the forward propagation equation is as follows:

$$p_e = (s_i + t_i)\vartheta_{ie} + \beta_e, \tag{8}$$

$$W = \partial\left(\sum_{l=1}^{a}(s_i + t_i)\vartheta_{ie} + \beta_e\right). \tag{9}$$

In the above equations, $\partial(k) = 1/1 + n^{-k}$, t_i is the deviation of the visible layer, β_e is the deviation of the hidden layer, and p_e is the hidden layer vector. To obtain the optimal fitting multimodal feature, the energy model is used to adjust the parameters, and the energy function is as follows:

$$H(x, y|\ell) = -\sum_{l=1}^{a} s_i t_i - \sum_{e=1}^{i} \beta_e p_e - \sum_{l=1}^{a}\sum_{e=1}^{i} t_i \vartheta_{ie} y_i. \tag{10}$$

In equation (9), $\ell = (t_i, \vartheta_{ie}, y_i)$, $H(x, y|\ell)$ represents the total energy of the module.

The marginal probability distribution is defined as follows:

$$p(x|\ell) = \frac{1}{Z(\ell)}\sum_{e} r^{-k(x,y|\ell)}, \tag{11}$$

$$p(y|\ell) = \frac{1}{Z(\ell)}\sum_{i} r^{-k(x,y|\ell)}. \tag{12}$$

In equations (10) and (11), $Z(\ell) = \sum_{il} r^{-k(x,y|\ell)}$, and the optimization function is defined as follows:

$$\ell_{nm} = \arg\max_{\ell}\sum_{j=1}^{o} \lg P\left(x_j|\ell\right). \tag{13}$$

In equation (12), o is the number of samples. When the function ℓ takes the maximum value, the energy proportion of the characteristic layer is high, and the energy of the hidden layer is small. When data is transmitted within the network, the direction of the data flow is also the direction of energy dissipation. After many iterations, the network energy shows a decay trend, the network tends to be ordered, or the probability distribution tends to be concentrated.

2.5. Evaluation Index. The performances of different models were quantitatively evaluated regarding the Accuracy, Recall, and AUC.

Accuracy refers to the proportion of the correct samples predicted by the model to the total samples, which is calculated as follows:

$$\text{Accuracy} = \frac{\text{TP} + \text{TN}}{\text{TP} + \text{FN} + \text{TN} + \text{FP}},$$
$$\text{Recall} = \frac{\text{TP}}{\text{TP} + \text{FN}}. \tag{14}$$

In the above equations, TP (true positive) means that the segmentation result and the gold standard result are both true, that is, true positive. FP (false positive) means that the segmentation result is false, and the gold standard results are all true. FN (false negative)) indicates that the segmentation result is true, and the gold standard results are all false.

The AUC value is defined as the area under the ROC curve enclosed by the coordinate axis. Since the ROC curve is generally above the line $y = x$, the value range of AUC is between 0.5 and 1. The closer the AUC is to 1.0, the higher the authenticity of the detection method is.

The observation of concomitant injury of ACL mainly included common combined injuries such as meniscus tear, bone contusion, medial and lateral collateral ligament injury, cartilage injury, and joint effusion.

2.6. Statistical Methods. SPSS 19.0 was employed for data statistics and analysis. Mean ± standard deviation ($\overline{x} \pm s$) was how measurement data were expressed, and the comparison of the mean between each group was performed by t test. Percentage (%) was how count data were expressed, and the χ^2 test was used. The difference was statistically considerable with $P < 0.05$.

3. Results

3.1. Analysis of the Results of ACL Damage Diagnosis Based on Deep Learning Algorithms. The results of ACL damage diagnosis based on deep learning algorithms were analyzed. Figure 1 showed that, after fusion of traditional features and deep learning features, the performance indicators of MRI were improved to a certain extent, especially in accuracy and AUC value. The accuracy was up to 90%, and the highest AUC value was 0.9726. The detection rate of this model for general positive samples was higher than 92%, and the detection rate for positive samples of ACL tear and meniscus tear was high, which was of great significance to assist physicians in diagnosing high-risk patients.

From the results in Figure 1, the sagittal plane detection had a great advantage and a high accuracy of 96.28% in the task of ACL tear prediction. The prediction accuracy of meniscus tear was low, which was 75.37% (Figure 1(a)). In the prediction of recall rate, the prediction of ACL tear was the best on the horizontal axis, the recall rate was 89.56% (Figure 1(b)), and the AUC value was 0.9726. In the prediction of meniscus tear, the sagittal plane was the best, with a recall rate of 90.57% and an AUC value of 0.923 (Figure 1(c)).

Since each prediction task had only two cases of positive and negative, the prediction probability of the model greater than or equal to 0.5 was deemed as a positive patient, and the prediction probability less than 0.5 was deemed as a negative patient, so as to better show the prediction effect of the model. The test results of ACL tear and meniscus tear were shown in Figure 2. The results showed that this prediction model had good performance for ACL tear and meniscus tear predictions, especially for ACL prediction accuracy and recall rate, and the maximum AUC value was above 0.96. It indicated that the prediction model based on deep learning used in this study can be used as a basis for diagnosing knee joint injuries and had certain value in clinical adoptions.

3.2. MRI Features of Patients with Knee Joint Injury Based on Deep Learning. Figure 3 was the schematic diagram of a 55-year-old male patient with bone contusion (axial displacement sign). In Figure 3(a), once the ACL was torn, the tibia would move forward relative to the femur, causing the lateral femoral condyle to collide with the outer and posterior tibia. Both sides had edema, and the degree of knee flexion determined the location of the femoral condyle. Figures 3(b) and 3(c) were images of ACL tears observed at different positions.

Figure 4 showed MRI images of some patients with knee injuries. Figure 4(a) showed ligament discontinuity. There was a low signal of the ligament, but the interruption was discontinuous, the path was low and flat, and the ligament was curled in a clumpy or wavy shape, which was generally seen in fresh injuries. In Figure 4(b), there was abnormal direction of ligament injury (ACL ptosis). There was a relatively intact ligament with low signal, but the direction was abnormal and pendulous, which was usually seen in the old injury of the femoral attachment, where the damaged ACL dropped and adhered to the PCL. In Figure 4(c), the ACL was absent. The intercondylar fossa was empty and there was no ligament signal. The symptoms were mainly present in prolonged injuries, where the damaged ACL tear was heavy and horse-tailed, did not enclose synovium, and was gradually corroded by enzymes in the joint.

In Figure 5(a), MRI T2WI showed a tear in the posterior horn of the medial meniscus of the knee. In Figure 5(b), MRI T2WI plain scan showed the high signal shadow within the low signal of the posterior cruciate ligament. The arrow indicated a partial rupture with hyperintensity bleeding around the rupture. The MRI diagnosis was an incomplete rupture of the right posterior cruciate ligament.

3.3. MRI Manifestations of ACL Injury. There are 60 knee joints in 30 patients with knee joint injury. In the examination results, the MRI examination showed that there were 34 cases of ACL grade III injury, 10 cases of grade II injury, 10 cases of grade I injury, and 6 cases of grade 0 injury.

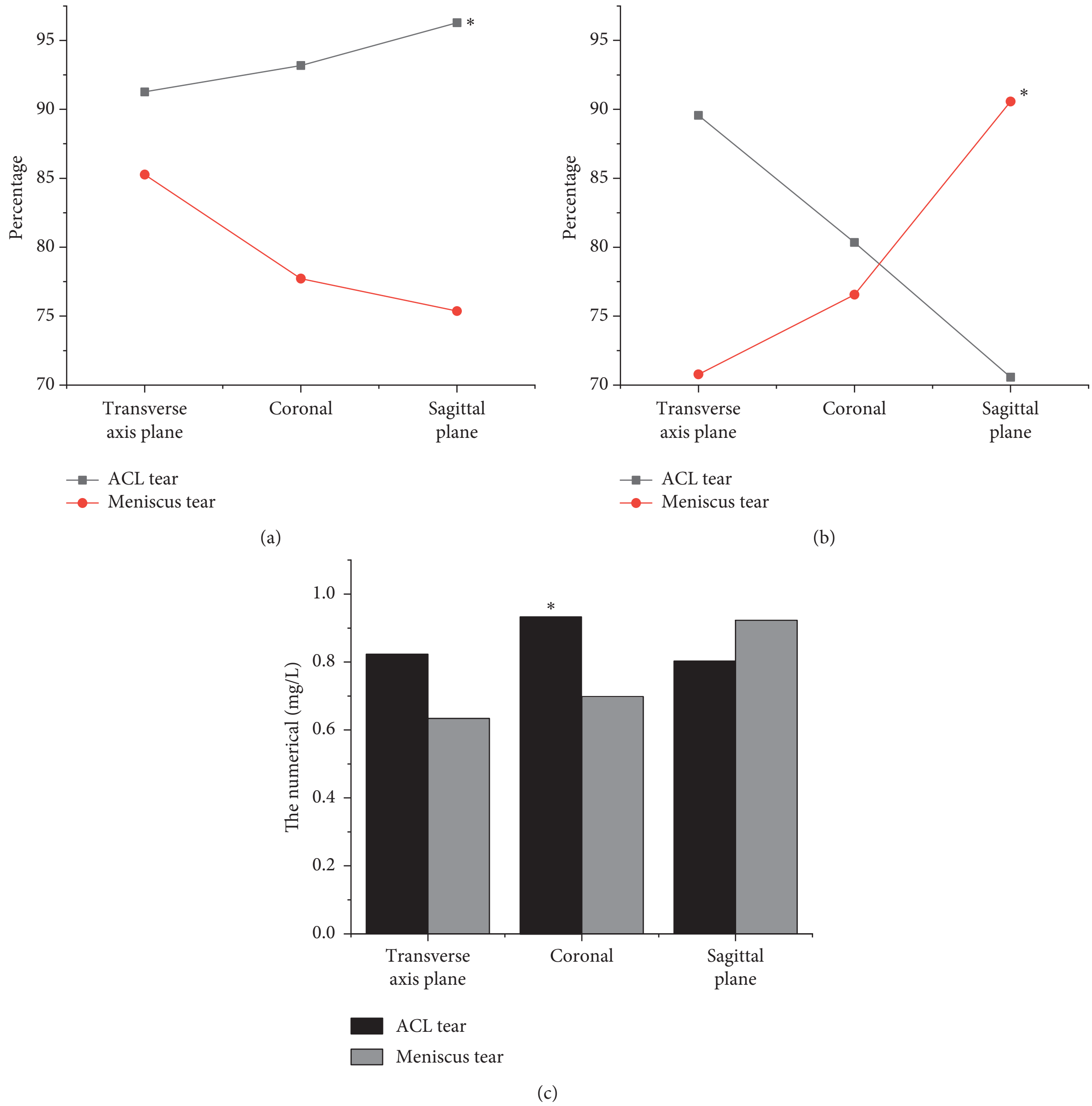

Figure 1: Analysis of diagnosis results of ACL injury based on deep learning algorithm. Accuracy comparison of transverse plane, coronal plane, and sagittal plane (a); recall rate comparison of transverse plane, coronal plane, and sagittal plane (b); AUC comparison of transverse plane, coronal plane, and sagittal plane (c). *indicated that the accuracy, recall rate, and AUC of ACL injury were statistically different from that of meniscus injury ($P < 0.05$).

Arthroscopy showed that there were 34 cases of ACL grade III injury, 13 cases of grade II injury, 11 cases of grade I injury, and 2 cases of grade 0 injury. Compared with the results of arthroscopy, 3 cases were misdiagnosed as intact ligaments, 3 cases were misdiagnosed as grade II ligament injuries, 1 case was misdiagnosed as grade I ligament injuries, 4 cases were misdiagnosed as grade 0 injuries, and 2 cases were missed (Figure 6).

Figure 7 showed that the sensitivity, specificity, and accuracy of MRI in the diagnosis of ACL injury was 96.78%, 90.62%, and 92.17%, respectively, with no substantial difference from the results of arthroscopy ($P < 0.05$), which showed that MRI can accurately diagnose ACL injury.

3.4. ACL Injury Classification and Concomitant Injury. In this research project, there were 34 cases of ACL grade III injury, including 10 cases of chronic injury and 24 cases of acute injury, 10 cases of grade II injury, 4 cases of chronic injury, and 6 cases of acute injury. Among grade I and grade 0 injuries, chronic injuries accounted for 3 cases and acute injuries accounted for 13 cases. There were 43 cases of acute injury and 17 cases of chronic injury.

Among the types of ACL injuries, there were meniscus tears, bone contusions, internal and external collateral ligament injuries, cartilage injuries, joint effusions, etc. The common concomitant injury was the torn meniscus. There were 30 patients with acute injury in concomitant injury and

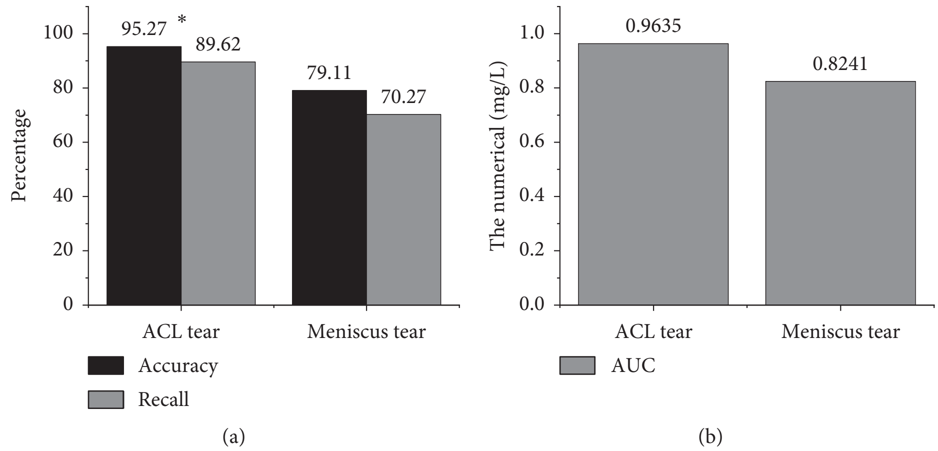

Figure 2: Performance comparison of regression models: (a) comparison of accuracy and recall rate of ACL and meniscus tear; (b) comparison of AUC of ACL and meniscus tear. *indicated that ACL injury was dramatically different versus meniscus injury ($P < 0.05$).

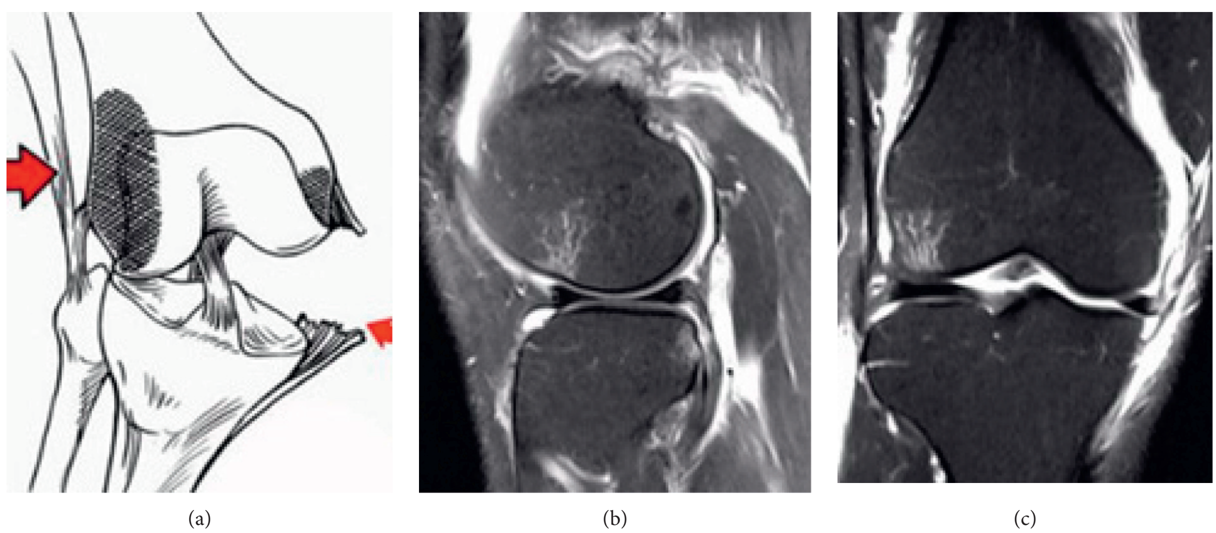

Figure 3: Schematic diagram of ACL injury. (a) The ACL tear, the arrow indicated the site of the ligament injury, (b) the coronal diagram of the ligament tear, and (c) the sagittal diagram of the ligament tear.

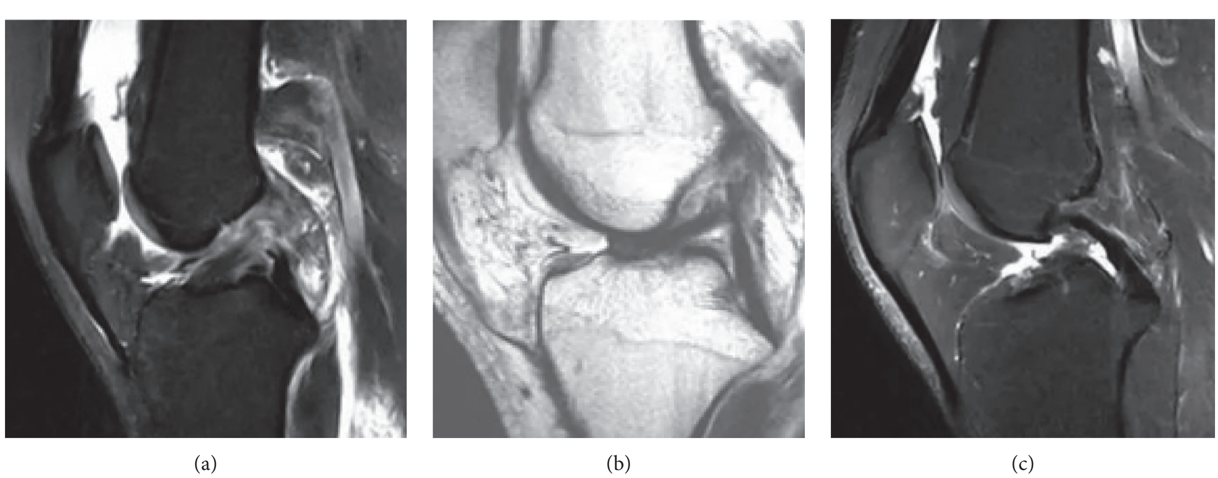

Figure 4: MRI images of the patients. (a) ACL discontinuity (49-year-old female patient), (b) ACL drooping sign (58-year-old male patient), and (c) ACL disappearance (55-year-old male patient).

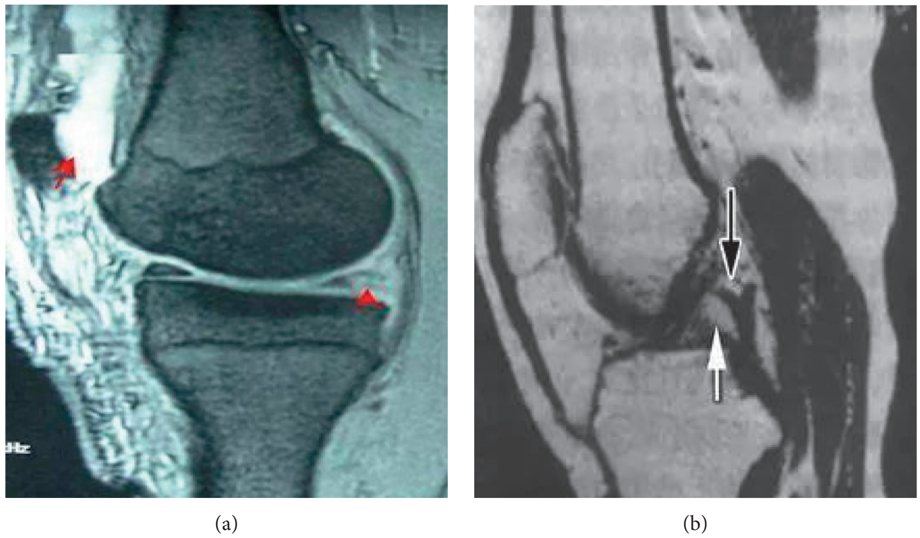

Figure 5: MRI T2WI images of the patients (male, 61 years old). (a) Tear of posterior corner of medial meniscus of knee joint (the arrow was the tear site); (b) MRI T2WI plain scan of posterior cruciate ligament (the arrow indicated a partial rupture of the ligament).

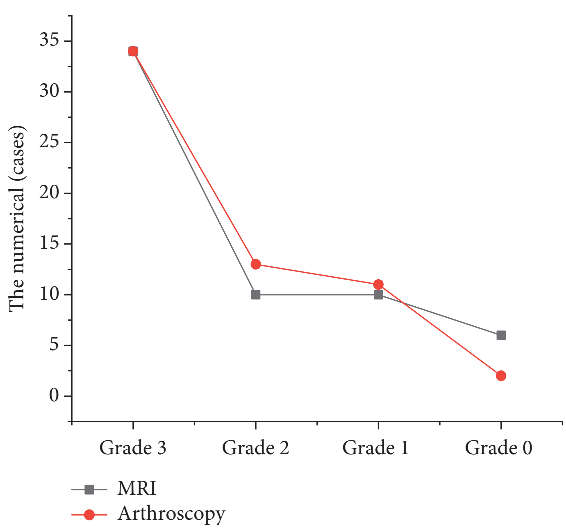

Figure 6: MRI diagnosis result of ACL injury.

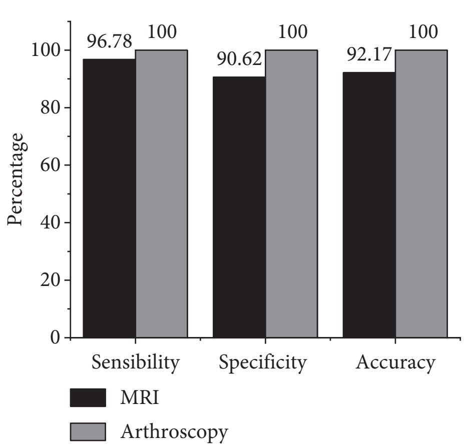

Figure 7: Contrast of MRI diagnosis performance of ACL injury.

meniscus injury. In addition, there were 20 patients with internal collateral ligament injury, 13 patients with lateral collateral ligament injury, 15 patients with cartilage injury, and 10 patients with bone contusion. Among chronic ACL injuries, 12 patients were accompanied by meniscus tears. In addition, there were 7 patients with collateral ligament injury, 5 patients with lateral collateral ligament injury, 7 patients with cartilage injury, and 3 patients with bone contusion. Figure 8 shows the positive rate of ACL concomitant injury. The positive rate of acute ACL patients with bone contusion and medial collateral ligament injury was considerably higher than that of the chronic patients. However, the incidence of ACL injury with meniscus tear and cartilage injury in the chronic group was substantially higher than that in the acute group, and there was a remarkable difference between the two ($P < 0.05$).

4. Discussion

The main function of the ACL is limiting the overdevelopment of the tibial plateau and the rotation of the knee joint. During the bending movement of the knee joint, the fiber bundles in the knee joint obtain the stability of the knee joint through various stretching modes. When the knee joint is straightened, the posterolateral branch (PLB) is in tension, and the anteromedial branch (AMB) is slightly relaxed. When the knee joint is bent, AMB is in tension and PLB is in a relaxed state. When an external force acts on the knee joint, resulting in excessive extension or rotation (for example, excessive internal and external rotation), it is easy to cause ACL damage or even fracture. MRI has become the most ideal examination method for the diagnosis of knee cruciate ligament injuries due to its advantages of high contrast, high resolution, noninvasive, and multipart imaging. MRI can not only clearly show the normal form of ACL but also show the location, extent, fracture, tear of meniscus, and other knee joint injuries of injured ACL. In this work, a

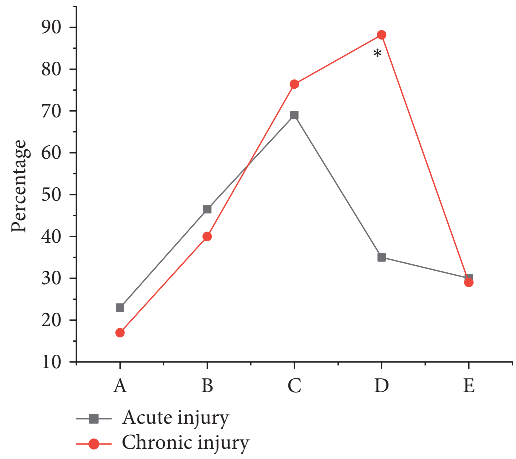

Figure 8: Contrast of positive rate of ACL concomitant injuries (A: bone contusion; B: medial collateral ligament injury; C: meniscus tear; D: cartilage injury; E: lateral collateral ligament injury) (*suggested remarkable differences in contrast to acute injury, $P < 0.05$).

multimodal feature fusion model based on deep learning was proposed for imaging diagnosis based on MRI. First, the knee joint MRI image was preprocessed, and the multimodal features of knee joint injury were extracted based on both traditional and deep learning. Then, the multilayer neural network was adopted to perform correlation fusion of the features. The results showed that the sagittal plane detection has a great advantage and a high accuracy rate of 96.28% in the task of ACL tear prediction. The prediction accuracy of meniscus tear was low, which was 75.37%. In the prediction of recall rate, the prediction of ACL tear was the best on the horizontal axis, the recall rate was 89.56%, and the AUC value was 0.9726. In the prediction of meniscus tear, the sagittal plane was the best, with a recall rate of 90.57% and an AUC value of 0.923. This prediction model showed good prediction performance for ACL tear and meniscus tear. In particular, the prediction accuracy and recall rate of ACL were relatively better, and the maximum AUC value was above 0.96. The results were similar to the conclusions of Miyaji et al. [17] and both showed that the prediction model based on deep learning used in this study can be used as a basis for diagnosing knee joint injuries and had certain value in clinical applications.

The model was applied to the MRI diagnosis of ACL injury. The MRI examination results showed that there were 34 cases of ACL grade III injury, 10 cases of grade II injury, 10 cases of grade I injury, and 6 cases of grade 0 injury. Arthroscopy showed that there were 34 cases of ACL grade III injury, 13 cases of grade II injury, 11 cases of grade I injury, and 2 cases of grade 0 injury. Compared with the results of arthroscopy, 3 cases were misdiagnosed as intact ligaments, 3 cases were misdiagnosed as grade II ligament injuries, 1 case was misdiagnosed as grade I ligament injuries, 4 cases were misdiagnosed as grade 0 injuries, and 2 cases were missed. The sensitivity, specificity, and accuracy of MRI in the diagnosis of ACL injury was 96.78%, 90.62%, and 92.17%, respectively, and there was no great difference from the results of arthroscopy ($P > 0.05$). Namiri et al. [18] found that the indirect signs of ACL tear had high specificity (91%~100%) and sensitivity in a retrospective study of the correlation between MRI imaging and arthroscopy in 100 patients. Therefore, these signs can determine whether the patient had an ACL tear, which was similar to the conclusion of this study, indicating that MRI can accurately diagnose ACL injury. The positive rate of acute ACL patients with bone contusion and medial collateral ligament injury was notably superior to the chronic group. However, the incidence of ACL injury with meniscus tear and cartilage injury in the chronic group was substantially higher than that in the acute group, with substantial differences ($P < 0.05$). Pedoia et al. [19] reported a high incidence of combined articular cartilage damage. However, the literature did not separate statistics on acute and chronic injuries. In this research topic, a clear analysis of the types of concomitant damage was carried out, and the results also provided a certain reference for the diagnosis of ACL concomitant damage.

5. Conclusion

A multimodal feature fusion deep learning model based on deep learning algorithms was established in this work and applied to the diagnosis of ACL injury patients, to explore the value of MRI based on deep learning in the diagnosis of ACL injury. The results revealed that deep learning-based MRI substantially improved the ability to diagnose ACL damage and increased the sensitivity, specificity, and accuracy of the diagnosis of ligament damage. However, this study still has some shortcomings. The number of patient samples selected is small, there is a lack of disease diversity research, and the scope of adoption of the research results has certain limitations. In the future work, the research area and research samples will be further expanded to ensure the universality of research results. In summary, the ability to diagnose ACL injuries in MRI images based on deep learning is improved, which provides a reference for the diagnosis and treatment of patients with knee joint injuries.

Data Availability

No data were used to support this study.

Conflicts of Interest

The authors declare that they have no conflicts of interest.

References

[1] B. Grawe, A. J. Schroeder, R. Kakazu, and M. S. Messer, “Lateral collateral ligament injury about the knee: anatomy, evaluation, and management,” *Journal of the American Academy of Orthopaedic Surgeons*, vol. 26, no. 6, pp. e120–e127, 2018.

[2] E. Alentorn-Geli, G. D. Myer, H. J. Silvers et al., “Prevention of non-contact anterior cruciate ligament injuries in soccer players. Part 1: mechanisms of injury and underlying risk factors,” *Knee Surgery, Sports Traumatology, Arthroscopy*, vol. 17, no. 7, pp. 705–729, 2009.

[3] Z. Lv, Li Xiaoming, W. Weixi, Z. Baoyun, Hu Jinxing, and F. Shengzhong, "Government affairs service platform for smart city," *Future Generation Computer Systems*, vol. 81, pp. 443–451, 2017.

[4] A. P. Dold, S. Swensen, E. Strauss, and M. Alaia, "The posteromedial corner of the knee: anatomy, pathology, and management strategies," *Journal of the American Academy of Orthopaedic Surgeons*, vol. 25, no. 11, pp. 752–761, 2017.

[5] Y. Dong and S. Y. Chen, "Improvement of arthroscopic thecnique to be helpful for the accurate treatment of knee joint injury," *Zhong Guo Gu Shang*, vol. 30, no. 4, pp. 293-294, 2017.

[6] F. Lecouvet, T. Van Haver, S. Acid et al., "Magnetic resonance imaging (MRI) of the knee: identification of difficult-to-diagnose meniscal lesions," *Diagnostic and Interventional Imaging*, vol. 99, no. 2, pp. 55–64, 2018.

[7] M. Englund, A. Guermazi, D. Gale et al., "Incidental meniscal findings on knee MRI in middle-aged and elderly persons," *New England Journal of Medicine*, vol. 359, no. 11, pp. 1108–1115, 2008.

[8] L. Zhang, M. Li, Y. Zhou, G. Lu, and Q. Zhou, "Deep learning approach for anterior cruciate ligament lesion detection: evaluation of diagnostic performance using arthroscopy as the reference standard," *Journal of Magnetic Resonance Imaging*, vol. 52, no. 6, pp. 1745–1752, 2020.

[9] F. Bruno, A. Barile, F Arrigoni et al., "Weight-bearing MRI of the knee: a review of advantages and limits," *Acta Bio-Medica: Atenei Parmensis*, vol. 89, no. 1-S, pp. 78–88, 2018.

[10] M. Javed Awan, M. Mohd Rahim, N. Salim, M. Mohammed, B. Garcia-Zapirain, and K. Abdulkareem, "Efficient detection of knee anterior cruciate ligament from magnetic resonance imaging using deep learning approach," *Diagnostics*, vol. 11, no. 1, Article ID 105, 2021.

[11] C. W. Shen and J. T. Ho, "Technology-enhanced learning in higher education: a bibliometric analysis with latent semantic approach," *Computers in Human Behavior*, vol. 14, no. 8, Article ID e0219586, 2019.

[12] M. H. Mayo, J. J. Mitchell, D. P. Axibal et al., "Anterior cruciate ligament injury at the time of anterior tibial spine fracture in young patients: an observational cohort study," *Journal of Pediatric Orthopaedics*, vol. 39, no. 9, pp. e668–e673, 2019.

[13] B. L. Young, J. A. Ruder, D. P. Trofa, and J. E. Fleischli, "Visualization of concurrent anterolateral and anterior cruciate ligament injury on magnetic resonance imaging," *Arthroscopy: The Journal of Arthroscopic & Related Surgery*, vol. 36, no. 4, pp. 1086–1091, 2020.

[14] S. H. Hong, J.-Y. Choi, G. K. Lee, J.-A. Choi, H. W. Chung, and H. S. Kang, "Grading of anterior cruciate ligament injury. Diagnostic efficacy of oblique coronal magnetic resonance imaging of the knee," *Journal of Computer Assisted Tomography*, vol. 27, no. 5, pp. 814–819, 2003.

[15] K. Simonyan and A. Zisserman, "Very deep convolutional networks for large-scale image recognition," 2014.

[16] B. A. Snoeker, F. W. Roemer, A. Turkiewicz, S. Lohmander, R. B. Frobell, and M. Englund, "Does early anterior cruciate ligament reconstruction prevent development of meniscal damage? results from a secondary analysis of a randomised controlled trial," *British Journal of Sports Medicine*, vol. 54, no. 10, pp. 612–617, 2020.

[17] N. Miyaji, Y. Hoshino, T. Tanaka et al., "MRI-determined anterolateral capsule injury did not affect the pivot-shift in anterior cruciate ligament-injured knees," *Knee Surgery, Sports Traumatology, Arthroscopy*, vol. 27, no. 11, pp. 3426–3431, 2019.

[18] N. K. Namiri, I. Flament, B. Astuto et al., "Deep learning for hierarchical severity staging of anterior cruciate ligament injuries from MRI," *Radiology: Artificial Intelligence*, vol. 2, no. 4, Article ID e190207, 2020.

[19] V. Pedoia, B. Norman, S. N. Mehany, M. D. Bucknor, T. M. Link, and S. Majumdar, "3D convolutional neural networks for detection and severity staging of meniscus and PFJ cartilage morphological degenerative changes in osteoarthritis and anterior cruciate ligament subjects," *Journal of Magnetic Resonance Imaging*, vol. 49, no. 2, pp. 400–410, 2019.

Hindawi
Journal of Healthcare Engineering
Volume 2023, Article ID 9836954, 1 page
https://doi.org/10.1155/2023/9836954

Retraction

Retracted: MiR-373 Inhibits the Epithelial-Mesenchymal Transition of Prostatic Cancer via Targeting Runt-Related Transcription Factor 2

Journal of Healthcare Engineering

Received 15 August 2023; Accepted 15 August 2023; Published 16 August 2023

This article has been retracted by Hindawi following an investigation undertaken by the publisher [1]. This investigation has uncovered evidence of one or more of the following indicators of systematic manipulation of the publication process:

(1) Discrepancies in scope
(2) Discrepancies in the description of the research reported
(3) Discrepancies between the availability of data and the research described
(4) Inappropriate citations
(5) Incoherent, meaningless and/or irrelevant content included in the article
(6) Peer-review manipulation

The presence of these indicators undermines our confidence in the integrity of the article's content and we cannot, therefore, vouch for its reliability. Please note that this notice is intended solely to alert readers that the content of this article is unreliable. We have not investigated whether authors were aware of or involved in the systematic manipulation of the publication process.

Wiley and Hindawi regrets that the usual quality checks did not identify these issues before publication and have since put additional measures in place to safeguard research integrity.

We wish to credit our own Research Integrity and Research Publishing teams and anonymous and named external researchers and research integrity experts for contributing to this investigation.

The corresponding author, as the representative of all authors, has been given the opportunity to register their agreement or disagreement to this retraction. We have kept a record of any response received.

References

[1] J. Pang, L. Dai, C. Zhang, and Q. Zhang, "MiR-373 Inhibits the Epithelial-Mesenchymal Transition of Prostatic Cancer via Targeting Runt-Related Transcription Factor 2," *Journal of Healthcare Engineering*, vol. 2021, Article ID 6974225, 9 pages, 2021.

Hindawi
Journal of Healthcare Engineering
Volume 2021, Article ID 6974225, 9 pages
https://doi.org/10.1155/2021/6974225

Research Article

MiR-373 Inhibits the Epithelial-Mesenchymal Transition of Prostatic Cancer via Targeting Runt-Related Transcription Factor 2

Jianyi Pang,[1] Limei Dai,[2] Chen Zhang,[3] and Qinglei Zhang[3]

[1]*Department of Urology Surgery, The Affiliated Weihai Second Municipal Hospital of Qingdao University, Weihai, Shandong 264200, China*
[2]*Department of Dermatology and STD, The Affiliated Weihai Second Municipal Hospital of Qingdao University, Weihai, Shandong 264200, China*
[3]*Department of Urology Surgery, The Affiliated Tengzhou Central People's Hospital of Jining Medical University, Tengzhou, Shandong 277500, China*

Correspondence should be addressed to Qinglei Zhang; zhangqinglei2021@163.com

Received 14 April 2021; Revised 20 May 2021; Accepted 20 June 2021; Published 29 June 2021

Academic Editor: Enas Abdulhay

Prostatic cancer (PCa) is a prevalent form of malignancy based on its high associated levels of mortality and morbidity across the world. MicroRNAs (miRNAs) are significant in the advancement of prostatic cancer. The current study is aimed at exploring the potential roles of miR-373 in PCa. In turn, the study conducted a qRT-PCR test to determine the levels of mRNA. A western blot test was also executed in determining the protein level. The processes of transwell assay and wound healing were integrated in the detection of the potential for PCa cells to invade and migrate. The integration of dual luciferase reporter assay is critical in determining the levels of luciferase activity among prostatic cancer cells. Then, the results showed a net decrease of miR-373 within prostatic cancer cells and tissues. Upregulated miR-373 reduced the invasion and migration potential of PCa cells. Moreover, overexpressed miR-373 increased the levels of E-cadherin and FSP1 as epithelial cell markers. Similarly, the overregulation of miR-373 brought about the upregulation of mesenchymal markers (N-cadherin, Snail, and vimentin). The study predicted runt-related transcription factor 2 (RUNX2) to be a target of miR-373. The luciferase activity of PCa cells was decreased after the cotransfection with miR-373 mimics and RUNX2 3′ untranslated region (3′UTR) wild type (WT). Moreover, RUNX2 became upregulated in PCa cells and tissues. The upregulation of miR-373 decreased the mRNA and protein level of RUNX2. However, overexpressed RUNX2 abated the roles of miR-373 in the intrusion and migration of PCa cells and in regulating the expression of epithelial cell markers and mesenchymal markers. In short, miR-373 may regulate the EMT of PCa cells via targeting RUNX2. The miR-373/RUNX2 axis provides a therapeutic target for PCa.

1. Introduction

PCa, characterized with high mortality and morbidity, is one of the most malignant tumors worldwide [1, 2]. The past years saw an increase of morbidity and mortality of PCa patients [3, 4]. The PCa-related deaths in 2012 reached 300,000 [5]. Additionally, the mortality of PCa increased from 3/100,000 to 30/100,000 in Asia [6]. Although prestigious breakthroughs have been realized in the management of PCa, the overall rates of survival in PCa are still unsatisfactory. In part, the diagnosis of patients at advanced stages is responsible for the low survival rates. The average survival rate over 5 years is 90% at early stage, while it is no more than 15% at advanced metastatic stage [7]. Lymph node metastasis and bone metastasis are the main challenges in the treatment of prostate cancer [8]. Epithelial-mesenchymal transition (EMT) remodels cell-cell and cell-extracellular matrix interactions, which induces the initiation and metastasis of cancer [9]. Therefore, to suppress the metastasis of PCa may be a promising therapy for the management of PCa.

MicroRNAs (miRNAs) are small endogenous noncoding RNAs, which play a crucial role in post-transcription [10].

Besides, miRNAs degrade gene level through their potential to bind to the 3′ untranslated region (3′UTR) within the target genes [11]. Intensive bodies of evidence have reported that miRNAs participate in multiple biological processes, including proliferation, cell differentiation, invasion, apoptosis, and migration, and epithelial-mesenchymal transition [12, 13]. Moreover, the aberrant expressed miRNAs are significant in facilitating the progression and emergence of cancer, including PCa. For instance, miR-373 is downregulated in non-small cell lung cancer (NSCLC), while overexpressed miR-373 suppresses EMT of NSCLC cells [14]. Upregulated miR-373 promotes EMT of tongue squamous cell carcinoma. MiR-373 is decreased in human epithelial ovarian cancer (EOC), while its overexpression suppresses the invasion and EMT of EOC cells [15]. MiR-373 inhibits the invasion of progression of PCa [16]. However, the underlying mechanisms is still unclear.

Still, RUNX2 is firstly reported to participate in the skeletal embryogenesis. In recent years, its oncogenic properties have been attracting increasing attention. RUNX2 is involved the initiation and progression of numerous cancers [17–19]. RUNX2 acts as an oncogene and regulates the apoptosis, migration, proliferation, invasion, and ETM of malignant cells via unchecked signaling pathways [18, 19]. In PCa, overexpressed RUNX2 is associated with high-grade prostatic intraepithelial neoplasia (HGPIN), cancerous lesions, and prostate tumorigenesis [20]. However, the possible roles of RUNX2 in EMT of PCa have not been elucidated.

In this study, transwell assay and wound healing were applied to examine the implications of overexpressed miR-373 on the processes of invasion and migration among PCa cells. The concept of luciferase assay has the potential of providing novel therapeutic target and was thus used in verifying whether RUNX2 was a target of miR-373. In summary, the study was based on the purpose of investigating the potential roles of miR-373 in the EMT of PCa and the underlying molecular mechanisms.

2. Methods

2.1. Clinical Samples. Tissue samples from the PCa as well as normal tissues in adjacent locations were selected from 30 patients diagnosed with PCa. Besides, the control population entailed patients that had benign prostatic hyperplasia (BPH) during August, 2017, to January, 2019, at The Affiliated Weihai Second Municipal Hospital of Qingdao University. The samples were immediately placed at a temperature of −80°C following the surgery. Besides, the participants have not received chemotherapy or radiotherapy prior to this study. The supervision of the research was conducted by the Institutional Review Board within the sponsoring institution. However, all participants were required to sign and provide informed consent.

2.2. Cell Culture. The researchers purchased their cell culture from ATCC and included normal prostate epithelia cell line alongside LNCaP, and DU145. Similarly, human PCa cell lines PC3 were also sourced from the cell culture in ATCC. Cells were incubated in a basal medium with 10% concentration of FBS and Penicillin-Streptomycin at 1%. Moreover, the temperature of the incubator was controlled at 37°C with 5% CO_2. The cells were subjected to a confluence of 80% through the process of being passaged.

2.3. Transfection. The transfection of PC3 cells was achieved using 50 nM of miR-373 mimics (Mimics) or miR-NC mimics (NC mimics) using Lipofectamine 2000 (Invitrogen, USA) for 48 h. pcDNA3.1 and pcDNA3.1-RUNX2 were synthesized and provided by GenePharma (Shanghai, China). The transfection of the cells was achieved using either pcDNA3.1-RUNX2 or pcDNA3.1 based on the manufacturer's protocols that use lipofectamine 2000.

2.4. qRT-PCR. The choice of reagent for isolating total RNA from the localized cells and tissues was TRIzol. The collected RNA was then transcribed into cDNA with PrimeScript RT kit (Takara, Japan) based on the manufacturer's instructions. The PCR was conducted using SYBR® Premix ExTaq™ II Kit (Takara, Japan) under the prescribed thermo cycling condition. Particularly, it was exposed to five minutes at 95°C, and 40 more cycles averaging 30 seconds at a temperature of 95°C. Finally, it was subjected to further cycles of 45 sec at 60°C. Then, a calculation of the expression level was made using $2^{-\Delta\Delta CT}$ method. In turn, U6 was regularized to the prescribed levels of miRNA and GAPDH to mRNA.

2.5. Western Blot. Cells or tissues were lysed. Total protein was collected with RIPA buffer (Sigma-Aldrich, USA). The concentration of the protein was calculated with BCA kit (Pierce, USA). Then, total protein was isolated with 12% SDS-PAGE. Afterwards, the protein was moved onto PVDF membranes, which was then blocked with milk that possessed nonfat attributes. The membranes would then be incubated over the night by relying on primary antibodies and being put in temperatures of 4°C in shade and then with secondary antibodies. Subsequently, the protein was visualized, and the relative protein level was calculated.

2.6. Wound Healing Assay. After 48 h transfection, cells became cultured with a 6-well plate (3 × 104 cells/well) overnight till the cells reached 80–90% confluency. Then, a pipette tip was applied to make a scratch. The cell movement was pictured and analyzed.

2.7. Transwell Assay. The cells were placed into a 24-well plate (2 × 103 cells/well) and then incubated in the upper chamber containing Matrigel and serum-free DMEM. Inherently, the bottom chamber was treated with 10% FBS. Within a day, the noninvasive cells were removed. Next, the invaded cells were corrected with 4% methanol while crystal violet was used for staining. Finally, the cells were captured before being calculated.

2.8. Dual Luciferase Reporter Assay. The online database across TargetScan 7.2 (https://www.targetscan.org/vert_72/) was utilized to forecast the target of miR-373. The 3′ untranslated region (3′UTR) sequences containing the potential target of miR-373 were synthesized and cloned into reporter gene plasmid vector pGL3 to build RUNX2 3′UTR wild type and RUNX2 3′UTR Mutant (MUT) plasmids. Then, the transfection of the cells is achieved using either miR-373 NC or the same variant with an accompanying Lipofectamine 2000 at 37°C with 5% CO_2. The determination of the cell luciferase activity was consistent with the Dual-Luciferase Reporter Assay System (Promega, USA).

2.9. Statistical Analysis. Data collected in the study was analyzed with SPSS22.0 software and represented through calculations of mean ± standard deviation (mean ± SD). The variances between the two groups were considered using Student's t-test, while the variances in multigroups were evaluated with one-way ANOVA. The statistical significance was set at $P < 0.05$.

3. Results

3.1. MiR-373 Is Downregulated in PCa Tissues. qRT-PCR was executed to identify the manifestation of miR-373 in PCa tissues as well as the normal tissues adjacent to the malignant cells. As shown in Figure 1, the expression of miR-373 was downregulated in PCa tissues relative to the normal tissues in adjacent locations, thereby suggesting that miR-373 may be an antitumor miRNA in PCa.

3.2. MiR-373 Is Decreased in PCa Cells. In exploring the roles of miR-373 in PCa, we also detected the expression of miR-373 in PCa cells. The findings also portrayed a decrease in the volume of miR-373 in PCa cell lines, such as PC3, LNCaP, and DU145, compared with prostate epithelial cell line RWPE-1, which was more potent in PC3 (Figure 2(a)). Then, PC3 cells were used in the following experiment. Moreover, the manifestation of miR-373 in PC3 cells that were transfected with miR-373 mimics was upregulated in comparison with control populations, which suggested PC3 were successfully transfected (Figure 2(b)).

3.3. MiR-373 Inhibits the EMT of PCa Cells. The processes of transwell assay and wound healing were executed to test the implications of miR-373 on the intrusion and migration of PCa cells. As shown in Figure 3(a), the scratch width of the miR-373 mimics transfected cells showed no significant difference. In turn, the healing rate was significantly decreased, suggesting that miR-373 inhibited the potential for PCa cells to migrate. Moreover, the ability of PCa cells to invade is significantly inhibited when transfected with miR-373 mimics, relative to the control group (Figure 3(b)). Meanwhile, overexpressed miR-373 downregulated N-cadherin, Snail, and vimentin and upregulated E-cadherin and FSP1, suggesting miR-373 played an inhibitory role in the EMT of PCa cells (Figure 3(c)).

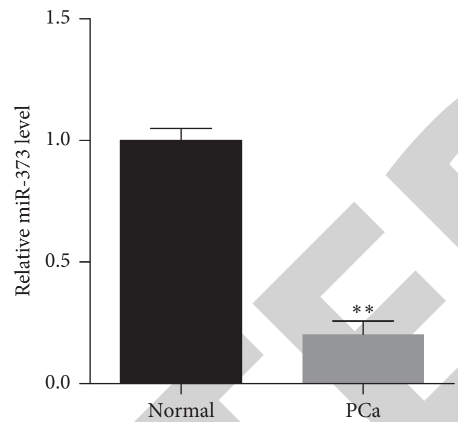

Figure 1: MiR-373 was downregulated in PCa tissues. The evidence of miR-373 was identified by qRT-PCR. $^{**}P < 0.01$ vs. normal tissues.

3.4. MiR-373 Directly Targets RUNX2. The research predicted RUNX2 as a target of miR-373 (https://www.targetscan.org/vert_72/). The binding locations between miR-373 and RUNX2 are shown in Figure 4(a). The findings from the luciferase assay portrayed the fact that the luciferase activity of PCa cells was transfected along with miR-373 mimics and RUNX 3′UTR WT was considerably decreased compared with NC mimics group (Figure 4(b)). The protein rates of RUNX2 were upregulated in PCa cells and tissues (Figures 4(c) and 4(d)). However, the mRNA of RUNX2 was also downregulated following its transfection with miR-373 mimics, which was paralleled with the protein level (Figures 4(e) and 4(f)).

3.5. Overexpressed RUNX2 Alleviates Inhibition of EMT Induced by MiR-373 Mimics in PCa. Rescue assay was performed to examine the roles of RUNX2 in the EMT of PCa cells. As shown in Figures 5(a) and 5(b), upregulated miR-373 reduced the potential for invasion and migration among PCa cells when compared with NC mimics, which was reversed by the overexpression of RUNX2. Moreover, the regulatory role of miR-373 in the depiction of EMT-related genes (such as N-cadherin, Snail, vimentin, E-cadherin and FSP1) was alleviated by RUNX2, where upregulated RUNX2 alleviated the effects of miR-373 on the EMT of PCa cells (Figure 5(c)).

4. Discussion

Augmenting bodies of evidence have revealed miRNAs have a significant role in the initiation and sustenance of PCa [16, 21, 22]. The aberrant expressed miRNAs suppress the identified tumors in PCa. For instance, downregulated miR-129-3p is associated with TNM staging, differentiation of PCA tumor, and lymph node metastasis, while its overexpression inhibited the spread and invasion of PCa cells [23]. miR-601 functions as an oncogene in PCa. As such, it alleviates the potential for migration, invasion, and progression of PCa cells [24]. Meanwhile, Qiu et al. demonstrated that the downregulation of miR-373-3p induces the

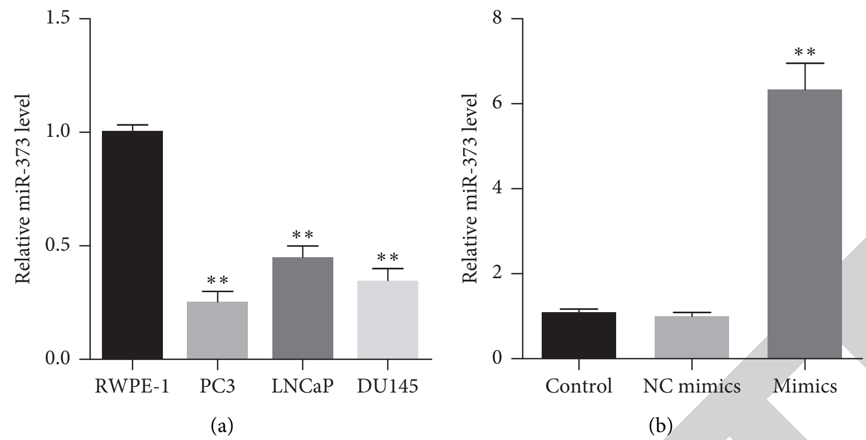

Figure 2: MiR-373 is decreased in PCa cells. (a) The manifestation of miR-373 in PCa cells. (b) The transfection efficacy of PCa cells determined by qRT-PCR. $^{**}P < 0.01$ vs. RWPE-1 cells or even control populations.

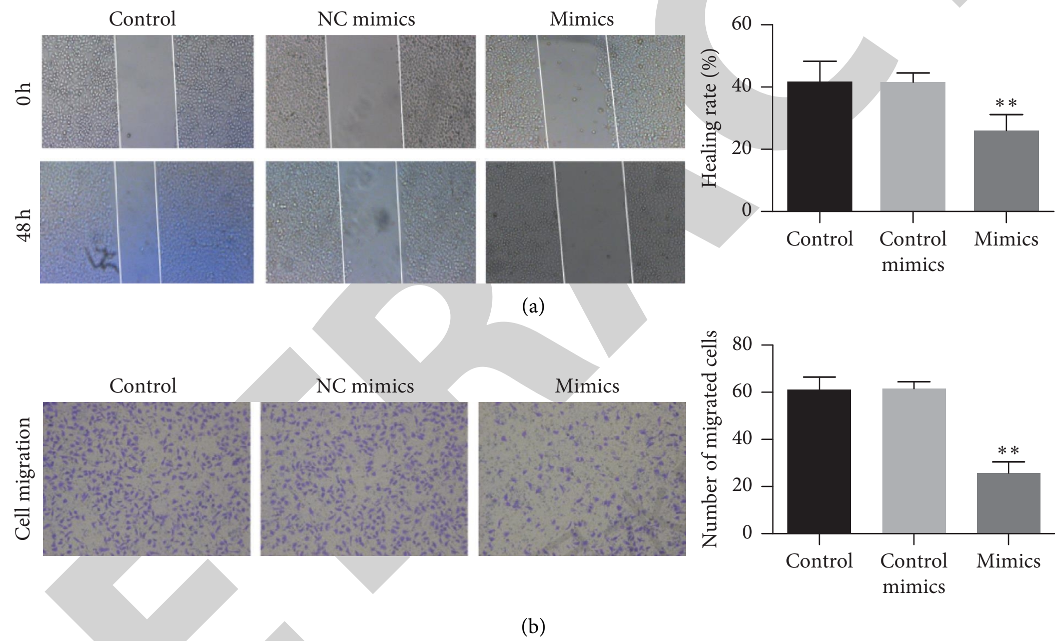

Figure 3: Continued.

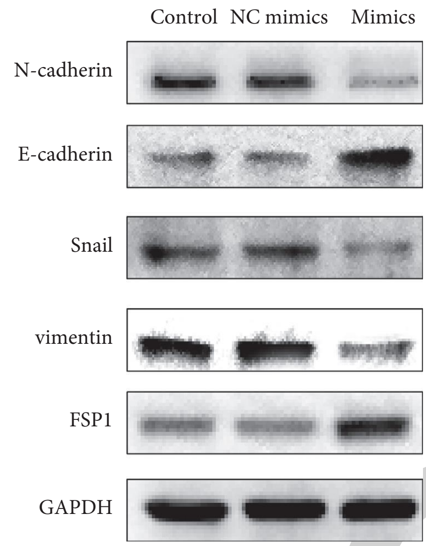

(c)

Figure 3: MiR-373 inhibits the EMT of PCa cells. (a) The potential for migration in PCa cells determined by wound healing assay. (b) The potential for invasion in PCa cells examined through transwell assay. (c) The protein level of N-cadherin, Snail, and vimentin and E-cadherin and FSP1 measured by western blot. $^{**}P < 0.01$ vs. control group.

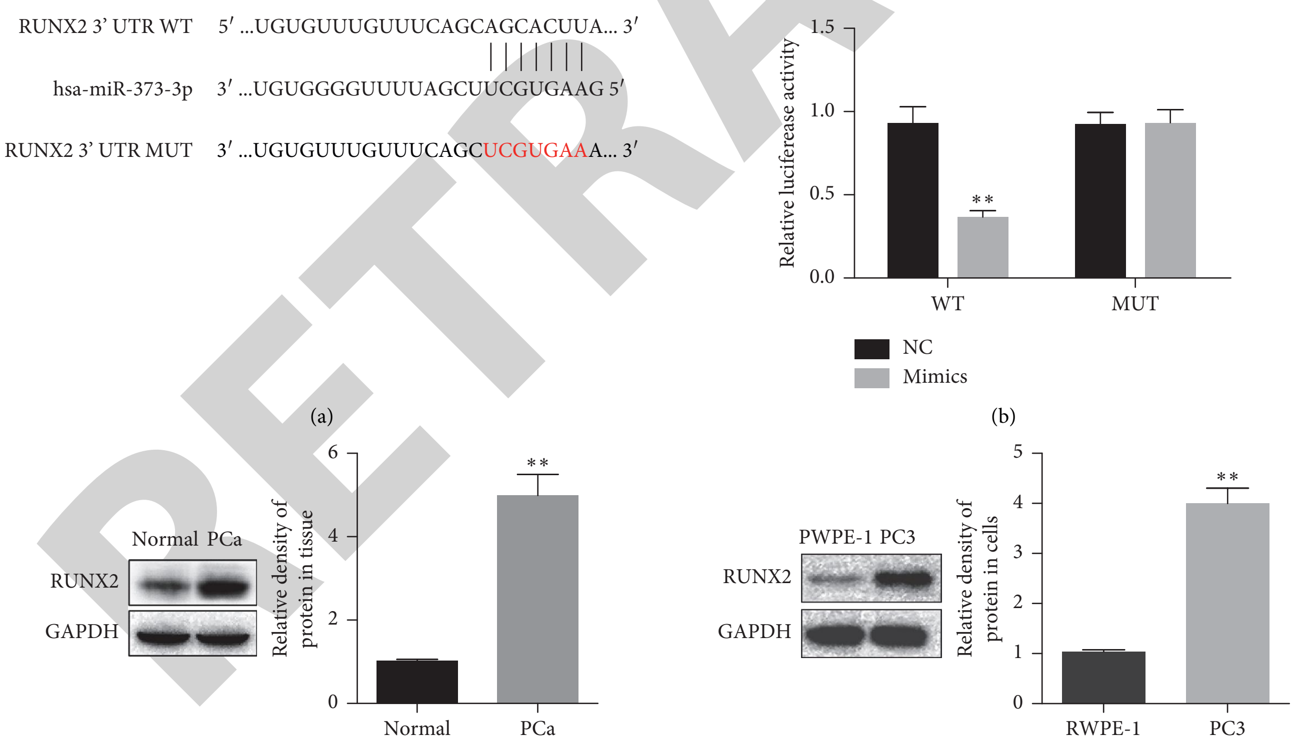

(a) (b) (c) (d)

Figure 4: Continued.

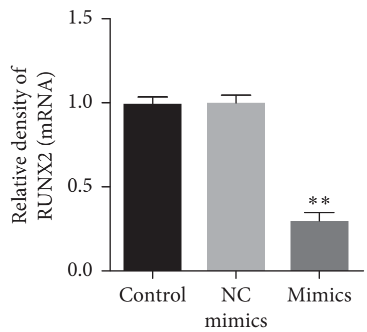

(e)

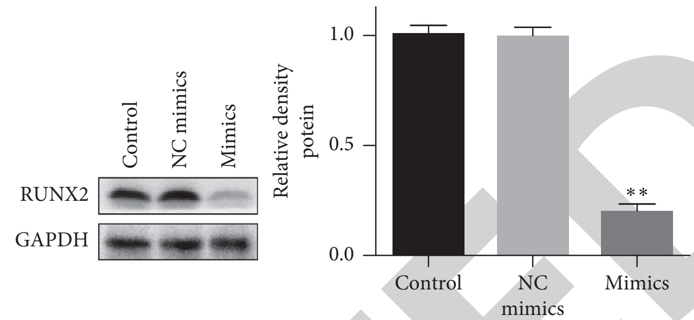

(f)

Figure 4: MiR-373 directly targets RUNX2. (a) The binding sites of miR-373 on RUNX2. (b) The activity of luciferase within PCa cells was established through Dual luciferase reporter assay. (c) The levels of protein in RUNX2 of PCa tissues determined by western blot. (d) The levels of protein of RUNX2 in PCa cells were identified by western blot. (e) The level of mRNA of RUNX2 in PCa cells calculated with qRT-PCR. (f) The level of protein in RUNX2 measured by western blot. $^{**}P < 0.01$ vs. normal tissues, RWPE-1 cells, or control group.

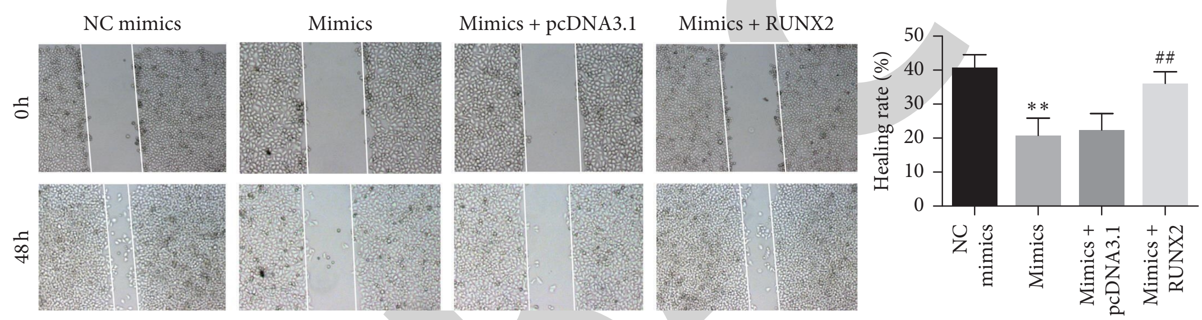

(a)

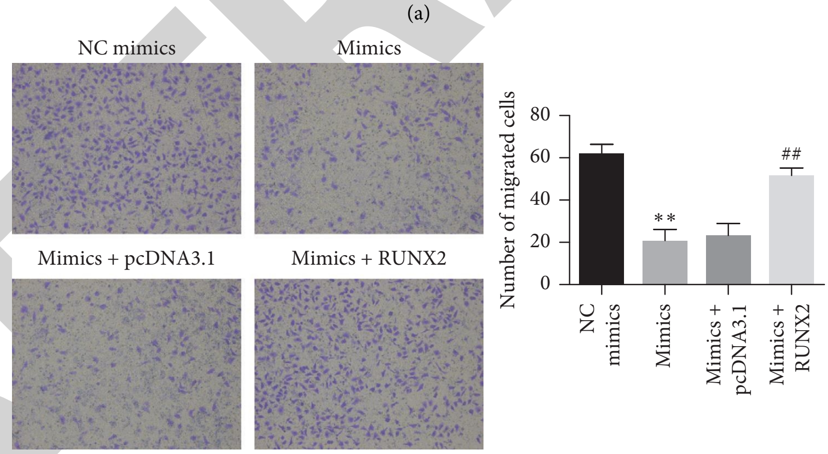

(b)

Figure 5: Continued.

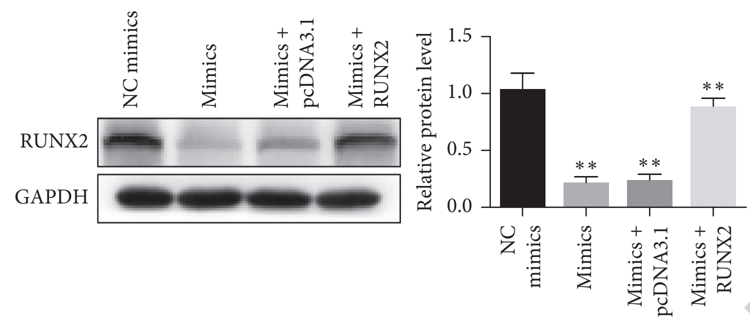

(c)

Figure 5: Overexpressed RUNX2 alleviates inhibition of EMT induced by miR-373 mimics in PCa. (a) The potential for migration in PCa cells is established through wound healing assay after miR-373 mimics transfection and pcDNA3.1 RUNX2. (b) The potential for invasion of PCa cells examined by transwell assay after miR-373 mimics transfection and pcDNA3.1 RUNX2. (c) The protein level of N-cadherin, Snail, and vimentin and E-cadherin and FSP1 determined by western blot after miR-373 mimics transfection and/or pcDNA3.1 RUNX2. $^{*}P < 0.01$ vs. control group. $^{\#\#}P < 0.01$ vs. miR-373 mimics group.

metastasis of PCa, and the silence of testicular nuclear receptor 4 (TR4) or the upregulation of miR-373-3p may be a likely target for PCa [25]. There was a reduction of miR-373 in PCa cells and tissues, thereby suggesting that miR-373 serves as an antitumor gene in PCa. These results are consistent with Qiu et al.'s study [25]. However, the possible mechanism that miR-373 regulated the progression of PCa is still unclear.

Epithelial-mesenchymal transition (EMT) is a complicated progress involved in the metastasis, stemness, and drug resistance of PCa [26]. EMT progresses with the loss of epithelial functions and acquisition of mesenchymal features [27]. This degradation from cuboidal to spindle-shaped in cell phenotype is accompanied with the downregulation of epithelial cell markers (E-cadherin, occludins, and FSP1). Similarly, mesenchymal markers such as vimentin and N-cadherin have been upregulated and further activating the master regulator of EMT, such as Snail and Twist [28, 29]. Thence, to explore the expected molecular mechanisms involved in the EMT of PCa cells to inhibit the metastasis is of vital importance. Still, miRNAs contribute to the initiation and sustenance of cancers via regulating multiple biological processes including EMT [12, 13]. In this study, upregulated miR-373 reduced the potential for invasion and migration among PCa cells. Moreover, its overexpression decreased the expression of mesenchymal markers (vimentin and N-cadherin) and the master regulator of EMT (Snail) and enhanced the manifestation of epithelial cell markers (E-cadherin and FSP1), which suggested the upregulation of miR-373 repressed the loss of epithelial functions and acquirement of mesenchymal features, and therefore inhibited the progression of EMT of PCa cells. However, the underlying mechanisms is still unknown.

miRNAs regulate biological functions through provision of bonds to the 3′UTR of the identified genes [11]. Runt-related transcription factor 2 (RUNX2) was predicted and proved to be a target of miR-373. Increasing studies have reported the upregulation of RUNX2 derived from epithelial tissues induces the progression of multitype cancers [17–19]. RUNX2, as a linage specific transcription factor, collectively participates in EMT and promotes the maturation of mesenchymal markers via interacting with specific pathways related to these pathophysiological processes [30, 31]. In PCa, the abnormal upregulation of RUNX2 contributes to EMT of PCa cells and PCa to bone metastasis [32]. In the current study, RUNX3 was upregulated in PCa cells and tissues. Interestingly, overexpressed RUNX2 reversed the alleviation of PCa invasion and migration and abrogated the upregulation of epithelial markers and the downregulation of mesenchymal markers in induced by miR-373. The findings suggested the regulatory role of miR-373 in PCa EMT was alleviated by RUNX2. Therefore, miR-373 may inhibit the EMT of PCa cells via targeting RUNX2.

In conclusion, miR-373 was downregulated in PCa cells and tissues. Overexpressed miR-373 inhibited the transition from epithelial to mesenchymal state for PCa through targeting PCa. In turn, the inhibition of this transition provides a significant strategy in the treatment of prostate cancer (PCa).

However, the present study has some limitations. Firstly, more patients are needed to make the results more convincing. Secondly, a miRNA may have more than one target, which may be targeted by various miRNAs. Therefore, the underlying mechanisms that miR-373 regulates the EMT of PCa need further research. Furthermore, this study needs to be combined with other hospitals for multicenter research in the future to promote the basic treatment of liver cancer.

Data Availability

The simulation experiment data used to support the findings of this study are available from the corresponding author upon request.

Conflicts of Interest

The authors declare no conflicts of interest.

Authors' Contributions

Jianyi Pang drafted the paper and cooperated with Limei Dai to conduct the experiment, with Qinglei Zhang to collect the data, and with Chen Zhang to interpret the data. Qinglei Zhang designed this work.

Acknowledgments

This paper was supported by the Research Support Fund for Teachers of Jining Medical University (No. JYFC2018FKJ169).

References

[1] M. C. S. Wong, W. B. Goggins, H. H. X. Wang et al., "Global incidence and mortality for prostate cancer: analysis of temporal patterns and trends in 36 countries," *European Urology*, vol. 70, no. 5, pp. 862–874, 2016.

[2] J. Ferlay, I. Soerjomataram, R. Dikshit et al., "Cancer incidence and mortality worldwide: sources, methods and major patterns in GLOBOCAN 2012," *International Journal of Cancer*, vol. 136, no. 5, pp. E359–E386, 2015.

[3] C. Liu, T. Liu, N. Zhang et al., "68Ga-PSMA-617 PET/CT: a promising new technique for predicting risk stratification and metastatic risk of prostate cancer patients," *European Journal of Nuclear Medicine and Molecular Imaging*, vol. 45, no. 11, pp. 1852–1861, 2018.

[4] R. L. Siegel, K. D. Miller, and A. Jemal, "Cancer statistics, 2015," *CA: A Cancer Journal for Clinicians*, vol. 65, no. 1, pp. 5–29, 2015.

[5] C. K. Zhou, D. P. Check, J. Lortet-Tieulent et al., "Prostate cancer incidence in 43 populations worldwide: an analysis of time trends overall and by age group," *International Journal of Cancer*, vol. 138, no. 6, pp. 1388–1400, 2016.

[6] B. Ha Chung, S. Horie, and E. Chiong, "The incidence, mortality, and risk factors of prostate cancer in Asian men," *Prostate International*, vol. 7, no. 1, pp. 1–8, 2019.

[7] K. P. Weinfurt, Y. Li, L. D. Castel et al., "The significance of skeletal-related events for the health-related quality of life of patients with metastatic prostate cancer," *Annals of Oncology*, vol. 16, no. 4, pp. 579–584, 2005.

[8] S. Lamouille, J. Xu, and R. Derynck, "Molecular mechanisms of epithelial-mesenchymal transition," *Nature Reviews Molecular Cell Biology*, vol. 15, no. 3, pp. 178–196, 2014.

[9] A. Dongre and R. A. Weinberg, "New insights into the mechanisms of epithelial-mesenchymal transition and implications for cancer," *Nature Reviews Molecular Cell Biology*, vol. 20, no. 2, pp. 69–84, 2019.

[10] N.-B. Hao, Y.-F. He, X.-Q. Li, K. Wang, and R.-L. Wang, "The role of miRNA and lncRNA in gastric cancer," *Oncotarget*, vol. 8, no. 46, pp. 81572–81582, 2017.

[11] D. P. Bartel, "MicroRNAs: target recognition and regulatory functions," *Cell*, vol. 136, no. 2, pp. 215–233, 2009.

[12] W. Chang, M. Liu, J. Xu et al., "MiR-377 inhibits the proliferation of pancreatic cancer by targeting Pim-3," *Tumor Biology*, vol. 37, no. 11, pp. 14813–14824, 2016.

[13] F. Huang, J. Tang, X. Zhuang et al., "MiR-196a promotes pancreatic cancer progression by targeting nuclear factor kappa-B-inhibitor alpha," *PloS One*, vol. 9, no. 2, Article ID e87897, 2014.

[14] L. Wang, J. Qu, L. Zhou, F. Liao, and J. Wang, "MicroRNA-373 inhibits cell proliferation and invasion via targeting BRF2 in human non-small cell lung cancer A549 cell line," *Cancer Research and Treatment*, vol. 50, no. 3, pp. 936–949, 2018.

[15] Y. Zhang, F.-J. Zhao, L.-L. Chen et al., "MiR-373 targeting of the Rab22a oncogene suppresses tumor invasion and metastasis in ovarian cancer," *Oncotarget*, vol. 5, no. 23, pp. 12291–12303, 2014.

[16] K. Yang, A. M. Handorean, and K. A. Iczkowski, "MicroRNAs 373 and 520c are downregulated in prostate cancer, suppress CD44 translation and enhance invasion of prostate cancer cells in vitro," *International Journal of Clinical and Experimental Pathology*, vol. 2, no. 4, pp. 361–369, 2009.

[17] J. Pratap, J. B. Lian, A. Javed et al., "Regulatory roles of runx2 in metastatic tumor and cancer cell interactions with bone," *Cancer and Metastasis Reviews*, vol. 25, no. 4, pp. 589–600, 2006.

[18] J. Akech, J. J. Wixted, K. Bedard et al., "Runx2 association with progression of prostate cancer in patients: mechanisms mediating bone osteolysis and osteoblastic metastatic lesions," *Oncogene*, vol. 29, no. 6, pp. 811–821, 2010.

[19] T. Ozaki, M. Yu, and D. Yin, "Impact of runx2 on drug-resistant human pancreatic cancer cells with p53 mutations," *BMC Cancer*, vol. 18, no. 1, p. 309, 2018.

[20] Y. Yang, Y. Bai, Y. He et al., "PTEN loss promotes intratumoral androgen synthesis and tumor microenvironment remodeling via aberrant activation of RUNX2 in castration-resistant prostate cancer," *Clinical Cancer Research*, vol. 24, no. 4, pp. 834–846, 2018.

[21] L. Xia, Q. Han, C. Chi et al., "Transcriptional regulation of PRKAR2B by miR-200b-3p/200c-3p and XBP1 in human prostate cancer," *Biomedicine & Pharmacotherapy*, vol. 124, Article ID 109863, 2020.

[22] Z. Xing, S. Li, Z. Liu, C. Zhang, and Z. Bai, "CTCF-induced upregulation of HOXA11-AS facilitates cell proliferation and migration by targeting miR-518b/ACTN4 axis in prostate cancer," *The Prostate*, vol. 80, no. 5, pp. 388–398, 2020.

[23] Y. Jia, Y. Gao, and J. Dou, "Effects of miR-129-3p on biological functions of prostate cancer cells through targeted regulation of smad3," *Oncology Letters*, vol. 19, no. 2, pp. 1195–1202, 2020.

[24] H. Du, X. Wang, R. Dong, D. Hu, and Y. Xiong, "MIR-601 inhibits proliferation, migration and invasion of prostate cancer stem cells by targeting KRT5 to inactivate the wnt signaling pathway," *International Journal of Clinical and Experimental Pathology*, vol. 12, no. 12, pp. 4361–4379, 2019.

[25] X. Qiu, J. Zhu, Y. Sun et al., "TR4 nuclear receptor increases prostate cancer invasion via decreasing the miR-373-3p expression to alter TGFβR2/p-Smad3 signals," *Oncotarget*, vol. 6, no. 17, pp. 15397–15409, 2015.

[26] Y. Du, X.-H. Liu, H.-C. Zhu, L. Wang, J.-Z. Ning, and C.-C. Xiao, "MIR-543 promotes proliferation and epithelial-mesenchymal transition in prostate cancer via targeting RKIP," *Cellular Physiology and Biochemistry*, vol. 41, no. 3, pp. 1135–1146, 2017.

[27] C. Zhiping, T. Shijun, W. Linhui, W. Yapei, Q. Lianxi, and D. Qiang, "MIR-181a promotes epithelial to mesenchymal transition of prostate cancer cells by targeting TGIF2," *European Review for Medical and Pharmacological Sciences*, vol. 21, no. 21, pp. 4835–4843, 2017.

[28] Y. Guan, H. Shi, and T. Xiao, "NUAK1 knockdown suppresses prostate cancer cell epithelial-mesenchymal transition, migration, and invasion through microRNA-30b-5p," *International Journal of Clinical and Experimental Pathology*, vol. 11, no. 12, pp. 5694–5704, 2018.

[29] S. Basu, A. Chaudhary, P. Chowdhury et al., "Evaluating the role of hsa-miR-200c in reversing the epithelial to mesenchymal transition in prostate cancer," *Gene*, vol. 730, Article ID 144264, 2020.

Hindawi
Journal of Healthcare Engineering
Volume 2021, Article ID 4109102, 10 pages
https://doi.org/10.1155/2021/4109102

Research Article

Smart Healthcare System Based on Cloud-Internet of Things and Deep Learning

Benzhen Guo, Yanli Ma, Jingjing Yang, and Zhihui Wang

College of Information Science and Engineering, Hebei North University, 11 Diamond South Road, Zhangjiakou 075000, China

Correspondence should be addressed to Yanli Ma; hebeinu_ma@163.com

Received 13 April 2021; Revised 31 May 2021; Accepted 20 June 2021; Published 29 June 2021

Academic Editor: Enas Abdulhay

Introduction. Health monitoring and remote diagnosis can be realized through Smart Healthcare. In view of the existing problems such as simple measurement parameters of wearable devices, huge computing pressure of cloud servers, and lack of individualization of diagnosis, a novel Cloud-Internet of Things (C-IOT) framework for medical monitoring is put forward. *Methods*. Smart phones are adopted as gateway devices to achieve data standardization and preprocess to generate health gray-scale map uploaded to the cloud server. The cloud server realizes the business logic processing and uses the deep learning model to carry out the gray-scale map calculation of health parameters. A deep learning model based on the convolution neural network (CNN) is constructed, in which six volunteers are selected to participate in the experiment, and their health data are marked by private doctors to generate initial data set. *Results*. Experimental results show the feasibility of the proposed framework. The test data set is used to test the CNN model after training; the forecast accuracy is over 77.6%. *Conclusion*. The CNN model performs well in the recognition of health status. Collectively, this Smart Healthcare System is expected to assist doctors by improving the diagnosis of health status in clinical practice.

1. Introduction

By the end of 2015, there were about 220 million people aged 60 or above in China, accounting for 16.1% of the total population. Among them, 140 million were over 65 years old, accounting for 10.5% of the total population. In this context, healthcare for the elderly has increasingly aroused social concern [1]. The rapid development of wearable devices, IOT, and cloud computing has brought about significant development opportunities and affected every aspect of people's lives. In the field of healthcare, the adoption of IOT can bring us health monitoring all the time [2]. With the popularity of smart phones, smart bracelets, and other devices, a variety of sensors can monitor health indicators timely and accurately [3–5]. Deep learning is an implementation method of machine learning, which is different from the traditional shallow models such as artificial neural network. Deep learning usually has a deeper model structure with five or six layers or even over ten layers or more hidden layers [6]. In addition, the importance of feature learning is highlighted [7, 8]. The feature representation of samples in the original space is transformed into a new feature space by means of feature transformation layer by layer. Deep learning is widely used in image and voice processing and develops rapidly in the medical and health field [8–10]. The study in [11] proposed a human fall early warning algorithm based on RNN and compared it with traditional machine learning algorithms such as SVM to verify its excellent performance. The study in [12] compared and studied the application of CNN, RNN, LSTM, and other deep learning models in the evaluation of sleep quality.

With the increase of the number of IOT devices and sensors, medical IOT system also highlights more problems in the development process, mainly including the following:

(1) The measurement parameters of existing wearable health monitoring devices are relatively simple, such as pedometers and intelligent sphygmomanometers. The common pedometer devices can connect with

smart phones via Bluetooth and other communication means, and upload data to the cloud server, so it is possible to view data such as exercise amount and sports assessment report through the phone APPs. Various forms of wearable health monitoring devices fail to share data due to different manufacturers and communication protocols.

(2) Limited by memory capacity and computing power, wearable devices may upload the collected data to the cloud server through smart phones or home gateways. The cloud server needs to store and process a large amount of collected data. The server and network have great transmission pressure, which reduces the real-time processing capacity.

(3) At present, many telemedicine monitoring systems based on IOT carry out certain disease early warning according to a set of diagnostic schemes, and it is difficult to develop personalized diagnosis and treatment schemes according to individual physiological characteristics and historical parameter changes.

(4) Intelligent diagnosis methods based on the uploaded data of health monitoring devices mainly include system-based diagnosis methods of experts and intelligent diagnosis methods based on sample data. Back Propagation (BP) neural network algorithm [13] and Support Vector Machines (SVM) algorithm have been applied to the classification of diagnosis results. Although deep learning algorithm has been applied in sleep quality and other fields [12], the application of intelligent diagnosis algorithm based on deep learning is rarely seen.

In view of the above problems, a healthcare monitoring system based on Cloud-Internet of Things (C-IOT) and deep learning is proposed, and the major work includes the following aspects:

(1) A health data acquisition system is designed based on C-IOT and the acquisition of parameters such as human blood pressure, body temperature, body weight/fat, and exercise amount is realized. The shortcoming that the acquisition of simple physiological parameters fails to evaluate and diagnose the user's health effectively is avoided.

(2) Data preprocessing of each acquisition device is realized locally to eliminate noise interference. By communicating with the user's smart phones through Bluetooth, the smart phones may display the collected data in real time, preprocess the data of each device, and upload them to the cloud server. The processing and integration of local data can reduce the computing pressure of cloud server and transmission pressure of network.

(3) The private doctor evaluates the user's health condition according to the data on the cloud server and establishes the initial data set. The cloud server uses the deep learning algorithm (CNN) to train the user health evaluation model according to the initial data set. The newly uploaded data are calculated by a depth model to automatically give health assessment results. The model is a process of dynamic change. The private doctor will manually evaluate the user's health status and update the user data set on a regular basis as well as the parameter values of the depth model. The model can realize personalized health assessment.

2. Materials and Methods

2.1. System Architecture. Figure 1 indicates the architecture of health monitoring system based on C-IOT and deep learning proposed in this paper. It is improved from the traditional three-layer architecture of the IOT, and described from the perspective of system implementation and data flow, including data collection layer, data preprocessing and net layer, data processing, and application layer.

Data collection layer is responsible for the acquisition of physiological parameters of health, which is mainly composed of a number of Internet-connected or wearable devices. Temperature, body fat/weight, blood pressure parameters, and exercise parameters are measured. In general, data collection layer devices have small data storage capacity and low computing capacity [14–16]. In order to reduce data redundancy, network transmission pressure, and power consumption, the data denoising, digital filtering, and power management based on rules can be realized locally. High-frequency noise is eliminated by digital low-pass filter and band-pass filter. In addition, the special value in the collected data is removed based on rules. The data collection layer device may be connected to smart phones or other mobile intelligent terminals through Bluetooth.

The data preprocessing and net layer are mainly composed of smart phones and other intelligent mobile terminals. Smart phone devices not only serve as network layer devices to realize data communication function of medical IOT gateway, but also install application layer APP software to realize local data preprocessing, parameter display, and device control. The smart phone connects to the data collection layer device through Bluetooth to receive measurement information reported by the blood pressure meter, weight/fat meter, pedometer, thermometer, and other data acquisition devices, and display the real-time information on the mobile APPs. Preprocessing data are uploaded to the cloud server through Wifi, 4G, and other communication means. Data preprocessing includes data normalization, data dimension transformation, data fusion, and other functions to generate images of health parameters. In terms of data normalization, body weight, body temperature, and other measurement parameters are normalized according to the grade to the gray value ranging from 0 to 255. In terms of data dimension transformation, original measurement parameters are extended in dimension, such as heart rate, systolic pressure and diastolic blood pressure measured by sphygmomanometer extended to ambulatory pulse pressure (APP), mean arterial pressure (MAP), and ambulatory rate-pressure product (ARPP), which are often used to diagnose cardiovascular diseases more effectively. The application

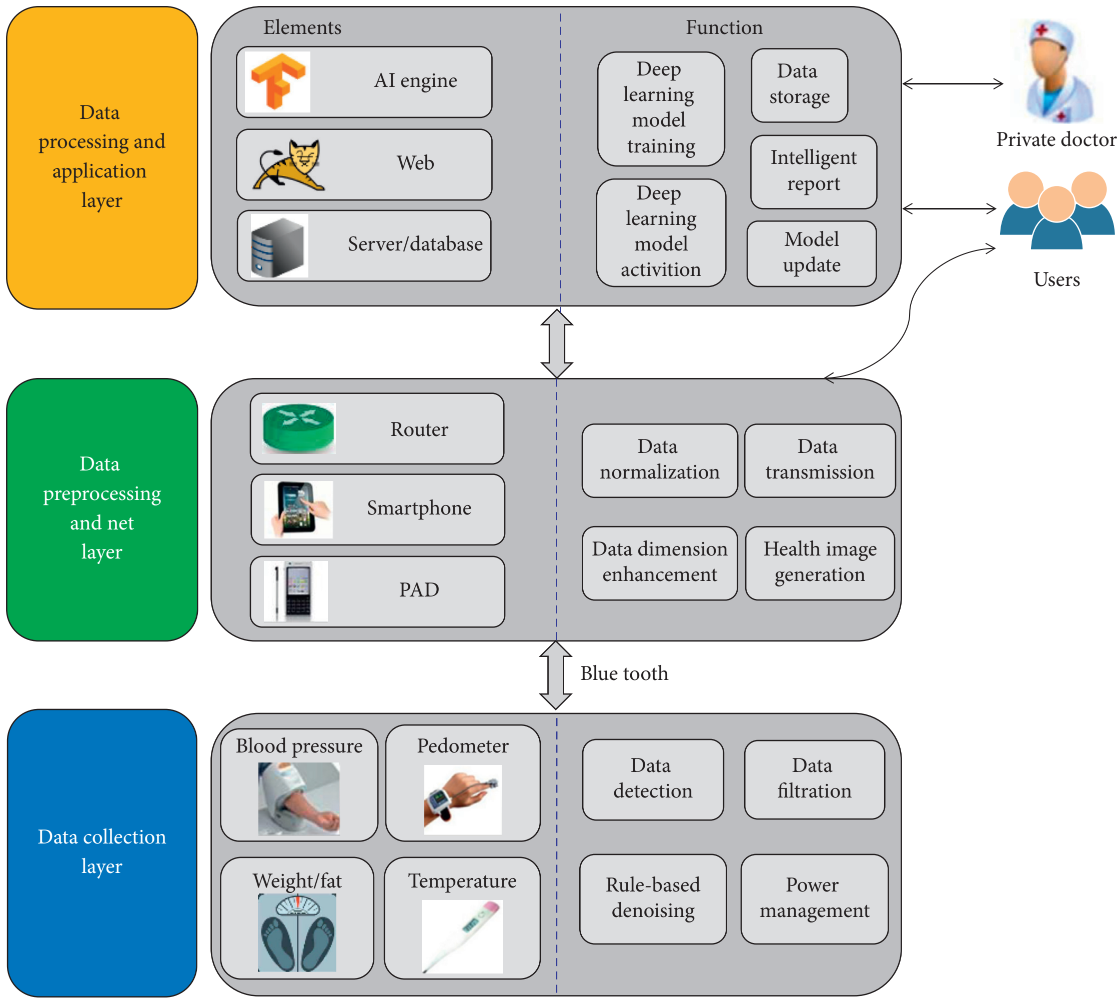

Figure 1: System architecture.

software of mobile phones can also fuse the physiological parameter measurement data after normalization of gray value and dimension expansion into the image of health parameters, upload them to the cloud server in the form of two-dimensional image, and use the deep learning model to solve the health parameter image to give the health index report. The users may receive and display the health report issued by the cloud server through smart phones. Making full use of the computing power of intelligent equipment for data preprocessing can effectively reduce the transmission pressure of database and network. With the rapid improvement of the computing power of intelligent terminal equipment, more and more data processing functions will be completed directly in the intelligent terminals.

The data processing and application layer mainly includes database and distributed server, web server, and deep learning model engine. The database stores and manages users' personal information/health monitoring data, personal doctor information, equipment information, etc., the distributed server realizes various business processing logic, and the web server provides users and personal doctors with friendly web interface for background operation. The deep learning model engine is used to train the deep learning model, and the trained deep learning model is used to solve the health parameter image. With the increase of user data, private doctors can annotate the data, enrich the personal health data set, and retrain and update the deep learning model.

2.2. Measurement of Blood Pressure. For blood pressure acquisition nodes, the oscillometric method is used to measure blood pressure [17], and the pressure value of the pressure sensor is filtered by low-pass filter and band-pass filter to obtain the static pressure value and the dynamic pressure value. In the measurement process, the dynamic pressure value amplitude increases gradually and then decreases. When the dynamic pressure value amplitude is multiplied by the normalized coefficients (Ks and Kd), the dynamic pressure value amplitude corresponding to the systolic pressure and the diastolic pressure can be obtained, respectively, and the human blood pressure value can be obtained by reverse check, as shown in Figure 2. According to the conclusions of Mauro's mathematical model, the normalized coefficient Ks was 0.46–0.64, and the normalized coefficient Kd was 0.43–0.73 [18]. In this paper, the amplitude coefficients commonly used in clinical medicine are $Ks = 0.48$ and $Kd = 0.58$ [19].

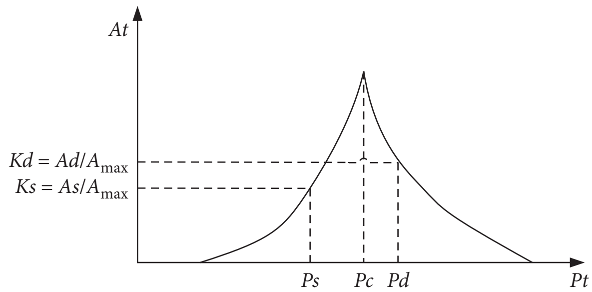

Figure 2: Blood pressure measurement method.

In order to obtain the optimal pulse oscillation amplitude envelope, Gaussian fitting method is used for data fitting: a set of sample data $(x_i, y_i)(i = 1, 2, 3 \ldots N)$ can be described by Gaussian functions as shown in the following equation:

$$y_i = y_{\max} * \exp\left[-\frac{(x_i - x_{\max})^2}{s}\right]. \quad (1)$$

Take the logarithm of both sides of this equation:

$$\ln y_i = \ln y_{\max} - \frac{(x_i - x_{\max})^2}{s} = \left(\ln y_{\max} - \frac{x_{\max}^2}{s}\right) + \frac{2x_i x_{\max}}{s} - \frac{x_i^2}{s}. \quad (2)$$

Assume

$$\begin{aligned} \ln y_i &= z_i, \\ \ln y_{\max} - \frac{x_{\max}^2}{s} &= b_0, \\ \frac{2x_{\max}}{s} &= b_1, \\ -\frac{1}{s} &= b_2. \end{aligned} \quad (3)$$

Taking all sample data into consideration, equation (2) is converted into a matrix as follows:

$$\begin{bmatrix} z_1 \\ z_2 \\ \vdots \\ z_n \end{bmatrix} = \begin{bmatrix} 1 & x_1 & x_1^2 \\ 1 & x_2 & x_2^2 \\ \vdots & \vdots & \vdots \\ 1 & x_n & x_n^2 \end{bmatrix} \begin{bmatrix} b_0 \\ b_1 \\ b_2 \end{bmatrix}. \quad (4)$$

It is simplified as

$$Z = XB. \quad (5)$$

According to the principle of least squares, the generalized solution of least squares for matrix B is

$$B = \left(X^T X\right)^{-1} X^T Z. \quad (6)$$

Then, the estimated parameters (b_0, b_1, b_2) are substituted into equation (1) to obtain the fitted Gaussian function. Both the measuring speed and accuracy are improved by using Gaussian fitting function.

2.3. Data Preprocessing. After the human physiological parameter monitoring equipment transmits the measurement results to a smart phone via Bluetooth, data preprocessing shall be conducted through the application software installed in the smart phone, which mainly includes dimensional transformation of data, data standardization, and generation of two-dimensional gray image for human health.

In order to optimize the input vector, the measurement data uploaded by monitoring equipment need to be transformed into a certain dimension. The measured data including heart rate (HR), systolic blood pressure (SP), and diastolic blood pressure (DP) are converted into three parameters, namely, mean arterial pressure (MAP), ambulatory pulse pressure (APP), and ambulatory rate-pressure product (ARPP).

$$\begin{aligned} \mathrm{APP} &= F1(\mathrm{SP}, \mathrm{DP}) = \mathrm{SP} - \mathrm{DP}, \\ \mathrm{MAP} &= F2(\mathrm{SP}, \mathrm{DP}) = \frac{\mathrm{DP} + (\mathrm{SP} - \mathrm{DP})}{3}, \\ \mathrm{ARPP} &= F3(\mathrm{HR}, \mathrm{SP}) = \mathrm{HR} * \mathrm{SP}. \end{aligned} \quad (7)$$

Step number, motion distance, fast motion time, fast motion distance, length of sleeping, and length of awakening are obtained according to the step number and time measured by the pedometer after dimension expansion. Data standardization converts the data of each index into the gray value ranged from 0 to 255 according to the scaling, so as to facilitate the synthesis of health status matrix for uploading to the cloud server for processing. The corresponding range relationship between the measured value of each index and the standardized value is shown in Table 1.

In this paper, the deep learning method is adopted to evaluate the human health status. The input data of the deep learning model are the measured values after the standardization of each physiological parameter of human body in a day. In order to better serve as the input of CNN, the standardized data need to be processed in two dimensions to generate the health status matrix. The health status matrix is

Table 1: Data standardization.

Index	Range of measurement value	Range of standard value
Weight	0–150 kg	0–255
Fat	0%–50%	0–255
SP	0–250 mmHg	0–255
DP	0–250 mmHg	0–255
HR	0–200 bpm	0–255
APP	0–200 mmHg	0–255
MAP	0–300 mmHg	0–255
ARPP	0–50000	0–255
Step num	0–30000	0–255
Distance	0–20 km	0–255
Fast motion time	0–24 h	0–255
Fast motion distance	0–20 km	0–255
Length of sleeping	0–24 h	0–255
Length of awakening	0–24 h	0–255
Body temperature	30–45°C	0–255

organized into 2D images. As required, the subjects shall have their blood pressure and body temperature measured once every morning and every evening, have their weight/fat measured once every day, and wear a pedometer 24 hours a day. On the smart phone side, 36-pixel 2D images of human health are generated every day, as shown in Table 2. Figure 3 is an example 2D image of health status matrix according to Table 2.

2.4. Collection of Data Set. The training of deep learning model shall be supported by a certain amount of labeled data set. In this study, the gray-scale chart of health monitoring parameters in one day is obtained by combining measurement and construction. Six volunteers are selected, including 3 males and 3 females (including 2 adolescents, 2 middle-aged, and 2 elderly). The volunteers are required to test the blood pressure each morning and evening, the body temperature once, and the weight/fat once. They are also required to wear a pedometer device for 24 hours and upload data to the cloud server at 6 o'clock each morning through the phone APP. Then, private doctors will grade their health status according to the uploaded data and user information such as age and gender and then divide them into three types: health, sub-health, and illness. The initial data set is generated by continuously tracking and annotating the user's data for 100 days. In addition, the initial data set of each user constructed and annotated by private doctors according to the user's historical data information is 3,000, and these three types account for 1/3. 80% of the extended initial data set is selected as the training sample to train the user's personalized deep learning model, and 20% is used as the test sample to test the model's performance.

2.5. Deep Learning Model. Deep learning model is constructed and trained in the cloud server, and CNN is the most commonly used deep learning model, which has been widely used in the field of image processing. The classic LeNet-5 [20] CNN model is adopted and modified to simplify a pooling layer. The CNN model constructed is shown in Figure 4, which contains two convolution layers, a pooling layer, and a full connection layer. The CNNs have 2×2 kernels for the convolutional layers with 3 and 9 filters, respectively, and a scaling of 2 for the max-pooling layers. The output layer outputs the health assessment results, including health, sub-health, and illness.

3. Results and Discussion

3.1. Measurement and Test of Blood Pressure. The method of using medical blood pressure meter and blood pressure measurement node at the same time for the same subject is used for comparative verification. A health monitor (PM-900S, Biocare Technology Co. Ltd., Shenzhen, China) is selected as the comparison device. The verification results are shown in Table 3, and the measurement results indicate that the relative error is within the range of 6%. Figure 5(a) is the photo of blood pressure measurement node device.

Also, the method of wearing commercial pedometer and step monitoring node is used for comparative verification. A sports bracelet (Honor 3, HUAWEI Technology Co. LTD, Shenzhen, China) is selected as the comparison experiment device. The test subjects wear sports bracelets and step monitoring nodes at the same time. The measured data of the previous day is read after the subjects get up at 6 o'clock in the morning. The verification results are shown in Table 4, and the measurement results indicate that the relative error is within the range of 9%. Figure 5(b) is the photo of step monitoring node.

3.2. Evaluation of Deep Learning Algorithm and Model. For each subject, the accuracy of average recognition of the three health states is studied. Apart from that, recall and precision and $F1$_score are used for model evaluation in respect of each category [21]. The data of test set in data set are used as model input. TP denotes number of true positive (labeled correctly). FP denotes number of false positive (other activity labeled as the sub-health and illness). Furthermore, TN denotes number of true negatives (correct rejection), and FN denotes number of false negatives (missed detections).

Table 2: Human health map.

	1	2	3	4	5	6
1	SP1	DP1	HR1	APP1	MAP1	ARPP1
2	SP2	DP2	HR2	APP2	MAP2	ARPP2
3		Weight			Fat	
4	Step num	Distance	Fast motion time	Fast motion distance	Length of sleeping	Length of awakening
5				Body temperature1		
6				Body temperature2		

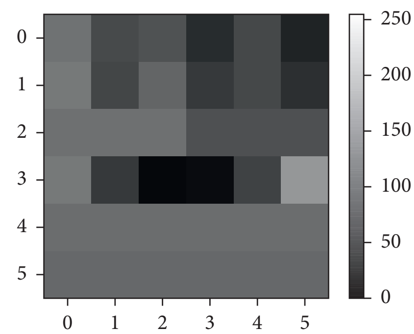

Figure 3: 2D images of human health.

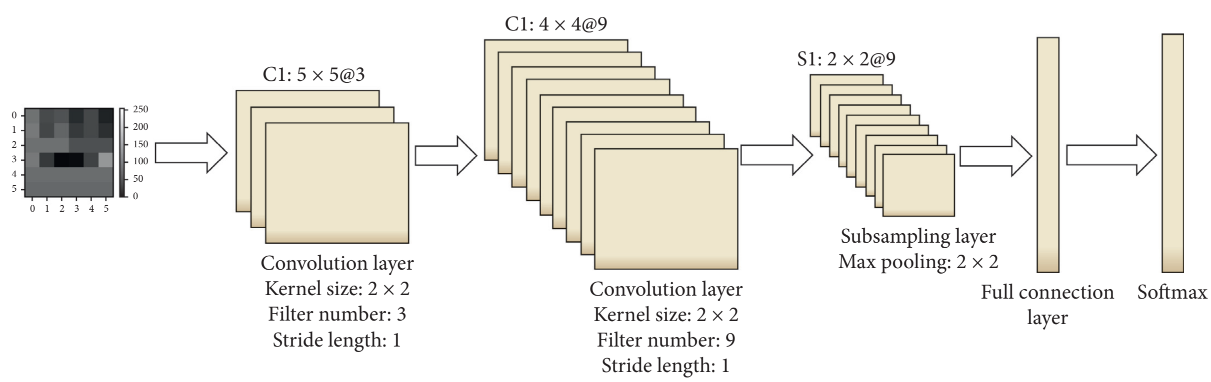

Figure 4: CNN model architecture.

$$\begin{aligned}
\text{Accuracy} &= \frac{\text{TP} + \text{TN}}{\text{TP} + \text{FP} + \text{FN} + \text{TN}},\\
\text{recall} &= \frac{\text{TP}}{\text{TP} + \text{FN}},\\
\text{precision} &= \frac{\text{TP}}{\text{TP} + \text{FP}},\\
F1_\text{score} &= \frac{2\text{precision} * \text{recall}}{\text{precision} + \text{recall}}.
\end{aligned} \tag{8}$$

Figure 6 exhibits the accuracy of the average classification of each subject. Error bars display the standard deviation of the recognition accuracy of the three health categories for each subject. As can be seen from the figure, the results of different subjects are of obvious differences. The highest recognition accuracy of CNN model is 84.2% (S4) and the lowest is 68.5% (S3). The standard deviation of recognition accuracy is all within 15 and the maximum is 14.94 (S5). For 6 subjects, the average accuracy of CNN model is 77.61%.

Figure 7 indicates the confusion matrices of 6 subjects acquired by CNN model. It can be revealed that the recognition performance of the model for health categories is obviously superior to the other two categories. In 200 samples, the highest recognition accuracy is 182 (S6). The capability to recognize sub-health categories is relatively poor, and S5 can only recognize 110 out of 200 samples correctly.

Figure 8 shows the precision, recall, and $F1$-score of 6 subjects in three categories acquired by CNN model. It can be seen that CNN model boasts higher precision for disease recognition than other two categories, except S2. Nevertheless, the value of recall is higher than that of

Table 3: Blood pressure measurement verification results.

	SP (mmHg) (PM-900S)	SP (mmHg) (test node)	Error (%)	DP (mmHg) (PM-900S)	DP (mmHg) (test node)	Error (%)
1	120	123	2.5	83	86	3.6
2	107	112	4.7	78	82	5.1
3	124	130	4.8	89	86	3.4
4	109	105	3.7	78	81	3.8
5	140	145	3.6	95	99	4.2

(a) (b)

Figure 5: (a) Blood pressure measurement node device. (b) Step monitoring node device.

Table 4: Step monitoring node verification results.

	Step num (honor3)	Step num (test node)	Error (%)	Amount of sleep (h) (honor3)	Amount of sleep (h) (test node)	Error (%)
1	5600	5743	2.6	6.5	6.3	3.1
2	8212	7920	3.6	7.4	7.0	5.4
3	15401	16280	5.7	8.2	7.7	6.1
4	7231	7102	1.8	7.1	6.6	7.0
5	11005	10098	8.2	9.4	9.0	4.3

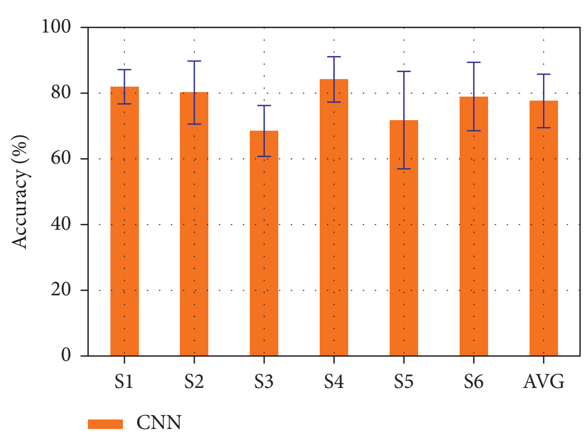

Figure 6: Classification accuracy of each subject. Each bar and the corresponding error bar show the average classification accuracy with standard deviation of three health patterns.

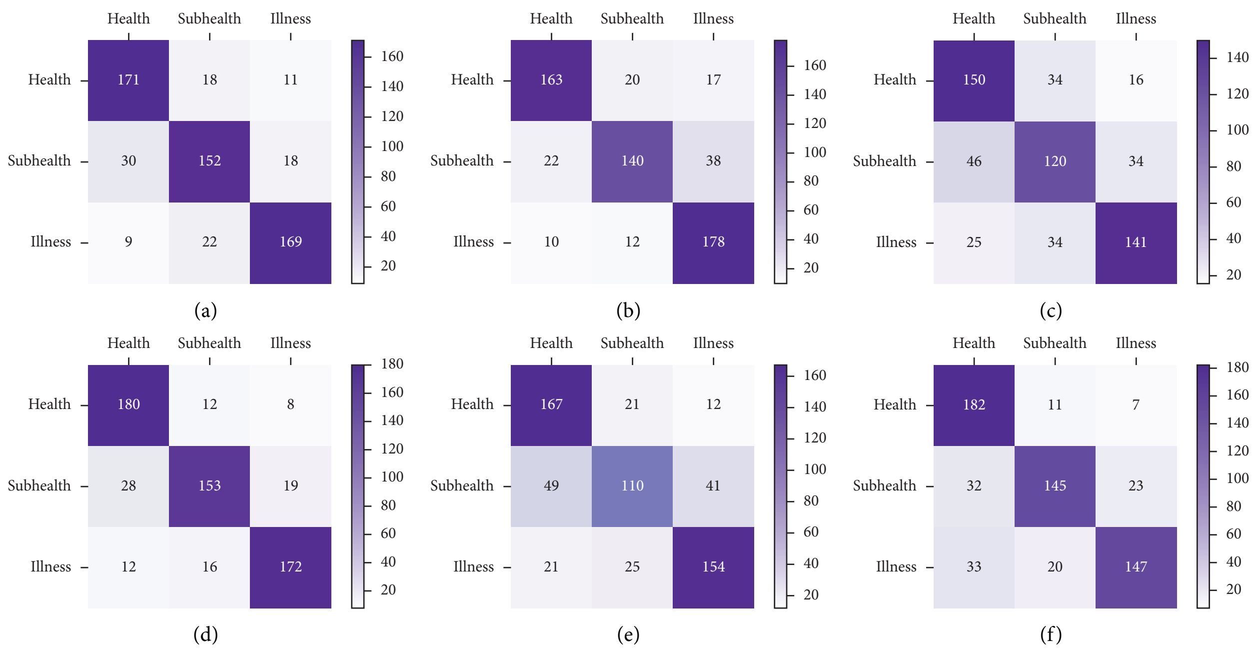

Figure 7: Confusion matrices acquired by the CNN model. (a–f) The confusion matrix of S1–S6.

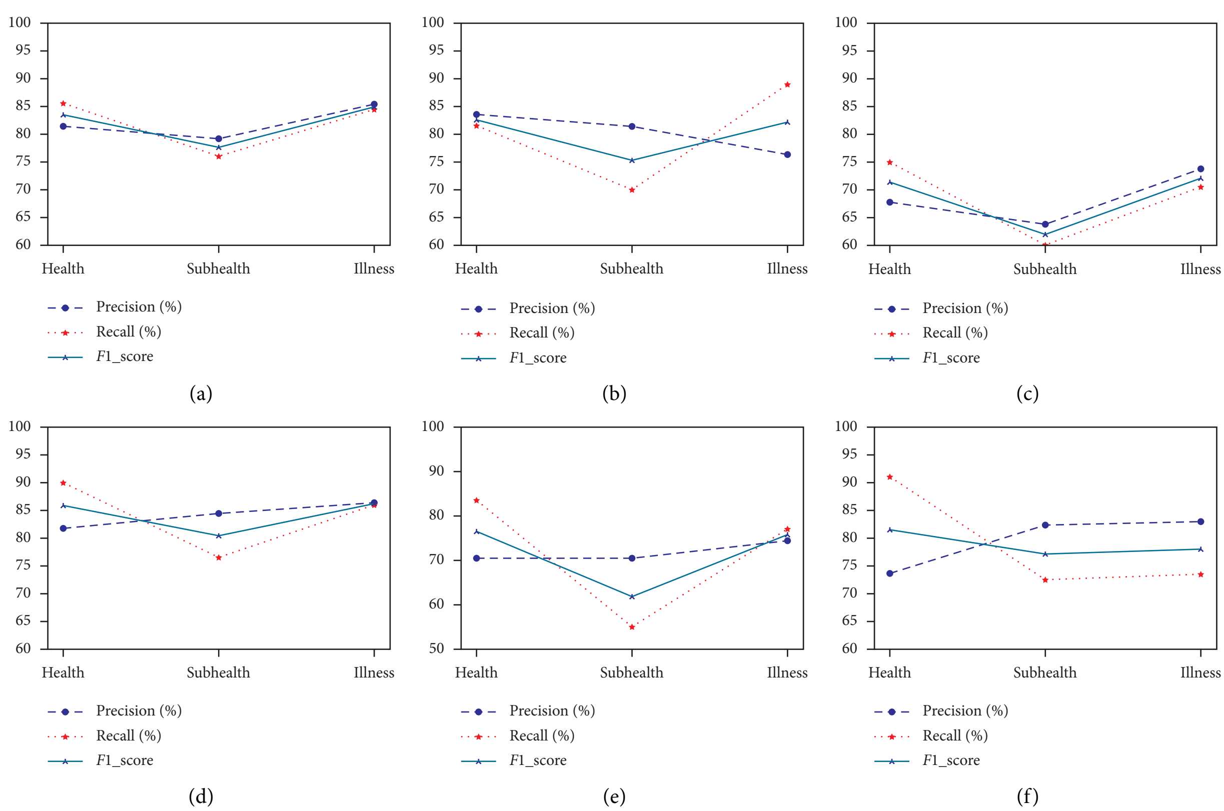

Figure 8: Precision, recall, and $F1$-score obtained by the CNN model. (a–f) The result curves of S1–S6.

precision except S2. $F1$_score is a comprehensive index reflecting the performance of the model. By observing the $F1$_score curve of 6 subjects, the recognition performance of the model for sub-health is worse than the other two categories, with a minimum of 61.8% (S5).

The current research suggests that it is feasible to recognize and intelligently diagnose the preprocessed data of the underlying devices of the medical Internet of Things with CNN model. In comparison with traditional machine learning methods such as SVM [22] and LDA

[23], the depth learning method for intelligent diagnosis does not require manual selection of data feature values. The depth model can automatically extract features and perform high-level abstraction. For different subjects, the optimal parameters of the model can be automatically acquired through training, which is more flexible and robust compared with traditional machine learning methods. The intelligent health management system architecture based on deep learning proposed in the current research can make the data set continuously grow under the condition of user data accumulation, and cooperate with doctors' manual annotation, and can optimize model training from time to time to achieve better recognition and diagnosis effects. Pretreatment of health data at the bottom layer of Internet of Things equipment enhances the robustness of data and can tremendously lower the computing pressure of servers.

For each subject, the accuracy of average recognition of the three health states is studied. Apart from that, recall and precision and $F1\_score$ are used for model evaluation in respect of each category.

4. Conclusions

In view of the existing problems in the existing IOT medical system, a new IOT architecture for medical monitoring is proposed in this paper, in which smart phones are used as gateway devices to realize data preprocessing of measurement node devices, thus greatly reducing the computing pressure of cloud servers and transmission pressure of network. Based on the data sets generated from such data annotated by private doctors, a CNN health recognition model is constructed to realize personalized diagnosis and treatment of human health. Six subjects are selected to wear wearable measuring devices for a long time and physiological parameters are measured as required. The test sample set is input into the deep learning model for identification, with a prediction accuracy of over 77%. In the future work, the measurement types of human health parameters will be added, such as ECG and EEG signals, etc. In addition, the scale of the data set will be expanded, and the training depth learning model will be updated continuously to improve the prediction accuracy.

Data Availability

The data used to support the findings of this study are available from the corresponding author upon request.

Conflicts of Interest

The authors declare that they have no conflicts of interest.

Acknowledgments

The work was supported by the Fundamental Research Funds for Hebei North University (JYT2019004) and Foundation of the Zhangjiakou Science and Technology Project (1411073B).

References

[1] S. Din and A. Paul, "Retracted: smart health monitoring and management system: toward autonomous wearable sensing for Internet of Things using big data analytics," *Future Generation Computer Systems*, vol. 91, pp. 611–619, 2019.

[2] W. Shi, J. Cao, Q. Zhang, Y. Li, and L. Xu, "Edge computing: vision and challenges," *IEEE Internet of Things Journal*, vol. 3, no. 5, pp. 637–646, 2016.

[3] B. Kwolek and M. Kepski, "Human fall detection on embedded platform using depth maps and wireless accelerometer," *Computer Methods and Programs in Biomedicine*, vol. 117, no. 3, pp. 489–501, 2014.

[4] Y. Kim and T. Moon, "Human detection and activity classification based on micro-doppler signatures using deep convolutional neural networks," *IEEE Geoscience and Remote Sensing Letters*, vol. 13, no. 1, pp. 8–12, 2016.

[5] M. Z. Uddin, "A wearable sensor-based activity prediction system to facilitate edge computing in smart healthcare system," *Journal of Parallel and Distributed Computing*, vol. 123, pp. 46–53, 2019.

[6] L. I. U. Dong, L. I. Yue, L. I. N. Jianping, L. I. Houqiang, and W. U. Feng, "Deep learning-based video coding: a review and a case study," *ACM Computing Surveys*, vol. 53, no. 1, pp. 1–35, 2020.

[7] M. Ghorbani, M. Bahaghighat, Q. Xin, and F. Özen, "ConvLSTMConv network: a deep learning approach for sentiment analysis in cloud computing," *Journal of Cloud Computing*, vol. 9, no. 1, pp. 1–13, 2020.

[8] L. Zheng, O. Wang, S. Hao et al., "Development of an early-warning system for high-risk patients for suicide attempt using deep learning and electronic health records," *Translational Psychiatry*, vol. 10, no. 1, pp. 1–11, 2020.

[9] Z. Liu, Y. Fu, Y. Zhang, F. Peng, and Z. Zhang, "Effect of CT image reconstruction methods on performance of pulmonary nodules detection algorithm based on deep learning," *Chinese Journal of Medical Imaging Technology*, vol. 35, no. 12, pp. 1775–1779, 2019.

[10] D. Spathis and P. Vlamos, "Diagnosing asthma and chronic obstructive pulmonary disease with machine learning," *Health Informatics Journal*, vol. 25, no. 3, pp. 811–827, 2019.

[11] T. R. Mauldin, M. E. Canby, V. Metsis, A. H. H. Ngu, and C. C. Rivera, "Smartfall: a smartwatch-based fall detection system using deep learning," *Sensors*, vol. 18, no. 10, pp. 1–19, 2018.

[12] A. Sathyanarayana, S. Joty, L. Fernandez-Luque et al., "Sleep quality prediction from wearable data using deep learning," *JMIR Mhealth and Uhealth*, vol. 4, no. 4, p. e125, 2016.

[13] X. F. Zhang, X. Li, J. T. Dai et al., "The design of a hemiplegic upper limb rehabilitation training system based on surface EMG signals," *Journal of Advanced Mechanical Design, Systems and Manufacturing*, vol. 12, no. 1, pp. 1–12, 2018.

[14] I. Kaur, K. S. Saini, and J. Khaira, "An effective architecture for smart city using advanced protocols of internet of things," *International Journal of Advanced Science and Technology*, vol. 28, no. 19, pp. 803–810, 2019.

[15] J. Mathew and R. Jemima Priyadarsini, "Enhancing security in IoT healthcare services using fog computing," *International Journal of Advanced Science and Technology*, vol. 28, no. 17, pp. 444–450, 2019.

[16] S. Pandya, R. Desai, D. Pathak, and K. Kotecha, "IoT based intelligent health surveillance & alert system with fault prediction using machine learning," *International Journal of*

Advanced Science and Technology, vol. 28, no. 18, pp. 660–676, 2019.

[17] W. Chen, T. Kobayashi, S. Ichikawa, Y. Takeuchi, and T. Togawa, "Continuous estimation of systolic blood pressure using the pulse arrival time and intermittent calibration," *Medical, & Biological Engineering & Computing*, vol. 38, no. 5, pp. 569–574, 2000.

[18] R. Gircys, A. Liutkevicius, E. Kazanavicius, V. Lesauskaite, G. Damuleviciene, and A. Janaviciute, "Photoplethysmography-based continuous systolic blood pressure estimation method for low processing power wearable devices," *Applied Sciences*, vol. 9, no. 11, p. 2236, 2019.

[19] J. Jilek and T. Fukushima, "Oscillometric blood pressure measurement: the methodology, some observations, and suggestions," *Biomedical Instrumentation & Technology*, vol. 39, no. 3, pp. 237–241, 2005.

[20] T. Wang, C. Lu, G. Shen, and F. Hong, "Sleep apnea detection from a single-lead ECG signal with automatic feature-extraction through a modified LeNet-5 convolutional neural network," *PeerJ*, vol. 7, no. 9, p. e7731, 2019.

[21] A. Khalaf, E. Sejdic, and M. Akcakaya, "EEG-fTCD hybrid brain-computer interface using template matching and wavelet decomposition," *Journal of Neural Engineering*, vol. 16, no. 3, Article ID 036014, 2019.

[22] K. Harimoorthy and M. Thangavelu, "Multi-disease prediction model using improved SVM-radial bias technique in healthcare monitoring system," *Journal of Ambient Intelligence and Humanized Computing*, vol. 12, no. 3, pp. 3715–3723, 2020.

[23] L. Zhu, I. Reychav, R. McHaney, A. Broda, Y. Tal, and O. Manor, "Combined SNA and LDA methods to understand adverse medical events," *The International Journal of Risk & Safety in Medicine*, vol. 30, no. 3, pp. 129–153, 2019.

Hindawi
Journal of Healthcare Engineering
Volume 2021, Article ID 6147434, 8 pages
https://doi.org/10.1155/2021/6147434

Research Article

miR-101-3p Contributes to α-Synuclein Aggregation in Neural Cells through the miR-101-3p/SKP1/PLK2 Pathway

Min Zhang, Wei Liu, Qingan Zhang, and Hongfeng Hu

Department of Neurology, Jingmen No. 1 People's Hospital, Jingmen, Hubei, China

Correspondence should be addressed to Hongfeng Hu; jingmenhuhongfeng@163.com

Received 12 April 2021; Accepted 2 June 2021; Published 14 June 2021

Academic Editor: Enas Abdulhay

Parkinson's disease (PD) is a neurodegenerative disorder characterized by progressive neuronal loss in different brain regions, including the dopaminergic (DA) neurons of the substantia nigra pars compacta (SNc). The aggregation of α-synuclein (α-Syn) plays an essential role in the progression of PD-related neuron toxicity. In this study, bioinformatic analysis was used to confirm differentially expressed genes between patients with PD and healthy donors. Immunofluorescence was used to study the aggregation of α-Syn. Flow cytometry was used to confirm the apoptosis of neurons. Western blot was used to investigate the underlying mechanism. Coimmunoprecipitation (co-IP) was used to verify the interaction between proteins. Luciferase activity assay was used to confirm the target gene of miRNA. In vitro protein ubiquitination assay was used to ascertain the role of S-phase kinase-associated protein 1 (SKP1) on the ubiquitination processes of polo-like kinase 2 (PLK2). The result indicated that miR-101-3p was overexpressed in the substantia nigra of the postmortem brains of patients with PD. The underlying role was investigated in the SH-SY5Y cell line. The overexpression of α-Syn did not result in toxicity or aggregation. However, the co-overexpression of miR-101-3p and α-Syn promoted aggregation and neuron toxicity. Luciferase activity assay indicated that SKP1 is a target gene of miR-101-3p. The co-IP experiment confirmed that SKP1 could directly interact with PLK2. In vitro protein ubiquitination assay confirmed that SKP1 could promote the ubiquitination and subsequent protein degradation of PLK2. We also observed that the cotransfection of short hairpin RNA that targets PLK2 and α-Syn overexpression plasmid results in the endoplasmic reticulum stress of neurons. Our results collectively provide evidence that miR-101-3p contributes to α-Syn aggregation in neurons through the miR-101-3p/SKP1/PLK2 pathway.

1. Introduction

PD is the most common severe movement disorder globally and affects about 1% of adults older than 60 years [1, 2]. The disease is attributed to the selective loss of neurons in the substantia nigra. Its cause is enigmatic in most individuals; PD is characterized by motor and nonmotor symptoms; patients with PD classically display rest tremor, rigidity, bradykinesia, and stooping posture [3–5]. PD can also be associated with neurobehavioral disorders (depression and anxiety), cognitive impairment (dementia), and autonomic dysfunction (e.g., orthostasis and hyperhidrosis) [6, 7]. α-Synuclein (α-Syn) plays a role in rare familial forms of PD and sporadic PD [8]. Human α-Syn is a protein with a molecular mass of ~14 kDa (containing 140 amino acid residues) and is highly expressed in the brain [8, 9]. The accelerated fibrillation of α-Syn may worsen the pathology of PD. Increased α-Syn protein levels in the neurons may facilitate its abnormal aggregation, which results in toxicity and diseased condition [10–12].

MicroRNAs (miRNAs) are small noncoding RNAs that are transcribed from miRNA genes and intronic sequences as primary miRNAs (pri-miRNAs) and stem-loop precursor miRNAs (pre-miRNAs), respectively [13]. The dysregulation of miRNAs may contribute to the development of various diseases, including brain disorder. Several studies have shown that miRNAs contribute to the progression or onset of PD [14].

A study showed that polo-like kinase 2 (PLK2) expression increased in aged monkeys. PLK2 might play an essential role in the modulation of α-Syn [15]. Abid Oueslati et al. reported that PLK2 could interact with α-Syn and subsequently promote the autophagic degradation of α-Syn [15, 16].

Ubiquitination, which is the process of tagging a protein with ubiquitin, is one of the most versatile cellular regulatory mechanisms [17]. Ubiquitination also participates in multiple cellular processes, including gene transcription and cell cycle progression; ubiquitin degrades protein via the ubiquitin-proteasome system or by selective autophagy [18, 19].

A comprehensive understanding of the association between PD and α-Syn is essential to prevent PD progression. In the present study, bioinformatic analysis was used to confirm the differential expression of miR-101-3p in patients with PD and healthy donors. The overexpression of α-Syn did not result in toxicity or aggregation, whereas the co-overexpression of miR-101-3p and α-Syn promoted aggregation and neuron toxicity. We also found that S-phase kinase-associated protein 1 (SKP1) is a target gene of miR-101-3p and could directly interact with PLK2. We also investigated the underlying mechanisms that contributed to these effects.

2. Materials and Methods

2.1. Cell Culture and Treatment. Cell line SH-SY5Y cells were purchased from American Type Culture Collection (Manassas, Virginia). The cells were incubated in RPMI-1640 medium (Thermo Fisher Scientific, Inc., Waltham, Massachusetts) supplemented with 10% fetal bovine serum (Gibco, USA) and 100 μg/mL penicillin-streptomycin (Sigma-Aldrich Co, St. Louis, Missouri) and cultured in a humidified atmosphere of 5% CO_2 in air at 37°C.

2.2. Transfection. Short hairpin RNAs (shRNAs) for PLK2 and SKP1, overexpression plasmids for PLK2 and α-Syn (pcDNA3.1-α-Syn), and corresponding negative controls were purchased from Shanghai GenePharma Co., Ltd. (Shanghai, China). miR-101-3p mimic, inhibitor, and negative control were purchased from RiboBio (Guangzhou, China). Transfection was conducted according to the instruction of the manufacturer.

2.3. Coimmunoprecipitation (Co-IP). Cells were lysed with lysis buffer. The lysates were centrifuged and purified by incubation with protein A/G magnetic beads at 4°C for 1 h. The precleared supernatant was then immunoprecipitated with the primary antibody Flag at 4°C overnight. The complexes were subjected to 1 h of incubation at 4°C using protein A/G magnetic beads and subsequently analyzed by Western blot. Of course, we repeated the experiment three times, and the results were recorded.

2.4. Western Blot. Western blot was carried out according to the standard protocols described previously. We used primary antibodies against GAPDH (1 : 500; Santa Cruz Biotechnology, CA, USA), α-Syn (1 : 1000; #2642), SKP1 (1 : 1000; # 2156S), PLK2 (1 : 1000; # 14812S), eIF2α (1 : 1000; #9722), P-eIF2α (1 : 1000; #9721), ERK (1 : 500), and P-ERK (1 : 500; Cell Signaling Technology, MA, USA). Goat anti-mouse and anti-rabbit antibodies conjugated with horseradish peroxidase were used as secondary antibodies (1 : 2000; Jackson ImmunoResearch, PA, USA). We detected the blots using enhanced chemiluminescence (Dura, Pierce, NJ, USA). We repeated the experiment three times.

2.5. Flow Cytometry. Cell apoptosis was measured by flow cytometry. The cells were harvested and washed with PBS after 24 h of incubation with 1-methyl-4-phenyl-pyridinium (MPP+). Then, the cells were resuspended and incubated with 5 μL of Annexin V-fluorescein isothiocyanate and 5 μL of propidium iodide (PI). Apoptosis percentage, including early apoptosis (Annexin V+/PI−) and late apoptosis (Annexin V+/PI+), was calculated. Experiments were repeated three times to ensure reproducibility. The labeled cells were analyzed using the BD FACSverse flow cytometer (BD, Bioscience), and the data were processed by the FlowJo software (Treestar).

2.6. Immunofluorescence Staining. SH-SY5Y cells were fixed with 4% paraformaldehyde for 10 min and permeabilized with PBS containing 0.1% Triton X-100 for 10 min after 72 h of transfection. The cells were blocked in 10% goat serum and incubated overnight with primary antibodies against α-Syn (1 : 500; Cell Signaling Technology, MA, USA) at 4°C. The cells were washed with PBS and incubated with fluorescent secondary antibody conjugated with Alexa Fluor®594 for 1 h. Subsequently, the cells were counterstained with 4',6-diamidino-2-phenylindole and imaged with a fluorescence microscope. Fluorescent intensities were measured using the ImageJ software.

2.7. Statistical Analysis. All statistical analyses in this study were performed using GraphPad Prism 5 for Windows. Data were expressed as mean ± standard deviation (SD) and were compared using a one-way analysis of variance (ANOVA) followed by Tukey's multiple-comparison test. The SPSS 21.0 software was used to analyze the experimental data. A value of $P < 0.05$ was considered statistically significant.

3. Results

3.1. miR-101-3p and α-Syn Co-Overexpression Promotes α-Syn Aggregation and Neurotoxicity. Initially, the Gene Expression Omnibus (GEO) database was used to predict the difference in the expression between patients with PD and healthy donors. Figures 1(a) and 1(b) show that the expression of 30 genes considerably changed. Among which, seven genes were upregulated and 24 genes were downregulated in patients with PD. miR-101-3p was the most considerably upregulated among the genes; therefore, miR-101-3p was used in the subsequent study.

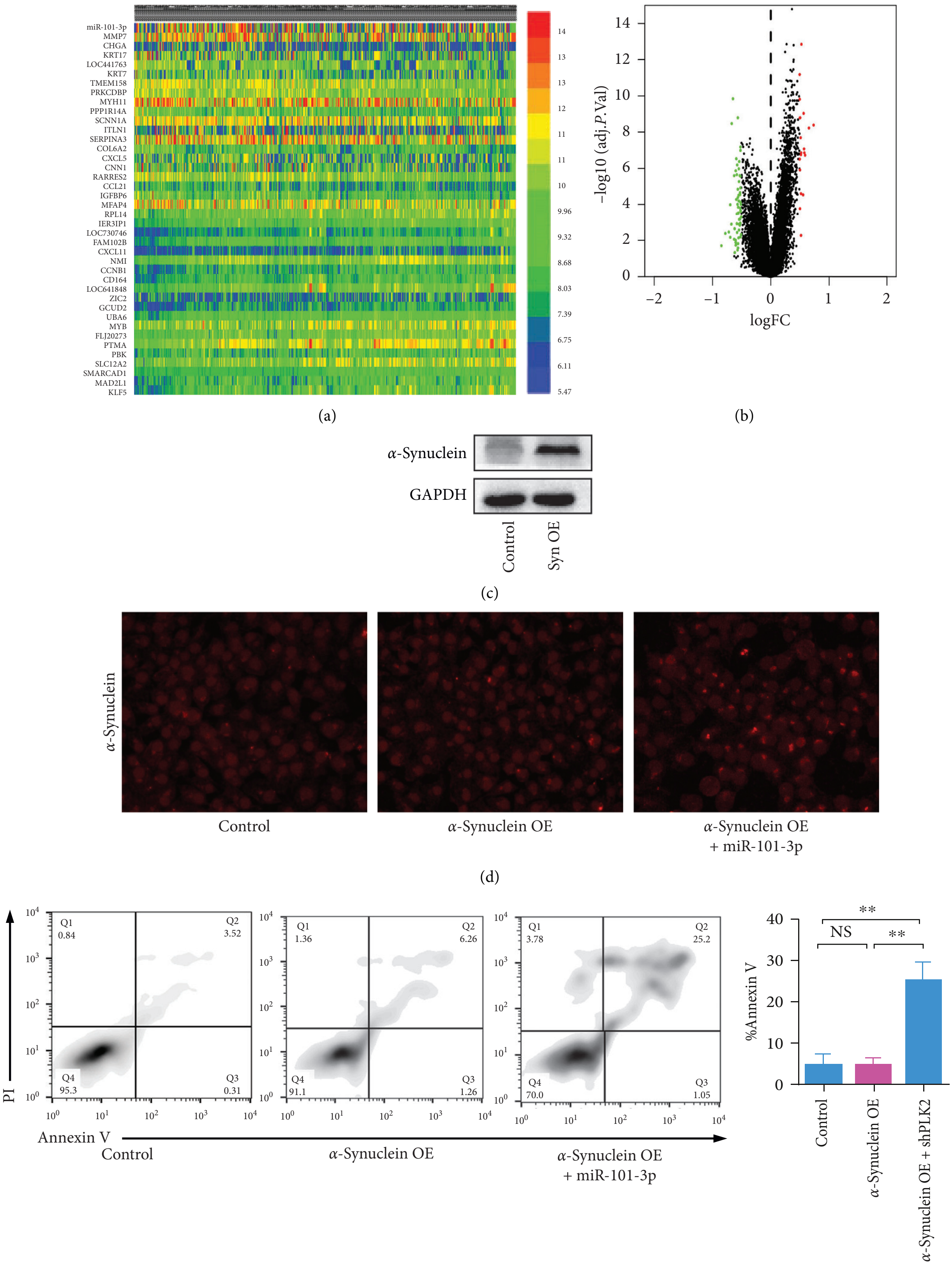

Figure 1: Co-overexpression of miR-101-3p and α-synuclein promotes α-Syn aggregation and neurotoxicity. (a) Heatmap of gene expression between substantia nigra from postmortem brains of patients with Parkinson's disease and health donors. (b) Volcano map of gene expression between substantia nigra from postmortem brains of patients with Parkinson's disease and health donors. (c) Western blot analysis of SH-SY5Y after transfection of α-synuclein overexpression plasmid. (d) Immunofluorescence of α-synuclein aggregation. (e) Flow cytometry analysis of cell apoptosis. Error bars represent mean ± SD. $^{**}P < 0.01$. n.s., not significant, by the paired two-sided Student's t-test.

The abnormal aggregation of α-Syn can promote PD progression and result in neuron toxicity. We confirmed this conclusion by constructing an α-Syn overexpression plasmid. The effect of the overexpression was confirmed by Western blot. As shown in Figure 1(c), α-Syn was overexpressed successfully. The impact of α-Syn overexpression on α-Syn aggregation was confirmed by immunofluorescence. Figure 1(c) demonstrates that no remarkable accumulation in SH-SY5Y cells after α-Syn was overexpressed. However, the cotransfection of miR-101-3p and α-Syn overexpression plasmid resulted in a considerable aggregation of α-Syn. Flow cytometry also confirmed that the cell apoptosis rate increased after the co-overexpression of miR-101-3p and α-Syn. This finding indicated that the co-overexpression caused substantial neurotoxicity.

Our result indicated that the co-overexpression of miR-101-3p and α-Syn promotes α-Syn aggregation and neurotoxicity.

3.2. miR-101-3p Binds to SKP1 mRNA and Suppresses SKP1 Expression. The public online dataset TargetScan was used to predict the possible target gene of miR-101-3p and confirm the downstream signal pathway of miR-101-3p. We found that SKP1 might serve as the target gene of miR-101-3p. Western blot was performed to confirm this prediction. As shown in Figure 2(a), SKP1 was downregulated after the transfection of miR-101-3p mimic and was upregulated after the transfection of the inhibitor. This result indicated that a regulation relationship might exist between SKP1 and miR-101-3p. Luciferase reporter assay was performed to further confirm their relationship. As shown in Figure 2(b), the 3'-untranslated regions (UTRs) in the predicted binding site of wild-type and mutated SKP1 were constructed, and cDNA was cloned into the luciferase reporter plasmid. The result confirmed that the transfection of miR-101-3p caused a substantial suppression of luciferase activity but did not substantially change the luciferase activity in the luciferase reporter plasmid with mutated UTR. This work demonstrated that miR-101-3p could directly bind to SKP1 mRNA and subsequently suppress SKP1 expression.

SKP1 is an essential component of the ubiquitin ligase complex. Therefore, the downstream signal of SKP1 was investigated. As shown in Figure 2(c), the STRING online dataset indicated that SKP1 could interact with PLK2. As shown in Figure 2(d), molecular docking confirmed that PLK2 might directly interact with SKP1. A co-IP experiment was performed based on the evidence. Figure 2(e) shows that PLK2 precipitated with SKP1; hence, PLK2 could directly interact with SKP1.

Our result confirmed that miR-101-3p targets SKP1 and SKP1 could interact with PLK2.

3.3. SKP1 Interacts with PLK2 and Promotes Ubiquitination of PLK2. SKP1 is an essential component of the ubiquitin ligase complex. Therefore, we speculated the interaction between SKP1 and PLK2 might influence the ubiquitination processes of PLK2. To confirm this hypothesis, shRNA targeting SKP1 was constructed, as shown in Figure 3(a); Western blot demonstrated that SKP1 was knocked down successfully, and we select shRNA#3 for subsequent study, as shown in Figure 3(b), after treatment of cycloheximide, a protein synthesis inhibitor, the half-life of PLK1 study. The result confirmed that after downregulation of SKP1, the half-life of PLK2 significantly increased, indicating that downregulation of SKP1 stabilized PLK2 and suppressed the protein degradation processes of PLK2.

To confirm whether SKP1 can influence the ubiquitination processes of PLK2, in vitro protein ubiquitination assay was performed. As shown in Figure 3(c), ubiquitination of PLK2 was enhanced significantly after overexpression of SKP1.

We next investigated the role played by PLK2 in neurotoxicity. To answer this question, PLK2 overexpression vector was constructed, as shown in Figure 3(d); Western blot indicated that PLK2 was overexpressed successfully after transfection of PLK2 overexpression vector.

Neurotoxin MPP+ is a classical neurotoxin that is used to generate a cell model of Parkinson's disease. As shown in Figure 3(e), the apoptosis rate increased after MPP+ treated neuron cells. However, the apoptosis rate was partly reduced after overexpression of PLK2. The result confirmed that PLK2 could partially alleviate neurotoxicity.

Our result confirmed that SKP1 interacts with PLK2 and promotes ubiquitination of PLK2, and PLK2 can partly alleviate neurotoxicity.

3.4. The Cotransfection of PLK2-Targeting shRNA and α-Syn Overexpression Plasmid Promotes Endoplasmic Reticulum (ER) Stress in Nerve Cells. PLK2 can interact with α-Syn and subsequently promote the autophagic degradation of α-Syn. Co-IP was performed to confirm this conclusion. Figure 4(a) shows that PLK2 could interact with α-Syn. To further investigate the role played by PLK2 in aggregation processes of α-syn, shRNA targeting PLK2 was constructed, as shown in Figure 4(b); Western blot indicated that PLK2 was knocked down successfully, and we select shRNA#1 for subsequently study. As shown in Figure 4(c), after cotransfection of PLK2-targeted shRNA and α-synuclein overexpression plasmid, P-ERK and eIF2α were overexpressed significantly, indicating that cotransfection of PLK2-targeted shRNA and α-synuclein overexpression plasmid promotes ER stress.

Flow cytometry was used to confirm our conclusion further. As shown in Figure 4(d), α-synuclein overexpression alone does not increase the apoptosis rate. However, cotransfection of PLK2-targeted shRNA and α-synuclein overexpression plasmid significantly enhanced apoptosis rate.

Taken together, our result confirmed that cotransfection of PLK2-targeted shRNA and α-synuclein overexpression plasmid promotes ER stress in nerve cells.

4. Discussion

PD is a severe neurological disease that results from the progressive degeneration of dopaminergic neurons located in the substantia nigra. PD influences about seven million

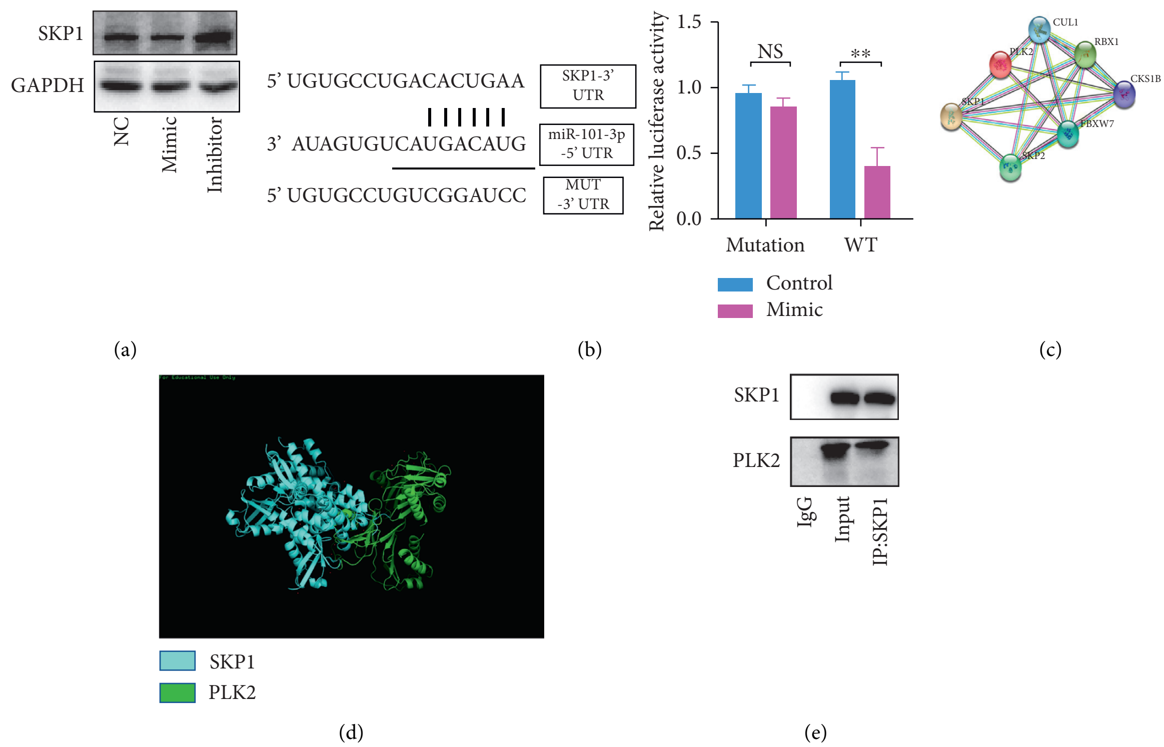

Figure 2: miR-101-3p binds to mRNA of SKP1 and suppress SKP1 expression. (a) Western blot analysis of SKP1 expression in SH-SY5Y after transfection of miR-101-3p mimic or inhibitor. (b) Illustration of SKP1 3'UTR and SKP1 3' UTR mutation. Right panel, quantification of the luciferase activity. (c) Protein-protein interaction predicted by the STRING online dataset. (d) Molecular docking of PLK2 and SKP1. (e) Co-IP experiment of SKP1 and PLK2. Error bars represent mean ± SD. $^{**}P < 0.01$. n.s., not significant, by the paired two-sided Student's t-test.

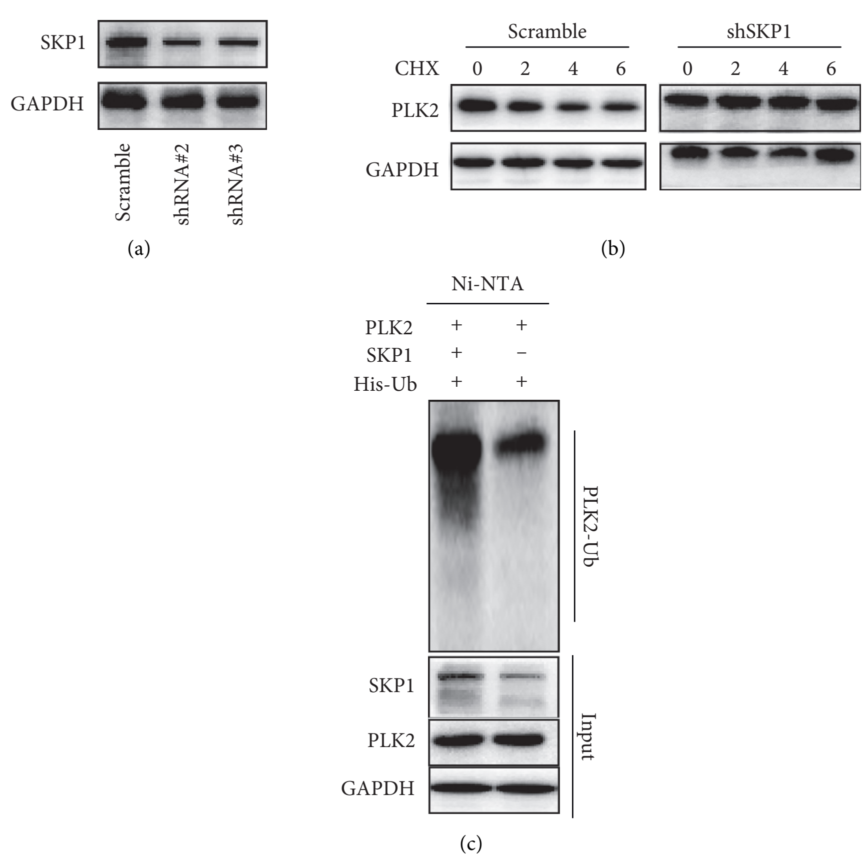

Figure 3: Continued.

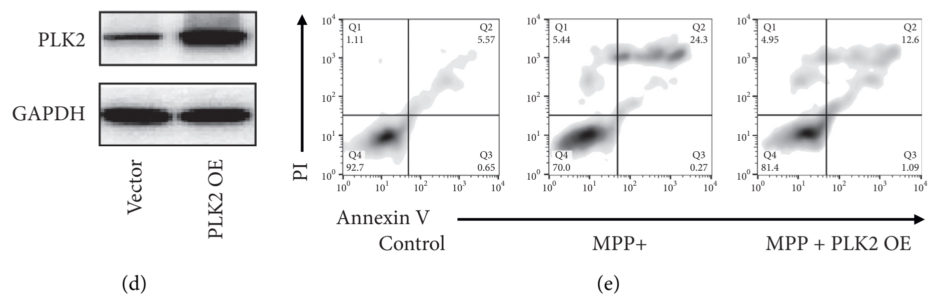

Figure 3: SKP1 interact with PLK2 and promotes ubiquitination of PLK2. (a) SKP1 expression after SH-SY5Y was transfected by shRNA targeting SKP1. (b) Half-life of PLK2 evaluated after treated by cycloheximide. (c) Ubiquitination assay of PLK2 with or without SKP1 overexpression. (d) Western blot analysis of PLK2 after transfection of PLK2 overexpression plasmid. (e) Flow cytometry analysis of cell apoptosis.

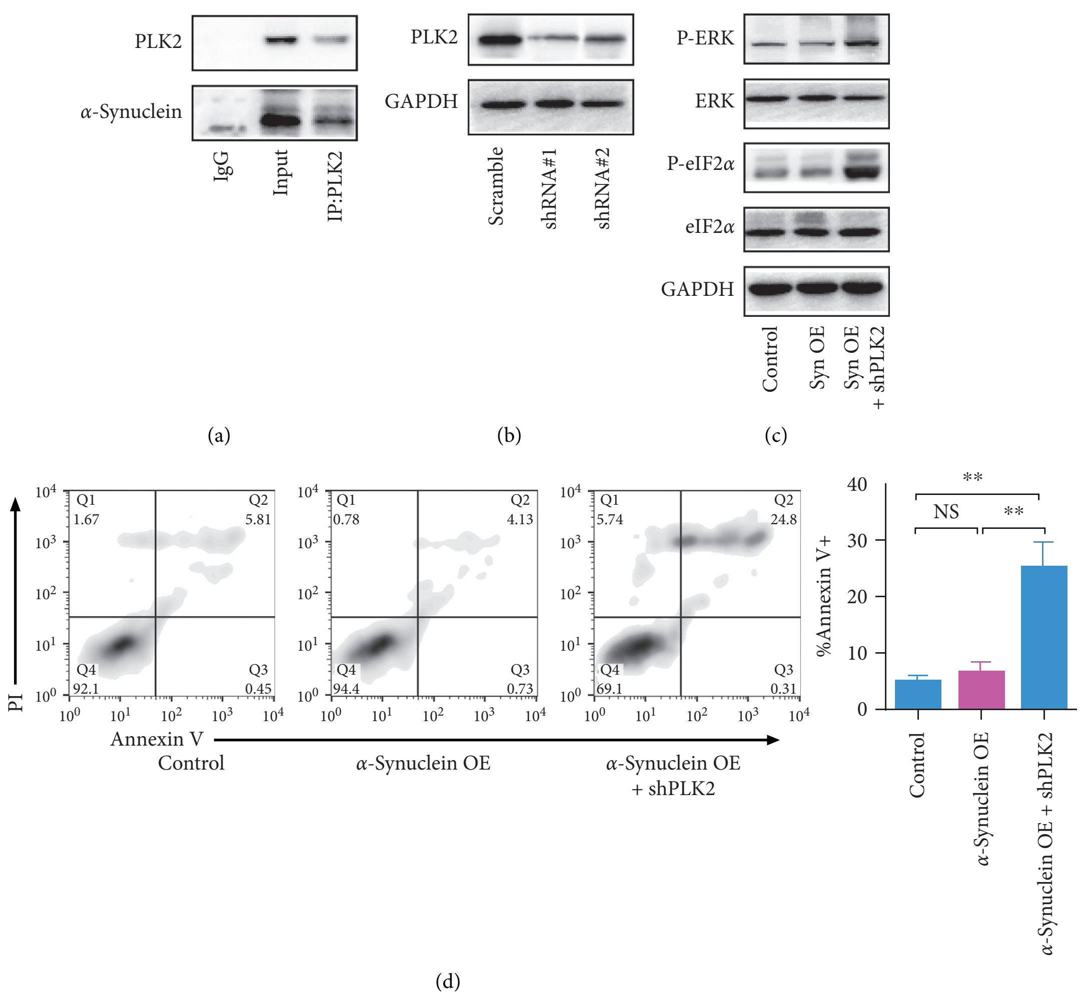

Figure 4: Cotransfection of PLK2-targeted shRNA and α-synuclein overexpression plasmid promotes ER stress in nerve cells. (a) Co-IP experiment of PLK2 and α-synuclein. (b) Western blot analysis of PLK2 after transfection of shRNA targeting PLK2. (c) Western analysis of P-ERK and P-eIF2α. (d) Flow cytometry analysis of cell apoptosis. Error bars represent mean ± SD. $^{**}P < 0.01$. n.s., not significant, by the paired two-sided Student's t-test.

people worldwide and occur among older adults; its prevalence increases from 1% in people aged more than 60 to 4% in those older than 80 [20–22].

MiRNAs with vast regulatory potential have been recently proposed as biomarkers or possible therapeutic targets for PD. MiRNAs are small (about 20–24 nucleotides long), endogenous noncoding RNAs that play a profound role in numerous biological processes in health and disease. Most miRNAs suppress gene expression through the promotion of mRNA degradation and translation inhibition [23]. Previous studies have revealed that miRNAs are implicated in neurodegeneration, and miRNA pathways are affected in almost all neurodegenerative disorders. In this study, the GEO database was used to predict the difference in expression between patients with PD and healthy donors [24]. We found that the expression of 30 genes considerably changed. Among which, seven genes were upregulated and 24 genes were downregulated in patients with PD. miR-101-3p was the most upregulated among the miRNAs. Therefore, miR-101-3p was used for subsequent study [25].

α-Syn is a 140-residue natively unfolded protein that is abundantly expressed at the presynaptic terminals. α-Syn participates in the regulation of synaptic transmission and dopamine biosynthesis; the overexpression and misfolding of α-Syn play an essential role in the progression of neurodegenerative disorders [26, 27]. In the present study, immunofluorescence was used to confirm α-Syn aggregation. No remarkable accumulation was observed in SH-SY5Y cells after α-Syn was overexpressed [28]. However, the cotransfection of miR-101-3p and α-Syn overexpression plasmid resulted in substantial α-Syn aggregation. Flow cytometry also confirmed that cell apoptosis rate increased after the co-overexpression of miR-101-3p and α-Syn. The results indicated that the co-overexpression caused considerable neurotoxicity.

SKP1 is an essential component of the ubiquitin ligase complex. In this study, we confirmed that SKP1 can bind to PLK2 and subsequently promote the ubiquitination of PLK2.

PLK2 can bind directly to α-Syn and regulate α-Syn clearance [29–31]. In the current study, we confirmed that α-Syn could directly interact with PLK2, and the overexpression of PLK2 can partly alleviate the neurotoxicity induced by MPP+. The binding between PLK2 and α-Syn is needed for α-Syn clearance.

Based on our result, miR-101-3p overexpression in neurons may suppress the expression of SKP1. SKP1 downregulation limited the clearance of α-Syn and subsequently caused the abnormal accumulation and aggregation of α-Syn.

Our result provides evidence that miR-101-3p contributes to α-Syn aggregation in neurons through the miR-101-3p/SKP1/PLK2 pathway.

Data Availability

The data used to support the findings of this study are available from the corresponding author upon request.

Ethical Approval

The Ethical Committee of Jingmen No. 1 People's Hospital approved this study.

Disclosure

Min Zhang and Wei Liu are the co-first authors.

Conflicts of Interest

The authors declare that they have no conflicts of interest.

Authors' Contributions

Min Zhang and Wei Liu contributed equally to this work.

Acknowledgments

The authors would like to thank Jingmen No. 1 People's Hospital and the original authors of references for their help in this work.

References

[1] T. Capriotti and K. Terzakis, "Parkinson disease," *Home Healthcare Now*, vol. 34, no. 6, pp. 300–307, 2016.
[2] R. B. Schneider, J. Iourinets, and I. H. Richard, "Parkinson's disease psychosis: presentation, diagnosis and management," *Neurodegenerative Disease Management*, vol. 7, no. 6, pp. 365–376, 2017, published online Epub2017/12/01.
[3] A. Samii, J. G. Nutt, and B. R. Ransom, "Parkinson's disease," *The Lancet*, vol. 363, no. 9423, pp. 1783–1793, 2004.
[4] O.-B. Tysnes and A. Storstein, "'Epidemiology of Parkinson's disease," *Journal of Neural Transmission*, vol. 124, no. 8, pp. 901–905, 2017, published online Epub2017/08/01.
[5] E. Tolosa, G. Wenning, and W. Poewe, "The diagnosis of Parkinson's disease," *The Lancet Neurology*, vol. 5, no. 1, pp. 75–86, 2006.
[6] M. Grayson, "Parkinson's disease," *Nature*, vol. 538, no. 7626, p. S1, 2016 published online Epub2016/10/01.
[7] P. M. A. Antony, N. J. Diederich, R. Krüger, and R. Balling, "The hallmarks of Parkinson's disease," *FEBS Journal*, vol. 280, no. 23, pp. 5981–5993, 2013, published online Epub2013/12/01.
[8] M. Fayyad, S. Salim, N. Majbour et al., "'Parkinson's disease biomarkers based on α-synuclein," *Journal of Neurochemistry*, vol. 150, no. 5, pp. 626–636, 2019, published online Epub2019/09/01.
[9] A. Atik, T. Stewart, and J. Zhang, "Alpha-synuclein as a biomarker for Parkinson's disease," *Brain Pathology*, vol. 26, no. 3, pp. 410–418, 2016, published online Epub2016/05/01.
[10] D. J. Irwin, V. M.-Y. Lee, and J. Q. Trojanowski, "'Parkinson's disease dementia: convergence of α-synuclein, tau and amyloid-β pathologies," *Nature Reviews Neuroscience*, vol. 14, no. 9, pp. 626–636, 2013, published online Epub2013/09/01.
[11] J. B. Koprich, L. V. Kalia, and J. M. Brotchie, "Animal models of α-synucleinopathy for Parkinson disease drug development," *Nature Reviews Neuroscience*, vol. 18, no. 9, pp. 515–529, 2017, published online Epub2017/09/01.
[12] P. Riederer, D. Berg, N. Casadei et al., "'α-synuclein in Parkinson's disease: causal or bystander?" *Journal of Neural*

Transmission, vol. 126, no. 7, pp. 815–840, 2019, published online Epub2019/07/01.

[13] Y. Gui, H. Liu, L. Zhang, W. Lv, and X. Hu, "Altered microRNA profiles in cerebrospinal fluid exosome in Parkinson disease and Alzheimer disease," *Oncotarget*, vol. 6, no. 35, pp. 37043–37053, 2015.

[14] K. S. Patil, I. Basak, I. Dalen et al., "Combinatory microRNA serum signatures as classifiers of Parkinson's disease," *Parkinsonism & Related Disorders*, vol. 64, pp. 202–210, 2019.

[15] A. Oueslati, B. L. Schneider, P. Aebischer, and H. A. Lashuel, "Polo-like kinase 2 regulates selective autophagic -synuclein clearance and suppresses its toxicity *in vivo*," *Proceedings of the National Academy of Sciences*, vol. 110, no. 41, pp. E3945–E3954, 2013.

[16] C. Guo, J. Zhu, J. Wang et al., "Neuroprotective effects of protocatechuic aldehyde through PLK2/p-GSK3β/Nrf2 signaling pathway in both in vivo and in vitro models of Parkinson's disease," *Aging*, vol. 11, no. 21, pp. 9424–9441, 2019.

[17] D. Popovic, D. Vucic, and I. Dikic, "Ubiquitination in disease pathogenesis and treatment," *Nature Medicine*, vol. 20, no. 11, pp. 1242–1253, 2014.

[18] S. Shaid, C. H. Brandts, H. Serve, and I. Dikic, "Ubiquitination and selective autophagy," *Cell Death & Differentiation*, vol. 20, no. 1, pp. 21–30, 2013, published online Epub2013/01/01.

[19] R.-H. Chen, Y.-H. Chen, and T.-Y. Huang, "Ubiquitin-mediated regulation of autophagy," *Journal of Biomedical Science*, vol. 26, no. 1, p. 80, 2019 published online Epub2019/10/21.

[20] A. Lee and R. M. Gilbert, "Epidemiology of Parkinson disease," *Neurologic Clinics*, vol. 34, no. 4, pp. 955–965, 2016, published online Epub2016/11/01.

[21] A. U. Khan, M. Akram, M. Daniyal, and R. Zainab, "'Awareness and current knowledge of Parkinson's disease: a neurodegenerative disorder," *International Journal of Neuroscience*, vol. 129, no. 1, pp. 55–93, 2019, published online Epub2019/01/02.

[22] M. Lew, "Overview of Parkinson's disease," *Pharmacotherapy*, vol. 27, no. 12 Part 2, pp. 155S–160S, 2007, published online Epub2007/12/01.

[23] S. Kumar, M. Vijayan, J. S. Bhatti, and P. H. Reddy, "MicroRNAs as peripheral biomarkers in aging and age-related diseases," in *Progress in Molecular Biology and Translational Science*, P. H. Reddy, Ed., vol. 146, pp. 47–94, Academic Press, Cambridge, UK, 2017.

[24] W. Wei, B. Zhou, D. Połap, and M. Woźniak, "A regional adaptive variational PDE model for computed tomography image reconstruction," *Pattern Recognition*, vol. 92, no. 3, pp. 64–81, 2019.

[25] W. Wei, H. Song, L. Wei, P. Shen, and A. Vasilakos, "Gradient-driven parking navigation using a continuous information potential field based on wireless sensor network," *Information Sciences*, vol. 408, pp. 100–114, 2017.

[26] S. Mehra, S. Sahay, and S. K. Maji, "'α-synuclein misfolding and aggregation: implications in Parkinson's disease pathogenesis," *Biochimica et Biophysica Acta (BBA) - Proteins and Proteomics*, vol. 1867, no. 10, pp. 890–908, 2019, published online Epub2019/10/01/.

[27] D. Ghosh, S. Mehra, S. Sahay, P. K. Singh, and S. K. Maji, "α-synuclein aggregation and its modulation," *International Journal of Biological Macromolecules*, vol. 100, pp. 37–54, 2017, published online Epub2017/07/01/(.

[28] W. Wei, X. Xu, W. Marcin, X. Fan, and L. Ye, "Multi-sink distributed power control algorithm for Cyber-physical-systems in coal mine tunnels," *Computer Networks*, vol. 161, pp. 210–219, 2019.

[29] M. Bergeron, R. Motter, P. Tanaka et al., "In vivo modulation of polo-like kinases supports a key role for PLK2 in Ser129 α-synuclein phosphorylation in mouse brain," *Neuroscience*, vol. 256, pp. 72–82, 2014, published online Epub2014/01/03/.

[30] E. Basso, P. Antas, Z. Marijanovic, S. Gonçalves, S. Tenreiro, and T. F. Outeiro, "PLK2 modulates α-synuclein aggregation in yeast and mammalian cells," *Molecular Neurobiology*, vol. 48, no. 3, pp. 854–862, 2013, published online Epub2013/12/01.

[31] R. Wang, Y. Wang, L. Qu et al., "Iron-induced oxidative stress contributes to α-synuclein phosphorylation and up-regulation via polo-like kinase 2 and casein kinase 2," *Neurochemistry International*, vol. 125, pp. 127–135, 2019, published online Epub2019/05/01/.

Hindawi
Journal of Healthcare Engineering
Volume 2021, Article ID 9929333, 6 pages
https://doi.org/10.1155/2021/9929333

Research Article

Impact of Portal Vein Thrombosis on Endoscopic Variceal Band Ligation in Liver Cirrhosis

Yue Huang

Department of Gastroenterology, The First Affiliated Hospital, College of Medicine, Zhejiang University, Hangzhou, China

Correspondence should be addressed to Yue Huang; 1313005@zju.edu.cn

Received 2 April 2021; Revised 26 April 2021; Accepted 10 May 2021; Published 22 May 2021

Academic Editor: Enas Abdulhay

Background. Portal vein (PV) thrombosis (PVT) is a common complication of liver cirrhosis and can refer to thrombosis within the PV that can extend to its left or right branches and in some cases to the superior mesenteric vein or the splenic vein (Chawla and Bodh, 2015). For severe PVT patients, there are possibilities of increasing PV resistance and reduction of the blood flow though PV towards liver, which exacerbate liver function damage meanwhile elevating the gastrointestinal variceal bleeding risk. Endoscopic Variceal band ligation (EVL) is often used to prevent esophageal variceal bleeding; postoperative complications such as severe gastrointestinal bleeding and bleeding-related death, fever, retrosternal pain, and esophageal stenosis may appear. There was absence of the research which evaluated the impact of PVT in liver cirrhosis on the complication of endoscopic Variceal band ligation for now. We herein aimed to compare cirrhosis patients with and without PVT of recent complications after EVL. *Method*. We established the retrospective investigation on 144 consecutive cirrhosis patients (excluding patients with hepatocellular carcinoma and who received portal vein-systemic circulation devascularization or shunt surgery, splenectomy, hepatectomy, liver transplantation, transjugular intrahepatic portal vein stent shunt (TIPS), endoscopic varices Variceal ligation, or sclerotherapy before) who have received first endoscopic esophageal varices band ligation in Gastrointestinal Endoscopy Center of the First Affiliated Hospital, College of Medicine, ZheJiang University, between January 2014 and December 2017. Portal vein Doppler ultrasonography, liver computerized tomography (CT), and angiography or liver-enhanced magnetic resonance imaging (MRI) were applied to evaluate the portal vein thrombosis of each patient before EVL. There were 18 patients confirmed with portal vein thrombosis while the other 126 patients without PVT. The primary end point for this research is the upper gastrointestinal hemorrhage and related death occurred from the date of ligation until leaving hospital, and the secondary end point is the appearance of postoperative fever and retrosternal pain. *Results*. There are no significant differences of gastrointestinal bleeding, bleeding-related death, fever, or retrosternal pain after EVL and the length of hospital stays between cirrhotic patients with or without PVT ($P = 0.34, 0.51, 0.58, 0.61, 0.88$). *Conclusion*. Liver cirrhosis with portal vein thrombosis did not increase incidence of recent complications of the endoscopic Variceal band ligation.

1. Introduction

The studies of the epidemiology of portal vein thrombosis (PVT) in cirrhosis are mainly established on liver transplant patients [1]. One study evaluated 41 indexes of the secondary PVT for liver transplant patients and finally reported that the prevalence of PVT is about 10% (2%–23%). A prospective cross section study established by 43 Italian research centers found that the prevalence of PVT for liver transplant patients is 7% [2]. According to the reports, PVT affects 0.6%–26% of liver cirrhosis patients, while the prevalence of PVT in healthy people is ~0.7–1/100000 [3].

As we know, different factors can drive risk of thrombosis including endothelial injury, hypercoagulability, and static blood flow from the PH [4]. Routine ultrasound is the most common means of incidentally detecting PVT in cirrhosis. The majority of the thrombus of portal vein is asymptomatic and chronic, but patients with acute PVT and hepatic decompensation may suffer from pain in the abdomen and/or worsening ascites. Follow-up imaging is generally necessary after ultrasound in order to confirm PVT diagnosis and exclude the possibility of tumor-related thrombosis, with MRI and CT being the primary imaging modalities used for this purpose.

The classification of PVT in early stage is mainly according to the anatomy position of thrombus. In 2002, a widespread application of classification standard raised by Yerdel and other scholars [5] has four different types and only defined by the anatomy position. The classification standard in the most recent guidance (from European Association for the Study of the Liver, EASL, and American Association for the Study of Liver Diseases, AASLD) has comprehensively gathered the past nomenclature (such as "acute" and "chronic"). At present, another "Anatomical-Functional Classification System"(Supplementary Table 1) has been indicated, which combined the anatomy position of thrombus, the duration of thrombosis formation, and the relationship with clinical outcomes [6]; this classification system is more capable to describe the disparity of different PVT types and provided a good standard for further clinical study.

The common treatments of PVT are anticoagulation, intravenous thrombolysis, and TIPS. However, considering the risk of gastrointestinal bleeding, the anticoagulant using is still controversial.

Endoscopic Variceal band ligation (EVL) is a frequently used treatment for the esophageal variceal bleeding, which is recommended by the Chinese guidance of the prevention and treatment of gastroesophageal variceal bleeding [7] and also 2016 Practice Guidance by AASLD as primary prevention for moderate to severe esophageal varices and secondary prevention for all severity of esophageal varices [8]. Common postoperative complications include ulcer-related bleeding after the ligation (which can cause fatal haemorrhage), fever, and retrosternal pain.

There was absence of the research which evaluated the impact of PVT in liver cirrhosis on the complication of endoscopic Variceal band ligation for now. Alessandra et al. made a retrospective research to assess the impact of PVT in the eradication effect of endoscopic ligation for esophageal varices. The results showed that the portal vein thrombosis will not elevate the incidence of gastrointestinal bleeding events of the group of PVT patients who received EVL during follow-up [9]. However, they did not evaluate the other complications of EVL. Therefore, we designed a retrospective cohort study, with detailed instruction as follows.

2. Method

2.1. Patients. We established retrospective investigation on 144 consecutive cirrhotic patients receiving endoscopic Variceal band ligation (EVL) in first time in Gastrointestinal Endoscopy Center of the First Affiliated Hospital, College of Medicine, Zhejiang University, from January 2014 to December 2017. This study was approved by the First Affiliated Hospital Ethics Committee of Zhejiang University College of Medicine.

Inclusion Criteria. First, the diagnosis of liver cirrhosis is based on the clinical history, laboratory inspection, and imageological examination. The etiology is separated into viral, alcoholic, and other reasons. Second, endoscopic esophageal varices were diagnosed by upper gastrointestinal endoscopy; meanwhile, the severity of esophageal varices was classified according to the endoscopic behaviors. Based on the form of the varices and whether had red signs with high risk of bleeding, the severity was separated into 3 types as follows: mild (G1): the appearance of endoscopic esophageal varices is linear or slightly tortuous and no red signs; moderate (G2): the appearance of endoscopic esophageal varices is linear or slightly tortuous and red sign appears or the appearance of endoscopic esophageal varices is serpentine, tortuously uplifted; severe (G3): the appearance of endoscopic esophageal varices is serpentine, tortuously uplifted along with red signs or the appearance of endoscopic esophageal varices is bead, nodular, or tuberculiform (no matter the red signs appeared or not).

Exclusion Criteria. First, patients who combined with hepatocellular carcinoma or once had hepatocellular carcinoma and treated by surgery are excluded. Second, patients who received endoscopic Variceal band ligation or sclerotherapy, TIPS, portal vein-systemic circulation devascularization or shunt surgery, splenectomy, and liver transplantation due to esophageal variceal bleeding are excluded. Patients selection is as shown in Figure 1.

2.2. Clinical Data Collection. Age, gender, etiology of liver cirrhosis, hemoglobin (HGB, g/dL), blood platelet count (PLT, 1000/mm3), serum total bilirubin (mg/dl), prothrombin time (PT, s), serum creatinine (mg/dl), international normalized ratio (INR), D-dimmer (μg/L), serum albumin (g/dL), severity of ascites, severity of hepatic encephalopathy, and status of portal thrombosis are collected retrospectively.

The Child-Pugh-Turcotte score (Table 1) and classification of patients and grade the model for end-stage liver disease (MELD) are calculated.

For primary biliary cirrhosis (PBC) or primary sclerosing cholangitis (PSC) patients, serum total bilirubin (umol/L) should be modified as follows: 17–68 as 1 point, 68–170 as 2 points, and > 170 as 3 points.

Child-Pugh-Turcotte classification is as follows:

(i) Class A： 5-6 points, low risk, the best prognosis
(ii) Class B： 7–9 points, moderate risk
(iii) Class C： ≥10 points, high risk, the worst prognosis

Computational formula of MELD score is as follows:
$R = 3.8\ln$ [bilirubin (mg/dl)] + 11.2ln (INR) + 9.6ln [creatinine (mg/dl)] + 6.4 (etiology: biliary or alcoholic = 0, others = 1). (Results in round numbers).

2.3. The Diagnosis and Evaluation Method for Portal Vein Thrombosis. Portal vein Doppler ultrasound is implemented for preliminary screening for all patients, the diagnosis is confirmed through liver-enhanced CT scan or liver CT angiography or liver-enhanced MRI, and the range of

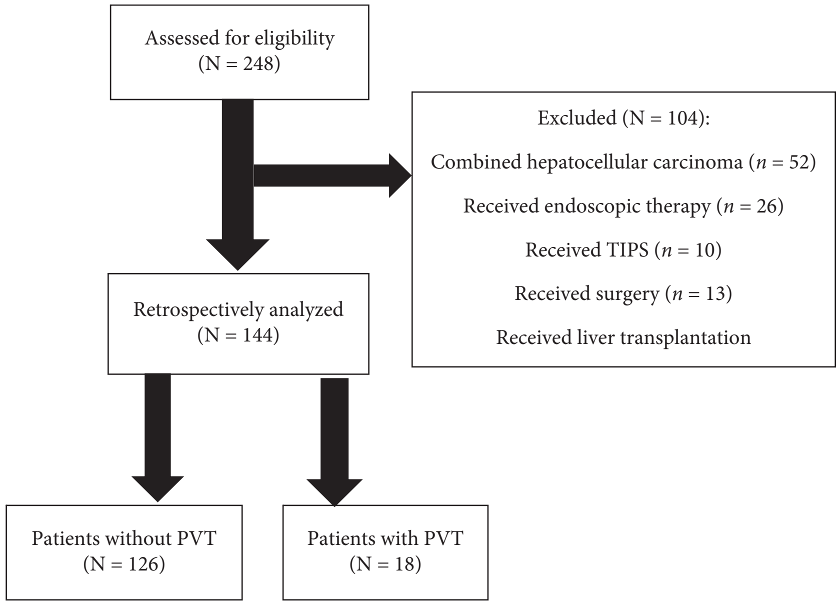

Figure 1: Patients enrollment and screening.

Table 1: The standards of Child-Pugh-Turcotte score.

Clinical biochemical indicators	1 point	2 points	3 points
Hepatic encephalopathy (stage)	Non	1–2	3–4
Ascites	Non	Mild	Moderate or severe
Serum total bilirubin (umol/L)	< 34	34–51	> 51
Serum albumin (g/L)	> 35	28–35	< 28
Prolonged PT (s)	< 4	4–6	> 6

thrombus, portal vein occlusion degree, and whether portal vein cavernous transformation appeared are evaluated.

2.4. The Implementation and Used Equipment of Endoscopic Variceal Band Ligation (EVL). All the endoscopic esophageal varices ligation (EVL) was operated by senior gastroenterologist. Type of applied endoscopy is as follows: Gif-Q260 J, Olympus Corporation, Japan. Type of ligation device is as follows: MBL-6-F, Wilson Cook Medical, America (Six Shooter Saeed Multi-Band Ligator, Wilson Cook Medical Inc. Winston-Salem, NC).

2.5. Endpoints

(a) Post-EVL gastrointestinal bleeding: hematemesis, melena, or HGB reduction greater than 2 g/dL during the period after EVL until patient leaving hospital

(b) Bleeding-related death: death caused by massive gastrointestinal hemorrhage after the EVL, which are judged by the clinician

(c) Post-EVL fever: body temperature greater than 37.5°C after the EVL

(d) Post-EVL retrosternal pain: pain behind the sternum after the EVL

2.6. Data Collection and Analyze. Data are analyzed with SPSS 17.0 software; statistical methods such as chi-square test or one-way analysis of variance will be implemented for analyzing influence factor of interblock or intraclass. P value less than 0.05 will be admitted as statistical significance.

3. Results

3.1. Baseline Characteristics. 144 patients were enrolled in the study in total, 67.46% men with the mean age of 54.79 ± 11.15 years. Study population characteristics are counted statistically. There were no significant difference between cirrhotic patients with or without PVT of etiology, prophylaxis level, Child-Pugh class, Child-Pugh score, MELD score, severity of esophageal varices, hemoglobin, platelets count, creatinine, PT, INR, albumin, bilirubin, and NSBB use. The D-dimer level of the PVT group is significantly higher than that of non-PVT group ($P < 0.001$)(Table 2).

We made a further analysis of the 18 cirrhosis patients with PVT classified by the anatomical-functional classification of PVT (Table 3). All the patients' portal vein thrombus is asymptomatic chronic thrombus, including 8 (44.4%) cases of Type 1, 3 (16.7%) cases of Type 2, and 7 (38.9%) cases of Type 3. There are 5 (27.8%) cases with superior mesenteric vein thrombosis and 2 (11.1%) cases with splenic vein thrombosis. Only 1 (5.6%) case was occlusive with cavernous transformation of portal vein, while the other 17 (94.4%) cases were nonocclusive. The chi-square test shows that the site of portal vein thrombus is significantly correlated to the severity of esophageal varices ($P = 0.004$). It seems that the trunk of portal vein involved patients has more severe esophageal varices. Besides, there

Table 2: Patients baseline characteristics.

	Cirrhosis without PVT (N%)	Cirrhosis with PVT (N%)	P value
N	126	18	
Age (year)	54.79 ± 11.15	53.39 ± 12.61	0.63
Male gender	85 (67.46)	12 (66.67)	0.95
Etiology			
Viral	76 (60.32)	7 (38.89)	0.05
Alcoholic	21 (16.67)	2 (11.11)	
Other	29 (23.02)	9 (50.00)	
Prophylaxis			
Primary	7 (5.47)	0	0.31
Secondary	119 (92.97)	18 (100)	
Child-Pugh class			
A	79 (62.70)	12 (66.67)	0.74
B	47 (37.30)	6 (33.33)	
C	0	0	
Child-Pugh score	6.20 ± 1.11	6.10 ± 1.02	0.75
MELD score	9.53 ± 2.11	9.67 ± 1.91	0.80
Esophageal varices			
G1	0	0	0.74
G2	11 (8.73)	2 (11.11)	
G3	115 (91.27)	16 (88.89)	
NSBB use	23 (18.25)	3 (16.67)	0.87
Hemoglobin (g/dl)	9.29 ± 2.40	8.48 ± 2.42	0.19
Platelets (×1000/mm3)	68.14 ± 38.18	66.83 ± 33.85	0.89
Creatinine (mg/dl)	0.80 ± 0.21	0.85 ± 0.19	0.33
PT (s)	13.85 ± 1.59	13.91 ± 1.67	0.90
INR	1.21 ± 0.14	1.23 ± 0.16	0.72
Albumin (g/dl)	3.66 ± 0.54	3.78 ± 0.45	0.36
Bilirubin (mg/dl)	1.15 ± 0.76	1.10 ± 0.54	0.78
D-dimer (μg/L)	1539.72 ± 1659.62	3513.61 ± 4370.17	<0.001

None of the patients with PVT are given anticoagulant therapy. PVT: portal vein thrombosis; MELD: the model for end-stage liver disease; NSBB: nonselective beta blockers; PT: prothrombin time; INR: international normalized ratio.

Table 3: The classification of PVT.

Site + extent	Frequency (N)	Percentage (%)
Type 1	6	33.3
Type 1+M	1	5.6
Type 1+S	1	5.6
Type 2	3	16.7
Type 3	2	11.1
Type 3+M	4	22.2
Type 3+S	1	5.6
Total	18	100.0
Degree		
NO	17	94.4
O	1	5.6
Total	18	100.0

All cases accord with symptomatic chronic thrombus. O: occlusive; NO: nonocclusive; S: splenic vein; M: mesenteric vein.

are no significant correlation between extension or degree of PVT and the severity of esophageal varices ($P = 0.49, 0.72$) (Table 4).

3.2. Primary End Points: Gastrointestinal Bleeding after EVL and Bleeding-Related Death. The chi-square test shows that the prevalence of gastrointestinal bleeding and bleeding-related death of the cirrhosis patients with or without PVT has no significant difference (0/18 versus 6/126, $P = 0.34$; 0/18 versus 3/126, $P = 0.51$) (Table 5).

3.3. Secondary End Points: Post-EVL Fever and Retrosternal Pain. The chi-square test shows that the prevalence of post-EVL fever and retrosternal pain of the cirrhosis patients with or without PVT has no significant difference (1/18 versus 12/126, $P = 0.58$; 1/18 versus 4/126, $P = 0.61$). One-way analysis of variance shows that the length of hospital stays of the two groups has no significant differences (20.61 ± 6.66 versus 20.87 ± 6.82; $P = 0.88$) (Table 5).

4. Discussion

Endoscopic ligation is often employed for treating patients with high risk of bleeding or rebleeding from esophageal varices, and its possible complications include gastrointestinal bleeding, fever, and retrosternal pain after ligation. PVT can worsen portal vein hypertension, can result in esophageal varices aggravated, and may finally raise the risk of gastrointestinal bleeding after ligation. Past studies have assessed the impact of PVT in the eradication effect of endoscopic ligation for esophageal varices. The results showed that the portal vein thrombosis will delay the time to eradicate esophageal varices but not increase the incidence

Table 4: The site\extension\degree of PVT with esophageal varices.

	Esophageal varices G2	Esophageal varices G3	P value
N	2	16	
Site of PVT			
Type 1	0	8	0.004
Type 2	2	1	
Type 3	0	7	
Extension of PV system			
PV alone	2	9	0.49
M	0	5	
S	0	2	
Degreen of PVT			
NO	2	15	0.72
O	0	1	

PV: portal vein; PVT: portal vein thrombosis; O: occlusive; NO: nonocclusive; S: splenic vein; M: mesenteric vein.

Table 5: Complications of EVL and the length of hospital stay.

	Cirrhosis without PVT （N%）	Cirrhosis with PVT （N%）	P value
N	126	18	
Post-EVL gastrointestinal bleeding	6 (4.76)	0	0.34
Bleeding-related death	3 (2.38)	0	0.51
Post-EVL fever	12 (9.52)	1 (5.56)	0.58
Post-EVL retrosternal pain	4 (3.17)	1 (5.56)	0.61
The length of hospital stays	20.87 ± 6.82	20.61 ± 6.66	0.88

PVT: portal vein thrombosis; EVL: endoscopic Variceal band ligation.

of recurrence of esophageal varices. The gastrointestinal bleeding events of the group of PVT patients during follow-up had not significantly increased [9]. This study aimed to evaluate the impact of cirrhosis with PVT on postoperative complications of endoscopic Variceal band ligation.

Despite the past study suggested the anticoagulant therapy in cirrhotic patients with PVT is safe [10], as all the PVT cases were clinically asymptomatic chronic thrombosis, according to the American association of liver disease recommendations [11], meanwhile, considering the risk of GI bleeding after EVL, none of the patients with PVT were given anticoagulant therapy.

The results of our study revealed no significant differences in postoperative gastrointestinal bleeding events, bleeding-related death events, fever, and retrosternal pain in cirrhotic patients with PVT compared with those without PVT. It suggests that endoscopic band ligation is still a safe treatment option for cirrhotic patients with PVT. Further analysis of the patients in the PVT group showed that the site of PVT was significantly associated with the severity of esophageal varices ($P = 0.004$), among which the degree of esophageal varices in the patients with the trunk of portal vein involvement was more serious, while the extension site and the degree of obstruction were not significantly correlated with the severity of esophageal varices. This result reveals the importance of classification of PVT, and further attention should be paid to the effect of different types of PVT on patient prognosis and endoscopic treatment in clinical practice and future studies. Considering this is a retrospective study, it has certain limitations. For one, inclusion bias cannot be ruled out since people experienced death threatening gastrointestinal bleeding may choose TIPS or surgery as the first treatment option rather than EVL, leaving only low-risk patients in the study cohort, such as Child-Pugh class A or class B patients. Second, this study included a limited number of cirrhotic patients with PVT, which might not be enough for statistical purposes. Hence, caution is required to interpret these conclusions, and we are looking forward a further scale up prospective research which could confirm the impact of PVT on EVL. Third, considering the risk of gastrointestinal hemorrhage, none of the patients with PVT were treated with anticoagulants; thus, we could not evaluate the impact of anticoagulants on PVT and EVL. Fourth, there was absence of the data of follow-up because of the poor treatment compliance of the patients. We are forward to promote prospective cohort study and find out a best strategy for the prevention of esophageal variceal bleeding of the cirrhotic patients with PVT.

In summary, endoscopic band ligation is an effective and safe treatment for cirrhotic patients without or with PVT. The incidence of GI bleeding and bleeding-related death after EVL is relatively low and does not get impacted by the presence of PVT and so does the incidence of fever and retrosternal pain after EVL.

Data Availability

The data used to support the findings of this study are available from the corresponding author upon request.

Conflicts of Interest

The author declares that there are no conflicts of interest.

Supplementary Materials

Supplementary Table 1: anatomical-functional classification of portal vein thrombosis in cirrhosis. (*Supplementary Materials*)

References

[1] Y. K. Chawla and V. Bodh, "Portal vein thrombosis," *Journal of Clinical and Experimental Hepatology*, vol. 5, no. 1, pp. 22–40, 2015.

[2] C. Francoz, J. Belghiti, V. Vilgrain et al., "Splanchnic vein thrombosis in candidates for liver transplantation: usefulness of screening and anticoagulation," *Gut*, vol. 54, no. 5, pp. 691–697, 2005.

[3] I. Gîrleanu, A. Trifan, C. Stanciu, and C. Sfarti, "Portal vein thrombosis in cirrhotic patients - it is always the small pieces that make the big picture," *World Journal of Gastroenterology*, vol. 24, no. 39, pp. 4419–4427, 2018.

[4] N. M. Intagliata, S. H. Caldwell, and A. Tripodi, "Diagnosis, development, and treatment of portal vein thrombosis in patients with and without cirrhosis," *Gastroenterology*, vol. 156, no. 6, pp. 1582–1599, 2019.

[5] M. A. Gunson and B. Mirza, "Portal vein thrombosis in adults undergoing liver transplantation," *Transplantation*, vol. 69, no. 9, pp. 1873–1881, 2000.

[6] S. K. Sarin, C. A. Philips, P. S. Kamath et al., "Toward a comprehensive new classification of portal vein thrombosis in patients with cirrhosis," *Gastroenterology*, vol. 151, no. 4, pp. 574–577, 2016.

[7] Hepatology Society of Chinese Medical Association, "Gastroenterology society of Chinese medical association, gastrointestinal endoscopy society of Chinese medical association, guideline for the diagnosis and treatment of esophageal and gastric variceal bleeding in cirrhotic portal hypertension," *Chinese Journal of Internal Medicine*, vol. 55, no. 1, pp. 57–72, 2016.

[8] G. Garcia-Tsao and J. G. Abraldes, "Portal hypertensive bleeding in cirrhosis: risk stratification, diagnosis, and management: 2016 practice guidance by the American association for the study of liver diseases," *Hepatology*, vol. 65, no. 1, pp. 311–335, 2017.

[9] A. Dell'Era, F. Iannuzzi, F. M. Fabris et al., "Impact of portal vein thrombosis on the efficacy of endoscopic variceal band ligation," *Digestive and Liver Disease*, vol. 46, pp. 152–156, 2014.

[10] C. N. Ferreira, D. Reis, H. Cortez-Pinto et al., "Anticoagulation in cirrhosis and portal vein thrombosis is safe and improves prognosis in advanced cirrhosis," *Digestive Diseases and Sciences*, vol. 64, pp. 2671–2683, 2019.

[11] J. G. O'Leary and S. Charles, "AGA clinical practice update: coagulation in cirrhosis," *Gastroenterology*, vol. 157, pp. 34–43, 2019.